Pumping of Nd:YAG with Electrodeless Arc Lamps

DAVID A. HUCHITAL, MEMBER, IEEE, AND GEORGE N. STEINBERG, MEMBER, IEEE

Abstract—**Optical pumping of Nd:YAG by electrodeless arc lamps is described. The lamps are annular, filled with 1-5-atm pressure of krypton and excited with 27-MHz electrical energy which is coupled to the lamp with approximately 80-percent efficiency. Optical energy is coupled from the lamp to the rod by a diffuse reflecting scheme. Overall efficiency and power output of the device are comparable to the dc-arc-lamp pumped case, while reliability and lifetime are greatly improved. The results of a successful 1000-h life test on a 25-W laser are described.**

I. INTRODUCTION

THE Nd:YAG laser is an attractive choice for a variety of applications by virtue of its relatively high power and efficiency at a generally useful wavelength. However, when the laser is continuously pumped at moderate-to-high power levels, the short lifetime and general unreliability of the krypton arc pumping source usually pose severe disadvantages. This paper describes an approach to this problem using electrodeless arc lamps that is based upon the realization that most of the failure modes of conventional arc lamps are associated with the electrodes and the glass-to-metal seals.

The primary function of the electrodes in a high-pressure arc lamp is to establish an electric field capable of delivering energy to the electrons in the arc. Since the electrodes are in actual contact with the arc, a small fraction of the free electrons are removed at the anode, and continuity of current requires that an equal number be supplied at the cathode. However, the circulation of this current is not basic to the operation of the arc which could be equally well maintained by a field created by currents flowing entirely within external circuitry. As we will show in the following, disposing with the electrodes leads to a device with similar output and efficiency to conventional krypton-pumped YAG but with markedly improved lifetime and reliability. A preliminary description of this effort has been published [1].

A. DC Excitation of Arc Lamps

The mechanism of the dc arc is widely discussed in the literature. In simple terms the arc lamp can be said to consist of an anode, a cathode, and a transparent envelope. As a rule the envelope is made of fused silica because of its good resistance to high temperatures. This choice results in some difficulty in designing the cathode seals since there will almost certainly be a mismatch of thermal-expansion coefficients. The electrodes are made of a refractory metal, and the cathode is sometimes doped with a low work-function material.

Manuscript received March 25, 1975; revised August 18, 1975. This work was supported in part by the U.S. Air Force Avionics Laboratory under Contract F33615-73-C-1280. R. L. Remski was the program monitor.

The authors are with the Perkin-Elmer Corporation, Norwalk, CT 06852.

The arc diameter is usually between 4 and 6 mm, and the length is in the range from 50 to 100 mm. Optical coupling between lamp and laser rod is usually accomplished by 1:1 imaging by locating the lamp and rod at the foci of an elliptical cylinder.

Lasers thus configured are relatively efficient. The radiation efficiency is about 30 percent for a krypton-filled lamp, and 25–50 percent of this energy is absorbed in the laser pump bands. Incremental or slope efficiencies over 3.0 percent have been reported.

However, the lifetime of high-pressure arc lamps is discouragingly short, particularly when operated in a laser cavity. Even when substantial pains are taken with the sealing techniques and with specially designed and cooled cathodes, lifetimes greater than 100 h or so are rare [2]. The electrodes and electrode seals are the source of most of the failure modes. Failures upon starting are common due to the fact that the cathode is initially cold and thus nonemitting, and it is necessary to deliver substantial energy to it in a fairly short time in order to heat it to thermionic temperatures. This is generally accomplished by ionizing the gas slightly with a spark and then driving a large current through it by means of a high-voltage capacitor. The current puts the cathode seal under particularly high stress as a result of the thermal-expansion mismatch. Catastrophic failure frequently results.

Should the lamp survive starting, there is a number of other effects which act in concert to limit its life. During operation, the electrodes are subjected to very high energy flux due both to radiation from the gas and bombardment by energetic charged particles. Most of the material that is either sputtered or evaporated from the electrodes is eventually deposited upon the tube walls. The deleterious effects thereof are twofold; first, envelope transmission is reduced, sometimes drastically, and second, the thermal wall loading is increased, often to the point of failure. Further, the cathode is usually pointed somewhat to facilitate starting. The erosion can wear the point away causing the lamp to require greater energy input to start and increasing the risk of failure. Finally, we should point out that dc arc lamps are fairly expensive, particularly when designed for lifetimes over 100 h. They often incorporate water-cooled electrodes, low work-function cathodes, and sophisticated fused silica-to-metal seals. The electrodeless lamp discussed in the following are all fused silica and can be fabricated easily by a skilled glassblower.

B. Electrodeless Excitation of Arc Lamps

In the frequency regime between one and a few hundred megahertz there exist two alternative methods for coupling electrical energy into a plasma. In the capacitive mode the discharge is maintained by displacement currents flowing through the walls of the vacuum container; in the inductive

mode, currents are induced in the plasma by other currents flowing through external circuitry. In either case, however, it is the electric field of the RF energy which actually delivers energy to the plasma electrons, which subsequently transfer it to the gas atoms leading to excitation and ionization. In fact, it is fairly readily shown that the magnetic field of the energy exerts very little force on the plasma electrons compared to the electric field unless the electron velocity is an appreciable fraction of the speed of light.

High-pressure gas discharges almost always operate in the arc mode. Here the neutral atom and ion gases are closely coupled, their temperatures are essentially equal, and of the order of several thousand degrees. The currents required are usually large enough that the capacitive mode of coupling is unfeasible due to the large voltage drop incurred at the tube walls. Since inductive coupling involves no current flow through the walls, it is the preferred mode of excitation for high-pressure gases. The field strength is usually on the order of tens of volts per centimeter, from which one can infer that it will take several cycles of the field to deliver sufficient energy to an electron to allow it to ionize a gas atom.

Most of the failure modes apparent in connection with dc arc lamps are not relevant in the case of RF excitation. To be sure, operation at too high a power level can result in a lamp failure. For example, the envelope may operate at too high a temperature leading to devitrification of the fused silica. Catastrophic failure will occur if the thermal gradient across the wall causes the thermal-expansion stress to exceed the strength of the material.

The use of RF energy does present additional constraints and potential problems. For example, materials used in the laser head must be good electrical conductors or good insulators and the designer must take care to minimize the level of radiated energy. However, since the problems thus posed are tractable, we have concluded that RF-excited arc lamps are a viable alternative to dc lamps in laser pumping applications.

II. Configuration of the Pump Lamp and Cavity

The fundamental problem in developing an electrodeless-lamp pump for an Nd:YAG rod lies in arranging the appropriate coupling of RF energy into the lamp, and of pump energy from the lamp into the rod. The difficulty lies in the fact that the respective requirements for efficient coupling are often contradictory.

Our initial efforts revolved about a conventional configuration wherein a capillary, electrodeless lamp was imaged on a laser rod by an elliptical reflector. RF energy was coupled to the lamp via a solenoidal coil and the impedance of the lamp-coil combination was matched to that of a 50-Ω transmission line by including it in a π-network with two vacuum-variable capacitors.

The radiation efficiency of a gas-filled lamp increases with the fill pressure. Further, efficient coupling of the radiated energy to the rod requires that the lamp diameter be small. Both these requirements make the task of coupling RF energy more difficult. A higher pressure lamp generally requires higher starting and operating voltage. Further, a small-diameter coupling coil has low inductance and thus requires uncomfortably large RF currents to generate the required voltage. The use of a higher RF frequency is of little value since, although the coil reactance can be increased, its resistance increases as well due to the skin effect. The use of heavier conductors would help; however, it would adversely impact the coupling of the optical energy to the rod.

Such considerations caused the abandonment of an imaging approach and led to the adoption of optical coupling means based upon an integrating sphere. Fig. 1 illustrates the two-lamp configurations studied subsequently. In both cases, the laser rod and lamp combination is surrounded by a diffuse reflective surface which serves to contain the optical energy until it is absorbed by the laser rod. The details of this part of the approach are discussed in Section III.

The lamps shown in Fig. 1 operate as single-turn secondary windings in transformers where the coupling coil serves as the primary winding. The immediate advantage, from the point of view of RF coupling efficiency is that the lamp links a large amount of flux. As discussed in the following, the annular geometry is the more efficient but in general is restricted to power inputs of less than 2 kW, and the racetrack arrangement, while slightly less efficient, is useful for power levels up to 6 kW.

A. Electrical Coupling Considerations

1) *Analysis of Coupling Losses:* The voltage gradient necessary to drive a high-pressure krypton arc E_p is generally of the order of 20 V/cm. The total voltage required is thus

$$V_p = E_p l \tag{1}$$

where l is the plasma length. In the case of the lamps shown in Fig. 1, l is the mean circumference of the lamp. When the lamps are excited by a coupling coil of n turns with inductance L and cross-sectional area A_c, the voltage induced in the coil

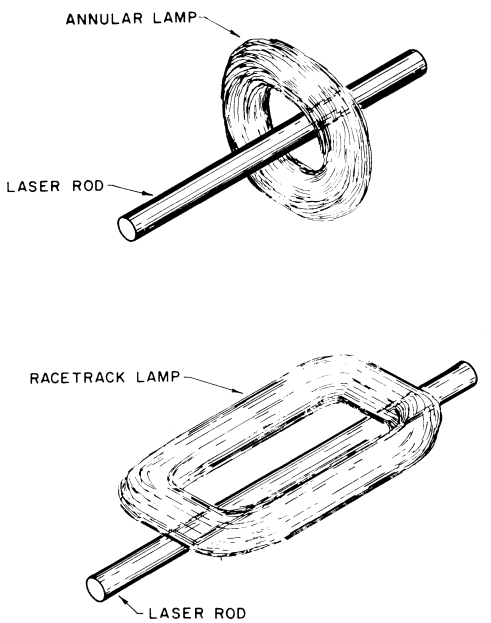


Fig. 1. Comparison of annular and racetrack laser configurations.

when driven a frequency ω is

$$V_c = \omega I_c L_c - V_b$$

where V_b is the back EMF due to the plasma current. Unless the coil is very closely coupled to the lamp, V_b can usually be neglected. If we make the useful, though not particularly rigorous assumption that the flux produced by the coil is uniform across it, then

$$V_p = (1/n)(A_p/A_c)\, V_c = (1/n)k\, V_c \tag{2}$$

where A_p is the area linked by the plasma. Finally, the power dissipated in the coil is

$$P_c = \frac{V_c^2}{\omega L_c Q} = \frac{n^2 V_p^2}{\omega L_c Q k^2} \tag{3}$$

where the Q of the coil is

$$Q = \frac{\omega L_c}{R}$$

and is nearly independent of frequency. Now in the annular geometry, if the coil length is approximately equal to its radius r_c in centimeters

$$L \approx 2 \times 10^{-2} n^2 r_c \quad \mu\text{H} \tag{4}$$

and

$$P_c \approx 10^2 \pi \frac{r_c E_p^2}{fkQ} \quad \text{W} \tag{5}$$

where f is the RF frequency in megahertz.

We can draw conclusions from (5) that are applicable to both the annular and racetrack geometries. As one would expect, the coil Q should be as high as possible, though a value of 500 would appear to be a practical limit [3]. The operating frequency should also be high; however, power-supply efficiency falls quickly for frequencies above 50 MHz. Further, when the coil is cooled by immersion in water the self-resonant frequency is generally around 30 MHz due to the large dielectric constant of water. Above its self-resonant frequency, of course, the coil behaves like a capacitor and energy cannot be coupled to the lamp. The coupling constant k should be as close to unity as possible; that is, the lamp should nearly fill the coil.

Since P_c is directly proportional to the radius of the coil, it is clear that the losses increase for larger structures. As a result, one should expect the racetrack lamp to involve higher coupling losses than does the annular lamp, and this indeed is the case.

Finally, the losses are proportional to the square of the electric field in the plasma E_p. In general, E_p can be lowered by increasing the diameter of the tubing used to make the lamp; however, this is often done at the expense of plasma stability. Similarly, a lower fill pressure will lead to reduced E_p at the expense of radiation efficiency.

2) *Coupling and Measurement of Losses:* Most commercially available RF power supplies are designed to drive 50-Ω coaxial cables. This is a convenient mode of operation as it allows the laser head to be physically separated from the power source. However, it requires the use of an impedance-matching network to transform the high impedance of the coil-lamp combination down to 50 Ω. The circuit shown in Fig. 2 is useful for this purpose. It is tuned to resonance to start the lamp, and subsequently both vacuum variable capacitors are adjusted for a 1 : 1 VSWR on the transmission line.

The same network allowed the measurement of the electrical coupling losses as summarized in Fig. 3 for typical annular and racetrack lasers. The data were gathered by measuring the coil voltage as a function of the RF power input. The lamp was then extinguished and the matching network tuned to match the coil impedance to the line. The power transmitted down the line necessary to generate the required voltage is equal to the power loss when the lamp is operating. Fig. 3 implies that at the usual input level, that is, 1.5 kW for the annulus and 3.0 kW for the racetrack, the coupling losses are of the order of 20 percent.

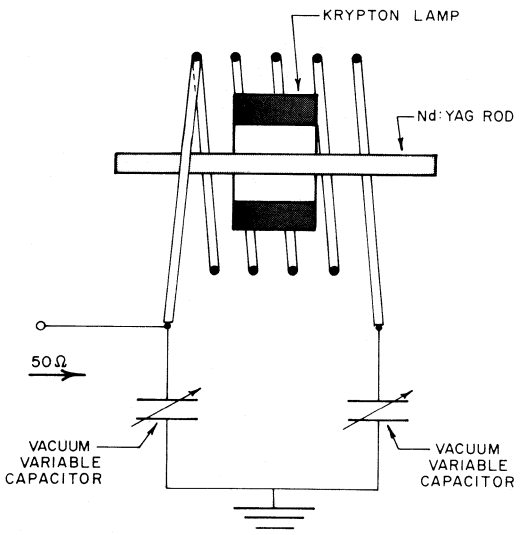


Fig. 2. Means for coupling energy to an electrodeless lamp.

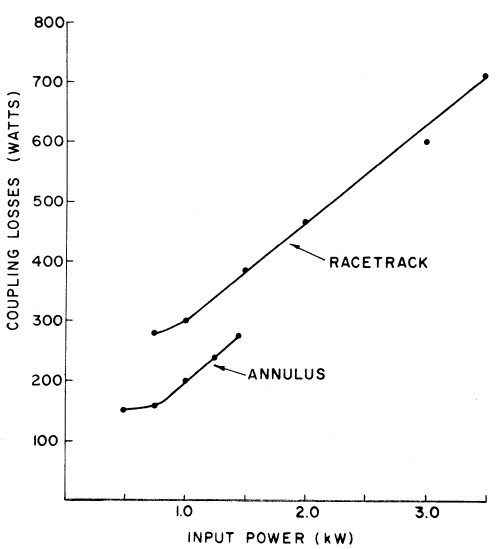


Fig. 3. Coupling loss as a function of input power for annular and racetrack lamps.

B. Optical Coupling Considerations

Diffusely reflecting surfaces have been used in the past to couple optical energy from a lamp to a laser medium. The lasers have, typically, been pulsed devices, and more importantly, the optical density of the absorbing medium has been fairly high.

As we will show in the following, the low absorbance of Nd:YAG places severe requirements upon the efficiency of the diffuse reflecting structure. Of course, low absorption also affects the efficiency of a conventional imaging scheme. We have measured the absorbance of Nd:YAG for the important krypton lines by passing the radiation from a 3-atm krypton lamp through a 10-mm-thick piece of 1-percent Nd in YAG. Table I summarizes the absorbance in units of mm^{-1} for the various lines.

The two strongest lines are 7601 and 8112 Å for which the absorbance is about 0.08 mm^{-1}. The weaker lines tend, with the exception of 8059 Å, to be even less strongly absorbed. Consequently, pumping energy incident upon a 3-mm-diam laser rod has a modest probability of being absorbed. If the average path length in the rod is 3 mm, Table I implies a fractional absorption of about 40 percent for 7601 and 8112 Å, and 32 percent for 8104 Å. Further, the optical properties of an elliptical reflector are such that the probability is low that the light will return through the lamp to be incident upon the rod a second time.

In the diffuse reflecting geometry, on the other hand, the reflector acts as the source, since little light is absorbed directly from the lamp. In this case, although a ray leaving the reflector has a low probability of encountering the rod before it strikes another wall, the energy is not lost until it is either absorbed by the wall or otherwise escapes. Clearly, a high premium is placed upon choosing a material with very high reflectivity and, equally important, one whose reflectivity does not deteriorate under intense UV exposure.

We can analyze the efficiency of a diffuse reflector by defining

- δ laser-rod diameter;
- D cavity diameter;
- r_i, r_o plasma inner and outer radii;
- ρ cavity reflectivity.

Both the lamp and the rod are considered to be infinitely long. If we consider a point in the plasma at a distance r from the center of the rod and assume the scattering from the cavity to be completely isotropic, we find that the fractional power incident upon the rod is

$$f(r) = \frac{\Omega_0}{2\pi} + \left(1 - \frac{\Omega_0}{2\pi}\right) \sum_{n=1}^{\infty} \rho^n \left(1 - \frac{\Omega_1}{\pi}\right)^{n-1} \tag{6}$$

where

$$\Omega_0 = \frac{\delta}{r}, \qquad \Omega_1 = \frac{2\delta}{D}.$$

The first term represents the light absorbed in the rod on the first pass, while the series describes the absorption of light after multiple reflections from the cavity walls.

TABLE I
ABSORBANCE OF KRYPTON LINES IN ND:YAG

Wavelength(Å)	Absorbance(mm^{-1})
7587	0.045
7601	0.083
7685	0.012
7694	0.007
7854	0.016
8059	0.146
8104	0.059
8112	0.074
8190	0.023
8263	0.006
8281	0.002
8298	0.008

Summing the series and integrating from r_i to r_o, we obtain

$$F = \frac{1}{\pi(r_o^2 - r_i^2)} [(1 - y)(r_o - r_i)\delta + \pi y(r_o^2 - r_i^2)] \tag{7}$$

where

$$y = \frac{\Omega_1}{\pi} \left(1 + \frac{\rho(1 - \Omega_1/\pi)}{1 - \rho(1 - \Omega_1/\pi)}\right). \tag{8}$$

As one would expect, (7) predicts that the transfer efficiency will depend critically upon the reflectivity of the diffuse reflector. Fig. 4 is a plot of the fractional collection efficiency as a function of ρ for a fairly typical choice of rod and diffuse reflector diameters. It is clear that the reflectivity must be in excess of 90 percent in order that half the emitted radiation be absorbed by the rod.

Several experiments were performed to verify the previous analysis. An apparatus that proved particularly useful is illustrated in Fig. 5. Light from a GaAs light-emitting diode (LED) (λ = 9400 Å) was directed against the wall of the chamber and the overall transfer efficiency was determined by observing the signal produced at the indicated detector.

The size of the output coupling hole is an important parameter as it simulates the absorbing power of the laser rod. The dependence of the transfer efficiency upon the output coupling is shown in Fig. 6. Three different ceramic diffuse reflectors were chosen. All measured 22 mm ID by 76 mm long. The transfer efficiency of the reflectors was measured for various coupling apertures in front of the detector. A typical rod might measure 3 mm in diameter by 50 mm long, and thus present an effective 150-mm^2 aperture. However, Table I implies that the actual absorption of light incident upon the rod will be between 30 and 40 percent, so its actual absorbing power will be the equivalent of a 30-60-mm^2 aperture as indicated by the hatched area in Fig. 6.

The parameter ρ in (5) can be taken to describe a net reflectivity comprising both the efficiency of the surfaces as well as any losses through openings and gaps in the structure. Such gaps are, of course, often unavoidable due to the need for a circulating coolant. For the initial experiment we chose an efficient structure consisting of an alumina tube and gold-coated end caps. The average reflectivity of the structure

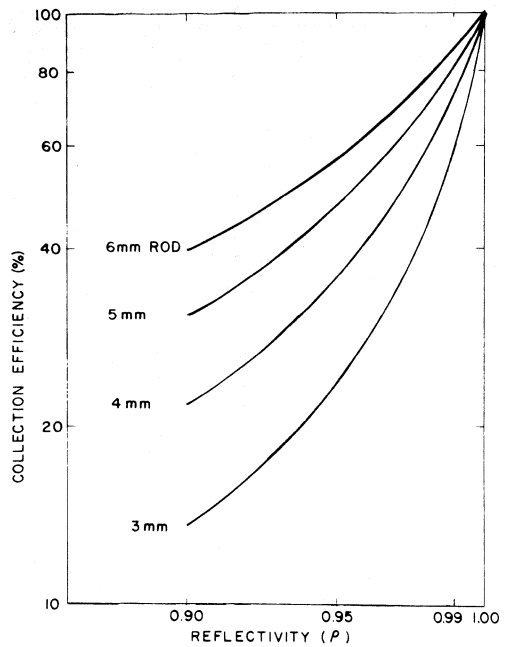


Fig. 4. Transfer efficiency as a function of the reflectivity of the diffuse reflector for various laser-rod sizes.

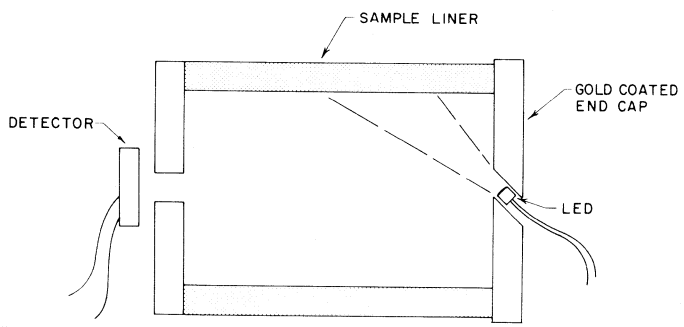


Fig. 5. Apparatus used to measure diffuse reflectivity.

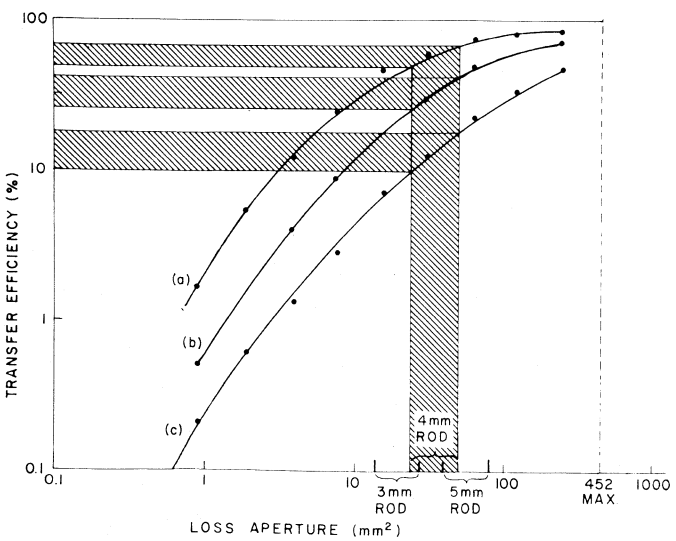


Fig. 6. Transfer efficiency of several diffuse reflectors as a function of the coupling aperture for (a) good, (b) fair, and (c) poor diffuse reflectors.

could be varied in a controlled way by progressively blackening the tube. Fig. 7 compares the results from the LED apparatus with the performance of the same diffuse reflector when used in a laser structure.

The effect of blackening is more drastic in the case of the laser output because of the laser threshold. In fact, the power input to the lamp was very nearly three times threshold for an unblackened diffuse reflector. Consequently, one would expect laser action to cease when the blackening reduced the transfer efficiency by a factor of 3, and this result is indeed apparent in Fig. 7.

One can conclude from the previous discussion that the ratio of rod diameter to reflector diameter should be as large as practical and that it is essential that the reflectivity of all surfaces inside the structure be as high as possible. The use of the dc arc lamps in such a structure is somewhat unattractive since the electrodes and associated leads will present an unavoidable loss, and any blackening of the lamp envelope will decrease the energy to the rod still further. Indeed, in an electrodeless-lamp configuration, it is necessary to ensure that the reflectivity of the structure does not deteriorate; otherwise, long lamp life, if achieved, would be of little value.

C. Power-Supply Considerations

In comparing the efficiency of the devices described here with the more conventional dc-arc-lamp pumped models, it is important to consider the efficiency with which the required RF energy can be generated. The efficiency of the power supply for a dc arc lamp, converting, for example, 208 VAC to 200 VDC can be over 90 percent. As we will show in the following, the corresponding conversion to 30-MHz RF can be accomplished with roughly 65-percent overall efficiency.

We designed a simple class *C* power stage around a type 3CX1500A7 ceramic triode. A triode was chosen rather than a tetrode or pentode because of our need to maximize overall efficiency, and screen grid dissipation in tubes of this size is usually of the order of several hundred watts. The unit could

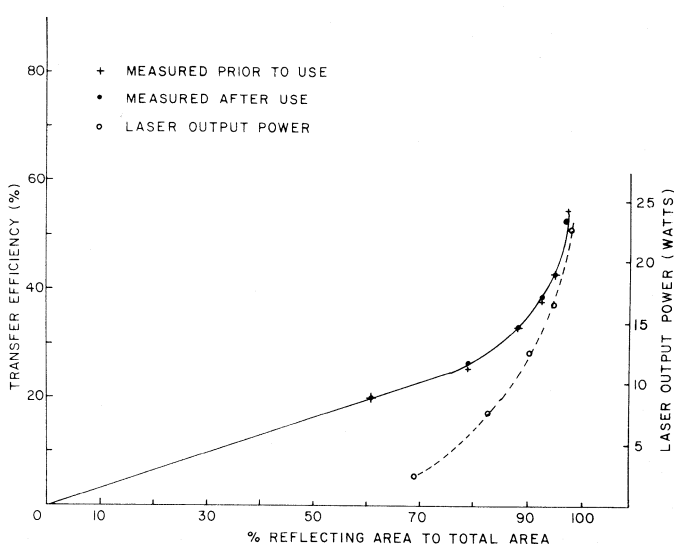


Fig. 7. Transfer efficiency and laser power for a progressively blackened diffuse reflector.

be operated as a high-level oscillator or in a master-oscillator-power-amplifier (MOPA) mode using a separate 100-W driver. As the driver requirements are compatible with modern transistor technology, the triode is, in principle, the only vacuum device needed in either case.

The plate efficiency (i.e., RF output for dc plate input) was measured to be as high as 78 percent in the oscillator mode and 85 percent in the MOPA mode. When all sources of power dissipation are included (e.g., filament power, fans, 208 VAC-3 kVDC conversion, and, for the MOPA, the driver requirements), overall efficiencies of 67 percent for the oscillator and 63 percent for the MOPA supply were achieved.

III. Performance and Operation

A. Results of a Parametric Study

Diffuse reflectivity of various materials was measured in the apparatus illustrated in Fig. 5, and we settled on alumina as a material with good optical and mechanical properties. Alumina tubes from several manufacturers behaved with noticeable differences in our experiments. Table II compares measurements performed in the test apparatus with performance in a laser configuration. The best material was supplied by the Ceram Corporation. Good correlation between performance in a test cavity and in a laser configuration is noted. Interestingly, a commercial white paint which used TiO_2 as a pigment did not have very high reflectivity in the wavelength region studied here.

The diffuse reflecting scheme allows a direct measurement of the efficiency of the optical coupling scheme to be made. Some of the radiation passing through a hole in the diffuse reflector was allowed to fall on the entrance slit of a spectrometer and spectra were obtained with the laser rod present and with the rod replaced by a glass rod. The Nd absorption could be clearly identified as shown by the portion of the spectrum illustrated in Fig. 8. The spectral region from 5000 to 9200 Å was studied in this manner. Fig. 9 compares the measured absorption with the Nd absorption spectrum. The maximum absorption measured was about 40 percent and is in good agreement with the analysis summarized by (7) and in Figs. 4 and 6. The black dots indicate wavelengths where there was no apparent absorption of the radiation. All the Nd absorption bands are present, though most of the 7300-7600-Å band was not apparent due to the very low lamp energy.

A series of experiments was performed to evaluate different materials for the end caps of the liner. Evaporated layers of gold and silver were considered, and it was soon discovered that a protective overcoat of evaporated SiO_2 was required to maintain high reflectivity. Table III compares the performance of those materials in the reflectance measuring apparatus.

A special selective coating was also tested. The coating was a dielectric specified to be highly reflecting in the 7000-9000-Å band and less than 60-percent reflecting from 3500 to 6000 Å. The performance was slightly poorer than with gold.

Questions of optimum lamp size and pressure are complicated because they involve two coupling processes; that is, coupling of RF energy from the coil to the lamp and coupling of optical energy from the lamp to the rod. The former process prefers large-diameter lamps and low pressures, while the latter is most efficient for small lamps at high pressure. Fig. 10 illustrates the performance of lamps filled with various krypton pressures pumping a 3 × 50-mm rod. Interestingly, there is little difference among the 3-, 4-, and 5-atm lamps. The 5-atm lamp undergoes a distinct and reproducible mode change near the 1-kW level. This datum is strikingly different

TABLE II
Efficiency of Various Diffuse Reflectors

Material	Efficiency in Test Apparatus	Relative Efficiency in Laser
Ceram	54%	1.
Wesgo AL600	38%	.78
Wesgo AL995	30%	.69
White Paint (TiO_2)	20%	not tested

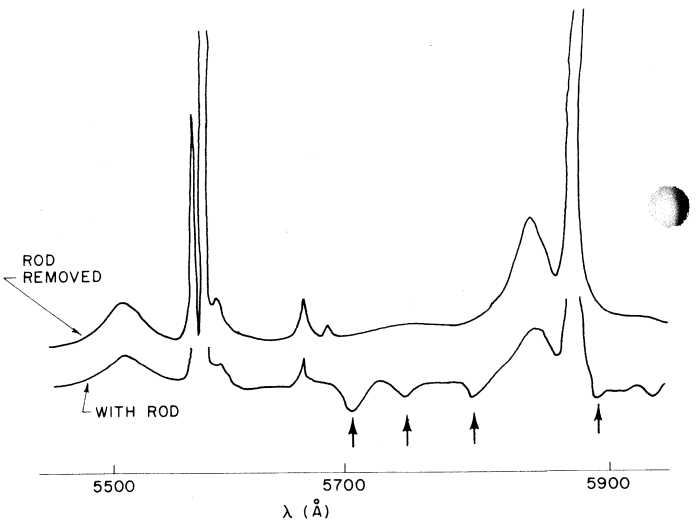


Fig. 8. Spectrum of optical energy inside the diffuse reflector with and without the laser rod (rod absorptions indicated by arrows).

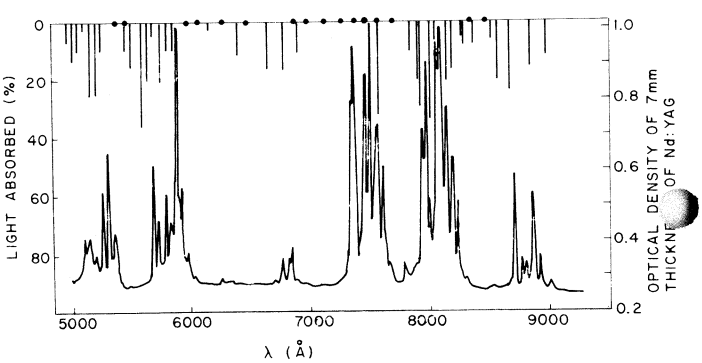


Fig. 9. Optical absorption by the rod in the diffuse reflector compared with optical density of Nd:YAG.

TABLE III
End-Cap Performance

Coating	Fractional Collection	Relative Laser Output
Gold + SiO_2	0.57	0.94
Silver + SiO_2	0.62	1.0

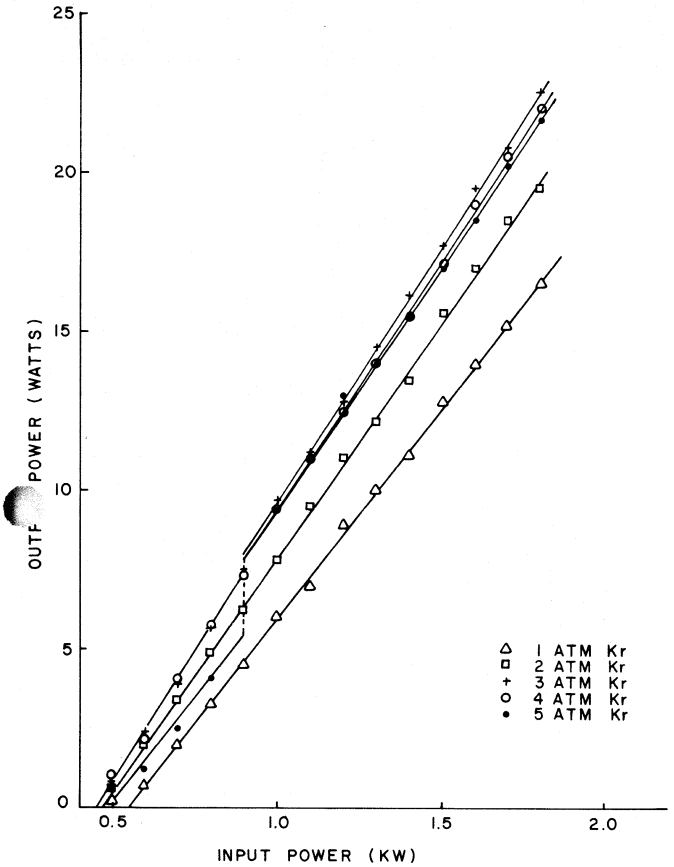


Fig. 10. Laser power output as a function of RF power input for various krypton fill pressures of an annular lamp.

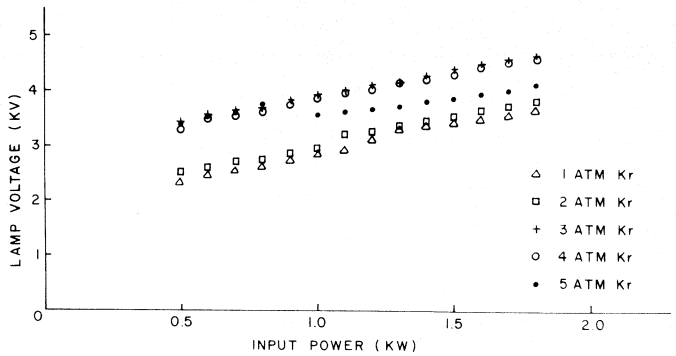


Fig. 11. Voltage across the coupling coil as a function of RF power input for various krypton fill pressures of an annular lamp.

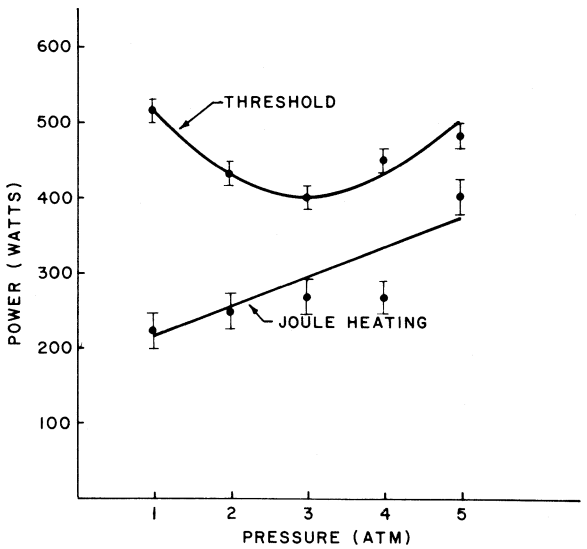


Fig. 12. Comparison of laser threshold with coupling loss for various krypton fill pressures of an annular lamp.

from that obtained with dc-arc-lamp pumping where useful light output continues to increase with lamp pressure up to pressures of 10 atm.

At least part of the explanation lies in the joule-heating losses in the coupling network. Fig. 11 illustrates the variation of the voltage across the coil with lamp pressure. Since the coil inductance and resistance are known, it is possible to infer an I^2R loss in the coil from these data. Fig. 12 compares the joule heating of the coil with the measured laser threshold. The implication is clearly that the threshold power is increased at high pressures as a consequence of joule heating of the coil. This is obviously a fruitful area for further investigation. Similar behavior is discovered in investigating the significance of lamp size, as the RF voltage required is fairly sensitive to lamp diameter. The I^2R loss, which can be expected to vary with the square of the voltage, is thus nearly twice as great for a 17-mm-OD lamp as for a 19-mm-OD one. The implied reduced RF coupling efficiency is, however, more than offset by enhanced optical coupling.

The effects of annular-lamp length were studied for lamps 7, 10, and 15 mm long that had been filled to 3 atm of krypton. Both of the longer lamps were observed to have two distinct modes of operation. At low input powers the discharge was unstable and substantial difficulty was encountered in tuning the impedance-matching network. However, both lamps switched into a stable mode when the output was raised. The phenomenon was completely reversible and reproducible although it exhibited some hysteresis. In the case of the 15-mm-long lamp, the mode changed at about 1.7 kW; for the 10-mm-long lamp it was closer to 1 kW. The 7-mm-long lamp showed no such switching in this case; however, a 7-mm lamp filled to 5 atm showed a mode change at 1 kW as shown in Figs. 10 and 11.

Fig. 13 shows the output of a phototube arranged to sample the intensity of the output beam. The low-frequency excursions of the output are demonstrated in Fig. 13(a) which is a 1-s exposure of the screen at 2 ms/sweep. The trace is only slightly broader than that obtained with the laser beam blocked. Fig. 13(b) shows a single sweep with the oscilloscope gain increased by a factor of 4. The peak-to-peak noise is of the order of 1-2 percent. It is also notable that no relaxation oscillations occur spontaneously although they could be induced by tapping sharply on the laser head or resonator structure. One can speculate that such increased stability as may be observed in this case is a consequence of optical coupling with a diffuse reflector. At least to first order, such a device should be unaffected by arc wander in the lamp, a phenomenon which is known to influence the stability of dc-arc-lamp pumped devices. It is, of course, necessary to pay careful attention to the suppression of various noise-generating phenomena in order that quiet operation like that of Fig. 13

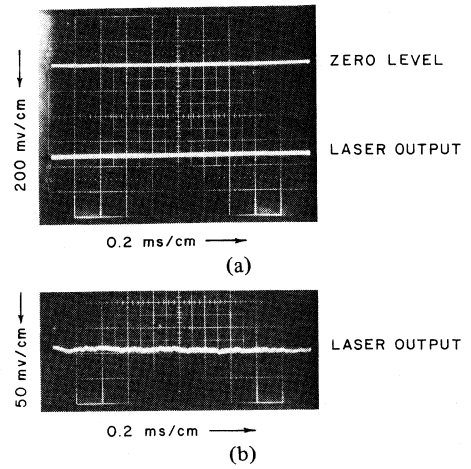


Fig. 13. Noise on output beam. (a) Automatic oscilloscope triggering, 1-s film exposure. (b) Single sweep at higher gain.

be observed. Some of the relevant considerations are discussed by Koechner [4].

Finally, Fig. 14 compares the multimode performance of typical racetrack and annular lasers using 4 X 50-mm laser rods. The racetrack could be safely operated up to the power-supply limit, while the input to the annular lamp was kept a factor of 2 below the calculated stress limit. The difference in efficiency is largely explained in terms of RF coupling losses as predicted by Fig. 3. A photograph of the laser with a racetrack lamp is shown in Fig. 15.

B. Life Test

An annular laser of the optimum design was life tested at an RF power level of 1.5 kW. All optics including the mirrors and antireflection coatings on the rod were carefully cleaned and the laser power was measured. Lasing action was allowed only for occasional monitoring purposes so as to avoid spurious effects associated with the deterioration of mirror surfaces. The arc was extinguished and restarted an average of once a day, the power level being changed both gradually and, on occasion, abruptly.

The first life test failed catastrophically at the 366-h mark due, we now believe, to a malfunction in the power supply. At the time of failure, the laser was energized by a commercial unit with a feedback-controlled output circuit. We tested the supply after the failure by operating it into a dummy load and observed it to break into oscillation when the power level was raised above 1.2 kW.

The lamp was replaced with an identical model and the test was repeated with the high-efficiency power supply previously described. The test methodology was unchanged, and the laser passed the 1000-h mark at which time the test was terminated. During the first 100 h the laser output was in the range from 23.7 to 24.0 W. Output data are summarized in Fig. 16. At the conclusion of the test the laser output was 22 W. At this point the ends of the laser rod and the mirrors were cleaned using the same procedure as was used at the beginning of the test. The arc was reignited and the power output was measured to be 23.7 W. Since the RF power input could not be measured to better than 10 W, corresponding

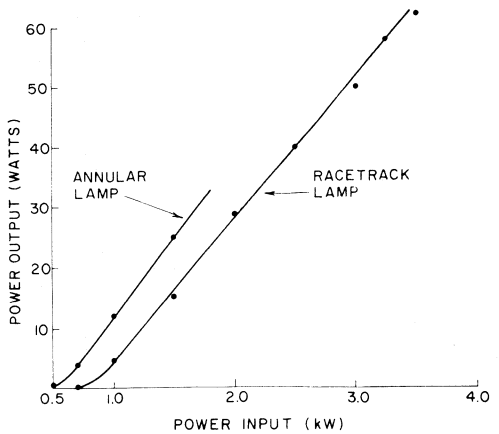


Fig. 14. Power output as a function of RF power input for annular and racetrack lamps.

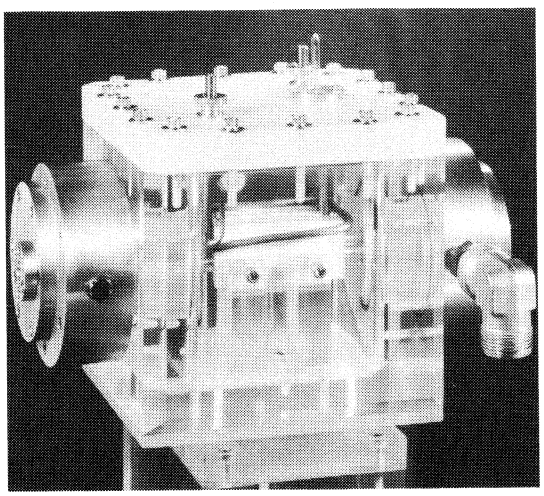


Fig. 15. Photograph of the laser head.

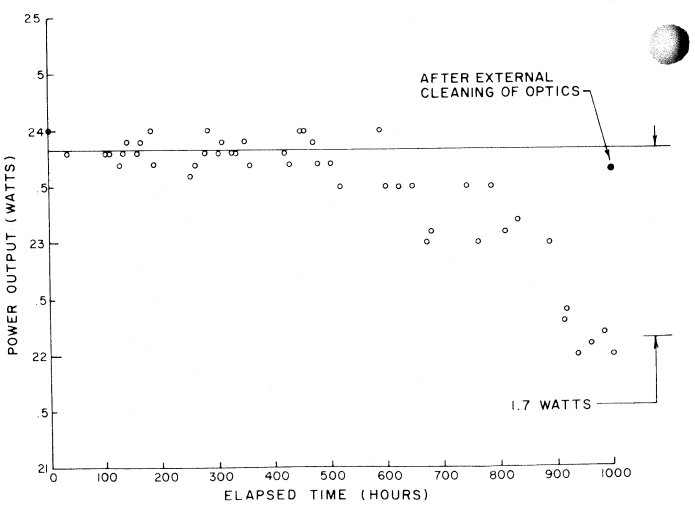


Fig. 16. Results of life test.

to a 0.3-W output uncertainty, the overall change in output level was within the accuracy of the measurements.

The lamp itself showed some slight changes. The annular region had a slight color which appeared either pink or gray depending upon the lighting condition. This overall change in transmission is most easily observed in the vicinity of the

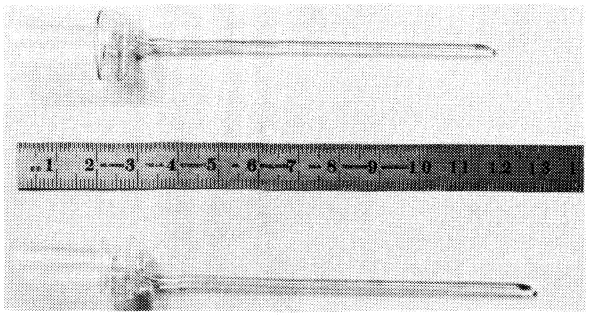


Fig. 17. Comparison of the 1000-h lamp (top) with a new lamp.

ring seal. Fig. 17 compares the 1000-h lamp with a new one. There was a slight frosting of the inner surface of the quartz which is not visible in Fig. 17.

IV. Conclusions

It seems reasonable to conclude that electrodeless-lamp pumping is a useful alternative to dc arc pumping for Nd:YAG. The device should prove particularly attractive in applications where reliability and lifetime are important.

The optical coupling efficiency achieved with the diffuse reflector seems to be comparable to that obtained with imaging schemes. The diffuse reflector has an obvious cost advantage over an imaging reflector; however, it may be that there are subtle performance advantages as well. Very low noise operation has been achieved, as shown in Fig. 13, and studies currently in progress indicate very attractive performance in low-order mode operation.

Adequate electrical-coupling efficiency has been demonstrated, though it should be clear that careful attention must be paid to the design of the coil and impedance-matching circuit. One attractive approach to reducing the electrical-coupling losses is to replace the circulating deionized water with a coolant exhibiting a low dielectric constant. This would reduce the coil self-capacitance and allow the use of coils with additional turns. The high Q of such coils should reduce the coil heating losses in accordance with (3).

Acknowledgment

The authors wish to thank J. F. Cunniff for designing the RF power supply described in this paper. They also wish to thank their colleagues R. S. Rowley and L. J. Rosenkrantz for their advice and suggestions.

References

[1] D. A. Huchital and G. N. Steinberg, "RF-excited krypton arc lamps for Nd:YAG lasers," *Proc. IEEE* (Lett.), vol. 60, p. 233, Feb. 1972.

[2] M. Grasis and L. Reed, "Long life krypton arc lamp for pumping Nd:YAG lasers," Air Force Avionics Lab. Tech. Rep. AFAL-TR-73-156, Aug. 1973.

[3] F. E. Terman, *Radio Engineer's Handbook*. New York: McGraw-Hill, 1943.

[4] W. Koechner, "Output fluctuations of CW-pumped Nd:YAG lasers," *IEEE J. Quantum Electron.*, vol. QE-8, pp. 656-661, July 1972.

10.6-μm Amplification in Metallic Waveguide by External Discharge Pumping

GERHARD A. KOEPF

Abstract—**Amplification of 10.6-μm radiation in a metallic waveguide and waveguide CO_2-laser action was achieved by excitation of the CO_2 (00^01) mode by vibrational energy transfer from metastable $N_2^*(v=1)$ molecules. Excitation of N_2 was accomplished in a separate dc discharge tube. The N_2-He mixture, after flowing through the discharge region, was pumped into the waveguide and there CO_2 was added. Maximum small-signal gain values of 25.6 and 15.3 dB/m were obtained at amplifying waveguide sections of 2 and 6-cm length, respectively.**

A theoretical analysis, based on rate equations for the (00^01) and the (10^00) states of CO_2 and the concentration of $N_2^*(v=1)$ molecules, is presented, which leads to predictions for the small-signal gain and the saturation intensity. In the pressure range covered by experiments the calculated gain values were found to be consistent with measurements.

Manuscript received April 2, 1975; revised July 10, 1975. This work was supported by the Austrian Government, Fonds zur Förderung der wissenschaftlichen Forschung, Vienna, Austria.

The author is with the Institut für Hochfrequenztechnik der Technischen Hochschule, Vienna, Austria, on leave at the NASA Goddard Space Flight Center, Greenbelt, MD.

Introduction

In flowing-gas systems CO_2-laser action may be achieved without electronic excitation of CO_2 molecules because of the following facts: 1) the very effective excitation of the asymmetrical stretching mode (00^01) of CO_2—which constitutes the upper laser level—by collisions with N_2 molecules in the lowest vibrational translational mode ($v=1$) [1], [2]; 2)

the extremely long lifetime of the $N_2^*(v = 1)$ mode [3], [4]; and 3) the high fraction of N_2 molecules that may be excited to the N_2^* $(v = 1)$ mode in a gas discharge [5], [6]. Therefore the design of a CO_2-N_2 laser amplifier or oscillator is possible with the discharge region being separated from the laser tube. Excitation of the $(00^0 1)$ state of CO_2 is accomplished by vibrational energy transfer from molecules in the $N_2^*(v = 1)$ mode which are pumped into the laser tube after being excited in the external discharge region. An increase of the gain will be obtained by the addition of He [7], [8]. Best results may be expected when the CO_2 gas is fed into the laser tube directly.

CO_2-N_2 lasers with an external RF discharge have been described in the very beginning of CO_2-laser research [4], [10]. Whereas the separation of discharge tube and laser tube was not found to be advantageous with large-diameter lasers, the use of an external discharge tube seems to be promising for waveguide lasers because metals can be used as guiding material.

The attenuation of coherent light beams propagating in optical hollow waveguides is determined essentially by the surface roughness and the complex index of refraction of the guiding material [11], [12]. Up to now, materials like glass and BeO have been used for the construction of waveguide CO_2 lasers [12]-[14]. Apart from easy availability glass offers good surface quality but has a low refractive index and poor thermal conductivity; BeO is well known for its excellent thermal conductivity and high refractive index at 10.6-μm wavelength, but the surface quality is not too high and it is rather difficult to work with. On the other hand, metals, e.g., brass with an inner gold or silver coating, combine the advantages of glass and BeO, and, beyond that, offer easy fabrication of waveguides of any desired cross section.

In this paper a theoretical treatment is presented for the calculation of the concentrations of molecules in the upper and lower laser states as a function of amplifier length for a CO_2 amplifier pumped by an external discharge. This leads to calculated small-signal gain and saturation intensity predictions. Further, small-signal gain measurements at 10.6 μm are reported for a metallic waveguide laser amplifier, and a waveguide CO_2-N_2-He laser oscillator with one internal mirror is described, both pumped by an external dc discharge. Measured gain values agree very well with the calculated results.

Theory

The physical processes along the CO_2 amplifier tube pumped by an external discharge may be characterized as follows (Fig. 1): at the point where the excited gas-mixture enters the amplifier tube, a simplified starting condition can be defined as CO_2 and He being in thermal equilibrium at partial pressures p_C and p_H, respectively. A second starting condition will be N_2 at a partial pressure p_N containing a fraction β_0 of metastable molecules N_2^* in the lowest translational-vibrational mode $(v = 1)$. Following the direction of the gas flow, a deactivation of vibrational energy in the N_2^* mode occurs by collisions with CO_2 molecules in different bending and stretching modes. These reactions have been studied, particularly in [2], [15], with the result that the main part of the vibrational

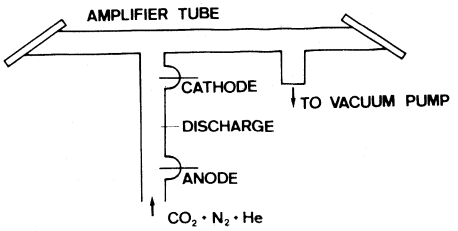


Fig. 1. Principle of a 10.6-μm amplifier using external discharge pumping.

energy of N_2^* is transferred to the asymmetrical stretching mode $(00^0 1)$ of CO_2. While increased by this reaction, the vibrational energy in the $(00^0 1)$ mode is deactivated by spontaneous and stimulated emission of radiation and by molecule-molecule collisions. After a certain time interval, while the gas is pumped down the waveguide, the total original vibrational energy in the N_2^* mode is consumed and the CO_2-N_2-He gas mixture reaches thermal equilibrium.

In order to calculate the gain of the amplifier at the 10.6-μm transition, rate equations are formulated for the variable time concentrations $n_2(t)$ and $n_1(t)$ of CO_2 molecules in the $(00^0 1)$ state and the $(10^0 0)$ state, respectively, and for the concentration of metastable $N_2^*(v = 1)$ molecules $\beta(t)n_N$. The quantity n_N is the total concentration of N_2 molecules per cubic centimeter at a pressure p_N. The following assumptions are made: 1) vibrational states of N_2^* higher than mode $(v = 1)$ are not considered because the cross sections for excitation of these modes by electron impact in a gas discharge are reported to be much less than for the $(v = 1)$ mode [6]; 2) collisional energy transfer from N_2^* to CO_2 is only considered through the resonancelike $N_2^*(v = 1)$-$(00^0 1)$ reaction by the rate k_0 (unit: $\text{torr}^{-1}\text{s}^{-1}$); 3) energy transfer from the $(00^0 1)$ to the $(10^0 0)$ state by collisions with CO_2 molecules in the ground state may be described by a rate k_{21}. All other reactions between the different bending and stretching modes CO_2 and between these modes and N_2 molecules are assumed to change *in summa* so little that they can be represented by constants R_1, R_2, R_3 in the rate equations. They contribute only to the steady-state solution; 4) rotational relaxation rates are very much faster than vibrational ones [1]. Introducing the induced emission and absorbtion rate coefficients S_{21} and S_{12} for the $P(20)$ line according to [15] (units: $\text{W}^{-1}\text{s}^{-1}\text{cm}^2$), the radiation density I in watts per square centimeters, the rate k_{10} for the collisional deactivation of the $(10^0 0)$ mode, and the radiative lifetime of the upper laser level τ, the following rate equations can be written:

$$\frac{dn_1}{dt} = \left(k_{21}p + \frac{1}{\tau}\right)n_2 - k_{10}pn_1 + I(S_{21}n_2 - S_{12}n_1) + R_1$$

$$\frac{dn_2}{dt} = k_0 p(\beta n_N - n_2) - \left(k_{21}p + \frac{1}{\tau}\right)n_2 - I(S_{21}n_2 - S_{12}n_1) + R_2$$

$$n_N \frac{d\beta}{dt} = -k_0 p(\beta n_N - n_2) + R_3. \qquad (1)$$

The solution of these equations is

$$n_1(t) = A_1 \exp(-x_1 t) + A_2 \exp(-x_2 t) + A_3 \exp(-x_3 t) + n_{10}$$
$$n_2(t) = y_1 A_1 \exp(-x_1 t) + y_2 A_2 \exp(-x_2 t) + y_3 A_3 \exp(-x_3 t) + n_{20}$$
$$n_N \beta(t) = z_1 A_1 \exp(-x_1 t) + z_2 A_2 \exp(-x_2 t) + z_3 A_3 \exp(-x_3 t) + \beta_\infty n_N. \quad (2)$$

A detailed discussion of this solution and the formulas for the constants y_i, z_i, and A_i are given in the Appendix. The time constants x_i are the roots of a third-order equation, and n_{10}, n_{20} such as $\beta_\infty n_N$ are the steady-state concentrations in the CO_2-N_2-He gas mixture at thermal equilibrium.

The net rate at which molecules are stimulated to emit photons can be calculated from the concentrations n_2 and n_1 as $I(S_{21} n_2 - S_{12} n_1)$. By multiplying this with the energy of one photon and dividing by I, the gain coefficient $\alpha(t)$ is obtained

$$\alpha(t) = \frac{hc}{\lambda}(S_{21} n_2 - S_{12} n_1) \quad (\mathrm{cm}^{-1}). \quad (3)$$

The gain of the amplifier as a function of waveguide length z is given by

$$G(z) = \exp\left[v \int_0^{z/v} \alpha(t)\, dt\right] \quad (4)$$

where v is the gas velocity. This result includes the further assumption that the total pressure is constant along the waveguide. However, in practice the input pressure p_0 decreases linearly toward the vacuum pump with a negative pressure gradient $-p'$. This affects the result for $G(z)$ in two ways: first, the collisional energy exchange between the different modes is decreased; and second, the flow rate is increased with increasing z. Whereas the first effect will be discussed after a numerical evaluation, the increase of the flow rate can be taken into consideration analytically. From the well-known fact that the product of pressure times volume is constant at constant temperature, the gas velocity follows immediately to increase as $v(z) \approx v_0 [1 + (p'/p_0) z]$ for small p'/p_0 values, with v_0 the input velocity. This corresponds to an exponential increase of v versus time according to

$$v(t) = v_0 \exp\left(\frac{p'}{p_0} v_0 \cdot t\right). \quad (5)$$

By integration and using a series expansion, a relation is found between the time variable t and z

$$t = \frac{z}{v_0}\left(1 - \frac{p'}{2p_0} z\right). \quad (6)$$

This leads to the new gain equation

$$G(z) = \exp\left[v_0 \int_0^t \alpha(t') \exp\left(\frac{p'}{p_0} v_0 \cdot t'\right) dt'\right]. \quad (7)$$

Experiment

A. Waveguide-Laser Amplifier

A 10.6-μm amplifier consisting of a 16-cm-long circular waveguide made of brass with KCl Brewster-angle windows and a separate glass discharge tube with three electrodes was constructed (Fig. 2). The inner diameters of the waveguide and the glass tube were 1.9 and 2.2 mm, respectively. Five brass hose liners were soldered to the waveguide at points 2 cm apart. To one of them, the external discharge tube, was connected by a short piece of silicon rubber hose. Two others served as CO_2 gas input and gas output, respectively, the latter being connected to the vacuum pump which produced an output flow rate of 190 ± 8 cm^3/s. The hose liners not used were sealed vacuum tight. Cooling of the discharge tube was simply achieved by partial immersion in a small water tank.

As a signal source, a stable CO_2-N_2-He laser locked to the $P(20)$ line of the $(00^0 1)$-$(10^0 0)$ transition by a Lansing lock-in stabilizer was used. The output beam of this laser was chopped mechanically, and after passing through the waveguide, directed on a pyroelectric infrared photodetector. The intensity at the detector was estimated to be 30–60 mW. The small-signal gain was determined from the enhancement of the output signal when the external discharge was ignited.

With the arrangement of the gas input and output shown in Fig. 2, that is for a CO_2-N_2-He gas flow region of 6-cm length, gain measurements were made for a variety of pressure conditions. The optimum CO_2 partial pressure p_C was observed to be 2–3 torr throughout all these experiments. In the absence of helium, gain was detected only for N_2 partial pressures p_N lower than 8 torr. The addition of He at partial pressures up to 10 torr very effectively increased the gain. The effect was most pronounced when He was added to the nitrogen gas before flowing through the discharge tube. Therefore, besides depopulating the lower laser level, He is seen to enhance the excitation of the $N_2^*(v = 1)$ state by decreasing the electron temperature in the discharge [6].

By choosing one of the electrodes $E1, E2, E3$ as anode and the brass hose liner $HL2$ as cathode, discharge regions of three different lengths were examined (Fig. 2). It can be derived from the corresponding gain measurements that a 2-cm-long N_2-He discharge region is too short for an adequate excitation of the $N_2^*(v = 1)$ state at high gas velocities (~60 m/s); whereas, the use of a 15-cm-long discharge did not give any

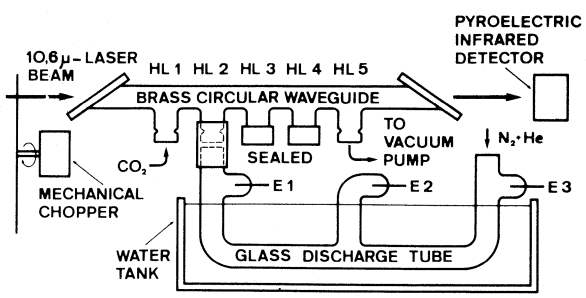


Fig. 2. Experimental setup for the measurement of small-signal gain of waveguide sections of different length with external discharge pumping.

improvement of the measured gain over a 9-cm-long discharge region. The distance between the discharge region and the waveguide proved to be quite uncritical. Even when choosing the electrodes $E2$ and $E3$ as anode and cathode, respectively, a decrease of the gain by less than 10 percent was observed. Variation of the discharge current revealed a very flat gain maximum at about 4–5 mA depending on the N_2–He pressure.

An N_2 partial pressure of 10–12 torr and an He partial pressure of 6–10 torr measured at the end of the laser tube, resulted in a maximum small-signal gain of 23.5 percent equivalent to 15.3 dB/m. By connecting the vacuum pump to the hose liners $HL4$ and $HL3$ the active waveguide section was reduced to a length of 4 and 2 cm, respectively. The corresponding gain values were measured to be 19.5 (19.4 dB/m) and 12.5 percent (25.6 dB/m). When p_H was increased the gain was found to decrease, reaching zero at a total pressure of 80 torr. Increasing the output power of the signal source by a factor of 10 resulted in a decrease of the maximum gain to 21 percent.

A reduction of the flow rate resulted in lower gain values, but different optimum pressure conditions and a slower decrease of the gain for increasing total pressure. With an output gas velocity of 30 m/s an optimum gain of 16 percent was measured for a pressure ratio of $p_C : p_N : p_H = 3:15:11$ torr. When He was added to a total pressure of 55 torr the gain decreased to 14 percent (see Fig. 6).

When mixing the CO_2 gas to N_2 and He in front of the discharge tube with the hose liner $HL1$ sealed, a maximum gain of 5 percent was observed. This relatively low value can be explained by a strong deactivation of the $N_2^*(v = 1)$ mode by collisions with CO_2 molecules on the way from the discharge region to the waveguide. In our case this section was 1.5 cm long, corresponding to a gas flow time of about 0.25 ms.

B. Waveguide-Laser Oscillator

A waveguide laser was constructed of a Pyrex glass tube of 18-cm length and an inner diameter of 1.8 mm. Glass was used instead of metal in order to allow comparison between operation with external discharge pumping on the one hand, and conventional operation with the discharge ignited in the waveguide on the other hand. The tube was equipped symmetrically with five hose liners, the one in the middle serving as a gas output, the others as input for CO_2 and N_2 + He, respectively, as shown in Fig. 3. The waveguide was sealed at one end with a gold-coated plane mirror, and at the other end with a KCl Brewster-angle window. As a second mirror, an aluminum-coated curved mirror was positioned at a distance from the waveguide end equal to its radius of curvature (79 cm). According to [16], this results in mode coupling losses of about 1.5 percent. The total losses in the resonator were estimated to be 8–12 percent. The flow rate at the output was again determined to be 190 cm^3/s. This yields a gas velocity of about 30 m/s at the input of each of the symmetrical waveguide sections.

For detection of the intensity inside the resonator the signal reflected by the Brewster-angle window was chopped and directed onto a pyroelectric infrared detector. The addition of He to N_2 was found to be necessary for laser action. A CO_2

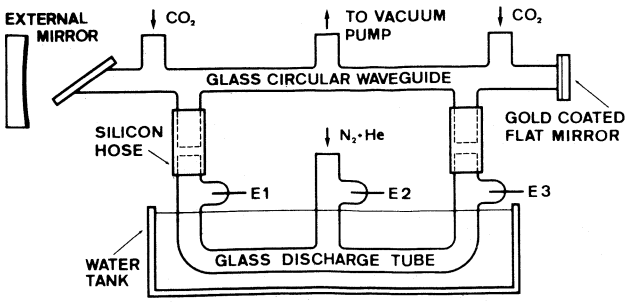


Fig. 3. Waveguide laser with one internal mirror and external discharge tube.

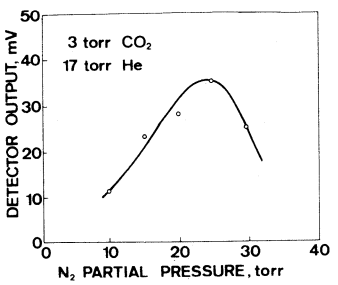


Fig. 4. Radiation density inside the waveguide laser resonator in terms of the detector output (millivolts) versus N_2 partial pressure for CO_2 and He partial pressures of 3 torr and 17 torr.

partial pressure of 3 torr and an He partial pressure of about 15 torr were found to result in maximum laser power inside the resonator. Fig. 4 shows the detector output signal in millivolts versus N_2 partial pressure with a maximum at 25 torr. For comparison with conventional operation, a discharge of 12-cm length inside the waveguide was ignited using the electrodes $E1$ and $E3$. An increase of intensity by a factor of 2 over the maximum value obtained by external discharge pumping was the result. As will be shown in the next section, this result is due to a reduction of the waveguide length where amplification occurs with increasing radiation intensity inside the resonator. In the external discharge operation, the active length was considerably shorter than 12 cm.

Results and Discussion

For a numerical evaluation of (2) and (7), the following parameter values given in the literature were used: k_0 has been determined to be 17 000 $torr^{-1}s^{-1}$ in a CO_2–N_2 mixture at room temperature [2], k_{10} and k_{21} in a CO_2–He mixture are reported to be 3400 $torr^{-1}s^{-1}$ and 85 $torr^{-1}s^{-1}$, respectively [15]. The radiative lifetime of the $(00^0 1)$ state is known to be 2.5 ms [2]. Values of 490 $W^{-1}s^{-1}cm^2$ and 470 $W^{-1}s^{-1}cm^2$ are given for S_{21} and S_{12} at the $P(20)$ rotational line of the 10.6-μm transition, for a Doppler line broadening, and the fraction of molecules in the $(10^0 0)$ state of CO_2 is 1.18×10^{-3} at room temperature [15]. The number of molecules per cubic centimeter of a gas at a partial pressure p can be calculated by Avogadro's law. This leads to a value of 8.3×10^{13} cm^{-3} for n_{10} at $p_C = 2$ torr. The quantity n_{20} that follows is equal to $0.011 \times n_{10}$ from Boltzmann's law. At a partial pressure p_N, there are $3.5 \times 10^{16} \times p_N$ molecules of nitrogen contained in one cubic centimeter, and from

the condition of thermal equilibrium of the CO_2-N_2-He mixture at the time $t = \infty$, $\beta_\infty n_N$ may be deduced to be equal to $n_{20} \cdot p_N/p_C$.

A plot of the concentrations n_1, n_2, and βn_N as functions of time shows the expected fast vibrational energy transfer from the $N_2^*(v = 1)$ state to the $(00^0 1)$ state of CO_2 (Fig. 5). These concentrations reach almost equilibrium after about 6 μs. The concentration of the $(10^0 0)$ state increases very fast, too, and shows a maximum after about 20 μs. The slope of decrease of all three concentrations depends essentially on the parameters k_{21} and I.

In order to study the effect of the rates for collisional energy exchange on the gain function, (7) was evaluated by varying the values of k_0, k_{21}, and k_{10} separately, and holding all other parameters constant: a total input pressure of 24 torr with $p_C : p_N : p_H = 2:12:10$, a pressure decrease of 4 torr along the waveguide section of 6-cm length, an input gas velocity of 60 m/s, and a β_0 of 5 percent were inserted. The value of k_0 was found to be uncritical: even a variation of ±50 percent caused no visible change of the plotted gain function. Varying k_{10} by ±20 percent resulted in a variation of the gain at $z = 6$ cm of less than 0.25 percent. However, $G(z)$ is modified by variations of k_{21} in two ways: at higher values of k_{21}, $G(z)$ shows a steeper initial increase, but levels off at lower values.

The previously stated assumption of constant pressure over the length of the waveguide may be discussed in terms of these results. As moderate variations of k_0 and k_{10} are not significant, the same is true for $k_0 p$ and $k_{10} p$. A space-dependent pressure will therefore affect $G(z)$ mainly in terms of $k_{21} p$, which corresponds to the vibrational energy loss of the $(00^0 1)$ state due to collisional deactivation. The reduction of these losses with increasing z leads to an increase of the gain coefficient with increasing z as compared with the gain coefficient at constant pressure. According to (7) this affects $G(z)$ in either the same way as a steeper increase of the exponential under the integral. From calculating $G(z)$ twice, once inserting for p_0 the input pressure, and once inserting the output pressure, a fictitious increase of p' by a factor of 1.4 in (7) could be estimated to correct the result for space-depending $k_{21} p$.

For the construction of a laser amplifier or a laser oscillator the gain as a function of waveguide length is interesting. The gain values measured at active waveguide sections of 2-,4-, and 6-cm length were found to fit very well to the calculated $G(z)$ curve with $\beta_0 = 5.8$ percent, if for all parameters, except for k_{21}, the previously stated values were inserted. For the rate k_{21}, 160 $\text{torr}^{-1}\text{s}^{-1}$ had to be used which is about twice as high as the previously given value. This can be explained by the fact that in (1) only collisional deactivation of the $(00^0 1)$ state to the $(10^0 0)$ state by molecule-molecule collisions with CO_2 in the ground state was considered. However, in [2] for CO_2-N_2 mixtures at room temperature a rate of about the same order as k_{21} is reported for the energy transfer from the $(00^0 1)$ state to the $(10^0 0)$ and the $(02^0 0)$ states by collisions with N_2 molecules in the ground state. Therefore the value of 160 $\text{torr}^{-1}\text{s}^{-1}$ seems to be more realistic than 85 $\text{torr}^{-1}\text{s}^{-1}$. It was used for all calculations described in this paper.

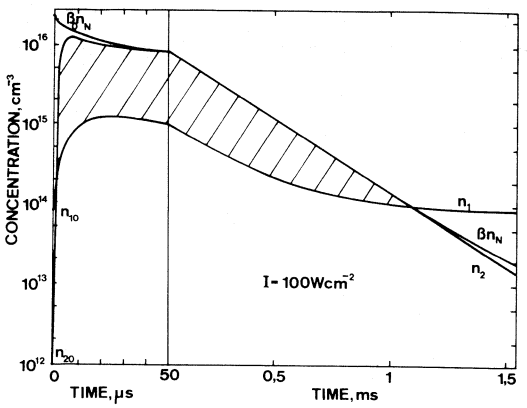


Fig. 5. Calculated concentrations of the $(00^0 1)$ and the $(10^0 0)$ states of CO_2 and of the $N_2^*(v = 1)$ mode versus time. The shaded area indicates inversion. Please note the change in time scale. Fixed parameters: $p_C = 2$ torr; $p_N = 12$ torr; $p_H = 10$ torr; $\beta_0 = 5.8$ percent; $k_0 = 17\,000$ $\text{torr}^{-1}\text{s}^{-1}$; $k_{21} = 160$ $\text{torr}^{-1}\text{s}^{-1}$; $k_{10} = 3400$ $\text{torr}^{-1}\text{s}^{-1}$; $S_{12} = 470$ cm^2/Ws; $S_{21} = 490$ cm^2/Ws; and $I = 100$ W/cm^2.

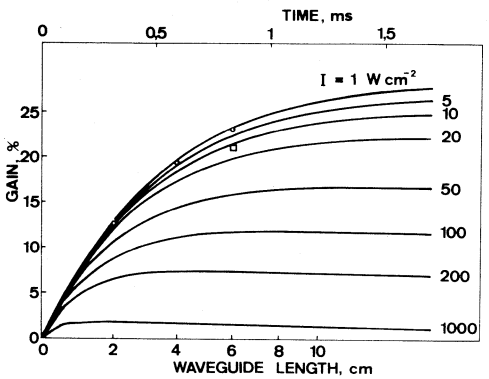


Fig. 6. Calculated gain versus waveguide length for varying radiation density I; the circles and the square correspond to measured results for $I \approx 1$-2 W/cm^2 and $I \approx 10$-20 W/cm^2. Fixed parameters: $p_C = 2$ torr; $p_N = 12$ torr; $p_H = 10$ torr; $p' = 4/3$ torr/cm; $v_0 = 60$ m/s; $\beta_0 = 5.8$ percent; $k_0 = 17\,000$ $\text{torr}^{-1}\text{s}^{-1}$, $k_{21} = 160$ $\text{torr}^{-1}\text{s}^{-1}$; $k_{10} = 3400$ $\text{torr}^{-1}\text{s}^{-1}$; $S_{12} = 470$ cm^2/Ws; and $S_{21} = 490$ cm^2/Ws.

In Fig. 6 the gain versus z is shown as calculated for $p_0 = 24$ torr, $v_0 = 60$ m/s, $\beta_0 = 5.8$ percent, and variable radiation density. The circles and the square correspond to the previously mentioned measured results. At higher radiation densities the faster deactivation of vibrational energy is seen to result in a reduction of the length of the waveguide necessary to achieve the maximum available gain. This has to be taken into account when constructing a laser, because CO_2 in thermal equilibrium at $p_C = 2$ torr introduces additional losses in the resonator, which can be calculated to be about 0.07 percent/cm.

The small-signal gain and the saturation intensity were calculated for a waveguide length of 6 cm, an input gas velocity of 30 m/s, a CO_2 partial pressure of 3 torr, and a pressure gradient of 2 torr/cm. The results are shown in Figs. 7 and 8 with the concentration $\beta_0 n_N$ of metastable N_2 molecules as a parameter. For a constant value of $\beta_0 n_N$ the gain is seen to decrease very fast with increasing total pressure. However, when the partial pressures p_N and/or p_H are increased also, the condition for the excitation of the $N_2^*(v = 1)$ mode in the discharge and the value of $\beta_0 n_N$ is changed. From Fig. 7 the

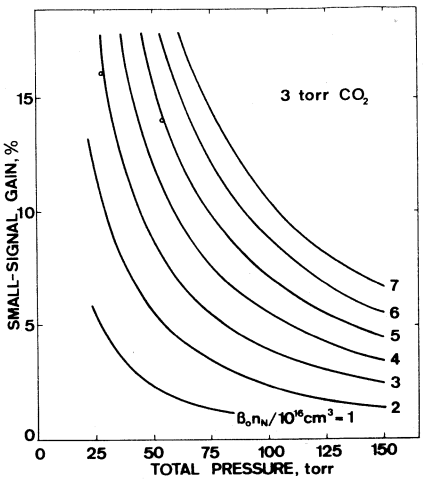


Fig. 7. Calculated small-signal gain versus total pressure for a p_C of 3 torr and varying input $N_2^*(v = 1)$ concentration. Circles indicate measured results. Fixed parameters: $v_0 = 30$ m/s; $z = 6$ cm; $p' = 2$ torr/cm; $k_0 = 17\,000$ torr^{-1}s^{-1}; $k_{21} = 160$ torr^{-1}s^{-1}; $k_{10} = 3400$ torr^{-1}s^{-1}; $S_{12} = 470$ cm^2/Ws; and $S_{21} = 490$ cm^2/Ws.

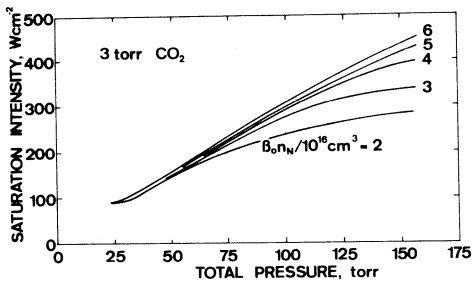


Fig. 8. Calculated saturation parameter versus total pressure for a p_C of 3 torr and varying input $N_2^*(v = 1)$ concentration. Fixed parameters: $v_0 = 30$ m/s; $z = 6$ cm; $p' = 2$ torr/cm; $k_0 = 17\,000$ torr^{-1}s^{-1}; $k_{21} = 160$ torr^{-1}s^{-1}; $k_{10} = 3400$ torr^{-1}s^{-1}; $S_{12} = 470$ cm^2/Ws; and $S_{21} = 490$ cm^2/Ws.

fraction of excited N_2 molecules entering the waveguide may be deduced if experimental results for the gain are at hand, e.g., from the measurements at $v_0 = 30$ m/s previously described, $\beta_0 n_N$ is seen to be about 3×10^{16} and 5×10^{16} cm^{-3} for total pressures of 28 and 55 torr, respectively. For constant $\beta_0 n_N$ the saturation intensity is seen (Fig. 8) first to increase about linearly with increasing pressure and then to level off. It has to be pointed out that the saturation intensity like the small-signal gain is a function of waveguide length. From Fig. 6 for active waveguide sections of 2- and 6-cm length, saturation intensities of about 200 and 100 W/cm^2, respectively, may be deduced.

Conclusions

Amplification of 10.6-μm radiation propagating in a metallic waveguide and 10.6-μm laser oscillation by external discharge pumping has been demonstrated. A small-signal gain of 15.3 dB/m in a 6-cm-long, 1.9-mm-ID waveguide was obtained at a total input pressure of 24 torr. This compares with 12.5 dB/m at 35 torr for a 12.5-cm-long, 2-mm-ID waveguide laser with internal gas discharge [17]. However, for such a comparison one has to take into consideration the relation between the small-signal gain and waveguide length. Whereas in conventional lasers the gain increases exponentially with waveguide length, in case of external discharge pumping it levels off after a steep increase reaching a maximum and then decreases slightly according to the absorption of CO_2 in thermal equilibrium. It follows that external discharge pumping offers a considerably higher small-signal gain only for short waveguide sections. For example, in a 2-cm-long section of the 1.9-mm-ID tube a gain of 25.6 dB/m was obtained. Considering the saturation intensity in the 25–150-torr pressure range, the value of 1–3 kW/cm^2 reported in the literature for conventional waveguide lasers [12], [17] has to be compared with our calculated 90–450 and 200–950 W/cm^2 for waveguide sections of 6- and 2-cm length, respectively.

For applications in communications CO_2 lasers exhibiting a large bandwidth of the gain profile are interesting [18]. In waveguide lasers with internal discharge the optimum working pressure, and hence the pressure broadening of the gain profile is essentially determined by the inner diameter of the waveguide. In case of external discharge pumping, the diameters of the waveguide and the discharge tube can be made independent of each other, offering a degree of freedom for the bandwidth of the gain profile. Further, the construction of such lasers by the use of metals as guiding material is promising because of low waveguide losses and easy fabrication of arbitrary waveguide cross sections. The scheme of external discharge pumping permits amplification of signals propagating in hollow waveguides in an easy way. Also the construction of a one-block laser modulator seems interesting for the generation of millimeter-wave-modulated 10.6-μm radiation [19].

However, further investigations are necessary to study the optimum excitation conditions for the metastable $N_2^*(v = 1)$ mode as a function of the N_2 and He partial pressures, and the gas velocity in the waveguide, respectively. Design of rectangular instead of circular waveguide cross sections may be advantageous in connection with transverse gas flow. High gain values should be obtainable for premixed CO_2-N_2-He gas mixtures than were measured in our corresponding experiment, by the use of the metallic waveguide itself as a cathode.

Appendix

Introducing the following abbreviations:

$$a = k_{10}p + S_{12}I$$

$$b = (k_0 + k_{21})p + \frac{1}{\tau} + S_{21}I$$

$$c = S_{12}I$$

$$d = k_0 p \qquad \text{(A1)}$$

(1) of the main text can be written in the form

$$\frac{dn_1}{dt} + an_1 = (b - d) \cdot n_2 + R_1$$

$$\frac{dn_2}{dt} + bn_2 = cn_1 + d \cdot \beta n_N + R_2$$

$$\frac{d\beta}{dt} n_N + d\beta n_N = dn_2 + R_3. \qquad \text{(A2)}$$

By elimination of n_2 and βn_N a differential equation of third

order for n_1 is obtained. The solution is

$$n_1(t) = A_1 \exp(-x_1 t) + A_2 \exp(-x_2 t) + A_3 \exp(-x_3 t) + n_{1\infty}. \quad \text{(A3)}$$

The x_i are the roots of a third-order equation, the A_i are constants, and $n_{1\infty}$ is the steady-state concentration of the lower laser state. For all interesting values of the parameters a, b, c, and d the roots x_i were found to be real and positive. Inserting (A3) into (A2) gives the solution for n_2 and βn_N

$$n_2(t) = y_1 A_1 \exp(-x_1 t) + y_1 A_1 \exp(-x_2 t) + y_3 A_3 \exp(-x_3 t) + n_{2\infty} \quad \text{(A4)}$$

$$n_N \beta(t) = z_1 A_1 \exp(-x_1 t) + z_2 A_2 \exp(-x_2 t) + z_3 A_3 \exp(-x_3 t) + \beta_\infty n_N \quad \text{(A5)}$$

where $n_{2\infty}$ and $\beta_\infty n_N$ again are the steady-state values of n_2 and βn_N, respectively, and the constants y_i and z_i are related to the constants x_i by the equations

$$y_i = \frac{-x_i + a}{b - d}$$

$$z_i = \frac{-x_i + b}{d} y_i - \frac{c}{d}. \quad \text{(A6)}$$

From the starting condition with $n_1 = n_{10}$ and $n_2 = n_{20}$ for $t = 0$ three equations for A_1, A_2, and A_3 are deduced. Because CO_2 is in thermal equilibrium at $t = 0$ and at $t = \infty$ at the same partial pressure, $n_{10} = n_{1\infty}$ and $n_{20} = n_{2\infty}$. With the abbreviation

$$\Delta = y_1(z_2 - z_3) + y_2(z_3 - z_1) + y_3(z_1 - z_2) \quad \text{(A7)}$$

one obtains

$$A_1 = \frac{1}{\Delta} n_N(\beta_0 - \beta_\infty)(y_3 - y_2)$$

$$A_2 = \frac{1}{\Delta} n_N(\beta_0 - \beta_\infty)(y_1 - y_3)$$

$$A_3 = \frac{1}{\Delta} n_N(\beta_0 - \beta_\infty)(y_2 - y_1).$$

Acknowledgment

The author wishes to thank Dr. G. Adam of the Institute für Theoretische Physik I, Technische Hochschule in Vienna, and his colleagues K. Kerschbaumer, H. Krammer, and A. L. Scholtz for helpful discussions. He also wishes to thank Dr. E. Bonek and M. J. Miltner for their critical reading of the manuscript.

References

[1] C. K. N. Patel, "CW high power N_2–CO_2 laser," *Appl. Phys. Lett.*, vol. 7, pp. 15–17, July 1965.
[2] W. A. Rosser, Jr., A. D. Wood, and E. T. Gerry, "Deactivation of vibrationally excited carbon dioxide (v_3) by collisions with carbon dioxide and nitrogen," *J. Chem. Phys.*, vol. 50, pp. 4996–5008, June 1969.
[3] M. F. Legay and N. Legay-Sommaire, "Sur les possibilities de realization d'un maser optique utilisant l'energie de vibration des gaz excites par l'azote active," *C. R. Acad. Sci.*, vol. 259, pp. 99–102, July 1964.
[4] C. K. N. Patel, "Selective excitation through vibrational energy transfer and optical maser action in N_2–CO_2," *Phys. Rev. Lett.*, vol. 13, pp. 617–619, Nov. 1964.
[5] K. Dressler, "Absorbtion spectrum of vibrationally excited N_2 in active nitrogen," *J. Chem. Phys.*, vol. 30, pp. 1621–1622, Feb. 1959.
[6] W. L. Nighan, "Electron energy distributions and collision rates in electrically excited N_2, CO, and CO_2," *Phys. Rev. A*, vol. 2, pp. 1989–2000, Nov. 1970.
[7] G. Moeller and J. D. Rigden, "High power laser action in CO_2–He mixtures," *Appl. Phys. Lett.*, vol. 7, pp. 274–276, Nov. 1969.
[8] C. K. N. Patel, P. N. Tien, and J. H. McFee, "CW high-power CO_2–N_2–He laser," *Appl. Phys. Lett.*, vol. 7, pp. 290–292, Nov. 1965.
[9] P. K. Cheo, "Effects of CO_2, He and N_2 on the lifetimes of the 00^01 and 10^00 CO_2 laser levels and on pulsed gain at 10.6 μm," *J. Appl. Phys.*, vol. 38, pp. 3563–3568, Aug. 1967.
[10] N. Legay-Sommaire, L. Henry, and F. Legay, "Realisation d'un laser utilisant l'energie de vibration des gàz excites par l'azote activè," *C. R. Acad. Sci.*, vol. 260, pp. 3339–3342, Mar. 1965.
[11] E. A. Marcatili and R. A. Schmeltzer, "Hollow metallic and dielectric waveguides for long distance optical transmission and lasers," *Bell Syst. Tech. J.*, vol. 43, pp. 1783–1809, July 1964.
[12] R. L. Abrams and W. B. Bridges, "Characteristics of sealed-off waveguide CO_2 lasers," *IEEE J. Quantum Electron.*, vol. QE-9, pp. 940–946, Sept. 1973.
[13] T. J. Bridges, E. G. Burkhardt, and P. W. Smith, "CO_2 waveguide lasers," *Appl. Phys. Lett.*, vol. 20, pp. 403–405, May 1972.
[14] R. E. Jensen and M. S. Tobin, "CO_2 waveguide gas laser," *Appl. Phys. Lett.*, vol. 20, pp. 508–510, June 1972.
[15] C. B. Moore, R. E. Wood, B. L. Hu, and J. T. Yardley, "Vibrational energy transfer in CO_2 lasers," *J. Chem. Phys.*, vol. 46, pp. 4222–4231, June 1967.
[16] J. J. Degnan and D. R. Hall, "Finite-aperture waveguide-laser resonators," *IEEE J. Quantum Electron.*, vol. QE-9, pp. 901–910, Sept. 1973.
[17] J. J. Degnan, H. E. Walker, J. H. McElroy, and N. McAvoy, "Gain and saturation intensity measurements of a waveguide CO_2 laser," *IEEE J. Quantum Electron.* (Corresp.), vol. QE-9, pp. 489–491, Apr. 1973.
[18] R. L. Abrams, "Gigahertz tunable waveguide CO_2 laser," *Appl. Phys. Lett.*, vol. 25, pp. 304–306, Sept. 1974.
[19] G. A. Koepf, "Integrierter CO_2-Kapillarlaser-Modulator mit externer Gasentladung," Austrian Patent Application No. 3949/75.

Application of Laser Q Switching for Infrared Spectroscopy

W. A. KREINER

Abstract—**Passive Q switching of IR lasers (N_2O as well as CO_2) has been applied for the detection of coincidences within a few 100 MHz between laser lines (ν_L) and molecular transitions (ν_M). Polar ($^{12}CH_3F$, $^{13}CH_3F$, C_2H_5OH, and $C_6H_5CH_3$) as well as nonpolar molecules (SiH_4, GeH_4, CCl_4, C_2H_4, C_3H_4, and C_6H_6) have been studied. The phenomenon depends strongly on the frequency mismatch $\Delta\nu = \nu_M - \nu_L$. 81 combinations between laser lines and molecular absorption lines were found to produce the Q-switch effect.**

I. Introduction

PASSIVE Q switching using gases as saturable absorbers is a well-known technique for producing laser pulses [1]-[10]. There is a large number of molecules producing this effect on certain lines of CO_2 and N_2O infrared lasers. For some polar molecules active Q switching was achieved by intracavity Stark modulation [11]-[14]. In this paper this phenomenon is used for detecting near coincidences between fixed-frequency CO_2 and N_2O lasers and molecular absorption lines. The work was originally undertaken in order to find suitable coincidences for laser-Stark and infrared-radio-frequency double-resonance experiments of nonpolar molecules [32]. This investigation was extended to some more polar as well as nonpolar molecules of spectroscopic interest in order to provide information about exact absorption frequencies. In particular the investigation was concentrated on the following.

1) The influence of the frequency mismatch $\Delta\nu$ between the laser line and the molecular absorption frequency on the performance of the Q-switching effect.

2) The determination of the maximum $\Delta\nu$ which still produces the effect under the conditions described.

In some favorable cases information could be obtained on whether the laser line is above or below the molecular absorption frequency.

The coincidences listed may be useful in various spectroscopic investigations [15]-[17], as calibration frequencies in tunable laser spectroscopy [18], in double resonance [32], as well as in two-photon experiments [25]. In total 10 molecules (SiH_4, GeH_4, CCl_4, $^{12}CH_3F$, $^{13}CH_3F$, C_2H_4, C_3H_4, C_6H_6, C_2H_5OH, and $C_6H_5CH_3$) have been investigated.

II. Experimental

A conventional CO_2 laser (tube length 260 cm, inner diameter 1.8 cm) with a cavity length of 379 cm giving a longitudinal mode spacing of about 40 MHz was used. Selection of a single line was provided by a blazed grating (PTR, 71 lines/mm) and longitudinal mode tuning (±20 MHz) by a gold mirror mounted on a piezoelectric crystal. Irises were inserted in the resonator in order to suppress transverse modes.

An absorption cell (length 61 cm, inner diameter 1.8 cm) with NaCl Brewster windows on both ends was placed near the grating inside the resonator. There was no electric field applied like some previous authors did in order to pull the absorption lines [11]-[14].

A liquid-nitrogen-cooled Pb:Sn:Te detector followed by an audio transformer (50 Ω/100 kΩ) was used to observe Q switching. The output was displayed on an oscilloscope.

Laser power could be varied continuously by changing the CO_2 gas pressure. The output power (taken from the 0th-order reflection of the grating) ranged typically between 10 and 100 mW. This corresponds to a power level inside the cavity of the order of 1 W. The same laser was used also for N_2O-laser lines.

III. Observation and Results

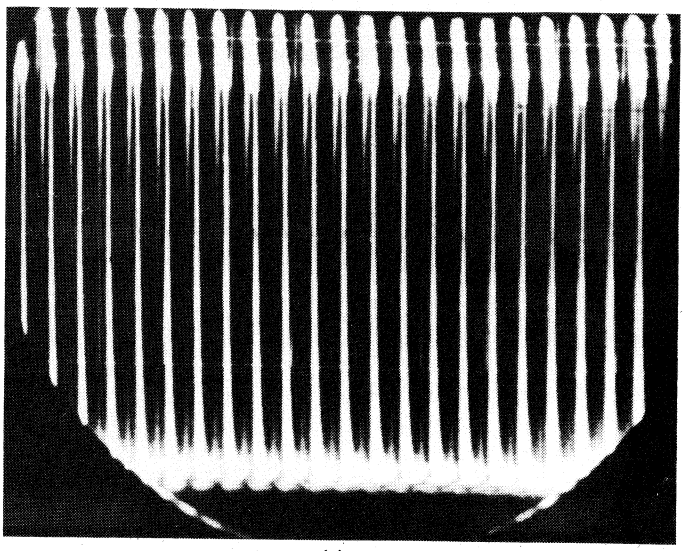
The technique was first tested on some absorption lines of SiH_4 ($R18$ of ν_4, $R21$ of ν_4) and CH_3F (see Tables I and III) for which the frequency mismatches with respect to the nearest laser line are already known from the measurement of the Stark effect [15], [16], [19]. When the laser was run with moderate power on a line nearly coinciding with a molecular transition, periodic saturation of the gas caused pulse modulation of the laser (Q switch). A typical sequence of spikes is shown in Fig. 1(a) and (b) for SiH_4. This technique was then applied to many other gases, GeH_4, CCl_4, C_2H_4, C_6H_6, C_2H_5OH, and $C_6H_5CH_3$. The pressure used in the experiments ranged from 6 mtorr to 1 torr. The observed features of the Q switch are summarized as follows.

1) Optimum sample pressure depends strongly on the absorption intensity of the transition. Below the Q-switch pressure level, absorption was still easily detectable. At higher pressures the laser tends to flip out to neighboring lines due to the limited resolution of the grating.

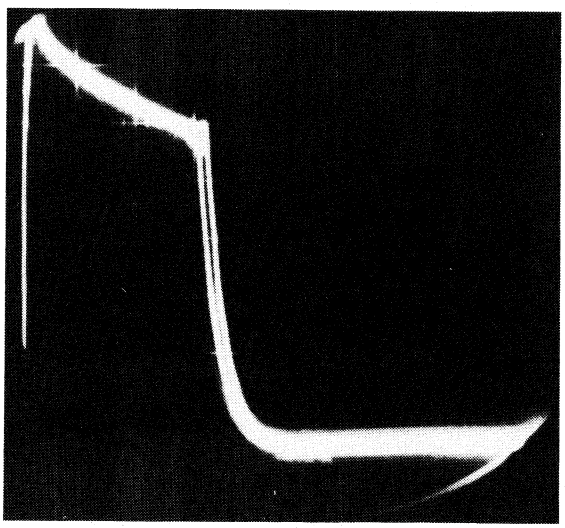
2) The effect is strongly influenced by a change of resonator length and hence the laser frequency. Fig. 2 shows the $P(20)$ line of CO_2 in the 9.4-μ band interacting with absorption lines of $^{12}CH_3F$. There are three lines near to the laser line, $Q(12,1)$, $Q(12,2)$, and $Q(12,3)$. Their frequency offset $\Delta\nu = \nu_M - \nu_L$ (where ν_M is the molecular absorption and ν_L the laser frequency) is -30, 44.2, and 165.0 MHz, respectively. Their relative intensity is 1:4:18 in the same order. The line at -30 MHz is very weak and most probably of minor importance for the effect. Here the output power of the laser is plotted versus the voltage moving the resonator mirror. The laser is oscillating mainly on one longitudinal mode. This was checked with a spectrum analyzer connected to the detector (resolution <1 MHz). The shadowed area indicates where

Manuscript received April 2, 1975; revised July 17, 1975.

The author was with the Division of Physics, National Research Council of Canada, Ottawa, Ont., Canada. He is now with the Abteilung für Physikalische Chemie, University of Ulm, Ulm, Germany.



(a)



(b)

Fig. 1. (a) Typical sequence of laser spikes produced by SiH_4 as a saturable absorber. Sample pressure is about 400 mtorr. $P(46)$ of CO_2 (10.4-μ band) is used. Scale: 1ms/div. (b) Single pulse which shows a steep increase of laser power followed by an exponential decay and wiggles before the cutoff. Scale: 100 μs/div.

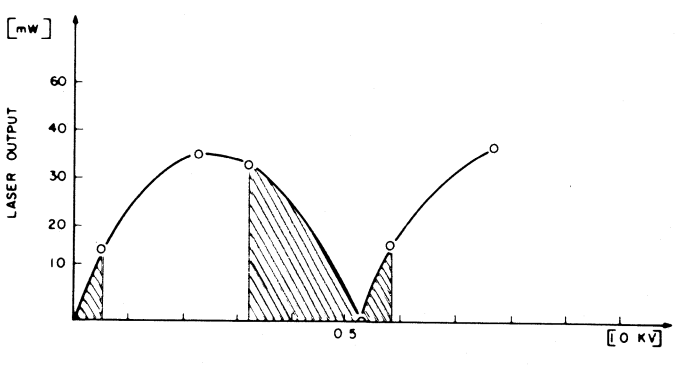


Fig. 2. Laser output versus cavity length which is given in terms of voltage applied to the piezocrystal. Laser frequency increases with voltage. The separation of the maxima corresponds to the separation of longitudinal modes (~ 40 MHz). 36 mtorr of $^{12}CH_3F$ are used to switch the $P(20)$ line of CO_2 in the 9.4-μ band.

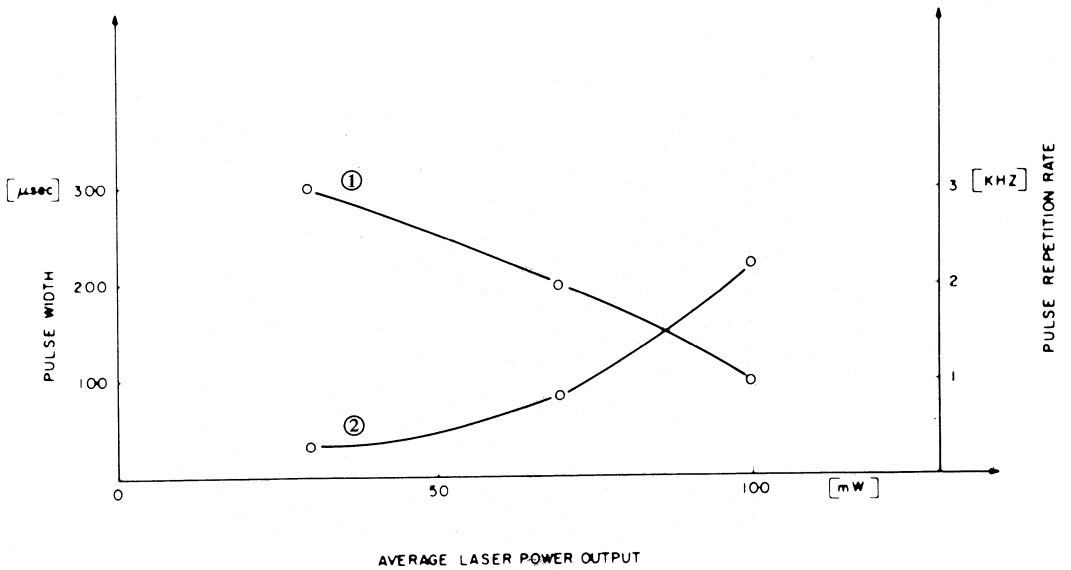


Fig. 3. Pulsewidth ① and pulse repetition rate ② versus laser output (0th order of the grating) for SiH_4 interacting with $P(46)$ of CO_2 in the 10.4-μ band. Sample pressure is about 400 mtorr. Laser power was varied via laser gas pressure.

laser spikes were observed. The distance between power maxima corresponds to the separation of two successive longitudinal modes. When the laser frequency ν_L is increased, the mode approaches the absorption line. Therefore we could use the asymmetric behavior of the Q switch to determine the sign of $\Delta\nu$.

3) Some absorption lines hardly produce spikes although they absorb strongly. This was observed for $R(4,3)$ of $^{13}CH_3F$ (ν_3 fundamental) using $P(32)$ in the 9.4-μ band of CO_2. $\Delta\nu$ is 25.8 MHz in this case. In toluene and carbon tetrachloride no Q switching was observed although they absorb most of the laser lines strongly.

4) The pulse repetition rate as well as the pulsewidth depends on the laser gain. An example is shown in Fig. 3. While the pulse repetition rate increases from 0.35 to 2.2 kHz the pulse length decreases from 300 to 100 μs. The pulses themselves show a sharp increase followed by an exponential decay as described by Burak *et al.* [8] and high-frequency wiggles before the steep cutoff [See Fig. 1(b)].

The results 2 and 3 seem to indicate that, for periodic switching, the laser line has to be in a certain position with respect to the absorption line. The result 3 indicates that when the laser line is very close to the center of an absorption line Q switching is hard to produce. This suggests that the mechanism responsible for Q switching is not merely absorption but absorption and dispersion with sufficient frequency dependence that the frequency of the laser has to be shifted during the transient phenomenon. This can be taken into consideration in the case of toluene and carbon tetrachloride where no effect was observed although absorption is nearly uniform over a wide spectral range because of the dense spectrum. A theory of the Q switch including absorption phenomena only was given by several authors. Their calculation of the pulse shape is done by rate equations based on absorption phenomena only [20]-[24]. Salomaa and Stenholm mention dispersion effects in the active medium, but

TABLE I

Silane SiH_4				N_2O Laser			
Laser Lines absorbed		Q-switching observed [m Torr]	$\Delta\nu = \nu_M - \nu_L$ [MHz]	Laser Lines absorbed		Q-switching observed [m Torr]	$\Delta\nu = \nu_M - \nu_L$ [MHz]
R(3)	s	-		P(12)	vs	>170	
R(4)	vvs	> 15		P(13)	vs	>160	
R(6)	m	-		P(14)	vs	> 90	
R(7)	vs	>140		P(15)	vs	> 90	
R(8)	vs	>180		P(17)	vw	-	
R(11)	vs	> 35		P(18)	s	200	
R(12)	w	-		P(19)	vw	-	
R(15)	m	-		P(20)	vw	-	
R(16)	vvs	> 10[a]	54 ± 2	P(21)	s	400	
R(17)	vs	200		P(22)	s	350	
R(24)	s	<200	-143 ± 5	P(23)	s	350	-
R(27)	vs	200		P(28)	s	> 70	-
R(28)	vw	-		P(30)	s	300	+
R(31)	w	-		P(31)	s	300	+
R(35)	m			P(32)	s	300	
P(4)	s	350		P(33)	s	200	+
P(5)	vs	10[b]		P(34)	s	200	+
P(6)	s	300		P(36)	s	200	-
P(7)	s	300		P(37)	s	>160	-
P(8)	s	380		P(38)	s	400	-
P(9)	vs	> 70		P(39)	m	-	
P(10)	vs	>180		P(40)	m	-	
P(11)	vs	> 90		P(41)	m	-	
P(6)	w	-	R(2)		250	P(18) vs	300
P(8)	w	-	R(12)		350	P(20) m	-
P(10)	m	-	R(20)	m	-	P(22) vw	-
P(20)	w	-	R(22)	m	-	P(24) m	-
P(26)	m	-	R(28)	m	-	P(26) vw	-
P(30)	w	-	R(32)	vs	>130	P(28) vs	300
P(32)	m	-	R(34)	vs	200	P(30) w	-
P(38)		-	R(36)	m	-	P(36)	400
P(40)		-	R(38)	vs	200	P(38)	450
P(44)	w	-	R(46)	vs	200	P(40)	450
P(46)	m	-	P(4)	w	-	P(44)	450
			P(12)	m	-	P(46)	450
10.8 μ band			P(22)	m			

[a] Q switching difficult to produce.
[b] The corresponding molecular transition was identified as $R9(F_1^{(3)} \rightarrow F_2^{(3)})$ in the ν_4 fundamental [32].

TABLE II

Germane GeH_4					
N_2O Laser			CO_2 Laser 10.4 μ band		
Laser Lines absorbed		Q-switching observed [m Torr]	Laser Lines absorbed	Q-switching observed [m Torr]	$\Delta\nu = \nu_M - \nu_L$ [MHz]
R(14)	s	250	P(10)	vs 300	
			P(18)	s 300	
P(6)	s	300	P(26)	vs 100[a]	-23 ± 1
P(31)	m	-	P(28)	s 200	
			P(30)	s 200[a]	

[a] Q switching difficult to produce.

TABLE III

Methylflouride				CO_2 Laser 9.4 μ band			
$^{12}CH_3F$				$^{13}CH_3F$			
Laser Lines absorbed[a]		Q-switching observed [m Torr]	$\Delta\nu = \nu_M - \nu_L$ [MHz]	Laser Lines absorbed	Q-switching observed [m Torr]		$\Delta\nu = \nu_M - \nu_L$ [MHz]
P(20)	vs	>6	-30 44.2 165.0[b]	P(32)	vs	-	- 25.8
				P(40)	w	-	-233.6

[a] Several other lines with $\Delta\nu$ between 4 and 12 GHz were tested. No absorption or Q swtiching could be detected up to a sample pressure of ≈1 torr.

[b] The line at $\Delta\nu = -30$ MHz is very weak and most probably of minor importance for the effect.

TABLE IV

Ethylene C_2H_4			N_2O Laser		
Laser Lines absorbed		Q-switching observed [m Torr]	Laser Lines absorbed		Q-switching observed [m Torr]
R(9)	s	400	P(15)	vs	400
			P(20)	vs	400
P(10)	vs	400	P(26)	m	400
CO_2 Laser 9.4 μ band					
R(10)	vs	<400	P(18)	s	-
P(6)	vs	400	P(34)	vs	400
P(8)	s	-	P(42)	400	400
CO_2 Laser 10.4 μ band					
R(2)	vs	400	P(6)	s	-
R(32)	m	400	P(8)	s	400
R(34)	m	400	P(34)	s	400
			P(44)	vs	400
			P(46)	s	400

neglect them as being small [22], [23]. The observed results on SiH_4, GeH_4, CH_3F, C_2H_4, C_3H_4, C_6H_6, and C_2H_5OH are given in Tables I-VII. For SiH_4, the molecule studied most extensively, all the laser lines are listed which show either Q switching or absorption only. The molecular transition interacting with $P(5)$ of N_2O was recently identified as $R9(F_1^{(3)} \rightarrow F_2^{(3)})$ in the ν_4 fundamental [32]. The frequency mismatch $\Delta\nu$ is given when it is known. From this an optimum value for $\Delta\nu$ between 30 and 200 MHz for Q switching to occur is derived.

TABLE V

Allene C_3H_4			N_2O Laser		
Laser Lines absorbed		Q-switching observed [m Torr]	Laser Lines absorbed		Q-switching observed [m Torr]
P(9)	vs	-	P(20)		-
P(13)	vs	-	P(25)	vs	300
P(15)	s	400	P(28)	s	400
P(18)	s	400			
CO_2 Laser 9.4 μ band					
P(24)	s	400	P(34)	s	400
CO_2 Laser 10.4 μ band					
P(32)	s	400	P(48)	s	400
P(46)	s	400			

TABLE VI

Benzene C_6H_6			CO_2 Laser 9.4 μ band		
Laser Lines absorbed[a]		Q-switching observed [m Torr]	Laser Lines absorbed		Q-switching observed [m Torr]
P(18)	s	250	P(44)	vs	250
P(30)	s	250	P(46)	vs	250
P(32)	s	250			

[a] Most of the CO_2-laser lines between ≈1020 and 1070 cm^{-1} are strongly absorbed.

TABLE VII

Ethanol C_2H_5OH			CO_2 Laser 9.4 μ band		
Laser Lines absorbed[a]		Q-switching observed [m Torr]	Laser Lines absorbed		Q-switching observed [m Torr]
R(2)	vs	>100	P(20)	s	200
R(4)	vs	> 35	P(22)	vs	> 40
R(12)	vs	> 80	P(32)	vs	> 40
R(18)	vs	>120	P(36)	vs	> 40
R(20)	s	>140	P(40)	vs	> 50
R(28)	vs	> 50	P(42)	vs	> 70
			P(50)	s	>160

[a] Most of the CO_2-laser lines above 960 cm^{-1} are strongly absorbed.

IV. Conclusion

The result of this paper indicates that the Q-switching technique is a useful tool for finding near coincidences between IR lasers and molecular transitions, expecially for a frequency offset of the order of 100 MHz. There exist several experimental techniques, e.g., two-photon absorption [25], [26] or laser-Stark spectroscopy [15], [16], [19], [27]-[31] which can be applied effectively in order to make spectroscopic use of the corresponding transitions.

References

[1] O. R. Wood and S. E. Schwarz, "Passive Q switching of a CO_2 laser," *Appl. Phys. Lett.*, vol. 11, pp. 88-89, 1967.

[2] J. T. Yardley, "Passive Q-switching of the CO_2 laser by vinyl chloride," *Appl. Phys. Lett.*, vol. 12, pp. 120-122, 1968.

[3] S. Marcus, "Two saturable absorbers for extending the wavelength limits of a passively Q-switched CO_2 laser," *Appl. Phys.*

Lett., vol. 15, pp. 217–219, 1969.
[4] T. Y. Chang, C. H. Wang, and P. K. Cheo, "Passive Q-switching of the CO_2 laser by CH_3F and PF_5 gases," *Appl. Phys. Lett.*, vol. 15, pp. 157–159, 1969.
[5] J. J. Wynne and F. Shimizu, "Passive Q switching of a CO_2 laser near 9.2 μ using CF_2Cl_2," *IEEE J. Quantum Electron.* (Corresp.), vol. QE-8, pp. 676–677, July 1972.
[6] J. R. Izatt, G. F. Caudle, and B. L. Bean, "Q switching and mode locking of CO_2 laser with aromatic halogenated hydrocarbons," *Appl. Phys. Lett.*, vol. 25, pp. 446–448, 1974.
[7] W. F. Krupke, "Passive Q-switching of a CO_2 laser using a mixture of SF_6 and C_2F_3Cl gases," *Appl. Phys. Lett.*, vol. 14, pp. 221–222, 1969.
[8] I. Burak, P. L. Houston, D. G. Sutton, and J. I. Steinfeld, "Mechanism of passive Q switching in CO_2 lasers," *IEEE J. Quantum Electron.*, vol. QE-7, pp. 73–82, Feb. 1971.
[9] R. E. Jensen and M. S. Tobin, "Passive Q switching of the CO_2 laser by C_2H_4 gas and CH_3OH vapor," *IEEE J. Quantum Electron.* (Corresp.), vol. QE-6, pp. 477–478, July 1970.
[10] H. Brunet and F. Voignier, "Passive Q-switching of a N_2O laser using ethylene," *Appl. Phys. Lett.*, vol. 15, pp. 423–425, 1969.
[11] D. R. Hall and Y.-H. Pao, "High-efficiency driven Q switching of the CO_2 laser using the Stark effect in molecular gases," *IEEE J. Quantum Electron.* (Corresp.), vol. QE-7, pp. 427–429, Aug. 1971.
[12] J. M. Martin, V. J. Corcoran, and W. T. Smith, "Identification of absorption lines in gases used to modulate the CO_2 laser," *IEEE J. Quantum Electron. (Part II of Two Parts: Special Issue on 1973 IEEE/OSA Conf. Laser Engineering and Applications)*, vol. QE-10, pp. 191–195, Feb. 1974.
[13] E. Weitz, G. Flynn, and A. M. Ronn, "Stark effects in $C^{13}H_3F$: Passive Q switching of the CO_2 laser using C^{13} enriched methyl-fluoride," *J. Appl. Phys.*, vol. 42, pp. 5187–5190, 1971.
[14] M. S. Tobin and R. E. Jensen, "Q switching of the CO_2 laser by molecular gases exhibiting the Stark effect," *IEEE J. Quantum Electron.* (Corresp.), vol. QE-8, pp. 21–22, Jan. 1972.
[15] W. A. Kreiner and T. Oka, "Infrared laser spectroscopy of SiH_4," presented at the 29th Symp. Molecular Structure and Spectroscopy, Columbus, OH, 1974.
[16] ——, "Observation of the linear Stark effect in some tetrahedral molecules," to be published.
[17] F. Meyer, J. Dupre, and C. Meyer, "Passive Q-switching of a CO_2 laser by allene molecule," *J. Mol. Spectrosc.*, vol. 55, pp. 28–30, 1975.
[18] G. P. Montgomery, Jr., and J. C. Hill, "High-resolution diode-laser spectroscopy of the 949.2 cm^{-1} band of ethylene," *J. Opt. Soc. Amer.*, vol. 65, pp. 579–585, 1975.
[19] S. M. Freund, G. Duxbury, M. Römheld, J. T. Tiedje, and T. Oka, "Laser Stark spectroscopy in the 10 μm region: The ν_3 bands of CH_3F," *J. Mol. Spectrosc.*, vol. 52, pp. 38–57, 1974.
[20] A. Szabo and R. A. Stein, "Theory of laser giant pulsing by a saturable absorber," *J. Appl. Phys.*, vol. 36, pp. 1562–1566, 1965.
[21] L. E. Erickson and A. Szabo, "Effects of saturable absorber lifetime on the performance of giant pulse lasers," *J. Appl. Phys.*, vol. 37, pp. 4953–4961, 1966.
[22] R. Salomaa and S. Stenholm, "Gas laser with saturable absorber. I. Single-mode characteristics," *Phys. Rev. A*, vol. 8, pp. 2695–2711, 1973.
[23] ——, "Gas laser with saturable absorber. II. Single-mode stability," *Phys. Rev. A*, vol. 8, pp. 2711–2726, 1973.
[24] L. W. Davis and Y. S. Lin, "Propagation of optical pulses in a saturable absorber," *IEEE J. Quantum Electron.*, vol. QE-9, pp. 1135–1138, Dec. 1973.
[25] T. Oka and T. Shimizu, "Observation of infrared-microwave two-photon transitions in NH_3," *Appl. Phys. Lett.*, vol. 19, pp. 88–90 1971.
[26] S. M. Freund, J. W. C. Johns, A. R. W. McKellar, and T. Oka, "Infrared-infrared double resonance experiments using a two-photon technique," *J. Chem. Phys.*, vol. 59, pp. 3445–3453, 1973.
[27] K. Sakurai, K. Uehara, M. Takami, and K. Shimoda, "Stark effect of vibration-rotation lines of formaldehyde observed by a 3.5 μm laser," *J. Phys. Soc. Jap.*, vol. 23, pp. 103–109, 1967.
[28] R. G. Brewer, M. J. Kelley, and A. Javan, "Precision infrared Stark spectra of $N^{14}H_2D$ using Lamb dip," *Phys. Rev. Lett.*, vol. 23, pp. 559–563, 1969.
[29] F. Shimizu, "Dipole moment of NH_3 in the ν_2 excited state," *J. Chem. Phys.*, vol. 51, pp. 2754–2755, 1969.
[30] G. Duxbury and R. G. Jones, "Electric field induced rotational transitions of ND_3 observed using a DCN maser," *Chem. Phys. Lett.*, vol. 8, pp. 439–441, 1971.
[31] F. Herlemont, J. Lemaire, J. Houriez, and J. Thibault, "Spectroscopie Stark du CH_3F par laser à CO_2," *C. R. Acad. Sci.*, ser. B, vol. 276, pp. 733–736, 1973.
[32] T. Oka and W. A. Kreiner, "Infrared-radiofrequency double resonance observations of $\Delta J = 0$ 'forbidden' rotational transitions of SiH_4," *Can. J. Phys.*, to be published.

High-Current Characteristics of the Continuous-Wave Hollow-Cathode He–I_2 Laser

JAMES A. PIPER AND COLIN WEBB

Abstract—**Output power versus current characteristics of a multiple-anode hollow-cathode He–I_2 laser have been studied using quasi-continuous excitation. Oscillation has been obtained on a total of 25 transitions of I^+ ranging in wavelength from the blue to near infrared and including 9 new CW transitions. For all transitions, upper level excitation is attributed to thermal-energy charge-transfer reactions. No saturation in laser output power has been detected for increasing discharge current up to 20 A in the 75-cm-long 2.5-mm-bore device. CW power levels up to 100 mW each for strong transitions and approaching 1 W total over all transitions have been achieved.**

INTRODUCTION

THE most striking feature of the output power versus current characteristics of laser transitions excited by Duffendack reactions[1] in hollow-cathode discharges reported to date [1]-[3] is the absence of saturation of output power. This behavior contrasts strongly with that observed [4]-[7] for Duffendack-excited transitions in positive-column discharges where laser power passes through a maximum (typically of order 10 mW) as the discharge current is increased. However, comparison of the characteristics of one and the same system (He–Hg) in hollow-cathode and positive-column discharges has lead us to the conclusion that the power turnover observed in the latter case does not constitute evidence for the existence of limiting processes *fundamental to the excitation mechanism* [8]. It is therefore of some interest to extend the study of Duffendack-excited laser systems in hollow-cathode discharges to a range of current well beyond that already investigated (typically up to 3 A in 50-cm-long 3-mm-bore tubes) so that the ultimate power capabilities of these systems might be explored.

Accordingly, we have extended our earlier studies [3] of the He–I_2 system in hollow-cathode discharges to currents up to 20 A in a specially constructed 75-cm-long 2.5-mm-bore tube. The He–I_2 system has the particular advantage over other rare gas–metal ion systems in that the required "metal" vapor pressure (typically of order 0.1 torr) is obtained near room temperature, thus allowing greater flexibility in design and in choice of materials for construction of the laser tube. The dissipation problems which set the limit to achievable currents on a fully continuous basis have been circumvented using long-pulse excitation at low repetition rates.

Laser oscillation in this quasi-CW mode has been observed on a total of 25 transitions of I^+ ranging from blue to near infrared and including 9 new CW transitions. Laser intensity increases linearly with discharge current beyond threshold to the 20-A limit (above which current the onset of discharge instabilities seriously degrades performance). CW power levels approaching 100 mW each for stronger transitions and 1 W total over all transitions have been achieved.

EXPERIMENTAL DETAILS

The laser tube used throughout these experiments has a discharge configuration similar to that of the hollow-cathode tubes we have employed in the past [10] except for the provision of a much larger number of anodes to give improved discharge uniformity along the tube length (Fig. 1). Seventy-four separately ballasted anodes are positioned at 1-cm intervals along the 2.5-mm-bore (square-cross-section) stainless-steel cathode. The 1-mm-diam tungsten anode rods are sleeved with recrystallized alumina tubes which terminate flush with the inner wall of the cathode. The end of each anode rod is recessed 1 mm from the bore so as to reduce the possibility of arcing direct to adjacent parts of the cathode wall. Vacuum joints at the outer extremities of the anodes are made with Torr Seal. The cathode unit comprises demountable upper and lower sections (the upper section incorporating the anode assembly) sealed by a nitrile O ring, and the entire struc-

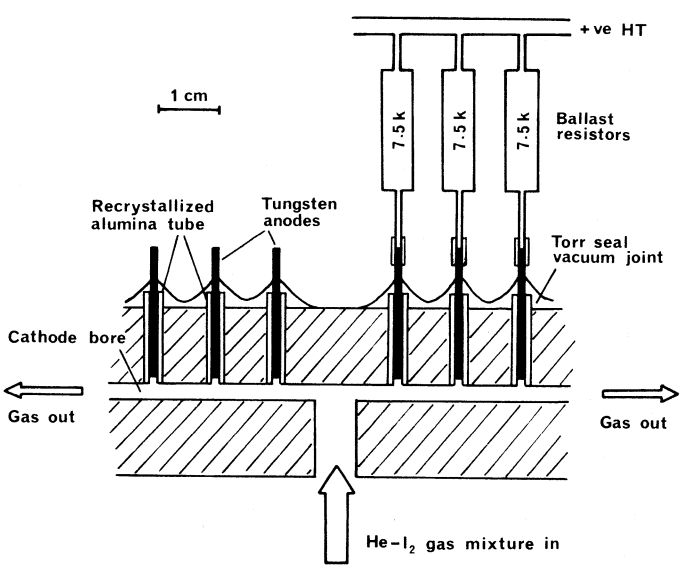


Fig. 1. Schematic diagram of the center section of the hollow-cathode laser tube.

Manuscript received April 8, 1975; revised September 16, 1975. This work was carried out as part of a program supported by the Procurement Executive, Ministry of Defence (sponsored by CVD) and by the Science Research Council.

J. A. Piper was with the Clarendon Laboratory, Oxford, England. He is now with the School of Mathematics and Physics, Macquarie University, Sydney, Australia.

C. Webb is with the Clarendon Laboratory, University of Oxford, Oxford, England.

[1] For brevity we refer to "thermal-energy charge-transfer reactions leading to excited-state formation" as "Duffendack reactions" following Green and Webb [9].

ture is water cooled. Brewster windows with simple O-ring seals are mounted in detachable end sections. In order to maintain gas purity, we employ a flow system: helium gas (purity > 99.995 percent) from a high-pressure cylinder and iodine vapor (purity > 99.9 percent) are premixed in a sidearm before entry midway along the cathode, and are pumped away symmetrically from both ends of the tube by a single rotary pump. The helium pressure (usually in the range 5–50 torr) and flow rate (of order 100 atm · cm^3 min^{-1}) are regulated by an inlet needle valve and a throttling valve on the pump line. The partial pressure of iodine in the gas mixture can be varied either by regulation of the sidearm temperature (usually 0–25°C) or, more conveniently, by regulation of the gas flow rate.

The laser cavity employed in these experiments was formed by spherical concave mirrors of radii of curvature 2 or 3 m separated by a distance about 1.6 m. The transmittances (T) of mirrors used were $T < 0.1$ percent for high-reflecting mirrors, and T in the range 1–3 percent for coupling mirrors. In some instances single wavelength operation of the laser was obtained using a high-reflecting (Littrow) prism selector in place of one concave mirror.

The choice of a pulsed excitation source was determined by the following two requirements. If meaningful conclusions concerning the CW performance of the laser are to be drawn from experiments using pulsed excitation, the duration of the pulses must be long compared with the important atomic interaction and gas equilibration times (see Table I). Further, the characteristic impedance of the source must be sufficient to match the discharge ballast resistance, the value of which must be high enough to ensure discharge stability. The excitation source used was a thyratron-switched simulated transmission line pulser (Z_c = 150 Ω) delivering approximately rectangular pulses of duration 1.6 ms and height variable up to 3 kV (Figs. 2 and 3). A low-current (100-mA) continuous discharge was maintained in addition to the pulsed discharge to avoid the necessity of achieving breakdown at the beginning of each pulse and assist in dissociation of I_2. In pure helium discharges pulsed currents up to 25 A could be obtained for the chosen ballast resistance 100 Ω (i.e., 7.5 kΩ per anode) at repetition rates up to 10 Hz.

TABLE I
ESTIMATED EQUILIBRATION TIMES

	PROCESS	CROSS SECTION cm^2	CHARACTERISTIC TIME τ, s
COLLISIONS	electron - electron electron - ion	$\sim 10^{-14}$	$\sim 10^{-7}$
	electron - He	6×10^{-16}	5×10^{-11}
	He^+ - He	10^{-15}	3×10^{-8}
	He^+ - I	3×10^{-16} [16]	3×10^{-5}
	Diffusion of I_2		$\sim 10^{-4}$
	Thermal desorption of I_2 from wall of tube		$\sim 10^{-4}$ to 10^{-3}

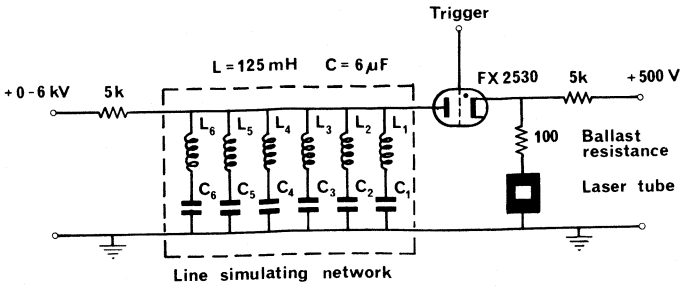


Fig. 2. Circuit diagram of the excitation source. Values of inductances and capacitances in the line simulating network are given by $L_n = (L/2)$ (L = 125 mH) and $C_n = (8C/\pi^2(2n-1)^2)$ (C = 6 μF).

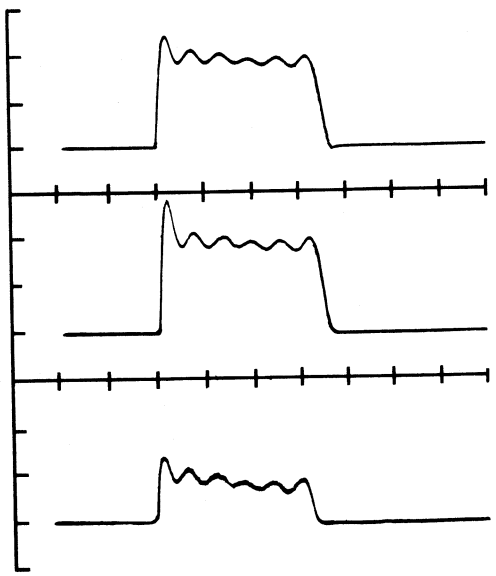


Fig. 3. Oscilloscope traces of (upper) the discharge current pulse (horizontal axis 0.5 ms/div, vertical axis 5 A/div), and (center and lower) laser output pulses at λ5761 and 6204 Å, respectively, for iodine vapor pressure 0.3 torr, helium pressure 10 torr, and discharge current 10 A (horizontal axis 0.5 ms/div).

Experimental Results and Discussion

Laser oscillation was observed over a range of gas conditions very similar to that reported previously for fully continuous operation of the hollow-cathode He-I_2 laser [3]. Satisfactory performance could be achieved for helium pressures from 2 to 30 torr, although maximum output power was obtained for all but one transition at pressures between 8 and 12 torr. (The sole exception was the transition λ 4675 Å for which maximum intensity was achieved at lower helium pressures, around 4–6 torr.) Sidearm temperatures at which laser intensity reached a maximum were in the range 15–20°C: the corresponding iodine partial pressure is estimated to be about 0.3 torr. In normal operation the sidearm temperature was held at 15°C by water cooling and the optimum proportion of I_2 vapor in the gas mixture achieved by small adjustments to the flow rate.

Oscilloscope traces of the current pulse and typical laser out-

put pulses for optimum conditions of the gas mixture are shown in Fig. 3. For *all* the laser transitions the output pulse follows closely the time dependence of the current pulse, even displaying the harmonic ripples of the simulated transmission line. Oscillation in this mode, which for reasons detailed in the following can surely be considered as interrupted continuous operation, has been observed on the 25 transitions of I^+ listed in Table II. The total includes 16 transitions on which fully CW oscillation has been observed previously in hollow-cathode

TABLE II
CW LASER TRANSITIONS OF SINGLY IONIZED IODINE (I II)

λ_{air} (measured) (Å)	λ_{air} (calculated)[a] (Å)	Transition upper level - lower level	ΔE[b] (cm^{-1})	Relative strength[c]
4675.6 ± 0.2	4675.53[d]	$6p'\ ^1D_2 - 6s'\ ^1D^o_2$	2480[e]	W
6204.9	6204.86[d]	$6p'\ ^1P_1 - 6s'\ ^1D^o_2$	150	W
6339.9	6339.97[d]	$6p'\ ^3F_3 - 6s'\ ^3D^o_3$	1555	W
8877.4	8877.61	$- 5d'\ ^3G^o_4$		M
4986.7	4986.92	$6p'\ ^3D_2 - 5d\ ^3D^o_1$	1785	M
5214.3	5214.08[d]	$- 5d\ ^3D^o_3$		M
5407.5	5407.36	$- 6s'\ ^3D^o_2$		S
5760.7	5760.72	$- 6s'\ ^3D^o_1$		S
6622.5	6622.35[d]	$- 5d'\ ^3D^o_2$		W
7139.0	7138.97	$- 5d'\ ^3D^o_3$		M
8170.2	8170.07	$- 5d'\ ^3F^o_3$		S
5216.3	5216.27	$6p'\ ^3F_2 - 5d\ ^3D^o_1$	2665	M
5678.2	5678.08	$- 6s'\ ^3D^o_2$		S
6069.0	6068.93[d]	$- 6s'\ ^3D^o_1$		W
6516.2	6516.18	$- 5p^5\ ^1P^o_1$		M
6825.2	6825.23[d]	$- 6s'\ ^3D^o_3$		M
7033.0	7032.99	$- 5d'\ ^3D^o_2$		S
7618.5	7618.50	$- 5d'\ ^3D^o_3$		M
8804.0	8804.23	$- 5d'\ ^3F^o_3$		S
4488.5	4488.55[d]	$6p'\ ^3D_1 - 5d\ ^5D^o_1$	3980	VW
5593.1	5593.12[d]	$- 5d\ ^3D^o_1$		W
6127.4	6127.49	$- 6s'\ ^3D^o_2$		S
6585.3	6585.21	$- 6s'\ ^3D^o_1$		S
7735.8	7735.78	$- 5d'\ ^3D^o_2$		M
8253.9	8253.84	$- 5d'\ ^3P^o_0$		W

[a] Identified from Martin and Corliss [13].
[b] Energy defect for Duffendack reaction (1).
[c] *S*: Strong. *M*: moderate. *W*: weak. *VW*: very weak.
[d] New CW transition.
[e] Energy defect for reaction (2).

He-I_2 discharge [3] (and, in some cases, positive-column He-I_2 discharges [6], [11]) as well as 9 transitions not formerly reported as oscillating on a CW basis, although pulsed operation has been reported on 2 of them [12]. The wavelengths were measured with a Spex 1802 (1-m Czerny-Turner) monochromator to within ±0.2 Å, and the transitions identified from published spectroscopic data [13]. The middle trace of Fig. 3 is the laser output on one of the 16 "old" transitions (5761 Å) and the lower trace is that of λ6204 Å—a "new" laser transition.

The fact that all lines (with the exception of λ4675 Å) have optimum laser performance under the same conditions, and that this set of discharge parameters is also optimum for fully CW oscillation is, we believe, very strong evidence that oscillation during the 1.6-ms-long discharge current pulse is effectively CW. A further check is that the output power on the transitions strong enough to permit absolute measurement corresponds very closely to the duty-cycle fraction of the fully CW power under equivalent conditions.

With the exception only of the transition λ4675 Å, the upper levels ($6p'$) $^1P_1$, $^3F_3$, $^3D_2$, $^3F_2$, and $^3D_1$ of the laser transitions of I^+ have positive energy defect (ΔE) values from 150 to 4000 cm^{-1} for the Duffendack (i.e., thermal energy charge transfer) reaction

$$He^+ + I \longrightarrow He + (I^+)^* + \Delta E \qquad (1)$$

where $(I^+)^*$ denotes the excited states of singly ionized iodine. We have evidence, from studies of many examples of reactions between He^+ ions and a variety of atomic metal species [9], that Duffendack reactions are most efficient for energy defects of order 1000-4000 cm^{-1}. Still further evidence supporting the identification of the reaction (1) as the source of excitation of the energetically accessible levels of the $6p'$ configuration of I^+ in He-I_2 discharges will be found in [14]-[16]. The upper level $6p'\ ^1D_2$ of the transition λ4675 Å would have a negative energy defect value for the reaction (1), and we propose that excitation in this case occurs by the reaction

$$He^+ + I^* \longrightarrow He + (I^+)^* + \Delta E' \qquad (2)$$

where I^* denotes the low-lying neutral iodine metastable excited state $5p^5\ ^2P^0_{1/2}$. The energy defect appropriate to the level $6p'\ ^1D_2$ of I^+ in the reaction (2) has a value $\Delta E' = +2480$ cm^{-1} quite consistent with efficient energy transfer by Duffendack reactions [9].[2]

The dependence of laser intensity on discharge current has been investigated for a number of the stronger transitions at currents up to 20 A for gas conditions corresponding to maximum intensity. The upper limit to the current range was set by the onset (at high currents) of gross discharge instabilities, characterized by instantaneous reduction of the discharge running voltage (normally about 300 V) at individual anodes to very low values and, simultaneously, by the appearance of

[2] Production of some excited states of the singly ionized metal in a He-As afterglow has recently been shown to result from analogous reactions involving low-lying metastable states of the neutral metal [17].

strong emission in the neutral iodine spectrum. The current dependence of relative intensity was very similar for all of the laser transitions studied. Data for each of the transitions λ5761, 5678, and 6127 Å, whose upper levels $(6p')\ ^3D_2$, $^3F_2$, and $^3D_1$ are the most strongly excited, are shown in Fig. 4. Laser intensity can be seen to increase approximately linearly with discharge current beyond threshold to the 20-A limit. Slight deviations from linearity do occur for currents exceeding about 16 A but we believe these result from the deterioration in discharge stability. For the two cases λ5761 and 6127 Å, CW power levels approaching 100 and 70 mW, respectively, have been achieved. These levels were deduced from an absolute measurement of the mean power of the laser in quasi-continuous operation at a repetition rate 2 Hz when a power 0.32 mW, corresponding to a CW power level 100 mW, was recorded for λ5761 and 6127 Å (combined) at a discharge current 12 A. The coupling mirror transmittance was $T = 2.2$ percent at 5761 Å and $T = 2.8$ percent at 6127 Å. In Fig. 4 the data appropriate to these two transitions have been normalized so that the intensity scale reads approximately in milliwatts. CW power levels of several tens of milliwatts have been achieved for a number of the other strong transitions and total CW output powers are estimated as approaching 1 W.

We note there is some evidence of competition between laser transitions; for example, between the two strong transitions λ5761 and 6585 Å. The latter, which shares a common lower level $(6s'\ ^3D_1^0)$ with λ5761 Å, was significantly depressed in power at high currents when oscillation was permitted at both wavelengths, but behaved normally when λ5761 Å was inhibited, say, by the use of a prism wavelength selector. Similarly, the transition λ8804 Å suffered in competition with λ8170 Å (common lower level $5d'\ ^3F_3^0$); oscillation throughout the excitation pulse at λ4986, 5216, and 5593 Å (common lower level $5d\ ^3D_1^0$) could only be obtained separately.

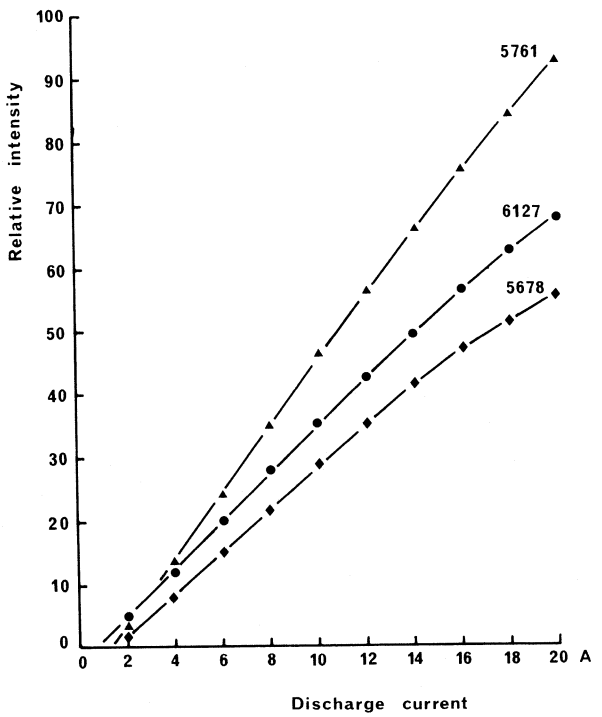


Fig. 4. Laser intensity as a function of discharge current for iodine vapor pressure 0.3 torr and helium pressure 10 torr. Data points for λ5761, 6127, and 5678 Å are denoted ▲, ●, and ◆, respectively. (Coupling mirror transmittances $T = 2.2$, 2.8, and 2.0 percent.)

Comparison of the data of Fig. 4 with those obtained recently for the positive-column He–I_2 laser by Hattori *et al.* [6] clearly illustrates the contrasting behavior of Duffendack-excited laser transitions in hollow-cathode and positive-column discharges, and lends support to our earlier conclusion that the power turnover characteristic of these transitions in positive-column lasers is not related to a fundamental limitation of the excitation process. It is our belief that the turnover in positive-column lasers is due to starvation of neutral metal (in this case iodine) in the active volume as a result of "imprisonment" of the available metal, partly in the form of ground-state metal ions (undergoing radial transport to the walls) and partly on the walls as neutral atoms awaiting thermal desorption. This explanation is supported by our observations in the present experiments of the laser pulse shape at low iodine partial pressures. Fig. 5 shows oscilloscope traces of the laser pulse for iodine vapor pressures approximately 0.02 and 0.1 torr (helium pressure 10 torr). The laser output takes the form of a short (100-μs-duration) "spike" at the onset of the current pulse, followed by a gradual buildup towards a stable continuous output. At even lower iodine vapor pressures only the initial short spike is present but at higher vapor pressures (i.e., approaching the optimum value 0.3 torr) the laser pulse shape assumes that of the current as in Fig. 3. Our interpretation of this behavior is as follows: at low iodine vapor pressures, the neutral iodine in the volume at the onset of excitation is very rapidly ionized so that the neutral concentration in the volume is depleted, and remains so until it is replenished by thermal desorption (and perhaps sputtering) from the cathode wall. The ambient neutral iodine concentration during fully continuous operation of the discharge must therefore be maintained by an equilibrium between the loss as a wall-directed ion current, and replenishment of neutral atoms from the wall. Since metal vapor pressures corresponding to normal operation of hollow-cathode lasers are typically a factor of 10 higher than those of analogous positive-column lasers, we should expect the occurrence of such metal starvation effects to be postponed to very much higher discharge currents than

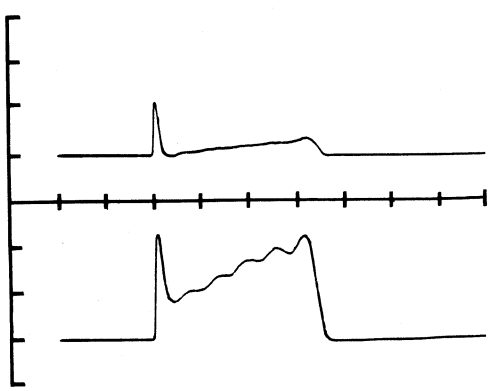


Fig. 5. Oscilloscope traces of laser output pulses for (upper) iodine vapor pressure approximately 0.02 torr and (lower) iodine vapor pressure 0.1 torr, helium pressure 10 torr and discharge current 10 A (horizontal axis 0.5 ms/div). The vertical deflection for the upper trace is × $2\frac{1}{2}$ magnified with respect to that of the lower trace.

is the case for positive-column lasers.[3] We believe that the discharge instabilities which set the upper limit to current, and hence laser output power, achieved in the present experiments originate from a catastrophic disturbance of this equilibrium. The disturbance takes the form of sudden gross overloading of the discharge volume with neutral iodine as a result of uncontrolled sputtering of material from the wall as arc spots develop.

Conclusion

The output characteristics of a hollow-cathode He-I_2 laser have been investigated for discharge currents up to 20 A using quasi-continuous excitation. The absence of power saturation with increasing current indicates there is no barrier to the attainment of CW powers at least of the order of 1 W set by the nature of the excitation process. However, a practical limitation to the ultimate power capabilities of the He-I_2 system in hollow-cathode discharges is set at present by the difficulty of maintaining a stable high-current discharge in such a gas mixture.

Acknowledgment

The authors wish to thank G. Krivaska for skilled technical assistance.

References

[1] Y. Sugawara, Y. Tokiwa, and T. Ijima, "New CW laser oscillations in Cd-He and Zn-He hollow-cathode lasers," *Japan. J. Appl. Phys.*, vol. 9, p. 1537, 1970.

[2] J. A. Piper and C. E. Webb, "Continuous-wave oscillation in singly ionized arsenic," *J. Phys. B: At. Mol. Phys.*, vol. 6, pp. L116-L120, 1973.

[3] J. A. Piper, "Increased efficiency and new CW transitions in the helium-iodine laser system," *J. Phys. D: Appl. Phys.*, vol. 7, pp. 323-328, 1974.

[4] R. C. Jensen, G. J. Collins, and W. R. Bennett, Jr., "Charge-exchange excitation and CW oscillation in the zinc-ion laser," *Phys. Rev. Lett.*, vol. 23, pp. 363-367, 1969.

[5] W. T. Silfvast and M. B. Klein, "CW laser action on 24 visible wavelengths in Se II," *Appl. Phys. Lett.*, vol. 17, pp. 400-403, 1970.

[6] S. Hattori, H. Kano, K. Tokutome, G. J. Collins, and T. Goto, "CW iodine-ion laser in a positive-column discharge," *IEEE J. Quantum Electron.* (Corresp.), vol. QE-10, pp. 530-531, June 1974.

[7] A. Ferrario, "Excitation mechanism in Hg^+ ion laser," *Opt. Commun.*, vol. 7, pp. 376-378, 1973.

[8] J. A. Piper and C. E. Webb, "Power limitations of the CW He-Hg laser," *Opt. Commun.*, vol. 13, pp. 122-125, 1975.

[9] J. M. Green and C. E. Webb, "The production of excited metal ions in thermal energy charge transfer and Penning reactions," *J. Phys. B: At. Mol. Phys.*, vol. 7, pp. 1698-1711, 1974.

[10] J. A. Piper and C. E. Webb, "A hollow-cathode device for CW helium-metal vapour laser systems," *J. Phys. D: Appl. Phys.*, vol. 6, pp. 400-407, 1973.

[11] V. I. Pugnin, S. A. Rudelov, and A. F. Stepanov, "Generation on ionic transitions of iodine," *Zh. Prikl. Spektrosk.*, vol. 18, pp. 912-913, 1973.

[12] C. S. Willett, "New laser oscillations in singly ionized iodine," *IEEE J. Quantum Electron.* (Notes and Lines), vol. QE-3, p. 33, Jan. 1967.

[13] W. C. Martin and C. H. Corliss, "The spectrum of singly ionized atomic iodine (I II)," *J. Res. Nat. Bur. Stand.*, vol. A64, pp. 443-479, 1960.

[14] I. A. Berezin, "Anomalous enhancement of iodine spectral lines in a hollow cathode discharge," *Opt. Spectrosc.*, vol. 26, p. 466, 1969.

[15] Yu. A. Tolmachev, "Measurement of the effective cross section for charge transfer in He^+-I," *Opt. Spectrosc.*, vol. 33, pp. 653-654, 1972.

[16] T. Shay, H. Kano, and G. J. Collins, "Excitation mechanism of the He-I^+ laser," *Appl. Phys. Lett.*, vol. 26, pp. 531-534, 1975.

[17] I. M. Littlewood, J. A. Piper, and C. E. Webb, "Production of excited levels of A II in thermal energy collisions," unpublished.

[18] A. L. McKenzie, "Radial profiles of upper laser level emission in a helium-selenium discharge," *J. Phys. B: At. Mol. Phys.*, vol. 7, pp. L141-L144, 1974.

[19] J. E. Allen and P. C. Thonemann, "Current limitation in the low-pressure mercury arc," *Proc. Phys. Soc.*, vol. 67, pp. 768-774, 1954.

[20] C. E. Webb, "A new technique for measurements of radial distribution of excited species in plasmas and its application to capillary discharges in argon," *J. Appl. Phys.*, vol. 39, pp. 5441-5470, 1968.

[3] Evidence of neutral metal starvation effects of this nature in positive-column He-Se discharges is provided by recent results of McKenzie [18]. It is well known that similar effects occur in mercury arc columns [19] and for the silicon content of low-pressure argon discharges in quartz tubes [20].

A CS_2/O_2 Electrochemical, Pulsed CO TEA Laser

JEFFREY L. AHL AND W. R. BINNS

Abstract—**This paper describes an experimental investigation of a pulsed CS_2/O_2 chemical CO laser initiated in a high-pressure double-discharge TEA-laser system. A distributed volumetric discharge was obtained and yielded a maximum pulse energy of 115 mJ with a chemical efficiency of 4.5 percent, an electrical efficiency of 2.5 percent, and a specific output energy of 1 J/l. Experimental results and modeling calculations indicate that chain-branching production of O atoms does not occur under the experimental conditions investigated.**

I. Introduction

THIS PAPER describes an experimental investigation of pulsed CO-laser action in a double-discharge CS_2/O_2-laser system. The purpose was to achieve higher laser energy output than has previously been achieved in this system by attempting to 1) obtain a distributed volumetric discharge in the CS_2/O_2 system, 2) obtain higher population densities of vibrationally excited CO (denoted CO*) by operating at higher CS_2 pressures than previously achieved, and 3) demonstrate chain branching via the chemical reaction $SO + O_2 \rightarrow SO_2 + 0$. Pollack [1] was the first to demonstrate pulsed laser action of CO* molecules which were formed as a result of the dissociation during flash photolysis of CS_2 and O_2 and subsequent chemical reactions of the product molecules. Subsequent to this, Jacobson and Kimbell [2] performed the first experiment using multiple, transverse spark discharges to initiate the chemical reactions leading to CO*. Several other authors have published work on this system, and these are summarized in [3].

II. Experiment

The experimental apparatus used to conduct this investigation was a double-discharge TEA laser similar to that of Richardson *et al.* [4] (see Fig. 1). The laser volume was filled with premixed CS_2, O_2, and in some cases He. It was then operated as a closed system yielding one laser shot for each filling. The initial discharge produced an array of sliding sparks on an etched circuit board with alternate conductor and dielectric surfaces. The ultraviolet radiation produced by these sparks penetrated the screen sustainer anode and photoionized the CS_2/O_2 mixture between the sustainer electrodes. This preionization discharge was followed 1-4 μs later by the main discharge across the sustainer electrodes which dissociated some of the O_2 and CS_2 molecules. The resultant products (CS_2, CS, O_2, O, and S) then reacted chemically to form vibrationally excited CO* molecules, the lasing species.

Manuscript received May 27, 1975; revised August 29, 1975. This research was conducted under the McDonnell Douglas Independent Research and Development Program.

The authors are with the McDonnell Douglas Research Laboratories, McDonnell Douglas Corporation, St. Louis, MO 63166.

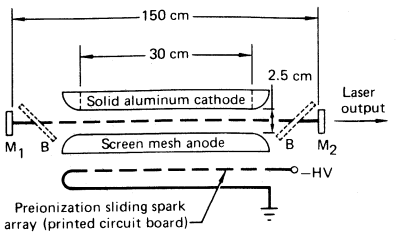


Fig. 1. Cross section of laser. M_1: gold-coated 10-m mirror (1-mm hole). M_2: dielectric-coated flat germanium mirror, 88-percent R. B: NaCl Brewster windows.

(The reactions believed to dominate the formation of CO* are given in Section IV.)

The sustainer electrodes are Rogowski contoured with an active length of 30 cm, an active width of 4 cm, and an electrode separation of 2.5 cm. The high voltage was switched from capacitors onto the preionization and sustainer electrodes using externally pulsed spark gaps. The sustainer voltage discharge waveform was a ringing pulse with a period of ~0.5 μs, a rise time of ~0.1 μs, and a duration of ~2 μs. A variable-delay pulse generator was used to vary the delay time between the two discharges continuously from 0.5 to 10 μs.

The optical cavity was formed by a 10-m gold-coated mirror with a 1-mm hole used for alignment opposite a flat 88-percent reflectivity (R) dielectric-coated germanium mirror. The initial experimental apparatus included NaCl flats mounted inside the optical cavity at Brewster's angle. Better laser performance was obtained, however, by mounting the mirrors inside the discharge cell.

A pyroelectric detector (Gentec LED-200) and a AuGe detector were used to measure the laser output energy and pulse shape, respectively. The output of these detectors was observed on an oscilloscope (Tektronix 7904).

III. Results

The laser output energy is plotted as a function of sustainer input energy in Fig. 2. A maximum output energy of 115 mJ was obtained for a CS_2/O_2 mixture of 1.8/35 torr. The decline in energy output for $E_{in} > 15$ J is probably caused by the onset of arcing between the sustainer electrodes. For the maximum output, the chemical efficiency (defined with respect to total conversion of CS_2 to CO*) is 4.5 percent assuming that 57 kcal/mole are available [5] from the reaction $CS + O \rightarrow CO^* + S$ for vibrational pumping of CO* and that the volume from which energy is extracted is that of a cylinder defined by the pyroelectric detector sensitive area (3.9 cm^2) and the active length of the sustainer electrodes (30 cm). The specific output energy is then 1.0 J/l and the electrical efficiency is 2.5 percent. The laser output pulse which was measured only for low-energy output levels was delayed by 3 μs

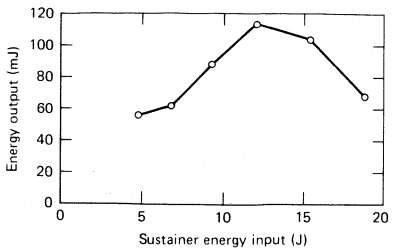


Fig. 2. Laser energy output plotted versus sustainer energy input for optimum CS_2/O_2 mixture. Data were obtained for a CS_2/O_2 mixture of 2.1/43 torr except for the maximum data point obtained for a CS_2/O_2 mixture of 1.8/35 torr. (NaCl Brewster windows were removed for these experiments.)

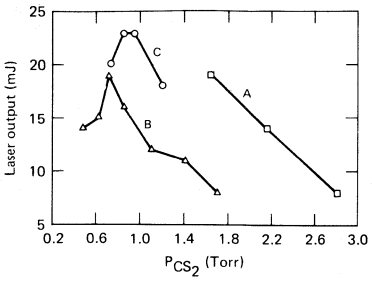


Fig. 3. Laser energy output plotted versus CS_2 pressure (P_{CS_2}). The CS_2/O_2/He pressure ratios are the same as those of Fig. 4. (NaCl Brewster windows were used in these experiments.)

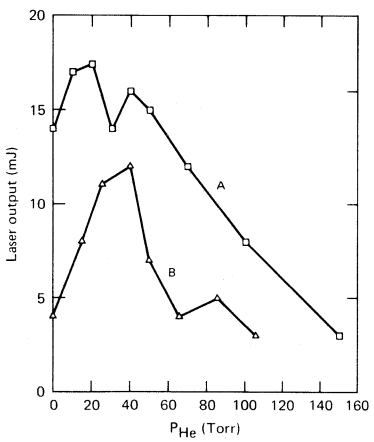


Fig. 4. Laser energy output plotted versus He pressure (P_{He}). Data plots labeled *A* and *B* were taken for fixed CS_2/O_2 pressures of 1.4/48 torr and 2.1/48 torr, respectively. (NaCl Brewster windows were used in these experiments.)

after the sustainer discharge, had a full width at half maximum pulsewidth of 5 μs, and a total duration of 30 μs.

Laser energy output for various mixtures of CS_2, O_2, and He as a function of total pressure and He pressure is plotted in Figs. 3 and 4, respectively. The sustainer input energy was 10 J. These data were taken with NaCl Brewster windows positioned in the laser cavity. (Brewster windows were not employed when data presented in Fig. 2 were obtained and mainly accounts for the higher output energy obtained in the Fig. 2 data.) Use of a 98-percent *R* dielectric mirror resulted in substantially lower energy output than was obtained with the 88-percent *R* mirror. Fig. 3 shows that attempts to increase CS_2 pressure and thereby obtain higher CO* population densities were unsuccessful. As the CS_2 pressure became larger than about 3 torr, the mixture became progressively more explosive upon discharge initiation and was accompanied by a substantial decrease in laser output. Modeling calculations (see Section IV) indicate that these higher CS_2 pressures result in lower CO* population densities because of an excessive loss of O atoms to CS_2 in reaction 1 (Table I) and/or CO* deactivation by unreacted CS_2. The characteristic deactivation time of CO* ($v = 1$) by 2 torr of CS_2 is ~30 μs [6]. Fig. 4 shows the effect of adding He to the gas mixture for two CS_2/O_2 mixtures. Contrary to the results obtained by Jacobson *et al.*, our data show little enhancement in laser output with the addition of He to the optimum CS_2/O_2 mixture, and, in fact, a deleterious effect is observed as the helium partial pressure increases (Fig. 4, curve *A*). This degraded output is believed to be caused by a deterioration of discharge quality with the addition of He for energy inputs near the limits of discharge stability. As the CS_2 partial pressure becomes larger, however, the addition of He initially augments laser performance, probably because of its cooling effect (Fig. 4, curve *B*). It should be noted that the optimum performance mixture in Fig. 2 does not correspond closely to the optimum mixtures in Figs. 3 and 4. This is not completely understood but is probably because of the effects of He on the electric-discharge quality and on the chemical kinetics.

TABLE I
REACTIONS USED IN MODELING THE LASER AND PRODUCTION AND CONSUMPTION RATES FOR CONDITIONS OF FIG. 5 AT $t = 10$ μs

	Reaction	Reaction Rate Constant[7] (k_i) [cm^3-molecule^{-1}-s^{-1}]	$R = k_i[N_1][N_2]$ [molecules-cm^{-3}-s^{-1}]
1.	$O + CS_2 \rightarrow CS + SO$	1.6×10^{-11} exp (- 1.03/RT)	7.7×10^{20}
2.	$O + CS \rightarrow CO^* + S$	7.9×10^{-11} exp (- 1.03/RT)	8.4×10^{20}
3.	$S + O_2 \rightarrow SO + O$	2.2×10^{-12}	1.24×10^{21}
4.	$O + CS_2 \rightarrow OCS + S$	1.8×10^{-12} exp (- 1.03/RT)	8.6×10^{19}
5.	$O + CS_2 \rightarrow CO + S_2$	2.0×10^{-12} exp (- 1.03/RT)	9.6×10^{19}
6.	$SO + O_2 \rightarrow SO_2 + O$	3.0×10^{-13} exp (- 5.6/RT)	3.0×10^{19}
7.	$CS + SO \rightarrow OCS + S$	6.7×10^{-11} exp (- 4.0/RT)	2.2×10^{19}
8.	$O + OCS \rightarrow CO + SO$	6.8×10^{-11} exp (- 5.08/RT)	5.5×10^{18}
9.	$S + CS_2 \rightarrow CS + S_2$	1.7×10^{-10} exp (- 4.0/RT)	4.6×10^{19}
10.	$CS + O_2 \rightarrow OCS + O$	1.7×10^{-16} exp (- 3.5/RT)	3.0×10^{16}
11.	$SO + O + M \rightarrow SO_2 + M$	$2.6 \times 10^{-28}/T$ [cm^6-molecule^{-2}-s^{-1}]	8.7×10^{19}

IV. MODELING CALCULATIONS

An attempt has been made to further our understanding of the O_2/CS_2 laser system and to aid in its optimization by computer modeling the kinetics using the McDonnell Douglas Research Laboratories (MDRL) laser code [7]. This model calculates the time evolution of the products of the reactions listed in Table I, taking into account the temperature rise resulting from the exothermicities of the reactions by modifying the kinetic rates accordingly. Rather than attempting to model the electrical discharge, we assume instantaneous initiation of the reaction and specify the O, CS, and S concentrations at $t = 0$ such that the output energy observed experimentally and the model's estimate for energy stored in CO vibration multiplied by an estimated chemical efficiency are approximately identical. We assume that 10 percent of the

discharge energy goes into translational heating, resulting in a 70 K rise in the gas temperature. The program also calculates the population and small-signal gain of the vibrational levels of CO, correcting for the temperature, vibrational deactivation, and line-broadening effects. The model does not include coupling to an optical field and cannot be used as an oscillator model. The initial distribution of CO* formed by the primary pumping reactions CS + O → CO* + S is used as reported by Powell and Kelley [5].

The reactions and rates used in the model are listed in Table I. These reactions appear to form a minimal set for modeling the system. There are a number of other reactions which have not been included, generally because of a lack of accurate rate data or because they are too slow to influence the first 50 μs of the reaction. Reactions 6 and 10 represent possible chain-branching mechanisms, since these reactions, together with reactions 1-3, produce several excited CO molecules for each initial O atom. Reaction 6 appears to be particularly favorable insofar as the rate listed is for ground-state SO molecules. The SO produced by reaction 1 is known to be vibrationally excited with an average internal energy of 4.1 kcal/mole [8]. If this energy is available as part of the activation energy of reaction 6, an enhancement of a factor of 62 is obtained for the rate at 500 K.

Results of a sample calculation taken for optimum experimental lasing conditions are shown in Fig. 5(a)-(c). The initial rate of production of vibrationally excited CO (i.e., CO*) is very large; half of the CO* production occurs within the first 7 μs. Calculations indicate that laser threshold is reached within 1 μs of initiation. The densities displayed can be used to calculate the rates of the reactions ($R = k_i[N_1][N_2]$). The production and consumption rates listed in Table I are for the conditions of Fig. 5 at 10 μs after initiation. Reactions 1-3 dominate the kinetics and account for 90 percent of the O-atom consumption and 98 percent of the O-atom production. The other reactions primarily affect the concentrations of vibrational deactivators of CO*. In particular, OCS is a very effective deactivator [9] of CO* and reaches an appreciable concentration within 10 μs. The energy stored in CO vibration during the first 30 μs in a 120-cm^3 volume is approximately 0.93 J. Vibrational deactivation is significant, as can be seen in Fig. 6, and may reduce available energy by a factor of 2. An estimate of the laser output energy can be obtained by assuming that the chemical efficiency (as defined in [10]) of the pulsed CO laser, $\eta_{chem} = (E_{out}/E_{stored\ in\ CO^*\ vib})$, is at least as large as for the CW CO laser. Jeffers *et al.* [10], [11] have reported efficiencies of 24 percent for a nonchain O-CS_2 chemical laser and 31 percent for a CS-fueled chain-reaction laser. This would result in an output energy of approximately 120 mJ as a lower limit, in good agreement with the measured output energy of 115 mJ for the optimum experimental conditions.

By varying the reactant species concentrations and noting the CO* population at 30 μs, we have been able to determine the pressure scalability of the device relative to the standard conditions of Fig. 5. Increasing the CS_2 pressure to 4 torr causes a 25-percent drop in the CO* population at 30 μs, principally because of an excessive loss of O atoms by reaction 1. Adding an additional 160 torr of O_2 also results in a 25-percent drop in CO* produced, possibly because of a reduction in temperature.

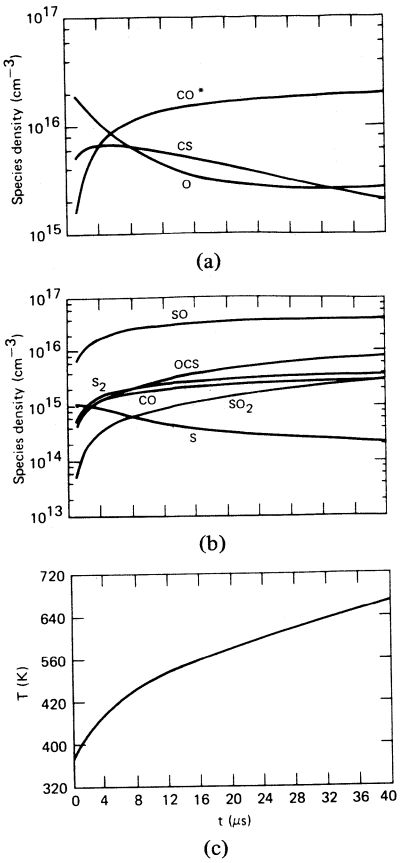


Fig. 5. (a), (b), (c) Kinetic modeling calculation of evolution of species for initial conditions: T = 370 K, O_2 = 38 torr, CS_2 = 1.8 torr, O = 0.8 torr, CS = S = 0.1 torr. CO* represents the CO production by the laser pumping reaction 2. CO is the product of reactions 5 and 8 of Table I.

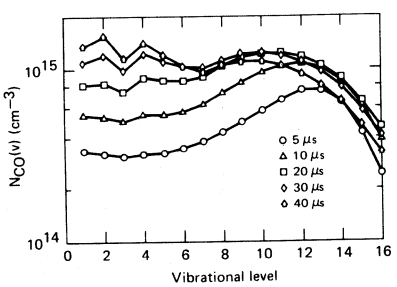


Fig. 6. Vibrational population distribution of CO* for the initial conditions of Fig. 5. Vibrational deactivation is clearly visible.

The addition of He diluent results in a decrease in output as a result of the decrease in gas temperature. Increasing the initial temperature from 370 to 550 K while maintaining a constant density results in a 10-percent increase in CO*. The CO* production appears to depend linearly on the total concentration of CS, S, and O initially produced. Increasing the energy deposited in the gas will raise the output energy density of this system, but will not substantially raise the electrical efficiency. There is no indication of a chain reaction occurring, as can be verified by observing that the rate of reaction 6, ($R = k_6[SO][O_2]$), is approximately 3×10^{19} cm^{-3}s^{-1}, while the rate of reaction 3, the nonchain O-atom production step, is 1.2×10^{21} cm^{-3}s^{-1} at 10 μs. Thus reaction 6 contributes less than 3 percent to the O-atom production rate. We have

been unable to find any conditions under which this system will operate as a branched chain. However, it should be noted that the rate constant for reaction 6 may be substantially higher in the presence of vibrationally excited SO. Non-optimized modeling calculations in which the activation energy of reaction 6 was reduced by 4.1 kcal/mole (the vibrational energy of the SO produced by reaction 1) [8] yielded chain lengths greater than 3. Thus the viability of this system depends on a favorable value of this rate.

V. Conclusions

A CS_2/O_2 electrochemical, pulsed CO-laser system has been operated with a maximum energy output of 115 mJ/pulse, a chemical efficiency of 4.5 percent, and a specific output energy of 1 J/l. Experimental results show no evidence of chain branching resulting in O-atom production. Modeling calculations also indicate that chain branching does not occur under optimum laser conditions. A significant increase in system energy density and efficiency for operating regimes other than those attempted experimentally is not predicted by this model unless the internal energy of SO produced in reaction 1 significantly enhances the rate of reaction 6. It is still possible that chain branching could be obtained by operating in a regime where reactions not included in this model (e.g., $SO + SO \rightarrow SO_2 + S$) become important. For example, higher input energy densities than were obtained in this experiment could lead to nonlinear production of O atoms.

Acknowledgment

The authors wish to thank H. C. Carpenter for his valuable technical assistance throughout the experiment. They also wish to thank W. Q. Jeffers for suggesting this experiment, and J. D. Kelley, T. J. Menne, and H. V. Lilenfeld for helpful discussions and encouragement in completing this research.

References

[1] M. A. Pollack, "Laser oscillation in chemically formed CO," *Appl. Phys. Lett.*, vol. 8, pp. 237–238, May 1966.
[2] T. V. Jacobson and G. H. Kimbell, "Transversely spark initiated laser with high pulse energies," *J. Appl. Phys.*, vol. 41, pp. 5210–5212, Dec. 1970.
[3] B. R. Bronfin and W. Q. Jeffers, "The CO chemical laser," in *Handbook of Chemical Lasers*, J. Bott and R. W. F. Gross, Ed. New York: Wiley-Interscience, to be published.
[4] M. C. Richardson, K. Leopold, and A. J. Alcock, "Large aperture CO_2 laser discharges," *IEEE J. Quantum Electron.*, vol. QE-9, pp. 934–939, Sept. 1973.
[5] H. T. Powell and J. D. Kelley, "Vibrational distribution of carbon monoxide from $O + CS \rightarrow S + CO(V)^*$," *J. Chem. Phys.*, vol. 60, pp. 2191–2192, May 1974.
[6] W. H. Green and J. K. Hancock, "Measurement of CO ($v = 1$) vibrational energy transfer rates using a frequency doubled CO_2 laser," *J. Chem. Phys.*, vol. 59, pp. 4326–4335, Oct. 1973.
[7] H. V. Lilenfeld, R. F. Webbink, W. Q. Jeffers, and J. D. Kelley, "Modeling of the CW CO chemical laser," *IEEE J. Quantum Electron. (Part II of Two Parts: 4th Conf. Chemical and Molecular Lasers)*, vol. QE-11, pp. 660–669, Aug. 1975.
[8] I. W. M. Smith, "Experimental and computer studies of the kinetics and distribution of vibrational energy in both products of the reaction: $O(^3P) + CS_2 \rightarrow SO + CS$," *Discuss. Faraday Soc.*, vol. 44, pp. 194–204, 1967.
[9] G. Hancock and I. W. M. Smith, "Quenching of infrared chemiluminescence. 1: The rates of de-excitation of CO ($4 \leqslant v \leqslant 13$) by He, CO, NO, N_2, O_2, OCS, N_2O, and CO_2," *Appl. Opt.*, vol. 10, pp. 1827–1842, Aug. 1971.
[10] W. Q. Jeffers and C. E. Wiswall, "Experimental studies of the $O/O_2/CS_2$ CW CO chemical laser," *IEEE J. Quantum Electron.*, vol. QE-10, pp. 860–869, Dec. 1974.
[11] W. Q. Jeffers and H. Y. Ageno, "CO chain reaction-chemical laser," *Appl. Phys. Lett.*, vol. 27, pp. 227–229, Aug. 1975.

Volume Ultraviolet Preionization from Bare Sparks

RICHARD V. BABCOCK, MEMBER, IEEE, IRVING LIBERMAN, AND W. D. PARTLOW

Abstract—**Volumetric photoionization in CO_2-laser gas mixtures by UV emission from bare sparks was studied in two ways: by spectroscopic emission and absorption measurements, and by direct collection of photoionized electrons. The physical processes were understood sufficiently to permit prediction of initial electron distributions in arbitrary geometries of CO_2, N_2, He gas mixtures containing known concentrations of ionizable impurity.**

Manuscript received May 29, 1975; revised August 18, 1975. This work was supported by the Air Force Weapons Laboratory, Kirtland Air Force Base, NM, under Contract 73-C-0121.

R. V. Babcock and W. D. Partlow are with the Westinghouse Research Laboratories, Pittsburgh, PA 15235.

I. Liberman was with the Westinghouse Research Laboratories, Pittsburgh, PA 15235. He is now with the Los Alamos Scientific Laboratory, University of California, Los Alamos, NM 87544.

Introduction

SELF-SUSTAINED electric discharges in CO_2 gas mixtures, initiated by UV preionization, have proven to be an excellent means of pumping compact, high-power, pulsed CO_2 lasers. Laser systems described in the literature [1]–[4] have employed a variety of auxiliary discharges to produce the pulse of ionization required to initiate growth of a uniform discharge. The mechanism of ionization can be a combination of UV photoionization of gas molecules in the discharge volume, UV photoelectron production from the cathode material, and perhaps direct injection of electrons from the auxiliary discharge.

By computer modeling of the discharge growth, Kline and

Denes [5] have shown that to obtain a uniform glow discharge with a uniformly applied electric field, the initial preionization n_{e0} must be uniform in the plane parallel to the electrodes and that its density must be orders of magnitude greater than the background preionization ($\sim$100 electrons/cm^3). Although nonuniformity in n_{e0} normal to the electrodes affects the discharge development, the final electron concentration is uniform throughout the field volume. Thus to understand the scaling of spatially uniform self-sustained discharges to larger dimensions requires that n_{e0} in a particular proposed device can be calculated. We have studied the physical mechanisms which determine the initial electron distribution produced by a particular initiation scheme–volume photoionization of gas molecules by UV from bare sparks generated in the laser medium. The controlling mechanisms are now sufficiently understood to specify n_{e0} in an arbitrary discharge volume containing CO_2, N_2, He, and known trace quantities of ionizable impurity. Some of our results have been previously reported [6]; similar conclusions were reached by Palmer and Wada [7]. Seguin *et al.* [8] have measured preionization electron densities from a variety of UV sources by microwave interferometry.

We determined the volumetric photoelectron production in two ways. First, detailed spectroscopic studies established the photon flux emitted from a standard bare-spark source in each of three reference-laser gas mixtures, and the subsequent transmission of this photon-flux distribution through the reference mixtures. From this, $n_{e0}(x_i)$ could be calculated for any assumed concentration of ionizable specie [6]. Secondly, $n_{e0}(x_i)$ was measured directly for the same standard bare-spark source and gas mixtures in a modified Faraday electron collector. When the observed background pressure in the evacuated electron collector was attributed to typical organic contaminants (all of which have roughly equal cross sections for direct photoionization over the appropriate photon energy range), the resulting $n_{e0}(x_i)$ calculated from the spectroscopic studies agreed with the measured values. Finally, the dependence of $n_{e0}(x_i)$ on the spark energy-supply parameters was determined with the electron collector.

UV Absorption of Laser Gas Mixtures

Reliable CO_2 absorption coefficients in the literature [9], [10] show that laser gases containing about 0.1 atm of CO_2 are essentially black for wavelengths shorter than 115 nm. Good data exist for CO_2 in the 115–167-nm region [9]. We therefore measured the absorption of CO_2 from 167 to 200 nm and the absorption of N_2 and He from 115 to 200 nm. There is no appreciable absorption in these gases at wavelengths longer than 200 nm. Absorption was measured in a 10.2-cm chamber at the exit slit of the 0.3-m McPherson monochromator by single-beam comparison of the gas-filled versus evacuated ($\sim 10^{-2}$-torr) chamber.

No absorption was seen in He that could not be attributed to expected impurities at the 10^{-2}-torr background pressure of the absorption chamber. Limiting values of this "impurity" absorption are: 120–145 nm

$$\alpha < 2 \times 10^{-3} \text{ cm}^{-1}\text{atm}^{-1}$$

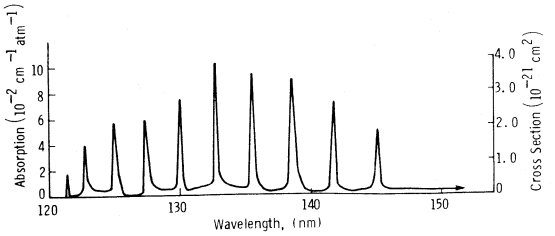
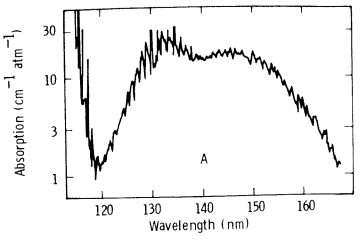
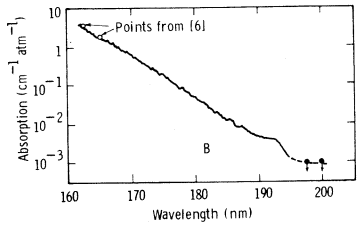


Fig. 1. Measured nitrogen absorption. Lyman-Birge-Hopfield series.



(a)



(b)

Fig. 2. CO_2 absorption. Curve *A* shows data of Nakata *et al.* [9], and curve *B* represents our extension.

and 145–200 nm

$$\alpha < 4 \times 10^{-3} \text{ cm}^{-1}\text{atm}^{-1}.$$

Measured nitrogen absorption is shown in Fig. 1. The sharp bands are from the forbidden Lyman-Birge-Hopfield series; the 145-nm line is the series limit. The very weak continuum between the peaks and extending beyond 145 nm is at our expected impurity absorption level.

CO_2 absorbs strongly below 115 nm. The absorption decreases to a few cm^{-1}atm^{-1} in an $\sim$10-nm band centered around 120 nm, then becomes strong again, falling to about 2 cm^{-1}atm^{-1} at 165 nm [see Fig. 2(a)]. The absorption continues to decrease at longer wavelengths [Fig. 2(b)], reaching a negligible level at about 195 nm.

Spark Emission

The UV emission from sparks was measured in three laser mixtures; CO_2:N_2:He = 1:1:8, 1:2:3, 1:7:0, and in the component gases, using an MgF_2-window McPherson monochromator. Because the MgF_2 does not transmit below 115 nm, spark emissions were also measured with a windowless vacuum UV monochromator. However, all emissions below 115 nm were completely absorbed in the $\sim$5-mm gas path length inside the monochromator spark chamber for all gas mixtures containing CO_2. The 0.3-m McPherson monochromator provided spectral resolution of 0.03 nm. We estimate a calibration accuracy of 20 percent.

The spark source was a 2-mm gap between sharpened Mo electrodes 1 mm in diameter. The energy supply was simply a storage capacitor C, charged to $V_c = 10$ kV, and discharged through a resistor R_s. Measured current-time behavior agreed within 10 percent for all cases with simple RLC circuit theory, with L as a fitted parameter, ranging from 0.68 to 1.95 μH for the four capacitors used. The theoretical spark current is

$$j = (V_c/\gamma L) \exp(-\beta t) \sin \gamma t, \qquad R_s^2 < 4L/C$$

$$j = (V_c/2\gamma L) \exp(-\beta t) [\exp(\gamma t) - \exp(-\gamma t)], \qquad R_s^2 > 4L/C$$

where $\beta = R_s/2L$ and $\gamma = \sqrt{|\beta^2 - (1/LC)|}$.

This relatively fast-rising current supply produced a hot spark having high UV emission efficiency. For one set of conditions ($R_s = 40\ \Omega$, $C = 0.005\ \mu$F) careful measurement of the voltage across the spark showed that 0.3 percent of the energy dissipated appeared as photons in the effective wavelength range of 117–124 nm.

The spectra of the 1:1:8, 1:2:3, and 1:7:0 mixes from 115 to 251 nm taken at atmospheric (720-torr) pressure are shown in Fig. 3. The spectra are redrawn to indicate the line strengths, corrected to give absolute spectral irradiance, with the continuum omitted. The spectral resolution was about 0.08 nm. From 251 to 350 nm, no emission was seen.

Spectral details of the radiation in the CO_2 "window" around 120 nm are shown for a 1:7:0 mix in Fig. 4. In spectrum (A) the current maximum (200 A) and the pulse-width are determined by R_s, L, and C. For spectra (B) and (C) inductance was added to reduce the peak spark current to 100 and 80 A, respectively. Some lines such as the 124-nm NI lines were only slightly affected. Other, high-lying energy transitions, such as the NIII lines at 118.4 nm and the CIII line at 124.7 nm, decreased dramatically with increasing inductance. The compound peak at 118 nm, which contains NI and CIII lines, was moderately affected. Within experimental accuracy, the energy into the spark, determined by $\int V \cdot Idt$, remained constant at about 2.8 mJ. We conclude that the peak spark current directly affects the peak temperature, which in turn strongly influences the population of the higher lying energy levels, but does not greatly affect lower energy levels. The continuum radiation (a large percentage of the total energy) also depends significantly on the peak current.

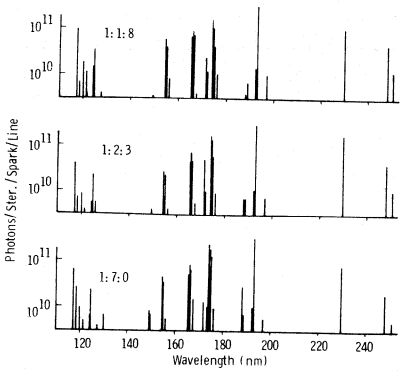


Fig. 3. Emission from bare spark in three reference mixtures. $P = 720$ torr; $C = 0.005\ \mu$F; and $R_s = 40\ \Omega$. Spark-to-window distance is 1 cm.

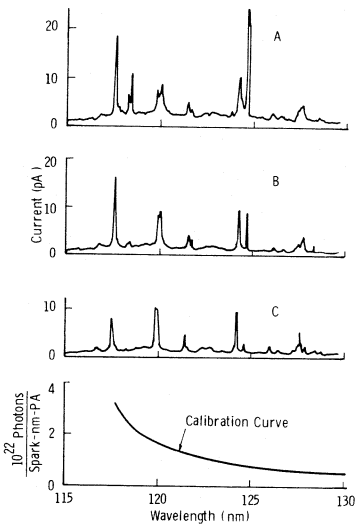


Fig. 4. Spectral detail of the emission in the 120-nm "window" for the 1:7:0 mixture. Spectrum A is an expansion of Fig. 3. Spectra B and C show the effect of adding inductance to reduce the spark temperature. The calibration curve shown applies to all three emission spectra.

Measured Photoelectron Production

The electron collection apparatus is shown in Fig. 5. The spark electrodes and energy supply were identical to those previously described. The emitted UV photons, collimated to a cone of solid angle Ω, passed between parallel planar electrodes which provided a collection field of typically 0.4 V/cm · torr. A semiconducting sheet 6 mm from the collimating hole supplied a uniform potential gradient across the gap, and also repelled secondary electrons and electrons from the spark.

The signal anode could be positioned a distance $d = 2$–22 cm from the spark. It collected photoelectrons generated in a disk-shaped volume of

$$V = \Omega d^2 w \qquad (1)$$

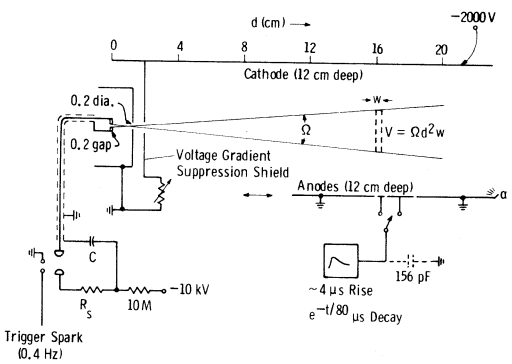


Fig. 5. Essential features of photoelectron collector.

where w is the effective width of the anode. Accurate data could be obtained for $d \geqslant 3$ cm. Collection efficiencies were verified by injecting alpha particles from the isotopic source shown, collecting electrons from the ionization track, with all four anodes connected in parallel, and measuring the maximum charge pulse. The indicated collection efficiency for all

gas fills was consistent with a collection efficiency for volumetric photoelectrons well in excess of 90 percent, as expected from proportional counter theory [11]. Mixtures having large CO_2 contents are a special case, because of the large electron-attachment rate of CO_2. As CO_2 partial pressure was increased above 150 torr, the collection efficiency decreased rapidly.

The UV-generated photoelectrons drifted to the anode in the order of 4 μs. The resulting voltage pulse was observed with a Tektronix 7A22 oscilloscope preamplifier. Each datum point represented an average of about ten observed pulses, with a typical pulse-to-pulse variation of about 10 percent. The smallest measurable signal was about 50 μV, representing 5×10^4 electrons.

The primary data were obtained using only a forepump for prior evacuation to a background pressure of roughly 0.03 torr. However, subsequent outgassing of the measurement chamber at 80°C for several days, diffusion pumping to a vacuum of about 6×10^{-4} torr, and slow admission of commercial-grade gas through a cold trap caused no significant change in the observed photoelectron production. Observed volumetric photoelectron production, in pure nitrogen and in the three laser mixtures chosen as standards, is shown by the solid lines in Fig. 6 for $P = 1$ atm. The volumetric production per spark is just $n_e = N_e d^{-2}$ electrons/cm^3. The much greater efficiency in pure N_2 was due to the prominent 108-nm spark-emission component, which is totally absorbed by the CO_2 component of the reference gas mixtures. The open circles give the observed electron production (normalized to the solid lines at $d = 20$ cm) when the measurement chamber is filled only with CO_2 to the same partial pressure. The good agreement implies that the variation of photoproduction with distance is determined solely by attenuation of the emitted photons (by nonionizing processes) due to the CO_2 content.

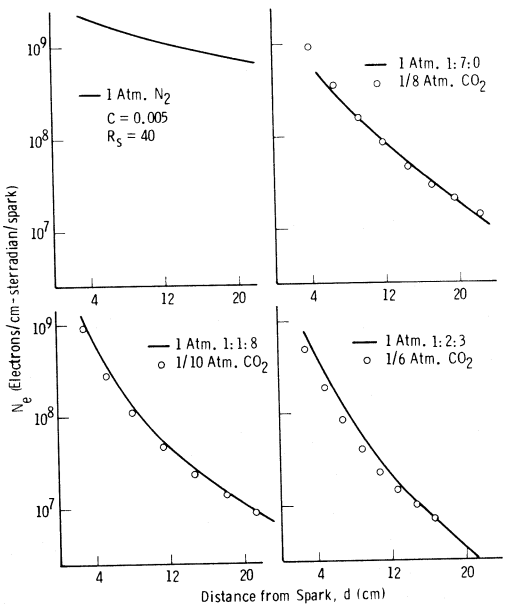


Fig. 6. Electron production in reference mixtures (solid curves). Open circles show electron production when CO_2 component alone is present, normalized to the solid curves at $d = 20$ cm. Except for N_2 data, spark supply was $C = 0.05$ μF, $R_S = 0.2$ Ω.

We showed previously that the only UV photons which could penetrate CO_2 sufficiently were the two groups 117 nm $< \lambda <$ 124 nm, and $\lambda >$ 160 nm. To determine which group accounted for the electron production, the collimating hole was covered first with 1 mm of MgF_2 (which passes $\lambda > 115$ nm), then with 1.5 mm of Al_2O_3 (which passes $\lambda > 143$ mm). With MgF_2 the dependence of N_e on d did not change, but the magnitudes of N_e were reduced ~50 percent, consistent with the known attenuation of the window in the 117-124-nm wavelength range. The Al_2O_3 window reduced photoelectron production more than 99.5 percent. Thus, in a typical laser geometry where the UV passes through a CO_2-laser gas mixture, only the band centered at 120 nm participates effectively in photoionization. In this wavelength range the N_2 and He absorptions are negligible compared to the CO_2 absorption.

Nature of Photoionizing Reaction

One-photon ionization of N_2, He, or CO_2 does not occur since each molecule has an ionization potential considerably above the highest photon energy, ~11 eV, which can be transmitted through the CO_2 window. The observed ionization must be either a two-photon process or a one-photon direct (or Penning) ionization of an impurity. To discriminate among these possibilities, the dependence of N_e on d and on P was observed, while holding constant the pressure in the spark chamber P_s (with the MgF_2 window sealing the spark chamber) and the spark energy supply.

Under these conditions, the effective photon flux from the bare spark is constant at I_0 photons/spark/sr. The photon-flux density at the range Pd is $i = I_0 d^{-2} \exp(-\bar{\alpha} Pd)$ photons/cm^2, where $\bar{\alpha}$ is the average absorption coefficient for the gas mixture. For a one-photon ionization of some target molecule present in a concentration n_t cm^{-3}, with an ionization probability of σ_i cm^2, the electron density will be $n_e = \sigma_i n_t i$ electrons/cm^3. From the collection volume given by (1), the number of electrons measured will be

$$N_e = n_e V = \Omega w \sigma_i n_t I_0 \exp(-\bar{\alpha} Pd). \quad (2)$$

For a two-step ionization, the density of intermediate species produced is $n_1 = \sigma_t n_t i$, and the final electron density is $n_e = \sigma_1 n_1 i = \sigma_1 \sigma_t n_t i^2$ electrons/cm^3, where σ_t and σ_1 are the cross sections for production and for ionization of the intermediate species. Then the number of electrons measured will be

$$N_e = n_e V = [\Omega w \sigma_1 \sigma_t n_t I_0^2] d^{-2} \exp(-2\bar{\alpha} Pd). \quad (3)$$

In Fig. 7, the observed N_e for a 1:1:8 mix is compared with (3), using the known minimum value of $\bar{\alpha} = 0.1$ cm^{-1} for a 10-percent CO_2 atmospheric mixture over the 117-124-nm wavelength range. The quantity in brackets is independent of d, and is normalized to the data at $d = 3$ cm. A discrepancy of two orders of magnitude is apparent, which thoroughly rules out two-photon ionization.

Possible one-photon ionizing reactions are: 1) direct ionization of an impurity in the gas feed; 2) excitation of N_2, He, or CO_2, followed by Penning ionization of an impurity; and 3) direct ionization of a background impurity from the appara-

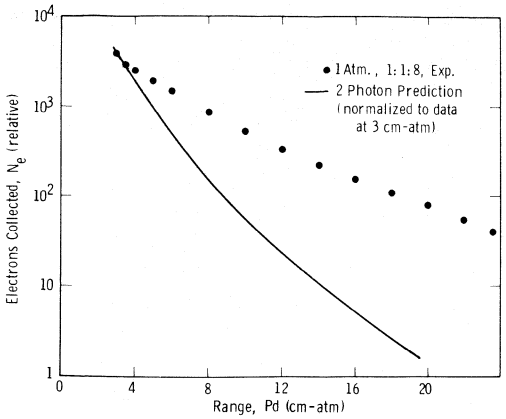


Fig. 7. Comparison of two-photon predictions to experiment.

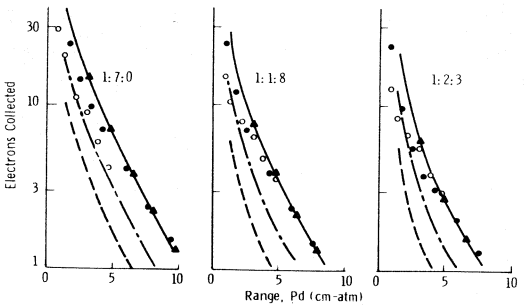


Fig. 8. Comparison of one-photon predictions to experiment at constant I_0. Triangles, filled circles, and open circles represent data at $P = 0.8$, 0.4, and 0.2 atm, respectively. Other curves show response predicted by (4) at $P = 0.8$ atm (——), $P = 0.4$ atm (—— · ——), and $P = 0.2$ atm (—— —— ——).

tus. In the first two cases, $n_t \propto P$. For a background impurity, n_t is constant. Thus (2) becomes; for cases 1) and 2)

$$N_e = f(Pd)P \tag{4}$$

and for a background impurity

$$N_e = f(Pd). \tag{5}$$

Fig. 8 compares observations at three values of P with the predictions of (4) and (5). For direct ionization of a background impurity, all the data points should lie on the solid curve, which represents (5) normalized to the 0.8-atm data. For cases 1) and 2), the low-pressure data should agree with the other curves. Although the low-pressure data points do tend to fall below the solid curve at the shorter ranges, they are clearly inconsistent with the curves representing cases 1) and 2). We therefore ascribe the electron production to direct ionization of a background impurity.

As an overall test of our inferences, we have computed the expected N_e versus d for a 1:7:0 mix at 720-torr total pressure from our absolute spectral-emission intensity measurements and published measurements of CO_2 attenuation versus photon frequency [Fig. 2(a)], under the following assumptions.

1) The photon flux is attenuated only by the CO_2 component in a nonionizing process.

2) Electrons are produced only by direct one-photon ionization of an impurity having an ionization cross section of 100 cm^{-1} atm^{-1} at a concentration of 0.5 ppm. This ionization cross section is typical of many organic molecules, and of NO, in the 117-124-nm wavelength range [12]. The results are compared to the measured N_e in Fig. 9; agreement is quite good. The assumed concentration of 0.5 ppm is in agreement with the measured background pressure in the electron collector of 6×10^{-4} torr (0.8 ppm).

Gas chromatographic and mass-spectrographic analyses showed no impurities. However, these analyses were sensitive to only a few ppm, and do not rule out the impurity mechanism. A direct test of background impurity ionization was attempted. With the spark chamber filled with 300-torr N_2, and the measurement chamber actively pumped at a pressure of 6×10^{-4} torr, N_e was seen to be a few $\times 10^7$ electrons/sr · cm, independent of position. Thus background impurity

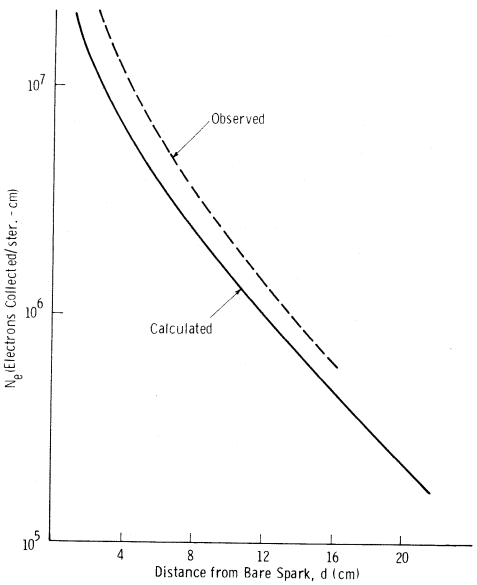


Fig. 9. Comparison of observed photoelectron production to calculation from spectroscopic measurements for a 1:7:0 mixture at 720 torr. Dashed curve shows observed response for $C = 0.005$ μF, $R_s = 40$ Ω, and background impurity concentration of ~0.8 ppm. Solid curve shows calculated response for an ionizing impurity concentration of 0.5 ppm.

ionization was significant, although the exact amount was not determined, because of difficulty in defining the collection efficiency at this low pressure.

Effect of Spark Energy Supply

The spark energy supply was varied to provide peak spark current j ranging from 12 to 1200 A, and spark-current durations T ranging from 20 ns to 40 μs. Fig. 10 shows N_e (observed at $d = 22$ cm) versus j for four values of energy stored in the capacitor J. To a good approximation $N_e \propto j$. At constant P the spark-emission intensity I_0 is proportional to N_e; therefore, $I_0 \propto j$. Taking values of N_e at constant j from the four curves we find, to an excellent approximation, $N_e \propto J^{0.5}$. Combining the two dependencies gives $N_e \propto I_0 \propto jJ^{0.5}$.

When P_s alone was varied we found that I_0 varied as $P_s^{0.5}$. When P alone was varied as in Fig. 8 we found that N_e (at constant Pd) was almost independent of P, ruling out Penning ionization. Empirically, over the range described, the electron

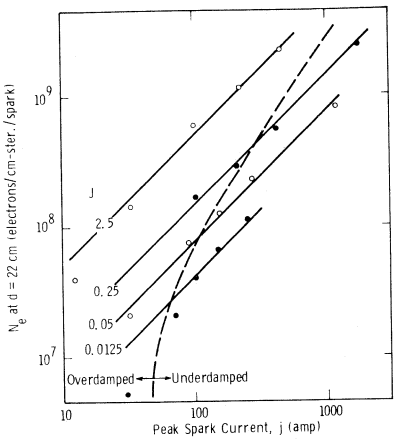


Fig. 10. Variation of N_e with peak spark current for 0.4-atm N_2. The dashed curve separates the region of overdamped current from the underdamped (ringing) region. Each line has a slope of 1.0 and is labeled by the stored energy in joules.

density was found to be

$$n_e = 4 \times 10^{-4}\, j(JP)^{0.5} d^{-2}\, N_e \text{ electrons/cm}^3 \qquad (6)$$

where j(A) is the peak spark current, J(J) is the capacitor energy, P(atm) is the total gas pressure, d(cm) is the distance to the spark, and N_e is obtained from Fig. 6 with the abscissa read as Pd(atm · cm).

Summary

We examined the physical mechanisms governing volumetric UV photoionization of CO_2-, N_2-, He-laser gas mixtures due to a bare-spark source, by high-resolution spectroscopic emission and absorption studies and by direct collection of photoionized electrons. The following mechanism for the volumetric photoelectron production has been established.

1) Electron production is due entirely to direct one-photon ionization of impurities, present at a partial pressure of the order of 10^{-6} atm, by photons in the wavelength range 117–124 nm.

2) The variation with distance is determined solely by nonionizing attenuation of these photons by the CO_2 fraction and straightforward geometric factors. The UV flux (proportional to electron production) decays as $\exp(-\alpha Pd)$, where α is roughly 1.5 (cm · atm)$^{-1}$ of CO_2.

3) Over the range studied, the effective photon flux from the spark varies directly with peak spark current, with the square root of energy (stored at 10 kV) discharged through the spark, and with the square root of gas pressure.

4) Typically, a single unfocused spark dissipating about 3 mJ can create 10^5 electrons/cm^3 at a distance of 10 cm, if one of literally hundreds of organic impurities is present at a partial pressure of 1×10^{-6} atm.

The description of volumetric photoelectron production is sufficiently complete to provide the initial electron distributions required for the discharge growth model of Kline and Denes [5], which is then used to describe the fully developed discharge conditions for a wide range of self-sustained electric-discharge CO_2-laser geometries. The ability to scale UV initiated, self-sustained discharges to large volumes is inherent in their model, which shows that an initial electron distribution, which is uniform parallel to the electrodes but highly nonuniform normal to the electrode plane, will result in a uniform electron density throughout the discharge volume.

Acknowledgment

The authors wish to thank Dr. W. J. Choyke for valuable advice concerning spectroscopy and J. Bogden for aid in preparing the spectrometers. They also wish to thank W. Fastie and R. Richardson of The Johns Hopkins University for making the spectroscopic calibration possible.

References

[1] H. M. Lamberton and P. R. Pearson, "Improved excitation techniques for atmospheric pressure CO_2 lasers," *Electron. Lett.*, vol. 7, pp. 141–142, 1971.

[2] L. J. Denes and O. Farish, "High-pressure pulsed carbon-dioxide laser with uniform excitation," *Electron. Lett.*, vol. 7, pp. 337–338, 1971.

[3] H. Seguin and J. Tulip, "Photoionitiated and photosustained laser," *Appl. Phys. Lett.*, vol. 21, pp. 414–415, 1972.

[4] O. P. Judd, "An efficient electrical CO_2 laser using preionization by ultraviolet radiation," *Appl. Phys. Lett.*, vol. 22, pp. 95–96, 1973.

[5] L. E. Kline and L. J. Denes, "Investigations of glow discharge formation with volume preionization," *J. Appl. Phys.*, vol. 46, pp. 1567–1574, 1975.

[6] I. Liberman and W. D. Partlow, "Mechanisms of UV preionization of CO_2 TEA lasers," *IEEE J. Quantum Electron. (1974 Int. Quantum Electronics Conf., Dig. Tech. Papers)*, vol. QE-10, pp. 750–751, Sept. 1974.

[7] A. J. Palmer and J. Y. Wada, "UV preionization mechanisms in CO_2 TEA lasers," *IEEE J. Quantum Electron. (1974 Int. Quantum Electronics Conf., Dig. Tech. Papers)*, vol. QE-10, p. 751, Sept. 1974.

[8] H. J. Seguin, J. Tulip, and D. C. McKen, "Ultraviolet photoionization in TEA lasers," *IEEE J. Quantum Electron.*, vol. QE-10, pp. 311–319, Mar. 1974.

[9] R. S. Nakata, K. Watanabe, and F. M. Matsunaga, "Absorption and photoionization coefficients of CO_2 in the region 580–1670Å," *Sci. Light*, vol. 14, pp. 54–71, 1965.

[10] R. D. Hudson, "Critical review of UV photoabsorption cross sections for molecules of astrophysical and aeronomic interest," U.S. Dept. of Commerce, NBS monograph NSRDS-NBS-38.

[11] F. H. Attix and W. C. Roesch, *Radiation Desimetry*, vol. II, 2nd ed. New York: Academic, 1966, pp. 30–36.

[12] J. H. Carver and P. Mitchell, "Ionization chambers for the vacuum ultraviolet," *J. Sci. Instrum.*, vol. 41, pp. 555–557, 1964.

A Canonical Formulation for Analyzing Multielement Unstable Resonators

ANTHONY E. SIEGMAN, FELLOW, IEEE

Abstract—**A simple but general formulation for the unified analysis of many different varieties of unstable optical resonators is obtained by expressing the round-trip Huygens' integral for the resonator in terms of the round-trip paraxial ray matrix. Complicated multielement resonators, ring resonators, and unstable resonators with variable-reflectivity output mirrors are thereby all reduced to a single equivalent collimated-beam diffraction problem. Essential assumptions in the analysis are that all elements in the resonator obey paraxial ray theory and that there is only one significant output coupler or limiting aperture per round trip inside the resonator. The only parameters needed to describe an arbitrary unstable resonator in this formulation are the round-trip magnification M and either the equivalent Fresnel number N_{eq} or else an equivalent collimated Fresnel number $N_c = [2M^2/(M^2 - 1)]N_{eq}$, plus for variable-reflectivity mirrors a specification of the mirror reflectivity profile.**

I. Introduction

UNSTABLE optical resonators [1] are now being designed in a variety of complex configurations, including ring resonators [2], [3], resonators with multiple intracavity elements, resonators having oddly shaped output couplers or output mirrors with variable-reflectivity profiles across the mirror [4], and resonators stable in one transverse dimension and unstable in the other [5]. It would be convenient to have a simple and general unstable-resonator mode analysis that would reduce any complex multielement unstable resonator to a simple equivalent unstable-resonator model. The geometrical mode solution for any such resonator could then be rapidly predicted. Also the limited supply of exact numerical calculations currently available for simple unstable resonators could be directly applied to complex multielement resonators as well. This paper presents such a simple canonical formulation for any unstable optical resonator, assuming only paraxial wave approximations everywhere in the resonator, and a single output coupler or dominant aperture stop inside the resonator.

In the following section we first review the *ABCD* ray-matrix analysis which gives the geometrical output beam and the geometrical magnification M for any arbitrary unstable resonator in terms only of its round-trip *ABCD* matrix. We then point out the sometimes overlooked fact that the Huygens' integral through any arbitrary paraxial optical system can be written in terms of the overall *ABCD*-matrix elements alone. Using this fact we can write the exact round-trip propagation integral for any unstable resonator, using only its round-trip *ABCD* matrix, and then convert this equation into a simple equivalent collimated-beam diffraction problem. The resulting canonical form depends on only two resonator parameters, the geometrical magnification M and either the equivalent Fresnel number N_{eq} or a collimated Fresnel number $N_c = [2M^2/(M^2 - 1)]N_{eq}$, plus the mirror transverse-reflectivity profile for the case of variable-reflectivity mirrors.

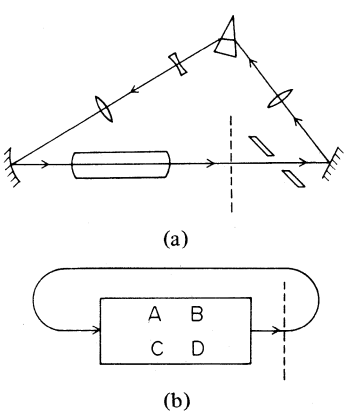
Manuscript received June 13, 1975; revised August 20, 1975. This work was sponsored by the Joint Services Electronics Program at Stanford University.

The author is with the Department of Electrical Engineering and the Microwave Laboratory, Stanford University, Stanford, CA 94305.

II. Ray Analysis of Unstable Optical Resonators

The following geometrical ray analysis of the unstable resonator does not contain any new physical content beyond that already given by Kahn [6]. However, the results are phrased in a manner closer to the current descriptions of unstable resonators.

Consider a transverse reference plane located inside an unstable optical resonator; for instance, the multielement ring resonator shown in Fig. 1(a). For purposes of a ray analysis the reference plane can be located anywhere inside the resonator. However, for a diffraction analysis to be done later, this plane is best located just before the output mirror, output coupling element, or dominant aperture stop inside the unstable resonator, as in Fig. 1(a). Disregarding any other aperture stops, we then assume that all of the optical elements encountered in one complete round trip around the resonator can be described by individual *ABCD* ray matrices [7] with respect to the resonator optical axis. This axis may, of course, be bent or folded as it encounters various elements such as prisms or tilted mirrors. For either a standing-wave or a ring-type resonator one can describe a complete round trip, starting from and returning to the reference plane, by an overall *ABCD* matrix. This matrix will, of course, be the matrix product of all the individual ray matrices arranged in *inverse* order (i.e., the last element encountered comes first if the matrix product is written out from left to right). Such a round trip is represented schematically in Fig. 1(b).



(a)

(b)

Fig. 1. (a) A typical multielement unstable resonator containing intracavity lenses, mirrors, and other paraxial optical elements. (b) The ray-matrix equivalent for one round trip inside such a resonator.

The ray displacement r and slope r' after one complete round trip, starting with r_0 and r'_0, are then given (for real $ABCD$ elements) by

$$\begin{bmatrix} r \\ r' \end{bmatrix} = \begin{bmatrix} A & B \\ C & D \end{bmatrix} \begin{bmatrix} r_0 \\ r'_0 \end{bmatrix} \tag{1}$$

in which $AD - BC = 1$. The wavefront radius of curvature $R = r/r'$ for a spherical wave after passing once around the resonator is given by

$$\frac{1}{R} = \frac{D/R_0 + C}{B/R_0 + A} \tag{2}$$

where $R_0 \equiv r_0/r'_0$. The geometrical solution for an unstable resonator is that spherical wave whose curvature is unchanged after one round trip, so that $R = R_0$. From (2), the unstable spherical-wave solution is

$$\frac{1}{R} = \frac{1}{B}\left[-\frac{A-D}{2} \pm \sqrt{\left(\frac{A+D}{2}\right)^2 - 1}\right]. \tag{3}$$

The choice of signs will be settled later. For the case of A and D real, the condition that the resonator be unstable is that R be purely real. This imposes the condition that

$$\left| g \equiv \frac{A+D}{2} \right| \geqslant 1. \tag{4}$$

The g parameter defined in this way is directly analogous to the g parameter of a conventional symmetric two-mirror resonator.

An unstable resonator will have a geometrical magnification M. For the self-consistent wave the displacement and slope will both be magnified by M after one round trip, i.e.,

$$\begin{aligned} r &= Ar_0 + Br'_0 = Mr_0 \\ r' &= Cr_0 + Dr'_0 = Mr'_0 \end{aligned} \tag{5}$$

where $|M| > 1$ for the magnifying solution that is of primary interest. Note, however, that M can either be a positive number $M > 1$ or a negative number with magnitude greater than one, i.e., $M < -1$. The latter case represents a "negative-branch" resonator [8], in which the ray emerges with a magnified displacement and slope on the opposite side of the resonator axis after each round trip. This implies that the resonator mode has at least one, if not a larger odd number, of internal axis crossings or focal points on each round trip around the resonator.

The magnification parameter M as defined by (5) is in fact identical with one of the matrix eigenvalues of the $ABCD$ matrix. Using the self-consistency condition that $r'/r = r'_0/r_0 = 1/R$ where $1/R$ is given by (3), one can solve for the two matrix eigenvalues which we will denote by M_p and M_n, with the values

$$M_p, M_n = \frac{A+D}{2} \pm \sqrt{\left(\frac{A+D}{2}\right)^2 - 1}. \tag{6}$$

The two eigenvalues are thus given by

$$M_p = g + \sqrt{g^2 - 1}$$

$$M_n = g - \sqrt{g^2 - 1} \tag{7}$$

with the general relationship

$$M_p M_n = 1. \tag{8}$$

Depending on the sign of g, one or the other of the two eigenvalues M_p and M_n corresponds to the expanding geometrical solution with $|M| > 1$. The other eigenvalue is then simply the converging or demagnifying reversed form of the same wave, with a demagnification by $|1/M|$ on each pass. Depending on which of the two eigenvalues M_p or M_n corresponds to the geometrical magnification M, one has the generalized equivalent of either a positive-branch or a negative-branch unstable resonator [8]. Examination of (3)-(7) shows that the resulting geometrical solutions are, in summary.

1) Positive-branch unstable resonators:

$$g = \frac{A+D}{2} > 1$$

$$M = M_p = g + \sqrt{g^2 - 1} > 1$$

$$\frac{1}{R} = \frac{1}{B}\left[-\frac{A-D}{2} + \sqrt{\left(\frac{A+D}{2}\right)^2 - 1}\right]. \tag{9}$$

2) Negative-branch unstable resonators:

$$g = \frac{A+D}{2} < -1$$

$$M = M_n = g - \sqrt{g^2 - 1} < -1$$

$$\frac{1}{R} = \frac{1}{B}\left[-\frac{A-D}{2} - \sqrt{\left(\frac{A+D}{2}\right)^2 - 1}\right]. \tag{10}$$

Note that the magnification M is essentially the same as the mode-stability factor F defined by Casperson [17].

In many cases with either a positive- or negative-branch resonator one may want to have a collimated output beam. From (9) and (10), obtaining $R \to \infty$ requires either $|B| \to \infty$ or else the generalized confocal condition

$$AD = 1. \tag{11}$$

This completes the purely geometrical ray analysis.

III. Diffraction Analysis of Unstable Resonators

The fundamental relationship between the $ABCD$ matrix and the Huygens' integral for a paraxial system has already been clearly pointed out in the literature [9]-[13]. However, it does not seem to be as widely realized as it might be that one can write the Huygens' integral for wave propagation through a multielement paraxial optical system in terms only of the overall $ABCD$-matrix elements of the system. The relation between the complex input and output wave amplitudes $\mathcal{E}_0(x_0)$ and $\mathcal{E}(x)$ in one transverse dimension is

$$\mathcal{E}(x) = \left(\frac{j}{B\lambda}\right)^{1/2} \int_{-\infty}^{\infty} \mathcal{E}_0(x_0) \cdot \exp\left[-j\frac{\pi}{B\lambda}(Ax_0^2 - 2xx_0 + Dx^2)\right] dx_0. \tag{12}$$

We have assumed wave propagation in the form $\exp j(\omega t - kz)$ and left out the plane-wave phase-shift term $\exp(-jkB)$.

Two transverse dimensions x and y, in an optical system which is possibly astigmatic but still separable in the x and y coordinates, can also be easily handled. One merely adds a second exponential factor involving y and y_0 inside the integral; puts an additional $(j/B\lambda)^{1/2}$ factor in front; and does a double integral in $dx_0 dy_0$ over the input plane. Optical systems having x-y astigmatism, such as may be caused by cylindrical lenses or by tilted curved mirrors, are then handled by using separate $ABCD$ matrices for the x and y directions. Still more general nonorthogonal systems having astigmatism about oblique axes and not possessing meridional planes of symmetry can also be handled if necessary [12], [13], but will not be treated here. For simplicity, in fact, we will present the following analysis in one transverse dimension only, since the extension to two transverse coordinates is obvious.

The Huygens' integral of (12) can represent the wave propagation for one complete round trip around the general unstable resonator of Fig. 1. To convert this integral into the simplest possible form we will first extract from the field expressions the quadratic phase variation of the geometrical spherical wave. That is, we write

$$\mathcal{E}_0(x_0) = u_0(x_0) \exp[-j\pi x_0^2/R\lambda]$$
$$\mathcal{E}(x) = u(x) \exp[-j\pi x^2/R\lambda] \tag{13}$$

where R is given by (9) or (10). This step is the same thing as completing the square in the exponent, or using the stationary-phase procedure, in evaluating (12). Also the wave amplitude $\mathcal{E}_0(x_0)$ before it propagates around the resonator must be multiplied by a mirror amplitude reflection function (or an output-coupler transmission function) which we will denote by $\rho(x)$. For the simplest results it is desirable, although not absolutely necessary, that any quadratic phase variation in the mirror reflection function $\rho(x)$ be absorbed in the overall round-trip $ABCD$ matrix rather than being retained in $\rho(x)$.

If there are not other significant apertures inside the resonator other than the output mirror or output coupler described by $\rho(x)$, the integral formula for round-trip propagation around the resonator can be written as

$$u(x) = \left(\frac{j}{B\lambda}\right)^{1/2} \int_{-\infty}^{\infty} \rho(x_0)\, u_0(x_0) \cdot \exp\left[-j\frac{\pi}{MB\lambda}(x - Mx_0)^2\right] dx_0. \tag{14}$$

In this form the integral involves only the magnification M, the ray-matrix element B, and the mirror reflection function $\rho(x)$.

By making the change of variables $x_0' = Mx_0$ (noting that M will be negative for negative-branch resonators) and then dropping the prime on the dummy variable of integration, one can convert this integral to the alternative form

$$u(x) = \pm\left(\frac{j}{MB\lambda}\right)^{1/2} \int_{-\infty}^{\infty} |M|^{-1/2}\, \rho(x_0/M)\, u_0(x_0/M) \cdot \exp\left[-j\frac{\pi}{MB\lambda}(x - x_0)^2\right] dx_0. \tag{15}$$

The $\pm$ sign in front represents an added π phase shift associated with negative-branch resonators and will henceforth be ignored. In the form given by (15) the round-trip wave propagation consists of three steps, which are illustrated schematically in Fig. 2.

1) Multiply the resonator wavefront $u_0(x)$ just before the reference plane by the mirror reflection function $\rho(x)$.

2) Magnify (interpolate) the resulting wavefront values radially outward by the magnification M to get $|M|^{-1/2} \cdot \rho(x/M)\, u_0(x/M)$.

3) Propagate the resulting wavefront forward by a free-space distance $L_{\text{eff}} = MB$ (or backward the same distance for negative values of MB) to get the wavefront $u(x)$ after one round trip.

The forward propagation in step 3 can be done using the Huygens' integral directly or, in a more efficient way, by using a plane-wave expansion plus the fast Fourier transform [14]. Repeated iteration of the three steps will then cause $u(x)$ to converge to a lowest order resonator mode in the manner pioneered by Fox and Li [22]. The converged lowest order solution for $u(x)$ should turn out to have close to a planar wavefront in most cases. The near-field output beam just outside the unstable resonator can then be obtained by multiplying the complex wavefront $u(x)$ by the transmission function of the output mirror or the output coupling function of the output coupling element.

We may consider in particular the case of a conventional sharp-edged unstable resonator with an output mirror of diameter $2a_m$, so that $\rho(x) = 1$ for $|x| < a_m$ and $\rho(x) = 0$ for $|x| > a_m$. By transforming to the dimensionless variables

$$y = x/a_m \qquad y_0 = x_0/a_m \tag{16}$$

one can further reduce the resonator equation to the form

$$u(y) = \sqrt{jN_c} \int_{-1}^{1} M^{-1/2}\, u_0(y_0/M) \cdot \exp[-j\pi N_c(y - y_0)^2]\, dy_0 \tag{17}$$

where we introduce the collimated Fresnel number N_c defined by

$$N_c \equiv \frac{(Ma_m)^2}{MB\lambda} = \frac{Ma_m^2}{B\lambda}. \tag{18}$$

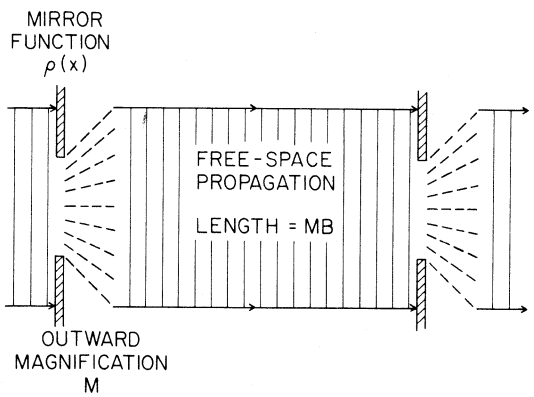


Fig. 2. The canonical model for one complete round trip in an arbitrary unstable resonator.

This collimated Fresnel number N_c is an important basic parameter for the unstable resonator. In particular, it determines the number of sample points and the width of the guard band that must be employed in evaluating the diffraction integral numerically [14]. Note that N_c as defined here carries the same explicit sign as does the magnification M.

We suggest as the primary conclusion of this paper that the formulation in terms of the resonator *ABCD* elements, as illustrated in Fig. 2, should be adopted as the standard form for all unstable-resonator mode calculations, at least for bare-resonator eigenmode and eigenvalue calculations.

IV. Discussion

A. Collimated and Equivalent Fresnel Numbers

The collimated Fresnel number N_c just introduced is related to the equivalent Fresnel number N_{eq} also widely used for unstable resonators in the following manner. The primary geometrical solution in an unstable resonator is a collimated uniform plane wave as shown schematically in Fig. 3(a). This plane wave remains planar but is magnified outward on each successive pass around the resonator. However, there also exists in an unstable resonator a converging or demagnifying geometrical solution. In the canonical formulation this demagnifying solution appears as a periodically refocused, inwardly converging spherical wave as shown in Fig. 3(b). It has been pointed out earlier [15], [16] that N_{eq} has a geometrical interpretation as the added phase lag in wavelengths with which the magnifying geometrical solution scatters into the demagnifying geometrical solution at the mirror edge, as compared to the mirror center. Applying this principle to the magnifying solutions shown in Fig. 3 leads, after a straightforward calculation, to a universal relationship between N_c and N_{eq}, namely

$$N_{eq} = \frac{M^2 - 1}{2M^2} N_c. \tag{19}$$

This general relation reduces to other expressions that have previously been obtained for specific cases, such as the symmetric and confocal unstable resonators. Formulas for a number of specific resonator designs are summarized in the Appendix.

B. Additional Aperture Stops

We have assumed in the previous analysis that only one aperture inside the resonator has any significant effect on the unstable-resonator mode pattern. This aperture is the output mirror, beam coupler, or aperture stop that is explicity included in $\rho(x)$. An unstable resonator will have minimum diffraction losses and probably the best beam quality, if only one aperture stop is present. On the other hand, additional apertures within a resonator may be necessary to suppress parasitic oscillations, to promote one-way oscillation in a ring resonator [2], [3], or simply because of mechanical constraints. If such additional apertures are present and have significant diffraction effects on the resonator mode, then the preceding analysis will not apply directly. Instead, it will be necessary to split the resonator round trip into two or more subsections, and apply an analysis like that previously given to each subsection individually.

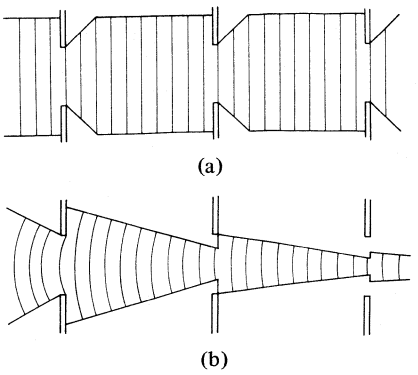


Fig. 3. The two geometrical modes, (a) the magnifying and (b) the demagnifying mode, for the canonical unstable-resonator model.

C. Transversely Varying Loss or Gain

A real laser device may have a transverse variation in gain or loss caused, for example, by a transverse gain variation across the laser medium or by a deliberately imposed transverse variation in the mirror reflectivity of the laser. To the extent that such transverse gain or loss variations can be approximated by a Gaussian transverse variation, with either a maximum or minimum on the resonator axis, they can be treated analytically by adding complex elements to the appropriate *ABCD* ray matrices.

Adding even a small amount of such radially increasing loss (or radially decreasing gain) to an unstable optical resonator that has otherwise unbounded optical elements (i.e., no other internal apertures) will convert this previously unstable resonator into a *stable* resonator having a stable Gaussian lowest order mode (at least within the paraxial degree of approximation). This result has recently been demonstrated for a variety of specific cases by various authors [17]-[20], and the proof can fairly readily be generalized to any arbitrary unstable resonator. Conversely, no stable and confined Gaussian mode can exist—at least not within the restrictions of a paraxial theory—in any resonator having a Gaussian gain minimum or loss maximum on axis.

As one consequence of this, if $\rho(x)$ in the analysis of Section III is a Gaussian mirror-reflectivity profile on a resonator that would otherwise be unstable, one can absorb this Gaussian mirror reflectivity into a complex overall *ABCD* matrix. One will then have an overall stable resonator that can be solved analytically for Gaussian modes without using the formalism of this paper.

As an alternative one can, of course, also handle this same Gaussian mirror case by leaving the Gaussian reflectivity profile in $\rho(x)$ and retaining the unstable *ABCD* matrix to describe the remainder of the resonator. The alternative choice will become essential if the Gaussian reflectivity profile must, as a practical matter, be terminated at some finite diameter where the Gaussian mode amplitude is not yet negligible. As a practical matter, terminating the Gaussian reflectivity profile at a finite diameter in an otherwise unstable resonator may prove to have unexpectedly large diffraction effects on the resulting quasi-Gaussian mode profiles. For example, Campillo *et al.* [21] have shown that in single-pass Fresnel diffraction, aperturing a Gaussian beam at an intensity level $\delta^2 \ll 1$ will

lead to Fresnel-diffraction intensity fluctuations that are as large as $\pm 2\delta$ if the Fresnel number is large compared to unity. Similar effects may be important in truncated-Gaussian resonators having otherwise unstable optics.

Appendix
Formulas for Specific Resonator Designs

In each case R_1 is the radius of curvature of the output mirror and R_2 the radius of curvature of the opposite mirror, both numbers being positive for mirrors concave inward toward the resonator, while $2a_m$ is the diameter (or width) of the output mirror for circular (or strip) resonators.

A. Symmetric Resonator ($R_1 = R_2$), One-Way Pass

$$A = 1 - 2L/R_1 \qquad B = L$$

$$C = -2/R_1 \qquad D = 1$$

$$g = 1 - L/R_1$$

$$M = \begin{cases} g + \sqrt{g^2 - 1}, & \text{(positive branch, } R_1 < 0) \\ g - \sqrt{g^2 - 1}, & \text{(negative branch, } 0 < R_1 < L/2) \end{cases}$$

$$N_c = \frac{Ma_m^2}{B\lambda} \qquad N_{eq} = \frac{M^2 - 1}{2M}\frac{a_m^2}{L\lambda}.$$

B. General Single-Ended Resonator (Full Round Trip)

$$g_1 = 1 - L/R_1 \qquad g_2 = 1 - L/R_2$$

$$A = 4g_1g_2 - 2g_2 - 1 \qquad B = 2g_2L$$

$$C = (2/L)(2g_1g_2 - g_1 - g_2) \qquad D = 2g_2 - 1$$

$$g = 2g_1g_2 - 1$$

$$M = \begin{cases} g + \sqrt{g^2 - 1}, & \text{(positive branch, } g_1g_2 > 1) \\ g - \sqrt{g^2 - 1}, & \text{(negative branch, } g_1g_2 < 0) \end{cases}$$

$$N_c = \frac{Ma_m^2}{B\lambda} \qquad N_{eq} = \frac{M^2 - 1}{2M^2} N_c.$$

C. Positive-Branch Confocal Resonator ($M > 1$)

$$R_1 = [2/(M-1)]\,L \qquad R_2 = [2M/(M-1)]\,L$$

$$A = M \qquad B = [(M+1)/M]\,L$$

$$C = 0 \qquad D = 1/M$$

$$g = (M^2 + 1)/2M \qquad M = M$$

$$N_c = \frac{M^2}{M+1}\frac{a^2}{L\lambda} \qquad N_{eq} = \frac{M-1}{2}\frac{a^2}{L\lambda}.$$

D. Negative-Branch Confocal Resonator ($M < -1$)

$$R_1 = [1/(1-2M)]\,L \qquad R_2 = [2M/(2M-1)]\,L$$

$$A = M \qquad B = L/M$$

$$C = 0 \qquad D = 1/M$$

$$g = (M^2 + 1)/2M \qquad M = M$$

$$N_c = \frac{M^2 a_m^2}{L\lambda} \qquad N_{eq} = \frac{M^2 - 1}{2}\frac{a_m^2}{L\lambda}.$$

Acknowledgment

Much of this work has grown out of consulting activities carried out in collaboration with Dr. E. A. Sziklas of the Florida Research and Development Center, Pratt and Whitney Aircraft, West Palm Beach, FL, as well as with Dr. J. Foster at GTE Sylvania Electro-Optics Organization, Mountain View, CA. Useful discussions were held earlier with Dr. C. Buczek of United Technology Research Laboratories, East Hartford, CT. Finally, the plane-wave equivalent model for the conventional two-mirror unstable resonator has been independently derived by J. F. Perkins and R. A. Shatas at the U.S. Army Missile Command, Redstone Arsenal, AL.

References

[1] A. E. Siegman, "Unstable optical resonators," *Appl. Opt.*, vol. 13, pp. 353–366, Feb. 1974.

[2] R. J. Freiberg, P. P. Chenausky, and C. J. Buczek, "Unidirectional unstable ring resonators," *Appl. Opt.*, vol. 12, pp. 1140–1144, June 1973.

[3] P. dal Pozzo, R. Polloni, O. Svelto, and F. Zaraga, "An unstable ring resonator," *IEEE J. Quantum Electron.*, vol. QE-9, pp. 1061–1063, Nov. 1973.

[4] a) E. A. Maunders, G. L. McAllister, and W. H. Steier, "Experiments on improved unstable mode profiles by aperture shaping," *IEEE J. Quantum Electron.* (Corresp.), vol. QE-10, pp. 821–822, Oct. 1974.
b) G. L. McAllister, W. H. Steier, and W. B. Lacina, "Improved mode properties of unstable resonators with tapered reflectivity mirrors and shaped apertures," *IEEE J. Quantum Electron.*, vol. QE-10, pp. 346–355, Mar. 1974.

[5] C. H. Weysenfeld, "Small dye laser in a semiunstable resonator pumped by an argon-jet guided spark," *Appl. Opt.*, vol. 13, pp. 2816–2822, Dec. 1974.

[6] W. K. Kahn, "Unstable optical resonators," *Appl. Opt.*, vol. 5, pp. 407–413, Mar. 1966.

[7] A. E. Siegman, *An Introduction to Lasers and Masers*. New York: McGraw-Hill, 1971, ch. 8.

[8] W. F. Krupke and W. R. Sooy, "Properties of an unstable confocal resonator CO_2 laser system," *IEEE J. Quantum Electron.*, vol. QE-5, pp. 575–586, Dec. 1969.

[9] P. Baues, "Huygens' principle in inhomogeneous isotropic media and a general integral equation applicable to optical resonators," *Opto-Electron.*, vol. 1, pp. 37–44, 1969.

[10] S. A. Collins, Jr., "Lens-system diffraction integral written in terms of matrix optics," *J. Opt. Soc. Amer.*, vol. 60, pp. 1168–1177, Sept. 1970.

[11] J. A. Arnaud, "Mode coupling in first-order optics," *J. Opt. Soc. Amer.*, vol. 61, pp. 751–758, June 1971.

[12] —, "Hamiltonian theory of beam mode propagation," in *Progress in Optics*, vol. 11, E. Wolf, Ed. New York: Elsevier, 1973.

[13] —, "Nonorthogonal optical waveguides and resonators," *Bell Syst. Tech. J.*, vol. 49, pp. 2311–2348, Nov. 1970.

[14] A. E. Siegman and E. A. Sziklas, "Mode calculations in unstable resonators with flowing saturable gain. II. Fast Fourier transform method," *Appl. Opt.*, vol. 14, pp. 1874–1889, Aug. 1975.

[15] Yu. A. Anan'ev and V. E. Sherstobitov, "Influence of edge effects on the properties of unstable resonators," *Sov. J. Quantum Electron.*, vol. I, pp. 263–267, Nov./Dec. 1971.

[16] G. R. Bisio, L. Ronchi, and V. Tognetti, "Some considerations about the diffraction loss of open resonators," *IEEE Trans. Microwave Theory Tech.* (Corresp.), vol. MTT-19, pp. 490–491, May 1971.

[17] L. W. Casperson, "Mode stability of lasers and periodic optical systems," *IEEE J. Quantum Electron.*, vol. QE-10, pp. 629–634, Sept. 1974.

[18] U. Ganiel and Y. Silberberg, "Stability of optical resonators with an active medium," *Appl. Opt.*, vol. 14, pp. 306–309, Feb. 1975.

[19] A. Yariv and R. Yeh, "Confinement and stability in optical resonators employing mirrors with Gaussian reflectivity tapers," *Opt. Commun.*, vol. 13, pp. 370–371, Apr. 1975.

[20] L. W. Casperson and S. D. Lunnam, "Gaussian modes in high loss laser resonators," *Appl. Opt.*, vol. 14, pp. 1193-1199, May 1975.
[21] A. J. Campillo, J. E. Pearson, S. L. Shapiro, and N. J. Terell, Jr., "Fresnel diffraction effects in the design of high-power laser systems," *Appl. Phys. Lett.*, vol. 23, pp. 85-87, July 1973.
[22] A. G. Fox and T. Li, "Modes in a maser interferometer with curved and tilted mirrors," *Proc. IEEE*, vol. 51, pp. 80-89, Jan. 1963.
[23] J. F. Perkins and R. A. Shatas, "Relationship between propagation in unstable and plane-mirror optical resonators," private communication.

Continuous-Wave CH_3F Waveguide Laser at 496 μm: Theory and Experiment

THOMAS A. DeTEMPLE, MEMBER, IEEE, AND EDWARD J. DANIELEWICZ, STUDENT MEMBER, IEEE

Abstract—**The kinetic processes controlling the conversion of CO_2 pump radiation into far-infrared (FIR) radiation in optically pumped waveguide lasers are discussed. It is found that pump saturation and excited-state FIR absorption play major roles in limiting the conversion. Good agreement between theory and experiment was obtained over a wide range of pump powers, gas pressures, and mirror reflectivities. For a well-optimized system, power-conversion efficiencies of 0.2-0.6 percent can be realistically achieved for CH_3F.**

I. Introduction

THE use of infrared lasers as the excitation source for far-infrared (FIR) lasers is now a demonstrated technique which has resulted in the generation of over 400 discrete spectral lines in the region 100-1000 μm [1]. One curious aspect of these lasers operating CW is that the resulting FIR power is approximately two orders of magnitude smaller than expected from the Manley-Rowe condition. For example, a 500-μm FIR laser pumped by a 10-W CO_2 laser could produce at best 200 mW. In practice, one observes a few milliwatts for this situation.

In this paper we address the specific details of the conversion of the infrared pump into FIR. Previous treatments by Yamanaka *et al.*, Tucker, and Henningsen and Jensen were concerned primarily with the qualitative aspects of the FIR lasers with little attention paid to factors controlling the absolute conversion efficiency [2]-[4]. In contrast, building upon these previous treatments, we present a simple but physically detailed model of the FIR laser which exhibits good quantitative agreement with experiments. In Section II the experimental configuration is discussed; in Section III the theoretical model is developed; and theory and experiment are compared in Section IV.

Manuscript received June 19, 1975; revised August 22, 1975. This work was supported in part by AFOSR Grant 71-1981, in part by NSF Grant ENG 74-23677, and in part by the University of Illinois Industrial Affiliates Program.

The authors are with the Electro-Physics Laboratory, Department of Electrical Engineering, University of Illinois, Urbana, IL 61801.

II. Experiment

In Fig. 1 is shown the experimental configuration under consideration. Central to this discussion is the waveguide FIR laser. Since diffusion has been shown to be an important relaxation process in these lasers, a waveguide as opposed to an open resonator is more desirable because of the smaller mode size and hence higher diffusion rate [3], [5], [6].

The incident pump is focused into the guide through a 1.5-mm-diam hole in the gold-coated flat mirror mounted on a translator. The guide itself is laboratory-grade Pyrex tubing 22 mm ID 120 cm long. Both FIR mirrors are located a few millimeters from the waveguide ends to minimize insertion loss on reflection [7].

Of particular importance is the recently developed FIR output mirror (MMD) [8]. This mirror has the property of reflecting over 98 percent of the infrared pump power while being semitransparent to the FIR. This is accomplished with the use of dielectric films for the infrared reflection and metallic films in the form of grids for the FIR reflection, both deposited on a rigid substrate. By simply changing the grid parameters, the FIR reflectivity may be varied over a wide range.

Pressure was measured with a thermocouple calibrated against a capacitive manometer with the particular gas being studied. The FIR power was measured with a Golay cell cali-

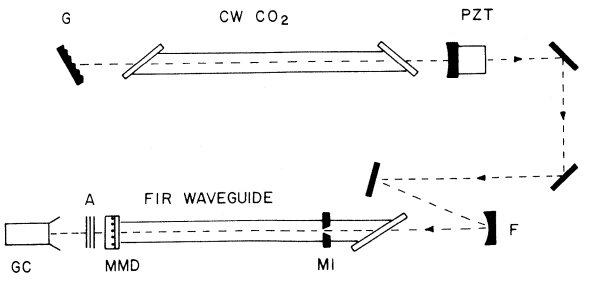


Fig. 1. Diagram of experiment: *G*: grating; PZT: translator; *F*: 30-cm focal-length mirror; *M*1: gold-coated entrance flat mounted on a mechanical translator; GC: Golay cell detector; *A*: attenuators; MMD: hybrid metallic-mesh multilayer dielectric mirror.

brated with an He-Ne laser. Calibrated FIR attenuators were used to extend the dynamic range of the Golay cell.

III. Theory

Of the many molecules and lines which are known to lase in both the conventional open resonator and the waveguide structure, we will be concerned only with the 496-μm transition ($^QR(11,2)$ $\nu_3 v = 1$) in CH_3F, first discussed by Chang, simply because of the availability of spectroscopic and relaxation data [1]. In Fig. 2 are shown the energy levels appropriate to the CH_3F system along with some known collision processes which are thought important. The population density notation used in this text is also indicated. In considering the conversion of infrared pump into FIR output, we must incorporate the various collision processes into the model as well as the passive cavity properties of the waveguide structure. We begin by resolving the problem into three separate areas: namely the determination of 1) the circulating pump power and hence the equivalent excitation rates to the various rotational states, 2) the FIR gain, and 3) the resulting FIR output.

A. Circulating Pump Power

Since the infrared pump is focused into the waveguide and suffers multiple specular reflections off the walls, we assume no radial variation of the pump. This ignores the existence of well-defined transverse-cavity modes in the infrared. Further, we assume that the infrared absorption coefficient is independent of radius and that the pump is not tuned to line center.

In terms of the infrared photon density Φ_I, the equation of evolution is

$$\frac{d\Phi_I}{dt} = \frac{-\eta L - \gamma_I}{t_1}\Phi_I + Z = 0 \tag{1}$$

where L is the cavity length, $t_1 = L/c$, γ_I is the total infrared cavity loss coefficient/pass, and Z is the equivalent volumetric source term due to the external pump given by

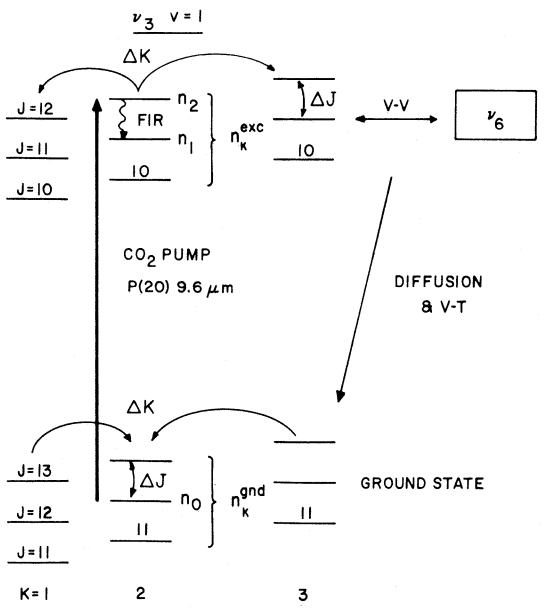


Fig. 2. Energy-level diagram of CH_3F showing various collision processes and level notation used in the text.

$$Z = P_{IR}/(\pi a^2 L \hbar\Omega_{IR})$$

where P_{IR} is the incident power and a is the guide radius [9].

In the low-pressure limit, the absorbing transition is Doppler broadened so that the absorption coefficient η is given by

$$\eta(I) = \frac{\alpha_0 e^{-\Delta^2/\Delta\nu_D^2}}{(1 + I/I_{SAT})^{1/2}} \tag{2}$$

where α_0 is the unsaturated absorption coefficient at line center, Δ is the detuning of the pump from line center, $\Delta\nu_D$ is the infrared Doppler half-width at the e^{-1} point, and I_{SAT} is the saturation intensity. Since the pump is not tuned to line center, the two traveling waves which make up Φ_I burn separate nonover-lapping holes in the Doppler profile so that we can simply write for the solution of (1) and (2) for the forward- and backward-traveling-wave intensities $I_{IR}^{\pm}$ [1]

$$I_{IR}^{+} = I_{IR}^{-} = \frac{1}{2}c\Phi_I = \frac{0.5ZL}{\gamma_I + \eta(I_{IR}^{+})L}. \tag{3}$$

The saturation intensity can be expressed in terms of the collision processes involved and is derived in Appendix I.

B. FIR Gain

We next consider the small-signal gain in the FIR. Due to the standing-wave infrared pump, rotational population is created at two axial velocities symmetric about $v_z = 0$. Competing with the creation of the inversion are ΔJ, ΔK, Δv, ΔM, and $\Delta\nu$ changing collisions. Recent work by Brewer *et al.* and by Oka *et al.* indicate that for high J transitions, ΔM and Δv collisions are weak compared to ΔJ collisions [10].

We assume a hard collision model without separate velocity or M cross relaxation. Setting the excitation source rate due to infrared absorption to be $S = I\eta(I)$, the appropriate bath equations of motion for the rotational populations at the FIR transition assuming rotational relaxation dominance are

$$\dot{n}_2(v_z) = S(v_z) - \Gamma_r n_2(v_z) + \Gamma_r f(v_z)\alpha_2 n_K^{exc}(r)$$
$$- (n_2(v_z) - \frac{g_2}{g_1} n_1(v_z))(\sigma_+ I_{FIR}^{+} + \sigma_- I_{FIR}^{-}) \tag{4a}$$

$$\dot{n}_1(v_z) = -\Gamma_r n_1(v_z) + \Gamma_r f(v_z)\alpha_1 n_K^{exc}(r)$$
$$+ (n_2(v_z) - \frac{g_2}{g_1} n_1(v_z))(\sigma_+ I_{FIR}^{+} + \sigma_- I_{FIR}^{-}) \tag{4b}$$

where the first two terms in (4b) represent rotational relaxation within the velocity distribution of the particular J level with rate Γ_r, α_J is the equilibrium fraction of the Jth rotational level in the $K = 2$ manifold (n_K^{exc}) within the $\nu_3 v = 1$ vibrational state, $f(v_z)$ is the speed distribution function, and the last term represents stimulated emission from the two

[1] Spatial hole burning is important if the mean free path between ΔJ collisions is less than the separation between standing-wave peaks. Thus, if $4\pi v_z/(\Gamma_r\lambda) \gtrsim 1$, we can, to a first approximation, ignore spatial hole burning and use axially averaged intensities. In the infrared the previously stated condition is satisfied for pressures below a few torr, while in the FIR the condition is satisfied below 0.1 torr.

traveling-wave components $I^{\pm}_{FIR}$ of the FIR standing wave. (Unlike the infrared absorption, the two traveling waves may interact with the same set of molecules because the homogeneous linewidth $\Delta\nu_H$ is comparable to the Doppler width for the pressures of interest.) The stimulated-emission cross sections are given by

$$\sigma_{\pm}(v_z, \nu) = \frac{\lambda^2_{FIR} A_{21} \Delta\nu_H}{16\pi^2} \frac{1}{(\nu - \nu_0 \pm \nu_0 v_z/c)^2 + (\Delta\nu_H/2)^2}$$

where ν_0 is the center frequency of the transition and ν is the laser frequency [9].

In (4), the population of the $K = 2$ manifold, n^{exc}_K, is a function of radial position due to the strong diffusion contribution to the relaxation [3], [5]. The inclusion of this population is very important because it leads to FIR absorption in the vibrationally excited state $\nu_3 v = 1$. The equivalent ground-state transition, $^{Q}R(11)v = 0$, is shifted a few gigahertz away and is thus negligible. The analytic expression for n^{exc}_K is derived in Appendix II.

Setting the population inversion to be $\Delta N(v_z) = n_2(v_z) - (g_2/g_1)n_1(v_z)$, the steady-state solution of (4) is found to be

$$\Delta N(v_z) = \frac{S(v_z) + \Gamma_r f(v_z) n^{exc}_K(r)(\alpha_2 - g_2\alpha_1/g_1)}{\Gamma_r + \left(1 + \frac{g_2}{g_1}\right)(\sigma_+ I^+_{FIR} + \sigma_- I^-_{FIR})} \tag{5}$$

which results in a small-signal gain in say the + direction of propagation of

$$g_+(r, \nu) = \int_{-\infty}^{\infty} \sigma_+(v_z, \nu)\, \Delta N(v_z)\, dv_z. \tag{6}$$

Further simplification is possible by considering the velocity smearing of the upper level due to hole burning by the pump. For a pump detuning from line center of Δ and strong saturation, a hole at axial velocity $v^+_z = \lambda_{IR}\Delta$ with a velocity width $2\delta v^+_z = \lambda_{IR}\Delta\nu_H(I_+/I_{SAT} + 1)^{1/2}$ is formed which results in population created in the $J = 12$, $K = 2$ level with the same velocity and velocity width [9]. However, considering the subsequent FIR transition, the frequency offset becomes $\Delta_{FIR} = v^+_z/\lambda_{FIR} = Q_q\Delta$ with a frequency width due to velocity smearing of

$$2\delta v^+_z/\lambda_{FIR} = Q_q\Delta\nu_H(I_+/I_{SAT} + 1)^{1/2} \ll \Delta\nu_H$$

where Q_q is the quantum efficiency of the transition defined to be $\hbar\Omega_{FIR}/\hbar\Omega_{IR} \approx 2$ percent. Hence we can neglect the finite velocity width of the population of the $J = 12$ state created directly by the pump and assume that the pump source terms in (5) can be replaced by δ-functions and written as

$$S(v_z) = \eta(I^+_{IR}) I^+_{IR}[\delta(v_z - v^+_z) + \delta(v_z + v^+_z)]$$

where both forward- and backward-traveling infrared waves are assumed to have the same intensity.

With these simplifications, (6) can be integrated and recast in the following form:

$$g_+(r, \nu) = \frac{\eta(I^+_{IR}) I^+_{IR}[\sigma_+(v^+_z, \nu) + \sigma_-(v^+_z, \nu)]}{\Gamma_r + \left(1 + \frac{g_2}{g_1}\right) I^+_{FIR}(\sigma_+(v^+_z, \nu) + \sigma_-(v^+_z, \nu))} + \frac{\left(\alpha_2 - \frac{g_2}{g_1}\alpha_1\right) n^{exc}_K(r)\, \sigma_D\, W(\nu, B)}{\sqrt{1 + B}} \tag{7}$$

where σ_D is the FIR cross section in the Doppler limit and B is the FIR saturation parameter given by

$$B = \left(1 + \frac{g_2}{g_1}\right) \frac{\lambda^2_{FIR} A_{21}}{4\pi^2 \Gamma_r \Delta\nu_H} I^+_{FIR}.$$

In (7) the function W is given by

$$W = \frac{1}{\pi} \int_{-\infty}^{\infty} \cdot \frac{y(1 + B)^{1/2}\, e^{-t^2}\, dt}{(x - t)^2 + y^2(1 + B) + By^2[(x - t)^2 + y^2]/[(x + t)^2 + y^2]}$$

with

$$x = \nu/\Delta\nu_{D,\,FIR}$$

$$t = 2\pi v_z/(\lambda_{FIR}\Delta\nu_{D,\,FIR})$$

$$y = \Delta\nu_H/2\Delta\nu_{D,\,FIR}$$

and $\Delta\nu_{D,\,FIR}$ is the half-width at the e^{-1} point of the FIR Doppler profile.

Although complicated, (7) has a simple physical interpretation. The first term is identified as the gain due to the two homogeneously broadened, overlapping (in frequency) velocity groups excited by the infrared standing-wave pump. The second term is simply the absorption due to the equilibrated excited-state population which is mixed broadened. The integral W expresses the mixed broadening, including saturation and power broadening by both FIR traveling waves. In the limit as $B \to 0$, W reduces to the usual expression of mixed broadening [9].

C. FIR Power

From the measured transverse-intensity variation of the FIR output using the hybrid output mirror, it was found that the EH_{11} mode was dominant [8]. We can thus express the FIR circulating intensity in terms of the mode profile and the total number ξ of FIR quanta in the cavity as

$$I^+_{FIR} = I^-_{FIR} = \frac{1}{2} \frac{c\xi J^2_0(u_1 r/a)}{\pi a^2 L J^2_1(u_1)}$$

where u_1 is the first zero of the Bessel function J_0 [11].[1] The FIR threshold gain is simply

$$g_{th} = (\gamma_{FIR} - \tfrac{1}{2} \ln R)/L$$

where R is the output mirror reflectivity and γ_{FIR} is the remaining FIR cavity loss coefficient per pass [9]. We solve for ξ subject to the constraint that the gain averaged over the

TABLE I
CH_3F WAVEGUIDE LASER PARAMETERS

α_2	.0528	
α_1	.0544	
α_K	.11	
α_V	.25	
Γ_r	1.3×10^{8}	$SEC^{-1}TORR^{-1}$
Γ_K	1.2×10^{7}	$SEC^{-1}TORR^{-1}$
Γ_v	1.2×10^{5}	$SEC^{-1}TORR^{-1}$
Γ_{vt}	600	$SEC^{-1}TORR^{-1}$
D	85	$CM^2TORR\,SEC^{-1}$
α_0	.047	$CM^{-1}TORR^{-1}$
σ_D	$3.4\times10^{-13}CM^2$	a
σ_{FIR}	7.4×10^{-15} CM^2TORR	a
σ_{IR}	2.4×10^{-16} CM^2TORR	
$\Delta\nu_H$	40	$MHZ\,TORR^{-1}$
γ_{IR}	.2 / PASS	
γ_{FIR}	.114 / PASS	

[a]Random spatial orientation.

mode profile is at the threshold value. Thus we require

$$g_{th} = \frac{2}{a^2}\int_0^a \frac{J_0^2(u_1 r/a)\, g_+(r,\nu)}{J_1^2(u_1)}\, rdr \tag{8}$$

with the small-signal gain g_+ given by (7). The output power is then given by [9]

$$P_{out} = -\tfrac{1}{2}\ln(R)\, c\hbar\Omega_{FIR}\xi/L. \tag{9}$$

IV. Comparison Between Theory and Experiment

The set of (2), (3), (7)–(9), (13), and (14) which comprise the model were solved using parameters appropriate to CH_3F and our cavity. The FIR cavity loss γ_{FIR} was calculated from the guide loss data of Marcatili and Schmeltzer with an added 2-percent/pass loss to account for guide irregularities and mirror losses [11]. The infrared cavity loss γ_I was estimated from a measured guide transmission of 80 percent. The fractional population constants α_2, α_1, and the FIR Einstein coefficient A_{21} were calculated using the spectroscopic constants of CH_3F [12], [13]. The homogeneous linewidth was estimated from the data of Murphy and Boggs [14]. The homogeneous infrared cross section was extracted from the unsaturated absorption measurement of Chang using the CO_2 line location (−44 MHz below $^{Q}Q(12,2)$) of Freund *et al.* [12], and Chang *et al.* [15]. We have estimated that the pump is tuned ~+10 MHz when the system is optimized, which places the pump −35 MHz off the $^{Q}Q(12,2)$ absorption. Absorption by $^{Q}Q(12,1)$ is small, typically <20 percent of the total. The rotational relaxation rate was found from the homogeneous linewidth while the VV, VT, and diffusion rates were taken from the work of Weitz and Flynn [16]. The K-K collision rate was estimated to be gas kinetic [17]. In comparing theory with experiment, we found it convenient to introduce an adjustable parameter multiplier to the FIR homogeneous cross section (or divisor of Γ_r), which had

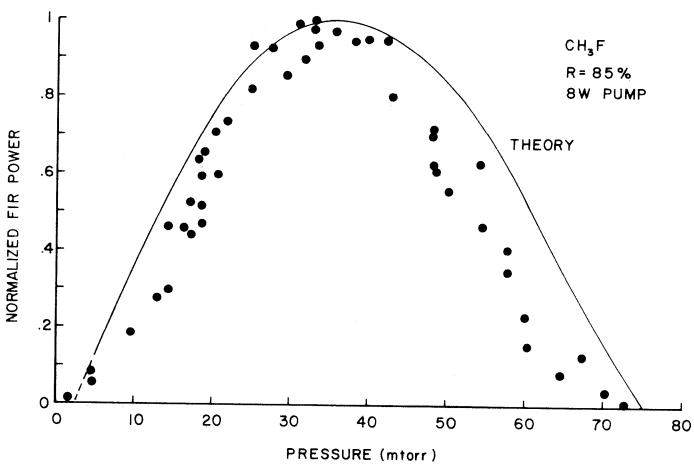


Fig. 3. Normalized FIR output power versus pressure for fixed pump power.

a value of 2 obtained by trial and error. This parameter presumably reflects the uncertainties of the various cavity parameters, the details of the ΔJ and ΔK relaxation processes, and the effect of an oriented population inversion including pump depolarization [1].[2] The pertinent parameters used are listed in Table I.

In Fig. 3 is shown the comparison between the measured and calculated output versus pressure. The scatter, which reflects measurement uncertainties and pump fluctuations, is typical of measurements with these unstabilized systems. The overall behavior of this curve can be understood with the aid of Figs. 4 and 5. The gain profile of Fig. 4 clearly shows the contribution due to the two velocity groups and that due to the

[2]There appear to be well-defined selection rules for ΔJ- and ΔK-type collisions which are not incorporated into our bath model. See [17] and T. Oka, "Collision-induced transitions between rotational levels," *Advan. At. Mol. Phys.*, vol. 9, pp. 127–206, 1973.

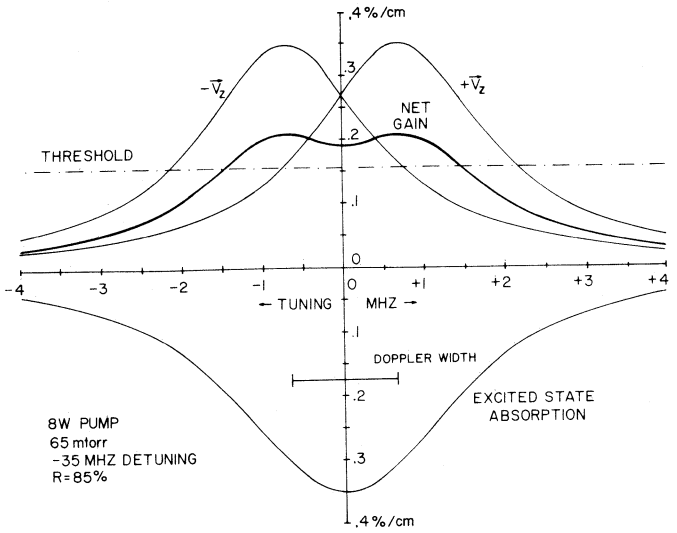


Fig. 4. Calculated net small-signal gain profile at $r = 0$ for the $^{Q}R(11,2)$ transition.

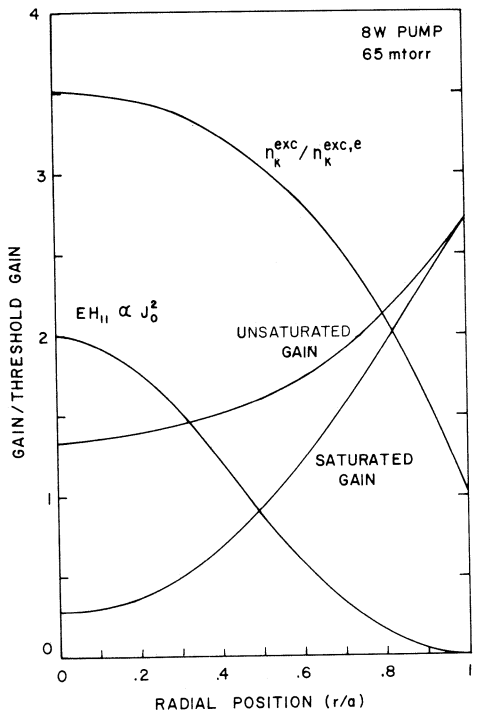


Fig. 5. Radial variation of the FIR mode, saturated and unsaturated gain, and the $K = 2$ excited-state manifold.

equilibrated excited-state population. The radial variation of the excited-state $K = 2$ manifold is exhibited in Fig. 5. As the pressure is reduced, diffusion is faster, which tends to reduce the excited-state absorption and hence increase the gain. Furthermore, the homogeneous cross section is increased which increases the gain contribution of each velocity group, further increasing the gain. At low pressure, the gain is very large so that to a good approximation the output is proportional to the absorbed infrared power. Thus the increased output with pressure in Fig. 3 simply reflects the increased infrared absorption, while the decreasing output with pressure reflects the effects of excited-state absorption, line broadening, and rotational relaxation. At the optimum pressure, less than 20 percent of the pump is actually absorbed by the gas with the rest dissipated in wall losses.

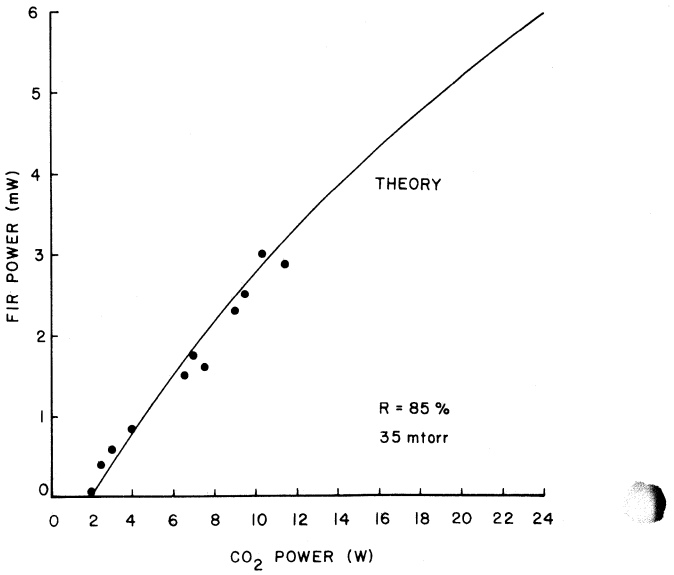


Fig. 6. FIR output power versus CO_2 input power at constant pressure.

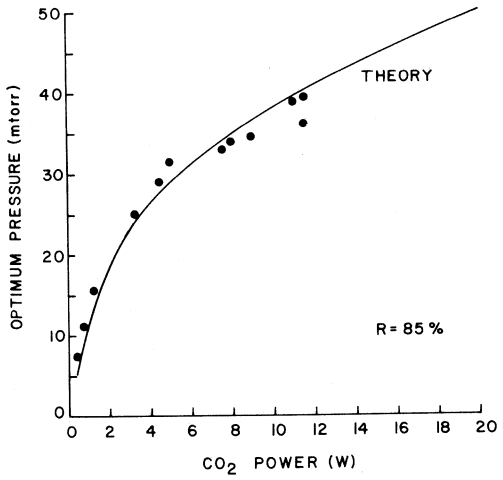


Fig. 7. Optimum pressure versus CO_2 power.

Returning to Fig. 5, also shown is the calculated radial variation of the gain with and without the FIR oscillating. In both cases a strong radial variation does exist which qualifies as a lens. The degree of waveguide mode distortion due to lensing is not known.

The central dip, evident in Fig. 4, might provide a convenient point for frequency stabilization. Cavity scans of this laser have not revealed the manifestation of the dip on output power. This might be due to strong power broadening reducing the effect of the dip or to the existence of infrared longitudinal-cavity resonances causing strong modulation of the FIR output versus cavity length [8].

In Figs. 6 and 7 are shown a comparison between theory and experiment for the optimum pressure and the output power versus pump power. Above a few watts, both the FIR output and the optimum pressure are approximately linear with pump power. However, for very strong pumps, the output becomes

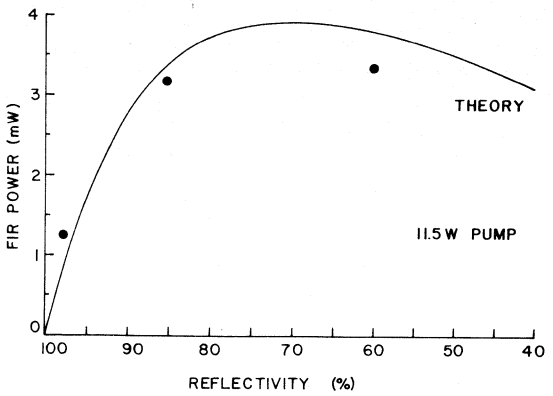


Fig. 8. Output power versus output reflectivity at fixed CO_2 power. All data at optimum pressure which is $\propto R$.

proportional to $P_{IR}^{1/2}$ due to a large saturation of the absorption.

In Fig. 8 is shown the FIR output at the optimum pressure versus output mirror reflectivity. These data indicate that the FIR laser does indeed have a very large gain, typically $\sim 0.5\ m^{-1}$, thus allowing considerable freedom in resonator configuration. The data also show that one reason for the low conversion efficiencies observed with simple hole-coupled optics lies in the fact that the equivalent reflectivity of >98 percent is far from the optimum value.

In view of the approximations employed and the uncertainties in the values of the parameters used, the overall agreement between theory and experiment is quite satisfactory. In practice, we have found that a change in a parameter which results in an increased net FIR gain shifts the theoretical curve of Fig. 3 to higher pressures. When this shift is corrected for by changing another parameter, which reduces the net gain such that the data of Fig. 3 are matched, the data of Figs. 6-8 are automatically matched by theory to within 25 percent. This gave us confidence that the important processes had been included and that the parameters listed in Table I, which form a self-consistent set, were close to reality.

V. Conclusion

Returning to Fig. 8, using the 60-percent-reflectivity mirror we calculate that because of the strong pump saturation ($I_{IR}^{+}/I_{SAT} \sim 4$) only 16 percent of the pump is absorbed. Full conversion of this pump would result in $11.5 \times 0.16 \times Q_q/(1 + g_2/g_1) = 18$-mW FIR power. The cavity efficiency ($-0.5 \ln R/(\gamma_{FIR} - 0.5 \ln R)$) is 70 percent, resulting in a maximum output of 12.5 mW. The difference between this value and the final value of ~4 mW is attributed to the radial variation of the FIR mode, excited-state absorption, and the threshold requirement.

Hence we identify weak infrared absorption, pump saturation, and excited-state FIR absorption as being the dominant processes limiting the efficient conversion of infrared into FIR in this laser. The mutually incompatible requirements of large infrared absorption (high pressure), weak saturation (high pressure, small radius), small excited-state absorption (low pressure, small radius), and a low FIR guide loss (large radius) can be partially met in small-diameter metallic guides which have a much lower FIR attentuation [6], [11]. There are a number of higher order TE waveguide modes which have losses <2 percent/m in metallic guides. Although it is not known which mode will dominate, we have performed calculations on a 5-mm-diam metallic guide assuming a guide loss of 1 percent/m and assuming, for simplicity, an EH_{11}-mode profile. The results of these calculations indicate that the optimum pressure is indeed increased to ~130 mtorr and that a 10-W pump will be 50 percent absorbed by the gas, assuming the same infrared guide loss as for the dielectric waveguide. Of the absorbed quanta, 25 percent are converted into useful output. Hence we anticipate that an overall conversion efficiency of between 0.2-0.6 percent, depending specifically on the infrared guide loss and the FIR mode structure, should be realistically obtainable from CH_3F in metallic waveguides. A 10-W pump would thus produce between 20-60 mW at 496 μm.

Appendix I

It is well known that rotational relaxation, VT, and diffusion all contribute to the saturation intensity of a molecular transition [18]. For the particular case of CH_3F we have the added feature of ΔK collisions which need to be incorporated. The equations of evolution of the various populations are simply

$$\dot{n}_2 = -\sigma_{IR} I_{IR}(n_2 - g_2 n_0/g_0) - \Gamma_{r2} n_2 + \alpha_2 \Gamma_{r2} n_K^{exc} - \Gamma(n_2 - n_2^e) \quad (10a)$$

$$\dot{n}_0 = \sigma_{IR} I_{IR}(n_2 - g_2 n_0/g_0) - \Gamma_r n_0 + \alpha_0 \Gamma_r n_K^{gnd} - \Gamma(n_0 - n_0^e) \quad (10b)$$

$$\dot{n}_K^{exc} = -\sigma_{IR} I_{IR}(n_2 - g_2 n_0/g_0) - \Gamma_K n_K^{exc} + \Gamma_K \alpha_K N^{exc} - \Gamma(n_K^{exc} - n_K^{exc,e}) \quad (11a)$$

$$\dot{n}_K^{gnd} = \sigma_{IR} I_{IR}(n_2 - g_2 n_0/g_0) - \Gamma_K n_K^{gnd} + \Gamma_K \alpha_K N^{gnd} - \Gamma(n_K^{gnd} - n_K^{gnd,e}) \quad (11b)$$

$$\dot{N}^{exc} = \Gamma_K n_K^{exc} - \Gamma_K \alpha_K N^{exc} - \Gamma(N^{exc} - N^{exc,e}) \quad (12a)$$

$$\dot{N}^{gnd} = \Gamma_K n_K^{gnd} - \Gamma_K \alpha_K N^{gnd} - \Gamma(N^{gnd} - N^{gnd,e}). \quad (12b)$$

In these equations, σ_{IR} is the homogeneous cross section, n_K^i are the populations of the $K = 2$ manifold in the ground and excited vibrational states, N^i are the remaining total populations in the ground and excited vibrational states, and the superscript e denotes the thermal equilibrium value. α_K is the equilibrium fraction of the $K = 2$ manifold within the particular vibrational state, and Γ_K and Γ are the ΔK and VT plus diffusion rates, respectively. For simplicity, the VV process has been ignored.

Solving these equations for the saturation intensity, we find

$$I_{SAT} = \frac{\hbar \Omega_{IR}(\Gamma_r + \Gamma)\Gamma(\Gamma_K + \alpha_K \Gamma_K + \Gamma)}{2\sigma_{IR}[m\Gamma(\Gamma_K + \alpha_K \Gamma_K + \Gamma) + \alpha_{J2}\Gamma_r(\alpha_K \Gamma_K + \Gamma)]}. \quad (13)$$

The existence of a saturating FIR field depleting the population of n_2 can be estimated by setting $\Gamma_{r2} \to \infty$ in (10a). This will clamp the population at the equilibrium value resulting in

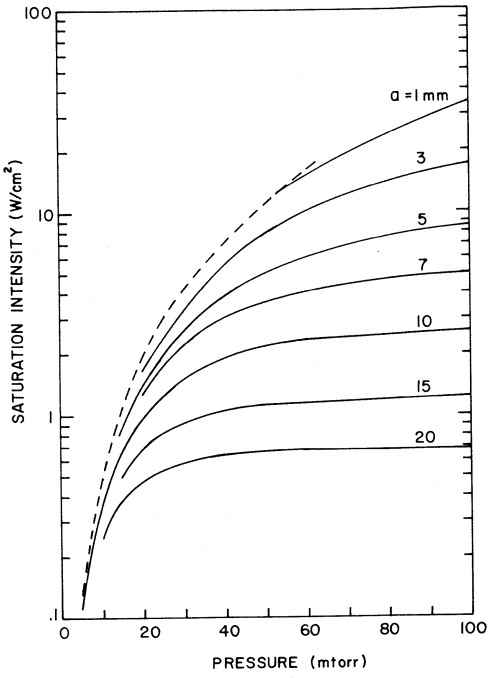


Fig. 9. Calculated saturation intensity for the $^{Q}Q(12,2)$ pump transition versus pressure with guide radius as a parameter. Calculations are not valid to the left of the dotted line – see text.

an m value of $\frac{1}{2}$ in (13). The usual case of $\Gamma_{r2} = \Gamma_r$ results in $m = 1$. The FIR contribution to the saturation intensity is a small correction resulting in an increase of <30 percent at low pressures <30 mtorr. The saturation intensity as a function of pressure with the radius a as a parameter is shown in Fig. 9 for the $^{Q}Q(12,2)$ transition ($m = 1$).[3] I_{SAT} for other K transitions can be found by noting that $I_{SAT}^{-1} \propto \sigma_{IR} \propto A_{IR} \propto K^2$ [13]. Hence the $K = 1$ transition, $^{Q}Q(12,1)$, has four times the saturation intensity but $\frac{1}{4}$ the line-center absorption as the $K = 2$ transition.

The previously stated calculation is valid, assuming no radial variation in the infrared absorption. This will be approximately true if the vibrational levels are only weakly populated. For our geometry, full infrared absorption would increase the population of the vibrational levels a factor of 10 above the thermal value which thus reduces the ground-state population by 10 percent. Hence $N^{gnd} \approx$ constant.

Appendix II

We now seek the radial dependence of the $K = 2$ manifold under the influence of ΔK, VV, VT, and diffusion. This simply entails adding terms of the form $D\nabla^2 N$ to (11) and (12) and introducing VV coupling to the ν_6 mode of CH_3F into (12) [16], [18]. Wall collisions are assumed to fully quench all levels. Defining the total excitation rate due to the infrared absorption to be $S = \eta(I_{IR}^{+})I_{IR}^{+} + \eta(I_{IR}^{-})I_{IR}^{-}$ we find that $n_K(r)$ is expressed in terms of modified Bessel functions as

$$n_K(r) = \frac{S(1-\alpha_K)}{\Gamma_K}\left[1 - \frac{I_0(\beta_K r)}{I_0(\beta_K a)}\right] + \frac{S\alpha_K(1-\alpha_v)}{\Gamma_v} \cdot \left[1 - \frac{I_0(\beta_w r)}{I_0(\beta_w a)}\right] + S\frac{\alpha_K\alpha_v}{\Gamma_{vt}}\left[1 - \frac{I_0(\beta_{vt} r)}{I_0(\beta_{vt} a)}\right] + n_K^e \quad (14)$$

where $\beta_K^2 = \Gamma_K/D$, $\beta_w^2 = \Gamma_v/D$, $\beta_{vt}^2 = \Gamma_{vt}/D$, Γ_v is the VV coupling rate, and α_v is the equilibrium fraction of the $\nu_3 + \nu_6$ coupled modes associated with the $\nu_3 v = 1$ level. Equation (14) describes the population for any pressure assuming only uniform excitation. For example, the VT limit can be found by noting that $\Gamma_K \gg \Gamma_{vv} \gg \Gamma_{vt} \gg D$ so for $r < a$, $n_K(r) \approx \alpha_K\alpha_v S/\Gamma_{vt} + n_K^e$, as expected. In the full diffusion limit $D \gg \Gamma_K$, so (13) reduces to

$$n_K(r) = \frac{Sa^2}{4D}(1 - r^2/a^2) + n_K^e$$

from which we deduce an effective relaxation rate due to diffusion of $\Gamma_{DIF} = 4D/a^2$. In practice, the latter limit is not reached because Γ_K is of the order of gas kinetic so that at least one hard collision must take place in order to have diffusion as opposed to molecular free flow [17]. The condition where $\Gamma_{DIF} = \Gamma_K$ is shown as the dotted line in Fig. 9, and $\Gamma_{DIF} \geqslant \Gamma_K$ is shown as the dotted extension of Fig. 3.

The major effect of incorporating ΔK and Δv processes is that at low pressures insufficient collision time exists for the distribution of excited-state population into the other K and v states. This is equivalent to a "bottleneck" which manifests itself as absorption.

Acknowledgment

The authors wish to thank T. Y. Chang, P. D. Coleman, G. W. Flynn, D. T. Hodges, T. Oka, T. K. Plant, R. Shoemaker, and J. Tucker for their helpful communications.

References

[1] T. Y. Chang, "Optically pumped submillimeter-wave sources," *IEEE Trans. Microwave Theory Tech. (Part I of Two Parts: Special Issue on the Proc. 1st Int. Conf. Submillimeter Waves and Their Applications)*, vol. MTT-22, pp. 983–988, Dec. 1974.

[2] a) M. Yamanaka and H. Yoshinaga, "Compact waveguide lasers in the submillimeter and millimeter wave regions," presented at the Int. Conf. Submillimeter Waves and Their Applications, Atlanta, GA, June 1974, Paper III-4.
b) M. Yamanaka *et al.*, "On the transverse mode in an optically pumped far-infrared NH_3 laser," *Japan. J. Appl. Phys.*, vol. 13, pp. 843–850, 1974.

[3] J. R. Tucker, "Theory of a FIR gas laser," presented at the Int. Conf. Submillimeter Waves and Their Applications, Atlanta, GA, June 1974, Paper I-3.

[4] J. O. Henningsen and H. G. Jensen, "The optically pumped far-infrared laser: Rate equations and diagnostic experiments," *IEEE J. Quantum Electron.*, vol. QE-11, pp. 248–252, June 1975.

[5] D. T. Hodges and T. S. Hartwick, "FIR waveguide laser performance in the 40 μm-1mm spectral region," presented at the Int. Conf. Submillimeter Waves and Their Applications, Atlanta, GA, June 1974, Paper IX-2.

[6] —, "Waveguide laser for the far infrared (FIR) pumped by a CO_2 laser," *Appl. Phys. Lett.*, vol. 23, pp. 252–253, 1973.

[7] R. L. Abrams, "Coupling losses in hollow waveguide laser resonators," *IEEE J. Quantum Electron.*, vol. QE-8, pp. 838–843, Nov. 1972.

[8] E. J. Danielewicz, T. K. Plant, and T. A. DeTemple, "Hybrid output mirror for optically pumped far infrared lasers," *Opt. Commun.*, vol. 13, pp. 366–369, 1975.

[9] A. Yariv, *Quantum Electronics*, 2nd ed. New York: Wiley-

[3] Preliminary measurements by D. T. Hodges (private communication) at small radii (~1 mm) agree to within a factor of 2 with these calculations.

Interscience, 1975, chs. 8, 9, 11, and 12.
[10] a) R. L. Shoemaker, S. Stenholm, and R. G. Brewer, "Collision-induced optical double resonance," *Phys. Rev. A*, vol. 10, pp. 2037–2050, 1974.
b) J. W. C. Johns, A. R. W. McKellar, T. Oka, and M. Römheld, "Collision induced Lamb dips in laser Stark spectroscopy," *J. Chem. Phys.*, vol. 62, pp. 1488–1496, 1975.
[11] E. A. J. Marcatili and R. A. Schmeltzer, "Hollow metallic and dielectric waveguides for long distance optical transmission and lasers," *Bell Syst. Tech. J.*, vol. 43, pp. 1783–1809, 1964.
[12] S. M. Freund, G. Duxbury, M. Römheld, J. T. Tiedje, and T. Oka, "Laser Stark spectroscopy in the 10 μm region: The ν_3 bands on CH_3F," *J. Mol. Spectrosc.*, vol. 52, pp. 38–57, 1974.
[13] C. H. Townes and A. L. Schawlow, *Microwave Spectroscopy*. New York: McGraw-Hill, 1955, ch. 3.
[14] T. S. Murphy and J. E. Boggs, "Collision broadening of rotational lines II. Self-broadening of symmetric top molecules," *J. Chem. Phys.*, vol. 47, pp. 4152–4158, 1967.
[15] T. Y. Chang, C. H. Wang, and P. K. Cheo, "Passive Q-switching of the CO_2 laser by CH_3F and PF_5 gases," *Appl. Phys. Lett.*, vol. 15, pp. 157–159, 1969.
[16] E. Weitz and G. W. Flynn, "Partial vibrational energy transfer map for CH_3F: A laser fluorescence study," *J. Chem. Phys.*, vol. 58, pp. 2781–2793, 1973.
[17] L. Frenkel, H. Marantz, and T. Sullivan, "Spectroscopy and collisional transfer in CH_3Cl by microwave-laser double resonance," *Phys. Rev. A*, vol. 3, pp. 1640–1651, 1971.
[18] C. P. Christensen, C. Freed, and H. A. Haus, "Gain saturation and diffusion in CO_2 lasers," *IEEE J. Quantum Electron.*, vol. QE-5, pp. 276–284, June 1969.

Analysis of Intensity Fluctuations in a Junction Laser with Low Quantum-Efficiency Regions

SEIJI MUKAI AND SHUN-ICHI GONDA

Abstract—**Fluctuation spectra due to quantum shot noise in the output from a junction laser are calculated using rate equations for a nonuniform double-sectioned laser with a low quantum-efficiency region. The pumping-rate dependence of the fluctuation spectra for the nonuniform model is found to be roughly the same as that for the ordinary uniform model. The degradation process is then simulated using the uniform and nonuniform models, and it is shown that qualitatively opposite changes, decay or growth of resonance phenomena, are expected in the fluctuations as the degradation proceeds uniformly or nonuniformly.**

I. Introduction

TWO TYPES of fluctuation in the microwave region have been reported, and thoroughly discussed, in the output intensity from junction lasers. One type is characterized by its large amplitude and regular periodicity of oscillation [1]-[4]. Repetitive Q switching [5] and second-order mode locking [6] are mainly proposed to explain this type of oscillation. For a Q-switched mechanism to exist the laser must contain a saturable absorbing as well as an amplifying region. The absorber is usually thought to appear due to nonuniform pumping, as in the case of the model calculated based on a double-sectioned laser.

The other type of fluctuation arises from the response of a dynamically interacting electron-photon system to the quantum shot noise. In general, the amplitude is relatively small and the periodicity is incomplete in this case. The noise spectrum for this type was first calculated by McCumber for a four-level laser system and has been shown to have a resonance peak in the gigahertz region [7]. Similar calculations have been made for GaAs lasers, and the dependence of the fluctuations on the temperature and injection current has been discussed [8], [9]. Experimentally, Paoli and Ripper [10] first observed the fluctuations caused by quantum shot noise from GaAs lasers operated continuously at 80 K and found that the results are in good agreement with previous calculations. Furthermore, Paoli [11] has investigated the intensity fluctuations at 300 K.

What behavior do the intensity fluctuations show as the degradation proceeds in junction lasers? Yang *et al.* [12] have reported that microwave oscillations occur in the output of a laser after a long-term operation, and they have pointed out that the result might be explained by the Q-switched model due to the appearance of locally degraded regions in a laser cavity. On the other hand, the present authors [13] have observed a decrease of the peak height in the spectra of the intensity fluctuations after a long-term operation. They have also shown that the result can be qualitatively explained by taking into account a uniform decrease of the quantum efficiency in a cavity in the quantum shot-noise model [14].

The internal changes which take place in a laser as the degradation proceeds are to be reflected in these two types of changes in the behavior of the fluctuations. An internal change of importance is the local appearance of low quantum-efficiency regions called "dark lines" [15]. It has been shown that the dark lines are mainly responsible for the degradation-induced changes in fundamental laser characteristics such as an increase of the threshold current and a decrease of differential quantum efficiency [16]. In this paper, the intensity fluctuations due to quantum shot noise in the output from a junction

Manuscript received June 25, 1975; revised August 11, 1975.
The authors are with the Electrotechnical Laboratory, Tanashi Branch, Tokyo, Japan.

laser are calculated using rate equations for a double-sectioned laser model with a low quantum-efficiency region, and the effect of the coexistence of the absorbing region and amplifying region in a degraded laser cavity on the quantum fluctuation spectra is discussed by comparison of the fluctuations of the nonuniform laser model with those of the uniform model [9], [14].

II. Rate Equations

The double-sectioned laser, which is the basic model of the following calculations, consists of two sections, 1 and 2, with volume V_1 and V_2 and internal quantum efficiency η_1 and η_2. It is assumed that electrons are distributed uniformly in each section, that electrons do not flow from one section into another, and that the photon distribution is uniform throughout the whole cavity. The last assumption is correct when the round-trip time of photons in a laser is sufficiently shorter than the period of the fluctuations concerned. When η_1 and η_2 differ from each other, the model is expected to represent the most simple case of degradation processes; i.e., the lower efficiency section corresponds to the degraded region in this case. It should be mentioned that neither normal nor degraded regions in an actual laser need to consist of only one spatial portion as sections 1 and 2 in the present double-sectioned laser. What is meant by "nonuniform model" in the following is that there are at least two kinds of regions with different electron densities in a laser cavity, and has nothing to do with the spatial distribution of each region. In an actual laser, relaxation of electron distribution may occur between degraded and undegraded regions, but, for simplicity, the relaxation process is neglected in the present model.

The rate equations with shot-noise terms are obtained for the photon number N_p, and the electron number in the section i, N_{ei}, in a nonuniform (double-sectioned) junction laser, by modifying rate equations for electron and photon numbers in a uniform laser [9].

$$\frac{dN_p}{dt} = N_p\left(R_{st1} + R_{st2} - \frac{1}{\tau}\right) + R_{sp1} + R_{sp2} + F_p(t) \qquad (1)$$

$$\frac{dN_{ei}}{dt} = P_i - R^T_{spi} - N_p R_{sti} + F_{ei}(t), \quad (i = 1, 2) \qquad (2)$$

where the subscript i takes values 1 and 2 and indicates the section to which each quantity is related. Here $N_p R_{sti}$ represents the stimulated-emission rate into the laser mode, τ is the photon lifetime, R_{sp} is the spontaneous-emission rate into the laser mode, and R^T_{sp} is the total spontaneous-emission rate into all modes. The pumping rate P_i is taken as $P(V_i/V)$, where P and V are the total pumping rate and the total volume, respectively. The photon and electron fluctuation operators $F_p(t)$ and $F_{ei}(t)$ are assumed to have shot-noise characters with the following average values [8]:

$$\langle F_p(t)\rangle = \langle F_{ei}(t)\rangle = 0$$

$$\langle F_p(t)F_p(s)\rangle = \delta(t-s)\,2(\bar{N}_p + 1)\,(\bar{R}_{sp1} + \bar{R}_{sp2})$$

$$\langle F_{ei}(t)F_{ej}(s)\rangle = \delta(t-s)\delta_{ij}\,2(\bar{R}^T_{spi} + \bar{N}_p\bar{R}_{spi})$$

$$\langle F_p(t)F_{ei}(s)\rangle = \delta(t-s)\,\{-\bar{N}_p(2\bar{R}_{spi} - \bar{R}_{sti}) - \bar{R}_{spi}\}$$

where the bracket $\langle\ \rangle$ means time-average values and the bars over the quantities indicate that they satisfy the time average of (1) and (2).

Using the linearization procedure explained in detail by Morgan and Adams [9], the following equations are obtained for the small fluctuations about the mean values:

$$\frac{d}{dt}\Delta N_p = A_{pp}\,\Delta N_p + A_{p1}\,\Delta N_{e1} + A_{p2}\,\Delta N_{e2} + F_p(t) \qquad (3)$$

$$\frac{d}{dt}\Delta N_{ei} = A_{ip}\,\Delta N_p + A_{ii}\,\Delta N_{ei} + F_{ei}(t), \quad (i = 1, 2) \qquad (4)$$

where

$$A_{pp} = \bar{R}_{st1} + \bar{R}_{st2} - 1/\tau$$

$$A_{pi} = \bar{N}_p\frac{d\bar{R}_{sti}}{dN_{ei}} + \frac{d\bar{R}_{spi}}{dN_{ei}}$$

$$A_{ip} = -\bar{R}_{sti}$$

$$A_{ii} = -\frac{d\bar{R}^T_{spi}}{dN_{ei}} - \bar{N}_p\frac{d\bar{R}_{sti}}{dN_{ei}}.$$

The photon-noise power spectrum

$$S(\omega) \equiv \int_{-\infty}^{+\infty} d\tau\,\langle N_p(t)\,N_p(t+\tau)\rangle \exp(i\omega\tau)$$

is obtained from the Fourier transforms of (3) and (4); that is,

$$S(\omega) = \frac{C_{pp}F_{pp} + C_{11}F_{11} + C_{22}F_{22} + C_{p1}F_{p1} + C_{p2}F_{p2}}{\omega^2(\omega^2 - A)^2 + (B - C\omega^2)^2} \qquad (5)$$

where

$$A = A_{11}A_{pp} + A_{22}A_{pp} + A_{11}A_{22} - (A_{p1}A_{1p} + A_{p2}A_{2p})$$

$$B = A_{pp}A_{11}A_{22} - A_{p1}A_{1p}A_{22} - A_{p2}A_{2p}A_{11}$$

$$C = A_{pp} + A_{11} + A_{22}$$

$$C_{pp} = (A^2_{11} + \omega^2)\,(A^2_{22} + \omega^2)$$

$$C_{ii} = (A_{pi}A_{jj})^2 + \omega^2 A^2_{pj}, \quad (i \neq j)$$

$$C_{pi} = -2A_{ii}A_{pj}, \quad (i \neq j)$$

$$F_{pp} = 2(\bar{N}_p + 1)\,(\bar{R}_{sp1} + \bar{R}_{sp2})$$

$$F_{ii} = 2(\bar{R}^T_{spi} + N_p\bar{R}_{spi})$$

$$F_{pi} = -\bar{N}_p(2R_{spi} - R_{sti}) - \bar{R}_{spi}.$$

III. Calculations and Results

Calculations have been made for the case of CW operation at room temperature, assuming parabolic bands and no k-selection rule in GaAs. Relevant expressions for the transition rates in (1) and (2) with these assumptions are [17]

$$R_{sti}(N_{ei}) = G_1(T)\,[G_{2i}(T)N_{ei} - 1]^3\left(\frac{V_i}{V}\right) \qquad (6)$$

$$R_{spi}(N_{ei}) = R_{sti}(N_{ei})\,[1 - \exp\{0.85\,(1 - G_{2i}(T)N_{ei})\}]^{-1} \qquad (7)$$

$$R_{spi}^{T}(N_{ei}) = \frac{B}{\eta_i V_i}\left(\frac{m_v}{m_c}\right)^{3/2} N_{ei}^2 \tag{8}$$

where

$$G_1(T) = 0.152\,\frac{B(m_c m_v)^{3/2}\,(kT)^2}{\Phi\pi^3\hbar^6}$$

$$G_{2i}(T) = \frac{5.08}{V_i}\left(\frac{\pi\hbar^2}{2m_c kT}\right)^{3/2} \quad \text{for } i = 1,2$$

$$V = V_1 + V_2 .$$

In these expressions B is the rate coefficient containing the matrix element for lasing transitions, m_c and m_v are the electron masses in the conduction and valence band, k is Boltzmann's constant, T is the absolute temperature in the active region, and Φ is the number of modes per unit energy per unit volume.

The values of the parameters are the same as those given in [9] except τ, η_1, and η_2. Here τ is 10^{-12} s and several values are used for η_1 and η_2. Using these values the fluctuations are calculated as follows. A series of pumping-rate values P are substituted into the mean stationary forms of (1) and (2) along with expressions (6)-(8). The equations are then solved for $\bar{N}_p$, $\bar{N}_{ei}$, and $\bar{N}_{e2}$. A typical example of the calculated results of $\bar{N}_p$ versus P is shown in Fig. 1. In order to calculate $S(\omega)$, the value of the threshold current is obtained, in the first place, as a point of intersection of the extrapolated straight line of $\bar{N}_p$ above threshold with the axis of abscissa $\bar{N}_p = 0$. In the next place, pumping rate P is calculated from a given value of normalized pumping rate P_N and then by the same procedure as previously stated $\bar{N}_p$, $\bar{N}_{ei}$, and $\bar{N}_{e2}$ are obtained for this pumping level. Using these values, fluctuations $S(\omega)$ are calculated from (5) for various frequencies up to 10 GHz.

When the difference between η_1 and η_2 is small, the fluctuation spectra calculated for the nonuniform model are almost the same as those obtained on the basis of the uniform model.[1] In the following we fix the values of η_1 and η_2 as 0.9 and 0.03, respectively, and show how different characteristic features appear in a really nonuniform ($\eta_1 \gg \eta_2$) laser. These values of η_i are rather arbitrary, and similar results which are peculiar to nonuniform lasers are also obtained using other values of η_i when $\eta_1 \gg \eta_2$.

Let us first discuss the typical dependence of $\bar{N}_p$, $\bar{N}_{e1}$, and $\bar{N}_{e2}$ on the pumping rate. This is calculated for the volume ratio $V_2/V = 0.374$ and is shown by solid lines in Fig. 1. Results for the uniform model are also shown with broken lines for comparison. Here and in Figs. 2-4 the value of the quantum efficiency η in the uniform model is adjusted so that both models give the same threshold current. In the nonuniform model, electron density in the low-efficiency section, $\bar{N}_{e2}/V_2$, remains very low due to fast nonradiative recombination and the calculated rate of stimulated emission, $R_{st}(\bar{N}_{e2})$, becomes less than zero; i.e., the section is absorbing rather than amplifying. In Fig. 1, $\bar{N}_{e1}$ has a sharp fold at threshold and begins to decrease above threshold, while $\bar{N}_{e2}$ continues to increase without discontinuity. The decrease of $\bar{N}_{e1}$ above threshold results from the following facts: The overall gain of the cavity saturates at threshold due to the onset of laser oscillation, and the gain of the low-efficiency section continues to increase due to the lack of those fast electron-dissipating processes, which accompany the onset of laser oscillation, in this section. Therefore the gain decreases in the highly pumped section. Another feature of interest is that the differential quantum efficiency calculated on the basis of the nonuniform model is smaller than that calculated for the uniform model. This is explained qualitatively by the pumping-rate dependence of the electron numbers $\bar{N}_{ei}$ in Fig. 1 in the following way. In a uniform laser, as the electron number saturates at threshold and the rate of the nonradiative recombination is proportional to the square of the electron number, the rate of nonradiative recombination does not increase above threshold. In the low-efficiency region of the nonuniform model the electron number $\bar{N}_{e2}$ does not saturate, and the efficiency is seen to be very low; i.e., the rate of nonradiative recombination is very high. Therefore, the smaller differential quantum efficiency in the nonuniform model is attributed to the successive increase in the rate of nonradiative recombination above threshold.

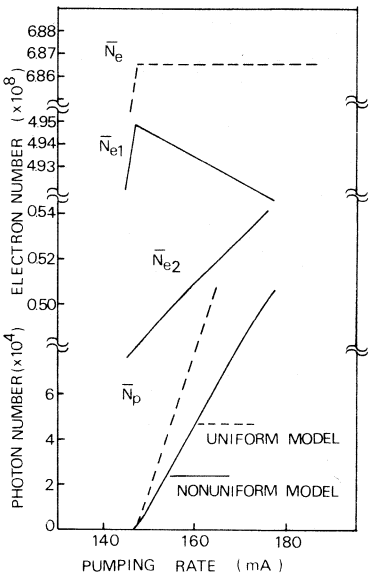


Fig. 1. The pumping-current dependence of $\bar{N}_{e1}$, $\bar{N}_{e2}$, and $\bar{N}_p$ in a double-sectioned laser model (solid lines). $\bar{N}_e$ and $\bar{N}_p$ are also shown for a uniform model with the same threshold current (broken lines).

The relative photon-noise spectra calculated for the nonuniform and uniform model using the previously given parameters are shown for various values of normalized pumping rate P_N by the solid and broken lines, respectively, in Fig. 2. In the nonuniform model, as the pumping current approaches the threshold value the noise becomes very large. Resonance begins at threshold and a gradual decrease in the peak height as well as the peak shift toward higher frequency is seen with a

[1] The actual coincidence of the fluctuations in the two models for $\eta_1 = \eta_2 = \eta$ is not self-evident because there is an essential difference in the physical background between the models. In the uniform model, a very fast relaxation process is assumed *a priori* for the spatially uniform distribution of electron density throughout the cavity, but any such process does not exist between the two sections in the double-sectioned laser model. The present result reveals that the interaction of photons and electrons itself in (1) and (2) serves as an effective mechanism to keep the uniformity of spatial electron distribution over the whole cavity with all independent statistical characteristics of electron shot noise in each section.

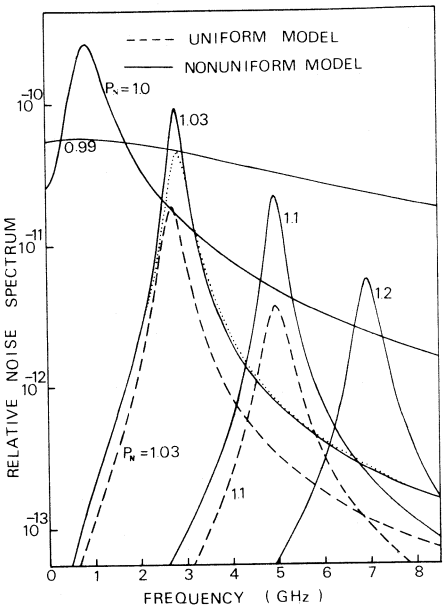


Fig. 2. Intensity-fluctuation spectra calculated for a double-sectioned laser model for various pumping rates (solid lines) and spectra for a uniform model (broken lines). The case of omitting the Q-switching-like mechanism, i.e., for putting A_{p2} to 0 in (3) in the nonuniform model, is also shown by a dotted line.

further increase of pumping. These are qualitatively the same characteristic features as those for the uniform model [8], [9]. Quantitative examination shows that the peaks are higher and the widths are narrower in the nonuniform model. The quantitative difference results from two types of difference in the mechanisms. One is the difference of parameters in the quantum shot-noise mechanism: In the nonuniform model, using the previously given parameters, photons are generated mainly in amplifying section 1 and the fluctuation spectra are determined basically by the interaction of fluctuations of photons in the cavity with fluctuations of electrons in section 1, but not of electrons in section 2. Relevant parameters such as the volume of amplifying regions, electron density, and coupling parameters have differences between the nonuniform and uniform models and additional absorption exists, even if the effect of the fluctuations of N_{e2} are omitted, in the nonuniform model. Therefore, some differences are expected in the fluctuation spectra between the two models. The other mechanism is the interaction of the electron-number fluctuation in the absorbing section 2 with photon-number fluctuation: The electron-number fluctuation ΔN_{e2} may at least amplify the fluctuations driven by quantum shot noises if ΔN_{e2} does not turn them into sustained Q-switched oscillations which need not be driven by any noises. This mechanism will be called, in the following, the Q-switching-like mechanism. In order to see how each of the two types of mechanism contributes to the difference in dashed and solid curves in Fig. 2, imaginary fluctuation spectra are calculated with the nonuniform model when the reaction of ΔN_{e2} to the photon number is omitted. These are obtained by putting A_{p2} as 0 in (3). A spectrum for $P_N = 1.03$ is shown by a dotted line in Fig. 2. Comparison of the dotted line with the dashed line shows that fluctuations in the nonuniform model without the Q-switching-like mechanism are larger than those in the uniform model by a factor of almost constant over the frequency region shown in the figure if a small frequency shift of the dotted curve is taken into account. The uniform increase in the noise spectrum suggests that the change in intensity is due to an increase of the quantum shot noises which have white-noise characters, F_p and/or F_{ei} in (1) and (2). For example, photon shot noise $F_p(t)$, which originates when a photon is emitted or disappears in a laser cavity, is expected to increase in the nonuniform model due to the existence of the absorbing section 2 and the highly emitting section 1. Comparison of the dotted line with the solid line shows that the addition of the Q-switching-like mechanism amplifies the fluctuations of frequencies only near the peak and does not affect the fluctuations in other frequency regions. Therefore, the sharpening of fluctuation peaks is attributed to the Q-switching-like mechanism.

Fig. 3 shows a plot of the squared-peak frequency ν_R^2 and the full width at half maximum (FWHM) of the resonant peak against normalized pumping rate P_N. Here dotted lines show the results for the previously mentioned imaginary nonuniform model; i.e., for the case of putting A_{p2} as 0 in (3). It is found that the linear dependence of ν_R^2 on the pumping rate $\nu_R^2 = \alpha^2 (I/I\text{th} - 1)$ exists just as in the uniform model [8], [9], and that the coefficient α scarcely differs between the uniform (broken line) and nonuniform (solid line) models when the threshold current is the same. The approximate coincidence in the values of α in both models results from compensation of the effect of the previously mentioned different parameters by the Q-switching-like mechanism, because the result for the nonuniform model (solid line) is closer to that for the uniform model (broken line) than the result for the case of omitting the Q-switching-like mechanism (dotted line) is. The width decreases abruptly just above threshold. The fact that the FWHM in the nonuniform model continues to decrease up to higher pumping current than in the uniform model may partly explain the disagreement pointed out in [14], where a decrease of FWHM with increasing pumping current is observed experimentally, while a gradual increase is obtained in calculations for the uniform model. The rate of increase after taking a minimum value is somewhat larger for the uniform model. The dependence of the peak height on the pumping rate is shown in Fig. 4. Qualitatively, both models show the same features, but the rate of its decrease with increasing pumping rate is larger for the uniform model than for the nonuniform one. At the pumping rate near threshold, where photon shot noise and the Q-switching-like mechanism are expected to play less of a role than at higher pumping rate, the difference between both models is small.

The differences of the fluctuations for both models discussed so far should disappear in the ultimate cases where the volume of lower efficiency section V_2 equals 0 and the higher quantum efficiency η_1 in the nonuniform model equals the value of the quantum efficiency η in the uniform model. The two models stand for the same laser with high efficiency and without lower efficiency regions which corresponds to an undegraded laser. In order to see how the differences in both models appear and become prominent as the degradation proceeds, changes of FWHM and the peak height have been

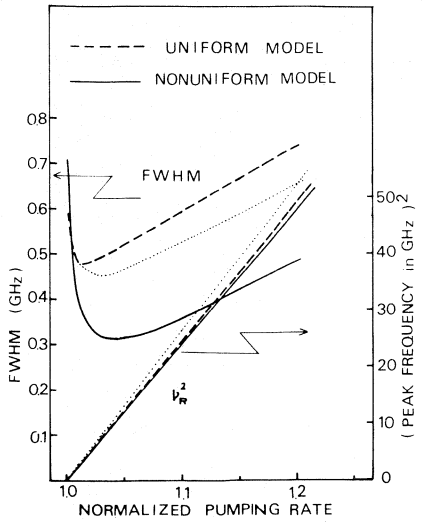


Fig. 3. The peak frequency ν_R and the FWHM of the fluctuation spectra for a nonuniform model (solid lines) and a uniform model (broken lines) as a function of pumping rate. The case of omitting the Q-switching-like mechanism in the nonuniform model is also shown by dotted lines.

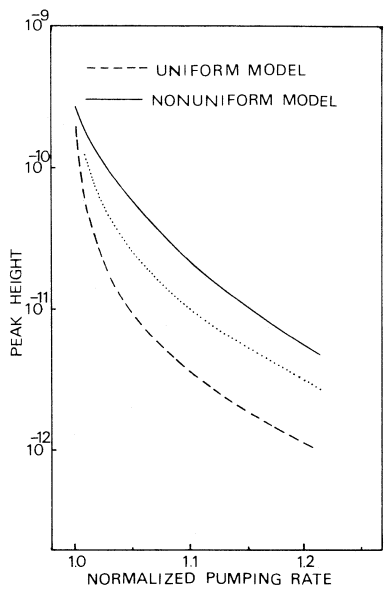


Fig. 4. The peak hight of fluctuation spectra as a function of pumping rate in a nonuniform model (solid line) and a uniform model (broken line) when the threshold current is the same. The case of omitting Q-switching-like mechanism in the nonuniform model is also shown by a dotted line.

calculated for the successive decrease of the efficiency η in the uniform model and for the successive increase of the volume V_2 in the nonuniform model. Fig. 5 shows the change of peak height for various pumping rates as a function of threshold current. The calculated threshold current before degradation is 120 mA. In the nonuniform model, shown by solid lines in the figure, the peaks grow rapidly as the low-efficiency region appears in a laser. As the degradation proceeds the growth becomes gradual and after taking a maximum value a slight decrease in the peak height occurs first for lower pumping and then for higher pumping rates. The change in the peak height when a laser degrades uniformly is shown with broken lines.

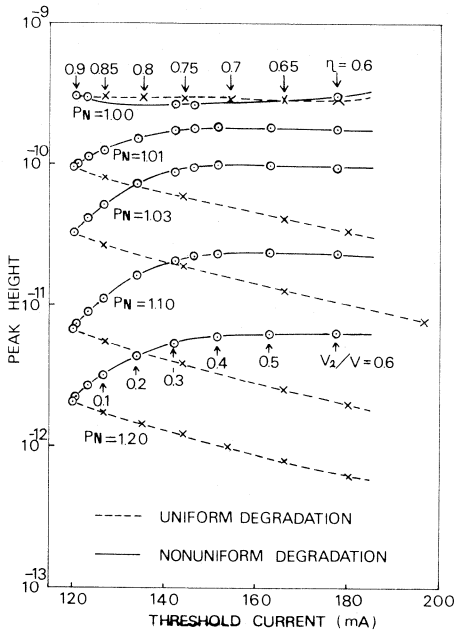


Fig. 5. Calculated change of the peak heights as a laser degrades nonuniformly (solid lines) or uniformly (broken lines) as a function of threshold current.

In this case, the peak height shows a monotonic decrease [14]. At $P_N = 1.0$ the values for the nonuniform and uniform models are nearly constant and almost coincide with each other. The characteristic features in Fig. 5 are understood as follows: As the quantum efficiency gradually decreases as a whole in the uniform model, the resonance becomes weaker and the peak height decreases monotonically. On the other hand, as the low-efficiency region corresponding to the absorbing region increases in the nonuniform model, something like the Q-switched mechanism occurs, and the photon shot noise which drives the intensity fluctuations increases in addition to a decrease of the quantum efficiency averaged over the whole cavity as in the uniform model. The first two of these changes tend to make fluctuation peaks grow and the last tend to make the peaks decay. When the ratio of the volume of the low-efficiency region to the total volume exceeds a value above which it is difficult for the Q-switching-like mechanism to appear, the change in the peak height is mainly governed by the second and third of the three changes and peaks grow only gradually, and with further increase in the volume V_2 the low-efficiency region begins to govern the characteristic features of the whole laser, and the peak height decreases monotonically in the same manner as in the uniform model.

The changes of FWHM for the uniform and nonuniform model are shown by broken and solid lines in Fig. 6 as a function of threshold current. The width increases monotonically as the degradation proceeds in the uniform model, while the curves for the nonuniform model exhibit minima. These minima take place at an earlier stage for a smaller pumping rate. With further degradation the width begins to increase almost at the same rate as the rate for the uniform model. The decrease of FWHM in the nonuniform model may be regarded as being due to the Q-switching-like mechanism. This is because the widths calculated for the nonuniform

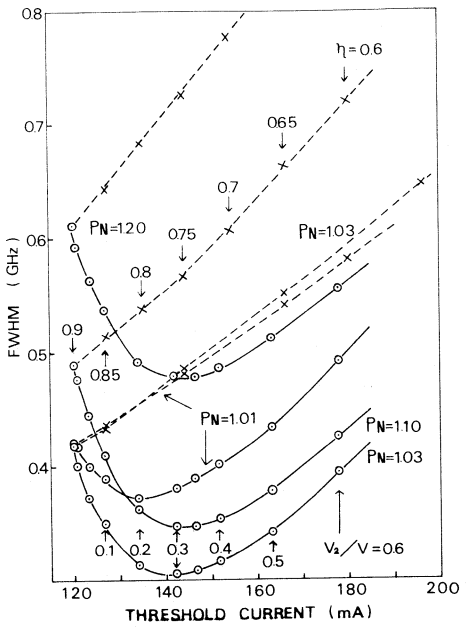


Fig. 6. Calculated change of the FWHM as a laser degrades nonuniformly (solid lines) or uniformly (broken lines).

model without the Q-switching-like mechanism (a dotted line in Fig. 3) are larger than the widths calculated for the same normalized pumping current P_N before degradation (at 120 mA in Fig. 6). The decrease of FWHM occurs only after including the Q-switching-like mechanism. This is not unexpected because the other two relevant changes accompanying nonuniform degradation do not seem to decrease the FWHM of fluctuation peaks: A decrease of the average quantum efficiency tends to make the resonance weaker and the fluctuation spectra broader, and an increase of photon shot noises with white-noise characters only makes the fluctuation grow uniformly and has no influence on the width.

IV. Discussion and Conclusion

The growth of the peak height and a decrease of FWHM in the fluctuation spectra for the nonuniform model indicate that at an early stage of degradation the fluctuations approach more intense oscillations with a longer correlation time with the appearance of local absorbing regions in the nonuniform model. It is well known that under certain conditions of the pumping rates a sustained oscillation can occur in a double-sectioned laser due to the Q-switched mechanism [5]. The present results show that even if the conditions for repetitive Q switching are not satisfied, nonuniformity in a laser can change the usual quantum fluctuations into more intense and oscillatory ones. This may explain the observation of Yang *et al.* [12] that the oscillations in the output from junction lasers grow as the degradation proceeds. According to our experiments [13] a decrease of peak height and an increase of FWHM have been observed and explained in terms of the uniform decrease of η [14].

These apparently opposite results may be explained by assuming different shapes or spatial distributions of pieces of low-efficiency regions for both cases. If the dark lines are very narrow in width and are distributed uniformly in a laser cavity, carriers which are injected into normal regions near each dark line may easily flow into this nonradiative region and compensate fast electron dissipation, so that electron distributions are uniform over the whole cavity and dark lines do not act as effective absorbing regions. In this case, the model, in which no electron relaxation occurs between the two sections, which is adopted here is not correct, and the uniform model is more appropriate and explains the decay of resonance. On the other hand, if each dark line has a large width or the distribution of dark lines is concentrated in a certain region of a cavity, compensation becomes difficult and the absorbing region may appear. The nonuniform model is thought to be appropriate in this case and explains the tendency of the growth of resonance phenomena.

In summary, the fluctuation spectra due to quantum shot noise are calculated for a nonuniform double-sectioned laser with two different internal quantum efficiencies and for an ordinary uniform laser. The pumping-rate dependence of the noise spectra for the nonuniform model is found to be qualitatively the same as that for the uniform model. The results calculated with parametric variations of η in the uniform model and of V_2 in the nonuniform model are then applied to the discussion of the degradation process. Qualitatively, opposite results are obtained for the changes of the fluctuations in the output from uniformly and nonuniformly degraded lasers. The differing behavior of the fluctuations is explained by the contributions of a Q-switching-like mechanism and of the differences of the parameters in the calculation of the quantum fluctuations. A possible explanation with the use of the present results is suggested for previous observations about the effect of degradation on fluctuations which apparently contradict each other.

References

[1] V. D. Kurnosov *et al.*, "Self modulation of emission from an injection semiconductor laser," *JETP Lett.*, vol. 4, pp. 303–305, Dec. 1966.

[2] L. A. D'Asaro, Sr., J. M. Cherlow, and T. L. Paoli, "Continuous microwave oscillations in GaAs junction lasers," *IEEE J. Quantum Electron.*, vol. QE-4, pp. 164–167, Apr. 1968.

[3] T. L. Paoli and J. E. Ripper, "Optical pulses from CW GaAs injection lasers," *Appl. Phys. Lett.*, vol. 15, pp. 105–107, Aug. 1969.

[4] T. P. Lee and R. Roldan, "Subnanosecond light pulses from GaAs injection lasers," *IEEE J. Quantum Electron.* (Corresp.), vol. QE-5, pp. 551–552, Nov. 1969.

[5] N. G. Basov, "Dynamics of injection lasers," *IEEE J. Quantum Electron.* (*Special Issue on 1968 Int. Quantum Electronics Conf.: Part II*), vol. QE-4, pp. 855–864, Nov. 1968.

[6] T. L. Paoli and J. E. Ripper, "Coupled longitudinal mode pulsing in semiconductor lasers," *Phys. Rev. Lett.*, vol. 23, pp. 1085–1088, May 1969.

[7] D. E. McCumber, "Intensity fluctuation in the output of cw laser oscillators I," *Phys. Rev.*, vol. 141, pp. 306–322, Jan. 1966.

[8] H. Haug, "Quantum-mechanical rate equations for semiconductor lasers," *Phys. Rev.*, vol. 184, pp. 338–348, Aug. 1969.

[9] D. J. Morgan and M. J. Adams, "Quantum noise in semiconductor laser," *Phys. Status Solidi* (*a*), vol. 11, pp. 243–253, 1972.

[10] T. L. Paoli and J. E. Ripper, "Observation of intrinsic quantum fluctuations in semiconductor lasers," *Phys. Rev. A*, vol. 2, pp. 2551–2555, Dec. 1970.

[11] T. L. Paoli, "Intrinsic fluctuations in the output intensity of double-heterostructure junction lasers operating continuously at 300°K," *Appl. Phys. Lett.*, vol. 24, pp. 187–190, Feb. 1974.

[12] E. S. Yang, P. G. McMullin, A. W. Smith, J. Blum, and K. K. Shih, "Degradation-induced microwave oscillations in double-heterostructure injection lasers," *Appl. Phys. Lett.*, vol. 24, pp. 324–327, Apr. 1974.
[13] S. Mukai, S. Gonda, and Y. Makita, "Effect of degradation on intensity fluctuation in cw AlGaAs double-heterostructure junction lasers," *Japan. J. Appl. Phys.*, vol. 14, pp. 737–738, May 1975.
[14] S.-I. Gonda and S. Mukai, "Degradation and intensity fluctuations in CW AlGaAs double-heterostructure junction lasers," *IEEE J. Quantum Electron. (Part II of Two Parts: Special Issue on 1974 IEEE Semiconductor Laser Conf.)*, vol. QE-11, pp. 545–550, July 1975.
[15] B. C. De Loach, Jr., B. W. Hakki, R. L. Hartman, and L. A. D'Asaro, "Degradation of CW GaAs double-heterojunction lasers at 300 K," *Proc. IEEE* (Lett.), vol. 61, pp. 1042–1044, July 1973.
[16] H. Yonezu, M. Ueno, T. Kamejima, and I. Sakuma, "Lasing characteristics in a degraded GaAs-$Al_xGa_{1-x}As$ double heterostructure laser," *Japan. J. Appl. Phys.*, vol. 13, pp. 835–842, May 1974.
[17] M. J. Adams, "A simple approximation for high-temperature properties of the injection laser," *Brit. J. Appl. Phys.*, vol. 2, pp. 1549–1553, 1969.

Multiply Resonant Distributed-Feedback Lasers

HAROLD M. STOLL AND DAVID H. SEIB

Abstract—**A modified distributed-feedback (DFB) laser, termed the multiply resonant distributed-feedback (MRDFB) laser, is described and demonstrated. The MRDFB-laser cavity incorporates a doubly periodic index-of-refraction variation which leads to the colinear generation of several preselected laser wavelengths simultaneously. A theoretical analysis of the MRDFB laser is given using the coupled-mode formalism, formulas are given for determining MRDFB-laser wavelengths, and estimates are made of required threshold gains. Experimental results obtained from MRDFB GaAs homojunction injection lasers are presented which verify important aspects of the theory.**

I. Introduction

BECAUSE of its configurational versatility, wavelength selectivity, and wavelength stability with varying temperature, the distributed-feedback (DFB) laser is currently the most promising candidate for incorporation into integrated optical circuitry. Since its original conception [1] and subsequent analysis [2], both optically [3]-[5] and electrically [6]-[9] pumped DFB lasers have been fabricated. In this paper, we propose, analyze, and experimentally demonstrate (using a GaAs homojunction injection laser) the feasibility of a new, modified DFB-laser structure which, for active media having broad, inhomogeneous or partially inhomogeneous gain lines, allows colinear lasing to occur at several preselected wavelengths simultaneously. We term this new device a multiply resonant distributed-feedback (MRDFB) laser.

One potential application of the MRDFB laser is in ultrahigh data-rate communications systems where modulator and detector bandwidth limitations (~1 GHz) necessitate frequency multiplexing in order to establish multigigabit/second transmission links. Toward the goal of realizing an integrated optical system of this type, the use of an MRDFB laser appears to offer definite fabricational and operational advantages over the use of a number of conventional single-frequency lasers. Fabricational advantages would include, for example, a reduction in the number of steps required for laser cavity construction (Section III) and elimination of the need for complicated frequency-selective directional couplers (a single optical waveguide could accommodate an MRDFB laser followed by an appropriate number of Bragg-reflector modulators [10]). Potential operational advantages include a reduction in total laser power requirements (Section II) and, when compared

Manuscript received July 17, 1975; revised September 2, 1975. This work was supported by the U.S. Air Force under Contract F04701-73-C0075.

The authors are with the Aerospace Corporation, Los Angeles, CA 90009.

with a system comprised of single-frequency DFB lasers operating within a common waveguide, the avoidance of possible intermodulation effects [11].

II. Theory of Operation

The general principle of operation of the MRDFB laser may be understood by examining the structure shown in cross section in Fig. 1(a). We assume that adjacent to the active medium there exists a high-frequency ($=1/\Lambda_2$) corrugation whose properties have been spatially modulated at a much lower mechanical frequency ($=1/\Lambda_1$). As in a conventional DFB-laser cavity, the period of the high-frequency corrugation is chosen to be equal to an integral multiple of one-half a guided, lasing wavelength, termed the fundamental wavelength in the case of an MRDFB cavity. The additional wavelengths, or "sidebands," of the MRDFB laser are generated as a result of the structural Fourier components introduced by the low-frequency modulation of the fundamental, high-frequency corrugation.

As an illustrative example, we now calculate the threshold gains and resonances of the MRDFB laser shown in cross section in Fig. 1(b). Here, for simplicity, the high- and low-frequency periodic surface corrugations have been taken to be of the square-wave type, i.e. [referring to Fig. 1(b)], $\Lambda_1 = 2b$ and $\Lambda_2 = 2c$. We assume that radiation is confined in the x-direction only within region II (active medium having a wavelength-independent amplitude gain γ) and that propagation is in the z-direction. The transverse electric modes of this structure are solutions of the following perturbed wave equation (the transverse magnetic modes may be found using the same approach, but with $\mathcal{E}_y$ replaced by $\mathcal{H}_y$):

$$\nabla^2 \mathcal{E}_y(x,z;t) = \frac{1}{c^2}\left[n_j^2 + 2in_2\frac{\omega}{c}\Gamma(x) + \Delta n^2(x) \cdot \sum_{l,m} \Pi_m^{(1)}(z)\cdot\Pi_l^{(2)}(z)\right]\cdot\frac{\partial^2 \mathcal{E}_y(x,z;t)}{\partial t^2}, \quad j = 1,2,3 \tag{1}$$

where the perturbation terms are given by

$$\Pi_m^{(1)}(z) \equiv \begin{cases} \frac{1}{2}, & m = 0 \\ \frac{2}{m\pi}\sin mK_1 z, & m = 1,3,5,\cdots \end{cases} \tag{2a}$$

$$\Pi_l^{(2)}(z) \equiv \begin{cases} \frac{1}{2}, & l = 0 \\ \frac{2}{l\pi}\sin lK_2 z, & l = 1,3,5,\cdots \end{cases} \tag{2b}$$

$$\Gamma(x) \equiv \begin{cases} \gamma, & -t \leqslant x \leqslant 0 \\ 0, & \text{otherwise} \end{cases} \tag{2c}$$

$$\Delta n^2(x) \equiv \begin{cases} n_1^2 - n_2^2, & -a \leqslant x \leqslant 0 \\ 0, & \text{otherwise.} \end{cases} \tag{2d}$$

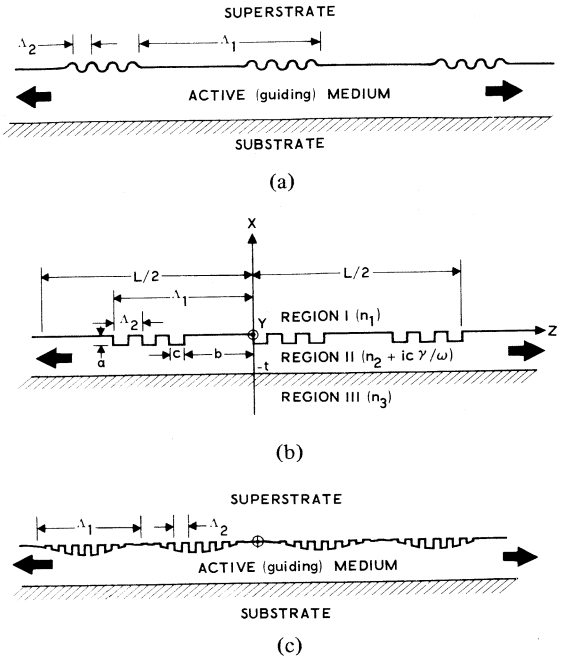


Fig. 1. Cross sections of MRDFB-laser structures. (a) General structure illustrating doubly periodic cavity configuration. (b) Square-wave-modulated structure with square-wave fundamental assumed for theoretical analysis. Only odd-order sidebands exist ($m = 1, 3, 5, \cdots$ in (2a)). Definitions of quantities used in the analysis are indicated. (c) Sine-wave-modulated structure; both even- and odd-order sidebands exist [$m = 1, 2, 3, \cdots$ in (2a)].

$K_1 = 2\pi/\Lambda_1$ and $K_2 = 2\pi/\Lambda_2$ are the magnitudes of the perturbation k-vectors, and n_j is the refractive index of region j [Fig. 1(b)].

Assuming that the active waveguiding region supports only the lowest order TE modes (associated with those resonant wavelengths of the MRDFB cavity which fall within the laser gain linewidth), the solution of (1) may be expressed as an expansion over the unperturbed, lowest order, forward- and backward-traveling modes $E_y(x,z;t)$ of the structure [12] as follows [13]:

$$\mathcal{E}_y^{(l,\pm m)}(x,z;t) = [C_{l,\pm m}^{(+)}(z)\exp(-i\beta_{l,\pm m}z) + C_{l,\pm m}^{(-)}(z)\cdot\exp(+i\beta_{l,\pm m}z)]\cdot E_y^{(l,\pm m)}(x)\cdot\exp(i\omega_{l,\pm m}t) \tag{3}$$

where the $C_{l,\pm m}^{(\pm)}(z)$ are expansion coefficients which are assumed to vary slowly over one guided-mode wavelength. Substituting $\mathcal{E}_y^{(l,\pm m)}(x,z;t)$ into (1) and making use of the modal orthonormality relation [13] yields the following set of coupled equations for the fundamental and sideband resonant modes:

$$\frac{d}{dz}(C_{l,0}^{(+)}(z)) = S_{l,0}C_{l,0}^{(-)}(z)\exp(+i\Delta_{l,0}z) + G_{l,0}C_{l,0}^{(+)}(z) \tag{4a}$$

$$\frac{d}{dz}(C_{l,0}^{(-)}(z)) = S_{l,0}C_{l,0}^{(+)}(z)\exp(-i\Delta_{l,0}z) - G_{l,0}C_{l,0}^{(-)}(z) \tag{4b}$$

$$\frac{d}{dz}(C_{l,\pm m}^{(+)}(z)) = \mp\frac{2i}{m\pi}S_{l,\pm m}C_{l,\pm m}^{(-)}(z)\exp(+i\Delta_{l,\pm m}z) + G_{l,\pm m}C_{l,\pm m}^{(+)}(z) \tag{4c}$$

$$\frac{d}{dz}(C^{(-)}_{l,\pm m}(z)) = \pm \frac{2i}{m\pi} S_{l,\pm m} C^{(+)}_{l,\pm m}(z) \exp(-i\Delta_{l,\pm m} z) - G_{l,\pm m} C^{(-)}_{l,\pm m}(z) \tag{4d}$$

where

$$S_{l,\pm m} \equiv \frac{\omega_{l,\pm m}\epsilon_0}{8\pi l}(n_1^2 - n_2^2)\int_{-a}^{0} |E_y^{(l,\pm m)}(x)|^2 dx \tag{5a}$$

$$G_{l,\pm m} \equiv \frac{n_2\gamma}{2c\mu_0}\int_{-t}^{0} |E^{(l,\pm m)}(x)|^2 dx \tag{5b}$$

and

$$\Delta_{l,\pm m} \equiv 2\beta_{l,\pm m} - (lK_2 \pm mK_1). \tag{5c}$$

Equations (4a) and (4b) give rise to the fundamental wavelength modes and (4c) and (4d) to the sideband wavelength modes. The choice of signs in (4a)-(5c) is dependent upon whether the low-frequency, mechanical k-vectors are added or subtracted from the high-frequency k-vectors. Phase-vector diagrams illustrating the situation are given in Fig. 2 where, for purposes of clarity, the small mismatch factors $\Delta_{l,\pm m}$ of (5c) have been neglected and a third-order ($l = 3$), fundamental, high-frequency perturbation has been assumed.

Finally, solution of (4a)-(4d), with the appropriate boundary conditions [2] applied to the $C^{(\pm)}_{l,\pm m}(z)$ at $z = \pm L/2$, yields the following complex transcendental equations for the resonant frequencies $\Delta_{l,\pm m}$ and threshold gains $G_{l,\pm m}$:

$$S_{l,0} = \pm i\sigma_{l,0}/\sinh(\sigma_{l,0}L) \tag{6a}$$

and

$$\frac{2}{m\pi} S_{l,\pm m} = \pm i\sigma_{l,\pm m}/\sinh(\sigma_{l,\pm m}L) \tag{6b}$$

where

$$\sigma_{l,0}^2 \equiv S_{l,0}^2 + \left(G_{l,0} + i\frac{\Delta_{l,0}}{2}\right)^2 \tag{7a}$$

and

$$\sigma_{l,\pm m}^2 \equiv \left(\frac{2}{m\pi} S_{l,\pm m}\right)^2 + \left(G_{l,\pm m} + i\frac{\Delta_{l,\pm m}}{2}\right)^2. \tag{7b}$$

In order to gain some feeling for the spectrum and relative thresholds (in the absence of loss) to be expected of a representative MRDFB laser, we now solve (6a) and (6b) for the case of a simple GaAs homojunction structure wherein regions II and III of Fig. 1(b) are heavily doped p- and n-type GaAs, respectively. Assuming that only the fundamental and the lowest ($m = 1$) order sideband wavelengths fall within the gain linewidth, (5c) yields (assuming $\Delta_{l,\pm m} \approx 0$)

$$\lambda_{3,0} \approx \tfrac{2}{3}\Lambda_2 n_2(\lambda_{3,0}) \tag{8a}$$

$$\lambda_{3,\pm 1} \approx \frac{2n_2(\lambda_{3,\pm 1})}{(3/\Lambda_2 \pm 1/\Lambda_1)}. \tag{8b}$$

For sidebands which are reasonably close to the fundamental,

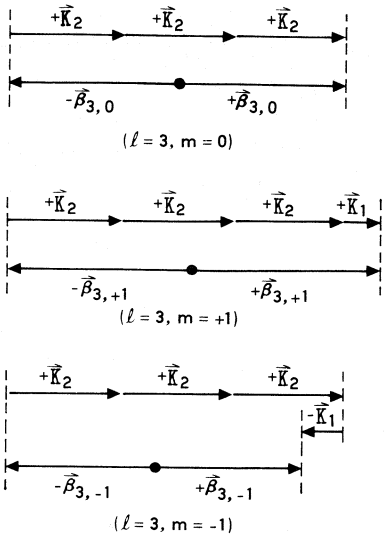


Fig. 2. Phase-vector diagram for the fundamental and lowest, odd-order sidebands of a square-wave-modulated MRDFB laser. $K_1 = 2\pi/\Lambda_1$, $K_2 = 2\pi/\Lambda_2$.

(8b) can be written

$$\lambda_{3,\pm 1} \approx \lambda_{3,0} \pm \frac{\lambda_{3,0}^2}{2\Lambda_1 F(\lambda)} \tag{8c}$$

where $F(\lambda)$ is the dispersion factor for GaAs defined by [14]

$$F(\lambda) = n - \lambda\frac{dn}{d\lambda}. \tag{9}$$

Taking $\Lambda_2 = 0.355$ μm (third-order fundamental corrugation), $\Lambda_1 = 50$ μm, $n_2(\lambda_{3,0}) = 3.57$, and $F(\lambda_{3,0}) = 5.0$, (8a) gives $\lambda_{3,0} = 0.8449$ μm and (8c) gives $\lambda_{3,-1} = 0.8463$ μm and $\lambda_{3,+1} = 0.8435$ μm. Finally, taking $n_1 = 1$ (air superstrate), $n_3 = 3.5$, and letting the corrugation groove depth $a = 0.18$ μm, the guide thickness $t = 1.5$ μm, and the active length $L = 1$ mm, (6a) and (6b) yield for the threshold amplitude gains in the absence of loss, $G_{3,0} = 1.4$ cm^{-1} and $G_{3,\pm 1} = 3.2$ cm^{-1}. These values compare with a threshold gain of 0.2 cm^{-1} for an unmodulated DFB laser whose cavity parameters are otherwise identical. In order to obtain a realistic comparison of threshold gains one must, of course, add cavity losses (on the order of 20 cm^{-1} for a GaAs homojunction laser operating at 77 K [15]) to the lossless threshold gains calculated here. Doing so, one notes that the percentage differences between the various threshold gains become relatively insignificant.

We conclude this section with two observations. First, by square-wave modulating the fundamental surface corrugation, only odd-ordered ($m = 1, 3, 5, \cdots$) sideband resonances exist; a full complement (i.e., $m = 1, 2, 3, \cdots$) of resonances would result, on the other hand, from the type of undulating spatial modulation of the fundamental corrugation depicted in Fig. 1(c). Second, as was previously shown, the threshold gains (including loss) for the lowest order sideband resonances (assuming square-wave modulation) are not much higher than the threshold gain for the fundamental resonance. Indeed, the three threshold gains previously calculated are seen to be only

slightly greater than the threshold gain associated with a singly resonant conventional DFB laser. This result suggests that optical multiplexing systems based upon an MRDFB-laser source might enjoy a greater drive power efficiency over systems utilizing several independently driven single-wavelength lasers; viz., several wavelengths can, in principle, be obtained for essentially the threshold "cost" of one. This argument, of course, ignores both the problem of competition between oscillating modes of a partially inhomogeneous gain medium such as GaAs and variations of gain and loss with wavelength.

III. Experimental Results

MRDFB homojunction injection lasers with cross sections similar to that shown in Fig. 1(a) have been fabricated from GaAs and tested using procedures similar to those previously reported [7]. Surface corrugations were introduced into the p-type surface layer (junction depth = 1.5 - 1.7 μm) by argon-ion milling through a specially prepared (Shipley AZ1350) photoresist mask. Modulation or segmentation of the high-frequency (third-order) photoresist mask was accomplished by placing a Ronchi grating with either a 25- or 50-μm period over an undeveloped holographic exposure and then exposing to normally incident 4579-Å light a second time before developing. A SEM photograph of a cleaved surface through a completed MRDFB-laser cavity is shown in Fig. 3. The high-frequency surface corrugations were sinusoidal in cross section and approximately 2000 Å deep. Ohmic contact to the p-type layer, directly over the grating, was made using a 3000-Å-thick evaporated layer of Ag-Mn alloy, applied in a stripe pattern as described previously [7].

Figs. 4 and 5 show output spectra obtained from MRDFB lasers fabricated using Ronchi masks having periods of 25 and 50 μm, respectivley. The 25-μm Ronchi was used to mask a 0.3550-μm-period fundamental grating and the 50-μm Ronchi a 0.3554-μm-period fundamental grating. Table I lists the observed wavelengths together with their approximate current thresholds and associated effective refractive indices. The effective refractive indices

$$n_{\text{eff}}^{(l,\pm m)} = \frac{\lambda_{l,\pm m}\beta^{(l,\pm m)}}{2\pi} \tag{10}$$

were calculated using (5c) with the $\Delta_{l,\pm m}$ assumed negligible. Fundamental wavelengths were identified by comparing the

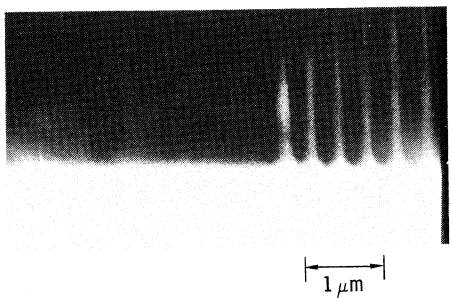


Fig. 3. SEM photomicrograph of a cleaved section of a square-wave-modulated MRDFB laser.

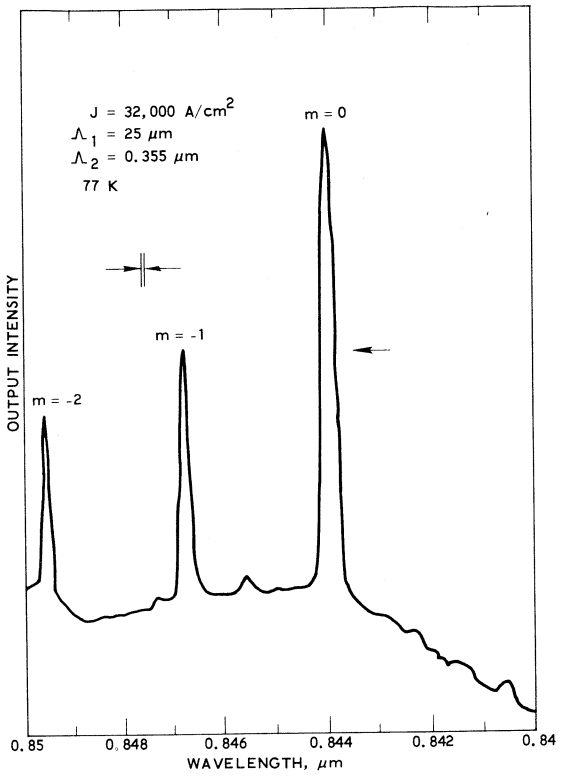


Fig. 4. Output spectrum of MRDFB laser showing the fundamental (denoted by arrow) and two long-wavelength sidebands ($m = -1$ and $m = -2$ in (2a)).

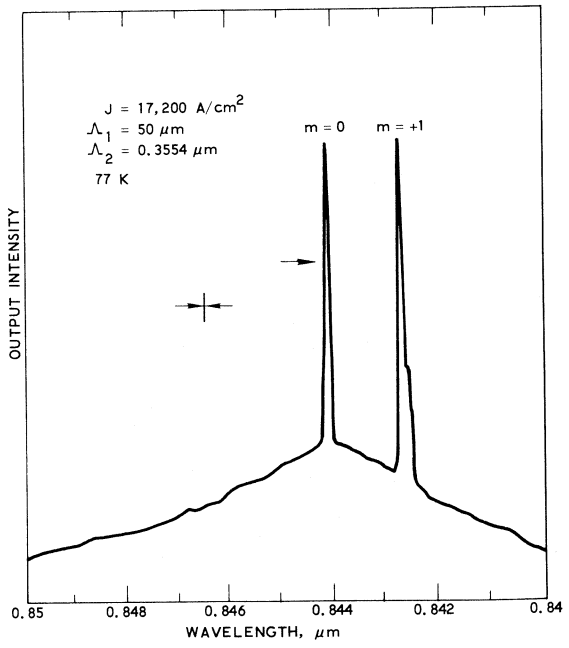


Fig. 5. Output spectrum of MRDFB laser showing the fundamental (denoted by arrow) and lowest order, short-wavelength sideband ($m = +1$ in (2a)).

MRDFB spectra with spectra obtained from conventional (unmodulated) DFB lasers which were otherwise identical.

Two observations are in order regarding the spectra of Figs. 4 and 5. First, we note that the spectrum of Fig. 4 includes the fundamental and both the lowest odd- *and* the lowest

TABLE I

	$(\ell, \pm m)$	$\lambda_{\ell,\pm m}(\mu m)$	$n_{eff}^{(\ell,\pm m)}$	$J_{th}(A/cm^2)$
$\Lambda_1 = 25 \mu m$, $\Lambda_2 = 0.3350 \mu m$	(3, 0)	0.8440	3.566	9,500
	(3, -1)	0.8467	3.561	16,000
	(3, -2)	0.8496	3.555	30,000
$\Lambda_1 = 50 \mu m$, $\Lambda_2 = 0.3554 \mu m$	(3, 0)	0.8441	3.562	14,000
	(3, +1)	0.8427	3.564	14,000

even- ($m = 2$) ordered sideband wavelengths. This result is explained by the fact that the low-frequency modulation was not perfectly square wave in character; measurements made of this unit revealed that the fundamental grating occupied 56.5 percent (instead of 50 percent) of a low-frequency period. Second, it is seen that the spectrum of Fig. 4 includes only long-wavelength sidebands, whereas the spectrum of Fig. 5 includes only the lowest, odd-order, *short*-wavelength sideband. Other lasers fabricated using the 50-μm-period Ronchi mask evidenced the opposite behavior; i.e., only the lowest, odd-order, *long*-wavelength sideband appeared. One possible explanation for this behavior is that the high- and low-frequency wave vectors and the normal-to-the-output face of the laser were not mutually parallel. This circumstance would result in the emission of the various wavelengths at different angles, thereby causing (because of the large index of refraction of GaAs) either the short- or long-wavelength sidebands to be emitted at angles unfavorable for collection by the measurement apparatus.

The thresholds listed in Table I, when considered relative to one another and after allowances have been made for gain variations with wavelength, approximate the trends predicted by theory. Indeed, the fundamental wavelength threshold observed for the three-wavelength MRDFB laser (9500 A/cm^2) was only slightly higher than the threshold (7400 A/cm^2) observed for its single resonant DFB counterpart (whose fundamental wavelength was identical). The relatively high thresholds observed for the long-wavelength sidebands of this laser are most likely due, at least in part, to coupling between guided and radiation modes [13] induced by the low-frequency k-vectors. This problem could, of course, be solved by employing GaAlAs heterojunction structures having large superstrate-guide and guide-substrate index discontinuities.

IV. Concluding Remarks

We have presented in this paper both a theoretical examination and an experimental demonstration of a new type of distributed-feedback laser—the MRDFB laser. The theory indicates that, for an active medium having a broad inhomogeneous or partially inhomogeneous gain line (such as GaAs), several preselected laser wavelengths can be generated colinearly and simultaneously by utilizing a laser cavity whose properties have been spatially modulated in a doubly periodic fashion. Spectra and pumping thresholds of MRDFB GaAs injection lasers have been obtained which substantially corroborate the theoretical predictions. Indeed, thresholds observed for similar single-wavelength DFB lasers were found to be only slightly lower than those observed for comparably configured MRDFB lasers. This result suggests the potential usefulness of MDRFB lasers in integrated optical circuits in which frequency multiplexing is desired.

While detailed consideration has been given to only one specific cavity configuration [Fig. 1(a)-(c)], other, possibly superior, geometries can be imagined. The high- and low-frequency corrugations could, for example, be fabricated on opposite sides of the active region. Another possibility might involve forming the high-frequency corrugation in a surface already provided with a low-frequency corrugation.

Further investigations should include an examination of inter-wavelength quenching effects (for the case of GaAs) and verification of both upper and lower sideband wavelength generation from a single unit. Experimental analysis should also be made of close-confinement MRDFB lasers wherein the avoidance of coupling to radiation modes might lead to lower sideband wavelength thresholds.

Acknowledgment

The authors wish to thank W. E. Soady for his fine technical assistance in fabricating the gratings and in taking the SEM photograph. They also wish to thank M. P. Ziegler for fabricating the units.

References

[1] S. E. Miller, "Integrated optics: An introduction," *Bell Syst. Tech. J.*, vol. 48, pp. 2059–2069, Sept. 1969.
[2] H. Kogelnik and C. V. Shank, "Coupled-wave theory of distributed feedback lasers," *J. Appl. Phys.*, vol. 43, pp. 2327–2335, May 1972.
[3] C. V. Shank, J. E. Bjorkholm, and H. Kogelnik, "Tunable distributed-feedback dye laser," *Appl. Phys. Lett.*, vol. 18, pp. 395–396, May 1971.
[4] a) M. Nakamura, H. W. Yen, A. Yariv, E. Garmire, and H. L. Garvin, "Optically pumped GaAs surface laser with corrugation feedback," *Appl. Phys. Lett.*, vol. 22, pp. 515–516, May 1973. b) M. Nakamura *et al.*, "Laser oscillation in epitaxial GaAs waveguides with corrugation feedback," *Appl. Phys. Lett.*, vol. 23, pp. 224–225, Sept. 1973.
[5] C. V. Shank, R. V. Schmidt, and B. I. Miller, "Double-heterostructure GaAs distributed feedback laser," *Appl. Phys. Lett.*, vol. 25, pp. 200–201, Aug. 1974.
[6] D. R. Scifres, R. D. Burnham, and W. Streifer, "Distributed feedback single heterojunction GaAs diode laser," *Appl. Phys. Lett.*, vol. 25, pp. 203–206, Aug. 1974.
[7] H. M. Stoll and D. H. Seib, "Distributed feedback GaAs homojunction injection laser," *Appl. Opt.*, vol. 13, pp. 1981–1982, Sept. 1974.
[8] M. Nakamura *et al.*, "GaAs-$Ga_{1-x}Al_xA_s$ double-heterostructure distributed feedback diode lasers," *Appl. Phys. Lett.*, vol. 25, pp. 487–488, Nov. 1974.
[9] D. B. Anderson, R. R. August, and J. E. Coker, "Distributed-feedback double-heterostructure GaAs injection laser with fundamental grating," *Appl. Opt.*, vol. 13, pp. 2742–2744, Dec. 1974.
[10] H. M. Stoll and A. Yariv, "Coupled-mode analysis of periodic dielectric waveguides," *Opt. Commun.*, vol. 8, pp. 5–8, May 1973.
[11] A. B. Fowler, "Quenching of gallium-arsenide injection lasers," *Appl. Phys. Lett.*, vol. 3, pp. 1–3, July 1963.
[12] A. Yariv, "Coupled-mode theory for guided-wave optics," *IEEE J. Quantum Electron.*, vol. QE-9, pp. 919–933, Sept. 1973.
[13] D. Marcuse, "Mode conversion caused by surface imperfections of a dielectric slab waveguide," *Bell Syst. Tech. J.*, vol. 48, pp. 3187–3215, Dec. 1969.
[14] T. S. Moss, G. J. Burrell, and B. Ellis, *Semiconductor Opto-Electronics*. New York: Wiley, 1973, p. 20.
[15] S. M. Sze, *Physics of Semiconductor Devices*. New York: Wiley, 1969, p. 707.

Correspondence

Positive Ion Spectra in He-CO-O_2-Laser Discharges

H. KEREN, P. AVIVI, AND F. DOTHAN

Abstract—**The ion spectra of He-CO-laser discharges with and without small addition of O_2 is presented. It is shown that upon addition of oxygen the dominant positive charge carriers in the discharge are O_2^+ ions. It is argued that the oxygen ion O_2^+ is populated in stage processes: the $a^3\Pi$ state of CO relaxes to a metastable state of oxygen, which in turn is ionized by electrons.**

INTRODUCTION

The influence of oxygen on CO-laser performance has been discussed by Keren *et al.* [1]. The influence of traces of O_2 in a CO–He mixture on the electron energy distribution function has been demonstrated and the effect of O_2 on emission spectra of CO in the UV, visible, and IR region, has been described.

A possible mechanism was suggested to explain the influence of O_2 on CO-laser performance. It was suggested that electrons excite CO to the $a^3\Pi$ level which is then efficiently quenched by O_2 molecules and its energy transferred to a metastable level of O_2. Furthermore, it was postulated that the ionization proceeds via the metastable level of the O_2 molecule. Such a mechanism implies a change of positive ions from CO^+ and CO^+ clusters to O_2^+.

It is the purpose of this correspondence to show striking experimental evidence that this is indeed what happens.

A detailed mapping of positive ions in CO–He mixtures with and without O_2 will be presented. This is of major importance to the understanding of kinetics of CO–He lasing mixtures.

EXPERIMENTAL ARRANGEMENT

A schematic drawing of the experimental setup is given in Fig. 1.

The discharge was maintained between two water-cooled gold electrodes, which were 50 cm apart. The inside diameter (ID) of the Pyrex tube was 3.3 cm. The gases used (Matheson research grade) were passed through liquid nitrogen traps before entering the discharge chamber.

For ion determination a quadrupole residual gas analyzer, Balzers QMG 111B was used. This instrument can be used as an ion detector by disconnecting the ionizing filament.

The quadrupole structure was matched to the discharge by a two-stage differential pumping system. The first stage was pumped by a 4-in diffusion pump to a base pressure of $\sim 10^{-6}$ torr and the second stage by a 3-in pump to a base pressure of $\sim 10^{-7}$ torr. At the operating pressure of the discharge (18 torr) the pressure in the first stage was 7×10^{-4} torr, while the analyzer in the second stage was kept at 2.5×10^{-6} torr.

An orifice of 0.3 mm midway between the electrodes and 5 mm from the axis of the discharge, which comprises the apex of a cone, allowed the ions from the discharge to flow into the first stage of the differential pumping system. The gas entered into the second stage through a stainless-steel cone which had a hole of 0.5 mm at its apex.

The 0.3-mm orifice at the first stage obviated recombination effects in the sheath which was in the experimental conditions about 0.1 mm thick. Moreover, the cone was made of Pyrex, coated internally with a silver layer, and thus comprised an equipotential surface at the floating plasma potential.

Manuscript received August 1, 1975.

The authors are with the Racah Institute of Physics, The Hebrew University of Jerusalem, Jerusalem, Israel.

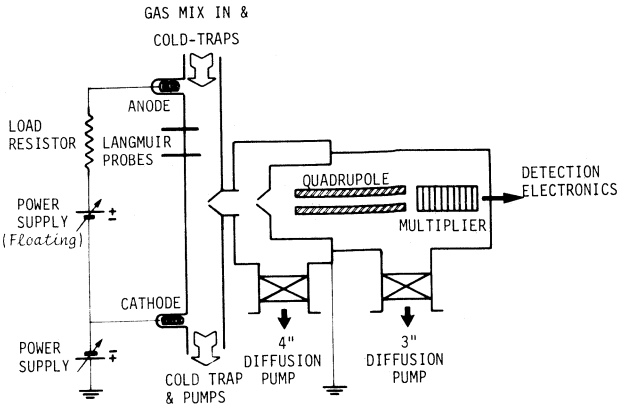


Fig. 1. Schematic of experimental setup.

The main difference between this system and others used was that the ions measured emanated from the bulk of the positive column and not from areas behind the cathode [2]–[4], and thus present a true picture of the ion composition in the lasing medium.

RESULTS

The ion spectra from a discharge in a mixture of 16.5-torr helium and 1.75-torr CO at 10-mA current with different amounts of O_2 are given in Fig. 2(a)–(d).

It is clearly seen [Fig. 2(a)] that without O_2 the dominant positive charge carriers are CO^+, CO^+:CO, and CO^+:CO:C_n (n = 1, 2, 3) clusters. Indeed the main carrier is CO^+:CO and not CO^+.

Upon introduction of O_2, the CO^+ ion and CO^+:CO:C_n charged clusters started to disappear and O_2^+ ions take over. These results are in accordance with the decrease in E/N and the increase in lasing power [1].

Fig. 3 shows the relative density of O_2^+ ions as a function of O_2 pressure. This curve was obtained from the measured ion signal by taking into account the factor $\sqrt{M}$ to allow for different ion masses M. It is seen that above 20-m · torr oxygen O_2^+ becomes the dominant ion and at about 50-m · torr oxygen about 70 percent of all the ions are O_2^+ ions.

DISCUSSION

The observed change in ion composition, when O_2 is added to a He–CO mixture, has indeed been predicted by Keren *et al.* [1] from indirect evidence. At a pressure of O_2 where maximum lasing power is obtained, the O_2^+ ion is three times more abundant than all other ions combined. The disappearance of CO^+:CO:C_n clusters is consistent with the disappearance of the C_2 Swan bands in the visible spectrum [1].

These results thus substantiate the model suggested in the previous paper [1] namely, the following three-stage ionization process:

$$e + CO \longrightarrow CO^*(a^3\Pi) + e \tag{1}$$

$$CO^*(a^3\Pi) + O_2 \longrightarrow CO + O_2^*(\text{metastable}) + KE \tag{2}$$

$$O_2^*(\text{metastable}) + e \longrightarrow O_2^+ + 2e. \tag{3}$$

In this model the role played by the metastable states of

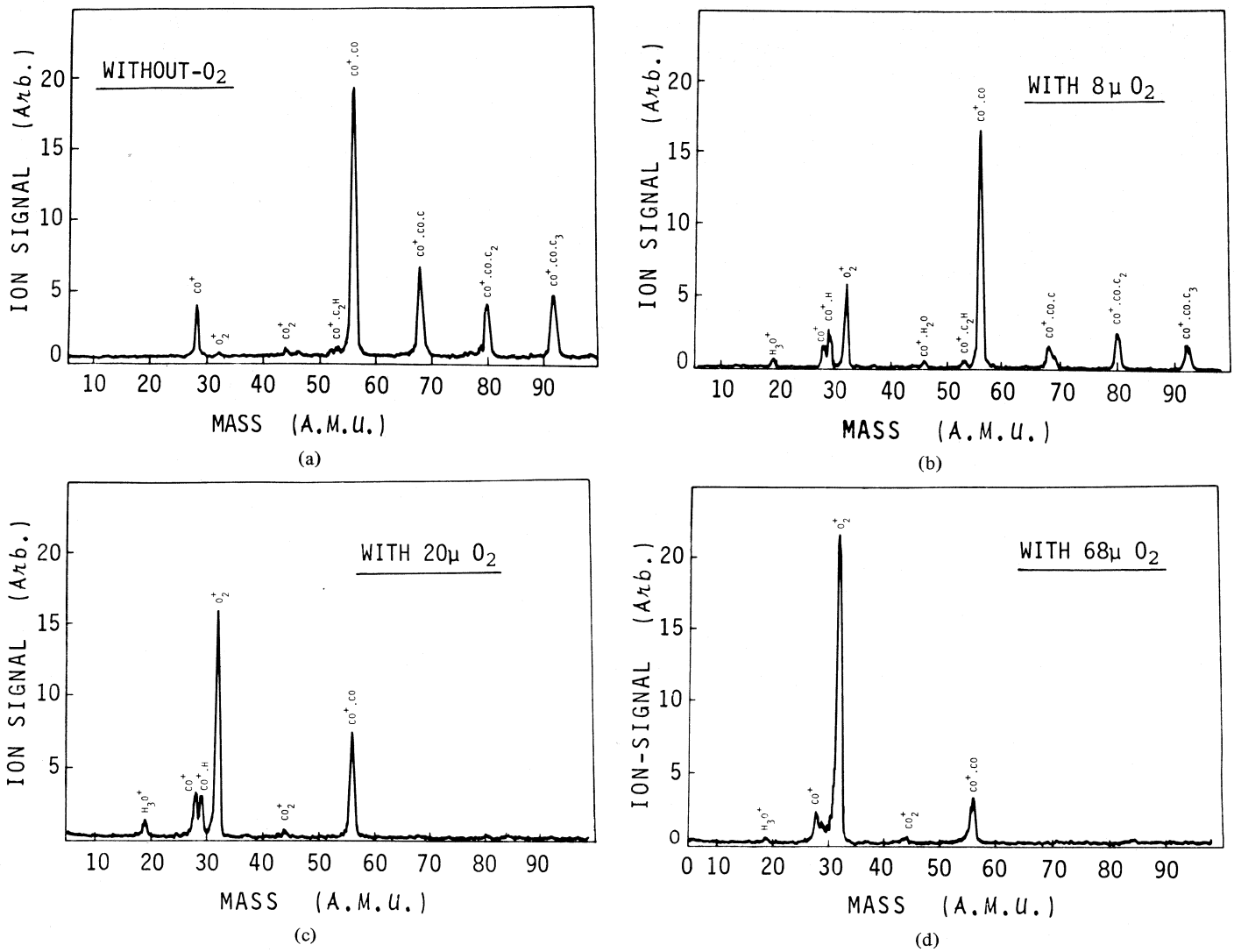


Fig. 2. (a) Positive ion mass spectra of He–CO mixture without oxygen. Discharge current–10 mA, He–16.5 torr, CO–1.75 torr. (b) Influence of 8-m · torr oxygen on positive ion mass spectra in the discharge at experimental conditions of Fig. 2(a). (c) Influence of 20-m · torr oxygen on positive ion mass spectra in the discharge at experimental conditions of Fig. 2(a). (d) Influence of 68-m · torr oxygen on positive ion mass spectra in the discharge at experimental conditions of Fig. 2(a).

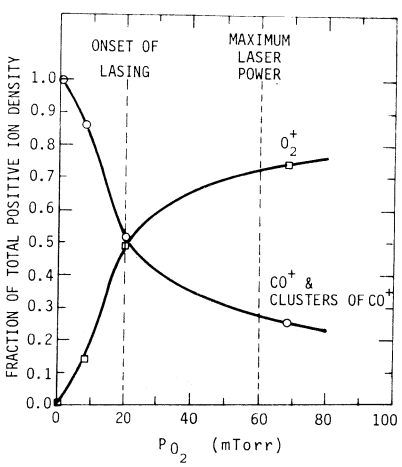


Fig. 3. Fractional positive ion density as function of partial oxygen pressure.

O_2 cannot be overemphasized. The ionization process through the O_2 metastable states is consistent with the observed decrease in E/N upon addition of O_2.

Simple calculations show that the probability of O_2^+ ions being produced by direct electron ionization is at least by a factor of 20 lower than the probability of ionizing O_2 through its metastable states which are populated by the relaxation of the $a^3\Pi$ level of CO. On the other hand, one could also surmize that the change in the relative ion abundance is due to charge exchange in the following process:

$$CO^+ + O_2 \longrightarrow O_2^+ + CO + KE.$$

This process, however, cannot explain the reduction in the axial field of the discharge and the change in the *E-I* curves from a positive to a negative slope. The latter is indicative of ionization by stage processes [5].

Moreover, in this process the density of O_2^+ should be proportional to the density of CO^+. The reduction in E/N with the concentration of O_2 should lead to a reduction in CO^+ and thus of O_2^+ which in turn means a drop in electron density. This is in contradiction to the experimental results.

The decrease in E/N is not due to a decrease in electron loss processes. Such processes would mean an extremely high volume recombination rate, which is much higher than that shown by Center [8] to be less than 10^{-7} cm^3s^{-1}.

The density of O_2^* (metastable) was calculated, assuming that O_2 ions are produced by ionization of the metastable states. The calculation was based on the electron energy distribution function derived in [1] and an estimate of the plasma losses. At a current of 18 mA and 25 m · torr oxygen, about 0.5 percent of the oxygen molecules are excited to metastable states.

Finally, one should note the ion composition in the CO–He mixture without oxygen. The fact that $CO^+:CO:C_n$ clusters dominate the discharge is of major importance in calculation and theories of the kinetics of the discharge, such as those performed by Nighan and Wiegand [6] and Lowke *et al.* [7]. In such calculations the ambipolar diffusion plays an important role; in particular in the onset of filamentation and constriction at higher gas pressures, where volume recombination cannot be neglected.

In order to obtain a more comprehensive understanding of the basic process involved in an He–CO–O_2 discharge, one should know more about the metastable states of oxygen involved in the relaxation and subsequent ionization.

References

[1] H. Keren, P. Avivi, and F. Dothan, "The influence of oxygen on CO-laser performance," *IEEE J. Quantum Electron. (Part I of Two Parts)*, vol. QE-11, pp. 590–594, Aug. 1975.

[2] P. D. Tannen, P. Bletzinger, and A. Garscadden, "Species composition in the CO_2 discharge laser," *IEEE J. Quantum Electron.*, vol. QE-10, pp. 6–11, Jan. 1974.

[3] J. M. Austin and A. L. S. Smith, "Analysis of positive ions in CO_2 gas laser systems," *J. Phys. D: Appl. Phys.*, vol. 5, pp. 468–475, 1972.

[4] J. Freudental, "Collision processes in a CO_2 laser plasma," *J. Appl. Phys.*, vol. 41, pp. 2447–2453, May 1970.

[5] A. Von Engel, *Ionized Gases*, 2nd ed. New York: Oxford, 1965, pp. 244–245.

[6] W. L. Nighan and W. J. Wiegand, "Influence of negative ion processes on steady state properties and striations in molecular gas discharges," *Phys. Rev. A*, vol. 10, pp. 922–945, Sept. 1974.

[7] J. J. Lowke, A. V. Phelps, and B. W. Irwin, "Predicted electron transport coefficients and operating characteristics of CO_2-N_2-He laser mixtures," *J. Appl. Phys.*, vol. 44, pp. 4664–4671, Oct. 1973.

[8] R. E. Center, "Electron-ion recombination measurements in CO at high pressures," *J. Appl. Phys.*, vol. 44, pp. 3538–3542, Aug. 1973.

1202.8-Å Generation in Hg Using a Parametrically Amplified Dye Laser

K. S. HSU, A. H. KUNG, L. J. ZYCH, J. F. YOUNG, AND S. E. HARRIS

Abstract—**We have generated 1202.8-Å radiation, one-half the frequency of the $1s^1S_0$–$2s^1S_0$ forbidden transition in He, using resonantly enhanced four-wave optical mixing in Hg vapor. Peak powers of 300 W in a ~ 15-ps pulse have been achieved using a tunable narrow-band source consisting of a parametrically amplified commercial dye laser. The dependence of the conversion efficiency on the spectral properties of this source is described. Hg is shown to be negatively dispersive for this process, and thus phase matchable.**

We report the generation of 1202.8-Å radiation by resonantly enhanced four-wave optical mixing [1]–[3] in Hg vapor. 1202.8-Å radiation is particularly interesting because it is the half frequency of the $1s^1S_0$–$2s^1S_0$ forbidden transition in He. Such a source could be used for the creation of high densities of metastable $2s^1S_0$ He by two-photon absorption, as well as for the generation of 400-Å radiation using resonantly enhanced harmonic generation in He. A peak power of 300 W in a ~15-ps pulse has been obtained at 1202.8 Å. Resonant optical mixing in Hg is achieved using a tunable picosecond-duration narrow-band source consisting of a commercial flashlamp pumped dye laser parametrically amplified using the frequency quadrupled output of a passively mode-locked Nd:YAG laser. The amplified tunable pulse is then frequency doubled and mixed with the output from a parametric generator-amplifier [4] to yield 1202.8-Å radiation.

Following the first demonstration of harmonic generation of UV and VUV radiation in metal vapors [5], Hodgson *et al.* [1] and Bloom *et al.* [3] demonstrated the advantages of using tunable sources to obtain resonant enhancement of the mixing process. The degree of enhancement achieved depends critically on the linewidth and stability of the source used. In addition, the efficiency of the mixing process depends on the ability to accurately control and adjust the interacting beams with respect to both time and space. In all of these respects, a source consisting of a parametrically amplified, stable, well-controlled laser has a number of attractive advantages, as recently described by Massey *et al.* [6], [7].

A schematic of our experimental arrangement is shown in Fig. 1. The output of a passively mode-locked Nd:YAG oscillator amplifier chain is frequency quadrupled to provide single mode-locked pulses of high-power 2660-Å radiation at 3 pulses per second. In addition to the usual system components, an electrooptic Pockel's cell is used in the oscillator cavity to determine a fixed time for the start of the laser buildup from noise. We found that by opening the Pockel's cell about 200 μs after triggering the flashlamp, the normal temporal jitter of the laser is reduced from $\pm$ 10 μs to less than $\pm$ 0.25 μs. When operating in this fashion the quality of the mode locking is not noticeably affected. It is possible, however, to destroy the mode locking by delaying the shutter opening too long.

The low temporal jitter of the 2660-Å pulse permits us to synchronize it reliably to a commercial (Chromatix CMX-4) flashlamp pumped dye laser of 1-μs pulsewidth. The bandwidth of the laser is narrowed to less than 1 cm^{-1} with an in-

Manuscript received September 2, 1975. This work was supported in part by the Advanced Research Projects Agency and in part by the Office of Naval Research.

The authors are with the Microwave Laboratory, Stanford University, Stanford, CA.

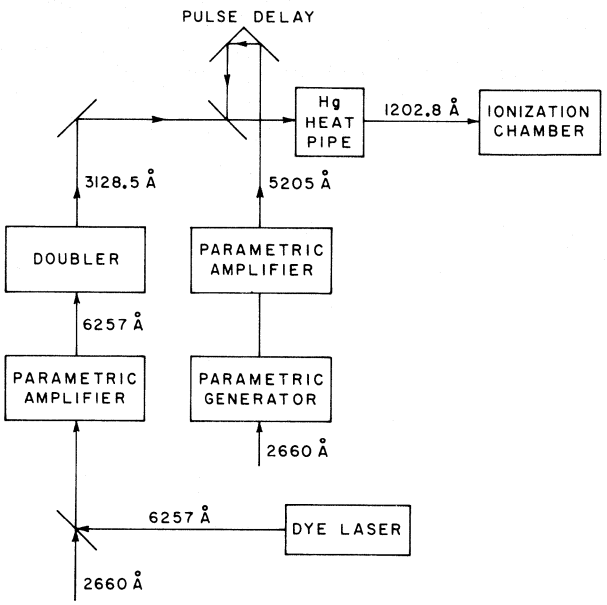


Fig. 1.

ternal etalon. A small portion of the dye laser output, ~ 100 W, and the 2660-Å pulse are incident collinearly into a parametric amplifier consisting of a 5 mm × 5 mm × 50 mm long $NH_4H_2PO_4$ crystal in a temperature controlled oven. For these experiments the laser is tuned to 6257 Å, four times the wavelength of the $6s^1S_0$–$7s^1S_0$ transition of Hg, and the temperature of the crystal oven is adjusted for maximum gain at this wavelength. For a power of 20 MW at 2660 Å focused to a density of 200 MW/cm^2, the theoretical small signal gain is 10^5. We measured peak output powers in excess of 1 MW each for the signal and idler waves, representing ~ 10-percent power conversion of the pump into tunable radiation.

The amplified output is frequency doubled in an angle-tuned crystal of KH_2PO_4 to 3128.5 Å and combined spatially and temporally with a second tunable, synchronized, picosecond pulse from a parametric generator-amplifier [4]. When tuned to 5205 Å (such that the sum wavelength is 1208.8 Å) the bandwidth of this source is ~ 30 Å due to its proximity to degeneracy of the parametric generator. However, because the efficiency of the mixing process is not affected by the spectral width of this (nonresonant) source, this somewhat simpler, more conventional approach is adequate. The collinear beams are focused at the center of a 12-cm-long stainless-steel Hg heat pipe cell. The VUV output signal passes through LiF windows into an ionization chamber used for energy measurements. The space between the Hg cell and the ionization chamber is purged with Ar to avoid absorption of the VUV signal by oxygen. The ionization chamber is filled with research grade p-xylene at 0.1 torr and is sensitive from the short wavelength cutoff of the LiF window at 1150 Å to 1400 Å, the long wavelength limit of the photoionization of p-xylene. We found the quantum yield at 1202.8 Å to be 0.275 based on an absolute calibration using a CW hydrogen discharge lamp through a McPherson 225 spectrometer and a calibrated CsSb photodiode.

For incident power densities of 6 GW/cm^2 at 3128.5 Å, 650 MW/cm^2 at 5205 Å, and an Hg pressure of 20 torr, we measured an output energy of 4.5 nJ, or 300-W peak in an estimated 15-ps-long pulse. This corresponds to a conversion efficiency of 0.5 percent from 5205 Å to 1202.8 Å in the overlapped beam areas. As expected, the output is very sensitive to the dye laser bandwidth and tuning. Tunings of a few angstroms off resonance results in signal decreases of greater than 100. Similarly, increasing the bandwidth from less than 1 cm^{-1} to 3 cm^{-1} by removal of the etalon, decreases the signal by about 10. This is in good qualitative agreement with the results of Stappaerts *et al.* [8]. We did not measure the bandwidth of the 1202.8-Å output, but based on the input bandwidths we expect it to be ~ 16 Å. A second parametrically amplified dye laser for the 5205-Å wavelength would probably be required to reduce the bandwidth to acceptable values for subsequent resonantly enhanced harmonic generation stages.

In these experiments the input radiation was tightly focused such that the effective focal region was short compared to the length of the nonlinear media. In this case the amplitude of the sum wavelength as a function of wave vector mismatch is no longer described by the familiar $\sin x/x$ function associated with plane-wave conditions [9]. Using the theory of [9] it is possible to determine the sign of the mismatch by adding a gas with known dispersion such as Ar. As Ar was introduced into the Hg cell the signal decreased monotonically by two orders of magnitude to below noise level. Since the signal from a positively dispersive vapor would have exhibited an oscillating signal amplitude with comparable peak heights as the Ar pressure was increased, while that from a negatively dispersive media would show no such oscillation, this indicates that Hg is negatively dispersive for the process. Thus the conversion efficiency could be increased using higher power sources to maintain the power density over a longer length and phase matching the process by adding the proper ratio of a positively dispersive vapor.

In summary, we have demonstrated the use of parametric amplification of a flashlamp pumped dye laser to obtain tunable, picosecond duration, high-power visible pulses. We have demonstrated the application of these pulses for efficient resonantly enhanced sum generation into the VUV region at 1202.8 Å. By tuning the second source from 4000 Å to 7000 Å, it should be possible to obtain tunable signals from 1125 Å to 1280 Å. This falls within the gain profiles of Ar excimer and hydrogen amplifiers, thus creating the possibility of sources of very high brightness in this region of the spectrum.

ACKNOWLEDGMENT

The authors wish to thank B. Yoshizumi for his expert technical assistance.

REFERENCES

[1] R. T. Hodgson, P. P. Sorokin, and J. J. Wynne, "Tunable coherent vacuum-ultraviolet generation in atomic vapors," *Phys. Rev. Lett.*, vol. 32, pp. 343–346, 1974.
[2] S. E. Harris and D. M. Bloom, "Resonantly two-photon pumped frequency converter," *Appl. Phys. Lett.*, vol. 24, pp. 229–230, 1974.
[3] D. M. Bloom, J. T. Yardley, J. F. Young, and S. E. Harris, "Infrared up-conversion with resonantly two-photon pumped metal vapors," *Appl. Phys. Lett.*, vol. 24, pp. 427–428, 1974.
[4] A. H. Kung, "Generation of tunable picosecond VUV radiation," *Appl. Phys. Lett.*, vol. 25, pp. 653–654, 1974.
[5] A. H. Kung, J. F. Young, G. C. Bjorklund, and S. E. Harris, "Generation of vacuum ultraviolet radiation in phase-matched Cd vapor," *Phys. Rev. Lett.*, vol. 29, pp. 985–988, 1972.
[6] G. A. Massey and J. C. Johnson, "Generation of frequency stable narrow-band optical pulses by high-gain parametric amplification," presented at the Conf. Laser Engineering and Applications, Washington, DC, May 28–30, 1975, Paper 17.5.
[7] G. A. Massey, J. C. Johnson, and R. A. Elliott, "Generation of frequency-controlled nanosecond and picosecond optical pulses by high-gain parametric amplification," *IEEE J. Quantum Electron.*, vol. QE-12, Feb. 1976, to be published.
[8] E. A. Stappaerts, G. W. Bekkers, J. F. Young, and S. E. Harris, "Two-photon-pumped frequency converters: Linewidth of nonallowed transition," in preparation.
[9] G. C. Bjorklund, "Effects of focusing on third-order nonlinear processes in isotropic media," *IEEE J. Quantum Electron.*, vol. QE-11, pp. 287–296, June 1975.

Notes and Lines

Millimeter and Submillimeter-Wave Laser Action in Symmetric Top Molecules Optically Pumped Via Perpendicular Absorption Bands

T. Y. CHANG AND J. D. McGEE

Abstract—**Ninety-nine new far infrared (FIR) laser lines from 227 μm to 1.965 mm have been observed in CH_3CN, CH_3CCH, CH_3Cl, CH_3Br, and CH_3I by optically pumping these gases with CO_2-laser pulses of 150-μs duration.**

Manuscript received July 22, 1975.
The authors are with Bell Laboratories, Holmdel, NJ 07733.

The purpose of this note is to report the observation of ninety-nine new far infrared (FIR) laser lines between 227 μm and 1.965 mm in acetonitrile (CH_3CN), methylacetylene (CH_3CCH), methylchloride (CH_3Cl), methylbromide (CH_3Br), and methyliodide (CH_3I) when they are optically pumped in the region of their perpendicular absorption bands by a CO_2 laser.

The experimental apparatus has been described previously [1]. Briefly, the CO_2 laser is a grating-tuned current-pulsed unit delivering 150-μs pulses of up to 200-W peak power at 120 pps. The optically pumped FIR laser cavity has 10-cm-diameter internal gold mirrors separated by approximately 93 cm. One mirror is concave with a 2.3-m radius of curvature. The other mirror is flat with a 2.16-mm-diameter coupling hole. The FIR laser wavelengths are measured with a scanning

TABLE I
CH_3CN LASER LINES

Wavelength (μm)	CO_2 Laser, Offset (μm), Line, (MHz)	Rel. Pol.	Max Out/In; Press (mW/W; mTorr)	Thresh. (W)
704.53	9.2,R(34),-15	∥	0.12/41;28	11
1351.78	9.3,R(20),-15	⊥	0.02/49;20	47
453.41[a]	9.3,R(16), 0	⊥	0.75/43;43	6
(466.25)		⊥	0.56/43;35	
(480.01)		⊥	0.20/43;17	
[441.15]		⊥	0.18/43;43	
1014.89	9.3,R(14),-20	⊥	0.018/43;20	24
387.31[a]	9.3,R(12),+15	⊥	0.38/44;40	11
741.62	9.3,R(8), +35	⊥	0.23/48;24	7
561.41	9.3,R(8), +40	∥	0.18/42;41	19
494.74[a]	9.4,P(6), -10	⊥	4.0/51;25	4
(510.16)		⊥	0.19/51;31	
1016.33	9.5,P(8), -40	∥	0.045/33;15	5
1164.83	9.5,P(10),+45	∥	0.050/45;20	24
854.41	9.5,P(16),-10	∥	0.13/70;35	18
346.32	9.5,P(16),-10	∥	0.45/70;95	7
388.39	9.6,P(22),+30	∥	0.005/69;24	43
427.04	9.6,P(26),+15	⊥	0.024/61;43	15
652.68[a]	9.6,P(30),-15	∥	0.32/77;20	29
281.18	9.7,P(34),-20	⊥	0.018/44;95	12
1086.89	9.7,P(40),+40	⊥	0.15/46;24	12
386.41	9.8,P(46),-15	∥	0.003/42;43	17
281.98	9.8,P(50),+50	∥	0.67/38;95	2
(286.88)		∥	0.29/38;95	

[a]Previously reported by Radford [3].

Fabry–Perot (FP) interferometer equipped with fine mesh-mirrors.

The measured FIR laser wavelengths corrected for the effect of finite aperture size in the FP interferometer are listed in the first column of Tables I–V, and are believed to have an accuracy of better than ±0.1 cm^{-1}. Some of the stronger FIR laser lines are accompanied by oscillation at one or two cascade transitions at somewhat longer wavelengths [2]. The wavelengths of these cascade transitions are listed in parentheses. Some strong laser lines are also accompanied by a refilling laser transition in the lower vibrational state [2], with a somewhat shorter wavelength. These are listed in square brackets.

The identity of the CO_2-laser line used and the required approximate offset of the pump frequency from the CO_2 line center are given in the second column of the tables. The third column gives the relative polarization between the pump and the FIR laser radiation. The maximum FIR output power (milliwatts), the pump power used (in watts), and the optimum gas pressure inside the FIR resonator (in mtorr) are given in the fourth column. The last column gives the threshold pump power (in watts) measured at $\frac{1}{5}$ of the optimum pressure (but not lower than 20 mtorr).

Four of the laser lines in CH_3CN (Table I) marked with a superscript a have been reported recently by Radford [3]. The wavelengths he reported are guide wavelengths in the waveguide resonator he used and are up to 1 percent longer than our values.

Fetterman *et al.* [4] observed a 364.5-μm line in CH_3Cl by using a high-power CO_2 TEA laser tuned to the 9.29-μm $R(16)$ line as the pump source. The same pump line produced laser action at 378.57 μm (Table III) in our apparatus. Because of the large difference in laser wavelengths, we believe two distinctly different FIR laser lines have been observed in two different experiments. The other three FIR laser lines in CH_3Cl reported by Fetterman *et al.* [4] have not been observed in our apparatus.

Three of the laser lines in CH_3I (Table V) marked with a superscript a have been reported by Dyubko *et al.* [5]. Their

TABLE II
CH_3CCH LASER LINES

Wavelength (μm)	CO_2 Laser, Offset (μm), Line, (MHz)	Rel. Pol.	Max Out/In; Press (mW/W; mTorr)	Thresh. (W)
428.87	9.2,R(38),+35	∥	0.012/20;51	9
516.77	9.3,R(12),+35	∥	0.006/47;39	25
531.08	9.4,P(6), 0	∥	0.004/45;92	9
1097.11	9.5,P(8),-20	∥	0.32/50;51	9
566.44	9.5,P(18),+25	∥	0.58/63;55	34
583.77	9.6,P(20),-15	∥	0.004/50;47	7
675.29	9.7,P(40), 0	∥	0.33/55;39	15

TABLE III
CH_3Cl LASER LINES

Wavelength (μm)	CO_2 Laser, Offset (μm), Line, (MHz)	Rel. Pol.	Max Out/In; Press (mW/W; mTorr)	Thresh. (W)
461.20	9.2,R(42),-25	⊥	0.027/11;140	2
275.09	9.2,R(36),+10	∥	0.05/60;310	6
378.57	9.3,R(16),+50	⊥	0.18/29;225	15
275.00	9.3,R(14),+45	∥	1.7/44;310	4
(281.67)				
943.97	9.3,R(12),-30	∥	13/45;100	2
236.25	9.4,R(2),-10	⊥	0.1/13;310	2
1886.87	9.6,P(26),+20	⊥	1.6/57;100	14
958.25	9.7,P(38),-50	∥	0.52/40;100	16
333.96	9.8,P(42),+40	⊥	44/47;225	1.3
227.15	9.8,P(48),+50	∥	0.072/26;140	5
870.80	9.9,P(52),+30	∥	1.3/16;49	5
511.90	10.1,R(52), 0	⊥	0.065/17;93	4
286.79	10.2,R(34),-35	⊥	0.31/69;225	22
568.81	10.2,R(26), +5	∥	0.022/97;120	70
349.34	10.3,R(18), -5	∥	7.4/89;180	3
240.98	10.5,P(10),-30	∥	1.3/90;260	12
271.29	10.6,P(20),-35	⊥	0.33/86;460	11
261.03	10.7,P(34),-20	∥	0.069/106;310	20
307.65	11.0,P(19)[a], -50	∥	0.57/23;225	2

[a](01^11)-(11^10) band of CO_2.

TABLE IV
CH_3Br Laser Lines

Wavelength (μm)	CO_2 Laser, Offset (μm), Line, (MHz)	Rel. Pol.	Max Out/In: Press (mW/W; mTorr)	Thresh. (W)
352.75	9.5,P(18),+25	⊥	2.3/66;550	24
407.72	9.6,P(28),-40	∥	0.013/57;115	34
245.04	9.6,P(28),-40	∥	0.89/57;650	7
585.72	9.7,P(40),+25	∥	3.3/49;150	6
658.53	9.9,P(56), 0	∥	5.2/52;82	9
279.81	10.1,R(52), 0	∥	0.012/51;230	8
311.21	10.1,R(50),+50	⊥	0.33/15;102	3
925.52	10.1,R(46),-35	∥	14/33;74	5
508.48	10.1,R(42),+30	∥	2.1/47;91	6
545.39	10.2,R(32),+20	∥	10/63;115	6
294.28	10.2,R(28),-40	∥	1.1/117;550	15
422.78	10.2,R(26),+50	∥	0.009/117;180	62
660.70	10.2,R(20),+25	⊥	15/68;450	13
380.02	10.3,R(18),+50	⊥	7.0/83;450	10
715.40	10.3,R(14),-15	⊥	1.6/63;91	8
(749.36)		⊥		
311.07	10.3,R(12),+30	⊥	0.019/69;300	11
264.05	10.3,R(10),+10	∥	5.3/73;375	15
332.86	10.3,R(6), 0	⊥	0.35/64;450	14
1310.38	10.4,R(4),-30	⊥	5.3/90;125	14
414.98	10.4,R(2),+45	⊥	17/46;180	10
1572.64	10.4,P(4), 0	∥	2.2/58;99	4
333.15	10.5,P(8),+35	∥	0.009/83;145	37
990.51	10.5,P(10), 0	∥	1.3/95;115	32
749.29	10.5,P(14),+5	⊥	2.8/73;91	7
631.93	10.6,P(16),+20	∥	0.0021/78;125	39
311.10	10.6,P(20),+10	∥	1.0/52;300	10
632.00	10.6,P(22), 0	⊥	0.025/88;300	11
531.06	10.6,P(24), -5	∥	5.5/108;300	23
418.31	10.7,P(26),+10	∥	0.49/101;375	17
1965.34	10.7,P(28), 0	∥	1.3/105;91	28
831.13	10.7,P(28),+10	∥	5.4/105;91	15
545.21	10.8,P(38), -5	⊥	8.8/39;180	2
(564.68)				
311.20	10.8,P(40),+45	⊥	1.5/21;300	4

TABLE V
CH_3I Laser Lines

Wavelength (μm)	CO_2 Laser, Offset (μm), Line, (MHz)	Rel. Pol.	Max Out/In; Press (mW/W; mTorr)	Thresh. (W)
377.45 [a]	9.3,R(16), +5	∥	5.1/47;435	7
392.48	9.3,R(14), +5	∥	0.017/40;100	24
583.87	9.4,P(4), 0	∥	0.12/32;192	4
525.32	9.4,P(4),-25	∥	0.093/26;130	6
639.73	9.4,P(6), +20	∥	0.17/35;79	30
477.87	9.6,P(26),+10	∥	0.021/82;110	58
508.37	9.7,P(34), 0	∥	13/66;192	7
578.90	10.2,R(34),-30	∥	0.98/68;375	54
459.18	10.5,P(8), 0	⊥	0.16/69;155	54
517.33	10.5,P(14),+30	∥	0.38/81;435	32
576.17	10.6,P(16),-30	∥	1.6/58;320	16
447.17 [a]	10.6,P(18), 0	∥	23/103;225	1.5
(457.25)		∥		
719.30	10.6,P(22),+25	∥	0.33/52;320	26
542.99	10.7,P(26),+10	∥	0.002/99;132	15
670.99	10.7,P(28),+20	∥	0.93/91;145	22
1253.67 [a]	10.7,P(32),+25	∥	13/98;170	5
529.28	10.8,P(36), 0	∥	3.2/60;320	20
1063.29	10.8,P(38),+5	∥	6.5/71;435	25
390.53	10.8,P(42),+25	∥	1.8/57;750	9

[a] Previously reported by Dyubko *et al.* [5].

wavelength values agree with ours within ±0.15 percent, which is apparently the accuracy of their measurements. (The identities of the CO_2-laser lines are misprinted in [5].)

In a previous publication [1], we investigated CH_3F, CH_3CN, and CH_3CCH in the region of their parallel absorption bands and presented spectroscopic interpretation of the laser lines based on correlations among absorption-emission frequency pairs in each molecule. A preliminary analysis of the present data indicates that the number of absorption-emission frequency pairs belonging to each of several overlapping absorption bands in each molecule is insufficient for an unambiguous spectroscopic interpretation. Consequently, a meaningful spectroscopic analysis of these laser lines will have to await the result of further investigations using isotopic CO_2 and N_2O

lasers, or even a tunable infrared (IR) source as the pump source. Suffice it to say that the main absorption bands involved in the present investigations are all associated with the CH_3-rocking mode in these molecules.

REFERENCES

[1] T. Y. Chang and J. D. McGee, "Millimeter and submillimeter wave laser action in symmetric top molecules optically pumped via parallel absorption bands," *Appl. Phys. Lett.*, vol. 19, pp. 103–105, 1971.

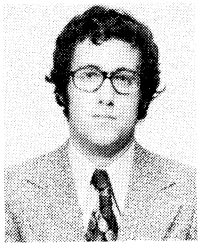
[2] T. Y. Chang and T. J. Bridges, "Laser action at 452, 496 and 541 μm in optically pumped CH_3F," *Opt. Commun.*, vol. 1, pp. 423–426, 1970.

[3] H. E. Radford, "New CW lines from a submillimeter waveguide laser," *IEEE J. Quantum Electron.*, vol. QE-11, pp. 213–214, May 1975.

[4] H. R. Fetterman, H. R. Schlossberg, and J. Waldman, "Submillimeter lasers optically pumped off resonance," *Opt. Commun.*, vol. 6, pp. 156–159, 1972.

[5] S. F. Dyubko, V. A. Svich, and L. D. Fesenko, "Submillimeter laser emission of CH_3I molecules excited by CO_2 laser radiation," *Opt. Spektrosk.*, vol. 37, p. 208, 1974; also *Opt. Spectrosc.* (USSR), vol. 37, p. 118, 1974.

Contributors



Jeffrey L. Ahl was born in New York, NY, on September 13, 1948. He received the B.S. degree in physics from Rensselaer Polytechnic Institute, Troy, NY and the M.S. degree in applied physics from Cornell University, Ithaca, NY, in 1970 and 1973, respectively.

Since 1973 he has been working in the McDonnell Douglas Research Laboratories in St. Louis, MO. He is currently engaged in research on pulsed visible lasers.

*



Richard V. Babcock (M'72) was born in Philadelphia, PA, in 1933. He received the B.S. degree in chemical engineering from Drexel Institute, Philadelphia, in 1956, and the Ph.D. degree in electrical engineering from Carnegie-Mellon University, Pittsburgh, PA, in 1970.

Joining the Central Research Laboratories of the Westinghouse Electric Corporation, Pittsburgh, in 1956, he studied nuclear radiation effects for 12 years with particular interest in the development of radiation detectors and in the vulnerability of electronic systems. Since joining the Westinghouse Research Laboratories in 1971 following his doctoral studies, he has worked on gaseous lasers, and is currently interested in improving self-sustained electrical-discharge pumping of large systems.

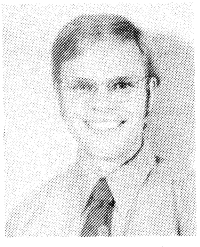
*



W. R. Binns was born in Ottawa, KS, on November 7, 1940. He received the B.S. degree in physics from Ottawa University, Ottawa, in 1962, and the M.S. and Ph.D. degrees, both from Colorado State University, Fort Collins, in 1966 and 1969, respectively.

Since 1969 he has been working at the McDonnell Douglas Research Laboratories, St. Louis, MO, where he is currently a Scientist in the Radiation Sciences Laboratories. From 1969 until 1973 his research was primarily directed at the study of heavy nuclei in the primary cosmic radiation. Since 1973 he has pursued research in pulsed infrared and visible lasers.

*

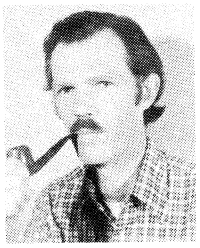


Edward J. Danielewicz (S'74) was born in Philadelphia, PA, on July 11, 1949. He received the B.S. degree in electrical engineering from the University of Pennsylvania, Philadelphia, in 1971, and the M.S. degree in electrical engineering from the University of Illinois, Urbana, in 1973.

He is currently working towards the Ph.D. degree in electrical engineering in the area of integrated optics using optically pumped far-infrared lasers at the University of Illinois, Urbana.

Mr. Danielewicz is a student member of the Optical Society of America and a member of Sigma Xi and Phi Kappa Phi.

*

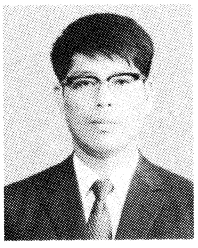


Thomas A. DeTemple (M'73) was born in New York, NY, in 1941. He received the B.S. and M.S. degrees in physics from San Diego State University, San Diego, CA, in 1965 and 1969, respectively, and the Ph.D. degree in electrical engineering from the University of California at Berkeley, Berkeley, in 1971.

From 1965 to 1969 he was engaged in high-power-gas laser research at the Navy Electronics Laboratory in San Diego. From 1971 to 1972 he was an Assistant Professor of Optical Sciences at the University of Arizona, Tucson. Since 1972 he has been at the University of Illinois, Urbana, where he is currently an Associate Professor engaged in gas laser research in the UV, visible, IR, and FIR regions. His interests also include nonlinear optics, quantum optics, gas dynamics, and gaseous electronics.

Dr. DeTemple is a member of the American Physical Society.

*

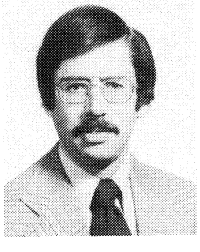


Shun-Ichi Gonda was born in Tokyo, Japan, on September 13, 1936. He received the M.Eng. and the D.Eng. degrees from Waseda University, Tokyo, Japan, in 1962 and 1973, respectively. The subject of his doctoral research was the electrical conduction of semiconductors at very low temperatures.

In 1962 he joined the Electrotechnical Laboratory, Tokyo, Japan, to work on research of the electrical properties of impure semiconductors at very low temperatures. Since 1970 he has been engaged in research on semiconductor lasers and integrated optics.

Dr. Gonda is a member of the Institute of Electronics and Communication Engineers of Japan, the Japan Society of Applied Physics, and the Physical Society of Japan.

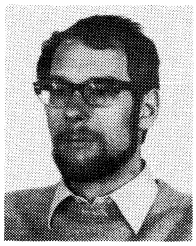
*



David A. Huchital (S'60-M'69) received the Ph.D. degree in plasma physics from Rensselaer Polytechnic Institute, Troy, NY, in 1965.

He joined the Perkin-Elmer Corporation, Norwalk, CT, as a Senior Scientist in 1966, and became Associate Director of Research in 1972. He has worked in the areas of plasma instabilities, gaseous electronics, electron spectroscopy, and gas and solid-state lasers.

Dr. Huchital is a member of Eta Kappa Nu, Tau Beta Pi, Sigma Xi, and the American Physical Society.



Gerhard A. Koepf was born in Innsbruck, Austria, on July 20, 1942. He received the Dipl. Ing. and Dr. Techn. degrees in electrical engineering (communications engineering) from the Technical University, Vienna, Austria in 1967 and 1972.

In 1967 he became Research Assistant and later Assistant Professor at the Institut für Hochfrequenztechnik, University of Technology, Vienna, where he did research in gas lasers, holography, and optical data processing. Since 1971 he has held a Lectureship on Optical Communications. In 1973 he worked out a feasibility study on direct satellite television for the Austrian Ministry of Science as a Project Leader. He became responsible for the laser efforts of the Institut für Hochfrequenztechnik in 1974. In 1976 he will be pursuing a Postdoctoral Resident Associateship from the National Research Council, National Academy of Science Washington, DC, at the NASA Goddard Space Flight Center, Greenbelt, MD.

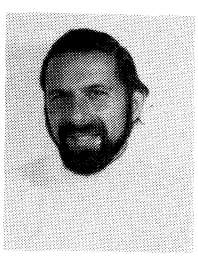
*



W. A. Kreiner was born in Graz, Austria, on January 3, 1942. He received the Ph.D. degree in physics from Graz University, Graz, in 1966.

In 1968 he joined Siemens AG in Munich, Germany, where he worked in the field of holography. From 1969 to 1973 he was at the University of Freiburg, Germany, as a Research Assistant, working on the application of IR lasers in rotational spectroscopy (infrared-microwave double resonance). In 1974 he held a Postdoctoral fellowship at the National Research Council of Canada, where he worked mainly in the field of spectroscopy. He is currently at the Abteilung für Physikalische Chemie, University of Ulm, Ulm, Germany. His main field of interest is laser spectroscopy.

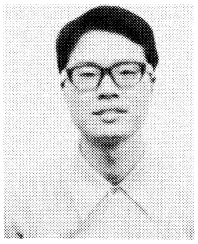
*



Irving Liberman was born in the Bronx, N.Y., on June 24, 1937. He received the B.S. degree from the College of the City of New York, and the M.S. and Ph.D. degrees from Northwestern University, Evanston, IL, all in electrical engineering, in 1958, 1960, and 1964, respectively.

He joined the Westinghouse Research Laboratories, Pittsburgh, PA, in 1963, where he first worked on thin-film technology. In 1965 he transferred to the Optical Physics Department, where he studied pulsed well-stabilized gas discharges which were primarily applied to the optical pumping of lasers. He then developed efficient, high-powered CW Nd:YAG lasers with emphasis on krypton lamps and on alkali lamps which spectrally matched the excitation spectrum of Nd:YAG. Since 1972 he has been interested in high-powered pulsed CO_2 lasers. In 1974 he became an Industrial Staff member at the Los Alamos Scientific Laboratory, Los Alamos, NM, where he is contributing to the development of short-pulsed CO_2 lasers for fusion applications.

Dr. Liberman is a member of the American Physical Society, the Optical Society of America, Eta Kappa Nu, Tau Beta Pi, and Sigma Xi.



Seiji Mukai was born in Osaka, Japan, on March 15, 1949. He received the B.S. degree in physical science and the M.S. degree in physics, both from Kyoto University, Kyoto, Japan, in 1971 and 1973, respectively.

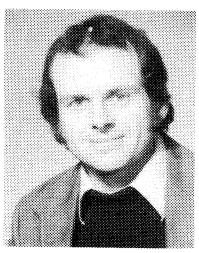
Since 1973 he has been with the Electrotechnical Laboratory, Tokyo, Japan, where he has been engaged in the research of semiconductor lasers.

Mr. Mukai is a member of the Physical Society of Japan and the Japan Society of Applied Physics.

*

W. D. Partlow, photograph and biography not available at the time of publication.

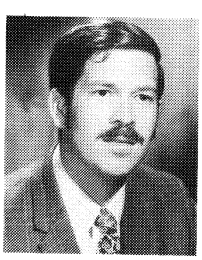
*



James A. Piper was born in Oamaru, New Zealand, in 1947. He received the B.Sc. (Hons) and Ph.D. degrees, both from the University of Otago, Dunedin, New Zealand, in 1967 and 1971, respectively.

From August 1971 to May 1975 he was engaged as a Postdoctoral Research Fellow at the Clarendon Laboratory, Oxford, England. His research activities centered on CW hollow-cathode rare gas–metal vapor lasers and, later, pulsed-metal vapor lasers. In June 1975 he took up an appointment at Macquarie University, Sydney, Australia.

*

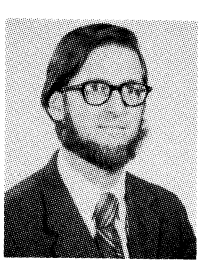


David H. Seib was born in Exeter, CA, on January 23, 1943. He received the B.S. degree in electrical engineering from the California Institute of Technology, Pasadena, in 1964, and the M.S. and Ph.D. degrees in electrical engineering from Stanford University, Stanford, CA, in 1965 and 1969, respectively. His thesis work was concerned with photoemission and optical studies of metals.

Since 1969 he has been employed by the Laboratories Division of the Aerospace Corporation, Los Angeles, CA, where he has been involved in semiconductor device research, including photodetectors, properties of III–V compounds, charge-coupled devices, and integrated optics.

Dr. Seib is a member of the American Physical Society.

*

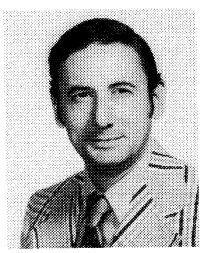


Anthony E. Siegman (S'54–M'57–F'66) was born in Detroit, MI, on November 23, 1931. He received the A.B. degree from Harvard College, Cambridge, MA, in 1952, the M.S. degree in applied physics from the University of California at Los Angeles, Los Angeles, in 1954, having studied under the Hughes Cooperative Plan, and the Ph.D. degree in electrical engineering from Stanford University, Stanford, CA, in 1957, where, from 1954 to 1957, he was a National Science Foundation Fellow and Research Assistant.

Since 1957 he has been on the Faculty of Stanford University, where he is now Professor of Electrical Engineering. He has published numerous technical articles in the fields of microwave electronics, parametric devices, microwave masers, and lasers and their applications, as well as *Microwave Solid-State Masers* (McGraw-Hill, 1970). He currently directs a research program in lasers and their applications at Stanford. He is also the inventor of the unstable optical-resonator concept widely used in high-power laser systems.

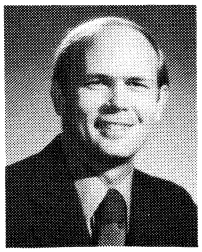
Prof. Siegman is a fellow of the Optical Society of America, and a member of the National Academy of Engineering. He was Program Chairman for the International Quantum Electronics Conference in Phoenix in 1966 and General Chairman of the 1968 International Quantum Electronics Conference held in Miami. In 1972, together with D. J. Kuizenga, he received the W. R. G. Baker Award of the IEEE TRANSACTIONS during 1971.

*



George N. Steinberg (S'54-M'57) was born in Brooklyn, NY, on June 12, 1935. He received the B.S.E.E. degree from the Massachusetts Institute of Technology, Cambridge, in 1956, and the M.S.E.E. degree from Cornell University, Ithaca, NY, in 1957.

He joined the Perkin-Elmer Corporation, Norwalk, CT, in 1956, where he has been employed in a variety of spectroscopic and laser-related assignments. He is currently engaged in the development of radio-frequency-excited electrodeless lamps for laser applications.



Harold M. Stoll was born in Detroit, MI, on January 7, 1947. He received the B.S. degree in electrical engineering from Stanford University, Stanford, CA, in 1968, and the M.S. and Ph.D. degrees in electrical engineering from the California Institute of Technology, Pasadena, in 1969 and 1974, respectively.

Since 1973 he has been employed at the Aerospace Corporation, Los Angeles, CA, where his research activities have concentrated in the field of integrated optics.

Dr. Stoll is a member of Phi Beta Kappa, Tau Beta Pi, and Sigma Xi.

*



Colin Webb was born in Erith, Kent, England, in 1937. He received the B.Sc. degree from the University of Nottingham, Nottingham, England, in 1960, and the D. Phil. degree from the University of Oxford, Oxford, England, in 1964 where, as a graduate student, he worked on an early gas laser research project at the Clarendon Laboratory.

In 1964 he joined the staff of Bell Laboratories, Murray Hill, NJ, where he worked on development and diagnostic studies of the rare-gas ion lasers. He returned to Oxford in 1968 to take up a Research Fellowship. Since then his research interests have been in the fields of discharge physics, gas laser excitation mechanisms—and, in particular, studies of thermal energy charge transfer collisions—and the development of hollow cathode lasers. He was appointed to a University Lectureship at the University of Oxford, in 1971, and in 1973 he became a Fellow of Jesus College, University of Oxford.

Dr. Webb is a member of the Institute of Physics and the American Optical Society.

Theory and Experiments on Grating Couplers for Thin-Film Waveguides

CESAR C. GHIZONI, STUDENT MEMBER, IEEE, BOR-UEI CHEN, AND CHUNG L. TANG, SENIOR MEMBER, IEEE

Abstract—A theoretical and experimental study is made of the grating couplers for thin-film waveguides. It is shown that the perturbation series expansion of the field based upon the Green's function approach can actually be summed to all orders to give an expression for the efficiency of grating couplers of arbitrary thickness. The results obtained by this theory are in good agreement with the experimental results obtained. It is also shown that the grating coupling efficiency depends strongly on the grating profile.

INTRODUCTION

OF the various methods for coupling light beams into the propagating modes of optical waveguides, the use of surface grating couplers [1] is particularly important because of its compatibility with thin-film technology. It was also thought to be highly efficient based upon earlier so-called "dip" measurements [1] in which the input coupling efficiency was inferred from the changes in the transmitted beam and various specularly reflected or diffracted beams when the incident angle was varied through the critical value for coupling. It is now generally agreed [2]-[5] that the dip measurements often overestimate the input coupling efficiency significantly, because of the reflection at the discontinuity at the end of a finite grating [2], [3] and the diffused scattering that were not taken into account in the measurements. On the theoretical side, previous results were based either upon what is essentially a first-order perturbation theory [2], [6], [7], which is valid for thin or shallow gratings only, or upon theories developed for infinite periodic structures [8], [9], which required the solution of either a system of infinite differential or algebraic equations and, in addition, did not take into account the discontinuity at the end of the finite grating. Comparison with experiments has been complicated by the fact that the models assumed in the theory did not always correspond to realistic gratings. The range of validity of the theories is therefore not known and the question of how good the grating couplers were and can be remains open.

In this paper, we report the measured input coupling efficiencies for a series of grating couplers. The results show that the perturbation results are valid only for thin or short gratings. For thick grating couplers the first-order perturbation theory leads to erroneous results and conclusions. It is shown that the perturbation series expansion of the field can actually be summed to all orders to give an expression for the efficiency of grating couplers of arbitrary thicknesses. We will see that the grating profile is a very important factor in determining the coupling efficiency and optimum coupling length of the grating coupler. This fact tends to be overlooked in earlier treatments [4]. It also adds an extra complication to the experimental part: the determination of the specific grating profile. The profile depends on so many parameters during the process of fabrication that it is almost impossible to predict the correct behavior of the final coupler. This, we believe, explains the disagreement between the predicted and the measured optimum coupling lengths [4]. Based upon scanning electron microscope (SEM) pictures of the actual grating profiles and upon diffraction efficiency measurements we can calculate theoretical efficiencies which agree quite well with the experimental results. The calculated results (Fig. 3) for a rectangular profile using the present theory and the perturbation theory of Ogawa *et al.* [6] show that the problem with the earlier perturbation results [6] is more than due to the particular profile assumed; there are essential differences in the results with the same assumed profile. In connection with the experimental results, it should be pointed out that Dalgoutte [3] has reported experimental efficiencies on the order of 70 percent. However, this figure refers to the efficiency of the grating as an output coupler. Unless the input beam can be shaped to match the radiation pattern of the output beam for such a coupler, the reciprocity theorem [2] implies that the input coupling efficiency would be far lower than this. This "aperture matching" problem is an unsolved experimental problem. In this work, we consider input beams that are unshaped plane waves of finite apertures.

Manuscript received July 21, 1975; revised September 26, 1975. This work was supported in part by the National Science Foundation under Grant GK-3384 and in part by the Materials Science Center of Cornell University, Ithaca, NY. One of the authors (C.C.G.) was supported by the Brazilian Space Research Institute, São José dos Campos-SP, Brazil.

The authors are with the School of Electrical Engineering, Cornell University, Ithaca, NY 14853.

BASIC THEORY

We summarize first the essential steps and results of the Green's function analysis for the grating coupler. Although the algebra involved is rather tedious, the basic idea is relatively simple to understand. The grating and waveguide structure are shown in Fig. 1. To avoid overly complicating the discussion, we restrict our consideration to the TE modes,

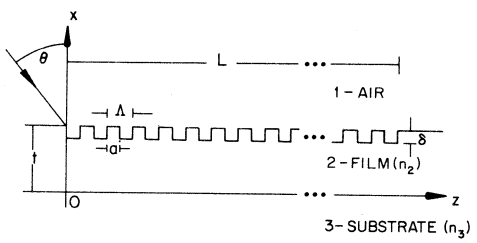


Fig. 1. Schematic diagram of an etched grating coupler.

although the same procedure can be readily extended to the TM modes also.

The transverse electric field E_y in the y direction can be given in terms of the Green's function $G(x', z'|x, z)$ of waveguide structure in the absence of the grating

$$E_y = E_y^0 + k_0^2 \iint \Delta n^2(x', z')\, G(x', z'|x, z)\, E_y(x', z')\, dx'\, dz' \tag{1}$$

and the spatially dependent change in the dielectric constant $\Delta n^2(x, z) = n^2(x, z) - n_i^2$, where k_0 is the free-space wavenumber of the incident wave, n_i is the constant index of refraction of the region i (= 1, 2, 3), and E_y^0 is the incident wave in the waveguide structure in the absence of the grating. $G(x', z'|x, z)$ can be calculated following the standard procedure of taking the Fourier transform in z followed by solving the appropriated differential equation in x subject to the appropriate boundary conditions and then inverse Fourier transform in k_z. The resulting G has three contributions: $G_g + G_r + G_L$, where G_g corresponds to the guided surface waves due to the residues of real poles in the complex k_z plane, G_r corresponds to the radiating modes due to the branch cuts, and G_L corresponds to the leaky-wave modes due to the complex poles. In considering the input coupling efficiency of the grating, the leaky-wave contribution can be neglected on the assumption that the incident angle is always adjusted for coupling into the guided modes, one at a time. Thus (1) leads to a pair of coupled integral equations for the E-fields of the guided and radiating modes, respectively

$$E_g = k_0^2 \iint \Delta n^2\, G_g(E_g + E_y^0 + E_r)\, dx'\, dz' \tag{2a}$$

$$E_r = k_0^2 \iint \Delta n^2\, G_r(E_g + E_y^0 + E_r)\, dx'\, dz'. \tag{2b}$$

Simultaneous solution of these equations will then give the E-field of the guided mode for a given incident wave including the effect of coupling between the guided and radiating modes. The input coupling efficiency is

$$\eta_c = \frac{k_g}{k_0} \int_{-\infty}^{+\infty} |E_g|^2\, dx / (L \cos\theta\, |E_{\text{inc}}|^2) \tag{3}$$

where k_g is the wavenumber of the guided wave in the z direction, θ is the incident angle, and L is the length of the grating coupler. Equation (2) can be further simplified on the basis of the Bragg condition. Such a condition for interaction between the guided modes cannot usually be satisfied; thus (2a) becomes

$$E_g = k_0^2 \iint \Delta n^2(x', z')\, G_g(x', z'|x, z)\, (E_r + E_y^0)\, dx'\, dz'. \tag{4a}$$

Similarly, the radiating mode that can be coupled into the guided mode through (4a) can only come from the same guided mode, thus reducing (2b) to

$$E_r = k_0^2 \iint \Delta n^2(x', z')\, G_r(x', z'|x, z) E_g\, dx'\, dz'. \tag{4b}$$

The problem is then reduced to finding the simultaneous solution of (4a) and (4b). The essential difference between the present theory and the earlier perturbation theory of, for example, Ogawa *et al.* [6] is this: instead of calculating E_g by solving (4a) and (4b) simultaneously, an approximate form of (4a) was used [6]. In this approximation, the very important effect due to the coupling between the radiating and guided modes was taken into account in an ad hoc fashion by replacing G_g by $G_g \exp(-\alpha|z - z'|)$ and neglecting E_r in (4a). This is clearly justified at best for very thin and short grating couplers so that the field in the grating region approximates that of the incident wave.

To solve (4), we introduce the formal operators $\mathcal{G}_g$ and $\mathcal{G}_r$ defined by the following relations:

$$\mathcal{G}_{g,r}\psi(x, z) = k_0^2 \iint \Delta n^2(x', z')\, G_{g,r}(x', z'|x, z) \cdot \psi(x', z')\, dx'\, dz'.$$

Thus (4) can be written as

$$E_g = \mathcal{G}_g(E_r + E_y^0)$$

and

$$E_r = \mathcal{G}_r E_g.$$

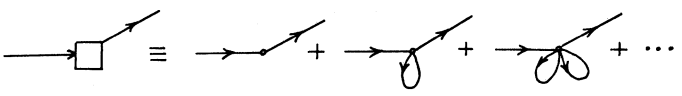
This can be solved formally for E_g

$$E_g = \mathcal{G}_g \frac{1}{1 - \mathcal{G}_r \mathcal{G}_g} E_y^0. \tag{5}$$

Formally, this is the most general form for the E-field of the guided surface wave excited by the incident wave E_y^0; it has meaning only when expanded in the form

$$E_g = (\mathcal{G}_g + \mathcal{G}_g \mathcal{G}_r \mathcal{G}_g + \mathcal{G}_g \mathcal{G}_r \mathcal{G}_g \mathcal{G}_r \mathcal{G}_g + \cdots) E_y^0. \tag{5a}$$

In the context of scattering theory [12], this is called the Born series. The term of nth order in $\mathcal{G}_r$ corresponds to n successive virtual scatterings of the wave by the scatterer as if the whole effect can be written:



in the notation of Feynman diagram technique [12]. It is important to note that E_g calculated this way is the actual field of the guided surface wave in the perturbed waveguide and the perturbation due to the grating is completely taken into account through the use of the Green's function so that any effect due to the discontinuities at the grating termina-

tions is automatically included in this formal result. However, to obtain actual numerical results, (5a) often cannot be evaluated simply without further approximations, even in the simple case of gratings with rectangular profiles. Under the condition where the gratings are sufficiently long in extent so that the reflections at the discontinuities at the grating terminations do not significantly modify the fields in the grating region and hence can be neglected, (5a) can be evaluated and summed in a closed form for the electric field of the guided surface wave without any further simplifications for gratings with rectangular profiles and with minor approximations for other shapes.

Using the series expansion (5a) for the electric field of the guided surface wave and assuming that the grating is long enough so that the reflection due to the discontinuity at the grating termination does not affect the field in the grating region significantly, the electric field is evaluated as follows: Applying $\mathcal{G}_g$ on E_y^0, a phase-matching condition between the z-components of the wave vector of the incident wave, the reciprocal vector of the periodic structure, and the real pole k_g (in the k_z plane) corresponding to the mode in question, is obtained; using this phase-matching condition, the integral involved can be readily evaluated. When operating with $\mathcal{G}_r$, which has a continuous spectrum of values of k_z, we have to keep in mind that $\mathcal{G}_g$ will always be operating on this quantity again, and therefore from the continuous spectrum of $\mathcal{G}_r$ only those values of k_z that satisfy the phase-matching condition will contribute. The integrals are reduced, therefore, to simple integrals of trigonometric functions in the x-coordinate and integrals of algebraic functions in the z-coordinate. The algebra involved is very tedious though straightforward [13]. We give here the final result

$$\eta_c = \frac{k_0^3(\Delta n^2)^2(p_{2g}^2 + p_{3g}^2)}{2k_g t_{\text{eff}}(p_{1g} + p_{3g})^2} \cdot \left(\frac{\sin p_{2g}t}{p_{2g}}\right)^2 \cdot \frac{L|C|^2\,|1 + r(\theta)|^2\,(1/\cos\theta)}{(\cos^2 p_{20}t + (p_{30}/p_{20})^2 \sin^2 p_{20}t)} \tag{6}$$

where k_g and p_{ig} are the wavenumbers of the unperturbed waveguide. They satisfy the eigenvalue equation

$$\tan(p_{2g}t) = \frac{p_{2g}(p_{1g} + p_{3g})}{p_{2g}^2 - p_{1g}p_{3g}}$$

with $p_{1g} = \sqrt{k_g^2 - k_0^2}$, $p_{2g} = \sqrt{n_2^2 k_0^2 - k_g^2}$, and $p_{3g} = \sqrt{k_g^2 - n_3^2 k_0^2}$. $p_{10} = k_0 \cos\theta$, $p_{20} = k_0\sqrt{n_2^2 - \sin^2\theta}$, $p_{30} = k_0\sqrt{n_3^2 - \sin^2\theta}$, where θ is the incident angle calculated from $\sin\theta = (k_g - 2\pi/\Lambda)/k_0$, $t_{\text{eff}} = t + 1/p_{1g} + 1/p_{3g}$, $r(\theta)$ is the reflection coefficient of structure from the air side

$$r(\theta) = \frac{(p_{10} - p_{30})p_{20} - i(p_{10}p_{30} - p_{20}^2)\tan(p_{20}t)}{(p_{10} + p_{30})p_{20} - i(p_{10}p_{30} + p_{20}^2\tan(p_{20}t)}$$

$$C = F_{11}\,[1 - \exp(-i\gamma L)]\,/i\gamma L$$

$$\gamma = \frac{k_0^4(\Delta n^2)^2 \sin(p_{2g}t)}{k_g t_{\text{eff}}(p_{1g} + p_{3g})} \cdot \sum_{l=1}^{l_{\max}} \left(\frac{F_{2l}F_{3l}}{\Delta(k_l)}\right)$$

where $l_{\max}$ is the integer such that $|k_{l\max}| \leqslant k_0 n_3$.

$$\Delta(k_l) = (p_{2l}^2 + p_{1l}p_{3l})\sin(p_{2l}t) + i(p_{1l} + p_{3l})p_{2l}\cos(p_{2l}t)$$

with

$$p_{1l} = \sqrt{k_0^2 - k_l^2}, \quad p_{2l} = \sqrt{n_2^2 k_0^2 - k_l^2}, \quad p_{3l} = \sqrt{n_3^2 k_0^2 - k_l^2}.$$

The F factors are integrals of trigonometric functions over the grating area; for rectangular profiles, the integrations involved can be evaluated and given explicitly. For more complicated shapes, the integrations involved can be carried out by slicing profiles by slices of simple rectangles [9] [see Fig. 2(b)]. Thus, in general, F is defined as

$$F(p_1, p_2, p_3, q_1, q_2, q_3, l) = \sum_{n=1}^{N} \left\{ \int_{x_{n-1}}^{x_n} [p_2 \cos p_2(x' - t) - p_1 \sin p_2(x' - t)] \cdot (\cos q_2 x' - i(q_3/q_2)\sin q_2 x')\,dx' \right\} \frac{\sin(\pi a_n l/\Lambda)}{l\pi}$$

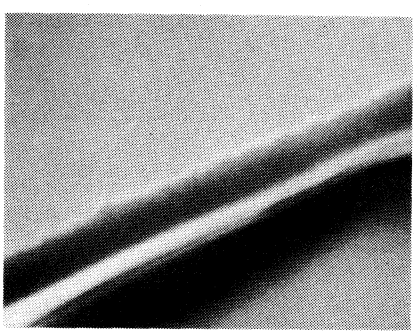
with

$$F_{11} \equiv F(p_{1g}, p_{2g}, p_{3g}, p_{10}, p_{20}, p_{30}, 1)$$

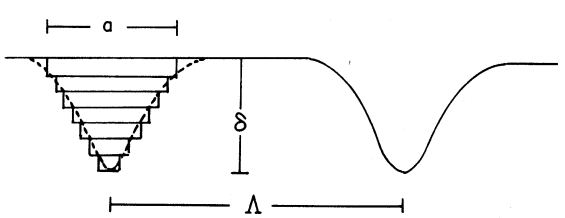
$$F_{2l} \equiv F(-ip_{1l}, p_{2l}, -ip_{3l}, ip_{1g}, p_{2g}, ip_{3g}, l)$$

$$F_{3l} \equiv F(p_{1g}, p_{2g}, p_{3g}, p_{1l}, p_{2l}, p_{3l}, l)$$

where $x_0 = t - \delta$, $x_N = t$, and a_n is the width of each rectangular slice, N being the total number of slices in which the grating profile is being approximated. For rectangular gratings,



(a)



(b)

Fig. 2. (a) SEM picture of the cross section of a 6500-Å spacing grating coupler showing the periodic corrugation on the top of the waveguide film. (b) Schematic diagram of the grating profile showing the grating parameters and illustrating the slicing approximation technique.

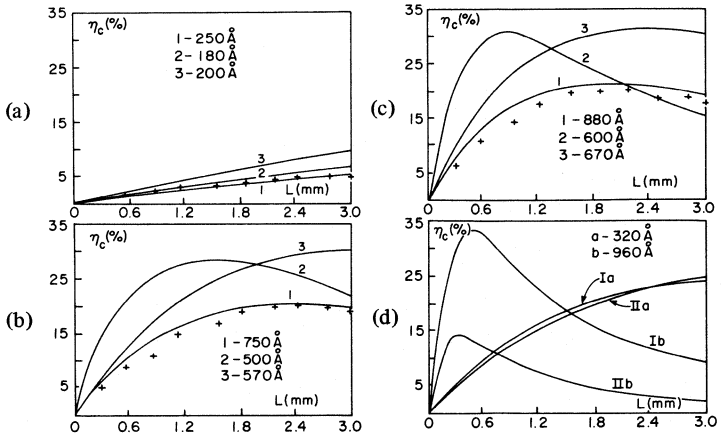


Fig. 3. (a), (b) and (c) Coupling efficiency versus coupling length (L) for different profiles and depths. Curve 1 refers to a triangular profile with $a/\Lambda = 0.4$; curve 2 to a rectangular profile with a $a/\Lambda = 0.4$; and curve 3 to the sinusoidal profile. The crosses are the experimental data. (d) Coupling efficiency versus coupling length for a rectangular profile calculated from the present theory (I), and from the perturbation theory (II) for 2 different equivalent depths.

$N = 1$; hence, F and η_c can be evaluated explicitly. Specific examples of calculated grating efficiencies are shown in Fig. 3.

Experimental Results and Conclusions

The gratings used had a periodicity of 6500 Å and were fabricated by exposing Shipley AZ 1350-B to the interference pattern of two 4880-Å $A\dot{r}$-laser beams followed by sputter-etching into a Corning 7059 glass thin-film waveguide through Mn masks. The experimental results shown were limited to grating depths less than about 900 Å due to difficulties encountered in trying to etch deeper gratings into the thin-film waveguides by this procedure. The glass waveguides were RF sputtered onto microscope slides ($n = 1.515$) in an atmosphere of 8-μ Ar and 2-μ O_2. The index of refraction and film thickness were measured by ellipsometry to be 1.55 and 8000 Å, respectively. The grating depth was estimated from SEM pictures and from diffraction efficiency measurements using the approaches described in [10] and [11] and in the Appendix. The coupling efficiency was measured using an He–Ne laser beam through a beam expander and variable slit to change the length of the grating coupler illuminated. The amount of light coupled into the waveguide was measured by using a prism output coupler which coupled out about 75–80 percent of the propagating wave in the waveguide. To get this figure we took into account the film loss (3.1 dB/cm) and the reflection at the prism–air interface. No attempt was made to account for the diffuse scattering which, for some of our samples, might not be insignificant. Fig. 3 displays the coupling efficiency versus length of the grating coupler for different depths and profiles. The measured coupling efficiency is accurate to 10 percent. For comparison with experimental results, we must know the shape and depth of the grating coupler. It is difficult to determine both accurately. For the calculated results in Fig. 3, we first assumed a specific profile (shape). After the profile was assumed, the depth could be estimated from diffraction efficiency measurements through the use of the formula outlined in the Appendix. Results for

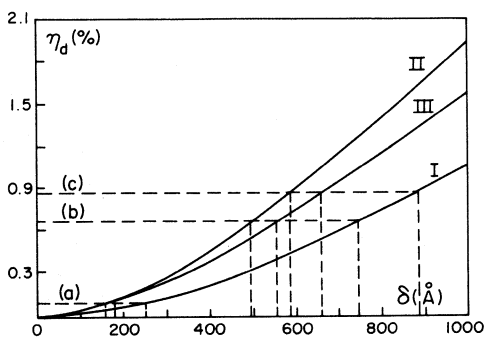


Fig. 4. Diffraction efficiency versus grating depth for (I) triangular; (II) rectangular; (III) sinusoidal profiles. The experimental diffraction efficiencies for the grating couplers used in Fig. 3 are indicated by the horizontal lines.

the various profiles are shown in Fig. 4. The triangular shape led to the best fit of the experimental data, as shown in Fig. 3. Such a shape is not unreasonable for sputter-etched gratings; this is confirmed to some extent by the SEM picture [Fig. 2(a)]. Although the SEM picture is not very clear due to experimental difficulties, the height-to-spacing ratio of the grating structure could be estimated fairly well; since the spacing was known precisely, a reasonable estimate of the height could be obtained using SEM pictures. The critical dependence of the coupling efficiency on the grating profile leads us to the conclusion that the prediction of the grating coupler efficiency cannot be done unless the exact profile is known. This imposes certain limitations on theories that require an analytical expression for the corrugated surface. The experimental results show that using our theory and the appropriate profile, chosen with the help of SEM pictures and diffraction efficiencies measurements, we can predict the coupling efficiency of a grating coupler as a function of the grating parameters. It is important to note that when the grating height is a significant fraction of the wavelength, the discontinuity at the grating terminations cannot be neglected

totally. In this case, the perturbation series expansion cannot be summed to all orders to give a closed form for the electric field of the guided surface wave. We have to use expression (5a) to calculate the field up to some desired order and then calculate an approximated expression for the coupling efficiency which accounts for the discontinuities at the grating terminations. Finally, Fig. 3(d) shows that while there is good agreement between our theory and the perturbation theory [6] for thin gratings, there are fundamental differences for thick gratings; namely, in the maximum coupling efficiency and in the optimum coupling length. The profile in the example of Fig. 3(d) was assumed to be rectangular.

Appendix

In this Appendix we will outline the diffraction efficiency formula used to estimate the equivalent grating depths. The diffracted electric field due to an incident plane wave on the grating structure of Fig. 1 is given by [11]

$$E_d = k_0^2 \iint \Delta n^2(x', z')\, E_y^0(x', z')\, G_r(x', z'|x, z)\, dx'\, dz'$$

if the angle of incidence is away from the coupling angle. Using well-known asymptotics methods for the evaluation of the integral in the far field [14], the diffraction efficiency of the grating is

$$\eta_d = \frac{n_3 k_0^4 (\Delta n^2)^2\, |1 + r(\theta)|^2 \cos\phi\, |F_d|^2}{[\cos^2 (p_{20} t) + ((p_{30}/p_{20}) \sin (p_{20} t))^2]\, |\Delta(k_d)|^2 \cos\theta}.$$

This diffraction efficiency refers to the first-order diffracted beam on the substrate side, so to account for the reflection at the glass-air interface, the previous formula must be multiplied by the transmission coefficient T given by

$$T = \frac{4 n_3 \cos\phi - \sqrt{1 - n_3^2 \sin^2\phi}}{[n_3 \cos\phi + \sqrt{1 - n_3^2 \sin^2\phi}]^2}.$$

Most of the parameters were defined before; the new ones are

$$\sin\phi = \frac{n_1 \sin\theta - \lambda_o/\Lambda}{n_3}, \qquad k_d = k_0 n_3 \sin\phi$$

and all the p'_{id} needed in the computation are defined by $p_{id} = \sqrt{k_0^2 n_i^2 - k_d^2}$. Finally,

$$F_d = F(-ip_{1d}, p_{2d}, -ip_{3d}, p_{10}, p_{20}, p_{30}, 1).$$

In Fig. 4 is shown the diffraction efficiency versus the grating depth for some assumed profiles calculated according to the formulas presented in this Appendix. The equivalent grating depth for an assumed profile is then obtained from this figure by using the measured diffraction efficiency on the vertical axis and reading the corresponding equivalent grating depth on the horizontal axis. In all the diffraction efficiency measurements we fixed the angle of incidence to be 20° for convenience.

Acknowledgment

The authors wish to thank J. J. Turner for taking the SEM pictures.

References

[1] M. L. Dakss, L. Kuhn, P. F. Heidrich, and B. A. Scott, "Grating coupler for excitation of optical guided waves in thin films," *Appl. Phys. Lett.*, vol. 16, pp. 523–525, June 1970.

[2] J. H. Harris, R. K. Winn, and D. G. Dalgoutte, "Theory and design of periodic couplers," *Appl. Opt.*, vol. 11, pp. 2234–2241, Oct. 1972.

[3] D. G. Dalgoutte, "Periodic couplers for the excitation of optical guided waves in thin films," Ph.D. dissertation, Univ. Glasgow, Glasgow, Scotland.

[4] A. Jacques and D. B. Ostrowsky, "The grating coupler: Comparison of theoretical and experimental results," *Opt. Commun.*, vol. 13, pp. 74–77, Jan. 1975.

[5] J. C. Tracy, L. F. Thompson, R. D. Heindenreich, and J. L. Merz, "Gratings for integrated optics by electron lithography," *Appl. Opt.*, vol. 13, pp. 1965–1702, July 1974.

[6] K. Ogawa, W. S. C. Chang, B. L. Sopori, and F. J. Rosenbaum, "A theoretical analysis of etched grating couplers for integrated optics," *IEEE J. Quantum Electron. (Part I of Two Parts)*, vol. QE-9, pp. 29–42, Jan. 1973.

[7] K. Ogawa and W. S. C. Chang, "Analysis of holographic thin film grating coupler," *Appl. Opt.*, vol. 12, pp. 2167–2171, Sept. 1973.

[8] N. Neviere, P. Vincent, R. Petit, and M. Cadilhac, "Determination of the coupling efficiency of a holographic thin film coupler," *Opt. Commun.*, vol. 9, pp. 240–245, Nov. 1973.

[9] S. T. Peng, T. Tamir, and H. L. Bertoni, "Theory of periodic dielectric waveguides," *IEEE Trans. Microwave Theory Tech. (Special Issue on Integrated Optics and Optical Waveguides)*, vol. MTT-23, pp. 123–133, Jan. 1975.

[10] W. J. Tomlinson and H. P. Weber, "Scattering efficiency of high-periodicity dielectric gratings: Experiment," *J. Opt. Soc. Amer.*, vol. 63, pp. 685–688, June 1973.

[11] G. W. Stroke, in *Handbuch der Physik*, vol. 29, S. Flügge, Ed. Berlin, Germany: Springer, 1967, pp. 426–754.

[12] J. M. Ziman, *Elements of Advanced Quantum Theory*. New York: Cambridge, 1969, ch. 4, pp. 94–131.

[13] C. C. Ghizoni, Ph.D. dissertation, Cornell Univ., Ithaca, NY, in preparation.

[14] D. S. Jones, *The Theory of Electromagnetism*. New York: Pergamon, 1964, ch. 8, pp. 438–449.

TM-Mode Coupling Coefficients in Guided-Wave Distributed Feedback Lasers

WILLIAM STREIFER, SENIOR MEMBER, IEEE, DON R. SCIFRES, MEMBER, IEEE, AND ROBERT D. BURNHAM

Abstract—**We derive an equation for TM-mode coupling coefficients in guided-wave distributed feedback (DFB) lasers. Results for GaAs:GaAlAs double-heterostructure lasers with rectangular, triangular, and sawtooth-shaped teeth, various Bragg diffraction orders, and transverse mode numbers are presented for TM modes and compared with those for TE modes. Generally, but not always, coupling coefficients for TE modes exceed those for TM modes.**

I. INTRODUCTION

CALCULATIONS of coupling coefficients in distributed feedback (DFB) heterostructure lasers published to date have considered TE modes. It is important to know TM-mode coupling coefficients as well to determine which types of modes will have lower thresholds and thus lase preferentially. The derivation of the TM coupling-coefficient equation is more complicated than that for TE modes. This has been noted by Peng and Tamir [3], who calculated radiation produced by TM modes and also by Weber *et al.* [2], who considered the effect of transverse variations in gain or loss on the propagation constant. The derivation for a corrugation in a heterostructure laser is still more complex than that of [2] since in the former case the index varies both axially and transversely. In this paper we present a derivation of the coupling constant equation and report comparative calculations of TE and TM coefficients. Generally, coupling of TE modes is stronger than that of TM modes.

II. DERIVATION

Consider a mode guiding structure with a corrugation as shown in Fig. 1. Only the y component of the H-field of TM modes is nonzero, and from Maxwell's equations with time dependence $e^{-i\omega t}$, H_y satisfies

$$\frac{\partial}{\partial z}\left(\nu\frac{\partial H_y}{\partial z}\right)+\frac{\partial}{\partial x}\left(\nu\frac{\partial H_y}{\partial x}\right)+k_0^2 H_y=0 \tag{1}$$

where $\nu = 1/n^2(x,z)$ and $k_0 = 2\pi/\lambda_0$. We consider only guided modes which propagate with approximately β_0, where

$$\beta_0 \triangleq \frac{m\pi}{\Lambda} \tag{2}$$

so that DFB can occur for mth-order Bragg scattering. In (2), Λ is the grating period. Thus we seek solutions of (1) in the form

$$H_y(x,z)=\sum_j f_j(z)\,\mathcal{H}_j(x)=\sum_j\left[R_j(z)\,e^{i\beta_0 z}+S_j(z)e^{-i\beta_0 z}\right]\mathcal{H}_j(x) \tag{3}$$

Manuscript received August 18, 1975; revised September 18, 1975.
The authors are with the Xerox Palo Alto Research Center, Palo Alto, CA 94304.

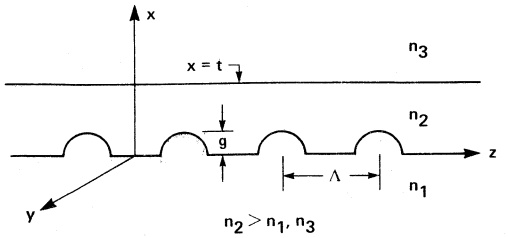


Fig. 1. Schematic of a guided-mode DFB laser.

where $R_j(z)$ and $S_j(z)$ are amplitudes of the right and left traveling jth TM mode, respectively. Upon substituting (3) into (1) and neglecting R_j'' and S_j'' (which assumes the amplitudes are slowly varying), we obtain

$$\sum_j\left\{f_j\frac{\partial}{\partial x}\left(\nu\frac{d\mathcal{H}_j}{dx}\right)-\beta_0^2\,\nu f_j\mathcal{H}_j+2i\beta_0\left(R_j' e^{i\beta_0 z}-S_j' e^{-i\beta_0 z}\right)\nu\mathcal{H}_j+i\beta_0\left(R_j e^{i\beta_0 z}-S_j e^{-i\beta_0 z}\right)\frac{\partial\nu}{\partial z}\mathcal{H}_j+k_0^2 f_j\mathcal{H}_j\right\}=0. \tag{4}$$

Here and in the preceding, primes denote derivatives with respect to z. Next, $\nu(x,z)$ is expressed as an unperturbed part $\nu_u(x)$ which describes the geometry without corrugations, plus a perturbed part $\nu_p(x,z)$ which characterizes the periodic corrugations. Because of the periodicity, $\nu_p(x,z)$ is expanded in a Fourier series in z, whose coefficients depend on x

$$\nu(x,z)=\nu_u(x)+\sum_{q=-\infty}^{\infty}A_q(x)e^{i2\pi qz/\Lambda} \tag{5}$$

where

$$A_q(x)=\frac{1}{\Lambda}\int_{-\Lambda/2}^{\Lambda/2}\nu_p(x,z)e^{-i2\pi qz/\Lambda}. \tag{6}$$

Upon substituting (5) into (4) and noting that R and S vary slowly compared to $e^{\pm i\beta_0 z}$, so that all terms multiplying $e^{i\beta_0 z}$ can be collected, we obtain

$$\sum_j\left\{R_j\frac{\partial}{\partial x}\left[(\nu_u+A_0)\frac{d\mathcal{H}_j}{dx}\right]-\beta_0^2(\nu_u+A_0)R_j\mathcal{H}_j+2i\beta_0 R_j'\cdot(\nu_u+A_0)\mathcal{H}_j+k_0^2 R_j\mathcal{H}_j+S_j\frac{\partial}{\partial x}\left[A_m(x)\frac{d\mathcal{H}_j}{dx}\right]-\beta_0^2 S_j A_m(x)\mathcal{H}_j-i\beta_0 S_j\left(\frac{i2\pi m}{\Lambda}\right)A_m(x)\mathcal{H}_j\right\}=0. \tag{7}$$

In deriving (7), two terms containing $\nu_p S_j'$ cancel and the relation

$$e^{-i\beta_0 z}\,e^{i2\pi mz/\Lambda}=e^{i\beta_0 z} \tag{8}$$

has been utilized. If $\mathcal{H}_j$ is then taken to be a solution of

$$\frac{d}{dx}\left\{[\nu_u + A_0(x)]\,\frac{d\mathcal{H}_j}{dx}\right\} - \beta_j^2\,[\nu_u + A_0(x)]\,\mathcal{H}_j + k_0^2\,\mathcal{H}_j = 0 \tag{9}$$

where β_j is the propagation constant of the jth TM mode, (7) is significantly simplified to read

$$\sum_j \left\{2i\beta_0 R_j'\,[\nu_u + A_0(x)]\,\mathcal{H}_j + (\beta_j^2 - \beta_0^2)\,R_j \cdot [\nu_u + A_0(x)]\,\mathcal{H}_j + S_j\frac{d}{dx}\left[A_m(x)\frac{d\mathcal{H}_j}{dx}\right] + \beta_0^2\,S_j A_m(x)\,\mathcal{H}_j\right\} = 0. \tag{10}$$

Equation (2) was invoked in obtaining (10) from (7). Finally, (10) is multiplied by $\mathcal{H}_k$, the particular transverse mode of interest, and the equation is integrated over $(-\infty, \infty)$. Since the modes are solutions of (9), they satisfy the orthogonality relation

$$\int_{-\infty}^{\infty} [\nu_u + A_0(x)]\,\mathcal{H}_j(x)\,\mathcal{H}_k(x)\,dx = 0, \qquad j \neq k \tag{11}$$

and we find

$$2i\beta_0 R_k' + (\beta_k^2 - \beta_0^2)\,R_k = S_k\left\{-\beta_0^2\int_{-\infty}^{\infty} A_m(x)\mathcal{H}_k^2\,dx + \int_{-\infty}^{\infty} A_m(x)\left[\frac{d\mathcal{H}_k}{dx}\right]^2 dx\right\}\Big/\int_{-\infty}^{\infty}[\nu_u + A_0(x)] \cdot \mathcal{H}_k^2\,dx. \tag{12}$$

The second integral in (12) was obtained by using integration by parts. The coupling coefficient κ is thus given by

$$\kappa = \frac{1}{2i\beta_0}\left\{-\beta_0^2\int_{-\infty}^{\infty} A_m\mathcal{H}^2\,dx + \int_{-\infty}^{\infty} A_m\left[\frac{d\mathcal{H}}{dx}\right]^2 dx\right\}\Big/\int_{-\infty}^{\infty}[\nu_u + A_0]\,\mathcal{H}^2 dx \tag{13}$$

where we have dropped the subscript k. In only retaining terms containing the k subscript, we have implicitly assumed that only coupling between oppositely going $\mathcal{H}_k$ modes is of interest. That is, integrals such as

$$\int_{-\infty}^{\infty} A_m(x)\,\mathcal{H}_j(x)\mathcal{H}_k(x)\,dx \neq 0$$

so that there could, in theory, exist coupling between oppositely going different TM modes if both had the same time dependence and approximately the same propagation constants (near β_0). An expression coupling R_k to S_k' follows from collecting all terms in (7) multiplied by $e^{-i\beta_0 z}$. Aside from interchanging R and S, and changing the sign of the derivative, $A_m(x)$ must be replaced by $A_{-m}(x)$ in (12) to obtain the other equation from (12).

It is important to examine (9) satisfied by $\mathcal{H}$. There $A_0(x)$ appears in addition to ν_u. For a corrugation of height g, $A_0(x) \neq 0$ only for $0 < x < g$. If the corrugation is rectangular, $A_0(x)$ is constant. Then (9) describes TM modes in the four-layer structure shown in Fig. 2, where the index for $0 < x < g$ is just the value of $\nu = 1/n^2$ averaged over the teeth. Thus the unperturbed geometry for TM modes differs slightly from that used both for TE and TM modes in [1] and [3], respectively, and for our checks on TE-mode DFB coupling coefficients [4]. In those cases the average of n^2 was employed in the corrugation region. One can show that the two unperturbed mode formulations do not differ to first order, and for the DFB calculation described previously, fewer terms need be neglected using the expansion of ν and thus the geometry of Fig. 2. If instead of $\nu = 1/\epsilon = 1/n^2$ we expand $\epsilon(x, z) = n^2(x, z)$ as

$$\epsilon(x, z) = \epsilon_u(x) + \sum_{q=-\infty}^{\infty} B_q(x)\,e^{i2\pi qz/\Lambda}$$

then after a slightly more complicated calculation than that presented above, we obtain

$$\kappa = \frac{1}{2i\beta_0}\left\{\beta_0^2\int_{-\infty}^{\infty}\frac{B_m\mathcal{H}^2}{(\epsilon_u + B_0)^2}\,dx - \int_{-\infty}^{\infty}\frac{B_m}{(\epsilon_u + B_0)^2}\left(\frac{d\mathcal{H}}{dx}\right)^2 dx\right\}\Big/\int_{-\infty}^{\infty}\frac{\mathcal{H}^2}{\epsilon_u + B_0}\,dx \tag{14}$$

where $\mathcal{H}$ is now computed from the four-layer geometry of [1] and [3]. Equations (13) and (14) are identical to first order since $\delta\nu = \delta(1/\epsilon) = -\delta(\epsilon)/\epsilon^2$.

It is also interesting to compare (14) with [2, eq. (10)]. The latter contains two integrals identical to those given in (14), but here they are of opposite signs whereas in [2] the signs are identical. The difference occurs because the term resulting from the axial variation in ν is exactly twice the negative of one term resulting from transverse variation in ν. In [2] only transverse ν variations are considered.

For other than rectangular corrugation shapes $A_0(x)$ varies within the layer $0 < x < g$, and the calculation of $\mathcal{H}$ [from (9)] and its integrals [in (13) or (14)] can be quite complicated.

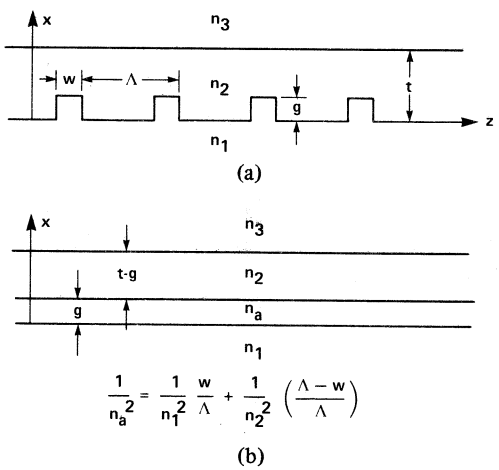


Fig. 2. (a) Schematic of a laser with rectangular teeth. (b) Equivalent geometry for calculating the unperturbed modes.

Therefore we consider a three-layer geometry for the computation. In this three-layer geometry the interface between regions 1 and 2 is shifted such that the tooth areas above and below the boundary are equal, i.e., the areas labeled A and B in Fig. 3 are equal. To illustrate the accuracy of this choice for rectangular teeth, we plot in Fig. 4 values of $|\kappa|$ versus tooth height computed from (13) and (14) for four-layer unperturbed structures and for the three-layer structure as shown in Fig. 3. In all cases $t = 0.8$ μm. Two curves are given for the three-layer structure; one uses the analog of (13) with an expansion of $\nu = 1/n^2$, the other is analogous to (14) with $\epsilon = n^2$ expanded. The agreement is quite good; however, we find that for large index differences at the corrugation boundary, such as occurs at an air-GaAs interface, the various formulations for TM-mode coupling coefficients do not agree well. Then, of course, $\delta\epsilon$ is large compared to ϵ in the grating region. In our opinion, further work is required to determine which four-layer geometry is the more suitable for calculating κ in the case of TM modes. In the remainder of this paper the unperturbed mode $\mathcal{H}$ is computed for the three-layer geometry previously described, and the expansion of ν is employed.

Consider the corrugation shown in Fig. 3. Clearly,

$$\nu_p(x,z) = \begin{cases} 0, & g_2 < x \\ \left(\frac{1}{n_1^2} - \frac{1}{n_2^2}\right) \sum_{p=-\infty}^{\infty} \{u[z - w_1(x) + p\Lambda] \\ \quad - u[z - w_2(x) + p\Lambda]\}, & 0 < x < g_2 \\ \left(\frac{1}{n_2^2} - \frac{1}{n_1^2}\right) \sum_{p=-\infty}^{\infty} \{u[z - w_3(x) + p\Lambda] \\ \quad - u[z - w_4(x) + p\Lambda]\}, & -g_1 < x < 0 \\ 0, & x < -g_1 \end{cases} \quad (15)$$

where x is measured from the new boundary and $u(z)$ is the unit step function. Upon integration, $A_m(x)$ is given by

$$A_m(x) = \frac{1}{2\pi m i}\left(\frac{1}{n_1^2} - \frac{1}{n_2^2}\right) \begin{cases} 0, & g_2 < x \\ e^{-i2\pi m w_2(x)/\Lambda} \\ \quad - e^{-i2\pi m w_1(x)/\Lambda}, & 0 < x < g_2 \\ e^{-i2\pi m w_3(x)/\Lambda} \\ \quad - e^{-i2\pi m w_4(x)/\Lambda}, & -g_1 < x < 0 \\ 0, & x < -g_1. \end{cases} \quad (16)$$

The coupling coefficient κ is found by substituting $A_m(x)$ from (16) together with expressions for $\mathcal{H}$ and $\mathcal{H}'$ (see the Appendix) in (13) and evaluating the integrals either numerically or analytically. Since the form of $\mathcal{H}$ is similar to that of $\mathcal{E}$ for TE modes, the analytic results given in our earlier paper [4] can be modified to evaluate (13).

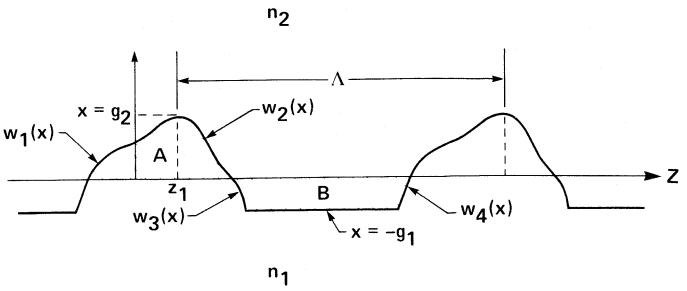


Fig. 3. Illustrating the functions defining tooth shape.

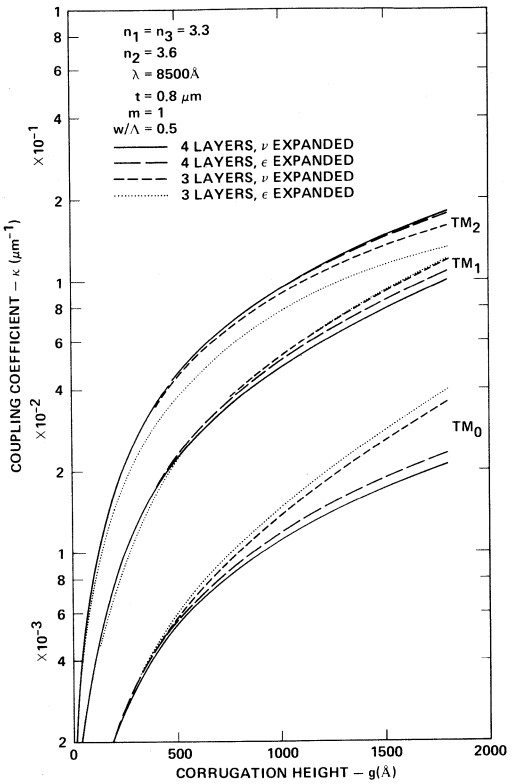


Fig. 4. Comparison of the theories for computing coupling coefficients of rectangular teeth.

III. Results

In Fig. 5(a)-(c) we plot TE and TM coupling coefficients for a double-heterostructure GaAs laser with rectangular, triangular, and sawtooth-shaped corrugations for various Bragg orders. The laser parameters are listed and t' is the center layer thickness measured to the center of the corrugations. Fig. 5(a)-(c) are for the three propagating TE and TM modes. The particular Bragg orders and tooth shapes were chosen to illustrate a variety of cases. Generally, κ for TE modes is found to be somewhat greater than that for TM modes. However, for large triangular corrugations the TM modes have greater values.

According to [1] and [3], results obtained using unperturbed modes computed from four-layer geometries are quite accurate

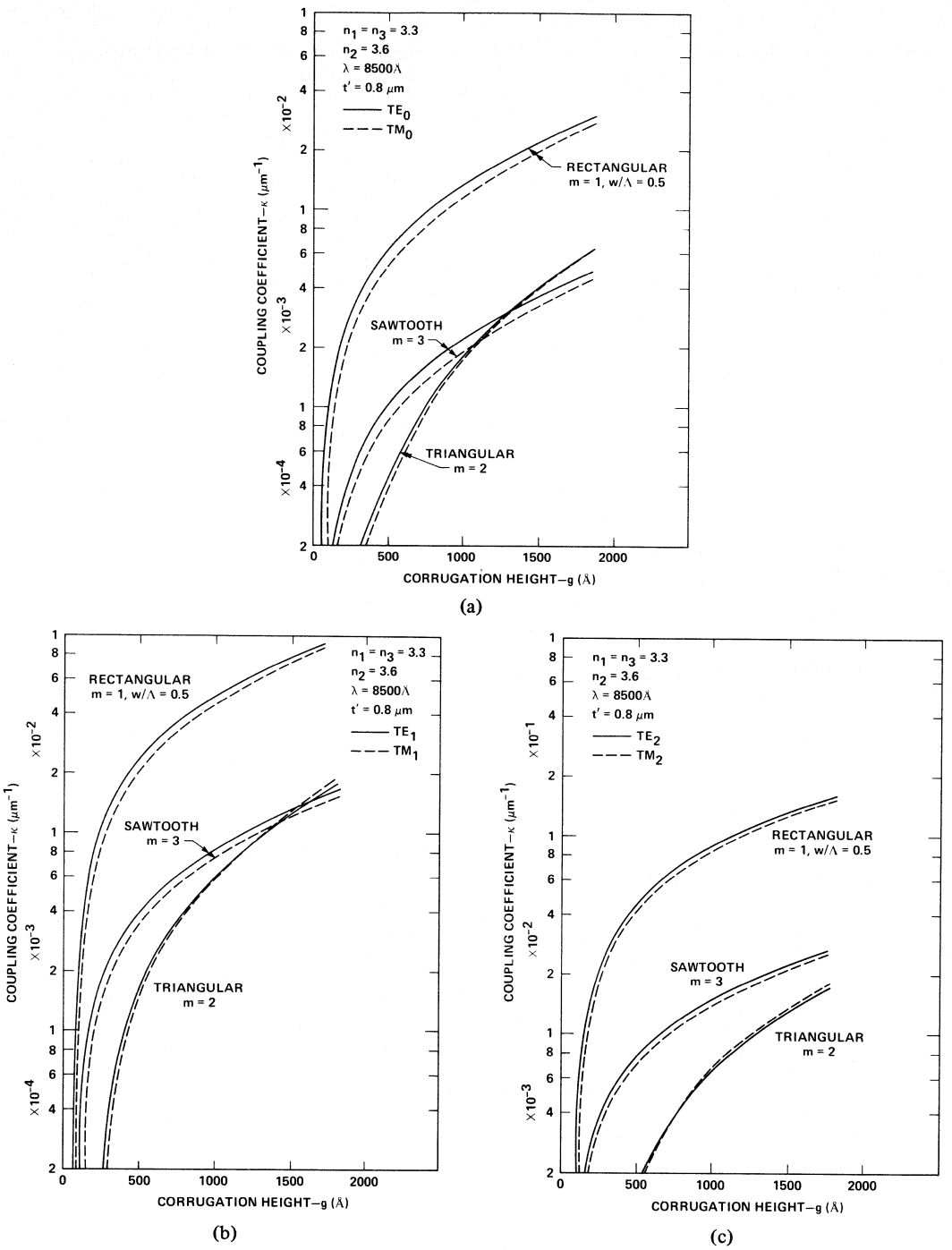


Fig. 5. Coupling coefficients versus tooth height for a double-heterostructure laser. (a) TE_0 and TM_0 modes. (b) TE_1 and TM_1 modes. (c) TE_2 and TM_2 modes.

even for grating heights comparable to a wavelength in the material. Since our results agree well with the four-layer results, at least for grating teeth less than 2000 Å high (see Fig. 4), we expect our results to be accurate in this range.

Appendix

The TM modes are given by [5]

$$\mathcal{H}(x) = \begin{cases} e^{qx}, & x < 0 \\ \cos(hx) + (\bar{q}/h)\sin(hx), & 0 < x < t' \\ [\cos(ht') + (\bar{q}/h)\sin(ht')]\, e^{-p(x-t')}, & t' < x \end{cases}$$

where

$$h = \sqrt{n_2^2 k_0^2 - \beta^2}$$

$$q = \sqrt{\beta^2 - n_1^2 k_0^2}$$

$$p = \sqrt{\beta^2 - n_3^2 k_0^2}$$

$$\bar{q} = n_2^2 q / n_1^2, \quad \bar{p} = n_2^2 p / n_3^2$$

and β is found by solving

$$\tan(ht') = \frac{h(\bar{p} + \bar{q})}{h^2 - \bar{p}\bar{q}}.$$

The normalization integral is

$$\int_{-\infty}^{\infty} \frac{\mathcal{H}^2(x)}{n^2(x)}\,dx = \frac{(h^2+\bar{q}^2)}{2h^2} \cdot \left\{ \frac{t'}{n_2^2} + \frac{(h^2+q^2)}{(h^2+\bar{q}^2)} \frac{1}{n_1^2 q} + \frac{(h^2+p^2)}{(h^2+\bar{p}^2)} \frac{1}{n_3^2 p} \right\}.$$

ACKNOWLEDGMENT

The authors wish to thank Dr. K. O. Hill for calling their attention to [2].

REFERENCES

[1] K. Handa, S. T. Peng, and T. Tamir, "Improved perturbation analysis of dielectric gratings," *Appl. Phys.*, vol. 5, pp. 325–328, 1975.
[2] W. H. Weber, S. L. McCarthy, and G. W. Ford, "Perturbation theory applied to gain or loss in an optical waveguide," *Appl. Opt.*, vol. 13, pp. 715–716, 1974.
[3] S. T. Peng and T. Tamir, "TM-mode perturbation analysis of dielectric gratings," *Appl. Phys.*, vol. 7, pp. 35–38, 1975.
[4] W. Streifer, D. R. Scifres, and R. D. Burnham, "Coupling coefficients for distributed feedback single- and double-heterostructure diode lasers," *IEEE J. Quantum Electron.*, vol. QE-11, pp. 867–873, Nov. 1975.
[5] A. Yariv, "Coupled-mode theory for guided-wave optics," *IEEE J. Quantum Electron.*, vol. QE-9, pp. 919–933, Sept. 1973.

Correspondence

On the Effect of the Addition of SF_6 to a N_2 Electrical Discharge Laser

O. JUDD

Abstract—**The electron distribution function has been calculated for simulated conditions of SF_6–N_2 gas mixtures under conditions typical of a N_2 electrical discharge laser. The results indicate that the electron distribution function, transport quantities, and electronic excitation rates change only a few percent in the presence of SF_6 provided E/N is unchanged. The enhancement in laser power output with the addition of SF_6 is attributed to an increased operating value of E/N in the electrical discharge.**

Recently, several experimental investigations have been reported concerning the effects of the addition of SF_6 to an electrically excited N_2 discharge laser operating on the second positive $C\,^3\pi_u \rightarrow B\,^3\pi_g$ electronic transition. The experiments may be classified into two types. In the first type, the discharge geometry and external circuitry are such as to allow a deposition of energy into the gas on a time scale of less than 50 ns [1]–[3]. With the addition of a small amount of SF_6 to the N_2 ($SF_6/N_2 \leqslant 0.2$), it is observed that the optical output intensity increases by 30–100 percent and that in some cases the optical pulsewidth (10 ns) increases by a factor of 2 [3]. The transition observed is the $v' = 0 \rightarrow v'' = 0$ transition at 337.1 nm. Typical discharge conditions are 20–30 torr of N_2 and a ratio of electric field E to total gas density N of $E/N \approx 2 \times 10^{-15}$ V/cm^2. In the second class of experiments, the energy is deposited into a discharge of 40 torr of N_2 on a time scale of 500 ns. As the ratio SF_6/N_2 was increased to 1.0, it was observed that the laser emission increased in intensity and a significant broadening of the optical pulsewidth occurred [4]. To date, optical pulsewidths in excess of 70 ns have been reported. In addition, both the $v' = 0 \rightarrow v'' = 0$ and $v' = 0 \rightarrow v'' = 1$ transitions at 337.1 and 357.6 nm, respectively, were observed.

Manuscript received August 1, 1975. This work was supported by the Energy Research and Development Administration.

The author is with the Los Alamos Scientific Laboratory, University of California, Los Alamos, NM 87544.

In this correspondence we will be concerned primarily with experiments of the first class. It has been suggested that the resulting laser behavior with the addition of SF_6 is due to a modification of the electron distribution function in the electrical discharge such as to favor excitation of the $C\,^3\pi_u$ and $B\,^3\pi_g$ states [2]. A theoretical simulation has been performed for the resulting electron distribution function in a N_2–SF_6 discharge for the conditions of the experiments. The results indicate that the electron distribution function, electron excitation rates, and discharge transport properties only change a few percent with the addition of SF_6 provided E/N is held constant. As an alternate explanation for the observed N_2 laser behavior, it appears that the enhanced laser output can be attributed to increases of E/N with the addition of SF_6.

The electron distribution function was calculated numerically from a self-consistent solution of the Boltzmann transport equation using well-known techniques which are summarized [5]. The N_2 electronic excitation cross sections for the $A\,^3\Sigma$, $B\,^3\pi$, $C\,^3\pi$, and $W\,^3\Delta$ were based on values revised by Cartwright *et al.* [6]. The electron vibrational cross sections for N_2 are those obtained by Schulz [7]. No published data on the electronic and vibrational excitation cross sections for electron impact on SF_6 were found in the literature. In order to determine the qualitative effects of SF_6 on the distribution function, it was necessary to simulate some of the SF_6 inelastic cross sections. Previous calculations of this type indicate that if the inelastic electron loss processes are distributed more or less uniformly in energy space, the form of the distribution function, and in particular the excitation rates, are rather insensitive to the exact character of the cross sections [5]. This cross-section behavior is assumed to be representative of SF_6. As a first approximation we simulate the electronic and vibrational cross sections in SF_6 by those that have been experimentally determined for CO_2. A much more important property of SF_6 that must be taken into account more accurately is electron attachment which tends to deplete the low-energy electron component of the distribution function. The cross sections for electron attachment and ionization in SF_6 were taken from Asundi and Craggs [8].

The calculated results for the electron distribution function $f(u)$ for two values of E/N are shown in Fig. 1. The solid lines are the electron distributions in pure N_2 and the dotted lines

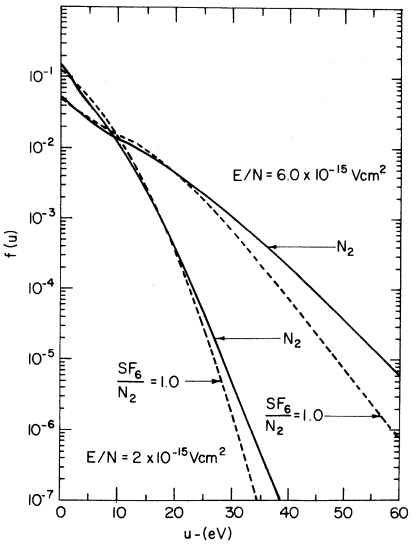


Fig. 1. Electron distribution function $f(u)$ in N_2-SF_6 gas mixtures for two values of E/N. The distribution is normalized such that $\int_0^\infty u^{1/2} f(u)\, du = 1$.

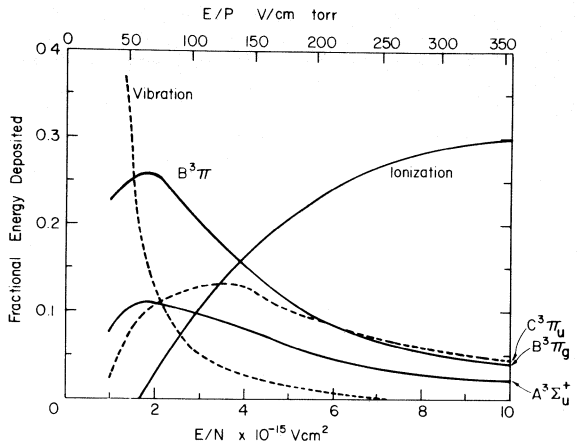


Fig. 2. Fractional energy deposition for several inelastic loss processes in N_2 as a function of E/N.

represent the results of the simulation for a mixture of $SF_6/N_2 = 1.0$. The distribution function in all cases is normalized such that $\int_0^\infty u^{1/2} f(u)\, du = 1$; the total number of electrons may, however, increase or decrease, a property not reflected in the figure. As indicated, the effect of the attachment is to reduce the low-energy electron component, increase the electron component in the range of 5–15 eV, and reduce the high-energy component. Even at equal SF_6 and N_2 concentrations, however, the effect of the SF_6 on the electron distribution is only a few percent in the energy range of interest in the laser. It was also verified that similar small corrections apply to the average electron energy and drift velocity in the discharge. It should be noted that to good approximation $f(u)$ is nearly Maxwellian even in the presence of SF_6. This is due to the large number of electrons accelerated to high energy as a result of the high value of E/N in the discharge. This behavior is in contrast to electron distribution functions calculated for N_2 discharges operating at low values of E/N (10^{-16} V/cm^2) where the distribution function is highly non-Maxwellian [9].

A plot of the E/N dependence of the fractional energy deposited in the various electronic states of N_2 is shown in Fig. 2. At a typical operating value E/N = 2.0×10^{-15} V/cm^2 in a pure N_2 laser, the major portion of input energy is transferred into the $B\,^3\pi$ state. The laser inversion results from the difference in Franck–Condon (FC) factors for electron excitation of the various vibrational levels in the $B\,^3\pi$ and $C\,^3\pi$ states connecting with the $v'' = 0$ vibration level in the ground electronic state. The FC factors for the $v' = 0$ and $v' = 1$ levels of the $B\,^3\pi$ and $C\,^3\pi$ are 0.06, 0.15 and 0.55, 0.31, respectively [6]. A more detailed laser kinetics model has been formulated taking into account the external circuitry of the discharge, the FC factors, and calculated electron excitation rates. The results, which will be described in a future publication, are in quantitative agreement with the observed experimental behavior of the N_2 laser.

The calculated results for the electron distribution function described up to this point assume that the E/N of the discharge remains constant as the ratio of SF/N_2 increases. In fact, the additional loss of electrons due to SF_6 attachment must be compensated by additional ionization, and therefore a higher value of E/N, to provide the self-sustained discharge condition. It is clear from Fig. 2 that as E/N increases from a value of 2×10^{-15} V/cm^2, the ratio of C to B energy deposition, which is also proportional to the population fraction, increases primarily due to the reduced electron excitation rate to the B state.

The data reported in [2] and [3] are consistent with this interpretation. In both experiments, a 10–20-ns-wide optical pulse was observed to increase approximately a factor of 2 when 3.3–5 torr of SF_6 was added to 30 torr of N_2 in the laser discharge. In [3], additional measurements to determine the value of E/N directly across the discharge electrodes were performed. The results indicated that the peak value of E/N varied from 70 V/cm torr (2×10^{-16} V/cm^2) to 140 V/cm torr as the SF_6/N_2 ratio increased from 0 to 0.6. This behavior was essentially independent of the total gas pressure, discharge electrode spacing, and charging voltage. It is doubtful that the optical intensity increase in these experiments can be attributed to a collisional deactivation or energy transfer process between SF_6 and N_2 since the time scale for the occurrence of a gas kinetic collision is 70 ns at 1 torr of SF_6. In order to account for the large temporal broadening of the optical pulse observed in [4], collisional energy transfer must assume a significant, if not a dominant, role in the laser kinetics.

In conclusion, calculations of the electron distribution function in a SF_6-N_2 discharge show an approximate invariant form with the addition of SF_6 to the gas mixture provided E/N is unchanged. The observed increase in laser output power in the short pulse N_2 laser experiments is attributed to an increased value of E/N obtained with the addition of SF_6 to the discharge.

References

[1] W. A. Fitzsimmons, L. W. Anderson, and J. M. Vrtilek, "Experimental investigations of high-power N_2 lasers," presented at the Gaseous Electronics Conf., Houston, TX, 1974, Paper CA-7.

[2] C. S. Willett and D. M. Litynski, "Power increase of N_2 UV and IR lasers by the addition of SF_6," *Appl. Phys. Lett.*, vol. 26, pp. 118–120, 1975.

[3] R. G. Wenzel and G. P. Arnold, Los Alamos Scientific Laboratory, Los Alamos, NM, 1973, unpublished work.

[4] a) S. N. Suchard and D. G. Sutton, "Quasi-cw laser emission from the second positive band of nitrogen," presented at the 4th Conf. Chemical and Molecular Lasers, St. Louis, MO, Oct. 1974.
b) S. N. Suchard, L. Galvan, and D. G. Sutton, "Quasi-cw laser emission from the second positive band of nitrogen," *Appl. Phys. Lett.*, vol. 26, pp. 521–523, 1975.

[5] O. Judd, "The effect of gas mixture on the electron kinetics in the electrical CO_2 gas laser," *J. Appl. Phys.*, vol. 45, pp. 4572–4575, 1974 (this work also contains references to the original literature on the subject).

[6] D. C. Cartwright, S. Trajmar, W. Williams, and A. Chutjian, *Phys. Rev.*, to be published.

[7] G. J. Schulz, "Vibrational excitation of N_2, CO, and H_2 by electron impact," *Phys. Rev.*, vol. 135, pp. A988–A994, 1964.
[8] R. K. Asundi and J. D. Craggs, "Electron capture and ionization phenomena in SF_6 and C_7F_{14}," *Proc. Phys. Soc.*, vol. 83, pp. 611–618, 1964.
[9] A. G. Engelhardt, A. V. Phelps, and C. G. Risk, "Determination of momentum transfer and inelastic collision cross sections for electrons in nitrogen using transport coefficients," *Phys. Rev.*, vol. 135, pp. A1566–A1574, 1964.

Extension of the CW CO–N_2–He Laser Capabilities

P. BRECHIGNAC AND J. P. MARTIN

Abstract—**CW laser action has been achieved from the $v = 1 \rightarrow v = 0$ band up to the $v = 36 \rightarrow v = 35$ band using a conventional electrical-discharge device filled with a mixture of CO, N_2, and He. The electronic systems used for frequency and intensity stabilization are described.**

The CW CO laser is now widely used as a probe instrument in a number of investigations including studies of the dynamics of CO expanding flows or shock-heated mixtures [1]–[4] and the kinetics of chemical reactions [5]–[8], in steady-state measurements of excited CO systems [9]–[13], in time-resolved measurements of molecular relaxation [14]–[17], and in such other fields of research as solid-state physics, astrophysics, atmospheric transmission [18], [19], and pollution control. For such diagnostic purposes it is of great practical interest to have a stable and broadly tunable source of CO wavelengths.

Recently, Djeu [20] obtained CW oscillation on low-lying bands of CO by the addition of xenon to the gas mixture. In the high vibrational bands laser action has been obtained up to $v = 37$ [21], [22] in the Q-switched regime, but to our knowledge, except in [12],[1] no CW oscillation has been reported on vibrational bands above $v = 19 \rightarrow v = 18$ [13]. In this correspondence we describe a CO–N_2–He laser system which enables us to obtain CW oscillation from the $v = 1 \rightarrow v = 0$ band up to the $v = 36 \rightarrow v = 35$ band without addition of xenon. Most of the numerous observed lines exhibit single-line single-mode oscillation sufficiently stable for a large number of the previously mentioned investigations, when electronic-feedback circuits acting on the cavity length and the discharge current intensity are employed.

The device used in this work is a conventional electrical discharge liquid-nitrogen-cooled CO–N_2–He laser as described in [12]. In such a device achievement of gain on the low-lying bands of CO, it has been found, depends very critically on the temperature of the medium. In order to keep this temperature as low as possible, the gas mixture is precooled (Fig. 1)

Manuscript received May 9, 1975; revised October 9, 1975. A part of this work, done by the Groupe de Recherches Thermiques, was supported by the Direction des Recherches et Moyens d'Essais.

P. Brechignac is with the Laboratoire de Photophysique Moléculaire, Centre National de Recherche Scientifique, University of Paris-Sud, Orsay, France.
J. P. Martin is with the Group de Recherches Thermiques, Centre National de Recherche Scientifique, Ecole Centrale des Arts et Manufactures, Chatenay-Malabry, France.

[1] We reported measurements with a CW CO–He–O_2 laser operating up to $v = 31 \rightarrow v = 30$.

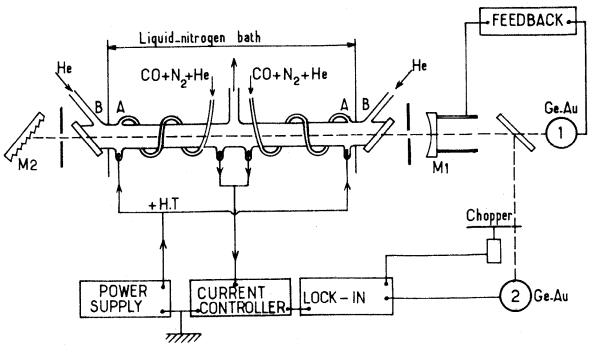


Fig. 1. Laser schematic with the frequency-stabilization loop (photoconductor 1) and the intensity-stabilization loop (photoconductor 2) shown.

by flowing it through a surrounding Pyrex coil before it enters the main discharge tube through a sonic injector, 2 mm in diameter, which is not represented on the figure (sidearm A). As already discussed by Djeu [20], oscillation on the $v = 1 \rightarrow v = 0$ band cannot be achieved if ground-state CO molecules are allowed to accumulate within the cavity. To sweep away unexcited CO from the regions beyond the ends of the discharge, a portion of the helium flow enters through the sidearms B. The 1.70-m-long 30-mm-ID Pyrex tube is cooled by a liquid-nitrogen bath along a 1.50-m length. The entire excited region is 1.20 m in length. The gas mixture is evacuated by a 25-m^3/h pumping system.

The optical cavity consists of a partially transmitting (nominally 2 percent at 4.8 μ) output coupling mirror M_1 (R = 12 m) mounted on a piezoelectric transducer and a gold-coated mirror M_2 (R = 6 m). Laser action from the $v = 1 \rightarrow v = 0$ band [$P(10)$, $P(11)$] up to $v = 15 \rightarrow v = 14$ band [$P(10)$, $P(11)$] was obtained with 3.6-torr He, 1.1-torr N_2, and 0.01-torr CO at a total current of 18 mA. Let us emphasize that up to this day, laser action on these low-lying bands, $v = 1 \rightarrow v = 0$ and $v = 2 \rightarrow v = 1$, absolutely needs the addition of xenon to the gas mixture in a long active discharge (1.5 m) [20]. In our device these low-lying bands oscillated without the addition of xenon, in a rather short active length discharge at moderate flow rates. These features permit inexpensive daily operation of a CW CO-laser device of this design.

For single-line operation, a grating (150 lines/mm blazed for 6 μ) replaces the mirror M_2. With this substitution oscillation was achieved from the $v = 2 \rightarrow v = 1$ band [$P(8)$, $P(9)$, $P(10)$, $P(11)$] up to the $v = 36 \rightarrow v = 35$ band [$P(9) \rightarrow P(13)$]. In each band $P(J)$ lines were generally obtained from $J = 5$ to $J = 15$ by varying laser conditions. For example, the J value decreases with decreasing discharge current as a result of the lower temperatures which accompany reductions in electrical power input. Oscillation of high-lying bands requires a larger amount of CO and a smaller amount of He than the low-lying bands since increasing CO pressure favors the ascension of vibrational quanta by VV exchange and decreasing the pressure reduces the quanta lost by VT processes [12]. To minimize cavity losses for the highest bands, mirror M_1 was replaced by a gold-coated mirror with a central output coupling hole (2 mm in diameter) and the CaF_2 windows were replaced by NaCl.

For absorption measurements, it is useful to have constant-intensity frequency-stable emission. The capabilities of our device with respect to these features are not comparable to the feats of the ultrahigh resolution spectroscopy which needs very sophisticated procedures [23], [24]. However, any of these numerous CO lines can be easily operated with a stability good enough for many usual applications. Adjustment of the

two variable-diameter irises placed in front of each reflector ensures a TEM_{00} single-mode operation on each line. This mode is maintained on line center by a conventional feedback technique [25]. The electronic feedback device provides a low-level 500-Hz modulation of the cavity length, receives the signal from the Ge–Au photoconductor 1, and suitably controls the cavity length. This system, which leaves a long-term[2] frequency jitter $\Delta f/f < 10^{-7}$, also reduces the fluctuation of the laser intensity which is about 10 percent in this case.

These fluctuations are further reduced by a second electronic feedback control circuit. The Ge–Au photoconductor 2 receives the 900-Hz chopped laser beam. Its signal is lock-in amplified and then compared with a constant-level voltage source. The error signal so generated is used to continuously adjust the excitation of the laser medium by means of the dc current controller. Time constants of the different parts of the loop must be finely adjusted to prevent undesired oscillations. Good results were obtained with a 300-ms time constant which was compatible with the working of the frequency loop. Utilizing these techniques long-term[2] fluctuations of the laser intensity were reduced to less than 2 percent.

In conclusion, we have demonstrated that a $CO–N_2–He$ laser can be operated readily with good stability across a very wide spectrum of wavelengths. Certainly, these features will serve to expand the areas of application for CW CO lasers of this type. This device should prove particularly suitable for detailed studies of CO vibrational relaxation where it is of great interest to reach both the lowest vibrational levels where VV processes are dominant and the highest ones where VT deexcitation is very efficient.

References

[1] J. H. Blom and R. K. Hanson, "Double discharge arrangement for cw electrical excitation of supersonic flows," *Appl. Phys. Lett.*, vol. 26, pp. 190–192, 1975.

[2] H. Rabitz, private communication.

[3] M. F. Weisbach and C. Chackerian, Jr., "Linewidths and transition probabilities for the carbon monoxide laser lines," *J. Chem. Phys.*, vol. 59, pp. 4272–4276, 1973.

[4] C. Chackerian, Jr., and M. F. Weisbach, "Relaxation of the v = 4, 5, 6, 7, Σ_g^+ vibrational levels of carbon monoxide studied by laser absorption," *J. Chem. Phys.*, vol. 59, pp. 807–811, 1973.

[5] N. Djeu, "Quantitative laser measurement of very small absorptions: Studies of the O + CS → CO (v) + S reaction," *J. Chem. Phys.*, vol. 60, pp. 4109–4115, 1974.

[6] H. T. Powell and J. D. Kelley, "Vibrational distribution of carbon monoxide from O + CS → S + CO (v)," *J. Chem. Phys.*, vol. 60, pp. 2191–2192, 1974.

[7] G. Hancock, C. Morley, and I. W. M. Smith, "Vibrational excitation of CO in the reaction O + CS → CO + S," *Chem. Phys. Lett.*, vol. 12, pp. 193–196, 1971.

[8] N. Djeu, H. S. Pilloff, and S. K. Searles, "Determination of optical gain for CO transitions in a CS_2-O_2 flame by oscillation-range measurements," *Appl. Phys. Lett.*, vol. 18, pp. 538–539, 1971.

[9] F. Legay, N. Legay, and G. Taïeb, "Mechanism of CO-N_2 laser: I–Study of the vibrational populations," *Can. J. Phys.*, vol. 48, pp. 1949–1955, 1970.

[10] G. Hancock and I. W. M. Smith, "Quenching of infrared chemiluminescence: 1–The rates of deexcitation of CO ($4 \leqslant v \leqslant 13$) by He, CO, NO, N_2, O_2 and CO_2," *Appl. Opt.*, vol. 10, pp. 1827–1842, 1971.

[11] N. Djeu and S. K. Searles, "Method for measuring relative transition probabilities of cascading molecular bands: Application to CO fundamental bands," *J. Chem. Phys.*, vol. 57, pp. 4681–4687, 1972.

[12] P. Brechignac, J. P. Martin, and G. Taieb, "Small-signal gain measurements and vibrational distribution in CO," *IEEE J. Quantum Electron.*, vol. QE-10, pp. 797–802, Oct. 1974.

[13] V. J. Corcoran, R. E. Cupp, W. T. Smith, and J. J. Gallagher, "CW measurements of the CO molecular laser," *IEEE J. Quantum Electron.*(Corresp.), vol. QE-7, pp. 246–248, June 1971.

[14] C. Wittig and I. W. M. Smith, "Vibrational relaxation of carbon monoxide ($4 \leqslant v \leqslant 10$) at T 100°K," *Chem. Phys. Lett.*, vol. 16, pp. 292–295, 1972.

[15] I. W. M. Smith and C. Wittig, "Vibrational energy transfer in carbon monoxide at low temperatures," *J. Chem. Soc.*, vol. 69, pp. 939–951, 1973.

[16] H. T. Powell, "Vibrational relaxation of carbon monoxide using a pulsed discharge," *J. Chem. Phys.*, vol. 59, pp. 4937–4941, 1973.

[17] P. Brechignac, F. Legay, and G. Taïeb, "V-V energy transfer in highly excited CO by infrared-infrared double resonance," *Chem. Phys. Lett.*, to be published.

[18] P. Varanasi, "Measurement of line widths of CO of planetary interest at low temperatures," *J. Quant. Spectrosc. Radiat. Transfer*, vol. 15, pp. 191–196, 1975.

[19] W. B. Lacina and G. L. McAllister, "Resonance self-absorption in CO lasers," *Appl. Phys. Lett.*, vol. 26, pp. 86–89, 1975.

[20] N. Djeu, "cw single line CO laser on the $v = 1 \rightarrow v = 0$ band," *Appl. Phys. Lett.*, vol. 23, pp. 309–310, 1973.

[21] J. T. Yardley, "Laser action in highly excited vibrational levels of CO," *J. Mol. Spectrosc.*, vol. 35, pp. 314–324, 1970.

[22] W. B. Roh and K. N. Rao, "CO laser spectra," *J. Mol. Spectrosc.*, vol. 49, pp. 317–321, 1974.

[23] C. K. N. Patel, "Saturation spectroscopy with a spin-flip Raman laser," *Appl. Phys. Lett.*, vol. 25, pp. 112–114, 1974.

[24] F. Y. Wu, R. E. Grove, and S. Ezekiel, "cw dye laser for ultrahigh resolution spectroscopy," *Appl. Phys. Lett.*, vol. 25, pp. 73–75, 1974.

[25] W. R. C. Rowley and D. C. Wilson, "Wave-length stabilization of an optical maser," *Nature*, vol. 200, pp. 745–747, 1963.

[2]Half an hour and more.

Comments on "Hyperfine Optical Pumping of Cesium with a CW GaAs Laser"

GURBAX SINGH, P. DiLAVORE, AND C. O. ALLEY

***Abstract*—Reference to our work [1] in a recent paper[1] by Picqué is clarified.**

In a recent paper,[1] Picqué has reported the complete depopulation of either one of the two ground-state hyperfine levels in cesium-133. The author is highly commended for advancing further the work [1] reported by us in 1971. He does refer to our work but by reading his text one can obtain the impression that in our work, matching of the GaAs-laser output to the D_2-line in Cs-133 was done by operating it in the pulsed mode. The fact is that we achieved population inversion among the two ground-state hyperfines by optically pumping cesium atoms with radiation from a CW-operated GaAs laser. It was conservatively stated in our paper [1] that the laser mode could be held for a few seconds on either

Manuscript received July 30, 1975; revised October 8, 1975.

G. Singh is with the University of Maryland at Eastern Shore, Princess Anne, MD 21853.

P. DiLavore is with Indiana State University, Terre Haute, IN 47809.

C. O. Alley is with the University of Maryland at College Park, College Park, MD 20742.

[1]J.-L. Picqué, *IEEE J. Quantum Electron.*, vol. QE-10, pp. 892–897, Dec. 1974.

hyperfine by manually controlling the injection current. However, Picqué has done a superb job in greatly improving the stability of the laser mode over extended periods and demonstrating complete depopulations.

REFERENCES

[1] G. Singh, P. DiLavore, and C. O. Alley, "GaAs-laser-induced population inversion in the ground-state hyperfine levels of Cs^{133}," *IEEE J. Quantum Electron.*, vol. QE-7, pp. 196-198, May 1971.

The Dependence of the Pulsed 10.6-μm Laser Damage Threshold on the Manner in Which a Sample is Irradiated

M. BASS AND K. M. LEUNG

Abstract—**The threshold for pulsed 10.6-μm laser-induced surface and bulk damage in transparent materials has been shown to depend on the manner in which the samples are irradiated. When a site is irradiated several times, starting at a very low intensity and increasing the flux a few percent on successive shots until damage occurs, the threshold is often higher than if each site were irradiated only once. In addition, it has been shown that the damage threshold also depends on the sample tested and so the use of relative damage-threshold measurements to identify the damage mechanism should be reexamined.**

Thresholds for pulsed laser damage to transparent media have been determined in a variety of experiments. The importance of the beam's spatial mode and the pulse's temporal waveform have been discussed [1]. There has also been extensive discussion of the relation between the size of the irradiated volume and the measured threshold [2]. In this correspondence, we point out the importance of the number of times a site is irradiated in determining the reported damage threshold at 10.6 μm and how this fact affects comparisons between materials.

We have reported experiments in which each site was irradiated only once and the intensity was increased at each successive site until damage was produced with some degree of consistency (i.e., 50 percent of the sites are damaged) [3]. Allen *et al.* reported damage thresholds obtained when each site was irradiated several times starting at a very low intensity and increasing the flux a few percent on successive shots until damage occurred [4]. Since our one shot on one site (1-on-1) and their several shots on one site (N-on-1) experiments gave different results for the same materials, we have undertaken a direct comparison of these procedures on the same samples.

Our experiment is described in detail in [3] and is summarized in Table I. The results of our 1-on-1 and N-on-1 comparison are given in Table II. Clearly, when the diameter of the irradiated region is ~100 μm, the 10.6-μm laser damage threshold of ZnSe is independent of the manner of irradiation. KCl and NaCl, on the other hand, have higher damage thresholds when measured in an N-on-1 experiment than in a 1-on-1 experiment. This increased threshold is observed for ~50 percent of the sites studied in both surface and bulk damage experiments. No dependence on interpulse interval was found for a range from 5 s to >1 min.

Manuscript received September 11, 1975. This work was supported by the Defense Advanced Research Projects Agency, and was monitored by the Air Force Cambridge Research Laboratory.

The authors are with the Center for Laser Studies, University of Southern California, Los Angeles, CA 90007.

TABLE I
SUMMARY OF EXPERIMENTAL PARAMETERS

Laser	CO_2 TEA
Wavelength	10.6 μm
Waveform	92 nsec gain switched pulse with self mode locked spikes $\lesssim$ 2.5 nsec duration and 8 nsec interpulse spacing
Transverse mode	TEM_{00}
Attenuation	ZnSe beamsplitter and two Brewster angle stacked plate polarizers
Focusing lens	Ge, 3.8 cm focal length, abberation free
Focal spot diameter	107 μm to $1/e^2$ in intensity
Detection system	Photon drag detectors and Tektronix 7844 Oscilloscope. Risetime = 2.5 nsec

As in [3], we also monitored the transmitted pulse waveform distortion during these experiments. We found that in an N-on-1 experiment no distortion could be detected during any pulse prior to the one which produced a spark and left residual damage in the sample. The distortion of the last pulse was, in all respects, similar to that seen in a 1-on-1 damage measurement.

The increase in surface damage threshold in an N-on-1 experiment might be due to either a cleaning of the surface by the laser at low intensities [5] or a smoothing out of the sharp edges of polishing scratches by some form of "laser polishing." If sharp edges are removed and "vee"-like scratches become more nearly cylindrical, Bloembergen [6] would predict a ratio of damage intensities for N-on-1 to 1-on-1 of

$$R = \frac{(\epsilon + 1)^2}{4}$$

where $\epsilon = n^2$ is the optical frequency dielectric constant, and R is the ratio of the square of Bloembergen's field-enhancement factors for "vee" grooves to that for cylindrical grooves. Thus, for NaCl where $n = 1.49$, we should have $R_{NaCl} = 2.59$ and for KCl where $n = 1.46$ we should have $R_{KCl} = 2.45$. From Table II we see that the experimental ratios are 3.06/3.33 and 2.36, respectively. In other words, the change in the surface damage threshold between the N-on-1 and 1-on-1 experiments does not disagree with the "laser-polishing" explanation. The fact that the surface damage threshold of ZnSe is independent of the type of experiment may be due to the fact that the damage mechanism in this material is absorption by particulate inclusions [3]. This mechanism is not sensitive to local field enhancement.

The foregoing model might explain the results for surface damage, but does not suffice when we consider the results for bulk damage. The increased damage flux in an N-on-1 experiment for bulk damage is both unexpected and troublesome. Consider, for example, the fact that the ranking of the two NaCl samples reverses when one goes from a 1-on-1 threshold to an N-on-1 value. Consider, in addition, comparing KCl to NaCl. For each type of experiment one gets a different relative damage threshold. The fact that the relative damage threshold also depends on which samples are compared suggests that the use of such comparisons to identify the damage mechanisms [7] be reexamined.

In studying the statistics of laser damage, at 1.06 and 0.69 μm the site was irradiated several times with pulses of fixed intensity [8]. The irradiation continued until either damage occurred or until some predetermined number of pulses had

TABLE II
COMPARISON OF *N*-ON-1 AND 1-ON-1 LASER DAMAGE THRESHOLDS

		10.6 μm Damage Threshold[a] in GW/cm^2									
Material		ZnSe		KCl				NaCl			
Supplier and Supplier's Designation		Raytheon ZnSe 1975		Harshaw Econoflat Grade		HRL RAP Grown		Harshaw Econoflat Grade		Harshaw Spectrophotometer Grade	
		Surface	Bulk	Surface	Bulk	Surface	Bulk	Surface	Bulk	Surface	Bulk
Type of Experiment	N on 1	0.35	0.41	1.3	2.0	-	2.6	4.9	7.1	2.8	14.0
	1 on 1	0.35	0.46	.56	0.65	-	1.5	1.6	6.1	0.84	3.9
$R = \frac{I_{threshold}^{(N \text{ on } 1)}}{I_{threshold}^{(1 \text{ on } 1)}}$		1.0	1.0	2.36	3.07	-	1.73	3.06	1.16	3.33	3.58

[a] Defined as that intensity which damages 50 percent of the sites.

been tried. At any particular intensity level the distribution of the number of pulses required to produce damage was given by the binomial distribution [8], [9]. This is a characteristic of a process having a constant probability of occurrence on each trial. If low-level irradiation caused an increase in the damage threshold of the materials studied at 1.06 and 0.69 μm, then the damage probability would not have been constant from pulse to pulse. The probability for damage would have decreased on each successive pulse so that if damage did not occur on the first pulse it would very likely not have occurred at all. The process would have appeared thresholdlike instead of statistical. We feel, therefore, that the increased threshold in an *N*-on-1 experiment at 10.6 μm does not conflict with the statistical properties of 1.06- and 0.69-μm laser damage. In fact, the statistics observed at the shorter wavelengths suggest that there would be no increase in threshold in an *N*-on-1 experiment performed with either an Nd or a ruby laser.

The measured 10.6-μm laser damage threshold for both bulk and surface damage in some materials has been shown to depend on the procedure used. This study has also shown that the relative ranking of materials according to their damage thresholds depends on which samples are compared and on the experimental procedure. As a result, the use of such rankings to identify the laser damage mechanism should be reexamined.

Note Added in Proof: No increase in bulk damage threshold for the sample of NaCl (Harshaw Spectrophotometer Grade) was observed in an *N*-on-1 experiment as compared to a 1-on-1 experiment performed with a ruby laser.

ACKNOWLEDGMENT

The authors wish to thank C. Tang and M. Chang for their assistance in this work. They also wish to thank V. Wang, who participated in the initial experiments.

REFERENCES

[1] M. Bass, "Laser induced damage to nonlinear crystalline materials," NBS Special Publ. 341, pp. 90–96, Dec. 1970.
[2] L. G. DeShazer, B. E. Newnam, and K. M. Leung, "The role of coating defects in laser-induced damage to thin films," NBS Special Publ. 387, pp. 114–123, Dec. 1973.
[3] K. M. Leung, M. Bass, and A. G. J. Balbin-Villaverde, "Damage to 10.6 μm window materials due to CO_2 TEA laser pulses," presented at the 1975 Laser Damage Symp., Boulder, CO, July 1975, and to appear in the proceedings of that meeting.
[4] S. D. Allen, M. Braunstein, C. Giuliano, and V. Wang "Pulsed CO_2 laser damage studies of RAP grown KCl," NBS Special Publ. 414, pp. 66–75, Dec. 1974.
[5] T. L. Barber, "Degradation of laser optical surfaces," ECOM Rep. 5237, Mar. 1969.
[6] N. Bloembergen, "The role of cracks, pores and absorbing inclusions on laser induced damage threshold at surfaces of transparent dielectrics," *Appl. Opt.*, vol. 12, pp. 661–664, Apr. 1973.
[7] E. Yablonovitch, "Optical dielectric strength of alkali-halide crystals obtained by laser induced breakdown," *Appl. Phys. Lett.*, vol. 19, pp. 495–497, Dec. 1971.
[8] M. Bass and H. H. Barrett, "Avalanche breakdown and the probabilistic nature of laser-induced damage," *IEEE J. Quantum Electron.*, vol. QE-8, pp. 338–343, Mar. 1972.
[9] M. Bass and D. W. Fradin, "Surface and bulk laser-damage statistics and the identification of intrinsic breakdown processes," *IEEE J. Quantum Electron.*, vol. QE-9, pp. 890–896, Sept. 1973.

A Thermostatic Control System for Nonlinear Optical Experiments at Low Temperatures

G. H. LESCH, J. C. JOHNSON, AND G. A. MASSEY

***Abstract*—A cryostat specifically designed for maintaining nonlinear optical crystals at temperatures between room temperature and −175°C is described. The sample is held in a vacuum environment, and its temperature is kept within 0.1°C of the desired value by applying regulated power to a sample holder which is connected to a liquid-nitrogen-cooled heat sink through a thermal resistance. The system is easily constructed and can be evacuated with a mechanical pump. It can operate longer than 6 h on a single filling of liquid nitrogen with the pump disconnected.**

In carrying out experiments in nonlinear optics, it is sometimes necessary to maintain the nonlinear crystal at temperatures well below ambient. This is particularly important as research interest has shifted to generation of ultraviolet wavelengths, because for nonlinear crystals of the ammonium dihydrogen phosphate (ADP) group the birefringence increases

Manuscript received October 6, 1975. This work was supported by the National Science Foundation under Grants GB 32808 and GB 43630.

G. H. Lesch is with the Institute of Molecular Biology, University of Oregon, Eugene, OR 97403.
J. C. Johnson and G. A. Massey are with the Department of Applied Physics and Electronic Science, Oregon Graduate Center, Beaverton, OR 97005.

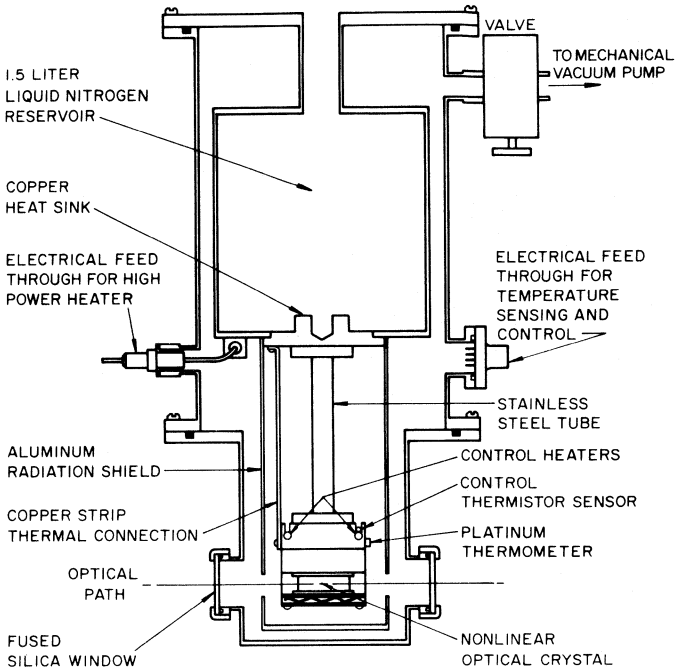


Fig. 1. Schematic diagram of cryostat system.

with decreasing temperature [1], [2], and increased birefringence is necessary to achieve phase-velocity synchronism of the interacting frequencies in the presence of the higher normal dispersion that is encountered at ultraviolet wavelengths [3]-[5]. The temperature tolerances for nonlinear optical generation using a second-harmonic or sum-frequency process can be as small as about 0.1°C, and in wavelength-tunable applications it may be necessary to maintain the crystal temperature at any point within a range that can extend below -100°C. The vacuum cryostat described here meets these requirements and is easily constructed and operated.

Cells for holding various types of samples at low temperatures with excellent thermal stability have been described previously in the literature; however, papers on nonlinear optical applications [4], [5] have not treated the design and operation of the cryostat systems in detail, and cryostats built for other applications [6], [7] must be substantially modified to permit optical access to the crystal and the use of large crystals which may require special handling. For example, ADP crystals are soft and hygroscopic, and in a typical experiment the crystal temperature should be maintained within 0.1°C over a crystal volume of several cubic centimeters. Evacuation of the cryostat eliminates water condensation at low temperatures and improves the thermal stability, but it introduces thermal contact resistance difficulties in the crystal holder. Silicone greases might be considered as contacting agents, but contamination of the optical surfaces of the crystal and subsequent optical damage are then a possibility. For these reasons we have developed a crystal mounting technique using a plastic solid which maintains good thermal contact over a wide range of temperatures without application of large pressures to the crystal.

The cryostat consists of an evacuated stainless-steel cylinder containing a liquid-nitrogen reservoir and copper heat sink at the upper end, as shown in Fig. 1. The capacity of the reservoir is 1.5-l, and the approximate volume of the copper heat sink is 100 cm^3. The crystal holder, which can accomodate crystals up to 1.3 cm square and 6 cm long in our device, is a rectangular aluminum block connected to the lower surface of the heat sink by a thin-walled stainless-steel tube. Heat to maintain the crystal at a temperature higher than the heat sink is provided by passing current through a pair of 1000-Ω resistors mounted in the top of the crystal holder. A radiation shield of aluminum tubing surrounds the crystal holder and its supporting tube and is secured to the heat sink at the top. The shield prevents heating of the interior components by infrared emission from the outer walls of the container. Light can be brought into the cryostat through fused-silica windows attached to the outer container with O-ring seals; holes in the heat shield allow the light to pass down the axis of the crystal. Electrical connections to the control heaters and thermal sensors are made through a multiple-pin vacuum feedthrough connector. In operation the cryostat is supported by a simple yoke assembly (not shown in Fig. 1) that allows the crystal axis to be aligned relative to the incident laser beam.

An important parameter of the system is the thermal conductance of the structure attaching the crystal holder to the heat sink. If this conductance is made too large, an excessive power input to the heater will be needed and the system will boil off nitrogen at a rapid rate. However, too small a conductance makes the temperature control slow and inaccurate, because the crystal temperature will drop too slowly when the heater is turned off. In our system this thermal connection is made with a type-321 stainless-steel tube having a diameter of 1.25 cm and a wall thickness of 0.83 mm. The length of the tube is 10 cm. In our first experiments we found that additional thermal conductance was desirable, and a copper strip 0.068 cm^2 in cross section and 11 cm long was later connected between the crystal holder and heat sink. The previous dimensions were chosen by measuring the input power required to stabilize the crystal-holder temperature as conducting strips of various sizes were attached. For our system an input of about 3.3 W maintains the crystal at -50°C when the heat-sink temperature is -196°C.

The temperature of the crystal holder is monitored by a

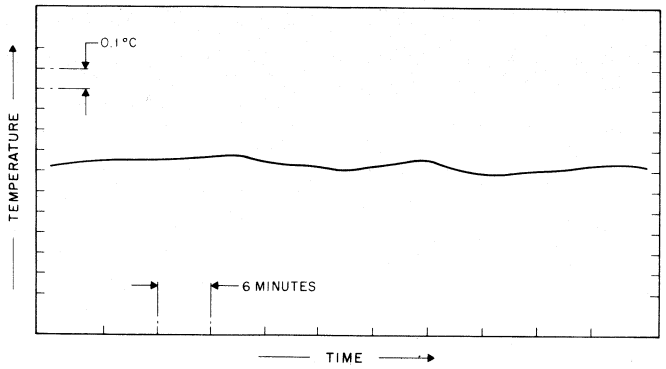


Fig. 2. Temperature variation of crystal holder with the control system turned off. Constant power was applied to the heater. Temperature of the holder was −55°C.

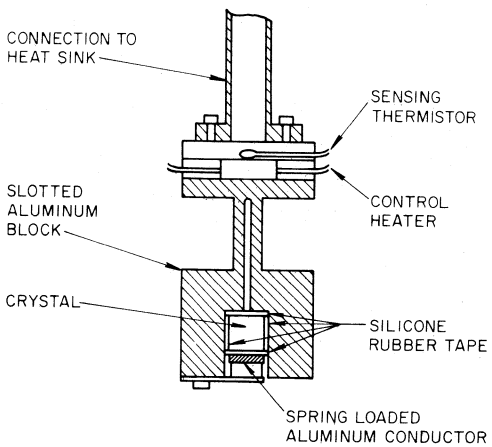


Fig. 3. Detail of crystal-holder assembly.

calibrated platinum thermometer with a temperature coefficient of 0.4 Ω/°C. For automatic thermostatic control a thermistor with a room-temperature resistance of about 500 Ω is cemented to one of the heater resistors. The large negative temperature coefficient of resistance of the thermistor permits accurate control of the heater current; the thermistor is connected to a simple 60-Hz ac bridge and comparator circuit which opens and closes a relay or silicon controlled rectifier connected in series with the heater resistors. We have obtained temperature stabilities better than 0.01°C with this method.

The loose coupling of the crystal to the laboratory environment also makes it practical to control the temperature manually by occasionally monitoring the thermistor resistance and then adjusting the heater current provided by a regulated variable power supply. With the heater turned off the crystal-holder temperature drops from ambient at a rate of about 1.7°C/min. When the temperature reaches −50°C, sudden application of about 3.3 W of continuous power reduces the drift rate to less than 0.1°C/h within 6 min, with less than 0.3°C overshoot. At this drift rate the system requires infrequent attention, and the temperature of the crystal holder varies with time as shown in Fig. 2.

Thermal contact resistance can present serious problems in thermostatic systems that must function in a vacuum environment, if careful attention is not given to the design. In crystal holders designed to be used at atmospheric pressure it is acceptable to mount the crystal directly between spring-loaded metal surfaces. However, in a vacuum environment the crystal/metal interfaces become poor thermal conductors, and we have observed that crystals can require up to 2 h to equilibrate with the holder to within 0.1°C if they are mounted in that way. After some experimentation we found that this problem can be overcome using the configuration shown in Fig. 3. The holder is a single piece of aluminum, slotted down the middle to achieve flexibility so that pressure can be applied to two opposite sides of the crystal. Silicone rubber tape is applied to the sides of the crystal before insertion into the holder. The silicone tape (we have used Scotch No. 70 electrical tape) retains some of its compliance even at low temperatures and achieves reasonably uniform heat flow between the crystal sides and the holder. This modification reduced the equilibration time and thermal gradients in our crystal by about an order of magnitude.

A very useful technique for sensing temperature changes and thermal gradients within the crystal is to monitor the birefringence of the crystal under 633-nm illumination from a linearly polarized helium–neon laser. The incident beam is polarized at 45° between the principal birefringence axes of the crystal and is expanded so that the entire crystal is illuminated. A polarizer placed in the emergent beam enables one to observe fringes of constant relative retardation. Since the birefringence is a function of temperature, the projected pattern can be interpreted as a mapping of isotherms averaged along the optical path. For crystals such as ADP and ammonium dihydrogen arsenate (ADA) with large thermal coef-

ficients of birefringence, the method can indicate temperature differences of the order of 0.1°C, and it immediately reveals contact resistance problems in the crystal/mount interfaces. Uneven thermal contact produces distortion of the fringe pattern as the crystal cools, and temporal changes in the pattern after the holder temperature is stabilized can be used to measure the equilibration rate of the crystal in the mount. At wavelengths and power levels for which appreciable heat is generated by optical absorption in the crystal, the fringes also reveal the temperature rise between the surfaces and the optical region in the crystal, as shown in Fig. 4. In the figure an ADP crystal 2.2 cm long with a 1-cm-square aperture was irradiated by a beam of 1064-nm light about 0.4 cm in diameter. At 1064-nm the absorption in ADP is approximately 0.2 cm^{-1}. The crystal was mounted in the vacuum cryostat using silicone tape as previously described. As the 1064-nm power was increased, the fringes were photographed in 633-nm light traveling nearly parallel to the 1064-nm beam. The fringe regularity indicates uniform heat flow at the crystal surfaces.

It is a great convenience to be able to operate the cryostat disconnected from its vacuum pump after its initial pump-down. This is accomplished in our device by mounting a small (~8 cm^3) container of Linde Type 5A sieve material on the bottom of the copper heat sink. The system is initially evacuated to a pressure of about 0.01 mmHg using a mechanical pump. The container is then valved off and disconnected from the pump, and the reservoir is filled with liquid nitrogen. The cold sieve material continues to adsorb the remaining gas, and the system can be used without further mechanical pumping as long as the reservoir contains liquid nitrogen. This system operates longer than 6 h without refilling the reservoir, and nitrogen can be added easily without interrupting an experiment.

The heat capacity of the heat sink in this cryostat is large, and some consideration must be given to the procedure for terminating an experiment if the refrigerated crystal is not to be cooled below some critical temperature. Crystals of the ADP family, for example, will shatter if cooled below their Curie temperatures. If the liquid nitrogen is removed and the control heater power is shut off immediately, the crystal-holder temperature can drop slowly to −100°C or lower before warming. If the heater power is left on, the holder will warm very slowly but may reach an excessively high temperature if the system is left unattended for several hours. When a highly reliable automatic control circuit is used this problem does not exist, of course. However, a simple alternative is to attach a high-power heater directly to the heat sink. We have found that application of about 50 W for 10 min after the nitrogen is removed will prevent a severe drop in temperature at the crystal holder.

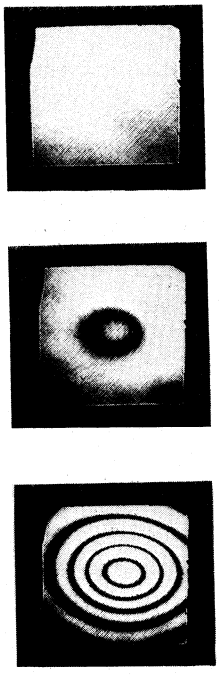


Fig. 4. Thermal birefringence patterns at 633 nm produced by absorption of 1064-nm light in a 2.2-cm crystal of ADP. The fringe separation corresponds to 0.75°C.

In conclusion, we have described the construction and operation of a cryostat for maintaining optical crystals (or other samples) at arbitrary temperatures down to −175°C with stabilities of the order of 0.1°C or better. The system can be evacuated with a mechanical pump, which is disconnected from the cryostat during an experiment, and it will operate for most of a working day with a single filling of liquid nitrogen.

References

[1] R. A. Phillips, "Temperature variation of the index of refraction of ADP, KDP, and deuterated KDP," *J. Opt. Soc. Amer.*, vol. 56, pp. 629–632, May 1966.
[2] R. S. Adhav and R. W. Wallace, "Second harmonic generation in 90° phase-matched KDP isomorphs," *IEEE J. Quantum Electron.* (Corresp.), vol. QE-9, pp. 855–856, Aug. 1973.
[3] F. B. Dunning, F. K. Tittel, and R. F. Stebbings, "The generation of tunable coherent radiation in the wavelength range 2300-3000 Å using lithium formate monohydrate," *Opt. Commun.*, vol. 7, pp. 181–183, Mar. 1973.
[4] R. K. Jain and T. K. Gustafson, "Second-harmonic generation of several argon-ion laser lines," *IEEE J. Quantum Electron.* (Corresp.), vol. QE-9, pp. 859–861, Aug. 1973.
[5] G. A. Massey, "Efficient upconversion of long-wavelength UV light into the 200-235 nm band," *Appl. Phys. Lett.*, vol. 24, pp. 371–373, Apr. 1974.
[6] R. H. Freeman, "A simple low temperature optical cryostat," *Rev. Sci. Instr.*, vol. 42, pp. 1263–1264, Aug. 1971.
[7] J. Bigeleisen, F. P. Brooks, T. Ishida, and S. V. Ribnikar, "Cryostat for thermal measurements between 2-300°K," *Rev. Sci. Instr.*, vol. 39, pp. 353–356, Mar. 1968.

Correction to "Far Infrared Frequency Synthesis with Stabilized CO_2 Lasers: Accurate Measurements of the Water Vapor and Methyl Alcohol Laser Frequencies"

F. R. PETERSEN, K. M. EVENSON, D. A. JENNINGS, J. S. WELLS, K. GOTO, AND J. J. JIMÉNEZ

Tables I and II (pages 841 and 842, respectively) from the above paper,[1] which were reduced to a size that makes for difficult reading, are reprinted here in a more readable form.

Manuscript received October 28, 1975.

F. R. Petersen, K. M. Evenson, D. A. Jennings, and J. S. Wells are with the Precision Laser Metrology Section, National Bureau of Standards, Boulder, CO 80302.
K. Goto is with the Toshiba Research & Development Center, Tokyo Shibaura Electric Company Ltd., Kawasaki, Japan.
J. J. Jiménez is with the Precision Laser Metrology Section, National Bureau of Standards, Boulder, CO 80302, on leave from the Laboratoire Primaire de Métrologie des Fréquences, Bureau National de Métrologie, Paris, France, and Centre National de la Recherche Scientifique, Paris, France.

[1] F. R. Petersen *et al.*, *IEEE J. Quantum Electron.*, vol. QE-11, pp. 838–843, Oct. 1975.

TABLE I
MEASURED FREQUENCIES FOR H_2O AND D_2O LASER LINES

WATER VAPOR LASER LINE λ (μm)	MEASURED FREQUENCY (MHz) (UNCERTAINTY: ± 1 MHz)	VACUUM WAVENUMBER (cm^{-1})	$^{12}C^{16}O_2$ SYNTHESIS COMBINATION
H_2O			
28[a]	10 718 068.3	357.516 276	$3\ P_{II}$ (10) - $3\ P_I$ (28)
78[b]	3 821 771.3	127.480 567	R_{II} (14) - P_I (16)
79[c]	3 790 474.5	126.436 620	R_{II} (10) - P_I (18)
119[d]	2 527 952.0	84.323 402	P_{II} (8) - R_I (16)
D_2O			
73[e]	4 120 984.3	137.461 240	R_{II} (22) - P_I (22)
84[f]	3 557 147.4	118.653 665	P_{II} (12) - P_I (30)
108	2 783 066.6	92.833 109	R_{II} (10) - R_I (26)

Note: Vacuum wavenumbers were calculated from the measured frequencies with c = 299 792 458 m/s ($\delta c/c = \pm 4 \times 10^{-9}$). The CO_2 synthesis combination with appropriate harmonic numbers is also listed for each measurement. In each case, the estimated 1-standard-deviation uncertainty in the CO_2 synthesized frequency was less than 30 kHz. Microwave frequencies up to 16 GHz were used. A total uncertainty of ±1.0 MHz has been assigned to each water vapor frequency, mainly because of the difficulty in determining the center of the Doppler and pressure-broadened laser gain curve.

[a]Evenson *et al.*, 10 718 073(2) MHz [17]. From HCN laser, 10 718 068.6(5) MHz (Lamb dip). Blaney *et al.*, 10 718 068.71(3) MHz [18] (Lamb dip).

[b]Evenson *et al.*, 3 821 775(3) MHz [17]. McDonald *et al.*, 3 821 774.4(3.0) MHz [5].

[c]From 78–79-μm difference, 3 790 477(3) MHz.

[d]Frenkel *et al.*, 2 527 952.8(1) MHz [19] (Lamb dip). Hocker and Javan, 2 527 954.0 MHz [20].

[e]The 72.7-μm line was the only CW line oscillating in our laser near this wavelength. Reference [12] reports CW oscillation at 71.9, but not at 72.7 μm.

[f]Hocker *et al.*, 3 557 143(2) MHz [21].

TABLE II
MEASURED FREQUENCIES OF 13 METHYL ALCOHOL LASER LINES

METHYL ALCOHOL LASER LINE λ (μm)	MEASURED FREQUENCY (MHz) (UNCERTAINTY: ±0.5 MHz)	VACUUM WAVENUMBER (cm^{-1})	ALCOHOL LASER VAPOR PRESSURE (Torr)	CO_2 PUMP LINE	CO_2 FREQUENCY SYNTHESIS COMBINATION
70.5	4 251 668.7	141.820 403	0.10	P_{II} (34)	R_{II} (30) - P_I (22)
96.5	3 105 936.8	103.602 901	0.20	R_{II} (10)	R_{II} (20) - R_I (18)
118.8[a]	2 522 781.6	84.150 935	0.10	P_{II} (36)	P_{II} (14) - R_I (8)
163.0	1 838 839.3	61.337 076	0.10	R_I (38)	P_{II} (20) - R_I (36)
170.6[b]	1 757 526.3	58.624 765	0.10	P_{II} (36)	P_{II} (30) - R_I (24)
232.9	1 286 999.5	42.929 683	0.20	R_{II} (10)	R_{II} (32) - P_{II} (24)
250.8	1 195 433.9	39.875 383	0.16	R_I (34)	R_I (34) - P_I (20)
251.1	1 193 727.3	39.818 455	0.20	R_I (38)	R_I (34) - P_I (20)
369.1	812 195.4	27.091 924	0.10	P_{II} (16)	R_I (10) - P_I (22)
392.1	764 642.6	25.505 733	0.15	P_{II} (36)	R_{II} (6) - P_{II} (24)
469.0	639 184.6	21.320 902	0.25	R_I (38)	P_I (8) - P_I (32)
570.6	525 427.5	17.526 375	0.15	P_{II} (16)	P_{II} (18) - P_{II} (36)
699.4	428 628.5	14.297 508	0.10	P_{II} (34)	R_I (38) - R_I (14)

Note: Vacuum wavenumbers were calculated from the measured frequencies with c = 299 792 458 m/s ($\delta c/c = \pm 4 \times 10^{-9}$). The 1-standard-deviation-type uncertainty for each frequency measurement is estimated to be ±0.5 MHz. The alcohol laser vapor pressure along with the CO_2 pump line are also given. The final column lists the two-laser CO_2 frequency synthesis combination. In each case, the estimated 1-standard-deviation uncertainty in the CO_2 synthesized frequency was less than 30 KHz.

[a]Fetterman *et al.*, 2522.78(1) GHz [4].

[b]Fetterman *et al.*, 1757.526(6) GHz [4].

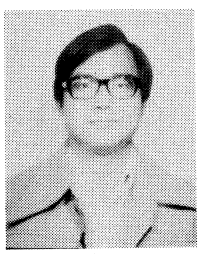
Contributors



Robert D. Burnham was born in Havre de Grace, MD, on March 21, 1944. He received the B.S., M.S., and Ph.D. degrees from the University of Illinois, Urbana, in 1966, 1968, and 1971, respectively. He held an NDEA Fellowship from 1966 to 1969 and a General Telephone and Electronics Fellowship from 1969 to 1971.

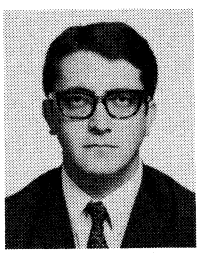
He has been a Member of the Research Staff at the Xerox Palo Alto Research Center, Palo Alto, CA, since 1971. His work has been centered on the growth and characterization of III-V compounds for device purposes.

*



Bor-Uei Chen was born in Taiwan, on August 1, 1949. He received the B.S. degree in physics from the National Taiwan University, Taipei, Taiwan, in 1970. He is currently working on integrated optics and thin-film optics at Cornell University, Ithaca, NY, where he is studying toward the Ph.D. degree.

*



Cesar C. Ghizoni (S'75) was born in Urubici-SC, Brazil, on February 16, 1945. He received the Degree of Engineer from the Federal University of Rio Grande do Sul, Porto Alegre, Brazil, in 1969, and the M.S. degree in electrical engineering from the Brazilian Space Research Institute (INPE), São José dos Campos-Sp, in 1971.

He joined INPE's research staff in 1971, where he worked on the design of low-noise microwave receivers. Since 1973 he has been at Cornell University, Ithaca, NY, working towards the Ph.D. degree in the area of quantum electronics.

Mr. Ghizoni is a member of the American Physical Society and Phi Kappa Phi.

*



Don R. Scifres (M'74) was born in Lafayette, IN, on September 10, 1946. He received the B.S. degree with honors in electrical engineering from Purdue University, West Lafayette, IN, in 1968, and the M.S. and Ph.D. degrees in electrical engineering from the University of Illinois, Urbana, in 1970 and 1972. While at the University of Illinois, he held a University of Illinois Doctoral Support Fellowship and a General Telphone and Electronics Fellowship.

In 1972 he joined the Xerox Palo Alto Research Center, Palo Alto, CA, as a Research Scientist and is currently working on the optical properties of semiconductor materials and injection lasers.

Dr. Scifres is a member of the American Physical Society and the Optical Society of America.

*



William Streifer (S'56-M'58-SM'74) was born in Poland on September 13, 1936. He received the B.E.E. degree (magna cum laude) from the City College of New York, NY, in 1957, the M.S. degree in electrical engineering from Columbia University, New York, NY, in 1959, and the Ph.D. degree from Brown University, Providence, RI, in 1962.

From 1957 to 1959 he was a Lecturer in the Department of Electrical Engineering, City College of New York, and from 1958 to 1959 he was a Research Engineer at the Heat and Mass Flow Analyzer Laboratory, Columbia University. In 1959 he accepted an NSF fellowship at Brown University, where he taught in the Division of Engineering and held a Bell Laboratories Fellowship. From 1962 to 1972 he was a Faculty Member at the University of Rochester, NY, where he held positions as Assistant Professor, Associate Professor, and Professor of Electrical Engineering. During the academic year 1969-1970 he was a Visiting Associate Professor at Stanford University, CA. He is presently a Principal Scientist at the Xerox Palo Alto Research Center, Palo Alto, CA. He has been a Consultant to several corporations including Xerox from 1969 to 1972. He has published numerous papers in the fields of optics, electromagnetism, applied mathematics, and mathematical ecology.

Dr. Streifer is a Fellow of the Optical Society of America.

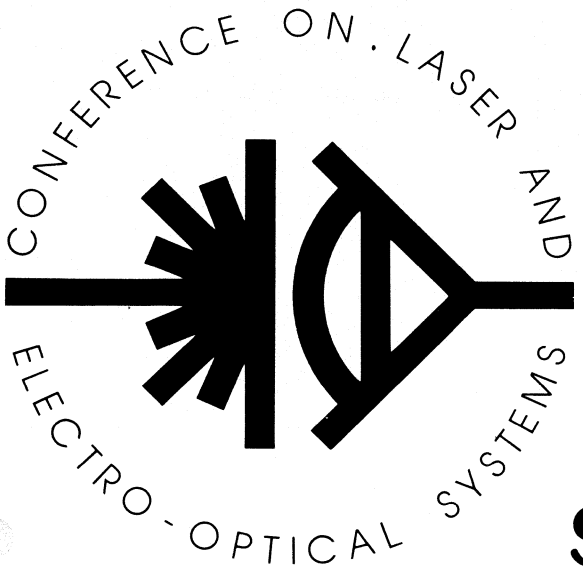
*



Chung L. Tang (SM'68) was born in Shanghai, China, on May 14, 1934. He received the B.S.E.E. degree from the University of Washington, Seattle, the M.S. degree from the California Institute of Technology, Pasadena, and the Ph.D. degree in applied physics from Harvard University, Cambridge, MA, in 1955, 1956, and 1960, respectively. As a recipient of a John Parker Traveling Fellowship from Harvard University, he also studied at the Institut für Theoretische Physik, Technische Hochschule, Aachen, Germany, during the academic year 1959-1960. During 1970-1971 he was a National Science Foundation Senior Postdoctoral Fellow on leave at Harvard University.

From 1960 to 1964, he was a Staff Member in the Research Division of the Raytheon Company, Waltham, MA. He joined the Faculty of Cornell University, Ithaca, NY, in 1964, where he is now a Professor of Electrical Engineering and a member of the Materials Science Center.

Dr. Tang is a member of Tau Beta Pi, Phi Beta Kappa, Sigma Xi, and the American Physical Society.



CLEOS
May 25-27, 1976
San Diego, California

The first Conference on Laser and Electro-Optical Systems (CLEOS) will be held at the Town and Country Hotel in San Diego, May 25-27, 1976, under the joint sponsorship of the Quantum Electronics Council of the Institute of Electrical and Electronics Engineers (IEEE) and the Technical Council of the Optical Society of America (OSA).

CLEOS aims to provide a professional technical forum for the presentation of engineering and manufacturing developments in the fields of lasers, laser applications, electro-optic devices, electro-optic systems, and the manufacturing and design techniques that have made these systems possible.

Original papers are solicited that describe new technical contributions to such areas as:

- laser engineering manufacturing
- measurement & alignment systems
- opto mechanical subsystems
- scanning systems
- optical signal & data processing systems
- optical display systems
- e-o component technology
- space & military e-o systems
- laser fusion & laser isotope separation systems
- optical communication systems
- medical e-o systems
- e-o systems for production of microelectronics
- pollution-monitoring systems
- consumer e-o systems
- imaging & surveillance subsystems
- ranging & designation subsystems
- adaptive optical techniques
- electro-optical systems for material processing

AN EXHIBIT WILL BE AN INTEGRAL PART OF THIS MEETING.

For general information on the conference write:

Leslie Hill
Hughes Aircraft Company
Electron Dynamics Division
3100 West Lomita Boulevard
Torrance, California 90509

For information on the exhibit and to receive the exhibitors package write:

Ed Greeley
American Institute of Physics
335 East 45th Street
New York, New York 10017

Preface

THE IEEE and the Optical Society of America (OSA) jointly sponsored the Fifth Biannual Conference on Laser Engineering and Applications in Washington, DC, May 28-30, 1975. This Special Issue of the IEEE JOURNAL OF QUANTUM ELECTRONICS contains 12 of the papers presented at the conference and which were subsequently submitted for a full review according to the standards of the JOURNAL. Additional papers edited by Tony DeMaria, Cochairman of the conference for OSA, are being published in *Applied Optics*.

Papers were assigned to one or the other journal on the basis of author preferences and the recommendations of reviewers. Many CLEA '75 papers appear in neither Special Issue, but abstracts of all the papers, including the post-deadline contributions, appear in the September 1975 IEEE JOURNAL OF QUANTUM ELECTRONICS.

CLEA '75 clearly extended the traditions of past successful conferences. Over 1100 people attended the three-day meeting and a record 74 exhibit booths displayed the latest laser hardware. There was a well-balanced program of 175 papers on laser devices and applications. Of these, there were 32 invited papers on far-ranging subjects, including special talks on "The Relevance of Lasers in the Energy Shortage" by Dr. E. Teller, and "Optical Communications in Prospective" by Dr. R. Kompfner. Thirty additional post-deadline papers were selected and presented. The success of the technical program is directly attributable to the Program Cochairmen Steve Halsted and Herwig Kogelnik and their 30-man program committee.

I would like to thank all the members of the CLEA '75 Conference Committee for their excellent work in running a successful conference. Special thanks are due the members of the Program Committee who thoughtfully and promptly reviewed the manuscripts for this issue. I also wish to acknowledge the vital help of my secretary, Bonnie Hoefer, for her patience and diligence in organizing all the paperwork. Most of all, thanks are expressed to the authors, whose efforts made this Special Issue possible.

—D. R. WHITEHOUSE
Guest Editor
Cochairman, CLEA '75

Photodegradation Mechanisms in Laser Dyes: A Laser Irradiated ESR Study

MIKIO YAMASHITA AND HIROSHI KASHIWAGI, MEMBER, IEEE

Abstract—**The photodegradation mechanisms in xanthene dye-laser solutions are investigated at 77 K by the direct detection of a decrease in the concentration of dye molecules in the lowest excited triplet state (T_1 state) and of free radicals produced after degradation using an ESR technique under UV (3511 + 3638 Å) or 5145-Å laser irradiations. It is shown that the ESR spectral shape of the radicals induced by an UV laser beam is quite different from that of those induced by a 5145-Å beam. For those radicals, the irradiation time and power dependences, the effects of dye and solvent molecular structures and the role of the T_1 state by the addition of cyclooctatetraene (COT) quenchers are examined in some detail. As a result the two following laser-induced photochemical reactions are proposed: in UV laser- or flashlamp-pumped dye lasers, the C-H bond rupture of a solvent molecule due to the energy transfer of a dye molecule in a higher excited triplet state, which is produced by a T-T absorption of a dye molecule in the T_1 state, results in a radical and a leuco compound of the dye. On the other hand, in the case of the 5145-Å laser excitation, a partially reversible change of a dye molecule in the T_1 state produced by only a one-photon absorption results in another radical which depends on the chromophoric structure of the dye.**

I. Introduction

PHOTODEGRADATION of organic dyes severely limits the lifetime of dye lasers, but the degradation mechanism is not yet well understood. Until now the studies on the degradation have been performed by detecting changes in the absorption and fluorescence spectra of dye-laser solutions before and after photodegradation [1]-[3]. In this paper we report the investigations on the photodegradation mechanism of xanthene laser dyes by a different method, in which the behaviors of the laser-induced free radicals and dye molecules in the lowest excited state (T_1 state) at 77 K are monitored directly, using an ESR technique during and after UV (3511 + 3638 Å) or visible (from 5145 to 4545 Å) laser irradiations [4]. Our method has the following advantages: 1) the dye molecules in the T_1 state and the free radicals occurring after degradation, photochemically produced, are directly detected; 2) the sensitivity to the paramagnetic products, induced by laser irradiations, is much higher; 3) as a result of cooling the ethanolic dye solution to 77 K, the solution becomes glassy [5], [6] and the products are stabilized at the irradiation point by being trapped in the rigid glass. On the other hand, because of the high intensity, wide tunability, and narrow spectral width of the pumping laser light, studies on the laser-induced photochemical reactions will be performed very often in the future and will exert significant influence on the field of photochemical physics.

At first we show that two different free radicals are induced in an R6G-ethanol solution by using either UV or visible laser irradiations. They differ in their ESR spectral shape according to the different wavelengths, and by increasing the laser power the amount of each increases, while the intensity of the $\Delta m = \pm 2$ ESR spectrum of the dye molecules in the T_1 state decreases. After that, the dependence of the radical concentration on the irradiation time and power, the effects of molecular structures of some laser dyes and solvents on the producing processes of radicals, and the role that the T_1 state of the dye molecules plays in the photochemical reactions are investigated. Finally, the laser-induced reaction sequences in the case of an UV laser irradiation and in that of a 5145-Å laser irradiation, which are quite different from each other, are proposed.

Manuscript received May 30, 1975; revised September 15, 1975.

The authors are with the Radio- and Opto-Electronics Division, Electrotechnical Laboratory, Tanashi, Tokyo, Japan.

II. Experimental

Each dye—rhodamine 6G (R6G), rhodamine B (RB), rhodamine S (RS), acridine red (AR), acridine orange (AO), and fluorescein disodium salt (FDS), all produced by the Eastman Kodak or Tokyo Kasei Kogyo Companies—was dissolved in ethanol, methanol, or dimethylsulfoxide (DMSO) at 1×10^{-3}-M concentration. We used Kanto Chemical's guaranteed reagent-grade ethanol, Tokyo Kasei's guaranteed reagent-grade methanol, and spectra-grade DMSO. The COT molecules, obtained from the Aldrich Chemical and Tokyo Kasei Kogyo Companies, were used as a triplet quencher for the R6G dye. In order to determine the photodegradation mechanism easily, the oxygen-free solution, outgassed by a freeze-thaw process, was sealed in a 4-mm-O.D. quartz tube. The experimental arrangement is nearly identical to the one we used previously to investigate the different behaviors of dye molecules in the T_1 state during laser excitation [4], [6]-[8]. Both the ESR spectrum of the H_{min} line corresponding to $\Delta m = \pm 2$ transitions in dye molecules in the T_1 state [4] and that of the free radicals, induced by laser light, were recorded with a Varian E-4 spectrometer with an optical transmission cavity. The peak-to-peak heights of the radical signal and of the H_{min} line were used in a first approximation to calculate the concentrations of the radicals and of the dye molecules in the T_1 state, respectively. The H_{min} line was recorded by using such a low-power 5145-Å laser beam (0.29 W/cm^2) that no measurable amount of radicals occurred. The solution, cooled by inserting it into liquid nitrogen in a quartz Dewar, was irradiated by an unfocused beam consisting of UV (3511 + 3638 Å) light or 5145-Å light of an Ar-ion laser (except for the AO dye solution, which was irradiated by a 4880-Å beam). The transmittances of the quartz tube without th dye solution, which was inserted into the Dewar vessel containing liquid nitrogen, were measured for UV and 5145-Å laser beams. The results were that the attenuations of the laser

irradiation power due to the air, the liquid nitrogen, and the cylindrical quartz sheets of the Dewar vessel and the sample tube were about 35 and 45 percent, and the beam diameters were about 3.2 and 3.5 mm for the UV and 5145-Å laser beams, respectively.

III. Results and Discussions

In both cases—UV (3511 + 3638 Å) and 5145-Å laser irradiations to the R6G in an ethanol solution at 77 K—an ESR spectrum in the free-radical region was observed, which grew in intensity while the $\Delta m = \pm 2$ spectrum of the dye molecule in the T_1 state decreased in intensity. The spectral shape of the radical (denoted by FR1) which appeared in the dye solution during or after the UV laser irradiation, was the same as that appearing during or after irradiation by a high-pressure Hg lamp, but was quite different from that of the radical (denoted by FR2) which appeared during or after the 5145-Å laser irradiation, as shown in Fig. 1. In the case of an Ar-ion laser irradiation in the blue-green region with a shorter wavelength than 5145 Å, the same spectral shape as that of the FR2 was always observed. The ESR spectrum of the FR1 obtained in the R6G-ethanol solution is quite good in comparison with that obtained in a hydrogen-peroxide-ethanol solution by Gibson *et al.* [9] using the photolysis method with a low-pressure Hg lamp. They assigned the hyperfine pattern to the ethanol radical, $CH_3\dot{C}HOH$, formed by an α-hydrogen abstraction from ethanol. Therefore, the FR1 spectrum appearing in the oxygen-free solution is considered to be due to the $CH_3\dot{C}HOH$ radical which arises by the abstraction of a hydrogen atom of an ethanol molecule by the laser-excited R6G molecule. On the other hand, the precise origin of the FR2 radical induced by the 5145-Å laser irradiation cannot be stated at present. However, there seems to be no doubt that the radical depends on the chromophoric structure of the R6G dye, which will be mentioned subsequently.

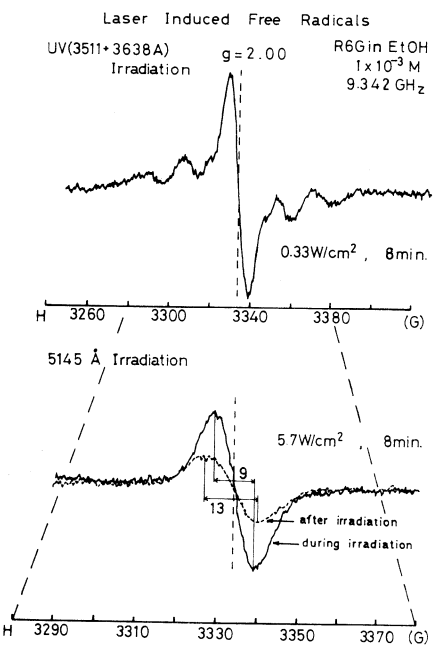


Fig. 1. Observed frequency-derivative ESR spectra of the free radical FR1 in a 1×10^{-3}-M R6G-ethanol solution at 77 K after UV laser irradiation (upper spectrum) and of the free radical FR2 during (solid line of the lower spectra) or after (dotted line of the lower ones) a 5145-Å laser irradiation. The UV and 5145-Å laser irradiation time and power are 8 min and 0.33 W/cm², and 8 min and 5.7 W/cm², respectively.

At first, for the cases of UV and 5145-Å laser irradiations to the R6G-ethanol solution, the dependence of the peak-to-peak heights of the radical and triplet signals on the increase of the repetition number of the irradiation, using a constant time (2 min) and a constant power (0.53 W/cm² for UV and 3.4 W/cm² for 5145 Å) was examined. Therefore, the spectra of the FR1 or the FR2 with the corresponding wavelengths were recorded, and afterwards the H_{min} signal which was used to calculate the concentration of the dye molecules in the T_1 state was recorded during a 5145-Å laser irradiation with such a weak power that no FR2 could increase. From the results shown in Figs. 2 and 3, we find that the increase in the concentration of the radicals is correlative with the decrease in the concentration of dye molecules in the T_1 state in the cases of the FR1 and FR2. This is considered to be due to the following causes: 1) the shortening of the triplet-state lifetime is due to the paramagnetic interaction between the induced radicals and the dye molecules in the T_1 state; and 2) the

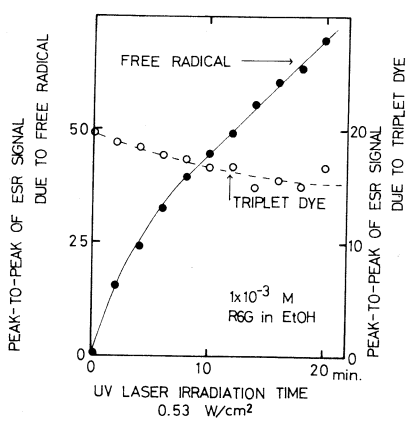


Fig. 2. Peak-to-peak heights of the FR1 radical spectrum (symbol •) induced after an UV laser irradiation and of the H_{min} line (symbol ○) in an R6G-ethanol solution versus the repetition number ($2 \times n$ min) of the irradiation using a fixed power (0.53 W/cm²) for 2 min. The H_{min} line corresponding to $\Delta m = \pm 2$ transitions in the T_1 state was recorded during a 5145-Å laser irradiation such a low power (0.29 W/cm²) that no other radical was produced.

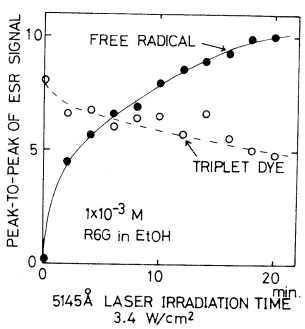


Fig. 3. Peak-to-peak heights of the FR2 radical spectrum induced after a 5145-Å laser irradiation and of the H_{min} line in an R6G-ethanol solution versus the repetition number ($2 \times n$ min) of the irradiation using a fixed power (3.4 W/cm²) for 2 min. The H_{min} line was recorded in the same way as in the case of Fig. 2. The symbols • and ○ correspond to those in Fig. 2.

decrease of the effective dye molecules is due to the change of its molecules into free radicals. But, on the basis of the experimental result that the triplet-state lifetime did not change significantly before and after UV or 5145-Å laser irradiations, it seems that the correlation between the increase of free radicals and the decrease of dye molecules in the T_1 state is mainly due to the last point.

Secondly, the variation of the concentration of the radicals was examined by increasing the irradiation power during a constant time (2 min for an UV irradiation and 5 min for a 5145-Å irradiation). The dependences of the peak-to-peak heights of the FR1 and FR2 on the irradiation power are shown in Fig. 4. This figure shows that the curve of the FR1 induced by an UV laser irradiation increases with the square of the irradiation power, while the one of the FR2 induced by a 5145-Å laser irradiation starts to increase linearly and then begins to saturate with increasing power. This saturation curve is similar to that of the concentration of dye molecules in the T_1 state depending on the pumping laser power [7]. Thus we can find that the FR1 and FR2 are produced by quite different optical processes, by two sequential single-photon absorptions including a T-T absorption and by a single-photon absorption, respectively. The fact that the T-T absorption is related to the producing process of the FR1 supports the foregoing assignment that the FR1 is a $CH_3\dot{C}HOH$ radical, because it is energetically sufficient to rupture the C-H bonds of ethanol by an energy transfer from the R6G molecules in a higher triplet state, which is produced by a stepwise single-photon absorption or a T-T absorption of a dye molecule in the T_1 state, to ethanol molecules [10], [11]. Furthermore, the comparison between the concentration dependence of the FR1 on the UV laser irradiation power and that of the FR2 on the 5145-Å laser irradiation power indicates that the FR1 is produced more easily by two orders in the production rate per unit power and unit time.

In order to investigate more thoroughly the effects of dyes and organic solvents on the producing processes of free radicals, we recorded the ESR spectra of those radicals occurring in dye-ethanol solutions for different dyes (R6G, RB, RS, AR, AO, and FDS) and occurring in R6G-organic solvents for different organic solvents (EtOH, MeOH, and DMSO). As shown in Figs. 5 and 6, the spectral shapes of the FR1 induced by the UV laser irradiation depend remarkably on the molecular structure of the solvents but only a little on that of the laser dyes. This also supports the previously mentioned conclusion that the FR1 is due to the solvent decomposition by the laser-excited dye molecule. On the other hand, the spectral shapes of the FR2 induced by the 5145-Å laser irradiation (only the AO dye solution was irradiated by a 4880-Å laser beam) depend more on the chromophoric structure of the dyes than on the molecular structure of the solvents, which is shown in Figs. 7 and 8. In the case of the visible laser irradiation the FR2 radical spectra of the dye solutions differ in the half-width only if their chromophoric structure is different. However, all the radicals we obtained have almost the same g-value of $g = 2.00$. Also it was evident that the FR1 or the FR2 in the AO- and FDS-ethanol and in the R6G-dimethylsulfoxide solutions were easily induced compared with those radicals induced in the other dye-ethanol and R6G-solvent solutions, respectively. Furthermore, it was observed for all the examined dyes that the signal intensities of the FR2 after the irradiation cutoff rapidly decreased to constant intensities when we used the visible laser irradiation, while those of the

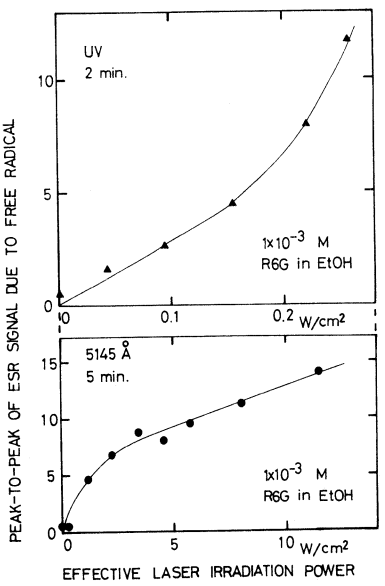


Fig. 4. Variation of the peak-to-peak heights of the FR1 and FR2 radical spectra induced in an R6G-ethanol solution after UV (upper curve) and 5145-Å (lower curve) laser irradiations as a function of the irradiation power for a constant time (2 and 5 min for UV and 5145-Å laser irradiations, respectively).

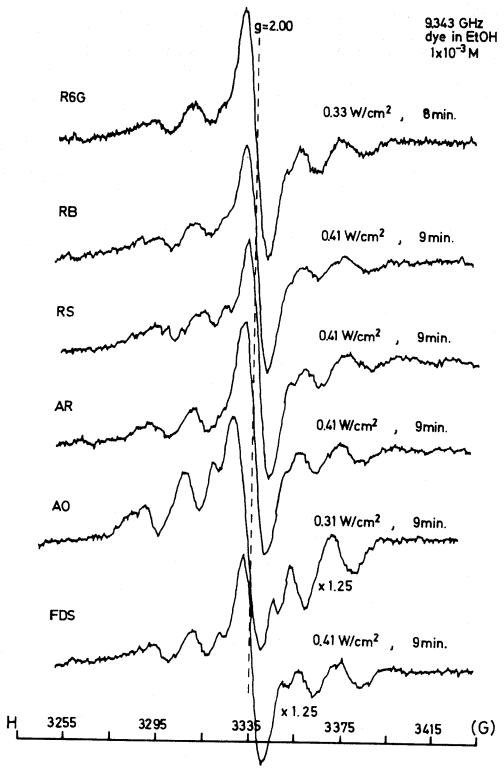


Fig. 5. Observed frequency-derivative ESR spectra of free radicals induced after an UV laser irradiation at 77 K for different dyes dissolved in ethanol.

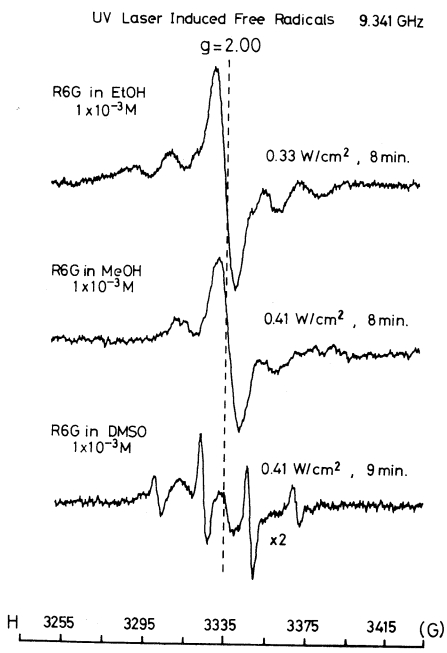


Fig. 6. Observed frequency-derivative ESR spectra of free radicals induced after an UV laser irradiation at 77 K for R6G in different solvents.

FR1 using the UV laser irradiation did not change. The decay times of the signal intensities of the FR2 in the R6G–ethanol solution at 77 K are about 1.0 s, which is a little less than the triplet-state lifetime of the solution [7]. This suggests that the

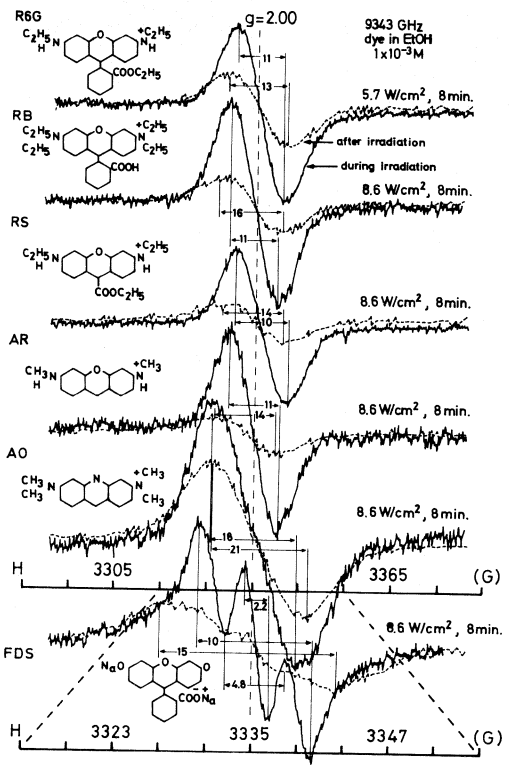


Fig. 7. Observed frequency-derivative ESR spectra of free radicals induced during (solid line) and after (dotted line) a 5145-Å laser irradiation at 77 K for different dyes dissolved in ethanol. Spectral half-widths in gauss units and dye molecular structures are also noted.

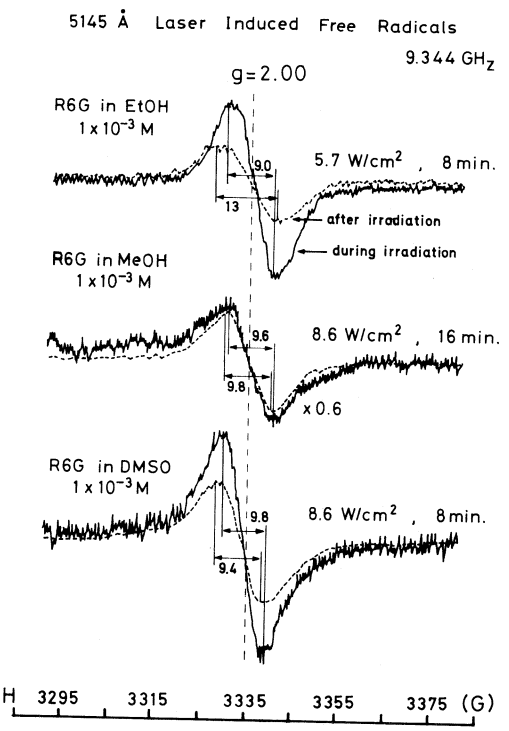


Fig. 8. Observed frequency-derivative ESR spectra of free radicals induced during (solid line) and after (dotted line) a 5145-Å laser irradiation at 77 K for R6G in different solvents. Spectral half-widths are again noted in gauss units.

FR2 arises from a partially reversible change of a laser-excited dye molecule.

Finally, in order to determine the connection of the amount of R6G molecules in the T_1 state with the producing processes of those radicals we examined the relation between the molecular concentration before the photochemical reaction and the radical concentration after the reaction for the R6G–ethanol solution, adding different amounts of a COT quencher. The result, which is shown in Figs. 9 and 10, is that the radical concentration (for the FR1 we got the same values during and after the UV laser irradiation and, for the FR2, different values during and after the 5145-Å laser irradiation) decreases as the concentration of the molecules in the T_1 state before the reaction decreases. This shows that the molecules in the T_1 state have direct effects upon those two laser-induced chemical reactions. In particular, the FR2 appearing during or after the 5145-Å laser irradiation decreases even more rapidly than the dye molecule in the T_1 state decreases due to the quenching by an energy transfer to a COT molecule. From this we conclude that the FR2, which depends on the chromophoric structure of the dye, is produced by a partially reversible change of one dye molecule in the T_1 state.

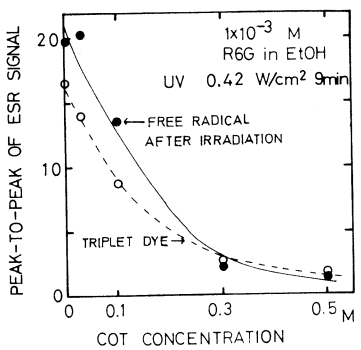


Fig. 9. Dependences of the peak-to-peak heights of the H_{min} line before the radicals occurred (symbol ○) and of the radical spectrum induced after an UV laser irradiation (symbol ●) on the COT concentration in an R6G–ethanol solution at 77 K. The H_{min} line was recorded in the same way as in the case of Fig. 2.

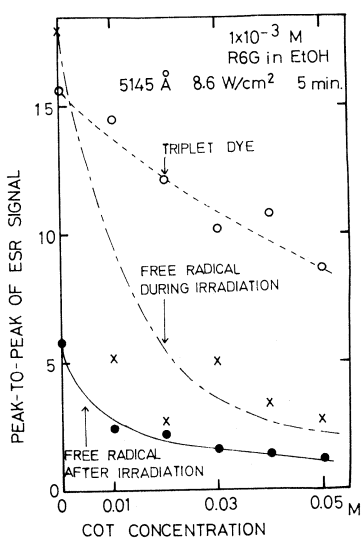


Fig. 10. Dependences of the peak-to-peak heights of the H_{min} line before the radicals occurred (symbol ○) and of the radical spectrum induced during (symbol X) or after (symbol ●) a 5145-Å laser irradiation on the COT concentration in an R6G–ethanol solution at 77 K. The H_{min} line was recorded in the same way as in the case of Fig. 2.

IV. Conclusion

Based on our considerations, we find that the mechanisms of the photodegradations occurring in R6G–ethanol laser solutions at 77 K are quite different for the two cases of UV and 5145-Å laser excitations, and the laser-induced photochemical reactions are explained in the following ways:

A) in the case of an UV laser irradiation including flashlamp excitation;

1) a few of the dye molecules excited to the S_1 state by the absorption of a photon decay to the T_1 state by an intersystem crossing process;
2) some of them return to the S_0 state, but others absorb another photon to produce a higher excited triplet state (T–T absorption);
3) the C–H bonds of the ethanol are ruptured by an energy transfer from a dye molecule in the higher triplet state to a solvent molecule, which results in the FR1 radical, and the dye is reduced to a leuco compound [12]:

B) in the case of a 5145-Å laser irradiation;

1) like A) 1), some dye molecules are excited to the T_1 state;
2) except for decaying to the S_0 state, the dye molecule in the T_1 state changes into another radical, FR2.

The schemes of the proposed reaction sequences in both cases A) and B) are shown in Fig. 11. Thus we think that one of the most important procedures to increase the lifetime of xanthene dye lasers is to use a triplet quencher and an unreduc-

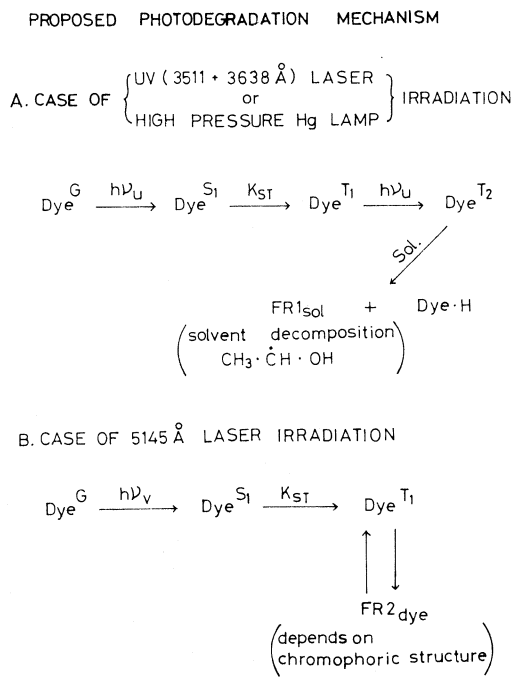


Fig. 11. Proposed photodegradation mechanisms occurring in a laser dye solution under UV laser or flashlamp excitations [case A)] and 5145-Å laser excitation [case B)].

ible solvent. Finally, it should be pointed out that there are still some problems to be solved. Mainly, what is the exact nature of the second reaction B) resulting in the FR2 radicals? But the information necessary to answer this question is not yet available.

ACKNOWLEDGMENT

The authors wish to thank Dr. K. Sakurai and Dr. T. Sato for their continuous encouragement. They also wish to thank H. Ikeda for his help with the experimental work.

REFERENCES

[1] E. P. Ippen, C. V. Shank, and A. Dienes, "Rapid photobleaching of organic laser dyes in continuously operated devices," *IEEE J. Quantum Electron.* (Corresp.), vol. QE-7, pp. 178-179, Apr. 1971.

[2] A. D. Britt and W. B. Moniz, "The effect of pH on photobleaching of organic laser dyes," *IEEE J. Quantum Electron.* (Corresp.), vol. QE-8, pp. 913-914, Dec. 1972.

[3] J. Weber, "Study of the influence of triplet quencher on the photobleaching of rhodamine 6G," *Opt. Commun.*, vol. 7, pp. 420-422, Apr. 1973.

[4] M. Yamashita and H. Kashiwagi, "Triplet-state esr of rhodamine 6G during laser irradiation," *J. Chem. Phys.*, vol. 59, pp. 2156-2157, Aug. 1973.

[5] R. A. Berg and A. Ron, "Phosphorescence lifetimes of cationic dyes: Concentration and temperature effects," *J. Chem. Phys.*, vol. 59, pp. 3289-3296, Aug. 1973.

[6] M. Yamashita and H. Kashiwagi, "Temperature effects on triplet lifetime of rhodamine 6G in ethanol and polymethylmethacrylate," *Japan. J. Appl. Phys.*, vol. 14, pp. 421-422, Mar. 1975.

[7] —, "Optical saturation and quenching effects in the triplet state of rhodamine 6G," *J. Phys. Chem.*, vol. 78, pp. 2006-2009, Sept. 1974.

[8] M. Yamashita, H. Ikeda, and H. Kashiwagi, "Laser pumped magnetophotoselection in triplet dyes," *J. Chem. Phys.*, vol. 63, pp. 1127-1132, Aug. 1975.

[9] J. F. Gibson, M. C. R. Symons, and M. G. Townsend, "Unstable intermediates. Part II. Photolysis of hydrogen peroxide in solid alcohols: Some reactions of hydroxyl radicals," *J. Chem. Soc.*, pp. 269-276, 1959.

[10] K. Shimokoshi, Y. Mori, and I. Tanaka, "An esr study of the aromatic-compounds-photosensitized decomposition of alcohol by the two-photon process," *Bull. Chem. Soc. Japan*, vol. 40, pp. 302-306, Feb. 1967.

[11] S. Siegel and K. Eisenthal, "Triplet-triplet absorption in sensitized solvent decomposition: An esr study," *J. Chem. Phys.*, vol. 42, pp. 2494-2502, Apr. 1965.

[12] K. Uchida, S. Kato, and M. Koizumi, "Photosensitized oxidation of leuco-uranine and the identification of the photobleached product of uranine in ethanol solution," *Bull. Chem. Soc. Japan*, vol. 35, pp. 16-22, Jan. 1962.

Lasing Efficiency and Photochemical Stability of IR Laser Dyes in the 710–1080-nm Spectral Region

PETER E. OETTINGER AND C. FORBES DEWEY, JR.

Abstract—**The lasing efficiencies and photochemical stabilities of laser dyes useful in the 710–1080-nm spectral region have been investigated using a *Q*-switched ruby laser pumping source. The measured bleaching rates *P* defined as the probability of irreversible decomposition of a dye molecule per absorbed photon, varied from $\leqslant 1 \times 10^{-5}$ to 3×10^{-4} for the different dye-solvent combinations investigated. Broad-band lasing efficiencies (the ratios of dye laser output to ruby radiation input) ranged from 4 to 43 percent. Shifts of wavelength tuning range with variations in solvent, dye concentration, and dye laser cavity geometry are reported.**

Manuscript received June 12, 1975. This work was supported in part by the Advanced Projects Agency under Grant N0014-67-A-0204-0092.

P. E. Oettinger is with the Thermo Electron Corporation, Waltham, MA 02154.

C. F. Dewey, Jr., is with the Department of Mechanical Engineering, Massachusetts Institute of Technology, Cambridge, MA 02139.

INTRODUCTION

THE lasing efficiency and photochemical stability of laser dyes useful in the near UV and visible portions of the spectrum (300-700 nm) have been characterized by numerous investigators [1]-[8]; the properties of laser dyes spanning the near IR region (700-1000 nm) are not as well defined [9]-[14]. Emission at these IR wavelengths is generally produced by long chain-like polymethine dyes, many of which are known to decompose readily in the presence of intense light. Major investigations of these polymethine dyes have been conducted by Miyazoe and Maeda [9], [11], and Maeda *et al.* [15], who found the general result that an increase in the length of the polymethine chain simultaneously shifted the lasing spectrum increasingly into the red and increased the propensity to photochemical degradation. Recently, an

attempt has been made by Webb *et al.* [13] to reduce such photochemical instabilities by introducing ring-like structures into the center of the chain, thereby "strengthening" the molecule. The maximum wavelength at which dye lasers will operate is speculated to be near 1.5 μm [16], [17], where internal conversions $S_1 \rightarrow S_0$ will become so large as to preclude the production of population inversions between the lasing levels.

Q-switched ruby lasers are the optical pumps most frequently used to excite dyes which lase in the near IR, although many of these dyes have more recently been excited with flashlamps [13], [18] with favorable results. In both flashlamp-pumped and laser-pumped systems, the experiments which have been reported in the literature have utilized a variety of laser cavity geometries, dye solvents [19], and dye concentrations so that comparison between different investigations is difficult at best. Only fragmentary quantitative information exists on the photochemical stability of these dyes [11], [20].

This investigation was undertaken to provide a systematic comparison of the lasing efficiency and photochemical stability of 16 promising laser dyes which have been reported in the literature. Included in this list are the first organic laser dyes reported by Schaefer *et al.* [21] and Sorokin *et al.* [19] as well as four of the new polymethine structures announced by Webb *et al.* [13]. We have also investigated the shifts in laser output tuning range which can be achieved by utilizing different optical pumping arrangements and cavity geometries.

Experimental Methods

Our experiments deal exclusively with ruby laser pumped dye lasers. Three different optical pumping arrangements were utilized, as illustrated in Fig. 1(a)–(c). Fig. 1(a) is an angle-pumping system, employed in the majority of our experiments, in which the dye laser cavity axis is offset from the ruby pump propagation direction by 14°. Wavelength tuning of the 25-cm-long dye laser cavity was accomplished with a 75-percent reflecting gold-coated 600-l/mm diffraction grating blazed for 1.6 μm and operated in second order. A 5-pps 50-ns Q-switched multimode ruby laser averaging 1.4 MW during the pulse was the optical excitation source. The dye cell was a stoppered quartz spectrophotometer cell with an active thickness of dye (as measured along the dye laser optical axis) of 2.30 mm. The diameter of the ruby pump beam at the dye cell was 2 mm. The output mirror was 45-percent reflective across the spectral region of interest. To obtain broad-band lasing action, the grating was replaced with a fully reflecting (99 percent) plane mirror.

Two other pumping configurations were also employed, and are illustrated in Fig. 1(b) and (c). In the end-pumping configuration, a dichroic mirror directs the ruby laser beam along the axis of the dye laser. The closed cell used here was 15 mm long, six times longer than that for angle pumping. A side-pumped system with a 20-mm-long active dye region is shown in Fig. 1(c); this cell exhibited peak dye laser output at dye concentrations substantially larger (roughly a factor of 2 to 4) than the angle-pumped system. The e^{-1} penetration depth of the ruby beam in the side-pumped cell was approximately 1 mm. For the arrangements of Fig. 1(b) and (c), the multimode Q-switched ruby laser produced a 30-ns 25-MW pulse with a 10-mm beam diameter.

Shown in Fig. 1(d) is the flashlamp-pumping geometry utilized by Webb *et al.* [13]. Their results for the wavelength of peak power broad-band lasing will be compared with ours. Note that their active dye length is 150 mm, or 65 times the length of the angle-pumped dye cell; comparable dye concentrations were utilized in the two systems.

The 16 dyes investigated are listed in Table I. Also included in Table I are four dyes which we did not study but for which substantial data are available in the literature. The numbering system follows that introduced in [22]; the numbers correspond (approximately) to the wavelength of peak laser power as reported by the original investigator. Inasmuch as many different dye solvents were tested in these early investigations, the numbers are only indicative of the spectral region covered.

Molar dye concentrations were established by adding a weighed amount of dye to a measured volume of solvent. All solvents were spectrophotometric grade, and several commercial sources of DMSO were used [14] with no measurable

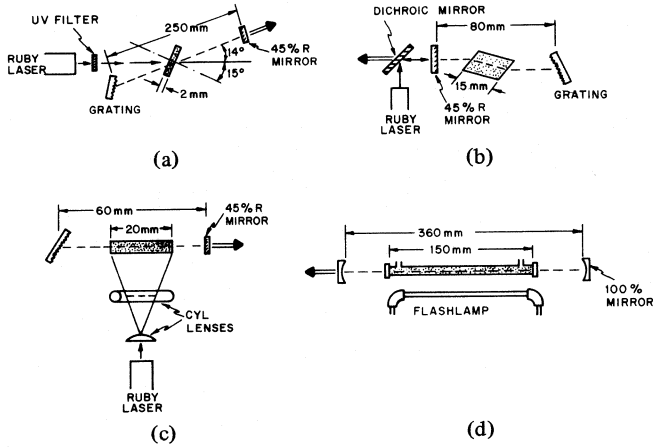


Fig. 1. Four dye laser optical pumping configurations. (a) Angle pumping. (b) End pumping. (c) Side pumping. (d) Flashlamp pumping.

TABLE I
IR LASER DYES INVESTIGATED[a]

715 [b]	–	3, 3'-diethyl-2, 2'-thiadicarbocyanine iodide (DTDC)
724	–	3, 3'-dimethyl-2, 2'-(5, 5'-dimethyl)-thiathiazolino-tricarbocyanine iodide
725	–	3, 3'-diethyl-2, 2'-oxatricarbocyanine iodide
735	–	3, 3'-dimethyl-2, 2'-oxatricarbocyanine iodide (DOTC)
757	–	3, 3'-diethyl-2, 2'-(6, 6'-dimethoxy)-thiadicarbocyanine iodide
771	–	1, 1'-diethyl-2, 2'-dicarbocyanine iodide (DDI)
800	–	1, 3, 3, 1', 3',3'-hexamethyl-2, 2'-indotricarbocyanine iodide (HITC)
809	–	6-(3-ethyl-2-benzothiazolylidene)-2, 4-hexadienylidene thioindosenid (Merocyanine B)
820 [b]	–	3, 3'-diethyl-2, 2'-thiatricarbocyanine iodide (DTTC iodide)
821	–	3, 3'-diethyl-2, 2'-thiatricarbocyanine bromide (DTTC bromide)
830	–	Kodak IR-123 tricarbocyanine salt
850	–	3, 3'-diethyl-2, 2'-(5, 6, 5', 6',-tetramethoxy)-thiatri-carbocyanine iodide
880	–	3, 3'-diethyl-2, 2'-(5, 5'-dimethoxy)-thiatricarbocyanine iodide
910	–	Kodak IR-144 tricarbocyanine salt
931	–	1, 1'-diethyl-4, 4'-dicarbocyanine iodide
940	–	Kodak IR-125 tricarbocyanine salt
950 [b]	–	Kodak IR-140 tricarbocyanine salt
972	–	Kodak IR-132 tricarbocyanine salt
980	–	3, 3'-diethyl-12-acetoxy-2, 2'-thiatetracarbocyanine perchlorate
1020 [b]	–	1, 1'-diethyl-4, 4'-quinotricarbocyanine iodide

[a]The numbers assigned to each dye signify (approximately) the center of the lasing band of each dye by the original reference in the literature.
[b]Dyes not investigated extensively but included because of considerable data from other sources.

differences in the results. After the solvent bottles were opened, no special precautions were employed (other than restoring the bottle cap after pouring the solvent) to inhibit trace moisture and oxygen from entering the DMSO. During and following dye solubilization, the laser solutions were exposed to the atmosphere for varying amounts of time. Convective mixing occurred in the solubilization process as well as in the stoppered dye laser cell during the bleaching tests. This suggests that the solutions contained substantial amounts of dissolved oxygen, but no attempts were made either to achieve oxygen saturation or to purge the solutions of dissolved oxygen. Bleaching tests with independently mixed solutions gave the same reproducibility in the bleaching probability P as replicate tests on a single solution (about ±15 percent).

Dye bleaching rates were calculated by comparing the ruby transmission through the dye cell as measured by a Hadron TRG Model 100 thermopile and Model 102 C energy meter and a Raytheon LA 31 vacuum silicon diode power meter, before and after exposure to 1500 laser pulses. Convective mixing assured uniform bleaching throughout the dye in the cell; this fact was substantiated by visual observations of the dye before and after bleaching.

Long-chain polymethine dyes are quite sensitive to the UV emission from the flashlamp used to pump the ruby laser, and to the fluorescent lights of the laboratory; exposure to these sources generally bleaches the dyes within a few days. Consequently, a Schott RG 665 UV filter was used to prevent exposure of the dye to the short wavelengths, and the dyes were shielded as much as possible from laboratory illumination.

Dye laser broad-band (~200-Å) and narrow-band (7-Å) output energies and powers were measured with the same diagnostic instrumentation as was used to quantitate the ruby laser performance. Dye emission was spectrally resolved with a $\frac{1}{4}$-m Jarrell Ash monochrometer.

DISCUSSION

The wavelength coverage, lasing efficiencies, bleaching probabilities, and quality factors of the sixteen dyes investigated are shown in Table II. Bleaching probabilities were obtained by first calculating the number ΔN of dye molecules bleached in a 2-mm-thick spectrophotometric cell when subjected to 50 mJ per pulse radiation at 5 pps for 5 min. Dye concentrations were adjusted for maximum lasing output; broad-band lasing was obtained from the dye cell throughout the bleaching tests.[1]

Let N and N' represent the number of intact dye molecules, respectively, before and after exposure to the ruby radiation. Their ratio may be related to the transmission of ruby laser light through the dye cell by

$$\frac{N'}{N} = \frac{\ln (I_0'/I')}{\ln (I_0/I)} \tag{1}$$

where I and I' are the initial and final ruby intensities transmitted through the dye, and I_0 and I_0' the corresponding incident intensities. Knowing the original dye concentration N (1) can be used to calculate the number of molecules bleached

$$\Delta N = N - N'. \tag{2}$$

(Equation (2) contains the premise that bleaching is irreversible and a bleached molecule no longer absorbs at the ruby wavelength; this assumption is consistent with our observations for all the dye-solvent combinations we have investigated.) A bleaching probability P, i.e., the number of dye molecules bleached per absorbed ruby photon, can be calculated from

$$P = \frac{h\nu \Delta N}{F} \tag{3}$$

where $h\nu$ is the energy per ruby photon and F is the total ruby laser energy absorbed by the dye during the bleaching test.

The lasing efficiencies E of the dyes, defined as the ratios of dye-output to absorbed ruby-input energies, were measured

[1]The bleaching probabilities were measured under actual lasing conditions, and are therefore indicative of the degradation which occurs under conditions of practical use. However, lasing action decreases the mean lifetime of the dye molecules in the excited singlet state and in any triplet state formed by singlet–triplet transitions [19]. If bleaching proceeds from the excited singlet or triplet state, the values of P we have measured would be lower bounds to the values which would be measured in a nonlasing configuration.

TABLE II
IR DYE LASER CHARACTERISTICS

Dye	Molar Concentration x 10^4	Wavelength Range (nm)	Lasing Efficiency E (%)	Bleaching Probability P x 10^5	Broadband Quality Factor Q x 10^{-3}	Comments
715 [b]	---	705-735	15 [a]	--	---	Also lases equally well in H_2O-surfactant and alcohols. Appears to be very stable against photochemical degradation.
724	4.1	710-765	43	30	1.4	Primary lasing 710-740 nm; secondary peak at 750 nm.
725	0.5	725-765	43,34 [a]	9	4.8	Primary lasing 725-745 nm; secondary peak at 760 nm. 3.9(10^{-4}) M concentration extends range to 790 nm.
735	1.0	725-780	39,36 [a]	9	4.3	Primary lasing 725-755 nm; secondary peak at 770 nm. Peak shifted 2.5 nm during bleaching test. Unstable in light. With H_2O- 5% triton as solvent E ∿ 36%, P ∿ 5(10^{-5}), poor shelf life.
757	1.4	710-755	23	20	1.2	Primary lasing 710-725 nm; secondary peak at 745 nm.
771	1.0	740-770	4	5	0.8	Solvent was ethylene glycol; does not lase in DMSO. Good lasing in glycerol with P < 10^{-5} and similar spectrum.
800	3.7	790-840	30	8	3.8	Peak intensity shifted 5 nm during bleaching test. Good lasing in H_2O-5% triton with similar spectrum.
809	1.3	780-823	5	24	0.2	Primary lasing 780-810 nm; secondary peak at 820 nm. Peak shifted 4 nm during bleaching test.
820 [b]	---	816-855	26 [a] (est.)	--	---	Very unstable to ruby laser light.
821	0.9	810-830	18,12 [a]	14	1.3	Peak shifted 5 nm during bleaching test. With H_2O-5% trition as solvent and 1.8(10^{-4})M mixture, lased 800-845 nm with E ∿ 18%, P ∿ 4.6(10^{-5}).
830	1.6	765-815	22 [a]	12	1.8	New Kodak "reinforced structure" dye. Rapid bleaching.
850	3.0	855-885	19	24	0.8	
880	1.7	820-875	24 [a]	11	2.2	Also lases efficiently when dissolved, at 150°F, in ethylene glycol [P = 5(10^{-5})].
910	2.2	835-890	21 [a]	6	3.5	New Kodak "reinforced structure" dye.
931	5.3	845-920	25	18	1.4	Good lasing in H_2O-5% trition, but poor shelf life.
940	2.3	840-920	14 [a]	≤ 1	14.0	New Kodak "reinforced structure" dye. Excellent resistance to bleaching.
950 [b]	---	∿850-930 (est)	> 35 (est)	--	---	New Kodak dye. Not available at time of these experiments. Should be comparable to 940 but with higher efficiency.
972	1.2	875-920	7 [a]	≤ 2	3.5	New Kodak "reinforced structure" dye. Heated to 150°F for good dissolution in DMSO.
980	0.8	920-950	20	17	1.2	Peak intensity shifted 6 nm during bleaching test. Poor shelf life.
1020 [b]	---	983-1081	--	--	---	Tested in end-pumped geometry only.

Note: Solvent is DMSO and angle-pumping configuration utilized unless specified otherwise.
[a]Narrow band; measured in grating-tuned configuration.
[b]Dyes not investigated extensively but included because of considerable data from other sources.

for the angle-pumped dye cell, generally in a broad-band configuration with the dye radiation oscillating between a totally reflecting mirror and a 45-percent reflecting output coupler. The polarization of the dye output was always the same as that of the ruby input. For certain dyes, as shown in Table I, a gold-coated grating replaced the fully reflecting mirror, and narrow-band (7-Å) efficiencies were measured. Peak output powers up to 1 MW were observed, with peak broad-band efficiencies as large as 43 percent.

A "quality factor" Q for a dye is defined as

$$Q = \frac{E}{P}. \tag{4}$$

Q is proportional to the total number of dye laser photons

which may be extracted from a given volume of dye prior to the onset of deleterious bleaching; Q increases with increasing efficiency and decreasing bleaching rate.

The dyes were tested in the following solvents: methanol, ethanol, propanol, glycerol, ethylene glycol, acetone, dimethyl sulfoxide (DMSO), and water containing 5-percent Triton X-100.[2] For almost all of these dyes, DMSO was found to be superior with respect to dissolving power, photochemical stability of the dye-solvent mixture, and lasing efficiency. Water containing 1-5-percent surfactant is a dye solvent exhibiting high heat capacity and low change of refractive index with temperature. It is therefore a useful solvent in minimizing Schlieren effects which have been found to degrade dye laser performance. The photochemical stability of water-surfactant solutions was generally poorer than for the DMSO, but frequently better than other solvents such as ethanol [20].[3] Other solvents are also useful; for example, 1,1′-diethyl-2,2′-dicarbocyanine iodide (DDI, number 771) did not lase when dissolved in DMSO, but did lase in glycerol or ethylene glycol.

The lasing efficiencies E which we measured in the angle-pumped configuration are comparable to, and somewhat larger than, those obtained by previous investigators [9], [14], [15], [19]. In agreement with other published results [23], we find that the dye laser output is reduced by only 5-20 percent when the cavity is changed from one with a broad-band mirror to one with a higher dispersive element to achieve narrow-band operation. This is to be expected for a laser medium with homogeneous broadening operated far above threshold with a low reflectivity output coupler.

Fig. 2 illustrates that the 710-950-nm spectral region can be covered using five dyes exhibiting high efficiency. The solid lines indicate the peak grating-tuned efficiency of each dye, and a small reduction in output power should be anticipated near the ends of the tuning range of each dye [14]. An examination of Table II shows that other combinations of five dyes covering this spectral region are also possible; Fig. 3 graphically illustrates the overlap of spectral coverage of the dyes listed in Table II.

The wavelength tuning ranges listed in Table II were obtained using DMSO as a solvent and using the angle-pumping configuration of Fig. 1(a). Sorokin *et al.* [19] demonstrated that substantial shifts in output wavelength occur with changes in dye concentration and solvent; a comparison of the wavelength tuning ranges of Table II and those obtained by Miyazoe and Maeda [9] and Webb *et al.* [13] suggest that the dye laser cavity configuration and pumping geometry are also important variables affecting the dye tuning range.

Fig. 4 presents data we obtained with dyes 821, 940, and 980 using different solvents and pumping geometries. The angle-pumped cell exhibits laser output at shorter wavelengths than either the end-pumped or side-pumped systems. We attribute this to the fact that there is substantially more self-absorption by the dye with the longer dye cells used in the latter two configurations. It is a general result [9], [13], [19] for polymethine dyes that increasing dye concentration increases the lasing wavelength. Fig. 5 presents our

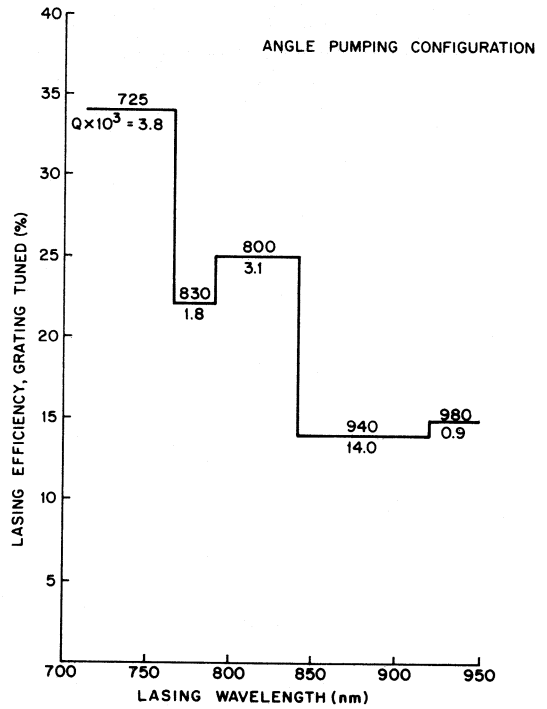


Fig. 2. Efficiency of laser dyes spanning the 710–950-nm spectral region. Efficiencies indicated are for a grating-tuned cavity angle pumped with a ruby laser.

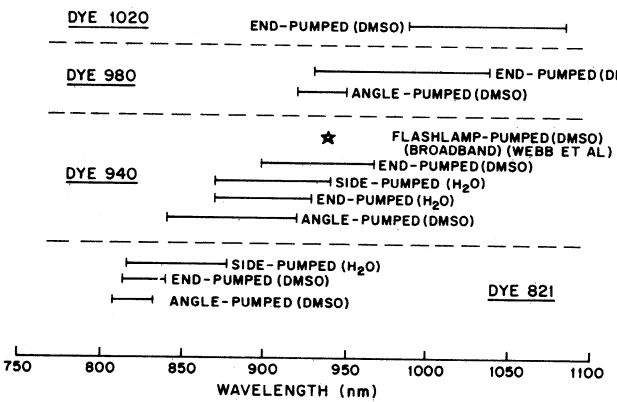


Fig. 3. Wavelength tuning ranges of 16 near-IR dyes in DMSO.

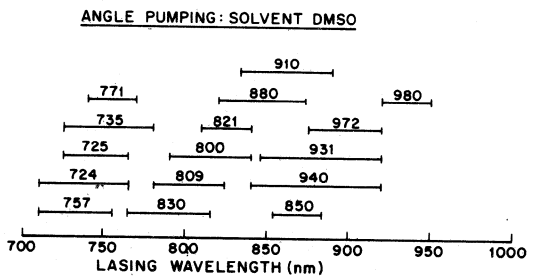


Fig. 4. Variation of wavelength tuning range with solvent and pumping configuration.

[2]Trademark of Rohm and Haas.

[3]Reference [20] indicates that H_2O-surfactant solutions of dye 735 exhibit excellent shelf life (at lease several hundred hours) in the absence of photochemical bleaching. We find that the shelf life is 4–6 days at ambient temperature when shielded from ambient light. This discrepancy remains unresolved.

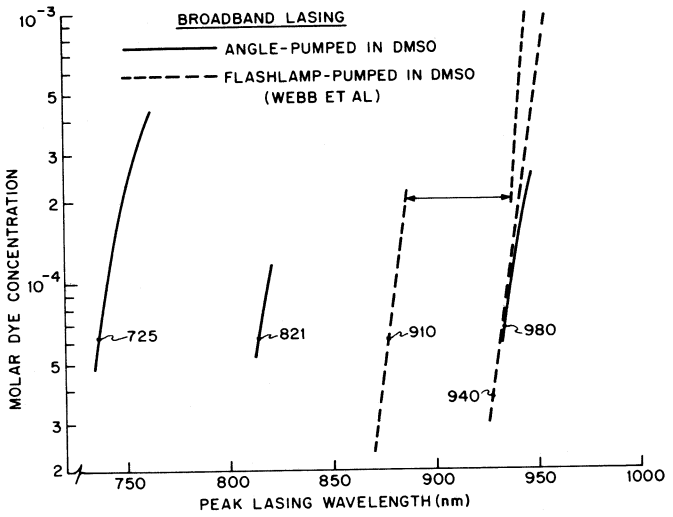


Fig. 5. Variation of peak lasing wavelength with dye concentration.

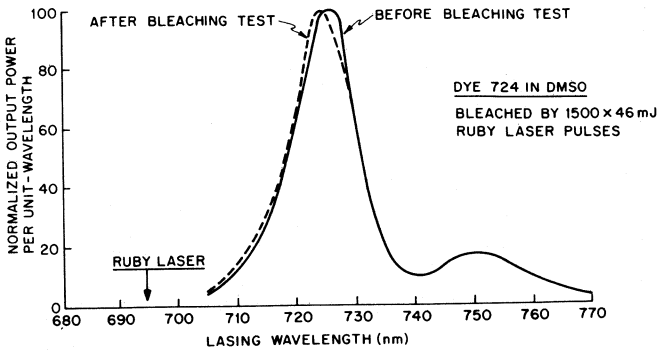


Fig. 6. Shift in spectral distribution of broad-band dye laser output with bleaching.

TABLE III
COMPARISON OF TYPICAL UV-VISIBLE AND IR LASER DYE BLEACHING RATES

	Dye	Solvent	Bleaching Rate P(x 10^5)	Ref.
UV-Visible	Rhodamine 6G	ethanol	0.05;0.1-1.1	1;6
		H_2O + 5% X-100	0.8;0.2-0.7;0.7	1;6;5
	Na-Fluorescein	methanol	1.8	5
		ethanol	0.4;1.1	1;6
	Cℓ-Fluorescein	methanol	9.5	5
IR	940 (minimum P)	DMSO	≤ 1	This Study
	724 (maximum P)	DMSO	30	" "

results and the results of Webb *et al.* [13] obtained in a flashlamp-pumped system. In general, the larger the product of dye concentration and cell length, the longer the lasing wavelength.

The tuning ranges given in Fig. 4 were obtained with dye concentrations corresponding to peak lasing efficiency. In order to achieve efficient lasing beyond 1000 nm, an end-pumped or side-pumped system is desirable. Most frequently DMSO also yields longer wavelengths than other solvents with a given dye, in accord with the results of Sorokin *et al.* [19].

If one adopts the premise that dye molecules which are irreversibly bleached by photochemical reactions do not participate in either the absorption process or the lasing process, then the effective concentration of dye should be decreased by bleaching and a shift of the peak spectral output to shorter wavelengths should occur as the dye is progressively bleached. This is in accord with our observations, as illustrated in Fig. 6. The magnitude of the spectral shift is in agreement with that which would be predicted from the measured value of ΔN and the wavelength-concentration curves of Fig. 5.

Several of the dyes we tested exhibited, in addition to a strong primary laser band, a weak secondary lasing peak at longer wavelength. Fig. 6 shows a monochrometer scan of the broad-band lasing output of dye 724 in the angle-pumping configuration. Such results have been noted before [14], [15]; an analogous result was also observed in the flashlamp-pumped geometry of Webb *et al.* [13], as noted in Fig. 5 (dye 910).

No systematic data regarding the bleaching rates of polymethine IR dyes have been reported previously. Miyazoe and Maeda [11] irradiated dyes 715, 935, 809, and 820 with the output of an intense tungsten projector lamp and noted rapid bleaching in acetone, DMSO, and methanol. Their conclusion, as well as ours, was that the high-efficiency dye DTTC iodide (820) used by Sorokin *et al.* [19] and others [9], [14] is extremely sensitive to bleaching, both by UV and ruby laser light. The bleaching characteristics of this dye were such that no accurate measurements were possible in our experimental system. Dye 821 (DTTC bromide [21]) provided nearly equal efficiencies, covered the same wavelength region, lased efficiently in both DMSO and H_2O-surfactant solutions, and exhibited a bleaching probability of 4.6×10^{-5} in H_2O surfactant.

Table III compares the bleaching rates of the polymethine IR dyes we have investigated under lasing conditions to the results obtained by others [1], [5], [6] who have measured, in nonlasing experiments, the degradation of laser dyes which are efficient in the visible and near UV. For the very best IR dyes, bleaching rates are comparable to those observed for shorter wavelength dyes, whereas some IR dyes bleach sufficiently rapidly (in ruby laser light) that their use is awkward at best.

Two of the new dyes manufactured by Eastman Kodak and reported by Webb *et al.* [13] (dyes 940 and 972) exhibited lower bleaching rates than any other IR dyes we have tested in the 840-920-nm spectral region. Dye 950 was not available to us during our experimental investigation, but according to the results of Webb *et al.* [13], the efficiency of this dye substantially exceeds that of 940 and 972, and should prove to be an excellent dye if the bleaching rate is as low as that of dyes 940 or 972.

CONCLUSIONS

Laser dyes spanning the near IR have been thought to be highly unstable and subject to rapid photochemical bleaching. This is indeed true for a number of dyes, but we have measured bleaching probabilities for some IR dyes which are comparable to values measured for dyes lasing in the visible.

The efficiency of ruby-pumped dyes can be very high. We have identified five dyes which span the 715–950-nm spectral region in a grating-tuned angle-pumping configuration, and for which the minimum efficiency is 13 percent.

Finally, we have investigated the effects of optical pumping

arrangement, solvent, and dye concentration on the lasing wavelength of several dyes. We determined that, of the solvents tested, DMSO generally produces the longest lasing wavelengths. The lasing wavelength of a given dye-solvent combination increases as the product of cell length and dye concentration increases. Many of the dyes exhibit low bleaching rates and high efficiencies in H_2O-surfactant solutions, a result which is particularly important in cases where thermally induced refraction effects may otherwise limit dye laser performance.

Acknowledgment

The authors wish to thank J. Fronduto for performing the angle-pumping experiments and L. O. Hocker for performing the end-pumped and side-pumped experiments reported here. They also wish to thank J. P. Webb and R. C. Hapeman of Eastman Kodak for making available small samples of dyes 830, 910, 940, and 972 at an early date in the investigation.

References

[1] E. P. Ippen, C. V. Shank, and A. Dienes, "Rapid photobleaching of organic laser dyes in continuously operated devices," *IEEE J. Quantum Electron.* (Corresp.), vol. QE-7, pp. 178–179, Apr. 1971.
[2] B. H. Winters, H. I. Mandelberg, and W. B. Mohr, *Appl. Phys. Lett.*, vol. 25, p. 723, 1974.
[3] E. J. Schimitschek, J. A. Trias, M. Taylor, and J. E. Celto, "New improved laser dye for the blue-green spectral region," *IEEE J. Quantum Electron.* (Corresp.), vol. QE-9, pp. 781–782, July 1973.
[4] J. Weber, *Opt. Commun.*, vol. 7, p. 420, 1973.
[5] D. Beer and J. Weber, *Opt. Commun.*, vol. 5, p. 307, 1972.
[6] A. Britt and W. B. Moniz, "The effect of pH on photobleaching of organic laser dyes," *IEEE J. Quantum Electron.* (Corresp.), vol. QE-8, pp. 913–914, Dec. 1972.
[7] I. P. Kaminow, L. W. Stutz, E. A. Chandross, and C. A. Pryde, *Appl. Opt.*, vol. 7, p. 1563, 1972.
[8] D. Kato and A. Sugimura, *Opt. Commun.*, vol. 10, p. 327, 1974.
[9] Y. Miyazoe and M. Maeda, *Appl. Phys. Lett.*, vol. 12, p. 206, 1968.
[10] L. D. Derkacheva, A. I. Krymova, A. F. Vompe, and I. I. Levkoev, *Opt. Spectrosc.* (USSR), vol. 25, p. 404, 1968.
[11] Y. Miyazoe and M. Maeda, *Opto-Electron.*, vol. 2, p. 227, 1970.
[12] A. Hirth, J. Faure, and D. Lougnot, *Opt. Commun.*, vol. 8, p. 318, 1973.
[13] J. P. Webb, F. G. Webster, and B. E. Plourde, "Sixteen new IR laser dyes," *IEEE J. Quantum Electron.* (Corresp.), vol. QE-11, pp. 114–119, Mar. 1975.
[14] C. D. Decker and F. K. Tittel, *Opt. Commun.*, vol. 7, p. 155, 1973.
[15] M. Maeda *et al.*, "Polymethine dyes used for laser emission," Bulletin 46, Japanese Research Institute for Photosensitizing Dyes Co., Ltd., 1973.
[16] K. H. Drexhage, *Laser Focus*, p. 35, Mar. 1973.
[17] F. P. Schaefer, *Laser Focus*, p. 33, Mar. 1974.
[18] M. Maeda and Y. Miyazoe, *Jap. J. Appl. Phys.*, vol. 11, p. 692, 1972.
[19] P. P. Sorokin, J. R. Lankard, E. C. Hammond, and V. L. Moruzzi, *IBM J. Res. Develop.*, vol. 11, p. 130, 1967.
[20] C. E. Hackett and C. F. Dewey, Jr., "Improved temporal stability of polymethine laser dyes in aqueous solutions," *IEEE J. Quantum Electron.* (Corresp.), vol. QE-9, pp. 1119–1120, Nov. 1973.
[21] F. P. Schaefer, W. Schmidt, and J. Volze, *Appl. Phys. Lett.*, vol. 9, p. 306, 1966.
[22] C. F. Dewey, Jr., "Excitation of gases using wavelength-tunable lasers," in *Modern Optical Methods in Gas Dynamic Research*, D. S. Dosanjh, Ed. New York: Plenum, 1971, pp. 221–270.
[23] A. J. Gibson, *J. Sci. Instrum. (J. Phys. E)*, vol. 2, p. 802, 1969.

Dependence of the $^4F_{3/2} \rightarrow {}^4I_{11/2}$ Induced-Emission Cross Section for Nd^{3+} on Glass Composition

RALPH R. JACOBS AND MARVIN J. WEBER

Abstract—**Systematic studies of spectral intensities using the Judd-Ofelt (J-O) theory for crystal-field-induced electric-dipole transitions demonstrate that Nd-doped glasses can be tailored for specific laser applications by proper selection of the glass constituents. Variations with glass composition are reported for the following properties: induced-emission cross section, peak fluorescence wavelength, effective fluorescence bandwidth, radiative lifetime, transition probabilities, and fluorescence branching ratios. Both glass network formers and network-modifier ions were changed. In these studies the induced-emission cross section for the Nd^{3+}, $^4F_{3/2} \rightarrow {}^4I_{11/2}$ laser transition was varied by more than a factor of 4 by changing the glass host.**

I. Introduction

SINCE the first demonstration of laser action in a neodymium-doped glass by Snitzer in 1961 [1], considerable progress has been made in evaluating the effects of these amorphous host materials on the rare-earth laser ion. Three review publications summarizing various aspects of glass lasers are Patek [2], Snitzer and Young [3], and Young [4]. Several reports have discussed the effect of glass composition on Nd^{3+} radiative or laser properties. Among these, Hirayama and Lewis [5] studied the effects of compositional variation on the line shape and decay time of Nd^{3+} fluorescence in alkali silicate glasses. Hauptmanova *et al.* [6] examined the absorption and emission spectra, fluorescence decay times and their temperature dependences, and quantum yields for three series of silicate glasses. Hirayama [7] also conducted similar studies on alkali borate glasses. Deutschbein [8], in a survey of Nd-doped phosphate glasses, noted the influence of composition on several spectral properties including linewidths and intensities. Deutschbein and Pautrat [9] evaluated various silicate, phosphate, and fluoride glass compositions with the aim of identifying suitable materials for room-temperature CW laser operation. This effort concentrated on obtaining absorption and emission spectra, upper level lifetimes, and laser thresholds. Hirayama *et al.* [10] determined the absorption and fluorescence properties, as well as the laser thresholds and slope efficiencies, of Nd^{3+} in potassium-barium germanate glasses. Sarkies *et al.* [11], using laser and fluorescence techniques, measured changes in the Nd^{3+} cross section for stimulated emission at 1.06 μm resulting from composition changes in a variety of silicate glasses. Rapp [12] measured the Nd^{3+} fluorescence decay in several silicate glasses, and hence the total transition probability from the $^4F_{3/2}$ level, assuming negligible effects from concentration quenching and nonradiative deactivation. Lipson *et al.* [13] obtained absorption and fluorescence spectra for Nd-doped alkali germanate and bismuth germanate glasses and crystals. Of these previous investigations, only that of Sarkies *et al.* [11] bears directly on the main topic of the present work: variations in laser cross section with variations in glass composition.

Recently, Krupke [14] applied the Judd-Ofelt (J-O) model for crystal-field-induced electric-dipole transitions to determine the induced-emission cross section at 1.06 μm for Nd^{3+} in four silicate laser glasses. The agreement between the calculated and measured cross sections was better than 10 percent. This technique permits relatively rapid determinations of induced-emission cross sections, radiative lifetimes, and fluorescence branching ratios and is utilized in the present work to investigate the dependence of these properties on systematic variations in glass composition. In conjunction with these determinations are measurements of absorption intensities and the related fluorescence bandwidths and fluorescence lifetimes. For a given glass composition, the calculated radiative lifetime and the measured fluorescence lifetime are combined to yield the radiative quantum efficiency.

The aforementioned quantities are presented for each of the glasses investigated, and general trends (or in some cases lack of them) are discussed for the following five glass groupings: 1) variations in glass network former; 2) variations in alkali-modifying ion in binary silicate glasses; 3) variations of a particular alkali concentration in a binary silicate glass; 4) variations in alkali additive for a fixed alkaline-earth concentration in ternary silicate glasses; and 5) variations in the alkaline-earth additive for a fixed alkali concentration in ternary silicate glasses. In addition, the properties of several selected Nd^{3+}-doped silicate and phosphate laser glasses are presented, including some which are commercially available. Finally, for promising glass candidates, a brief description is given of an evaluation procedure that incorporates the spectroscopic and J-O information to yield predicted system performance of large Nd:glass amplifiers.

II. Judd-Ofelt Model

The basis of the present glass compositional studies is the theory for crystal-field-induced electric-dipole transitions between $4f$ states developed by Judd [15] and Ofelt [16] for trivalent rare earths. This theory has been successfully applied to rare-earth ions in solids, liquids, and gases [17]. In this

Manuscript received July 21, 1975. This work was performed under the auspices of the United States Energy Research and Development Administration. Reference to a company or product name does not imply approval or recommendation of the product by the University of California or the U.S. Energy Research and Development Administration to the exclusion of others that may be suitable.

The authors are with the Lawrence Livermore Laboratory, University of California, Livermore, CA 94550.

section the relevant aspects of the J-O model are presented; for consistency, the notation of [14] is used. The electric-dipole transition line strength between an initial J' manifold $|(S', L')J'\rangle$ and final $\bar{J}$ manifold $|(\bar{S}, \bar{L})\bar{J}\rangle$ is expressed as

$$S = \sum_{t=2,4,6} \Omega_t |\langle (S', L')J' || U^{(t)} || (\bar{S}, \bar{L})\bar{J}\rangle|^2 \quad (1)$$

where the three terms $\langle || U^{(t)} || \rangle$ are the doubly reduced unit tensor operators calculated in the intermediate coupling approximation, and the coefficients Ω_2, Ω_4, and Ω_6 contain the effects of the odd-symmetry crystal-field terms, radial integrals, and energy denominators. The unit tensor operators have been numerically evaluated for Nd^{3+} and are given in [14]. Also, it has been shown that the values for the unit tensor elements exhibit negligible change with host constituents [17].

The line strength in (1) is related to the integrated absorbance of an electric-dipole transition $\int k(\lambda)\, d\lambda$ via the relation

$$\int_{\text{band}} k(\lambda)\, d\lambda = \frac{8\pi^3 e^2 \bar{\lambda}\rho}{3ch(2J+1)} \frac{1}{n}\left[\frac{(n^2+2)^2}{9}\right] S \quad (2)$$

where $k(\lambda)$ is the absorption coefficient at wavelength λ, ρ is the concentration of Nd^{3+} (ions/cm^3), $\bar{\lambda}$ is the mean wavelength of the absorption band, J is the total angular momentum of the initial level, which for Nd^{3+} is 9/2, $n(\bar{\lambda})$ is the index of refraction, and $(n^2+2)^2/9$ is the local field correction using the tight binding approximation. At this point the essence of the J-O technique is apparent. 1) Spectrophotometer traces are taken for a given glass composition and the various absorption bands are integrated. 2) A computerized least squares fitting routine then determines the best fit phenomenological parameters Ω_2, Ω_4, and Ω_6 using (1) and (2) to eliminate S. With these parameters, and as described in [14], the following radiative properties for a particular glass composition can be evaluated.

Property 1: The spontaneous emission probability from an initial manifold $|(S', L')J'\rangle$ to a final manifold $|(\bar{S}, \bar{L})\bar{J}\rangle$

$$A[(S', L')J'; (\bar{S}, \bar{L})\bar{J}] = \frac{64\pi^4 e^2}{3h(2J'+1)\bar{\lambda}^3} n \left[\frac{(n^2+2)^2}{9}\right] \cdot \sum_{t=2,4,6} \Omega_t |\langle (S', L')J' || U^{(t)} || (\bar{S}, \bar{L})\bar{J}\rangle|^2. \quad (3)$$

Property 2: The fluorescence branching ratio for transitions from an initial manifold $|(S', L')J'\rangle$ to lower levels $|(\bar{S}, \bar{L})\bar{J}\rangle$

$$\beta[(S', L')J'; (\bar{S}, \bar{L})\bar{J}] \equiv \frac{A[(S', L')J'; (\bar{S}, \bar{L})\bar{J}]}{\sum_{\bar{S},\bar{L},\bar{J}} A[(S', L')J'; (\bar{S}, \bar{L})\bar{J}]} \quad (4)$$

where the sum is over all possible terminal manifolds.

Property 3: The radiative lifetime given by

$$\tau_{\text{rad}}^c = \left\{\sum_{\bar{S},\bar{L},\bar{J}} A[(S', L')J'; (\bar{S}, \bar{L})\bar{J}]\right\}^{-1} = A_{\text{total}}^{-1}. \quad (5)$$

Property 4: The radiative quantum efficiency of the $|(S', L')J'\rangle$ manifold defined as

$$\eta_c \equiv \tau_f^M / \tau_{\text{rad}}^c \quad (6)$$

where τ_f^M is the *measured* fluorescence lifetime.

Property 5: The peak induced-emission cross section σ_p for the Nd^{3+}, $^4F_{3/2} \rightarrow {}^4I_{11/2}$ transition expressed as

$$\sigma_p(\lambda_p) = \frac{\lambda_p^4}{8\pi c n^2 \Delta\lambda_{\text{eff}}} A[(^4F_{3/2}); (^4I_{11/2})] \quad (7)$$

where λ_p is the peak fluorescence wavelength of the emission band and $\Delta\lambda_{\text{eff}}$ is the effective fluorescence bandwidth determined by integrating the fluorescence line shape and dividing by the intensity at λ_p [11], [14]. The effective linewidth is used since the Nd^{3+} emission bands in glass are asymmetric and, as noted in [8], use of the linewidth at full width at half maximum (FWHM) can yield misleading results. In addition to these spectroscopic properties, the J-O intensity parameters can also be used to evaluate the effects of excited state absorptions and the probability for ion-ion interactions which enter into energy transfer and fluorescence quenching phenomena.

In the absence of excited state absorption from the $^4F_{3/2}$ level, $\sigma_p(\lambda_p)$ describes the exponential growth in spatial laser intensity. As noted in [14], J-O calculations of the excited state line strengths from the $^4F_{3/2}$ level indicate that this effect on the net laser cross section should be small (<10 percent) at 1.06 μm so that σ_p can then be equated to the stimulated-emission cross section.

Once the three Ω_t parameters are obtained from absorption spectra for a given sample, radiative transition probabilities, branching ratios, and lifetime are obtained according to (3), (4), and (5), respectively. In addition, with measurements of the fluorescence lifetime τ_f^M, peak fluorescence wavelength λ_p, and effective fluorescence bandwidth $\Delta\lambda_{\text{eff}}$, one obtains the radiative quantum efficiency and induced-emission cross section described by (6) and (7). These quantities are tabulated in the following tables.

III. Experimental Procedure

Absorption spectra were taken at room temperature using a dual-beam Cary 14 spectrophotometer. For each sample typically nine absorption bands lying between 430 and 880 nm and originating from the $^4I_{9/2}$ ground state were integrated using a Hewlett-Packard 9810 digitizer. These data, along with values for the Nd^{3+} concentration and refractive indices for the various bands, were fitted by a computerized least squares program describing (1) and (2) to yield the best fit values for Ω_2, Ω_4, Ω_6. Occasionally, two other additional absorption bands at 1.62 and 0.35 μm were utilized in the fitting procedure; however, their inclusion did not affect the values of the resultant Ω_t parameters. Thus for reasons of experimental convenience, the same nine bands lying between 430 and 880 nm were used consistently for all the glasses in this study. The measured absorption line strengths could be matched with the best fit Ω_t results to typically 3-6 percent (rms) accuracy for all the glasses examined. Nd-ion concentrations were determined from the nominal mole fractions of constituent mate-

rials and measured sample density. The glasses were doped with a Nd_2O_3 concentration typically of 0.3–0.5 mol % corresponding to approximately $2\text{–}3 \times 10^{20}$ ions/cm^3. A dispersion relation yielding the linear index of refraction for a desired wavelength was obtained for all the glass samples by use of a commercial refractometer. Fluorescence spectra in the 1.06-μm region were excited with either a Chromatix 1000 frequency-doubled Nd:YAG laser ($\approx$150-ns pulsewidth at 532 nm) or a 1-kW xenon arc lamp and recorded with a PbS detector–0.3-m scanning grating monochromator combination. The spectral resolution was $\approx$3 nm. The relative spectral response of the detection system was calibrated in the 1.06-μm range using a quartz-tungsten-iodine standard lamp. Negligible deviations (<2 percent) were found over the spectral range of interest near 1.06 μm, thus the peak wavelength λ_p and the effective bandwidths $\Delta\lambda_{eff}$ were evaluated directly from the recorded traces with no further corrections. The fluorescence lifetime τ_f^M was measured with the aforementioned pulsed laser source. The temporal behavior of the fluorescence signal for each sample was detected by an *S*-1 photomultiplier tube whose output was recorded by a computerized data acquisition system. All samples exhibited a nonexponential behavior in the decay of the $^4F_{3/2}$ fluorescence intensity. Therefore, in the tables which follow, the values for τ_f^M are given for the times of the first and third *e*-folding intensities. The subject of nonexponential fluorescence decay in Nd:glasses and its dependence on concentration of the active species, energy migration, and local field site variations will be treated in a future publication [18]. The uncertainties in the listed values of λ_p, $\Delta\lambda_{eff}$, τ_f, and σ_p are estimated to be no greater than $\pm$2 nm, $\pm$2 nm, $\pm$10 percent, and $\pm$10 percent, respectively.

Most of the samples investigated were of experimental composition, although several commercially available glasses were also studied. The suppliers of the various glasses, listed alphabetically, are: Heraeus-Quarzschmelze:9016; Hoya(H):1 → 14, LHG-5, LSG-91H, LSG-95; Kigre: P25, P107; National Bureau of Standards (L): 41, 65, 213, 215, 217, 220, 223, 235; Owens-Illinois: 162M, ED-2, ED-8, EV 1; Schott: LG 650. We note that the parenthetical manufacturer designations in this list, used for brevity in the text and tables, do not always correspond to the suppliers' identifications.

IV. Experimental Results

Table I presents examples of the quality of fits obtained from absorption spectra of Nd^{3+} in glass. Calculated S_c and measured S_m line strengths, derived from (1) and (2), are given for a phosphate and a silicate glass (the compositions are listed in Table II). These glasses typify the differences in absorption intensities observed for the various glass compositions studied. Also listed in Table I are the best fit J-O parameters that reflect such changes in the absorption line strengths.

Differences in the $^4F_{3/2} \rightarrow {}^4I_{11/2}$ fluorescence spectra, both with respect to wavelength of the fluorescence maximum λ_p and the effective bandwidth $\Delta\lambda_{eff}$, are illustrated in Fig. 1 for these two glasses. Similar observations were reported by Deutschbein and Pautrat [9]. For all the glasses investigated,

TABLE I
Measured (S_m) and Calculated (S_c) Absorption Line Strengths (10^{-20}cm^2) for Nd^{3+} in a Phosphate (H14) and a Silicate (H11) Glass

	H(14)		H(11)	
$\bar{\lambda}$(μm)	S_m	S_c	S_m	S_c
0.88	1.33	1.54	0.74	0.83
0.81	4.43	4.14	2.18	2.09
0.75	3.63	3.83	1.76	1.82
0.68	0.26	0.27	0.15	0.13
0.63	0.06	0.07	0.03	0.03
0.58	6.11	6.11	6.25	6.25
0.53	2.00	2.07	1.29	1.29
0.47	0.53	0.45	0.26	0.24
0.43	0.17	0.23	0.12	0.12
Rms deviation	6%		3%	

J-O Parameters (10^{-20} cm^2):

	H(14)	H(11)
Ω_2	2.7 ± 0.3	4.4 ± 0.1
Ω_4	5.4 ± 0.4	3.0 ± 0.1
Ω_6	5.4 ± 0.2	2.6 ± 0.1

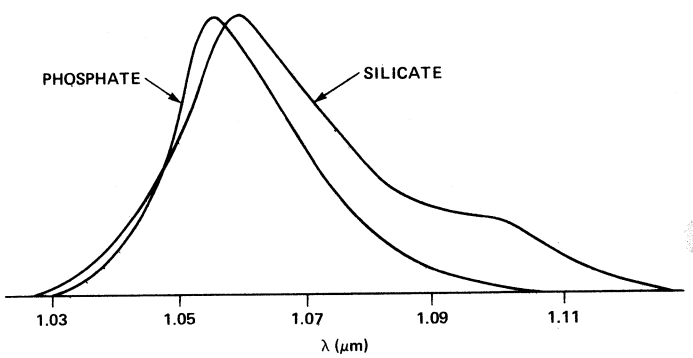


Fig. 1. $^4F_{3/2} \rightarrow {}^4I_{11/2}$ fluorescence spectra of Nd^{3+} for a phosphate (H14) and silicate glass (H11) illustrating the effect of network former on the peak emission wavelength and bandwidth. Table I lists the measured and calculated absorption line strengths for these two glasses.

the emission bands are inhomogeneously broadened. This is a characteristic feature of the spectra of ions in amphorous materials and arises from the site-to-site variations in the local ligand fields. The fluorescence bands are also generally asymmetric. As noted earlier, the effective bandwidth is therefore used to evaluate σ_p. Comparative bandwidths based upon the FWHM can be misleading if the exact band shape is not taken into account.

A. Series I—Variations in Glass Network Former

A summary of the $^4F_{3/2}$ radiative properties of Nd^{3+} in eight different host glasses is given in Table II. These include four simple oxide glasses where only the glass network former is changed (P_2O_5, B_2O_3, GeO_2, SiO_2), three additional oxide

TABLE II
SUMMARY OF THE Nd^{3+}, $^4F_{3/2}$ RADIATIVE PROPERTIES FOR NETWORK FORMER VARIATIONS (SERIES I)

PROPERTY Glass →	PHOSPHATE (H14)	BORATE (H13)	GERMANATE (H12)	SILICATE (H11)	TELLURITE (162M)	ALUMINATE (L65)	TITANATE (L220)	FLUORO-PHOSPHATE (L-223)
COMPOSITION (mol. %) (all but the last sample contain 0.3 - 0.5 % Nd_2O_3)	67 P_2O_5 18 BaO 15 K_2O	67 B_2O_3 18 BaO 15 K_2O	67 GeO_2 18 BaO 15 K_2O	67 SiO_2 18 BaO 15 K_2O	80 TeO_2 20 BaO	11 SiO_2 5 BaO 32 Al_2O_3 52 CaO	50 SiO_2 25 Na_2O 25 TiO_2	80 LiF 20 $Al(PO_3)_3$ (0.5% NdF_3)
$^4F_{3/2}$ FLUORESCENCE:								
A_{Total} ($^4F_{3/2}$), sec^{-1}	2888	2386	2299	1602	4193	2660	3232	2695
$\beta(^4F_{3/2}; {}^4I_{9/2})$	0.43	0.42	0.46	0.45	0.45	0.45	0.43	0.42
$\beta(^4F_{3/2}; {}^4I_{11/2})$	0.48	0.49	0.45	0.46	0.46	0.46	0.47	0.48
$\beta(^4F_{3/2}; {}^4I_{13/2})$	0.09	0.09	0.08	0.08	0.08	0.08	0.09	0.09
$\beta(^4F_{3/2}; {}^4I_{15/2})$	0.005	0.005	0.004	0.004	0.004	0.004	0.004	0.005
τ^c_{rad} ($^4F_{3/2}$), μsec	346	419	435	624	239	392	309	371
$^4F_{3/2} \rightarrow {}^4I_{11/2}$ TRANSITION:								
λ_p, nm	1055	1061	1062	1060	1063	1069	1064	1054
$\Delta\lambda_{eff}$, nm	25.3	36.8	34.7	34.9	28.9	43.1	38.6	27.2
$\sigma_p(10^{-20}cm^2)$	4.1	2.2	1.9	1.5	2.9	1.8	2.5	3.5

glasses, and a fluorophosphate glass. For these host materials, the basic glass former networks are different: borates are made up of BO_3 triangles; silicates, phosphates, and germanates have SiO_4, PO_4, and GeO_4 tetrahedra; and tellurites have TeO_6 octahedra. This series, while representing significant differences in the host glass, by no means exhausts the large number of known inorganic glass former possibilities [19]. It does, however, include many glasses of interest for laser materials.

For the first four glasses in Table II, σ_p decreases by a factor of 2.7 in the order phosphate → borate → germanate → silicate. The relatively large cross section for the phosphate arises in part from larger intensity parameters Ω_t and from the fluorescence bandwidth which is much narrower than for the other three glasses. Note, however, that large variations in σ_p for a given network former can also be obtained by varying the network-modifier ions. This is shown in what follows for silicate glasses. Since these variations are not identified for all glasses, otpimization of the composition to obtain particular radiative parameter values must be done for each glass network. The results in Table II demonstrate that these radiative properties can be significantly disparate for different glasses, but do not represent optimum compositions or extreme values possible for each case.

For the glasses in Table II, the two phosphates have the lowest values of λ_p, whereas the calcium aluminate has the highest. The total radiative probability A_{Total} varies by more than a factor of 2.5; however, the radiative branching ratios for the four possible transitions from the $^4F_{3/2}$ level change by only a few percent.

Another variation with glass composition arises from the dependence of the spontaneous-emission probability and cross section on the refractive index of the host via the local field correction. This is usually treated in a simple isotropic tight-binding approximation, where the field is given by

$$\frac{E_{eff}}{E_0} \approx 1 + \frac{n^2 - 1}{3} + \cdots . \tag{8}$$

Such a consideration introduces the factor $n(n^2 + 2)^2/9$ in the expression for A [see (3)]. Since n ranges from ≈1.5 to >2 for the oxide glasses listed in Table II, this last factor can range from 3 to 8. This factor for the cross section is further multiplied by $1/n^2$ and, though smaller in effect, is still a nonnegligible variation with host material. Because of the strong dependence on refractive index, the radiative decay rates for equal Ω_t values can be significantly different. For example, this has been observed for the tellurite glasses.

B. Series II—Variations in Alkali-Modifying Ion in Binary Silicates

Here and in the subsequent glass compositional variations we concentrate only on silicate host systems, although phosphate systems have been investigated and will be the subject of a future report. Table III presents results for a simple series of alkali disilicate glasses M_2O:2 SiO_2, where M = Li, Na, K, and Rb. For this series the J-O parameters are also given. There is a pronounced dependence of the intensity parameters on alkali ion variation, and different trends are evident for Ω_2 as compared to Ω_4 and Ω_6. The physical interpretation of these dependences, which are related to changes in the odd-parity terms in the expansion of the local crystal field, will be discussed in a separate publication [20]. Suffice it to indicate here that the J-O parameters change with alkali-network-modifying ions (M^+). The magnitude of σ_p for the Nd^{3+},

TABLE III
SUMMARY OF Ω_t VALUES AND Nd^{3+}, $^4F_{3/2}$ RADIATIVE PROPERTIES FOR BINARY SILICATE GLASSES (SERIES II)

PROPERTY	L215	L213	L217	L235
COMPOSITION (mol. %) (all samples contain 66.5% SiO_2, 33% M_2O, 0.5% Nd_2O_3)	Li_2O	Na_2O	K_2O	Rb_2O
J-O PARAMETERS ($10^{-20}cm^2$):				
Ω_2	3.4 ± 0.2	4.3 ± 0.2	5.1 ± 0.1	5.7 ± 0.1
Ω_4	4.5 ± 0.2	3.2 ± 0.2	2.4 ± 0.2	2.2 ± 0.2
Ω_6	4.6 ± 0.1	3.2 ± 0.1	2.0 ± 0.1	1.9 ± 0.1
$^4F_{3/2}$ FLUORESCENCE:				
$A_{Total}(^4F_{3/2})$, sec^{-1}	2523	1661	1100	1061
$\beta(^4F_{3/2}; {}^4I_{9/2})$	0.43	0.43	0.45	0.45
$\beta(^4F_{3/2}; {}^4I_{11/2})$	0.48	0.48	0.46	0.46
$\beta(^4F_{3/2}; {}^4I_{13/2})$	0.09	0.09	0.08	0.08
$\beta(^4F_{3/2}; {}^4I_{15/2})$	0.004	0.004	0.004	0.004
$\tau^c_{rad}(^4F_{3/2})$, μsec	396	602	909	942
τ^M_f, sec (for 0.05 mole% Nd_2O_3)	370 → 460	450 → 600	600 → 1000	*
$^4F_{3/2} \rightarrow {}^4I_{11/2}$ TRANSITION:				
λ_p, nm	1061	1060	1059	1058
$\Delta\lambda_{eff}$, nm	33.8	33.4	35.6	37.7
$\sigma_p(10^{-20}\ cm^2)$	2.6	1.8	1.1	0.97

$^4F_{3/2} \rightarrow {}^4I_{11/2}$ transition is directly related to the values of the Ω_4 and Ω_6 parameters, and thus exhibits similar variations since the bandwidth $\Delta\lambda_{eff}$ increases only slightly with increasing alkali size (for phosphates we observe an opposite behavior for $\Delta\lambda_{eff}$ in agreement with [9]).

The calculated radiative lifetime and the measured fluorescence lifetime show similar behavior with alkali ion variation. The observed fluorescence decays in neodymium glass are typically nonexponential even at low concentrations where ion-ion interactions are negligible. This arises from the inhomogeneous nature of glass. Different sites have different local fields and the odd harmonics in the expansion of these fields, which enter into the J-O parameters, exhibit a site-to-site variation. The parameters determined from integrated absorption spectra are therefore an effective average over the different sites. The decay, on the other hand, reflects a summation of the decays of different sites having different decay rates. In general, one finds the decay rate at early times may be less than the calculated radiative rate, while at later times in the decay it is more. The measured decay times τ_f^M listed in Table III are the rates for the first and third e-foldings of the decay intensity. The average measured rates, however, are in good agreement with the predictions based on the J-O parameters. At higher neodymium concentrations, concentration quenching by ion-ion interactions becomes important. These interactions, however, are also dependent upon the line strength and hence also reflect the effects of compositional changes via the J-O parameters [18].

Three previously published works [5], [11], [12] have observed similar effects on σ_p or the fluorescence lifetime with the M^+ variations employed in this series. These results are summarized in Table IV. Qualitatively, the trends in Tables III and IV are in good agreement; both the total transition probabilities A_{Total} and peak emission cross sections σ_p decrease with increasing M^+ radius in the sequence Li → Na → K → Rb. Quantitatively, there is a 10-percent agreement between the results of Tables III and IV if one compares *ratios* of transition probabilities and emission cross sections. Differences in the absolute values of lifetimes are due to concentration quenching effects and the specific glass compositions used. Cross-section differences are also attributed to the latter feature.

C. Series III—Variation of Alkali Concentration in Binary Silicates

The effect of varying the alkali concentration was examined for one of the aforementioned binary silicates, specifically Na_2O. The results are summarized in Table V for [Na_2O] contents ranging from zero to 35 mol %. Except for pure SiO_2, which is discussed in what follows, the effects are small. There is a small decrease of radiative probability and $^4F_{3/2} \rightarrow {}^4I_{11/2}$ cross section with decreasing Na_2O content. The decrease in σ_p is barely beyond experimental uncertainty; however, the observed corresponding increase in fluorescence lifetime confirms this result. Similar lifetime studies with changing alkali concentration have been reported for K_2O [5], [12] in the ranges 29–12 and 35–15 mol % where monotonic increases in τ_f^M with decreasing alkali content were also ob-

TABLE IV
SUMMARY OF PREVIOUS DETERMINATIONS OF FLUORESCENCE LIFETIMES τ_f^M AND PEAK CROSS SECTIONS σ_p FOR THE Nd^{3+}, $^4F_{3/2} \rightarrow {}^4I_{11/2}$ TRANSITION IN SILICATE GLASSES WITH ALKALI SPECIES VARIATIONS

REFERENCE	CONCENTRATION (mole %)	τ_f^M(μsec)	σ_p(units 10^{-20} cm^2)
[5]	33 Li_2O, 66.5 SiO_2, 0.5 Nd_2O_3	237	
	34.5 Na_2O, 65 SiO_2, "	475	
	33 K_2O, 66.5 SiO_2, "	635	
[11]	20.5 Li_2O, 66 SiO_2, 10.7 CaO, 2 Al_2O_3, 0.8 Nd_2O_3	260	2.21
	20.5 Na_2O " "	388	1.59
	20.5 K_2O " "	550	0.93
[12]	27.5 Li_2O, 70 SiO_2, 2.5 Al_2O_3, 0.5 Nd_2O_3	340(a)	
	27.5 Na_2O " " "	520	
	27.5 K_2O " " "	710	
	27.5 Rb_2O " " "	770	

TABLE V
SUMMARY OF Nd^{3+}, $^4F_{3/2}$ RADIATIVE PROPERTIES FOR VARIATIONS OF Na_2O CONCENTRATION IN BINARY SILICATE GLASSES (SERIES III)

PROPERTY / GLASS →	H1	H2	H3	H4	9016
COMPOSITION (mol. %) (all samples have 0.3% Nd_2O_3 except for 0.1% Nd_2O_3 in 9016)	35 Na_2O 65 SiO_2	30 Na_2O 70 SiO_2	35 Na_2O 75 SiO_2	20 Na_2O 80 SiO_2	100 SiO_2
$^4F_{3/2}$ FLUORESCENCE:					
A_{Total} ($^4F_{3/2}$), sec^{-1}	1669	1655	1526	1434	2072
$\beta(^4F_{3/2}; {}^4I_{9/2})$	0.44	0.44	0.44	0.44	0.44
$\beta(^4F_{3/2}; {}^4I_{11/2})$	0.47	0.47	0.47	0.47	0.47
$\beta(^4F_{3/2}; {}^4I_{13/2})$	0.09	0.09	0.09	0.09	0.09
$\beta(^4F_{3/2}; {}^4I_{15/2})$	0.004	0.004	0.004	0.004	0.004
τ_{rad}^c ($^4F_{3/2}$), μsec	599	604	655	697	483
τ_f^M, μsec	403 → 584	450 → 613	477 → 677	515 → 700	420 → 520
$^4F_{3/2} \rightarrow {}^4I_{11/2}$ TRANSITION:					
λ_p, nm	1059	1061	1061	1061	1088
$\Delta\lambda_{eff}$, nm	33.0	34.4	34.3	34.6	44.8
$\sigma_p(10^{-20}$ $cm^2)$	1.8	1.7	1.6	1.5	1.9

TABLE VI
SUMMARY OF Nd^{3+}, $^4F_{3/2}$ RADIATIVE PROPERTIES FOR VARIED ALKALI SPECIE WITH A FIXED ALKALINE-EARTH CONCENTRATION IN TERNARY SILICATE GLASSES (SERIES IV)

PROPERTY / GLASS →	H5	H6	H7
COMPOSITION (mol. %) (all samples have 65% SiO_2, 20% BaO, and 0.3% Nd_2O_3)	15 Li_2O	15 Na_2O	15 K_2O
$^4F_{3/2}$ FLUORESCENCE:			
A_{Total} ($^4F_{3/2}$), sec^{-1}	2427	2109	1523
$\beta(^4F_{3/2}; {}^4I_{9/2})$	0.43	0.42	0.45
$\beta(^4F_{3/2}; {}^4I_{11/2})$	0.47	0.48	0.46
$\beta(^4F_{3/2}; {}^4I_{13/2})$	0.09	0.09	0.08
$\beta(^4F_{3/2}; {}^4I_{15/2})$	0.004	0.004	0.004
τ_{rad}^c ($^4F_{3/2}$), μsec	412	474	657
τ_f^M, μsec	341 → 433	375 → 508	424 → 641
$^4F_{3/2} \rightarrow {}^4I_{11/2}$ TRANSITION:			
λ_p, nm	1062	1061	1061
$\Delta\lambda_{eff}$, nm	33.6	34.6	36.0
$\sigma_p(10^{-20}$ $cm^2)$	2.3	2.0	1.4

served. In the present case, the measured lifetimes are slightly shorter than the radiative lifetimes on the average because of the presence of some concentration quenching at 0.3 mol % [Nd_2O_3]. Table V also reveals a small change in λ_p and $\Delta\lambda_{eff}$ with alkali content.

Pure fused silica is an obvious exception to the trends with decreasing alkali concentration shown in Table V. The J-O parameters and resulting radiative probabilities are the largest of the series. The peak fluorescence wavelength λ_p is shifted to the largest value and the effective bandwidth is the biggest. Because of this latter feature, the peak cross section is comparable to those of the other glasses in the series. Two recent studies on laser action in fused silica are Stone and Burrus [21] and Galant *et al.* [22].

D. Series IV—Variations in Alkali Additive for a Fixed Alkaline-Earth Concentration in Ternary Silicates

This series is similar to species Series II except for the presence of an alkaline-earth. The alkali specie (M = Li, Na, K) was varied for a fixed alkaline-earth concentration in a ternary silicate of the form (mol %) 15 M_2O:20 BaO:65 SiO_2. The results are given in Table VI. The qualitative behavior of the cross sections and lifetimes for varied alkali species in this ternary silicate series corresponds directly with results for the binary silicates (Table III). While not shown, the Ω_t param-

TABLE VII
SUMMARY OF Nd^{3+}, $^4F_{3/2}$ RADIATIVE PROPERTIES FOR VARIATION OF ALKALINE-EARTH SPECIE FOR A FIXED ALKALI CONCENTRATION IN TERNARY SILICATES (SERIES V)

PROPERTY GLASS →	H8	H9	H10	H7
COMPOSITION (mole %) (all samples have 65% SiO_2, 15% K_2O, and 0.3% Nd_2O_3)	20 MgO	20 CaO	20 SrO	20 BaO
$^4F_{3/2}$ FLUORESCENCE:				
A_{Total} ($^4F_{3/2}$), sec^{-1}	1765	1829	1700	1523
$\beta(^4F_{3/2}; {}^4I_{9/2})$	0.46	0.44	0.45	0.45
$\beta(^4F_{3/2}; {}^4I_{11/2})$	0.46	0.47	0.46	0.46
$\beta(^4F_{3/2}; {}^4I_{13/2})$	0.08	0.09	0.08	0.08
$\beta(^4F_{3/2}; {}^4I_{15/2})$	0.004	0.004	0.004	0.004
$\tau^c_{rad}(^4F_{3/2})$, μsec	567	547	588	657
τ^M_F, μsec	391 → 523	410 → 557	417 → 579	424 → 641
$^4F_{3/2} \rightarrow {}^4I_{11/2}$ TRANSITION:				
λ_p, nm	1061	1061	1061	1061
$\Delta\lambda_{eff}$, nm	41.2	37.0	35.1	36.0
$\sigma_p(10^{-20}\ cm^2)$	1.5	1.7	1.6	1.4

eters also behave similarly, that is, Ω_2 increases and Ω_4 and Ω_6 decrease in the sequence Li → Na → K.

E. Series V—Variations in the Alkaline-Earth Additive for a Fixed Alkali Concentration in Ternary Silicates

In contrast to the preceding series, in this series the alkali concentration [K_2O] is kept fixed and the alkaline earth (M = Mg, Ca, Sr, Ba) is varied in a ternary silicate of the form (mol %) 15 K_2O:20 MO:65 SiO_2. The results are presented in Table VII. The radiative transition probabilities and cross sections show a tendency to decrease with increasing ion size in the sequence Ca → Sr → Ba. The data for Mg do not continue this trend; however, the deviation is small and is within the total experimental uncertainties in measurement and composition. Overall, the changes in radiative properties in Table VII with varying alkaline-earth are small. Note, however, that whereas in the alkali Series IV the alkali represents 26 percent of the cations, in the alkaline-earth Series V the alkaline earth represents only 17 percent of the cation concentrations. The effects may therefore be expected to be smaller on a number-of-ions basis, albeit the charge for each ion is doubled.

A further study was done in which the CaO concentration was varied from 5 to 40 mol % with a corresponding reduction in SiO_2 content in a multicomponent silicate glass. No appreciable differences, i.e., >10 percent in A_{total} and σ_p resulted for such large modifications, although a tendency toward larger values was observed with increasing CaO content.

F. $^4F_{3/2} \rightarrow {}^4I_{11/2}$ Radiative Properties of Nd^{3+} in Selected Laser Glasses

The J-O technique was used to determine the Nd^{3+} cross sections and other radiative properties for several commercially available and selected silicate and phosphate laser glasses. These results are listed in Table VIII. (Corresponding values for the $^4F_{3/2} \rightarrow {}^4I_{13/2}$ transitions are reported in [23].) As evident in Table VIII, variations in σ_p by a factor of approximately 2.5–3.0 are obtainable for both silicate and phosphate hosts by compositional changes. By combining silicate and phosphate host possibilities, σ_p variations of almost five are observed. The peak cross sections for the phosphate glasses are larger than for the silicate glasses in many cases because of the narrower bandwidths.

To correlate the results of the preceding compositional studies with these commercial laser glasses, we note two examples. One sees from Tables III and VII that for silicate glasses larger laser cross sections are obtained for small alkali ions, such as lithium, and small alkaline-earths, such as calcium. High cross-section laser glasses such as ED-2 and ED-8 contain large quantities of lithia and calcia. LG 650, on the other hand, has a small cross section and, in contrast, contains larger sized alkali and alkaline-earths such as potassium and barium. Thus the trends in Nd^{3+} cross-section values can be inferred from the species variations given in Tables III and VII for addition of alkali and alkaline-earth network-modifying ions into the silicate network former. Similar findings have recently been reported by Dianov *et al.* [24].

V. DISCUSSION AND CONCLUDING REMARKS

The aforementioned results demonstrate that large changes in induced-emission cross sections for Nd^{3+} can be achieved by varying the glass composition. This was shown for several different glass forming networks in Table II. For a given glass network (silicate), further changes were obtained by varying the network-modifying ions (alkali, alkaline-earth). Therefore

TABLE VIII
$\Delta\lambda_{eff}$, λ_p, AND σ_p FOR THE $^4F_{3/2} \rightarrow {}^4I_{11/2}$ TRANSITION AND τ^c_{rad} ($^4F_{3/2}$) IN SELECTED Nd-DOPED SILICATE AND PHOSPHATE LASER GLASSES

	SILICATES					PHOSPHATES			
PROPERTY / GLASS →	LSG-91H (a)	LSG-95	ED-2 (a)	ED-8	LG 650	LHG-5	P107	EV 1	L-41
$\Delta\lambda_{eff}$, nm	33.5	35.1	34.0	36.1	33.5	25.5	26.5	21.7	32.5
λ_p, nm	1062	1063	1062	1063	1059	1054	1054	1054	1056
$\tau^c_{rad}(^4F_{3/2})$, μsec	361	250	326	287	856	351	322	314	564
$\sigma_p(10^{-20}$ cm$^2)$	2.7	2.8	2.9	3.1	1.1	3.9	3.9	4.7	1.9

for each glass type, additional studies are needed to identify the optimum composition to tailor σ_p for a particular application.

Peak cross sections are dependent on the intensity parameters Ω_t and the bandwidth $\Delta\lambda_{eff}$. Both are affected by compositional changes. The effective bandwidth is a measure of the overall extent of the Stark splitting of the J manifolds, and is inhomogeneous due to the site-to-site variations in the local field seen by rare-earth ions in glass. The intensity of the $^4F_{3/2} \rightarrow {}^4I_{11/2}$ laser transition is dependent only on the Ω_4 and Ω_6 parameters because of the triangle rule $|J' - \bar{J}| \leqslant t \leqslant |J' + \bar{J}|$ [17]. For a large cross section one wants Ω_4 and Ω_6 to be as large as possible (assuming constant $\Delta\lambda_{eff}$). In addition, the fluorescence branching ratio to $^4I_{11/2}$ should be as favorable as possible. Since Ω_2 does not enter, the branching ratios for the Nd^{3+}, $^4F_{3/2}$ fluorescence can be expressed in terms of the ratio Ω_4/Ω_6. The results are plotted in Fig. 2 and show that large changes in β are possible if the Ω_4/Ω_6 ratio varies. To maximize the intensity to $^4I_{11/2}$, one wants $\Omega_6 \gg \Omega_4$. The results in Tables II, III, V, VI, and VII show, however, that for the glasses studied thus far, Ω_4/Ω_6 varies over only a narrow range of approximately 0.9-1.1.

The desired value of σ_p for a given laser application may be dependent upon whether the system is pump-limited or parasitic-limited. In a long amplifier chain both conditions may exist at different stages, thus giving rise to a mixed requirement. The availability of glasses with different gain coefficients can affect the staging methodology. The time domains with respect to 1) storage of energy in the Nd system and 2) extraction and saturation flux for short-pulse operation are also considerations in selecting the induced-emission cross section. Finally, it should be noted that for constant $\Delta\lambda_{eff}$ and for β to be approximately constant, changes in σ_p translate inversely into changes in τ_{rad}.

Although this paper is devoted to the effects of composition on stimulated-emission cross sections, several other properties of greater or lesser importance may also vary with host composition. These include 1) the linear and nonlinear refractive indices which are important for effects such as self-focusing and laser beam breakup, 2) the vibrational spectrum of the glass which determines the homogeneous linewidths and nonradiative relaxation rates for multiphonon emission, 3) thermal properties such as expansion coefficient, conductivity, and dn/dT, 4) chemical durability, 5) optical quality obtainable, and 6) threshold for laser-induced damage and solarization. For example, tellurite glasses have high refractive indices and hence are unattractive for applications involving high intensities although other properties may be satisfactory. For glasses having high vibrational frequencies, such as borates, nonradiative quenching of the $^4F_{3/2}$ fluorescence reduces the overall quantum efficiency for long pumping and extraction times [25]. Thermally dependent properties such as the quantity $dn/dT + \alpha(n - 1)$, where α is the linear expansion coefficient, can be controlled to some degree by compositional changes [26] and may be more significant in effect than σ_p. It is evident, therefore, that the optimum glass composition for a specific application requires exploration of a multidimensional parameter space.

The J-O theory of electric-dipole transitions combined with fluorescence line shapes has provided a convenient way to de-

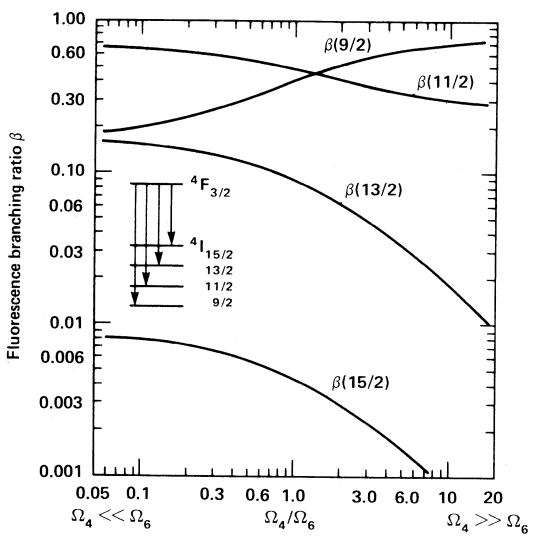


Fig. 2. Fluorescence branching ratios for Nd^{3+} from the $^4F_{3/2}$ state to the ^4I_J levels versus the ratio of J-O parameters Ω_4/Ω_6.

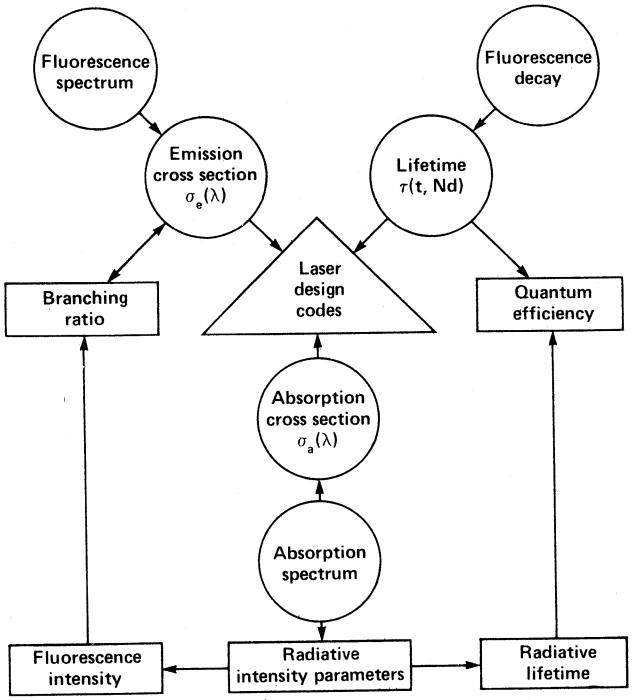


Fig. 3. Schematic description of a procedure for evaluating Nd^{3+}-doped glasses for use as laser amplifier media.

termine stimulated-emission cross sections of Nd laser materials and has been applied herein to investigate the effects of systematic changes in composition on σ_p. The overall approach has further utility in selecting materials for large laser systems to be used in fusion experiments. Computer programs have been developed [27] to aid in the design of Nd:glass rod and disk amplifiers. Inputs to these codes include the absorption spectrum and cross sections, the emission cross section as a function of wavelength, and the fluorescence decay as a function of time and Nd content (concentration quenching). These inputs are depicted schematically in Fig. 3. Given this information, the program, which contains a model for the xenon flashlamp spectrum, determines the optimum pump pulse duration and flashlamp current density to match the lasing material absorption and flashlamp emission spectra, in addition to optimizing the Nd concentration and amplifying media dimensions. Fig. 3 also shows that from the absorption intensities, the J-O parameters are derived and, in turn, are used to calculate 1) the radiative lifetime which when compared to the observed lifetime yields the quantum efficiency, and 2) the branching ratios and intensities required to normalize the fluorescence spectra.

Finally, while the J-O approach discussed in this report was applied only to Nd:glass, other rare earths and host materials are amenable to the same evaluation.

Acknowledgment

The authors wish to thank C. Dobler, D. Downs, J. Lynch, and D. Morgret for the excellent technical assistance in data acquisition and reduction, and Dr. J. Paisner for performing the spectral calibration. They also wish to thank the following for generously providing samples and for helpful discussions of glass properties: D. Blackburn, National Bureau of Standards; T. Izumitani, Hoya Glass Works; J. Myers, Kigre; C. Rapp, Owens-Illinois; and K. Rau, Heraeus-Quarzschmelze.

References

[1] E. Snitzer, "Optical maser action of Nd^{3+} in a barium crown glass," *Phys. Rev. Lett.*, vol. 7, pp. 444–446, Dec. 1961.
[2] K. Patek, *Glass Lasers*, J. G. Edwards, Ed. London, England: Butterworth, 1970.
[3] E. Snitzer and C. G. Young, "Glass lasers," in *Advances in Lasers*, vol. 2, A. Levine, Ed. New York: Dekker, 1968, pp. 191–256.
[4] C. G. Young, "Glass lasers," *Proc. IEEE*, vol. 57, pp. 1267–1289, July 1969.
[5] C. Hirayama and D. W. Lewis, "The effect of neodymium environment on its absorption and emission characteristics in glass," *Phys. Chem. Glasses*, vol. 5, pp. 44–51, Apr. 1964.
[6] K. Hauptmanova, J. Pantoflicek, and K. Patek, "Absorption and fluorescence of Nd^{3+} ion in silicate glass," *Phys. Status Solidi*, vol. 9, pp. 525–537, May 1965.
[7] C. Hirayama, "Nd^{3+} fluorescence in alkali borate glasses," *Phys. Chem. Glasses*, vol. 7, pp. 52–55, Apr. 1966.
[8] O. K. Deutschbein, C. C. Pautrat, and I. M. Svirchevsky, "Phosphate glasses, new laser materials," *Rev. Phys. Appl.*, vol. 2, pp. 29–37, Mar. 1967.
[9] O. K. Deutschbein and C. C. Pautrat, "CW laser at room temperature using vitreous substances," *IEEE J. Quantum Electron.*, vol. QE-4, pp. 48–51, Feb. 1968.
[10] C. Hirayama, F. E. Camp, N. T. Melamed, and K. B. Steinbruegge, "Nd^{3+} in germanate glasses: Spectral and laser properties," *J. Non-Cryst. Solids*, vol. 6, pp. 342–356, 1971.
[11] P. H. Sarkies, J. N. Sandoe, and S. Parke, "Variation of Nd^{3+} cross section for stimulated emission with glass composition," *Brit. J. Appl. Phys. (J. Phys. D)*, vol. 4, pp. 1642–1649, 1971.
[12] C. Rapp, "The influence of the composition on the gain of Nd-doped glasses," in *Physics of Electronic Ceramics Part B*, L. L. Hench and D. B. Dove, Ed. New York: Dekker, 1972, pp. 1011–1020.
[13] H. G. Lipson, J. R. Buckmelter, and C. O. Dugger, "Neodymium environment in germanate crystals and glasses," *J. Non-Cryst. Solids*, vol. 17, pp. 1–17, 1975.
[14] W. F. Krupke, "Induced-emission cross sections in neodymium laser glasses," *IEEE J. Quantum Electron.*, vol. QE-10, pp. 450–457, Apr. 1974.
[15] B. R. Judd, "Optical absorption intensities of rare-earth ions," *Phys. Rev.*, vol. 127, pp. 750–761, 1962.
[16] G. S. Ofelt, "Intensities of crystal spectra of rare-earth ions," *J. Chem. Phys.*, vol. 37, pp. 511–520, 1962.
[17] L. A. Riseberg and M. J. Weber, "Relaxation phenomena in rare-earth luminescence," in *Progress in Optics*, vol. XIV, E. Wolf, Ed. Amsterdam, The Netherlands: North Holland, 1975, to be published.
[18] C. Layne, W. Lowdermilk, and M. Weber, "Relaxation processes in laser glass," 1974 Laser Program Annu. Rep., Lawrence Livermore Lab., Livermore, CA, Rep. UCRL 50021-74, pp. 271–273 (available from National Technical Information Service, Springfield, VA).
[19] H. Rawson, *Inorganic Glass-Forming Systems*. London, England: Academic, 1967.
[20] M. J. Weber and R. R. Jacobs, to be published.
[21] J. Stone and C. A. Burrus, "Neodymium-doped silica lasers in end-pumped fiber geometry," *Appl. Phys. Lett.*, vol. 23, pp. 388–389, Oct. 1973.
[22] E. I. Galant *et al.*, "Stimulated emission of neodymium ions in quartz glass," *JETP Lett.*, vol. 18, pp. 372–373, 1974.
[23] R. R. Jacobs and M. J. Weber, "Induced-emission cross sections for the $^4F_{3/2} \rightarrow {}^4I_{13/2}$ transition in neodymium laser glasses," *IEEE J. Quantum Electron.* (Corresp.), vol. QE-11, pp. 846–847, Oct. 1975.
[24] E. M. Dianov, A. Ya. Karasik, L. S. Kornienko, A. M. Prokhorov,

and I. A. Shcherbakov, "Laser transition measurements for Nd-glass," in *1975 IEEE/OSA Conf. Laser Engineering and Applications Digest Tech. Papers*, 1975, p. 18.
[25] W. H. Lowdermilk, C. B. Layne, and M. J. Weber, "Nonradiative relaxation of rare-earth ions in glasses: (II) Dependence on vibrational spectrum," *Bull. Amer. Phys. Soc.*, Ser. II, vol. 20, p. 448, 1975, and to be published.
[26] M. M. Bubnov *et al.*, "Enhancement of the brightness of the output of neodymium-glass lasers by selection of the composition of the active-element matrix," *Sov. J. Quantum Electron.*, vol. 3, pp. 349–350, 1974.
[27] J. Trenholme, 1974 Laser Program Annu. Rep., Lawrence Livermore Lab., Livermore, CA, Rep. UCRL 50021-74, pp. 71–77 and pp. 84–88 and previous reports.

Two-Photon Laser Isotope Separation of Atomic Uranium: Spectroscopic Studies, Excited-State Lifetimes, and Photoionization Cross Sections

G. SARGENT JANES, IRVING ITZKAN, MEMBER, IEEE, CHARLES T. PIKE, RICHARD H. LEVY, MEMBER, IEEE, AND LAWRENCE LEVIN

Abstract—Experimental studies are described wherein an atomic beam of uranium vapor produced by electron-beam evaporation is selectively excited and ionized by light from two short-pulse narrow-bandwidth, tuned dye lasers, and detected and analyzed by a mass spectrometer. The total number of ions per pulse produced is small; however, the time of production is known precisely. By counting single ions, using digital logic, and multiplexing the mass spectrometer between U^{238} and U^{235}, it is possible to measure isotope ratios as a function of exciter wavelength and to correct for background effects and spurious ions. These results demonstrated 50 percent enrichment of U^{235}/U^{238}. Excited-state lifetimes were measured by observing yields as a function of the delay between the two laser pulses. In addition, for an excitation wavelength of 4266.325 Å, the variation of two-step photoionization efficiency was measured as a function of the wavelength of the ionizing laser. The maximum yield at an ionizing wavelength of 3609 Å corresponds to a cross section of 2×10^{-17} cm^2 for matched linewidths. Also the ionization potential of uranium was determined to be 6.187 ± 0.002 eV.

I. Introduction

It has been apparent for a number of years that there would be a serious shortage of facilities for the isotopic enrichment of uranium for use in light-water reactors sometime after 1980; i.e., when the existing gaseous-diffusion capacity had become fully committed. Furthermore, the gaseous-diffusion process is very inefficient from an energy viewpoint, as can be seen from the observation that approximately 3 MeV of electrical energy is consumed for each U_{235} atom which is separated. Indeed, the electrical energy represents about 50 percent of the gaseous-diffusion-process cost. By way of contrast, however, the ionization potential for uranium, the quantity more generally used in comparing chemical-processing costs, is only about 6.2 eV.

It was thus apparent that greatly reduced energy costs might be possible with a laser isotope separation (LIS) process involving the preferential ionization of U_{235} atoms from the vapor phase in conjunction with an MHD separation technique [1]. Such a process has three basic steps.[1] The first step involves the efficient production of a monatomic nonexcited metal vapor, presumably by evaporation from the liquid phase at temperatures well above 2000 K. Uranium is highly corrosive at these temperatures and the energy requirements are indeed considerable; however, electron-beam evaporation and the use of rhenium in the melt have both been offered as possible routes for solving this set of difficulties [1], [2]. The second requirement is for a multiple-step excitation scheme which will selectively ionize a significant fraction of the U_{235} atoms without ionizing U_{238} atoms. Finally, one must have a scheme, either chemical or physical, for removing the ions from the

Manuscript received June 6, 1975.

G. S. Janes, I. Itzkan, and C. T. Pike are with the AVCO Everett Research Laboratory, Inc., Everett, MA 02149.
R. H. Levy was with the AVCO Everett Research Laboratory, Inc., Everett, MA 02149. He is now with the Exxon Nuclear Company, Inc., Bellevue, WA.
L. Levin was with the AVCO Everett Research Laboratory, Inc., Everett, MA 02149. He is now at P.O. Box 9001, Beer-Cheva, Israel.

[1] The laser requirements, although not discussed here, are also difficult and will likewise influence the selection of color schemes quite strongly.

flow. It is clear that these three steps cannot be treated completely separately and that the collisional process will limit the permissible range of densities [1], [2]; however, some attempts to deal with these considerations have been discussed in the patent literature [1].

Thus, although the first and third requirements are difficult and warrant careful attention, there are several possible approaches [1], [3]. This paper deals with the second requirement for selective ionization of U_{235} which is fundamental to any atomic LIS scheme. It describes our initial experiments which not only illustrate "proof of principle" on an atomic scale but also demonstrate an experimental technique usable for subsequent, more detailed studies.

II. Spectroscopic Considerations

Uranium has one of the most complex optical spectra of any element with over 900 identified energy levels, 9000 classified transitions, and perhaps as many as 300 000 visible lines [4].

Of the 92 electrons in neutral uranium, 86 are arranged in closed shells sufficiently bound so that they are unaffected by optical excitation. In the ground state the other six electrons are in the configuration $5f^3\ 6d\ 7s^2$. The energies of the three lowest levels, all of which have odd parity, are 0, 620, and 3801 cm^{-1} with J values of 6, 5, and 7, respectively. At a temperature of 2500 K and thermal equilibrium 47 percent of the atoms would be in the ground state and 28 percent in the 620 level. Although the uranium atom has been studied rather extensively [4] most of the data have been obtained by conventional spectroscopic techniques which are rather tedious and there is a great deal of information missing, particularly on odd levels above 19 000 cm^{-1} and even levels above 39 000 cm^{-1}.

In order to utilize photons efficiently, the first step in the ionization process should be selective. Furthermore, this transition must be made to a bound state if it is to have a linewidth which is small relative to the isotope shift (typically of order 0.1 Å). Thus any selective ionization process will most likely involve at least 2 steps. In addition, the lifetime of the excited state must be long relative to the duration of the light pulses in order to minimize decay losses. Finally, transition schemes would be chosen which have large cross sections in order to minimize the requirements for laser intensity. Detailed information is available on isotope shifts for most of the first-step transitions [4], but data on excited-state lifetimes, and on photoexcitation and photoionization cross sections, are not. In Fig. 1 we show the level diagram for a two-photon laser ionization scheme which is typical of those investigated in these studies. Note that the selective exciting step is made to a state which is approximately halfway to the ionization limit. The lifetimes and cross sections indicated on this diagram are approximate only. In these studies we demonstrate two-step selective ionization of U_{235} atoms in a low-density apparatus ($\approx 10^{10}$ atoms/cm^3) and measure the lifetime of the upper state. The technique described herein utilizes short-pulse tuned lasers, and is particularly well suited for the quantitative measurement of many relevant physical parameters as well as to proof of principle demonstrations.

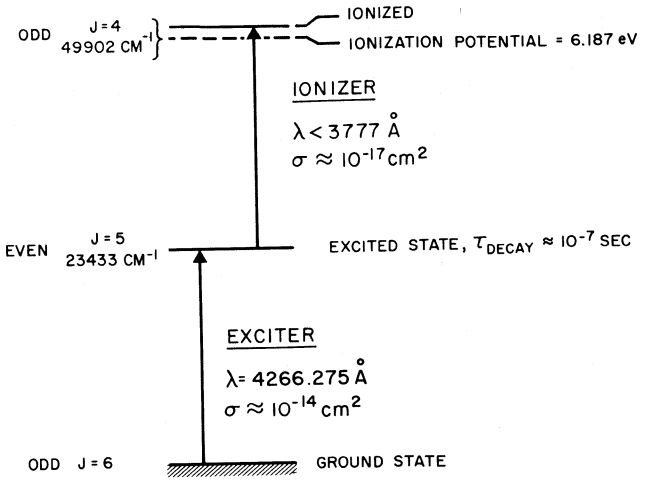


Fig. 1. Schematic level diagram for a typical two-photon selective laser ionization scheme investigated in these studies. Wavelengths are given in air, but wavenumbers are given in vacuum. The 4266.275-Å excitation color corresponds to a U^{235} ground-state transition. Lifetime and cross-section data given on this diagram are to be interpreted as approximate only (see Section V).

III. Experimental Apparatus

In this experiment uranium atoms are excited and ionized by light from tuned lasers. The ions are detected and analyzed by a mass spectrometer. The apparatus consists of three systems.

1) A uranium evaporation system consisting of a vacuum tank enclosing an electron-beam evaporator, atomic-beam collimators, and evaporation monitoring and control equipment.

2) Tuned lasers with their associated electronics and monitoring equipment.

3) An ion-detection system consisting of a quadrupole mass spectrometer with associated timing circuits and digital-detection electronics.

A. Uranium Evaporation System

The vacuum tank is drawn schematically in Fig. 2. Uranium vapor is produced by electron-beam evaporation at the bottom of the tank. Most of the vapor collects on the walls of a shield surrounding the evaporator assembly. Only the small fraction of the vapor which passes through a hole in the top of the shield reaches the sensitive region of the mass spectrometer. Further collimation of the uranium atomic beam is provided just below this region. Laser light is incident on the vacuum tank horizontally through a window on the right and intercepts the uranium atoms in the sensitive region of the mass spectrometer. Most of the laser light leaves the tank through a window on the left where its characteristics can be monitored. An additional "reference" E-beam is provided whose electrons can ionize the vapor in the sensitive region. The function of this E-beam will be described later.

The uranium evaporation rate can be monitored both by the mass spectrometer and by deposition-monitoring crystals placed near the top of the shield. The uranium density in the sensitive region of the mass spectrometer is typically maintained at about 10^{10} atoms/cm^{-3}.

A vacuum of 10^{-6} torr is maintained by two oil-diffusion

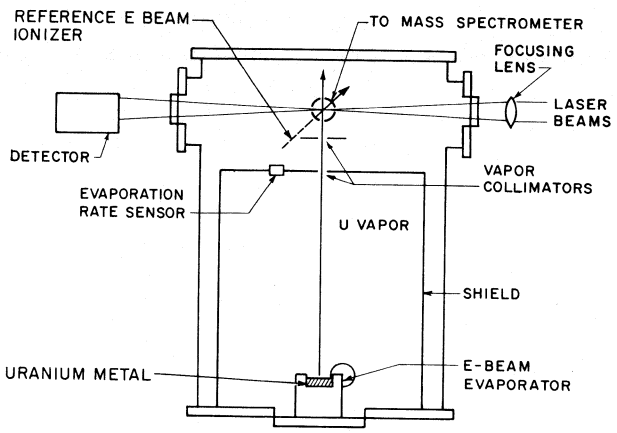


Fig. 2. Schematic diagram of vapor source and vacuum chamber.

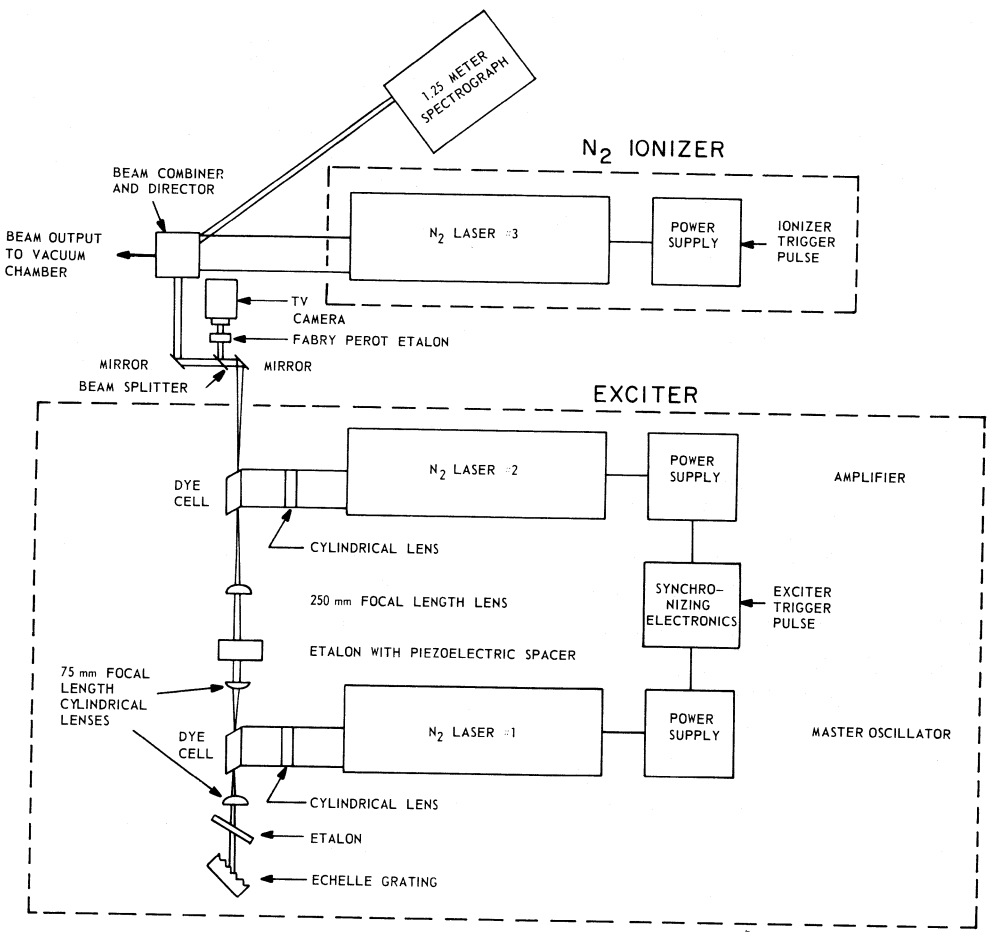


Fig. 3. Schematic diagram of nitrogen-laser-pumped tunable dye-laser master oscillator-power amplifier with echelle grating and Fabry–Perot etalon to narrow laser linewidth to 0.02 Å.

pumps with cryopanels, one for the main tank and one for the mass spectrometer. A series of interlocks protects the system from electrical vacuum, and water-cooling failures.

B. Laser System

The tuned laser light is provided by either a pair of dye-laser systems or else by a single dye-laser system for excitation followed by a pulsed nitrogen laser (3371 Å) for ionization. The latter version of the system is shown schematically in Fig. 3. The laser used for selective excitation of the uranium atoms is called the exciter. The laser which ionizes the selectively excited atoms is called the ionizer. The wavelengths of the exciter and ionizer will be designated λ_E and λ_I, respectively. The exciter consists of two synchronized nitrogen lasers which transversely pump a dye oscillator and a dye amplifier [7]. The dye oscillator is basically an AVCO "Dial-A-Line"® laser

®Registered service mark of the AVCO Corporation.

with some tuning modifications. The wavelength and linewidth of this dye laser are determined by the grating used as the rear reflector of the oscillator and two Fabry-Perot etalons. One etalon is located inside the optical cavity and the other serves as the output mirror. The output etalon has a piezoelectric spacer. The diverging dye-laser beam emerging from each end of the dye cell is collimated by cylindrical lenses whose cylinder axis is parallel to the grating grooves.

This combination of elements gave an oscillator linewidth of about 0.02 Å. A lens focuses the oscillator output into the amplifier.

The wavelength of the exciter is monitored by a 1.25-m spectrometer with a resolution of 0.02 Å. The wavelength of the exciter laser is also monitored with a stable etalon used as a Fabry-Perot spectrometer. The Fabry-Perot interference pattern is focused on the photosensitive surface of a TV camera. The enlarged image produced on a TV screen provides a means of observing the linewidth and adjusting the wavelength. Fig. 4 is a typical TV screen image.

The delay of the ionizer with respect to the exciter is variable. It is monitored by means of a fast photodiode placed at the exit window of the vacuum tank (Fig. 2). This calibrated photodiode is also used to measure the energy incident on the uranium atomic beam.

The ionizer and exciter beams are combined prior to entering the vacuum tank by means of a dichroic mirror. A lens is used to focus the combined beams into the interaction region.

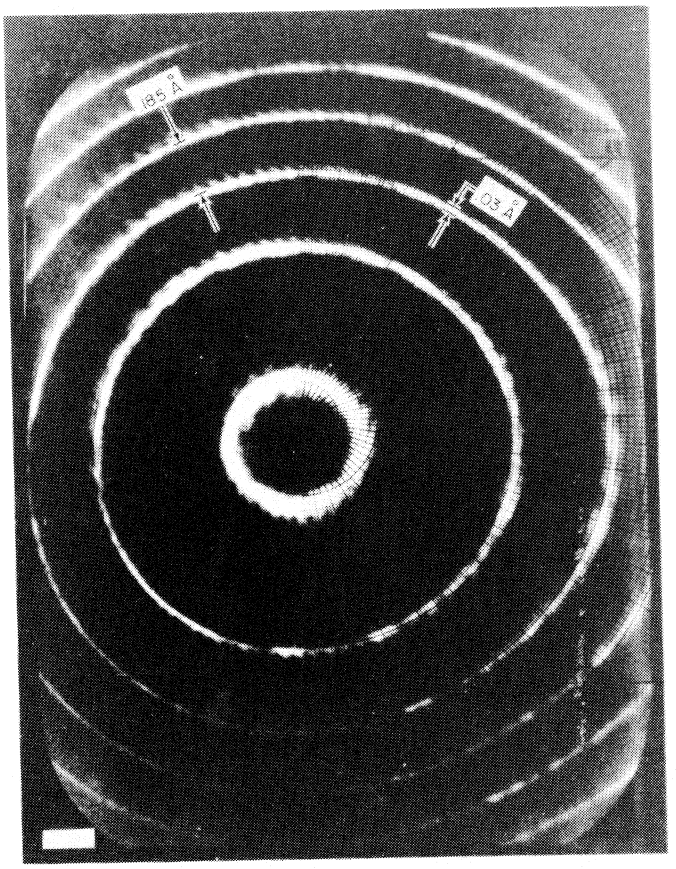


Fig. 4. Photograph of the interference pattern produced on a TV monitor by an etalon which monitors the output of the exciting laser. The distance between fringes is 0.185 Å and the width of each line is less than 0.03 Å. The transparent grid is used in making quantitative measurements of linewidth and of relative wavelength.

The optical spectrometer has a shaft encoder and digital readout such that 14 units change in the digital readout corresponded to 0.01 Å. Thus, when an argon spectra line at 4266.2854 Å was used to calibrate the spectrometer, the correct setting for the uranium line at 4266.324 Å was obtained by stepping the appropriate number of units on the shaft encoder. Coarse adjustment of the laser was accomplished by tuning the grating, fine adjustment by manually tilting the rear etalon, and very fine adjustment by means of a piezoelectric spacer in the front etalon. These adjustments were optimized by maximizing the U_{238} count rate. The position of the Fabry-Perot rings on the TV screen was noted and provided a reference for tuning to U_{235}.

IV. Measurement Techniques

The total number of ions per pulse produced by two-step laser photoionization was expected to be small; however, their time of production would be known precisely. Hence, from a knowledge of the kinematics of charged particles in a known potential distribution, it was possible to predict their expected time of arrival at the detector of the mass spectrometer. These facts led us to select a single-particle counting system rather than an analog output system. This selection permitted the use of pulse amplifiers, pulse discriminators, gate generators, coincidence circuits, and gated scalers for handling the output. These components were, however, used in a slightly unorthodox manner. A single sensor, the output of the electron multiplier, is amplified, discriminated, and fanned out into a number of counters which are gated on in sequence as the experimental conditions vary. In addition, the tuning of the mass spectrometer was also capable of multiplexing between U_{235} and U_{238} for measurement of isotope ratios.

The details of the electronics used to accomplish this objective are relatively complex and will not be given here; however, the basic technique can be understood in principle by reference to Figs. 5 and 6 which are timing diagrams illustrating the basic clock cycles for these measurements. The two basic objectives were to understand the nature of the two-step photoionization process in uranium, and to demonstrate isotope separation using lasers. The first objective was accomplished with the clock cycle shown in Fig. 5, while separation was demonstrated with the clock cycle shown in Fig. 6. Because of the flexibility of the apparatus, it was possible to convert back and forth between these cycles in a short time merely by changing a few electrical connections.

The cycles shown were designed to minimize the possibilities for introducing systematic errors due to variations in the evaporation rates, in the laser parameters (wavelength, intensity, or geometry), and in the mass spectrometer detection efficiency. This was accomplished by using a simple electron-beam impact ionizer as a normalizing reference. Thus we counted the number of laser-produced events in the signal gate per 4000 events in the mass-238 *E*-beam gate. This typically required about 80 repetitions of the cycle which, at the 11.8 pulses per second (pps) laser pulse rate, takes about 13-s run time for the dual clock cycle (Fig. 5) and 26 s for the quadruple clock cycle (Fig. 6). Note that this reference *E*-beam ionizer is turned off temporarily during the time interval when the laser pulses occur.

It was also possible to turn off the evaporator temporarily

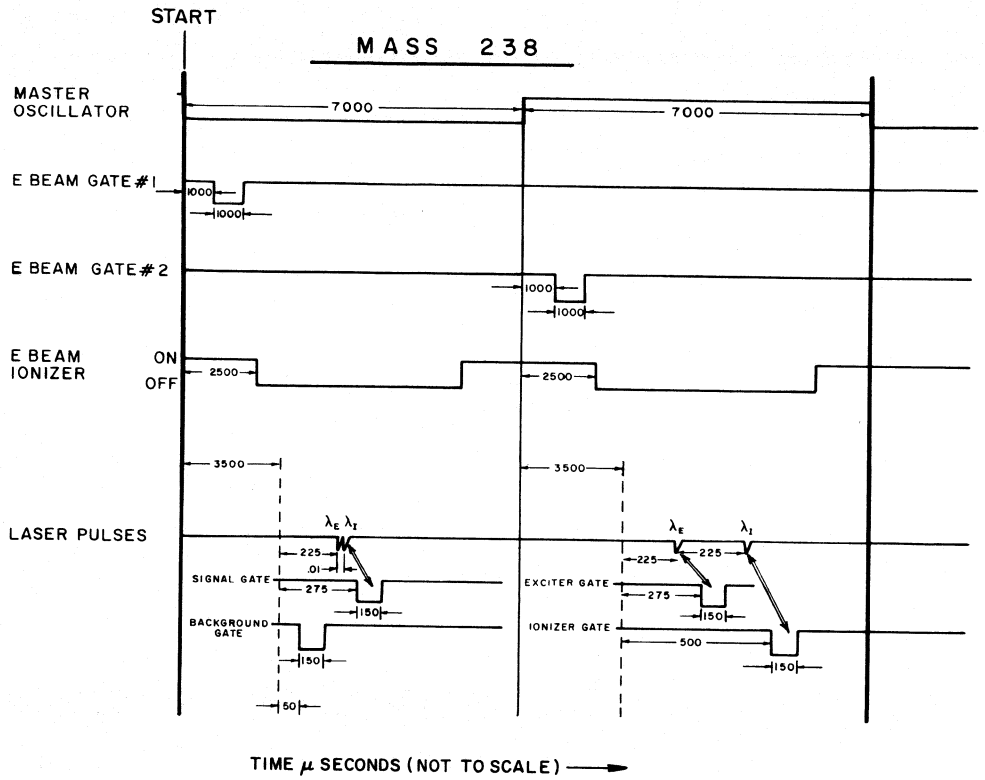


Fig. 5. Time diagram of the dual-electronic clock cycle used for obtaining measurements in investigating the nature of the two-step laser-induced photoionization process in uranium. (See Section IV.) Note that the time intervals are not shown to scale.

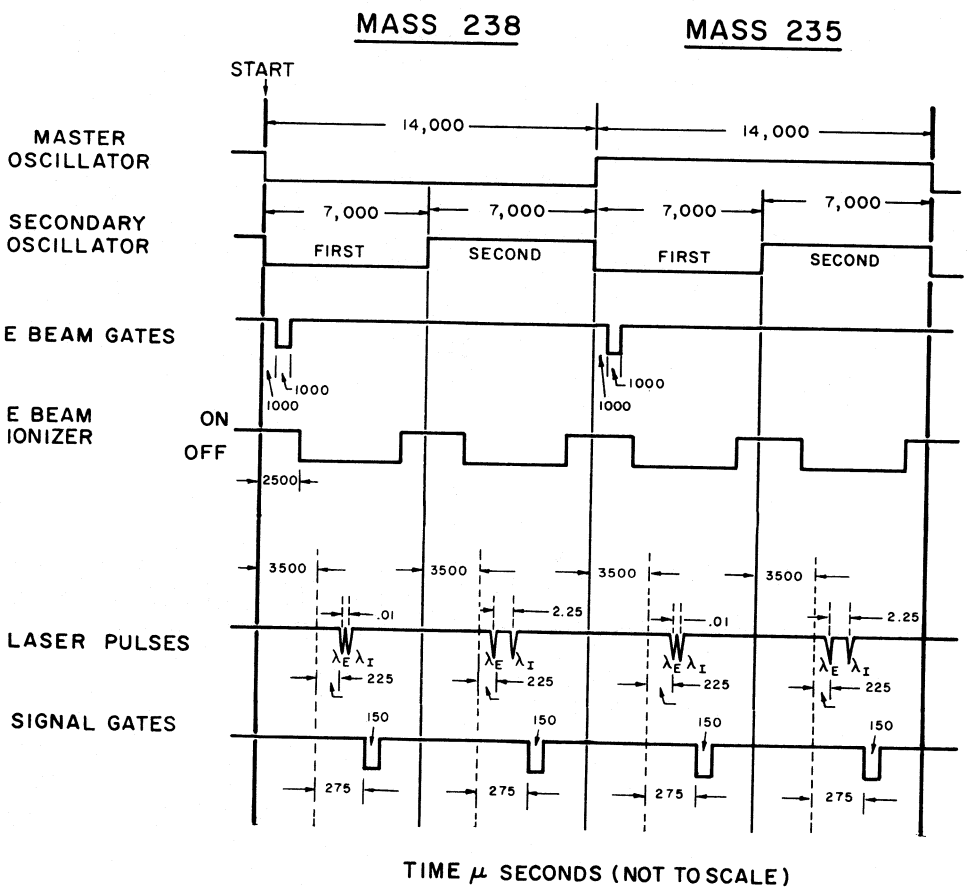


Fig. 6. Time diagram of the quadruple-electronic clock cycle used for obtaining measurements in demonstrating isotope separation with a two-step laser-induced photoionization process in uranium. (See Section IV). Note that time intervals are not shown to scale.

in order to avoid counting ions produced initially by the E-beam evaporation process; however, this turned out not to be necessary and was hence omitted. The absence of such ions is probably a consequence of the positive voltage bias on the ionizer section of the mass spectrometer and should not be taken as an indication that no ions were produced in the evaporation process.

Four sequential gates, 2 laser pulses, and an ionizer inhibit pulse, were generated during each part of the cycle. These gates were in turn multiplexed with the output of the master and secondary square-wave oscillators (using TTL logic circuits) in order to generate the matrix of 16 gates from which the appropriate gate subset was selected for the experiment being conducted. Thus the limits on the information-gathering capabilities of the apparatus were determined by the number of available scalers. Other cycles than those outlined in Figs. 5 and 6 were easily obtainable. This arrangement had the additional advantage of avoiding the possibilities for systematic errors as a consequence of fluctuations in gate length and gate delays. The lengths of the four gates are themselves controlled by use of 10-MHz oscillator.

The dual clock cycle shown in Fig. 5 was designed to permit detailed study of laser-produced photoionization of atoms of a single mass number (generally mass 238). A typical ion required about 100 μs to reach the multiplier. Thus, during the first half of this cycle, an ion produced by a closely spaced laser pulse pair occurring 225 μs after the first (dotted line) 3500-μs delay would arrive at the detector after about a 325-μs delay. It would, therefore, register in the scaler counter activated by the "signal" gate. Since the "background" gate was unrelated to any laser pulse(s), the number of counts registered in the scaler gated by the background gate provided an estimate of the background contribution to all gates. Not all laser-related events registering in the signal gate were due to a two-step ionization process involving excitation by a photon of wavelength λ_E followed by ionization by a photon of wavelength λ_I. The inverse two-step process involving excitation by a photon of wavelength λ_I followed by ionization by a photon of wavelength λ_E was ruled out by a sequence in which λ_E clearly precedes λ_I. However, it is sometimes possible for a laser of wavelength λ_E or λ_I to produce ions individually. The contributions to signal-gate events due to lasers at wavelength λ_E and λ_I individually were estimated separately during the "second" half of the cycle by introducing a 225-μs delay between λ_E and λ_I (this is very long relative to atomic lifetimes), and counting the events due to λ_E and λ_I alone during separate exciter and ionizer gates. Thus the counting rate due to a true two-step photoionization process involving excitation by a laser of wavelength λ_E and power P_E followed by photoionization by a laser of wavelength λ_I and power P_I can best be estimated by taking the sum of the signal and background gates and subtracting therefrom the sum of the exciter and ionizer gates. For the case where either λ_I or λ_E corresponds to more than half the ionization potential, it is easy to see that the counts in the corresponding exciter or ionizer gate will represent a significant fraction of the signal-gate counting rate, when λ_I or λ_E corresponds to and is close to a ground-state resonance line. This suggests, of course, that a two-photon experiment will be simpler to interpret (although not necessarily more interesting or relevant) for cases where λ_E does not correspond to more than half the ionization potential. Since, however, some of the uranium atoms are already excited thermally, we anticipate that additional ions N_E and N_I will be produced in the exciter or ionizer gates from previously excited atoms even when neither λ_E nor λ_I correspond to a resonance from the ground state. This can be expected to occur as a result of frequency doubling, as a single-photon process from a high-lying state, or (most probably) as a resonant transition from a partially populated, relatively low-lying excited state to a much higher excited state followed by photoionization. Although the latter process sounds improbable, it is important to keep in mind both the complexity of the uranium atom and the finite linewidth of the lasers (particularly the ionizing laser).

With the exception of the case where contributions arise as a consequence of ionization from sparsely populated upper levels, we would expect contributions to the exciter and ionizer gates to exhibit a quadratic dependence upon the laser powers P_E and P_I. Thus, in the absence of saturation in the excitation process, the functional dependence of the counting rate of the signal gate may be expected to take the form given in (1)

$$N_{\text{signal}} = \alpha P_E P_I e^{-t/\tau} + \beta P_E^2 + \gamma P_I^2 + N_{\text{background}}. \quad (1)$$

In the equation α, β, and γ are constants which depend upon both the vapor state and wavelengths involved, τ is the mean life of the excited state, and t is the time delay between the exciting and ionizing laser pulses, assuming that they do not overlap. The true selective "yield," Y, due to two-step photoionization, can be estimated from (2)

$$Y = (N_{\text{signal}} + N_{\text{background}}) - (N_E + N_I). \quad (2)$$

The quadruple clock cycle shown in Fig. 6 was used to demonstrate separation with a finely tuned narrow-bandwidth laser. This is a similar electronic arrangement to that shown in Fig. 5 with the exception that the mass spectrometer is tuned for mass 238 during the first 170 000-μs half of the cycle, and for mass 235 during the corresponding second half of the cycle. In addition, the arrangement of gates used in the dual cycle was slightly simplified in order to reduce the number of scalers required. In this case the delay between the laser pulses was increased to 2.25 μs in the second and fourth quarters of each cycle. Thus the background, N_E and N_I, contribution to the signal-gate counts in the second and fourth quarters of each cycle are the same as in the corresponding first and third quarters, while the yield due to a two-step photoionization process will have decayed exponentially with time. If the mean life is short relative to 2.25 μs, then the yields computed by subtracting the first and second signal gates for each mass number will be equivalent to those computed from (2).

V. Experimental Results

The two-step ionization process in uranium was first observed using a single 0.25-Å-bandwidth laser. In this and subsequent experiments the atom density was in the range of 10^9-10^{10} atoms/cm^3. Uranium is known to have a resonance

level at 26 920.695 wavenumbers corresponding to a wavelength of 3713.557 Å. Since this level is more than halfway to the ionization limit, a single laser can accomplish both steps. We observed that we could detect a signal during the proper time interval when and only when 1) the mass spectrometer was tuned to mass 238; 2) uranium vapor was passing through the mass spectrometer; 3) the laser beam was present; and 4) the laser beam was tuned to the proper wavelength. These observations clearly established a two-step ionization process in metallic uranium vapor. Subsequently, the electronics was refined as outlined in Section IV, and the resolution of the mass spectrometer was checked using two-step laser-induced photoionization. These measurements, shown in Fig. 7, were taken with a broad-band exciting laser which did not preferentially excite either isotope. It is important to observe that the mass spectrometer clearly distinguishes between the 238 and 235 isotopes (note the dip in the middle), and also that the ratio of the heights of the 238 and 235 peaks corresponds to the natural isotope ratio.

For the reasons discussed in Section III, it was decided to select for study an exciting wavelength corresponding to less than half the ionization potential. Accordingly, an exciting wavelength of 4266.324 Å (mass 238) was selected since it is a moderately strong line with a relatively long lifetime and a reasonable isotope shift. The corresponding resonance line for mass 235 is 4266.266 which is displaced by 0.058 Å. Also, argon is known to have a spectral line between these two uranium lines at 4266.2854 Å. This argon line serves as a convenient tuning reference.

Our initial studies were made with the dual clock cycle of Fig. 5 and a broadly tuned 4266-Å laser. These studies served to confirm the βP_E^2 and γP_I^2 hypothesis contained in (1), and also to provide a measurement of the mean life for the excited state. The latter result is illustrated in Fig. 8 where we plot the "yield" as a function of the delay between the two laser pulses. The duration of each laser pulse was approximately 5 ns. Note that this yield is asymmetrical around zero delay indicating that in this case (where $\lambda_I = 3371$ Å) the ionizing laser does not excite effectively. Note also that the observed mean life of 0.155 μs is indeed long relative to the 0.01-μs laser delay interval used in the first and third quadrants of the quadruple clock cycle (Fig. 6), but short compared to the 2.25-μs laser delay interval used in the second and fourth quadrants. Several other excited-state lifetimes for two-step processes as measured by this technique are given in Table I.

Subsequently, the bandwidth of the exciting laser was reduced with two etalons and attempts were made to demonstrate isotope separation. This was first done with the quadruple clock cycle of Fig. 6, a 4266-Å exciting laser, and a 3371-Å pulsed-nitrogen ionizing laser. Success was initially achieved when, with natural uranium, we varied the observed isotope ratio between 0.09 and 18 percent by changing the wavelength of the exciting laser. Following some improvement in techniques, the experiment was repeated with the results shown in Figs. 9 and 10. In these figures we have plotted the total "first-signal" counting rate and the two-step photoionization yield as corrected for background, respectively, as a function of the wavelength of the exciting laser. The raw-yield data shown in Fig. 9 correspond to 30-percent enrichment from a single pulse while Fig. 10 shows that the same data, corrected for background contributions, correspond to

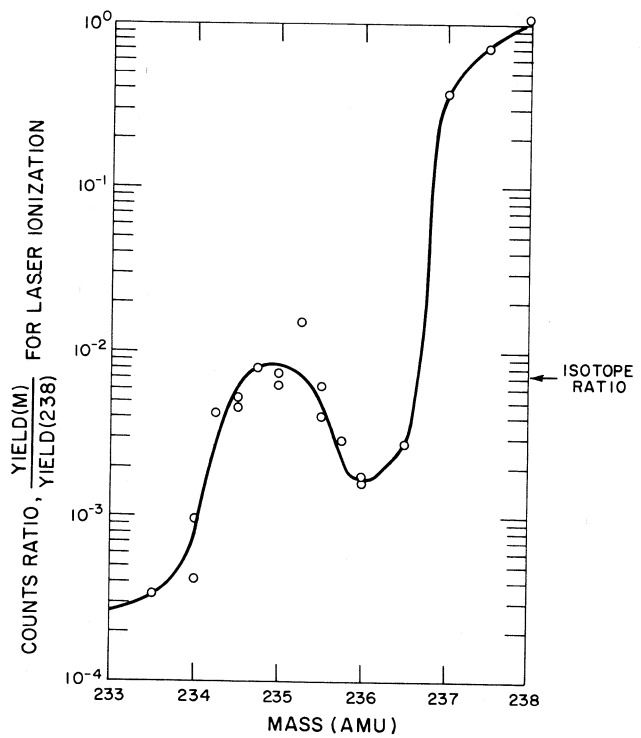


Fig. 7. Plot of data obtained with a relatively broad-band exciting laser illustrating the dependence of counting rate on mass numbers. These data confirm the adequacy of the resolution of the mass spectrometer.

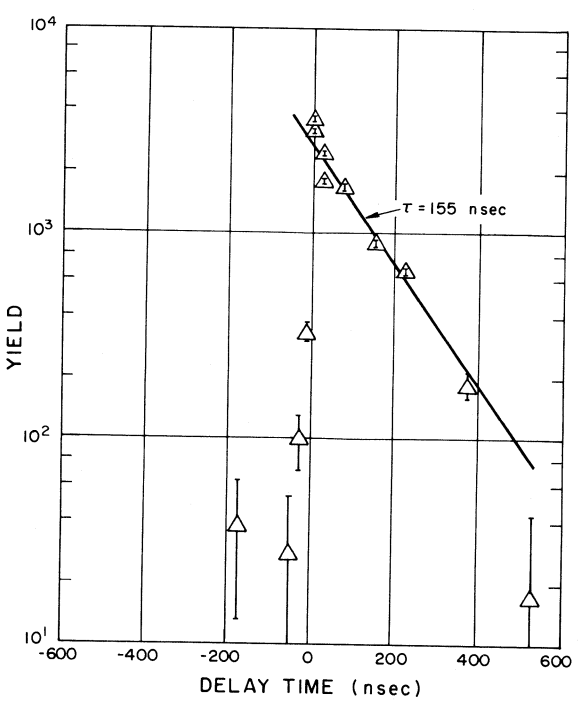


Fig. 8. Measurement of the counting rate yield due to two-step photoionization of uranium as a function of the delay between the exciting- and the ionizing-laser pulses. The error bars shown are due to counting statistics. The mean life of the excited state is seen to be close to 150 ns.

TABLE I
EXCITED STATES WITH LARGE ISOTOPE SHIFTS

Energy (cm^{-1})	Exciting Wavelength in Air (Å)	J	Isotope Shift (Å)	Lifetime (Nsec.)
24 907	4013.8	6	-.055	
24 671	4052.1	6	-.061	
24 560	4070.4	7	-.076	
24 334	4108.4	7	-.059	
24 186	4133.5	7	-.064	
24 067	4154.0	7	-.072	
23 849	4191.9	7	-.052	
23 572	4241.1	6	-.076	60
23 543	4246.3	7	-.051	
23 534	4247.9	5	-.054	
23 487	4256.5	5	-.082	
23 433	4266.3	5	-.057	155
23 212	4306.8	5	-.080	170
22 862	4372.8	6	-.061	135
22 583	4426.9	6	-.055	130
22 056	4532.6	6	-.081	300
21 768	4592.6	7	-.073	
21 767	4592.9	6	-.090	
21 637	4620.4	5	-.075	

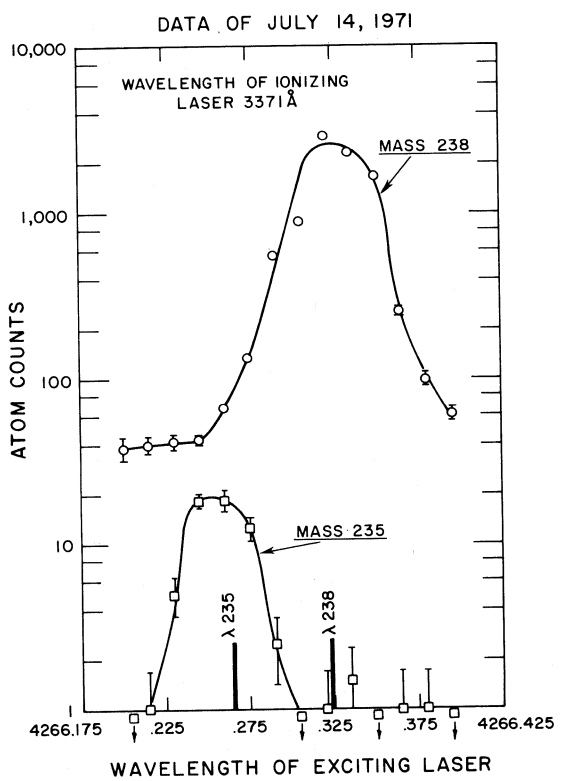


Fig. 9. Measurement of the total counting rates in the first (mass 238) and third (mass 235) quadrants of the separation clock cycle as a function of the wavelength of the exciting laser. λ_{235} and λ_{238} are the predicted values for the wavelengths of the mass 235 and mass 238 resonance lines. The plateau on the left of the 238 curve is due to a βP_I^2 as outlined in the text. In this case, the effect limits the isotope ratio to 30 percent. The error bars are due to counting statistics.

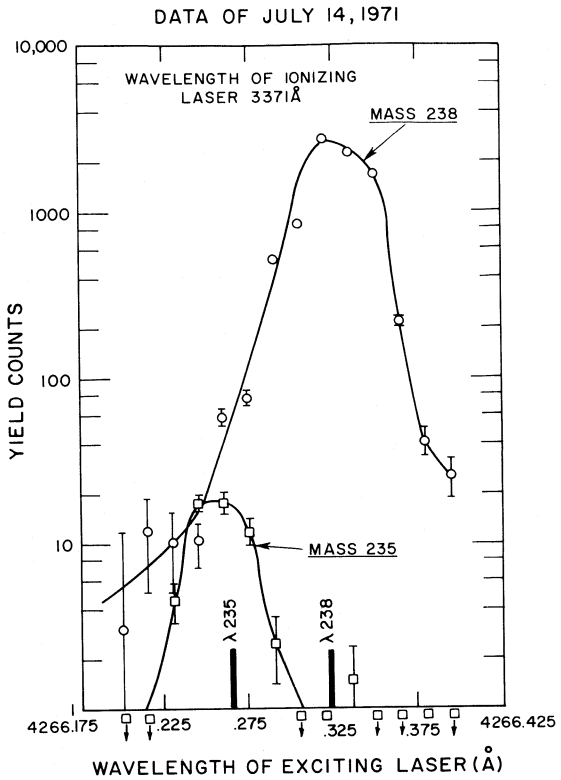


Fig. 10. Measurements of the two-step laser-induced yield (see Section V) for the mass 235 and mass 238 as a function of the wavelength of the exciting laser. These data include corrections for background, and for the βP_I^2 and αP_E^2 effects discussed in Section IV. The error bars are due to counting statistics. Note that 50-percent enrichment has been obtained.

50-percent enrichment. Note that the ratio of the 238 and 235 peaks is 140:1 corresponding to the natural-isotope ratio and also that the peaks occur at the predicted wavelengths. In addition, the 3000:1 yield ratio of 238–235 ions at λ_E = 4266.325 Å constitutes an independent check on the resolution of the mass spectrometer.

The flat portion of the 238 curve on the left side of Fig. 9 is due to the βP_I^2 effect. There is a spectral line in U_{238} near 3371 Å corresponding to a transition whose lower level is at 7645.6213 wavenumbers. This constitutes a near-resonance level for atoms which are already in this lower state. A 1-percent contribution from this effect would not be surprising. This suggests another criterion for selecting the ionizing wavelength and its linewidth.

Fig. 9 clearly indicates that given a pure two-step photoionization process, very high levels of isotope separation are possible. Using essentially this technique, we have also demonstrated two-photon selective ionization and isotope separation utilizing a number of the other excited states listed in Table I with similar results.

We have also used this apparatus to measure photoionization spectra (Fig. 11) in the dual clock cycle configuration (Fig. 5). The exciter was set at the 4266.324-Å uranium resonance line (corresponding to a photon energy of 2.905 eV) and the ionizer wavelength was varied between 3605 and 3830 Å. The dashed curve in Fig. 11 represents the results of this experi-

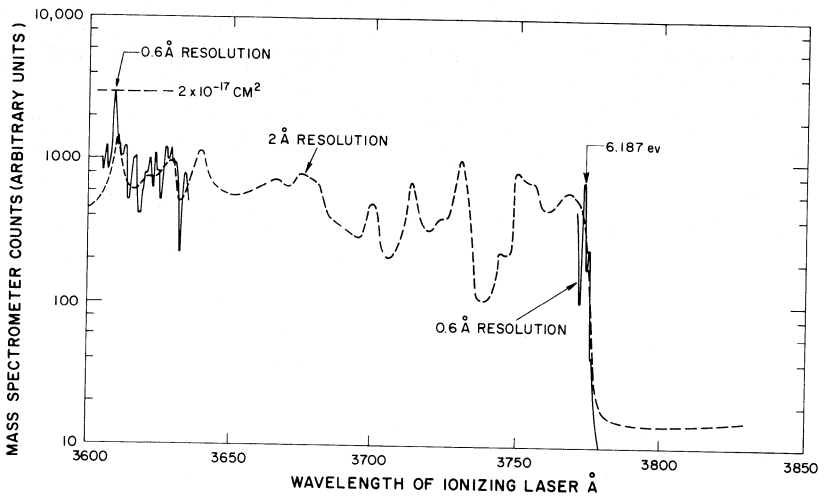


Fig. 11. Photoionization spectrum. The exciting laser was set at the 4266.324-Å uranium resonance line.

ment. The resolution, due to the linewidth of the ionizer, was 2 Å. The threshold for ionization was found to be 3777 ± 2 Å (corresponding to a photon energy of 3.282 ± 0.002 eV). The uranium ionization potential, which is the sum of the two-photon energies, is therefore 6.187 ± 0.002 eV. This result is in agreement with previous experiments (6.19 ± 0.06 eV) [5], [6], but is more precise by a factor of 30. This precision, which could be increased still further by narrowing the ionizing-laser linewidth, illustrates the potential of the tunable laser method for measuring physical constants of complex atomic systems.

In order to increase resolution, the linewidth of the ionizing laser was decreased from 2 to 0.6 Å. The results of these increased-resolution studies are shown in the two solid curves in Fig. 11. These curves were taken over the two most interesting regions in the photoionization spectrum. The peak at 3609 Å represents the maximum yield attained in the wavelength range studied initially. The curve at the ionization potential shows the extremely sharp ionization cutoff. Both 0.6-Å resolution curves show features whose width is clearly resolution limited.

We have also used this apparatus to measure absolute photoionization cross sections. For the two-step process, these measurements were made using a technique wherein the ion yield due to laser flux was compared to the ion yield produced by a 1.4-keV electron beam of known flux. The electron and laser beams were truncated by identical masks just prior to entering the saturation region in order to provide comparable geometries. In this particular case, the initial photoexcitation transition was essentially saturated as shown by no further increase in yield with increase in exciter-laser power. Thus the photoionization cross section could be determined in terms of a ratio with the theoretically calculated electron-impact ionization cross section [8]. The details of this technique are not treated here; however, the peak yield in Fig. 11 at 3609 Å corresponds to a photoionization cross section of $2 \times 10^{-17}\ \Gamma_L/\Gamma\ \text{cm}^2$ where Γ is the linewidth of the optical transition and Γ_L is the laser linewidth.

VI. Conclusions

We have described an experiment using a beam of atomic uranium of natural isotopic abundance, two fine-tuned short-pulse laser beams, and a mass spectrometer, with which we have been able to demonstrate up to 50-percent isotopic enrichment of U_{235}/U_{238} by selective excitation of the U_{235}. With this experimental apparatus, we have been able to demonstrate two-photon ionization with a single laser when the laser photon energy is greater than half the ionization potential. The apparatus is also useful for measuring photon-absorption cross sections and lifetimes of excited states. In addition, the variation of two-step photoionization efficiency with wavelength of the ionizing laser has been measured, and the ionization potential of uranium determined to be 6.187 ± 0.002 V.

This experiment should prove to be a very useful tool for the future study of the spectroscopy of other atomic vapors as well.

Subsequent to the performance of this work (1971) measurements on noble gases using somewhat similar techniques were described in papers by Dunning and Stebbings [9]-[11].

Acknowledgment

The authors wish to thank H. A. Bethe, H. E. Petschek, and A. R. Kantrowitz for numerous valuable discussions. They also wish to thank J. P. Dotson, F. Cunningham, D. F. Twombly, K. H. Gerber, L. N. Litzenberger, and A. Capucci for their assistance with the experiment, and R. L. Dickeman and L. P. Bupp of Exxon Nuclear Company, Inc., for their encouragement and support.

References

[1] R. H. Levy and G. S. Janes, "Method of and apparatus for the separation of isotopes," U.S. Patent 3 772 519, Nov. 13, 1973.

[2] S. A. Tuccio *et al.*, "Two-step, selective photoionization of ^{235}U in uranium vapor," presented at the Quantum Electronics Conf., San Francisco, CA, June 10-13, 1974.

[3] I. Nebenzahl, "Some technical aspects of the laser isotope separation method," presented at the Int. Conf. Uranium Isotope Separation, London, England, 1975.

[4] D. W. Steinhaus *et al.*, "Present status of the analysis of the first and second spectra of uranium (U I and U II) as derived from measurements of optical spectra," Los Alamos Scientific Lab., Los Alamos, NM, Rep. LA-4501, Oct. 1971; also Rep. LA-3475, Apr. 1966.
[5] D. H. Smith and G. R. Hertel, *J. Chem. Phys.*, vol. 51, p. 3105, 1969.
[6] A. M. Emel'yanov, Yu. S. Khodeev, and L. N. Gorokhov, *High Temp.* (USSR), vol. 8, p. 279, 1970.
[7] I. Itzkan and F. W. Cunningham, "Oscillator-amplifier dye-laser system using N_2 laser pumping," *IEEE J. Quantum Electron. (Part II of Two Parts: Special Issue on 1971 IEEE/OSA Conf. Laser Engineering and Applications)*, vol. QE-8, pp. 101–105, Feb. 1972.
[8] H. A. Bethe, private communication.
[9] R. F. Stebbings and F. B. Dunning, *Phys. Rev. A*, vol. 8, p. 665, 1973.
[10] F. B. Dunning and R. F. Stebbings, *Phys. Rev. A*, vol. 9, p. 2378, 1974.
[11] —, *Phys. Rev. Lett.*, vol. 32, p. 1286, 1974.

Laser-Generated *RC* Networks

MANSOOR A. SAIFI AND OTTO T. MASOPUST, JR.

Abstract—**Laser machining is the basis of a new technique for manufacturing integrated *RC* networks. The technique involves the generation of resistance patterns by laser machining nonconductive paths in capacitor plates composed of polyester film metallized with 400 Å of zinc. The reliability of such networks under operating conditions is largely dependent upon the electrical isolation provided by the laser-machined line. Good adherence of the metal film at the edges of the machined line is required, with no loose metal particles. This entails careful control of the laser pulse intensity and spot overlap. A further restriction on the laser-machining parameters is imposed by the fact that the 6-μm-thick polyester film (the dielectric body of the network) should not be thermally damaged due to evaporating metal film. In this paper we discuss the laser-machining aspects and the electrical characteristics of the laser-generated networks.**

I. Introduction

RESISTIVE and capacitive components are used in almost all electronic circuits. An important application of a series *RC* network in a telephone switching system is that of contact protection. At present these networks are an assembly of a discrete resistor and a capacitor.

A typical assembly [Fig. 1(b)] consists of a $\frac{1}{2}$-W 120-Ω resistor encased in a metal tube around which two polyester films and metal foils are wound in sandwich form to create a capacitor of about 0.1 μF. The physical dimensions of such a network are generally 1.1-cm diameter by 3 cm long. The physical size of these networks can be substantially reduced if the two metal foil–polyester films are replaced by two metallized polyester films. A further size reduction can be achieved if the discrete resistor is eliminated by developing the resistive component within the metallized film. This can be accomplished by generating nonconductive paths in the metallized polyester film, as shown in Fig. 2. The nonconductive paths can be generated by using laser-machining techniques.

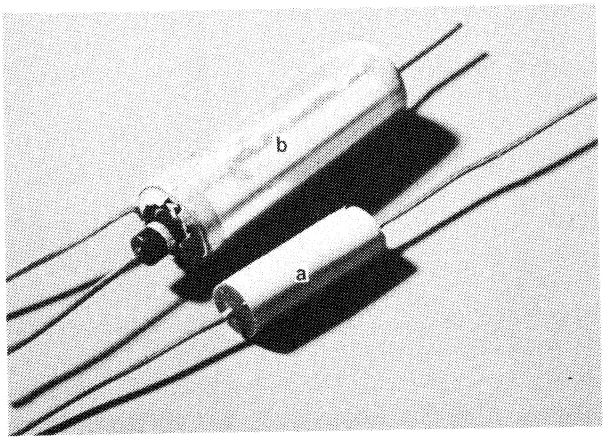


Fig. 1. (a) Laser-generated *RC* network. (b) Polyester-film–metal-foil capacitor and carbon-resistor network.

In this paper we report the development of a process in

Manuscript received July 14, 1975.
M. A. Saifi is with the Engineering Research Center, Western Electric Company, Inc., Princeton, NJ 08540.
O. T. Masopust, Jr., is with the Hawthorne Station, Western Electric Company, Inc., Chicago, IL 60623.

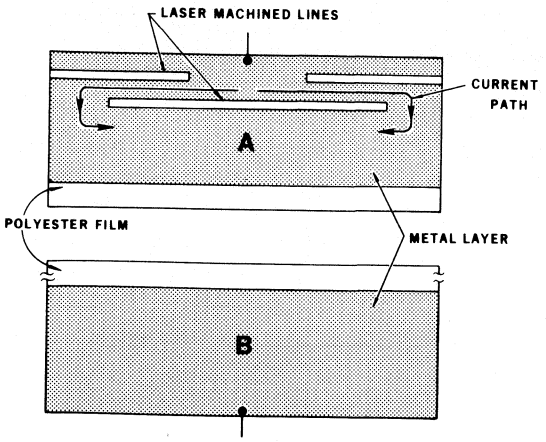


Fig. 2. Laser-machining pattern for an *RC* network.

which a *Q*-switched YAG laser is used to generate the desired resistance values during the capacitor winding operation. For the same electrical performance as the discrete-component network, the laser-generated networks occupy only $\frac{1}{9}$ the volume, and have many other attractive economic and design features. In particular, the geometry of the laser-machined lines can be readily varied to produce networks with a wide spectrum of electrical characteristics.

In the following we shall first discuss the laser-machining aspects, followed by the electrical characteristics of the networks.

II. Laser-Machining Threshold—Analysis

Laser machining of thin metal films on dielectric substrates for generating and/or trimming resistive components is used in the electronic industry [1]-[3]. In most of these applications the thin or thick films are on ceramic alumina or glass substrates. What makes this application different is that the substrate itself is very thin, i.e., 6-μm-thick polyester versus 0.75-mm-thick alumina. Furthermore, since the polyester film itself is the dielectric body of the capacitor and is wound under tension at high speeds, it is essential that the laser-machining process be carefully controlled to minimize any thermal damage. This is important since the thin zinc film vaporizes at 920°C, whereas the polyester film melts at 250°C. The advantage of using zinc film on the electrode material is that it allows use of solder blocks for end connections. It is apparent from this that in any thermal process requiring zinc evaporation, the interface temperature will reach 920°C. Thin-film machining can be done with high-intensity short-duration pulses from *Q*-switched or cavity-pumped lasers. The advantage of this process is that the machining is done within tens of nanoseconds, a time interval much less than the thermal time constant τ of the irradiated spot [$\tau = (d^2/k_1)$, where d is the focused spot diameter and k_1 is defined in (1)]. In this case, the process is aided by the fact that while zinc absorbs strongly at the radiation wavelength (1.06 μm for a YAG laser), the polyester film is practically transparent. Furthermore, the low thermal conductivity of the polyester film coupled with the short duration of the radiation pulse confines the temperature rise to within a submicron layer of its surface.

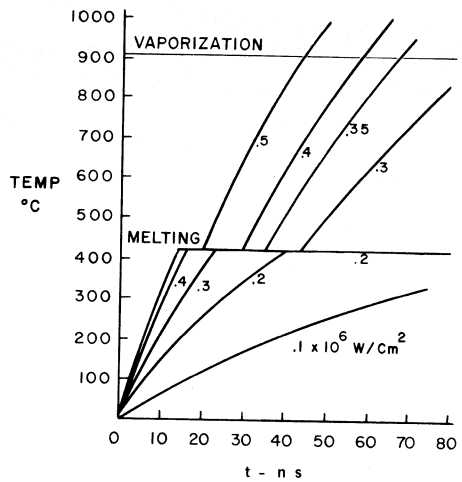


Fig. 3. Calculated zinc and polyester film interface temperature versus time for several radiation intensities.

Laser machining of thin films has been studied by several investigators [4], [5]. Maydan [6] considered the machining of thin bismuth films on transparent dielectric substrates for image recording. For a short-duration pulse of constant intensity in time and space, the temperature rise within the film is given by [5]

$$T(x,t) \cong \frac{P_0}{K_1} \sum_{n=0}^{\infty} \left\{ 2\sqrt{k_1 t}\, \alpha^{n+1}\, i\,\mathrm{erfc}\left(\frac{2(n+1)\,d \pm x}{2\sqrt{k_1 t}}\right) \right.$$
$$-2\sqrt{k_1 t}\, e^{-d/\delta}\, \frac{\Lambda \alpha^n}{1+\Lambda}\, i\,\mathrm{erfc}\left(\frac{2(n+1)\,d \pm x}{2\sqrt{k_1 t}}\right)$$
$$+2\sqrt{k_1 t}\, e^{-d/\delta}\, \frac{\alpha^n}{1+\Lambda}\,\mathrm{erfc}\left(\frac{2(n+1)\,d \pm x}{2\sqrt{k_1 t}}\right)$$
$$\left. -\delta e^{-xk} + 2\sqrt{k_1 t}\, i\,\mathrm{erfc}\left(\frac{x}{2\sqrt{k_1 t}}\right) \right\} \qquad (1)$$

where

P_0	transmitted intensity at the air-film interface;
K_1, k_1	metal-film thermal conductivity and diffusivity, respectively;
K_2, k_2	substrate thermal conductivity and diffusivity, respectively;
δ	radiation skin depth;
t	time;
Λ	$= (K_1/K_2)\sqrt{k_2/k_1}$;
α	$= (\Lambda - 1)/(\Lambda + 1)$;
T	temperature in degrees Kelvin.

Using (1), one can calculate the metal-film temperature rise as a function of time for constant radiation intensity. Fig. 3 shows temperature at the film-substrate interface for several different values of P_0 and zinc thickness of 400 Å. The optical and the thermal properties on which these curves are based are listed in Table I. At 418°C, the temperature of zinc remains constant for a while as the film absorbs energy corresponding to its latent heat of fusion. This is estimated from the time required to raise the zinc-film temperature by the amount

TABLE I
OPTICAL AND THERMAL PROPERTIES

	Zinc	Polyester Film
Relfection Coefficient	.7	.06
Absorption Coefficient (cm^{-1})	--	12.5
Thermal Conductivity ($J \cdot s^{-1}\ cm^{-1}\ {}^{o}C^{-1}$)	1.13	1.67×10^{-3}
Thermal Diffusivity ($cm^2\ s^{-1}$)	.41	1.1×10^{-3}
Melting Point	419°C	250°C
Boiling Point	908°C	--
Latent Heat of Fusion (J)	9.6	--

$\Delta T = (L_f/C_p)$.[1] In Fig. 3 only the metal film-substrate interface temperature is plotted, since the temperature gradient across the film for $t \geqslant 10$ ns is always less than 10 percent [5].

It should be noted that (1) describes the temperature distribution across the film but does not describe the evaporation process. This is because the radiation intensity is not uniform in the focused spot, as assumed here, but has a Gaussian distribution. Therefore, the portion of the film which is in the center of the optical spot will first reach the vaporization temperature, while the surrounding regions are still in liquid state. Once a small portion of the film starts vaporizing, the escaping vapor will tend to remove some of the film in liquid form and the surface tension of the film may tend to increase the machined-spot diameter [7]. Thus it may not be necessary to provide latent heat of vaporization to all of the metal film removed from a certain spot.

This model can be used to determine the machining threshold intensity. An accepted definition of threshold intensity is the intensity which for a given pulse length raises the film temperature to its boiling point. The calculated results based on the present model and for various intensity values are shown in Fig. 3. For a 70 ns (pulsewidth at $\frac{1}{2}$-power points) the calculated threshold intensity is about 0.35×10^6 W/cm^2.

III. Machined-Spot Structure

In the previously described model the metal-film temperature was calculated for uniform illumination. However, the intensity distribution in the focused spot (for TEM_{00} mode) is Gaussian; i.e.,

$$I = I_0\, e^{-r^2/r_0^2}.$$

It has been shown that for thin-film machining with short pulse lengths, the radial heat conduction can be neglected [5], [6]. From (1) the temperature is directly proportional to the incident radiation density; hence, one can assume the temperature distribution in the focused spot to be Gaussian. The occurrence of phase transformation (solid to liquid, liquid to vapor) of course distorts the Gaussian temperature profile [6]. However, considerable insight into the machined-spot structure can be gained from this simple model.

[1] Where L_f is the latent heat of fusion and C_p is the heat capacity.

First consider the effect of machining with the threshold intensity. Several curves showing the intensity distribution (Gaussian) in the focused spot are plotted in Fig. 4. The intensity values are normalized in terms of vaporization threshold, and the radial distance in terms of r_0. Based on the data of Fig. 3, both the vaporization and melting thresholds are also marked. The region between the melting and vaporization threshold will be in molten condition. For zinc on polyester, if machining is done at the threshold intensity, then the region up to $0.9r_0$ is at temperature between T_v and T_m. At this intensity only a small spot in the center is vaporized. Zinc in the molten region adheres poorly to the polyester film, and on cooling the forces due to surface tension tend to break it apart. This explains the clover-leaf structure of the laser irradiated spot shown in Fig. 5(a) wherein machining was done at the threshold intensity.

Next consider the effect of machining with intensities above the threshold value. This not only increases the diameter of the machined spot, but also reduces the width of the molten zone. The present model can be used to estimate their dependence on radiation intensity.

Let

I_v vaporization threshold intensity;
I_m melting threshold intensity;
r_0 optical-spot radius, $(1/e^2)$ point;
r_v vaporized-spot radius;
r_m molten-spot radius.

Since for a given pulse length the temperature is directly proportional to radiation intensity, we obtain

$$I_v = I_0\, e^{-r_v^2/r_0^2} \tag{2a}$$

$$I_m = I_0\, e^{-r_m^2/r_0^2}. \tag{2b}$$

In (2), r_v is the radius at which the thin-metal-film temperature has reached a temperature $T_v = T$ (boiling point) + (L_f/C_p), where L_f and C_p are the latent heat of fusion and the specific heat of zinc, respectively. The term (L_f/C_p) is the temperature equivalent of the latent heat of fusion. Solving (2) for r_m and r_v, the width of the molten region W_m is estimated to be

$$W_m = r_m - r_v = r_0\left[\sqrt{\ln I_0/I_m} - \sqrt{\ln I_0/I_v}\right]$$

$$= r_0\left[\sqrt{\ln I_0/I_m}\left\{1 - \sqrt{\frac{\ln I_0/I_v}{\ln I_0/I_m}}\right\}\right].$$

For $I_0 \gg I_v$, this reduces to

$$W_m \approx \frac{r_0}{2}\frac{\ln I_m/I_v}{\sqrt{\ln I_0/I_m}}. \tag{3}$$

This is a monotonically decreasing function of I_0, and has no minimum for finite values of I_0. Experimentally, several spots were irradiated each with a single Q-switched pulse and examined optically. The spot structure as a function of radiation intensity is shown in Fig. 5. If we assume that the width of the molten zone corresponds to that of the folded film, it is apparent that this width decreases with increasing intensity. A large molten-zone width increases the machined-spot rugged-

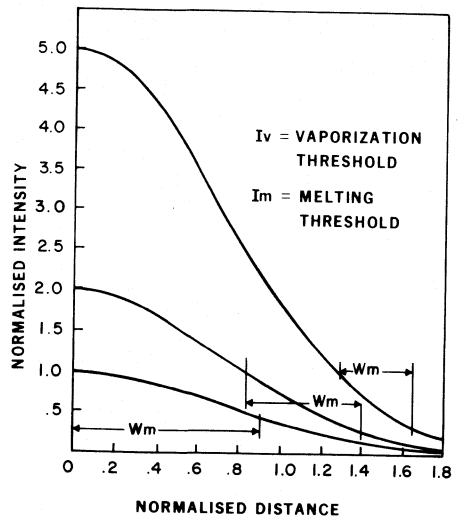


Fig. 4. Normalized temperature versus normalized distance for Gaussian intensity distribution.

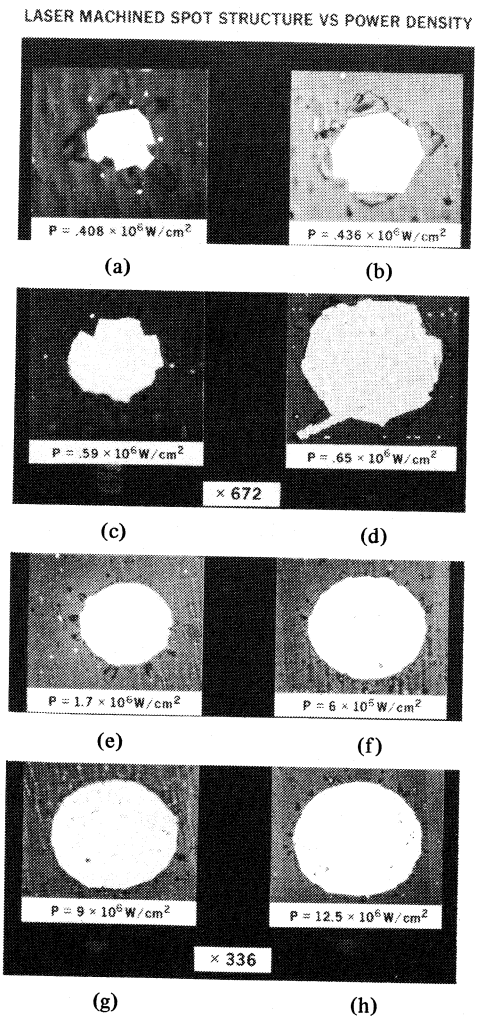


Fig. 5. Machined-spot structure for various radiation intensities.

ness, because the zinc film breaks up on sudden cooling at the end of the laser pulse. This will be discussed further in the experimental section.

Next consider the effect of intensity on the diameter of the machined spot. This is obtained from (2a).

$$r_v = r_0 \sqrt{\ln I_0/I_v} \tag{4a}$$

$$\frac{dr_v}{dI_0} = \frac{r_0}{2I_0} \frac{1}{\sqrt{\ln I_0/I_v}}. \tag{4b}$$

In a manufacturing environment we can expect the laser to have pulse-to-pulse stability within ±5 percent and, depending upon the tuning and lamp condition, day-to-day variation in laser output of ±5 percent. This means one should expect overall variation in laser intensity to be less than ±10 percent. Our goal is to maintain the machined-spot diameter within ±2.5 percent. According to (4b) this can be accomplished if machining is done at 8 times the threshold intensity.

IV. Threshold Intensity—Experimental

The laser-machining threshold intensity was determined by machining a series of lines with a focused beam but with nonoverlapping spots at a pulse repetition rate of 200 Hz. In order to vary the incident-radiation intensity a series of attenuators was introduced in the beam path before the lens. To determine the attenuation factor, the laser-pulse repetition rate was increased to 10 kHz and the average power with and without the attenuators measured. The experimental data are given in Table II. The structure of the laser-machined spot for various pulse peak power and focused intensities is shown in Fig. 5. For an intensity level below 0.4×10^6 W/cm² no machining was observed. Thus the experimentally determined threshold intensity is 0.4×10^6 W/cm², which compares well with the calculated value of 0.35×10^6 W/cm².

The structure of the machined spots, for intensity close to the threshold value, is shown in Fig. 5(a)-(d). The cloverleaf structure due to the large molten zone is evident here, and has been discussed earlier. As the radiation intensity is increased the molten zone shrinks, which can be seen in the progressive reduction of this region in Fig. 5(a)-(h). Furthermore, machining between 9-20 times the threshold intensity, the spot size increased by about 10 percent only. This is in

TABLE II

	Repetition Rate Hz	Average Power mW	Peak Pulse Power kW	Power Density* $I_0=(1-R)I$ MW/cm²
1	197	1.90	.128	.408
2	197	2.02	.136	.436
3	191	2.66	.185	.59
4	208	2.82	.18	.575
5	204	3.14	.204	.65
6	206	8.25	.532	1.7
7	206	29.0	1.88	6
8	210	46.5	2.84	9
9	211	62.5	3.95	12.5
10	213	110	6.25	19.9

accord with our earlier prediction that for good machined linewidth stability, intensities above 8 times the threshold value should be used.

V. Network Electrical Characteristics

The network electrical properties of interest are its frequency response and life under actual operating conditions. We first discuss the frequency response of the laser-generated networks (LGN) and compare it with that of the discrete film–foil (DFF) type. The impedance as a function of frequency for a typical LGN/DFF *RC* network is shown in Fig. 6. This figure clearly shows that between 100 Hz and 100 kHz there is little difference in the overall impedance of the LGN and the DFF. However, if one considers the variation in the resistive and the capacitive components, some interesting differences are observed. For example, Fig. 7 shows the percent change in the effective series resistance (ESR) and the effective capacitance for the LGN and DFF, respectively. Normalizing the values at 1 kHz, note that ESR drops down with frequency. However, the drop in ESR for LGN is larger compared to that for DFF, 9.1 versus 6.5 percent. On the other hand, up to 10 kHz, the capacitance remains practically constant and above 10 kHz it drops down for LGN, whereas it increases for DFF. Both the variation in ESR and effective capacitance can be understood from the equivalent circuit and the pattern in which the plate current flows. The low-frequency equivalent circuit of LGN is shown in Fig. 8(a). The resistance R_0 in parallel with the capacitance C_0 represents the dielectric-loss component, and the series resistance R_2 is that due to the laser-machined lines. An equivalent series circuit for this combination is shown in Fig. 8(b). In terms of the Mylar dissipation factor δ the series resistance R_1 is given by

$$R_1 = \frac{1}{\omega C_0} \frac{\delta}{1+\delta^2} \tag{5}$$

where ω is frequency in radians/second. This shows that R_1 decreases with frequency and increases with δ. Assuming that R_2 remains constant with frequency, the resistance variation is due to changes in R_1 only. Calculations show that the variation in ESR can be accounted by the changes in R_1 with frequency.

Considering the capacitive reactance, the equivalent series capacitance is given by

$$C = C_0(1+\delta^2).$$

Since $\delta \ll 1$, this shows that capacitance is practically independent of frequency. However, so far we have not considered the fact that both R_0 and C_0 for the LGN are essentially distributed. This can be seen from the current path shown in Fig. 2. The plate current in LGN enters from both ends of the plate and flows across the width towards the central section of the plate. At high frequencies the shunting effect of the end portions reduces the overall plate capacitance.

In the DFF network the plate connections are made at the two opposite ends. The distributed effect in this case also tends to lower the effective series capacitance. However, this reduction is overshadowed by an increasing inductance. In particular, note that for DFF (see Fig. 9) the current in both

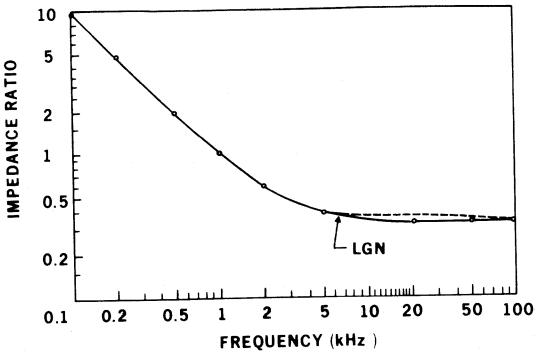


Fig. 6. Network impedance versus frequency for LGN and DFF.

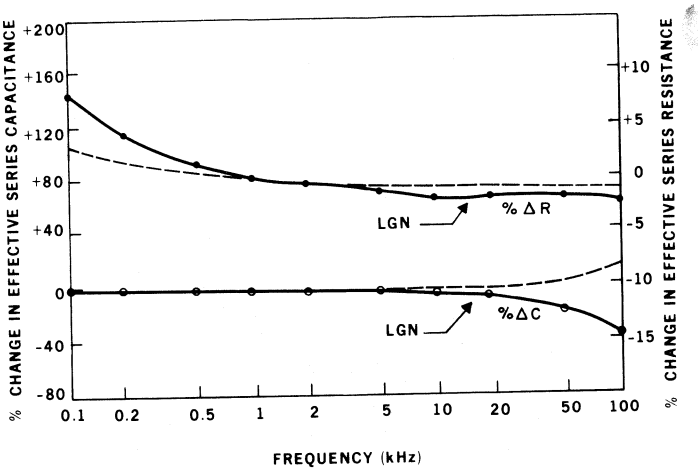


Fig. 7. Percent of effective series resistance and percent of capacitance variation with frequency for LGN and DFF.

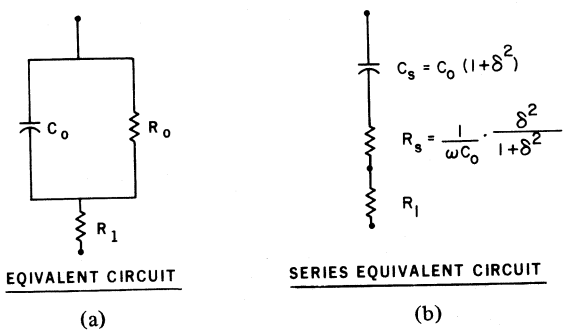


Fig. 8. (a) Low-frequency LGN equivalent circuit. (b) Series equivalent circuit. C_0: capacitance; R_0: dielectric loss component; R_1: laser-generated path resistance; δ: dielectric-loss factor ≈ 0.004.

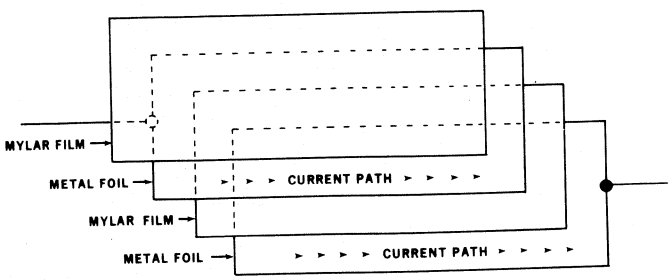


Fig. 9. Current path in DFF.

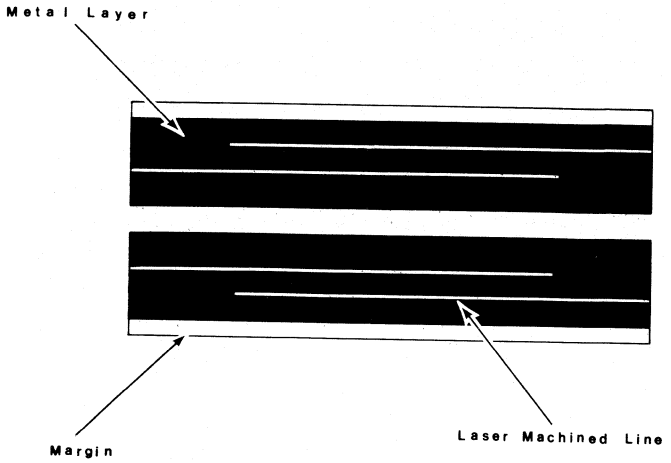


Fig. 10. Laser-machining pattern for distributed-parameter network.

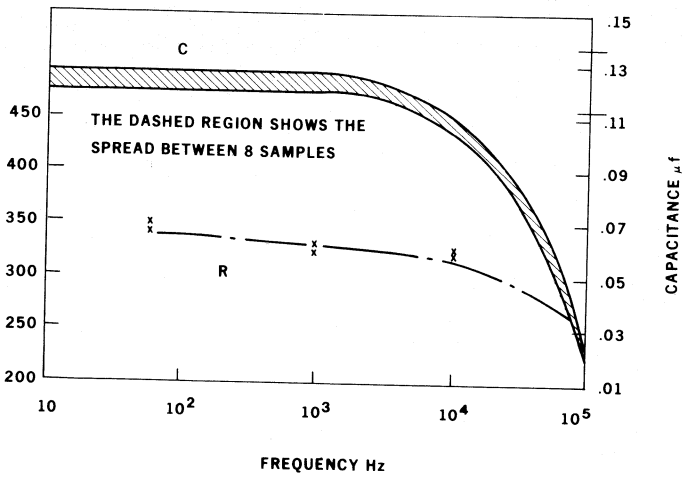


Fig. 11. LGN distributed-parameter network resistance and capacitance versus frequency.

the plates flows in the same direction, whereas in LGN the current in each plate flows in the opposite directions. In LGN this essentially eliminates any inductive reactance, and in DFF a large inductive reactance is present at high frequencies. Since these reactive components are of opposite signs, it has the effect of increasing the effective capacitance in DFF at high frequencies.

An important advantage of the present technique is that one can modify the laser-machining pattern to obtain a host of different electrical characteristics. For example, another network configuration investigated is shown in Fig. 10. In this case, the resistance path of plate *A* is capacitively coupled to plate *B*. This is unlike the pattern shown in Fig. 2 wherein the resistance section of plate *A* (shown enlarged for clarity) lies over the margin (nonmetallized region) of plate *B*. The capacitive coupling of the resistance path (Fig. 10) causes the network frequency response to be that of a distributed-parameter network. In this case, therefore, both resistance and capacitance drop down with frequency. Typical network characteristics of this pattern are shown in Fig. 11. Note that in this case both the resistance and the capacitance drop off with frequency. Such networks are of interest in electronic circuits where impedance matching with frequency may be desired.

VI. Conclusions

We have shown that laser machining of nonconducting paths on metallized polyester films can be used to produce *RC* networks. Compared to discrete-component networks, size reduction of over 500 percent is accomplished in this manner. Furthermore, by varying the machining pattern, networks with widely different frequency responses can be made. The effect of focused-radiation intensity on the machined-spot structure has been investigated. It is shown that to maintain the electrical integrity and for a production process machining should be done at over 8 times the threshold intensity.

Acknowledgment

The authors wish to thank several persons of both the Western Electric Engineering Research Center and the Hawthorne Works for their technical assistance and cooperation in making this work possible; particularly, R. Borutta for his technical assistance, and R. D. Berg for his assistance in developing the system. They also wish to thank M. I. Cohen, B. R. Kasik, S. S. Charschan, and D. R. Brown for their encouragement and thoughtful criticism.

References

[1] J. L. Hokanson and B. A. Unger, *J. Appl. Phys.*, vol. 40, p. 3157, 1969.

[2] M. I. Cohen, B. A. Unger, and J. F. Milkosky, "Laser machining of thin films and integrated circuits," *Bell Syst. Tech. J.*, vol. 47, pp. 385–405, 1968.

[3] F. M. Barlage, "A stability study of laser-patterned thermally stabilized tantalum nitride and tantalum aluminum films," *IEEE Trans. Parts, Hybrids, Packag.*, vol. PHP-9, pp. 123–130, June 1973.

[4] W. W. Weick, "Laser generation of conductor patterns," *IEEE J. Quantum Electron.* (*Part II of Two Parts: Special Issue on 1971 IEEE/OSA Conf. Laser Engineering and Applications*), vol. QE-8, pp. 126–131, Feb. 1972.

[5] U. C. Paek and A. Kestenbaum, "Thermal analysis of thin-film micromachining with lasers," *J. Appl. Phys.*, vol. 44, pp. 2260–2268, 1973.

[6] D. Maydan, "Micromachining and image recording on thin-films by laser beams," *Bell Syst. Tech. J.*, vol. 50, p. 1761, 1971.

[7] R. Sard and D. Mayden, "A structural investigation of the laser machining of thin bismuth films," *J. Appl. Phys.*, vol. 42, pp. 5084–5094, 1971.

Investigations on Laser Welding

MARCO MONTANARINI AND JÜRG STEFFEN

Abstract—A welding method has been developed that makes use of fundamental mode laser pulses. These pulses show single-mode relaxation oscillations with a high peak power first spike causing breakdown of the material surface. The laser emission following the first spike can be adapted to the welding requirements and the material properties. Metallurgical problems of intermixing of dissimilar materials in the weld puddle have been investigated with an electron beam microprobe analysis. In the case of materials which normally show bad weldability uniform welds with maximum strength could be achieved by local addition of welding agents to the weld puddle. The lap weld of a stainless-steel spring with a nickel-iron baseplate has been performed with Nb as welding agent.

Introduction

LASER welding has become an important method in many industrial manufacturing processes because of several laser properties [1]-[3]. The heat affected region can be extremely small, and the heating and intermixing of different materials in the melt puddle as well as the subsequent solidification can be controlled by the energy-time behavior of the laser emission. Laser welding of high reflectivity materials, especially the welding of thin foils of highly reflective metals to any baseplate, have proven difficult due to the high intensity required to overcome the reflective losses [4], [5]. In addition some materials tend to form hot cracks by intergranular precipitation of material constituents [6].

This paper summarizes some aspects of the formation of a lap weld of a 60-μm-thick stainless-steel spring to an iron-nickel baseplate. The material surface shows a high reflectivity at the YAG laser wavelength. State of the art laser welds showed cracks in the melt puddle and at the weld-spring interface. These put in question the strength of the joint during vibration of the spring. In order to solve this welding problem, the intermixing of the weld materials and their metallurgical properties were studied.

Choice of Laser Radiation

Independence of material surface properties and its reflecting behavior can be achieved if the laser output consists of a high intensity first spike followed by an emission adapted to the welding process. The high intensity of the first spike decreases the reflection of the workpiece to a residual value of about 20 percent for the subsequent laser emission [14], leading to a welding process independent of surface properties. In addition the transfer efficiency of light energy into heated material is maximized. The beam intensity required to decrease the initially bigger surface reflectivity is less by a factor of 100-1000 than the one required for the welding process.

The power limits required for the welding process are determined by the heat conduction of the material and by its boiling and subsequent splattering characteristics [7]-[13].

The weld spots were made with a pulsed YAG laser oscillating in the transverse fundamental mode [15]. The temporal emission of these pulses shows the well-known relaxation oscillations of a single-mode laser pulse [16]. Typical pulse to pulse reproducibility is ±1 percent. The corresponding spatial intensity distribution has a Gaussian shape. The characteristic time performance of the relaxation oscillations can be controlled and the intensity of the first spike relative to the continuous emission may be changed. By varying the leading and trailing edges of the pulse, the heating and solidification of the material can be influenced. The small beam divergence of fundamental mode radiation allows the use of reasonably large focal length focusing systems which simplifies the optical and lens protection problems.

Fig. 1 shows a lap weld of two stainless-steel foils, to the left is a top view and on the right a metallurgical section. The power density on the surface was $2 \cdot 10^5$ W/cm^2, whereas the peak intensity of the first spike was $5 \cdot 10^7$ W/cm^2. The cross section shows the low thermal influence in the surrounding material; the depth of penetration and width of the melt puddle could be reproduced within some few percents. The etched section shows the well-known large elongated grains in the microstructure of the laser affected zone and also the initiation of solidification at parent grains at the liquid-solid interface. The grains are orientated in the direction of the heat flow, because the heat is removed through the growing interface.

Fig. 2 shows three sections of lap weld spots of a stainless-steel spring with a nickel-iron baseplate. Welding was per-

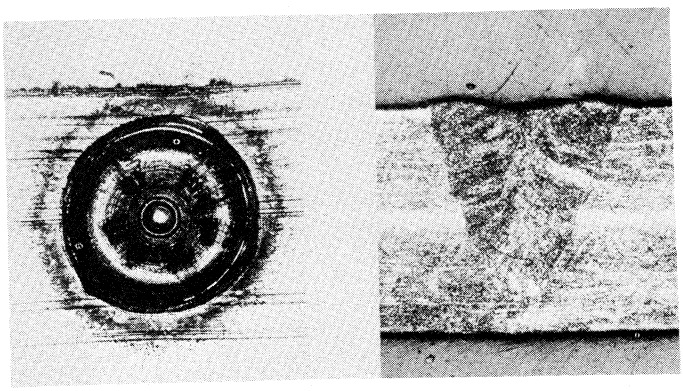


Fig. 1. Top view (at left) and metallurgical section (at right) of a lap weld of two stainless-steel foils (thickness 0.2 mm).

Manuscript received June 23, 1975. This paper was presented at CLEA 75.

The authors are with LASAG S. A., Thun, Switzerland.

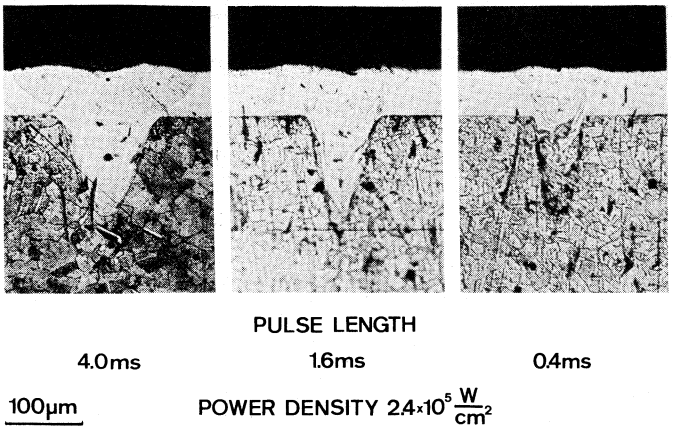


Fig. 2. Sections of three lap welds of a stainless-steel spring (thickness 60 µm) with a nickel-iron baseplate. Pulse length 4.0 ms, 1.6 ms, 0.4 ms; power density 2.4×10^5 W/cm^2.

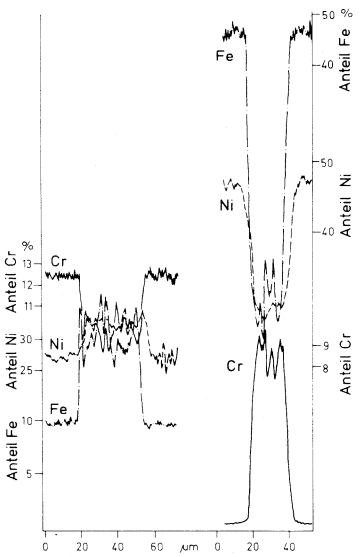


Fig. 3. Concentration diagrams of Cr, Ni, and Fe across the spot weld at left in the upper and at right in the lower material of the 0.2 ms pulse weld.

formed with laser pulses of different duration but equal power density. The state of intermixing of the two materials is improved with longer pulses. Weld cracks occur at the edges of the weld in the spring for all three pulse lengths which results in a very brittle weak weld.

An electron beam microprobe concentration analysis of the welding elements was made to study the intermixing of the two materials. Concentration profiles were taken along a line in the upper and in the lower material for the two pulse lengths 0.4 ms and 4 ms. The spatial resolution of the microprobe was 2 µm and the scanning speed was 24 µm/min. The profiles in Fig. 3 show strong variations of the concentration across the weld which are correlatable to the visible striations in the metallurgical section. The concentration of the weld components along the line in the upper material differs from the one in the lower demonstrating the incomplete mixing.

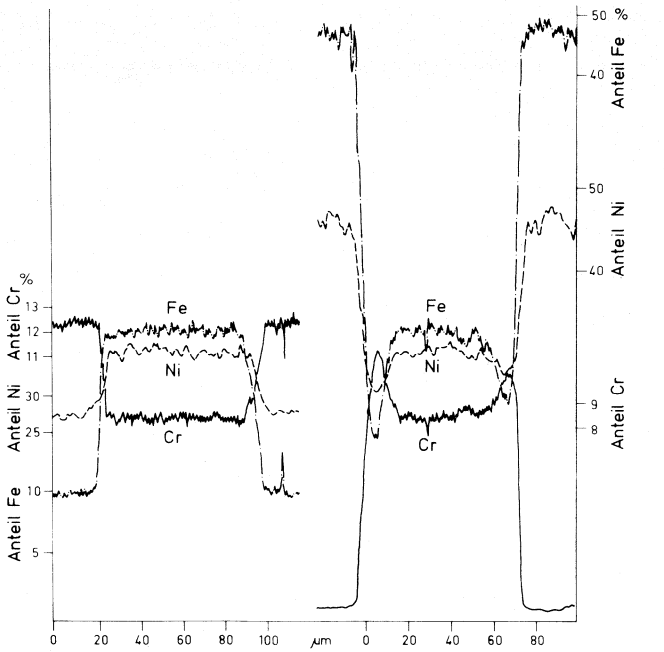


Fig. 4. Concentration diagrams of Cr, Ni, and Fe across the spot weld at left in the upper material and at right in the lower material of the 4.0-ms pulse weld in Fig. 2.

Fig. 4 shows the behavior of the long pulse weld. It can be seen that the intermixing is more complete and that the concentrations in the upper part correspond with the ones in the lower. The concentration peaks of Cr at the edge of the melt of the upper section can be seen as spikes of unmixed stainless-steel (see Fig. 2, 4.0 ms) extending into the weld puddle. From the evidence we can deduce that the laser pulse duration must be appropriately long if homogeneous mixing is to be achieved.

The thermal expansion coefficients and phase diagrams of Cr, Fe, Ni, Co alloys are known [17]-[20]. From these and the microprobe analysis we can estimate that the thermal expansion coefficient of the melted zone and the spring material must be approximately equal. The calculated values of the thermal stresses in the weld [21] are smaller than the tensile strength of the stainless-steel spring (>145 kg weight/mm^2). These calculations lead to the conclusion that the weld cracks (Fig. 5) are due to other metallurgical causes. Some characteristics of the welded materials are shown in the following table:

	Stainless-Steel Spring Duratherm 2602	Ni, Fe Baseplate Permenorm
Melting Point (K)	1663	1713
Thermal Diffusivity (cm^2/s)	0.04	0.04
Specific Heat (Ws/g) (288–873 K)	0.51	0.53
Expansion Coefficient 10^{-7} (1/K) (300–473 K)	131	100
Hardness V (kg weight/mm^2)	>500	160–200

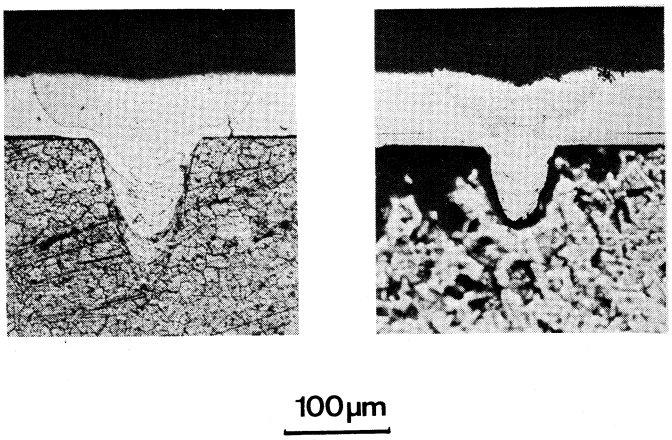


Fig. 5. Weld sections without (at left) and with an inserted 10-µm-thick Nb foil (at right).

Welding Agents

It is known that Nb prevents weld cracks in low carbon Cr-Ni steels by forming intermetallics as Fe_2Nb and Fe_2Nb_3 and thereby increasing weld strength [22]-[24]. Nb could change the properties of the materials to be joined if alloyed to the Ni, Fe baseplate or to the stainless-steel spring, which was inadmissible in the present practical problem. For this reason Nb was inserted as a thin foil between the materials in order to act as welding agent only in the melt puddle. Fig. 5 compares the sections of two welds, at left without and at right with welding agent. Pulse length and power density were the same for both welds. As a consequence of the addition of Nb the weld cracks could be avoided and a higher welding strength is reached. The success of this procedure depends evidently on a homogeneous intermixing of the different elements which requires a pulse of appropriate length and shape.

The electron microprobe analysis of the elements (Fig. 6) along the Nb foil shows a Nb-Fe ratio in the puddle corresponding to the intermetallic compound Fe_2Nb. At the weld interface an enrichment of Fe occurs, due to eutectic separation of the (Fe, Nb) solid solution.

As a consequence of the addition of Nb the softening of the weld is avoided. Without Nb the hardness of the weld corresponds to the one of the Fe-Ni baseplate and a sharp hardness step results at the spring. With the welding agent the hardness of the weld corresponds to the one of the spring.

A series of 3500 weld spots have been produced and tested in respect to static strength and dynamic properties. No changes in the weld spots could be observed after 10^8 vibrations; the static strength was >3 N/weld (~0.3 kg weight/weld) spot with a reproducibility of ±8 percent.

Conclusion

The demonstrated welding problem is an example of how materials that are difficult to weld could be joined by laser radiation. The use of fundamental mode laser pulses made the process independent of the material surface quality; the high intensity first spike pretreated the surface of the weld area to cause high absorption of the subsequent low power part of the pulse. This emission could be optimized for the particular weld and material properties, and the reproducible temporal and spatial intensity distributions produced a well-defined heat region.

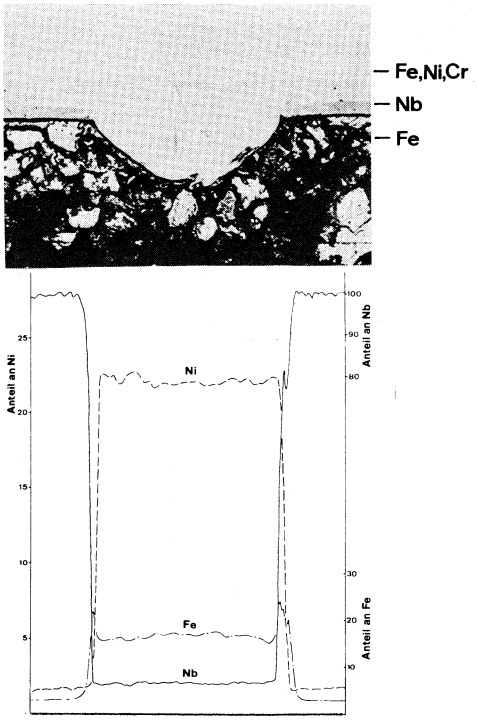


Fig. 6. Weld section and concentration diagram of Nb, Fe, Ni along the inserted Nb foil.

Metallurgical characteristics were investigated with an electron beam microprobe analysis. Weldability could be influenced by local addition of welding agents such that the joined material remained unchanged in their physical properties.

References

[1] J. E. Anderson and J. E. Jackson, "Theory and application of pulsed laser welding," *Weld. J.*, vol. 12, pp. 1018-1026, Dec. 1965.
[2] F. P. Gagliano, R. M. Lumley, and L. S. Watkins, "Lasers in industry," *Proc. IEEE*, vol. 57, pp. 114-147, Feb. 1969.
[3] M. M. Schwartz, "Laser welding and cutting," Welding Res. Council Bull. 167, pp. 1-24, Nov. 1971.
[4] M. I. Cohen, "Laser beams and integrated circuits," *Bell. Lab. Rec.*, vol. 45, pp. 247-251, Sept. 1967.
[5] S. R. Bolin, "Pulsed laser welding of clad metals," presented at the IEEE/OSA Conf. Laser Engineering Applications, Paper 12.8, May 1975.
[6] J. C. Borland, "Suggested explanation of hot cracking in mild and low alloy steel welds," *Brit. Weld. J.*, pp. 526-540, Nov. 1961.
[7] R. H. Fairbank and C. M. Adams, "Laser beam fusion welding," *Weld. J.*, vol. 43, pp. 97s-102s, Mar. 1964.
[8] D. M. Newitt, N. Dombrowski, and F. H. Knelman, "Liquid entrainment," *Trans. Inst. Chem. Eng.*, vol. 32, pp. 244-261, 1954.
[9] F. Erdmann-Jesnitzer and G. Pysz, "Position, time, and cause of spatter during electric-arc welding," *Schweissen und Schneiden*, vol. 8, pp. 303-311, 1958.
[10] A. F. Ellis and J. Glover, "Mechanism of fume formation in oxygen steelmaking," *J. Iron Steel Inst.* (London, England), vol. 209, pp. 593-599, Aug. 1971.
[11] M. B. C. Guigley and J. M. Webster, "Observations of exploding droplets in pulsed-arc GMA welding," *Weld. J.*, vol. 11, pp. 461s-466s, Nov. 1971.
[12] J. R. Collins, "High silicon welding wire," *Weld. J.*, vol. 3, pp. 169-172, Mar. 1972.
[13] M. J. Bibby, G. Burbidge, and J. A. Goldak, "Gas evolved from

electron beam welds in plain carbon steels," *Weld. J.*, vol. 12, pp. 844–846, Dec. 1972.
[14] J. Steffen, unpublished.
[15] J. Steffen, J. P. Lörtscher, and G. Herziger, "Fundamental mode radiation with solid-state lasers," *IEEE J. Quantum Electron. (Part II of Two Parts)*, vol. QE-8, pp. 239–245, Feb. 1972.
[16] H. Statz and G. de Mars, "Transients and oscillation pulses in masers," in *Quantum Electronics*, C. Townes, Ed. New York: Columbia University Press, 1960, p. 530.
[17] *Metals Handbook, Constitution of Ternary Alloys*, The American Society of Metals, Cleveland, OH, 1948, pp. 1260–1261.
[18] Roesch and Zimmermann, *Stahlguss.* Düsseldorf, Germany: Stahl and Eisen, 1969, p. 228.
[19] H. Masumoto, "On the thermal expansion of the alloys of Fe, Ni, and Co and the cause of the small expansibility of alloys of Invar type," Science Rep., Tôhoku University, 1931, vol. 20, pp. 101–123.
[20] M. E. Fine and W. C. Ellis, "Thermal expansion properties of Fe-Co alloys," *Trans. AIME*, vol. 175, pp. 242–254, 1948.
[21] B. A. Boley and J. H. Weiner, *Theory of Thermal Stresses.* New York: Wiley, pp. 290–291, 1960.
[22] T. E. Kihlgren and C. E. Lacy, "The control of weld hot cracking in nickel chromium iron alloys," *Weld. J.*, vol. 25, pp. 768s–775s, 1946.
[23] S. I. Ornichev, V. A. Savchenkov, and N. I. Lipskii, "Effect of niobium on the properties of welded joints," *Welding Production*, vol. 4, pp. 30–33, 1972.
[24] E. N. Sivov and B. A. Kartashkin, "Interaction of molten steel with solid niobium and the formation of intermetallics," *Welding Production*, vol. 1, pp. 6–8, 1973.

Laser Spot Welding and Real-Time Evaluation

MANSOOR A. SAIFI AND SOTIRIOS J. VAHAVIOLOS, MEMBER, IEEE

Abstract—**The high-repetition-rate pulsed-YAG-laser welding of insulated copper wires to terminal posts and their real-time evaluation with stress-wave emission (SWE) are discussed. It is shown that to minimize damage to the wire from the incident radiation a shoulder terminal, wherein the shoulder covers the wire, is desirable. The experimental and the analytical results show that for the geometry a terminal made out of higher melting-point material than copper is desirable.**

SWE techniques have been used to predict the quality of a laser weld in real time. An experimental criterion has been established for such a prediction. This criterion has been verified by resistance measurement, visual observation, and, to a limited extent, mechanical-pull testing. It is shown that an almost linear relation exists between the threshold crossings of an SWE signal and the quality of the weld.

I. Introduction

FUSION WELDING is an important fabrication process where lasers are finding an increasingly wide field of applications. Bahun and Engquist [1], Buddenhagen [2], and others demonstrated, in early experiments, the feasibility of laser welding and some of its advantages such as localized heat zone and the ability to weld dissimilar metals and dissimilar geometries. The application of pulsed laser welding to small electrical and electronic components has been discussed by Fluger and Mass [3], Gagliano and Lockhart [4], and Cohen *et al.* [5]. Several articles have appeared in the literature which review these applications [6], [7].

Initially, the laser welding was limited to the interconnection of cross-sectional thicknesses of less than 0.5 mm. However, the recent development of multikilowatt CW CO_2 lasers allows deep-penetration welding of large parts, such as automotive bodies [8]. Another important development in the area of laser welding is the emergence of high repetition rate [up to 40 pulses per second (pps)] high power, and more efficient pulsed Nd-YAG lasers. This makes possible laser welding of small components at high production rates hitherto done by conventional welding techniques, such as resistance and capacitance discharge welding.

In many electrical applications it is necessary to join insulated copper wires to terminals which provide connection to the external world. Such terminations often cannot be done by conventional welding techniques and in many cases require removal of insulation. Using special insulation, such as polyurethane, and a high-temperature soldering gun, insulation can be removed during a soldering operation. However, such methods are not amenable to mass-soldering techniques, such as wave soldering. Laser welding for such applications is very advantageous, since the incident radiation can be used to remove the insulation and cause a weld in the precise area.

However, to fully exploit the economic potential of this development, the need for an on-line real-time weld-evaluation technique is clearly seen. We shall show in our paper that this can be done with stress-wave emission (SWE) techniques. SWE is defined as the white acoustic noise generated in a material by an applied stress. This white acoustic noise is usually detected by means of a piezoelectric transducer. The first basic study of the SWE phenomenon appears to have been done in the late 1940's and early 1950's in the United States [9] and Germany [10]. Efforts to develop the potential of the SWE

Manuscript received July 14, 1973.
The authors are with the Engineering Research Center, Western Electric Company, Inc., Princeton, NJ 08540.

for high-resolution nondestructive surveillance of structures and pressure systems to detect growing flaws, however, are of more recent origin (1967 to present).

SWE techniques have been applied throughout the world to prevent catastrophic failure of expensive and/or high-reliability structures. Examples of these applications are too numerous to delineate here, but a few will be discussed to provide somewhat of a background for those unfamiliar with SWE technology. The aerospace industry has successfully used SWE to save time, money, and loss of almost irreplaceable structures [11]-[13]. Since the inception of SWE in the aerospace industries they have "saved" Polaris rocket chambers from destruction in proof test [14], performed many hydrotests on pressure vessels [15], studied SWE from structures such as bridges [16], and completed many contract studies for the military services.

In the nonaerospace fields, SWE is now being used to study crack growth in nuclear plants, oil and natural gas pipelines, on bearing surfaces, in the petrochemical industry, and in the welding applications to improve weld quality and yield [17], [18]. Recently, SWE was introduced as a process-control tool in the manufacturing of semiconductors and hybrid integrated circuits [19].

In this paper we shall first discuss the welding geometry and material considerations. This discussion will be followed by a discussion of the welding mechanics and its analysis. In the remaining sections of this work we shall discuss the theoretical aspects of SWE and its experimental correlation to the present experiment of laser welding.

II. Welding Geometry

A. Welding Insulated Wires to Terminals

The welding geometry to be considered is shown in Fig. 1. The copper wires are 12.5 mils (312 μ) in diameter and polyurethane insulated. The terminal could be of any electrically conducting material. The terminal shoulder under which the wire is wound protects the wire from direct irradiation with the laser beam. We have found this geometry to be useful where it is desirable to protect the wire from severe necking in the welding process. However, this imposes certain restrictions on the choice of the terminal or more correctly the shoulder material, which will be discussed later. It is well known but worth emphasizing that, as in any welding process, the two materials to be welded must be in intimate contact. In many other welding techniques this contact is accomplished by proper fixturing and application of mechanical pressure during the welding operation. In laser welding this is not always possible, since the high-intensity incident radiation will damage any external component used for this purpose. Hence one has to rely on proper winding and geometric considerations to keep the wire in contact with the shoulder terminal.

B. Material Consideration

Laser welding of insulated copper wires to terminal posts has been attempted and reported by Gagliano and Zaleckas [6], and Cohen and Epperson [7]. One common feature of all these investigations has been that the terminals did not extend much beyond the termination point. This feature permits

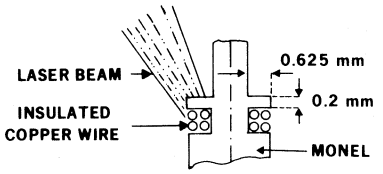


Fig. 1. Welding geometry.

focusing of the laser beam on the terminal head, causing the head to flow over and weld to the wire. In the present case, the terminal geometry is more restrictive and extends much beyond the termination point for later wave soldering to a printed circuit board. Furthermore, the system geometry restricts the incident-beam angle to within 15° of the terminal axis. For a wire completely protected by the terminal shoulder, as shown in Fig. 1, several terminal materials such as phosphor bronze, brass, and monel were investigated. For the particular geometry and laser parameters (pulse length $\leqslant$3.5 ms, energy $\leqslant$20 J) most reliable welding results were obtained with monel. The analytical results and their experimental verification will be discussed later. However, it is important to note here that monel melting and vaporization temperatures are higher than those of copper, whereas for phosphor bronze and brass the opposite is true. Moreover, copper and nickel are metallurgically compatible in the sense that they make solid solutions [20] in almost all proportions. The higher melting point of monel together with its excellent metallurgical compatibility with copper make this combination very useful for laser welding.

C. Effect of Insulation

The polyurethane insulation, while it can be removed by the incident welding pulse, does affect the weld quality and welding mechanics. First, it is apparent that even if the insulated wire is kept in contact with the shoulder, removal of its insulation during the welding cycle will create a gap between the wire and the shoulder. This can be avoided if the wire is wound with sufficient tension and the proper geometry is used so as to allow its movement towards the shoulder. Second, there is some evidence that the optical properties of polyurethane, particularly the absorption coefficient at the laser wavelength (1.06 μm), have a marked effect on welding mechanics. As will be discussed later, even with a shoulder design, part of the wire is directly exposed to laser radiation. Hence focused-spot diameter should be carefully tailored to avoid direct exposure of the wire to the maximum beam intensity.

III. Welding Mechanics

A. Analytical Results

In order to understand the welding process, we consider a simplified one-dimensional model first analyzed by Cohen [21]. In this model, one considers melting of a semi-infinite body (Fig. 2) with constant optical and thermal properties in both the solid and molten regions. Another model based on a Gaussian heat-distribution circular spot and finite thickness [22] has been discussed. The later referenced model, however, does not account for the molten region,

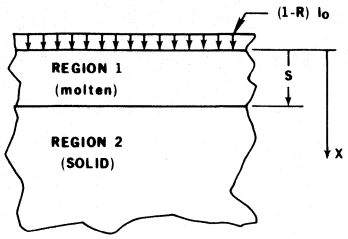


Fig. 2. Semi-infinite heating model.

since its inclusion makes the governing equations nonlinear. Furthermore, it can be shown that for the spot size and pulse lengths under consideration all the other models give results very close to that of a semi-infinite body. The problem is further complicated by the facts that in the real welding geometry considered here, the beam is incident on two orthogonal axes (see Fig. 1) and one cannot completely avoid some surface vaporization. The analysis carried out here is therefore to support the qualitative arguments to be presented later in the welding process. It will also become evident that these conclusions are corroborated with the SWE results and experiments carried out on welding of thin plates.

In the Cohen [21] model one first calculates t_m and t_v, the time required for the surface to reach the melting and the vaporization temperatures, respectively. These times and the thermal properties of the material are then used to estimate the depth of the molten zone. The optical and thermal properties of interest for monel and the laser-welding parameters are shown in Table I. The time (t_m) required for the monel surface to reach melting point is given by

$$t_m = \frac{\pi}{K}\left(\frac{kT_m}{2I_0}\right)^2 \tag{1}$$

where

K thermal diffusivity;
k thermal conductivity;
I_0 absorbed radiation intensity;
T_m monel melting temperature.

Substituting the values from Table I

$$t_m = 0.39 \text{ ms}.$$

From the curves given by Cohen, the time for the surface to reach vaporization temperature and the depth of the molten zone is estimated to be 1.66 ms and 0.07 mm, respectively. Once the surface reaches boiling temperature, the molten zone could penetrate further, before heavy surface vaporization sets in. This is because the surface temperature would stabilize as the material takes its latent heat of vaporization. Furthermore, the existence of vapor pressure itself causes the vaporization temperature to increase. Hence the significance of the previous calculations lies in the fact that it predicts a minimum pulse length of about 1.6 ms. We have experimentally confirmed this prediction by showing that small welds can be made with 2 ms, but not with 1.5-ms-long pulses. At shorter pulse lengths and higher incident-radiation intensity (constant energy/pulse) extensive evaporation occurs.

TABLE I
THERMAL AND OPTICAL PROPERTIES OF MONEL AND LASER-WELDING PARAMETERS

Thermal conductivity, k	0.466 W/cm K
Thermal diffusivity, K	0.123 cm^2/s
Specific heat, C_p	0.427 J/g °C
Melting temperature, T_m	~ 1400°C
Vaporization temperature, T_v	~ 2800°C
Reflection coefficient at 1.06 μm	~ 0.6
Pulse length	3.5 ms
Pulse energy, J	8–10 J
Lens focal length, cm	150 cm
Spot size (defocused)	0.125 cm

The previous discussion and the fact that in the actual process heating is done from two sides supports our experimental results of being able to produce good welds between monel shoulder and insulated copper wire with 3.5-ms-duration laser pulses.

The laser-welding experiments were also carried out with shoulder terminals made out of phosphor bronze and brass. In both cases it was rather difficult to obtain good welds to copper wire, and in most cases heavy surface vaporization was observed.

The previous analytical and experimental results suggest a welding model which we outline in the following section.

B. Experimental Results

Typical cross sections of the welds produced between a shoulder monel terminal and polyurethane-insulated copper wires are shown in Figs. 3 and 4. These welds were made with a 9-J 3.5-ms-duration pulse focused to about a 1.25-mm-diam spot.

Note that because of the excellent solid solubility of nickel and copper the weld region indicates good material mixing. Also note the absence of voids and residual polyurethane insulation. Several of these welds were pull tested to determine the weld strength and the strength of the wire in the vicinity of the weld region. The tensile strength of the welded wire was found to lie between 50 and 75 percent of its "parent" value. However, in no case were we able to break the weld joint itself. The welds were also subjected to an electrical test by passing current through several series-connected welded terminals. In all cases wire melted and broke, without any deleterious effects or heating of the weld region itself. This result is perhaps due to the large thermal mass of the terminal itself.

Several authors have reported satisfactory laser welding of Ni and Cu alloys [6], [7]. In this experiment we have exploited the higher melting temperature of monel to produce good welds between it and insulated copper wire. The welding mechanics we propose are as follows. We suggest that the wire interface reaches insulation vaporization temperature (~600°C) prior to the time when the monel shoulder surface begins to vaporize. This is estimated by assuming a constant surface temperature and then calculating the temperature at the wire-monel interface from the expression [24]

$$T(x, t_m) = T_s \operatorname{erfc} \frac{x}{2\sqrt{kt_m}}$$

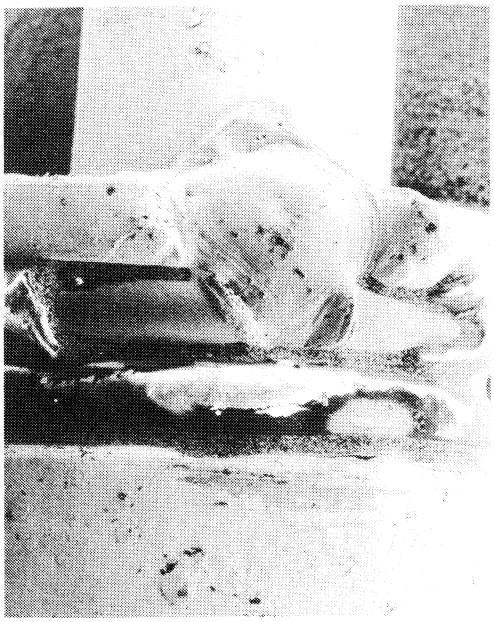
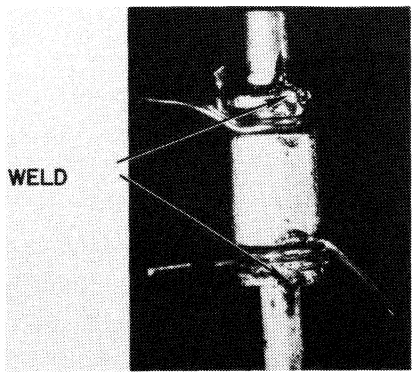
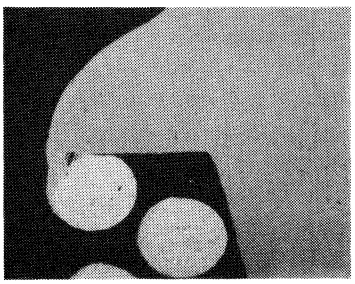


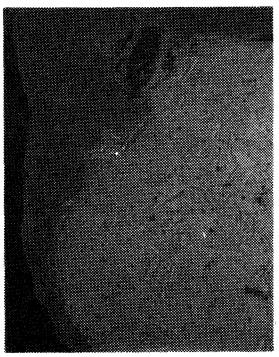
Fig. 3. Front view of typical laser weld produced with a 3.5-ms 9-J pulse. Note that the necking down of the copper wire is minimal.



(a)



(b)



(c)

Fig. 4. Typical welds and cross sections. (a) Terminal with two welded wires. (b) Weld cross section 10×. (c) Enlarged view of the weld region 50×. Note the good intermixing of the two metals at the interface and smooth flow of the molten monel.

where

T_s surface temperature ~ 3000°C;
x shoulder thickness in centimeters.

If the wire is wound under tension, the copper surface comes in intimate contact with monel. When monel at the interface approaches its melting point, copper, because of its lower melting point, melts and begins to develop a fusion zone. The higher thermal conductivity of the copper inhibits heavy melting and destruction of the wire. This and the fact that the fusion-zone melting temperature is higher than that of copper, but lower than that of monel, tends to stabilize the process.

IV. Real-Time Evaluation: Theory

As previously mentioned, in many applications it is important to determine the weld quality during the welding cycle. This is particularly important in order to realize the economic potential of high-speed spot welding now possible with high-repetition-rate pulsed lasers. We have investigated SWE techniques. Introductory theoretical models and preliminary results will follow.

A. Generation of SWE

1) *Definition:* SWE is a phenomenon arising from energy released as a solid material undergoes (elastic) plastic deformation and fracture. A laser-spot-welding operation releases SWE energy and thus it constitutes an SWE source. The released energy is then converted to elastic waves which propagate through the material and can be detected at the material surface using highly sensitive sensors. A detection technique of these waves is shown in Fig. 5.

During the laser-welding cycle and the SWE detection time, losses due to reflection at the specimen boundaries can be neglected if the acoustic impedance of the surrounding medium approaches that of the specimen. The amount of energy transmitted to the adjacent medium is equal to the ratio of acoustic impedances

$$U_E' = \frac{\rho_m v_m}{\rho_s v_s} \times 100 \tag{2}$$

where

U_E' percent of energy transmitted;
ρ_m, ρ_s density of the medium, specimen;
v_m, v_s wave-propagation velocity in medium, specimen.

In our specific experiment the medium is steel and the sensor is a PZT transducer. An $U_E' \simeq 80$ percent of SWE energy transfer is expected.

Since SWE pulses are considered to have emanated from point sources, they can be considered as spherical waves, shown in Fig. 5, whose sound pressure decreases inversely with distance from the source. Geometrical losses are independent of frequency and material properties, and of the form [23]

$$p = p_0 (x_0/x) \tag{3}$$

where

p_0 the sound pressure in newtons per square centimeter;
x_0 some arbitrary point (usually sensor location).

When the frequency and material-dependent attenuation is considered

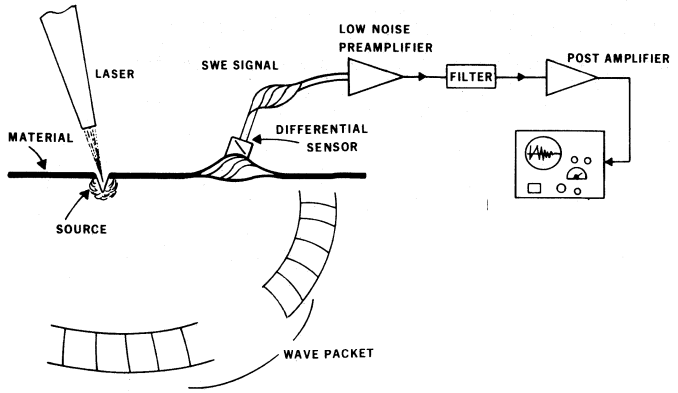


Fig. 5. Laser generation of SWE wave packets and their detection.

$$p = p_0 e^{-\alpha x} \tag{4}$$

where α is the attenuation coefficient in decibel/unit distance (frequency dependent).

In the preliminary stages of our experiment we determined that for a transducer frequency of 500 kHz and small intertransducer distances, signal losses should be attributed to geometrical losses. This is clearly shown in the SWE AM detection of Fig. 6. An important note should be made that the attenuation introduced does not affect the proportionality of the transducer output to initial displacement of the lattice other than to introduce a dissipative factor. To obtain optimum performance from a piezoelectric device, the circuit to which it is connected must have high input impedance and frequency match. Hence, depending on the application, some crystals are more desirable than others.

B. Detection of SWE

When the laser beam is absorbed by the surface of the material under consideration a stress-wave packet is generated due to the elastic behavior of the material as well as to the thermal stresses generated. As the wave packet travels it excites a differential piezoelectric crystal (preferably PZT) that in turn generates an electrical SWE signal. This signal is then amplified in order to obtain usable voltage levels.

Two outstanding features of SWE as an integrity-monitoring device are: 1) the ability to detect melting, plastic deformation, resolidification, and crack formation or movement at the time it occurs, and 2) to accomplish this remotely. Also simultaneous interrogation of multiple sensors ($\geqslant 3$) provides the necessary information to locate the source of the signals by triangulation.

For the static case of a pressure wave at normal incidence to a crystal which deforms only in the thickness dimension the maximum peak voltage of the transducer is shown to be by [23]

$$V = g_{33} dp \tag{5}$$

where

d the thickness of the transducer;
g_{33} the transducer sensitivity constant.

Assuming a U_E' of 100 percent, the minimum theoretical detectable displacement of a material could be calculated

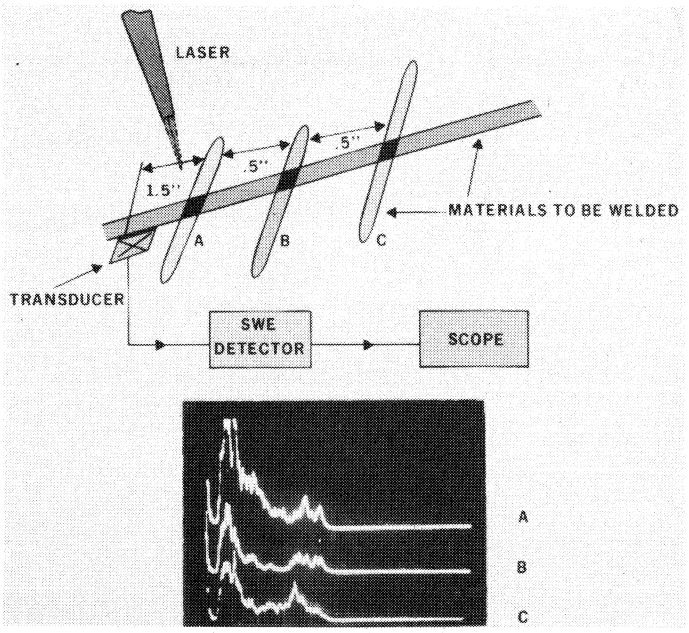


Fig. 6. Experimental setup indicating that attenuation of SWE is attributed to geometrical losses only.

from [19]

$$\delta_{\min} = \frac{V_n}{g_{33}\, Y_{33}^E} \tag{6}$$

where

V_n system electrical noise;
Y_{33}^E transducer modulus constant.

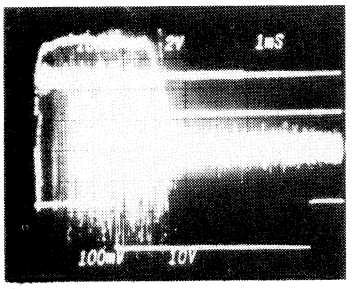
Our theoretical $\delta_{\min} \simeq 9.5 \times 10^{-10}$ cm. Problems associated with high transducer sensitivity and ringing are shown in Fig. 7. It can be seen that in Fig. 7(a) the saturated transducer hides signals associated with information concerning the quality of the weld (second distinct burst). Waveforms of the form of Fig. 7(b) are preferable. Thus extreme sensitivity might be undesirable due to the finite time constant associated with the ringdown of the piezoelectric transducer according to the equation

$$V_T(t) = V_0 f(t) e^{-\beta_0 t} \sin \omega_0 t \tag{7}$$

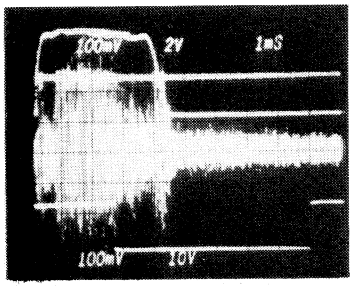
where

$f(t)$ a function of time (associated to Rayleigh waves);
β_0 time constant of the transducer;
ω_0 angular resonant frequency of the transducer.

Equation (7) clearly defines a single SWE event. The SWE's detected during laser welding could be thought of as a summation of events resulting from a series of discrete thermal-stress sources similar to the shot effect of a semiconductor device. Also the elastic behavior as well as the material expulsion resulting from the laser beam could contribute to the overall source of SWE signals. Let us then characterize these discrete sources by saying that they result in mechanical waves that are governed by some kind of a wave equation having these properties: 1) they are random in time, and 2) their stress-

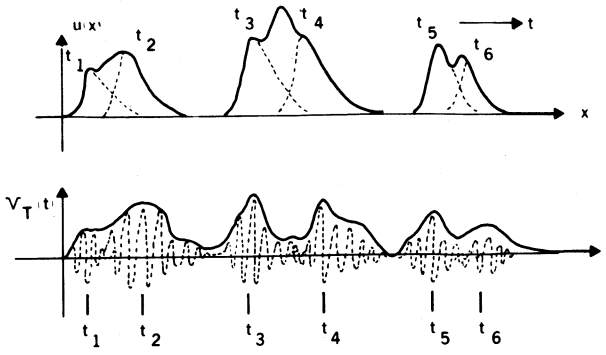


(a)

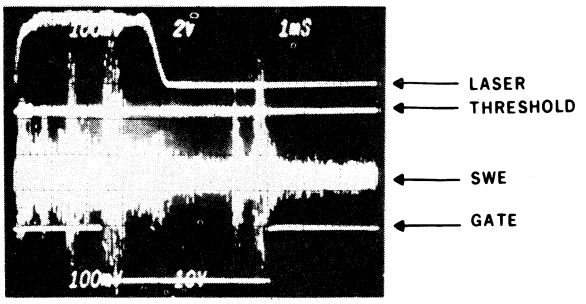


(b)

Fig. 7. Detected SWE from laser weld. Photos show that oversensitivity is not acceptable in detecting SWE. (a) Transducer is attached to the welder part. (b) Transducer is attached in proximity to the welded part.



(a)



(b)

Fig. 8. The model of generation and detection of SWE.

displacement relation behaves as a function of the form

$$u(x) = \psi f(x) e^{-\gamma x} \tag{8}$$

where

$u(x)$ displacement function;
ψ the random amplitude of the displacement;
γ the displacement coefficient;
$f(x)$ the displacement function.

If we assume that the width of the displacement caused by the laser remains constant, the following wave, shown in Fig. 8(a), arrives at the transducer

$$u(x) = \sum_{i=0}^{N} \psi_i f(x - x_i) e^{-\gamma(x - x_i)} \mu(x - x_i) \tag{9}$$

where

N the number of stress emissions;
$\mu(x - x_i)$ the unit step function.

Thus the output of the transducer will consist of a function similar to (7), but random in time and amplitude. Therefore

$$V_T(t) = \sum_{i=0}^{N} V_i f(t - t_i) e^{-\beta_i(t - t_i)} \sin \omega_0(t - t_i) \mu(t - t_i) \tag{10}$$

where $\mu(t - t_i)$ is the unit-time step function.

This is clearly illustrated in Fig. 8(b). For simplicity, the envelope of the detected SWE signal is also displayed. It is this envelope that enables us to evaluate the quality of a good versus bad microelectronic laser spot weld. The widths of these envelopes define such parameters as melting time, cooling time, and particulate-material removal time. It should be clear that for low-ringing transducers the SWE signal could be characterized as a composite Poisson process. Some preliminary work on the previous distribution assumption is now in progress by one of the authors.

V. Experimental Correlation

A. Electronic Setup

The electronic setup used for real-time evaluation of laser welds is shown in Fig. 9. Whenever a weld is made an SWE is generated due to the fusion of the material. This mechanical-stress signal is then detected by a differential piezoelectric transducer whose output is amplified and filtered by blocks 1 and 2. The output of the filter is then subjected to a threshold crossing and counting quantization procedure that is based on the assumption of having an amplitude and time-invariant transducer time constant. Thus the larger the V_0 in (7), the greater the number of threshold crossings. It is shown in [19] that an upper bound of the number of crossings exists, assuming $f(t) = 1$, and can be calculated from

$$N = \frac{f_0}{\beta_0} \ln\left(\frac{V_0}{V_t}\right) \tag{11}$$

where N is the number of crossings at threshold V_t.

B. Experimental Results

Since signals detected from a laser-welding operation are multiple events, the previously given number should be multi-

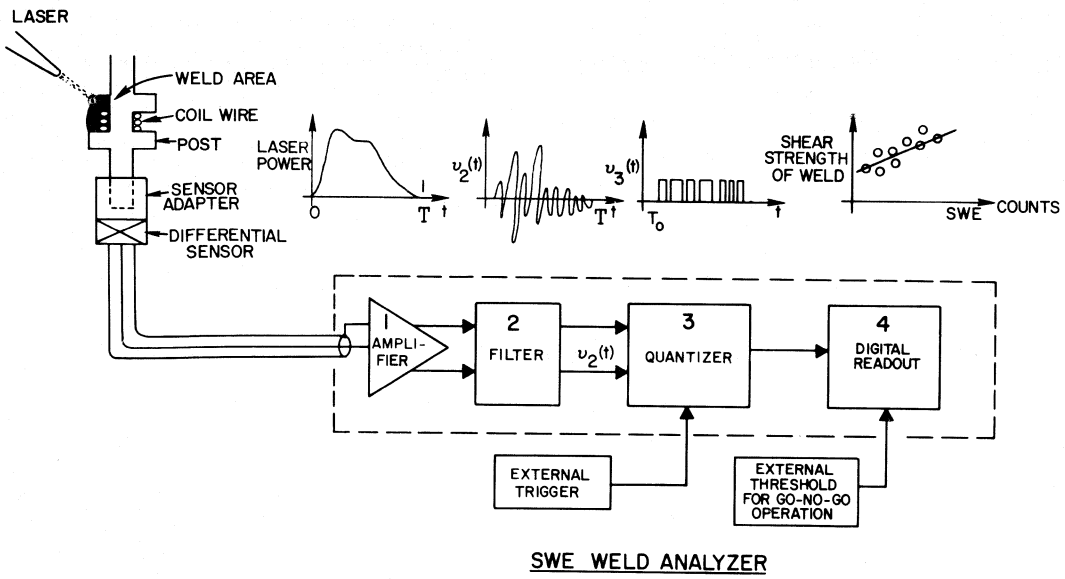


Fig. 9. The electronic system for evaluation laser welds in real time.

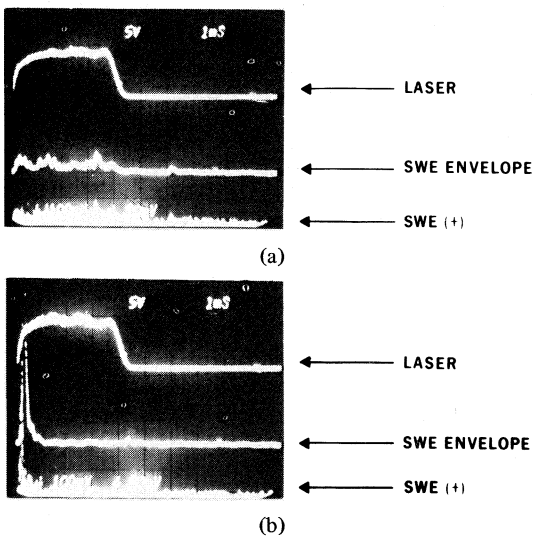


Fig. 10. The criterion of recognizing SWE generated by (a) a terminal only and by (b) burned insulation.

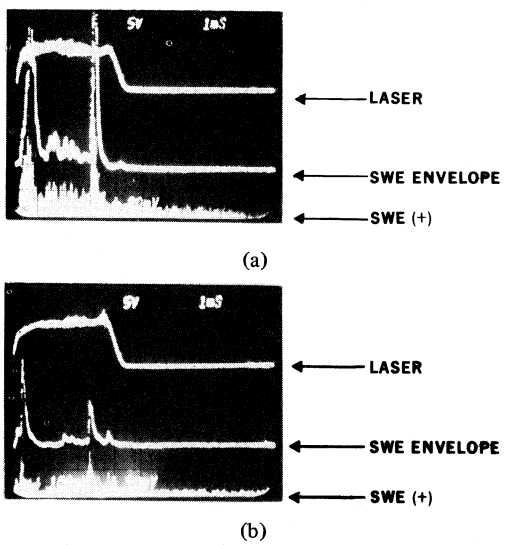


Fig. 11. The criterion of recognizing SWE generated by an (a) excellent and a (b) good weld.

plied by the number of events. Note that these events are only counted during the proper external triggering that is set by the laser-intensity window. The authors have also investigated time-division signal processing and its relation to the various physical parameters associated with welding. This investigation will be reported elsewhere.

Whenever a correlation is necessary the previously given count is compared to a weld-destructive test and, as indicated in Fig. 9, the results favor an almost linear relation [25]. Thus the relative quality of a weld can be obtained by reading the digital readout of the SWE evaluation system. The previously given relation can also be shown pictorially. But, before that, let us first characterize the envelope of the signals detected during welding. As shown in Fig. 10, the laser striking a terminal will generate the signal of Fig. 10(a), and when burning the wire insulation will generate that of Fig. 10(b).

Finally, the second event generated in Fig. 11(a) and (b) is attributed to the fusion of two materials which is indicative of the weld quality. When the welds made were subjected to visual inspection, it was found that they were in full agreement with the pictures in the figure. Obviously, a go-no-go signal can be generated using a comparator that compares the magnitude of the weld envelope to a variable threshold externally adjusted and indicative to an acceptable weld. The flexibility of choosing a good weld based on a variable externally set threshold is self-evident.

VI. Conclusions

Welding of insulated copper wires to terminal posts with a high-repetition-rate pulsed YAG laser has been demonstrated. The advantages of a shoulder terminal made out of higher melting point than wire has been discussed. It is shown that

the welds so produced have good mechanical and electrical integrity. The technique can also be used for the welding of thin plates. The evaluation of these welds was done nondestructively in real time for the first time, using SWE techniques.

This evaluation method has been demonstrated to be a potentially effective tool for real-time analysis of laser-weld quality. Prediction of the failure mechanisms such as insulation burning and striking high or low on the terminal has been done successfully. Preliminary data indicate that an almost linear relation exists between the number of threshold crossings of an SWE signal and the pull strength of a laser weld. A go-no-go signal can be generated using a comparator that compares the magnitude of the laser-weld envelope signal to a variable threshold externally adjusted and indicative to an acceptable weld.

Acknowledgment

The authors wish to thank Dr. M. C. Jon, J. M. Palmquist, and H. Maddox for their fruitful discussions concerning laser welding and real-time evaluation. They also wish to thank D. A. Bear, V. Palazzo, and L. P. Griswold for setting up the electronics.

References

[1] C. J. Bahun and R. D. Engquist, in *Proc. National Electronic Conf.* (vol. 18, 1963), p. 607.
[2] D. A. Buddenhagen, presented at the Automotive Engineering Congr., 1964, SAE Paper 819A.
[3] A. R. Fluger and P. M. Mass, "Laser beam welding electronic-component leads," *Welding J.*, vol. 44(6), pp. 264–269, 1965.
[4] F. P. Gagliano and D. H. Lockhart, "Pulsed laser welding of transistor and other electronic component parts," in *IEEE Dig.* (1969), pp. 150–151, 69C-14-IEEE.
[5] M. I. Cohen, F. J. Mainwaving, and T. G. Melone, "Laser interconnection of wires," *Welding J.*, vol. 48, pp. 191–197, 1969.
[6] F. P. Gagliano and V. J. Zaleckas, "Laser processing," in *Lasers in Industry*, S. S. Charschan, Ed. New York: Van Nostrand-Reinhold, 1972, ch. 4.
[7] M. I. Cohen and J. P. Epperson, "Application of lasers to microelectronic fabrication," in *Advances in Electronics and Electron Physics*, A. B. El-Kareh, Ed. New York: Academic, 1968.
[8] M. Yessik and D. J. Schmatz, "Laser processing in the automotive industry," in *Dig. Tech. Papers, 1975 IEEE/OSA Conf. Laser Engineering and Applications.*
[9] W. P. Mason, H. J. McSkimin, and W. Shockley, "Ultrasonic observations of twinning in tin," *Phys. Rev.*, vol. 73, pp. 1213–1214, May 1948.
[10] J. Kaiser, "Information and conclusions from the measurements of noises in tensile stressing of metallic materials," *Arch. Eisenhuettenw.*, vol. 24, pp. 43–45, 1953.
[11] J. Drawley and J. Edgar, "Investigation of hydrotest failure of Thiokol Chemical Corporation, 260 inch SL-1 motor case," NASA Lewis Research Center, Cleveland, OH, NTIS NASA Rep. TM-X01194, 1966.
[12] A. Green, C. Lockman, and R. Steel, "Acoustic verification of structural integrity of Polaris chambers," *Mod. Plast.*, July 1964.
[13] A. Green, H. Dunegan, and A. Tetelman, "Nondestructive inspection of aircraft structures and materials via acoustic emission," Air Transport Ass., San Antonio, TX, 1970.
[14] A. Green, "Stress wave detection–Saturn A-1A," Aerojet General Corp., Sacramento, CA, NTIS Rep. X67-18378, 1966.
[15] N. O. Cross, L. L. Loushin, and J. L. Thompson, "Acoustic emission testing of pressure vessels for petroleum refineries and chemical plants," *Amer. Soc. Test. Mater., Spec. Tech. Publ. 505*, pp. 270–296, May 1972.
[16] C. Hartbower, C. Morais, and W. Reuter, "Development of NDI technique to determine flaw critically," AFML Rep. TR 71-71-218, 1971.
[17] C. Hartbower, W. Reuter, G. Morais, and P. Crimmins, "Use of acoustic emission for the detection of weld and stress corrosion cracking," *Amer. Soc. Test. Mater., Spec. Tech. Publ. 505*, pp. 187–221, May 1972.
[18] S. J. Vahaviolos and H. E. Meadows, "A model of the transfer function of a capacitance discharge welding using stress wave emission (SWE) techniques," in *Proc. 18th Midwest Symp. Circuits and Systems* (Aug. 1975).
[19] S. J. Vahaviolos, "Real time detection of microcracks in brittle materials using stress wave emission (SWE)," *IEEE Trans. Parts, Hybrids, Packag.*, vol. PHP-10, pp. 152–159, Sept. 1974.
[20] M. Hansen, *Constitution of Binary Alloys*. New York: McGraw-Hill, 1958, pp. 602–603.
[21] M. I. Cohen, "Melting of half-space subjected to a constant heat input," *J. Franklin Inst.*, vol. 283, pp. 271–285, 1967.
[22] T. P. Lin, *IBM J. Res. Develop.*, vol. 11, p. 527, 1967.
[23] W. P. Mason and H. J. McSkimin, "Attenuation and scattering of high frequency sound waves in metals and glasses," *J. Acoust. Soc. Amer.*, vol. 19, pp. 464–473, 1947.
[24] H. S. Carslaw and J. C. Jaeger, *Conduction of Heat in Solids*. New York: Oxford, 1959.
[25] S. J. Vahaviolos, U. C. Paek, and G. E. Kleinedler, "Network approach to capacitance discharge welding using stress wave emission techniques (SWE)," *IEEE Trans. Ind. Electron. Contr. Instrum.*, to be published.

Change of Reflectivity of Metallic Surfaces During Irradiation by CO_2-TEA Laser Pulses

JOHN F. READY

Abstract—**Measurements of the decrease in reflectivity of metallic surfaces as a function of time during irradiation by pulses from a CO_2-TEA laser are described. The TEA laser delivered power densities up to 3×10^8 W/cm^2 in a 100-ns-duration pulse. The reflectivity was monitored as a function of time by a probing beam from a low-power continuous CO_2 laser operating at 9.6 μm, and focused onto the same area struck by the TEA laser pulse. This paper presents data on the decrease in specular reflectivity as a function of time under various conditions of laser power density, laser pulse duration, ambient air pressure, and cumulative number of pulses on the same area.**

I. Introduction

THE reflectivity of all metallic surfaces is high at the CO_2 laser wavelength of 10.6 μm. This fact has significance for laser applications in material processing, such as welding and drilling. The high reflectivity of certain metals may dictate the choice of laser to be used in a particular application. It has long been recognized that the reflectivity of a metallic surface, although initially high, can decrease rapidly during the irradiation by a high-power laser beam. Measurements at 1.06 μm [1], [2] indicated that the reflectivity could decrease considerably for laser power densities around 10^8 W/cm^2. Energy balance measurements [3] indicated that a large fraction of the incoming laser energy could be absorbed in the target. More recent measurements at 1.06 μm [4] indicate that the reflectivity during irradiation drops to values lower than can be attributed to the effects of increased surface temperature. A model of the physical processes involved has been developed [5], involving a phase change from a liquid metal to a liquid dielectric.

Although this phenomenon has special importance for the application of CO_2 lasers, there is a scarcity of quantitative data at the wavelength of 10.6 μm. Some time-integrated data have been obtained with a TEA laser [6]. These data indicate that for laser power densities in excess of 10^5 W/cm^2, the reflectivity does decrease.

In this paper we describe time-resolved measurements of the specular reflectivity of a metal surface while it is being disrupted by a CO_2 laser beam. We believe that these are the first such time-resolved measurements. In addition, we present data on the influence of the ambient air pressure, the laser power density, the laser pulse duration, and the accumulated number of pulses on the same spot. Also, we present non-time-resolved measurements of the absorptivity and the integrated hemispherical reflectivity for areas irradiated by the TEA laser.

Such measurements as these are important for understanding how much of the incoming laser radiation actually is reflected by the target surface, and for understanding the physical processes involved in the laser-induced disruption of the surface.

Manuscript received May 30, 1975. This work was supported by the Air Force Office of Scientific Research under Contract F44620-73-C-0022.

The author is with the Honeywell Corporate Research Center, Honeywell, Inc., Bloomington, MN 55420.

II. Experimental Arrangement

The experimental arrangement is shown in Fig. 1. The TEA laser is a Lumonics model 801 TEA laser, which operates at a wavelength of 10.6 μm. The wavelength was measured with a grating monochromator in order to insure that it remained stable at 10.6 μm and did not vary from pulse to pulse. The TEA laser operated reliably in a single narrow wavelength interval near 10.6 μm. The TEA laser beam was focused onto the target surface by a cadmium telluride lens.

The TEA laser emits pulses with peak power up to 10 MW. The pulse shape can be varied by varying the gas mixture. When the gas mixture is deficient in nitrogen, the output consists of a single narrow spike with duration (full width at half maximum) around 100 ns. The shape of this pulse is shown in Fig. 2. When nitrogen is added to the gas mixture, the laser pulse develops a lower power tail with duration around 3 μs.

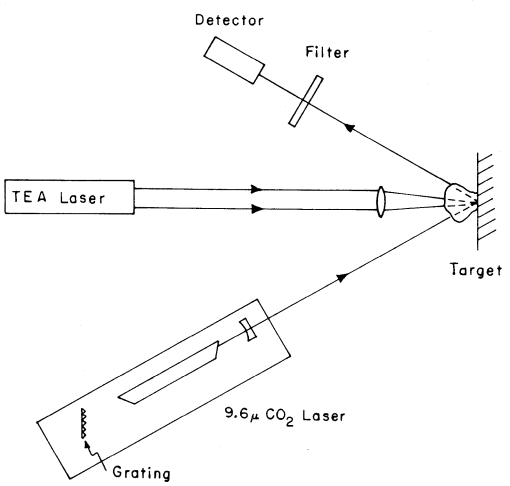


Fig. 1. Diagram of experimental arrangement.

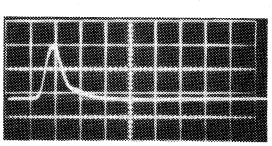


Fig. 2. TEA laser pulse shape with nitrogen off. Sweep speed: 100 ns/div.

Although the power in the tail is much lower, the tail does contain approximately twice as much energy as the initial peak. The initial peak is still present and is unchanged in duration or amplitude by the addition of nitrogen.

The TEA laser pulse can be focused to a spot with dimension around 1 mm. The peak power density on the target surface can be as high as 10^9 W/cm^2. In order to achieve accurate alignment of the TEA laser beam with the probing beam, it was necessary to defocus the TEA laser beam slightly. The maximum power density actually used was approximately 3×10^8 W/cm^2. The power density in the focal region was monitored as a function of position by driving a razor edge mounted on a micrometer across the focal region and measuring the transmitted power. The spatial distribution of laser power in the focal area was found to be approximately uniform.

The probe laser was a Coherent Radiation Laboratories model 41 continuous CO_2 laser operating with an internal grating. The wavelength was tuned to 9.6 μm. The beam from this laser is focused onto the same area as that struck by the TEA laser pulse. The probe laser beam is reflected from the target surface. Variations in the probe laser beam reaching the detector define the temporal history of the surface reflectivity. The value of reflectivity at 9.6 μm is similar to that at 10.6 μm. A blocking filter is inserted in the probe-laser-beam path to separate the 9.6-μm radiation from 10.6-μm radiation that may be scattered from the target or from the blowoff material. Any such scattered radiation would interfere with the measurement of the reflected probe beam. A germanium filter with a multilayer dielectric coating was used. This filter had a reflectivity greater than 80 percent at 9.6 μm and less than 1 percent at 10.6 μm. With the filter in place, no signal was observed by the detector when the TEA laser was fired with the probe laser beam turned off.

Several different detectors were employed. These included photovoltaic mercury cadmium telluride, with rise time of 150 ns, and lithium tantalate pyroelectric detectors with rise times less than 100 ns.

In addition, a vacuum chamber was constructed to carry out measurements as a function of ambient air pressure. The chamber has Irtran II ports for introduction of the TEA laser beam and for introduction and exit of the probe laser beam. The target is mounted on a pedestal which can be moved through a vacuum bellows assembly. It is possible to present a fresh target area on each TEA laser pulse. Measurements have been carried out which involve variations of many of the possible parameters. The parameters include the following.

1) Target material. We used both steel and aluminum targets so as to have initially two different values of reflectivity near 10 μm. The target surfaces were polished to a surface finish of approximately 0.3 μm. We have not carried out any experiments on the effect of surface finish. Work at other laboratories [7] has indicated that the threshold for laser-supported detonation waves is dependent on the surface perfection. We have not investigated this phenomenon.

2) Ambient pressure. The ambient pressure was varied over the range from 0.01 to 760 torr.

3) Wavelength of the probe beam. We carried out measurements using the probing wavelength of 0.6328 μm (a He–Ne laser) in addition to the measurements at 9.6 μm. The measurements at 0.6328 μm were done initially to develop alignment procedures with a visible laser. During the course of this work we obtained data of interest. In particular, the results at the probing wavelength of 0.6328 μm can be compared to those at 9.6 μm for determining the mechanisms of damage to the surface.

4) The TEA laser pulse shape. This is varied by turning nitrogen on or off in the TEA laser, as described previously. The variations of surface reflectivity are sensitive to the presence of the lower power tail in the laser pulse.

5) TEA laser power density. The peak power in the TEA laser pulse has been varied up to 3×10^8 W/cm^2. This maximum value is dictated by the necessity of assuring that the probing laser beam is accurately focused entirely within the area struck by the TEA laser beam.

6) Accumulative effects when a number of pulses strike the same area in succession.

In addition, a number of other measurements have been performed in order to interpret the data obtained. These measurements include measurement of the transmission of the laser-produced blowoff material, which absorbs part of the incoming 9.6-μm probe beam radiation. Also, non-time resolved measurements of the absorptivity of the irradiated area, the integrated hemispherical reflectivity of the area, and the diffuse reflectivity into a small cone of solid angles surrounding the specular direction have been performed. Scanning-electron-microscope photographs of the irradiated areas were obtained.

III. Experimental Results

A typical data shot is shown in Fig. 3. The trace shows the output of a lithium tantalate pyroelectric detector viewing the reflected probe beam light. This signal decreases rapidly over a period of several hundred nanoseconds, and then recovers slightly. It is necessary to correct the raw data for the effect of the absorption of the probe laser light in the blowoff material. At low-ambient air pressure the absorption is relatively small, but it can be large at values near 760 torr. Measurements of the transmission of the blowoff material as a function of time, laser power density, and ambient air pressure were used to correct the raw data to give the effect of surface changes alone.

Fig. 4 shows results for the specular reflectivity of a stainless-steel target surface at an ambient pressure of 50 torr for irradiation by a laser power density of 2.4×10^8 W/cm^2. These data are the 9.6-μm specular reflectivity normalized to its initial value as unity. When the effect of absorption in the blowoff material is removed, we see that there is no recovery of the reflectivity. This is confirmed by measurements on the static value of the reflectivity taken after the TEA laser pulse is over. The static reflectivity is indicated by the points shown at infinity in Fig. 4. This shows that the decrease in reflectivity is permanent. This result is different from data at 1.06 μm at

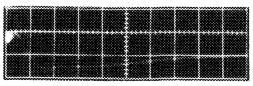


Fig. 3. Output of pyroelectric detector viewing reflection of 9.6-μm probe beam from steel target. Sweep begins with start of TEA laser pulse. Sweep speed: 500 ns/div.

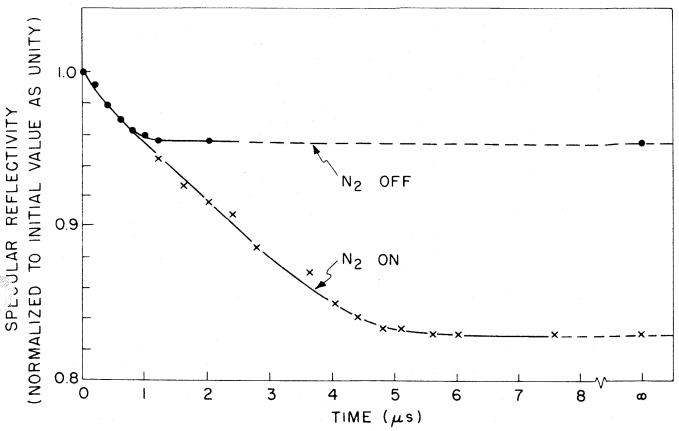


Fig. 4. Specular reflectivity (normalized to initial value as unity) of stainless-steel target at 9.6 μm as a function of time after start of TEA laser pulse, for peak TEA laser power density of 2.4×10^8 W/cm^2 and ambient pressure 50 torr.

power densities around 10^8 W/cm^2 [4], which show some recovery of the lowered reflectivity. The effect of changing laser pulse shape is apparent. When the longer lower power tail is present, the reflectivity continues to decrease for a longer period of time than when only the initial short spike is present. In addition, it decreases to a lower final value. With nitrogen off, the decrease in reflectivity continues for about 1 μs, much longer than the laser pulse duration. We shall consider this point later.

Fig. 5 shows data on the change in reflectivity due to one laser shot on a steel target as a function of pressure. For these data, nitrogen was on in the laser and peak power density was 2.7×10^8 W/cm^2. This is the permanent change in reflectivity. The effect is much enhanced at reduced values of ambient air pressure. At 760 torr there is a well-developed laser-supported detonation wave above the target surface. This laser-supported detonation wave is strongly absorbing and cuts off most of the TEA laser radiation from the surface. As the ambient air pressure is reduced, the laser-supported detonation wave is diminished [8]. More of the TEA laser radiation reaches the target surface and the effect on the surface increases. Below 1 torr the laser-supported detonation wave has disappeared, and there is little further change when the pressure is reduced further.

Fig. 6 shows the effect of peak laser power density with nitrogen on in the TEA laser for a steel target at an ambient pressure of 5 torr. For laser power densities below 1×10^8 W/cm^2 there is relatively little effect. Between 1 and 2×10^8 W/cm^2 the effect increases considerably. Above 2×10^8 W/cm^2 it appears to saturate.

Fig. 7 shows comparable data for an aluminum target. This

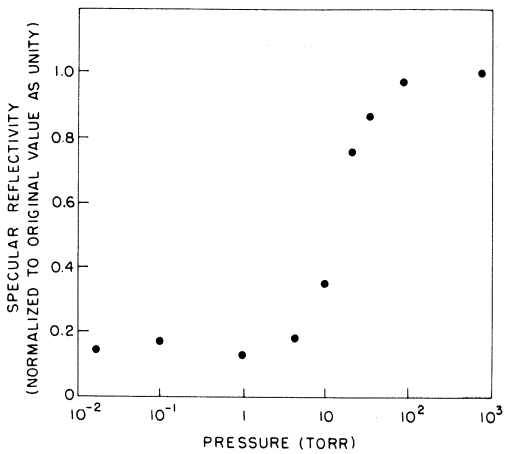


Fig. 5. Specular reflectivity at 9.6 μm for stainless-steel target after irradiation by one laser pulse at 2.7×10^8 W/cm^2 (nitrogen on in TEA laser) as a function of ambient air pressure.

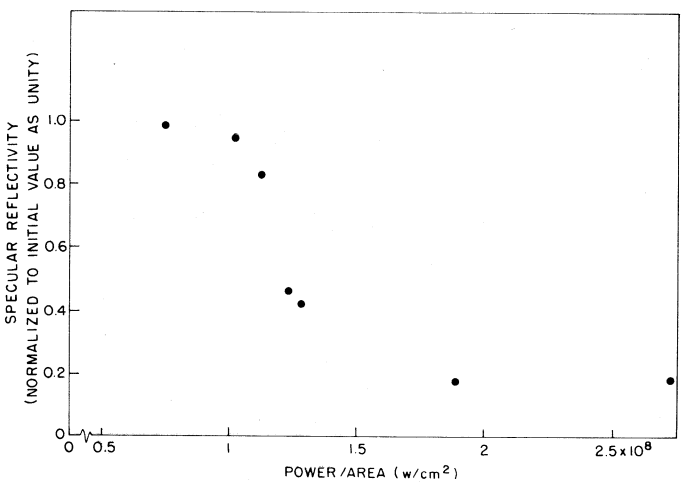


Fig. 6. Specular reflectivity at 9.6 μm for stainless-steel target after one laser shot at 5-torr ambient air pressure, as a function of peak incident power density (nitrogen on in TEA laser).

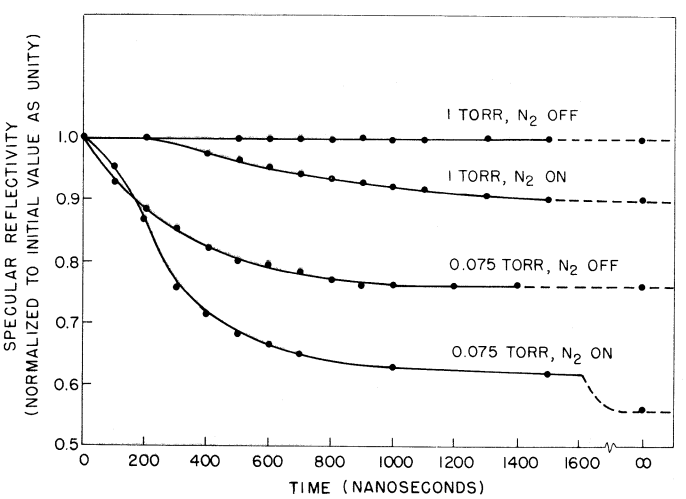


Fig. 7. Specular reflectivity (normalized to initial value as unity) for aluminum target at 9.6 μm as a function of time after start of TEA laser pulse, for peak TEA laser power density of 1.5×10^8 W/cm^2.

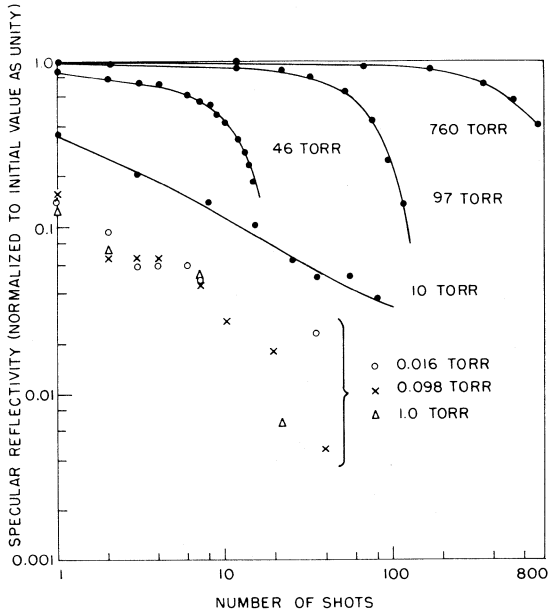


Fig. 8. Specular reflectivity of stainless-steel target at 10.6 μm as a function of the accumulated number of laser shots on the same area. The data are normalized to the initial value before the first shot as unity. The data are relevant to irradiation at a peak power density of 3×10^8 W/cm^2 with nitrogen on in the TEA laser.

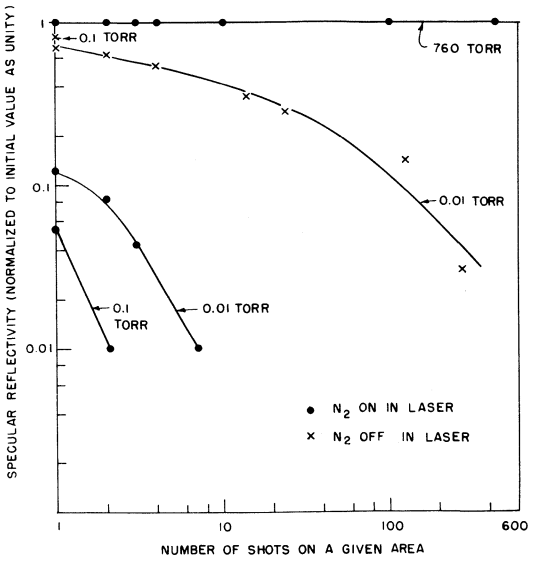


Fig. 9. Specular reflectivity of aluminum target at 10.6 μm as a function of the accumulated number of laser shots on the same area. The data are normalized to the initial value before the first shot as unity. The data are relevant to irradiation at a peak power density of 3×10^8 W/cm^2.

shows the specular reflectivity as a function of time for an aluminum target irradiated by 1.5×10^8 W/cm^2 for two different values of ambient pressure. When the nitrogen is on in the TEA laser, the decrease in reflectivity drops to a lower final value. The points shown at infinity represent the static values of reflectivity measured after the pulse was over. As with the data in Fig. 4, these results have been corrected for absorption in the plume and do not show a recovery of the reflectivity after the laser pulse is over.

When the data in Fig. 7 are compared with Figs. 4 and 6, one sees that the effect on aluminum is less than that on steel. This is not surprising because the initial 10.6-μm reflectivity of the aluminum target is higher. One would expect increased requirements on laser power density in order to produce the same observed effect. For values of ambient air pressure above 1 torr it was not possible to produce an observable change in the reflectivity of the aluminum target surface within a single shot.

Data on cumulative effects are presented in Fig. 8 for a steel target and a laser power density of 3×10^8 W/cm^2, with nitrogen on in the TEA laser. The data presented are the permanent decrease in reflectivity as a function of the cumulative number of laser pulses delivered to the same area on the target. These data were obtained under static conditions with the probe laser wavelength at 10.6 μm. Data taken with nitrogen off in the laser indicate similar behavior, but it takes more pulses to produce the same effect. For ambient air pressure below 1 torr there is little variation with pressure. For higher values of pressure it takes more pulses to produce the same effect. When many pulses are incident on the same area, a large decrease in reflectivity is observed even when no effect was observed within a single shot.

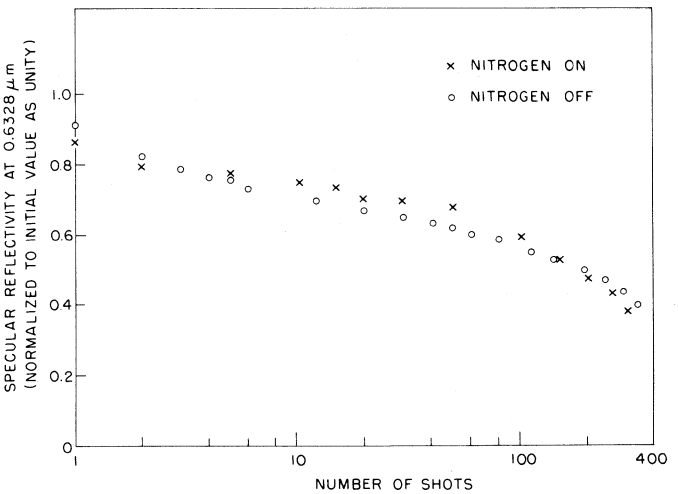


Fig. 10. Specular reflectivity of aluminum at 0.6328 μm as a function of accumulated number of laser shots on the same area. The data are normalized to the initial value before the first shot as unity. The data are relevant to irradiation at a peak power density of 3×10^8 W/cm^2.

Comparable data are shown for an aluminum target in Fig. 9, which combines data for nitrogen on and off in the laser. We see that the effect is greater when nitrogen is present. In addition, the effect decreases as ambient air pressure increases. At 760 torr we did not observe any change, even when a large number of pulses impacted the same area.

However, when a probe laser beam operating at 0.6328 μm was used, an effect was easily observable. Some data are shown in Fig. 10 for the effect on an aluminum target in ambient air at 760 torr as a function of the number of shots when a He-Ne laser beam was used as the probe. A considerable effect was noted, even at 760 torr. There appeared to be little dependence on the pressure of nitrogen in the TEA laser.

Even within a single shot, a 10-percent decrease in reflectivity was observed. Much greater effects were observed with steel targets or with aluminum targets at reduced ambient pressure.

IV. Discussion

Comparison of the 0.6328-μm data and 9.6-μm data suggests that the decrease of specular reflectivity is due to disruption of the surface by irregularities with a scale size between that of the two wavelengths. Such an effect would produce relatively little change at 9.6 μm, but could produce a large change at the He-Ne laser wavelength. This hypothesis is strengthened by scanning-electron-microscope photographs of the damaged area. An example is shown in Fig. 11. This is an area on the steel surface which has been heavily damaged and has been struck by a large number of laser pulses at 3×10^8 W/cm^2. The surface is roughened on a scale size of approximately 2-3 μm.

Additional measurements of the radiation diffusely scattered into a small cone of solid angles around the specular beam also support this hypothesis. Some data are shown in Fig. 12 which represent results for a steel target at ambient pressure 100 torr and laser power density around 3×10^8 W/cm^2. The fraction of the probe laser light scattered into the indicated cone of solid angles surrounding the specular angle is plotted for several different values of the solid angle. After a single shot there is no difference in the fraction of the light scattered into the solid angle as the solid angle is varied. This suggests that the initial effect is small angle scattering. As the number of shots increases, the radiation is scattered into an increasingly large cone of solid angles. For a given solid angle, as a function of number of shots, the amount of scattered radiation increases to a maximum and then begins to decrease. The amount of radiation scattered into a 4.6×10^{-3}-sr cone can be as great as 25 percent of the initial probe laser light under some conditions. This suggests that most of the decrease in specular reflectivity is due to an increase in diffuse reflectivity. This interpretation is compatible with the appearance of the surface in Fig. 11, which should be a highly scattering surface. Apparently, the scattering begins in a small cone of solid angles. As damage progresses it spreads into an increasingly large cone of solid angles. With reference to Fig. 12, after several hundred shots, most of the radiation is being scattered into a cone of solid angles much larger than 4.6×10^{-3} sr. Only a small fraction of the diffusely scattered light is seen within this cone.

Additional measurements on the total hemispherical reflectivity have been obtained using an integrating sphere. In addition, we performed measurements of the absorptivity of the damaged areas by monitoring the temperature increase when a low-power beam struck these areas. The results of these measurements are summarized in Table I for a stainless-steel surface. The initial values indicate high specular reflectivity, with some relatively smaller values for hemispherical diffuse reflectivity and absorptivity. These numbers, measured independently, add to approximate unity. After one shot the specular reflectivity has decreased considerably. The hemispherical diffuse reflectivity has increased. We have no data for the absorptivity for this area. On a heavily damaged area, struck by a large number of pulses, the specular reflectivity has dropped to a very low value. The absorptivity at the same time has increased to approximately 15 percent. Thus, even though the specular reflectivity is much decreased, most of the incident light will still be reflected diffusely. However, there is approximately a sixfold increase in absorptivity on this heavily damaged area.



Fig. 11. Scanning-electron-microscope picture of area on steel target which has been struck by many laser pulses at 3×10^8 W/cm^2. The total width covered by the photograph is approximately 20 μm.

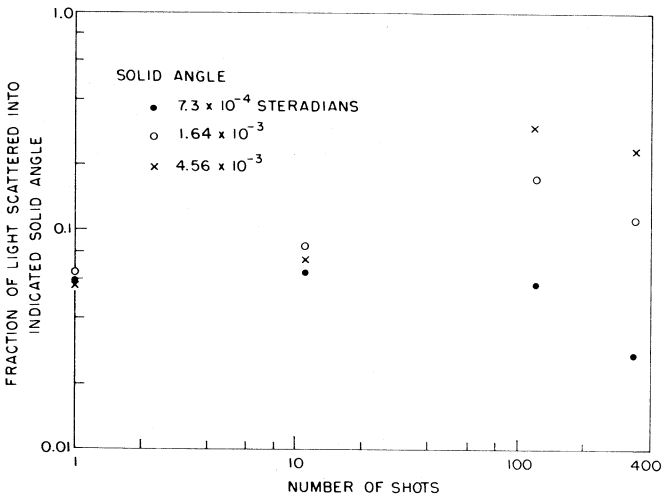


Fig. 12. Fraction of 10.6-μm probe beam light diffusely scattered into the indicated cone of solid angles surrounding the specular angle, as a function of the number of TEA laser shots delivering 3×10^8 W/cm^2 to a steel target at a pressure of 100 torr. The original value of this fraction, before the first laser shot, was less than 0.001. Nitrogen was on in the TEA laser.

TABLE I
Characteristics of Stainless-Steel Surface

	Initial values	Values after 1 shot (1 torr, 1.5×10^8 W/cm^2)	Values for heavily damaged areas
Specular reflectivity	0.91	0.74	<0.001
Hemispherical diffuse reflectivity	0.065	0.20	~0.85
Absorptivity	0.025	–	~0.15

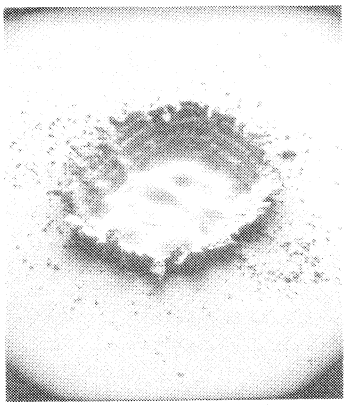


Fig. 13. Scanning-electron-microscope photograph of the impact area on a steel target struck by 40 TEA laser pulses at 3×10^8 W/cm^2. Flow patterns produced by successive pulses are visible. The total width covered by the photograph is 2.2 mm.

We can now interpret the temporal dependence of the decrease in specular reflectivity shown in Figs. 4 and 7. With nitrogen off in the laser, the reflectivity continues to decrease even after the end of the laser pulse. We hypothesize that the main effect in producing these results is that the surface begins to melt and flow. Some flow patterns are shown in Fig. 13, a scanning-electron-microscope picture of an area hit by 40 laser pulses. The flow produced by successive individual pulses is clearly demonstrated. The main effect in producing the observed changes is a roughening of the surface due to melting and flow of the target surface, leading to irregularities which have a scale size of the order of 2 μm. This decreases the specular reflectivity, with maximum effect at shorter wavelengths. It also tends to make the diffuse reflectivity increase. Since part of the effect is due to physical flow and motion of material, the variation can last for a period of time longer than the laser pulse. This accounts for the continued decrease of the curves in Figs. 4 and 7 for several hundred nanoseconds after the end of the laser pulse. In interpretation of these results, we do not need to invoke any mechanisms involving a phase change such as were suggested in [5].

V. Conclusions

These experiments have obtained time-resolved data on the change of specular reflectivity of metallic surfaces struck by CO_2-TEA laser radiation with peak power density up to 3×10^8 W/cm^2. A single shot can produce large changes, reducing the specular reflectivity to 15 percent of its original value under some conditions. The effect diminishes with increasing target reflectivity and with increasing ambient air pressure, as the laser-supported detonation wave increases. The results indicate that the primary effect is a disruption of the target surface with melting, flow, and redistribution of the target material so as to produce a diffusely reflecting surface. Most of the decrease in specular reflectivity goes into diffuse reflectivity; however, there can be considerable increase in the absorptivity of the surface. Further work is in progress to obtain the power density actually absorbed by the surface as a function of time.

Acknowledgment

The author wishes to thank D. Brinda, who set up the experimental apparatus and carried out many of the measurements, T. Koehler, Honeywell Radiation Center, who supplied the photovoltaic mercury cadmium telluride detector, and R. Heinisch, Honeywell Systems and Research Center, who performed the measurements on hemispherical reflectivity. He also wishes to thank M. Liu and D. Heaps for providing information on the fabrication of lithium tantalate pyroelectric detectors, and D. George for performing the scanning-electron-microscope photography.

References

[1] N. G. Basov, V. A. Boiko, O. N. Krokhin, O. G. Semenov, and G. V. Sklizkov, "Reduction of reflection coefficient for intense laser radiation on solid surfaces" (in Russian), *Zh. Tekh. Fiz.*, vol. 38, pp. 1973–1975, Nov. 1968 (transl.: *Sov. Phys.–Tech. Phys.*, vol. 13, pp. 1581–1582, May 1969).

[2] A. M. Bonch-Bruevich, Ya. A. Imas, G. S. Romanov, M. N. Libenson, and L. N. Mal'tsev, "Effect of a laser pulse on the reflecting power of a metal" (in Russian), *Zh. Tekh. Fiz.*, vol. 38, pp. 851–855, May 1968 (transl.: *Sov. Phys.–Tech. Phys.*, vol. 13, pp. 640–643, Nov. 1968).

[3] M. K. Chun and K. Rose, "Interaction of high-intensity laser beams with metals," *J. Appl. Phys.*, vol. 41, pp. 614–620, Feb. 1970.

[4] T. E. Zavecz, M. A. Saifi, and M. Notis, "Metal reflectivity under high-intensity optical radiation," *Appl. Phys. Lett.*, vol. 26, pp. 165–168, Feb. 15, 1975.

[5] A. M. Prokhorov, V. A. Batanov, F. V. Bunkin, and V. B. Fedorov, "Metal evaporation under powerful optical radiation," *IEEE J. Quantum Electron.*, vol. QE-9, pp. 503–510, May 1973.

[6] B. A. Sanders and V. G. Gregson, Jr., "Optical reflectivity of some metals using a CO_2 TEA laser," in *Proc. Tech. Program, Electro-Optical Systems Design Conf.* (New York, NY), Sept. 18–20, 1973, pp. 24–29.

[7] C. T. Walters, "Surface scattering at LSD-wave initiation sites on nonmetallic materials," *Appl. Phys. Lett.*, vol. 25, pp. 696–698, Dec. 15, 1974.

[8] J. F. Ready, "Impulse produced by the interaction of CO_2 TEA laser pulses," *Appl. Phys. Lett.*, vol. 25, pp. 558–560, Nov. 15, 1974.

Generation of Frequency-Controlled Nanosecond and Picosecond Optical Pulses by High-Gain Parametric Amplification

GAIL A. MASSEY, MEMBER, IEEE, JOEL C. JOHNSON, MEMBER, IEEE, AND RICHARD A. ELLIOTT, STUDENT MEMBER, IEEE

Abstract—An ADP parametric amplifier pumped by the 266-nm fourth harmonic of Q-switched or mode-locked Nd lasers has been used to produce nanosecond or picosecond pulses at a number of wavelengths across the visible spectrum. The input signal to the parametric amplifier was obtained either from pulsed parametric fluorescence passed through a Fabry-Perot (FP) filter, or from CW noble gas lasers. Peak powers to 60 kW and pulse lengths of the order of 10 ps have been generated by amplifying the beam from a CW He-Ne laser.

I. Introduction

THIS paper describes experiments in which a high-gain visible optical parametric amplifier is used to generate nanosecond and picosecond visible optical pulses which are accurately stabilized to an arbitrary wavelength standard and synchronized to an external time reference. It has been demonstrated previously [1], [2] that parametric gains as high as 10^{13} can be achieved in crystals of ammonium dihydrogen phosphate (ADP) because 90° phase matching for generation of visible wavelengths is possible and the crystal is resistant to damage by UV pump beam intensities as high as 10^9 W/cm^2, depending on the pulse length.

When an ADP crystal is pumped by intense UV pulses of nanosecond or picosecond duration, it can be used as a parametric oscillator or parametric fluorescence generator [1], [2] but the output of such a device ordinarily is spread over a few nanometers in wavelength and is not diffraction limited in angle. Alternatively, the very high gain makes it practical to use this parametric interaction as an efficient pulsed amplifier of low-level injected signals which can have nearly ideal spectral and spatial characteristics. The injected signal can be provided by a continuous-wave (CW) visible laser with a few milliwatts of average output power, a very narrow and stable frequency spectrum, and a Gaussian spatial mode profile. If the 266-nm fourth harmonic of a neodymium laser is used as the pump, a variety of pulse durations and repetition rates are available. For the generation of subnanosecond pulses this technique is particularly useful because the crystal serves as a traveling-wave amplifier with gain only when the pump pulse is present; there is no resonator or inverted population with its associated buildup or relaxation rate to alter the synchronism between the pump and the generated signal. Other harmonics of the same pumping laser can, of course, be generated in synchronism with the wavelength-tunable pulses produced in the parametric amplifier. This can be used to advantage in a variety of pulse probe and optical mixing applications. An additional characteristic of the high-gain parametric interaction is that the output signal pulse can be substantially shorter than the incident pumping pulse, when the amplified signal is below saturation and group velocity dispersion effects are negligible.

This paper considers the following three types of parametric amplifier experiments:

1) nanosecond pulse amplification of filtered parametric fluorescence;
2) nanosecond pulse amplification of wavelength-tunable CW laser emission;
3) picosecond amplification of an injected CW laser signal.

Manuscript received May 22, 1975. This work was supported by the National Science Foundation under Grant GK 40812.

The authors are with the Department of Applied Physics and Electronic Science, Oregon Graduate Center, Beaverton, OR 97005.

II. Gain and Noise Considerations

The power gain of an optical parametric amplifier of length L in the plane-wave approximation can be written as [3]

$$\frac{P_s(L)}{P_s(0)} = \cosh^2 \Gamma L \tag{1}$$

where

$$\Gamma^2 = 2(\mu_0/\epsilon_0)^{3/2}\, d^2\, [\omega_s \omega_i/(n_s n_i n_p)]\, (P_p/A) \tag{2}$$

and where μ_0 and ϵ_0 are the free-space permeability and permittivity, d is the effective nonlinear coefficient [4], ω_s and ω_i are the signal and idler radian frequencies, P_p is the pump power, and A is the beam area. The refractive indices at signal, idler, and pump frequencies are n_s, n_i, and n_p, respectively. Perfect phase matching is assumed in (1); that is

$$n_i \omega_i + n_s \omega_s = n_p \omega_p \tag{3}$$

where

$$\omega_i + \omega_s = \omega_p. \tag{4}$$

For high gain, $\Gamma L \gg 1$ and (1) reduces to

$$\frac{P_s(L)}{P_s(0)} \approx \frac{1}{4} \exp(2\Gamma L). \tag{5}$$

The experiments considered here were all carried out with ADP and a pump wavelength of 266 nm, a combination which permits 90° phase matching for generation of all visible wavelengths by adjusting the crystal temperature from 50 to 110°C. The pump, signal, and idler beams are collinear, propagating at 90° to the optic (Z) axis and 45° between the X and Y crystallographic axes. The pump polarization is extraordinary, and the signal and idler polarizations are ordinary. The appropriate nonlinear coefficient is therefore $d_{36} = 1.36 \times 10^{-9}$

ESU [5] = 5.04×10^{-24} C/V^2. For generation of visible light in this configuration, the refractive indices in (3) are all near 1.53, and (5) therefore indicates that a power gain $P_s(L)/P_s(0) = 10^6$ in a 5-cm crystal would require pump-power densities between 241 MW/cm^2, if $\omega_i = \omega_s$, and 264 MW/cm^2, at the extremes of the tuning range. We have found that these power densities are not far below the damage threshold of ADP for 10-ns pulses but are well below the damage threshold for pulses of 50-ps length. Therefore, parametric gains up to 60 dB can be reliably achieved using either Q-switched or mode-locked pump pulses and readily available crystal lengths in a single-pass amplifier geometry.

Kleinman [6] has shown that the EM zero-point power fluctuations produce an effective noise power per mode at the input surface of the crystal equal to $\frac{1}{2} h\nu_s \Delta\nu_s$ at the signal frequency ν_s and $\frac{1}{2} h\nu_i \Delta\nu_i$ at the idler frequency ν_i, where the $\Delta\nu$'s are the bandwidths of the parametric gains at ν_s and ν_i as limited by phase-matching tolerances. At pump power densities high enough to produce gains of the order of 60 dB, the observed fluorescence output from the crystal can have linewidths up to about 5 nm and linear divergences about 20 times the diffraction limit, corresponding to roughly 400 spatial modes. The broad spectrum is due partly to generation of noncollinear signal and idler beams at high gains that must satisfy different wave vector conservation conditions from those of the collinear beams, and partly to a dilation of the amplifier half-power bandwidth for phase matching at high gains [3], [7]. This bandwidth expansion corresponds to a factor of 1.75 greater tolerance in the collinear wave vector matching condition at a gain of 10^6 than for small gains. The equivalent noise input to the parametric amplifier under these conditions typically is about 1 μW/mode or a total of about 0.5 mW for all modes with significant gain. These values indicate the feasibility of exceeding the input noise of the ADP amplifier with an injected CW laser signal of very modest power. Since CW signals of the order of 10 mW or more are readily available at a variety of visible wavelengths from noble gas or flowing dye lasers, the ADP amplifier should be able to generate pulses with peak powers of the order of 10 kW or more with nanosecond or picosecond durations. Our experiments show that these theoretical predictions can be realized.

III. Pump Source

The UV pump beam in our experiments was the fourth harmonic of the 1064-nm output of a flash-pumped Nd:YAG laser. The effective length of the laser cavity was 75 cm, and a 2-mm intracavity aperture was used to produce oscillation in the TEM$_{00}$ mode. Pockels cell Q-switching was used to generate pulses of 15-ns duration, and for the mode-locked experiments a saturable absorber cell was substituted in place of the Q-switch. The mode-locking cell was connected to a small pump which circulated a solution of nickel complex dye [8] (Eastman Kodak Type 14015) in dimethyl sulfoxide. The cell itself, which terminated one end of the laser cavity, consisted of an antireflection coated window, a 1.5-mm thickness of flowing dye solution, and a totally reflecting dielectric mirror in contact with the solution. An unbleached dye transmission of 75 percent or less (double pass) was necessary for stable generation of a single burst of mode-locked pulses, but we found that variation of the dye concentration over a range of 30 percent had little effect on the laser output. With a 50-percent transmissive mirror for output coupling in the Nd:YAG laser, we obtained approximately 1 mJ in an entire train of mode-locked pulses, and the energy of the largest picosecond pulse was about 0.25 mJ. The duration of the mode-locked pulses at 1064 nm was measured by means of a second-harmonic correlation technique [9] using a thin crystal of ADP, and it was found that the pulse length was 44 ± 5 ps. In many of the experiments a Nd:YAG laser amplifier was used between the oscillator and the first frequency doubler to increase the output power. The pulse repetition frequency was 5 pulses/s in mode-locked operation and 10 pulses/s in Q-switched operation.

Frequency doubling of the 1064-nm light to 532 nm was accomplished with a 20-mm crystal of cesium dideuterium arsenate maintained at 100°C in a thermostatic oven. The energy conversion efficiency of this first doubling step was about 20 percent with the unfocused IR beam incident on the crystal. The second harmonic was converted with similar efficiency to fourth harmonic in a 5-cm ADP crystal at 50°C. With the Nd:YAG laser operating in the Q-switched mode we obtained 266-nm pulses with energies about 2 mJ and lengths about 10 ns. With the laser mode locked, the UV pulse train usually contained three major pulses, with 13 μJ in a typical single pulse. Since we were not equipped to measure picosecond pulse lengths at this wavelength, we have estimated the length by assuming that the 1064-nm pulse is Gaussian and that the frequency doubling steps exhibit negligible saturation and band limiting effects. Under the preceding conditions these appear to be good approximations. The UV pulses would then be half as long as the IR pulses, or about 22 ps in duration. We therefore had peak powers at 266 nm of 200 kW in the Q-switched experiments and 600 kW in the mode-locked pulses. In each of the parametric amplifier experiments the UV pump beam was focused by fused silica lenses to a spot size calculated to produce a peak-power density corresponding to the desired gain according to (5).

IV. Fluorescence Amplification

In these experiments the parametric fluorescence from one 5-cm ADP crystal was passed through a narrow-band filter and injected into a second 5-cm ADP amplifier, as shown in Fig. 1.

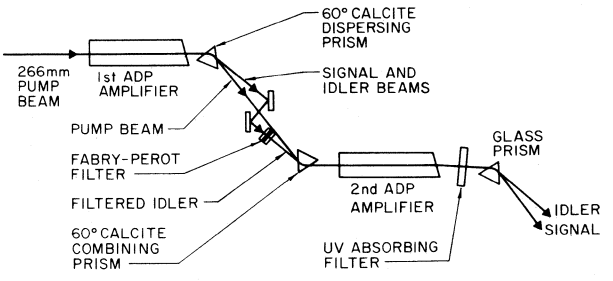


Fig. 1. Configuration for amplification of filtered parametric fluorescence.

The experiment is similar to one described by Kung [2] except that the presence of the narrow-band filter in our experiment requires separation of the pump, signal, and idler frequencies at the output of the first crystal. The pump beam waist was located between the ADP crystals, but since the confocal distance was approximately 50 cm and the separation of the crystals was 30 cm, a small spot size was obtained in both amplifiers. This choice of confocal distance and spacing also provided spatial filtering of the fluorescence, since the only fluorescence which reaches the second crystal and is further amplified is that with a divergence similar to that of the diffraction-limited pump beam. One end of each crystal was polished at an 85° angle to the direction of propagation to avoid optical feedback.

Both ADP crystals were mounted in thermostatically controlled ovens. For these experiments the temperatures of the crystals were set at 55°C, providing fluorescence at a signal wavelength of 500 nm and an idler at 568 nm. Precise coincidence of the phase-matching wavelengths was obtained by careful angular adjustment of the second crystal in the plane of its optic axis, using a grating monochromator to view the overlapping spectra. Energy measurements were carried out using a calibrated silicon photodiode mounted behind a diffuser.

Spectral filtering of the fluorescence was accomplished using a narrow-gap Fabry-Perot (FP) etalon between the crystals. The etalon was formed by two plane fused silica substrates coated for reflectivity between 95 and 97 percent over the band 475-630 nm. The reflecting surfaces of the two mirrors were separated from each other by three carefully selected segments of 0.05-mm-diameter tungsten wire, with slight pressure applied to the outer surfaces of the mirrors to hold them together. This choice of spacing and reflectivity gave us a free spectral range of about 3 nm and a finesse of 50. Adjustment of the transmission frequency of the filter was done by tilting the etalon slightly.

With the Q-switched UV beam incident on the first crystal, the fluorescence spectrum produced by that crystal at 568 nm was found to be up to 6 nm wide, with a total energy output of 1.3 μJ when the pump pulse energy was 1 mJ. Insertion of the filter lowered the total idler fluorescence to 3×10^{-8} J at the input to the second crystal. This corresponded to roughly 10^{-10} J of input over the area on the second crystal irradiated by the pump. With the entire system in the best possible alignment, the amplified fluorescence leaving the second crystal was measured to be 0.7-1.0 μJ for a typical pulse. The spectral width of the amplified output was approximately 0.1 nm as observed with a second FP etalon. The amplified energy appeared in the far-field pattern of the amplifier as a bright spot surrounded by less intense broad-band fluorescence from the second crystal. The energy in the output fluorescence with the filtered input beam blocked was approximately 0.3 μJ.

The pulse shape of the amplifier output was observed with a Tektronix Model 519 oscilloscope and HP Type 4203 silicon photodiode. Generally, there appeared to be one significant pulse, with a duration of about 1 ns; on some shots there were two pulses, and an occasional pulse had a duration as long as 2 ns. Any substructure within the pulse with time variations significantly faster than 1 ns was not observable with this equipment. The pulse energy variation from shot to shot was typically within a factor of 2 of the average level; this variation is easily understood because of the sensitivity of the gain to pump intensity fluctuations [see (5)], and because the relative phases of the pump laser modes vary from shot to shot in Q-switched operation.

From the preceding data we conclude that the peak amplified fluroescence output power was about 1 kW, far from saturating the 200-kW pump beam. Since the fluorescence output in the absence of injected input was about 300 W from the second amplifier, a gain near 10^6 was realized as expected, but the injected energy did not appear to be amplified by this factor, but instead by a lower gain of the order of 10^4. We attribute this discrepancy to the following factors.

1) The difficulty of obtaining simultaneous alignment, overlap, and optimum spectral tuning of the filter in this injected beam geometry.

2) The probable existence of subnanosecond structure in the pulses, so that the differential delay between arrival times of the pump and injected idler at the second crystal results in highest gain when the visible input is weak and lower gain at the peak of the input. We estimate this differential delay to be of the order of 0.2 ns in our experiment.

3) The possibility that higher peak powers were actually obtained, but on a time scale not resolved by our electronic detection and display equipment.

It is worth noting that the two frequency doubling steps required to generate the pump beam act to enhance the internal intensity variations within a Q-switched pulse so that the pump pulses tend to have some of the characteristics of mode-locked pulses.

V. Nanosecond Amplification of CW Laser Beams

The advantage of the fluorescence injection approach is that only one input light source, the pump beam, is required. However, even narrower spectral linewidths, with better frequency stability, can be obtained by injecting a CW laser signal into the parametric amplifier, as shown in Fig. 2. This configuration is much easier to align than that of Fig. 1, since there is no filter in the path and there is no requirement to minimize the delay of the injected beam. From the noise considerations presented earlier it is clear that a laser supplying at least 1 mW CW will be required to produce an output well above the fluorescence noise. The Q-switched 266-nm pump beam was

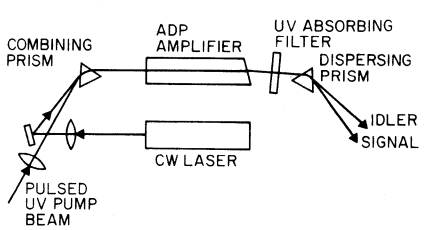


Fig. 2. Parametric amplification of a CW laser beam.

focused to an area about 10^{-3} cm^2 in the ADP crystal, providing a power density near 200 MW/cm^2 which should correspond to a gain of about a million in the 6-cm length of ADP used in this experiment.

Two CW lasers were used in these experiments: a mixed gas Ar-Kr ion laser which could be operated at any of eight transitions between 476.5 and 676.4 nm to provide inputs to the ADP amplifier greater than 10 mW, and a large He-Ne laser with which we could obtain inputs to the crystal in the 20-30-mW range at 632.8 nm. The beam from one of these lasers was focused to have a confocal parameter similar to that of the pump, and it was polarized as an ordinary ray in the ADP crystal, perpendicular to the pump polarization. The spectral linewidth of the transitions varied from about 1.5 GHz at 632.8 nm in Ne to about 6 GHz for the 488-nm transition in Ar. Observation of the linewidth of the Q-switched pump laser was carried out at the second harmonic with a FP interferometer. At 532 nm the spread was typically 2 GHz for a single pulse, with occasional jumps in the center frequency as large as 10 GHz. We assume that the 266-nm harmonic had about twice this bandwidth. The amplified pulses at the CW laser wavelength therefore were expected to have a spectral width comparable to the input radiation if pulse lengths greater than about a nanosecond were produced. Output pulses at the difference frequency between the CW laser and the pump should have a spectrum which is the convolution of the line shapes of the two input beams. If the mode structure of the CW laser or the pump laser were narrowed by means of intracavity filtering, the ultimate limit to the spectral purity of the parametric amplifier output would be set by the Fourier transform of the pulse envelope, of course.

The results of our Q-switched experiments are summarized in Table I. For each input wavelength the ADP crystal temperature was adjusted to make the parametric fluorescence overlap the injected wavelength, as observed with a grating monochromator. The pump beam was focused to produce an expected gain of about 10^6. The output pulse length was measured with the equipment described in Section IV in the preceding and found to be about 1 ns. Most of our measurements were made on the output pulses at the difference frequency between the pump and input frequencies, to avoid problems with the substantial CW beam power leaving the crystal at the input frequency. The spectral width of the difference-frequency pulses typically was about 5 GHz, and the pulse energies were in the 1-10-μJ range, corresponding to 1-10-kW output powers. The amplified beam divergence was similar to that of the input beam. From pulse to pulse, fluctuations in output energy were observed; the variations usually were within a factor of 2 of the average level.

TABLE I
EXPERIMENTAL DATA: ADP PARAMETRIC AMPLIFIER PUMPED AT 266 NM

Input Wavelength (nm)	Laser Medium	Difference Frequency Wavelength (nm)	Visible Input Power (mW)	Approximate Output Power (kW)
476.5	Ar	602.3	35	5
488.0	Ar	584.7	70	6
501.7	Ar	566.2	5	3
514.5	Ar	550.8	60	5
530.9	Kr	533.2	35	5
568.2	Kr	500.2	15	2
632.8	He - Ne	458.9	19	3
647.1	Kr	451.7	70	5
676.4	Kr	438.5	10	2

In the Q-switched experiments, permanent optically induced damage to the surfaces of the ADP crystal was sometimes observed after extended exposure (e.g., 10 min or more) to the 266-nm pump beam. Damage was not found when picosecond pump pulses, rather than nanosecond pulses, were used.

VI. Picosecond Amplification of CW Beams

In these experiments the pump beam was the fourth harmonic of the mode-locked Nd:YAG laser described earlier, and the visible input signal was a 28-mW beam from a CW He-Ne laser. The total pump input energy per shot was about 40 μJ, with a pulse shape as shown in Fig. 3. Usually, two or three strong subnanosecond pulses, whose duration we believe to be about 22 ps, appeared during each pump pulse train. The peak power was therefore about 600 kW. The pulse train in Fig. 3 was recorded using a silicon photodiode and Tektronix R7912 transient digitizer display system, a combination that provided a time resolution of the order of 1 ns. The geometry of the experiment was as shown in Fig. 2, with a 50-cm lens converging the 266-nm pump beam to an area about 1.5×10^{-3} cm^2 on the amplifier crystal. The pump power density was estimated to be approximately 400 MW/cm^2, which should provide a gain of about 4×10^7 in a 5-cm interaction length according to (5).

The output radiation at the difference frequency (458.9-nm wavelength) exhibited the pulse train shown in Fig. 4. The total output energy per shot at the difference frequency, stimulated by the 632.8-nm input, was about 1.3 μJ, or about 0.5 μJ for the largest pulse in the train. The fluorescence produced in the absence of an injected signal was about 2.5 μJ, spread over about 400 spatial modes and 5 nm in wavelength. The spectral spread of the stimulated difference frequency pulse was about 0.1 nm.

To estimate the peak powers obtained in these experiments, we must have an approximate value for the output pulse duration. This can be done using a result derived by Becker *et al.* [10] for the case of transient amplification without saturation of the pump

$$\tau_s/\tau_p = (1/2 \ln G)^{-1/2} \tag{6}$$

where τ_s is the duration of the generated pulse, τ_p is the length of the pump pulse, and G is the gain. We have carried out numerical solutions of the coupled wave equations including the effects of saturation and group velocity dispersion, and we find excellent agreement with (6) under the experimental conditions reported here. For a gain of 4×10^7 and a pump pulse length of 22 ps, the expected signal pulse length is about 7.5 ps. Pulses of this length can be accommodated by the parametric amplifier bandwidth if they have transform-limited spectral spread. The corresponding peak power, assuming an

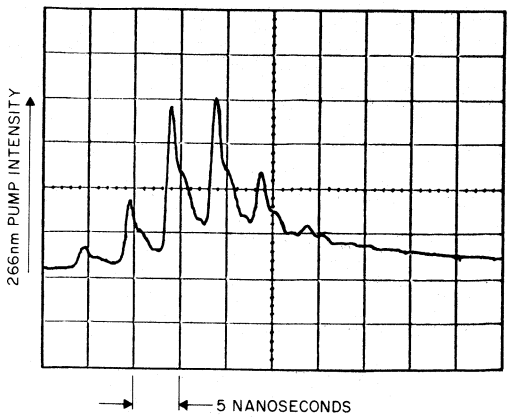


Fig. 3. Mode-locked pulse train at 266 nm.

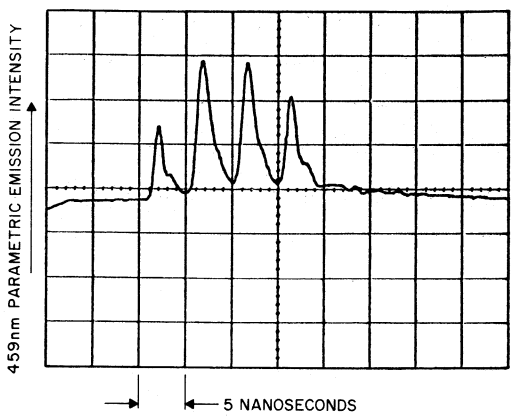


Fig. 4. Parametric amplifier output at 458.9 nm produced by a CW input beam at 632.8 nm and a pump pulse similar to that in Fig. 3.

energy of 5×10^{-7} J, would be about 67 kW at 458.9 nm, and the corresponding output at 632.8 nm would have to be 49 kW, since equal numbers of photons are produced at the signal and idler wavelengths. Since the sum of these powers is well below the 600-kW peak power of the pump beam, the use of (6) is justified. The gain at 632.8 nm for the injected signal was therefore about 1.8 million, about 100 times lower than the estimated value for the fluorescence, which is thought to have grown from about 0.5×10^{-3} W to 10^5 W under the same conditions. This difference in apparent gains may be the result of accidental mismatch of the input spot diameters, imperfect relative beam positioning and angular alignment, and perhaps too low an estimate of the number of modes contributing significantly to the spontaneous fluorescence.

These results show that it is feasible to use this technique to generate picosecond visible-wavelength pulses with peak-power efficiencies about 10 percent and total energy efficiencies near 3 percent for conversion of UV pump light into output at a selected visible wavelength. This can be accomplished in ADP without optical damage.

VII. Conclusions

We have demonstrated that one can obtain narrow-band pulses at arbitrary wavelengths in the visible spectrum by pulsed high-gain parametric amplification of relatively weak optical signals having high spectral purity and frequency stability. When injected parametric fluorescence is amplified, the bandwidth and wavelength stability can be determined by a passive filter inserted at the amplifier input, and only one coherent source, the pump, is needed. Since the filtering is done before the final amplification, the efficiency of the device is not seriously affected by loss of the signal power rejected by the filter.

Amplified pulses shorter than the pump pulse also can be generated by injecting a signal from a low powered laser instead of the filtered fluorescence. In this case the divergence and wavelength stability are limited by the input, and the spectral width can be as narrow as the pulse length permits. An additional output at the difference frequency between the pump and the visible input is of course generated.

Peak-power conversion efficiencies (pump to signal) about 10 percent have been obtained in ADP, and kilowatt pulses of 1-ns duration have been produced at 18 wavelengths between 438 and 676 nm by injecting CW signals from laser transitions in Ne and in ionized Ar and Kr. Pulses of 60-kW peak power and of durations estimated to be less than 10 ps have been obtained in the same way using the fourth harmonic of a mode-locked Nd:YAG laser as the pump. An extremely uniform pump intensity from pulse to pulse is necessary if nearly constant output power is desired, however, because of the exponential dependence of the parametric amplifier gain on the pump field strength. Parametric amplifiers with large gains in the IR have recently been demonstrated [11], [12] and the injection technique described here might be extended to cover that portion of the spectrum as well.

References

[1] J. M. Yarborough and G. A. Massey, "Efficient high-gain parametric generation in ADP continuously tunable across the visible spectrum," *Appl. Phys. Lett.*, vol. 18, pp. 438-440, May 15, 1971.

[2] A. H. Kung, "Generation of tunable picosecond VUV radiation," *Appl. Phys. Lett.*, vol. 25, pp. 653-654, Dec. 1, 1974.

[3] S. E. Harris, "Tunable optical parametric oscillators," *Proc. IEEE*, vol. 57, pp. 2096-2113, Dec. 1969.

[4] G. D. Boyd and D. A. Kleinman, "Parametric interaction of focused Gaussian light beams," *J. Appl. Phys.*, vol. 39, pp. 3597-3639, July 1968.

[5] G. E. Francois, "CW measurement of the optical nonlinearity of ammonium dihydrogen phosphate," *Phys. Rev.*, vol. 143, pp. 597-600, Mar. 1966.

[6] D. A. Kleinman, "Theory of optical parametric noise," *Phys. Rev.*, vol. 174, pp. 1027-1041, Oct. 1968.

[7] R. G. Smith, "Effects of momentum mismatch on parametric gain," *J. Appl. Phys.*, vol. 41, pp. 4121-4124, Sept. 1970.

[8] K. H. Drexhage and G. A. Reynolds, "New dye solutions for mode-locking infrared lasers," *Opt. Commun.*, vol. 10, pp. 18-20, Jan. 1974.

[9] H. E. Rowe and T. Li, "Theory of two-photon measurement of laser output," *IEEE J. Quantum Electron.*, vol. QE-6, pp. 49-67, Jan. 1970.

[10] M. F. Becker, D. J. Kuizenga, D. W. Phillion, and A. E. Siegman, "Analytic expressions for ultrashort pulse generation in mode-locked optical parametric oscillators," *J. Appl. Phys.*, vol. 45, pp. 3996-4005, Sept. 1974.

[11] G. A. Massey and R. A. Elliott, "Tunable infrared parametric generation in cesium dihydrogen arsenate," *IEEE J. Quantum Electron.* (Corresp.), vol. QE-10, pp. 899-900, Dec. 1974.

[12] A. Laubereau, L. Greiter, and W. Kaiser, "Intense tunable picosecond pulses in the infrared," *Appl. Phys. Lett.*, vol. 25, pp. 87-89, July 1, 1974.

Electrooptical Compensation for Self-Heating in CD*A During Second-Harmonic Generation

DAVID T. HON

Abstract—A pulsed electric field is used to fine tune the phase-matching conditions in temperature-tuned CD*A for second-harmonic generation (SHG) to 0.53 μ from a 1.06-μ laser. By changing the pulsewidth of the E field, the clamped and unclamped electrooptic (EO) effects are studied, resulting in the determination of $r_{63} = 14.1 \pm 0.4 \times 10^{-10}$ cm/V (electrooptic constant) and the product $p_{66}d_{36} = 10.2 \pm 0.4 \times 10^{-10}$ cm/V (elastooptic and piezoelectric constants, respectively) at 102°C.

A steady 57-percent efficient SHG was obtained for 10.4 W of 1.06 μ laser light in CD*A. The usual instability caused by self-heating was eliminated electrooptically.

I. Introduction

NONLINEAR optical processes involving crystals, such as frequency doubling and parametric oscillation, have provided great latitudes in frequency agility. Such processes can be very efficient and very simple to operate, and many such systems have established themselves firmly in laser engineering.

However, these systems are all limited to low average powers: they cannot handle more than 5, 15, or 20 W before thermal effects create serious problems. It is not crystal damage. It is the thermal absorption of the strong radiations passing through the crystal which in turn disrupts the phase-match condition on which the efficiency of these processes critically depends. Such self-heating is manifested in two ways: 1) output instability, and 2) loss of efficiency due to thermal profile. The need for high average power frequency conversion systems is continuing and increasing, particularly in such applications as isotope separation. A certain degree of improvement will undoubtedly come from purer and less absorbing crystals. But in recent years we at Hughes Aircraft Company have been working toward solving the more fundamental problems of self-heating instability and loss of efficiency as stated in the preceding. In both aspects, definite gains have been made toward the goal of systems capable of handling several hundred watts of laser throughput. We report here a solution of 1), viz., the control of output instabilities by electrooptic (EO) effect [1]-[3].

This solution is more practical than either the preprogrammed oven temperature or the angular tuning approaches. In the latter approach, the acceptance angle decreases significantly if a 90° phase-match condition is relinquished.

II. Electrooptic Effects

An isomorph of KDP, CD*A has a $\bar{4}2m$ point group symmetry. The optimal SHG orientation is shown in Fig. 1. The normally degenerate x_1 and x_2 axes are at 45° with the propagation direction $\bar{k}$ of the 1.06-μ fundamental beam which

Manuscript received June 9, 1975.

The author is with the Department of Laser Physics and Systems Design Laser Division, Hughes Aircraft Company, Culver City, CA 90230.

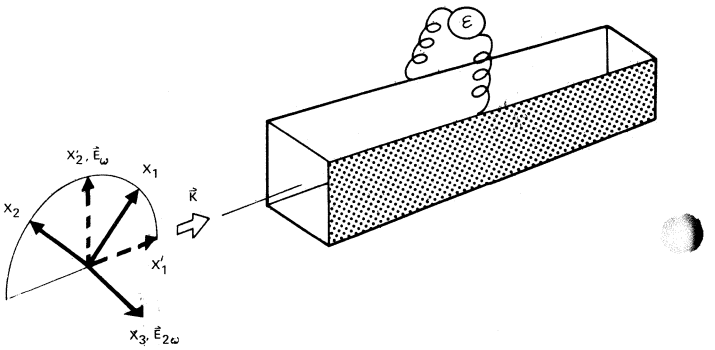


Fig. 1. Crystal orientation of CD*A in SHG. The fundamental 1.06-μ E_ω is polarized in the degenerate x_1x_2 (or xy) plane at 45° with either axis. The green light $E_{2\omega}$, produced by SHG, is polarized along the x_3 (or z, or c) axis. Voltage applied along x_3 results in a 45° rotation of x_1 and x_2 to x_1' and x_2', and the changes in (1).

is polarized in the x_1x_2 plane. The 0.53-μ SHG beam is polarized along the x_3 axis. The effect of ΔE along the x_3 direction is a rotation of x_1 and x_2 axes by 45° to x_1' and x_2' in their own plane [13], with the principal indices now given by

$$n_1 = n_0 - (n_0^3 \Delta E/2)(r_{63} + p_{66}d_{36})$$
$$n_2 = n_0 + (n_0^3 \Delta E/2)(r_{63} + p_{66}d_{36})$$
$$n_3 = n_e \text{ (unchanged)} \qquad (1)$$

where r_{ij}, p_{ij}, and d_{ij} are components of the electrooptic (EO), elastooptic, and piezoelectric constant matrices [14].

The r_{63} term is the "primary effect." The $p_{66}d_{36}$ term is the "secondary effect;" it represents an indirect contribution by the strain ϵ induced by the E field, or a piezoelectric elastooptic effect in reverse. If the pulse duration of the applied field is short compared to the typical mechanical response time of the bulk crystal of 1 to 2×10^{-5} s, this "secondary effect" would be absent. Depending on whether it is absent or present, we have in (1) a *clamped* or *unclamped* EO effect.

III. EO Effects and SHG in CD*A

Such an E field has no effect on the 0.53-μ beam, but will modify the phase velocity of the 1.06-μ fundamental, thus providing a means of fine tuning the phase-matching condition, i.e., the phase-match temperature can be shifted.

In our experiments, electrodes are painted onto the x_1x_2 faces (see Fig. 1) of a CD*A crystal grown by quantum technology, which is then placed in a Hughes-made oven. A partially focused beam from a multimode, 10 Hz, 100 mJ per pulse Q-switched Nd:YAG laser is made to frequency double, and the efficiency versus temperature curve is taken. CD*A has a low resistivity of about 5×10^5 $\Omega \cdot$ cm and a dc field

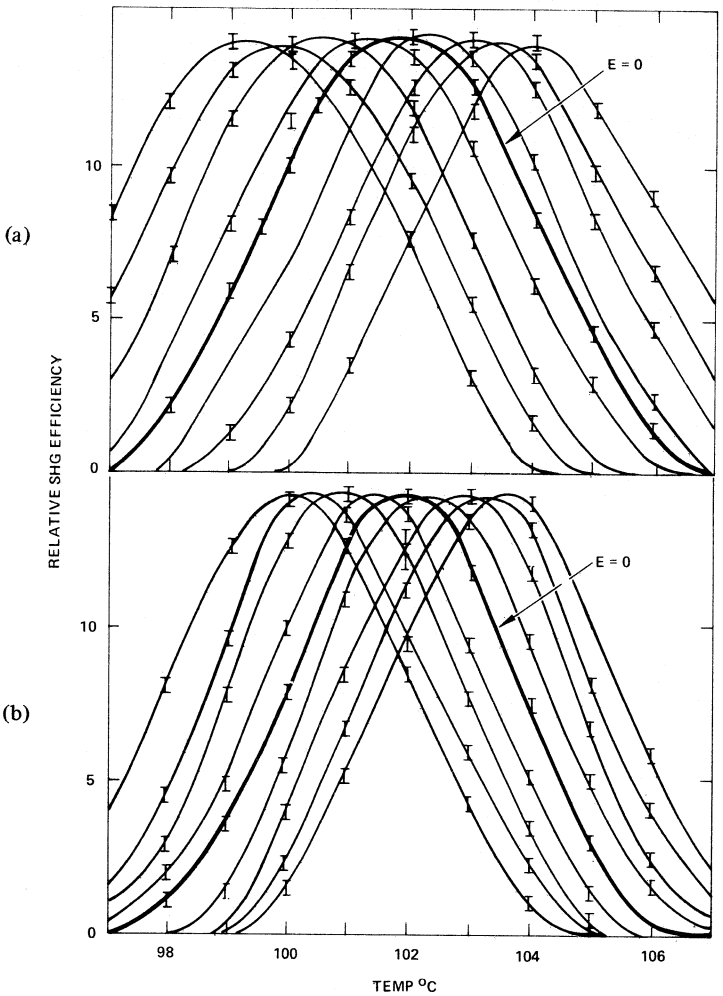


Fig. 2. Electrooptic effects in SHG. Efficiency versus temperature for different applied E fields. (a) Clamped electrooptic effect: pulse duration ~200 ns, $\Delta E = \pm 1450, \pm 2800, \pm 5700, \pm 7400$ V/cm. (b) Unclamped electrooptic effect: pulse duration ~200 μs, $\Delta E = \pm 850, \pm 1800, \pm 2750, \pm 3250$ V/cm.

cannot be used. E-field pulses of various magnitudes are then applied to the crystal synchronously with the laser pulses, and the efficiency versus temperature curve is caused to shift and to eventually form a family of E-dependent curves (Fig. 2). Basically, two families of curves are obtained, for the two representative pulsewidths of ~200 ns (clamped) and ~200 μs (unclamped). The ratio $(\Delta T/\Delta E)$, where ΔT is the effective change of temperature as a result of a change of the applied E field, is then obtained from the curves of Fig. 2. The result is shown in Fig. 3. The unclamped effect is found to be almost twice as large.

We now use the familiar equation [13]

$$\frac{P_{2\omega}}{(P_{2\omega})_{\max}} = \frac{\sin^2 (\Delta Kl/2)}{(\Delta Kl/2)^2} \tag{2}$$

for the relative SHG efficiency as a function of crystal length l and phase mismatch ΔK. $\Delta K = K_{2\omega} - 2K_{\omega}$, where $K_{2\omega} = 2\pi n_{2\omega}/\lambda_{2\omega}$ and $K_{\omega} = 2\pi n_{\omega}/\lambda_{\omega}$ are the wavenumbers of the $\lambda_{2\omega} = 0.53\,\mu$ and the $\lambda_{\omega} = 1.06\,\mu$ beams, respectively. Since the applied field only affects n_{ω} and thus K_{ω}, we may write, for a crystal already temperature phase matched at $E = 0$

$$\Delta K = -2\Delta K_{\omega} = -2\Delta K_{\omega} = -4\pi\Delta n_{\omega}/\lambda_{\omega}$$

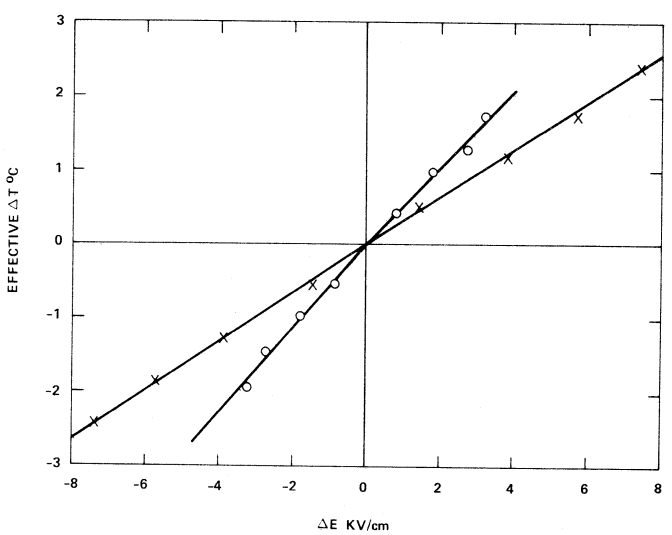


Fig. 3. Effective ΔT versus ΔE for clamped and unclamped electrooptic effects in SHG as obtained from Fig. 2.

$$\Delta K = (2\pi n_0^3 \Delta E/\lambda_{\omega})(r_{63} + p_{66} d_{36}) \tag{3}$$

the last equality making use of (1).

Comparing the first minima of (2) at $\Delta K = (2\pi)/l$ and the

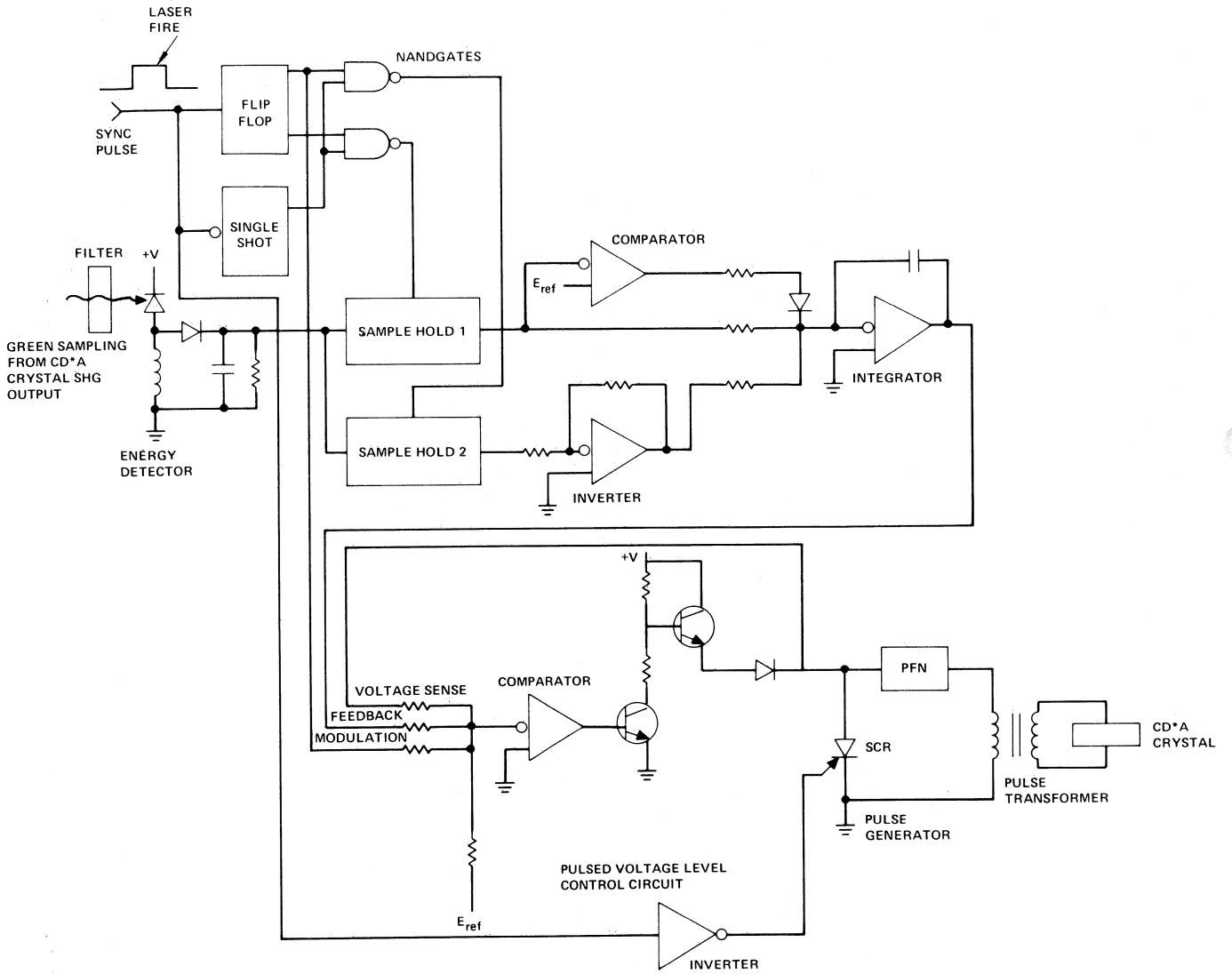


Fig. 4. Electronic schematics of the automatic electrooptic SHG fine-tuning device.

experimental data of Fig. 2, we can write

$$(\Delta K/\Delta T) = 2\pi/l\delta T \tag{4}$$

where δT is the temperature difference between the maximum and the first minimum in Fig. 2. Dividing (3) by (4)

$$(\Delta T/\Delta E) = (ln_0^3 \delta T/\lambda_\omega)(r_{63} + p_{66} d_{36}). \tag{5}$$

Using the values of $(\Delta T/\Delta E) = 0.32$ and 0.55°C cm/kV for the clamped and unclamped cases from Fig. 3, $n_0 = 1.5 \pm 0.01$, $l =$ 1.39 cm, $\delta T = 5.15$°C, and setting $p_{66} d_{36} = 0$ [15][1] for the clamped case, we calculate from (5)

$$r_{63} = 14.1 \pm 0.4 \times 10^{-10} \text{ cm/V}$$

and

$$p_{66} d_{36} = 10.2 \pm 0.4 \times 10^{-10} \text{ cm/V [7]}$$

[1] Unclamped values at room temperature have been reported by Adhav [15]. A strong temperature dependence of these constants is not unusual and the values reported have agreed quite well with the extrapolation of temperature-dependent data in the 25–50°C range taken by Adhav.

for CD*A at the phase-match temperature of 102°C. For a second crystal of CD*A with $l = 2.4$ cm, $\delta T = 3.33$°C, and a phase-match temperature of 97°C, it was found that $r_{63} = 14 \pm 0.6 \times 10^{-10}$ cm/V and $p_{66} d_{36} = 10 \pm 0.4 \times 10^{-10}$ cm/V.

IV. EO Fine Tuning of SHG

By modulating the amplitude of the E-field pulses by a small set amount between pulses, and by comparing the respective SHG outputs, it can be established whether more or less E field would increase the efficiency. A closed loop has been built (Fig. 4) that quickly compensates for any thermal fluctuations within the crystal. In addition to the ±3°C EO compensation range, the oven temperature is also controlled by the same electronics to give an almost arbitrarily large total range. An 0.52-J/15-ns/20-Hz laser was used with an uncoated 1 × 1 × 2-cm CD*A housed in a Hughes-built dry oven with maximum thermal conductivity and minimum thermal mass. The output normally vanished after 1 min–long compared with other oven types (Fig. 5). But EO compensation kept it steady indefinitely at an efficiency of 57 percent (Fresnel reflection considered). The EO compensation response time of the loop

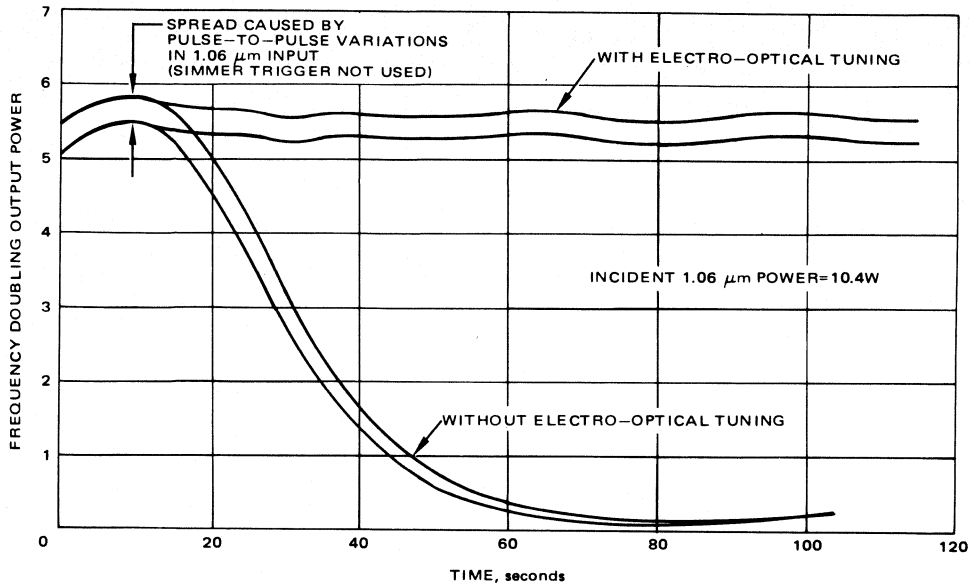


Fig. 5. Frequency doubling conversion efficiency versus time for an uncoated 1 × 1 × 2-cm CD*A crystal with and without EO tuning. 1.06-μ source was a multimode 0.52-J per pulse 20-Hz Q-switched Nd:YAG laser.

was four times faster than the maximum self-heating rate of ~0.5°C/s. Oven response is slow but adequate. Ambient fluctuations of ±60°C had not affected the performance.

This technique should be useful in other SHG materials and also in parametric oscillators. It will work for considerably higher powers than the equipment limited 10.4 W reported here until severe crystal temperature gradients cause unacceptable loss of efficiencies. Substantial gains have also been made toward controlling temperature gradients.

Acknowledgment

The author wishes to thank Dr. W. K. Ng and Dr. E. J. Woodbury for their encouragement and G. C. Atchison and R. W. Wyeth for their contributions to the electronics.

References

[1] J. P. Fan der Ziel, *Appl. Phys. Lett.*, vol. 5, p. 27, 1964.
[2] N. I. Adams and J. J. Barrett, presented at the Int. Conf. Quantum Electronics, Phoenix, AZ, Apr. 1966, Paper 5A-6.
[3] B. H. Soffer and I. M. Winder, *Appl. Phys. Lett.*, vol. 24A, p. 5, 1967.
[4] R. C. Miller, G. D. Boyd, and A. Savage, *Appl. Phys. Lett.*, vol. 6, 1965.
[5] V. S. Suvorov, A. S. Sonin, and I. S. Rez, "Some nonlinear optical properties of crystals of the KDP group," *Sov. Phys.–JETP*, vol. 26, pp. 33–37, 1968.
[6] R. S. Adhav, "Linear electro-optic effects in tetragonal phosphates and arsenate," *J. Opt. Soc. Amer.*, vol. 59, pp. 414–418, 1969.
[7] V. S. Suvorov and I. S. Rez, "Second harmonic generation of CDA (CsH_2AsO_4) crystals having no birefringence at room temperature," *Opt. Spectrosc.* (USSR), vol. 27, pp. 94–95, 1969.
[8] J. H. Boyden, E. G. Erikson, J. E. Murray, and R. Webb, "Second harmonic generation," Final Tech. Rep. ARPA 306, Oct. 1971.
[9] T. A. Rabson, H. J. Ruiz, P. L. Shah, and F. K. Tittel, "Efficient second harmonic generation of picosecond laser pulses," *Appl. Phys. Lett.*, vol. 20, pp. 282–284, 1972.
[10] J. M. Yarborough and E. O. Amman, "High-average-power optical second-harmonic generation and optical parametric oscillation," *IEEE J. Quantum Electron. (1973 IEEE/OSA Conf. Laser Engineering and Applications, Dig. Tech. Papers)*, vol. QE-9, pp. 702–703, June 1973.
[11] Y. D. Golyaev *et al.*, "Efficient frequency doubler utilizing a cesium dihydrogen arsenate crystal," *Sov. J. Quantum Electron.*, vol. 3, pp. 72–73, July–Aug. 1973.
[12] K. Kato, "Efficient second harmonic generation in CDA," *Opt. Commun.*, vol. 9, pp. 249–251, 1973.
[13] See, e.g., A. Yariv, *Quantum Electronics*. New York: Wiley, 1967.
[14] J. F. Nye, *Physical Properties of Crystals: Their Representation by Tensors and Matrices.* New York: Oxford, 1957.
[15] R. S. Adhav, "Research on electrooptic crystals for display systems," Tech. Rep. RADC-TR-68-307, Canada, Nov. 1968.

The Asterix III Pulsed High-Power Iodine Laser

G. BREDERLOW, K. J. WITTE, ERNST FILL, K. HOHLA, AND R. VOLK

Abstract—**A system description and first results of the Asterix III high-power iodine laser built at IPP Garching are given. This laser is designed to yield an output energy of 1 kJ in about 1 ns. Until now pulses with output energies up to 300 J and pulse lengths ranging from 1 to 3 ns have been obtained.**

I. Introduction

THE feasibility of high-power operation of the iodine laser has been demonstrated in several experiments [1]-[4]. This photochemical gas laser has the potential for delivering subnanosecond pulses with multikilojoule energies, with a diffraction-limited beam quality and a high repetition rate. It is less subject to problems of optical damage than solid-state lasers and shows a greater flexibility in choosing the most suitable optical parameters and operational conditions. To check these properties and test the applicability of the iodine laser for fusion experiments, we built the Asterix III single-beam high-power laser with a planned output energy in the 1-kJ range.

II. Basic Features of the Iodine Laser

The iodine laser operates on the magnetic dipole allowed transition $^2P_{1/2}$-$^2P_{3/2}$ of atomic iodine at 1.315 μm. The laser medium is the perfluor-alkyliodide C_3F_7I. It decomposes upon irradiation with UV light (in the wavelength region of 280 nm) into C_3F_7 radicals and I* ($^2P_{1/2}$). After photolysis a series of chemical reactions takes place, recombination of C_3F_7 and I to C_3F_7I and formation of I_2 being the most important ones [5]. The degree of inversion $\alpha = \Delta n/n$ produced by flashlamp pumping ranges between $0.1 \leqslant \alpha \leqslant 0.2$. The radiation lifetime of the excited iodine atoms is 130 ms; but collisional deactivation processes caused by molecular iodine and by impurities will reduce it to the region of about 1 ms depending on the type and the partial pressure of the impurities. But this time will, in any case, be much longer than the pumping and release times of the laser, which have to be shorter than 15 μs. This is because the pump light will evaporate condensed components from the walls, thus causing shock waves traveling towards the center and disturbing the optical homogeneity of the laser medium.

The iodine laser provides optimum flexibility for high-energy storage and extraction because the stimulated-emission cross section σ can easily be adjusted to its maximum tolerable value by adding a certain amount of foreign gas to the laser medium [6]-[9]. The species of foreign gas has to be chosen such that the pressure broadening constant is as high as possible, while the deactivation rate is as low as possible.

Manuscript received May 30, 1975; revised September 19, 1975.

The authors are with the Euratom Association, Max-Planck-Institut für Plasmaphysik, D-8046 Garching, Germany.

In order to avoid parasitic oscillations, the σ value in conjunction with the inversion density has to be such that the small-signal amplification of an amplifier does not exceed a factor of around 10^3. As the σ value ranges for amplifier operation from 2 to $5 \cdot 10^{-19}$ cm^2, energy densities from 2 to 5 J/cm^2 can then be stored.

The stored energy cannot be completely extracted. The efficiency of this process depends on the spectrum and the length of the pulse to be amplified. This is because both levels of the laser transition show hyperfine splitting resulting in two and four sublevels, respectively (Fig. 1). As a consequence of the addition of a foreign gas for σ reduction, the sublevels of both the upper and lower levels overlap under amplifier conditions. According to calculations of Yukov [10], the relaxation within the lower sublevels is fast in relation to a nanosecond pulse, whereas the relaxation within the upper sublevels is slow. Thus each group of the three transitions starting from both the $F = 2$ and $F = 3$ sublevels of the excited state can be imagined to form for pulse durations down to subnanoseconds one homogeneously broadened line, with both lines coupled by the sublevels of the ground state. For optimal energy extraction a pulse should therefore contain frequencies of both groups of lines. The maximum amplifier extraction efficiency η^* is then $\eta^* = 0.66$. If only the $F = 3 \rightarrow F = 4$ line—this is the line with the highest σ value—is fed into the amplifier, η^* has a value of 0.46, when there is no overlapping with the lines originating from the $F = 2$ sublevel [8].

The minimum pulse length (bandwidth limited) to be generated and amplified can be expected to be in the 50-ps range at atmospheric pressure (C_3F_7I plus CO_2). At this pressure the combined linewidth of the laser transition due to the hyperfine splitting is 20 GHz. Until now minimum pulse lengths of 300 ps have been measured [11].

To run an amplifier, the C_3F_7I pressure has to be adjusted in

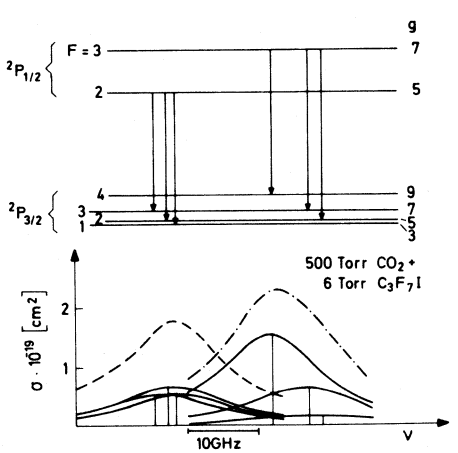


Fig. 1. Hyperfine splitting of iodine laser levels. Lower plot shows cross sections for stimulated emission for different transitions.

such a way that the illumination of the amplifier volume is as homogeneous as possible. This is achieved at a certain ratio of the C_3F_7I pressure to the amplifier diameter. With this ratio known [12] and the information reported here and given in the references, one has the basic information for constructing the laser.

III. Description of Asterix III

The schematic setup of this laser is shown in Fig. 2. The system consists of an acoustooptically mode-locked oscillator operating in the TEM_{00} mode and four amplifiers of increasing diameter and energy content. The distance between the amplifiers is chosen such that the beam widening due to its natural divergence fits the diameter of the following amplifier. To improve the spatial beam quality, soft apertures were placed before the second and third amplifiers, respectively.

The oscillator consists of a 1-cm-diam quartz tube illuminated by four Xe flashlamps, the optical pumping time being 2 μs. It delivers a pulse train from which a single pulse is switched out by means of a Pockels cell. The selected pulse has a length of about 1 ns and a diffraction-limited beam divergence of $0.9 \cdot 10^{-3}$ rad. The design of the first, second, and third amplifiers is similar to the oscillator. The internal effective diameters of the quartz tubes vary from 1 cm over 2.5 to 6 cm and the pumping times from 6 μs (first and second) to 15 μs. The inner surfaces of the quartz tubes were etched to avoid inhomogeneities in the inversion profile caused by the optical pumping configuration. In the third amplifier a metal spiral lying close to the wall was placed to eliminate diffuse parasitic oscillations.

The laser medium of the oscillator and the amplifiers consists of a mixture of C_3F_7I and argon or CO_2. The partial pressures of the C_3F_7I which give the most homogeneous inversion profile and the partial pressure of the foreign gas which reduces the σ value to its maximum tolerable value under the present conditions are specified in Fig. 2. The oscillator and the first three amplifiers were connected to a gas recycling system which cleans the used gas by removing the photolytic reaction products by condensing them in a cooling trap, and which replaces the used C_3F_7I by passing the gas through a vessel where stored C_3F_7I is cooled to a temperature at which its vapor pressure corresponds to the required partial pressure. Measurements have shown that one iodine atom can lase up to 15 times. The repetition time of this system ranges between 1 and 2 min.

The fourth amplifier provides the main energy for the pulse (Fig. 3). It consists of a stainless-steel tube with a diameter of 20 cm. This tube is assembled from eight sections. Each section has eight Xe flashlamps with an active length of 1 m mounted inside. From section to section the flashlamps are slightly displaced relative to each other in order to improve the homogeneity of the inversion in the axial direction. Each section is connected to its own capacitor bank with an energy of 36 kJ at 40 kV. The laser medium was replaced after every shot by pumping and refilling. Therefore the repetition rate of the total system is restricted so far to one shot every 10 min.

For the runs reported, the total system has not been in its final state. Especially the optical isolation of the amplifiers

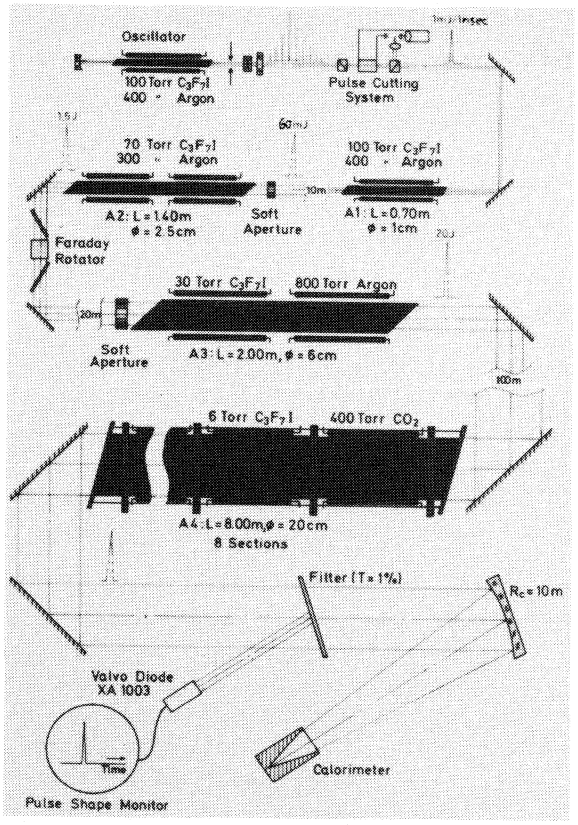


Fig. 2. Schematic setup of the iodine laser currently tested.

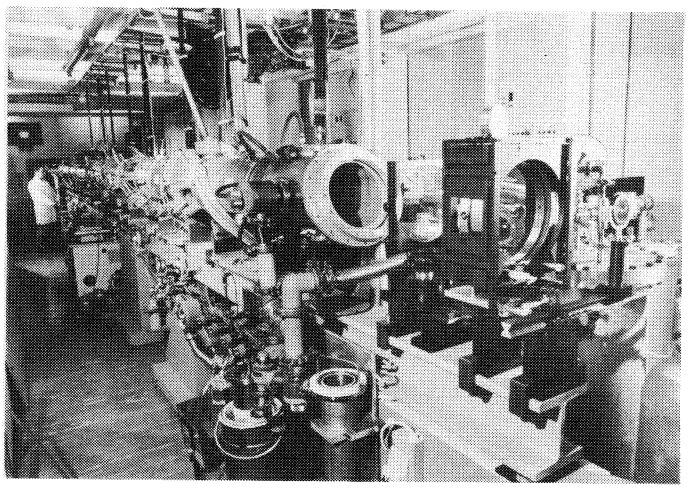


Fig. 3. Fourth amplifier of Asterix III.

and the suppression of the prepulses have to be improved. Optical isolation was achieved mainly by means of distance except between the second and third amplifiers, where a Faraday rotator was placed. With the Faraday rotator having a backward-forward extinction ratio of 10^4 and solid angles with which an amplifier sees the other of some 10^{-6} rad, a small-signal amplification of the total system between 10^8 and 10^9, each amplifier yielding 10^2-10^3, can be sustained. In our laser, prepulses were reduced by a factor of 10^4 after passing through the pulse-selecting system. But as the small-signal gain is higher than the real gain, the prepulses after the last amplifier were down by a factor of 20 only. The optical iso-

lation and the suppression of the prepulses will be improved by additional measures in the future.

IV. Results of Asterix III

In contrast to the well-tested first three amplifiers of the system [3], there was no experience in reliably scaling an amplifier of the size and concept of the fourth. Therefore we concentrated our investigations on finding the conditions for optimal performance of this amplifier. Our main interest was focused on five topics.

1) The inversion density $\langle \Delta n \rangle$ averaged over the laser cross section has been investigated as a function of the pumping energy. As shown in Fig. 4, it increases linearly with the pumping energy up to a value of 40 kJ. The smaller increase at higher energies is a consequence of the decreasing efficiency of the flashlamps. These results and the decreasing lifetime of the flashlamps with increasing energy input prompted us to operate the system at 40 kV.

2) To determine the C_3F_7I pressure at which the amplifier had to be operated, $\langle \Delta n \rangle$ has also been measured as a function of $P_{C_3F_7I}$. Fig. 5 shows that in the linear region at a pressure up to 4 torr the degree of inversion α remains practically constant and then decreases at higher pressures. In addition, Δn has to be investigated as a function of the radius of the amplifier, with $P_{C_3F_7I}$ as a parameter (Fig. 6). As a compromise between high inversion density and a sufficient homogeneity of the inversion profile, $P_{C_3F_7I} = 6$ torr has been chosen.

3) The average small-signal amplification $\langle V \rangle$ of the fourth amplifier should not exceed a value of $\langle V \rangle = 5 \cdot 10^2$. To adjust $\langle V \rangle$ to this value, V has been measured as a function of the foreign gas pressure at different positions of the amplifier cross section. It turns out that the appropriate value of $\langle V \rangle$ will be obtained at a foreign gas pressure of 400 torr CO_2.

4) To ensure that the pumped energy can be stored at $\langle V \rangle = 5 \cdot 10^2$, the maximum sustainable small-signal amplification should be higher than the maximum value of the amplification profile of around 10^3. A maximum sustainable small-signal amplification of $2 \cdot 10^4$ has been measured. Until now, after around 270 shots, there has been no indication that this value would be affected by deposits on the walls.

At the given parameters the measured inversion stored in the fourth amplifier was around 1 kJ. First runs with the whole laser system yielded pulse energies of up to 300 J with pulse lengths ranging between 1 and 3 ns. The beam quality of these pulses was investigated. As already mentioned in the previous section, the temporal quality of the pulse is affected by prepulses leaking through the pulse cutting system. The prepulses contain up to 5 percent of the total energy. It is, however, planned to suppress the prepulses further by a saturable iodine absorber and an additional Pockels cell. Fluorescence radiation from the laser is negligible. This is a result of both the small pumping time ($t \leqslant 15$ μs) and the small Einstein coefficient ($A = 7\ s^{-1}$). The spatial beam quality was measured by taking burn patterns. These patterns always showed a fairly homogeneous intensity distribution. There was no evidence of any beam deterioration due to nonlinear effects such as gas breakdown and self-focusing. By increasing the output energy density by a factor of 6 in a separate experiment ($e_{out} = 6\ J/cm^2$) a 1-ns pulse could still be propagated through the amplifier with no signs of beam instabilities.

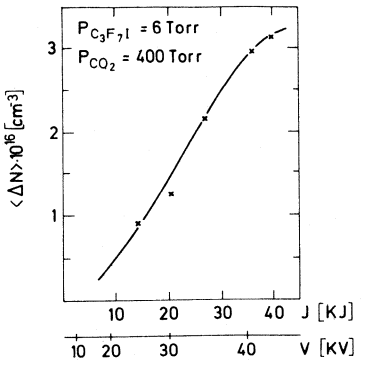


Fig. 4. Inversion density averaged over the laser cross section versus pumping energy.

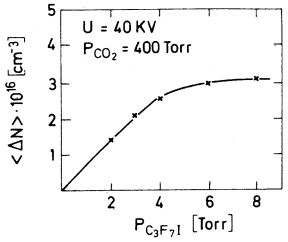


Fig. 5. Inversion density averaged over the laser cross section versus C_3F_7I pressure.

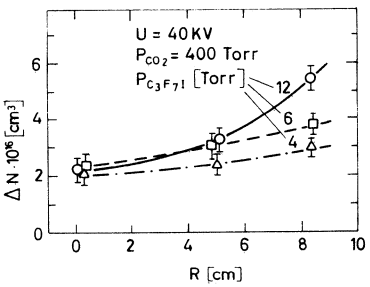


Fig. 6. Inversion density versus radius of the amplifier with C_3F_7I pressure as a parameter.

The entire system was pumped with an electric energy input of 360 kJ. The output pulse energy of around 300 J then corresponds to a total efficiency η_t of the system of $\eta_t = 0.08$ percent. Calculations of the total efficiency cannot be performed accurately because of the uncertainty in the conversion efficiency of the electrical input energy to the UV light absorbed in the active medium. Only an interval can be given ranging from 0.07 percent $\leqslant \eta_t \leqslant$ 0.23 percent. Measurements with around 270 shots have shown that η_t decreases within the first 40 shots by around 20 percent and then remains constant. This behavior is due to a certain equilibrium between deposition and vaporization of pyrolysis products on the surface of the flashlamps, thus causing absorption of the pumping light. But there is still a possibility of reducing the influence of this effect by using a different quartz material for the flashlamps.

For the fourth amplifier the output energy was calculated. These calculations were made by taking the measured inversion density profile of the amplifier, as well as the profile and energy of the input pulse (20 J), and assuming that the oscillator delivers a pulse containing only the line of the $F = 3 \rightarrow F = 4$ transition. (This assumption was confirmed by spectroscopic measurements made with a similar oscillator.)

The calculated value of 330 J is nearly equivalent to the measured one. An output energy of 460 J was calculated for the case where all lines of the laser transition were fed into the amplifier.

The output energy of the laser shall now be increased by improving the pumping efficiency as well as the optical isolation of the amplifiers and by operating the oscillator under conditions where it emits lines of both groups of the laser transition. Further plans involve better suppression of the prepulses and the reduction of the pulse length to the region of a few hundred ps. If we succeeded in getting pulses shorter than 100 ps, because of the pressure broadening of the laser transition this would be an alternative to the two-line operation proposed to increase the amplifier extraction efficiency.

V. Conclusion

The investigations reported have demonstrated that the iodine laser practically behaves as expected theoretically and that there are no technical impediments which impair the performance of the laser.

In conclusion, it can be stated that the iodine laser offers the advantages of high flexibility, good energy extraction efficiency, high beam quality, short pulse length, simple technical structure, and low construction and operation costs. Therefore this laser has good prospects of becoming a valuable tool for laser fusion research.

References

[1] K. Hohla and K. L. Kompa, *IEEE J. Quantum Electron.*, vol. QE-8, p. 198, 1972.
[2] N. G. Basov *et al.*, *Kvantovaya Elektron.*, vol. 6, p. 116, 1973.
[3] K. Hohla *et al.*, *J. Appl. Phys.*, vol. 46, p. 808, 1975.
[4] V. A. Gaidash *et al.*, *ZUETF Lett.*, vol. 20, p. 243, 1974.
[5] W. Fuss and K. Hohla, to be published.
[6] F. T. Aldridge, "Stimulated-emission cross section and inverse lifetime in a three-atmosphere iodine photodissociation laser," *IEEE J. Quantum Electron.* (Corresp.), vol. QE-11, pp. 215–217, May 1975.
[7] V. S. Zuev, V. A. Katulin, V. Yu. Nosach, and O. Yu. Nosach, *Zh. Eksp. Teor. Fiz.*, vol. 62, p. 1673, 1972.
[8] W. Fuss and K. Hohla, IPP Rep. IV/67, 1974, and *Z. Naturforsch.*, to be published.
[9] T. D. Padrick and R. E. Palmer, *J. Chem. Phys.*, vol. 62, p. 3350, 1975.
[10] E. A. Yukov, *Kvantovaya Elektron.*, vol. 2, p. 53, 1973.
[11] R. Volk, to be published.
[12] G. Brederlow, K. Hohla, and K. J. Witte, IPP Rep. IV/74, 1974.

High-Repetition-Rate TEA-Laser Discharge Using Integrated Preionization and Switching

JOHN TULIP, HERB J. SEGUIN, MEMBER, IEEE, AND WAYNE FASZER

Abstract—**A high-pressure high-repetition-rate pulsed-discharge technique is described. Ultraviolet preionization and voltage switching are integrated using spark-gap switches in a geometry such that they will irradiate the discharge gas. A repetition rate of 4000 pulses per second (pps) has been achieved.**

I. Introduction

THE PROBLEM of extending the operation of the TEA CO_2 laser to a high repetition rate has been largely neglected in the literature. This neglect is in contrast with the extensive development of the very high-energy single-pulse version. Those high-repetition-rate systems which have been described are all of the double-discharge type rather than externally controlled with an E beam [1]-[4], [6]. The double-discharge system (preionization followed by an overvolted self-sustained discharge) is sensitive to the presence of its own discharge products so that as a consequence convective flow has been used in the previously mentioned lasers more to stabilize the discharge than to achieve cooling of the CO_2 bending mode [3]. One might think that one gas change per pulse would be adequate to ensure complete cleanup of the discharge gas. However, Dzakowic and Wutzke [3] have pointed out that the shock from the discharge will backstream the discharge products so that several gas changes are in fact necessary for cleanup. Another closely related problem is one of poisoning [2] in closed-cycle operation. After a short period of operation in such a system the level of discharge products accumulates to that extent that discharge arcing occurs. This poisoning has an associated recovery time [2] implying that the detrimental species has a finite lifetime. The nature of the species and the cause of discharge instability are as yet unknown. The discharge products may inhibit preionization, for example, by absorbing the ionizing radiation. Alternatively, the instability may be associated with attachment as in the bulk-dominated continuous discharge.

Manuscript received May 30, 1975.
The authors are with the Department of Electrical Engineering, University of Alberta, Edmonton, Alta., Canada.

II. Concept and Apparatus

In this paper another high-repetition-rate TEA CO_2 laser of the double-discharge type is described. This structure embodies a convenient combination of switching means and preionization means and is shown schematically in Fig. 1.

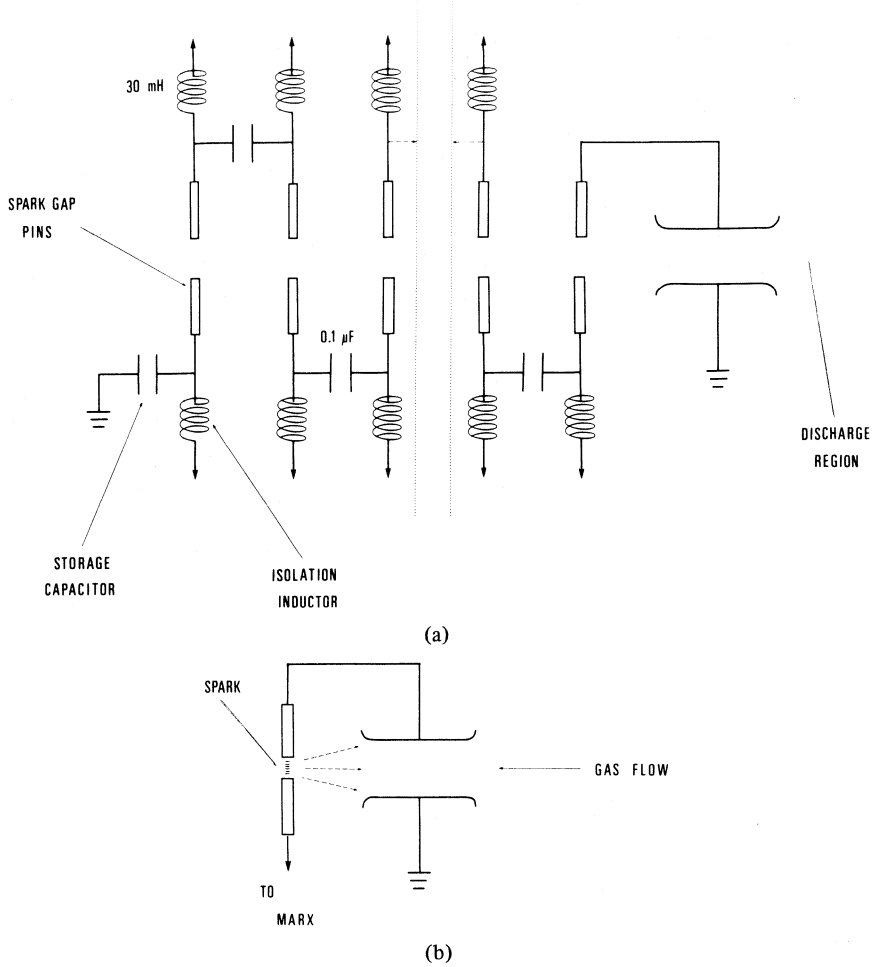


Fig. 1. Marx-generator integral to the flowing laser gases to provide discharge preionization.

Switching is achieved with spark gaps which are maintained within the laser gases so that they also serve to preionize, via ionizing radiation, the discharge gases. As shown in Fig. 1 the spark gaps are arranged along the length of the profiled electrodes in a Marx-generator circuit. Gap voltages of more than 10 kV are difficult to obtain in the laser mixture of gases (80-percent He) so that a Marx-generator circuit is necessary to multiply the gap voltage to some desired level. Moreover, the resulting array of gaps along the electrodes provides a strong uniform UV preionization. In this structure it is essential that the spark gaps lie downstream of the main electrodes since, if the discharge products from the sparks are swept into the main discharge, arcing will occur. Table I summarizes the essential features of the discharge described in this paper. The ten-element capacitors of 0.1 μF charged to 6 kV give a total stored energy of 20 J. Though a small energy value by TEA-laser standards this compromise must be made if a high-repetition-rate operation is to be achieved with limited supply capacity. In order to maintain the high peak power needed for efficient operation at atmospheric pressure, a discharge volume of only 0.37 l is used. The discharge structure forms part of a closed-cycle duct which blows the laser gases transverse to the electrodes at approximately 100 m/s. This represents a volumetric flow of 1500 l/s; less than half of the rated flow for the blower used. A heat exchanger is incorporated into this closed-cycle system.

TABLE I
TYPICAL GEOMETRY OF THE LASER DISCHARGE

ELECTRODE LENGTH	60 cm
ELECTRODE MATERIAL	carbon or copper
DISCHARGE VOLUME	0.37 l
DISCHARGE CROSS – SECTION	2.5 cm x 2.5 cm
ELEMENT CAPACITOR	0.1 μF
ELEMENT INDUCTOR	30 mH
NUMBER OF STAGES	10
CHARGING VOLTAGE	6 kV
ENERGY STORAGE	20 J
PIN SPACING	1 cm
PIN – ELECTRODE DISTANCE	5 cm
GAS MIXTURE	1:1:8
FLOW VELOCITY	100 m/s
GAP RECOVERY STRENGTH	60 kV/ms

III. EXPERIMENTAL RESULTS

The use of the Marx generator described in Section II to successfully preionize the discharge gases depends upon the commutation time of the Marx circuit being short. In Fig. 2 the commutation time for the circuit with a single trigger at the first gap is shown. Sinusoidal ringing at the first gap is caused by the trigger and is not important. Fig. 2 shows that breakdown takes approximately 15 μs to propagate along the circuit, and with this long commutation time discharge

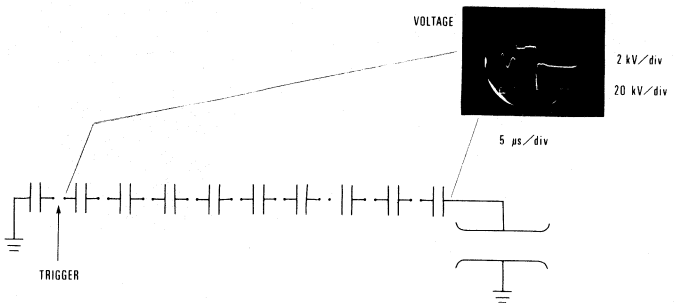


Fig. 2. Commutation delay seen in Marx generator with single trigger.

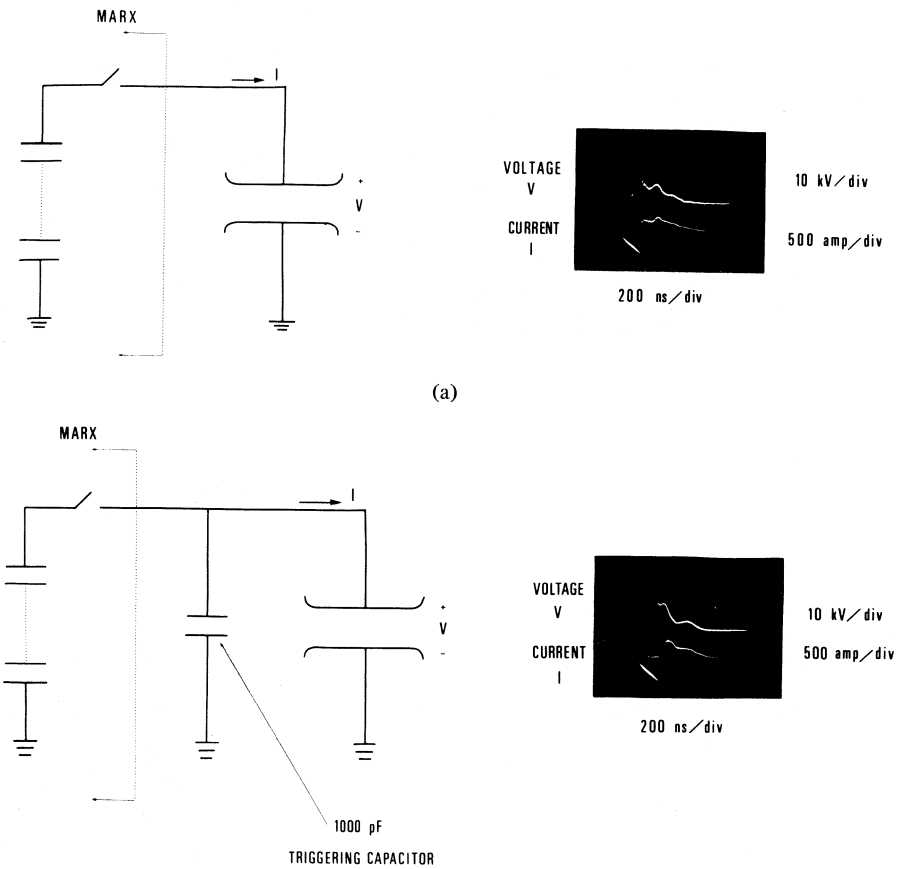


Fig. 3. Voltage current waveform of the discharge. (a) Without load capacitor. (b) With load capacitor.

arcing will occur frequently. The problem may be solved by triggering the first and every other gap, in which case the commutation time is less than 100 ns and a stable discharge is obtained for every pulse.

Fig. 3(a) shows a typical discharge-pulse waveform. The voltage switches onto the electrodes in a period of less than 100 ns. The voltage does not rise all the way to the open-circuit voltage of 60 kV but is limited to 30 kV because of the discharge loading after breakdown. The current pulse is approximately a half sine wave 800 ns long. Experiment has shown that the resistance of the discharge to the glow-to-arc transition at a high repetition rate is improved by placing a small capacitance across the electrodes as shown in Fig. 3(b). The capacitance slows the growth of applied voltage but sharpens up the rise of current once the discharge forms. The reason for improved stability of the discharge with this capacitor is not clear. The capacitor acts possibly as a low-impedance source which allows the plasma to form unimpeded.

The peak current of about 1000 A may be reduced by placing an inductor in-series with the discharge, as shown in Fig. 4. In order to "start" the discharge a small capacitance shunts the 360-μH inductor. As can be seen in Fig. 4 the current is reduced to 100 A and the pulse is stretched to several microseconds. Unlike the results of other work [5] the voltage across the discharge does not settle to some quasi-steady-state value, but has almost a sinusoidal character. Some overshoot and ringing of the voltage can also be seen. If the current pulse is stretched beyond approximately 10 μs, the discharge appears to degenerate. For short pulses the plasma appears visually to be distributed uniformly across the electrode sur-

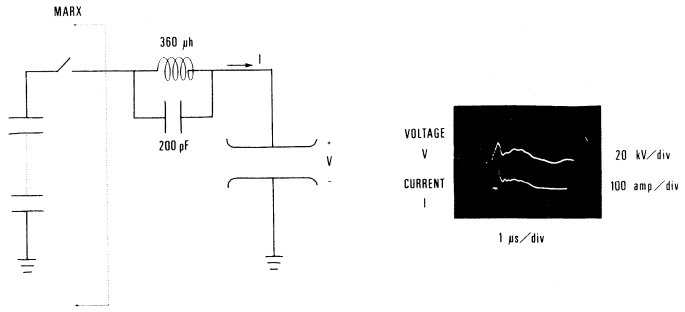


Fig. 4. Discharge pulsewidth is stretched using an inductance in-series with the discharge.

face. However, when the current duration is increased the plasma becomes localized and patchy, following the small irregularities of the electrode surface. The plasma distribution also becomes critically sensitive to electrode alignment. Clearly, small variations of electric field greatly influence the local growth and decay of the discharge. In fact, the large sensitivity of current to change in electric field is a documented feature of these discharges [5]. The nonuniform development of the discharge is accompanied by cathode filaments which form the "seeds" of the glow-to-arc transition. We conclude that the atmospheric-pressure discharge as we have described here is poorly adapted to long pulse lengths. If, however, the gas pressure is reduced, the difficulties just described are resolved. For example, at a gas pressure of 250 torr a uniform glow discharge of 30-μs duration can be obtained in the discharge geometry just described. For discharge duration in excess of 30 μs, current leakage into the 30-mH holdoff inductors becomes significant.

The maximum repetition frequency of this structure is limited not by discharge instabilities as others have observed [2], but by the recovery strength of the discharge spark gaps. Fig. 5 shows the recovery strength of the spark gaps in the absence of the discharge. This corresponds to linear charging of a 0.1-μF capacitor, which is used to drive a 100-Ω resistive load through a single spark gap. At atmospheric pressure these data indicate that 10 000 pulses per second (pps) operation with 6-kV charging should be possible. When the spark gaps are operated in the discharge structure that has been described, a maximum operating frequency of much less than 10 000 pps was observed. The recovery strength of the spark gaps is modified by the presence of the glow discharge which is upstream of the gaps. For example, with a stored energy of 20 J/pulse we find a maximum pulse repetition frequency (PRF) of 2000 pps. If the stored energy per pulse is reduced to 3 J, that is, by almost an order of magnitude, the maximum PRF does increase. The increase, however, is only to 4000 pps. One explanation for this modified recovery strength is that the discharge reduces the gas flow. Recurrent shock waves moving against the flow might be expected to slow the gases. Measurement, however, has shown that the flow velocity is very little modified by the discharge. The other and probable explanation for the observed derating of the spark-gap recovery is that ionized gases from the discharge flow into the spark gaps. The transit time from the discharge to the gaps is less than 1 ms so that substantial ionization can be expected to

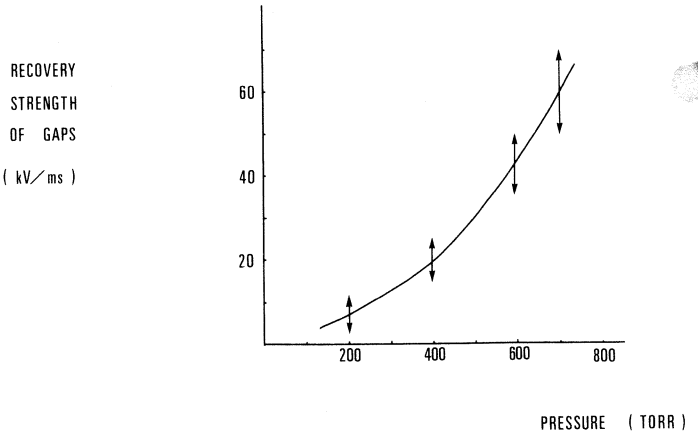


Fig. 5. Recovery strength of the Marx-generator spark gaps in the absence of the discharge.

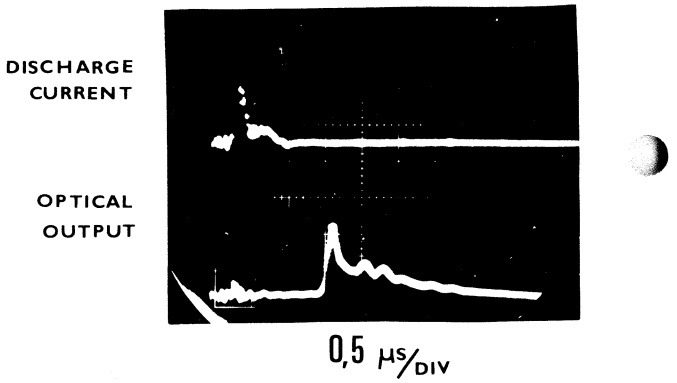


Fig. 6. Typical optical output pulse.

remain in the gases. A blown gap will recover much faster than a nonblown gap simply because of the convective removal of charge from the gap. It is clear that a contrary effect will occur if charge is blown into the gap. The presence of ionized gases from the discharge also influences the breakdown potential of the gaps. At a low repetition rate for the conditions summarized in Table I the minimum breakdown voltage with the trigger used is 6 kV. However, at close to 2000 pps the minimum breakdown voltage is reduced to 4 kV. This indicates the presence of highly ionized gases flowing into the gaps.

In Fig. 6 a typical optical output pulse is shown with reference to the discharge current. The usual gain switching effect and optical delay can be seen. The optical pulse shown in Fig. 6, though uncalibrated, corresponds to an energy out-

put of 1 J. This result was obtained using the parameters of Table I and a cavity coupling of 10 percent (10-percent-reflectivity output mirror). With a molecular gas concentration of approximately 40 percent the optical energy has a maximum of 2 J. The laser is very sensitive to losses in the cavity which suggests rather low gain. For example, when NaCl Brewster-angle windows of apparently good quality are introduced into the cavity the optical energy is substantially reduced.[1]

Our experience with other systems indicates that this difficulty may be resolved either by using a longer discharge or by increasing the specific input energy to the discharge.

IV. Conclusions

This technique has demonstrated the integration of switching and preionization using Marx-generator spark gaps within the flowing laser gases. A maximum PRF of 2000 pps and an average discharge power of approximately 30 kW show great promise for the utility of the high-repetition-rate CO_2 laser. Of note is the very high power density achieved. The discharge volume of 0.37 l results in a power density of approximately 80 kW/l.

[1] For the parameters given in Table I the optical output energy is reduced by a factor of 5.

References

[1] R. Dumanchin, M. Michon, J. C. Farcy, G. Boudinet, and J. Rocca-Serra, "Extension of TEA CO_2 laser capabilities," *IEEE J. Quantum Electron. (Part II of Two Parts: Special Issue on 1971 IEEE/OSA Conf. Laser Engineering and Applications)*, vol. QE-8, pp. 163-165, Feb. 1972.

[2] C. W. Glanford, M. F. Paris, P. R. Pearson, and D. C. Tyte, "High repetition-rate operation of a double Rogowski TEA CO_2 laser," presented at the IEEE/OSA Conf. Laser Engineering and Applications, Washington, DC, June 1973.

[3] G. S. Dzakowic and S. A. Wutzke, "The influence of transverse gas flow upon high pressure high repetition rate glow discharge," presented at the 25th Gaseous Electronics Conf., London, Ont., Canada, 1972.

[4] D. B. Nichols and W. M. Brandenberg, "Radio-frequency preionization in a supersonic transverse electrical discharge laser," *IEEE J. Quantum Electron.* (Corresp.), vol. QE-8, pp. 718-719, Aug. 1972.

[5] L. J. Denes and J. J. Lowke, "*V-I* characteristics of pulsed CO_2 laser discharges," *Appl. Phys. Lett.*, vol. 23, pp. 130-132, Aug. 1973.

[6] O. P. Judd and J. Y. Wada, "Investigations of a UV preionized electrical discharge and CO_2 laser," *IEEE J. Quantum Electron.*, vol. QE-10, pp. 12-20, Jan. 1974.

Contributors



G. Brederlow was born in Pakulent, Germany, on October 23, 1929. He received the M.S. degree and the Dr. rer. nat. degree, both in physics, from Greifswald University, Greifswald, Germany, in 1955 and 1957, respectively.

From 1957 to 1959 he was engaged in plasma physics at the Institute for Gas Discharges, Greifswald. In 1960 he joined the Max-Planck-Institut für Plasmaphysik, Garching, Germany, where he worked on shock tubes and noble-gas MHD generators until 1973. In 1969 he was a Guest Scientist at the Department of Mechanical Engineering, Stanford University, Stanford, CA. Since 1973 he has been active in the iodine laser field.

Dr. Brederlow is a member of the Deutsche Physikalische Gesellschaft.

*

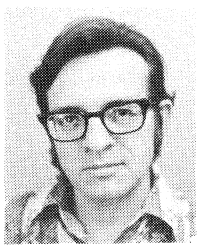


C. Forbes Dewey, Jr., was born in Pueblo, CO, on March 27, 1935. He received the B.E. degree from Yale University, New Haven, CT, the M.S. degree from Stanford University, Stanford, CA, and the Ph.D. degree from the California Institute of Technology, Pasadena, in 1956, 1957, and 1963, respectively.

From 1963 to 1968 he was an Assistant Professor of Aerospace Engineering Sciences at the University of Colorado, Boulder. Since 1968 he has been an Associate Professor of Mechanical Engineering at the Massachusetts Institute of Technology, Cambridge. He was a Visiting Scientist at the Institut für Plasmaphysik, Garching, Germany, in 1966–1967, during which period he held a University of Colorado Faculty Fellowship and lectured throughout Europe for the Advisory Group for Aeronautical Research and Development. Since 1960 he has been a Consultant to numerous academic and industrial organizations, including the RAND Corporation, Sansum Clinic Research Foundation, and Thermo Electron Corporation. Currently, he is Chairman of the Board of Sensoresearch Corporation and a Trustee of the Cardiovascular Charitable Trust of Boston. His research interests, which are reflected in over fifty scientific and technical papers and patents, have been in the fields of high-speed aerodynamics, boundary layer theory, free-molecular flow, low-density plamas, nonlinear optics and laser applications, biomedical fluid mechanics, and industrial and medical instrumentation.

Dr. Dewey is a member of Tau Beta Pi, Sigma Xi, the American Physical Society, and the Yale Engineering Association.

*

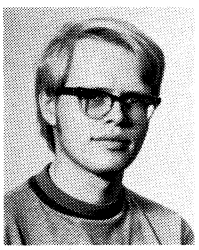


Richard A. Elliott (S'71) was born in Canada in 1937. He received the B.A. degree and the B.Sc. and M.Sc. degrees in physics, all from Queen's University, Kingston, Ont., Canada, in 1960, 1961, and 1963, respectively. He received the Ph.D. degree from the University of British Columbia, Vancouver, B.C., Canada, in 1966, where he specialized in kinetic theory and nonequilibrium statistical mechanics.

He was a Research Associate of Prof. E. W. Montroll at the Institute for Fundamental Studies, University of Rochester, Rochester, NY, from 1966 to 1969. While there he worked on random walk theory and its application to exciton conduction in macromolecules and molecular crystals. Since 1969 he has been with the Department of Applied Physics and Electronic Science, Oregon Graduate Center, Beaverton, OR. His research interests have expanded to include laser propagation through turbulent media, statistical models of small-scale turbulence, high-gain optical parametric interactions, and laser pulse shaping.

Dr. Elliott is a member of the Canadian Association of Physicists.

*



Wayne Faszer was born in Edmonton, Alta., Canada, in 1952. He received the B.Sc. degree in physics from the University of Alberta, Edmonton, Alta., Canada, in 1973. He is currently working towards a Ph.D. in electrical engineering at the University of Alberta.

*



Ernst Fill was born in Kufstein, Austria, in November 1940. He received the Ph.D. degree in physics and mathematics from the University of Innsbruck, Innsbruck, Austria. He then pursued one-and-a-half years of postdoctoral study at the University of Vermont, Burlington.

In 1969 he joined the Max-Planck-Institut für Plasmaphysik, Garching, Germany, where he has been engaged in experimental studies of various high-power lasers, notably the Nd-$POCl_3$, the CO_2, and the iodine laser.

Dr. Fill is a member of Sigma Xi, Chapter-at-Large.

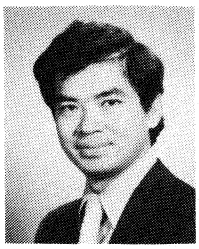
*



K. Hohla was born in Prague, Czechoslovakia, on June 11, 1943. He received the M.S. degree and the Dr. rer. nat. degree, both in physics, from Ludwig Maximilians University of Munich, Munich, Germany, in 1968 and 1971, respectively.

In 1970 he joined the Max-Planck-Institut für Plasmaphysik, Garching, Germany, and was at first engaged in chemical laser physics. Since 1972 he has worked in the iodine laser field.

Dr. Hohla is a member of the Deutsche Physikalische Gesellschaft.



David T. Hon was born in Kwangtung, China, on August 9, 1941. He received the B.A. degree from the University of California, Berkeley, in 1964, the M.S. degree from the University of Oregon, Eugene, in 1966, and the Ph.D. degree in physics from the University of Southern California, Los Angeles, in 1972.

He was an Assistant Professor at California Polytechnic University from 1967 to 1968. He has been with the Laser Division, Hughes Aircraft Company, Culver City, CA, since 1972 where he is now a Senior Staff Physicist and leader of the laser technology group. His thesis on plasmon–phonon interaction was an invited paper in *Applied Physics*. His current interest includes isotope separation involving the use of the frequency up-converted high-power Nd: YAG laser.

Dr. Hon is a member of Sigma Xi.

*



Irving Itzkan (M'57) received the B.S. degree in engineering physics from Cornell University, Ithaca, NY, in 1952, the M.S. degree in electrical engineering from Columbia University, New York, NY, in 1961, and the Ph.D. degree in physics from New York University, New York, NY, in 1969.

He joined the Sperry Rand Corporation in 1956 as an Engineer assigned to research on the formation and control of high-density electron beams and fast-response electron beam-switching tubes. He became a Senior Engineer in 1958 and was involved with studies of slow-wave interaction circuits for traveling-wave tubes and electron-beam parametric amplifiers. In 1962 he advanced to Engineering Section Head for microwave tube research and led projects that concerned transverse-wave tubes and hollow-beam electron guns. He joined the Sperry Electro-optics Group in 1964 as Engineering Section Head for Laser Research and assumed responsibility for problems dealing with the physics of lasers, nonlinear optics, and optical components. During this period he was in charge of numerous research projects, both company sponsored and government sponsored. He joined the AVCO Everett Research Laboratory, Inc., Everett, MA, in 1969 where he has been principally concerned with research on high-power lasers, tunable dye lasers, atmospheric seeing, and high-power beam propagation. In 1970 he became Chairman of the Optics Research Committee with responsibility for maintaining the high level of performance of the laboratory in all phases of optics research. His most recent research involves the use of lasers for remote-sensing applications, and the use of highly tuned lasers for isotope separation. He is the author of 31 publications and holds 9 patents with several other patent applications pending.

Dr. Itzkan is a member of the American Physical Society, the Optical Society of America, Sigma Pi Sigma, and Tau Beta Pi.

*



Ralph R. Jacobs was born in Niagara Falls, NY, on December 31, 1942. He received the B.S. degree (physics) from New York University, New York, and the Ph.D. degree (physics) from Yale University, New Haven, CT, in 1964 and 1969, respectively. His dissertation was concerned with studies on the fine structure He^+.

He then joined the GTE Laboratories, Bayside, NY, and was involved in various research on gas and CW dye lasers. Since 1972 he has been in the laser fusion program at the Lawrence Livermore Laboratory, University of California, Livermore, and has conducted investigations on rapid relaxations in CO_2 and in the areas of laser spectroscopy and new gas lasers.

Dr. Jacobs is a member of the American Physical Society, the Scientific Research Society of America, Tau Beta Pi, and Sigma Pi Sigma.

*



G. Sargent Janes received the B.A. degree from Cornell University, Ithaca, NY, in 1949, and the Ph.D. degree from the Massachussetts Institute of Technology, Cambridge, in 1953. His area of study for the Ph.D. was in radioactivity, the interaction of high-energy particles with matter, and radiation monitoring techniques.

He served on the staff of the Synchrotron Laboratory at the Laboratory for Nuclear Science at the Massachussetts Institute of Technology, working in high-energy nuclear physics. He conducted research in that field and also in cosmic rays, and the interaction of energetic particles with matter. He also obtained extensive experience with a 300-MeV electron synchrotron, taught courses in undergraduate physics, conducted research in the areas of nuclear particle detectors, electronic-pulse technology, and high-vacuum techniques. Since joining the AVCO Everett Research Laboratory, Inc., Everett, MA, in 1956, he has been active in the fields of plasma physics and magnetohydrodynamics, and has worked on the acceleration of high-temperature plasmas. He has investigated the properties of pure electron plasmas with a view towards evaluating their possible applications to the generation and containment of ultrahigh temperature ions, and to the production of superheavy ions. He has also made original contributions to the design of time-of-flight mass spectrometers, and to the development of lasers. He was recently appointed Vice President of the AVCO Everett Research Laboratory, Inc., with technical and administrative responsibilities as Director of the Isotope Research Program Office. In this capacity, he is currently leading a program directed towards the development of a new process which utilizes laser technology for the enrichment of uranium as a fuel for nuclear power plants. He has published papers on electrical space propulsion, radiation phenomena, plasma acceleration and electron diffusion phenomena in crossed electric and magnetic fields, generation and containment of pure electron plasmas in time-dependent magnetic fields, calibration and monitoring of gamma-ray beams, and the design of targets for nuclear physics experiments. He holds patents and patent applications in a number of areas including laser isotope enrichment.

Dr. Janes is a member of the American Physical Society and the American Institute of Aeronautics and Astronautics.

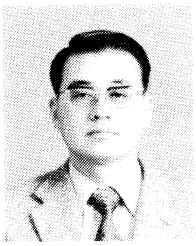
*



Joel C. Johnson (S'72-M'67) was born in Park Rapids, MN, on January 25, 1950. He received the B.S. degree in applied science from Portland State University, Portland, OR, in 1972, where he is now pursuing the M.S. degree in the area of pollutant monitoring using dye lasers.

Currently, he is on the staff of the Oregon Graduate Center, Beaverton, OR, where his interests are in solid, liquid, and gas lasers and nonlinear optics.

Mr. Johnson is a member of the Optical Society of America.



Hiroshi Kashiwagi (M'68) was born in Tokyo, Japan, on June 21, 1943. He received the M.S. and Ph.D. degrees in electrical engineering in 1960 and 1967, respectively.

In 1964 he joined the Electrotechnical Laboratory, Tokyo, Japan, and since then he has been engaged in research on millimeter- and submillimeter-wave technology, lasers, and optical communication and display. He is currently a Chief of the Laser Section, Radio- and Opto-Electronics Division. Currently, his fields of interest are efficient high-power lasers and optical communication.

Dr. Kashiwagi is a member of the Institute of Electronics and Communication Engineers of Japan, the Japan Society of Applied Physics, and the Institute of Electrical Engineers of Japan.

*



Lawrence Levin received the B.A. degree in physics from Columbia University, New York, NY, in 1961, the M.S. degree in physics from Yale University, New Haven, CT, in 1962, and the Ph.D. degree in physics from the Hebrew University of Jerusalem, Jerusalem, Israel, in 1967. His doctoral dissertation covered experimental studies of optical pumping of excited states of atomic vapors and paramagnetic ions in solids, and a theoretical analysis of the results.

He was an Assistant Professor of Physics at Columbia University, and at the Columbia Radiation Laboratory he studied stimulated Raman scattering in a theoretically simple system (atomic thallium vapor) to develop a new technique, the "Raman echo," for studying excited states of more complex systems. He also advised graduate students who were working on photon echoes and electron-spin echoes in ruby and neodymium-doped materials, multiphoton absorption phenomena, and the interaction of incoherent radiations with matter. He has worked at the AVCO Everett Research Laboratory, Inc., Everett, MA, as a Senior Scientist in the isotopes research program. He is now with the Nuclear Research Center, Negev, Beer-Cheva, Israel.

*



Richard H. Levy (M'65) was born in London, England, in 1932. He attended Cambridge University, Cambridge, England, and received the Ph.D. degree in engineering from Princeton University, Princeton, NJ, in 1958.

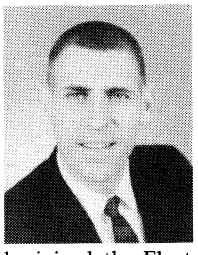
Since 1960 he has been with the AVCO Everett Research Laboratory, Inc., Everett, MA, a subsidiary of the AVCO Corporation, specializing in advanced research and development activities. In November 1972 he was appointed Vice President of the AVCO Corporation. He was Vice President and Director of a joint venture company established by the AVCO Corporation and the Exxon Corporation to exploit a new technique for uranium enrichment. He is currently Manager of Jersey Nuclear-AVCO Isotopes Program Planning, Exxon Nuclear Company, Inc., Bellevue, WA. His activities have involved research and management of research in a variety of areas, including plasma physics, aerodynamics, super-conducting magnets, blood flow, high-voltage electron devices, and laser applications. He is the author of a score of scientific papers and several patents.

Dr. Levey is a member of many professional and technical societies, including the American Physical Society and the American Nuclear Society.



Otto T. Masopust, Jr., is a Development Engineer in the Capacitor Design Control, Manufacturing and Development Engineering Group at Western Electric's Hawthorne Works, Chicago, IL. His present professional interests concern capacitor designs with thin metallized dielectric films, various laser generated network designs, and the development of process facilities for capacitor and network manufacture. He holds five patents involving metallized film capacitor and laser generated network manufacture.

*



Gail A. Massey (M'67) received the B.S.E.E. degree from the California Institute of Technology, Pasadena, and the M.S. and Ph.D. degrees from Stanford University, Stanford, in 1959, 1967, and 1970, respectively.

From 1959 to 1963 he was a member of the engineering staff of the Raytheon Company, Santa Barbara, CA, where he worked in the areas of optical communications, modulator device development, and laser range-finders. In 1963 he joined the Electro-optics Group of GTE Sylvania, Mountain View, CA, where as a Senior Engineering Specialist his activities included development of laser vibration sensors and acoustooptical devices, research in acoustical holography, and acoustical imaging systems, laser mode locking and development of high-power lasers, new materials for solid-state lasers, and nonlinear optical devices. He joined the faculty of the Oregon Graduate Center, Beaverton, OR, in 1972 and currently holds the position of Professor in the Department of Applied Physics and Electronic Science. His current research activities include nonlinear optical devices, dye lasers, and laser remote sensing techniques.

Dr. Massey is a member of the Optical Society of America and the Acoustical Society of America.

*



Marco Montanarini was born in Aarau, Switzerland, in 1941. He received the Diploma in physics and the Ph.D. degree from the Swiss Federal Institute of Technology, Zürich, in 1967 and 1973, respectively.

From 1968 to 1973 he worked as a Research Assistant in the Institute of Crystallography of the Swiss Federal Institute of Technology, on Order–Disorder phenomena in mixed crystals of YIG and YAG. He joined the LASAG Company, Thun, Switzerland, in 1973 where he is currently a member of the Research Group engaged in high-precision laser material processing.



Peter E. Oettinger received the Ph.D. degree from Stanford University, Stanford, CA, in 1966.

Thereafter, he taught at the University of Colorado, Boulder, and conducted research at its Joint Institute for Laboratory Astrophysics. Prior to joining Thermo Electron, he was a member of the technical staff at the Aerospace Corporation. He is now a Senior Scientist at the Thermo Electron Corporation's Research and Development Center, Waltham, MA, and head of its Laser Instruments Development Program.

*



Charles T. Pike received the B.S. degree in physics from Union College, Schenectady,NY, in 1960, and the M.S. degree, also in physics, from Fairleigh Dickinson University, Rutherford, NJ, in 1964.

In 1960 he joined the Isomet Corporation as an Associate Research Physicist and assisted in research and development of lasers and electro-optic light modulators. In 1964 he joined the GCA Corporation as a Senior Scientist assigned to the research and development of lasers and the application of lasers to physical measurements of the atmosphere. His primary contribution was the development of a tuned optical radar for the detection of atomic species in the upper atmosphere. During the period 1964–1968 he developed efficient nonlinear optical techniques: Raman shifting, and second and fourth harmonic generation. He also developed mode selection techniques for line narrowing and tuning of lasers. He developed laser pumped and flashpumped tunable dye lasers for application to atmospheric probing during the period 1969–1971. He joined the AVCO Everett Research Laboratory, Inc., Everett, MA, in 1971 as a specialist in optics and lasers and since that time has been developing stable dye lasers and dye laser systems for use in isotope separation. He is the author of several publications and holds two patents with others pending.

Mr. Pike is a member of the Optical Society of America.

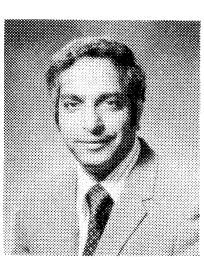
*



John F. Ready was born in St. Paul, MN, on July 13, 1932. He received the M.S. degree in physics from the University of Minnesota, Minneapolis, in 1956.

He is currently a Senior Principal Scientist with the Honeywell Corporate Research Center, Honeywell, Inc., Bloomington, MN, where he is engaged in research on the interaction of high-power laser radiation with materials.

*

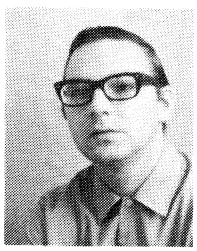


Mansoor A. Saifi received the B.E. degree in electrical engineering and the B.E. degree in mechanical engineering from Osmania University, Hyderabad, India, in 1953 and 1958, respectively. He received the M.S. degree from the University of Idaho, Moscow, and the Ph.D. degree from the Pennsylvania State University, University Park, both in electrical engineering, in 1960 and 1968, respectively.

From 1953 to 1962 he was associated with several electrical machinery manufacturers in India and the United States. His work in this area encompassed all aspects of rotating electrical machines, i.e., development, design, and manufacturing. From 1963 to 1968 he was an Instructor in Electrical Engineering at the Pennsylvania State University. Since 1968 he has been a member of the Research Staff with the Engineering Research Center of the Western Electric Company, Inc., Princeton, NJ. His main research interests are in the interaction of high-intensity electromagnetic radiation with materials and its application to materials processing.

Dr. Saifi is a member of the American Physical Society and its division on solid-state physics.

*

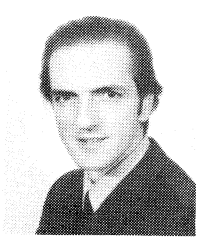


Herb J. Seguin (M'71) was born in Alberta, Canada, in 1935. He received the B.Sc. degree in electrical engineering from the University of Alberta, Edmonton, Alta., Canada, and the Ph.D. and D.I.C. degrees from the Imperial College of Science and Technology, University of London, London, England, in 1959 and 1963, respectively.

From 1963 to 1966 he was an Assistant Professor at the U.C.L.A. Physics Department. In 1966 he joined the Department of Electrical Engineering at the University of Alberta in Edmonton where he currently acts as Laser Group Leader.

Dr. Seguin is a member of Sigma Xi, the Optical Society of America, and CAP.

*

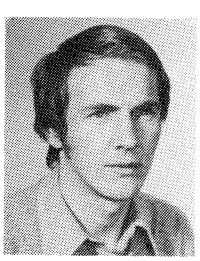


Jürg Steffen was born in Zürich, Switzerland, in 1942. He received the M.S. degree in physics from the Swiss Federal Institute of Technology, Zürich, and the Ph.D. degree from the Institute of Applied Physics, University of Berne, Berne, Switzerland, in 1966 and 1970, respectively. The M.S. thesis concerned work on CN-lasers, and the Ph.D. dissertation concerned solid-state lasers for high precision material processing.

From 1968 to 1971 he was head of the Laser Material Processing Group of the Institute of Applied Physics, University of Berne. Since 1972 he has been Research Head of the Research Institute Pierres Holding and of the LASAG Company, Thun, Switzerland, working on industrial laser applications.

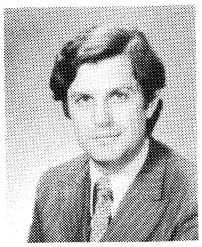
Dr. Steffen is a member of the Optical Society of America.

*



John Tulip was born in Durham, England, on September 2, 1943. He received the B. Eng. degree in electrical engineering in 1966 from the University of Sheffield, Sheffield, England. He then did graduate work on lasers at the University of Sheffield and at University College, London, England. He received the Ph.D. degree in electrical engineering from the University of Sheffield in 1969.

In 1968 he received a postdoctoral fellowship from the University of Alberta, Edmonton, Alta., Canada, where, since 1972, he has been Associate Professor in the Department of Electrical Engineering. His principal research interests include pulsed and continuous gas discharge lasers, and optically pumped long-wavelength lasers.

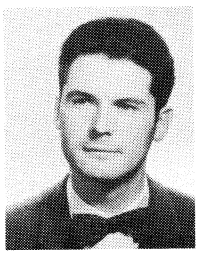


Sotirios J. Vahaviolos (S'69–M'72) was born in Mistras Sparta, Greece, in 1946. He received the B.S.E.E. degree from Fairleigh Dickinson University, Rutherford, NJ, and the M.S.E.E. degree from Columbia University, New York, in 1970 and 1972, respectively. Currently, he is completing thesis work on signal processing techniques at Columbia.

As a member of the Research Staff of the Engineering Research Center, Western Electric Company, Inc., Princeton, NJ, he has been involved in IC testing, real-time measurement, and failure mode analysis. His published work has been concerned with active filters, graph theory, and stress wave emission source modeling and signal processing.

Mr. Vahaviolos is a member of Pi Zeta Kappa, Phi Chi Psi, Eta Kappa Nu, Sigma Chi, and holds three patents. He is currently serving as an Associate Editor of the IEEE TRANSACTIONS ON INDUSTRIAL ELECTRONICS AND CONTROL INSTRUMENTATION and is the Program Chairman of IECI'76.

*



R. Volk was born in Buchen/Odenwald, Germany, on June 15, 1940. His study of physics began at the Technical University of Karlsruhe, Karlsruhe, Germany, and he received the M.S. degree in physics from the Technical University of Munich, Munich, Germany, in 1965. He received the Dr. rer. nat. degree in 1970 with a thesis on Rayleigh scattering of gamma rays.

He joined the Max-Planck-Institut für Plasmaphysik, Garching, Germany, where he worked on combustion MHD until 1973. Since then he has been active in the iodine laser field.

*



Marvin J. Weber was born in Fresno, CA. He received the A.B., M.A., and Ph.D. degrees in physics from the University of California, Berkeley, in 1954, 1956, and 1959, respectively.

From 1959 to 1973 he was a Principal Scientist with the Raytheon Research Division, Waltham, MA. In 1966 he was a Visiting Research Associate at Stanford University. His research has been in the areas of luminescence, quantum electronics, and optical spectroscopy and magnetic resonance in solids. Since 1973 he has been a group leader in the laser fusion program at the Lawrence Livermore Laboratory, University of California, Livermore.

Dr. Weber is a fellow of the American Physical Society.

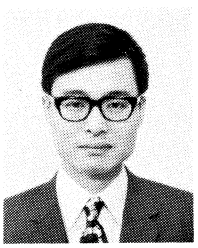
*



K. J. Witte was born in Bromberg, Poland, on January 27, 1939. He received the M.S. degree in mechanical engineering and the Dr.-Ing. degree in engineering science, both from the Technical University of Darmstadt, Darmstadt, Germany, in 1964 and 1968, respectively. From 1969 to 1970 he held a postdoctoral fellowship at the Massachussetts Institute of Technology, Cambridge, where he was engaged in the study of noble-gas MHD generators.

In 1971 he joined the Max-Planck-Institut für Plasmaphysik, Garching, Germany, where he continued the investigation of noble-gas MHD generators up to the end of 1973. Since then he has worked on the iodine laser.

*



Mikio Yamashita was born in Kyoto, Japan, on February 15, 1946. He received the B.E. degree in electrical engineering from the Kyoto University of Industrial Arts and Textile Fibers, Kyoto, Japan, and the M.E. degree in electronic engineering from Kyoto University, Kyoto, Japan, in 1968 and 1970, respectively.

Since joining the Laser Research Group, Radio- and Opto-Electronics Division, Electrotechnical Laboratory, Tokyo, Japan, as a Research Scientist in 1970, he has been engaged with laser excitation ESR studies on laser dyes. He has been working toward the Ph.D. degree in electronic engineering in the area of dye lasers at Kyoto University. His research interests are also in laser-induced photochemical reactions including isotope separation and biophysics.

Mr. Yamashita is a member of the Physical Society of Japan, the Japan Society of Applied Physics, and the Institute of Electronics and Communication Engineers of Japan.

Threshold Behavior of CW GaAs–AlGaAs Injection Lasers

JEROME K. BUTLER, MEMBER, IEEE, AND CHUNG-SHU WANG, STUDENT MEMBER, IEEE

Abstract—**This paper investigates some of the properties of continuous wave (CW) (AlGa)As–GaAs injection lasers with Al in the active region. The active region gain at threshold g_{th} is estimated as a function of Al concentration in the active region. The basic configuration is a five-layer structure with GaAs as the two outer regions; the center region is $Al_yGa_{1-y}As$ and the two surrounding layers are $Al_xGa_{1-x}As$.**

Introduction

CONTINUOUS WAVE (CW) lasers [1]-[4] have geometrical structures different from those used in the pulsed mode [5], [6]. Generally, CW structures have the active region in the proximity of a heat sink so that efficient heat transfer from the active region can be obtained.

This study determines the threshold gain characteristics of CW lasers as a function of Al concentration in the active region. For certain device geometries, we show that the gain at threshold can be reduced by the addition of Al to the active region. Since GaAs is usually employed as a substrate and for "capping off" the AlGaAs growth, there is a strong interaction of the lasing field with the GaAs "cap" since the absorption coefficient of GaAs is very large at lasing wavelengths around 8000 Å.

The basic device structure used for the fabrication of CW lasers is shown in Fig. 1 [1], [2]. The active region 3 where the lasing wavelength is determined by the fraction of Al concentration y is bounded by two $Al_xGa_{1-x}As$ layers with $x > y$. The two outside regions 1 and 5 are, respectively, p- and n-GaAs. The widths of the inner regions are illustrated in the figure. A laser structure similar to that shown in Fig. 1 has been used to produce low-threshold devices emitting short wavelengths [7], [8]; the largest fraction Al was $y \cong 0.37$ which is the approximate upper bound for y to produce a direct bandgap material [8]. Lasers which are used for CW operation are generally made with $y \cong 0.1$ and with the outer p- and n-walls having $x = 0.3$ [1], [2]. The basic configuration can be modeled theoretically as a five-layer device where the two outer regions extend to infinity along the positive and negative x directions [9].

Theoretical Model

The fraction Al used in the confining regions 2 and 4 will have a fixed relation with respect to the values used in the active region so that a given index of refraction discontinuity can be maintained between the active region 3 and the p- and n-$Al_xGa_{1-x}As$ regions 2 and 4. The refractive index variation

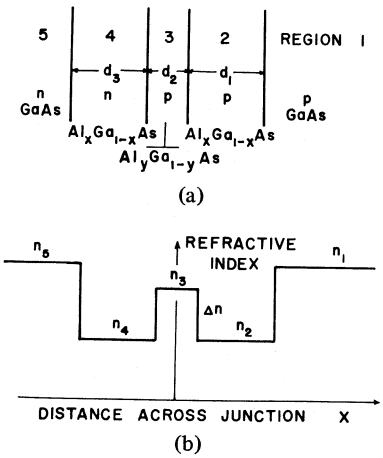


Fig. 1. Five-layer model of the CW laser. (a) The layer thickness and Al composition are indicated with $y < x$. (b) The refractive index variation as a function of the distance across the layers.

of a given region is approximately proportional to the mole fraction of Al. For example, if n_0 is the index of GaAs at $\lambda_0 \sim 9000$ Å, then the index of $Al_xGa_{1-x}As$ at $\lambda \sim \lambda_0$ is

$$n(x, \lambda) \sim n_0 + n_x x + n_\lambda(\lambda - \lambda_0)$$

where $n_x = (\partial n/\partial x)_{x=0,\lambda=\lambda_0}$ and $n_\lambda = (\partial n/\partial \lambda)_{x=0,\lambda=\lambda_0}$. The index discontinuity between GaAs and $Al_xGa_{1-x}As$ at $\lambda = \lambda_0$ is $n_0 - n(x, \lambda_0) = -n_x x$. The index discontinuity between $Al_yGa_{1-y}As$ and $Al_xGa_{1-x}As$ is

$$n = n(y, \lambda) - n(x, \lambda) = n_x(y - x).$$

The preceding expression is a linear approximation for the index discontinuity and it is valid only over a limited range near $x, y = 0$ and $\lambda = \lambda_0$. Over a wide range of x and λ values, the exact value $n(x, \lambda)$ of $Al_xGa_{1-x}As$ should be determined from experimental data [10], [11].

The Al in the active region is the predominant factor which determines the lasing wavelength [8]. Another factor affecting the lasing energy is the dopant and its concentration. For example, lasers fabricated with GaAs active regions have had lasing wavelengths varying from approximately 8800–9200 Å. To simplify this study, we will not be concerned with the changes in lasing wavelength due to the active region doping; we assume that all active regions with different Al concentrations are fabricated identically with respect to doping.

At lasing energies greater than the bandgap of GaAs, the absorption constants α_1 and α_5 in regions 1 and 5 are very large while if the lasing energies are less than the energy gap of GaAs then α_1 and α_5 are relatively small and will be strongly doping-level dependent; we use here the absorption constant of p-GaAs [12] with $p \sim 10^{18}$ cm^{-1}. The value of the photon energy is correlated with the lasing wavelength determined by

Manuscript received July 14, 1975; revised October 14, 1975. This work was supported in part by the National Science Foundation under Grant ENG 74-22946.

The authors are with the Department of Electrical Engineering, Southern Methodist University, Dallas, TX 75275.

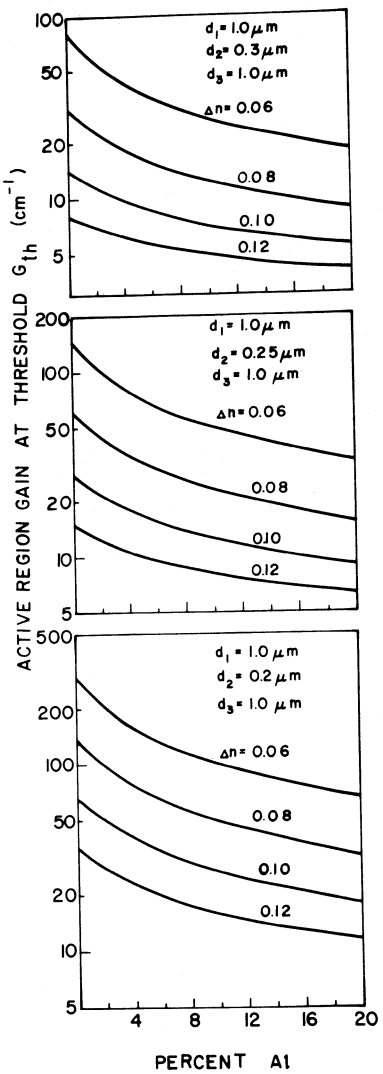


Fig. 2. Dependence of G_{th} with respect to Al content y of the active region. The geometrical structure is symmetrical with $d_1 = d_3 = 1$ μm. The refractive index discontinuities Δn are 0.06, 0.08, 0.10, and 0.12. The absorption coefficient in regions 2 and 4 is 10 cm^{-1}.

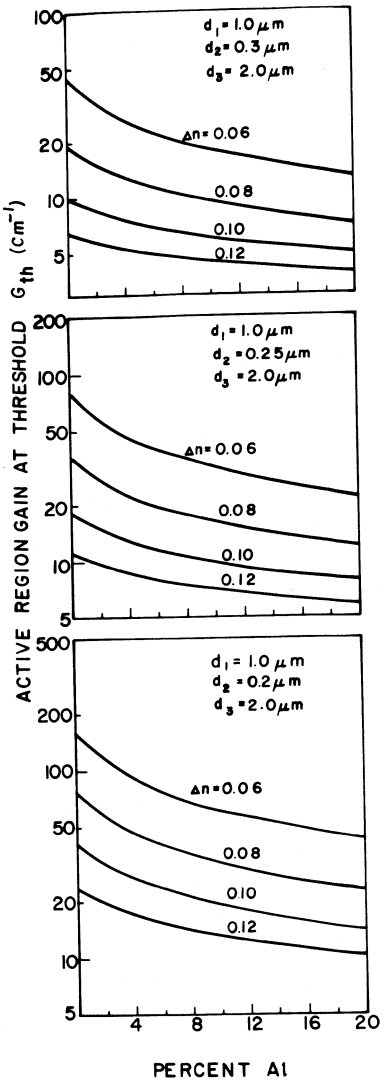


Fig. 3. Dependence of G_{th} with respect to Al content y of the active region. The structure is asymmetrical with $d_1 = 1$ μm and $d_3 = 2$ μm. $\alpha_2 = \alpha_4 = 10$ cm^{-1}.

the mole fraction y of Al used in the active region [8]. For $y = 0$, corresponding to a free-space wavelength of 0.9 μm, the absorption constant $\alpha_1, \alpha_5 = 100$ cm^{-1}, while for $y = 0.2$, which corresponds to $\lambda_0 = 0.771$ μm, $\alpha_1, \alpha_5 \sim 18\,000$ cm^{-1}. Consequently, the wave absorption in regions 1 and 5 are extremely large at short wavelengths leading one to expect relatively large values of g_{th} and J_{th} for such devices. However, these calculations lead to a different conclusion which we discuss in the following.

Numerical Examples

In the examples here, performance curves are calculated for d_2 values of 0.2, 0.25, and 0.3 μm. The index of refraction discontinuities between the optical cavity and the two confining layers which we treat as parameters, are assumed to be 0.06, 0.10, and 0.12. The indices n_1, n_5 of the outer regions are wavelength dependent [11] and their values can be determined once λ_L is specified. The results presented later are almost independent of the actual values of n_1 and n_5 provided $n_1, n_5 > n_3$; however, the values of α_1 and α_5 play a major role in the device performance by confining the light to the vicinity of the optical waveguide. The widths d_1 and d_3 of the optical confining layers are also assumed to be constants; we assume the following two different cases: 1) $d_1 = d_3 = 1$ μm and 2) $d_1 = 1$ μm and $d_3 = 2$ μm. The confining wall thicknesses were chosen because of previous calculations [2] concerned with the effects of device performance with respect to the confining wall thicknesses. It was found that the threshold gain of devices increased very rapidly as the widths d_1 and d_3 decreased below 1 μm.

The absorption constants of regions 2 and 4 are assumed to be 10 cm^{-1} since the bandgaps are well above the lasing energy, while that of regions 1 and 5 are correlated with the lasing wavelength λ_L. Although α_1 is determined from experimental data of p-GaAs, α_5 for n-GaAs is not, but it is chosen here to be identical to α_1 (calculations with exact values of α_5 produce only slight perturbations in the results presented).

Figs. 2 and 3 show a series of calculations giving the threshold gain G_{th} for a laser of infinite length and without free-carrier absorption α_{fc} in the active region. If Γ is the optical

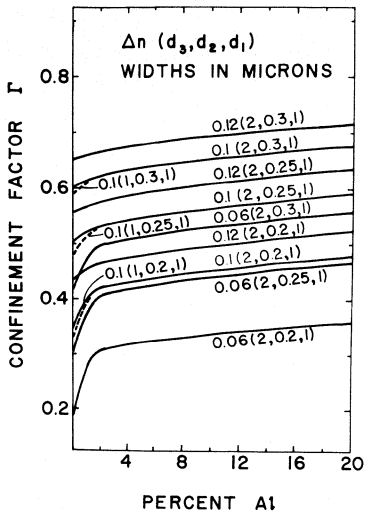


Fig. 4. Confinement factor Γ. The symmetrical and asymmetrical structures differ only near $y = 0$. The value of Γ varies most rapidly near $y = 0$ and is monotonically increasing.

wave confinement to the active region, the quantity

$$\bar{\alpha} = \Gamma G_{th}$$

represents the modal wave absorption due to losses in all regions other than that of the active region 3. The gain g_{th} of a laser of finite length and which has free-carrier losses in the active region is

$$\Gamma g_{th} = \Gamma(G_{th} + \alpha_{fc}) + \alpha_{end}$$

where $\alpha_{end} = 1/L \ln(1/R)$ is the equivalent absorption due to mirror losses, L is the laser length, and R is the mirror reflection coefficient. The external quantum efficiency is given by

$$\eta_{ext} = \eta_i \frac{\alpha_{end}}{\alpha_{end} + \Gamma(G_{th} + \alpha_{fc})}$$

where η_i is the internal quantum efficiency.

Figs. 2 and 3 illustrate the functional dependence of G_{th} with respect to the Al concentration y of the active region. The different plots correspond to the various cavity widths. In Fig. 2, the structure is symmetrical in the sense that $d_1 = d_3 = 1$ μm while in Fig. 3, $d_1 = 1$ μm and $d_3 = 2$ μm. The important result illustrated by this series of plots is that G_{th} decreases as y increases. Consequently, the lasers with a given active region width and index discontinuity $\Delta n = n_3 - n_2 = n_3 - n_4$, have the smallest G_{th} for the largest y.

The confinement factor Γ is shown in Fig. 4. Note that the behavior for the symmetrical structures is almost identical to that for the asymmetrical one. The value of Γ varies most rapidly near $0 < y < 0.02$ and is monotonically increasing with respect to y. For a typical laser [1] with $d_2 = 0.2$ and $\Delta n = 0.1$, Γ varies from 0.34 to 0.48 which is an approximate 40-percent change.

The behavior of G_{th} and Γ can be understood by examining the transverse cavity field for two different values of y. For $\Delta n = 0.1$, $d_1 = d_3 = 1$ μm, and $d_2 = 0.3$ μm, we show in Fig. 5 the cavity fields for $y = 0$ and 0.2. When y is increased, the value of Γ increases because 1) the decreasing lasing wavelength affects the effective cavity width, and 2) the increasing absorption in regions 1 and 5 increases the confinement of the cavity field to the active region. For $0 < y < 0.04$, the absorption constants α_1 and α_5 change rapidly because of the change of the lasing wavelength; this result is reflected in Fig. 4 by the rapid increase of Γ in the vicinity $y = 0$. For tightly bound fields occurring when Δn is large, the dependence of Γ on α_1 and α_5 is minor since a negligible fraction of the mode energy propagates in regions 1 and 5.

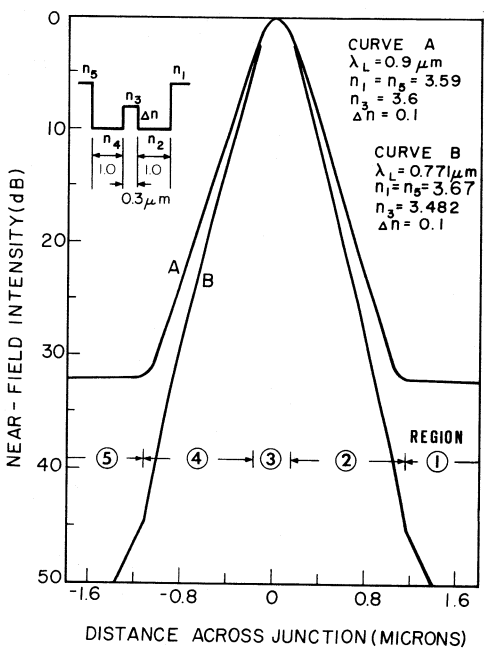


Fig. 5. The cavity modal fields for two similar laser structures. For curve A, there is no Al in the active region while for curve B, the active region has 20-percent Al. The fields in regions 1 and 5 attenuate rapidly for curve B.

Another important characteristic associated with these lasers is the radiation half-power beamwidth in the plane perpendicular to the p-n junction [13]. As expected, the lasers with the smallest index discontinuity have the smallest beam divergence

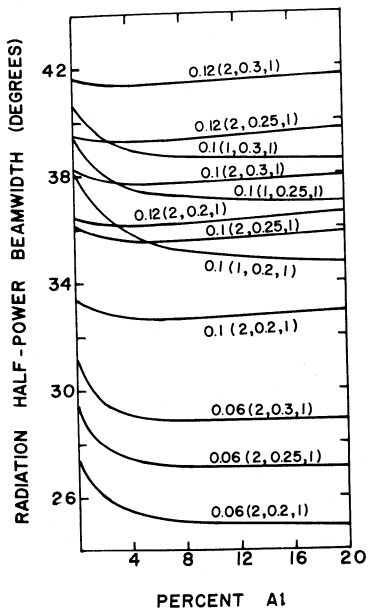


Fig. 6. Far-field radiation half-power beamwidth. The lasers having the smallest beam divergence correspond to the small Δn's. Each curve is labeled by four numbers corresponding to the index step and the various cavity dimensions.

as seen in Fig. 6. Note that for a given index step Δn the smallest half-power beamwidth is obtained with maximum Al concentration in the active region; however, the change in the half-power beamwidth with respect to y is only gradual above $y \sim 5$–10 percent.

Discussion

The primary aim of this study is to determine the effects on the active region gain g_{th} as a function of the lasing wavelength λ_L determined by the fraction y of Al used in the active region.

With the data given for G_{th} and Γ, it is possible to calculate g_{th} and η_{ext} for lasers with specific reflection coefficients R and active region free-carrier absorption α_{fc}. As an example, we take $\Delta n = n_3 - n_2 = n_3 - n_4 = 0.1$, $d_1 = 1\ \mu m$, $d_2 = 0.2\ \mu m$, and $d_3 = 2\ \mu m$. If $\alpha_{fc} = 20\ cm^{-1}$ and $\alpha_{end} = 30\ cm^{-1}$, then we find for the case $y = 0$, $g_{th} = 147\ cm^{-1}$, while if $y = 0.2$, $g_{th} = 97\ cm^{-1}$. If J_{th} is linearly related to g_{th}, then the laser with $y = 0$ will have an approximate 50-percent higher threshold current compared to the laser with $y = 0.2$.

Assuming $\eta_i = 0.65$ for $y = 0$ [8], the external quantum efficiency will vary from approximately 38–41 percent, the larger value corresponding to $y \cong 0.1$. For $y = 0.2$, $\eta_{ext} \cong 36$ percent. Consequently, the external quantum efficiency rises and drops with the optimum value occurring at $y \cong 0.1$. The reason for the drop in η_{ext} is due to the fact that internal quantum efficiency starts to decrease at approximately 0.8 μm [8]. However, it is important to note that the value of η_{ext} is strongly dependent on α_{fc}. The value we have chosen is arbitrary with the actual values being dependent upon the exact fabrication of the active region. When the active region is doped heavily p-type, the value of α_{fc} will be much larger than 20 cm^{-1} [12]. On the other hand, for lightly doped active regions, the injected carrier, both holes and electrons, will be large resulting in large values of α_{fc}.

References

[1] I. Ladany and H. Kressel, "The influence of device fabrication parameters on the gradual degradation of (AlGa)As CW laser diodes," *Appl. Phys. Lett.*, vol. 25, pp. 708–710, Dec. 15, 1974.

[2] J. K. Butler, H. Kressel, and I. Ladany, "Internal optical loss in very thin CW heterojunction laser diodes," *IEEE J. Quantum Electron. (Part II of Two Parts)*, vol. QE-11, pp. 402–408, July 1975.

[3] T. L. Paoli and B. W. Hakki, "CW degradation at 300°K of GaAs double-heterostructure junction lasers. I. Emission spectra," *J. Appl. Phys.*, vol. 44, pp. 4108–4112, Sept. 1973.

[4] B. W. Hakki and T. L. Paoli, "CW degradation of GaAs double-heterostructure junction lasers. II Electronic gain," *J. Appl. Phys.*, vol. 44, pp. 4113–4119, Sept. 1973.

[5] H. Kressel and F. Z. Hawrylo, "Fabry-Perot structure $Al_xGa_{1-x}As$ injection lasers with room-temperature threshold current densities of 2530 A/cm^2," *Appl. Phys. Lett.*, vol. 17, pp. 169–171, Aug. 15, 1970.

[6] I. Hayashi, M. B. Panish, and F. K. Reinhart, "GaAs-$Al_xGa_{1-x}As$ double heterostructure injection lasers," *J. Appl. Phys.*, vol. 42, pp. 1929–1941, Apr. 1971.

[7] K. Itoh, "6190-Å emission at 77K of $Ga_{1-x}Al_xAs$ double heterostructure lasers," *Appl. Phys. Lett.*, vol. 24, pp. 127–129, Feb. 1, 1974.

[8] H. Kressel, H. F. Lockwood, and H. Nelson, "Low-threshold $Al_xGa_{1-x}As$ visible and IR-light-emitting diode lasers," *IEEE J. Quantum Electron. (Special Issue on Semiconductors Lasers)*, vol. QE-6, pp. 278–284, June 1970.

[9] J. K. Butler, "Theory of transverse cavity mode selection in homojunction and heterojunction semiconductor diode lasers," *J. Appl. Phys.*, vol. 42, pp. 4447–4457, Oct. 1971.

[10] H. Kressel, H. F. Lockwood, and J. K. Butler, "Measurement of refractive index step and of carrier confinement at (AlGa)As-GaAs heterojunctions," *J. Appl. Phys.*, vol. 44, pp. 4095–4097, Sept. 1973.

[11] H. C. Casey, Jr., D. D. Sell, and M. B. Panish, "Refractive index of $Al_xGa_{1-x}As$ between 1.2 and 1.8 eV," *Appl. Phys. Lett.*, vol. 24, pp. 63–65, Jan. 15, 1974.

[12] I. Kudman and T. Seidel, "Absorption edge in degenerate p-type GaAs," *J. Appl. Phys.*, vol. 33, pp. 771–773, Mar. 1962.

[13] J. K. Butler and J. Zoroofchi, "Radiation fields of GaAs-(AlGa)As injection lasers," *IEEE J. Quantum Electron.*, vol. QE-10, pp. 809–815, Oct. 1974.

Parameter Ranges for CW Passive Mode Locking

HERMANN A. HAUS, FELLOW, IEEE

Abstract—CW passive mode locking of a homogeneously broadened laser is considered. In the coordinate plane, whose abscissa is proportional to the small-signal saturable absorber loading, and whose ordinate is proportional to the small-signal gain, the following regimes are laid out:

1) steady-state single-pulse mode-locking solutions;
2) stability against relaxation oscillations;
3) self-starting of mode locking.

The assumption is made that CW mode locking can be obtained only for a choice of parameters for which all three regimes overlap. We require further that the overlap regime be reached by a monotonic increase of small-signal gain (pumping), without passing outside regime 2). Under these conditions one may state requirements on the system parameters for the obtainment of single-pulse mode locking by a saturable absorber. The analysis explains why it has been impossible to mode lock passively the CW Nd:YAG laser, but passive mode locking of the CW dye-laser system is possible.

I. Introduction

In two previous papers [1], [2] we presented the theory of CW mode locking of a homogeneously broadened laser by a "fast" and a "slow" saturable absorber. The relaxation time of the fast absorber was assumed to be short compared with the duration of the mode-locked pulse τ_p, and that of the slow absorber was assumed to be long compared with τ_p.

The existence of steady-state mode-locked pulse solutions does not guarantee that these will be realized in practice. In fact, the scarcity of successful experiments of mode locking of a homogeneously broadened CW laser by a saturable absorber suggests that, more likely than not, the mode locking may be prevented by some other instability such as the well-known relaxation oscillations [3],[1] or may not be self-starting. The only successful mode locking of CW, or quasi-CW, homogeneously broadened lasers by a saturable absorber was that of Ippen *et al.* [4] on the CW dye laser, and Jung *et al.* [5] on the CO_2 laser. We emphasize that we are discussing homogeneously broadened systems. Inhomogeneously broadened systems are much easier to mode lock because they tend to oscillate in the steady state in a number of axial modes. The sole function of mode locking is to provide an injection signal to phase the different oscillation frequencies with respect to each other. This is a relatively easy task.

In this paper we explore explicitly the requirements for the self-starting of the mode-locked state and for the suppression of relaxation oscillations. Since the relaxation time of the absorber will always be fast compared to the cavity round-trip time, even in the case of the slow saturable absorber, the analyses for both the fast and the slow absorber cases are identical. We shall overlay the parameter regimes of stability against relaxation oscillation, of self-starting of mode locking, and of the mode-locking solution. Only when these three regimes overlap can one expect self-starting and steady-state excitation of mode-locked pulses. We shall see that the parameters of the Nd:YAG laser are incompatible with CW mode-locked operation. This explains why no CW mode locking with a saturable absorber has been reported for this system. We shall also see that the CW dye-laser system fits rather snugly into the region of overlap of these three regimes.

We shall illustrate the regimes of stable mode locking in the q_0-g_0 plane, where[2] $q_0 = Q/Q_A^0$ is the small-signal value of the inverse Q of the saturable absorber Q normalized to the inverse cavity Q, and g_0 is the small-signal value of the gain per pass normalized to the cavity loss per pass. One traverses the q_0-g_0 plane in a vertical direction when the pump power to the laser medium is raised. At fixed pump power the q_0-g_0 plane is traversed horizontally through addition of absorber dye to the solvent in the absorber cell. In the previous papers we have not presented the data in this form. In the fast absorber case we used the variables $g_0/1 + q_0$ and $q_0K/1 + q_0$ where K is the parameter [1]

$$K \equiv \frac{1}{4}\frac{P_L}{P_A}\omega_L T_R \tag{1}$$

with P_L as the laser medium saturation power, P_A as the saturation power of the saturable absorber, ω_L as the laser linewidth, and T_R as the cavity round-trip time. K is a parameter representing the ease with which the saturable absorber is bleached; the smaller P_A compared with P_L, the easier is the bleaching of the saturable absorber. K also contains a measure of the cavity round-trip time normalized to the inverse laser linewidth. In the analysis of the fast absorber [1], the relaxation time of the laser medium T_L was assumed long compared with cavity round-trip time T_R, so that no appreciable gain modulation occurred within the duration of the pulse. The overall gain pulldown was due to the inversion depletion of many successive pulses. If this condition is relaxed and T_L is made comparable to T_R, it is still possible to find mode-locked pulses. We shall assume, in the present analysis, that $T_L >> \tau_p$ but not necessarily $T_L >> T_R$.

It is an easy task to replot the boundary of mode-locking solutions of [1, fig. 4] in the g_0-q_0 plane, now with K as a parameter. Fig. 1 shows a sequence of such curves labeled for

Manuscript received July 28, 1975; revised November 10, 1975.

The author was with Bell Laboratories, Holmdel, NJ 07733, on leave from the Department of Electrical Engineering and the Research Laboratory of Electronics, Massachusetts Institute of Technology, Cambridge, MA 02139. He is now with the Department of Electrical Engineering and the Research Laboratory of Electronics, Massachusetts Institute of Technology, Cambridge, MA 02139.

[1] The "giant pulsing" is a fully developed relaxation oscillation. Ours is essentially the study of incipient giant pulsing.

[2] We use a subscript 0 on q to emphasize that it is a small-signal value. References [1] and [2] did not use a subscript.

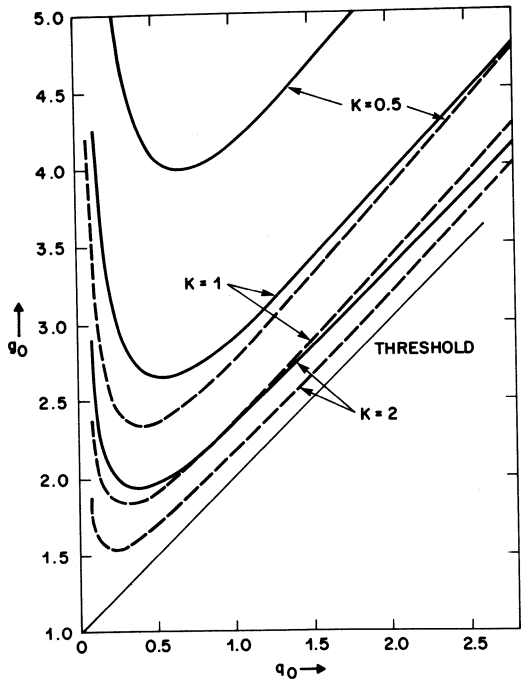


Fig. 1. Regimes of single-pulse mode locking by fast saturable absorber. Solid curves give stability boundary; dashed curves give boundary determined by $1/(\omega_L \tau_p) > 0.1$. The regimes between solid and dashed curve pair contain g_0-q_0 values that lead to single-pulse mode-locking solutions.

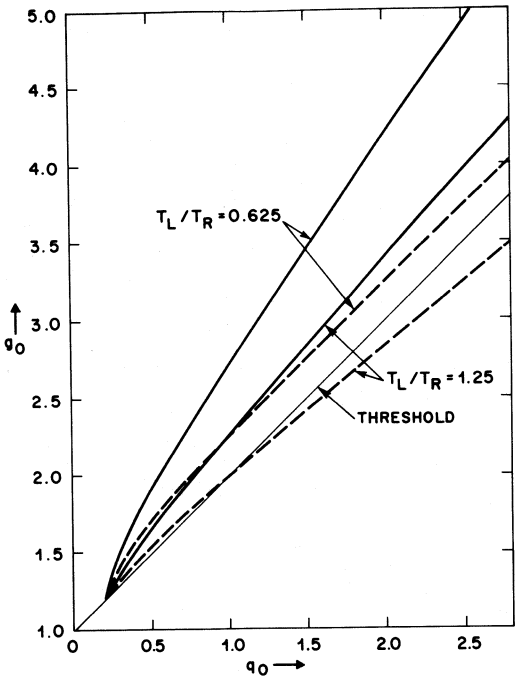


Fig. 2. Regimes of single-pulse mode locking by slow saturable absorber for $s = 6$. Solid curves give upper stability boundary; dashed curves give lower stability boundary. The regimes between solid and dashed curves contain g_0-q_0 values that lead to single-pulse mode-locking solutions.

different K values. Each curve pair bounds the region within which single-pulse mode-locking solutions can be obtained. The top boundary shown solid is the stability boundary of [1]. Above this boundary multiple-pulse solutions occur. The lower boundary shown dashed is drawn for an assumed pulse duration τ_p of magnitude $1/\omega_L \tau_p = 0.1$. Below the boundary the pulses are excessively long. Note the dependence of the mode-locking regime upon K. The regime gets very narrow for $K \geqslant 2$. Hence values of K of the order of unity should be striven for in practical systems so as not to make mode locking too sensitive to (unavoidable) variations in q_0 and g_0.

In the analysis of the slow absorber it was found to be necessary to include the relaxation process of the laser medium in order to assure stability of the mode-locked pulse with respect to (noise) perturbations following the pulse. This requirement was previously pointed out by New [6].

Fig. 2 shows regimes in the g_0-q_0 plane for which mode-locking solutions are found. For any given value of q_0 there is a range of gain (g_0) values for which single-pulse mode-locking solutions exist. The top boundary is shown solid and the bottom boundary dashed for two different values of the ratio T_L/T_R. We have picked

$$s = E_L/E_A = 6$$

where E_A is the saturation energy of the absorber and E_L that of the laser medium. The parameter s plays a role somewhat similar to that of K in the fast saturable absorber case. The lower boundary for $T_L/T_R = 1.25$ (T_L is the laser medium relaxation time) dips below the threshold line $g_0 = 1 + q_0$, indicative of the presence of a hysteresis effect for $q_0 > 1$: as the small-signal gain is raised by increased pumping and threshold is reached, the laser oscillates and mode locks. As the gain is lowered while the laser oscillates, the laser will keep oscillating and mode locking even when the threshold line is passed from above.

In Section II we determine the basic equations for the stability analysis. Section III is devoted to determination of the self-starting regime and Section IV determines the region in the g_0-q_0 plane for which no relaxation oscillations occur.

II. The Basic Equation

The fast absorber analysis [1] contains a relation between the nth and $(n+1)$th pulse passing through the laser. This relation may be adapted both to the analysis of self-starting and the study of relaxation oscillations. The relation is [1]

$$v_{n+1}(t) = v_n(t - T_R) - \frac{\omega_0 T_R}{2Q}\left[1 + \frac{Q}{Q_A(t)} - g\left(1 + \frac{1}{\omega_L^2}\frac{d^2}{dt^2}\right) + \frac{g}{\omega_L}\frac{d}{dt}\right] v_n(t - T_R). \quad (2)$$

Here $v_n(t)$ is the pulse envelope at one of the end mirrors after nth passage, T_R is the cavity round-trip time, ω_0 is the optical carrier frequency, Q is the empty cavity Q, $1/Q_A(t)$ is the time-dependent contribution of the absorber to the inverse Q, and g is the normalized gain of the medium.

Whereas the detailed derivation of (2) appears in [1], the meaning of (2) is rather self-evident. We see from (2) that v_{n+1} is a delayed and modified version of v_n. The modification is treated as small—and hence additive. There is the loss

$$\Delta v_n|_{\text{loss}} = -\frac{\omega_0 T_R}{2}\left[\frac{1}{Q} + \frac{1}{Q_A(t)}\right] v_n(t - T_R)$$

due to the cavity Q and time-dependent saturable absorber Q.

The laser medium modifies v_n by

$$\Delta v_n|_{\text{gain}} = \frac{\omega_0 T_R}{2Q} g \left[1 + \frac{1}{\omega_L^2}\frac{d^2}{dt^2} - \frac{1}{\omega_L}\frac{d}{dt}\right] v_n(t - T_R).$$

This modification is of operator character which entails growth (first term), spreading via "diffusion in time" (second term), and a delay due to the change in dielectric susceptibility as caused by the laser medium (third term).

We note first of all that a startup of single mode-locked pulses is characterized by the period T_R; relaxation oscillations usually have a much longer period. The laser linewidth affects the process only for time durations of the order of the mode-locked pulsewidth, which is much shorter than T_R. Therefore the terms $(g/\omega_L^2)\, d^2/dt^2$ and $(g/\omega_L)\, d/dt$ can be disregarded in a study of self-starting and of relaxation oscillations. The time dependence of the gain cannot be disregarded, but is easily included by making the remaining g in (2) time dependent.

In the study of the stability of mode-locked solutions against small perturbations [1] we have used two time parameters, a fast time parameter in terms of which the short pulse was described, and a slow time parameter expressing the number of passages through the laser cavity. Once one disregards the operators d^2/dt^2 and d/dt, such a distinction is not necessary; the time t used henceforth describes both the oscillating behavior of a perturbation (real part of the frequency) as well as the growth or decay of the perturbation (imaginary part of the frequency).

If one considers the limit where the change per pass is small enough, so that

$$\frac{v_{n+1}(t) - v_n(t - T_R)}{T_R} \simeq \frac{d}{dt} v$$

then one has the basic equation for v

$$\frac{dv}{dt} = -\frac{\omega_0}{2Q}[1 + q - g]\, v \tag{3}$$

where we have defined the normalized inverse Q of the saturable absorber

$$Q/Q_A(t) \equiv q(t). \tag{4}$$

In addition to the equation for the field envelope $v(t)$ in the cavity, one needs equations for the time-dependent gain $g(t)$ and the time-dependent inverse Q of the absorber, i.e., $q(t)$. We assume that the population difference n_A of the saturable absorber obeys the rate equation

$$\frac{d}{dt} n_A = -\frac{n_A - n_A^0}{T_A} - n_A \frac{P}{E_A} \tag{5}$$

and a similar equation for the population difference of the laser medium. Here n_A^0 is the equilibrium difference, T_A is the relaxation time, and E_A is the saturation energy. Now

$$\frac{n_A}{n_A^0} = \frac{Q_A^0}{Q_A} \tag{6}$$

where Q_A^0 is the small-signal value of Q_A. Using (6) in (5) and the definition (4), we obtain the equation of motion for q

$$\frac{d}{dt} q = -\frac{q - q_0}{T_A} - q\frac{P}{E_A}. \tag{7}$$

The equation of motion for the gain is correspondingly

$$\frac{d}{dt} g = -\frac{1}{T_L}(g - g_0) - g\frac{P}{E_L}. \tag{8}$$

These equations assume that $1/Q_A$ and g follow the time variation of P in the same way as they adjust to its time average (i.e., the same saturation energy is used for both). This is only correct if the laser medium and saturable absorber medium are near the end mirrors. Modifications to take into account other positions will be considered later.

Equation (3) has a different interpretation when the period of the process under study is a submultiple of the cavity round-trip time T_R (self-starting of mode locking) from the one when the period of the process is much longer than T_R (relaxation oscillations).

The first case is, to a certain extent, analogous to the perturbation of a free-running oscillator, of frequency $2\pi/T_R$. The frequency of the perturbation is close to this "unperturbed" frequency. In the second case of a relaxation oscillation with a period much greater than T_R one has the analog of a system which selects its own frequency of oscillation; the frequency is not prescribed by the round-trip condition itself. A relaxation oscillation is one in which the energy inside the cavity grows at a rate usually much slower than the round-trip time. The laser gain gets progressively depleted, gain gives way to loss, the energy decays. The pumping restores the gain while the field in the cavity is low, and the process repeats itself. For a certain parameter range the regimes of relaxation oscillation and self-starting merge and cannot be distinguished. We shall show later that in practical systems this is never the case.

III. Study of Self-Starting

Let us set up the equations for self-starting of mode locking from a CW time-independent state of operation. Suppose that the amplitude of the field in the cavity consists of a constant time-independent part v_s and a perturbation δv which changes upon each round trip. The time-independent part must obey the relation, using (3),

$$[1 + q_s - g_s]\, v_s = 0 \tag{9}$$

where we use subscripts s to denote the steady state (in distinction of the zero-power small-signal values indicated by 0). Because $v_s \neq 0$, the coefficient in brackets must vanish. This is a condition from which we may evaluate the power of the steady state $P_s = |v_s|^2$. Using the time-independent forms of (7) and (8), one has from (9)

$$1 + \frac{q_0}{1 + \dfrac{P_s T_A}{E_A}} - \frac{g_0}{1 + \dfrac{P_s T_L}{E_L}} = 0. \tag{10}$$

Equation (10) yields two roots for P_s, one of which is negative if $1 + q_0 - g_0 < 0$, i.e., the system is above threshold. Hence

only one root is acceptable. A perturbation of (3) gives

$$\frac{d}{dt}\delta v = -\frac{\omega_0}{2Q}[\delta q - \delta g]v_s. \tag{11}$$

We note first of all that self-starting of a mode-locked pulse is characterized by growth of a periodic perturbation on the time-independent laser output. The perturbation must have a period which is a submultiple of T_R. We set

$$\delta v = a \exp j\phi \exp j\frac{2\pi m}{T_R}t \tag{12}$$

where a and ϕ are time dependent. The time dependence of ϕ accounts for deviations of the repetition period from T_R.

The power δP caused by the perturbation is, with a convenient nomalization for v,

$$P = |v_s|^2 + \left[a \exp j\phi \exp\left(j\frac{2\pi m}{T_R}t\right) + a \exp j\phi \exp\left(-j\frac{2\pi m}{T_R}t\right)\right]v_s. \tag{13}$$

The perturbation of the gain may be written, using (8),

$$\delta g = -Y_L \frac{a}{v_s} \exp j\phi \exp j\frac{2\pi}{T_R}t + \text{c.c.} \tag{14}$$

where

$$Y_L \equiv \frac{g_s \dfrac{P_s}{P_L}}{1 + \dfrac{P_s}{P_L} + j\dfrac{2\pi m}{T_R}T_L} \tag{15}$$

and $P_L = E_L/T_L$. Similarly, one finds for δq from (7)

$$\delta q = -Y_A \frac{a}{v_s} \exp j\phi \exp j\frac{2\pi}{T_R}t + \text{c.c.} \tag{16}$$

where

$$Y_A = \frac{q_s \dfrac{P_s}{P_A}}{1 + \dfrac{P_s}{P_A} + j\dfrac{2\pi m}{T_R}T_A} \tag{17}$$

and $P_A = E_A/T_A$. The equation for the perturbation δv becomes, after separation of the positive and negative frequency components,

$$\dot{a} + j\dot{\phi}a = \frac{\omega_0}{2Q}(Y_A - Y_L)a. \tag{18}$$

The perturbation will grow, ($\dot{a} > 0$) mode locking will be self-starting, if

$$\text{Re}\,[Y_A - Y_L] > 0 \tag{19}$$

or

$$\frac{\dfrac{q_0}{P_A}}{\left(1 + \dfrac{P_s}{P_A}\right)^2 + \left(\dfrac{2\pi m T_A}{T_R}\right)^2} > \frac{\dfrac{g_0}{P_L}}{\left(1 + \dfrac{P_s}{P_L}\right)^2 + \left(\dfrac{2\pi m T_L}{T_R}\right)^2}. \tag{20}$$

One may eliminate P_s from (20) using (10), and thus one obtains a relation between g_0 and q_0 with $(2\pi m T_L/T_R)$, T_L/T_A, and P_L/P_A as parameters. A boundary for self-starting in the q_0-g_0 plane is shown in Fig. 3 which is plotted for the following assumed parameter values: $(2\pi m T_L/T_R) = 2$; $(T_L/T_A) = 4$; and $(P_L/P_A) = 0.5, 0.75$, and 1.0.

Self-starting of mode locking occurs within the q_0-g_0 plane below the curve(s) shown in Fig. 3. Only those portions of the curves above the threshold line are shown because a precondition for the analysis of self-starting of mode locking was the existence of a time-independent solution. In a monotonic increase of the pumping this is the case only when the threshold line has been passed. The curves change for different choices of parameters, but certain general characteristics may be noted. The threshold line is

$$g_0 = 1 + q_0. \tag{21}$$

At threshold the power approaches zero, and hence one may find the intercept of the self-starting boundary with the threshold line by eliminating g_0 from the two equations (20) and (21) with $P_s = 0$ and the inequality replaced by an equality. One finds

$$q_0 = \frac{1}{\dfrac{P_L}{P_A}\dfrac{1 + (2\pi m T_L/T_R)^2}{1 + (2\pi m T_A/T_R)^2} - 1}.$$

In order to obtain an intercept at a finite q_0, one requires that

$$\frac{P_L}{P_A}\frac{1 + (2\pi m T_L/T_R)^2}{1 + (2\pi m T_A/T_R)^2} > 1. \tag{22}$$

If there is no intercept, there are no regions of self-starting above the threshold line. Hence raising the pumping power

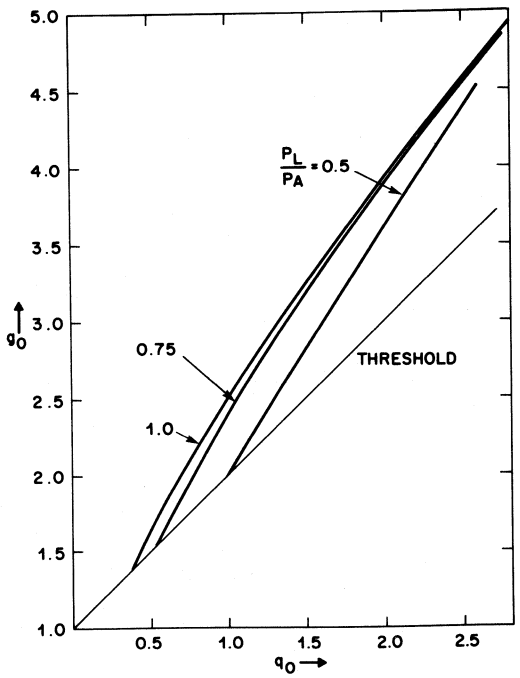


Fig. 3. Self-starting regimes in q_0-g_0 plane; the regimes to right of respective curves correspond to self-starting. Only regimes above threshold line are shown.

(g_0) until the threshold line is crossed will result in operation with a time-independent power output—no mode locking. Equation (22) shows that a value of P_L/P_A that is too small (the saturable absorber is too hard to saturate) can result in no self-starting of mode locking.

IV. Relaxation Oscillation

We consider next the question whether relaxation oscillations may exist in the system. If one finds such oscillations, one may expect, at the very least, that the mode-locked pulse train is modulated by the relaxation oscillation. It is more likely that the existence of relaxation oscillations suppresses mode locking if the period of the relaxation oscillation is too short to allow for the buildup of mode-locked pulses within one cycle of the oscillation.

The equation for the radiation inside the cavity is now a simple rate equation. It follows from (3) by multiplication by v^* and addition of the complex conjugate. One may normalize v so that $|v|^2 = P$, the power traveling in one direction in the cavity. The differential equation for P is

$$\frac{d}{dt}P = -\frac{1}{T_C}[1 + q - g]P \tag{23}$$

where

$$\frac{1}{T_C} = \frac{\omega_0}{Q}.$$

The perturbation of (23) gives

$$\frac{d}{dt}\delta P + \frac{1}{T_C}[\delta q - \delta g]P_s = 0 \tag{24}$$

where we have taken into account the fact that for the CW steady state the quantity $1 + q_s - g_s = 0$. If T_A is taken as short compared to the period of interest, a condition always met when relaxation oscillations tend to occur, then δq is an instantaneous function of $\delta P/P_A$

$$\delta q = -\frac{q_0}{\left(1 + \frac{P_s}{P_A}\right)^2}\frac{\delta P}{P_A}. \tag{25}$$

Using (25) in (24) and the differential equation (8) for δg, one has two coupled first-order differential equations for δP and δg. Assuming the time dependence $\exp st$, one obtains the determinantal equation

$$s^2 - s\left\{\frac{q_0\frac{P_s}{P_A}}{\left(1 + \frac{P_s}{P_A}\right)^2 T_C} - \left(1 + \frac{P_s}{P_L}\right)\frac{1}{T_L}\right\} - \frac{1}{T_C T_L}\left[\frac{\left(1 + \frac{P_s}{P_L}\right)}{\left(1 + \frac{P_s}{P_A}\right)^2} q_0 \frac{P_s}{P_A} - \frac{g_0}{1 + \frac{P_s}{P_L}}\frac{P_s}{P_L}\right] = 0. \tag{26}$$

Instabilities are found (Re $s > 0$) when either the s-independent term is negative, i.e.,

$$\frac{q_0\frac{1}{P_A}}{\left(1 + \frac{P_s}{P_A}\right)^2} > \frac{g_0\frac{1}{P_L}}{\left(1 + \frac{P_s}{P_L}\right)^2} \tag{27}$$

or the coefficient of s is negative

$$\frac{q_0\frac{P_s}{P_A}}{\left(1 + \frac{P_s}{P_A}\right)^2} > \left(1 + \frac{P_s}{P_L}\right)\frac{T_C}{T_L}. \tag{28}$$

Condition (27) corresponds to exponential growth of a perturbation. It has the simple interpretation

$$\left|\frac{d}{dP}q\right| > \left|\frac{d}{dP}g\right| \quad \text{at } P = P_S. \tag{29}$$

This condition is met when the loss characteristic $1 + q(P)$ and gain characteristic $g(P)$ intersect so that the slope of the loss characteristic is steeper than the slope of the gain characteristic. If the small-signal value of the gain g_0 is greater than $1 + q_0$, i.e., the system is above threshold, then the slope of g is always steeper than the slope of q at the intersection point $P = P_s$, and hence (27) is not satisfied for a system above threshold. Therefore condition (27) is not of interest in our present investigation which treats only self-starting systems ($g_0 > 1 + q_0$).

Condition (28) is of interest and gives regimes of instability in the q_0-g_0 plane. The regime of instability is circumscribed by the curve obtained from (28) by replacing the inequality by an equality. The curve has for one asymptote the threshold line $g_0 = 1 + q_0$, and for the other asymptote the straight line

$$g_0 = \frac{P_A}{P_L}q_0. \tag{30}$$

The minimum value of q_0 is found to occur at a power $P_{\min}$

$$P_{\min}/P_A = -\frac{1}{4}\frac{P_L}{P_A} + \sqrt{\left(\frac{1}{4}\frac{P_L}{P_A}\right)^2 + \frac{1}{2}\frac{P_L}{P_A}}$$

and has the value

$$q_{\min} = \frac{T_C}{T_L}\frac{(1 + P_{\min}/P_L)(1 + P_{\min}/P_A)^2}{P_{\min}/P_A}.$$

Thus the instability regime lies above the threshold line for $P_L/P_A < 1$ and covers more and more of the q_0-g_0 plane for smaller and smaller values of T_C/T_L. Fig. 4 shows some typical stability boundaries.

From (28) we see that an excessive value of q_0 leads to the instability, as is to be expected because the bleaching of the absorber is the cause of the instability. The smaller T_C/T_L, or the larger the laser medium relaxation time compared to the cavity relaxation time, the greater the tendency toward an instability. This may be understood by recalling the stabilizing influence of the gain changes. If T_L is too long, the gain change shifts out of phase with the change of absorption of the saturable absorber and hence the gain change cannot stabilize against the destabilization of the absorption change.

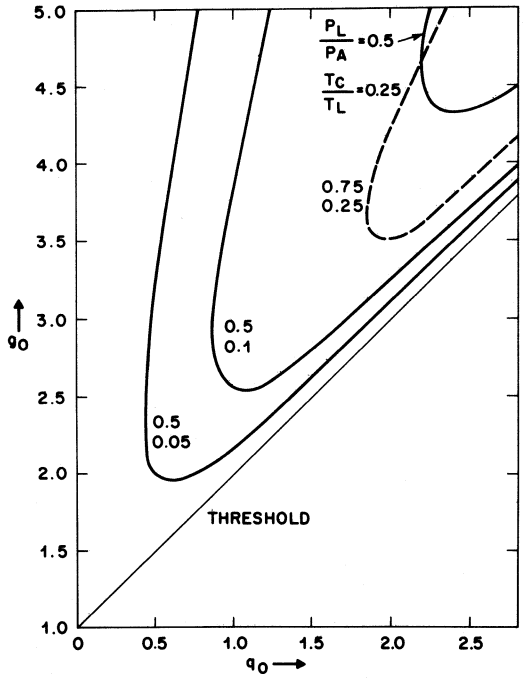


Fig. 4. Instability contours in q_0-g_0 plane for relaxation oscillations; $P_L/P_A < 1$, regions within curves are unstable.

The stability boundary of Fig. 4 illustrates the difficulty of avoiding relaxation oscillations in the Nd:YAG system. Indeed, for the values displayed in Table I, which are typical of the system of Liao and Weber [7] in which they attempted mode locking, we find that $P_L/P_A < 1$ except for the longest relaxation times of the saturable absorber. When $P_L/P_A < 1$ and $T_C/T_L \ll 1$ (as is by necessity the case for an Nd:YAG system with a cavity of reasonable length and loss), the relaxation oscillation regime covers pretty much all of the q_0-g_0 plane above threshold. Indeed, the regime stable with regard to relaxation oscillation is practically invisible on the scale of Fig. 4. Hence no mode locking is possible for $P_L/P_A < 1$. A different situation prevails when T_A approaches the longest value attempted, 100 ps. Then the relaxation oscillation instability region moves below the threshold line. We find, however, that the K parameter becomes extremely large ($K \to 630$). On the scale of Fig. 1 in this limit of large K, the mode-locking region is of "infinitesimal" extent, and hence stable mode locking is unachievable, even though no relaxation oscillations need occur.

It is worth noting that relaxation oscillations have been observed in various situations. The brief theory presented here explains properly the growing oscillations of [8] observed in the aftermath of passive Q switching. In the experiment of [8], $P_L/P_A < 1$, and hence the instability boundary occurred above the threshold line. As the gain and loss gradually recovered, the operating point moved upward and to the upper right in the g_0-q_0 plane and entered the instability region. The predicted period of the order of $2\pi\sqrt{T_C T_L}$ checks with the observed period of 10 μs, using the parameter values of the experiment [9].

One may ask why transient saturable absorber mode locking of the Nd:YAG or Nd:glass laser is possible [10], [11], whereas steady-state mode locking is prevented by relaxation oscillations. Clearly, if one obtains mode-locked pulses before the relaxation oscillations set in, then transient mode locking is assured. But why, then, did Liao and Weber not observe the mode-locked substructure of the relaxation oscillations? We believe that the reason for this is that the excess gain achieved in transient excitation tends to be much higher than the gain in steady-state excitations. Hence mode locking can build up faster in the transient case than under CW excitation. The transient excitation is usually over by the time relaxation oscillations have a chance to build up.

TABLE I

	Nd YAG	Dye Laser
T_L	230 μs	4 ns
T_A	10 <—> 100 ps	1.2 ns
T_R	10 ns	10 ns
σ_A	10^{-16} cm^2	3×10^{-16} cm^2
σ_L		10^{-16} cm^2
A_A	$[10\mu]^2$	$[10\mu]^2$
A_L	10^{-2} cm^2	$[20\mu]^2$
P_L/A_L	2.3×10^3 w cm^{-2}	7.7×10^5 w cm^{-2}
P_A/A_A	1.8×10^8 w cm^{-2} <—> 1.8×10^7	8.4×10^5 w cm^{-2}
P_L/P_A	.13 <—> 1.3	3.7
ω_L	2.1×10^{11} s^{-1}	
$K = \frac{1}{4}\frac{P_L}{P_A}\omega_L T_R$	63 <—> 630	

V. Discussion

We have identified three regions in the q_0-g_0 plane (the plane of saturable absorber loading and small-signal gain) whose disposition determines whether one can obtain self-starting single mode-locked pulses without running into relaxation oscillations. The dependence of the three regions upon the system parameters determines the required choice of system parameters. Here we shall briefly review the ranges of parameters found appropriate by the analysis.

A. Fast Absorber Case

The determining parameter for the width of the single-pulse mode-locking regime is K

$$K = \frac{1}{4}\frac{P_L}{P_A}\omega_L T_R.$$

The larger K the narrower the regime in the q_0-g_0 plane within which mode-locked single-pulse solutions are obtained. Now, it is clear that generally $\omega_L T_R >> 1$, because ω_L will be of the order of the inverse pulsewidth $1/\tau_p$ or larger ($\omega_L \tau_p > 1$ as indicated by the analysis of [1, fig. 2]), and $T_R/\tau_p >> 1$. In order to keep K on the order of unity, one needs

$$P_L/P_A < 1. \tag{31}$$

The saturable absorber should not saturate easily compared with the laser medium. A further requirement for the fast absorber case is that

$$T_L \geqslant T_R \tag{32}$$

so that the laser medium does not fully recover between pulses. Indeed, the leading edge of the mode-locked pulse must experience loss, $1 + q_0 - g > 0$, so that it is stable against perturbations preceding the pulse. If the laser medium recovered fully between pulses, $T_L << T_R$, then $g = g_0$ and the condition holds $1 + q_0 - g_0 > 0$. This means that the laser is below threshold and can never get started.

Condition (31) applied to (30) implies that a regime of relaxation oscillations occurs above the threshold line. In order to prevent a severe overlap of the instability regime, one needs

$$T_C/T_L \gtrsim 1. \tag{33}$$

The cavity relaxation time should be of the order of or larger than the laser relaxation time.

Finally, in order to have self-starting of mode-locked pulses one must satisfy (22). This condition can be met in spite of (31) as long as

$$\frac{P_L}{P_A} > \frac{1 + \left(\frac{2\pi T_A}{T_R}\right)^2}{1 + \left(\frac{2\pi T_L}{T_R}\right)^2}. \tag{34}$$

B. Slow Absorber Case

Mode locking with a slow absorber requires that the laser medium do some pulse shaping of its own. In order that the pulse is stable against perturbations preceding the pulse, one requires, as in the fast absorber case, that the laser medium not recover fully between pulses, or

$$T_L/T_R \gtrsim 1. \tag{35}$$

Further, one requires that the s parameter be greater than unity

$$s = \frac{E_L}{E_A} > 1. \tag{36}$$

It has been assumed in the analysis of mode locking by a slow absorber that the absorber fully recovers between pulses or

$$T_A/T_R < 1. \tag{37}$$

This is a necessary condition since the absorber must recover faster than the laser medium; recovery of the laser medium before that of the absorber would lead to net gain preceding the occurrence of the next pulse and lead to instability of the pulse train.

In order to have self-starting of the mode-locked solution, one needs

$$\frac{P_L}{P_A} > \frac{1 + \left(\frac{2\pi T_A}{T_R}\right)^2}{1 + \left(\frac{2\pi T_L}{T_R}\right)^2}. \tag{38}$$

No direct requirement on P_L/P_A is found. Indeed, P_L/P_A could be made greater than unity, making it easy to meet (38) and, at the same time, preventing relaxation oscillations above the threshold line (compare Fig. 4). For this reason it is less difficult to satisfy the three conditions for a slow saturable absorber than for the fast absorber.

So far we have assumed implicitly that the laser medium is at one of the end mirrors of the cavity. This assumption is inherent in using the same saturation energy E_L for all time dependences of g. If the laser medium is in the center of the cavity, then a perturbation of frequency $2\pi/T_R$ does not excite a corresponding perturbation of g. This is a consequence of the fact that a frequency of $2\pi/T_R$ is produced by the beating of two adjacent axial modes. But two adjacent axial modes do not couple via a medium in the cavity center. An immediate consequence of this fact is that the gain will not tend to stabilize against absorber changes—perturbations of period $2\pi/T_R$ are all unstable; the mode locking is always self-starting. Thus when the laser medium is in the cavity center one may disregard conditions (34) and (38).

In one of the realizations of the Shank-Ippen mode-locked dye-laser system the laser medium was mixed with the absorber dye and near one of the end mirrors. In another realization the laser medium was put into the center of the cavity. Fig. 5 is a plot of regimes 1), steady-state single-pulse mode-locking solutions, and 3), self-starting of mode locking, for the Shank-Ippen system in the first configuration, using

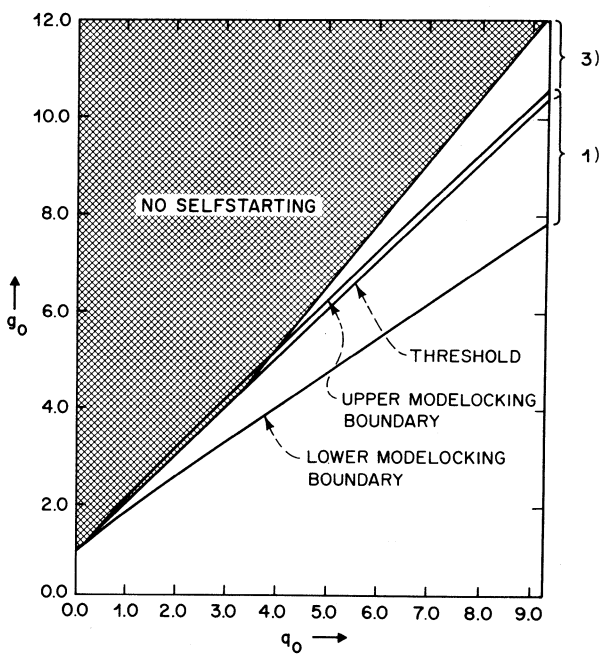


Fig. 5. Plot of regimes 1) and 3) for system of Shank and Ippen. Regime 2) occurs for $q_0 > 590$ and does not appear on this scale.

the values of Table I. Regime 2), the regime stable against relaxation oscillations, covers the plane above the threshold line in Fig. 5. In the second configuration one may simply disregard the self-starting boundary because the system is automatically self-starting. We have disregarded group velocity dispersion in plotting the mode-locking regime, thus overestimating slightly the extent of the regime [10].

We have mentioned earlier that relaxation oscillations and self-starting conditions might merge if the frequency of oscillation is comparable to $2\pi/T_R$. In this case the relaxation oscillations would not represent a threat to successful mode locking because they are indistinguishable from self-starting conditions. Now, (26) shows that the frequency of the relaxation oscillations is of the order of $1/\sqrt{T_C T_L}$. Hence when $\sqrt{T_C T_L} \simeq T_R/2\pi$, one could disregard the contour of stability against relaxation oscillations. But we have pointed out that $T_L > T_R$ so that the laser medium does not fully recover between pulses. Because $T_C >> T_R$ for low-loss systems, one finds that this condition is never met in practice.

VI. Conclusions

We have stated conditions for the self-starting of CW passively mode-locked pulse trains of single pulses. The available experimental facts on successful passive mode locking of CW laser systems seem to bear out our results. Also, we can explain why attempts at passive mode locking of the CW Nd:YAG laser have failed. In the process we have developed criteria for the choice of laser and saturable absorber parameters so that passive mode locking of the system will be successful.

Acknowledgment

The author wishes to thank Dr. H. P. Weber and Dr. P. F. Liao for discussions concerning their experiments on the CW Nd:YAG system. He also wishes to thank Dr. T. Y. Chang for data on his observation of growth of relaxation oscillations, and Dr. E. P. Ippen and Dr. C. V. Shank for stimulating discussions.

References

[1] H. A. Haus, "Theory of modelocking with a fast saturable absorber," *J. Appl. Phys.*, vol. 46, pp. 3049–3058, 1975.
[2] ——, "Theory of mode locking with a slow saturable absorber," *IEEE J. Quantum Electron.*, vol. QE-11, pp. 736–746, Sept. 1975.
[3] W. G. Wagner and B. A. Lengyel, "Evolution of the giant pulse in a laser," *J. Appl. Phys.*, vol. 34, pp. 2040–2046, 1963.
[4] E. P. Ippen, C. V. Shank, and A. Dienes, "Passive modelocking of the CW dye laser," *Appl. Phys. Lett.*, vol. 21, pp. 348–350, 1972.
[5] C. K. Jung, A. M. Ronn, and J. T. LaTourette, "Passive Q-switching and modelocking of a CO_2 laser with CH_3Br, PF_5, SF_6 and self-modelocking using electrical pulse excitation," *J. Appl. Phys.*, vol. 41, pp. 4240–4242, 1970.
[6] G. H. C. New, "Pulse evolution in mode-locked quasi-continuous lasers," *IEEE J. Quantum Electron. (Part I of Two Parts)*, vol. QE-10, pp. 115–124, Feb. 1974.
[7] P. F. Liao and H. P. Weber, private communication.
[8] T. Y. Chang, C. H. Wang, and P. K. Cheo, "Passive Q-switching of the CO_2 laser by CH_3F and PF_5 gases," *Appl. Phys. Lett.*, vol. 15, pp. 157–159, 1969.
[9] T. Y. Chang, private communication.
[10] H. A. Haus, "Model of CW modelocked dye laser," unpublished.

Substrate Radiation Losses in GaAs Heterostructure Lasers

WILLIAM STREIFER, SENIOR MEMBER, IEEE, ROBERT D. BURNHAM, MEMBER, IEEE, AND DONALD R. SCIFRES, MEMBER, IEEE

Abstract—Double-heterostructure (DH) diode lasers with a thin $Ga_{1-x}Al_xAs$ layer between the active GaAs region and the GaAs substrate or superstrate are analyzed. In these devices power flows through the thin $Ga_{1-x}Al_xAs$ layer and is radiated into the substrate or superstrate. Three methods for computing the laser thresholds are developed and compared. The first is an analytic perturbation technique, which yields accurate results in many cases of practical interest. The second and third are rapidly convergent numerical iteration techniques. The former utilizes overlap integrals to compute absorption losses and thresholds; the latter includes all losses and gains directly in the formulation. We show that conventional DH diode lasers can be designed with thick active GaAs layers and still achieve lowest order TE-mode operation. These devices will produce better collimated, higher power output beams than do similar devices with thinner active regions. Transverse-mode control is achieved because all higher order modes have increased penetration through the thin $Ga_{1-x}Al_xAs$, and therefore exhibit increased radiation losses into the substrate or superstrate. A design example is included in which it is shown that with proper choice of the $Ga_{1-x}Al_xAs$-layer thickness the TE_0-mode threshold increases by 5 percent compared with a 110-percent increase in the TE_1 threshold. These results are virtually independent of the substrate power-absorption coefficient. Threshold current densities are computed for a set of diodes studied experimentally by Casey and Panish and the results are shown to be in excellent agreement.

I. Introduction

IN THIS PAPER we analyze double-heterostructure (DH) lasers with a thin $Ga_{1-x}Al_xAs$ (hereafter GaAlAs) layer between the active GaAs region and an external GaAs region (substrate or superstrate). The study of such structures is important for several reasons. First, these lasers exhibit transverse-mode selectivity. Second, the use of a thin GaAlAs layer in any DH laser increases the thermal conduction between the active region and the heat sink through the poorly conducting GaAlAs layer [1], [2]. Third, a thin GaAlAs region enables the modes to interact with a substrate corrugation to obtain distributed feedback action [3] or grating coupled output [3]. In the latter two situations it is desirable to calculate the optimum GaAlAs thickness which maximizes the desired effect without excessively increasing the laser threshold.

Conventional DH lasers with thick active regions have advantages of better output beam collimation and higher output power at the expense of higher thresholds and poor transverse-mode control. Attempts to increase beam collimation and power output have led to versions of the large optical cavity (LOC) laser [4]-[6]. In some LOC lasers higher order transverse modes tend to lase and produce less well-collimated output beams. Furthermore, LOC lasers are somewhat more difficult to fabricate than conventional lasers. To achieve TE-mode control in a conventional DH diode with a thick active region, one or both GaAlAs regions is grown thin. This layer thickness is judiciously selected such that all higher order TE modes experience high radiation loss into the substrate or superstrate because of their greater penetration through the thin GaAlAs layer. In the same geometry the TE_0-mode does not exhibit a significantly increased threshold. The calculations described in the following indicate that transverse-mode control utilizing radiation into the substrate or superstrate is entirely feasible.

Previous calculations of mode losses were confined mainly to waveguides. Reisinger [7] considered the use of various techniques to account for absorption, but did not treat radiation losses. Suematsu and Furuya [8] considered radiation losses of the type discussed herein, but used a rather complex perturbation technique and gave only approximate solutions. Kawakami and Nishida have published perturbation results for circular [9] and slab [10] geometries, but have not considered the effects on laser threshold nor do they give comparisons with more exact numerical solutions. Finally, Butler *et al.* [2] have published numerical results for GaAs DH lasers. Their calculations use overlap integrals to determine the laser threshold. In Section II of this paper we develop a simple perturbation technique to determine TE-mode radiation losses and a test which generally indicates the accuracy of the perturbation. Next, in Section III, we use these results as the starting point in a rapidly converging numerical calculation, which together with the application of overlap integrals yields results similar to those of [2]. In Section IV linear gain within the active region as well as absorption and transmission losses are included in the formulation, and mode propagation constants, field patterns, and thresholds are determined. No overlap integrals are employed in the last calculation; rather it is an exact solution to the linear problem. These sections are followed by some examples and a comparison with previously published results [1].

II. Perturbation Calculation

A schematic of a conventional DH laser is shown in Fig. 1. The p-GaAs material, region 5, is grown to facilitate metallic contact. To determine the increase in threshold resulting from radiation losses into the substrate (the calculation also applies to radiation losses into region 5) we begin with E_y for TE modes in a diode with very thick GaAlAs regions, i.e., $t_2, t_4 \to \infty$ (see Adams and Cross [15]),

Manuscript received August 18, 1975; revised October 22, 1975.
The authors are with the Xerox Palo Alto Research Center, Palo Alto, CA 94304.

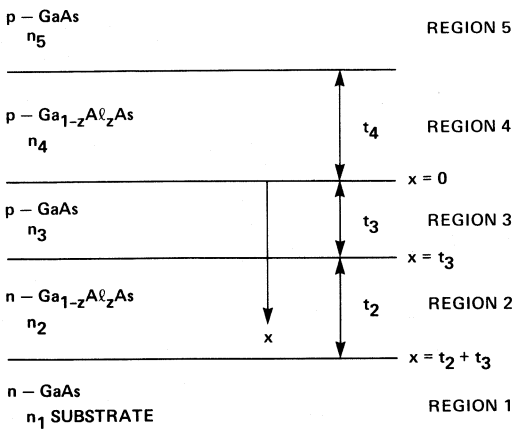


Fig. 1. Schematic of a conventional DH laser.

$$E_y = \begin{cases} \exp(qx), & x \leqslant 0, \text{ region 4} \\ \cos(hx) + (q/h)\sin(hx), & \\ & t_3 \geqslant x \geqslant 0, \text{ region 3} \\ [\cos(ht_3) + (q/h)\sin(ht_3)]\exp[-p(x - t_3)], & \\ & t_2 + t_3 \geqslant x \geqslant t_3, \text{ region 2} \end{cases} \quad (1)$$

where

$$q = \sqrt{\beta^2 - n_4^2 k^2}$$
$$h = \sqrt{n_3^2 k^2 - \beta^2}$$
$$p = \sqrt{\beta^2 - n_2^2 k^2} \quad (2)$$

and $k = 2\pi/\lambda_0$ with λ_0 the free-space wavelength. The mode propagation constant β (the z and time dependence are exp $[i(\beta z - \omega t)]$) is found by requiring continuity of $H_z \propto \partial E_y/\partial x$ at $x = t_3$. (E_y and $\partial E_y/\partial x$ as given by (1) are continuous at $x = 0$.) To approximate the field in the substrate (region 1) we solve the wave equation in that region using the previous propagation constant for the z variation. If the material absorption is characterized by a plane-wave field decay of $\alpha_s/2$ (a power decay of α_s) the result is

$$E_y = A_1 \exp[-\gamma(x - t_2 - t_3)] \exp[ir(x - t_2 - t_3)] \quad (3)$$

where r, γ are, respectively, the real and imaginary parts of

$$r + i\gamma = [n_1^2 k^2 - \beta^2 - \alpha_s^2/4 + i\alpha_s n_1 k]^{1/2}. \quad (4)$$

The constant A_1 is determined by requiring E_y and H_z continuity at the substrate-GaAlAs interface. To accomplish this

$$B_2 \exp[p(x - t_3)] \quad (5)$$

must also be included in the E_y-field of region 2. This term cannot exist in the unperturbed geometry since it grows without limit as x increases. Upon matching the fields at $x = t_2 + t_3$ we obtain

$$B_2 = U \exp(-2pt_2)\left(\frac{p - \gamma + ir}{p + \gamma - ir}\right) \quad (6a)$$

and

$$A_1 = U \exp(-pt_2)\left(\frac{2p}{p + \gamma - ir}\right) \quad (6b)$$

where

$$U = \cos(ht_3) + (q/h)\sin(ht_3). \quad (6c)$$

The ith-mode power-decay exponent in the propagation direction, α_{is}, caused by radiation into the substrate is now computed as follows. First, we perturb the propagation constant β by letting

$$\beta = \beta_0 + \delta\beta \quad (7)$$

and the E_y-fields in regions 3 and 4 by multiplying *both* with

$$1 + \delta E \quad (8)$$

where $\delta\beta \ll \beta_0$ and $\delta E \ll 1$. This form of field perturbation ensures continuity at $x = 0$. By imposing continuity at $x = t_3$ and consistently retaining only first powers of $\delta\beta$ and δE we find

$$\delta\beta = \left(\frac{2B_2}{\beta_0}\right)\left\{U_0\left(\frac{1}{p_0^2} + \frac{1}{h_0^2}\right)(1 + p_0 t_3) + q_0\left(\frac{1}{q_0^2} + \frac{1}{h_0^2}\right) \cdot \left[\frac{\cos(h_0 t_3)}{p_0} + \frac{\sin(h_0 t_3)}{h_0}\right]\right\}^{-1} \quad (9)$$

and

$$\delta E = \frac{B_0}{U_0} - \frac{\beta_0 \delta\beta}{h_0}\left\{\frac{p_0 t_3}{h_0} + \frac{q_0}{U_0}\left(\frac{1}{q_0^2} + \frac{1}{h_0^2}\right)\sin(h_0 t_3)\right\} \quad (10)$$

where the subscript 0 refers to evaluation at β_0. Since B_2 is complex, so too are δE and $\delta\beta$. Thus α_{is} is approximately given by

$$\alpha_{is} = 2 \text{ Im}(\delta\beta). \quad (11)$$

Laser threshold gain is not only determined by α_{is}, but also by the free-carrier absorption [11] α_{if} and the transmitted power through the cleaved end faces. The former is approximately

$$\alpha_{if} = (\alpha_{fc2} I_2 + \alpha_{fc3} I_3 + \alpha_{fc4} I_4) \Big/ \sum_{j=2}^{4} I_j \quad (12)$$

where α_{fcj}, $j = 2, 3, 4$ is the free-carrier absorption in region j and I_j, $j = 2, 3, 4$ is proportional to the power flow in each region. They are given by

$$I_4 = \int_{-\infty}^{0} E_y^2(x)\,dx = \frac{1}{2q} \quad (13a)$$

$$I_3 = \int_0^{t_3} E_y^2(x)\,dx = \frac{1}{2}\left\{\left(1 + \frac{q_0^2}{h_0^2}\right)t_3 + \frac{q_0}{h_0^2} \cdot [1 - \cos(2h_0 t_3)] + \left(1 - \frac{q_0^2}{h_0^2}\right)\frac{\sin(2h_0 t_3)}{2h_0}\right\} \quad (13b)$$

and

$$I_2 = \int_{t_3}^{t_2+t_3} E_y^2(x)\,dx = \frac{U_0^2}{2p_0}(1 - \exp[-2p_0 t_2]) + \frac{|B_2|^2}{2p}(\exp[2p_0 t_2] - 1) + 2U_0 t_2\,\mathrm{Re}(B_2). \quad (13c)$$

The corrected field in region 2 was used to calculate (13c), since that correction is not a small perturbation as is δE. The transmitted power loss is

$$\alpha_{ir} = \frac{1}{L}\ln\left(\frac{1}{R_i}\right) \quad (14)$$

where R_i is the ith-mode power reflected back into that mode by the end face and L is the laser length. Values of R_i are given in [12] and [13]. The required mode threshold gain is

$$g_i = \alpha_{is} + \alpha_{ir} + \alpha_{if} \quad (15)$$

but the actual gain available to each mode also depends on the degree to which the mode overlaps the active region [4] Γ_i. Thus the gain required at threshold in the active region G_i must be greater than g_i and is given by

$$G_i = g_i/\Gamma_i \quad (16)$$

where

$$\Gamma_i = I_3 \Big/ \sum_{j=2}^{4} I_j. \quad (17)$$

As shown in the following these results are quite accurate so long as $|\delta E| \ll 1$ (say $|\delta E| < 0.05$). In the remainder of this paper we refer to the method previously developed as A.

III. Numerical Solution With Overlap Integrals

Consider next satisfying the field-continuity conditions exactly including the effect of radiation into and absorption by the substrate, but neglecting free-carrier absorption losses, transmission losses, and gain. We write

$$E_u = \begin{cases} \exp(qx), & x \leqslant 0, \ \text{region 4} \\ \cos(hx) + (q/h)\sin(hx), & 0 \leqslant x \leqslant t_3, \ \text{region 3} \\ U(1+V)^{-1}\{\exp[-p(x-t_3)] + V\exp[p(x-t_3)]\}, & t_3 \leqslant x \leqslant t_2 + t_3, \ \text{region 2} \\ \dfrac{2pU}{(p+\gamma-ir)}\exp(-pt_2)\exp[(-\gamma+ir)(x-t_2-t_3)], & t_2 + t_3 \leqslant x, \ \text{region 1} \end{cases} \quad (18)$$

where

$$V = \left(\frac{p-\gamma+ir}{p+\gamma-ir}\right)\exp(-2pt_3) \quad (19)$$

and the other symbols are defined by (2)-(6c). The form of (18) is such that E_y and H_z are continuous for any β at all boundaries except $x = t_3$, where β must be chosen for $H_z \propto \partial E_y/\partial x$ continuity, i.e.,

$$F(\beta) = -h\cos(ht_3) + q\sin(ht_3) + pU(1-V)/(1+V) = 0. \quad (20)$$

To determine $\beta = \beta_s$, the complex propagation constant which satisfies (20), we expand about β_s and retain one term

$$F(\beta_s) = F(\beta) + (\beta_s - \beta)\,dF/d\beta = 0 \quad (21)$$

to obtain

$$\beta_s = \beta - F(\beta)/(dF/d\beta). \quad (22)$$

Then the numerical value of β obtained in Section II is substituted in the right side of (22), an approximation to β_s is obtained, and the iteration process is continued until β_s is found. In practice, very few iterations are required for convergence.

To approximate G_i, the procedure previously described via (12)-(17) is repeated, but now in place of (13a)-(13c), we have

$$I_4 = 1/2q_r \quad (23a)$$

$$I_3 = \frac{1}{2}\left\{\left(1 + \left|\frac{q}{h}\right|^2\right)\frac{\sinh(2h_i t_3)}{2h_i} + \left(1 - \left|\frac{q}{h}\right|^2\right)\cdot\frac{\sin(2h_r t_3)}{2h_r} + \mathrm{Re}\left(\frac{q}{h}\right)\frac{[1-\cos(2h_r t_3)]}{h_r} + \mathrm{Im}\left(\frac{q}{h}\right)\frac{[1-\cosh(2h_i t_3)]}{h_i}\right\} \quad (23b)$$

$$I_2 = \frac{|U|^2}{2|(1+V)|^2}\left\{\frac{1}{p_r}[1 - |V|^2 - \exp(-2p_r t_3) + |V|^2\cdot\exp(2p_r t_3)] + \frac{2}{p_i}\mathrm{Re}[iV^*[\exp(-i2p_i t_3) - 1]]\right\} \quad (23c)$$

where power flows transverse to the propagation direction have been neglected, and the subscripts r and i on g, h, and p refer to real and imaginary parts, respectively. Hereafter, the method of this section is referred to as B.

IV. Formulation and Solution With Gain and Absorption

To solve for the modes exactly with absorption loss in all regions plus gain in region 3 and transmission loss, we begin with the same field patterns as in (18). Now, however, each of the refractive indices n_2, n_3, and n_4 is complex, viz.,

$$n_2 = \mathrm{Re}(n_2) + i\alpha_{fc2}/2k_0 \quad (24a)$$

$$n_4 = \mathrm{Re}(n_4) + i\alpha_{fc4}/2k_0 \quad (24b)$$

and

$$n_3 = \mathrm{Re}\,(n_3) + i\,(\alpha_{fc3} - G_i)/2k_0 \tag{24c}$$

where α_{fcj}, $j = 2, 3, 4$ are power absorption coefficients in the same units as k_0. The unknown threshold power gain in the active region for the ith mode G_i is expressed in the same units. Furthermore

$$\beta = \mathrm{Re}\,(\beta) - i\alpha_{ir}/2k_0 \tag{25}$$

where α_{ir} (in the same units as k_0) is the net power gain of the mode required to compensate for transmission losses through the cleaved end facets and Re (β) is an unknown. The equation which results from imposing H_z continuity at t_3 is identical to (20), but now instead of calculating the complex propagation constant β, we must solve for G_i and Re (β).

If β_s and G_i^s are the solutions we expand (20) as previously shown and obtain

$$F(\beta_s, G_i^s) = F(\beta, G_i) + (\beta_s - \beta)\frac{\partial F}{\partial \beta} + (G_i^s - G_i)\frac{\partial F}{\partial G_i} = 0. \tag{26}$$

Since the quantities F, $\partial F/\partial\beta$, and $\partial F/\partial G_i$ are all complex, whereas $\beta_s - \beta$ and $G_i^s - G_i$ are real, (26) is actually two real simultaneous linear equations solvable for $\beta_s - \beta$ and $G_i^s - G_i$. To solve for β_s and G_i^s, we begin with the values determined from the calculation of Section III, substitute, and iterate to convergence. Once again very few iterations are required. In the following this method is called C.

V. Examples

As a first example of the previous analysis, we choose a diode with cleaved end faces, refractive indices $n_1 = n_3 = 3.59$, $n_2 = n_4 = 3.385$, active-layer thickness $t_3 = 0.8$ μm, length $L = 350$ μm, substrate power absorption coefficient $\alpha_s = 50$ cm^{-1}, free-carrier power absorption coefficients $\alpha_{fc4} = \alpha_{fc2} = \alpha_{fc3} = 10$ cm^{-1}, and free-space wavelength $\gamma_0 = 0.9$ μm. For this diode, the TE-mode power reflectivities [12] (see also [13]) are $R_0 = 0.35$, $R_1 = 0.45$, and $R_2 = 0.49$ so that $\alpha_{0r} \approx 30$ cm^{-1}, $\alpha_{1r} \approx 22.8$ cm^{-1}, and $\alpha_{2r} \approx 20.4$ cm^{-1}. Fig. 2 is a plot of the ith-mode threshold gain G_i versus t_2, the thickness of the GaAlAs layer adjacent to the substrate, obtained using the perturbation calculation of Section II (method A). The asymptotic values are the threshold gains for very thick GaAlAs regions and for this diode they indicate that the TE_1 mode will lase at a lower pumping current than the TE_0 mode because of the higher reflectivity for the TE_1 mode. However, with decreasing GaAlAs thickness, G_i increases quite dramatically and most noteworthy is the fact that the increase for the TE_0 mode occurs significantly below that for the TE_1 mode. Thus, for $0.3 < t_2 < 0.5$, there exists substantial discrimination between the mode thresholds. Furthermore, in this range the TE_0 threshold has changed only slightly from its asymptotic value. Specifically, for $t_2 = 0.4$ μm the TE_0 threshold increase is 5 percent, whereas the TE_1 threshold increase is 110 percent. Thus, even though

$$G_i \sim J_i^m, \quad m \geqslant 1 \tag{27}$$

where J_i is the threshold pumping current, there will be substantial differences in J_i for these modes. It should be noted that the asymptotic TE_0-mode threshold gain for this diode

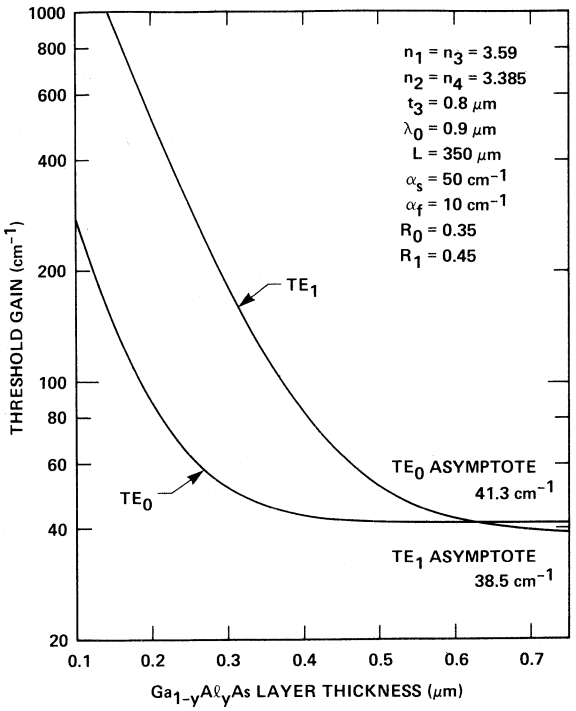


Fig. 2. Threshold gain versus GaAlAs-layer thickness t_2 for the TE_0 and TE_1 modes.

with $t_3 = 0.8$ μm is approximately three times that for similar diodes with $t_3 \leqslant 0.3$ μm.

To illustrate the accuracy of the perturbation procedure we list in Table I values of G_i computed by method A of Section II and the numerical methods B and C. Values are given for two GaAlAs thicknesses, viz., $t_2 = 0.1$ μm and $t_2 = 2.0$ μm. For $t_2 = 0.1$ μm, in which case the losses and thresholds are quite high, the perturbation technique still yields fairly accurate results for the TE_0 and TE_1 modes. The good agreement of methods A and B correlates with the listed values of $|\delta E|$. For the TE_2 mode, which is poorly confined in this geometry, the perturbation technique is completely inaccurate and $|\delta E|$ is large. Furthermore, methods B and C do not agree well. This occurs because method B neglects transverse power flow and uses inexact fields for computing I_j. For $t_2 = 2.0$ μm, methods A and B agree well for all modes and $|\delta E| \ll 1$. With this value of t_2 and indeed even for larger t_2, method C does give slightly different results. Also listed in Table I are the number of iterations required to achieve at least the listed precision.

Clearly, the mode patterns are influenced by the complex character of the refractive indices and the propagation constant. In Fig. 3 we plot $|E_y|$ and the phase front of the TE_0 mode in the previously described laser with $t_2 = 0.1$ μm obtained by using method C. The curvature of the phase front in the active region is indicative of the transverse power flow, which must exist to transfer energy from the active region to the radiated substrate wave and to a lesser extent to the absorbing GaAlAs. In the substrate the mode amplitude appears constant because the absorption is quite low. The linear phase variation in the substrate determines the plane-wave radiation direction, which for this particular diode is 6.65° to the waveguide plane. Upon refraction at the cleaved diode face the plane wave escapes at an angle of approximately

TABLE I
COMPARISONS OF THE METHODS FOR A LASER

GaAlAs THICKNESS = 0.1 μm

	METHOD A		METHOD B		METHOD C	
	THRESHOLD GAIN	|δE|	THRESHOLD GAIN	ITERATION #	THRESHOLD GAIN	ITERATION #
TE_0	266.56	0.155	287.06	4	286.88	2
TE_1	1554.9	0.0009	1552.0	4	1540.9	3
TE_2	476.89	0.733	3836.6	7	5693.4	3

GaAlAs THICKNESS = 2.0 μm

	METHOD A		METHOD B		METHOD C	
	THRESHOLD GAIN	|δE|	THRESHOLD GAIN	ITERATION #	THRESHOLD GAIN	ITERATION #
TE_0	41.296	3×10^{-6}	41.296	2	41.054	2
TE_1	38.522	3×10^{-6}	38.522	2	37.671	2
TE_2	87.484	0.005	88.077	2	83.669	2

Note: $n_1 = n_3 = 3.59$; $n_2 = n_4 = 3.385$; $t_3 = 0.8$ μm; $L = 350$ μm; $\lambda_0 = 0.9$ μm.

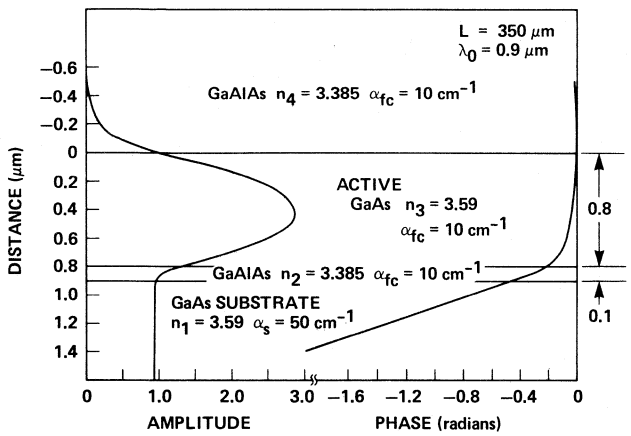


Fig. 3. Amplitude and phase of the TE_0 mode.

24.5° to the normal. Of course, because of the finite aperture the wave is not plane in the far field (see [21]). The substrate plane wave will experience total internal reflection at a substrate-air interface for this diode.

The role of substrate absorption is clarified by studying the dependence of G_i on α_s. In Fig. 4 we plot this variation with $t_2 = 0.4$ μm for the TE_0 and TE_1 modes. The results of all three methods are indistinguishable on this plot. Over the range of α_s plotted (and indeed even for $\alpha_s = 0.0$) G_0 for the TE_0 mode is essentially independent of α_s; TE_0-mode losses result from radiation into the substrate, which does not vary until α_s achieves unrealistically high values. The TE_1 threshold gain G_1 is relatively independent of α_s, but does decrease at large values. Then substrate absorption begins to influence the mode patterns as γ becomes comparable to r and p in (6a) and (6b).

Next we consider diodes with $n_3 = n_5 = 3.59$, $n_2 = n_4 = 3.385$, $L = 350$ μm, $\lambda_0 = 0.9$ μm, an active GaAs region of thickness $t_3 = 0.12$ μm, a thick GaAlAs layer t_2 on the substrate, and various GaAlAs-region thicknesses t_4 between the active region and the umpumped absorbing GaAs superstrate region 5. We take [14] $\alpha_s = 500$ cm^{-1} for region 5 and plot the TE_0-mode threshold current J_0 versus t_4 in Fig. 5. The previous parameter values characterize a set of diodes studied experimentally by Casey and Panish [1] and measurements from their paper

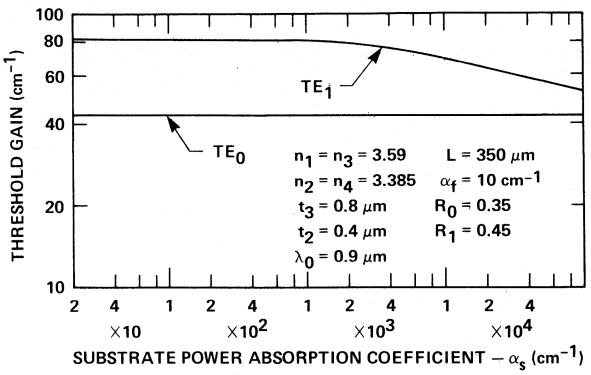


Fig. 4. Threshold gain versus substrate power absorption coefficient α_s for the TE_0 and TE_1 modes.

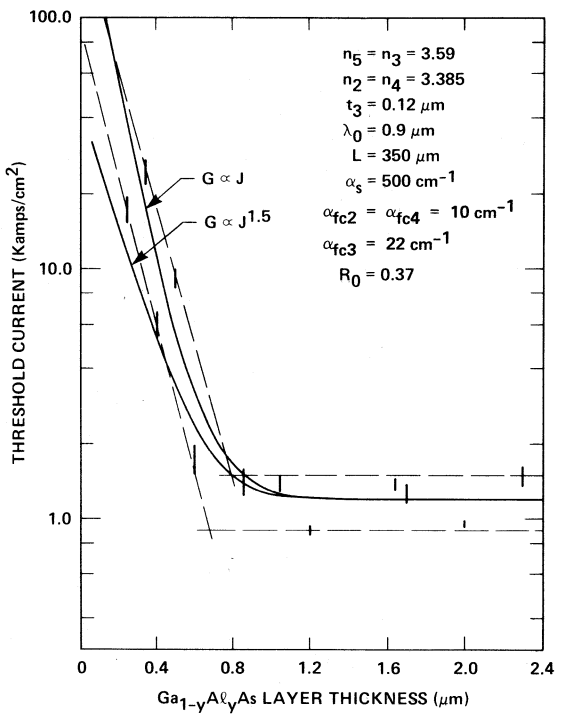


Fig. 5. Threshold current versus GaAlAs-layer thickness t_4 for the TE_0 mode in a diode with a 0.12-μm-thick active region.

are shown as vertical bars in Fig. 5. The dashed lines, also taken from [1], are approximate boundaries on the data. The two solid curves are the results of our calculations for G_0 using method *C*. These were carried out with $\alpha_{fc3} = 22$ cm^{-1} in Si-doped GaAs [1] and $\alpha_{fc2} = \alpha_{fc4} = 10$ cm^{-1} in the GaAlAs; the reflectivity was taken as $R_0 = 0.37$ from the graphs of [12]. Values of G_0 were converted to J_0 via (27) with both $m = 1.5$ and $m = 1.0$, which holds for Si-doped GaAs [11] at low and high pumping currents, respectively. The curves were normalized to $J_0 = 1200$ A/cm^2 in the case of infinitely thick GaAlAs layers and this value was chosen as the mean of the dashed lines given in [1]. Clearly, the curve for $m = 1$ fits the data much better than the one for $m = 1.5$. This is not surprising since even with infinitely thick GaAlAs, $G_0 = 121.6$ cm^{-1} and at $t_4 = 0.4$ μm, $G_0 = 1081.7$ cm^{-1}, which gain certainly requires high excitation. It is also interesting to note that the shapes of the calculated curves are not strongly dependent of the free-carrier absorptions and the reflectivity R_0.

The threshold gain obtained by methods A and B for this laser with a thick GaAlAs region ($t_2 \to \infty$) is 126.7 cm^{-1} compared with 121.6 cm^{-1} from method C. However, plots using data obtained from method B, normalized to 1200 A/cm^2 for $t_2 \to \infty$, are virtually indistinguishable from the results shown in Fig. 5. The perturbation method, on the other hand, yields significantly erroneous results for $t_2 \lesssim 0.3$ μm for this laser with a thin active region. At $t_2 = 0.4$ μm with $G \propto J$ and J normalized to 1200 A/cm^2, method A yields 9361 A/cm^2 compared with 10 672 A/cm^2, an error of 12.3 percent. For that value of t_2, $|\delta E| = 0.0335$. With $t_2 = 0.3$, the threshold error (method A compared to C) is 21.3 percent and $|\delta E| = 0.0693$. It thus appears that method A yields usable results for $|\delta E| \lesssim 0.05$, but it should be noted that for lasers with thicker active regions the accuracy of method A is better even for larger values of $|\delta E|$. Methods B and C also agree more closely for lasers with thicker active regions.

VI. Conclusion

We have presented and compared one rather simple analytic method and two numerical methods for calculating mode losses and thresholds for DH lasers with a thin GaAlAs layer. These lasers exhibit transverse-mode selectivity without significant increases in the TE_0-mode threshold. The calculations are also of use in determining minimum GaAlAs-layer thicknesses to promote thermal conduction between the active layer and a heat sink and to permit mode interaction with a substrate corrugation.

Acknowledgment

The authors wish to thank Dr. H. C. Casey for useful discussions and critically reading an early version of the manuscript.

References

[1] H. C. Casey, Jr., and M. B. Panish, "Influence of $Al_xGa_{1-x}As$ layer thickness on threshold current density and differential quantum efficiency for GaAs-$Al_xGa_{1-x}As$ DH lasers," *J. Appl. Phys.*, vol. 46, pp. 1393–1395, 1975.

[2] J. K. Butler, H. Kressel, and I. Ladany, "Internal optical losses in very thin CW heterojunction laser diodes," *IEEE J. Quantum Electron. (Part II of Two Parts: Special Issue on 1974 Semiconductor Laser Conf.)*, vol. QE-11, pp. 402–408, July 1975.

[3] D. R. Scifres, R. D. Burnham, and W. Streifer, "Output coupling and distributed feedback utilizing substrate corrugations in double heterostructure GaAs lasers," *Appl. Phys. Lett.*, vol. 27, pp. 295–297, Sept. 1, 1975.

[4] H. Kressel, H. F. Lockwood, and F. Z. Hawrylo, "Large-optical-cavity (AlGa) As-GaAs heterojuction laser diode: Threshold efficiency," *J. Appl. Phys.*, vol. 43, pp. 561–567, 1972.

[5] H. C. Casey, Jr., M. B. Panish, W. O. Schlosser, and T. L. Paoli, "GaAs-$Al_xGa_{1-x}As$ heterostructure laser with separate optical and carrier confinement," *J. Appl. Phys.*, vol. 45, pp. 322–333, 1974.

[6] B. W. Hakki and C. J. Hwang, "Mode control in GaAs large-cavity double-heterostructure lasers," *J. Appl. Phys.*, vol. 45, pp. 2168–2173, 1974.

[7] A. Reisinger, "Characteristics of optical guided modes in lossy waveguides," *Appl. Opt.*, vol. 12, pp. 1015–1025, 1973.

[8] Y. Suematsu and K. Furuya, "Quasi-guided modes and related radiation losses in optical dielectric waveguides with external higher index surroundings," *IEEE Trans. Microwave Theory Tech. (Special Issue on Integrated Optics and Optical Waveguides)*, vol. MTT-23, pp. 170–175, Jan. 1975.

[9] S. Kawakami and S. Nishida, "Characteristics of a doubly clad optical fiber with a low-index inner cladding," *IEEE J. Quantum Electron.*, vol. QE-10, pp. 879–887, Dec. 1974.

[10] Y. Ohtaka, S. Kawakami, and S. Nishida, "Transmission characteristics of a multi-layer dielectric slab optical waveguide with strongly evanescent wave layers," *Trans. Inst. Electron. Commun. Eng. Japan*, vol. 57-C, pp. 187–194, 1974.

[11] E. Pinkas, B. I. Miller, K. Hayashi, and P. W. Foy, "GaAs-$Al_xGa_{1-x}As$ double heterostructure lasers–Effect of doping on lasing characteristics of GaAs," *J. Appl. Phys.*, vol. 43, pp. 2827–2835, 1972.

[12] T. Ikegami, "Reflectivity of mode at facet and oscillation mode in double-heterostructure injection lasers," *IEEE J. Quantum Electron.*, vol. QE-8, pp. 470–476, June 1972.

[13] F. K. Reinhart, I. Hayashi, and M. B. Panish, "Mode reflectivity and waveguide properties of double-heterostructure injection lasers," *J. Appl. Phys.*, vol. 42, pp. 4466–4479, 1971.

[14] H. C. Casey, Jr., D. D. Sell, and K. W. Wecht, "Concentration dependence of the absorption coefficient for n- and p-type GaAs between 1.3 and 1.6 eV," *J. Appl. Phys.*, vol. 46, pp. 250–257, 1975.

[15] M. J. Adams and M. Cross, "Electromagnetic theory of heterostructure injection lasers," *Solid-State Electron.*, vol. 14, pp. 865–883, 1971.

Compact High-Power N_2 Laser: Circuit Theory and Design

ADOLF J. SCHWAB, SENIOR MEMBER, IEEE, AND FRITZ W. HOLLINGER

Abstract—**Based on measurements of the transient voltage across the cavity of a transversely excited N_2 laser an equivalent circuit is developed which provides better understanding of the contribution of all individual components to maximum peak power. Consideration of the design criteria established guarantees about one million light pulses with more than 1 MW from simple high-efficiency construction.**

I. Introduction

MANY papers on transversely excited N_2 lasers published recently describe various modifications of the original versions reported by Leonard [1], Gerry [2], and Shipman [3]. Improvement of cavity design, high-voltage circuitry, and spark-gap switch resulted in lasers with output peak power in the megawatt range. Most of the information given deals with constructive details and the dependency of the laser output from various parameters as gas pressure, high-voltage magnitude, etc. Whereas the time history of the light pulse is well known, little information is available on voltage and current waveforms in the gas discharge of the cavity, as well as on the electromagnetic (EM) interaction of the individual laser components. This is due to the fact that the laser cavity is generally an integral part of the high-voltage circuitry with terminals barely accessible. Both laser electrodes are floating with respect to ground, Fig. 1.

In transversely excited N_2 lasers a gas volume between two electrodes whose length is large compared with their distance is pumped by an electric pulsed gas discharge perpendicular to the laser axis. The pulse forming network consists of two parallel-plate transmission lines located at both sides of the cavity. Both sides are charged to ten or more kilovolts by a dc power supply or Marx generator. When one of the transmission lines is short circuited at its end, for instance, by a pressurized spark gap, a transient voltage occurs across the laser cavity creating a powerful gas discharge between the electrodes. Measurement of this voltage with a conventional unbalanced method, choosing one of the laser electrodes as ground reference, and rendering the base plate live would yield erroneous results because of the strong coupling by stray capacitances. Hence an electrooptic differential method has been chosen requiring none of the cavity electrodes to be grounded.

II. Voltage Waveforms Across the Laser Cavity and the Spark Gap

It is generally assumed that after the firing of the spark gap a traveling wave occurs in one of the transmission lines initiating the gas discharge and generating a second traveling wave

Manuscript received September 9, 1975; revised November 5, 1975. This work was supported by the Deutsche Forschungsgemeinschaft.

The authors are with the University of Karlsruhe, Karlsruhe, Germany.

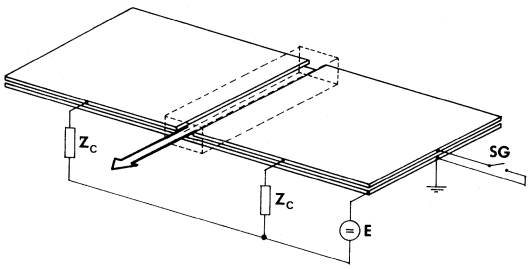


Fig. 1. Basic transversely excited N_2 laser with Blumlein circuit. Z_C: charging impedance; E: high-voltage power supply; SG: spark gap.

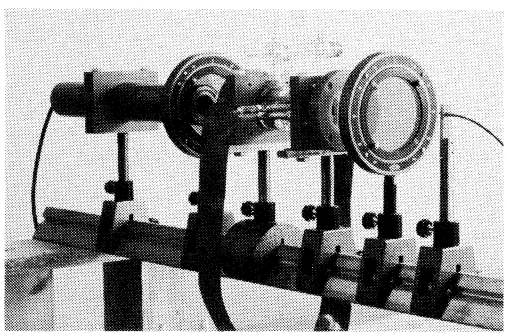


Fig. 2. Kerr-cell voltage measuring system.

in the other line. Superposition of both traveling waves causes a complex voltage across the laser electrodes that sustains the discharge. Measurement of the voltage waveform by conventional differential methods, i.e., via two high-voltage probes and a differential amplifier, will not be successful because of the inadequate common-mode rejection due to the inherently asymmetrical signal channels, particularly at high frequencies. Abundant common-mode rejection is provided by Kerr-cell measuring system employing an He–Ne laser, two polarizers, high-voltage Kerr cell, and a photodetector [4], Fig. 2.

Depending on the voltage applied to the Kerr-cell electrodes the laser beam is intensity modulated when it leaves the analyzer. The modulated beam is guided via a glass fiber optic to a photomultiplier and cascaded CRO inside a Faraday cage (photomultiplier: Valvo UVP 56, T_r = 3.5 ns, oscilloscope: Tektronix 7904 with plug-in 7A19, T_r = 0.7 ns). Applying Kerr's $\sin^2$ law the pulse shape of the high voltage applied to the Kerr cell can be computed [5]. The resonant frequency of the high-voltage lead and Kerr-cell arrangement is beyond 100 MHz and adequate for the rise times encountered. For even faster measurements the Kerr cell and the polarizers could be mounted immediately on top of the laser cavity providing resonant frequencies beyond 400 MHz.

Fig. 3(a) shows the voltage waveform across the cavity obtained by the Kerr-cell method and Fig. 3(b) shows the voltage breakdown across the spark gap measured with a conventional

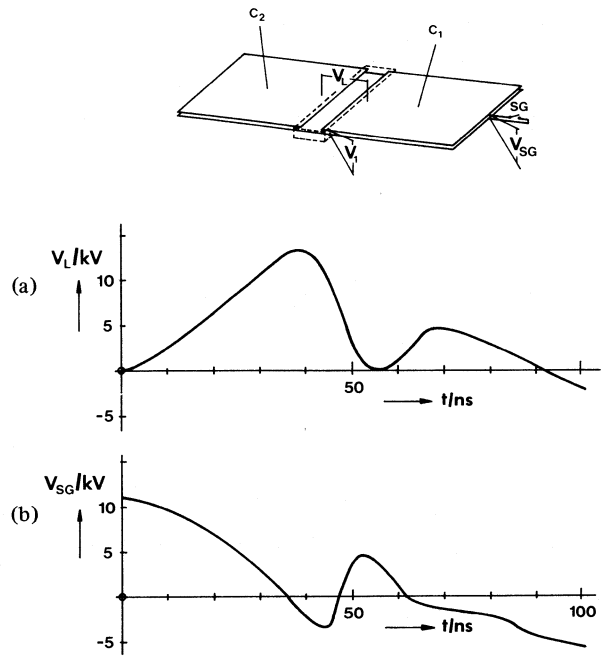


Fig. 3. Voltage waveform V_L across the cavity, evaluated by Kerr-cell measurement and voltage waveform V_{SG} across the spark-gap switch measured with a conventional high-voltage probe.

high-voltage probe (Tektronix P6015, T_r = 4 ns). In contrast to rapidly changing voltages so far assumed to exist, the oscillographs exhibit voltage waveforms with rise times on the order of 25 ns. This value is very large compared to a few nanoseconds usually encountered for pressurized spark gaps. To check the validity of these results the voltages between both laser electrodes and ground were individually measured by a high-voltage probe, Fig. 4.

The voltage waveform of the laser electrode adjacent to the spark gap and the spark-gap voltage are identical. The voltage of the opposite electrode remains constant until breakdown. Then with approximately the same rate of decay, this voltage also approaches zero. From the graphic superposition of both voltages, the transient voltage across the laser gap can be synthesized, Fig. 4(c), yielding a curve which is in good agreement with the voltage measured by the Kerr-cell system, Fig. 3(a). Due to the different arrangement of the voltage sensing leads, the probe measurement includes a larger portion of the inductive voltage drop across the cavity and hence exhibits two zeros at 50 and 60 ns.

The surprisingly low rates of the voltage variation can be explained by the large time constant $T = L/R$ with L the inductance of the switch and R the characteristic impedance of the lines. For example, to obtain a rise time of 2 ns in an N_2-laser Blumlein generator with 0.160-Ω characteristic impedance, L should be less than 0.2 nH, which is unrealizable using a single spark gap. For large time constants the velocity of voltage breakdown in the spark gap is no longer determined by the formation time of the gas discharge, but rather is controlled by the circuit inductance. In the original Blumlein circuit employing transmission lines with high characteristic impedance, rise times of a few nanoseconds were easily ob-

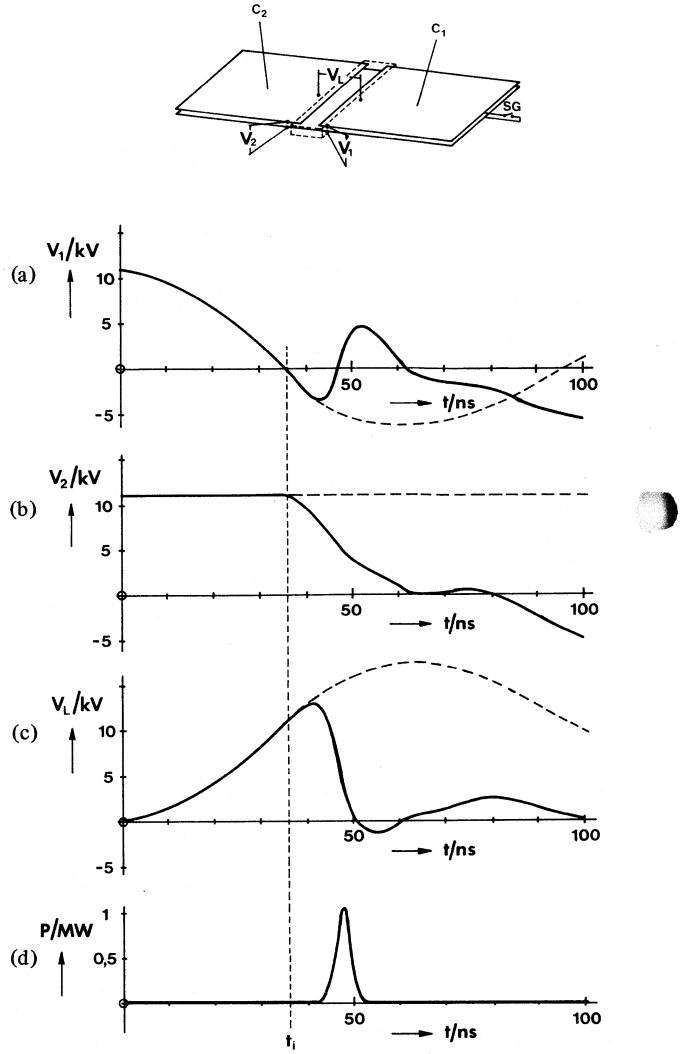


Fig. 4. Voltages V_1 and V_2 between laser electrodes and ground, voltage waveform V_L across the cavity, evaluated graphically by superposition, and laser output P. (Dotted lines show voltage waveforms at high pressure, i.e., without cavity breakdown.) t_i = start of cavity discharge.

tained and the transmission-line concept was justified. For low-impedance Blumlein generators (as used with N_2 lasers), propagation time on the transmission lines is on the order of 5 ns/m. Considering rise times of about 25 ns, which are inherent to many reported N_2 lasers, the traveling-wave concept becomes obsolete. This is particularly important in view of N_2 lasers operating with wedge-shaped or parabolic transmission lines [6], [7]. Obviously, the improvement of performance in those lasers cannot be explained by the time match between the laser light and the tapered arrival of the voltage wave at the electrodes, but must rather be explained by the different impedances between the short circuit and the particular starting points of the gas discharge. Of course, in order to obtain a higher output and small power variation from pulse to pulse it is advantageous that the discharge starts reproducibly at one end of the cavity. However, this goal can be achieved more efficiently by a tapered electrode gap. If the advantages of true traveling-wave excitation shall be utilized,

either multiple spark gaps [8], solid-dielectric spark gaps [3], or lines with high characteristic impedance (e.g., 20 Ω) [9] must be employed.

III. Current Waveform in the Laser Cavity

Having evaluated the voltage waveform across the laser cavity, measurement of the associated current seems desirable. Direct measurement of this current by a Rogowski coil or a specially adapted shunt is not possible without significantly changing the integrated cavity arrangement. However, to a first approximation, the current waveform can be evaluated from the cavity voltage V_L and the cavity impedance.

As the discharge current in a spark gap is growing from zero to its maximum value, eventually limited by the source impedance, the spark impedance is decreasing from its infinitely high value towards a minimum determined by the short-circuit current of the source. Simultaneously, the voltage across the spark gap is decreasing from the static breakdown voltage to the arc voltage. When the voltage V_L across the cavity, measured with the Kerr-cell system, becomes almost zero during the interval between 50 and 60 ns (the arc voltage being too small to be recognized in Fig. 3), the current in the cavity possesses its maximum. The location of this maximum can be determined more precisely from the probe measurement where, because of the inclusion of the induced voltage, a voltage zero must correspond to $di/dt = 0$. These considerations permit a qualitative sketch of the current rise and the location of the current maximum with respect to time. Fig. 5 shows clearly the time correlation between cavity voltage, cavity current maximum, and the occurrence of the laser pulse. Population inversion requires only 10 ns, beginning at t_i. Of course, almost nothing can be said about the current waveform beyond 60 ns which, on the other hand, does not contribute to the laser action and hence need not be considered. Measurement of the complete cavity current waveform and current magnitude by a magnetooptic method currently done in our laboratory will sustain the considerations made in the preceding.

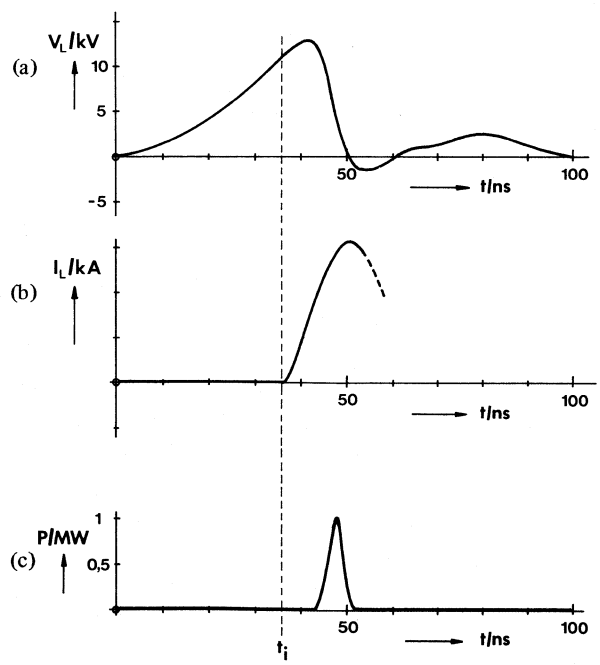


Fig. 5. Probe measurement voltage V_L, graphically evaluated cavity current I_L, and laser output P. t_i = start of cavity discharge.

IV. Equivalent Circuit of an N_2 Laser with One Pressurized Spark Gap

Since pulse forming networks of N_2 lasers must not necessarily be treated as circuits with distributed parameters, a network with lumped components has been developed which can be evaluated by a computer program, Fig. 6. In this equivalent circuit C_2 represents the open stripline, C_1 the stripline adjacent to the spark gap, L_L, R_{L1}, and R_{L2} the cavity impedance before and after the ignition of the gas discharge, and L_{SG} and R_{SG} the spark-gap impedance. Inductances L_1 and L_2 take into account the transmission-line character of the Blumlein circuit, if any. The quantities C_1, L_1, C_2, L_2 can be estimated from the stripline dimensions, L_L, L_{SG}, R_{L1}, R_{SG} from the resonant frequencies and the attenuation, both of which can be evaluated from oscillographs. The nonlinear behavior of the cavity discharge is represented by a thyristor characteristic which provides a fast resistance change and offers different voltage levels for the conducting and nonconducting state. The capacitance C_L lies typically in the picofarad range and is considered negligible here.

Assuming the inductance L_1 and L_2 to be small compared with the inductance of the short circuit the following results can be obtained from the computation.

1) Given a fixed line capacitance the rate of voltage variation across the cavity is almost exclusively determined by the inductance of the spark-gap switch, Fig. 7. Likewise, this applies to the voltage V_L, because V_2 remains constant until breakdown (cf. Fig. 4). To obtain a high overvoltage across the cavity a spark-gap switch with extremely low inductance is essential.

2) The rate of current change is limited by the inductance of the cavity, Fig. 8. It must be emphasized that even slightly higher inductances significantly reduce the rate of current variation and the peak current, thereby favoring arc formation and output degeneration.

3) Given a fixed spark-gap and cavity inductance and a particular thickness of the dielectric, the rate of current varia-

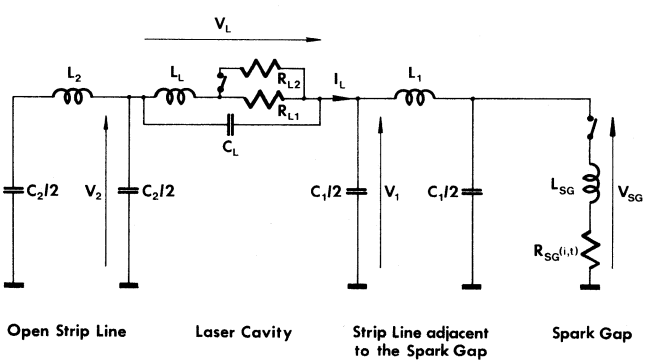


Fig. 6. Equivalent circuit of N_2 lasers with one pressurized spark gap.

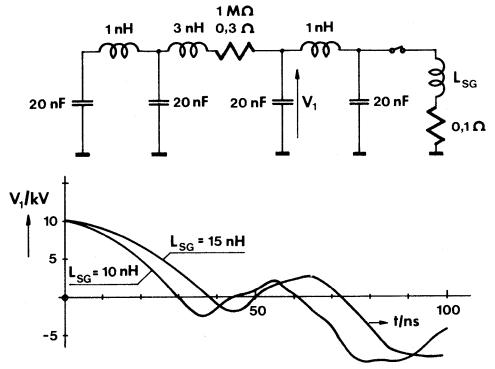


Fig. 7. Voltage waveform V_1 showing the influence of spark-gap inductance on dV_1/dt.

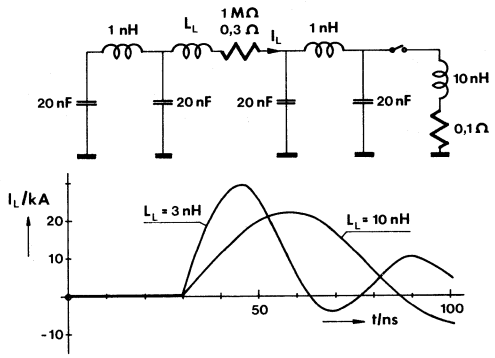


Fig. 8. Current waveform I_L showing the influence of cavity inductance on dI_L/dt.

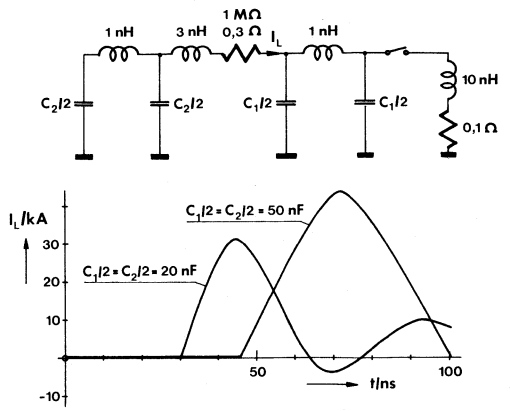


Fig. 9. Current waveform I_L showing the influence of the line capacitance on dI_L/dt and time of ignition.

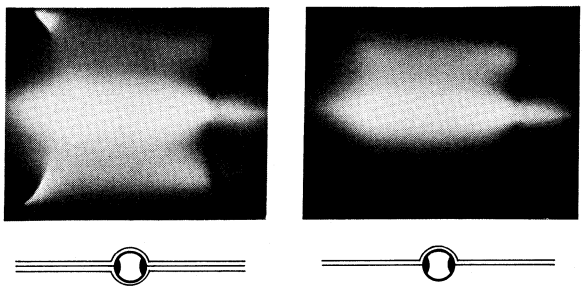


Fig. 10. Photographs of a symmetrical and asymmetrical cavity arrangement.

tion depends slightly of the length of the line. The shorter the length, i.e., the smaller the capacitance, the higher dI/dt in spite of $I_{L\,max}$ being smaller, Fig. 9. This tendency is limited when arcing occurs (cf. Section VI).

Computed and experimentally obtained results generally show good agreement. It should be emphasized that the establishment of the equivalent circuit profited from the experimental diagnosis to a high degree and likewise the design criteria for an optimization took advantage of the feedback provided by the equivalent circuit analysis.

V. Influence of Skin Effect and Stray Ground Capacitances

The major goal in TEA laser pumping is the generation of a diffuse, uniform gas discharge in the cavity. Having solved the problem of arc formation a further improvement can be achieved by utilization of the skin effect in the gas discharge and by taking into account stray ground capacitances. The magnetic fields of the current in the discharge and of the current in the ground planes, as well as their interaction (proximity effect), tend to expand the discharge. Likewise, the stray ground capacitances between the main electrodes in the cavity and the adjacent external ground planes tend to smooth the electric field between the electrodes. Skin effect is definitely dominant during later stages of the discharge, whereas stray ground capacitances contribute to discharge fidelity at the start. The beneficial influence of both effects can be recognized from Fig. 10, showing discharge photographs of a symmetrical and asymmetrical cavity arrangement.

The asymmetrical cavity arrangement exhibits an asymmetrical, smaller discharge pattern and possesses less output power. Hence optimization of peak power, i.e., generation of a uniform discharge profile as wide as possible, requires careful placement of the ground return path with respect to the discharge electrodes.

VI. N_2-Laser Design

A. Striplines

A powerful arc-free discharge in the cavity requires a certain amount of electrical energy stored in the capacitors C_1 and C_2. These capacitors should be physically realized by short electrodes with small conductor spacing. Then the isolation of the distributed components by the inductors L_1 and L_2 becomes negligible. However, the electrode length must not be too short (e.g., 50 cm for a cavity length of about 60 cm) in order to avoid arcing between the electrodes due to excessive impedance differences between the location of the short circuit and the particular starting points of the gas discharge (cf. Section II). Increasing the total capacitance by either enlarging the capacitor electrode length or reducing the thickness of the dielectric will not contribute to the laser output without limit because the resonant frequency of the circuit will decrease resulting in lower rates of voltage and current variation.

B. Spark Gap

The spark gap consists of four parts, the top part "1" accommodating the trigger pin and compressed gas inlet, the

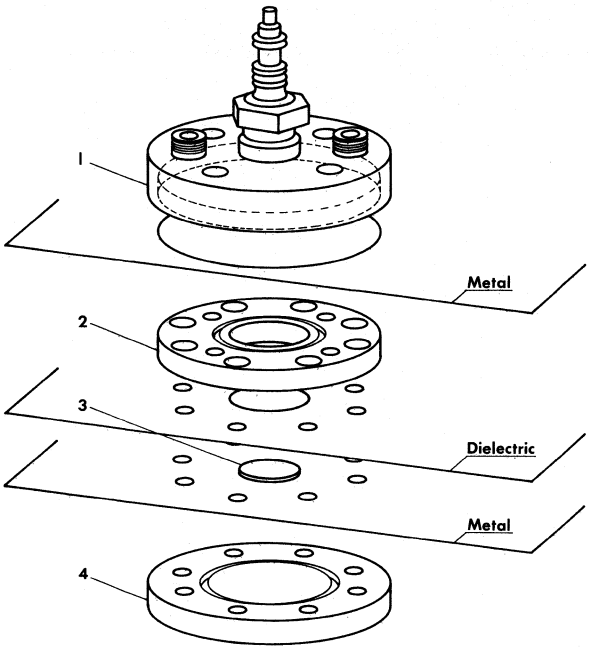


Fig. 11. Low-inductance spark gap of the N_2 laser, $L < 5$ nH. (Determined from the resonant frequency.)

high-pressure envelope "2" and the bottom part "4," both made from Lucite, and the high-voltage electrode "3," Fig. 11.

Mounting of the spark gap requires three steps.

1) Part 3 is soldered to the live electrode at the desired location.

2) Parts 2 and 4 are bolted together with nylon screws through eight holes punched concentrically in the dielectric. The high-voltage seal against the ground electrodes is a silicon rubber ring (RTV) extruded into concentric grooves of parts 2 and 4.

3) Part 1, soldered to the ground electrode, is slipped over the Lucite envelope and fixed by four metal screws.

This spark gap possesses an inductance of less than 5 nH. Its breakdown voltage is coarsely controlled by the distance between the high-voltage and ground electrodes, fine adjustment is accomplished by pressure variation.

C. Cavity Design

Depending on the desired cross section of the laser beam two different approaches can be recommended.

1) The inner diameter of the cavity is only about 20 mm, the main electrodes consist of thin cylindrical brass rods, (Fig. 12). This is about the most trivial design if one neglects even simpler arrangements, where the live electrodes of the transmission lines or saw blades serve as the main electrodes. Sharp electrodes require moderate operating voltages; however, the cross section of the discharge is small, particularly at the electrodes. Since the output is approximately proportional to the pumped cross section, broadening of the discharge by electrodes of larger diameter is preferable. Given a particular diameter of the electrodes their distance must be adjusted in such a way that breakdown occurs at a voltage V_L higher than the charging voltage V_{dc} (cf. Fig. 4(a), oscillating voltage V_1 permits $V_L > V_{dc}$).

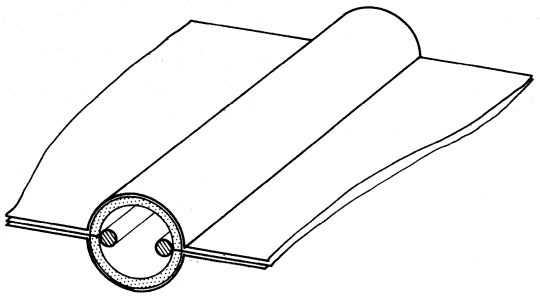


Fig. 12. Small cavity with cylindrical brass electrodes.

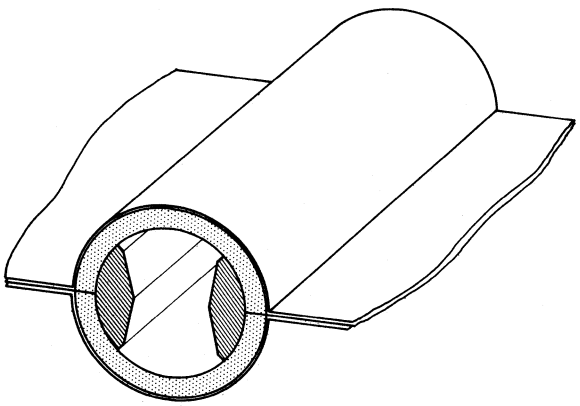


Fig. 13. Cavity of larger diameter with milled electrodes.

According to Section V, the choice of the inner diameter of the cavity must take into account the influence of skin effect and stray capacitances. Arranging external ground electrodes close to the main electrodes expands the discharge along the cavity walls. Close approximation between the external ground electrodes and the discharge path contributes to a low cavity inductance.

2) The cavity diameter is about 40–50 mm, the main electrodes consist of milled bars, smoothly fitting to the curvature of the cavity, Fig. 13. This design permits discharges of larger cross section. However, the gain provided by the larger, uniformly ionized cross section is balanced by the increased cavity inductance.

VII. Compact N_2 Laser

Application of an N_2 laser for dye laser pumping or as an irradiation source in high-voltage laboratories [10] requires a compact, conveniently handled instrument. Flat solid striplines, spread on a laboratory table, are no longer tolerable. In an earlier paper the authors have described a more compact version, wherein the spiraled striplines formed two cylinders located at both sides of the cavity [11]. In this paper an improved version is presented, possessing even smaller dimensions, Fig. 14.

Both striplines are rolled up around the cavity offering minimum space requirements. Finally, Fig. 15 shows the N_2 laser including spark gap and all necessary instrumentation except dc power supply in a metal cabinet providing adequate suppression of EM interferences. Reproducible peak power is

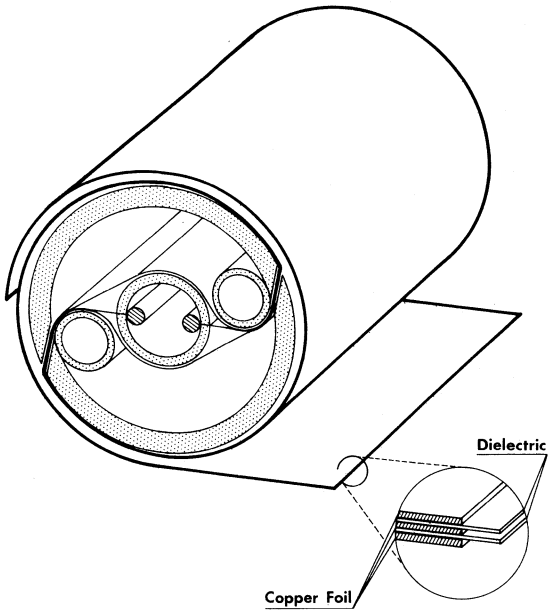


Fig. 14. Schematic cross section of the compact N_2 laser.

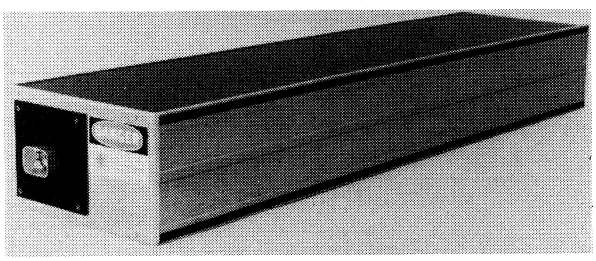


Fig. 15. Compact N_2 laser in a metal cabinet housing all necessary components except high-voltage power supply (courtesy Schwab).

1.2 MW at 12-kV charging voltage. Total efficiency is about 0.3–0.4 percent, the higher efficiency obtained with a mirror attached to the cavity.

Acknowledgment

The authors wish to thank Prof. H. Lau of the Hochspannungsinstitut of the University of Karlsruhe, Germany, for his assistance and great interest in their work.

References

[1] D. Leonard, "Saturation of the molecular nitrogen second positive laser transition," *Appl. Phys. Lett.*, vol. 7, pp. 4–6, Jan. 1965.
[2] E. Gerry, "Pulsed-molecular-nitrogen laser theory," *Appl. Phys. Lett.*, vol. 7, pp. 6–8, Jan. 1965.
[3] J. Shipman, "Traveling wave excitation of high-power gas lasers," *Appl. Phys. Lett.*, vol. 10, pp. 3–4, Jan. 1967.
[4] A. Schwab, *High-Voltage Measurement Techniques.* Cambridge, MA: M.I.T. Press, 1972.
[5] R. Klein, "Étude de la mesure d'impulsion haute tension rapides au moyen de capteurs éléctro-optiques," Ph.D. dissertation, University of Strasburg, Strasburg, France, 1974.
[6] D. Basting, F. P. Schäfer, and B. Steyer, "A simple high power nitrogen laser," *Opto-Electron.*, vol. 4, pp. 43–49, 1972.
[7] B. Godard, "A simple high-power large efficiency N_2 ultraviolet laser," *IEEE J. Quantum Electron. (Part II of Two Parts)*, vol. QE-10, pp. 147–153, Feb. 1974.
[8] M. Geller, D. Altmann, and T. DeTemple, "Some considerations in the design of a high power pulsed N_2-laser," *Appl. Opt.*, vol. 7, pp. 2232–2237, 1968.
[9] H. Salzmann and A. Strohwald, "High-power, subnanosecond pulse from a TEA nitrogen laser," *Opt. Commun.* (Amsterdam), vol. 12, pp. 370–372, Apr. 1974.
[10] A. Schwab and F. Hollinger, "Triggerung von Funkenstrecken mit ultraviolettem Laserlicht," *Elektrotech. Z. Ausg. A.*, vol. 96, pp. 236–238, May 1975.
[11] —, "UV-Laser Zur Bestrahlung von Messfunkenstrecken," *Elektrotech. Z. Ausg. A.*, vol. 94, pp. 459–462, Aug. 1973.

Spiking Oscillations in Diode-Pumped NdP_5O_{14} and $NdAl_3(BO_3)_4$ Lasers

STEPHEN R. CHINN, MEMBER, IEEE, HENRY Y-P. HONG, AND JAMES W. PIERCE

Abstract—**Using quasi-CW sinusoidally modulated excitation from a 0.8-μm-wavelength laser diode, we have obtained driven spiking oscillations in miniature, high-Nd-concentration room-temperature lasers of NdP_5O_{14}, and $NdAl_3(BO_3)_4$. With modulation indices of 0.25 or less, peak-power enhancements of 11 (at 35 kHz) and 7 (at 124 kHz), respectively, have been observed for these materials. Theoretical calculations of these and other characteristics of the driven oscillations are in good agreement with experiment.**

IN AN EFFORT to enhance the peak powers of miniature high-Nd-concentration lasers, we have obtained driven spiking oscillations in NdP_5O_{14} (NPP) and $NdAl_3(BO_3)_4$ (NAB) lasers excited by a 0.8-μm-wavelength laser diode. Quasi-CW laser operation of diode-pumped NPP [1] and dye-laser-excited NAB [2] has been described previously. Both of these materials have low optical pump thresholds and good power conversion efficiencies, making them attractive candidates for applications such as sources in fiber optic communications, where large average output powers are not required. In some circumstances, it might be desirable to increase the peak laser power in order to increase the signal-to-noise ratio (SNR) in pulsed or gated detection systems, and even possibly to reach large enough intracavity optical power densities for useful nonlinear applications such as second-harmonic generation. The peak power may be conveniently increased, at no increase in average optical pump power with no additional optical components, by sinusoidally modulating the laser loss or gain to obtain periodic output peaks, called spiking oscillations. Such behavior was observed by Kimura and coworkers [3], [4], who modulated the cavity loss of a lamp-pumped Nd:YAG laser by vibrating one of the optical cavity mirrors at approximately 10 kHz. Danielmeyer and Ostermayer [5] later obtained 4–6-kHz spiking output of a Nd:YAG laser pumped by a sinusoidally modulated luminescent diode array. In this paper, we report much higher frequency spiking in laser-diode-pumped NPP and NAB lasers with similar sinusoidal pump modulation, and show that the experimentally observed output is in excellent agreement with theoretical calculations of the spiking frequencies, peak-power enhancement, and spike width.

A diagram of the experimental setup, which is similar to the one described in [1], is shown in Fig. 1. The laser crystal was located in the center of a nearly concentric optical cavity ~ 10 cm long, with 99.7-percent- and 100-percent-reflecting, 5-cm-radius mirrors. Pump radiation was collected from a 100-μm-wide double-heterostructure $Ga_{1-x}Al_xAs$ laser diode (provided by Ladany of RCA Laboratories) by two $f/0.9$ lenses, and focused with ~ 1:1 imaging onto the side of the crystal. The laser diode was mounted on the cold finger of a liquid-nitrogen Dewar to increase its bandgap and shift the output wavelength into the 0.8-μm absorption band of Nd^{3+}. In these experiments, unlike those in [1], the pump wavelength was not optimized by fine temperature tuning the diode, and all results reported are for 7915-Å pump radiation with 27-Å bandwidth, full width at half maximum (FWHM). Because of thermal limitations imposed by the laser diode, not by the Nd laser crystals, quasi-CW excitation with 300-μs pulses was used. These pulses were synchronized with the sinusoidal modulation by the triggering scheme shown in Fig. 1. The pulse repetition rate, 100 Hz, was determined by the 10-ms oscilloscope sweep of the sinusoid-triggered oscilloscope trace. In order to excite the laser diode only during the 300-μs pulse, the sinusoidal modulation current was gated by this pulse and then amplified. The modulation and pulse currents, passing, respectively, through 25-Ω and 50-Ω impedance-matching load resistors, were summed at the diode, which had a low

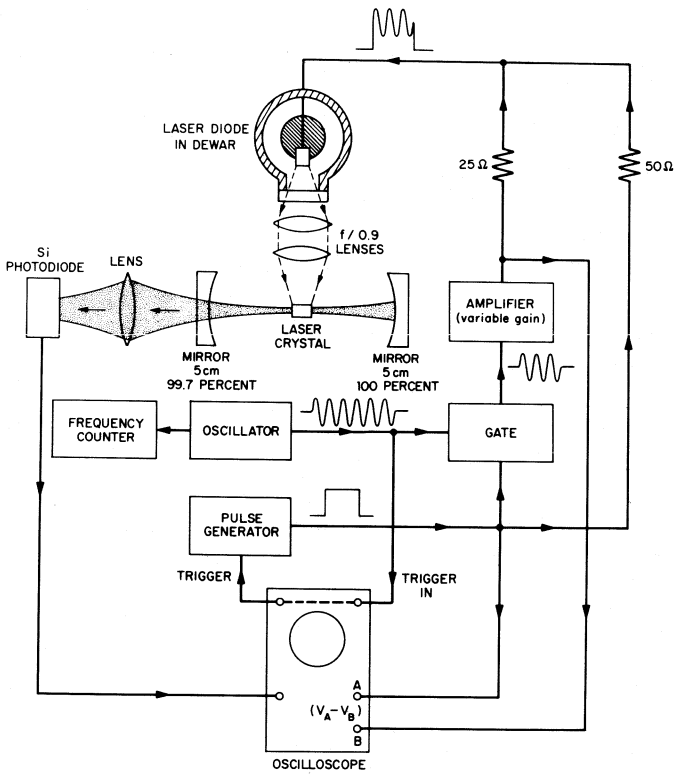


Fig. 1. Schematic diagram of apparatus for pulsed sinusoidally modulated diode pumping of NPP and NAB lasers with driven spiking output.

Manuscript received November 3, 1975. This work was supported by the U.S. Air Force.

The authors are with the Lincoln Laboratory, Massachusetts Institute of Technology, Lexington, MA 02173.

resistance during the forward bias of the pulse. The NPP or NAB laser output was partially focused and then detected by a calibrated Si photodiode. The diode pump power was calibrated against current by using another Si photodiode placed at the laser crystal position.

An as-grown NPP crystal used in most of these experiments was the same one described in [1], with a pair of parallel natural laser facets normal to the *a* axis. The laser length was 760 μm. The side pump facet was parallel, and the pump direction was therefore perpendicular, to the lasing axis. The NAB sample was a four-faceted rhombohedral rod (lacking two of its hexagonal-symmetry facets), with pairs of natural laser facets parallel to the *c* axis. The laser length was 173 μm. This crystal was not as suitable for transverse pumping as the NPP crystal, because the side pump facet was tilted 60° from the lasing axis.

Experimental results for unmodulated and modulated pumping are shown in Fig. 2(a)-(c) for NPP and in Fig. 2(d)-(f) for NAB. In each of these figures the bottom trace is the Nd laser output. The top traces in Fig. 2(a) and (d) are the unmodulated pulse voltages, while those in Fig. 2(b) and (e) are the difference voltages between the pulsed and sinusoidal voltages ($V_A - V_B$ in Fig. 1). These top traces (200 μs/cm), taken from a 5 × expansion of the oscilloscope channel used in the modulation triggering circuit (Fig. 1), have a compressed time scale relative to the bottom traces (50 μs/cm). In Fig. 2(c) and (f), the top traces represent scattered optical output from the pump diode measured without calibrated vertical amplitude; in these figures the top and bottom traces have the same expanded time scale (10 μs/cm) and show the actual phase relation between the modulated pump and Nd laser outputs. Note that for each laser the output amplitude scales are the same for the unmodulated and modulated cases. Each of the figures shows roughly three repetitive oscilloscope sweeps occurring within the 1/30-s camera exposure. The lasers were aligned to give a single, stable damped relaxation oscillation in the absence of modulation. This configuration generally did not give either maximum output power or minimum threshold, but neither of these parameters showed more than 50-percent degradation. Although we have not made a detailed investigation of the nature of such detuning effects, it is most likely that the stable relaxation oscillations occur when higher loss modes are discriminated against. These modes may either be the usual higher order Gaussian modes, or in the present concentric resonator, slightly off-axis modes whose minimum loss condition is determined by etalon effects of the laser crystal. Previous coaxial pumping experiments have shown a correlation between complex, unstable relaxation oscillations and lasing spectra with wavelengths additional to the usual axial modes of the crystal etalon.

The data of Fig. 2 were obtained with each laser pumped at approximately twice the threshold optical power of 17.5 mW for NPP and 16.5 mW for NAB. The measured optical modulation index, defined as the ratio of the sinusoidal pump output amplitude to the amplitude of the unmodulated pump pulse was 0.25 for NPP and 0.21 for NAB, leaving the lasers at or above threshold throughout the 300-μs pump pulse.

For a given pump power, the spiking oscillations occurred over a frequency range determined primarily by the small-signal damped relaxation oscillation frequency, ω_0 [6]. With unmodulated pumping, this decaying sinusoidal output was observed after a few initial large-amplitude spikes. In the present discussion, by spiking oscillations we mean periodic output peaks with zero amplitude between them. At very low modulation frequencies, output peaks with intermediate weaker pulsed or sinusoidal output occurred. At much higher frequencies, the spiking decreased in amplitude and eventually turned into a sinusoidal output. Typically, the range of spiking frequencies extends from $\sim\omega_0/2$ (the approximate frequency of undriven spiking output in the initial, highly nonlinear regime) to a higher frequency, somewhat below ω_0, that depends on the pump power and modulation index.

In order to gain a more general insight into the driven spiking oscillations, we have numerically simulated the operation of the Nd lasers by solving the coupled nonlinear laser rate equations with a digital computer and have also obtained approximate analytic expressions for the output during the individual peaks. The coupled rate equations have been formulated and solved in various regimes by several authors [3], [4], [6]-[11]. We write the simplified single-mode equations as

$$\dot{n} = nN - n \tag{1a}$$

$$\dot{N} = -nN\lambda(\bar{\rho} - 1) - N\lambda + \rho\lambda \tag{1b}$$

where the dimensionless variables n and N, normalized to their CW values, are

- n number of photons;
- N population inversion;
- λ ratio of cavity lifetime (τ_Q) to fluorescence lifetime (τ);
- ρ pumping rate (normalized to *threshold* value);
- $\bar{\rho}$ average (quasi-CW) normalized pumping rate.

In these equations, the unit of dimensionless time (t) is $\tau_Q = [2\mathcal{L}/c(T + L)]$, where

- $\mathcal{L}$ optical length of laser cavity;
- c velocity of light;
- L internal loss/pass;
- T output mirror transmission.

As shown in [8], (1) also applies to multimode lasers if the modes have the same parameters.

Two typical solutions of (1), obtained by using a standard Runge-Kutta method on a digital computer, are shown in Fig. 3. A step excitation is applied at $t = 0$. The dash-dotted curve shows the damped oscillations that occur in the absence of sinusoidal modulation, and the solid curve shows the driven spiking oscillations (both outputs are given by the left-hand scale); the modulated pump power used to drive the oscillations is shown by the dashed curve (right-hand scale). The dimensionless parameters used in computing the results in Fig. 3 were chosen to correspond approximately to the experimental parameters of Fig. 2(a)-(c). Thus the value of λ was taken to be 0.001. Since $\tau_Q \approx 0.1$ μs for the NPP laser, this

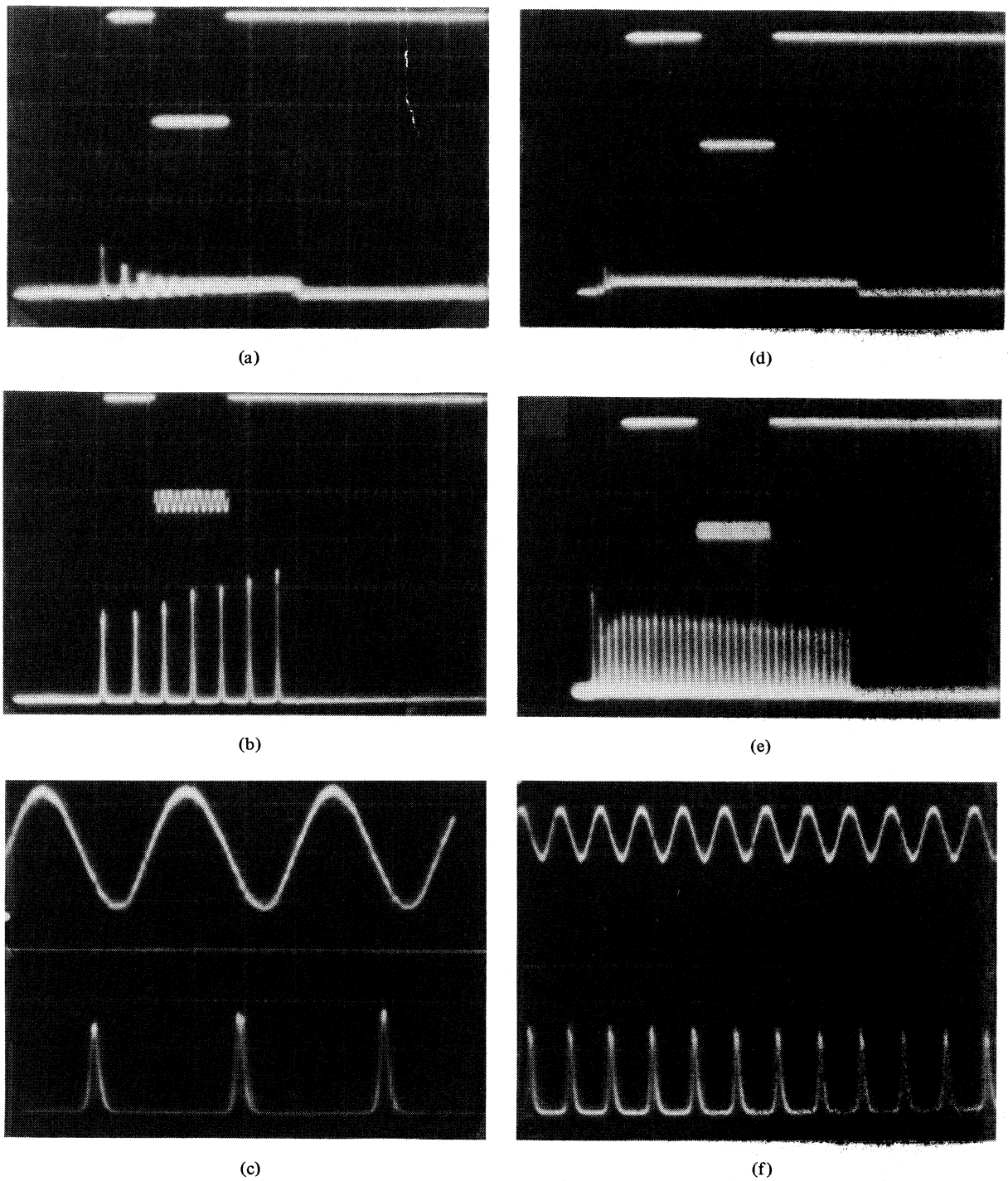


Fig. 2. Oscilloscope traces showing diode pump levels and laser outputs for NPP laser (left side) and NAB laser (right side). Photographs (a) and (d) on each side were obtained with unmodulated pumping, photographs (b), (c), (e), and (f) with modulated pumping. The bottom trace in each photograph is the laser output. The top traces in (a), (b), (d), and (e) are the diode voltages, $V_A - V_B$ (see Fig. 1) on a compressed time scale. The top traces in (c) and (f) represent scattered optical output from the pump diode on an uncalibrated vertical scale, shown in their actual phase relation to the laser output.

The scales are as follows.

		Top		Bottom	
		Vertical V/cm	Horizontal μs/cm	Vertical mW/cm	Horizontal μs/cm
NPP	(a)	20	200	2.4	50
	(b)	20	200	2.4	50
	(c)	(Uncalibrated	10	2.4	10
NAB	(d)	20	200	0.85	50
	(e)	20	200	0.85	50
	(f)	(Uncalibrated	10	0.85	10

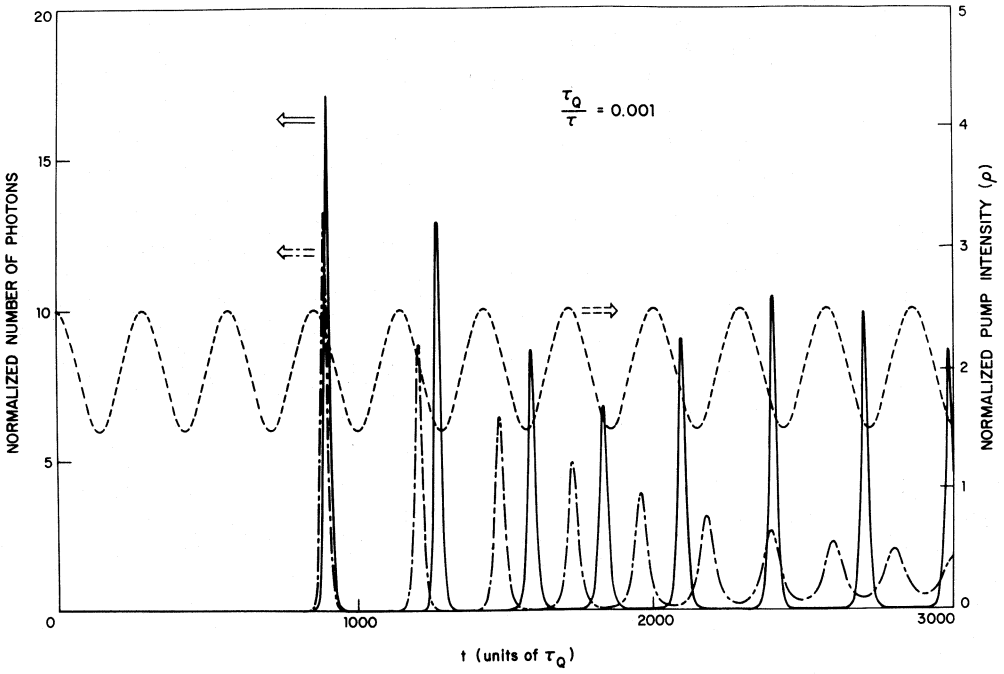


Fig. 3. Calculated solutions of (1) for laser output due to step excitation at $t = 0$. The normalized time scale, 0–3000, corresponds to 300 μs for $\tau_Q = 0.1$ μs. The dash-dotted curve is the damped oscillatory output produced by unmodulated pumping and the solid curve is the driven spiking output (both measured on left-hand scale). The dashed curve (right-hand scale) is the modulated pump power, normalized to the laser threshold power.

gives $\tau \approx 100$ μs, close to the value for NPP, 115–120 μs [12], [13]. The pump level, $\rho \approx 2$, and modulation index of 0.25 at 35 kHz are also taken from the experiment, and the full-time scale of Fig. 3 corresponds to $3000\,\tau_Q \approx 300$ μs. The calculations are carried out for the interval 0–$3000\tau_Q$ during an infinite duration step, corresponding to the finite pulse duration, and do not show the rapid output decay (within a few times τ_Q) at the end of the pump pulse.

The calculated results for the initial turnon delay, number of peaks, and the peak amplitude, width, and phase are in good agreement with the experimental data, allowing for both the slight inaccuracy of the parameters ρ and λ, and the experimental errors in measuring the laser output. The most serious discrepancy is in the relative amplitudes of the first few spikes, which depend very strongly (both experimentally and theoretically) on the phase of the sinusoidal modulation with respect to the step excitation. Similar results hold for the NAB laser output shown in Fig. 2(d)–(f), which was driven at 124 kHz. In this case, parameters for NAB used in the numerical calculations to obtain close agreement with the data were $\rho = 2.2$, modulation index = 0.21, $\tau_Q = 0.067$ μs, and $\tau = 20$ μs (giving $\lambda = 0.0033$). Much more rapid spiking frequencies can be obtained for NAB than for NPP because of the former's shorter fluorescence lifetime, $\tau \simeq 15$–20 μs [2], [14]. (It should be stressed that concentration quenching is no more severe in NAB than in NPP. The shorter lifetime is due primarily to the larger radiative transition probability in NAB [2]. Even at low Nd concentrations in $Nd_xGd_{1-x}Al_3(BO_3)_4$, τ is only 50 μs [2], [14].)

We have also obtained approximate analytic solutions of (1) for the driven spiking mode by making the same approximations used by Carlson [10], i.e., neglecting spontaneous emission and pumping during an output peak and taking $\dot{n} \ll n$. The solution for an individual peak centered about $t = 0$ is

$$n(t) = n_m \{\cosh^2 (\sqrt{\lambda(\bar{\rho} - 1)n_m/2t})\}^{-1} \tag{2}$$

where n_m is the normalized peak number of photons (enhancement factor). Using the fact that average laser power is conserved [5], as is observed and numerically calculated, we find for the enhancement factor

$$n_m = \frac{(\bar{\rho} - 1)}{8f^2\,\tau\tau_Q} \tag{3}$$

and FWHM width of the peak

$$\Delta t = \frac{7.051\tau\tau_Q f}{(\bar{\rho} - 1)} \tag{4}$$

where f is the modulation and spiking frequency. The conservation of average power with varying amounts of sinusoidal modulation can also be derived from (1) by taking time averages, and approximating the time average of N as 1, which holds for the present mode of operation. In (3) and (4), we have returned to actual time units, i.e., seconds, for $1/f$, τ, τ_Q, and Δt. Substituting into (3) and (4) the parameter values given in the preceding, corresponding to Figs. 2 and 3, we obtain the results for n_m and Δt listed in Table I.

Further verification of (3) has been obtained with another NPP sample, at similar pulse and modulation powers, by measuring n_m as a function of f. This 565-μm-long sample, also described in [1], had the same orientation as the previous NPP crystal, but was polished parallel to the lasing axis and mounted on a mirror to increase the pumping efficiency and allow slightly larger values of ρ. Over the range of spiking frequencies

TABLE I

Laser	n_m		Δt (μs)	
	Calc.	Obs.	Calc.	Obs.
NPP	10.2	11.3	2.5	2.0
NAB	7.3	7.1	1.0	1.0

from 31 to 63 kHz, n_m decreased from 18 to 7. A least squares linear fit to 8 data points on a logarithmic plot showed $n_m \propto f^{-2.2}$ (with r^2 correlation = 0.986), in good agreement with the predicted inverse square dependence. Arbitrarily, large power enhancements or arbitrarily narrow pulsewidths cannot be achieved—by decreasing τ_Q or f, for example—because f is limited to the range in which spiking oscillations can be obtained. If we take as a low-frequency limit $f \sim (\frac{1}{2}) \times (\omega_0/2\pi)$, where $\omega_0^2 \simeq (\bar{\rho} - 1)/\tau\,\tau_Q$, (3) and (4) give

$$n_m \simeq 19.7$$

and

$$\Delta t = 0.561\,[\tau\tau_Q/(\bar{\rho} - 1)]^{1/2}.$$

One approximation made in deriving the preceding analytic results that is not always valid is the neglect of the pumping term in the coupled rate equations. Experimentally, this term manifests itself by the need for a minimum modulation index in order to obtain spiking. In our experiments this minimum value is typically on the order of 0.2–0.3. With larger modulations, the spiking frequency range has been extended and peak power further increased.

Another factor of practical importance is the internal power within the laser cavity. In the experiments reported here, a low-transmission (0.3-percent) output mirror was used both to minimize the pump threshold and to maximize the internal power. With NPP we have obtained driven spike outputs up to 10 mW, corresponding to over 3-W peak internal power. With an estimated minimum mode radius $\sim$ 10–15 μm, the internal peak-power density is conservatively $\sim$ 0.5 MW/cm^2. With only slightly higher power densities, useful nonlinear interactions such as second-harmonic generation or passive mode locking could become practical in miniature Nd lasers in spite of their low average output power. Finally, as pointed out in [5], we emphasize that driven spiking output can be obtained by sinusoidal pump modulation with no additional intracavity components and no increase in laser threshold.

ACKNOWLEDGMENT

The authors wish to thank H. Heckscher, C. H. Anderson, Jr., and E. J. Delaney for their expert assistance. They also wish to thank Dr. P. L. Kelley and Dr. A. J. Strauss for helpful comments and discussion and Dr. I. Ladany of RCA Laboratories for supplying the laser diode used in this work.

REFERENCES

[1] S. R. Chinn, J. W. Pierce, and H. Heckscher, "Low-threshold, transversely-excited NdP_5O_{14} laser," in *Dig. Tech. Papers, IEEE/OSA Conf. Laser Engineering Applications* (Washington, DC, 1975); also in *Appl. Opt.*, to be published.

[2] S. R. Chinn and H. Y-P. Hong, "CW laser action in acentric $NdAl_3(BO_3)_4$ and $KNdP_4O_{12}$," *Opt. Commun.*, vol. 15, pp. 345–350, 1975.

[3] T. Kimura and K. Otsuka, "Response of a CW Nd^{3+}: YAG laser to sinusoidal cavity perturbations," *IEEE J. Quantum Electron.*, vol. QE-6, pp. 764–769, Dec. 1970.

[4] T. Kimura, K. Otsuka, and M. Saruwatari, "Spatial hole-burning effects in a Nd^{3+}:YAG laser," *J. Appl. Phys.*, vol. 43, pp. 2911–2913, 1972.

[5] H. G. Danielmeyer and F. W. Ostermayer, Jr., "Diode-pump-modulated Nd:YAG laser," *IEEE J. Quantum Electron.*, vol. QE-7, pp. 225–230, June 1971.

[6] H. G. Danielmeyer, "Low-frequency dynamics of homogeneous four-level CW lasers," *J. Appl. Phys.*, vol. 41, pp. 4014–4018, 1970.

[7] R. Dunsmuir, "Theory of relaxation oscillations in optical masers," *J. Electron. Contr.*, vol. 10, pp. 453–458, 1961.

[8] C. L. Tang, H. Statz, and G. deMars, "Spectral output and spiking behavior of solid-state lasers," *J. Appl. Phys.*, vol. 34, pp. 2289–2295, 1963.

[9] R. Polloni and O. Svelto, "Static and dynamic behavior of a single-mode Nd–YAG laser," *IEEE J. Quantum Electron.*, vol. QE-4, pp. 481–485, Aug. 1968.

[10] D. G. Carlson, "Dynamics of a repetitively pump-pulsed Nd:YAG laser," *J. Appl. Phys.*, vol. 39, pp. 4369–4374, 1968.

[11] J. E. Jackson and R. R. Rice, "Output fluctuations of high-frequency pulse-pumped Nd:YAG laser," *J. Appl. Phys.*, vol. 45, pp. 2353–2355, 1974.

[12] H. Y-P. Hong and K. Dwight, "Crystal structure and fluorescence lifetime of a laser material $NdNa_5(WO_4)_4$," *Mater. Res. Bull.*, vol. 9, pp. 775–780, 1974.

[13] B. C. Tofield, H. P. Weber, T. C. Damen, and G. A. Pasteur, "On the growth of neodymium pentaphosphate crystals for laser action," *Mater. Res. Bull.*, vol. 9, pp. 435–948, 1974.

[14] H. Y-P. Hong and K. Dwight, "Crystal structure and fluorescence lifetime of $NdAl_3(BO_3)_4$, a promising laser material," *Mater. Res. Bull.*, vol. 9, pp. 1661–1666, 1974.

Suppression of the Relaxation Oscillation in the Modulated Output of Semiconductor Lasers

ROY LANG AND KOHROH KOBAYASHI

Abstract—**Practical rates of direct pulse modulation of semiconductor lasers have so far been limited to below several hundred megahertz, owing to serious distortion in the output signal caused by the relaxation oscillation of the light intensity. Based on theoretical analysis of the dynamic properties of lasing under constant injection of external radiation into the cavity modes, light injection is proposed as a method for suppressing the relaxation oscillation. The effectiveness of this method has been confirmed in a series of preliminary experiments which employed GaAs injection lasers both as the modulated laser and as the external source of the injected radiation.**

I. Introduction

THE ability of semiconductor lasers to be modulated directly at high speed is among the unique features of those lasers which make them especially desirable sources for optical communication systems [1]. In principle, direct modulation at a gigabit rate is expected to be feasible. However, the practical rate of pulse modulation has been limited to below several hundred megahertz, owing to the serious distortion of the output waveform caused by the relaxation oscillation (RO) of the light intensity.

The typical repetition frequency ω_R of the intensity spikes is a few gigahertz, with the spike height decreasing exponentially with the time constant of a few nanoseconds. This transient oscillation of the light intensity presents increasingly more serious problems in the detection of the light signal, as the modulation rate increases to become comparable to the repetition frequency of RO.

Aside from the distortion in the output waveform, the oscillation of the carrier density which accompanies RO of the light intensity degrades the spectral quality of the output. The optical gain varies with the carrier density causing the number of lasing modes, and hence the width of the spectral envelope to increase. In addition, the spectral width of an individual lasing mode has been found to broaden with RO, which can be explained [2] as a result of the change in time of the part of the dielectric constant which depends on the carrier density. While both types of spectral broadening can have adverse effects in various practical applications, the increase of the number of the lasing modes can be a serious drawback in case the output is to be transmitted through an optical fiber with material dispersion.

In order to attain practical rates of direct modulation in the gigahertz range, it therefore appears essential to suppress RO in the modulated output of semiconductor lasers. Through an analysis of the transient behaviors of semiconductor lasers, we have found that RO can be essentially eliminated by constantly injecting external radiation into one or more modes with sufficient gain of a modulated laser. The effects of the light injection on the dynamical properties of lasing are analyzed in the next section. The results of the preliminary experiments are presented in Section III.

Manuscript received September 12, 1975; revised November 11, 1975. A part of this work was presented at the IEEE/OSA Conference on Laser Engineering and Applications, Washington, DC, May 28-30, 1975.

R. Lang is with the Central Research Laboratories, Nippon Electric Company, Ltd., Kawasaki, Japan.

K. Kobayashi is with the Laser Equipment Development Division, Nippon Electric Company, Ltd., Kawasaki, Japan.

II. Theory

It will become apparent that the realistic means to modify the response characteristics of the modulated laser is to utilize narrow-band or quasi-monochromatic radiation as the injected external radiation. However, the effects of the injected radiation on the modulation characteristics can be most succinctly analyzed in case the injected radiation is incoherent and of a broad band. Moreover, the essential results obtained for the case of injection of broad-band radiation will be found to apply as well to the case of injection of narrow-band radiation. For these reasons, we shall consider first the effects of the injection of broad-band external radiation in the following.

A. Injection of Broad-Band Radiation

In case the injected radiation is incoherent or of a broad band, whose spectral width is broad compared with the separation of the longitudinal modes of the laser cavity, its effect can be accounted for by adding a term Q, representing the part of the external radiation injected into the lasing modes, to the rate equation for the photon density N. That is, the rate equations for the laser under *constant* injection of broad-band radiation become

$$\dot{N} = (G - \Gamma)N + Q \tag{1}$$

and

$$\dot{n} = -n/\tau_{sp} - GN + P \tag{2}$$

where n is the density of the excited carrier, G and Γ represent, respectively, the mode gain and cavity loss, and τ_{sp} is the lifetime of the excited carrier. The P in (2) represents the rate of carrier injection into unit volume.

The same form of the rate equation as (1) is obtained when the spontaneous emission into lasing modes is taken explicitly into account [3]. The magnitude Q_{sp} of the constant Q

resulting from the spontaneous emission is, however, of the order of 10^{21} $cm^{-3} \cdot s^{-1}$ in a GaAs laser operating at room temperature, while the appreciable modification of the response characteristics will result when the injected radiation increases the value of Q to the order of 10^{24} $cm^{-3} \cdot s^{-1}$ or greater.

In the following we shall be mainly concerned with lasers near or above threshold in which carrier density is close to its threshold value n_{th}. In this case we may approximate the mode gain G as

$$G(n) \cong G(n_{th}) + g\Delta n = \Gamma + g\Delta n \tag{3}$$

where

$$g \equiv \left.\frac{\partial G(n)}{\partial n}\right|_{n=n_{th}}, \qquad \Delta n \equiv n - n_{th}.$$

Experimentally, the gain is known to vary near theshold as $G(n) \sim n^m$ where $1 < m < 3$, which implies

$$g = m\Gamma/n_{th}. \tag{4}$$

At a steady state, the simultaneous solution of (1) and (2) with the help of (3) becomes

$$N = \{Q + \Delta P + [(Q + \Delta P)^2 + 4\Gamma Q/g\tau_{sp}]^{1/2}\}/2\Gamma \tag{5}$$

and

$$\Delta\Gamma \equiv -g\Delta n = Q/N \tag{6}$$

where $\Delta P \equiv P - P_{th}$. The first of the preceding equations indicates that photon density in lasing modes at the excitation levels below threshold (with $|\Delta P| \gg Q$) is increased by light injection approximately by a factor of Q/Q_{sp}. The second equation implies that a laser, even with the pumping above threshold, operates under light injection at a gain level below its threshold value by an amount $\Delta\Gamma$. The effects of those changes on transient behaviors of the laser will be discussed in turn.

It follows from Kleinman's general analysis [4] that the height of the initial intensity spike at the onset of lasing, i.e., the initial amplitude of RO, is lower, the greater the initial photon density in lasing modes at the beginning of the exciting current pulse. Therefore, the increase by light injection of the subthreshold photon density results in the decrease of the initial spike height. Similar reduction of the initial amplitude of RO can be achieved by applying dc bias current greater than the threshold current ($P > P_{th}$) to the modulated laser. However, in order to maintain a certain level of on-off ratio, the bias current cannot be so large, in practice, as to eliminate RO altogether. In contrast, light injection can achieve essentially complete suppression, because the injected light not only reduces the initial spike height, but also enhances the damping of the residual RO. The mechanism of the enhancement of the damping of intensity fluctuations by light injection is examined in the following.

The effects of the residual loss $\Delta\Gamma$ on transient behaviors of lasers can be analyzed through the linearized form of (1) and (2). Defining δn and δN as the small deviations of n and N from their respective stationary values $\bar{n}$ and $\bar{N}$, those equations can be linearized with respect to the newly defined variables as

$$\delta\dot{n} = -\delta n/\tau_{sp} - (\Gamma - \Delta\Gamma)\,\delta N - g\bar{N}\delta n \tag{7}$$

$$\delta\dot{N} = g\bar{N}\delta n - \Delta\Gamma\delta N. \tag{8}$$

The solutions of the preceding equations take form as e^{Zt}, where the real and the imaginary parts of Z give the decay constant $1/\tau_d$ and the frequency ω_R of RO, respectively. They are found as

$$2/\tau_d = 1/\tau_{sp} + g\bar{N} + \Delta\Gamma \tag{9a}$$

$$\omega_R^2 = g\bar{N}\Gamma + \Delta\Gamma/\tau_{sp}. \tag{9b}$$

Since typical values of $1/\tau_{sp}$ and Γ are 10^9 s^{-1} and 10^{12} s^{-1}, respectively, $\Delta\Gamma$ as small as $10^{-2}\Gamma$, corresponding to $Q = 10^{-2}\Gamma\bar{N}$, increases the damping constant by a factor of 10. Since $\Gamma\bar{N}$ is the contribution from unit volume in the active region to the laser output, this implies that the injection into a lasing mode of external radiation amounting only to a few percent of the output of the modulated laser is sufficient to affect the transient behaviors drastically.

Dependence of $1/\tau_d$ and ω_R on Q is plotted in Fig. 1 in which τ_d^0, ω_0, and N_0 denote, respectively, the values of these variables without light injection at the given pumping level P. Values of m in (4) and product $\Gamma\tau_{sp}$ are assumed, respectively, to be 2 and 10^3 in this and the following figures, Figs. 2 and 3.

The reduction of the initial amplitude of RO together with the enhanced damping of the residual oscillation can result in the complete suppression of RO in the modulated output as demonstrated in Fig. 2. The curves in Fig. 2 are the output responses to a stepwise increase of the pumping at $T = 0$ obtained through the direct integration of (1) and (2). The normalized time T has been defined as $T = \Gamma t$. In addition

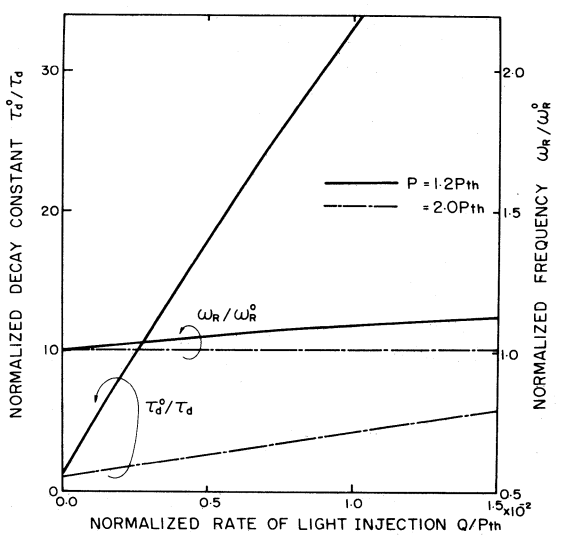


Fig. 1. Calculated dependence of the decay constant and the frequency of relaxation oscillation on the injected light intensity. τ_d^0 and ω_R^0 denote the values of these parameters at respective pumping levels without light injection.

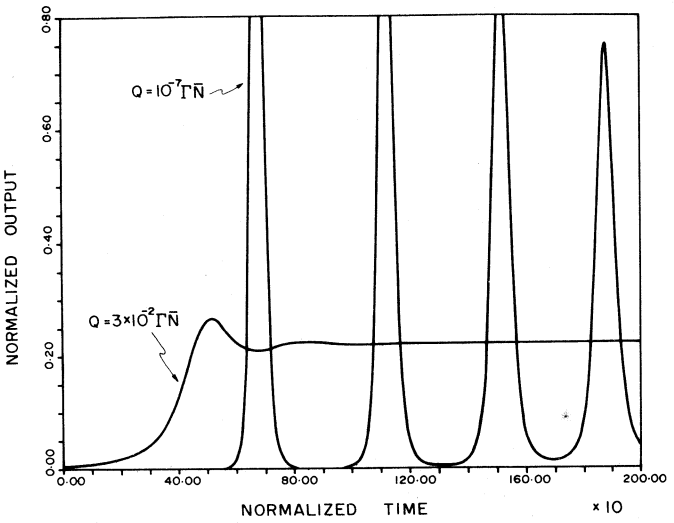


Fig. 2. Calculated output response with ($Q = 3 \times 10^{-2}\Gamma\bar{N}$) and without ($Q = 10^{-7}\Gamma\bar{N}$) light injection to a stepwise increase of the pumping rate P at $T = 0$. Assumed $P = 0.9P_{th}$ for $T < 0$ and $1.2P_{th}$ for $T > 0$.

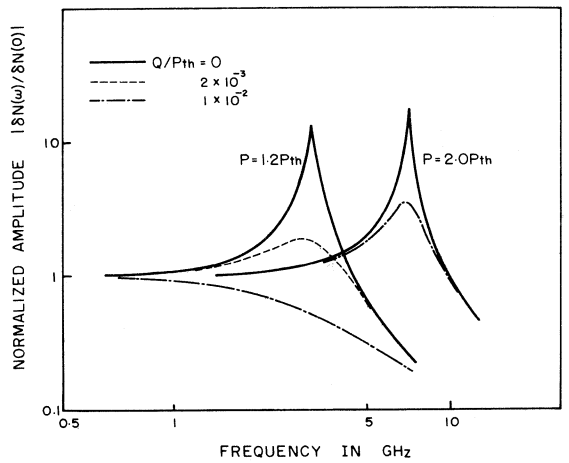


Fig. 3. Calculated frequency spectrum of the modulated depth (normalized to the modulation depth at zero frequency) of the light intensity in response to sinusoidal modulation of a small but fixed amplitude imposed on a dc bias current.

to the suppression of RO, light injection is seen to reduce the delay in the onset of lasing.

The changes in $1/\tau_d$ and ω_R caused by light injection imply the change in the frequency dependence of modulation depth. In fact, when a modulation term $P_m e^{i\omega t}$ is added to the right-hand side of (2), the modulation depth $|\delta N(\omega)|$ of the photon density at the given small amplitude $|P_m|$ is found to vary with the frequency as

$$|\delta N(\omega)/\delta N(0)| = [(1 - \omega^2/\omega_R^2)^2 + (2\omega/\tau_d\omega_R^2)^2]^{-1/2}. \quad (10)$$

The response spectrum is plotted in Fig. 3. The characteristic peak in the response of a laser without light injection is seen to broaden with increase of the injected light. This is an effect of light injection which can be utilized to reduce the distortion in direct amplitude modulation (AM) of semiconductor lasers. Light injection brings about similar changes in the frequency spectrum of the intensity fluctuation of the output. It is to be noted that these changes do not take place if, instead of light injection, dc bias current is employed to reduce RO.

B. Injection of Narrow-Band Radiation

It has been found that only a small amount of external radiation needs to be injected into lasing modes to suppress RO. However, since the density of modes (including nonlasing transverse modes) of a laser cavity is $\nu^2/c^3\pi^2$ per unit angular frequency and unit volume, the total intensity of the broad-band incoherent radiation required to realize the injection rate Q per mode per unit volume turns out to be quite large. This difficulty can be avoided by injecting narrow-band radiation, for which the description by the rate equation (1) is not adequate.

By regarding a laser as a one-dimensional Fabry-Perot (FP) cavity filled with gain medium, the equation for the complex amplitude α_ν of the traveling wave in the cavity generated by a frequency component $s_\nu \exp(-i\nu t)$ of the external radiation can be derived as

$$\dot{\alpha}_\nu = (i\delta\nu - \Delta\Gamma/2)\alpha_\nu + S_\nu \quad (11)$$

where, as defined earlier, $\Delta\Gamma = \Gamma - G$, $\delta\nu$ is the difference between ν and the resonant frequency ν_R of the longitudinal mode which is closest to ν, and

$$S_\nu = t_0 s_\nu / T. \quad (12)$$

The t_0 and T in the preceding expression denote, respectively, the amplitude transmission coefficent at the cavity wall and the round-trip time for photons in the cavity.

The photon density in the cavity can be expressed as $N = \int d\nu \alpha_\nu^* \alpha_\nu$. When the injected radiation has a Lorentzian profile with the half-width W and the peak frequency ν_0, equations of the form of (11) can be combined to give

$$\dot{N} = -\Delta\Gamma N + 2Q_R \quad (13a)$$

$$\dot{Q}_R = -(\Delta\Gamma/2 + W)Q_R + \delta\nu_0 Q_I + C \quad (13b)$$

$$\dot{Q}_I = -(\Delta\Gamma/2 + W)Q_I - \delta\nu_0 Q_R \quad (13c)$$

where $\delta\nu_0 = \nu_0 - \nu_R$ and $C \equiv \int d\nu S_\nu^* S\nu$ is proportional to the total intensity of the injected radiation. Q_R and Q_I are the real and the imaginary parts of the integral $\int d\nu \alpha_\nu^* S_\nu$. By replacing (1) with a set of coupled equations (13), influences of the injected narrow-band coherent radiation can be analyzed in a similar fashion to those of broad-band radiation.

In particular, when $W \ll \Delta\Gamma$, the effective rate $2Q_R$ of the injection of external radiation into a lasing mode is given, at a steady state, by

$$2Q_R = \Delta\Gamma C/[(\Delta\Gamma/2)^2 + \delta\nu_0^2] \quad (14)$$

while the residual loss $\Delta\Gamma$ becomes, sufficiently above threshold

$$\Delta\Gamma \simeq 2(\Gamma C/\Delta P - \delta\nu_0^2)^{1/2}. \quad (15)$$

That is, the residual loss $\Delta\Gamma$ as well as $\bar{N} = 2Q_R/\Delta\Gamma$ now depends on the frequency mismatch $\delta\nu_0$.

Despite these added complexities, the examination of the small amplitude oscillation through the linearized version of (13) and (2) reveals that the frequency and the damping

constant of RO depend on $\Delta\Gamma$ and $\bar{N}$ in the same manner as in (9). Direct integration of (13) and (2) indicates also that the injection of narrow-band radiation leads, in essentially the same way as that of broad-band radiation, to suppression of RO and reduction of the response delay, as long as $\Delta\Gamma$ given approximately by (15) is made sufficiently large ($\Delta\Gamma \gtrsim 10^{-2}\Gamma$).

III. Experimental Results

The experimental arrangements are depicted in Fig. 4. Pairs of GaAs double-heterostructure lasers with a planar stripe geometry [5] were used in the experiments. The two lasers in a pair, which are referred to as lasers A and B, were separated by ~30 cm or ~1 ns in terms of the transit time of the light. The output of laser B was fed into the other using a combination of objective lenses. The temporal behavior of the output from laser A was detected by an Si avalanche photodiode and displayed on a sampling oscilloscope; the rise time of the system was less than 150 ps. Each of the lasers was connected to a grating monochromator by SELFOC® cables and their emission spectra were recorded by an X-Y recorder. The near-field pattern of laser A was monitored by an Si vidicon camera. The heat sink of laser B was placed on a Pertier element so that temperature control of the emission wavelength was possible.

In the analysis in the previous section, light injection has been assumed to be one sided; that is, the output of the modulated laser has been assumed to affect little the source of the external radiation. In order to realize this situation experimentally, laser B was driven at a considerably higher current level than laser A. Moreover, since the two diodes were separated by a distance corresponding to 2 ns in the round-trip time of the light, the injection during the initial 2-ns period after the commencement of lasing in laser A can be considered to be unidirectional to a good approximation.

Experiments were first carried out on a pulsed basis in which the two lasers were driven by current pulses of 10-ns duration and the repetition frequency of about 1 kHz. The current pulse to laser A was delayed by 5 ns with respect to that to laser B so that RO in laser B had been essentially damped out by the time laser A started to lase.

The output responses of laser A with (upper trace) and without (lower trace) light injection are contrasted in Fig. 5. The sharp intensity peaks in the lower trace disappeared entirely in the upper trace with light injection. In addition, the delay in the onset of lasing is seen to be reduced as expected. It is to be noted that the actual changes in the response patterns are likely to be more drastic than those which are apparent in the oscilloscope traces, since the width of the intensity spikes are expected to be small compared with the response time (~150 ps) of the detection system.

The changes in the output spectra of the two lasers associated with the changes in the output response are shown in Fig. 6. In this figure, the spectrum of laser A (laser B) without light injection is denoted as A_0 (B_0), while that with the light injection is denoted as A_B (B_A). The scales of intensities for different diodes are different, because the coupling efficiencies between the SELFOC cables and the monochromator or the laser diodes were not precisely reproduced. It is apparent in

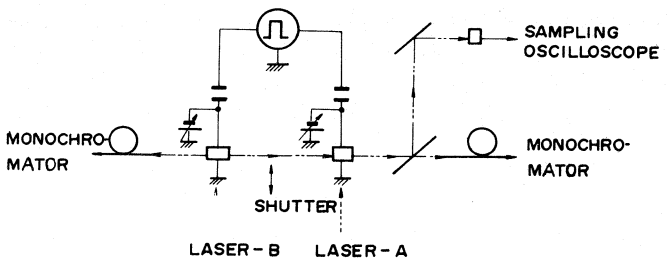


Fig. 4. Schematic diagram of the setup of the light injection experiment which employed two GaAs injection lasers. Laser A was the modulated laser, while laser B was used as the source of the external radiation.

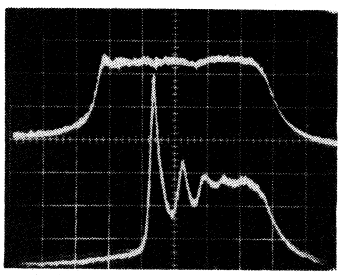


Fig. 5. Observed output responses with and without light injection of the laser diode modulated by a current pulse of 10-ns duration with the peak current of 120 mA. The threshold current for pulse operation of the diode was 110 mA. Upper trace: With light injection. Lower trace: Without light injection. (1 ns/div.)

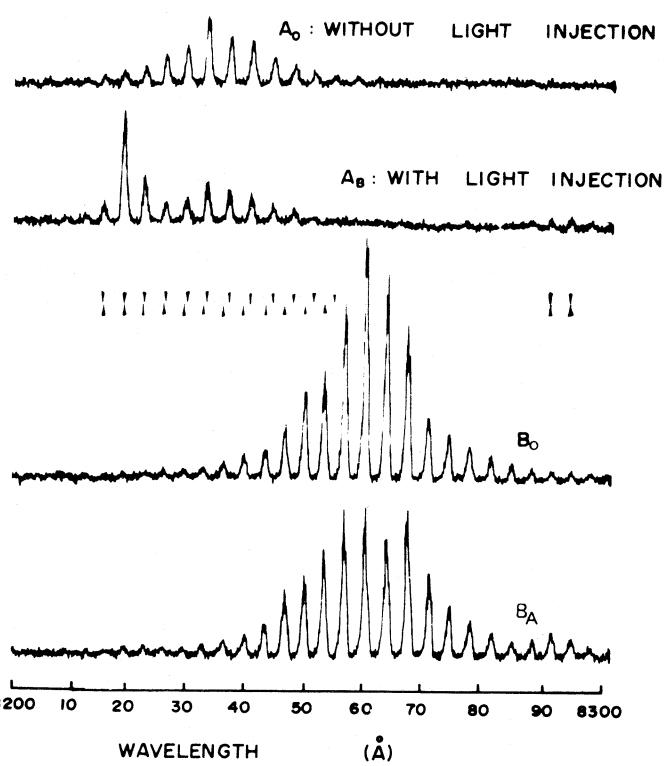


Fig. 6. Observed output spectra of two diodes. A_0 (B_0) denotes the spectrum of laser A (laser B) observed with the shutter between the diodes closed, while A_B (B_A) denotes that with the shutter open. The scales of intensities for different diodes are different. Arrows indicate the positions of longitudinal modes.

the figure that the light injection affected the spectrum of laser A more strongly than that of laser B. This indicates that the light injection was effectively one sided as intended.

Detailed comparison of the spectra of laser A with those of laser B reveals that the enhancement of the mode intensities by light injection took place in laser A at around 8220 Å where the wavelengths of the injected light coincide very closely with those of the longitudinal modes of laser A. The separations Δ_A and Δ_B of the longitudinal modes in the two lasers are found, respectively, to be 3.7 and 3.9 Å. Therefore, the close matching of the wavelengths of longitudinal modes of the lasers is expected to occur at every $\Delta_A\Delta_B/|\Delta_A - \Delta_B| \simeq$ 70 Å in the spectrum. In fact, enhancement of the mode intensities in A_B is also visible at around 8290 Å. On the other hand, the mode intensities in other modes are seen to be reduced with the light injection. The increase in selected modes and reduction or quenching in other modes of mode intensities can be understood as the enhanced excitation of those modes to which external radiation is injected and the reduction over the spectrum of the gain level due to the presence of residual loss in the excited modes.

The total amount of the external radiation was not measured directly, but it was estimated to correspond to at most a few percent of the total output of laser A. The dependence of the output response on the relative intensity of the injected radiation was examined by inserting neutral density (ND) filters in the optical path between laser B and laser A. The decay constant $1/\tau_d$ and the frequency ω_R of RO were deduced, respectively, from the envelop of the intensity peaks and the time interval T_{12} between two initial peaks. Dependence of $1/\tau_d$ and $f_{12} = 1/T_{12}$ on the relative intensity of the injected radiation as plotted in Fig. 7 agrees qualitatively with the theoretical results given in Fig. 2.

Experiments were also carried out on a dc basis in which laser B was excited by a dc current and laser A was driven by 400-Mbit/s signal of 50-percent duty imposed on a dc bias current close to or slightly above the threshold. Examples of the output responses of the modulated laser are shown in Fig. 8.

The diodes used in these experiments had approximately same length (~230 μm) and width (~15 μm) of the active region, but they were cut out from a few different wafers. Pairs of diodes were selected in such a way that the wavelengths of the highest emission peaks of the two diodes differed less than 50 Å or so. Substantial suppression of RO was observed in all of the several pairs examined, although no deliberate attempts were made to insure close matching between the wavelengths of emission lines of laser B and those of longitudinal modes of laser A.

The reason for the successful suppression of RO without fine tuning of the emission wavelength of laser B can be understood from Fig. 6. The separation in wavelengths of the longitudinal modes (~4 Å) was small compared with the gain breadth which was estimated to be over 100 Å and, therefore, there were many longitudinal modes in laser A which had sufficient gain to be candidates for the modes for light injection. Similarly, the output of laser B was distributed in many modes. Moreover, the separations of the longitudinal modes of the

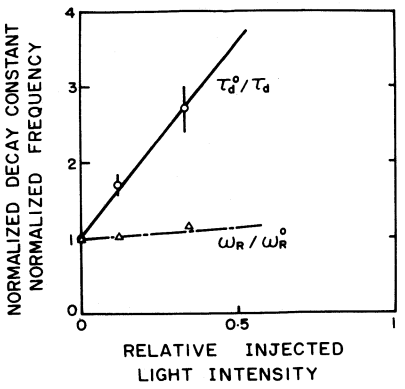
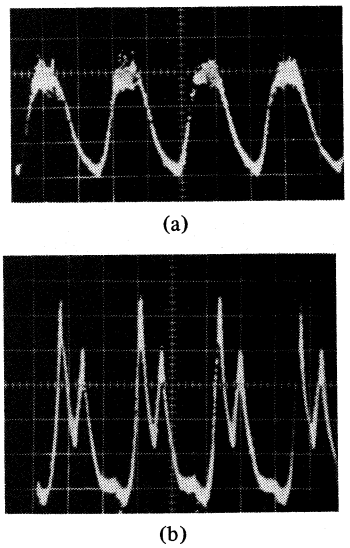


Fig. 7. Observed dependence of the decay constant and the frequency of the relaxation oscillation (normalized to the values of respective constants without light injection) on the relative intensity of the injected radiation.



(a)

(b)

Fig. 8. Observed output response of laser A driven by 400-Mbit/s RZ current signal of 50-percent duty. Height of the current pulse was 30 mA which was imposed on the dc bias current of 150 mA (Ith = 145 mA). (a) With light injection. (b) Without light injection. (1 ns/div.)

two diodes in a pair differed typically by 5-10 percent owing to the scatter in the cavity lengths. Consequently, there happened to be one or more pairs of the longitudinal modes of the two diodes with the resonant wavelengths sufficiently close to each other to insure effective injection. To check this point, the emission wavelengths of laser B were varied gradually by ~20 Å by slowly varying the temperature of the laser mount; the degree of suppression of RO was seen to change only slightly in a periodic fashion during the process, while the output spectra of laser A indicated that the mode with maximum injection kept shifting from one to another.

As the emission wavelengths of laser B were varied further, suppression of RO and quenching of the intensities of the uninjected modes in laser A could be observed until the separation between the wavelength of the emission peak in laser B and that of the gain peak (the highest emission peak without light injection) in laser A became as large as ~140 Å.

The broadness of the gain spectrum and the homogeneous nature of gain saturation implied by this result add further support to the reasoning in the preceding paragraph.

IV. Discussions and Conclusions

Comparison of the output responses in Figs. 5 and 8 appears to prove the remarkable effectiveness of light injection as a method for suppressing RO and reducing the response delay in direct pulse modulation of semiconductor lasers. The changes in the output spectrum of the modulated laser with light injection and the dependence on the injected intensity of the decay constant $1/\tau_d$ and the frequency ω_R of RO indicate that the suppression does result through the mechanism analyzed in Section II.

The suppression of RO in the output intensity is expected to eliminate the broadening of the output spectrum associated with the oscillation of the carrier density discussed in Section I. Furthermore, the selective excitation of longitudinal modes by the injected radiation, which has a close resemblance to the coupled cavity effect [6], tends to reduce the number of lasing modes. The tendency is evident in Fig. 6, but better results can be obtained with finer control of the wavelength of the injected radiation.

When the modulation rate is high, the output response to a current pulse tends to depend on the pulse pattern of the preceding bits. The suppression of RO will also reduce this pattern effect. This is expected because the absence of RO results in the uniformity of the densities of the photons and the carriers at the end of an exciting current pulse irrespective of the length of the current pulse.

The changes with light injection in the frequency dependence of the modulation depth suggest that this method can also be used for improving the response characteristics in direct AM of semiconductor lasers. With injection of an appropriate amount of external radiation, reduction of distortion in output signal will result without appreciable reduction in the modulation bandwidth.

When two laser diodes are used, one as the modulated laser and the other as the source of external radiation, the necessary alignment of the diodes is somewhat troublesome. This problem will be eliminated by integrating the two diodes into a double-section diode with two independent optical cavities.

In conclusion, the results of the theoretical and experimental investigations indicate that light injection in which a small amount of external radiation is constantly injected into one or more modes of a modulated laser is quite effective as a means for suppressing the relaxation oscillation and reducing the response delay in the modulated output of a semiconductor laser.

The suppression of relaxation oscillation is expected to prevent the degradation of the output spectrum associated with the relaxation oscillation of the carrier density. The selective excitation of longitudinal modes by the injected radiation can further improve the spectral quality of the output. Furthermore, the elimination of the oscillations in the photon density and the carrier density is expected to reduce the pattern effect. It is hoped that those improvements in response characteristics brought about by light injection make direct modulation of semiconductor lasers at gigabit rates practicable.

After completion of the present work, the authors received the summary of the talk entitled "Modulation Behavior of Injection Lasers With Coherent Irradiation Into Their Oscillating Mode" presented by P. Russer at the meeting "Optoelektronische Komponenten in der Nachrichtentechnik," February 17–18, 1975. In the summary theoretical analysis is given, which resembles closely with the content of Section II-A of the present paper.

Acknowledgment

The authors wish to thank T. Uchida for his encouragement and valuable comments. They also wish to thank I. Hayashi, S. Sugimoto, Y. Mita, and A. Ueki for their critical reading of the manuscript and helpful comments. The laser diodes used in the experiments were kindly supplied by the Semiconductor Laser Group at Central Research Laboratories of Nippon Electric Company, Ltd.

References

[1] T. L. Paoli and J. E. Ripper, "Direct modulation of semiconductor lasers," *Proc. IEEE (Special Issue on Optical Communication)*, vol. 58, pp. 1457–1465, Oct. 1970.
[2] T. Ikegami, private communication.
[3] H. Haug, "Quantum mechanical rate equations for semiconductor lasers," *Phys. Rev.*, vol. 184, pp. 338–348, Aug. 1969.
[4] D. A. Kleinman, "The maser rate equation and spiking," *Bell Syst. Tech. J.*, vol. 43, pp. 1505–1532, July 1964.
[5] H. Yonezu *et al.*, "A GaAs-$Al_xGa_{1-x}As$ double heterostructure planar stripe laser," *Japan. J. Appl. Phys.*, vol. 12, pp. 1585–1592, Oct. 1973.
[6] R. Salathe, C. Voumard, and H. Weber, "Optical coupling of two diode lasers with variable coupling coefficient," *Phys. Status Solidi*, vol. 23, pp. 675–682, June 1974.

Correspondence

Self-Heated, Multiple-Metal-Vapor Laser

THEODORE S. FAHLEN

Abstract—**The design and performance of a self-heated metal-vapor laser utilizing copper, gold, and copper plus gold as active laser materials are described. A total average power of 17 mW at a pulse-repetition rate of 1.7 kHz was obtained simultaneously at 5106 Å (green), 5782 Å (yellow), and 6278 Å (red).**

The purpose of the research reported here was to obtain multiple-wavelength laser operation by mixing, in a single laser tube, metals known to lase individually. The design and operating characteristics of a discharge-heated metal-vapor laser utilizing copper, gold, or a mixture of copper and gold as the active laser materials are described. Although gold has been used as the active laser material previously, we believe this is the first report of a self-sustained (the only source of heat to vaporize the metal is the discharge used to excite it) gold-vapor laser and the first report of a multiple-metal-vapor laser.

The longitudinal discharge tube is of very simple construction and allows the rapid changing of tube bores or metal laser material. A diagram of one end of the laser is shown in Fig. 1. The laser consists of an Al_2O_3 ceramic tube contained within ceramic insulation, two water-cooled copper end fixtures containing quartz Brewster windows, and pulse-forming circuitry. The Al_2O_3 tube bore has an inside diameter (ID) of 0.64 cm and a length of 30 cm. Each end of the tube slips 1.3 cm into a water-cooled copper end fixture with an "O"-ring forming the vacuum seal between the outside diameter of the ceramic tube and the ID of the copper end fixture. The copper end fixture contains a Brewster angle window epoxied to a copper tube, which is likewise O-ring sealed to the copper end fixture.

The laser electrodes consist of two layers of tungsten wire mesh which are clamped in each of the copper end fixtures and extends 8.2 cm along the inside of the ceramic laser tube. The tungsten-mesh electrodes serve also to prevent the molten metal from pooling within the tube bore. The electrical connections from the pulse-forming circuitry are made to the copper end fixtures. The longitudinal discharge path in the tube is 15 cm.

The insulation for the tube consists of two machinable fused silica blocks, each 23 cm long by 15 cm wide by 8 cm thick. A half-circle groove is machined into these blocks along the 23-cm dimension and into the 8-cm dimension to contain the laser tube when they are clamped together.

The pulse-forming circuitry consists of a thyratron and a 5-nF capacitor resonantly charged through an inductor and diode with a dc power supply. Short, heavy electrical leads joining these components keep the stray circuit inductance at a minimum to facilitate the generation of a short discharge-pulse duration.

The tube is initially loaded by placing a wire or pellet of the metal within the tube between the tube electrodes. The Brewster-window tube is then slipped into place and the tube is evacuated and filled with several torr of inert buffer gas. Although He as a buffer gas was tried, the discharge stability was better with argon. Upon application of the 140-ns-wide current pulse at a sufficient voltage and pulse-repetition frequency, the metal is vaporized and laser action occurs.

Manuscript received July 30, 1975; revised September 15, 1975.

The author is with the GTE Sylvania, Inc., Electro-Optics Organization, Mountain View, CA 94042.

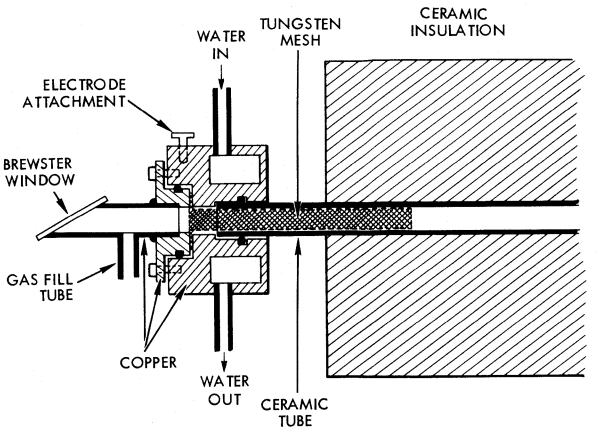


Fig. 1. Diagram of one end of laser tube.

The tube is placed between two cavity mirrors of 40-cm separation. One mirror is a maximum-reflectivity mirror having a radius of curvature of 5 m. The output mirror is a flat mirror with a reflectivity that is variable for different experiments.

The results reported in the following paragraphs were obtained with a tube temperature of approximately 1600°C and with 4 torr of argon as the buffer gas. Although maximum output power was obtained at a pressure of 4 torr, the power decreased only about 10 percent at 2.5 and 6 torr.

A similar tube of 0.48-cm ID loaded with pure copper produced a total power of 70 mW at 5106 and 5782 Å at a pulse-repetition frequency of 4 kHz, and a capacitor voltage of 3.4 kV. Here maximum output power was obtained with a sapphire etalon of 13-percent reflectivity as the output coupler although the device was strongly superradiant. The efficiency (output pulse energy/stored capacitor energy) was therefore 0.15 percent. The laser could be turned off and on at will, and several runs of approximately 2-h duration were made. The tube failed due to melting of the ceramic tube when the average input power was increased 20 percent.

When loaded with 99.999-percent pure gold, the 0.64-cm-diameter tube produced 4 mW of output power at 6278 Å at a 3-kHz pulse rate. The tube temperature was approximately 1600°C. Although the laser operated without any output mirror, maximum output was obtained with the sapphire etalon.

With the ceramic laser tube of 0.64-cm diameter loaded with both copper and gold, the laser produced green, yellow, and red beams simultaneously. The total power was 17 mW at a capacitor voltage of 7.6 kV and a pulse-repetition rate of 1.7 kHz. Here a (nonoptimized) mirror having a transmission of 16 percent at 5106 Å, 31 percent at 5782 Å, and 50 percent at 6278 Å maximized the red output power. The three colors were separated with a grating, and the powers were found to be 13 mW of green, 4 mW of yellow, and 0.04 mW of red light. Of course, an output mirror having a different transmission characteristic would yield a different ratio. The FWHM pulse-widths were measured to be 12 ns for the green, 5 ns for the yellow, and 5 ns for the red.

In conclusion, operation of a simple, reliable, self-heated metal-vapor laser utilizing two metals simultaneously has been

demonstrated. Efforts in the future will be directed toward reduction of the applied pulsewidth to achieve improved efficiency, increasing the pulse-repetition frequency, and investigating other metals.

ACKNOWLEDGMENT

The author wishes to thank M. Conroy for his expert technical assistance.

REFERENCES

[1] W. T. Walter, "Metal vapor lasers," *IEEE J. Quantum Electron. (Dig. Tech. Papers, 1968 International Quantum Electronics Conference)*, vol. QE-4, pp. 355-356, May 1968.

External Cavity CO_2-Pumped InSb Spin-Flip Laser

S. R. J. BRUECK AND A. MOORADIAN

Abstract—**A pulsed CO_2-pumped external cavity spin-flip laser has been operated with the output frequency governed to a large extent by the Fabry-Perot (FP) modes of resonant output couplers. An output spectral width of 0.027 ± 0.003 cm^{-1} has been attained.**

The use of an external cavity spin-flip laser is described here in which the axial and transverse modes are carefully controlled to provide a device that is useful for spectroscopic and photochemical applications. In the past, spin-flip lasers in the usual form of a rectangular parallelepiped produced a spectrally poor output when operated at high drive levels [1], [2]. This is particularly true for high carrier concentration InSb crystals ($n \sim 1 \times 10^{16}$ cm^{-3}) operated in high magnetic fields because the spontaneous spin-flip linewidth [3] (~0.2 cm^{-1}) is comparable to the Fabry-Perot (FP) cavity linewidths. These high carrier concentration samples are needed for high energy pulsed operation in the 11-13-μm region. The spin-flip output then has limited tuning within a mode with large jumps between modes. This is in contrast to low-concentration samples at low magnetic fields (1-10 kG) where the spontaneous linewidths [4], [5] are only a few hundred megahertz. In addition, internal bounce mode operation can degrade the spectral characteristics as well as substantially limit the external conversion efficiency. In order to improve this situation, we have operated the spin-flip laser in an external cavity geometry where bounce modes are eliminated and the cavity mode frequencies can be altered independently of the magnetic field to allow complete control of the spin-flip laser output frequency. In addition, the use of resonant output couplers results in a narrowed spin-flip spectral output. At present, with a low-finesse uncoated Ge-output coupler, we have obtained a spin-flip output spectral width of less than 0.027 cm^{-1}.

The cavity geometry consists of an antireflection coated InSb crystal ($n \sim 1.2 \times 10^{16}$ cm^{-3}) mounted on a cold finger ($T \sim 20$ K) in the bore of a split superconducting solenoid. Sample dimensions are $\frac{3}{4} \times \frac{3}{4}$-cm cross section by 1.5 cm long. A 1-m-radius gold mirror was mounted on the Dewar output window flange with a bellows arrangement that allowed its alignment to be adjusted under vacuum. A NaCl Brewster angle window was mounted in the opposite window flange and an output coupler completed the optical cavity. Both ZnSe- and Ge- (uncoated) output couplers were used. The overall cavity length was 30 cm. Pump laser radiation was introduced through the output coupler and the spin-flip output was separated out using a dichroic beamsplitter and a spectrometer. In order to provide a spectrally narrow pump source, a CW gain cell was operated in the CO_2 TEA laser cavity to force the laser to operate in a single longitudinal mode [6], [7]. Apertures constrained the output to the TEM_{00} transverse mode. The CO_2 beam was collimated to a spot size of approximately 2-mm diameter which matches the 12-μm spot size for the spin-flip cavity parameters.

The reflectivity of the Ge-output couplers varies as a function of wavelength because of FP resonances. The spin-flip laser will operate near the frequencies of maximum reflectivity; thus the uncoated Ge window serves a dual role as both output coupler and frequency selective etalon. The set of coupled FP cavities involved in the observed tuning characteristics with their free spectral ranges (fsr) are the following.

Overall cavity—30 cm fsr = 0.017 cm^{-1};
Ge etalon 2.23 mm fsr = 0.56 cm^{-1};
Ge etalon 3.2 mm fsr = 0.39 cm^{-1}.

The spin-flip laser output tuning characteristics at a wavelength of 12.2-μm were measured with a 1-cm^{-1} fsr FP interferometer and are shown in Fig. 1(a) for the case of a 3.2-mm-thick Ge-output coupler. The output spectrum is dominated by the FP modes of the output coupler; the overall cavity FP modes are too finely spaced to be observed. The average mode spacing of 0.38 ± 0.04 cm^{-1} is in good agreement with the

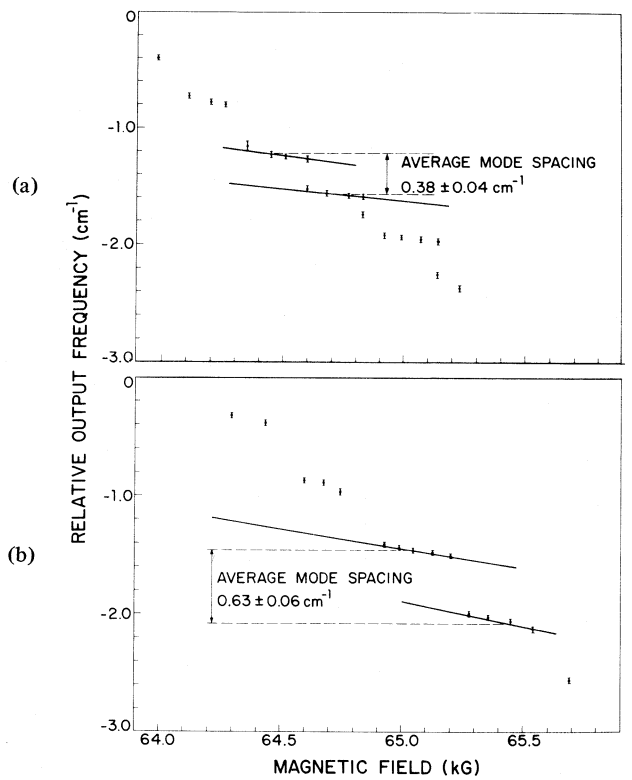


Fig. 1. Tuning characteristics of the external cavity spin-flip laser. (a) 3.2-mm-thick Ge-output coupler. (b) 2.23-mm-thick Ge-output coupler.

Manuscript received August 18, 1975. This work was sponsored by the Department of the Air Force and the U.S. Energy Research and Development Administration under a subcontract from the Los Alamos Scientific Laboratory.

The authors are with the Lincoln Laboratory, Massachusetts Institute of Technology, Lexington, MA 02173.

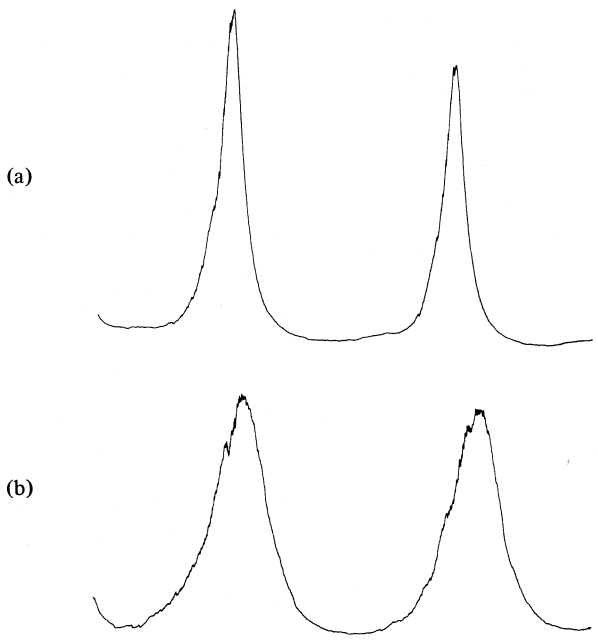


Fig. 2. Fabry–Perot (FP) spectral traces, 0.13-cm^{-1} free spectral range. (a) CO_2-pump laser. (b) 12-μm spin-flip laser output ($H = 60$ kG, $T \sim 20$ K, $n = 1.2 \times 10^{16}$ cm^{-3}).

calculated etalon spacing of 0.39 cm^{-1}. The tuning rate within a mode is 9.3 MHz/G and the tuning range of a single mode is about 0.13 cm^{-1}. More complex spectra were observed with the 2.23-mm Ge-output coupler because of broader etalon modes. A plot of the dominant output line of the spin-flip laser with magnetic field for the 2.23-mm etalon is shown in Fig. 1(b). The mode spacing of 0.63 ± 0.06 cm^{-1} is in agreement with the calculated etalon spacing.

With a 9.6-mm-thick output coupler, the spin-flip output frequency was determined solely by the FP modes of the output coupler to within the 0.05-cm^{-1} resolution of the measurement. Varying the magnetic field resulted in the spin-flip laser output frequency jumping from one etalon mode to the next. The narrowest spectral output was obtained with this output coupler. Fig. 2 shows a 0.13-cm^{-1} fsr FP trace of the output spectrum. The top trace shows the CO_2 pump laser spectral output and the bottom trace is the spin-flip laser output. The measured spectral width is 0.027 ± 0.003 cm^{-1} after allowing for the FP resolution. The modes of the overall cavity, of which there were probably no more than two, could not be resolved in this trace. Single frequency operation should be possible with higher finesse output couplers.

The control of the spin-flip laser output frequency by the resonant output coupler provides a convenient means of fine tuning this frequency. A tunable output coupler could be constructed from two Ge windows, AR coated on one side, which are separated by a piezoelectric cylinder which can be voltage tuned over a free spectral range. Alternatively, the temperature dependence of the Ge index of refraction $(1/n)\ (dn/dT) = 6.9 \pm 0.4 \times 10^{-5}$/K) could be exploited to temperature tune the output coupler. For a 1-cm-thick Ge etalon, a temperature variation of only 2 K is required to tune over a free spectral range. By sweeping the magnetic field in synchronism with the temperature, continuous tuning over a relatively broad range should be readily attainable.

The spin-flip output pulse shape does not simply follow the time dependence of the pump laser, but rather shows only a short (~50-ns) output pulse even when long input pulses of about 1-μs duration are used. This behavior is due to a combination of transient behavior of the saturable Raman medium and gain reduction due to free carrier absorption. These effects will be discussed in more detail in a subsequent publication [8]. The spectral data presented in the preceding were obtained at maximum output energy levels of about 50–60 μJ.

In summary, the CO_2-pumped spin-flip laser has been operated in an external cavity geometry in which the output frequency of the spin-flip laser is governed to a large extent by the FP modes of a resonant output coupler. By tuning this output coupler in tandem with the magnetic field, essentially complete frequency coverage with single-mode operation can be obtained and should enhance the usefulness of the spin-flip laser for many applications.

ACKNOWLEDGMENT

The authors wish to thank W. E. DeFeo for expert technical assistance.

REFERENCES

[1] C. K. N. Patel and E. D. Shaw, "Tunable stimulated scattering from conduction electrons in InSb," *Phys. Rev. Lett.*, vol. 24, pp. 451–455, Mar. 2, 1970.

[2] J. T. Ganley, F. B. Harrison, and W. T. Leland, "Spin-flip Raman laser as a tunable infrared source," *J. Appl. Phys.*, vol. 45, pp. 4980–4981, Nov. 1974.

[3] S. R. J. Brueck, A. Mooradian, and F. A. Blum, "Near-resonance spontaneous-spin-flip light scattering in InSb," *Phys. Rev. B.*, vol. 7, pp. 5253–5271, June 15, 1972.

[4] S. R. J. Brueck and A. Mooradian, "Spontaneous spin-flip Raman linewidth and nonlinear processes in InSb," *Opt. Commun.*, vol. 8, p. 263, 1973.

[5] C. S. DeSilets and C. K. N. Patel, "Characteristics of a low-field spin-flip Raman laser: Measurement of Raman gain," *Appl. Phys. Lett.*, vol. 22, pp. 543–545, 1973.

[6] A. Gondhalekar, E. Holzhauer, and N. R. Heckenberg, "Single longitudinal mode operation of high pressure pulse CO_2 lasers," *Phys. Lett.*, vol. 46A, pp. 229–230, Dec. 17, 1973.

[7] A. Girard, "The effects of the insertion of a cw, low-pressure CO_2 laser into a TEA CO_2 laser cavity," *Opt. Commun.*, vol. 11, pp. 346–351, Aug. 1974.

[8] S. R. J. Brueck and A. Mooradian, to be published.

Laser Frequency Doubling in the Presence of Small-Scale Beam Breakup

D. T. ATTWOOD, E. S. BLISS, E. L. PIERCE, AND L. W. COLEMAN

Abstract—**Frequency multiplication of intense laser pulses in narrow acceptance angle crystals is commonly accomplished with large conversion efficiency. However, the conversion efficiency can be seriously affected by degradation of the laser pulse, such as occurs when small-scale intensity fluctuations exponentiate due to nonlinear refractive effects within the laser. We present evidence that beam breakup such as this can cause a significant fraction of the laser energy to lie outside the acceptance angle of the crystal, thus diminishing conversion efficiency.**

Optical frequency conversion of intense laser beams is well understood [1]-[3] and routinely practiced with great proficiency [4]-[6]. A limitation to this conversion process, not clearly identified previously, is that of small-scale beam breakup due to nonlinear propagation effects in solid-state lasers [7]-[9]. In this correspondence we describe experiments which demonstrate that small-scale beam breakup in a high-intensity Nd laser can adversely affect subsequent frequency multiplication with nonlinear crystals of narrow acceptance angle. Angle tuned crystals of potassium dihydrogen phosphate (KDP), which are often used to frequency double Nd laser pulses at 1.064 μm because of their excellent optical quality, are available with typical dimensions of several centimeters and acceptance angles of several hundred microradians [10]. Frequency doubling with such crystals is utilized in laser fusion experiments [11] both for target irradiation [12] and plasma diagnostics [13], [14]. Since efficient conversions are essential for these applications, it is important that all limiting mechanisms be well understood. The mechanism examined here, small-scale beam breakup, can cause a significant fraction of the laser output energy to emerge at angles larger than the acceptance angle of the crystal. Our frequency doubling experiments confirm previous observations [9] regarding the angular distribution of light in intense laser beams which have propagated through nonlinear material.

Fig. 1 is a schematic diagram of the experiment. A Nd:YAG oscillator is followed by two Nd:YAG and two Nd:glass rod amplifiers. The final amplifier is a 2.5-cm-diameter glass rod. Operating without an etalon in the oscillator, and with a mode-locking dye transmission of 58-percent nominal pulsewidths of 50-ps full width at half maximum (FWHM) are obtained.[1] An uncoated wedge and a long focal length lens are used to monitor the fraction of laser energy within a full angle of 500 μrad. A dielectric mirror is then used to reflect a selected fraction of the main beam to the crystal. In these experiments full data runs were made with both 100- and 22-percent reflecting mirrors. Collimation optics provide a factor of 2.3 linear reduction following the mirrors. The 1.064-μm pulse entering the crystal has an approximately Gaussian spatial profile with a $1/e$ diameter of 8.5 mm. The KDP crystal is a 2.5-cm cube cut at 41° to the (z) optic axis and at 45° to the crystallographic (x) axis, for type I conversion. The FW$1/e$ acceptance angle for this crystal is 500 μrad, while the spectral acceptance [10] is approximately 80 Å. An absorption filter passes the 5320-Å radiation to a calorimeter.

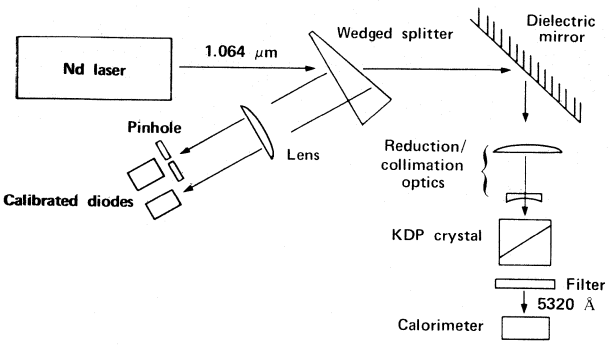


Fig. 1. Schematic diagram showing the Nd laser, beam-breakup monitor, and frequency conversion system. As discussed in the text, mirror reflectivities of both 22 and 100 percent have been used.

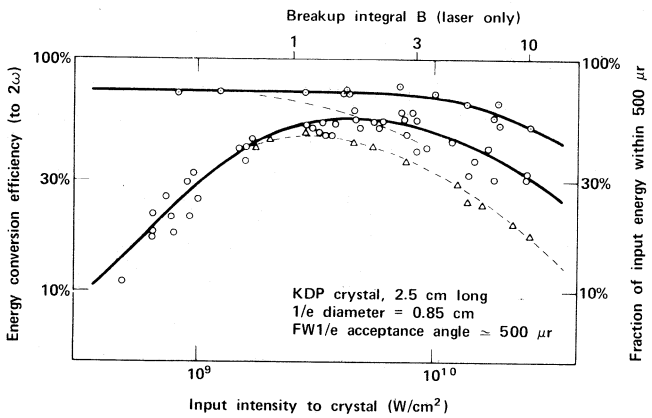


Fig. 2. Frequency doubled energy conversion efficiency versus 1.064-μm pump intensity at the crystal. The effect of beam breakup on the fraction of pump energy within an angle of 500 μrad is also displayed using the top and right-side axes. The solid lines correspond to 100 percent of the laser light reaching the crystal. The dashed lines correspond to 22 percent reaching the crystal.

Fig. 2 shows the results of frequency doubling the 1.064-μm laser energy to 5320 Å. The lower solid line, obtained with a 100-percent reflecting mirror, plots energy conversion efficiency as a function of pump intensity. The curve rises in the expected linear fashion, appears to approach a depletion-limited regime, and finally rolls over after reaching a peak conversion of approximately 60 percent. We correlate this rollover with the upper solid line which shows, on the right-side ordinate, that a diminishing fraction of the input beam is within the acceptance angle of the crystal as measured directly by the pinhole/diode monitor. That is, beam-breakup effects in the laser are causing sufficient degradation in beam quality at the crystal to dominate the otherwise increasing conversion due to higher pump intensity. Although this degradation of beam quality had a significant impact on frequency conversion, it did not produce damage in the KDP crystals.

We note on the upper scale of Fig. 2 that this beam breakup corresponds to rather large values of the beam-breakup integral B, a convenient parameter which characterizes the growth of small-scale beam perturbations due to nonlinear refractive effects. Linearized instability theory shows that the intensity ΔI of the most unstable spatial irregularities grows approxi-

Manuscript received August 18, 1975; revised November 11, 1975. This work was performed under the auspices of the United States Energy Research and Development Administration.

The authors are with the Lawrence Livermore Laboratory, University of California, Livermore, CA 94550.

[1] Using a frequency selective etalon within the oscillator cavity, the measurements reported here were repeated with 150-ps, 1.064-μm pulses, yielding essentially identical results.

mately as [15], [16]

$$\Delta I = (\Delta I)_0 e^B \tag{1}$$

where B is given by

$$B = \frac{2\pi\gamma}{\lambda} \int_0^L Idl \tag{2}$$

where λ is the laser wavelength in vacuum, I is the laser intensity, L is the propagation distance in the nonlinear medium, and the constant γ is defined by the relation between total refractive index n and its linear component n_0, viz., $n = n_0 + \gamma I$. The intensity, spectrum, and growth of spatial irregularities vary with position within a given laser, and from one laser to the next, because of differences in noise sources, beam divergence, and other important properties. Consequently, the breakup integral B must be regarded as a somewhat system-dependent parameter. Nevertheless, we find that with some care this parameter is useful for predicting the performance of various laser systems. The values of B indicated in Fig. 2 are calculated[2] for the laser system only and do not include the relatively small[3] contributions from propagation in the KDP crystal; location of B values in Fig. 2 assumes a 100-percent mirror between laser and crystal.

To avoid ambiguity in the interpretation of Fig. 2, all data points were obtained with identical pumping of the laser rods. The nearly two orders of magnitude range of pump intensity is achieved by statistical variation of the oscillator output and by the use of attenuating filters between the single pulse switchout and the first rod amplifier. To further demonstrate the correlation between beam breakup in the laser and rollover in the frequency conversion curve, the measurements were repeated with a 22-percent reflecting mirror between laser and crystal. In this configuration the laser accumulates five times as much B to reach the same pump intensity at the crystal. This effectively shifts the breakup curve to the left in Fig. 2, as indicated by the upper dashed line. The corresponding measurements of energy conversion efficiency to 5320 Å are shown by the lower dashed line. We again observe a strong correlation between beam breakup and reduced conversion efficiency. In this case, with the laser operating further into the nonlinear regime the rollover occurs at lower pump intensity, thus resulting in a lower peak conversion efficiency.

In conclusion, we find that small-scale beam breakup in solid-state lasers can limit ultimate frequency conversion efficiencies in narrow acceptance angle crystals. In our present experimental configuration we are limited to energy doubling efficiencies of approximately 60 percent. Higher conversion efficiencies should be obtainable by redesigning the overall laser system to reduce the deleterious growth of small-scale spatial irregularities.

References

[1] J. A. Armstrong, N. Bloembergen, J. Ducing, and P. S. Pershan, "Interactions between light waves in a non-linear dielectric," *Phys. Rev.*, vol. 127, pp. 1918–1939, Sept. 15, 1962.

[2] D. A. Kleinman, "Optical harmonic generation in non-linear media," in *Laser Handbook*, F. T. Arecchi and E. O. Schulz-DuBois, Ed. Amsterdam, The Netherlands: North-Holland, 1972, pp. 1229–1258.

[3] K. F. Hulme, "Nonlinear optical crystals and their applications," *Rep. Progr. Phys.* (London), vol. 36, pp. 497–540, May 1973.

[4] A. H. Kung, J. F. Young, C. G. Bjorklund, and S. E. Harris, "Generation of vacuum ultraviolet radiation in phase-matched Cd vapor," *Phys. Rev. Lett.*, vol. 29, pp. 985–988, Oct. 9, 1972.

[5] V. D. Volosov, V. N. Krylov, V. A. Serebryakov, and D. V. Sokolov, "Highly effective generation of the second and fourth harmonics of high power picosecond pulses," *JETP Lett.* (USSR), vol. 19, pp. 23–25, Jan. 1974.

[6] D. T. Attwood, E. L. Pierce, and L. W. Coleman, "Conversion efficiency and pulse shortening of a frequency tripled, subnanosecond, 1.064 μm pulse," *Opt. Commun.* (Amsterdam), vol. 15, pp. 10–12, Sept. 1975.

[7] A. J. Campillo, S. L. Shapiro, and B. R. Suydam, "Periodic breakup of optical beams due to self-focusing," *Appl. Phys. Lett.*, vol. 23, pp. 628–630, Dec. 1973.

[8] E. S. Bliss, D. R. Speck, J. F. Holzrichter, J. H. Erkkila, and A. J. Glass, "Propagation of a high intensity laser pulse with small-scale intensity modulation," *Appl. Phys. Lett.*, vol. 25, pp. 448–450, Oct. 15, 1974.

[9] E. S. Bliss, J. T. Hunt, P. A. Renard, G. E. Sommargren, and H. J. Weaver, "Effects of nonlinear propagation on laser focusing properties," unpublished.

[10] W. F. Hagan and P. C. Magnante, "Efficient second-harmonic generation with diffraction limited and high spectral radiance Nd-glass lasers," *J. Appl. Phys.*, vol. 40, pp. 219–224, Jan. 1969.

[11] J. L. Emmett, J. Nuckolls, and L. Wood, "Fusion power by laser implosion," *Sci. Amer.*, vol. 230, pp. 24–37, June 1974.

[12] A. Carion, J. Lancelot, J. deMetz, and A. Salares, "Fusion reactions in a plasma created by the second harmonic of a Nd:glass laser", *Phys. Lett.* (Amsterdam), vol. 45A, pp. 439–440, Nov. 5, 1973.

[13] D. T. Attwood, L. W. Coleman, and D. W. Sweeney, "Holographic microinterferometry of laser produced plasmas with frequency tripled probe pulses," *Appl. Phys. Lett.*, vol. 26, pp. 616–618, June 1, 1975.

[14] J. A. Stamper and B. H. Ripin, "Faraday rotation measurements of megagauss magnetic fields in laser produced plasmas," *Phys. Rev. Lett.*, vol. 34, pp. 138–141, Jan. 20, 1975.

[15] V. I. Bespalov and V. I. Talanov, "Filamentary structure of light beams in nonlinear liquids," *JETP Lett.*, vol. 3, pp. 307–310, June 1966.

[16] J. Trenholme *et al.*, "Small scale instability growth," Lawrence Livermore Laboratory, Livermore, CA, Laser Program Annu. Rep.–1974, UCRL-50021-74, pp. 179–199, Mar. 1975.

[17] E. S. Bliss, D. R. Speck, and W. W. Simmons, "Direct interferometric measurements of the nonlinear refractive index coefficient n_2 in laser materials," *Appl. Phys. Lett.*, vol. 25, pp. 728–730, 1974.

[2] Typical values of γ are 4.1×10^{-7} cm^2/GW for ED-2 laser glass and 8.6×10^{-7} cm^2/GW for YAG [17]. The refractive index is often expressed as $n = n_0 + n_2 \langle E^2 \rangle$ where E is the electric-field amplitude, $n_2 = nc\gamma/4\pi$ in electrostatic units, and c is the speed of light in vacuum.

[3] The small contribution from KDP is estimated on the basis of a direct interferometric measurement of n_2 by Milam and Weber. In a private communication they report a preliminary value of $(0.9 \pm 0.2) \times 10^{-13}$ ESU for propagation along the optic axis.

Computer Solution for the Traveling-Wave-Excited N_2 Laser

J. B. MORENO

Abstract—**A computer solution is presented for the nitrogen laser excited by a longitudinal relativistic electron beam. The solution demonstrates efficient extraction by amplified spontaneous emission, and preferential radiation parallel to the electron beam, caused by the traveling-wave nature of excitation. These observations tend to validate approximations used to calculate extraction in an earlier study.**

Manuscript received August 26, 1975. This work was performed under the auspices of the United States Energy Research and Development Administration.

The author is with Sandia Laboratories, Albuquerque, NM 87115.

In a recent publication [1], a calculation was presented for the 3371-Å power produced by a nitrogen laser excited by a longitudinal relativistic electron beam. The results showed that the excitation contribution of cascade electrons is negligible, and that the experiments could be explained in terms of excitation by plasma electrons drifting in the inductive field of the electron beam. Among those approximations which the authors used to simplify their calculation, two related to the extraction process are examined here. These are 1) that all the laser power is emitted in the forward direction, and 2) that efficient energy extraction begins upon satisfaction of a threshold-gain condition. The threshold-gain condition at a point is considered to be satisfied when photons, originating at the electron-beam entrance, are amplified by exp(13), as calculated under small-signal-gain conditions. In the present work, these approximations are tested by solving the exact transport equations, which describe the detailed time- and space-dependent process of radiation buildup by amplification of spontaneous emission.

The configuration analyzed here is the same as in [1]. The electron beam is propagated through a cylindrical slug of nitrogen 5 cm in diameter and about 200 cm long. It is assumed that the physical space can be divided into optically independent cylindrical annuli. The kinetic model used in [1] is carried over directly in the present treatment and will not be described in detail again. It is only necessary to repeat that the model includes P-branch laser transitions between rotational levels of the $v' = 0$ vibrational state of the $C\,^3\pi_u$ electronic level, and the $v'' = 0$ vibrational state of the $B\,^3\pi_g$ electronic level. The rotational levels corresponding to each electronic level are again taken to be uncoupled so that each transition is pumped and lases independently.

The small-signal-gain equations of [1] form the basis of the present upper and lower level rate equations. They are modified by deletion of the terms representing plasma–electron interaction with excited states, which can be shown to be of secondary importance [2], and by the addition of radiative interaction terms

$$\frac{\partial N}{\partial t} = fX - \frac{N}{\tau} \mp \frac{\alpha}{h\nu}(P^+ + P^-). \tag{1}$$

Here N represents either the upper or lower level population density, and f is the rotational Boltzmann factor for the ground state. X is the excitation rate and τ is the total lifetime for the respective levels. For each P-branch transition, the gain α can be calculated from expressions given in [1]. The radiant-energy flux parallel and antiparallel to the electron beam is denoted by P^+ and P^-. The radiative transport equations for $P^\pm$ are

$$\left(\frac{\partial}{\partial t} \pm C\frac{\partial}{\partial z}\right) P^\pm = C\alpha P^\pm + S^\pm \tag{2}$$

where $S^\pm$ is the spontaneous-emission contribution into solid angle $\Delta\Omega^\pm$ and frequency width $\Delta\nu$. An expression for $S^\pm$ follows from (2) by application of the principle of detailed balance. For the present calculations, $\Delta\nu$ was taken to be the Doppler linewidth and $\Delta\Omega^\pm$ was calculated at each axial location as the solid angle subtended by the area at the appropriate end of the laser tube.

To complete the governing equations, the excitation rates X must be specified. These have been kindly supplied by the authors [1] for representative conditions (P-9 transition, 15-torr pressure, zero-radius location). The traveling-wave nature of the excitation permits the supplied rate data to be fit by

$$X(z, t) = X\left(z_0, t - \frac{z - z_0}{V_b}\right)\exp\left(-\frac{z - z_0}{152}\right) \tag{3}$$

where $V_b = 7.7$ cm/ns is the traveling-wave speed, and $z_0 = 3.8$ cm. Equations (1) and (2), together with these data, constitute a determinate set. The initial conditions for the equations are taken to correspond to thermodynamic equilibrium at 300 K, and the boundary conditions are $P^+(0, t) = P^+(0, 0)$ and $P^-(L, t) = P^-(L, 0)$.

The governing equations just described are of the same form as those used to describe the superradiant H_2F_2 laser in [3]. There it was pointed out that the equations constituted a hyperbolic partial differential set, integrable by an implicit method-of-characteristics numerical procedure [3]. This numerical technique has as its principal advantage the avoidance of undue stability constraints on integration step size. Although the present problem introduces the additional phenomenon of traveling-wave excitation, no new difficulties were encountered in applying the technique.

Results calculated by the present approach are illustrated in Figs. 1–4. Fig. 1 shows the excitation wave, moving parallel to the electron beam, and computed small-signal-gain distributions at various instants in time. One can see that, at each axial location, the gain increases steadily until the excitation wave passes. Thus the gain distribution moves parallel to the electron beam at the excitation-wave speed. Notice that small-signal gain in excess of 1000 percent/cm is attained.

Figs. 2 and 3 show the computed gain and radiative-flux distributions when the influence of amplified spontaneous emission is admitted. The gain is everywhere strongly suppressed, but a prominent peak is evident, propagating at about one-third the excitation-wave speed. It is also evident that except for very early times, extraction occurs mainly in the forward direction. This behavior is explained in Fig. 4, which shows time histories of pumping, radiative power, and gain for a single axial location. Because of differences in wave speeds, forward radiation reaches the location before excitation can begin, thus pinning the gain at relatively low levels and extracting most of the available energy. Once the forward radiation wave has passed, the gain increases sharply in response to the tail of the excitation wave. Finally, backward radiation arrives from the most recently excited region. This forces the gain down again, leaving the gain peak seen in Fig. 2.

The threshold-gain condition has been calculated from the small-signal-gain results. Except for the first few nanoseconds, this condition is found to be satisfied over virtually the entire length of the excited medium, implying that practically all of the pumped energy is extracted by amplified spontaneous emission. To test this approximation, the previous calculations were repeated with the addition of a steady, high-intensity

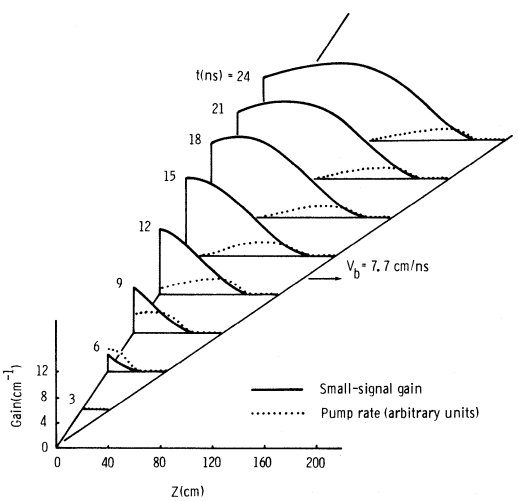


Fig. 1. Excitation-wave and small-signal-gain distributions.

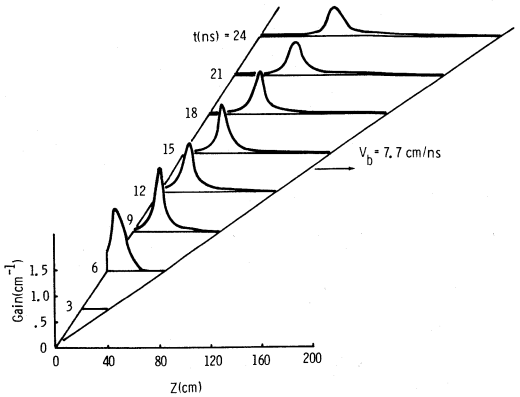


Fig. 2. Gain distributions under the influence of amplified spontaneous emission.

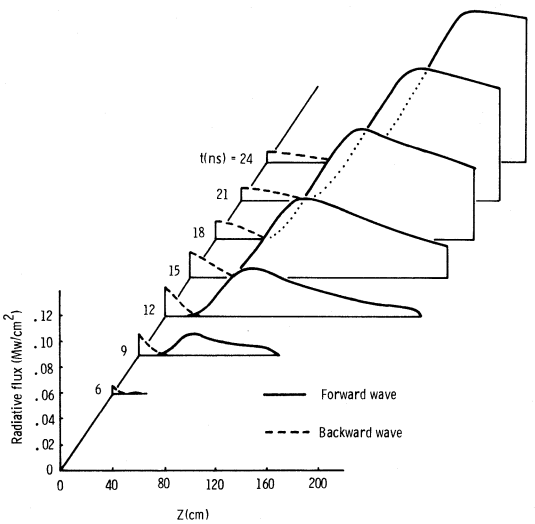


Fig. 3. Forward and backward radiant-flux distributions.

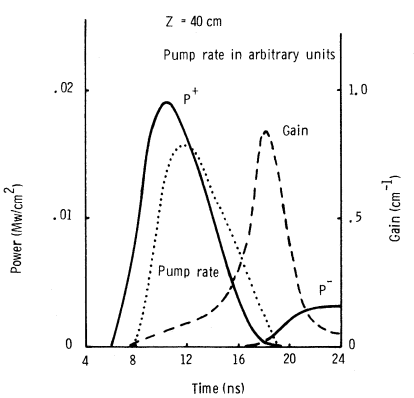


Fig. 4. Pumping, gain and radiant-flux time histories at z = 40 cm.

probe-laser beam parallel to the electron beam. Increasing the probe intensity to 10^9 W/cm^2 resulted in suppression of the backward radiation and complete extraction of all the pumped energy in the forward direction. Thus the difference between the power output in the forward direction, with and without the probe, represents the error attributable to the threshold-gain condition and the neglect of backward radiation. The calculated results indicate an error of about 30 percent, not enough to alter the conclusions of [1].

In summary, another application has been demonstrated for the implicit method of characteristics developed in [3]. Although the present problem introduces the additional phenomenon of traveling-wave excitation, no new difficulties were encountered in applying the method. Finally, the results and observations presented here tend to validate the approximations used to calculate extraction in [1].

ACKNOWLEDGMENT

The author wishes to thank Dr. D. A. McArthur for useful discussions.

REFERENCES

[1] D. A. McArthur and J. W. Poukey, "Theory of the nitrogen laser excited by a relativistic electron beam," *IEEE J. Quantum Electron.*, vol. QE-11, pp. 892-902, Nov. 1975.
[2] D. A. McArthur, private communication.
[3] J. B. Moreno, "Computer model for the $H_2 + F_2$ superradiant laser," presented at the American Institute of Aeronautics and Astronautics 13th Aerospace Sciences Meet., 1975, Paper 75-36.

Influence of Spatial Hole Burning on the Output Power of a CW Dye Ring Laser

GERD MAROWSKY AND KONRAD KAUFMANN

Abstract—**The output power of a single-mode CW dye ring laser can be enhanced by 50 percent by changing over from standing-wave (SW) operation to traveling-wave (TW) operation. This effect is attributed to smoothing out the SW pattern in the active medium, which gives rise to spatial inhomogeneities of the inversion.**

The standing-wave (SW) pattern of the electric field intensity leads to a nonuniform distribution of the inverted population in the active medium of an organic dye laser. It has recently been shown that this effect of spatial hole burning can be successfully exploited to achieve single-mode operation with only a few narrowing elements [1] or to restrict the laser emission to two simultaneously oscillating lines of narrow bandwidth [2]. It is the purpose of this correspondence to study the influence of spatial hole burning on the output power of a CW dye ring laser by comparison of the power obtainable in SW and traveling-wave (TW) operation of the laser.

The theoretical treatment of the problem (cf. Appendix) starts from the general laser equations [3], thus avoiding the introduction of a sinusoidally modulated inversion density into the rate equations, a procedure which turns out to be justified only in the limit of pumping rates just above threshold. The result of the theoretical calculation can be summarized as follows. Let I_0 be the measured output power of one of the oppositely circulating waves, then the total output power in the SW case (A) is given by $I_A = 2I_0$. According to (6) given in the Appendix, the output power in the TW case (B) near threshold is then $I_B = 3I_0$. The factor 3 instead of 2 is strictly valid only for single-mode operation. For multimode operation output power values between $2I_0$ and $3I_0$ are to be expected. The considerable increase in efficiency in TW single-mode operation could be successfully demonstrated with a dye ring laser.

Since details of the construction have been published elsewhere [4], [5], the description of the setup is limited to the essential properties for the TW experiment (Fig. 1). The moderately dispersive prism ring laser starts to oscillate at 150 mW input power of the Ar^+ pump laser. By reflection of the CW traveling wave onto itself with the mirror R_1, unidirectional TW operation can be achieved. To restrict the laser oscillation to a single longitudinal mode, a set of two Fabry-Perot etalons can be inserted into the cavity. The interferometrically measured bandwidths are 0.5 Å in broad band and 0.001 Å in

Manuscript received October 9, 1975; revised November 7, 1975.

The authors are with the Max-Planck-Institute for Biophysical Chemistry, Göttingen, Germany.

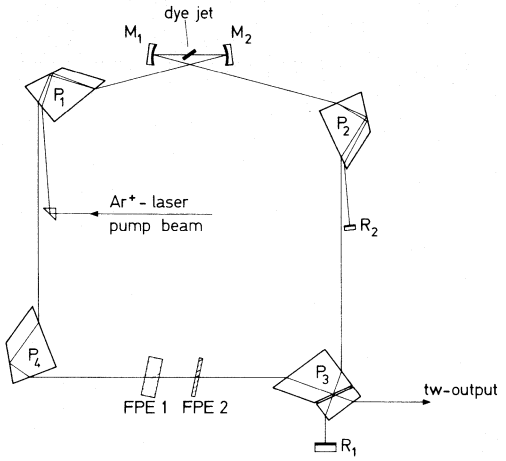


Fig. 1. Optical schematic of Ar^+-laser-pumped CW dye ring laser P_1, P_2, P_3, P_4: Abbé or Pellus-Broca prisms, R_1, R_2: flat 100-percent reflectors, M_1, M_2: concave mirrors of 40-mm radius of curvature. FPE 1: quartz Fabry-Perot etalon of 0.25-mm thickness and 40-percent reflectivity, FPE 2: uncoated quartz etalon of 12-mm thickness. The quantity I_0 is measured after removal of R_1.

single-mode operation. No special care is taken to minimize the internal cavity losses [6]. For the quantity I_0—the SW single-mode output power in either CW or CCW sense—typically $I_0 = 12$ mW were measured. With mirror M_1 inserted, the threefold value of I_0, 36 mW, was obtained within an experimental uncertainty of ±1 mW.

In multimode operation 30 mW in either direction and 60 mW under TW condition were obtained. (All output-power values refer to an input power of 310 mW of the 514.5-nm Ar^+-laser line.) With only one etalon inserted, values between $2I_0$ and $3I_0$ were observed. In the case of a few simultaneously oscillating modes, the output power strongly depended on the position of the etalon within the cavity with respect to the position of the active medium. Especially in the case of two not adjacent modes all values between $2I_0$ and $3I_0$ could be produced by a slight variation of the longitudinal position of the etalon creating either a $\lambda/4$ phase shift or an in-phase superposition in the active medium. The exact agreement with the theoretical prediction concerning output power for more than one mode is linked to the condition that the active medium be thin compared to the resonator length. This condition usually no longer holds for flashlamp-pumped systems. In the Appendix it has been shown that far above threshold the output powers of the SW and TW cases tend to be asymptotically equal (cf. Fig. 3). This can be intuitively understood taking into consideration the SW pattern leading to the effect of spatial hole burning. In Fig. 2 the normalized inversion for the SW case and for the TW case is depicted versus the spatial coordinate z for a few optical wavelengths for various values of the SW energy as parameter. The figure shows that whereas the inversion of the TW case σ_B remains constantly equal to its threshold value σ_I, σ_A, the SW inversion, is strongly modulated. While a sinusoidal hole burning appears near threshold in agreement with perturbation theoretical result [8], the exact solution [(3) and (6)] shows a strong deviation from the sinusoidal shape far above threshold. In the latter case the excess inversion $\sigma_A(z) - \sigma_I$ shows a strong tendency to be utilized completely and to approach the TW case. It has proved experimentally to be impossible to obtain single-mode operation so far above threshold to check for the validity of the asymptotic expansion. It has been shown theoretically [9] that the effect of spatial hole burning favors

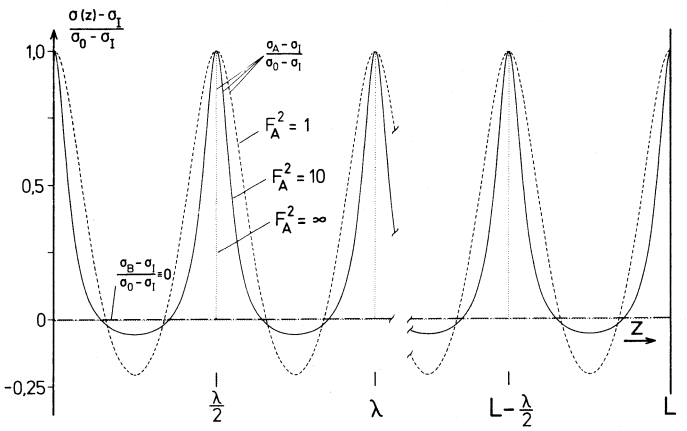


Fig. 2. Normalized inversion $\sigma(z) - \sigma_I/\sigma_0 - \sigma_I$ versus axial coordinate z at different values of F_A^2, with F_A^2 equal to normalized energy as defined in (7) of the Appendix. In the TW case the inversion $\sigma_B(z) = \sigma_I$ coincides with the abscissa. The spatial holes burned by the laser electromagnetic field in the SW case clearly show the tendency to smooth out at higher pumping.

the appearance of other modes which tend to consume the available excess inversion. In fact, a system of two modes spatially spaced within the active medium by $\lambda/4$ will consume the whole inversion and consequently will yield the same output power as under TW operation.

APPENDIX

The basic laser equations for the electric field $\boldsymbol{E}(\boldsymbol{r}, t)$, the macroscopic polarization $\boldsymbol{P}(\boldsymbol{r}, t)$, the microscopic polarization $\boldsymbol{e}p_{12}a(\boldsymbol{r}, t)$, and the microscopic inversion $\sigma(\boldsymbol{r}, t)$ of homogeneously broadened two-level atoms are [3]

$$\left(\frac{\partial}{\partial t} + \gamma_{\parallel}\right)\sigma(\boldsymbol{r}, t) = \gamma_{\parallel}\sigma_0 + \frac{2i}{\hbar}\boldsymbol{e}p_{12}\boldsymbol{E}[a(\boldsymbol{r}, t) - \text{c.c.}] \tag{1a}$$

$$\left(\frac{\partial}{\partial t} - i\omega + \gamma_{\perp}\right)a(\boldsymbol{r}, t) = +\frac{i}{\hbar}\boldsymbol{e}p_{12}\boldsymbol{E}\sigma(\boldsymbol{r}, t) \tag{1b}$$

$$\Delta\boldsymbol{E}(\boldsymbol{r}, t) - \frac{2\kappa\mu}{c^2}\frac{\partial}{\partial t}\boldsymbol{E} - \frac{\epsilon\mu}{c^2}\frac{\partial^2}{\partial t^2}\boldsymbol{E} = \frac{4\pi\mu}{\partial t^2}\boldsymbol{P}(r, t) \tag{1c}$$

$$\boldsymbol{P}(\boldsymbol{r}, t) = n\boldsymbol{e}p_{12}[a(\boldsymbol{r}, t) + \text{c.c.}]$$

with vacuum velocity of light c, Planck's constant $\hbar = 2\pi h$, space vector $\boldsymbol{r}$, time t, dielectric constant ϵ, magnetic susceptibility μ of the host medium for the atoms, and the dissipation constant κ which accounts for the resonator losses phenomenologically. The two-level system of atoms with density n is described by a dipole matrix element of amount p_{12} parallel to the unit vector $\boldsymbol{e}$, a transition frequency ω, longitudinal and transversal relaxation constants $\gamma_{\parallel} = 1/T_1$ and $\gamma_{\perp} = 1/T_2$, and the "pump inversion" σ_0 which is established in the absence of an electromagnetic field. We consider only the single-mode case in a one-dimensional cavity, length L, of either standing (SW) or traveling (TW) eigenmodes $f(z)$ in resonance $k = (\omega/c) = m(\pi/L)$; m integer; normalized to $\int_0^L |f(z)|^2\, dz = 1$

$$\boldsymbol{E}(\boldsymbol{r}, t) = \boldsymbol{e}\tilde{E}f(z)e^{i\omega t} + \text{c.c.} \tag{2}$$

$$f(z) = \sqrt{\frac{2}{L}}\sin kz \tag{2A}$$

$$f(z) = \sqrt{\frac{1}{L}}e^{-ikz}. \tag{2B}$$

Making use of (2) and the normalization, we rewrite the laser equations (1) neglecting antiresonant terms in rotating wave approximation

$$\sigma(z) = \frac{\sigma_0}{1 + \dfrac{4p_{12}^2}{\hbar^2\gamma_{\parallel}\gamma_{\perp}}|\tilde{E}|^2\,|f(z)|^2} \tag{3a}$$

$$a(z, t) = +\frac{i}{\hbar}p_{12}\,\sigma(z)\,\tilde{E}f(z)e^{i\omega t} \tag{3b}$$

$$1 = \frac{\sigma_0}{\sigma_I}\int_0^L dz\,\frac{|f(z)|^2}{1 + \dfrac{4p_{12}^2}{\hbar^2\gamma_{\parallel}\gamma_{\perp}}|\tilde{E}|^2\,|f(z)|^2} \tag{3c}$$

with $\sigma_I = h\kappa/2\pi\omega n p_{12}^2$. These equations describe spatial hole burning of the inversion if $|f(z)|^2$ depends on z, which is the case only in SW operation of the laser [compare (2A)], but not in TW operation. It follows from (3c) that the threshold inversion σ_I is identical in both cases

$$|\tilde{E}|^2 > 0 \quad \text{for} \quad \sigma_0 > \sigma_I. \tag{4}$$

At a given transmission of the output coupler the measured values of the output power I_0 of the laser are proportional to the energy loss per round-trip time of the electromagnetic field. On the other hand, this energy in the cavity is related to the energy density $(1/4\pi)\boldsymbol{E}^2$ by

$$\int_0^L dz\,\frac{1}{4\pi}|\boldsymbol{E}|^2 = |\tilde{E}|^2 \tag{5}$$

again neglecting antiresonant terms. Hence $|\tilde{E}|^2$ is an observable of the system. The influence of spatial hole burning on the output power of the laser can now be calculated without any approximation of the nonlinearity [8]. The exact solution can be given not only for the TW but also for the SW case

$$\text{SW case:}\quad \frac{F_A^2}{2}\left[1 - (1 + F_A^2)^{-1/2}\right]^{-1} = \frac{\sigma_0}{\sigma_I} \tag{6a}$$

$$\text{TW case:}\quad 1 + \frac{F_B^2}{2} = \frac{\sigma_0}{\sigma_I} \tag{6b}$$

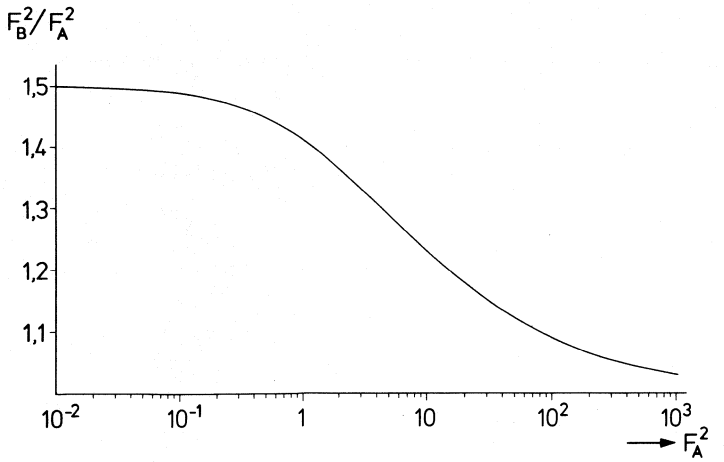


Fig. 3. F_B^2/F_A^2 versus F_A^2 to show near-threshold and asymptotic behavior of the ratio of TW to SW energy given in (8).

with

$$F^2 = \frac{4p_{12}^2}{\hbar^2 \gamma_\parallel \gamma_\perp} \frac{2}{L} |\tilde{E}|^2 . \tag{7}$$

The parameter σ_0/σ_I, i.e., the pump normalized to the laser threshold, can be directly measured by the input power of the Ar^+ laser. Eliminating for our purposes σ_0/σ_I from (6a) and (6b), we obtain a relation between $|\tilde{E}_A|^2$ and $|\tilde{E}_B|^2$, abbreviated again by F_A^2 and F_B^2 as in (6)

$$\frac{F_B^2}{F_A^2} = -\frac{2}{F_A^2} + [1 - (1 + F_A^2)^{-1/2}]^{-1} . \tag{8}$$

Fig. 3 shows this relation. The deviation of the output power of the SW case from that of the TW case, hence from $F_B^2/F_A^2 = 1$, is due to the spatial hole burning. This deviation is maximal near threshold and vanishes only extremely far above threshold.

M. Sargent, III, brought to our attention a prediction (J. A. White, *Phys. Rev.*, vol. 137A, p. 1651, 1965) that due to spatial hole burning a ring laser with a homogeneously broadened medium should automatically oscillate in bistable unidirectional operation. This discrepancy with our observations could well be due to the neglect in that analysis of cavity anisotropies, well known from the frequency locking of counterrunning waves in ring lasers. Spatial hole burning has been discussed in this and other contexts by M. Sargent, *Appl. Phys.*, vol. 9, to be published.

References

[1] H. W. Schröder, H. Dux, and H. Welling, "Single mode operation of CW dye lasers," *Appl. Phys.*, vol. 7, pp. 21–28, 1975.
[2] I. V. Hertel and A. S. Stamatović, "Spatial hole burning and oligomode distance control in CW dye lasers," *IEEE J. Quantum Electron.*, vol. QE-11, pp. 210–212, May 1975.
[3] H. Risken, "Zur Statistik des Laserlichts," *Fortschr. Phys.*, vol. 16, pp. 261–308, 1968.
[4] G. Marowsky and F. Zaraga, "A comparative study of dye prism lasers," *IEEE J. Quantum Electron.*, vol. QE-10, pp. 832–837, Nov. 1974.
[5] G. Marowsky, "Astigmatism- and coma-free prism dye ring laser," *Appl. Phys. Lett.*, vol. 26, pp. 647–649, 1975.
[6] G. Marowsky and R. Polloni, "Experimental determination of CW dye laser parameters by loss variation," *Appl. Phys.*, vol. 8, pp. 29–33, 1975.
[7] C. T. Pike, "Spatial hole burning in CW dye lasers," *Opt. Commun.*, vol. 10, pp. 14–17, 1974.
[8] W. E. Lamb, Jr., "Theory of an optical maser," *Phys. Rev.*, vol. 134A, pp. 1429–1450, 1964.
[9] K. Kaufmann and W. Weidlich, "Mode interaction in a spatially inhomogeneous laser," *Z. Phys.*, vol. 217, pp. 113–127, 1968.

Contributors

Robert D. Burnham (M'76), for a photograph and biography please see page 88 of the February 1976 issue of this JOURNAL.

*

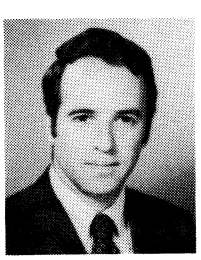


Jerome K. Butler (S'59–M'65) was born in Shreveport, LA, on September 27, 1938. He received the B.S. degree from Louisiana Polytechnic University, Ruston, and the M.S. and Ph.D. degrees from the University of Kansas, Lawrence, in 1960, 1962, and 1965, respectively.

From 1960 to 1965 he was a Research Assistant at the Center for Research in Engineering Sciences, University of Kansas. His research was related to electromagnetic-wave propagation in anisotropic media and to the optimization and synthesis techniques of antenna arrays. In 1965, he joined the staff of the Institute of Technology, Southern Methodist University, Dallas, TX, where he is now Professor of Electrical Engineering. His primary research areas have been in theoretical antenna array studies, wave scattering, electromagnetic-wave propagation in semiconductors, semiconductor lasers, and quantum electronics. He has held consulting appointments with Texas Instruments, Inc., the Geotechnical Corporation of Teledyne, Inc., and Earl Cullum Associates of Dallas, TX. In the summers from 1969 to 1974 he was a Member of the Technical Staff, RCA Laboratories, Princeton, NJ, where he did research concerned with electromagnetic-wave propagation in solid-state injection lasers.

Dr. Butler is a member of Sigma Xi, Tau Beta Pi, Eta Kappa Nu, and the American Society for Engineering Education.

*



Stephen R. Chinn (M'75) was born in Baltimore, MD, on November 20, 1942. He received the B.S. and M.S. degrees in electrical engineering and the Ph.D. degree in electrical science and engineering from the Massachusetts Institute of Technology, Cambridge, MA, in 1965 and 1970, respectively.

He has worked in the areas of electron paramagnetic resonance, magnetism, and Raman scattering. In 1970 he became a Postdoctoral Fellow at the Massachusetts Institute of Technology Lincoln Laboratory, Lexington, MA, and since 1971 has been a member of the staff there, studying semiconductor lasers.

Dr. Chinn is a member of the American Physical Society, Tau Beta Pi, Eta Kappa Nu, and Sigma Xi.

*

Hermann A. Haus (S'50-A'55-SM'58-F'62) attended the Technische Hochschule, Graz, Austria, from 1946 to 1948, and the Technische Hochschule, Vienna, Austria, in 1948. He received the B.S. degree from Union College, Schenectady, NY, the M.S. degree from the Rensselaer Polytechnic Institute, Troy, NY, and the Sc.D. degree from



the Massachusetts Institute of Technology, Cambridge, MA, all in electrical engineering, in 1949, 1951, and 1954, respectively.

He is Elihu Thomson Professor of Electrical Engineering and a Research Staff Member of The Research Laboratory of Electronics, Massachusetts Institute of Technology. He also serves as a Consultant to the Raytheon Company. From 1959 to 1960 he was a Visiting Professor and Guggenheim Fellow at the Technische Hochschule, Vienna. He is coeditor of the recent book *Noise in Electron Devices*, coauthor of the monographs *Circuit Theory of Linear Noise Networks* and *Electrodynamics of Moving Media*, and coauthor of the book *Case Studies in Electromagnetism.*

Dr. Haus is a member of Sigma Xi.

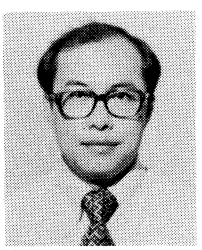
*



Fritz W. Hollinger was born in Lauterecken, Germany, on November 16, 1944. He received the Dipl. Ing. degree from the University of Karlsruhe, Karlsruhe, Germany, in 1971.

He is currently working as a Research Assistant at the Hochspannungsinstitut of the University of Karlsruhe, where he is involved in the electrical breakdown of gases and the application of UV lasers in the field of high-voltage technology.

*



Henry Y-P. Hong was born in Taiwan on October 17, 1943. He came to the United States in September 1967 as a graduate student, receiving the M.S. degree in chemical engineering from the University of New Hampshire, Durham, and the Ph.D. degree in chemical engineering from the University of Texas, Austin (where he worked under Prof. H. Steinfink on structural chemistry), in 1971.

He came to the M.I.T. Lincoln Laboratory, Lexington, MA, in October 1971, where he is in charge of the X-ray facility. He has been studying the relationship between crystal structures and the physical properties of solid electrolytes and of rare-earth compounds used as laser materials. His single-crystal X-ray determinations have played a critical role in the development of three-dimensional network structures for fast alkali-ion transport in solid electrolytes and in establishing that isolation of the rare-earth polyhedra sharply reduces "concentration quenching"and that fluorescence lifetime is determined by the rare-earth local site symmetry.

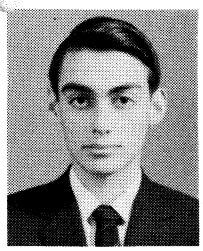


Kohroh Kobayashi was born in Nagano, Japan, in 1944. He received the B.E. and M.E. degrees in electronic engineering, both from the Tokyo Institute of Technology, Tokyo, Japan, in 1968 and 1970, respectively.

In 1970 he joined the Central Research Laboratories, Nippon Electric Co., Ltd., Kawasaki, Japan. Since 1975 he has been working at the Laser Equipment Development Division of the same company. He has been engaged in development of semiconductor lasers and their application to optical fiber communications.

Mr. Kobayashi is a member of the Japan Society of Applied Physics and the Institute of Electronics and Communication Engineering.

*

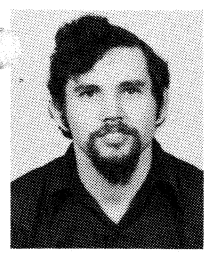


Roy Lang was born in Tokyo, Japan, in 1942. He received the B.S. degree from the University of Tokyo, in 1966, and the Ph.D. degree from the Massachusetts Institute of Technology, Cambridge, in 1971.

From 1971 to 1973 he was a Research Associate at the Joint Institute for Laboratory Astrophysics of the University of Colorado and the National Bureau of Standards, Boulder, CO. Since 1973 he has been with the Central Research Laboratories of the Nippon Electric Co., Ltd., Kawasaki, Japan, where he has been working mainly on the theoretical problems related to the development and applications of GaAs injection lasers.

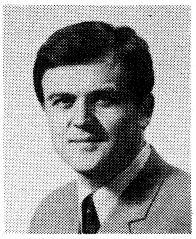
Dr. Lang is a member of the Physical Society of Japan and the Japan Society of Applied Physics.

*



James W. Pierce was born in Sandwich, MA, on September 25, 1943. He received the B.S. degree in chemistry from Worcester Polytechnic Institute, Worcester, MA, and the Ph.D. degree in chemistry from Brown University, Providence, RI, in 1965 and 1970, respectively.

He has worked in preparative and structural chemistry of transition metal and rare-earth oxides and fluorides, correlating structure and composition with optical, magnetic, and transport properties. At the Massachusetts Institute of Technology Lincoln Laboratory, Lexington, MA, his primary emphasis has been on rare-earth fluorides and oxides for infrared-to-optical up-conversion and on improved laser hosts.



Adolph J. Schwab (SM'71) was born in Mannheim, Germany, on June 20, 1937. He received the Dip. Ing. and Dr.-Ing. degrees from the University of Karlsruhe, Karlsruhe, Germany, in 1961 and 1963, respectively.

Since 1964 he has been Assistant Professor and in 1971 he was appointed Associate Professor at the High-Voltage Laboratory of the University of Karlsruhe. He does research in high-voltage measurements, electrical breakdown of gases, and electromagnetic compatibility. He is a Consultant in electromagnetic interference and has published a number of articles in the field of high-voltage research and is author of the book *High-Voltage Measurement Techniques*, which has been edited in English, German, and Russian.

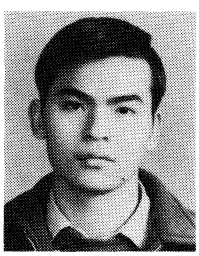
*

Donald R. Scifres (M'74), for a photograph and biography please see page 88 of the February 1976 issue of this JOURNAL.

*

William Streifer (S'56-M'58-SM'74), for a photograph and biography please see page 88 of the February 1976 issue of this JOURNAL.

*



Chung-Shu Wang (S'73) was born in Taiwan on April 8, 1949. He received the B.S. degree in electrophysics from Chiao-Tung University, Hsin-Chu, Taiwan, in 1970, and the M.S.E.E. degree from the University of New Mexico, Albuquerque, in 1972.

Since 1973 he has held a Research Assistantship in the Department of Electrical Engineering, Southern Methodist University, Dallas, TX, where he is currently working toward the Ph.D. degree on semiconductor lasers and optical communications.

Mr. Wang is a member of Sigma Tau.



QUANTUM ELECTRONICS

AMSTERDAM the NETHERLANDS JUNE 14–18, 1976

SPONSORS: EUROPEAN PHYS. SOC., DUTCH PHYS. SOC., PHYSICA (Neth.), A.I.P. and I.E.E.E. through the JOINT COUNCIL on QUANT. ELECTR. (USA)

TOPICS:
- Physics and chemistry with lasers
- Laser-induced isotope separation and chemical reactions
- Interaction of extremely intense radiation with matter
- Laser spectroscopy and environmental measurements
- Advances in coherent light sources
- Photon statistics and coherence effects
- Nonlinear optics, modulators and detectors
- New optical materials
- Integrated optics and guided waves

EXHIBITION: – During the conference at the congress site

Chairman Technical Program Committee
Prof. Dr. O. Svelto
c/o Prof. Dr. H. J. Frankena
Dept. Applied Physics
University of Technology
Lorentzweg 1
Delft/the Netherlands

Local Program Committee USA/Canada
Dr. J. A. Armstrong
IBM Thomas J. Watson
Research Center
P.O. Box 218
Yorktown Heights
NY 10598

Secretary Organizing Committee
Dr. J. Langelaar
Lab. for Physical Chemistry
University of Amsterdam
Nieuwe Prinsengracht 126
Amsterdam-C/
the Netherlands

REGISTRATION For a smooth organization, advance registration is highly desirable. Advance registration fee: Dfl 175,-; deadline April 14, 1976. Registration fee after April 14, 1976: Dfl. 275,-

GENERAL INQUIRIES
to be directed to Dr. Langelaar only.

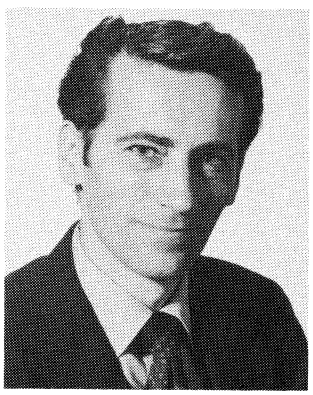
Announcement

EFFECTIVE December 1975, two of our Associate Editors have retired from their positions and are being replaced by two new editors.

E. I. Gordon has been an Associate Editor since the first edition of this JOURNAL was published in April of 1965. E. Schulz-DuBois has been an Associate Editor since October of 1967. Both have served long and conscientiously, and deserve much thanks for their contributions to the current stature of this JOURNAL.

Their places are being taken by P. W. Smith and J. Ducuing, whom we hereby welcome on the staff.

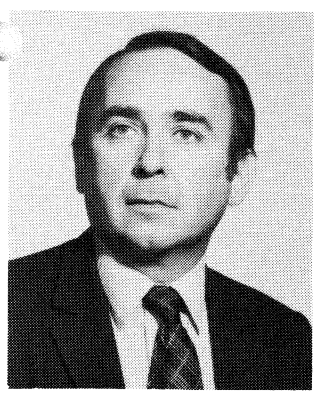
A. GARDNER FOX
Editor



Peter W. Smith (M'67-SM'75) was born in London, England, in 1937. He received the B.Sc. degree in mathematics and physics in 1958 and the M.Sc. and Ph.D. degrees in physics in 1961 and 1964, all from McGill University, Montreal, P.Q., Canada. His thesis work was on the paramagnetic relaxation of iron-group ions in dilute single crystals.

After obtaining the Ph.D. degree he joined the Bell Telephone Laboratories, Holmdel, NJ, where he has conducted research on the fundamental properties of gas lasers. He has investigated the use of guided-wave techniques for producing miniature gas lasers, and is currently studying dye-vapor laser systems. In 1970 he spent nine months at the University of California, Berkeley, as Visiting Mackay Lecturer in the Department of Electrical Engineering.

Dr. Smith is a member of the American Physical Society and the Optical Society of America.



Jacques Ducuing was born in Tarbes, France, in 1932. He graduated from the Ecole Polytechnique, Paris, France, and obtained the D.Sc. degree from the University of Paris.

He began his research at CSF Laboratories, followed by four years at Harvard in Professor Bloembergen's group. He taught and conducted research at the Massachusetts Institute of Technology and at the Institut d'Optique in Orsay. In 1968 he was appointed Professor of Physics at the Faculté des Sciences d'Orsay, and in 1973 was appointed Professor of Physics at the Ecole Polytechnique. Since 1970 he has been Director of the Laboratoire d'Optique Quantique du CNRS.

Dr. Ducuing is a member of the French and American Physical Societies, and is the recipient of the Prix Aimé Cotton of the French Physical Society and of the Silver Medal of CNRS.

Stabilization of Oscillating Modes in a $LiNdP_4O_{12}$ Laser

KENJU OTSUKA AND HIROSHI IWASAKI

Abstract—**Suppression of mode competition in a $LiNdP_4O_{12}$ (LNP) laser is reported. The stabilization of the oscillating modes was achieved with a quartz quarter-wave plate placed within an optical resonator without any external modulation.**

In a typical laser, there are many modes of the optical resonator which fall within the frequency region over which the gain of the laser medium exceeds the resonator losses. The output of such a laser will depend on amplitudes and relative phases of all of these oscillating modes. In a free-running laser, the amplitudes and relative phases of all of oscillating modes are fluctuating randomly due to the mode competition. Mode-locking or FM-laser operation by an intracavity modulator is useful to stabilize the oscillating modes.

Recently, we have reported the room-temperature CW operation of the $LiNdP_4O_{12}$ (LNP) laser [1]. In this paper, a new method to stabilize the oscillating modes is reported. Stabilization of the LNP laser is achieved using the intracavity quarter-wave plate.

The crystal used was 1.85 mm long (pseudoorthorhombic *a* axis), 0.7 mm thick (*b* axis), and 1.2 mm wide (*c* axis). The surfaces were not antireflection coated. The crystal was mounted on a Cu heat sink and placed within an optical resonator.

The experimental arrangement is shown in Fig. 1. The resonator consisted of the mirror M_1 (radius of curvature $R_1 = \infty$ and transmission $T_1 = 1$ percent at 1.047(7) μm, $T' = 83$ percent at 5145 Å) and M_2 ($R_2 = 9$ cm and $T_2 = 0.1$ percent). These two mirrors were separated by about 9 cm. The LNP crystal was located just in front of M_1. A CW argon laser (5145 Å) was used as a pump and pumped the LNP longitudinally. A quartz quarter-wave plate P, whose surfaces were antireflection coated at 1.047(7) μm, was placed between the crystal and M_2. The fast axis of the quartz lies at 45° to the *c* axis of the LNP crystal ($\theta = 45°$).

In a free-running LNP laser, the laser emission was linearly polarized along the *c* axis of the crystal, since the emission cross section for the electric vector along the *c* axis of the crystal, which is 3.2×10^{-19} cm^2, is larger than those for the electric vectors along the *b* and *a* axes which are 1.3×10^{-19} cm^2 and 1.5×10^{-19} cm^2, respectively [2].

With an insertion of the quarter-wave plate, the output light beam from the mirror M_2 was circularly polarized and two orthogonal modes from the mirror M_1 were divided into two passes by the Wollaston prism. Passage through P toward the right along the resonator introduces a relative phase shift of $\pi/2$ in the fast axis component of the electric vector along the *c* axis of the LNP laser and results in a circularly polarized wave. After reflecting back from M_2 and passing through P in the opposite direction, the laser beam is then linearly polarized along the *b* axis of the LNP crystal. After the next round trip within the resonator, the linearly polarized wave along the *b* axis of the LNP crystal is coverted into the linearly polarized wave along the *c* axis in the same manner. Therefore, a stable mode is formed after the *double* round trip within the resonator.

The output waveform was detected with an S-1 photomultiplier. The results are shown in Fig. 2. Fig. 2(a) shows the

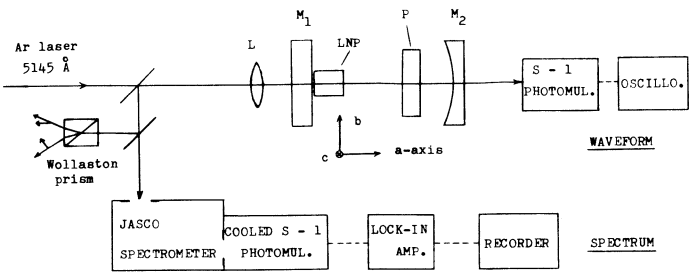


Fig. 1. Experimental arrangement. The fast axis of the quarter-wave plate P lies at 45° to the pseudoorthorhombic *c* axis of the LNP.

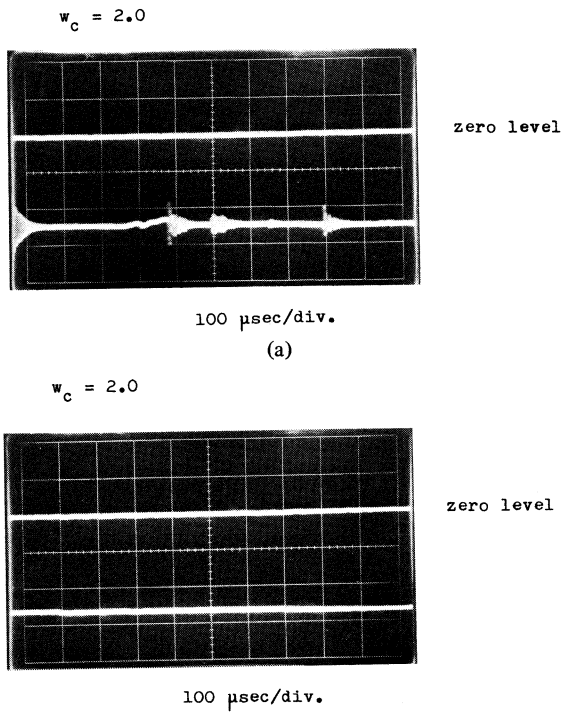


Fig. 2. CW output observed with an S-1 photomultiplier. The upper and lower traces represent the zero level and output of the LNP laser. w_c is the relative pump power P/P_{th} (P_{th}: threshold pump power). (a) Free-running (without the quarter-wave plate). (b) With the quarter-wave plate.

Manuscript received June 26, 1975; revised December 8, 1975.

The authors are with the Musashino Electrical Communication Laboratory, Nippon Telegraph and Telephone Public Corporation, Musashino-shi, Tokyo, Japan.

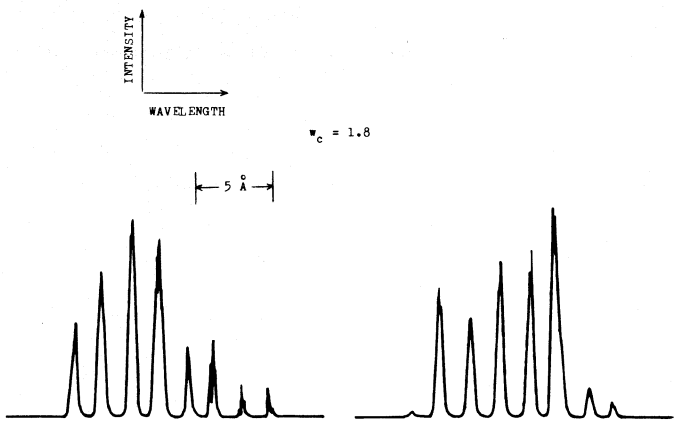


Fig. 3. Emission spectrum of the free-running laser measured at different times. $w_c = 1.8$.

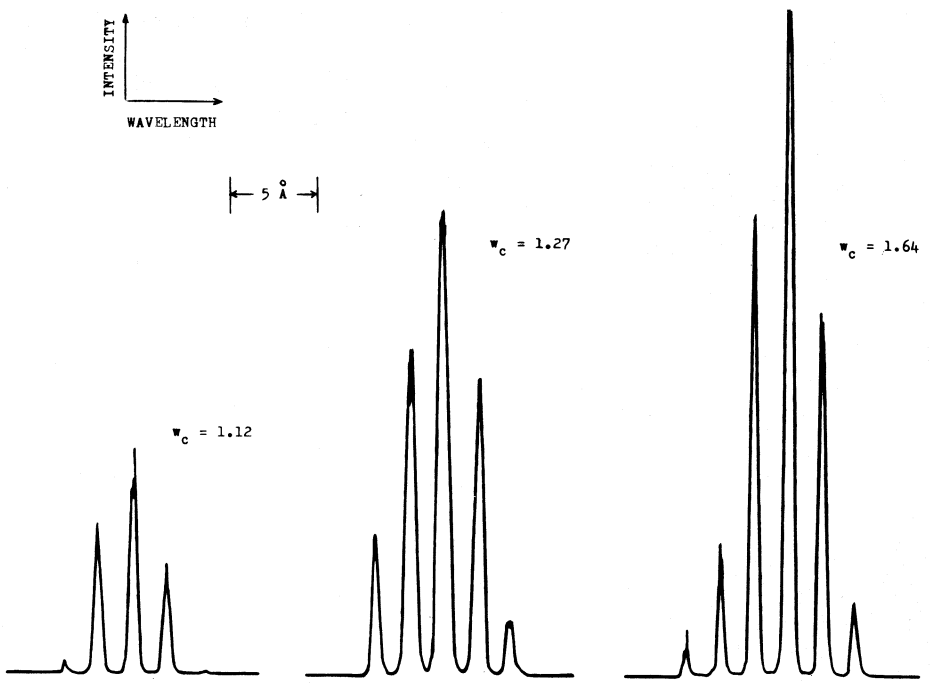


Fig. 4. Emission spectrum of the laser with the intracavity quarter-wave plate at various pump powers. $\theta = 45°$.

output from the free-running laser and Fig. 2(b) shows the output from the laser with the quarter-wave plate. In the free-running condition, the output exhibits relaxation spikings while the output from the laser with the wave plate shows stable radiation without spikings.

The oscillating mode spectrum was analyzed with a JASCO single grating spectrometer with a resolution of 0.1 Å. The cooled S-1 photomultiplier and a lock-in amplifier were used to record the laser spectrum.

Without the quarter-wave plate, the amplitude of each oscillating axial mode was unstable and the mode spectrum was not reproducible. This is due to the mode competition between the oscillating modes. Fig. 3 shows the output spectrum of the free-running laser measured at different times. The oscillating spectrum consists of multilongitudinal modes separated by 51 GHz. The mode spacing coincides with that resulting from the mode-selecting laser crystal $c/2nL$, i.e., etalon effect (c, velocity of light; n, refractive index of the crystal; L, crystal length). The longitudinal modes of the cavity, with $\Delta\nu = c/2 \times 9 = 1.67$ GHz, were not observed.

Fig. 4 shows the measured output spectrum from the laser with the quarter-wave plate at various pump powers, where w_c is the relative pump power P/P_{th}(P_{th}, threshold pump power). The output spectrum was stable and reproducible. When the quarter-wave plate was rotated in the cavity ($\theta \neq 45°$), the output spectrum changed and dual-peak spectra were observed as shown in Fig. 5.

To confirm the mode competition in the LNP laser, the pump light was chopped and the relaxation oscillation at the onset of the laser output was observed. In the free-running laser, the output varies in an uncontrolled way and shows unreproducible relaxation oscillations as shown in Fig. 6(a). This means that the amplitude and relative phases of all of oscillating modes are fluctuating as a consequence of the mode

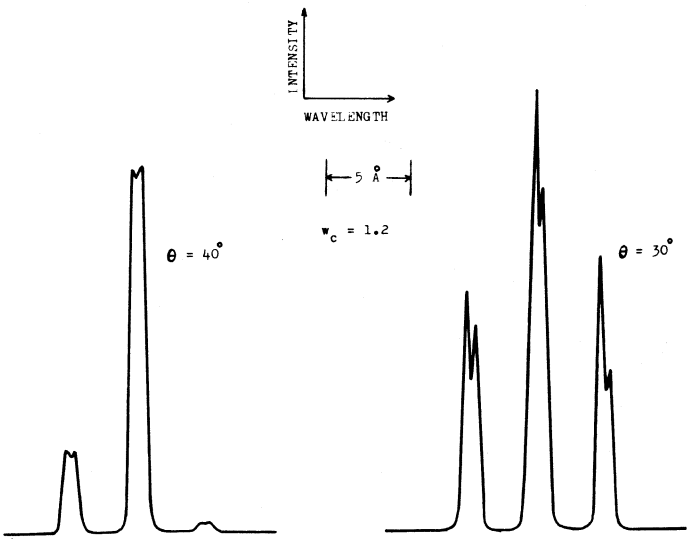


Fig. 5. Emission spectrum of the laser when the quarter-wave plate was rotated in the cavity.

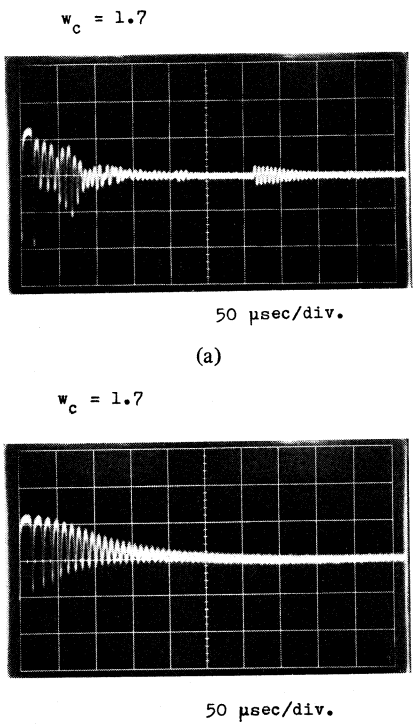


Fig. 6. Relaxation oscillations observed with an S-1 photomultiplier when the pump light was chopped. Pump pulse: width = 10 ms, duty factor = 40 percent. $w_c = 1.7$. (a) Without the quarter-wave plate. (b) With the quarter-wave plate.

competition [3]. The output of the LNP laser with the intracavity quarter-wave plate shows the reproducible ideal relaxation oscillation which can be represented by the rate equation [Fig. 6(b)]. One possible explanation for this result is that each mode in Fig. 4 is undergoing a relaxation oscillation at the same frequency and that the phases of the different modal relaxations are fixed.

The polarization eigenmodes and eigenvalues of the laser which has the intracavity polarization element and birefringence crystal have been analyzed by Carlson *et al.* [4]. The round-trip matrix of a resonator having intracavity elements is the successive product of the matrices of the elements forming the resonator [5].

The resonator matrix for the electric vectors E_c and E_b, which are polarized along the c and b axes of the LNP crystal, respectively, is given by

$$M = \begin{pmatrix} m_{11} & m_{12} \\ m_{21} & m_{22} \end{pmatrix}$$

$$= L_r \exp(\sigma_c \Delta N L) \begin{pmatrix} p^2 \cos 2\theta & -p \sin 2\theta \\ -p \sin 2\theta & -\cos 2\theta \end{pmatrix} \quad (1)$$

where L_r is the amplitude round-trip loss factor of the resonator, σ_c is the emission cross section for the c axis, ΔN is the population inversion density, $p = \exp\{(\sigma_b - \sigma_c)\Delta N L/2\}$ (σ_b, emission cross section for b axis), and θ is the angle between the fast axis of the quartz and the c axis of the LNP crystal.

The condition for stationarity is that after a *single* round trip the electric vector reproduces itself. According to the rules of matrix calculus the eigenvalues $\lambda_{1,2}$ are given by

$$\lambda_{1,2} = \frac{m_{11} + m_{22}}{2} \pm \sqrt{\left(\frac{m_{11} + m_{22}}{2}\right)^2 - (m_{11}m_{22} - m_{12}m_{21})}$$

$$= \frac{1}{2} L_r \exp(\sigma_c \Delta N L) \{(p^2 - 1)\cos 2\theta \pm \sqrt{(p^2 - 1)^2 \cos^2 2\theta + 4p^2}\}. \quad (2)$$

These eigenvalues yield the rotation dependent gain induced by the quarter-wave plate and the eigenpolarization of the resonator. The threshold population inversion density is obtained from $|\lambda_{1,2}/L_r|^2 = 1$.

Eigenpolarization components E_{cl} and E_{bl} are calculated from

$$|E_{cl}|^2 = 1/(1 + q_l^2) \quad |E_{bl}|^2 = q_l^2/(1 + q_l^2)$$

$$q_l = |(\lambda - m_{11})/m_{12}|, \quad l = 1, 2. \quad (3)$$

A typical result is shown in Fig. 7, assuming $p = 0.7$.

The power ratio of the two orthogonal modes E_b^2/E_c^2 was measured to come near to unity when θ approached to 45°. This can be explained by Fig. 7. Moreover, the power ratio of the two orthogonal modes was found to change depending on the position of the LNP crystal within the resonator. This effect may result from a combination of the localized scattering at the surfaces of the crystal and spatial hole burning [6]. In particular, the coupling coefficient between the two modes along the laser axis changes through both the self- and cross-saturation of the population inversion, since the maxima and minima of the population inversion for the two modes are spatially shifted to each other because of the difference of refractive indices for c and b axes [7].

For the case of *single* round trip ($\theta \neq 45°$), the two polarization eigenmodes are different in frequency due to the difference of the optical cavity lengths for the two modes as shown

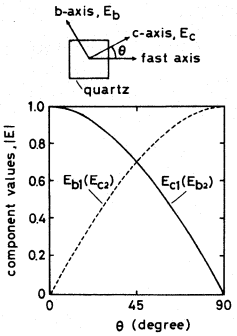


Fig. 7. Amplitudes of the two components of the two eigenvectors for the case $p = 0.7$ versus the angle between the fast axis of the quartz and the c axis of the LNP crystal.

Fig. 5 while a stable mode is formed by a *double* round trip within the resonator for $\theta = 45°$. Therefore, the two eigenmodes are degenerate in frequency in this case as shown in Fig. 4.

The adjacent axial modes for the c- or b-polarized mode couple together through the power coupling between the two orthogonal modes resulting from the spatial overlapping of the population inversion; the mode competition between axial modes would be reduced by a suitable coupling.

The quarter-wave plate also causes a higher degree of transverse mode selectivity probably due to the elimination of the beam distortion by compensating the birefringence which would be introduced by the thermal stress and stabilizes low-order modes of the unstable resonator [8], [9].

Acknowledgment

The authors wish to thank Dr. N. Niizeki and T. Yamada for valuable discussions. The LNP crystal was grown by T. Yamada and J. Nakano. They also wish to thank K. Kubodera for his fruitful discussions and comments.

References

[1] T. Yamada and K. Otsuka, "CW laser operation of $LiNdP_4O_{12}$ by transverse pumping," presented at 1975 IEEE/OSA Conf. Laser Engineering and Applications, Paper S 16.8.

[2] K. Otsuka, T. Yamada, M. Saruwatari, and T. Kimura, "Spectroscopy and laser oscillation properties of lithium neodymium tetraphosphate," *IEEE J. Quantum Electron. (Part I of Two Parts)*, vol. QE-11, pp. 330-335, July 1975.

[3] C. L. Tang, H. Statz, and G. deMars, "Spectral output and spiking behavior of solid-state lasers," *J. Appl. Phys.*, vol. 34, pp. 2289-2295, Aug. 1963.

[4] D. G. Carlson and A. E. Siegman, "Intracavity electrooptic frequency tuning, polarization switching, and Q-switching of a Nd:YAG laser oscillator," *IEEE J. Quantum Electron.*, vol. QE-4, pp. 93-98, Mar. 1968.

[5] J. Junghans, M. Keller, and H. Weber, "Laser resonators with polarizing elements—eigenstates and eigenvalues of polarization," *Appl. Opt.*, vol. 13, pp. 2793-2798, Dec. 1974.

[6] D. A. Draegert, "Selection and stabilization of longitudinal modes by spacing of laser cavity components," *IEEE J. Quantum Electron.*, vol. QE-10, pp. 476-479, May 1974.

[7] M. F. Becker, D. J. Kuizenga, and A. E. Siegman, "Harmonic mode locking of the Nd:YAG laser," *IEEE J. Quantum Electron.*, vol. QE-8, pp. 687-693, Aug. 1972.

[8] L. M. Osterink and J. D. Foster, "Experimental compensation of thermally induced stress birefringence in solid-state laser rods," presented at the IEEE Int. Electron Devices Meeting, 1969.

[9] W. C. Scott and M. de Wit, "Birefringence compensation and TEM_{00} mode enhancement in a Nd:YAG laser," *Appl. Phys. Lett.*, vol. 18, pp. 3-4, Jan. 1, 1971.

Theory of Spin-Flip Laser Modes—I: Threshold Modulation and Tuning Behavior

WILLIAM J. FIRTH, BRIAN S. WHERRETT, AND D. WEAIRE

Abstract—**Theoretical calculations of threshold intensity and output frequency, as functions of magnetic field, are presented for the InSb spin-flip Raman laser (SFRL). These are based on a numerical solution of Maxwell's equations for the case of a pump beam of Gaussian profile, and various analytical results for more approximate models. The results are used to discuss nonlinear tuning characteristics, mode jumping, and the dependence of threshold power upon beam size. These are the first calculations to include the effects of finite beam size, which are found to be quite significant and consist chiefly of a marked asymmetry of the variation of threshold power and tuning rate across each mode. This asymmetry is in qualitative agreement with recent experimental observations. The model may be readily generalized to include higher modes and extended to the case of constant input power.**

I. Introduction

As the spin-flip Raman laser (SFRL) becomes established as an instrument for high-resolution infrared spectroscopy [1], it is increasingly desirable to understand its modulation and tuning characteristics in detail. The necessary theory of the mode structure of such a laser is developed in this paper and some preliminary results are presented.

The SFRL system, as used to date, consists of a plane-parallel-sided semiconductor (InSb) cavity with a Fabry–Perot mode structure defined by natural reflectivity. It is pumped by a beam of fixed frequency laser radiation. Stimulated Raman scattering induces in the cavity a negative absorption coefficient or gain, which has its peak value at the frequency

$$\nu_s = \nu_p - h^{-1}|g^*|\beta B \tag{1}$$

where ν_p is the pump frequency, B is the magnetic field, β is the Bohr magneton, and g^* is the effective g factor of the conduction electrons. Variation of the magnetic-field strength allows a tuning of ν_s by ~70 MHz/G. The Raman gain has a linewidth [full width at half maximum (FWHM)] Γ_s, which is highly dependent upon sample free-carrier concentration and magnetic field [2]. It is now established [3], [4] that under continuous-wave operating conditions the SFRL output frequency displays some form of mode pulling and hopping as the applied magnetic field is varied.

The following questions present themselves.

1) For a fixed magnetic field and fixed pump laser focusing, what are the frequency and spatial mode structure of the Stokes field in the cavity when the pump power is just sufficient to induce Stokes cavity oscillation?

2) What is this threshold pump power?

3) How are the frequency and mode structure affected by increasing either the focusing or the pump power?

4) As the threshold is magnetic-field dependent, for fixed pumping conditions the magnetic-field tuning varies the amount by which threshold is exceeded. What is the resultant SFRL tuning behavior and what is the associated output power modulation?

5) Does laser action always involve the lowest order transverse cavity mode of the Stokes radiation or do higher order modes operate preferentially, or perhaps simultaneously? For example, as one axial mode "hops" to the next, is there a succession of intermediate jumps involving high-order transverse modes?

6) In what way can we exploit the experimental variables (sample reflectivity, length and free-carrier concentration, and pump laser characteristics) in order to modify the SFRL tuning characteristics to our advantage?

The purpose of the present paper is to establish a theoretical model of the SFRL system which may be used to answer the aforementioned questions.

The major innovation of this paper is the exact treatment of *diffraction* in the problem of stimulated Raman scattering in a plane-parallel cavity for a pump laser beam of finite cross section. We show that this significantly alters the SFRL output characteristics otherwise predicted. The tuning behavior becomes nonlinear, there is an asymmetry in the output power modulation, and we can predict a pump power dependence of the SFRL frequency.

Relevant experimental investigations have been made by Brueck and Mooradian [3] and Mackenzie *et al.* [4]. The former authors have presented single-mode tuning curves for various sample free-carrier concentrations and magnetic-field regions. They are able to explain qualitatively the degrees of mode pulling and hopping observed, by invoking their experimental data for the magnetic field and frequency dependences of the natural cavity mode and Raman gain frequencies and linewidths [2], [3], and using a model based on the plane-wave approximation. They are unable to explain the nonlinear behavior obtained for the fine tuning within a mode since, as we shall see, this is not found in such a model. They do not attempt to discuss the output power levels of the system. Their analysis is based on the expression

$$\nu = \frac{\nu_c\Gamma_s + \nu_s\Gamma_c}{\Gamma_s + \Gamma_c} \tag{2}$$

which gives the cavity oscillation frequency that would be obtained under plane-wave pump and output conditions, that is, when diffraction is ignored. The parameters ν_c and Γ_c are the natural cavity-mode frequency and bandwidth of a given longitudinal mode; for a sample of length L, with reflectivity $\mathcal{R}$, absorption coefficient α, and refractive index n

$$\nu_c = qc/2Ln \tag{3a}$$

$$\Gamma_c = (\alpha L - \ln \mathcal{R})\, c/2\pi Ln = \alpha' c/2\pi n. \tag{3b}$$

Manuscript received July 11, 1975; revised December 3, 1975.

The authors are with the Department of Physics, Heriot-Watt University, Edinburgh, Scotland.

Here q is an integer which takes values, in the present case, of the order of 10^4, and α' is the effective absorption coefficient for the complete cavity. To avoid the possibility of confusion apparent in some papers on this subject, we define both frequencies and linewidths in hertz.

In principle, it is possible to include in Γ_c a term which takes approximate account of the *losses* due to diffraction. To do so one must presuppose a value or expression for the spot size of the cavity modes. However, in the case of the SFRL the spot size is itself determined primarily by diffraction, and the self-consistent treatment used here leads to effects which are qualitatively different to those that would be predicted using an effective Γ_c.

In the experiments carried out by Mackenzie *et al.* [4] similar tuning characteristics to those reported by Brueck and Mooradian are observed. In addition, these authors present data for output power levels. The modulation of output power within each mode is found to have significant asymmetry with respect to the mode center. Again, this is inconsistent with the simple plane-wave theory.

In the present paper we confine ourselves to the threshold situation in which the Stokes field becomes vanishingly small. We shall determine an asymmetry, across a mode, of the pump power at threshold and are therefore able to infer a corresponding asymmetry in the output power. In order to determine the precise output power modulation, it would be necessary to treat for SFRL action above threshold. Theoretical treatments of this problem [5], [6] have been confined to the geometric optics approximation in which the spatial cross section of the pump beam is included but diffraction is neglected. In future work we intend to adapt existing saturation theories to include diffraction in order to calculate the output power modulation in a manner consistent with the present threshold calculations.

We calculate here the detailed mode pulling and hopping as a function of magnetic field, under pumping conditions (focusing and power) that are just sufficient to induce SFRL action. These conditions are also determined by our calculations, as are the spatial mode structures of the Stokes field. As far as the tuning is concerned, we are interested in deviations of the "active" cavity-mode oscillation frequency from either ν_c or ν_s and from the frequency determined by the plane-wave approximation. That is, we do not attempt to include explicitly the magnetic field and frequency dependence of the sample parameters (n, g^*, and Γ_s) but assume that such dependences are accounted for in defining ν_c and ν_s [2], [3].

II. The Theoretical Model

A proper study of the role of diffraction requires an investigation of the Maxwell's equations and the divergence equation for the problem

$$\nabla \wedge \nabla \wedge \boldsymbol{E} + \frac{1}{c^2}\,\epsilon \cdot \ddot{\boldsymbol{E}} = -\frac{4\pi}{c^2}\,\ddot{\boldsymbol{P}}^{\mathrm{NL}} \tag{4a}$$

$$\nabla \cdot (\epsilon \cdot \boldsymbol{E}) = -4\pi\, \nabla \cdot \boldsymbol{P}^{\mathrm{NL}}. \tag{4b}$$

Defining the x direction as that of the applied magnetic field, the linear dielectric tensor ϵ, related to absorption coefficient and refractive index in the usual manner, has the form

$$\epsilon = \begin{bmatrix} \epsilon_{xx} & 0 & 0 \\ 0 & \epsilon_{yy} & \epsilon_{yz} \\ 0 & -\epsilon_{yz} & \epsilon_{yy} \end{bmatrix}. \tag{5}$$

$\boldsymbol{P}^{\mathrm{NL}}$ represents any nonlinear polarization source. In particular, we are interested in that at the Stokes cavity oscillation frequency due to stimulated Raman scattering.

$$\boldsymbol{P}^{\mathrm{NL}} = \chi\, [(\boldsymbol{j} - i\boldsymbol{k}) \wedge \boldsymbol{E}_p]\ [(\boldsymbol{j} + i\boldsymbol{k}) \cdot \boldsymbol{E}_p^* \wedge \boldsymbol{E}]. \tag{6}$$

Here χ is the nonlinear Raman susceptibility and $\boldsymbol{E}_p$ and $\boldsymbol{E}$ are the pump and Stokes radiation fields.

We consider only the conventional configuration for SFRL operation. Collinear propagation of the pump and Stokes beams is obtained (in the z direction) with the pump field polarized in the x direction. The dominant and only direct nonlinear Stokes source term is in the y direction, perpendicular to the magnetic field, and we keep only this term.

The nondiagonal terms in ϵ are neglected in the treatment of diffraction, although their effect on refractive indices appears automatically in the definition of ν_c.

We neglect multiple Stokes and anti-Stokes fields [7], [8]. We can also neglect pump depletion herein as the Stokes field is vanishingly small at threshold.

Equation (4) now reduces to

$$-\nabla^2 E_y - \left(\frac{2\pi\nu}{c}\right)^2 (\epsilon + 4\pi\chi |E_{px}|^2)\, E_y = 0 \tag{7}$$

written in such a way that the Raman term appears as a correction to the linear dielectric constant.

We consider only the resonant susceptibility, so that

$$\chi = \chi^R \left(\frac{\Gamma_s/2}{(\nu - \nu_s) + i\Gamma_s/2}\right). \tag{8}$$

The Raman gain is manifested in the negative value of the imaginary part of χ. Mode pulling in the sample cavity is associated with the real part, for it describes a change in the effective linear refractive index in the cavity. The cavity oscillation frequencies (2) are obtained by using this changed refractive index (n') self-consistently, in the equation $\nu = qc/2Ln'$. We are interested in this plane-wave result only as a limiting case; in general, the pump beam intensity varies transversely across the cavity and in consequence so does n'. This variation of the effective refractive index tends to focus the Stokes radiation for frequencies ν greater than ν_s, while for ν less than ν_s there is a defocusing effect.

The pump radiation is generally considered to be of Gaussian spatial cross section, of spot radius w constant down the sample length:

$$|E_{px}|^2 = |E_p|^2 \exp\{-2(x^2 + y^2)/w^2\}.$$

The resulting mathematical problem is now soluble using separation of variables in cylindrical coordinates:

$$E_y = R(\rho) \exp[-im\phi] \exp[iKz]. \tag{9}$$

Here m is an integer, K is a complex propagation constant, and the radial function $R(\rho)$ satisfies the equation

$$\left[\frac{1}{\rho}\frac{\partial}{\partial\rho}\rho\frac{\partial}{\partial\rho}-\frac{m^2}{\rho^2}-K^2+\left(\frac{2\pi\nu}{c}\right)^2(\epsilon+4\pi\chi|E_p|^2 \cdot \exp\{-2\rho^2/w^2\})\right]R(\rho)=0. \tag{10}$$

The phase change over a full path length ($2L$) in the cavity must be an integral multiple of 2π. Thus the real part of K equals $q\pi/L$. The imaginary part of K describes the net gain in the cavity, which must balance the transmission losses at the sample ends,

$$\mathrm{Im}K=\frac{1}{2L}\ln\mathcal{R}. \tag{11}$$

It is interesting to note that for a plane-parallel-sided cavity the preceding separation of variables, which removes from the problem any variation of spot size along the propagation direction, is an exact treatment. The point is that such solutions are the only ones that can exist in the steady state; they are "matched" solutions for the cavity [10]. The only stable situation is the one discussed; an arbitrary mode will tend to this matched form after very few cavity passes [10].

A change of variables, $\rho \rightarrow Lr/(q\pi)^{1/2}$, then places (10) in dimensionless form, suitable for computation:

$$\left[\frac{1}{r}\frac{\partial}{\partial r}r\frac{\partial}{\partial r}-\frac{m^2}{r^2}+\left(-X+i\alpha'L+\frac{\alpha'Lt\exp\{-\gamma r^2\}}{\beta(X_0-X)+i}\right)\right]\cdot R\left(\frac{Lr}{\sqrt{q\pi}}\right)=0. \tag{12}$$

The parameters X_0 and X are defined by the deviations of ν_s and ν, respectively, from the frequency ν_c of the natural mode from which the mode under consideration is derived.

$$\nu_s=\frac{[q-(X_0/2\pi)]\,c}{2Ln} \qquad \nu=\frac{[q-(X/2\pi)]\,c}{2Ln}. \tag{13}$$

Magnetic-field tuning is therefore investigated by obtaining solutions for X as X_0 is varied. A given mode has a lower threshold than those derived from other values of q only over a range of 2π extent, such that the thresholds at the ends of this range are equal.

α' has already been defined by (3b). The remaining parameters are

$$\beta=\frac{c}{2\pi\Gamma_s nL}=\frac{1}{\alpha'L}\frac{\Gamma_c}{\Gamma_s} \qquad \gamma=\frac{2L^2}{q\pi w^2}. \tag{14}$$

$\beta\rightarrow 0$ and ∞ are therefore the limiting cases for which the cavity modes are well defined with respect to a broad Raman gain and vice versa. One therefore expects tuning to be along the natural Stokes frequency ($X=X_0$) for $\beta\rightarrow\infty$. In studying the case of finite β, we make the arbitrary choice $\beta=1$ for our calculations. In the limit $\gamma\rightarrow 0$ the pump field is effectively plane wave and tuning should be expressed by (2) so that, in particular, $X=(X_0/2)$ for $\beta=1$. It may be noted that γ^{-1} is the Fresnel number for a cavity of cross section πw^2, that is, of the "area" of the pump beam.

The factor t represents the pump intensity required to achieve threshold and is determined as a solution to (12).

$$t=\frac{1}{\alpha'L}\frac{\pi q}{n^2}4\pi\chi^R|E_p|^2=\frac{g}{\alpha'} \tag{15}$$

where g is the Raman gain at the center of the pump beam and at frequency ν_s. The parameter t is the amount by which threshold intensity at the center of a Gaussian pump beam exceeds the minimum threshold (plane-wave) intensity. There is a set of solutions to (12) for each value of m.

III. Plane-Wave Pumping

Equation (12) becomes trivial in the plane-wave limit $\gamma\rightarrow 0$. The solution to (12) yields

$$\alpha'Lt-\alpha'L-\beta X(X_0-X)=0 \tag{16a}$$

$$X+\alpha'L\beta(X-X_0)=0. \tag{16b}$$

Equation (16b) is precisely equivalent to (2); it defines the mode-*pulling* of a single axial mode. Equation (16a) then gives the threshold as a function of tuning and therefore determines the absolute positions of the mode *hops;* these positio[illegible] have not previously been discussed in relation to the SFR[illegible] In frequency terms

$$t=1+\left[\frac{2(\nu_s-\nu_c)}{\Gamma_s+\Gamma_c}\right]^2. \tag{17}$$

t takes its minimum value of unity, as expected, when the Stokes frequency ν_s falls on any natural cavity-mode frequency ν_c. Here the mode hop occurs halfway between the passive mode frequencies, where

$$t=t_{\max}=1+\left[\frac{\Delta\nu_c}{\Gamma_c+\Gamma_s}\right]^2. \tag{18}$$

$\Delta\nu_c$ is the separation of the passive modes,

$$\Delta\nu_c=\frac{c}{2Ln}=\Gamma_c\frac{\pi}{\alpha'L}. \tag{19}$$

The magnitude of the mode hop $\Delta\nu$ is

$$\Delta\nu=\Delta\nu_c\Gamma_s/(\Gamma_c+\Gamma_s). \tag{20}$$

As shown in Fig. 1, as the output frequency is tuned the threshold is modulated by the cavity-mode structure. The resulting modulation of the output intensity (I_s) may be obtained by accounting for saturation [5]. For an input intensity a factor p above the minimum threshold

$$I_s=I_L(1-t/p) \tag{21}$$

where I_L is the limit to the output intensity, determined by the rate at which electrons become available for the spin-flip mechanism [5].

For device applications one obviously wants to minimize both the mode hop and mode modulation. It is a striking feature of (18) that the modulation in the continuous tuning region is greatest when the Raman gain profile is very narrow with respect to the cavity bandwidth $\Gamma_s \ll \Gamma_c$, even though the mode pulling is least in this situation. Reduction of both the output modulation and mode pulling can be achieved by use of antireflection coatings to lower the cavity finesse.

IV. Solution for a Gaussian Pump Profile

In this section we shall restrict solutions to (12) to the case $\Gamma_c=\Gamma_s$, $\alpha'L=1$; that is, $\beta=1$. We look only for $m=0$ modes, which now satisfy the equation

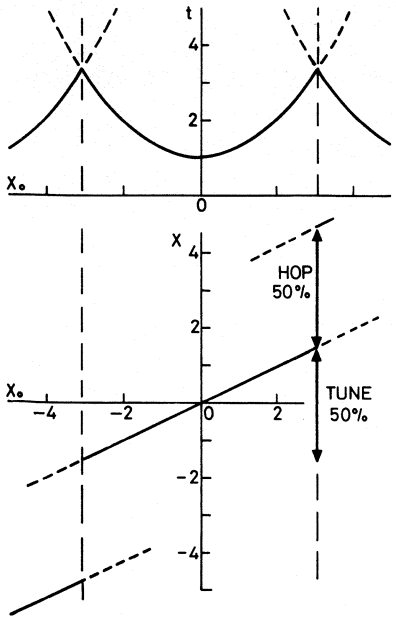


Fig. 1. SFRL threshold and tuning for a plane-wave pump beam for the case of equal Raman gain and cavity linewidths ($\Gamma_S = \Gamma_C$). (Top) normalized SFRL threshold intensity t versus magnetic field (represented by X_0). Minima occur wherever the Stokes frequency coincides with a passive cavity mode. The cusps mark the crossover from one mode to the next ($q \rightarrow q + 1$). (Bottom) SFRL tuning, (oblique lines) frequency shift X versus magnetic field X_0. The dimensionless parameters t, X_0, and X are defined in Section II.

$$R'' + r^{-1}R' + (-X + i + t(X_0 - X + i)^{-1} \exp\{-\gamma r^2\})R = 0. \tag{22}$$

Numerical solutions are obtained for various magnetic-field strengths (represented by X_0) and pump spot sizes (γ).

The problem is to find real t and X such that (22) has a physically acceptable solution, i.e., one which obeys the additional boundary conditions that R is finite everywhere, falling to zero as r tends to infinity. We normalize R to unity at the origin.

$$\left.\begin{aligned} R &= 1 \\ R' &= 0 \end{aligned}\right\} \text{at } r = 0. \tag{23}$$

The equation may be integrated by straightforward numerical methods starting from $r = 0$, for chosen values of X and t. By numerical integration, values of t and X can be found for given X_0, such that the solutions decay exponentially as $r \rightarrow \infty$. We find in this way a solution having the least threshold parameter t which we will designate the $n = 0$ solution, and a sequence of solutions of higher threshold ($n = 1, 2, 3, \cdots$) as expected on physical grounds.

In Fig. 2 we show the $n = 0$ mode structure for typical values of the input parameters ($\gamma = 1$ implies a spot size of the order of 70 μm). The modulus and phase are, respectively, exponentially decreasing and linear in r as $r \rightarrow \infty$.

Much of the physical interest of this problem is centered on the dependence of t and X on X_0, as explained in Section II. Results for the threshold and tuning behavior are shown in Figs. 3 and 4 for the $n = 0$ mode.

The most obvious feature of the results for the threshold is that t is considerably greater than 1, which is not surprising

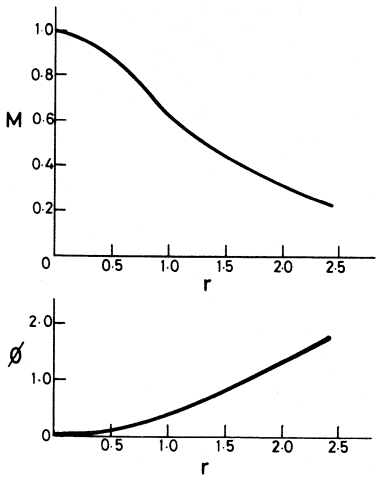


Fig. 2. Transverse mode structure of a typical lowest order Stokes mode. Modulus M and phase ϕ of the field amplitude (R) are plotted as functions of radius r. The calculation is for case $\nu_S = \nu_C$, $\Gamma_S = \Gamma_C$ and a Gaussian pump beam of radius $w = (2L^2/q\pi)^{1/2}$ which corresponds to $\gamma = 1$, where γ is defined in dimensionless form in Section II.

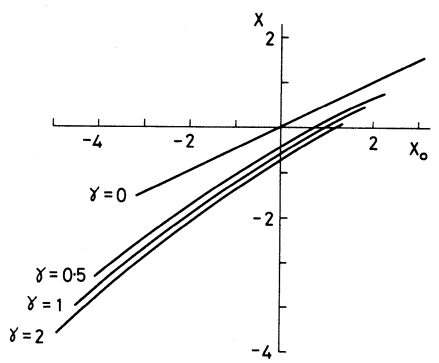


Fig. 3. SFRL tuning behavior for a Gaussian pump beam. Frequency shift X versus magnetic field X_0 is plotted for the case $\Gamma_S = \Gamma_C$ and various beam spot sizes. The spot size is proportional to $\gamma^{-1/2}$ as defined in (14).

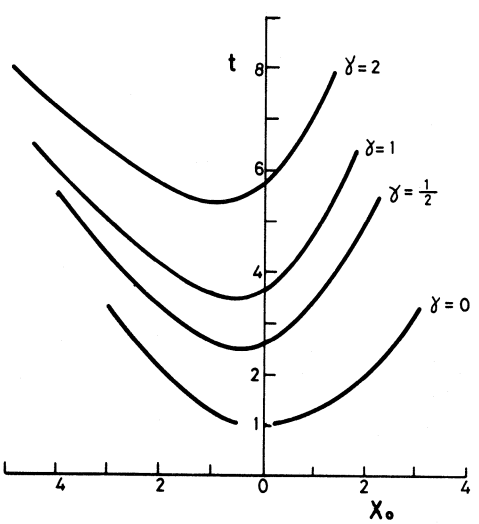


Fig. 4. SFRL normalized threshold intensity t versus X_0 computed for the same conditions as Fig. 3. Mode hops occur at the end points of the curve where $\Delta X_0 = 2\pi$ with $\Delta t = 0$ (compare Fig. 1).

since we require the gain to balance the loss over the whole Stokes mode, which includes regions where exp $[-\gamma r^2]$ is much less than unity. The other obvious feature is not so easy to explain – t is now an asymmetrical function of X_0 with its maximum shifted to low field (negative X_0) by an amount which increases with γ.

The tuning curve is shifted to high frequency (low X) vis-à-vis the plane-wave curve, which can be explained as a typical "waveguide" effect due to the confinement of the mode within a finite cross section.

The most interesting feature of the curves, however, is that they are bent: the tuning rate varies across the mode from around the plane-wave rate ($dX/dX_0 = 0.5$) at the high field end to approach the "spontaneous" rate ($dX/dX_0 = 1$) at low fields. As a result the tuning range is greater, with a "tune-to-hop" ratio of 70:30 as against 50:50 in the plane-wave limit.

The way in which this nonlinear tuning comes about is not yet entirely clear, but we give some qualitative arguments in the Conclusion after the analytic parabolic model has been discussed in Section V. It is worth noting, however, that experimental tuning curves [3], [4] are also nonlinear, with the bend in the same sense as in Fig. 3. Uncertainties in the precise experimental values of such parameters as Γ_s and γ, however, preclude a conclusive quantitative test of this explanation at this stage.

The asymmetry of t (Fig. 4) can be regarded as arising from the fact that $(X - X_0)$ is much smaller at the low field end of the mode, making the gain denominator more resonant, and hence requiring a lower pump intensity to make the gain offset the losses.

It may also be noted that we predict some "spot-size tuning," i.e., focusing down the pump beam increases the Stokes frequency. The effect is not large–around 50 MHz for doubling γ.

We plot in Fig. 5 the minimum threshold power level $t_{\min}/\gamma$ for a given spot size. As expected, in the plane-wave limit of zero γ, $t_{\min}$ falls to unity at the position $X_0 = 0$, $X = 0$. The opposite limit is an awkward one to treat analytically. By examining instead the problem in which the pump is a delta function at r_0 and letting r_0 tend to zero, it is possible to find the limiting behavior of t and X as $\gamma \to \infty$:

$$t/\gamma \longrightarrow 4/\pi \text{ at } X \sim -\pi^{-1} \ln \gamma. \tag{24}$$

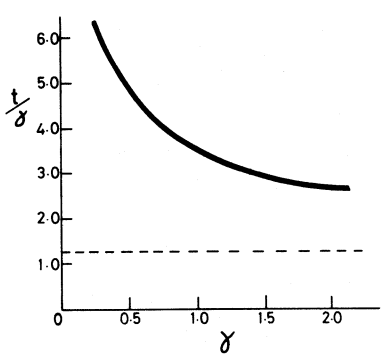


Fig. 5. Minimum threshold power t/γ versus spot-size parameter γ for the same conditions as Fig. 3. Note that t/γ asymptotes to a *finite* value in contrast to the geometric-optics approximation (γ^{-1}).

This does not, of course, prove that the same limiting value applies for t minimized with respect to X_0, but results obtained so far are consistent with this limiting value. It can be seen that, in general, reducing the pump spot size (increasing γ) reduces the power threshold of the SFRL. However, this reduction ceases to be particularly beneficial beyond $\gamma \sim 2$ (50 μm). Moreover, in the real situation tight focusing will eventually lead to detrimental effects not considered here (such as increasing Γ_s).

V. The Parabolic Approximation

In this approximation we replace the Gaussian profile with a parabolic function, so that (22) becomes

$$R'' + r^{-1}R' + (-X + i + t(X_0 - X + i)^{-1}(1 - \gamma r^2))\, R = 0. \tag{25}$$

While this has the advantage of an analytic solution, it has the somewhat unphysical characteristic of negative pump intensity for large r. If the parabolic form is regarded as an approximation to the Gaussian of Section IV, it is to be expected that it will become increasingly inadequate for the higher modes. This is because such modes have their maximum intensity where the approximation is a poor one, at large r. However, the parabolic model gives results for $m = n = 0$ remarkably similar to those of the Gaussian model–indeed we shall arrive at the surprising conclusion that the two problems are intimately related. The solution is set out in the following for $n = 0$. (It is closely related to the familiar problem of a two-dimensional harmonic oscillator in quantum mechanics.)

The solution takes the form of a Gaussian beam

$$R = \exp(-\lambda r^2) \tag{26}$$

where

$$\lambda = x - iy.$$

Given γ and y one may solve for x, X, X_0, and t by means of the following equations:

$$x = \frac{1}{8y}\gamma(4y + 1) \tag{27a}$$

$$-X = 4x + 4\gamma^{-1}(x^2 - y^2) \tag{27b}$$

$$X_0 = X + (x^2 - y^2)/2xy \tag{27c}$$

$$t = 4\gamma^{-1}\langle (x^2 - y^2)(X_0 - X) + 2xy \rangle. \tag{27d}$$

Results for a particular X_0, if required, can be found by interpolation. One attractive feature of this model is that the minimum value of t (for fixed γ) can be found analytically. It is given by

$$t_{\min} = \frac{(1 + 4y)(1 + 2y)^2}{(1 + y)(1 + 3y)}, \qquad \gamma = \frac{8y^2}{1 + 4y}\left(\frac{1 + 3y}{1 + y}\right)^{1/2} \tag{28}$$

and is closely similar to the Gaussian result shown in Fig. 5. It is worthy of note that in this case t/γ tends to a finite value $(8/3\sqrt{3})$ as γ tends to infinity, while for small γ, $t_{\min} \sim 1 + (2\gamma)^{1/2}$ (a qualitative form which we suspected but were unable to verify analytically in the Gaussian case).

The Stokes intensity profile is the simple Gaussian exp

$[-2xr^2]$. The spot size $\sim x^{-1/2}$ is zero in the limit $X_0 \to +\infty$, and asymptotes to the pump beam radius as $X_0 \to -\infty$. It is obvious by comparison with the results of the previous section that this is the $n = 0$ mode. Furthermore, the higher order modes may similarly be obtained in the form of Hermite Gaussians, analogous to the solutions of the harmonic oscillator problem.

Fig. 6 compares typical results for the parabolic and Gaussian models. Surprisingly, it is found that the results are not only similar but essentially *identical* if displaced according to $X \to X + \gamma$, $X_0 \to X_0 + \gamma$. This remarkable result can be derived theoretically by means of first-order perturbation theory. It is therefore not exact but is an excellent approximation. Furthermore, this transformation does not change any of the readily measured experimental quantities related to the variation of X and t with X_0!

The analytic solution of the parabolic model, suitably interpreted, is thus a reliable guide to the understanding of at least some aspects of the more difficult Gaussian model.

VI. Variation of the Spontaneous Linewidth

It is found experimentally that the spontaneous linewidth Γ_s can be strongly dependent on magnetic-field strength (2). For an InSb sample of concentration 10^{21} m^{-3} free carriers, Γ_s varies by a factor of 40 in the range 0–10 kG. It is therefore essential in practice to generalize the solution to (12) to the case $\Gamma_s \neq \Gamma_c$. This is simply achieved by the substitution

$$\frac{\Gamma_c}{\Gamma_s}(X_0' - X) = (X_0 - X). \tag{29}$$

Having obtained solutions for R and the parameters t and X for a given X_0 (fixed magnetic field) under the restriction $\Gamma_s = \Gamma_c$, these solutions apply to an arbitrary Γ_s for the magnetic field represented by X_0'. The result of (29) is simply to narrow or broaden the t versus magnetic-field curve for Γ_s less than or greater than Γ_c, respectively. Similarly, the tuning curve approaches or separates from $X = X_0$, as in the plane-wave model. The crossover point $X = X_0$ is invariant (although it may be outside the actual tuning range). Since the mode hops now occur at intervals of 2π in X_0', the depth of modulation and size of hop is altered. Fig. 7 shows the tuning and threshold modulation for the cases $\Gamma_s = 10\,\Gamma_c$ and $0.1\,\Gamma_c$, obtained from the parabolic model for the condition $\gamma = 1$, $\alpha' L = 1$. The characteristics are compared with the plane-wave case in Table I. In particular, for the lower Γ_s/Γ_c values, we can see that the finite spot size of the pump is beneficial in reducing both the mode pulling and modulation.

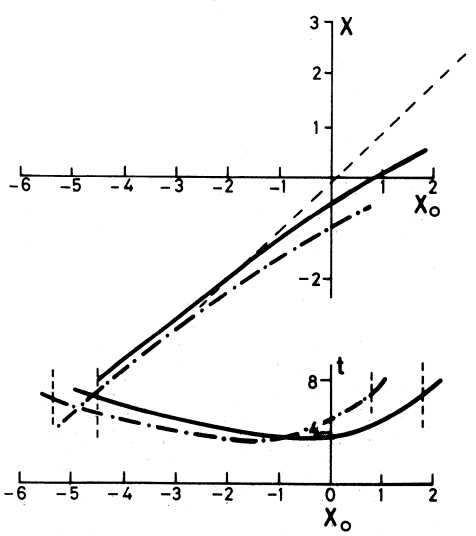


Fig. 6. Comparison of analytic results for the parabolic model (chain curves) and computed results for the Gaussian model (full lines). The threshold t and tuning x, versus X_0 for $\gamma = 1$. Note that the curves are closely similar but displaced from each other.

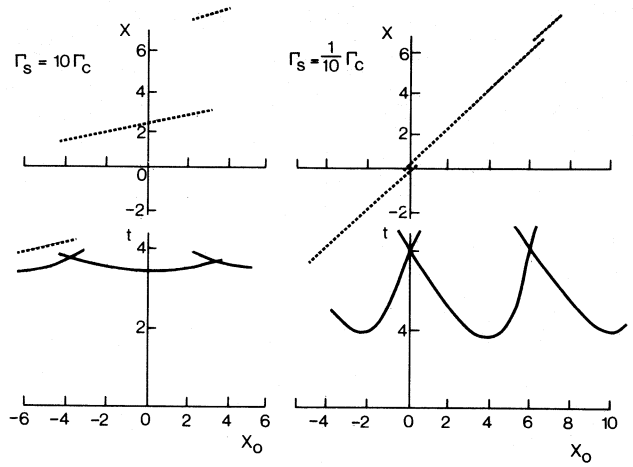


Fig. 7. Threshold and tuning behavior for $\Gamma_s = 10\Gamma_c$ and $\Gamma_s = 0.1\Gamma_c$ for The parabolic model, with $\gamma = 1$. This figure demonstrates the significance of the ratio of the Raman gain and cavity linewidths in determining the characteristics.

TABLE I

Model	Plane-wave ($\gamma \to 0$)			Parabolic ($\gamma = 1$)		
Γ_s/Γ_c	0.1	1	10	0.1	1	10
Fraction of frequencies tuned over	0.91	0.5	0.1	0.97	0.71	0.2
t_{max}/t_{min}	9.2	3.5	1.1	2.5	1.9	1.1

Finally, it is interesting to note that the "γ-shift" connection between the Gaussian and parabolic models discussed in Section V is preserved under the transformation (29) and thus holds for all values of the gain linewidth.

VII. Discussion and Conclusion

In this paper we have presented the first extensive discussion of the active cavity modes of the SFRL, taking account of its particular characteristics, namely, the gain is tunable, its linewidth can be considerably less than the cavity-mode spacing, and the cavity has low finesse—the photon lifetime is typically only a single pass. We have given a full analysis of the problem from first principles, leading via various approximations to a complex modification of Bessel's equation whose parameters determine the thresholds and tuning behavior. This equation

must be solved numerically in general, and we have presented some preliminary computer results for physically relevant situations.

We have also found that the equation is analytically solvable for a parabolic intensity profile, and that the results are similar to those of the corresponding Gaussian profile. Indeed we have found a close mathematical connection between the two problems.

The most important result of our models in comparison with the plane-wave model (for which we have given a fuller and more general treatment than previously available) is the noticeable asymmetry in the threshold and tuning rates across each Stokes mode, qualitatively similar to those observed. There is an asymmetry built into the finite beam size case which is absent from the plane-wave model.

A tentative explanation of these results may be developed as follows. It is to be expected that the tuning curve, when compared to that of the plane-wave case, will be shifted to lower X (higher frequency) on account of the finite transverse size of the mode. There is an additional effect, however, which is due to the necessity to balance gain against loss. In the limit of large positive X_0 (high magnetic-field strength) for which $X \ll X_0$, refraction has a *focusing* effect and the mode is confined well within the pump beam, but in the opposite limit of large negative X_0 the mode is of larger extent than the beam. In the latter case the gain varies strongly with defocusing. Consider $X_0 - X$ (the departure from the Stokes resonance) in the denominator of the Stokes term as our "input parameter" rather than X_0. A small increase of $X_0 - X$ produces an increase in the mode size, which in turn necessitates a larger value of t to balance gain against loss. This in turn increases the defocusing, enlarges the mode, and so on. Thus t and X should vary *strongly* with $X_0 - X$ in this regime, which means that $X_0 - X$ should be *constant* as a first approximation.

These arguments suggest a tuning rate tending to that of the plane-wave model as $X \to \infty$ and tending to the (higher) *spontaneous* tuning rate as $X \to -\infty$, and hence they explain the curvature of the tuning curve which is predicted by the calculations.

The analytic solution of the parabolic model gives a tuning rate which is consistent with the previous reasoning; $(dX/dX_0) \to [\Gamma_c/(\Gamma_s + \Gamma_c)]$ and 1 in the two limits, respectively.

At this point it is worthwhile to discuss how far we have gone in answering the questions posed in the Introduction. Questions 1) and 2) have been the main subject matter of the paper. We have shown that diffraction effects severely limit the advantage of focusing down the pump spot size. The effect of increasing the pump power above threshold is, however, of major importance: it is, of course, the practical situation. The problem is complicated, however, because for finite Stokes power the gain is reduced by spin saturation and pump depletion. Saturation is dominant in much recent high-resolution CW SFRL work. One may formulate a modified (nonlinear) mode equation to handle this problem, and a full treatment of the saturation problem is being undertaken. We can only affirm, for the present, that *power tuning* does exist within such a model, that is, the tuning curve moves with pump power. We do not expect this effect to be very large—typically a few hundred megahertz—but it will alter the detail of the tuning curves, in particular the nonlinearity of the tuning rate (tuning curves are obtained experimentally at fixed pump power, not at threshold).

We also defer the discussion of the influence of higher order modes [question 5)]. The problem is a straightforward generalization of the cases considered, and the parabolic approximation again yields an analytic solution. We shall also have to consider the problem of mode overlap—do both modes operate simultaneously in the neighborhood of a mode hop?

Clearly, the practical situation has many dimensions that we are yet to explore. However, the idealized model treated in this paper contains, we believe, important aspects of the problem and should provide a foundation for further theoretical investigations which should eventually be of practical importance. Even at the present preliminary stage we have arrived at a reasonable explanation of observed asymmetries in output power modulation and tuning rate.

Since submission of this paper, D. C. Hanna has kindly brought to our attention previous work [10]-[12] on the propagation of Gaussian beams in media with parabolic gain and/or dispersion profiles. Our solution for the oscillation mode in the parabolic approximation corresponds directly to the case of the stationary complex beam parameter in the references mentioned. The main objective of our work, however, has been a study of threshold pump intensities and tuning behavior versus magnetic field; i.e., we have concentrated on the frequency and threshold of the modes whereas the earlier authors were mainly interested in mode spot sizes and phase-front curvatures. Further, in order to tackle the relationship between the parabolic and Gaussian profiles and to take account of saturation as the pump power goes above threshold, we have developed a novel perturbation-theory approach which may well have applications to the propagation of Gaussian beams.

Acknowledgment

The authors wish to thank S. D. Smith for posing many of the questions which we have tried to answer, and P. G. Harper, R. B. Dennis, and H. Mackenzie for helpful discussions. They also wish to acknowledge the Science Research Council for assistance with backup experimental work.

References

[1] a) R. J. Butcher, R. B. Dennis, and S. D. Smith, "The tunable spin-flip Raman laser, II. Continuous wave molecular spectroscopy," *Proc. Roy. Soc. A* (London), vol. 344, pp. 541-561, Aug. 1975.
b) C. K. N. Patel, "Spin-flip Raman laser and applications," in *Proc. Int. Conf. Laser Spectroscopy*. New York: Plenum, June 1973, pp. 471-491.
c) S. D. Smith, C. R. Pidgeon, R. A. Wood, A. McNeish, and N. Brignall, "Kilowatt spin-flip outputs in the 5 μm region. Application to chemical spectroscopy and resonant non-linear mixing," in *Proc. Int. Conf. Laser Spectroscopy*. New York: Plenum, June 1973, pp. 523-532.

[2] S. R. J. Brueck and A. Mooradian, "Spontaneous spin-flip Raman linewidth and non-linear processes in InSb," *Opt. Commun.*, vol. 8, pp. 263-266, July 1973.

[3] ——, "Frequency stabilization and fine-tuning characteristics of a CW InSb spin-flip laser," *IEEE J. Quantum Electron.*, vol. QE-10,

pp. 634–642, Sept. 1974.
[4] H. Mackenzie, S. D. Smith, and R. B. Dennis, "Tuning and mode characteristics of the cw InSb spin-flip Raman laser determined by use of a Fabry–Perot interferometer," *Opt. Commun.*, vol. 15, pp. 151–156, Oct. 1975.
[5] B. S. Wherrett and W. J. Firth, "Spin saturation and pump depletion in continuous spin-flip Raman oscillation," *IEEE J. Quantum Electron.*, vol. QE-8, pp. 865–868, Dec. 1972.
[6] S. Y. Yuen, B. Lax, and P. A. Wolff, "Theory of travelling wave electronic Raman lasers—Stokes-anti-Stokes coupling in the steady state," *Phys. Rev. A*, vol. 10, pp. 416–434, July 1974.
[7] B. S. Wherrett, "Stokes-anti-Stokes spin-flip cavity oscillation," *Opt. Commun.*, vol. 6, pp. 402–406, Dec. 1972.
[8] M. A. Guerra, S. R. J. Brueck, and A. Mooradian, "Gradient-field permanent-magnet spin-flip laser," *IEEE J. Quantum Electron.* (Corresp.), vol. QE-9, pp. 1157–1159, Dec. 1973.
[9] M. Abramowitz and I. A. Segun, Ed., *Handbook of Mathematical Functions*. New York: Dover, 1965.
[10] H. Kogelnik, "On the propagation of Gaussian beams of light through lenslike media including those with a loss or gain variation," *Appl. Opt.*, vol. 4, pp. 1562–1569, 1965.
[11] L. W. Casperson and A. Yariv, "Gain and dispersion focussing in a high gain laser," *Appl. Opt.*, vol. 11, pp. 462–466, 1972.
[12] L. W. Casperson, "Mode stability of lasers and periodic optical systems," *IEEE J. Quantum Electron.*, vol. QE-10, pp. 629–634, Sept. 1974.

Rotation of Polarization Axis of Injection Lasers with Viewing Direction

HENRY S. SOMMERS, JR., AND DWIGHT O. NORTH, FELLOW, IEEE

Abstract—**It is shown theoretically that in lasers with box modes and polarization determined by facet reflectivity, the axis of polarization rotates with viewing direction. For thin double-heterojunction (DHJ) cavities, the angle ρ between the junction plane and the E field of the radiation depends on the angles θ and ϕ in the junction plane and transverse to it, $\rho \approx 10^{-2}\theta\phi$ in degrees. It is suggested that this behavior is a useful test for control of polarization by facet reflection. Measurements show the relation is followed in wide sawed lasers with good box modes prepared from a thin DHJ wafer and in a narrow stripe laser from the same wafer. A second narrow stripe laser from the wafer and a single-heterojunction (SHJ) cavity have no such dependence. Qualitative discussion of the measurements reveals information about polarization and mode properties not previously available.**

I. Introduction

We present a useful technique for studying polarization in injection lasers, the measurement of the dependence of the plane of polarization on the position of the detector. It gives a test for control of polarization by facet reflectivity as well as new information about lasers where the source of polarization is not clear.

Many cavity properties can influence the laser polarization, among which are the propagation constant [1], [2], the gain if the energy bands are distorted [3], [4] and the loss arising from the transmissivity of the end facets [5]-[7], the difference in confinement of the propagating modes [8], and scattering at internal or surface inhomogeneities. Probably all are operative, and it is seldom that the measured polarization can be traced to a single cause. Positive identification of the presence of a particular effect has been possible only when the polarization could be switched. The clearest case was the change of polarization from electric field parallel to the junction to nearly perpendicular by uniaxial stress [9], which was linked to the stress-induced splitting of the degenerate valence band. An opposite switch accompanying a change of facet transmission was attributed to the polarization dependence of facet reflection [6], but without detailed analysis, while measurement of the difference in loss between TE and TM modes of the laser lacked the precision needed to define the cause of polarization [10].

We show that for lasers with many excited modes, there is a distinctive relation between polarization axis and angle to the facet if the polarization is controlled by facet reflectivity. While we have no theorem that this relation is unique to facet control of reflectivity, we are not aware of any other mechanism which gives it, and so we discuss the test as if it were a necessary and sufficient condition for dominance by reflection at the facet.[1] Experimental examples reveal in addition that different types of cavity modes have different behaviors, giving new data to test calculations of propagating modes.

II. Theory

Marcatili [11] has developed an approximate description of the hybrid modes in a perfect rectangular dielectric waveguide and showed that they correspond exceedingly well to the exact solutions of Maxwell's equations. While this description could be used to deduce the polarization at any position in

Manuscript received August 5, 1975; revised November 12, 1975.
The authors are with the RCA Laboratories, Princeton, NJ 08540.

[1] Our analysis of the interaction of box modes with the granular sidewalls of sawed lasers [12] leads to a similar relation; however, this mechanism favors TM radiation because of the higher scattering loss of the TE waves and so it is probably not important for lasers with TE dominant.

the radiation field, we do not feel the involved mathematical analysis is warranted in light of the obvious departures of our cavities from the ideal model. These imperfections consist not only of material inhomogeneities but of gross imperfections in the sidewalls, whether they are formed by cutting with a string saw or by dielectric changes due to lateral confinement of the current driving the laser. Instead we use a semi-rigorous analysis, in terms of propagating plane waves inside the cavity, which gives a direct geometrical interpretation of the relation between direction of the electric field and the angular position of the detector.

The modes of the rectangular cavity (box modes), a cavity of width W and thickness D with front and back facets separated by length L, Fig. 1(a), are described in terms of the modes of a rectangular waveguide. The waveguide is treated as a homogeneous rectangular dielectric core of refractive index n separated from a material of lower dielectric constant surrounding it by four plane interfaces, for instance, by a pair of heterojunctions and the sidewalls, where

$$W >> D. \tag{1}$$

Because of relation (1), the modes can be constructed by first treating the modes of a one-dimensional guide, considering W as infinite, which we call D modes, and then describing the two-dimensional modes as modifications of the original D modes resulting from addition of the sidewalls. The term mode signifies a configuration of the electromagnetic (EM) field which propagates along the guide axis without alteration of its character. For every such wave there is another obtained by interchanging E and H, i.e., the polarization is rotated 90°; the slight difference of the propagation constants we ignore.

Fig. 1(b) gives a set of instantaneous wavefronts of one propagating mode. The field of the mode decomposes into the two plane waves whose Poynting vectors Q make angles $\pm\phi_{mi}$ with the guide axis, where [12]

$$\sin \phi_{mi} = m\lambda_0/2nD, \qquad m = 1, 2, 3, \cdots, M. \tag{2}$$

The λ_0 is the wavelength in air. The upper limit to ϕ_{mi} is the critical angle at the sidewall, set by the smaller of the index steps Δn, detail Fig. 1(c). The subscript i designates an angle inside the guide. For the one-dimensional guide, the modes are pure TE or pure TM, that is E or H perpendicular to the guide axis. Choice of polarization corresponds to selecting E parallel to the walls (TE) or perpendicular to them (TM).

For simplicity we consider only TE waves in the following analysis. The extension to TM is straightforward. The pair of dots in Fig. 2(a) shows the directions of the pair of Poynting vectors of mode m. The coordinates are the lateral angle (in the plane of the junction) and transverse angle ϕ (transverse to the junction), which are $\theta = 0$, $\phi = \pm\phi_{mi}$; that is each Q lies in the transverse plane through the guide axis. Since for each decomposition wave E is perpendicular to both Q and the guide axis, it lies in the facet plane and is parallel to the guide walls. The instantaneous E vectors of each of the waves are shown by the arrows through the respective dots in Fig. 2(a). [The TM wave follows the same construction except that both E vectors would be rotated 90° in Fig. 2(a). In this case, however, H lies in the facet plane and E does not. Since reflection at the end facet is maximum for E in the facet, the TE wave is favored in a one-dimensional waveguide cavity with plane end facets.]

The direction of E in the radiation field is our interest. Fig. 2(b) shows the two Poynting vectors approaching the front facet; each radiates a principal lobe of half-width λ/D in the

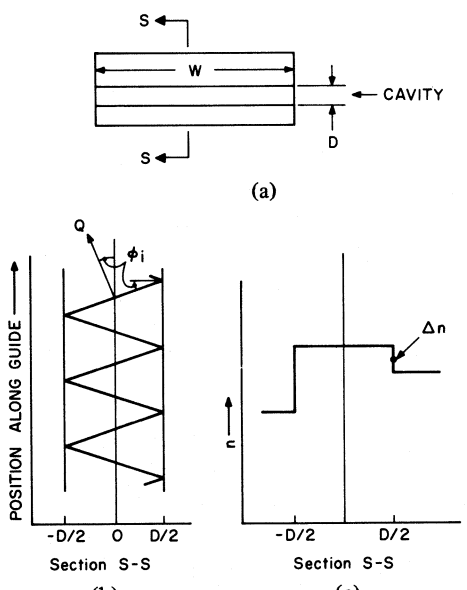


Fig. 1. Sections through one-dimensional dielectric slab waveguide. Q is the Poynting vector of a traveling wave making angle ϕ_i with the guide axis. (a) View of front facet. (b) Instantaneous wavefronts. (c) Index of refraction.

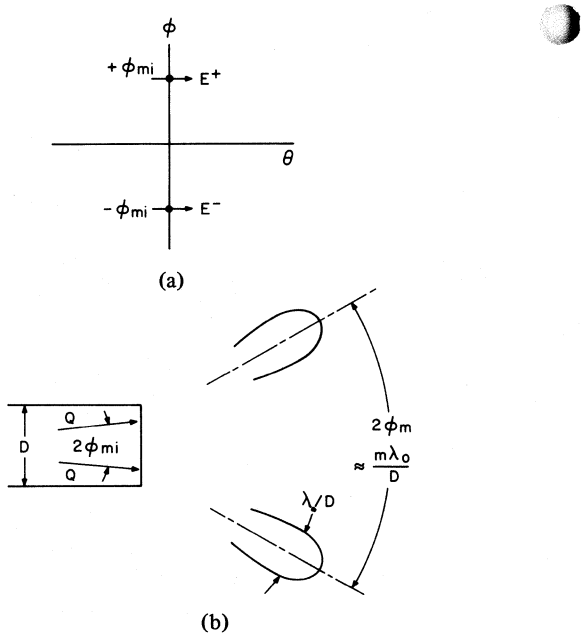


Fig. 2. One-dimensional waveguide terminated at a facet. (a) Lateral and transverse angles of Q for the two-component waves of mode m (heavy dots). (b) Principal lobes radiated by Poynting vectors Q.

refracted direction $\phi_m \approx n\phi_{mi} \approx \pm m\lambda_0/2D$. (For the lowest mode $m = 1$, the lobes overlap and the profile is a single lobe of half-width λ/D.) The electric field at any point will be the sum of the contributions from the two Poynting vectors; since both have E in the facet and parallel to the junction, E will be parallel to the junction for any position of the detector.

When the sidewall is added to make a two-dimensional guide, several things change. To discuss the new mode structure, we should first choose a D mode of the one-dimensional guide; we then recognize that the addition of the sidewalls splits each of the original Q vectors into a pair making angles $\pm\theta_{si}$ with the guide axis, where

$$\sin\theta_{si} = s\lambda_0/2nW, \qquad s = 1, 2, 3, \cdots \tag{3}$$

as determined by the condition that each plane wave generate one of the others by reflection at the *sidewalls*. Hence the decomposition of the *two-dimensional mode* (s, m) is the *four plane waves* with Poynting vectors making angles $(\pm\theta_{si}, \pm\phi_{mi})$ with the guide axis. These radiate four principal lobes in the refracted directions $(\pm\theta_s, \pm\phi_m)$.

Next, although the modes can still be classified to good accuracy as TE and TM [11], the E vectors of the four decomposition waves of a mode no longer lie parallel to the junction plane; however, each of the decomposition waves of a TE mode still has its E vector in the facet plane. Since the E associated with a Poynting vector is also perpendicular to the vector Q, its direction is tangent to the circle common to the four Poynting vectors at the corresponding point Q Fig. 3. The four arrows show the instantaneous directions of E for the four decomposition waves.

Now the direction of E in the radiation field does depend on detector position, since it is made up of the overlap of four lobes each with its own direction of E. From symmetry, E will be in the junction plane whenever the detector lies on the axes ($\theta = 0$ or $\phi = 0$). For instance, at position $(\theta_s, 0)$, the lobes will contribute equal intensities of E^- and E^+ (lower detail of Fig. 3), and the resultant E is in the junction plane. On the other hand, if the detector is so far off axis that it collects the radiation from only one of the four lobes, the angle ρ between E and the junction plane will approach its limiting values ρ_m

$$\rho_m = \tan^{-1}(\pm\theta_{si}/\pm\phi_{mi}).$$

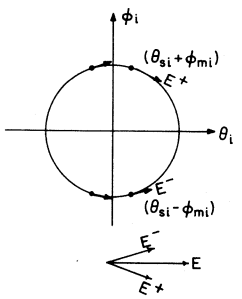


Fig. 3. Direction of Poynting vectors (heavy dots) and associated electric fields of TE mode (s, m) of a two-dimensional rectangular dielectric waveguide.

In the extreme case of a double-heterojunction (DHJ) cavity so thin that only one D mode can propagate, the complete set of transverse angles is the single pair $(\pm\phi_{1i})$. Moreover, for narrow cavities and large Δn such that these two angles approach the critical angle at the end facet $\phi_c \approx 1/n$, the angle ρ_m becomes

$$\rho_m = \tan^{-1}(\theta_{si}/\phi_c) \approx n\theta_{si}. \tag{4}$$

For a given lateral mode (s), this value would be observed for a detector near the direction of any of the refracted Poynting vectors, or at the angles $(\pm n\theta_{si}, \pm\pi/2)$. For smaller transverse angles, the interference from the conjugate D wave would reduce the angle below ρ_m, dropping it to zero in the junction plane as already described. Using a linear interpolation between $\pi/2$ and zero, the relation between the angle of E and the detector position becomes

$$\rho \approx \theta_s\phi/(\pi/2) \tag{5}$$

or

$$\rho \approx 10^{-2}\theta_s\phi. \tag{6}$$

In (6), all angles are measured in degrees. For the box modes assumed, the subscript can be dropped because the bulk of the radiation in direction θ is from modes with $\theta_s \approx \theta$, giving

$$\rho \approx 10^{-2}\theta\phi, \tag{7}$$

again in degrees.

Two comments on (7) are important. First the numerical factor and the range of ϕ are uncertain because of the crude approximation that Q is at the critical angle of the facet. Second, although the equation looks symmetrical in the two angles, the aspect ratio (1) introduces an asymmetry in profile of a lobe which makes the scans differ in an interesting way. The *transverse* scan at fixed lateral angle θ plots the changing overlap at fixed s of the single pair of wavefronts describing the D mode. For the *lateral* scan at fixed transverse angle ϕ, the D overlap is fixed and the scan studies the changes associated with a single wavefront of successive s modes. Because of this difference, we expect that ρ will change smoothly in angle for the transverse scan but will probably have considerable structure in the lateral scan. This structure records differences in the detailed character of successive s modes—departures from the perfect box modes assumed in the derivation.

We now propose a generalization: For a beam consisting of a single broad transverse profile, a large number of s modes, and polarization controlled by facet reflection, the angle of E is given by (7).

This assumes that the radiation at a particular angle θ originates in a small range of s, which is certainly valid for box modes [12]. We believe it should apply to other symmetrical types of lateral mode providing the output is linearly polarized and many indices are excited, including ideal Hermite-Gaussian (H-G) [14]. Although for H-G modes the wavefronts are curved, giving a different overlap, they still have approximately the character needed to replace θ_s of (6) by θ. The reason is that for high orders, a large part of

the power is in the outer lobe, whose direction is the refracted direction of the internal Poynting vector as for box modes.

III. Experiments

The terms TE and TM have already been used to describe the waveguide modes. The polarization of the laser output is specified in terms of the relative powers transmitted by a polarization analyzer inserted in the output beam. P_2 is the transmitted power with analyzer set for minimum transmission and P_1 with the analyzer rotated 90°. The angle ρ is then the angle of the analyzer setting for P_1. The equation $\rho = 0$ means that the polarization in P_1 has E parallel to the junction plane.

The plane of polarization was measured by passing the beam through a motor-driven Polaroid analyzer [10]. A synchronous detector locked to twice the rotational frequency of the analyzer measured the amplitude and phase of the modulation. The only improvement over the earlier technique was the use of the automatic gain control (AGC) signal to control the voltage on the photomultiplier rather than the amplifier gain [10].

All measurements used current pulses of 100-ns nominal width and 500/s repetition, and a peak detector with 10-ns gate. The cavity facets were cleaved and uncoated, and the back facet was enclosed in black wax to suppress scattered radiation. The cavity front slightly overlapped the mounting block to avoid forward reflection of the beam. The facet was oriented with respect to the scanning plane by viewing through a low power microscope mounted on the optical bench, and the normal to the facet located with an He-Ne laser. Details of the techniques have been published [15].

A. Box Modes: E Controlled by the Facet

The first laser is a good approximation to the model yielding (7). Laser 3/74-15 #11 has a cavity 310 μm long × 100 μm wide sawed from wafer CLW-14. It has an undoped active layer 0.4 μm thick defined by symmetrical heterojunctions with index step of 3 percent. The lasing wavelength is 8200 Å and the threshold 0.82 A, corresponding to quality CW material of the alloy (GaAl)As.

The laser dispersion was quadratic in lateral angle. In addition, the structure in the monochromatic lateral profile could be associated with successive q modes and index of refraction of 3.38, a reasonable value. These factors show that the dispersion corresponds to box modes [15], a dispersion assumed in our derivation of (7). The radiation is linearly polarized ($P_1/P_2 > 20$ dB, the discrimination of our analyzer), and $\rho = 0°$ for the power in a small cone along the normal to the laser facet.

Fig. 4 is a recording of the angle of polarization against viewing direction at full drive of 650 mW. Detail Fig. 4(c) is the lateral profile, detail Fig. 4(b) the polarization ratio, and detail Fig. 4(a) the angle of E in respect to the junction plane. The pair of intersecting traces corresponds to lateral scans with the laser cocked from the junction plane by the two angles (±15°). Details Fig. 4(b) and (c) have $\phi = +15°$.

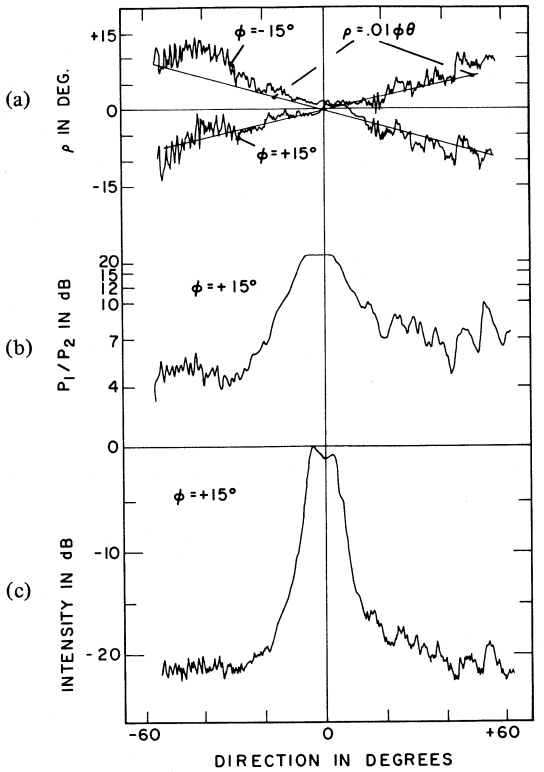


Fig. 4. Lateral scan through beam of laser 3/74-15 #11 at 650 mW. (a) Polarization angle of electric field from plane of junction, laser tilted at +15° and −15°. Solid lines are the prediction of (7). (b) Polarization ratio, P_1/P_2, same scan. (c) Lateral profile with laser tilted +15° from plane of junction.

The important features are as follows.

1) The lateral profile is typical for a sawed laser, following the theoretical shape [12] to reasonable approximation but with structure associated with peculiarities of the sawing.

2) Complete TE polarization over the half-width of the profile, dropping slightly as the direction moves into the skirts but remaining high to all scan angles.

3) Angle of E changing fairly smoothly with scan until the intensity has dropped two orders of magnitude, and even then having only small excursions from its average trend.

4) Reasonable agreement with (7), the two straight lines drawn to intersect on the normal to the facet in detail Fig. 4(a).

5) Slight systematic excursion from the equation at small lateral mode number s (small angles).

Fig. 5 is the complementary measurement, laser tilted in the lateral direction to ($\theta = \pm 15°$) and transverse scan. The half-width of the profile in this truncated section is 38° compared to 46° in the junction plane. Only mode $m = 1$ is excited. Top detail, Fig. 5(a), is the polarization angle, which roughly follows the slope of (7). The displacement of the intersection from the normal is probably an artifact.

The smooth behavior of the phase angle in the transverse scan compared to the lateral scan (which shows a hump near the normal and noticeable fluctuations at angles where the coherent power is still large) we attribute to the differences in the modal content [second comment following (7)].

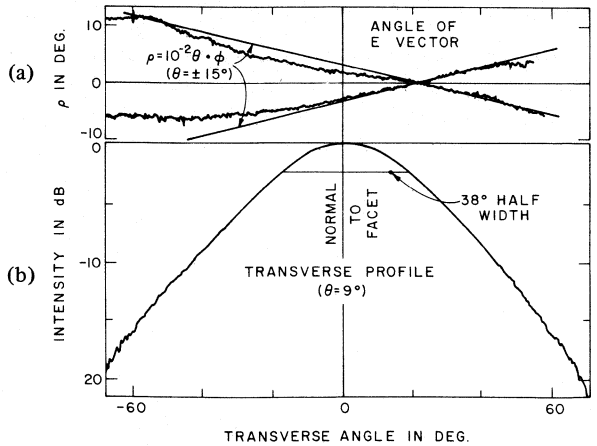


Fig. 5. Transverse scan corresponding to Fig. 4. (a) Angle of electric field from plane of junction, laser tilted in junction plane by +15° and −15°. Solid lines are the prediction of (7). (b) Profile with laser tilted +9° in junction plane.

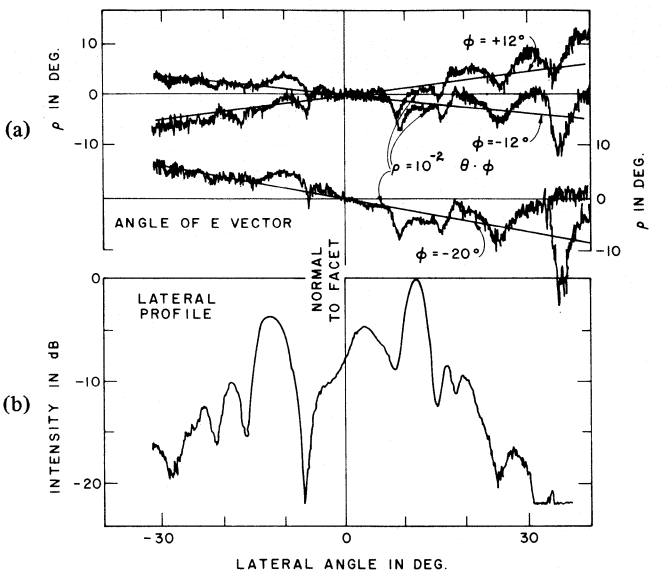


Fig. 6. Lateral scan through beam of narrow stripe laser, unit 3/74-15 #4 at 90 mW. (a) Angle of electric field from junction plane, laser tilted −20°, −12°, and +12° from junction plane. Solid lines are (7). Polarization is complete, with $\rho = 0°$. (b) Profile, showing H-G type of modes.

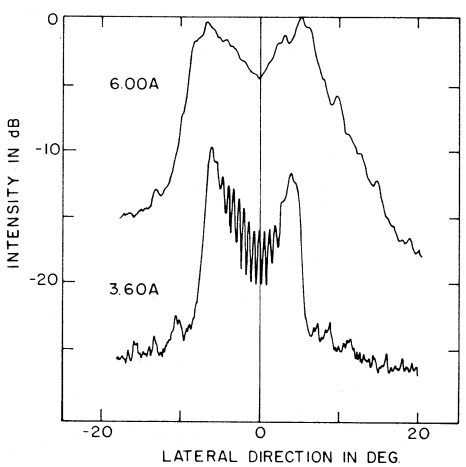


Fig. 7. Lateral scan through beam of wide stripe laser 1/74-5 #14. Top: Profile at 1.6 W, showing many unresolved modes peaking around $N = 22$. Bottom: Profile at 100 mW showing presence of a few H-G modes around $N = 15$.

A scan with the laser rotated 45° about its axis (scan at $\theta = \phi$), gave a polarization angle parabolic in scan over the central portion of the profile, in agreement with (7).

Because of the contrasting behavior of later examples, we recapitulate certain points as follows.

1) When the transverse profile is composed of a symmetrical pair of unstructured lobes of mode $m = 1$, the angle ρ will be a smooth function of transverse direction over the major part of the beam profile. If in addition the facet controls the polarization, ρ will approximate (7).

2) If the lateral profile is due to good box modes, ρ will be a reasonably smooth function of lateral direction. Equation (7) gives the trend for polarization controlled by the facet.

3) Structure in ρ indicates complexity in the modes. In the lateral scan in Fig. 4 the complexity probably arises in an additional modal dependence of polarization angle from interaction with the sawed sidewalls.

4) This same general behavior we have found repeatedly in thin lasers with hard polarization; the trend of ρ is described by (7), but the structure in the lateral scan varies widely.

B. H-G Modes

An interesting variation is a narrow stripe cavity prepared by proton bombardment [16] of the same wafer. Laser 3/74-15 #4 is 290 μm long by a nominal 10 μm wide. Fig. 6 is the lateral scan at 700 mA, $p = 90$ mW. The profile has well defined lobes and deep minima suggestive of H-G modes [14] although the lateral-mode type could not be determined from the lateral dispersion and spectrum. The top traces are the angle of E for facet cocked to ±12°, while the middle trace has tilt of $\phi = -20°$. Again the straight lines are (7). Unfortunately, the laser was damaged before the transverse scan was made.

Laser 1/74-5 #14 shows the behavior when an appreciable number of H-G modes is excited. It has an LOC cavity with the DHJ's separated by 1.9 μm with the p/n junction 0.6 μm into the cavity from the p side. It has an oxide stripe 100 μm wide, length 170 μm and lases at 8860 Å. The transverse profile is a single lobe with 24° half-width. The lateral profile at 3.6 A ($P = 100$ mW) and 6.0 A (1.6 W) are shown in Fig. 7. The pattern at low power looks like a mixture of a few high-order H-G modes, an impression supported by the near field. Both near and far fields were consistent with the assignment of $N = 15$ [14] being dominant and dielectric curvature coefficient $\omega_0 = 9.6$ μm [17]. At high drive there is still a suggestion of unresolved H-G modes, with the strongest mode now around $N = 22$.

Fig. 8 is the lateral scan at 1.6 W with the laser tilted 18.5° from the scan axis. The top is the profile, the middle the angle of E from the junction plane, and the bottom the polarization ratio. Interesting features which we cannot predict theoreti-

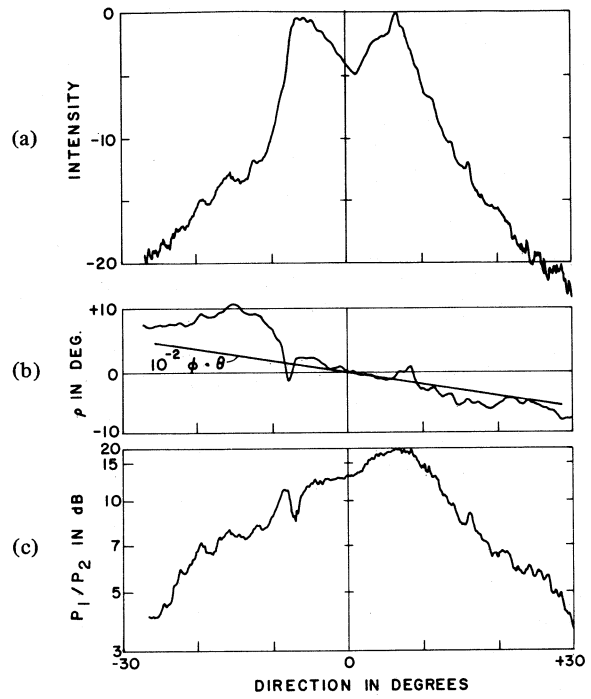


Fig. 8. Lateral scan, laser 1/74-5 #14 tilted 18.5° from scan axis, 1.6-W output. (a) Lateral profile. (b) Angle of electric field from plane of junction. The straight line is (7). (c) Polarization ratio; polarization is strong but not 100 percent, $\rho = 0°$.

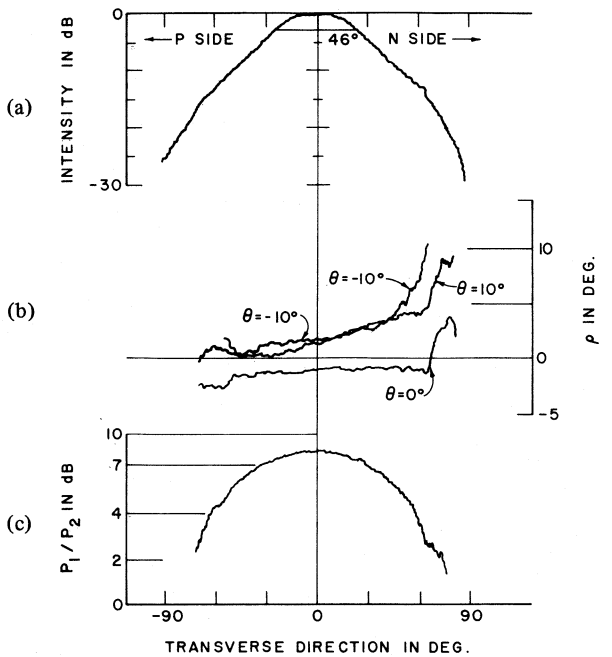


Fig. 9. Transverse scan through beam of narrow stripe laser, unit 3/74-15 #13. (a) Profile. (b) Angle of electric field E from junction plane, laser tilted 0°, −10°, and +10° from junction plane. (c) Polarization ratio.

cally are the strong polarization at such high drive [10], the general trend of ρ with scan angle, and its structure near the two peaks in the profile. The facet does not seem to be controlling the polarization, for in such a narrow transverse profile as 24° half-width the discrimination by facet reflectivity between TE and TM is too weak to maintain hard polarization. We have no theory of the dependence of ρ on scan direction, the generalization of (7) being inapplicable on the two counts of lack of facet control and narrow transverse profile.

C. Unknown Lateral Modes and Cause of Polarization

In contrast is 3/74-15 #3, a laser from the proton-bombarded wafer cut from the same cleaved strip as 3/74-15 #4. The lateral scan revealed a profile with central maximum and no obvious character. The transverse profile Fig. 9 is a clean single lobe, half-width 46°. The polarization is not complete, about 10 dB in the forward direction and dropping steadily toward the sides. The polarization is E parallel to the junction and ρ is independent of current. The change of ρ with scan angle was affected by tilting the laser, but the scans for tilts of +10° and −10° were indistinguishable. Obviously, for this cavity the polarization is *not* determined by the facet.

D. Single Heterojunction (SHJ)

The SHJ lasers [18], [19] have very different behavior of polarization from any of the preceding. Laser 11/72-67 #3 has a 100-μm-wide cavity sawed from SHJ wafer SHF-31. Fig. 10 is the near field at 4 W measured by a scanning photomultiplier with slit 125 μm × 4 mm in the focus plane of a microscope with 200 × magnification. The transverse scan shows a

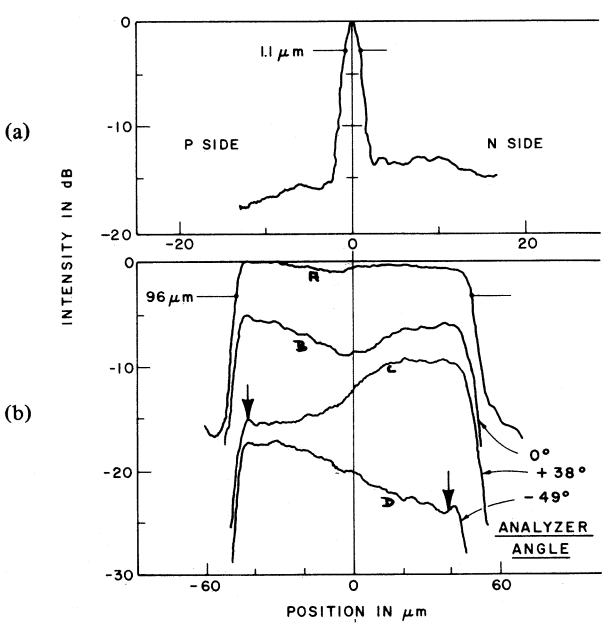


Fig. 10. Intensity distribution at laser facet, SHJ laser 11/72-67 #3 at 4-W power. (a) Transverse; distribution across junction, scan from P side to N side. (b) Lateral; distribution parallel to junction. A–Unfiltered output. B–Polaroid analyzer set to transmit radiation with E parallel to junction, giving maximum rejection at center of scan. C–Polaroid rotated +38°, maximum rejection at position of heavy arrow. D–Polaroid at −49°, maximum rejection at arrow at right. Such steady change of direction of E field with position on facet is frequently observed with SHJ lasers.

single line. In the lateral scan, trace A shows a very uniform emission, variation ±0.5 dB. Trace B has a Polaroid set to reject $E \perp$ junction (set to an angle we call zero). In trace C, the angle is +38°, and in D the Polaroid is at −49°. These give maximum rejection for the positions indicated by the heavy arrows. Smooth change of axis of polarization across the facet with E roughly ⊥ to the junction is frequently found in SHJ lasers with sawed sides.

Transverse scans of the beam are given in Fig. 11. The profile, top trace, Fig. 11(a), is a single lobe with 21° half-width and fine structure on the N side, a characteristic of SHJ lasers which has been attributed to extension of the wave into the passive N material [20]. The middle detail, Fig. 11(b), shows that the angle of the E field oscillates strongly on the N side of the normal, a structure obviously related to the beam profile. On the P side, no such variations occur. The polarization ratio is quite constant at about 2 dB with $\rho \sim 90°$ [detail Fig. 11(c)].

The lateral profile Fig. 12 is normal for sawed cavities [12]. The angle of the E field is more interesting; $\rho \approx 90°$ in the central lobe but with pronounced dips, and changing to 0° at large angles from the normal. The linear plot of the polarization difference $(P_1 - P_2)/(P_1 + P_2)$ shows a drastic change in character from the central region dominated by TM, where changes with angle are smooth, to very noisy character in the TE region. The smooth "parabola" is the expected behavior for transmission of incoherent radiation through the front facet, Fresnel's law of transmission [21]. In the wings the trace follows it to large angles but then drops, probably because of radiation which has not come through the front facet. As reference points, the two arrows are the Brewster angles. Scans with the facet tilted are not useful because of the lack of understanding of the profiles shown. In any case, facet reflection favors TE in injection lasers and cannot produce TM dominant as here observed.

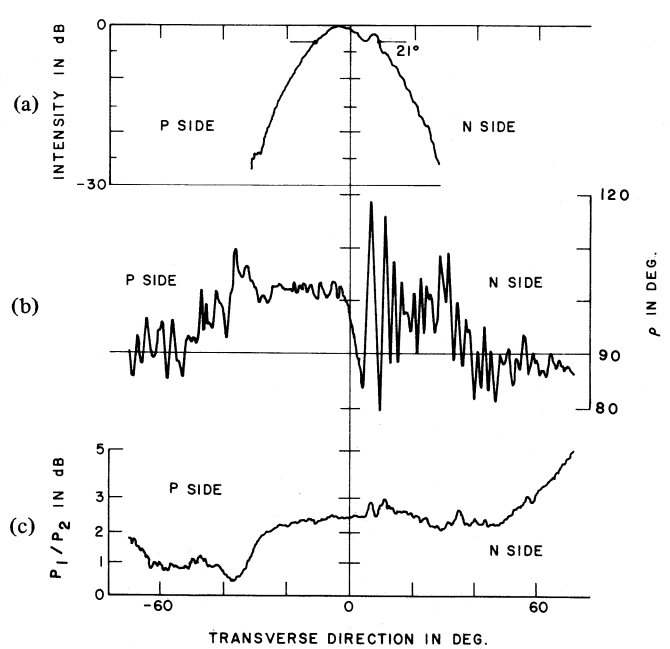


Fig. 11. Transverse scan through beam corresponding to Fig. 10. (a) Profile, scan from P side to N side. Note structure on N side characteristic of SHJ lasers. (b) Angle of E field showing correlation with structure in profile on N side of normal to facet. (c) Ratio of P_1 to P_2. Note polarization is weak at all angles.

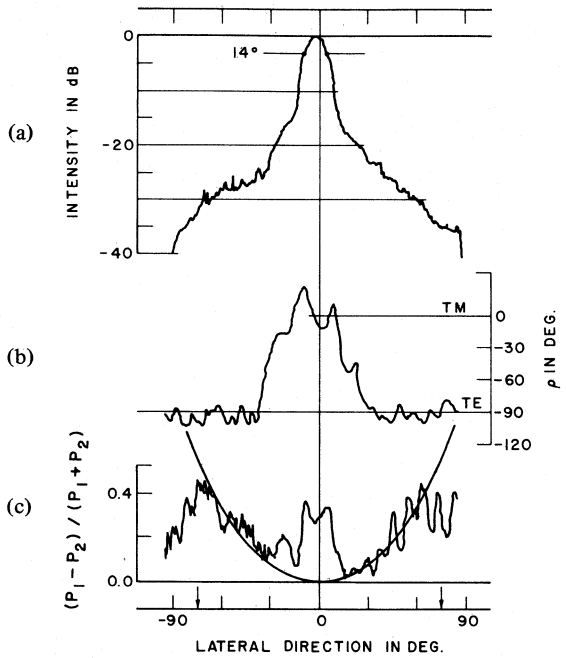


Fig. 12. Lateral scan corresponding to Figs. 10 and 11. (a) Profile. (b) Angle ρ of E field showing reversal of polarization away from forward lobe. (c) Polarization difference. Smooth curve is difference calculated from Fresnel's equations for facet transmission of unpolarized incoherent light [21].

IV. Conclusion

Study of the dependence of the angle of the polarization on direction gives information about the cavity modes not previously available. In some cases it can determine whether or not the polarization is controlled by the facet reflectivity. It also reveals details of the overlap of wavefronts in the transmitted beam which can be used to check theories of the propagating modes. Of particular interest is the difference in polarization between the two narrow stripe lasers from the same thin DHJ wafer, showing that even in thin cavities there are competing sources of polarization.

Acknowledgment

The authors wish to thank I. Ladany and F. Z. Hawrylow, who supplied the lasers, and V. M. Cannuli, M. G. Harvey, and D. P. Marinelli for their assistance. They also wish to thank H. Kressel and H. F. Lockwood for helpful discussions and E. C. Douglas for the proton bombardment.

References

[1] W. W. Anderson, "Mode confinement and gain in junction lasers," *IEEE J. Quantum Electron.*, vol. QE-1, pp. 228–236, Sept. 1965.

[2] Y. Suematsu and M. Yamada, "Transverse mode control in semiconductor lasers," *IEEE J. Quantum Electron.*, vol. QE-9, pp. 305–311, Feb. 1973.

[3] P. R. Emtage, "Theory of the effect of strain in GaAs electroluminescent diodes," *J. Appl. Phys.*, vol. 36, pp. 1408–1411, Apr. 1965.
[4] Alyamovskii, Bagaev, Berozashvili, and Vul, "Polarization of radiation from GaAs diodes," *Sov. Phys.–Solid State*, vol. 8, pp. 871–875, 1966.
[5] M. J. Adams and M. Cross, "On the polarization of radiation from double heterostructure injection lasers," *Electron. Lett.*, vol. 7, pp. 569–570, Sept. 1971.
[6] F. K. Reinhart, I. Hayashi, and M. B. Panish, Jr., "Mode reflectivity and waveguide properties of double heterostructure injection lasers," *J. Appl. Phys.*, vol. 42, pp. 4466–4480, Oct. 1971.
[7] T. Ikegami, "Reflectivity of mode at facet and oscillation mode in double-heterostructure injection lasers," *IEEE J. Quantum Electron.*, vol. QE-8, pp. 470–476, June 1972.
[8] J. Hatz and E. Mohn, "Calculation of intrinsic threshold for TE and TM mode in GaAs laser diodes," *IEEE J. Quantum Electron.*, vol. QE-3, pp. 656–662, Dec. 1967.
[9] J. E. Ripper, N. B. Patel, and P. Brosson, "Effect of uniaxial pressure on the threshold current of double heterostructure GaAs lasers," *Appl. Phys. Lett.*, vol. 21, p. 124, Aug. 15, 1972.
[10] H. S. Sommers, Jr., "Experimental properties of injection lasers. V. Strong polarization," *J. Appl. Phys.*, vol. 45, pp. 237–242, Jan. 1974.
[11] E. A. J. Marcatili, "Dielectric rectangular waveguide and directional coupler for integrated optics," *Bell Syst. Tech. J.*, vol. 48, pp. 2071–2102, Sept. 1969.
[12] H. S. Sommers, Jr., "Experimental properties of injection lasers: Modal distribution of laser power," *J. Appl. Phys.*, vol. 44, pp. 1263–1276, Mar. 1973.
[13] I. Ladany and H. Kressel, "(AlGa)As double heterojunction CW lasers: The effect of device fabrication parameters on reliability," in *Inst. Phys. Conf. Ser. 24, Inst. Phys.*, London, England, 1975, pp. 192–199.
[14] L. I. Schiff, *Quantum Mechanics*, 2nd ed. New York: McGraw-Hill, 1955, pp. 60–66.
[15] H. S. Sommers, Jr., "Experimental properties of injection lasers. IV. Modes of large cavities with sawed sides," *J. Appl. Phys.*, vol. 44, pp. 3601–3608, Aug. 1973.
[16] J. C. Dyment, L. A. D'Asaro, J. C. North, B. I. Miller, and J. E. Ripper, "Proton-bombardment formation of stripe-geometry heterostructure lasers for 300 K CW operation," *Proc. IEEE* (Lett.), vol. 60, pp. 726–728, June 1972.
[17] T. H. Zachos and J. E. Ripper, "Resonant modes of GaAs junction lasers," *IEEE J. Quantum Electron.*, vol. QE-5, pp. 29–37, Jan. 1969.
[18] H. Kressel and H. Nelson, "Close confinement GaAs P/N junction lasers with reduced optical loss at room temperature," *RCA Rev.*, vol. 30, pp. 106–113, Mar. 1969.
[19] I. Hayashi, M. B. Panish, and P. W. Foy, "A low-threshold room temperature injection laser," *IEEE J. Quantum Electron.* (Co resp.), vol. QE-5, pp. 211–212, Apr. 1969.
[20] J. K. Butler, H. Kressel, and I. Ladany, "Internal optical losses in very thin CW heterojunction laser diodes," *IEEE J. Quantum Electron. (Part II of Two Parts: Special Issue on 1974 IEEE Semiconductor Laser Conference)*, vol. QE-11, pp. 402–408, July 1975.
[21] D. H. Menzel, Ed., *Fundamental Formulas of Physics*, vol. 2. New York: Dover, 1960, p. 367.

Strip-Loaded Diffused Optical Waveguides

G. BENJAMIN HOCKER, MEMBER, IEEE

Abstract–**A strip-loaded diffused optical waveguide consists of a one-dimensional diffused guide with a narrow loading strip of dielectric deposited on the surface. Two-dimensional modes can exist in the diffused material, confined in depth by the diffusion and in width by the loading strip. The propagation constants of these two-dimensional modes are calculated. The requirements for the index of refraction and width of the loading strip are discussed along with the rate of decay of electric-field amplitude away from the strip. A numerical example typical of Ti-diffused $LiNbO_3$ is given.**

I. Introduction

OPTICAL WAVEGUIDES have been formed by diffusion techniques in various materials, most notably in ferroelectric materials such as $LiNbO_3$ [1] and $LiTaO_3$ [2], [3]. Diffused guides in such ferroelectrics with strong electrooptic effects promise to be of great importance in the fabrication of modulators, switches, and other active devices for integrated optics. Several such devices have been demonstrated [2], [4], and work in this area is proceeding in many laboratories.

Most waveguides have employed a uniform diffusion over the surface of the ferroelectric material, forming a one-dimensional waveguide. However, several attractive types of devices have been proposed or demonstrated which utilize coupling between adjacent channel or two-dimensional guides [5]. While channel guides have been formed by diffusion of selected narrow strips in the substrate material [6], we present here the theory of an alternative method of providing two-dimensional confinement of modes in diffused guides.

We show that if a uniform one-dimensional diffusion is followed by deposition of a narrow strip of dielectric on the surface, modes can exist in the diffused material which are confined in width under this dielectric strip. We term this structure a strip-loaded diffused waveguide, an analogy with the strip-loaded thin-film guides which have already been analyzed and demonstrated [7], [8]. The analysis of these strip-loaded diffused guides is based on our previous theory of diffused waveguide modes [9], in which a universal chart de-

Manuscript received September 7, 1975. This work was sponsored by the Defense Advanced Research Projects Agency.

The author is with the Department of Electrical Engineering, University of Minnesota, Minneapolis, MN 55455.

scribing all guides of a given diffusion shape is obtained in terms of several normalized parameters.

An advantage of all strip-loaded guides is that a lack of edge smoothness in the loading strip does not cause significant scattering losses. Additional potential advantages of the strip-loaded diffused guide over other two-dimensional diffused guides are shown to be increased dimensional tolerance, making for ease of fabrication, and a more easily analyzed structure, for more accurate design of devices.

II. Modes of Diffused Optical Waveguides with Covering Material

In this section we extend our previous theory of the modes of diffused optical waveguides [9] to include the effects of a dielectric material covering the diffused guide. A third normalized parameter, involving the index of refraction of the covering material, is added to the two previously used.

Suppose that the material being diffused into occupies the space $x \geq 0$ and that a diffusion is carried out over its surface, increasing the index of refraction near the surface and producing a one-dimensional optical waveguide. The resulting index-of-refraction profile can be specified by the undiffused bulk index n_b, the index at the surface n_s, the diffusion depth D, and the diffusion shape $f(\alpha)$

$$n(x)^2 = n_b^2 + (n_s^2 - n_b^2) f(x/D) \tag{1}$$

where $f(\alpha)$ takes on values between 0 and 1, and it is assumed $f(0) = 1$ while $f(\alpha) \to 0$ for large α. $f(\alpha)$ may, for instance, be given by $\exp(-\alpha)$, $\exp(-\alpha^2)$, or $\operatorname{erfc}(\alpha)$.

Light can be confined in the x direction while propagating as a waveguide mode in the y-z plane. Such a mode is described by its propagation constant β, or equivalently by its effective index n_{eff}

$$\beta = n_{\text{eff}} k \tag{2}$$

where $k = 2\pi/\lambda$ is the free-space propagation constant. The limits on β and n_{eff} for guided modes are

$$n_s k > \beta > n_b k$$

$$n_s > n_{\text{eff}} > n_b. \tag{3}$$

As is the case for the modes of a thin-film waveguide [10], the modes of a diffused guide may be found in terms of a normalized effective index b, and a normalized guide thickness V [9]

$$b = (n_{\text{eff}}^2 - n_b^2)/(n_s^2 - n_b^2) \tag{4}$$

$$V = kD(n_s^2 - n_b^2)^{1/2}. \tag{5}$$

Following the theory of [9], these parameters must satisfy a mode dispersion equation

$$2V \int_0^{\alpha_t} [f(\alpha) - b]^{1/2}\, d\alpha + 2\Phi_1 + 2\Phi_2 = 2m\pi \tag{6}$$

where the turning point α_t is defined by $f(\alpha_t) = b$, and where $m = 0, 1, 2, \cdots$ for the different order modes. $2\Phi_1$ and $2\Phi_2$ represent the phase shifts for a wave reflected at the top surface and at the point of maximum penetration $y_t = \alpha_t D$, respectively. In [9] it was shown that $2\Phi_2 = -\pi/2$, and it was assumed that $2\Phi_1 = -\pi$. This assumption was made for a guide bounded by air with $n_s \gg 1$. It is equivalent to assuming that the electric-field amplitude drops to zero at $x = 0$ and does not penetrate into the air.

If we let the diffused guide be bounded for $x < 0$ by a dielectric covering material of index $n_c (n_c \leq n_b)$, then the phase shift at the surface is given by

$$2\Phi_1 = -2 \tan^{-1} [(n_{\text{eff}}^2 - n_c^2)^{1/2}/(n_s^2 - n_{\text{eff}}^2)^{1/2}] \tag{7}$$

for TE modes [9], [11].

Following the theory of thin-film waveguides [10], we introduce a third normalized parameter, the asymmetry index a

$$a = (n_b^2 - n_c^2)/(n_s^2 - n_b^2). \tag{8}$$

The phase shift (7) can then be written in terms of normalized parameters as

$$2\Phi_1 = -2 \tan^{-1} [(b + a)/(1 - b)] \tag{9}$$

and the mode dispersion equation becomes

$$2V \int_0^{\alpha_t} [f(\alpha) - b]^{1/2}\, d\alpha = (2m + \tfrac{1}{2})\pi + 2 \tan^{-1} \cdot [(b + a)/(1 - b)]. \tag{10}$$

For a particular diffusion shape $f(\alpha)$, choosing a value of the asymmetry index a permits easy computer calculation of b versus V. Fig. 1(a)-(c) consist of universal charts of b versus V for various values of a, with $f(\alpha) = \operatorname{erfc}(\alpha)$, $\exp(-\alpha^2)$, and $\exp(-\alpha)$, respectively. All diffused guides having a given diffusion shape $f(\alpha)$ are described by one such chart, although interpolation or calculation for values of a other than those shown may be needed.

It should be noted that a covering material of higher index n_c results in a smaller value of a, and, for a given V, a larger b and larger n_{eff}. This technique of increasing n_{eff} by using a higher index covering material is employed in the strip-loaded guide described in Section III.

As shown in [10], the same dispersion equation (10) and charts of b versus V as in Fig. 1 may be used for TM modes as long as $(n_s - n_b) \ll 1$, a requirement which is easily met for diffused guides. However, the asymmetry index must be redefined for TM modes as

$$a' = (n_s^4/n_c^4)[(n_b^2 - n_c^2)/(n_s^2 - n_b^2)]. \tag{11}$$

Thus the distinction between TE and TM modes is reintroduced, a distinction which was removed in [9] when assuming $2\Phi_1 = -\pi$.

III. Strip-Loaded Diffused Waveguides

We now use the preceding theory to analyze strip-loaded two-dimensional waveguides made from one-dimensional diffused guides. These waveguides are made by placing on top of the diffused guide a narrow strip of dielectric having an index lower than or equal to the bulk index of the diffused material, the remainder of the surface being bounded by material of lower index such as air. Light in the waveguides under the strip propagates with a higher effective index than

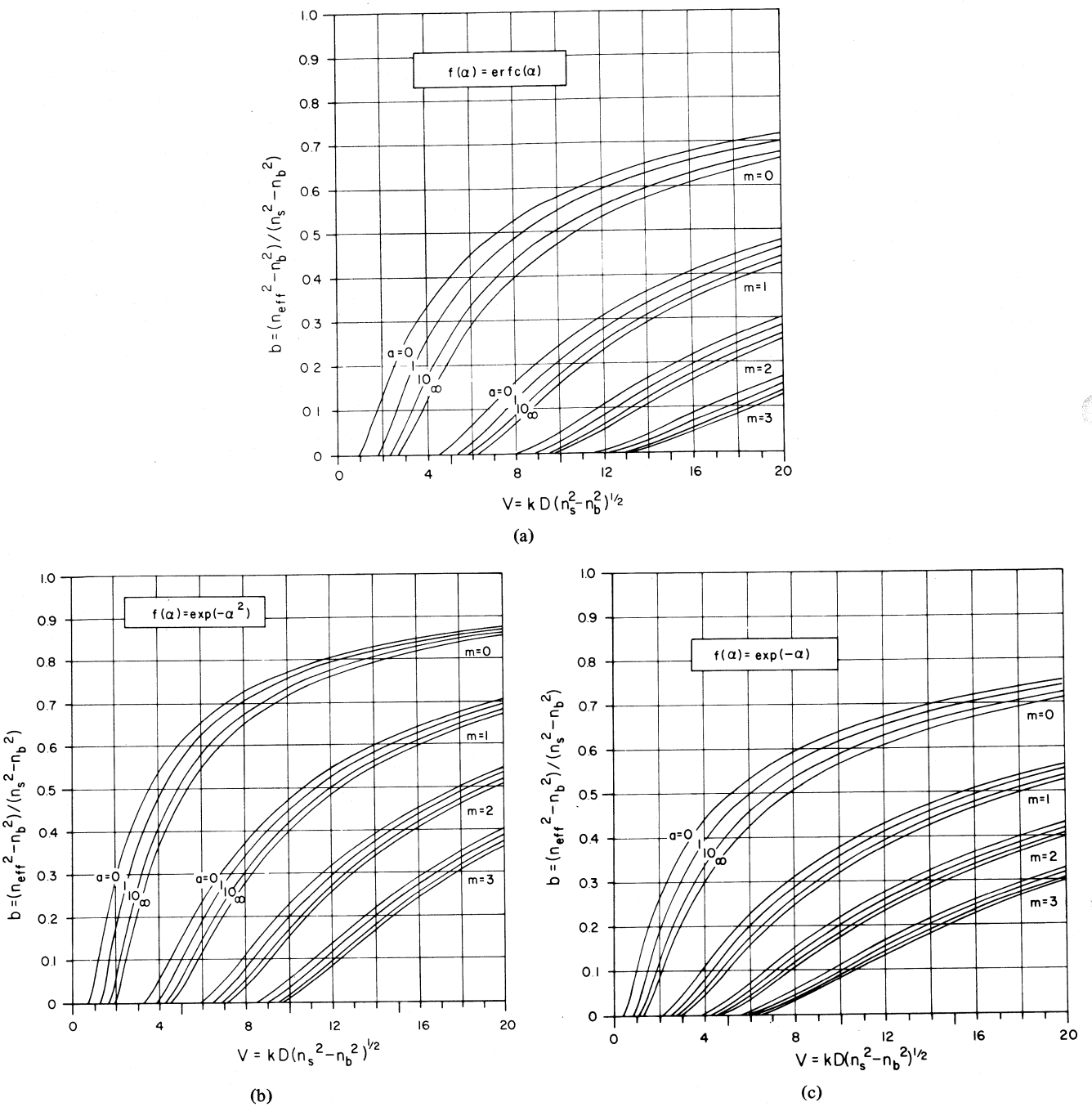


Fig. 1. Universal chart of normalized mode index b versus normalized diffusion depth V for several values of the asymmetry index a. The diffusion shape $f(\alpha)$ is as follows. (a) A complementary error function. (b) A Gaussian. (c) An exponential.

away from the strip. Thus light can be confined under the strip by total reflection at the strip boundary, forming a two-dimensional waveguide.

Consider a strip-loaded diffused waveguide as shown in Fig. 2(a). A one-dimensional diffused guide has had a strip of covering material of index n_c and width W applied as shown. Elsewhere, the diffused guide is covered with material of lower index $n_a < n_c$, the simplest case being where $n_a = 1$. This structure will support modes propagating in the z direction and confined in both the x and y directions.

The modes of this strip-loaded structure will be analyzed by the equivalent index-of-refraction method [8]. This method involves a succession of one-dimensional waveguide mode calculations, in which the x and y dependences of the index profile are separated, and employs an equivalent one-dimensional guide model.

First, consider a wave traveling in the structure of region I with $W = \infty$. The covering material has index n_c and the index profile is a function of x alone. The wave is constrained only in the x direction and propagates in the y-z plane with an effective index n_I which can be calculated using the theory of Section II. Similarly, a wave traveling in the structure of

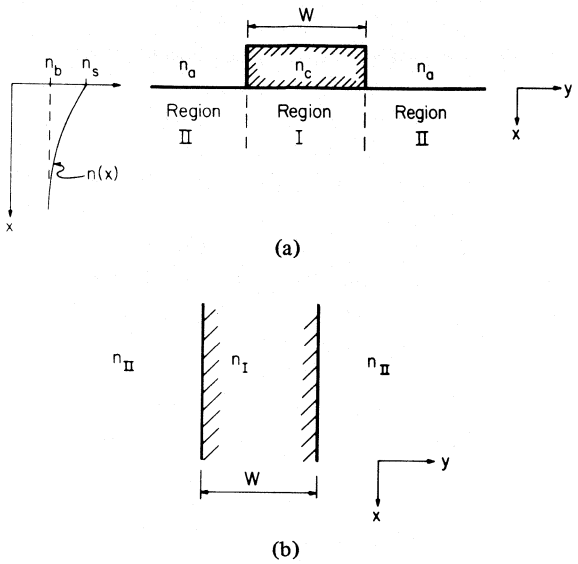


Fig. 2. (a) Geometry of a strip-loaded diffused optical waveguide. (b) The equivalent symmetrical one-dimensional guide.

region II differs only in that the covering material has index $n_a (n_a < n_c)$, and it propagates with effective index n_{II} where $n_{II} < n_I$. Because of this difference in effective index between regions I and II, a wave launched under the strip at a small angle to the z axis could undergo total reflection at the strip boundary, confining it in the y direction as well.

In the y direction, this behavior can be represented by an equivalent symmetrical one-dimensional guide as shown in Fig. 2(b). It consists of a thin film of index n_I and thickness W in the y direction bounded by material of index n_{II}. The equivalent guide is of infinite extent in the x and z directions. The modes of this equivalent one-dimensional guide are confined in the y direction, and their effective indices are, to a good approximation, the effective indices of the two-dimensional modes of the original structure. As an example of the validity of the equivalent index approach, it has been applied to the problem of the modes of a rectangular dielectric waveguide [12], giving results identical to the method of Marcatili [13].

The analysis of the strip-loaded diffused waveguide structure uses the normalized parameters of Section II. The parameter V has the same value in both region I and region II

$$V = kD\sqrt{n_s^2 - n_b^2}. \tag{12}$$

The values of the asymmetry index in regions I and II can be calculated from (8) as a_I and a_{II}, respectively, with $a_{II} > a_I$ since $n_c > n_a$. For propagation in region I, b_I can be obtained from the universal charts of Fig. 1 for the calculated V and a_I; b_{II} is similarly obtained, describing propagation in region II. The values of the effective index for modes in region I and region II can finally be obtained, using (4), as n_I and n_{II}, respectively.

The equivalent one-dimensional symmetrical guide of Fig. 2(b) is now used to describe the confinement of light in the y direction, and thus to obtain the two-dimensional mode indices. This equivalent guide has discrete, rather than diffused, changes in index and hence can be described by normalized parameters V_{eq} and b_{eq} [9]

$$V_{eq} = kW(n_I^2 - n_{II}^2)^{1/2} \tag{13a}$$

$$b_{eq} = (n_{eq}^2 - n_{II}^2)/(n_I^2 - n_{II}^2) \tag{13b}$$

where n_{eq} is the mode effective index of the equivalent guide. Expressing V_{eq} and b_{eq} in terms of the normalized parameters of the two regions gives

$$V_{eq} = V\sqrt{b_I - b_{II}}\, W/D \tag{14a}$$

$$b_{eq} = (b_0 - b_{II})/(b_I - b_{II}) \tag{14b}$$

where $b_0 \equiv (n_{eq}^2 - n_b^2)/(n_s^2 - n_b^2)$. b_{eq} and V_{eq} are related by the theory of thin-film guides of [10] for $a = 0$, and this relationship is plotted as the universal chart of Fig. 3.

Therefore, once b_I, b_{II}, and V are calculated for a structure, V_{eq} is found from (14a) for any value of the ratio W/D, and b_{eq} is then obtained from Fig. 3. Finally, the effective index of the equivalent guide, and hence of the two-dimensional mode, is just

$$n_{eq}^2 = [b_{eq}(b_I - b_{II}) + b_{II}](n_s^2 - n_b^2) + n_b^2. \tag{15}$$

The requirement that the strip-loaded guide have M modes in the y direction is that the equivalent guide have M modes

$$(M - 1)\pi < V_{eq} < M\pi \tag{16}$$

which can be written as

$$(M - 1)\pi < V\sqrt{b_I - b_{II}}\, W/D < M\pi \tag{16'}$$

or

$$(M - 1)\pi < 2\pi\sqrt{n_I^2 - n_{II}^2}\, W/\lambda < M\pi. \tag{16''}$$

As a numerical example, consider a typical single-mode Ti-diffused $LiNbO_3$ guide having a complementary error function profile with $n_b = 2.20$, $n_s = 2.209$, and $D = 3$ μm [12], so that $V = 6$ at $\lambda = 0.6328$ μm. If $n_c = 1.0$, then $a_{II} = 97 (\cong \infty)$ and from Fig. 1(a) we find $b_{II} = 0.290$, and hence $n_{II} = 2.20261$.

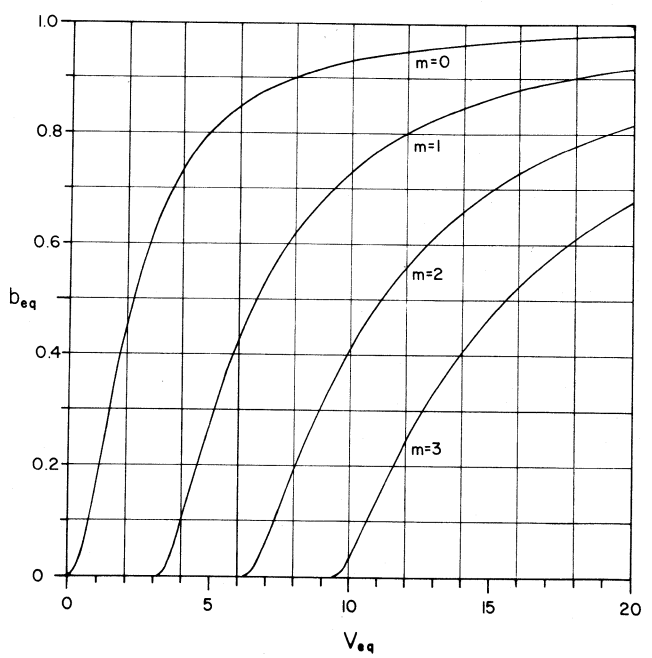


Fig. 3. Universal chart of normalized mode index b_{eq} versus normalized guide width V_{eq} for a symmetrical thin-film guide, plotted using the theory of [10] with $a = 0$.

Suppose a covering film with $n_c = 2.11$ is deposited to give $a_I = 10$. Then $b_I = 0.337$ and $n_I = 2.20307$. From (16) we see that this covering material can be used to construct a strip-loaded guide with a single mode in the y dimension as long as $W < 7.3$ μm. If $W = 7$ μm, then $V_{eq} = 3.04$ and, from Fig. 3, $b_{eq} = 0.635$. Such a strip-loaded guide will have a single two-dimensional mode propagating with an effective index $n_{eq} = 2.20288$.

This example illustrates one advantage of a strip-loaded diffused guide, in that a single mode guide can be obtained using a relatively wide strip W. By contrast, if a two-dimensional diffused guide were formed by diffusing in a narrow strip of Ti, this stripe would have to be appreciably narrower than 7 μm to give a single mode guide [14]. This is because diffusion occurs in the y direction as well as the x direction, making the diffused guide about two diffusion lengths wider than the original stripe.

Another advantage of the strip-loaded guide is that, because confinement is weak in the y direction, the field amplitude away from the loading strip decays slowly in the y direction. Moreover, the decay constant (an important parameter in the coupling between parallel guides) is easily calculated

$$\gamma_{II} = k\sqrt{b_{eq}(n_I^2 - n_{II}^2)}. \tag{17}$$

For the numerical example, $\gamma_{II} = 0.355$ μm^{-1}, or a decay length of 2.8 μm. The slow decay and easy calculation should simplify the design and construction of devices using coupling between parallel two-dimensional waveguides, such as directional couplers, branching waveguides, and tapered velocity couplers.

A limitation of the strip-loaded diffused waveguide structure is the requirement that the strip material have index n_c close to the bulk index n_b. In particular, to obtain guiding in the y direction we infer from Fig. 1 that we require $a_I \lesssim 10$. Since, for diffused waveguides, n_c is close to n_b, this requirement can be written as

$$(n_b - n_c) \lesssim 10(n_s - n_b). \tag{18}$$

However, suitable covering materials may be found for a given substrate material, such as perhaps Ta_2O_5 or Nb_2O_5 on $LiNbO_3$. It may also be possible to form the loading strip from the same material as the substrate by sputtering, so that $n_c = n_b$ and $a_I = 1$.

Because the confinement is weak in the y direction, the allowable minimum radius of curvature in the y-z plane must be chosen to limit radiation losses. For the numerical example previously given, using Marcatili's theory [15], losses will be limited to 0.1/rad if the minimum radius of curvature is 15 cm. This should not be a problem for many devices where little path curvature is required.

IV. Conclusions

We have discussed the theory of strip-loaded diffused waveguides, in which a two-dimensional guide is formed from a one-dimensional diffused guide by adding a dielectric loading strip. A method of calculating the propagation constants of the modes is presented. Also discussed are the requirements on the index of refraction of the strip material, the effects of strip width, and the decay of field amplitude away from the loading strip. Strip loading appears to be an attractive way of adding a second dimension of mode confinement to diffused waveguides, especially when applied to ferroelectric materials with strong electrooptic effects. The structure should be applicable to a wide variety of both active and passive devices for integrated optical circuits.

References

[1] R. V. Schmidt and I. P. Kaminow, "Metal-diffused optical waveguides in $LiNbO_3$," *Appl. Phys. Lett.*, vol. 25, pp. 458–460, Oct. 15, 1974.

[2] J. M. Hammer and W. Phillips, "Low-loss single-mode optical waveguides and efficient high-speed modulators of $LiNb_xTa_{1-x}O_3$ on $LiTaO_3$," *Appl. Phys. Lett.*, vol 24, pp. 545–547, June 1, 1974.

[3] J. Noda, T. Saku, and N. Uchida, "Fabrication of optical waveguiding layer in $LiTaO_3$ by Cu diffusion," *Appl. Phys. Lett.*, vol. 25, pp. 308–310, Sept. 1, 1974.

[4] a) I. P. Kaminow, J. R. Carruthers, E. H. Turner, and L. W. Stulz, "Thin-film $LiNbO_3$ electro-optic light modulator," *Appl. Phys. Lett.*, vol. 22, pp. 540–542, May 15, 1973.
b) I. P. Kaminow and L. W. Stulz, "A planar electrooptic-prism switch," *IEEE J. Quantum Electron.* (Corresp.), vol. QE-11, pp. 633–635, Aug. 1975.

[5] a) E. A. J. Marcatili, "Dielectric rectangular waveguide and directional coupler for integrated optics," *Bell Syst. Tech. J.*, vol. 48, pp. 2071–2102, Sept. 1969.
b) J. C. Webster and F. Zernike, "Push-pull thin-film optical modulator," *Appl. Phys. Lett.*, vol. 26, pp. 465–467, Apr. 15, 1975.
c) M. G. F. Wilson and G. A Teh, "Improved tolerance in optical directional couplers," *Electron. Lett.*, vol. 9, pp. 453–455, Sept. 20, 1973.

[6] M. Papuchon *et al.*, "Electrically switched optical directional coupler: Cobra," *Appl. Phys. Lett.*, vol. 27, pp. 289–291, Sept. 1, 1975.

[7] H. Furuta, H. Noda, and A. Ihaya, "Novel optical waveguide for integrated optics," *Appl. Opt.*, vol. 13, pp. 322–326, Feb. 1974.

[8] V. Ramaswamy, "Strip-loaded film waveguide," *Bell Syst. Tech. J.*, vol. 53, pp. 697–704, Apr. 1974.

[9] G. B. Hocker and W. K. Burns, "Modes in diffused optical waveguides of arbitrary index profile," *IEEE J. Quantum Electron.*, vol. QE-11, pp. 270–276, June 1975.

[10] H. Kogelnik and V. Ramaswamy, "Scaling rules for thin-film optical waveguides," *Appl. Opt.*, vol. 13, pp. 1857–1862, Aug. 1974.

[11] M. Born and E. Wolf, *Principles of Optics*. New York: Pergamon, 1965.

[12] W. K. Burns, Naval Res. Lab., private communication.

[13] E. A. J. Marcatili, "Slab-coupled waveguides," *Bell Syst. Tech. J.*, vol. 53, pp. 645–674, Apr. 1974.

[14] G. B. Hocker, unpublished.

[15] E. A. J. Marcatili, "Bends in optical dielectric guides," *Bell Syst. Tech. J.*, vol. 48, pp. 2103–2132, Sept. 1969.

Waveguide CO_2 Laser Gain: Dependence on Gas Kinetic and Discharge Properties

STEVEN C. COHEN

Abstract—**Using a simple rate equation approach we examine the gas kinetic and discharge properties of waveguide CO_2 lasers. We calculate the dependence of the population inversion and laser small-signal gain on gas pressure, gas mixture, pumping rate (discharge current), tube bore diameter, and wall temperature. The results indicate, for example, that at a pressure of 50 torr and a tube-bore diameter of 0.125 cm, the gain is optimized with a gas mixture in the ratio CO_2:N_2:He of 1:0.75:1.5. At higher pressures the gain is optimized by using more helium-rich mixtures. We also calculate the dependence of laser tunability on the gas kinetic properties and cavity losses. We find that for low-loss cavities the laser tunability may substantially exceed the molecular full width at half-maximum. Furthermore, the more helium-rich gas mixtures give greater tunability when cavity losses are small, and less tunability when cavity losses are large. The roles of the various gases in the waveguide CO_2 laser are the same as those in conventional devices. By contrast with conventional lasers, however, the waveguide laser transition is homogeneously broadened. Thus the dependence of gain on gas pressure and other kinetic properties differs substantially from that predicted by scaling results from conventional low-pressure lasers.**

I. Introduction

THE waveguide CO_2 laser is a compact, high-gain, tunable CO_2 laser. It is an attractive device for many applications including, in particular, laser communications and high-resolution spectroscopy. For these applications it is essential to know the variations in laser gain and tunability with gas mixture, pressure, discharge current, bore diameter, and wall temperature.

We will calculate the gain in CO_2-N_2-He waveguide lasers using an approach which centers around the rate equations for the vibrational modes of the CO_2 and N_2 molecules. Our analysis draws heavily on the formulation of Gordietz *et al.* [1] and Moore *et al.* [2] for conventional lasers. The essential differences here are the smaller tube-bore diameters, higher gas pressures, and higher current densities. These differences manifest themselves in faster rates of electron-molecule and molecule-molecule energy transfer and in a faster diffusion rate to the tube wall. The higher operating pressures also ensure that the gas is homogeneously broadened in contrast to the inhomogeneous broadening of low-pressure (several-torr) devices.

Before proceeding with this paper we should point out that the gas discharge scaling laws [3], [4] can also provide much information about waveguide lasers via a transformation to a laser with a larger tube diameter whose characteristics have been completely determined. Thus, for example, a laser with a 0.1-cm bore diameter, current density of 150 mA/cm^2, and with a total gas pressure of 100 torr is similar to one with a 1-cm bore, 15-mA/cm^2 current density, gas pressure of 10 torr, and the same gas mixture. While the two discharges have the same relative population distributions, their gains differ due to the different absolute populations and different broadening mechanisms. Furthermore, the scaling laws may be difficult to apply for practical computation of gain since complete characterization of all the required similar discharges is rarely available.

In the next section of this paper we discuss the theory of laser kinetics, then in Section III we will discuss the numerical techniques employed in gain computations. In Section IV we present and analyze selected computational results which illustrate the dependence of laser gain on the external parameters. Section V contains our concluding remarks.

Manuscript received November 3, 1975; revised December 1, 1975.

The author is with the Laser Technology Branch, Goddard Space Flight Center, Greenbelt, MD 20771.

II. Theory

The relevant features of the familiar CO_2-N_2 vibrational energy level diagram are shown in Fig. 1. We assume that both the vibrational mode of N_2 and the asymmetric stretch mode (ν_3) of CO_2 are excited by electron impact. Energy exchange between the excited N_2 molecules and the ν_3 mode of CO_2 occurs via nearly resonant V-V energy transfer. Rapid intramode relaxation ensures that the energy level occupancy of the ν_3 mode is characterized by a Boltzmann distribution at temperature T_3. The fraction, $f_2(T_3)$, of the CO_2 molecules whose asymmetric stretch mode is excited is in the upper lasing level (designated 001). De-

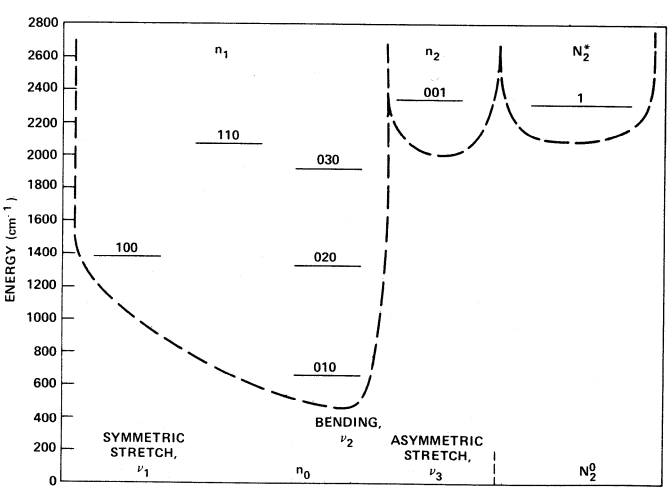


Fig. 1. Energy level diagram for low-lying vibrational states of CO_2 and N_2. The combined population density of the CO_2 bending and symmetric stretching modes (assumed in equilibrium) is n_1; the population densities of the CO_2 asymmetric mode, CO_2 ground state, N_2 excited states, and N_2 ground states are n_2, n_0, N_2^*, and N_2^0, respectively.

excitation of the ν_3 mode occurs both via molecular collisions and wall interactions. The molecular collisions result in the excitation of the ν_1 and ν_2 modes which are assumed to maintain equilibrium due to the rapid Fermi resonance interaction. The equilibrium distribution is characterized by the temperature T_2. A fraction, f_1, of the molecules in the combined ν_{12} mode is in the lower laser level (assumed in the present calculation to be the 100 level). De-excitation of the ν_{12} mode occurs via diffusion loss to the walls and via molecular energy transfer, in particular, via V-T processes from the 010 level. Thus, for a fixed gas mixture, total pressure, and electron temperature, the system is described by the density, n_2, of CO_2 molecules in the ν_3 mode, the density, n_1, of CO_2 molecules in the ν_{12} mode, the density of excited nitrogen molecules, N_2^*, and kinetic temperature. The vibrational population inversion is $\Delta n = f_2 n_2 - f_1 n_1$.

The steady-state rate equations for a closed gas system are

$$\frac{dn_2}{dt} = \alpha n_0 - \rho n_2 + K n_0 N_2^* - K n_2 N_2^0 + K_{12} n_1 - K_{21} n_2 - \frac{\beta_2 D_{CO_2}}{\Lambda^2} n_2 = 0 \tag{1a}$$

$$\frac{dn_1}{dt} = \omega K_{21} n_2 - \omega K_{12} n_1 + \tfrac{1}{2} K_{01} n_0 - \tfrac{1}{2} K_{10} n_1 - \frac{\beta_1 D_{CO_2}}{\Lambda^2} n_1 = 0 \tag{1b}$$

$$\frac{dN_2^*}{dt} = \gamma N_2^0 - \zeta N_2^* - K n_0 N_2^* + K n_2 N_2^0 - \frac{\beta_{N_2} D_{N_2}}{\Lambda^2} N_2^* = 0 \tag{1c}$$

where

α	rate of electron excitation of the ν_3 mode of CO_2 (s^{-1});[1]
ρ	rate of electron de-excitation of the ν_3 mode of CO_2 (s^{-1});[1]
K	rate constant for vibrational energy exchange between excited states of N_2 and the ν_3 mode of CO_2 ($cm^{-3} \cdot s^{-1}$);
K_{21}	rate of collisional transfer of energy from the ν_3 to the ν_{12} mode of CO_2 (s^{-1});
K_{12}	rate for inverse process of K_{21} (s^{-1});
K_{10}	rate of collisional de-excitation from the ν_{12} mode to ground state (s^{-1});
K_{01}	rate for inverse process of K_{10} (s^{-1});
γ	rate of electron excitation of N_2 vibration (s^{-1});[1]
ζ	rate of electron de-excitation of N_2 vibration (s^{-1});[1]
D_{CO_2}	diffusion coefficient for CO_2 molecules (cm^2/s);
D_{N_2}	diffusion coefficient for the N_2 molecule (cm^2/s);
Λ	($=R/2.4$ where R is the tube radius) diffusion distance factor (cm);
n	density of CO_2 molecules (cm^{-3});
n_0	density of CO_2 molecules in ground state (cm^{-3});
n_1	density of CO_2 molecules with the ν_{12} mode excited (cm^{-3});[1]
n_2	density of CO_2 molecules with the ν_3 mode excited (cm^{-3});[1]
N_2	density of nitrogen molecules (cm^{-3});
N_2^0	density of nitrogen molecules in ground state (cm^{-3});
N_2^*	density of excited nitrogen molecules (cm^{-3});[1]
$\beta_1, \beta_2, \beta_{N_2}, \omega$	numerical coefficients.

The first two terms in (1a) are the electron excitation and de-excitation of the CO_2 ν_3 mode. The next two terms give the resonant exchange between ν_3 and the excited N_2 molecules, the terms with K_{21} and K_{12} express the energy transfer between the ν_3 and ν_{12} modes, and the final term represents the de-excitation due to diffusion to the walls. In (1b) the terms containing K_{10} and K_{01} express the relaxation and excitation of the ν_{12} mode to and from the ground state, and the final term is the diffusion loss. Finally, in (1c) the first two terms give the rate of vibrational excitation and de-excitation of nitrogen due to electron impact, and the last term is again a diffusion loss. In the present work we do not consider the decomposition of CO_2 in the laser discharge.

Several of the numerical coefficients appearing in (1a)-(1c) require more detailed explanation. Each of the diffusion terms contains a numerical coefficient, β, which is an estimate of the average number of quanta lost per wall de-excitation of that mode. Thus, for example, Gordietz *et al.* [1] have estimated that, on the average, 1.5 quanta of ν_3 oscillation are lost in a wall de-excitation of n_2, i.e., $\beta_2 = 1.5$. The coefficient ω appearing in front of the $K_{21}n_2$ and $K_{12}n_1$ terms in (1b) takes into account the fact that a molecular collision deactivation of the ν_3 mode in favor of the ν_{12} mode usually results in the excitation of more than 1 quantum of ν_{12} oscillation. (We consider 2 quanta of ν_2 oscillation to be equivalent to 1 quantum of ν_1 oscillation.) Typical de-exciting reactions include

$$(001) + M \longrightarrow (030) + M \tag{2a}$$

$$(001) + M \longrightarrow (040) + M \tag{2b}$$

$$(001) + M \longrightarrow (110) + M \tag{2c}$$

where M can be a CO_2, N_2, or He molecule. Reactions (2a) and (2c), for example, result in a factor of $\frac{3}{2}$ appearing before the $K_{21}n_2$ and $K_{12}n_1$ terms in (1b); reaction (2b) results in a factor of 2. The factor of $\frac{1}{2}$ appearing in the third and fourth terms of (1c) can be explained by considering the collisional deactivation of the ν_{12} mode which occurs primarily through the reaction

$$(010) + M \longrightarrow (000) + M \tag{3}$$

where, in most cases, helium is the dominant collision partner. Since each deactivation of one ν_2 quantum via the

[1] These symbols refer to peak (on-axis value) in (5) and thereafter.

reaction described by (3) is equivalent to the deactivation of only $\frac{1}{2}$ quantum of ν_1 oscillation, and since the (100) state is the lower laser state, terms $K_{10}n_1$ and $K_{01}n_0$ have to be multiplied by a factor of $\frac{1}{2}$.

A few comments should be made about the collision-rate constants K_{21} and K_{10} which refer to the relaxation rate of the ν_3 mode to the ν_{12} mode, and the ν_{12} mode to ground, respectively. Each rate is a composite sum of reaction rates with each of the gas constituents, e.g.,

$$K_{21} = K_{21}^{CO_2} P_{CO_2} + K_{21}^{N_2} P_{N_2} + K_{21}^{He} P_{He} \tag{4}$$

where the specific rate constants, K_{21}^X, are given in units of $(\text{torr} \cdot \text{s})^{-1}$ and the P_X are the partial pressures of the gases. Each of these specific rate constants can be, in turn, the sum of several reactions. For example, three prime contributors to K_{21} are given by reactions (2a)-(2c).

With the exception of the inclusion of diffusion terms in the rate equations, we have, to this point, ignored any spatial variation of the electron and molecule densities. We will now assume that the discharge electrons and the excited states of CO_2 and N_2 have a zeroth-order Bessel function radial distribution, $J_0(r/\Lambda)$, which is centered on the bore axis. Then redefining n_1, n_2, and N_2^* so that they refer to the on-axis (peak) density, the rate equations become

$$\alpha n_0[1] - \rho n_2[2] + K n_0 N_2^*[1] - K n_2 N_2^0[1] + K_{12} n_1[1] - K_{21} n_2[1] - \beta_2 \frac{D_{CO_2}}{\Lambda^2} n_2[1] = 0 \tag{5a}$$

$$\omega K_{21} n_2[1] - \omega K_{12} n_1[1] + \tfrac{1}{2} K_{01} n_0 - \tfrac{1}{2} K_{10} n_1[1] - \beta_1 \frac{D_{CO_2}}{\Lambda^2} n_1[1] = 0 \tag{5b}$$

$$\gamma N_2^0[1] - \zeta N_2^*[2] - K n_0 N_2^*[1] + K n_2 N_2^0[1] - \beta_{N_2} \frac{D_{N_2}}{\Lambda^2} N_2^*[1] = 0 \tag{5c}$$

where

$$[1] = \frac{1}{\pi R^2} \int_0^{2\pi} d\phi \int_0^R r J_0\left(\frac{r}{\Lambda}\right) dr \approx 0.434$$

$$[2] = \frac{1}{\pi R^2} \int_0^{2\pi} d\phi \int_0^R r J_0^2\left(\frac{r}{\Lambda}\right) dr \approx 0.270$$

and where α, ρ, γ, and ζ, which are proportional to electron density, now also refer to the on-axis (peak) excitation and de-excitation rates. Equations (5a)-(5c) can be cast in the form of (1a)-(1c) by dividing each equation by [1] and defining

$$\rho' = \rho[2]/[1] \tag{6a}$$

$$K_{01}'' = K_{01}/[1] \tag{6b}$$

$$\zeta' = \zeta[2]/[1]. \tag{6c}$$

We then reproduce (1a)-(1c) with ρ', K_{01}'', ζ', replacing ρ, K_{01}, ζ. To this set of equations we add the equations for particle conservation, namely,

$$n = n_0 + n_1[1] + n_2[1] \tag{7a}$$

$$N_2 = N_2^0 + N_2^*[1]. \tag{7b}$$

Now eliminating n_0 and N_2^0 by way of (7a) and (7b), combining (5a) and (5c) to eliminate N_2^*, and using (5b) to express n_2 in terms of n_1 we derive a quadratic expression for n_1

$$n_1^2 [K''(\alpha'' + \bar{s}\Omega)] - n_1 [K''(\gamma N_2 + \alpha n - \delta\Omega) + K\bar{s}\theta N_2 + (\alpha'' + \bar{s}\Omega)(\theta + Kn)] - (\gamma N_2 + \alpha n - \delta\Omega)(\theta + Kn) - \theta N_2(\gamma + K\delta) = 0 \tag{8}$$

where

$$\gamma'' = \gamma/[1] \tag{6d}$$

$$K'' = K/[1] \tag{6e}$$

$$\alpha'' = \alpha/[1] \tag{6f}$$

$$\bar{s} = \frac{\frac{K_{01}}{2} + \frac{K_{10}}{2} + \frac{\beta_1 D_{CO_2}}{\Lambda^2}}{\omega K_{21} - \frac{K_{01}}{2}} \tag{9}$$

$$\delta = \frac{-\frac{1}{2} K_{01}'' n}{\omega K_{21} - \frac{K_{01}}{2}} \tag{10}$$

and

$$\Omega = \alpha'' + \rho' + K_{21} + \beta_2 \frac{D_{CO_2}}{\Lambda^2} \tag{11}$$

$$\theta = \gamma'' + \zeta' + \beta_{N_2} \frac{D_{N_2}}{\Lambda^2}. \tag{12}$$

In (8) we have ignored the small excitation of the ν_3 mode from the ν_{12} mode.

The rate constants appearing in the preceding equations are functions of the gas temperature. This temperature is controlled by the rate of energy transfer from electron to gas kinetic energy and by the gas thermal conductivity. We will ignore any spatial variation in the gas temperature and assume that all the energy transferred by electrons to molecular vibration contributes to the temperature rise after vibrational relaxation. We can write [1]

$$\Delta T = T - T_W = \frac{1.36 R^2 [\gamma N_2^0 - \zeta' N_2^* + \alpha n_2 - \zeta' n_0]}{18.9\,\kappa} E_3 \tag{13}$$

where T_W is the wall temperature, E_3 is the energy of the ν_3 quantum, and κ is the thermal conductivity given by [1]

$$\kappa = \kappa_{CO_2}\left[1 + 0.81\frac{P_{N_2}}{P_{He}} + 0.23\frac{P_{He}}{P_{CO_2}}\right]^{-1} + \kappa_{N_2}\left[1 + 1.4\frac{P_{CO_2}}{P_{N_2}} + 0.34\frac{P_{He}}{P_{N_2}}\right]^{-1} + \kappa_{He}\left[1 + 3.4\frac{P_{CO_2}}{P_{He}} + 2.7\frac{P_{N_2}}{P_{He}}\right]^{-1}. \tag{14}$$

Equation (13) is an extension of the result quoted in [1]; the extension takes into account the direct excitation of the ν_3 mode of the CO_2. The numerator of the equation is proportional to the heat input to the gas.

We have noted that the vibrational energy level population inversion is $(f_2 n_2 - f_1 n_1)$ [1]. However, up to now we have not considered the rotational sublevels of each vibrational level (except to implicitly assume that the rotational relaxation is very rapid compared to that of vibration). We now take explicit note of the Boltzmann distribution of rotational sublevels at the gas kinetic temperature, T. The vibration-rotation population inversion is

$$\Delta n_J = f_2 n_2 [1] \frac{2hcB_2}{k_B T} d_2 e^{-J_2(J_2+1)(hcB_2/k_B T)} - f_1 n_1 [1] \frac{2hcB_1}{k_B T} d_1 e^{-J_1(J_1+1)(hcB_1/k_B T)} \quad (15)$$

where d_2 and d_1 are the degeneracies of the upper and lower state rotational sublevels, B_2 and B_1 are the sublevel energies (in cm^{-1}), J_2 and J_1 are the sublevel rotational quantum numbers, h is Planck's constant, c is the speed of light, and k_B is Boltzmann's constant.

Given the population inversion it is a simple matter to calculate the small-signal gain, which for a homogeneously broadened laser line is

$$g(\nu) = \frac{\lambda^2 d_2}{8\pi t_s} \left\{ f_2 n_2 [1] \frac{2hcB_2}{k_B T} e^{-J_2(J_2+1)(hcB_2/k_B T)} - f_1 n_1 [1] \frac{2hcB_1}{k_B T} e^{-J_1(J_1+1)(hcB_1/k_B T)} \right\} \frac{\Delta\nu/2\pi}{(\nu - \nu_0)^2 + \left(\frac{\Delta\nu}{2}\right)^2} \quad (16)$$

where λ is the wavelength of the transition, t_s is the spontaneous-emission lifetime, and $\Delta\nu$ is the linewidth. The gain is a function of the vibration-rotation inversion and the linewidth, both of which vary with temperature, gas mixture, and pressure. The inversion also depends on the discharge current (excitation rate) and the tube wall temperature.

Once we know the line center gain of a laser oscillator as well as the length of the gain medium and the reflectivity of the cavity mirrors, r_1 and r_2, then we can also determine the laser frequency tuning range from line center, Δf [5]

$$\Delta f = \frac{\Delta\nu}{2} \sqrt{\frac{g_0(\nu_0)L}{\ln(1/\sqrt{r_1 r_2})^{-1}}}. \quad (17)$$

III. Computational and Numerical Considerations

While the theory developed in Section II is sufficiently detailed to accurately predict the dependence of laser gain, population inversion, and gas temperature on the kinetic and discharge properties of the laser, it also has simple computational requirements. In practice, for a given set of independent variables, namely, gas mixture, total pressure, pump rate, and wall temperature, an initial estimate is made for the gas temperature (for simplicity our usual estimate is $T = T_W$). The quadratic equation for n_1 is solved, from which the other molecular state populations are computed. From this information we calculate an updated gas temperature using (13). The updated temperature is then reinserted in the loop and the iterative process is continued until temperature convergence has been achieved. After convergence, we calculate f_2, f_1, $\Delta\nu$, and other parameters required to compute the gain. A flow diagram for this process appears in Fig. 2.

This computational procedure has been programmed on an HP model 9820A desk-top calculator with a 429-storage-register memory (about $\frac{3}{4}$ of these registers are required in the current version of our program). Computation of the gain for a particular set of operating conditions requires, typically, a few seconds. The output is either plotted on an HP model 9862A plotter or written on paper tape. The program is input either by magnetic card or magnetic tape using the HP9865A cassette reader.

The rate constants which enter into our calculations are K, $K_{21}(M = CO_2, N_2, He)$, $K_{10}(M = CO_2, N_2, He)$, α, and γ. The rate constants for the inverse processes are determined by detailed balancing. The numerical values for the rate constants and other factors which we have used in our calculations can be found in the references cited in Table I.[2] We have found, however, that the qualitative features of population inversion, gain, and gas temperature are insensitive to the exact values of the rate constants. Thus, for example, replacing the theoretical rate constants of [1] by the somewhat different experimental rate constants quoted in [11]

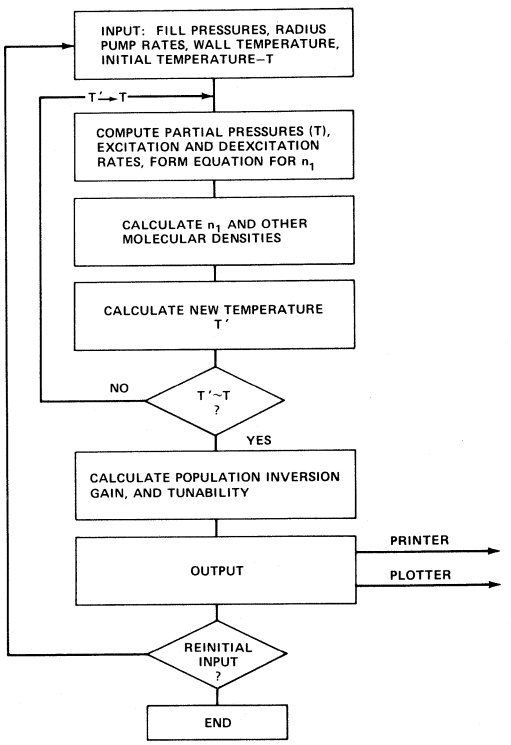


Fig. 2. Logic flow diagram for computation of laser kinetic and discharge properties.

[2]In addition we have chosen $\omega = 1.5$, $\beta_1 = 1.5$, $\beta_2 = 1.0$, $\beta_{N_2} = 1.5$.

TABLE I
REFERENCES FOR RATE CONSTANTS USED TO OBTAIN NUMERICAL RESULTS

Quantity	Reference
$K_{21}^{CO_2}, K_{21}^{N_2}, K_{21}^{He}$	[1]
$K_{10}^{CO_2}, K_{10}^{N_2}, K_{10}^{He}$	[1]
K	[6]
D_{CO_2}, D_{N_2}	[1]
$\kappa_{CO_2}, \kappa_{N_2}, \kappa_{He}$	[7]
$\Delta\nu$	[8]
B_1, B_2	[9]
t_2, t_S	[10], [2]
$\alpha \simeq \gamma/5$	

produces little change in the qualitative dependence of gain on the independent variables.

We should note that in calculating the absolute magnitude of the gain, the spontaneous-emission lifetime for a particular P- or R-branch transition must be used. This quantity, t_S, is related to the radiative lifetime of the upper vibration-rotation level, t_2, by $1/t_S = (S_J/d_2)(1/t_2)$ where $S_J = J_2 + 1$ for a P-branch transition and $S_J = J_2$ for an R-branch transition.

IV. RESULTS

The gas population inversion, gain, gas temperature, and laser tunability have been computed as a function of gas mixture, total pressure, pump rate, bore diameter, and wall temperature. Space limitations require that we present here only selected results which illustrate the salient features of waveguide laser performance.

In Fig. 3 we present the pressure dependence of gain for several gas mixtures. The small-signal gain is evaluated for the line center of the $P(20)$ $001 \rightarrow 100$ transition. We see that the following statements are true.

1) For each mixture there is an optimal operating pressure for maximum gain. The more helium rich the mixture, the higher the optimal pressure.

2) The maximum available gain tends to decrease with increasing helium fraction.

3) The more helium-rich mixtures show less gain variations with pressure.

Similar conclusions have been reached by Abrams and Bridges [4]. In Fig. 3 we also reproduce for comparison purposes experimental data on the laser gain [12]. It is evident that the experimental and theoretical curves agree quite well. The modest reduction in gain from theory to experiment may be due, in part, to decomposition effects.

In Fig. 4, we plot the laser gain versus mixture for two total pressures. At 50 torr, the theoretical optimum gas mixture is very close to that found experimentally to be optimum by Burkhardt *et al.* [13], namely, $CO_2:N_2:He$ in the ratio 1:0.6:1.4. At 150 torr we find that a mixture in the approximate ratio 1:1:5–1:1:7 gives optimum gain even though less helium-rich mixtures have higher gains at lower pressures. Since high laser tunability implies high operating pressures it is clear that the tunable CO_2 waveguide lasers require mixtures that give less than optimal gain at lower pressures.

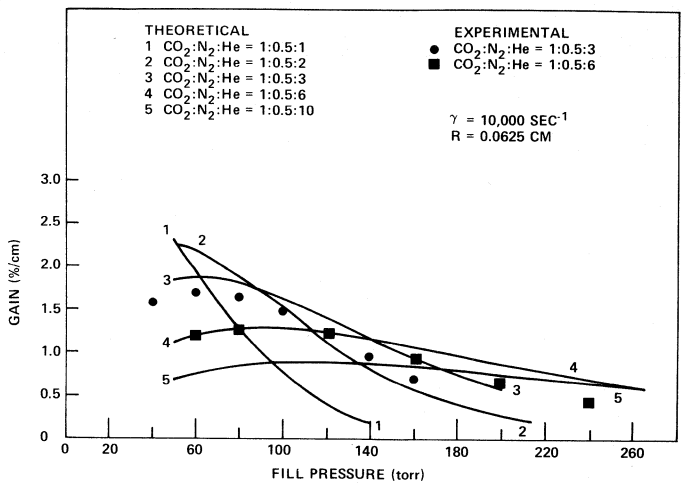


Fig. 3. Small-signal gain versus fill pressure for several gas mixtures. Gain is evaluated at line center assuming homogeneous line broadening. The experimental points are extracted from [12]. We assume that $\gamma = 10\,000\ s^{-1}$ corresponds to a current of 2–3 mA for a 0.0625-cm bore radius.

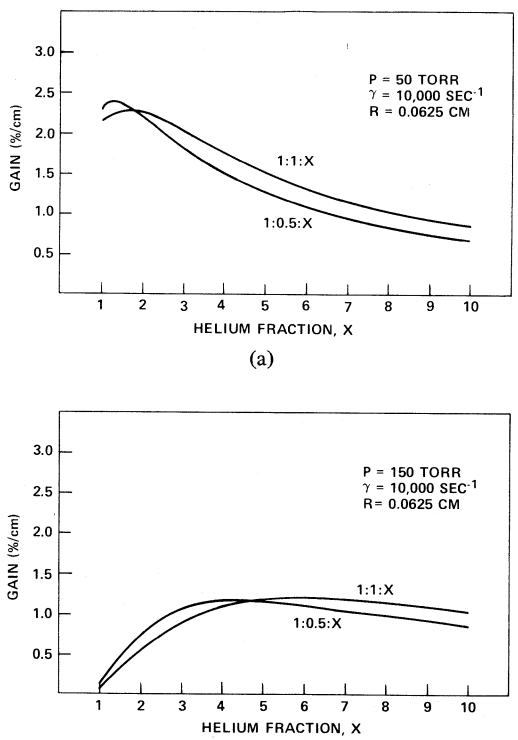


Fig. 4. Small-signal gain versus mixture for total fill pressure of (a) 50 torr. (b) 150 torr.

Fig. 5 shows the dependence of gas temperature on fill pressure for three of the gas mixtures whose gain is plotted in Fig. 3. It is apparent that the decreased sensitivity of the gain of helium-rich mixtures to pressure increases is a reflection of cooler, less pressure-dependent gas temperature. Furthermore, Fig. 6 shows that the reason that these more helium-rich mixtures are required at higher operating pressures is to prevent adversely large rises in the temperature. At 150 torr, the presence of helium in the laser discharge prevents a gas-temperature rise of several hundred degrees above the wall

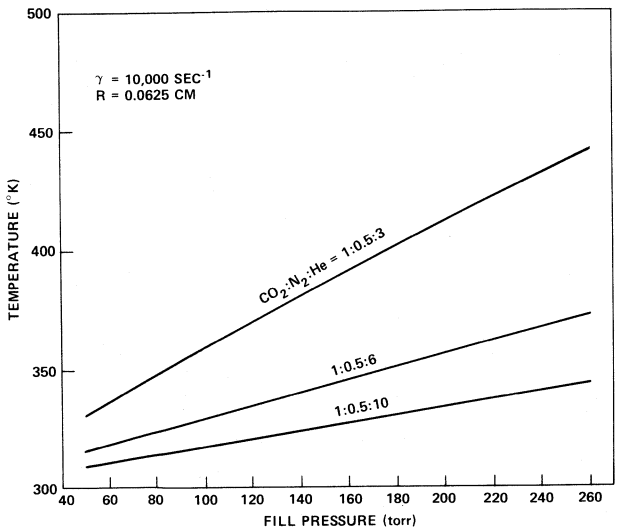


Fig. 5. Temperature versus fill pressure for several gas mixtures.

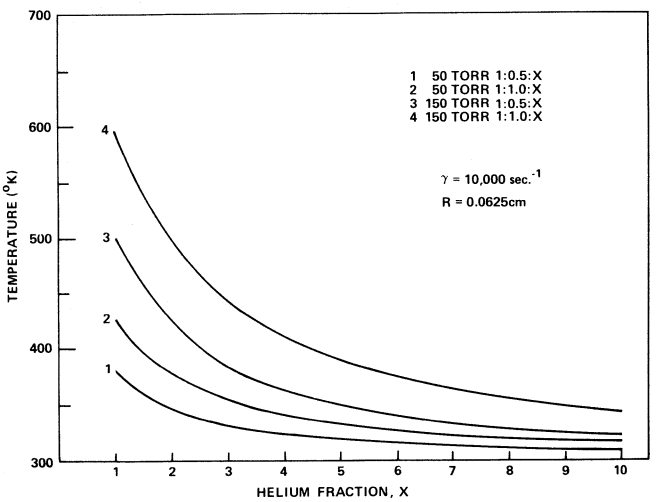


Fig. 6. Temperature versus gas mixture for fill pressures of 50 and 150 torr.

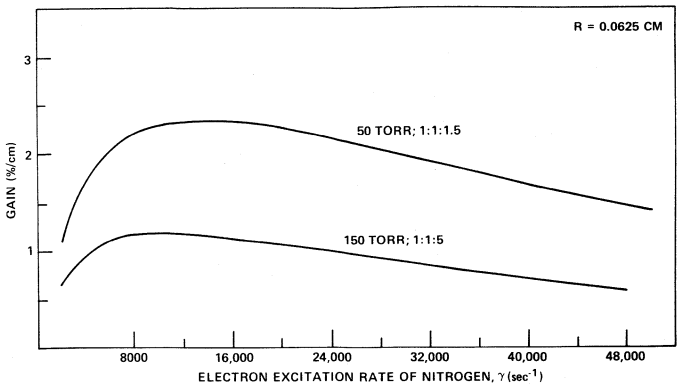


Fig. 7. Small-signal gain versus pump rate.

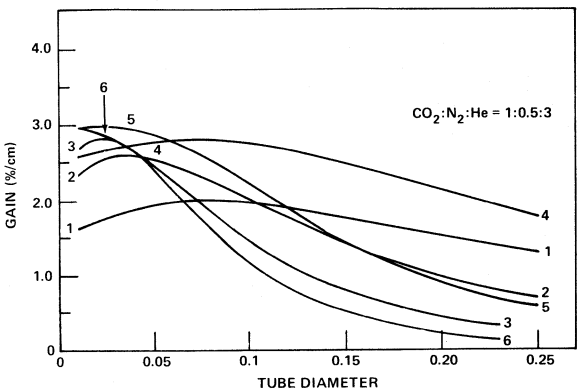


Fig. 8. Small-signal gain versus tube-bore diameter: 1, pressure = 50 torr, $\gamma R^2 = 39$; 2, pressure = 100 torr, $\gamma R^2 = 39$; 3, pressure = 150 torr, $\gamma R^2 = 39$; 4, pressure = 50 torr, $\gamma R^2 = 117$; 5, pressure = 100 torr, $\gamma R^2 = 117$; 6, pressure = 150 torr, $\gamma R^2 = 117$; $\gamma R^2 = 39$ (117) corresponds approximately to a current of 2 (6) mA.

temperature. At 50 torr, the potential temperature rise is less dramatic; as a consequence less helium is required in the gain-optimized mixture. The role of helium in gas-temperature control is, as in conventional CO_2 lasers, to enhance the gas thermal conductivity over that of an N_2-CO_2 mixture.

Calculations of gain versus typical pump rates (discharge currents) have revealed a somewhat decreasing gain sensitivity to pump-rate variations at higher pressures. As shown in Fig. 7 the gain for a 1:1:1.5 mixture at 50 torr and with a bore radius of 0.0625 cm rises to a peak at a nitrogen pump rate of about 14 000 s^{-1}. Assuming (very approximately) that the pump rate is related to the current density by $J = 0.016\gamma$ where J is in mA/cm^2 and γ is in s^{-1}, we find this optimal pump rate corresponds to a current of about 2.7 mA. At 150 torr with a 1:1:5 mixture, the optimal pump rate is reduced to about 10 000 s^{-1}, corresponding to a current of about 2.0 mA.

Another factor influencing gain is the tube diameter. The decreased bore width of a waveguide as compared to a more conventional laser manifests itself in several competing effects. First, since the walls are closer there is a greater rate of molecular diffusion to the walls with subsequent vibrational de-excitation; second, the thermal transport of energy out of the discharge is more rapid; and finally, there is a higher current density. Fig. 8 shows the variation in laser gain as the bore diameter is changed but with the pressure and current held fixed. It is evident that for each pressure there is an optimal bore diameter and current which maximizes the gain. In general, however, smaller bore diameters permit operation at higher gas pressures.

As expected and shown in Fig. 9 the laser wall temperature has significant impact on gain. With lower wall temperatures, the excited gas remains cooler; hence there are fewer adverse vibrational de-excitations and the population inversion and gain are greater. We find, for example, that for a 1:1:1.5 mixture at 50 torr the gain increases from 1.7 percent/cm, to 2.9 percent/cm as the wall temperature is lowered from 350 K to 250 K.

In Fig. 10 we plot the laser tunability as a function of pressure. The parameter $(2/L)$ ln $[1/(r_1 r_2)^{1/2}]$ is approximately equal to the loss divided by gain-medium length. It is important to note that for high losses the less helium-rich mixtures provide maximum tunability while for low losses, the non helium-rich mixtures are preferred. Thus, for example, with a loss of 0.2 percent/cm the 1:0.5:3 mixture has a maximum tunability of 460 MHz at 110 torr while the 1:0.5:6 mixture has a maximum tunability of 300 MHz at 125 torr. By contrast, with a loss of 0.5

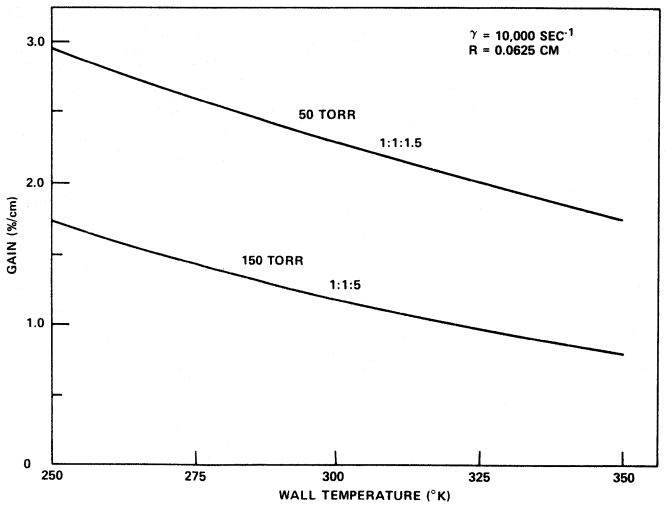


Fig. 9. Small-signal gain versus wall temperature.

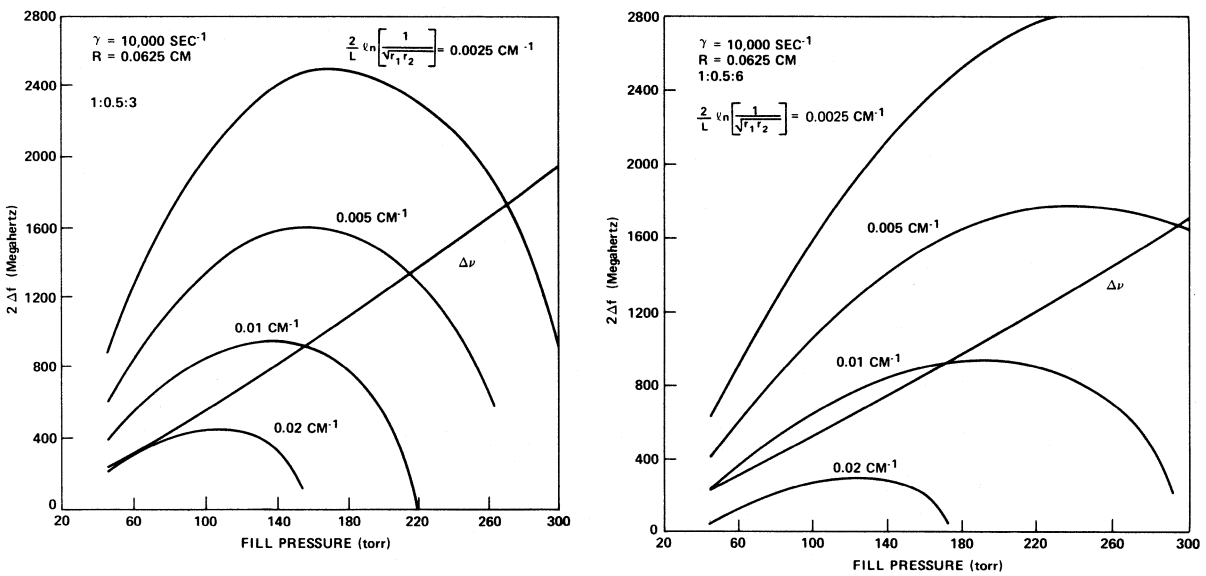


Fig. 10. Laser tunability, $2\Delta f$, versus fill pressure. The parameter $(2/L)\ln[1/(r_1r_2)^{1/2}]$ is essentially the loss divided by gain-medium active length. (a) Gas mixture $CO_2:N_2:He$ in the ratio 1:0.5:3. (b) Gas mixture $CO_2:N_2:He$ in the ratio 1:0.5:6.

percent/cm the 1:0.5:3 mixture has a maximum tunability of 1600 MHz at 160 torr while the 1:0.5:6 mixture has a tunability of 1780 MHz at 240 torr. In all cases it is apparent that the tunability peaks at some optimal pressure, a consequence of the dependence of both the gain and the linewidth on pressure. The value of the optimal pressure and the associated tunability depends on the cavity losses and length [5].

V. Concluding Remarks

The role of the three gases in the waveguide laser mixture is essentially the same as in conventional lasers. The nitrogen acts as a pump for the inversion in CO_2. The helium assures rapid depopulation of the lower laser level and increases the gas thermal conductivity over that of CO_2-N_2 mixtures.

The population inversion in the laser discharge is determined by the competition among several kinetic processes including electron-molecule collisions, inter- and intramolecule energy transfer, molecular diffusion, and molecule-wall interaction. In particular, the diffusion to the walls and subsequent de-excitation as well as direct collisional de-excitation are responsible for the vibrational deactivation of the CO_2 molecule. At low pressures the diffusion loss dominates the de-excitation. As the pressure increases, the rate of collisional de-excitation increases, but the diffusion rate is reduced; hence wall losses become less significant and collisional de-excitation dominates. At the higher operating pressures collisions further reduce the gain by homogeneous broadening of the laser transition. Thus the gain peaks at substantially lower pressures than does the population inversion.

ACKNOWLEDGMENT

The author wishes to thank J. Degnan and W. Leeb for stimulating discussions on several aspects of the work.

REFERENCES

[1] a) B. F. Gordietz, N. N. Sobolev, V. V. Sokovikov, and L. A. Shelepin, "Vibrational level inversion population of polyatomic molecules, CO_2 laser," *Phys. Lett.*, vol. 25A, pp. 173–175, July 1967.
b) B. F. Gordietz, N. N. Sobolev, and L. A. Shelepin, "Kinetics of physical processes in CO_2 lasers," *Sov. Phys. JETP*, vol. 26, pp. 1039–1045, May 1968.
c) B. F. Gordietz, N. N. Sobolev, V. V. Sokovikov, and L. A. Shelepin, "Population inversion of the vibrational levels in CO_2 lasers," *IEEE J. Quantum Electron. (Special Issue–1968 Int. Quantum Electron. Conf.: Part II)*, vol. QE-4, pp. 796–802, Nov. 1968.
d) J. Tulip, "Gain saturation of the carbon dioxide laser," *IEEE J. Quantum Electron.*, vol. QE-6, pp. 206–211, Apr. 1970.

[2] C. B. Moore, R. E. Wood, B-L. Hu, and Y. T. Yardley, "Vibrational energy transfer in CO_2 lasers," *J. Chem. Phys.*, vol. 46, pp. 4222–4231, June 1967.

[3] V. K. Konyukhov, "Similar gas discharges for CO_2 lasers," *Sov. Phys.–Tech. Phys.*, vol. 15, pp. 1283–1287, Feb. 1967.

[4] R. L. Abrams and W. B. Bridges, "Characteristics of sealed-off waveguide CO_2 lasers," *IEEE J. Quantum Electron.*, vol. QE-9, pp. 940–946, Sept. 1973.

[5] J. J. Degnan, "Phenomenological approach to the design of highly tunable pressure broadened gas lasers," *J. Appl. Phys.*, vol. 45, pp. 257–262, Jan. 1974.

[6] W. A. Rosser, A. D. Wood, and E. T. Gerry, "Deactivation of vibrationally excited carbon dioxide by collisions with carbon dioxide or nitrogen," *J. Chem. Phys.*, vol. 50, pp. 4996–5007, June 1969.

[7] D. E. Gray, Ed., *American Institute of Physics Handbook*, 3rd ed. New York: McGraw-Hill, 1972, pp. 4–149.

[8] a) O. Judd, Hughes Res. Labs., Internal Res. Rep. 452, 1971.
b) R. L. Abrams, "Broadening coefficients for the $P(20)$ CO_2 laser transition," *Appl. Phys. Lett.*, vol. 25, pp. 609–611, Nov. 1974.

[9] R. A. McClatchey *et al.*, "AFCRL atmospheric absorption line parameters compilation," AFCRL Tech. Rep. 73-0096, p. 24, Jan. 1973.

[10] C. P. Christensen, C. Freed, and H. A. Haus, "Gain saturation and diffusion in CO_2 lasers," *IEEE J. Quantum Electron.*, vol. QE-5, pp. 276–283, June 1969.

[11] R. L. Taylor and S. Bitterman, "Survey of vibrational relaxation data for processes important in the CO_2–N_2 laser system," *Rev. Mod. Phys.*, vol. 41, pp. 26–47, Jan. 1969.

[12] "Design report for NASA contract NAS 5-20623," Hughes Aircraft Co., Hughes Res. Rep. D0460, May 1975.

[13] E. G. Burkhardt, T. J. Bridges, and P. W. Smith, "BeO capillary CO_2 waveguide laser," *Opt. Commun.*, vol. 6, pp. 193–195, Oct. 1972.

Measurement of Optical Gain in CO Gas Excited Only by Fission Fragments

DAVID A. McARTHUR AND PHILIP B. TOLLEFSRUD

Abstract–**Gain has been measured in high-density (~0.5 amagat) CO gas, which was cooled to 77 K and excited with an intense burst of fission fragments induced by a fast-burst reactor (Sandia SPR II). Peak-gain coefficients $\lesssim$0.5 percent/cm were measured in pure CO over the wavelength range 5.1–5.33 μ, for fission-fragment energy depositions ~200 J/l. Interpreting the measured gains with an approximate steady-state vibrational distribution implies that ~25–70 percent of the fission-fragment energy deposited in the CO is appearing as excitation of the vibrational modes of the CO molecule.**

I. INTRODUCTION

THE goal of achieving laser excitation directly with nuclear reaction products has been pursued since shortly after the invention of the laser [1]. Nuclear-reactor-excited lasers are of interest because of the possibility that such lasers would have unique characteristics, and because typical reactors store very large amounts of energy in their cores and can be scaled to produce very high powers. The potential high power and scalability of a reactor-excited laser is particularly attractive in view of the recent proposals to use lasers in such large-scale industrial processes as isotope separation and industrial photochemistry [2], or to heat fusion plasmas [3]. Preliminary conceptual designs for reactor-excited lasers are also much simpler than corresponding designs for scaled-up electrically excited gas lasers [4], which may increase laser reliability and ease of maintenance significantly.

Fig. 1 shows the general scheme of excitation of a gas laser medium by fission fragments emerging from a foil. The ^{235}U fission fragments created initially in the foil are heavy, highly charged particles moving with a velocity about equal to that of a 500-eV electron. The energy and charge of the fragment will have decreased somewhat by the time it enters the laser gas, if the fragment was created deep within the foil. The fragment moves approximately in a straight line, exciting and ionizing gas molecules along its path. The laser medium can either be excited solely by the fission fragments, or the fission fragments can be used merely to preionize the medium, which is then pumped primarily by an electric discharge. Enhancement of the power output of electrically excited lasers has been ob-

Manuscript received November 6, 1975.
The authors are with the Sandia Laboratories, Albuquerque, NM 87115.

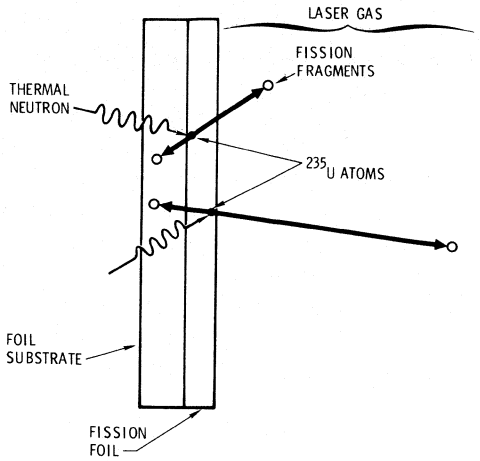


Fig. 1. Schematic diagram of excitation of a laser medium by fission fragments emerging from a fission foil. Typical properties of fission fragments from ^{235}U fission are in the range $\sim 3 \times 10^{-3}$ g/cm^2, mass ~95 or 138 μ, initial charge ~ +20 electron charges, and initial velocity $\sim 10^9$ cm/s. To obtain significant excitation of the laser medium, an intense source of neutrons is required.

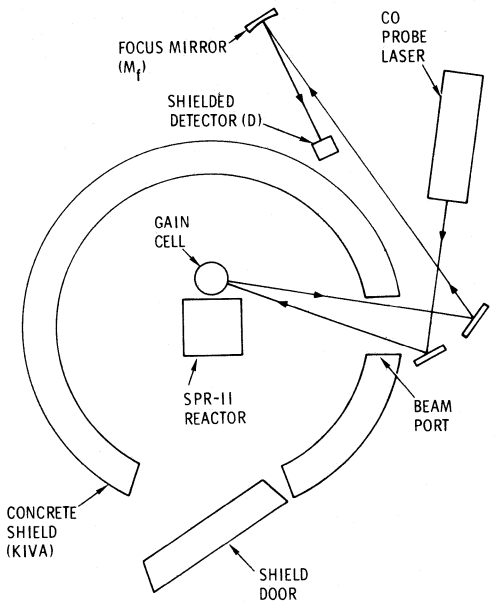


Fig. 2. Overall view of reactor-excited CO gain experiment. Lead shielding was required around the sensitive Ge:Au detector. After a reactor burst, the reactor can be lowered beneath a lead plate, so that the gain cell apparatus can be adjusted if necessary.

served in several cases, when the electrically operating laser was irradiated with energetic nuclear reaction products induced by neutrons from a reactor [5], or with a beam of energetic particles from an accelerator [6]. Since electrical power supplies are still required as the major energy source for such "reactor-enhanced" lasers, they would not have some of the advantages of compact energy storage, rugged construction, and large energy potential which can be envisioned for pure reactor-excited lasers. Gain and laser action have also been reported in media pumped by intense bursts of gamma radiation from underground nuclear explosions [7], but we shall not discuss this work further because of its apparently limited potential for development of large laboratory and industrial lasers.

More recently, laser action has been observed in cooled CO [8], in He/Xe [9], and in Ne/N_2 mixtures [10] which were excited only by intense bursts of nuclear reaction products which were induced by neutrons from pulsed laboratory nuclear reactors. These reactor-excited systems are of great interest for understanding the physical processes of laser excitation by energetic heavy charged particles. Careful measurements on these systems are also needed to evaluate their potential as efficient laser media for construction of very large lasers excited by reactors.

We report here in detail an initial series of gain measurements on fission-fragment-excited CO-laser media [11], which reveal some characteristics of this new excitation method, as well as several areas of uncertainty in the understanding of the physical processes occurring. As will be shown in greater detail in the following, the gain data indicate that a relatively large fraction of the fission-fragment energy deposited in the gas is rapidly converted to vibrational excitation of the CO gas.

II. Experimental Apparatus

Fig. 2 shows the overall experimental arrangement, which consisted of the pulsed neutron source (the Sandia Pulse Reactor II, or SPR II) [12], the CO gain cell located adjacent to the SPR II, and a CW-CO probe laser and shielded Ge:Au

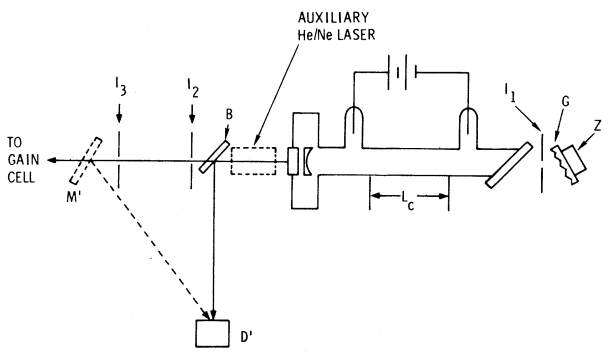


Fig. 3. CO probe laser system. The cooled length $L_c \approx 67$ cm, and the laser tube ID ≈ 1.3 cm.

detector D located outside the reactor shielding at distances of ~15 m from the reactor. The SPR II is a fast-burst reactor which typically produced a 50-μs-wide fast neutron pulse with peak flux at the center of the gain apparatus of about 5×10^{17} neutron/cm^{2}s [12].

The probe laser shown in Fig. 3 was a single-line single-transverse-mode CO laser cooled with liquid nitrogen. A mixture of CO, N_2, He, and O_2 at a total pressure of about 10 torr was used. To align the infrared (IR) beam through the distant gain cell and back to the detector D, a pair of adjustable iris diaphragms I_2 and I_3 was first used to locate the IR beam accurately, by maximizing the signal on an auxiliary detector D'. An auxiliary He–Ne laser beam was then directed accurately through I_2 and I_3, and this beam was used to align the rest of the mirrors in the system. Final adjustments were made to the mirrors outside the reactor shield to maximize the probe laser signal from D, up until about 10 min before the reactor burst. The size and position of the intracavity iris I_1 was very critical in maximizing the probe laser signal at the detector D, because it was necessary to force the probe laser to oscillate only in the lowest order transverse mode to minimize

beam divergence. A 0.3-m MacPherson monochromator with a 75-grooves/mm 8-μ blaze wavelength grating was used to measure the wavelength λ of the particular laser transition selected by the intracavity grating G. The monochromator was calibrated with higher orders of a He-Ne laser beam, and the accuracy of quoted wavelengths is ± 0.003 μ. Once the laser wavelength was chosen, the piezoelectric translator Z in the laser grating mount was manually adjusted to compensate for slow laser cavity length changes. To monitor the probe laser beam intensity continuously without disturbing its orientation, the BaF_2 beam splitter B was used.

Typical probe laser beam intensities on a single line at the position of the gain cell were ~ 0.1 mW/cm^2, much smaller than the estimated saturation intensity of the CO gas in the gain cell ($\sim 2 \times 10^4$ W/cm^2) [13]. Typical probe laser signals at the detector D were about 1.0 V; to reduce visible-wavelength fluorescence D was covered with a narrow-band interference filter centered at 5.243-μ wavelength.

Fig. 4 shows the gain cell apparatus in relation to the SPR II reactor. Early attempts to cool the CO gas below room temperature at pressures of the order of 1 atm were frustrated by heat leaks into the gas, which resulted in significant density variations, which in turn strongly deflected the alignment laser beams. To overcome this problem, in the apparatus of Fig. 4 the gas fill comes into contact only with walls which are either in direct contact with liquid nitrogen or which are conduction cooled by liquid nitrogen and well insulated from heat sources. The apparatus was oriented vertically for simplicity and to eliminate convection currents which might be caused by slight heating of the window inside the gain cell. The gain cell consisted of a stainless-steel cylinder of 3.5-cm inside diameter (ID) divided into two chambers separated by a CaF_2 window 2.5 cm in diameter. A vacuum seal between the two chambers was maintained at the CaF_2 window by Teflon O rings. Standard copper-gasket vacuum flanges were used where possible in the apparatus. The upper chamber was evacuated to provide thermal insulation for the inner CaF_2 window, and the probe laser beam was admitted through an outer CaF_2 window in the top of the apparatus.

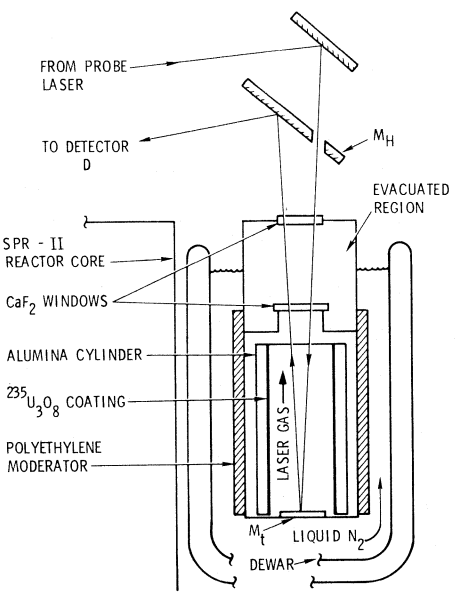


Fig. 4. Details of cooled gain cell. Neutrons diffuse readily through the stainless-steel walls of the apparatus.

The lower chamber contained the laser gas in which gain was being measured, and the fission foil exciter. The foil substrate was a 2.7-cm-ID alumina tube 20 cm long, coated on its inner surface with about a 10-μ-thick coating of 93-percent enriched U_3O_8 ceramic. The laser gas mixtures chosen were typically pure CO and CO/N_2 mixtures at total pressures of 50 and 100 torr at 77 K. A flat totally reflecting mirror on a Ge substrate was mounted at the bottom of the lower chamber to reflect the probe laser beam back to the mirror M_H and then to the detector D.

The stainless-steel cylinder was immersed in a liquid nitrogen bath contained in a stainless-steel Dewar. The lower part of the cylinder was surrounded with polyethylene cylinders 1.6 or 2.0 cm thick to moderate the fast neutrons from the reactor and thus enhance the fission rate in the foil. The moderator was placed as close as possible to the cylinder to minimize the width of the fission-fragment pulse and to minimize the thickness of thermal-neutron-absorbing liquid nitrogen between the moderator and the fission foil.

In early experiments it was found that the later part of the gain pulse could not be studied accurately, because large probe laser signal variations set in suddenly at about 40 μs after the fast neutron pulse peak. These variations could not be attributed to real gain or absorption, since they were present even when the CO was replaced by an equal pressure of N_2. Since N_2 is a homopolar diatomic molecule, the probe laser beam does not interact with its vibrational modes, yet because of the similarity of the mass and electronic structure of CO and N_2 the energy deposition profiles of the two gases should be almost identical. It was, therefore, concluded that small density variations in the heated gas were deflecting the probe laser beam off the 2-mm diameter of the sensitive area of D.

The 0.8-cm-diameter hole in the mirror M_H served to restrict the probe laser beam to the center of the gain cell where the fission-fragment energy deposition was most uniform at the pressure chosen. Other than the lost reflectivity of the hole, the mirror M_H and the rest of the mirrors in the optical path to the detector D also did not block light which might be scattered through small angles. The mirror M_f (Fig. 2) was adjusted to image the gain cell onto the detector D. This arrangement reduced the beam-deflection noise background at D to less than the other noise backgrounds, for about 800 μs following the neutron pulse. This can be seen in Fig. 5, where the probe laser signal passing through N_2 is almost identical to the background signal observed from an equal pressure of CO, for the first ~ 800 μs. At late times large pressure waves pass through the gas and reduce the detector signal to zero for short periods. Whenever they were well defined, these zero-signal regions were used to obtain the probe laser signal amplitude at the instant of the reactor burst.

III. Results of Gain Measurements

Measurements were made on several CO-laser gas compositions, at total pressures of either 50 or 100 torr, as measured at the 77 K initial temperature of the laser gas before the reac-

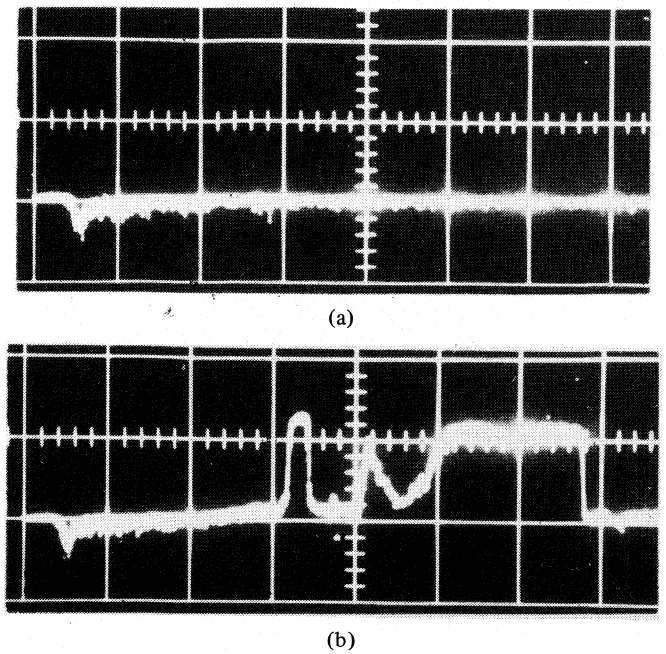


Fig. 5. Demonstration that the mirror arrangement of Fig. 4 nearly eliminates the early-time effects of probe laser beam deflection by nonuniform energy deposition in the gas. (Vertical = 0.5 V/div, horizontal = 500 μs/div.) (a) Fluorescent background (laser off, 100-torr CO). (b) Beam-deflection background (laser on, 100-torr N_2).

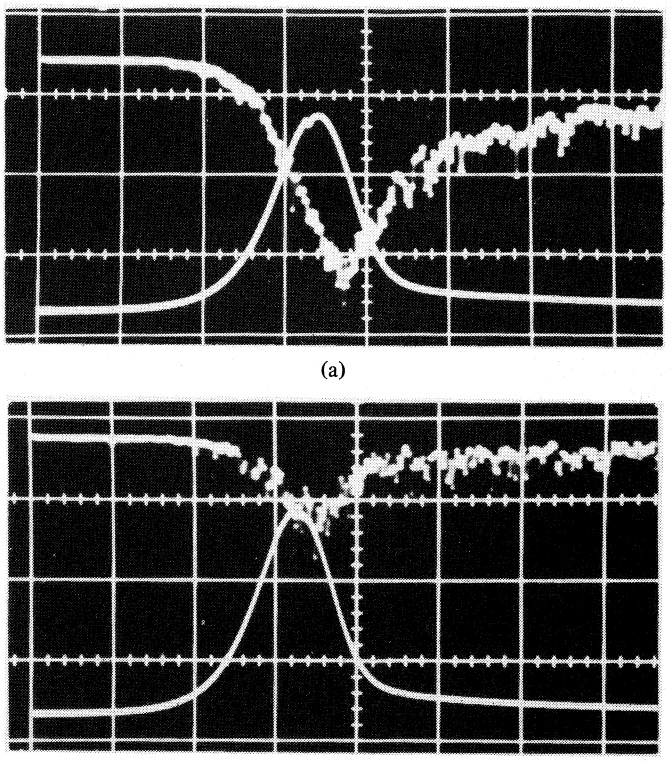


Fig. 6. Gain signal in 100-torr CO at λ = 5.270 μ. (a) Raw gain signal (laser on). (b) Fluorescence and radiation noise background signal with probe laser beam blocked (laser off). (Vertical = 0.2 V/div, horizontal = 50 μs/div.)

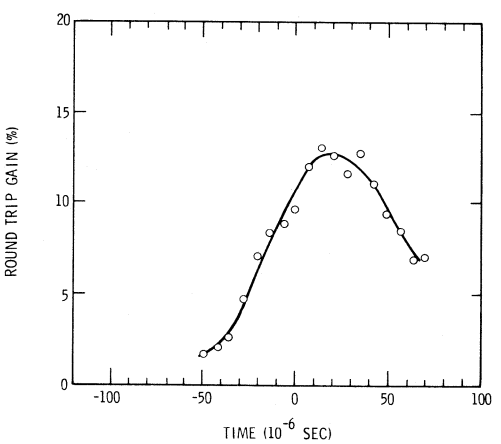


Fig. 7. Corrected round-trip gain signal obtained by subtracting the signal of Fig. 6(b) from Fig. 6(a).

tor burst. Very consistent and repeatable gain data were observed with pure CO, but large fluctuations in the magnitude and time dependence of the gain (or absorption) were observed in 50-percent CO/50-percent N_2 and 25-percent CO/75-percent N_2 mixtures. The gases were admitted separately to the cooled gain cell and diffusion was relied upon to mix them during the wait before the reactor burst (typically about 30 min). Since diffusion times over the length of the gain cell at this low temperature and high density (~0.5 amagat) are comparable to the waiting period, incomplete mixing of the gases may have contributed significantly to the inconsistent results obtained with gas mixtures. Therefore, we report here only the gain data measured in pure CO gas.[1]

The general features of the gain pulses in pure CO are illustrated in Fig. 6. The upper trace in Fig. 6(a) shows the time dependence of a typical gain pulse (referred to as a laser-on signal), and the lower trace is the time dependence of the pulse of fast neutrons from the SPR II reactor. The upper trace in Fig. 6(b) is the radiation and fluorescence background signal obtained by repeating the reactor burst with the CO probe laser beam blocked. Taking the difference of the two detector signals in Fig. 6(a) and (b) (neglecting the noise spikes) yields the gain signal shown in Fig. 7, where the zero of time has been taken to be the peak of the fast neutron pulse from the reactor, and the round-trip gain is expressed as a fraction of the probe laser signal.

The major sources of noise in the data were the spikes of radiation-induced detector noise, the fluorescence signal from the gas, and slow variations in the probe laser signal. The error in the probe laser signal was about 5 percent, which is negligible compared to the other sources of noise. The gas fluorescence signal varied slowly in time and slowly with the size of the reactor burst, so that it would be possible to subtract this contribution from the laser-on signal to obtain the gain signal. However, the large radiation-induced noise spikes seen in Fig. 6 made it difficult to define the signal amplitudes. Ideally, it would be possible to make these noise contributions negligible by increasing the probe laser signal, but in practice the

[1]The apparatus has recently been modified to premix the gas fill mechanically, and laser action has been observed in 50/50 CO/Ar mixtures [4].

signal-to-noise (S/N) of the gain data on each line depends strongly on the amplitude of the probe laser signal used to measure the gain, as well as the gain magnitude.

Two methods were used to subtract the background signals from the laser-on signal to obtain the gain signal. In the first method the laser-on and background signal amplitudes were defined by the envelope of the bottoms of the radiation noise spikes, to an uncertainty of about ±25 mV. Since the peaks of the background and laser-on signals were coincident in time to within the experimental error, the peak-gain signal was defined as the peak laser-on signal L_p [cf. Fig. 6(a)] minus the peak background signal B_p [cf. Fig. 6(b)]. The measured B_p was a slowly increasing function of the reactor burst size (Fig. 8), where the burst size was characterized by the peak temperature rise in the reactor core ΔT measured in degrees centigrade. The peak-gain coefficient for data taken with the full detector system bandwidth (BW) then becomes

$$\alpha_p \text{ (full BW)} = (L_p - B_p)/2LS_0 \tag{1}$$

where $L = 20.3$ cm is the length of the fission foil in the gain cell, and S_0 is the probe laser signal at the time of the reactor burst for the particular CO-laser line being studied. Fig. 8 also shows the dependence of α_p (full BW) on the reactor ΔT for a probe laser wavelength $\lambda = 5.270$ μ. The error bars are determined by the magnitude of the net gain signal in relation to the ±25-mV uncertainty in its determination.

The second method of obtaining α_p involved smoothing the same laser-on and background signals used to obtain α_p (full BW), by observing them on an oscilloscope plug-in containing filters with a passband of 0–30 kHz. The filtered laser-on signal $S(t)$ and background signal $B(t)$ were digitized at 10-μs time intervals, and the $B(t)$ signals for several ΔT were averaged to obtain a background signal $\bar{B}(t)$. Using a computer, the difference signal was calculated, and a peak value obtained by fitting a parabola to the five highest points. A peak-gain signal was then obtained in analogy to α_p (full BW)

$$\alpha_p(\text{smoothed}) = [S(t) - \bar{B}(t)]_p/2LS_0. \tag{2}$$

These data for the $\lambda = 5.270$-μ CO-laser line are shown in Fig. 9 as a function of reactor ΔT. The error bars are obtained from the residual noise after smoothing. Since $2LS_0\alpha_p \lesssim 0.20$ for all data, the linear approximation to the exponential gain is accurate compared to the experimental error.

The magnitude of the peak gain varies strongly with ΔT, appearing to have a threshold at about $\Delta T = 200$°C for both methods of analyzing the data, and increasing approximately logarithmically with ΔT at about the same slope (to ±25 percent). The total energy deposited in the gas is accurately proportional to ΔT, although the rate of energy deposition may rise slightly faster than ΔT when the SPR II reactor kinetics and the incomplete moderation of the neutrons are taken into consideration. Figs. 8 and 9 show that a threshold energy deposition is required to produce gain, which is characteristic of the CO-laser medium. Above the threshold ΔT the gain rises rapidly but less than linearly. The method chosen to plot the data has no theoretical significance, and more detailed data may show a slightly different ΔT dependence. This functional form was not checked in detail for other laser transitions, but scattered data taken on other lines are consistent with this functional form.

The safety rules for operation of the SPR II reactor make it difficult to reproduce the same ΔT value for many bursts, if the time between bursts varies appreciably. Because of the strong variation of α_p with ΔT, it is necessary to normalize the gain data to a common ΔT in order to compare different laser lines. We have, therefore, made the assumption that all laser lines obey the same ΔT dependence as the $\lambda = 5.270$-μ line, and normalized all α_p data to a common ΔT value of 320°C. Since $\Delta T = 320$°C lies near the average ΔT of all gain data taken, the extrapolations are small for many data points. Fig. 10 shows the resulting peak gain $\bar{\alpha}_p$, normalized to $\Delta T = 320$°C and averaged for the two methods of averaging the radiation noise. Based on the measured λ these data represent transitions from the upper laser levels with vibrational quantum number $v = 10$, 9, and 7, and for the higher v values the gain appears to peak near $J = 9$. The overall dependence of

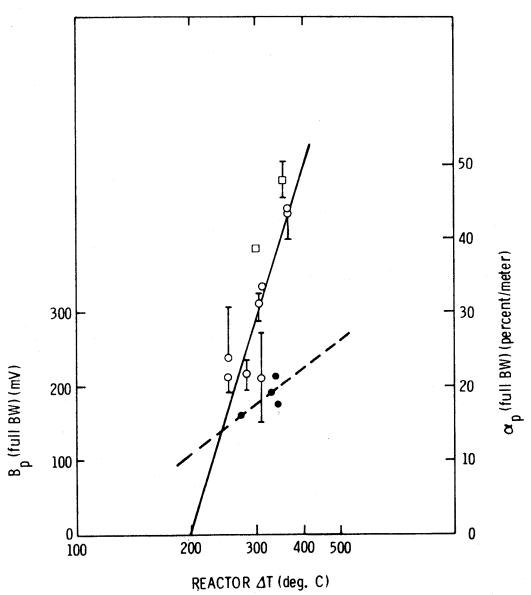


Fig. 8. Dependence of background signal B_p and peak-gain coefficient α_p on reactor burst size, for the "full bandwidth" gain data ($\lambda = 5.270$ μ). ○ – 1.6-cm polyethylene; □ – 2.0-cm polyethylene; ● – Background.

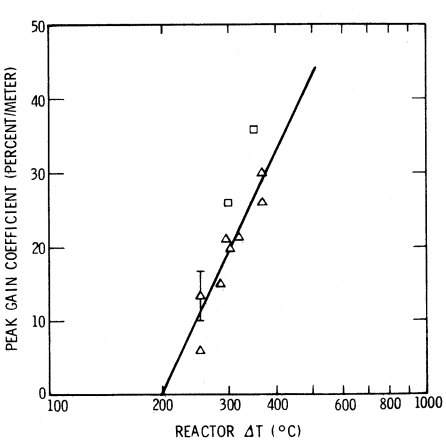


Fig. 9. Dependence of "smoothed" peak-gain coefficient on reactor burst size ($\lambda = 5.270$ μ). Typical error bars are shown. Polyethylene thickness: Δ – 1.6 cm; □ – 2.0 cm.

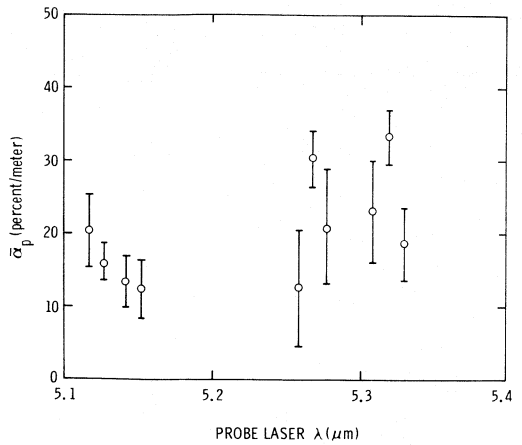


Fig. 10. Dependence of peak-gain coefficient $\bar{\alpha}_p$ on probe laser wavelength normalized to $\Delta T = 320°C$ and averaged.

the gain versus λ is similar to that in low-pressure CW-CO lasers [13]. The observation is confirmed by the fact that gain was first observed using a free-running CO probe laser which was oscillating intermittently on many different transitions in the wavelength range of Fig. 10. In spite of this, the initially observed gains were only about a factor of 2 or 3 lower than the peak gains observed with a single-line CO probe laser.

The full width at half maximum (FWHM) of the gain pulses was somewhat larger for the higher lying vibrational levels. Fig. 11 shows the average pulse width $\bar{\tau}$ obtained from the "full-bandwidth" and "smoothed" data, as a function of the vibrational quantum number v' of the upper laser level.

To calculate the average fission-fragment energy input into the gas as a function of time, a neutron-transport calculation was performed for the actual three-dimensional geometry of the gain experiments [14]. This calculation yielded the time-dependent neutron spectrum at the fission foil, which could then be used to calculate both the ^{235}U fission rate in the foil, and the time-integrated flux (or fluence) of thermal neutrons with energies below 0.4 eV. The fluence of neutrons with energy $E_n \leq 0.4$ eV was also measured at three axial positions along the fission foil with Au and Au–Cd foils (Fig. 12). This measurement shows considerable axial variation, but the average thermal neutron fluence agrees with the calculated average fluence within 15 percent.

Using the calculated fission rate in the foil, the spatially averaged energy deposition rate in the gas was calculated by using a continuous-slowing-down approximation for the fission-fragment transport out of the foil, and approximating the fission-fragment distribution by two groups. It was then assumed that all the fission-fragment energy emerging from the foil was deposited uniformly in the cylinder of laser gas. Fig. 13 shows this calculated average energy deposition rate in the gas for $\Delta T = 320°C$ and 1.6 cm of polyethylene moderator, corresponding to an average energy deposition of 210 J/l. Fig. 13 represents an upper limit to the energy deposition in the laser gas, since effects such as the distribution of fragment ranges and the angular distribution of the fragments emitted from the foil will tend to deposit a portion of the emitted fragment energy in the foil walls.

When the polyethylene moderator thickness was increased from 1.6 to 2.0 cm, the calculated energy deposition was increased by about 40 percent to 293 J/l, and the measured gain on the 5.270-μ line increased by 20–35 percent. The peak of the measured gain pulses shifted from 10 μs to about 30 μs after the peak of the fast neutron pulse. Since the observed gain approximately follows the time dependence of the calcu-

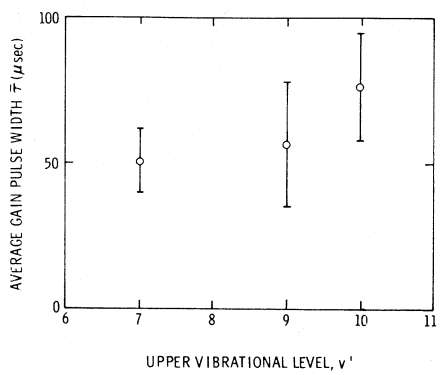


Fig. 11. Measured width of gain pulses.

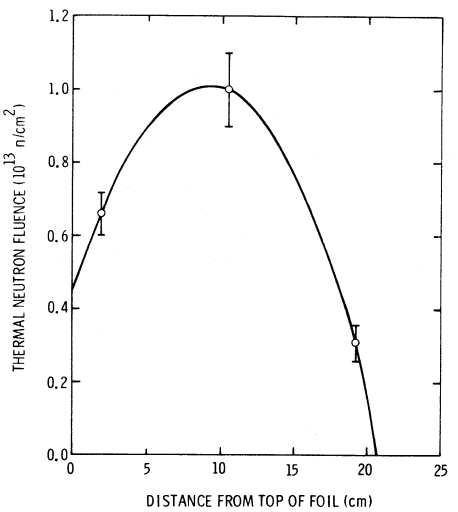


Fig. 12. Axial dependence of measured fluence of thermal neutrons (energy < 0.4 eV), with a parabolic fit to the data.

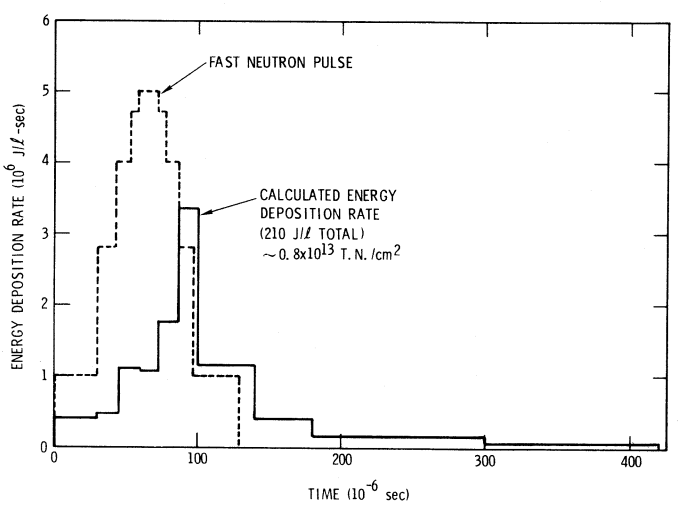


Fig. 13. Calculated rate of fission-fragment energy deposition in the CO, averaged over the volume excited by the fission foil.

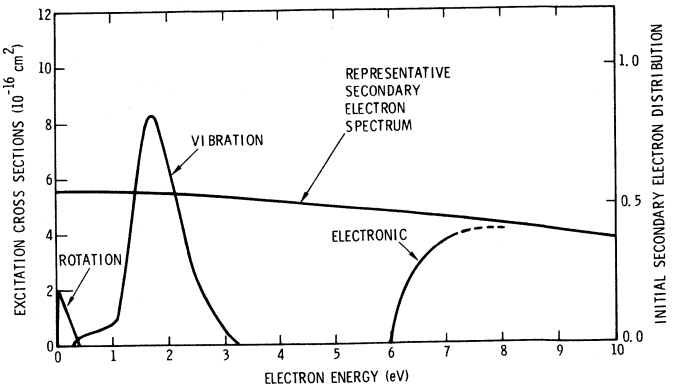


Fig. 14. Schematic drawing of the cross sections for the excitation of the CO molecule by electrons of low energy. The secondary electron spectrum is that measured for 500-eV electrons incident on N_2 [17].

lated energy deposition rate, this time shift may be associated with changes in the details of the neutron moderation process.

Since data were taken primarily at 100 torr where a well-defined gain signal was initially observed, the precise pressure dependence of the gain is unknown. The few data taken at 50 torr of pure CO show slightly wider gain pulses of approximately the same magnitude.

Some gain was observed on every line studied in pure CO. The wavelength range studied was limited by the wavelength passband of the narrow-band interference filter over the Ge:Au detector. Because of time limitations, no data were taken for the $v = 8$ band.

After the series of gain measurements (more than 40 reactor bursts), no damage to the fission foil or the mirror at the bottom of the gain cell was noted. A thin brownish coating, which was soluble in alcohol, was once observed on the mirror, however.

IV. Interpretation of the Gain Data

The paths by which a heavy charged particle such as a fission fragment creates vibrational excitation in a high-pressure gas are not known in detail. Some processes analogous to those in electrically excited laser media are likely to be present, but their relative importance is not known. Detailed calculations [15] for simple monatomic gases show that both ionization and electronic excitation by both the charged particle and secondary electrons occur. From measurements of the average energy a fission fragment loses in creating an ion pair [16], about 40 percent of the fission-fragment energy initially produces ionization in the gas. The secondary electrons so created are expected to have a broad spectrum of initial energies, by analogy to measurements of secondary electron spectra created by fast electrons [17]. The broad range of secondary electron energies would permit the excitation of the electronic, vibrational, and rotational levels of the CO molecule [18], as shown in Fig. 14. In addition the fission fragment itself may excite these levels directly, and also create energetic recoil ions and atoms which could cause further excitation.[2] Finally, the conversion of electronic excitation to vibrational excitation has been observed to be a 60–80-percent efficient process for the $d^3\Delta$ and $a^3\pi$ levels of the CO molecule [19]. This conversion to vibrational energy may also be quite rapid compared to the radiative lifetimes of many electronic levels. From measurements [19] of the collisional quenching rate we estimate that the $a^3\pi$ level would be quenched in about 0.9 ns at 100 torr and 77 K.

The excitation rates to each of the vibrational levels of CO by most of the foregoing processes are unknown, so that any assumptions for those rates would be highly arbitrary. In the absence of the detailed information required to make an accurate time-dependent calculation of the gain from the total energy input rate, we have interpreted the gain data in terms of a simple, approximate steady-state vibrational distribution. The transient gas temperature is unknown, except that some heating can be inferred from the late-time modulation of the probe laser intensity. The pressure of CO in these experiments is about a factor of 10 higher than the partial pressure of CO used in typical high-efficiency electrical CO lasers. Using measured CO $v - v$ relaxation rates at 100 K [20], it can be seen that for our conditions the vibrationally excited CO molecules can transfer their excitation to vibrationally unexcited CO molecules with time constants $\lesssim 10$ μs, which are considerably shorter than the $\sim$150-μs width of the fission-fragment pulse which excites the gas (Fig. 13). Therefore, it is reasonable to assume a form of steady-state nonequilibrium vibrational distribution as a first approximation.

From numerical calculations [21] of the steady-state vibrational distribution of CO molecules (including spontaneous emission and vibrational–translational relaxation), one finds that a reasonable form for an analytical approximation to the steady-state distribution would be given by

$$N_v = N_0 \exp\left(-\frac{vE_1}{kT_v} + \frac{vE_1 - E_v}{kT_g}\right), \quad (v < v_0) \tag{3a}$$

and

$$N_v = N_{v-1}\{(v-1)/(v+1)\}^{1/2}, \quad (v \geq v_0) \tag{3b}$$

where v_0 is the quantum number of the vibrational state at the minimum of the Treanor distribution given by (3a). E_v is the energy of the vth vibrational state assuming $E_0 = 0$, $T_v = -E_1/(k \ln (N_1/N_0))$ is the effective temperature as determined by

[2]The possible importance of these mechanisms was pointed out by G. H. Miller of Sandia Laboratories.

the population of the $v = 1$ level, T_g is the rotational and translational temperature of the gas, and k is Boltzmann's constant. The normalization of the distribution is $\Sigma_{v=0}^{30} N_v = n_0$, where n_0 is the initial CO gas density.

The following procedure was therefore used to compare the peak measured gain at $\Delta T = 320°C$ with an approximate calculated gain: An arbitrary value of T_g was assumed, and T_v was varied through a range, yielding varying distributions N_v. Small-signal gains were calculated for each T_g and T_v for the P-branch transitions of the 10 - 9 through the 6 - 5 vibrational bands of the CO molecule. The gain expression for the P-branch transition with upper level vibrational and rotational quantum numbers v and $J - 1$ is given by [13]

$$\alpha_{v,J-1} = A_{10} \frac{\lambda_0^3}{\lambda} \frac{JvS}{8\pi k T_g} \cdot \{N_v B_v \exp[-B_v J(J-1)/kT_g] - N_{v-1} B_{v-1} \exp[-B_{v-1} J(J+1)/kT_g]\}$$

where $A_{10} = 30.3\ s^{-1}$, $\lambda_0 = 4.608\ \mu$, λ is the probe laser wavelength, and B_v is the rotational constant of the vth vibrational level. Because collisional broadening dominates Doppler broadening at our pressures

$$S \cong 1.109 \sqrt{\pi}/(n_0 \sigma v_{rel})$$

where $\sigma \cong 3.1 \times 10^{-15}\ cm^2$, $v_{rel} = (16RT_g/\pi M)^{1/2}$, $R = 8.317 \times 10^7$ erg/mole K, and $M \cong 28$ g/mole.

For each band the magnitude of peak gain and the wavelength of peak gain were compared with the measured gains shown in Fig. 10. Fig. 15(a)-(c) shows the best fits obtained, as T_v was varied for T_g values of 80, 115, and 150 K. Since the initial temperature is 77 K, 80 K is very close to the lowest reasonable gas temperature. For temperatures greater than 150 K, gain on the $9 \rightarrow 8$ band begins to be much lower than the gain of the $10 \rightarrow 9$ band, which does not agree with experiment. For each T_g, the calculated gains typically varied within the range of experimental uncertainty, as T_v was varied within only about ±25 K around the values shown in Fig. 15. As can be seen from Fig. 15, no one assumption of T_g and T_v fits the entire wavelength dependence of the observed gain. At high T_g the gain magnitude and wavelength peaking within the higher bands are approximately correct, but at shorter wavelengths absorption is predicted rather than gain. At low T_g gain is predicted at shorter wavelengths, but at longer wavelengths the rotational level J of maximum gain is too low. Some of these discrepancies are undoubtedly associated with the piecewise nature of the approximate steady-state distribution, coupled with the fact that calculation of the gain involves taking differences of almost equal populations.

Detailed time-dependent calculations can be made using the energy input rate of Fig. 13, if an arbitrary T_g is chosen and it is assumed that a certain fraction η_v of the fission-fragment energy goes into vibrational excitation of the gas. A few calculations have been made [22], assuming for simplicity that all vibrational excitation goes into the $v = 1$ level. At late times these time-dependent calculations approach the N_v distribution of (3) within ±10 percent, if the steady-state distribution chosen for comparison has the same T_g and the same total vibrational energy. The gains from the time-dependent calculation also agree with the "steady-state" gains within ~ ±5 percent for $v' \gtrsim v_0$, but are about a factor of 2 low for $v' \lesssim v_0$. The time-dependent calculation also shows that the gain rises too slowly on the $v' \geqq 9$ bands. These discrepancies could be related to our ignorance of T_g, and the restrictive assumption that only the $v = 1$ level is directly excited by the fission-fragment energy deposition. Without better knowledge of T_g and the vibrational excitation rates, it appears pointless to continue the time-dependent calculations, although they do confirm the choice of steady-state vibrational distribution used to calculate the gain.

The T_g and T_v values derived from Fig. 15 imply certain increases in the translational, rotational, and vibrational energy of the gas as a result of fission-fragment energy deposition (Table I). Since a ΔT of 320°C corresponds to a calculated input fission-fragment energy of 110 J/l at the peak of the gain pulses, the vibrational pumping efficiency η_v and the gas heating efficiency η_H are defined by

$$\eta_v = (\text{vibrational energy (from } T_v))/(110\ \text{J/l})$$

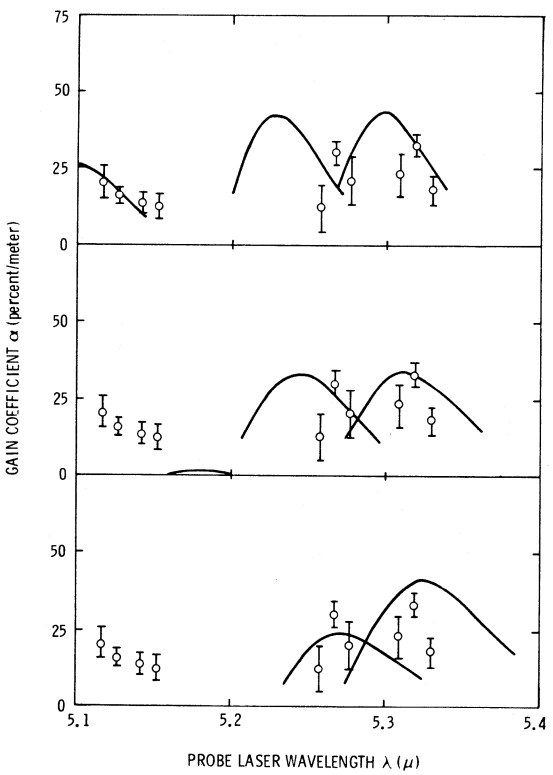


Fig. 15. Fits to peak-gain data for various T_g assumptions. The solid lines are smooth curves drawn through the calculated gain coefficients for various discrete wavelengths. The points are the normalized gain data from Fig. 10. (a) $T_g = 80$ K; $T_v = 1000$ K. (b) $T_g = 115$ K; $T_v = 1200$ K. (c) $T_g = 150$ K; $T_v = 1400$ K.

TABLE I
IMPLIED VIBRATIONAL PUMPING EFFICIENCIES

T_g(°K)	T_v(fit)	η_v(%)	η_H(%)	Energy Discrepancy(%)
80	1000	25	1	73
115	1200	45	15	40
150	1400	70	30	0

and

η_H = (rotational and translation energy (from T_g))/(110 J/l).

Table I thus implies that between 25 and 70 percent of the fission-fragment energy deposited in the gas is appearing as vibrational excitation of the gas. The implied vibrational excitation efficiency is not greatly sensitive to the precise magnitude of the measured gain. For example, if the gain at $t = 70$ μs in Fig. 7 is used (about 45 percent of the peak gain), the implied η_v for the $T_g = 115$ K assumption drops only to 39 percent from 45 percent.

If a low T_g is assumed, a substantial portion of the deposited energy is appearing neither as heat, nor as excitation of the longest lived levels of the gas at this high pressure (the vibrational levels). Current density measurements in fission-fragment-excited CO indicate an instantaneous plasma density of $\lesssim 10^{+14}$ cm^{-3}, which implies a total plasma energy density of $\lesssim 0.25$ J/l, if we include the CO ionization potential and assume an average plasma electron energy of ~ 10 eV. This means that energy which is not accounted for would probably have to reside in relatively long-lived species which eventually undergo chemical reactions to release their energy. One source of energetic atoms might be the dissociative recombination of CO^+ ions, which would presumably result in loss (to the vibrational modes) of some of the ionization energy of the CO^+ ions. However, the measured rate of formation of the $(CO)_2^+$ ion in three-body collisions implies that CO^+ ions are converted to $(CO)_2^+$ ions in ~ 0.1 ns under our conditions, if we neglect the possible temperature dependence of the rate [23]. This conversion rate is fast compared to measured radiative lifetimes of the CO^+ ion and CO molecule [24]. Measured plasma decay rates [25] in high-pressure CO gas are also consistent with recombination of $(CO)_2^+$ ions. If the $(CO)_2^+$ ion breaks up into electronically or vibrationally excited CO molecules after recombination with an electron, it is conceivable that a large fraction of the ionization energy of the CO^+ ion could also be converted to vibrational excitation of ground-state CO molecules. Finally, C and O^- are produced by dissociative attachment of ~ 10-eV electrons to CO molecules [26]. However, the peak attachment cross section of CO is only ~ 1 percent as large as typical peak excitation cross sections to electronic states of diatomic molecules. Since 10 eV is above the excitation threshold of several CO electronic states, it seems likely that only a small fraction of the secondary electrons suffer attachment as they pass through the 10-eV region.

The gain pulse has approximately the shape of the calculated fission-fragment energy deposition pulse, and also resembles the measured gain pulses in electrically excited CO lasers at similar total pressures [27]. The time-dependence of the gain is not well understood, since in the pure CO at low temperatures the vibrational relaxation times are calculated to be much longer than 10^{-3} s even for high-lying vibrational levels. Although the initial gas fill was relatively pure ($\lesssim 0.1$ torr of residual gas before filling), the gas composition after the burst has not been checked. In laser experiments [8] it was noted that a brownish film was formed on the lower laser mirror as a result of irradiation of the gas. Therefore, it is possible that some of the CO decomposition products formed might quench the CO vibrational excitation strongly (e.g., if the brownish film is C_3O_2, it is likely that gaseous CO_2 is also formed in the same reaction [28]). Finally, since the CO-laser gain is very sensitive to the gas temperature, it is also possible that the gain decays as a result of continued heating of the gas later in the excitation pulse.

V. Conclusions

We have measured gain in CO gas initially cooled to 77 K and then excited by an intense pulse of fission fragments induced by neutrons from a fast-burst nuclear reactor. Lines from the 10 - 9, 9 - 8, and 7 - 6 vibrational bands of the CO molecule showed peak gains of up to 0.5 percent/cm. The time dependence of the gain pulse was qualitatively similar to that observed in high-pressure CO gas mixtures used for high-efficiency CO lasers. The peak gains observed here were about an order of magnitude lower than those observed in CO gas mixtures diluted with Ar and N_2, presumably because the excitation per CO molecule was considerably lower in our experiments. The vibrational excitation efficiencies implied by the gain data reported here depend on the value assumed for the unknown gas temperature, but are in the range of 25–70 percent. These high efficiencies are of interest from the standpoint of the physical processes involved, and also for the construction of large reactor-driven CO lasers for possible applications requiring a very high energy, simply constructed laser system with very compact energy storage.

Note Added in Proof: Recently, A. M. Hunter, II, R. D. Franklin, and C. P. Holmes of the Air Force Weapons Laboratory have undertaken more sophisticated calculations of the vibrational excitation of CO by secondary electrons. These calculations include electron–electron interactions and transfer of electronic excitation to vibrational excitation. One result of their calculations is that a small amount of energy deposited in one of the high v levels (perhaps by electronic–vibrational transfer) can significantly change the shape of the vibrational distribution at high v. Therefore, it seems that future theoretical work should treat this type of mechanism in detail.

Acknowledgment

The authors wish to thank A. E. Greene and A. M. Hunter, II, of the Air Force Weapons Laboratory for their cooperation in making several calculations in an effort to understand the possible excitation mechanisms. They also wish to thank Dr. G. H. Miller, J. F. Schulze, and F. A. Morgan for their technical assistance.

References

[1] a) K. Thom and R. T. Schneider, "Nuclear pumped gas lasers," *AIAA J.*, vol. 10, pp. 400-406, Apr. 1972.
b) G. H. Miley, "Nuclear radiation effects on gas lasers," in *Laser Interaction and Related Plasma Phenomena*, vol. 2, H. J. Schwarz and H. Hora, Ed. New York: Plenum, 1972.

[2] a) R. S. Chang and G. J. Wolga, "A laser induced chemical reaction–HF ($v = 3$) + $D_2 \rightarrow$ HD + DF," *IEEE J. Quantum Electron.* (1974 Int. Quantum Electronics Conf. Dig. Tech. Papers), vol. QE-10, p. 702, Sept. 1974.
b) S. A. Tuccio, J. W. Dubrin, O. G. Peterson, and B. B. Snavely, "Two-step, selective photoionization of ^{235}U in uranium vapor," *IEEE J. Quantum Electron.* (1974 Int. Quantum Electronics Conf. Dig. Tech. Papers), vol. QE-10, p. 790, Sept. 1974.

[3] a) J. L. Emmett, J. Nuckolls, and L. Wood, "Fusion power by

laser implosion," *Sci. Amer.*, vol. 230, pp. 24–37, June 1974.
b) J. M. Dawson, "CO_2 gas laser fusion," *Bull. Amer. Phys. Soc.*, ser. II, vol. 19, p. 932, Oct. 1974.

[4] D. A. McArthur, T. R. Schmidt, P. B. Tollefsrud, and J. S. Philbin, "On high-energy (~1 MJ) nuclear-driven gas laser systems," *Trans. Amer. Nucl. Soc.*, vol. 21, pp. 21–22, June 1975.

[5] T. Ganley, J. T. Verdeyen, and G. H. Miley, "Enhancement of CO_2 laser power and efficiency by neutron irradiation," *Appl. Phys. Lett.*, vol. 18, pp. 568–569, June 15, 1971.

[6] S. A. Golubev, V. D. Pismennyi, and T. V. Rakhimova, "Effects of proton beam on the generation of a CO_2 gas laser," *Sov. Phys.–JETP*, vol. 35, pp. 244–247, Aug. 1972.

[7] a) P. J. Ebert, L. J. Ferderber, H. A. Koehler, R. W. Kuckuck, and D. L. Redhead, "Amplified spontaneous emission in xenon pumped by gamma rays," *IEEE J. Quantum Electron.* (1974 Int. Quantum Electronics Conf. Dig. Tech. Papers), vol. QE-10, p. 736, Sept. 1974.
b) P. B. Lyons, J. S. Clarke, and D. S. Metzger, "Gamma initiated HF laser," *IEEE J. Quantum Electron.* (1974 Int. Quantum Electronics Conf. Dig. Tech. Papers), vol. QE-10, p. 736, Sept. 1974.

[8] D. A. McArthur and P. B. Tollefsrud, "Observation of laser action in CO gas excited only by fission fragments," *Appl. Phys. Lett.*, vol. 26, pp. 187–190, Feb. 1974.

[9] H. H. Helmick, J. L. Fuller, and R. T. Schneider, "Direct nuclear pumping of a helium-xenon laser," *Appl. Phys. Lett.*, vol. 26, pp. 327–328, Mar. 15, 1975.

[10] R. J. DeYoung, W. E. Wells, J. T. Verdeyen, G. H. Miley, "A direct nuclear pumped Ne–N_2 laser," in *Proc. 1975 IEEE/OSA Conf. Laser Engineering and Applications*, Washington, DC, May 28–30, 1975.

[11] D. A. McArthur and P. B. Tollefsrud, "Measurement of optical gain on vibrational transitions of CO gas excited only by fission fragments," *Trans. Amer. Nucl. Soc.*, vol. 19, p. 356, Oct. 1974.

[12] L. L. Bonzon and J. A. Snyder, "Sandia pulsed reactor II (SPR II): Experimenter's manual," Sandia Laboratories, Albuquerque, NM, Rep. SLA-73 0551, 1973.

[13] M. L. Bhaumik, W. B. Lacina, and M. M. Mann, "Characteristics of a CO laser," *IEEE J. Quantum Electron. (Part II of Two Parts: Special Issue on 1971 IEEE/OSA Conference on Laser Engineering and Applications)*, vol. QE-8, pp. 150–160, Feb. 1972.

[14] J. Kimlinger and E. F. Plechaty, "SORS Monte Carlo neutron-transport code for the CDC-6600," Lawrence Radiation Laboratory, Livermore, CA, Rep. UCRL-50532, Oct. 1968.

[15] P. E. Thiess and G. H. Miley, "Calculations of ionization-excitation source rates in gaseous media irradiated by fission fragments and alpha particles," in *Research on Uranium Plasmas and Their Technological Applications*, NASA SP-236, pp. 369–396, 1971.

[16] L. O. Herwig and G. H. Miller, "Relative ionization yields for fission fragments in various gases," *Phys. Rev.*, vol. 95, pp. 413–417, July 15, 1954.

[17] C. B. Opal, W. K. Peterson, and E. C. Beaty, "Measurements of secondary-electron spectra produced by electron impact ionization of a number of simple gases," *J. Chem. Phys.*, vol. 55, pp. 4100–4106, Oct. 15, 1971.

[18] a) G. J. Schulz, "Measurement of excitation of N_2, CO, and He by electron impact," *Phys. Rev.*, vol. 116, pp. 1141–1147, Dec. 1, 1959.
b) —, "Vibrational excitation of N_2, CO, and H_2 by electron impact," *Phys. Rev.*, vol. 135, pp. A988–A994, Aug. 17, 1964.
c) R. D. Hake, Jr., and A. V. Phelps, "Momentum-transfer and inelastic-collision cross sections in O_2, CO, CO_2," *Phys. Rev.*, vol. 158, pp. 70–84, June 5, 1967.

[19] a) T. G. Slanger, G. Black, and J. Fournier, "Electronic-to-vibrational energy transfer between molecules," to be published.
b) T. G. Slanger and G. Black, "Electronic-to-vibrational energy transfer efficiency in the $O(^1D) - N_2$ and $O(^1D)$ – CO systems," *J. Chem. Phys.*, vol. 60, pp. 468–477, Jan. 15, 1974.
c) G. W. Taylor and D. W. Setser, "Quenching rate constants for $CO(a^3\pi;\ v' = 0, 1, 2)$," *J. Chem. Phys.*, vol. 58, pp. 4840–4851, June 1, 1973.

[20] C. Wittig and I. W. M. Smith, "Vibrational relaxation of carbon monoxide ($4 \leqslant v \leqslant 10$) at $T = 100°K$," *Chem. Phys. Lett.*, vol. 16, pp. 292–295, Oct. 1, 1972.

[21] G. E. Caledonia and R. E. Center, "Vibrational distribution functions in anharmonic oscillators," *J. Chem. Phys.*, vol. 55, pp. 552–561, July 15, 1971.

[22] A. E. Greene and A. M. Hunter, II, Air Force Weapons Laboratory, Kirtland Air Force Base, Albuquerque, NM.

[23] J. H. Schummers *et al.*, "Measurement of the rate coefficient of the reaction $CO^+ + 2\ CO \rightarrow CO^+ \cdot CO + CO$ in a drift-tube mass spectrometer," *Phys. Rev. A*, vol. 7, pp. 689–693, Feb. 1973.

[24] J. E. Hesser, "Absolute transition probabilities in ultraviolet molecular spectra," *J. Chem. Phys.*, vol. 48, pp. 2518–2535, Mar. 15, 1968.

[25] R. E. Center, "Electron-ion recombination measurements in CO at high pressures," *J. Appl. Phys.*, vol. 44, pp. 3528–3542, Aug. 1973.

[26] D. Rapp and D. D. Briglia, "Total cross sections for ionization and attachment in gases by electron impact. II. Negative-ion formation," *J. Chem. Phys.*, vol. 43, Sept. 1, 1965.

[27] M. J. W. Boness and R. E. Center, "Observations of small-signal gain in high-pressure pulsed CO electric discharge laser," *Appl. Phys. Lett.*, vol. 26, pp. 511–514, May 1, 1975.

[28] S. C. Lind, *Radiation Chemistry of Gases*. New York: Van Nostrand-Reinhold, 1961, pp. 112.

Correspondence

Optical Design of a Frequency-Doubled Nd:YAG Laser

J. D. BARRY

Abstract—The design and laboratory manipulation of the optical resonator of a frequency-doubled Nd:YAG laser has been aided by a unique computer program written for the desk-top HP 9820 calculator-plotter. The program is a self-consistent treatment of Gaussian mode propagation and includes the thermooptical effects of intracavity elements. The optimization of the frequency-doubled laser is greatly aided by use of the computer program. A listing and narrative of the computer program and its use in optimization of the frequency-doubled Nd:YAG is available upon request.

The optical design of an intracavity frequency-doubled Nd:YAG laser for space use which has an optically folded three-mirror geometry has been greatly simplified by the use of a unique self-consistent computer program. The computer program has allowed for the design and experimental verification to be completed with greater ease than normally possible. The computer program was written for the desk-top HP 9820 calculator with plotter. We have used the calculator within the laboratory for rapid theory–experiment verification. The program is used to calculate the optical resonator parameters required for Gaussian-mode operation and is based upon the well-known 2 X 2 *ABCD* matrix method. The computer program is the first widely available to include the important thermooptical influences which affect the laser operation. A listing of the computer program called 405B – AJAX, a discussion of effects which influence the laser operation, and a discussion of its use are available upon request.

A schematic of the intracavity frequency-doubled Nd:YAG laser is shown in Fig. 1 and defines the arrangement and nomenclature used herein. An optically folded cavity is used to enable the 532-nm light to exit the laser in one direction. The frequency-doubled light is generated by an intracavity $Ba_2Na(NbO_3)_5$ crystal. The intracavity lens is used to collimate the circulating laser power through the laser rod, and to optimally focus the light into the $Ba_2Na(NbO_3)_5$ crystal. The intracavity lens is positioned at the confocal position for thermal and mechanical insensitivity [1].

The program calculations are based upon the simultaneous solution of the complex beam parameter, $q^{-1} = R^{-1} - j\lambda/\pi w^2$ and the Gaussian-mode propagation equation $q_2 = (q_1A + B)/(q_1C + D)$ where R is the wavefront radius of curvature; w is the e^{-1} beam radius; λ is the wavelength, 1064 nm; and *ABCD* is the 2 X 2 matrix for the optical system [2]. The system matrix is defined by the single-direction, one-mirror-to-the-other, ordered individual-element 2 X 2 matrix multiplication. Each cavity element or space is represented by an appropriate 2 X 2 matrix [3].

The resonator program is self-consistent by mathematically defining the radius of curvature of the intracavity beam to be equal the radius of curvature of each end mirror at its terminating position. The appropriate equations for the beam e^{-1} size and radius of curvature at any position in the cavity result from the q equations as

Manuscript received February 17, 1975; revised December 1, 1975.

The author is with the Department of Space Laser Communications, Headquarters of the Space and Missile Systems Organization, Los Angeles AFS, CA 90009.

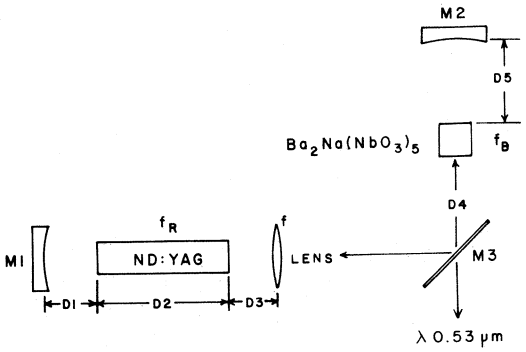


Fig. 1. Diagram of the arrangement of the intracavity frequency-doubled Nd:YAG laser. $M2$ is highly reflective at both 532 and 1064 nm and $M3$ is highly reflective at 1064 nm but transmissive at 532 nm.

$$w_2^2 = w_1^2\left(\frac{A + B/R_1}{D - B/R_2}\right)$$

$$R_2 = \frac{A + B/R_1 + B^2\lambda^2/\pi^2 w_1^4(A + B/R_1)}{C + D/R_1 + BD\lambda^2/\pi^2 w_1^4(A + B/R_1)}$$

$$w_1^4 = \frac{\lambda^2 B}{\pi^2(A + B/R_1)} \frac{R_2D - B}{A + B/R_1 - R_2(C + D/R_1)} \tag{1}$$

where R is positive for concave surfaces viewed from the left. These relations are sufficient to define the beam parameters at each mirror when the system *ABCD* is used, and at any position when appropriate *ABCD* for that propagation is used. The computer program uses the normal Gaussian equations where appropriate, and accepts concave, convex, and flat surfaces.

The computer program requires only four inputs after the individual-element 2 X 2 matrices and the thermooptical parameters have been defined. The inputs are R_1, R_2, f, and D_3 where f is the focal length of the intracavity lens, and D_3 is a probable lens-to-rod-separation operating distance. These parameters are operator input in response to the display, for example, "R_1 = ?". The stability of a resonator configuration is defined in the normal manner, $0 \leqslant g_1g_2 \leqslant 1$; $g_1 = A + B/R_1$, and $g_2 = D - B/R_2$. These parameters are calculated within the program and the word UNSTABLE is displayed and the program halted if the inequality is violated.

The laser resonator program is the first known to us to have incorporated the influences of the thermooptical effects in both the laser rod and in the $Ba_2Na(NbO_3)_5$ crystal. These thermal effects distort the optical configuration and influence a frequency-doubled laser to some degree [4]–[7]. These thermooptical effects include a thermally induced lens in the laser rod and a similar distortion to the $Ba_2Na(NbO_3)_5$ crystal. A value for the focal length of these thermally induced lenses is needed in order to provide the parameters for the *ABCD* matrix used for the two elements.

The rod is treated as a lens-like medium with the index modified by radial variation [3]. The induced focal length is normally experimentally measured, thereby defining the parameters for the appropriate 2 X 2 matrix describing the rod. The thermally induced focal length in the Nd:YAG rod is also related to the heat absorbed per unit volume, Q [2]. The induced focal length measurement may be independently

verified by measuring heat input to the rod and calculating the related focal length.

The $Ba_2Na(NbO_3)_5$ crystal is thermally perturbed by 1064-nm absorption and is also treated as a lens-like medium with the C element of the matrix for the crystal set equal to $+1/f$ rather than $-1/f$, due to the negative value for the thermal coefficient of the index of refraction $\partial n/\partial T$ for $Ba_2Na(NbO_3)_5$. If the influence to the $Ba_2Na(NbO_3)_5$ crystal is ignored, the theoretical optimum intracavity lens position will not agree with the position experimentally determined. Additionally, the laser 532-nm power will not be optimized and will not agree with the calculated value. The induced focal length has a practical value in centimeters of [7]

$$f_B = -1.5 \times 10^{-7} w_B^2 / I \tag{2}$$

where $2w_B$ is the beam diameter in the $Ba_2Na(NbO_3)_5$ crystal, I is the circulating intracavity power, and a 1064-nm absorption coefficient of 0.002 cm^{-1} is assumed.

The values of the beam diameter in the $Ba_2Na(NbO_3)_5$ crystal and in the laser rod are of extreme importance in the design of an optimized frequency-doubled laser. Even though we input R_1, R_2, f, and D_3 to the program, these are used only to generate the optimum values so that requirements on w_B and w_R are satisfied; w_R is the beam size on the laser rod. The influence of w_B and w_R is illustrated by the laser power and associated relations. The 532-nm power for CW operation is

$$P = 2\epsilon I^2 \tag{3}$$

where it must be recognized that the thermooptical effects modify and influence the circulating power, as [8]

$$I = \frac{\alpha\beta + \epsilon}{2\epsilon\beta}\left[\sqrt{1 + \frac{4\epsilon\beta(G_0 - \alpha)}{(\alpha\beta + \epsilon)^2}} - 1\right] \tag{4}$$

where G_0 is the unsaturated gain, α is the passive cavity loss, and β is the saturation parameter given by

$$\beta = 2.9 \times 10^{-4} / w_R^2 \tag{5}$$

for Kr and KRb lamp pumping, and ϵ is the frequency-doubling parameter, given by [2],

$$\epsilon = 5.64 \times 10^{-8} L^2 / w_B^2 \tag{6}$$

where L is the interaction length in the $Ba_2Na(NbO_3)_5$ crystal and $\epsilon = \alpha\beta$ at optimum coupling. Diameter dimensions are in centimeters and power is in watts. Additionally, the depth of modulation required during the mode-locked operation to achieve an e^{-2} pulsewidth of time τ is also influenced by the thermooptical effects and is equal to

$$\delta_l = (4L_1/\pi c)^2(\sqrt{2}\epsilon I/3\sqrt{3}\tau^2)$$

where L_1 is the mode-lock crystal length [9].

Numerical data generated by the computer program presently include: the beam diameter at both end mirrors, the beam diameter at each end of the Nd:YAG laser rod, the beam diameter at the frequency-doubling crystal, the beam waist diameter and location of the waist relative to the end dichroic mirror and the resonator stability factor.

Graphical results are generated as well. Variations in the position of the intracavity lens, for example, will cause changes in the size of the beam in the laser rod and in the $Ba_2Na(NbO_3)_5$ crystal, and in the size of the beam waist and its location. These diameters can be sequentially plotted versus the lens-to-rod separation, and these data are necessary to optimize the laser design for maximum 532-nm power. An example of the data output is illustrated in Fig. 2 for $R_1 = -300$ cm, $R_2 = 2.5$ cm, and $f_R = 11.0$ cm, with $D_1 = 3.3$ cm, $D_2 = 6.6$ cm, $D_5 = 0.94$ cm, and total length of 30 cm. The graph shows the variations of the beam diameters in the laser rod, the $Ba_2Na(NbO_3)_5$ crystal, and the waist diameter caused by movement of the intracavity lens; these are denoted as $2w_R$, $2w_B$, and $2w_0$, respectively. The position of zero slope in the $2w_R$ curve is the confocal position and is chosen as the operating location for the intracavity lens [1]. The laser is designed so that the optimum w_R and w_B values are consistent with the confocal position on the positive-slope side of the curve due to stability considerations. We have found that such theoretical curves are verified by experiment, and that the laser is most stable at or near the confocal position [10]. We use the theory to drive experimental arrangements.

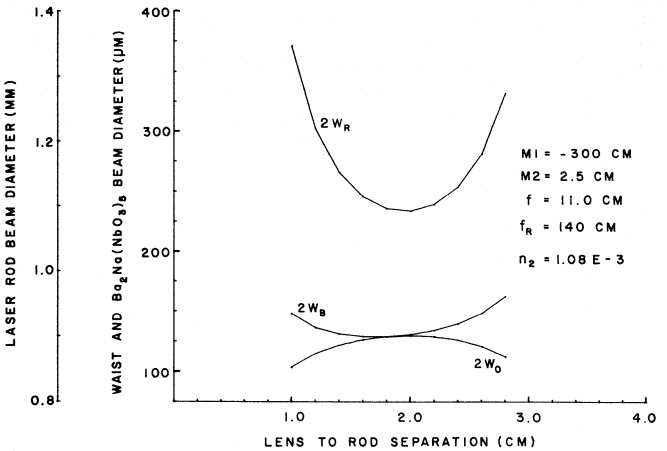


Fig. 2. Variation in beam diameters in the laser rod, in the $Ba_2Na(NbO_3)_5$ crystal, and in the waist diameter caused by motion in the lens-to-rod separation. These are denoted by $2w_R$, $2w_B$, and $2w_0$, respectively.

The computer program denoted 405B - AJAX has been used to provide the optical design for a space-qualifiable frequency-doubled Nd:YAG laser [10], and has already been furnished to several commercial companies and universities. The laboratory use of the program has made rapid analysis of experimental results possible and provided the essential direction for the experimental work. A program listing for the HP 9820 calculator-plotter, a discussion of the program, and the optimization direction of the frequency-doubled Nd:YAG laser with the use of the program are available upon request at no charge.

REFERENCES

[1] J. Steffan, J.-P. Lörtscher, and G. Herziger, "Fundamental mode radiation with solid-state lasers," *IEEE J. Quantum Electron. (Part II of Two Parts–Special Issue on 1971 IEEE/OSA Conf. on Laser Engineering and Applications)*, vol. QE-8, pp. 239–245, Feb. 1972.

[2] A. Yariv, *Introduction to Optical Electronics*. New York: Holt, Rinehart, and Winston, Inc., 1971, pp. 30–39.

[3] H. Kogelnik, "Imaging of optical modes–Resonators with internal lenses," *Bell Syst. Tech. J.*, vol. 44, pp. 455–595, 1965.

[4] A. Stein, "Thermooptically perturbed resonators," *IEEE J. Quantum Electron.*, vol. QE-10, pp. 427–434, Apr. 1974.

[5] J. D. Forster and L. M. Osterink, "Thermal effects on a Nd:YAG laser," *J. Appl. Phys.*, vol. 41, pp. 3656–3663, 1970.

[6] A. R. Clobes and A. Stein, "Thermal effects in intracavity frequency doubling crystals," presented at the 1973 Spring Meeting of the Optical Society, Denver, CO, Paper C15.

[7] J. D. Barry and C. J. Kennedy, "Thermooptical effects of intracavity $Ba_2Na(NbO_3)_5$ on a frequency-doubled Nd:YAG laser," *IEEE J. Quantum Electron.*, vol. QE-11, pp. 575–579, Aug. 1975.

[8] C. J. Kennedy and J. D. Barry, "Stability of an intracavity frequency-doubled Nd:YAG laser," *IEEE J. Quantum Electron.*, vol. QE-10, pp. 596–599, Aug. 1974.

[9] C. Kennedy, "Frequency-domain analysis of the mode-locked and frequency-doubled homogenous laser," *IEEE J. Quantum Electron.*, vol. QE-11, pp. 857–862, Nov. 1975.
[10] D. Radecki, "Lamp pumped engineering feasibility model laser," presented at the 1975 Conf. Laser Engineering and Application, Washington, DC, May 28, 1975.

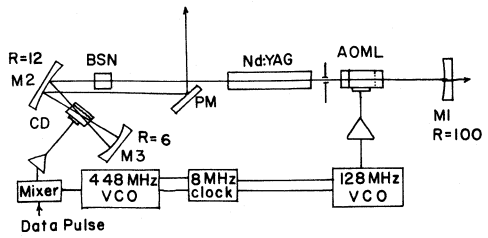


Fig. 1. Experimental layout of mode-locked and cavity-dumped laser. AOML, acoustooptic mode locker; CD cavity dumper; PM pick-off mirror; BSN $Ba_2Na(NbO_3)_5$ frequency doubler and oven. CD is 6 cm from $M3$. Radii are in centimeters.

A Stabilizer for Cavity-Dumped Nd:YAG

C. J. KENNEDY

Abstract—**Relaxation oscillations induced by cavity dumping in a Nd:YAG laser have been suppressed by an intracavity frequency doubler, thereby increasing the useful output of this laser for communications purposes by an order of magnitude. The additional loss induced by frequency doubling was negligible even at high damping constants.**

The author has previously shown [1] that nonlinear losses in a laser, such as those occuring when an intracavity frequency doubler is used, produce an enhancement of the damping coefficient for relaxation oscillations. A potentially useful device is therefore apparent for those lasers which are troubled by these oscillations—the intracavity frequency doubler. It is used this time as an output stabilizer instead of a source for 0.53-μ operation. Indeed, since the frequency doubler appears as a loss to the laser, its coupling must be minimized so as not to degrade the circulating power in the laser to a significant degree. Since large nonlinear coupling is undesirable, the frequency doubler may be located anywhere in the cavity, regardless of the beam size of its location.

Our particular application involved the use of a mode-locked and cavity-dumped Nd:YAG laser for a pulse-interval-modulation (PIM) communication system. Cavity dumping in Nd:YAG induces relaxation oscillations with a fairly long damping time. This makes medium-data-rate communication with these lasers in a PIM cavity dump mode difficult since the circulating power at the dumping time is highly uncertain. The result is a noisy transmission which forces an unnaturally low receiver threshold and results in increased error rates. A stabilizer would be of considerable value to this system to damp out relaxation oscillations from one dumping event before it became necessary to dump again.

Fig. 1 shows the layout of the laser used in our experiments. The circulating power was monitored as leakage through $M1$ by a P-I-N photodiode. A proportional controller was used to keep the $Ba_2Na(NbO_3)_5$ (BSN) crystal near phase-match temperature for maximum second-harmonic conversion. About 10-mW, single-directional 0.53-μ power was generated at most. The laser was mode-locked to eliminate free-running noise, and cavity dumped at the maximum available percentage which was determined by the RF pulsewidth and power-amplifier gain. The cavity dumper operated in the PIM data mode in which the spacing between pairs of pulses was random between 15- and 45-s intervals. Fig. 2 was the result and

Manuscript received March 3, 1975; revised December 17, 1975.

The author is with the Department of Space Laser Communications, Headquarters of the Space and Missile Systems Organization, Los Angeles AFS, CA 90009.

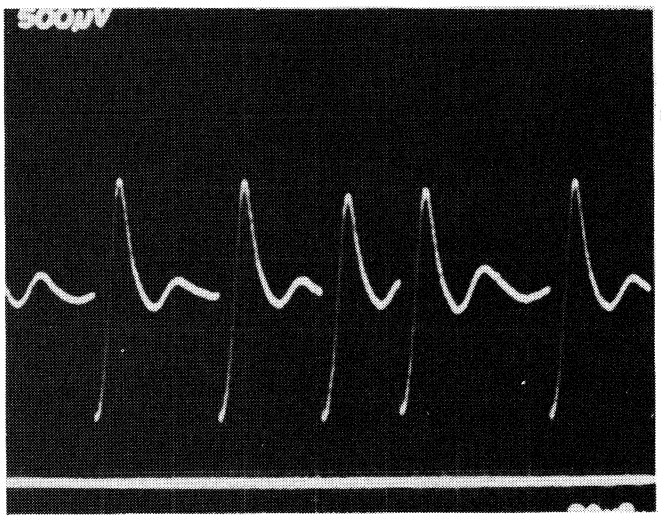


Fig. 2. Circulating power fluctuations as a result of cavity dumping the stabilized laser. Lower line represents $P_c = 0$.

shows the reaction of the circulating power at a sweep rate of 20 μs/cm. The reduction in circulating power at a dump indicated that 70 percent of the power was dumped each time. The damping factor for the ensuing oscillations wa about 1.3×10^5, which is an order of magnitude above typical damping factors for this laser. Theoretically, when nonlinear damping dominates

$$\gamma = \epsilon P_c/\tau$$

where $P_{SH} = \epsilon P_c^2$ is the single-directional second-harmonic power. Therefore

$$\gamma = \frac{P_{SH}}{\tau P_c}$$

and from the observed γ and P_c, P_{SH} must be 13 mW which is close to the measured output at 0.53 μ.

In order to observe the effect of reduced damping, the temperature of the BSN was reduced to 85°C from the 91°C phase-match temperature. Fig. 3 shows the greatly exaggerated oscillations which result. The damping constant here is 3.3×10^4, which is yet four times the damping without the BSN. Some small second-harmonic power was still being generated—about a milliwatt, but the circulating power of 25 W remained unchanged from the previous measurement. We concluded that no observable degradation in power was involved in achieving high damping constants.

The reader will note that the circulating power at dumping varies considerably in Fig. 3, but hardly at all in Fig. 2. This demonstrates the reduction in noise on the dumped output

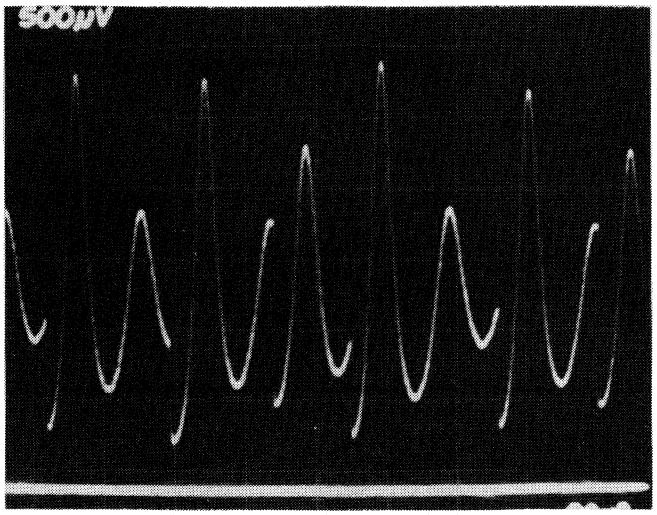


Fig. 3. Circulating power fluctuations with lowered nonlinear coupling compared to Fig. 2, but with all other parameters the same.

as a result of intracavity frequency doubling. Ordinarily, the same amount of noise would have been produced by an 8-percent dump and thus the usable power of the laser has increased about tenfold. This improvement in performance could open new doors for the application of this type of laser communicator in the medium-data-rate category.

References

[1] C. J. Kennedy and J. D. Barry, "Stability of an intracavity frequency doubled Nd:YAG laser," *IEEE J. Quantum Electron.*, vol. QE-10, pp. 596-599, Aug. 1974.

Operation of TEA CO_2 Lasers with Rough Surface Electrodes

N. KARASIKOV AND J. SHAMIR

Abstract—**In contrast with the normally accepted concepts in the construction of transversely excited atmospheric (TEA) CO_2 lasers it is found that homogeneously roughened electrodes perform better then polished ones.**

It is usually accepted that in order to obtain a uniform and stable glow discharge in a transversely excited atmospheric (TEA) CO_2 laser, the electrodes must be well polished [1]. Unfortunately, well-polished electrodes are very vulnerable to small surface perturbations that will cause local distortions of the electric field which leads to arc discharges instead of a homogeneous glow discharge.

These perturbations may be induced by sputtering [2], by dust particles, or by inaccurate milling resulting in small deviations from the theoretically ideal electrode profile.

Demanding well-polished electrodes and avoiding any local perturbations is most desirable, but cannot be achieved in practice. It seemed to be worthwhile to try to deliberately generate a fine homogeneous roughness of the electrode surface. Such a homogeneous roughness may diminish the effect of local surface perturbations, resulting in a more stable and uniform glow discharge. Apart from this there are several additional advantages to electrodes with rough surfaces.

1) The rough surface may be characterized by a large number of edges producing field concentrations. As a result, the required breakdown voltage will be reduced. This effect is important both for stabilizing the electrical discharge and for improving the pumping mechanism by the reduction of the E/N ratio. (In self-sustained lasers, this ratio is usually higher than the optimal value [3], [4].)

2) The roughness of the surface increases the active cathodic area resulting in a stronger photoemission and hence better preionization. This is most essential in laser systems preionized by cathodic photoemission.

3) Rough-surfaced electrodes might store ions (remaining from previous discharges) on the surface. These ions will be transferred to the active volume supporting the preionization process.

In order to investigate the influence of roughened electrode surfaces, we performed a series of experiments with two lasers constructed according to the Lamberton–Pearson method [1], [5].

The two lasers differed by the profile of the electrodes, one had cylindrical electrodes while the other was built with a Rogowski profile [6]. First the performance of both lasers was investigated with polished electrodes. We checked the stability and uniformity of the discharge, discharge voltage, laser pulse energy, peak power, and reproducibility under a large variety of gas mixtures and pressures up to 850 torr. After accomplishing these measurements, the electrodes were sandblasted to produce the rough surface and the previously mentioned measurements were repeated.

By comparing the two sets of measurements, the improvement caused by the sandblasting was evident and may be summed up as follows.

1) The homogenity and stability of the glow were found by observation to be improved.

2) The required discharge voltage (optimal) was reduced by about 10 percent.

3) Reproducibility of output pulses was improved, and the number of false discharges was reduced.

4) Pulse power peaks and energy were also improved, though not considerably.

In conclusion we may point out that electrodes with rough surfaces performed better than polished electrodes. However, the optimal amount of roughness remains to be determined.

References

[1] H. N. Lamberton and P. R. Pearson, "Improved excitation techniques for atmospheric pressure CO_2 lasers," *Electron. Lett.*, vol. 7, pp. 141-143, Mar. 1975.

[2] G. F. Weston, *Cold Cathode Glow Discharge Tubes*. London: Iliffe, 1968, ch. 2, p. 2.1.

[3] W. L. Nighan and H. H. Bennet, "Electron energy distribution functions and vibrational excitation rates in CO_2 laser mixtures," *Appl. Phys. Lett.*, vol. 14, pp. 240-243, Apr. 1969.

[4] W. L. Nighan, "Electron energy distribution and collision rates in electrically excited N_2, CO and CO_2," *Phys. Rev.*, vol. A2, pp. 1989-2000, Nov. 1970.

[5] P. R. Pearson and H. N. Lamberton, "Atmospheric pressure CO_2 lasers giving high output energy per unit volume," *IEEE J. Quantum Electron. (Part II of Two Parts: Special Issue on 1971 IEEE/OSA Conf. Laser Engineering and Applications)*, vol. QE-8, pp. 145-149, Feb. 1972.

[6] H. J. Seguin, M. Manes, and J. Tulip, "Simple inexpensive laboratory-quality Rogowski TEA laser," *Rev. Sci. Instr.*, vol. 43, pp. 1134-1139, Aug. 1972.

Manuscript received October 24, 1975.

The authors are with the Faculty of Electrical Engineering, Technion, Israel Institute of Technology, Haifa, Israel.

Oscillator Strengths of Nd^{3+} in $Nd_xLa_{1-x}P_5O_{14}$ and Concentration Quenching in Stoichiometric Rare-Earth Laser Materials

F. AUZEL

Abstract—**Oscillator strengths of Nd^{3+} in $Nd_xLa_{1-x}P_5O_{14}$ for $0.01 \leqslant x \leqslant 1$ are shown to be constant. Consequently, through the whole concentration range Nd^{3+} behaves essentially as one center with respect to transition probabilities. This situation is discussed in relation to concentration quenching.**

As is now well known, $(Nd_xY_{1-x})_3Al_5O_{12}$(YAG) and $Nd_xLa_{1-x}P_5O_{14}$ (NdLaUP) behave differently with respect to concentration quenching. At 10^{21} Nd^{3+} ions/cm^3 for instance, YAG shows a stronger decrease in efficiency compared to NdLaUP [1], [2].

An interesting hypothesis has recently been suggested to explain the concentration dependence of NdUP and of other so-called "stoichiometric laser materials" [3].

For Nd–Nd spacing of the order of 5 Å, the average distance in NdUP, hybrid exchange between ion pairs may take place; the $5d$ configuration of one ion being mixed with the $4f$ configuration of the neighboring ion, gives rise to an additional transition probability in analogy to one-center parity crystal field mixing. Then at high concentration, lifetimes decrease not through concentration quenching but through concentration enhancement of transition probabilities by crystal field overlap mixing. This in turn would explain why efficiencies do not drop much in stoichiometric materials.

A way to test this hypothesis is to estimate the additional emission probability obtained through this crystal field overlap mixing of pairs in stoichiometric laser materials such as NdUP. We report on such measurements.

Oscillator strengths of Nd^{3+} in NdLaUP have been measured by the experimental technique already described elsewhere [5] for a wide variation of Nd^{3+} concentrations (from 4×10^{19} ions/cm^3, $x = 0.01$ to 4×10^{21} ions/cm^3, $x = 1$).

The following transitions have been studied:

$$^4I_{9/2} \longrightarrow {}^2P_{1/2}; \quad {}^4I_{9/2} \longrightarrow {}^4F_{3/2};$$

$$^4I_{9/2} \longrightarrow {}^2G_{5/2}, {}^4G_{7/2}; \quad {}^4I_{9/2} \longrightarrow {}^4S_{3/2}, {}^4F_{7/2}.$$

Within experimental errors, due mainly to polarization effects by Wood's anomalies of the spectrophotometer on our unpolarized spectra, Fig. 1 shows that the considered oscillator strengths are constant with respect to concentration. This indicates that pairing effects cannot contribute by more than a few percent to transition probabilities and so cannot explain the 260-percent variation found in the $^4F_{3/2}$ level lifetime [1] in the same concentration range.

According to Judd's theory, the oscillator strength f of any transition depends on three parameters T_2, T_4, T_6 only.

The choice of the measured transitions is one where according to this theory [5] and results shown in Fig. 1, T_2, T_4, T_6 are constant

$$f {}^4I_{9/2} \longrightarrow P_{1/2} \propto T_4$$

$$f {}^4I_{9/2} \longrightarrow {}^4F_{3/2} \propto (0.23T_4 + 0.05T_6)$$

$$f {}^4I_{9/2} \longrightarrow {}^4S_{3/2}, {}^4F_{7/2} \propto (0.044T_4 + 0.662T_6)$$

$$f {}^4I_{9/2} \longrightarrow {}^9G_{5/2}, {}^4G_{7/2} \propto (0.96T_2 + 0.57T_4 + 0.06T_6).$$

So any other transitions can be considered as having a constant oscillator strength. This is, of course, the case for transitions linked by Einstein relations to the radiative lifetime of $^4F_{3/2}$ which in turn is constant with concentration. This is consistent with results in [1] showing that peak cross sections were the same for the $^4F_{3/2} \rightarrow {}^4I_{11/2}$ transition for the two concentration values $x = 0.25$ and 1.

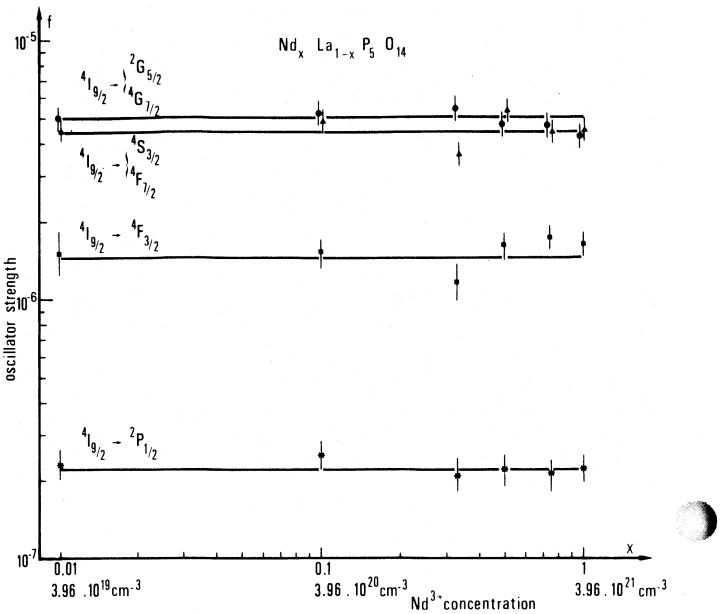


Fig. 1. Oscillator strengths of Nd^{3+} in $Nd_xLa_{1-x}P_5O_{14}$ for $0.01 \leqslant x \leqslant 1$ (from 3.9610^{19} to 3.9610^{21} ions · cm^{-3}) for the following transitions: • $^4I_{9/2} \rightarrow {}^2G_{5/2}$, $^4G_{7/2}$; ▲ $^4I_{9/2} \rightarrow {}^4S_{3/2}$, $^4F_{7/2}$; ■ $^4I_{9/2} \rightarrow {}^4F_{3/2}$; * $^4I_{9/2} \rightarrow {}^2P_{1/2}$.

Parameter T_2 being constant is of particular interest since it is well known [4], [5] that changes in hosts usually modify the T_2 parameter more strongly than others and so lines involving T_2 are the most sensitive to varying environments of the ion. Then $^4I_{9/2} \rightarrow {}^4G_{7/2}$, $^2G_{3/2}$ could also be the most sensitive line to crystal field overlap mixing. From Fig. 1 this does not seem to be the case.

In conclusion, it has been experimentally demonstrated that increase in transition probabilities through rare-earth ions pairing is smaller than a few percent of the one-ion oscillator strength even in NdUP, the "prototype of stoichiometric materials." One may argue it could even be much smaller: oscillator strengths for pair lines in $PrCl_3$ were reported in the order of 10^{-10} [6]; this means that variations of only 10^{-4} could be the entire increase in transition probabilities by such pairing effect. Provided Einstein relations between absorption and emission are not too much modified by local field effects [7] at high concentration, the crystal field overlap mixing concentration enhancement hypothesis does not seem to apply to stoechiometric materials.

References

[1] S. Singh, D. C. Miller, J. R. Potopowicz, and L. R. Shick, "Emission cross-section and fluorescence quenching of Nd^{3+} lanthanum pentaphosphate," *J. Appl. Phys.*, vol. 46, pp. 1191–1196, 1975.

[2] H. G. Danielmeyer and M. Blätte, "Fluorescence quenching in Nd: YAG," *Appl. Phys.*, vol. 1, pp. 269–274, 1973.

[3] a) G. Huber, J. P. Jeser, W. W. Krühler, and H. G. Danielmeyer, "Laser action in pentaphosphate crystals," *IEEE J. Quantum Electron. (1974 Int. Quantum Electronics Conf., Dig. Tech. Papers)*, vol. QE-10, p. 766, Sept. 1974.

b) H. G. Danielmeyer, "Efficiency and fluorescence quenching of stoichiometric RE laser materials," presented at the Int. Conf. Luminescence (Tokyo Sept. 1975); also *J. Lum.* (Abstracts), Mar. 1976.

Manuscript received October 29, 1975.

The author is with the CNET, 92220 Bagneux, France.

[4] F. Auzel, "Contribution à l'étude spectroscopique de verres dopés avec Er^{3+}," *Ann. Telecommun.*, vol. 24, pp. 199–229, 1969.
[5] B. R. Judd, "Optical absorption intensities of rare earth ions," *Phys. Rev.*, vol. 127, pp. 750–761, 1962.
[6] E. Dorman, "Concentration broadening and oscillator strengths in Pr: $LaCl_3$," *J. Chem. Phys.*, vol. 44, pp. 2910–2916, 1966.
[7] W. B. Fowler and D. L. Dexter, "Relation between absorption and emission probabilities in luminescent centers in ionic solids," *Phys. Rev.*, vol. 128, pp. 2154–2165, 1962.

Single-Mode Operation of a Repetitively Pulsed Dye Laser

M. D. LEVENSON AND G. L. EESLEY

Abstract—**A Hansch-type dye laser pumped by a xenon ion laser achieves single-mode operation with a frequency jitter of 32 MHz and a peak power of 2 kW.**

A number of techniques of high-resolution spectroscopy require laser intensities greater than those conveniently obtained from presently available single-mode CW dye lasers. The nitrogen-laser-pumped Hansch-type dye laser has been used to perform some of these experiments [1]–[4]. However, the maximum resolution attainable with these dye lasers has been limited by the short duration of the pumping pulse. The short pulse excitation allows the light to make fewer than three round trips through the dye-laser cavity. The usual steady-state mode structure of a laser cavity has no time to build up, and the output resembles filtered and amplified spontaneous emission. The linewidth of the output is limited by the Fourier transform of the pulse length [90-MHz full width at half maximum (FWHM) for a 10-ns FWHM Gaussian dye-laser pulse]. With a sacrifice of intensity, resolutions on the order of 10 MHz can be obtained by filtering the output with a passive interferometer [1], [5].

We have succeeded in pumping a narrow-band dye laser with the visible output of a 20-kW pulsed xenon ion laser [6]. The 160-ns pulses allow the formation of the familiar longitudinal and transverse cavity modes within the resonator structure diagramed in Fig. 1. The cavity consists of a plane 50-percent-reflecting output mirror, a transversely pumped dye cell with an active length of 1 cm, a 20-power telescope, and an aluminized diffraction grating used in fifth-order Littrow mount. An iris and a Fabry–Perot etalon can be inserted between the telescope and grating. The telescope is corrected to $\lambda/6$ and consists of a Spectra Physics Model 332-L1 expanding lens and a Model 333 collimating lens. The xenon laser beam is focused to a line at the inside surface of the front window of the dye cell by means of an 11-cm focal length cylindrical lens. The overall length of the cavity is 32.5 cm, which corresponds to a longitudinal mode separation of 429 MHz. For mechanical rigidity the entire apparatus is supported on three 1-in-diam Invar rods. All optical elements are held in three-point kinetic mounts.

Intracavity insertion of a plane airspaced Fabry–Perot etalon with a finesse of 40 and a plate spacing of 8-mm results in single-longitudinal-mode oscillation. The transverse mode structure is TEM_{00} with a beam waist radius of 0.10 mm. For a dye solution of 0.125 g/l of rhodamine 6G in ethanol and oscillation at 588 nm, the pumping threshold is 1.0 mJ. Without the etalon the threshold is reduced by 50 percent, and the linewidth obtained is 0.2-cm^{-1} FWHM.

Manuscript received November 4, 1975. This work was supported by the Research Corporation under Grant 7510.

The authors are with the Departments of Physics and Electrical Engineering, University of Southern California, Los Angeles, CA 90007.

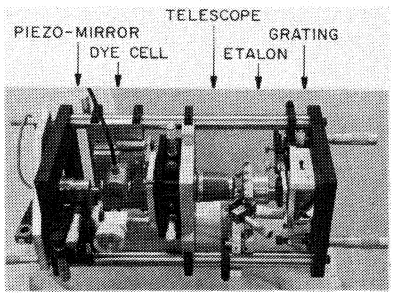


Fig. 1. Resonator structure; relative position of basic components indicated by arrows.

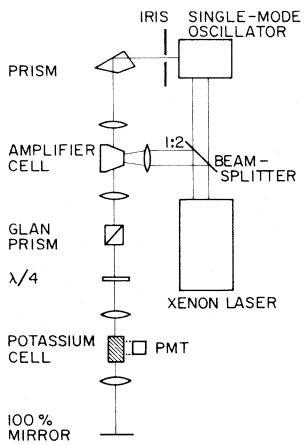


Fig. 2. Two-photon absorption oscillator–amplifier system.

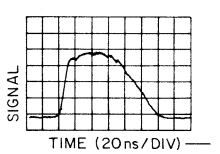


Fig. 3. Oscillator output pulse.

Stable single-mode oscillation can only be obtained near threshold. Hence the traveling-wave amplifier shown in Fig. 2 was added to achieve greater peak intensities. With 3.2 mJ of pump energy divided in a 1:2 ratio between the amplifier and oscillator, the total laser output was 0.2 mJ in a 100-ns pulse (FWHM). A typical single-mode pulse appears in Fig. 3. When the pump laser was pulsed at 30 Hz, the oscillator–amplifier provided 3.5-W rms output.

This laser was assembled in order to study two-photon absorption without Doppler broadening in atomic potassium [2], [7]. Intensities of 10 MW/cm^2 are needed to excite the $4S$–$11D$ transition with calculated two-photon absorption cross section, 1.30×10^{-18} cm^2 [8].

In the two-photon absorption experiment shown in Fig. 2, the amplified output is focused into a potassium vapor cell with one lens and then recollimated and refocused into the cell from the opposite direction by a lens–mirror combination. An isolator consisting of a glan laser prism and a quarter-wave plate inhibited return beam feedback into the laser and subsequent destabilization of the mode frequency. Prisms between the oscillator and amplifier stages also helped prevent oscillation in the cavity formed by the output mirror of the oscillator and the return beam mirror. The decay fluorescence from the $11D$ state to the $4P$ levels was detected by a photomultiplier and interference filter.

The frequency of the laser mode was scanned continuously

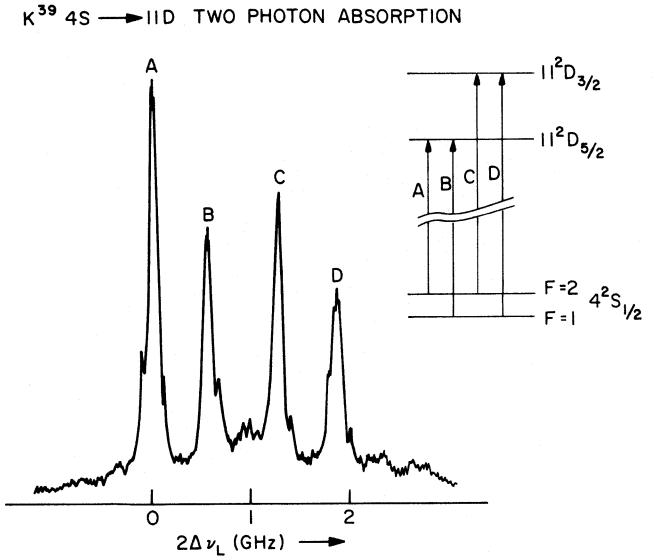


Fig. 4. TPA fluorescence signal.

over the four components of the $4S$–$11D$ TPA transition by translating the output mirror of the oscillator piezoelectrically. The passband of the etalon was also scanned by manually tilting the etalon in order to prevent hopping from one longitudinal mode to another. The resulting fluorescence signal appears in Fig. 4. By comparing the widths of the peaks to the known splitting between peaks A and B and between C and D due to the hyperfine interaction in the ground state, we find a resolution of 32-MHz FWHM. This linewidth corresponds to the residual frequency jitter of the laser due to mechanical vibrations in the resonator structure (induced largely by the dye pump) and possibly also due to turbulence in the dye solution. The splitting between peaks A and C and between B and D is the fine structure interval in the $11D$ state of potassium. We find that the $11D_{5/2}$ and $11D_{3/2}$ levels are inverted with a splitting of 1.03 ± 0.04 GHz. A more complete account of the experiments performed with this laser will be published elsewhere.

References

[1] T. W. Hansch, "Repetitively pulsed tunable dye laser for high resolution spectroscopy," *Appl. Opt.*, vol. 11, pp. 895–898, 1972.
[2] M. D. Levenson and M. M. Salour, "Fine and hyperfine structure in highly excited states of sodium," *Phys. Lett. A*, vol. 48A, p. 331, 1974.
[3] M. Lambropoulos, S. Moody, S. Smith, and C. Lineberger, "Observation of electric quadrupole transitions in multiphoton ionization," *Phys. Rev. Lett.*, vol. 35, p. 159, 1975.
[4] T. W. Hansch, S. A. Lee, R. Wallenstein, and C. Wieman, "Doppler free two-photon spectroscopy of hydrogen $1S$–$2S$," *Phys. Rev. Lett.*, vol. 34, p. 307, 1975.
[5] T. W. Hansch, "Powerful dye laser oscillator-amplifier system for high resolution spectroscopy," *Opt. Commun.*, vol. 14, p. 353, 1975.
[6] C. Harper and M. Gunderson, "Construction of a high power xenon ion laser," *Rev. Sci. Instrum.*, vol. 45, p. 400, 1974.
[7] M. D. Levenson and N. Bloembergen, "Observation of two-photon absorption without Doppler broadening on the $3S$–$5S$ transition in sodium vapor," *Phys. Rev. Lett.*, vol. 32, p. 645, 1974.
[8] H. Eicher, "Third-order susceptibility of alkali metal vapors," *IEEE J. Quantum Electron.*, vol. QE-11, pp. 121–130, Apr. 1975.

Notes and Lines

New Far-Infrared Laser Lines in $N^{15}H_3$

A. H. BUSHNELL AND MARTIN GUNDERSEN

Abstract—**Several isotopes of NH_3 have been studied as laser candidates, including ND_2H, NH_2D, ND_3, and $N^{15}H_3$. Lasing was observed in $N^{15}H_3$ at 15.08 and 15.91 μ. Tentative assignments of transitions to the $2\nu_2 \rightarrow \nu_2$ vibrational levels have been made. Enhanced energy output was observed in $N^{14}H_3$ with the addition of helium.**

New laser lines have been observed from the ammonia isotope $N^{15}H_3$ at 15.08 and 15.91 μ. These two lines appear to correlate with the 14.78- and 15.47-μ transitions reported by Akitt and Wittig [1] in $N^{14}H_3$. In addition, the isotopes ND_3, NH_2D, and NHD_2 were studied, with negative results.

A pulsed 7-m longitudinal-discharge laser, with a 7.5-cm-diam plasma tube, was used. The laser is divided electrically into two sections, each section driven by a 1500-A 3-μs full width at half-maximum (FWHM) peak current pulse. The optical cavity consists of a 10-m-focal-length gold-coated mirror and an aluminum-coated flat with a 5-mm hole for output coupling. Both mirrors are within the vacuum system, and a polycrystalline ZnSe flat is used as a window. Wavelengths were measured using a Bausch and Lomb 500-mm-grating monochromator. An HgCdTe photoconductive detector peaked at 16 μ, along with a Tektronix 446 storage oscilloscope, was used for detection.

$N^{15}H_3$ was produced from $(N^{15}H_4)_2$ SO_4 and passed through an acetone, dry-ice-cooled trap. The high cost of $N^{15}H_3$ required that some care be taken in gas handling, because NH_3 breaks down rapidly in the pulsed discharge. The laser was filled to a static pressure of 1 torr and sealed off. The stronger line (15.08 μ) was observed for approximately 18 pulses before lasing ceased, while the line at 15.91 would lase for 7 shots. The lack of sufficient $N^{15}H_3$ made it impossible to run a complete scan; in fact, lasing was observed by setting the monochromator to predetermined wavelengths calculated assuming the transitions to be $2\nu_2+ \rightarrow \nu_2-$. The laser light pulse was approximately 2 μs for 15.08 μ and 1 μs for 15.91 μ.

ND_3, ND_2H, and NH_2D were studied, and no laser transitions were observed. NH_2D probably will not lase because rapid isotopic exchange reactions dilute the NH_2D concentration to approximately 45 percent, the remaining gas being NHD_2, NH_3, and ND_3. This was pointed out to us by Shoemaker [2]. The lack of laser action in ND_3 is a little more

Manuscript received December 1, 1975. This work was supported by ERDA Contract E(29-2)-3572.

The authors are with the Department of Electrical Engineering, Texas Technological University, Lubbock, TX 79409.

surprising. The detector limited observations to wavelengths shorter than 18 μ. However, it should be noted that the seperation between $2\nu_2$ and ν_4 in ND_3 is about 5 times greater than the same separation in NH_3. A Coriolis coupling occurs between the close ν_4 and $2\nu_2$ vibrational levels in NH_3. Several additional details suggest that $2\nu_2$ is the upper laser level in $N^{14}H_3$.

1) The shift of vibrational levels in $N^{15}H_3$ is such that if the upper level were ν_4, the wavelengths would be shorter rather than longer.

2) Assuming the upper level is $2\nu_2$ allows a fairly accurate prediction of the observed isotopic shift.

3) Garing *et al.* [3] observed a $\nu_2 \rightarrow 2\nu_2$ absorption at 15.47 μ [$2a$ $Q(8, 5)$] in $N^{14}H_3$.

The addition of helium in the ratio of approximately 1:1, 2-torr total pressure, was observed to double energy output in $N^{14}H_3$. This is probably a gas cooling effect similar to that observed in H_2O by Pichamuthu *et al.* [4], reducing thermal pumping of the lower laser level. The addition of N_2 produced no observable enhancement of laser power or energy.

In conclusion, laser transitions have been observed in $N^{15}H_3$ analogous to those previously reported in $N^{14}H_3$. The transitions are slightly stronger than the corresponding $N^{14}H_3$ transitions.

ACKNOWLEDGMENT

The authors wish to thank Professor C. Wittig for helpful discussions, and W. Hacke, G. F. Erickson and E. Brown for valuable assistance.

REFERENCES

[1] D. P. Akitt and C. F. Wittig, "Laser emission in ammonia," *J. Appl. Phys.*, vol. 40, p. 902–903, 1969.
[2] R. Shoemaker, private communication.
[3] J. S. Garing, H. H. Nielsen, and K. Nurahari Rao, "The low-frequency vibration rotation bands of the ammonia molecule," *J. Mol. Spectrosc.*, vol. 3, pp. 496–527, 1959.
[4] J. P. Pichamuthu, J. C. Hassler, G. H. Sherman, and P. D. Coleman, "The role of helium in the H_2O laser," *IEEE J. Quantum Electron.* (Corresp.), vol. QE-9, pp. 244–245, Feb. 1973.

Higher Order Harmonics of CO_2 and N_2O Laser Difference Frequencies

B. G. WHITFORD

Abstract—**The generation of the fourth and fifth harmonics of the difference frequency between two 28-THz laser lines, by a tungsten–nickel diode, was observed.**

Manuscript received December 8, 1975.

The author is with the Physics Division, National Research Council, Ottawa, Ont., Canada.

Difference frequencies produced by mixing individual CO_2 laser lines, as well as harmonics of these differences, provide a convenient substitute for direct far-infrared laser emissions. Frequencies generated in this way form the basis of a proposed new technique for the absolute frequency measurement of CO_2 laser transitions [1], and are also generally useful as secondary standards in infrared spectroscopy, as has been recently demonstrated by Petersen *et al.* [2]. In [1], successful generation of the third harmonic of a difference frequency was reported. However, the feasibility of the CO_2 frequency measurement scheme depends on generating harmonics of order 4 or greater: higher order harmonics of differences would also be useful in general spectroscopy applications.

The purpose of this note is to report the observation of the fourth and fifth harmonics of difference frequencies between two infrared laser lines. As in the previous work [1], mixing and harmonic generation were performed in a tungsten–nickel point contact diode. Grating controlled CO_2 and N_2O lasers were used. Laser power in the vicinity of 100–400 mW at each frequency was focused on the diode with a 3-cm-focal length NaCl lens. Microwave power was directed at the diode by the open end of RG-98/U waveguide. Microwave frequencies were always chosen to produce a diode output frequency near 500 MHz, which was observed on a Tektronix 1L20 spectrum analyzer preceded by a 3-dB noise figure wide-band amplifier.

Three results are reported here. The first and second concern fourth harmonics, while the third result pertains to a fifth harmonic. In the first case two CO_2 laser frequencies differing by 53549 MHz were mixed with the third harmonic of a microwave frequency. In the second and third cases one CO_2 laser frequency and one N_2O laser frequency, differing by 17905 and 14554 MHz in the two cases, respectively, were mixed with a fundamental microwave frequency. The three observed interactions are as follows:

$$4\,(\underset{28359774}{P(18),\,CO_2} - \underset{28306225}{P(20),\,CO_2}) - 3\,(71232) = 500\ \text{MHz} \quad (1)$$

$$72118 - 4\,(\underset{28665705}{P(6),\,CO_2} - \underset{28647800}{R(20),\,N_2O}) = 498\ \text{MHz} \quad (2)$$

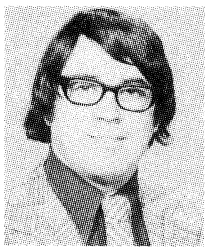
$$5\,(\underset{28616542}{P(8),\,CO_2} - \underset{28601988}{R(18),\,N_2O}) - 72268 = 502\ \text{MHz}. \quad (3)$$

The spectrum analyzer was set for a sweep speed of 500 kHz/cm and a resolution of 10 kHz. As observed on the display, both fourth-harmonic interactions produced a beat with a signal-to-noise (S/N) ratio of 19 dB. In the fifth-harmonic case the best observed S/N was 12 dB.

REFERENCES

[1] B. G. Whitford, K. J. Siemsen, H. D. Riccius, and K. M. Baird, "New frequency measurements and techniques in the 30-THz region," *IEEE Trans. Instrum. Meas.* (*1974 Conference on Precision Electromagnetic Measurements*), vol. IM-23, pp. 535–539, Dec. 1974.
[2] F. R. Petersen *et al.*, "Far infrared frequency synthesis with stabilized CO_2 lasers: Accurate measurements of the water vapor and methyl alchohol laser frequencies," *IEEE J. Quantum Electron.*, vol. QE-11, pp. 838–843, Oct. 1975.

Contributors



Steven C. Cohen was born in New Kensington, PA, on August 27, 1947. He received the B.S. degree in physics from Drexel University, Philadelphia, PA, in 1970, and the M.S. and Ph.D. degrees from the University of Maryland, College Park, in 1972 and 1973, respectively.

From 1966 to 1970 he was an undergraduate cooperative education student in the physical sciences at the NASA Goddard Space Flight Center, Greenbelt, MD. Since 1970 he has been a member of Goddard's Laser Technology Branch, where he has carried out research in heterodyne detection principles and applications, molecular energy-transfer theory, and gas-laser kinetics. His current interests are in geophysics and laser applications in the geosciences.

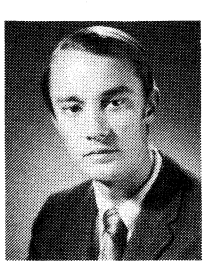
Dr. Cohen is a member of the American Physical Society, Phi Kappa Phi, Sigma Xi, Sigma Pi Sigma, and Pi Mu Epsilon.

*

William J. Firth was born in Orkney, Scotland, in 1945. He received the B.Sc. degree from Edinburgh University, Edinburgh, Scotland, in 1966, and took a postgraduate diploma in elementary particle physics. He received the Ph.D. degree from Heriot-Watt University, Edinburgh, Scotland, in 1973.

He was appointed to the Lecturing Staff of Heriot-Watt University in 1967.

*

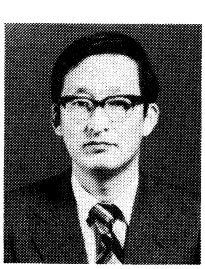


G. Benjamin Hocker (S'69–M'69) was born in Harrisburg, PA, in September 1942. He received the B.E.P. degree and the Ph.D. degree in applied physics, both from Cornell University, Ithaca, NY, in 1965 and 1970, respectively.

Since 1970 he has been an Assistant Professor in the Department of Electrical Engineering at the University of Minnesota, Minneapolis. He has done research on mass-spectroscopic studies of molecular-gas lasers, and on materials and devices for integrated optics.

Dr. Hocker is a member of the Optical Society of America and the American Society for Engineering Education.

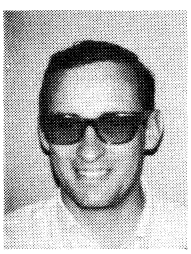
*



Hiroshi Iwasaki was born in Kobe, Japan, on December 23, 1933. He received the B.S. degree in pure chemistry from Kobe University, Kobe, Japan, in 1956, and the M.S. and D.S. degrees in crystal chemistry from Osaka University, Osaka, Japan, in 1958 and 1963, respectively.

Since joining the Electrical Communication Laboratory, Nippon Telegraph and Telephone Public Corporation, Tokyo, Japan, he has done research on dielectric materials, especially ferroelectrics for electrooptic and acoustooptic device applications. His current research interest include new solid-state laser materials, optical waveguide and optical integrated circuits.

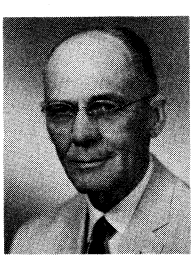
*



David A. McArthur was born in Meridian, MS, on August 14, 1938. He received the B.S. degree in physics from the University of Arizona, Tucson, and the Ph.D. degree in physics (nuclear magnetic resonance) from the University of California, Berkeley, in 1960 and 1967, respectively. He attended the University of Munich, Germany, from 1960 to 1961 on a Fulbright Scholarship.

He was a member of the Technical Staff at Bell Laboratories, Holmdel, NJ, from 1967 to 1969 where he worked in far-infrared nonlinear optics using the water vapor laser. Since 1969 he has been a member of the Technical Staff at Sandia Laboratories, Albuquerque, NM, where he has worked experimentally on optical techniques to measure the current, voltage, charge deposition, and plasma properties of relativistic electron beams. He has also worked on theoretical models of the plasma created and laser action induced by intense electron beams. More recently, he has experimentally studied the excitation of laser media by nuclear reactions, using laboratory nuclear reactors.

*



Dwight O. North (A'35–M'38–F'43) is a native of Hartford, CT. He received the B.S. degree in physics from Wesleyan College, Middletown, CT, and the Ph.D. degree from the California Institute of Technology, Pasadena, both in physics, in 1930 and 1933, respectively.

He is now a retired Fellow of the Technical Staff, RCA Laboratories, Princeton, NJ. He joined the Research and Development Laboratory of the RCA Manufacturing Company in Camden in 1934, where he worked on the design theory of small vacuum tubes, contributing particularly to the theory of conventional amplifying tubes at high frequencies. His early investigations were of the physical origin of noise in almost every branch of communications. It was in the course of this work that he developed the theory of the space-charge suppression of noise in vacuum tubes. His papers on this work have become classic and established him as a world authority on fluctuation phenomena. One of them issued as a military-security-classified report during World War II and cited as a source in numerous subsequent reports and papers by other scientists, was reprinted in the *Proceedings of the IEEE* in 1963 because of its historical importance. In 1942 he transferred to Princeton with the establishment of the RCA Laboratories, where he led some of the earliest fundamental studies of solid-state electronics. Since that time he has continued the study of noise ranging from optimum design of radar systems to studies of noise processes in semiconductors, transistors, and other solid-state devices. He has served as a Consultant on many phases of solid-state research, including luminescence of solids, physics of thermoelectric cooling, and the tunneling effect in diodes. In 1954 he was a Visiting Lecturer at Princeton University, conducting seminars on noise in electronic systems. He was named a Fellow of the Technical Staff, RCA Labora-

tories, in 1959. In 1961 he was the recipient of the David Sarnoff Outstanding Achievement Award in Science "for insight in interpreting the role of the theorist at RCA Laboratories and for resourcefulness in translating theory into practical results."

Dr. North is a Fellow of the American Physical Society and a member of Sigma Xi.

*

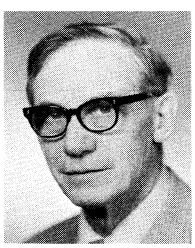


Kenju Otsuka (A'73) was born in Anto, Manchuria, on January 2, 1946. He received the B.S. degree in communication engineering from Tohoku University, Sendai, Japan, in 1968.

In 1968 he joined the Musashino Electrical Communication Laboratories, Nippon Telegraph and Telephone Public Corporation, Tokyo, Japan. He has been engaged in the research of the technique of mode locking in solid-state lasers and more recently in the investigation of Nd-ultraphosphate lasers for high bit-rate optical transmission systems.

Mr. Otsuka is a member of the Institute of Electronics and Communication Engineers of Japan and the Japan Society of Applied Physics.

*

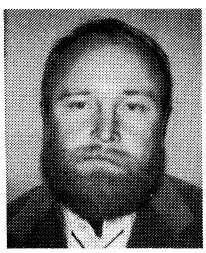


Henry S. Sommers, Jr., was born in St. Paul, MN, in 1914. He attended Stanford University, Stanford, CA, in 1933 and 1934, and received the B.A. degree in physics from the University of Minnesota, Minneapolis, and the Ph.D. degree in nuclear physics from Harvard University, Cambridge, MA, in 1936 and 1941, respectively.

He has made basic contributions to science and electronics in fields ranging from nuclear and low-temperature physics to radar, high-frequency semiconductor devices, and optical detectors. He served as n Instructor of Physics at Harvard University during 1942. From 1942 to 1945 he was a Staff Member at the M.I.T. Radiation Laboratory. As Assistant Project Engineer in the development of the Mark 56 Gunfire Control System and Project Engineer in the development of the Mark 35 Fire Control Radar at the M.I.T. Laboratory, he made wartime contributions for which he received the Naval Ordnance Development Award in 1945. After the war, Dr. Sommers was appointed Assistant Professor of Physics at Rutgers University, where he also conducted research and development work on a precision current control for a large electromagnet. In 1949, he joined the Research Staff at the Los Alamos Scientific Laboratories in New Mexico, where he carried out fundamental studies on the thermodynamic properties of liquid helium and on the scattering of neutrons by liquid helium. He joined the Technical Staff of RCA Laboratories at Princeton, NJ, in 1954. His work at RCA has been devoted to the study of electrical and optical properties of insulators and semiconductors, including the development of tunnel diodes for which he received an RCA Laboratories Achievement Award and a David Sarnoff Outstanding Team Award in Science. He spent the year 1960–1961 at the Laboratories of RCA Ltd. in Zurich, Switzerland, and as a Guggenheim Fellow and Fulbright Lecturer at the Hebrew University in Jerusalem, Israel. He is the author of a variety of papers in the fields of solid-state physics, electronics, cryogenics, nuclear physics, and chemical kinetics.

Dr. Sommers is a Fellow of the American Physical Society and a member of the Federation of American Scientists and the American Association for the Advancement of Science.

*



Philip B. Tollefsrud was born in Fargo, ND, on June 11, 1938. He received the B.A. degree in physics from the University of North Dakota, Grand Forks, in 1964, and the M.A. and Ph.D. degrees in physics from the University of Wisconsin, Madison, in 1966 and 1969, respectively.

Since 1969 he has been a member of the Technical Staff at Sandia Laboratories, Albuquerque, NM.

Dr. Tollefsrud is a member of the American Physical Society, Phi Beta Kappa, and Sigma Xi.

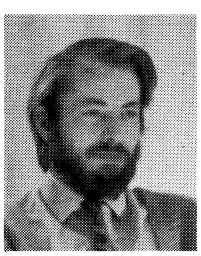
*



D. Weaire was born in 1942. After receiving the B.A. degree in mathematics from Cambridge University, Cambridge, England, he spent two years as a Harkness Fellow studying theoretical physics at the University of California, Berkeley, and the University of Chicago, Chicago, IL. He received the Ph.D. degree from Cavendish Laboratory, Cambridge, England.

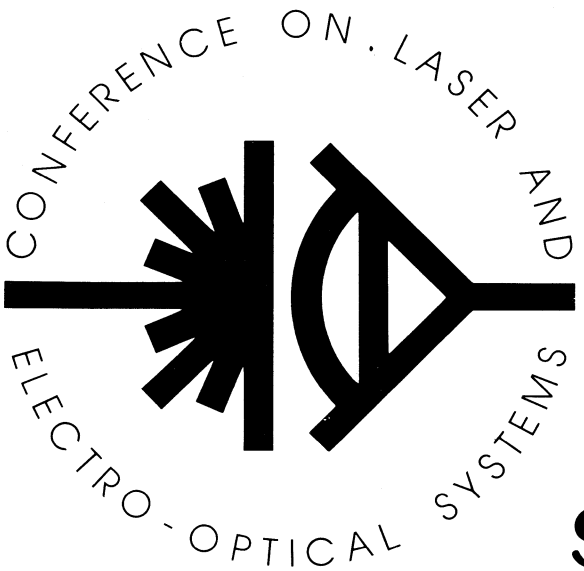
He has since been a Research Fellow at Clare College, Cambridge, England, and also at Harvard University, Cambridge, MA. He was an Associate Professor at Yale University, New Haven, CT, before taking up a Senior Lectureship position at Heriot-Watt University, Edinburgh, Scotland.

*



Brian S. Wherrett was born in Bromley, England, on May 8, 1946. He received the B.Sc. and Ph.D. degrees from the University of Reading, Reading, England, in 1966 and 1969, respectively.

He held postdoctoral appointments at the University of Reading and Heriot-Watt University, Edinburgh, Scotland, until his appointment as a Lecturer in the Department of Physics at Heriot-Watt University in 1971.



CLEOS
May 25-27, 1976
San Diego, California

The first Conference on Laser and Electro-Optical Systems (CLEOS) will be held at the Town and Country Hotel in San Diego, May 25-27, 1976, under the joint sponsorship of the Quantum Electronics Council of the Institute of Electrical and Electronics Engineers (IEEE) and the Technical Council of the Optical Society of America (OSA).

CLEOS aims to provide a professional technical forum for the presentation of engineering and manufacturing developments in the fields of lasers, laser applications, electro-optic devices, electro-optic systems, and the manufacturing and design techniques that have made these systems possible.

Original papers were solicited in the following fields:

- laser engineering manufacturing
- measurement & alignment systems
- opto mechanical subsystems
- scanning systems
- optical signal & data processing systems
- optical display systems
- e-o component technology
- space & military e-o systems
- laser fusion & laser isotope separation systems
- optical communication systems
- medical e-o systems
- e-o systems for production of microelectronics
- pollution-monitoring systems
- consumer e-o systems
- imaging & surveillance subsystems
- ranging & designation subsystems
- adaptive optical techniques
- electro-optical systems for material processing

AN EXHIBIT WILL BE AN INTEGRAL PART OF THIS MEETING.

For general information on the conference write:

Leslie Hill
Hughes Aircraft Company
Electron Dynamics Division
3100 West Lomita Boulevard
Torrance, California 90509

For information on the exhibit and to receive the exhibitors package write:

Ed Greeley
American Institute of Physics
335 East 45th Street
New York, New York 10017

Valkyrie: A CO_2 Laser System for Laser Fusion Experiments

KENNETH R. MANES, WALTER B. LINDQUIST, PAUL A. RENARD, H. E. EDDLEMAN, DONALD L. SMITH, MEMBER, IEEE, STANLEY S. GLAROS, TED C. STEWART, AND ROGER A. HAAS

Abstract—**A short-pulse CO_2 laser system fabricated from commercially available components for laser fusion experimentation is described. Simulation calculations are sketched, amplifier testing is discussed, overall laser system performance is reported, and the requirements for a typical target irradiation experiment are described.**

I. Introduction

THE prospect of achieving controlled thermonuclear burn by means of laser-driven implosions has motivated the construction of the most powerful lasers in the world. As soon as nanosecond 10.6-μm pulses became available from CO_2 TEA lasers, several laboratories began to study the feasibility of large CO_2 laser systems. While the CO_2 laser, by virtue of its excessively long wavelength, has never seemed to be a good candidate for compression experiments, its very fault makes it a good research tool to study laser-plasma interaction phenomena. Besides X-ray, charged particle, and optical measurements usually made on target plasmas heated by shorter wavelength lasers, much additional information is available in a 10.6-μm interaction since the critical density surface is easily accessible to optical interferometric and holographic techniques. With laser target interaction measurements as its goal, a short-pulse CO_2 laser system code named Valkyrie was assembled at the Lawrence Livermore Laboratory.

II. Valkyrie

Valkyrie is a single-beam CO_2 laser designed to produce 50 J in ~1 ns with good beam quality, for use as a target irradiation facility. The system has been largely constructed with commercially available amplifiers.

The oscillator, located in the background of Fig. 1, employs a specially designed ultraviolet preionized TEA gain medium (Lumonics 142 A), a germanium Brewster's angle acousto-optic mode locker, and a sodium chloride etalon as an output mirror. This oscillator, indicated schematically in Fig. 2, generates a burst of ~1-ns-duration pulses with peak pulse energies of ~10 mJ distributed among approximately six rotational lines centered on the P20 transition of the 10.4-μm band. A single pulse is selected by a two-stage switch-out assembly consisting of a laser-triggered spark gap, two Ge polarizers, and two CdTe Pockels cells. Exiting from the system, the selected pulse contains a measured 1-2 mJ. The pulse is then directed through a second Lumonics 142 A 1 m long that serves as a preamplifier and into a 3X Keplerian beam expander with a 25-μm-thick replaceable Mylar film at its focus. At the output of this stage the pulse contains a measured 20-40 mJ. Expanded and collimated, the pulse propagates through a 9-cm-aperture 1-m-long ultraviolet-preionized TEA amplifier (Lumonics 602A, output 0.5-0.7 J) followed by two 11-cm-aperture 1-m-long cold-cathode *e*-beam sustained amplifiers operated at 2-atm pressure. Emerging in the target area, measurements show the pulse contains 40 ±

Manuscript received August 18, 1975; revised December 29, 1975. This work was performed under the auspices of the U.S. Energy Research and Development Administration.

The authors are with the Lawrence Livermore Laboratory, University of California, Livermore, CA 94550.

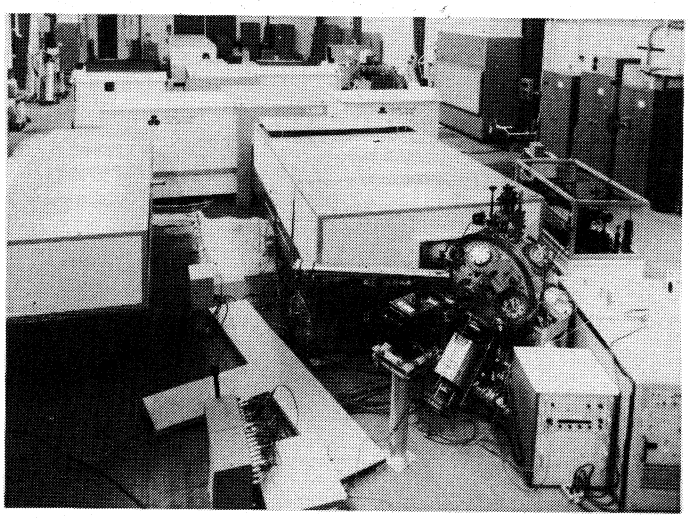


Fig. 1. The Valkyrie CO_2 laser system is seen from the south with its oscillator-amplifier chain in the background, beam diagnostics tables, and target chamber in the foreground. All cables and plumbing are routed through trenches to a remote control room.

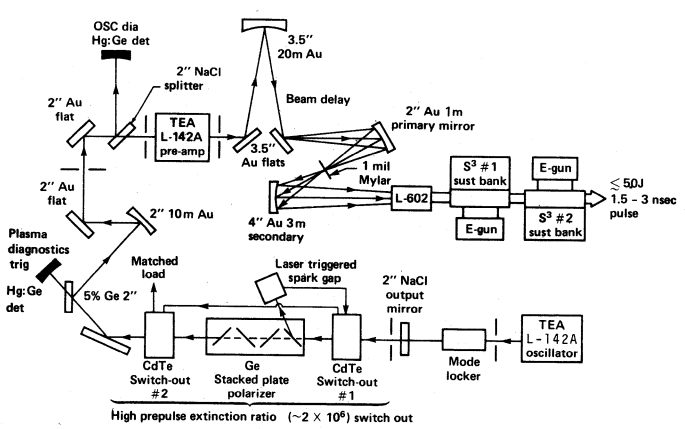


Fig. 2. Schematic diagram of Valkyrie showing its oscillator, switch-out system, and beam delays for streak camera triggering, beam expander, and amplifier chain.

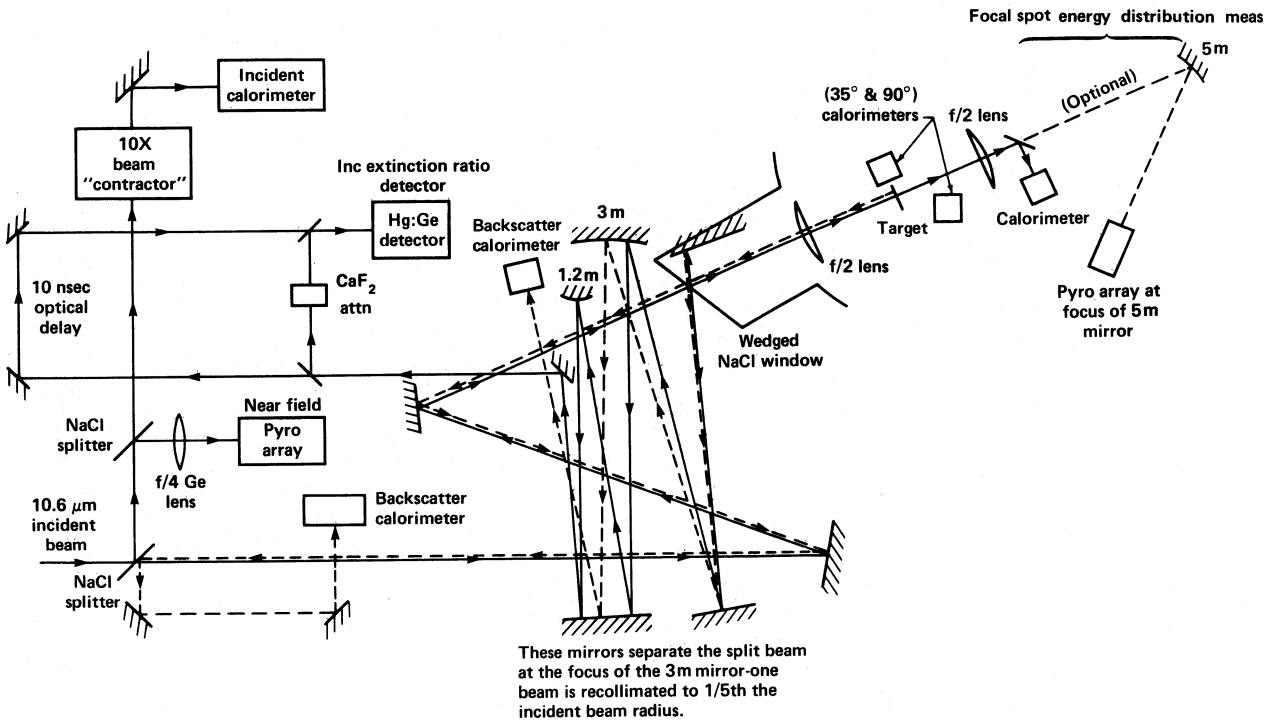


Fig. 3. Schematic diagram of Valkyrie laser-beam diagnostics designed to measure beam energy, temporal pulse shape, prepulse extinction ratio, and near- and far-field beam profile.

10 J in ~1.5 ns with a uniform spatial intensity distribution. Three sodium chloride beam splitters, wedged and antireflection coated with sodium flouride on one face, provide diagnostic beams for intensity profile, energy, temporal character, and prepulse measurements as shown in Fig. 3. The main beam is finally focused to an ~80-μm full width at half maximum (FWHM) spot by an $f/2$ aspheric sodium chloride lens mounted inside the spherical vacuum vessel shown in the foreground of Fig. 1. On the output side of the target chamber a second sodium chloride lens recollimates the beam for forward scatter and focal spot intensity measurements.

III. CO_2 Laser System Simulation

To arrive at a design for Valkyrie, a CO_2 amplifier modeling program predicted the performance of each amplifier module. Any five-temperature model for CO_2 at pressures of a few atmospheres may be extended to model nanosecond pulse propagation by the addition of rate equations describing rotational cross relaxation and vibrational intramode relaxation. Once such a model for gain was developed, it was incorporated into a plane-wave pulse propagation code valid in the regime where coherent propagation effects may be ignored. At $t = 0$ a discharge is turned on and the amplifier's gain begins to develop. At some later time, generally chosen to be near the time of peak gain, an optical pulse of arbitrary temporal shape is launched down the amplifier. This pulse enters the first "bologna"-like slice of gain medium and alters its gain history by saturation. The temporal shape of the pulse reaching the second slice of gain medium has been changed by propagation through the time-varying gain of the first slice. This process is repeated until the end of the amplifier is reached. In a typical calculation several hundred spatial steps are required and each spatial step through a "bologna" slice of medium represents several hundred temporal steps.

The basic rate equation for energy flow from any given rotational state, $|\nu, n, J\rangle$, where ν identifies the vibrational mode, n the vibrational level in that mode, and J the rotational level in that manifold, to any other state may be written

$$\frac{d\rho_{\nu nJ}}{dt} = -\sum_{K\neq J}^{\infty} \gamma_{\nu n}(J,K)\rho_{\nu nJ} + \sum_{K\neq J}^{\infty} \gamma_{\nu n}(K,J)\rho_{\nu nK}$$

$$- \sum_{L} W_{\nu\xi\lambda\beta L} I_{\nu\xi\lambda\beta L} \left[\rho_{\nu\lambda L} - \frac{2L+1}{2L+3}\rho_{\xi\beta(L+1)}\right] \delta_{n\lambda}\delta_{LJ}$$

$$+ \{\text{vibrational intramode relaxation terms}\}$$

$$+ \{\text{direct electronic pumping terms}\}$$

where

$\rho_{\nu nJ}$ $\equiv$ the population density of $|\nu, n, J\rangle$;
$\gamma_{\nu n}(J,K)$ $\equiv$ the rate of population transfer from the Jth rotational level to the Kth rotational level within the (ν, n) manifold;
$W_{\nu\xi\lambda\beta L}$ $\equiv$ the stimulated-emission cross section for the P-type transition between $|\nu, \lambda, L\rangle$ and $|\xi, \beta, L+1\rangle$ (all others being ignored);
$I_{\nu\xi\lambda\beta L}$ $\equiv$ the light intensity resonant with that transition.

The central issue in nanosecond CO_2 pulse propagation calculations is the character of $\gamma_{\nu n}(J,K)$ which describes rapid rotational cross relaxation. Burak *et al.* [1] provided two rota-

tional relaxation models in their study of absorber kinetics. Their first model presumes that $\gamma_{vn}(J, K)$ couples adjacent rotational states only; i.e., $\gamma_{vn}(J, K) = 0$ for $K \neq J \pm 2$ in this case. Their second model groups those levels not directly involved in the lasing process into a reservoir whose kinetics is described by a single equation. Stark *et al.* [2] and Feldman [3] proposed a model similar to Burak *et al.*'s reservoir model in which it is assumed that $\gamma_{vn}(J, K) = \gamma_0 P(K)$; i.e., the rate of population transfer depends only on the Boltzmann occupation probability of the terminal level. In this model levels not involved in lasing relax together maintaining their thermal equilibrium distribution. Jacobs *et al.* [4] provided direct experimental evidence on the character of $\gamma_{31}(J, K)$, i.e., rotational cross relaxation in the (001) rotational manifold of CO_2. In analyzing their results, Jacobs *et al.* realized that no reservoir model could fit their data and were led to a model similar to Burak *et al.*'s first model. The set of equations which result from a $\Delta J = \pm 2$ assumption are second difference equations, and as a result their numerical solutions have the character of solutions to the diffusion equation. That is, energy collisionally "diffuses" in J space to reestablish Boltzmann equilibrium when the population of a level or levels is disturbed by the optical pulse. Jacobs *et al.* noted that $\Delta J \pm 2$ was too short range to fit their data, reservoir models were too long range, and that a third intermediate model would be required.

In designing Valkyrie, therefore, two models were studied. The first was a "reservoir" model in which $\gamma_{vn}(J, K) = \gamma_0 P(K)$. The second was an empirically derived "diffusion" model where

$$\gamma_{vn}(J, K) = \gamma_0 \sqrt{\frac{P(K)}{P(J)}} \exp - \left(\frac{J - K}{\sigma_J}\right)^2$$

which satisfies detailed balance. Fig. 4 is a comparison of the prediction of this model with the data of Jacobs *et al.* A choice of $\sigma_J \cong 8$ comes closest to fitting the data. These assumptions, together with vibrational intramode relaxation constants estimated from the work of Burak *et al.* [5], patched onto the five-temperature model described by [6] and [7], make up the amplifier simulation model for Valkyrie.

As mentioned previously, the pulses from our mode-locked TEA oscillator contain energy in several rotational lines distributed according to the spectrum shown in Fig. 5 [8], [9]. Fig. 6 is a typical energy extraction calculation showing the predicted result of propagating a 1-ns pulse with this spectrum through one of Valkyrie's 11-cm-aperture e-beam sustained amplifiers. The two models predict approximately the same performance in the regime of interest with the diffusion model suggesting about 6 percent less extraction. Both models' predictions lie within the scatter of the data reported in [2].

By inserting the output of this propagation code into a general laser system simulation routine capable of tracing rays through components typically found in laser systems, an overall prediction for the performance of Valkyrie was made. For example, the effects of saturation in the radial dimension may be seen in Fig. 7, an output from this program. More energy may be extracted at the expense of reduced beam quality and increased danger of parasitic oscillations; however, 30-50 J was deemed adequate for target studies.

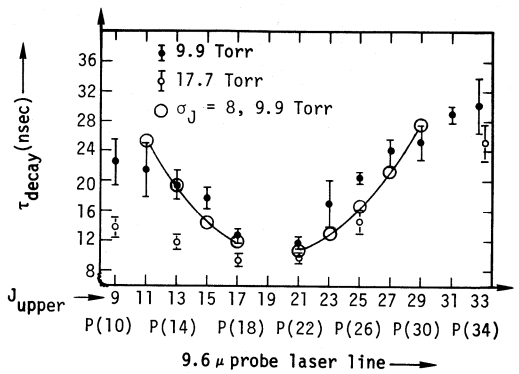


Fig. 4. Jacobs *et al.*'s non-$P(20)$ decays in the 9.4-μm band as a function of J fitted by $\sigma_J = 8$.

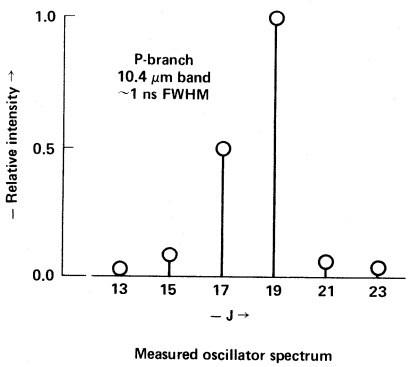


Fig. 5. Measured oscillator spectrum [8].

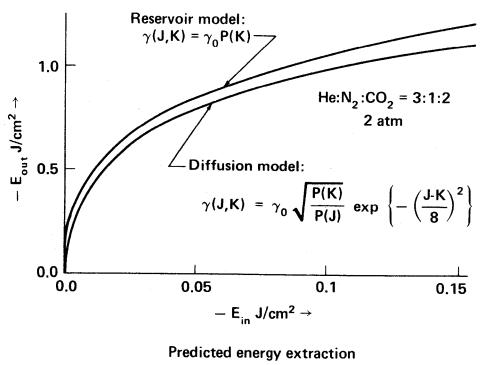


Fig. 6. Predicted energy extraction for a 1-ns pulse propagated through Valkyrie's output amplifier.

IV. Amplifier Testing

With Valkyrie's staging established, a search was initiated to find reliable amplifier modules with the requisite spatial gain uniformity. After testing and rejecting several designs, the devices listed previously were specified and built. A gain measuring apparatus was assembled and used to study the spatial and temporal properties of CO_2 laser amplifiers [10]. An 8-W TEM_{00} CW probe laser beam operating on the P20 rotational transition of the 10.4-μm band was passed through the amplifier. Using a single detector, the amplitude of the emerging beam before, during, and after the amplification-producing discharge was recorded. The detector and oscilloscope were checked for calibration and linearity before each run.

The 9-cm-aperture UV preionized preamplifier, Lumonics

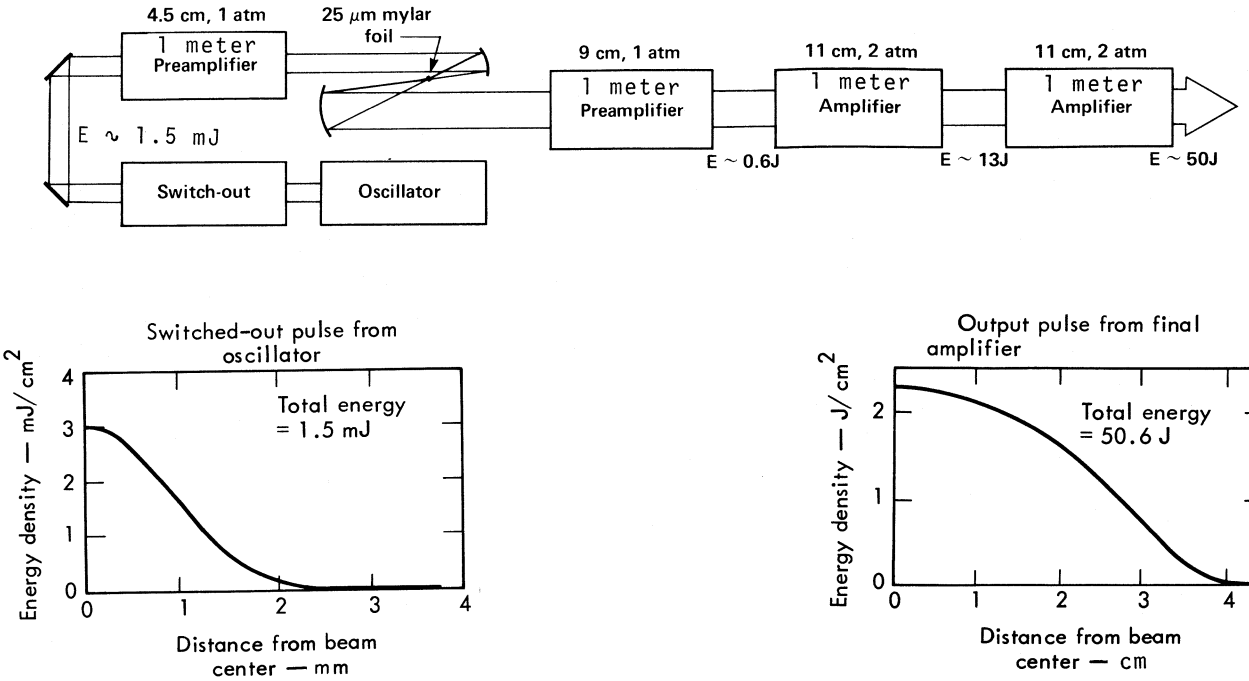


Fig. 7. Simulation calculation showing the predicted performance of the Valkyrie chain.

602A, was built according to Richardson's design [11], and its testing is described in [12]. While axial gains as high as 4.5 percent/cm have been observed, this device is usually operated at 3.0-3.5 percent/cm for improved reliability. The Lumonics 142 A preamplifier is simply a scaled-down version of this unit.

The acquisition of large-aperture *e*-beam sustained power amplifiers presented a more complex problem. A detailed account of the testing of these devices is to be found in [13]. Cold-cathode *e*-beam sustained amplifiers were chosen because of their simplicity, high reliability, and wide operating range. The devices studied are shown in the cut-away drawing in Fig. 8. Two identical power amplifiers of this design built by Systems, Science and Software, Inc., make up Valkyrie's output stages as shown in the insert in Fig. 8. A 10-cm-aperture device was the prototype for these amplifiers, and data taken on the prototype guided the design of the other two units installed in the system. The cylindrical electron-gun vacuum vessel shown in Fig. 8 is evacuated to about 10^{-6} torr. At t = 0, 200 kV are impressed on the array of tantalum strips that constitute the electron gun's "cold" cathode. As a result, a sheet beam of electrons about 10 cm wide by 1 m long emerges through a 25-μm-thick titanium foil window, supported by the hibachi structure drawn in Fig. 8.

A Faraday cup array was used to establish the primary electron-beam current density distribution *in vacuo* 1 cm from the foil window. The variation was slight along the 1-m dimension, but important variations were observed transverse to the electron gun along the 10-cm dimension, as shown in Fig. 9. The primary electron-beam current was approximately retangular in time.

After penetrating the titanium foil window, the electron beam passes through a coarse-mesh stainless-steel screen, not shown, and produces a partial ionization of about 10^{-6} in the 11 X 11 X 100-cm discharge volume located between this cathode screen and the large profiled graphite anode in Fig. 8. The graphite anode is connected to a capacitor bank charged

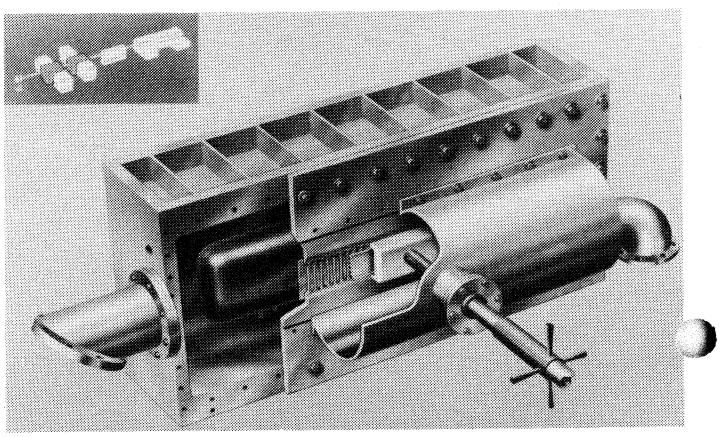


Fig. 8. Exploded view of an S^3 *e*-beam sustained amplifier. The insert shows the location of these units in the Valkyrie chain.

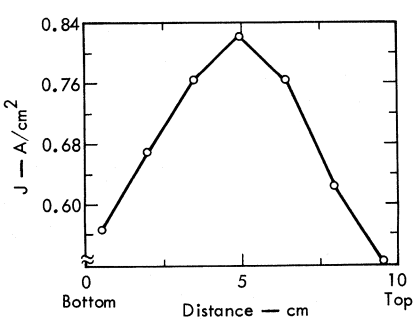


Fig. 9. Variation of primary electron beam current transverse to the electron gun along the 10-cm dimension.

to provide an E/N ratio of about 1.6×10^{-16} V · cm^2 in the discharge volume filled with a mixture of He, CO_2, and N_2. In normal operation the primary electron-beam current is terminated after 2 μs by crowbarring the electron gun's Marx bank. The discharge bank is crowbarred simultaneously, with the net result that about 200 J/l · atm are deposited in the laser gas. The unique features of Valkyrie's amplifiers are their careful electrical shielding, low inductance circuitry, and high electric-field uniformity in the discharge region.

While an exhaustive parameter study required more time than was available, the operating parameters of the amplifiers were explored using five gas mixtures. During each experimental run a gas sample was taken and subjected to mass spectrometric analysis to establish the mixture. Pressure was measured by two Wallace and Tiernan gauges, which always agreed within reading accuracy. Fig. 10 is a typical data set taken at one of the five gas mixtures. The upper trace in Fig. 10(a) shows the chopped probe laser-beam amplitude at a slow sweep rate, while the lower trace records the amplified probe laser beam at 2 μs/division.

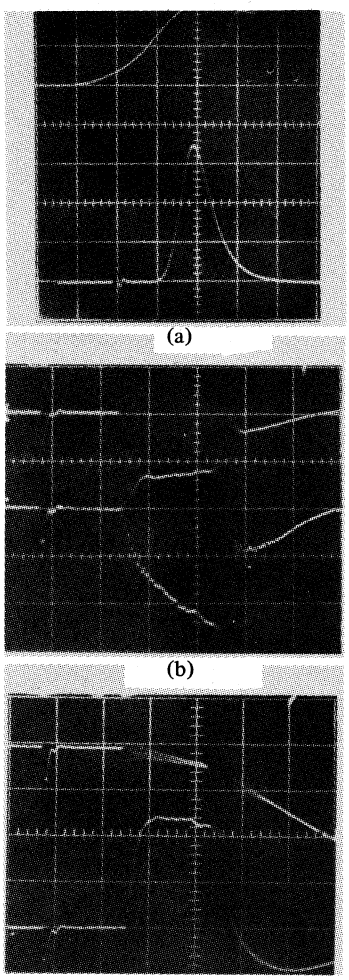


Fig. 10. Typical oscillographs. (a) Gain. Upper trace: probe laser amplitude. Vertical scale = 2 mV/div. Horizontal scale = 100 μs/div. Lower trace: gain = 5.17 percent/cm. Vertical scale = 0.2 V/div. Horizontal scale = 2 μs/div. (b) Electron-gun voltage and current. Upper trace: electron-gun voltage. Vertical scale = 140 kV/div. Horizontal scale = 1 μs/div. Lower trace: electron-gun current. Vertical scale = 3 kA/div. Horizontal scale = 1 μs/div. (c) Discharge bank voltage of 88 kV and a gas mixture of 52 percent He, 17.5 percent N_2, and 29.8 percent CO_2 at 1520 torr. Upper trace: discharge voltage. Vertical scale = 35 kV/div. Horizontal scale = 1 μs/div. Lower trace: discharge current. Vertical scale = 15 kA/div. Horizontal scale = 1 μs/div.

To change the discharge E/N ratio, the charging voltage on the discharge bank was varied from 76 to 96 kV. This resulted in a static E/N variation of 1.38×10^{-16} -1.75×10^{-16} V · cm^2. No attempt was made to measure the electric field, pressure, or temperature variations in the presence of the discharge plasma, so E/N refers to $t = 0$ values only. To explore a range of energy depositions at each charging voltage, the pulse duration was varied from 0.5 to 3.0 μs with a fixed gas mixture at 1520 torr. It was found, as shown by Fig. 11, that small-signal gain usually increased as pulsewidth and discharge voltage increased. The numbers adjacent to the curves in Fig. 11 are pump pulse durations in microseconds.

Depositing more than 300 J/l · atm did not increase the measured gain either because of thermal population of the lower laser level or perhaps even because of probe laser-beam scattering due to pump-induced thermal lensing. A maximum energy deposition of ~400 J/l · atm was recorded at 96 kV and a 3-μs pump pulsewidth. At no time during the testing were any arcs, striations, or other evidence of discharge instabilities observed when the system staged correctly.

The amplifier's gain at several locations within its aperture was determined by carefully translating the probe laser beam. Early measurements on the 10-cm-aperture prototype revealed a disappointingly nonuniform gain profile, shown in Fig. 12. The nearly linear reduction in α from anode to cathode was attributed to a corresponding calculated static electric-field variation as shown in Table I. Readily achievable geometry changes were incorporated into the design of Valkyrie's 11-cm-aperture amplifiers to guarantee good static electric-field uniformity.

To evaluate Valkyrie's 11-cm-aperture amplifiers' gain uniformity, a 3:1:2 gas mixture of $He:N_2:CO_2$ at 1520 torr,

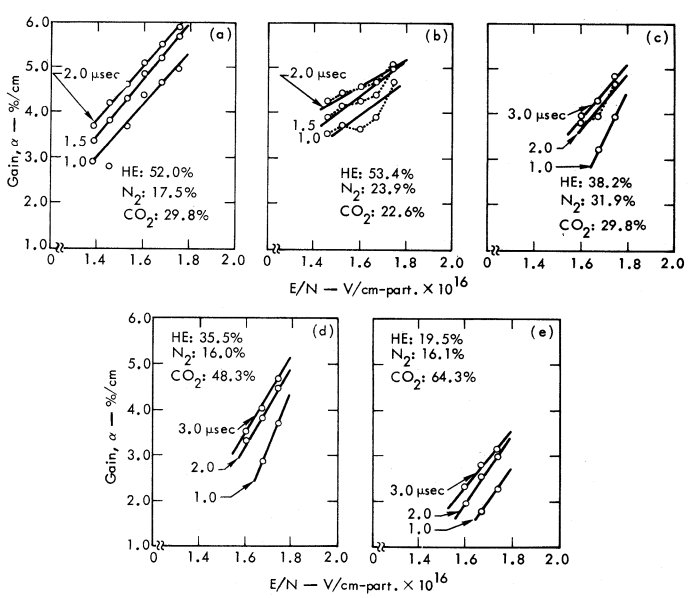


Fig. 11. Gain versus E/N for five gas mixtures. Numbers for curves are pump pulse durations. Solid lines fit data; dashed lines connect data points for clarity.

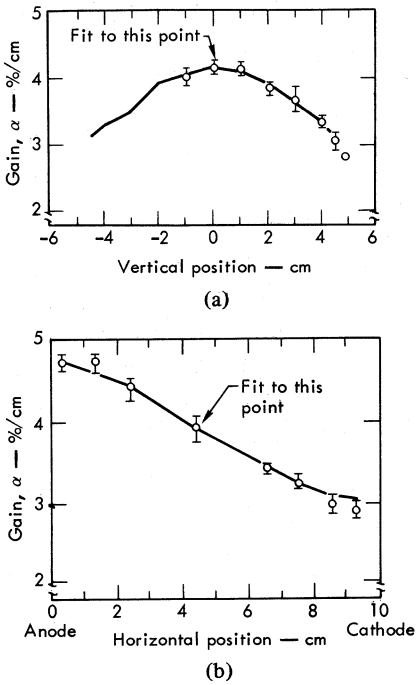


Fig. 12. Comparison of simple gain uniformity model to measured prototype gain for a gas mixture of 50 percent He, 16.7 percent N_2, and 33.3 percent CO_2 at 760 torr. (a) Energy deposition ~200 J/l · atm and discharge bank voltage ~37 kV. (b) Energy deposition ~180 J/l · atm and discharge bank voltage ~37 kV.

TABLE I
PROTOTYPE GAIN UNIFORMITY

Position (cm)		α	σ_α	Calc static e-field (kV/
x	y	(%/cm)	(%/cm)	cm-atm)
		Horizontal scan		
0.4	0.0	4.72	0.08	4.44
1.4	0.0	4.72	0.08	4.36
2.4	0.0	4.44	0.10	4.19
4.4	0.0	3.92	0.12	3.72
6.5	0.0	3.44	0.04	3.33
7.5	0.0	3.24	0.05	3.18
8.5	0.0	2.96	0.06	3.07
9.3	0.0	2.90	0.04	3.00
		Vertical scan		
5.0	-1.0	4.04	0.12	3.61
5.0	0.0	4.12	0.10	3.62
5.0	1.0	4.12	0.08	3.61
5.0	2.0	3.84	0.10	3.59
5.0	3.0	3.70	0.16	3.54
5.0	4.0	3.35	0.08	3.47
5.0	4.5	3.10	0.12	3.45

and E/N of ~1.6×10^{-16} V · cm^2, and a 2-μs pump pulse duration were used. Five shots were taken in each of the 17 positions indicated in Fig. 13. The electrostatic field was calculated for each position probed and these values, together with the measured peak gains, are given in Table II. The gains reported for Unit No. 1 are larger than those for Unit No. 2, although the devices were supposedly identical. This discrepancy was traced to a poorly calibrated voltmeter, which allowed the first unit to be charged about 2 percent more than

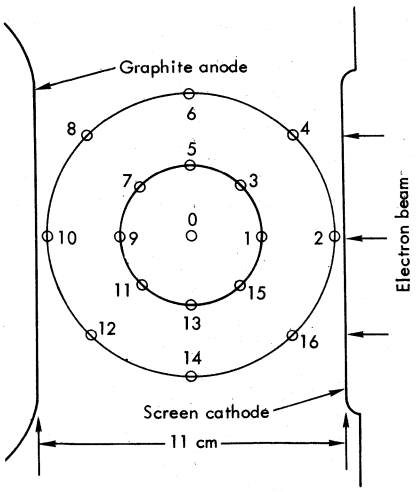


Fig. 13. Location of gain measurements within the amplifier's aperture.

TABLE II
GAIN UNIFORMITY FOR 11-CM-APERTURE AMPLIFIERS

	Unit 1			Unit 2		
Position[a]	α (%/cm)	σ_α (%/cm)	Calc static e-field (kV/cm-atm)	α (%/cm)	σ_α (%/cm)	Calc static e-field (kV/cm-atm)
00	5.45	0.08	4.08	5.14	0.22	4.00
01	5.21	0.10	4.05	5.22	0.17	3.97
02	5.20	0.09	4.03	4.80	0.09	3.95
03	5.25	0.09	4.05	4.91	0.04	3.97
04	5.09	0.17	4.00	4.87	0.27	3.92
05	5.52	0.14	4.10	5.21	0.06	4.02
06	4.90	0.11	4.07	4.44	0.15	3.99
07	5.37	0.24	4.15	5.25	0.12	4.07
08	5.21	0.16	4.24	5.04	0.02	4.16
09	5.65	0.04	4.17	5.30	0.04	4.09
10	5.62	0.07	4.19	5.27	0.09	4.11
11	5.36	0.15	4.15	5.28	0.19	4.07
12	5.12	0.06	4.24	5.35	0.22	4.16
13	5.34	0.08	4.10	5.17	0.12	4.02
14	4.77	0.14	4.07	4.54	0.05	3.99
15	5.11	0.15	4.05	5.00	0.05	3.97
16	4.79	0.03	4.00	4.84	0.10	3.92
Av overall locations	5.23	0.26	4.10	5.04	0.27	4.02

[a]See Fig. 13.

the 88 kV required to provide an E/N of ~1.6×10^{-16} V · cm^2. All shots were charged to an indicated 88 kV and crowbarred after 2 μs. An energy of 212 ± 6 J/l · atm was deposited on each shot. These data are displayed in Fig. 14 to indicate the gain uniformity along vertical and horizontal directions. Whereas the prototype amplifier's small-signal gain varied by ± 20 percent about its average, attention to field uniformity reduced this variation to ± 6 percent in Valkyrie's output stages.

The nearly linear relationship observed between α and E/N in the operating range yields a simple gain uniformity model which largely explains remaining gain nonuniformities. The small-signal gain coefficient α is related to the cross section σ and the inversion density ΔN by $\alpha = \sigma \Delta N$. The cross section is not strongly dependent on E/N or energy deposition, so variations in α across an amplifier's aperture reflect variations in ΔN. The population difference ΔN may be written in terms of the energy stored in the symmetric stretch mode E_1, the bending mode E_2, and the antisymmetric stretch mode E_3.

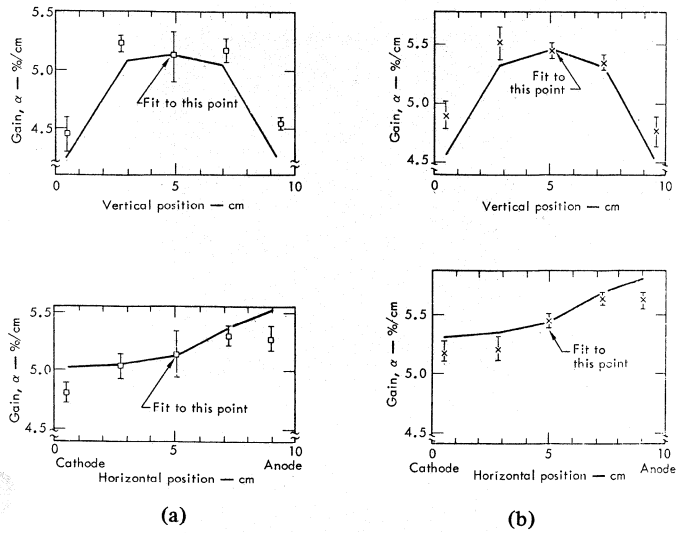


Fig. 14. (a) Comparison of simple gain uniformity model to first 11-cm-aperture unit. (b) Comparison of simple gain uniformity model to the second 11-cm-aperture unit.

Pumping of these modes, and hence the laser levels, in the CO_2 molecule depends on the product of secondary electron density and E/N dependent dynamic excitation rates. The secondary electron density is proportional to the square root of the primary beam current density given that the current pulse is rectangular in time. E_1 and E_2 equilibrate with the translational temperature of the gain medium in a time short compared to the 2-μs pumping time, while E_3 and the energy stored in nitrogen do not. Two more or less independent thermal baths are therefore created with the upper laser level coupled tightly to the hotter one and the lower laser level coupled to the cooler one near the translational temperature. The hotter one, containing the upper laser level, dominates α, and its stored energy is proportional to the time integral of the secondary electron density times an E/N dependent excitation rate. Consequently, in addition to the almost linear dependence of α on E/N evident in Fig. 11, α is also proportional to $\sqrt{J}$. The measured e-beam current uniformity in Fig. 9 was used to estimate the spatial variation of J. Fig. 11 gave the slope of the linear E/N dependence and the resulting predictions for α were fit to the axial measurements and displayed as solid lines in Fig. 12 and Fig. 14. The good agreement between this simple model and measurement confirms its usefulness in amplifier design. Our search for a published numerical model to predict this behavior from first principles was fruitless because of the high CO_2 concentrations used in our amplifiers.

V. Laser System Performance

Targets employed in laser fusion studies tend to be small and fragile. CH_2 foil targets 5 and 10 μm thick and parylene disks 5 μm thick by ~200 μm in diameter have been irradiated. Consequently, besides being sufficiently energetic and of high quality, the output from a laser system designed for laser fusion experiments must be virtually free of prepulses and parasitic oscillations which might prematurely disassemble the target. From the outset Valkyrie yielded 40-60-J 1.5-3.0-ns pulses into a calorimeter. With a target at the focus of the sodium chloride lens, however, about 50 percent of the pulses were accompanied by unacceptably large parasitic oscillations. The e-beam sustained amplifiers' gains were reduced by using a 1:1:1 gas mix rather than the 3:1:2 mix used previously. Configured in this way Valkyrie produced ~25-J pulses with no detectable parasitic oscillations and prepulses 33 dB or more down from the main pulse.

Fig. 2 contains a schematic of the pulse selection system used for target experiments [15]. Low-level pulses separated by 20 ns eventually produced enough ionization in the laser-triggered spark gap to cause it to close launching a 10-kV square wave of 20-ns duration. When this voltage appeared across the CdTe electrooptic crystal, it caused the next mode-locked pulse's polarization to be rotated by $\pi/2$ and consequently that pulse was eventually reflected off the output Brewster plate. Fig. 3 includes a diagram of the experimental arrangements used to determine the efficacy of this pulse selection technique by measuring the ratio of the amplitude of the switched-out pulse to that of the immediately preceding pulse, i.e., the prepulse extinction ratio. A photograph obtained with this apparatus is shown in Fig. 15. This switch-out system had a measured extinction ratio of 2×10^6 at the oscillator which was degraded by amplifier saturation to 2×10^3 at the target. Tests of a single-stage switch-out system had previously shown an extinction ratio of $2\text{-}5 \times 10^4$ at the oscillator which was reduced to only 20-50 at the target. Separate target damage studies established that 10-μm CH_2 foils could usually survive irradiation by pulses with energies of ~100 mJ and showed negligible damage after exposure to $\leqslant$ 40-mJ pulses. Consequently, the single-stage system was found to be inadequate, but the two-stage system guaranteed that the target would not be prematurely disassembled.

Fig. 3 indicates the location of the near- and far-field laser beam diagnostics. Fig. 16(a) is a measurement of the spatial intensity distribution at the output of the laser system as observed by the near-field pyroelectric detector array. A burn pattern of the beam is included in Fig. 16(b). The rear $f/2$ lens and an external mirror were used to reimage the focal intensity distribution with a magnification of ~30 on a second pyroelectric detector array [Fig. 16(c)]. The focal intensity distribution observed in this way shows most of the energy in a diffraction limited peak. A burn pattern, Fig.

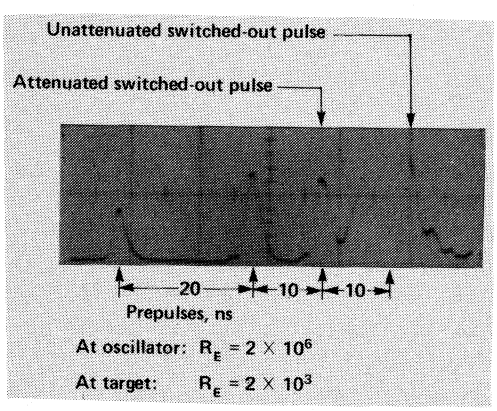


Fig. 15. Oscillograph of extinction ratio measurement.

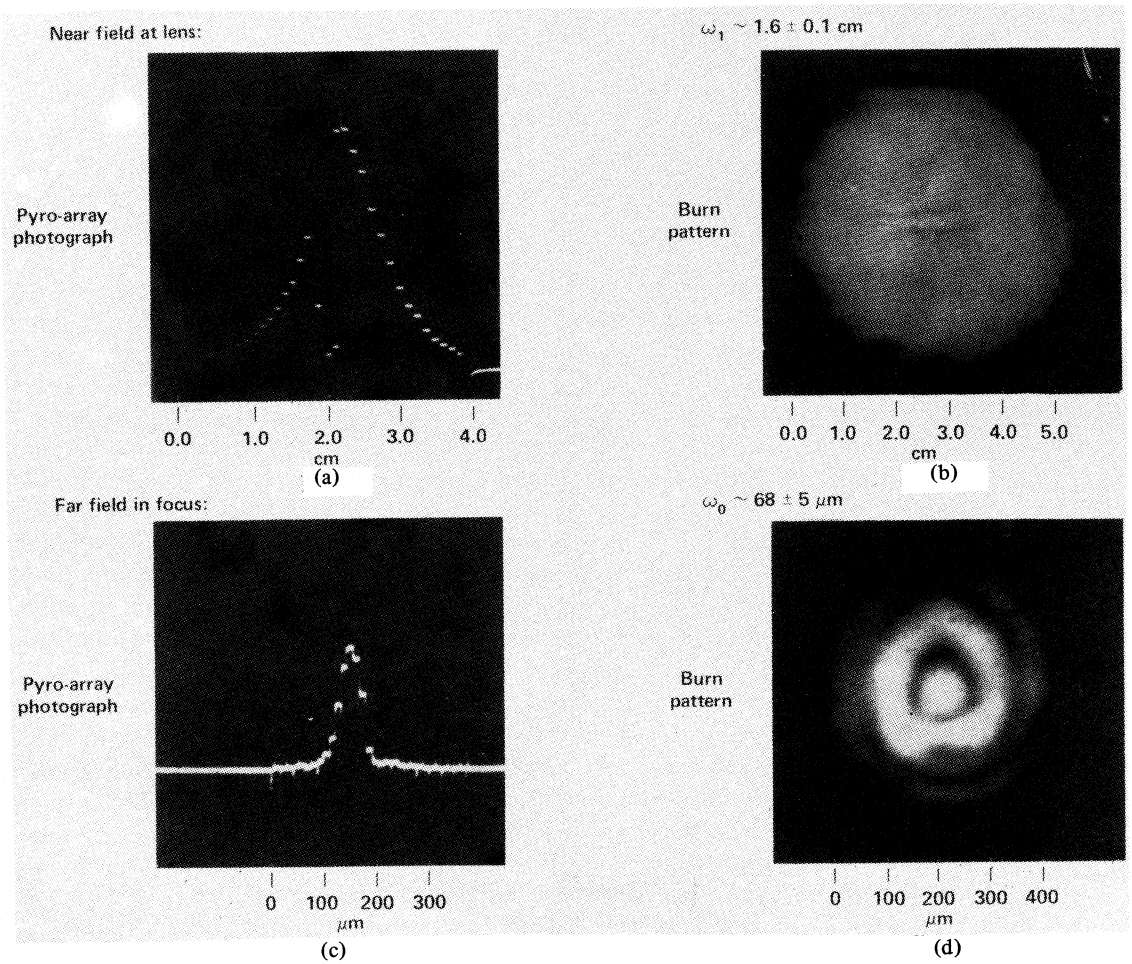


Fig. 16. Near- and far-field beam patterns displayed with pyroelectric arrays and burn patterns.

16(d) on exposed Polaroid film taken in the focal region using only the oscillator, greatly exaggerates the weak ring structure apparent in the pyroarray trace. Estimates of focal intensity distributions based on burn patterns are, therefore, suspect since such a threshold measurement is often misleading.

The smooth output beam profile shown in Fig. 16 was found to be sensitive to the pumping of the preamplifiers. Fig. 17 shows the distortion of a 1-ns pulse by an overdriven preamplifier. The discharge induced thermal lensing effects discussed by O'Neil *et al.* [16] cause the preamplifier medium to behave like an aberrated cylindrical lens. This problem was avoided by a reduction in preamplifier pumping and/or by launching the 1-ns pulse ~0.5 μs before the gain peaked.

Each of Valkyrie's amplifiers was carefully shielded to minimize electrical noise. Even with the entire system firing, only 10–15 mV of RFI were observed on an unterminated 50-ft piece of RG58 cable in the target area. The largest source of electrical noise was the pulse selection system. This relatively small noise level greatly facilitated gathering of target data.

With targets in place, back reflections of 1–6 percent were observed. The 25-μm Mylar foil located in the focal plane of the Keplerian beam expander was broken down by the amplified returning pulse and protected the switch-out and oscillator optics. In summary, Valkyrie provided a high-quality

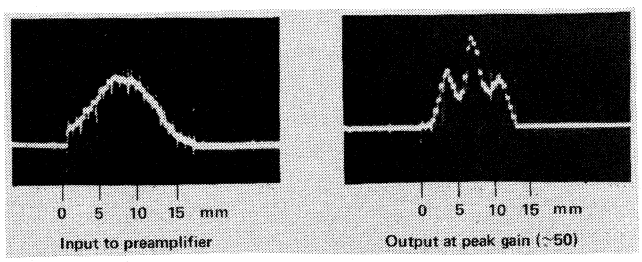


Fig. 17. Beam distortion caused by pump induced thermal lensing in the preamplifiers is shown in these pyroelectric array traces. The distortion depends on total energy deposition and delay before the 1-ns pulse passes through the amplifier. The preamplifier medium behaves like an aberrated cylindrical lens.

10.6-μm source capable of reaching intensities of $\sim 10^{14}$ W/cm^2 on fragile laser fusion targets.

Laser-target interaction studies performed using Valkyrie on three target geometries were reported in [17] and will not be discussed here. Target plasmas produced by a 10.6-μm source were found to be tangibly different from those heated by 1.06-μm light. Evidence of localized heating in CO_2 laser produced plasmas is presented in [18]; however, the coupling of 10.6-μm energy into the target was less efficient than corresponding 1.06-μm irradiations, and the plasmas produced were relatively cooler.

ACKNOWLEDGMENT

The authors wish to thank G. Loda of Systems, Science and Software, Inc., and J. Nilson of Lumonics, Inc., for their help with design, specification, assembly, and testing of Valkyrie's amplifiers. They also wish to thank M. Boyle and V. Rupert for their help in carrying out experiments with Valkyrie, and R. Jacobs, C. Phipps, Y. Pan, and J. Holzrichter for many helpful discussions.

REFERENCES

[1] I. Burak, P. I. Houston, D. G. Sutton, and J. I. Steinfeld, "Mechanism of passive Q switching in CO_2 lasers," *IEEE Journal of Quantum Electronics*, vol. QE-7, pp. 73-89 1971.

[2] E. E. Stark, Jr., W. H. Reichelt, G. T. Schappert, and T. F. Stratton, "Comparison of theory and experiment for nanosecond pulse amplification in high gain CO_2 amplifier systems," *Appl. Phys. Lett.*, vol. 23, pp. 322-324, 1973.

[3] B. J. Feldman, "Short pulse multiline and multiband energy extraction in high pressure CO_2 laser amplifiers," *IEEE Journal of Quantum Electronics*, vol. QE-9, p. 1070, 1973.

[4] R. Jacobs, S. Thomas, and K. Pettipiece, "J-dependence of rotational relaxation in the CO_2 00°1 vibrational level," *IEEE Journal of Quantum Electronics*, vol. QE-10, pp. 480-486, 1974.

[5] I. Burak, Y. Noter, and A. Szoke, "Vibration-vibration energy transfer in the ν_3 mode of CO_2," *IEEE Journal of Quantum Electronics*, vol. QE-9, pp. 541-544 1973.

[6] K. Manes and H. Seguin, "Analysis of the CO_2 TEA laser," *J. Appl. Phys.*, vol. 43, p. 5073, 1972.

[7] A. Davies, K. Smith, and R. Thomson, Rep. 31, Centre for Computer Studies, University of Leeds, Leeds, England, 1974.

[8] C. Phipps, K. Manes, and S. Thomas, Lawrence Livermore Lab. Rep. UCRL 50021-72-2, pp. 20-23, 1972.

[9] M. C. Richardson, "Multiline mode locked uv preionized CO_2 laser," *Appl. Phys. Lett.*, vol. 25, pp. 31-33, 1974.

[10] R. Jacobs, "Technique for gain determinations in pulsed CO_2 TEA lasers," *Rev. Sci. Instr.*, vol. 44, p. 1146, 1973.

[11] M. Richardson, K. Leopold, and A. Alcock, "Large aperture CO_2 laser dicharges," *IEEE Journal of Quantum Electronics*, vol. QE-9, p. 934, 1973.

[12] S. Glaros, J. Nilson, and K. Manes, "Characterization of a large aperture CO_2 amplifier," *IEEE Journal of Quantum Electronics*, vol. QE-9, p. 1122, 1973.

[13] K. Manes *et al.*, "Cold cathode, electron beam sustained CO_2 amplifier gain studies," Lawrence Livermore Lab. Rep. UCRL 51728, 1975.

[14] W. Nigham and J. Bennet, "Electron energy distribution functions and vibrational excitation rates in CO_2 laser mixtures," *Appl. Phys. Lett.*, vol. 14, p. 240, Apr. 1969.

[15] K. Manes, D. Smith, R. Haas, and S. Glaros, "Prepulse extinction ratio measurements in a CO_2 laser system," *IEEE Journal of Quantum Electronics*, vol. QE-11, pp. 635-636, 1975.

[16] R. O'Neil, R. Carbone, H. Granek, and H. Kleiman, "TEA laser medium diagnostics," *Appl. Phys. Lett.*, vol. 20, pp. 461-463, June 1972.

[17] a) R. Haas, K. Manes, M. Boyle, and V. Rupert, presented at the IEEE Conf. Plasma Science, Ann Arbor, MI, May 15, 1975.
b) K. R. Manes, R. A. Haas, V. C. Rupert, and M. J. Boyle, presented at the APS Plasma Physics Conf., St. Petersburg, FL, Nov. 10-14, 1975.

[18] R. A. Haas, M. J. Boyle, K. R. Manes, and J. W. Swain, "Evidence of localized heating in CO_2 laser produced plasmas," *J. Appl. Phys.*, to be published.

Electrooptic Guided-to-Unguided Mode Converter

YONG-KYUNG LEE, STUDENT MEMBER, IEEE, AND SHYH WANG, SENIOR MEMBER, IEEE

Abstract—**Experimental demonstration of electrooptic polarization conversion from a guided TE wave to an unguided TM wave in a thin-film light guide is reported. In the specific device we fabricated utilizing Ta_2O_5 film and $LiTaO_3$ substrate, we have observed a 40-percent modulation when 500 V were applied across two electrodes spaced 50 μm apart. We present here a ray-optics analysis of the conversion process. With the inclusion of the Goos-Haenchen shifts, the analysis agrees well with the experiment.**

Manuscript received September 22, 1975. This work was sponsored in part by the Joint Services Electronics Program under Contract F44620-71-C-0087 and in part by the U.S. Army Research Office, Durham, Grant DAHCO4-74-G-0070.

Y.-K. Lee was with the Department of Electrical Engineering and Computer Sciences and the Electronics Research Laboratory, University of California, Berkeley, CA 94720. He is now with the Department of Information Engineering, University of Illinois at Chicago Circle, Chicago, IL 60680.

S. Wang is with the Department of Electrical Engineering and Computer Sciences and the Electronics Research Laboratory, University of California, Berkeley, CA 94720.

I. INTRODUCTION

THE permittivity tensor of a medium is generally denoted by

$$\overleftrightarrow{\epsilon} = \epsilon \begin{bmatrix} K_{11} & K_{12} & K_{13} \\ K_{21} & K_{22} & K_{23} \\ K_{31} & K_{32} & K_{33} \end{bmatrix} = \epsilon_0 \overleftrightarrow{K} \tag{1}$$

where ϵ_0 is the free-space permittivity. The relative permittivity tensor $\overleftrightarrow{K}$ is a Hermitian matrix in a lossless medium and reduces to a symmetric matrix ($K_{ij} = K_{ji}$) if the medium is electrooptic. When the off-diagonal elements K_{12} or K_{23} are nonzero in a chosen coordinate system, the solutions of Maxwell's equations can no longer be pure TE or pure TM waves, but become admixtures of TE and TM waves.

The electrooptic polarization-converter being discussed here

utilizes the matrix element K_{12} electrooptically to control the coupling between TE and TM waves. Wang *et al.* have proposed and analyzed TE $\leftrightharpoons$ TM mode converters consisting of an isotropic thin film and an anisotropic or electrooptic substrate [1]. Its feasibility has been demonstrated by Shah *et al.* [2] and by Sosnowsky and Weber [3] using anisotropic substrates where the off-diagonal elements were made nonzero by misaligning the substrate crystals (passive mode converters). The experiment to be presented here uses electrooptic effects in the substrate. We believe it is the first electrooptic operation of such mode converters (active mode converters). Similar devices but using magnetooptic effects in the film have been previously reported by Tien *et al.* [4] and by Tseng *et al.* [5].

In the present device, the light guide (isotropic Ta_2O_5 film on $LiTaO_3$ crystal) is made to support only TE_0. When the TE wave is converted into a TM wave, it can no longer be guided because the guide dimension is smaller than the cutoff dimension for TM waves. The converted wave will then leak into the substrate or superstrate (substrate mode or superstrate mode) [6]. While the device is based on the same principle as the active guided mode converter [1], [4] in the sense that it utilizes polarization coupling, it does not require strict phase degeneracy between the TE and TM waves due to the following considerations.

The spacing between the guided modes is approximately inversely proportional to the guide thickness. If we regard a substrate mode as a guided mode with the substrate as its guiding layer, the spacing between substrate modes is much smaller than that between (film-) guided modes (the ratio being 10^{-3} for the case of a film 1 μm thick and a substrate 1 mm thick, for example). Therefore, the substrate modes can be considered as forming a continuum for all practical purposes. For efficient mode conversion, the modes which are involved in the conversion process should propagate with the same phase velocity. This phase degeneracy condition is more easily met in the guided-to-unguided (or film-mode-to-substrate-mode) converter, where the conversion is taking place from a discrete mode to a continuous mode, than in the guided-to-guided mode (or film-mode-to-film-mode) converter, where the conversion is from a discrete mode to a discrete mode.

In Section II we will analyze the present electrooptic polarization converter following the ray-optics approach. The fabrication and operation of the device will be discussed in Section III, and the present limitations and prospective improvements of the structure will be discussed in Section IV.

II. Ray-Optics Analysis of Thin-Film Electrooptic Polarization Converter

The analysis of wave propagation in anisotropic guide can be carried out in both ray-optics and wave-optics approaches. While the wave-optics approach is more general and presents a more comprehensive treatment of all physical effects, the ray-optics approach is simpler in its mathematics and easier to understand in its physics. In the ray-optics approach, it is first assumed that a ray is totally reflected from the geometrical interface. However, the ray actually penetrates into the spaces adjacent to the waveguide through evanescent fields, and the effect which accounts for the evanescent nature of the field is known as the Goos-Haenchen effect [7]-[9]. In this section, we will adopt the ray-optics analysis and start by reviewing the analysis by Wang *et al.* [1]. This analysis will be made complete by including the Goos-Haenchen effect in the final stage of our calculation.

The three-layer guide structure being discussed here is shown in Fig. 1. The top layer and the film are isotropic, while the substrate is anisotropic. The refractive indices of the three layers are assumed to be such that $n_t^2 < K_{11}, K_{22}, K_{33} < n_f^2$ and $K_{12} \ll K_{11}, K_{22}, K_{33}$. We first study the reflections at the top layer and the substrate interface and then combine them with the phase retardation across the film.

A. Reflection from Anisotropic Substrate

Let us consider an electromagnetic (EM) wave impinging on an anisotropic boundary as shown in Fig. 2. $k_0 = \omega(\mu_0 \epsilon_0)^{1/2}$ is the free-space wavenumber, and p and β are the normalized propagation constants in the x and z direction, respectively. It is assumed that $K_{11} > K_{22} = K_{33}$. The reflected and refracted waves at such boundaries can be found by solving Maxwell's equations in regions I and II separately and then requiring them to satisfy the necessary boundary conditions at the interface.

For the given permittivity tensor, the normal modes (1 and 2) in region II are admixtures of TE and TM waves. These two normal modes reduce to pure TE and TM waves when K_{12} is made zero (i.e., when the coupling is removed). The normalized propagation constants p_1 and p_2 in the substrate can be obtained by solving the characteristic equations of region II and their expressions are given in Appendix I. The modes are numbered such that mode 1 is a TE-like wave and mode 2 is a TM-like wave. The reason for such an assignment becomes clear shortly.

Let us consider the case when $K_{12} = 0$. The p_1^2 and p_2^2 of (A1) become

$$p_1^2 = \beta^2 - K_{22}$$

$$p_2^2 = \frac{K_{33}}{K_{11}} (\beta^2 - K_{11}) \tag{2}$$

and it is apparent that p_1 corresponds to pure TE wave and p_2 to pure TM wave. When β of the incident wave is such that

$$K_{22} = K_{33} < \beta^2 < K_{11} \tag{3}$$

p_1 is real (mode 1 is an evanescent wave) and p_2 is imaginary (mode 2 is a propagating wave). An incident TE wave will then be totally reflected while a TM wave will have both reflected and refracted components.

When $K_{12} \neq 0$ and $K_{22} = K_{33} < \beta^2 < K_{11}$, the situation becomes more complicated. The TE incident wave will no longer be totally reflected at the boundary but will have both reflected and refracted waves. The reflected wave, in this case, will consist of both TE and TM components, and the refracted wave is a TM-like wave (mode 2). Thus the incident TE wave is partially converted into a TM wave upon reflection and refraction. The incident TM wave will go through an analogous

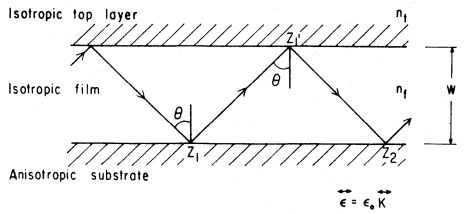


Fig. 1. Ray-optics picture of light guiding in a three-layer lightguide. Goos–Haenchen shift is not shown here.

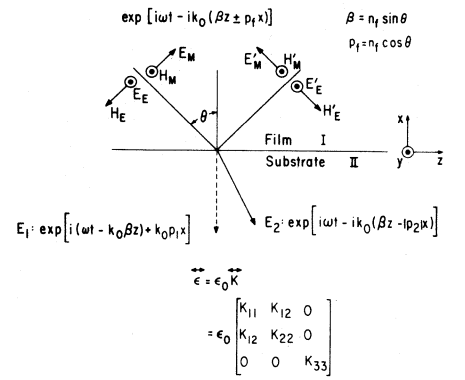


Fig. 2. Reflection and refraction of EM wave at the interface between an isotropic film and an anisotropic substrate. E_1 is an evanescent field and E_2 is a propagating wave.

process except that no "actual" polarization conversion is involved in the refraction because the refracted (propagating) wave in region II is always a TM-like wave.

The reflection and refraction at the boundary can be summed up in terms of a scattering matrix $[S]$ which relates the electric fields in both regions as follows:

$$\begin{bmatrix} E'_E \\ E'_M \\ E_1 \\ E_2 \end{bmatrix} = [S] \begin{bmatrix} E_E \\ E_M \end{bmatrix} = \begin{bmatrix} r_{EE} & r_{EM} \\ r_{ME} & r_{MM} \\ t_{EE} & t_{EM} \\ t_{ME} & t_{MM} \end{bmatrix} \begin{bmatrix} E_E \\ E_M \end{bmatrix}. \tag{4}$$

In the preceding equation, E_E and E_M are the electric fields of the impinging TE and TM waves, and E'_E and E'_M are those of the reflected TE and TM components, while E_1 and E_2 are the y components of the two refracted waves. The other components of the electric and magnetic field vectors can be obtained from Maxwell's equations. The mathematical expressions of the various matrix elements are given in Appendix II. Of these, the elements r_{EM}, r_{ME}, t_{EM}, and t_{ME} signify the conversion of TE to TM polarization or vice versa due to the anisotropy of the medium involved. Since the conversion factors (r_{EM} and r_{ME}) are proportional to the product of the two modes involved [10]-[12], the polarization conversions from TE to TM and from TM to TE are always reciprocal to each other and $r_{EM} = r_{ME}$.

Among other relations that should hold between the different matrix elements, the conservation of energy requires that the sum of the energies of the reflected and refracted waves be equal to the incident wave energy. This means that the x component of the Poynting's vectors of these waves should add up to zero. For the case of incident TE wave, remembering that mode 2 is the only propagating wave in the substrate, we have

$$\frac{1}{2}\sqrt{\frac{\epsilon_0}{\mu_0}} k_0 p_f |E_E|^2 = \frac{1}{2}\sqrt{\frac{\epsilon_0}{\mu_0}} \frac{K_{11}|p_2|(p_1^2 + |p_2|^2)}{L_2} |E_2|^2 + \frac{1}{2}\sqrt{\frac{\epsilon_0}{\mu_0}} k_0 p_f |E'_E|^2 + \frac{1}{2}\sqrt{\frac{\epsilon_0}{\mu_0}} k_0 p_f |E'_M|^2. \tag{5}$$

When $E'_E = r_{EE}E_E$, $E'_M = r_{ME}E_E$, and $E_2 = t_{ME}E_E$ are substituted, (5) reduces to

$$|r_{EE}|^2 + |r_{ME}|^2 + \frac{K_{11}|p_2|}{p_f} \frac{p_1^2 + |p_2|^2}{L_2} |t_{ME}|^2 = 1 \tag{6}$$

where L_2 is defined in Appendix II. We define

$$|T|^2 = \frac{K_{11}|p_2|}{p_f} \frac{p_1^2 + |p_2|^2}{L_2} |t_{ME}|^2 \tag{7}$$

for future reference. A similar relationship can be derived for TM wave incidence, namely

$$|r_{MM}|^2 + |r_{EM}|^2 + \frac{K_{11}|p_2|^2}{p_f} \frac{p_1^2 + |p_2|^2}{L_2} |t_{MM}|^2 = 1. \tag{8}$$

B. Scattering Matrices along the Zig-Zag Ray Path

The scattering matrix for one complete zig-zag ray path (1-1'-2 in Fig. 1) can be obtained by combining the results of the preceding section with the reflection effect at the top-layer interface and the additional phase shift from the round trip across the film layer. The reflection at the top layer is treated in the same way as from the substrate. Since $\beta > n_t$ and the top layer is isotropic, the field existing beyond the top boundary is evanescent and no polarization conversion is involved in this total reflection. Thus the reflection coefficient has a magnitude of unity and a phase shift [6] of

$$\exp(-i\phi_E) = \exp\left[i \tan^{-1}\left(\frac{p_t}{p_f}\right)\right] \tag{9}$$

for the TE wave and

$$\exp(-i\phi_M) = \exp\left[i \tan^{-1}\left(\frac{p_t/n_t^2}{p_f/n_f^2}\right)\right] \tag{10}$$

for the TM wave, where $p_t^2 = \beta^2 - n_t^2$. Finally, the round trip across the film of thickness W introduces a phase delay of $\exp(-i\phi_d) = \exp(-i2k_0 p_f W)$.

The resultant scattering matrix for one complete zig-zag path is then obtained by cascading these matrices in proper order, and is given by

$$\begin{bmatrix} E_E \\ E_M \end{bmatrix}_2 = [r] \begin{bmatrix} E_E \\ E_M \end{bmatrix}_1 = \begin{bmatrix} |r_{EE}| \exp(i\phi^E) & |r_{EM}| \exp(i\phi_{EM}) \\ |r_{MM}| \exp(i\phi_{EM}) & |r_{MM}| \exp(i\phi^M) \end{bmatrix} \begin{bmatrix} E_E \\ E_M \end{bmatrix}_1 \tag{11}$$

where

$$\phi^{E} = \phi_{EE} + \phi_{E} - \phi_{d}$$

$$\phi^{M} = \phi_{MM} + \phi_{M} - \phi_{d}$$

and ϕ_{EE}, ϕ_{MM}, and ϕ_{EM} are the phases of r_{EE}, r_{MM}, and r_{EM}, respectively. The equality $r_{EM} = r_{ME}$ is recalled in the preceding equation. The electric fields of TE and TM waves at z_n (after making $n-1$ zig-zag paths) are obtained by simply multiplying the matrix $[r]$ $(n-1)$ times:

$$\begin{bmatrix} E_E \\ E_M \end{bmatrix}_n = [r]^{(n-1)} \begin{bmatrix} E_E \\ E_M \end{bmatrix}_1 \equiv [R]_n \begin{bmatrix} E_E \\ E_M \end{bmatrix}_1$$

$$= \begin{bmatrix} R_{EE} & R_{EM} \\ R_{ME} & R_{MM} \end{bmatrix} \begin{bmatrix} E_E \\ E_M \end{bmatrix}. \tag{12}$$

Under the condition of (3), let us assume that the TE wave is a proper guided mode of the light guide satisfying the "mode equation" [1], [6] of

$$\phi^{E} = 2m\pi, \quad (m = \text{integer}) \tag{13}$$

and that any TM wave which leaks into the substrate is lost in the substrate. Under these assumptions, the characteristics of matrices $[r]$ and $[R]_n$, and their implications concerning the electrooptic polarization converter can be summarized as follows.

1) $[r]$ and $[R]_n$ are always symmetric matrices (i.e., polarization conversions always happen in both directions).

2) $|r_{MM}| < 1$ and hence $|R_{MM}| < 1$. A TM wave is a leaky wave.

3) When the applied electric field is zero ($K_{12} = 0$): a) $r_{EM} = r_{ME} = 0$ and $R_{EM} = R_{ME} = 0$ (no polarization conversion happens), and b) the TE wave is totally reflected from the substrate ($|r_{EE}| = 1$) and is a proper guided mode.

4) When an electric field is applied to make $K_{12} \neq 0$: a) TE and TM waves are coupled together and the polarization conversion happens in both directions; $r_{EM} = r_{ME} \neq 0$, and $R_{EM} = R_{ME} \neq 0$, and b) part of the TE wave is converted and refracted into the substrate TM wave, thus making $|r_{EE}| < 1$ and $|R_{EE}| < 1$.

In summary, the application of an electric field causes the guided TE mode to convert into a TM wave upon reflections from and refractions into the substrate. The refracted TM wave is eventually lost in the substrate. The fraction of TE wave energy still remaining in the waveguide at z_n is represented by $|R_{EE}|^2$ of the matrix $[R]_n$ (12).

The distance $z_n - z_1$ is $(n-1)$ times the distance Z_0 by which the ray advances in one complete zig-zag path. As is shown in Fig. 3, Z_0 consists of two components: 1) the lateral displacements in going from one boundary to another, $W \tan\theta$, and 2) the additional displacements, known as the Goos-Haenchen shifts, at the substrate and top-layer interfaces. Since the TM wave is not a guided wave, only the Goos-Haenchen shifts for the TE wave are involved.

Here we follow the analysis carried out by Kogelnik *et al.* [9], and borrow their expressions for the displacements shown in Fig. 3. We have

$$Z_{EE} = \frac{1}{k_0} \frac{d\phi_{EE}}{d\beta} \tag{14}$$

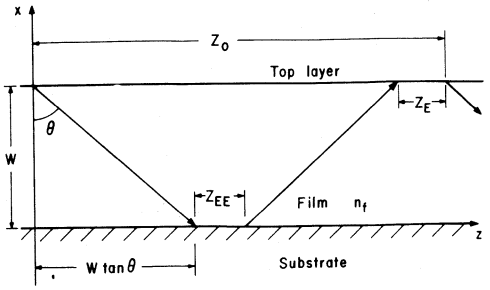


Fig. 3. Ray-optics picture of light guiding with the Goos-Haenchen shifts, z_E and z_{EE}, included. $Z_0 = 2W \tan\theta + Z_{EE} + Z_E$. Compare with Fig. 1.

$$Z_E = \frac{1}{k_0} \frac{d\phi_E}{d\beta} \tag{15}$$

and

$$Z_0 = 2W \tan\theta + Z_{EE} + Z_E. \tag{16}$$

In the wave-optics analysis, the Goos-Haenchen shifts are automatically incorporated into the analysis [13]. Addition of these extra shifts to the ray-optics analysis makes up the discrepancies between the two analyses.

III. Electrooptic Polarization Conversion Experiment

A. Experiment

The configuration of a thin-film electrooptic polarization converter used in the experiment is shown in Fig. 4. A Ta_2O_5 light-guiding layer of 7000 Å was deposited on top of a *c*-cut $LiTaO_3$ crystal ($n_o = 2.1763$ and $n_e = 2.1807$ at $\lambda = 6328$ Å) following the procedure outlined in [14]. A pair of 1000-Å-thick *Al* electrodes were fabricated directly onto the film using photolithographic technique. The electrodes were 8 mm long, spaced 50 μm apart, and were measured to have a capacitance of 4 pF. Epoxy was coated on top of it to increase its breakdown voltage.

A He-Ne laser beam ($\lambda = 6328$ Å) was first TE-polarized using a Glan-Thompson prism (PL1) and was focused onto an input prism coupler (PR1). After the beam was passed between the electrodes, it was coupled out by an output prism coupler (PR2) and then fed into a photomultiplier through an analyzer (PL2) which passed TE waves only. An oscilloscope was used to examine the output signal.

Light-coupling experiments on this light guide using a $SrTiO_3$ prism ($n = 2.38618$ at $\lambda = 6328$ Å) showed that it supported only the TE_0 mode with $\beta_E = 2.17809$, which confirms the requirement $K_{22}, K_{33} < \beta_E^2 < K_{11}$. The actual light-guiding picture taken while looking into the end of the film is shown in Fig. 5. In Fig. 5(a), a TE-polarized beam was coupled into the film, and we indeed see it was confined in the film plane. However, when the polarizer was rotated to select a TM-polarized input, the beam confinement in the film disappeared, and it is seen that the optical beam had completely leaked into the substrate, as shown in Fig. 5(b). Substituting the measured values of W and β_E into the mode equation, (13), we find that the TE refractive index of the film n_{fE} is 2.1930. A more de-

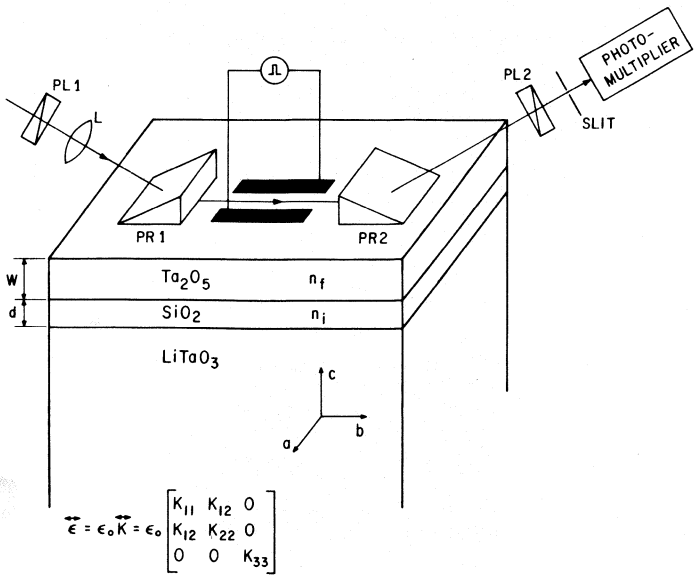


Fig. 4. Configuration of thin-film electrooptic polarization converter.

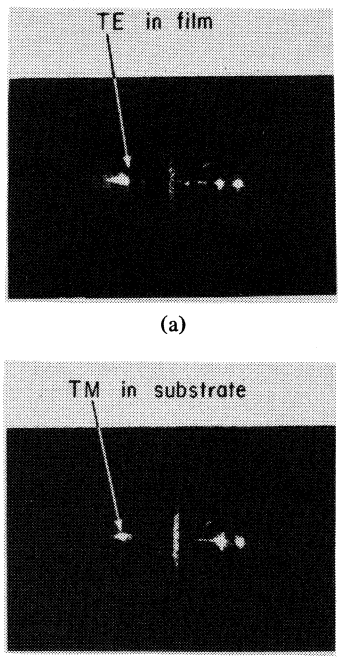


Fig. 5. Photographs of the guide edge. (a) TE input. (b) TM input. Note the beam confinement in the thin-film layer in (a), while the beam is entirely in the substrate in (b).

tailed discussion regarding the film index will be given in Section III-B.

The electric field was applied along the a-axis of the crystal. It penetrates through the film and into the substrate to induce a nonzero K_{12} by means of the electrooptic coefficient r_{51} ($r_{51} = 20.0 \times 10^{-12}$ m/V in $LiTaO_3$).

$$K_{12} = K_{11}K_{22}r_{51}E. \tag{17}$$

The oscilloscope display of the actual decrease of the optical beam strength is shown in the upper trace of Fig. 6(a) along with the applied voltage pulse in the lower trace. It vividly demonstrates that when the electric field is applied, part of the

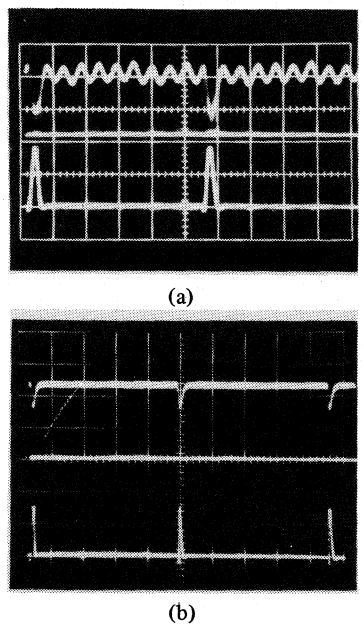


Fig. 6. (a) Oscilloscope photographs of the coupled-out TE intensity (upper trace; 0.1 V/div. × 5 μs/div.) and the applied voltage pulses (lower trace; 500 V/div. × 5 μs/div.) using prism couplers. (b) The interpulse modulation effects have disappeared when the grating couplers were used. Same scale as in (a).

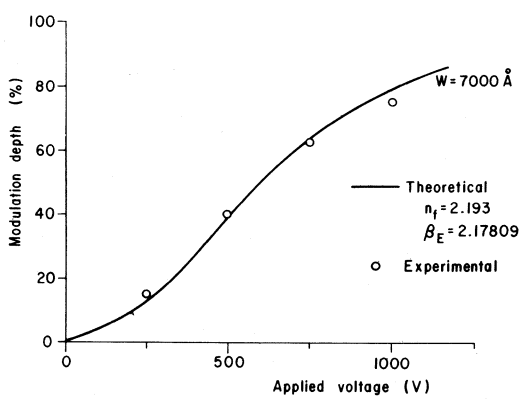


Fig. 7. Modulation (polarization conversion) versus applied voltage curve.

TE_0 wave is converted into a TM wave and then is lost into the substrate, because the guide cannot support a TM wave. The modulation depth versus the applied voltage is plotted in Fig. 7. Typically, about 40 percent of the guided energy was converted when 500 V was applied.

In Fig. 6(a), the variation of the optical beam strength between the electric pulses, i.e., when the applied electric field was actually off, can be attributed to the acoustic surface wave that was excited unintentionally during the time when the applied electric field was on. The large applied electric field ($E = 100$ kV/cm at $V = 500$ V, for example) excited a very strong acoustic surface wave which propagated toward the prism coupler sites and set up a lattice vibration in the crystal. Under the prism, this lattice vibration changed the air gap spacing between the prism and the film, which, in turn, changed the coupling efficiency [15]. This conjecture is verified by another experiment where the prism couplers were

replaced by grating couplers [16] in order to eliminate the air gap. Input and output grating couplers with 3200-Å periodicity were fabricated directly on the film following the procedures developed by Cordero [17]. The modulation picture using these grating couplers is shown in Fig. 6(b), and, indeed, the spurious modulation effect is eliminated. The existence of propagation of an acoustic wave could be detected by an acoustic wave probe [18], which simply consisted of a bare end of a coaxial cable. Fig. 8 shows the experimental arrangement and the detected acoustic signal. Note that the acoustic surface wave did not show any considerable decay in the first 20–30 μs after the electric pulse was removed. This explains why the amplitude of the spurious variation in Fig. 6(a) did not decay between pulses.

B. Discussion of the Experimental Results

When the film thickness was below about 7700 Å, the Ta_2O_5 light guide on a c-cut $LiTaO_3$ crystal ceased to support any TM mode. The TE_0 mode, however, could still be guided at $W = 6900$ Å. To ascertain the value of the film index and the initial thickness for waveguiding, several samples with different film thicknesses W were prepared. The measured values of β_E and β_M are plotted in Fig. 9 for film thicknesses ranging from 6900 Å to 1.1 μm. At 7700 Å, β_M was measured to be 2.1814, which is very close to the extraordinary index of the substrate 2.1807. As the thickness is reduced further, β_M would eventually become smaller than the substrate index and the TM wave will start leaking into the substrate.

Due to the peculiar behavior of the refractive index of thermally oxidized Ta_2O_5 films, it was not possible to find a unique value for n_f which would satisfy the mode equation for all the data points simultaneously. As Hensler *et al.* [19] have pointed out, and as we have observed ourselves during this investigation, the refractive index was different not only for TE and TM polarizations but also for different film thicknesses. In the following discussions, we assume that $n_f = 2.1930$ based on the measurement at $W = 7000$ Å.

Let us now calculate the theoretical modulation depth based on the ray-optics formulation presented in Section II, and compare it with the experimental results. We will proceed by first estimating the electric field E between the electrodes when a voltage V is applied. The electrode configuration in Fig. 4 can be approximated by two semi-infinite conducting planes separated by a distance D. This problem is solved as an example in the EM field text [20], and we adopt the formula given in [20] directly with the following considerations.

1) Since the film thickness W is much smaller than the electrode gap D ($W = 7000$ Å and $D = 50$ μm), we assume that the electric field is constant in the x direction (c direction in Fig. 4) within the range of interest because the decay constant of the electric field into the substrate would be on the order of tens of microns.

2) Since the major portion of the optical energy is centered around the axis in a Gaussian beam, the electric field at the middle of the electrode gap is taken and assumed constant across the gap.

3) The anisotropy of the substrate is ignored. The resulting expression for the electric field is

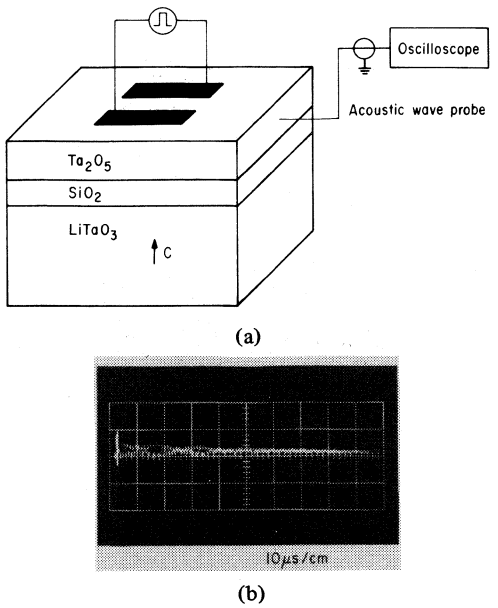


Fig. 8. Probing of the acoustic surface wave launched by the electrodes.

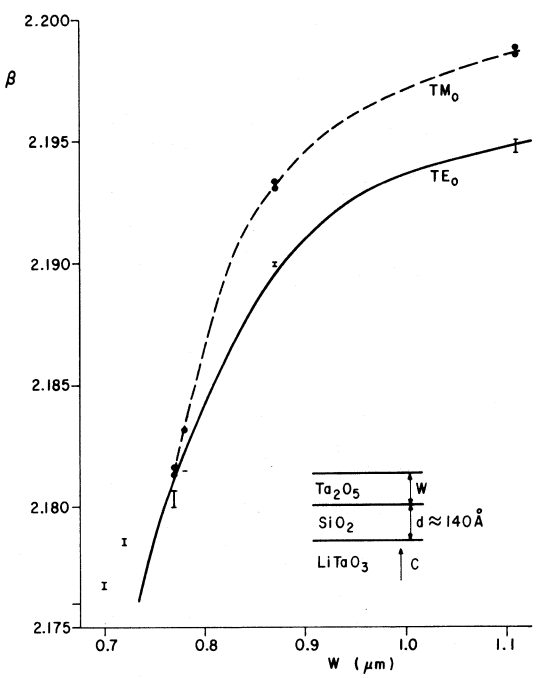


Fig. 9. Experimental plot of β–W variation of the Ta_2O_5–SiO_2–(c-cut) $LiTaO_3$ light guide.

$$E = \frac{2}{\pi}\frac{V}{D} = 0.636\,\frac{V}{D}. \tag{18}$$

Using the estimated values of n_f and E together with other structural parameters, we can now compute the scattering matrices $[S]$ and $[R]_n$ of (4) and (12) as well as the Goos–Haenchen shifts of (16). In Fig. 10, the variations of the matrix elements, r_{EE}, r_{ME}, and T, the Poynting vector of the refracted wave normal to the substrate interface and normalized to the incident E [refer to (7)], are plotted for different

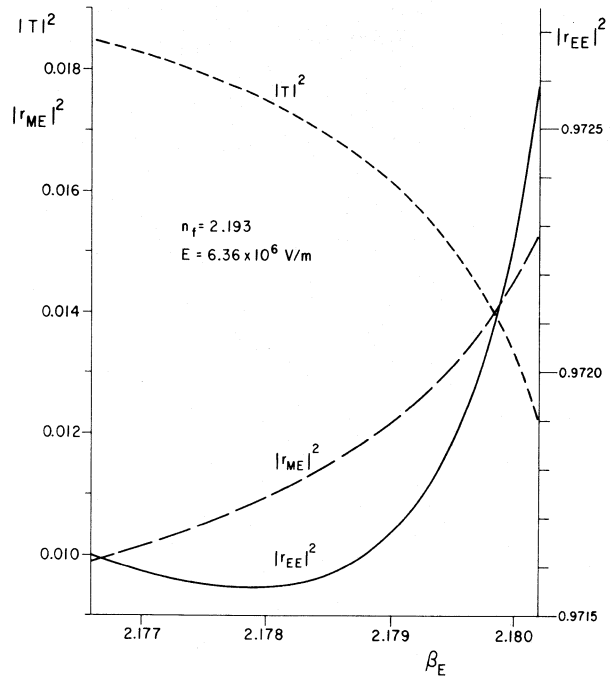


Fig. 10. Variation of $|r_{EE}|^2$, $|r_{ME}|^2$, and $|T|^2$ with respect to β_E. The sum of the preceding three variables always should be one. See text for detail.

values of β_E and for an applied voltage of 500 V. The power lost into the substrate $|T|^2$ increases as β_E decreases toward the TE substrate index. This is so because the decay constant p_1 of the evanescent field in the substrate becomes smaller which means a larger penetration depth. Throughout the β_E variation, the sum of $|r_{EE}|^2$, $|r_{ME}|^2$, and $|T|^2$ is always 1, as demanded by (6).

The variation of $|R_{EE}|^2$, which represents the energy of the TE optical beam in the guide, is plotted with respect to the electrode length L in Fig. 11. As expected, the TE wave energy decays as more and more of it is converted into TM and subsequently lost into the substrate. When we read $|R_{EE}|^2$ for different voltages at $L = 8$ mm, which is the electrode length in our device, and plot it against the applied voltages in Fig. 7 as the solid curve, the agreement between the experiment and the analysis is rather good.

Finally, we discuss the relationship between modulation depth (η) and β_E. While Fig. 10 indicates that more energy is lost into the substrate per bounce when β_E is decreased toward the cutoff value of the TE wave, it should be pointed out that the propagation distance Z_0 per one zig-zag path increases at the same time as it is inversely proportional to β_E (16). Thus, for fixed electrode length L, the number of bounces (NB) that can be accommodated within the interaction region will be smaller for smaller β_E. The optimum modulation efficiency is obtained when these two competing factors are compromised. Fig. 12 shows the variation of these values versus β_E. For the structural and operating parameters of the present device, the optimum operation is obtained when $\beta_E = 2.1780$. This value of β suggests a film thickness of 7250 Å from Fig. 9 as compared to the value 7000 Å used in the experiment.

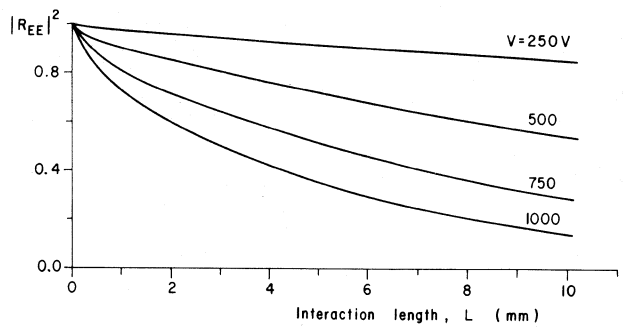


Fig. 11. Variation of $|R_{EE}|^2$, TE wave energy remaining in the guide, versus L the electrode length.

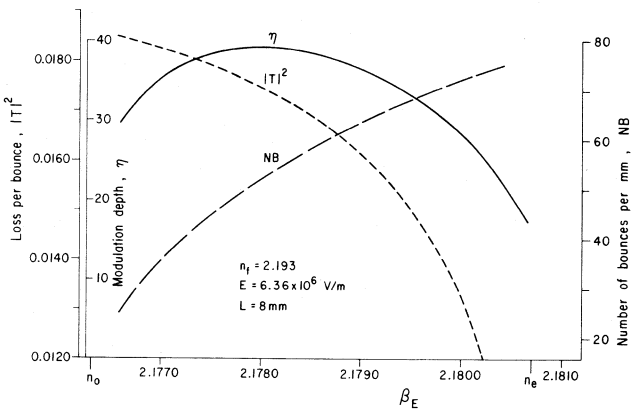


Fig. 12. Opposite behaviors of $|T|^2$ and NB (number of bounces per millimeter) for β_E variation. The conversion efficiency η is optimized at the compromising point of $|T|^2$ and NB.

IV. Summary and Discussions

We have demonstrated electrooptic polarization conversion from a guided TE wave to an unguided TM wave in a thin-film light-guiding structure. Since the amount of polarization conversion can be controlled by varying the applied electric field, this configuration of electrooptic modulators may be useful for optical communications. In the specific device we fabricated using Ta_2O_5 film and $LiTaO_3$ crystal, we have observed a 40-percent modulation when 500 V was applied across two electrodes spaced 50 μm apart.

We have presented here a ray-optics analysis of the conversion process and have shown that the analysis explains the experimental results rather well with the inclusion of the Goos-Haenchen shifts. Since the conversion loss per bounce and the propagation distance per zig-zag path show opposite behaviors for β_E variation (Fig. 12), these two competing factors should be optimized in order to obtain a maximum modulation efficiency.

While this study shows that the optical beam can be modulated by such a guided-to-unguided mode conversion scheme, it has two drawbacks. First, it is practically impossible to achieve 100-percent conversion even with a long electrode. As is depicted in Fig. 11, the guided mode energy decays exponentially for increasing interaction length, and will never be depleted completely. Second, its power performance is considerably inferior to other schemes [21] due to the high modulating voltage required. For example, at 40-percent

modulation, the present device has a power-per-bandwidth factor of 1.57 W/MHz which is three orders of magnitude larger than that for the deflection modulators [21]. Since the power-per-bandwidth factor is proportional to the capacitance and to the square of the required voltage, it can be lowered by a factor of 5 to 314 mW/MHz by reducing the electrode gap to 10 μm.

A proper way to improve the modulation efficiency would be to employ the guided-to-guided mode conversion scheme, which was discussed in [1]. When the two modes participating in the conversion process have the same phase velocity and a proper coupling is provided between them (electrooptically or magnetooptically, for example), the guided EM energy will keep oscillating between these two modes. We have made preliminary, theoretical calculations regarding the performance of such a device made of Ta_2O_5 film with proper refractive index ($n_f = 2.2$) and thickness ($W = 1.14$ μm), and the analysis indicates a 100-percent mode conversion for $L < 1$ cm and $E = 20$ kV/cm.

Our attempt to fabricate such a device has not been successful so far because of the difficulties in achieving the phase degeneracy. Exact matching of the phase velocities of TE and TM waves would require a precise control of the film thickness and the film index. Our difficulty was compounded by the fact that the film index changes during thermal oxidation (Fig. 10).

It should be possible, however, to compensate any phase mismatch by employing a periodic structure similar to that used by Tien *et al.* in their magnetooptic mode conversion experiment [4]. By periodically inverting the polarity of the applied electric field with a periodicity of $\Lambda = 2\pi/(k_0\Delta\beta) = \lambda/\Delta\beta$, we can sustain the growth of the converted field until it reaches a complete mode conversion. For example, a phase mismatch of $\Delta\beta = 0.011$ at $W = 7700$ Å in Fig. 9 will require electrodes with 282-μm periodicity. This dimension falls into the range in which the electrodes can be easily fabricated using photolithographic techniques. Fabrication of such structures to realize an electrooptic guided-to-guided mode converter will be a natural extension of this work.

Appendix I

Decay Constants p_1 and p_2 in the Substrate

By borrowing the results in [1] directly, we have

$$p_{1,2}^2 = \frac{1}{2K_{11}}\left[A + K_{12}^2 \pm (B^2 + 2K_{12}^2 C + K_{12}^4)^{1/2}\right] \tag{A1}$$

where

$$A = \beta^2(K_{11} + K_{33}) - K_{11}(K_{22} + K_{33})$$

$$B = \beta^2(K_{11} - K_{33}) + K_{11}(K_{33} - K_{22})$$

$$C = \beta^2(K_{11} + K_{33}) + K_{11}(K_{33} - K_{22}).$$

Appendix II

Expression of the Scattering Matrix Elements

When the results of [1] are modified for the condition of (3), we obtain

$$r_{EE} = \frac{1}{F}\left(\frac{G_1 J_2^-}{L_1} - \frac{J_1^* G_2^+}{L_2}\right) \tag{B1}$$

$$r_{MM} = \frac{1}{F}\left(\frac{G_1^* J_2^+}{L_1} - \frac{J_1 G_2^-}{L_2}\right) \tag{B2}$$

$$r_{EM} = r_{ME} = \frac{2i(p_1 - i|p_2|)n_f \cos\theta}{F\beta K_{12}} \tag{B3}$$

$$t_{EE} = -\frac{2}{F}\frac{G_2^+}{L_2} n_f \cos\theta \tag{B4}$$

$$t_{ME} = \frac{2}{F}\frac{G_1}{L_1} n_f \cos\theta \tag{B5}$$

$$t_{EM} = \frac{2}{F}\frac{J_2^+}{K_{12}}\frac{\cos\theta}{\sin\theta} \tag{B6}$$

and

$$t_{MM} = -\frac{2}{F}\frac{J_1}{K_{12}}\frac{\cos\theta}{\sin\theta} \tag{B7}$$

where

$$F = \frac{G_1 J_2^+}{L_1} - \frac{J_1 G_2^+}{L_2}$$

$$G_1 = K_{33}\cos\theta - ip_1 n_f$$

$$G_2^\pm = K_{33}\cos\theta \pm n_f|p_2|$$

$$J_1 = n_f\cos\theta - ip_1$$

$$J_2^\pm = n_f\cos\theta \pm |p_2|$$

$$L_1 = \beta^2 K_{33} - K_{11}K_{33} - K_{11}p_1^2$$

$$L_2 = \beta^2 K_{33} - K_{11}K_{33} + K_{11}|p_2|^2.$$

Acknowledgment

The authors wish to thank T. R. Ranganath for helpful discussions they had with him during the development of this work.

References

[1] S. Wang, M. Shah, and J. D. Crow, "Studies of the use of gyrotropic and anisotropic materials for mode conversion in thin-film optical waveguide applications," *J. Appl. Phys.*, vol. 43, pp. 1861–1875, Apr. 1972.

[2] M. Shah, J. D. Crow, and S. Wang, "Optical-waveguide mode-conversion experiments," *Appl. Phys. Lett.*, vol. 20, pp. 66–69, Jan. 15, 1972.

[3] T. P. Sosnowsky and H. P. Weber, "Polarization conversion of light in thin-film waveguides," *Opt. Commun.*, vol. 7, pp. 47–50, Jan. 1973.

[4] P. K. Tien, R. J. Martin, R. Wolfe, R. C. LeCraw, and S. L. Blank, "Switching and modulation of light in magneto-optic waveguides of garnet films," *Appl. Phys. Lett.*, vol. 21, pp. 394–396, Oct. 15, 1972.

[5] S. C-C. Tseng, A. R. Reisinger, E. A. Giess, and C. G. Powell, "Mode conversion in magneto-optic waveguides subjected to a periodic permalloy structure," *Appl. Phys. Lett.*, vol. 24, pp. 265–267, Mar. 15, 1974.

[6] P. K. Tien, "Light waves in thin-films and integrated optics," *Appl. Opt.*, vol. 10, pp. 2395–2413, Nov. 1971.

[7] H. K. V. Lotsch, "Reflection and refraction of a beam of light at a plane interface," *J. Opt. Soc. Amer.*, vol. 58, pp. 551–561, Apr. 1968.
[8] N. S. Kapany and J. J. Burke, *Optical Waveguides* (Quantum Electronics Ser.). New York: Academic, 1973, pp. 73–80.
[9] H. Kogelnik, T. P. Sosnowsky and H. P. Weber, "A ray-optical analysis of thin-film polarization converters," *IEEE J. Quantum Electron.*, vol. QE-9, pp. 795–800, Aug. 1973.
[10] S. Yamamoto, Y. Koyamada and T. Makimoto, "Normal-mode analysis of anisotropic and gyrotropic thin-film waveguides for integrated optics," *J. Appl. Phys.*, vol. 43, pp. 5090–5097, Dec. 1972.
[11] A. Yariv, "Coupled-mode theory for guided-wave optics," *IEEE J. Quantum Electron.*, vol. QE-9, Sept. 1973.
[12] T. P. Sosnowski and G. D. Boyd, "The efficiency of thin-film optical-waveguide modulators using electrooptic films or substrates," *IEEE J. Quantum Electron.*, vol. QE-10, pp. 306–311, Mar. 1974.
[13] S. Wang, J. D. Crow, S. L. Wong, and M. Shah, "Eigenmode analysis of wave propagation in optical waveguides deposited on gyrotropic and anisotropic substrates," *J. Appl. Phys.*, vol. 44, pp. 3232–3239, July 1973.
[14] Y. K. Lee and S. Wang, "Tantalum oxide lightguide on lithium tantalate," *Appl. Phys. Lett.*, vol. 25, pp. 164–166, Aug. 1, 1974.
[15] P. K. Tien and R. Urlich, "Theory of prism-film coupler and thin-film lightguides," *J. Opt. Soc. Amer.*, vol. 60, pp. 1325–1337, Oct. 1970.
[16] M. L. Dakss, L. Kuhn, P. F. Heidrich, and B. A. Scott, "Grating coupler for efficient excitation of optical guided waves in thin films," *Appl. Phys. Lett.*, vol. 16, pp. 523–525, June 15, 1970.
[17] R. Cordero, private communication.
[18] R. M. White, private communication.
[19] D. H. Hensler, J. D. Cuthbert, R. J. Martin, and P. K. Tien, "Optical propagation in sheet and pattern generated films of Ta_2O_5," *Appl. Opt.*, vol. 10, pp. 1037–1042, May 1971.
[20] S. Ramo, J. R. Whinnery, and T. Van Duzer, *Fields and Waves in Communications Electronics*. New York: Wiley, pp. 184–186, 1965.
[21] J. Noda, N. Uchida, S. Saito, T. Saku, and M. Minakata, "Electro-optic amplitude modulation using three-dimensional $LiNbO_3$ waveguide fabricated by TiO_2 diffusion," *Appl. Phys. Lett.*, vol. 27, pp. 19–21, July 1, 1975.

Saturation Effects and Lamb-Dip Formation in Molecular Lasers

J. S. GOELA AND T. F. MORSE

Abstract—**With the use of velocity-dependent kinetic equations to account properly for collisional relaxation behavior in molecular lasers, new results for gain saturation formulas have been obtained for intermediate values of pressure. These results, for a traveling-wave field, are exact and, in proper limits, reduce to known results. Further, a more complete description of the behavior of the Lamb dip as a function of molecular parameters has been obtained, and it is shown how the Lamb dip depends not only upon molecular parameters, but upon the total cavity loss parameter itself.**

I. Introduction

THE influence of collisions on the saturation characteristics of atomic transitions and vibration-rotation transitions in molecular lasers has been considered by several authors [1]–[5]. These authors treat the problem either by means of the density matrix or a rate equation formalism. Various collision parameters are introduced phenomenologically and their values determined by curve fitting to experimental data. However, previous results have not led to expressions which properly account for collisional effects and are simultaneously valid for all ranges of pressure; from the Doppler to the collision broadened limit. Djeu and Wolga [3], by considering a variable source term for rotational transfer, modified the gain saturation formula obtained by Close [2] to account for molecular relaxation effects, and in [4] the important effect of elastic collisions on molecular laser parameters was introduced for the Doppler broadened limit.

In this paper an attempt has been made to present a more complete theory of gain saturation and Lamb-dip formation in molecular lasers. In particular, it will be seen how new results arise for the case in which the Doppler and collisional broadening are of the same order of magnitude. The two-level gas is described by a suitably modified relaxation form of the Boltzmann equation and the radiation is treated by the equation of radiative transfer. The formulation takes into account homogeneous as well as inhomogeneous broadening effects, velocity changing elastic collisions and rotational level changing inelastic collisions. The theory gives new insight into the "hole burning" phenomenon and the dependence of the Lamb-dip formation on the cavity-loss parameter in molecular lasers. In the proper limits our results reduce to those obtained by several other authors [1]–[5].

II. Kinetic Relaxation Equations

Consider a single rotational-vibrational lasing transition, resonant external collisional pumping, and velocity-changing elastic and inelastic collisions. In order to account properly for various collisional processes and radiative interactions that quantitatively predict inhomogeneous as well as homogeneous broadening effects, it is necessary to consider kinetic equations, i.e., velocity-dependent rate equations. These equations for

Manuscript received October 17, 1975. This work was supported by the Air Force Office of Scientific Research, Mechanics Branch, under Contract AFOSR-74-2645.

The authors are with the Division of Engineering and Center for Fluid Dynamics, Brown University, Providence, RI 02912.

molecular systems with rotational fine structure have been discussed elsewhere [4]-[9]. The details of dynamic collisional processes and radiative interaction that determine the saturating response of a rotation-vibration transition are shown in Fig. 1. A kinetic relaxation equation for the upper lasing state 2_J can be written as follows:

$$\frac{Df_{2_J}}{Dt} = \Gamma_{2_J} M - R_2 f_{2_J} + \sigma_{2_J}(n_{2_J} M - f_{2_J}) + \sigma_{2_J x} \cdot \left[\left(\frac{n_{2_J}}{n_2}\right)_{eqm} n_2 M - f_{2_J}\right] - 4\pi A_{2_J 1_{J+1}} f_{2_J} - A_{2_J 1_{J+1}} Q_{2_J 1_{J+1}} (f_{2_J} - f_{1_{J+1}}). \quad (1)$$

Here f_{2_J} is the velocity distribution function for rotational state J of vibrational level 2. On the right-hand side the terms correspond respectively to external collisional pumping of the upper lasing state which is assumed to be Maxwellian, vibrational relaxation, source and sink terms for elastic collisions, inelastic collisions that change rotational levels, spontaneous emission, and finally a radiative interaction term which accounts for the effects of stimulated emission and absorption by selective interaction with particles in a certain range of the velocity spectrum. The elastic and rotational rate constants are given respectively as σ_{2_J} and $\sigma_{2_J x}$. The Maxwellian velocity distribution function is given as $M = (m/2\pi kT_0)^{3/2} \exp(-\xi^2 m/2kT_0)$, $A_{2_J 1_{J+1}}$ is the Einstein coefficient for the transition $2_J \leftrightarrow 1_{J+1}$, $Q_{2_J 1_{J+1}}$ represents the number of photons per unit volume capable of being absorbed by a molecule in a given velocity range, and f_ν is the photon distribution function

$$Q_{2_J 1_{J+1}}(f_\nu) = \int_{-\infty}^{\infty} d\zeta_{2_J 1_{J+1}} \int_{4\pi} d\Omega\, f_\nu(l, \zeta_{2_J 1_{J+1}}) \cdot q_{2_J 1_{J+1}} \frac{\Delta\nu_D}{(\ln 2)^{1/2}} \quad (2a)$$

where the Doppler width is given as

$$\Delta\nu_D \equiv \nu_{2_J 1_{J+1}} (2RT_0)^{1/2} (\ln 2)^{1/2}/c.$$

c is the velocity of light, and T_0 is the translational temperature. The line shape function $q_{2_J 1_{J+1}}$, which is Lorentzian in the rest frame of the molecule, is normalized such that

$$\int_{-\infty}^{\infty} q_{2_J 1_{J+1}}\, d\nu = \int_{-\infty}^{\infty} \cdot \frac{\Delta\nu_D\, b\, d\nu}{\pi\left[\left\{\nu - \nu_{2_J 1_{J+1}}\left(1 + \frac{\xi \cdot l}{c}\right)\right\}^2 + \left(\frac{\Delta\nu_H}{2}\right)^2\right](\ln 2)^{1/2}} = 1 \quad (2b)$$

$\nu_{2_J 1_{J+1}}$ is the line center frequency, and

$$b \equiv \frac{\Delta\nu_H (\ln 2)^{1/2}}{2\,\Delta\nu_D}$$

$$\zeta_{2_J 1_{J+1}} \equiv \frac{(\nu - \nu^L_{2_J 1_{J+1}})(\ln 2)^{1/2}}{\Delta\nu_D}$$

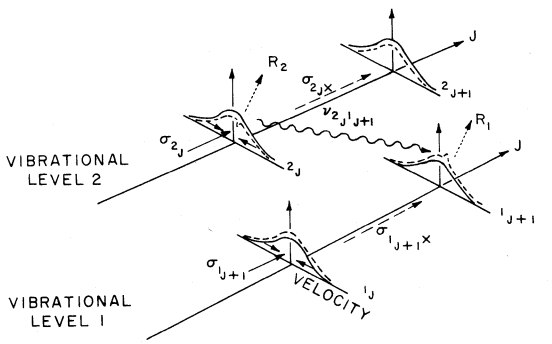


Fig. 1. The details of dynamic collisional processes and radiative interaction for a rotation-vibration transition. ----- population with saturating laser. ——— population without saturating laser. ·····→ vibrational relaxation. ——→ velocity cross relaxation. — — → rotational relaxation.

where $\nu^L_{2_J 1_{J+1}}$ is the lasing frequency, considered to be at a cavity resonance.

In a similar manner, for a P-branch transition the kinetic equation for the lower lasing level 1_{J+1} may be written as

$$\frac{Df_{1_{J+1}}}{Dt} = \Gamma_{1_{J+1}} M - R_1 f_{1_{J+1}} + \sigma_{1_{J+1}}(n_{1_{J+1}} M - f_{1_{J+1}}) + \sigma_{1_{J+1}x}\left[\left(\frac{n_{1_{J+1}}}{n_1}\right)_{eqm} n_1 M - f_{1_{J+1}}\right] - 4\pi (A_{1_{J+1}0} f_{1_{J+1}} - A_{2_J 1_{J+1}} f_{2_J}) + A_{2_J 1_{J+1}} Q_{2_J 1_{J+1}} (f_{2_J} - f_{1_{J+1}}). \quad (3)$$

For steady-state conditions (1) and (3) can be solved for the velocity distribution functions to yield

$$(f_{2_J} - f_{1_{J+1}}) = \frac{M\left[\left(\frac{\Gamma_{2_J}}{\gamma_{2_J}} - \frac{\Gamma_{1_{J+1}}}{\gamma_{1_{J+1}}}\right) + \left(\frac{\sigma_{2_J} n_{2_J}}{\gamma_{2_J}} - \frac{\sigma_{1_{J+1}} n_{1_{J+1}}}{\gamma_{1_{J+1}}}\right) + \left(\frac{B_2 \sigma_{2_J x} n_2}{\gamma_{2_J}} - \frac{B_1 \sigma_{1_{J+1}x} n_1}{\gamma_{1_{J+1}}}\right)\right]}{1 + A_{2_J 1_{J+1}} Q_{2_J 1_{J+1}} \frac{(\gamma_{2_J} + \gamma_{1_{J+1}})}{\gamma_{2_J}\gamma_{1_{J+1}}}}. \quad (4)$$

In this expression spontaneous-emission terms, being small, are neglected. The particle number density is denoted by n_{i_J} and

$$\gamma_{2_J} \equiv R_2 + \sigma_{2_J} + \sigma_{2_J x}$$

$$\gamma_{1_{J+1}} \equiv R_1 + \sigma_{1_{J+1}} + \sigma_{1_{J+1}x}$$

$$B_2 \equiv \left(\frac{n_{2_J}}{n_2}\right)_{eqm} \quad B_1 \equiv \left(\frac{n_{1_{J+1}}}{n_1}\right)_{eqm}.$$

The vibrational rate constants for the upper and lower levels are R_2 and R_1. In (3), $Q_{2_J 1_{J+1}}$ is a function of f_ν. Since all significant radiation will be in the lasing transition, it will be assumed that the photon distribution is given as follows:

$$f_\nu = L^0 \delta(\nu - \nu^L_{2_J 1_{J+1}}) \delta(1 \pm l_x) \delta(l_y) \delta(l_z). \quad (5)$$

All photons propagate along the lasing axis with a δ-function in frequency, thus l_x is the component of a unit vector l in the direction of the lasing axis. The only unknown in (5) is L^0, the lasing intensity which is related to the more familiar specific intensity I as follows:

$$L^0 = \frac{Ic^2}{2h\nu^3_{2J^1J+1}}.$$

With (5) and (2a) we calculate Q_{2J^1J+1}. For a traveling-wave field, Q_{2J^1J+1} can be written as

$$Q_{2J^1J+1} = \frac{bc^2 I\,(\ln 2)^{1/2}}{2\pi h\nu^3_{2J^1J+1}\,\Delta\nu_D}\,\frac{1}{[(\phi+\eta_x)^2+b^2]} \tag{6}$$

where

$$\phi \equiv \frac{(\nu^L_{2J^1J+1} - \nu_{2J^1J+1})c}{\nu_{2J^1J+1}\,(2RT_0)^{1/2}}$$

and

$$\eta_x = \frac{\xi_x}{(2RT_0)^{1/2}}.$$

Substituting (6) in (4) we obtain

$$(f_{2_J} - f_{1_{J+1}}) = \frac{M\left[\left(\frac{\Gamma_{2_J}}{\gamma_{2_J}} - \frac{\Gamma_{1_{J+1}}}{\gamma_{1_{J+1}}}\right) + \left(\frac{\sigma_{2_J} n_{2J}}{\gamma_{2_J}} - \frac{\sigma_{1_{J+1}} n_{1_{J+1}}}{\gamma_{1_{J+1}}}\right) + \left(\frac{B_2\sigma_{2Jx}\,n_2}{\gamma_{2_J}} - \frac{B_1\sigma_{1_{J+1}x}\,n_1}{\gamma_{1_{J+1}}}\right)\right]}{1 + b^2\,\frac{I}{I_0}\,\frac{1}{[(\phi+\eta_x)^2+b^2]}} \tag{7}$$

where the saturation parameter is given as

$$I_0 = \frac{\pi h\nu^3_{2J^1J+1}\,\Delta\nu_H\,\gamma_{2_J}\,\gamma_{1_{J+1}}}{c^2\,A_{2J^1J+1}\,(\gamma_{2_J}+\gamma_{1_{J+1}})}.$$

It should be noted that the definition of I_0 differs from the usual definition as a consequence of the introduction of additional relaxation processes represented by the γ's.

III. Inversion Density and Differential Inversion

We now make the following simplifying assumptions: $\gamma_{2_J} = \gamma_{1_{J+1}}$, $B_2 = B_1$, $\sigma_{2_J} = \sigma_{1_{J+1}}$, $\sigma_{2Jx} = \sigma_{1_{J+1}x}$, $R_2 = R_1$. The collision rate constants are assumed to be independent of the rotational quantum number. It should be noted that these simplifications help make expressions more amenable to analysis without significantly affecting the generality of the results derived.

Integrating (7) over velocity space with the above assumptions leads to an expression for the population inversion.

$$(n_{2_J} - n_{1_{J+1}}) = \frac{1}{\gamma_{2_J}}\,[\Gamma_p + \sigma_{2_J}(n_{2_J} - n_{1_{J+1}}) + B_2\sigma_{2Jx}\,(n_2 - n_1)] \times \left[1 - b\sqrt{\pi}\,\frac{I}{I_0}\,\frac{\operatorname{Re} W(-\phi+iy)}{(1+I/I_0)^{1/2}}\right] \tag{8}$$

where

$$y = b(1+I/I_0)^{1/2} \qquad \Gamma_p = (\Gamma_{2_J} - \Gamma_{1_{J+1}}).$$

Re $W(-\phi+iy)$ is the real part of the complex error function [11]

$$W(\phi+iy) = \frac{2}{\sqrt{\pi}}\exp[-(\phi+iy)^2]\int_{-i(\phi+iy)}^{\infty}\exp[-t^2]\,dt.$$

The pump rates, or source terms, for the rotational levels are variable and are functions of the saturating radiation intensity. In order to determine the saturating characteristics of the population inversion, it is necessary to know the dependence of these variable pump rates on lasing intensity.

Integrating (1) and (3) over velocity yields the usual rate equations.

$$\frac{Dn_{2_J}}{Dt} = \Gamma_{2_J} - R_2 n_{2_J} + \sigma_{2Jx}\,(B_2 n_2 - n_{2_J}) - 4\pi A_{2J^1J+1}\,n_{2_J} - \mathrm{SI} \tag{9}$$

$$\frac{Dn_{1_{J+1}}}{Dt} = \Gamma_{1_{J+1}} - R_1 n_{1_{J+1}} + \sigma_{1_{J+1}x}\,(B_1 n_1 - n_{1_{J+1}}) - 4\pi(A_{1_{J+1}0}\,n_{1_{J+1}} - A_{2J^1J+1}\,n_{2_J}) + \mathrm{SI} \tag{10}$$

where the stimulated-emission term SI is given as

$$\mathrm{SI} = \int_{-\infty}^{\infty} A_{2J^1J+1}\,Q_{2J^1J+1}\,(f_{2_J} - f_{1_{J+1}})\,d\xi.$$

The rate equations for particle number density for vibrational levels 1 and 2 are obtained on summing (9) and (10) over all rotational states. Since only one line is permitted to oscillate, the stimulated-emission term is not summed.

$$\frac{Dn_2}{Dt} = \Gamma_2 - R_2 n_2 - 4\pi A_{2J^1J+1}\,n_2 - \mathrm{SI} \tag{11}$$

$$\frac{Dn_1}{Dt} = \Gamma_1 - R_1 n_1 - 4\pi\,(A_{1_{J+1}0}\,n_1 - A_{2J^1J+1}\,n_2) + \mathrm{SI}. \tag{12}$$

For steady-state conditions, subject to the aforementioned assumptions, (8)-(12) can be solved exactly for the population inversion $(n_{2_J} - n_{1_{J+1}})$ to yield

$$(n_{2_J} - n_{1_{J+1}}) = \frac{(1-p)\,\Delta N^0_J}{\left[1 + p\left\{\frac{B_2\sigma_{2Jx}}{R_2} + z\left(1 + \frac{B_2\sigma_{2Jx}}{R_2}\right)\right\}\right]} \tag{13}$$

$$p = b\sqrt{\pi}\,\frac{I}{I_0}\,\frac{\operatorname{Re} W(-\phi+iy)}{(1+I/I_0)^{1/2}}, \quad z = \sigma_{2_J}/(R_2+\sigma_{2Jx}).$$

$$\Delta N^0_J = \left\{\Gamma_p + \frac{B_2\sigma_{2Jx}}{R_2}(\Gamma_2 - \Gamma_1)\right\} \Big/ (R_2 + \sigma_{2Jx}).$$

With the neglect of velocity changing collisions, $z \to 0$, (13) reduces identically to the result obtained in [3]. Since z is of

the order of 1-10 for many molecular gases, its appearance in (13) is significant.

As noted by Kan and Wolga [4], further significant information can be obtained by considering how elastic collisions influence the population inversion. For a Doppler-broadened transition, diffusion in velocity space contributes in two ways. As the saturating field "burns" a hole in the Doppler profile, molecules, whose Doppler shift is too large to permit significant interaction with the field, can do so by diffusing through velocity space in the same rotation-vibration line. A larger contribution, however, is made due to the presence of collisional coupling among the rotational levels. This coupling funnels the available population inversion in the adjacent rotational levels into the pair being stimulated. However, only those particles that diffuse in velocity space into the field interaction region contribute to the stimulated emission.

We can define a differential inversion (δI) as the difference between the saturated and unsaturated velocity-dependent inversion [4].

$$\delta I \equiv (f_{2_J} - f_{1_{J+1}})_{I=0} - (f_{2_J} - f_{1_{J+1}})_{I \neq 0}$$
$$\equiv \delta I_D + \delta I_L.$$

From (7), (8), and (13) we find that the Lorentzian (δI_L) and Doppler (δI_D) components of δI are given as

$$\delta I_L(\xi, \phi, b) = \frac{b^2 (I/I_0)\, M\, \Delta N_J^0}{\left[1 + p\left\{\frac{B_2 \sigma_{2_{Jx}}}{R_2} + z\left(1 + \frac{B_2 \sigma_{2_{Jx}}}{R_2}\right)\right\}\right][(\phi + \eta_x)^2 + y^2]} \quad (14)$$

$$\delta I_D(\xi, \phi, b) = \frac{M p\, \Delta N_J^0 \left\{\frac{B_2 \sigma_{2_{Jx}}}{R_2} + z\left(1 + \frac{B_2 \sigma_{2_{Jx}}}{R_2}\right)\right\}}{\left[1 + p\left\{\frac{B_2 \sigma_{2_{Jx}}}{R_2} + z\left(1 + \frac{B_2 \sigma_{2_{Jx}}}{R_2}\right)\right\}\right]}. \quad (15)$$

These results are more general and present greater physical detail than those given in [4] and [5]. Also, within the framework of the kinetic relaxation equations and the equation of radiative transfer, they are valid for any b and arbitrary I/I_0. In the limit of b small and I/I_0 small, the preceding results reduce to those of [4].

Examining the preceding equations we observed, as noted in [4], that the Lorentzian component saturates over a nondimensional velocity width y, which can be small compared with the full distribution width. It is a measure of the number of particles able to interact directly with the radiation field in a given velocity range. The Doppler component, however, saturates over the whole velocity profile, and this mechanism is associated with the diffusion in velocity space that collisionally replenishes those particles in the upper lasing state that are stimulated to emit.

In order to determine the dominant mechanism of molecular interaction with radiation, we define a new parameter γ as the ratio of the integrated Lorentzian component (area B, Fig. 2) to the integrated Doppler component (area A, Fig. 2).

$$\gamma = \frac{\int_{-\infty}^{\infty} \delta I_L\, d\xi}{\int_{-\infty}^{\infty} \delta I_D\, d\xi} = \frac{1}{\left\{\frac{B_2 \sigma_{2_{Jx}}}{R_2} + z\left(1 + \frac{B_2 \sigma_{2_{Jx}}}{R_2}\right)\right\}}. \quad (16)$$

This definition of γ differs from that of [4] and [5]. In order to compare our results with those of [4], define γ' as

$$\gamma' = \frac{\delta I_L(\xi = 0, \phi = 0)}{\delta I_D(\xi = 0, \phi = 0)} = \frac{\gamma}{b\sqrt{\pi}\,(1 + I/I_0)^{1/2} \exp\{b^2(1 + I/I_0)\} \operatorname{erfc}\{b(1 + I/I_0)^{1/2}\}}$$

$$\gamma'_{b \to 0,\, (I/I_0) \to 0} = \frac{\gamma}{b\sqrt{\pi}}. \quad (17)$$

In the limit of $b \to 0$ and $I/I_0 \ll 1$, this result reduces to that of [4]. It should be noted that γ' compares the Lorentzian and Doppler components of δI only at the center of the Doppler profile, whereas γ compares the total number of Lorentzian component molecules that take part in stimulated emission to the total number of Doppler component molecules interacting with radiation. For this reason it would seem that γ is a better indicator of mixed saturation effects over the whole velocity profile. Further, as seen from (16), γ depends only on collisional parameters and is independent of saturation intensity, frequency, and b, even though these parameters would appear in the nonintegrated ratio of (14) and (15). As b increases, more particles can interact with radiation by burning a hole of larger width in the velocity profile. Simultaneously, indirect processes of cross relaxation are also enhanced so that γ remains independent of b. The significance of (16) is schematically shown in Fig. 2. As we move away from line center, there are fewer particles available for resonant interaction and this correspondingly reduces the diffusion of particles through the velocity profile. At first glance expression (16) seems somewhat surprising. It can, however, be explained once it is realized that cross relaxation is not an independent process in itself. If there is no hole burning there will not be any cross-relaxation effect. For homogeneous broadening the separation of δI into two parts is artificial. The significance of cross relaxation is observed only when there is selective interaction of molecules within the velocity profile. The radiation field saturates one part of the velocity profile and collisions tend to restore

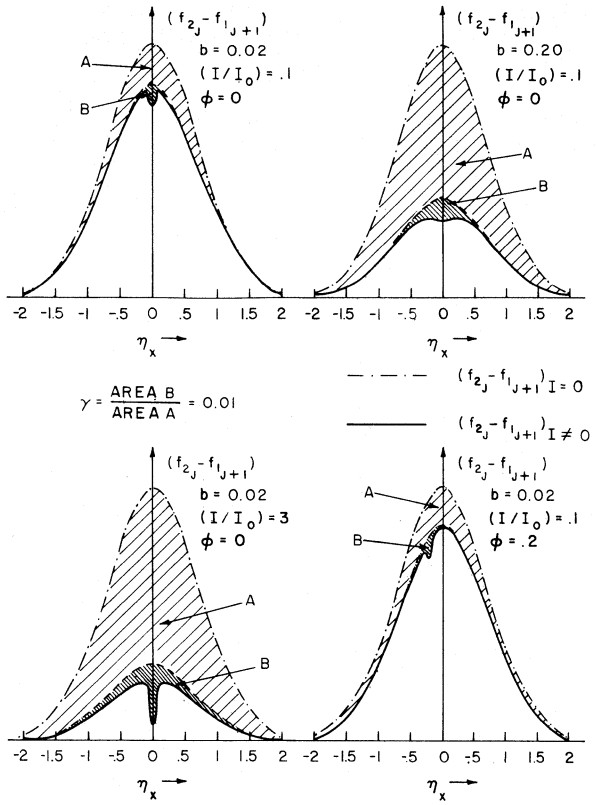


Fig. 2. The significance of molecular parameter γ.

the equilibrium distribution. For these reasons the ratio of the areas A and B in Fig. 2 is independent of b, ϕ, and I/I_0.

For a given gas γ is independent of pressure. As $\gamma \rightarrow \infty$, cross relaxation is unimportant and stimulated emission occurs through Lorentzian hole burning. However, if $\gamma \rightarrow 0$ saturation occurs throughout the velocity profile and the preferential interaction of the field with molecules disappears.

IV. Gain Saturation

The steady-state equation of radiative transfer may be written as follows, assuming that only radiation in the $2_J - 1_{J+1}$ line is of importance:

$$l \cdot \frac{dfv}{dx} = \frac{A_{2_J 1_{J+1}} c^2}{2 \nu^2_{2_J 1_{J+1}}} [H_{21}(f_{2_J}) + fv\, H_{21}(f_{2_J} - f_{1_{J+1}})] \quad (18)$$

where $H_{21}(f_{1_{J+1}})$ is defined as the number of particles per unit volume per unit solid angle about a unit vector l capable of absorbing a photon on a line centered about $\nu_{2_J 1_{J+1}}$. Thus, by definition,

$$H_{21}(f_{2_J} - f_{1_{J+1}}) \equiv \int_{-\infty}^{\infty} (f_{2_J} - f_{1_{J+1}})\, q_{2_J 1_{J+1}}\, d\xi. \quad (19)$$

In (18) the first term on the right-hand side represents spontaneous emission. For an intense lasing field this term may be neglected for a rotation-vibration transition, and the gain may be immediately inferred to be

$$G(\zeta_{2_J 1_{J+1}}) = \frac{A_{2_J 1_{J+1}} c^2}{2 \nu^2_{2_J 1_{J+1}}} H_{21}(f_{2_J} - f_{1_{J+1}}). \quad (20)$$

From (7), (8), (13), and (20) we obtain the frequency dependence of saturated gain.

$$G(\phi) = \frac{A_{2_J 1_{J+1}} c^2 (\ln 2)^{1/2}\, \Delta N^0_J\, \text{Re}\, W(-\phi + iy)}{2\sqrt{\pi}\, \nu^2_{2_J 1_{J+1}}\, \Delta\nu_D\, (1 + p/\gamma)\, (1 + I/I_0)^{1/2}}. \quad (21)$$

For a traveling-wave field this expression is exact within the framework of the formulation carried out in this paper. This result can be further simplified to yield

$$G(\phi) = \frac{G_0\, \text{Re}\, W(-\phi + iy)}{\left[(1 + I/I_0)^{1/2} + \frac{b\sqrt{\pi}}{\gamma} \frac{I}{I_0}\, \text{Re}\, W(-\phi + iy)\right]} \quad (22)$$

where

$$G_0 = \frac{A_{2_J 1_{J+1}} c^2 (\ln 2)^{1/2}}{2\sqrt{\pi}\, \nu^2_{2_J 1_{J+1}}\, \Delta\nu_D} \Delta N^0_J.$$

This is the expression for the inhomogeneous limit of zero field gain, which differs from the corresponding homogeneous limit by a factor of b.

Equation (22) is the frequency-dependent gain saturation formula for both homogeneous and inhomogeneous broadening, and incorporates effects of velocity changing elastic collisions and rotational-level changing inelastic collisions. If elastic velocity changing collisions are neglected, $z \rightarrow 0$, and this expression reduces to that of [3].

Let us now consider gain saturation in certain limits, in particular, when $\phi = 0$. For homogeneous broadening $b \rightarrow \infty$, and at line center we obtain the following from (22):

$$G(\phi = 0) = \frac{G_0/b}{\left[1 + \frac{I}{I_0}\left(1 + \frac{1}{\gamma}\right)\right]}. \quad (23)$$

Although this expression has the same algebraic form as that obtained in [3], the appearance of the ratio of the integrated differential inversion for the Doppler and Lorentzian components presents a new physical result to be discussed in the following discussion. Thus γ is an important new parameter in a description of saturated gain in molecular lasers. In the limit of frozen rotational relaxation $\sigma_{2_J x} \rightarrow 0$ and $I/\gamma \rightarrow 0$, (23) reduces to the form obtained for an atomic system. When the rotational rate constant $\sigma_{2_J x}$ is large, the effective saturation parameter $I_0\gamma/(\gamma + 1)$ is increased by a Boltzmann factor showing that all the other rotational levels are now indirectly participating in the lasing process.

As b decreases, the collisional processes become very significant in determining the saturation characteristics of a rotation-vibration transition. For inhomogeneous broadening (small b) at line center (22) reduces to

$$G(\phi = 0) = \frac{G_0}{\left[\left(1 + \frac{I}{I_0}\right)^{1/2} + \frac{2b}{\gamma} \frac{I}{I_0}\right]}. \quad (24)$$

The discussion thus far has been kept general in terms of molecular parameters. In order to illustrate the significantly different results in the behavior of gain saturation at inter-

mediate to low pressures, we consider the value of γ for a typical CO_2 system. At 300 K, $z \sim 0$ (1), $B_2 = 15$, $R_2 \sim 0$ (10^4), $\sigma_{2_{Jx}} \sim 0$ (5×10^7) [9]. Thus $\gamma = 0.0015$. Consequently, for $b \ll 1$ we can still have $2b/\gamma \gg 1$. Equation (23) then becomes

$$G(\phi = 0) = \frac{G_0}{\left[1 + \frac{2b}{\gamma}\frac{I}{I_0}\right]}. \tag{25}$$

This is a significantly different saturation formula for intermediate values of b (for a CO_2 laser this intermediate region would correspond to $0.001 < b < 0.1$). In the usual saturation formula both for homogeneous as well as for inhomogeneous broadening, saturation effects occur when $I/I_0 \geqslant 1$. Since $2b/\gamma$ may be quite large, even for b small, the saturation effects occur when $I/I_0 \geqslant \gamma/2b$.

In order to understand clearly the physical significance of (25), we redefine the saturation parameter.

$$I_0' = \frac{\pi h \nu_{2_{J^1J+1}}^3 \gamma \gamma_{2_J} \Delta\nu_D}{2c^2 A_{2_{J^1J+1}} (\ln 2)^{1/2}}$$

$$G(\phi = 0) = \frac{G_0}{(1 + I/I_0')}. \tag{26}$$

Thus comparing (26) (inhomogeneous limit) with (23) (homogeneous limit) in the limit $1/\gamma \gg 1$, we find that they are essentially the same except that $\Delta\nu_H$ in $I_0\gamma$ is replaced by $[\Delta\nu_D/(\ln 2)^{1/2}]$ in I_0', and the zero field gain differs by a factor of b. If we assume that b and collision rate constants are directly proportional to pressure, we find that I_0 varies as the square of the pressure, while I_0' varies as pressure. The saturation parameter is independent of homogeneous linewidth but instead depends upon the Doppler linewidth. Therefore the value of homogeneous linewidth becomes immaterial and selective interaction disappears as long as $2b/\gamma \gg 1$ and $b \ll 1$. This means that Doppler saturation occurs, all particles participate in the lasing process, and hole burning is insignificant even though $b \ll 1$.

Returning to (24) we see that for very small values of b and $2b/\gamma \ll 1$ we have the usual inhomogeneous broadening saturation formula for atomic systems.

$$G(\phi = 0) = \frac{G_0}{(1 + I/I_0)^{1/2}}. \tag{27}$$

For CO_2 lasers this occurs when $b < 0.001$. Thus collisions extend the range of homogeneous broadening to very small values of b.

We may also consider the effect of collisional coupling on the saturation parameter in the limit of inhomogeneous broadening ($b \to 0$). Since $\sigma_{2_{Jx}} \leqslant \sigma_{2_J}$, we find that I_0 differs only by a factor of 2 in the two limits $\sigma_{2_{Jx}} \to 0$ and $\sigma_{2_{Jx}} = \sigma_{2_J}$. Thus rotational level changing collisions are less effective in increasing the saturation parameter in the limit of very small values of b.

V. Lamb-Dip Formation

For a standing-wave field, with the assumptions previously introduced, we obtain the following result from a spatially homogeneous solution of (1) and (3):

$$(f_{2_J} - f_{1_{J+1}}) = \frac{M\left[\Gamma_p + \sigma_{2_J}(n_{2_J} - n_{1_{J+1}}) + B_2\sigma_{2_{Jx}}(n_2 - n_1)\right]}{\gamma_{2_J}\left[1 + b^2\frac{I}{I_0}\left\{\frac{1}{(\phi + \eta_x)^2 + b^2} + \frac{1}{(\phi - \eta_x)^2 + b^2}\right\}\right]}. \tag{28}$$

This cannot be integrated exactly over velocity space. However, for $(I/I_0) \ll 1$, the denominator can be expanded in powers of (I/I_0) and (28) reduces to

$$(f_{2_J} - f_{1_{J+1}}) = \frac{M}{\gamma_{2_J}}\left[\Gamma_p + \sigma_{2_J}(n_{2_J} - n_{1_{J+1}}) + B_2\sigma_{2_{Jx}}(n_2 - n_1)\right] \times \left[1 - b^2\frac{I}{I_0}\left\{\frac{1}{(\phi + \eta_x)^2 + b^2} + \frac{1}{(\phi - \eta_x)^2 + b^2}\right\}\right]. \tag{29}$$

We can determine gain from (20). Using (29) and a modified form of expressions (8), (13), (14), and (15) valid for a standing-wave field, we obtain

$$G(\phi) = G_0'(\phi) - \frac{p}{(\gamma + p)}G_0'(\phi) - \frac{A_{2_{J^1J+1}} b^3 c^2 (\ln 2)^{1/2} I \Delta N_J^0}{2\pi\nu_{2_{J^1J+1}}^2 \Delta\nu_D I_0 \left(1 + \frac{p}{\gamma}\right)} \cdot \int_{-\infty}^{\infty} M\left\{\frac{1}{(\phi + \eta_x)^2 + b^2} + \frac{1}{(\phi - \eta_x)^2 + b^2}\right\}^2 d\xi \tag{30}$$

where

$$G_0'(\phi) = \frac{A_{2_{J^1J+1}} c^2 (\ln 2)^{1/2} \Delta N_J^0 \operatorname{Re} W(-\phi + ib)}{\sqrt{\pi}\,\nu_{2_{J^1J+1}}^2 \Delta\nu_D} = G_0 \operatorname{Re} W(-\phi + ib) \tag{31}$$

and

$$p = 2b\sqrt{\pi}\frac{I}{I_0}\operatorname{Re} W(-\phi + ib).$$

The integral in (30) can be solved exactly in terms of the error function of complex argument. This is given in the Appendix. Using this result we obtain

$$G(\phi) = G_0'(\phi)\left\{1 - \frac{p}{\gamma + p} - b^2\frac{I}{I_0}\frac{\gamma}{2(\gamma + p)(\phi^2 + b^2)} - \frac{\gamma}{2}b^3\frac{I}{I_0}\frac{\operatorname{Im} W(\phi + ib)}{\phi(\phi^2 + b^2)(\gamma + p)\operatorname{Re} W(\phi + ib)} - \frac{\gamma}{2}\frac{I}{I_0}\frac{1}{(\gamma + p)} + \frac{\gamma b}{\sqrt{\pi}}\frac{I}{I_0}\frac{1}{\operatorname{Re} W(\phi + ib)(\gamma + p)} + \frac{\gamma\phi b}{(\gamma + p)}\frac{I}{I_0}\frac{\operatorname{Im} W(\phi + ib)}{\operatorname{Re} W(\phi + ib)} - b^2\frac{I}{I_0}\frac{\gamma}{\gamma + p}\right\}. \tag{32}$$

Equation (32) can be solved for laser intensity $I(\phi)$ subject to the condition that saturated gain $G(\phi)$ be equal to the sum of cavity loss α_0 plus mirror transmittance t.

$$I(\phi) = \frac{k\left[1 - \dfrac{\alpha}{G_0 \operatorname{Re} W(\phi + ib)}\right]\gamma_{2_J}\,\Delta\nu_H}{\left[1 + \dfrac{\alpha}{G_0}\dfrac{4\sqrt{\pi}\,b}{\gamma} + \dfrac{b^2}{\phi^2 + b^2} + \dfrac{b^3 \operatorname{Im} W(\phi + ib)}{\phi(\phi^2 + b^2)\operatorname{Re} W(\phi + ib)} + \dfrac{2}{\sqrt{\pi}}\dfrac{b}{\operatorname{Re} W(\phi + ib)} - 2b^2 - \dfrac{2\phi b \operatorname{Im} W(\phi + ib)}{\operatorname{Re} W(\phi + ib)}\right]} \tag{33}$$

$$I(\phi)\big|_{\phi\to 0} = \frac{k\left[1 - \dfrac{\alpha}{G_0 \operatorname{Re} W(ib)}\right]\gamma_{2_J}\,\Delta\nu_H}{\left[2 + \dfrac{\alpha}{G_0}\dfrac{4\sqrt{\pi}\,b}{\gamma} + \dfrac{4}{\sqrt{\pi}}\dfrac{b}{\operatorname{Re} W(ib)} - 4b^2\right]}$$

$$\alpha = \alpha_0 + t$$

where k is a constant proportional only to t.

Equation (33) is perhaps the most significant result of this analysis. It contains new terms and additional parameters characterizing the Lamb dip for both molecular as well as atomic lasers. If the fourth through seventh terms in the denominator are neglected, b taken small so that Re $W(\phi + ib)$ becomes a Gaussian in ϕ, and α, the total loss, is set equal to G_0, the unsaturated gain at line center in the inhomogeneous limit (denominator only), we recover the results of [4].

Before considering (33) in detail, we should note that the appearance of the cavity-loss parameter α in the denominator is significant in that different behavior of the Lamb dip is to be expected in experimental situations that have the same molecular gas but different losses. The parameters that determine the behavior of the Lamb dip are ϕ, α/G_0, γ, and b. In Fig. 3 we show the behavior of the Lamb dip as a function of $\alpha\sqrt{\pi}/G_0$, essentially a dimensionless total cavity-loss parameter, for one fixed value of b and γ. In this it is seen that as the cavity-loss parameter increases, all other parameters (other than ϕ) remaining fixed, the effect of hole burning diminishes. That is, in a given experiment, if only the mirror transmission were increased by a large enough value, we should expect the disappearance of the Lamb dip. Increasing cavity losses is analogous to decreasing excitation, so that Fig. 3 illustrates how decreasing excitation power diminishes the effect of the Lamb dip. Since this phenomenon is associated with the second term in the denominator of (33), it is essentially an effect to be noted in molecular lasers, when this second term is important. For comparison, $\alpha/G_0 = 1$ (in the denominator only) corresponds to the results obtained in [4] (dashed curves, Fig. 3). It is seen that although the widths of the two results are comparable, it is thus the addition of this new parameter in the denominator that must determine the depth of the Lamb dip. Since α, the total loss parameter, is one over which the experimentalist has control, the Lamb dip can be enhanced significantly by decreasing laser output coupling, reducing α, and thus the second term of (33). Only when this term is small does the Lamb dip appear. Alternatively, by increasing G_0, we can also cause the Lamb dip to be more pronounced. For these reasons it would appear questionable to depend upon the values of molecular parameters obtained from curve fitting experimental results to a formula that does not contain this parameter. The effect of γ, the ratio of integrated Lorentzian component to the integrated Doppler component, is shown in Fig. 4. We note that in the limit of γ large (or α small) the second term becomes negligible, and the Lamb dip takes on those features of an atomic laser. Thus (33) is an extension of previous results for atomic lasers. In Fig. 4 we see how the dominant effect of cross relaxation eliminates hole burning for b small. In Fig. 5 we hold the ratio of b/γ constant, and vary b and γ individually to see clearly how the hole width is influenced. The hole width varies approximately as b for small I/I_0. In Fig. 5 the parameter γ' is held constant as b varies. From this figure it is seen that both the width and height of the Lamb dip vary significantly for γ' constant. Two independent parameters, b and γ, are necessary to characterize the Lamb dip. To consider the dependence of (33) on b, we may consider the following. If pressure is increased through the addition of an inert gas or a gas that does not participate in the

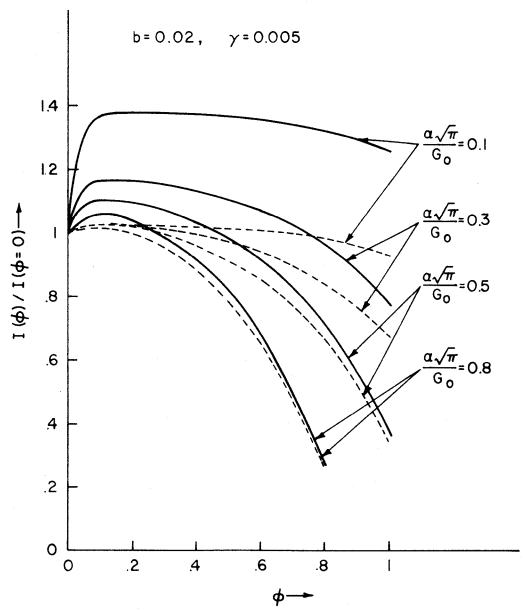


Fig. 3. The behavior of Lamb dip as a function of $\alpha\sqrt{\pi}/G_0$ for one fixed value of b and α. Dashed curves are drawn for $\alpha/G_0 = 1$ (in the denominator only) of (33).

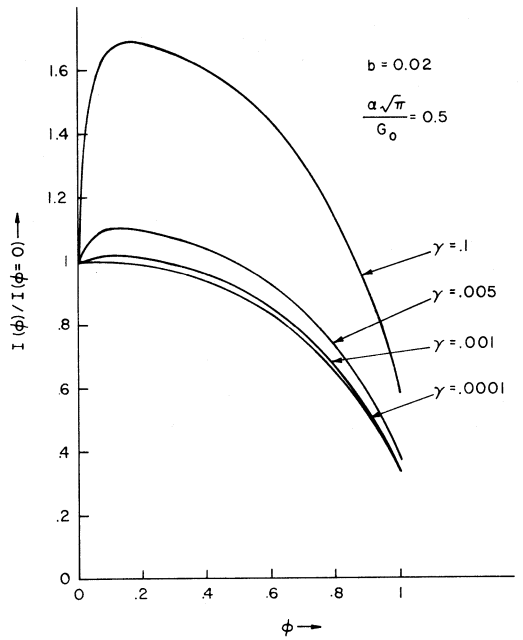


Fig. 4. The effect of molecular parameter γ on Lamb dip for one fixed value of b and $\alpha\sqrt{\pi}/G_0$.

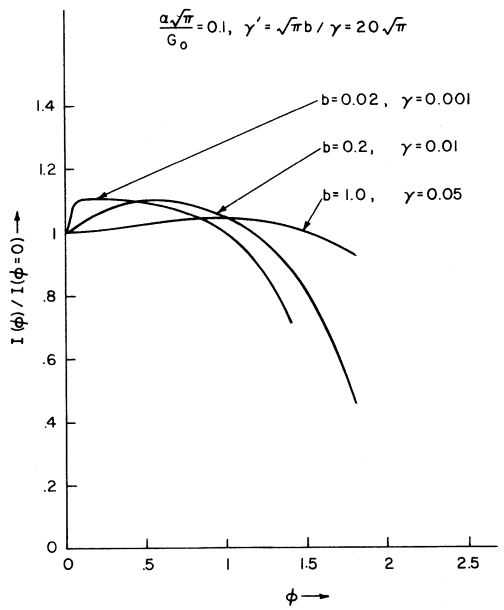


Fig. 5. The effect of simultaneous variation in b and γ on Lamb dip for one fixed value of γ' and $\alpha\sqrt{\pi}/G_0$.

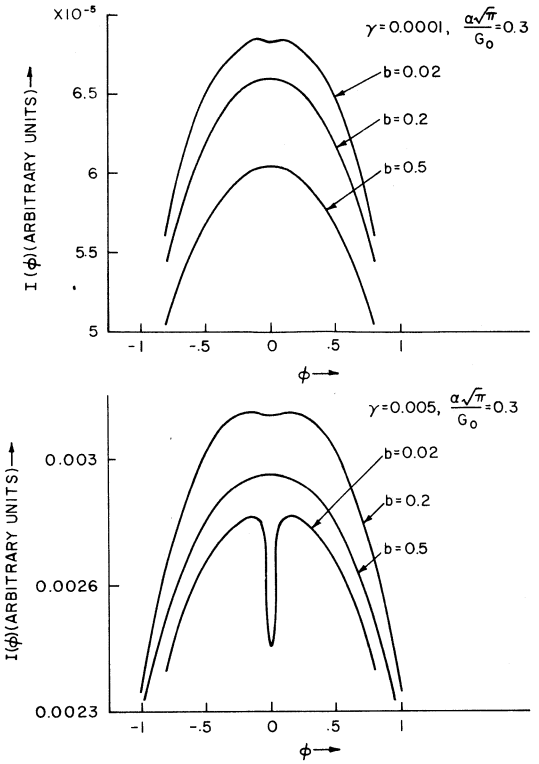


Fig. 6. The behavior of Lamb dip as a function of b for two different values of γ.

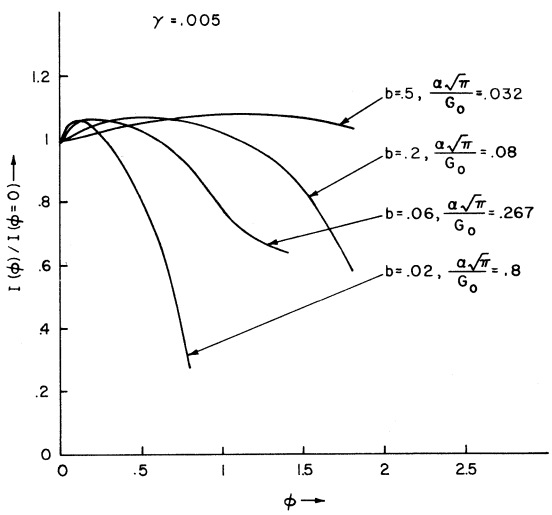


Fig. 7. The effect of varying pressure on Lamb dip keeping a particular gas, γ, and losses fixed.

inversion, then only b increases and G_0 remains constant. For two different values of γ, in Fig. 6 we see that changing b can have dramatically different results. If γ is small enough, only homogeneous-type broadening appears, and there is no Lamb dip.

We now wish to examine the behavior of (33) by varying pressure keeping a particular gas and losses fixed. Thus density, hence G_0, varies as pressure; b and all rate constants vary as pressure. There is no pressure dependence of γ. This effect is shown in Fig. 7 in which G_0 is proportional to pressure, and it is assumed that the inversion density ΔN_J^0 varies as pressure. We note that the Lamb dip vanishes in Fig. 6 as pressure is increased through the addition of an inert gas keeping excitation (ΔN_J^0) constant. However, as seen in Fig. 7, if pressure increases and inversion density increases with pressure, there is a significant broadening of the power versus frequency curve, and a shift of the maximum, but the ratio $I(\phi)/I(\phi = 0)$ increases slightly with increasing pressure. Conclusions drawn in this study seem to be in agreement with previous experiments on CO_2 lasers [10].

Finally, in order to see the effects of the new terms (4 through 7) in the denominator of (33), we note Fig. 8. Curves A represent values of (33) neglecting these terms, and B corresponds to their inclusion. For γ very small, the second term of (33) clearly dominates, and the additional terms are

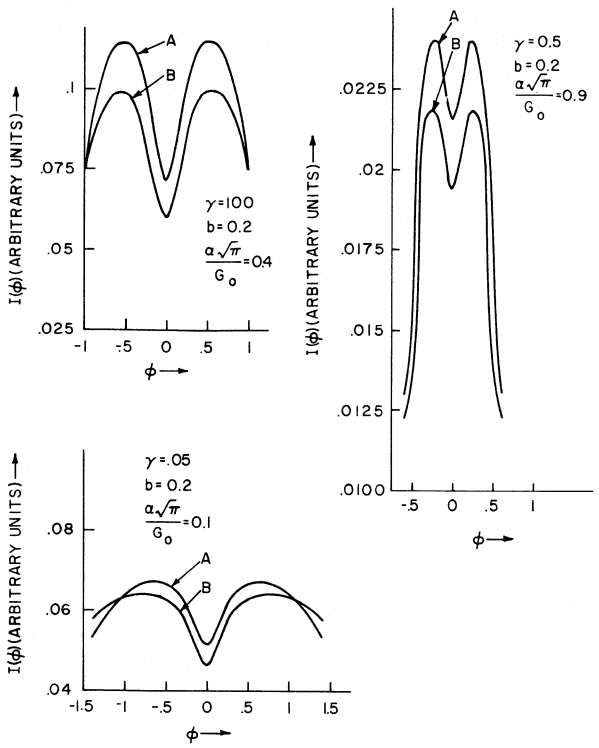


Fig. 8. The influence of the new terms in the denominator of (33) on Lamb dip. Curve A: The additional terms are neglected. Curve B: These terms are included.

not significant. However, for atomic systems, $\gamma \to \infty$, and the additional terms are important, as can be seen in Fig. 8 for $\gamma = 100$. The results of (33), it again is noted, are valid for all values of b, as long as I/I_0 is small.

VI. Conclusions

By a consideration of molecular lasers in the framework of kinetic equations, a new parameter appears that is the ratio of the integrated Lorentzian and Doppler components of the differential inversion. For a traveling-wave field exact results for gain saturation have been obtained that are valid for arbitrary b and I/I_0 for any ϕ. New simple results involving the molecular parameter γ are obtained for intermediate values of b. For a standing-wave field in the limit of small I/I_0, for any b, the behavior of the Lamb dip is analyzed. In addition, the ratio of total cavity loss to unsaturated gain (inhomogeneous limit at line center) appears. Additional terms are obtained for the Lamb-dip formation that can be significant for atomic as well as molecular gases.

Appendix

Error function of the complex argument is defined as [11]

$$W(x+iy) = \frac{i}{\pi}\int_{-\infty}^{\infty} \frac{\exp[-t^2]}{(x+iy-t)}\,dt$$

$$= \frac{i}{\pi}\int_{-\infty}^{\infty} \frac{\exp[-t^2]\,(x-t-iy)}{(x+iy-t)\,(x-t-iy)}\,dt$$

$$= \frac{y}{\pi}\int_{-\infty}^{\infty} \frac{\exp[-t^2]}{[(x-t)^2+y^2]}\,dt$$

$$+ i\,\frac{1}{\pi}\int_{-\infty}^{\infty} \frac{\exp[-t^2]\,(x-t)}{[(x-t)^2+y^2]}\,dt$$

$$= \text{Re } W(x+iy) + i \text{ Im } W(x+iy). \tag{A1}$$

Now

$$I = \int_{-\infty}^{\infty} M\left\{\frac{1}{(\phi+\eta_x)^2+b^2} + \frac{1}{(\phi-\eta_x)^2+b^2}\right\}^2 d\xi$$

$$= \frac{1}{\sqrt{\pi}}\int_{-\infty}^{\infty} \exp[-\eta_x^2]\left\{\frac{1}{[(\phi+\eta_x)^2+b^2]^2}\right.$$

$$\left. + \frac{1}{[(\phi-\eta_x)^2+b^2]^2}\right\} d\eta_x + \frac{2}{\sqrt{\pi}}\int_{-\infty}^{\infty}$$

$$\cdot \exp[-\eta_x^2]\,\frac{1}{[(\phi+\eta_x)^2+b^2]\,[(\phi-\eta_x)^2+b^2]}\,d\eta_x$$

$$= I_1 + I_2$$

$$\frac{1}{[(\phi+\eta_x)^2+b^2]^2} = \left[\frac{1}{(\phi+\eta_x+ib)\,(\eta_x+\phi-ib)}\right]^2$$

$$= -\frac{1}{4b^2}\left[\frac{1}{(\eta_x+\phi-ib)} - \frac{1}{(\eta_x+\phi+ib)}\right]^2$$

$$= -\frac{1}{4b^2}\left[\frac{1}{(\eta_x+\phi-ib)^2} - \frac{2}{[(\eta_x+\phi)^2+b^2]} + \frac{1}{(\eta_x+\phi+ib)^2}\right]$$

$$\therefore I_1 = \frac{2}{\sqrt{\pi}}\int_{-\infty}^{\infty} \frac{\exp[-\eta_x^2]}{[(\phi+\eta_x)^2+b^2]^2}\,d\eta_x$$

$$= \frac{1}{\sqrt{\pi}}\,b^2\int_{-\infty}^{\infty} \frac{\exp[-\eta_x^2]}{[(\eta_x+\phi)^2+b^2]}\,d\eta_x$$

$$- \frac{1}{2\sqrt{\pi}\,b^2}\int_{-\infty}^{\infty} \frac{\exp[-\eta_x^2]}{(\eta_x+\phi-ib)^2}\,d\eta_x$$

$$- \frac{1}{2\sqrt{\pi}\,b^2}\int_{-\infty}^{\infty} \frac{\exp[-\eta_x^2]}{(\eta_x+\phi+ib)^2}\,d\eta_x$$

$$= \frac{\sqrt{\pi}}{b^3}\,\text{Re } W(-\phi+ib) + \frac{1}{2b^2}$$

$$\cdot\left\{-\frac{1}{\sqrt{\pi}}\int_{-\infty}^{\infty} \frac{\exp[-\eta_x^2]}{(\eta_x-t)^2_{t=-\phi+ib}}\,d\eta_x\right.$$

$$\left. - \frac{1}{\sqrt{\pi}}\int_{-\infty}^{\infty} \frac{\exp[-\eta_x^2]}{(\eta_x+t)^2_{t=\phi+ib}}\,d\eta_x\right\}.$$

Substituting $\eta_x = -\eta_x$ in the last integral, we obtain

$$I_1 = \frac{\sqrt{\pi}}{b^3} \operatorname{Re} W(-\phi + ib) + \frac{1}{2b^2} \left\{ -\frac{1}{\sqrt{\pi}} \int_{-\infty}^{\infty} \cdot \frac{\exp[-\eta_x^2]}{(\eta_x - t)^2_{t=-\phi+ib}} d\eta_x - \frac{1}{\sqrt{\pi}} \int_{-\infty}^{\infty} \frac{\exp[-\eta_x^2]}{(\eta_x - t)^2_{t=\phi+ib}} d\eta_x \right\}.$$

Differential-equation characterization of the error function of a complex argument is given as [11]

$$W'(t) = \frac{2i}{\sqrt{\pi}} - 2tW(t), \qquad t = (x + iy)$$

$$W'(t) = \frac{dW(t)}{dt} = \frac{-i}{\pi} \int_{-\infty}^{\infty} \frac{\exp[-u^2]}{(t-u)^2} du$$

$$\therefore I_1 = \frac{\sqrt{\pi}}{b^3} \operatorname{Re} W(-\phi + ib) + \frac{\sqrt{\pi}}{2b^2 i} \left\{ \frac{2i}{\sqrt{\pi}} - 2(-\phi + ib) \cdot W(-\phi + ib) \right\} + \frac{\sqrt{\pi}}{2b^2 i} \left\{ \frac{2i}{\sqrt{\pi}} - 2(\phi + ib) W(\phi + ib) \right\}.$$

On simplification, we obtain

$$I_1 = \frac{\sqrt{\pi}}{b^3} \operatorname{Re} W(-\phi + ib) + \frac{2}{b^2} - \frac{2\sqrt{\pi}}{b^2} \phi \operatorname{Im} W(\phi + ib) - \frac{2\sqrt{\pi}}{b} \operatorname{Re} W(-\phi + ib)$$

$$I_2 = \frac{2}{\sqrt{\pi}} \int_{-\infty}^{\infty} \frac{\exp[-\eta_x^2]}{[(\phi + \eta_x)^2 + b^2]\,[(\phi - \eta_x)^2 + b^2]} d\eta_x$$

$$= \frac{1}{2\sqrt{\pi}\phi(\phi^2 + b^2)} \int_{-\infty}^{\infty} \exp[-\eta_x^2] \left\{ \frac{(\eta_x + 2\phi)}{[(\phi + \eta_x)^2 + b^2]} - \frac{(\eta_x - 2\phi)}{[(\phi - \eta_x)^2 + b^2]} \right\} d\eta_x.$$

Making use of (A1), we obtain

$$I_2 = \frac{\sqrt{\pi} \operatorname{Im} W(\phi + ib)}{\phi(\phi^2 + b^2)} + \frac{\sqrt{\pi} \operatorname{Re} W(\phi + ib)}{b(\phi^2 + b^2)}.$$

Hence

$$I = \frac{\sqrt{\pi}}{\phi(\phi^2 + b^2)} \operatorname{Im} W(\phi + ib) + \frac{\sqrt{\pi}}{b} \frac{\operatorname{Re} W(\phi + ib)}{(\phi^2 + b^2)} + \frac{\sqrt{\pi}}{b^3} \operatorname{Re} W(-\phi + ib) + \frac{2}{b^2} - \frac{2\sqrt{\pi}\phi}{b^2} \operatorname{Im} W(\phi + ib) - \frac{2\sqrt{\pi}}{b} \operatorname{Re} W(-\phi + ib). \tag{A2}$$

References

[1] E. I. Gordon, A. D. White, and J. D. Rigden, "Gain saturation at 3.39 microns in the He Ne maser," *Symp. Optical Masers*, Polytechnic Inst. Brooklyn, Brooklyn, N.Y., pp. 309–318, Apr. 1963.

[2] D. H. Close, "Strong field saturation effects in laser media," *Phys. Rev.*, vol. 153, pp. 360–371, Jan. 1967.

[3] N. Djeu and G. J. Wolga, "Frequency dependence of the optical saturation of vibration-rotation transitions," *J. Appl. Phys.*, vol. 42, pp. 3226–3230, July 1971.

[4] T. Kan and G. J. Wolga, "Influence of collisions on radiative saturation and Lamb dip formation in CO_2 molecular lasers," *IEEE J. Quantum Electron.*, vol. QE-7, pp. 141–150, Apr. 1971.

[5] H. Granek, C. Freed, and H. A. Haus, "Experiment on cross relaxation in CO_2," *IEEE J. Quantum Electron.*, vol. QE-8, pp. 404–414, Apr. 1972.

[6] J. W. Cipolla and T. F. Morse, "Kinetic theory of an optically pumped gas," *Phys. Fluids*, vol. 14, pp. 1850–1862, Sept. 1971.

[7] J. J. Healy and T. F. Morse, "Theory of an optically pumped gas laser," *J. Quan. Spectrosc. Radiat. Transfer*, vol. 13, pp. 235–254, Sept. 1972.

[8] —, "Cavity detuning and multimode operation of an optically pumped gas laser," *Phys. Rev. A*, vol. 6, pp. 2459–2469, Dec. 1972.

[9] J. S. Goela, J. J. Healy, and T. F. Morse, "Inhomogeneous broadening and rotational relaxation effects in a molecular gas flow laser," to be published.

[10] C. Bordé and L. Henry, "Study of the Lamb dip and of rotational competition in a carbon dioxide laser," *IEEE J. Quantum Electron. (1968 International Quantum Electronics Conference: Part II)*, vol. QE-4, pp. 874–880, Nov. 1968.

[11] V. N. Faddeyeva and N. M. Terentev, *Tables of Values of the Error Function for Complex Argument*. New York: Pergamon, 1961.

Output Coupling for Closely Confined $Pb_{1-x}Sn_xTe$ Double-Heterostructure Lasers

RICHARD W. DAVIES AND JAMES N. WALPOLE

Abstract—**The output coupling of an idealized, symmetric model of a double-heterostructure (DH) laser is analyzed theoretically using parameters suitable to $Pb_{1-x}Sn_xTe$. For the TE_0 mode incident at the laser mirror and for thin optical guiding regions such that only the TE_0, TE_1, TM_0, and TM_1 modes may propagate, an exact formulation of the coupling problem is obtained including mode coupling at the mirror into the continuum of unguided radiation modes. Using this formulation, the power reflection and transmission coefficients, the fraction of incident power coupled into the radiation modes, the mirror illumination, and the far-field pattern are calculated for typical parameters. Significant mode coupling can occur, limiting the maximum external efficiency of such lasers. This and other potentially undesirable characteristics resulting from close optical confinement, such as large output beam divergence, must be considered in design criteria for DH structures in this alloy system.**

I. Introduction

RECENTLY, heterostructure diode lasers [1]-[3] and waveguides [4] have been successfully fabricated in the $Pb_{1-x}Sn_xTe$ alloy system. The purpose of this paper is to analyze the output coupling of such devices, specifically double-heterostructure (DH) lasers with thin active regions, less than about 4 μm thick. The solution of this problem requires a more complete treatment of the boundary conditions at the waveguide termination or laser end mirror than is usually necessary. In the model treated here, mode coupling (or conversion) at the mirror into the continuum of unguided radiation modes is important because of the unusual optical parameters which apply to $Pb_{1-x}Sn_xTe$ DH lasers. Comparison with the parameters of the widely studied $Ga_{1-x}Al_xAs$ alloy system brings out this point more clearly.

The optical dielectric constant in the $Pb_{1-x}Sn_xTe$ system is larger by a factor of 3 to 4 than that of $Ga_{1-x}Al_xAs$ and varies more rapidly with alloy composition x, and the wavelength of operation (ranging from about 6.5 to over 20 μm compared to about 1 μm in $Ga_{1-x}Al_xAs$ devices) is roughly an order of magnitude longer. The larger dielectric constant and its stronger dependence on x result in larger variations in the optical dielectric constant across the profile of a heterostructure dielectric waveguide, and consequently, greater optical confinement. The confinement may be further enhanced by the doping profile of the structure because of relatively large free carrier contributions to the dielectric constant at the longer wavelengths. The larger dielectric constant also increases the mode reflectivity at the laser end mirror. Finally, the longer wavelength results in more beam spread or diffraction of the output for comparable waveguide thicknesses.

As an example, it is possible in principle to make a $Pb_{1-x}Sn_xTe$ DH laser operating at 10.6-μm wavelength having 70 percent of the energy of the lowest order transverse mode confined to an active region only 1 μm in width. Simple treatments of output coupling and output beam diffraction do not apply to such a device. The plane wave components of the sinusoidal variation of the mode (in the ray-optics approach) are incident on the cavity mirror at angles well beyond the critical angle for total internal reflection, [5] and the mode width is much less than the free-space wavelength. In order to obtain a rigorous, exact formulation of this problem a simple, idealized model of a DH laser discussed below is used here. For this model we obtain: the fraction of the power incident in the lowest order TE_0 mode on the laser end mirror which is reflected back into the mode, i.e., the power reflection coefficient R; the fraction of incident power coupled into the waveguide radiation modes and hence lost or scattered into the bulk, which we term the scattering coefficient of the mirror S; and the fraction of power transmitted or coupled into the output beam T. The latter quantity, which is given by $T = 1 - S - R$, is not of particular interest alone. Instead, results are shown for the quantity, $T/(T+S)$, which, together with R, comprises the coupling parameters of practical importance. As discussed below, the quantity $T/(T+S)$ limits the maximum possible external efficiency in the presence of the scattering S. For $Pb_{1-x}Sn_xTe$ parameters, S may become as large as 10 percent or more and at the same time R may approach 70 percent or more, with the result that output efficiency is degraded. The maximum efficiency can become less than 50 percent. This situation is not encountered to any significant degree when the theory presented here is applied to $Ga_{1-x}Al_xAs$. Even for worst case parameters the calculated mode coupling for the TE_0 mode incident is never larger than a few percent, and the reflectivity remains relatively small (less than 40 percent). Since the resulting losses are not significant, parameters suitable to $Ga_{1-x}Al_xAs$ will not be discussed further.

To determine the output beam diffraction, both the fields at the mirror and the far-field pattern are calculated for typical parameters, and general trends are discussed including the effects of the waveguide radiation modes excited at the mirror.

Section II of this paper discusses further some of the matters mentioned above in order to provide a perspective in which to view the results. These include the model used, its limitations, the parameters of the model, and the relevance of the results to $Pb_{1-x}Sn_xTe$ DH lasers. Sections III and IV, together with the Appendix, present the theory and the techniques of the

Manuscript received November 3, 1975. This work was supported in part by the Department of the Air Force and in part by the Defense Advanced Research Projects Agency.

The authors are with the Lincoln Laboratory, Massachusetts Institute of Technology, Lexington, MA 02173.

numerical calculation. For completeness, this material is entirely self-contained and includes mathematical derivations and proofs of general interest in the type of problem [6],[1] [7],[2] [8] considered here. A reader interested primarily in the results, however, should be able to omit many of the details, particularly Section IV and the Appendix. These results are presented in Section V and discussed further there. Finally, a brief summary is given in Section VI.

II. Preliminary Considerations

A. Waveguide Model

In order to obtain an exact formulation of the output coupling problem, it is desirable to simplify the theoretical model as much as possible. Fig. 1 shows the geometry of the waveguide model to be treated. It is an idealized three-layered structure terminated by free space in the plane $z = 0$, which is normal to the direction of propagation through the guide. The two-dimensional guide is made symmetric and free of irregularities so that no coupling can exist between modes of different parity (even or odd) or different polarization (TE or TM). We shall treat the case where only the lowest order TE_0 mode is incident on the waveguide termination. The theory is valid for guiding regions sufficiently thin ($2d \lesssim 4$ μm for the parameters to be used) so that only the four lowest order modes can propagate (i.e., the TE_0, TM_0, TE_1, and TM_1 modes). By restricting the thickness in this manner, we need consider mode conversion only to the continuum of unguided radiation modes rather than to the TE_2, TE_4, etc., as well. The limitation on guiding region thickness is not a serious one at the present state-of-the-art, since it is the thin devices which are of interest for low laser threshold. However, more advanced devices, using separate carrier and optical confinement, would require examination of a different model where mode conversion to higher order propagating modes could occur. The treatment for the TE_0 mode incident on the mirror can easily be generalized for any one of the other three allowed modes incident, but in practice the lowest order TE_0 mode is of most interest [4].

The dielectric constant ϵ is treated as totally real (i.e., the waveguide is treated as lossless and passive) since, at worst, one can estimate $\text{Im}\,\epsilon \leqslant 10^{-2}\,\text{Re}\,\epsilon$. Because variations much larger than 1 percent occur in Re ϵ, mode confinement in this case is not influenced by Im ϵ [9], [10].

It is important to appreciate the limitations of the theory imposed by the idealized, symmetric model used. The abrupt changes in dielectric constant shown in Fig. 1 at the interfaces of different alloy composition would be smoothed or graded in a real structure to one degree or another, although grading could be accounted for theoretically and may in principle be minimized. Perhaps more important ways in which real devices differ from the assumed model are these.

[1] An approach similar to that used here has been presented by Ikegami who, however, finally discards the radiation modes from his calculations of reflectivity for the case of $Ga_{1-x}Al_xAs$ DH lasers.

[2] These authors obtain a result similar to that derived here for the far-field pattern at large angles. The differences are due to their approximate treatment of the boundary conditions at the laser mirror.

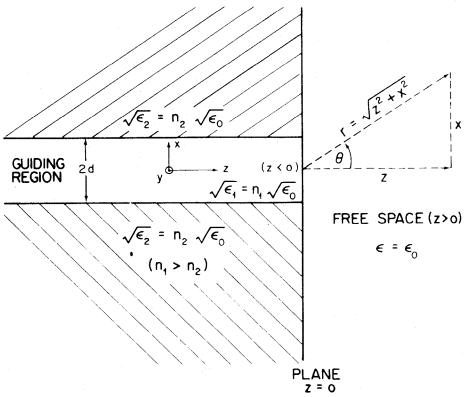


Fig. 1. Geometry for symmetric waveguide with guiding region of width $2d$. The free-space interface is located at the plane $z = 0$. Also shown are the polar coordinates r, θ used in the discussion of the far-field power distribution.

1) The end mirrors of $Pb_{1-x}Sn_xTe$ lasers are not, in general, optically smooth nor perfectly normal to the cavity axis [11].

2) In order to improve heatsinking the (assumed infinite) dielectric medium may be terminated close (compared to a wavelength) to the active layer on one side of the waveguide by the electrical contact and heatsink.

Neither of these deviations from an ideal geometry is necessarily a small perturbation nor easily accounted for theoretically. In order to satisfy the more irregular boundary conditions, it would be expected that mode coupling at the mirror would increase, particularly, it would seem, where significant coupling already exists in the idealized geometry.

B. Variation of Optical Dielectric Constant

The optical dielectric constant for $Pb_{1-x}Sn_xTe$ alloys varies with the composition x, the free carrier concentration N, the temperature T, and the free-space optical wavelength λ. Although the dependence on these variables has been established experimentally [12]-[14] and is well understood theoretically, a precise value of the optical dielectric constant or refractive index for a given set of variables is not generally available. Reasonable estimates can be made, however. In addition to the dispersion due to free carriers, the index has a sizeable peak near the band-gap wavelength [15].[3] For a laser operating at $\lambda \simeq 10$ μm ($x \simeq 0.12$ to 0.18 for $4.2 < T < 80$ K), the relative dielectric constant of the active region n_1^2 could be anywhere between 40 and 55. If PbTe ($x = 0$), having a free carrier concentration $N \simeq 4 \times 10^{18}$ cm^{-3}, is used in region 2, then n_2^2 at the 10-μm wavelength would be about 30. This value establishes an approximate lower limit likely to be encountered for n_2^2, since significantly heavier doping (which further decreases n_2) should not be required for electrical purposes, and x could be increased somewhat (increasing n_2) without losing carrier confinement.

For the calculations here, the value used for n_1^2 will be kept

[3] The position, height, and width of this peak depends on carrier density through the Burstein shift and, in theory, is sensitive to the lifetime or damping constant used (without damping it is a logarithmic singularity). Experimentally, ϵ at the peak may be 10 to 20 percent larger than the high-frequency asymptotic value ϵ_∞.

constant at a typical value of 45 and n_2^2 will be varied. If a different value for n_1^2 is used, 40 or 50, the values found for R and S will also differ, but these variations are not very significant numerically and, as discussed below, have little consequence for device performance. The quantity $T/(T+S)$, the maximum possible external efficiency, is quite insensitive to the value chosen for n_1^2. It depends, instead, primarily on the difference $n_1^2 - n_2^2$. As can be seen from the estimates given above, this difference may range from an arbitrarily small value up to a maximum value of about 25. For the numerical calculations presented in this paper, excessive computer time is required to obtain accurate results for values of $(n_1^2 - n_2^2)$ greater than about 20. Hence, we limit this parameter to values less than 20, which includes most situations of practical interest. The exception is epitaxial $Pb_{1-x}Sn_xTe$ devices on low-index substrates such as BaF_2 [16]. Although the calculations do not cover this case, the trends indicate that severe scattering or mode coupling might be expected.

C. Device Coupling Parameters

As mentioned above, since $R+S+T=1$, the output coupling of the laser is characterized by any two of the three power coefficients (excluding for the moment distributed waveguide losses) together with the beam angle or divergence of the output. The latter is determined by the far-field pattern, i.e., the power density as a function of the angle θ in Fig. 1 at distances $r \gg \lambda, 2d$. The beam angle can then be specified as the half-width at half-power (or any other convenient definition).

As discussed earlier, the most meaningful coupling parameters involving the power coefficients are R and $T/(T+S)$. This is seen by considering the expressions for incremental external quantum efficiency.

In the absence of mode conversion or any other scattering into the bulk at the mirrors, the incremental (above threshold) external quantum efficiency is approximately [17]

$$\eta'_{\text{ext}} \simeq \eta_{\text{int}} \left(\frac{\ln 1/R}{\alpha L + \ln 1/R} \right) \tag{2.1}$$

where η_{int} is the internal quantum efficiency above threshold, including the pumping or injection efficiency, and α is the loss coefficient of the laser waveguide. In our model this loss is completely independent of the optical parameters of the calculation and is determined by the free carrier absorption and scattering from any irregularities distributed throughout the guide. The parameter L is the cavity length.

When scattering at the mirror is considered, it is easy to see that internally the cavity remains characterized by the parameters αL and R. The only difference is that a portion of the power not reflected is also not transmitted. Hence, the external efficiency is degraded by the ratio of the transmitted power to the unreflected power $T/(1-R) = T/(T+S)$, i.e.,

$$\eta_{\text{ext}} = \eta'_{\text{ext}}\, T/(T+S). \tag{2.2}$$

In the limit that the internal quantum efficiency approaches unity and $\alpha L \ll \ln 1/R$, the maximum external efficiency is

$$\eta_{\text{ext}}(\max) = T/(T+S). \tag{2.3}$$

Scattering at the mirror affects laser threshold only to the extent that it affects the reflective feedback. For the idealized model treated here, this effect is insignificant.

With the outlined considerations in mind, we now continue with the theoretical formulation of the coupling problem.

III. Theoretical Formulation

We begin with Maxwell's equations (MKS units) for the symmetric waveguide structure shown in Fig. 1, and for a wave propagating with time dependence $e^{i\omega t}$

$$\nabla \times \boldsymbol{E}(\boldsymbol{r}) = -i\omega\mu_0 \boldsymbol{H}(\boldsymbol{r}) \tag{3.1}$$

$$\nabla \times \boldsymbol{H}(\boldsymbol{r}) = i\omega\epsilon(x)\boldsymbol{E}(\boldsymbol{r}). \tag{3.2}$$

In (3.2), $\epsilon(x)$ is the discontinuous dielectric constant as illustrated in Fig. 1. Combining (3.1) and (3.2) yields

$$\nabla^2 \boldsymbol{E}(\boldsymbol{r}) + \mu_0 \epsilon(x) \omega^2 \boldsymbol{E}(\boldsymbol{r}) = 0. \tag{3.3}$$

We shall consider the case of TE modes such that

$$\boldsymbol{E}(\boldsymbol{r}) = \hat{y} E(x, z); \tag{3.4}$$

then from (3.1)

$$\boldsymbol{H}(\boldsymbol{r}) = \frac{i}{\mu_0 \omega} \left[-\hat{x} \frac{\partial E(x,z)}{\partial z} + \hat{z} \frac{\partial E(x,z)}{\partial x} \right]. \tag{3.5}$$

The boundary conditions are that the tangential components of $\boldsymbol{E}$ and $\boldsymbol{H}$ are everywhere continuous. From (3.4), (3.5), and the geometry of Fig. 1, this is equivalent to the requirement that $E(x,z)$ and $\partial E(x,z)/\partial x$ be continuous at $x = \pm d$ inside the dielectric structure, while on the free-space interface at $z=0$ we must have $E(x,z)$ and $\partial E(x,z)/\partial z$ continuous.

The time average of the Poynting vector is given by

$$\boldsymbol{S}_{\text{ave}} = \frac{1}{2\mu_0 \omega} \operatorname{Im} \left\{ \hat{x} E(x,z) \frac{\partial E(x,z)^*}{\partial x} + \hat{z} E(x,z) \frac{\partial E(x,z)^*}{\partial z} \right\}. \tag{3.6}$$

We shall be interested in the equation for power flow across any plane of constant z, i.e., we are interested in the $\hat{z}$ component of $\boldsymbol{S}_{\text{ave}}$ integrated over all x. Since the waveguide is treated as lossless and passive, the power flow in the $\hat{z}$ direction must be independent of z, and hence it is the power transmitted into free space. By normalizing the fields of the mode incident on the mirror to unite power [see (3.9)] the integral over x of the $\hat{z}$ component of $\boldsymbol{S}_{\text{ave}}$ is by definition the power transmission coefficient T at the mirror. Hence,

$$T = \frac{1}{2\mu_0 \omega} \int_{-\infty}^{\infty} dx \operatorname{Im} \left\{ E(x,z) \frac{\partial E(x,z)^*}{\partial z} \right\}. \tag{3.7}$$

It can be seen here that the continuity of T at $z=0$ is guaranteed by the requirement that $E(x,z)$ and $\partial E(x,z)/\partial z$ be continuous.

As discussed in Section II, the waveguide parameters will be restricted such that we need consider only the coupling of an incident TE_0 bound mode to the continuum of even TE radiation modes. In this case, the field inside the waveguide can be

written as

$$E(x,z) = E_0(x)e^{-i\beta_0 z} + \mathcal{R}E_0(x)e^{i\beta_0 z} + \int_0^\infty d\gamma g(\gamma)E_\gamma(x)e^{i\beta\gamma z}. \quad (3.8)$$

In the above equation, the first two terms are the incident and reflected fields for the bound mode, and $\mathcal{R}$ is the (complex) reflection coefficient. The third term in the equation represents reflected waves belonging to the continuum of even TE radiation modes. The coefficients $\mathcal{R}$ and $g(\gamma)$ need to be determined.

As derived in Marcuse [18] the fields $E_0(x)$ and $E_\gamma(x)$ normalized for unit power are given as follows:

$$E_0(x) = \left(\frac{2\mu_0\omega}{\beta_0(d+\gamma_0^{-1})}\right)^{1/2} \cdot \begin{cases} \cos(\kappa_0 x) & \text{for } |x|<d \\ \cos(\kappa_0 d)e^{d\gamma_0}e^{-|x|\gamma_0} & \text{for } |x|>d. \end{cases} \quad (3.9)$$

Here, κ_0 is the lowest order eigenvalue solution of

$$(\kappa_0 d)^2[1+\tan^2(\kappa_0 d)] = (k_0 d)^2(n_1^2 - n_2^2) \quad (3.10)$$

where

$$k_0 = \sqrt{\mu_0\epsilon_0\omega^2} = 2\pi/\lambda \quad (3.11)$$

is the free-space wave vector. The coefficients β_0 and γ_0 are then determined from

$$(\beta_0 d)^2 = (k_0 d)^2 n_1^2 - (\kappa_0 d)^2 \quad (3.12)$$

$$(\gamma_0 d) = (\kappa_0 d)\tan(\kappa_0 d). \quad (3.13)$$

Similarly, for the even parity TE radiation modes, we have

$$E_\gamma(x) = A\cos\kappa x \quad \text{for } |x|<d$$
$$= A\left[\cos\kappa d\cos\gamma d + \frac{\kappa}{\gamma}\sin\kappa d\sin\gamma d\right]\cos\gamma x + A\left[\cos\kappa d\sin\gamma d - \frac{\kappa}{\gamma}\sin\kappa d\cos\gamma d\right]\sin\gamma|x| \quad \text{for } |x|>d \quad (3.14)$$

with

$$A = \left[\frac{2\mu_0\omega}{\pi|\beta_\gamma|(\cos^2\kappa d + \kappa^2/\gamma^2\sin^2\kappa d)}\right]^{1/2}. \quad (3.15)^4$$

Here γ is an arbitrary (continuum) wave vector in the range $0 \cong \gamma \cong \infty$, and κ and β_γ are then determined from

$$(\kappa d)^2 = (\gamma d)^2 + (k_0 d)^2(n_1^2 - n_2^2) \quad (3.16)$$

$$(\beta_\gamma d) = \sqrt{(k_0 d)^2 n_2^2 - (\gamma d)^2}. \quad (3.17)$$

In (3.17) it should be noted that β_γ can be imaginary for $\gamma > k_0 n_2$, i.e., this is the case of evanescent modes. In this case the meaning of (3.17) is

$$(\beta_\gamma d) = -i\sqrt{(\gamma d)^2 - (k_0 d)^2 n_2^2} \quad (3.18)$$

where the sign is determined from (3.8) by requiring that the reflected evanescent waves be decaying exponentials in the dielectric region $z<0$. The fields described by (3.9) and (3.14) are orthonormal according to

$$\int_{-\infty}^{\infty} E_0(x)^2\,dx = \frac{2\mu_0\omega}{\beta_0} \quad (3.19)$$

$$\int_{-\infty}^{\infty} E_\gamma(x)E_{\gamma'}(x)\,dx = \frac{2\mu_0\omega}{|\beta_\gamma|}\delta(\gamma-\gamma') \quad (3.20)$$

$$\int_{-\infty}^{\infty} E_0(x)E_\gamma(x)\,dx = 0. \quad (3.21)$$

Next, we can write the free-space field for $z>0$ as

$$E(x,z) = \int_{-\infty}^{\infty} a(\sigma)e^{-i\sigma x}e^{-i\beta(\sigma)z}\,d\sigma \quad (3.22)$$

where the Fourier components $a(\sigma)$ need to be determined, and from Maxwell's equations

$$\beta(\sigma)d = \sqrt{(k_0 d)^2 - (\sigma d)^2} \quad \text{for } k_0 > \sigma$$
$$= -i\sqrt{(\sigma d)^2 - (k_0 d)^2} \quad \text{for } k_0 < \sigma. \quad (3.23)$$

Again, the sign in (3.23) for $k_0 < \sigma$ is determined from (3.22) by requiring that the evanescent transmitted waves decay in the $+z$ direction.

The next step is to solve [6] for the complex reflection coefficient $\mathcal{R}$, and the coefficients $g(\gamma)$ and $a(\sigma)$ in (3.8) and (3.22). These coefficients are obtained by requiring that $E(x,z)$ and $\partial E(x,z)/\partial z$ as given by (3.8) and (3.22) be continuous on the mirror plane $z=0$. This immediately yields the two equations

$$E_0(x)(1+\mathcal{R}) + \int_0^\infty d\gamma g(\gamma)E_\gamma(x) = \int_{-\infty}^{\infty} a(\sigma)e^{-i\sigma x}\,d\sigma \quad (3.24)$$

$$E_0(x)\beta_0(1-\mathcal{R}) - \int_0^\infty d\gamma g(\gamma)\beta_\gamma E_\gamma(x) = \int_{-\infty}^{\infty} a(\sigma)e^{-i\sigma x}\beta(\sigma)\,d\sigma. \quad (3.25)$$

We may now solve for $a(\sigma)$ by multiplying (3.24) by $e^{i\sigma' x}$ and integrating over x. Using

$$\int_{-\infty}^{\infty} e^{i(\sigma'-\sigma)x}\,dx = 2\pi\delta(\sigma'-\sigma)$$

and defining the Fourier transforms of $E_0(x)$ and $E_\gamma(x)$ as

$$\mathcal{E}_0(\sigma) = \frac{1}{2\pi}\int_{-\infty}^{\infty} E_0(x)e^{i\sigma x}\,dx \quad (3.26)$$

[4] The quantity A in our treatment is identical to the quantity C_e defined in [18, eq. 8.4-18]. Note, however, when β_γ becomes negative imaginary, the normalization of the power is to unit (negative) imaginary power. This leads to the factor of $|\beta_\gamma|$ in (3.15) of this paper.

$$\mathcal{E}_\gamma(\sigma) = \frac{1}{2\pi}\int_{-\infty}^{\infty} E_\gamma(x)e^{i\sigma x}\,dx \tag{3.27}$$

we obtain from (3.24)

$$a(\sigma) = (1+\mathcal{R})\,\mathcal{E}_0(\sigma) + \int_0^\infty d\gamma g(\gamma)\,\mathcal{E}_\gamma(\sigma). \tag{3.28}$$

Inserting this expression into (3.25) gives

$$E_0(x)\beta_0(1-\mathcal{R}) - \int_0^\infty d\gamma g(\gamma)\beta_\gamma E_\gamma(x) = \int_{-\infty}^{\infty} d\sigma\beta(\sigma)e^{-i\sigma x}\left[(1+\mathcal{R})\,\mathcal{E}_0(\sigma) + \int_0^\infty d\gamma g(\gamma)\,\mathcal{E}_\gamma(\sigma)\right]. \tag{3.29}$$

The coefficients $\mathcal{R}$ and $g(\gamma)$ may now be determined by multiplying (3.29) by $E_0(x)$ or $E_{\gamma'}(x)$, integrating on x, and using the orthonormality relations (3.19)–(3.21). The result is

$$\mathcal{R} = \frac{1 - F_0 - \int_0^\infty d\gamma g(\gamma)F(\gamma)}{1+F_0}, \tag{3.30}$$

where the F's will be defined below, and where $g(\gamma)$ satisfies the Fredholm integral equation

$$g(\gamma) = \frac{|\beta_\gamma|}{\beta_\gamma}\left[\varphi(\gamma) + \int_0^\infty d\gamma' K(\gamma,\gamma')g(\gamma')\right]. \tag{3.31}$$

In (3.31), the quantities $\varphi(\gamma)$ and $K(\gamma,\gamma')$ are given by

$$\varphi(\gamma) = \frac{-2F(\gamma)}{1+F_0} \tag{3.32}$$

$$K(\gamma,\gamma') = \frac{F(\gamma)F(\gamma')}{1+F_0} - F(\gamma,\gamma') \tag{3.33}$$

where the F's are given by

$$F_0 = \frac{\pi}{\mu_0\omega}\int_{-\infty}^{\infty} d\sigma\beta(\sigma)\,\mathcal{E}_0(\sigma)^2 \tag{3.34}$$

$$F(\gamma) = \frac{\pi}{\mu_0\omega}\int_{-\infty}^{\infty} d\sigma\beta(\sigma)\,\mathcal{E}_0(\sigma)\,\mathcal{E}_\gamma(\sigma) \tag{3.35}$$

$$F(\gamma,\gamma') = \frac{\pi}{\mu_0\omega}\int_{-\infty}^{\infty} d\sigma\beta(\sigma)\,\mathcal{E}_\gamma(\sigma)\,\mathcal{E}_{\gamma'}(\sigma) \tag{3.36}$$

and where $\beta(\sigma)$ is given by (3.23). These results also depend on the fact that $\mathcal{E}_0(-\sigma) = \mathcal{E}_0(\sigma)$ and $\mathcal{E}_\gamma(-\sigma) = \mathcal{E}_\gamma(\sigma)$, because the modes $E_0(x)$, $E_\gamma(x)$ are real and even. The problem now reduces to the calculation of the F's as given by (3.34)–(3.36), and the solution of the integral equation (3.31). We shall take up this problem in detail in Section IV. Here we wish to complete some formal aspects of the theory.

We first consider power balance. Inserting (3.8) into (3.7) and using (3.19)–(3.21), we find that T for $z<0$ is indeed independent of z and given by

$$T = 1 - |\mathcal{R}|^2 - \mathrm{Re}\int_0^\infty d\gamma\frac{\beta_\gamma|g(\gamma)|^2}{|\beta_\gamma|}. \tag{3.37}$$

It should be noted that in the last term of the foregoing equation the evanescent continuum modes having β_γ imaginary do not contribute to the power flow. Similarly, by inserting (3.22) into (3.7), we find that T for $z>0$ is also independent of z and given by

$$T = \frac{\pi}{\mu_0\omega}\mathrm{Re}\int_{-\infty}^{\infty} d\sigma\beta(\sigma)|a(\sigma)|^2. \tag{3.38}$$

We see from this result that the free-space evanescent modes having $\beta(\sigma)$ imaginary also make no contribution to the power flow. Equations (3.37) and (3.38) must be equal at $z=0$ because of the imposed continuity of $E(x,z)$ and $\partial E(x,z)/\partial z$ at the free-space interface. Hence, equating (3.37) and (3.38), we obtain the fundamental equation of power balance

$$1 = |\mathcal{R}|^2 + \mathrm{Re}\int_0^\infty d\gamma\frac{\beta_\gamma|g(\gamma)|^2}{|\beta_\gamma|} + \frac{\pi}{\mu_0\omega}\mathrm{Re}\int_{-\infty}^{\infty} d\sigma\beta(\sigma)|a(\sigma)|^2. \tag{3.39}$$

The left-hand side of this equation represents the incident power in the bound TE_0 mode. The three terms on the right-hand side are, respectively, the bound mode reflected power, the reflected power in the radiation modes (which represent a loss due to scattering at the mirror interface), and the transmitted power into free space. In the notation discussed in the Introduction, we may rewrite (3.39) as

$$1 = R + S + T. \tag{3.40}$$

In addition to the equation for power balance, we are also interested in the mirror illumination at $z=0$ and in the far-field pattern $r \gg \lambda$. By setting $z=0$ in either (3.8) or (3.22) we obtain

$$E(x,0) = (1+\mathcal{R})E_0(x) + \int_0^\infty d\gamma g(\gamma)E_\gamma(x) \tag{3.41}$$

as the mirror illumination pattern.

To obtain an approximation for the far-field pattern, we apply the method of stationary phase [19] to (3.22). The stationary point, σ_s, of the integrand is the solution of

$$\frac{d}{d\sigma}[\sigma x + \beta(\sigma)z] = 0$$

or

$$x + z\frac{d\beta(\sigma)}{d\sigma} = 0$$

which from (3.23) yields $\sigma_s = k_0\sin\theta$, $\beta(\sigma_s) = k_0\cos\theta$, where $\theta = \arctan(x/z)$ is the polar coordinate shown in Fig. 1. For

the far-field pattern [7] we then find

$$E(x, z) \simeq a(k_0 \sin\theta) \cos\theta \, e^{i(\pi/4)} \sqrt{\frac{2\pi k_0}{r}} \, e^{-ik_0 r} \tag{3.42}$$

where $r^2 = x^2 + z^2$ and

$$a(k_0 \sin\theta) \equiv a(\sigma)_{\sigma = k_0 \sin\theta}.$$

Similarly, in the far field, one calculates

$$\frac{\partial E(x, z)^*}{\partial z} \simeq i k_0 \sin\theta \, a(k_0 \sin\theta)^* \cos\theta \, e^{-i\pi/4} \sqrt{\frac{2\pi k_0}{r}} \, e^{ik_0 r}. \tag{3.43}$$

Inserting (3.42) and (3.43) into (3.7), and performing the integration over x yields

$$T = \frac{\pi k_0^2}{\mu_0 \omega} \int_{-\pi/2}^{\pi/2} d\theta \cos^2\theta \, |a(k_0 \sin\theta)|^2. \tag{3.44}$$

Note that the integrand of (3.44) is the far-field pattern, or the relative power density as a function of angle θ. By making the change of variables $\sigma = k_0 \sin\theta, d\sigma = k_0 \cos\theta \, d\theta$ in (3.44), we recover the *exact* expression given previously in (3.38) for the transmitted power. Thus the stationary phase approximation preserves exactly the result for the *total* transmitted power. Finally, we should note that the quantity $a(\sigma)$, which appears in (3.42) and (3.43) for the far-field pattern, has the interpretation of being the Fourier transform of the mirror illumination $E(x, 0)$ [via (3.22)].

IV. Analysis of the Integral Equation

In order to treat the integral equation (3.31), the first step is to evaluate the Fourier transforms [(3.26), (3.27)] of the bound and radiation modes as given by (3.9) and (3.15). For the bound mode this is straightforward and we find

$$\mathcal{E}_0(\sigma) = \frac{1}{\pi} \left[\frac{2\mu_0 \omega}{\beta_0 (d + \gamma_0^{-1})} \right]^{1/2} \left(\frac{\gamma_0^2 + \kappa_0^2}{\gamma_0^2 + \sigma^2} \right) \cdot \frac{(\sigma \sin\sigma d \cos\kappa_0 d - \kappa_0 \sin\kappa_0 d \cos\sigma d)}{\sigma^2 - \kappa_0^2}. \tag{4.1}$$

It should be noted that the last factor in the above equation is *not* singular at $\sigma = \kappa_0$.

Calculation of $\mathcal{E}_\gamma(\sigma)$ requires slightly more caution because the result contains principal value and δ-function singularities. We obtain the result

$$\mathcal{E}_\gamma(\sigma) = \frac{1}{\pi} \left[\frac{2\mu_0 \omega}{\pi |\beta_\gamma| (\cos^2 \kappa d + (\kappa^2/\gamma^2) \sin^2 \kappa d)} \right]^{1/2} \cdot \left\{ \frac{\pi}{2} \delta(\sigma - \gamma) (\cos\kappa d \cos\gamma d + \frac{\kappa}{\gamma} \sin\kappa d \sin\gamma d) + (\kappa^2 - \gamma^2) \frac{(\sigma \sin\sigma d \cos\kappa d - \kappa \sin\kappa d \cos\sigma d)}{\sigma^2 - \kappa^2} \cdot \Pr \frac{1}{\sigma^2 - \gamma^2} \right\}. \tag{4.2}$$

This expression is not singular at $\sigma = \kappa$, but it has a δ-function and principal value singularity at $\sigma = \gamma$. In obtaining the above result we have made use of the following representations [20]:

$$\lim_{L \to \infty} \int_d^L dx \, e^{ikx} = ie^{ikd} \left[\Pr\left(\frac{1}{k}\right) - i\pi\delta(k) \right] = ie^{ikd} \lim_{0^+ \to \infty} \frac{1}{k + i0^+}. \tag{4.3}$$

We have also checked the above results for $\mathcal{E}_0(\sigma)$, $\mathcal{E}_\gamma(\sigma)$ by Fourier inversion, which yields exactly (3.9) and (3.15) for $E_0(x)$ and $E_\gamma(x)$.

From the above expressions for $\mathcal{E}_0(\sigma)$ and $\mathcal{E}_\gamma(\sigma)$ one must next calculate the functions F_0, $F(\gamma)$, and $F(\gamma, \gamma')$ as given by (3.34)-(3.36). Unfortunately, it does not appear to be possible to carry out in closed form the integration over $d\sigma$ which gives these functions. The main source of difficulty in accomplishing this arises from the branch cut singularities of the function $\beta(\sigma)$ as given by (3.23). Thus we have resorted to direct numerical integration of (3.34)-(3.36). In doing this, F_0 presents no problem since the integrand of (3.34) is well behaved. The calculation of $F(\gamma)$ and $F(\gamma, \gamma')$ is more complex due to the principal value singularities of $\mathcal{E}_\gamma(\sigma)$ as given by (4.2). The calculation of $F(\gamma, \gamma')$ is especially delicate, as it involves integration of a product of two principal value factors. Further consideration of this difficulty will be discussed presently.

In order to monitor the accuracy of our numerical integration of the functions $F_0, F(\gamma), F(\gamma, \gamma')$, we have performed the following test. We note that if the factor of $\beta(\sigma)$, which appears in the integrand of (3.34)-(3.36), is replaced by $\beta(\sigma) \to 1$, then by Parseval's theorem for Fourier transforms, and from (3.19)-(3.21), we should obtain

$$F_0 = \frac{1}{\beta_0} \tag{4.4}$$

$$F(\gamma) = 0 \tag{4.5}$$

$$F(\gamma, \gamma') = \frac{1}{|\beta_\gamma|} \delta(\gamma - \gamma'). \tag{4.6}$$

Although (4.6) appears to be difficult to verify numerically (since the result is singular), we shall presently show how it can be made meaningful. Our numerical integration of (3.34)-(3.36) for the case $\beta(\sigma) \to 1$ satisfied (4.4)-(4.6) to a high degree of accuracy, and therefore we have good confidence in the numerical results for $F_0, F(\gamma), F(\gamma, \gamma')$ when the factor of $\beta(\sigma)$ is restored in the integrand of (3.34)-(3.36).

Before proceeding further with the discussion of the integral equation, we introduce a number of dimensionless quantities, and we make a transformation to eliminate a square root singularity in $g(\gamma)$ as given by (3.31).

We define

$$x_0 = \kappa_0 d \quad x = \kappa d \quad x' = \kappa' d \quad t = \gamma d \quad t' = \gamma' d$$

and from (3.10) and (3.16) we note

$$x_0^2 [1 + \tan^2 x_0] = (x^2 - t^2) = (x'^2 - t'^2) = (k_0 d)^2 (n_1^2 - n_2^2). \tag{4.7}$$

We also define $\beta_t = \beta_\gamma d$; then from (3.17) and (3.18)

$$\left.\begin{aligned}\beta_t &= \sqrt{(k_0 d)^2 n_2^2 - t^2} \quad \text{for} \quad k_0 d n_2 > t \\ &= -i\sqrt{t^2 - (k_0 d)^2 n_2^2} \quad \text{for} \quad k_0 d n_2 < t\end{aligned}\right\}. \tag{4.8}$$

Also, in place of the variable of integration σ in (3.34)-(3.36), we introduce the dimensionless variable $y = \sigma d$.

Next, we make the following transformation to barred quantities:

$$F_0 = \bar{F}_0 \text{ no change} \tag{4.9}$$

$$F(t) = \frac{d^{1/2}}{|\beta_t|^{1/2}} \bar{F}(t), \qquad t = \gamma d \tag{4.10}$$

$$F(t, t') = \frac{d\bar{F}(t, t')}{[|\beta_t|\,|\beta_{t'}|]^{1/2}}, \qquad t = \gamma d, t' = \gamma' d \tag{4.11}$$

$$g(t) = \frac{d^{1/2}\,|\beta_t|^{1/2}}{\beta_t} \bar{g}(t). \tag{4.12}$$

In terms of these reduced variables, we then find that $\bar{g}(t)$ satisfies the integral equation

$$\bar{g}(t) = \bar{\varphi}(t) + \int_0^\infty \frac{dt' \bar{K}(t, t')}{\beta_{t'}} \bar{g}(t') \tag{4.13}$$

with

$$\bar{\varphi}(t) = \frac{-2\bar{F}(t)}{1 + \bar{F}_0} \tag{4.14}$$

and

$$\bar{K}(t, t') = \frac{\bar{F}(t)\bar{F}(t')}{1 + \bar{F}_0} - \bar{F}(t, t'). \tag{4.15}$$

The expression for the complex reflection coefficient now takes the form

$$\mathcal{R} = \frac{1 - \bar{F}_0 - \int_0^\infty \frac{dt}{\beta_t} F(t)\bar{g}(t)}{1 + \bar{F}_0} \tag{4.16}$$

and the equation for power balance becomes

$$1 = |\mathcal{R}|^2 + \int_0^{n_2 k_0 d} \frac{|\bar{g}(t)|^2\, dt}{\sqrt{n_2^2 (k_0 d)^2 - t^2}} + \frac{\pi}{\mu_0 \omega} \operatorname{Re} \int_{-\infty}^{\infty} d\sigma\, \beta(\sigma)\, |a(\sigma)|^2. \tag{4.17}$$

It should be noted that (4.13), (4.16), and (4.17) all involve a square root singularity when β_t or $\beta_{t'}$ vanish, i.e., for t or t' equal to $n_2 k_0 d$. Such a square root singularity is, of course, integrable, and the point of the transformation (4.10)-(4.12) was to isolate these singularities, and to remove them from the unknown function $\bar{g}(t)$, which is subsequently well behaved.

A result similar to the ones discussed above also obtains in the calculation of the mirror illumination field. If we make the transformation

$$E_t(x) = \frac{d^{1/2} \bar{E}_t(x)}{|\beta_t|^{1/2}}, \qquad t = \gamma d \tag{4.18}$$

then the mirror illumination is given by

$$E(x, 0) = (1 + \mathcal{R}) E_0(x) + \int_0^\infty \frac{dt \bar{g}(t) \bar{E}_t(x)}{\beta_t}. \tag{4.19}$$

Again, there appears an integrable square root singularity for $t = k_0\, \mathrm{dn}_2$ ($\beta_t \to 0$).

We now return to the discussion of the quantities $\bar{F}_0, \bar{F}(t)$, $\bar{F}(t, t')$ in terms of the reduced dimensionless variables. For $\bar{F}_0$ we have

$$\bar{F}_0 = \frac{x_0}{(\beta_0 d)} \frac{x_0^4 (1 + \tan^2 x_0)^2}{x_0 + \cot x_0} \frac{4}{\pi} \int_0^\infty \frac{dy \sqrt{(k_0 d)^2 - y^2}}{(y^2 + x_0^2 \tan^2 x_0)^2} \cdot \frac{(y \sin y \cos x_0 - x_0 \sin x_0 \cos y)^2}{(y^2 - x_0^2)^2}. \tag{4.20}$$

In (4.20) (and throughout the paper), the square root factor is to be interpreted as defined by (3.23). We note for $y \to x_0$ that the last factor in (4.20) has the limiting value

$$\left[\frac{1}{2}\left(1 + \frac{\sin x_0 \cos x_0}{x_0}\right)\right]^2.$$

Thus the integrand of (4.20) is well behaved for all y and presents no difficulty for numerical integration.

Turning next to $\bar{F}(t)$, we obtain the result

$$\begin{aligned}\bar{F}(t) = {} & \left[\frac{1}{\pi(\beta_0 d)} \frac{x_0}{x_0 + \cot x_0} \frac{1}{t^2 \cos^2 x + x^2 \sin^2 x}\right]^{1/2} \\ & \cdot \left\{ 2\sqrt{(k_0 d)^2 - t^2}\,(t \cos x \cos t + x \sin x \sin t) \right. \\ & \cdot \frac{(t \sin t \cos x_0 - x_0 \sin x_0 \cos t)}{t^2 - x_0^2} \frac{x_0^2 (1 + \tan^2 x_0)}{t^2 + x_0^2 \tan^2 x_0} \\ & + \frac{4t}{\pi}(x^2 - t^2) \int_0^\infty dy\, \mathrm{Pr}\left[\frac{1}{y^2 - t^2}\right] \sqrt{(k_0 d)^2 - y^2} \\ & \cdot \frac{(y \sin y \cos x_0 - x_0 \sin x_0 \cos y)}{y^2 - x_0^2} \\ & \left. \cdot \frac{(y \sin y \cos x - x \sin x \cos y)}{y^2 - x^2} \frac{x_0^2 (1 + \tan^2 x_0)}{y^2 + x_0^2 \tan^2 x_0} \right\}.\end{aligned} \tag{4.21}$$

Some further remarks on this expression are in order. The values of x are related to the values of t through (4.7). The function $\bar{F}(t)$ has no singularities (other than the branch cut singularities introduced by the factors of $\sqrt{(k_0 d)^2 - t^2}$ and $\sqrt{(k_0 d)^2 - y^2}$), but the principal value integral in the second term of (4.21) must be performed accurately in the numerical integration. The first term in (4.21) arises from the δ-function contribution of $\mathcal{E}_\gamma(\sigma)$ as given by (4.2), and similarly, the second (integral) term in the equation arises from the principal value part of $\mathcal{E}_\gamma(\sigma)$. The Parseval's theorem result in (4.5) implies that if the two square root factors in the curly bracket of (4.21) are replaced by any constant, then the first term in (4.21) must exactly cancel the integral term. We have verified

that our numerical integration procedure satisfies this test to a high degree of accuracy.

Finally, we consider the function $\bar{F}(t, t')$ given by

$$\bar{F}(t,t') = \left[\frac{1}{t^2\cos^2 x + x^2\sin^2 x}\,\frac{1}{t'^2\cos^2 x' + x'^2\sin^2 x'}\right]^{1/2} \cdot \Big\{\sqrt{(k_0d)^2 - t^2}\,(t\cos x\cos t + x\sin x\sin t)^2\delta(t-t') + \frac{2}{\pi}\,\frac{(x^2 - t^2)}{t^2 - t'^2} \cdot \Big[t'\sqrt{(k_0d)^2 - t^2}\,(t\cos x\cos t + x\sin x\sin t) \cdot \frac{(t\sin t\cos x' - x'\sin x'\cos t)}{t^2 - x'^2} - t\sqrt{(k_0d)^2 - t'^2} \cdot (t'\cos x'\cos t' + x'\sin x'\sin t') \cdot \frac{(t'\sin t'\cos x - x\sin x\cos t')}{t'^2 - x^2}\Big] + \frac{4}{\pi^2}(x^2 - t^2)^2 \cdot \int_0^\infty dy\sqrt{(k_0d)^2 - y^2}\,\Pr\frac{t}{y^2 - t^2}\,\Pr\frac{t'}{y^2 - t'^2} \cdot \frac{(y\sin y\cos x - x\sin x\cos y)}{y^2 - x^2} \cdot \frac{(y\sin y\cos x' - x'\sin x'\cos y)}{y^2 - x'^2}\Big\}. \tag{4.22}$$

Although this expression is rather complicated, it is easy to see the origin of the various terms. The first term, proportional to $\delta(t - t')$, arises from the product $\delta(\sigma - \gamma)\delta(\sigma - \gamma')$ in the expression $\mathfrak{E}_\gamma(\sigma)\mathfrak{E}_{\gamma'}(\sigma)$ of (3.36). On integration over σ this leads to a $\delta(\gamma - \gamma') \propto \delta(t - t')$ contribution. The second term (in square brackets) of (4.22) arises from the products $\delta(\sigma - \gamma)$ $\Pr 1/(\sigma^2 - \gamma'^2)$ and $\delta(\sigma - \gamma')\Pr 1/(\sigma^2 - \gamma^2)$ in the expression for $\mathfrak{E}_\gamma(\sigma)\mathfrak{E}_{\gamma'}(\sigma)$. On integration over σ this leads to contributions of the form $\Pr 1/(\gamma^2 - \gamma'^2) \propto \Pr 1/(t^2 - t'^2)$. It may be noted that we have dropped the principal value symbol in the second term of (4.22). This was done because there really is no singularity in this term $t \to t'$ since the expression in the square bracket also approaches zero in this limit.

The last (integral) term of (4.22) arises from the principal value products $\Pr 1/(\sigma^2 - \gamma^2)\Pr 1/(\sigma^2 - \gamma'^2)$ in the expression for $\mathfrak{E}_\gamma(\sigma)\mathfrak{E}_{\gamma'}(\sigma)$. This term must be treated with a great deal of caution because the product of principal values leads to an additional singular contribution to $\bar{F}(t, t')$ at $t = t'$. In the Appendix, we show that it is possible to manipulate the last term in (4.22) to produce the result

$$\bar{F}(t,t') = \sqrt{(k_0d)^2 - t^2}\,\delta(t - t') + \bar{F}_2(t,t') \tag{4.23}$$

where the δ-function term contains the *entire* singular behavior of $\bar{F}(t, t')$ at $t = t'$, and where $\bar{F}_2(t, t')$ is perfectly well behaved. The explicit expression for the regular term $\bar{F}_2(t, t')$ is also presented in the Appendix. A little consideration shows that when the square root factors in (4.22) and (4.23) are replaced by an appropriate constant, the δ-function term in (4.23) by itself satisfies the Parseval's theorem result of (4.6). It follows in this case that $\bar{F}_2(t, t')$ must vanish. It is this test which we have applied to our numerical integration scheme which computes $\bar{F}_2(t, t')$.

In solving the integral equation (4.13) for $\bar{g}(t)$, it is convenient to extract explicitly the singular part of the kernel in (4.23). From (4.13)-(4.15), and using the result in (4.23), we obtain

$$\bar{g}(t) = \psi(t) + \int_0^\infty dt'\left(\frac{\beta_t}{\beta_{t'}}\right)\frac{\bar{K}_2(t,t')\bar{g}(t')}{\beta_t + \sqrt{(k_0d)^2 - t^2}} \tag{4.24}$$

where

$$\psi(t) = \frac{-2\bar{F}(t)}{1 + \bar{F}_0}\,\frac{\beta_t}{[\beta_t + \sqrt{(k_0d)^2 - t^2}]} \tag{4.25}$$

and where

$$\bar{K}_2(t,t') = \frac{\bar{F}(t)\bar{F}(t')}{1 + \bar{F}_0} - \bar{F}_2(t,t') \tag{4.26}$$

is the part of the kernel which is regular at $t = t'$.

Having evaluated the functions $\bar{F}_0$, $\bar{F}(t)$, and $\bar{F}_2(t, t')$ numerically, we have solved the integral equation (4.24) on the IBM 370 computer. This was done by using the trapezoidal rule to approximate (4.24) by a large finite set of N inhomogeneous linear equations in N unknowns $\bar{g}(t_1)\cdots\bar{g}(t_N)$, and then solving by a standard scientific subroutine.

We have found that throughout much of the parameter space of interest for $Pb_{1-x}Sn_xTe$ heterostructure lasers, the complete solution of (4.24) is unnecessary. That is, for most cases of interest, the lowest approximation $\bar{g}(t) \simeq \psi(t)$ gives a sufficiently accurate approximation to the solution of the integral equation. Situations where this is not the case will be discussed in Section V, where we present the numerical results of our calculations.

V. Results

A. Power Coefficients

Fig. 2 shows the calculated results for the scattering coefficient S (the fraction of the incident power coupled into the waveguide radiation modes). The contours of constant S for variable normalized guiding region thicknesses k_0d, and for variable difference in dielectric constants $(n_1^2 - n_2^2)$ are shown with $n_1^2 = 45$, the typical value chosen for most of these calculations as discussed in Section II-B. Above the curve given by

$$k_0d\sqrt{n_1^2 - n_2^2} = \pi \tag{5.1}$$

the next higher order, even TE mode (TE_2) propagates and the theory does not apply. S increases monotonically with $(n_1^2 - n_2^2)$, but maxima occur as a function of k_0d. The maximum scattering at fixed $(n_1^2 - n_2^2)$ occurs very near the minimum effective width of the TE_0 mode, where the effective width W_{eff} is defined by

$$W_{\text{eff}} = 2(d + 1/\gamma_0). \tag{5.2}$$

The minimum of W_{eff} with respect to d at fixed $(n_1^2 - n_2^2)$ oc-

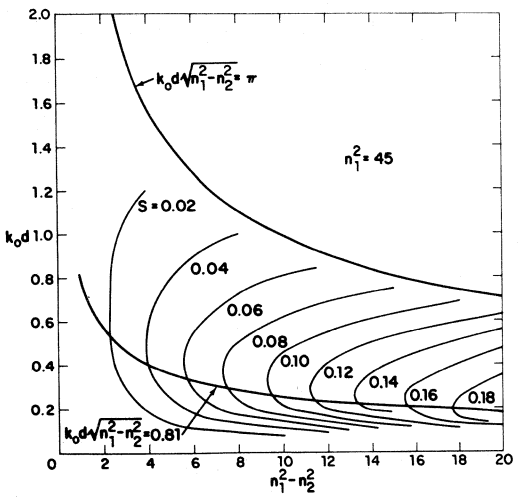


Fig. 2. Contours of constant S, the fraction of power incident on the mirror in the TE_0 mode which is coupled into the radiation modes of the laser waveguide, for variable normalized thickness of the guiding region k_0d and variable difference in relative dielectric constant $n_1^2 - n_2^2$. The dielectric constant of the guiding region is fixed, $n_1^2 = 45$. Above the curve labeled $k_0d\sqrt{n_1^2 - n_2^2} = \pi$, the TE_2 mode propagates and the theory does not apply. The curve labeled $k_0d\sqrt{n_1^2 - n_2^2} = 0.81$ is the locus of minimum effective width for the TE_0 mode given by (5.2).

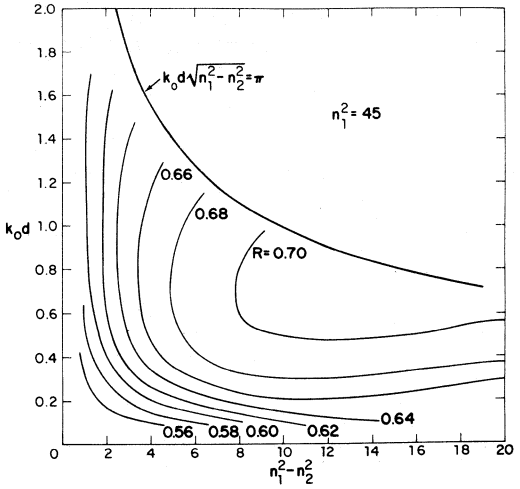


Fig. 3. Contours of constant power reflection coefficient R for variable normalized guide thickness k_0d and variable difference in dielectric constant $n_1^2 - n_2^2$ with $n_1^2 = 45$. Above the curve labeled $k_0d\sqrt{n_1^2 - n_2^2} = \pi$, the theory does not apply.

curs at approximately

$$(k_0d)_{\min}\sqrt{n_1^2 - n_2^2} \simeq 0.81. \tag{5.3}$$

For values of d less than the value determined by (5.3), W_{eff} increases because the exponential decay constant γ_0 decreases more rapidly than d. The locus of the minimum W_{eff} given by (5.3) is shown in Fig. 2.

As mentioned earlier, calculations were not done for values of $n_1^2 - n_2^2 > 20$. For larger values, the approximate solution of the integral equation neglecting the kernel [i.e., setting $\bar{g}(t) \simeq \psi(t)$ in (4.24)] is no longer accurate. At the same time, the numerical integrations over t needed to evaluate R and S [(4.16)-(4.17)] require values of $\bar{g}(t)$ for a higher density of points in t. As a result, the inversion of the $N \times N$ matrix to find $\bar{g}(t_n)$ rapidly becomes infeasible.

The calculated power reflection coefficients $R = |\mathcal{R}|^2$ are shown in Fig. 3, again for $n_1^2 = 45$. These curves have the same general appearance as those for the scattering coefficients. However, the maximum reflectivity as a function of k_0d is shifted to larger values of k_0d than those corresponding to the minimum effective mode width and the dependence of R on $n_1^2 - n_2^2$ is not entirely monotonic. Comparison of Figs. 2 and 3 suggests that these trends are due to the coupling to the waveguide radiation modes, i.e., the reflected power is decreased where the scattering is largest.

The maximum external efficiency, $\eta_{\text{ext}}(\max) = T/(T + S)$, is shown in a similar contour plot in Fig. 4. These results were calculated again for $n_1^2 = 45$, but are reasonably accurate for a broad range of this parameter. In Fig. 5, where $\eta_{\text{ext}}(\max)$ is plotted versus k_0d for $(n_1^2 - n_2^2) = 5$, 10, and 20, results are compared using $n_1^2 = 40$ and using $n_1^2 = 50$, which represents ±11-percent change from the value of 45 used in the previous figures. The variation found in $\eta_{\text{ext}}(\max)$ is less than ±3 per-

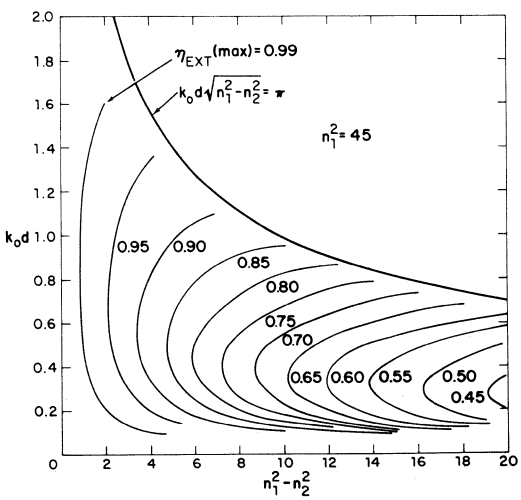


Fig. 4. Contours of constant η_{ext} (max) = $T/(T + S)$, the maximum incremental external quantum efficiency, for variable normalized guide thickness k_0d and variable difference in dielectric constant $n_1^2 - n_2^2$ with $n_1^2 = 45$. Above the curve labeled $k_0d\sqrt{n_1^2 - n_2^2} = \pi$, the theory does not apply.

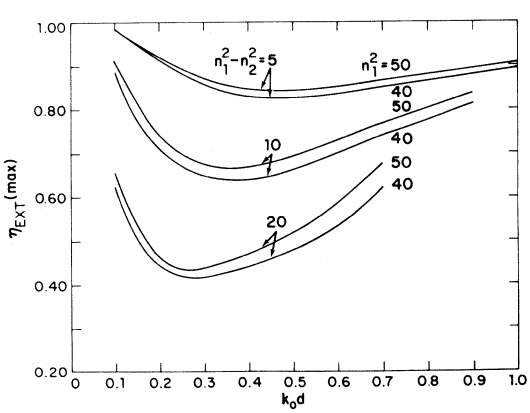


Fig. 5. The maximum external quantum efficiency η_{ext} (max) for $n_1^2 - n_2^2 = 5$, 10, and 20. Results calculated with $n_1^2 = 50$ and 40 differ from the results for $n_1^2 = 45$, used elsewhere, by less than ±3 percent.

cent. As n_1^2 is increased from 40 to 50, the reflectivity increases. However, the scattering decreases so that the net result is a small increase in $\eta_{ext}(\max)$. The decrease in the scattering as n_1^2 is made larger for fixed difference $(n_1^2 - n_2^2)$ can be understood in the limit n_1^2 approaching infinity. Here, the interface with free space becomes a perfect mirror and no scattering at all is needed to satisfy boundary conditions.

B. Field Patterns

Fig. 6 shows the field at the mirror using the complete expression (4.19) with $n_1^2 = 45$, $n_2^2 = 35$ and $k_0 d = 0.4$ compared to the field $E_0(x, 0)$ neglecting the radiation modes. Since neither absolute magnitude nor absolute phase has any physical significance, it is convenient to divide the field by the complex number $\sqrt{2\mu_0\omega}\,(1 + \mathcal{R})$ so that in the absence of the radiation modes the mirror field is entirely real. It can then be seen that the total field at the mirror has a large component in phase with the incident TE_0 mode and an out-of-phase component. In other words, the field due to the radiation modes has an x-dependent phase. It is interesting that the total "wave packet" at the mirror remains essentially as tightly confined as the incident mode and much smaller than the free-space wavelength. However, there are small but very slowly decaying oscillatory tails. Because the fields due to the radiation modes extend further in x than the incident mode, termination of the dielectric medium ϵ_2 by the diode contact and heat sink near the active layer, as discussed in Section II, may affect coupling to the radiation modes even more than initially might be expected. The long oscillatory tails are integrable since there is no singularity (nor even an indication of a peak) in the Fourier transform of the fields $a(\sigma)$ at $\sigma = 0$. The latter is shown in Fig. 7 plotted as $|a(k_0 \sin\theta)|^2$ versus θ for the same parameters used in Fig. 6. Again for comparison, the results obtained neglecting the radiation modes, $|a_0(k_0 \sin\theta)|^2$, are shown. The modulus squared of the Fourier transforms of the mirror fields represents the usual expression for the far-field pattern for small angles.

As we have shown, for large angles the correct expression includes the factor $\cos^2\theta$. The complete expression $|a(k_0 \sin\theta)|^2 \cos^2\theta$ is also plotted in Fig. 7. As can be seen, the inclusion of the radiation modes flattens or broadens the Fourier transform and increases the beam spread. It is interesting to note that the two components of the mirror field, Re $E(x, 0)$ and Im $E(x, 0)$, act as independent, noninterfering sources for the far-field pattern because of the dependence on the modulus squared of their Fourier transforms. The actual far-field pattern, however, is dominated by the $\cos^2\theta$ term, the half-width at half-power is approximately 0.68 rad $\simeq 39°$ neglecting mode coupling, and approximately 0.74 rad $\simeq 42°$ with the complete solution. Since the radiation modes broaden the far-field pattern but the maximum half-width is limited to 45° by the $\cos^2\theta$ term, it is clear that mode coupling at the mirror never influences strongly the far-field pattern.

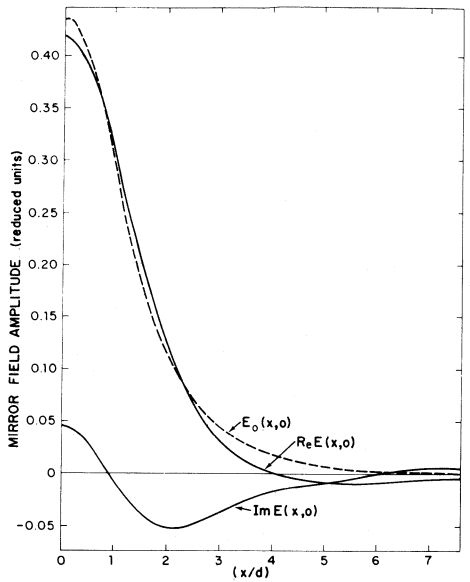


Fig. 6. Mirror electric field pattern $E(x, 0) = E(x, z = 0)$. The absolute amplitude and phase are arbitrary and plotted here is the expression given by (3.41) divided by the complex factor $[(1 + \mathcal{R})\,(2\mu_0\omega)^{1/2}]$. The dashed curve is the result obtained neglecting the radiation modes $E_0(x, 0)$. The parameters used are $k_0 d = 0.4$, $n_1^2 = 45$, and $n_2^2 = 35$.

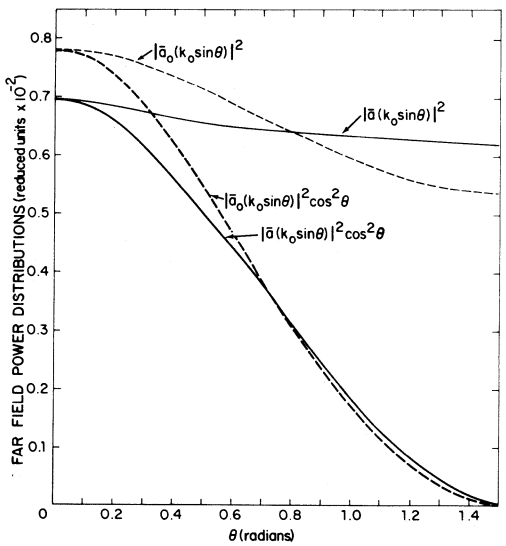


Fig. 7. Far-field power distributions. The quantity $\bar{a}(k_0 \sin\theta) = a(k_0 \sin\theta)k_0/[(1 + \mathcal{R})\,(2\mu_0\omega)^{1/2}]$, where $a(k_0 \sin\theta) = a(\sigma = k_0 \sin\theta)$, is defined by (3.28). The dashed curves are the results neglecting the radiation modes. The factor $\cos^2\theta$ dominates the far-field pattern even at quite small angles because of the extremely broad small-angle approximation $|\bar{a}(k_0 \sin\theta)|^2$. The parameters used are $k_0 d = 0.4$, $n_1^2 = 45$, and $n_2^2 = 35$.

VI. Summary

The analysis of the idealized symmetric structure presented here shows that mode conversion or scattering into the continuum of unguided radiation modes can be significant at the end mirrors of tightly confined $Pb_{1-x}Sn_xTe$ DH lasers. The most important consequence of the scattering is that it can limit the external quantum efficiency, thus reducing the output power and increasing internal heating of the device.

The analysis also shows that excitation of the radiation modes at the mirror does not in any way facilitate the output coupling. Mirror reflectivity remains large, and although a slight broadening of the mirror illumination occurs, the effect on the beam spread is a slight increase rather than a decrease.

As mentioned in Section II-A, the same physical parameters (the dielectric constant and its variation, and the wavelength compared to guide dimensions) which cause significant mode coupling at the mirror in the ideal model would also cause the

mode coupling to be sensitive to the asymmetries and irregularities of actual devices, which are often severe.

In conclusion then, the theory presented here indicates that close optical confinement in $Pb_{1-x}Sn_xTe$ DH lasers leads to potentially important limitations in external efficiency and output beam angle and may aggravate the problems associated with irregularities and assymetries at the mirror.

Optimization of devices may require use of the minimum dielectric discontinuity $(n_1^2 - n_2^2)$ compatible with carrier confinement. Multiheterostructure devices may also be desirable to achieve separate carrier and optical confinement.

Appendix

Here we show how to extract the singular portion of the function $\bar{F}(t, t')$ as given by (4.22). We need only concentrate on the last (integral) term in this expression which has the form

$$Q(t,t') = \int_0^\infty dy \sqrt{(k_0 d)^2 - y^2}\, \Pr \frac{t}{y^2 - t^2} \Pr \frac{t'}{y^2 - t'^2} S_y(t,t') \tag{A.1}$$

where $S_y(t, t')$ is symmetric in $t \rightleftarrows t'$ and is an *even* function of y. Explicitly, we have from (4.22)

$$S_y(t,t') = \frac{4}{\pi^2}(x^2 - t^2)^2 \frac{(y \sin y \cos x - x \sin x \cos y)}{y^2 - x^2} \cdot \frac{(y \sin y \cos x' - x' \sin x' \cos y)}{y^2 - x'^2}. \tag{A.2}$$

That this expression is actually symmetric in $t \rightleftarrows t'$ follows from $(x^2 - t^2)^2 = (x^2 - t^2)(x'^2 - t'^2)$, because of (4.7).

Since the integrand of (A.1) is an even function of y, we can replace $\int_0^\infty dy \to \frac{1}{2}\int_{-\infty}^\infty dy$, and also, we invoke the identity

$$\frac{1}{y^2 - t^2} = \frac{1}{2t}\left[\frac{1}{y - t} - \frac{1}{y + t}\right] \tag{A.3}$$

which gives

$$Q(t,t') = \frac{1}{4}\int_{-\infty}^\infty dy \sqrt{(k_0 d)^2 - y^2}\, \Pr\left[\frac{1}{y - t} - \frac{1}{y + t}\right] \cdot \Pr \frac{t'}{y^2 - t'^2} S_y(t,t'). \tag{A.4}$$

In the term involving $1/(y + t)$, we send $y \to -y$, use the fact that the rest of the integrand is an even function of y, and obtain

$$Q(t,t') = \frac{1}{2}\int_{-\infty}^\infty dy \sqrt{(k_0 d)^2 - y^2}\, \Pr \frac{1}{y - t} \cdot \Pr \frac{t'}{y^2 - t'^2} S_y(t,t'). \tag{A.5}$$

Again using

$$\frac{1}{y^2 - t'^2} = \frac{1}{2t'}\left[\frac{1}{y - t'} - \frac{1}{y + t'}\right]$$

we obtain

$$Q(t,t') = \frac{1}{4}\int_{-\infty}^\infty dy \sqrt{(k_0 d)^2 - y^2} S_y(t,t') \Pr \frac{1}{y - t} \cdot \Pr\left[\frac{1}{y - t'} - \frac{1}{y + t'}\right]. \tag{A.6}$$

In the product of the principal values, we make use of the identities

$$\lim_{0^+ \to 0} \frac{1}{x \mp i0^+} = \Pr \frac{1}{x} \pm i\pi\delta(x) \tag{A.7}$$

to write

$$\Pr \frac{1}{y - t} \Pr\left[\frac{1}{y - t'} - \frac{1}{y + t'}\right] = \mathrm{Re}\left[\frac{1}{y - t - i0^+}\frac{1}{y - t' - i0^+} - \frac{1}{y - t - i0^+}\frac{1}{y + t' - i0^+}\right] + \pi^2\delta(y - t)\delta(y - t') - \pi^2\delta(y - t)\delta(y + t'). \tag{A.8}$$

The last δ-function term in (A.8) can be dropped because t and t' are *both* positive. The other δ-function term can be written $\pi^2\delta(t - t')\delta(y - t)$. Inserting (A.8) into (A.6) then gives

$$Q(t,t') = \frac{\pi^2}{4}\sqrt{(k_0 d)^2 - t^2} S_t(t,t')\delta(t - t') + \frac{1}{4}\int_{-\infty}^\infty \cdot dy \sqrt{(k_0 d)^2 - y^2} S_y(t,t') \mathrm{Re}\left[\frac{1}{y - t - i0^+} \cdot \frac{1}{y - t' - i0^+} - \frac{1}{y - t - i0^+}\frac{1}{y + t' - i0^+}\right]. \tag{A.9}$$

From the above manipulations we have been able to extract a singular δ-function contribution. It remains to show that the second term of (A.9) is actually well behaved at $t = t'$. We begin by invoking the identities

$$\frac{1}{y - t - i0^+}\frac{1}{y - t' - i0^+} = \frac{1}{(t - t')}\left[\frac{1}{y - t - i0^+} - \frac{1}{y - t' - i0^+}\right] \tag{A.10}$$

$$\frac{1}{y - t - i0^+}\frac{1}{y + t' - i0^+} = \frac{1}{(t + t')}\left[\frac{1}{y - t - i0^+} - \frac{1}{y + t' - i0^+}\right]. \tag{A.11}$$

This gives

$$\mathrm{Re}\left[\frac{1}{y - t - i0^+}\frac{1}{y - t' - i0^+} - \frac{1}{y - t - i0^+}\frac{1}{y + t' - i0^+}\right] = \frac{1}{(t - t')}\mathrm{Re}\left[\frac{1}{y - t - i0^+} - \frac{1}{y - t' - i0^+}\right] - \frac{1}{(t + t')} \cdot \mathrm{Re}\left[\frac{1}{y - t - i0^+} - \frac{1}{y + t' - i0^+}\right] = \frac{1}{(t - t')} \cdot \left[\Pr \frac{1}{y - t} - \Pr \frac{1}{y - t'}\right] - \frac{1}{(t + t')}\left[\Pr \frac{1}{y - t} - \Pr \frac{1}{y + t'}\right] \tag{A.12}$$

where, in the last step, we have again used (A.7). We are going to insert (A.12) into (A.9) and integrate on y. In doing this we can send $y \to -y$ in the term Pr $(1/y + t')$ of (A.12), because the rest of the integrand is an even function of y. Hence, in effect, we can replace (A.12) by

$$\mathrm{Re}\left[\frac{1}{y-t-i0^+}\frac{1}{y-t'-i0^+}-\frac{1}{y-t-i0^+}\frac{1}{y+t'-i0^+}\right]$$
$$=\left[\frac{1}{(t-t')}-\frac{1}{(t+t')}\right]\mathrm{Pr}\frac{1}{y-t}-\left[\frac{1}{(t-t')}+\frac{1}{(t+t')}\right]$$
$$\cdot\,\mathrm{Pr}\frac{1}{y-t'}=\frac{2}{t^2-t'^2}\left[\mathrm{Pr}\frac{t'}{y-t}-\mathrm{Pr}\frac{t}{y-t'}\right]. \quad \text{(A.13)}$$

Inserting the above result into (A.9) yields

$$Q(t,t')=\frac{\pi^2}{4}\sqrt{(k_0d)^2-t^2}\,S_t(t,t')\delta(t-t')$$
$$+\frac{1}{2}\int_{-\infty}^{\infty}dy\sqrt{(k_0d)^2-y^2}\,S_y(t,t')\frac{1}{t^2-t'^2}$$
$$\cdot\left[\mathrm{Pr}\frac{t'}{y-t}-\mathrm{Pr}\frac{t}{y-t'}\right]. \quad \text{(A.14)}$$

Note that this expression is still symmetric in $t \rightleftarrows t'$.

It is evident that the second term in (A.14) is well behaved as long as $t \neq t'$. For $t' \to t$, one can easily verify that

$$\lim_{t'\to t}\frac{1}{t^2-t'^2}\left[\mathrm{Pr}\frac{t'}{y-t}-\mathrm{Pr}\frac{t}{y-t'}\right]=-\frac{1}{2t}\mathrm{Pr}\frac{1}{y-t}$$
$$-\frac{1}{2}\frac{\partial}{\partial y}\mathrm{Pr}\frac{1}{y-t}. \quad \text{(A.15)}$$

The first term in (A.15) causes no problems, and while the expression $(\partial/\partial y)$ Pr $1/(y - t)$ is a highly singular function, it is evident that one can use integration by parts to convert the contribution from this term to an expression of the form

$$\frac{1}{4}\int_{-\infty}^{\infty}dy\,\mathrm{Pr}\frac{1}{y-t}\frac{\partial}{\partial y}\{\sqrt{(k_0d)^2-y^2}\,S_y(t,t')\} \quad \text{(A.16)}$$

which is a well-defined (and finite) integral.

Now if we replace the last term in the curly brackets of (4.22) by $Q(t, t')$ as given by (A.14), (A.2), and combine the terms proportional to $\delta(t - t')$, we obtain (4.23), where the nonsingular part of $\bar{F}(t, t')$ may be written as

$$\bar{F}_2(t,t')=\left[\frac{1}{t^2\cos^2x+x^2\sin^2x}\frac{1}{t'^2\cos^2x'+x'^2\sin^2x'}\right]^{1/2}$$
$$\cdot\left\{\frac{2}{\pi}\frac{(x^2-t^2)}{t^2-t'^2}\left[t'\sqrt{(k_0d)^2-t^2}(t\cos x\cos t\right.\right.$$
$$+x\sin x\sin t)\frac{(t\sin t\cos x'-x'\sin x'\cos t)}{t^2-x'^2}$$
$$-t\sqrt{(k_0d)^2-t'^2}(t'\cos x'\cos t'+x'\sin x'\sin t')$$
$$\left.\cdot\frac{(t'\sin t'\cos x-x\sin x\cos t')}{t'^2-x^2}\right]+\frac{2}{\pi^2}(x^2-t^2)^2$$
$$\cdot\int_{-\infty}^{\infty}dy\sqrt{(k_0d)^2-y^2}\frac{1}{t^2-t'^2}\left[\mathrm{Pr}\frac{t'}{y-t}\right.$$
$$\left.-\mathrm{Pr}\frac{t}{y-t'}\right]\frac{(y\sin y\cos x-x\sin x\cos y)}{y^2-x^2}$$
$$\left.\cdot\frac{(y\sin y\cos x'-x'\sin x'\cos y)}{y^2-x'^2}\right\}. \quad \text{(A.17)}$$

Finally, as mentioned previously, if the square root factors in the curly brackets of (A.17) are replaced by a constant, then by Parseval's theorem $\bar{F}_2(t, t')$ must vanish. Our numerical integration scheme which computes $\bar{F}_2(t, t')$ was able to achieve this result to a high degree of accuracy, both for $t \neq t'$ and $t = t'$.

Acknowledgment

The authors wish to thank Dr. S. R. Chinn for suggesting the theoretical approach presented in this paper, and also for a careful reading of the final manuscript.

References

[1] J. N. Walpole, A. R. Calawa, R. W. Ralston, T. C. Harman, and J. P. McVittie, "Single Heterojunction $Pb_{1-x}Sn_xTe$ Diode Lasers," *Appl. Phys. Lett.*, *23*, 620–622, (1973).

[2] T. R. Tomasetta and C. G. Fonstad, "Liquid Phase Epitaxial Growth of Laser Heterostructures in $Pb_{1-x}Sn_xTe$," *Appl. Phys. Lett.*, *24*, 567–570, (1974).

[3] S. H. Groves, K. W. Nill, and A. J. Strauss, "Double Heterostructure $Pb_{1-x}Sn_xTe$-PbTe Lasers with CW Operation at 77 K," *Appl. Phys. Lett.*, *25*, 331–333, (1974).

[4] R. W. Ralston, J. N. Walpole, T. C. Harman, and I. Melngailis, "Double Heterostructure $Pb_{1-x}Sn_xTe$ Waveguides at 10.6 μm," *Appl. Phys. Lett.*, *26*, 64–66, (1975).

[5] J. T. Boyd, "Totally Internally Reflecting Thin-Film Optical Cavities," *Appl. Opt.*, *11*, 2635–2638, (1972).

[6] T. Ikegami, "Reflectivity of Mode at Facet and Oscillation Mode in Double-Heterostructure Injection Lasers," *IEEE J. Quantum Electronics*, *QE-8*, 470–476, (1972).

[7] J. K. Butler and J. Zoroofchi, "Radiation Fields of GaAs-(AlGa)As Injection Lasers," *IEEE J. Quantum Electronics*, *QE-10*, 809–815, (1974).

[8] J. McKenna, "The Excitation of Planar Dielectric Waveguides at p-n Junctions, I," *Bell Systems Tech. J.*, *XLVI*, 1491–1526, (1967).

[9] W. O. Schlosser, "Gain-Induced Modes in Planar Structures," *Bell Systems Tech. J.*, *52*, 887–905, (1973).

[10] F. R. Nash, "Mode Guidance Parallel to the Junction Plane of Double-Heterostructure GaAs Laers," *J. Appl. Phys.*, *44*, 4696–4707, (1973).

[11] J. N. Walpole, A. R. Calawa, R. W. Ralston, and T. C. Harman, "High-power Output in $Pb_{1-x}Sn_xTe$ Diode Lasers with Improved Mirror Quality," *J. Appl. Phys.*, *44*, 2905–2907, (1973).

[12] J. N. Zemel, J. D. Jensen, and R. B. Schoolar, "Electrical and Optical Properties of Epitaxial Films of PbS, PbSe, PbTe and SnTe," *Phys. Rev.*, *140*, A330–A342, (1965).

[13] G. Dionne and J. C. Woolley, "Optical Properties of Some $Pb_{1-x}Sn_xTe$ Alloys Determined from Infrared Plasma Reflectivity Measurements," *Phys. Rev.*, *B6*, 3898–3913, (1972).

[14] J. R. Lowney, "Band-Inversion Studies in $Pb_{1-x}Sn_xTe$," M.I.T. Ph.D. dissertation (unpublished), 1975. This author finds a stronger dependence of the optical dielectric constant on alloy composition x than do the authors of [13]. The discrepancy is attributed to the neglect by the former authors of a complete allowance for dispersion. The upper estimates given here for n_1^2 are based on Lowney's results.

[15] P. Asbeck, "Optical and Minority Carrier Confinement in PbSe Homojunction Lasers," M.I.T. Ph.D. dissertation, 1974 (unpublished).

[16] W. H. Weber and K. F. Yeung, "Waveguide and Luminescent Properties of Thin-Film Pb-Salt Injection Lasers," *J. Appl. Phys.*,

44, 4991-5000, (1973).
[17] J. R. Biard, W. N. Carr, and B. S. Reed, "Analysis of a GaAs Laser," *Trans. Met. Soc. AIME*, *230*, 286-290, (1964).
[18] D. Marcuse, *Light Transmission Optics*. (Van Nostrand Reinhold Co., New York, 1972), Chapter 8.
[19] H. Jeffreys, *Asymptotic Approximations*. (Oxford Press, London, 1962), Chapter 2.
[20] W. Heitler, *The Quantum Theory of Radiation*, Third Edition. (Oxford Press, London, 1954), pp. 66-71.
[21] L. Lewin, "A Method for the Calculation of the Radiation-Pattern and Mode-Conversion Properties of a Solid-State Heterojunction Laser," *IEEE Trans. Microwave Theory and Techniques*, *MTT-23*, 576-585, (1975).[5]
[22] F. K. Reinhart, I. Hayashi, and M. B. Panish, "Mode Reflectivity and Waveguide Properties of Double-Heterostructure Injection Lasers," *J. Appl. Phys.*, *42*, 4466-4479, (1971).

[5] References [21] and [22], which were pointed out to us by referees, also deal with the general theoretical problem considered here.

Second-Harmonic Generation in $KB_5O_8 \cdot 4H_2O$ from 217.1 to 315.0 nm

HARRY J. DEWEY

Abstract—**Second-harmonic generation (SHG) has been observed in $KB_5O_8 \cdot 4H_2O$ (KB5) between 217.1 and 315.0 nm by angle tuning in a single crystal using a single cut. A conversion efficiency of 9.2 percent was observed for type I noncritical phase matching at 217.1 nm for a peak power of 15 kW at 434.2 nm. The nonlinear coefficients d_{31} and d_{32} are estimated to be approximately 1.1×10^{-10} ESU (4.0×10^{-25} m/V) and 0.08×10^{-10} ESU (0.29×10^{-25} m/V), respectively.**

Introduction

RECENT demonstration of second-harmonic generation (SHG) at wavelengths as short as 217.3 nm using crystalline potassium pentaborate tetrahydrate [1] ($KB_5O_8 \cdot 4H_2O$ or KB5, for brevity) has opened up an important region of the spectrum around 220 nm where numerous molecules absorb. Interest in this laboratory concerning excitation of the $^1B_2$ state of SO_2 and the 1*s*-2*s* transition in hydrogen [2] has led to an investigation of the properties of KB5, which is the subject of this paper.

Although two possible orientations for type I SHG have been discussed previously [1], no experimental data concerning one of these orientations, namely the one which uses a fundamental beam propagating in the *ab* plane, have been reported. The present report concentrates on this orientation.

Experimental

KB5 crystallizes as an orthorhombic crystal of class mm2 having lattice parameters $a = 1.1065$ nm, $b = 1.1171$ nm, and $c = 0.9054$ nm [3]. The crystalline material is relatively soft [3] (2.5 mho) so that considerable care needs to be taken in polishing the faces. The crystals were polished on a lap which was moistened with ethanol. The lap was made of beeswax in which 0.05 μ levigated alumina had been suspended. The problem of slow deterioration of the polished surfaces under normal atmospheric conditions has been noted previously [1] and is probably due to the loss of water of hydration.

The dye-laser oscillator used in these studies was constructed according to the design of Hänsch [4]. The output coupler was a wedged quartz flat, the beam expander provided an expansion of 20X, and the grating was 316-grooves/mm echelle grating used in high order near the blaze angle of 64°. About 25 percent of the output from a Molectron UV-1000 1-MW nitrogen laser was used to pump the oscillator. The remainder of the output was used to pump an amplifier. The amplifier was positioned about 25 cm from the output coupler of the oscillator. This configuration provided increased efficiency from the doubling crystal compared with using only an oscillator operating at comparable power levels. This increase in efficiency is presumably due to elimination of some of the off-axis modes of this system which do not illuminate the active region of the dye in the amplifier. The temporal characteristics of the amplified pulses were examined using a silicon photodiode having a rise time of 0.5 ns. The pulse durations depended on the particular dye being used, ranging from 2.4 to 4.8 ns. The pulse durations for the doubled light were shorter than the corresponding fundamental pulses in accordance with their expected dependence on the square of the fundamental power. The amplified pulses were found to be 85-90 percent linearly polarized, as was observed by spatially resolving the two components using a calcite crystal and measuring the average power in each beam. The bandwidth of the dye laser was measured interferometrically and was found to range from 0.01 to 0.025 nm. A system of two lenses, each of 17-cm focal length, was used to focus the dye-laser output into the doubling crystal. These lenses were positioned to produce a beam hav-

Manuscript received November 4, 1975; revised December 15, 1975. This work was supported in part by the Measures for Air and Water Quality Program, National Bureau of Standards. The mention of brand name equipment does not constitute an endorsement by NBS nor does it imply that such equipment is either the only or the best available equipment for these applications.

The author was with the Optical Physics Division, National Bureau of Standards, Washington, DC 20234. He is now with the Department of Chemistry, University of Utah, Salt Lake City, UT 84112.

ing a confocal parameter of approximately 1 cm (assuming a Gaussian beam). This appeared to optimize second-harmonic operation in accordance with theory [5].

Four crystals of KB5, 8–10 mm in length and having different orientations, were used. All were cut from a single sample which was purchased from Cleveland Crystals, Inc. Crystals were oriented using X-ray techniques to an accuracy of about 1°. One crystal was cut so that its face normal was 20° from the *b* axis in the *ab* plane, the second was cut with its face normal 65.5° from the *b* axis in the *ab* plane, the third crystal was cut with its face normal parallel to the *c* axis, and the fourth crystal was cut with its face normal 27° from the *b* axis in the *bc* plane. These will be referred to as crystals I, II, III, and IV, respectively.

The fundamental and second-harmonic beams emerging from the crystal were collimated by a 15-cm-focal-length quartz lens and separated with a 33° quartz prism. The average power in the second-harmonic and fundamental beams was measured using an electrically calibrated pyroelectric detector [6] whose output was measured with an Ithaco dynatrac 391 lock-in amplifier. This detector allowed the detection of average power levels as low as 0.5 μW with a signal-to-noise ratio of approximately 2. At higher power levels (≥0.5 mW average power), where a calibrated thermopile could be used, measurements with the two devices were in excellent agreement. No attempt was made to correct the measured powers for reflections and scattering from the various optical elements.

Results and Discussion

The tuning curve for critical phase matching with propagation in the *ab* plane is shown in Fig. 1. Crystal I was used to obtain these results. Phase-matched SHG was observed from 217.1 to 315.0 nm in a single crystal for internal angles (measured from the *b* axis) of 0 to 59°, respectively. At the long wavelength limit, corresponding to an internal angle of about 39° from the face normal, internal reflection of the second-harmonic light, which is polarized parallel to the crystal face, becomes significant. Since the wave surfaces for the incident fundamental radiation in this configuration are elliptical in the *ab* plane, the internal angles were calculated from the measured external angles using the appropriate Huygen's constructions. External angles from −31.4 to +60.0° from the face normal were used to obtain the range of internal angles shown in Fig. 1. The uncertainties in the internal angles range from ±0.1° near the *b* axis to about ±1° at the largest internal angles. The increase in uncertainty with increasing angle is due to the uncertainties in alignment of the *c* axis with the axis of rotation. Using published values of the refractive indices n_a and n_b in the visible region [1] and the phase-matching angles shown in Fig. 1, values of n_c from 217.1 to 300.0 nm were calculated from the phase-matching condition

$$n_c(2\omega) = \left(\frac{\cos^2\phi}{n_a^2(\omega)} + \frac{\sin^2\phi}{n_b^2(\omega)}\right)^{-1/2}. \quad (1)$$

The results of these calculations are shown in Fig. 2.

Fig. 3 shows the tuning curve for propagation in the *bc* plane. Crystals III and IV were used to obtain this curve. Phase-matched SHG was observed between 217.1 and 239.8 nm. The

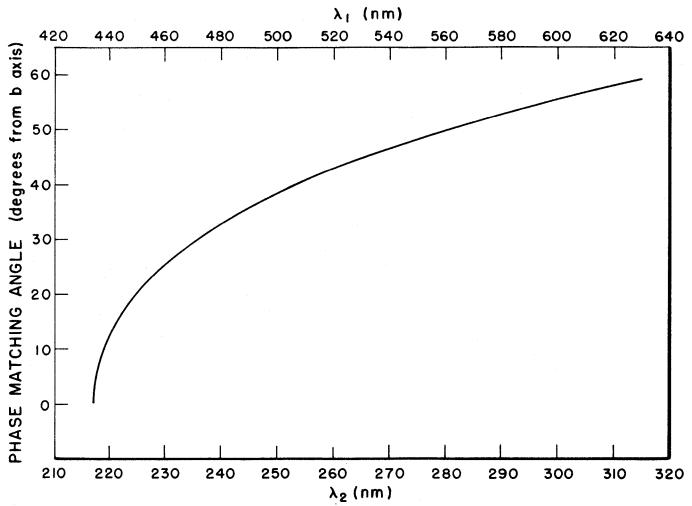


Fig. 1. Tuning curve for critical phase-matched SHG in KB5 with the fundamental beam propagating in the *ab* plane, polarized in the *ab* plane.

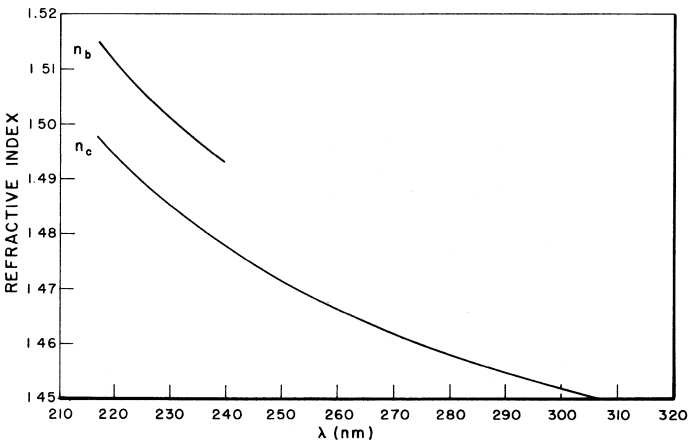


Fig. 2. Refractive indices n_b and n_c for KB5 in the UV calculated from n_a and n_b in the visible and the phase-matching angles shown in Figs. 1 and 3.

c and *b* axes were located optically in crystals III and IV, respectively, as a check on the X-ray crystallographic orientation. In crystal IV, an elliptical cone of angles about the *b* axis was found for which phase-matched SHG at one particular wavelength was observed. In crystal III, symmetric points in the *bc* plane were found on either side of the *c* axis for each wavelength near 239.8 nm for which SHG was observed. In an analogous fashion, the *bc* plane in each crystal was optically located. SHG is not observed along the *c* axis since d_{21} is equal to zero in a class mm2 orthorhombic crystal [7]. Internal angles were calculated from the measured external angles using Snell's law and published values of $n_a(\omega)$. Values of n_b between 217.1 and 239.8 nm were calculated from the phase-matching condition

$$n_b(2\omega) = \left(\frac{1}{n_a^2(\omega)} - \frac{\cos^2\phi}{n_c^2(2\omega)}\right)^{-1/2} \sin\phi. \quad (2)$$

Boyd and Kleinman [5] have derived an expression for the second-harmonic power P_2 obtainable from a Gaussian funda-

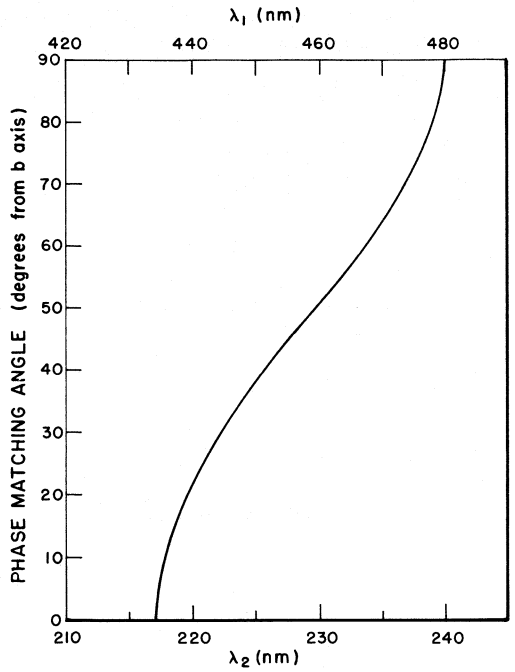


Fig. 3. Tuning curve for critical phase-matched SHG in KB5 with the fundamental beam propagating in the *bc* plane, polarized along the *a* axis.

mental beam for the case in which both focusing and phase matching are optimized. For a fundamental power P_1 at wavelength λ in a crystal of length l, assuming no absorption in the crystal, the second-harmonic power may be written as

$$P_2 = \frac{1024\Pi^5 d^2 P_1^2 l h_{mm}(B)}{c n_1 n_2 \lambda^3} \tag{3}$$

where c is the speed of light, n_1 and n_2 are the refractive indices at the fundamental and second-harmonic frequencies, respectively, d is the effective nonlinear coefficient for SHG, and $h_{mm}(B)$ is a parameter which takes into account losses due to double refraction. The double-refraction parameter B is given by

$$B = \rho\left(\frac{\Pi n_1 l}{2\lambda_1}\right)^{1/2} \tag{4}$$

where ρ is the double-refraction angle. For a fundamental beam propagating in the *ab* plane of KB5 at an angle ϕ from the *b* axis, polarized in the *ab* plane, the double-refraction angle is given by

$$\rho = \tan^{-1}\left(\frac{n_a(\omega)\{n_a^2(\omega) - n_c^2(2\omega)\cos^2\phi\}^{1/2}}{n_b(\omega) n_c(2\omega)\cos\phi}\right) - \phi \tag{5}$$

and the effective nonlinear coefficient is given by

$$d = d_{31}\cos^2\phi + d_{32}\sin^2\phi. \tag{6}$$

For propagation in the *ab* plane, then, (3) may be rewritten in the form

$$\left[\frac{c n_1 n_2 \lambda^3 P_2}{1024\Pi^5 P_1^2 h_{mm}(B)}\right]^{1/2} \cos^{-2}\phi = d_{31} + d_{32}\tan^2\phi. \tag{7}$$

P_1 and P_2 were evaluated by measuring pulse energies and durations at various phase-matching angles while values of $h_{mm}(B)$ were taken from Boyd and Kleinman [5]. Crystal I was used for shorter wavelengths and crystal II was used for longer wavelengths. The results of a least squares fit of the data to (7) is shown in Fig. 4 where the percent conversion efficiency, $100P_2/P_1$, is shown as a function of second-harmonic wavelength from 217.1 to 300.0 nm, for a crystal length of 8 mm. The efficiencies were normalized to a peak power of 15 kW which corresponds to the highest power used for noncritical phase-matched SHG at 217.1 nm. In this case a conversion efficiency of 9.2 percent was observed and the efficiency was proportional to the fundamental peak power for peak powers between 15 and 2.5 kW. The conversion efficiencies at 295 nm were also found to be proportional to the fundamental peak powers up to the highest peak powers used in this study of 33 kW. The least squares fit of the data to (7) yielded values for d_{31} and d_{32} of 1.09×10^{-10} ESU (4.01×10^{-25} m/V) and 0.08×10^{-10} ESU (0.29×10^{-25} m/V), respectively. The least squares fit yielded a standard deviation for both quantities of 0.08×10^{-10} ESU (0.29×10^{-25} m/V). These values yield a ratio d_{32}/d_{31} which is in substantial disagreement with estimates [1] based on Miller's rule [8]. Deviations from (3) have been observed in the frequency doubling of a nitrogen laser pumped dye laser [9]. These deviations were ascribed to the lack of stable, well-defined modes in the dye-laser output. The extent to which this problem has been corrected by using an oscillator-amplifier configuration for the dye laser is not known. However, an independent investigation using nonphase-matched SHG at 200 nm in both ADP and KB5 gave results indicating that d_{31} in KB5 is about 1/10 d_{36} in ADP [10]. This estimate is in fairly close agreement with the results of the present investigation and would seem to indicate that mode quality can be consider-

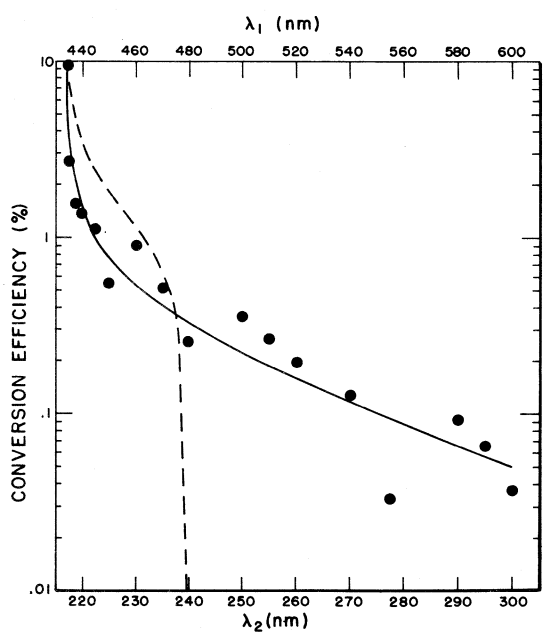


Fig. 4. Conversion efficiencies for critically phase-matched SHG in KB5 for a crystal 8 mm long normalized to a fundamental peak power of 15 kW. —— a least squares fit to (7) of data obtained for propagation in the *ab* plane. ---- efficiencies predicted from (3) and (9) for propagation in the *bc* plane.

ably improved by using an amplifier stage following the dye-laser oscillator.

The broken line in Fig. 4 is the efficiency predicted from (3), with $d_{31} = 1.09 \times 10^{-10}$ ESU (4.01×10^{-25} m/V) for angle tuning with the fundamental beam propagating in the *bc* plane at an angle ϕ from the *b* axis and polarized along the *a* axis. In this case, the double-refraction angle is given by

$$\rho = \tan^{-1}\left(\frac{n_c(2\omega)\{n_c^2(2\omega) - n_a^2(\omega)\cos^2\phi\}^{1/2}}{n_b(2\omega)n_a(\omega)\cos\phi}\right) - \phi \qquad (8)$$

and the effective nonlinear coefficient is given by

$$d = d_{31}\cos\phi. \qquad (9)$$

The significantly higher conversion efficiencies in this configuration for second-harmonic wavelengths between 218 and 230 nm result from smaller double-refraction angles which vary between 1 and 11 mrad. For the other orientation, in which the light propagates in the *ab* plane, the double-refraction angles vary from 8 to 280 mrad over the same wavelength range. This, in turn, is due to the relatively large differences between $n_a(\omega)$ and $n_b(\omega)$ compared to the differences between $n_b(2\omega)$ and $n_c(2\omega)$.

Temperature tuning may be used to obtain phase matching at wavelengths shorter than 217.1 nm. However, the tuning range available by this method appears to be very small. By cooling the crystal from 22.5 to 4.5°C, a shift of only 0.46 nm was observed near the noncritical phase-matching orientation. Cooling to lower temperatures was not attempted for fear of cracking the crystal.

Conclusions

In summary, the tuning curves for type I phase-matched SHG in KB5 for propagation in either the *ab* or *bc* planes are reported. These curves were used to calculate the refractive indices n_b and n_c in the UV. The conversion efficiencies were measured for the case of propagation in the *ab* plane and were then used to obtain estimates of the nonlinear coefficients, d_{31} and d_{32}. These results lead to the prediction that conversion efficiencies will be as high, if not higher, in the case of propagation in the *bc* plane, compared with efficiencies when propagation is in the *ab* plane over the spectral range from 217.1 to 230.0 nm due to large differences in the double-refraction angles for these two orientations.

Acknowledgment

The author would like to thank R. D. Deslattes for initiating this project and for his continuing interest and encouragement in this work, J. C. Geist for the use of the pyroelectric detector, E. Farabaugh for orienting the crystal, and G. G. Luther for many helpful discussions.

References

[1] C. F. Dewey, Jr., W. R. Cook, Jr., R. T. Hodgson, and J. J Wynne, "Frequency doubling in $KB_5O_8 \cdot 4H_2O$ and $NH_4B_5O_8 \cdot 4H_2O$ to 217.3 nm," *Appl. Phys. Lett.*, vol. 26, pp. 714–716, June 1975.

[2] a) E. V. Baklanov and V. P. Chebotaev, "On the precise measurement of the frequency transition 1*s*–2*s* of the hydrogen atom," *Opt. Commun.*, vol. 12, pp. 312–314, Nov. 1974.
b) T. W. Hänsch, S. A. Lee, R. Wallenstein, and C. Wieman, "Doppler-free two-photon spectroscopy of hydrogen 1*s*–2*s*," *Phys. Rev. Lett.*, vol. 34, pp. 307–309, Feb. 1975.

[3] W. R. Cook and H. Jaffe, "The crystallographic, elastic, and piezoelectric properties of ammonium pentaborate and potassium pentaborate," *Acta Crystallogr.*, vol. 10, pp. 705–707, 1957.

[4] T. W. Hänsch, "Repetitively pulsed tunable dye laser for high resolution spectroscopy," *Appl. Opt.*, vol. 11, pp. 895–898, Apr. 1972.

[5] G. D. Boyd and D. A. Kleinman, "Parametric interaction of focused Gaussian light beams," *J. Appl. Phys.*, vol. 39, pp. 3597–3639, July 1968.

[6] J. Geist, H. Dewey, and M. A. Lind, to be published.

[7] F. Zernike and J. E. Midwinter, *Applied Nonlinear Optics*. New York: Wiley, 1973, p. 37.

[8] R. C. Miller, "Optical second harmonic generation in piezoelectric crystals," *Appl. Phys. Lett.*, vol. 5, pp. 17–19, July 1964.

[9] F. B. Dunning, E. D. Stokes, and R. F. Stebbings, "The efficient generation of coherent radiation continuously tunable from 2500 Å to 3250 Å," *Opt. Commun.*, vol. 6, pp. 63–66, Sept. 1972.

[10] J. J. Wynne, private communication.

Correspondence

Electrooptic Phase Modulation in CdS Optical Waveguides

J. A. McMURRAY AND C. R. STANLEY

Abstract—**Thin polycrystalline films of CdS have been successfully adapted into a multilayer configuration to form the basis of low-electrical-drive-power optical phase modulators.**

An experimental structure with a guide thickness of 1.4 μm, buffer thicknesses of 0.45 μm and an electrode area of 10 × 0.5 mm^2 requires 11.2 mW · MHz^{-1} drive power for a phase change of 1 rad.

I. Introduction

Electrooptic waveguide modulators employing various materials such as $LiNbO_3$ [1], GaAs [2], and Cd(S,Se) [3] have all been demonstrated. These modulators rely, in the majority of cases, on the electrooptic effect in the waveguiding film. However, some modulators have utilized the interaction of the evanescent field of a guided mode with an electrooptic substrate to provide the requisite phase change. Single crystal substrates are required for all these modulators.

The electrooptic phase modulator to be described here has the advantage that it is a completely evaporated system and does not depend on epitaxial growth on to a single crystal substrate. The modulator is based on a CdS waveguiding region and exploits the fact that the evaporated films of CdS grow with a high degree of *c*-axis orientation perpendicular to the plane of the film. A multilayer configuration is employed, as illustrated schematically in Fig. 1, making use of the r_{13} linear electrooptic coefficient of CdS. Buffer layers of SiO are essential to isolate the guiding film from the metal electrodes and hence eliminate additional propagation losses. Further, the band edge of CdS at ~520 nm precludes the use of visible radiation, and consequently all experiments reported in this correspondence were carried out with infrared sources, either a 1.15-μm He–Ne laser or a 900-nm GaAs laser.

II. Theory of Operation

Single crystal CdS is a hexagonal material with 6-mm symmetry. The refractive index changes resulting from the application of an electric field parallel to the *c* axis are

$$\Delta n_{1,2} = \Delta n_0 = -\tfrac{1}{2} r_{13} n_0^3 E_3$$
$$\Delta n_3 = \Delta n_e = -\tfrac{1}{2} r_{33} n_e^3 E_3 \qquad (1)$$

where the subscripts 1, 2, 3 relate to the orthogonal x, y, z axes of Fig. 1 with z parallel to the crystallographic *c* axis. The TE waveguide modes propagate in the x direction with their E-field polarized in the y direction and will therefore experience a refractive index change associated with r_{13}. Since the refractive index changes in the x and y directions are the same, the crystallographic orientation in the x-y plane is of no consequence for a useful electrooptic effect. This point is particularly relevant in view of the polycrystalline nature of CdS films on amorphous substrates.

The equation relating phase change to refractive index change is obtained by differentiation of the transcendental equation for a five-layer waveguide structure in which the refractive indices and propagation constant are considered complex. This yields an expression of the form

$$d\beta' = \mathrm{Re}\,[F(W, d, \beta)] \cdot dn$$
$$= -\tfrac{1}{2} r n^3 E \cdot \mathrm{Re}\,[F(W, d, \beta)] \qquad (2)$$

where $F(W, d, \beta)$ is a function of film thickness, buffer thickness, and propagation constant β ($\beta = \beta' + j\beta''$).

The electric field of (2) must be correlated with the voltage applied between the metal electrodes, V_{TOT}, by treating the various layers as individual capacitors, all connected in series. The phase change $\Delta\varphi$ in terms of the voltage driving the modulator is then given by

$$\Delta\varphi = -\frac{\tfrac{1}{2} r n^3 \,\mathrm{Re}\,[F(W, d, \beta)]\; V_{TOT} \epsilon_1'^2}{(2d\epsilon_1'\epsilon_2' + W\epsilon_1'^2)} \qquad (3)$$

where ϵ_1' and ϵ_2' are real parts of the complex dielectric constants of the buffer and guiding films, respectively.

In a practical modulator structure, buffer layer thickness cannot be reduced indefinitely to take advantage of the concomitant increase in $\Delta\varphi$. The effects of increasing attenuation rate must also be considered. A compromise is therefore reached between a useful value of $\Delta\varphi$ and an acceptable, additional attenuation resulting from the presence of the metal electrodes. A series of constant attenuation rate and phase change contours are therefore drawn on axes of buffer layer thickness versus guide thickness. The contours for the Al–SiO–CdS–SiO–Al structure are shown in Fig. 2 and are similar to those presented by Chang and Loh [4] for two 10.6-μm modulator structures based on single-crystal GaAs films. It is important to emphasize that the attenuation rate contours represent the additional attenuation introduced by the Al metal electrodes and do not include the inherent losses of the waveguide, i.e., scatter and absorption losses.

The modulator design is optimized by minimizing a figure of merit, the power-per-unit bandwidth P, where

$$P = \pi C_m V_{TOT}^2 \qquad (4)$$

and C_m is the modulator capacitance. A reduction in voltage is therefore more effective in minimizing P than a reduction in C_m. This is equivalent to maximizing the phase change $\Delta\varphi$ of Fig. 2. An acceptable additional loss figure, say 1 dB · cm^{-1}, is chosen and the corresponding guide and buffer

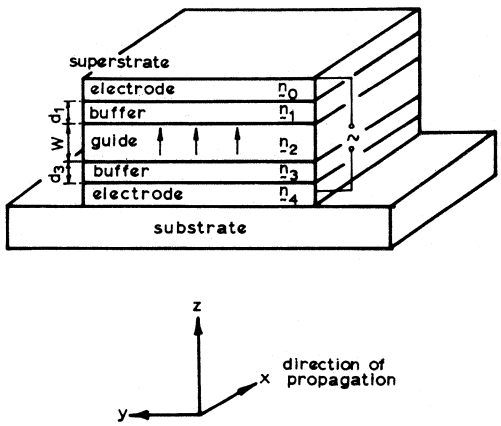


Fig. 1. Schematic diagram of the multilayer electrooptic phase modulator structure.

Manuscript received July 28, 1975; revised January 26, 1976. This work was supported by a grant from the Science Research Council.

The authors are with the Department of Electronics and Electrical Engineering, University of Glasgow, Glasgow, G12 8QQ, Scotland.

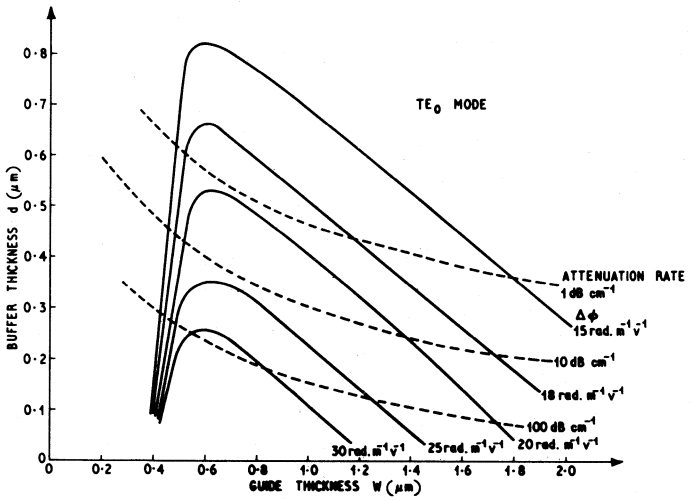


Fig. 2. Constant phase change and attenuation rate contours plotted on axes of buffer thickness versus guide thickness for the Al-SiO-CdS-SiO-Al system.

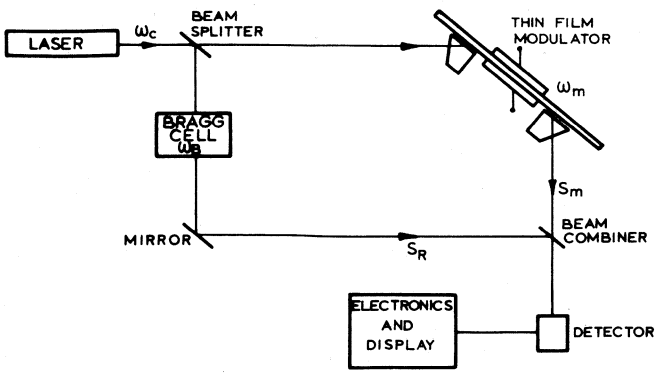


Fig. 3. Schematic diagram of optical modulator and heterodyne detection system used for studying phase change and frequency response. The Bragg cell is removed for homodyne detection.

layer thicknesses for maximum $\Delta\varphi$ are noted; the values taken from Fig. 2 are $\Delta\varphi_{max} = 19.5$ rad $\cdot$ m^{-1} $\cdot$ V^{-1} for $W = 0.65$ μm and $d = 0.55$ μm. When the mode is unbounded in the lateral direction, the minimum permissible electrode width inclusive of a safety factor [5] $s = 6$ is $\sim$500 μm. For an electrode length of 10 mm, the total capacitance of the modulator equals 122 pF and the maximum base bandwidth with a 50-Ω load is 50 MHz. The theoretical power-per-unit bandwidth figure for a 1.15-μm TE_0 guided mode and 1-rad phase change is 10.0 mW $\cdot$ MHz^{-1}.

III. Device Preparation

The aluminum electrodes and silicon monoxide buffer layers were evaporated in a conventional diffusion-pumped coating unit while the CdS films were grown by electron beam evaporation in an ion-pump CHV system capable of 10^{-9} torr. The successive layers were deposited through straight-edged masks. The top electrode pattern with electrodes of differing widths was defined in photoresist and the aluminum electrodes formed by using the "lift-off" technique. Silicon monoxide was chosen for its thermal compatibility to CdS and acceptable dielectric constant. A high dielectric constant is of advantage in minimizing P by increasing the proportion of the total applied voltage appearing across the waveguide.

The cadmium sulphide was previously grown [6] from Eagle Picher grade A single crystal starting material, with the substrate temperature heated to 100°C for films of apparent optimum stoichiometry. These films were on fused silica and glass slides and had a minimum observed loss of 5 dB $\cdot$ cm^{-1} for the TE_0 mode at 1.15 μm. Subsequently a different source material, polycrystalline B.D.H. Optran grade CdS, has been investigated. It has shown equally good results on glass substrates but with the substrate temperature for minimum loss much higher at 260°C. Lower temperatures tended to yield a dark film indicating an excess of cadmium while at temperatures in excess of 260°C the films became milky in appearance suggesting an excess of sulphur. These changes in film composition were reflected in a number of recorded parameters; namely the resistivity, band edge, and photoconductivity.

The films are subject to two loss mechanisms; free carrier absorption, and scattering from both grain boundaries and an amorphous region adjacent to the substrate. The latter scattering mechanism dominates in the thinner films. The theoretical minimum power-per-unit bandwidth predictions in Section II must therefore be reconsidered because the basic film loss is not tolerable at film thicknesses much less than 1 μm.

The phase measurements were made in the interferometer illustrated in Fig. 3; both homodyne and heterodyne detection were employed as means of determining the electrooptically induced phase changes.

IV. Experimental Results

Several modulators were constructed with various guide and buffer layer thicknesses in order to verify experimentally the predictions of the curves in Fig. 2. Table I lists the results obtained from 6 modulators and includes for comparison the theoretically calculated performances. Sample curves of applied voltage versus frequency for modulator C are shown in Fig. 4. The guide thicknesses and the refractive index contrast between CdS and SiO were such that no modulation enhancement effects [7] occurred.

As expected from loss measurements on basic CdS waveguides, modulators with guide thicknesses of <1 μm showed unacceptably high propagation losses. A new optimum design must therefore be sought in which the scatter and absorption losses of the CdS are taken into account. This is achieved by following the 0.5 dB $\cdot$ cm^{-1} additional loss contour of Fig. 2 until a guide thickness is reached for which the contribution to loss from the amorphous film region is not dominant. The corresponding value of $\Delta\varphi$ represents the maximum attainable in a *realistic* modulator, i.e., a modulator in which the total losses including guide and electrode losses are acceptable. A guide thickness of 1.4 μm and buffer layer thicknesses of 0.45 μm give a phase change of 0.16 rad $\cdot$ V^{-1} for an electrode length of 10 mm. The associated modulator capacitance and power per unit bandwidth are 94 pF and 11.2 mW $\cdot$ MHz^{-1}, respectively. The maximum base bandwidth into a 50-Ω load is 68 MHz. The results obtained from a modulator made to this design are given in Table II. Again, agreement between theory and experiment is good. The structures have tolerated 150 V without breakdown.

Frequency response measurements on the phase modulators have shown the expected RC cutoff at high frequencies. However, at frequencies <1 MHz an unanticipated rolloff occurred. This is attributed to dielectric relaxation in the CdS and SiO which is illustrated in the ϵ' versus frequency plots of Fig. 4. It is evident that the low-frequency (<1 MHz) rolloff of the phase modulators is largely due to the increasing dielectric constant of the CdS guide. The electrical loss associated with dielectric relaxation, tan δ, does not appear to be significant.

V. Conclusions

The phase modulation properties of Al-SiO-CdS-SiO-Al waveguiding structures have been analyzed both theoretically and experimentally. Experimental observations have been adequately explained assuming the r_{13} electrooptic coefficient of the polycrystalline CdS films is equal to the value for bulk single crystals. The important feature of the modulators de-

TABLE I
COMPARISON BETWEEN THEORETICAL CALCULATIONS AND EXPERIMENTAL RESULTS FOR SIX MULTILAYER ELECTROOPTIC PHASE MODULATORS

Modulator	Guide Thickness (μm)	Buffer Thickness (μm)	Electrode Area (mm^2)	Theoretical Power per Unit Bandwidth (mW MHz^{-1})	Experimental Power per Unit Bandwidth (mW MHz^{-1})	Theoretical Cut-Off Frequency with 600Ω Load (MHz)	Experimental Cut-Off Frequency with 600Ω Load (MHz)
A	1.45	0.4	5.0 x 5.0	226.5	230.0	1.1	1.4
			5.0 x 2.0	90.6	90.0	2.2	2.1
			5.0 x 1.0	45.3	45.7	5.5	5.2
B	1.0	0.6	5.0 x 5.0	227.5	225.0	1.09	1.2
			5.0 x 1.0	45.5	46.0	5.45	5.3
C	1.5	0.5	5.0 x 5.0	276.0	270.0	1.2	1.6
			5.0 x 2.0	110.4	105.0	3.0	4.0
			5.0 x 1.0	55.2	55.0	6.0	6.5
			5.0 x 0.5	27.6	27.0	12.0	13.0
D	1.1	0.4	5.0 x 5.0	194.0	205.0	0.94	1.2
			5.0 x 2.0	77.6	85.0	2.35	2.4
			5.0 x 1.0	38.8	39.5	4.7	5.0
E	1.05	0.5	5.0 x 5.0	200.0	215.0	1.01	0.95
			5.0 x 2.0	80.0	81.0	2.02	2.2
			5.0 x 1.0	40.0	45.0	5.05	5.4
F	1.5	0.95	5.0 x 5.0	339.0	340.0	1.7	2.0
			5.0 x 2.0	135.6	125.0	4.2	4.0
			5.0 x 1.0	67.8	70.0	8.4	8.5
			5.0 x 0.5	33.9	34.0	16.8	17.0

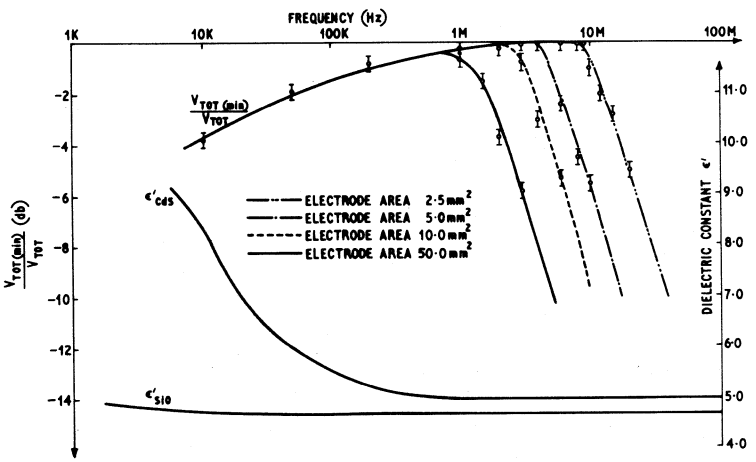


Fig. 4. Frequency response plot for modulator *C*, W = 1.5 μm and d = 0.5 μm, and dielectric constant versus frequency for thin films of CdS and SiO showing dielectric relaxation effects.

TABLE II
COMPARISON BETWEEN THEORETICAL AND EXPERIMENTAL FIGURES FOR AN OPTIMIZED AL–SIO–CDS–SIO–AL STRUCTURE IN WHICH BUFFER AND GUIDE THICKNESSES HAVE BEEN SELECTED TO CONTAIN ADDITIONAL PROPAGATION LOSS TO 0.5 DB · CM^{-1}

Guide Thickness (μm)	Buffer Thickness (μm)	Electrode Area (mm^2)	Theoretical Power per Unit Bandwidth (mW MHz^{-1})	Experimental Power per Unit Bandwidth (mW MHz^{-1})	Theoretical Cut-Off Frequency with 600Ω Load (MHz)	Experimental Cut-Off Frequency with 600Ω Load (MHz)
1.4	0.45	10.0 x 5.0	112.0	115.0	0.56	0.6
		10.0 x 2.0	44.8	45.0	1.41	1.6
		10.0 x 1.0	22.4	22.5	2.83	3.0
		10.0 x 0.5	11.2	11.5	5.65	6.0

scribed in this paper is that all films are vacuum evaporated onto an amorphous substrates. Unlike most other modulators, epitaxial growth onto single crystal substrates is not required in order to achieve the desired electrooptic effect.

The measured performance figures for a diffraction-limited device with no lateral confinement suggest that a 2-*D* guide modulator assembly requiring less than 450 μW · MHz^{-1} drive power (1-rad phase change) is feasible with a guide width of ~20 μm. The base bandwidth of the proposed modulator would be 1.7 GHz with a 50-Ω drive-source impedance.

ACKNOWLEDGMENT

The authors are indebted to R. H. Hutchins for capable technical assistance at various stages of the work. The Bragg cell was designed by R. M. De La Rue and C. D. Wilkinson, and the photolithography masks were produced by G. Boyle.

REFERENCES

[1] I. P. Kaminow, V. Ramaswamy, R. V. Schmidt, and E. H. Turner, "Lithium niobate ridge waveguide modulator," *Applied Physics Letters*, vol. 24, pp. 622-624, June 1974.
[2] D. Hall, A. Yariv, and E. Garmire, "Optical guiding and Electro-optic modulation in GaAs epitaxial layers," *Optics Communications*, vol. 1, pp. 404-405, Apr. 1970.
[3] W. E. Martin, "Waveguide electro-optic modulation in II-VI compounds," *Journal of Applied Physics*, vol. 44, pp. 3703-3707, Aug. 1973.
[4] W. S. C. Chang and K. W. Loh, "Theoretical design of guided wave structure for electro-optical modulation at 10.6 μm, *IEEE Journal of Quantum Electronics*, vol. 8, pp. 463-470, June 1972.
[5] I. P. Kaminow and E. H. Turner, "Electro-optic light modulators," *Proceedings of the IEEE*, vol. 54, pp. 1374-1390, Oct. 1966.
[6] C. R. Stanley, W. Duncan, and J. A. McMurray, "Infrared waveguides in thin films of CdS," *Applied Physics Letters*, vol. 24, pp. 380-382, Apr. 1974.
[7] J. F. Lotspeich, "Modulation-sensitivity enhancement in electro-optic slab waveguides," *Journal of the Optical Society of America*, vol. 65, pp. 797-803, July 1975.

A Calibrated, Knife-Edge Attenuator for Optimization of the Output Mirror Transmission of TEM_{00} Lasers

T. F. JOHNSTON, JR.

Abstract—**A simple optical attenuator consisting of a mirrored edge of a glass prism inserted into the intracavity beam of a TEM_{00} mode laser may be used to measure directly the optimum output mirror transmission, the output power at optimum transmission, and the small-signal gain of the laser.**

The problem of determining the output transmission, t_{opt} which maximizes the output power from a laser is often encountered [1]. It is possible to compute t_{opt} if the optical gain and losses of the system are known by an equation derived from a gain-saturation treatment of the laser output [2]. However, in many cases the gain is not known, and for lasers operating with an applied magnetic field or isotopic splitting of the laser transition, the applicable form of gain saturation may be uncertain. An experimental method for determining t_{opt} is then of value, and for this, a Brewster plate inserted in the laser cavity and rotated slightly off Brewster's angle [3]-[5] is commonly employed. The Brewster plate suffers from the three problems [4]-[6] of interference of the multiply reflected, overlapping beams (if the plate is too thin), the parallel displacement of the beam across the opposite cavity mirror with rotation of the plate, and a sensitivity of the fraction of the laser power coupled out of the cavity to any slight ellipticity of the beam polarization. An appartus as simple as the Brewster plate but with none of these difficulties when used with a TEM_{00}-mode beam is shown in Fig. 1(a). In our experiment, lowest order mode operation was ensured by choosing a resonator geometry having a high ratio [7] of TEM_{10}- to TEM_{00}-mode diffraction loss, with the bore as the limiting aperture.

Manuscript received November 21, 1975.

The author was with Hughes Electron Dynamics Division, Torrance, CA. He is now with Coherent Radiation, Palo Alto, CA 94304.

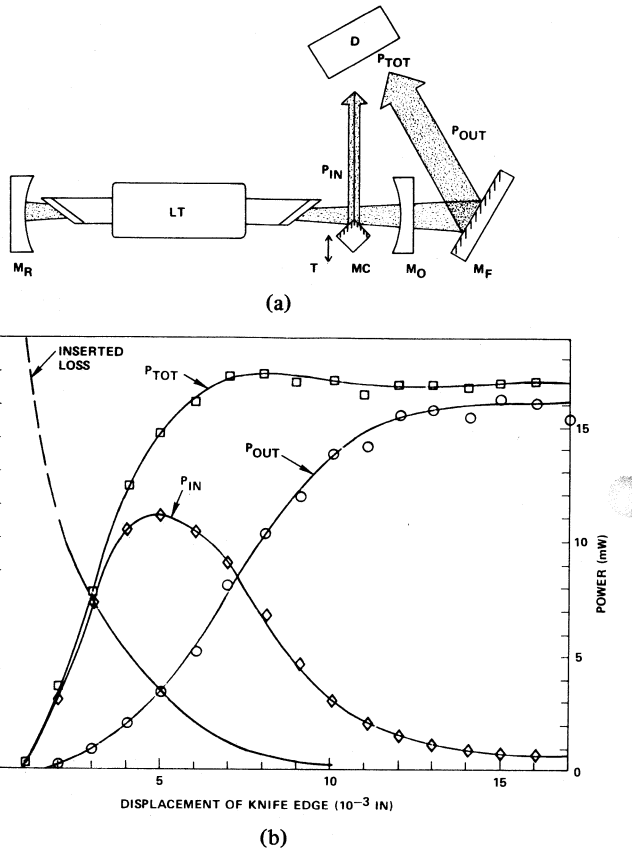


Fig. 1. Apparatus for the optimum mirror transmission measurement and an example of the resulting data. (a) M_R, maximum reflector; LT, laser tube; T, translation stage; MC, mirrored glass cube (knife-edge); M_O, output mirror of known transmission; M_F, folding mirror; D, laser power detector. (b) Plots of the measured powers as a function of the distance of insertion of the mirrored edge. P_{IN}, power coupled out of the cavity by the inserted loss; P_{OUT}, the ordinary laser output; P_{TOT}, the sum of these powers. The inserted loss is calculated from a ratio of measured powers.

A small glass prism or cube[1] that has been mirrored on the two faces meeting at a sharp 90° edge is inserted into the laser cavity by means of a micrometer-driven translation-stage. The part of the beam occluded by this knife-edge is reflected out of the cavity as the beam of power level P_{IN}, the fraction of intracavity power coupled out by the inserted loss. The amount of loss L (for a given edge position d read on the micrometer) represented by the beam P_{IN} is calibrated by comparison with the output power P_{OUT} transmitted through the output mirror of known transmission t. That is, for small inserted loss and output transmission

$$L = \frac{P_{IN}}{P_{OUT}} t \tag{1}$$

since both the knife-edge and output mirror sample have nearly the same level of intracavity power. [If the folding mirror M_F of Fig. 1(a) is coated with the same mirror material as the knife-edge and both are used at about the same angle of incidence, no correction for mirror reflectivity to either P_{IN} or P_{OUT} need be made in computing L from (1).]

To determine the optimum mirror transmission, the three power levels P_{IN}, P_{OUT}, and their sum P_{TOT} (measured by alternately blocking the beams incident on the detector D) are plotted as a function of insertion distance as in Fig. 1(b).

[1]The cube used here was from the Edmund Scientific Co., Barrington, NJ, part no. 3305.

The combination of the edge MC plus output mirror M_O acts as a variable-transmission end reflector, with the optimized output being that at the maximum of the total power curve [this occurs at 8×10^{-3}-in displacement in Fig. 1(b)]. The optimum mirror transmission is the sum of t and the inserted loss at that point

$$t_{opt} = \left(1 + \frac{P_{IN}}{P_{OUT}}\bigg|_{opt\ d}\right) t. \tag{2}$$

For Fig. 1(b), $t = 0.70$ percent and thus $t_{opt} = 1.16$ percent.

In performing the measurement an output mirror should be used which undercouples the resonator, since for an overcoupling transmission, *adding* inserted loss cannot maximize the output, and the P_{TOT} curve will then rise steadily without going through a maximum [a P_{TOT} curve taken with an overcoupled t will look like the P_{OUT} curve in Fig. 1(b)]. The output power at optimum transmission is just the maximum P_{TOT}, divided by the reflectivity of the mirrors MC, M_F. The data of Fig. 1(b) are for a 0.12-cm bore diameter by 40-cm active length 442-nm He-Cd laser, for which the mean reflectivity of our aluminum mirror coatings at 45° incidence was $R = 0.84$, yielding an optimized output for this tube of 20.7 mW.

The small-signal gain is determined by adding the inserted loss required to put the laser at threshold (which occurs in Fig. 1(b) for $d = 1 \times 10^{-3}$ in) to the other known losses in the cavity. Since both P_{IN} and P_{OUT} go to zero as threshold is approached, (1) becomes indeterminate and it is desirable to extrapolate L from above-threshold data according to the expected theoretical form to fix the threshold loss (dashed line in Fig. 1(b), and see (3) below). For the data of the figure the tube gain is calculated as 7.2 percent/pass as shown in Table I.

Note that any means of variable coupling of the intracavity power (with a Brewster plate or otherwise) can give a value of t_{opt} when calibrated by comparison with a known mirror transmission. The advantage of the present method is in producing no beamshift, no polarization change, and (for an initial TEM_{00}-mode and moderate insertion distances) no mode change so that the coupling function is known and a reliable extrapolation may be done to get the small-signal gain. The knife-edge attenuates by diffracting light out of the laser cavity mode and by occultation. The diffracted component may be estimated from Fresnel diffraction theory, with the result that if the space between the tube and output mirror (where the edge is inserted) is no more than about 10 cm long, then the ray direction of the main diffraction maximum is at an angle of less than 1/5 mrad from the beam axis. This is less than the typical divergence angle of a laser cavity mode, so the diffracted light stays in the mode (experimentally the large angle diffracted part of the P_{IN} beam is observed to be very slight), and the primary means of edge attenuation is by occultation.

The theoretical form of the inserted loss due to occultation is the same as twice the transmission past a half-plane of a lowest order Gaussian beam of $1/e^2$-intensity radius w. (The factor of 2 arises because the edge picks off light from the traveling waves going in both directions inside the cavity so (1) represents the double-pass loss.) Thus

$$L(y) = 2\,T(y) = \left[1 - 2\sqrt{\frac{2}{\pi}}\int_0^y \exp(-2v^2)\,dv\right]. \tag{3}$$

Here $y = (d - d_0)/w$ is the separation of the knife-edge from the beam axis, measured in beam radii.

The integral in (3) is evaluated in terms of the tabulated error function. By (3), insertions approaching to within $w/\sqrt{2}$ of the axis give single pass losses up to 8 percent, which is adequate to reach the threshold of oscillation of most lasers. Edge insertions up to this distance are "moderate," as experimentally they are found to produce little distortion of the transverse intensity distribution.

TABLE I
SMALL-SIGNAL GAIN CALCULATION

Threshold inserted loss (2 passes) from Fig. 1(b)		13 ± 2%
Inserted loss, per pass		6.5 ± 1 percent
Diffraction loss [7] per pass		0.2 percent
Absorption and scatter loss per pass		0.1 percent
Brewster window reflection per pass		0.06 percent
Mean mirror transmission		0.35 percent
Small signal gain/pass	(total)	7.2 ± 1 percent

In summary, the knife-edge attenuator described here has these advantages.

1) Simple and inexpensive construction of all-reflective optics useful from the UV to the IR is possible.

2) No beam shift or polarization change results from attenuation.

3) Only a short (≃1-cm) insertion length is required and the device can go in at any orientation with respect to the beam polarization or tube Brewster windows.

4) The picked-off beam P_{IN} is clean enough to serve as the laser output in noncritical applications like cutting with a focused CO_2 beam.

The disadvantages of the device are that it only works with a TEM_{00}-mode beam (the edge forces mode changes in higher order mode lasers), the picked-off beam contains a small diffracted component, and for a tube gain estimate an extrapolation is required.

REFERENCES

[1] P. Laures, "Variation of the 6328 Å Gas Laser Output Power with Mirror Transmission," *Physics Letters*, 10, pp. 61–62, 15 May 1964.

[2] W. W. Rigrod, "Gain Saturation and Output Power of Optical Masers," *J. Applied Physics*, 34, pp. 2602–2609, September 1963.

[3] T. M. Sporton, "Optical Transmission Through Windows Set Near the Brewster Angle," *Journal of Scientific Inst.*, 44, pp. 720–724, 1967.

[4] H. P. Brandli, "Method of Measuring Small Optical Losses Using a HeNe Laser," *Rev. Sci. Inst.*, 39, pp. 583–587, April 1968.

[5] R. Dandliker, "Eigenstates of Polarization in Optical Resonators with Partial Polarizers," *JOSA*, 58, pp. 1062–1069, August 1968.

[6] B. S. Patel, S. Charan, A. Mallik, and P. Swarup, "Determination of He-Ne Laser Parameters Using An Intra-cavity Rotatable Reflector," *J. Phys. D. (Applied Physics)*, 7, pp. L40–L44, 1974.

[7] T. Li, "Diffraction Loss and Selection of Modes in Maser Resonators with Circular Mirrors," *Bell System Tech. Journal*, 44, pp. 917–932, May–June, 1975.

A 100-W-Average-Power Flashlamp-Pumped Dye Laser

W. W. MOREY AND W. H. GLENN

Abstract—**Average dye laser output powers greater than 100 W have been demonstrated at pulse repetition frequencies (PRF) up to 350 Hz. The dye flow was transverse to the laser axis and was pumped by a vortex-stabilized flashlamp in an elliptical reflector. Indications are that considerably more average power is attainable.**

Manuscript received November 24, 1975. This work was supported in part by ARPA and monitored by ONR.

The authors are with United Technologies Research Center, East Hartford, CT 06108.

Flashlamp-pumped dye lasers that produce average powers in the 5–10-W range have been reported [1], [2]. We recently reported an axial-flow dye laser (dye flow along the laser axis) that produced 42 W of average power at a pulse repetition frequency (PRF) of 100 Hz [3]. For efficient operation the axial-flow laser was limited to a PRF of 65 Hz. At PRF's above 65 Hz the laser pulse intensity fell off, and a maximum in the laser output occurred around 100 Hz. The limiting feature of the axial-flow laser was the maximum rate at which dye solution could be replaced in the active region. The maximum replacement rate occurred at a flow of 12 m/s, and a faster flow speed caused cavitation and release of bubbles [4].

We have since developed a transverse flow laser that has given 114-W output at a PRF of 250 Hz. A key element in the high-power dye laser is a vortex-stabilized flashlamp. This flashlamp is an extensively modified version of one reported earlier [5]. A rotary spark gap was used to discharge a low-inductance 2-μF capacitor into the flashlamp [6]. A continuous glow-type discharge of a few milliamperes was maintained in the flashlamp. The flashlamp was placed at the focus of an elliptical reflector. The ellipse was cut at the opposite focus along the latus rectum, in a plane perpendicular to the major axis. A tapered channel, butted up against the reflector, guided a sheet of flowing dye solution through the focus of the elliptical reflector. In addition, a water lens was placed in front of the dye channel to help collect and focus the pump light into the dye solution. The flow channel was 3 mm thick and 11 cm long; 1.9 cm of channel height was exposed to the pump light. The transverse flow laser had an electrical efficiency of 0.23 percent compared to 0.4 percent for the axial-flow laser. The loss in efficiency, which is inherent in the transverse flow design, is more than compensated by the improvement in the dye replacement in the active region. For the maximum flow of 2.5 l/s, the replacement rate of dye in the active region is 390 s^{-1}.

Fig. 1 shows the average laser power measured at different PRF's with a concentration of 2.5×10^{-4} M of rhodamine 6G (pilot 559). A high-reflectivity flat mirror and a 50-percent flat output coupler spaced 13 cm apart formed the laser resonator. The discharge energy per pulse was 211 J. We measured an average laser power of 26.1 W at 53 Hz with a CRL model 201 power meter calibrated at ± 5-percent accuracy. For PRF's greater than 100 Hz the rotary spark gap would, on occasion, draw a continuous arc that overloaded the power supply. To avoid the overloads, the laser was run for only about a second at the higher input powers. Since longer running times are required for a measurement with the CRL power meter, we recorded the laser pulse intensity with a photodiode and oscilloscope. A few hundred overlaying traces of the flashlamp and laser intensity are shown in Fig. 2. Using the area under the pulse traces and the PRF, we calculated the average power for the higher PRF's. The error bars in Fig. 1 represent the estimated measurement accuracy from the pulse intensity traces.

In Fig. 1 we see that the average laser power was linear with increasing PRF up to 150 Hz. Above 150 Hz the laser power fell slightly from linearity, reached a maximum at 250 Hz, and saturated at a lower power level for PRF's up to 350 Hz. The dye solution replacement rate for these measurements was 330 s^{-1}.

At PRF's above 150 Hz we found that the flashlamp intensity, and, correspondingly, the laser intensity would fall to a steady-state value after the first 4 or 5 pulses. We believe that the flashlamp intensity fell because of a preheating of the incoming argon that flows through the flashlamp and drives the vortex (see [4]). The preheated gas is less dense, and consequently, the light output is reduced. This effect is particularly severe if the flashlamp gas flow is reduced. For the results in Fig. 1 the gas flow was 9.8 l/s (STP). If the flow was reduced to 5 l/s, for example, the laser pulse intensity dropped to a steady-state value of about one-half of the initial value for a 200-Hz PRF.

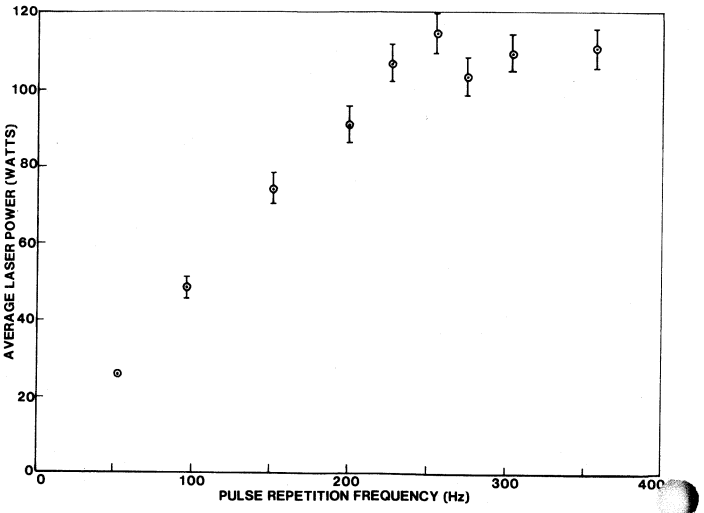
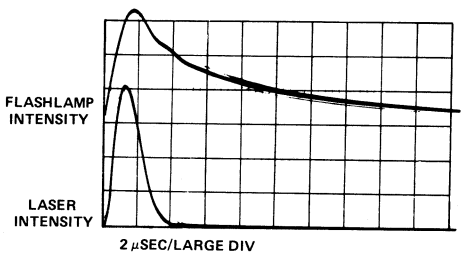
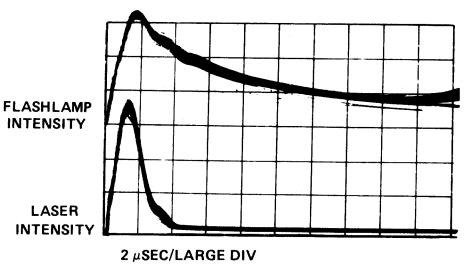


Fig. 1. Dye laser average output power for different pulse repetition frequencies.



(a)



(b)

Fig. 2. Laser and flashlamp pulses: (a) at 52-Hz PRF, 0.47 J/pulse; (b) at 249-Hz PRF.

Optical distortion in the dye solution from the absorption of flashlamp light causes the laser beam to deflect away from the flashlamp side of the channel. As a consequence, optimum alignment of the laser mirrors occurred when they were tilted approximately 10 mrad towards the flashlamp axis. In Fig. 2 we see that the laser pulse was terminated before the flashlamp intensity had fallen to one-half of its peak value. The dye solution was oxygen equilibrated so that the triplet state was sufficiently quenched to allow long-pulse operation [7]. Optical distortion from the flashlamp, then, is probably the major factor in the early pulse termination.

The average power of the transverse-flow laser is currently limited by the flashlamp gas flow and the dye solution replacement rate. In addition, the elliptical reflector was made by hand polishing aluminum and was measured to be only 68-percent specular reflecting. We estimate that with an increased flashlamp gas flow, a narrower channel to increase the dye replacement rate, and a well-polished and coated reflector output powers greater than 150 W could be attained. More interestingly, however, Burlamacchi and Pratesi have shown that a waveguide configuration for a dye laser can give efficiencies up

to 1.7 percent [8]. This geometry takes advantage of the flashlamp-induced distortion and reflection from the walls to contain the laser light to the high-gain region of the dye cell. We estimate that well over 500-W output could be achieved with the waveguide design if the dye solution could be replaced as rapidly as in the present system.

ACKNOWLEDGMENT

The authors would like to acknowledge valuable discussions with C. M. Ferrar and the technical assistance of R. Preisach, A. Wilson, and J. Ryan.

REFERENCES

[1] J. Jethwa and F. P. Schafer, "A reliable high average power dye laser," *Appl. Phys.*, vol. 4, pp. 229-302, 1974.
[2] H. W. Friedman and R. G. Morton, "Transverse flow flashlamp pumped dye laser," presented at the *1975 IEEE/OSA Conf. Laser Engineering and Applications*, May 1975, Paper 1.7.
[3] W. H. Glenn, W. W. Morey, and C. M. Ferrar, "High power dye lasers," presented at the *1975 IEEE/OSA Conf. Laser Engineering and Applications*, May 1975, Paper 1.10.
[4] S. G. Varnado, "Degradation in long pulse dye laser emission under fast flow conditions," *J. Appl. Phys.*, vol. 44, pp. 5067-5068, 1973.
[5] M. E. Mack, "Vortex stabilized flashlamps for dye laser pumping," *Appl. Opt.*, vol. 13, pp. 46-55, 1974.
[6] C. M. Ferrar, "Rotary spark gap switching for high power dye lasers," *Appl. Opt.*, vol. 13, pp. 1998-1999, 1974.
[7] F. P. Schafer, Ed., *Dye Lasers*. New York: Springer, 1973, pp. 54-66.
[8] P. Burlamacchi and R. Pratesi, "High efficiency coaxial waveguide dye laser with internal excitation," *Appl. Phys. Lett.*, vol. 23, p. 475, 1973.

Correction to "Analysis of Curved Optical Waveguides by Conformal Transformation"

MORDEHAI HEIBLUM AND JAY H. HARRIS

In the above paper,[1] at the bottom of the left-hand column of page 79, the proper expression for the transformed index in the case of a diffused guide should be

$$n(u) = n_1 \exp u/R_2 + (n_2 - n_1) \exp\left[-\frac{\zeta}{R_2}(\rho - R_2) + u/R_2\right]$$

and the initial slope is $-b/R_2$ (the minus sign had been omitted in two occasions on page 79, once at the bottom of the left-hand column and once at the top of the right-hand column). Equation (29) on page 80 should be replaced by the following equation:

$$n(u_5) = n_1 \frac{1+b}{b}[b(n_2/n_1 - 1)]^{1/(b+1)}$$

$$[n(u_5)\partial^2 n(u_5)/\partial u^2]^2 = R_2 b^{-1/2}. \quad (29)$$

In Table I, in the column headed $\exp(2ih_{4+,6-})$, k_1 should be replaced by k_2 for the single-boundary case, and by k_3 for the two-boundary case.

An important point should be mentioned about the accuracy of the closed-form expressions for bends with radii close to R_{min}. At this region the approximation introduced by (A12) is not good any more and the attenuation constant has to be found by solving (A9) numerically with $D_{1,6} = 0$. As a result of this inaccuracy, the expressions (26) and (27) for R_{min} are only approximate, but the order is correct. More exact numerical calculations will be presented elsewhere.

Manuscript received December 10, 1975.

M. Heiblum is with the Department of Electrical Engineering and Computer Science, University of California, Berkeley, CA 94720.
J. H. Harris is with the National Science Foundation, Washington, DC.

[1] H. Heiblum and J. H. Harris, *IEEE J. Quantum Electron.*, vol. QE-11, pp. 75-83, Feb. 1975.

Discharge-Heated Lead Vapor Laser

R. S. ANDERSON, B. G. BRICKS, T. W. KARRAS, AND L. W. SPRINGER

***Abstract*—Operation of a discharge-heated lead vapor laser with emission at 4062 and 4057 Å is reported. In contrast to previous reports, the output was obtained at 4057 Å using a relatively slowly rising discharge pulse.**

INTRODUCTION

An interest in the development of high-efficiency lasers which operate in the visible portion of the spectrum has existed for some time. One of the most significant areas of investigation has centered on those elements in which lasing can be achieved between a resonant and a metastable level of the atom, because such transitions inherently offer a high quantum efficiency [1].

Lasers which operate on this principle have been demonstrated with several different elements (e.g., Cu, Mn, Pb, Tl, Au). Laser oscillation in the PbI (Fig. 1) system was first observed on the high-gain 7229-Å transition in an oven-heated apparatus [2]. Subsequently, also in an oven, lasing was achieved on the 4057-, 4062-, and 3639-Å lines using a more sophisticated pulse-discharge method [3]. In particular, a fast-rise time current pulse was found to be essential for producing an inversion on these lines because the lifetimes of the upper levels are quite short.

More recently, the discharge-heated technique, which has been developed into a useful form for the copper vapor laser [4]-[7] has been applied to lead, and the 7229-Å line has been observed [5], [8]. Here we report the development of a discharge-heated lead vapor laser and an investigation of the lasing conditions of the near-UV lines (4057 and 4062 Å).

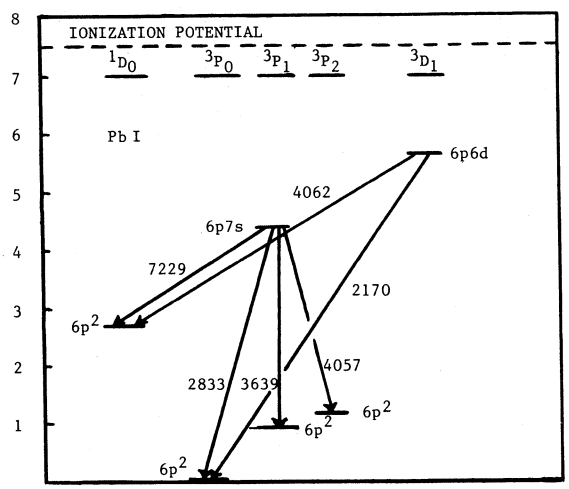


Fig. 1. Energy level diagram of the lead atom showing the laser transitions and the resonance transitions from the ground state to the upper laser states.

Manuscript received December 12, 1975. This work was supported in part by General Electric I.R. & D. and in part by the Lawrence Livermore Laboratory under Contract P09093105.

The authors are with the Space Sciences Laboratory, Space Division, General Electric Company, Philadelphia, PA 19101.

Experimental Techniques

The discharge-heated lead vapor laser was similar in design to the one developed for copper vapor as the active medium [5]. The alumina discharge tube was supported in the vacuum chamber by coaxial, cylindrical tantalum electrodes at each end. The electrodes were 32 cm apart, and the inside diameter of the tube was 7.9 mm. However, the bore of the tube was restricted by alumina inserts having an inside diameter of 3.9 mm. Four of these spacers, each 4.4 cm in length, were positioned with pieces of lead between them such that the overall length of the small bore region was 20 cm.

The discharge tube and electrodes were surrounded by a single radiation shield which was a larger diameter alumina tube. Only minimal radiation shielding was required because a sufficient lead vapor pressure can be achieved with temperatures in the range of 800–1000°C where radiative losses are small. This is in contrast to the copper vapor laser where the thermal radiation shielding is of crucial importance because temperatures of at least 1400–1500°C must be reached.

Particular attention was given to implementing low-inductance discharge circuitry. The vacuum housing was used to provide a coaxial ground return, and the capacitors were mounted symmetrically around the discharge tube. Similarly, pulse-charging techniques were used to reduce the cirucit inductance by eliminating the thyratron from the laser discharge circuit. For most experiments, capacitances of 7.5 or 10 nF were used, and charging voltages were in the range of 8–10 kV.

Laser power was measured with an EG&G Model 580 radiometer system. The wavelengths were identified with a half-meter Ebert monochromator which was calibrated with a mercury lamp. All temporal pictures of the laser pulse were made with a fast photomultiplier at the output of the monochromator.

Experimental Results

Laser oscillation was observed at 4062 Å when the leading edge of the discharge current pulse had a rate of rise of 5×10^{11} A/cm^2 · s (300 A in 6 ns), and the buffer gas pressure was less than 4 torr. Neon, argon, helium, or air was used as the buffer gas, and each produced approximately equal results. Unfortunately, this emission was too weak and erratic to allow a systematic parametric study. Nonetheless, the results support the conclusions of [7] that a steep leading edge of the excitation pulse is required in order to obtain a population inversion on this transition.

Laser oscillation at 4057 Å was not observed under the above conditions. However, lasing at 4057 Å was obtained when the rate of rise of the current density was reduced to 8×10^{10} A/cm^2 · s while maintaining 8 torr of neon as the buffer gas.

The temporal behavior of the laser pulse at 4057 Å was somewhat complex. The majority of the energy was in an initial spike which occurred during the early rise of the current pulse, less than 20 ns after the tube had begun to conduct. The 7229 Å transition was also lasing, but it was delayed by 12–14 ns relative to the 4057-Å-line emission. Both lines had a full width at half-maximum (FWHM) of approximately 10 ns. However, the 4057-Å line continued to lase at a greatly reduced power level throughout the remainder of the current pulse, and a second, smaller spike occurred during the voltage reversal across the tube (Fig. 2).

The power at 4057 Å was measured over a wide range of operating conditions. The maximum output recorded was 3.5-mW total from both ends of the tube. However, under these conditions the 7229-Å line was also lasing because appropriate mirrors to enhance the 4057-Å output relative to that of 7229 Å were not available. In addition, it was noted that at the optimum tube temperature a momentary increase in input power of about 20 percent produced a 100-percent increase in output power. This implies that the lead vapor was not being excited efficiently, and hence an optimization of the thermal shielding and discharge parameters to permit larger input pulses should increase the output.

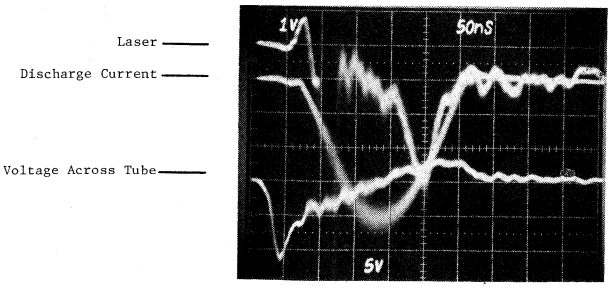


Fig. 2. Oscilloscope trace showing the time dependences of the laser pulse, discharge current, and voltage across the tube. Laser amplitude, uncalibrated; discharge current, 200 A/cm; voltage, 5 kV/cm.

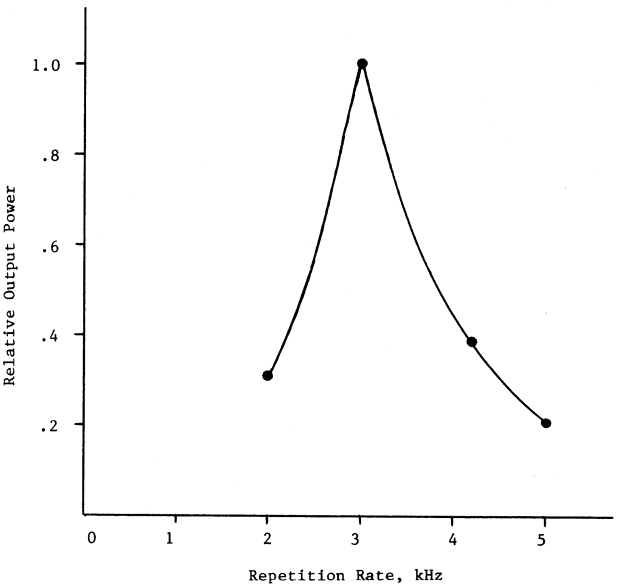


Fig. 3. The variation of the 4057-Å laser energy per pulse with repetition rate.

The laser energy per pulse was strongly dependent upon repetition rate as shown in Fig. 3. The maximum in output was observed to be in the range of 2.5–3.5 kHz, and lasing ceased altogether at rates greater than 6.0 kHz. The falloff at high rates is presumably related to the quenching rate of the metastable lower laser state. The reason for the decrease in output at low rates is unclear. However, it may be due to slow breakdown of the discharge at these rates, which in turn can probably be attributed to less residual ionization in the tube resulting from more recombination during the longer interpulse period.

The gain of the 4057-Å line was sufficiently high that only a single pass was needed to produce a collimated beam. The small signal gain was measured using various attenuators and mirrors of known reflectivities and assuming that the active region was the total length of the segmented, small-bore section. The resulting value was 165 dB/m.

Conclusions

The laser results found at 4062 Å with the fast-rising current pulse generally agree with the results at low voltage (5–6 kV) in [7].

In contrast, the lasing at 4057 Å with slow rise times and long pulsewidth has not been observed previously and, in fact, would appear to be in conflict with the known lifetime

of the upper state and the metastable nature of the lower level. However, the experimental results do suggest that improvements in the laser should lead to moderately powerful output at 4057 Å.

ACKNOWLEDGMENT

The authors wish to thank T. E. Buczacki and B. Fox for technical assistance. In particular, they appreciate the support of and discussions with C. E. Anderson.

REFERENCES

[1] W. T. Walter, N. Solimene, M. Piltch, and G. Gould, "Efficient pulsed gas discharge lasers," *IEEE J. Quan. Elec.*, vol. QE-2, p. 474, Sept. 1966.
[2] G. R. Fowles and W. T. Silfvast, "High-Gain laser transition in lead vapor," *Appl. Phys. Lett.*, vol. 6, p. 236, June 15, 1965.
[3] A. A. Isaev and G. G. Petrash, "New generation and superradiance lines of lead vapor," *JETP Lett.*, vol. 10, p. 119, 1969.
[4] A. A. Isaev, M. A. Kazaryan, and G. G. Petrash, "Effective pulsed copper-vapor laser with high average generation power," *JETP Lett.*, vol. 16, p. 27, July 5, 1972.
[5] R. S. Anderson, L. W. Springer, B. G. Bricks, and T. W. Karras, "High current density pulsed metal vapor laser," *Bull. Am. Phys. Soc.*, vol. 20, p. 238, Feb. 1975.
[6] —, "A discharge-heated copper vapor laser," *IEEE J. Quan. Elec.*, vol. QE-11, p. 173, Apr. 1975.
[7] R. S. Anderson, B. G. Bricks, L. W. Springer, and T. W. Karras, "A discharge-heated copper vapor master oscillator power amplifier," *IEEE J. Quan. Elec.*, vol. QE-11, p. 56D, Sept. 1975.
[8] G. G. Petrash, A. A. Isaev, M. A. Kazaryan, "Pulsed metal vapor lasers," *IEEE J. Quan. Elec.*, vol. QE-9, p. 644, June 1973.

Correction to "A Canonical Formulation for Analyzing Multielement Unstable Resonators"

A. E. SIEGMAN

In (16) of the above paper,[1] the change of variables should be $y = x/Ma_m$ and $y_0 = x_0/Ma_m$. Also one must interpret $u(y)$ and $u_0(y_0/M)$ in (17) as meaning $u(x)$ with $x = Ma_m y$ and $u_0(x_0/M)$ with $x_0 = Ma_m y_0$, where $u(x)$ and $u_0(x_0/M)$ are defined as in (15). In physical terms the range $-1 \leqslant y \leqslant 1$ in the dimensionless coordinate system then corresponds to $-Ma_m \leqslant x \leqslant Ma_m$ in the real coordinate system. Equation (17) remains correct and none of the conclusions of the paper are altered.

Manuscript received January 12, 1976. This work was supported by the Joint Services Electronics Program at Stanford University.

The author is with the Department of Electrical Engineering and the Microwave Laboratory, Stanford University, Stanford, CA 94305.

[1] A. E. Siegman, *IEEE J. Quantum Electron.*, vol. QE-12, pp. 35–40, Jan. 1976.

Notes and Lines

New Laser Oscillations in the N Atom Quartet Manifold

DAVID G. SUTTON

Abstract—**Three new laser oscillations have been observed in a pulsed discharge of He and N_2. These oscillations at 1.0568, 1.0611, and 1.0623 μm are fine-structure components of the 3d $^4P \rightarrow 3p\ ^4P^0$ transition of N(I). The three observed transitions (out of a possible seven) are those with the largest transition matrix elements that do not share a common lower state.**

Three new laser oscillations in the N(I) atom have been observed. The measured wavelengths are 1.0611, 1.0568, and 1.0623 μm and correspond to the fine-structure components $\frac{5}{2} \rightarrow \frac{5}{2}$, $\frac{5}{2} \rightarrow \frac{3}{2}$, and $\frac{3}{2} \rightarrow \frac{1}{2}$ of the 3d $^4P \rightarrow 3p\ ^4P^0$ multiplet [1].

The laser apparatus used for these experiments has been described elsewhere [2]. Briefly, the laser tube consists of two 1.25-m (2.5-cm ID) Lucite pipes, which are fitted with 251 pairs of 470-Ω resistors in a double-helical-configuration coaxial with the optical axis. The gap between resistor pairs is 1.9 cm. One of these helices is connected to ground, which forms the cathode of the discharge circuit; the other is connected to a pulsed power supply triggered by a spark gap. The ends of the laser tube are sealed by CaF_2 windows at Brewster's angle. A stable optical cavity is formed about the laser tube by two silver-coated mirrors: a total reflector with a radius of curvature of 11.5 m and a flat output coupler with a 1-mm hole in its center. The entire length of the optical cavity is 3.2 m.

Laser output is directed into a screen room where the beam is split into two parts by a sapphire flat. One of these beams is directed to an InSb detector to monitor the total laser emission; the other is directed through a 0.5-m monochromator to an identical InSb detector to monitor the spectrally resolved emission. Detector response is monitored with a fast oscilloscope.

The pulses are observed in the afterglow of a condensed discharge through 100 torr He containing 0.2 torr N_2. Threshold is obtained on the $\frac{5}{2} \rightarrow \frac{5}{2}$ and $\frac{5}{2} \rightarrow \frac{3}{2}$ components 1 μs after cessation of the discharge. The pulse duration full width at half-maximum (FWHM) of all three components is 3 μs. Threshold of the $\frac{3}{2} \rightarrow \frac{1}{2}$ component occurs 3 μs after the current pulse. The well-known 1.358-μm N atom transition ($3p\ ^2S^0_{1/2} \rightarrow 3s\ ^2P_{3/2}$) is also observed [3]. Its width is 9 μs.

The excitation mechanism for this type of laser is generally accepted as dissociative excitation transfer from He metastable species. Although production of one ground state and one 3d ^4P N atom by the He ($^3S_1$) species is 3 eV endothermic, dissociation of high vibrational levels of N_2 has been invoked to explain production of equally energetic N atoms in He afterglows [4].

For a set of fine-structure components, one might expect the stimulated emission intensities to reflect the variation in statistical weights and matrix elements within that transition. Functions that account for the squares of the matrix elements and assume a statistical population distribution among upper levels have been tabulated [5]. Table I reproduces the results for a $^4P \rightarrow {}^4P$ transition. The upper entries in the table are the

Manuscript received August 22, 1975. This work was supported by the Energy Research and Development Administration under Contract AT(04-3)-1056.

The author is with the Aerospace Corporation, El Segundo, CA 90245.

TABLE I
INTENSITIES OF FINE-STRUCTURE COMPONENTS

Lower Level	Upper Level $^4P_{5/2}$	Upper Level $^4P_{3/2}$	Upper Level $^4P_{1/2}$
$^4P^0_{5/2}$	35.0 / 35.0	15.0 / 0	0 / 0
$^4P^0_{3/2}$	15.0 / 30.1	4.4 / 0	13.9 / 0
$^4P^0_{1/2}$	0 / 0	13.9 / 3.5	2.8 / 0

calculated values, which, of course, can only be compared directly to spontaneous emission intensities. They will, however, be proportional to gain provided the lower level populations are small relative to the upper state and the statistical population distribution is maintained. The lower entries are the normalized peak stimulated emission intensities observed experimentally.

We observe that the three fine-structure components observed in stimulated emission are the three expected to show highest initial gain that do not share a common lower state. Perhaps filling of a lower level by stimulated emission on the highest gain transition suppresses the other possibilities, or the populations are otherwise curiously distorted. Use of a frequency-selected cavity or individual gain measurements could resolve the question.

REFERENCES

[1] C. E. Moore, *Atomic Energy Levels* (circular 467). Washington, DC: NBS, June 1949.

[2] D. G. Sutton, L. Galvan, P. R. Valenzuela, and S. N. Suchard, "Atomic laser action in rare gas-SF_6 mixtures," *IEEE J. Quantum Electron.*, vol. QE-11, pp. 54-57, Jan. 1975.

[3] R. J. Pressley (Ed.), *Handbook of Lasers*. Cleveland, OH: Chemical Rubber Co., 1971.

[4] J. B. Atkinson and J. H. Sanders, "Laser action in C and N following dissociative excitation transfer," *J. Phys. B. (Proc. Phys. Soc.)*, vol. 1, pp. 1171-1179, 1968.

[5] C. H. Townes and A. L. Shawlow, *Microwave Spectroscopy*. New York: McGraw-Hill, 1955.

New Pulsed Xe-Neutral Laser Line

ROBERT A. OLSON, PETER BLETZINGER, AND ALAN GARSCADDEN

Abstract—**A previously unreported xenon-neutral laser line at 4.02 μ has been observed in high-pressure He-Xe mixtures excited by a pulsed electrical discharge.**

A new pulsed Xe-neutral laser line at 4.02 μ was observed during studies of a closed-cycle, fast-flow, high-pressure, high-repetition-rate He-Xe transversely excited atmospheric (TEA) laser. The laser system was essentially the same as that described in [1] except that internal mirrors (53-cm cavity-formed by 2-m reflector and Ge output flat) were used.

Simultaneous lasing of the five lines listed in Table I was observed under the appropriate excitation conditions. All of these transitions obey the selection rules of $j-l$ coupling [2]: $\Delta j = 0$; $\Delta K = 0, \pm 1$; $\Delta J = 0, \pm 1$, $J = 0 \not\leftrightarrow J = 0$. Faust and McFarlane [2] have pointed out that transitions with $\Delta K = \Delta J$ are comparatively strong. The first four lines of Table I, for which $\Delta K = \Delta J$, exhibited high gain by lasing in a short-gain-length cavity ($\sim$ 12 cm) with an output transmittance of 40 percent or more. For the 4.02-μ line, however, an output transmittance of less than 5 percent (2 percent for the present results) was required for lasing.

TABLE I
XE-I LASER LINES OBSERVED IN PULSED HIGH-PRESSURE HE-XE DISCHARGE

λ_{vac} (μ) Calculated	Measured	Transition (Racah Notation)
2.0268	2.0271	$5d[3/2]^0_1 - 6p[3/2]_1$
2.6518	2.6516	$5d[3/2]^0_1 - 6p[1/2]_0$
3.4344	3.4349	$7p[5/2]_2 - 7s[3/2]^0_1$
3.6518	3.6516	$7p[1/2]_1 - 7s[3/2]^0_2$
4.0207	4.0208	$7p[1/2]_1 - 7s[3/2]^0_1$ [a]

[a] Previously unreported laser transition.

The oscillograms of the laser pulses shown in Fig. 1 were obtained at a pressure of 300 torr He-Xe (200:1), a charging voltage of 14 kV, and a pulse-repetition frequency (PRF) of 4 kHz. A CaF_2 lens was used to focus the laser output on the entrance slit of a Jarrell-Ash 0.5-m Ebert scanning spectrometer equipped with an infrared grating blazed at 5 μ. A liquid-nitrogen-cooled PbSnTe detector was used at the exit slit. The spectrometer was calibrated with a He-Ne laser.

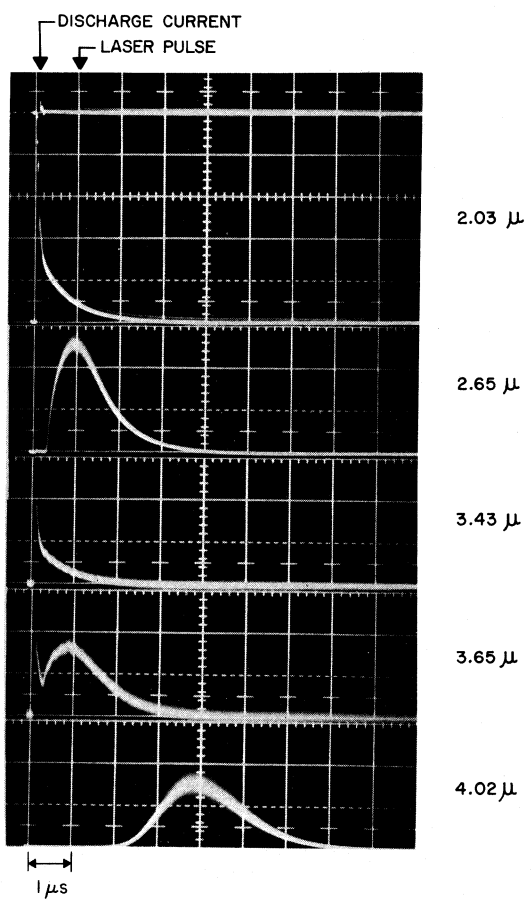


Fig. 1. Oscillograms of laser pulses obtained at a pressure of 300 torr He-Xe (200:1).

Manuscript received December 17, 1975. This work was supported in part under USAF Contract F33615-73-C-4130 and funded jointly by the Air Force Aero Propulsion Laboratory, the Air Force Avionics Laboratory, and the Air Force Weapons Laboratory.

R. A. Olson is with the Systems Research Laboratories, Inc., Dayton, OH 45440.

P. Bletzinger and A. Garscadden are with the Air Force Aero Propulsion Laboratory, Wright-Patterson Air Force Base, OH 45433.

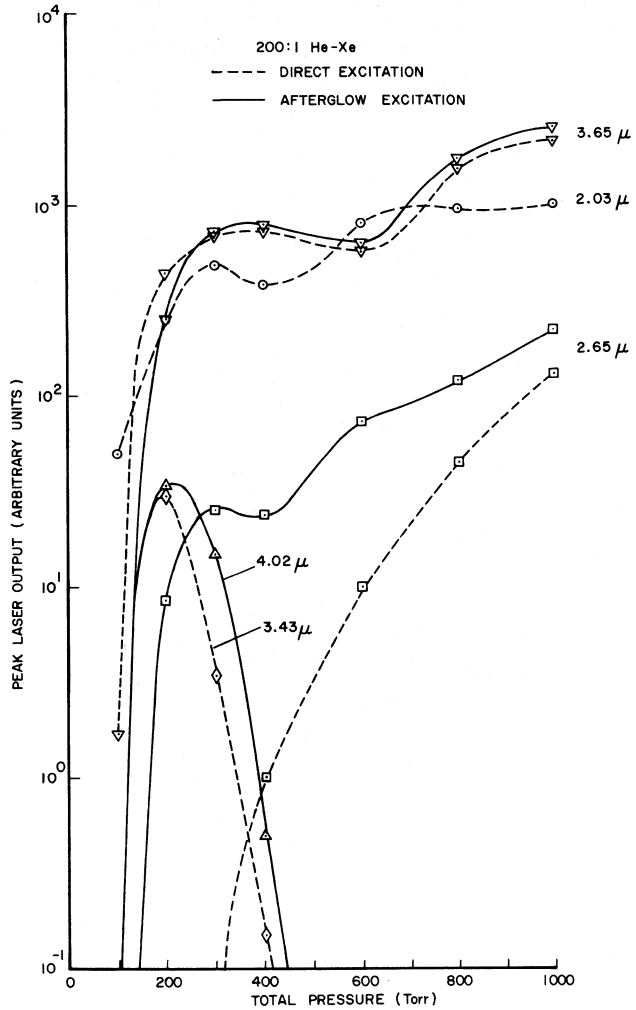


Fig. 2. Peak output of laser pulses as a function of total pressure.

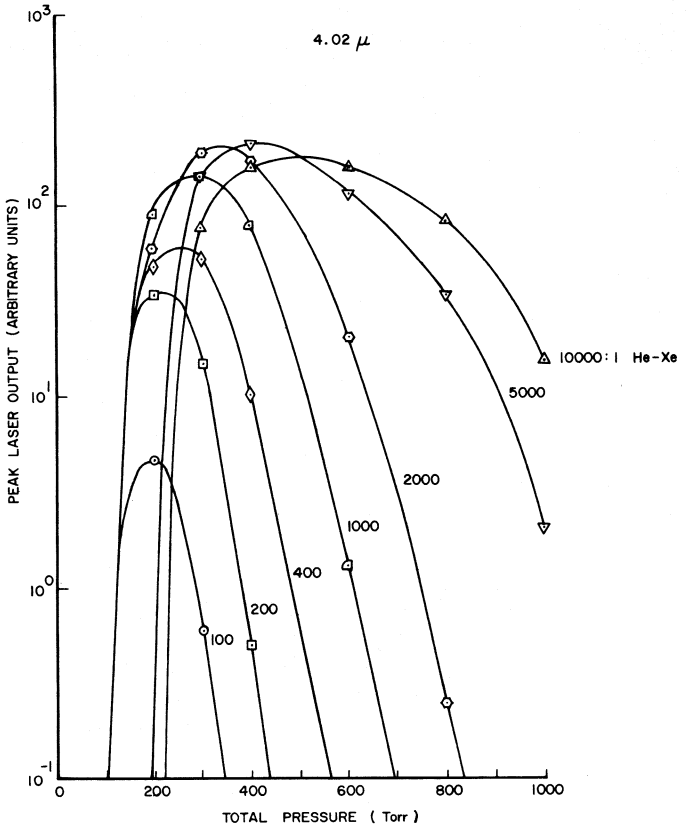


Fig. 3. Peak output of 4.02-μ laser pulse as a function of total pressure with partial-pressure ratio as parameter.

As can be seen in Fig. 1, the temporal behavior of the laser pulses varies considerably. The 2.03- and 3.43-μ pulses peak during the 100-ns discharge current pulse; the 2.65- and 4.02-μ pulses peak at $\sim$ 1 and 4 μs, respectively, after the current pulse; and the 3.65-μ pulse peaks both during the current pulse and $\sim$ 1 μs afterward. The peak values of the directly excited and afterglow pulses at the various wavelengths are plotted in Fig. 2 as a function of total pressure. The pressure dependence of the 4.02-μ pulse for various He–Xe mixture ratios is shown in Fig. 3. Whereas the magnitude of the directly excited pulses decreased with decreasing Xe partial pressure, the afterglow-pulse magnitude increased with decreasing Xe partial pressure, as in Fig. 3. This enhancement of afterglow lasing at low Xe partial pressures is consistent with the observation by Shuker *et al.* [3] that the number of excited Xe atoms in a pulsed He–Xe discharge grew rapidly as the Xe/He concentration ratio was lowered to 2×10^{-5}. These investigators attributed the enhanced Xe excitation and emission to energy transfer from atomic and molecular He metastables to Xe atoms via Penning ionization. This appears to be a reasonable explanation for the present results.

ACKNOWLEDGMENT

The authors wish to thank B. Sarka, Jr., and J. R. DeKock for technical assistance.

REFERENCES

[1] R. A. Olson, D. Grosjean, B. Sarka, A. Garscadden, and P. Bletzinger, "High-repetition-rate closed-cycle rare-gas electrical-discharge laser," *Rev. Sci. Instrum.*, Apr. 1976.

[2] W. L. Faust and R. A. McFarlane, "Line strengths for noble-gas maser transitions; calculations of gain/inversion at various wavelengths," *J. Appl. Phys.*, vol. 35, pp. 2010–2015, July 1964.

[3] R. Shuker, A. Szoke, E. Zamir, and Y. Binur, "Energy transfer in noble-gas mixtures, Penning ionization in He/Xe," *Phys. Rev.*, vol. A-11, pp. 1187–1192, April 1975.

Quasi-CW High-Power Mercury Laser

H. R. LÜTHI, W. SEELIG, AND A. STADLER

Abstract—**Laser action on a new line (λ = 6501.5 Å) with true CW potential has been achieved in a pulsed low-pressure Hg discharge. The highest power observed was 40 W. A laser pulsewidth of 0.5 ms, limited by the apparatus, was achieved.**

Continuous high-power laser action of visible lines excited in a low-pressure high-current Hg discharge has been proved in a recent work [1]. In this letter we report the quasi-CW laser action from a new Hg line.

In contrast to previously reported He–Hg lasers [2], the discharge in our laser is operated in pure Hg vapor in a 10-mm-bore quartz tube with a thermionic cathode. The active length is 1.2 m. The whole discharge apparatus can be heated to 70°C. The Hg vapor pressure is controlled by the temperature of two reservoirs (10^{-3} torr $< p < 2 \cdot 10^{-2}$ torr).

Manuscript received January 19, 1976. This work was supported by the Kommission zur Förderung der wissenschaft Lichen Forschung des EVD.

The authors are with the Institute of Applied Physics, University of Berne, Berne, Switzerland.

The current pulses for the discharge are generated by means of an RCL network operated in the aperiodic limit. The pulse-width varies from 25 μs to 2 ms; the maximum current is 300 A. Current density j and particle density N_{Hg} are about the same as in the discharges of high-power noble-gas ion lasers [3].

The axis of the optical resonator is collinear with the discharge tube. The laser power is measured with a calibrated semiconductor diode (SGD-444 EG_8G). Lasing occurs on a red line which has not been reported before. The wavelength of $\lambda = 6501.5$ Å $\pm$ 0.5 Å was measured with a Jarrel-Ash 0.5-m-grating monochromator. In that range an Hg^{2+} line due to a transition from a $5d^8 6s^2$ level at 118 926.5 cm^{-1} to a $5d^9 6p^\circ_{1/2}$ level at 103 594.4 cm^{-1} is reported by Foster [4], [5]. Between these level groups laser action had also been reported on a blue line ($\lambda = 4797$ Å) [6].

Quasi-CW laser action is proved in the following way: an increase of the current pulse length from 25 μs to 2 ms leads to an increase of the duration of the laser emission from 10 μs to 0.5 ms without remarkable change in the laser peak power.

The dependence of the laser power on the vapor pressure and the discharge current has been investigated with short (25-μs) and long (1-ms) current pulses. For the short pulses the optimum pressure for laser action is $p \simeq 2 \cdot 10^{-3}$ torr. Laser action does not occur for $p > 10^{-2}$ torr. The maximum measured power is 40 W (Fig. 1), and by optimizing the system larger values may be expected.

Output powers in the same range are obtained with long pulses (Fig. 2). The optimum gas pressure for the long pulses is $p > 10^{-2}$ torr, i.e., one order of magnitude larger than for the short pulses. This difference in pressure is due to the onset of neutral gas depletion during the current flow, a process which is well known in CW discharges [7].

In our system neutral gas depletion also determines the upper limit of the actual pulse length: The discharge apparatus can be heated to a maximum temperature of 70°C corresponding to a maximum Hg pressure of $3 \cdot 10^{-2}$ torr, which is too low for high-current CW operation. For pulses longer than 2 ms, the gas heating and the depletion become so strong that the stability limit of the discharge is reached [8]. However, this effect does not seem to be a principal limitation for CW operation. It can be overcome by the use of a discharge apparatus which can be heated to higher temperatures corresponding to Hg vapor pressures of $p > 0.1$ torr. Such efforts are currently on the way.

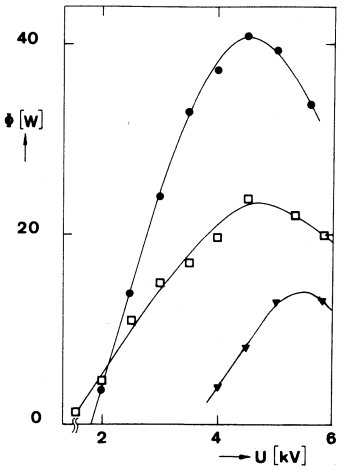


Fig. 1. Peak output power versus capacitor voltage ($\tau_{pulse} \simeq 25$ μs, C = 2 μF). □: $p_{Hg} = 1.5 \cdot 10^{-3}$ torr; ●: $p_{Hg} = 2.5 \cdot 10^{-3}$ torr; ▼: p_{Hg} $6 \cdot 10^{-3}$ torr.

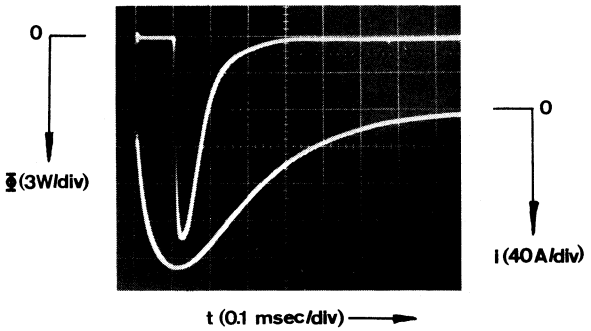


Fig. 2. Current dependence of laser power for 1-ms pulses (Hg pressure $\simeq 10^{-2}$ torr). Upper trace: laser power Φ. Lower trace: discharge current i.

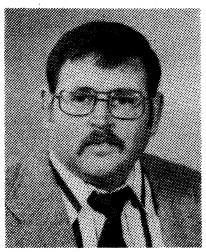
ACKNOWLEDGMENT

The authors wish to thank Prof. K. P. Meyer for his stimulating interest and acknowledge J. Steinger and P. Burkhard for experimental assistance.

REFERENCES

[1] K. Banse, G. Herziger, and W. Seelig, "Metalldampfionenlaser mit reinem Hg," *Verhandl. DPG* (VI), vol. 8, p. 704, Apr. 1973.
[2] W. E. Bell, "Visible laser transitions in Hg^+," *Appl. Phys. Lett.*, vol. 4, pp. 34–35, 1964.
[3] G. Herziger and W. Seelig, "Ionenlaser hoher Leistung," *Z. Physik*, vol. 219, pp. 5–31, 1969.
[4] E. W. Foster, "New terms of the $5d^8 6s^2$ and $5d^8 6s6p$ configurations of the spectrum of Hg III," *Proc. Royal Soc.* (London), vol. 200A, pp. 429–437, 1949.
[5] —, "Hyperfine structure in $5d^9 6p$ and $5d^8 6s^2$ configurations of the spectrum of Hg III," *Proc. Royal Soc.* (London), vol. 208, pp. 367–391, 1951.
[6] H. J. Gerritsen and P. V. Goedertier, "Blue gas laser using Hg^{2+}," *J. Appl. Phys.*, vol. 35, pp. 3060–3061, 1964.
[7] G. Herziger, H. R. Lüthi, and W. Seelig, "Temperaturen in Ionen Laserplasmen," *Z. Physik*, vol. 264, pp. 61–71, 1973.
[8] S. Torven and M. Babic, "Current chopping space layers in a low pressure arc plasma," in *Proc. 12th Int. Conf. Phenomena in Ionized Gases* (Contributed Papers), p. 124, 1975.

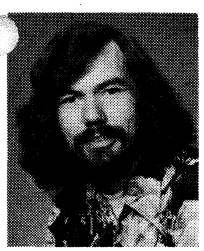
Contributors



Richard W. Davies was born on May 27, 1936. He received the B.S., M.S., and Ph.D. degrees in Physics from the Carnegie-Mellon University, Pittsburgh, PA.

Since 1964 he has been a Staff Member at the M.I.T. Lincoln Laboratory, Lexington, MA. His primary area of research has been theoretical solid-state physics.

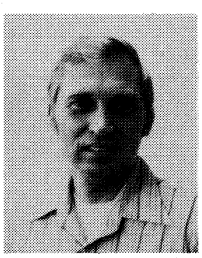
*



Harry J. Dewey was born in Sacramento, CA, on September 30, 1948. He received the B.S. degree in chemistry from the University of California, Davis, in 1970, and the Ph.D. degree in physical chemistry from the University of Utah, Salt Lake City, in 1973.

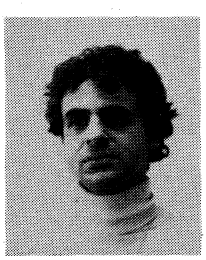
He was a National Research Council/National Bureau of Standards (NBS) Postdoctoral Research Associate at NBS from 1973 to 1975. He is presently with the Department of Chemistry, University of Utah, Salt Lake City.

*



H. E. Eddleman entered the United States Navy in 1957. Upon completion of flight training, he was given tour assignments which included several fighter squadrons, USNPGS, Monterey, CA, and aircraft carriers. He is currently on a Military Research Associate tour at the Lawrence Livermore Laboratory, University of California, Livermore. Upon arrival, he was assigned to the CO_2 laser program as an Electronics Engineering Team Member working primarily in the area of system operation and computerized data reduction.

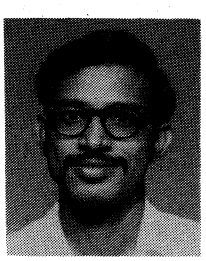
*



Stanley S. Glaros was born in San Francisco, CA, on April 6, 1942. He received the B.S.M.E. degree in 1965 from the California State Polytechnic University, San Luis Obispo. He received the M.S. degree in nuclear engineering with primary work in plasma physics from the University of Washington, Seattle.

From 1965 to 1970 he was an Aerospace Engineer with the Boeing Corporation, Seattle, WA. From 1971 to 1972 he headed the New Products Research and Development Department at ILC Technology, Sunnyvale, CA. Currently, he is an Engineer in support of the Laser/Plasma Interaction Group of Y-Program, Lawrence Livermore Laboratory, University of California, Livermore.

*



J. S. Goela was born in New Delhi, India, on April 20, 1951. He received the B. Tech. degree in mechanical engineering from the Indian Institute of Technology, Delhi, India, in June 1972, and the M.Sc. degree in engineering from Brown University, Providence, RI, in June 1974. He expects to receive the Ph.D. degree in Engineering from Brown University in June 1976.

Currently, he is a Research Assistant in the Division of Engineering at Brown University. He is working on the interaction of radiation with a two- and three-level gas. His research interests include work related to nonlinear spectroscopy, chemical lasers, laser isotope separation techniques, and low-pressure molecular lasers.

Mr. Goela is a member of Sigma Xi and a student member of the American Society of Mechanical Engineers, the Optical Society of America, and the American Institute of Aeronautics and Astronautics.

*

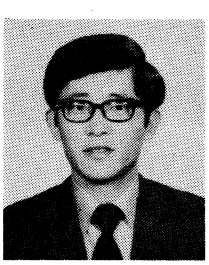


Roger A. Haas was born September 27, 1942. He received the B.E.S. degree in engineering science from the University of Florida, Gainesville, in 1964. He received the M.S. and Ph.D. degrees in engineering science and physics from the California Institute of Technology, Pasadena, in 1965 and 1969, respectively. While at the University of Florida his studies were supported by a Robert O. Law Scholarship and at the California Institute of Technology he was aided by several scholastic fellowships including a California State Scholarship, a California Institute of Technology Tuition Scholarship, an Alfred P. Sloan Fellowship, a Florence and Daniel Guggenheim Fellowship, a Ford Foundation Fellowship, and a National Science Foundation Traineeship.

From 1969 to 1973 he was a Research Scientist at the United Aircraft Research Laboratories, East Hartford, CT. His work there included an analysis of the plasma stability of electric discharges in molecular gases with emphasis on CO_2 laser plasmas. Since coming to the Lawrence Livermore Laboratory, University of California, Livermore, in 1974 he has been concerned with experimental and analytical investigations of the interaction of intense laser radiation with matter.

Dr. Haas is a member of the American Physical Society and several scholastic honor societies.

*



Yong-Kyung Lee (S'75) was born in Korea on June 11, 1943. He received the B.S. degree in electronics engineering from the Seoul National University, Seoul, Korea, in 1964. After serving the Korean Army as an instructor at the Korean Army Signal School, Taejon, Korea, he came to the United States to receive the M.E. degree from the University of Oklahoma, Norman, in 1969, and the Ph.D. degree from the University of California, Berkeley, in 1975, all in electrical engineering.

In 1969 he worked on the development of an infrared intrusion detection system at Optical Controls, Inc., Woburn, MA. He is currently an Assistant Professor in the Department of Information Engineering, University of Illinois at Chicago Circle, Chicago, where his current research interest includes integrated optical devices, fiber optics communications, and electrooptic modulation.

Dr. Lee is a member of the American Physical Society, Optical Society of America, and Eta Kappa Nu.

*

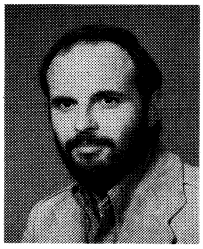


Walter B. Lindquist was born in San Francisco, CA on August 7, 1940. He received the B.S.E.E. degree in 1964, and the M.S.E.E. degree in 1969, from San Jose State University, San Jose, CA.

Since 1964 he has been with the Electronics Engineering Department of the Lawrence Livermore Laboratory, University of California, Livermore. He became an Electronics Engineering Department Group Leader for Gas Lasers in the Laser Fusion Program in 1971. In addition

to his Group Leader duties, he served as Project Engineer on the CO_2 Laser System (Valkyrie). Currently, he is Group Leader for the Pulsed Energy Group of the Electronics Engineering Department.

*

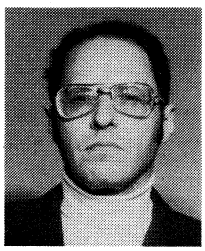


Kenneth R. Manes was born in New York, NY, on October 9, 1942. He received the B.S. degree in electrical engineering from Purdue University, Lafayette, IN, in 1965, and the M.S. and Ph.D. degrees from Stanford University, Stanford, CA, in 1967 and 1970, respectively. While at Stanford University, he studied under a National Science Foundation Fellowship.

From 1970 to 1972 he was a Killam Postdoctoral Fellow and Lecturer in Electrical Engineering at the University of Alberta, Edmonton, Alta., Canada. He joined the CO_2 Laser Group at the Lawrence Livermore Laboratory, University of California, Livermore, in 1972 and subsequently led that group until mid-1975. Currently, he is Assistant Group Leader of the Laser Plasma Interaction Group.

Dr. Manes is a member of the American Physical Society and several physics, engineering, and scholastic honor societies.

*



T. F. Morse was born in New York, NY, on February 28, 1932. He received the B.A. degree and the M.A. degree from Duke University, Durham, NC, in 1953 and 1954, respectively. He received the B.Sc. degree in mechanical engineering from the University of Hartford, Hartford, CT, in 1957, the M.Sc. degree from the Rensselaer Polytechnic Institute, Hartford, CT, in 1958, and the Ph.D. degree in engineering from Northwestern University, Evanston, IL, in 1961.

From 1955 to 1958 he was a Research Engineer with the Pratt and Whitney Aircraft Company, East Hartford, CT. After two years with the Aeronautical Research Associates of Princeton, Inc., he joined the faculty of Brown University, Providence, RI, in 1963 and has been a Professor of Engineering since 1967. His research interests are concerned with kinetic theory, gas lasers, membrane theory, isotope separation, and problems of nonlinear spectroscopy.

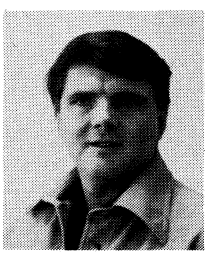
Dr. Morse was the recipient of a Senior Fulbright Research Fellowship at the DVFLR in Porz-Wahn, Germany, during 1969–1970. He is a member of the Optical Society of America and the American Physical Society.

*

Paul A. Renard was born in Detroit, MI, on June 23, 1950. He received the B.S. degree in mathematics from the honor college at the University of Michigan, Ann Arbor.

He joined the Computations Department at the Lawrence Livermore Laboratory, University of California, Livermore, in July, 1972. Since that time he has been involved with the computer simulations of strategic missile defense systems, CO_2 laser oscillators and amplifiers, models of atomic and molecular physics, and the propagation and focusing properties of laser light through nonlinear media.

*



Donald L. Smith (M'70) received the B.S.E.E. degree from California State University, San Jose, in 1970. He has done graduate course work at the University of California, Davis.

He began work at the Lawrence Livermore Laboratory, University of California, Livermore, in 1960 as an Electronic Technician and was promoted to Electrical Engineer after receiving the B.S.E.E. degree. He has contributed to the design and development of electrooptic systems that include a laser telemetry system with automatic gain control for compensating for the effects of atmospheric turbulence and a laser time-resolved pinex used in nuclear weapons diagnostics. From 1971 to 1973 he supported the Laser Fusion Program by designing and developing CO_2 oscillators with single 1-ns pulse generation. He also developed several high-voltage fast-rise pulse generators. From 1973 to 1975 he participated in the development and operation of Valkyrie. His responsibilities included the CO_2 oscillator, overall system alignment, beam diagnostics, and target diagnostics instrumentation.

Mr. Smith is a member of Eta Kappa Nu.

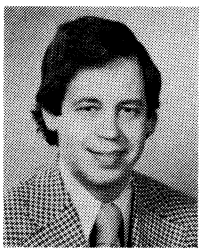
*



Ted C. Stewart was born on January 28, 1920.

He was employed at N.A.S., Alameda, CA, from 1942 to 1958. From 1958 to the present he has progressed from Technician to Technic Associate at the Lawrence Livermore Laboratory, University of California, Livermore. His principal interests include control design troubleshooting and test equipment maintenance.

*



James N. Walpole was born February 27, 1939, in Brownsville, TN. He received the B.S.E.E. degree in 1961 from Duke University, Durham, NC. His graduate degrees were from the Department of Electrical Engineering, Massachusetts Institute of Technology, Cambridge, MA, where he received the M.S. degree in 1962 and the Ph.D. degree in 1966.

He was an Assistant Professor of Electrical Engineering at M.I.T. from 1966 to 1971 and was appointed Associate Professor in 1971 Since 1972 he has been a Staff Member at the M.I.T. Lincoln Laboratory, Lexington, MA. His research activities have centered around semiconductor devices and physics with emphasis on the IV–VI compounds and alloys. Currently he is engaged in work on lead-salt semiconductor diode lasers.

*

Shyh Wang (S'49–A'52–M'57–SM'74) was born in Wusih, China, on June 15, 1925. He received the B.S. degree in electrical engineering from Chiao Tung University, Shanghai, China, and the M.A. and the Ph.D. degrees from Harvard University, Cambridge, MA, both in applied physics.

From 1951 to 1953 he was a Postdoctoral Research Fellow at Harvard University investigating high-power saturation and nonlinear effects in paramagnetic and ferrimagnetic substances. From 1953 to 1958 he was an Engineering Specialist with Sylvania Electric Products (now a part of General Telephone and Electronics), where he worked on the property of semiconductor device theories. In 1958 he joined the faculty of the University of California, Berkeley. In the academic year 1965–1966 he furthered his research studies in the Institut für Angewandte Physik, University of Bern, Switzerland, on a John Simon Guggenheim Memorial Fellowship. Currently, he is a Professor of Electrical Engineering and Computer Sciences at the University of California. He is the author of *Solid State Electronics* (New York: McGraw-Hill, 1966). His current research interests are in magnetoelastic and magnetooptic interactions in ferrimagnetic materials, in nonlinear optical effects in semiconductors and dielectrics, and in integrated optics.

Dr. Wang is a member of the American Physical Society.

Editorial

Integrated Optics

A QUESTION has been raised as to the desirability of this JOURNAL's arranging a Special Issue on Integrated Optics. In discussing this with knowledgeable people I soon discovered that there is a wide difference of opinion on whether integrated optics is the white hope for optical communications, or whether it is a momentary flash in the pan. It appeared that such an issue would benefit from having a pair of invited papers argue these opposing views. However, I also discovered that no one who valued his reputation was willing to sign his name to a paper on either side of this issue. In hasty retrenchment, potential authors modified their statements so that it was no longer clear which side of the fence they were straddling. This left only your Editor, who could repeat what he had heard, but who, like a disavowed spy, could not depend upon anyone to back him up. Accordingly, I shall attempt a brief resumé of these interesting speculations.

What is integrated optics? So far most of the contributions to this field are more properly described as "thin-film optical devices." Substrates coated with dielectric films can confine radiation to a plane; and by forming stripes of higher refractive index, filamentary beams may be guided within the plane. Thin-film directional couplers, lenses, gratings, and modulators have been made. One can conceive of assemblies of such elements including laser diodes and active devices, all incorporated on a single substrate, performing complex optical functions. Could this revolutionize optical communications in the way that integrated circuits are revolutionizing information processing at lower frequencies? The vision is appealing. But is it practical?

Here is where anti-integrationists argue that some healthy debunking is needed to give a balanced view. Without claiming that these visionary things cannot be done, they point out that for the near future most of the necessary functions can be performed more conveniently by integrated circuits at lower frequencies. Among optical systems engineers, the advent of low-loss optical fibers has changed their vision of what optical systems should look like. As long as the transmission medium was conceived as a beam guide of precision lenses spaced along a carefully aligned and buried tube of several centimeters diameter, the cost of such a link could be justified only if many channels were multiplexed over the same light path. But with the advent of low-loss fibers of only 100-μm diameter, so many channels could be easily provided by putting each channel on a separate fiber that the complexities of multiplexing channels on a single light path appear unwarranted. In fact, it can be argued that for short voice links (less than a kilometer), the cheapest system might use only one voice per fiber. This would make the optics for terminals very simple: a current-modulated LED for the transmitter, and a photodiode for the detector. Even for many channels digitally multiplexed into bands several hundred megahertz wide, a directly modulated laser diode at one end, and direct detection at the other end may be best. Such a system would be able to take advantage of presently available integrated circuits for multiplexing, amplification, and channel dropping, leaving only the simplest operations to be performed at optical frequencies.

This line of thinking is predicated on the extremely sophisticated state of the art for large-scale integrated circuits. It is here now. Optical integration undoubtedly will make advances, but it has a long way to go. Indeed, it can be argued that an optical waveguide in a thin film can never have transverse dimensions much smaller than a wavelength. Directional couplers, gratings, and other such elements frequently are many wavelengths long. This is to be compared with the trend in integrated circuits where improvement in mask-making techniques may make possible operational elements as small as 0.01 μm, much less than an optical wavelength. Thus integrated circuits may eventually have higher packing densities and lower power requirements than optical integrated circuits can ever hope to attain.

Is there any reason then to continue research on integrated optics? Of course there is. Not until the field has been much more thoroughly explored will we know what is doable, and where it can be most advantageously applied. What is needed now is the ability to build the hardware. There seems to be agreement that the brainstorming of wild-blue-yonder possibilities has largely been done. There must be real progress in the technology of crystal growing, etching, ion milling, molecular beam epitaxy, contacting, and so forth before the dreams can come true. In fact, progress in these endeavors has already been made during the last two years. Even without integration, some of the thin-film devices which have been built appear so attractive as to provide sufficient justification for the research effort. In addition, there have been several demonstrations of true, though modest, integration of several components in a single waveguiding structure.

Because we believe this developing field is both fascinating and potentially important, we are devoting a special issue of the JOURNAL OF QUANTUM ELECTRONICS to it. Prof. William S. C. Chang has agreed to serve as Guest Editor, and we invite your attention to the Call for Papers on the back page of this issue.

A. GARDNER FOX
Editor

Trapped Radiation in Injection Lasers

V. P. GRIBKOVSKII, V. K. KONONENKO, G. I. RYABTSEV, AND V. A. SAMOILYUKOVICH

Abstract—**The effect of trapped radiation on the stimulated emission threshold and power in injection lasers is investigated theoretically and experimentally. The density of trapped radiation is determined by the relation between the gain and the loss coefficients for this radiation in the active region. The last value depends upon treatment of the cavity sidewalls and laser diode geometry. The absorption of spontaneous emission in the active diode region provides for an additional optical excitation of the crystal and can result in a decrease of threshold current.**

The GaAs laser diodes with Fabry-Perot cavities and four-ended resonators were studied. The lasing threshold for the axial modes is increased with the diode width and that for the nonaxial radiating modes is decreased with it. The luminescence spectra from the cavity ends and sidewalls are investigated as a function of diode length and current density. It is shown that the gained luminescence can be an essential source of energy losses in injection lasers and leads to limitations of dimensions of laser diodes with planar p-n-junctions.

Various methods for suppression of harmful radiation and for increase of the stimulated emission power in injection lasers are discussed.

I. Introduction

THOUGH injection laser power is not so high in comparison with solid-state laser power and makes up some tens of watts, its energy output per unit volume of active medium reaches great magnitudes, up to 10 MW/cm^3. Radiant energy concentration in the cavity is so high that its further increase results in crystal damage and catastrophic degradation of laser diodes. Therefore, all the ways of increasing injection-laser stimulated emission power involve volume enlargement of the active medium. However, as soon as $k\sqrt{s} > 1$, where k is the gain coefficient and s the active layer area, the effect of trapped radiation on laser threshold and power rises noticeably; i.e., the threshold current density j_t sharply increases and the stimulated emission power S_{st} drops to zero. Hence the necessity of studying and researching the ways of harmful radiation suppression in injection lasers is evident.

There are a number of works on investigation of trapped radiation in solid-state lasers [1]. However, the problem of trapped radiation is the most undeveloped in semiconductor quantum electronics to date.

This paper is concerned with theoretical and experimental investigation data dedicated to this problem.

II. Theory

Trapped radiation in injection lasers includes the following: 1) luminescence, 2) radiation arising due to scattering of stimulated emission flow, 3) emission, corresponding to lasing modes, having no output from the cavity, and 4) thermal radiation. Planck radiation is insignificant at room and lower temperatures and may be neglected. The closed modes can be eliminated as well. As is known, the amplified luminescence is exhibited before the lasing threshold and leads to an evident narrowing of the emission spectrum of laser diodes [2]. The scattering of the stimulated emission flow in an active diode region has been established experimentally in [3].

The effect of trapped luminescence on the threshold current value has been considered theoretically in [4]. When operating in CW, accumulation of trapped radiation in an active layer of the laser diode in consequence of light amplification is fully compensated by its loss while going out of active region and absorption in the bulk of the active region itself. Loss value can be characterized by the trapped radiation loss coefficient k_{tr}, averaged over the volume of the active region and over all directions of light propagation. Then the equation for lasing threshold, taking into account induced transitions under the influence of the luminescence, will be of the form [4]

$$j_t = j_{t0}\left[1 + \eta_l \frac{\int \frac{k(\nu)}{k_{tr} - k(\nu)} r_l(\nu)\, d\nu}{\int r_l(\nu) d\nu}\right], \tag{1}$$

where

- j_{t0} threshold current density, when the effect of trapped radiation is negligible;
- $k(\nu)$ gain coefficient;
- $r_l(\nu)$ spectral spontaneous recombination rate in the active region;
- ν light frequency;
- η_l luminescence quantum efficiency.

The contribution of optical transitions induced by luminescence in the threshold current, as is evidenced by (1), is determined by the value of k_{tr} and the spectral distribution of $k(\nu)$ and $r_l(\nu)$. The second term in (1) is decomposed into two parts, positive and negative, depending on the sign of $k(\nu)$. The first part yields a rise of lasing threshold because of a recombination rate increase caused by amplified luminescence. The negative term characterizes a role of the part of luminescence which is absorbed in the active region and increases the inverted population. Additional optical pumping of a crystal is provided by this part of the luminescence. The effect on the threshold is enhanced by the increase of luminescence quantum efficiency η_l.

In accordance with the condition of CW lasing, the gain coefficient $k(\nu)$ at stimulated emission frequency ν_{st} is equal to the loss coefficient

$$k(\nu_{st}) \equiv k_l = k_r + \rho, \quad k_r = \frac{1}{l} \ln \frac{1}{\sqrt{r_1 r_2}} \tag{2}$$

Manuscript received June 5, 1975; revised February 19, 1976.

V. P. Gribkovskii, V. K. Kononenko, and G. I. Ryabtsev are with the Institute of Physics, Academy of Sciences of the BSSR, Minsk, USSR.

V. A. Samoilyukovich is with the Department of Physics, Polytechnical Institute of the BSSR, Minsk, USSR.

where l is the diode length, r_1 and r_2 are the reflection coefficients of the cavity ends, and ρ is the internal optical loss of the stimulated emission. If k_{tr} is close to the value of k_l, then as a result of the gained luminescence contribution, the value of j_t noticeably exceeds j_{t0}. In the limiting case when k_{tr} tends to k_l the threshold current reaches infinite values, i.e., the stimulated emission of axial modes is impossible. If luminescence reabsorption is more essential than its amplification, then j_t can be less than j_{t0}.

The estimation of gain coefficient $\bar{k}$ averaged over the luminescence spectrum may be used for preliminary evaluation of the relative contribution of luminescence amplification and absorption into the threshold current. If $\bar{k} > 0$, then at any k_{tr} the gained luminescence prevails. On the contrary, when $\bar{k} < 0$, at large k_{tr} the luminescence reabsorption results in decreasing j_t.

The loss coefficient for trapped radiation k_{tr} is determined by diode geometry and depends upon treatment of the cavity sidewalls. To lower the luminescence density in the active volume of laser diodes k_{tr} must be increased. As is evident from the calculation [4], the value of k_{tr} is approximately equal to

$$k_{tr} = \frac{\Delta}{\sqrt{s}}. \tag{3}$$

Here Δ is the dimensionless proportionality factor and the junction area $s = lw$, where w is the diode width. On the other hand, $k_l \sim 1/l$. As the stimulated emission of resonator axial modes can occur only when meeting the condition of $k_l < k_{tr}$, then it is apparent that trapped luminescence limits both the laser diode length and width.

In a number of cases the trapped radiation affects the dependence of threshold current density on diode length and results in a rise of j_t with the increase of the diode width w. In particular, the experimentally observable tendency to a rise of j_t at an increase of diode length in a large l region [5]-[7] can be explained not only by the disalignment of p-n-junction planarity but also by a rise of recombination rate induced with trapped luminescence.

About the radiation density inside of the diode and the value of k_{tr} one can judge from the intensity and spectral distribution of the luminescence emitting from the resonator. The intensity of emitting luminescence $S_l(\nu)$ is proportional to the luminescence density in the active layer $u_l(\nu)$ which is equal to [1], [4]

$$u_l(\nu) = \frac{W_l(\nu)}{v\,[k_{tr} - k(\nu)]} \tag{4}$$

where $W_l(\nu)$ is the luminescence output per unit volume of the active layer and v is the light velocity in the crystal. When radiation density level is, relatively, not so high and $k(\nu)$ does not depend on u_l, using [6]-[8] we consider the gain coefficient to be increased linearly with the current at the frequencies similar to the stimulated emission frequency

$$k(\nu) = \beta(j - j_0). \tag{5}$$

Here β is the gain factor and j_0 is the zero current density. Consider $W_l(\nu) \sim j$, and measuring relative change of luminescence intensity with the current, one can easily estimate the value k_{tr} and determine the internal parameters of injection laser. For this purpose, putting up on the ordinate axis the values

$$\delta = j_1\left(\frac{S_l(j_1)}{S_l(j_2)} - 1\right)\left(\frac{S_l(j_1)}{S_l(j_2)} - \frac{j_1}{j_2}\right)^{-1} \sim j_0 + \beta^{-1} k_{tr}$$

$$= j_0 + \beta^{-1}\frac{\Delta}{\sqrt{s}} \tag{6}$$

for different currents j_1 and j_2 independent of $1/\sqrt{s}$ and using a cutoff we get j_0, and by an angle of slope, knowing β, we find parameter Δ and obtain k_{tr} as a function of l or w. The results of experimental approbation of the given method and the limits of its application are discussed in the next section.

Stimulated emission flow from the both ends of laser diode is given in linear approximation by the formula [6], [7]

$$S_{st} = s\frac{h\nu_{st}}{e}\eta_{st}(j - j_t)\frac{k_r}{k_r + \rho} \tag{7}$$

where η_{st} is the internal quantum efficiency of the stimulated emission.

Energy losses due to the rise of trapped radiation density above lasing threshold are difficult to eliminate. One of the causes of it is the scattering of stimulated emission. At k_{tr} close to k_l, the harmful radiation influence upon the value S_{st} can be essential [4]. In this case decreasing S_{st} is conditioned not only by the threshold current increase but by the decrease of η_{st}. In particular, the influence of the trapped radiation which involves internally circulating nonradiating modes upon the value η_{st} was investigated experimentally in [9].

III. Experiment

Experiments were performed with diffused GaAs laser diodes either with Fabry-Perot cavities or four-ended resonators at liquid nitrogen temperature in pulsed operation.

Observing the far-field pattern of diodes with four-ended resonators one finds axial and nonaxial modes, the latter having the output under an angle to the cavity axis and being conditioned by the reflection at the sidewalls. In the Fabry-Perot cavity diodes only axial modes were observed.

The increase of diode width was accompanied by the increase of axial mode lasing threshold j_t^a and by the decrease of nonaxial mode lasing threshold j_t^n [10]. If the length of a laser diode is less than its width, then the value j_t^a for a four-ended resonator is ten times more than j_t^n. Axial modes were not observed in a four-ended cavity at $w/l \approx 3$, and the threshold for nonaxial modes decreased to a minimum value. With the grinding of the four-ended resonator sidewalls, the value j_t^a decreased by more than one order.

Experimental results are explained as follows. According to the theory the value k_{tr} decreases with increasing w for a given cavity length and current density; therefore the luminescence density increases sharply and the gain coefficient may decrease [11] as a result of nonlinear effects. Consequently, larger current densities are required for obtaining the axial mode lasing threshold. The decrease of the nonaxial mode lasing threshold

with increasing w may be caused by a decrease of the loss coefficient for these types of modes as the result of propagation length increasing.

Luminescence spectra from the Fabry-Perot cavity mirror $S_l^m(\nu)$ and sidewall $S_l^s(\nu)$ were investigated in detail. As is evident from Fig. 1 the band maximum of S_l^m is shifted to the long-wave region in respect to the maximum of S_l^s. This shift depends on the cavity length and injection current density [12]. With the decrease of l the maximum of S_l^m shifts to the short-wave spectrum region reaching the maximum of S_l^s at $l \approx w$. The dependence of spectral position of the luminescence band maximum on l is caused by a change of single-pass gain in the active region. So long as the value $k(\nu)$ remains invariable at a given j, the relation (4) allows the estimation of a change of the loss coefficient k_{tr}.

If the Fabry-Perot cavity mirrors are treated roughly then the shift of the maximum of S_l^m in respect to the maximum of S_l^s decreases in comparison with the shift for the diode of the same length, but with better mirror qualities. It proves that with grinding of the diode mirrors the increase of k_{tr} and decrease of luminescence density occur in the cavity.

Using the formula (4) for spectral luminescence density in cavity $u_l(\nu)$ one can calculate k_{tr} for radiation propagating in a perpendicular direction towards cavity mirrors. In this case knowing $W_l(\nu)$ and $k(\nu)$ we choose a value of k_{tr} at which the maxima of the calculated density $u_l(\nu)$ and luminescence power from the cavity mirror observed experimentally, $S_l^m(\nu)$, coincide. Spectral distribution of the magnitude $W_l(\nu)$ is replaced by distribution $S_l^s(\nu)$ in a diode with a small cavity width $w = 0.1$ mm ($l/w > 10$) at a given j. Spectral distribution of the gain coefficient in the active region $k(\nu)$ is determined from the universal relation between absorption and emission spectra [13], [14].

In Fig. 1 the dotted lines represent the calculated luminescence spectra for three lengths of Fabry-Perot cavity. The corresponding values of k_{tr} are given in Table I. The difference of distributions $u_l(\nu)$ and $S_l^m(\nu)$ on spectrum edges for the diode with $l = 1.06$ mm can be explained by the frequency dependence of the trapped radiation loss coefficient. Another possible cause of this difference likely to be involved is the gain saturation effect [11] because of high radiation density in the frequency range of the maximum gain. For the smaller cavity lengths ($l = 0.36$ mm) the divergence in the form of $u_l(\nu)$ and $S_l^m(\nu)$ is noticeable only in the long-wave spectral range.

The trapped radiation loss coefficient was also measured according to the method described in Section II. The experiments were undertaken both on the diodes with Fabry-Perot cavities and diodes having four roughly treated sidewalls. The measurements of radiation intensity emitted from the diode sidewall S_l^s were carried out at the frequency ($h\nu = 1.44$ eV), close to the laser frequency but at current densities which are smaller than threshold values (Fig. 2).

Ten pairs of values j_1 and j_2 for a given l and cavity type were chosen on the basis of the dependence curve of S_l^s on the current, and δ was calculated according to (6). Fig. 3 gives the dependence of δ on $1/\sqrt{s}$ for the diode DI with a

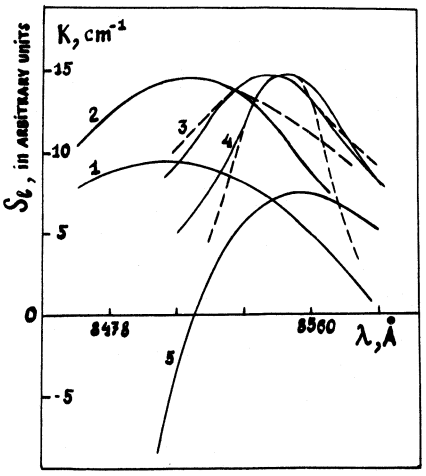


Fig. 1. Spectra of laser diode radiation at $j = 450$ A/cm^2. 1: luminescence spectrum emitting from the diode sidewall and small $w = 0.1$ mm; 2, 3, 4: spectra $S_l^m(\nu)$ for the diode DI with the Fabry-Perot resonator at $l = 0.36$, 0.73, 1.06 mm, respectively, $w = 0.3$ mm; 5: gain coefficient $k(\nu)$ at given j.

TABLE I
TRAPPED RADIATION LOSS COEFFICIENT VALUES k_{tr} FOR THE DIODE DI WITH FABRY-PEROT CAVITY CALCULATED FROM THE DISPLACEMENT OF SPECTRUM MAXIMA S_l^m AND S_l^s AS A FUNCTION OF DIODE LENGTH l, $w = 0.3$ MM

l, mm	1.06	0.73	0.36
k_{tr}, cm^{-1}	12	18	110

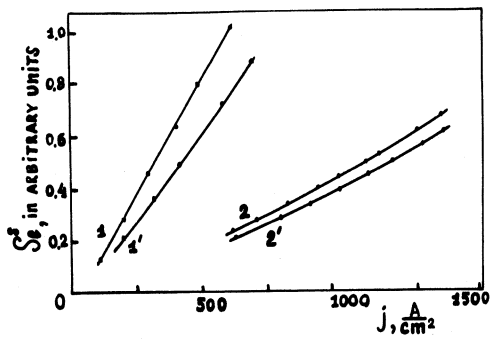


Fig. 2. Dependence of radiation intensity S_l^s on the current for the diode DI. 1, 2: With the Fabry-Perot resonator ($l = 1.75$ and 0.36 mm, $j_t = 670$ and 1400 A/cm^2 accordingly), 1', 2': with four ground walls ($l = 1.70$ and 0.32 mm, respectively), $w = 0.3$ mm.

Fabry-Perot cavity. The analogous dependence was obtained for this particular diode but possessing four ground sidewalls.

As can be seen from Fig. 3 the value $j_0 = 750$ A/cm^2 determined by the cutoff of the straight line $\delta \sim 1/\sqrt{s}$ is of the same order with parameter $j_0 = 350$ A/cm^2 measured in accordance with the method [6]-[8]. The linear dependence of δ on $1/\sqrt{s}$ in the limits of the experimental error means that $k_{tr} \sim 1/\sqrt{s}$. To define k_{tr} from the value of δ for a given s, parameter $\beta = 2.7 \times 10^{-2}$ cm/A was measured additionally [8] and coefficient Δ was obtained from the slope $\delta \sim 1/\sqrt{s}$. For the diode DI having Fabry-Perot cavity $\Delta = 3.2$, with four

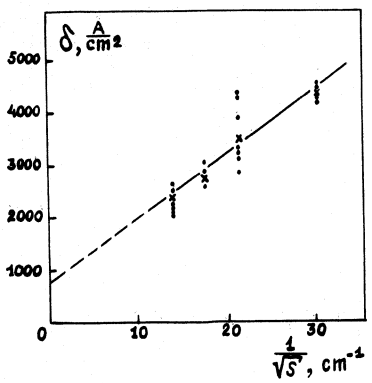


Fig. 3. Dependence of the value $\delta = j_0 + \beta^{-1} k_{tr}$ on $1/\sqrt{s}$ for the diode DI with the Fabry-Perot resonator. The average δ for ten current couples j_1 and j_2 is marked by ×.

ground sidewalls $\Delta = 3.4$, which practically coincides with theoretical data [4].

While comparing the trapped radiation loss coefficient, calculated from the displacement of maxima S_l^m and S_l^s (Table I), with k_{tr}, determined from the data measurements of $S_l^s(j)$ (Table II) for the diode with Fabry-Perot resonator, it becomes evident that the greatest coefficient difference is characteristic of the diode with greater cavity length. This is apparently conditioned by the spatial nonuniformity of the trapped radiation loss coefficient. When $l \approx w$, the values of k_{tr} measured according to both methods are approximately equal.

The value of k_{tr} given in Table I for large l defines mainly the gained luminescence, propagating perpendicularly to the resonator mirrors, as $S_l^m(\nu)$ measurements were undertaken in a small space angle. And the value of k_{tr} from Table II determines the averaged radiation density over all directions of light propagation.

The method for the determination of the trapped radiation loss coefficient suggested in Section II is convenient to use in the frequency range close to the frequency range of the stimulated emission. It should be noted, however, that the laser parameter values obtained in accordance with the given method and from the threshold characteristics [6], [7] may differ slightly from one another. In particular, the exceeding of the zero current, found from the luminescent measurements over threshold parameter j_0 may be the consequence of the fact that the threshold measurements correspond to the variable frequency at which the stimulated emission occurs rather than to the fixed frequency as in case of estimation of δ. The nonlinearity of $W_l(\nu)$ and $k(\nu)$ dependences on injection current should be taken into account for ν, far from the lasing frequency. Furthermore, large trapped radiation densities inevitably cause nonlinear optical effects resulting in the gain saturation [11].

IV. Discussion

The theoretical and experimental investigation given in Sections II and III lead to the conclusion that under certain conditions the trapped radiation level in injection lasers becomes considerable. This is accompanied by a sharp increase

TABLE II
THE VALUES k_{tr} FOR THE DIODE DI WITH FABRY-PEROT CAVITY AND FOUR GROUND SIDEWALLS MEASURED ACCORDING TO δ VERSUS $\sqrt{s}$, $w = 3.3$ MM

Diode with Fabry-Perot cavity		Diode with four ground sidewalls	
ℓ, mm	K_{ℓ}, cm^{-1}	ℓ, mm	K_{ℓ}, cm^{-1}
1.75	44	1.70	47
1.06	57	0.93	64
0.73	68	0.70	74
0.36	97	0.32	110

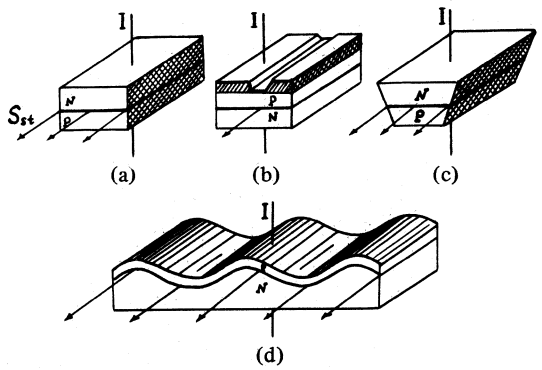


Fig. 4. Possible constructions of injection lasers for harmful radiation suppression in the active region.

of axial mode laser threshold and decrease of power and quantum efficiency of the stimulated emission. Therefore, for effective work of laser diodes it is necessary to undertake special measures, leading to a decrease of trapped radiation density within the active region.

Our experiment results testify that k_{tr} is more in the diode with the Fabry-Perot resonator than in the diode with a four-ended resonator, but less than in the diode with four ground sidewalls. The harmful radiation level in the injection laser can be decreased due to the rough treatment of the diode sidewalls [Fig. 4(a)].

As is expected, u_l is minimum for the diode having a small value of s. The construction of the laser diode with a long but narrow active region (the diode with the stripe geometry) is shown in Fig. 4(b). Using such diodes the lowest thresholds of the injection lasers [15], [16] were obtained.

In the diode with the trapezoidal cross section [Fig. 4(c)] the part of radiation reflected from the lateral surfaces is absorbed in the low passive region and does not return to the resonator, and then k_{tr} increases.

The common defect is peculiar to injection lasers shown in Fig. 4(a) and (c). The effectiveness of suppression of harmful radiation sharply falls at the considerable increase of the diode width w. The expansion of the stimulated emission layer area can be achieved only by rejection of planar p-n-junctions. Such an injection laser is shown in Fig. 4(d) in which the surface of the p-n-junction is similar to a cylindrical surface, the generating line of which is perpendicular to the resonator mirrors, and the guide path resembles a sinusoid [17]. The radius of curvature of the guide path should be chosen to

suppress the amplified luminescence in the lateral direction. The lasers with a nonplanar p-n-junction will make possible the obtaining of a coherent beam of large power.

References

[1] "Metody rascheta opticheskikh kvantovykh generatorov," in *Nauka i Tekhnika*, B. I. Stepanov, Ed. Minsk, BSSR, vol. 1, 1966, vol. II, 1968.

[2] T. N. Danilova, L. M. Kogan, S. S. Meskin, D. N. Nasledov, and B. V. Tsarenkov, *Fiz. Tverd. Tela*, vol. 8, p. 2462, 1966.

[3] R. Ulbrich and M. H. Pilkuhn, *Appl. Phys. Lett.*, vol. 16, p. 516, 1970.

[4] V. K. Kononenko and V. P. Gribkovskii, *Fiz. Tekh. Poluprov.*, vol. 5, p. 1875, 1971.

[5] V. G. Karnauchov, I. V. Krvyukova, and A. I. Petrov, *Fiz. Tekh. Poluprov.*, vol. 1, p. 1362, 1967.

[6] V. A. Samoilyukovich, V. P. Gribkovskii, R. V. Efremova, L. A. Kravtsov, and A. K. Lyakhovich, *Zh. Prikl. Spektr.*, vol. 8, p. 50, 1968.

[7] V. P. Gribkovskii, V. K. Kononenko, and V. A. Samoilyukovich, *Phys. Stat. Sol. (a)*, vol. 3, p. 353, 1970.

[8] V. P. Gribkovskii, V. K. Kononenko, and V. A. Samoilyukovich, in *Kvantovaya Electronica i Lazernaya Spektroskopiya*, Minsk, 1971, p. 285.

[9] M. Ettenberg, H. F. Lockwood, and H. S. Sommers, *J. Appl. Phys.*, vol. 43, p. 5047, 1972.

[10] G. I. Ryabtsev, V. P. Gribkovskii, and V. A. Samoilyukovich, *Zh. Tekh. Fiz.*, vol. 45, p. 919, 1975.

[11] V. K. Kononenko and V. P. Gribkovskii, *Opt. i Spektr.*, vol. 29, p. 975, 1970.

[12] V. A. Zyulkov, G. I. Ryabtsev, and V. A. Samoilyukovich, *Zh. Prikl. Spektr.*, vol. 21, p. 337, 1974.

[13] V. P. Gribkovskii and B. I. Stepanov, *Dokl. Skad. Nauk.* (USSR), vol. 183, p. 67, 1968.

[14] V. P. Gribkovskii and V. A. Samoilyukovich, *Zh. Prikl. Spektr.*, vol. 11, p. 170, 1969.

[15] J. C. Dyment, L. A. D'Asaro, J. C. North, B. I. Miller, and J. E. Ripper, *Proc. IEEE*, vol. 60, p. 726, 1972.

[16] T. Tsukada, *et al.*, *Appl. Phys. Lett.*, vol. 20, p. 344, 1972.

[17] V. P. Gribkovskii, V. A. Samoilyukovich, and V. A. Andreichev, *Zh. Prikl. Spektr.*, vol. 18, p. 140, 1973; see also V. P. Gribkovskii, "Theory of light absorption and emission in semiconductors," *Nauki i Tekhnika.* Minsk, BSSR, 1975.

Increased Tuning Range of $Pb_{1-x}Sn_xSe$ Diode Lasers Using Small Magnetic Fields

HERBERT FLICKER, SENIOR MEMBER, IEEE, AND NORRIS NERESON

Abstract—A $Pb_{0.96}Sn_{0.04}Se$ laser diode emitting in the 815-835-cm^{-1} region with current tuning has been examined with applied magnetic fields at 7 kG and below. With increasing magnetic field the laser gain curve broadens, allowing more laser cavity modes (separated by 1.8 cm^{-1}) to oscillate at a given current, and yielding a larger tuning range with current for each cavity mode. Using a combination of current tuning and a constant magnetic field, laser emission was achieved from 800 to 850 cm^{-1} with 90 percent coverage of the spectral interval.

I. Introduction

PREVIOUS WORK [1] on combined current and magnetic tuning of semiconductor laser diodes has shown that with magnetic fields in the 7.5-50-kG range a continuous tuning range of about 90 cm^{-1} was achieved in the region of 1200 cm^{-1}. The present investigation confirms that the total wavenumber tuning coverage as well as individual mode tuning intervals can be greatly extended by employing small magnetic fields below 7.5 kG. The particular diode employed in this work yielded only 3 or 4 modes of limited tuning range ($\Delta\nu \sim 0.4$ cm^{-1}) in the region between 815-835 cm^{-1} with current tuning at zero field. These few modes at zero field were consistently observed over five months of working with this same diode. The main objective of the present work was to determine if the above restricted frequency coverage could be enhanced by placing the diode in small magnetic fields. The experimental results verified that current tuning combined with applied fields below 7.5 kG extended the emission over the 800-850-cm^{-1} range with 90-percent coverage and increased the tuning-width interval of individual modes ($\Delta\nu \sim 1.0$ cm^{-1}). Current tuning of the individual modes at constant magnetic field was stable and showed a linear response between diode current and output frequency; however, the energy output of individual modes with magnetic field was reduced by factors of 3 to 100 as compared with the energy output at zero field.

Manuscript received December 2, 1975; revised February 25, 1976. This work was performed under the auspices of the U.S. ERDA.

The authors are with the Los Alamos Scientific Laboratory, University of California, Los Alamos, NM 87545.

II. Experimental

The diode laser employed in the present work was a commercial single crystal, $Pb_{0.96}Sn_{0.04}Se$, fabricated by the A. D. Little Co.; the approximate dimensions were 0.2 × 0.2 × 0.5 mm. The threshold current was about 1.2 A and the maximum recommended current was 2.0 A. The diode was mounted on the copper cold finger of a helium cryostat. The current flow along the ⟨100⟩ crystallographic axis of the diode was parallel to the applied magnetic field. The cryostat outer dimensions limited the magnetic field intensity to 7.5 kG.

A simple optical arrangement was employed as shown in Fig. 1. The diode laser energy was collected by a T1 (Br, I) $f/1.5$ lens and focused into the entrance slit of a Jarrell-Ash 0.5-m spectrometer or a Spex 1-m spectrometer. The energy

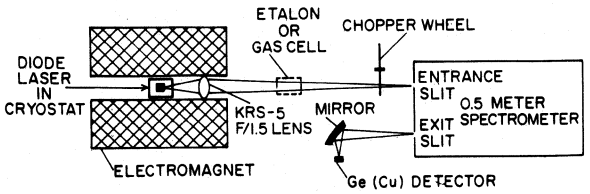


Fig. 1. Optical arrangement for studying laser diode emission modes with small magnetic fields applied to the diode.

output of the spectrometer was collected by an ellipsoidal mirror which was focused onto a Ge (Cu-doped) detector. A mechanical chopper (∿700 Hz) mounted in front of the spectrometer entrance slit modulated the laser beam for electrical detection by a lock-in amplifier. The diode could be current tuned by programming a regulated current supply from an external ramp generator. Single laser modes typically tuned over a current interval of about 0.5 A.

Fig. 2 shows the increased number of emission modes obtained with applied fields of 6 and 7 kG compared with the modes at zero field. These data were obtained by recording the detector output at constant diode current (1.9 A) as a function of the motor-driven spectrometer reading in wavenumbers. The mode amplitudes with the 6- and 7-kG fields applied are considerably less than the strongest mode at zero field but are still sufficiently intense for a satisfactory detector signal to noise ratio. This was experimentally verified with absorption-line observations on an ammonia gas cell. The emission modes obtained with the magnetic field applied shifted towards higher wavenumbers than the zero-field modes. However, magnetic field modes at lower wavenumbers than the zero-field case were also observed (Fig. 2) at 6 kG when the Landau level moves below the zero-field Fermi level. In Fig. 2 the width of the recorded mode lines represents the slit function of the monochromator (∿1.3 cm^{-1}) rather than the linewidth of the diode laser which is less than 10^{-4} cm^{-1}.

A more detailed presentation of the diode emission modes with magnetic field strength at a constant diode current of 1.7 A is shown in Fig. 3. These data show two predominant effects from the applied magnetic field: 1) an increased number of modes appear with application of the field; and 2) the majority of the modes show a slight shift to higher wavenumbers as the field strength is increased. The latter effect is similar to the tuning effect that is observed from current tuning a diode. In both cases the frequency change is produced by a change in the index of refraction of the diode cavity. The lines drawn through the observed points or modes in Fig. 3 show the wavenumber trend of individual modes as the field is changed.

The data in Fig. 3 show that 9 modes with an average spacing of $\delta\nu = 1.8 \pm 0.1$ cm^{-1} appear at a field strength of 7 kG and a diode current of 1.7 A. This permitted quasi-continuous frequency coverage over the 825-845-cm^{-1} emission region by varying the diode current around 1.7 A. Several low wavenumber modes in Fig. 3 with a mode spacing less than the cavity mode separation disappear at the higher fields. Using a diode cavity length, l, of 0.5 mm, the dispersive index of refraction, n, of the diode crystal can be calculated as $n = 1/(2l\delta\nu) = 5.6$. This value for the dispersive index of refraction is reasonable for $Pb_{1-x}Sn_xSe$ at the energy gap.

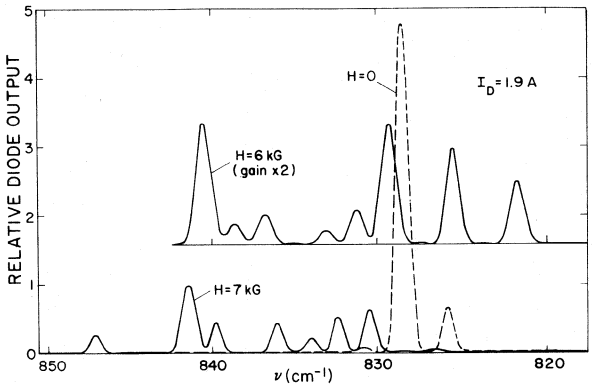


Fig. 2. Detector signal amplitudes of laser diode modes versus wavenumber for applied magnetic fields of H = 7, 6, and 0 kG. Amplifier gain was the same for H = 7 and 0 kG but was increased by a factor of 2 for H = 6 kG.

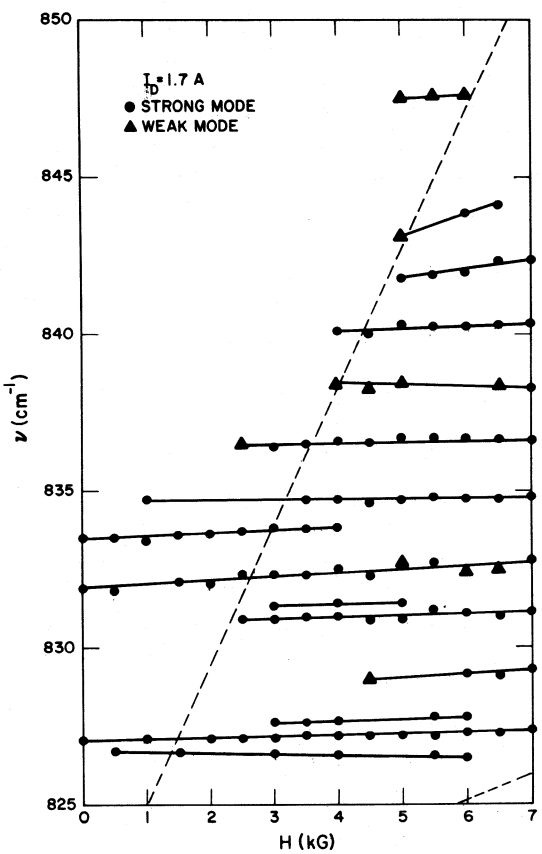


Fig. 3. Observed emission modes from laser diode versus applied magnetic field. Guide lines have been drawn through the observed points so as to easily identify the individual modes. The dashed lines show magnetic field tuning values of 4.4 and 0.77 cm^{-1}/kG for $Pb_{0.95}Sn_{0.05}Se$[5].

Fig. 3 shows that the cavity modes do not all tune at the same rate, $d\nu/dH$. Two modes, at 826.5 and 838.5 cm^{-1}, have negative $d\nu/dH$ which makes the derivative of the index of refraction, dn/dH, positive; the mode at 834.7 cm^{-1} has a zero $d\nu/dH$ and dn/dH. All the other modes have the positive $d\nu/dH$ previously reported for PbSe [1], [2].

For these modes $dv/dH = 0.12\ cm^{-1}/kG$, which yields $(\partial n/\partial H)_v = -n/v\ (dv/dH) \simeq -7 \times 10^{-4}/kG$. Allario *et al.* [1] report that $(\partial n/\partial H)_v$ for PbSe increased from -0.8×10^{-4} to -7×10^{-4} kG as the field went from 11 to 21 kG. The present results, obtained at lower fields and in an alloy semiconductor, indicate that $(\partial n/\partial H)_v$ depends upon the wavenumber of the mode and can vary from -7×10^{-4} to 7×10^{-4} kG.

The application of a small magnetic field to the laser diode usually resulted in a larger mode wavenumber tuning interval for a given current ramp. A germanium etalon inserted in the beam path provided information concerning this mode tuning range. Fig. 4 shows a recorder trace of the detector output at $H = 0$ and $H = 7$ kG for the same current ramp at approximately the same spectrometer setting. With the 7-kG field, a mode was obtained which covered a tuning range of 1.2 cm^{-1}, whereas a range of only 0.4 cm^{-1} was obtained with zero field. The extremities of the 7-kG mode in Fig. 4 show the decreased signal-to-noise ratio existing with applied fields because of the smaller energy output; however, the etalon pattern shows that a useful signal is obtained over 80 percent of the mode tuning range. The etalon response in this figure also verifies that the diode current tuning rate remains linear with the constant applied magnetic field. Fig. 5 shows mode tuning ranges obtained from current tuning at intermediate magnetic field values. The data show that increased mode tuning ranges occur at the higher magnetic fields; the detailed behavior of this curve is not understood, but a qualitative explanation is offered in the following section. The vertical bars indicate the range of repeated measurements.

The data in Fig. 6 summarize the Ge:Cu detector signal amplitudes obtained from the laser diode modes at magnetic fields of 7 and 0 kG. The modes in this figure were obtained from two diode currents of 1.3 and 1.7 A. As mentioned previously, the zero-field modes show the largest signal amplitudes but a restricted number of emission modes. Combining the above two fixed current values and an applied 7-kG field, emission is obtained over about 90 percent of the 800-850-cm^{-1} range but with reduced signal amplitudes, especially at the extremeties of the above wavenumber interval. By summing the signal amplitudes of the modes it can be seen that the total power output of the diode drops by approximately 20 percent when a 7-kG field is applied.

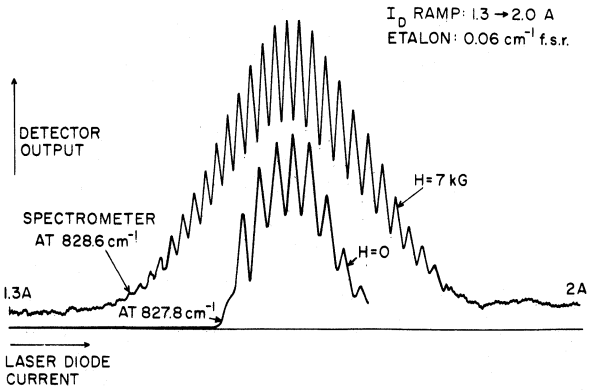


Fig. 4. Laser diode tuning range interval obtained with current ramp at applied magnetic fields of $H = 7$ kG and $H = 0$. A germanium etalon inserted in the beam path verifies the frequency change.

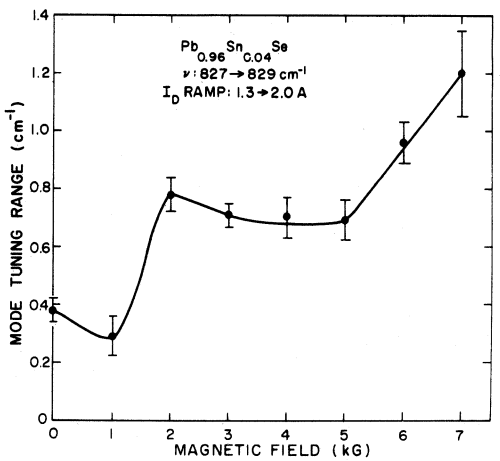


Fig. 5. Laser diode mode tuning ranges obtained from current tuning at different applied magnetic fields.

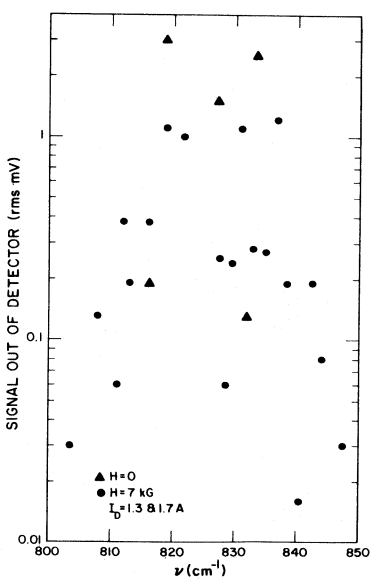


Fig. 6. Summary of Ge:Cu detector output signals from $Pb_{0.96}Sn_{0.04}Se$ laser diode versus wavenumber at $H = 7$ kG and $H = 0$.

III. Theoretical

The increase in the number of oscillating cavity modes and the tuning range of modes with magnetic field implies a broadening of the laser gain curve with magnetic field. Existing theory is adequate for a qualitative explanation of the effect.

A magnetic field in the Z direction quantizes the energy of the charge carriers of the semiconductor with respect to motion in the XY plane. The lowest Landau level in the conduction band and the highest Landau level in the valence band, both having quantum numbers equal to zero, are shown in Fig. 7. The two cyclotron levels are further split into the two spin states, as shown in the figure. Four transition energies are possible

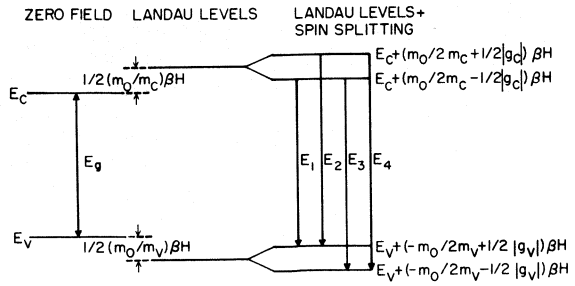


Fig. 7. Quantized energy levels of the charge carriers in a magnetic field, and the radiative recombination transitions E_1, E_2, E_3, and E_4.

$$E_1 = hc\nu_1 = E_g + 1/2m_0\left[\frac{1}{m_c}+\frac{1}{m_v}-|g_c|-|g_v|\right]\beta H$$

$$E_2 = hc\nu_2 = E_g + 1/2m_0\left[\frac{1}{m_c}+\frac{1}{m_v}+|g_c|-|g_v|\right]\beta H$$

$$E_3 = hc\nu_3 = E_g + 1/2m_0\left[\frac{1}{m_c}+\frac{1}{m_v}-|g_c|+|g_v|\right]\beta H$$

$$E_4 = hc\nu_4 = E_g + 1/2m_0\left[\frac{1}{m_c}+\frac{1}{m_v}+|g_c|+|g_v|\right]\beta H$$

where the symbols are defined as

$E_g = E_c - E_v$ = The semiconductor energy gap;
m_c, m_v = appropriate effective masses for electrons and holes, respectively;
m_0 = the free electron mass;
g_c, g_v = the gyromagnetic ratios of electrons and holes, respectively;
β = Bohr magneton = $e/2m_0c$;
H = magnetic field.

It is known that in the lead salt system the gyromagnetic ratios of holes and electrons are of opposite sign and approximately equal in absolute magnitude [3], [4].

The selection rules allow the spin flip transitions E_1 and E_4 but previous studies [1], [5]-[7] have shown that the spin-conserving transitions E_2 and E_3 dominate the laser process at low fields (below 10 kG). Furthermore, in the lead salt semiconductors, $|g_c| \simeq |g_v|$ causing the transitions E_2 and E_3 to be degenerate. As the field is increased the upper conduction band state is driven above the quasi-Fermi level for electrons, and the lower valence band state is driven below the quasi-Fermi level for holes, cutting off first the E_4 transition at relatively low fields and then the E_2, E_3 transitions at $H > 10$ kG. The problem of laser transitions between the Landau levels in the conduction and valence bands is more complex than the model given in Fig. 7. The momentum k_z in the direction of the magnetic field is not quantized, and each Landau level has a continuum of states having an energy quadratic in k_z. In addition, the density of states in the conduction and valence bands are severely altered when the magnetic field is imposed, splitting the free states into Landau levels. The results of this experiment indicate that it is not only possible for the E_1, E_2, and E_3 laser gain curves to be simultaneously above threshold, but that the wavelength region of overlap between the broad gain curves can also be above threshold. The magnetic field dependence of the energy of the transitions in $Pb_{0.95}Sn_{0.05}Se$ are [7]

$$\frac{d\nu_1}{dH} \simeq 0.77 \text{ cm}^{-1}/\text{kG}$$

$$\frac{d\nu_2}{dH} \simeq \frac{d\nu_3}{dH} \simeq 4.4 \text{ cm}^{-1}/\text{kG}.$$

These two slopes are superimposed on the experimental data in Fig. 3, with the value at zero field arbitrarily chosen to enclose the maximum number of modes. The zero-field intercept falls below the observed frequency of oscillation because of a Burstein shift (i.e., an apparent increase in energy gap due to deep penetration of the quasi-Fermi levels into the bands). The slope of the E_1 transition has only a weak dependence on the alloy composition, but the slope of the E_2, E_3 transition increases rapidly with increasing SnSe [7]. Thus the data for our $Pb_{0.96}Sn_{0.04}Se$ laser diode lie below the straight line having a slope for the E_2, E_3 transition derived from a $Pb_{0.95}Sn_{0.05}Se$ laser diode.

In the experimental section mention was made of two modes that show a positive dn/dH. Calculations of the magnetodispersion in low-band-gap semiconductors have been performed yielding the result that dn/dH is negative [8]. These two modes appear to lie near the peak of the laser gain curves of the E_1, E_2, and E_3 transitions, as drawn in Fig. 3. The magnetoabsorption of the spin-split Landau levels may be sharply peaked in this region, causing the index of refraction to have a pole. The index would decrease as the magnetic field moved the pole away from the cavity mode frequency.

IV. Conclusion

It has been shown that significant improvement in the tunability of lead salt diode lasers is accomplished by relatively small magnetic fields. A change in sign of the derivative of the index of refraction with respect to magnetic field has been observed and appears to be related to the position of the Landau levels.

Acknowledgment

The authors wish to thank F. Allario, J. Butler, and C. Cantrell, III, for helpful conversations. R. Hinsley aided in performing the experiments. This paper benefited from excellent criticism and editing by an anonymous reviewer.

References

[1] F. Allario, C. H. Bair, and J. F. Butler, "High resolution spectral measurements of SO_2 from 1176.0 to 1265.8 cm^{-1} using a single PbSe laser with magnetic and current tuning," *IEEE J. Quantum Electron.*, vol. QE-11, pp. 205-209, May 1975.

[2] F. Allario, private communication. The authors of [1] observed a negative dv/dH at 7.5 kG when they were measuring an absorption line in a current scan.

[3] D. R. Mitchell, E. D. Palik, and J. N. Zemel, "Magneto-optical band studies of epitaxial PbS, PbSe, and PbTe," in *Physics of Semiconductors, Proc. 7th Int. Conf. Semiconductors.* Paris: Dunod, 1964, p. 325.

[4] E. D. Palik, D. L. Mitchell, and J. N. Zemel, "Magneto-optical

studies of the band structure of PbS," *Phys. Rev.*, vol. 135, pp. A763–A778, Aug. 1964.
[5] J. F. Butler and A. R. Calawa, "Magneto-emission studies of PbS, PbTe, and PbSe diode lasers," in *Physics of Quantum Electronics*, P. L. Kelley, B. Lax, and P. E. Tannewald, Ed. New York: McGraw-Hill, 1966, p. 458.
[6] J. F. Butler, "Magneto-emission experiments in $Pb_{1-x}Sn_xTe$," *Solid State Communications*, vol. 7, p. 909, July 1969.
[7] A. R. Calawa, J. O. Dimmock, T. C. Harmon, and I. Melngailis, "Magnetic field dependence of laser emission in $Pb_{1-x}Sn_xSe$ diodes," *Phys. Rev. Lett.*, vol. 23, pp. 7–10, July 1969.
[8] B. Lax, "Progress in magneto-optical effects," in *Physics of Semiconductors, Proc. 7th Interim Conf. on Semiconductors*. Paris: Dunod, 1964, p. 253.

The Effect of Linewidth on the Efficiency of Two-Photon-Pumped Frequency Converters

EDDY A. STAPPAERTS, STUDENT MEMBER, IEEE, GERHARD W. BEKKERS, JAMES F. YOUNG, MEMBER, IEEE, AND STEPHEN E. HARRIS, FELLOW, IEEE

Abstract—**The efficiency of two-photon-pumped frequency converters as a function of the pump laser detuning and linewidth, and of the linewidth of the selected nonallowed atomic transition is studied. We show that pressure broadening of the atomic transition is a key parameter in the design of these converters. A technique is developed to measure this linewidth as a function of either self- or foreign-gas broadening using a broad-band pump laser. Measurements of the linewidth of the $3s^2S$–$3d^2D$ transition of Na, and its device implications, are presented.**

I. Introduction

TWO-PHOTON-PUMPED frequency converters are useful for the generation of tunable vacuum ultraviolet radiation, and provide an excellent technique for the conversion of infrared radiation into the visible and near ultraviolet [1]–[3]. Such a converter consists of a pumping laser whose frequency ω_0 equals approximately one-half the frequency of a nonallowed transition in an atomic vapor. The pump radiation sets up a strong excitation in the atom at a frequency $2\omega_0$ which cannot radiate because of the absence of a dipole moment. A third photon of frequency ω couples this excitation to an oscillation mode which does have a dipole moment, producing output radiation at frequencies $2\omega_0 \pm \omega$. The strength of the atomic excitation at $2\omega_0$, and thus the conversion efficiency, depends directly on the laser detuning, and on the atomic and laser linewidths.

In Section II below we calculate the functional dependence of the conversion efficiency of two-photon-pumped converters on the laser detuning and linewidth, and on the atomic linewidth, including both pressure and Doppler broadening. Our results show that the pressure broadening of the nonallowed transition is a key parameter in the design of UV generators and IR up-converters. Although a number of spectroscopic techniques currently exist to measure such broadening [4]–[7], they require rather sophisticated, narrow-bandwidth, tunable lasers. In Section III we describe a technique for measuring the pressure broadening of a nonallowed transition based on the results of Section II. The technique uses the broad-band laser source which would be used as the pump for the converter under evaluation. Section IV describes such measurements for an IR up-converter operating around 9 μ utilizing the $3s^2S$ to $3d^2D$ transition in Na [3].

Manuscript received December 8, 1975. This work was supported in part by the Air Force Cambridge Research Laboratory under Contract F19628-75-C-0046, and in part by the U.S. Army Research Office.

E. A. Stappaerts, J. F. Young, and S. E. Harris are with the Microwave Laboratory, Stanford University, Stanford, CA 94305.
G. W. Bekkers is with the Microwave Laboratory, Stanford University, Stanford, CA 94305, on leave from the IBM Corporation, San Jose, CA, under the Resident Study Program.

II. Calculation of Conversion Efficiency

The pumping radiation is described by a superposition of randomly phased discrete laser modes with center frequency ω_0, mode spacing $\Delta\omega$, amplitudes E_n, and phases φ_n. The second field is also assumed to be made up of a superposition of independent modes. Because of the randomness of the phases, each of these modes will be up-converted independently, and the power up-conversion efficiency is the same as that of a single mode. Therefore, in what follows, we treat this field as monochromatic with frequency ω and amplitude E. The dipole moment at the generated frequencies $2\omega_0 \pm \omega$ is given by [8]

$$P^{(3)}(t) = K_1 E e^{i\omega t} \sum_{k,n} E_n E_{k-n} \cdot \left\{ \frac{e^{-i(2\omega_0 + k\Delta\omega)t + i(\varphi_n + \varphi_{k-n})}}{(\omega_{02} - 2\omega_0 - k\Delta\omega) - i\gamma/2} \right\} + \text{c.c.} \qquad (1)$$

where

$$K_1 = \sum_{\text{paths}} \frac{N \mu_{01}\mu_{12}\mu_{23}\mu_{30}}{8\hbar^3 (\omega_{01} - \omega_0)[\omega_{03} - (2\omega_0 \pm \omega)]}.$$

In this equation the ω_{0j} and μ_{ij} are atomic transition frequencies and matrix elements, γ is the pressure-broadened linewidth of the individual atoms, and N is the number density of the nonlinear species. A summation over all possible paths for the first and third steps in the perturbation sequence is also included [9]. To incorporate Doppler broadening in the theory we note that, for an observer traveling with the incident electric field, atoms moving at different velocities have different apparent resonance frequencies: $\omega_{02}(x) = \omega_{02} + x$. For a Maxwellian velocity distribution, the frequency deviation x has a Gaussian distribution function

$$p(x) = \frac{1}{\sqrt{2\pi\gamma_D^2}} e^{-x^2/2\gamma_D^2} \tag{2}$$

where

$$\gamma_D = \sqrt{\frac{kT\omega_{02}^2}{Mc^2}}.$$

Combining (1) and (2), and substituting into Maxwell's equations, we find that the power conversion efficiency for the second field is given by

$$\mathcal{E}(\gamma, \gamma_D, \delta, \Delta\omega) = K_2 \frac{P_{av}^2}{\gamma_D^2} \sum_k G(k) \left[F_R^2(k) + F_I^2(k)\right] \tag{3}$$

where

$$P_{av} = \frac{1}{2}\sum_n E_n^2$$

$$G(k) = \sum_n \frac{E_n^2 E_{k-n}^2}{P_{av}^2}$$

$$F_R(k) = \int_{-\infty}^{\infty} \frac{(\omega_{02} - 2\omega_0 + x - k\Delta\omega)\, e^{-x^2/2\gamma_D^2}\, dx}{(\omega_{02} - 2\omega_0 + x - k\Delta\omega)^2 + (\gamma/2)^2}$$

$$F_I(k) = \int_{-\infty}^{\infty} \frac{(\gamma/2)\, e^{-x^2/2\gamma_D^2}\, dx}{(\omega_{02} - 2\omega_0 + x - k\Delta\omega)^2 + (\gamma/2)^2}$$

$$K_2 = \frac{2\eta_0^2\omega_s^2 L_c^2 K_1^2}{\pi^3} \sin^2\left(\frac{\pi}{2}\frac{L}{L_c}\right).$$

In these expressions, P_{av} is the average power in the pump field, $G(k)$ is the normalized autoconvolution of the power spectrum of the pump field, $F_R(k)$ and $F_I(k)$ are the real and imaginary parts of the plasma dispersion function [10], η_0 is the impedance of vacuum, ω_s is the generated frequency, L is the length of the medium, and L_c is the coherence length for the process [9]. If the coherence length is set by the nonlinear species itself (no phase matching), then its value is inversely proportional to N and the factor K_2 is independent of pressure.

Given the values of the parameters δ, $\Delta\omega$, γ_D for a particular system it is quite easy to evaluate the efficiency given by (3) numerically as a function of the atomic linewidth γ. In most cases of practical interest, however, (3) can be reduced to a simple closed-form relationship. Generally the laser spectrum consists of a large number of modes with a spacing much smaller than both the atomic and Doppler linewidths, in which case the summations over n and k in (3) can be approximated by integrals. In addition, the spectrum of the laser can usually be represented by a Gaussian distribution:

$$E_n^2 = E_0^2\, e^{-4n^2\Delta\omega^2/\delta^2} \tag{4}$$

where δ is the laser linewidth, defined as $(\ln 2)^{-1/2}$ times the full width at half-maximum (FWHM).

Consider first the case when the laser is detuned several linewidths from one-half the two-photon transition frequency. For this case (3) reduces to

$$\mathcal{E} = \frac{8\pi K_2 P_{av}^2}{(\omega_{02} - 2\omega_0)^2}. \tag{5}$$

This is the well-known quadratic reduction of efficiency with detuning, independent of the laser, atomic, and Doppler linewidths.

When the laser is tuned on-resonance and the pressure is low enough so that Doppler broadening dominates pressure broadening, i.e., $\gamma_D > \gamma$, then

$$\mathcal{E} = 4(\pi^2\sqrt{2} + 8\sqrt{\pi})\, K_2 \frac{P_{av}^2}{\gamma_D \delta}. \tag{6}$$

In the high-pressure region where pressure broadening dominates

$$\mathcal{E} = 16\pi^2 \sqrt{\frac{2}{\pi}} K_2 \frac{P_{av}^2}{\gamma\delta}. \tag{7}$$

In view of (5) one might not initially expect the *linear* reduction of efficiency with laser linewidth of (6) and (7). Physically, however, it is clear that a resonant atomic response is produced not only by the pump mode exactly at half the transition frequency, but also by all combinations of two modes whose sum is within the atomic linewidth [11]. Thus efforts to significantly narrow the pump linewidth, usually at the expense of simplicity and peak power, are often not effective in improving efficiency. A similar analysis of two-photon absorption can be used to show that, on resonance, the absorption cross section is also a linear, rather than quadratic, function of laser linewidth.

For image up-converters of this type it is easy to show that the conversion efficiency for a given resolution and pump power increases quadratically with the atomic number density [12]. As the density is increased, however, pressure broadening will dominate the atomic linewidth, and (7) indicates that the efficiency obtainable in a single coherence length will be reduced. In some cases there may also be a significant contribution to the broadening from a foreign buffer gas. Thus the pressure broadening of the selected nonallowed transition is a key parameter in the design of two-photon-pumped frequency converters.

III. Measurement of Pressure Broadening

Conceivably one could determine the limiting efficiency of a given frequency converter by merely measuring conversion efficiency while raising the atomic and/or buffer gas density. However, other effects such as atomic and molecular absorp-

tion, change of coherence length caused by the foreign gas, thermal defocusing, and the Kerr effect also influence the efficiency. Thus an independent measurement of pressure broadening (both self- and foreign-gas) is required to optimize the performance of the device.

Several methods are currently available to measure the linewidth of nonallowed transitions [4]-[7] but the required laser sources are not often available. Using the results of Section II, it is possible to quickly and conveniently measure these parameters in cases of practical interest using just the unnarrowed pump laser.

Equation (5) shows that when the laser is sufficiently detuned, the efficiency is independent of the linewidth of both the laser and the atomic transition, but it will still be influenced by the other processes mentioned above. Thus these effects may be normalized out by making efficiency measurements both on-resonance and off-resonance as a function of pressure, and taking a ratio. The theoretical result, in the high-pressure region where $\gamma > \gamma_D$, is the ratio of (7) to (5)

$$R = 2\sqrt{2\pi} \times \frac{(\omega_{02} - 2\omega_0)^2}{\gamma \times \delta}. \tag{8}$$

The detuning and laser linewidth can be eliminated by normalizing to the low-pressure asymptote of R, R_0 found from (6) and (5):

$$\frac{R}{R_0} = \frac{4\pi}{\pi\sqrt{\pi} + 4\sqrt{2}} \frac{\gamma_D}{\gamma}. \tag{9}$$

Thus one can determine the pressure-broadened linewidth γ from the measured values of R and R_0:

$$\gamma = 1.12 \times \gamma_D \times \frac{R_0}{R}. \tag{10}$$

The procedure does not require detailed knowledge of the laser linewidth and spectral composition, but is valid only in the higher pressure regime where $\gamma > \gamma_D$. Practically, this is usually the only region where values of γ are of interest, and extrapolation to lower pressures can usually be made with confidence.

A more rigorous determination of γ, valid at all pressures, can be made using an exact evaluation of (3) for the efficiency. This is useful if detailed knowledge of γ at intermediate pressures is required, and/or the assumptions used to reduce (3) to closed form are not valid. The experimental procedure is identical to that explained above. Two sets of efficiency measurements, on- and off-resonance, are made and the normalized ratio R_m/R_{m0} is plotted versus the pressure of the broadening agent (the subscript m refers to measured values, c to calculated values). Using the fixed parameters γ_D, δ, and $\Delta\omega$, the ratio R_c/R_{c0} is computed as a function of γ from (3) and also plotted. Note that since the efficiency off-resonance is a constant independent of γ, only one numerical evaluation of (3) per point is required to calculate R_c/R_{c0}. The normalized curves of measured and calculated efficiency are used to determine γ from the relation $[R_m(P)/R_{m0}] = [R_c(\gamma)/R_{c0}]$. Thus for any given pressure P, the linewidth γ may be read from the point on the calculated curve associated with the value $R_m(P)/R_{m0}$. Although this technique requires more detailed knowledge of the system, and also some computation, it is completely general and can determine pressure-broadened linewidths considerably smaller than the Doppler linewidth. The two procedures are illustrated below in Section IV.

IV. Measurement of the Na $3s^2S$-$3d^2D$ Transition

We have measured the foreign-gas broadening by He of the $3s^2S$-$3d^2D$ transition in Na using the above techniques. A pumping wavelength of 6856 Å was obtained from an optical parametric oscillator, and the idler frequency at 2.37 μ was used as the input frequency ω to generate the observed lower sideband signal at $2\omega_0 - \omega$ (4006 Å). The pumping radiation had a linewidth of 2 cm^{-1} and a mode spacing of 0.028 cm^{-1}. Both incident beams had a peak power of about 1 kW and were focused into a small Na heat pipe at a temperature of about 700 K, yielding a Doppler linewidth γ_D = 0.049 cm^{-1}, and an Na pressure of 0.75 torr (1×10^{16} cm^{-3}).

Efficiency measurements were made both on- and off-resonance while varying the He pressure from a few torr to 2 atm. Fig. 1 shows the ratio $R_m(P)/R_{m0}$ as a function of the He pressure, and Fig. 2 is a plot of the computed ratio $R_c(\gamma)/R_{c0}$ for this case. Fig. 1 also shows the atomic linewidth γ as a function of pressure, both using the exact method and, for $P > 800$ torr, using the approximate method. Note that the two techniques are consistent, and that the numerical technique permits one to measure pressure broadenings sev-

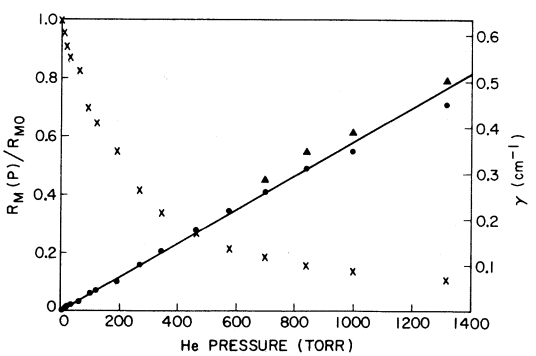


Fig. 1. Measured radio $R_m/R_{m0}(x)$ and corresponding atomic linewidth γ of the Na $3s^2S$-$3d^2D$ transition versus He pressure. Linewidths indicated by (▲) are from the simplified, high-pressure procedure; those indicated by (•) are found from the numerical technique.

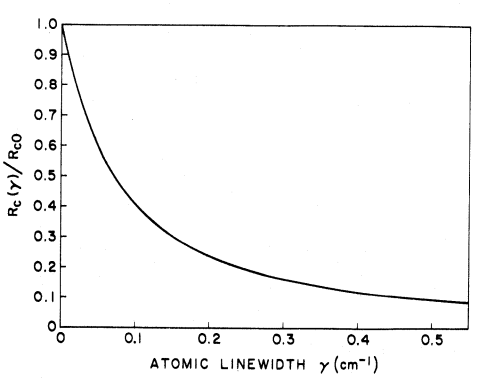


Fig. 2. Calculated ratio R_c/R_{c0} versus atomic linewidth.

eral times smaller than the Doppler broadening. The measured broadening coefficient is 0.3 cm^{-1}/atm.

A similar procedure was used to determine the self-broadening of this transition by varying the Na density from 0.75 torr to 150 torr. Unfortunately, at these high Na densities, it was necessary to introduce 300 torr of He buffer gas to protect the cell windows, and the Na self-broadening was not observable above the 0.1-cm^{-1} He broadening. Thus we infer a self-broadening of less than 0.1 cm^{-1} at a density of 10^{18} cm^{-3}. From a device point of view this result is important in two respects. First, it indicates that the converter may be operated at Na pressures of at least 150 torr without a significant reduction of efficiency, and second, it indicates that it is very important to keep the buffer gas pressure as low as possible. Fig. 1 shows, for example, that at an He buffer gas pressure of about 300 torr, the efficiency is about a factor of 3 less than the value with no He at all.

Using the results of these measurements, we predict that a Na image up-converter operating on this transition at an Na pressure of 150 torr will require 2.5 MW of pump power at 6856 Å to up-convert 10^5 resolvable spots from the 9.0-9.5-μ band to the 3302-3308-Å band at a photon conversion efficiency of 10 percent. Development of devices of this type is currently underway in our laboratory.

Acknowledgment

We thank Prof. T. W. Hänsch for an important early discussion, and B. Yoshizumi for help in constructing the apparatus.

References

[1] R. T. Hodgson, P. P. Sorokin, and J. J. Wynne, "Tunable coherent vacuum-ultraviolet generation in atomic vapors," *Phys. Rev. Lett.*, vol. 32, pp. 343–346, Feb. 18, 1974.

[2] S. E. Harris and D. M. Bloom, "Resonantly two-photon pumped frequency converter," *Appl. Phys. Lett.*, vol. 24, pp. 229–230, Mar. 1, 1974.

[3] D. M. Bloom, J. T. Yardley, J. F. Young, and S. E. Harris, "Infrared up-conversion with resonantly two-photon pumped metal vapors," *Appl. Phys. Lett.*, vol. 24, pp. 427–428, May 1, 1974.

[4] F. Biraben, B. Cagnac, and G. Grynberg, "Experimental evidence of two-photon transition without Doppler broadening," *Phys. Rev. Lett.*, vol. 32, pp. 643–645, Mar. 25, 1974.

[5] M. D. Levenson and N. Bloembergen, "Observation of two-photon absorption without Doppler broadening on the 3*s*–5*s* transition in sodium vapor," *Phys. Rev. Lett.*, vol. 32, pp. 645–648, Mar. 25, 1974.

[6] T. W. Hänsch, K. C. Harvey, G. Meisel, and A. L. Schawlow, "Two-photon spectroscopy of Na 3*s*–4*d* without Doppler broadening using a CW dye laser," *Opt. Comm.*, vol. 11, pp. 50–53, May 1974.

[7] D. Pritchard, J. Apt, and T. W. Ducas, "Fine structures of Na $4d^2D$ using high-resolution two-photon spectroscopy," *Phys. Rev. Lett.*, vol. 32, pp. 641–642, Mar. 25, 1974.

[8] P. N. Butcher, *Nonlinear Optical Phenomena*, Eng. Experiment Station, Ohio State Univ., Columbus, OH, 1965, bulletin 200, ch. 8.

[9] R. B. Miles and S. E. Harris, "Optical third-harmonic generation in alkali metal vapors," *IEEE J. Quant. Elect.*, vol. QE-9, pp. 470–484, Apr. 1973.

[10] B. D. Fried and S. D. Conte, *The Plasma Dispersion Function*. New York: Academic, 1961.

[11] K. M. Leung and J. F. Ward, "Two-photon resonant optical third-harmonic generation in cesium vapor," *Phys. Rev. A*, vol. 9, pp. 2440–2448, June 1974.

[12] E. A. Stappaerts, S. E. Harris, and J. F. Young, "Image up-conversion in alkali vapors," to be published.

Output Mode Spectra, Comparative Parametric Operation, Quenching, Photolytic Reversibility, and Short-Pulse Generation in Atomic Iodine Photodissociation Lasers

CHRISTOPHER C. DAVIS, ROBERT J. PIRKLE, ROSS A. McFARLANE, MEMBER, IEEE, AND GEORGE J. WOLGA, MEMBER, IEEE

Abstract—**The advantages and disadvantages of the atomic iodine photodissociation laser for high-energy operation have been considered. Laser excitation by both slow and fast flashlamps has been investigated; in slow flash excitation, self-mode-locking occurs frequently and the output-mode characteristics of the laser operated in this way have been studied. The comparative performance of different parent materials for photodissociation has been investigated in the fast flash mode of excitation. This mode of excitation gives higher energy laser output and efficiency and less pyrolysis of the parent material. These observations, and the photolytic reversibility characteristics of different materials in repetitively photolyzed operation, have been discussed in the light of the most recently available kinetic data; i-C_3F_7I is the material of choice for laser operation. Finally, limits to the ability of atomic iodine photodissociation laser/amplifier(s) systems to generate and amplify short duration, high-energy pulses set by intralevel relaxation effects and coherent interactions are discussed.**

Introduction

THE atomic iodine laser based on the photodissociation of perfluoroalkyl iodides, particularly n-C_3F_7I and i-C_3F_7I has demonstrated practical ability to generate high-energy short-duration laser pulses. To date, outputs of at least 60 J in 0.7 ns have been obtained (from a system utilizing an acoustooptically mode-locked oscillator and two amplifiers [1]). Consequently the iodine photodissociation laser is of interest in connection with laser-produced plasma and fusion experiments. This laser system has a number of advantages and some disadvantages relative to existing high-energy laser systems in this context. Its main advantages are as follows.

1) Scalability: no serious problems have presented themselves so far in reaching currently available output energies.

2) The amplifying medium is capable of storing large amounts of energy. At a pressure of 100 torr of C_3F_7I, which is near the optimum pressure for laser operation of this material in oscillators of about 1-cm diameter, the laser medium, if completely photodissociated, stores 534 $J \cdot l^{-1}$. However, in the absence of coherent phenomena, in principle only $\frac{2}{3}$ of this stored energy can be extracted, an amount of 356 $J \cdot l^{-1}$. Volumetric outputs of up to 110 $J \cdot l^{-1}$ have in fact been achieved [2]. The volumetric output available does, however, depend in practice on the diameter of the tube where the perfluoroalkyl material is photolyzed. For homogeneous photolysis in such a tube, the optimum filling pressure is inversely proportional to tube diameter over a wide range of pressure and tube diameter, so the volumetric output will vary similarly.

3) The operating wavelength of 1.315 μm, while not as short as is desirable for laser-induced fusion experiments, is comparable with that available from Nd^{3+} glass lasers, while the iodine system has none of the undesirable internal material damage and self-focusing problems associated with the former.

4) It seems possible that the iodine laser will have a higher internal breakdown threshold in $J \cdot cm^{-2}$ than the high-pressure CO_2 laser. This higher internal breakdown threshold is predicated on the ability of I_2 molecules to rapidly attach free electrons and prevent the formation of plasmas. Some I_2 molecules are always present in the medium of an iodine photodissociation laser following the photolytic process. However, this mechanism of internal breakdown prevention may not be effective on a very short time scale.

5) High output-beam quality should be obtainable from an oscillator/amplifier(s) system. This beam quality should be comparable to or better than can be obtained from Nd^{3+} glass, CO_2, or HF lasers. The main phenomenon which can present a problem in obtaining a high-quality output beam from an iodine laser is the occurence of shock waves, traveling approximately radially, which give rise to refractive index inhomogeneities of the amplifying medium [3], [4]. These shock waves arise from adsorbed material evaporated from the walls of the amplifier tube by the exciting flashlamp, and by the heating of the laser medium which occurs following photolysis.

The main disadvantages of the iodine photodissociation laser are as follows.

1) Relatively low overall electrical efficiency. The quantum efficiency of the laser (= laser photon energy out/photolysis photon energy in) is relatively high, >20 percent, but this is offset by the inability of flashlamps to generate ultraviolet photons efficiently in the photodissociative absorption band of the perfluoroalkyl iodides around 2700 Å. The best overall efficiency from an oscillator which has been achieved to date is ~0.6 percent [2].

2) Photolytic irreversibility. Following the photolysis process not all the parent perfluoroalkyl iodide compound regenerates itself; some irreversible conversion into molecular iodine, the appropriate perfluoroalkane, and other products

Manuscript received December 12, 1975. This work was supported in part by the National Science Foundation through the Materials Science Center, Cornell University, in part by the U.S. Army Missile Command under Contract DAA-H01-71-C-0840, and in part by the U.S. Army Research Office Durham under Grant DAHC04-74-G-0120.

C. C. Davis was with the School of Applied and Engineering Physics and the Materials Science Center, Cornell University, Ithaca, NY 14853. He is now with the Department of Electrical Engineering, University of Maryland, College Park, MD 20742.

R. J. Pirkle was with the Laboratory of Plasma Studies, Cornell University, Ithaca, NY 14853. He is now with the Department of Chemistry, Cornell University, Ithaca, NY 14853.

R. A. McFarlane and G. J. Wolga are with the School of Electrical Engineering, Materials Science Center, and Laboratory of Plasma Studies, Cornell University, Ithaca, NY 14853.

occurs. Thus the composition of the laser medium alters in successive shots and eventually necessitates refilling the system with fresh material.

Neither of the two main disadvantages listed above does, however, prevent the use of an iodine photodissociation laser system for the generation and amplification of short-duration pulses, although in practical terms, irreversibility is unfortunate.

The basic physical and chemical processes which occur in the medium of an iodine photodissociation laser are responsible for both its technological advantages and disadvantages. Clearly an improved understanding of as many of these processes as possible is interesting and technologically desirable. Although much is known about certain phenomena which are very important in this laser system, many more phenomena still are only partially understood, or have been little considered. We have carried out a series of experiments on an iodine photodissociation laser oscillator operated in two different modes which, we believe, give further insight into a number of important characteristics, in particular:

1) the longitudinal and transverse output mode spectra, mode competition and self-mode-locking of these lasers;
2) the parametric behavior of iodine photodissociation laser oscillators using different perfluoroalkyl and deuterated alkyl materials;
3) the role of photolytic reversibility of the laser medium in determining the behavior of the laser in repetitively pulsed operation.

We will also present calculations concerning the possible occurrence of coherent phenomena in iodine amplifiers and what limits these phenomena may impose on the generation of very short, high-energy pulses by iodine photodissociation lasers. In the sections which follow we will, where necessary, review the current state of knowledge regarding certain aspects of the behavior of these lasers, and physical and chemical phenomena which occur in them.

Experimental

The iodine photodissociation laser system used in our experiments consisted of a quartz tube of 10-mm ID and 30-cm length whose central 15-cm region lay along one focal line of a polished aluminum elliptical cavity. The tube was terminated with spectrosil windows set at Brewster's angle. The tube could be evacuated with a rotary pump/cryogenic sorption trap combination to $<10^{-4}$ torr and filled with perfluoroalkyl iodide vapor to a known pressure measured with a Leybold Diavac B gauge. This material was photolyzed with a linear xenon-filled flashlamp which lay along the other focal line of the elliptical cavity. Two different types of flashlamp excitation were used which we call "slow" and "fast" flash excitation. The characteristics of these two modes of operation follow.

A. Slow Flash Excitation

This mode of operation used an I.L.C. 10L6 flashlamp in series with a 20-μH series inductor through which a 200-μF capacitor bank charged at voltages up to 3 kV could be discharged. The flashlamp was triggered by a 20-kV pulse applied to an external wire wrapped around it to give a flash duration $\simeq 140$-μs FWHM.

B. Fast Flash Excitation

This mode of operation used an I.L.C. 7D6 flashlamp in series with a nitrogen-pressurized hemispherical spark gap, through which a 2.5-μF low-inductance (20-nH) capacitor (Maxwell Laboratories, Inc., 31100 series) could be discharged. The spark gap was triggered by a 20-kV pulse applied to a field distortion plate placed symmetrically between the two hemispheres. All connections in the circuit were designed to minimize inductance. The resulting flash had a duration in the ultraviolet below 3900 Å of 2.7-μs FWHM with a 10-90-percent rise time of 1.1 μs. At longer wavelengths, the flash duration increased. For example, beyond 5000 Å, as observed through a Corning 3-70 glass filter with an S-1 photomultiplier, the flash duration had an FWHM of 5.4 μs. No such dramatic change in spectral output was observed with the slow flashlamp. In the case of both fast and slow flash excitation the energy of the laser pulse could be measured with an ITL laser energy output meter. Since the absorption band leading to the dissociation of the various perfluoroalkyl iodides studied is a 500-Å-wide (FWHM) band centered around 2700-Å, only flashlamp emission in this region is useful in generating a population inversion. The fast flashlamp is much more efficient than the slow one in this respect; the fast lamp approximates in the visible to a very high temperature black body and has a significant fraction of its emission at short wavelengths, whereas the slow lamp generates most of its emission at longer wavelengths than lead to photodissociation. However, the most subtle way in which the flashlamp interacts with the laser medium is through the magnetic field produced by the flashlamp current pulse, which splits the hyperfine levels of the iodine laser transition into magnetic sublevels, thereby producing time-dependent lineshape and gain coefficient changes which are not simply related to the overall population inversion generated by the flashlamp [5]-[8].

Hyperfine Structure

The effect of the magnetic field from the flashlamp on the hyperfine structure of the iodine laser transition and how it may affect laser oscillation can be illustrated with reference to Figs. 1 and 2. Fig. 1 shows the hyperfine structure of the magnetic dipole laser transition in zero, weak, and strong fields. In zero field the $\frac{5}{2}$ nuclear spin of I^{127} couples to the total angular momentum of the $5p^5$ electrons to give two hyperfine levels of the $^2P_{1/2}$ upper laser level and four hyperfine levels of $^2P_{3/2}$. The zero field splittings of the ground $^2P_{3/2}$ level have been determined by Jaccarino *et al.* [9]; they are $4 \leftrightarrow 3 = 0.142$ cm^{-1}, $3 \leftrightarrow 2 = 0.065$ cm^{-1}, and $2 \leftrightarrow 1 = 0.025$ cm^{-1}. The zero field splitting of the $^2P_{1/2}$ level has been determined by Onaka [10], Verges [11], Belousova *et al.* [12], and Zuev *et al.* [13]; the value obtained by the latter authors appears to be the most reliable, 0.662 ± 0.009 cm^{-1}.

In a weak magnetic field (what we strictly mean by "weak" will become clear later) the F states split according to the value of M_F and are characterized as $|JIFM_F\rangle$ states. In a

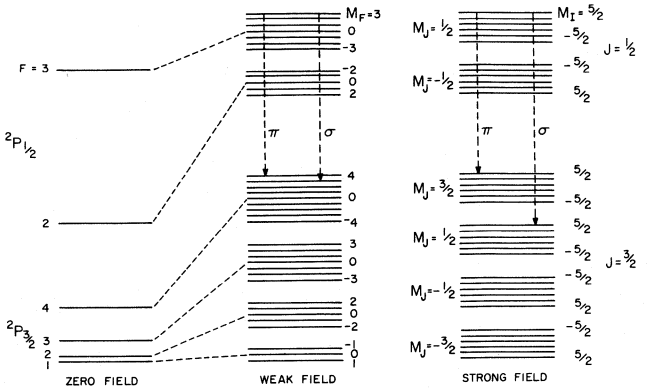


Fig. 1. Schematic diagram of the hyperfine structure of the iodine $^2P_{1/2} \rightarrow {}^2P_{3/2}$ transition in zero, weak, and strong external magnetic fields.

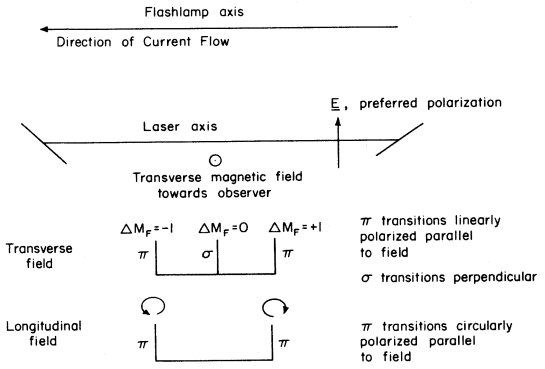


Fig. 2. Characteristics of σ and π polarization components of a magnetic dipole laser transition in a flashlamp-produced magnetic field.

strong field, the perturbation due to the external field breaks down the coupling between the angular momenta of the electrons and the nucleus, and the states are split according to the values of M_J and M_I and can be classified as $|JIM_JM_I\rangle$ states. In intermediate fields only $M_F = M_J + M_I$ is a good quantum number.

Neglecting the very small octupole moment of the iodine nucleus and the small perturbation introduced by the interaction of external magnetic fields with the nucleus, the Hamiltonian of the *hfs* interaction in an external magnetic field may be written as

$$\mathcal{H} = a\underline{I} \cdot \underline{J} + \underline{Q} \cdot \underline{U} + \beta H \cdot (\underline{L} + 2\underline{S}) \tag{1}$$

where a is the magnetic dipole interaction constant, $\underline{Q} \cdot \underline{U}$ is the quadrupole interaction operator (see Shore and Menzel, [14]) and β is the Bohr magneton. The operators $\underline{I}, \underline{J}, \underline{L}$, and $\underline{S}$ have their usual significance.

In zero or weak fields, the Hamiltonian is diagonal in an F, M_F representation and the relative position of the energy levels is given by

$$\Delta E_{F,M_F} = \frac{aK}{2} + b \cdot \frac{\frac{3}{4}K(K+1) - I(I+1)J(J+1)}{2I(2I-1)J(2J-1)} + \beta H g_F M_F \tag{2}$$

where

$$K = F(F+1) - I(I+1) - J(J+1)$$

and

$$g_F = g_J \frac{(F(F+1) + J(J+1) - I(I+1))}{2F(F+1)}$$

where g_J is the Landé g factor. b is the quadrupole interaction constant which is zero for a $J = \frac{1}{2}$ state. (Specific expressions for the hyperfine structure interaction constants a and b, and detailed discussions of hyperfine interactions in general have been given by several authors [15]-[19].)

In strong fields the Hamiltonian is diagonal in an M_I, M_J representation, and the relative position of the energy levels is now

$$\Delta E_{M_IM_J} = aM_IM_J + \frac{b[3M_J^2 - J(J+1)][3M_I^2 - I(I+1)]}{4[2I^2 - I][2J^2 - J]} + \beta H g_J M_J. \tag{3}$$

In intermediate fields the only good quantum number is M_F and the position of the energy levels must be found by solving the secular equation of the energy matrix. This calculation has been carried out by Belousova *et al.* [8].

In the above, an external magnetic field can be regarded as weak only if it introduces an energy perturbation significantly smaller than the nuclear magnetic dipole interaction, that is, from (2) if $\beta H g_F M_F \ll aK/2$. For example, for the $^2P_{1/2}$, $F = 3$, $M_F = 3$ state with $a = 0.221$ cm^{-1} [13], $g_F = 1/9$, and $K = 5/2$, this implies $H \ll 17.8$ kG. For the $^2P_{3/2}$, $F = 4$, $M_F = 4$ state with $a = 0.0276$ [9], $g_F = 1/2$, $K = 15/2$ this implies $H \ll 1.11$ kG. These examples imply that for magnetic fields considerably below 1 kG, the frequency of all the components of the $(^2P_{1/2})\, F = 3 \rightarrow (^2P_{3/2})\, F = 4$ transition vary linearly with applied field. The frequency shift of a component arising from the transition between the magnetic sublevels M_{F_1} of $^2P_{1/2}$, $F = 3$, and M_{F_2} of $^2P_{3/2}$, $F = 4$ is

$$\Delta\nu = \frac{\beta H}{h}(g_{F_1}M_{F_1} - g_{F_2}M_{F_2}) \tag{4}$$

which is largest for the $M_{F_1} = 3 \rightarrow M_{F_2} = 4$ component, having a value of

$$\Delta\nu_M = \frac{-5}{3}\frac{\beta H}{h}, \qquad |\Delta\nu_M| = 2.33 \text{ MHz} \cdot \text{G}^{-1}.$$

In the present experiments the maximum current passing through the flashlamp in the slow flash mode of operation was measured to be 1124 A, which gave rise to a transverse field of 44 G at the photolysis tube 2 in away. This field caused a maximum frequency shift in the components of the $F = 3 \rightarrow F = 4$ transition of 103 MHz. This shift is considerably smaller than the homogeneous linewidth of the $F = 3 \rightarrow F = 4$ transition, measured to be 1.8 GHz by Zuev *et al.* [13] at a pressure of 100 torr, which is near the optimum for laser operation. Thus with slow flash excitation the observed behavior of the laser should be very little influenced by hyperfine structure effects. The opposite is true in the case of fast flash excitation; at 15 kV the peak current in the fast flashlamp in the present experiments is estimated to be 15 kA which causes a maximum frequency shift of the $F = 3 \rightarrow F = 4$ transition in the photolysis tube of 1.4 GHz. Therefore with fast flash excita-

tion the effect of hyperfine structure on the behavior of the laser will be important.

There is one further mechanism by which the magnetic field from the flashlamp might be expected to interact with the laser transition. This is illustrated in Fig. 2. The magnetic field at the laser tube is transverse to the direction in which laser oscillation occurs. This field splits the individual hyperfine components of the laser transition into σ components polarized perpendicular to the field and π components polarized parallel to the field. For the magnetic dipole laser transition $\Delta M_F = \pm 1$ for the π transitions and $\Delta M_F = 0$ for the σ transitions. The orientation of the Brewster windows on the laser will affect which of these subcomponents appear in the laser output. In Fig. 2, Brewster windows oriented as shown will pass the σ components but present a considerable reflection loss to the π components. Since there are more π than σ components of a given hyperfine transition, it might be expected that the laser would exhibit an output power dependence on the orientation of its Brewster windows relative to the magnetic field. We have observed no such dependence when operating our present system in the slow flash mode where only a small magnetic field is generated by the lamp. In such small fields, which only split the laser transition by a small fraction of its homogeneous width, no significant dependence of the laser output on Brewster window orientation relative to the field should be expected [90] and the laser output should be linearly polarized in the preferred direction. In larger fields the relative gains of the π and σ components of the laser alter and the laser will then exhibit a preferred Brewster window orientation for maximum linearly polarized power output. The orientational dependence of the gain and polarization characteristics of the iodine magnetic dipole laser transition in a magnetic field have been discussed in more detail by Davis [90] and examined experimentally by Belousova *et al.* [7].

Longitudinal and Transverse Mode Spectra

In order to eliminate as much as possible the complications introduced by time-dependent hyperfine structure, Einstein coefficient, and polarization effects, all our observations of the mode behavior of an iodine laser have been made in the slow flash mode of operation. A schematic diagram of the experimental arrangement used for these observations is shown in Fig. 3. The laser output was attenuated before being detected with an RCA 7102 S-1 photomultiplier. The output of the photomultiplier could be recorded in the time domain with a Biomation model 8100 transient digitizer and Northern Scientific NS-575 digital signal analyzer or analyzed at a particular frequency with a Tektronix L-20 0.01 4-GHz spectrum analyzer. The transient digitizer/analyzer combination allows a very accurate, convenient digital record of the laser output to be obtained which can be kept permanently on magnetic tape. However, as the overall response of this arrangement is 20 ns, we used long laser cavities so that any self-mode-locked pulse trains which appeared could be recorded reliably. In our present experiments we have used a number of concave spherical mirrors in four different length cavities: mirror *A*, 2-m radius, 95 percent reflecting, dielectric coated; mirror *B*, 3-m radius, gold coated; mirror *C*, 10-m radius, gold coated; mirror

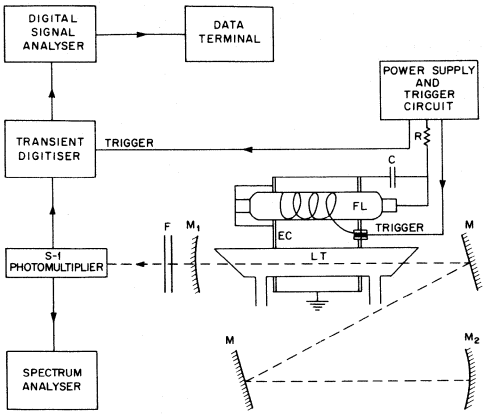


Fig. 3. Schematic diagram of apparatus used for studying self-mode-locking and output mode beat frequencies of a slow-flash-excited iodine photodissociation laser.

D, 3.9-m radius, gold coated with a 0.5-mm-diam centered coupling hole; mirror *E*, 4.5-m radius, gold coated. The cavities used were:

1) mirrors *A* and *B*, 5.4 m apart (this is an unstable cavity);
2) mirrors *A* and *C*, 11.75 m apart;
3) mirrors *C* and *D*, 11.75 m apart;
4) mirrors *D* and *E*, 7.5 m apart.

The 5.4-m and 7.5-m cavities were folded with one plane gold-coated mirror, the 11.75-m cavities with two such mirrors. Some transverse mode control was possible in all of these cavities with an adjustable intracavity iris. In all cases the amplifying medium was situated near one of the cavity end mirrors.

Because the laser transition is predominantly homogeneously broadened at pressures near the optimum for maximum energy output, we deliberately carried out our investigations of output mode spectra using a lower pressure of 20 torr of n-C_3F_7I where the homogeneous and inhomogeneous contributions to the line broadening are approximately equal, but where the homogeneous width is still larger than the maximum frequency shift of the components of a particular hyperfine transition produced by the magnetic field of the slow flashlamp. Thus, at this low pressure, in a long cavity whose longitudinal modes are closely spaced, the conditions exist for potential multimode operation and self-mode-locking. At higher pressures the laser is homogeneously broadened and single-mode operation is likely to result, particularly in short cavities.

In our present experiments we have observed both partial and complete mode-locking and mode beating. This behavior seemed to be the rule rather than the exception and has been reported elsewhere [20]. The laser output typically began as a damped relaxation oscillation consisting of pulses approximately 3 μs wide and 6 μs apart followed by a region of smaller envelope modulation and frequently terminated in another burst of relaxation oscillations [for example see Fig. 5(a) and (c)]. Some or all of the early relaxation "spikes" were partially or completely mode-locked. Fully mode-locked relaxation spikes could be obtained by suitably adjusting the cavity end mirrors, although completely reproducible operation was not generally obtained in successive firings of

the laser. Similar self-mode-locked behavior was observed on successive shots using the same sample of n-C_3F_7I. Fig. 4(a) shows two typical mode-locked relaxation spikes observed using cavity 3). Fig. 4(b) shows the second of these two spikes on an expanded time scale; the spots in the display correspond to different memory channels in the analyzer and are 10 ns apart. The measured time separation of the pulses in Fig. 4(b) is $2L/c$ where L is the length of the cavity. This is regular longitudinal mode-locking. We have observed self-mode-locked pulse trains whose pulse separation was L/c corresponding to longitudinal mode-locking when every other longitudinal mode has been suppressed by mode competition. We have also observed pulse trains whose time separation was not a simple submultiple of $2L/c$ which correspond to locking of adjacent longitudinal modes of different transverse modes, or to simple beating between these modes (when only two are involved). Periodic fluctuations at the cavity round trip frequency in the output of higher pressure iodine photodissociation lasers operated with high-current fast flashlamps have been observed [21], [22]. These fluctuations were, however, only observed for short periods of time (<50 ns) and are not self-mode-locking but rather manifestations of the way the stimulated emission process builds up from noise, as discussed originally by Fleck [23], [24]. This may also be true in other reports of self-mode-locking observed for short periods of time, particularly in high-pressure homogeneously broadened gas lasers, for example in [25]. The self-mode-locking and mode-beating we observed frequently persisted for long periods of time ~10 μs, more than 100 cavity round trip times.

The reason why self-mode-locking should occur in the present experimental arrangement is uncertain. There is a region of n-C_3F_7I in the photolysis tube just beyond the elliptical cavity at each end which is nonuniformly irradiated by the flashlamp but whether this could act as a saturable absorber is unclear. The laser output is almost certainly on the $F=3 \rightarrow F=4$ transition alone under the present experimental conditions of low flashlamp energy and small magnetic field [12], [13], [6], [7]. The burst of relaxation oscillations which occur just before laser action terminates is quite possibly due to an increase in the gain of the $F=3 \rightarrow 4$ transition which occurs as the flashlamp-produced magnetic field decreases [87].

We have correlated the observation of self-mode-locking with multimode operation of the laser by studying the time dependence of the beats between different longitudinal and transverse modes. Fig. 5(a) and (b) shows the laser output recorded by the signal analyzer and the corresponding time dependence of the fundamental beat frequency $c/2L$ near 20 MHz recorded with the spectrum analyzer and an oscilloscope, observed using cavity 4). The apparent different time origins and time scales of the two signals result because the triggering and time bases of the analyzer and oscilloscope were not exactly synchronized. It is clear that for at least part of its oscillation period, the laser is operating in at least two modes with time intervals of single-mode operation. The duration of the intervals of multimode operation cannot be determined exactly because the response time of the spectrum analyzer,

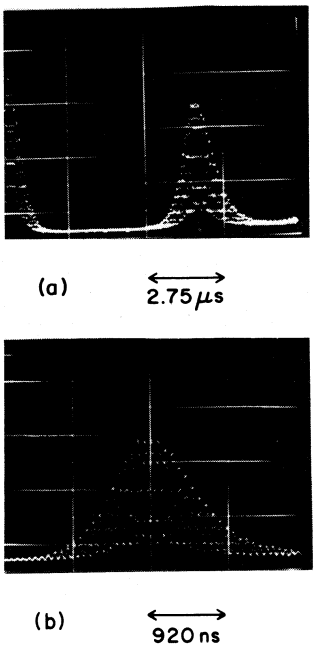


Fig. 4. (a) Typical mode-locked relaxation spikes observed with cavity 3). (b) Expanded view of the second mode-locked relaxation spike in (a): pulse spacing ≃80 ns = $2L/c$.

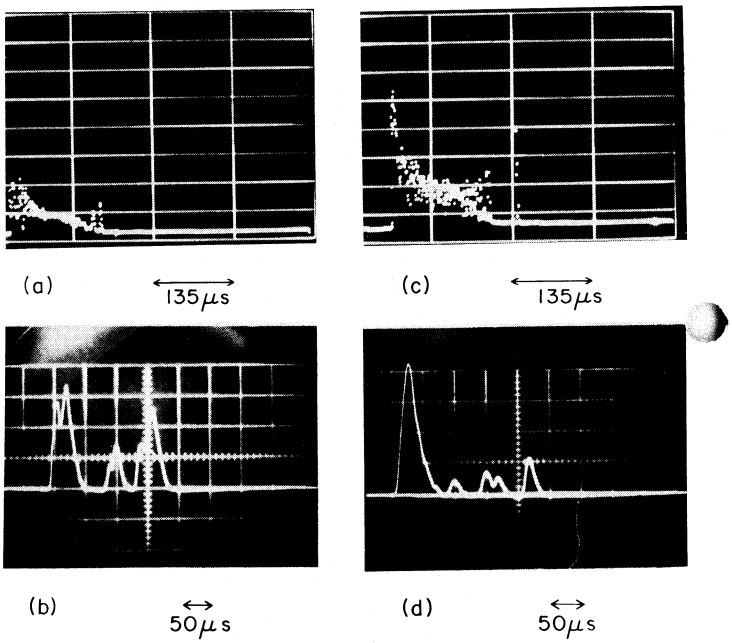


Fig. 5. Laser outputs (a) and (c) with corresponding beat frequencies near 20 MHz (b) and 40 MHz (d) observed using cavity 4) and slow flash excitation of 20 torr of n-C_3F_7I.

when it is set to a fixed frequency, is only about 5 μs. Fig. 5(c) and (d) shows similar recordings of the laser output together with the beat frequency c/L near 40 MHz in cavity 4). We were able to monitor beat frequencies with this cavity out to 140 MHz. The intensity of these beats decreased progressively towards the higher frequencies, and beyond 140 MHz it was difficult to distinguish whether an observed signal was a true beat or due to electrical pickup. The time duration of the beats also decreased progressively towards higher frequencies

and for the beats at 80 MHz and above, the beat was only observed for a short period $\lesssim 10\ \mu s$ at the onset of laser oscillation. We conclude that at least 8 longitudinal modes of a single transverse mode oscillate at least for a short time when laser oscillation starts, but that mode competition quenches all but three or four of the strongest modes. Periods of single- or two-mode operation correlated quite well with times when the laser oscillation showed the smallest degree of modulation due to relaxation oscillations. This is consistent with the approach to equilibrium in a largely homogeneously broadened laser when a single mode can suppress all the others. Spatial nonuniformities in the population inversion can result from relaxation oscillations and reduce the effect of this mode competition. For example, the burst of relaxation oscillations just before laser oscillation terminates has been observed to involve four modes. We were also able to observe beats in cavity 4) at nonmultiple frequencies of 20 MHz which arise from the beating of longitudinal modes of the fundamental transverse mode with higher order transverse modes. These beats could not be completely suppressed even by closing the in-cavity iris but only occurred for a short time immediately after the onset of laser oscillation. It is possible that the optical pumping of the laser medium in the elliptical cavity used produces a higher population inversion in the photolysis tube on the side directly facing the flashlamp than it does on the other. This may give some off-axis modes higher gains than TEM_{00} which would compensate for the increased loss they suffer at the in-cavity iris. However, this situation would only be expected to persist for a short time before a radially traveling shockwave starts to propagate with subsequent equalization of the gain distribution.

Comparative Performance of Different Iodides

Kinetic Processes

Although very many different iodine-bearing materials have been shown to produce population inversion and laser oscillation following photolysis, namely: CH_3I, CF_3I [26], C_2H_5I, n-C_3H_7I, n-C_4H_9I, i-C_4H_9I, C_2F_5I, n-C_3F_7I [27], i-C_3F_7I [28], CF_3CH_2I [29], CD_3I [30], $(CF_3)_2AsI$, $CF_3(C_2F_5)AsI$, $CF_3(C_3F_7)AsI$, $(C_2F_5)_2AsI$, $(C_3F_7)_2AsI$, $(CF_3)_2PI$, $CF_3(C_2F_5)PI$, $CF_3(C_3F_7)PI$, $(C_2F_5)_2PI$, $(C_3F_7)_2PI$, $CF_3(CH_3)PI$, $CF_3PI(CN)$, $CF_3(CF_2Cl)(CFH)PI$, F_3PI, OPF_2I, and $(CF_3)_2SbI$ [31], only i-C_3F_7I, n-C_3F_7I, C_2F_5I, CF_3I, and CD_3I appear to be of practical importance. There are a number of reasons for this which can be best illustrated by considering the most important kinetic processes which occur in an iodine photodissociation laser during and following photolysis:

$$RI + h\nu \longrightarrow R(\text{hot?}) + I^*(^2P_{1/2}) \quad (1)$$

$$RI + h\nu \longrightarrow R(\text{hot?}) + I(^2P_{3/2}). \quad (2)$$

The fractional yields of I* following the broad-band ultraviolet (UV) photolysis of various alkyl, perfluoroalkyl, and deuteroalkyl iodides have been measured by Donohue and Wiesenfeld [32], [33] whose results are summarized in Table I. These results illustrate the superiority of the perfluoroalkyl iodides and CD_3I over the alkyl iodides in their predominant photodissociation to yield excited iodine atoms. They also illustrate why Kasper *et al.* [27] were unable to obtain laser action following photolysis of i-C_3H_7I and HI; these compounds, and others, have fractional yields of I* below the $33\frac{1}{3}$ percent needed to achieve a population inversion. The radicals produced following photodissociation are almost certainly translationally and vibrationally "hot." This has been demonstrated in the photolysis of CH_3I, C_2H_5I, n-C_3H_7I and i-C_3H_7I [34]-[36].

TABLE I
Fractional Yields p^* of Excited Iodine Atoms Following the Broad-Band UV Photolysis of Various Alkyl Iodides [32], [33]

COMPOUND	p^* [a]
CH_3I	0.92 ± 0.02
C_2H_5I	0.69 ± 0.05
n-C_3H_7I	0.67 ± 0.04
i-C_3H_7I	<0.10
n-C_4H_9I	0.82 ± 0.04
s-C_4H_9I	<0.10
i-C_4H_9I	0.69 ± 0.04
t-C_4H_9I	<0.10
CD_3I	0.99
CF_3I	0.91 ± 0.03
C_2F_5I	>0.98
n-C_3F_7I	>0.99
i-C_3F_7I	0.90 ± 0.02
HI	0.10 ± 0.05

[a] $p^* = [I^*]_0/([I^*]_0 + [I]_0)$ where $[I^*]_0$ and $[I]_0$ are the initial concentrations of excited and ground state iodine atoms produced following photolysis.

The quenching reaction

$$I^* + RI \longrightarrow I + RI \quad (3)$$

strongly influences the efficiency of the iodide as a laser material.

$$I^* + I_2 \longrightarrow I + I_2. \quad (4)$$

Reaction (4) is the quenching reaction with the largest rate constant. Its importance increases with time following photolysis as iodine molecules accumulate from the recombination of ground state iodine atoms in the presence of a third body M

$$I + I + M \longrightarrow I_2 + M. \quad (5a)$$

Iodine molecules also accumulate following pyrolysis, the thermal decomposition of parent alkyl iodide molecules by excessive heat deposition in the laser medium from the flashlamp. The formation of I_2 molecules also leads to irreversibility of the photodissociation process. Beyond a critical temperature, which depends on the exact composition of the laser medium, pyrolysis increases rapidly and the accumulation of molecular iodine accelerates leading to rapid quenching of laser oscillation [88]. In the absence of pyrolysis, whose occurrence can be minimized by adding a buffer gas such as helium to the laser medium, the rate of accumulation of iodine molecules due to reaction (5a) is a slow, but accelerat-

ing process. The most efficient third body for promoting reaction (5a) is an I_2 molecule itself, in which case the rate constant is $3.9 \cdot 10^{-30}$ $cm^6 molecule^{-2} s^{-1}$ [37]. Reaction (5a) may, in principle, involve one or two excited iodine atoms, for example

$$I^* + I + M \longrightarrow I_2 + M \quad (5b)$$

$$I^* + I^* + M \longrightarrow I_2 + M. \quad (5c)$$

On energetic considerations these recombination reactions should have smaller rate constants than reaction (5a) as any intermediate complex MI formed during the recombination process might be expected to be less stable when an excited iodine atom is involved. Andreeva *et al.* [55] estimate the rate constants of (5b) and (5c) to be at least 25 times smaller than for reaction (5a).

The best available values of the rate constants for the quenching of excited iodine by various species in reactions like (3) and (4) are collected in Table II. A number of the quenching species listed are not specifically important under the usual operating conditions in atomic iodine photodissociation lasers but they are listed for completeness. Rate constants for the quenching of excited iodine atoms by additional molecules are listed in [46] and [47]. The rate constants listed in Table II for quenching by alkyl iodide molecules include a contribution from the chemical quenching reaction

$$I^* + RI \longrightarrow I_2 + R. \quad (6)$$

However, the contribution of this reaction to the overall quenching is probably much smaller than from reaction (3) [38], [48], [51], [54]. Further, in a consideration of quenching by free radicals it is difficult to separate the contributions due to

$$I^* + R\,(+M) \longrightarrow RI\,(+M) \quad (7)$$

and

$$I^* + R \longrightarrow I + R. \quad (8)$$

Donohue and Wiesenfeld [51] conclude that these two reactions have a large combined rate constant for some of the alkyl radicals and are therefore potentially important in determining photodissociation laser kinetics, particularly when a large degree of photodissociation is produced by the flashlamp.

It is important to note from Table II that the order of quenching efficiency for various parent alkyl iodide molecules is

$$CH_3I > CD_3I > CF_3I, n\text{-}C_3F_7I, i\text{-}C_3F_7I, C_2F_5I.$$

The perfluoroalkyl iodides, particularly, are very inefficient quenchers of excited iodine atoms. Molecular iodine however, is a very efficient quencher and reaction (4) will quickly quench laser oscillation if molecular iodine builds up sufficiently following photolysis [65], [67], [88], [89]. This buildup of molecular iodine becomes very rapid if pyrolysis of the parent alkyl iodide sets in. Reversibility of the photodissociation process occurs as a result of reaction (7) above and from

TABLE II
RATE CONSTANTS FOR COLLISIONAL DEACTIVATION OF $I(^2P_{1/2})$ AT 300 K

QUENCHING SPECIES	$k(cm^3\text{-}molecule^{-1}\ s^{-1})$	REFERENCES
He	$< 5 \cdot 10^{-18}$	[39], [46], [47]
Ar	$< 2 \cdot 10^{-18}$	[38], [41], [42], [46], [47]
Xe	$< 1.6 \cdot 10^{-18}$	[40], [46], [47]
$I(^2P_{3/2})$	$< 1.6 \cdot 10^{-14}$	[38], [46], [47]
H_2	$8.8 \cdot 10^{-14}$	[39]
D_2	$2.2 \cdot 10^{-15}$	[42]
N_2	$1.5 \cdot 10^{-16}$	[42]
CO	$1.2 \cdot 10^{-15}$	[40], [42]
CO_2	$1.3 \cdot 10^{-16}$	[40]
N_2O	$1.7 \cdot 10^{-16}$	[42]
	$1.3 \cdot 10^{-15}$	[45]
SF_6	$3.1 \cdot 10^{-15}$	[40]
CH_4	$5.9 \cdot 10^{-14}$	[40]
	$1 \cdot 10^{-13}$	[42]
CF_4	$4.5 \cdot 10^{-15}$	[40]
	$4.6 \cdot 10^{-16}$	[42]
HI	$1.5 \cdot 10^{-13}$	[43], [51]
	$1.3 \cdot 10^{-13}$	[39]
DI	$1.2 \cdot 10^{-13}$	[39]
H_2O	$2.3 \cdot 10^{-12}$	[50]
ICN	$6.0 \cdot 10^{-14}$	[45]
NO	$1.1 \cdot 10^{-11}$	[40]
O_2	$2.5 \cdot 10^{-11}$	[50]
$i\text{-}C_3H_7$	$3 \cdot 10^{-10}$	[51]
I_2	$3.6 \cdot 10^{-11}$	[49]
CH_3I	$2.6 \cdot 10^{-13}$	[48]
	$5.7 \cdot 10^{-13}$	[51]
C_2H_5I	$1.9 \cdot 10^{-13}$	[44]
	$6.1 \cdot 10^{-13}$	[51]
$n\text{-}C_3H_7I$	$2.0 \cdot 10^{-13}$	[44]
	$6.3 \cdot 10^{-13}$	[51]
$i\text{-}C_3H_7I$	$2.0 \cdot 10^{-13}$	[44]
	$6.3 \cdot 10^{-13}$	[51]
CD_3I	$4.6 \cdot 10^{-15}$	[48]
	$1.8 \cdot 10^{-14}$	[51]
CF_3I	$3.5 \cdot 10^{-16}$	[42]
C_2F_5I	$1.1 \cdot 10^{-16}$	[53]
$n\text{-}C_3F_7I$	$8 \cdot 10^{-16}$	[53]
	$\sim 2 \cdot 10^{-16}$	[52]
$i\text{-}C_3F_7I$	$\sim 3 \cdot 10^{-16}$	[52]

$$R + I\,(+M) \longrightarrow RI\,(+M). \quad (9)$$

The presence of a third body is necessary to stabilize the highly vibrationally excited molecule produced by the recombination of the radical and the iodine atom. By kinetic modeling of experimental photodissociation laser systems, quite large rate constants have been estimated for reactions (7) and (9); for example: $5 \cdot 10^{-11}$ $cm^3 molecule^{-1} s^{-1}$ [28] for reaction (9) and $4 \cdot 10^{-12}$ $cm^3 molecule^{-1} s^{-1}$ [28], [55] for reaction (7) when the radical is CF_3; between 10^{-11}-10^{-12} cm^3 $molecule^{-1} s^{-1}$ for reaction (9) when the radical is normal or iso C_3F_7; between $4 \cdot 10^{-13}$ and 10^{-12} $cm^3 molecule^{-1} s^{-1}$ for reaction (7) when the radical is $n\text{-}C_3F_7$ [52]. In a laser where a substantial fraction of the parent alkyl iodide molecules are dissociated, reactions (7) and (9) are likely to be the dominant contributors to the removal of excited iodine atoms. However, since these reactions remove ground-state atoms at an even faster rate, they do not destroy a population inversion.

The exothermic radical recombination reaction, for example,

$$C_3F_7 + C_3F_7(+M) \longrightarrow C_6F_{14}(+M) \quad (10)$$

also causes irreversibility of the photodissociation process and has a large rate constant, between 10^{-12}-10^{-11} $cm^3 molecule^{-1} s^{-1}$ for n-C_3F_7, and between $3 \cdot 10^{-13}$-$2 \cdot 10^{-12} cm^3$ $molecule^{-1} s^{-1}$ for i-C_3F_7 radicals [52]. The corresponding rate constant for CF_3 radicals is between $5 \cdot 10^{-12}$ and $4 \cdot 10^{-11}$ $cm^3 molecule^{-1} s^{-1}$ [28], [52], [55]. A simple consideration involving molecular complexity and steric factors indicates reaction (10) being of increasing importance in the order

$$\text{i-}C_3F_7 < \text{n-}C_3F_7 < C_2F_5 < CF_3.$$

One further reaction which has been considered of possible importance by several authors [55]-[57], [53], [58], [28], [59], [60] is the chemical pumping reaction, for example,

$$C_3F_7(\text{hot?}) + C_3F_7I \longrightarrow C_6F_{14} + I^*. \qquad (11)$$

This reaction has been suggested as a possible explanation of the "late time gain" apparently observed in some laser experiments [28], [59]. However, the existence of this "late time gain" has not been confirmed in subsequent investigations [61], [62]. Gusinow *et al.* [63] have suggested that a nonuniform initial production of I*, with a maximum I* concentration off axis, followed by diffusion, could account for an apparent late time increase of the axial gain. This is, no doubt, correct in a simple model which ignores all the other complexities of the system such as, for example, radially traveling shockwaves. However an off-axis maximum in I* production under the experimental conditions reported in [28], [59] is extremely unlikely. The radial dependence of the energy density in a uniformly side-pumped cylinder has been considered by Cooke *et al.* [64] who show that no off-axis maxima in this monochromatic energy density occur for values of the parameter $R\alpha \lesssim 1$ where R is the radius of the cylinder and α is the intensity absorption coefficient. For CF_3I the value of α at the peak of the UV pumping band is $\simeq 1.9 \cdot 10^{-2}$ $cm^{-1} torr^{-1}$ and in [28] the radius was 5.5 mm and operating pressures were $\lesssim 40$ torr, giving a peak value of $R\alpha \lesssim 0.42$. When it is taken into consideration that photodissociation occurs over a relatively broad band with an average value of α below the peak it seems unlikely that any off-axis pumping maximum should have occurred for pressures below 100 torr. The observation of an increase in the late time gain can as easily be explained on the basis of cooling of the laser medium following photolysis. Immediately following photolysis the laser medium is heated to a temperature above ambient, typically 500-1000 K by the thermalization of the hot radicals produced in the photolysis process, their recombination, and the thermalization of the vibrational energy acquired by undissociated parent molecules. As the gas cools by heat transport to the photolysis tube walls, its gain will depend on the quantity $\Delta N/\Delta\nu$, where ΔN is the population inversion and $\Delta\nu$ is the linewidth of the amplifying transition. As the Doppler contribution to $\Delta\nu$ falls with cooling, the gain may show an initial increase before quenching of excited iodine atoms takes over. Observations of the kinetics of photolyzed alkyl iodides by Donovan and Husain [39] and by Donohue and Wiesenfeld [51] have failed to reveal any evidence for the occurrence of the chemical pumping reaction (11). We conclude that it is doubtful whether this reaction is of any real significance in the kinetics of the atomic iodine photodissociation laser.

The reactions that we have considered above do not constitute an exhaustive survey of all possible reactions in a photolyzed alkyl iodide medium. Some previous discussion of the kinetics of such systems have considered very many more reactions, up to several tens in number [60], [28], [68], [94], but in order to arrive at a manageable kinetic model have concluded that only relatively few reactions, namely some of those discussed above, are important. Several other discussions of kinetic models for the iodine photodissociation laser have appeared in the literature [93], [65], [66], [53], [55], [67], [59], [51], [52]. Some of these models [92], [65]-[67] consider too few reactions and present an oversimplified picture of the kinetic processes occurring. In many cases, apparently quite good agreement between the predictions of a model and experimental observations may be artificially generated, by fitting the experimental data to the model using the rate constants of the reactions considered, as adjustable parameters. Most of the kinetic models that have been proposed, even those which are oversimplified, generally predict some of the gross qualitative features of laser behavior, for example: the initial rise of population inversion following the start of the flash excitation process, the subsequent decay of the inversion produced by quenching, the partial reversibility of the photodissociation process to regenerate the parent iodide, the buildup of molecular iodine and the existence of a pressure optimum for maximum laser energy output. The latter, in fact, is generally controlled by optical thickness effects of the laser medium and not by any kinetic considerations. This is particularly true for fast flash excitation of the perfluoroalkyl iodides, where quenching of excited iodine by either parent iodide molecules or molecular iodine is neglible on the time scale of laser excitation. To be useful a kinetic model should make at least semiquantitative predictions about the behavior of the laser and some models have had some success in this regard, for example, in predicting the time scale of energy storage in the system before quenching of excited iodine atoms destroys the population inversion, [65], [53], [60], [28], [59], [52], [69], [94] and laser energy outputs [60], and should be capable of predicting the fractional degree of photolysis which results with given flashlamp energy inputs, and the amount of irreversibile photolysis which results under given excitation conditions. We will not formulate a new kinetic model here or discuss critically the advantages or deficiencies of previous models. However, we feel that in the light of currently available kinetic data, consideration of the most important reactions occurring in the system, namely, reactions (1)-(5), and (7)-(10) makes possible semiquantitative predictions about the behavior of the laser. More accurate predictions probably cannot be obtained without considering other complexities of the system, for example, gas heating, which changes reaction rate constants and ultimately leads to pyrolysis [65], [72], [88], [94]; gas transport (shock waves) [3], [4]; the spectral dis-

tribution of the exciting flash and its interaction with the parent iodide and photolysis products [95]; and magnetic field effects.

Experimental Observations

In any comparison of the relative performance of different alkyl materials in a photodissociation laser system a very basic consideration is the efficiency of the different materials in absorbing pumping radiation from the exciting flashlamp [reaction (5a)]. Since the fundamental parameters of the ultraviolet photodissociative absorption band of different important materials do not appear to be convenviently tabulated anywhere, we have measured them with carefully purified material on a Cary 14 UV absorption spectrophotometer. The most important features of the various absorption peaks are summarized in Table III. The absorption peaks themselves are approximately Gaussian. One would expect the efficiency of coupling of the absorption band to the flashlamp to be dependent both on the peak absorption coefficient and on the peak absorption wavelength, with compounds absorbing at longer wavelength being more efficiently pumped. The useful long wavelength absorption of both n-C_3F_7I and i-C_3F_7I extends to about 3300 Å.

Fig. 6 shows the pressure dependence of the energy output of the oscillator used in our experiments when excited in the fast flash mode. This energy output is a measure of the number of excited iodine atoms which contribute to the stimulated emission process before quenching occurs. The exact pressure at which maximum energy outputs are observed is specific to the size of photolysis tube used in our experiments, being in part determined by its optical thickness when filled with alkyl iodide, and its ability to efficiently and uniformly absorb radiation from the pumping flashlamp. The energy outputs shown in Fig. 6 are well below the maximum which could be obtained from an oscillator of the size used in these experiments. No attempt at achieving optimum coupling for maximum energy output was made. All the compounds used in our experiments were purified by multiple *in vacuo* distillations between dry-ice/isopropanol and liquid-nitrogen-cooled traps.

The main conclusions which can be drawn from Fig. 6, and which should be generally applicable to atomic iodine photodissociation laser/amplifier systems are as follows.

1) Compound maximum energy output follows the sequence: i-C_3F_7I > n-C_3F_7I > CF_3I > C_2F_5I > CD_3I although iso and normal C_3F_7I are not significantly different.

2) Since the fractional yield of I* from photolysis of i-C_3F_7I is lower than for n-C_3F_7I (Table I) and since the self-quenching coefficient of i-C_3F_7I is also the larger (Table II), one would expect n-C_3F_7I to be the better laser material. The fact that it is not suggests that perhaps reaction (7) is more efficient in the case of a linear C_3F_7 radical.

3) CF_3I provided greater energy outputs than C_2F_5I in our experiments even though the fractional yield of I* from C_2F_5I is greater and its peak absorption coefficient is higher. The differing pressures for maximum energy output of these two materials are partially determined by differences in their absorption coefficients. For example, the material with the higher absorption coefficient might be expected to exhibit the lower optimum pressure as it becomes optically thick and nonuniformly irradiated at lower pressures. However this dependence may be reversed by differences in the rate of quenching of excited iodine atoms by parent molecules. A high rate for this quenching reaction will help to move the optimum operating conditions to lower pressure. The more rapid decrease in energy output of C_2F_5I over CF_3I at high pressures may indicate that C_2F_5I has a larger rate constant for this quenching reaction than the value listed in Table II.

4) CF_3I provides substantially greater energy outputs than CD_3I at all but the lowest pressures we studied. There is a crossover point at very low pressures when CD_3I becomes marginally more efficient [92]. This is in agreement with comparative observations of CF_3I and CD_3I made at a pressure of 2.5 torr by Butcher *et al.* [30].

TABLE III
PARAMETERS OF PHOTODISSOCIATIVE ABSORPTION BANDS

COMPOUND	λ_{peak} (Å)	α_{peak} (cm^{-1} $torr^{-1}$)	$\Delta\lambda$ [a] (Å)
CD_3I	2555	$3.7 \cdot 10^{-2}$	235
CF_3I	2665	$1.9 \cdot 10^{-2}$	370
C_2F_5I	2665	$2.3 \cdot 10^{-2}$	400
n-C_3F_7I	2705	$2.5 \cdot 10^{-2}$	430
i-C_3F_7I	2735	$2.2 \cdot 10^{-2}$	435

[a] $\Delta\lambda$ is the full width of the absorption band between the wavelengths where $\alpha = \alpha_{peak}/2$.

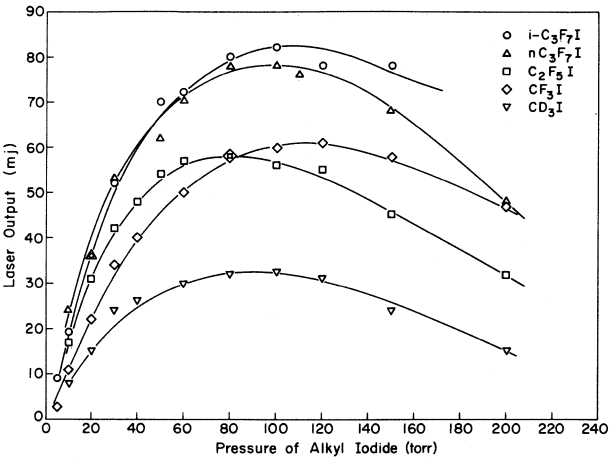


Fig. 6. Pressure dependence of photodissociation laser energy output for various alkyl iodides, observed using fast flash excitation.

Quenching and Photolytic Reversibility

Following the UV photolysis of a pure perfluoroalkyl iodide such as n-C_3F_7I some irreversible dissociation into the main products I_2 and, in this case, C_6F_{14} occurs. Other products can be produced if heating of the laser medium causes pyrolysis and liberates free fluorine and carbon atoms; for example, free fluorine will attack the parent molecule,

$$C_3F_7I + F \longrightarrow C_3F_8 + I.$$

The larger the alkyl iodide molecule, the more stable it should

be against pyrolytic breakup as it possesses more internal degrees of freedom and a resultant greater heat capacity.

Pyrolysis is usually most severe in iodine photodissociation lasers driven by high-energy slow flashlamps. It has been assumed that such lamps deliver large amounts of energy in the infrared which can be absorbed in vibrations of the alkyl iodide leading to gas heating [69]. However, this assumption appears to be unjustified. We will consider CF_3I as an example, as this should be the perfluoroalkyl iodide most subject to pyrolytic breakup. If this material is irradiated in a high-quality fused silica photolysis tube, then radiation out to about 5 μm reaches the interior of the tube. CF_3I has only very weak absorption bands below 8 μm [70], [71], and it is doubtful whether these bands could absorb sufficient energy to heat the gas significantly. We estimate from the data in [70] that the mean absorption coefficient in these infrared bands, which peak near 4.4 μm and have an effective total width $\sim$1.5 μm, is $\sim 4.6 \cdot 10^{-4}$ cm^{-1}torr^{-1}. The emission from conventional slow xenon-filled flashlamps in the region of these absorption bands (3.5–5 μm) is very small. To illustrate this, it is useful to compare the relative rates of photodissociation and infrared absorption produced by slow and fast xenon flashlamps.

If we assume that a conventional slow xenon flashlamp approximates to a black body source at 6000 K, which peaks in the visible at 4800 Å, then its radiant emmittance is $3.6 \cdot 10^{3}$ W $\cdot$ cm$^{-2}\mu$m^{-1} at 2700 Å and $3.8 \cdot 10^{-3}$ W $\cdot$ cm^{-2} μm^{-1} at 4.4 μm (the strongest infrared absorption peak of CF_3I below 5 μm). The corresponding figures for a fast flashlamp, assumed to approximate a much hotter black body at $\sim$15 000 K, are $7.7 \cdot 10^{5}$ W $\cdot$ cm$^{-2}\mu$m^{-1} at 2700 Å and $9.3 \cdot 10^{-3}$ W $\cdot$ cm$^{-2}\mu$m^{-1} at 4.4 μm. We approximate the photodissociative absorption band by a square profile 500 Å wide with a peak absorption coefficient of $1.9 \cdot 10^{-2}$ cm^{-1} torr^{-1}. At 100 torr of CF_3I if the spectral irradiance at the photolysis tube is equal to the emittance from the lamp, the value of the ratio infrared energy absorbed/ultraviolet energy absorbed is $\sim 2 \cdot 10^{-6}$ for the 6000 K source and $\sim 2 \cdot 10^{-8}$ for the 15 000 K source (assuming an average absorption path length of 1 cm). These calculations indicate that, even if the exact spectral emittance of the flashlamp used deviates widely from a black body, direct absorption of flashlamp energy by vibrations is entirely negligible compared to ultraviolet absorption leading to photodissociation. This absorption leads to heating of the gas because of the translational and vibrational energy acquired by the radical following photolysis and because of the exothermicity of the radical recombination reaction (11) [72].

It remains unclear, therefore, why long-duration flashlamps produce more pyrolysis than fast flashlamps delivering comparable energies. The only significant difference between these two modes of excitation is that the fast flash terminates before a significant quantity of the photolysis products have been produced, whereas the slow flash persists during the time when such products have reached significant concentrations. Absorption of some of the substantial quantity of visible radiation from the lamp by the photolysis products, for example by molecular iodine or by hot parent molecules [72], would provide a pathway for lamp radiation to heat the laser medium. However, these considerations are of largely academic interest, as pyrolysis can be minimized by the addition of large quantities of a suitable buffer gas to the laser medium to increase its heat capacity. Without such a buffer gas, pyrolysis will eventually become detrimental to laser performance even when fast flashlamps are used.

We have observed the effect which the products of photolysis have on laser operation by repetitively pulsing single fills of different alkyl iodide materials at successive time intervals and recording changes in the temporal characteristics and output energy of the laser. Because there is a substantial volume of alkyl iodide beyond the region which is irradiated by the flashlamp, the time interval between shots must be carefully chosen so that diffusion of fresh material into, and photolysis products out of the pumping region does not mask the changes in laser behavior due to product buildup.

Diffusional Mixing

If we photolyze a cylindrical tube of, for example, C_3F_7I, then following photolysis a number of the original molecules, N_1 per unit volume, are irreversibly decomposed to give concentrations of mainly I_2 and C_6F_{14} each with a concentration of $N_1/2$. If the photolyzed region extends from $-l$ to $+l$, after photolysis diffusional mixing will begin to equilibrate the concentration of all the species present between the photolyzed and unphotolyzed regions of the system. This diffusional mixing will be governed approximately by the one-dimensional diffusion equation giving the concentration N_i of species i in the tube as a function of time and position

$$\frac{\partial N_i}{\partial t} = D_i \frac{\partial^2 N_i}{\partial x^2} \tag{5}$$

where D_i is the diffusion coefficient of species i in the surrounding mixture. If we take as the boundary condition the distribution of species i at time zero, $N_i(x, 0) = \phi_i(x)$, immediately following photolysis, then (5) has the solution

$$N_i(x, t) = 1/2(\pi D_i t)^{-1/2} \int_{\infty}^{\infty} \phi_i(u) \exp\left(-(x-u)^2/4D_i t\right) du \tag{6}$$

where x is the distance measured from the center of the photolysis region. In the present experiments the fractional irreversible photolysis per shot is relatively small, so the parent alkyl iodide molecule remains the dominant species present for very many shots. Thus the diffusion coefficient applicable to all the species present approximates well to the self-diffusion coefficient D of the parent alkyl iodide molecule; that is

$$D_i = D = 1/3\lambda\bar{c}$$

where $\bar{c}$ is the mean velocity of the alkyl iodide molecule and λ is its mean free path

$$\bar{c} = (8KT/\pi m)^{1/2}$$

where m is the molecular weight; for C_3F_7I

$\bar{c} = 1.465 \cdot 10^4$ cm $\cdot$ s^{-1} at 300 K.

In a mixture of n gases the mean free path of species i is [73]

$$\lambda_i = 1 \Big/ \left(\pi \sum_{j=1}^{n} N_i S_{ij}^2 (1 + m_j/m_i)^{1/2} \right) \tag{7}$$

where $S_{ij} = \frac{1}{2}(\sigma_i + \sigma_j)$ and σ_i, σ_j are the diameters of the molecules i and j (assumed to be spherical). When one component dominates

$$\lambda_1 = 1/(2^{1/2} \pi N_1 \sigma_1). \tag{8}$$

We can estimate the mean free path of a C_3F_7I molecule by taking the value of σ appropriate to C_3H_8, namely 5.06 Å [73]. At a pressure of 20 torr the value obtained is $\lambda = 1.243 \cdot 10^{-4}$ cm, which gives a value for the diffusion coefficient D at 300 K and 20 torr of 0.607 cm^{2}s^{-1}. We can solve (6) for the distribution of I_2 and C_6F_{14} molecules after photolysis. In an excess of C_3F_7I both these species diffuse at the same rate. The I_2 concentration $[I_2](x, t)$ when the initial I_2 concentration is $[I_2]_0 (|x| \leqslant l)$ and zero elsewhere is from (6),

$$[I_2] = [I_2]_0 (\operatorname{erf}((l - x)/2(Dt)^{1/2}) + \operatorname{erf}((l + x)/2(Dt)^{1/2}))/2. \tag{9}$$

The dimensionless parameter which determines the shape of this distribution is $K = l^2/Dt$. Fig. 7 shows this distribution for iodine (or C_6F_{14}) molecules in the photolysis tube for values of $K = 1$ and 6 normalized to an initial unit I_2 concentration of uniform density from $x = -l$ to $x = +l$. In our present apparatus $K = 1$ corresponds to a time 96 s after photolysis at 20 torr, 480 s after photolysis at 100 torr. Even after these relatively long times the I_2 concentration has fallen only to a little below half its initial value. For $K = 6$ the corresponding times are 16 s and 80 s, respectively, and a substantial part of all the photolysis products remains in the initially photolyzed region. Fig. 7 also shows the C_3F_7I concentrations at times corresponding to $K = 1$ and 6 which would result following 50-percent irreversible photolysis in a single shot, assuming the same value for the diffusion coefficient. (This assumption is not unreasonable since C_3F_7I, C_6F_{14}, and I_2 treated as spherical molecules are all approximately the same size; compare: C_3H_8, $\sigma = 5.06$ Å, n-C_6H_{14}, $\sigma = 5.91$ Å, I_2, $\sigma = 4.98$ Å, and all have similar molecular weights.) This C_3F_7I distribution is given by

$$N_1 = N_1(t = 0)(1 - \tfrac{1}{2}(1 - p)(\operatorname{erf}((l - x)/2(Dt)^{1/2}) + \operatorname{erf}((l + x)/2(Dt)^{1/2})) \tag{10}$$

where p is the fractional irreversible photolysis, 0.5 in the case of Fig. 7.

Fig. 8 shows the time dependence of the laser output resulting from the slow flash photolysis of 20 torr of n-C_3F_7I. Fig. 8(a)-(d), respectively, shows the output on the first, second, fourth, and ninth firings of the laser with the same gas fill with a 120-s interval between shots. It is clear that the most marked change occurs after the first shot. This is further illustrated in Fig. 9 which shows the changes in the duration

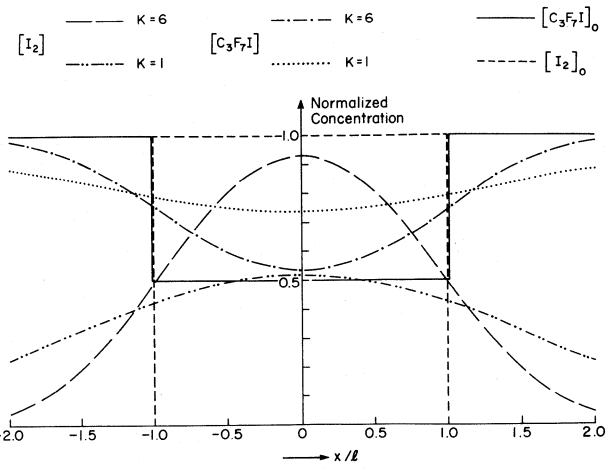


Fig. 7. Longitudinal concentration distribution of various species at two dimensionless times following photolysis at $t = 0$.

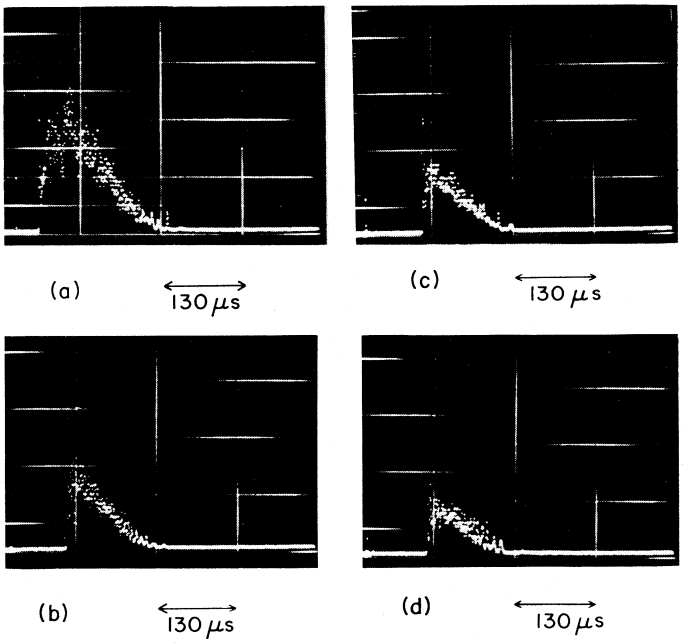


Fig. 8. Laser output on the (a) first, (b) second, (c) fourth, and (d) ninth shots of a single fill of 20-torr n-C_3F_7I. A 120-s time interval between shots using slow flash excitation and a flash energy of 400 J.

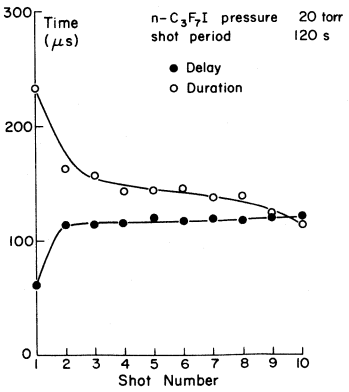


Fig. 9. Variation in the delay before laser oscillation begins, and the duration of lasing, observed in successive shots of a single fill of 20-torr n-C_3F_7I. A 120-s time interval between shots using slow flash excitation and a flash energy of 400 J.

of lasing, and the delay after flashlamp triggering at which laser oscillation starts, in successive firings of the laser under the above conditions. The instant of flashlamp triggering is visible as a spike on the left of the analyzer displays shown in Fig. 8. Fig. 10(a)-(d) shows the behavior of the laser at 20 torr on the first, second, third, and fourth shots of the same gas fill, with a 15-s interval between shots. Once again the most marked change occurs after the first shot. Fig. 11(a)-(d) shows the output in four successive firings of the laser at 100 torr with a 75-s time interval between shots. Here there is a marked monotonic decrease in output from the first shot onwards, with no lasing on the fourth shot. This behavior is even more marked when the time interval is reduced to 15 s. These observations are all compared in Fig. 12. The total energy input to the flashlamp in all the above slow flash observations was 400 J.

Our observations made at 20 torr indicate that longitudinal diffusional mixing is not very important in determining the behavior of the laser in repetitive operation since we observed very little change between 15-s and 120-s interval firings. However there is a marked change at 100 torr with a 75-s interval where the diffusional mixing is the same as at 20 torr with a 15-s interval. At 100 torr the gas absorbs much more UV radiation and significantly more irreversible photolysis and pyrolysis will occur. The most undesirable product of this process is molecular iodine which will quench laser oscillation if its concentration is high enough. Saturation of the C_3F_7I vapor with molecular iodine at ambient temperature gives a partial I_2 pressure of about 0.25 torr; we have observed laser action in such mixtures without difficulty. Kasper *et al.* [27] reported that 1.5 torr of I_2 vapor was necessary to quench laser oscillation in a CF_3I photodissociation laser. It would appear from our observations at 100 torr that at high enough pressures, heating of the laser medium by the photolysis process allows a high enough concentration of I_2 to be held in the vapor phase, without solidification on the photolysis tube wall, for laser oscillation to be quenched after very few shots. The iodine concentration builds up to a critical level by successive cycles of irreversible photolysis or pyrolysis. The behavior we observed at 20 torr would indicate much less gas heating, and a constant I_2 concentration below the critical quenching value being maintained by radial diffusion and solidification on the tube walls. The marked change after one or two shots suggests the buildup of molecular iodine until the C_3F_7I vapor becomes saturated.

The slow flash method of excitation is unsuitable for producing and storing excited iodine atoms as a high concentration of quenchers builds up and generally terminates laser

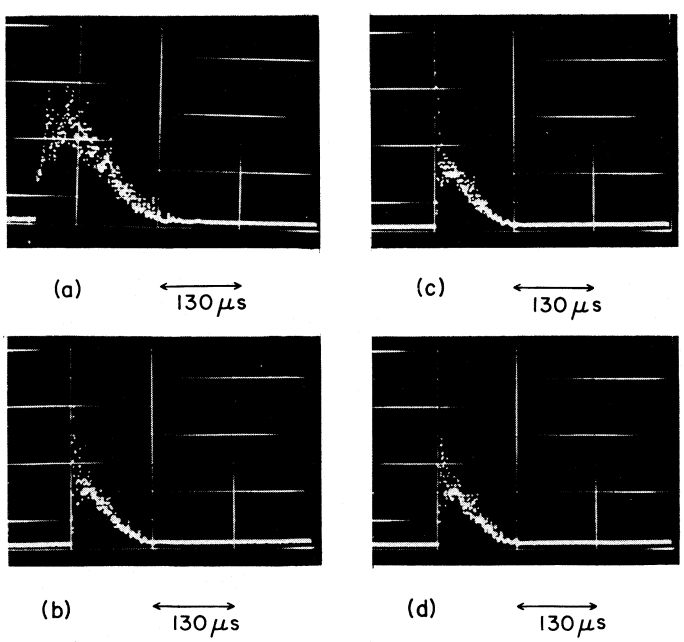


Fig. 10. Laser output on the (a) first, (b) second, (c) third, and (d) fourth shots of a single fill of 20-torr n-C_3F_7I. A 15-s time interval between shots using slow flash excitation and a flash energy of 400 J.

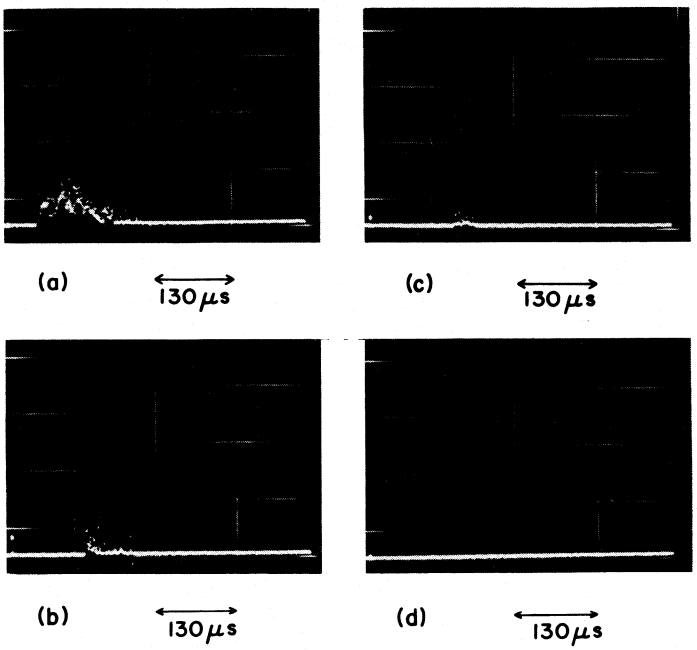


Fig. 11. Laser output on the (a) first, (b) second, (c) third, and (d) fourth shots of a single fill of 100-torr n-C_3F_7I. A 75-s time interval between shots using slow flash excitation and a flash energy of 400 J.

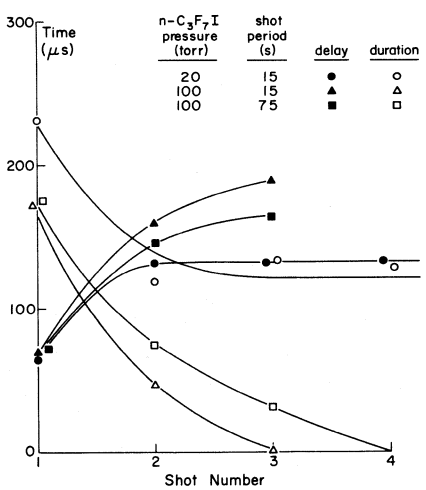


Fig. 12. Variation in the delay before laser oscillation begins, and the duration of lasing, observed in successive shots of a single fill of n-C_3F_7I.

action before the end of the flash. We operated our present oscillator in a Q-switched mode using a rotating mirror but could not obtain any laser output at times beyond the end of the slow flash. This is in contrast to observations made in an oscillator/amplifier experiment with fast flash excitation where amplification could be obtained several milliseconds after the end of the flash, demonstrating the ability of the system to store excited iodine atoms [59].

Under conditions of fast flash excitation with comparable energy inputs to the flashlamp, the behavior of the laser in our experiments is quite different from that with slow flash excitation, as is illustrated by Figs. 13–15. Fig. 13 shows the comparative performance of the most useful alkyl iodides in repetitively pulsed operation with the fast flashlamp, a constant input energy of 380 J, and a time interval between shots of 60 s. All the compounds show irreversibility to some degree, the largest change in performance in every case occurs after the first shot, although this is smallest for i-C_3F_7I. The smallest change in performance in successive shots after the first appears to be for C_2F_5I, but its total energy output is below i-C_3F_7I. The most interesting feature of these curves is that laser oscillation is not quenched, even at this input energy and pressure, after 8 shots whereas with slow flash excitation of 100 torr of n-C_3F_7I at 400 J it occurs after 3 shots at 75-s intervals. When one considers the greater output of the fast flashlamp in the UV, and the correspondingly larger energy absorbed by the gas fill than is the case for slow flash excitation, it is clear that some as yet uncertain mechanism of pyrolysis must result when the latter form of excitation is used. Fig. 14 illustrates the behavior of i-C_3F_7I in repetitive operation at 60-s intervals at different pressures with a constant energy input to the flashlamp of 240 J. Reversibility improves at lower pressures as the total energy absorbed from the flashlamp and the concentration of undesirable photolysis products falls. These results indicate that in large-diameter photodissociation laser amplifiers which operate at lower optimum pressures, even without a buffer gas, reversibility ought to be very good. The results in Fig. 14 do not show evidence for significant pyrolytic production of undesirable photolysis products and the low-pressure curves show excellent reversibility. Fig. 15 shows further evidence of this; the repetitive behavior of i-C_3F_7I at a fixed pressure does not appear very strongly dependent on the input flash energy. These results are consistent with the production of molecular iodine which saturates the laser medium at a pressure lower than necessary for complete quenching, coupled with a gradual depletion of the concentration of C_3F_7I molecules. The tendency of the curves to almost level off after the first few shots is evidence that the concentration of quenching molecules is becoming saturated. We conclude that in the fast flash mode of excitation the laser system does not show significant evidence of pyrolysis at energy inputs below about 40-J flash energy/ml of laser medium at 100 torr (the maximum used in our experiments). This is only true for the compounds indicated in Fig. 13. CH_3I exhibited intense laser action in our system but only when operated with a fresh gas fill; repetitive operation was never observed with this material in our experiments, which indicates that this material may have a very high tendency to pyrolyze. When pyrolysis is unimportant, the formation of undesirable quenching molecules following photolysis will not be reduced by the addition of a buffer gas.

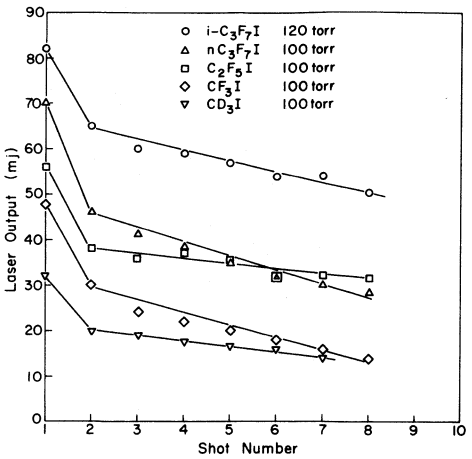


Fig. 13. Comparative performance of a single fill of different alkyl iodides in repetitively photolyzed operation, using fast flash excitation and a flash energy of 380 J.

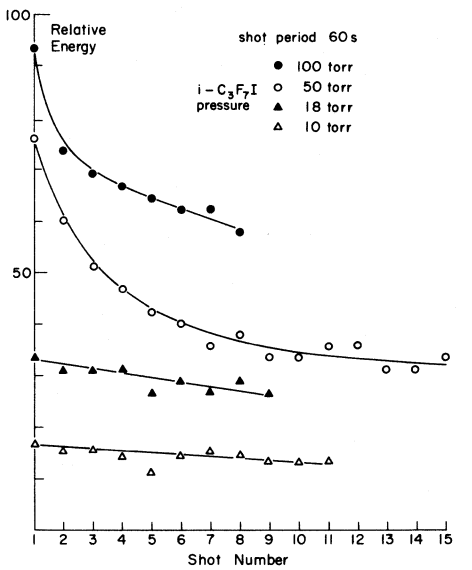


Fig. 14. Comparative performance of a single fill of i-C_3F_7I at different pressures in repetitively photolysed operation, using fast flash excitation and a flash energy of 240 J.

High-Energy Short-Pulse Generation with Iodine Photodissociation Lasers

A number of the problems associated with the use of atomic iodine laser/amplifier systems to generate short-duration high-energy pulses have been solved. Short-duration oscillator pulses suitable for feeding into an amplifier chain can be generated either by mode-locking [74], [1], [22] or by pulse cutting methods [75]; amplified spontaneous emission problems in the amplifier sections can be eliminated by pressure broadening of the amplifying transition with a suitable buffer gas [76], [1], [77]; and diffraction-limited beam quality should be attainable by injecting the oscillator pulse into the amplifier stages before the flashlamp-induced shock waves have propagated far from the photolysis tube walls [78]. Pressure broadening of the transition in the amplifier has the additional advantage of ensuring good overlap between the oscilla-

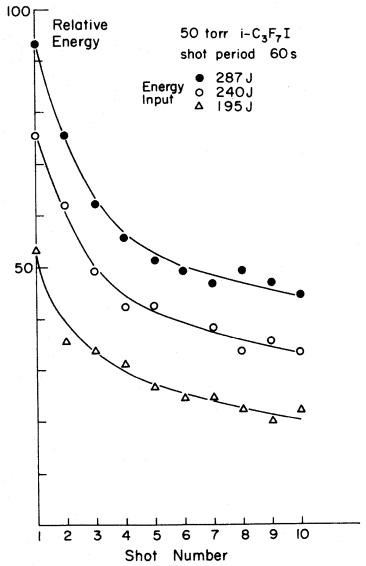


Fig. 15. Comparative performance of a single fill of i-C_3F_7I in repetitively photolyzed operation, using fast flash excitation and different flash energies.

tor output, on the $F = 3 \rightarrow F = 4$ hyperfine component and this transition in the amplifiers by producing effective degeneracy of the Zeeman components of the amplifying transition in the presence of flashlamp magnetic fields. It is possible to eliminate such magnetic effects by operating the oscillator in a Q-switched mode after its pumping flash has ceased [58], or by operating the amplifier flashlamps in an underdamped mode, and feeding the oscillator pulse to the amplifiers as the current through the amplifier flashlamp passes through zero [79]. The disadvantage of this latter scheme of operation is that refractive index inhomogeneities will result from the shock waves in both oscillator and amplifiers and affect beam quality.

Intralevel Relaxation

Two other phenomena also influence the efficiency and ability of amplifying stages in increasing the energy of pulses transmitted through them. If the duration of the pulse to be amplified τ_p is comparable to, or shorter than, the relaxation time between hyperfine levels, then less than $\frac{2}{3}$ of the stored energy can be extracted from the amplifier. If relaxation among the hyperfine levels of $^2P_{3/2}$ is faster than the time scale of the pulse, while relaxation among the hyperfine levels of $^2P_{1/2}$ is slower, then a fraction 14/31 of the stored energy can be extracted. If relaxation among all hyperfine levels is slower than the time scale of the pulse, then only a fraction 21/64 of the stored energy can be extracted. Yukov [80] has concluded that relaxation among the hyperfine levels of $^2P_{3/2}$ is fast and results from the Van der Waals interaction in collisions with any particle in the laser medium. This relaxation time is estimated to be 0.1-1 ns under typical laser conditions. However, relaxation among the hyperfine levels of $^2P_{1/2}$ may be much slower, depending on the exact composition of the laser medium, as such relaxation only occurs efficiently when the collision partner has degenerate electronic angular momentum. Collisional relaxation among the hyperfine levels of an isolated $^2P_{1/2}$ state by species with zero electronic angular momentum, for example, ground-state noble-gas atoms, is generally very slow because the selection rules $\Delta M_J = 0, \pm 2$, $\Delta M_I = 0$ prevent coupling except between sublevels with the same M_F [81]. Consequently, in a photodissociation laser using C_3F_7I, only the C_3F_7 radicals and iodine atoms present after photolysis are effective in distributing population between all the hyperfine levels of the iodine $^2P_{1/2}$ atoms. However, the cross sections for these relaxation processes are of the same order as in the case of collisional relaxation among the hyperfine levels of $^2P_{3/2}$ by Van der Waals interactions [80]. The relative rates of relaxation within the $^2P_{1/2}$ and $^2P_{3/2}$ levels will depend on the fraction $([I] + [I^*] + [C_3F_7] + [M])/N_0$ where square brackets indicate particle densities and N_0 is the total particle density in the laser medium, M is any additional species present which possesses degenerate angular momentum. If the fraction above is ~1/10, as might be typical in a C_3F_7I system where 5-percent dissociation is produced, then the relaxation time within the $^2P_{1/2}$ levels will be in the 1-10-ns region and pulses on this time scale will experience some loss in amplification even if the amplifier is saturated.

Coherent Phenomena

The second group of phenomena which serve to limit the ability of an amplifier to increase the energy of short duration input pulses is the onset of coherent interactions, in particular, self-induced transparency [82]-[85]. These phenomena arise when the duration of the pulse being amplified τ_p becomes comparable to or shorter than T_2', the inverse of the homogeneous broadening contribution to the optical linewidth. In the case of the iodine transition, homogeneous broadening is likely to dominate, particularly if a high-pressure buffer gas is present to minimize pyrolysis and effects of amplified spontaneous emission. In pure C_3F_7I, $1/T_2' \sim 18$ MHz · torr^{-1} [13]. For high pressures of added helium we estimate from the data given in [76] that $1/T_2' \sim 3.65$ GHz · atm^{-1}. In contrast, the inhomogeneous dephasing time, T_2^*, is larger than T_2', except at relatively low pressures (<20 torr) and at temperatures above ambient. T_2^*, taken as the reciprocal of the inhomogeneous contribution to the linewidth, is ~4 ns at 300 K. These figures indicate that unless very high buffer gas pressures are used, pulsewidths with $\tau_p \lesssim 0.1$ ns will satisfy the condition $\tau_p < T_2'$, T_2^* and coherent effects should occur strongly. Pulsewidths in the region 0.1 ns $< \tau_p <$ 10 ns will be in an intermediate region where effects such as pulse breakup ought to be discernible at sufficiently high power levels. In general, for pulse durations short enough for coherent effects to occur, the critical power level necessary for the observation of phenomena such as self-induced transparency and pulse breakup is set by the π pulse criterion. McCall and Hahn [82]-[84] have shown that in the simple case of a plane wave pulse of duration $\tau_p \ll T_2'$ interacting with an inhomogeneously broadened nondegenerate transition at resonance, the area of the pulse, A, obeys

$$\frac{dA}{dz} = \frac{1}{2} g \sin A \tag{11}$$

where z is distance measured through the medium along the direction of propagation and g is the gain coefficient. A pulse

whose area is π will propagate through the medium as if it were transparent, and suffer no gain in energy; a pulse whose area is below π will be amplified until it becomes a π pulse, while a pulse whose area obeys $\pi < A < 2\pi$ will be attenuated until it becomes a π pulse. Pulses with area $>2\pi$ are likely to suffer pulse breakup effects. (While the exact validity of these statements has only been demonstrated for $T_2^* \ll \tau_p \ll T_2'$, they are also believed to hold true for $\tau_p \ll T_2^*, T_2'$ [84].)

The pulse area, for interaction with a magnetic dipole transition, is, by analogy with an electric dipole transition [84],

$$A = \frac{|\underset{\sim}{\mu}|}{\hbar} \int_{-\infty}^{\infty} H(z,t)\, dt \tag{12}$$

where $\underset{\sim}{\mu}$ is the magnetic dipole moment of the transition and $H(z,t)$ is the magnetic field component of the pulse. In the case where the interacting transition is degenerate, as is the case for the iodine laser in all but very large magnetic fields, we replace $\underset{\sim}{\mu}$ by $\underset{\sim}{\mu}_{\mathrm{MAX}}$, the largest dipole moment of the various degenerate components of the transition. For the $F = 3 \rightarrow F' = 4$ transition we can evaluate $\underset{\sim}{\mu}_{\mathrm{MAX}}$ from the Einstein A coefficient of the strongest component of the transition. For the σ components of this transition, the strongest is $F = 3, M_F = 0 \rightarrow F' = 4, M_{F'} = 0$ (see Table IV). For this transition between magnetic sublevels the Einstein coefficient $A_{M_F M_{F'}}$ is related to the overall Einstein coefficient $A_{FF'}$ by $A_{M_F M_{F'}} = (28/63) A_{FF'}$ [14], ($A_{FF'} = 3.47\ \mathrm{s}^{-1}$ for $F = 3 \rightarrow F' = 4$ [13]). For the π components of the $F = 3 \rightarrow F' = 4$ transition, the strongest is $F = 3$, $M_F = 3 \rightarrow F' = 4, M_{F'} = 4$. For this transition $A_{M_F M_{F'}} = (7/9)\, A_{FF'}$.

The magnetic dipole moment of a transition between magnetic sublevels is [14]

$$|\underset{\sim}{\mu}_{M_F M_{F'}}| = |\langle JIFM_F | M_m^{(1)*} | J'I'F'M_{F'}\rangle| \tag{13}$$

where J, I, F, M_F are the quantum numbers of the upper level of the transition and $J', I', F', M_{F'}$ are those of the lower. $M_m^{(1)}$ is the mth component of the magnetic dipole tensor operator

$$\underline{M}^{(1)} = \sum_j \beta[\underline{l}(j) + 2\underline{s}(j)]^{(1)} \text{ [14]}$$

where β is the Bohr magneton.

Now

$$A_{M_F M_{F'}} = \frac{4}{3}\frac{k^3}{\hbar} |\langle FM_F | M_m^{(1)*} | F'M_{F'}\rangle|^2 \tag{14}$$

where $k = 2\pi/\lambda$; so from (13) and (14) we can write

$$|\mu_{M_F M_{F'}}|^2 = 3A_{M_F M_{F'}}\hbar/4k^3. \tag{15}$$

Substituting the appropriate values for $A_{M_F M_{F'}}$ in (15) we find that for the σ components of the $F = 3 \rightarrow F' = 4$ transition

$$|\mu_{\mathrm{MAX}}|^2 = 0.13 \text{ (Bohr magneton)}^2$$

and for the π components

$$|\mu_{\mathrm{MAX}}|^2 = 0.228 \text{ (Bohr magneton)}^2.$$

In MKS units the intensity of an electromagnetic wave is related to its magnetic field component by

$$I = ZH^2 \tag{16}$$

where Z is the characteristic impedance of the medium, which, in this case, we take to be the same as for free space. For a square pulse of duration τ_p the intensity I_0 necessary for a π pulse is, therefore, from (12) and (16)

$$I_0 = Z(\hbar\pi/|\mu_{\mathrm{MAX}}|\tau_p)^2. \tag{17}$$

The calculated collimated intensity necessary for a 0.1 ns π pulse is $2.34 \cdot 10^{10}\ \mathrm{W \cdot cm^{-2}}$ for the σ components of the $F = 3 \rightarrow F' = 4$ transition and $1.34 \cdot 10^{10}\ \mathrm{W \cdot cm^{-2}}$ for the π components. The total energies in these pulses are 2.34 $\mathrm{J \cdot cm^{-2}}$ and 1.34 $\mathrm{J \cdot cm^{-2}}$, respectively. (It is worth noting that the mode-locked pulses observed in our experiments were not π pulses [86]; their peak power we estimate to be of the order of 5 kW, far below that necessary for even a 10-ns duration π pulse, even if such a long pulse could exhibit coherent interactions with the laser medium.)

The propagation of π pulses through an iodine amplifier is not, however, given simply by (11). We must consider both the effect of the degeneracy of the $F = 3 \rightarrow F' = 4$ transition and the spatial mode of the incident pulse. The generalized area theorem in this case is [84]

$$\frac{dA}{dz} = \frac{1}{2} g' \left[\sum_i \int dx \int dy\, N_i(x,y,z)\, D_i \sin(D_i A) \right] \cdot \left[\sum_i \int dx \int dy\, N_i(x,y,z)\, D_i^2 \right]^{-1} - \frac{1}{2}\alpha A \tag{18}$$

where

$$D_i = \frac{\mu_i}{\mu_{\mathrm{MAX}}} \frac{|\hat{\underset{\sim}{\mu}}_i(x,y,z) \cdot \underset{\sim}{\xi}^*(x,y,z)|}{|\hat{\underset{\sim}{\mu}}_{\mathrm{MAX}}(0,0,z) \cdot \underset{\sim}{\xi}^*(0,0,z)|} \tag{19}$$

μ_i is the dipole moment matrix element of the ith component of the transition, $\xi(x,y,z)$ is the spatial mode amplitude of the input wave, such that its magnetic field component is $\xi(x,y,z)\, H(z,t)$; $\hat{\underset{\sim}{\mu}}_i(x,y,z)$ is a unit vector in the direction of $\underset{\sim}{\mu}_i$; $N_i(x,y,z)$ is proportional to the inversion density of the ith component of the transition; α is a distributed loss coefficient; and g' is a complicated factor involving ξ, N_i, etc. In a gas we take $\hat{\underset{\sim}{\mu}}_i$ parallel to the magnetic field of the incident wave and the N_i to be initially equal and spatially uniform.[1] For a plane wave in this case, (18) reduces to

$$\frac{dA}{dz} = \frac{1}{2} g' \left(\sum_i D_i' \sin D_i' A \right) \Big/ \sum_i D_i'^2 - \frac{1}{2}\alpha A \tag{20}$$

where $D_i' = \mu i/\mu_{\mathrm{MAX}}$.

For a TEM_{00}-mode pulse

$$\hat{\underset{\sim}{\mu}}_i(x,y,z) \cdot \underset{\sim}{\xi}^*(x,y,z) = \exp[-(x^2+y^2)/w_0^2] \tag{21}$$

where w_0 is the spot size, and the area theorem becomes

[1] If relaxation between magnetic sublevels becomes slower than the time scale of a propagating short-duration light pulse, as the pulse propagates the various population inversion densities N_i will cease to be equal, and analysis of the propagation characteristics of the medium become even more complex than the discussion here implies.

$$\frac{dA}{dz} = g' \left(\sum_i (1 - \cos (D_i' A)) |A \right) \Big/ \sum_i D_i'^2 - \frac{1}{2} \alpha A \qquad (22)$$

where $D_i' = \mu_i / \mu_{MAX}$.

Relative values of $A_{M_F M_{F'}}$ and $\mu_{M_F M_{F'}}$ for the σ and π components of the $F = 3 \rightarrow F' = 4$ transition, calculated from the appropriate $3 - j$ symbol [91] are tabulated in Table IV. In (18), (20), and (22), g' is chosen so that for small pulse areas the area theorem reduces to

$$\frac{dA}{dz} = \frac{1}{2} (g - \alpha) A \qquad (23)$$

the familiar linear form. We can, in general, write (18) in the form

$$\frac{dA}{dz} = \frac{1}{2} g S(A) - \frac{1}{2} \alpha A \qquad (24)$$

where $S(A)$ is an area function.

Explicitly, for a plane wave pulse which interacts only with the σ components of the $F = 3 \rightarrow F' = 4$ transition (a situation which occurs, for example, when an external magnetic field is present transverse to the plane of polarization of a linearly polarized input wave, as shown in Fig. 2)

$$\begin{aligned} S(A) = 4 \{ & \sin A + (15/4)^{1/2} \sin [(15/16)^{1/2} A] \\ & + (7/4)^{1/2} \sin [(7/16)^{1/2} A] \\ & + (3)^{1/2} \sin [(3/4)^{1/2} A] \} / 21. \end{aligned} \qquad (25)$$

In the case where an input plane wave interacts with the π transitions alone (a situation which occurs, for example, when the input wave is linearly polarized parallel to an external transverse magnetic field, or in an axial magnetic field),

$$\begin{aligned} S(A) = \{ & \sin A + (1/28)^{1/2} \sin [(1/28)^{1/2} A] + (3/4)^{1/2} \\ & \cdot \sin [(3/4)^{1/2} A] + (3/28)^{1/2} \sin [(3/28)^{1/2} A] \\ & + (15/28)^{1/2} \sin [(15/28)^{1/2} A] + (3/14)^{1/2} \\ & \cdot \sin [(3/14)^{1/2} A] + (5/14)^{1/2} \sin [(5/14)^{1/2} A] \} / 3. \end{aligned} \qquad (26)$$

For a TEM_{00}-mode wave which interacts with the σ transitions alone

$$\begin{aligned} S(A) = 8 \{ & 7 - \cos A - 2 \cos [(15/16)^{1/2} A] \\ & - 2 \cos [(7/16)^{1/2} A] - 2 \cos [(3/4)^{1/2} A] \} / 21 A \end{aligned} \qquad (27)$$

while for interaction with the π components alone

$$\begin{aligned} S(A) = 2 \{ & 7 - \cos A - \cos [(1/28)^{1/2} A] - \cos [(3/4)^{1/2} A] \\ & - \cos [(3/28)^{1/2} A] - \cos [(15/28)^{1/2} A] \\ & - \cos [(3/14)^{1/2} A] - \cos [(5/14)^{1/2} A] \} / 3 A. \end{aligned} \qquad (28)$$

When there is no external magnetic field acting on the transition, an input wave, whatever its state of polarization, will interact with both the π and σ components of the amplifying transition, in which case, for a plane wave pulse

TABLE IV

RELATIVE VALUES OF $A_{M_F M_{F'}}$ AND $\mu_{M_F M_{F'}}$ FOR THE σ AND π COMPONENTS OF THE ATOMIC IODINE $(^2P_{1/2})\, F = 3 \rightarrow (^2P_{3/2})\, F' = 4$ TRANSITION. CALCULATED FROM

$$A_{M_F M_{F'}} = \text{CONSTANT} \; |(^{F'}_{-M_F} \; ^{1}_{m} \; ^{F}_{M_F})|^2 \; S(F, F')$$

[14] WHERE $S(F, F')$ IS THE LINE STRENGTH OF THE $F = 3 \rightarrow F' = 4$ TRANSITION.

M_F	$M_{F'}$	$A_{M_F M_{F'}}$	$\mu_{M_F M_{F'}}$	σ or π
3	3	0·50	- 1/6	σ
-3	-3			
2	2	0·8571	$1/(21)^{1/2}$	σ
-2	-2			
1	1	1·0714	$(5/84)^{1/2}$	σ
-1	-1			
0	0	1·1428	$2/(63)^{1/2}$	σ
3	4	2·0	1/3	π
-3	-4			
3	2	0·0714	$1/(252)^{1/2}$	π
-3	-2			
2	3	1·50	$-1/(12)^{1/2}$	π
-2	-3			
2	1	0·2143	$-1/(84)^{1/2}$	π
-2	-1			
1	2	1·0714	$(5/84)^{1/2}$	π
-1	-2			
1	0	0·4286	$1/(42)^{1/2}$	π
-1	0			
0	1	0·7143	$(5/126)^{1/2}$	π
0	-1			

$$\begin{aligned} S(A) = \tfrac{1}{9} \{ & \sin (A/2) + (12/7)^{1/2} \sin [(3/7)^{1/2} A] \\ & + (15/7)^{1/2} \sin [(15/28)^{1/2} A] + (4/7)^{1/2} \\ & \cdot \sin [(4/7)^{1/2} A] + 2 \sin A + (1/7)^{1/2} \\ & \cdot \sin [(1/28)^{1/2} A] + 3^{1/2} \sin [(3/4)^{1/2} A] \\ & + (3/7)^{1/2} \sin [(3/28)^{1/2} A] + (15/7)^{1/2} \\ & \cdot \sin [(15/28)^{1/2} A] + (6/7)^{1/2} \sin [(3/14)^{1/2} A] \\ & + (10/7)^{1/2} \sin [(5/14)^{1/2} A] \} \end{aligned} \qquad (29)$$

while for a TEM_{00}-mode pulse

$$\begin{aligned} S(A) = \tfrac{2}{9} \{ & 21 - 2 \cos (A/2) - 2 \cos [(3/7)^{1/2} A] \\ & - 2 \cos [(15/28)^{1/2} A] - \cos [(4/7)^{1/2} A] \\ & - 2 \cos A - 2 \cos [(1/28)^{1/2} A] - 2 \cos [(3/4)^{1/2} A] \\ & - 2 \cos [(3/28)^{1/2} A] - 2 \cos [(15/28)^{1/2} A] \\ & - 2 \cos [(3/14)^{1/2} A] - 2 \cos [(5/14)^{1/2} A] \} / A. \end{aligned} \qquad (30)$$

These area functions are plotted in Figs. 16 and 17 which show the area functions appropriate to plane wave and TEM_{00}-mode pulses both without an external magnetic field (the ($\pi + \sigma$) transitions) and in an external field (where the input wave interacts with either the π or the σ components of the $F = 3 \rightarrow F' = 4$ transition).

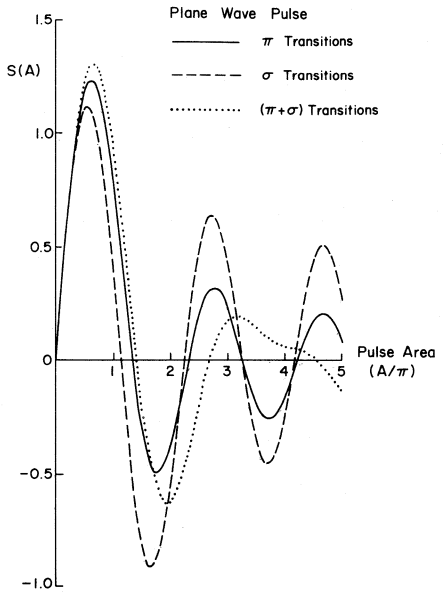


Fig. 16. The area function for the $(^2P_{1/2})\ F = 3 \rightarrow (^2P_{3/2})\ F = 4$ magnetic dipole transition in atomic iodine for a plane wave input.

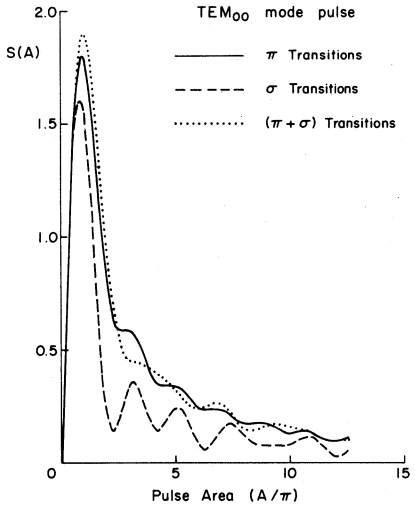


Fig. 17. The area function for the $(^2P_{1/2})\ F = 3 \rightarrow (^2P_{3/2})\ F = 4$ magnetic dipole transition in atomic iodine for a TEM_{00}-mode input.

For small, or zero values of the distributed loss coefficient α, pulse areas where $S(A)$ crosses, or approaches close to the pulse area (horizontal axis, represent solutions of (24) such that $dA/dz = 0$. Such pulse areas represent stable or unstable propagating pulse areas appropriate to an iodine laser amplifier. For example, in Fig. 16 pulse areas $A \simeq 1.14\pi$, 2.24π, 3.25π, 4.15π correspond to $S(A) = 0$ for interaction with the σ transitions such that for $\alpha \simeq 0$, $dA/dz \simeq 0$. The pulse areas $\simeq 1.14\pi$ and 3.25π are stable, an input pulse of area $< 1.14\pi$ will be amplified until it reaches this value and will then experience no further amplification. A pulse of area $> 2.24\pi$ will experience pulse breakup effects. Similar conclusions can be drawn for a plane wave interacting with the π and the $(\pi + \sigma)$ transitions. However from Fig. 17, for an input TEM_{00}-mode pulse there are no exact solutions of (24) for small α and $A \lesssim 12\pi$. Input pulses of area $\lesssim 12\pi$ will not be stable propagating pulse areas. Pulse areas $\lesssim \pi$ will continue to grow but may be unstable against pulse breakup effects. For maximum small pulse gain, for either plane wave or TEM_{00}-mode inputs, it is marginally advantageous to ensure a zero magnetic field situation in the amplifier. This is likely to be difficult however, in which case the polarization state of the input pulse should be chosen so that preferential interaction with the π transitions occurs, as here the small pulse gain reaches higher values, and slightly larger pulse areas are stable against pulse breakup effects.

Summary

We have considered the advantages and disadvantages of atomic iodine photodissociation lasers for the generation and amplification of short duration high-energy pulses. Self-mode locking has been observed in this largely homogeneously broadened system, and output mode spectra were studied in a low-magnetic-field situation where Zeeman effect complications were minimized. Immediately after the laser reached threshold, it oscillated on several longitudinal modes for a short time, but only continued to operate on a few modes, presumably because of mode competition effects.

We reconsidered the kinetics of the laser system following photolysis in the light of the most recent data on pertinent rate coefficients. By studying the behavior of the laser system, following photolysis with flashlamps which have very different temporal and spectral characteristics, we have concluded that some as yet unclear mechanism of pyrolysis is responsible for the degradation of laser performance which occurs when long-duration flash excitation is used. A careful comparison of different parent compounds for laser operation indicates a slight preference for operation with iso rather than normal C_3F_7I, particularly when repetitive operation is required. All the perfluoroalkyl compounds studied performed better than CD_3I or CH_3I. The reversibility characteristic of different materials has been studied under conditions where diffusional mixing following each photolytic cycle was negligible. The most undesirable aspect of the partial irreversibility of all the materials studied is the buildup of molecular iodine in the laser medium. Limitations on the amplification of short-duration, high-energy pulses have been considered, namely intralevel relaxation and coherent phenomena and those conditions of operation indicated where these problems can be best avoided. Some loss of amplification under typical laser conditions is to be expected for pulse duration $\lesssim 10$ ns because of intralevel relaxation times, while for subnanosecond pulses, severe self-induced transparency problems should be avoidable up to energy densities $\sim 20\ J \cdot cm^{-2}$ in a 100-ps pulse.

Acknowledgment

We are grateful to Dr. H. J. Baker and Dr. T. A. King for helpful discussions and access to their results prior to publication. We are also grateful to D. H. Burde, Dr. T. Donohue, and Prof. J. R. Wiesenfeld for details of their results prior to publication.

REFERENCES

[1] K. Hohla *et al.*, "60-J 1-nsec iodine laser," *J. Appl. Phys.*, vol. 46, pp. 808–809, 1975.

[2] H. J. Baker and T. A. King, private communication.

[3] I. M. Belousova, O. B. Danilov, I. A. Sinitsina, and V. V. Spiridonov, "Investigation of the optical inhomogeneities of the active medium of a CF_3I photodissociative laser," *Sov. Phys.-JETP*, vol. 31, pp. 791–793, 1970.

[4] L. E. Golubev, V. S. Zuev, V. A, Katulin, V. Yu. Nosach, and O. Yu. Nosach, "Investigation of optical inhomogeneities which appear in an active medium of a photodissociation laser during coherent emission," *Sov. J. Quantum Electron.*, vol. 3, pp. 464–467, 1974.

[5] I. M. Belousova, V. M. Kiselev, and V. N. Kurzenkov, "Linewidth for induced emission due to the $^2P_{1/2}$-$^2P_{3/2}$ transition of atomic iodine," *Opt. and Spectrosc.*, vol. 33, pp. 115–117, 1972.

[6] W. C. Hwang and J. V. V. Kasper, "Zeeman effects in the hyperfine structure of atomic iodine photodissociation laser emission," *Chem. Phys. Lett.*, vol. 13, pp. 511–514, 1972.

[7] I. M. Belousova, B. D. Bobrov, V. M. Kiselev, V. N. Kurzenkov, and P. I. Krepostnov, "Photodissociative I^{127} laser in a magnetic field," *Sov. Phys.-JETP*, vol. 38, pp. 258–263, 1974.

[8] —, "I^{127} atom in a magnetic field," *Opt. and Spectrosc.*, vol. 37, pp. 20–24, 1974.

[9] V. Jaccarino, J. G. King, R. A. Satten, and H. H. Stroke, "Hyperfine structure of I^{127}—Nuclear magnetic octupole moment," *Phys. Rev.*, vol. 94, pp. 1798–1799, 1954.

[10] R. Onaka, "Hyperfine splitting in the $p^5\ ^2P_{1/2}$ metastable state of I^{127}," *Phys. Rev.*, vol. 106, p. 1178, 1957.

[11] J. Verges, "Etude des spectres d'emission dans l'infrarouge par l'emploi d'un SISAM-I. Spectre de l'iode entre 1.31μ et 2.24μ et l'effet Zeeman de la raie interdite $5s^25p^5\ ^2P_{3/2}$-$5s^25p^5\ ^2P_{1/2}$ à 7603K," *Spectrochimica Acta*, vol. 24B, pp. 177–185, 1969.

[12] I. M. Belousova, V. M. Kiselev, and V. N. Kurzenkov "Induced emission spectrum of atomic iodine due to the hyperfine structure of the transition $^2P_{1/2}$-$^2P_{3/2}$ (7603 cm^{-1})," *Opt. and Spectrosc.*, vol. 33, pp. 112–113, 1972.

[13] V. S. Zuev, V. A, Katulin, V. Yu. Nosach, and O. Yu. Nosach, "Investigation of the luminescence spectrum of atomic iodine ($^2P_{1/2}$-$^2P_{3/2}$) laser transition," *Sov. Phys.-JETP*, vol. 35, pp. 870–873, 1972.

[14] B. W. Shore and D. H. Menzel, *Principles of Atomic Spectra*. New York: Wiley, 1968.

[15] H. B. G. Casimir, *On the Interaction Between Atomic Nuclei and Electrons*. San Francisco, CA: Freeman, 1963.

[16] C. Schwartz, "Theory of hyperfine structure," *Phys. Rev.*, vol. 97, pp. 380–395, 1955.

[17] H. Kopfermann, *Nuclear Moments*. New York: Academic, 1958.

[18] I. Lindgren and A. Rosen, "Relativistic self-consistent-field calculations with application to atomic hyperfine interaction. Part I: Relativistic self-consistent fields. Part II: Relativistic theory of atomic hyperfine interaction," in *Case Studies in Atomic Physics*, vol. 4. Amsterdam, The Netherlands: North-Holland, pp. 93–196.

[19] —, "Relativistic self-consistent-field calculations with application to atomic hyperfine interaction. Part III: Comparison between theoretical and experimental hyperfine structure results," in *Case Studies in Atomic Physics*, vol. 4. Amsterdam, The Netherlands: North-Holland, pp. 197–298.

[20] R. J. Pirkle, C. C. Davis, and R. A. McFarlane, "Self-mode-locking of an iodine photodissociation laser," *J. Appl. Phys.*, vol. 46, 1975.

[21] H. J. Baker and T. A. King, "Mode-beating in-gain-switched iodine photodissociation laser pulses," *J. Phys. D: Appl. Phys.*, vol. 8, pp. L31–L34, 1975.

[22] K. Hohla, W. Fuss, R. Volk, and K. J. Witte, "Iodine laser oscillator in gain switch mode for ns pulses," *Opt. Commun.*, vol. 13, pp. 114–116, 1975.

[23] J. A. Fleck, Jr., "Mode-locked pulse generation in passively switched lasers," *Appl. Phys. Lett.*, vol. 12, pp. 178–181, 1968.

[24] —, "Emission of pulse trains by *Q*-switched lasers," *Phys. Rev. Lett.*, vol. 21, pp. 131–133, 1968.

[25] J. Gilbert and J. L. Lachambre, "Self-locking of modes in a high-pressure CO_2 laser with transverse pulse excitation," *Appl. Phys. Lett.*, vol. 18, pp. 187–189, 1971.

[26] J. V. V. Kasper and G. C. Pimentel, "Atomic iodine photodissociation laser," *Appl. Phys. Lett.*, vol. 5, pp. 231–233, 1964.

[27] J. V. V. Kasper, J. H. Parker, and G. C. Pimentel, "Iodine-atom laser emission in alkyl iodide photolysis," *J. Chem. Phys.*, vol. 43, pp. 1827–1828, 1965.

[28] K. Hohla and K. L. Kompa, "Kinetische Prozesse in einem photochemischen jodlaser," *Zeit. Naturforsch.*, vol. 27a, pp. 938–946, 1972.

[29] M. Y. De Wolf Lanzerotti, "Iodine-atom laser emission in 2-2-2 trifluoroethyliodide," *IEEE J. Quantum Electron.*, vol. QE-7, pp. 207–208, 1971.

[30] R. J. Butcher, R. J. Donovan, C. Fotakis, D. Fernie, and A. G. A. Rae, "Photodissociation laser isotope effects," *Chem. Phys. Lett.*, vol. 30, pp. 398–402, 1975.

[31] G. N. Birich, G. I. Drozd, V. N. Sorokin, and I. I. Struck, "Photodissociation iodine laser using compounds containing Group-V atoms," *Sov. Phys.-JETP Lett.*, vol. 19, pp. 27–29, 1974.

[32] T. Donohue and J. R. Wiesenfeld, "Relative yields of electronically excited iodine atoms, I ($5^2P_{1/2}$), in the photolysis of alkyl iodides," *Chem. Phys. Lett.*, vol. 33, pp. 176–180, 1975

[33] —, "Photodissociation of alkyl iodides," *J. Chem. Phys.*, vol. 63, pp. 3130–3135, 1975.

[34] J. R. Majer and J. P. Simons, "Photochemical processes in halogenated compounds," *Adv. Photochem.*, vol. 2, pp. 137–182, 1964.

[35] S. J. Riley and K. R. Wilson, "Excited fragments from excited molecules: Energy partitioning in the photodissociation of alkyl iodides," *Faraday Disc. Chem. Soc.*, vol. 53, pp. 132–146, 1972.

[36] G. M. Harris and J. E. Willard, "Photochemical reactions in the system methyl iodide-iodine-methane: The reaction $C^{14}H_3 + CH_4$–$C^{14}H_4 + CH_3$," *J. Amer. Chem. Soc.*, vol. 76, pp. 4678–4687, 1954.

[37] J. A. Blake and G. Burns, "Kinetics of iodine atom recombination between 300 and 1164°K," *J. Chem. Phys.*, vol. 54, pp. 1480–1486, 1971.

[38] R. J. Donovan and D. Husain, "Deactivation of excited iodine atoms I($5^2P_{1/2}$)," *Trans. Faraday Soc.*, vol. 62, pp. 11–17, 1966.

[39] —, "Electronically excited iodine atoms. Part 2—I($5^2P_{1/2}$) in the photolysis of hydrogen iodide," *Trans. Faraday Soc.*, vol. 62, pp. 1050–1055, 1966.

[40] —, "Electronically excited iodine atoms I($5^2P_{1/2}$). Part 3," *Trans. Faraday Soc.*, vol. 62, pp. 2023–2029, 1966.

[41] D. Husain and J. R. Wiesenfeld, "Study of electronically excited iodine I($5^2P_{1/2}$) by time resolved emission," *Nature*, vol. 213, pp. 1227–1228, 1967.

[42] —, "Time-resolved emission studies of electronically excited iodine atoms I($5^2P_{1/2}$)," *Trans. Faraday Soc.*, vol. 63, pp. 1349–1357, 1967.

[43] P. Cadman, J. C. Polanyi, and I. W. M. Smith, "Production of electronically excited atoms. Part I: $HI + h\nu$ ($\lambda = 2537$Å) $\rightarrow H + I^*$ ($^2P_{1/2}$) and $H + HI \rightarrow H_2 + I^*$ ($^2P_{1/2}$)," *J. Chem. Phys.*, vol. 64, pp. 111–118, 1967.

[44] R. J. Donovan, F. G. M. Hathorn, and D. Husain, "Study of electronically excited iodine atoms, I($5^2P_{1/2}$) in the presence of alkyl iodides," *Trans. Faraday Soc.*, vol. 64, pp. 3192–3199, 1968.

[45] F. G. M. Hathorn and D. Husain, "Some reactions of electronically excited iodine atoms I ($5^2P_{1/2}$) with halides and oxides," *Trans. Faraday Soc.*, vol. 65, pp. 2678–2684, 1969.

[46] R. J. Donovan and D. Husain, "Recent advances in the chemistry of electronically excited atoms," Chem. Rev., vol. 70, pp. 489–516, 1970.

[47] D. Husain and R. J. Donovan, "Electronically excited halogen atoms," *Adv. Photochem.*, vol. 8, pp. 1–75, 1971.

[48] R. J. Donovan and C. Fotakis, "Isotope effects in the quenching of electronically excited atoms: Photolysis of CD_3I," *J. Chem. Phys.*, vol. 61, pp. 2159–2160, 1974.

[49] D. H. Burde, R. A. McFarlane, and J. R. Wiesenfeld, "Collisional quenching of excited iodine atoms I($5p^5\ ^2P_{1/2}$) by I_2," *Chem. Phys. Lett.*, vol. 32, pp. 296–299, 1975.

[50] D. H. Burde and R. A. McFarlane, to be published.

[51] T. Donohue and J. R. Wiesenfeld, "Photochemistry of alkyl iodides," to be published.

[52] S. V. Kuznetsova and A. I. Maslov, "Investigation of the reactions of atomic iodine in a photodissociation laser using n-C_3F_7I and i-C_3F_7I molecules," *Sov. J. Quantum Electron.*, vol. 3, pp. 468–

471, 1974.
[53] V. Yu. Zalesskii and T. I. Krupenikova, "Deactivation of metastable iodine atoms by collision with perfluoroalkyliodide molecules," *Opt. and Spectrosc.*, vol. 30, pp. 439–443, 1971.
[54] S. Aditya and J. E. Willard, "Chemical reactivity of $I(^2P_{1/2})$ atoms," *J. Chem. Phys.*, vol. 44, pp. 418–419, 1966.
[55] T. L. Andreeva, S. V. Kuznetsova, A. I. Maslov, I. I. Sobelman, and V. N. Sorokin, "Investigation of reactions of excited iodine atoms with the aid of a photodissociation laser," *Sov. Phys.-JETP Lett.*, vol. 13, pp. 449–452, 1971.
[56] A. J. Demaria and C. J. Ultee, "High-energy atomic iodine photodissociation laser," *Appl. Phys. Lett.*, vol. 9, pp. 67–69, 1966.
[57] T. L. Andreeva, V. I. Malyshev, A. I. Maslov, I. I. Sobelman and V. N. Sorokin, "Possibility of obtaining excited iodine atoms as a result of chemical reactions," *Sov. Phys.-JETP Lett.*, vol. 10, pp. 271–274, 1969.
[58] P. Gensel, K. Hohla, and K. L. Kompa "Energy storage of CF_3I photodissociation laser," *Appl. Phys. Lett.*, vol. 18, pp. 48–50, 1971.
[59] K. Hohla and K. I. Kompa, "Energy transfer in a photochemical iodine laser," *Chem. Phys. Lett.*, vol. 14, pp. 445–447, 1972.
[60] V. Yu Zalesskii, "Kinetics of a CF_3I photodissociation laser," *Sov. Phys.-JETP*, vol. 34, pp. 474–480, 1972.
[61] R. E. Palmer and M. A. Gusinow, "Late-time gain of the CF_3I iodine photodissociation laser," *J. Appl. Phys.*, vol. 45, pp. 2174–2179, 1974.
[62] —, "Gain versus time in the CF_3I iodine photodissociation laser," *IEEE J. Quantum Electron.* (Corresp.), vol. QE-10, pp. 615–616, 1974.
[63] M. A. Gusinow, J. K. Rice, and T. D. Padrick, "The apparent late-time gain in a photodissociation iodine laser," *Chem. Phys. Lett.*, vol. 21, pp. 197–199, 1973.
[64] C. H. Cooke, J. McKenna, and J. G. Skinner, "Distribution of absorbed power in a side-pumped ruby rod," *Appl. Opt.*, vol. 3, pp. 957–961, 1964.
[65] V. Yu Zalesskii and A. A. Venediktov, "Mechanism of generation termination at the $5^2P_{1/2}$-$5^2P_{3/2}$ transition in iodine," *Sov. Phys.-JETP*, vol. 28, pp. 1104–1107, 1969.
[66] D. E. O'Brien and J. R. Bowen, "Kinetic model for the iodine photodissociation laser," *J. Appl. Phys.*, vol. 40, pp. 4767–4769, 1969.
[67] A. A. Filyukov and Ya. Karpov, "A criterion for probable laser quenching," *Sov. Phys.-JETP*, vol. 35, pp. 63–65, 1972.
[68] H. J. Baker, C. C. Davis, and T. A. King, "High power photodissociation laser," Rep. Contract KE 68456, Manchester Univ., U.K.A.E.A., 1973.
[69] H. J. Baker and T. A. King, "Iodine photodissociation laser oscillator characteristics," *J. Phys. D: Appl. Phys.*, vol. 8, pp. 609–619, 1975.
[70] E. K. Plyler and N. Acquista, "Infrared absorption spectra of five halomethanes," *J. Res. N.B.S.*, vol. 48, pp. 92–97, 1952.
[71] M. Hauptschein, E. A. Nodiff, and A. V. Grosse, "Perfluorolkyl halides prepared from silver perfluoro-fatty acid salts. II Perfluorolkyl bromides and chlorides," *J. Amer. Chem. Soc.*, vol. 74, pp. 1347–1350, 1952.
[72] V. Yu. Zalesskii and E. I. Moskalev, "Optical probing of a photodissociative laser," *Sov. Phys.-JETP*, vol. 30, pp. 1019–1023, 1970.
[73] J. O. Hirschfelder, C. F. Curtiss, and R. B. Bird, *Molecular Theory of Gases and Liquids*. New York: Wiley, 1964.
[74] C. M. Ferrar, "*Q* switching and mode locking of a CF_3I photolysis laser," *Appl. Phys. Lett.*, vol. 12, pp. 381–383, 1968.
[75] K. Hohla and K. L. Kompa, "Gigawatt photochemical iodine laser," *Appl. Phys. Lett.*, vol. 22, pp. 77–78, 1973.
[76] F. T. Aldridge, "High-pressure iodine photodissociation laser," *Appl. Phys. Lett.*, vol. 22, pp. 180–182, 1973.
[77] —, "Stimulated-emission cross section and inversion lifetime in a three-atmosphere iodine photodissociation laser," *IEEE J. Quantum Electron.*, vol. QE-11, pp. 215–217, 1975.
[78] G. Brederlow, K. Hohla, and K. J. Witte, "Pulsed high power iodine laser at IPP," presented at the 7th European Conf. Plasma Production by High Power Lasers, Apr. 22–26, 1974, Garching, Germany.
[79] N. G. Basov *et al.*, "Iodine laser emitting short pulses of 50J energy and 5nsec duration," *Sov. J. Quantum Electron.*, vol. 3, p. 524, 1974.
[80] E. A. Yukov, "Elementary processes in the active medium of an iodine photodissociation laser," *Sov. J. Quantum Electron.*, vol. 3, pp. 117–120, 1973.
[81] F. A. Franz and J. R. Franz, "Excited state mixing in the optical pumping of alkali-metal vapors," *Phys. Rev.*, vol. 148, pp. 82–89, 1966.
[82] S. L. McCall and E. L. Hahn, "Self-induced transparency by pulsed coherent light," *Phys. Rev. Lett.*, vol. 18, pp. 908–911, 1967.
[83] —, "Self-induced transparency," *Phys. Rev.*, vol. 183, pp. 457–485, 1969.
[84] —, "Pulse-area-pulse-energy description of a travelling-wave laser amplifier," *Phys. Rev.*, vol. 2A, pp. 861–870, 1970.
[85] A. Icsevgi and W. E. Lamb, Jr., "Propagation of light pulses in a laser amplifier," *Phys. Rev.*, vol. 185, pp. 517–545, 1969.
[86] A. G. Fox and P. W. Smith, "Mode-locked laser and the 180° pulse," *Phys. Rev. Lett.*, vol. 18, pp. 826–828, 1967.
[87] I. M. Belousova, B. D. Bobrov, V. M. Kiselev, and V. N. Kurzenkov, "Characteristics of the stimulated emission from iodine atoms in pulsed magnetic fields," *Sov. J. Quant. Electron.*, vol. 4, pp. 767–769, 1974.
[88] I. M. Belousova, N. G. Gorshkov, O. B. Danilov, V. Yu. Zalesskii, and I. L. Yachnev, "Accumulation of iodine molecules in flash photolysis of CF_3I and $\eta - C_3F_7I$ vapor," *Sov. Phys.-JETP*, vol. 38, pp. 254–257, 1974.
[89] I. M. Belousova, O. B. Danilov, N. S. Kladovikova, and I. L. Yachnev, "Quenching of excited atoms in a photodissociation laser," *Sov. Phys.-Tech. Phys.*, vol. 15, pp. 1212–1213, 1971.
[90] C. C. Davis, "Orientational dependence of the gain and polarization characteristics of the hyperfine components of a magnetic dipole laser transition in a magnetic field," unpublished.
[91] M. Rotenberg, R. Bivens, N. Metropolis, and J. K. Wooten, Jr., *The 3-j and 6-j Symbols*. Cambridge, MA: M.I.T. Technology Press, 1959.
[92] R. J. Pirkle, C. C. Davis, and R. A. McFarlane, "Comparative performance of CF_3I, CD_3I and CH_3I in an atomic iodine photodissociation laser," *Chem. Phys. Lett.*, vol. 36, pp. 305–307, 1975.
[93] M. A. Pollack, "Pressure dependence of the iodine photodissociation laser peak output," *Appl. Phys. Lett.*, vol. 8, pp. 36–38, 1966.
[94] V. Yu. Zalesskii, "Analytic estimate of the maximum duration of stimulated emission from a CF_3I photodissociation laser," *Sov. J. Quant. Electron.*, vol. 4, pp. 1009–1014, 1975.
[95] L. K. Gavrilina, V. Ya. Karpov, Yu. S. Leonov, V. A. Sautkin, and A. A. Filyukov, "Selective pumping effect of a photodissociative laser," *Sov. Phys.-JETP*, vol. 35, pp. 258–259, 1972.

Sustainer Enhancement of the VUV Fluorescence in High-Pressure Xenon

ERNEST E. HUBER, JR., LAWRENCE R. JONES, MEMBER, IEEE, EDWARD V. GEORGE, AND ROBERT M. LERNER, SENIOR MEMBER, IEEE

Abstract—A low-energy (20–60 kV), high-repetition-rate (~60-Hz) electron-beam system is used to excite xenon at pressures up to 600 psi. The salient features of the temporal and spatial measurements of the VUV fluorescence, corresponding to the $^1\Sigma_g^+ - ^{3,1}\Sigma_u^+$ transitions in xenon, are presented. Experimentally, it is found that in a regime where more than 20 percent of the electron-beam energy incident on the gas is converted to VUV fluorescence, the maximum incremental efficiency due to the addition of a sustainer discharge is about 7 percent. A kinetic model is described which attributes the low sustainer efficiencies to electron interactions with the excited state populations.

THE experimental verification of VUV laser action in high-pressure rare-gas excimers has generated a considerable interest in these systems. Coherent oscillation has been observed in xenon [1], krypton [2], argon [3], and rare-gas mixtures [2], [4]. In all these works the lasing media were excited by a high-energy relativistic electron beam. In this work the VUV fluorescence characteristics from high-pressure xenon excited by a low-energy (20–60-kV), high-repetition-rate (60-Hz) electron beam are presented. We also present a detailed study on the enhancement of the VUV fluorescence when additional energy is deposited by means of a sustainer discharge. A kinetic model is described which explains the salient features of the experimental results.

A lower limit of 20 percent was measured for the conversion efficiency of pulsed electron-beam energy to VUV energy, while an upper limit of 7 percent was measured for the incremental energy conversion efficiency of sustainer discharge to VUV. These experimental results are shown to be in agreement with the kinetic model.

I. Experimental Apparatus

The experimental apparatus consisted of a high-pressure gas facility, an electron-beam-generation system, a vacuum system, and monitoring electronics. Major features of the experimental arrangement are presented in Figs. 1 and 2.

The high-pressure gas was excited in a multiport cell having MgF_2 windows mounted in the vacuum chamber, which also has MgF_2 windows. The gas was introduced into and withdrawn from this cell via a gas-handling system external to the vacuum chamber.

Manuscript received December 16, 1975. This work was supported by the Department of the Air Force.

E. E. Huber, Jr., L. R. Jones, and R. M. Lerner are with the Lincoln Laboratory, Massachussetts Institute of Technology, Lexington, MA.

E. V. George was with the Research Laboratory of Electronics, Massachussetts Institute of Technology, Cambridge, MA. He is now with the Lawrence Livermore Laboratory, University of California, Livermore, CA 94550.

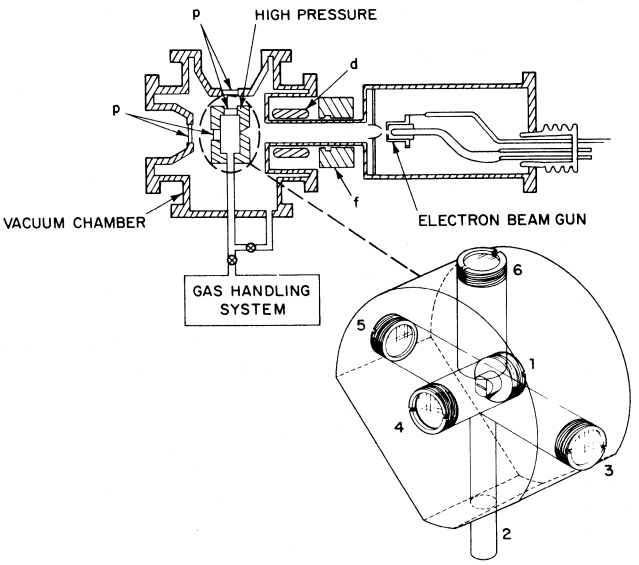


Fig. 1. Experimental apparatus. Viewing ports are labeled p, deflector coils d, focus coils f. Circle contains enlarged view of high-pressure multiport cell with ports for: 1: electron-beam window holder; 2: gas inlet/outlet; 3, 4, 5, and 6: MgF_2 windows.

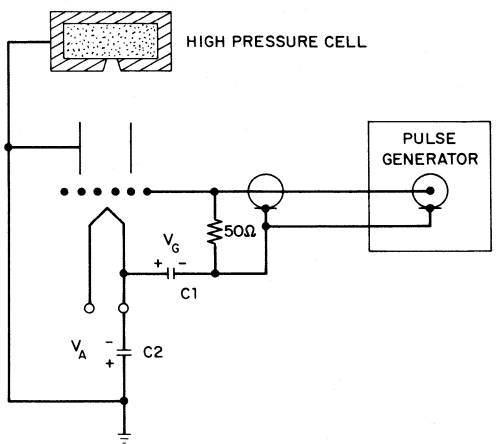


Fig. 2. Schematic of electron gun and pulser.

The multiport cell shown in the circle of Fig. 1 has removable MgF_2 windows on four sides which allow spectral monitoring of the fluorescent volume. The MgF_2 windows, and the holder for the e-beam window, were sealed with small Viton O-rings. The leak rate through all these seals could be made less than detectable (1×10^{-9} std cm^3/s) for either internal pressure (1000 psi) or external pressure (15 psi). In one series of experiments, the window at port 4 was replaced with an insu-

lated feedthrough assembly used to support a small copper electrode a short distance from the electron-beam window ("sustainer" experiments). By charging this electrode via a dc power supply and then exciting the gas with an electron-beam pulse, it was possible to deposit controlled amounts of energy into the intervening gas volume. The electrode spacing was small, typically $\sim 2.7 \times 10^{-2}$ cm.

The electron beam was typically generated by a tantalum ribbon filament shaped and pulse-modulated by a single slotted steel grid and magnetically focused and deflected by coils external to the vacuum system. Either defocused or intense focused beams of low energy (20–60 kV) could be obtained. Utilizing high negative potential on the electron-beam gun electronics allowed the use of a grounded high-pressure gas cell. The grid drive for the electron gun was provided by a $\sim$2-ns-rise-time 0-to-1-kV coaxial delay-line pulse generator, as shown in Fig. 2.

By mounting an insulated copper plate on the pressure cell around port 1 and magnetically deflecting the beam, it was possible to directly monitor the electron-beam pulse shape. In addition, it was also possible to obtain dc electron beams. Fig. 3 illustrates a typical electron-beam pulse shape.

It is important to note that although the maximum electron-beam current density, J_B (about 30 A/cm^2) which we could obtain from our equipment was lower than that obtainable from the typical high-energy machines used in the laser experiments, we could achieve comparable power density depositions in the gas. The reason for this is the fact that the energy dissipation gradient, dE/dx, is much larger at our low electron energies than at high electron energies. Measurements indicate that we have achieved power density depositions of approximately 10^7 W/cm^3 using the e-beam alone, and also for the combined influence of e-beam and sustainer discharge.

The electron beam entered the high-pressure gas cell through an extremely thin (2-μ-thickness) window. This window covered a small slotted opening, typically 2.5×10^{-1} cm long by 2.5×10^{-3} cm wide in the pressure cell. Two types of window materials were employed in our work [5]. The first was 2-μ-thick titanium foil epoxy-mounted on an electroformed copper support structure; the second and most successful was a silicon monolithic structure. The silicon windows were made by first diffusing a p-type dopant into a 100-μ-thick n-type substrate. Photolithographic procedures [6] were then used to etch through the n-type material to the thin p-type layer. These silicon windows have exceeded our most optimistic expectations in their ability to hold off high pressures (pressures to 500 psia were routinely used) and in the ease with which they could be mounted in their holder.

The gas fluorescence was monitored by several methods. A calibrated solar-blind photodiode (ITT F4115) was used for absolute radiance measurements and study of transient fluorescent phenomena. A McPherson 218 VUV grating monochrometer was used in conjunction with a broad-spectrum photomultiplier (RCA 4837) and a gated boxcar averager for time-resolved spectroscopy. A magnesium fluoride lens and scanning apparatus were used with an apertured photomultiplier tube to obtain spatial radiance profiles of the fluorescing volume.

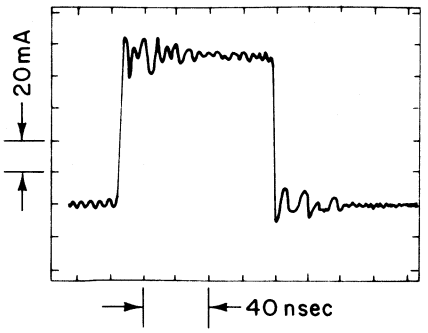


Fig. 3. Typical pulse shape for beam current at target.

II. Kinetic Model

The kinetic model is completely described elsewhere [7]; here, we discuss only its salient features. The model considers three atomic excited states, namely the ^3P manifold corresponding to the $^6s_{3/2}$ excited electron orbital, a representative upper excited state, and the ground ionic state; the three molecular states considered include the $A^2\pi$ ionic and the $^{1,3}\Sigma_u^+$ excimer states. We neglect excited ionic states due to the typically low levels of ionization ($\leqslant$0.1 percent) in these systems. Three-body processes convert the excited (and ionic) states into their molecular equivalents. Dissociative recombination of the $A^2\pi$ ionic state channels energy into the representative upper state. The subsequent decay of this upper molecular state to the ^3P manifold can proceed either via radiation, or by kinetic channeling through collisional pathways which arise on account of curve crossings of the interaction potentials. (Curve crossings between higher lying bound molecular states and lower lying states are possible because each atomic level is, in general, associated with both an attractive and a repulsive interaction potential corresponding to a bonding and nonbonding configuration.) The lower lying excimer states then radiate to the ground repulsive state (corresponding to the $^1\Sigma_g^+ - ^{1,3}\Sigma_u^+$ transition) emitting photons at wavelengths around 1700 Å. This completes the kinetic channeling. In Table I we list some of the more important reactions used in the calculational model, with the rates for kT_e = 1 eV and kT_g = 0.025 eV (unless otherwise specified).

The energy deposition by the electron beam into the various atomic states and background plasma was treated in a manner similar to that described by Bass and Green [8]. In addition, we allow for the interaction of the background plasma with the excited states, as indicated in Table I. We assumed that the distribution function for the background electron plasma was a Maxwellian (see [7] for a discussion of this matter). It is further assumed that the time evolution of the plasma is sufficiently rapid that we may neglect its directed motion and heat conduction. Also, we assume that the plasma is sufficiently homogeneous that "local" parameters can be compared with experiment. For the case of the sustainer experiments at pressures above approximately 100 psia, this assumption becomes progressively worse (see discussion in the Section III).

The volume rate at which power is delivered to the plasma electrons due to the sustainer current is given by

TABLE I
NUMERICAL VALUES OF IMPORTANT REACTION PARAMETERS USED IN THE COMPUTATIONAL MODEL

	Reaction	Coefficient	Value (Xe)
1.	$X^+ + 2X \rightarrow X_2^+ + X$	$\beta^+(cm^6\ sec^{-1})$	3.5×10^{-31}
2.	$X_2^+ + e \rightarrow X^{**} + X$	$\alpha(cm^3\ sec^{-1})^\dagger$	1.4×10^{-6}
3.	$X^*[S(3/2,1)] + 2X \rightarrow X_2^*(^1\Sigma) + X$	$\beta_1(cm^6\ sec^{-1})$	1.7×10^{-32}
4.	$X^*[(3/2,2)] + 2X \rightarrow X_2(^3\Sigma) + X$	$\beta_3(cm^6\ sec^{-1})$	3.00×10^{-32}
5.	$X_2^* + e \rightarrow X_2^+ + 2e$	$\langle Qv\rangle\ (cm^3\ sec^{-1})$	5×10^{-9}
6.	$X_2^* + X_2^* \rightarrow X_2^+ + 2X + e$	$\langle Qv\rangle\ (cm^3\ sec^{-1})$	8×10^{-11}
7.	$X_2^*(^1\Sigma) \rightarrow 2X + h\nu$	$\tau(sec)$	5×10^{-9}
8.	$X_2^*(^3\Sigma) \rightarrow 2X + h\nu$	$\tau(sec)$	1×10^{-7}
9.	$X_2^*(^1\Sigma) + e \rightarrow X_2^*(^3\Sigma) + e$	$\langle Qv\rangle\ (cm^3\ sec^{-1})$	1×10^{-7}
10.	$X_2^*(^1\Sigma) + X \rightarrow X_2^*(^3\Sigma) + X$	$\langle Qv\rangle\ (cm^3\ sec^{-1})$	4.0×10^{-12}
11.	$X_2^* + h\nu \rightarrow X_2^* + e$	$Q(cm^2)$	1.7×10^{-18}

$^\dagger KT_e = kT_g = 0.025$ eV.

$$P_{\text{sustainer}} = en_e\mu\mathcal{E} \quad (1)$$

where n_e is the plasma electron density, $\mathcal{E}$ is the local electric field, and μ is the electron mobility obtained by convolving the momentum transfer cross section and the electron distribution function in the usual manner.[1]

The electric field $\mathcal{E}$ in (1) is determined by dividing the sustainer voltage by the sustainer electron-beam window spacing d. One may well argue that this overestimates the actual electric field in the positive column due to the neglect of the anode and cathode falls. For example, in cold cathode discharges, cathode falls of the order of a few hundred volts are typical. However, the large VUV fluxes incident on the cathode surfaces provide ample photoelectron emission for the conduction (sustainer) current. Under these conditions, the cathode fall is substantially reduced. Our experiments indicate that this is indeed the case.

The temporal evolution of the power density deposited in the plasma by the sustainer discharge was calculated by solving the appropriate state equations for the electrical network used, treating the plasma contained between the sustainer and e-beam window as a nonlinear resistor. For our experiment, the following circuit best represented the sustainer electrical discharge system (see Fig. 4). Here, $\mathcal{E} = V_{c2}/d$, where d is the sustainer e-beam window spacing and $R_{\text{plasma}} = (e\mu n_e)^{-1}(d/A)$, where A is the measured cross-sectional area of the plasma (see Section III).

A set of rate equations was written which described the time evolution of the excited state densities, the electron density and temperature, the gas temperature, and for the case of the sustainer experiments, the state variables of the circuit model. These resulting nonlinear differential equations were numerically integrated using an interactive Gear package. It is important to point out that the inputs for the sustainer discharge model are only the circuit values and initial capacitor voltages.

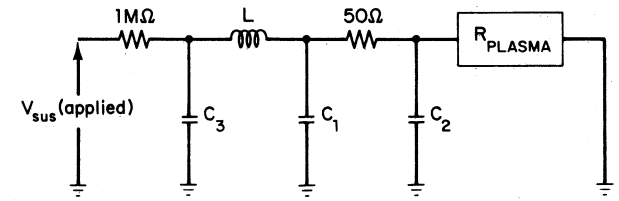


Fig. 4. Sustainer charge/discharge circuit model. L_1 and C_1 represent 15 cm of coaxial cable. C_2 is the capacitance of the electrode. C_3 is the primary charge storage capacitor.

III. Fluorescence Studies and Comparisons with Theory

In this section we present the experimental results of our fluorescence studies for both the cases of electron-beam excitation only, and electron-beam excitation in conjunction with a sustainer discharge. Also shown are the comparisons of these experimental results with the kinetic model discussed previously.

A. Electron-Beam Excitation

Fig. 5 illustrates the temporal development of the VUV fluorescence for three values of xenon-fill pressure, using the ITT photodiode mounted in an enclosure adjacent to viewing window 4 (see Fig. 1), which was flushed with dry N_2. The 100-ns-wide electron-beam excitation pulse is as shown in Fig. 3, and the corresponding current density and incident electron energy were 10 A/cm^2 and 45 kV, evident in this figure. As the pressure in the target cell is increased, one ob-

[1]We include the action of the sustainer discharge in the energy balance equation for the electrons; the resulting change in electron temperature then affects the ionization and excitation rates. Treating this problem using published values of the Townsend α or η coefficients is not justified since they are measured under discharge conditions which are very different from those we have here.

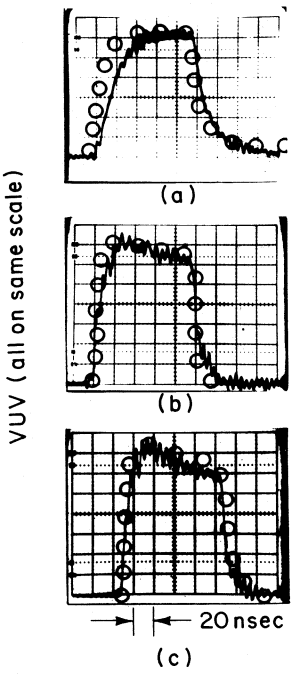


Fig. 5. Transient output waveforms in response to 100-ns pulse. o, theory; —, experiment. (a) At 100 psia. (b) At 200 psia. (c) At 400 psia xenon in cell. Peak output is approximately 50 W in each case. [Time origin is offset in (c).]

serves 1) a steepening of both the rise and fall portions of the flourescent pulses, and 2) a noticeable "droop" in the temporal shape of the fluorescence pulse which, for this value of electron-beam current density, becomes apparent at a pressure of 150 psia. As shown, the peak fluorescent output is approximately independent of pressure; this result is a consequence of the fact that the detector observes, for all of the pressures studied, the entire radiating volume.

The circles shown in this figure are the theoretical predictions obtained from our kinetic model. For comparisons of the temporal development to be made, we have normalized the respective curves to their experimental counterparts. The steepening of the rise and fall portions of the fluorescence pulse is a consequence of the fact that at low pressures the formation rates of the $^{1,3}\Sigma_u^+$ excimer states and the collisional collapse of the excited state manifolds are much longer than the radiative lifetimes for these states. Therefore, in this case the output pulse is dominated by formation and decay processes. As the pressure is increased, these rates increase dramatically; hence the rise and fall times are dominated by a convolution of the lifetimes and the temporal characteristics of our electron-beam pulse. The pulse droop is a result of excited state loss processes (reactions 5 and 6 in Table I), which become more important at large excited state and electron density values. Two facts substantiate this postulate: 1) lowering the electron-beam current density removes the droop, resulting in a flat-topped pulse; and 2) removing excited state loss processes in our kinetic model also yields a "flat-topped" fluorescent pulse.

Measurements of the intrinsic conversion efficiency of electron-beam energy into VUV fluorescence were subject to considerable experimental difficulties, in part because only a small fraction (typically, 10 percent) of the total beam energy was able to enter the cell, and in part because of the large variability of this fraction with operating conditions. A lower bound of 20-percent conversion efficiency of electron-beam energy to VUV was established in the following manner. A special structure was employed to measure total electron-beam current transmitted through each of several typical electron-beam windows, with the electron-beam gun adjusted for maximum transmitted current. Adjusting for primary electron energy loss in the window and secondary electron effects, the maximum peak power of the beam beyond the window was 95 W, with far lower values being more typical. Using the high-pressure cell under similar operating conditions, the peak VUV power was between 20 and 40 W. Fluorescent power was measured with calibrated ITT F4115 photodiodes on both ports 4 and 5 (see Fig. 1), and corrected for window transmittance and aperture size. Hence, our measurements give a lower bound on efficiency of 20 percent, with 40 percent being more likely.

B. Electron-Beam Excitation Plus Sustainer Action

The sustainer electrode consisted of a shaped copper disc spaced 2.7×10^{-2} cm from the electron-beam window. The electrode, its supporting structure, and associated electrical circuitry were mounted in place of viewing window 4, Fig. 1. Destruction of the electron-beam window was minimized by operating the copper disc as a cathode. Operation in this polarity is possible because of the relatively small applied sustainer voltages ($V_{sus} \leqslant 1$ kV). In the electron-beam sustainer mode of operation, a variety of discharge phenomena were observed. These include: 1) a visually very intense cathode spot; or 2) a spatially constricted yet diffuse arc-like discharge; or 3) a bright spark discharge; or 4) a uniform enhancement of a discharge in the fluorescing region. The occurrence of a particular phenomenon (mode) depended in a complicated manner on pressure, sustainer voltage, electron-beam excitation level, and circuit parameters. After some experimentation, it was found that operation in mode 4) was always possible and least likely to precipitate *e*-beam window failure.

The application of a sustainer voltage changed both the temporal and spatial character of the VUV fluorescence. We first discuss the spatial changes. In this experiment a magnesium fluoride lens was placed at a distance from the fluorescing source, imaging the source onto a 25-μ slit at the image plane. The slit was oriented parallel to the sustainer electrode (perpendicular to the current flow direction in the discharge). A 175-nm bandpass filter (having a half-power bandwidth of 27 nm) was placed on the source side of the slit, and a VUV-sensitive photomultiplier tube was mounted immediately behind the slit. The entire apparatus was mounted in a VUV-compatible environment (gaseous withdrawal from liquid nitrogen). The photomultiplier tube, slit assembly, and bandpass filter were mounted on a servo-controlled lead screw which allowed the magnified image of the source to be scanned along an axis parallel (or antiparallel) to the current flow direction. Fig. 6 illustrates the spatial plots of the VUV fluorescence

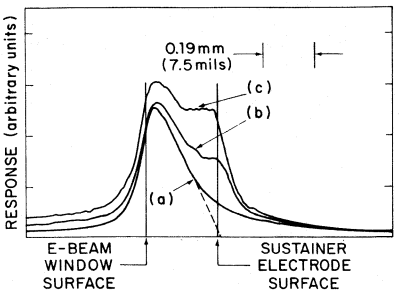


Fig. 6. Spatial distribution of VUV fluorescence in the pressure cell. Electron-beam window to sustainer electrode gap approximately is 0.25 mm. $P = 225$ psia. (a) Sustainer electrode not energized, $V_{sus} = 0$. (b) $V_{sus} = -400$ V, (c) $V_{sus} = -500$ V. Dashed line indicates extrapolation to obtain the electron range, R.

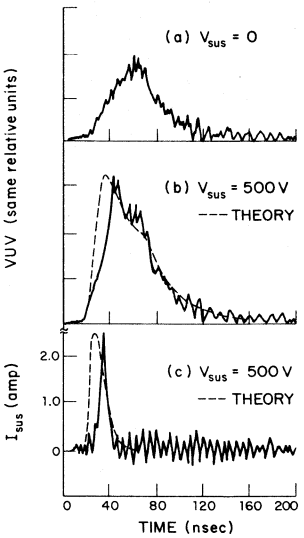


Fig. 7. Sustainer action on VUV fluorescence (temporal response). (a) $V_{sus} = 0$, unenhanced output. (b) $V_{sus} = -500$ V. (c) Sustainer current corresponding to (b). All at 100 psia.

for several values of applied sustainer voltage (V_{sus}). These data were obtained using boxcar integrating techniques (Keithly 881) and positioning the 50-ns gate in the temporal region of the VUV pulse which possesses the maximum enhancements with applied V_{sus} (see Fig. 7 and accompanying discussion).

In Fig. 6, the unenhanced fluorescence curve (curve *a*) can be extrapolated in the manner shown in order to define an electron range, R. Doing this for different pressures, we find good agreement with the range formula of Gruen [9], who found R can be expressed as

$$R(\text{cm}) = 4.57 E_B^{1.75}/\rho \qquad (2)$$

where E_B is the energy in keV of electrons entering the gas and ρ is the xenon mass density in g · cm^{-3}. As can be seen, the application of a sustainer voltage not only increases the peak value of the VUV fluorescence, but (at sufficiently high pressures) broadens its spatial extent as well until the region between the sustainer electrode and electron-beam window is uniformly excited. Data taken at other pressures yielded similar results. The spatial "wings" of the measured fluorescence (see Fig. 6) are thought to be due to radiation entering the detector assembly after a reflection off of the sustainer electrode or electron *e*-beam window. Because of the spatially inhomogeneous nature of the fluorescence (for $V_{sus} \neq 0$) at high pressures, the comparisons of experiment with theory were carried out at a pressure such that $R > d$ (the sustainer-window spacing).

Fig. 7 illustrates the temporal evolution of the VUV enhancement by means of the sustainer discharge. The values for the circuit parameters in this case were (Fig. 4) $C_3 = 22$ pF, $C_1 + C_2 = 10$ pF, and $V_{sus} = -500$ V. Temporally resolved spectral measurements showed that the enhanced VUV emission was indeed at the same wavelength as that due to the electron-beam excitation alone. Experimentally, peak enhancements up to an order of magnitude were possible in VUV output.

As can be seen in this figure, the enhanced VUV follows basically the sustainer current, which is to be expected. The sustainer current reaches a maximum value of ~2 A and falls with a temporal half-width of ~10 ns. The sustainer current was measured using a wide-band current transformer which was designed to have a pulse rise and fall time of less than 3 ns. It also had less than 4-percent droop, and no measurable ringing when detecting a 100-ns current pulse. Not shown in the figure is the sustainer voltage (across C_1 of Fig. 4), which was also measured and which fell to ~60 V in ~15 ns. Experimentally, it was found that this low-voltage component of the sustainer voltage temporal evolution was dependent upon (for a given pressure) J_B, V_{sus} and the circuit parameters.

Experimentally, we found that for a given V_{sus}, circuit parameters, and pressure, the value of the peak VUV output caused by the sustainer discharge was reasonably independent of the electron-beam current density, J_B, over an order-of-magnitude variation. It was found, however, that if J_B was *below* a critical value ($J_{B\,\text{critical}} \simeq 0.2$ A/cm^2 for the conditions in Fig. 7), constricted arc performance was always observed for some value of V_{sus}. Thus, in contradistinction to the case of the CO_2 laser sustainer schemes, the enhancements here were seen concurrently with an increased conductivity of the plasma. This is to be expected since the levels of excitation and ionization produced solely by the electron beam are so large that attempts to alter only the electron temperatures T_e with V_{sus} (as is done in CO_2) are always accompanied by sizeable changes in n_e as well. In the xenon system, our experimental results indicate that the electron beam provides a good uniform level of ionization, which is then enhanced by the sustainer action. In support of this hypothesis, we found that for a fixed V_{sus}, the percentage enhancement decreased with increasing J_B. This is to be expected since the density ratio, defined as the ratio of sustainer to electron-beam power density, was decreasing. Increasing V_{sus} to offset this decrement resulted ultimately in arc formation. We found, therefore, that the maximum percentage enhancement occurs in a region where J_B is near J_B critical.

The predictions from the kinetic model are shown by the dashed lines in Fig. 7, where the theory has been normalized to experiment. As can be seen, the comparisons between

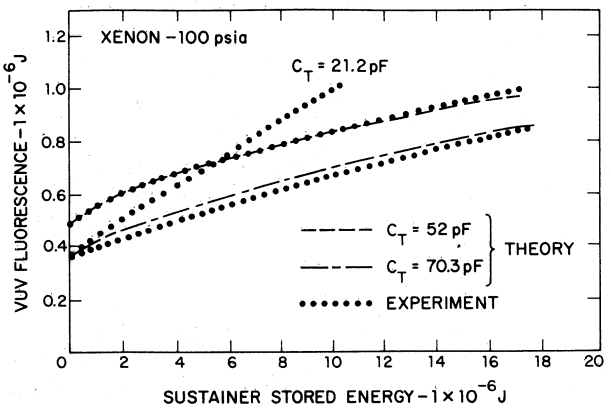


Fig. 8. Time-integrated VUV fluorescence output versus stored energy in the sustainer network for different total capacitance values. All at 100 psia.

theory and experiment are in qualitative agreement; however, we do overestimate the effectiveness of the sustainer action by about a factor of two as was also the case for the V_{sus} = 0 data of Fig. 5. This is reasonable agreement considering 1) that small departures from the assumed electron velocity distribution (Maxwellian) and from the velocity dependence of cross section lead to a large change in the pumping or ionization rate, and 2) that normalization of the per-unit-volume theory to experiment requires knowing an effective or average experimental volume, about which there is some doubt.

In Fig. 8 we show the time-integrated VUV fluorescent power output in xenon at 100 psia as a function of stored energy in the sustainer network for several values of the circuit parameters. Here the total energy output U_0 was determined using the solid angle of the detector and assuming an isotropic radiation source; whereas the stored energy in the sustainer U_s was obtained from $U_s = (C_T V_{sus}^2/2)$, where $C_T = C_1 + C_2 + C_3$ represented the total circuit capacitance and V_{sus} represented the initial charging voltage. Several features are noteworthy in this figure. Defining dU_0/dU_s to be the incremental slope efficiency due to the sustainer action, we see that the "faster" circuit, that is, the circuit which deposits the sustainer energy in the shortest possible time, yields the largest slope efficiency. The maximum slope efficiency is seen to be ~7 percent for C_T = 20 pF for these experimental conditions. This value drops to ~4 percent for larger C_T values.

It is important to point out that whereas the enhancement efficiencies are between 4 and 7 percent, the efficiency due to the presence of the electron-beam pumping alone is at least 20 percent. Theoretically, we can explain this fact by considering the role of those electron interactions with the excited state populations which result in additional ionization at the expense of the excited state populations (reaction 5, Table I). In the limit, where this process dominates, the stored energy is simply dissipated in circulating particles from the excited states to the ionic states; these return to the excited states via the kinetic channeling previously discussed. The recoil heating contribution is negligible for the case of xenon and for electron temperatures of ~1 eV because of the large mass value of xenon and the fact that at ~1 eV we are operating near the Ramsauer minimum. Roughly speaking, one may estimate that excited state loss processes will begin to reduce the efficiency (below its electron-beam pumped value) when

$$N_x[{}^x_e Q^i(v)v] \gtrsim N_0[{}^o_e Q^i(v)v] \tag{3}$$

where N_x, N_0 are the excited and ground state densities and $[{}^x_e Q^i v(v)]$, $[{}^o_e Q^i(v)v]$ are the velocity-averaged cross sections for ionization from the excited state and ground state, respectively. Such processes as ionization of excited states have been well known in gas discharge studies, and lead to a reduced electron temperature as the ionization (and correspondingly the excitation) level increases (for the case of argon see the article by Wojaczek [10]). As can be seen, the efficiency for converting the stored sustainer energy into VUV will be a decreasing function of initial excited state populations, which is in accord with experiment. The reason for the larger efficiency values for the faster circuits is also in accord with the above discussion when one considers the fact that for a faster electrical circuit the sustainer energy is deposited in the gaseous media at a time when the excited densities are below their peak values. The per-unit-volume theoretical values have been normalized to the experiment in Fig. 8, and are seen to be in accord, although again the theory somewhat overestimates the experiment as in Figs. 5 and 7.

In conclusion, we have measured the fluorescence characteristics from a low-energy high-repetition-rate electron-beam facility with and without a sustainer discharge. Although accurate measurements of the conversion of e-beam energy to fluorescent energy were not possible, we believe this efficiency to be high, at least 20 percent, with greater than 40 percent being more likely. On the other hand, efficiencies less than ~7 percent are obtainable for sustainer-enhanced discharges. These results are in accord with our theoretical model. As a side issue, we find, using the theoretical model, that it may be possible to obtain efficient conversion of electrical energy to fluorescent output from a preionized electrical discharge if fast, high $\mathcal{E}/p$, electrical pulses are applied to the system.

ACKNOWLEDGMENT

The authors are indebted to the efforts of C. W. Werner of M.I.T. for his assistance in developing the computational model used in these experiments. D. A. Emmons provided much helpful interaction and discussion, as well as experimental assistance. They also wish to thank P. Murray for his help in designing and constructing much of the experimental apparatus.

REFERENCES

[1] a) H. A. Koehler, L. J. Ferderber, D. L. Redhead, and P. J. Ebert, "Stimulated VUV emission in high-pressure xenon excited by high current relativistic electron beams," *Appl. Phys. Lett.*, vol. 21, pp. 198–200, 1972.
b) J. B. Gerardo and A. W. Johnson, "High-pressure xenon laser at 1730 Å," *IEEE J. Quant. Electron.*, vol. 9, pp. 748–755, 1973.
c) C. K. Rhodes and P. W. Hoff, "Oscillation on the ultraviolet bound-free continuum of diatomic molecular xenon and molecular krypton," in *Laser Spectroscopy*, R. G. Brewer and A. Mooradian, Ed. New York: Plenum, 1973, p. 113.
d) C. K. Rhodes, "Review of ultraviolet laser physics," *IEEE J. Quant. Electron.*, vol. QE-10, pp. 153–174, 1974 (a compendium of references).

[2] P. W. Hoff, J. C. Swingle, and C. K. Rhodes, "Observations of stimulated emission from high pressure krypton and argon/xenon mixtures," *Appl. Phys. Lett.*, vol. 23, pp. 245–246, 1973.

[3] W. M. Hughes, J. Shannon, and R. Hunter, "126.1 nm molecular argon laser," *Appl. Phys. Lett.*, vol. 24, 488–490, 1974.

[4] A. W. Johnson and J. B. Gerardo, "Diluent cooling of a vacuum-ultraviolet high pressure xenon laser," *J. Appl. Phys.*, vol. 45, pp. 867–872, 1974.

[5] *Space Communications*, M.I.T. Lincoln Laboratory, Lexington, MA, Tech. Reps. Div. 6, Sept. 15, 1973–June 15, 1974 (the window development is reported).

[6] R. A. Cohen *et al.*, "Fabrication procedure for silicon membrane X-ray lithography masks," Tech. Note 1973-38, M.I.T. Lincoln Laboratory, Lexington, MA, Sept. 20, 1973.

[7] C. W. Werner, "Radiative and kinetic mechanisms in bound-free excimer systems," Ph.D. dissertation, Phys. Dep., M.I.T., Cambridge, MA, 1975.

[8] J. N. Bass and A. E. S. Green, "Energy deposition of electrons in gas lasers," *J. Appl. Phys.*, vol. 44, pp. 3726–3728, 1973.

[9] A. E. Grün, "Luminescent-photometric measurements of energy absorption in the radiation field of electron sources for the unidimensional case in air" (in German), *Z. Naturforschg.*, vol. 12a, pp. 89–95, 1957.

[10] K. Wojaczek, "The positive column of the low pressure argon discharge in the transition region III" (in German), *Beitr. Plasma Phys.*, vol. 5, pp. 307–329, 1965.

Very High Radiance Edge-Emitting LED

MICHAEL ETTENBERG, HENRY KRESSEL, FELLOW, IEEE, AND JAMES P. WITTKE, SENIOR MEMBER, IEEE

Abstract—**In this paper we describe a new light-emitting diode (LED) whose radiance is 1000 W/cm^{2}sr, an order of magnitude higher than any previous LED. The LED is an (AlGa)As double-heterojunction edge-emitting structure. This structure acts as a waveguide for the internally generated light, and with appropriate Al concentration difference at the heterojunctions ($\Delta x \approx 0.3$) and active region width (~500 Å), the radiation pattern perpendicular to the junction can be less than 30° (FWHM). For fiber-optic communications this LED is capable of coupling 850 μw, at a coupling loss of only −10 dB into a 0.14-numerical-aperture (NA), 90-μm-diam low-loss fiber. The LED is capable of being directly modulated at 250 MHz and has a spectral width of less than 300 Å.**

I. Introduction

DUE to the small diameters and acceptance angles of low-loss, low-dispersion optical fibers, incoherent light-emitting diodes (LED's) must act as high-radiance light sources if they are to couple significantly into the propagating modes of such a fiber. To date, the best reported values for both surface [1], [2] and edge [3] emitters have been about 100 W/cm^{2}sr, obtained with heterojunction diodes of (AlGa)As. The radiance can be increased in two ways: by increasing the overall light efficiency, and/or by making the emitted light more directional. In this paper, we describe a new edge-emitting diode structure that has demonstrated a greatly increased radiance, primarily by decreasing the solid angle into which the light is emitted. Radiances of over 1000 W/cm^{2}sr have been measured. Also, the new type of diode inherently has very high speed modulation capabilities, in excess of 200 MHz.

II. Diode Structure

The diodes were deposited on (100)-oriented Si-doped (~ 1×10^{18} cm^{-3}) GaAs substrates by a thin-solution liquid phase epitaxy technique described previously [4]. A growth temperature between 800 and 860°C and a cooling rate of 0.75°C/min were employed.

The diode structure consists of a symmetrical double heterojunction, as illustrated schematically in Fig. 1. In all, five layers are grown: a Te-doped ($n \sim 1 \times 10^{18}$ cm^{-3}) GaAs substrate layer, an Sn-doped $Al_{0.45}Ga_{0.55}As$ layer ($n \sim 1 \times 10^{17}$ cm^{-3}), an undoped active region of either GaAs or $Al_{0.1}Ga_{0.9}As$, a p-type $Al_{0.45}Ga_{0.55}As$ layer doped with Ge to a density of ~ 5×10^{17} cm^{-3}, and, finally, a GaAs layer doped with Ge to a density of 1×10^{19} cm^{-3}. All of the layers except the active region are 3–4 μm thick. The active region is about 0.05 μm thick.

Manuscript received January 21, 1976. This work was supported in part by the Office of Naval Research, Arlington, VA, under Contract N00014-75-C-0365.

The authors are with the RCA Laboratories, Princeton, NJ 08540.

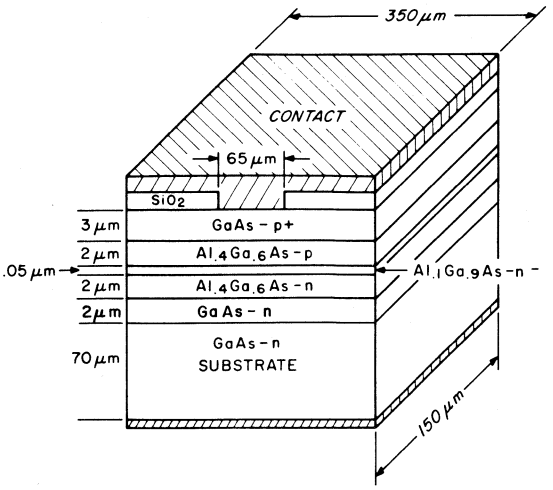


Fig. 1. Schematic representation of the structure of the edge-emitting diode with directed emission.

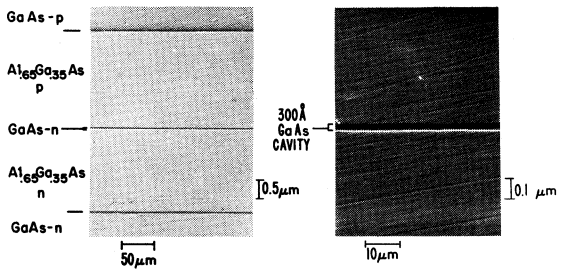


Fig. 2. Cross section of wafer 344 at two different magnifications (sample beveled at 1° to the plane of growth and etched in sodium hypochlorite).

A cross section of one of the wafers after growth is shown in Fig. 2 at two different magnifications. The sample has been mechanically polished at an angle of 1° from the plane of the junction and etched in sodium hypochlorite. The beveled samples were also used to determine the Al concentrations of the n- and p-type $Al_{0.45}Ga_{0.55}As$ confining layers by electron probe microanalysis.

Contacts were applied in either of two forms: a broad area contact, consisting of alloyed Sn on the n-side followed by plated Ni and Au on both sides, or the same contact on the n-side and an oxide-defined stripe contact 65 μm wide on the p-side (Fig. 1). The stripe geometry allows better heat sinking and coupling to fibers and was therefore used for the power and coupling measurements described in this paper.

III. Diode Characteristics

Far-field distributions were measured by rotating the diodes in an optical system described previously [5]. The system has a resolution of 1° and a signal-to-noise ratio greater than

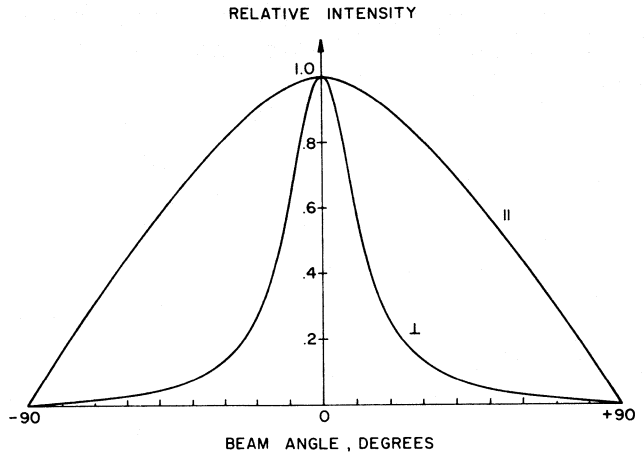


Fig. 3. Far-field light output distribution from an edge-emitting LED, (wafer 295) both ⊥ and || to the junction plane.

TABLE I
SUMMARY OF DIODE PROPERTIES

sample no.	d(μm)	Δx_{Al}	$\theta_{\perp}$ degrees (exp)	λ (μm)	$\theta_{\perp}^{*}$ (calc degrees)
295	0.08	0.25	35	0.88	26
297	0.05	0.48	25	0.88	31
298	0.08	0.45	65	0.82	50
305	0.04	0.32	30	0.81	18
309	0.06	0.35	25	0.81	17
313	0.06	0.35	28	0.83	29
314	0.10	0.50	67	0.81	70
321	0.10	0.25	30	0.81	35
327	0.07	0.35	31	0.80	35
344	0.03	0.65	29	0.87	25

*From (1).

20 dB. To prevent scattering from light emitted from the sides and back of these edge-emitting LED's, black wax was applied to these surfaces before measurement. The radiated beams are characterized by two parameters, the angular beamwidth at the half-maximum point in the direction perpendicular to the junction plane, $\theta_{\perp}$, and the beamwidth in the plane of the junction, $\theta_{\parallel}$. The focus of this paper is on $\theta_{\perp}$, which is affected by the structure; $\theta_{\parallel}$ remained invariant for all the devices at ~120°, as expected for a Lambertian distribution.

The far-field distribution in planes both perpendicular and parallel to the junction for one of the LED's is shown in Fig. 3. For this diode with an active region of $d = 0.05$ μm, $\theta_{\perp} = 25°$, compared to 120° for a Lambertian source such as a surface-emitting LED. While this pattern is for a diode from one of the wafers exhibiting the narrowest beams, this general beam shape and beamwidths of 35° or less have been found to be typical for all of the diodes with narrow active regions, as shown in Table I.

It is important to note that the far-field patterns of the diodes perpendicular to the junction plane closely resemble those of lasing diodes with similarly narrow active regions. This is because, in both cases, the radiation is into the fundamental guided transverse mode. With a laser, all stimulated emission is into this mode, while with an incoherent LED, the spontaneously emitting electrons are coupled much more strongly to this mode than to the unguided ones, as shown theoretically in detail by Wittke [6]. Dumke's [7] approximate calculation gives an estimate of the far-field beamwidth in the direction perpendicular to the junction

$$\theta_{\perp} \approx \frac{20\Delta x d}{\lambda} \text{ (rad)}. \tag{1}$$

Here Δx is the fractional aluminum concentration difference across the heterojunctions, d is the thickness of the active region, and λ is the emission wavelength. The calculation is compared to measured beam angles for the incoherent LED's from a variety of grown wafers in Table I. Considering the estimated accuracy (15 percent) of the measurements of active region width, the agreement, over a large range of Δx and d values, is good.

The agreement between the far-field beamwidth calculated for the coherent mode and experimentally determined for the incoherent mode might suggest that these diodes are operating in a superradiant mode near lasing. However, it should be

emphasized that these diodes are operating incoherently. Evidence for this contention includes the following.

1) The far-field pattern is Lambertian in the plane *parallel* to the junction (see Fig. 3).

2) The spectral width is determined by the doping in the active region (65 nm for Si-doped active regions and 25 nm for undoped active regions, see Fig. 7).

3) The aforementioned parameters are independent of the drive current density, from 10 A/cm^2 to near the lasing threshold, ~2000 A/cm^2.

IV. Power Output and Radiance

Because in these new diodes the light output is directed toward the emitting facet in the plane perpendicular to the junction, more of the internally generated light is able to be externally extracted than from diodes with the usual thicker active region. Thus, these new devices have a relatively high emission quantum efficiency, ~ 1 percent from a single emitting edge. The light output from one edge as a function of drive current for one of the best diodes is shown in Fig. 4. This diode is 150 μm long, with an oxide stripe contact 65 μm wide on the p-side, and is mounted p-side down on a Cu heat sink. It has reflective and antireflective coatings on the back and emitting cleaved facets, respectively. At a drive current of 400 mA, the applied voltage was 1.8 V; hence the power efficiency of this device under these conditions is ~ 1 percent. The nonlinear behavior of this diode near the origin is due to leakage in the metal reflective coating, but in general these diodes exhibit linear output versus diode characteristics, as shown in Fig. 5. The data of Fig. 5 are for a broad area diode in the pulsed mode of operation. The deviation from linearity at the higher drive currents is due to the onset of lasing.

The radiance of this device was measured in two ways: first, by using a previously described [3] lens and pinhole arrangement, and, second, by measuring the emission area and the power emitted into a cone of numerical aperature (NA) 0.1. For the lens and pinhole measurement, a 16 X, 0.15-NA microscope objective lens was used, and the power through a 50-μm-diam pinhole was 5.7 μW, giving a (peak) source radiance of 1100 W/cm^{2}sr. Using the second method, the source size was first determined to be 6 X 75 μm (to -6 dB from peak level) by scanning in the image plane of the lens used in the first method. From this source size, the power collected in a 0.1-NA cone was 0.25 mW, at a 400-mA drive level. This corresponds to a radiance of 1700 W/cm^{2}sr. Part of the discrepancy in the two measurements may be due to the neglect of losses in the microscope lens. In any case, the source radiance was measured to be over 1000 W/cm^{2}sr, about 10 times greater than the highest value reported previously [1]-[3].

Because of the high radiance of this source, large amounts of power can be coupled into small-diameter low-NA fibers, with relatively high coupling efficiency. Fig. 4 shows total output power and the power through 0.3 km of a 0.14-NA 90-μm-diam low-loss step-index fiber as a function of drive current. Assuming a 2-dB loss for this fiber length, the maximum power coupled into the fiber is 800 μW, which is nearly an

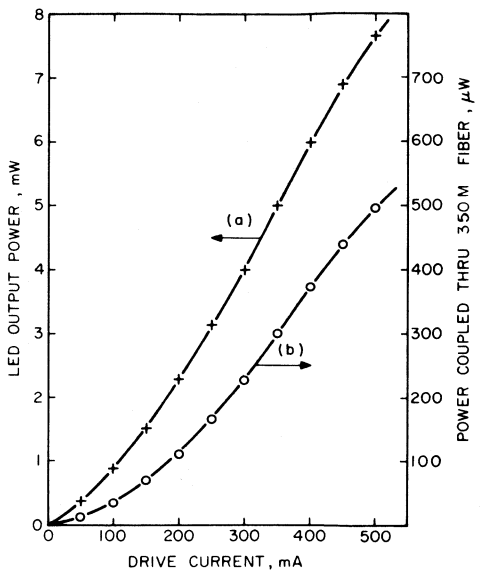


Fig. 4. Total power output from one edge of a stripe diode, and power coupled through 350 m of 8-dB/km 0.14-NA 90-μm-diam low-loss fiber. All measurements made with a 1-cm-diam calibrated Si photodiode.

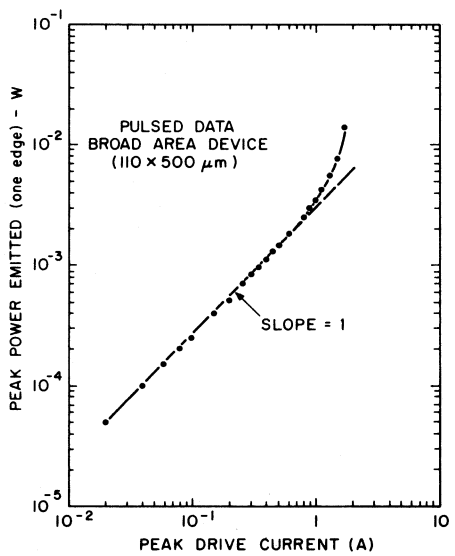


Fig. 5. Log plot of peak light output as a function of peak current input for a diode from wafer 313. Pulse length 200 ns, 10^3 pps.

order of magnitude higher than previously reported [8]. The coupling loss is ~10 dB, compared to calculated values of 17 dB for a Lambertian surface-emitting LED. A long length of fiber was employed for these measurements, because measurements with relatively short lengths (< 10 m) may include power coupled into the cladding, and lossy skew modes.

Modulation Capability

In order that these high-efficiency LED's be most useful in optical communications systems, they must be capable of being modulated at high speed; as we will describe below, the very narrow active region of these devices enhances their capability for direct modulation at very high frequencies. In a

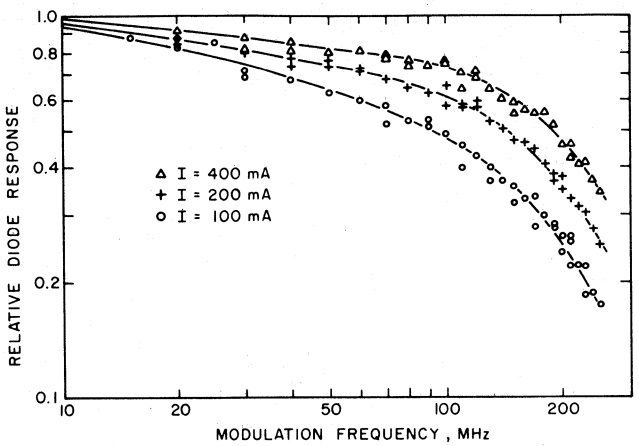


Fig. 6. Modulation response as a function of drive current for stripe diode (see Figs. 1 and 4).

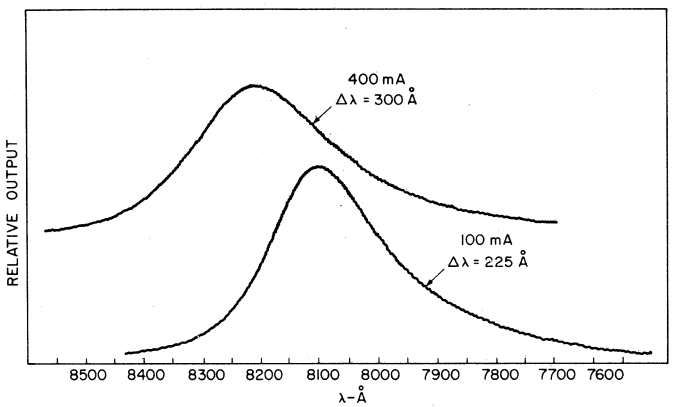


Fig. 7. Emission spectra of a stripe diode whose properties are shown in Fig. 4, at 100- and 400-mA dc drive current.

Steady state, the average injected carrier density in a recombination region of width d is given by

$$\Delta n = \frac{J\tau}{qd}. \tag{2}$$

Here, J is the injected current density, τ is the minority carrier lifetime, and q is the electronic charge. In an LED with a narrow 0.05-μm active region, and with $\tau = 10^{-8}$ s, which is appropriate for the relatively low carrier recombination ($n \sim 5 \times 10^{17}$) in our active region, the injected carrier density equals the background carrier density at $J = 40$ A/cm^2. At substantially higher current densities, the carrier lifetime decreases with injection level because of a bimolecular recombination process [9], and in the regime of bimolecular recombination

$$\tau \propto J^{-1/2}. \tag{3}$$

For the diode described above, the carrier lifetime would decrease from ~10 ns at 40 A/cm^2 to ~1 ns at 4000 A/cm^2. Since the diode modulation frequency response $R(\omega)$ is related to the drive-current modulation frequency ω by [10]

$$R = \frac{1}{[1 + (\omega\tau)^2]}^{1/2} \tag{4}$$

the frequency response (at the 3-dB points) of the diode increases from 40 MHz at low current density (~100 A/cm^2) to ~250 MHz at 4000 A/cm^2.

This bimolecular recombination process also means that for narrow recombination regions, short recombination times and high modulation capabilities can be obtained at reasonable operating current densities (a few thousand amperes per centimeter squared) independent of the initial minority carrier lifetime. In Fig. 6, we show the effects of drive current on the modulation response of the diode described in the previous section. The diode exhibits the expected dependence of modulation capability on current density. At 400 mA (3500 A/cm^2), the response extends to 250 MHz. Since the recombination region doping density or type does not control the modulation capability of these edge emitters, one can design the recombination region for highest output efficiency or narrow spectral width. The diode whose properties are illustrated in Figs. 3-5 is one with an unintentionally doped $\sim 1 \times 10^{17}$-cm^{-3} active region. This low doping in the active region creates an LED which combines high efficiency and a narrow spectral width, as shown in Fig. 7, at both relatively low and high dc drive currents. The diode emission spectra peaks at ~830 nm. The difference in the two spectra is due

to joule heating. This relatively narrow spectral width is useful in reducing fiber material dispersion effects.

V. Summary and Conclusions

Very narrow active region ($\lesssim 0.1$-μm) double-heterojunction edge-emitting stripe diodes have been shown to be useful as high-radiance ($\gtrsim 1000$ W/cm^{2}sr) incoherent emitters capable of modulation at frequencies in excess of 200 MHz. These properties result from: 1) an unusually low beam divergence in the direction perpendicular to the junction plane, about 30° compared to 120° for a conventional Lambertian diode source, and 2) a very high injected carrier density for a given current density. The beam divergence is shown to be similar to that which would be observed from these diodes in stimulated emission; however, no evidence of superradiance was found in the current density range investigated here. (A model for this effect is given elsewhere [6].) The diode quantum efficiency measured on diodes provided with antireflective coatings is about 1 percent. Because of the high diode radiance, the coupling efficiency into low-numerical-aperture fibers (NA = 0.15) suitable for long distance communication, is the highest reported to date for LED's, -10 dB. A power level of 800 μW has been coupled into such a fiber at a diode current of 500 mA.

References

[1] C. A. Burrus, "Radiance of small-area high-current-density electroluminescent diodes," *Proc. IEEE* (Lett.), vol. 60, p. 231–232, Feb. 1972.

[2] E. D. King and A. J. Springthorpe, "The integral lens coupled LED," *Journal of Electronic Materials*, vol. 4, p. 243–253, Apr. 1975.

[3] M. Ettenberg, K. C. Hudson, and H. F. Lockwood, "High-radiance light-emitting diodes," *IEEE Journal of Quantum Electronics*, vol. QE-9, p. 987, Oct. 1973.

[4] H. F. Lockwood and M. Ettenberg, "Thin solution multiple layer epitaxy," *Journal of Crystal Growth*, vol. 15, p. 81–83, July 1972.

[5] H. S. Sommers, Jr., "Experimental properties of injection lasers–IV modes of large cavity with sawed sides," *Journal of Applied Physics*, vol. 44, p. 3601–3608, Aug. 1973.

[6] J. P. Wittke, "Spontaneous-emission-rate alteration by dielectric and other waveguiding structures," *RCA Review*, vol. 36, p. 655–660, Dec. 1975.

[7] W. P. Dumke, "The angular beam divergence in double-heterojunction lasers with very thin active regions," *IEEE Journal of Quantum Electronics*, vol. QE-11, p. 400–403, July 1975.

[8] H. Kressel and M. Ettenberg, "A new edge-emitting (AlGa)As heterojunction LED for fiber-optic communications," *Proc. IEEE* (Lett.), p. 1360–1361, Sept. 1975.

[9] H. Namizaki, H. Kan, M. Ishii, and A. Ito, "Current dependence of spontaneous carrier lifetime in GaAs-$Ga_xAl_{1-x}As$ double heterojunction lasers," *Appl. Phys. Lett.*, vol. 24, p. 486–487, May 1974.

[10] H. F. Lockwood, J. P. Wittke, and M. Ettenberg, "LED for high data rate optical communications," *Optics Communications*, vol. 16, p. 193–195, Jan. 1976.

Correspondence

Propagation of Waves in Optical Waveguides with Various Dielectric and Metallic Claddings

H. J. FINK

Abstract—A new graphic method of obtaining easily the phase constant for a propagating wave is described and illustrated by a number of solutions for an optical waveguide covered with various dielectric and metallic claddings. It contains, implicitly, solutions for surface waves.

I. Introduction

We here describe a new graphic method to obtain simple solutions for the phase constant β of a propagating electromagnetic wave when all dielectric constants are real. This method is also approximately correct for an optical waveguide clad with silver for free-space wavelengths between 0.45 and 0.65 μm. For example, one obtains from the experimental values [1] of the optical constants an effective dielectric constant for silver at $\lambda = 0.55$ μm which is: $\epsilon_{\text{eff}}/\epsilon_0 = -11 - j0.36$, indicating that ϵ'' may be neglected with respect to ϵ' to first approximation.

Our method is illustrated by an example in which an optical waveguide with a refractive index of 2 is clad by various dielectric and metallic materials. The equations are simple enough so that they can be solved by slide rule or hand calculator.

II. Propagation Constant

We assume that an electromagnetic wave is propagating in the positive z direction in a slab of thickness $2a$ with dielectric constant ϵ_1. The x direction is perpendicular to the surfaces of medium 1; medium 2 with ϵ_2 extends from $x = -a$ to $x = -\infty$, and medium ϵ_3 from $x = a$ to $x = \infty$. All media are assumed to be of infinite extent in the y direction.

The electric and magnetic fields of a positively traveling wave are proportional to $\exp(j\omega t - \gamma z)$ and the propagation constant $\gamma = \alpha + j\beta$ is complex in general. In a medium with dielectric constant ϵ, permeability μ, and conductivity $\sigma(\omega)$ we define

$$k^2 = \omega^2\mu\epsilon - j\omega\mu\sigma \equiv \omega^2\mu\epsilon_{\text{eff}} \tag{1}$$

and

$$K^2 = k^2 + \gamma^2 \tag{2}$$

where

$$K = K' + jK''.$$

In general, the eigenvalue equation which determines the solution for the propagation constant γ is [2]

$$\frac{1+\rho_2}{1-\rho_2}\,\frac{1+\rho_3}{1-\rho_3} = e^{j4K_1a} \tag{3}$$

where (for $i = 2, 3$)

$$\rho_i = -\frac{\epsilon_{i\,\text{eff}}}{\epsilon_{1\,\text{eff}}}\,\frac{K_1}{K_i} \quad \text{for TM modes} \tag{4}$$

$$\rho_i = -\frac{\mu_i}{\mu_1}\,\frac{K_1}{K_i} \quad \text{for TE modes} \tag{5}$$

and $\text{Im}\,[K_i] < 0$. Equation (3) may be recast into

$$\tan 2K_1a = -j\,\frac{\rho_2 + \rho_3}{1 + \rho_2\rho_3}. \tag{6}$$

Assuming all $\epsilon''_{\text{eff}} = 0$, then $\rho_2 = jb_2$ and $\rho_3 = jb_3$, where b_2 and b_3 are real, and (6) reduces to

$$2K_1a - n\pi = \arctan\frac{b_2 + b_3}{1 - b_2b_3} \equiv Y(\epsilon_\beta) \tag{7}$$

with $n = 0, 1, 2, \cdots$ the order of the modes. Introducing the arbitrary but convenient definition $\beta^2 \equiv \omega^2\mu\epsilon_\beta$, where ϵ_β is an effective dielectric constant, we may write for the parameters in (7) (all μ are the same)

$$K_1 = \frac{2\pi}{\lambda}\left(\frac{\epsilon_1}{\epsilon_0} - \frac{\epsilon_\beta}{\epsilon_0}\right)^{1/2} \tag{8}$$

$$b_i = -\left(\frac{\epsilon_1 - \epsilon_\beta}{\epsilon_\beta - \epsilon_i}\right)^{1/2} \quad \text{for TE modes} \tag{9}$$

$$b_i = -\frac{\epsilon_i}{\epsilon_1}\left(\frac{\epsilon_1 - \epsilon_\beta}{\epsilon_\beta - \epsilon_i}\right)^{1/2} \quad \text{for TM modes.} \tag{10}$$

$K_1[(8)]$ must be real, not imaginary; and $\beta^2 > 0$ if the signal is to be mainly contained and propagate inside the guide. Therefore, ϵ_β is restricted to the region $0 < \epsilon_\beta < \epsilon_1$. From the solution of (7) the value of ϵ_β may be obtained and from it, β^2. If $\beta^2 > 0$ exists, the wave propagates through the guide. The principal values of $\arctan u \equiv Y(\epsilon_\beta)$ are within the region $-\pi/2 < Y(\epsilon_\beta) < \pi/2$ and these are plotted in the figures which follow.

III. Optical Waveguides with Various Claddings

In Fig. 1(a) we have plotted $2K_1a$ as a function of $\epsilon_\beta/\epsilon_0$ for various guide thicknesses $2a$ normalized by the free-space wavelength λ for $\epsilon_1 = 4\epsilon_0$. In the following figures we have plotted on the same scale

$$Y(\epsilon_\beta) = \arctan\,[(b_2 + b_3)/(1 - b_2b_3)]$$

always with $\epsilon_1 = 4\epsilon_0$, for various metallic and dielectric claddings. For a given normalized guide thickness $2a/\lambda$ we may find ϵ_β for the $n = 0$ mode by direct superposition of Fig. 1(a) on the other figures by the points of intersection of the superimposed curves. For $n = 1, 2, 3$, etc., the corresponding $2a/\lambda$ curve in Fig. 1(a) must be shifted downward by π, 2π, 3π, etc. to satisfy (7). Thus the propagation constants β for the higher order modes are readily found.

We have investigated a number of typical cases: the symmetric and asymmetric dielectric–dielectric–dielectric (*DDD*) guides, the symmetric and asymmetric metal–dielectric–metal (*MDM*) guides, and the metal–dielectric–dielectric (*MDD*) guide when the dielectric in the center is always $4\epsilon_0$ (refractive index of 2). A special case exists for TM modes for which the thick-

Manuscript received July 21, 1975; revised January 26, 1976.

The author is with the Department of Electrical Engineering, University of California, Davis, CA 95616.

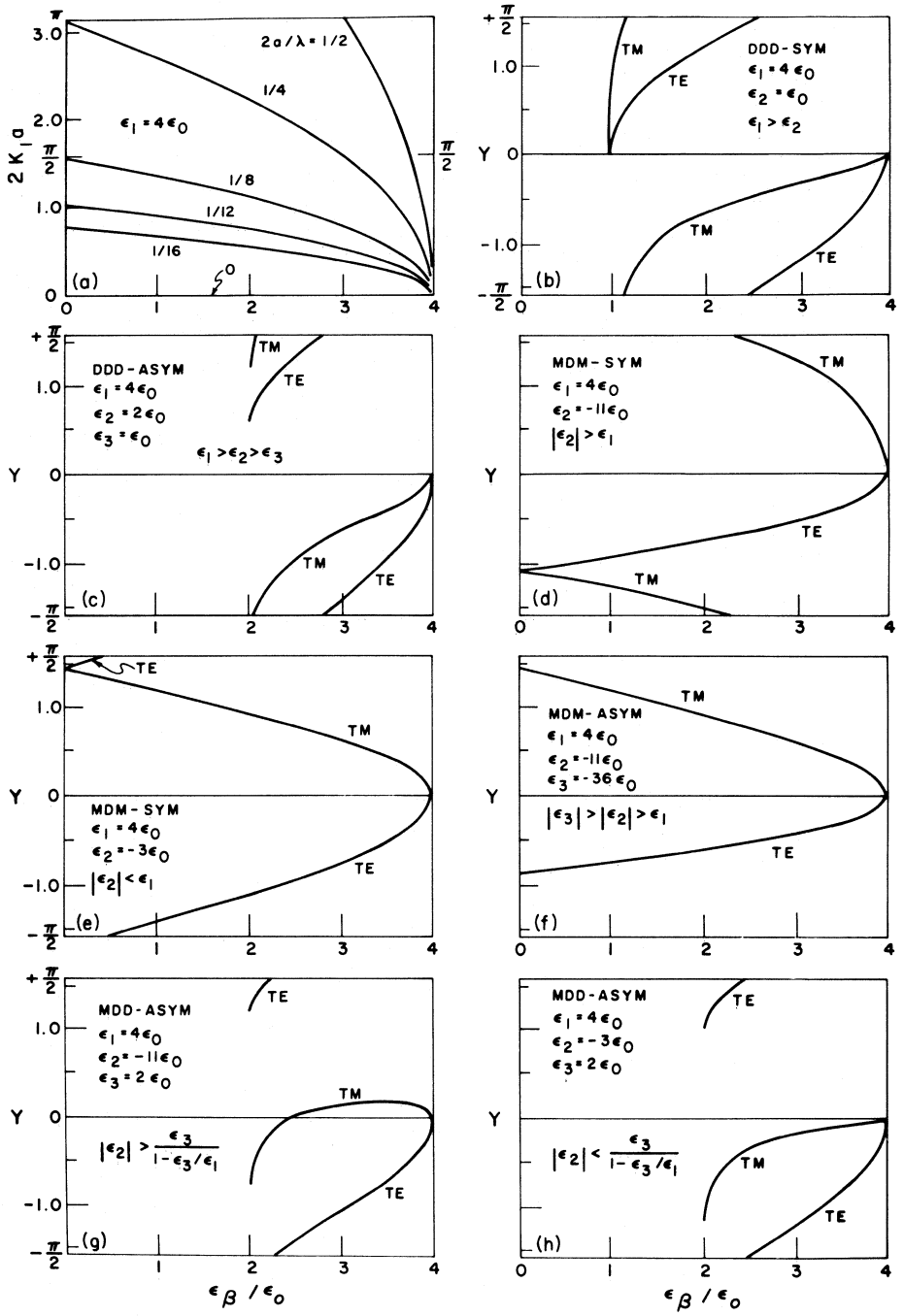


Fig. 1. (a) Solution of the left-hand side of (7), $2K_1a$, with $n = 0$ as a function of $\epsilon_\beta(\beta^2 \equiv \omega^2\mu\epsilon_\beta)$ with $\epsilon_1 = 4\epsilon_0$ for various guide thicknesses $2a$. λ is the free-space wavelength. (b) Solution of the right-hand side of (7), $Y(\epsilon_\beta)$, with $\epsilon_1 = 4\epsilon_0$ for a symmetric dielectric (*D*) guide. (c) Same for an asymmetric *D* guide. (d) Same for a symmetric *MD* guide. (e) Same for a symmetric *MDM* guide. (f) Same for an asymmetric *MDM* guide. (g) Same for an *MDD* guide. (h) Same for an *MDD* guide.

ness of the center dielectric may approach zero ($2a \to 0$). The guide then consists only of a metal–dielectric (*MD*) which may propagate a surface wave (surface polariton [3], [4]).

Fig. 1(b) shows the well-known [5] symmetric *DDD* guide which has real solutions of β for $\epsilon_1 > \epsilon_2$. Superposition of Fig. 1(a) on (b) shows that there are always solutions for β for any guide thickness $2a > 0$. No real solutions exist when $\epsilon_\beta < \epsilon_2$ as can be seen readily from (9) and (10) or Fig. 1(b).

Fig. 1(a) and (c) shows that for certain small thicknesses $2a/\lambda$ no real solutions of β can be found for an asymmetric *DDD* guide [5]. Therefore, a cutoff always exists for small thicknesses of medium 1. For $\epsilon_\beta < \epsilon_2$ there are no real values of $Y(\epsilon_\beta)$ where ϵ_2 is the larger dielectric constant of the two cladding materials ($\epsilon_2 > \epsilon_3$).

Again, the *MDM* symmetric and asymmetric guides rule out solutions for smaller values of $2a/\lambda$, in general, and in particular for $n = 0$ for large values of $2a/\lambda$. This can be seen readily from the superposition of Fig. 1(a) on Fig. 1(d), (e), and (f).

The *MDD* guide, which by its nature is always asymmetric, has no real β values for small values of $2a/\lambda$ for TE modes in

general, as can be seen readily from the superposition of Fig. 1(a) on the Fig. 1(g) and (h). Real solutions of β for TM modes exist for very small values of $2a/\lambda$ and for $2a \to 0$ provided $|\epsilon_2| > \epsilon_3/(1 - \epsilon_3/\epsilon_1)$ is satisfied. Depending on the values of ϵ_1, ϵ_2, and ϵ_3, there is also a certain range of guide thicknesses for which neither TM nor TE modes can propagate. When $2a \to 0$ and the guide degenerates to an *MD* guide [3], [4], the value of the phase constant for propagation of a surface wave (for $n = 0$) is from (7) with $b_2 + b_3 = 0$ [see also Fig. 1(a) and 1(g)]

$$\beta_{TM} = \omega \left(\frac{\mu \epsilon_3}{1 - \epsilon_3/|\epsilon_2|} \right)^{1/2}. \tag{11}$$

This surface wave exists only if $\epsilon_2 < 0, (\epsilon_2 + \epsilon_3) < 0$ and $0 < \epsilon_3 < |\epsilon_2|$. For very large guide thicknesses $2a/\lambda$ there exist always real solutions of β for $n \geqslant 1$ for TE and TM modes.

When $|\epsilon_2| < \epsilon_3/(1 - \epsilon_3/\epsilon_1)$ there exist neither TM nor TE modes for small values of $2a/\lambda$, nor does a TM mode exist for $n = 0$ for any guide thickness [Fig. 1(h)] of an *MDD* guide. For large values of $2a/\lambda$ and $n \geqslant 1$, solutions for both TM and TE modes exist.

IV. Conclusion

We have described a new graphic method of easily obtaining the phase constant β for a propagating wave when all dielectric constants are real. This method is illustrated for an optical waveguide clad with various dielectric and metallic materials. This method contains implicitly the case of surface waves, e.g., when the guide thickness approaches zero and a TM mode clings to and propagates along the interface between a dielectric and a metal.

Acknowledgment

The author thanks J. D. Swalen for helpful discussions.

References

[1] *American Institute of Physics Handbook*. New York: McGraw-Hill, 1972.
[2] V. A. Pruzhanovskii, "Metal Optical Waveguides," *Sov. Phys.-Techn. Phys.*, vol. 13, pp. 784-786, 1968.
[3] D. L. Mills and E. Burstein, "Polaritons: The electromagnetic modes of media," *Rep. Prog. in Phys.*, vol. 37, pp. 817-926, 1974; see also references therein.
[4] A. Otto, "Experimental investigation of surface polaritons on plane interfaces," *Festkörperprobleme*, vol. 14, pp. 1-37, 1974; see also references therein.
[5] D. Marcuse, *Theory of Dielectric Optical Waveguides*. New York: Academic, 1974; see references therein.

Nonlinear Optical Susceptibility of $HgGa_2S_4$

B. F. Levine, C. G. Bethea, H. M. Kasper, and F. A. Thiel

Abstract—**The second harmonic coefficient d_{36} of $HgGa_2S_4$ has been measured to be 5 times larger than d_{31} ($LiNbO_3$). The birefringence is usefully large.**

Manuscript received December 29, 1975.
The authors are with Bell Laboratories, Murray Hill, NJ 07974.

As discussed previously [1], [2], the thiogallate structure has very favorable optical and crystallographic properties. For this reason we had measured $CdGa_2S_4$ and found it [1] to have a very large nonlinear optical coefficient d_{36} which was in fact, five times larger than d_{31} of $LiNbO_3$. Unfortunately, $CdGa_2S_4$ has only a small birefringence $n_e - n_o \sim 0.006$ which is due to an accidental isotropy point at 4900 Å. Thus we were led to investigate a new thiogallate crystal $HgGa_2S_4$ [3]-[7]. We have found that d_{36} is the same as for $CdGa_2S_4$ but that the birefringence is an order of magnitude larger, making $HgGa_2S_4$ a promising new material with good device potential.

$HgGa_2S_4$ was first prepared as a powder by Hahn *et al.* [3] from HgS and Ga_2S_3. Beun *et al.* [6] and Krausbauer *et al.* [4] obtained yellow needles of $HgGa_2S_4$ by vapor transport with iodine. Our first crystals were obtained by vapor transport. Stoichiometric amounts of HgS and Ga_2S_3 were weighed into a quartz ampoule and iodine amounting to 4 mg/cm^3 was added. The ampoule was placed vertical in a resistance furnace and the $HgGa_2S_4$ was transported from 750°C to the cooler upper end at 700°C. The crystals obtained were yellow needles about $10 \times 1 \times 0.3$ mm in size; we found it difficult to obtain larger crystals of $HgGa_2S_4$ by the vapor transport method and therefore tried to grow $HgGa_2S_4$ from a melt. The starting composition of $(HgS)_{1.05}Ga_2S_3$ was enclosed in a sealed quartz ampoule with 3-mm walls. This ampoule was placed in a horizontal furnace enclosed in a pressure vessel and then the vessel was filled with Argon and pressurized to 1000 psi. Then the furnace was heated to 950°C, soaked at that temperature for 12 h, and then slowly cooled to room temperature. Orange chunks of $HgGa_2S_4$ crystals were found enclosed in a black matrix. There was some indication that the yellow needles might have a larger birefringence than the orange crystals, but the small size of the needles made accurate measurement difficult. If this were true, it suggests the possibility of controlling the birefringence by the growth process. From consideration of Beun's result that the luminescence depends on deviations of stoichiometry, we suspect that the needles are deficient and the bulk crystals richer in HgS.

We found it convenient to use a [1, 1, 2] crystal orientation polished flat and parallel. The size of the crystal which was available was ~ 1 mm^3 and it had a few internal defects. The indices of refraction were measured and are given in Table I. These indices are consistent with the measured coherence lengths of

$$l_c^V = 1.9\ \mu\text{m} \pm 5\ \text{percent}, \quad l_c^H = 2.9\ \mu\text{m} \pm 5\ \text{percent} \tag{1}$$

at 1.06 μm. The transmission of the [1, 1, 2] plate was measured using unpolarized light and is given in Fig. 1. The average absorption coefficients for our sample at 1.06 μm and 0.53 μm were

TABLE I
Measured Indices of Refraction and Birefringence at Several Wavelengths

$\lambda(\mu m)$	n_θ	n_o	n_e	$(n_o - n_e)$
0.5145	2.73	2.79	2.71	0.08
0.5320	2.65	–	–	–
0.6328	2.57	2.61	2.55	0.06
1.064	2.51	2.56	2.50	0.05
1.318	–	–	–	0.04

Note: The ordinary n_o and extraordinary n_e indices are given as is n_θ which is the index appropriate for a vertically polarized beam traveling perpendicular to the [1, 1, 2] plate, i.e., for a polarization at an angle θ to the c axis.

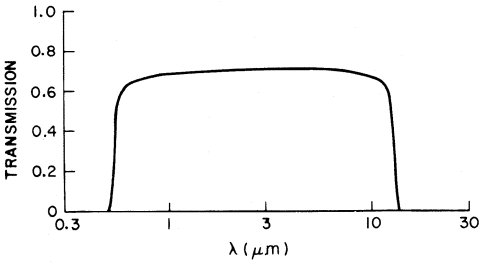


Fig. 1. Percent transmission of a 0.98-mm plate of $HgGa_2S_4$. The transparency range is approximately 0.55–13 μm.

$$\alpha_\omega \simeq 0, \quad \alpha_{2\omega} = 11 \text{ cm}^{-1}. \tag{2}$$

The second harmonic coefficient d_{36} was measured with the Maker-fringe technique [8], using a single TEM_{00} mode YAG laser operating at 1.06 μm. The sample rotation was about a vertical axis which contained the projection of the c axis. The effective nonlinear coefficient for both fundamental and harmonic polarized vertically (at normal incidence) is [1]

$$d_{\text{eff}}^{V} = 3 \sin^2 \theta \cos \theta d_{36} \tag{3}$$

while that for a horizontal fundamental and a vertical harmonic (at normal incidence) is [1]

$$d_{\text{eff}}^{H} = -\cos \theta \, d_{36}, \tag{4}$$

where θ is the angle between the c axis and the crystal plate. For a [1, 1, 2] plate of $HgGa_2S_4$ (for which [7] $c/2a = 0.929$) this angle is 33.3°. By comparing the second harmonic generated to that produced by a quartz reference plate (for which we use [9] $d_{11}(SiO_2) = 0.80 \times 10^{-9}$ ESU) we obtain

$$d_{36}(HgGa_2S_4) = 64 \times 10^{-9} \text{ ESU} \pm 30 \text{ percent} \tag{5}$$

where both the vertical fundamental-vertical harmonic [i.e., (3)] and the horizontal fundamental-vertical harmonic [i.e., (4)] experiments gave values which were in agreement to within the experimental error. The 30-percent error given for d_{36} is a result of the sample size and quality.

In conclusion, $HgGa_2S_4$ has a very large nonlinearity with $d_{36}(HgGa_2S_4)$ being five times larger than $d_{31}(LiNbO_3)$. Further, $HgGa_2S_4$ has an order of magnitude larger birefringence than $CdGa_2S_4$ and thus this crystal has good device potential. The birefringence of $HgGa_2S_4$ is large enough to allow phase matching for a fundamental wavelength longer than ~1.5 μm. For a nondegenerate mixing or parametric generation process even shorter pump and signal wavelengths can be used.

References

[1] B. F. Levine, C. G. Bethea, and H. M. Kasper, "Nonlinear optical susceptibility of $CdGa_2S_4$," *IEEE J. Quantum Electron.*, vol. QE-10, pp. 904–906, 1974.

[2] B. F. Levine, "Bond charge calculation of nonlinear optical susceptibilities for various crystal structures," *Phys. Rev. B*, vol. 7, pp. 2600–2626, 1973.

[3] H. Hahn, G. Frank, W. Klinger, A. D. Störger, and G. Störger, "Ternary chalcogenides of aluminum, gallium and indium with zinc, cadium and mercury," *Z. Anorg. Allg. Chem.*, vol. 279, pp. 241–270, 1955.

[4] R. Nitsche, H. U. Bolsterli, and M. Lichtensteiger, "Crystal growth by chemical transport reactions," *J. Phys. Chem. Sol.*, vol. 21, pp. 199–205, 1961.

[5] W. A. Shand, "The preparation and growth of some ternary sulphides," *J. Cryst. Growth*, vol. 5, pp. 203–205, 1969.

[6] J. A. Beun, R. Nitsche, and M. Lichtensteiger, "Optical and electrical properties of ternary chalcogenides," *Physica*, vol. 27, pp. 448–452, 1961.

[7] L. Krausbauer, R. Nitsche, and P. Wild, "Mercury gallium sulfide, $HgGa_2S_4$, a new phosphor," *Physica*, vol. 31, pp. 113–121, 1965.

[8] J. Jerphagnon and S. K. Kurtz, "Maker fringes: A detailed comparison of theory and experiment of isotropic and uniaxial crystals," *J. Appl. Phys.*, vol. 41, pp. 1667–1681, 1970.

[9] B. F. Levine and C. G. Bethea, "Nonlinear susceptibility of GaP; Relative measurement and use of measured values to determine a better absolute value," *Appl. Phys. Lett.*, vol. 20, pp. 272–275, 1972.

Characteristics of RF Injection Locking of Self-Pulsing in an AlGaAs DH Junction Laser

T. P. LEE AND THERESINHA J. B. SERRA

Abstract—**The minimum RF power required for injection locking of the light pulsations in the output of a CW room-temperature AlGaAs double-heterostructure (DH) junction laser was found to depend exponentially on $(f - f_r)$, where f is the RF injection frequency and f_r is the self-pulsing frequency, and also, to depend inversely on the self-pulsing strength of the laser. Nearly 100-percent modulation depth is achievable at $f = f_r$, and slight reduction of modulation depth occurs when $f >> f_r$.**

It is well known [1]–[3] that diode lasers often show self-pulsing of their light output at microwave frequencies. Regular pulsations usually occur at specific pump current levels and within a certain range of device temperatures. Stabilization [2]–[7], narrowing [4], and frequency pulling [7] of the optical pulses by applying either optoelectronic, electrical or optical feedback [4], and by microwave injection-locking methods [2]–[7] have been demonstrated in homostructure CW GaAs lasers at 77 K. It is observed that the frequency of pulsation, which ranges from 0.5 to 3 GHz increases with the drive current, and that the pulsations first occur at about 1.3 times the threshold current in some lasers and at more than twice the threshold current in others. RF injection locking reported previously indicated the following information.

1) The minimum RF power for locking was 10^{-4} to 10^{-6} W.

2) The maximum locking range from the self-pulsing frequency increased with RF power P_L.

3) It is more difficult to pull the oscillation frequency away from the self-pulsing frequency for lasers having strong oscillation.

4) Locking could also be achieved at harmonic frequencies and fractional harmonic frequencies with increased RF power.

Although previous work on homostructure lasers was extensive, there has been little reported for CW double-heterostructure (DH) lasers at room temperature. It is the purpose of this correspondence to report on such a study and to compare the results with the RF locking characteristics of conventional oscillators.

The laser diode was a stripe-geometry DH AlGaAs type with a 12.5-μm stripe width. The laser was mounted on a stripline circuit so that both dc and RF signals could be applied simul-

Manuscript received January 8, 1976: revised February 12, 1976.

T. P. Lee is with Bell Laboratories, Holmdel, NJ 07733.

T. J. B. Serra is with the Instituto de Fisica "Gleb Watghin," Universidade Estadual de Campinas, Campinas, Brazil.

taneously. The frequency response of the RF circuit was flat up to 2 GHz at least. The laser output was detected by a fast photodiode with 200-ps resolution, and then analyzed by a microwave spectrum analyzer.

In the absence of the RF injection signal, the peak of the self-resonance frequency versus dc driving current I is shown in Fig. 1(a). At current less than 1.05 times the threshold current I_{th}, a single resonance peak was obtained, and its peak frequency increased with current approximately as $\sqrt{I/I_{th} - 1}$, as expected from theory (quantum noise fluctuations) [8]-[10]. At current larger than 1.05 I_{th}, however, the spectrum showed harmonically related multiresonance peaks, which implied that the light output was composed of deeply modulated light pulses. The fundamental frequency of the multiple-peaked RF spectrum varied as $(I/I_{th} - 1)^{3/2}$. The latter frequency-current dependence is in good agreement with computed results based on a saturable-absorber Q-switched model previously reported [11]. Thus we could identify two regions of operation: at lower current, there is a weak self-oscillation region induced by quantum noise fluctuations; and at slightly higher current, there is a much stronger self-oscillation of Q-switched pulsations.

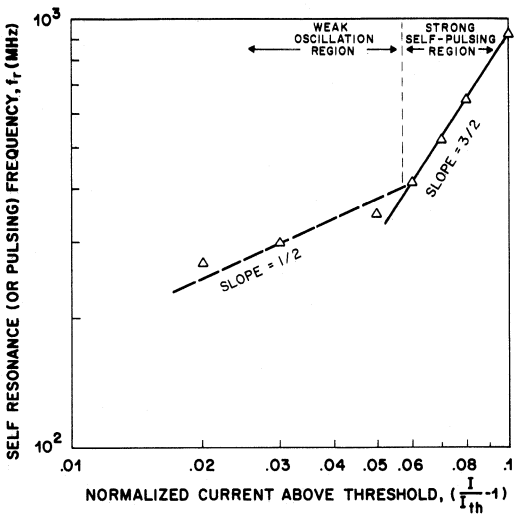
Fig. 1(b) shows the detected relative RF output power at the RF fundamental frequency plotted against $(I/I_{th} - 1)$. The RF power reaches a peak at about 1.07 I_{th}, which corresponds to the region of the strongly Q-switched pulsations shown in Fig. 1(a).

One complication arose when the current was increased above 1.1 I_{th} at which point the output of the laser began to saturate as indicated in the output-power-versus-current plot of Fig. 2, with the appearance of a "step" between 200 mA (1.1 I_{th}) and 250 mA (1.4 I_{th}). When the near field of the laser was examined, we observed a well-defined light spot approximately 4-6 μm wide along the junction plane at a current below 200 mA. As the current increased the width of the light spot widened. At higher currents, the light spot tended to break into two or more spots whose sizes were irregular. As current increased still higher, one of these spots became the brightest one which usually was near the edges of the stripe. In the diode reported here, the brightest spot occurred at 250 mA (1.4 I_{th}), thus contributing to the second steeper slope in Fig. 2. We observed that the second "filament"[1] generally had a similar self-pulsing behavior, but its pulsing frequency was not the same as that of the first filament, thus resulting in a random noise-like pulsation.

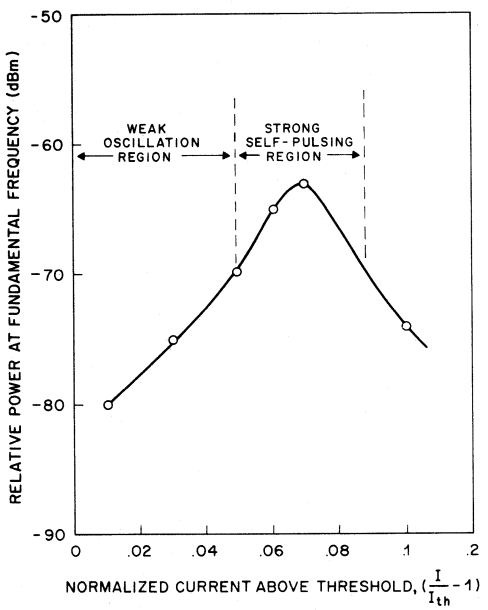
When the laser was biased for self-pulsing at frequency f_r and an RF signal of the same frequency $f = f_r$ was injected, the depth of modulation of the light pulses increased with increasing RF power as shown by the solid curve in Fig. 3. Depth of modulation as high as 95 percent has been achieved. Pulsewidth of about 200 ps was measured, which is limited by our detector diode resolution. When the injected locking frequency f was different from the self-pulsing frequency, f_r, the laser tended to be pulled to the frequency f. However, more RF power was required to obtain the same depth of modulation as that in the case for $f = f_r$, as shown by the dashed curve in Fig. 3. Also, it appeared that the maximum attainable depth of modulation decreased with increasing deviation of the locking frequency from the self-pulsing frequency.

The maximum frequency pulling range of the laser from its self-pulsing frequency f_r to the injected signal frequency f

[1]The term "filament" is used here rather loosely. In a detailed study, Paoli has found that the loss of guiding in the waveguide along the junction plane causes the light intensity distribution to change. In this case the term "filament" would be misleading.



(a)



(b)

Fig. 1. (a) The self-resonance frequency, as measured by the fundamental frequency in the RF spectrum, versus normalized dc current above threshold. (b) The relative RF power of the optical pulses at the fundamental frequency versus normalized dc current above threshold.

increased with the RF power in the fashion shown in Fig. 4 for two bias conditions. From these plots, an experimental relationship of the RF injection locking range versus RF power can be derived as given below

$$\frac{\Delta f}{f_r} = \eta \ln \frac{P_L}{P_0} \tag{1}$$

where P_L is the minimum RF power to achieve a frequency pulling range of $\Delta f = f - f_r$; P_0 is obtained by extrapolation of P_1 at $\Delta f = 0$. P_0 is about equal to the minimum RF power required to double the depth of modulation of the self-pulsation at $f = f_r$, and η is a constant equal to the slope of the curves of Fig. 4. For the two currents $I/I_{th} = 1.03$ and 1.06 in Fig. 4, the values for P_0 and η are -30 dBm, 0.2, and -37.5 dBm, 0.14, respectively. Comparison of Fig. 1(b) and

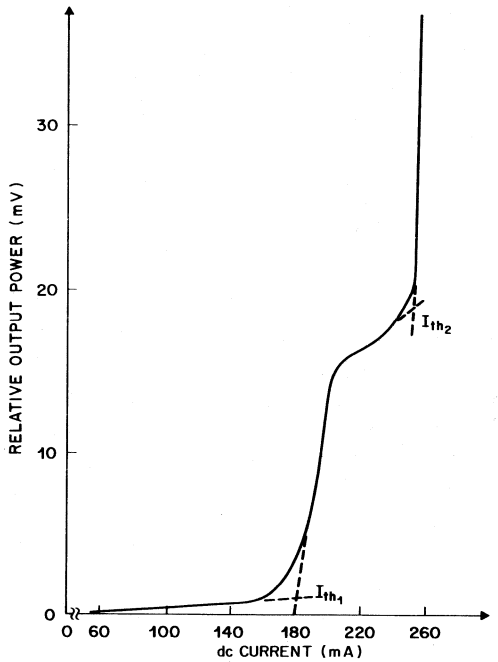


Fig. 2. Laser output power versus dc current. The step in the curve indicates the existence of "multifilament" lasing.

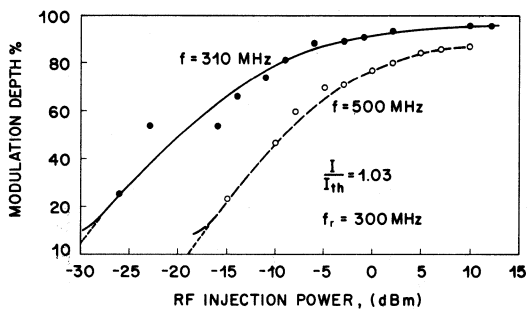


Fig. 3. Depth of modulation of light pulses as a function of injected RF power.

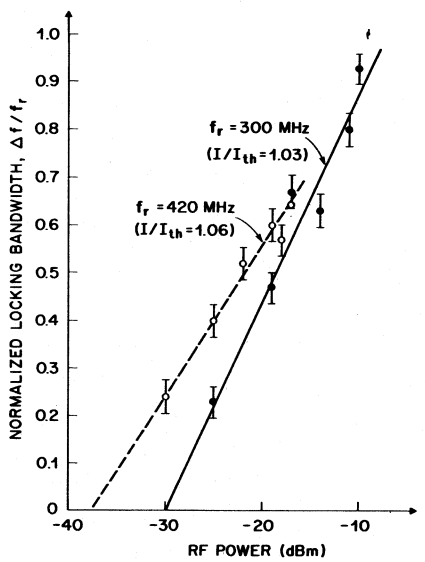


Fig. 4. Normalized locking range as a function of RF power.

Fig. 4 indicates that higher RF power is required to lock the weaker self-oscillation mode (at $I = 1.03\ I_{th}$) for a given fractional locking bandwidth, thus its P_0 is larger. Thus, unlike locking of electronic oscillators where the frequency of oscillation is more difficult to pull for stronger free-running oscillators, the reverse is true in the case of self-pulsing injection lasers. The slight difference in η values for the two curves in Fig. 4 is not clearly understood. It may involve the details of the self-pulsing mechanism. A theoretical justification of (1) warrants further investigation.

Because our laser exhibited the existence of more than one filament at a large driving current, the present study of RF injection locking was conducted for a limited dc current range, namely, from $I = 1.01\ I_{th}$ to $1.1\ I_{th}$. At the latter current, regular pulsations at 920 MHz with 80-percent modulation depth has been achieved with RF injection locking. Presumably, pulsing frequency at a few gigahertz would be possible if filamentary lasing behavior could be eliminated.

In conclusion, we have studied the characteristics of RF injection locking for enhancement and stabilization of the self-pulsing of DH lasers operating continuously at room temperature. The minimum RF power required to achieve locking depends exponentially on the difference of the RF signal frequency and the laser self-pulsing frequency, and depends inversely on the laser self-pulsing strength. The depth of modulation can attain 100 percent if the laser is locked at its self-pulsing frequency. Modulation depth is reduced as the injection frequency moves away from the self-pulsing frequency.

ACKNOWLEDGMENT

The authors would like to express their gratitude to T. L. Paoli for many comments, and to H. M. Marcos and R. W. Dixon for supplying the DH lasers.

REFERENCES

[1] V. D. Kurnosov *et al.*, "Self-modulation of emission from an injection semiconductor laser," *JETP Lett.*, vol. 4, pp. 303–305, 1966.

[2] V. I. Magalyas, A. A. Pleshkov, L. A. Rivlin, A. T. Semenov, and V. V. Tsvetkov, "Modulation and synchronization of the emission of a semiconductor injection laser," *JETP Lett.*, vol. 6, pp. 68-70, 1967.
[3] L. A. D'Asaro, Sr., J. M. Cherlow, and T. L. Paoli, "Continuous microwave oscillations in GaAs junction lasers," *IEEE J. Quantum Electron.*, vol. QE-4, pp. 164-167, Apr. 1968.
[4] T. L. Paoli and J. E. Ripper, "Frequency stabilization and narrowing of optical pulses from CW GaAs injection lasers," *IEEE J. Quantum Electron.*, vol. QE-6, pp. 335-339, June 1970.
[5] —, "Locking of spontaneously pulsing CW GaAs injection laser by fractional-harmonic current modulation," *IEEE J. Quantum Electron.*, vol. QE-6, pp. 326-328, June 1970.
[6] —, "Optical pulses from CW GaAs injection lasers," *Appl. Phys. Lett.*, vol. 15, pp. 105-107, Aug. 1969.
[7] J. E. Ripper and T. L. Paoli, "Frequency pulling and pulse position modulation of pulsing CW GaAs injection lasers," *Appl. Phys. Lett.*, vol. 15, pp. 203-205, Oct. 1969.
[8] D. E. McCumber, "Intensity fluctuation in the output of CW laser oscillators," *Phys. Rev.*, vol. 141, pp. 306-322, Jan. 1966.
[9] H. Haug, "Quantum mechanical theory of fluctuations and relaxation in semiconductor lasers," *Zeit. Phys.*, vol. 200, pp. 57-68, 1967.
[10] T. L. Paoli and J. E. Ripper, "Observation of intrinsic quantum fluctuation in semiconductor lasers," *Phys. Rev. A*, vol. 2, pp. 2551-2555, Dec. 1970.
[11] T. P. Lee and R. Roldan, "Repetitively *Q*-switched light pulses from GaAs injection lasers with tandem double-section stripe geometry," *IEEE J. Quantum Electron.*, vol. QE-6, pp. 339-352, June 1970.

Correction to "Surface-Wave Radiation Loss from Curved Dielectric Slabs and Fibers"

EDWARD F. KUESTER AND DAVID C. CHANG

In the above paper,[1] on p. 903, (2) should read

$$\Delta = \frac{1}{R}\int_S \hat{x}\left[\omega\mu_0 \bar{H}_0 \cdot \bar{H}_0 + \omega\epsilon \bar{E}_0 \cdot \bar{E}_0\right] dS \qquad (2)$$

and on p. 904 the second equation above (11) should be amended to

$$\Delta = \frac{1}{R}\left\{\frac{1}{\omega\mu_0}\int_{-\infty}^{\infty} \hat{x}\left[k_0^2(\nu_0^2 + n^2)E_{0\hat{z}}^2 - \left(\frac{\partial E_{0\hat{z}}}{\partial \hat{x}}\right)^2\right] d\hat{x}\right\}.$$

The following equation for Δ is, however, correct, as is (11), and the conclusions of the paper regarding the slab remain unchanged. The local coordinates are defined by

$$\hat{x} = \rho - R = \hat{r}\cos\hat{\phi}$$

$$\hat{y} = R\theta$$

$$\hat{z} = z = -\hat{r}\sin\hat{\phi}.$$

Manuscript received February 13, 1976.
The authors are with the Electromagnetics Laboratory, Department of Electrical Engineering, University of Colorado, Boulder, CO 80309.
[1] E. F. Kuester and D. C. Chang, *IEEE J. Quantum Electron.*, vol. QE-11, pp. 903-907, Nov. 1975.

Notes and Lines

Additional Ultraviolet Laser Transitions in Cu II

J. R. McNEIL AND G. J. COLLINS

***Abstract*—We have observed three additional ultraviolet laser transitions in Cu II at 2529, 2600, and 2707 Å. To our knowledge, this is the first time these lines have been observed to oscillate.**

We report three new Cu II laser transitions, two of which arise from the $3d^9 5s\ (^1D)$ term of Cu II and one which originates from the $3d^9 5s\ (^3D)$ term. These three new laser transitions are shown in Fig. 1. We have previously observed four ultraviolet laser transitions at 2486, 2506, 2591, and 2599 Å, all of which originate from the $3d^9 5s\ (^3D)$ term of Cu II [1]. The upper and lower levels of these four transitions are also shown in Fig. 1.

A rectangular slotted hollow cathode 2 mm × 6 mm in cross section and 50 cm in length was used as the active medium. This device has already been described in the literature [2].

The 2600-Å transition, $5s\ (^1D_2)$–$4p\ (^1F_3^0)$, was inverted on

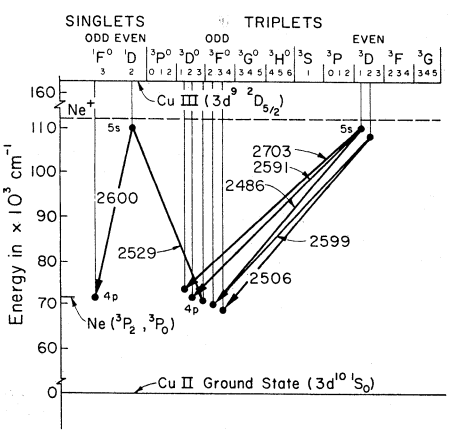


Fig. 1. A partial term diagram of Cu II indicating the seven ultraviolet laser wavelengths and transition assignments. The energy available from Ne^+ and $Ne^M(^3P_2, ^3P_0)$ in a collision of the second kind is also shown.

Manuscript received March 1, 1976. This work was supported by ERDA Grant E2723 and by NASA (Lewis) and was submitted in partial fulfillment of the Ph.D. requirements of J. R. McNeil at Colorado State University.
The authors are with the Department of Electrical Engineering, Colorado State University, Fort Collins, CO 80523.

TABLE I
ULTRAVIOLET LASER TRANSITIONS OF Cu II AND LEVEL ASSIGNMENTS

λ_{air} (Å) Measured ± 0.1 Å	λ_{air} (Å) Actual[a]	Transition assignment[a] Upper	Lower	Threshold Current[b] (A)
2485.8	2485.8	$3d^9 5s\ ^3D_1$	$3d^9 4p\ ^3F^0_2$	14[c]
2506.5	2506.3	$3d^9 5s\ ^3D_2$	$3d^9 4p\ ^3F^0_3$	40[c]
2529.2	2529.3	$3d^9 5s\ ^1D_2$	$3d^9 4p\ ^3D^0_3$	35[c]
2590.6	2590.5	$3d^9 5s\ ^3D_1$	$3d^9 4p\ ^3D^0_2$	6
2599.0	2598.8	$3d^9 5s\ ^3D_2$	$3d^9 4p\ ^3F^0_2$	7
2600.3	2600.3	$3d^9 5s\ ^1D_2$	$3d^9 4p\ ^1F^0_3$	7
2703.1	2703.2	$3d^9 5s\ ^3D_1$	$3d^9 4p\ ^3D^0_1$	32[c]

[a] Identification from [3].
[b] Threshold currents are measured using 12 torr of neon excited in a copper hollow cathode with a cross section of 2 × 6 mm and 50 cm long.
[c] Observed only on a quasi-CW (200-μs duration) basis.

a continuous basis with a threshold current of 7 A. Our dc power supply was limited to 10 A. As a consequence, the 2529-Å $5s\ (^1D_2)$–$4p\ (^3D^0_3)$ and 2703-Å $5s\ (^3D_1)$–$4p\ (^3D^0_1)$ transitions were inverted using a high-current pulse generator. The threshold currents for the 2529- and 2703-Å transitions were 35 and 32 A, respectively. The current pulses employed were of 200-μs duration and laser action occurred throughout the entire 200 μs. Hence, we conclude that true CW oscillation has been obtained on all three transitions. Our results to date are summarized in Table I.

Using dielectric mirrors which cover the spectral range from 2450 to 2650 Å, we have observed simultaneous oscillation on six of the seven ultraviolet laser transitions. At the current limit of our pulse generator, 50 A, we observed 350 mW of multiline output power in the ultraviolet using a coupling mirror of 0.6-percent transmittance. The peak power was calculated by measuring the average power, 2.8 mW, and dividing by the duty cycle (0.008). Unlike our previous results we have *not* observed any saturation of the output power with increasing discharge current.

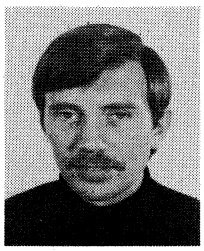
ACKNOWLEDGMENT

The authors express their gratitude to Dr. K. B. Persson of the National Bureau of Standards, Boulder, CO for helpful technical discussions and encouragement.

REFERENCES

[1] J. R. McNeil, G. J. Collins, K. B. Persson, and D. L. Franzen, "Ultraviolet laser action from Cu II in the 2500 Å region," *Appl. Phys. Lett.*, vol. 28, pp. 207–209, 1976.
[2] —, "CW laser oscillation in Cu II," *Appl. Phys. Lett.*, vol. 27, pp. 595–598, 1975.
[3] J. Reader *et al.*, *J. Opt. Soc. Amer.*, vol. 50, p. 221, 1960.

Contributors



Gerhard W. Bekkers was born in Walsum, Germany in 1938. He received the Electrotechnisch Ingenieur degree from the Technische Hogeschool Rindhoven, Rindhoven, Germany, in 1964.

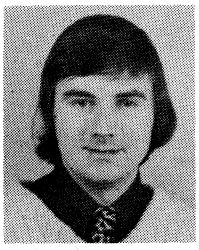
In 1964 he joined IBM, The Netherlands, and worked on optical character recognition and disk file memories. In 1968 he transferred to IBM, San Jose, where he worked on mass storage systems. He received his M.S.E.E. degree from Stanford University, Stanford, CA, in 1972. In September 1973 he was assigned an IBM Resident Study Program Fellowship and started working toward a Ph.D. degree at Stanford University. His thesis work has been directed at the study of high-efficiency nonlinear optical processes in metal vapors using high-powered laser systems and low-powered systems with two-photon enhancement.

Mr. Bekkers is a member of the Koninklijk Instituut van Ingenieurs.

*

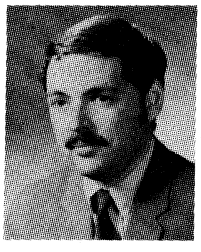
Christopher C. Davis was born in Manchester, England, on July 7, 1944. He received the B.A. and M.A. degrees from Trinity College, Cambridge, England, in 1965 and 1970, respectively, and the Ph.D. degree in physics from the University of Manchester, Manchester, in 1970. His doctoral research involved studies of excitation and relaxation processes in noble-gas lasers.

From 1969 to 1973 he was a Research Associate in the Department of Physics at the University of Manchester, where he carried out research on atomic-iodine gas-discharge lasers, electronegative plasmas, and atomic-iodine photodissociation lasers. From 1973 to 1975 he was a Research Associate with the Materials Science Center, Cornell University, Ithaca, NY. He is now with the Department of Electrical Engineering, University of Maryland, College Park. His current research interests include photodissociation and chemical lasers, photochemical kinetics, and molecular-energy transfer.



Dr. Davis is a member of the Institute of Physics (London).

*



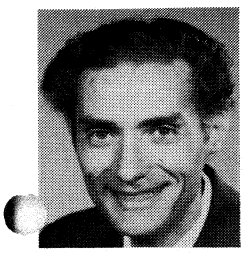
Michael Ettenberg received the B.S. degree in metallurgy from the Polytechnic Institute of Brooklyn, New York, NY, in 1964. From 1964 to 1969 he attended New York University, New York, NY, and received the M.S. degree in 1967 and the Ph.D. degree in 1969. His dissertation was concerned with thermodynamic studies of the interaction of point defects in intermetallic compounds.

He joined RCA Laboratories, Princeton, NJ, in 1969 and has been involved in studies con-

cerning factors which affect the reliability of electroluminescent diodes, improved liquid-phase techniques for the synthesis of III-V compounds and theoretical studies of the thermodynamics of crystal synthesis. He has published several papers on his work.

Dr. Ettenberg is a member of the American Institute of Metallurgical Engineers, the American Society of Metals, and the Alpha Sigma Mu Metallurgical Honor Society.

*

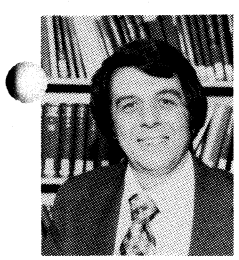


Herbert Flicker (SM'66) was born in Brooklyn, NY, on January 28, 1930. He received the A.B. degree in physics from Cornell University, Ithaca, NY, in 1951, the M.S. and Ph.D. degrees in physics from the University of Pennsylvania, Philadelphia, in 1953 and 1959, respectively.

From 1959 to 1964 he was at RCA Laboratories, Princeton, NJ, performing experiments on III-V semiconductors, radiation damage to silicon, construction of a Promethium-147 nuclear battery, and a photoconductive detector using microwave bias. During 1964–1965 he was a Visiting Associate Professor in the Division of Engineering, Brown University, Providence, RI. He studied the room-temperature anneal of radiation damage in lithium-doped silicon at TRW Systems during 1965–1966. From 1966 to 1972 he was at Electro-Optical Systems, a Xerox company, in Pasadena, CA. During this time he worked on light-emitting diodes and lasers in $Pb_{1-x}Sn_xTe$ and mixed III-V alloy semiconductors, as well as analysis and conceptual design of electrooptical systems operating from visible to long-wavelength infrared wavelengths. Since 1972 he has been with the Laser Division of Los Alamos Scientific Laboratory, University of California, Los Alamos, NM, where he has been active in tunable diode laser spectroscopy in support of the laser isotope separation program.

Dr. Flicker is a member of Sigma Xi and the American Physical Society.

*



Edward V. George was born in Chicago, IL on December 8, 1938. He received the B.S. degree in electrical engineering from the Illinois Institute of Technology, Chicago, in 1961, and the Ph.D. degree in physics from the Massachussetts Institute of Technology, Cambridge, in 1969.

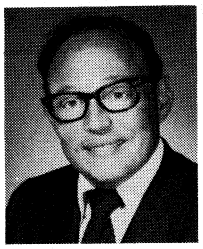
He then joined the Faculty of the Physics Department at M.I.T. and conducted research in the areas of gaseous electronics and laser physics. In 1974 he was made an Associate Professor in the Physics Department at M.I.T. In 1975 he joined the Research Staff at the Lawrence Livermore Laboratory, University of California, Livermore, and he is currently in charge of the Advanced Lasers Group of the Y-Program. He directs an experimental research and technology effort in all areas of lasers for both fusion and isotope separation applications.

*



V. P. Gribkovskii was born in Astashkovitchy, BSSR, on April 30, 1932. He graduated from the Byelorussian State University, Minsk, BSSR, in 1956.

Since 1959 he has worked at the Institute of Physics, Byelorussian Academy of Sciences, Minsk. He is Supervisor of the Laboratory of Optics of Semiconductors. He worked out the theory of nonlinear absorption and amplification of light in molecular, atomic, and semiconductor systems. He is the author of the monographs: "Theory of luminescence" (with B. I. Stepanov), "Theory of light absorption and emission in semiconductors," and a number of works in the field of quantum electronics.



Stephen E. Harris (S'59–M'64–F'72) was born in New York, NY, on November 29, 1936. He received the B.S. degree in electrical engineering from Rensselaer Polytechnic Institute, Troy, NY, in 1959, and the M.S. and Ph.D. degrees in electrical engineering from Stanford University, Stanford, CA, in 1961 and 1963.

Since 1963 he has been on the faculty of Stanford University where he is now a Professor of Electrical Engineering. His present research interests are concerned with selective collisions caused by intense tunable electromagnetic radiation, and holographic studies in the vacuum ultraviolet spectral regions.

Dr. Harris is a member of Sigma Xi, Tau Beta Pi, and Eta Kappa Nu. He is a Fellow of the Optical Society of America and the American Physical Society.

*

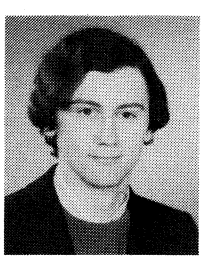


Ernest E. Huber, Jr., was born in Washington, DC, on January 1, 1929. He received the B.S. degree in physics in 1951, the M.S. degree in physics in 1954, and the Sc.D. degree in physical metallurgy in 1962, all from the Massachusetts Institute of Technology, Cambridge, MA.

Since 1957 he has been a Staff Member at the Lincoln Laboratory, Massachussetts Institute of Technology, Lexington, MA, where his earlier work was in research on magnetic materials, magnetic thin-film devices, thin-film active devices, surface physics, and electron-beam accessed memory devices. Since 1970 he has primarily been engaged in optical source development and in optical engineering.

Dr. Huber is a member of Sigma Xi and the Americal Physical Society.

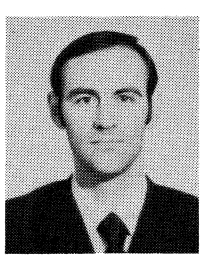
*



Lawrence R. Jones (S'72–M'73) was born in Baltimore, MD, on December 10, 1948. He received the B.E.E. and M.S.E.E. degrees from the Georgia Institute of Technology, Atlanta, GA, in 1971 and 1973, respectively.

From 1967 to 1970 he was employed in the cooperative work-study program at the Government Products Division, Texas Instruments, Inc., Dallas, TX. He joined the Lincoln Laboratory Optical Communications Group, Massachussetts Institute of Technology, Lexington, MA, in 1973, engaging in optical source development. Since 1974 he has been with the Special Communications Technology Group at the Lincoln Laboratory developing satellite communications equipment.

*



V. K. Kononenko was born in Petropavlovsk-Kamchatskii, USSR, on January 23, 1943. He received the diploma of radio-physicist from the Byelorussian State University, Minsk, BSSR, in 1965. In 1972 he received the candidate degree in physics and mathematical sciences from the Institute of Physics, Byelorussian SSR Academy of Sciences, Minsk.

He is currently a Senior Scientific Collaborator and a Chief of the Group at the Laboratory of Optics of Semiconductors at the Institute of Physics, BSSR Academy of Sciences, Minsk. His current work includes injection lasers and metal-semiconductor structures.

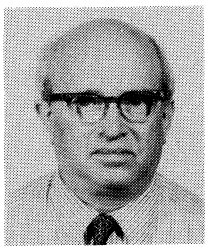


Henry Kressel (M'61–SM'73–F'74) received the B.A. degree from Yeshiva University, New York, NY, in 1955, the M.B.A. degree from Harvard University, Cambridge, MA, in 1959, and the Ph.D. degree from the University of Pennsylvania, Philadelphia, in 1965.

He has been with RCA since 1959. As a member of the RCA Solid State Division he contributed to the development of high-frequency planar silicon transistors and subsequently led a group responsible for the development of high-power varactor diodes subsequently used for the Lunar Excursion Module Communication System. He joined the RCA Laboratories, Princeton, NJ, in 1966 and became Head of the Semiconductor Optical Devices Research Group in 1969. He pioneered in the field of (AlGa)As–GaAs heterojunction devices, in particular, laser diodes, and has been actively engaged in the study of optoelectronic and power devices. He is presently Head, Semiconductor Device Research, with responsibility in the area of silicon power and III–V compound devices.

Dr. Kressel is the recipient of three RCA Research Achievement Awards as well as a 1974 David Sarnoff Medal for Outstanding Technical Achievement, RCA's highest award. He is a Fellow of the American Physical Society, and a member of the IEEE Quantum Electronics Council.

*



Robert M. Lerner (M'48–SM'57) received the B.S. and M.S. degrees from the Worcester Polytechnic Institute, Worcester, MA, in 1948 and 1950, respectively. He received the Sc.D. degree in electrical engineering from the Massachussetts Institute of Technology in 1959.

For the past twenty-five years he has held various posts at the Lincoln Laboratory, Massachussetts Institute of Technology, Lexington, MA, including recently, Assistant Leader of the Optical Communications Technology Group. Since 1950 he has published papers in a variety of specialities relating to communications technology: noise analysis, signal design, network theory, data transmission, electromagnetic propagation, and optical signaling. In the mid-1960's he served on the National Administrative Committee of the IEEE Professional Group on Information Theory.

*

Ross A. McFarlane (S'52–M'71) was born in Toronto, Ont., Canada, on June 10, 1931. He received the B.Sc. degree in physics from McMaster University, Hamilton, Ont., Canada, in 1953, and the M.S. and Ph.D. degrees in physics from McGill University, Montreal, P.Q., Canada, in 1955 and 1959, respectively.

From 1959 to 1961 he was a member of the Division of Space and Research, Research Laboratory of Electronics at the Massachusetts Institute of Technology, Cambridge, engaged in research on broad-band microwave masers. In 1961 he joined the Bell Laboratories in Murray Hill, NJ, where he worked on atomic and molecular-gas lasers and precision spectroscopy. He joined the Faculty of Cornell University, Ithaca, NY, in 1969, and is currently Professor of Electrical Engineering. His current research interests include molecular-energy transfer, chemical lasers, and photochemical kinetics.

*



Norris Nereson was born in Gaylord, MN, on November 4, 1918. He received the B.A. degree from Concordia College, Moorhead, MN, in 1939, and the Ph.D. degree in physics from Cornell University, Ithaca, NY, in 1943.

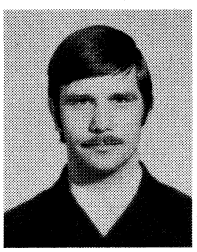
Except for two years (1947–1949) as an Assistant Professor of physics at the University of New Mexico, Albuquerque, and a year (1966) as an international Atomic Energy Agency expert in Brazil, he has worked at the Los Alamos Scientific Laboratory, University of California, Los Alamos, NM, in nuclear physics, weapon testing and diagnostics, and on the magnetic properties of rare-earth intermetallic compounds at low temperatures. During the last two years, he has been working with semiconductor laser diodes and their applications to molecular spectroscopy.

*

Robert J. Pirkle received the B.S. and M.S. degrees in chemistry from Auburn University, Auburn, AL, in 1963 and 1965, respectively, and the Ph.D. degree in physical chemistry, from the University of Western Ontario, London, Ont., Canada, in 1972. He studied the visible electronic spectrum of NO_2 while at this last university.

From 1965 to 1969 he worked in the Molecular Spectroscopy Branch of the Physical Sciences Laboratory DR&D at the U.S. Army Missile Command, Redstone Arsenal, AL. From 1972 through 1974 he worked as a Postdoctoral Associate in the Laboratory for Plasma Studies at Cornell University, Ithaca, NY, where he studied several chemical-laser systems and also the photodissociation iodine laser. He is currently studying the kinetics of electronically excited atomic species in the Department of Chemistry at Cornell University.

*



G. I. Ryabtsev was born in Orehovsk, BSSR, on October 18, 1948. He graduated from the Byelorussian State University, Minsk, BSSR, in 1971. He is currently engaged in postgraduate work at the Laboratory of Optics and Semiconductors, Institute of Physics, BSSR Academy of Sciences, Minsk.

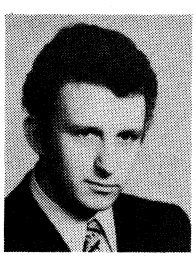
*



V. A. Samoilyukovich was born in Pruzhany, BSSR, on April 17, 1931. In 1954 he graduated from the Pushkin Pedagogical Institute, Brest, USSR. In 1964 he received the candidate degree in science from the Institute of Physics, Byelorussian Academy of Sciences, Minsk, BSSR, where he had been working in the field of semiconductor lasers since 1964.

He now works in the Department of Physics, Byelorussian Polytechnical Institute, Minsk.

*



Eddy A. Stappaerts (S'74) was born in Tielen, Belgium, on January 23, 1946. He received the Electrotechnisch Ingenieur degree from the University of Louvain, Louvain, Belgium, in 1970. From August 1970 to August 1971 he worked as a Research Assistant on optical modulators at the University of Louvain. Since September 1971 he has been at Stanford University, Stanford, CA, where he received his M.S. degree in 1972 and is currently working towards his Ph.D. degree. His thesis work has been directed at the study of nonlinear interactions at very high intensities, two-photon spectroscopy, and the use of two-photon-

resonant processes in alkali vapors for IR image up-conversion into the visible and UV.

Mr. Stappaerts is a member of Koninklijke Vlaamse Ingenieurs Vereniging and the Optical Society of America.

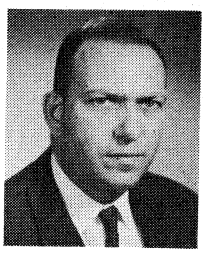
*



James P. Wittke (M'58-SM'72) was born in Westfield, NJ, in 1928. He received the M.E. degree from the Stevens Institute of Technology, Hoboken, NJ, in 1949, and the M.A. and Ph.D. degrees in physics from Princeton University, Princeton, NJ, in 1952 and 1955, respectively. His doctoral research concerned precision microwave determination of the hyperfine splitting in atomic hydrogen.

He was an Instructor in physics at Princeton for one year before joining the Technical Staff of RCA Laboratories, Princeton, NJ. At RCA he has engaged in paramagnetic resonance and microwave maser studies, in research on optically excited crystal lasers, and in investigations of the motions and properties of impurities in rutile. He has also worked on various classified projects. In 1967 he was awarded an RCA Fellowship for a year of study abroad, which he spent at the Clarendon Laboratory at Oxford, England. Since then he has studied the luminescence of heavily doped GaAs, helped develop new infrared-stimulated light-emitting phosphors, and worked on the generation of ultrashort laser pulses, using mode-locking techniques. He has studied optical-fiber communications systems, making measurements of the transmission properties of various fibers and on the frequency response of light-emitting diodes, and developing techniques for coupling the light from semiconductor light sources into fibers. Currently, he is investigating applications of CW injection lasers for optical information handling, and working on problems connected with microsonic filters. He is the author of numerous technical papers and the coauthor of a text on quantum mechanics.

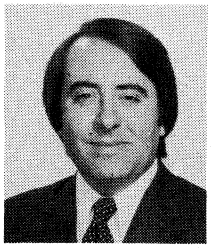
Dr. Wittke is a Fellow of the American Physical Society and a member of the Optical Society of America and Tau Beta Pi.



George J. Wolga (M'71) received the B.Eng. Phys. degree from Cornell University, Ithaca, NY, in 1953, and the Ph.D. degree in physics from the Massachusetts Institute of Technology, Cambridge, in 1957.

He was an Instructor and Assistant Professor of Physics at the Massachusetts Institute of Technology through 1961 when he returned to Cornell University where he is now Professor of Electrical Engineering and Applied Physics. He spent 1968-1969 at the Naval Research Laboratory, where he was Branch Head of the Laser Physics Branch. His current research interests are tunable infrared lasers, molecular-energy transfer and relaxation as studied with lasers, laser-induced chemistry, and the development and study of new laser systems.

*



James F. Young (M'72) was born in Pennsylvania in 1943. He received the B.S. and M.S. degrees in electrical engineering from the Massachusetts Institute of Technology, Cambridge, in 1965 and 1966, and the Ph.D. degree in electrical engineering from Stanford University, Stanford, CA, in 1970. For his Master's thesis he studied and developed a model for the cells which sense the blood pressure in mammals. He began his Ph.D. research in nonlinear optics in 1967 under the direction of Prof. S. E. Harris. His thesis research included the development of the first visible CW optical parametric oscillator, and subsequent improvements in cavity design and nonlinear materials.

Following his graduation he joined Prof. Harris as a Research Associate with primary responsibility for the experimental activities of the group. In 1975 he was appointed Adjunct Professor of Electrical Engineering at Stanford University. His research interests include parametric oscillators, the generation of coherent UV and VUV radiation, VUV holography, and molecular bound-free laser systems.

Dr. Young is a member of the American Physical Society, the Optical Society of America, the Federation of American Scientists, Tau Beta Pi, and Sigma Xi.

Call for Papers
IEEE Journal of Quantum Electronics

Special Issue
on
Integrated Optics

Publication Date
April 1977

Deadline for Submission
October 1, 1976

Authors are invited to submit original contributions to this special issue as either regular papers or correspondence in the various areas of integrated optics. Examples:

Semiconductor devices	Couplers
Nonlinear devices	Waveguiding
Modulators	Resonators
Lasers	Measuring techniques
Deflectors	Theory and Fundamentals

Whatever the subject, its relevance to integrated optics should be clear. Other information for authors will be found on the inside back cover of current issues of the IEEE JOURNAL OF QUANTUM ELECTRONICS.

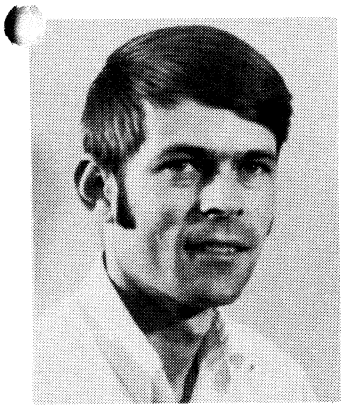
Papers should be submitted directly to the Guest Editor:

Prof. William S. C. Chang
Laboratory for Applied Electronic Sciences
Box 1115
Washington University
St. Louis, MO 63130
Telephone (314) 863-0100, X4162

Announcement

WE wish to extend a most cordial welcome to Prof. Robert Byer of Stanford University and to Dr. William Streifer of the Xerox Corporation who are joining our staff as two new Associate Editors. With their appointments, effective May 1, 1976, the number of Associate Editors is increased to nine as directed by the Quantum Electronics Council.

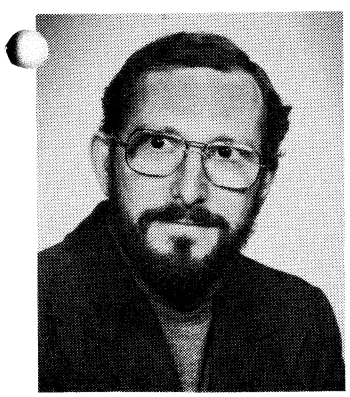
A. GARDNER FOX
Editor



Robert L. Byer (M'75) received the B.S. degree in physics from the University of California, Berkeley, in 1964, and the M.S. and Ph.D. degrees in applied physics from Stanford University, Stanford, CA, in 1967 and 1969, respectively.

After completing his undergraduate studies he joined Spectra Physics in the Research and Development Department for one year before beginning graduate studies in quantum electronics. After receiving the Ph.D. degree he joined the Department of Applied Physics at Stanford University as an Assistant Professor. Throughout his graduate work and since, his research has been primarily concerned with nonlinear optical materials, parametric devices, and applications of tunable coherent sources to spectroscopy. His present work is concerned with the absorption and very narrow Lamb dip spectra of I_2 in the visible region and also with tunable infrared generators for the 2-15 μm region.

Dr. Byer received the Adolf Lomb Medal of the Optical Society of America in 1972, and he is also the holder of a Sloan Fellowship (1974-1976).



William Streifer (S'56-M'58-SM'74) was born in Poland on September 13, 1936. He received the B.E.E. degree (magna cum laude) from the City College of New York, New York, NY, in 1957, the M.S. degree in electrical engineering from Columbia University, New York, NY, in 1959, and the Ph.D. degree from Brown University, Providence, RI, in 1962.

From 1962 to 1972 he was, successively, Assistant Professor, Associate Professor, and Professor of Electrical Engineering at the University of Rochester, Rochester, NY. During the academic year 1969-1970 he was a Visiting Associate Professor at Stanford University, Stanford, CA. In 1972 he joined the Xerox Palo Alto Research Center, Palo Alto, CA, as a Principal Scientist. He has studied stable and unstable laser resonator modes, wave and ray properties of graded index fibers, tunable dye lasers, and most recently, integrated optical devices, in particular, gratings as applied to GaAs distributed feedback lasers and couplers.

Dr. Streifer is a Fellow of the Optical Society of America.

Analysis of the Guided Modes in Slab-Coupled Waveguides Using a Variational Method

MASATO OHTAKA, MEMBER, IEEE, MASANORI MATSUHARA, AND NOBUAKI KUMAGAI, SENIOR MEMBER, IEEE

Abstract—The waveguiding properties of the slab-coupled waveguides (i.e., the optical stripline and the rib waveguide) are investigated by the vector variational method. The slab-coupled waveguides are low-loss optical waveguides which are easy to fabricate and design. In this paper, the propagation constants and the field intensity distributions of the slab-coupled waveguides are presented, and the effects on the waveguiding properties caused by changing their geometrical parameters are discussed. The results obtained by employing the variational method are compared with those obtained by using other methods.

I. Introduction

OPTICAL integrated circuits have received considerable attention as components of various optical devices used in optical communication and/or optical data processing systems. It is apparent that waveguides for optical integrated circuits are required to possess three-dimensional guiding properties. The dielectric rectangular waveguide is one of the typical examples which possess such properties, but it is difficult to fabricate the guide with sufficiently smooth-faced side walls. Kumagai *et al.* [1] proposed an inhomogeneous dielectric thin-film waveguide for guidance of millimeter waves [see Fig. 1(a)]. Although this guide was originally developed with the intention of supporting a thin-film guide without disturbing the guided field, it also meets the basic requirements for optical integrated circuits use.

Recently, several waveguide structures which are similar to the above-mentioned waveguide have been reported for use in optical integrated circuits. They are the optical stripline or the strip-loaded film waveguide [see Fig. 1(b)], the single material fiber [see Fig. 1(c)], and the rib waveguide or the ridge waveguide [see Fig. 1(d)]. They are called, generally, slab-coupled waveguides [2]. The optical stripline was proposed by Furuta *et al.* [3]. It is a planar waveguide with a strip of slightly lower index on a higher index film. The strip acts as loading. The rib waveguide was proposed by Goell [4] and the single material fiber by Kaiser *et al.* [5]. These guides are also planar slab waveguides with an increased thickness film portion. The portion with the increased thickness can be considered as a strip which loads a planar slab waveguide. The last two guides can be treated in the same manner because the guiding properties of the single material fiber are scarcely affected by its supporting shell. An advantage of these waveguides is a relaxation of the stringent requirements for smoothness of waveguide side walls because only a small portion of the electromagnetic-wave energy impinges on the side walls in these waveguides.

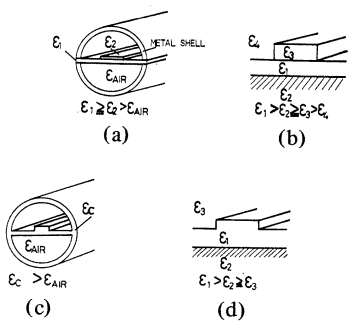


Fig. 1. Geometries of various dielectric waveguides. (a) Inhomogeneous thin-film guide. (b) Optical stripline. (c) Single material fiber. (d) Rib waveguide.

In the case of the slab-coupled waveguides it is quite difficult to solve the Maxwell's equations rigorously under the imposed boundary conditions. Furuta *et al.* [3] and Ramaswamy [6] obtained the propagation constant of the optical stripline using the effective index method. Marcuse analyzed the single material fiber employing an equivalent model of the fiber and a point-matching method [7]. Marcatili also gave an approximate method to solve the slab-coupled waveguides which employed an equivalent guide model of the waveguides [2].

The authors have studied several optical dielectric guides using the variational method previously [8]-[10]. The slab-coupled waveguides can be analyzed by the same method without introducing any approximation. In this paper, two types of slab-coupled waveguides (i.e., the rib waveguide and the optical stripline) are studied using the vector variational method, and their propagation constants and field intensity distributions are presented. The effects on the guiding properties caused by changing the geometrical dimensions of the waveguides are also discussed. Finally, the results obtained by the variational method are compared with the results given by Furuta *et al.* and Marcatili, employing the analytical approximation method.

II. Vector Variational Expression and Rayleigh-Ritz Procedure

In this section, we will derive the vector variational expression of the propagation constant and the Rayleigh-Ritz procedure for obtaining the solution of the variational problem.

A. Vector Variational Expression

The magnetic field $\boldsymbol{H}$ of the transmission line which is uniform along the z axis is expressed as

Manuscript received April 23, 1975; revised March 5, 1976.

M. Ohtaka was with the Department of Communication Engineering, Osaka University, Osaka, Japan. He is now with the Department of Electrical Engineering, Faculty of Engineering, Fukui University, Fukui, Japan.

M. Matsuhara and N. Kumagai are with the Department of Communication Engineering, Faculty of Engineering, Osaka University, Osaka, Japan.

$$H = [h_t(x, y) + h_z(x, y) \cdot i_z] \exp [j(\omega t - \beta z)] \quad (1)$$

where h_t and h_z are the transverse part and the longitudinal component of the magnetic field vector, respectively, i_z is a unit vector in the longitudinal direction z, and β is the propagation constant in the z direction.

The vector variational expression of the propagation constant β for a lossless, linear, and isotropic dielectric waveguide, which is uniform in the axial (z) direction of the guide, is given by

$$\beta^2 = N/D \quad (2)$$

where N and D are

$$N = \int \left[\epsilon \left(\omega^2 \mu h_t - \nabla \times \frac{1}{\epsilon} \nabla \times h_t \right)^2 - \omega^2 \frac{1}{\mu} (\nabla \cdot \mu h_t)^2 \right] dS + 2 \int \left[\left(\frac{1}{\mu} \nabla \cdot \mu h_t \right) \cdot \left\{ n \cdot \left(\omega^2 \mu h_t - \nabla \times \frac{1}{\epsilon} \nabla \times h_t \right) \right\} \right] dl$$

and

$$D = \int \left[\omega^2 \mu h_t - \frac{1}{\epsilon} (\nabla \times h_t)^2 \right] dS + 2 \int \left[\left(\frac{1}{\epsilon} \nabla \times h_t \right) \cdot (n \times h_t) \right] dl.$$

Here the surface integrals must be carried out over the whole transverse cross section, and the line integrals must be evaluated along the closed contour selected on the opposite sides of the boundary where the material constants change discontinuously [11]. n is a unit outward vector normal to the boundary. μ, ϵ, ω, and ∇ are the permeability, permittivity, angular frequency, and Hamiltonian operator, $\nabla = i_x (\partial/\partial x) + i_y (\partial/\partial y) + i_z (\partial/\partial z)$, respectively.

It should be noted in this connection that we can assume any approximate trial function h_t so long as $(1/\mu)\nabla \cdot \mu h_t$ and $i_z \cdot (n \times h_t)$ are continuous across the boundary between the different media. Equation (2) was derived by Matsuhara [11] modifying Kurokawa's variational expression [12].

B. Rayleigh-Ritz Procedure

Because the parabolic cylinder functions form a system of complete orthogonal functions in the infinite domain $(-\infty, \infty)$, it is possible and adequate to express the trial function h_t as

$$h_t = h_x i_x + h_y i_y \quad (3)$$

where

$$\begin{cases} h_x = \sum_{i,j} A_{xij} \Phi_{ij} \\ h_y = \sum_{i,j} A_{yij} \Phi_{ij} \end{cases}$$

$$\Phi_{ij} = (2\pi\xi\eta i! j!)^{-1/2} D_i(x/\xi) D_j(y/\eta)$$

and

$$D_n(z) = (-1)^n \exp\left(\frac{z^2}{4}\right) \frac{\partial^n}{\partial z^n} \exp\left(-\frac{z^2}{2}\right).$$

Here $D_n(z)$ is the parabolic cylinder function, and the characteristic parameters A_{xij}, A_{yij}, ξ, and η are constants determined by the Rayleigh-Ritz procedure, which requires the vector variational expression to be stationary over the characteristic parameters. Substituting (3) into (2), the propagation constant β can be expressed as

$$\beta^2 = \sum_{p,q} \sum_{i,j} \sum_{k,l} N_{pqijkl} A_{pij} A_{qkl} \Big/ \sum_{p,q} \sum_{i,j} \sum_{k,l} D_{pqijkl} A_{pij} A_{qkl} \quad (4)$$

where

$$N_{pqijkl} = \int \left[\epsilon \left(\omega^2 \mu \Phi_{ij} i_p - \nabla \times \frac{1}{\epsilon} \nabla \times \Phi_{ij} i_p \right) \cdot \left(\omega^2 \mu \Phi_{kl} i_q - \nabla \times \frac{1}{\epsilon} \nabla \times \Phi_{kl} i_q \right) - \omega^2 \frac{1}{\mu} (\nabla \cdot \mu \Phi_{ij} i_p)(\nabla \cdot \mu \Phi_{kl} i_q) \right] dS + \int \left[\left(\frac{1}{\mu} \nabla \cdot \mu \Phi_{ij} i_p \right) \cdot \left\{ n \cdot \left(\omega^2 \mu \Phi_{kl} i_q - \nabla \times \Phi_{kl} i_q \right) \right\} + \left(\frac{1}{\mu} \nabla \cdot \mu \Phi_{kl} i_q \right) \cdot \left\{ n \cdot \left(\omega^2 \mu \Phi_{ij} i_p - \nabla \times \frac{1}{\epsilon} \nabla \times \Phi_{ij} i_p \right) \right\} \right] dl$$

and

$$D_{pqijkl} = \int \left[\omega^2 \mu (\Phi_{ij} i_p) \cdot (\Phi_{kl} i_q) - \frac{1}{\epsilon} (\nabla \times \Phi_{ij} i_p) \cdot (\nabla \times \Phi_{kl} i_q) \right] dS + \int \left[\left(\frac{1}{\epsilon} \nabla \times \Phi_{ij} i_p \right) \cdot (n \times \Phi_{kl} i_q) + \left(\frac{1}{\epsilon} \nabla \times \Phi_{kl} i_q \right) \cdot (n \times \Phi_{ij} i_p) \right] dl$$

and the subscripts p and q, represent both x and y simultaneously. Applying the stationary condition for A_{qkl},

$$\partial \beta^2 / \partial A_{qkl} = 0 \quad (5)$$

to (4), we get

$$\sum_{p} \sum_{i,j} (N_{pqijkl} - \beta^2 D_{pqijkl}) A_{pij} = 0. \quad (6)$$

From (6), $\beta^2(\xi, \eta)$ and $A_{pij}(\xi, \eta)$ can be obtained. Furthermore, applying the stationary conditions for ξ and η,

$$\begin{cases} \partial \beta^2(\xi, \eta)/\partial \xi = 0 \\ \partial \beta^2(\xi, \eta)/\partial \eta = 0 \end{cases}$$

to $\beta^2(\xi, \eta)$, the parameters ξ and η are determined. Finally, we can obtain the solutions β^2 and h_t which satisfy the stationary conditions.

The above procedure can be performed easily using a digital computer. In the case of numerical examples shown in the next section, we represent the trial function h_t in (3) using the parabolic cylinder functions with 9 to 18 terms.

III. Numerical Examples and Discussions

In this section, we investigate the guiding properties of the rib waveguide and the optical stripline. We also compare our numerical results with those obtained by Furuta's and Marcatili's analytical approximation.

We introduce the symbol $h_p(m, n)$ to distinguish each guided mode. The $h_p(m, n)$ mode is the mode whose largest expansion coefficient in (3) is A_{pmn}. The guided modes of the slab-coupled waveguides are essentially hybrid modes, but the principal field components of the $h_x(m, n)$ mode are H_x and E_y, and those of the $h_y(m, n)$ mode are H_y and E_x. The difference in the propagation constants between the $h_x(m, n)$ mode and $h_y(m, n)$ mode is small, and the propagation constant of the $h_x(m, n)$ mode is always slightly smaller than that of the $h_y(m, n)$ mode in the case of the waveguides shown in this paper. Therefore, we show the numerical results only for the $h_y(m, n)$ modes except the $h_x(0, 0)$ mode. Also in the following numerical results, the transverse magnetic field h_t is normalized to have a maximum value of unity.

A. Rib Waveguide

The cross section and the permittivity distribution of the rib waveguide are shown in Fig. 2. Numerical results are presented in Figs. 3–5 for the case of $\epsilon_2 = 0.95\epsilon_1$ and $\epsilon_3 = 0.4\epsilon_1$. This permittivity distribution corresponds to the case where the thin film and the substrate are glass and the ambience is the air. The normalized frequency ω_n and the normalized propagation constant $\Delta\beta^2$ are given by

$$\omega_n = \left(\frac{\epsilon_1 - \epsilon_2}{\epsilon_1}\right)^{1/2} \frac{a}{\lambda}$$

and

$$\Delta\beta^2 = \frac{\beta^2 - k_2^2}{k_1^2 - k_2^2}$$

where $k_i^2 = \omega^2 \epsilon_i \mu_0$ and $\lambda = 2\pi/k_1$.

Fig. 3 shows the dispersion curves of the first four h_y-type guided modes and the $h_x(0, 0)$ mode in the rib waveguide with $b = 2a$ and $c = 0.5a$. The intensity distributions of h_t of the guided modes are shown in Fig. 4 for $\omega_n = 1$. In Fig. 3, the difference of the propagation constants between the $h_x(0, 0)$ mode and the $h_y(0, 0)$ mode is very small, and the $h_y(2, 0)$ mode is not shown because its cutoff frequency is higher than the maximum normalized frequency selected in the figure. In the case of the rib waveguide, the region of the increased thickness (i.e., the rib structure) confines the electromagnetic field in the x direction. Since the field of the $h_y(1, 1)$ mode spreads wider than that of the $h_y(1, 0)$ mode in the y direction and the $h_y(1, 1)$ mode suffers much more from the effect of the rib part than the $h_y(1, 0)$ mode does, the magnetic field of

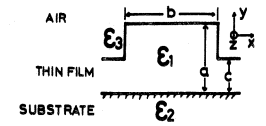


Fig. 2. The cross sectional geometry and the permittivity distribution of the rib waveguide.

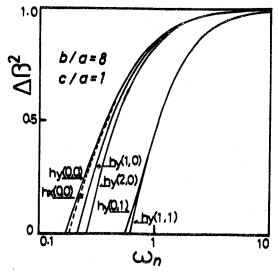


Fig. 3. Dispersion curves of the rib waveguide.

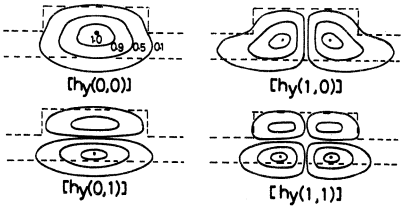


Fig. 4. Intensity distributions of the transverse magnetic field h_t in the rib waveguide.

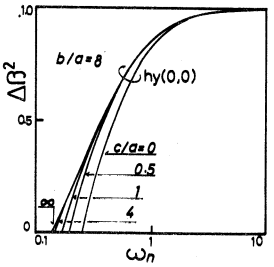


Fig. 5. Dispersion curves of the $h_y(0, 0)$ mode in the rib waveguide for some values of c/a.

the $h_y(1, 1)$ mode is confined better than that of the $h_y(1, 0)$ mode in the x direction.

Fig. 5 shows the dispersion curves of the $h_y(0, 0)$ mode in the rib waveguide for $b = 2a$ and some values of c/a. The cases of $c/a = 0$ and $c/a = 1$ correspond to the cases of the dielectric rectangular waveguide and the dielectric thin-film guide, respectively. In the case of $c/a \leqq 0.5$, the value of c/a affects the propagation constant slightly. If the value of c/a is close to unity, the propagation constant is affected strongly by the value of c/a. Hence the deviation of the guiding properties caused by the fabrication errors may be minimized by selecting the waveguide with $c/a \leqq 0.5$. In this case the guiding properties are controlled chiefly by the value of b/a.

B. Optical Stripline

Fig. 6 shows the cross-sectional geometry and the permittivity distribution of the optical stripline. Numerical data are presented in Figs. 7–9 for the case of $\epsilon_2 = \epsilon_3 = 0.95\epsilon_1$ and $\epsilon_4 = 0.4\epsilon_1$. The dispersion curves of the first five h_y-type

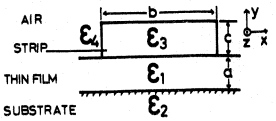


Fig. 6. The cross sectional geometry and the permittivity distribution of the optical stripline.

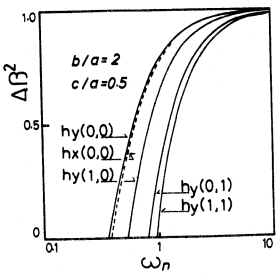


Fig. 7. Dispersion curves of the optical stripline.

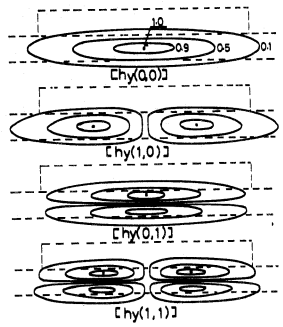


Fig. 8. Intensity distributions of the transverse magentic field h_t in the optical stripline.

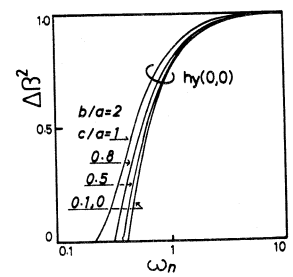


Fig. 9. Dispersion curves of the $h_y(0, 0)$ mode in the optical stripline for some values of c/a.

modes and the $h_x(0, 0)$ mode in the optical stripline are shown in Fig. 7 where $b = 8a$ and $c = a$. In Fig. 8 the intensity distributions of the transverse magnetic field $\boldsymbol{h}_t$ are presented for $\omega_n = 1$.

The difference of the propagation constants between the $h_x(0, 0)$ mode and the $h_y(0, 0)$ mode is small as in the case of the rib waveguide. But there is a large difference of the propagation constants between the $h_y(m, 0)$ mode and the $h_y(m, 1)$ mode. This is a typical property of the optical stripline [3], [6]. For the case shown here, the electromagnetic field is well confined in the x direction by the dielectric strip since the width b of the dielectric strip is large compared with the thin-film thickness a and the wavelength λ.

In Fig. 9, the propagation constants of the $h_y(0, 0)$ mode in the optical stripline are shown for $b = 8a$ and for several values of c/a. It is found that the effect on the propagation constants due to the change of c/a is not so pronounced in the case of $c/a \geqq 1$ except in the neighborhood of the cutoff frequency. Therefore, if we choose the strip thickness c larger than the thin-film thickness a, the guiding properties of the optical stripline are almost determined by the strip width b.

C. Comparison with the Results Obtained by the Analytical Approximations

Approximate methods which have been reported for the slab-coupled waveguides are the effective index method [3], [6], and the Marcatili method [2]. Here we compare our numerical results with those of Furuta and Marcatili. Table I shows the numerical results obtained by our method, the Furuta effective index method, and the Marcatili method for the case of the optical stripline shown in Fig. 7.

The propagation constants obtained by the effective index method are in good agreement with those obtained by the variational method. The difficulty encountered in the effective index method is that the propagation constants of the guided modes in the slab-coupled waveguides cannot be calculated in the neighborhood of the cutoff frequency $\Delta\beta^2 = 0$ since we cannot determine the effective index around this frequency region. Numerical results of the Marcatili method are not in good agreement with those of the variational method and the Furuta method, especially near the cutoff frequencies. Consequently, we believe that the effective index method is more appropriate than the Marcatili method for a simple calculation of the propagation constants of the guided modes in the slab-coupled waveguides.

Since the numerical results of two analytical approximation methods are inaccurate near the cutoff frequency of the guided mode, the variational method shown in this paper must be employed in this frequency region to obtain the accurate result. We have to use the variational method to obtain the field intensity distribution since the other two analytical approximation methods are powerless to calculate the field intensity distribution.

IV. Conclusions

The slab-coupled waveguides (i.e., the rib waveguide, the single material fiber, and the optical stripline) are developed to decrease scattering losses and undesired mode conversion caused by imperfections of etched side walls of the optical waveguide. The slab-coupled waveguides are based on the two-dimensional dielectric thin-film guide, but these waveguides get three-dimensional guiding properties by means of changing the thickness of the thin film or putting a loading dielectric strip on it.

The deviation of the guiding properties caused by the fabrication errors can be minimized when the variation in the thickness of thin film is large enough in the case of the rib waveguide, and the thickness of the dielectric strip is chosen to be larger than that of the thin film in the case of the optical stripline. In this case, the propagation constant and the field distribution are controlled primarily by the width b of the increased film thickness of the rib waveguide and the dielectric strip width b of the optical stripline.

Numerical results of the propagation constant of the slab-

TABLE I
NUMERICAL EXAMPLES FOR THE OPTICAL STRIPLINE OF FIG. 7

Mode	ω_n	$\Delta\beta^2$ Vari.	$\Delta\beta^2$ E.I.	$\Delta\beta^2$ Marcatili's
$h_y(0, 0)$	0.63	0.720	0.725	0.716
	0.25	0.256	0.278	0.167
$h_y(1, 0)$	0.63	0.695	0.706	0.695
	0.25	0.119	0.178	0.042
$h_y(0, 1)$	1.58	0.724	0.727	0.723
	0.79	0.261	0.270	0.187

Note: Vari.: The variational method shown in this paper.
E. I. : The Furuta effective index method.

coupled waveguides obtained by the Furuta analytical approximation method and the Marcatili method are compared with numerical results given by the variational method. The analytical approximation methods are less accurate but simpler than our variational method employed in this paper. We find that the Furuta method (the effective index method) gives good agreement with ours.

The variational method is a general and useful method to analyze the guided mode in the dielectric waveguide with arbitrary transverse shape and permittivity distribution. Also, it is possible to investigate the guiding properties of the dielectric waveguide including an anisotropic medium by this method.

ACKNOWLEDGMENT

The authors wish to thank Dr. T. Yamaguchi for his helpful comments and discussions. They also wish to thank M. Geshiro, K. Kitayama, and N. Yamaguchi for their kind assistance.

REFERENCES

[1] N. Kumagai, S. Kurasono, S. Sawa, and N. Yoshikawa, "Surface waveguide consisting of inhomogeneous dielectric thin-film," *Trans. Inst. Electron. Commun. Eng. Jap.*, vol. 51-B, pp. 82–87, Mar. 1968.
[2] E. A. J. Marcatili, "Slab-coupled waveguides," *Bell Syst. Tech. J.*, vol. 53, pp. 645–674, Apr. 1974.
[3] H. Furuta, H. Noda, and A. Ihaya, "Novel optical waveguides for integrated optics," *Appl. Opt.*, vol. 13, pp. 322–326, Feb. 1974.
[4] J. E. Goell, "Rib waveguide for integrated optical circuits," *Appl. Opt.*, vol. 12, pp. 2797–2798, Dec. 1973.
[5] P. Kaiser, E. A. J. Marcatili, and S. E. Miller, "A new optical fiber," *Bell Syst. Tech. J.*, vol. 52, pp. 265–269, Feb. 1973.
[6] V. Ramaswamy, "Strip-loaded film waveguide," *Bell Syst. Tech. J.*, vol. 53, pp. 697–704, Apr. 1974.
[7] D. Marcuse, "Theory of the single-material fiber," *Bell Syst. Tech. J.*, vol. 53, pp. 1619–1641, Oct. 1974.
[8] M. Ohtaka, M. Matsuhara, and N. Kumagai, "Analysis of lens-like media using the variational method," *Trans. Inst. Electron. Commun. Eng. Jap.*, vol. 55-B, pp. 332–333, June 1972.
[9] M. Matsuhara, "Analysis of TEM modes in dielectric waveguides, by a variational method," *J. Opt. Soc. Amer.*, vol. 63, pp. 1514–1517, Dec. 1973.
[10] M. Geshiro, M. Ohtaka, M. Matsuhara, and N. Kumagai, "Analysis of wave modes in slab waveguide with truncated parabolic index," *IEEE J. Quantum Electron.*, vol. QE-10, pp. 647–649, Sept. 1974.
[11] M. Matsuhara and N. Kumagai, "Theory of coupled open transmission lines and its application," *IEEE Trans. Microwave Theory Tech.*, vol. MTT-22, pp. 378–382, Apr. 1974.
[12] K. Kurokawa, "Electromagnetic waves in waveguides with wall impedance," *IRE Trans. Microwave Theory Tech.*, vol. MTT-10, pp. 314–320, Sept. 1962.

Theory and Operation of High-Power CW and Long-Pulse Dye Lasers

O. TESCHKE, MEMBER, IEEE, ANDREW DIENES, AND JOHN R. WHINNERY, FELLOW, IEEE

Abstract—A complete theoretical model for CW and long-pulse dye lasers is developed. The effects of excited singlet-state absorption of pump and laser light and triplet absorption of pump and laser light are included. Expressions are derived for gain, actual dye transmission, and output power. Experimental work is presented to verify the theory and to obtain values of excited-state absorption cross sections for rhodamine 6G by matching experimental to theoretical curves.

I. Introduction

THE BASIC MODEL for CW dye lasers is well known [1] and predicts most aspects of gain, output, and dye transmission well. One aspect left out of earlier models and investigated by two of the authors in a recent work [2] is that of excited singlet-state absorption, especially of the pump light. This absorption can have important effects upon the output power of high-intensity CW (or quasi-CW) dye lasers. In earlier models the absorption of the pump light was assumed to be equal to the small-signal ground-state absorption. However, saturation and excited-state absorption may cause significant departures from this simple picture.

The effect of crossovers from the upper laser level to the triplet state is well known [1], but rates have not been available for all of the dyes and solvents of concern. We have recently measured crossover rates and triplet lifetimes [3], [4] for rhodamine 6G in various solvents. An additional triplet effect which decreases power output in the same manner as the singlet-state absorption of pump power is the triplet absorption of the pump.

In this paper we include all of the above effects in order to provide a relatively complete model of the laser action. Limiting cases are compared with results previously available, and calculations show the ranges in which the additional effects are important. Several practical matters, including thermal effects and the effects due to laser and pump misalignment, are discussed. Experiments on the efficiency of the dye laser and on determination of the excited singlet-state absorption cross sections for several pumping wavelengths are described, extending our earlier work on this subject [2].

Manuscript received December 15, 1975; revised March 8, 1976. This work was sponsored in part by the National Science Foundation under Grant ENG73-08077-A02, and in part by the Joint Services Electronics Program under Contract F44620-71-C-0087.

O. Teschke was with the Department of Electrical Engineering, University of California, Berkeley, CA 94720. He is now with Bell Laboratories, Holmdel, NJ 07733.

A. Dienes is with the Department of Electrical Engineering, University of California, Davis, CA 95616.

J. R. Whinnery is with the Electronics Research Laboratory, University of California, Berkeley, CA 94720.

II. Theory

A. Model for the Theory

1) Dye Properties: The energy level diagram of the laser dye is shown in Fig. 1 with the customary designation for the singlet and triplet states. Since the photophysical properties of dyes have been discussed extensively in the literature, no detailed description will be given here. Instead, in what follows, the pertinent physical parameters will be defined and, where necessary, briefly described. The usual assumptions and approximations, used in existing dye laser theories, will be made. The most important of these is that the thermalization time within the vibrational-rotational continuum of a given electronic level band is very fast and the dye therefore can be considered to be homogeneously broadened. Consequently, the population of each level is considered *in toto*, and emission and absorption from and to a given band influence its entire population regardless of the wavelength of the radiation. A change in wavelength only changes the relative magnitude of the interaction, which is described by the wavelength-dependent cross sections. It is also assumed that the dye laser radiation is essentially monochromatic, the narrow bandwidth being achieved with the help of a frequency-selective tuning element. The bandwidth is determined by a combination of factors, including the bandwidth of the tuning element, spatial inhomogeneities of the dye, properties of the cavity, etc. This problem will not be examined in this paper.

The ground-state absorption cross sections at the pump, and laser wavelength will be designated σ_{ap}^0 and σ_{al}^0, respectively. These quantities are readily measurable, and are well known for most dyes. The absorption cross section from the lowest triplet level at the laser wavelength is σ_{al}^t. This quantity is more difficult to determine, but has been carefully measured for some important dyes. We assume here no measurable absorption by the triplet at the pump wavelength, as is usually the case. In Section II-C the theory will be modified to include this possibility as well.

Stimulated emission takes place at the laser wavelength with cross section σ_e, given by

$$\sigma_e = E(\lambda)\lambda^4/8\pi\tau_1 cn^2 \tag{1}$$

where n is the index of refraction, τ_1 is the fluorescence decay time (lifetime of the S_1 state) and $E(\lambda)$ is the fluorescence line shape normalized such that

$$\int_0^\infty E(\lambda)\,d\lambda = \phi \tag{2}$$

where ϕ is the quantum efficiency.

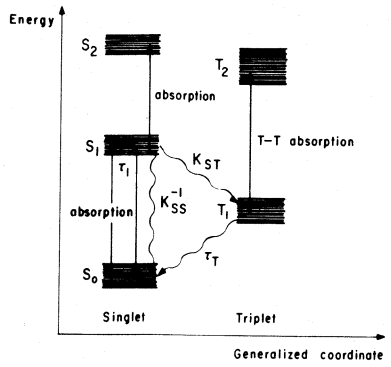


Fig. 1. Schematic dye energy diagram.

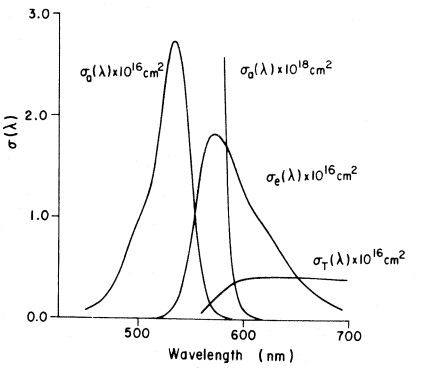


Fig. 2. Stimulated cross sections versus wavelength for rhodamine 6G. σ_a is singlet absorption, σ_t is triplet absorption, and σ_e is singlet emission cross section (from [1]).

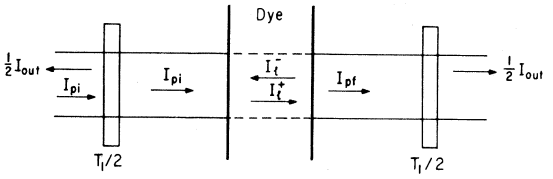


Fig. 3. Idealized dye laser geometry used for the theoretical calculations.

In Fig. 2 the above-described stimulated cross sections are shown as a function of wavelength for rhodamine 6G, the dye used in the experimental section of this work. In addition to the above, we assume that absorption of both laser and pump radiation can take place from the excited singlet (S_1) state which is the lasing level. These excited-state absorption cross sections are designated σ_{al}^1 and σ_{ap}^1, respectively. In general, very little is known about excited-state absorption in dyes. As we shall describe later the theoretical and experimental results will allow determination of these quantities. Additional parameters needed are the singlet-triplet crossover rate k_{st} and the triplet decay rate τ_t. The triplet crossover rate is included in the total fluorescent lifetime, i.e.,

$$\tau_1^{-1} = \tau_{1r}^{-1} + k_{ss} + k_{st} \tag{3}$$

where τ_{1r} is the radiative lifetime of S_1, and k_{ss} is the nonradiative singlet ($S_1 \rightarrow S_0$) relaxation rate. The fluorescence quantum efficiency ϕ is related to these quantities by

$$\phi = \frac{\tau_{1r}^{-1}}{\tau_{1r}^{-1} + k_{ss} + k_{st}} = \frac{\tau_1}{\tau_{1r}}. \tag{4}$$

2) Pumping and Laser Geometry–The Photon Rate Equations: The simplified dye laser geometry on which the theory is based is shown in Fig. 3. The pump and laser beams are collinear and have uniform intensities over identical cross sections. (Deviations from these idealized conditions are discussed in Section II-D.) The pump beam propagates in one direction only, while the laser beam consists of two oppositely running waves. The quantities I_p, I_l^+, and I_l^- are the photon intensities of the respective beams measured in photons/s · cm^2. The total laser intensity at any point is $I_l = I_l^+ + I_l^-$. The length of the dye cell is $\mathcal{L}$. We can now write the photon transport equations for the pump:

$$\frac{1}{c}\frac{dI_p}{dt} + \frac{dI_p}{dx} = -I_p\,[\sigma_{ap}^0 N_0 + \sigma_{ap}^1 N_1]. \tag{5}$$

The first term on the right-hand side (RHS) is the ground-state absorption of the pump, by which the excited state S_1 is populated. The second term indicates absorption of the pump by the excited state. The effect of this latter process is expected to be detrimental to the laser. Similarly, we have for one of the laser beams

$$\frac{1}{c}\frac{dI_l^+}{dt} + \frac{dI_l^+}{dx} = I_l^+\,[\sigma_e N_1 - \sigma_{al}^1 N_1 - \sigma_{al}^0 N_0 - \sigma_{al}^t N_t] \tag{6}$$

where we have stimulated emission into the laser beam, and absorption of the laser beam by the excited singlet, by the ground state, and by the triplet, in this order.

3) The Population Rate Equations: The rate equation for the population density N_1 of the first excited singlet level (S_1) is

$$\frac{dN_1}{dt} = \sigma_{ap}^0 N_0 I_p - N_1 \frac{1}{\tau_1} - N_1 \sigma_e I_l + N_0 \sigma_{al}^0 I_l - N_1 \sigma_{ap}^1 I_p - N_1 \sigma_{al}^1 I_l + N_2 \frac{1}{\tau_2}. \tag{7}$$

This equation can be simplified considerably if we consider that the decay time τ_2 from the S_2 to the S_1 state is, usually, very fast, of the order of 10^{-11} s [5]. The pump intensity required to lift a significant portion of the population of the S_1 state to the S_2 state is $\approx(\tau_2 \sigma_{ap}^1)^{-1}$. This is some 100 times larger than the ground state to first excited-state saturation intensity $(\tau_1 \sigma_{ap}^0)^{-1}$. Thus the sum of the last three terms in (7) is essentially zero for normal pump and laser intensities. In other words, there is no effective population change of the S_1 state due to $S_1 \rightarrow S_2$ transitions, because the molecules in the S_2 states immediately return to S_1. With this simplification (7) becomes

$$\frac{dN_1}{dt} = \sigma_{ap}^0 N_0 I_p - N_1 \frac{1}{\tau_1} - N_1 \sigma_e I_l + N_0 \sigma_{al}^0 I_l. \tag{8}$$

The lifetimes of the higher lying triplet states have not been measured. However, from qualitative data and theoretical considerations it is known [6] that they also decay nonradiatively with lifetimes of the order of 10^{-11} s or shorter. Thus, we can, by the same argument, neglect absorptive depopulation of the triplet state also. Then we have

$$\frac{dN_t}{dt} = k_{st} N_1 - \frac{1}{\tau_t} N_t \tag{9}$$

and finally,

$$N_0 + N_1 + N_t = N_{tot} = \text{constant}. \tag{10}$$

The photon transport (5), (6) and the population rate (8)-(10) constitute the basic equations of the dye laser medium. We shall solve these for steady-state conditions, obtaining results valid for CW or quasi-CW lasers. By the latter we mean pulses longer than the slowest decay rate (usually τ_t). As will be discussed later, the results can also be used for pulses shorter than the triplet lifetime (but much longer than the fluorescent lifetime) provided appropriate correction for the triplet effect is made. Before proceeding with the solution we must consider the properties of the cavity.

4) Cavity Properties: Following Rigrod [7] we consider the cavity to be symmetrical, with the output coupling transmission T_1 distributed equally between the two end mirrors. In addition we may have some residual loss l which includes mirror diffraction losses, scattering in the dye and from windows and mirrors, etc. Thus the total loss L in a one-way pass plus reflection from the end mirror is

$$L = \frac{I_{lf}^+}{I_{li}^+} = 1 - T_1/2 - l. \tag{11}$$

We define the total gain of the laser medium in a one-way pass in the absence of losses as

$$G = \frac{I_{lf}^+}{I_{li}^+}. \tag{12}$$

In both the above equations the subscripts i and f indicate initial and final values. Under steady-state conditions we have

$$G = 1/L = (1 - T_1/2 - l)^{-1}. \tag{13}$$

The total output power is

$$I_{out} = (I_l^+ + I_l^-)\, T_1/2 = I_l\, T_1/2. \tag{14}$$

B. Solution of the Laser Equations–Results

Under steady-state conditions all time derivatives vanish and the laser equations become

$$N_0 [\sigma_{ap}^0 I_p + \sigma_{al}^0 I_l] = N_1 \left[\frac{1}{\tau_1} + \sigma_e I_l\right] \tag{15}$$

$$\frac{dI_p}{dx} = -I_p [\sigma_{ap}^0 N_0 + \sigma_{ap}^1 N_1] \tag{16}$$

$$\frac{dI_l^+}{dx} = I_l^+ [N_1 \sigma_{ef} - \sigma_{al}^0 N_0] \tag{17}$$

where

$$\sigma_{ef} = \sigma_e - \sigma_{al}^1 - \sigma_{al}^t k_{st} \tau_t. \tag{18}$$

The solution of (9), $N_t = N_1 k_{st} \tau_t$, has been used in the foregoing equations. First, let us solve (17), rewriting it as

$$\frac{1}{I_l^+} dI_l^+ = (N_1 \sigma_{ef} - N_0 \sigma_{al}^0) \frac{dx}{dI_p} dI_p. \tag{19a}$$

Combining with (16) and integrating through the length of the dye

$$\ln \frac{I_{lf}^+}{I_{li}^+} = -\int_{I_{pi}}^{I_{pf}} \frac{dI_p}{I_p} \frac{\sigma_{ef} N_1/N_0 - \sigma_{al}^0}{\sigma_{ap}^0 + \sigma_{ap}^1 N_1/N_0}. \tag{19b}$$

Upon substitution of (15) into the above we obtain

$$\ln G = -\int_{I_{pi}}^{I_{pf}} \frac{dI_p}{I_p} \frac{\sigma_{ef}(\sigma_{ap}^0 I_p + \sigma_{al}^0 I_l) - \sigma_{al}^0 (1/\tau_1 + \sigma_e I_l)}{\sigma_{ap}^1 (\sigma_{ap}^0 I_p + \sigma_{al}^0 I_l) + \sigma_{ap}^0 (1/\tau_1 + \sigma_e I_l)}. \tag{20}$$

We note that the laser intensity occurring inside the integral sign is I_l, the *total* laser intensity. It has been shown, both theoretically and experimentally, that to a very good approximation I_l is constant with respect to x [8]. This approximation is good even in rather high gain lasers. With this approximation the integral is straightforward. After some simple manipulation we obtain

$$\ln G = -\frac{\sigma_{ef}}{\sigma_{ap}^1} \ln \left[\frac{1 + I_l/I_s + I_p/I_1}{1 + I_l/I_s + TI_p/I_1}\right] + y \frac{1 + I_l/I_2}{1 + I_l/I_s} \ln \left[T \frac{1 + I_l/I_s + I_p/I_1}{1 + I_l/I_s + TI_p/I_1}\right] \tag{21a}$$

where

$$y = \sigma_{al}^0/\sigma_{ap}^0 \tag{21b}$$

$$I_s^{-1} = (\sigma_e + y\sigma_{ap}^1)\, \tau_1 \tag{21c}$$

$$I_1^{-1} = \sigma_{ap}^1 \tau_1 \tag{21d}$$

$$I_2^{-1} = (\sigma_{al}^1 + \sigma_{al}^t k_{st} \tau_t)\, \tau_1 \tag{21e}$$

and $T = I_{pf}/I_{pi}$ is the transmission of the dye cell. For simplicity of notation, the symbol of the input pump intensity, I_{pi}, has been replaced by I_p.

Equation (21) gives the saturated gain with absorption of the pump light by the excited singlet state and absorption of the laser light by the ground, excited singlet, and triplet states all included. For a particular laser the saturated gain is, of course, constant and is given by (13). This will allow calculation of the laser intensity I_l and hence the output intensity. Let us now examine this expression more closely and look at some limiting cases to compare with already known results.

The first term in the RHS of (21a) is the gain without the effects of ground-state absorption of the laser light, but including triplet effects and excited-state absorption. In the limit as σ_{ap}^1 and σ_{al}^1 become zero (i.e., no excited-state absorption), this term can be reduced to the well-known expression for saturated gain. To see this, let us ignore the second term of (21a) and let $\sigma_{ap}^1 \to 0$. Then, $I_1^{-1} \to 0$ and the fraction to first order in I_p/I_1 is

$$\ln G \Longrightarrow \frac{\sigma_{ef}}{\sigma_{ap}^1} \ln \left[1 + \frac{(1 - T)\, I_p/I_1}{1 + I_l/I_s}\right] = \frac{\sigma_{ef}(1 - T)\, I_p \tau_1}{1 + I_l/I_s} = \ln G_0. \tag{22}$$

With $\sigma_{al}^1 = 0$ also, $\sigma_{ef} = \sigma_e [1 - k_{st} \tau_t \sigma_{al}^t/\sigma_e] = \sigma_e f_t$ and we have obtained the well-known expression for gain [1]. Expanding to the second order in I_p/I_1 we obtain the first-order correction to the gain due to σ_{ap}^1. We find in a straightforward manner

$$\ln G = \ln G_0 \left[1 - \frac{\sigma_{ap}^1}{\sigma_{ef}} \frac{1+T}{2} \ln G_0\right] \tag{23}$$

where G_0 is the gain with $\sigma_{ap}^1 = 0$ as given by (22). Note that the correction is proportional to $\sigma_{ap}^1/\sigma_{ef}$ and also to the uncorrected logarithmic gain. The effect of excited-state absorption of the laser wavelength is also apparent in (21a). The cross section σ_{al}^1 subtracts directly from the emission cross section σ_e [see (18)], as does the triplet absorption $k_{st}\tau_t \sigma_{al}^t$, to result in an effective emission cross section. The gain is proportional to this σ_{ef}. While the detrimental effect of the triplet absorption can be decreased by influencing $k_{st}\tau_t$, that of the excited-state absorption of the laser light cannot be remedied. It is easily seen that if $\sigma_{al}^1 > \sigma_e$, gain cannot be achieved regardless of how strong the pumping is. The second term in (21a) represents the ground-state losses (modified somewhat by the presence of excited-state absorption). If we consider no laser action ($I_l = 0$) and weak pumping only, the pump transmission T is

$$T \approx T_0 = e^{-\sigma_{ap}^0 N_{\text{tot}} \mathcal{L}}. \tag{24}$$

With these assumptions, and in the limit $\sigma_{ap}^1 \to 0$, the second term becomes

$$\text{S.T.} = \frac{\sigma_{al}^0}{\sigma_{ap}^0}(-\sigma_{ap}^0 N_{\text{tot}} \mathcal{L}) = -\sigma_{al}^0 N_{\text{tot}} \tag{25}$$

which is just the logarithmic ground-state absorption of the laser light for this limiting case. It is important to note that the pump transmission T is, in general, not equal to the small-signal transmission (T_0). This is because the ground-state population $N_0 \neq N_{\text{tot}}$ and is not constant with distance x. Rather, N_0 is an unknown function of x and its values depend on the pump and laser intensities. Let us therefore calculate the value of T. Starting again with the phenomenological rate (15)-(17), we again assume steady-state conditions. We also have

$$N_{\text{tot}} = N_0 + N_1(1 + k_{st}\tau_t). \tag{26}$$

Combining (15) and (26) we can write

$$N_1 = \frac{N_{\text{tot}}(\sigma_{ap} I_p + \sigma_{al}^0 I_l)}{(1 + k_{st}\tau_t)(\sigma_{ap}^0 I_p + \sigma_{al}^0 I_l) + \dfrac{1}{\tau_1} + \sigma_e I_l} \tag{27}$$

$$N_0 = \frac{N_{\text{tot}}(1/\tau_1 + \sigma_e I_l)}{(1 + k_{st}\tau_t)(\sigma_{ap}^0 I_p + \sigma_{al}^0 I_l) + \dfrac{1}{\tau_1} + \sigma_e I_l}. \tag{28}$$

Substituting these into the photon transport (16) we obtain

$$\frac{dI_p}{dx} = -I_p \left\{ N_{\text{tot}} \sigma_{ap}^0 \frac{1/\tau_1 + \sigma_e I_l}{(1 + k_{st}\tau_t)(\sigma_{ap}^0 I_p + \sigma_{al}^0 I_l) + \dfrac{1}{\tau_1} + \sigma_e I_l} + N_{\text{tot}} \sigma_{ap}^1 \frac{\sigma_{ap}^0 I_p + \sigma_{al}^0 I_l}{(1 + k_{st}\tau_t)(\sigma_{ap}^0 I_p + \sigma_{al}^0 I_l) + \dfrac{1}{\tau_1} + \sigma_e I_l} \right\}. \tag{29}$$

After some rearrangement this equation can be integrated to give

$$T_0 = T^{\gamma} \left[\frac{1 + TI_p/I_3}{1 + I_p/I_3}\right]^{-\gamma+\beta} \tag{30}$$

where

$$I_3 = I_1(1 + I_l/I_s) \tag{31}$$

$$\gamma = \frac{1 + I_l[\sigma_e \tau_1 + (1 + k_{st}\tau_t)\sigma_{al}^0 \tau_1]}{1 + I_l(\sigma_e + \sigma_{al}^0)\tau_1} \tag{32}$$

and

$$\beta = (1 + k_{st}\tau_t)\sigma_{ap}^0/\sigma_{ap}^1. \tag{33}$$

Equation (30) is an extension of the results of Hercher *et al.* [9]. In our expression the effects of the triplet crossover and of the laser action are included. If the laser is below threshold we set $I_l = 0$, then $\gamma = 1, I_3 = I_1$ and (33) becomes

$$\frac{T}{T_0} = \left[\frac{1 + I_p/I_1}{1 + TI_p/I_1}\right]^{(1+k_{st}\tau_t)\sigma_{ap}^0/\sigma_{ap}^1 - 1} \tag{34}$$

If we also set $k_{st}\tau_t = 0$ this expression becomes identical to the result of [9].

It is also instructive to set $k_{st}\tau_t = 0$, but have lasing fairly strong. Then if $TI_p/I_3 \ll 1$ we may expand T/T_0 to obtain

$$T = T_0[1 + I_p/I_3]^{\sigma_{ap}^0/\sigma_{ap}^1 - 1}. \tag{35}$$

In the limit as σ_{ap}^1 approaches zero this becomes

$$T \approx T_0 \left[1 + \frac{I_p}{I_a} \frac{1}{1 + I_l/I_s}\right] \tag{36}$$

where $I_a = 1/\sigma_{ap}^0 \tau_1$, the saturation intensity for absorption. Equation (36) clearly shows that while strong pumping increases the transmission (bleaching), laser action decreases it by returning the dye molecules to the ground state.

Equation (34) also shows that excited-state absorption reduces the transmission of the pump. However, this increased pump absorption does not result in gain, but only in a rapid circulation of the dye molecules between the S_1 and S_2 states. In Figs. 4 and 5 we plot G and T as functions of the excited-state cross section σ_{ap}^1 for $I_l = 0$. Both transmission and gain are seen to decrease with increasing σ_{ap}^1. It may also be noted that for low values of I_p, curves II and III, the initial slope increases with increasing G_0, in agreement with the approximate (23).

Equation (30) for the dye transmission T under lasing conditions is not easy to use, since it involves the cavity laser intensity I_l. The value of I_l can be calculated from the gain (21), but it is evident that I_l is in turn a function of T. However, an alternate expression for T can be derived, which does not explicitly involve I_l. From (16) and (17) we have by integration that

$$\ln T = -\mathcal{L}\bar{N}_0 \sigma_{ap}^0 - \mathcal{L}\bar{N}_1 \sigma_{ap}^1 \tag{37}$$

$$\ln G = \mathcal{L}\bar{N}_1 \sigma_{ef} - \mathcal{L}\bar{N}_0 \sigma_{al}^0 \tag{38}$$

where

$$\bar{N}_i = \frac{1}{\mathcal{L}} \int_0^{\mathcal{L}} N_i \, dx \tag{39}$$

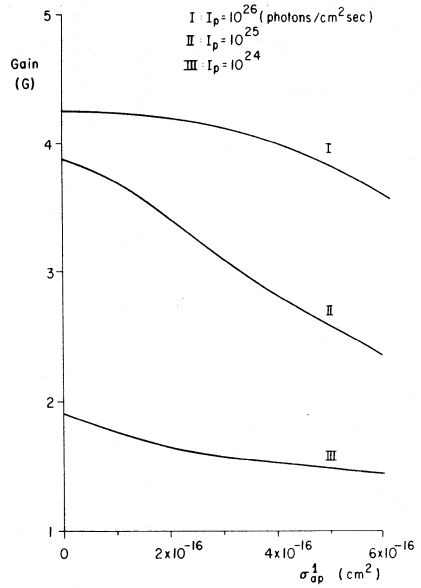


Fig. 4. Variation of the dye gain with excited-state absorption of the pump: G versus σ^1_{ap}, for various values of pumping intensity, calculated from (21a). The following other parameters apply: $\sigma_e = 2.1 \times 10^{-16}$, $\sigma^1_{al} = 0$, $\sigma^0_{ap} = 1.53 \times 10^{-16}$, $\sigma^0_{al} = 0$, $\sigma^t_{al} = 0.45 \times 10^{-16}$ (all in cm²), $\tau_1 = 5 \times 10^{-9}$ s, $k_{st}\tau_t = 0.8$. Length of dye cell $\mathcal{L} = 0.03$ cm. The values of the dye transmission are calculated from (34) and are plotted in Fig. 5.

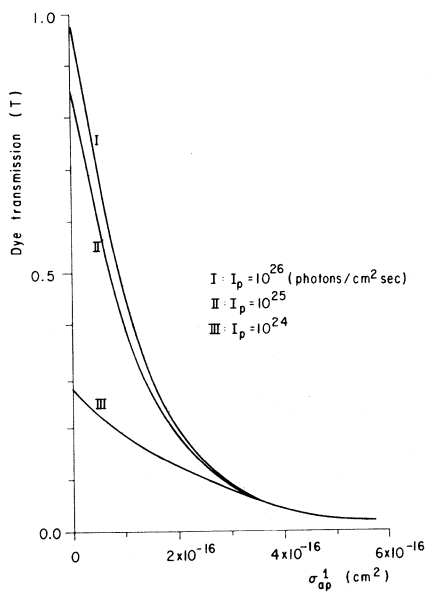


Fig. 5. Variation of the dye transmission with excited-state absorption of the pump: T versus σ^1_{ap} (with no lasing) as calculated from (34). The same parameters apply as in Fig. 4.

is the average population of the ith state over length of the active dye. After some straightforward manipulation of (37) and (38) we obtain

$$\ln T = -\sigma^0_{ap}\mathcal{L}N_{\text{tot}} + \frac{\sigma^0_{ap}(1 + k_{st}\tau_t) - \sigma^1_{ap}\ln G + \mathcal{L}\sigma^0_{al}N_{\text{tot}}}{\sigma_{ef} + \sigma^0_{al}(1 + k_{st}\tau_t)} \tag{40}$$

where the saturated gain G is a constant when the laser is above threshold and is given by (13). For the case when $\sigma^0_{al} = 0$ (no ground-state reabsorption of the laser light), (40) becomes

$$\ln T = \mathcal{L}N_{\text{tot}}\sigma^0_{ap} + \frac{\sigma^1_{ap}}{\sigma_{ef}}(\beta - 1)\ln\frac{1}{1 - T_1/2 - l}. \tag{41}$$

The first term of this expression is the small-signal transmission $\ln T_0$. The other term is the correction due to the pumping of the molecules to the excited singlet state. The number of molecules in the excited state is determined by the losses of the cavity. For a particular laser the dye transmission T is constant when the laser is above threshold.

Having obtained expressions for G and T we are now in the position to calculate the in-cavity laser intensity I_l and hence the output intensity I_{out}. To do this we solve for I_l from (21) and use (13) and (14). In general, this cannot be done in an explicit form, and numerical methods may have to be used. However, an explicit expression may be obtained for the case when there is no ground-state reabsorption of the laser light ($\sigma^0_{al} = 0$). Since for many laser dyes this is the situation over a significant portion of the laser bandwidth (see Fig. 2 for Rd 6G), such a result is useful. Setting $y = 0$ in (21b) we have

$$(1 + I_l/I_s + TI_p/I_1)\,G^{\sigma^1_{ap}/\sigma_{ef}} = 1 + I_l/I_s + I_p/I_1. \tag{42}$$

Solving for I_l, and combining with (13) and (14) it follows that

$$I_l = I_p\frac{\sigma^1_{ap}}{\sigma_e}\frac{1 - TQ}{Q - 1} - \frac{1}{\sigma_e\tau_1} \tag{43}$$

or

$$I_{\text{out}} = \frac{T_1}{2}\left[\frac{\sigma^1_{ap}}{\sigma_e}\frac{1 - TQ}{Q - 1}I_p - \frac{1}{\sigma_e\tau_1}\right] \tag{44}$$

where

$$Q = \left[1 - \frac{T_1}{2} - l\right]^{-\sigma^1_{ap}/\sigma_{ef}} = G^{\sigma^1_{ap}/\sigma_{ef}}. \tag{45}$$

In a slightly different form the expressions have been reported by Teschke and Dienes in a recent communication [2]. The first term gives the slope efficiency, while the second term indicates a threshold.

To gain some physical insight into the influence of the excited-state absorption on the output power, (44) can be expanded for $\sigma^1_{ap}/\sigma_{ef} \ll 1$ and $T_1/2 + l \ll 1$. Then, keeping terms to second order in $\sigma^1_{ap}/\sigma_{ef}$, we obtain

$$I_{\text{out}} = I_p\frac{T_1/2}{T_1/2 + l}\frac{\sigma_{ef}}{\sigma_e}\left\{(1 - T) - (l + T_1/2)\frac{\sigma^1_{ap}}{\sigma_{ef}}\frac{1 + T}{2}\right\} - \frac{T_1}{2}\frac{1}{\sigma_e\tau_1}. \tag{46}$$

If $\sigma^1_{al} = 0$, then $\sigma_{ef} = \sigma_e f_t$ and

$$I_{\text{out}} = I_p\,T_1/2\left[\frac{f_t}{T_1/2 + l}(1 - T) - \frac{\sigma^1_{ap}}{\sigma_e}\frac{1 + T}{2}\right] - \frac{T_1}{2}\frac{1}{\sigma_e\tau_1}. \tag{47}$$

The first term of this expression is equivalent to the well-known expression for output power [1] and is proportional to the amount of pump power absorbed in the dye. The second term is the correction due to excited-state absorption of the

pump. The correction is proportional to σ_{ap}^1/σ_e and also to $1 + T$. Equations (46) and (47) can also be obtained from the approximate gain equation (23). Finally, any of the equations for output intensity may be written as

$$I_{out} = \eta(I_p - I_{th}) \tag{48a}$$

or, since laser and pump beam areas are equal, in terms of power

$$P_{out} = \eta(P_p - P_{th}) \tag{48b}$$

where η is the slope efficiency and I_{th} and P_{th} are threshold values given by

$$I_{th} = \frac{1}{\eta}\frac{T_1}{2}\frac{1}{\sigma_e \tau_1} \tag{49a}$$

and

$$P_{th} = I_{th} \times \text{(effective beam area)}. \tag{49b}$$

Equations (41) and (44) are used to calculate the dye transmission and the output intensity when the laser is above threshold. Alternately, (30) and (41) may be used, but these are coupled and an iterative approach must be employed. The two methods give identical results, but the first is more convenient. Below threshold (34) is used to calculate the transmission.

In Fig. 6 the in-cavity laser intensity, I_l, is plotted as a function of the excited-state absorption cross section σ_{ap}^1 for various values of the output-mirror transmission T_1. I_l, and hence I_{out}, are seen to decrease essentially linearly with increasing σ_{ap}^1. For high pump power and high output coupling the population of the S_1 state is high and the excited-state absorption has a significant effect. For low-loss cavities the population of the S_1 state is small and only a minor effect is detectable. The corresponding curves for dye cell transmission are shown in Fig. 7. The transmission changes from one curve to the next because the laser intensity inside the cavity is a function of the losses. For exactly the same reason as described above, the influence of the excited-state absorption on the dye transmission is small in low-loss cavities and large in high-loss cavities. In Fig. 8(a) I_{out} and T are shown together as functions of the pump power. The output intensity increases linearly with pump power. The dye transmission starts at $T = T_0$, and for $I_p > I_{th}$ becomes constant with pump power at a value different from T_0. The difference between T and T_0 is a function of the dye parameters and of the cavity losses. In Fig. 8(b), transmission curves only are shown for various values of the mirror transmission T_1. The value of $T = T_{th}$ increases with increasing mirror losses. The dashed line is the dye transmission with laser action prevented by making $T_1/2 = 1$. It is well known that in any laser there is an optimum mirror transmission for a given pumping level. From (44) and (47) for the output intensity it may be expected that the presence of excited-state absorption changes the value of this optimum. In Fig. 9 we show curves of output intensity versus mirror transmission for $\sigma_{ap}^1 = 0$ and for a finite value of σ_{ap}^1. The other laser parameters are typical for Rd 6G and the pumping level is equivalent to moderately strong CW pumping. There is a shift

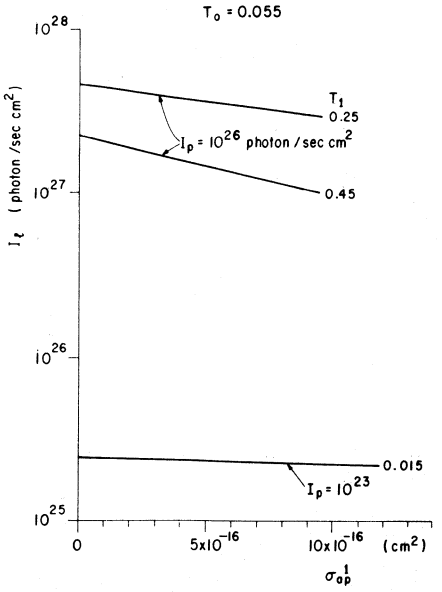


Fig. 6. Dependence of the cavity laser intensity on excited-state pump absorption: I_l versus σ_{ap}^1, for various values of mirror transmission T_1 and pumping intensity I_p calculated from (43). Other parameters are as in Fig. 4 except $\sigma_{ap}^0 = 3.2 \times 10^{-16}$, $T_0 = 0.055$, $l = 0.015$. The values of the dye transmission T are calculated from (41) and are plotted in Fig. 7.

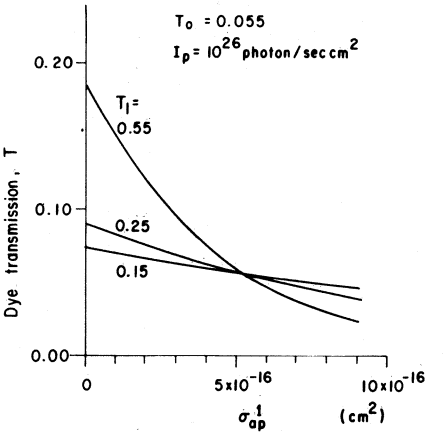
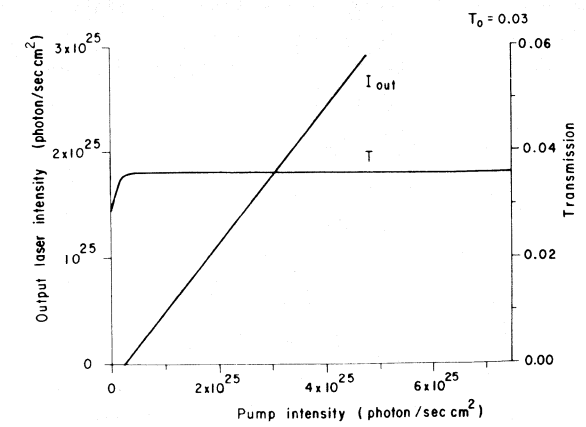
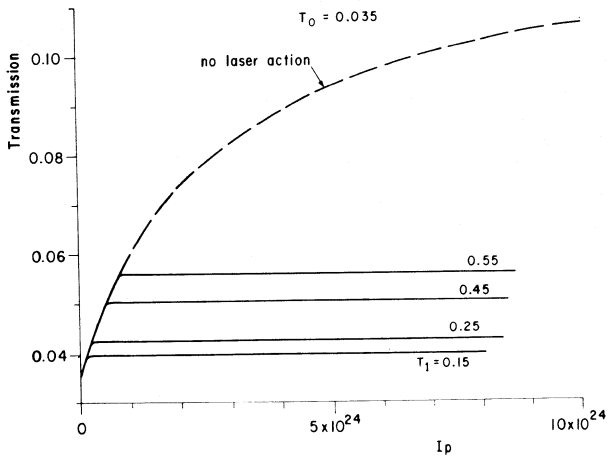


Fig. 7. Variation of the dye transmission with excited-state pump absorption under lasing conditions. T versus σ_{ap}^1, calculated from (41). The same parameters apply as in Fig. 6.

in the peak when $\sigma_{ap}^1 \neq 0$, as well as a reduction of the output power. Thus, excited-state absorption can substantially alter the design of a CW dye laser. It is evident that by matching experimental curves of output versus input intensity to the theoretical (44) the values of σ_{ap}^1/σ_e can be determined. Such results have been reported by us in [2] and will be further discussed in the experimental section of this work. Another way of finding the excited-state absorption cross sections is by transmission measurements with no laser action. Fig. 10 shows plots of T versus I_p as determined from (34). It can be observed that for $\beta > 1$ the transmission increases with pump power, for $\beta = 1$ it is constant and for $\beta < 1$ it decreases with increasing pump power. If the value of $k_{st}\tau_t$ is known, the values of $\sigma_{ap}^0/\sigma_{ap}^1$ can be found by matching theoretical and



(a)



(b)

Fig. 8. (a) Output intensity I_{out} and dye transmission T as a function of pump intensity I_p. $T_1 = 0.06$. $T_0 = 0.03$, $\sigma_{ap}^1 = 1.75 \times 10^{-16}$ cm^2. Other parameters are the same as in Fig. 6. (b) Dye transmission for various values of mirror transmission T_1. Dashed line is transmission with laser action prevented.

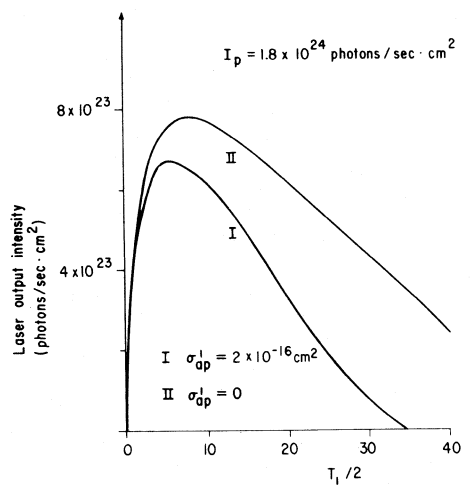


Fig. 9. Laser output intensity (I_{out}) versus output mirror transmission T_1 with and without excited-state absorption. The dye parameters are the same as in Fig. 4, except $\sigma_e = 1.3 \times 10^{-16}$ cm^2, $l = 0.02$.

expanded curves. The gains corresponding to Fig. 10 are shown in Fig. 11. The gain, ln G, does not increase linearly with pump power except at low pump intensities, because the useful $S_0 \rightarrow S_1$ absorption saturates with increasing pump power. We note that the gain plotted here is small-signal gain, since $I_l = 0$.

C. Inclusion of Pump Absorption by the Triplet

Although in all the above theory it was assumed that no absorption of the pump by the triplet state is present, the theory can be easily modified to include such an effect. To do this we must include in the photon rate equation (16) an additional term

$$\frac{dI_l}{dx} = -I_p \left[\sigma_{ap}^0 N_0 + \sigma_{ap}^1 N_1 + \sigma_{ap}^t N_t\right]. \tag{50}$$

But since $N_t = k_{st}\tau_t N_1$, (50) is in fact identical to (16), with σ_{ap}^1 replaced by

$$\sigma_{ap}^1 \Longrightarrow \sigma_{ap}^1 \left[1 + k_{st}\tau_t \sigma_{ap}^t/\sigma_{ap}^1\right]. \tag{51}$$

Thus all derivations proceed the same way and every result given in Section II-B is valid, provided that the above replacement is everywhere made. It is evident from the above that triplet absorption of the pump has the same effect on the dye laser as excited-state pump absorptions.

D. Additional Consideration for Real Dye Lasers

The above theory was based on a somewhat idealized model that neglected a number of factors that are or may be present in our actual dye laser. Some of these follow.

1) The pump and laser beams are not of equal areas of uniform intensity, but are Gaussian beams which may have different beam parameters.

2) The pump and laser beams may not be exactly coaxial.

3) There may be residual thermal effects.

4) The laser and pump lights are linearly polarized and the molecular dipoles of the dye are randomly oriented.

In the following we shall examine some of these factors and attempt at least a partial theoretical description of some of them. The most important of these is the Gaussian beam character of the pump and laser light. With both assumed to be in the fundamental Gaussian mode, the radial intensity distributions are

$$I_l(r,z) = \frac{P_l}{0.5\pi w_l^2(z)} e^{[-2r^2/w_l^2(z)]} \tag{52a}$$

$$I_p(r,z) = \frac{P_p}{0.5\pi w_p^2(z)} e^{[-2r^2/w_p^2(z)]}. \tag{52b}$$

Thus an accurate description of the dye laser would include transverse as well as longitudinal dependence of the variables. To solve the complete nonlinear problem including this additional complication would be a formidable task, without hope of finding analytical form solutions. A much simpler problem, however, has been considered by Pike [10]. For the case when the active region is confined to within a distance

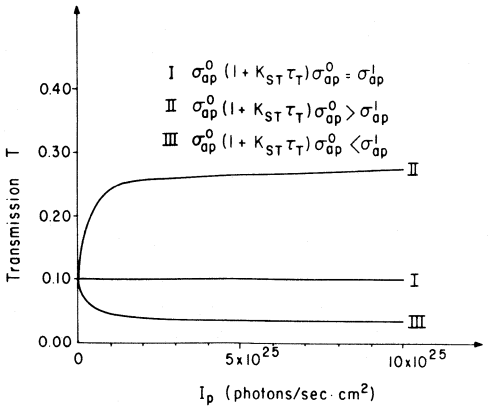


Fig. 10. Dye transmission T versus pump intensity I_p (with laser action prevented), for various values of excited-state absorption cross section σ_{ap}^1. The values of σ_{ap}^1 are I: 2.7×10^{-16} cm², II: 4×10^{-16} cm², III: 1.5×10^{-16} cm². The following other parameters apply: $\sigma_{ap}^0 = 1.5 \times 10^{-16}$ cm², $k_{st}\tau_t = 0.8$, $\tau_1 = 0.5 \times 10^{-9}$ s, $\mathcal{L} = 0.03$ cm.

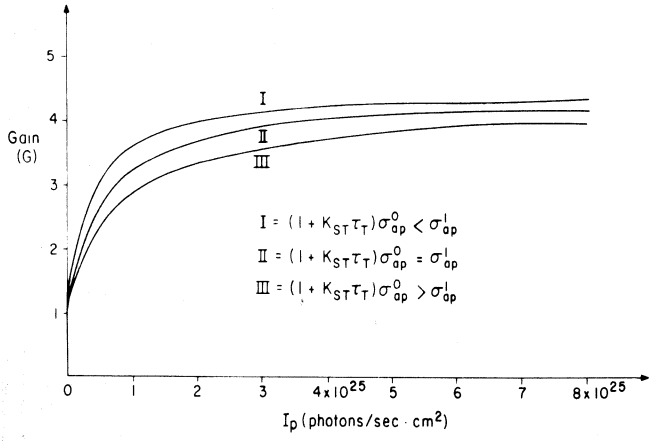


Fig. 11. Dye gain G versus pump intensity I_p (with laser action prevented) corresponding to the cases shown in Fig. 10. Additional parameters are: $\sigma_e = 2.1 \times 10^{-16}$ cm², $\sigma_{al}^0 = \sigma_{al}^1 = 0$.

less than the confocal parameter of the beam waists, i.e., the Gaussian beams can be considered to be of constant diameter, for no excited-state absorption, and considering small-signal absorption of the pump, Pike has shown that (using our notation)

$$P_{\text{out}} = \frac{\mu}{\sqrt{1+\mu^2}}\left[\frac{T_1/2}{l+T_1/2} f_t(1-T)P_p - \frac{T_1}{2}\frac{1+\mu}{2}\frac{\pi w_p^2}{\sigma_e \tau_1}\right] \tag{53}$$

where the parameter μ is defined as the ratio of the areas of the dye laser and pump beams

$$\mu = \frac{\pi w_l^2}{\pi w_p^2}. \tag{54}$$

Since the beam areas are no longer the same, power (in photons/s), rather than intensity, is used in this expression. We note that the slope efficiency in (53) is the same as the first term of (47) (without the excited-state absorption correction) except for the factor $\mu/(1+\mu^2)^{1/2}$. Similarly, the thresholds are in agreement, but with an additional $(1+\mu)/2$ factor in Pike's results. On the basis of this comparison we may make a phenomenological correction for the effect of Gaussian beams in our expression for the efficiency of the CW dye laser. We assume that the power slope efficiency *including excited-state absorption* is given by

$$\eta = \frac{\mu}{\sqrt{1+\mu^2}} \frac{T_1}{2} \frac{\sigma_{ap}^1}{\sigma_e} \frac{1-TQ}{Q-1}. \tag{55}$$

For $\sigma_{ap}^1 = 0$ this reduces to Pike's result, and for $\mu \to \infty$ it becomes identical with our expression. There is, of course, no proof that the Gaussian beam correction factor would apply the same way with excited-state absorption as without, the overall problem being very complex. Nonetheless, given its correct limiting forms (55) appears to be reasonable. Note that the correction factor is always smaller than unity. No attempt is made to account for the Gaussian beam shapes in the transmission expressions. Similarly we write for the corrected threshold pump power

$$P_{\text{th}} = \frac{1+\mu}{2}\frac{1}{\eta}\frac{T_1}{2}\frac{\pi w_p^2}{\sigma_e \tau_1}. \tag{56}$$

To account quantitatively for the possibility of the beams being at an angle to each other is exceedingly difficult. The variable of differentiation is not the same then in (16) and (17), and additionally, the two beams only partially overlap. Referring to Fig. 12 it is evident that detrimental effects are minimized if the dye concentration is high and the pump light is therefore absorbed in a short distance. However, the concentration cannot be increased at will for most dyes. The factors limiting the dye concentration are: solubility, dimer formation, and concentration quenching of flouresence. It is generally possible to make the angle between the beams small and the overlap nearly the same as with perfect coaxial pumping. Under such conditions only a very small decrease in the output is caused by off-axis pumping. We will assume that this effect can also be accounted for by a multiplicative factor in the slope efficiency.

The thermal problem in dye lasers is well known as is its usual remedy: rapid flow of the dye. We have theoretically examined thermal defocusing in an axially pumped dye laser solution and have performed experiments to verify the theory. This work will be reported in a separate paper [11]. A minimum rate of flow is necessary to avoid thermal defocusing for a given pump power level in a given dye solution. For all practical dye lasers and for all the experiments reported in the experimental section of this paper, the flow rate well exceeded this minimum. However, it may be assumed that small amounts of optical inhomogeneities may still be present. These would also tend to decrease the output efficiency of the dye laser from the theoretical value given above. On the basis of the above discussion we assume that the actual (power) slope efficiency η of our dye laser is given approximately by (55).

III. Experiments

Experiments were performed with two purposes: first, to test the validity of the theory and second, to determine excited-state absorption cross sections. All experiments were

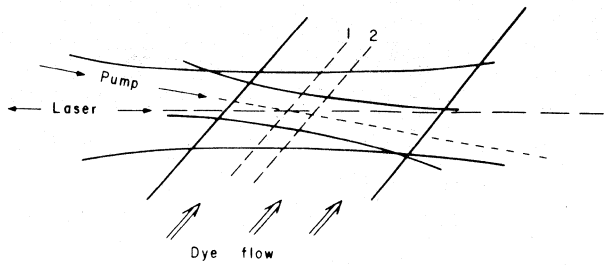


Fig. 12. Pumping geometry in the actual CW dye laser. Beams are Gaussian and pumping is slightly off-axis. Dashed lines 1 and 2 represent $1/e$ absorption planes for two different dye concentrations.

carried out with the dye rhodamine 6G, because most of its relevant parameters are known with reasonable accuracy. The solvent was ethylene glycol for jet-stream operation. Two groups of experiments were carried out:

1) measurements of the dye transmission T under both lasing and nonlasing conditions;

2) measurements of the output slope efficiency of the dye laser.

To accomplish both of the above-stated purposes, a number of pump wavelengths and a wide range of powers were needed.

A. The Experimental Arrangement

Two different lasers were used as pump sources, a commercial CW argon laser, capable of delivering 7 W at 514.5 nm (15 W, all lines) and a pulsed xenon laser with peak powers up to 40 kW in 8 lines. The pulse length of this laser was 250 ns (FWHM). This time is much longer than the fluorescent decay rate τ_1 but is of the same order as the triplet decay time τ_t. Thus, strictly speaking, CW dye laser theory does not appear to be applicable for xenon laser pumping. However, following the suggestion of Peterson *et al.* [12] the theory may be applied with the following modification: the equilibrium triplet population $N_t = N_1 k_{st} \tau_t$ is replaced by

$$N_t = N_1 k_{st} \tau_t \left[\frac{1}{\tau_t} \int_0^{t_0} e^{-t'/\tau_t} \, dt' \right] \tag{57}$$

$$= N_1 k_{st} \tau_t \kappa .$$

Thus the triplet factor f_t in all the theory is replaced by

$$f_t' = 1 - k_{st} \tau_t \kappa \, \sigma_{al}^t / \sigma_e . \tag{58}$$

The xenon laser was constructed in our laboratory. Its plasma tube consisted of an 8-mm ID Pyrex tubing with indium electrodes. A liquid-nitrogen-cooled reservoir of xenon was provided, which allowed some pressure adjustment. Optimum lasing occurred at a pressure of approximately 0.012 torr. The electrical energy source was a 6-kV 0.7-μF capacitor discharging through the tube after breakdown is initiated by a 30-kV trigger pulse into a trigger electrode wrapped close to the cathode. Repetition rates from 5 to 30 pps were used.

Fig. 13 shows the experimental setup. The dye laser cavity is the folded three-mirror design analyzed by Kogelnik *et al.* [13], with mirror radii $R_1 = 5$ cm, $R_2 = 5$ cm, $R_3 = \infty$. For angular and length stability an Invar rod of 2-in diameter was used to hold all the optical elements. The cell position and the

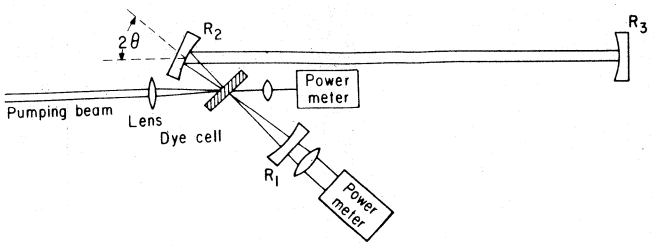


Fig. 13. The experimental setup.

spacing between mirrors 1 and 2 could be accurately adjusted. The pumping arrangement is according to the modification of Yarborough [14] whereby the pump and dye laser beams are slightly off axis; by judicious design the angle between the beams was held to approximately 15°. The pump beam is focused by an achromatic lens. The tuning element shown is a one-element Lyot filter by which the dye laser could be tuned over the entire gain bandwidth with an oscillation bandwidth of 0.5 nm [15]. The Brewster-angle dye cell is the free-flow (jet-stream) type utilizing a nozzle designed especially to give a jet stream of good optical quality with flow speeds to 15 m/s and of adjustable thickness. After the interaction region, the stream is deflected to remove part of its kinetic energy and collected in a collecting box which prevents droplets from hitting the mirror and eliminates bubbles from the recirculating line.

The dye is circulated by a gear pump with flexible Teflon tubing used in the circuit to eliminate vibrations coming from the pump. Power measurements were made with two accurately calibrated power meters. In addition, for transmission measurements, a low-power HP radiant flux meter was used. The values of the cavity residual loss l and the output-mirror transmission T_0 were found by first measuring the total cavity losses from plots of small-signal gain versus pump power as reported in [3] and then measuring the mirror transmission separately.

A. Transmission Measurements

1) CW Excitation: Previous transmission measurements [9] in organic dyes have been performed mainly with Q-switched or mode-locked solid-state lasers, and the characteristic studied was the suitability of the dye for a saturable absorber. The pulse duration of the incident light was short and no triplet effects had to be considered. Our interest lies in the measurement of transmission for CW lasing dyes so that triplet effects must be included. As can be seen from (30) and (34), derived in Section II, the effect of the triplet state on the dye transmission is the reduction of the number of absorbing molecules by storing them in the triplet state. By measuring the transmission as a function of pump power it is possible to determine the value of $k_{st}\tau_t$ if the value of the excited-state absorption cross section σ_{ap}^1 is known, or, more usually, to determine σ_{ap}^1 if $k_{st}\tau_t$ is known from another experiment. The latter is the approach used in this work. The value of $k_{st}\tau_t$ for rhodamine 6G in ethylene glycol is 0.8, as reported by us in an earlier paper [3]. To measure the transmission without lasing, the end mirror of the cavity was removed. The pump beam was focused to a Gaussian beam radius

$w_0 \approx 20$ μm. This value was determined by measuring the spot size of the reflection from the Brewster-angle surface at some distance away and using the well-known beam formula. The cell thickness was adjusted to 0.3 mm. A Brewster angle of 57.2° (set for 514.5 nm) gave a path length of 0.55 mm. The concentration of the dye was adjusted to give at 514.5 nm a small-signal transmission of 0.03 for the cell thickness used. For the other pump wavelengths, the small-signal transmission was both measured and calculated from the known values of the ground-state absorption cross sections. Measured and calculated values of T_0 are shown in Table I. We have assumed throughout the experiments that there is no excited-state absorption of the laser light ($\sigma_{al}^1 = 0$) and thus $\sigma_{ef} = \sigma_e f_t$.

The results for the four argon lines are shown in Fig. 14. With increasing pump power the transmission is flat for 488.0 nm and for 496.5 nm. The solid lines in the figures are fitted from the theory [(34)]. The values of $\sigma_{ap}^1/\sigma_{ap}^0$ used for these fits are shown also in Table I. We observe that there is a probable error for $\lambda = 476.5$ nm due, most likely, to the fact that since an interference filter was not available for this wavelength, an absorption filter was used.

Next, the end mirror of the dye laser cavity was replaced and the transmissions of the dye cell under both lasing and nonlasing conditions were simultaneously measured by alternately blocking off the cavity. This experiment was carried out only for the 514.5-nm line. The cavity had an output mirror with $T_1 = 4.2$ percent and, if properly aligned, a residual loss $l = 4$ percent. However, for this experiment an additional 2.5-percent loss was introduced by a deliberate slight misalignment. The lasing wavelength was set to $\lambda_l = 610$ nm, where there is no ground-state reabsorption ($\alpha_{al}^0 = 0$), and the dye concentration was adjusted to give $T_0 = 0.1$. The dye laser beam waist was adjusted to be approximately the same as that of the pump beam ($w_p \approx w_l \approx 20$ μm). This is necessary in order for the theory to be valid. Otherwise, the stimulated emission drives down the population N_1 only in a part of the pumping beam and the measured transmission is an average of the values with and without lasing. In addition to measuring T, the output power of the dye laser was also measured. The results are shown in Fig. 15. The solid line for T with no lasing was fitted from (34) as before, giving $\sigma_{ap}^1/\sigma_{ap}^0 = 1.31$ in agreement with the previous experiment (which had a different T_0). The line for T with lasing was determined in two different ways, first, from (30) and (43) using a method of successive approximations for each value of input intensity. This gave $\sigma_{ap}^1/\sigma_{ap}^0 = 1.29$, close to the value from the no-lasing transmission curve. This method also gave values for output intensity and thus a value for the slope efficiency. Secondly, (41) was used. For this fitting $\sigma_{ap}^0/\sigma_{ef}$ was needed and was calculated from the data of Fig. 2 ($\sigma_{ap}^0/\sigma_{ef} = 0.485$). This second method gave $\sigma_{ap}^1/\sigma_{ap}^0 = 1.37$. Although the output powers were not measured very carefully in this experiment, an attempt was made to fit the theory to these data as well. The theoretical slope efficiency calculated from (44) is 0.13. This does not fit the experimental data shown. However, if a correction is made for the fact that pump and laser beams are Gaussian beams with $\mu = 1$, as described in Section II-D, the fit becomes quite good. The corrected slope efficiency, from (55), is $\eta = 0.13/\sqrt{2} = 0.092$. We also calculate the threshold power from (56), $P_{th} = 2.2$ W. The resulting straight line for P_{out} versus P_p is shown in Fig. 15.

TABLE I

Wavelength λ (nm)	476.5	488.0	496.5	514.5	527.0	536.0
T_0 (calculated)	0.5	0.25	0.14	0.03		
T_0 (measured)	0.8	0.26	0.16	0.03		
$\sigma_{ap}^1/\sigma_{ap}^0$ (fitted)	–	1.8	1.8	1.29 1.31	1.32	1.05
σ_{ap}^1/σ_e (fitted)[1]	0.60	0.71	0.82	0.92		
σ_{ap}^1/σ_e (fitted)[2]	1.25	1.52	1.69	1.90		
P_{th} (calculated watts)	1.10	0.71	0.69	0.55		
P_{th} (measured watts)	1.25	0.79	0.78	0.65		

Notes: [1]From (55): includes Gaussian beam correction.
[2]From (47).
σ_e is at 610 nm for all the pumping wavelengths.

2) Xenon Laser Excitation: These experiments gave transmission curves for a larger range of input intensities and for several new wavelengths of excitation. As described earlier, since the pulse length of the xenon laser is shorter than the time required to reach the steady state, the triplet factor f_t is replaced by f_t' given by (58). The calculated value of κ is 0.67. The experiment and the fitting of the curves were carried out in the same manner as for the CW case, except that a different focusing lens was used which gave a beam radius of 35 μm. The results are shown in Fig. 16 and in Table I.

B. Output Power Measurements

In the previous experiments the output power of the dye laser was measured for only two pump lines and not with high accuracy. To further test the validity of the theory and to demonstrate and measure the effect of the excited-state absorption of the pump on the efficiency we accurately measured output versus input power curves for four different CW pump lines. If accurate fitting of theory and experiment is to be achieved it is important to minimize factors that could make the slope efficiency different from the theoretical value. The following steps were taken to this effect.

1) The ratio μ of pump beam area to laser beam area was made fairly large ($\mu = 2.5$).

2) A high dye concentration was used (to minimize off-axis effects); $T_0 = 0.03$.

3) Flow speed was increased somewhat beyond the point for which no further improvement was noted.

4) The entire experiment was carried out in one continuous run and special care was taken to maintain identical conditions.

The results of the measurements are shown in Fig. 17(a). The main cause of the differences in slope efficiency and threshold is the different fraction of power absorbed at the different wavelengths. Assuming for the moment no excited-

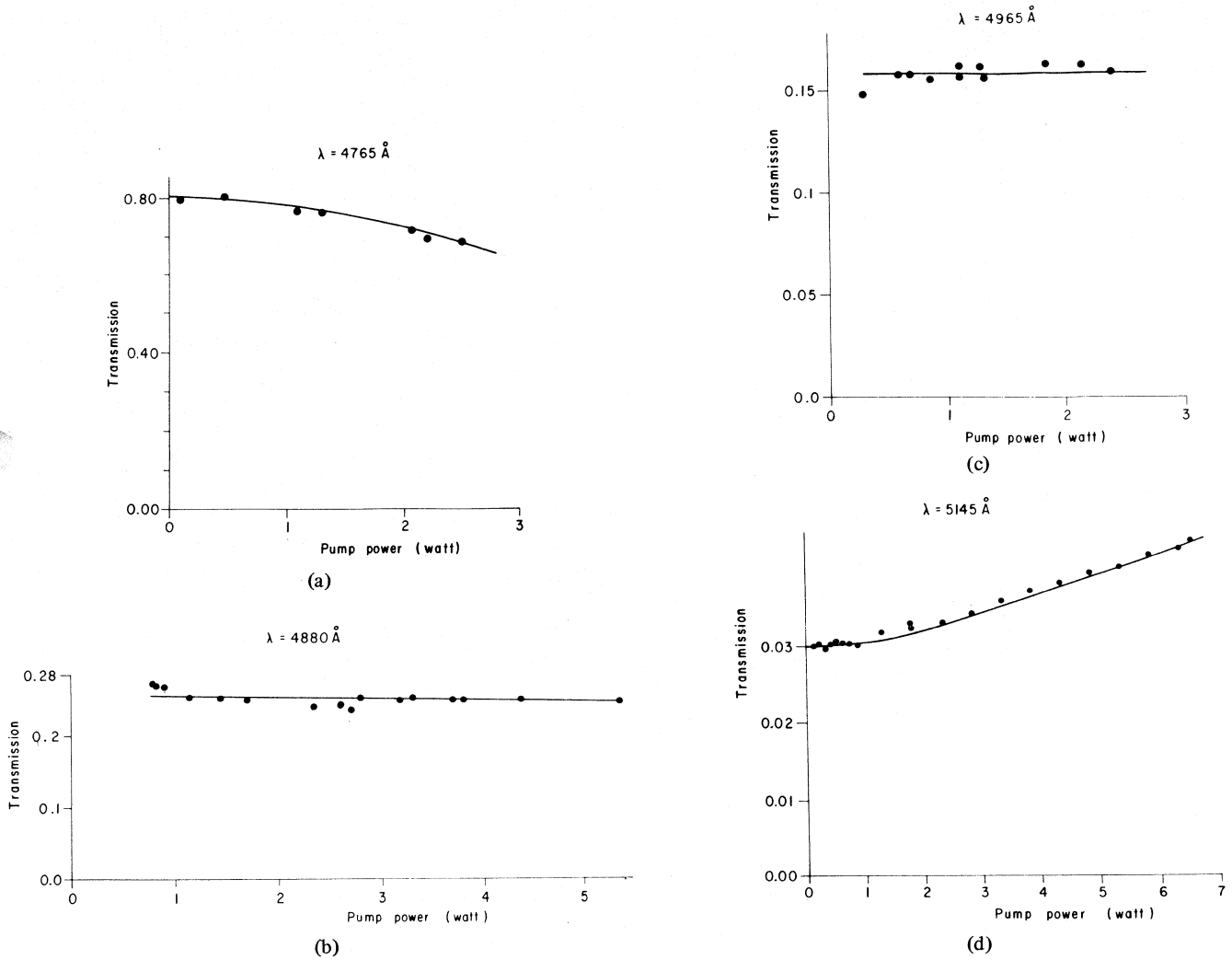


Fig. 14. Dye transmission as a function of pump power for the four different A laser lines with dye laser action prevented. Solid lines are theoretical curves matched from (34). Beam radius $w_p = 20$ μm, $k_{st}\tau_t = 0.8$. The values of $\sigma_{ap}^1/\sigma_{ap}^0$ used in the matching are given in Table I.

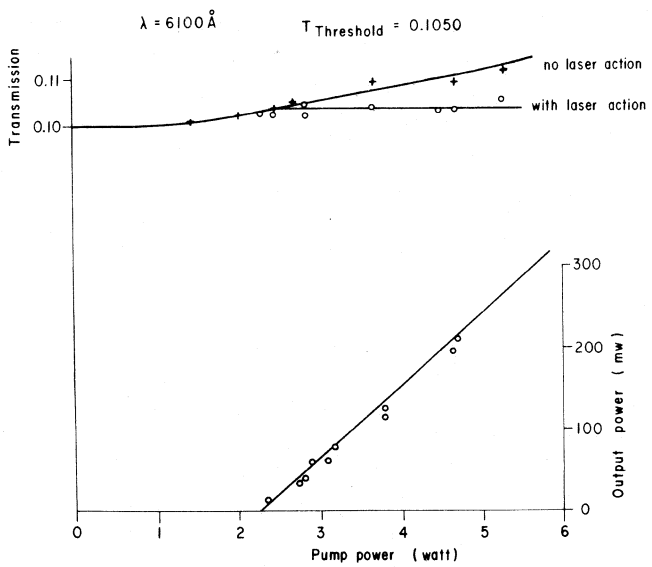


Fig. 15. Dye cell transmission and output power versus pump power for the 514.5-nm argon line. Solid lines are theoretical curves matched to the experimental points as described in the text.

state absorption, the output intensity is then given by the first term of (47) and the only differences are due to the $1 - T$ factor. In Fig. 17(b) we show the same data with the pump power coordinate of each point shifted by the $1 - T$ factor. As was discussed before, T is not, in general, equal to T_0 but $T = T_{th}$. However, observing the transmission data shown in Fig. 14 we note that for this low-loss low-threshold cavity $T = T_0$ for each of the pumping lines within a few-percent error.

It is seen that the plots of P_{out} versus $P_p(1 - T)$ have different slopes for the four pump lines. Since the differences are not too large, considerable care was taken to eliminate all possible external causes. We attribute the differences in slopes in Fig. 17(b) to excited-state absorption of the pump light as predicted by (44) or (47). Let us therefore use the complete theoretical expression to fit the experimental data. In this manner we can determine the ratio σ_{ap}^1/σ_e. It should be noted at this point that since in this low-loss cavity excited-state absorption results in only a small correction of the slope efficiency, values of σ_{ap}^1/σ_e thus determined are strongly

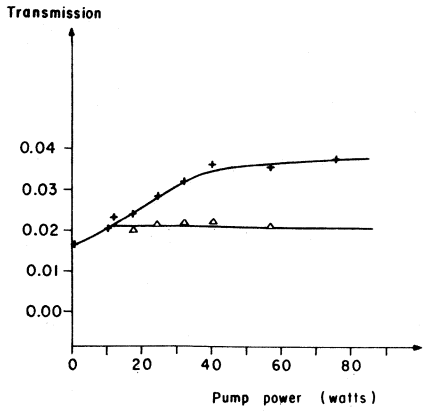


Fig. 16. Dye cell transmission with and without laser action for the 536.0-nm xenon pump line. Solid lines are matched from theory.

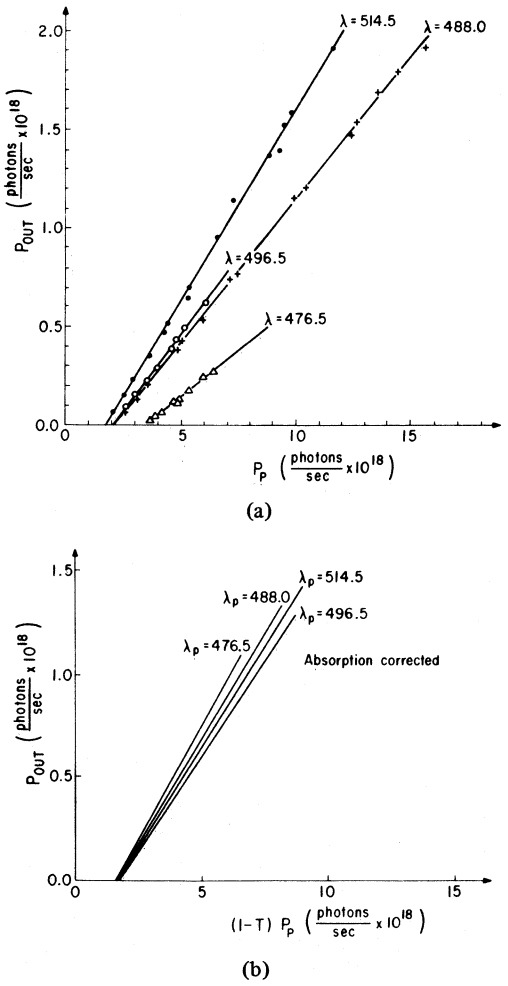


Fig. 17. (a) Dye laser output power versus pump power for four different pump lines. (b) Dye laser output power versus absorbed pump power.

affected by small changes and errors in the other parameters ($T_1/2$, l, f_t, etc.). For this reason, this is not a very suitable method for measuring absolute values of the excited-state-absorption cross sections. However, it does give reliably the relative change of σ_{ap}^1 with wavelength and it does demonstrate clearly the influence of excited-state absorption on the efficiency of the dye laser. Using the measured value of $\mu = 2.5$ we fit the theoretical slope efficiency from (55) to the experimental points. The resulting values of σ_{ap}^1/σ_e are given in Table I. If the $\mu/(1+\mu^2)^{1/2} = 0.94$ correction factor is ignored [(44)], we arrive at values of σ_{ap}^1/σ_e that are approximately two times larger (also shown in Table I).

Next we attempt to fit the threshold pump powers. For this the value of the pump beam area in the dye is needed. The radius of the Gaussian pump beam was measured to be 10 μm. It should be pointed out that the accuracy of this measurement was somewhat poor, with a probable error of $\approx$20 percent. For this reason, we do not expect a very good fit in the threshold values, since the threshold power is a sensitive function of the beam radius.

As pointed out by Tuccio and Strome [16] it is necessary to take into account the effects of concentration quenching on the fluorescent decay rate τ_1. For the dye concentration used ($N_{tot} = 0.416 \times 10^{18}$ cm^{-3}) the value of τ_1 obtained from [16] is $\tau_1 = 3.8 \times 10^{-9}$ s. Using this value the threshold pump powers are calculated from (56). These are shown in Table I, together with the experimentally measured values. The agreement is well within possible errors.

We have made output power measurements with xenon laser pumping as well. However, due to fluctuations of the pump power the slope efficiency could not be measured with enough accuracy to obtain values of σ_{ap}^1/σ_e. Qualitatively, the results agreed with those of the argon laser pumping.

IV. Discussion and Conclusions

In the above sections we have developed a theory of CW and long-pulse dye lasers that include excited-state and triplet absorption of both pump and laser light. We have developed expressions for gain and output power and treated the absorption of the pump rigorously. The effects of the Gaussian beam characteristics were also included by applying Pike's results [10] to our equations without proof. The theory shows that the influence of excited-state absorption can be important in the behavior of the dye laser, especially at high intensities. Excited-state absorption of the laser light reduces the effective emission cross section and thus reduces the gain and output efficiency in the same manner as triplet absorption of the laser light. Excited-state absorption of the pump changes the dye transmission and causes a portion of the pump power to go unused. Its main effect is to reduce the gain and the slope efficiency. At high power levels it can substantially change the value of the optimum output coupling. The effects of the triplet absorption of the laser light on the gain and output power are well known but we have also shown that the dye transmission is also affected by the storing of molecules in the triplet state. Triplet absorption of the pump, if present, acts in the same manner as excited-state pump absorption. The theory also shows that the absorption of the dye cell is different from the small-signal absorption. For low power and low cavity loss this difference is negligible but it can be substantial for high-power, high-output coupling lasers.

In the experimental part we have verified the theory and have also shown that if all other parameters are known, excited-state absorption cross sections may be found by fitting theory

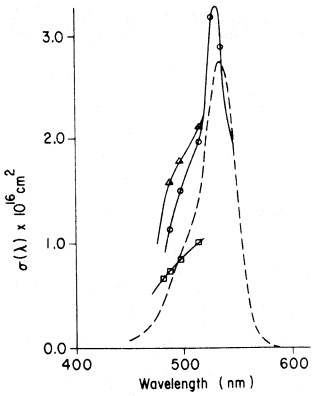


Fig. 18. Excited-state absorption spectrum for rhodamine 6G as determined from transmission and output power measurements. Dashed line is ground-state absorption spectrum. Dots are from transmission measurements; triangles are from output power measurements, using (47); squares are from output power measurements using (55).

to experiment. The transmission measurements gave us the ratio of excited-state- to ground-state-absorption cross sections $\sigma_{ap}^1/\sigma_{ap}^0$ while the output power measurements resulted in the determination of the ratio of the excited-state absorption cross section to the emission cross section σ_{ap}^1/σ_e. Of these two results the first one is considerably more reliable since it depends on fewer known parameters and the fits are much less sensitive to errors in these known parameters. In Fig. 18 these ratios (from Table I) are translated into absolute values of cross sections by using values of σ_{ap}^0 and σ_e from the literature. It must be pointed out that substantial disagreements exist in the published values. We have used the latest data [1] but they were measured for a water solution rather than for the ethylene glycol solution used in our experiments. In Fig. 18 the cross section versus wavelength curves have the same general shape, but those from the output power experiments are smaller by a factor of 1.5 to 2. As mentioned above, we consider the transmission data the more reliable.

In conclusion, we have derived and verified a complete theory for the dye laser and have used it to obtain excited-state absorption cross sections for the dye rhodamine 6G.

References

[1] B. B. Snavely, "Continuous wave dye lasers," in *Dye Lasers*, F. P. Schafer, Ed. New York: Springer-Verlag, 1973, pp. 91–120. (An excellent review.)

[2] O. Teschke and A. Dienes, "Influence of excited state absorption on the output power of CW dye lasers," *Appl. Phys. Letters*, vol. 26, pp. 13–15, Jan. 1975.

[3] ——, "Solvent effects on the triplet state population in jet stream CW dye lasers," *Optics Commun.*, vol. 9, pp. 128–131, Oct. 1973.

[4] O. Teschke, A. Dienes, and G. Holtom, "Measurement of triplet lifetime in a jet stream CW dye laser," *Optics Commun.*, vol. 13, pp. 318–320, Mar. 1975.

[5] C. Lin and A. Dienes, "Direct measurement of radiationless internal conversion rate from the second excited singlet to the first excited singlet state of laser dye molecules," *Optics Commun.*, vol. 9, pp. 21–24, Sept. 1973.

[6] R. S. H. Liu and R. E. Kellog, "Triplet–triplet energy transfer from the second triplet state of anthracene," *J. Amer. Chem. Soc.*, vol. 91, pp. 250–252, Jan. 1969.

[7] W. W. Rigrod, "Saturation effects in high gain lasers," *J. Appl. Phys.*, vol. 36, pp. 2487–2490, Aug. 1965.

[8] U. Ganiel, A. Hardy, G. Neumann, and D. Treves, "Amplified spontaneous emission and signal amplification in dye laser systems," *IEEE J. Quantum Electron.*, vol. QE-11, pp. 881–892, Nov. 1975.

[9] M. Hercher, W. Chu, and D. L. Stockman, "An experimental study of saturable absorbers for ruby lasers," *IEEE J. Quantum Electron.*, vol. QE-4, pp. 954–968, Nov. 1968.

[10] H. A. Pike, unpublished thesis, Univ. of Rochester, Rochester, NY (results described in [1]).

[11] O. Teschke, J. R. Whinnery, and A. Dienes, "Thermal effects in jet-stream dye lasers," to be published.

[12] O. G. Peterson, J. P. Webb, W. C. McColgin, and J. H. Eberly, "Organic dye laser threshold," *J. Appl. Phys.*, vol. 42, pp. 1917–1928, Apr. 1971.

[13] H. Kogelnik, E. P. Ippen, A. Dienes, and C. V. Shank, "Astigmatically compensated cavities for CW dye lasers," *IEEE J. Quantum Electron.*, vol. QE-8, pp. 373–379, Mar. 1972.

[14] J. M. Yarborough, "CW dye laser emission spanning the visible spectrum," *Appl. Phys. Letters*, vol. 24, pp. 629–630, June, 1974.

[15] G. Holtom and O. Teschke, "Design of birefrigent filter for high power dye lasers," *IEEE J. Quantum Electron.*, vol. QE-10, pp. 577–579, Aug. 1974.

[16] S. A. Tuccio and F. C. Strome, "Design and operation of a tunable continuous dye laser," *Appl. Optics*, vol. 11, pp. 64–67, Jan. 1972.

Switched Directional Couplers with Alternating $\Delta\beta$

HERWIG KOGELNIK, FELLOW, IEEE, AND RONALD V. SCHMIDT, MEMBER, IEEE

Abstract—Coupled waveguide structures with sections of alternating phase mismatch are proposed as switched directional coupler configurations in which complete conversion of light from one guide to the other can be achieved by an electrical adjustment. These structures can be used to make electrooptic switches and amplitude modulators in integrated optics form with improved conversion and on-off ratios. Couplers with 2, 3, 4, and N sections of alternating phase mismatch are analyzed, and diagrams describing their switching characteristics are given.

I. Introduction

OPTICAL directional couplers, such as those formed by two parallel strip waveguides [1], are characterized by 1) the interaction length L, 2) the coupling coefficient κ or the corresponding conversion length $l = \pi/2\kappa$ indicating the minimum length required to obtain complete crossover of light from one guide to the other, and 3) the mismatch $\Delta\beta = \beta_1 - \beta_2$ between the propagation constants β_1 and β_2 of the two guides. Complete crossover is achieved when the guides are phase matched ($\Delta\beta = 0$) and when the interaction length is an exact odd multiple of the coupling length, i.e., when $L = (2\nu + 1)l$. It has been proposed [2]-[5] that an optical switching device can be built by electrically switching the directional coupler from the crossover state to the straight-through state where no net crossover occurs. One way to do this is by fabricating the coupler on electrooptic material and applying a voltage which induces a mismatch $\Delta\beta$ via the electrooptic effect. An early switching experiment of this kind is that of Tada and Hirose [6] who employed planar film guides in GaAs. Recently, Papuchon *et al.* [7] and Campbell *et al.* [8] have demonstrated experimental switches by using Ti-diffused strip guides in $LiNbO_3$ and metal-gap strip guides in GaAs, respectively. When the interaction length L is not made exactly equal to the coupling length l (or an odd multiple thereof), then the crossover is not complete in these devices and crosstalk results. It does not appear to be possible to eliminate the crosstalk in the crossover state of these devices by an electrical adjustment. However, crosstalk requirements are relatively stringent if such optical switches are to be used to switch optical transmission channels (some 25 dB are required for digital systems). This imposes stringent fabrication tolerances which may be hard to meet ([7] does not report measured crossover values and [8] reports crossover values of about 75 percent). In addition, we know that the conversion length l is a function of wavelength [1], which may make it impossible to operate these switches properly beyond the design wavelength.

In this paper we propose switched coupler configurations in which such an electrical adjustment can be made for both the crossover and the straight-through states for just about any interaction length L that is larger than the conversion length l. They are called alternating-$\Delta\beta$ couplers because the technique used to achieve complete crossover in the coupler is to provide along the interaction length two or more sections with a mismatch or asynchronism $\Delta\beta$ of alternating sign.[1] A simple way to induce this alternating $\Delta\beta$ is to provide sectioned electrodes and apply voltages of alternating polarity along the interaction length. There is no requirement for an exact L/l ratio in this configuration, and we find that there is always a voltage that will make the light cross over completely, and another voltage that will make the light go straight through. If the switch has to be operated at another wavelength and l is wavelength dependent, the only adjustment that seems necessary is a change of these voltage values.

In this paper we discuss the principle of operation of alternating-$\Delta\beta$ couplers and present their theory based on coupled-wave theory. The first successful operation of a switched alternating-$\Delta\beta$ coupler with two sections using Ti-diffused strip guides in $LiNbO_3$ is reported elsewhere [9].

To simplify our discussion, we shall call the switching state where the light crosses over completely from one guide to the other the "cross" state, and we associate with this state the symbol ⊗; the state in which the light passes straight through, appearing at the output in the same guide that it entered at the device input, we shall call the "bar" state associated with the symbol ⊖. We have found it convenient to describe the various switching configurations in a diagram which, for a given L/l value, gives the mismatch values $\Delta\beta$ required to drive the switch into the cross and bar states, respectively. In Section II we work out the transfer matrix and the switching diagram for the conventional switched directional coupler. In Sections III-V we derive the transfer matrices and the switching diagrams for couplers with alternating $\Delta\beta$ with 2, 3, and 4 sections, respectively. In Section VI we discuss alternating-$\Delta\beta$ couplers with N sections.

II. The Switched Directional Coupler

A sketch of a conventional switched directional coupler is shown in Fig. 1. We give here the transfer matrix and the cross-bar diagram of this known coupler in order to provide the basis for the discussion of the following sections. For simplicity, the electrodes are shown in the COBRA configuration [7]. Application of a voltage V to these electrodes induces a mismatch $\Delta\beta(V) = \beta_1 - \beta_2$ between the propagation constants of guides 1 and 2. We describe the coherent light in

Manuscript received December 18, 1975.
The authors are with Bell Laboratories, Holmdel, NJ 07733.

[1] It is interesting to note that in a patent disclosure filed in 1957, Miller [13] proposed reversals in the sign of $\Delta\beta$ or of κ for the purpose of broadening the frequency band of operation of microwave directional couplers.

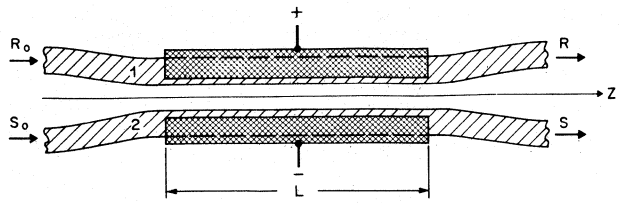


Fig. 1. Switched directional coupler consisting of two optical strip waveguides, with an interaction length L. The electrodes are shown in the COBRA configuration [7].

the two guides by complex amplitudes $R(z)$ and $S(z)$ which vary slowly in the propagation direction chosen coincident with the z axis. We assume that the energy exchange between the two guides can be regarded as a codirectional coupled-wave process which is governed by the coupled-wave equations [10]-[12]

$$R' - j\delta R = -j\kappa S \tag{1}$$

$$S' + j\delta S = -j\kappa R \tag{2}$$

where the prime indicates differentiation with respect to z, $\delta = \Delta\beta/2$, and κ is the coupling coefficient. For arbitrary input amplitudes R_0 and S_0 the solution of the coupled-wave equations can be written in matrix form

$$\begin{pmatrix} R \\ S \end{pmatrix} = \begin{pmatrix} A_1 & -jB_1 \\ -jB_1^* & A_1^* \end{pmatrix} \begin{pmatrix} R_0 \\ S_0 \end{pmatrix} \tag{3}$$

where the asterisk indicates a complex conjugate and the subscript 1 refers to a single section of uniform $\Delta\beta$. The matrix coefficients are [10]-[12]

$$A_1 = \cos z\sqrt{\kappa^2 + \delta^2} + j\delta \sin z\sqrt{\kappa^2 + \delta^2}/\sqrt{\kappa^2 + \delta^2} \tag{4}$$

$$B_1 = \kappa \sin z\sqrt{\kappa^2 + \delta^2}/\sqrt{\kappa^2 + \delta^2}. \tag{5}$$

For $z = L$ the matrix

$$M_1^+ = \begin{pmatrix} A_1 & -jB_1 \\ -jB_1^* & A_1^* \end{pmatrix} \tag{6}$$

may be called the transfer matrix of the coupler. Note that its determinant is unity, B_1 is real for this special case, and that the transfer matrix M_1^- of coupler with a mismatch of $-\Delta\beta$ has the form

$$M_1^- = \begin{pmatrix} A_1^* & -jB_1 \\ -jB_1^* & A_1 \end{pmatrix}. \tag{7}$$

The switched coupler is in the cross state $\otimes$ when $A_1 = 0$. As is well known, this requires that $\delta L = 0$ and that

$$\kappa L = (2\nu + 1)\pi/2$$

or

$$L/l = 2\nu + 1 \tag{8}$$

where ν is an integer.

The bar state $\ominus$ is obtained when $B_1 = 0$, which occurs if

$$(\kappa L)^2 + (\delta L)^2 = (\nu\pi)^2$$

or

$$\left(\frac{L}{l}\right)^2 + \left(\frac{\Delta\beta L}{\pi}\right)^2 = (2\nu)^2. \tag{9}$$

The conditions for the cross and bar states can be graphically represented in a switching diagram where we use the values of L/l and $\Delta\beta L/\pi = 2\delta L/\pi$ as coordinates. This is shown in Fig. 2. According to (8) the cross states are represented by isolated points on the L/l axis, and (9) predicts concentric circles for the bar states as shown in the figure. While in this switch configuration the L/l value is essentially independent of the applied voltage, the $\Delta\beta$ values can be controlled electrically. An increase in the voltage moves the point representing the state of the coupler parallel to the $\Delta\beta L/\pi$ axis to the right. We note that, for any L/l value, there is always a $\Delta\beta L$ (or voltage) value that will drive the switch into the bar state. To obtain the cross state, however, exact odd-integer values of L/l must be produced during device fabrication and no voltage adjustment can compensate for fabrication errors. We shall see in the next sections that an electrical adjustment of the cross state is possible for the alternating-$\Delta\beta$ configurations.

III. Single Step $\Delta\beta$ Reversal

Fig. 3 shows a sketch of a switched coupler configuration in which the interaction length L is divided into two equally long sections. The asynchronism introduced in the two sections is equal in magnitude but reversed in sign, i.e., we have $\Delta\beta$ in the left section and $-\Delta\beta$ in the right section. The figure indicates a simple way to achieve this; one can bisect the electrodes and apply equal voltages of opposite polarity. The transfer matrix M_2 of this alternating-$\Delta\beta$ coupler with two sections can be obtained with the help of the single-section matrices M_1^+ and M_1^- by matrix multiplication

$$M_2 = M_1^- \cdot M_1^+ = \begin{pmatrix} A_2 & -jB_2 \\ -jB_2^* & A_2^* \end{pmatrix} \tag{10}$$

where we assume that there are no reflections at the interface between the two sections. The matrix elements are calculated to be

$$A_2 = A_1A_1^* - B_1^2 = 1 - 2B_1^2 \tag{11}$$

$$B_2 = 2A_1^*B_1 \tag{12}$$

where A_1 and B_1 are given in (4) and (5) where we put $z = L/2$.

The switch is in the cross state when $A_2 = 0$, i.e., when

$$2B_1^2 = 1. \tag{13}$$

With (4) this condition can be written in the form

$$\frac{\kappa^2}{\kappa^2 + \delta^2} \sin^2 \frac{L}{2}\sqrt{\kappa^2 + \delta^2} = \frac{1}{2} \equiv \sin^2 \frac{\pi}{4}. \tag{14}$$

In the switching diagram this condition leads to a family of curves shown in Fig. 4. The curves intersect the vertical axis at the points $L/l = 1, 3, 5, 7$, etc. which are isolated $\otimes$ points in the case of the single section coupler discussed in the preceding section. Near the vertical axis these curves are very nearly circles, and all curves are tangent to a 45° line through the origin (i.e., the line $\delta = \kappa$).

The switch is in the bar state if $B_2 = 0$ which occurs either

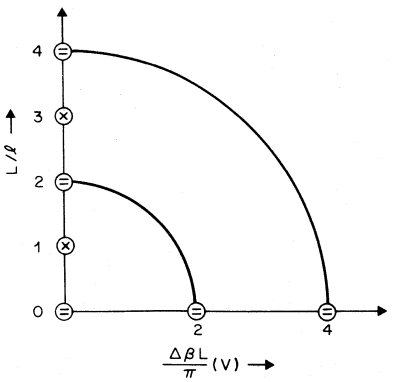


Fig. 2. The switching diagram for a switched directional coupler. The isolated points marking the conditions required for complete energy crossover are marked by an ⊗, and the circles indicating the conditions required for zero net crossover are marked by a ⊖.

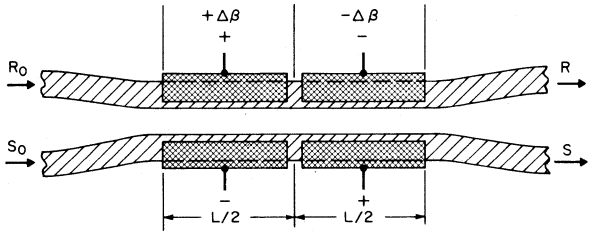


Fig. 3. Split electrode configuration for a switched coupler with stepped $\Delta\beta$ reversal (alternating $\Delta\beta$ with two sections).

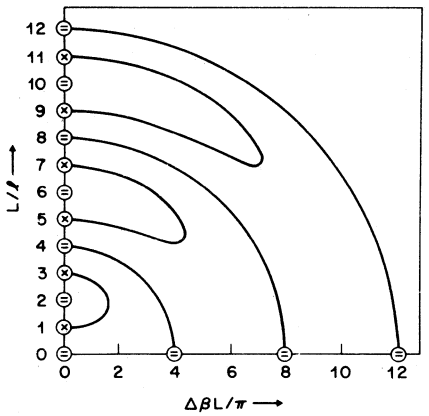


Fig. 4. Switching diagram for a switched coupler with two sections of alternating $\Delta\beta$. The ⊗ sign marks the cross-state conditions and the ⊖ sign marks the bar-state conditions.

for $A_1 = 0$ or for $B_1 = 0$. The first condition implies $\Delta\beta = 0$ and

$$L/l = 2(2\nu + 1) \tag{15}$$

which represents the isolated points at $L/l = 2$, 6, 10, etc., shown for the ⊖ state in Fig. 4. The second condition can be written in the form

$$\left(\frac{L}{l}\right)^2 + \left(\frac{\Delta\beta L}{\pi}\right)^2 = (4\nu)^2. \tag{16}$$

This condition for the ⊖ states corresponds to the concentric circles with radius 4, 8, 12, etc. in the switching diagram. The diagram indicates that the stepped-$\Delta\beta$ configuration makes available ranges of L/l values (e.g., the range from $L/l = 1$ to 3) in which complete crossover can be achieved. The diagram also gives the $\Delta\beta$ or voltage adjustments which are required for this purpose. These adjustment values are of the same order of magnitude as those required for the bar state in the uniform-$\Delta\beta$ configuration. In the next sections we will find that similar L/l ranges for the cross state and the associated possibility for electrical adjustment can be obtained for three or more sections of alternating $\Delta\beta$.

IV. Three Sections of Alternating $\Delta\beta$

In the following we discuss coupler configurations with three and more sections of alternating $\Delta\beta$. As the analysis of these configurations and the associated arguments are very similar in kind to those presented in Section III for couplers with two sections, we can and shall keep the following discussion very brief.

Fig. 5 shows a sketch of a coupler with three sections of alternating $\Delta\beta$. By matrix multiplication we obtain the transfer matrix M_3 of this configuration

$$M_3 = M_1^+ \cdot M_1^- \cdot M_1^+ = \begin{pmatrix} A_3 & -jB_3 \\ -jB_3^* & A_3^* \end{pmatrix}. \tag{17}$$

The matrix elements are

$$A_3 = A_1(1 - 4B_1^2)$$

and

$$B_3 = B_1(3 - 4B_1^2) \tag{18}$$

where we obtain A_1 and B_1 from (4) and (5) by putting $z = L/3$. The condition for the cross state is $A_3 = 0$, which is obtained either when $A_1 = 0$ or when

$$4B_1^2 = 1. \tag{19}$$

The first condition demands that $\Delta\beta = 0$ and that

$$L/l = 3(2\nu + 1) \tag{20}$$

which corresponds to the isolated cross-state points at $L/l = 3$, 9, 15, etc., which are indicated in the diagram of Fig. 6. Condition (19) can be written in the form

$$\frac{\kappa^2}{\kappa^2 + \delta^2} \sin^2 \frac{L}{3}\sqrt{\kappa^2 + \delta^2} = \frac{1}{4} = \sin^2 \frac{\pi}{6}. \tag{21}$$

In the diagram this condition is represented by the curves which intersect the vertical axis at $L/l = 1$, 5, 7, 11, 13, etc., and which are tangent to a 30° line through the origin.

Setting $B_3 = 0$ we obtain the bar-state conditions. The first of these is $B_1 = 0$ or

$$(L/l)^2 + (\Delta\beta L/\pi)^2 = (6\nu)^2 \tag{22}$$

which corresponds to the concentric circles through $L/l = 6$, 12, etc. in the diagram. The second condition is

$$4B_1^2 = 3 \tag{23}$$

which we can write in the form

$$\frac{\kappa^2}{\kappa^2 + \delta^2} \sin^2 \frac{L}{3}\sqrt{\kappa^2 + \delta^2} = \frac{3}{4} \equiv \sin^2 \frac{\pi}{3}. \tag{24}$$

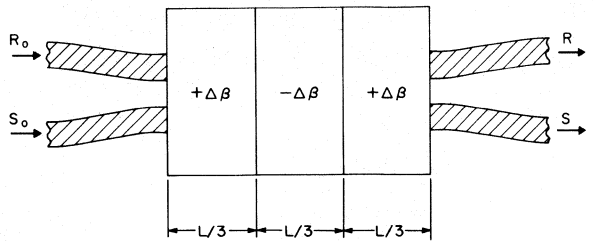


Fig. 5. Sketch of switched coupler with three sections of alternating $\Delta\beta$.

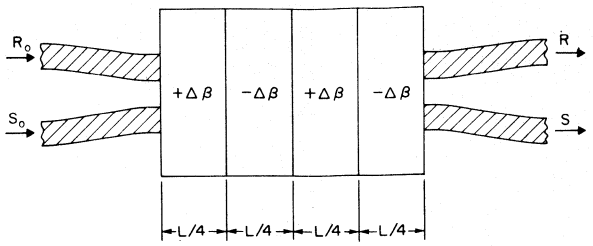


Fig. 7. Sketch of switched coupler with four sections of alternating $\Delta\beta$.

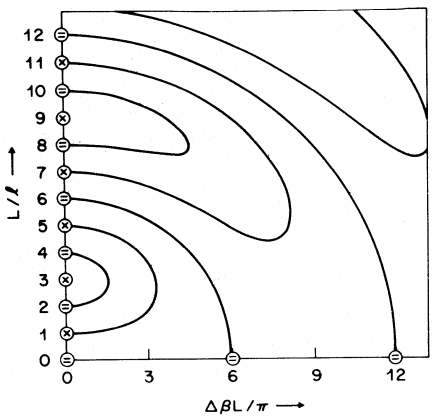


Fig. 6. Switching diagram for a coupler with three sections of alternating $\Delta\beta$. The ⊗ and ⊖ signs mark the conditions required for the cross and the bar states, respectively.

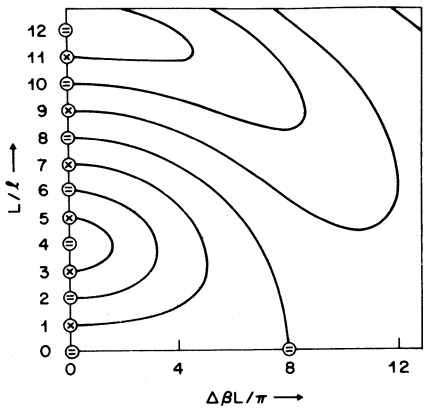


Fig. 8. Switching diagram for a coupler with four sections of alternating $\Delta\beta$.

In the diagram this condition is represented by the curves intersecting the vertical axis at $L/l = 2, 4, 8, 10, 14$, etc., which are tangent to a 60° line through the origin.

V. Four Sections of Alternating $\Delta\beta$

Fig. 7 shows a sketch of a coupler with four sections of alternating $\Delta\beta$. For the transfer matrix M_4 of this configuration we obtain

$$M_4 = M_1^- \cdot M_1^+ \cdot M_1^- \cdot M_1^+ = M_2^2 = \begin{pmatrix} A_4 & -jB_4 \\ -jB_4^* & A_4^* \end{pmatrix} \tag{25}$$

where the matrix elements are

$$A_4 = 2(1 - 2B_1^2)^2 - 1 \tag{26}$$

$$B_4 = 4A_1^* B_1 (1 - 2B_1^2) \tag{27}$$

and A_1 and B_1 are obtained from (4) and (5) with $z = L/4$.

Letting $A_4 = 0$ we get the two conditions for the cross state

$$B_1^2 = \frac{1}{2}\left(1 \pm \frac{1}{\sqrt{2}}\right) \tag{28}$$

which we can write in the form

$$\frac{\kappa^2}{\kappa^2 + \delta^2} \sin^2 \frac{L}{4}\sqrt{\kappa^2 + \delta^2} = \frac{1}{2}\left(1 \pm \frac{1}{\sqrt{2}}\right) \equiv \begin{cases} \sin^2 3\pi/8 \\ \sin^2 \pi/8. \end{cases} \tag{29}$$

These conditions correspond to two sets of curves shown in the diagram of Fig. 8. Taking the − sign we get the curves that intersect the vertical axis at $L/l = 1, 7, 9, 15$, etc., which are tangent to a 22.5° line through the origin; the plus sign yields the curves through $L/l = 3, 5, 11, 13$, etc., which are tangent to the 67.5° line.

Letting $B_4 = 0$ we get three conditions for the bar state. The first is $A_1 = 0$, or $\Delta\beta = 0$ and

$$L/l = 4(2\nu + 1) \tag{30}$$

which yields the isolated points at $L/l = 4, 12$, etc. shown in the diagram. The second condition is $B_1 = 0$ or

$$(L/l)^2 + (\Delta\beta L/\pi)^2 = (8\nu)^2 \tag{31}$$

represented in the diagram by the circles through $L/l = 8, 16$, etc. The third condition is

$$2B_1^2 = 1 \tag{32}$$

or

$$\frac{\kappa^2}{\kappa^2 + \delta^2} \sin^2 \frac{L}{4}\sqrt{\kappa^2 + \delta^2} = \frac{1}{2} \equiv \sin^2 \frac{\pi}{4}. \tag{33}$$

In the diagram this corresponds to the curves through $L/l = 2, 6, 10, 14$, etc., tangent to a 45° line through the origin.

VI. N Sections of Alternating $\Delta\beta$

From the results of the previous discussion we can already make a fairly good guess at the characteristics of a coupler with an arbitrary number of sections of alternating $\Delta\beta$. Using matrix multiplication and Sylvester's theorem, it is also fairly straightforward to analyze these structures. Assuming N to be an even number, we will distinguish between couplers with an even number (N) of sections and couplers with an odd number ($N + 1$) of sections.

Fig. 9(a) shows a coupler with an even number of sections of

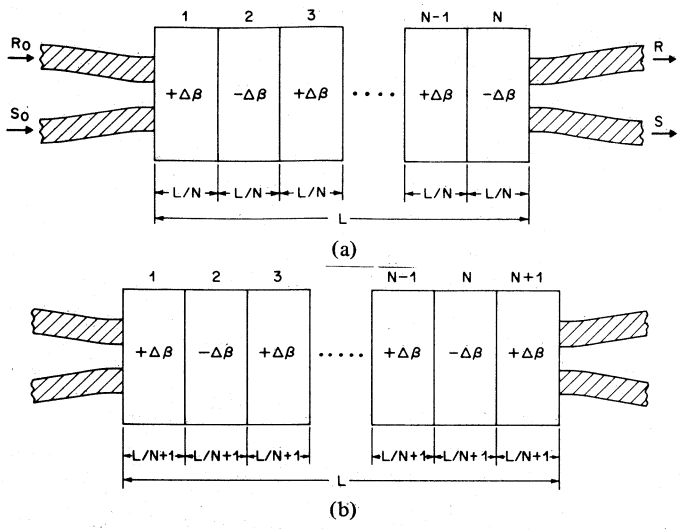


Fig. 9. Sketches of switched couplers with N and $N+1$ sections of alternating $\Delta\beta$. (a) Even number of sections. (b) Odd number of sections.

alternating $\Delta\beta$ and equal length L/N. The mismatch of the first section is $\Delta\beta$ and that of the last section is $-\Delta\beta$. The transfer matrix M_N of this coupler can be written as a power of the two-section matrix M_2 in the form

$$M_N = M_2^{N/2} = \begin{pmatrix} A_N & -jB_N \\ -jB_N^* & A_N^* \end{pmatrix}. \tag{34}$$

The matrix elements are determined with the help of Sylvester's theorem with the result

$$A_N = \cos(N\theta/2) \tag{35}$$

$$B_N = 2A_1^* B_1 \sin(N\theta/2)/\sin\theta \tag{36}$$

where

$$\cos\theta = A_2 = 1 - 2B_1^2 \tag{37}$$

and A_1 and B_1 are determined from (4) and (5) letting $z = L/N$. We rewrite (37) as

$$B_1^2 = \sin^2\theta/2 \tag{38}$$

in order to cast the subsequent results into our standard form.

To determine the cross-state conditions we let $A_N = 0$ and find

$$N\theta/2 = (2\nu+1)\pi/2 \tag{39}$$

where ν is an integer. Combining this with (5) and (38) we obtain

$$\frac{\kappa^2}{\kappa^2+\delta^2}\sin^2\frac{L}{N}\sqrt{\kappa^2+\delta^2} = \sin^2\left(\frac{2\nu+1}{N}\cdot\frac{\pi}{2}\right). \tag{40}$$

In the switching diagram, these conditions correspond to sets of curves similar to those discussed for couplers with two and four sections. The curves intersect the vertical axis ($\delta = 0$) at the points

$$L/l = 2N\mu \pm (2\nu+1) \tag{41}$$

where μ is another integer.

For $B_N = 0$, we obtain the bar-state following conditions:

1) $A_1 = 0$ indicating isolated points at $\Delta\beta = 0$ and

$$L/l = N(2\nu+1) \tag{42}$$

2) $B_1 = 0$ or

$$(L/l)^2 + (\Delta\beta L/\pi)^2 = (2N\nu)^2 \tag{43}$$

corresponding to concentric circles of radius $2N\nu$; and, finally,

$$N\theta/2 = \nu\pi \tag{44}$$

or

$$\frac{\kappa^2}{\kappa^2+\delta^2}\sin^2\frac{L}{N}\sqrt{\kappa^2+\delta^2} = \sin^2\frac{\nu\pi}{N} \tag{45}$$

corresponding to the now familiar curves which, in this case, intersect the vertical axis of the diagram at the points

$$L/l = 2N\mu \pm 2\nu. \tag{46}$$

For couplers with an odd number of sections, we obtain similar results, with the exception that we get isolated points for the cross states rather than the bar states. Fig. 9(b) shows such a coupler with sections of equal length $L/(N+1)$ starting and terminating with a section of mismatch $+\Delta\beta$. The transfer matrix of this coupler is

$$M_{N+1} = M_1 \cdot M_N = \begin{pmatrix} A_{N+1} & -jB_{N+1} \\ -jB_{N+1}^* & A_{N+1}^* \end{pmatrix} \tag{47}$$

with the matrix elements

$$A_{N+1} = A_1 \cos[\theta(N+1)/2]/\cos(\theta/2) \tag{48}$$

and

$$B_{N+1} = B_1 \sin[\theta(N+1)/2]/\sin(\theta/2). \tag{49}$$

A_1 and B_1 are obtained from (4) and (5) letting $z = L/(N+1)$.

For $A_{N+1} = 0$ we obtain the cross-state conditions, which include now $A_1 = 0$, or $\Delta\beta = 0$ and

$$L/l = (N+1)(2\nu+1) \tag{50}$$

which are the isolated points mentioned before. The other cross-state condition is

$$\theta(N+1) = (2\nu+1)\pi \tag{51}$$

or

$$\frac{\kappa^2}{\kappa^2+\delta^2}\sin^2\left(\frac{L}{N+1}\sqrt{\kappa^2+\delta^2}\right) = \sin^2\left(\frac{2\nu+1}{N+1}\cdot\frac{\pi}{2}\right). \tag{52}$$

The curves corresponding to this relation intersect the vertical axis in the switching diagram at the points

$$L/l = 2\mu(N+1) \pm (2\nu+1). \tag{53}$$

Letting $B_{N+1} = 0$ we get the bar-state conditions, which include, first, the condition $B_1 = 0$ or

$$(L/l)^2 + (\Delta\beta L/\pi)^2 = [2\nu(N+1)]^2 \tag{54}$$

which is represented by circles of radius $2\nu(N+1)$ in the diagram. The second condition is

$$\theta(N+1)/2 = \nu\pi \tag{55}$$

or

$$\frac{\kappa^2}{\kappa^2+\delta^2}\sin^2\left(\frac{L}{(N+1)}\sqrt{\kappa^2+\delta^2}\right)=\sin^2\left(\frac{\nu}{N+1}\pi\right). \quad (56)$$

The curves representing these conditions in the diagram intersect the vertical axis at the points

$$L/l=2\mu(N+1)\pm 2\nu. \quad (57)$$

VII. Conclusions

We have examined switched directional couplers in which we have assumed the coupling coefficient κ to be constant and the mismatch $\Delta\beta$ adjustable by an applied voltage, e.g., via the electrooptic effect. We have found that the providing of sections with alternating $\Delta\beta$ (e.g., by providing applied voltages of alternating polarity) makes it possible to induce complete crossover of the light from one guide to the other by an electrical adjustment. This adjustment is possible as long as L/l is larger than unity and can be used to reduce undesired crosstalk. We have used the switching diagram to depict graphically the $\Delta\beta$ adjustments required for each value of L/l to induce either the crossover (cross) or the straight-through (bar) states. In this diagram these states are represented either by isolated points, or by circles, or by curves belonging to a family, all described by equations of the same form. The circles always represent bar states only. The isolated points represent cross states when the number of sections is odd (i.e., 1, 3, $N+1$), and they represent bar states when the number of sections is even (2, 4, N). The isolated point with the lowest L/l value is always the point where L/l equals the number of sections. Beyond the electrical adjustability for both switching states obtained when we divide the coupler into two sections of reversed $\Delta\beta$, nothing essentially new seems to happen when we provide 3 or more sections of alternating $\Delta\beta$. Three or more sections, however, offer a low-voltage (low $\Delta\beta$) adjustment for the cross state when the L/l value is large, with the best choice being a number of sections approximately equal to L/l.

References

[1] E. A. J. Marcatili, "Dielectric rectangular waveguide and directional coupler for integrated optics," *Bell Syst. Tech. J.*, vol. 48, pp. 2071–2102, Sept. 1969.

[2] S. Kurazono, K. Iwasaki, and N. Kumagai, "New optical modulator consisting of coupled optical waveguides," *Electron. Commun. Jap.*, vol. 55, pp. 103–109, Jan. 1972.

[3] H. F. Taylor, "Optical switching and modulation in parallel dielectric waveguides," *J. Appl. Phys.*, vol. 44, pp. 3257–3262, July 1973.

[4] S. Somekh, E. Garmire, H. L. Garvin, and R. G. Hunsperger, "Channel optical waveguides and directional couplers in GaAs–Imbedded and ridged," *Appl. Optics*, vol. 13, pp. 327–330, Feb. 1974.

[5] J. M. Hammer, "Modulation and switching of light in dielectric waveguides," in *Integrated Optics*, vol. 7, T. Tamir, Ed. Berlin, Germany: Springer, pp. 140–198, 1975.

[6] K. Tada and K. Hirose, "A new light modulator using perturbation of synchronism between two coupled guides," *Appl. Phys. Lett.*, vol. 25, pp. 561–562, Nov. 1974.

[7] M. Papuchon *et al.*, "Electrically switched optical directional coupler: COBRA," *Appl. Phys. Lett.*, vol. 27, pp. 289–291, Sept. 1975.

[8] J. C. Campbell, F. A. Blum, D. W. Shaw, and K. L. Lawley, "GaAs electro-optic directional coupler switch," *Appl. Phys. Lett.*, vol. 27, pp. 203–205, Aug. 1975.

[9] R. V. Schmidt and H. Kogelnik, "Electroptically switched coupler with stepped $\Delta\beta$ reversal using Ti diffused $LiNbO_3$ waveguides," *Appl. Phys. Lett.*, vol. 28, pp. 503–506, May 1976.

[10] S. E. Miller, "Coupled-wave throy and waveguide applications," *Bell Syst. Tech. J.*, vol. 33, pp. 661–719, May 1954.

[11] A. Yariv, "Coupled mode theory for guided wave optics," *IEEE J. Quantum Electron.*, vol. QE-9, pp. 919–933, Sept. 1973.

[12] H. Kogelnik, "Theory of dielectric waveguides," in *Integrated Optics*, vol. 7, T. Tamir, Ed. Berlin, Germany: Springer, pp. 15–79, 1975.

[13] S. E. Miller, "Broad-band electromagnetic wave coupler," U.S. patent 2 948 864, Aug. 9, 1960.

Effects of Nonlinear Propagation on Laser Focusing Properties

E. S. BLISS, ASSOCIATE MEMBER, IEEE, J. T. HUNT, P. A. RENARD, G. E. SOMMARGREN, AND H. J. WEAVER

Abstract—In a high-power laser system both the nonlinear growth of small-scale spatial irregularities on a pulse (beam breakup) and the accumulation of self-induced phase-front distortion on the spatial envelope of the pulse (whole-beam self-focusing) alter the focusing properties of the system output. We present experimental results which show simultaneously and in detail the influence of these two effects on the spatial and temporal profiles of the focused output of a simple system. In an extreme case the focused on-axis intensity is observed to be reduced by beam breakup to 20 percent of the value obtained in the absence of breakup. Diffraction code calculations of whole-beam self-focusing, which in these experiments tends to *enhance* the focused on-axis intensity, are found to agree closely with the measured results and demonstrate that whole-beam self-focusing effects depend strongly on the plane being observed.

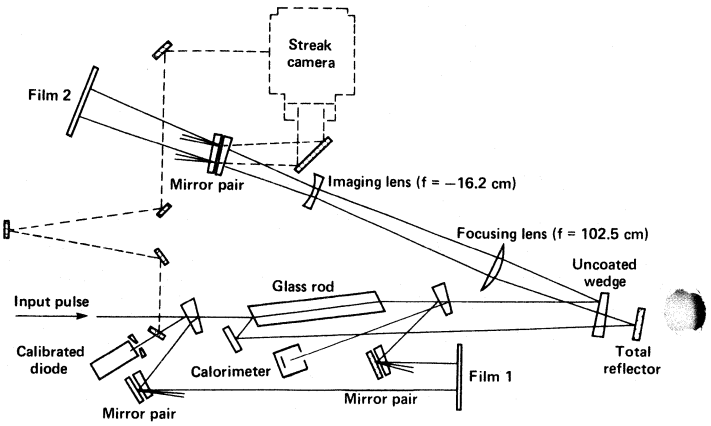


Fig. 1. Experimental arrangement for recording the effects of nonlinear propagation on laser focusing properties. Components indicated by dashed lines were not used in the initial set of measurements.

I. INTRODUCTION

THE GROWTH of small-scale intensity and phase irregularities on an intense laser pulse propagating in an optically nonlinear medium is predicted by linearized instability theory and is well documented experimentally [1]-[6]. Qualitatively one expects that focusing a beam which has significant high-frequency intensity and phase modulation over its spatial cross section will lead to a far-field pattern in which a corresponding fraction of the energy lies outside of the diffraction-limited spot size achieved by focusing a similar unmodulated beam [7]. Some attempts have been made to calculate features of the resulting far-field distribution for the early stages of beam degradation [8], but quantitative predictions are difficult because, in actual laser systems, intensity and phase profiles are complicated and not easily characterized in detail. Much of this complexity arises from the fact that sources for beam perturbations are distributed throughout the system in the form of dirt particles, small damage sites, and various material imperfections.

II. INITIAL MEASUREMENTS

As a first step in empirically determining the detailed consequences of small-scale beam degradation we have conducted experiments which measure the effects of nonlinear propagation on the focusing properties of an initially high-quality beam propagating through the simplest possible system, a single unpumped rod of ED-2 laser glass [9], [10]. The experimental arrangement is shown in Fig. 1. A collimated 1.06-μ input beam enters from the left and contains 0.5-0.7 J in a 100-200-ps (full-width half-maximum) pulse with a $1/e$ beam diameter of approximately 1 cm. Since the beam has been reduced in size by a factor of at least $2\frac{1}{2}$ after leaving the last laser amplifier, it propagates through the sample rod at an intensity more than 6 times higher than the highest intensity reached in the laser system itself. The energy in the central 2 mm of the input beam is measured by a calibrated photodiode, and an absorbing glass disk calorimeter [11] monitors the transmitted energy. Film 1 records multiple-image photographs [12] of the near-field intensity profile both before and after passage through the sample rod. Both the beam which propagates through the rod and a reference beam directed around the rod then pass through the 1-m focusing lens, and the focal plane of this lens is imaged with a magnification of 10 onto film 2. Each photograph contains all the information needed for accurately determining the response characteristics of the film and thus for converting from film density to laser energy density [13]. The sample is a high-optical-quality amplifier rod and does not introduce any detectable aberrations at low intensity.

Fig. 2 shows several exposures from each of the four photographs taken for a typical intense pulse. Severe beam breakup is evident in the near-field picture of the output beam, and in the far-field some distortion of the focused beams can be seen. The input focuses to an essentially diffraction-limited spot with some evidence of astigmatism while the output beam focuses to an equally small spot but with some side lobes resulting from a combination of nonlinear effects and weak astigmatism.

III. ENERGY LOSS

What is not obvious from Fig. 2 is that the focused output beam as recorded in the photograph does not contain all of the energy which entered the experiment. In fact, the fraction of input energy which contributes to this exposure decreases as the input intensity and corresponding beam breakup

Manuscript received December 18, 1975. This work was performed under the auspices of the U.S. Energy Research and Development Administration under Contract W-7405-Eng-48.

The authors are with the Lawrence Livermore Laboratory, University of California, Livermore, CA 94550.

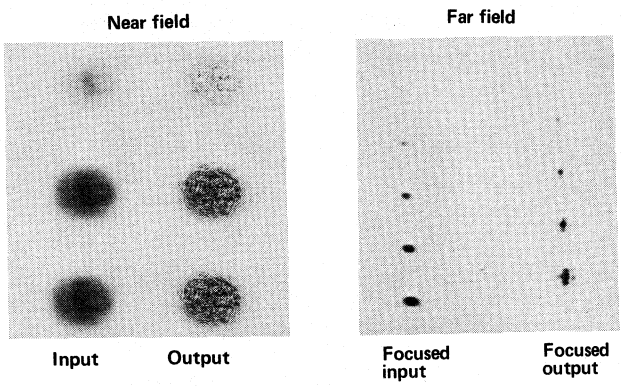


Fig. 2. Representative photographs obtained using the apparatus shown in Fig. 1.

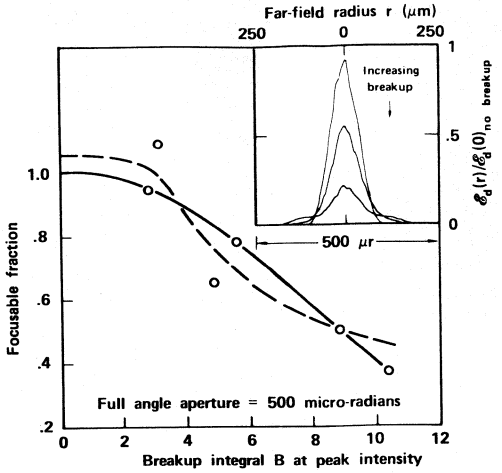


Fig. 3. Inset: Radial scans through the far-field energy-density profiles for shots with three different pulse energies. Main figure: The fraction of laser energy entering the focusing lens within a 500-μrad full-angle cone as a function of B accumulated in the sample rod at the temporal peak of the pulse. The B values do not include contributions from the laser itself. Representative accumulations in the laser are approximately 0.3 at $B = 2$ and 3.0 at $B = 10$. The ordinate is normalized to 1 at $B = 0$ for the solid curve. In reading the dashed curve the values should be renormalized accordingly.

increase. This effect is illustrated by the inset in Fig. 3, which shows radial scans through far-field energy-density profiles obtained from shots with a range of pulse energies. Each profile is normalized to the on-axis energy density obtained in the corresponding focused input photograph, and integrating over the area of these recorded profiles confirms that there is a significant loss of energy when breakup occurs [14]. The missing energy must be focused outside the 500-μ aperture of the photograph, or, equivalently, it entered the 1-m focusing lens with a full-angle divergence exceeding 500 μrad. This is consistent with both the approximately 0.5-mm structure seen in the near-field output and with the 2-mrad half-angle scattering predicted by linearized instability theory for the fastest growing instabilities at an intensity of 7 GW/cm^2 [1], near the maximum intensity used in these measurements.

In a system where the laser intensity does not change drastically with propagation distance, the total ripple gain predicted by linearized instability theory for the fastest growing spatial frequency is approximately [15][1]

$$\Delta I/(\Delta I)_0 = \exp\left[\int_o^L (2\pi\gamma I/\lambda)\, dz\right] \equiv \exp B \qquad (1)$$

where L is the propagation distance in the nonlinear medium, I is the laser intensity, λ is the laser wavelength in vacuum, and the intensity-induced change in the index of refraction is given by $\Delta n = \gamma I$.[2] Therefore, to the extent that all systems of interest have approximately the same input beam quality, the integral B is expected to serve as a useful parameter for characterizing accumulated beam breakup [18].[3] The main part of Fig. 3 shows the fraction of the input energy that entered the focusing lens within a 500-μrad full-angle cone as a function of B accumulated in the sample rod. Given the extent of scatter in the data, considerable uncertainty exists in choosing a "best fitting" curve. The solid curve results from constraining the initial slope to be zero and postulating that there should be no point of inflection over the range of B studied. The dashed curve results from more elaborate considerations [19]. Whatever the details of the curve one chooses, however, the unavoidable conclusion is that beam breakup in lasers containing optically nonlinear materials can lead to a severe reduction in the fraction of the output which can be usefully focused.

IV. Time-Resolved Measurements

It is important to remember that the photographic data discussed to this point necessarily give information about breakup effects averaged over both the temporal and spatial profiles of the input beam. Since the modulation depth of the beam profile grows exponentially with intensity and the loss from the focal spot increases nonlinearly with modulation depth [7], [8], the fraction lost from the temporal and spatial peak of the pulse is expected to be considerably larger than the average over the whole pulse. Severe temporal and spatial distortion could occur as a result of preferentially depleting the high-intensity parts of the pulse. Recognition of this fact led us to add a 10-ps-resolution streak camera [20] to the experiment as shown by the dashed lines in Fig. 1. With this arrangement we obtain a much more detailed picture of the effects of nonlinear propagation.

A. Whole-Beam Self-Focusing

The time-integrated far-field photographs, which record an image of the beam in a plane slightly ahead of the low-intensity focus, typically show a central bright spot surrounded by concentric rings of gradually decreasing intensity and rather low contrast as seen in Fig. 4. The central maximum and the rings are also detected on the streak camera,

[1] A similar expression for perturbation growth expressed in terms of the electric field and a nonlinear dielectric-constant coefficient can be found in [16].

[2] The value of γ for ED-2 glass is 4.1×10^{-7} cm^2/GW [17]. The change in refractive index is often expressed as $\Delta n = n_2 < E^2 >$, where E is the electric field amplitude, $n_2 = nc\gamma/4\pi$ in electrostatic units, and c is the speed of light in a vacuum.

[3] It is also a measure of the accumulated nonlinear phase delay, the number of waves of phase delay being given by $B/2\pi$.

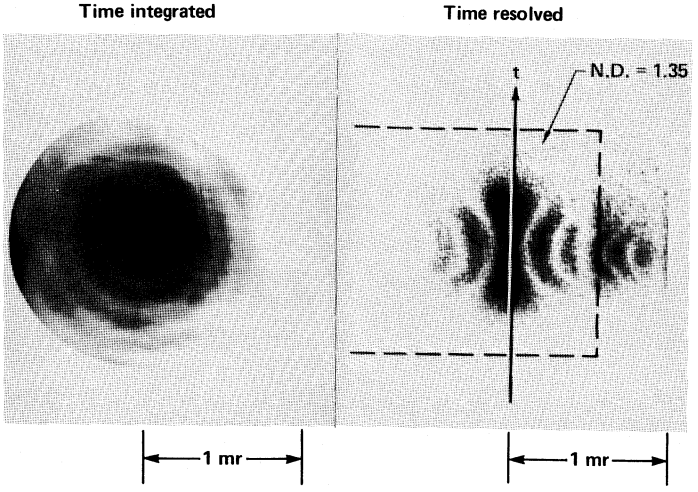


Fig. 4. Comparison of time-integrated and time-resolved far-field photographs for a plane slightly ahead of best focus. The time-resolved photograph records the temporal development of a radial slice through the intensity distribution in the same plane as the time integrated photo. It shows clearly the intensity dependence of the diffraction ring diameters.

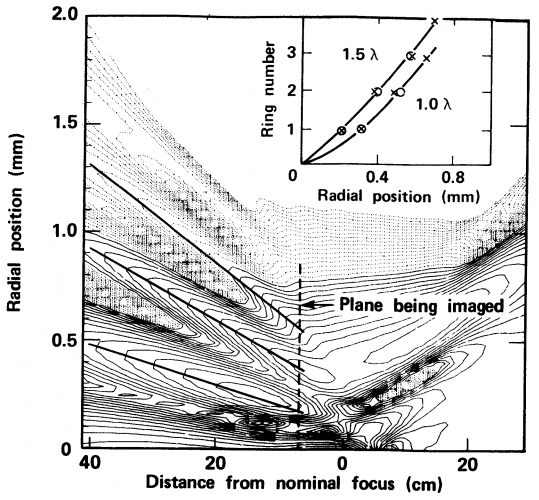


Fig. 5. Main figure: Calculated constant intensity contours in the focal region for an accumulated on-axis phase delay of 1.5λ. The solid dark lines identify the positions of diffraction rings. Inset: Calculated (○) and measured (×) diffraction ring radii in the plane imaged in Fig. 4 for accumulated phase delays of 1.0λ and 1.5λ.

which is aligned to record the temporal development of a radial slice through the far-field intensity distribution in the same image plane. The streak camera photograph in Fig. 4 shows that the rings have an intensity-dependent radius with the smallest radius occurring at the temporal peak of the pulse. The useful dynamic range of the camera has been increased by use of a filter with an optical density of 1.35 in the central, most intense part of the image.

The formation of these rings, and the details of their motion can be accurately predicted by calculations of the self-focusing properties of the beam as a whole. Using a nonlinear optical-ray tracing code for propagating the initially Gaussian spatial-intensity profile through the glass sample [21] and a linear diffraction code for propagating the resulting distorted beam through the lens to the focus [22], we have generated constant-intensity contour plots of the focal region for a range of input intensities. Fig. 5 shows the focal region for an accumulated phase delay on the beam axis of 1.5λ, which corresponds to the peak input intensity reached by the pulse in Fig. 4. The beam comes from the left, and in the region ahead of the focus the intensity contours confirm the presence of several diffraction rings, which are identified by solid dark lines.

In the inset of Fig. 5 the radial position of each ring in the plane indicated by the dashed line is plotted (○) both for the 1.5λ calculation and for 1.0λ. On the same plot (×) are the corresponding ring positions measured on the streak picture in Fig. 4 at peak intensity, and two-thirds peak intensity. The shift in the radial position of a given ring as the intensity is changed results from the combined effects of intensity-dependent aberrations and intensity-dependent focal position, the point of best focus being drawn closer to the lens as the intensity increases. If an image plane more than 12 cm further from the focusing lens had been chosen for the experiment, the contour plot shows that an on-axis minimum would have been observed at the peak of the pulse, and such on-axis reductions have been previously reported [23]. It is important to recognize, however, that the effects of whole-beam self-focusing on beam-focusing properties depend strongly on the plane being observed and, of course, on the radial intensity and phase profiles of the initial beam [24].

B. Small-Scale Beam Breakup

Small-scale nonlinear effects are superimposed on the whole-beam behavior just described, and they lead to additional intensity-dependent far-field features which account for the energy loss observed in the initial experiments. The time-integrated far-field picture in Fig. 6 has been intentionally overexposed on the beam axis in order to record light with several orders of magnitude lower intensity at large radii. As a result the central ring pattern is not visible and is drawn in schematically. Now at radii corresponding to scattering angles as large as 4 mrad, blotches of light are seen which, when integrated over the extremely large area involved, account for a significant portion of the total beam energy.

The streak camera picture in Fig. 6 confirms our initial suspicion that the high-divergence components of the far-field energy distribution are coming from the temporal peak of the pulse (and, by inference, from the spatial peak as well). The on-axis intensity, as determined by a densitometer scan with appropriate allowance for camera and film response characteristics [25], behaves in an apparently normal fashion as a function of time except near the time corresponding to the peak of the input pulse when losses from the center of the far-field pattern suddenly increase and light appears at an angle of about 1.5 mrad. From the time-integrated photograph it seems quite plausible that a blotch of light could fall on the streak camera slit at 1.5 mrad, and we believe that all of the energy in the rather random pattern of large-angle light is generated in the same way, namely, by being scattered during beam breakup in the high-intensity parts of the pulse. Some energy may also be lost completely from the beam, absorbed

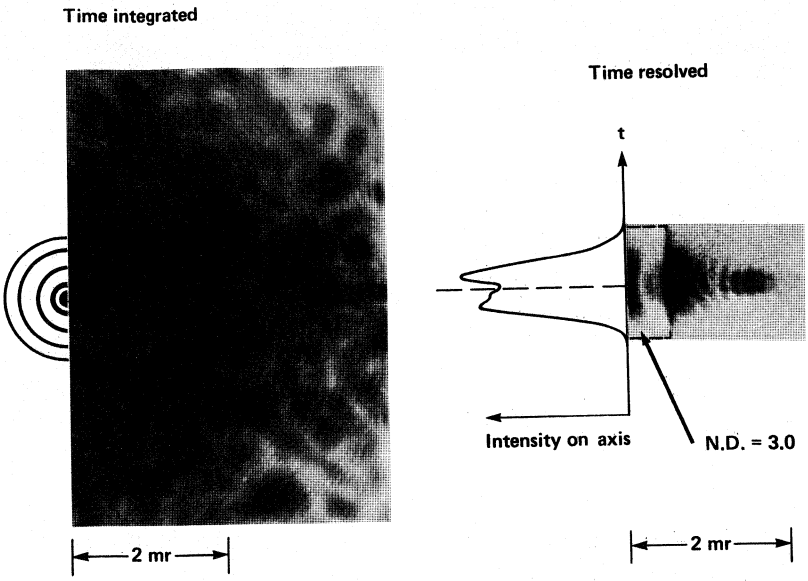


Fig. 6. Time-integrated and time-resolved far-field photographs of a plane slightly ahead of best focus. The exposure levels are chosen to show the energy which is scattered out of the central part of the beam at angles on the order of milliradians. The time-resolved photo confirms that the scattered light appears predominantly at the peak of the pulse and that depletion of the on-axis intensity occurs at the same time.

nonlinearly, for example. However, earlier measurements in ED-2 have shown the intensity dependent absorption to be less than 10 percent at the maximum intensity used here [26], and some portion of that 10 percent may actually have been due to beam breakup.

Loss from beam breakup is observed in varying degrees over a range of peak B values, and the depletion of the temporal peak of the pulse can be quite severe. For the pulse in Fig. 7, for example, the power in the central 12 μ of the focused beam is reduced to less than 20 percent of its expected value at the peak of the pulse, with smaller but significant losses being measured as the streak photo is integrated over larger apertures. This large loss and the steepness of the time-resolved focusable fraction versus the B curve obtained for this pulse suggest that there is no real limit on the extent to which focusing can be degraded by small-scale beam breakup in a rod. It has been correctly noted [8] that calculations which predict such a limit on the loss of focusability, but which are based on a formalism that assumes small perturbations on the beam, cannot be applied to the advanced stages of self-focusing.

The time-resolved power focused inside of the 12-μ aperture is actually influenced by both whole-beam and small-scale self-focusing. Initially, as the intensity of the input pulse increases, whole-beam self-focusing draws the point of best focus toward the lens, thus enhancing the measured on-axis intensity in a plane ahead of the low-intensity focus. As the input intensity continues to rise, however, high angle losses from beam breakup increase abruptly and dominate the focusing properties for large B values. A feature of Fig. 7 not yet understood is the leading- and trailing-edge asymmetry of the power versus time curves. This asymmetry may not be real, and may simply be an indication of the amount of uncertainty inherent in the experiment. On the other hand, it has been seen on several shots and the sense of the asymmetry has never been reversed. In plotting the focused fraction curves for Fig. 7 the leading and trailing edges of the pulse have been averaged.

V. Conclusions

The results of the experiments described above strongly suggest that a high-power solid-state laser system must not only be carefully designed and built to minimize beam irregularities caused by dirt particles, material imperfections, diffraction from apertures, and other "noise" sources, some provision must also be made for removing the remaining small-scale structure, which will inevitably appear in spite of good design, before it becomes large enough to cause severe degradation of the laser's focusing properties as well as component damage. Vacuum spatial filters meet this need. They are now being used in present systems [27] and are recognized as crucial components in the optimization of new and larger laser systems, forcing the exponential growth of small-scale irregularities to start over again for those spatial frequencies which are removed [28]-[29].

At the same time, the effects of whole-beam self-focusing on focal properties must be kept within tolerable limits, and the close agreement shown in this paper between calculated and measured whole-beam distortions demonstrates a capability for modeling such effects accurately.

The results reported here also have important implications for the use of solid-state lasers in irradiating small targets. Target diagnostics must be capable of determining how much energy actually reached the target and to what extent the spatial and temporal profiles of the focused beam were altered by the effects of nonlinear propagation in the laser [30]. Tar-

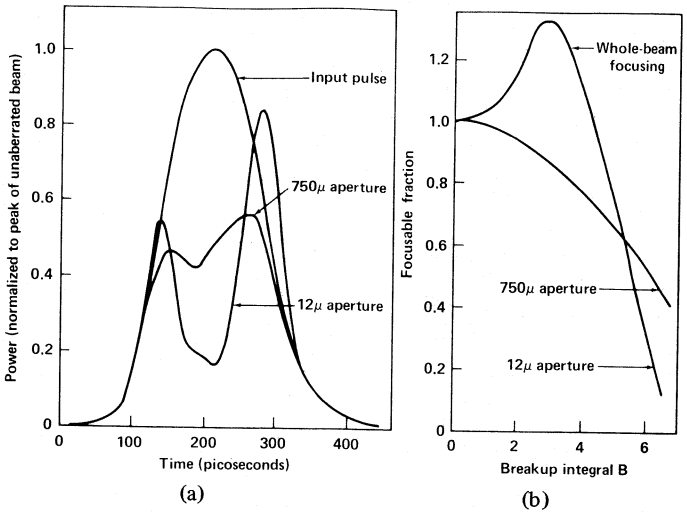


Fig. 7. (a). An example of the severe temporal distortion which can be caused by nonlinear propagation. (b) Corresponding plots of the fraction of the pulse power which is focused through two different diameter apertures as a function of the breakup integral B. The initial rise of the "12-μ aperture" curve is explained in the text.

get designers must also take note of the dynamic nature of the focusing properties of high-power solid-state lasers and model the laser/target interactions accordingly.

Acknowledgment

The authors acknowledge the important experimental contributions of G. E. Murphy and the densitometry services of the LLL Technical Photography Group. We have also benefited from frequent discussions with LLL Laser Program colleagues, many of whose names are found among the references.

References

[1] V. I. Bespalov and V. I. Talanov, "Filamentary structure of light beams in nonlinear liquids," *JETP Lett.*, vol. 3, pp. 307-310, June 1966.

[2] A. J. Campillo, S. L. Shapiro, and B. R. Suydam, "Periodic breakup of optical beams due to self-focusing," *Appl. Phys. Lett.*, vol. 23, pp. 628-630, Dec. 1973.

[3] J. R. Jokipii and J. Marburger, "Homogeneity requirements for minimizing self-focusing damage by strong electromagnetic waves," *Appl. Phys. Lett.*, vol. 23, pp. 696-698, Dec. 1973.

[4] A. J. Campillo, S. L. Shapiro, and B. R. Suydam, "Relationship of self-focusing to spatial instability modes," *Appl. Phys. Lett.*, vol. 24, pp. 178-180, Feb. 1974.

[5] E. S. Bliss, D. R. Speck, J. F. Holzrichter, J. H. Erkkila, and A. J. Glass, "Propagation of a high-intensity laser pulse with small-scale intensity modulation," *Appl. Phys. Lett.*, vol. 25, pp. 448-450, Oct. 1974.

[6] J. M. McMahon, "Limitations on high peak power lasers," in *Tech. Dig. Int. Electron Devices Meeting*, Dec. 1974, pp. 307-310.

[7] J. W. Goodman, *Introduction to Fourier Optics.* New York: McGraw-Hill, 1968, pp. 65-70.

[8] B. R. Suydam, "Effect of refractive index nonlinearity on the optical quality of high power laser beams," *IEEE J. Quantum Electron.*, vol. QE-11, pp. 225-230, June 1975.

[9] E. S. Bliss, G. E. Sommargren, and H. J. Weaver, "Far-field consequences of nonlinear propagation," in the *1974 Lawrence Livermore Laboratory Laser Program Ann. Rep.* (UCRL-50021-74), Mar. 1975, pp. 193-196.

[10] —, "Loss of focusable energy due to small-scale nonlinear effects," *1975 IEEE/OSA Conf. on Laser Engineering and Applications—Technical Dig.*, May 1975, p. 29.

[11] S. R. Gunn, "Volume-absorbing calorimeters for high-power laser pulses," *Rev. Sci. Instrum.*, vol. 45, pp. 936-943, July 1974.

[12] D. C. Burnham, "Laser beam photography by a multiple beam technique," *Appl. Opt.*, vol. 9, p. 1482, June 1970.

[13] I. M. Winer, "A self-calibrating technique for measuring laser beam intensity distributions," *Appl. Opt.*, vol. 5, pp. 1437-1439, Sept. 1966.

[14] Bliss *et al.*, Talk D.6, presented at the 8th Int. Quantum Electron. Conf., San Francisco, CA, June 1974 (unpublished), first presentation and discussion of this data.

[15] J. B. Trenholme, "Small-scale instability growth: Review of small signal theory," in the *1974 Lawrence Livermore Laboratory Laser Program Ann. Rep.* (UCRL-50021-74), Mar. 1975, pp. 179-191.

[16] B. R. Suydam, "Self-focusing of very powerful laser beams II," *IEEE J. Quantum Electron.*, vol. QE-10, pp. 837-843, Nov. 1974.

[17] E. S. Bliss, D. R. Speck, and W. W. Simmons, "Direct interferometric measurements of the nonlinear refractive index coefficient n_2 in laser materials," *Appl. Phys. Lett.*, vol. 25, pp. 728-730, Dec. 1974.

[18] J. B. Trenholme, private communication, May 1974.

[19] —, "Deconvolution of spatial-filter curves," in the *1974 Lawrence Livermore Laboratory Laser Program Ann. Rep.* (UCRL-50021-74), Mar. 1975, pp. 197-199.

[20] S. W. Thomas, G. R. Tripp, and L. W. Coleman, "Ultrafast streaking camera for picosecond laser diagnostics," *Proc. 10th Int. Congress on High Speed Photography* (Paris, France: National Association of Technical Research, 1972), pp. 127-133.

[21] J. T. Hunt, R. G. Nelson, and P. A. Renard, "Numerical calculations of nonlinear propagation," in the *1974 Lawrence Livermore Laboratory Laser Program Ann. Rep.* (UCRL-50021-74), Mar. 1975, pp. 206-211.

[22] J. T. Hunt, P. A. Renard, and R. G. Nelson, "Focusing properties of an aberrated laser beam," *Appl. Opt.*, June 1976.

[23] A. J. Campillo, Robert A. Fisher, R. C. Hyer, and S. L. Shapiro, "Streak camera investigation of the self-focusing onset in glass," *Appl. Phys. Lett.*, vol. 25, pp. 408-411, Oct. 1974.

[24] J. T. Hunt and P. A. Renard, "Propagation of super-Gaussian and quadratic intensity profiles-A numerical study," in the *1974 Lawrence Livermore Laboratory Laser Program Ann. Rep.* (UCRL-50021-74), Mar. 1975, pp. 203-206.

[25] H. J. Weaver, G. E. Sommargren, and E. S. Bliss, "Self-calibration and analysis of image formation in the subnanosecond domain," in *Proc. 18th Ann. Tech. Meeting of the Society of Photo-Optical Instrumentation Engineers*, Aug. 1974, pp. 63-68.

[26] D. R. Speck and E. S. Bliss, "Studies of material properties for solid-state laser design," in the *1973 Lawrence Livermore Laboratory Laser Fusion Program Semiann. Rep. Jan.-June 1973* (UCRL-50021-73-1), Aug. 1973, pp. 20-29.

[27] W. W. Simmons, S. Guch, Jr., F. Rainer, and J. E. Murray, "A high energy spatial filter for removal of small scale beam instabilities in high power solid state lasers," *1975 IEEE/OSA Conf. Laser Engineering and Applications—Technical Dig.*, May 1975, p. 30.

[28] J. B. Trenholme, "Optical chain design with spatial filtering," in the *1974 Lawrence Livermore Laboratory Laser Program Ann. Rep.* (UCRL-50021-74), Mar. 1975, pp. 84-88.

[29] J. A. Glaze, "High energy glass lasers," *Opt. Eng.*, vol. 15, pp. 136-141, Mar. 1976.

[30] J. F. Holzrichter and D. R. Speck, "Laser focusing limitations from non-linear beam instabilities," *J. Appl. Phys.*, May 1976.

Effect of Fabry–Perot Interference on Second Harmonic Generation in a GaAs Plate

J. P. VAN DER ZIEL

Abstract—**The transmitted and reflected second harmonic generation is computed for a parallel-plate Fabry–Perot structure including all the effects of interference and multiple reflections. As a function of wavelength, the spectra consist of rapid Fabry–Perot oscillations superimposed on the more slowly varying coherence-length fringes. The harmonic generation from a 97.5-μm-thick GaAs plate, obtained using a fundamental near 2 μm from a wavelength-tunable parametric oscillator, is in good agreement with the theoretical calculations.**

I. Introduction

THE measurement of nonlinear optical coefficients usually requires a determination of the second harmonic intensity and the index mismatch between the fundamental and harmonic waves [1], [2]. This can be obtained by measuring the intensity as a function of optical thickness, and is normally accomplished by either rotating a flat nonlinear plate about an axis perpendicular to the plane of incidence [3]–[5], or by translating a slightly wedged sample transverse to the beam [6], [7]. In each case the harmonic intensity shows a well-known oscillatory pattern which, for the rotation of the flat plate, is known as Maker fringes [3].

In a detailed analysis of Maker fringes, Jerphagnon and Kurtz have included the effects of multiple reflections, but have purposely neglected the interference effects due to multiple reflections from the front and back surfaces [4]. This is justified for the translation technique, as well as for the rotation method where the data are normally taken away from normal incidence and extrapolated to zero angle. In Section II we compute the second harmonic intensity for a flat nonlinear plate including the effects due to interference. It is shown that the interference effects become important when Fabry–Perot interference is observed in the spectrum of the transmitted fundamental.

The experimental spectrum of second harmonic generation obtained from a thin GaAs plate utilizing a fundamental beam from a temperature-tuned optical parametric oscillator is discussed in Section III. Multiple interference effects are quite important here because of the ~30-percent reflection, both at the fundamental and harmonic, at the GaAs–air interfaces. In this experiment the sample is kept at normal incidence, and the optical phase thickness varied both with the direct dependence of the phase on wavelength, and the indirect wavelength dependence of the difference in the refractive indices at ω and 2ω. Then the analog of the coherence length in the Maker fringe experiment is the wavelength shift of the fundamental which is required for the intensity to vary from zero to a maximum

$$\delta\lambda_{CL} = \frac{\lambda_\omega^2}{4L\left[\lambda_\omega \dfrac{\partial \Delta n}{\partial \lambda_\omega} - \Delta n\right]} \tag{1}$$

where L is the length of the crystal and $\Delta n = n_{2\omega} - n_\omega$. The corresponding spacing for the Fabry–Perot fringes is

$$\Delta\lambda_{FP} = \frac{\lambda^2}{4L\left[\lambda \dfrac{\partial n}{\partial \lambda} - n\right]}. \tag{2}$$

Since $\delta\lambda_{CL} \gg \delta\lambda_{FP}$, the fringe pattern of the second harmonic appears as a coherence-length envelope modulating the more rapidly varying Fabry–Perot patterns at the fundamental and harmonic which result from the standing waves in the crystal.

Manuscript received January 7, 1976.
The author is with Bell Laboratories, Murray Hill, NJ 07974.

II. Theory

In this section we treat harmonic generation in a plane parallel plate including the effects due to interference of the multiple reflections at the fundamental and second harmonic. As shown in Fig. 1 the plate, denoted by region 2, is immersed in linear media labeled 1 and 3. The plate is assumed to be an isotropic nonlinear crystal. In particular, the results apply directly to the (110)-oriented GaAs plate, discussed in Section III, with the fundamental polarized along $[\bar{1}10]$ and the harmonic consequently polarized along [001]. The fundamental of power P_ω is incident normal to the surface from the left. In medium 1 it has field amplitude F_{1R} and wave vector $\kappa_1 = 2\pi n_1/\lambda_\omega$. The transmitted fundamental and reflected amplitudes are F_{3R} and F_{1L} and the field amplitudes inside the crystal are F_{2R} and F_{2L}. The solution of the boundary value problem yields the field amplitudes in terms of F_{1R}:

$$F_{3R} = t_{12}t_{23}\exp(i\kappa_2 L)F_{IR}/D_\omega \tag{3}$$

$$F_{1L} = (r_{12} + r_{23}\exp(i2\kappa_2 L))F_{IR}/D_\omega \tag{4}$$

$$F_{2R} = t_{12}F_{1R}/D_\omega \tag{5}$$

$$F_{2L} = t_{12}r_{23}\exp(i\kappa_2 L)F_{1R}/D_\omega \tag{6}$$

where from the Fresnel formulas at the fundamental

$$r_{ij} = \frac{n_i - n_j}{n_i + n_j} \tag{7a}$$

$$t_{ij} = \frac{2n_i}{n_i + n_j} \tag{7b}$$

and the effect due to multiple reflections is given by

$$D_\omega = 1 + r_{12}r_{23}\exp(2i\kappa_2 L). \tag{8}$$

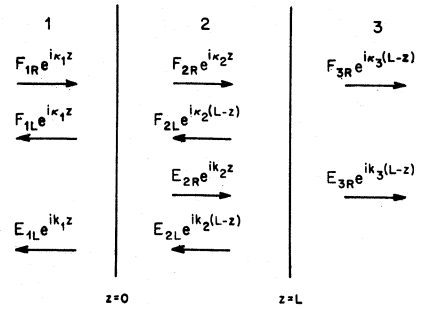


Fig. 1. The nonlinear crystal 2 immersed in linear media 1 and 3. The fundamental field amplitudes are identified by F with $F_{1R}\exp(i\kappa_1 z)$ incident from the left. The free harmonic waves are denoted by $E_l \exp(ik_l z)$. The bound harmonic waves are not shown.

The wave equation for the harmonic in the nonlinear medium is

$$\nabla^2 E + k_2^2 E = -\mu_0(2\omega)^2 [P_R^{NL} + P_L^{NL}] \tag{9}$$

where for the GaAs plate having the previously discussed orientation,

$$P_R^{NL} = -\epsilon_0 d_{14} F_{2R}^2 \exp(2i\kappa_2 z) \tag{10a}$$

$$P_L^{NL} = -\epsilon_0 d_{14} F_{2L}^2 \exp(2i\kappa_2 (L - z)) \tag{10b}$$

are the nonlinear polarizations propagating to the right and left, respectively. The solution of the inhomogeneous equation yields the bound wave propagating with a wave vector $2\kappa_2$ and amplitude

$$E_{2BR} = \frac{\mu_0 \epsilon_0 (2\omega)^2}{(k_2^2 - (2\kappa_2)^2)} d_{14} F_{2R}^2 \tag{11}$$

with a similar expression for the bound harmonic wave traveling to the left (E_{2BL}). The solution of the homogeneous part of (9) yields the free electric field amplitudes in each region as shown in the bottom half of Fig. 1. Matching of the free and bound waves at the boundaries then yields the complete solutions in terms of the forced wave amplitudes. Let p_i denote the refractive index of the harmonic in layer i, and let ρ_{ij} and τ_{ij} denote the Fresnel reflectivity and transmission at the i,j interface at the harmonic. We obtain

$$\begin{aligned} E_{1L} = {} & (p_2 + p_3) \cdot D_{2\omega}^{-1} \{E_{2BR} [(p_2 - n_2) \\ & - (p_2 + n_2)\rho_{23} \exp(2ik_2 L) \\ & - (p_3 - n_2)\tau_{23} \exp(i(k_2 + 2\kappa_2)L)] \\ & + E_{2BL} [(p_2 + n_2) - (p_2 - n_2)\rho_{23} \exp(2ik_2 L)) \\ & \cdot \exp(2i\kappa_2 L) - (p_3 + n_2)\tau_{23} \exp(ik_2 L)]\} \end{aligned} \tag{12}$$

and

$$\begin{aligned} E_{3R} = {} & (p_1 + p_2) D_{2\omega}^{-1} \{E_{2BR} [((p_2 + n_2) - (p_2 - n_2)\rho_{21} \\ & \cdot \exp(2ik_2 L)) \exp(2i\kappa_2 L) - (p_1 + n_2)\tau_{21} \\ & \cdot \exp(ik_2 L)] + E_{2BL} [(p_2 - n_2) - (p_2 + n_2)\rho_{21} \\ & \cdot \exp(2ik_2 L) - (p_1 - n_2)\tau_{21} \exp(i(k_2 + 2\kappa_2)L)]\} \end{aligned} \tag{13}$$

where

$$D_{2\omega} = (p_1 + p_2)(p_2 + p_3)\{1 + \rho_{12}\rho_{23} \exp(2ik_2 L)\}. \tag{14}$$

The second harmonic intensity outside the crystal is

$$P_l(2\omega) = \frac{1}{2\mu_0} \left(\frac{k_l}{2\omega}\right) |E_l|^2 \tag{15}$$

where the subscript l denotes either the left-traveling wave in medium 1, ($1L$), or the right-traveling wave in medium 3 ($3R$). Spatial integration over the cross section of the Gaussian beam yields the total harmonic power.

The terms in the numerator of (12) and (13) give rise to the coherence-length fringe pattern. In (12) the first term in E_{2BR} is the reflected wave from the (1, 2) interface which was first observed by Ducuing *et al.* [8]. The remaining terms involve the effects due to the (2, 3) interface. The first term in E_{2BL} is due to the harmonic transmitted from 2 to 1 due to the reflected bound wave E_{2BL}. In (13) the first and third terms in E_{2BR} yield the usual expression for second harmonic generation from a plate [2], [9]. The remaining terms are due to the effects of the reflections.

The denominator of $P_l(2\omega)$ contains the factor $D(\omega)^2 \cdot D(2\omega)$ which yields the Fabry-Perot interference effects. Fig. 2 is a plot of the transmitted fundamental power between 1.9 and 2.1 μm for a 97.5-μm-thick GaAs plate in air, and was computed using the published dispersion data [10]. The intensity maxima of the transmitted power coincide with the minima in the reflected power and from (3), (5), (6), also with the maxima of the fields within the crystal. Because of dispersion the Fabry-Perot spacing of the harmonic differs from the spacing of the fundamental, and the peaks in the second harmonic intensity, due to interference effects of the fundamental and harmonic, occur generally at different wavelengths.

The computed second harmonic spectrum is shown in Fig. 3(a) and (b), and consists of the previously mentioned rapid oscillations due to interference with a more slowly varying coherence-length envelope. The strongest harmonic peaks are, in general, close to the peaks in the fundamental power density in the plate. The small shifts are due to a pulling effect of the harmonic Fabry-Perot modes. There are weaker subsidiary peaks which are identified with the second harmonic Fabry-Perot modes. This fine structure is due to the interference effect and is absent for a slab which is not an interferometer which exhibits only coherence-length fringes [4]. The intensity of the reflected harmonic is about a factor of 8 weaker than the transmitted harmonic, and this is due to the smaller $P_{2L}(\omega)$ relative to the $P_{2R}(\omega)$ and the index factors appearing in (12) and (13). In addition, the coherence-length fringe pattern of the transmitted harmonic is more sharply peaked than the reflected harmonic. For the latter the intensity near the peak is reduced because of partial destructive interference of the forward- and backward-traveling bound wave terms, and results from an effective doubling of the crystal length for this configuration. This is most evident for the symmetric patterns near 2.025 and 2.062 μm in Fig. 3(b) where these peaks are less intense than the neighboring peaks.

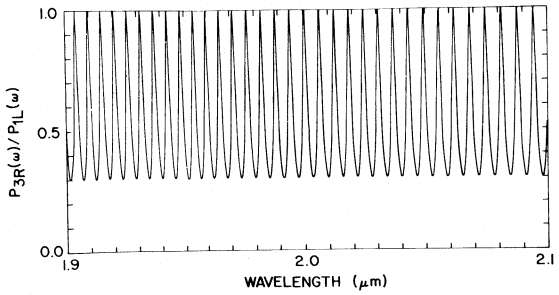


Fig. 2. The computed transmitted spectrum $P_{3R}(\omega)/P_{1R}(\omega)$ of the fundamental intensity outside a 97.5-μm-thick GaAs plate in vacuum.

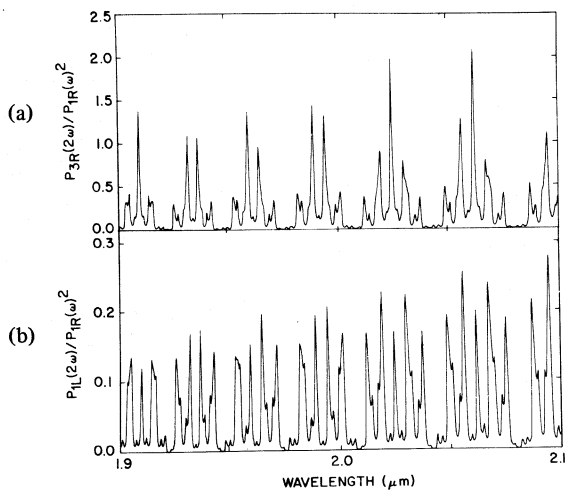


Fig. 3. Computed spectrum of the second harmonic intensity outside a 97.5-μm-thick GaAs plate in vacuum. (a) $P_{3R}(2\omega)/P_{1R}(\omega)^2$. (b) $P_{1L}(2\omega)/P_{1R}(\omega)^2$.

III. Experimental

The experimental arrangement is shown in Fig. 4. The fundamental is obtained from a temperature-tuned Chromatix optical parametric oscillator (*OPO*) which was pumped by 0.659-μm radiation from a doubled YAG:Nd laser. The output from the laser and oscillator had a zeroth-order Gaussian transverse mode shape. The glass and antireflection-coated germanium filter eliminated all radiation except the fundamental near 2 μm. The fundamental is polarized in the vertical plane along [$\bar{1}$10] by *POL*1, and focused by the 15-cm f.l. lens into the crystal. For radiation from the *OPO* the confocal parameter of this lens is 3.1 mm, and for a crystal with $L = 97.5$ μm, $L/b = 0.031$. Thus this lens has enough focusing power to yield an appreciable second harmonic signal, and yet has a sufficiently parallel beam so that the unfocused wave approximation remains approximately valid. The transmitted harmonic is polarized along [001], and passes through *POL*2, the filters *F*2, and is detected by the photomultiplier (*PMT*). The reflected harmonic signal is collimated by the 15-cm lens, reflected by *POL*1 and mirror *M*1, and detected by *PMR*.

The GaAs plate was Cr doped ($\rho \sim 10^8$ $\Omega \cdot$ cm) with faces polished parallel to better than 10^{-3} rad. Fig. 5 shows the spectrum of the transmitted fundamental, and was obtained using a pyroelectric detector in place of the *PMT* in Fig. 4.

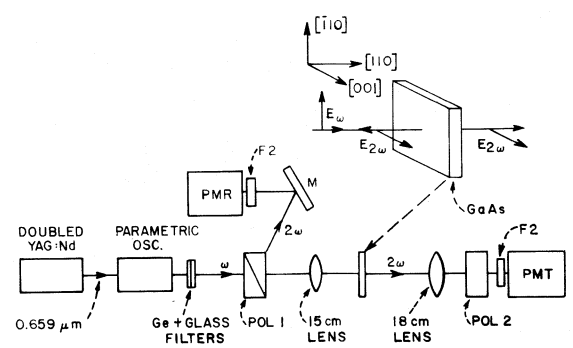


Fig. 4. Experimental arrangement for observing the wavelength dependence of forward- and backward-traveling harmonic generation. The insert shows the orientation of the GaAs sample.

The sample thickness was obtained from the fringe pattern at ω and 2ω and the index data [10]. The small difference between the transmission peaks of the fundamental and the measured intensity without the crystal (shown by the dashed curve) is due to the slight nonparallelism of the surfaces and a slight misalignment of the beam. From measurements on thick samples we have found the absorption at ω and 2ω to be less than 0.6 cm^{-1} which is sufficiently small to be neglected. Measurements were also made on n-type ($\sim 10^{18}$) GaAs sam

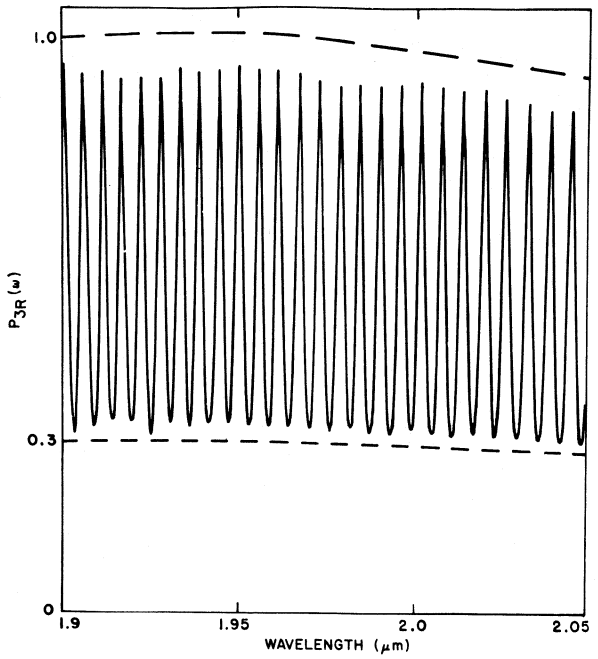


Fig. 5. Measured transmitted fundamental intensity through the 97.5-μm-thick GaAs plate.

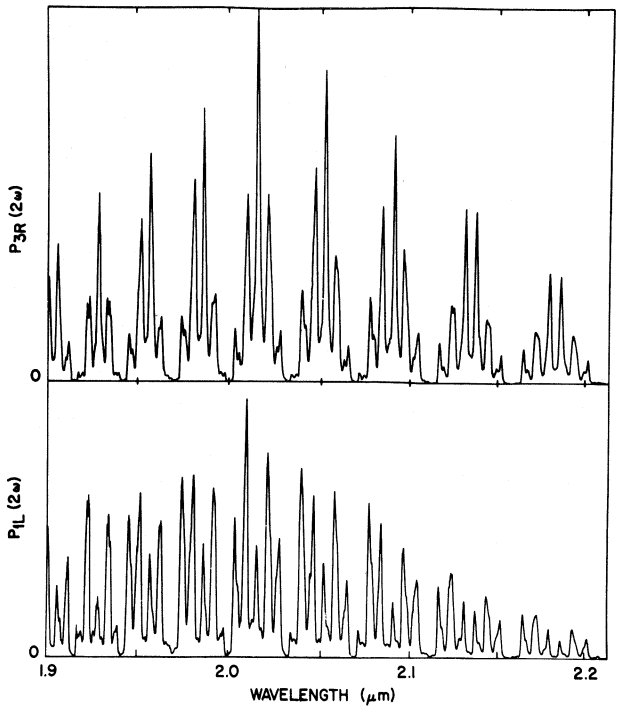


Fig. 6. Measured forward- and backward-traveling second harmonic intensities from the 97.5-μm-thick GaAs plate.

ples which had significant absorption, and hence had lower quality Fabry-Perot fringes and second harmonic interference effects.

The experimental spectrum of second harmonic generation shown in Fig. 6 is qualitatively similar to the computed spectrum (Fig. 3). It differs in detail because the Fabry-Perot oscillations are strongly dependent on small differences in the refractive indices and crystal thickness. As was mentioned for the computed spectra, the strongest harmonic intensity occurs at the Fabry-Perot peaks in the fundamental, and the weaker structure is associated with the Fabry-Perot structure of the harmonic.

The decrease in intensity at long wavelengths is primarily due to the decrease in photomultiplier sensitivity, and the decrease at short wavelength is caused by reduced filter transmission. The relative sensitivities of the photomultipliers and filters were obtained at 1.15 μm using an He-Ne laser. With this calibration the ratio of the transmitted to reflected peak harmonic intensities between 2.0 and 2.1 μm in Fig. 6 is 7.5 ± 1 which agrees well with the calculated ratio from Fig. 3. In this wavelength range the laser is focused in the center of the crystal, and all the harmonic intensity is collected by the detectors. Because of the dispersion of the refractive indices of the lenses the focus moves from the front to the back of the crystal with increasing wavelength. Consequently, the detected, transmitted, and reflected signal is a function of wavelength, and the ratio also varies.

IV. Conclusions

In this paper we have given expressions for the transmitted and reflected second harmonic intensity from a uniformly thick nonlinear plate, including the effects of interference. The Fabry-Perot interference at the fundamental and second harmonic gives rise to sharp peaks in the harmonic intensity, with the most pronounced effects due to the interference of the fundamental. The measured spectrum of the second harmonic from a 97.5-μm-thick GaAs plate is in good agreement with the calculated spectrum. The interference effects are especially important when the air-to-crystal index difference is high. This effect complicates the measurements of nonlinearities and can be avoided by using wedged or tilted samples for which the correction for the multiple reflections [4] should be applied.

Acknowledgment

The author is grateful to R. M. Mikulyak for experimental assistance and to S. Bortas for polishing the GaAs crystals.

References

[1] J. Armstrong, N. Bloembergen, J. Ducuing, and P. S. Pershan, "Interaction between light waves in a nonlinear dielectric," *Phys. Rev.*, vol. 127, pp. 1918–1939, 1962.

[2] G. D. Boyd and D. A. Kleinman, "Parametric interaction of focused Gaussian light beams," *J. Appl. Phys.*, vol. 39, pp. 3597–3639, 1968.

[3] P. D. Maker, R. W. Terhune, M. Nisenhoff, and C. M. Savage, "Effects of dispersion and focusing on the production of optical harmonics," *Phys. Rev. Lett.*, vol. 8, pp. 21–25, 1962.

[4] J. Jerphagnon and S. Kurtz, "Maker fringes: A detailed comparison of theory and experiment for isotropic and uniaxial crystals," *J. Appl. Phys.*, vol. 41, pp. 1667–1681, 1970.

[5] —, "Optical nonlinear susceptibilities: Accurate relative values for quartz, ammonium dihydrogen phosphate, and potassium dihydrogen phosphate," *Phys. Rev. B*, vol. 1, pp. 1739–1744, 1970.

[6] J. J. Wynne and N. Bloembergen, "Measurement of the lowest order nonlinear susceptibility in III–V semiconductors by second-harmonic generation with a CO_2 laser," *Phys. Rev.*, vol. 188, pp.

1211-1220, 1969.
[7] G. D. Boyd, H. M. Kasper, and J. H. McFee, "Linear and nonlinear optical properties of $AgGaS_2$, $CuGaS_2$, and $CuInS_2$, and the theory of the wedge technique for the measurement of nonlinear coefficients," *IEEE J. Quantum Electron.*, vol. QE-7, pp. 563-573, 1971.
[8] J. Ducuing and N. Bloembergen, "Observation of reflected light harmonics at the boundary of piezoelectric crystals," *Phys. Rev. Lett.*, vol. 10, pp. 474-476, 1963.
[9] R. C. Miller and W. A. Nordland, Jr., "Absolute signs of second harmonic generation coefficients of piezoelectric crystals," *Phys. Rev. B*, vol. 2, pp. 4896-4902, 1970.
[10] M. A. Afromowitz, "Refractive index of $Ga_{1-x}Al_xAs$," *Solid State Comm.*, vol. 15, pp. 59-63, 1974.

Pulse Propagation Stability in Absorbing and Amplifying Media

JEAN-CLAUDE DIELS AND ERWIN L. HAHN

Abstract—**Simple stability conditions are obtained for pulse propagation in a two-level system with linear scattering and combined homogeneous and inhomogeneous broadening. Properties of steady-state π and $\pi\sqrt{2}$ area pulses are reviewed. Computer simulation of an approach to equilibrium pulse propagation is presented in a few cases for initially perturbed pulses.**

I. Introduction

THE simple approximation of continuous weak signal propagation in an absorbing medium, leading to Beer's law of linear attenuation, ceases to be valid for high-power laser radiation and for pulses short compared with atomic damping times. Even in the simplest approximation of a two-level system which is used in the discussion to follow, it is very difficult to find general expressions for the evolution in time and distance of a coherent radiation pulse on- and off-resonance. Nonlinear amplitude and phase modulation effects build up cumulatively during propagation. An expression for the evolution of the average carrier frequency has been derived previously [1]. A related new formula is established here for the evolution of the pulse mean-square spectral width. The medium is represented by an ensemble of two-level atoms in which we take into account both homogeneous and inhomogeneous broadening as well as linear scattering. The two-level system is either initially inverted (amplifier) or initially in the ground state (absorber).

The study of the evolution of the pulse spectral width is important in understanding the function of high-power laser amplifiers and associated saturable absorbers. The analysis to be presented provides a criterion which determines whether or not a small initial phase modulation of a pulse entering the medium will grow or disappear after propagation through the medium.

Distortionless propagation of several pulse shapes in absorbing or amplifying media in the steady state has been shown analytically [1]-[4]. Pulse shapes, such as the hyperbolic secant function for the 2π pulse of self-induced transparency [2], and the traveling-wave laser π pulse of Arecchi and Bonifacio [3a)] and Armstrong and Courtens [3b)] are examples. It is impossible to draw any conclusion as to the stability or instability of these distortionless pulses from a steady-state analysis alone. The spectral evolution equations developed in this paper are seen to provide criteria for stability.

II. Spectral Evolution Equations

The same notation and basic equations are used as in [1] and [2] to describe the pulse propagation of a plane wave in the slowly varying envelope approximation through a medium which contains a two-level system. The combination of Maxwell's equations with macroscopic dipole source terms v (absorptive) and u (dispersive) is written in the retarded reference frame as

$$\frac{\partial \mathcal{E}}{\partial z} = \left\{ -\frac{2\pi\omega}{\eta c} \int_{-\infty}^{\infty} vg(\delta)\, d\delta \right\} - \frac{\sigma \mathcal{E}}{2} \tag{1}$$

$$\mathcal{E}\frac{\partial \varphi}{\partial z} = -\frac{2\pi\omega}{\eta c} \int_{-\infty}^{\infty} ug(\delta)\, d\delta. \tag{2}$$

The inhomogeneous spectral distribution for the two-level system is given by $g(\delta)$ where δ is the spectral deviation from the average resonance ω_0 of the systems. The linear scattering coefficient is given by σ, and η is the host-medium refractive index assumed to be constant. With the traveling wave given by

Manuscript received January 8, 1976. The work of J. C. Diels was supported by the Los Alamos Scientific Laboratory, University of California. The work of E. L. Hahn was supported by the National Science Foundation.

J. -C. Diels is with the Center for Laser Studies, University of Southern California, University Park, Los Angeles, CA 90007.
E. L. Hahn is with the Department of Physics, University of California, Berkeley, CA 94720.

$$E(z,t) = \mathcal{E}(z,t)\exp[\omega t - kz + \varphi(z,t)] + \text{c. c.}$$

the coupling of (1) and (2) to the optical Bloch equations for the polarization in the rotating wave approximation yields the following evolution equation for the average pulse frequency:

$$\frac{d\langle\Omega\rangle}{dz} = -\frac{1}{\mathcal{T}}\int_{-\infty}^{\infty} \Delta W(\omega_0 + \delta - \langle\Omega\rangle)\, g(\delta)\, d\delta + \frac{2\langle k'\rangle}{T_2} \tag{3}$$

where

$$\langle\Omega\rangle = \omega + \langle\dot{\varphi}\rangle = \omega + \left(\int_{-\infty}^{\infty} \dot{\varphi}\,\mathcal{E}^2\, dt\right)\Big/\int_{-\infty}^{\infty} \mathcal{E}^2\, dt \tag{4}$$

$$\mathcal{T} = (\eta c/4\pi)\cdot\int_{-\infty}^{\infty} \mathcal{E}^2\, dt, \quad \Delta\omega = \omega_0 - \omega \ll \omega_0,$$

$$\Delta W = W_\infty - W_0$$

and T_2 is the inverse homogeneous linewidth of the two-level system. The initial and final values of the energy density of the medium are W_0 and W_∞, respectively, where $W_0 = \pm N\hbar\omega_0/2$ (+ for an emitter, - for an absorber), and N is the number density of the two-level atoms. The average contribution of the near resonant two-level system to the wave vector is

$$\langle k'\rangle = -\left(\int_{-\infty}^{\infty} \mathcal{E}^2\,\frac{\partial\varphi}{\partial z}\,dt\right)\Big/\int_{-\infty}^{\infty}\mathcal{E}^2\,dt$$

$$= \frac{\omega}{2}\int_{-\infty}^{\infty}\int_{-\infty}^{\infty} u\mathcal{E}\, g(\delta)\, d\delta\, dt. \tag{5}$$

If the pulse phase modulation is small (pulse spectral width of the order of the inverse pulsewidth), the term on the right side of (3) produces a frequency change opposite to that of the second term. There are two mechanisms which will phase modulate a pulse for the initial condition $\dot{\varphi}(z=0) = 0$. If homogeneous broadening is dominant, where T_2 is short, saturation of the line will produce frequency pulling of the carrier wave toward the resonance at ω_0 for an absorber and pushing for an emitter. If inhomogeneous broadening is dominant, and $T_2 \to \infty$, the opposite effects occur (pushing for an absorber and pulling for an emitter).

An evolution for the second moment of the phase derivative was also derived in [1]:

$$\frac{d\langle\dot{\varphi}^2\rangle}{dz} = \frac{1}{\mathcal{T}}\left\{\int_{-\infty}^{\infty}\int_{-\infty}^{\infty} dt d\delta\, g(\delta)\left[\omega v\mathcal{E}\left(\langle\dot{\varphi}^2\rangle + \frac{1}{T_2^2} - \Delta\omega^2\right)\right.\right.$$

$$\left.\left. + \kappa^2\mathcal{E}^2\left(\frac{W}{T_2} - \frac{\dot{W}}{2}\right) + \frac{2\omega\delta\mathcal{E}u}{T_2}\right)\right\}$$

$$+ \frac{4\Delta\omega_0}{T_2}\langle k'\rangle - \frac{1}{\mathcal{T}}\left[\frac{d}{dz}\left(\frac{\mathcal{T}}{2}\right) + \frac{\sigma\mathcal{T}}{\tau^2}\right] \tag{6a}$$

with

$$\frac{d\mathcal{T}}{dz} = \int_{-\infty}^{\infty} dt d\delta g(\delta)\,\omega v\mathcal{E} - \sigma\mathcal{T} \tag{6b}$$

and $\dot{W} = \omega\mathcal{E}v$. Equation (6a) is of little practical use because of the difficulty in evaluating the last terms which contain space derivatives. The equation can, however, be used to determine the evolution of the pulse mean-square spectral width:

$$\langle\Omega^2\rangle = \frac{\int_{-\infty}^{\infty}\Omega^2\,|\mathcal{E}(z,\Omega)|^2 d\Omega}{\int_{-\infty}^{\infty}|\mathcal{E}(z,\Omega)|^2 d\Omega} = \langle\dot{\varphi}^2\rangle + \frac{\int_{-\infty}^{\infty}\dot{\mathcal{E}}^2(z,t)dt}{\int_{-\infty}^{\infty}\mathcal{E}^2(z,t)dt}$$

$$= \langle\dot{\varphi}^2\rangle + \frac{1}{\tau^2} \tag{7}$$

where $1/\tau^2$ is the reciprocal mean-square pulse envelope width. Note that

$$\langle\Omega\rangle = \int_{-\infty}^{\infty}\Omega\,|\mathcal{E}(z,\Omega)|^2 d\Omega\Big/\int_{-\infty}^{\infty}|\mathcal{E}(z,\Omega)|^2 d\Omega$$

also defines $\langle\Omega\rangle$, stated in (4). Combination of (6) and (7) yields

$$\frac{d\langle\Omega^2\rangle}{dz} = \frac{1}{\mathcal{T}}\left\{\int_{-\infty}^{\infty}\int_{-\infty}^{\infty} dt\, d\delta\, g(\delta)\left[\omega v\mathcal{E}\left(\langle\Omega^2\rangle + \frac{1}{T_2^2}\right.\right.\right.$$

$$\left.\left.\left. - (\omega_0 + \dot{\varphi} - \langle\Omega\rangle)^2\right) + \kappa^2\mathcal{E}^2\left(\frac{W}{T_2} - \frac{\dot{W}}{2}\right) + \frac{2\omega\delta u}{T_2}\right]\right.$$

$$\left. + 4\left(\frac{\omega_0 + \delta - \langle\Omega\rangle}{T_2}\right)\langle k'\rangle. \tag{8}$$

Equation (8) defines a more general and directly measured mean-square spectral derivative than (6a), because it includes the spectrum due to the pulsewidth as well as frequency modulation. In the approximation $T_2 = \infty$, and for a pulse applied at resonance, (8) reduces to

$$\frac{d\langle\Omega^2\rangle}{dz} = \frac{\omega}{\mathcal{T}}\int_{-\infty}^{\infty} g(\delta)\, d\delta\int_{-\infty}^{\infty}\dot{W}\left\{\langle\Omega^2\rangle - \delta^2\right.$$

$$\left. - \frac{\kappa^2\mathcal{E}^2}{2}\right\} dt. \tag{9}$$

The last term of the right-hand side accounts for the spectral broadening due to the strong radiation transition rate $\kappa\mathcal{E}$. For weak short pulses such that $\langle\Omega^2\rangle \gg \kappa^2\mathcal{E}^2$, this term can be neglected, and the time integration in (9) gives

$$\frac{d\langle\Omega^2\rangle}{dz} = \frac{1}{\mathcal{T}}\int_{-\infty}^{\infty}\Delta W(\langle\Omega^2\rangle - \delta^2)\, g(\delta)\, d\delta. \tag{10}$$

For weak pulses, the energy absorbed at the frequency $\omega_0 + \delta$ is proportional to the spectral intensity of the light at that same frequency [1]:

$$\Delta W(\delta) = -\frac{1}{2}(\kappa^2 W_0)|\tilde{\mathcal{E}}(\delta)|^2 \tag{11}$$

where $\tilde{\mathcal{E}}(\delta)$ is the Fourier component of the envelope $\mathcal{E}(t)$ at

the frequency δ. If we apply (11) to (10) in the case of an infinitely broad inhomogeneous line ($g(\delta) = 1$ for all values of δ), then

$$\frac{d\langle\Omega^2\rangle}{dz} = -\frac{\kappa^2 \cdot W_0}{2\mathcal{T}} \int |\tilde{\mathcal{E}}(\delta)|^2(\langle\Omega^2\rangle - \delta^2)\, d\delta = 0 \qquad (12)$$

since

$$\frac{\int_{-\infty}^{\infty} |\tilde{\mathcal{E}}(\delta)|^2 \delta^2\, d\delta}{\int_{-\infty}^{\infty} |\tilde{\mathcal{E}}(\delta)|^2\, d\delta} = \langle\Omega^2\rangle$$

for weak pulses. It is only in this particular circumstance that a short coherent weak pulse is amplified or absorbed without distortion. For the case of bell-shaped-type functions, $g(\delta)$ not constant over the pulse spectrum, it follows that

$$\int |\mathcal{E}(\delta)|^2 \delta^2\, g(\delta)\, d\delta \ll \langle\Omega^2\rangle \int |\mathcal{E}(\delta)|^2\, g(\delta)\, d\delta \qquad (13)$$

and linear distortion will occur. Therefore from (12), $d\langle\Omega^2\rangle/dz$ is positive for an absorber and negative for an amplifier in the linear regime of weak excitation. If $\langle\dot{\varphi}^2\rangle = 0$ at $z = 0$, the negative sign of $d\langle\Omega^2\rangle/dz$ in an inverted medium implies that the pulsewidth will increase with propagation distance because of the finite bandwidth of the amplifying medium. The wings of the pulse spectrum are amplified less than its center, giving it a more monochromatic character. In an absorbing medium the opposite effect occurs, and the pulsewidth decreases. These effects will be enhanced by any initial chirp ($\langle\dot{\varphi}^2(0)\rangle$). Inspection of (8) shows, on the other hand, that for a sharp line absorber ($\delta = 0$) there is a competition between terms, including those with finite T_2, which can produce a shift in the sign of $d\langle\Omega^2\rangle/dz$ as a function of z, depending upon the initial value of $\langle\Omega^2\rangle$ at $z = 0$. The positive coefficient of $\langle\Omega^2\rangle$ in (8), together with negative terms involving T_2, accounts for the spectral instability of weak resonant pulses in absorbing media.

III. Criteria for Instability of Steady-State Pulses

By definition of steady-state propagation, the derivatives (4) and (8) have to be identically zero if a pulse is to propagate without distortion through the medium. In addition, the energy transfers from and to the pulse should be in equilibrium:

$$\frac{d\mathcal{T}}{dz} = \int_{-\infty}^{\infty} \Delta W g(\delta)\, d\delta - \sigma\mathcal{T} = 0. \qquad (14)$$

One can apply the method of "virtual displacements" to (3) to determine the stability around the equilibrium situation. Let us assume that the frequency $\langle\Omega_0\rangle$ of a steady-state pulse is given a "displacement" $\Delta\langle\Omega\rangle$ where $\langle\Omega\rangle = \langle\Omega_0\rangle + \Delta\langle\Omega\rangle$. To terms in first order in $\Delta\Omega$, (3) gives

$$\frac{1}{\Delta\langle\Omega\rangle}\frac{d\Delta\langle\Omega\rangle}{dz} = \frac{1}{\mathcal{T}}\int_{-\infty}^{\infty} \Delta W g(\delta)\, d\delta. \qquad (15)$$

The steady-state pulse is unstable if this expression is positive. Similarly by applying the pulse mean-square spectral width $\langle\Omega^2\rangle = \langle\Omega_0^2\rangle + \Delta\langle\Omega^2\rangle$ to (8), the return to steady state will not take place if

$$\frac{1}{\Delta\langle\Omega^2\rangle}\frac{d\Delta\langle\Omega^2\rangle}{dz} = \frac{1}{\mathcal{T}}\int_{-\infty}^{\infty} \Delta W g(\delta)\, d\delta \qquad (16)$$

is positive. The instability criteria (15) and (16) are seen to be identical. Since ΔW is positive for an absorbing medium, and negative for an amplifying medium, steady-state pulses are seen to be, in general, *unstable* against phase modulation or frequency mismatch in absorbing media. The right-hand side of (15) and (16) is the ratio of the energy absorbed by the medium to the pulse energy. This quantity is negative for steady-state pulses in amplifying media, and therefore, the necessary (but not sufficient) condition given by (15) and (16) for stability is satisfied. The stronger the depletion of the medium (relative to the pulse energy) by the steady-state pulses, the faster the return to stability.

IV. Case of the Absorbing Media—The 2π Self-Induced Transparency Pulse

In the approximation $T_2 = 0$ and $\sigma = 0$ a steady-state hyperbolic-secant-shaped pulse can propagate through an absorbing medium (2π sech pulse) [2]. Since $\Delta W = 0$ in this special case for this particular pulse, the right sides of (15) and (16) are zero. This form of stability is called "indifferent equilibrium" in mechanics. The lossless properties of the 2π sech pulse are independent of the assigned carrier frequency. However, ΔW is always finite and positive for any departure from the 2π sech exact steady-state solution, and one is therefore tempted to conclude that the 2π sech pulse is basically unstable because of (15) if any fluctuation from $|\Delta W| = 0$ takes place. Computer simulation of pulse propagation confirms that a 2π sech pulse perturbed either by amplitude bump or chirp is unstable in terms of *local* short time and distance analysis, but demonstrates a dynamic stability after a long distance of propagation. The example of Fig. 1 demonstrates the stabilization mechanism that preserves the 2π sech pulse. The initial pulse injected at resonance into the medium is a 2π sech with a small 90° out-of-phase Gaussian "disturbance" added to it in the middle of the main pulse. This amounts to a perturbation both in amplitude and phase. The spectral width of the input signal is therefore larger than the spectral width of the perfect 2π sech, and is further increased in the early stage of propagation. In the example of Fig. 1, the 2π sech does not remain unaffected, but reshapes into a longer 2π sech pulse, losing in the process roughly twice the amount of energy contained in the small initial disturbance. The latter is seen to propagate at nearly the velocity of light and sees its phase modulation strongly enhanced. Although the energy in the disturbance has grown with increasing propagation distance, the large separation in time and frequency between the disturbance and the main 2π sech pulse allows the latter to persist independently. If one limits the bandwidth of observation to roughly two linewidths and/or time of observation to $(t - z/V) \pm 2\tau$, where V is the wave velocity, the 2π

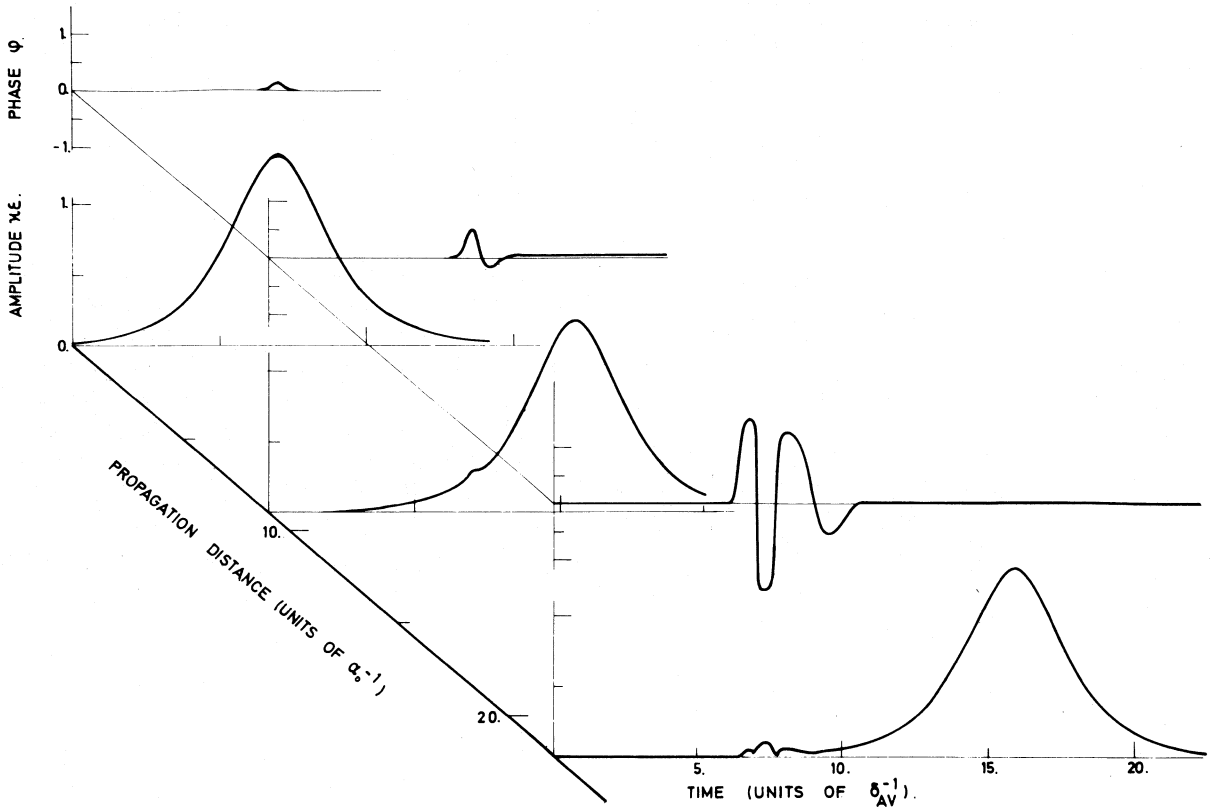


Fig. 1. Propagation of a 2π sech pulse at resonance, with a small 90° out-of-phase Gaussian disturbance initially superimposed on it. The pulse is applied on-resonance on an inhomogeneously broadened line with profile: $g(\delta) = (1/\sqrt{\pi})$ exp $\{-(\delta/\delta_{AV})^2\}$. The input signal is given by: $\kappa\mathscr{E}(t) = (2/1.5)$ sech $[(t-7)/1.5] + i \cdot (0.1/0.3\sqrt{\pi})$ exp $-\{(t-7)/0.3\}^2$ where the time t is expressed in units of δ_{AV}^{-1}, and the amplitude $\kappa\mathscr{E}$ in units of δ_{AV}. The amplitude and phase of the electric field are represented as a function of time and distance. Propagation distance is expressed in units of α_0^{-1}, where $\alpha_0 = 4\pi\kappa^2 W_0 g(0)/\eta c$. In amplitude, the disturbance of the 2π sech envelope is seen as a thicker line at the top of the initial pulse. The phase modulation is continuously amplified with propagation distance, rejecting the corresponding Fourier components of the signal far away from resonance. When the slow 2π sech pulse has separated in time from the "noise" signal, it has reshaped in a lower energy broader pulse fitting the equation: $\kappa\mathscr{E}(t') = (2/1.509)$ sech $(t'/1.509)$ (t' being the time t retarded to the appropriate origin).

sech pulse is seen to be filtered of its noise and becomes dynamically stable against amplitude or phase modulation.

V. The Homogeneously Broadened Amplifier

The pulse of Arrechi and Bonifacio [3a)] and Armstrong and Courtens [3b)] has been previously investigated by our approach [1] and its stability was confirmed by an analytic study and numerous computer simulations [1], [6]. It is often assumed that any pulse in an homogeneously broadened amplifier will evolve toward a π pulse. This assumption will be disproved here by showing that another steady-state pulse may exist which is actually chirped and stable. We call it the $\pi\sqrt{2}$ pulse [1]. It is still unclear where the dividing line is, that is, which initial pulse conditions determine evolution toward a π pulse, and which conditions favor evolution toward a $\pi\sqrt{2}$ pulse. However, in the presence of host dispersion, computer calculations of Gieszelman [6] have shown that weak pulses sent into homogeneously broadened amplifiers can evolve toward a chirped, one-linewidth-below-resonance, steady-state pulse which approximately fits the $\pi\sqrt{2}$ pulse. From the propagation equations in the retarded frame of [1] and [2], a steady-state solution for the $\pi\sqrt{2}$ pulse is possible if the dispersive and absorptive macroscopic dipole moments have solutions

$$v = \frac{\eta c \sigma}{4\pi\omega}\,\mathscr{E}$$

and

$$u = -v.$$

The π and $\pi\sqrt{2}$ pulse parameters are shown in Table I, together with the corresponding quantities for each pulse. Both sets of parameters satisfy the three steady-state conditions $d\langle\Omega\rangle/dz = 0$, $d\langle\Omega^2\rangle/dz = 0$, and $d\mathcal{T}/dz = 0$. It was shown in [1] that the velocity of the $\pi\sqrt{2}$ pulse is slightly less than c/η. This small velocity correction is of physical importance. The steady-state condition implies distortionless propagation over infinite distance. A velocity mismatch of the order of $\sigma\lambda c/\eta$ can therefore make a significant difference. Since the $\pi\sqrt{2}$ pulse is off-resonance, the resonant dispersion of the two-level system is expected to have an effect on the steady-state pulse velocity. A simplified derivation for the determination of the velocity of the $\pi\sqrt{2}$ pulse is given in Appendix A of this paper. (A more rigorous derivation can be found in [1, appendixes A and C].) The calculation of [1] is consis-

TABLE I

	"π" Pulse	"$\pi\sqrt{2}$" Pulse
$\kappa\mathcal{E}$	$\frac{1}{\tau_0}\operatorname{sech}\left(\frac{t'}{\tau_0}\right)$	$\frac{\sqrt{2}}{\tau_0}\operatorname{sech}\left(\frac{t'}{\tau_0}\right)$
$\dot{\Phi}$	0	$\frac{1}{\tau_0}\tanh\left(\frac{t'}{\tau_0}\right)$
	$t' = t - z/v$	
v	c/η	$\frac{c/\eta}{1+\frac{\lambda\sigma}{2\pi}}$
ω	ω_0	$\omega_0 + \frac{1}{T_2}$
$\frac{1}{\tau_0}$	$\left(\frac{\alpha_0}{\sigma} - 1\right)\frac{1}{T_2}$	$\left(\frac{\alpha_0}{2\sigma} - 1\right)\frac{1}{T_2}$
	$\alpha_0 = \frac{4\pi\kappa^2 W_0 T_2}{\eta c}$	
u	0	$\frac{\eta c\sigma}{4\pi\omega}\mathcal{E}$
v	$-\frac{\eta c\sigma}{4\pi\omega}\mathcal{E}$	$-\frac{\eta c\sigma}{4\pi\omega}\mathcal{E}$
W	$W_0\frac{\sigma}{\alpha_0}\left(1 - \frac{T_2}{\tau_0}\tanh\left(\frac{t'}{\tau_0}\right)\right)$	$2\frac{W_0\sigma}{\alpha_0}\left(1 - \frac{T_2}{\tau_0}\tanh\left(\frac{t'}{\tau_0}\right)\right)$
$\frac{W_\infty}{W_0}$	$2\frac{\sigma}{\alpha_0} - 1$	$4\frac{\sigma}{\alpha_0} - 1$

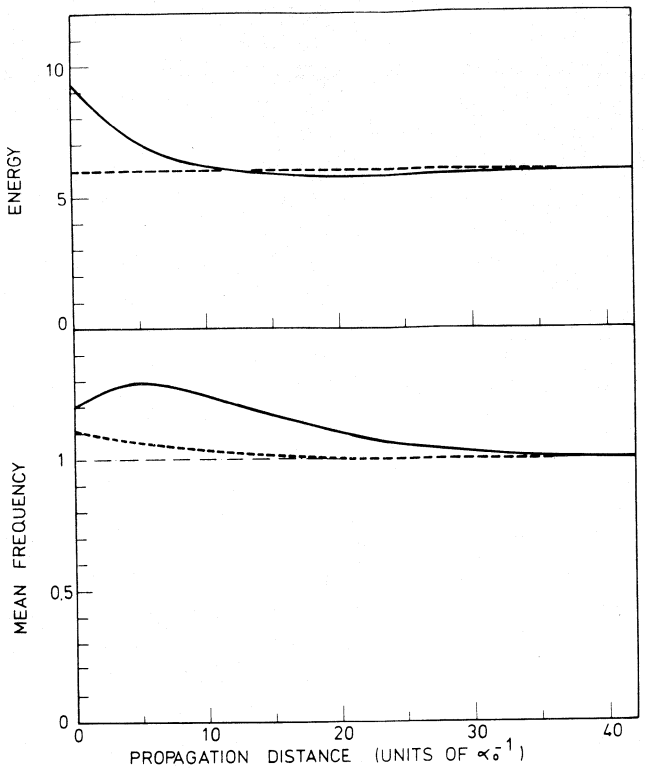


Fig. 2. Stability of $\pi\sqrt{2}$ pulses. The mean carrier frequency $\omega + \langle\dot{\varphi}\rangle - \omega_0$ (units of T_2^{-1}) and the pulse energy ($\int_{-\infty}^{\infty}\kappa^2\mathcal{E}^2\,dt$ in units of T_2^{-1}) are represented as a function of propagation distance (in units of linear gain length at the resonance frequency ω_0). The scattering coefficient of the medium is $\sigma = 0.2\alpha_0$. The initial pulse shape is $A \cdot \operatorname{sech}(t/0.25)$ with $A = \sqrt{2}/0.25$ (dashed curves) and $A = 1.24\sqrt{2}/0.25$ (full curves). The initial amounts of off-resonance are $(1 + \frac{1}{9})/T_2$ (dashed line, and $(1 + \frac{1}{5})/T_2$ (full line). The parameters of the $\pi\sqrt{2}$ steady-state pulse are 1 for the mean frequency and 6 for the energy.

tent with the slowly varying envelope approximation (SVEA): all second derivatives of the envelope functions are neglected. The exact phase factor of the radiation is conserved, which is not inconsistent with the SVEA.

In order to investigate the stability of the $\pi\sqrt{2}$ pulse, computer simulation of the propagation of such a pulse disturbed from steady state is made. An example of such a $\pi\sqrt{2}$ pulse displaced one-ninth of a linewidth ($\omega = \omega_0 + 1/9T_2$) from its "equilibrium frequency" ($\omega_{eq} = \omega_0 + 1/T_2$) is shown in Fig. 2 (dashed line). The average pulse frequency is seen to return to equilibrium according to the analytic stability criteria of (15) and (16). The latter apply if only the frequency of the $\pi\sqrt{2}$ pulse is changed, and all other parameters are left unchanged. The mean frequency is seen to shift initially away from the steady-state value, given an initial change of both the amplitude ($=1.25 \times \sqrt{2}/\tau$) and the mean frequency (0.2 linewidths above equilibrium) of the $\pi\sqrt{2}$ pulse. The computer simulation shows that the pulse ultimately returns to the $\pi\sqrt{2}$ steady-state area.

It has previously been shown by computer simulations [1] that a π pulse develops from propagation and amplification of a small unchirped pulse. This suggests that a $\pi\sqrt{2}$ pulse will not appear because of instabilities. Indeed, if we assume that a fabricated $\pi\sqrt{2}$ pulse is preceded by a weak pulse at resonance, the latter is expected to grow, thus changing the medium gain and initial conditions in front of the $\pi\sqrt{2}$ pulse. This argument, however, applies to an idealized two-level system where the π pulse has been seen to develop [1]. In real amplifiers, the symmetry of the ideal two-level system is broken by the host dispersion, and the π and $\pi\sqrt{2}$ pulses are then only approximate steady-state solutions (the host dispersion is negligible compared to the resonant dispersion of the two-level system if the pulse duration is larger than or of the order of T_2). In the presence of host dispersion, a third steady-state pulse has been found by Armstrong and Courtens [7]. Pulse propagation through homogeneous amplifiers with host dispersion was computer simulated by Gieszelman [6], using a succession of "slices" (an alternation of passive quadratic dispersers and homogeneous amplifiers). In this numerical simulation, weak pulses are seen to evolve toward a chirped steady-state quite different from the solutions of Arecchi and Bonifacio [3a)] and Armstrong and Courtens [7]. However, under conditions of small (quadratic) dispersion, the numerical steady-state pulse has all the characteristics of the $\pi\sqrt{2}$ pulse (one linewidth below resonance, approximately hyperbolic-secant envelope shape, and hyperbolic-tangent-shaped chirp). We suggest therefore that a weak dispersion in glass amplifiers would tilt the stability balance from the π pulse towards the $\pi\sqrt{2}$ pulse. Further work should be done in order to prove or disprove this statement. Measure of the time-resolved spectrum of picosecond pulses shows that the frequency of a single pulse sweeps from a lower to a higher frequency [8]. This experimental observation, coupled with the simulation of Gieszelman, suggests that the $\pi\sqrt{2}$ pulse may be a physical reality.

VI. Conclusions

The conditions given by (15) or (16) could be applied to study the stability conditions of other types of pulses not mentioned here in which multiple pulses with areas greater than 2π occur. Equation (8) can also be applied to specific systems of amplifiers. We have not included inhomogeneous broadening in our amplifier examples since analytic expressions could be found for homogeneously broadened amplifiers only. However, our stability arguments apply under conditions in which homogeneous and inhomogeneous broadening together with linear scattering are simultaneously present. In general, the existence of steady-state pulses and corresponding solutions to the Bloch optical equations do not guarantee their existence. The stability conditions expressed by (15) and (16) are necessary but not sufficient. Assurance that quasi-steady-state pulses can develop is given by the existence of an area theorem [2]. Such a theorem exists for purely inhomogeneously broadened media, in which convergence of pulse area towards 2π (absorber) and π (amplifier) is demonstrated. In all other cases, the absence of an area theorem casts doubt upon the existence of a particular steady state.

Appendix A
Velocity of the $\pi\sqrt{2}$ Pulse

A more accurate form than (2) of the real part of Maxwell's wave equation in the slowly varying envelope approximation is

$$\mathcal{E}\left\{\left(k-\frac{\partial\varphi}{\partial z}\right)^2-\frac{\eta^2}{c^2}(\omega+\dot{\varphi})^2\right\}=\frac{4\pi}{c^2}\cdot(\omega+\dot{\varphi})^2 u. \tag{A1}$$

Equation (A1) is usually approximated as

$$\mathcal{E}\left(k^2-\frac{\eta^2}{c^2}\omega^2\right)-2\mathcal{E}\left(\frac{\partial\varphi}{\partial z}-\frac{\eta^2\omega}{c^2}\right)+\left\{\left(\frac{\partial\varphi}{\partial z}\right)^2-\frac{\eta^2}{c^2}\dot{\varphi}^2\right\}\mathcal{E}\simeq\frac{4\pi\omega^2}{c^2}u. \tag{A2}$$

When the first term of the right-hand side of (A2) is put equal to zero, and the third one is neglected, the usual form of the slowly varying approximation (2) is obtained. This is an unnecessary approximation. If a chirped steady-state pulse is to exist, thus a pulse with an amplitude-dependent frequency, each component of the pulse has to propagate at the same velocity. The variation of the phase factor of the light fields has to be zero:

$$\delta\phi=0=(\omega+\dot{\varphi})\,\delta t-\left(k-\frac{\partial\varphi}{\partial z}\right)\delta z. \tag{A3}$$

A constant phase velocity

$$V_w=\frac{(\omega+\dot{\varphi})}{\left(k-\frac{\partial\varphi}{\partial z}\right)} \tag{A4}$$

must be associated with the chirped steady-state pulse. Therefore, (A1) should be rewritten:

$$\left(1-\frac{\eta^2V_w^2}{c^2}\right)\mathcal{E}=\frac{4\pi V_w^2}{c^2}u. \tag{A5}$$

Introducing the steady-state solution for the $\pi\sqrt{2}$ pulse $u=\mathcal{E}\eta c\sigma/4\pi\omega$ in (A5) yields the solution for the wave velocity:

$$V_w=\frac{c/\eta}{\sqrt{1+\frac{\lambda\sigma}{2\pi}}} \tag{A6}$$

which is the result obtained after a systematic and rigorous but more tedious derivation of the $\pi\sqrt{2}$ solution in [1].

References

[1] J. -C. Diels and E. L. Hahn, "Carrier-frequency distance dependence of a pulse propagating in a two-level system," *Phys. Rev. A*, vol. 8, pp. 1084–1110, 1973.

[2] S. L. McCall and E. L. Hahn, "Self-induced transparency," *Phys. Rev.*, vol. 183, pp. 457–485, 1969.

[3] a) F. T. Arecchi and R. Bonifacio, "Theory of optical maser amplifiers," *IEEE J. Quantum Electron.*, vol. QE-1, pp. 169–178, July 1965.
b) J. A. Armstrong and E. Courtens, "Exact solution of a π-pulse problem," *IEEE J. Quantum Electron.*, vol. QE-4, pp. 411–419, June 1968.

[4] G. L. Lamb, Jr., "Analytical descriptions of ultrashort optical pulse propagation in a resonant medium," *Review of Modern Physics*, vol. 43, pp. 99–121, 1971.

[5] M. D. Crisp, "Distortionless propagation of light through an optical medium," *Phys. Rev. Lett.*, vol. 22, pp. 820–823, 1969.

[6] E. L. Gieszelman, "Chirped pulses in laser amplifier," Tech. Rep. 80, Optical Science Center, University of Arizona, Tucson, p. 88, 1973.

[7] J. A. Armstrong and E. Courtens, "π-pulse propagation in the presence of host dispersion," *IEEE J. Quantum Electron.*, vol. QE-5, pp. 249–259, May 1969.

[8] A. N. Rubinov, M. C. Richardson, K. Sala, and A. J. Alcock, "Time resolved spectroscopy of picosecond laser pulses with the aid of optical Kerr effect photography," *Optics Comm.*, vol. 12, pp. 188–190, 1974.

CN* Production Efficiencies from Active Nitrogen–Hydrocarbon Flames

GENE A. CAPELLE AND STEVEN N. SUCHARD

Abstract—Various hydrocarbons have been reacted with active nitrogen in a supersonic flow system. The resulting chemiluminescence was invariably dominated by CN $A^2\Pi$ and $B^2\Sigma^+ \rightarrow X^2\Sigma^+$ emission. The intensity of this emission and the excited-state vibrational temperatures were strongly dependent upon the reactant hydrocarbon. Photon yields as high as 18.5 percent were measured for CN $A^2\Pi \rightarrow X^2\Sigma^+$ emission when C_2F_4 was used as a reactant, which makes this system a very promising chemically pumped laser candidate. Calculations have shown that if the populations in the electronically excited states can be vibrationally cooled, it should be possible to achieve positive gain in the system.

INTRODUCTION

SOME of the most promising reactions for use as potential chemically pumped electronic transition laser systems are those reactions that produce Group IVa oxides, halides, and nitrides [1]. The Group IVa oxides and halides have been discussed elsewhere [2], [3]. To date, however, little, if any, attention has been given to photon production efficiencies of reactions that produce Group IVa nitrides, which stems in part from the fact that emission from the free radicals, PbN, SnN, and GeN has not been observed. SiN and CN are the only Group IVa nitrides for which spectra have been observed and measured. CN, in particular, has been extensively studied [4]. The reaction of nearly any hydrocarbon with active nitrogen produces CN emission; very little, however, has been reported on the reaction mechanisms producing the CN radicals. We reacted several hydrocarbons with active nitrogen and measured the photon production efficiencies for CN emission under various experimental conditions. We also measured vibrational temperature distributions of the excited states of the CN reaction product. The minimum reactive branching ratios that we calculate to be required for positive gain on various transitions in CN are compared with our experimental measurements.

EXPERIMENT

The CN production system is shown schematically in Fig. 1. Room-temperature N_2 gas is passed through a dc electric arc [5] at the rate of 0.1 to 0.2 mole/s at a pressure (cold) near 140 torr. The effect of the dc discharge (typically, 350 V and 250 A) is to convert the N_2 thermally into active nitrogen at roughly 6000 K. The active nitrogen is a mixture of vibrationally and electronically excited N_2. This mixture is expanded through a plug nozzle into the reaction chamber at velocities on the order of 1.5×10^6 cm/s for a 10-torr reaction chamber pressure; the dwell time in the 15-cm-long observation and reaction area, consequently, is about 10 μs. The hydrocarbon is injected at right angles into the expanding active nitrogen flow, which results in the production of a bright flame. The total pressure can be varied between 2 and 100 torr by changes in the pumping speed. For photon-yield measurements, small amounts of hydrocarbon are titrated into the reaction region through a calibrated flowmeter system, which results in a nearly closed flame. Flame spectra are measured with a scanning monochromator and a phototube combination sensitive from 300 to 900 mm. The spectra are compared with the spectrum recorded from a lamp of known output intensity placed at the position of the flame in order to determine the absolute output, in photons/s, of the chemiluminescence.

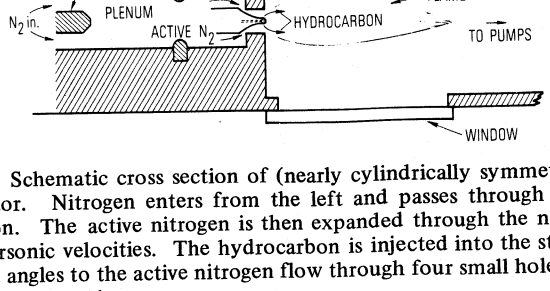


Fig. 1. Schematic cross section of (nearly cylindrically symmetric) arc reactor. Nitrogen enters from the left and passes through the arc region. The active nitrogen is then expanded through the nozzle at supersonic velocities. The hydrocarbon is injected into the stream at right angles to the active nitrogen flow through four small holes at the tip of the nozzle.

RESULTS

The chemiluminescent flames resulting from the reaction of CH_4, C_3H_8, CH_3Cl, C_2H_2, and C_2F_4 with the active nitrogen stream were similar in appearance. At 20 torr, the flames were very bright (white with pinkish tinges) when large hydrocarbon flows were used; the C_2F_4 flame, however, was considerably redder than the others. Often, pinched zones (constrictions) were visible in the flame. These regions were shock zones and were brighter than other parts of the flame because of the higher densities and temperatures at these points. At pressures above 20 torr, the flame was compressed toward the nozzle as might be expected from the lower gas-flow velocities and faster reaction rates at the higher pressures, and the tail of the flame, which was previously lost from view in the jet catcher became visible.

Two strong band systems were identified in the hydrocarbon flames: CN $B^2\Sigma \rightarrow X^2\Sigma^+$ in the blue and near-ultraviolet regions and CN $A^2\Pi \rightarrow X^2\Sigma^+$ extending from approximately

Manuscript received January 17, 1976. This work was supported by the Defense Advanced Research Projects Agency of the Department of Defense under U.S. Air Force Space and Missile System Organization (SAMSO) Contract F04701-75-C-0076.

The authors are with the Aerospace Corporation, El Segundo, CA 90245.

500 to beyond 900 nm, the limit of our detection system. Experiments in which an infrared-sensitive (1 to 2 μm) vidicon [6] and a cooled InSb detector with various filters (to 2.5 μm) were used to observe the chemiluminescence revealed emission that extended to greater than 2.5 μm. The only other band system of significant intensity was $C_2 d^3\Pi_g \rightarrow a^3\Pi_u$, which was usually of much lower intensity than either CN system. On the intensity scale of the CN emission, no nitrogen molecule emission was observed. A typical flame spectrum is shown in Fig. 2. With a small and constant hydrocarbon flow, it was found that the CN emission intensity increased to a maximum value, and then decreased, as the system pressure was increased, i.e., there was an optimum system pressure, Fig. 3(a). At higher pressures, there was an intensity decrease that resulted from quenching effects; and at lower pressures, there was a decrease in the observed intensity as the flame extended into the jet catcher and out of the observation region. When the hydrocarbon flow was adjusted at each pressure for maximum flame intensity, Fig. 3(b), the $A \rightarrow X$ intensity continued to increase with decreasing pressure down to ~ 2 torr, the lowest pressure that could be reached with the system; however, increasingly higher flow rates of hydrocarbon were needed as the pressure was reduced in order to attain this maximum intensity. This phenomenon can be explained by the decreasing amount of collisional quenching that occurs with reduced pressure; the ever-increasing hydrocarbon concentration keeps the reaction rate high, despite the decreasing pressure. It was found that if the system pressure was held constant, the CN intensity went through a definite maximum as the hydrocarbon flow was varied, i.e., there was an optimum hydrocarbon flow.

CN $A^2\Pi$-state vibrational temperatures were calculated [7] by plotting relative v' population versus $G(v')$ (Fig. 4). Relative vibrational level populations were calculated from measured $A \rightarrow X$ bandhead intensities, corrected for instrument response, and the appropriate Franck-Condon factors [8]. With the possible exception of CH_3Cl at $P \leqslant 10$ torr, the vibrational distributions were all Boltzmann in the range observed. The temperatures calculated for the same system from different Δv sequences were usually in excellent agreement, giving credibility both to the measurements and the Franck-Condon factors that were employed. Results of the temperature measurements are given in Table I. All the temperatures measured were high, and in some cases they were as high as the temperature of the nitrogen in the plenum (Fig. 1). This plenum N_2 temperature, accurate probably to ±750 K, was determined from the relation [9]

$$\left(\frac{P_1}{P_2}\right)^2 (300\ \mathrm{K}) = T$$

where P_1 is the pressure of the N_2 in the plenum with the arc current on, and P_2 is the pressure with no current. In one case, i.e., CH_4 at 100 torr, it was possible also to determine a vibrational temperature for the upper state of the C_2 Swan bands ($d^3\Pi_g \rightarrow a^3\Pi_u$); this temperature was the same as that measured for CN $A^2\Pi$. Expansion of the N_2 through the supersonic nozzle had little effect on its vibrational distributions; measurement of the N_2 $B^3\Pi_g$-state vibrational distribution, through the observation of the weak N_2 first-positive emission system (with the hydrocarbon turned off to eliminate

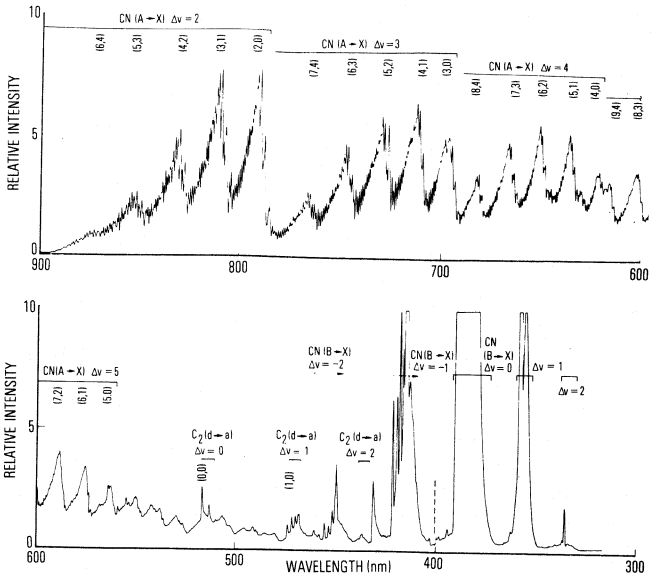


Fig. 2. Spectrum of emission that results on mixing C_3H_8 (ethane) with arc-produced active nitrogen at 25 torr. Spectrum is not corrected for instrument response. Spectral scans taken on two different days were joined at 400 nm.

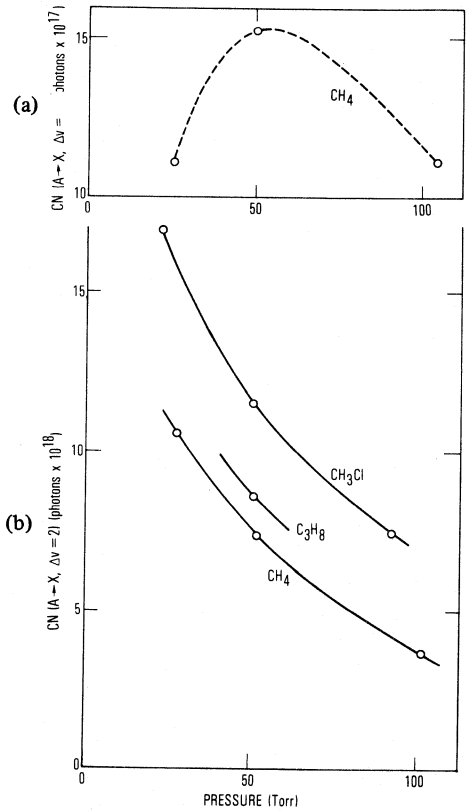


Fig. 3. CN ($A^2\Pi \rightarrow X^2\Sigma^+$) emission intensity versus pressure (a) at small and constant CH_4 flow and (b) with hydrocarbon flow adjusted for maximum CN chemiluminescence at each pressure.

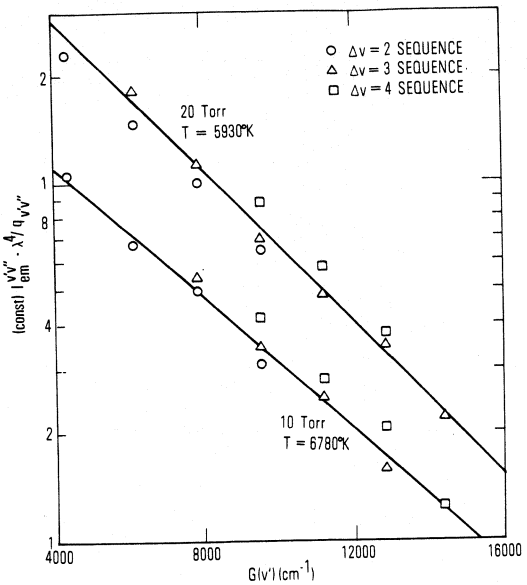


Fig. 4. Relative v' population of CN $A^2\Pi$ versus $G(v')$ for vibrational temperature determination. Measurements were made from $A^2\Pi \rightarrow X^2\Sigma$ bands of CN produced from C_3H_8.

TABLE I
CN $A \longrightarrow X$ VIBRATIONAL TEMPERATURES[a]

Fuel	Pressure (Torr)	Temperature (°K)	N_2 Temperature[c] (°K)
CH_4	100	6040[b]	----
C_3H_8	10	5930	6000
	20	6780	6000
CH_3Cl	10	Slightly non-Boltzmann	----
	20	7180	----
C_2H_2	10	4960	6000
	20	4390	6000
C_2F_4	10	4710	6000
	20	4520	6000

[a]Because of the lack of reliable Franck-Condon factors, no temperature could be calculated for the CN $B \rightarrow X$ system bands.
[b]A calculation based on the C_2 Swan bands gave 6020 K.
[c]Temperature of N_2 calculated from ratio of measured pressures of hot and cold N_2 in plenum.

the overpowering CN emission), showed it to be approximately Boltzmann with a temperature similar to the plenum N_2 temperature.

The photon yields, which are accurate to better than a factor of 2, were measured for CN emission from the reaction of CH_4, C_3H_8, CH_3Cl, C_2H_2, and C_2F_4 with active nitrogen and are given in Table II. For CH_4, the yield is divided into the contributions from the individual Δv sequences; the relative contributions from the Δv sequences are roughly the same for the other hydrocarbons. For $A \rightarrow X$ emission, two numbers are given: the total observed photon yield, i.e., counting all the photons within the spectral range of our detection system ($\lambda \leqslant 900$ nm), and the total calculated photon yield in which the $A \rightarrow X$ photons that are emitted at $\lambda > 900$ nm are also taken into account. The Franck-Condon factors of [8] were used for this calculation, together with the assumption of a 4700-K Boltzmann distribution for the $A^2\Pi$-state vibrational levels. The number of emitted photons was divided by the number of hydrocarbon molecules titrated into the active nitrogen in order to obtain the photon yields.

DISCUSSION

In the cases investigated, the upper state vibrational temperature decreased and the $A^2\Pi \rightarrow X^2\Sigma^+$ photon yield increased when the basic hydrocarbon fuel was changed from a single-bonded to a double-bonded or triple-bonded carbon type, or to a halogenated type. C_2F_4, which is both double-bonded and halogenated, gave both the lowest excited-state vibrational temperature and the highest photon yield of all the hydrocarbons investigated, about 18.5 percent for the $A \rightarrow X$ transition. This high yield, coupled with the relatively long radiative lifetime of 7 μs for the $A^2\Pi$ state [10], makes the system relatively promising as an electronic transition chemical laser; the 0.06-μs radiative lifetime [11] of the CN $B^2\Sigma^+$ state makes it unattractive. The 18.5 percent CN $A^2\Pi$ yield must, however, be viewed with caution. Because two carbon atoms are available from each C_2F_4 molecule, it is possible, in the worst case, that for every 100 C_2F_4 molecules that react, 18.5 CN molecules are produced in the $A^2\Pi$ state and that the remaining 181.5 carbon atoms form CN $X^2\Sigma^+$, which makes the effective branching ratio into the $A^2\Pi$ state $\sim$ 10 percent. Furthermore, it is also possible that some CN molecules are initially produced in the $X^2\Sigma^+$ state, are excited to the $A^2\Pi$ state by transfer from the bath gas, and subsequently radiate before leaving the observation zone. Although a CN molecule can experience 10 to 100 two-body collisions while traveling through the 15-cm reaction and observation area, the fact that the flame is essentially closed suggests that this reexcitation process is not the sole or primary process that leads to CN emission. On the positive side, there is also the effect of quenching collisions, which causes a photon yield to be measured that is lower than the true branching ratio. The data in Fig. 3 indicate that quenching effects do indeed play a significant role.

In order to evaluate the CN $A^2\Pi \rightarrow X^2\Sigma^+$ transition as a potential electronic transition laser, the minimum reactive branching ratio R_b^0 required for this transition to display zero gain, i.e., no overall gain or absorption, has been calculated [1]. Since these calculations are performed for a hypothetical $Q(0)$ transition, the zero-gain condition on this transition necessarily implies positive gain on either the P-branch or R-branch transitions [1]. The results of these calculations for the $\Delta v > 0$ sequences and for equal vibrational temperatures of the $A^2\Pi$ and $X^2\Sigma^+$ states of 5000 and 1000 K are given in Table III. The $\Delta v > 0$ sequences comprise what are referred to as the "red" bands of CN and have been studied previously as a potential laser [12]. The results given in Table III do not show promise for the production of positive gain. Since the definition of the reactive branching ratio is

$$R_b^0 = \frac{N'}{N' + N''} \tag{1}$$

TABLE II
CN PHOTON YIELDS

	Yield (%)						
	CH_4			CH_3Cl	C_3H_8[a]	C_2H_2	C_2F_4
$A^2\Pi - X^2\Sigma$	25 Torr	50 Torr	100 Torr	25 Torr	25 Torr	15 Torr	20 Torr
$\Delta v = 2$[b]	0.53	0.72	0.52	1.0	2.2	2.8	3.3
$\Delta v = 3$[c]	0.40	0.53	0.36	0.88	1.4	1.7	1.9
$\Delta v = 4$	0.29	0.37	0.24	0.54	0.85	0.8	0.78
$\Delta v = 5$	----	----	----	----	----	----	0.20
Total Observed $A \rightarrow X$	1.3	1.7	1.2	2.5	4.6	5.5	6.2
Total Calculated[d] $A \rightarrow X$	----	----	----	----	----	16	18.5
Observed $B^2\Sigma \rightarrow X^2\Sigma$	----	----	----	~4%	----	~3	~3

[a]Data for C_3H_8 represent one experimental run only; therefore, the yields for C_3H_8 should be considered less accurate than the numbers given for the other hydrocarbons.
[b]$\Delta v = 2$ band is ≥ 25 percent (2, 0) and ≥ 25 percent (3, 1).
[c]$\Delta v = 3$ band is ≥ 25 percent (4, 1) and ≥ 25 percent (5, 2).
[d]Includes observed bands plus calculated contribution from strongest (but unobserved in this work) infrared emission.

TABLE III
MINIMUM REQUIRED $A^2\Pi$ BRANCHING RATIOS

Sequence	Transition	λ (nm)	R_b^o 5000°K[a]	R_b^o 1000°K[a]
$\Delta v = 1$	(1, 0)	914	0.81	0.96
$\Delta v = 2$	(2, 0)	787	0.87	0.99
	(3, 1)	807	0.86	1.00
$\Delta v = 3$	(4, 1)	709	0.91	1.00
	(5, 2)	726	0.90	0.99
$\Delta v = 4$	(6, 2)	648	0.94	1.00
	(7, 3)	663	0.93	1.00
$\Delta v = 5$	(8, 3)	599	0.96	1.00
	(9, 4)	613	0.95	1.00
	(10, 5)	628	0.95	1.00

[a]Calculated for strongest observed transitions with 5000-K (1000-K) Boltzmann vibrational distributions assumed for upper and lower electronic states.

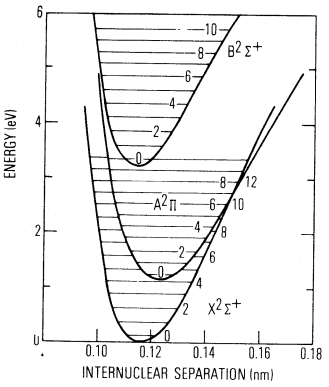


Fig. 5. Potential energy curves of CN.

where N' and N'' are the populations of the $A^2\Pi$ and $X^2\Sigma^+$ states, respectively, the results given in Table III indicate that at a 5000-K system vibrational temperature, a minimum of 81 percent of the CN radicals formed must be formed in the $A^2\Pi$ state in order for the zero-gain condition to be attained. As the system vibrational temperature is lowered to 1000 K, the situation becomes even worse; at this point, 96 percent of the CN radicals must be in the $A^2\Pi$ state.

These results are not surprising when the potential energy curves for the CN radical are inspected (Fig. 5). The shift in the internuclear separations between the $A^2\Pi$ and $X^2\Sigma^+$ states is only 5.34×10^{-3} nm, and the vibrational spacings are similar; consequently, all of the transitions originating from the small internuclear separation side of the potential curve of the $A^2\Pi$ state terminate on (numerically) lower levels of the ground state, i.e., $v' > v''$. Under the conditions of Boltzmann vibrational distributions in both the $A^2\Pi$ and $X^2\Sigma^+$ states, the fact that $v' > v''$ necessarily implies that $R_b^0 \approx 1$ since the relative amount of the X-state population in the vibrational level v'' must always be greater than the relative amount of A-state population in the vibrational level v'.

The results given in Table IV for the $\Delta v < 0$ transitions however, are quite promising. At a system vibrational temperature of 5000 K, reactive branching ratios as small as 25 percent are required for the zero-gain condition, and at 1000 K, this requirement decreases to ~0 percent. This type of R_b^0 requirement behavior is, however, expected because now $v' < v''$. Under this condition, the R_b^0 requirement should be extremely temperature dependent.

With a total measured photon yield of 18.5 percent for the production of $A^2\Pi$-state CN from the reaction of active nitrogen with C_2F_4 and the R_b^0 requirements listed in Table IV, this reaction system appears to be an excellent potential electronic transition laser system. In our calculations, it is assumed that no electronic deactivation occurs; consequently, the R_b^0 values should be increased in order to approximate a realistic laser system. The small R_b^0 requirements, however, indicate that even when considerable deactivation occurs, the measured photon yields will still exceed the R_b^0 required if the system vibrational temperature can be lowered to $\lesssim 2500$ K.

Initial attempts to cool the CN vibrationally have been unsuccessful. These attempts included increasing the N_2 mass flow and adding cold N_2, CO_2, or SF_6 just before expansion through the nozzle. Experiments by previous investigators [4] indicate that the high vibrational temper-

TABLE IV
MINIMUM REQUIRED $A^2\Pi$ BRANCHING RATIOS

Sequence	Transition	λ (μm)	R_b^o 5000°K[a]	R_b^o 1000°K[a]
Δv = -1	(0,1)	1.4	0.58	0.11
Δv = -2	(1,3)	2.1	0.42	0.005
	(2,4)	2.2	0.41	0.004
Δv = -3	(3,6)	4.1	0.27	0.0002
	(4,7)	4.5	0.27	~0
	(5,8)	4.8	0.26	~0
	(6,9)	5.3	0.25	~0

[a]Calculated for infrared transitions having strongest Franck-Condon factors, with 5000-K (1000-K) Boltzmann vibrational distributions assumed for upper and lower electronic states.

atures result, at least in part, from the reaction mechanism that produces CN and are not entirely attributable to the high vibrational temperature of the N_2 "bath" alone. Further efforts to cool the CN vibrationally should, therefore, be directed toward gaining a better understanding of the reaction mechanism.

ACKNOWLEDGMENT

The authors wish to thank D. Durran for assistance in designing the plug nozzle and H. Bixler and R. Cook for their assistance in performing the experiments on the arc facility.

REFERENCES

[1] D. G. Sutton and S. N. Suchard, "Potential electronic transition chemical laser: parametric evaluation," *Appl. Opt.*, vol. 14, pp. 1898-1910, 1975.
[2] G. A. Capelle and J. M. Brom, Jr., "Reactions of germanium vapor with oxidizers: Photon yields and a new GeO band system," *J. Chem. Phys.*, vol. 63, pp. 5168-5176, 1975.
[3] G. A. Capelle and C. Linton, "Photon yields for several Sn-oxidizer reactions," to be published.
[4] T. Iwai, M. I. Savadatti, and H. P. Broida, "Mechanisms of populating electronically excited CN in active nitrogen flames," *J. Chem. Phys.*, vol. 47, pp. 3861-3874, 1967; and also, other papers by H. P. Broida in *J. Chem. Phys.*
[5] D. Durran (to be published).
[6] M. A. Kwok, E. F. Cross, and T. A. Jacobs, "Spectroscopy of pulsed HF chemical lasers using an infrared vidicon camera tube," *Rev. Sci. Instr.*, vol. 43, pp. 1043-1045, 1972.
[7] G. Herzberg, *Spectra of Diatomic Molecules*. Princeton, NJ: Van Nostrand, 1950, pp. 203-204.
[8] J. C. McCallum, W. R. Jarmain, and R. W. Nicholls, *Franck-Condon Factors and Related Quantities for Diatomic Molecular Band Systems*, Spectroscopic Rep. 1, York University, Toronto and Ontario, Ont., Canada, Mar. 1970.
[9] D. Durran, The Aerospace Corporation, El Segundo, CA, private communication.
[10] M. Jeunehomme, "Oscillator strength of the CN red system," *J. Chem. Phys.*, vol. 42, pp. 4086-4088, 1965.
[11] T. J. Cook and D. H. Levy, "Lifetimes of the $A^2\Pi$ and $B^2\Sigma$ states of the CN radical," *J. Chem. Phys.*, vol. 57, pp. 5059-5064, 1972; and also, C. K. Luk and R. Bersohn, "Time dependence of the fluorescence of the B state of CN," *J. Chem. Phys.*, vol. 58, pp. 2153-2163, 1973.
[12] T. T. Kikuchi and H. P. Broida, "Laser possibilities of chemically excited molecules formed with atomic species," *Appl. Opt., Suppl. 2, Chemical Lasers*, pp. 171-178, 1965.

Analysis of Grating-Coupled Radiation in GaAs:GaAlAs Lasers and Waveguides

WILLIAM STREIFER, SENIOR MEMBER, IEEE, DON R. SCIFRES, MEMBER, IEEE, AND ROBERT D. BURNHAM, MEMBER, IEEE

Abstract—Grating-coupled radiation in GaAs:GaAlAs lasers and waveguides is analyzed. A general formulation is developed for arbitrary-shaped gratings which need not be small in size. Two methods are used to solve the resulting equations in the case of rectangular-shaped gratings. The first is a perturbation technique and the second is iterative in nature. The iterative procedure converges to a numerical exact solution in many cases of practical interest and indicates that the perturbation results are quite accurate. Curves are presented for radiated power from traveling waves as a function of grating tooth height, tooth width, refractive index, waveguide thickness, and period for rectangular gratings in heterostructure waveguiding geometries. It is shown that radiation is not a monotonically increasing function of tooth height, but rather maxima occur when the teeth are half the optical wavelength in the material. Also, in particular geometries with an air:GaAs grating interface, radiated power of a mode can exceed 100 cm^{-1}.

I. Introduction

THE phenomenon of radiation from periodic structures in waveguides is utilized in couplers and lasers. In the former situation one generally deals with a structure which contains a wave propagating in one direction. Through its interaction with the periodic grating the propagating wave excites one or more radiating waves which provide the output coupling. If the grating period is approximately an integral multiple of half the propagating wavelength in the guide (the Bragg condition) then a strong coupling also exists between the propagating wave and an identical contradirectional wave. This is, of course, just the situation which exists in a distributed feedback (DFB) or Bragg reflection (DBR) laser [1]. If one of the latter devices functions such that the grating provides the feedback, two contradirectional propagating waves always exist and both simultaneously contribute to the radiation field. However, laser devices which contain gratings for output coupling, but obtain feedback away from the Bragg condition from external reflectors [2]-[5] (such as cleaved crystal facets) may be considered to radiate as two independent contradirectional waves in a waveguide.

In this paper we study analytically the radiation properties of gratings in GaAs:GaAlAs structures which are used either as waveguides or as lasers, where in the latter case the oscillation wavelength is not in the immediate vicinity of that determined by the Bragg condition. An exact formulation for arbitrary grating tooth shape is presented. The first-order solution of these equations in the case of rectangular-shaped corrugations corresponds to the perturbation technique given by Handa *et al.* [6]. Starting with the perturbation results, numerical iterations converge, in many cases of practical interest, to a more accurate solution. Specifically, we present results of radiated power as a function of grating tooth height, tooth width, refractive index, waveguide thickness, and period for rectangular gratings in heterostructure waveguiding geometries.

Manuscript received January 22, 1976; revised March 9, 1976.
The authors are with the Xerox Palo Alto Research Center, Palo Alto, CA 94304.

II. Formulation

Consider TE modes of the structure shown in Fig. 1. The E-field is in the y direction and satisfies

$$\frac{\partial^2 E_y}{\partial x^2} + \frac{\partial^2 E_y}{\partial z^2} + k_0^2 n^2(x,z) E_y = 0 \tag{1}$$

where a time dependence $\exp(-i\omega t)$ has been assumed, $k_0 = 2\pi/\lambda_0$, λ_0 is the free-space wavelength, and $n^2(x,z)$ is the squared refractive index which is equal to the relative dielectric constant. Next, we express the mode field E_y as an infinite summation of partial waves in a form dictated by Floquet's theorem,

$$E_y(x,z) = \sum_{m=-\infty}^{\infty} \mathcal{E}_m(x) \exp(i\beta_m z) \tag{2}$$

with

$$\beta_m = \beta_0 + \frac{2\pi m}{\Lambda} \tag{3}$$

where Λ is the grating period. If no grating were present, then all $\mathcal{E}_m(x)$ with $m \neq 0$ would be zero, whereas $\mathcal{E}_0(x)$ and β_0 are the mode pattern and propagation constant of that unperturbed waveguide structure.

Next we express $n^2(x,z)$ analytically as

$$n^2(x,z) = \begin{cases} n_1^2, & x < 0 \\ \sum_{p=-\infty}^{\infty} [n_1^2\{u[z - w_1(x) - p\Lambda] - u[z - w_2(x) - p\Lambda]\} \\ \quad + n_2^2\{u[z - w_2(x) - p\Lambda] \\ \quad - u[z - w_1(x) - (p+1)\Lambda]\}], & 0 < x < g \\ n_2^2, & g < x < t \\ n_3^2, & t < x \end{cases} \tag{4}$$

where the functions $w_1(x)$ and $w_2(x)$ express the tooth shape as shown in Fig. 1 and u is the unit step function. Then since $n^2(x,z)$ is periodic in z, we write

$$n^2(x,z) = n_0^2(x) + \sum_{\substack{q=-\infty \\ q\neq 0}}^{\infty} A_q(x) \exp(i2\pi qz/\Lambda) \tag{5}$$

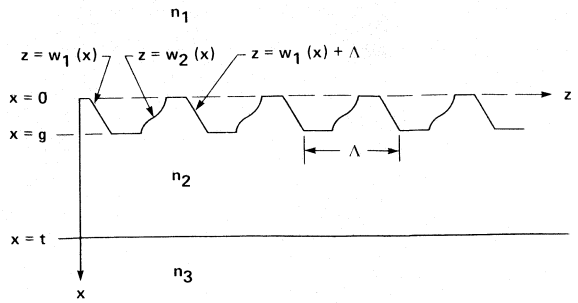


Fig. 1. A waveguide with a grating.

where

$$n_0^2(x) = \begin{cases} n_1^2, & x < 0 \\ \{n_1^2 [w_2(x) - w_1(x)] + n_2^2 [\Lambda + w_1(x) - w_2(x)]\}/\Lambda, & 0 < x < g \\ n_2^2, & g < x < t \\ n_3^2, & t < x. \end{cases} \tag{6}$$

This quantity just equals $n^2(x, z)$ outside the grating region, and inside that region it equals the Fourier series term with no z-dependence which would correspond to $A_0(x)$. Thus $A_0(x) \equiv 0$. The other Fourier coefficients ($q \neq 0$) are given by

$$A_q(x) = \begin{cases} 0, & x < 0, g < x \\ \dfrac{1}{\Lambda} \displaystyle\int_{-\Lambda/2}^{\Lambda/2} n^2(x, z) \exp(-i2\pi qz/\Lambda)\, dz \\ = \dfrac{(n_2^2 - n_1^2)}{i2\pi q} \{\exp[-i2\pi q w_2(x)/\Lambda] \\ - \exp[-i2\pi q w_1(x)/\Lambda]\}, & 0 < x < g. \end{cases} \tag{7}$$

Upon substituting (5) and (2) in the differential equation (1) and collecting all terms with the same z-dependence we obtain

$$\frac{d^2 \mathcal{E}_m}{dx^2} + [k_0^2 n_0^2(x) - \beta_m^2]\, \mathcal{E}_m = -k_0^2 \sum_{\substack{q=-\infty \\ q \neq m}}^{\infty} A_{m-q}(x)\, \mathcal{E}_q(x), \forall_m \tag{8}$$

where the $q = m$ term has been omitted from the summation since $A_0(x) \equiv 0$.

The system of (8), satisfied by $\mathcal{E}_m$, determines a single mode of the corrugated waveguide when summed according to (2). The solution of (8), subject to the boundary conditions of E_y and $H_z \propto \partial E_y/\partial z$ continuity at $x = 0$, g, and t, determines β_0 and through (3), β_m. (Note that E_y continuity ensures $H_x \propto \partial E_y/\partial x$ continuity.) Partial waves with $|\mathrm{Re}\,(\beta_m)| < \min(k_0 n_1, k_0 n_3)$ radiate power into both regions 1 and 3, whereas those with $|\mathrm{Re}\,(\beta_m)| > \max(k_0 n_1, k_0 n_3)$ exponentially decay in both regions [7]. For (say) $n_3 > n_1$, there may exist partial waves with $k_0 n_1 < |\mathrm{Re}\,(\beta_m)| < k_0 n_3$, which radiate into region 3 and not into region 1. If any radiation occurs, the mode loses power as it propagates and this loss is represented by a complex β_0:

$$\beta_0 = \beta_r + i\beta_i \tag{9a}$$

with

$$\mathrm{Im}\,(\beta_0) = \beta_i > 0. \tag{9b}$$

All the partial waves decay at the same rate since

$$\beta_m = \beta_r + \frac{2\pi m}{\Lambda} + i\beta_i. \tag{10}$$

Thus the mode power decay with propagation in z is given by $\exp(-\alpha z) = \exp(-2\beta_i z)$.

Next consider only the left side of (9) for $m = 0$,

$$\frac{d^2 \mathcal{E}_0}{dx^2} + [k_0^2 n_0^2(x) - \beta_0^2]\, \mathcal{E}_0 = 0 \tag{11}$$

with $n_0^2(x)$ given by (7). Clearly $n_0^2(x)$ describes a four-layer waveguiding structure; outside the grating region for $x < 0$ and $x < g$ this waveguide is identical to the original, for $g > x > 0$, $n_0^2(x)$ is equal to $n^2(x, z)$ in the grating region averaged along z for each x. For example, $n_0^2(x)$ for rectangular teeth is a constant equal to the average of n^2 in the grating region (see [6] and [8]). For any trapezoidal- (including all triangular-) shaped teeth $n_0^2(x)$ varies linearly across the grating region.

If (11) is solved for $\mathcal{E}_0$ and β_0, and then only $\mathcal{E}_0$ is used to drive other $\mathcal{E}_m (m \neq 0)$ in the right side of (8), i.e.,

$$\frac{d^2 \mathcal{E}_m}{dx^2} + [k_0^2 n_0^2(x) - \beta_m^2]\, \mathcal{E}_m = -k_0^2 A_m(x)\, \mathcal{E}_0(x) \tag{12}$$

we obtain a first-order perturbation solution for $\mathcal{E}_m$. This is just the technique carried out in [6] for rectangular-shaped gratings.

The value of β_0 determined by (11) alone is real and therefore does not reflect power lost through radiation. Instead, the time-averaged power lost by the partial wave $\mathcal{E}_m$ per unit length is found, using the Poynting vector, to be

$$P_m = \frac{1}{2\omega\mu_0} \mathrm{Re}\,\{\sqrt{k_0^2 n_1^2 - \beta_m^2}\, |\mathcal{E}_m(0)|^2 + \sqrt{k_0^2 n_3^2 - \beta_m^2}\, |\mathcal{E}_m(t)|^2\}. \tag{13}$$

Here the first and second bracketed terms are the parts radiated into regions 1 and 3, respectively, and if β_m^2 exceeds $k_0^2 n_1^2$ and/or $k_0^2 n_3^2$, imaginary terms occur in (13) which do not contribute to P_m. Thus $P_m = 0$ for all terms with $m \geq 0$ and with sufficiently large negative m, which could be $m = -1$ for small Λ. Since the radiated power is proportional to the guided power it is convenient to use the normalized measure of radiated power given by α, the exponential rate at which power is lost by the $\mathcal{E}_0$ wave. From (13)

$$\alpha = \sum_m P_m / \{(\beta_0/2\omega\mu_0) \int_{-\infty}^{\infty} |\mathcal{E}_0(x)|^2\, dx\}. \tag{14}$$

To solve (8) more accurately, we use the approximate solutions obtained in the perturbation technique above to evaluate the right side of (8) for $m = 0$ and thereby obtain more accurate solutions for $\mathcal{E}_0$ and β_0. Then (8) is solved for all other values of m using the current partial wave solutions to evaluate the right side. This process is continued until convergence. The above remarks are illustrated by calculations for rectangular gratings presented in the next section.

III. Results for Rectangular Gratings

Algebraic details of solutions for rectangular-shaped gratings are given in Appendix A and some comments concerning the numerical techniques employed are included in Appendix B. The results presented below for α in the form of continuous curves were obtained utilizing the perturbation technique and (13) and (14). This procedure yields accurate data in many cases of practical interest with little expenditure of computer time. Specific points computed by the numerical iteration technique using summations of the partial waves with $-8 \leqslant m \leqslant 5$ are also shown for comparison purposes. Here $\alpha = 2$ Im (β). In all cases, iterations were continued to convergence as determined by changes in the Im (β) of less than 1 part in 10^4. This calculation requires a comparatively large amount of computer time, which explains the few "exact" points computed and plotted.

In the results w is the grating tooth width of n_1^2 material so that $\Lambda - w$ is the width of n_2^2 material. The refractive index squared in the grating region is

$$n_4^2 = [n_1^2 w + n_2^2 (\Lambda - w)]/\Lambda. \tag{15}$$

Fig. 2 is a plot of α for total radiated power versus grating tooth height, g, in a double-heterostructure waveguide or laser geometry with $n_1 = n_3 = 3.4$, $n_2 = 3.6$, and a 1.0-μm-thick guiding region as measured to the outside of the grating. The grating period is $\Lambda = 2100$ Å, $w/\Lambda = 0.25$, and the free-space wavelength is $\lambda_0 = 8800$ Å. With these values of λ_0 and Λ, only the $m = -1$ partial wave radiates and that wave radiates in a backward direction into both media 1 and 3. The radiation directions are equal in regions 1 and 3 only because $n_1 = n_3$. Since the waveguiding geometry as described by (6) in which the partial waves $\mathcal{E}_m(x)$ are determined varies with grating height, g, the propagation constants of the guided modes vary with g, and so too does the angle at which light is radiated. Specifically, the radiation in regions 1 and 3 makes angles of 100.3°-100.6°, 101.2°-101.7°, 102.6°-102.9° with the propagation direction in the waveguide for the TE_0, TE_1, and TE_2 modes, respectively, where the lower values apply in the limit $g = 0.0$ μm and the higher values apply for $g = 0.5$ μm. Of course, in passing through a GaAlAs (index 3.4): air interface the wave is refracted.

The calculation reveals that for this particular situation the powers radiated into regions 1 and 3 are approximately equal. Since the differences would be difficult to discern if plotted on the scale of Fig. 2, we have shown only α resulting from the sum of power radiated into 1 and 3.

Consider first the plot for the TE_0 mode. The radiated power is an increasing function of g with a superimposed oscillation, whose period is approximately equal to the wavelength of light in the material, λ. As expected, radiation is strongest for $g \approx \lambda/2$, $3\lambda/2$, and $5\lambda/2$. For $g \approx \lambda$ and 2λ, power is trapped in the grating region by resonance in the transverse direction. Radiated power generally increases with g because the overlap of $\mathcal{E}_0$ and the radiating partial wave $\mathcal{E}_{-1}$ increases. A comparison of the points obtained from the iterated solution and the perturbation solution curve leads to the perhaps surprising conclusion that the perturbation results are quite accurate even for gratings which are several λ in height. This

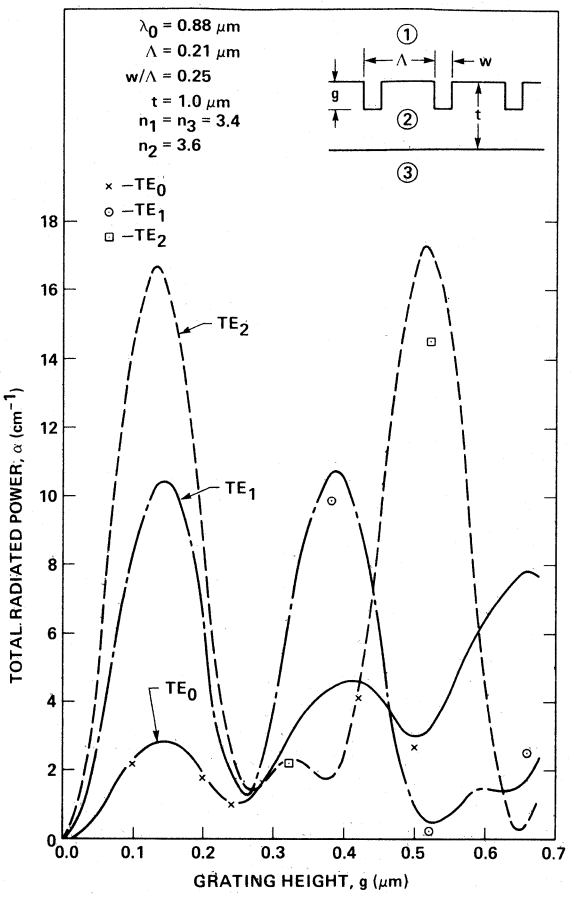


Fig. 2. Total radiated power versus tooth height for a rectangular grating. Discrete points are iterative solution results.

is the case when the index differential at the grating is not large as in this figure.

The TE_1 and TE_2 modes also exhibit oscillations in radiated power, but in addition there exist irregularities in these curves. These occur for $0.5 < g < 0.6$ for the TE_1 mode and for $0.3 < g < 0.4$ for the TE_2 mode. An examination of the TE_i mode pattern of $\mathcal{E}_0$ reveals that the mode undergoes a 180° phase shift near the base of the teeth for $0.5 < g < 0.6$. Thus $\mathcal{E}_0$ exciting the TE radiating partial wave $\mathcal{E}_{-1}$ actually reduces its integrated driving effect just as the tooth height approaches $5\lambda/2$. The net effect of these competing phenomena is to produce the curve shape shown. The situation is identical for the TE_2 mode with $0.3 < g < 0.4$.

For small values of g the TE_2 radiated power exceeds that of the TE_1, which in turn exceeds that of the TE_0. This occurs because of the greater percentage of higher mode power in the grating vicinity. It is also important to note that even for relatively small grating heights, i.e., 1500 Å, α is comparable in value to mode decay produced by free-carrier absorption losses, e.g., 10 cm^{-1}.

In Fig. 3 we plot radiated power as a function of w for the same waveguide geometry as in Fig. 2 with $g = 0.2$ μm. All three modes have a radiation peak near $w/\Lambda = 0.5$ because the dependence of the dominant coefficient coupling $\mathcal{E}_0$ and $\mathcal{E}_{-1}$, i.e., A_{-1}, on w is given by $A_{-1} \propto \sin(\pi w/\Lambda)$ [see Appendix A]. However, the peak occurs just below $w/\Lambda = 0.5$ and the curves are not symmetric about that value. The asymmetry results

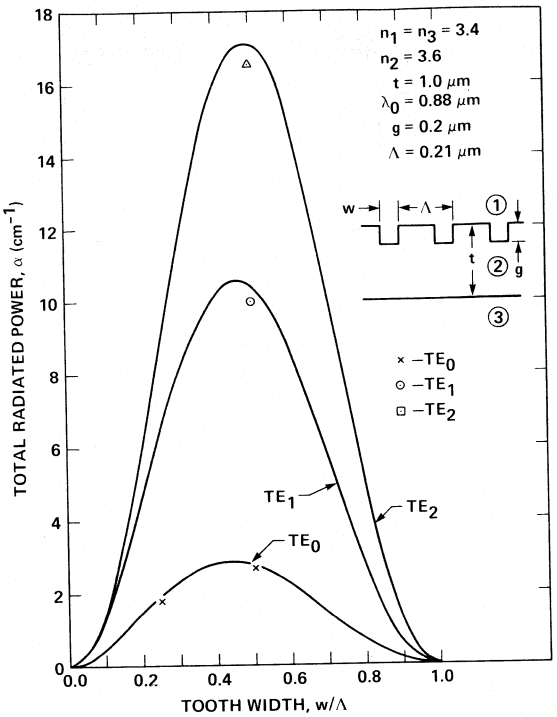


Fig. 3. Total radiated power versus tooth width for a rectangular grating. Discrete points are iterative solution results.

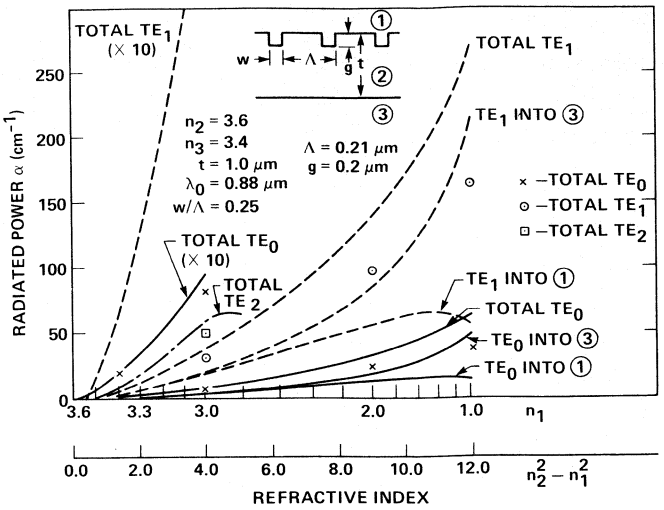


Fig. 4. Radiated power versus $n_2^2 - n_1^2$ for a rectangular grating. Discrete points are iterative solution results.

from the decreased penetration of $\mathcal{E}_0$ into the grating region with decreasing n_4^2 [increasing w according to (15)]. Furthermore, the higher order transverse modes are less sensitive to variations in w in this respect because their equivalent refractive indices as determined by their propagation constants are smaller.

Fig. 4 is a plot of radiated power versus the refractive index n_1 of the outer medium at the corrugated interface for the same waveguiding geometry as above with $w/\Lambda = 0.25$. The actual horizontal scale is in equal increments of $n_2^2 - n_1^2$, which is the difference in relative dielectric constant at the grating teeth and is the quantity occurring naturally in the analysis. Equally spaced increments in n_1 of 0.2 between 1.0 and 3.0, and of 0.1 between 3.0 and 3.6 are also shown on the abscissa. Values of n_1 between 3.6 and 2.9 may be obtained in practice by varying Al composition in $Ga_{1-x}Al_xAs$ from $x = 0.0$ to $x = 1.0$. The interesting and important result illustrated by this figure is the dramatic increase in radiated power with increasing $n_2^2 - n_1^2$. The continuous curves for total radiated power are approximately quadratic. This dependence occurs because the A_{-1} coefficient coupling $\mathcal{E}_0$ and $\mathcal{E}_{-1}$ [see (A1)] is proportional to $n_2^2 - n_1^2$ and the radiated power is proportional to $|\mathcal{E}_{-1}|^2$. Again we observe that for this rectangular grating radiated power divides approximately equally between regions 1 and 3 for smaller values of $n_2^2 - n_1^2$, but for increasing $n_2^2 - n_1^2$ more power is radiated into region 3, whose refractive index n_3 is significantly higher than n_1. The curve for the TE_2 mode exists only for $n_1 > 2.8$ since below that value this mode is beyond cutoff. It is also important to examine the accuracy of the perturbation calculation as a function of $n_2^2 - n_1^2$. Clearly since all coefficients A_q are proportional to $n_2^2 - n_1^2$, all partial waves are coupled more strongly with increases in this parameter. The perturbation technique used to compute the continuous curves in Fig. 5 includes only the first-order effect between $\mathcal{E}_0$ and $\mathcal{E}_{-1}$, which is proportional to $n_2^2 - n_1^2$ as noted above, whereas the points marking exact solutions contain all partial waves with $-8 \leqslant m \leqslant 5$ including coupling effects which depend on higher powers of $n_2^2 - n_1^2$. Thus the accuracy of the perturbation solution decreases significantly with increasing $n_2^2 - n_1^2$, but even for large differences, e.g., as occur with $n_1 = 1.0$, the perturbation technique yields results accurate to much better than an order of magnitude.

In Fig. 5 we plot radiated power versus the refractive index of region 3 for the TE_0 mode in the same waveguiding geometry as above with $n_1 = 3.4$. We observe that the total radiated power increases with decreasing n_3. For n_3 near 3.6 there is a rapid increase in radiated power as n_3 decreases because the mode then experiences a greater degree of confinement, i.e., the mode power in region 3 decreases rapidly as n_3 decreases. As n_3 continues to decrease (say, below 3.4) the mode penetrates the grating region more strongly since then n_3 is much less than n_4 and n_1. We note, too, that for larger values of n_3 power radiates approximately equally into regions 1 and 3, but for smaller values of n_3 more power is radiated into region 1.

Radiated power versus waveguide thickness t is plotted in Fig. 6 for the same geometry as studied above. The curve for each TE mode shows a rapid increase as t exceeds the value corresponding to mode cutoff. This increase occurs because the mode confinement improves rapidly above the cutoff thickness value. With continued increases in t there is a gradual decrease in radiated power resulting from the decreased field penetration into the grating region.

Fig. 7 is a plot of radiated power by each partial wave versus grating period for the TE_0 mode in the same waveguide as above with $t = 1.0\ \mu m$. The figure also contains broken curves of radiation angle versus Λ, where the angle is measured from the horizontal and is zero in the forward direction. The angle is computed from

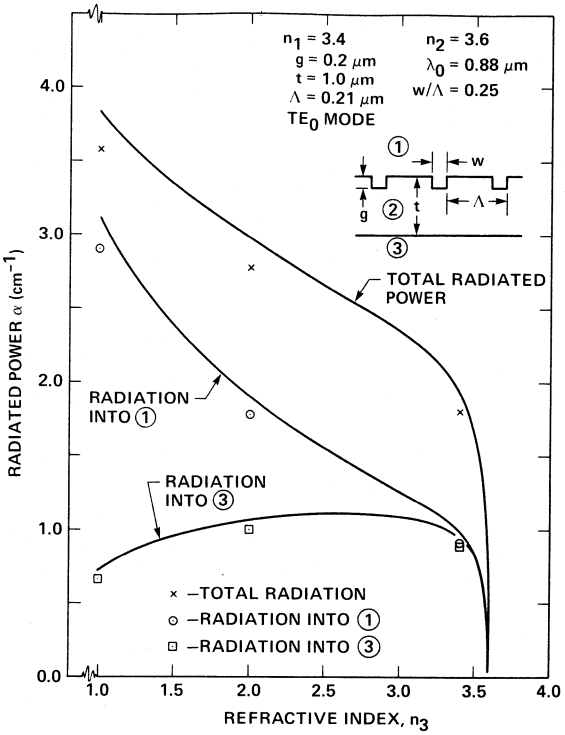


Fig. 5. TE_0 mode radiated power versus n_3 for a rectangular grating. Discrete points are iterative solution results.

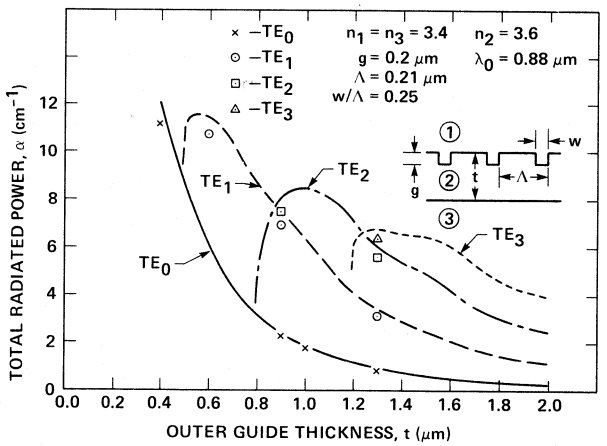


Fig. 6. Total radiated power versus outer guide thickness for a rectangular grating. Discrete points are iterative solution results.

$$\theta_i = \cos^{-1}\left[\beta_m/(2\pi n_i/\lambda_0)\right], \quad i = 1,3 \tag{16}$$

where β_m is given by (3), λ_0 is the free-space wavelength, and n_i is the refractive index of media 1 or 3. In this plot, $n_1 = n_3 = 3.4$ so that the radiation angles are equal in the two media. For small values of Λ, all partial waves are trapped within the waveguide. At $\Lambda = 0.1229\ \mu m$, $\beta_{-1} = -\beta_0$, and the grating functions to provide distributed feedback (DFB) in the first Bragg order. For very slightly larger Λ, $|\beta_{-1}| < \beta_0$, but since the equivalent refractive index, as given by

$$n_{eq} = \frac{\lambda_0 |\beta_{-1}|}{2\pi} \tag{17}$$

exceeds n_1, n_3 there exists no radiated partial wave; rather a guided wave propagating with β_{-1}. However, at $\Lambda = 0.1261\ \mu m$, radiation begins to escape from the waveguide.

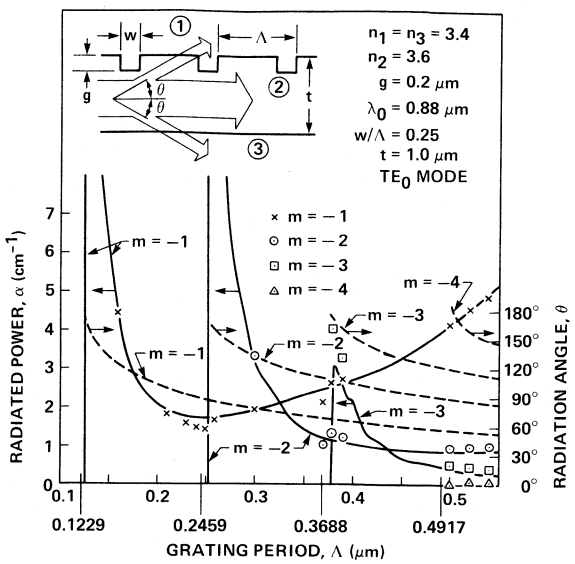


Fig. 7. TE_0 mode radiated power (solid curves) and radiation angle (broken curves) versus grating period for each partial wave. Discrete points are iterative solution results.

This value of Λ is obtained from (17) and (3) with $n_{eq} = 3.4$. At that value $\theta_1 = \theta_3 = 180°$. With continuing increases in Λ, the radiated power in the $m = -1$ partial wave rapidly peaks and then starts to decrease as the radiation angle moves toward the vertical ($\theta = 90°$). We note that as Λ approaches $\Lambda = 0.2459\ \mu m$, at which value $\beta_{-2} = -\beta_0$, the accuracy of the perturbation technique decreases. At $\Lambda = 0.2459\ \mu m$ the grating functions in the second Bragg order to provide DFB, and the grating resonantly couples the partial traveling wave $\mathscr{E}_0$ to its oppositely traveling identical wave $\mathscr{E}_{-2}$. Since the perturbation theory used to obtain the curve does not take into account the coupling between $\mathscr{E}_{-2}$ and $\mathscr{E}_{-1}$, but only between $\mathscr{E}_0$ and $\mathscr{E}_{-1}$, it becomes inaccurate. For this Λ, $\beta_{-1} = 0.0$ and therefore, according to (16), the $m = -1$ radiating partial wave is emitted normally. This is also the region in which the $m = -1$ radiated power is a minimum.

At $\Lambda = 0.2522\ \mu m$ the $m = -2$ partial wave begins to radiate and with increasing Λ, the process continues. Third-order Bragg scattering to produce DFB occurs at $\Lambda = 0.3688\ \mu m$, and the $m = -3$ partial wave begins to radiate at $\Lambda = 03783\ \mu m$. The perturbation calculations are again inaccurate in this region. At $\Lambda = 0.4917\ \mu m$, $\beta_{-4} = -\beta_0$ and $\beta_{-2} = 0.0$ so that the $m = -2$ partial wave radiates normally. Then at $\Lambda = 0.5044\ \mu m$ the $m = -4$ partial wave begins to radiate. For the particular tooth width $w/\Lambda = 0.25$, $A_{-4} = 0$, since $A_{-4} \propto \sin(4\pi w/\Lambda)$ [see Appendix A]. Thus the perturbation technique predicts no $m = -4$ partial wave and therefore no radiation. The iterative solution indicates that some small $m = -4$ partial wave does exist; it is produced by partial waves other than $\mathscr{E}_0$ coupling to $\mathscr{E}_{-4}$. Since all $\mathscr{E}_m$ ($m \neq 0$) are generally small compared to $\mathscr{E}_0$, the partial wave $\mathscr{E}_{-4}$ is very weak and radiates very little power.

IV. Concluding Remarks

We have employed an accurate perturbation technique and an iterative procedure to calculate radiation from gratings in waveguide geometries. The results indicate optimum parameter values to maximize radiation. In particular it was shown

that there exist optimal tooth heights and that the index difference at a grating should be as large as possible to maximize radiated power. In a particular geometry with an air:GaAs interface at the grating, radiated power of a mode exceeds 100 cm^{-1}.

Appendix A

Analysis for Rectangular Gratings

Consider a rectangular grating with a tooth width w of n_1^2 material as shown in Fig. 8. For this grating $w_2(x) = -w_1(x) = w/2$ and from (7)

$$A_q(x) = \begin{cases} \dfrac{-(n_2^2 - n_1^2)}{\pi q} \sin(\pi q w/\Lambda), & 0 < x < g \\ 0, & x < 0,\ g < x \quad q \neq 0 \end{cases} \tag{A1}$$

and

$$n_0^2(x) = \begin{cases} n_1^2 & \\ n_4^2 = [w n_1^2 + (\Lambda - w) n_2^2]/\Lambda, & 0 < x < g \\ n_2^2, & g < x < t \\ n_3^2, & t < x. \end{cases} \tag{A2}$$

We next rewrite (8) in the form

$$\frac{d^2 \mathcal{E}_m}{dx^2} + k_n^2(x)\, \mathcal{E}_m = \mathcal{F}_m(x), \qquad \forall_m \tag{A3}$$

where

$$\mathcal{F}_m(x) = \begin{cases} -k_0^2 \sum\limits_{\substack{q=-\infty \\ q \neq m}}^{\infty} A_{m-q}(x)\, \mathcal{E}_q(x), & 0 < x < g \\ 0, & x < 0,\ g < x, \end{cases} \tag{A4}$$

$$k_m^2(x) = k_0^2 n_0^2(x) - \beta_m^2 = k_{mj}^2, \qquad j = 1,2,3,4, \tag{A5}$$

and the subscript j in (A5) for $j = 1,2,3$ refers to regions 1,2,3 whereas $j = 4$ refers to the grating region.

Each equation in (A3) is formally solved using variation of parameters. Then imposing continuity conditions on $\mathcal{E}_m$ and $d\mathcal{E}_m/dx$ at $x = 0$ and t, we obtain

$$\mathcal{E}_m(x) \begin{cases} C_{m1} \exp(-ik_{m1} x), & x < 0 \\ C_{m1} [\cos(k_{m4} x) - (ik_{m1}/k_{m4}) \sin(k_{m4} x)] & \\ \qquad + T_m(x), & 0 < x < g \\ C_{m3} \{\cos[k_{m2}(t - x)] - (ik_{m3}/k_{m2}) & \\ \qquad \cdot \sin[k_{m2}(t - x)]\}, & g < x < t \\ C_{m3} \exp[ik_{m3}(x - t)], & t < x \end{cases} \tag{A6}$$

where

$$T_m(x) = \frac{1}{k_{m4}} \int_0^x \mathcal{F}_m(\xi) \sin[k_{m4}(x - \xi)]\, d\xi. \tag{A7}$$

Since $T_m(x)$ and its derivative are zero at $x = 0$, i.e., $T_m(0) = 0$, $dT_m/dx|_0 = 0$, the solution as given by (A6) is continuous and since T_m satisfies

$$\frac{d^2 T_m}{dx^2} + k_{m4}^2 T_m = \mathcal{F}_m, \qquad 0 < x < g \tag{A8}$$

(A6) also satisfies the differential equation (A3) with $\mathcal{F}_m$ given by (A4). In (A6) and (A7), k_{mj} as defined by (A5) is, in general, complex and thus also are the sine and cosine functions and the coefficients C_{m1} and C_{m3}. For $m = 0$, we set $C_{01} = 1$, solve for C_{03} by requiring continuity of $\mathcal{E}_0$ at $x = g$, and solve for β_0, which determines k_{0j}, by requiring continuity of $d\mathcal{E}_0/dx$ at $x = g$ [see Appendix B]. For $m \neq 0$, with k_{mj} assumed known, the coefficients are determined by requiring continuity of $\mathcal{E}_m$ and $d\mathcal{E}_m/dx$ at $x = g$. In both situations $T_m(g)$ is given by (A7) with $x = g$ and

$$\left.\frac{dT_m}{dx}\right|_g = \int_0^g \mathcal{F}_m(\xi) \cos[k_{m4}(g - \xi)]\, d\xi. \tag{A9}$$

It is necessary to clarify the calculation of k_{mj} as defined by (A5). The choice of sign is unimportant in the case of k_{m2} and k_{m4} since the expressions in (A6) apply if either sign is chosen. However, in the outer regions the partial wave fields must decay away from the waveguide if the partial wave is confined and must travel away from the guide if it radiates [9]. Specifically, from (A5) for a particular partial wave if

$$k_0^2 n_0^2 > \mathrm{Re}(\beta_m^2) = \mathrm{Re}\{(\beta_0 + 2\pi m/\Lambda)^2\} \tag{A10}$$

in either outer region, the partial wave radiates in that region; otherwise it decays there. Thus all partial waves with $m \geq 0$ decay in both outer regions, all partial waves with sufficiently negative m also decay outside the guide, and some partial waves with $m \leq -1$ radiate in one or both outer regions if (A10) is satisfied. The conditions on radiating waves imply that those which radiate in a forward direction actually increase in intensity along lines normal to the guide. In this case the partial wave at some distance from the guide was radiated by the mode before it decayed to its current value [10].

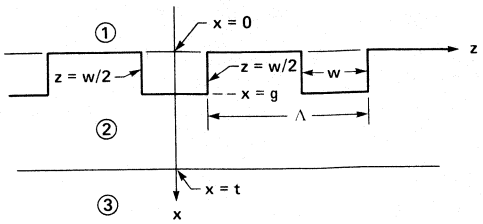


Fig. 8. Illustrating the geometry of a rectangular grating.

Appendix B

Solution Technique

It was demonstrated in Appendix A that knowledge of β_0 and $\mathcal{F}_m(x)$ enable one to compute all the partial waves, but $\mathcal{F}_m(x)$ itself depends on the partial waves and β_0 is also an unknown. The procedure used to resolve this problem is as follows.

First we set $\mathcal{F}_0(x) \equiv 0$ [and therefore $T_0(x) \equiv 0$] and calculate $\mathcal{E}_0(x)$ and β_0. Next this value of β_0 is used in (A5) to calculate k_{mj}, and $\mathcal{E}_0(x)$ is used to estimate $\mathcal{F}_m(x)$, $m \neq 0$; all

$\mathcal{E}_m(x)$ other than $\mathcal{E}_0(x)$ are ignored in this calculation of $\mathcal{F}_m(x)$. With these estimates of k_{mj} and $\mathcal{F}_m(x)$, all $\mathcal{E}_m(x)$, $m \neq 0$ are determined. This constitutes the perturbation calculation of the partial wave fields and, together with (13) and (14), yields α.

To obtain more accurate solutions, all $\mathcal{E}_m(x)$ are employed to determine first $\mathcal{F}_0(x)$, and then, simultaneously, $\mathcal{E}_0(x)$ and β_0 (β_0 is computed numerically as described below). Next, β_0 and all the current estimates of the partial wave fields are used to determine $\mathcal{F}_m(x)$, noting that $\mathcal{F}_m(x)$ as given by (A4) does not depend on $\mathcal{E}_m(x)$. Finally all $\mathcal{E}_m(x)$, $m \neq 0$, are computed and used to obtain first $\mathcal{F}_0(x)$ and then, simultaeously, $\mathcal{E}_0(x)$ and β_0. This entire process, which is illustrated by the flow chart of Fig. 9, is repeated until convergence.

The solution for β_0 is as follows. After C_{01} is set equal to 1, we obtain

$$C_{03} = \frac{\cos(k_{04}g) - (ik_{01}/k_{04})\sin(k_{04}g) + T_0(g)}{\cos[k_{02}(t-g)] - (ik_{03}/k_{02})\sin[k_{02}(t-g)]} \tag{B1}$$

by requiring $\mathcal{E}_0$ to be continuous at $x = g$. Then $d\mathcal{E}_0/dx$ will be continuous at $x = g$ if

$$\begin{aligned} R(\beta_0) = {} & k_{04}\sin(k_{04}g) + ik_{01}\cos(k_{04}g) - dT_0/dx|_g \\ & + C_{03}\{k_{02}\sin[k_{02}(t-g)] \\ & + ik_{03}\cos[k_{02}(t-g)]\} = 0 \end{aligned} \tag{B2}$$

where C_{03} is given by (B1). It should be recalled that all k_{0j} and C_{03} are functions of β_0. To solve (B2), we expand $R(\beta_0)$ about the unknown solution value β_{0s}, i.e., $R(\beta_{0s}) = 0$, retain one term of the series, and solve for β_{0s},

$$\beta_{0s} = \beta_0 - R(\beta_0)/[dR/d\beta_0]. \tag{B3}$$

An estimate of β_0 is used in the right side of (B3), β_{0s} is calculated and this process is repeated until $|R(\beta_0)|$ is sufficiently small. For the first calculation, in which case $T_0(x) \equiv 0$, β_0 is real and the procedure presents no difficulties. For later calculations we employ the β_{0s} value from the previously determined partial waves as a starting point. Convergence occurred in almost all cases, except for very large grating teeth, i.e., $g = 0.66\ \mu$m in the geometry of Fig. 2. There, no solutions of (B2) for the TE_0 and TE_2 modes exist with the initially calculated values of $T_0(g)$ and $dT_0/dx|_g$. Of course the formulation still applies, but the iterative solution will not converge without modification.

The calculation of $T_m(x)$ according to (A7) requires numerical evaluation of the integral since after the first iteration $\mathcal{F}_m(x)$ is known only numerically. However, direct evaluation of (A7) proved to be quite inaccurate and wasteful of computer time for large values of $|m|$, in which case k_{m4} is a large complex number. Indeed, the sine function evaluation often produced floating point overflows in the computer. This situation was aggravated by the fact that $T_m(x)$ and $C_{m1}[\cos(k_{m4}x) - (ik_{m1}/k_{m4})\sin(k_{m4}x)]$ in (A6) were both large and added to yield a small difference. We therefore abandoned this approach and instead solved (A3) directly for $\mathcal{E}_m(x)$ with $0 < x < g$. This was accomplished by dividing the grating region into twenty segments and using difference methods to solve for the field at these points. Even here care had to be taken to avoid roundoff problems in solving the resultant matrix equation.

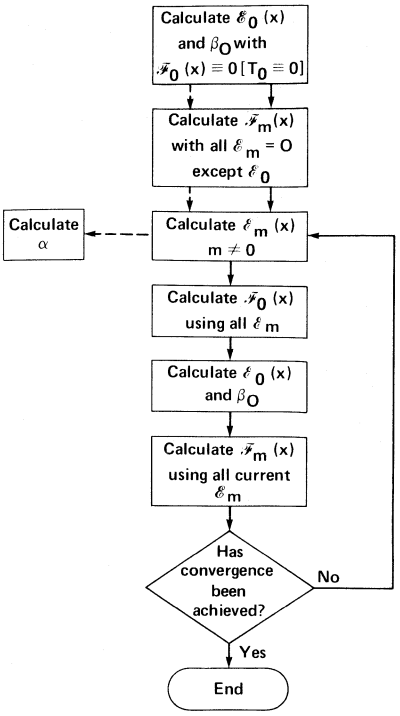


Fig. 9. Flow chart illustrating the solution procedure. The perturbation method follows the dashed path; the iterative technique follows the solid path.

References

[1] H. Kogelnik and C. V. Shank, "Coupled mode theory of distributed feedback lasers," *J. Appl. Phys.*, vol. 43, pp. 2327-2335, 1972.

[2] Zh. I. Alferov *et al.*, "Semiconductor laser with extremely low divergence of radiation" (in Russian), *Sov. Phys.-Semicond.*, vol. 8, pp. 832-833, 1974; also (in English), *Sov. Phys.-JETP*, pp. 541-542, 1974.

[3] R. D. Burnham, D. R. Scifres, and W. Streifer, "Low divergence beams from grating coupled composite guide heterostructure GaAlAs diode lasers," *Appl. Phys. Lett.*, vol. 26, pp. 644-647, 1975.

[4] P. Zory and L. D. Comerford, "Grating-coupled double-heterostructure AlGaAs Diode Lasers," *IEEE J. Quant. Elect.*, vol. QE-11, pp. 451-457, 1975.

[5] D. R. Scifres, R. D. Burnham, and W. Streifer, "Output coupling and distributed feedback utilizing substrate corrugations in double-heterostructure GaAs lasers," *Appl. Phys. Lett.*, vol. 27, pp. 295-297, 1975.

[6] K. Handa, S. T. Peng, and T. Tamir, "Improved perturbation analysis of dielectric gratings," *Appl. Phys.*, vol. 5, pp. 325-328, 1975.

[7] T. Tamir, "Inhomogeneous wave types at planar interfaces: III-Leaky waves," *Optik*, vol. 38, pp. 269-297, 1973.

[8] W. Streifer, D. R. Scifres, and R. D. Burnham, "TM mode coupling coefficients in guided wave distributed feedback lasers," *IEEE J. Quant. Elect.*, vol. QE-12, pp. 74-78, Feb. 1976.

[9] A. Hessel, "General characteristics of traveling wave antennas," in *Antenna Theory-Part II*, R. E. Collin and F. J. Zucker, Ed. New York: McGraw-Hill, 1969, ch. 19, pp. 151-258 (particularly, p. 203 ff.).

[10] A. A. Oliner, "Leaky waves in electromagnetic phenomena," in *Electromagnetic Theory and Antennas, Part II*, E. C. Jordan, Ed. New York: Pergamon, 1963, pp. 837-856.

Infrared Third-Harmonic Generation in Molecular Gases

HELGE KILDAL, MEMBER, IEEE, AND THOMAS F. DEUTSCH, MEMBER, IEEE

Abstract—We report the first observation of third-harmonic generation (THG) in molecular gases. Using a CO_2 TEA laser and choosing molecules with vibrational transitions that contribute to a resonance enhancement of the third-order susceptibility tensor we have studied absolute conversion efficiencies, spectral response, and pressure dependences for THG in SF_6, BCl_3, and CO and compared the results to theoretical predictions.

I. Introduction

We report optical third-harmonic generation (THG) of CO_2 laser radiation in SF_6, BCl_3, and CO. Although THG in the visible and ultraviolet spectral regions has previously been observed in atomic vapors [1], [2] this is the first observation of THG in molecular gases. The conversion efficiencies for atomic systems can be quite high (up to 10 percent) when phase-matching techniques are employed and when the nonlinear susceptibility tensor is enhanced by choosing twice the pump laser frequency to be near an atomic resonance. At 10.6 μm it is not possible to use electronic states for resonance enhancement of THG. However, by using molecules one can take advantage of vibrational resonances. While THG of 10.6-μm radiation has been observed in crystals with conversion efficiencies of 10^{-6} [3], the use of gases suggested some potential advantages; large-aperture systems can readily be made and optical damage is not a problem. In practice, saturation effects appear to limit the conversion efficiencies available.

II. Theory—Outline

Fig. 1(a) and (b) illustrates two different approaches to THG, each of which we have demonstrated experimentally. In process *a* depicted in Fig. 1(a), the molecule has a fundamental vibrational transition near the pump frequency and only vibrational intermediate states, each of them in near resonance, contribute to the third-order susceptibility. In *b*, Fig. 1(b), there is only one vibrational resonance, a two-photon transition, and in addition, two nonresonant electronic intermediate states are involved.

The third-order susceptibility for the first process, which was first discussed by Ueda and Shimoda [4], is given by the expression [5]

$$\chi_a^{(3)} = \frac{N}{\hbar^3} \frac{\vec{\mu}_{03}\vec{\mu}_{32}\vec{\mu}_{21}\vec{\mu}_{10}}{(\omega_{10} - \omega - i\Delta\omega_{10}/2)(\omega_{20} - 2\omega - i\Delta\omega_{20}/2)(\omega_{30} - 3\omega - i\Delta\omega_{30}/2)} \tag{1}$$

where N is the density of molecules in the vibrational ground state, $\vec{\mu}_{ab}$ is the dipole matrix element between the vibrational-rotational states a and b, ω_{10}, ω_{20}, and ω_{30} are the fundamental, first, and second overtone frequencies of the vibrational transition, and $\Delta\omega_{10}$, $\Delta\omega_{20}$, and $\Delta\omega_{30}$ are the linewidths of these transitions. The matrix elements μ_{32} and μ_{21} are proportional to the μ_{10}; in addition μ_{03} is also approximately proportional to μ_{10}; hence $\chi_a^{(3)}\alpha(\mu_{10})^4$. Since the absorption line strength f is proportional to $(\mu_{10})^2$, it follows that third-harmonic conversion efficiency, which is proportional to $|\chi_a^{(3)}|^2$, (see (4) below) has an f^4 dependence. The THG will thus be very sensitive to the strength of the molecular absorption.

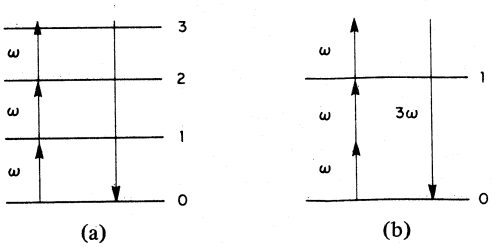


Fig. 1. Energy levels contributing to the third-order susceptibility tensor in (a) SF_6 and BCl_3, and (b) CO.

Because the susceptibility tensor has three resonant denominators it is highly frequency dependent. This threefold resonance enhancement is somewhat reduced, however, by the anharmonic effects. While minimizing the mechanical anharmonicity maximizes the possible resonant enhancement, it is not necessarily the molecule with the smallest mechanical anharmonicity that has the largest susceptibility tensor since the matrix element μ_{03} is zero for a perfect harmonic oscillator and its magnitude depends on both the electric as well as the mechanical anharmonicity.

A disadvantage of using three resonant denominators for THG is the substantial absorption of the pump laser radiation. This causes the maximum in conversion efficiency to occur at relatively low pressure-times-cell-length products, typically 50 torr · cm for SF_6. Thus the total conversion is low in spite of a large resonance enhancement in the susceptibility tensor. To avoid this, one can instead choose a system where the susceptibility tensor is enhanced only by a two-photon absorption resonance. In this case the contribution from the energy denominators is smaller since there is only one resonance; however, this may be partially compensated for by the fact that the transitions can be electronic and hence have much larger matrix elements.

Manuscript received January 30, 1976. This work was supported by the Department of the Air Force.

The authors are with the Lincoln Laboratory, Massachusetts Institute of Technology, Lexington, MA 02173.

This second scheme was recently suggested by She and Billman [6] who estimated a potential conversion efficiency of 10 percent in H_2. However, no pump laser is available at the H_2 two-photon absorption frequency. The third-order susceptibility for this process is given by [5], [6]

$$\chi_b^{(3)} \approx \frac{N}{\hbar^3}\frac{2}{\Omega^2}\frac{\left|\sum_e \vec{\mu}_{0e}\vec{\mu}_{e1}\right|^2}{(\omega_{10} - 2\omega - i\Delta\omega_{10}/2)} \tag{2}$$

where Ω is an average electronic transition frequency which has been assumed to be much larger than 3ω, and $\vec{\mu}_{0e}$ and $\vec{\mu}_{e1}$ are vibronic dipole matrix elements.

It is interesting to make an order-of-magnitude comparison between the susceptibilities for the two schemes. It can be shown that $\Sigma_e \mu_{0e}\mu_{e1} \sim \mu_{el}\mu_{vib}$ where μ_{el} and μ_{vib} are typical electronic and vibrational dipole moments and $\mu_{03} \sim 3 \times 10^{-3}\mu_{10} = 3 \times 10^{-3}\mu_{vib}$. With one exact resonance satisfied in (1) and denoting the anharmonic defect by $\Delta\omega_{anh}$ it follows that the ratio between the susceptibilities is given by

$$\frac{\chi_a^{(3)}}{\chi_b^{(3)}} \sim 3 \cdot 10^{-3}\left(\frac{\mu_{vib}/\Delta\omega_{anh}}{\mu_{el}/\Omega}\right)^2 \tag{3}$$

when we neglect the difference between the rotational matrix elements. Inserting typical values such as $\mu_{vib} \sim 0.1\,\mu_{el}$, $\Delta\omega_{anh} \sim 5\ \text{cm}^{-1}$, and $\Omega \sim 50\,000\ \text{cm}^{-1}$ into (3) gives $\chi_a^{(3)}/\chi_b^{(3)} \sim 3000$ for equal molecular densities. This ratio can be made smaller, however, since the second scheme allows operation at higher pressures.

The third-harmonic conversion efficiency for a laser operating in a TEM_{00}-order mode is given by

$$\frac{P_3}{P_1} = \frac{3}{4}\frac{\eta^4\omega^2|\chi^{(3)}|^2}{\lambda^2}P_1^2|\mathcal{J}|^2\exp(-\alpha_3 l) \tag{4}$$

where

$$\mathcal{J} = \frac{2}{b}\int_0^l \frac{\exp(i\Delta kz' - \alpha z'/2)}{(1 - i2(z' - z_0)/b)^2}\,dz' \tag{5}$$

is the phase-mismatch integral given by Ward and New [7] generalized to include the absorption $\alpha = 3\alpha_1 - \alpha_3$ where α_1 and α_3 are the absorption constants at the pump and the third-harmonic frequency, respectively. Furthermore $b = 2\pi w_0^2/\lambda$ is the confocal parameter with the spot size equal to w_0; z_0 is the distance from the cell entrance window to the focal point, l is the cell length, $\eta = \sqrt{\mu_0/\epsilon_0}$ is the free-space impedance, and $\Delta k = k_3 - 3k_1$ is the wave-vector mismatch. Neglecting absorption, the integral reduces to $|\mathcal{J}|^2 = (2l/b)^2\,\text{sinc}^2(\Delta kl/2)$ for weak focusing ($b > 3l$); for strong focusing ($b < l/3$) we have $|\mathcal{J}|^2 = 0$ for $\Delta k > 0$ and $|\mathcal{J}|^2 = (\pi\Delta kb)^2\exp\Delta kb$ for $\Delta k < 0$. In the case of perfect phase matching ($\Delta k = 0$) and no absorption losses, maximum conversion efficiency is obtained for confocal focusing into the cell ($b = 2z_0 = l$). The integral $\mathcal{J}$ is then equal to unity and so the third-harmonic conversion efficiency is independent of cell length as long as the input power is kept constant and there is no optical breakdown.

III. Experimental

THG was obtained using both the schemes discussed above: generation by the triply resonant process, scheme *a*, was demonstrated in SF_6 and BCl_3, while the two-photon scheme *b* was realized using CO. The experiments were motivated in part by recent demonstrations that SF_6 can be excited by a CO_2 laser to high vibrational levels without the assistance of collisions [8], [9]. It follows that the molecules should radiate coherently at these highly excited transitions and it suggested that THG might be observed under similar conditions.

A grating-controlled single-line multimode CO_2 TEA laser producing 0.75-J pulses with a width of 175-ns (FWHM) was used in the experiments. The energy was measured using a Gen-Tec ED-200 joule meter and the intensity was monitored by a photon drag detector. The CO_2 laser beam was passed through an 8-μm long-wavelength pass filter to block the 4.3-μm fluorescence from the CO_2 laser as well as the third-harmonic signal from the germanium CO_2 laser output coupler before being focused into the 10-cm-long 1.8-cm ID Teflon cell equipped with KCl windows. Except where indicated, the beam was focused by an *f*/3 off-axis paraboloid mirror to a spot size of 400 μm corresponding to a confocal parameter of 11 cm at either 2.5 or 5 cm from the front of the cell. (Although the CO_2 laser did not operate in a perfect TEM_{00}-order mode, an effective spot size w_0 was determined by measuring transmission through different apertures and defining the spot size as the diameter of the aperture for 39-percent transmission.)

The CO_2 laser radiation emerging from the exit window of the cell was blocked by an LiF absorption filter whereas the third-harmonic radiation was focused onto a 0.125-m-focal-length *f*/3.7 monochromator equipped with a grating blazed at 4 μm and then detected by an InSb photovoltaic detector. The detector had a time constant of 0.3 μs which did not allow temporal resolution of the third-harmonic signal. The overall sensitivity of the detection system was calibrated using a 3.39-μm He-Ne laser. The third-harmonic-signal intensities and conversion efficiencies given below are based on this calibration, with no correction for the fact that the detector time constant was slower than the third-harmonic rise time. The limited detector speed also prevented us from observing temporal behavior of saturation phenomena.

The most extensive studies were performed on SF_6; frequent refillings of the cell were used to minimize depletion of the initial SF_6 fill due to dissociation of the gas by the focused CO_2 laser beam. In addition, third-harmonic intensity versus pressure measurements were performed using both increasing and decreasing pressure to check that no hysteresis effects were present. Fig. 2 shows normalized third-harmonic output as a function of frequency together with the absorption curve for SF_6. Note that the third-harmonic signal falls to zero on the high-frequency side of *P*(20). The pressure dependence was examined for each of the CO_2 laser *P* lines. Fig. 3 shows the behavior for *P*(20) and *P*(26) with the focus 2.5 cm from the front of the cell. The third-harmonic output power reached a maximum at approximately 4.5 torr. The oscillations in the signal that occur using the *P*(20) line become weaker and less pronounced as the laser frequency decreases. The oscillations also depend on the location of the focal plane within the cell; with the focus in the middle of the cell, only two maxima are observed in the third-harmonic output versus pressure curve for *P*(20).

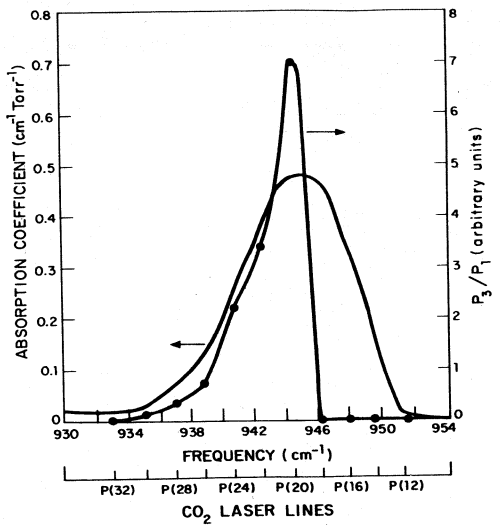


Fig 2. Relative third-harmonic conversion efficiency in SF_6 versus laser frequency at a pressure of 5 torr together with the spectral dependence of the absorption coefficient. The latter was measured by a Beckman 4250 IR spectrophotometer at a resolution of 2 cm^{-1} for a 0.5 torr SF_6-1 atm He mixture.

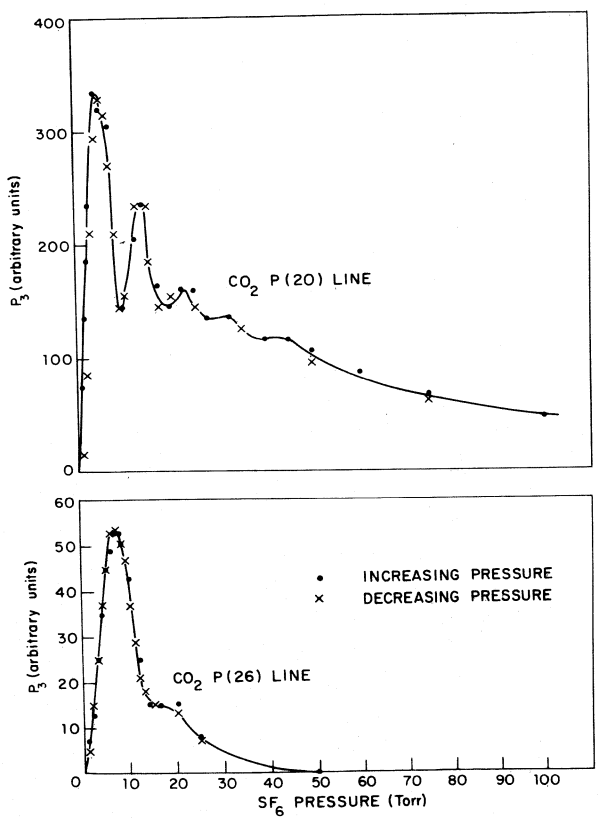


Fig. 3. Pressure dependence of the third-harmonic signal generated in SF_6 in a 10-cm cell using two different CO_2 laser lines in the 10.6-μm band.

The dependence of the third-harmonic signal, P_3, on the pump power, P_1, was measured for the $P(20)$ line. At low intensities this dependence was close to P_1^3, with a transition to a P_1^2 behavior at higher intensities. Such deviations from a simple P_1^3 dependence have been observed with metal vapors and attributed to saturation of the two-photon transitions [10], [11]. In our case the deviations are probably due to saturation of the SF_6 absorption, with attendant changes in the third-order susceptibility and the wave-vector mismatch, as discussed below. The presence of saturation was demonstrated by a measurement of the SF_6 absorption for the $P(20)$ CO_2 laser line; under tight focusing conditions with pump powers of ~4 MW an absorption coefficient of 0.0065 $cm^{-1} \cdot torr^{-1}$ was found, about 50 times less than the unsaturated value obtained using a spectrophotometer. The third-harmonic power from an optimized SF_6 system pumped with 4.0 MW of CO_2 $P(20)$ line power was approximately 2.2×10^{-5} W, corresponding to a conversion efficiency of 5×10^{-12}. A comparable signal was also generated in SF_6 using a weakly focused beam having a spot size of 0.75 cm at the center of the cell. In this case the third-harmonic signal versus pressure curve still peaked at 4.5 torr, but then declined smoothly at higher pressures without the oscillatory behavior seen in Fig. 3, and the third-harmonic signal versus frequency curve showed a much sharper peak around the $P(20)$ line with no output on the high-frequency side, and intensities of 0.03 and 0.007 of the $P(20)$ third-harmonic signal for the $P(22)$ and $P(24)$ lines, respectively.

THG was also obtained in BCl_3. Fig. 4 shows the spectral dependence of the third-harmonic conversion efficiency along with the absorption coefficient. Before the absorption measurements, special care was taken to passivate the Teflon-coated stainless steel spectrophotometer cell. It was filled with 1 torr of BCl_3 and then left standing overnight before refilling the cell with the same BCl_3 pressure and making the transmission measurements. Without this procedure reproducible spectrophotometer measurements could not be obtained. THG resulting from contributions of the $^{10}BCl_3$ isotope (near 978 cm^{-1}) and $^{11}BCl_3$ (near 939 cm^{-1}) is evident. The maximum third-harmonic signal occurs at the low-frequency side of the absorption lines. The asymmetrical structure obtained with SF_6 is absent. Fig. 5 shows the pressure dependence of the third-harmonic output; in contrast to the SF_6 case, no oscillations were observed. The conversion efficiency for the $P(26)$ line at the optimum pressure, 15 torr, and under the same tight focusing conditions as for SF_6, was about $\frac{3}{4}$ of that obtained with SF_6. Under the same loose focusing conditions used with SF_6, no detectable third-harmonic signal was obtained from BCl_3.

Other gases having absorption bands within the range of the CO_2 laser, such as CH_3F which absorbs the $P(10)$-$P(24)$ transitions of the 9.6-μm CO_2 band, and CCl_2F_2 which absorbs the $P(16)$-$P(36)$ transitions of the 10.6-μm band, were also examined but produced no observable third-harmonic signal.

THG according to scheme *b* was obtained using a two-photon resonance between the CO_2 laser transitions and the Q-branch transitions of CO near 2143 cm^{-1}. Table I lists the Q-branch frequencies of CO, calculated using measured spectroscopic constants [12], together with some doubled CO_2 laser frequencies in the 9.3-μm band [13]. Twice the CO_2 $R(8)$-line frequency lies within 0.036 cm^{-1} of the CO $Q(11)$ line. THG was observed using this CO_2 line, as well as $R(10)$ which lies on the high-frequency side of the Q-branch 0.5 cm^{-1} away from CO $Q(0)$; no THG was found with $R(12)$. The laser did not operate on $R(6)$ and $R(4)$, other lines of possible interest.

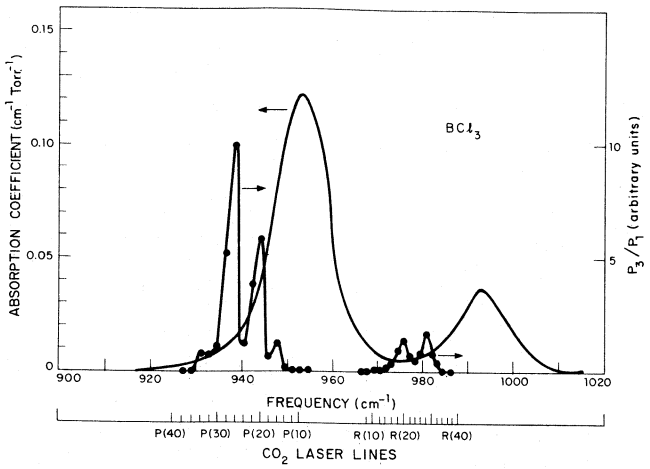


Fig. 4. Relative third-harmonic conversion efficiency in BCl_3 versus laser frequency at a pressure of 15 torr together with the spectral dependence of the absorption coefficient. The latter was measured by a Beckman 4250 IR spectrophotometer at a resolution of 2 cm^{-1} using a preconditioned cell with a BCl_3 pressure of 1 torr.

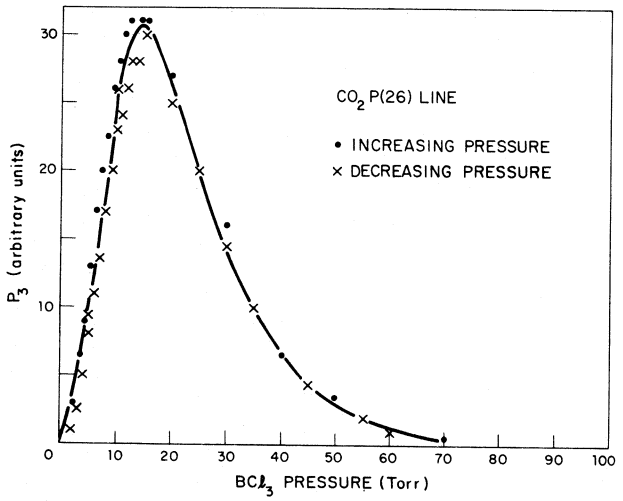


Fig. 5. Pressure dependence of the third-harmonic signal generated in BCl_3 in a 10-cm cell using the CO_2 $P(26)$ line in the 10.6-μm band.

In these experiments a 65-cm f.l. ZnSe lens was used to focus the beam, which had an intensity of 2.5 MW for $R(10)$, to a spot size of 1.8 mm in the center of a 1-m-long cell. Fig. 6 shows the third-harmonic signal versus CO pressure for this configuration; THG was detectable ($\sim 2 \times 10^{-7}$ W) at pressures as low as 300 torr. The third-harmonic output for the $R(10)$ line was proportional to the pressure squared up to 1 atm, the limit of our pressure handling system; for the $R(8)$ line the pressure dependence deviated from square-law behavior at pressures above 500 torr. At a CO pressure of 1 atm the third-harmonic conversion efficiency was 0.4×10^{-12} for both the $R(8)$ and the $R(10)$ line with input powers of 2.2 and 2.7 MW, respectively.

IV. Discussion

A. SF_6

The magnitude of the third-order susceptibility for SF_6 can be estimated using (1) [14]. The 10.6-μm absorption in SF_6 is due to the threefold degenerate ν_3 mode which has a dipole moment μ_{10} of approximately 0.3 D [15]. For the higher vibrational transitions we have $\mu_{21} \approx \sqrt{2}\,\mu_{10}$ and $\mu_{32} \approx \sqrt{3}\,\mu_{10}$ and we estimate that the third overtone transition has a dipole strength μ_{03} of approximately $3 \times 10^{-3}\,\mu_{10}$. The latter value is based on absorption measurements made using a Beckman 4250 spectrophotometer together with a White cell with a 2-m path. The SF_6 line spectrum near 10.6 μm is very rich, with over 1000 lines/cm^{-1} [16], so that above 1 torr the line spectrum merges into a continuum. We will therefore neglect the vibrational-rotational fine structure and treat the molecule as a single anharmonic oscillator with transition frequencies and linewidths (FWHM) of $\nu_{10} \approx 946$ cm^{-1}, $\nu_{20} \approx 1888$ cm^{-1}, $\nu_{30} \approx 2827$ cm^{-1}, $\Delta\nu_{10} \approx 11$ cm^{-1}, $\Delta\nu_{20} \approx 16$ cm^{-1}, and $\Delta\nu_{30} \approx 22$ cm^{-1}, as estimated from our spectrophotometer measurements. Assuming a pressure of 1 torr ($N = 3.3 \times 10^{16}$ cm^{-3} at 22°C) we calculate a third-order susceptibility which has a peak value $|\chi_a^{(3)}|_{max} \approx 3.2 \times 10^{-35}$ $A \cdot s \cdot m/V^3$ at 944 cm^{-1}. The maximum occurs on the low-frequency side of the absorption line because of the anharmonic defect. We have multiplied the result obtained using (1) by 3 to account for the threefold degeneracy of the ν_3 mode and performed the angular averaging classically which gives rise to a factor of $\frac{1}{5}$. We have neglected the possibility of using combinations of the degenerate modes as intermediate states. A rigorous treatment of this possibility requires de-

TABLE I

CO (0-1) Q branch		CO_2 (00°1-02°0)	
J	$\nu_{Q(J)}$ (cm^{-1})	Line	$2\nu_{CO_2}$ (cm^{-1})
		R(10)	2143.768
0	2143.272		
1	2143.237		
2	2143.166		
3	2143.061		
4	2142.921		
5	2142.746		
6	2142.536		
7	2142.291		
8	2142.011		
9	2141.696		
10	2141.346		
11	2140.961	R(8)	2140.925
12	2140.541		
13	2140.086		
14	2139.596		
15	2139.071		
16	2138.511		
17	2137.916	R(6)	2138.028
18	2137.285		
19	2136.620		
20	2135.920		
21	2135.185	R(4)	2135.078
22	2134.415		
23	2133.610		
24	2132.770		
25	2131.895		

tailed investigation of the selection rules and complicates the calculation beyond the scope of our simplified model. Insertion into (4) results in a third-harmonic conversion efficiency of

$$P_3/P_1 \approx 4.4 \times 10^{-21} P_1^2 |\mathcal{J}|^2 \exp(-\alpha_3 l) \quad (6)$$

at a pressure of 1 torr and with the powers in watts. The conversion efficiency depends on the phase mismatch

$$\Delta kl = (k_3 - 3k_1)l = 6\pi l(n_3 - n_1)/\lambda.$$

We estimate the index of refraction difference due to dispersion to be $\delta n = n_3 - n_1$ assuming the main contribution arises from the 10.6-μm transition, and neglect any electronic contribution. With a triply degenerate oscillator at ω_{10} the difference is given by

$$\delta n \approx -\frac{N|\mu_{10}|^2}{2\epsilon_0\hbar}\left\{\frac{\omega_{10}-\omega}{(\omega_{10}-\omega)^2+(\Delta\omega_{10}/2)^2} + \frac{\omega_{10}+\omega}{(\omega_{10}+\omega)^2+(\Delta\omega_{10}/2)^2}\right\}. \quad (7)$$

Using the values for SF_6 we find that the maximum negative dispersion occurs at 940.5 cm^{-1} and at 1 torr it is given by $\delta n_{max} = -8.5 \times 10^{-6}$ which gives a coherence length of $l_c = \pi/\Delta k = \lambda/6\delta n_{max} = 21$ cm. At pressures below a few torr in a 10-cm-long cell the process is therefore phase matched.

The integral in (5) under weak focusing conditions and including absorption losses is given by

$$|\mathcal{J}|^2 = (2/b)^2 \frac{(1-\exp(-\alpha l/2))^2 + 4\exp(-\alpha l/2)\sin^2(\Delta kl/2)}{(\alpha/2)^2 + \Delta k^2}. \quad (8)$$

Since SF_6 has negligible absorption at the third-harmonic frequency we have $\alpha = 3\alpha_1$. At a pressure of 4.5 torr with 4 MW incident on the cell, the saturated absorption coefficient at 944 cm^{-1} was measured to be 0.03 cm^{-1}. Furthermore, the wave-vector mismatch calculated from (7) is $\Delta k = 0.44$ cm^{-1}. Using the parameters $l = 10$ cm and $b = 3.3 \times 10^3$ cm for our weak-focusing SF_6 experiment, we find $|\mathcal{J}|^2 = 3.4 \times 10^{-6}$. When this is inserted into (6) we obtain a predicted third-harmonic conversion efficiency of $P_3/P_1 = 1.1 \times 10^{-12}$ for $P_1 = 4$ MW and a pressure of 4.5 torr. This estimate agrees reasonably well with the measured conversion efficiency of 5×10^{-12}.

As pointed out, the maximum conversion efficiency did not increase with tighter focusing into the cell, but the spectral widths did depend on the focusing conditions. For both weak and strong focusing the THG cut on sharply below 946 cm^{-1}. However, for weak focusing the spectral width was about 1 cm^{-1} while under tight focusing it increased to 3 cm^{-1}.[1] In contrast, our simple oscillator model, which neglects absorption losses and wave-vector mismatch, predicts a width of 5 cm^{-1} for the third-harmonic signal versus frequency curve.

[1] It is of interest to note that the relatively narrow spectral widths observed in THG differ from the wide width of 18 cm^{-1} observed in photodissociation experiments on SF_6 with a CO_2 laser at comparable intensities [18].

We believe this dependence on focusing is due to depletion of the ground-state population by absorption at the fundamental frequency. At pressures of a few torr we estimate a few kW/cm^2 is sufficient to saturate the fundamental ν_3 absorption [15], [17]. With tight focusing at the optimum frequency for THG the molecules are driven up the vibrational ladder where the anharmonicity causes them to get out of resonance during the pump laser pulse reducing the effective susceptibility tensor. The asymmetric shape of the third-harmonic curve is probably due to the contribution of molecules in excited vibrational levels which have been populated due to the absorption. Because of anharmonicity the resonance enhancement for these excited molecules is shifted to lower frequencies.

The third-harmonic versus pressure curve in Fig. 3 shows oscillations with maxima at pressures of approximately $p = p_0(1+2q)$ where $q = 0, 1, 2, \cdots$ and $p_0 = 4.5$ torr for the $P(20)$ line and 7 torr for the $P(26)$ line. The oscillations are due to the phase mismatch, and at p_0 we have $\Delta kl/2 = \pi/2$ which gives $\Delta k = 0.3$ cm^{-1} in reasonable agreement with our calculation [(7)]. The third-harmonic output versus pressure curve for weak focusing in SF_6 did not show a similar structure. The absorption is less saturated than for tight focusing so that the first term in the numerator in (8) could dominate over the second one. The oscillations would then disappear.

The drop in SF_6 third-harmonic conversion efficiency at pressures above a few torr for a 10-cm cell is due to increased absorption of the fundamental.

B. BCl_3

The spectral dependence of THG in BCl_3 shows more structure than in SF_6. Associated with $^{11}BCl_3$ there are 4 peaks spaced approximately 5 cm^{-1} apart and for $^{10}BCl_3$ there are two peaks also spaced by 5 cm^{-1}. We are not certain of the origin of this structure, but we do not believe it is caused by coherence length effects since otherwise they would have been present in Fig. 5 which shows the pressure dependence of the third-harmonic conversion efficiency.

C. CO

In principle the third-order susceptibility for CO can be calculated from (2). However, this is not a practicable approach since the matrix elements are not well known. Instead we can recast (2) in terms of the two-photon absorption constant $\alpha^{\text{two-ph}}$ between the ground state and the first excited vibrational state. We have

$$|\chi_b^{(3)}| \approx (1 + (2(\omega_{10} - 2\omega)/\Delta\omega_{10})^2)^{1/2}\, \alpha^{\text{two-ph}}/\eta^2\omega I_1 \quad (9)$$

where I_1 is the laser intensity. The magnitude of $\alpha^{\text{two-ph}}$ has been discussed in [17]. The two-photon absorption constant can be related to the spontaneous Raman scattering cross section by the expression

$$\alpha^{\text{two-ph}} = \frac{16\pi^2(d\sigma^r/d\Omega)I_1\omega c^2 N}{\hbar\omega_r\omega_s^3\Delta\omega_{10}(1+(2(\omega_{10}-2\omega)/\Delta\omega_{10})^2)} \quad (10)$$

where ω_r and ω_s are, respectively, the Raman pump and the Stokes frequency. The latter equation is valid when the Raman pump frequency is sufficiently below the electronic transition frequencies to avoid any electronic resonance enhancement. The spontaneous Raman scattering cross section $d\sigma^r/d\Omega$ is for polarized light with the output polarization parallel to the input polarization. For the CO Q-branch $d\sigma^r/d\Omega = 4.3 \times 10^{-31}$ cm$^2 \cdot$ St^{-1}($\lambda_r = 5145$ Å) [19]. The main contribution to the third-order susceptibility for the CO_2 $R(8)$ line comes from the CO(0-1) $Q(11)$ transition. There are also contributions from $Q(10)$ and $Q(12)$, but they have opposite signs leading to partial cancellation [see (2)]. For this CO_2 laser line we consider therefore only the $Q(11)$ transition. The number density in (10) is then the population in a single rotational state given by $N_J = n_J N_t$ where n_J is the Boltzmann factor and N_t is the total density of molecules in the vibrational ground state. For the CO(0-1) $Q(11)$ transition the pressure-broadened linewidth is $\Delta\nu_{10} = 0.14$ cm^{-1}/atm [20]. Furthermore $n_J = 0.063$, $\nu = 1070.46$ cm^{-1}, and $\nu_{10} - 2\nu = 0.036$ cm^{-1}. Inserting these values into (10) we find

$$\alpha^{\text{two-ph}}/I_1 = 4.3 \times 10^{-14} \quad \text{(cm/W)} \tag{11}$$

at a pressure of 1 atm, where we have neglected the finite laser linewidth of approximately 0.03 cm^{-1}. Using (9) and (4) we find that the susceptibility is $|\chi_b^{(3)}| = 1.7 \times 10^{-35}$ A $\cdot$ s $\cdot$ m/V^3 and the third-harmonic conversion efficiency is

$$P_3/P_1 = 2.0 \times 10^{-21} P_1^2 |\mathcal{J}|^2 \exp(-\alpha_3 l) \tag{12}$$

with the powers in watts. The CO has no absorption at ω and 3ω so that $\alpha_1 = \alpha_3 = 0$. The change in the index of refraction due to the CO vibrational transition at $\omega \approx \omega_{10}/2$ is given by

$$\delta n = n_3 - n_1 \approx -16N|\mu_{10}|^2/45\epsilon_0\hbar\omega \tag{13}$$

where $|\mu_{10}| = 0.1$ D [21]. At 1 atm, $\delta n = -5.2 \times 10^{-6}$ and the coherence length is $l_c = 30$ cm. The actual index change will be somewhat smaller since the electronic transitions add a positive contribution to the dispersion making the coherence length longer. The coherence length according to Fig. 6 is longer than 1 m at pressures of up to 1 atm since the third-harmonic signal for the CO_2 $R(10)$ line shows no deviation from a square-law pressure dependence. Using the experimental parameters $l = 1$ m, $b = 2.18$ m, and $P_1 = 2.2$ MW, and neglecting the phase mismatch we have $|\mathcal{J}|^2 = 0.76$ which gives an estimated third-harmonic conversion efficiency for the CO_2 (00°1-02°0) $R(8)$ line of $P_3/P_1 = 7.4 \times 10^{-9}$ in CO at 1 atm. The measured conversion efficiency is several orders of magnitude smaller. Part of the discrepancy might be explained by the pump laser which operated multimode. This reduces the efficiency with confocal focusing.

The $R(10)$ line is much further from any two-photon resonance than the $R(8)$ line (0.50 cm^{-1} compared to 0.036 cm^{-1}). However, the third-order susceptibilities for the two lines are almost the same. The reason is that the doubled $R(10)$ line lies outside the Q-branch (on the $Q(0)$-side) so that the contributions from the individual $Q(J)$ transitions add constructively to the susceptibility tensor. We can estimate the ratio between the susceptibilities for the two pump lines by considering the denominator in (2) together with appropriate

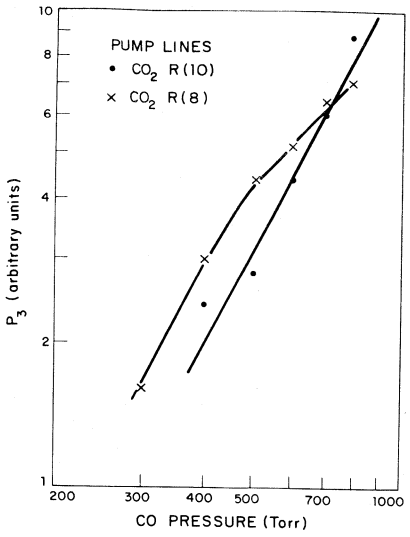


Fig. 6. Pressure dependence of the third-harmonic signal generated in CO in a 1-m cell with input powers of 2.2 MW in the $R(8)$ line and 2.7 MW in the $R(10)$ line.

Boltzmann factors. We have $\chi_b^{(3)}(R(10))/\chi_b^{(3)}(R(8)) \approx 0.6$ which is in agreement with the experimental result shown on Fig. 6.

The third-harmonic signal shows a different pressure dependence for the two CO_2 laser lines. At low pressures the susceptibility tensor increases linearly with pressure. However, saturation will occur when the pressure-broadened linewidth approaches the frequency mismatch between the pump laser and the resonant CO transition. For the $R(8)$ line this occurs at about 400 torr which agrees well with the observed value of 500 torr in Fig. 6. The third-order susceptibility for the $R(10)$ line should not show any saturation before 7 atm, and the saturation should be less pronounced since the frequency mismatches are different for the various Q-branch transition contributing to the susceptibility tensor. For optimization of the THG efficiency in CO it is therefore best to use the $R(10)$ line and in general, the doubled pump frequency should lie slightly on the side of the Q-branch.

It is interesting to insert (9) directly into (4) assuming weak focusing, no absorption losses, and an exact two-photon resonance. We have

$$P_3/P_1 = 3/16(\alpha^{\text{two-ph}} l \operatorname{sinc} \Delta kl/2)^2 \tag{14}$$

showing that efficient THG by utilizing one exact two-photon resonance is possible only when two-photon absorption losses become significant.

V. Conclusion

We have observed THG of CO_2 laser radiation in several molecules. Two approaches have been examined to obtain resonance enhancement of the third-order susceptibility tensor. In SF_6 and BCl_3 the CO_2 laser is in resonance with a fundamental vibrational transition and in CO there is a two-photon resonance. Comparing the two schemes, the second is more attractive because there is no absorption leading to saturation. The coherence lengths are also longer since the pump laser is far away from any resonance. The second scheme is also more

general allowing sum and difference frequency generation of two lasers with the same efficiency as long as the two-photon resonance is maintained.

THG can also be used as a sensitive technique in two-photon absorption spectroscopy. Information about states with no dipole moment to the ground state can be obtained by observing the resonances in the third-harmonic signal when the pump laser is tuned through two-photon transitions [22].

Acknowledgment

We acknowledge helpful discussions with P. L. Kelley and A. Mooradian, and the expert technical assistance of J. W. Burke is greatly appreciated.

References

[1] J. F. Young, G. C. Bjorklund, A. H. Kung, R. B. Miles, and S. E. Harris, "Third harmonic generation in phase-matched Rb vapor," *Phys. Rev. Lett.*, vol. 27, pp. 1551–1553, 1971.

[2] D. M. Bloom, G. W. Bekkers, J. F. Young, and S. E. Harris, "Third harmonic generation in phase-matched alkali metal vapors," *Appl. Phys. Lett.*, vol. 26, pp. 687–689, 1975.

[3] H. Kildal, R. F. Begley, M. M. Choy, and R. L. Byer, "Efficient second and third harmonic generation of 10.6 μm in $CdGeAs_2$," *J. Opt. Soc. Am.*, vol. 62, p. 1398, 1972.

[4] Y. Ueda and K. Shimoda, "Optical third harmonic generation by molecular vibration," *J. Phys. Soc. Japan*, vol. 28, pp. 196–204, 1970.

[5] P. N. Butcher, *Nonlinear Optical Phenomena*, bulletin 200, Engineering Experiment Station, Ohio State Univ., Columbus, 1965, p. 98.

[6] C. Y. She and K. W. Billman, "Infrared-pumped third-harmonic and sum-frequency generation in diatomic molecules," *Appl. Phys. Lett.*, vol. 27, pp. 76–79, 1975.

[7] J. F. Ward and G. H. C. New, "Optical third-harmonic generation in gases by a focused laser beam," *Phys. Rev.*, vol. 185, pp. 57–72, 1969.

[8] R. V. Ambartsumyan, Yu. A. Gorokhov, V. S. Letokhov, and G. N. Makarov, "Separation of sulfur isotopes with enrichment coefficient $>10^3$ through action of CO_2 laser radiation on SF_6 molecules," *JETP Lett.*, vol. 21, pp. 171–172, 1975.

[9] J. L. Lyman, R. J. Jensen, J. Rink, C. P. Robinson, and S. D. Rockwood, "Isotopic enrichment of SF_6 in S^{34} by multiple absorption of CO_2 laser radiation," *Appl. Phys. Lett.*, vol. 27, pp. 87–89, 1975.

[10] C. C. Wang and L. I. Davis, Jr., "Saturation of resonant two-photon transitions in thallium vapor," *Phys. Rev. Lett.*, vol. 35, pp. 650–653, 1975.

[11] J. F. Ward and A. V. Smith, "Saturation of two-photon-resonant optical processes in cesium vapor," *Phys. Rev. Lett.*, vol. 35, pp. 653–656, 1975.

[12] H. Kildal, R. S. Eng, and A. H. M. Ross, "Heterodyne measurements of $^{12}C^{16}O$ laser frequencies and improved Dunham coefficients," *J. Mol. Spectrosc.*, vol. 53, pp. 479–488, 1974.

[13] F. R. Petersen, D. G. McDonald, J. D. Cupp, and B. L. Danielson, "Accurate rotational constants, frequencies, and wavelengths from $^{12}C^{16}O_2$ lasers stabilized by saturated absorption," in *Proc. Laser Spectroscopy Conf.* (Vail, CO, 1973), A. Mooradian and R. G. Brewer, Ed. New York: Plenum, 1974, pp. 555–569.

[14] M. F. Becker, private communication (a more detailed calculation).

[15] J. I. Steinfeld, I. Burak, D. G. Sutton, and A. V. Nowak, "Infrared double resonance in sulfur hexafluoride," *J. Chem. Phys.*, vol. 52, pp. 5421–5434, 1970.

[16] E. D. Hinkley, "High-resolution infrared spectroscopy with a tunable diode laser," *Appl. Phys. Lett.*, vol. 16, pp. 351–354, 1970.

[17] P. L. Kelley, H. Kildal, and H. R. Schlossberg, "Highly selective excitation of atoms and molecules using two-photon processes," *Chem. Phys. Lett.*, vol. 27, pp. 62–66, 1974.

[18] R. V. Ambartsumyan, private communication.

[19] C. M. Penney, L. M. Goldman, and M. Lapp, "Raman scattering cross sections," *Nature Physical Science*, vol. 235, pp. 110–112, 1972.

[20] G. M. Hoover and D. Williams, "Infrared absorptance of carbon monoxide at low temperatures," *J. Opt. Soc. Am.*, vol. 59, pp. 28–33, 1969.

[21] S. S. Penner, *Quantitative Molecular Spectroscopy and Gas Emissivities*. Reading, MA: Addison-Wesley, 1959.

[22] P. P. Sorokin *et al.*, "Generation of vacuum ultraviolet radiation by nonlinear mixing in atomic and ionic vapors," *Lecture Notes in Physics* 43, *Laser Spectroscopy, Proc. 2nd Int. Conf.*, (Megève, France, 1975), S. Haroche, J. C. Pebay-Peyroula, T. W. Hänsch, and S. E. Harris, Ed. New York: Springer, 1975, pp. 46–54.

Correspondence

Second-Harmonic Generation in $KB_5O_8 \cdot 4H_2O$

T. S. CHEN AND W. P. WHITE

Abstract—**Theoretical calculations on the nonlinear crystal potassium pentaborate tetrahydrate (PPT) indicate that frequency doubling may be achieved over a wide spectral region of fundamental wavelengths (434 to >700 nm) using a single crystal cut. To test these results, second-harmonic generation of the ruby laser and the argon laser was investigated.**

INTRODUCTION

Dewey *et al.* [1] recently observed second-harmonic generation in potassium pentaborate tetrahydrate (PPT) for the fundamental wavelength region: 434–469 nm. The fundamental wave propagated in the b–c plane with polarization parallel to the a axis. Using the published refractive indices [1], [2], we investigated various index-phase-matching second-harmonic generation schemes for PPT. These calculations predict that second-harmonic generation may be obtained for a wide range (434 to >70 nm) of fundamental wavelengths using a single crystal cut. To test these results, second-harmonic generation of the ruby (694 nm) and the argon ion laser was investigated. Conversion efficiencies of $\sim 10^{-5}$ for the ruby laser were easily achieved.

THEORETICAL

Our interest in PPT originated in our search for a nonlinear material suitable for second-harmonic generation of dye lasers which permitted maximum wavelength coverage in a single crystal cut. Dewey *et al.* [2] found that second-harmonic generation can be achieved in PPT over a wide wavelength region if the fundamental wave propagates in the a–b plane with the fundamental polarization perpendicular to the c axis. This scheme is shown in [2] Fig. 2(b). Our calculations, using the refractive indices given in [1], yield the relationship between index-matching angle and fundamental wavelength shown in Fig. 1. We measure the matching angle, θ, relative to the a axis.

EXPERIMENTAL

The experimental arrangement for second-harmonic generation of the ruby laser is shown in Fig. 2. The fundamental source was an unfocused Q-switched ruby laser (Holobeam Model 264) which produced an 18-ns 2-J pulse. The beam splitter diverted 2 percent of the incident radiation. The crystal supplied by Cleveland Crystals, Inc., was a polished 1-cm cube cut so that the c axis was perpendicular to, and the a axis made an angle of 27° with the normal to the entrance face. The photodiode was a Holobeam Model HPD-1. In some experiments the diode was replaced by a calorimeter energy detector for calibrations of beams I_1 and I_2. Second-harmonic generation was observed for a phase-matching angle of 26.5° in good agreement with the theoretical value of 26.4°. The crystal angular orientation is critical. When the external angle was detuned by ±0.1° the second-harmonic generation energy decreased by over half the peak value. Theoretically

Manuscript received September 22, 1975; revised March 12, 1976. This work was supported by the National Aeronautics and Space Administration, Johnson Space Center, under Contract NAS9-12200.

The authors are with the Aerospace Systems Division, Lockheed Electronics Company, Inc., Houston, TX 77058.

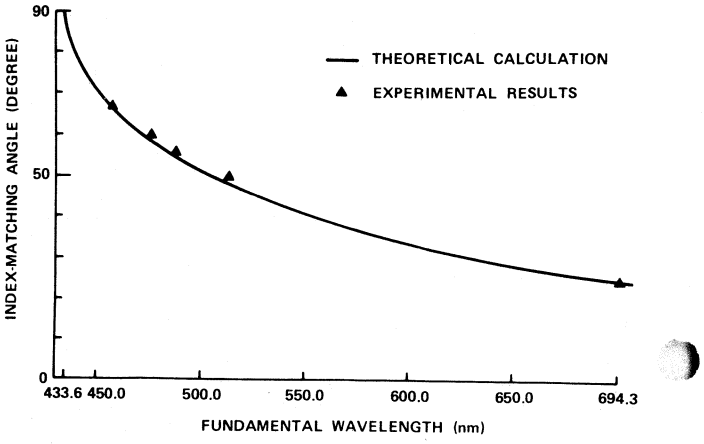


Fig. 1. Index-matching angles versus fundamental wavelength for the proposed propagating mode.

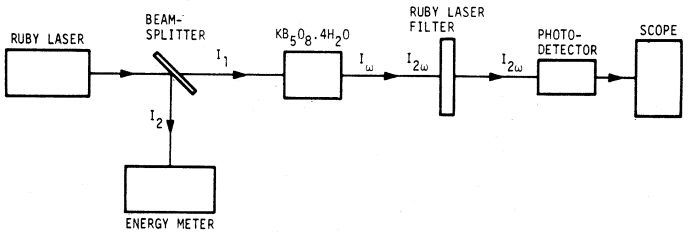


Fig. 2. Schematic diagram of experimental arrangement.

[3], the angular deviation, $\Delta\theta$, from θ, from a half-power reduction is given by

$$\pm\Delta\theta = 0.44 \frac{\lambda_\omega}{(n_{c,2\omega})^3 \{[n_{a,\omega}]^{-2} - [n_{b,\omega}]^{-2}\} \sin^2\theta}. \quad (1)$$

For $\lambda_\omega = 694.3$ nm, we calculate $\Delta\theta$ to be $\sim 0.02°$, consistent with the experimental result. Therefore, the alternative propagation scheme used by Dewey *et al.* [1] is more convenient for fundamental wavelengths <470 nm.

The dependence of harmonic energy on fundamental energy over the range of 0.25–2.0 J was measured. The result is shown in Fig. 3. The conversion efficiency at 2.0 J was $\sim 10^{-5}$. The optimum conversion efficiency should greatly exceed 10^{-5}. Our crystal sustained some damage during an earlier experiment using a weakly focused fundamental beam. Therefore, the unfocused ruby laser beam was directed onto the lower half of the crystal face resulting in a slight loss of beam energy.

Some additional experiments using an argon laser were carried out to confirm the form of the curve in Fig. 1. The laser used was a Spectra-Physics Model 164-03. A 10-cm focal length lens was used to focus the fundamental radiation into the crystal. The detection of second-harmonic generation was achieved by using a McPherson $\frac{1}{2}$-m Seya Namioka monochromator and solar-blind photomultiplier tube, EMR 542P-09-18. Second-harmonic generation was detected for wavelengths of 457.9 nm, 476.5 nm, 488.0 nm, and 514.5 nm at the measured angles of 67.2°, 60.2°, 56.6°, and 50.2°, respectively. The results are included in Fig. 1.

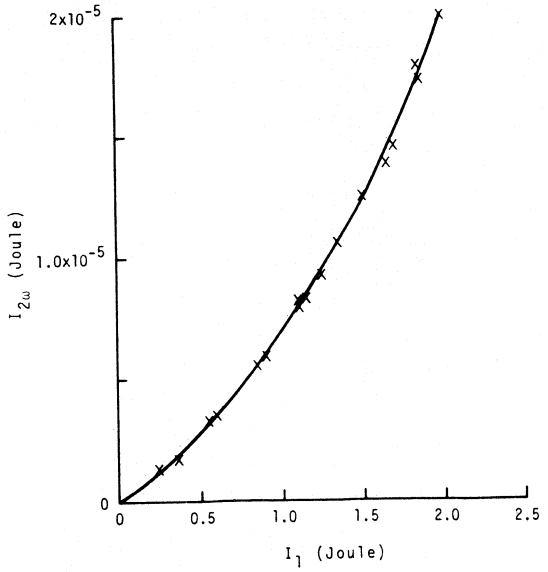


Fig. 3. Power dependence of SHG on ruby laser output power.

SUMMARY

Theoretical calculations and confirming experiments indicate that a single crystal cut of $KB_5O_8 \cdot 4H_2O$ can be used for reasonably efficient second-harmonic generation over a broad spectral region.

REFERENCES

[1] C. F. Dewey, Jr., W. R. Cook, Jr., R. T. Hodgson, and J. J. Wynne, "Frequency doubling in $KB_5O_8 \cdot 4H_2O$ to 217.3 nm," *IEEE J. Quantum Electron.*, vol. QE-10, pp. 707–708, Sept. 1974.

[2] C. F. Dewey, Jr., W. R. Cook, Jr., R. T. Hodgson, and J. J. Wynne, *Appl. Phys. Lett.*, vol. 26, pp. 714–716, 1975. Note that Fig. 3 of this paper shows a tuning curve obtained from experiments utilizing the tuning scheme of [1]. Our calculations for this scheme differ from the published tuning curve by about 20° at 450 nm.

[3] A. Yariv, *Quantum Electronics.* New York: Wiley, 1967.

A Stacked Blumlein N_2 Laser

J. S. LEVINE, K. BEZDJIAN, AND R. RAPPAPORT

***Abstract*—A novel device for producing fast-rise-time, large-volume electrical-discharge excitation of gas lasers is described. Some operating characteristics of an N_2 ultraviolet (UV) laser are presented.**

INTRODUCTION

During recent years, the Blumlein transmission line has been utilized in a novel way for producing extremely short-pulse high-current-density electrical excitation of gas lasers. Using devices of this design, several authors [1] have observed superradiant laser emission in the second positive band system of molecular nitrogen at 3371 Å with pulse energy as high as 10 to 20 mJ. This letter describes a new laser device utilizing a modified Blumlein circuit which permits the rapid electrical pumping of larger volumes of gas than that obtainable in a simple Blumlein system. A small model of the new device has been built and has demonstrated laser oscillation at 3371 Å.

Manuscript received February 23, 1976; revised April 12, 1976.

J. S. Levine performed preliminary work on this project at the Lincoln Laboratory, Massachusetts Institute of Technology, Lexington, MA 02139. He is with the Laser Development Corporation, Lexington, MA 02173.

K. Bezdjian and R. Rappaport are with the Department of Physics, Massachusetts Institute of Technology, Cambridge, MA 02139.

DESCRIPTION OF THE DEVICE

The device consists of a stack of double-clad epoxy circuit boards, each etched as shown in Fig. 1 to produce two low-inductance capacitors. A hole is drilled through the center of each board; when triggered, each set of capacitors produces a fast-rise-time sheet discharge across the hole. The laser device consists of a multitude of these epoxy boards stacked so that the optical axis is perpendicular to the large area of the boards and along the center of the resultant cavity. The boards are wired in parallel; one capacitor on each board is connected to a source of high voltage, the second capacitor is connected via low-inductance copper strips to a common spark gap, and a common charging resistor connects each capacitor on each board. To prevent arcing from one side of each board to the other through the hole, as well as to prevent arcing between adjacent boards, a piece of $\frac{1}{32}$-in fiberglass cut to the identical outline as the circuit board is epoxied to the back of each board. The seal is made on the etched annular region surrounding each hole. Flat rubber gaskets with holes larger than the holes in the boards are placed between adjacent circuit board/fiberglass board pairs and the whole sandwich is held together in compression by a four rod-end plate arrangement. Brewster windows are mounted on the end plates along with pumping leads. The gasket vacuum construction readily permits evacuation to several-tenths of torr pressure with a mechanical pump.

The prototype device described here comprised 45 Blumlein circuit boards, each containing two capacitors of dimensions 10 cm × 5 cm × 0.16 cm thick; the total capacitance of the device is measured to be 0.01 μF. The central hole is 0.95 cm (electrode separation) × 1.3 cm. The overall length of the discharge region of the assembled laser is 12 cm, and it is terminated in quartz Brewster angle windows. The optical resonator consists of a flat totally reflecting aluminum mirror and a 50-percent transmitting flat separated by 45 cm.

PERFORMANCE CHARACTERISTICS

In investigating the operating parameters of the prototype device, pulse shape was observed with a fast ultraviolet (UV) photomultiplier and a Tektronix 519 oscilloscope; energy measurements were made with a Scientech energy meter.

UV laser oscillation was observed over the range of pressures 25–90 torr of N_2 at the maximum available charging voltage of 16 kV. Fig. 2 summarizes the variations of peak laser power with pressure. A typical laser pulse shape is shown in Fig. 3. Laser energy was found to be too small to be measured directly with the energy meter, so a comparison technique was adopted. The energy and pulse shape of a larger, conventional N_2 laser was measured directly. Its output was then reduced with calibrated attenuators until its peak power and the peak power of the prototype device were equalized as determined with the photodiode. Then by a graphical determination of areas under the power versus time traces, the pulse energy and power of the new device were determined as 0.05 mJ and 10 kW ± 50 percent, respectively. Total energy stored in all of the stacked capacitors is 0.85 J at the charging voltage of 13 kV. This implies an efficiency of about 0.005 percent, rather low in comparison to other N_2 lasers. We attribute this low efficiency to the short gain path length involved here, estimated to be approximately 5 cm. We believe that in scaling this device in size, it will be possible to extract UV laser

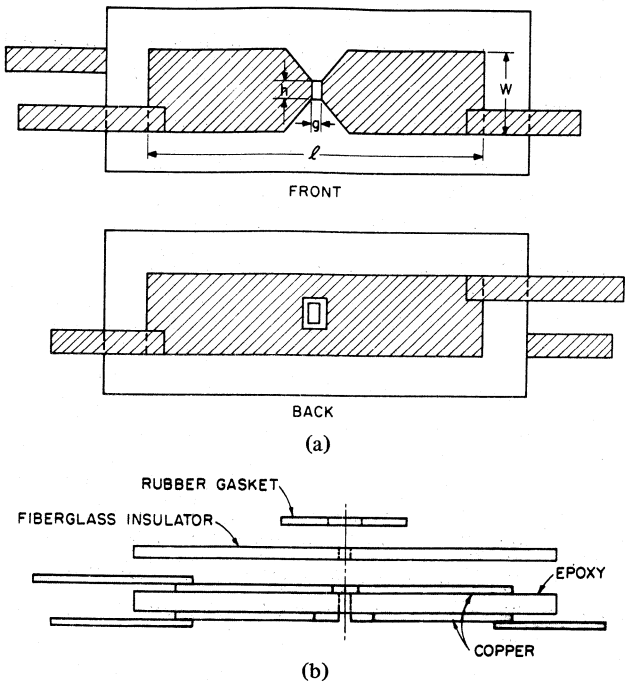


Fig. 1. (a) Etched copper-clad epoxy board. $h = 1.3$ cm, $g = 0.95$ cm, $w = 5$ cm, $l = 24$ cm. (b) Cross section of copper-clad epoxy board, fiberglass insulator, and rubber gasket.

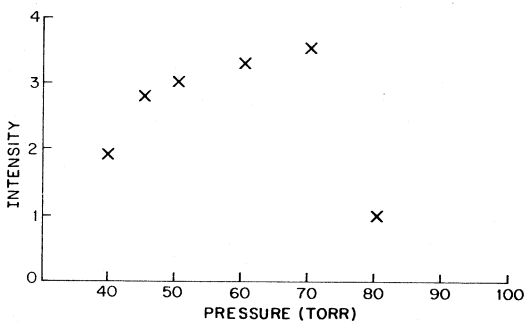


Fig. 2. Relative pulse intensity versus N_2 pressure at 16-kV charging voltage.

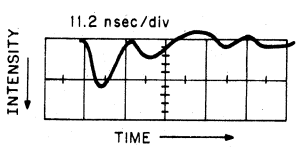


Fig. 3. Temporal behavior of laser pulse. Laser N_2 pressure = 70 torr, 16-kV charging voltage; horizontal scale: 11.2×10^{-9} s/div.

pulses from large volumes of N_2 with efficiency on the order of 0.1 percent.

Conclusions

During the course of experimentation it was observed that laser output intensity and pulse shape had excellent shot-to-shot reproducibility. This is due to the independence of the 45 discharge circuits along the length of the lasing medium which minimizes the effects of localized electrical arcing. Therefore, this new device may be especially useful in excitation of rare-gas-halogen systems where discharges in homogeneities are troublesome.

The discharge cavity may be tailored to be circular or rectangular in cross section. Because of the greater cross sectional area as compared to conventional Blumlein lasers, we find the beam has cleaner mode structure.

Acknowledgment

The authors wish to thank Prof. A. Javan for his interest in and support of this work.

References

[1] J. I. Levatter, S. Lin, *Appl. Phys. Lett.*, vol. 25, p. 703, Dec. 15, 1974; and I. Nagata and Y. Kimura, *J. of Physics E: Scientific Instr.*, vol. 6, p. 1193, 1973.

Analysis of the Response of Lasers to External Signal Injection

KENJU OTSUKA

Abstract—**The rate equation including the injection term was extended and solved numerically. The relation between the peak photon number in the onset of relaxation oscillations of lasers and the injected photon number is shown. The step response of the CW laser to the external signal injection and the reshaping property of the laser for the distorted optical pulse are reported.**

Introduction

In solid-state and semiconductor lasers, there exist relaxation oscillations during the onset of laser oscillations. Especially in the semiconductor laser, the relaxation spikings cause a spectrum-broadening effect associated with the direct pulse modulation. Ikegami reported that spectrum broadening increases with the increase of the peak photon number of the first spike in relaxation oscillations [1]. This effect forms an obstacle to the realization of a several-hundred-megabits-per-second optical PCM system using the semiconductor laser.

Kleinman has suggested that an external weak signal applied to the cavity influences the spiking patterns of the laser [2]. Kobayashi *et al.* have demonstrated the suppression effect of relaxation oscillations in semiconductor lasers due to the injection of a weak laser beam into the resonator [3], [4].

The effect of external signals on the laser oscillator has been analyzed using the van der Pol oscillator including an external signal [5]. The transient response of the laser oscillator to an external signal has not been analyzed.

From a numerical calculation of the rate equations, it is shown that the optimum injection for reduction of the peak photon number in relaxation oscillations exists and depends on the pumping power.

The transient response of the CW laser oscillator to the external signal is analyzed numerically using the nonlinear rate equation. The peak signal gain and extinction ratio of the laser oscillator for the step injection of the external signal are found to depend on the magnitudes of the injected signal, pumping power, and the ratio of the fluorescence lifetime to the cold-cavity lifetime of the resonator with the peculiar exponents.

Numerical solutions corresponding to the response of the laser oscillator to the Gaussian optical pulse injection are given. In this case it is found that the laser acts as a reshaping oscillator.

Manuscript received February 23, 1976; revised March 8, 1976.

The author is with the Musashino Electrical Communication Laboratory, Nippon Telegraph and Telephone Public Corporation, Tokyo, Japan.

Optimum Injection

The rate equations including the *source* term, which indicates the rate of production of laser photons by spontaneous emission or any external signal applied to the cavity, have been given by Kleinman [2]. After normalizing the population inversion, photon number, injected signal in the cavity, and pump power, we obtained the following differential equations for the four-level lasers:

$$dn/dt' = w - n - ns \tag{1}$$

$$ds/dt' = K(ns - s + s_i) \tag{2}$$

where

$w = P/P_{th}$	relative pump power;
P_{th}	threshold pump power;
$n = N/N_{th}$	normalized population inversion;
N_{th}	threshold population inversion;
$s = S/p$	normalized photon number;
p	number of modes of the spontaneous emission;
$s_i = S_i/p$	normalized injected signal;
$K = \tau_f/\tau_c$	ratio of lifetimes;
τ_f	fluorescence lifetime;
τ_c	cold-cavity lifetime;
$t' = t/\tau_f$	normalized time.

The coupled equations of (1) and (2) have been solved numerically by the Runge–Kutta–Gill method assuming $K = 10^3$, $w = 1.10$ and 1.20 for various values of the injected signal.

Numerically obtained values of the first spike in relaxation oscillations and the steady-state photon number are plotted as a function of the injected signal in Fig. 1. In this figure it is noticed that the peak photon number decreases at first (*spiking region*), then increases (*suppression region*) with the increase of the injected photon number and the *optimum region* of the injection for reduction of the spectrum broadening exists since the spectrum broadening increases with the increase of the peak photon number [1].

In the *spiking region*, the peak value of the first spike s_p obtained from the numerical calculation agrees well with the theoretical value given by [2]

$$\psi_p - \exp \psi_p = \psi_v - \exp \psi_v \tag{3}$$

$$\ln s = \psi + \ln(w - 1) \tag{4}$$

$$s_v = 2s_i \{(w - 1)/K\}^{-1/2}. \tag{5}$$

Response to Step Injection

The response of the CW laser oscillator to step injection of the external signal can be solved using the rate equations (1) and (2). In this case, the laser oscillation for no injection is in the steady state, therefore initial conditions of the population inversion and the photon number for computation are $n = 1$ and $s = w - 1$, respectively.

Fig. 2 shows the response of the CW laser oscillator to the step injection of the external signal assuming $w = 1.02$ and $K = 3.3 \times 10^3$ for various values of the external signal.

Fig. 3 shows the peak signal gain defined as $G = (s_p - \bar{s}_0)/s_i$ ($\bar{s}_0$: steady-state photon number before injection, i.e., $w - 1$), the extinction ratio defined as $E = s_p/\bar{s}_0$, and the buildup time t_b' as a function of the injected photon number s_i. From Fig. 3, it is found that $G, t_b' \propto s_i^{-1/3}$ and $(s_p - \bar{s}_0), E \propto s_i^{2/3}$.

Similar calculations were made for the peak photon numbers as a function of w or K, and the following relations were obtained from the computer experiment:

$$s_p \sim w^{-1/2} K^{1/3} s_i^{2/3} + w - 1 \tag{6}$$

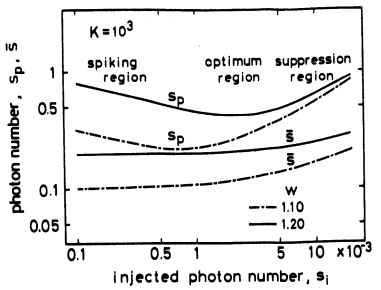


Fig. 1. The peak value of the first spike of relaxation oscillations and the steady-state photon number as a function of the injected signal for $w = 1.10$ and 1.20.

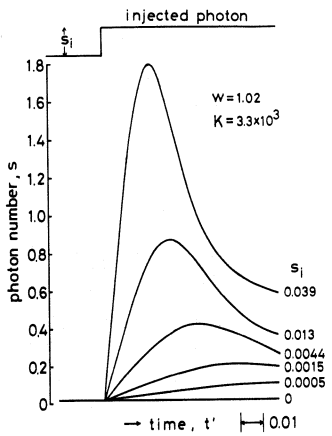


Fig. 2. Response of the CW laser oscillator to the step injection of the external signal. $w = 1.02$, $K = 3.3 \times 10^3$.

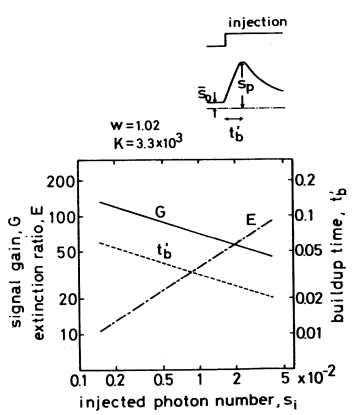


Fig. 3. The peak signal gain, extinction ratio, and buildup time as a function of the injected signal. $w = 1.02$, $K = 3.3 \times 10^3$.

$$G \sim w^{-1/2} K^{1/3} s_i^{-1/3} \tag{7}$$

$$E \sim w^{-1/2} K^{1/3} s_i^{2/3}/(w - 1) + 1. \tag{8}$$

Laser as Reshaping Oscillator

In this section, we discuss the response of the laser to the Gaussian pulse signal numerically. We will consider the most general Gaussian optical pulse with the envelope of

$$s_i(t') = s_0 \exp(-2\alpha t'^2). \tag{9}$$

The pulsewidth is defined as the time between half-intensity points

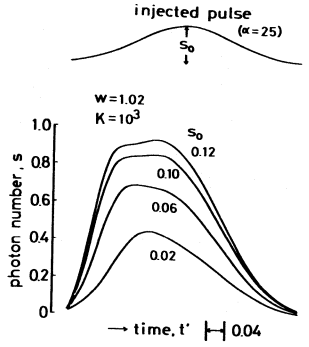


Fig. 4. Response of the CW laser oscillator to the Gaussian pulse injection. $w = 1.02$, $K = 10^3$, $\alpha = 25$.

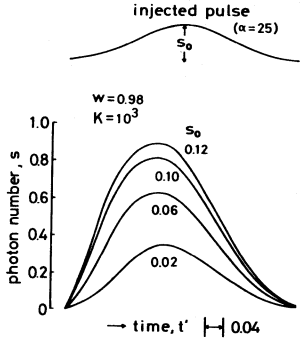


Fig. 5. Response of the laser below threshold to the Gaussian pulse injection. $w = 0.98$, $K = 10^3$, $\alpha = 25$.

$$\tau_p' = \sqrt{2\ln 2/\alpha}. \tag{10}$$

Inserting (9) into (2), the rate equations are solved numerically. Figs. 4 and 5 show the numerical results for $w = 1.02$ and 0.98, respectively, assuming $K = 10^3$ and $\alpha = 25$.

Figs. 4 and 5 indicate that the response time as well as the buildup and decay times of the output photon number decrease with the increase of the injected pulse hight s_0. These results are due to the nonlinear gain and response time for the injected photon number described in the previous section. In this case, the laser acts as a reshaping oscillator.

CONCLUSION

The first conclusion from the work presented here is that there exists an *optimum region* of the injection for suppression of relaxation oscillations in lasers, and the optimum injection to the resonator depends on pumping power.

Another conclusion that we can draw from the numerical analysis is that the transient behavior of the CW laser oscillator for the step injection is related to the injected signal power, pumping power, and the ratio of lifetimes with simple peculiar exponents; and the laser may be utilized as a reshaping oscillator for the distorted optical pulse using its nonlinear gain coefficient for the injected signal.

ACKNOWLEDGMENT

The author would like to thank Dr. H. Iwasaki for his fruitful discussions and encouragement.

REFERENCES

[1] T. Ikegami, "Spectrum broadening and tailing effect in directly modulated injection lasers," presented at the 1st European Conf. Optical Fibre Communication, 1975.

[2] D. A. Kleinman, "The maser rate equations and spiking," *Bell Syst. Tech. J.*, vol. 43, pp. 1505–1532, July 1964.

[3] K. Kobayashi, R. Lang, and K. Minemura, "Novel optical methods for high speed direct modulation of semiconductor lasers," in *Dig. Tech. Papers 7th Conf. Solid State Devices* (Tokyo, Japan, 1975), B-6-1.

[4] R. Lang and K. Kobayashi, "High speed modulation of semiconductor lasers with suppressed spiking by optical injection," *Proc. Inst. Electron. Commun. Eng. Japan*, vol. OQE-75-47, 1975.

[5] K. Shimoda and T. Yajima, *Quantum Electronics*. Tokyo, Japan: Syokabo, 1972.

Dye-Laser Cavity Employing a Reflective Beam Expander

G. L. EESLEY AND M. D. LEVENSON

Abstract—**A repetitively pulsed dye laser employing a reflective intracavity beam expander achieves a 50-MHz full width at half-maximum (FWHM) linewidth. A geometrical technique for partially correcting the expander astigmatism and maintaining cavity stability is derived. The use of reflective cavity elements minimizes cavity losses and eliminates spurious reflections.**

Cavity designs employing reflective and refractive beam-expanding optics have been presented by many authors [1]–[4]. To date, the most successful cavity design for high-gain pulsed lasers is that of Hansch, which employs a refractive beam expander [5]. On the other hand, reflective beam expanders have the advantage that the insertion loss can be readily minimized by an appropriate choice of dielectric coatings. Chromatic aberrations and spurious reflections are also avoided.

We have designed a dye-laser cavity employing an internal 18-power reflective beam expander to magnify and collimate the stimulated emission. The first-order aberration, which results from the use of spherical mirrors off-axis, is corrected geometrically in our folded-cavity configuration. Narrow-band operation comparable to that obtained with more conventional designs has been achieved using rhodamine 6G dye. Pumping of this dye laser via a commercial nitrogen laser or a xenon-ion laser provides high pulse-repetition rates and high peak powers. The principles outlined here may also be applied to the cavity of an electron beam pumped, rare gas excimer laser, enabling the generation of tunable, coherent, narrow-band radiation in the ultraviolet.

A schematic representation of the dye laser is shown in Fig. 1. The folded cavity is composed of three basic branches: 1) the output mirror and dye cell; 2) the beam expander formed by the convex and concave mirrors; 3) the mode selection branch, composed of a tunable grating, preceded by an iris and Fabry–Perot etalon if necessary.

In the first branch, the pump beam is focused to a line just inside the dye cell front window via a cylindrical lens. The output mirror is flat and may be optionally mounted on a piezoelectric translator for varying the overall cavity length.

Manuscript received March 5, 1976; revised April 12, 1976. This work was supported by the Department of the Navy under Contract N00014-C-75-0950.

G. L. Eesley is with the Department of Electrical Engineering, University of Southern California, Los Angeles, CA 90007.

M. D. Levenson is with the Departments of Physics and Electrical Engineering, University of Southern California, Los Angeles, CA 90007.

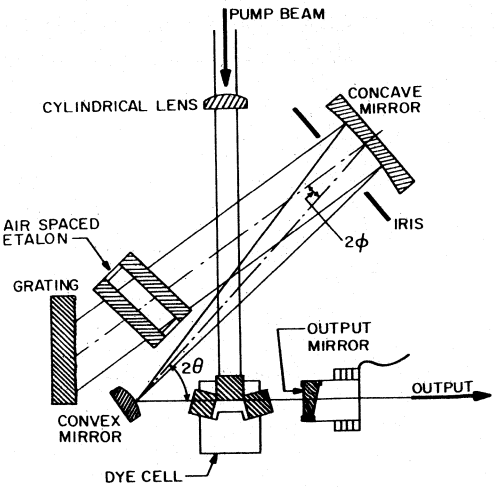


Fig. 1. Folded cavity with internal reflective beam-expander.

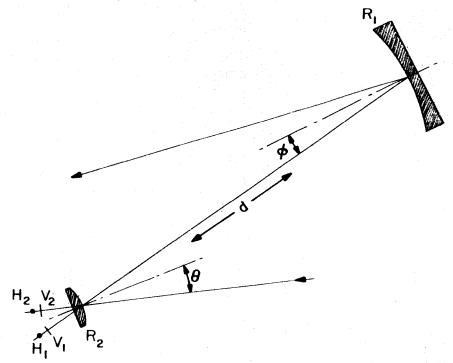


Fig. 2. Beam-expander angles of incidence; corresponding horizontal and vertical foci of mirrors R_1 and R_2.

The intracavity beam expander is composed of two spherical mirrors, both tilted off-axis. The small-diameter light beam which emerges from the transversely pumped dye cell diverges from the convex mirror of 2.5-cm radius and is then recollimated by the concave mirror of 46-cm radius. Together these mirrors provide a beam magnification of 18. The magnified and collimated beam then strikes a Littrow-mount grating which reflects desired frequency components back into the cavity for amplification. Further linewidth reduction may be achieved by insertion (into the third branch) of an iris, and if required, a Fabry–Perot etalon.

As previously noted, the use of spherical mirrors off-axis results in an aberration commonly referred to as astigmatism. From a geometrical optics point of view, incident parallel rays in a vertical plane normal to the mirror surface will focus at a point preceding the focus of rays incident in the horizontal plane. This first-order effect is described by the following two equations [6]:

$$H = \frac{R}{2\cos\phi} \quad \text{and} \quad V = \frac{R\cos\phi}{2}.$$

Here, R is the mirror radius, ϕ the angle of incidence, and V and H the foci distances along the reflected rays. Shown in Fig. 2 is the cavity beam expander with angles of incidence θ and ϕ indicated for each mirror. The notation V_1, H_1, V_2, H_2 indicates the vertical and horizontal ray foci for mirrors 1 and 2. Since the input and exit beams from the expander are to be collimated, the astigmatic distortion of the exit beam spot may be corrected by placing the real foci of the concave mirror on the virtual foci of the convex mirror. The following solution results:

$$\cos\theta = \{-2(H_1 - V_1) \pm \sqrt{4(H_1 - V_1)^2 + 4R_2^2}\}/2R_2.$$

Thus, once the parameter ϕ is chosen, θ and the mirror separation

$$d = H_1 - (R_2/2\cos\theta)$$

may be calculated. For our cavity, an angle of $\phi = 6^\circ$ was chosen with the angle $\theta = 25.27^\circ$ and mirror separation of $d = 21.743$ cm resulting.

Generally, any resonator possessing mirrors with different focal lengths in the x–z and y–z planes (z being the ray propagation direction) will produce beams of an elliptic-Gaussian nature [7]. Since the wave equation for this geometry is separable in Cartesian coordinates, the familiar $ABCD$ ray matrix technique may be applied independently in each of the two planes to yield a condition for overall stability [8], [9]. With our beam expander perfectly compensated, a ray matrix analysis shows that the cavity approaches a positive branch unstable resonator [9]. It is desirable to slightly overcompensate the cavity by increasing the spherical mirror separation beyond the compensated distance and "focus" the beam into predictable cavity mode patterns. Calculations were made by writing the ray matrix for the vertical and horizontal cavity ray planes individually and thereby accounting for the astigmatic focal lengths of the spherical mirrors. This analysis indicates that increasing the mirror separation to 21.790 cm will result in a Gaussian beam waist with semiaxes 0.131 mm and 0.195 mm at the output mirror. As expected, a slightly elliptical TEM_{00} output beam results.

Higher order transverse modes with intensity profiles analogous to those of an axially symmetric cavity will also exist with resonant frequencies

$$\nu_{mnp} = \frac{c}{2l}\left[p + \frac{(2m+1)}{2\pi}\arctan\left(\frac{\lambda l}{\pi W_{x0}^2}\right) + \frac{(2n+1)}{2\pi}\arctan\left(\frac{\lambda l}{\pi W_{y0}^2}\right)\right]$$

where p, m, and n are the longitudinal and transverse mode numbers, l is the overall cavity length and W_{x0} and W_{y0} are the semiaxes of the lowest order mode at the output mirror. Using our values of $W_{x0} = 0.131$ mm, $W_{y0} = 0.195$ mm, $\lambda = 5885$ Å, and $l = 52.5$ cm, reveals that several higher order transverse modes lie within 50 MHz of the TEM_{00p} mode. Thus while an intracavity etalon with a 300-MHz passband may select a particular longitudinal mode, spatial filtering is necessary within the cavity to discourage higher order transverse modes.

The dye laser design was optimized for nonlinear spectroscopy experiments in the red–orange region of the spectrum. A dye concentration of 3×10^{-4} M rhodamine 6G in ethanol proved most suitable for pumping with the blue–green output of a pulsed xenon-ion laser [10]. A 50-percent reflective dielectric output coupler was used in conjunction with aluminized beam-expander mirrors and a 600-lines/mm ruled grating. The pump light was focused into the dye cell by an 11-cm focal length cylindrical lens. With 20 kW of incident power in a 160-ns full width at half-maximum (FWHM) pulse, the dye laser output was 600 W in a 100-ns (FWHM) pulse, at a 10-pps repetition rate.

The overall linewidth was 0.3 cm^{-1} (FWHM), when the 600-lines/mm grating was used in fifth order as the only

frequency-selective cavity element. When the intracavity etalon, with 1.2-cm spacing and a reflectivity finesse of 40, was inserted in the third cavity branch, further narrowing resulted. The output power was reduced to 300 W when single-mode operation was achieved. Doppler-free two-photon absorption traces taken in potassium vapor then indicated a total frequency jitter of 50 MHz (FWHM).

The transverse beam profile was found to be effectively Gaussian when all cavity adjustments were optimized. By measuring the beam divergence in the vertical and horizontal planes, we estimated the semiaxes of the beam waist to be 0.099 mm and 0.137 mm. Alignment of the cavity, however, was extremely difficult due to the strong interdependence of the individual cavity adjustments.

Pumping the dye laser with a commercial nitrogen laser resulted in a peak output power of 17.5 kW in a 7-ns pulse, at a 10-pps repetition rate. Due to the shorter pulse duration, an output linewidth of approximately 1.5 cm^{-1} was obtained with the grating alone. Beam divergence measurements resulted in beam waist semiaxes of 0.090 mm and 0.102 mm. The formation of familiar Gaussian cavity modes is not as clearly defined in this case, since stimulated emission can make only two round trips through the cavity during the short pump pulse.

All-reflective laser cavities of the sort proposed here have several advantages. A convenient means of tuning a single-mode frequency is realized when the cavity is enclosed in a vacuum vessel. By changing the vessel gas pressure, the resonant frequencies of the cavity, etalon, and grating can be varied simultaneously [11]. Since refractive optics for use in the ultraviolet may be prohibitively expensive, an all-reflective cavity for narrow-band tunable operation in that region may be more feasible. Furthermore, reflective beam expanders are more easily scalable to the large dimensions needed in tunable lasers for certain industrial-level isotope separation schemes. The intensity level at the grating of a discretely tunable infrared molecular laser could be reduced if a reflective beam expander were incorporated into the cavity. Gratings ruled with fewer lines per millimeter and with lower damage thresholds, could be used and still provide adequate frequency selection. In general, the cavity design proposed here can be scaled and modified to fulfill the user's specific applications.

REFERENCES

[1] R. W. Wallace, "Generation of tunable UV from 2610 to 3150A," *Opt. Comm.*, vol. 4, p. 316, Dec. 1971.

[2] A. Dienes, E. P. Ippen, and C. V. Shank, "A mode-locked CW dye laser," *Appl. Phys. Lett.*, vol. 19, p. 258, Oct. 1971.

[3] R. L. Kohn, C. V. Shank, E. P. Ippen, and A. Dienes, "An intracavity-pumped CW dye laser," *Opt. Comm.*, vol. 3, p. 177, 1971.

[4] H. Kogelnik, E. P. Ippen, A. Dienes, C. V. Shank, "Astigmatically compensated cavities for CW dye lasers," *IEEE J. Quantum Electron.*, vol. QE-8, p. 373, 1972.

[5] T. W. Hansch, "Repetitively pulsed tunable dye laser for high resolution spectroscopy," *Applied Opt.*, vol. 11, pp. 895-898, 1972.

[6] F. A. Jenkins and H. E. White, *Fundamentals of Optics*, 3rd ed. New York: McGraw-Hill, 1957, pp. 94-95.

[7] A. Yariv, *Quantum Electronics*, 2nd ed. New York: Wiley, 1975, pp. 123-124.

[8] H. Kogelnik and T. Li, "Laser beams and resonators," *Applied Opt.*, vol. 5, pp. 1550-1556, Oct. 1966.

[9] A. E. Siegman, "A canonical formulation for analyzing multielement unstable resonators," *IEEE J. Quantum Electron.*, vol. QE-12, p. 35, Jan. 1976.

[10] C. Harper and M. Gundersen, "Construction of a high power xenon ion laser," *Rev. Sci. Instrum.*, vol. 45, p. 400, 1974.

[11] R. Wallenstein, T. W. Hansch, "Powerful dye laser oscillator-amplifier system for high resolution spectroscopy," *Opt. Comm.*, vol. 14, p. 353, 1975.

Near-Infrared Dye Laser Pumped by a Carbazine-122 Dye Laser

K. KATO

Abstract—**Efficient generation of a high-power near-infrared dye laser has been achieved by pumping longitudinally with a 5321-Å pumped carbazine-122 dye laser at 7000 Å. A peak power as high as 3.5 MW at 8630 Å and peak powers in excess of 0.5 MW from 7680 to 9170 Å have been obtained.**

Although numerous laser-pumped high-power dye lasers have been described in the literature, considerably less work has so far been reported for a high-repetition-rate high-peak-power infrared dye laser. Recently the utility of the second harmonic of a repetitively pulsed Nd:YAG laser for pumping infrared laser dyes has been demonstrated [1]. However, direct pumping of infrared laser dyes by the 5321-Å radiation does not allow conversion efficiencies as high as those reported for ruby-laser pumping [2]-[4] because of the unsatisfactory overlap between the pump wavelength and the principal absorption bands of dyes or their reduced fluorescence quantum yields when exicted at 5321 Å. One possible way of surmounting this problem is to use a high-peak-power deep-red dye laser pumped by a frequency-doubled Nd:YAG laser as an optical pump source for infrared laser dyes. Here we report the efficient generation of a high-peak-power and high-average-power near-infrared dye laser at 7680-9170 Å using a cascade pumping scheme.

Fig. 1 is a schematic diagram of the experimental setup. The basic pump source was a repetitively Q-switched Nd:YAG oscillator-amplifier system working in the TEM_{00} transverse mode and in 2-4 axial modes with a peak power of 50 MW and 12-ns pulse duration. The angular divergence of the 5-mm-diam fundamental beam was 1.1 mrad. As shown in Fig. 1, the 10-ns 24-MW second-harmonic radiation at 5321 Å generated from a temperature-tuned, 1.9-cm-long deuterated cesium dihydrogen arsenate (CD*A) crystal [5] was physically separated from the fundamental by a high-quality Glan polarizer, and was used to pump a deep-red dye laser in an off-axis longitudinal pumping scheme. The 30-cm-long dye-laser cavity was formed by a 99.9-percent reflectivity, broad-band flat mirror and an uncoated sapphire etalon used for output coupling. The 1-cm-thick dye cell consisted of two antireflection-coated sapphire windows wedged at about 8° in a stainless steel housing. The dye flow was transverse to the optical axis of the dye-laser cavity. Among several different combinations of dye compounds and solvents tested, an ethanol solution (basic) of recrystallized high-purity carbazine-122 [6]-[8] has been found to lase most efficiently around 7000 Å with an energy conversion efficiency of 35 percent, which was comparable to that of fluorescein disodium salt in methanol. Both nile blue A perchlorate and oxazine-1 perchlorate did not lase in this system when directly pumped at 5321 Å, although these dyes dissolved in methanol lased very efficiently when pumped by a cresyl violet perchlorate dye laser at 6470 Å. Naphthofluorescein-126 [6] was not commercially available at the time of this experiment.

The 10-ns 8.5-MW carbazine-122 dye-laser radiation was then used to pump a second infrared dye laser in the off-axis longitudinal pumping scheme. The 40-cm-long dye-laser cavity had the same configuration as that has been used for the carbazine-122 dye laser except that a Brewster-angle dispersion prism was inserted between the dye cell and the high-reflectivity mirror. Wavelength tuning was achieved by rotation of the

Manuscript received March 9, 1976; revised April 12, 1976.

The author is with the First Research Center, Japan Defense Agency, Tokyo, Japan.

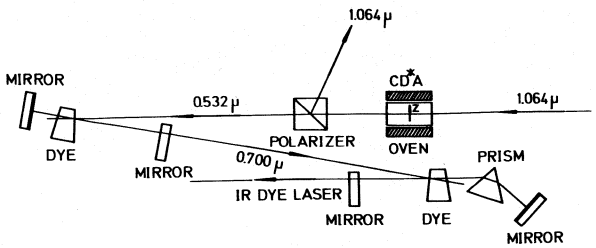


Fig. 1. Schematic diagram of experimental setup.

rear mirror. All polymethine dyes used in this experiment were dissolved in dimethyl sulfoxide (DMSO) and the solutions were purified through 5-μ filters. The dye concentration was adjusted to maximize the output power in the untuned system. This gave molar concentration of, typically 2×10^{-4} mole/liter. The detection of the dye-laser pulses was made by high-speed photodiode-oscilloscope system having an overall risetime of less than 1 ns, and the output power was monitored by a calibrated CW power meter. The spectral linewidth of the dye-laser output analyzed with a 1-m-grating spectrograph was 12–15 Å, which was stable within a frequency jitter of about 20 Å.

Table I represents the central lasing wavelength and the average output power achieved with six different laser dyes. The tunability range (defined as the wavelength separation between laser output power points extrapolated to zero power) of the dye-laser output for individual dye solutions was 400–500 Å, which could probably be somewhat extended by using a high-reflectivity output mirror. We note that in excess of 20-percent energy conversion efficiency from the 7000-Å radiation to the infrared dye-laser output has been obtained with all the dye solutions at their central lasing wavelength. The best conversion efficiency obtained was 40 percent for Eastman Kodak IR-144 [9] which has been continuously tuned from 8440 to 8850 Å with peak powers greater than 0.5 MW. IR-123 produced dye-laser pulses greater than 0.5 MW in the range 7680–8190 Å. The utility of the cascade pumping scheme has been clearly demonstrated by the fact that 1,3,3,1′,3′,3′-hexamethylindotricarbocyanine iodide (HITC iodide) and 3,3′-diethylthiatricarbocyanine iodide (DTTC iodide) lased, respectively, at 8220 and 8340 Å with about 9-percent overall energy conversion efficiency from the 5321-Å radiation to the dye-laser output. Direct pumping of these dyes by the 5321-Å radiation has resulted in an energy conversion efficiency of less than 1 percent in our apparatus. We note also that IR-125 lased very efficiently around 9030 Å with a conversion efficiency somewhat higher than that of IR-140, in contrast to previous measurements [1]. The excellent conversion efficiencies observed in this experiment were due to the near-optimum matching of the pump wavelength to the principal absorption bands of the dye compounds utilized, and to the excellent spatial overlap between the dye-laser mode and the pump beam in the near-longitudinal pumping scheme ($\sim 6^{\circ}$).

The polarization direction of the untuned dye-laser beam was found to be parallel to that of the 5321-Å pump beam irrespective of the dye solutions. In addition, saturation of the dye-laser output has not been observed in any dye solutions listed in Table I, and thus more energetic 7000-Å pump pulses should lead to a corresponding increase in the dye-laser output. The spatial profile of the $\sim$5-mm-diam dye-laser beam was close to Gaussian having an angular divergence of 1.2 mrad.

In summary, we have reported the efficient operation of a high-peak-power and high-average-power near-infrared dye laser using the cascade pumping arrangement. The system described in the preceding has an immediate application for investigating the wavelength dependence of laser-induced phenomena with an important advantage of higher-repetition-rate than the dyes pumped by a ruby laser.

TABLE I
DYE-LASER PERFORMANCE PUMPED BY CARBAZINE-122 DYE LASER AT 7000 Å

dye	central lasing wavelength	average output power
IR-123	7890 Å	280 mW
1,3,3,1',3',3'-hexamethylindotricarbocyanine iodide	8220	210
3,3'-diethylthiatricarbocyanine iodide	8340	220
IR-144	8630	340
IR-140	8980	170
IR-125	9030	180

Note: The pump power at 7000 Å is 8.5 MW at a pulse repetition rate of 10 pps.

ACKNOWLEDGMENT

The author wishes to thank Dr. R. T. Hodgson of the IBM Thomas J. Watson Research Center for his helpful comments on the deep-red laser dyes.

REFERENCES

[1] C. D. Decker, "Excited state absorption and laser emission from infrared dyes optically pumped at 532 nm," *Appl. Phys. Lett.*, vol. 27, pp. 607–609, 1975.
[2] Y. Miyazoe and M. Maeda, "Stimulated emission from 19 polymethine dyes–Laser action over the continuous range 710–1060 mμ," *Appl. Phys. Lett.*, vol. 12, pp. 206–208, 1968.
[3] C. D. Decker and F. K. Tittel, "Broadly tunable, narrow linewidth dye laser emission in the near infrared," *Opt. Commun.*, vol. 7, pp. 155–157, 1973.
[4] P. E. Oetinger and C. F. Dewey, Jr., "Lasing efficiency and photochemical stability of IR laser dyes in the 710–1080-nm spectral region," *IEEE J. Quantum Electron.*, vol. QE-12, pp. 95–101, Feb. 1976.
[5] K. Kato, "Second-harmonic generation in CDA and CD*A," *IEEE J. Quantum Electron.* (Corresp.), vol. QE-10, pp. 616–618, Aug. 1974.
[6] K. H. Drexhage, "Structure and properties of laser dyes," in *Dye Laser*, F. P. Schafer, Ed. Berlin: Springer, 1973, pp. 144–179.
[7] J. B. Marling, J. G. Hawley, E. M. Liston, and W. B. Grant, "Lasing characteristics of seventeen visible-wavelength dyes using a coaxial-flashlamp-pumped laser," *Appl. Opt.*, vol. 13, pp. 2317–2320, 1974.
[8] C. A. Moore and L. S. Goldberg, "Tunable uv and IR picosecond pulse generation by nonlinear mixing using a synchronous mode-locked dye laser," *Opt. Commun.*, vol. 16, pp. 21–25, 1976.
[9] J. P. Webb, F. G. Webster, and B. E. Plourde, "Sixteen near IR laser dyes," *IEEE J. Quantum Electron.* (Corresp.), vol. QE-11, pp. 114–119, Mar. 1975.

Second-Harmonic Generation at 0.659 μ in CD*A

K. KATO AND R. S. ADHAV

***Abstract*—The efficient generation of the second-harmonic radiation of an Nd:YAG laser operating at 1.318 μ has been achieved in a deuterated cesium dihydrogen arsenate (CD*A) crystal. An overall peak**

Manuscript received March 12, 1976.

K. Kato is with the First Research Center, Japan Defense Agency, Tokyo, Japan.
R. S. Adhav is with Quantum Technology, Ltd., Agincourt, Ont., Canada.

power conversion efficiency of 40 percent was obtained for the experimental conditions described.

The deuterated cesium dihydrogen arsenate (CD*A) crystal has proved highly successful for frequency doubling of high-power Nd:YAG laser radiation at 1.064 μ [1], [2] due to its 90° phase matchability as well as large nonlinear optical constant and high damage threshold. In addition, however, if 90° phasematching is not possible, CD*A appears to be a superior material for the second-harmonic generation of a high-power Nd:YAG laser operating at 1.318 and 1.338 μ due to its large angular acceptance angle expected from the small birefringence of the refractive indices [2], [3] and high transmission ranging from 0.3 to 1.4 μ. In this correspondence we wish to report the highly efficient generation of high-power red radiation at 0.659 μ in CD*A. Although the second-harmonic generation of an Nd:YAG laser operating at 1.318 μ has previously been reported by several workers [4]–[7], they did not disclose the second-harmonic output powers and conversion efficiencies. The second-harmonic generation reported here has produced a peak power as high as 1.4 MW at 0.659 μ with an overall power conversion efficiency of 40 percent.

The basic pump source was a rotating-mirror Q-switched Nd:YAG oscillator–amplifier system working in the TEM_{00} transverse mode with a peak power of 3.5 MW and 25-ns pulse duration. The frequency discrimination of the 1.318-μ line against the higher gain 1.064-μ line was accomplished by three Brewster-angle dispersion prisms placed between the 7.5-cm-long Brewster-angle-cut Nd:YAG rod and the rotating mirror. The flat dielectric-coated output mirror had 45-percent reflectivity at 1.318 μ. The transverse mode selection of the oscillator was made by a 3-mm-diam aperture inserted between the Nd:YAG rod and the Brewster-angle prism. The 25-ns 1.2-MW fundamental beam emerging from the oscillator was then amplified by a 10.5-cm-long Nd:YAG amplifier rod wedged at about 8° and AR-coated at 1.318 μ. A single-pass gain of 2.9 was obtained with a corresponding output power of 3.5 MW. The spatial profile of the 3-mm-diam fundamental beam was close to Gaussian having an angular divergence of 0.94 mrad. Although Goto and Higuchi [6] have previously obtained a peak power as high as 1.4 MW at 1.318 μ and 1.2 MW at 1.338 μ using an oscillator similar to the one described above, we did not attempt to lase the 1.338-μ line in this experiment.

The CD*A crystal used in this experiment was 13.5 mm long and cut at $45°z70°y$ to achieve type-1 frequency doubling of the 1.318-μ radiation near normal incidence. The transmission loss of this crystal at 1.318 and 0.659 μ was measured by means of the fundamental and second-harmonic of an Nd:YAG laser. The absorption loss per centimeter was approximately 5 percent at 1.318 μ and 1.5-percent at 0.659 μ.

At 20°C the phase-matching angle in CD*A was measured to be 70°23′ in fairly good agreement with the theoretical value of 69°29′ calculated with the fundamental and second-harmonic indices of $n_1^o = 1.5452$, $n_2^o = 1.5612$, and $n_2^e = 1.5430$, which were extrapolated from the data presented in [2]. Fig. 1 shows the angular dependence of the second-harmonic power in CD*A measured with constant pump power of 3.5 MW and a pulse repetition rate of 10 pulses per second (pps). The dashed line is the theoretical curve calculated in terms of the above refractive indices. The small difference between theoretical and experimental curves is partly due to the error in the measurements of the output power at low levels and to the laser beam divergence. As can be seen from the experimental curve, the product of the crystal length and its internal angular acceptance angle at full width at half-maximum (FWHM) is approximately 5.4 mrad · cm which is considerably larger than that of $LiIO_3$ for which this parameter is calculated to be 0.6 mrad · cm at

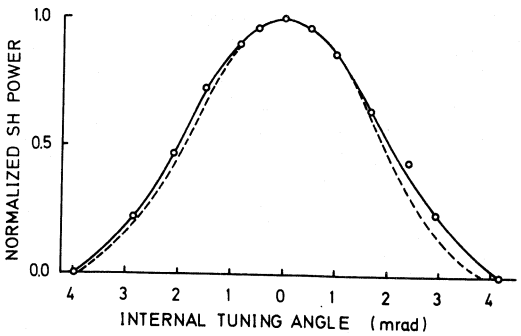


Fig. 1. Angular dependence of second-harmonic power at 0.659 μ in a 13.5-mm-long CD*A crystal. The phase-matching angle is 70°23′ at 20°C. The dashed line is the theoretical curve.

a phase-matching angle of 22°19′. The second-harmonic power obtained at the optimum crystal orientation was about 0.3 MW with 20-ns pulse duration. When a 1-m-focal-length lens was used to focus the fundamental beam in the CD*A crystal, the conversion efficiency increased to 40 percent, yielding the second-harmonic power of 1.4 MW with 22-ns pulse duration. For direct comparison of the conversion efficiency, a 15.2-mm-long KD*P crystal cut for type-2 phase matching was used as a harmonic generator. At the same pump power and pulse repetition rate, the KD*P crystal was found to yield the second-harmonic power of 1.1 MW with 22-ns pulse duration. Since the polarization loss of the fundamental beam does not affect the conversion efficiency for type-2 phase-matching process and KD*P has a higher transmission than CD*A at both fundamental and second-harmonic frequencies, the significant difference in the conversion efficiency observed between CD*A and KD*P is apparently due to the difference in the effective nonlinear optical constant and the angular acceptance angle which has been measured to be 1.9 mrad for the KD*P crystal. Although no measurement was made with normal CDA crystal, it is estimated that CDA is less effective than CD*A due to its large transmission loss at 1.318 μ.

The system described above has been operated for several hours at a pulse repetition rate of 10 pps without any noticeable deterioration in the second-harmonic output power and no surface or internal damage was observed in the CD*A crystal. In addition, the spatial profile of the second-harmonic beam was more uniform when using CD*A than when using KD*P. The high-peak-power 0.659-μ radiation reported in this correspondence has proved to be a good pump source for infrared laser dyes Eastman Kodak IR-123 and IR-144. Furthermore, it is an attractive pump source to scale up the output of a 90° phase-matched $LiNbO_3$ parametric oscillator reported in [5].

References

[1] E. O. Ammann, C. D. Decker, and J. Falk, "High-peak-power 532-nm pumped dye laser," *IEEE J. Quantum Electron.* (Corresp.), vol. QE-10, pp. 463–465, Mar. 1974.

[2] K. Kato, "Second-harmonic generation in CDA and CD*A," *IEEE J. Quantum Electron.* (Corresp.), vol. QE-10, pp. 616–618, Aug. 1974.

[3] R. S. Adhav, "Linear electro-optic effects in tetragonal phosphates and arsenates," *J. Opt. Soc. Amer.*, vol. 59, pp. 414–418, 1969.

[4] U. Deserno, D. Ross, and G. Zeidler, "Quasicontinuous giant pulse emission of $^4F_{3/2} - {}^4I_{13/2}$ transitions at 1.32 μm in YAG: Nd^{3+}," *Phys. Lett.*, vol. 28A, pp. 422–423, 1968.

[5] R. W. Wallace, "Stable, efficient, optical parametric oscillators pumped with doubled Nd:YAG," *Appl. Phys. Lett.*, vol. 17, pp. 497–499, 1970.

[6] K. Goto and Y. Higuchi, "Sum-frequency generation at 0.59 μ using Nd:YAG laser operating at 1.06 and 1.32 μ" (in Japanese),

Preprints of the Ann. Meeting of the Japan. Soc. of Appl. Phys., Quantum Electron., 29a-G-10, 1972 (unpublished).
[7] C. G. Bethea, "Megawatt power at 1.318 μ in Nd^{3+}:YAG and simultaneous oscillation at both 1.06 and 1.318 μ," *IEEE J. Quantum Electron.* (Corresp.), vol. QE-9, p. 254, Feb. 1973.

Proposed Wide-Band and Low-Drive-Power Electrooptic Modulators

JYONG CHI AN, YOSHIO CHO, AND YUKITO MATSUO

Abstract—**Novel methods for the wide-band and low-drive-power electrooptic modulators are proposed. This wide-band and low-drive-power performance is obtained by the utilization of relative electrical and optical delays. Both a lumped and a traveling-wave configuration are described.**

INTRODUCTION

Realization of a wide-band and low-drive-power optical modulator is particularly important for optical communications with larger information capacities. It is well known that light modulation using the Pockels effect, which is exhibited by a number of electrooptic crystals, is suitable for such a purpose [1], [2]. Pockels-effect-type modulators have been developed in a number of forms such as lumped, cavity, and traveling-wave types. All of these realizations have certain disadvantages including low modulation efficiency, narrow bandwidth, or complex construction. Recently planar optical waveguides were produced on $LiNbO_3$ crystals by an out-diffusion process [3]; an efficient diffraction-limited electrooptic modulator was demonstrated [4], and further improvement in efficiency was realized using a ridge [5] or a strip [6] waveguide structure for confining the optical beam in transverse dimensions. On the other hand, the modulation bandwidth is considerably limited by the geometry of the modulator that presents a capacitance load to the driver amplifier.

For the traveling-wave modulator, it was pointed out that large bandwidth and high efficiency could be obtained without the velocity compensation between electrical and optical signals in the crystal [7]. The device is based on the compensation for the electrical and optical velocity differences by adjusting the relative electrical and optical delays between the two modulators [8].

In this correspondence, novel configurations for the wide band with the low-driving-power performance based on the utilization of relative electrical and optical delays are proposed, and for those configurations lumped and a traveling-wave designs are outlined and discussed.

LUMPED MODULATOR

A lumped circuit configuration is shown in Fig. 1. It consists of a tandem array of electroded electrooptic crystals and focusing lenses. Each crystal is connected to an independent driver amplifier driven by a single modulating signal source through each variable delay unit and is terminated with a load resistance that is matched to the driver amplifier output impedance.

Let us consider the polarized light entering the array from the left. At a certain instant the modulating voltage is applied to the first crystal while no voltage is yet applied to the second crystal because of its delay unit, and at the next instant this delayed modulating voltage, which is delayed by an amount of time necessary for transit of light in the first crystal and lens, is applied to the second crystal and so on. For such operation, as the electrical and optical signals interact constructively in each crystal, the modulation depth is cumulated according to the number of crystals while the bandwidth is essentially independent of the number.

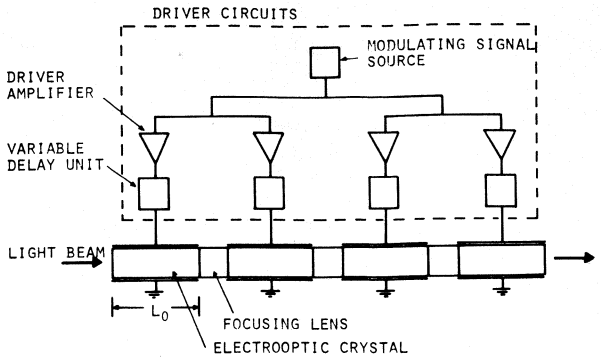


Fig. 1. Lumped modulator.

Assuming that the modulator presents a certain half-wave voltage v_π with the total length of crystals, in order to obtain the half-wave retardation, for example, v_π must be applied to each crystal. Thus, in general, assuming that each crystal is attached with a matched load, the total required driving power P_L, compared with the required driving power $P_L^{(0)}$ of the ordinary type modulator, in which a modulating electrode is not partitioned, is given by

$$P_L = N \cdot P_L^{(0)} \tag{1}$$

where N is the number of crystals. While the bandwidth f_L of the proposed modulator comprising N electrooptic crystal rods, compared with the bandwidth $f_L^{(0)}$ of the ordinary type modulator, is written as

$$f_L = N \cdot f_L^{(0)}. \tag{2}$$

From the combination of (1) and (2), the driving power per unit bandwidth is same for both modulators, but the bandwidth of the proposed modulator is N times that of the ordinary type, and the required power per driver amplifier is the same for both.

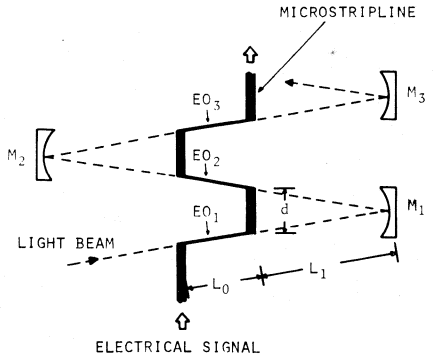
Also for a given bandwidth, the proposed configuration can offer the reduction in the driving power required by each driver amplifier. In Fig. 1, assuming N modulator units, each of which has a certain half-wave voltage and bandwidth with the crystal of a length of L_0, the required voltage for each unit can be reduced to $1/N$ of that for the case of a single unit ($N = 1$); accordingly, the required power for each driver amplifier can be reduced to $1/N^2$, by holding the bandwidth to a single unit.

In the previous discussion although we have neglected the half-wave plate and compensator in the configuration, in practice they must be included.

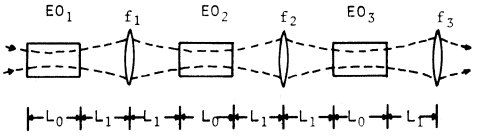
TRAVELING-WAVE MODULATOR

The traveling-wave modulator consists of a zig-zag microstrip line containing electrooptic crystals in its light-traversing sections and concave mirrors as shown in Fig. 2. The modulating signal travels through the zig-zag line and is absorbed by a load resistance with the line characteristic impedance. In Fig. 2 an optically equivalent transmission scheme of the beam is shown. We consider that both the electrical and optical signals enter the first crystal ($E0_1$) at a certain instant and travel in

Manuscript received March 22, 1976.
The authors are with the Institute of Scientific and Industrial Research, Osaka University, Suita, Japan.



(a)



(b)

Fig. 2. (a) Cascaded traveling-wave modulator. (b) Equivalent transmission scheme of light beam.

the same direction so that a traveling-wave interaction is obtained. After the two signals emerge from the crystal, they travel in different paths with the transit time difference t_d

$$t_d = \frac{L_0}{v_0}(\sqrt{\epsilon_1} - n) \tag{3}$$

where v_0 is the velocity of light in the vacuum, and ϵ_1 and n are the effective dielectric permittivity and the refractive index, respectively, in the rod. The compensation operation which cancels the transit time difference can be accomplished by the relative electrical and optical delays between two crystals. This compensation condition at the entrance of each crystal is given by

$$2L_1 = (\sqrt{\epsilon_1} - n)L_0 + \sqrt{\epsilon_2}\, d \tag{4}$$

where L_0 is the length of a crystal, L_1 and d are the lengths of the optical and electrical paths between the adjacent two crystals, respectively, and ϵ_2 is the effective dielectric permittivity in nonactive material. For such operation, as in the lumped case, the modulation index is cumulated according to the number of crystals while the bandwidth is essentially independent of the number.

In general, the bandwidth of the proposed modulator comprising N electrooptic crystal rods will be increased by N times that of the ordinary noncompensating type modulator, while the half-wave voltage remains at the value of the focusing-type (noncompensating) modulator [9].

Discussion

Lumped modulator

The proposed method may be applied to the waveguide modulators. The structure consists of a tandem array of electrodes evaporated on a waveguide electrooptic crystal as shown in Fig. 3 (case of four electrodes). As in the bulk case, each electrode is connected to the driver circuits.

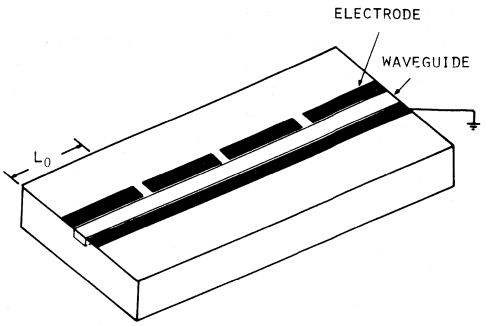


Fig. 3. Waveguide modulator structure.

Traveling-wave modulator

The proposed method allows the wide-band performance in addition to the low-driving-power performance obtained by the use of a focusing structure. Assuming that the crystal has a square cross section and the zig-zag microstrip line is matched with a load resistance, the bandwidth–length product for the $LiTaO_3$ crystal is

$$f_T \cdot L \cong 7.8\,N \quad \text{GHz} \cdot \text{cm}$$

and for the $LiNbO_3$ crystal,

$$f_T \cdot L \cong 16.5\,N \quad \text{GHz} \cdot \text{cm}$$

where it is also assumed that the nonactive material is air, and the calculation on ϵ_1 is done with the aid of [9]. In practice, in order to obtain such wide bandwidths, microwave characteristics in the microstrip line are very important.

References

[1] I. P. Kaminow and E. H. Turner, "Electrooptic light modulators," *Proc. IEEE*, vol. 54, pp. 1374–1390, Oct. 1966.
[2] F. S. Chen, "Modulators for optical communications," *Proc. IEEE*, vol. 58, pp. 1440–1457, Oct. 1970.
[3] I. P. Kaminow and J. R. Carruthers, "Optical waveguiding layers in $LiNbO_3$ and $LiTaO_3$," *Appl. Phys. Lett.*, vol. 22, pp. 326–328, Apr. 1973.
[4] I. P. Kaminow, J. R. Carruthers, E. H. Turner, and L. W. Stulz, "Thin film $LiNbO_3$ electro-optic light modulator," *Appl. Phys. Lett.*, vol. 22, pp. 540–542, May 1973.
[5] I. P. Kaminow, V. Ramaswamy, R. V. Schmidt, and E. H. Turner, "Lithium niobate ridge waveguide modulator," *Appl. Phys. Lett.*, vol. 24, pp. 622–624, June 1974.
[6] I. P. Kaminow, L. W. Stulz, and E. H. Turner, "Efficient strip-waveguide modulator," *Appl. Phys. Lett.*, vol. 27, pp. 555–557, Nov. 1975.
[7] J. C. An, Y. Cho, and Y. Matsuo, "A configuration for wideband of optical modulators," *J. Inst. Electron. Commun. Eng. Jap.*, vol. 58C, pp. 495–496, Aug. 1975.
[8] G. White, "Optical modulation at high information rates," *Bell Syst. Tech. J.*, vol. 50, pp. 2607–2645, Oct. 1971.
[9] S. Uehara, "Focusing-type optical modulator," *IEEE J. Quantum Electron.*, vol. QE-9, pp. 984–986, Oct. 1973.

Notes and Lines

Effect of a Small Capacitor in Parallel with a Pulsed CO_2 TEA Laser

A. H. BUSHNELL, M. GUNDERSEN, AND T. R. BURKES

Abstract—**A simple circuit theory model is used to explain why discharge stability improves when a small capacitor is added in parallel with a CO_2 TEA laser. The small capacitor is a simple way to improve the discharge stability at low cost.**

In a recent article, Tulip *et al.* [1] reported enhancement of discharge stability through addition of a small capacitor in parallel with the electrodes of a CO_2 TEA laser. The laser was driven by a 10-stage 0.1-μF-per-stage Marx generator. The Marx generator produced an 800-ns current pulse in the shape of a half sine wave. The authors observed that arcs formed less often when a 1000-pF capacitor was placed in parallel to the laser electrodes [1]. Presented here is an explanation of the improved discharge stability observed by Tulip *et al.*

A Marx generator is connected to the TEA laser and a small capacitor as in Fig. 1. When the Marx generator erects, the 1000-pF capacitor begins to charge. Initially the current in the laser is very small since Townsend breakdown has not begun to occur. The voltage on C_1 rises above the voltage to which the Marx generator was first charged. This is due to the distributed inductance. After breakdown begins to occur and the impedance drops, the voltage on C_1 will drop back to the voltage that occurs if C_1 is not present. Therefore, a high-voltage spike occurs at the beginning of the discharge of the Marx generator. This spike produces many free electrons that help prevent arc formation and is probably similar to the "poker" described by Hill [2].

To estimate the rise time and maximum voltage on C_1, the Marx generator may be modeled as in Fig. 2. The Marx generator is modeled as a capacitor that represents the series capacitors and an inductor that models the stray inductance in the Marx generator. A switch closes at $t = 0$ to represent the spark gaps firing. $R_L(t)$ represents the laser discharge and is a function of time. Initially the current in $R_L(t)$ will be assumed small compared to the current in C_1 since breakdown has not occurred. Using these assumptions, the voltage on C_1 may be shown to be [3]

$$V_{C_1}(t) = \frac{V_0}{1 + \dfrac{C_1}{C}}\left(1 - \cos\frac{t}{\sqrt{LC'}}\right)$$

where

$$C' = \frac{CC_1}{C + C_1}$$

and

V_0 = initial charge on Marx.

Manuscript received March 24, 1976. This work was supported by ERDA Contract E(29-2)-3572.

The authors are with the Department of Electrical Engineering, Texas Tech University, Lubbock, TX 79409.

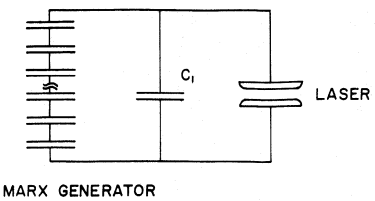


Fig. 1. Marx generator in parallel with TEA laser. C_1 provides spike at beginning of pulse.

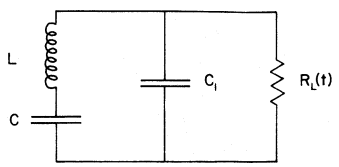


Fig. 2. Circuit model of circuit in Fig. 1. L and C model the Marx generator. $R_L(t)$ represents TEA laser.

From this equation it is seen that V_{C_1} reaches $2V_0$ at

$$t = \pi\sqrt{LC'}.$$

Using the pulse length reported by Tulip *et al.*, the value of L may be estimated to be

$$L \approx 6\ \mu\text{H}$$

and

$$C_1 = 1000\ \text{pF}$$
$$C = 0.01\ \mu\text{F}$$

so

$$C' = \frac{C_1 C}{C_1 + C} \approx 900\ \text{pF}.$$

The pulse reaches its maximum at

$$t = \pi\sqrt{LC'} = 80\ \text{ns}.$$

Breakdown would probably begin to occur before C_1 reached $2V_0$.

Placing a small capacitor in parallel with a CO_2 TEA laser is a simple method of achieving high electron density at the beginning of a current pulse. A simple model has been presented to explain the observed effect.

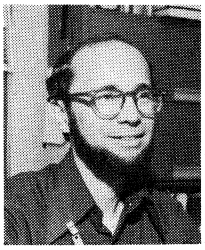
References

[1] J. Tulip, H. J. Seguin, and W. Faszer, "High-repetition-rate TEA-laser discharge using integrated preionization and switching," *IEEE J. Quantum Electron.*, vol. QE-12, pp. 155–159, Feb. 1976.

[2] A. Hill, "Continuous uniform excitation of medium pressure CO_2 laser plasma by means of controlled avalanche ionization," *Appl. Phys. Lett.*, vol. 22, pp. 670–673, June 15, 1973.

[3] C. A. Desoer and E. S. Kuh, *Basic Circuit Theory*. New York: McGraw-Hill, 1969.

Contributors



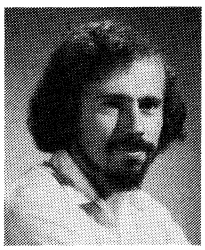
E. Bliss (A'54) received the B.A. degree in physics from Lawrence University, Appleton, WI, in 1963 and the M.S. and Ph.D. degrees in physics from Carnegie-Mellon University, Pittsburgh, PA, in 1965 and 1968, respectively.

From 1968 to 1972 he worked in the Laser Physics Branch at the Air Force Cambridge Research Laboratories, Bedford, MA, on the problem of laser induced damage to dielectric materials. Since coming to Lawrence Livermore Laboratory, University of California, Livermore, CA, in 1972, Dr. Bliss has directed his efforts toward the study of intense pulse propagation in large laser systems. This has involved measurements of nonlinear material properties, characterization of degraded beams, comparison with theoretical propagation models, and evaluation of proposed solutions to the intense pulse propagation problem. In 1975 he supervised preparation of the 1 TW CYCLOPS laser chain for target irradiation experiments. In addition to continuing propagation studies, he is now the Responsible Physicist for alignment systems on the 20 beam SHIVA laser.

*

Robert D. Burnham (M'76), for a photograph and biography please see page 88 of the February 1976 issue (Part I) of this JOURNAL.

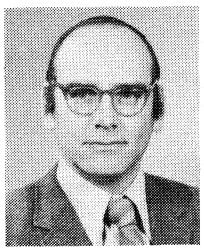
*



Gene A. Capelle was born in Oakland, CA, on October 6, 1944. He received the B.A. degree in physics from the University of California, Berkeley, in 1966 and the M.A. and Ph.D. degrees in physics from the University of California, Santa Barbara, in 1968 and 1972, respectively.

From 1972 to 1973 he was a Visiting Scientist at the Department of Physical Chemistry of the University in Bonn, Germany. From 1973 to 1974 he was a postdoctoral fellow at the Quantum Institute, University of California, Santa Barbara, where his research related to the spectroscopy of diatomic metal oxides. He is currently with the Aerospace Corporation, El Segundo, CA, and is engaged in measuring photon yields of various reactions producing diatomic Group IVa oxides, halides, and nitrides, and transfer rates from NF ($a^1\Delta$) to atomic species.

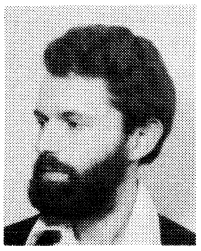
*



Thomas F. Deutsch (S'56-M'61) was born in Vienna, Austria in 1932. He received the B.S. degree in engineering physics from Cornell University, Ithaca, NY, in 1955, and the Ph.D. degree from Harvard University, Cambridge, MA, in 1961.

From 1960 to 1974 he was a Principal Research Scientist with the Raytheon Research Division, Waltham, MA, where his research interests included dye lasers, CO_2 and chemical lasers, and window materials for infrared lasers. In 1974 he joined the staff of the Lincoln Laboratory, Massachusetts Institute of Technology, Lexington, where he has been working in the areas of optically pumped molecular lasers and laser photochemistry.

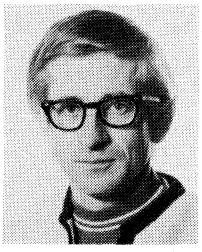
*



Jean-Claude Diels was born in Brussels, Belgium, on December 12, 1943. He received the Ph.D. in physics from the University of Brussels, Brussels, Belgium, for research performed at the University of California, Berkeley.

He has been a Research Associate at the Ecole Royale Militaire, Brussels, Belgium, the Philips Research Laboratories, Eindhoven, The Netherlands, the University of California, Berkeley, and the Max Planck Institute für Biophysikalische Chemie, Göttingen, Germany. He is currently a Research Scientist with the Center for Laser Studies, University of Southern California, Los Angeles. He has published many papers in the fields of laser materials and optics and delivered several papers to conferences on quantum electronics and quantum optics.

*



Andrew Dienes was born in Hungary on October 22, 1939. He left Hungary in 1956 and studied at McGill University, Montreal, P.Q., Canada, where he received the B.Sc. degree in electrical engineering in 1962. He received the M.Sc. degree in electrical engineering in 1963 and the Ph.D. degree in physics in 1967, both from the California Institute of Technology, Pasadena.

From 1967 to 1973 he was a Member of the Technical Staff at Bell Laboratories, Holmdel, NJ. From 1972 to 1973 he was a Visiting McKay Lecturer at the University of California, Berkeley. Since 1973 he has been with the Faculty of the Department of Electrical Engineering, University of California, Davis, and also of the Department of Electrical Engineering/Computer Sciences, University of California, Berkeley.

*



Erwin L. Hahn was born in Sharon, PA, on June 9, 1921. He received the B.S. degree from Juniata College, Huntindon, PA, in 1943, and the M.S. and Ph.D. degrees from the University of Illinois, Urbana, in 1947 and 1949, respectively.

Since graduation he has held teaching positions at several universities and done research for private industry. He has also been a Consultant for the U.S. Atomic Energy Commission and the U.S. Navy. Since 1961 he has held the

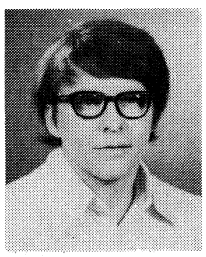
position of Professor with the Department of Physics, University of California, Berkeley. He is involved in the fields of nuclear and electron spin magnetic resonance, molecules and solids, and laser physics. He was responsible for the discovery of spin echoes in 1949 and was the codiscoverer (with S. L. McCall) of self-induced transparency by pulsed coherent light. He has also done research on spin echoes, nuclear moments in molecules, nuclear and electron spin magnetism in solids, nuclear electric quadrupole moments, and laser light propagation in matter.

Dr. Hahn has received the American Physical Society Solid State Physics Buckley Prize for 1971 and the prize of the International Society of Magnetic Resonance. He is a member of the National Academy of Sciences of the United States and the American Academy of Arts and Sciences, and a Fellow of the American Physical Society.

*

J. T. Hunt, photograph and biography not available at the time of publication.

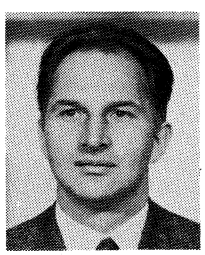
*



Helge Kildal (S'70-M'71) was born in Oslo, Norway. He received the B. Eng. degree in physics (Sivilingenior degree) from the Norwegian Institute of Technology, Trondheim, Norway, in 1967, and the M.S. and Ph.D. degrees, both in applied physics, from Stanford University, Stanford, CA, in 1969 and 1972, respectively.

He has been with the Lincoln Laboratory, Massachusetts Institute of Technology, Lexington, since 1972. His more recent research interests include infrared nonlinear materials, absolute frequency calibration, and new optically pumped infrared lasers.

*

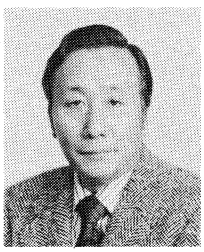


Herwig Kogelnik (M'61-F'73) was born in Graz, Austria, in 1932. He received the Dipl.-Ing. and Doctor of Technology degrees, both from the Technische Hochschule Wien, Vienna, Austria, in 1955 and 1958, respectively, and the Ph.D. degree from Oxford University, Oxford, England, in 1960.

From 1955 to 1958 he was Assistant Professor at the Institut für Hochfrequenztechnik, Vienna, engaged in microwave research and teaching. He won a British Council Scholarship to Oxford from 1958 to 1960, where he did research on electromagnetic radiation in magnetoplasmas and anisotropic media. He joined Bell Laboratories, Holmdel, NJ in 1961, where he has been concerned with research in optics, electronics and communications, including work on lasers, holography, optical guided-wave devices, and integrated optics. Since 1967 he has been Head of the Coherent Optics Research Department.

Dr. Kogelnik is a member of the American Physical Society, the American Association for the Advancement of Science, the Electrotechnischer Verein Osterreichs (Austria), and a Fellow of the Optical Society of America.

*

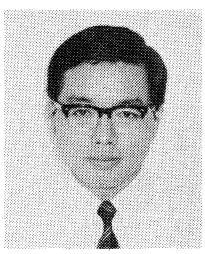


Nobuaki Kumagai (M'59-SM'71) was born in Ryojun, Japan, on May 19, 1929. He received the B.Eng. and Dr.Eng. degrees both from Osaka University, Osaka, Japan, in 1953 and 1959, respectively.

From 1958 to 1960 he was a Visiting Senior Research Fellow at the Electronics Research Laboratory of the University of California, Berkeley, where he was engaged in research on electromagnetic wave scattering and parametric amplifiers. From 1960 to 1970, he was an Associate Professor of Communication Engineering at Osaka University. In 1966, he was invited to the 11th G-MTT International Symposium as an Invited Speaker. Since 1971, he has been a Professor of Communication Engineering at Osaka University where he is engaged in research and education in electromagnetic theory, microwave and millimeter-wave engineering, optical waveguides and devices, and lasers and their applications. He is the coauthor of *Microwave Circuits* (Tokyo, Japan: OHM-sha, 1963) and *Introduction to Relativistic Electromagnetic Field Theory* (Tokyo, Japan: Corona, 1971).

Dr. Kumagai is a member of the Institute of Electronics and Communication Engineers of Japan, the Institute of Electrical Engineers of Japan, the Japan Society of Applied Physics, and the Physical Society of Japan.

*

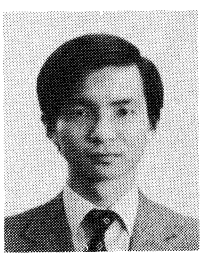


Masanori Matsuhara was born in Fukui, Japan, on February 14, 1941. He received the B.E. degree in electrical engineering from Fukui University, Fukui, Japan, in 1963, and the M.E. and Ph.D. degrees in electrical communication engineering from Osaka University, Osaka, Japan, in 1965 and 1968, respectively.

He was a Research Associate from 1968 to 1972, and since 1972 he has been an Associate Professor of Communication Engineering at Osaka University. Also, he was a Research Fellow at the Communication Research Center, the Department of Communications, Ottawa, Canada, from 1973 to 1975. He is engaged in studies of optical transmission lines and optical integrated circuits.

Dr. Matsuhara is a member of the Institute of Electronics and Communication Engineers of Japan.

*



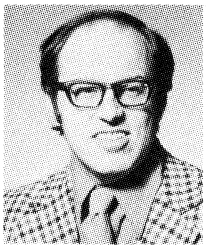
Masato Ohtaka (S'72-M'76) was born in Hyogo, Japan, on March 28, 1947. He received the B.E. and M.E. degrees in electrical communication engineering from Osaka University, Osaka, Japan, in 1970 and 1972, respectively.

He is currently a Research Associate of the Department of Electrical Engineering at Fukui University, Fukui, Japan. He has been engaged in research on optical transmission lines and integrated optical circuits.

Mr. Ohtaka is a member of the Institute of Electronics and Communication Engineers of Japan.

P. A. Renard, for a photograph and biography please see page 320 of the May 1976 issue of this JOURNAL.

*



Ronald V. Schmidt (S'68–M'75) was born in San Francisco, CA, on March 31, 1944. He received the Ph.D. degree in electrical engineering from the University of California, Berkeley, in 1970.

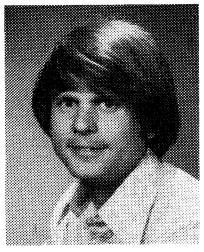
In 1971 he had a post-doctoral position at University College, London. Presently he is with Bell Laboratories, Holmdel, NJ, where he is concerned with optical waveguide devices and acoustic wave devices.

Dr. Schmidt is a member of Phi Beta Kappa.

*

Don R. Scifres (M'74), for a photography and biography please see page 88 of the February 1976 issue (Part I) of this JOURNAL.

*



G. E. Sommargren was born in Rockville Centre, NY, on April 21, 1944. He received the B.S. and M.S. degrees in physics from Stevens Institute of Technology, Hoboken, NJ, in 1966 and 1968, respectively, and the Ph.D. degree from the Institute of Optics, University of Rochester, Rochester, NY, in 1972.

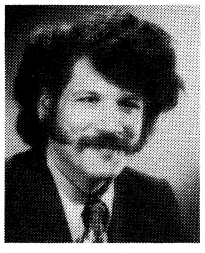
He joined the Lawrence Livermore Laboratory, University of California, Livermore, CA, in 1972 where he has been working on beam propagation, interferometry, and holography.

Dr. Sommargren is a member of the Optical Society of America and the Society of Photo-Optical Instrumentation Engineers.

*

William Streifer (S'56–M'58–SM'74), for a photograph and biography please see page 88 of the February 1976 issue (Part I) of this JOURNAL.

*

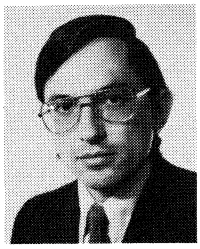


Steven N. Suchard was born in Chicago, IL, on February 8, 1944. He received the B.S. degree in chemistry from the University of California, Berkeley, and the Ph.D. degree in chemical physics from the Massachusetts Institute of Technology, Cambridge, in 1965 and 1969, respectively. During his graduate career he was awarded a NASA Traineeship from 1965 to 1968 and an NIH Predoctoral Fellowship from 1968 to 1969.

From 1969 to 1970 he was a Postdoctorate Research Fellow in the College of Chemistry at the University of California, Berkeley, where his work involved the demonstration of the first hydrogen halide chemical laser to operate on an overtone transition. He joined the Aerophysics Laboratory of the Aerospace Corporation, El Segundo, CA, in 1970, and has studied pulse-chain and transfer chemical lasers and chemically pumped electronic transition lasers.

Dr. Suchard is a member of the American Physical Society.

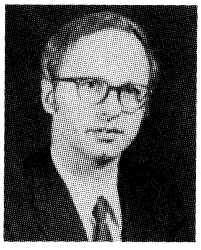
*



O. Teschke (M'75) received the Ph.D. degree in electrical engineering from University of California, Berkeley, in 1975, where he investigated CW dye laser operation and mode locking.

He is currently with Bell Laboratories, Holmdel, NJ, involved in picosecond spectroscopy of semiconductors.

*

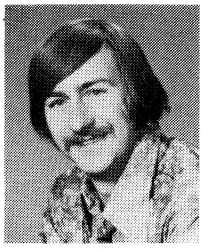


Jan P. van der Ziel was born in The Netherlands on August 17, 1937. He received the B.S. degree in electrical engineering from the University of Minnesota, Minneapolis, in 1959, and the M.S. and Ph.D. degrees in applied physics from Harvard University, Cambridge, MA, in 1961 and 1964. From 1964 to 1965 he was a Postdoctoral Fellow at Harvard University.

In 1965 he joined Bell Laboratories, Murray Hill, NJ, and is currently working on the linear and nonlinear optical properties of semiconductor materials.

Dr. van der Ziel is a member of the American Physical Society.

*



H. J. Weaver, Jr. was born in Auburn, NY on April 16, 1942. He graduated from the University of Notre Dame, South Bend, IN, receiving the B.S. and M.S. degrees in mechanical engineering and the Ph.D. degree in systems theory in 1964, 1966, and 1969, respectively.

In 1969 he joined the Lawrence Livermore Laboratory, University of California, Livermore, CA, where he has specialized in physical systems modeling and Fourier analysis. For the last four years he has worked specifically in the Laser Fusion Program in the areas of wave propagation, laser systems design, and laser diagnostic analysis. He is currently assigned to the Nuclear Test Engineering Division Research and Development Group working in the area of time dependent nuclear radiation imaging. He has been active for several years in the Laboratory's Mechanical Engineering Continuing Education Program as both a Lecturer and Committee Member. He is also a Faculty Member of two local colleges where he lectures in mathematics.



John R. Whinnery (A'41-SM'44-F'52) was born in Read, CO, on July 26, 1916. He received the B.S. and Ph.D. degrees in electrical engineering from the University of California, Berkeley, in 1937 and 1948, respectively.

From 1937 to 1946 he was with the General Electric Company, Schenectady, NY, working on problems in microwave electron tubes and circuits. He was also a Part-Time Lecturer at Union College, Schenectady, NY. Since 1946 he has been on the Faculty of the University of California, Berkeley, holding positions of Associate Professor, Professor, Director of the Electronics Research Laboratory, Chairman of the Electrical Engineering Department, and Dean of the College of Engineering. On leaves from the University he was Head of Microwave Tube Research at the Hughes Aircraft Company in 1952–1953; a Guggenheim Fellow at Eidgenössische Technische Hochschule, Zurich, Switzerland, in 1959; a Visiting Member of the Technical Staff, Bell Laboratories, Murray Hill, NJ in 1963–1964; and Visiting Professor of Electrical Engineering at the University of California, Santa Cruz, in 1967–1968 and at Stanford University, Stanford, CA, in 1970.

Dr. Whinnery has served on various professional and government advisory committees. He was a member of the Board of Directors of the IRE from 1956 to 1959, a member of the Board of Directors of the IEEE from 1967 to 1970, and Secretary of the IEEE in 1970. He is also a member of the American Physical Society, the Optical Society of America, Sigma Xi, the National Academy of Engineering, and the National Academy of Sciences.

Call for Papers for Topical Conferences on Optical Phenomena in Infrared Materials

Annapolis, MD, December 1-3, 1976
Sponsored by the Optical Society of America

Deadline for papers: September 3, 1976

Papers are solicited in the areas of optical phenomena, properties, and processes in infrared optical materials. Special emphasis will be given to materials for components (such as windows, lenses, filters, waveguides, modulators, absorbers, and AR and protective coatings) and to modern infrared applications (especially in the 3-5 and 10 μm regions) such as high-energy laser systems, communications, imaging and scanning, solar-energy conversion, infrared detection, and spectroscopy.

A 25 word abstract and a 300-500 word summary should be sent to:

Optical Society of America
2000 L Street, N.W.
Washington, DC 20036

Rotational Nonequilibrium and Line-Selected Operation in CW DF Chemical Lasers

ROBERT J. HALL

Abstract—A numerical analysis of rotational nonequilibrium effects in CW DF chemical lasers is presented. The rotational master equations incorporate the effects of simultaneous mixing, chemical pumping, rotational cross relaxation, and radiative emission. Rotational cross relaxation is described by "exponential gap" models in which ΔJ is unrestricted. Results of this analysis indicate that rotational equilibrium can be a poor assumption for high J levels even under small-signal conditions. The model predictions are in good qualitative agreement with observed multiline resonator spectra. Performance loss due to rotational nonequilibrium is predicted to be modest (~15 percent) for multiline operation, with larger losses predicted for line-selected modes. Criteria for efficient line-selected operation are presented.

I. Introduction

UNTIL RECENTLY, most theoretical analyses of HF/DF chemical laser performance have been based on the assumption that an equilibrium (thermal) distribution of rotational states is maintained at all times [1]-[5]. It has been recognized, however, that stimulated emission rates can be competitive with rotational cross-relaxation rates under certain conditions, in which case significant departures from thermal equilibrium would be expected. Also, it is known that the chemical reactions which pump the vibration-rotation population inversions are characterized by highly non-Boltzmann product rotational distributions. These primitive distributions might be expected to influence the spectral distribution of power output. In general, the rotational distribution in HF or DF will be determined by a competition between chemical pumping, stimulated emission, and collisional thermalization; depending on the experimental conditions and the rotational state of interest, the time scales for these processes may all overlap. For pulsed HF chain lasers there is experimental evidence that suggests a significant degree of rotational nonequilibrium, at least for the higher vibrational bands [6]. For CW HF/DF lasers, the most notable qualitative discrepancy between experiment and (rotational equilibrium) theory is the experimental observation of spatially overlapping emission belonging to different P branches of the same vibrational band [7]. Also, the high-lying P branches are observed to begin lasing simultaneously with the lowest P branches [7]. These results are at variance with the theoretical (rotational equilibrium) predictions that only one P branch per vibrational band can oscillate at a given axial location, and that lasing on the higher P branches should only begin well downstream from the point at which mixing begins.

Manuscript received December 18, 1975. This work was supported by the Office of Naval Research under Contract N00173-76-C-004 and by the UTRC Corporate Research Program.

The author is with the United Technologies Research Center, East Hartford, CT 06108.

On the theoretical side, several investigators have provided rate equation analyses of pulsed HF lasers in which the time histories of individual vibration-rotation (VR) state densities are given by the solution to kinetic master equations [8]-[11]. The results of [8] indicated that inclusion of this effect was particularly important for accurate prediction of line-selected power output. For multiline operation, however, the gross power output differed appreciably from the rotational equilibrium calculations only for an effective cross-relaxation cross section of about 0.01 gas kinetic.

Skifstad and Chao [12] have studied rotational nonequilibrium effects in CW HF amplifiers. Assuming $|\Delta J| = 1$ selection rules and single-line operation, they concluded that finite cross relaxation significantly limits the power output obtainable in amplifier configurations. Rotational nonequilibrium in CW HF resonators has been examined by Sentman [13], who employed a simplified chemical-vibrational kinetics model. For operation on one vibrational band, it was found that rotational nonequilibrium caused a 20-30 percent performance decrease.

This paper represents an attempt to assess the importance of rotational nonequilibrium in CW DF chemical laser resonators. Although the calculations are specialized to the DF system, the conclusions should be valid for HF chemical lasers as well. One important question which this analysis seeks to answer is whether rotational nonequilibrium can cause significant multiline performance reductions. The investigation is also motivated in part by the importance of operating on selected lines for improved beam quality and atmospheric propagation.

II. Nomenclature

A_s	constant appearing in expression for rotational cross-relaxation rate constant;
b_{vJ}	thermal equilibrium distribution of rotational states J in DF vibrational state v;
C_s	constant appearing in expression for rotational cross-relaxation rate constant;
c_{ps}	constant pressure molar heat capacity of chemical species s (equilibrium modes);
d_J	degeneracy of rotational state = 2J + 1;
DF(v, J)	DF vibration-rotation state;
$D_2(v)$	D_2 vibrational quantum state;
E_{vJ}	energy of DF quantum state;
$g^{v,J-1}_{v-1,J}$	line-center gain coefficient of transition DF(v, J - 1) → DF(v - 1, J);
g_c	cavity threshold gain;
H	total enthalpy stored in nonequilibrium modes;
h	Planck's constant;

$I^{v,J-1}_{v-1,J}$ intracavity flux on transition DF(v, J - 1) → DF(v - 1, J);
K_f overall forward rate constant for F + D_2 → DF + D;
$KCR^{(M)}_{JJ'}$ rate coefficient for rotational cross-relaxation process DF(v, J) + M → DF(v, J') + M ($s^{-1} \cdot torr^{-1}$);
k Boltzmann's constant;
L_c distance between cavity mirrors;
$L^{v,J-1}_{v-1,J}$ stimulated emission rate for transition DF(v, J - 1) → DF(v - 1, J);
l_{mix} characteristic mixing length used in mixing model;
$\tilde{M}$ average molecular weight in mixed zone;
M collision partner M = DF, D_2, D, F, He, HF, ⋯;
$\dot{m}$ mass flow rate in mixed zone;
N number of primary-secondary nozzle pairs between mirrors;
N_A Avogadro's number;
P_{vJ} product distribution for chemical pumping process F + D_2 → DF(v, J) + D;
vP(J) denotes P-branch transition DF(v, J - 1) → DF(v - 1, J);
p static pressure of gas in mixed zone;
Q_{opt} total optical power removed from gas;
R_1, R_2 reflectivities of cavity mirrors;
T translational temperature in mixed zone;
$\langle T^0 \rangle_s$ average temperature in free streams of chemical species s;
u flow velocity in mixed zone;
$\left\langle \frac{u^2}{2} \right\rangle^0$ average bulk kinetic energy per gram of primary and secondary zones;
w width of mixed zone in optic direction;
x flow coordinate;
y optical axis;
Y_s concentration of chemical species s (s = DF, D_2, D, F, He, HF, ⋯) in mixed zone (moles/gram);
Y^0_s concentration of chemical species s in primary and secondary streams;
y_{vJ} concentration of DF(v, J);
$\hat{y}_v$ concentration of D_2(v).

A. Greek Symbols

Δ difference of two quantities;
ν frequency of transition DF(v, J - 1) → DF(v - 1, J);
ρ mass density of gas in mixed zone.

B. Subscripts

J Jth rotational level;
s sth chemical species;
v vth vibrational state.

III. Analysis

A. Governing Conservation Equations

Because the inclusion of rotational nonequilibrium kinetics represents a considerable increase in analytical complexity, the portions of this analysis dealing with fluid mechanics and stimulated emission have been simplified. Mixing and gas dynamic phenomena are assumed to be quasi-one-dimensional, and the optical configuration is taken to be a transverse Fabry-Perot resonator. Fig. 1 illustrates the flow and optical configurations modeled in this analysis.

The phenomenological mixing model is similar to that given

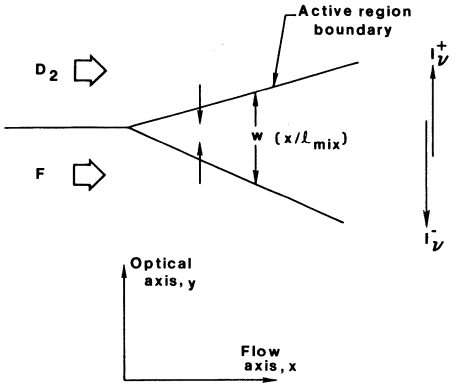


Fig. 1. Illustration of mixing nozzles and optical configuration.

by Broadwell [14]; parallel primary and secondary reactant streams are assumed to mix at a prescribed rate, beginning at $x = 0$. Although the widths of the reactant zones at $x = 0$ are generally different, it is assumed that the two zones have equal characteristic mixing lengths, so that the width of the mixed zone has the functional form $w = w(x/l_{mix})$. The mass flow rate in the mixed zone is proportional to w. Variations in species concentrations in the y direction within the mixed stream are neglected. For turbulent mixing a linear mixing rate ($w \alpha x$) should be employed, while for laminar, diffusive mixing the appropriate function is $w \alpha x^{1/2}$. In the numerical examples to follow, the approximation

$$w = (L_c/N)\,(\tanh\,(x/l_{mix}))^{1/2} \tag{1}$$

to the laminar mixing function has been employed.

The species conservation equations valid in the mixed zone reflect the simultaneous effects of kinetic processes and the entrainment of molecules from the free streams. For equal primary and secondary mixing lengths, these equations have the following simple form:

$$\frac{dY_s}{dx} = \frac{\dot{Y}_s}{u} + (Y^0_s - Y_s)\frac{1}{w}\frac{dw}{dx} \quad \text{(chemical species)} \tag{2}$$

$$\frac{dy_{vJ}}{dx} = \frac{\dot{y}_{vJ}}{u} - y_{vJ}\frac{1}{w}\frac{dw}{dx} \quad \text{(DF vibration-rotation states } v \leqslant 4) \tag{3}$$

$$\frac{dy_v}{dx} = \frac{\dot{y}_v}{u} - y_v\frac{1}{w}\frac{dw}{dx} \quad \text{(DF vibrational states } v > 4). \tag{4}$$

For D_2 vibrational states, the equations have the same form as those for DF, except for D_2(v = 0) whose rate equation can be written

$$\frac{d\hat{y}_0}{dx} = \frac{\dot{\hat{y}}_0}{u} + (Y^0_{D_2} - \hat{y}_0)\frac{1}{w}\frac{dw}{dx} \quad [D_2(v = 0)]. \tag{5}$$

The first term on the right-hand side of the above equations represents the time rate of change of species concentration due to kinetic processes; the second term represents the effect of mixing in primary and secondary constituents. The quantity Y^0_s represents the concentration (moles/gram) of chemical species s in premixed (but unreacted) primary and secondary flows.

A summary of the chemical and vibrational mechanisms governing DF laser performance has been given in [15]. In the present analysis, the chemical mechanism is assumed to consist

solely of the reaction

$$F + D_2 \longrightarrow DF(v, J) + D. \tag{6}$$

The overall forward rate constant is derived from the data of Hohmann *et al.* [16] and Persky [17]. Choice of vibration-vibration (VV) and vibration-translation (VT) rate coefficients has been guided by the recommendations of [15], with some minor variations. Rate data for the chemical and vibrational processes are far from complete, however, particularly for DF-DF VV exchange and DF relaxation by atoms. This portion of the analysis is itself subject to considerable uncertainty. The mathematical formulation of chemical and vibrational master equations has been given elsewhere [1].

The DF rotational distributions and optical gain will be influenced by translational temperature rises due to chemical reaction. A simple energy equation consistent with the assumption of quasi-one-dimensional flow can be written

$$\dot{m}\left(\left(\sum_s c_{ps} Y_s\right) T + \frac{u^2}{2} + H\right) + Q_{\text{opt}}/N = (\text{constant})\, w. \tag{7}$$

The right-hand side of (7) is equal to the difference between the total enthalpy flux in the unmixed zone at $x = 0^-$ and the remaining enthalpy flux in the unmixed zones at $x > 0$. The quantity H in the above equation represents the energy per unit mass of mixed gas stored in "nonequilibrium" modes (DF VR, D_2 vibration, and enthalpy of formation of reacting species). If a constant pressure jet is assumed, differentiation of the energy equation leads to the following expression for the translational temperature derivative:

$$\left(\sum_s c_{ps} Y_s\right)\frac{dT}{dx} = -\frac{\dot{H}}{u} - \sum_s c_{ps} T\left(\frac{\dot{Y}_s}{u}\right) + \left[\left\langle\frac{u^2}{2}\right\rangle^0 - \frac{u^2}{2}\right] \cdot \frac{1}{w}\frac{dw}{dx} + \left[\sum_s c_{ps} Y_s^0 (\langle T^0\rangle_s - T)\right]\frac{1}{w}\frac{dw}{dx}. \tag{8}$$

Note that (8) contains terms reflecting the fact that fluid ingested into the mixed zone generally possesses a different temperature and bulk kinetic energy than the mixed zone. The symbol $\dot{H}$ represents the time rate of change of H due to collisional (nonradiative) processes only.

B. Rotational Relaxation Mechanisms and Rate Constants

The time rate of change of y_{vJ} due to collisional and radiative processes can be expressed as

$$\begin{aligned}\dot{y}_{vJ} = {} & (\rho N_A) P_{vJ} K_f Y_F Y_{D_2} && \text{(chemical pumping)}\\ & + b_{vJ}\dot{y}_v\big|_{\substack{VV\\VT}} && \text{(vibration-vibration-rotation (VVR), VR exchange)}\\ & + \dot{y}_{vJ}|_{CR} && \text{(cross relaxation)}\\ & - L^{v,J}_{v-1,J+1} + L^{v+1,J-1}_{v,J} && \text{(stimulated emission).}\end{aligned} \tag{9}$$

There is also a contribution to the chemical pumping term from the reverse of reaction (6); this process is important only for $v \geqslant 4$, however. The primitive product distribution, P_{vJ}, is taken from Polyani and Woodall [18], who reported initial rotational distributions peaked at J = 13 (estimated), 11, 9, and 5 for vibrational states v = 1, 2, 3, and 4, respectively.

Processes such as VV and VT exchange in reality involve rotational quantum number changes as well, and these must be accounted for in the rotational master equations. An exact formulation of VVR and VR transfer is extremely complex, and this effect has been included in the master equations (9) in a simplified way. The formulation in (9) reflects the assumption that the VV and VT processes are unaffected by the rotational state distribution of the molecules involved, and that these processes interact with the rotational distribution in accordance with the Boltzmann distribution. Because the time scales associated with VV and VT processes are typically much longer than those associated with cross relaxation, the rotational distributions are not significantly perturbed by vibrational relaxation.

Rotational sublevels belonging to the same vibrational state will relax toward a thermal or Boltzmann distribution through cross-relaxation processes

$$DF(v, J) + M \longrightarrow DF(v, J') + M + \Delta E$$
$$\Delta E = E_{vJ'} - E_{vJ}. \tag{10}$$

Depending upon the collision partner M, this transfer will be dominated by rotation-rotation (RR) or rotation-translation (RT) processes. Although no experimental data exist for DF rotational relaxation, reasonable estimates can be derived from the results of experimental investigations into HF rotational relaxation by Hinchen and Hobbs [19], [20]. For the processes

$$HF(1, J) + HF \longrightarrow HF(1, J') + HF \tag{11}$$

time constants on the order of 10^7 s^{-1} · torr^{-1} were measured for the lower J levels. These investigators found multiquantum transfer processes ($|\Delta J| > 1$) to be important, and preliminary experiments with H_2 and He indicated that these molecules are at least an order of magnitude less efficient than HF itself in promoting HF rotational relaxation.

The DF rotational relaxation model is based on the assumption that the rate coefficients for DF-DF rotational transfer involving lower J levels will be comparable to those for HF-HF collisions. In particular, the time constant for

$$DF(v = 1, J = 2) + DF \longrightarrow DF(v = 1, J = 3) + DF \tag{12}$$

has been normalized to the value 2×10^7 s^{-1} · torr^{-1}. Hinchen and Hobbs interpreted HF rotational relaxation by HF in terms of RR transfer, and proposed a rate constant model that can be expressed in the form

$$KCR^{(HF)}_{JJ'} = A_{HF} d_{J'} \exp(-E_{vJ'}/kT) \exp(-|\Delta E|/kT) \tag{13}$$

where A_{HF} is a normalization factor. In this analysis it has been assumed that this functional form also suffices to scale the rates for DF-DF interactions (12) to $J > 2$ and $|\Delta J| > 1$. DF relaxation by HF (present in combustion-driven systems) is assumed to proceed with rates given by (13) multiplied by an efficiency factor. The calculations to follow are relatively insensitive to variations in the efficiency factor over the range 0.5 to 1.0. The value 0.5 is employed in the sample calculations.

Rate constants for DF rotational relaxation by other foreign

gases are assumed to proceed with the efficiency of the analogous process in the HF system. Consequently, the processes analogous to (12) involving D_2, He, D, and F are assigned relative efficiencies of 0.1, 0.03, 0.03, and 0.03, respectively. It is also assumed that RT transfer dominates DF relaxation by these collision partners. Scaling of these rate coefficients to higher J states and $|\Delta J| > 1$ consequently employs the Polyani-Woodall model [21]

$$KCR_{JJ'}^{(s)} = A_s \frac{d_{J'}}{d_J} \exp(-C_s|\Delta E|/kT) \quad (J' < J) \tag{14}$$

where A_s and C_s are empirical constants. Upward rates ($J' > J$) are computed from detailed balance. For the base rate model, the C_s are set equal to 1, and the A_s are assigned values determined by the relative efficiency of the species. The Polyani-Woodall model has been used instead of other rate coefficient models [22], [23] because of its success in explaining the RT relaxation pattern of nascent rotational distributions [21], [24]. The A_s are assumed to have no dependence on temperature or vibrational quantum number.

In the absence of experimental data for DF RR and RT transfer, this cross-relaxation rate model is subject to considerable uncertainty. The assumptions about the equivalence of the HF and DF rate coefficients for small J may prove to be reasonably accurate, but the use of (13) and (14) for scaling to high J and $|\Delta J| > 1$ is speculative. The RR scaling function (13) may be particularly uncertain for large J.

Typical chemical laser mixtures contain only a small mole fraction (~10 percent) of the efficient rotational relaxation partners DF and HF, and one is often interested in higher J states for which ΔE is comparable to or exceeds kT. As will be seen, these factors produce an effective time constant for rotational relaxation that is considerably slower than the value of 10^{-7} s · torr associated with low-J DF-DF interactions.

The cross-relaxation term $\dot{y}_{vJ}|_{CR}$ is expressed in the form

$$\dot{y}_{vJ}|_{CR} = -p\tilde{M} \sum_s Y_s \sum_{J'} KCR_{JJ'}^{(s)} \cdot \left[y_{vJ} - \frac{d_J}{d_{J'}} \exp(-\Delta E/kT)\, y_{vJ'} \right] \tag{15}$$

which reflects the absence of selection rules on rotational relaxation and the application of detailed balance. It should be mentioned that while (15) is in a form appropriate to RT transfer, it will be a valid representation for RR processes such as (12) if the "rotator bath" is close to thermal equilibrium. For most conditions of interest, this will be the case.

For the Fabry-Perot optical configuration shown in Fig. 1, the cavity threshold gain is given by

$$g_c = -\frac{1}{2Nw} \ln(R_1 R_2). \tag{16}$$

In the optical flux calculation, variations in total optical intensity along the optical axis are neglected, along with all considerations of diffraction and cavity mode structure. Further, a Maxwellian distribution of DF molecular velocities is assumed at all times. Instantaneous velocity redistribution may not be a good assumption for lasing conditions, however, because momentum relaxation may be slower than rotational relaxation [19]. Non-Maxwellian DF velocity distributions would affect the magnitudes of the various DF relaxation rates and the form taken by the principle of detailed balance. When the line-center gain coefficient on a transition vP(J) reaches the cavity threshold, the rotational master equations (9) are solved for the stimulated emission rates (L's) which maintain the equal gain-loss condition

$$\frac{d}{dx}(g_{v-1,J}^{v,J-1} w) = 0. \tag{17}$$

The total intracavity fluxes are then computed from the L's:

$$L_{v-1,J}^{v,J-1} = \frac{g_c I_{v-1,J}^{v,J-1}}{\rho N_A (h\nu)}. \tag{18}$$

All molecular spectroscopic data have been taken from [25].

This analysis individually treats 17 rotational levels per DF vibrational state (for $v \leqslant 4$). Adding the master equations for chemical species, D_2 vibrational states, and translational temperature results in a total of 92 independent rate equations which are integrated simultaneously when making multiline calculations. For line-selection calculations, rotational equilibrium is assumed in all vibrational levels not involved in stimulated processes, and the rotational master equations for these states are removed from the equation set. Numerical integration is carried out using an implicit, Gauss-type finite-difference representation of (2)-(5) and (8). A Newton-Raphson iteration is used to solve the finite-difference expressions.

Because of the simplifications associated with mixing and optical extraction, the power levels predicted by this model will be approximate. The model will be most useful as an indicator of trends.

IV. Results

Sample calculations have been performed for a set of conditions representative of a combustion-driven DF laser (Table I). Although the calculations are presented for a specific set of flow conditions and device dimensions, the results will be pressure-size scalable. As long as attention is restricted to pressures sufficiently low that three-body processes and Lorentz broadening are unimportant, the various species concentrations ($Y_s, y_{vJ}, \cdots$) and extraction efficiency can be correlated by the product of jet pressure and a characteristic length in the system (such as the mixing length). Small-signal gains will scale directly with pressure. Consequently, all of the results to follow are presented in terms of the independent variable px (in torr · centimeters). It is to be understood that for pressures other than that listed in Table I, the mixing length and cavity mirror separation values which apply are determined from the constraint that pl_{mix} and pL_c have the values of Table I. All of the scaling considerations given in the more complete discussion by Warren [26] apply to the rotational nonequilibrium case as well.

For those calculations dealing with line-selected operation it has been assumed that an unspecified line-selection technique (e.g., gas cell absorber, diffraction grating) has succeeded in suppressing oscillation on all unwanted lines. Because losses

TABLE I
INPUT CONDITIONS FOR SAMPLE CALCULATIONS

Primary	Secondary
$T = 300^{\circ}K$	$T = 300^{\circ}K$
$p = 1$ torr	$p = 1$ torr
$u = 2.16 \times 10^5$ cm/sec	$u = 2.12 \times 10^5$ cm/sec
$Y^{\circ}_F = .075$	$Y^{\circ}_{D_2} = .35$
$Y^{\circ}_{He} = .15$ (rel. units)	$Y^{\circ}_{He} = .35$
$Y^{\circ}_{HF} = .075$	

Mixed Zone (x = 0)	Cavity
$T = 300^{\circ}K$	$a_1 = a_2 = 5 \times 10^{-3}$
$p = 1$ torr	$t_1 = 5 \times 10^{-2}$
$u = 2.13 \times 10^5$ cm/sec	$pL_c = 100$ torr-cm
Mach No. = 2.75	
$pl_{mix} = 12.5$ torr-cm	

associated with intracavity gratings have not been taken into account, the calculated line-selected powers will be optimistic.

Fig. 2 displays the axial variation of the DF (v = 2) rotational distribution under small-signal conditions. At $px = 0$ the states have the primitive distribution of [18]. At $px = 0.5$ torr · cm, the distribution has assumed the doubly peaked pattern observed in [18], [21], and [24]. The primitive distribution peak at J = 11 decreases in magnitude while a thermal peak at J = 3 grows. This pattern persists until the relative populations have assumed a Boltzmann distribution.

Because the higher J levels are directly pumped chemically, and possess cross-relaxation rates that are somewhat slower than those for small J, there is a tendency for molecules to become trapped in high-J states. Appreciable nonequilibrium is predicted for high J at relatively large downstream distances. Fig. 3 compares the calculated and equilibrium rotational distributions for three values of px. For $px = 2$ and 4 it can be seen that significant departures from equilibrium are predicted, particularly for $J > 8$. At $px = 10$, the distribution is essentially thermalized. It is evident that the relaxation of the v = 2 rotational manifold cannot be characterized by a single time constant. Experimental observation of the nonequilibrium from sidelight emission would, of course, depend on the pressure level and the location of the viewing port. There is experimental evidence which suggests the presence of rotational nonequilibrium at low pressure [27]. It is also possible that the high-J states could relax through stimulated emission on pure rotational transitions; as will be seen, the calculated gains on such transitions are quite large.

Fig. 4 displays the calculated small-signal gain coefficients for $2P(4)$, $2P(9)$, and $2P(12)$. As seen, the thermal equilibrium gain for $2P(4)$ and $2P(9)$ is in error for low values of px, but is generally adequate for most axial locations of interest. For $2P(12)$, however, the thermal equilibrium assumption is in serious error over a significant range, and is valid only for $px > 10$ torr · cm. As will be seen, experimental support for

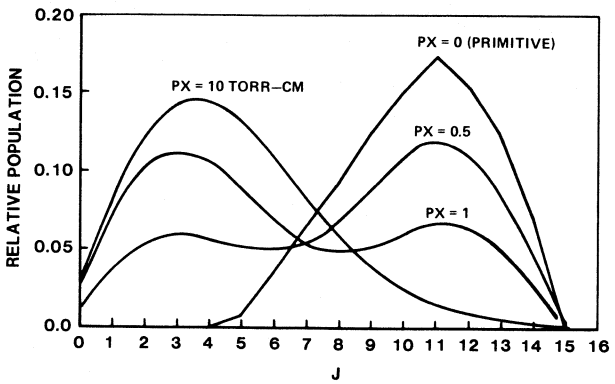


Fig. 2. Relaxation of DF(v = 2) rotational levels.

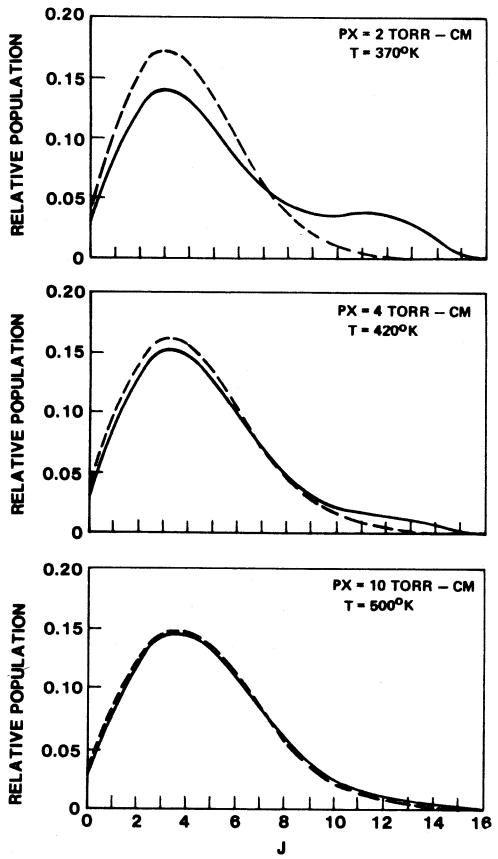


Fig. 3. Rotational distribution of DF(v = 2) compared with thermal equilibrium at selected axial locations. ——— nonequilibrium rotational kinetics; ----- thermal equilibrium.

this predicted behavior is provided by the fact that these high-J P branches have been observed to begin lasing very close to the nozzle exits [7]. The gains presented in Fig. 4 are the calculated gains in the mixed zone, and have not been averaged over the active and inactive regions of the flow.

One feature of these calculations is that gain coefficients on pure rotational transitions can be calculated. Lasing on HF(v, J) → HF(v, J - 1) transitions has been observed experimentally in pulsed and optically pumped systems [28], [29]. Fig. 5 presents the results of such calculations for pure rotational transitions within the v = 2 manifold. As seen, the predicted peak gains for $p = 5$ torr are very large (>100 percent/centimeter) but persist over a relatively short length scale

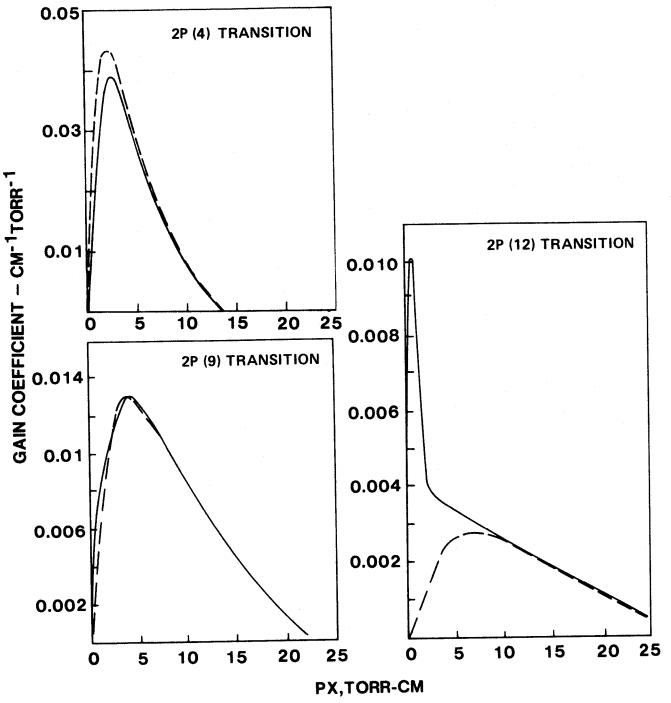


Fig. 4. Small-signal gain profiles for $2P(4)$, $2P(9)$, and $2P(12)$. ——— nonequilibrium rotational kinetics; ------ thermal equilibrium.

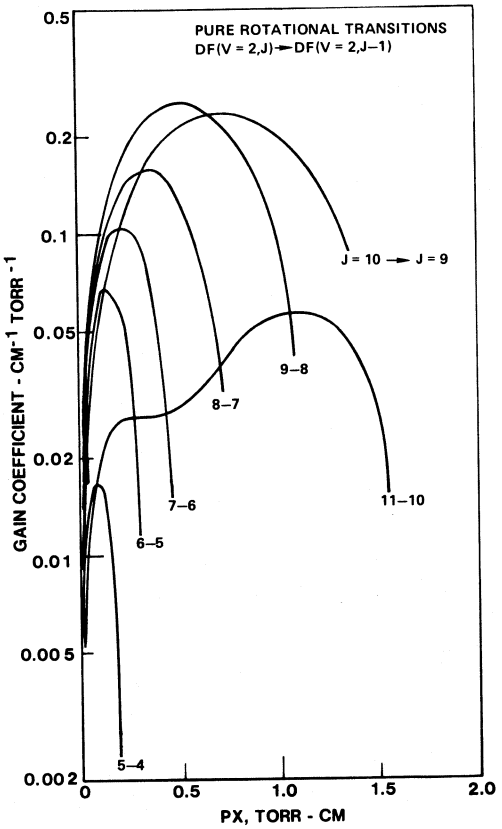


Fig. 5. Calculated small-signal coefficients on pure rotational transitions for DF(v = 2).

(<0.5 cm). Despite the short lifetime of these pure rotation inversions, there appears to be a possibility that lasing would be observed on them; transitions possessing such large gains would probably be subject to parasitic oscillations. The magnitude of the predicted gains is consistent with the estimates of [29].

The results of a multiline optical flux calculation are shown in Fig. 6. Intracavity fluxes for the P branches belonging to DF(v = 2 → v = 1) transitions have been plotted as a function of px. The most obvious difference between these flux profiles and those computed on the basis of rotational equilibrium is the fact that spatially overlapping P-branch emission is predicted. In the nonequilibrium model, numerous P branches belonging to the same vibrational transition oscillate simultaneously. The nonequilibrium model does predict sequential switching off of P branches with distance, although profiles are always overlapped. The highest P branches begin oscillating close to the nozzle exits; for the 2-1 band the actual P-branch initiation sequence follows the v = 2 nascent rotational distribution fairly closely. The intensity profiles for $2P(11)$ and $2P(12)$ actually exhibit two maxima; the first is due to the initial dominance of the chemical pumping rate, and the second reflects the tendency for maximum gain to switch to higher P branches downstream. Maximum intensity shifts from $P(6)$ to $P(9)$ over the distance shown. This shifting, which is also predicted by the rotational equilibrium models, is due to translational temperature increase and a decreasing effective vibrational temperature resulting from deactivation and stimulated emission.

The variation of P-branch spectra with vibrational band is shown in Fig. 7 for an axial distance of 2.87 torr · cm from the nozzle exits. High-lying P-branch emissions are observed for 1-0 and 2-1 transitions close to the nozzle exits. As the vibrational quantum number increases, the maximum intensity tends to occur on lower J lines. This behavior reflects the influence of cascades and the fact that the primitive rotational distribution of the pumping reaction (6) becomes less energetic as the vibrational quantum number increases. The qualitative behavior of these theoretical spectra is in very good agreement with experimental measurements. Fig. 8 presents a measured output spectrum from the combustion-driven DF laser experiments described in [7]. In this particular experiment the cavity mode diameter is 1.8 mm and is centered 3.2 mm downstream from the nozzle exits. As seen, high-lying P branches are observed at this relatively close axial location, as is the downward shift of maximum intensity P branch with increasing vibrational band. A comparison of these experimental results with the predictions of the Fabry-Perot flux model should be valid because of the narrow width of the mode (1.8 mm) relative to the farthest downstream distance at which stimulated emission was observed (15.2 mm). Inclusion of rotational nonequilibrium effects in the theoretical model thus resolves the discrepancy between theory and experiment concerning the spatial distribution of high P-branch emission. Rotational equilibrium codes or nonequilibrium analyses which assume thermal primitive distributions will be in disagreement with experiment on this point.

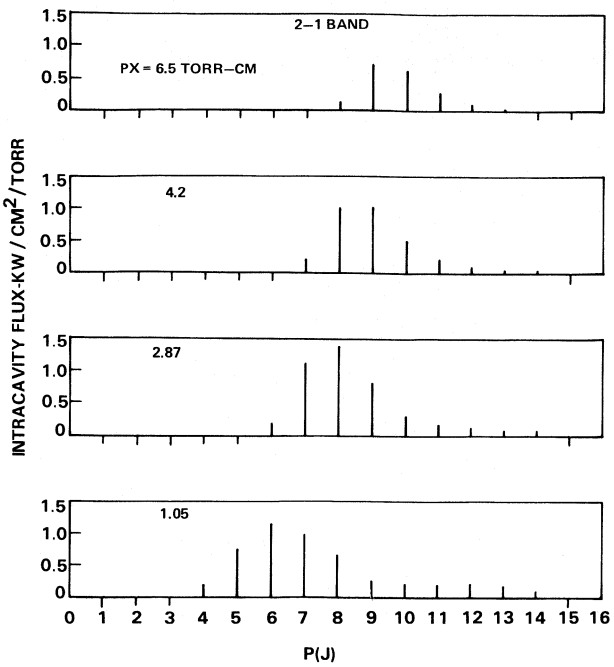


Fig. 6. Optical flux values for v = 2 → v = 1 P branches at selected axial locations.

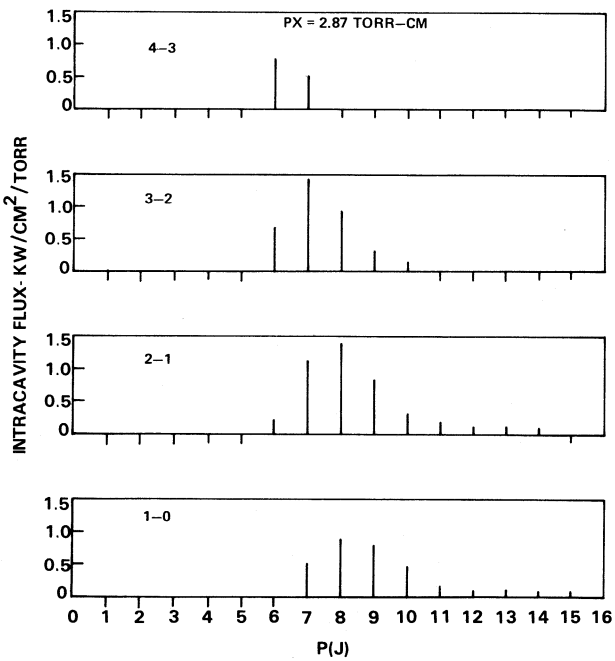


Fig. 7. Variation of spectral distribution with vibrational band at fixed axial location.

Finite-rate rotational relaxation also results in quantitative changes in predicted output power. In rotational-equilibrium flux calculations the oscillating P branch can draw energy instantaneously from all other rotational states having the same vibrational quantum number. In the nonequilibrium model, however, energy is supplied from adjacent J levels at a finite rate, during which time the upper laser level can be subjected to loss processes (such as VT relaxation). It is of interest to

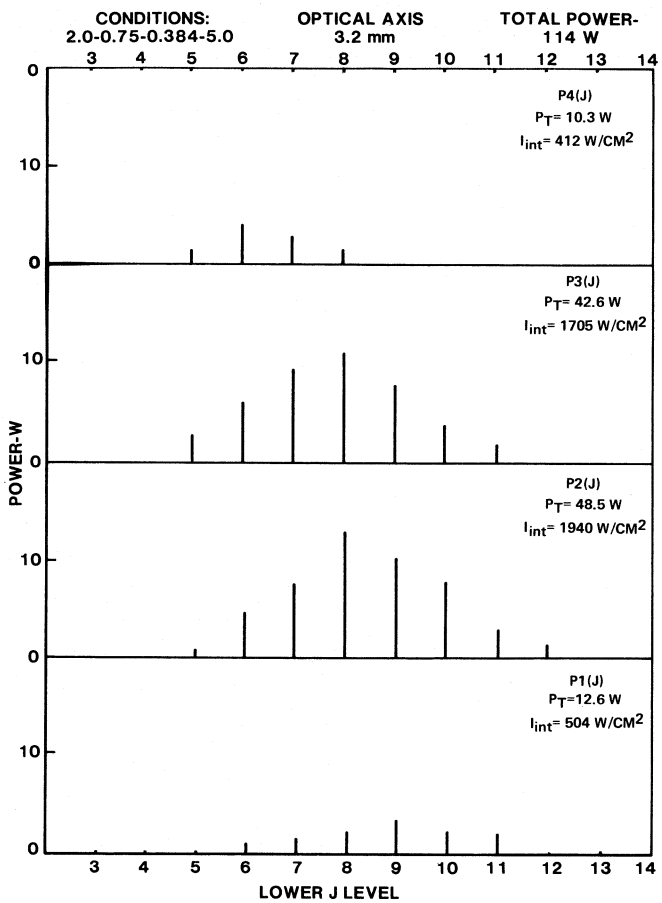


Fig. 8. Experimental power spectrum at fixed axial location for combustion-driven DF laser. Reproduced from [7, p. 184, fig. 90]. P_T and I_{int} are total extracted power and intensity for each vibrational band, respectively.

examine the predicted power loss due to finite cross-relaxation rates.

Table II compares the predictions of the equilibrium and nonequilibrium models for multiline, cascade, and single-line operation. The power output is given in efficiency units, defined as the extracted optical power divided by the product of reaction (6) enthalpy release and total molar flow of F atoms. Considering the rotational equilibrium calculations first, it is interesting to note that operation on a straight-channel cascade such as $4P(7)$-$3P(8)$-$2P(9)$-$1P(10)$ is predicted to be highly efficient (~90 percent) relative to multiline operation. Single-line operation on $2P(9)$ is predicted to involve a power loss of about 75 percent relative to the multiline case. Overall power output for the nonequilibrium mulitline case is about 86 percent that computed assuming rotational equilibrium. The assumption of rotational equilibrium may, therefore, give rise to slightly overoptimistic multiline performance projections. For single-line operation [$2P(9)$] the difference between the two models is more significant; the finite rate prediction is about 65 percent that of the rotational equilibrium model.

If the nonoptically connected sequence of transitions $4P(7)$-$3P(9)$-$2P(8)$-$1P(10)$ (mixed cascade) is chosen for lasing, the predicted power is only 70 percent that predicted

TABLE II
SUMMARY OF LINE-SELECTED POWER OUTPUT EFFICIENCY

	Multiline All P-branches	Quartet 4P(7)-3P(8)-2P(9)-1P(10)	Doublet 2P(9)-1P(10)	Singlet 2P(9)
Equilibrium Rotational States	.274	.237	.131	.065
Nonequilibrium Rotational Kinetics	.236	.193	.104	.043

for the straight-channel cascade sequence $4P(7)$-$3P(8)$-$2P(9)$-$1P(10)$. The mixed doublet $2P(9)$-$1P(9)$ produces an optical power output that is 89 percent that of the straight-channel doublet $2P(9)$-$1P(10)$. These results emphasize a tendency for power output to occur in optically connected channels.

Adding adjacent doublets to the transition sequence $2P(9)$-$1P(10)$ results in relatively modest power increases. It appears that additional doublets belonging to the same vibrational bands merely compete for available inversion. This result would also be expected for the singlet, triplet, and quartet modes. It appears, therefore, that it is most important to have one P branch per band that is optically connected to lines in adjacent vibrational bands. However, as will be seen, very low and very high P branches must be avoided for maximum efficiency.

Calculations have also been performed to determine to what extent the foregoing conclusions are functions of cavity output coupling, t, and active medium length, L_c. It might be expected that the power loss due to rotational nonequilibrium would be increased in the limits $t \to 0$ (closed cavity) and $L_c \to \infty$. For single-line $2P(9)$ operation it has been found that the absolute power loss due to rotational nonequilibrium does increase as $t \to 0$, but that the ratio of nonequilibrium to equilibrium efficiency is sensibly independent of t. Similarly, at fixed t the efficiency ratio is independent of L_c for larger values of L_c. Because the unsaturated gain is not too much different for the equilibrium and finite rate models (Fig. 4), it appears that this behavior can be interpreted simply in terms of different saturation intensities [30]. The saturation intensity for single-line $2P(9)$ operation is apparently reduced by about 35 percent due to rotational nonequilibrium.

Fig. 9 displays the magnitudes of some of the rate processes contributing to the time rate of change of DF (v = 2, J = 8) for single-line operation on $2P(9)$. In the rotational equilbrium calculation, the stimulated emission rate rises rapidly to a value comparable to the total chemical production rate for DF(v = 2). Considering the rotational nonequilibrium case, it is evident that finite rotational kinetics significantly retards the stimulated emission rate. Near the nozzle exits the lasing is driven by direct chemical pumping of DF(v = 2, J = 8), with little cross relaxation. The stimulated emission rate then rises as cross relaxation supplies population from adjacent states. However, the maximum emission rate is limited by finite cross relaxation to a value well below that for rotational equilibrium. In the downstream portion of the cavity the optical intensity decreases, and the emission rate approaches the equilibrium value. The slowed removal of optical energy in the upstream region of the flow gives the various kinetic processes time to act, and hence accounts for the power loss due to rotational nonequilibrium.

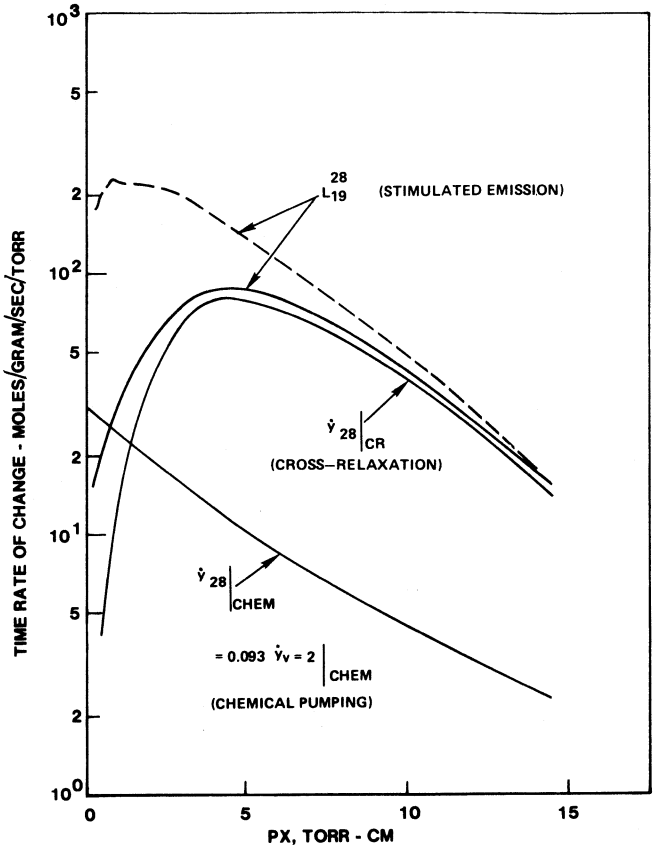


Fig. 9. Magnitude of kinetic processes affecting upper laser level in single-line operation. ——— nonequilibrium rotational kinetics; ----- thermal equilibrium.

The question of single-line efficiency has been found to be dependent on the particular P branch selected for operation. Table III presents the calculated efficiencies for operation on $2P(6)$, $2P(9)$, and $2P(12)$. It can be seen that the equilibrium and nonequilibrium models predict much different trends with $P(J)$. Considering the rotational nonequilibrium calculations, it is apparent that the least efficient line is $2P(12)$. This relative inefficiency is a consequence of the slower cross-relaxation rates affecting the higher J levels; this effect appears to override the fact that the upper laser level, v = 2, J = 11, is the most strongly pumped state in the v = 2 manifold. Because RR and RT relaxation rates are most rapid for low J, $2P(6)$ shows the smallest power decrease relative to the equi-

TABLE III
POWER OUTPUT EFFICIENCY FOR SINGLE-LINE OPERATION

	2P(6)	2P(9)	2P(12)
Nonequilibrium	.035	.043	.019
Equilibrium	.041	.065	.075

librium calculation. However, the largest absolute power output can be expected from an intermediate-J transition such as $2P(9)$.

Because of the uncertainty surrounding the rotational cross-relaxation model, the sensitivity of the calculated results to variations in these rates has been considered. In the cross-relaxation model there are numerous unknown parameters governing the magnitude and scaling of the rate coefficients; rather than varying all of these systematically, the rate model uncertainty has been simulated by multiplying all rate constants by a constant factor. Table IV presents the results of calculations in which the base relaxation rates have been increased and decreased by a factor of 5. Moderate departures from the multiline base rate prediction are predicted for both the fast and slow rates. For single-line operation, however, the sensitivity of predicted power output to relaxation rates is much larger. The changes that occur in the spectral distribution of cumulative power output for 2-1 transitions are shown in Fig. 10. As the cross-relaxation rate constants are increased, the spectrum maximum shifts toward higher $P(J)$ and assumes a narrower distribution over the $P(J)$. Rapid cross-relaxation rates enable a few lines to suppress oscillation on other P branches. The rotational equilibrium spectrum is shown for comparison.

Variations in mixing length can cause noticeable changes in the spectral distribution of power output for the rotational nonequilibrium case. As the mixing length approaches zero, there is more of a tendency for the spectral distribution to reflect the nascent rotational distributions. In this limit, high-lying P-branch emission becomes more dominant near the nozzle exits, and a relatively large number of P branches per vibrational band oscillate simultaneously. For very long mixing lengths, however, the rotational distribution will be substantially thermalized before cavity threshold (16) is reached. High-lying P branches will then be absent from the upstream portion of the cavity. Because the rotational distribution at threshold will be nearly Boltzmann, relatively few P branches per vibrational band will oscillate at a given axial location.

V. CONCLUSIONS

While it is difficult to generalize the results of calculations for one set of conditions to a whole class of laser devices, it does appear that rotational nonequilibrium is an important effect in DF/HF CW chemical lasers. Because of uncertainties surrounding the rotational relaxation rate constants for DF, the conclusions which can be drawn must be qualitative at this time. It appears that the question of whether or not rotational equilibrium is a valid approximation in CW devices depends strongly on the rotational quantum state of interest.

TABLE IV
VARIATION OF POWER OUTPUT EFFICIENCY WITH CROSS-RELAXATION RATES

	Multiline	Single Line (2P(9))
Base Rates	.236	.043
$(\frac{1}{5})$ x Base Rates	.197	.02
5 x Base Rates	.260	.058

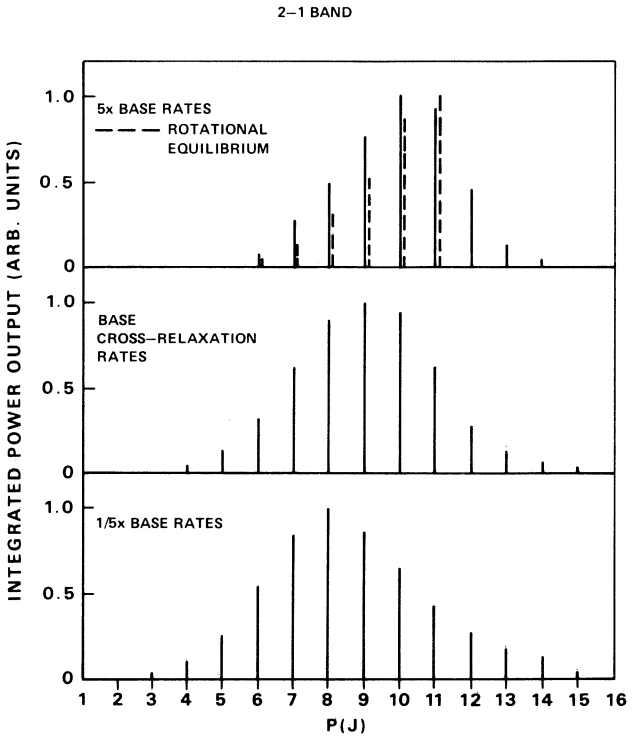


Fig. 10. Variation of cumulative spectral distribution with cross-relaxation rates. Multiline operation.

For high-J levels there appears to be appreciable overlap of the time scales associated with chemical pumping and collisional thermalization; substantial departures from thermal equilibrium are predicted for high-lying rotational states even under small-signal conditions. Most importantly, the rotational nonequilibrium model explains qualitative features of observed DF chemical laser spectra that rotational equilibrium models cannot explain. In addition to predicting spatially overlapping P-branch emission, the model explains the appearance of high-lying P-branch emission near the nozzle exits, and indicates the possibility of pure rotational lasing. The primitive rotational distributions play an important role in the explanation of these effects. The analysis suggests that rotational nonequilibrium causes a modest (~15-percent) performance decrease for multiline operation, and predicts that straight-channel cascades will be highly efficient. Single-line operation is predicted to involve larger performance penalties. However, quantitative conclusions about the efficiency of line-selected operation are not warranted at this time because of uncertainties in rotational relaxation rates, particularly those for high J. Modeling of CW DF/HF chemical

lasers is incomplete without consideration of rotational nonequilibrium phenomena; however, much more information on cross-relaxation rate coefficients must be made available before the predictions of analyses such as this can be regarded as quantitative.

ACKNOWLEDGMENT

The author wishes to acknowledge helpful conversations with Dr. J. J. Hinchen, Dr. R. H. Hobbs, and Dr. L. Lynds.

REFERENCES

[1] G. Emanuel, W. D. Adams, and E. B. Turner, "RESALE-1: A chemical laser computer program," Aerospace Corporation, El Segundo, CA, Rep. TR-0172 (2776)-1, Mar. 1972.

[2] R. L. Kerber, G. Emanuel, and J. S. Whittier, "Computer modelling and parametric study for a pulsed $H_2 + F_2$ laser," *Appl. Optics*, vol. 11, pp. 1112–1123, June 1972.

[3] R. A. Meinzer, R. J. Hall, and B. R. Bronfin, "CW combustion-mixing laser: HF, DF," presented at 6th Int. Quantum Electronics Conf., Kyoto, Japan, Sept. 1970.

[4] J. G. Skifstad, "Theory of an HF chemical laser," *Combustion Science and Technology*, vol. 6, pp. 287–306, 1972.

[5] W. S. King and H. Mirels, "Numerical study of a diffusion-type chemical laser," *AIAA Journal*, vol. 10, pp. 1647–1654, 1972.

[6] S. N. Suchard *et al.*, "Time-resolved spectroscopy of a flash-initiated $H_2 + F_2$ laser," *Appl. Phys. Lett.*, vol. 19, pp. 411–413, 1971.

[7] A. W. Angelbeck *et al.*, "Investigation of master oscillator power amplifier systems for chemical lasers," United Technologies Research Center, East Hartford, CT, Final Tech. Rep. under Contract AFWL-TR-F29601-73-C-0072, Sept. 1975.

[8] J. J. T. Hough and R. L. Kerber, "Theoretical investigation of the effect of rotational nonequilibrium on predicted performance of pulsed HF chemical lasers," Paper TA7, presented at 4th Conference on Chemical and Molecular Lasers, St. Louis, MO, Oct. 21–23, 1974.

[9] T. D. Padrick and M. A. Gusinow, "Evidence for rotational nonequilibrium in the $CH_3I + N_2F_4$ chemical laser," *Chem. Phys. Lett.*, vol. 24, pp. 270–274, 1974.

[10] J. R. Creighton and R. K. Pearson, "Calculation of rotational nonequilibrium in a pulsed HF laser," Paper TA8, 4th Conference on Chemical and Molecular Lasers, Paper TA8, St. Louis, MO, Oct. 21–23, 1974.

[11] J. B. Moreno, "Computer model for the $H_2 + F_2$ super-radiant laser," presented at AIAA 13th Aerospace Sciences Meeting, Paper 75–36, Pasadena, CA, Jan. 20–22, 1975.

[12] J. G. Skifstad and C. M. Chao, "Rotational relaxation in a line-selected continuous HF chemical laser," *Applied Optics*, vol. 14, pp. 1713–1718, 1975.

[13] L. H. Sentman, "Rotational nonequilibrium in cw chemical lasers," *J. Chem. Phys.*, vol. 62, pp. 3523–3537, 1975.

[14] J. E. Broadwell, "Effect of mixing rate on HF chemical laser performance," *Applied Optics*, vol. 13, pp. 962–967, 1974.

[15] N. Cohen, "A Brief review of rate coefficients for reactions in the D_2–F_2 chemical system," Aerospace Corporation Rep. SAMSO-TR-74-14, Jan. 1974.

[16] K. H. Homann *et al.*, "Eine Methode zur Enzengang von Fluorstomer in Inerten Atmosphäre," *Ber. Bunsen, F. Phys. Chem.*, vol. 74, pp. 585–589, 1970.

[17] A. Persky, "Kinetic isotope effects in the reaction of fluorine atoms with molecular hydrogen, I. H_2/D_2 kinetic isotope effect," *J. Chem. Phys.*, vol. 59, pp. 3612–3615, 1973.

[18] J. C. Polyani and K. B. Woodall, "Energy distribution among reaction products. VI. $F + H_2$, D_2," *J. Chem. Phys.*, vol. 57, pp. 1574–1586, 1972.

[19] J. J. Hinchen and R. H. Hobbs, "Rotational relaxation studies of HF using double I.R. resonance," United Technologies Research Center, East Hartford, CT, Final Tech. Rep. under Office of Naval Research Contract N00014-74-C-0378, July 1975.

[20] J. J. Hinchen, "Rotational population transfer in HF," *Appl. Phys. Lett.*, vol. 27, pp. 672–673, 1975.

[21] J. C. Polyani and K. G. Woodall, "Mechanism of rotational relaxation," *J. Chem. Phys.*, vol. 56, pp. 1563–1572, 1972.

[22] R. Herman and K. E. Shuler, "Studies in nonequilibrium rate processes, IV. The rotational and vibrational relaxation of a system of rotating oscillators," *J. Chem. Phys.*, vol. 29, pp. 366–374, 1958.

[23] L. M. Raff and T. G. Winter, "Origin of the temperature dependence of the ultrasonic 'rotational relaxation' time," *J. Chem. Phys.*, vol. 48, pp. 3992–4000, 1968.

[24] W. H. Duewer and D. W. Setser, "Infrared chemiluminescence and energy partitioning from reactions of fluorine atoms with hydrides of carbon, silicon, oxygen, sulfur, nitrogen, and phosphorous," *J. Chem. Phys.*, vol. 58, pp. 2310–2320, 1973.

[25] R. E. Meredith and F. G. Smith, "Investigations of fundamental laser processes, vol. II: Computation of electric dipole matrix elements for hydrogen fluoride and deuterium fluoride," Willow Run Laboratories, Final Tech. Rep. under ARPA Contract DAHC-15-67-C-0062, Nov. 1971.

[26] W. R. Warren, "Chemical lasers," *Astronautics and Aeronautics*, vol. 13, pp. 36–49, 1975.

[27] F. Mastrup *et al.*, "Hydrogen fluoride laser technology study," TRW Systems Group, Final Tech. Rep. under AFWL Contract TR-72-28, Feb. 1972.

[28] T. F. Deutsch, "Laser emission from HF rotational transitions," *Apply. Phys. Lett.*, vol. 11, pp. 18–20, 1967.

[29] N. Skribanowitz *et al.*, "Anisotropic ultrahigh gain emissions observed in rotational transitions in optically pumped HF gain," *Appl. Phys. Lett.*, vol. 20, pp. 428–431, 1972.

[30] W. W. Rigrod, "Saturation effects in high-gain lasers," *J. Appl. Phys.*, vol. 36, pp. 2487–2491, 1965.

The Prism Coupler and the Dielectric Bend: Similarities and Anomalous Behavior

MORDEHAI HEIBLUM, STUDENT MEMBER, IEEE

Abstract—**Properties of the output prism coupler and the dielectric bends are investigated near cutoff. A decrease in the attenuation very close to cutoff is exhibited by the prism coupler and might be possible also in the bend case. Range of validity of the established approximated solutions is discussed.**

I. Introduction

A CONFORMAL transformation approach to curved dielectric waveguides was recently presented [6]. In carrying out calculations of attenuation for bends with radii close to cutoff, we unexpectedly found that attenuation appears to reach a maximum and then decrease for smaller radii of curvature, a result which might be of importance in very sharp bends. Since the WKB approximation is made in the analysis, we had to examine the result very carefully, and to attempt to explain it physically. The approach to this has been to note the similarity to the prism coupler, equations for which can be solved exactly although they are usually done approximately also. This paper then is to show the similarity between the radiation in curved dielectric bends and the energy transfer phenomenon in an output prism coupler, and to present calculated results for both in regimes for which they are not usually available.

Many papers were written about the prism coupler; among them the most important ones are those by Harris and Shubert [1] and by Tien and Ulrich [2]. The curved waveguides were investigated thoroughly by Marcatili [3] and Marcuse [4] in the limit of large radii. The theory has been extended to small radii—utilizing a conformal transformation—in [5] and [6]. While in [5] the transformed index is approximated by straight lines but the solution of this modeling is accurate, in [6], the transformed index profile is accurate but a WKB-type solution is adopted leading to a very similar solution to that of a prism coupler. In both cases, when the leaky modes approach cutoff, the well-known closed-form expression for the attenuation in the prism coupler case ([1] and [2]) and the expression for the attenuation in bends (given in [6]), fail to give correct results. A numerically *accurate* solution for the prism coupler and an improved numerical solution for the bend lead to similar results.

The results are not expected, since they predict that in many cases the attenuation constant drops from a maximum value, when the modes approach cutoff. At this regime, in the prism-coupler case, the real part of the longitudinal propagation constant and the thickness of the film at cutoff diverge considerably from the approximated values that are known.

In the following sections the similarity between the prism coupler and the bend configurations will be demonstrated, while reviewing the approximated methods of solutions (Section II). Then the limitation of the approximated results will be discussed, and numerical results for the propagation constants in a few different cases will be presented (Section III).

Manuscript received January 21, 1976; revised April 11, 1976. This work was supported by the National Science Foundation under Grant ENG73-08077.

The author is with the Departments of Electrical Engineering and Computer Sciences and the Electronics Research Laboratory, University of California, Berkeley, CA 94720.

II. Perturbation-Type Solutions for the Prism Coupler and the Dielectric Bend

The usual approach in attacking the prism-coupler problem is to look on the prism as a perturbation to a three-layer configuration, which supports guided modes (Fig. 1).

To solve first the substrate-film-superstrate problem one considers the boundary conditions by forming four homogeneous equations (two for the electric field and two for the magnetic field). These will have a solution only if the determinant of the coefficients is zero

$$D_{1,3} = 0 \tag{1}$$

where D denotes the determinant and the subscripts 1 and 3 refer to the substrate and superstrate, respectively. Solving for (1), one obtains the following equation [1]:

$$u_2 t_2 - \tan^{-1}\left(\frac{K_1}{iK_2}\right) - \tan^{-1}\left(\frac{K_3}{iK_2}\right) = m\pi \tag{2}$$

where $u_i = (k_0^2 n_i^2 - k_z^2)^{1/2}$ is the transverse propagation constant in layer i, k_z is the longitudinal propagation constant, K_i is u_i/n_i^2 for TM waves (E_z, Ex, Hy) and u_i for TE waves (Hz, Hx, Ey), k_0 is the wavenumber of free space, n_i is the index of refraction of layer i, t_2 is the film thickness, and m is an integer (0, 1, 2, $\cdots$) that describes the mode order. Solutions for (2) are found numerically and result in a real k_z. When the prism is mounted on top of the waveguide leaving a narrow tunneling gap, the longitudinal propagation constant k_z changes to give

$$D_{1,4} = 0. \tag{3}$$

The solution of (2) will be denoted as the zeroth-order approximation ($k_z^{(0)}$), for (3). The commonly made assumption is that $|k_z - k_z^{(0)}| \ll k_z^{(0)}$, and as a result of this assumption, $D_{1,3}(k_z) - D_{1,3}(k_z^{(0)}) = D_{1,3}(k_z) = \epsilon$, where ϵ is very close to zero. Following this line of thought, the following identity for the determinants is used (for more details about the determinants $D_{r,s}$ and notation see [7]):

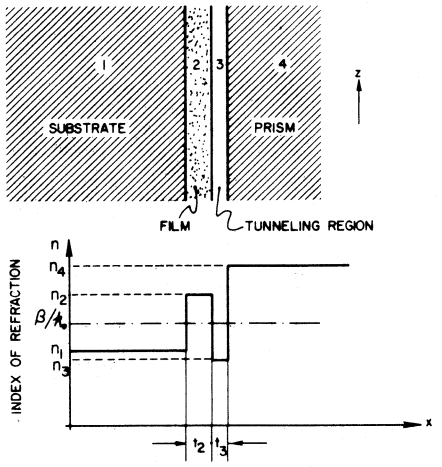


Fig. 1. A two-dimensional prism-coupler configuration, and its index profile.

$$D_{1,4} = D_{1,3}D_{3,4} - D'_{1,3}{}'D_{3,4} \tag{4}$$

when the postprimes and preprimes are defined as follows:

$$D'_{i,j}(u_i, \cdots, u_j) = D_{i,j}(u_i, \cdots, -u_j)$$
$$'D_{i,j}(u_i, \cdots, u_j) = D_{i,j}(-u_i, \cdots, u_j). \tag{5}$$

Using (5) in (4) and (3) gives

$$\frac{D'_{1,3}(k_z)}{D_{1,3}(k_z)} = \frac{D_{3,4}(k_z)}{'D_{3,4}(k_z)}. \tag{6}$$

Since $D_{1,3}(k_z) = \epsilon$, (6) can be approximated by

$$\frac{D'_{1,3}(k_z^{(0)})}{\frac{\partial}{\partial k_z} D_{1,3}(k_z^{(0)})(k_z - k_z^{(0)})} = \frac{D_{3,4}(k_z^{(0)})}{'D_{3,4}(k_z^{(0)})}. \tag{7}$$

$k_z - k_z^{(0)}$ is a complex correction to $k_z^{(0)}$ and will be denoted as $k_z^{(1)} + i\alpha$. Evaluation of (7) leads to

$$k_z^{(1)} + i\alpha = \frac{u_2}{\left(t_2 + \frac{1}{|K_1|} + \frac{1}{|K_3|}\right) k_z^{(0)}} \frac{2|K_3|K_2}{K_2^2 + |K_3|^2} \exp(-2|u_3|t_3)$$
$$\times \left[\frac{|K_3|^2 - K_4^2}{|K_3|^2 + K_4^2} + i\frac{2|K_3|K_4}{|K_3|^2 + K_4^2}\right]. \tag{8}$$

The imaginary part in (8) is the common expression for the leaking rate from the output prism coupler. Obviously (8) fails near cutoff, namely, when either K_3 or K_1 approaches zero, depending on whether $n_3 > n_1$ or $n_1 > n_3$, respectively.

Let us turn our attention now to the dielectric curved two-dimensional waveguide. The extension of the results obtained in [3] and [4] to the regime of small radii was possible by employing the conformal transformation

$$W = R \ln Z/R \tag{9}$$

where $W = u + iv$, $Z = x + iy$, and R is the radius of some circle in the x-y plane. As a result of (9) the boundaries of a guide with arcs as boundaries in the x-y plane become parallel straight lines in the u-v plane. The index of refraction varies as $n \exp(u/R)$ in the transverse direction u, and remains constant along the coordinate v. Fig. 2 describes transformations of a two-boundary bend and a single-boundary ($R_1 = 0$) bend, where R in (9) was chosen to be R_2. The transformed index profile of the bend resembles strongly the index profile of the prism-coupler configuration, and the higher index to the right forces all the modes to be leaky. Whenever $k_v/k_0 > n_2(R_1/R_2)$ where k_v is the longitudinal propagation constant and k_0 is the wavenumber in vacuum, or for small radii when $n_2(R_1/R_2) < n_3$, the two-boundary bend behaves approximately as a one-boundary bend (namely, the left-hand-side turning point is continuous and not abrupt). The expressions for a single-boundary bend will be used since they are easier to deal with (the extension to double-boundary bends can be found in [6]).

In Fig. 2, associating the region $u < u_1 = -R_2 \ln k_0 n_2/\beta$, where β stands for k_v, with the substrate, $u_1 < u < 0$ with the film, and $u > 0$ with the superstrate, $D_{1,3} = 0$ has the following form for TE waves [6]:

$$\int_{u_1}^{0} k_u(u)du - \tan^{-1}\frac{k_u(0+)}{ik_u(0-)} - \frac{\pi}{4} = m\pi \tag{10}$$

where $k_u(u) = (n^2(u)k_0^2 - k_v^2)^{1/2}$, k_v is the longitudinal wavenumber, and $0+$ and $0-$ are close points to the right and to the left of $u = 0$, respectively. A first-order WKB-type solution was employed to calculate $D_{1,3}$, and $k_u(u_{1+})/k_u(u_{1-})$ was assumed to take the value unity, where u_{1+} and u_{1-} are points to the right and to the left of the turning point u_1. Carrying out the integration in (10) leads to the eigenvalue equation of a single-boundary bend:

$$R_2 k_v \left[\left(\frac{k_0^2 n_2^2}{k_v^2} - 1\right)^{1/2} - \cos^{-1}\frac{k_v}{k_0 n_2}\right] - \tan^{-1}\left(\frac{k_v^2 - k_0^2 n_3^2}{k_0^2 n_2^2 - k_v^2}\right)^{1/2}$$
$$- \frac{\pi}{4} = m\pi. \tag{11}$$

A numerical solution of (11) results in a real $k_v^{(0)}$ that is assumed to be the zeroth-order approximated solution to the complete index profile.

The index profile to the right of $u = 0$ is introduced now as a perturbation. Following the same steps as in (3)-(8), the first-order correction to $k_v^{(0)}$ is a pure imaginary number that is denoted as $i\alpha$:

$$i\alpha = i\frac{2k_u(0-)|k_u(0+)|}{k_u^2(0-) + |k_n(0+)|^2}$$
$$\cdot \exp\left\{2R_2|k_u(0+)| - 2\beta R_2 \ln\frac{\beta + |k_u(0+)|}{k_0 n_3}\right\}$$
$$\times \left[\frac{\beta}{k_u(0-)\cdot|k_u(0+)|} + R_2 \cos^{-1}\frac{\beta}{k_0 n_3}\right]^{-1} \tag{12}$$

where $\beta \equiv k_v^{(0)}$. The above expression for $i\alpha$ collapses when $k_u(0+)$ approaches zero, namely when β is close to $k_0 n_3$.

In the next section the limitations of the perturbation-type solution will be investigated and (8) and (2) will be compared with more rigorous numerical results.

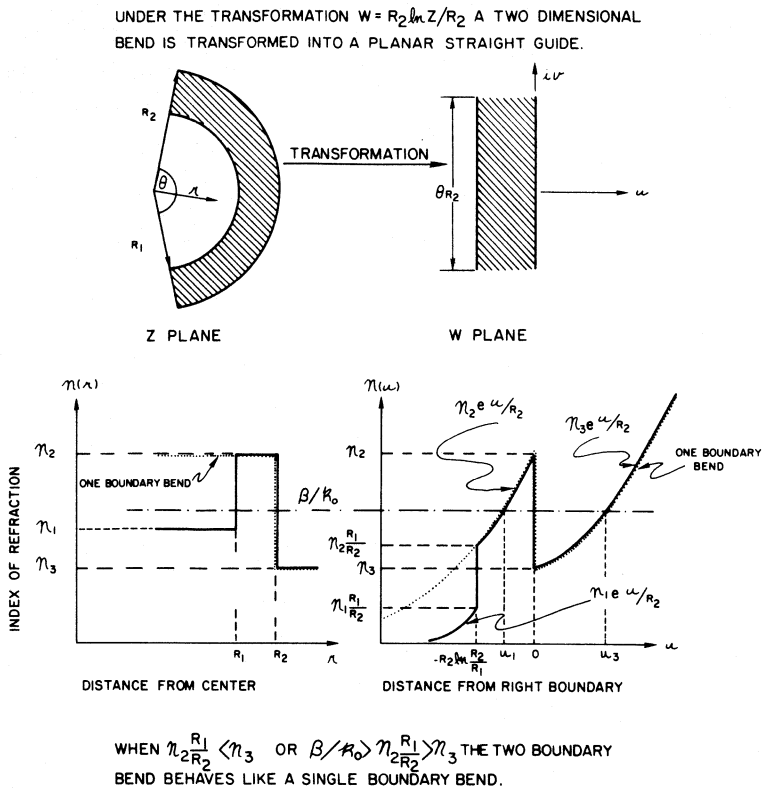


Fig. 2. A conformal transformation of a double- and single-boundary, two-dimensional dielectric bend. The transformed index profile is exponential. A possible mode (β/k_0) is illustrated for example. The mode has three turning points, two of them are continuous (u_1, u_3) and one is abrupt ($u = 0$).

III. Improved Solutions for the Prism Coupler and the Dielectric Bend

The reason that (8) and (2) collapse near cutoff is that the higher index regimes to the right of the guiding regions are no longer small perturbations. Mathematically, $D_{1,3}(k_z)$ and $D_{1,3}(k_v)$ are no longer small numbers. If one again checks the first-order approximation for $D_{1,3}$ in the case of the prism coupler, one finds

$$\frac{\partial}{\partial k_z} D_{1,3}(k_z^{(0)}) = -\frac{k_z^{(0)}}{u_2}\left[t_2 + \frac{1}{|K_1|} + \frac{1}{|K_3|}\right]$$
$$= -t_2' \cdot \tan\theta = -L. \tag{13}$$

Since $1/|K_3|$ is the decay distance in region 3 and $1/|K_1|$ is the decay distance in region 1

$$t_2' \equiv t_2 + \frac{1}{|K_1|} + \frac{1}{|K_3|}$$

is usually called the "effective width" of the waveguide. Tan $\theta = k_z^{(0)}/u_2$ is the slope of the wave normal in the guide with respect to the normal to the walls, and so $L = t_2' \cdot \tan\theta$ describes the "effective longitudinal ray length" between two successive bounces of a ray with the waveguide walls (Fig. 3). Away from cutoff L decreases with $k_z^{(0)}$, but close to cutoff, the evanescent regions take over (K_1 and K_3 become small) and L starts increasing sharply with the reduction of $k_z^{(0)}$. In this regime $D_{1,3}(k_z) = -L \cdot (k_z - k_z^{(0)})$ is a growing quantity not much smaller than unity anymore, causing the first-order approximation to collapse. Exactly the same flaw occurs in

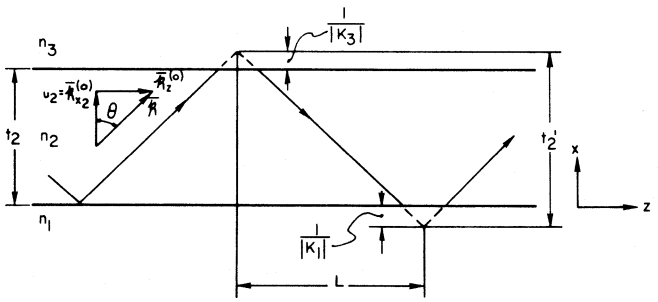


Fig. 3. The "effective thickness" (t_2') and the "effective longitudinal ray length" (L) in a two-dimensional planar waveguide. $1/|K_1|$ and $1/|K_3|$ are the decay distances and $k_z^{(0)}$ is the zeroth-order approximation for the longitudinal wavenumber.

the curved waveguide solution near cutoff. The exact solutions of $D_{1,4} = 0$ can be found rather easily by sacrificing the convenience of having a closed-form expression for $i\alpha$.

To begin with, the prism coupler, $D_{1,4}$ is evaluated (as in [1]). Using (4), we find

$$\sin\left[\tan^{-1}\frac{K_1}{iK_2} + \tan^{-1}\frac{K_3}{iK_2} - u_2 t_2\right]$$
$$- \sin\left[\tan^{-1}\frac{K_1}{iK_2} - \tan^{-1}\frac{K_3}{iK_2} - u_2 t_2\right]$$
$$\times \exp\left\{-2i\tan^{-1}\frac{K_3}{iK_2} - 2|u_3|t_3\right\} = 0. \tag{14}$$

For a tunneling region of infinite thickness ($t_3 = \infty$), (14) is simplified to (2). Numerical results for the accurate propaga-

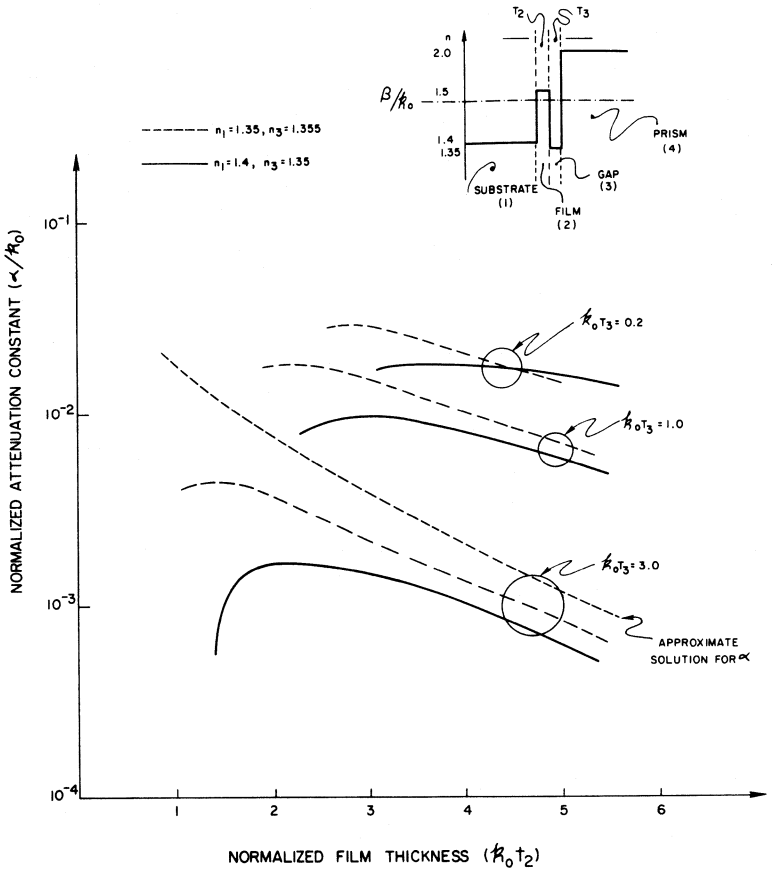


Fig. 4. An illustration of the attenuation constant in the output-prism-coupler configuration for the TE_0 mode shown with six different selections of parameters. The tunneling region is one parameter, and the attenuation is seen to have a peak near cutoff. For comparison, one approximate solution for α is given, using (2) and (8).

tion constant of the zeroth-order TE mode in the prism-coupler configuration near cutoff are shown in Figs. 4 and 5 for both cases: $n_1 > n_3$ (the usual case) and $n_1 < n_3$ (an oil gap, for example, instead of the usual air gap). In the shown graphs, the tunneling region was chosen as a parameter and the waveguides approach cutoff when their film thickness (t_2) is decreased. Unexpectedly, the attenuation constant (α) *decreases* near cutoff from its maximum value (more numerical calculations show that this phenomenon occurs only for $n_1 > n_3$, and $n_3 > n_1$ but only by a small percentage). The reason for α to pass through a maximum near cutoff is the domination of the substrate that stores more of the energy. In other words, the effective longitudinal ray length becomes considerably larger, the ray interacts fewer times with the tunneling region, resulting in a decrease of the attenuation.

Figs. 4 and 5 present also for comparison the results of (2) and (8), the well-known formulas given in the literature. Evidently the accurate results diverge rapidly from the approximate ones when $1/|K_3|$ reaches the same order of magnitude as t_3. The easiest test for the validity of the approximate formulas is to evaluate $k_z^{(0)}$ from (2), and then if

$$(k_z^{(0)} - k_0^2 u_3^2)^{-1/2} \ll t_3 \tag{15}$$

equation (8) can be used for evaluating α; otherwise, $\beta + i\alpha$ will be found by a numerical solution of (14). It is worth mentioning that when (15) is not satisfied (which usually happens when the prism is pressed against the waveguide, leaving a fraction of a micron tunneling gap) the cutoff value for t_2 is considerably higher than the one predicted by (2). This is shown in Fig. 5.

In the single-boundary curved waveguide configuration, $D_{1,4}$ is evaluated for TE waves. Use of the first-order WKB approximation results in an expression similar to (14),

$$\sin\left\{k_v R_2\left[\left(\frac{k_0^2 n_2^2}{k_v^2} - 1\right)^{1/2} - \cos^{-1}\frac{k_v}{k_0 n_2}\right] - \tan^{-1}\left(\frac{k_v^2 - k_0^2 n_3^2}{k_0^2 n_2^2 - k_v^2}\right)^{1/2} - \frac{\pi}{4}\right\} - \sin\left\{k_v R_2\left[\left(\frac{k_0^2 n_2^2}{k_v^2} - 1\right)^{1/2} - \cos^{-1}\frac{k_v}{k_0 n_2}\right]\right.$$
$$\left. + \tan^{-1}\left(\frac{k_v^2 - k_0^2 n_3^2}{k_0^2 n_2^2 - k_v^2}\right)^{1/2} - \frac{\pi}{4}\right\} \times i \exp\left\{2R_2(k_v^2 - k_0^2 n_3^2)^{1/2} - 2k_v R_2 \ln\frac{k_v + (k_v^2 - k_0^2 n_3^2)^{1/2}}{k_0 n_3}\right\} = 0. \tag{16}$$

In (16) the approximation is again made: $k_u(u_{3+})/k_u(u_{3-}) = 1$ where u_{3+} and u_{3-} are points to the right and to the left of u_3, respectively. Numerical results for the attenuation of a few

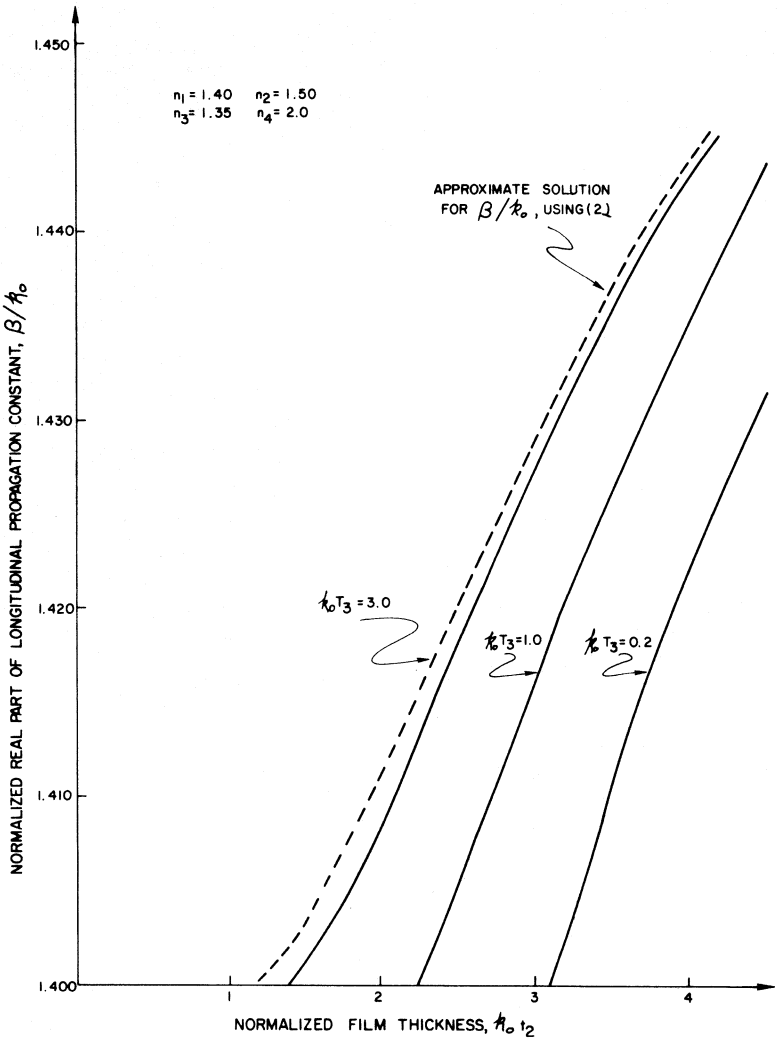


Fig. 5. The real part of the longitudinal propagation constant near cutoff. The smaller the tunneling region is, the worse the approximate solution. Note the big change in the cutoff thickness (t_2) as a function of t_3.

TE modes are shown for two different bends in Fig. 6. This time the modes are forced to approach cutoff by decreasing the radius of the bend, but the calculations near cutoff are limited. As is well known, the first term in a WKB-type solution is a good approximation only if the index changes by a small amount in a region compared to a wavelength, mathematically, only if $|\partial k_u/\partial u| \ll 2|k_u|^2$. This constraint excludes the solution from the vicinity of turning points (where $k_u \simeq 0$) and from the regimes where the slope of the index of refraction is very large. When the modes in a curved waveguide approach cutoff, the turning point u_3 approaches $u = 0$, and $k_u(0)$ becomes very small. Then the first term in the WKB solution cannot be trusted anymore and in Fig. 6 this region is noted by broken lines. In this region more accurate solutions have to be used (our method does not provide these), but as is seen from the figure, the results are accurate up to radii extremely close to cutoff. More meaningful results are those for the attenuation over a period length along the bend. Two model calculations are presented for the attenuation of 90° bends ($I_{out}/I_{in} = \exp(-\alpha\pi R_2)$); they predict that for even a slight decrease of α, the overall attenuation of the arc decreases. Even though the accurate behavior of α in the regimes close to cutoff is not yet available, the anomalous behavior of α or I_{out}/I_{in} (as in the prism-coupler case) might occur, as the rough WKB approximation suggests. The explanation for this phenomenon (if true) will involve, as before, the change in the effective longitudinal ray length between two bounces with the curved surface. The first experimental work had been done recently on curved (three-dimensional) diffused guides [8]. The results, if accurate enough, show a definite slowdown in the rate that α increases near cutoff and a reduction in the overall attenuation. For reference, sample results are shown in Fig. 7. If this anomalous behavior of α is true, it will enable one to reduce the sizes of elements in integrated optical circuits. It should be stressed that the overall attenuation in a practical case also includes the transition losses from the straight guide to the bend and this part of the attenuation might grow monotonically with the reduction of R_2, thus losing some of the advantage predicted here.

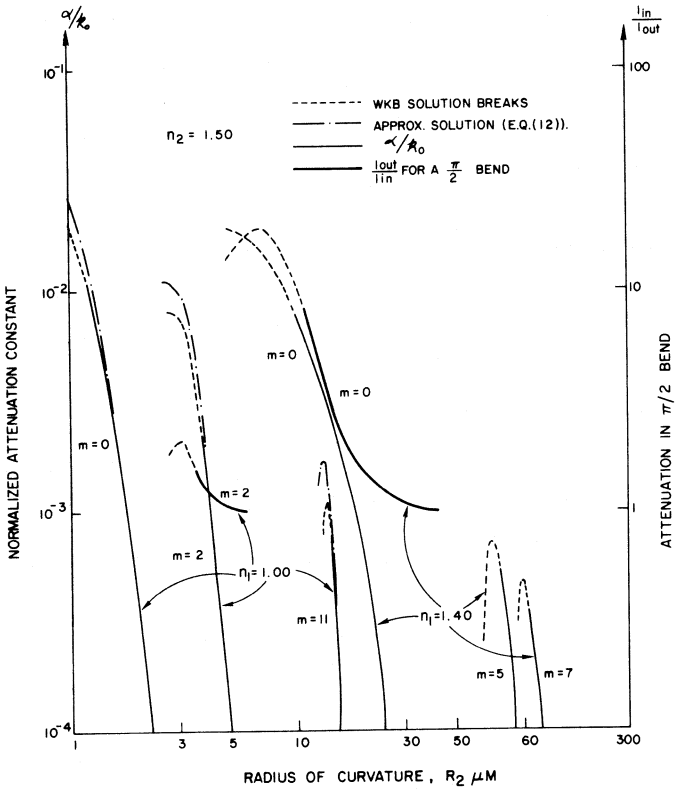


Fig. 6. Comparison between solutions for α/k_0 based on (11) and (12) and those given by (16). The ratio between the output intensity (I_{out}) and the input intensity (I_{in}) for $\pi/2$ bends are given for two modes. Note, broken lines are the solutions in the regions that WKB solution is in question. $k_0 = 2\pi/\lambda_0$ and $\lambda_0 = 0.6328$ Å.

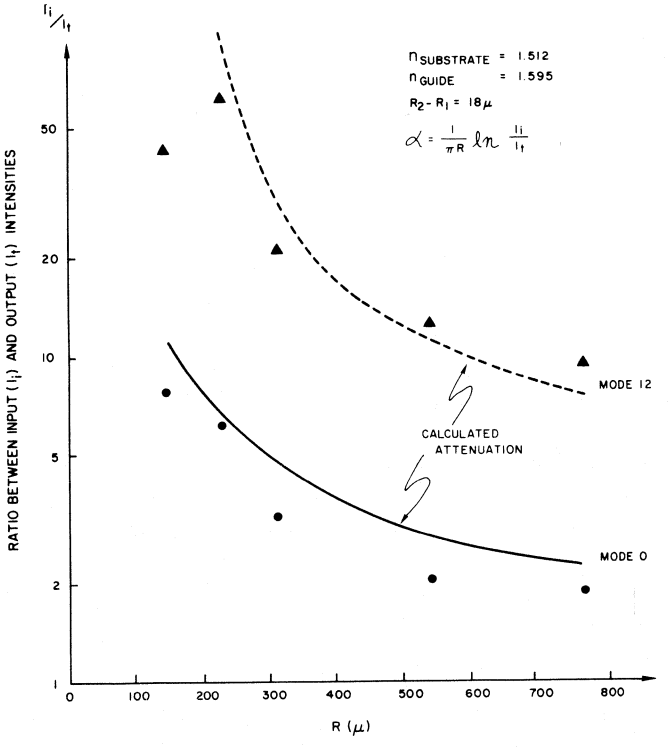


Fig. 7. Experimental results for the attenuation of TE modes in diffused $\pi/2$ bends. The two modes shown are the zeroth and twelfth with respect to waveguide depth, and the calculated results were done by summing up the attenuation of all the transverse modes in each case. (Work done by A. Gedeon and B. Carnstan, Sweden.)

The approximated solutions for $\beta(11)$ and $\alpha(12)$ will be valid only if $1/k_u(0+) \lll u_3$ (the much much smaller sign has been used since the tunneling region does not have a constant index of refraction). Since $u_3 = R_2 \ln(\beta/k_0 n_3)$, (11) and (12) are valid only if

$$(\beta^2 - k_0^2 n_3^2)^{-1/2} \lll R_2 \ln(\beta/k_0 n_3); \tag{17}$$

otherwise (16) has to be used to find the complex root $\beta + i\alpha$. For comparison, we have plotted the approximate solutions for α for three different modes in Fig. 6. It is clearly seen that the approximate and the improved solutions diverge only in the region where the validity of the WKB-type solutions is in question[1] (the real part of k_u given by (16) and $k_v^{(0)}$ given by (11) are in even better agreement and are not shown here!). So, it may be concluded that the approximated convenient solutions can be used whenever the WKB-type solution is sufficiently accurate and criterion (17) holds. (The numerical results show that they hold together.)

As a final point we would like to mention a rather interesting case that can be considered as a hybrid case between the prism-coupler and the bend configurations: an output prism coupler on top of a diffused waveguide. This case was investigated by Marcuse [9]. He employed the WKB-type solution to the region of the diffused guide and an accurate solution to the tunneling-prism regimes. The configuration and model results are shown in Fig. 8. The attenuation constants are plotted—for TE modes—as a function of the mode order, or in other words, as a function of the real part of the longitudinal propagation constant. When the mode order increases, β decreases with a lower limit of $k_0 n_2$. When the mode order is high (or β is close to cutoff), the attenuation constant goes through a peak and then drops down, like our previous results. Note that the abrupt drop in α is due to the approximation of the index profile by two straight lines. The abrupt change in α occurs when the modes switch from one straight line to another. These results again show the domination of the substrate for small longitudinal propagation constants.

IV. Conclusions

It has been shown that a curved waveguide and waveguide-prism configurations have similar guiding characteristics. One must pay attention to the validity of the equations he uses when the mode under consideration is close to cutoff. A simple test is to check if the approximated evanescent field is of the same order as the tunneling region. It was shown exactly for the prism coupler and approximately for the curved waveguide that the attenuation peaks before cutoff and then drops down almost at cutoff. If verified for the curved guide, this phenomenon could be employed in constructing bends, and especially in cases that do not involve transitions from different curvature guides, for example in a ring laser.

[1] It is worth mentioning at this point that in the first order WKB-type solution the radiation condition is neglected, since only near-zone fields are being considered, and reflections from the exponentially growing index to infinity are assumed to be small. They are really small if the criterion $[2k_0 R_2 n_3 (\beta^2 - k_0^2 n_3^2)^{3/2}]^{-1} \ll 1$ is satisfied, and then the solution presented above is very good. For regimes in which the above criterion is not satisfied, a second-order WKB-type solution (that adds the contribution of first-order reflection of the region beyond u_3) must be considered and the radiation condition has to be satisfied.

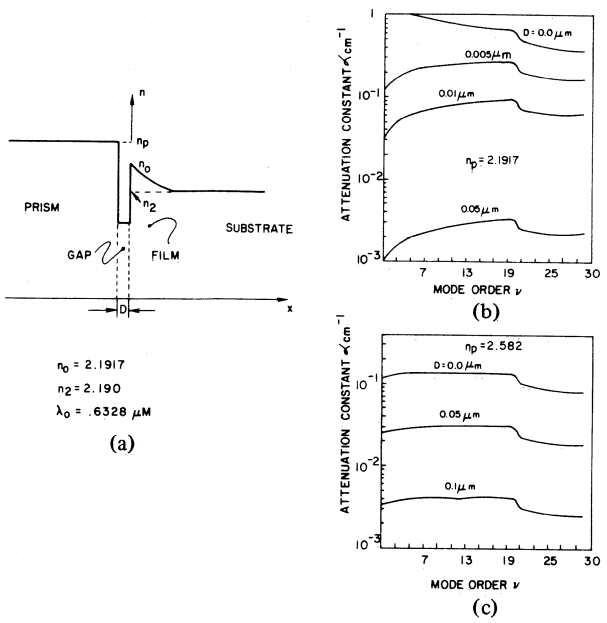


Fig. 8. Radiation loss from a two-dimensional diffused waveguide whose index profile is described above. ν is the mode order and D is the tunneling region thickness. (a) Index profile of an output prism coupler above an outdiffused guide. Two prism materials were chosen, (b) n_p = 2.1917 and (c) n_p = 2.582 (rutile prism). Note a peak in α near cutoff. (Taken from [9].)

Acknowledgment

The author would like to thank J. R. Whinnery and J. H. Harris for valuable discussions and helpful suggestions.

References

[1] J. H. Harris and R. Shubert, "Variable tunneling excitation of optical surface waves," *IEEE Trans. Microwave Theory Tech.*, vol. MTT-19, pp. 269–276, Mar. 1971.

[2] P. K. Tien and R. Ulrich, "Theory of prism-film coupler and thin-film light guides," *J. Optical Society Amer.*, vol. 60, pp. 1325–1337, Oct. 1970.

[3] E. A. Marcatili, "Bends in optical dielectric guides," *Bell Syst. Tech. J.*, vol. 48, pp. 2103–2132, Sept. 1969.

[4] a) D. Marcuse, "Bending losses of the asymmetric slab waveguide," *Bell Syst. Tech. J.*, vol. 50, pp. 2551–2563, Oct. 1971.
b) —, "Bent optical waveguide with lossy jacket," *Bell Syst. Tech. J.*, vol. 53, pp. 1079–1101, July 1973.

[5] S. Sheem and J. R. Whinnery, "Guiding by single curved boundaries in integrated optics," *Wave Electron.*, vol. 1, pp. 105–116, 1975.

[6] M. Heiblum and J. H. Harris, "Analysis of curved optical waveguides by conformal transformation," *IEEE J. Quantum Electron.*, vol. QE-11, pp. 75–83, Feb. 1975.

[7] J. H. Harris, R. Shubert, and J. N. Polky, "Beam coupling to films," *J. Optical Society Amer.*, vol. 60, pp. 1007–1016, Aug. 1970.

[8] A. Gedeon and B. Carnstam, "Attenuation in bends of diffused stripe waveguides," *Integrated Optics* (Conf. Abstracts), Jan. 1976.

[9] D. Marcuse, "TE modes of graded-index slab waveguides," *IEEE J. Quantum Electron.*, vol. QE-9, pp. 1000–1006, Oct. 1973.

Photoionization Parameters in the Carbon Dioxide Laser Gases

DON C. McKEN, HERB J. SEGUIN, MEMBER, IEEE, AND JOHN TULIP

Abstract—**The data and results of an extended investigation of the more salient parameters associated with the application of ultraviolet (UV) photoionization processes in TEA CO_2 lasers are presented. The study encompasses emission spectra, wavelength dependence, and influence of circuit parameters for a typical UV spark source. This investigation and a companion study utilizing a specialized charge collection apparatus on a monochromator provides further insight into the primary mechanisms involved in these photoinitiated laser devices and has, in addition, provided design criteria for the development of more efficient photoionization sources.**

INTRODUCTION

THE application of photoionization techniques to CO_2 lasers has advanced rapidly over the past few years [1]-[7] in that several such TEA devices are now commercially available. In addition, new experimental photoionized laser systems have demonstrated output characteristics comparable to electron-beam sustained machines [8]-[10]. Despite these advances in device technology there has been a scarcity of investigation on the precise processes at work in these lasers. In an attempt to gain some understanding of the dominant physical processes, an initial series of microwave density measurements were performed on a variety of ultraviolet- (UV) produced plasmas. For convenience, the results of this study [11] are reproduced in Figs. 1 and 2. Helium gas was found to support a very high level of photoionization, which was unexpected since the ionization potential of He is near 25 eV. On the other hand, very little photoion density was obtained in carbon dioxide or the normal laser gas mixture. Extrapolation of the laser mix curve indicated that a photoplasma density as low as $10^4/cm^3$ was to be expected in a photoionized TEA laser operating at atmospheric pressure. It was not immediately obvious how such a low level of preionization could play any significant role in discharge stabilization as this is little more than background. However, the electron density measurements obtained with "seed" materials added to the laser mix, and shown in Fig. 2, indicate that relatively large photoelectron densities could, in fact, be readily achieved with simple UV spark sources and an appropriate low-ionization-threshold additive. The pressure dependence of this enhancement effect was seen to be nonsimple and best characterized by two intersecting curves. Moreover, the maximum enhancement in photoelectron density did not correspond to the additive with the lowest ionization threshold.

It can thus be appreciated that, far from providing a clearer understanding of the relevant processes in the spark-initiated photoionized TEA laser, this initial study introduced more questions to be resolved. Several of these were as follows.

1) How does ionizing radiation propagate to such distances from the UV source at high pressure?

2) What emission spectrum do such spark sources produce?

3) What wavelength bands are primarily responsible for the photoionization observed?

Manuscript received February 3, 1976; revised March 29, 1976. This work was supported in part by the Canadian National Research Council and the Defence Research Board.

The authors are with the Department of Electrical Engineering, University of Alberta, Edmonton, Alta., Canada.

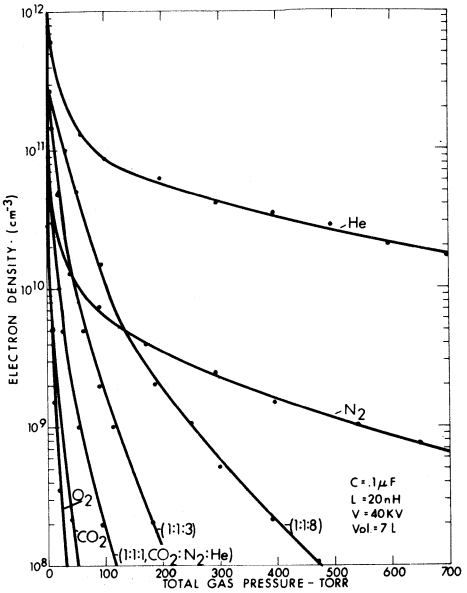


Fig. 1. Photoelectron density versus gas pressure for the primary CO_2 laser gases and mixtures. Measured at 12 cm from single UV source.

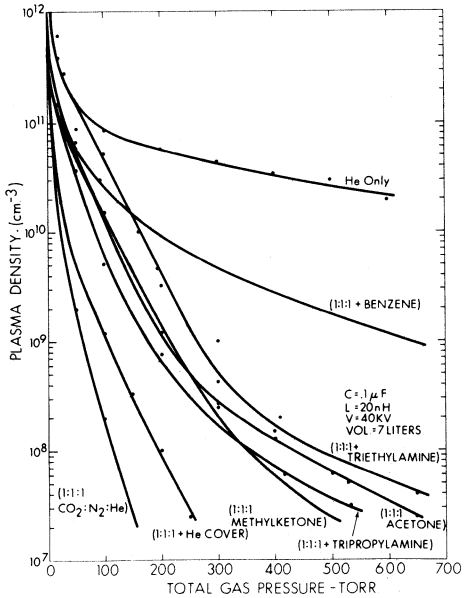


Fig. 2. Photonelectron density versus gas pressure for (1:1:1) CO_2 laser mixture with selected additives. Measured at 12 cm from single UV source.

4) Is the ionization mechanism a first- or second-order process?

5) What gas species is ionized in He gas and the laser mix?

6) How does such a low level of preionization produced in the normal laser mix stabilize the main discharge?

7) Do other processes become significant when low-ionization-threshold additives are used?

8) What source wavelength bands are utilized in doped TEA lasers?

Some insight into question 6 was initially obtained from a Russian study of pulsed nanosecond discharges in gases [12]. This theoretical contribution analyzed the stabilizing influence of an initial electron density on the evolution of a high-current discharge. A uniform preionization density as low as $10^4/cm^3$ was predicted to be adequate for discharge stabilization. A subsequent analysis employing a multichannel streamer model also featured high-current discharge stabilization with low-level preionization [13]. This paper describes measurements of photoionization parameters aimed at providing answers to some of these other questions.

Apparatus

The study was performed on a specially adapted vacuum UV monochromator shown in Fig. 3. The basic modifications to the autoscan Jarrel-Ash monochromator consist of a special spark source chamber and a sample chamber in which all parameters may be independently controlled. This allows measurement of the emission spectrum produced by a spark source, the effects of a laser gas media on propagation of such radiation, and the ionization subsequently produced in various laser gases and mixtures.

Spark Chamber

The source chamber consists of a double-shielded ferromagnetic cylinder inside of which is mounted a simple two-pin spark source. These electrodes are fabricated from 1-mm-diam pointed tungsten pins adjusted to a 2-mm spacing. This unit is in turn bolted to the outside mounting of the inlet-adjustable slit assembly on the monochromator. A well-shielded and low-inductance 0.01-μF capacitor charged to 50 kV is used as the power source, while a pressurized spark gap, repetitively pulsed at a 1-Hz rate serves as the switch. A removable lithium fluoride window is incorporated into the exit of the spark chamber so that its gas environment can be separately controlled when desired.

Sample Chamber

All emission and plasma density measurements are performed in the sample chamber, which is fitted with both a photon and an ionization detector. Appropriate control, sampling, and display electronics are incorporated into the device such that continuous and simultaneous chart recordings of both photon and ionization spectra are obtained automatically as the monochromator slowly autoscans from 500 to 3800 Å.

Photon Detector

The photon detector used in these investigations consists of a fast photomultiplier fitted with a sodium salicylate scintillator. This scintillator film is sprayed onto a 5-mm-thick acrylic substrate and provides a broad-band response from 500 to 3800 Å with satisfactory quantum yield [14]. In this manner it is possible to utilize the low-pass transmission characteristics of the acrylic to guard against direct short-wavelength excitation of the *S*1 photomultiplier photoemissive surface [15]. In operation, UV photons excite the sodium salicylate atoms over the normal monochromator scanning range of 500 to 3800 Å; the scintillator, in turn, produces an optical output centered at 4200 Å which is then transmitted by the acrylic filter into an RCA 8645 photomultiplier. The high-impedance electrical output from this photomultiplier is subsequently used to charge a small, low-loss, storage capacitor. The integrated charge stored in this capacitor, corresponding to the photomultiplier output signal, is sampled and reset by an ultrasensitive, high-speed and high-impedance electronic preamplification system shown in Fig. 4(a). The electrical signal from this unit is then used for driving the y axis of an x-y pen recorder, while the x axis slowly drives in synchronism with the monochromator wavelength scan. In this manner it is possible to obtain a broad-band and sensitive photon detection system, the output display of which consists of sequential vertical line plots on an x-y recorder. The y amplitude is directly proportional to the integrated photon intensity and the x-axis position of this vertical line is directly proportional to the particular momentary wavelength scanning position of the monochromator. In order to achieve adequate sensitivity and immunity from the spark-source discharge interference, all the detection components and associated battery packs are built inside a well-shielded enclosure, integral with the sample chamber.

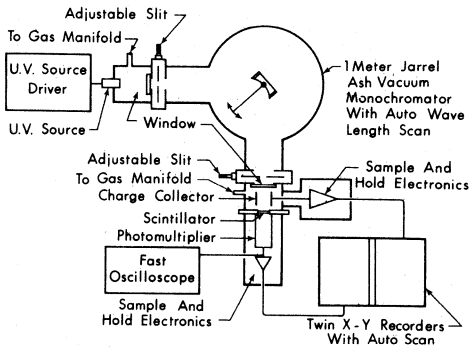


Fig. 3. Schematic diagram of measurement apparatus showing vacuum UV monochromator fitted with source and sample chambers.

Ionization Detector

Essentially the same charge collecting, sampling, and resetting technique as is used in the photon detection system is also utilized for the ionization detector. In this case, however, the current source for charging the sampling storage capacitor is simply a pair of parallel charge collection plates mounted internally along the length of the sample chamber, sufficiently removed from the optical path to prevent photoemission. Collection of charge is accomplished through incorporation of an adjustable bias battery pack in the sampling capacitor circuit, see Fig. 4(b).

In this measurement system the output signal is also used to

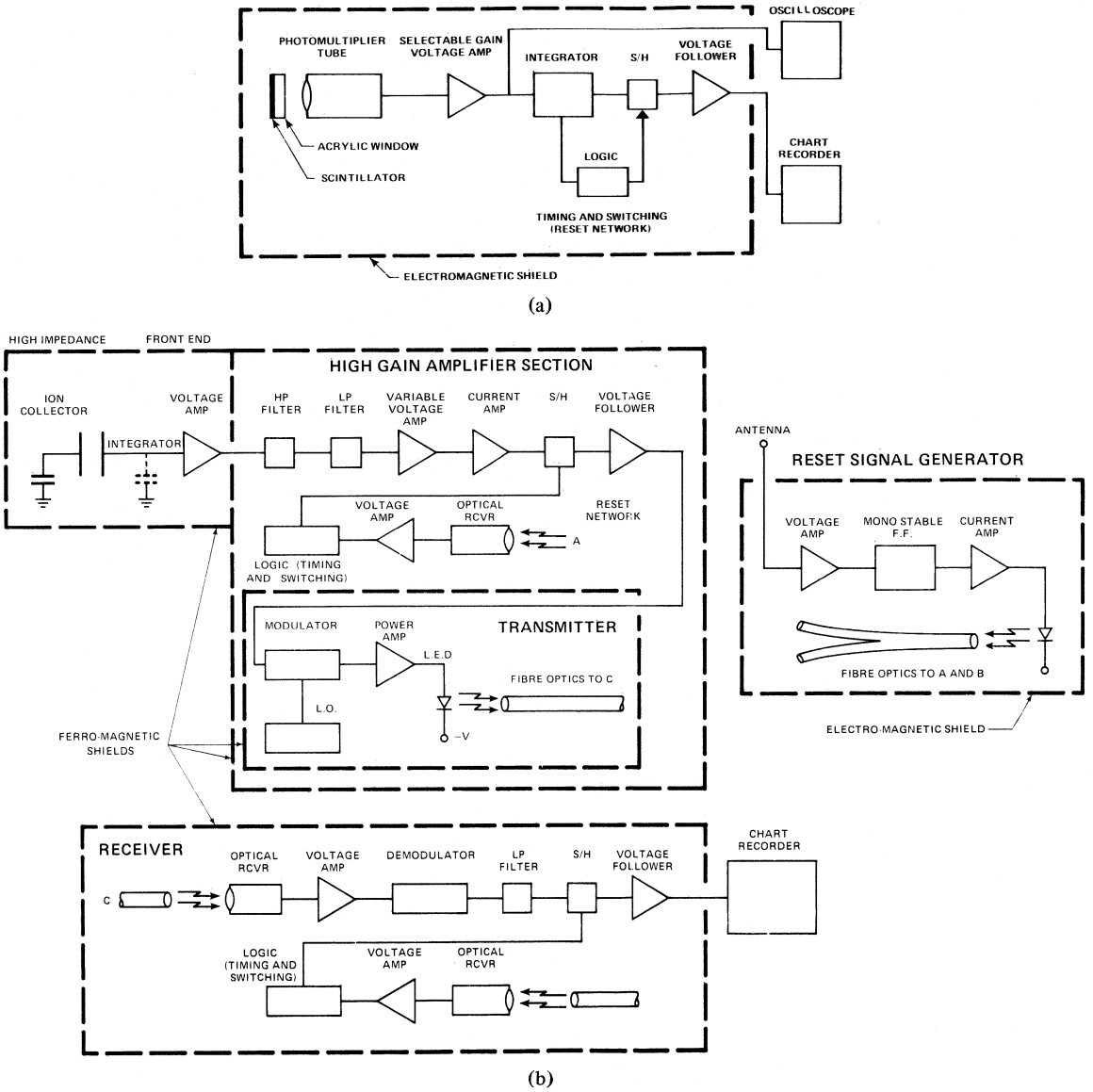


Fig. 4. (a) Schematic diagram of photon measurement electronic system. (b) Schematic diagram of ionization measurement electronic system.

drive the y-axis display of another identical x-y recorder. Here in this detection technique also, the vertical-recorder display is directly proportional to the total charge collected and hence gives an ionization measurement, integrated at a particular wavelength. The x-axis scan of the two recorders are ganged together which thus gives a simultaneous display of the photon and ionization spectrum. Extremely high standards of circuit fabrication and shielding are again mandatory to achieve sufficient immunity from the high RFI levels present in the spark system.

Data Display Format

By proper circuit design and utilization of fast integrated-circuit modules the sensitivity of both the photon and ionization detection systems is sufficient to allow repeatable measurements with a scanning bandwidth as small as 5 Å. This sensitivity coupled with a monochromator wavelength scan drive of 50 Å/min, a pulse repetition rate of 1 pulse/s, and a linear x-axis recorder displacement of 1 in/50 s yields the typical data display shown in Fig. 5. Before photographic reduction each major 1-in division encompassed a 50-Å wavelength spectrum and the data recorded over these intervals consisted of 50 separate vertical line samples. Thus the composite multiline structures displayed in Figs. 5–16 are real sampled data measurements having an overall run-to-run repeatability of 80 percent or better. Although the Jarrel-Ash monochromator is capable of automatic scan from 500 to 4000 Å, most of the data presented here were restricted to a 1000–2500-Å band, as this was the region of primary interest. Approximately $\frac{1}{2}$ h automatic data sampling was required to acquire the scan spectra shown in Fig. 5.

Results

Source Spectrum

Although the measurement system was built to simultaneously record both photon and ionization spectra, the first

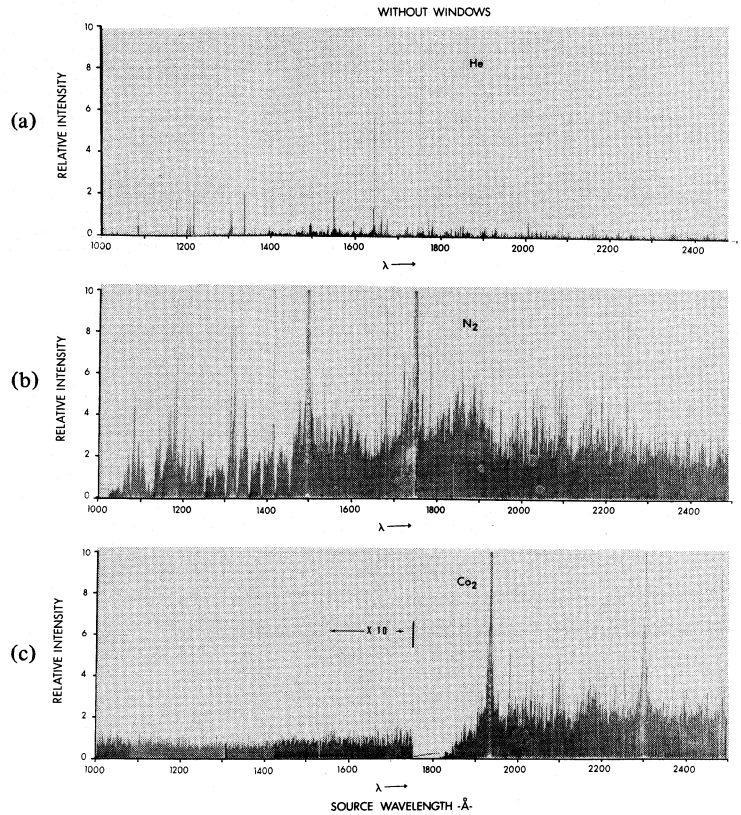


Fig. 5. Spark source emission spectrum obtained in primary laser gases (a) for He, (b) N_2, (c) for CO_2.

data acquired utilized only the photodetector. These investigations were performed to precisely characterize the emission spectrum of simple UV spark sources of the type commonly used in photoionized TEA laser devices. Uniqueness with respect to specific gas environments and/or circuit parameters were of particular attention in these initial measurements.

It is to be noted here that *all* windows were removed for this data collection and the entire system was filled with the particular gas under test. This was found to be of major significance, as will be evident.

Fig. 5 shows the radiation emitted by a pair of pointed tungsten pins spaced with a 2-mm gap and driven by a 0.01-μF low-inductance capacitor, charged to 50 kV. The upper scan was obtained in He and shows very little UV intensity over the 1000–2500-Å range. This result appears to prove an error in initial speculations of strong UV production from the Hopfield continuum in He [11], [16]. The increased plasma density observed in nitrogen when a helium cover gas was used on the UV source in [11] was most probably due to an increased concentration of low-ionization-threshold impurity entrained in the helium flow. See discussion on ionization measurements.

The lower spectrum, also in Fig. 5, similarly suggests that CO_2 plays no significant role in hard UV production. Note here that the sensitivity of the vertical display has been increased by a factor of 10 for the scan of 1000–1750 Å. The absence of a vertical-line display in the 1750–1825-Å interval indicates that the product of preamplified gain and signal level has fallen below the sampling threshold of the electronics. On the other hand, the spectrum obtained in nitrogen (middle display) leaves little doubt that it is this particular gas that dominates the hard UV production in a two-pin discharge geometry.

Fig. 6 demonstrates the influence of circuit inductance upon UV production in such a spark. The upper and lower recordings were obtained under identical gas and circuit conditions except for an additional 300-μH inductor placed in-series with the spark source of display Fig. 6(b), thereby decreasing the peak current through the source. These data suggest that driving circuits which promote high peak currents are desirable if maximum UV production is to be realized.

The emission spectrum of Fig. 7(a) was obtained when the system was filled with a standard (1 : 1 : 8), (CO_2 : N_2 : He), laser mix. Here it is seen that the resultant photon emission is drastically altered by the mixture in that only 2 bands of useful photons remain; one approximately 50 Å wide centered at 1200 Å and the other about 100 Å wide centered at 1750 Å. Careful examination and comparison of Fig. 7(a) with Fig. 5(b), reveals that it is still the nitrogen present in the laser gas mixture that controls the photons produced within these 2 narrow bands, even though all other portions of the pure nitrogen emission spectrum have been eliminated. Further examination of Fig. 7(a) in relation to Fig. 8 gives some insight into the photon loss experienced here. Fig. 8 represents a wide collection of photoabsorption measurements for pure CO_2 [17]. It is evident that the absorption length μ is large for all wavelengths shorter than 1150 Å but that a window about 50 Å wide exists in the gas at 1200 Å. CO_2 again becomes transparent for radiation longer than 1700 Å. The spectra measured in the laser mixture of Fig. 7(a) obviously

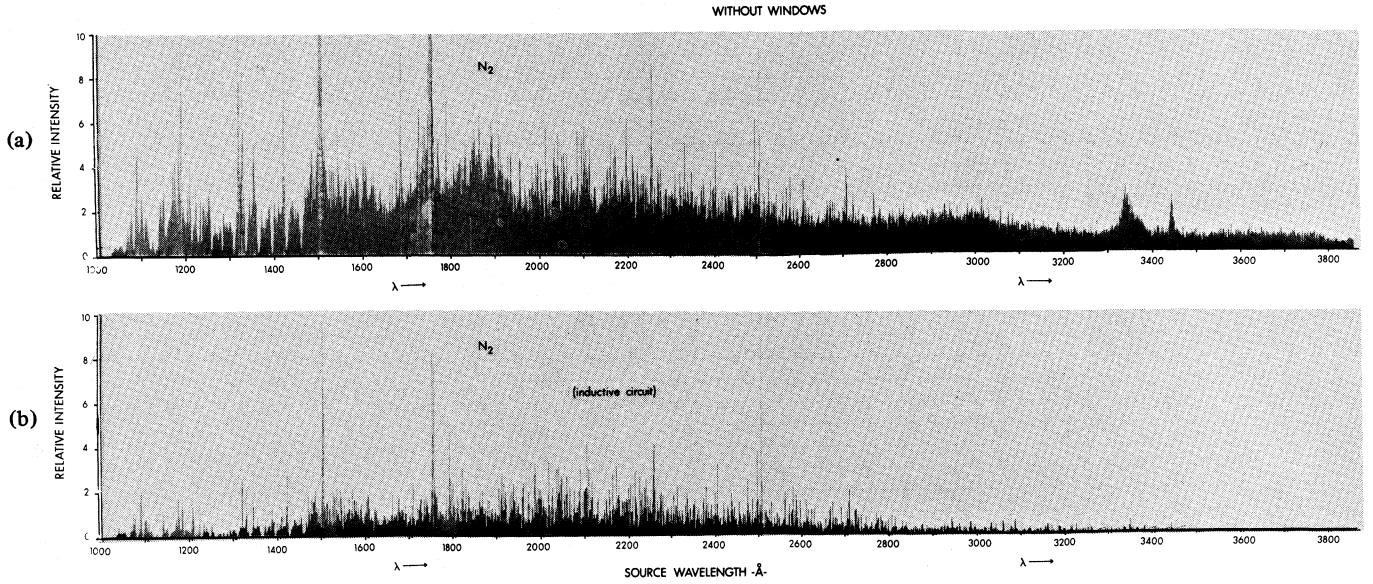


Fig. 6. Spark source emission spectrum obtained in high-purity nitrogen gas and showing effect of circuit inductance. Circuit inductance is approximately 1 and 300 μH for upper and lower traces, respectively.

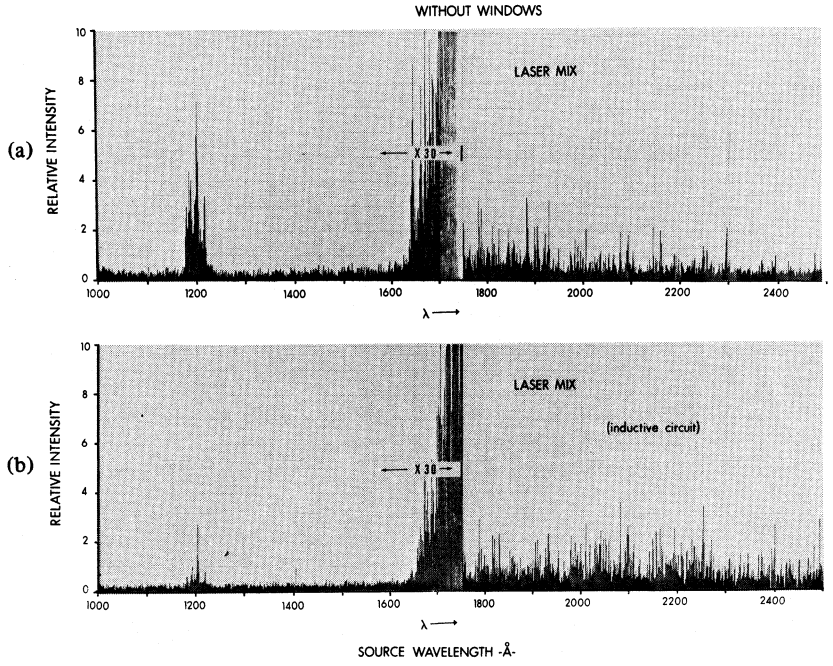


Fig. 7. Spark source emission spectrum obtained in laser mix (1:1:8) (CO_2:N_2:He). $L \approx 1$ and 300 μH as in Fig. 6.

correlate well with this CO_2 absorption profile. From these results it would appear logical to conclude that in a normal spark photoionized TEA CO_2 laser, the nitrogen gas serves as the dominant UV photon source while the CO_2 component present absorbs most of this short wavelength emission such that only 2 narrow UV photon bands remain; one centered at 1200 Å and the other at 1750 Å. The trace of Fig. 7(b) further demonstrates the effect of circuit response on hard UV production in a 2-pin spark discharge.

Windows

It was desired at this point in the study to investigate photoelectron production in various laser gases and to accomplish this it is necessary to isolate the sample chamber from the main monochromator body by means of a UV window. Consequently, it was important to determine exactly what effect such a window had on the source emission spectrum. Fig. 9 demonstrates the results of this measurement using high-purity nitrogen gas as the spark source environment. Nitrogen was subsequently used as the photon source in all later tests because of its intense emission spectrum. The display in Fig. 9(b) is a recording of the photon emission measured by the photodetector without any windows in the system. Fig. 9(a) shows the same spectrum after passing through a carefully prepared lithium fluoride window. As can be seen, there has been considerable attenuation, especially below 1300 Å. Fig.

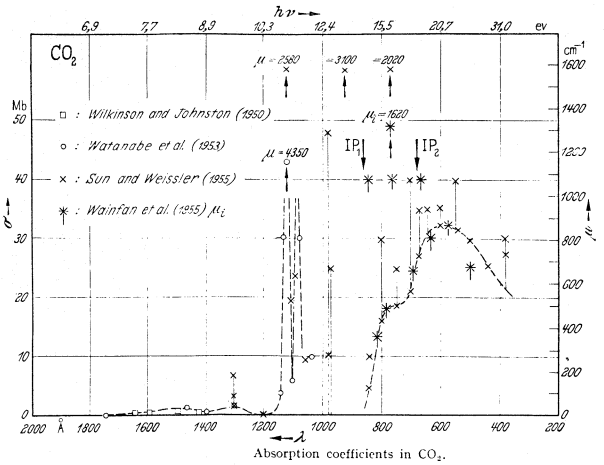


Fig. 8. Absorption coefficient versus wavelength for pure CO_2. Taken from [17].

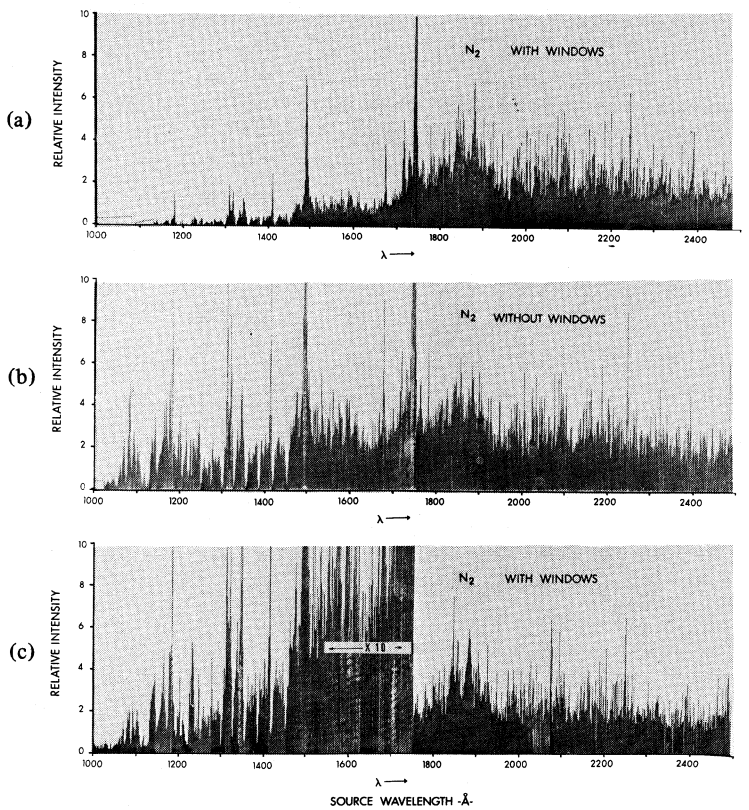


Fig. 9. Spark source emission spectrum obtained in high-purity nitrogen gas and showing absorption of lithium fluoride window placed at entrance of sample chamber.

9(c) shows the transmitted spectrum, amplified by a factor of 10, which is used as the reference spectrum in the ensuing tests. It is interesting to note at this point that useful transmission is obtained down to 1000 Å, however, this is only achieved in selected LiF crystals and after special preparation. Slight contamination reduces the short wavelength cutoff to about 1200 Å. In addition, it was discovered that the hard UV transmission of such LiF windows rapidly deteriorates when the crystal is subjected to an intense UV flux. Thus when a LiF window is placed at the spark chamber location, where it is subjected to the full broad-band spark source emission intensity, the transmitted intensity is soon cut off at 1400 Å. A similar but less dramatic effect has also been experienced with CaF windows. Consequently for all the tests reported here, no window is used at the spark chamber but rather only at the entrance to the sample chamber. In this manner the photon flux incident on the window is drastically reduced and no significant window deterioration is experienced. The extent of reduction in the hard UV transmission characteristics of these window materials under intense irradiation was not initially

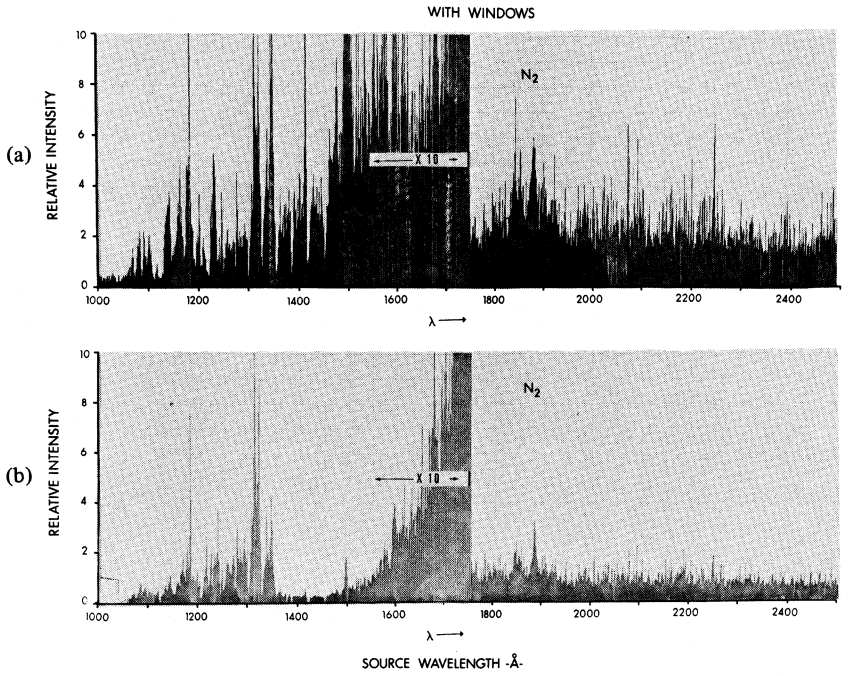


Fig. 10. Spark source emission spectrum obtained in (1) high-purity- (upper trace) and (b) industrial- (lower trace) grade nitrogen gas, showing effect of increased oxygen impurity concentration on short wavelength production.

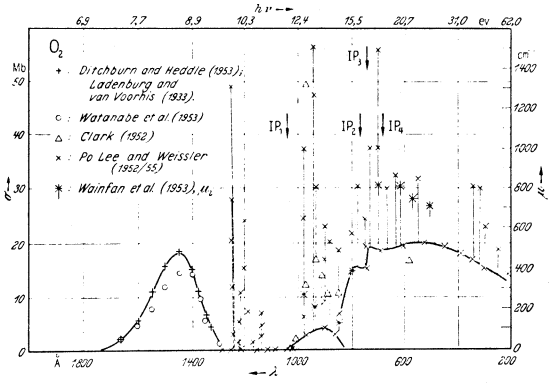


Fig. 11. Absorption coefficient of oxygen versus wavelength for pure oxygen. Taken from [17].

appreciated by the present authors and was thus responsible for the early belief that the ionizing radiation was mainly shorter than 1200 Å [7], [11].

The data of Fig. 10 illustrate the effect of gas purity upon UV radiation produced in a spark. The upper trace shows the normal spectrum generated in a "high-purity" grade of commercial nitrogen gas. However with "industrial" grade N_2 in the spark chamber, Fig. 10(b) is obtained. The attenuation of emission is clearly significant and may be attributed to the increased oxygen impurity content found in the industrial grade gas. High-purity nitrogen is specified at 20 ppm O_2 while industrial grade has an oxygen impurity level in excess of 100 ppm. Additional evidence against oxygen is afforded in Fig. 11. Here it is seen that O_2 has a strong absorption band between 1700 Å and 1300 Å, which correlates well with the reduction in the photon spectrum of Fig. 10 [17].

Ionization Measurement

Ionization data were collected using selected gases in the sample chamber. For these measurements the spark emission spectrum produced by high-purity nitrogen and transmitted through an LiF window is utilized, having previously been established as a reliable and broad-band photon source and shown in Fig. 9. Fig. 12 shows those data obtained for the primary laser gases. Here it is also seen that by far the highest photoionization was observed in He gas while CO_2 and N_2 contribute little. This correlates with the results obtained in the previous microwave measurements [11]. It is interesting to note also that in helium there is strong photoionization below 1500 Å, but negligible ionization between 1550 Å and 1700 Å even though Fig. 9 reveals a strong source photon flux over the entire band. In addition, appreciable photoionization again appears from 1750 to 1900 Å. Note here that the spectrum displayed from 2100 to 2500 Å is to be discounted as it has been conclusively identified as the second grating order of the data displayed below 1300 Å. Fig. 13 displays further measurements made with the sample chamber evacuated and then filled with two different grades of helium gas. The upper trace provides a check on the cleanliness of the system in that negligible photoplasma is observed in the pumped-out cham-

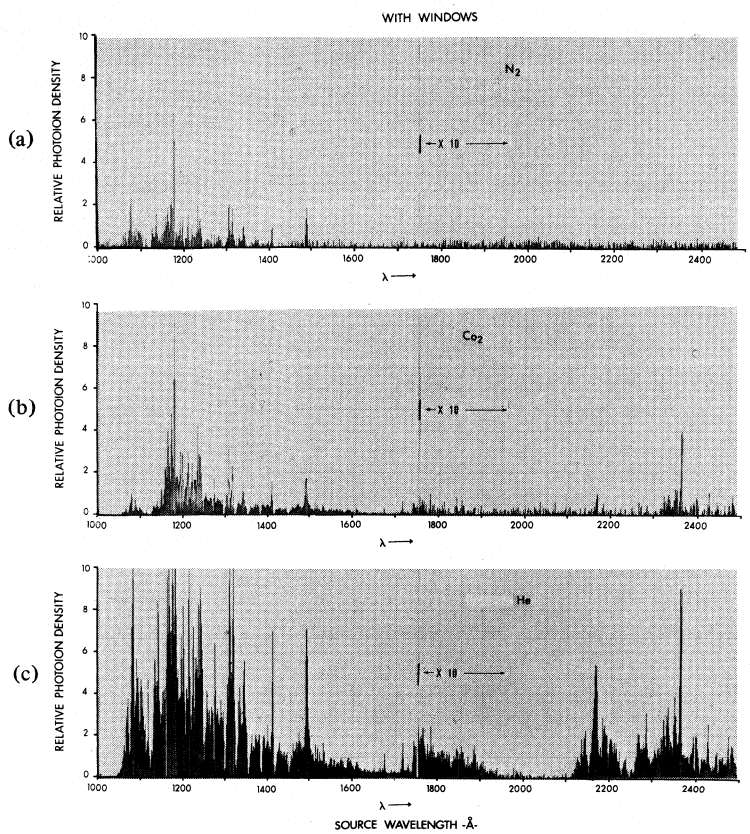


Fig. 12. Photoionization versus wavelength obtained in primary laser gases using high-purity nitrogen gas as photon source. Charge collection performed with $E/p \leqslant 3$ V/cm · torr. Pressure ≈ 50 torr. (a) For high-purity N_2. (b) For CO_2. (c) For industrial-grade He.

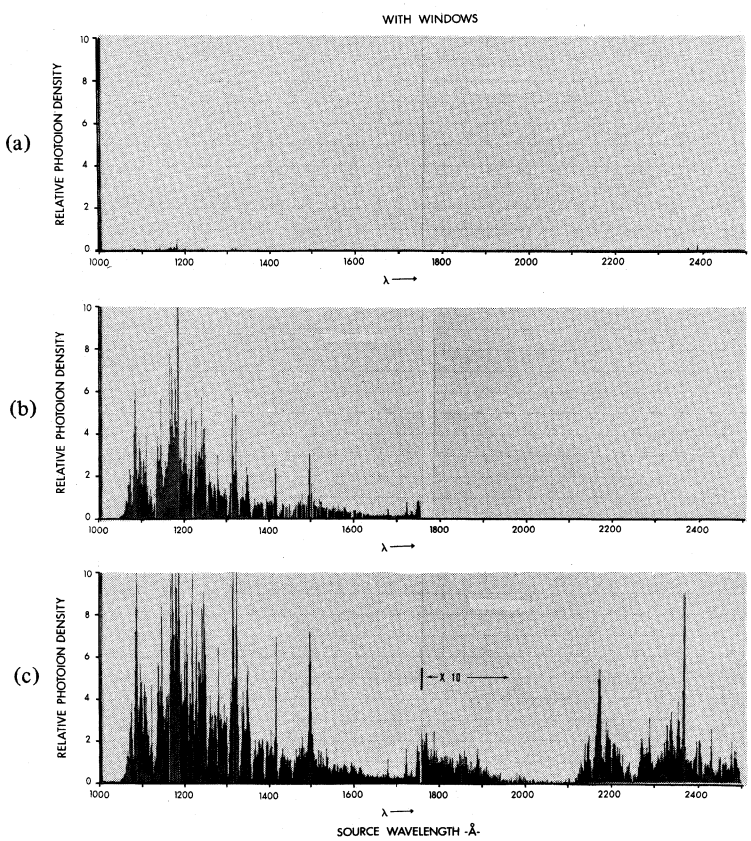


Fig. 13. Photoionization versus wavelength obtained in (a) evacuated chamber, maximum sensitivity; (b) spectroscopic-grade helium; (c) industrial-grade helium.

ber. In the other two curves it is apparent that less ionization is obtained in helium gas with the highest purity. The relatively large photoionization levels produced in He at these wavelengths require an explanation other than direct ionization of He atoms since the photons present are not sufficiently energetic [8]. The results of Fig. 13 can be explained by postulating a trace impurity with an ionization potential of approximately 1600 Å.[1] Further evidence for the presence of such an impurity was afforded by a series of photoelectron density scans performed on the sample chamber over an extended time period while helium was slowly flushed through the chamber via a small orifice. Under these conditions the photoion density continues to increase with time when industrial grade He is used. However, if higher purity spectroscopic He gas was then flowed through the sample chamber, a reduction in photoion density was experienced. Such an effect is consistent with a gradual accumulation of impurity concentration within the sample chamber as a function of time, most probably due to the larger viscosity and molecular weight characteristic of easily photoionized atoms.

The simultaneously transmitted photon spectrum and resulting photoelectron density obtained with a (1:1:8) laser mixture is shown in Fig. 14. Here the upper curve displays the photon spectrum entering the sample chamber, while the middle trace shows the photons that propagate through the gas to the detector, a distance of approximately 20 cm. The lower display records the photoplasma density produced within the gas sample as a consequence. Comparison of Figs. 14(b) and 7(a) immediately reveals that again only two bands of photons penetrate the chamber; moreover, the photoion density scan, Fig. 14(c), clearly shows that it is only these two narrow bands that give rise to photoionization. It follows from these data that the only useful photons produced in a photoionized TEA device lie within a 50-Å-wide band centered at 1200 Å and also a 100-Å-wide band centered at 1750 Å. From further comparison of the data in Figs. 14(c), and 13(c) while taking due account of the photon loss from CO_2 absorption, it becomes apparent that in the laser mixture also, it is the impurity present in helium that dominates the ionization process.

Additives

It is of interest at this point to examine in some detail the photon intensity and resultant photoionization density obtained when a specific trace impurity with low ionization threshold is added to the laser mix. Such data are given in Fig. 15. The upper display corresponds to the source spectrum obtained at the detector after passing through the sample chamber containing the additive. Here the figure appears very similar to that obtained in the undoped laser mixture except for an enhanced absorption of photons in the 1200- and 1750-Å bands. The dominating influence of such an additive or seed on photoion production is, however, clearly manifest in the middle recording. Comparison of this curve, for a mixture seeded with tripropylamine, to that of the unseeded mix, Fig. 15(c), reveals a photoion density enhancement of about three orders of magnitude. Note here that the ionization reading of Fig. 15(b) is off-scale despite an order of magnitude reduction in gain of the ionization detection system. This display also shows an enhanced photoionization effect centered around 1750 Å and extending to 2100 Å.

It should also be noted that the data recorded around 2400 Å are again due to the second grating order. Examination of the display in Fig. 15(b) clearly demonstrates that even in the presence of an easily ionized additive, the useful source photons are still only those contained in the 1200- and 1750-Å bands, as was the case in the undoped laser mix. Another interesting implication of these results is that, since the ionization threshold for tripropylamine is 1705 Å, the relatively high level of ionization experienced at long wavelengths (up to 2100 Å), would seem to imply a two-step photoionization mechanism in this wavelength region. Further insight into this aspect is afforded in a series of scans, similar to Fig. 15, which were obtained under conditions of increasing additive concentration. With a low seed concentration (approximately 10 ppm), the ionization process is dominated by the more energetic photons centered at 1200 Å. As the additive concentration is increased, up to 100 ppm, the ionization at 1200 Å is seen to go through a maximum and then decrease, while that at 1750 Å continues to increase. At even higher additive concentrations the contribution at 1200 Å decreases still further and eventually disappears while that at 1750 Å goes through a maximum. At excessive doping levels all ionization is lost. These observations may be explained in terms of two separate and competing ionization mechanisms. At low seed concentrations an efficient one-step process, with a characteristic short penetration depth, dominates at 1200 Å. With medium doping levels a longer range two-step process, utilizing photons around 1750 Å, begins to make a significant contribution to the plasma density. Under still higher additive concentrations the one-step process is effectively restricted to the area near the input window and only the longer range mechanism is observed. Finally, with excessive seed concentration all useful photons are quickly absorbed in a narrow region adjacent to the photon source.

The existence of two such processes, one of long, and the other of shorter range, is consistent with previous microwave measurements shown in Fig. 16. Here photoion density is plotted as a function of distance from a single UV source, for typical doped laser mixes. It can be seen that the curves are not well fitted by a single absorption length over any appreciable distance. In this context a direct one-step process with a photon mean free path of about 5 cm would appear to describe measurements up to a distance of about 12 cm from the source. However, at twice this range an effective mean free path of 17 cm is observed. It follows from the results in Fig. 16 that in small-aperture lightly doped TEA lasers, a single-step photoionization process, which utilizes a 50-Å-wide band of photons at 1200 Å, dominates the plasma density. In larger

[1] At the field-pressure ratio used in the measurements of Fig. 13, ($E/p \leqslant 3$ V/cm-torr), it can be shown that the Townsend cascade makes a negligible contribution to the electron density in carbon dioxide and nitrogen. This is not necessarily so in the case of helium where the impurity level can significantly alter the Townsend coefficient [19]. Nevertheless, best available estimates for α give a worst case cascade enhancement of less than an order of magnitude [19], [20]. Operation was generally restricted to a linear or saturated region of the charge collection V–I characteristic.

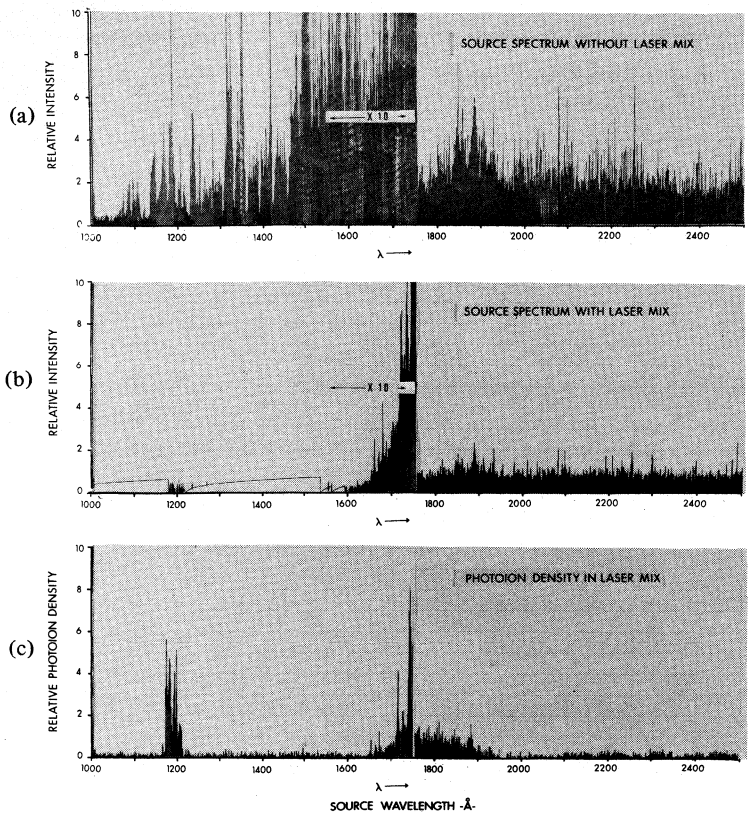


Fig. 14. Photon intensity and photoionization density versus wavelength obtained in (1 : 1 : 8) (CO_2 : N_2 : He) laser mix.

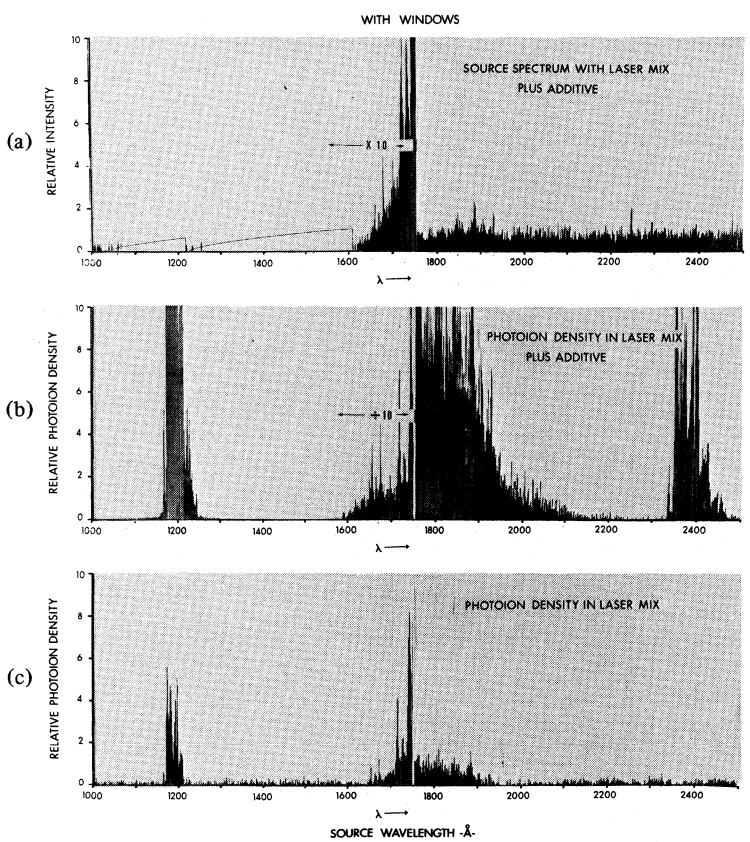


Fig. 15. Photon intensity and photoionization density versus wavelength obtained in (1 : 1 : 8) (CO_2 : N_2 : He) laser mixture with tripropylamine additive.

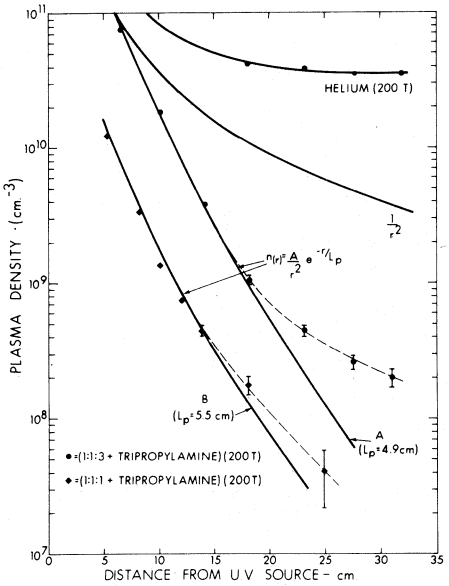


Fig. 16. Photoelectron density versus distance from a single UV source obtained in laser mix with tripropylamine additive showing effective photon mean free path.

aperture or highly doped devices, however, a two-step process centered on a 100-Å-wide photon band at 1750 Å serves as the major contributor to volume ionization. The above statements are consistent with experience obtained with a variety of experimental photoionized TEA lasers. In large-aperture or highly doped machines no significant change in performance was observed while using several different UV source geometries and driving circuits even though many of these systems were known to be poor generators of very short wavelength radiation.

UV Source Considerations

A series of measurements of spark source intensity as a function of time were performed. Fig. 17 demonstrates a typical result. Both optical intensity and discharge current are shown versus time for 2000-Å emission. A delay of about 50 ns is generally observed before the onset of appreciable UV production. Moreover, the variation in optical intensity occurs at double the ringing frequency of the discharge circuit. Such a condition is consistent with maximum generation of UV intensity occurring when discharge current is maximum. If this is indeed the case, then for a given maximum operating supply voltage V_0, usually determined by insulation considerations of the UV source structure, optimum utilization of input electrical energy should be achieved with spark source discharge circuits of minimum inductance. If, however, V_0 is not limited, increased overall efficiency in UV production should be attained through a reduction of both inductance and capacitance of the discharge circuit. This implies that circuits with high ringing frequencies are then desirable.

In contrast, some previous, though limited, evidence suggests that hard UV production may not, in fact, occur at the current maximum but rather when the rate of change of current is a maximum [21]. This situation would also yield a double frequency in the optical intensity, as in Fig. 17. This being the case, it is desirable at this point to more closely examine the

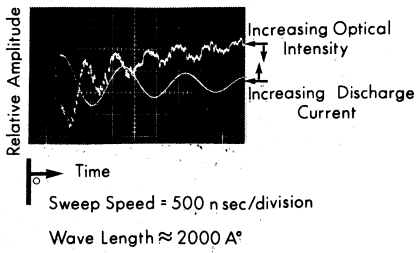


Fig. 17. Time-resolved emission intensity and discharge current for a UV spark source.

UV source circuit parameters in an effort to resolve the uncertainty.

In a typical series *RCL* circuit of the type used to drive spark sources, it is easily shown that for small R the time-dependent discharge current is given as

$$i_{(t)} = I_0 \sin \omega t$$

where

$$I_0 = V_0 \frac{\sqrt{c}}{\sqrt{L}}$$

is the peak value of the discharge current, and $\omega = 1/\sqrt{LC}$ is the ringing frequency of the circuit. Correspondingly, the rate of change of current is simply

$$\frac{di_{(t)}}{dt} = \omega I_0 \cos \omega t$$

and so the maximum value of di/dt becomes

$$\frac{di}{dt_{(\max)}} = \frac{V_0}{L}.$$

Consequently, if the UV production is directly proportional to the rate of change of current, a plot of log photon intensity versus log inductance should give a straight line with unity slope. On the other hand, if the UV emission is directly controlled by the maximum current density, a line with a slope of $\frac{1}{2}$ should be obtained. To further clarify the above situation, additional measurements shown in Fig. 18 were performed. Here the spark source intensity measured at both the 1200- and 1750-Å bands is plotted as a function of circuit inductance. The slope of both curves is nearly 0.5 to 1 which suggests that maximum current density is the controlling parameter in hard UV production.

In actual practice it is usually found that the minimum spark circuit inductance is limited by geometrical and scale considerations imposed by the laser structure itself; consequently it becomes expedient in such instances not to attempt operation at highest efficiency but rather to use the largest supply voltage feasible and to select the energy storage capacitance to generate the required photon flux.

Plasma Jet UV Source

From the previous data displayed in Fig. 15 it becomes clear that in a photoionized laser most of the source emission spectrum is not utilized, but rather, only two narrow bands play any significant role in photo plasma production. This being the case, for both doped and undoped devices, it seems pru-

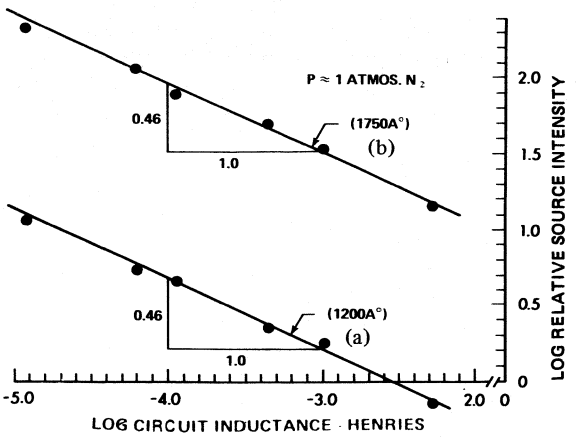


Fig. 18. Relative photon intensity versus circuit inductance for a UV spark source. (a) For 1200-Å band. (b) For 1750-Å band.

dent to attempt development of a special UV source, the emission spectrum of which more closely approaches that which the laser can effectively utilize. It follows, therefore, that for maximum efficiency a source which emits most of its radiation in either or both of the bands at 1200 and 1750 Å should be designed. To this end several UV source geometries were investigated, the most promising of which is the "plasma jet" shown in Fig. 19. Examination of the sectional view reveals that the device resembles a Garton Flash tube, which is known to be an effective but low-pressure hard UV source [22]. The major design changes in this plasma jet are that the output is open to the high-pressure laser gas environment and the primary internal dimensions have been scaled to allow operation in a similar field-pressure regime. Under these conditions the emission spectrum produced by this atmospheric pressure plasma jet source begins to approach that of the Garton Flash tube in that many of the photons are emitted in a 1000- to 1800-Å range. During operation a hot dense plasma is formed inside the ceramic capillary which subsequently expands out of the open end in the form of a highly luminous "jet" or plume. Most of the short-wavelength photons are contained within a 30° cone of radiation, thus giving the device a useful measure of directionality. Experiment has shown that UV performance comparable to that of simple sparks can be achieved in the plasma jet with near an order of magnitude reduction in driving energy. Satisfactory operation has been achieved with as little as 10 mJ of input electrical energy delivered to the plasma jet source. In a typical TEA laser structure a linear array of these devices is mounted along the length of the discharge region, in either a mesh electrode or side-illuminated configuration.

Discussion

An extensive series of measurements of the spark source emission and companion photoionization spectra for the primary CO_2 laser gases has been presented. The results clearly identify nitrogen gas as the dominant source of hard UV photons and CO_2 as the controlling transmittance. It is also shown that in a typical CO_2 laser device only 2 narrow photon bands are utilized in photoelectron production; one 50 Å wide centered at 1200 Å and the other 100 Å wide centered at

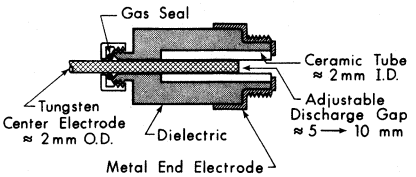


Fig. 19. Sectional diagram of a plasma jet UV source.

1750 Å. The 1200-Å band exhibits a short photon mean free path and as such appears most effective in small-aperture devices whereas the longer range 1750-Å band is more useful in large or heavily doped structures. In the normal undoped CO_2 laser a low-level impurity present in the helium gas appears to dominate the ionization process. This impurity, still to be isolated and identified, shows an ionization threshold of approximately 1600 Å. Further results with spark sources demonstrate that low-energy driving circuits possessing very high ringing frequencies are best for efficient hard UV production.

Conclusion

The data presented give some additional insight into the mechanisms and salient parameters associated with photoionized TEA CO_2 lasers. It is hoped that these results may ultimately provide a focus for further optimization in device performance.

References

[1] A. Javan and J. S. Levine, "The feasibility of producing laser plasmas via photoionization," *IEEE J. Quantum Electron.*, vol. QE-8, pp. 827-832, Nov. 1972.

[2] H. Seguin and J. Tulip, "Photoinitiated and photo sustained laser," *Appl. Phys. Lett.*, vol. 21, pp. 414-415, Nov. 1972.

[3] J. S. Levine and A. Javan, "Observation of laser oscillation in a 1-atm CO_2-N_2-He laser pumped by an electrically heated plasma generated via photoionization," *Appl. Phys. Lett.*, vol. 22, pp. 55-57, Jan. 1973.

[4] O. P. Judd, "An efficient electrical CO_2 laser using preionization by ultraviolet radiation," *Appl. Phys. Lett.*, vol. 22, pp. 95-96, Feb. 1973.

[5] M. C. Richardson, A. J. Alcock, K. Leopold, and P. Burtyn, "A 300-J multigigawatt CO_2 laser," *IEEE J. Quantum Electron.*, vol. QE-9, pp. 236-243, Feb. 1973.

[6] D. B. Cohn and E. R. Ault, "Photo initiated and transversely sustained CO_2 laser," *Appl. Phys. Lett.*, vol. 22, pp. 128-140, Feb. 1973.

[7] O. P. Judd and J. Y. Wada, "Investigations of a UV preionized electrical discharge and CO_2 laser," *IEEE J. Quantum Electron.*, vol. QE-10, pp. 12-20, 1974.

[8] A. E. Hill, "Continuous uniform excitation of medium pressure CO_2 laser plasma by means of controlled avalanche ionization," *Appl. Phys. Lett.*, vol. 22, p. 670, June 1973.

[9] R. C. Lind, "High energy CO_2 laser pumped by a UV sustained discharge," *IEEE J. Quantum Electron.*, vol. QE-11, p. 710, Sept. 1975.

[10] H. J. J. Seguin, K. Nam, and J. Tulip, "High power continuous CO_2 laser Using U.V. stabilized, sustained discharge," to be published.

[11] H. J. J. Seguin, J. Tulip, and D. C. McKen, "Ultraviolet photoionization in TEA lasers," *IEEE J. Quantum Electron.*, vol. QE-10, pp. 311-319, Mar. 1974.

[12] G. A. Mesyats, I. Bychkov, and V. Kremnev, "Pulsed nano second discharges in gases," *Sov. Phys. Uspekhi*, vol. 15, pp. 282-297, Nov. 1972.

[13] A. J. Palmer, "A physical model on the initiation of atmospheric pressure glow discharges," *Appl. Phys. Lett.*, vol. 25, pp. 138-140, Aug. 1974.

[14] J. R. Samson, *Techniques of Vacuum Ultraviolet Spectroscopy*. New York: Wiley, 1967, pp. 212-216.

[15] M. Ross, *Laser Receivers*. New York: Wiley, 1967, pp. 135-137.
[16] H. J. J. Seguin, J. Tulip, and D. McKen, "UV photoionization density measurements in TEA lasers," *Appl. Phys. Lett.*, vol. 23, pp. 344-346, Sept. 1973.
[17] G. L. Weissler, "Photoionization in gases and photo electric emission from solids," *Handbuch der Physik*, vol. 21. Berlin, Germany: Springer, 1965, pp. 304-341.
[18] K. Watanabe, T. Nakayama, and J. Mottle, "Ionization potentials of gases and vapors," *J. Quant. Spectrosc. Radiat. Transfer*, vol. 2, pp. 369-382, 1962.
[19] S. C. Brown, *Basic Data of Plasma Physics*, 2nd ed. Cambridge, MA: M.I.T. Press, ch. 5, 1966.
[20] L. B. Loeb, *Basic Process of Gaseous Electronics*. Berkeley, CA: Univ. California Press, 1961, pp. 690-695.
[21] W. H. Bostick, V. Nardi, and W. Prior, "X-ray fine structure of dense plasma in a coaxial accelerator," *J. Plasma Phys.*, vol. 8, pp. 7-20, Mar. 1972.
[22] W. R. S. Garton, "Improved lyman continuum flash source of large aperture," *J. Sci. Instrum.*, vol. 36, pp. 11-16, Jan. 1959.

Addendum

Since submission of this paper a report of similar work has been published; see R. V. Babcock, I. Liberman, and W. D. Partlow, "Volume ultraviolet preionization from bare sparks," *IEEE J. Quantum Electron.*, vol. QE-12, pp. 29-34, Jan. 1976.

The Self-Heated 442-nm He–Cd Laser: Optimizing the Power Output, and the Origin of Beam Noise

THOMAS F. JOHNSTON, JR., AND WILLIAM P. KOLB

Abstract—**Power output and beam noise parametric results are obtained for the blue transition of the self-heated He-Cd laser in tubes of 0.10–0.16-cm bore diameter. Presentation of this data in the form of performance contour maps shows that the usual scaling laws for laser discharges are accurate for this laser (<12-percent parameter variation for a 60-percent diameter variation) and is a convenient form for use in tube design. The contour maps imply the existence of a direct connection between the output and noise of this laser. A theory is proposed that the noise in the He-Cd discharge arises from the rapid increase in ionization rate due to Penning collisions as Cd is added to the He discharge. This produces a high gain in the discharge column for the growth of striation waves (which modulate the output). The theory correctly predicts the details of the laser noise behavior, showing that both the noise and output share a common origin in the Penning effect. The dependence of Cd vapor density on tube current is found, from sidelight studies, to be more pronounced in self-heated tubes (as opposed to tubes with externally heated Cd sources). A threshold dissipation value is given for puncture of the hot glass bore by the discharge (this is a common failure mode in the He-Cd laser).**

I. Introduction

A. Background and Summary of Results

FOLLOWING the discovery [1]-[3] of laser action at 442 nm in the helium-cadmium discharge by Silfvast, Fowles, and Hopkins using external ovens to heat the metal to the vapor state, the practicality of this laser was greatly enhanced by the introduction [4], [5] of the cataphoretic technique [6] for filling the bore with metal vapor. Using this technique and a constant-current power supply, the discharge is sufficiently stable that the ohmic power drop of the tube can provide the heat to maintain the metal in vapor form (a "self-heated" tube) [7], [8]. These improvements made the He-Cd laser much simpler to build, led to the commercial production of this laser, and focused attention on the refinement of tube characteristics other than output power such as the level of noise on the output beam [8], [9]. Concurrently with these engineering advances, a theoretical understanding was developed for this laser in terms of Penning collisions of helium metastables with neutral Cd atoms as the source of the population inversion in the discharge [10]-[13].

The present paper reports detailed output power and noise parametric results for the self-heated 442-nm He-Cd laser, and then these performance results are applied to discussions of scaling laws, the origin of the noise, and tube design. The primary new results from this study are as follows.

1) The current dependence of the Cd vapor density is shown to be much more pronounced in self-heated tubes (than in tubes with the Cd source in an appendage) due to the direct coupling of the Cd temperature with the tube current (Section III).

2) The noise in the He-Cd laser discharge is shown to arise from the rapid increase in ionization rate, due to Penning collisions, as Cd is added to the He discharge. The large rate of change of ionization frequency produces a high gain for growth of striation waves down the discharge column, and these waves modulate the laser output power (Section IV-C).

3) By operating the tube slightly on the low-Cd-partial-pressure side of the output power maximum, 85 percent of the maximum possible output at 3-percent rms noise can be maintained from a tube of the simple Silfvast [8] construction over

Manuscript received February 17, 1976; revised April 26, 1976.

T. F. Johnston, Jr., was with the Electron Dynamics Division, Hughes Aircraft Company, Torrance, CA 90509. He is now with Coherent Radiation, Palo Alto, CA 94304.

W. P. Kolb was with the Electron Dynamics Division, Hughes Aircraft Company, Torrance, CA 90509. He is now with the Industrial Products Division, Hughes Aircraft Company, Carlsbad, CA 92008.

the operating time required for a 23-percent cleanup of the initial He fill (Section IV-D). (There is a slow loss of He in this discharge which can be reduced to low rates by the means suggested in [14] of separating the Cd deposition region from the active discharge where He^+ ions are produced.)

4) A threshold dissipation estimate for the collapse of a Pyrex bore wall of 250 W/cm^3 is given (Section IV-E). This is the level where the ohmic power generated by conduction of current through the hot bore wall melts the glass locally. From this limit, safe cooling times to protect the tube upon restarting may be calculated.

B. Self-Heated Tube Construction

All of the tubes built in this study were of Silfvast's design [8]. The tube bore in this design is made by slipping Pyrex insert sections of a precision outside diameter into a support tube of a precision (slightly larger) inside diameter as in Fig. 1(a). This permits ready fabrication of the containment section [6] and placement of the machined Cd pellet in the discharge channel, as well as any desired step changes (such as additional Cd sources [8]) along the bore length. (All of the data presented here, however, are for tubes with a single Cd source near the anode.)

In addition in this self-heated design, the dissipation of the discharge input power radially through the glass wall automatically maintains the temperature T_B of the inside diameter of the bore at the 50°C or more greater than the pellet temperature T_{Cd} necessary to prevent deposition of the metal in the bore [7]. For a typical input power per unit length of $W/L = 3.3$ W/cm, the temperature drop between the inner wall of diameter $D = 0.12$ cm to the outer diameter $D_0 = 0.63$ cm of the Pyrex bore insert is given by [15]

$$T_B - T_0 = \frac{W}{2\pi L k} \ln (D_0/D) \tag{1}$$

as 69°C where the thermal conductivity of Pyrex is $k = 3.0 \times 10^{-3}$ cal · cm^{-1} · s^{-1} · (°C)$^{-1}$.

Due to the much larger thermal conductivity of Cd of 0.22 cal · cm^{-1} · s^{-1} · (°C)$^{-1}$, the radial temperature drop through the Cd pellet of the same dimensions is only 0.9°C so that the pellet may be considered isothermal at temperature T_{Cd}. The outer wall of the support tube dissipates heat to the surrounding convective air flow, and within a few degrees, the same outer wall temperature is measured at the location of the Cd pellet (wall temperature T_W) as along the bore insert. Thus the difference in radial temperature drops maintains the desired condition $T_B > T_{Cd} + 50$°C. Note that according to (1) the wall temperature T_W measured at the Cd pellet is typically 19°C less than the actual T_{Cd}.

Tubes with this bore design were constructed in two versions as summarized in Table I. The sidearm version of Fig. 1(b) used a neon-sign cathode and was convenient for direct measurement of wall temperatures as part of the parametric data. The coaxial version of Fig. 1(c) using an aluminum cold cathode is simpler to heat properly to produce a small He gas cleanup rate and the greater tube symmetry simplifies the laser head package. All output powers measured here are for TEM_{00} transverse mode operation.

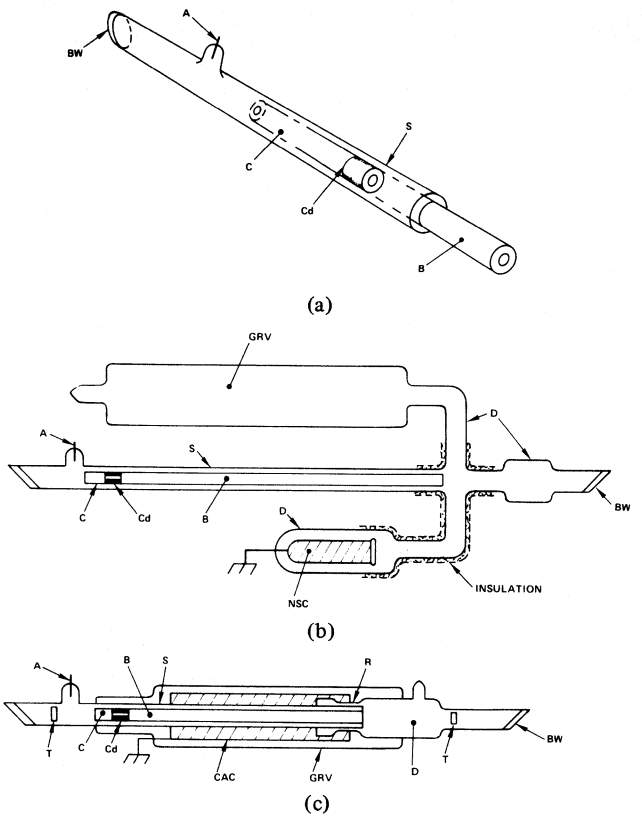


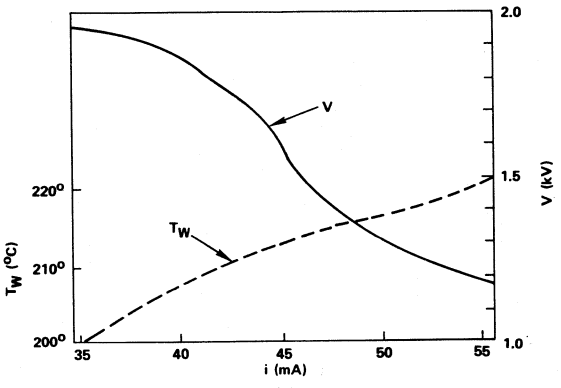
Fig. 1. Tube construction. (a) Insert geometry: *A*, anode; *B*, bore insert (0.630-cm OD); *BW*, Brewster window; *C*, containment insert; Cd, cadmium pellet (0.630-cm OD by 0.63 cm long); *S*, support tube (0.635-cm ID × 0.99-cm OD). (b) Sidearm tube cross section: *D*, cadmium deposition region; *GRV*, gas reservoir volume; *NSC*, neon-sign cathode. (c) Coaxial tube cross section: *CAC*, cold aluminum cathode; *R*, reentrant discharge region; *T*, cadmium vapor trap.

TABLE I
TUBE DIMENSIONS

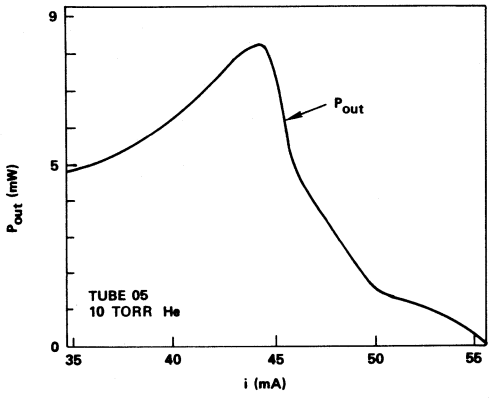
Tube No.	Sidearm	Coaxial	Bore Insert ID (cm)	Bore Insert Length (cm)	Containment Insert ID (cm)	Containment Insert Length (cm)
03	X		0.160	24	0.180	5.0
05	X		0.100	20	0.160	3.8
06	X		0.160	32.5	0.180	5.0
08	X		0.119	38.1	0.160	2.0
16		X	0.140	40.1	0.180	2.5
22		X	0.119	40.1	0.160	2.5
23		X	0.119	40.1	0.160	2.5
LR-1		X	0.251	75	0.40	4.1

C. Discharge Characteristics

The typical characteristics of a tube of either construction are shown in Fig. 2. With increasing current i, the wall temperature T_W at the cadmium pellet increases until a few millitorr partial pressure of Cd enters the bore. The easily ionized Cd decreases the anode voltage, and the T_W rise with current slows somewhat. Maximum laser output occurs just prior to the knee of the V versus i curve, where the discharge color turns from the pink of a pure He discharge to the white of an He-Cd discharge (due to a balance between the yellow He



(a)



(b)

Fig. 2. Tube characteristics with constant heat sinking. (a) Anode voltage and wall temperature at the location of the Cd pellet versus tube current for a 0.10-cm diameter × 20-cm bore tube. (b) Output power for the same tube.

spectral line at 587.5 nm, and the Cd ion line at 441.6 nm and Cd neutral-blue lines). At higher tube currents the discharge turns bright blue as the neutral Cd visible triplet spectra dominate. The heat capacity of the surrounding glass inserts can maintain an excessive Cd pellet temperature for a few seconds after the anode voltage falls, and these regions of blue discharge can propagate in bursts down the tube from anode to cathode (with a time constant on the order of a second), an effect called a "blue wave." (Goldsborough [4] referred to this as a "shock wave" discontinuity.) To avoid this and maintain the proper Cd temperature control, a power supply regulated for constant current is used with this tube construction [8], and operation is restricted to currents less than that at the output power maximum.

II. Parametric Data

A. Experimental Arrangement

The most difficult variable to control in metal vapor lasers is the metal source temperature, because the heat capacity of the metal pellet and adjacent materials makes this variable depend on the previous discharge input power. Thus the arrangement of Fig. 3 is convenient for taking parametric data. The pellet is first cooled by adding external heat sinking (either forced air or a finned heat sink) and then as T_W freely rises upon removal of the heat sink, an X-Y recorder plots the dependent variable versus T_W. Adjustments to the amount of glass wool

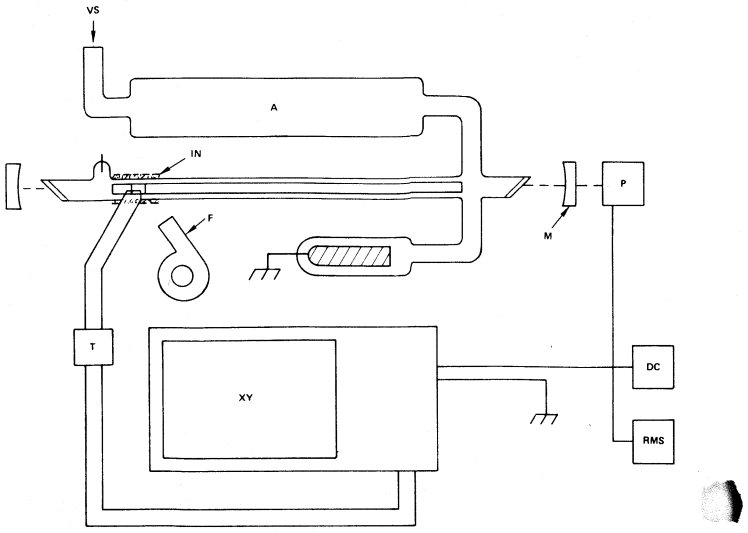


Fig. 3. Apparatus used for parametric measurements. A, He-Cd laser tube; DC, dc voltmeter; F, fan used to cool Cd pellet; IN, glass wool insulation; M, resonator mirror; P, silicon solar cell power meter; RMS, rms voltmeter (10 Hz–4 MHz bandwidth); T, thermocouple monitoring the Cd pellet temperature; VS, connection to vacuum station; XY, X-Y recorder.

insulation draped over the tube at the pellet location are made to keep the time per recorder trace constant (with input power variations) at about 4 min.

Data taken this slowly are reproducible if rising T_W traces are compared (the same trace, if recorded with T_W falling, is shifted to higher temperatures by about 4°C). The independent variables (isotopic He^3 or He^4 fill pressure, tube current) are stepped a fixed amount between traces to generate a family of curves. The dependent variables recorded are the laser output power P_{out} and the rms noise on the output beam (taken as the ratio of the rms noise voltage in a 10-Hz-1-MHz bandwidth to the dc signal level). Data on tubes of several different bore diameters (see Table I) were taken to account for this geometrical variable.

If the mounting of the thermocouple to the tube shown in Fig. 3 is altered slightly, a shift in the T_W axis can result due to a change in thermal contact resistance. When such changes occurred, a correction was made by shifting the low T_W scale upward to make the output power peaks for identical discharge conditions coincide. The same correction of a few degrees centigrade shift of the temperature scale was made when comparing data taken statically (point by point, with constant T_W) with rising T_W data. All of the noise data were taken point by point.

The output data are most accurate near the peak of the profile, away from the threshold for lasing. The resonator was slightly undercoupled to reduce the effect of threshold; but an optimum output power was separately determined for each tube for use in discussing scaling laws.

B. Profiles with p_{He} Stepped

A typical family of curves generated when the helium fill pressure p_{He} is stepped (with constant current) is shown in Figs. 4 and 5. The output power traces peak asymmetrically with a width at half-maximum of about 20°C. Maintaining the

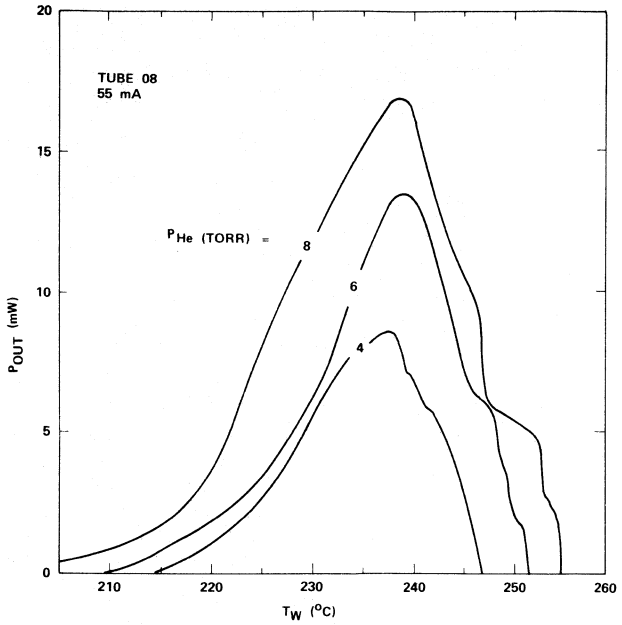


Fig. 4. Parametric data with the pressure of the He^4 component decreasing from optimum. For each p_{He}, the output power as a function of cadmium pellet temperature is given for a tube of 0.119-cm bore diameter.

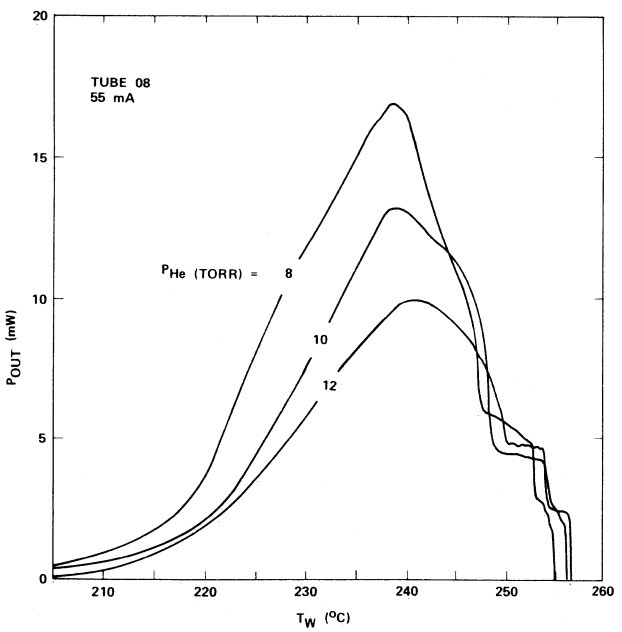


Fig. 5. Parametric data with the pressure of the He^4 component increasing from optimum. For each p_{He}, the output power as a function of cadmium pellet temperature is given for a tube of 0.119-cm bore diameter.

proper Cd pellet temperature is critical; for outputs of 90 percent of maximum or greater, T_W must be within ±3°C of the optimum value. The trace asymmetry is due to the exponential rise of p_{Cd} (Cd partial pressure) with pellet temperature which compresses the horizontal scale of the trace after the peak. The same discharge color changes discussed for Fig. 2 occur here, with the staircase-like drops in power at the high-temperature end of the trace coinciding with episodes of "blue waves." Note that the temperature giving maximum output power changes very little with helium fill pressure.

C. Profiles with i Stepped

With p_{He} fixed and 10-mA steps made in the tube current i, data such as those given in Fig. 6 are generated. The obvious new feature here is that T_W at maximum output decreases systematically with increasing tube current. This is understood as follows. The anode voltage varies with T_W in the fashion shown in Fig. 2 for each trace; and in particular, the same value of anode voltage is observed for all traces at the output power maximum. The 10-mA current change then represents a fixed input power step $\Delta W = \Delta iV$ between traces, which by (1) implies a 3.7°C increase in the temperature gradient $T_{Cd}-T_W$ through the support tube wall for each step increase in i. This is just the size of the backward (decreasing) temperature step between traces; thus, by referring back to the actual pellet temperature, we find the optimum value of T_{Cd} is a constant, independent of i.

Thus in the self-heated He-Cd laser, the main dependence of the laser output on discharge current is seen to be through the heating effect of the current on the Cd pellet. If the Cd temperature is optimized independently of i, the output dependence follows the envelope of the traces in Fig. 6 which gives a broad curve similar in form to that reported [9] for a laser with external heating control. The intrinsic dependence of output power on tube current (the current saturation effect) is so slight that it becomes practical in the self-heated laser to use small adjustments (of a few milliamperes) of the tube current around the nominal value to tune T_{Cd} to the critical, optimum pellet temperature.

In Fig. 6 the traces were taken starting with 70 mA, then decreasing in steps to 50 mA, followed by increasing steps from 80-100 mA. The slight distortion of the 80-mA trace would have been avoided if the tube had been run a few minutes longer at 80 mA to fully heat the bore before allowing the T_W rise to begin. The distorted trace was included in Fig. 6 as an indication of the limits of reproducibility of the present method of recording data.

D. Contour Plots.

The large amount of data collected can be presented compactly in the form of contour plots (Figs. 7-10). Data such as those given in Fig. 4 represent a set of profiles of the "elevation" of the output-power "hill," along a constant-p_{He} path, in the p_{He}, T_W plane. To construct contours from the profiles, the power scale is normalized (at 100 percent) to the maximum power observed, the points representing 80 percent (60 percent, etc.) of this power are plotted in the plane of the independent variables, and a smooth curve (contour line) is drawn through the plotted points. Similar contour lines describe the beam-noise "valley." The plots are made using the quantities $p_{He}D$, or i/D on the axes so that contour results from tubes of different bore diameters may be directly overlaid in evaluating the scaling laws [4], [8], [9] (Section IV-A) proposed for the He-Cd laser.

In general shape, the output power rises as an elliptically contoured hill elongated in the direction of the p_{He} axis and compressed along the Cd temperature axis. In Fig. 7, for example, the region where P_{out} is 80 percent or more of the

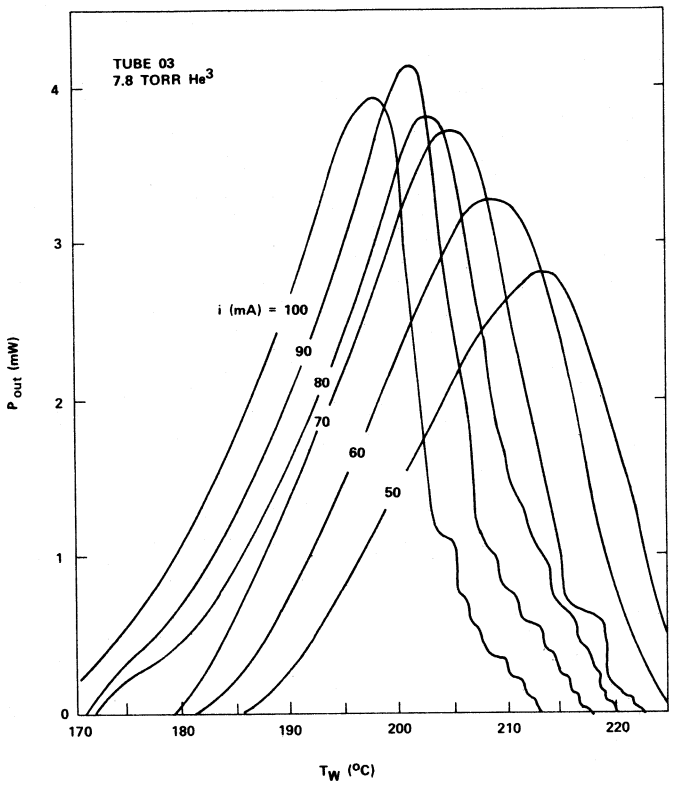


Fig. 6. Parametric data with 10-mA step changes in tube current as a parameter. For each i, the output power as a function of cadmium pellet temperature is given for a tube of 0.160-cm bore diameter.

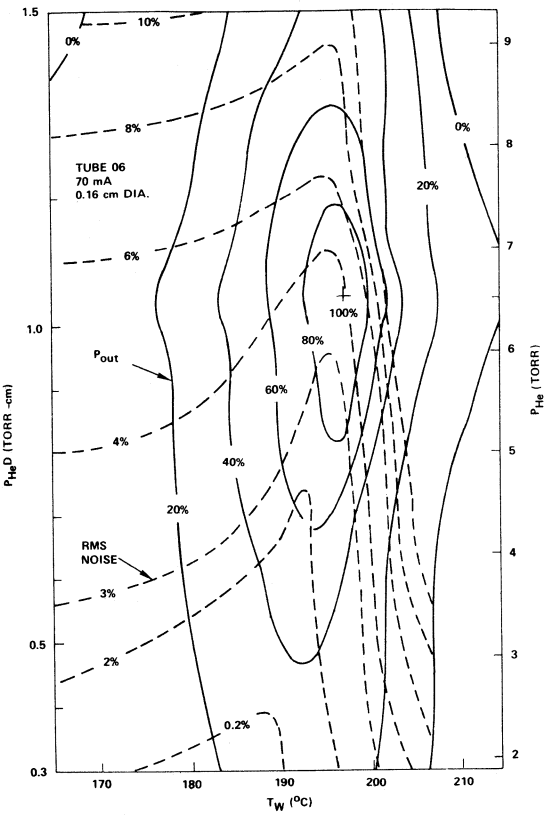


Fig. 8. Power output and beam noise contour plot for a constant 70-mA current in a tube of 0.160-cm bore diameter; the normalization power (100 percent) is 14.5 mW.

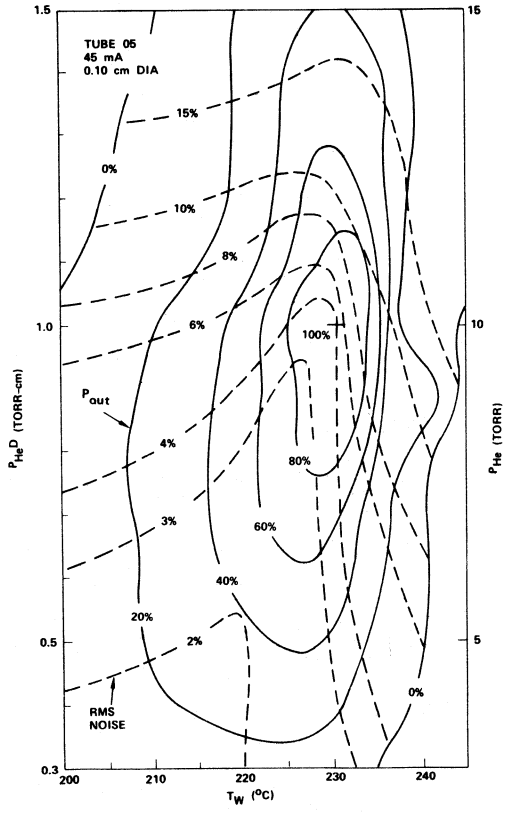


Fig. 7. Power output and beam noise contour plot for a constant 45-mA current in a 0.100-mm-bore-diam tube; the normalization power (100 percent) is 9.0 mW.

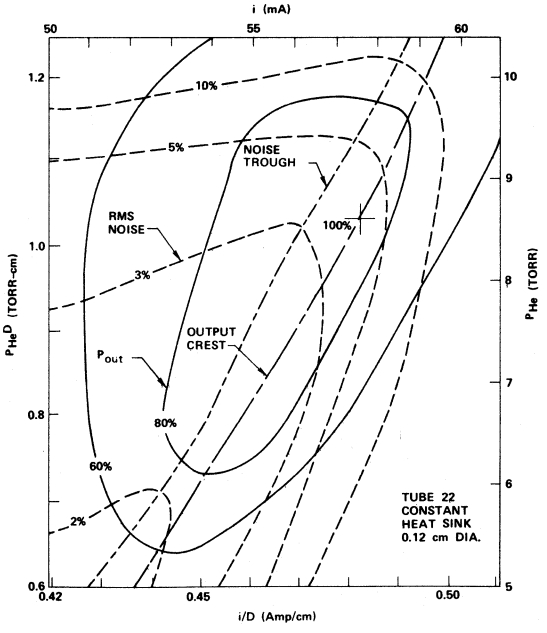


Fig. 9. Power output and beam noise contour plot constructed from data taken point by point on a coaxial tube of 0.119-cm bore diameter; the normalization power (100 percent) is 25 mW.

maximum encompasses about a 40-percent change in helium pressure but only a 4-percent change in the temperature rise of the Cd source above the 25°C ambient air. The crest of the hill follows a constant temperature line at high He-fill pressures, and then swings slightly towards lower T_W as the input power

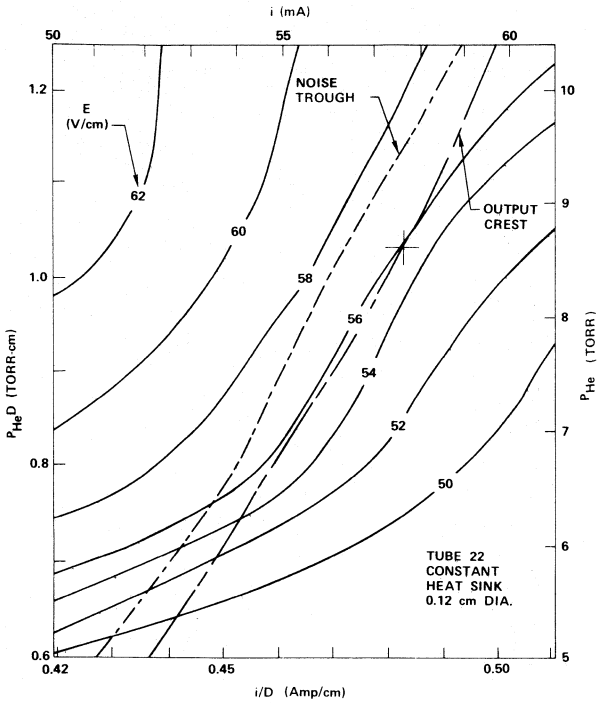


Fig. 10. Axial voltage contour plot constructed from point-to-point data taken along with those for Fig. 9.

(and thus according to (1), the temperature gradient through the support tube wall) drops with lower He pressures.

The noise contours describe a valley rising steeply in the direction of increasing pellet temperature, and rising more gently with He pressure. The valley trough or minimum closely parallels the output crest, but is offset from it by from 2° to 3°C lower T_W values; this relationship is discussed further in Section IV-C. The frequency spectrum of the noise is complex, with many independent components in the range from 200-500 kHz. Frequencies in the high end of this range dominate in the low-noise regions of the valley, with the large-amplitude components dropping in frequency with the increase of either helium or cadmium partial pressures.

Figs. 9 and 10 are constructed from data taken point by point on a coaxial tube; here T_W increases with i (in proportion to the input power iV). The offset between the minimum of the noise valley and maximum along the top of the output power hill is emphasized by drawing these extremes in as dashed lines. Note in Fig. 10 that both extremes follow contours of constant axial electric field, E, near the output-power maximum [4].

III. Sidelight Studies

The data presented so far are averaged over the active volume of the tube. There has been some question in the literature [8], [9] about the uniformity of discharge conditions along the bore in self-heated tubes. This question was examined experimentally here by means of sidelight studies similar to [6] to assess the effect of axial changes on the foregoing parametric results. As in Sosnowski's case, to correct for tube-wall transmission variations due to dark deposits which build up along the bore of the He-Cd laser, calibration scans of the 492.1-nm He-line sidelight intensity were taken at low current, with no Cd in the tube bore. This wall transmission was used to correct the 479.9-nm (neutral Cd) and 441.6-nm (ionized Cd) spontaneous intensities measured versus distance along the bore under discharge conditions appropriate for lasing. A fiber-optic bundle conducted the sidelight to an 0.5-m Jarrel-Ash monochrometer used for line selection, with the data plotted on an X-Y recorder.

The results, Fig. 11, show that a discharge-heated tube behaves very differently from one with the metal source contained in an appendage with the source temperature controlled by an external oven, such as was studied in [2]. There the increase of Cd neutral density with current began to level off (saturate) with increasing current, while here the Cd density continues to rapidly increase since the heat input to the source rises with i. The average Cd density in the blue discharge which occurs at 70 mA is about a factor of 10 greater than the Cd neutral density at the optimum lasing conditions of 50 mA.

Sosnowski analyzed the axial Cd density profile to be expected when cataphoresis in the discharge distributes the metal from a hot source near the anode, to a condensation sink near the cathode. This case is described by a dimensionless cataphoretic-pumping parameter β (the ratio of the forced diffusion effect for ions, due to the axial electric field, to the ordinary diffusion effect [16]). A simplified method was used here to determine the β values associated with the profiles of Figure [11]. Let z_f be the axial distance from the source where the density profile drops to a fraction $f < 1$ times the initial density n_0 at the source, and L be the distance between source and sink. Then for large $\beta(\beta > 3)$, an approximate solution for β, (2) below, may be derived from Sosnowski's profile equation describing the source to cathode region:

$$\beta \cong \frac{-\ln(1-f)}{(1-z_f/L)}. \tag{2}$$

In using (2), the flat portion of the profile was extrapolated back (dotted lines in Fig. 11) to the origin as in [6] to find the initial density n_0, since the experimental value exactly at the source $z = 0$ is anomalously large. The fractional ionization α of the Cd vapor in the discharge is given [6] from β by

$$\alpha = \frac{\beta k T_{\text{gas}}}{eEL}. \tag{3}$$

Our gas temperature was 313°C and the measured axial voltage gradients E for our $L = 38$-cm tube are given in Table II. The results for β (obtained from (2) with the choice $f = 0.8$), for α [via (3)], and the output powers and wall temperatures for the profiles of Fig. 11 are also shown in Table II.

Over the 40-60-mA range of currents where maximum lasing occurs, β exceeds 10 and the neutral Cd density variation over 80 percent of the bore length is less than ±10 percent of the average value, so that the bore-averaged parametric results are representative of the incremental discharge conditions. Thus valid scaling laws for changes in bore diameter and length can be derived from our parametric data (Section IV-A).

The axial variation of several other variables was measured, including the 441.6-nm spontaneous sidelight intensity and the inversion ratio $INR = n_2^+/n_1^+$. The inversion ratio was obtained

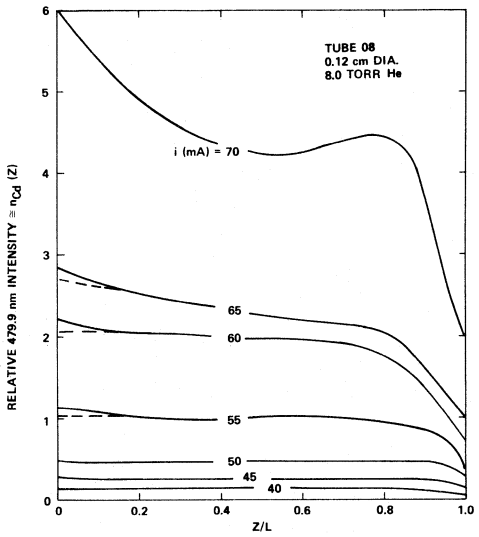


Fig. 11. Neutral Cd sidelight intensity as a function of axial distance along the bore ($z = 0$ is the Cd source and $z = L$ is the Cd sink) with the tube current as parameter.

TABLE II
CATAPHORETIC PUMPING PARAMETERS DERIVED FROM THE NEUTRAL CD DENSITY AXIAL PROFILES OF FIG. 11

i (mA)	E (V/cm)	P_{out} (mW)	T_W (°C)	β	α
40	70	7	196°C	31	5.9×10^{-4}
45	68	10	200°C	21	4.2×10^{-4}
50	61	16	205°C	13	2.9×10^{-4}
55	58	10	209°C	13	3.1×10^{-4}
60	51	5	209°C	10	2.5×10^{-4}
65	50	3.5	215°C	4	1.1×10^{-4}
70	38	0	212°C	2	7.5×10^{-5}

by the method [17] of analyzing the fractional change in upper laser level population as a function of intracavity beam intensity. Here n_2^+ is the density of Cd ions in the upper laser level and n_1^+ that in the lower level. From this, several conclusions may be drawn. There is a 4-5-cm-long length on the cathode side of the Cd pellet in which the cataphoretic pumping "catches hold" of the metal vapor and the normal (cataphoretic profile) Cd density and normal inversion ratio are established. The inversion ratio is $INR = 3.0$ over most of the bore, but is $INR = 2.7$ at the Cd pellet. The Cd pellets in a multiple-pellet design [8] should not be spaced too closely or this effect will reduce the output power. Fig. 11 can, in fact, be interpreted as showing that a single pellet is sufficient for bore diameters as small as 0.12 cm.[1]

[1]For the largest bore diameter (of the sidearm tubes) of 0.16 cm, six magnets were placed along the bore to provide a transverse, inhomogeneous magnetic field of 500-G peak value, oriented at right angles to the light polarization. This raised the output power +38 percent and brought the P_{out}/LD constant for this bore up to that for the other bore diameters. Much smaller effects (+4 percent) were seen with magnets on the smaller bore diameters. About half the increase for the 0.16-cm bore was reached only after 2 h of stabilization when dark Cd deposits appeared in the bore opposite the magnets. This much power change can therefore be attributed to a more uniform Cd distribution over the bore length, which is apparently more difficult to achieve in larger bore diameters (see [8]). The other half is due to a Zeeman effect, probably causing reduced radiation trapping in the decay of the lower laser level, which is significant only in large diameters.

Over the range of currents giving lasing, the 441.6-nm Cd ion density profiles closely followed the 479.9-nm Cd neutral density profiles. This supports the assumption made in Sosnowski's analysis [6] that the fractional ionization α in the discharge is a constant independent of the axial distance from the metal source. The rms noise level on the 441.6-nm sidelight increased in moving down the bore from 4.5 percent at the Cd source (near the anode) to 1.8 times this at the cathode end of the tube.

From the inversion ratio measurement, there may be derived the factor by which the total upper level population exceeds the difference between laser level populations. By measuring the output power and using the analysis of [17], an upper level population density $n_2^+ = 4.1 \times 10^{10}$ cm^{-3} is obtained for optimum conditions (50 mA) in our 0.12-cm-diam tube. Combining the percentage ionization $\alpha = n^+/n_0$ results from Table II with the neutral density n_0 (computed from the vapor pressure curve [11] for Cd and the measured source temperature $T_{Cd} = 257$°C) gives an estimate of the total Cd ion density n^+. At currents up to the optimum value of 50 mA, comparison of these values shows that most of the Cd ions are in the upper laser level. This level is preferentially pumped [10]-[13] by Penning collisions with He metastables. Thus the present results support the conclusion reached previously by other authors [10], [12] that the Penning effect is the dominant Cd ionization process in the He-Cd laser discharge. This fact leads to the propagation of large-amplitude ionization waves (striations) in the discharge which generate noise on the laser output beam (see Section IV-C).

IV. APPLICATIONS OF THE PERFORMANCE CONTOURS

A. Scaling Laws

If the parameters of independently optimized laser tubes of different bore diameters are compared, there result several rules describing the effect of this change in scale. General discussions of discharge scaling [18], [19] show that the rates of many processes remain the same if the total pressure p of a gas fill of fixed mix ratio is adjusted to maintain

$$pD = \text{constant} \tag{4}$$

with changes in diameter. In particular, where ionization occurs by the Penning effect or single-step electron impact, and electron loss is determined by ambipolar diffusion (conditions expected in the positive column He-Cd discharge), then (4) results in

$$E/p = \text{constant} \tag{5}$$

$$kT_e = \text{constant} \tag{6}$$

where kT_e is the mean energy of the Maxwellian electron-energy distribution. If the pressure which maximizes the laser output is used to evaluate the constant in (4) for one bore diameter, then for other diameters, p is proportional to D^{-1} and (5) becomes

$$ED = \text{constant}. \tag{7}$$

In a laser like He-Cd where the population inversion depends on the population of helium metastables, a rate-equation analysis (such as that given by Gordon and White [20]-[22] for the He-Ne laser) shows that there is an optimum value of

TABLE III
SCALING LAWS FOR SELF-HEATED 442 NM He^4-Cd^{nat} LASERS (VARIATION OVER 60-PERCENT DIAMETER CHANGE)

Quantity Units	$p_{He}D$ torr · cm	ED volts	i/D A/cm	g_0D	P_{out}/LD mW/cm^2	ϵ/D cm^{-1}	$p_{Cd}D$ torr · cm	$\Delta p_{He}D$ @ 0.5 P_{max} torr · cm	Noise (10 Hz–1 MHz) @ P_{max} percent rms
Mean	1.00	7.6	0.43	1.4×10^{-4}	4.3	1.4×10^{-3}	2.5×10^{-4}	0.93	4.0
Fractional standard deviation	±4 percent	±6 percent	±5 percent	±13 percent	±5 percent	±12 percent	±90 percent	±12 percent	±30 percent

n_e/p which maximizes the gain

$$n_e/p = \text{constant}. \tag{8}$$

(n_e is the electron density.) Since $n_e \sim i/D^2$, with (4) this becomes

$$i/D = \text{constant}. \tag{9}$$

Also at optimum pD and n_e/p, the incremental gain g_0 is proportional to the active species density, or by (4),

$$g_0D = \text{constant}. \tag{10}$$

The laser output is proportional to the gain times the active volume $P_{out} \sim g_0LD^2$ and the laser efficiency ϵ is the ratio of output to input power iEL so that by (9) and (10)

$$\frac{P_{out}}{LD} = \text{constant} \tag{11}$$

and

$$\frac{\epsilon}{D} = \text{constant}. \tag{12}$$

The six scaling laws (4), (7), and (9)–(12) are tested and found valid in Table III from parameters evaluated at the output-power maxima (100 percent points) of the contour plots for sidearm tubes of 1.00-, 1.19-, and 1.60-mm diameter (a 60-percent bore diameter change).

The mean m and fractional standard deviation $\pm\sigma/m$ (in percent) calculated for these constants from the three data points are also listed.

Data on coaxial tubes were not included in the table, as the insulation added by this construction has the two adverse effects of increasing the hysteresis in laser performance with temperature changes and making the tube parameters depend slightly on the tube packaging.

Although the mix ratio p_{Cd}/p_{He} was not held constant in our parametric measurements, each partial pressure was optimized as previously described. The cadmium partial pressure was calculated [11] from the measured wall temperature and the large standard deviation for the $p_{Cd}D$ constant is due to inaccuracies in measuring T_W (mainly variations in thermal contact resistance between tubes). As shown in Fig. 2 and elsewhere [4], the tube voltage is sensitive to the cadmium partial pressure and a better estimate of the true variation of $p_{Cd}D$ with diameter is given by the fractional standard deviation of ED. (The analysis of Fig. 6 demonstrated that constancy of i/D is also a measure of the constancy of $p_{Cd}D$ in self-heated tubes.) Included in Table I is $\Delta p_{He}D$, a measure of the change of helium pressure encompassed by the 50-percent output-power contour, which shows that in laser scaling [where (8) is valid] the slopes of the output-power hill do not scale as accurately as the peak.

For each tube at optimum discharge conditions, the output coupling was experimentally varied with an intracavity reflecting attenuator, where both the power reflected out of the resonator and that transmitted through the output mirror are summed to measure the output power under optimum-coupling conditions. These optimized P_{out} values[1] were used in computing P_{out}/LD. The inserted loss, with the attenuator adjusted to put the laser at threshold, was added to the known cavity diffraction, transmission, and absorption losses to determine the gain per pass g_0L (and thus g_0D), for each tube. This gain constant is about half that found by Silfvast and Szeto [8]; both results are for the naturally occurring isotopic mixture of Cd (but note below a correction to the output power and gain constants listed in Table III).

The performance results reported in Table III for sidearm tubes were improved upon when coaxial tubes (Figs. 1(c), 9, and 10) were constructed. All self-heated tubes require a few hours when the Cd is first brought up to temperature for the pellet to develop a stable vapor-emitting surface and, thus, a uniform Cd vapor profile along the bore. Studies with coaxial tubes showed that this process can require 50–100 h of operation to reach completion, during which time the maximum obtainable power from the tube slowly rises. Most of the parametric studies on sidearm tubes were done after 10 h but before 50 h of operation.

Also, the suggestion [23] has been made that the addition of an insulator coaxial with the bore (making the bore temperature more uniform) improves performance. The full-length coaxial aluminum cathode and coaxial gas reservoir bottle of Fig. 1(c) serve in this capacity.

Our experiments indicated that the pellet aging probably has the most influence on P_{out} and this effect applies to tubes of both constructions. In any event, several coaxial tubes of 0.12-cm diameter were found to optimize with current, voltage, and pressure constants compatible with Table III, but with an output constant of $P_{out}/LD = 5.1$ mW/cm^2, an 18-percent increase for this and the efficiency constants. The measured increase in the gain constant was about double this amount (to 2.0×10^{-4}). This improvement makes the difference negligible between the output performance of self-heated tubes of Silfvast's design and those of the more complicated vented-bore construction [9].

B. Noise Behavior with He^3 and He^4 Fills

The behavior of the noise on the output beam is too complicated to be adequately described just by the scaling law

implied in Table III, that is, the noise at maximum output power is a constant independent of diameter. The observed noise frequency spectrum, sidelight observations, and noise waveforms on the discharge current and voltage clearly tie the beam noise to moving striations (waves of excessive ionization) propagating in the discharge [8], [9], [24], [25]. In general, many fundamental striation frequencies are present; the difference-beat frequencies between them have long wavelengths and produce large modulations of the output beam at the difference frequencies. The noise on the 442-nm sidelight emission increases in moving from anode to cathode showing that gain exists for striation waves.[2] To reduce noise both this gain and the boundary conditions for launching waves at the tube ends should be controlled. In our experiments, the noise at optimum output (the 100 percent point of the contour plots) increased systematically (although slightly) with bore diameter. But if the larger bore tubes were underfilled ($p_{He}D$ less than 0.65 torr · cm) and the current critically adjusted, the discharge could be made to support only a single-frequency striation wave [8] which does not modulate the output beam (rms beam noise less than 0.2 percent—see the lowest noise contour in Fig. 8).

The beam noise is greater with He^3 fills than with He^4, which is why the fills of the heavier isotope were emphasized in this work. The optimum pressure (the $p_{He}D$ constant of Table III) was found to be 1.10 times larger for He^3. Since the noise increases with p_{He}, this nearly accounts for the 1.25 times larger magnitude of the noise contours found for the lighter fill around the output power maximum. The P_{out}/LD constant was larger by a factor of 1.07 for the lighter isotope, but if the He^3 were underfilled so that outputs at the same noise level were compared, this advantage disappeared.

C. The Origin of the Beam Noise in Penning Ionizations

A concise explanation of the noise behavior of the He-Cd laser is obtained by ignoring the single-striation wave case [8] and the complications introduced by special boundary conditions [9], and concentrating on how the striation-wave gain depends on the discharge parameters.

In modern discharge theory, moving striations are "understood in principle" [27] in the region where the gas pressure and tube current are high enough that axial ambipolar diffusion conditions prevail [27] (as in the He-Cd laser discharge). Then the cycle generating striations is as follows [25].

1) A local variation δZ in the ionization frequency Z (the number of ion pairs produced per electron per second) generates a region of excessive ionization.

2) Axial ambipolar diffusion of electrons depletes the local electron concentration, leaving an excess positive ion concentration.

3) This space-charge separation produces a local variation δE in the axial electric field E, and thus a variation $\theta = k(T_e - T_e|_{equilibrium})$ in mean electron energy.

4) θ generates a variation in ionization frequency δZ to complete the cycle.

For small-amplitude striations the theory is linearized and δZ is calculated as

$$\delta Z = \frac{\partial Z}{\partial kT_e}\bigg|_{\text{equilibrium}} \theta = Z'_\theta \theta. \tag{13}$$

The source term (13) is put into the integro-differential equation describing the cycle outlined above [25], [27], and a solution for the striation-wave incremental gain is found which increases monotonically with Z'_θ, the slope of the Z versus kT_e curve. Large changes in $Z(kT_e)$ occur in the He-Cd discharge with changes in p_{Cd} due to Penning ionizations. While data on the He-Cd mixture are scant, extensive data are available for the Ne-Ar mixture originally studied by Penning [28], [29] which are representative of the form of $Z(kT_e)$ where ionization by collisions with metastables is important. Townsend's second ionization coefficient η is given [28] as a function of E/p ($V \cdot cm^{-1} \cdot torr^{-1}$) and a (the fraction of the low-ionization-potential component in the mixture). η (units of ions V^{-1}) is the number of ions produced per volt of potential drop and is related to Townsend's first ionization coefficient α (ion pairs cm^{-1}) by $\eta = \alpha/E$. The ionization frequency is [25] $Z = \alpha v_d$, where the electron drift velocity v_d is proportional [19, p. 123, eq. (4.21)] to $(E/p)^{1/2}$. Generally, kT_e is proportional [19, p. 244, eq. (8.41)] to (E/p) so we finally arrive at

$$Z = (\text{constant})\, p\eta(E/p)^{3/2} \tag{14}$$

$$Z'_\theta = (\text{constant})\frac{\partial Z}{\partial(E/p)}$$

$$= (\text{constant})\, p\left(\frac{E}{p}\right)^{1/2}\left[\frac{E}{p}\frac{\partial\eta}{\partial(E/p)} + \frac{3}{2}\eta\right]. \tag{15}$$

In Fig. 12 we show the computed function Z'_θ determining the striation-wave gain, obtained from (15) and the η-contour plot given in [28]. The quantities η and $\partial\eta/\partial(E/p)$ were determined graphically along a straight-line trajectory on the contour map from $E/p = 10$ $V \cdot cm^{-1} \cdot torr^{-1}$ at $a = 0$ to $E/p = 5$ $V \cdot cm^{-1} \cdot torr^{-1}$ at $a = 10^{-2}$. Since the ionization potentials of Ne and He are similar, we used the same E/p values in Ne-Ar as were observed in the He-Cd discharge. This E/p versus a trajectory accounts approximately for the variation of axial voltage drop E as Cd enters the discharge with rising T_W (along a constant p_{He} profile that for $p_{He}D$ = 1.00 torr · cm). The resulting $Z'_\theta(a)$ dependence is not sensitive to the precise trajectory chosen. The striation-wave gain is found to go through a shallow minimum near $a = 10^{-5}$ and then rise to a large maximum near $a = 10^{-3}$; this occurs even though E/p was taken as slowly and montonically decreasing[3] with a. From $a = 0$ to $a = 10^{-3}$, η is montonically increasing; the Z'_θ minimum results because the $\partial\eta/\partial(E/P)$ term in (15) decreases (and goes negative) faster than the η term rises at small a.

[2]The noise in hollow-cathode He-Cd lasers is low (less than 0.4 percent rms) due to the short gain length between anode and cathode (typically less than 0.2 cm) in the transverse discharge [26].

[3]If Penning collisions produced a local kT_e maximum as a function of p_{Cd} as was suggested in Silfvast's data [10] on a 10-mm-bore tube, then the existence of a noise minimum (and, in general, the increase of noise amplitude with either p_{He} or p_{Cd}) could be explained in terms of the noise being some monotonically decreasing function of kT_e. Measurements of kT_e by other authors [13], [30] with tubes of the smaller bore diameters more typical of He-Cd lasers have not shown this local kT_e rise, however.

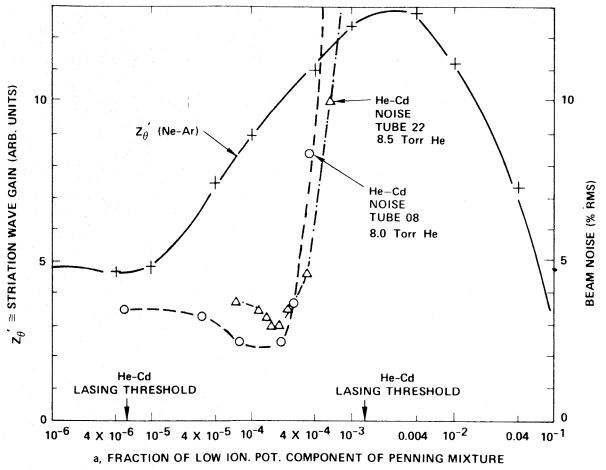


Fig. 12. Comparison of the striation wave gain calculated for a typical Penning mixture (Ne-Ar) with the measured rms beam noise in an He-Cd laser as a function of the fraction of the low ionization-potential component in the mixture.

For comparison, in Fig. 12 there are also plotted data on the rms noise in the He-Cd laser as a function of a. The fraction of Cd in the gas fill was determined by multiplying the value of a for maximum output power (from Table III)

$$a_{\text{opt}} = \frac{p_{\text{Cd}}D}{p_{\text{He}}D} = 2.5 \times 10^{-4}$$

by the ratio of 479.9-nm sidelight intensities (Fig. 11) for other values of T_W or tube current i.

The observed noise minimum and subsequent rise with the Cd fraction are more pronounced than given by the Z_θ' calculation, but this is probably due to differences to be expected between the He-Cd and Ne-Ar Penning mixtures. Since He is considerably lighter than Ne, the mean relative velocity between collision partners is greater in the He-Cd case; and the Penning-collision cross section [11], [12] in He-Cd is somewhat greater than that [31] in Ne-Ar, both of which effects would cause the peak in η values due to Penning collisions occurring over a narrower range of a values. The calculated drop in striation gain with continued increase in a occurs in the He-Cd mixture also (though out of the range of lasing operation), since for large p_{Cd} the quiet, neutral-Cd-dominated discharge [32] typical of fluorescent lamps [33] results.

A decrease in the He-fill pressure in the He-Cd discharge raises the E/p value (see Fig. 10). A computation of Z_θ' for double the E/p values used to generate Fig. 12 was done (corresponding to $p_{\text{He}}D = 0.39$ torr · cm). (The proportionality $Z_\theta' \sim p$ of (15) favors lower noise at reduced pressure.) This gave a broader, deeper striation-gain minimum and a less steep striation-gain rise, in accordance with noise behavior observed for $p_{\text{He}} = 3$ torr in tube 08 (see also Figs. 7, 8). The increased noise with He^3 fills can probably also be ascribed to the pressure factor in (15).

The striation-wave theories [25], [27] also predict the frequencies of the striation waves but the observations [23] of these in He-Cd are too complex to be fit without detailed measurement of $Z(a, E/p)$ for the He-Cd mixture. The single-striation-wave case frequently observed in the 442-nm laser is certainly possible in the striation theory of He-Cd laser noise presented here.

In summary, the noise and the output power of the 442-nm He-Ce laser are related (refer to the parallel loci of extremes shown in Figs. 9, 10) by their common origin in the Penning effect. The Penning collisions greatly increase the rate of ionizations in the discharge, giving rise to gain for ionization waves and thus also the beam noise. At the same time the Cd ions are preferentially produced in these collisions in the Cd^+ ($5s^2\ ^2D_{5/2}$) state, giving rise to a population inversion and thus the laser output. The agreement between theoretical predictions and He-Cd noise observations is remarkably good for a theory based by analogy on measurements in another Penning mixture. A definite need has been demonstrated here for detailed measurements of η, the frequencies of striation waves, etc., to allow a more thorough comparison of experiment with striation theory in the He-Cd discharge.

D. Tube Design with Contours

An example of a tube design based on the preceding sections may be developed as follows. First, Section III showed that only one Cd source was necessary. The scaling laws for this laser (Section IV-A) are the same as those for the He-Ne laser [4], [9], [20]-[22]. Thus the laser output power will be determined in the usual way largely by the active length of the tube, because the bore diameter will be chosen small enough to select TEM_{00} transverse-mode operation (without requiring alignment-sensitive [34] long-radius mirrors). Resonators with Fresnel numbers $N = 1$ to 1.5 give [35] a high ratio of diffraction loss for the TEM_{10} mode to that for the TEM_{00} mode in a short-radius symmetrical cavity. If the maximum practical resonator length l is chosen as 60 cm, there results for $N = 1.2$ a bore diameter $D = (4\lambda lN)^{1/2} \cong 0.11$ cm for $\lambda = 442$ nm. To allow room for a containment discharge, Cd deposition region, and Brewster windows, the active length L is about $(\frac{2}{3})l$ or 40 cm.

The gain per pass for a coaxial tube will be (Section IV-A) $g_0 L = (2.0 \times 10^{-4}/0.11) \cdot (40) = 7.3$ percent/pass. With a TEM_{10} to TEM_{00} mode diffraction-loss ratio of 13 (obtained

[35] for a symmetrical cavity of two 1.2-m radius mirrors), a lowest order mode diffraction loss [35] of 0.2-0.4 percent is found. Together with a measured optimum output mirror transmission of 0.9 ± 0.1 percent, and a mean mirror absorption and scattering loss of 0.2 percent per pass, the gain-to-loss ratio for the TEM_{00} mode is 6.7 to 8.1 and for the TEM_{10} mode it is 1.2 to 2.2. This difference is adequate to secure lowest order mode operation well above threshold while suppressing operation in the next highest order mode. The symmetrical short-radius cavity provides a mode volume with good filling of the bore (this was assumed in deriving the P_{out} constant of Section IV-A), while retaining a low sensitivity [34] to output power decrease from mirror misalignment.

A coaxial tube can then be expected to give a maximum output power (Section IV-A) of $P_{out} = (5.1\ mW/cm^2)\ LD = 24.5$ mW at 4-percent rms beam noise. A better choice of operating point (see Fig. 9) is to provide more stability against temperature drift bringing on a blue wave condition, by reducing the operating current 2-4 percent, cooling the Cd pellet down to the noise-minimum point where 20-21.5 mW at 3-percent rms noise is obtained. The performance contour plot for a tube of this design (see Fig. 9, upper and right-side coordinates) provides a compact description of the changes expected in the tube over its operating life. With running hours, the He fill pressure slowly drops due to gas cleanup (Section I-A). Since the discharge tube is operated with a constant-current power supply, this change with time traces out on Fig. 9 a vertical line (a "life-history" line). Thus if the tube were sealed off at $p_{He} = 8.5\ T$ and the current set up at $i = 56$ mA, over the operating time required to produce a 1-torr loss of helium, we would expect the output power to rise to 23 mW and the noise to fall to 2.8 percent rms from the initial values given above.

E. Erosion and Puncture of the Glass Bore by the Discharge

A type of tube failure peculiar to the He-Cd laser is the puncturing of the bore wall by the discharge in a coaxial design, which can occur if the high potential used to start the tube is applied while the bore is still hot from previous operation.

When heated from room temperature to 400°C, the electrical resistivity of Pyrex drops by a factor [36] of 10^{-8}. It is this great change that creates the restart failure mode where the tube current is conducted through the wall and down the coaxial chamber to the cathode, bypassing the remaining length of bore. This occurs at the hottest spot on the bore closest to the high voltage end; the conduction current through the wall further heats the glass leading to the local melting and puncture of the wall shown in Fig. 13.

The "finger" in the center of the photo is a hollow zone formed in the softened glass projecting from the inner capillary surface about two-thirds of the way through the 0.33-cm-thick Pyrex wall. The exiting electron flow has raised a small dome on the outer surface of the bore, indicating the whole column of glass in the region of the finger was softened. The dark U-shaped object surrounding the finger is a crack in a region which evidently remained cool, caused by the strain from the melted region.

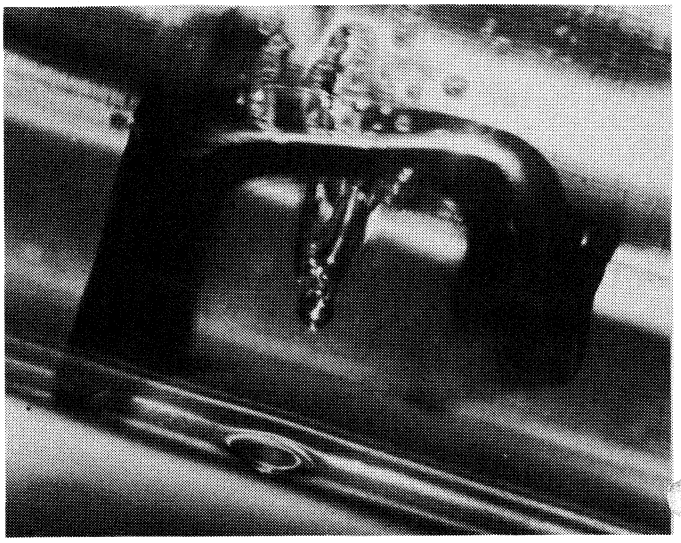


Fig. 13. Local melting of the wall of the bore of a coaxial tube caused by restarting tube *LR*-1 while still hot.

This tube was restarted several times before the crack occurred, so the tube conditions then represented the threshold values for this sort of collapse. Note that the cross section of the column of glass heated by the conduction current was about equal to that of the bore. The electrical resistance R of a column of glass of area S is $R = \rho t/S$, where ρ is the tabulated [36] volume resistivity (a function of temperature), and t is the column height (wall thickness). The power per unit volume W/v dissipated on starting tube *LR*-1 at potential V, just before the collapse of the wall, was $W/v = V^2/RtS = V^2/\rho t^2 = 250\ W \cdot cm^{-3}$. Knowing this critical dissipation limit, and the heat dissipation properties of the tube construction, the time delay may be calculated, which should be built into the laser power supply to allow sufficient cooling for a safe restart (upon any interruption of tube current). This time is typically 2 min.

Scrap analysis of tubes that were life tested showed that a slower type of Pyrex glass erosion occurs with long-term exposure (10^3 h) to high voltages (2 kV) and temperatures (300°C). The hotter regions of the bore show radial cracks or checks extending from the inner surface about halfway through the bore wall, and the inner surface has a scoured appearance. Another bore material (such as [36] quartz) with a higher resistivity at temperature should be considered for tubes with a design life in excess of 2000 h.

V. Conclusions

The simple tube design of Silfvast and Szeto [8] was shown here to be capable of essentially the same performance as the alternative [9], more complex design. Since the discharge striations, which modulate the laser output, arise from the same source (the Penning effect) as the population inversion, neither can be eliminated without the other.[4] Further reduction of noise levels in the He-Cd laser would seem to require tube designs, like the hollow cathode tube, where striation

[4]While a single-frequency striation wave may be set up in the discharge if special boundary conditons are met, the laser is then subject to "bursts" of noise when environmental influences perturb these special conditions.

waves are prevented from growing to significant amplitudes by the very short gain length (electrode spacing). The noise levels obtained in the present, positive-column tube construction are already low enough to make the He-Cd laser of interest in applications where the blue wavelength is an advantage (film recording and light-scattering instruments).

Acknowledgments

The capable technical assistance of J. R. Garcia throughout this work is gratefully acknowledged. The Lansing Research Corporation, Ithaca, NY, kindly gave permission for the use of Fig. 13.

References

[1] W. T. Silfvast, G. R. Fowles, and B. D. Hopkins, "Laser action in singly ionized Ge, Sn, Pb, In, Cd and Zn," *Appl. Phys. Letters*, vol. 8, pp. 318-319, June 15, 1966.
[2] G. R. Fowles and B. D. Hopkins, "CW laser oscillation at 4416Å in cadmium," *IEEE J. Quantum Electron.*, vol. QE-3, p. 419, Oct. 1967.
[3] W. T. Silfvast, "Efficient CW laser oscillation at 4416Å in Cd (II)," *Appl. Phys. Letters*, vol. 13, pp. 169-171, Sept. 1, 1968.
[4] J. P. Goldsborough, "Stable, long life cw excitation of helium-cadmium lasers by dc cataphoresis," *Appl. Phys. Letters*, vol. 15, pp. 159-161, Sept. 15, 1969.
[5] J. R. Fendley, Jr., I. Gorog, K. G. Hernqvist, and C. Sun, "Characteristics of a sealed-off He^3-Cd^{114} laser," *RCA Review*, vol. 30, pp. 422-428, Sept. 1969.
[6] T. P. Sosnowski, "Cataphoresis in the helium-cadmium laser discharge tube," *J. Appl. Phys.*, vol. 40, pp. 5138-5144, Dec. 1969.
[7] W. T. Silfvast and L. H. Szeto, "A simple high temperature system for cw metal vapor lasers," *Appl. Optics*, vol. 9, pp. 1484-1485, June 1970.
[8] —, "Simplified low-noise He-Cd laser with segmented bore," *Appl. Phys. Letters*, vol. 19, pp. 445-447, Nov. 15, 1971.
[9] K. G. Hernqvist, "Vented-bore He-Cd lasers," *RCA Review*, vol. 34, pp. 401-407, Sept. 1973.
[10] W. T. Silfvast, "Penning ionization in a He-Cd dc discharge," *Phys. Rev. Letters*, vol. 27, pp. 1489-1492, Nov. 29, 1971.
[11] G. J. Collins, "Excitation mechanisms in He-Cd and He-Zn ion lasers," *J. Appl. Phys.*, vol. 44, pp. 4633-4652, Oct. 1973.
[12] K. Miyazaki, Y. Ogata, T. Fujimoto, and K. Fukuda, "Excitation mechanism of 3250 and 4416Å laser lines in the cataphoretic He-Cd laser discharge," *Japan. J. Appl. Phys.*, vol. 13, pp. 1866-1874, Nov. 1974.
[13] J. K. Mizeraczyk, "On saturation mechanisms in PC He-Cd^+ lasers," *IEEE J. Quantum Electron.*, vol. QE-8, pp. 218-220, May 1975.
[14] T. P. Sosnowski and M. B. Klein, "Helium clean-up in the helium-cadmium laser discharge," *IEEE J. Quantum Electron.*, vol. QE-7, pp. 425-426, Aug. 1971.
[15] M. W. Zemansky, *Heat and Thermodynamics*. New York: McGraw-Hill, 1957, p. 82.
[16] F. H. Shair and D. S. Remer, "A theoretical model for gas separation in a glow discharge: Cataphoresis," *J. Appl. Phys.*, vol. 39, pp. 5762-5767, Nov. 1968.
[17] T. F. Johnston, Jr., "Measurement of the lower-level population of the argon ion laser using laser induced population changes," *Appl. Phys. Letters*, vol. 17, pp. 161-164, Aug. 15, 1970.
[18] G. Francis, "The glow discharge at low pressure," in *Handbuch der Physik, Gas Discharges II*. Berlin, Germany: Springer, pp. 70-80, 1956.
[19] A. von Engel, *Ionized Gases*. London, England: Oxford, 1965, appendix 1.
[20] E. I. Gordon and A. D. White, "Similarity laws for the effects of pressure and discharge diameter on the gain of He-Ne lasers," *Appl. Phys. Letters*, vol. 3, pp. 199-201, Dec. 1, 1963.
[21] A. D. White and E. I. Gordon, "Excitation mechanisms and current dependence of population inversion in He-Ne lasers," *Appl. Phys. Letters*, vol. 3, pp. 197-199, Dec. 1, 1963.
[22] R. L. Field, Jr., "Operating parameters of dc-excited He-Ne gas lasers," *Rev. Sci. Inst.*, vol. 38, pp. 1720-1722, Dec. 1967.
[23] D. C. Brown and N. Ginsburg, "Study of noise in He-Cd^+ laser," *Appl. Phys. Letters*, vol. 24, pp. 287-289, Mar. 15, 1974.
[24] R. A. Willgoss and G. C. Thomas, "Excitation mechanisms in the presence of moving striations in an He/Cd cataphoretic laser discharge," *J. Phys. D, Appl. Phys.*, vol. 7, pp. 2269-2276, Nov. 1974.
[25] D. A. Lee, P. Bletzinger, and A. Garscadden, "Wave nature of moving striations," *J. Appl. Phys.*, vol. 37, pp. 377-387, Jan. 1966.
[26] J. R. McNeil, private communication.
[27] N. L. Oleson and A. W. Cooper, "Moving Striations," in *Advances in Electronics and Electron Physics*, vol. 24, pp. 155-278, 1968.
[28] A. A. Kruithof and F. M. Penning, "Determination of the Townsend ionization coefficient α for mixtures of neon and argon," *Physica*, vol. 4, pp. 430-449, June 1937; see, especially, p. 448, Fig. 12. This figure also appears in [29].
[29] M. J. Druyvesteyn and F. M. Penning, "The mechanism of electrical discharges in gases at low pressure," *Rev. Mod. Phys.*, vol. 12, pp. 87-174, Apr. 1940.
[30] T. Goto, A. Kawahara, G. J. Collins, and S. Hattori, "Electron temperature and density in positive column He-Cd^+ lasers," *J. Appl. Phys.*, vol. 42, pp. 3816-3818, Sept. 1971.
[31] A. A. Kruithof and M. J. Druyvesteyn, "The Townsend ionization coefficient α and some elementary processes in neon with small admixtures of argon," *Physica*, vol. 4, pp. 450-463, June 1937.
[32] R. H. Springer and B. T. Barnes, "Intensities of 2288Å and 3261Å radiation from low-pressure cadmium rare-gas discharges," *J. Appl. Phys.*, vol. 39, pp. 3100-3104, June 1968.
[33] J. F. Waymouth and F. Bitter, "Analysis of the plasma of fluorescent lamps," *J. Appl. Phys.*, vol. 27, pp. 122-134, Feb. 1956.
[34] A. L. Bloom, "Properties of laser resonators giving uniphase wave fronts," Spectra-Physics Laser Technical Bulletin 2, pp. 1-7, Aug. 1963.
[35] T. Li, "Diffraction loss and selection of modes in maser resonators with circular mirrors," *Bell Sys. Tech. J.*, vol. 44, pp. 917-932, May-June 1965.
[36] "Engineering with Glass," Corning Glass Works Booklet 62-19567, Corning, NY, p. 10.

Analysis of Grating-Coupled Radiation in GaAs:GaAlAs Lasers and Waveguides—II: Blazing Effects

WILLIAM STREIFER, SENIOR MEMBER, IEEE, ROBERT D. BURNHAM, MEMBER, IEEE, AND DONALD R. SCIFRES, MEMBER, IEEE

Abstract—Grating-coupled radiation in lasers and waveguides is analyzed for trapezoidal-shaped grating teeth which includes all triangular shapes. A perturbation technique is used which involves calculating the modes in a geometry with an inhomogeneous refractive index profile in the grating region. Curves are presented for radiated power from traveling waves as a function of blazing angle, grating tooth height, refractive index, and grating period. It is shown that the ratio of power radiated into the outer media depends greatly on tooth shape and size. By judiciously selecting parameters this ratio can exceed 50:1.

I. Introduction

In a recent paper [1] we presented a formulation for calculating radiation from arbitrary-shaped gratings excited by traveling waves in lasers and waveguides. Perturbation and exact numerical solutions were given for radiation from rectangular-shaped gratings. This paper contains extensions of the previous results to trapezoidal-shaped grating teeth which includes all triangular shapes. The results are interesting and important because, as we show, both directionality and increased radiated power can be obtained by judiciously selecting tooth angles (blazing angle) (see also [2]) and heights as well as guide geometry. The discussion is restricted to radiation from traveling waves in which case the grating periodicity is such that it does not provide feedback for laser oscillations. Laser feedback, if present, is provided by external reflectors. We consider only TE modes and present results for radiated power versus blazing angle, grating height, refractive index, and grating period.

II. Solutions for Trapezoidal-Shaped Gratings

The basic ideas developed in [1] are as follows. First, the TE mode field E_y, which satisfies

$$\frac{\partial^2 E_y}{\partial x^2} + \frac{\partial^2 E_y}{\partial z^2} + k_0^2 n^2(x,z) E_y = 0, \tag{1}$$

is expressed as a sum of partial waves

$$E_y = \sum_{m=-\infty}^{\infty} \mathcal{E}_m(x) \exp(i\beta_m z) \tag{2}$$

where

$$\beta_m = \beta_0 + \frac{2\pi m}{\Lambda}. \tag{3}$$

In these equations a time dependence $\exp(-i\omega t)$ has been assumed, the z-dependence of $\mathcal{E}_0(x)$ is given by $\exp(i\beta_0 z)$, $k_0 = 2\pi/\lambda_0$; λ_0 is the free-space wavelength, $n^2(x, z)$ is the squared refractive index, and Λ is the grating period. Second, $n^2(x, z)$ in the grating region is expanded in a Fourier series whose coefficients vary in the transverse direction x. Third, the Fourier component independent of z is used to modify the original geometry. Fourth, accurate initial estimates of $\mathcal{E}_0$ and β_0 are obtained in this geometry. Fifth, $\mathcal{E}_0$, β_0, and the periodic Fourier components are used to compute the particular partial waves among the $\mathcal{E}_m$ which radiate. The above process constitutes the perturbation solution; the "exact" numerical solution consists of repeating this procedure until self-consistent solutions are obtained. Here we discuss only the perturbation solution.

Consider first the Fourier expansion. As shown in [1] the squared refractive index is written

$$n^2(x,z) = n_0^2(x) + \sum_{\substack{q=-\infty \\ q\neq 0}}^{\infty} A_q(x) \exp(i2\pi q z/\Lambda) \tag{4}$$

where $n_0^2(x)$ equals $n^2(x, z)$ outside the grating region and

$$n_0^2(x) = n_1^2 + (n_2^2 - n_1^2)[w_1(x) - w_2(x)]/\Lambda, \quad 0 < x < g. \tag{5}$$

For the trapezoidal-shaped grating teeth shown in Fig. 1, the functions describing the tooth shape $w_1(x)$ and $w_2(x)$ are linear in x, and therefore $n_0^2(x)$ is linear in the grating region. The functions $A_q(x)$ are given by [1]

$$A_q(x) = \begin{cases} 0, & x < 0, g < x \\ \dfrac{(n_2^2 - n_1^2)}{i2\pi q} \{\exp[-i2\pi q w_2(x)/\Lambda] \\ \quad - \exp[-i2\pi q w_1(x)/\Lambda]\}, & 0 < x < g \end{cases} \tag{6}$$

with $q \neq 0$ and $A_0(x) \equiv 0$ since that Fourier term has been absorbed into $n_0(x)$.

The field $\mathcal{E}_0(x)$ and propagation constant β_0 are found by imposing continuity conditions on the solutions of

$$\frac{d^2 \mathcal{E}_0}{dx^2} + [k_0^2 n_0^2(x) - \beta_0^2]\mathcal{E}_0 = 0 \tag{7}$$

at $x = 0$, g, and t. The variation of $n_0^2(x)$ in (7), shown in Fig. 2, is given by

$$n_0^2(x) = n_l^2 + (n_r^2 - n_l^2)(x/g), \quad 0 < x < g \tag{8}$$

where

$$n_l^2 = n_0^2(0+)$$

and

$$n_r^2 = n_0^2(g-).$$

For $x < 0$, $g < x$, the solution functions are exponential

Manuscript received February 23, 1976.

The authors are with the Palo Alto Research Center, Xerox Corporation, Palo Alto, CA 94304.

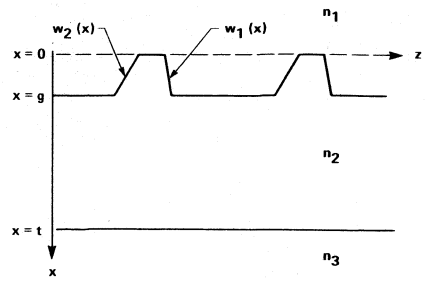


Fig. 1. The waveguide geometry and grating tooth shape.

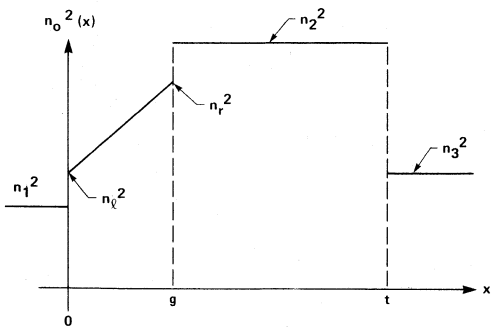


Fig. 2. The variation in squared refractive index.

(trigonometric), but for $0 < x < g$ they are expressed in terms of the Airy functions Ai and Bi [see Appendix A]. The detailed solution of (7) is given in Appendix B (see also [3]).

Next, to determine the radiating waves, we must solve (see [1, eq. (12)])

$$\frac{d^2\mathcal{E}_m}{dx^2} + [k_0^2 n_0^2(x) - \beta_m^2]\,\mathcal{E}_m = -k_0^2 A_m(x)\mathcal{E}_0(x) \tag{9}$$

and it should be recalled that $A_m(x) = 0$ for $x < 0, g < x$. Furthermore, $\mathcal{E}_m(x)$ must either decay or radiate away from the waveguide in regions 1 and 3. Equation (9) is solved in Appendix B. Then the average power lost by $\mathcal{E}_m$ per unit length is

$$P_m = \frac{1}{2\omega\mu_0}\{|\mathcal{E}_m(0)|^2 R_e[\sqrt{k_0^2 n_1^2 - \beta_m^2}] + |\mathcal{E}_m(t)|^2 R_e[\sqrt{k_0^2 n_3^2 - \beta_m^2}]\} \tag{10}$$

where the first term represents radiation into region 1 ($x < 0$) and the second, radiation into region 3 ($x > t$). If in (10) the argument of one or both square roots is positive, the real part should be taken as positive and the wave $\mathcal{E}_m$ radiates power into that region; if one or both arguments are negative, the real part is zero and no power is radiated into that region. Thus all partial waves with $m \geq 0$ and with m sufficiently negative do not radiate, whereas some partial waves with $|m|$ sufficiently small and $m < 0$ may radiate depending on β_0, Λ, and the refractive indices.

Normalized radiated power is generally measured by the exponential rate at which power is lost by the $\mathcal{E}_0$ wave, $\exp(-\alpha z)$; and α is given by

$$\alpha = \sum_m P_m \Big/ \left[(\beta_0/2\omega\mu_0)\int_{-\infty}^{\infty} |\mathcal{E}_0(x)|^2\,dx\right]. \tag{11}$$

Finally the radiation angle that the mth partial wave makes with the propagation direction is given by

$$\theta_i = \cos^{-1}[\beta_m/(2\pi n_i/\lambda_0)], \quad i = 1, 3 \tag{12}$$

where the subscript refers to region 1 or 3.

III. Results

First we consider the double-heterostructure waveguide geometry shown as an insert in Fig. 3. This structure supports three TE modes and for the given values of λ_0, Λ, and refractive indices, only the $m = -1$ wave radiates. For each mode we plot total radiated power and power radiated into regions 1 and 3 as a function of grating tooth shape for triangular teeth. The shape parameter is

$$\delta = \Delta/\Lambda \tag{13}$$

where Δ is defined in the insert. Also shown is the wave direction in the guide. With $\delta = 0.0$ the teeth are sawtooth shaped and open in the propagation direction; with $\delta = 1.0$ they are sawtooth shaped opening opposite to the propagation direction. In fact, results for any value of δ and $1 - \delta$ simply correspond to the same grating interacting with two contradirectional traveling waves. The plots of total radiated power are symmetrical about $\delta = 0.5$, which indicates that the total radiated power is independent of the propagation direction even for asymmetric teeth. This result has been confirmed analytically using the first-order perturbation theory for arbitrarily shaped asymmetrical teeth (not just trapezoidal). It may well be true more generally. Radiated power into regions 1 and 3 also appears symmetric about $\delta = 0.5$ in Fig. 3 for each mode, but the curves are actually asymmetrical. The degree of asymmetry increases with differing refractive indices n_1 and n_3. For sawteeth with $\delta = 0.0$, power radiated into region 1 is approximately 10X that radiated into region 3 and conversely for $\delta = 1.0$. Physically this may occur because the guide widens as the wave passes under a sawtooth with $\delta = 0.0$. Thus power is allowed to leak out through the corrugated interface. A wave traveling in the opposite direction, $\delta = 1.0$, however, sees a contracting guide under each sawtooth and power is forced toward the uncorrugated interface in a manner similar to that of a tapered coupler. A similar result was observed by Peng and Tamir [4], using a step-wise approximation to a sawtooth. Finally, note the increase in radiated power with mode number. This effect occurs because higher order modes more strongly penetrate the grating region. An expanded plot for the TE_0 mode has been published in our earlier paper [5].

Fig. 4 is another plot of TE_0 radiated power versus tooth shape for the same waveguide geometry. Here the distance γ shown in the insert is varied. We observe that the total radiated power peaks when $\gamma/\Lambda \approx 0.25$ at which value the tooth slope is $\approx 45°$; however, a similar plot (not shown) for the same geometry with a tooth height of 0.1 μm also peaks at $\gamma/\Lambda \approx 0.25$ in which case the tooth angle is $\approx 34°$. As in Fig. 2 most of the power radiated with the wave direction shown enters region 1. A contradirectional wave radiates exactly the same total power, but most of that power enters region 3 rather than 1. The ratio of radiated powers is approximately equal for both traveling waves.

In Fig. 5 we plot radiated power versus grating tooth height

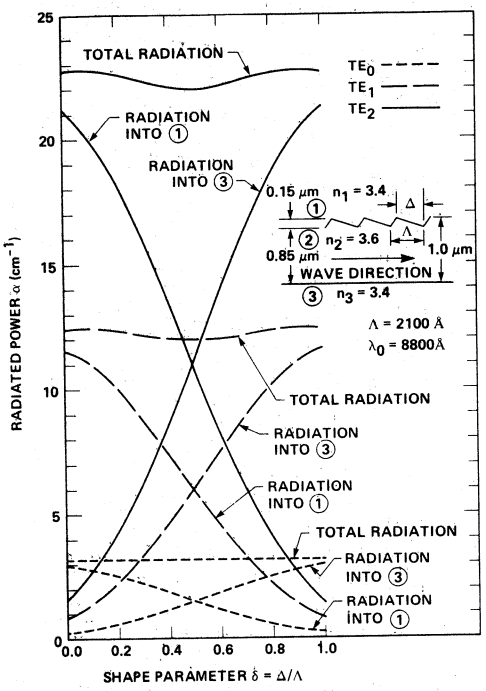


Fig. 3. Radiated power versus grating tooth shape for the TE_0, TE_1, and TE_2 modes.

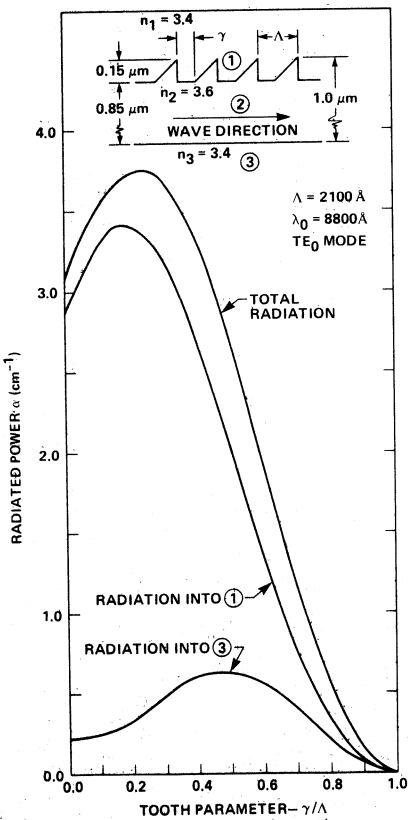


Fig. 4. Radiated power versus grating tooth shape for the TE_0 mode.

for the same waveguiding geometry as above. The accuracy of such perturbation results for these large tooth heights was illustrated in our earlier paper [1]. Consider first the curves for $\delta = 0.0$, which value, as shown in the insert, corresponds to a sawtooth-shaped grating with the teeth opening in the propagation direction. In this case the total radiated power and the power radiated into region 1 both peak at approxi-

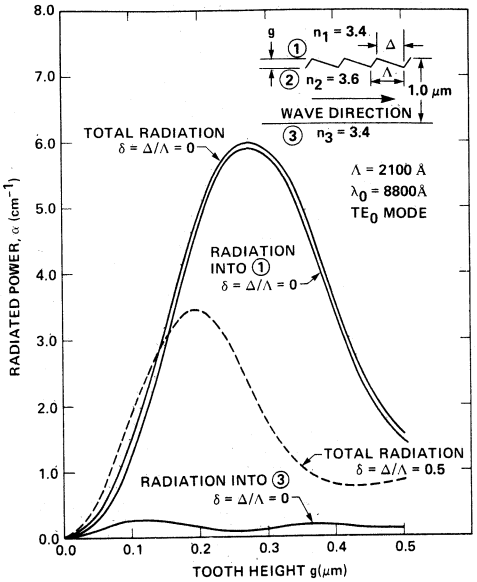


Fig. 5. Radiated power versus grating tooth height for the TE_0 mode.

mately $g = 0.27$ μm. It is important to note that almost all the radiated power enters region 1; in fact for $0.2\ \mu m < g < 0.3\ \mu m$, the ratio of power radiated into region 1 to power radiated into region 3 is in the vicinity of 50:1. For $\delta = 1.0$ (not shown), which describes sawteeth opening in the opposite direction, or, equivalently, a contradirectional wave interacting with the $\delta = 0.0$ grating, the total radiated power is identical to that shown for $\delta = 0.0$, but the powers radiated into regions 1 and 3 are approximately the reverse of that shown in the figure. For the symmetric triangular case we plot only the total radiated power. To a good approximation this power is radiated equally into regions 1 and 3.

Radiated power versus the refractive index n_1 is plotted in Fig. 6 for the same waveguiding geometry as above with g 0.15 μm. Values of n_1 in increments of 0.2 between 1.0 and 3.0 and in increments of 0.1 for $3.0 < n_1 < 3.6$ are shown on the axis, but the linear scale used is $n_2^2 - n_1^2$, which is the difference in relative dielectric constant at the grating interface. The coefficient $A_{-1}(x)$ is proportional to this quantity, and in [1] we observed that radiated power given by (10) in terms of $|\mathcal{E}_{-1}|^2$ was approximately proportional to $(n_2^2 - n_1^2)^2$. With triangularly shaped teeth, however, radiated power is better described as a linear function of $n_2^2 - n_1^2$. In this case the field $\mathcal{E}_0$ penetration into the grating region decreases more rapidly with increasing $n_2^2 - n_1^2$ and so the net effect of the product $A_{-1}\mathcal{E}_0$ is to produce a linear power dependence. For the parameter values shown in the insert, symmetric triangular teeth ($\delta = 0.5$) radiate more total power than do sawteeth ($\delta = 0.0$ or 1.0) for $n_2^2 - n_1^2 \geq 3.0$ (equivalently $n_1 \leq 3.2$). This phenomenon does not necessarily occur generally as we see from the radiated power curves of Fig. 5 for larger gratings. The total radiated power by the sawtooth grating is identical regardless of the incident guided wave direction, i.e., for $\delta = 0.0$ and $\delta = 1.0$; but the power separation into regions 1 and 3 no longer follows the pattern described above in connection with Figs. 3-5. Now, for example, as $n_2^2 - n_1^2$ increases, the power radiated into region 1 with $\delta = 0.0$ does not approximate that radiated into region 3 with $\delta = 1.0$ as well. It

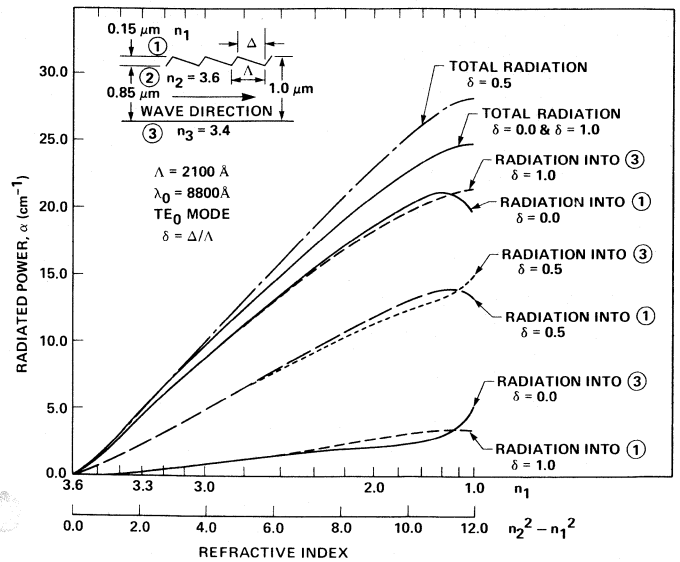


Fig. 6. Radiated power versus refractive index at the grating for the TE_0 mode.

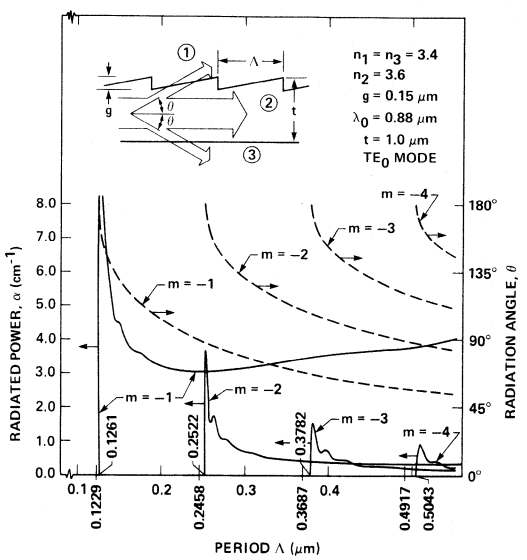


Fig. 7. Radiated power versus grating period for a sawtooth grating shape.

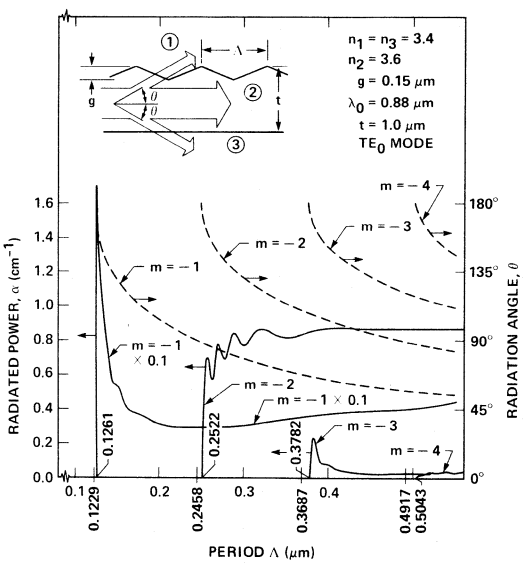


Fig. 8. Radiated power versus grating period for a symmetrical triangular grating shape.

should also be noted that the accuracy of the results presented in this figure decreases substantially with increasing $n_2^2 - n_1^2$ as shown in [1].

Fig. 7 is a plot of TE_0 mode radiated power versus grating period Λ for each wave $\mathcal{E}_m$ in the same waveguide geometry as above with $n_1 = 3.4$. This plot applies to sawtooth-shaped grating teeth with both $\delta = 0.0$ and $\delta = 1.0$. Solid curves are for radiated power and are to be read on the left axis, whereas the broken curves are the radiation angles and are to be read on the right axis. These perturbation results do not apply in the immediate vicinity of the Bragg condition for DFB, when $\beta_m = -\beta_0$ for some m, since with those values of Λ, a single propagating wave cannot exist alone, but must be accompanied by a contradirectional wave. The values of Λ for DFB are shown on the axis as 1229 Å, 2458 Å, 3687 Å, and 4917 Å for $m = -1, -2, -3$, and -4, respectively. For Λ just above these values, the contradirectional wave with β_m still has an equivalent refractive index which is greater than 3.4 and so that wave remains trapped in the waveguide and does not radiate. The values of Λ, i.e., Λ_m, at which new radiating waves emerge is found by setting $\theta = 180°$ in (12) and using (3) to obtain

$$\Lambda_m = 2\pi|m|/(\beta_0 + 2\pi n_i/\lambda_0) \tag{14}$$

and these are indicated on the figure. With increasing Λ above these values the radiated power curves oscillate. This behavior probably results from interference effects in the grating region. The general shape of the curves shown is similar to that of [1, fig. 8] plotted for rectangular-shaped teeth, but here the $m = -2$ wave is substantially smaller than the $m = -1$ wave. To maximize the power radiated in a near-orthogonal direction to the propagating wave thus requires using the $m = -1$ wave as output rather than the $m = -2$ wave. Finally, for most values of Λ ($\theta \lesssim 150°$) with $\delta = 0.0$ the power is radiated primarily into region 1 rather than region 3 and with $\delta = 1.0$ the reverse is the case; however, this is not true for $\theta \gtrsim 150°$ in which case radiated power into region 3 exceeds that radiated into region 1 for $\delta = 0.0$ and conversely for $\delta = 1.0$.

A similar plot for symmetrical triangular teeth ($\delta = 0.5$) is given in Fig. 8. Note that the scale for the $m = -1$ curve is to be multiplied by 10. Aside from the more pronounced oscillations of the $m = -2$ curve the principal difference between the results of Figs. 7 and 8 is the more rapid decrease in radiated power of the higher orders (larger $-m$) for the symmetric triangular grating than for the sawtooth grating.

In Fig. 9 we plot radiated power versus grating height for a waveguide [6] and grating profile [7] similar to that employed by Reinhart *et al.* [6]. Region 1 was an index matching oil with $n_1 = 1.5$. This guide supports only one TE mode. As in Fig. 8 we note that the $m = -1$ radiated power is much greater than the $m = -2$ power, which, in turn, is greater than the $m = -3$ power. The $m = -1$ radiation into region 1 was that measured in the experiment and for an estimated tooth height of 0.12 μm the radiated power is 20.8 cm^{-1}, which is quite substantial. This radiation is at an angle of 38.71° with the propagation direction and assuming a 45° prism with a refractive index of 1.5, the output radiation is at an angle of 54.46° with the normal to the propagation direction. In [6]

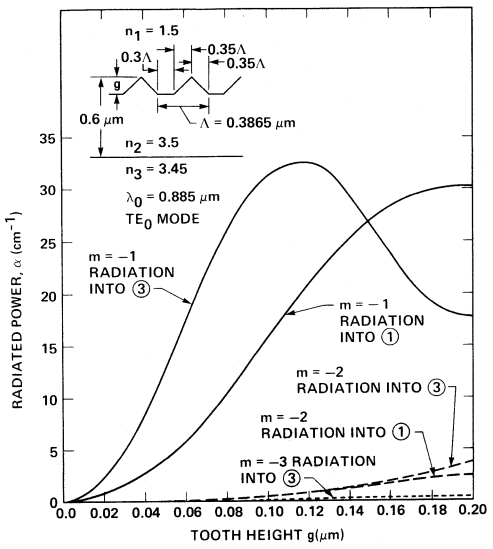


Fig. 9. Radiated power versus grating height for a symmetric triangular grating in the waveguide of [6].

an angle of 51.2° is reported, but this discrepancy is not surprising since the particular parameters used to compute Fig. 9 cannot be those of the experiment. With the values shown in Fig. 9 the grating does not act as a DBR for the TE_0 mode, because for a DBR the $m = -3$ wave would not radiate, but rather would be the reflected mode. However, if the refractive indices of regions 2 and 3 were decreased just slightly, which is likely the case in the experiment, the geometry functions as a DBR for $\lambda_0 = 0.885$ μm and $\Lambda = 3865$ Å. The perturbation analysis does not apply to the DBR without modification.

Appendix A
The Airy Functions

The Airy functions [8], [9] satisfy

$$\frac{d^2y}{d\xi^2} - \xi y = 0 \tag{A1}$$

and generally the two linearly independent solutions are denoted by Ai(ξ) and Bi(ξ). For $\xi > 0$, Ai exponentially decays and Bi exponentially grows; for $\xi < 0$ both functions oscillate. The functions are easily computed from rapidly convergent power series for small values of $|\xi|$ and from asymptotic series expressed in terms of trigonometric or exponential functions for large values of $|\xi|$. Since the series about $\xi = 0$ converges for all ξ, albeit slowly for $|\xi| >> 1$, the functions can be computed for all ξ. The Wronskian relation required in the analysis of Appendix B is

$$\mathrm{Ai}(\xi)\mathrm{Bi}'(\xi) - \mathrm{Ai}'(\xi)\mathrm{Bi}(\xi) = 1/\pi, \tag{A2}$$

where the primes denote derivatives and (A2) holds for all ξ.

Appendix B
Solution for the Fields

Consider first (7) with $n_0^2(x) = n_i^2$, $i = 1, 2, 3$ and $n_0^2(x)$ given by (8) for $0 < x < g$. Thus for $0 < x < g$

$$\frac{d^2\mathcal{E}_0}{dx^2} - (\eta_0 - \nu x)\mathcal{E}_0 = 0 \tag{B1}$$

where

$$\eta_0 = \beta_0^2 - k_0^2 n_l^2 \tag{B2a}$$

and

$$\nu = k_0^2(n_r^2 - n_l^2)/g. \tag{B2b}$$

If we substitute

$$\xi = \eta_0/\nu^{2/3} - \nu^{1/3}x \tag{B3}$$

then (B1) is exactly in the form of (A1) and its solutions are Airy functions. Thus $\mathcal{E}_0(x)$ is given by

$$\mathcal{E}_0(x) = \begin{cases} \exp(-ik_{01}x), & x < 0 \\ C_{04}\mathrm{Ai}(\xi) + D_{04}\mathrm{Bi}(\xi), & 0 < x < g \\ C_{04}\{\cos[k_{02}(t-x)] - (ik_{03}/k_{02}) \\ \quad \cdot \sin[k_{02}(t-x)]\}, & g < x < t \\ C_{03}\exp[ik_{03}(x-t)], & t < x \end{cases} \tag{B4}$$

where

$$k_{0i} = \sqrt{k_0^2 n_i^2 - \beta_0^2}, \quad i = 1, 2, 3 \tag{B5}$$

and C_{04}, D_{04}, C_{03}, and β_0 are to be determined by imposing continuity conditions on $\mathcal{E}_0$ and $d\mathcal{E}_0/dx$ at $x = 0$ and $x = t$. The sign of k_{0i} is selected for field decay with $x < 0$, $x > t$. For $g < x < t$, $\mathcal{E}_0(x)$ does not depend on the sign of k_{02}.

At $x = 0$

$$\xi = \xi_l = \eta_0/\nu^{2/3} \tag{B6a}$$

and at $x = g$,

$$\xi = \xi_r = \eta_0/\nu^{2/3} - \nu^{1/3}g. \tag{B6b}$$

With these definitions, continuity at $x = 0$ yields

$$C_{04}\mathrm{Ai}(\xi_l) + D_{04}\mathrm{Bi}(\xi_l) = 1 \tag{B7a}$$

and

$$-\nu^{1/3}[C_{04}\mathrm{Ai}'(\xi_l) + D_{04}\mathrm{Bi}'(\xi_l)] = -ik_{01} \tag{B7b}$$

so that

$$C_{04} = \pi[\mathrm{Bi}'(\xi_l) - (ik_{01}/\nu^{1/3})\mathrm{Bi}(\xi_l)] \tag{B8a}$$

and

$$D_{04} = -\pi[\mathrm{Ai}'(\xi_l) - (ik_{01}/\nu^{1/3})\mathrm{Ai}(\xi_l)] \tag{B8b}$$

where (B2) has been invoked. At $x = g$, continuity of $\mathcal{E}_0$ gives an expression for C_{03},

$$C_{03} = [C_{04}\mathrm{Ai}(\xi_r) + D_{04}\mathrm{Bi}(\xi_r)]/\{\cos[k_{02}(t-g)] - (ik_{03}/k_{02})\sin[k_{02}(t-g)]\} \tag{B9}$$

and finally β_0 is determined by requiring continuity of $d\mathcal{E}_0/dx$ at $x = g$, viz., satisfaction of

$$C_{03}\{k_{02}\sin[k_{02}(t-g)] + ik_{03}\cos[k_{02}(t-g)]\} = -\nu^{1/3}[C_{04}\mathrm{Ai}'(\xi_r) + D_{04}\mathrm{Bi}'(\xi_r)]. \tag{B10}$$

The numerical solution for β_0 is accomplished by first combining (B8a), (B8b), and (B9) with (B10) to eliminate all the constants and then employing the bisection technique [10] to obtain the value of β_0 which satisfies the resulting equation.

Given $\mathcal{E}_0(x)$ and β_0 as determined above we now solve (9)

for $\mathcal{E}_m(x)$. That function is given by

$$\mathcal{E}_m(x) = \begin{cases} C_{m1} \exp(-ik_{m1}x), & x < 0 \\ C_{m4}\mathrm{Ai}(\xi_m) + D_{m4}\mathrm{Bi}(\xi_m) + T_m(x), & 0 < x < g \\ C_{m3}\{\cos[k_{m2}(t-x)] - (ik_{m3}/k_{m2}) \\ \quad \cdot \sin[(k_{m2}(t-x)]\}, & g < x \\ C_{m3} \exp[ik_{m3}(x-t)], & t < x \end{cases} \tag{B11}$$

where

$$\xi_m = \eta_m/\nu^{2/3} - \nu^{1/3}x \tag{B12a}$$

$$\eta_m = \beta_m^2 - k_0^2 n_i^2 \tag{B12b}$$

and

$$k_{mi} = \sqrt{k_0^2 n_i^2 - \beta_m^2}. \tag{B13}$$

Here k_{m1} and k_{m3} are either positive imaginary or positive real to produce decay or outward radiation, respectively, in regions 1 and 3. In (B11)

$$T_m(x) = -\frac{\pi}{\nu^{1/3}} \int_0^x [\mathrm{Ai}(\phi)\mathrm{Bi}(\xi_m) - \mathrm{Bi}(\phi)\mathrm{Ai}(\xi_m)] \cdot [-k_0^2 A_m(u)\mathcal{E}_0(u)]\, du \tag{B14}$$

where $\phi = \eta_m/\nu^{2/3} - \nu^{1/3}u$. The function $T_m(x)$ is a particular solution of (9) which satisfies

$$\frac{d^2T_m}{dx^2} - (\eta_m - \nu x)T_m = -k_0^2 A_m \mathcal{E}_0. \tag{B15}$$

Since $T_m(0) = 0$ and

$$\frac{dT_m(x)}{dx} = \pi \int_0^x [\mathrm{Ai}(\phi)\mathrm{Bi}'(\xi) - \mathrm{Bi}(\phi)\mathrm{Ai}'(\xi)] \cdot [-k_0^2 A_m(u)\mathcal{E}_0(u)]\, du \tag{B16}$$

evaluated at $x = 0$ is zero, the continuity conditions imposed at $x = 0$ yield

$$C_{m4} = \pi C_{m1}[\mathrm{Bi}'(\xi_{ml}) - (ik_{m1}/\nu^{1/3})\mathrm{Bi}(\xi_{ml})] \tag{B17a}$$

and

$$D_{m4} = -\pi C_{m1}[\mathrm{Ai}'(\xi_{ml}) - (ik_{m1}/\nu^{1/3})\mathrm{Ai}(\xi_{ml})] \tag{B17b}$$

where ξ_{ml} equals ξ_m evaluated at $x = 0$. Next from continuity of $\mathcal{E}_0$ and $d\mathcal{E}_0/dx$ at $x = g$, we obtain

$$C_{m4}\mathrm{Ai}(\xi_{mr}) + D_{m4}\mathrm{Bi}(\xi_{mr}) + T_m(g) = C_{m3}\{\cos[k_{m2}(t-g)] - (ik_{m3}/k_{m2}) \sin[k_{m2}(t-g)]\} \tag{B18a}$$

and

$$-\nu^{1/3}[C_{m4}\mathrm{Ai}'(\xi_{mr}) + D_{m4}\mathrm{Bi}'(\xi_{mr})] + dT_m/dx|_g = C_{m3}\{k_{m2} \sin[k_{m2}(t-g)] + (ik_{m3}) \cos[k_{m2}(t-g)]\} \tag{B18b}$$

where ξ_{mr} is ξ_m evaluated at $x = g$. The four equations, (B17a)-(B18b) are solved for the four constants, C_{m1}, C_{m4}, D_{m4}, and C_{m3}, and thereby $\mathcal{E}_m(x)$ is determined.

References

[1] W. Streifer, D. R. Scifres, and R. D. Burnham, "Analysis of grating-coupled radiation in GaAs:GaAlAs lasers and waveguides," *IEEE J. Quantum Electron.*, vol. QE-12, pp. 422–428, July 1976.

[2] S. T. Peng and T. Tamir, "Directional blazing of waves guided by asymmetrical dielectric gratings," *Optics Comm.*, vol. 11, pp. 405–409, 1974.

[3] W. W. Rigrod, J. H. McFee, M. A. Pollack, and R. A. Logan, "Index-profile determination of heterostructure GaAs planar waveguides from mode-angle measurements at 10.6 μm wavelength," *J. Opt. Soc. Amer.*, vol. 65, pp. 46–55, 1975.

[4] S. T. Peng and T. Tamir, "Effects of groove profile on the performance of dielectric grating couplers," in *1974 Proc. Symp. Optical and Acoustical Micro-Electronics* (Apr. 16–18, 1974). New York: Polytechnic, pp. 377–391 (see fig. 9).

[5] W. Streifer, R. D. Burnham, and D. R. Scifres, "Grating coupled output beams from distributed feedback diode lasers," in *Proc. Electro-Optics Int. Laser Conf.* (Nov. 11, 1975, Anaheim, CA).

[6] F. K. Reinhart, R. A. Logan, and C. V. Shank, "GaAs–$Al_xGa_{1-x}As$ injection lasers with distributed Bragg reflectors," *Appl. Phys. Lett.*, vol. 27, pp. 45–48, 1975.

[7] F. K. Reinhart, private communication.

[8] J. C. P. Miller, "The Airy integral," in *British Association for the Advancement of Science, Mathematical Tables*, vol. B. Cambridge, England: University Press, 1946, pp. B1–B56.

[9] M. Abramowitz and I. Stegun, *Handbook of Mathematical Functions*, Nat. Bur. Std. (U.S.) Handbook 55, Washington, DC: U.S. Gov. Printing Office, 1964, pp. 446–452.

[10] C. F. Gerald, *Applied Numerical Analysis*. Reading, MA: Addison-Wesley, 1970, p. 2.

Coherent Effects in Spin-Flip Light Scattering

PETER A. WOLFF, ROGER N. NUCHO, AND ROSHAN L. AGGARWAL

Abstract—**A pulsed, coherent, spin-flip Raman experiment is proposed. Calculations show that if narrow pulses are used to drive the spin system in InSb via the Raman coupling, the equivalent of an NMR $\pi/2$-pulse experiment may be achieved. The free induction decay signal is expected to be about 10^{-6} J/pulse and might serve as an intense, pulsed, magnetically tunable source of far-infrared (IR) generation.**

I. Introduction

RECENT experiments [1] have demonstrated that in certain semiconductors, spin-flip Raman scattering is a surprisingly strong process. The outstanding example of such material is n-type InSb, in which CW stimulated spin-flip scattering has been achieved [2] with pump powers of a few milliwatts. This threshold is far below that of any other stimulated Raman process. Such observations indicate that in n-InSb (and other semiconductors) there is a large, nonlinear interaction between two light waves and the spins of mobile electrons. This coupling is responsible for the strong Raman scattering, but might also be used for other purposes. For example, by injecting two light signals with difference frequency at the spin resonance frequency into an InSb sample, it should be possible to perform a type of nonlinear, spin resonance experiment. This goal has, in fact, been successfully accomplished in InSb by Nguyen and Bridges [3]. The pump beams were obtained in their initial experiment from two fixed-frequency Q-switched CO_2 lasers and in a subsequent experiment from a tunable InSb spin-flip Raman laser. In both cases the laser pulses were of ~250-ns duration. The purpose of this paper is to study this effect in the subnanosecond pulsed regime. In particular, we wish to investigate the possibility of achieving pulsed, coherent excitation of the spin system via the Raman interaction.

In conventional nuclear magnetic resonance [4] (or NMR), a standard experiment is that in which a spin system is turned through 90° by a short, intense burst of radiation at the spin resonance frequency. The RF signal is then removed, and the total spin vector of the sample freely precesses about the static magnetic field. This motion gives rise to considerable radiation (the free induction decay) since all spins in the sample rotate in phase for a time T_2^*, the dephasing time for spin precession. The crucial feature of the experiment is one's ability to turn the spins through 90° in a time short compared to T_2^*. This action prepares the superradiant state which gives rise to the subsequent emission.

An interesting question to consider is the possibility of achieving a similar effect via the *Raman* coupling. Imagine, for example, that two intense pulses of radiation (with frequencies ω_1 and ω_2) simultaneously impinge on an n-type sample of InSb. If the difference frequency is at the spin resonance frequency ($\omega_1 - \omega_2 = \omega_s$), there will be strong interaction with the electron spins. With appropriate powers in the optical pulses, the spins can be turned through 90°, and will subsequently radiate (coherently) at the spin resonance frequency. This experiment is the optical analogue of the standard free induction decay experiment of NMR. Note, however, that in the optical case the driving fields are high-frequency waves, whereas the radiated signal is at the *difference* frequency ($\omega_s = \omega_1 - \omega_2$). In InSb, ω_s will generally be in the far-infrared (IR) region because of the large g-values ($g \simeq -50$ for electrons in n-InSb). It would be exceedingly interesting to observe such Raman-induced IR spin resonance radiation. Signals of this type could provide considerable information concerning the spin dynamics of electrons in n-InSb; they might also serve as intense, pulsed, magnetically tunable sources of far-IR radiation. Our subsequent calculations will show that an experiment along these lines is within reach of present laser technology, and might actually be fairly easy to carry out.

II. The Raman Coupling

There are two approaches leading to an expression for the Raman coupling. Both start with the usual Hamiltonian:

$$H = \frac{p^2}{2m} + v(r) - \frac{\hbar}{4m^2c^2}\,[\vec{\sigma}\cdot\vec{p}\times\vec{\nabla}v] \tag{1}$$

in which the standard replacement $\vec{p} \to (\vec{p} - (e/c)\vec{A})$ must be made in the presence of electromagnetic fields. The first approach is due to Yafet [5] who first discovered the spin-flip Raman process and studied it theoretically. In his method the scattering cross section is determined by second-order, virtual, interband processes due to the $(\vec{p}\cdot\vec{A})$ portion of the Hamiltonian. Alternatively, one can remove the interband $(\vec{p}\cdot\vec{A})$ interaction via a canonical transformation (in the Kohn-Luttinger representation). The advantage of the latter method is that one obtains an effective one-band spin Hamiltonian, which, for narrow-gap materials, was found to be [6]

$$H_{NL} = \frac{e^2}{2c^2}\,\frac{\hbar E_g}{E_g^2 - (\hbar\omega_1)^2}\left(\frac{1}{m_s} - \frac{1}{m}\right)\vec{\sigma}\cdot\vec{A}\times\frac{\partial\vec{A}}{\partial t}. \tag{2}$$

This expression has been carefully checked and confirmed by experiment [7].

With two incident waves propagating along the y axis and polarized, respectively, along the z and x axes as in Fig. 1, the

Manuscript received March 22, 1976; revised April 23, 1976. The work of P. A. Wolff and R. N. Nucho was supported by the U.S. Air Force Office of Scientific Research, Air Force Systems Command under Contract/Grant AFOSR-76-2894. The Francis Bitter National Magnet Laboratory is supported by the National Science Foundation.

P. A. Wolff and R. N. Nucho are with the Department of Physics, Massachusetts Institute of Technology, Cambridge, MA 02139.

R. L. Aggarwal is with the Francis Bitter National Magnet Laboratory and the Department of Physics, Massachusetts Institute of Technology, Cambridge, MA 02139.

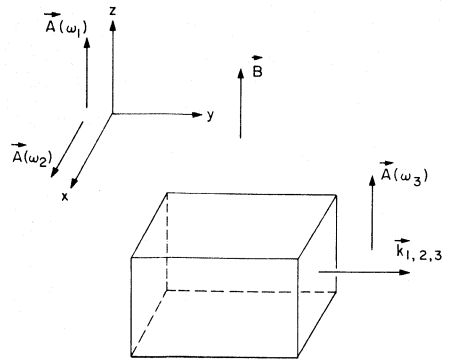


Fig. 1. Schematic showing the geometry of the proposed nonlinear spin resonance experiment. $\vec{B}$ is the applied magnetic field. $\vec{A}(\omega_1)$ and $\vec{A}(\omega_2)$ indicate the polarization of the two pump beams at the frequencies ω_1 and ω_2, respectively. $\vec{A}(\omega_3)$ indicates the polarization of the spin resonance radiation in the far IR. $\vec{k}_1, \vec{k}_2$ and $\vec{k}_3$ represent the propagation direction of the three beams at the frequencies ω_1, ω_2, and ω_3, respectively.

nonlinear term becomes

$$H_{\mathrm{NL}} = \frac{e^2}{4c^2} \cdot \frac{\hbar(\omega_1 + \omega_2)}{2} \frac{E_g}{E_g^2 - (\hbar\omega_1)^2} \left(\frac{1}{m_s} - \frac{1}{m}\right) \vec{\sigma} \cdot (\hat{e}_1 \times \hat{e}_2) \times [iA_1 A_2 e^{i(k_1 - k_2)y} e^{-i(\omega_1 - \omega_2)t} + \text{c.c.}] \tag{3}$$

where $\hat{e}_1$ and $\hat{e}_2$ are the polarization vectors, E_g the band gap, and m_s the spin mass. As there exists some confusion in the literature in the notation of spin mass, it is well to specify here our definition [8]:

$$\frac{m}{m_s} = \frac{g^*}{2} = \left[1 - \left(\frac{m}{m^*} - 1\right) \frac{\Delta}{3E_g + 2\Delta}\right]$$

where g^* is the total g value of the electrons in the crystal, and m^* is the conduction band effective mass. Note that as the spin orbit coupling, Δ, goes to zero, m_s tends to m and H_{NL} vanishes, as it should. Introducing the effective magnetic moment $\vec{\mu}^* = -\mu(g^*/2)\vec{\sigma}$ and noting that $m_s \ll m$ in InSb, we can rewrite the above equation as

$$H_{NL} \simeq -\left[\frac{ie}{4c} \cdot \frac{(\omega_1 + \omega_2)E_g}{E_g^2 - (\hbar\omega_1)^2}\right] \vec{\mu}^* \cdot [\vec{A}(\omega_1) \times \vec{A}^*(\omega_2) - \text{c.c.}] \tag{4}$$

where

$$\vec{A}(\omega_i) = \hat{e}_i A_i e^{i(k_i y - \omega_i t)}$$

is the vector potential associated with the pump beam at frequency ω_i. This "magnetic dipole" interaction is responsible for spin-flip Raman scattering. One can easily check to see that it yields the cross sections and polarization selection rules for this process that have been discussed by Yafet.

III. Coherent Spin Excitation

Having established the form of the Raman coupling, we next wish to consider the possibility of using this interaction to perform spin-resonance-type experiments in n-InSb. For this purpose, we imagine that the fields A_1 and A_2 are optical waves whose frequency difference is at the electron spin resonance frequency. The waves are assumed to propagate in the y direction, perpendicular to the z-directed dc magnetic field, and with x and z polarizations. Since the spins are, in effect, driven by an effective magnetic field which may be derived from (4), the spin-flip process can be viewed as a type of "nonlinear spin resonance," and we can use a standard method in resonance physics to describe the system. Under these conditions, the electron spin Hamiltonian has the relatively simple form

$$H = -\hbar \begin{bmatrix} \frac{\omega_s}{2} & \Omega e^{-i[(k_1 - k_2)y - \omega_3 t]} \\ \Omega e^{+i[(k_1 - k_2)y - \omega_3 t]} & -\frac{\omega_s}{2} \end{bmatrix} \tag{5}$$

where

$$\Omega = \left(\frac{e^2}{4m_s c^2}\right) \frac{E_g}{E_g^2 - \hbar^2\omega_1^2} \cdot \frac{\omega_1 + \omega_2}{2} A_1 A_2. \tag{6}$$

$\omega_3 = \omega_1 - \omega_2$, and $\omega_s = 2\mu^* B/\hbar$ is the spin resonance frequency. We have used the rotating wave approximation [4] in the off-diagonal terms of (5). If the electron is initially in the lower energy state, its wave function (at resonance $\omega_3 \simeq \omega_s$) at a later time is given by the expression

$$\Psi(t) = -i \sin \Omega t \, e^{-i(\omega_s/2)t} |\beta> + \cos \Omega t \, e^{i(\omega_s/2)t} |\alpha>. \tag{7}$$

Note the occupation probability alternates, with frequency Ω, between the lower and upper spin states. In particular, the electron spin is turned through 90° (into the x-y plane) when $\Omega\tau_{\pi/2} = \pi/4$. Thus, the $\pi/2$-pulse condition [from (6)] is

$$\left(\frac{e^2}{4m_s c^2}\right) \frac{E_g}{E_g^2 - (\hbar\omega_1)^2} \cdot \frac{\omega_1 + \omega_2}{2} A_1 A_2 \tau_{\pi/2} = \frac{\pi}{4}. \tag{8}$$

In order to observe a significant free precession signal after the $\pi/2$-pulse, it is necessary that the spins be turned in a time comparable with (or less than) the dephasing time, T_2^*. Thus

we require $\tau_{\pi/2} \leqslant T_2^*$, a condition which sets a lower limit [via (8)] on the powers required for our experiment. To make numerical estimates of these powers, we need a value of T_2^* for electron spins in n-InSb. Recent (spontaneous) spin-flip light scattering experiments by Brueck [9] gave a linewidth of 0.3 cm^{-1}, corresponding to a T_2^* of about 10^{-10} s. This figure is for an n-InSb sample containing about 10^{16} electrons/cm^3 at 4 K. Larger values of T_2^* are expected in less heavily doped

$$\rho = \begin{bmatrix} \frac{1}{2} + \frac{1}{2}(\rho_0^{\uparrow\uparrow} - \rho_0^{\downarrow\downarrow}) \cos 2\Omega t & -\frac{i}{2}(\rho_0^{\uparrow\uparrow} - \rho_0^{\downarrow\downarrow}) \sin 2\Omega t\, e^{+i(\theta+\omega_s t)} \\ \frac{i}{2}(\rho_0^{\uparrow\uparrow} - \rho_0^{\downarrow\downarrow}) \sin 2\Omega t\, e^{-i(\theta+\omega_s t)} & \frac{1}{2} - \frac{1}{2}(\rho_0^{\uparrow\uparrow} - \rho_0^{\downarrow\downarrow}) \cos 2\Omega t \end{bmatrix} \tag{10}$$

crystals. However, in our subsequent estimates we will generally use the number $T_2^* \simeq 10^{-10}$ s.

With this figure, and other parameters appropriate to n-InSb, one may estimate from (8) the intensities needed to turn the spins through 90° in the time T_2^*.

$$\sqrt{I_1 I_2} = n\left(\frac{c}{8\pi}\right)\frac{\omega_1\omega_2}{c^2} A_1 A_2 \simeq \frac{n\omega}{32c} \cdot \frac{E_g^2 - \hbar^2\omega^2}{E_g} \frac{1}{T_2^*} \frac{1}{\frac{g^*}{2}\left(\frac{e^2}{4mc^2}\right)} \tag{9}$$

where $n \simeq 4$ is the index of refraction of n-InSb, $\omega = (\omega_1 + \omega_2)/2$, and I_1 and I_2 are the intensities at the frequencies ω_1 and ω_2, respectively. For $T_2 \simeq 10^{-10}$ s, (9) yields $\sqrt{I_1 I_2} \simeq 10^5$ W/cm^2. Intensities in this range are now attainable via stimulated spin-flip scattering in n-InSb. Such sources would also naturally provide the two optical signals whose difference frequency is at the spin resonance frequency of electrons in this material. For example, Aggarwal *et al.* [10] have achieved Raman powers exceeding 10^3 W when pumping n-InSb with high-powered (10^6 W) atmospheric-pressure CO_2 lasers. For these two optical signals it is possible to obtain a value of $\sqrt{I_1 I_2}$ in excess of 10^5 W/cm^2.

The preceding discussion indicates that presently available optical powers (from spin-flip lasers) are adequate for coherent spin-flip excitation in InSb. A more difficult problem is that of achieving the very short pulses ($<10^{-10}$ s) needed in such experiments. Mode-locked CO_2 lasers currently produce pulses in the 10^{-9}-s range [11]. This figure is determined by the linewidth of the pressure-broadened CO_2 transition, and cannot be easily reduced. Calculations [12], however, show that if such short (and powerful $\simeq$ 1 MW) pulses are used to drive a spin-flip laser, the Raman pulse is much shorter. In fact, it was found that the Raman pulsewidth, for large y, was $\tau_p/\sqrt{yg}$, where τ_p is the pump pulse width, g is the gain of the Raman pulse, and y is the distance from the front edge of the sample. With high gains ($\simeq$30 cm^{-1}) and long crystals (1-1.5 cm), we may thus expect to have Raman pulses close to one order of magnitude narrower than the pump pulse.

IV. The Free-Induction Decay

In the preceding section, we have seen that $\pi/2$-pulses might be obtained, via Raman coupling to electron spins in n-InSb. We next wish to estimate the power radiated, due to the free precession mechanism, after the $\pi/2$-pulses. For this purpose, we may first follow the standard spin resonance procedure, with the two-term Hamiltonian $H = H_0 + H_{NL}$. Using the density matrix approach, we solve the equation of motion $i\hbar(\partial\rho/\partial t) = [H, \rho]$ for ρ (we assume no relaxation effects because the flipping process occurs in $\tau \ll T_2^*$). We find, at resonance,

where

$$\theta = (k_2 - k_1)y.$$

In equilibrium in InSb, most of the spins point along the field, i.e., $\rho_0^{\uparrow\uparrow} - \rho_0^{\downarrow\downarrow} \simeq 1$. We thus obtain for the individual spin magnetizations during the pulsing

$$m_z(t) = T_r(\rho\mu_z^*) = \frac{\mu|g^*|}{2}\cos 2\Omega t$$

$$m^+(t, y_\lambda) = m_x + im_y = \frac{\mu|g^*|}{2} e^{i(\pi/2) - i(\omega_\lambda t + \theta_\lambda)} \sin 2\Omega t.$$

Here ω_λ is the spin resonance frequency of the λth spin, and y_λ is its position. (We assume relatively little diffusion across the magnetic field [13].)

Now the spins precess freely about the dc magnetic field. The back reaction of the radiated field on the spins will be ignored. It can be shown to be unimportant unless the spins radiate a large fraction of their energy (unlikely in InSb). We can thus write the total precessing magnetization density as

$$M^+(r,t) = \sum_\lambda m^+(\tau, y_\lambda)\, e^{i\omega_\lambda t}\, \delta(r - r_\lambda) \quad \text{where} \quad \Omega\tau = \frac{\pi}{4}$$

$$= \frac{\mu|g^*|}{2} e^{-i(\pi/2)} \sum_\lambda \delta(r - r_\lambda)\, e^{i\omega_\lambda(t-\tau)} \cdot e^{-i(k_2 - k_1)y_\lambda}.$$

Note the fanning out of the spins. Moreover, $\omega_\lambda\tau = (\bar{\omega} + \delta\omega_\lambda)\tau$ where $\bar{\omega}$ is some average frequency, and since $\delta\omega_\lambda\tau \lesssim \tau/T_2 \ll 1$ in our approximation, we are left with only an overall phase factor which we need not be concerned with. We can finally write

$$M^+(r,t) \simeq \frac{\mu|g^*|}{2} \sum_\lambda \delta(r - r_\lambda)\, e^{i\omega_\lambda t}\, e^{-i(k_2 - k_1)y_\lambda}. \tag{11}$$

This expression is next used to estimate the power radiated. For this purpose, we imagine that the InSb crystal constitutes an optical cavity at the spin resonance frequency. The magnetic field is expanded in a series of cavity modes as follows:

$$H(r,t) = \sum_\alpha [c_\alpha(t) h_\alpha(r)\, e^{i\omega_\alpha t} + \text{c.c.}]. \tag{12}$$

The h_α are the modes which are assumed to be a complete,

orthonormal set:

$$\int_{\text{cavity}} h_\alpha^*(r) \cdot h_\beta(r)\, d^3r = \delta_{\alpha\beta}. \tag{13}$$

An equation for the (slowly varying) expansion coefficient $c_\alpha(t)$ can easily be derived by integrating Maxwell's equation against the eigenfunction $h_\alpha^*(r)$. One finds

$$2i\omega_\alpha \frac{\partial c_\alpha}{\partial t} + i\omega_\alpha \frac{c_\alpha}{\tau_\alpha} = 4\pi\left(\frac{\mu|g^*|}{2}\right)\sum_\lambda \omega_\lambda^2\, e^{i(\omega_\lambda - \omega_\alpha)t} \cdot \int h_\alpha^*(r)\delta(r - r_\lambda)\, e^{-i(k_1 - k_2)y_\lambda}\, d^3r \tag{14}$$

where $1/2\tau_\alpha$ is the decay rate of the αth mode. It is important to notice that (14) involves a phase-matching condition. Only cavity modes whose propagation vectors are in the y direction will couple to the radiating spins. Hence, the free precession signal is quite directional, being emitted only in the y direction. With the linewidths quoted by Brueck [9], and a cavity length of 1 mm, there is, in general, only a single mode that effectively couples to the precessing spins. Even for that mode there is a slight phase mismatch due to dispersion of the refractive index between the 10-μ and far-IR regions. The coherence length $l_{\text{coh}} = \tau/\delta k$ for the far-IR emission is of the order of 1 mm.

To solve (14), we must first transform the summation on the right-hand side (RHS) into an integral, using the line-shape function for spin resonance, $g(\omega)$, and the electron density $n(r)$, which will be taken to be uniform. We then have $\Sigma_\lambda \to \int g(\omega)n(r)\, d\omega\, d^3r$ and (14) can be rewritten as

$$\frac{\partial c_\alpha}{\partial t} + \gamma c_\alpha = -\frac{i\pi\mu|g^*|}{V^{1/2}}\frac{N}{Y}\left[\frac{e^{i\delta kY} - 1}{i\delta k}\right]\frac{1}{\omega_\alpha} \cdot \int_{-\infty}^{+\infty} \omega^2 g(\omega)\, e^{i(\omega - \omega_\alpha)t}\, d\omega \tag{15}$$

where $V = AY$ is the volume of the cavity, and Y is its length in the y direction; $\gamma = 1/2\tau_\alpha$; N is the total number of spins; and δk is the wave vector mismatch. With the initial condition $c_\alpha(t) = 0$ at $t = 0$, the solution of (15) is

$$c_\alpha(t) = \frac{\pi\mu|g^*|}{V^{1/2}} \cdot \frac{N}{Y}\left[\frac{e^{i\delta kY} - 1}{i\delta k}\right]\frac{1}{\omega_\alpha}\int_{-\infty}^{+\infty} \frac{\omega^2 g(\omega)}{(\omega_\alpha - \omega) + i\gamma} \cdot [e^{i(\omega - \omega_\alpha)t} - e^{-\gamma t}]\, d\omega. \tag{16}$$

Assuming a Lorentzian shape for $g(\omega)$ with width Γ, and that its effect on the ω^2 in the integrand is to give it the value ω_α^2, we find, after some calculation,

$$|c_\alpha(t)|^2 = 4\pi^2(\mu g^*)^2 Nn\, \frac{1}{Y^2\delta k^2} \cdot \frac{\omega_\alpha^2}{\left(\frac{\Gamma}{2} - \gamma\right)^2} \cdot [e^{-(\Gamma/2)t} - e^{-\gamma t}]^2. \tag{17}$$

The power radiated per unit area is given by the quantity

$$\frac{P}{A} = \frac{c}{4\pi}\frac{|c_\alpha|^2}{V}.$$

Hence the energy radiated is

$$\epsilon_{\text{rad}} = \frac{c}{Y\pi}(\mu g^*)^2 Nn\, \frac{\omega_s^2}{\gamma\Gamma\left(\frac{\Gamma}{2} + \gamma\right)}. \tag{18}$$

Assuming 10^{16} electrons/cm^3, $\Gamma \simeq 10^{10}$ s^{-1}, and $\gamma \simeq 4 \times 10^{10}$ s^{-1}, one finds [3], [9]

$$\epsilon_{\text{rad}/N} \simeq 10^{-15} \text{ erg/electron}.$$

This is a small, though not inappreciable, fraction of the spin energy ($\simeq 10^{-14}$ erg) per electron. Note, moreover, that the total energy radiated is about 10 erg in 10^{-10} s, corresponding to a power of 10^4 W. With only a single pulse per second, the *average* power is about 10^{-6} W in a well-collimated beam. Such powers can be easily detected. Higher powers could be achieved by pulsing the whole experiment many times per second.

V. Discussion

In the preceding sections, we have suggested that the extraordinarily large Raman coupling in InSb might be used to perform nonlinear, pulsed, spin resonance experiments. Such processes are also favored by the relatively long (by solid-state standards) dephasing times observed in this material.[1] The optical powers required to achieve $\pi/2$-spin rotation are now available. There is reason to believe that the Stokes pulses generated by driving a spin-flip laser with a mode-locked CO_2 laser would be sufficiently short ($\sim 10^{-10}$ s) to perform the experiment proposed herein.

Assuming $\pi/2$-rotation can be achieved, we have made estimates of the (tunable) IR power that might be radiated. Average powers in the 10^{-6}-W range, in a collimated beam, are attainable from single-pulse-per-second operation; higher powers could be achieved with higher repetition rates.

References

[1] a) R. E. Slusher, C. K. N. Patel, and P. A. Fleury, "Inelastic light scattering from Landau-level electrons in semiconductors," *Phys. Rev. Lett.*, vol. 18, pp. 77–79, Jan. 1967.
b) C. K. N. Patel and R. E. Slusher, "Light scattering by plasmons and Landau levels of electron gas in InAs," *Phys. Rev.*, vol. 167, pp. 413–415, Mar. 1968.
c) —, "Electron spin-flip Raman scattering in PbTe," *Phys. Rev.*, vol. 177, pp. 1200–1202, Jan. 1969.
d) C. K. N. Patel and E. D. Shaw, "Tunable stimulated Raman scattering from conduction electrons in InSb," *Phys. Rev. Lett.*, vol. 24, pp. 451–455, Mar. 1970.
e) P. A. Fleury and J. F. Scott, "Spin-flip Raman scattering from conduction electrons in CdS and ZnSe," *Phys. Rev.*, vol. B3, pp. 1979–1985, Mar. 1971.
f) T. W. Walker *et al.*, "Electron spin-flip-Raman scattering in II–VI compounds," in *Proc. 11th Int. Conf. Physics of Semiconductors* (Warsaw, Poland, July 1972), pp. 376–381.
g) T. W. Walker *et al.*, "Spin-flip Raman scattering in semicon-

[1] It has been brought to our attention that CdS may be an even better material for the experiment described in this paper since for CdS at 4 K T_2 has a large value of 4×10^{-9} s. The nonlinear Hamiltonian, however, is not necessarily described by (2) which was derived for III–IV compounds with large spin-orbit splitting. Therefore, the theory, as presented in this paper, may have to be modified for CdS.

ductors," *Bull. Am. Phys. Soc.*, vol. 18, p. 300, 1973.
h) R. Romestain, S. Geschwind, G. E. Devlin, and P. A. Wolff, "Raman scattering from coherent spin states in n-type CdS," *Phys. Rev. Lett.*, vol. 33, pp. 10–13, July 1974.

[2] a) S. R. J. Brueck and A. Mooradian, "Efficient, single-mode, cw, tunable spin-flip Raman laser," *Appl. Phys. Lett.*, vol. 18, pp. 229–230, Mar. 1971.
b) A. Mooradian, private communication.

[3] a) V. T. Nguyen and T. J. Bridges, "Resonant optical nonlinearity due to conduction-electron spins in InSb," *Phys. Rev. Lett.*, vol. 29, pp. 359–361, Aug. 1972.
b) T. J. Bridges and V. T. Nguyen, "Generation of tunable far-infrared radiation by difference frequency mixing using conduction electron spin nonlinearity in InSb," *Appl. Phys. Lett.*, vol. 23, pp. 107–109, July 1973.

[4] A. Abragam, *The Principles of Nuclear Magnetism*. Oxford, England: Oxford University Press, 1961.

[5] Y. Yafet, "Raman scattering by carriers in Landau levels," *Phys. Rev.*, vol. 152, pp. 858–862, Dec. 1966.

[6] a) T. L. Brown and P. A. Wolff, "Theory of resonant, far-infrared generation in InSb," *Phys. Rev. Lett.*, vol. 29, pp. 362–364, Aug. 1972.
b) R. N. Nucho and P. A. Wolff, to be published.
c) P. M. Platzman and P. A. Wolff, *Waves and Interactions in Solid State Plasmas*. New York: Academic, 1973, p. 111.

[7] a) S. R. J. Brueck and A. Mooradian, "Near-resonance spin-flip Raman scattering in indium antimonide," *Phys. Rev. Lett.*, vol. 28, pp. 161–165, Jan. 1972.
b) V. T. Nguyen, E. G. Burkhardt, and P. A. Wolff, to be published.

[8] a) Y. Yafet, *Solid State Physics*, vol. 14. New York: Academic, 1963, p. 40.
b) L. M. Roth, B. Lax, and S. Zwerdling, "Theory of optical magneto-absorption effects in semiconductors," *Phys. Rev.*, vol. 114, pp. 90–104, Apr. 1959.

[9] S. R. J. Brueck, private communication.

[10] R. L. Aggarwal *et al.* "High-intensity tunable InSb spin-flip Raman laser," *Appl. Phys. Lett.*, vol. 18, pp. 383–385, May 1971.

[11] a) O. R. Wood, R. L. Abrams, and T. J. Bridges, "Mode locking of a transversely excited atmospheric pressure CO_2 laser," *Appl. Phys. Lett.*, vol. 17, pp. 376–378, Nov. 1970.
b) D. L. Lyon, E. V. George, and H. A. Hans, "Observation of spontaneous mode locking in a high-pressure CO_2 laser," *Appl. Phys. Lett.*, vol. 17, pp. 474–476, Dec. 1970.
c) A. F. Gibson, M. F. Kimmitt, and C. A. Rosito, "Passive mode locking of a high-pressure CO_2 laser with a CO_2 saturable absorber," *Appl. Phys. Lett.*, vol. 18, pp. 546–548, June 1971.

[12] R. N. Nucho and P. A. Wolff, to be published.

[13] S. Y. Yuen, P. A. Wolff, and B. Lax, "Theory of spin-flip Raman-scattering line shape in narrow-gap semiconductors," *Phys. Rev.*, vol. B9, pp. 3394–3406, Apr. 1974.

Correspondence

Field Configurations and Propagation Constants of Modes in Hollow Rectangular Dielectric Waveguides

HERMANN KRAMMER

Abstract—**The field configurations and propagation constants of linearly polarized low-loss modes in hollow dielectric waveguides with rectangular cross section are computed analytically under the assumption that the dimensions of the rectangular cross section are much larger than the free-space wavelength. The attenuation constant is then equal to the sum of the corresponding TE- and TM-mode attenuation constants in parallel-plate waveguides.**

Hollow dielectric waveguides with square cross sections have recently been used for the construction of waveguide gas lasers [1], [2]. In the following, the field configurations and propagation constants of modes in a hollow dielectric rectangular waveguide will be calculated. The waveguide shown in Fig. 1 consists of an infinitely long prism of rectangular cross section $2a \times 2b$ (free-space dielectric constant ϵ_0) which is embedded in another medium with the complex dielectric constant $\epsilon = \epsilon_0(\epsilon' - j\epsilon'')$, where $j = (-1)^{1/2}$. The magnetic permeability μ_0 is assumed to be that of free space for both media. It is impossible to satisfy the boundary conditions exactly by a separation method solution, e.g., $f(x) \cdot g(y)$ in Cartesian coordinates, but one can find approximate solutions in a way similar to Marcatili's method for the dielectric rectangular fiber [3]. The results are developed in two steps.

1) An approximation method is given to obtain separate boundary equations in x and y.

2) The two boundary equations are solved by a perturbation technique.

The dimensions of the rectangle are assumed to be much larger than the free-space wavelength λ,

$$ka \gg |n|, \quad kb \gg |n| \tag{1}$$

where $k = 2\pi/\lambda$ is the free-space phase constant and n is the complex refractive index defined by $n^2 = \epsilon' - j\epsilon''$. Further, the analysis shall be restricted to low-loss modes,

$$|\gamma/jk - 1| \ll 1. \tag{2}$$

$\gamma = \alpha + j\beta$ is the axial complex propagation constant of the mode under consideration. Modes which satisfy (1) and (2) are approximately of the TEM kind. As the waveguide structure is symmetric with respect to the planes $x = 0$ and $y = 0$, the modes must be either symmetric or antisymmetric with respect to these planes.

With reference to Fig. 1, two classes of field configurations

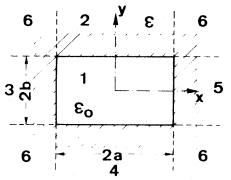


Fig. 1. A hollow rectangular waveguide is embedded in a medium with the complex dielectric constant ϵ. The z axis is perpendicular to the drawing plane. The cross section is divided into regions 1 to 6 for calculation.

in the regions 1 to 5 can be established which satisfy the boundary conditions along the boundary of region 1. The magnetic field of the modes of the first class is almost completely polarized in the x direction (symbol H^xE^y); that of the second class in the y direction (symbol E^xH^y). At first we consider H^xE^y modes symmetric with respect to $x = 0$ and $y = 0$. The trial solution for the magnetic field components satisfying the boundary conditions are

$$H_x = \begin{cases} M_1 \cdot \cosh(\gamma_x x) \cdot \cosh(\gamma_y y) & \text{in region 1} \\ M_2 \cdot \cosh(\gamma_x x) \cdot \exp[-\gamma_{y2}(|y| - b)] & \text{in regions 2, 4} \\ M_3 \cdot \exp[-\gamma_{x3}(|x| - a)] \cdot \cosh(\gamma_y y) & \text{in regions 3, 5} \end{cases} \tag{3}$$

$$H_y = 0$$

where factor $\exp(-\gamma z + j\omega t)$ has been omitted and γ_x, γ_y, γ_{x3}, γ_{y2} are propagation constants in the x and y directions. They satisfy the relations

$$\gamma_x^2 + \gamma_y^2 + \gamma^2 = -k^2 \tag{4a}$$

$$\gamma_x^2 + \gamma_{y2}^2 + \gamma^2 = -n^2k^2 \tag{4b}$$

$$\gamma_{x3}^2 + \gamma_y^2 + \gamma^2 = -n^2k^2. \tag{4c}$$

The other field components can be derived from Maxwell's equations.

The fields in regions 2 to 6 may be considered to be generated by the refraction of waves propagating in region 1 and impinging at grazing angles on the interface between the two media. Therefore they are much smaller than the fields in region 1 and the inequalities $|M_2| \ll |M_1|$, $|M_3| \ll |M_1|$ hold.

Even less power arrives at region 6. For this reason we do not explicitly consider the fields and boundary conditions of region 6.

A further simplification is the neglect of the components H_z in regions 2 and 4, and E_z in the regions 3 and 5. This is justified because they contain products of small quantities M_2, M_3 and γ_x/k, γ_y/k, where

$$|\gamma_x/k| \ll 1, \quad |\gamma_y/k| \ll 1$$

is valid because of (2) and (4a).

The remaining boundary conditions require the continuity of H_x along the boundary 1–2 and of E_y along 1–5:

$$M_2 = M_1 \cosh(\gamma_y b), \quad M_3 = M_1 \cosh(\gamma_x a). \tag{5}$$

Continuity of E_z along 1–2 and of H_z along 1–5 leads to the eigenvalue problems

Manuscript received October 13, 1975; revised March 5, 1976.

The author is with the Institut für Hochfrequenztechnik, University of Vienna, Vienna, Austria.

TABLE I
FIELDS AND PROPAGATION CONSTANTS OF MODES OF THE HOLLOW RECTANGULAR WAVEGUIDE

$H^xE^y_{pq}$ modes

$$H_x = -E_y/Z = M\begin{Bmatrix}\cos(p_1\pi x/2a)\\ \sin(p_2\pi x/2a)\end{Bmatrix}\begin{Bmatrix}\cos(q_1\pi y/2b)\\ \sin(q_2\pi y/2b)\end{Bmatrix}$$

$$H_z = \pi M/2jka\begin{Bmatrix}-p_0\sin(p_1\pi x/2a)\\ p_e\cos(p_2\pi x/2a)\end{Bmatrix}\begin{Bmatrix}\cos(q_1\pi y/2b)\\ \sin(q_2\pi y/2b)\end{Bmatrix}$$

$$E_z = j\pi MZ/2kb\begin{Bmatrix}\cos(p_1\pi x/2a)\\ \sin(p_2\pi x/2a)\end{Bmatrix}\begin{Bmatrix}-q_1\sin(q_1\pi y/2b)\\ q_2\cos(q_2\pi y/2b)\end{Bmatrix}$$

$$\alpha = \frac{(p\pi)^2}{4k^2a^3}\operatorname{Re}(N_1) + \frac{(q\pi)^2}{4k^2b^3}\operatorname{Re}(N_2)$$

$$\beta = k\left\{1 - \frac{1}{2}\left[\left(\frac{p\pi}{2ka}\right)^2\cdot\left(1 - \frac{2}{ka}\operatorname{Im}(N_1)\right) + \left(\frac{q\pi}{2kb}\right)^2\cdot\left(1 - \frac{2}{kb}\operatorname{Im}(N_2)\right)\right]\right\}$$

$E^xH^y_{pq}$ modes

$$H_y = E_x/Z = M\begin{Bmatrix}\cos(p_1\pi x/2a)\\ \sin(p_2\pi x/2a)\end{Bmatrix}\begin{Bmatrix}\cos(q_1\pi y/2b)\\ \sin(q_2\pi y/2b)\end{Bmatrix}$$

$$H_z = \pi M/2jkb\begin{Bmatrix}\cos(p_1\pi x/2a)\\ \sin(p_2\pi x/2a)\end{Bmatrix}\begin{Bmatrix}-q_1\sin(q_1\pi y/2b)\\ q_2\cos(q_2\pi y/2b)\end{Bmatrix}$$

$$E_z = \pi MZ/2jka\begin{Bmatrix}-p_1\sin(p_1\pi x/2a)\\ p_2\cos(p_2\pi x/2a)\end{Bmatrix}\begin{Bmatrix}\cos(q_1\pi y/2b)\\ \sin(q_2\pi y/2b)\end{Bmatrix}$$

$$\alpha = \frac{(p\pi)^2}{4k^2a^3}\operatorname{Re}(N_2) + \frac{(q\pi)^2}{4k^2b^3}\operatorname{Re}(N_1)$$

$$\beta = k\left\{1 - \frac{1}{2}\left[\left(\frac{p\pi}{2ka}\right)^2\cdot\left(1 - \frac{2}{ka}\operatorname{Im}(N_2)\right) + \left(\frac{q\pi}{2kb}\right)^2\cdot\left(1 - \frac{2}{kb}\operatorname{Im}(N_1)\right)\right]\right\}$$

$$Z = \sqrt{\frac{\mu_0}{\epsilon_0}} \qquad N_1 = \frac{1}{\sqrt{n^2-1}} \qquad N_2 = \frac{n^2}{\sqrt{n^2-1}}$$

Note: M, arbitrary amplitude factor.

$$\gamma_x \cdot \tanh(\gamma_x a) = -\gamma_{x3} \tag{6a}$$

$$n^2 \cdot \gamma_y \cdot \tanh(\gamma_y b) = -\gamma_{x2}. \tag{6b}$$

In order to obtain solutions satisfying (2), (6a) and (6b) can be transformed with (4) to

$$\tanh^2(\gamma_x a) = -(n^2 - 1)\,k^2a^2/(\gamma_x a)^2 \tag{7a}$$

$$\tanh^2(\gamma_y b) = -(n^2 - 1)\,k^2b^2/n^4(\gamma_y b)^2. \tag{7b}$$

Equations (7a) and (7b) were solved by a perturbation technique using the fact that the absolute values of the right-hand sides of the equations are much greater than unity. This is true within assumption (1) for sufficiently large values of the refractive index $|n^2 - 1| \gtrsim 1$.

The results for the propagation constants γ_x and γ_y are then

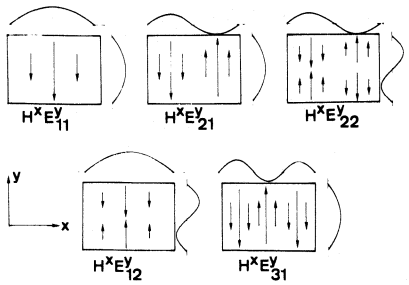


Fig. 2. Electric field lines of modes $H^xE^y_{pq}$. The amplitude of H_x or E_y is shown as it depends on x and y.

$$\gamma_x a = -(2\nu - 1)\,\pi/2ka \cdot \operatorname{Re}((n^2 - 1)^{-1/2}) + j \cdot (2\nu - 1)\,\pi/2 \cdot [1 - Im((n^2 - 1)^{-1/2})/ka] \tag{8a}$$

$$\gamma_y b = -(2\mu - 1)\,\pi/2kb \cdot \operatorname{Re}(n^2(n^2 - 1)^{-1/2}) + j \cdot (2\mu - 1)\,\pi/2 \cdot [1 - \operatorname{Im}(n^2(n^2 - 1)^{-1/2})/kb]. \tag{8b}$$

ν and μ are the mode numbers ($\nu, \mu = 1, 2, \cdots$). The propagation constant γ follows from (4a):

$$\gamma = jk[1 + (\gamma_x^2 + \gamma_y^2)/2k^2]. \tag{9}$$

Note that only low-order modes obey the inequality (2). Antisymmetric fields with respect to the x or y axis are calculated in an analogous way. Caution has to be exerted in applying the results to metallic waveguides for which $|n|$ might be very high. Thus the right-hand side of (7b) is not large compared to unity, and the approximation developed for solving (6b) is not applicable.

Table I gives the field components in region 1 and the propagation constants of modes $H^xE^y_{pq}$ and $E^xH^y_{pq}$. New indices p and q are defined which state the number of extrema of the magnetic or electric transverse field components. The odd numbers p_1 and q_1 ($p_1 = 2\nu - 1$, $q_1 = 2\mu - 1$) correspond to modes with transversal field components symmetric with respect to the planes $x = 0$ and $y = 0$, respectively. The even numbers p_2 and q_2 ($p_2 = 2\nu$, $q_2 = 2\mu$) correspond to antisymmetric modes with respect to these planes.

Inspection of Table I reveals that the attenuation constant is equal to the sum of the corresponding TE- and TM-mode attenuation constants in parallel-plate waveguides with heights $2a$ and $2b$, respectively. The phase constant β is equal to the free-space phase constant k minus two small terms, which correspond to the terms of the TE- and TM-mode of parallel-plate waveguides in an analogous way.

For illustrative purposes, the lines of the electric field in the inner waveguide region are shown for the first few $H^xE^y_{pq}$ modes in Fig. 2. In a waveguide with square cross section ($a = b$) the modes $H^xE^y_{pq}$ and $E^xH^y_{qp}$ are degenerate.

ACKNOWLEDGMENT

The author is grateful to his colleagues at the Institute, particularly to Dr. E. Bonek, for their critical reading of the manuscript and to a reviewer of an earlier version of this correspondence for his comment that the results are not applicable to metallic waveguides of high conductivity.

REFERENCES

[1] R. L. Abrams and W. B. Bridges, "Characteristics of sealed-off waveguide CO_2 lasers," *IEEE J. Quantum Electron.*, vol. QE-9, pp. 940–946, Sept. 1973.

[2] R. L. Abrams, "Gigahertz tunable waveguide CO_2 laser," *Appl. Phys. Lett.*, vol. 25, pp. 304–306, Sept. 1, 1974.

[3] E. A. J. Marcatili, "Dielectric rectangular waveguide and directional coupler for integrated optics," *B.S.T.J.*, vol. 48, pp. 2071–2102, Sept. 1969.
[4] H. Nishihara, T. Inoue, and J. Koyama, "Low-loss parallel-plate waveguide at 10.6 μm," *Appl. Phys. Lett.*, vol. 25, pp. 391–393, Oct. 1, 1974.

A $Gd_2(MoO_4)_3$ Longitudinal Electrooptic Modulator at 6328 Å

N. G. THEOPHANOUS

Abstract—**A $Gd_2(MoO_4)_3$ light modulator operating at low frequencies, from 100 Hz up to 1 MHz, is examined. Experimental results concerning the thermal behavior and stability, frequency response, and linearity performance characteristics of the system are presented. Advantages and disadvantages of the modulator are discussed.**

Gadolinium molybdate (GMO) belongs to the mm2 (C_{2v}) orthorombic group up to 159°C [1] and exhibits interesting ferroelectric, ferroelastic, electrooptic, and optical properties [2]–[4]. GMO crystals do not exhibit thickness modes along the c axis, the piezoelectric constants d_{32} and d_{33} being quite small [4]. This fact suggests that a GMO Z-cut crystal excited under longitudinal electrooptic modulation conditions would be essentially free of acoustic piezoelectric resonances in the low-frequency region from 0 to 100 kHz or more, providing an important advantage over other electrooptic modulation systems operating in this frequency band. The present work deals with the study of the above modulator.

The experimental setup is indicated schematically in Fig. 1. The GMO modulator crystal and the optical components have been arranged according to a typical Senarmont compensator configuration [5]. The light source was a 2.5-mW stabilized He–Ne Laser at 6328 Å and the detector a photomultiplier set followed by an amplifier and a camera oscilloscope. The GMO crystal was bar shaped with 20-mm length along the $Z(c)$ axis, parallel to the laser beam, and with a 5×5-mm^2 cross section. All crystal surfaces were perpendicular to the three crystallographic axes and two Al electrodes were attached to the end faces normal to the Z axis.

A modulating voltage $V = U_0 \sin \omega_m t$ adds to the spontaneous (static) optical retardation $\Gamma^{(0)}$ of the crystal an ac component with peak value [6], [13]

$$\Gamma_0 = \pi \frac{U_0}{V_{\lambda/2}} = \pi n_0^3 r_c U_0 / \lambda_0 \qquad (1)$$

where

$\lambda_0 = 6328$ Å	vacuum wavelength;
$n_0 = 1.848$	refractive index;
$r_c \simeq r_{13} - r_{23}$	electrooptic coefficient equivalent of GMO for the particular configuration [1];
$V_{\lambda/2}$	corresponding half-wave voltage of the crystal.

Manuscript received October 20, 1975; revised April 5, 1976.

The author is with the Electronics Laboratory, Athens University, Athens, Greece. He is on leave at the Fundamental and Applied Physics Group, University of Metz, Metz, France.

With the analyzer adjusted at extinction for the unmodulated beam, its incident intensity being I_0, one gets an intensity-modulated beam having at the output a modulation amplitude $J_0 = \Delta I = I_0 \Gamma_0^2/4$ at a principal frequency $2\omega_m$, thus twice the modulating one; this "frequency doubling" observed on the scope is very abrupt and sharp and has been used for the detection of the extinction position of the analyzer with an accuracy greater than that of the usual visual or photoelectric methods [13]. A $\pi/4$ rotation of the analyzer from its extinction position leads to the linear modulation position where the beam comes out modulated at the fundamental modulating frequency ω_m with modulation amplitude $J_0 = \Delta I = I_0 \Gamma_0/2$ [7], [16].

The temperature dependence of the modulation depth $m = 2J_0/I_0$ and of the spontaneous retardation $\Gamma^{(0)}$ of the crystal, in the temperature range of 20–28°C, has been measured with a 300-V peak value modulating voltage at 2 kHz; results are shown in Figs. 2 and 3. For these measurements the extinction position has been used and the retardation was determined from the extinction angle of the analyzer [16], while the modulation depth was calculated for the case of linear modulation position from oscilloscope observations. From the obtained $\Gamma^{(0)}$ versus T curves, the mean temperature variation of the static birefrigence of GMO crystal was calculated equal to

$$l^{-1}(\partial l |\Delta n^{(0)}|/\partial T) = 8.5 \times 10^{-7}/°\text{C}$$

a value much lower than that of several other modulators, e.g., KDP and/or $LiNbO_3$ types [8]–[10]. Following the method of Denton *et al.* [8] it was found that a ±0.35°C control of the crystal temperature is sufficient to maintain the optical bias in its proper value for 0.1-percent modulation stability. The observed periodical fluctuation on the m versus T curves must be attributed mainly to the interaction of thermal expansion with multiple beam optical interference effects [15] in the crystal along the c axis; obviously, the elimination of these effects would cancel corresponding fluctuations of m. By taking into account these effects and the positions of maxima on the m versus T curves, a mean coefficient of linear thermal expansion along the c axis equal to 6.5×10^{-6} $(°\text{C})^{-1}$ was obtained; this value is in close agreement with thermal expansion data for GMO [4]. Using values of m corrected for such interference effects we determined, by means of (1) (see also [7]), the electrooptic coefficient r_c of GMO as a function of temperature; the resulting r_c versus T curve, shown in Fig. 2, is consistent with similar results of other authors [1], [3].

The frequency response of the modulator at 23.5°C in the frequency band from 100 Hz up to 1 MHz has been investigated by means of a precision frequency synthesizer in 1–10-Hz steps, under operation at the extinction position; corresponding results are shown in Figs. 4 and 5. Both curves m_0 versus f_m and φ versus f_m indicate that the system is free of resonances and phase distortion practically in the whole range of audio and low frequencies from 100 Hz to 100 kHz, in spite of the great length of the utilized crystal that ought to favor the generation of acoustic piezoelectric resonances in the lower frequency region. These characteristics of a GMO modulator represent a useful advantage over similar widely used longitudinal electrooptic modulators for the same frequency band, such as ADP- and KDP-type Z-cut modulators, which demonstrate embarassing resonance peaks perturbing the modulation performance [5], [11], [12]. It would be interesting to compare with other, e.g., $LiNbO_3$-type, modulators if their frequency response data were available for the particular configuration and frequency band.

The linearity characteristics of our system, operating at the

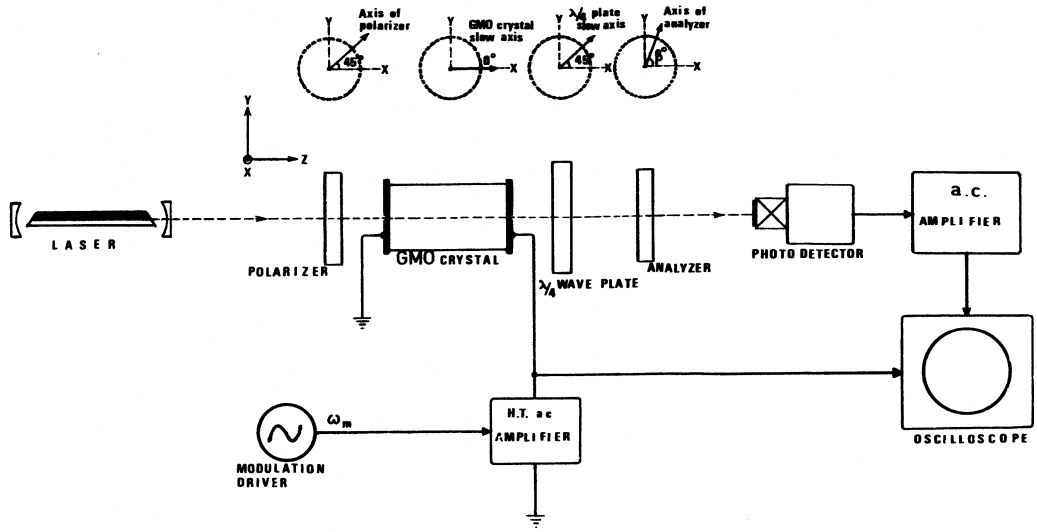


Fig. 1. Schematic of the experimental arrangement.

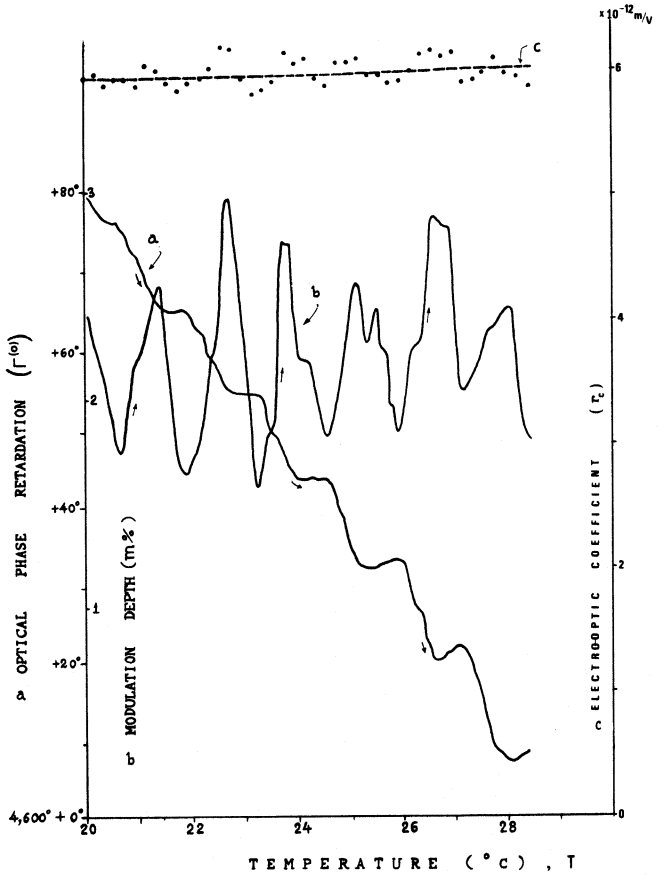


Fig. 2. Behavior of GMO modulator for increasing temperatures. Curve *a:* spontaneous optical retardation $\Gamma^{(0)}$ of the GMO crystal versus temperature T. Curve *b:* intensity (linear) modulation depth m versus temperature T. Curve *c:* electrooptic coefficient r_c of GMO for the examined configuration versus temperature T.

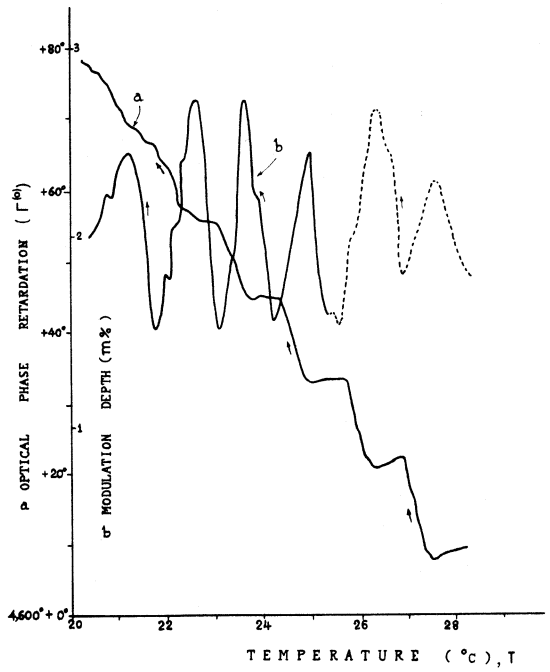


Fig. 3. Behavior of GMO modulator for decreasing temperatures. Curve *a:* spontaneous optical retardation $\Gamma^{(0)}$ versus temperature T. Curve *b:* intensity (linear) modulation depth m versus temperature T. (Dashed segments correspond to not completely trustworthy results.)

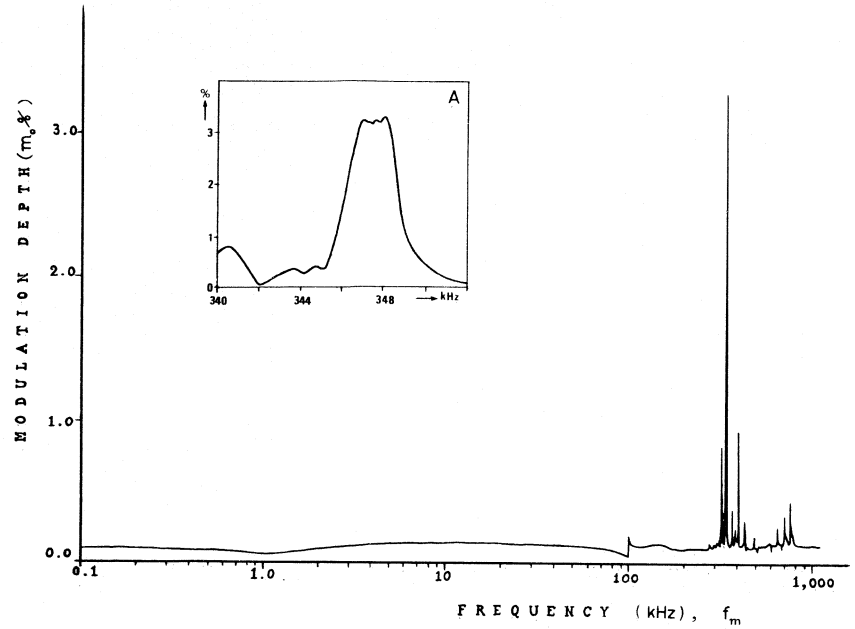


Fig. 4. Intensity modulation depth m_0 at the extinction position of operation versus modulating signal frequency f_m. The upper curve enclosed in rectangle A represents explicitly the response near principal resonance (at 348.22 kHz).

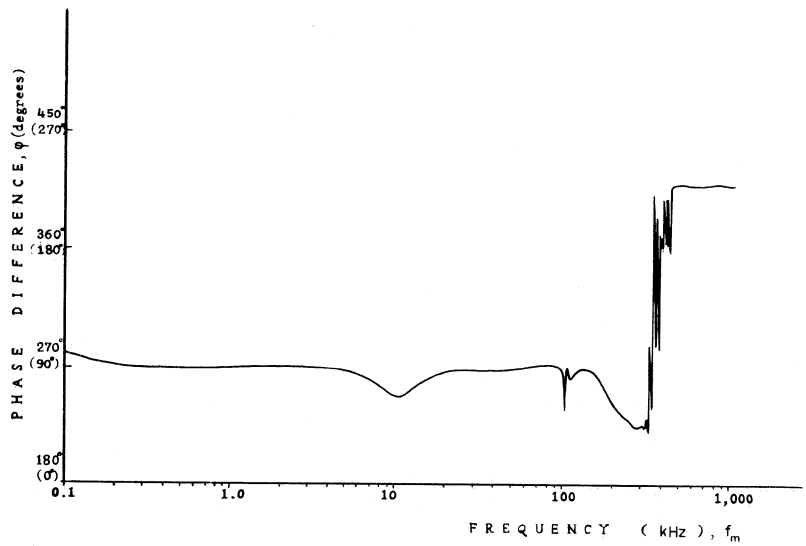


Fig. 5. Phase difference (shift) φ between the modulating signal and the ac variation of the modulated beam at the output of the analyzer versus modulating signal frequency f_m.

linear modulation position, were checked with modulating voltages up to 270-V peak value; the modulation under these conditions was linear in this range. The corresponding modulation sensitivity is found such that 77 V (thus a field of 38.5 V/cm) are required for 1-percent modulation; this sensitivity is relatively small compared to that of currently used simple light modulators. The good linearity response and the poor sensitivity of the GMO modulator are inherently connected with the large value of $V_{\lambda/2}$ (20.2 kV at 23.5°C, in our case) and with the rather small value of the $n_0^3 r_c$ product (38×10^{-12} m/V at 23.5°C, in our case), characteristics that constitute the more serious disadvantages of the system. On the other hand, the low dielectric constant of GMO ($\simeq 10$), unusually small for a ferroelectric [4], appears to be an advantageous parameter increasing the figure of merit [14] and leading to reduced performance conditions for the case of a GMO lumped modulator [6], [10].

ACKNOWLEDGMENT

It is a pleasure to acknowledge Prof. C. Carabatos for helpful hints and discussions and A. Arapoghianni for useful assistance.

REFERENCES

[1] A. W. Smith and G. Burns, "Optical properties and switching in $Gd_2(MoO_4)_3$," *Phys. Letters*, vol. 28A, pp. 501-503, Jan. 1969.
[2] A. Kumada, "Optical properties of gadolinium molybdate and their device applications," *IEEE Trans. Sonics and Ultrasonics*, vol. SU-19, pp. 115-123, 1972.
[3] T. Nakamura, T. Kondo, and A. Kumada, "Spontaneous birefrigence and electrooptic response in $Gd_2(MoO_4)_3$," *Phys. Letters*, vol. 36A, pp. 141-143, Aug. 1971.
[4] S. E. Cummins, "Electrical, optical and mechanical behavior of ferroelectric $Gd_2(MoO_4)_3$," *Ferroelectrics*, vol. 1, pp. 11-17, 1970.
[5] R. O'B. Carpenter, "The electro-optic effect in uniaxial crystals

of the dihydrogen phosphate type, (III) Measurements of coefficients," *J. Opt. Soc. Amer.*, vol. 40, pp. 225–229, Apr. 1950.
[6] I. P. Kaminow and E. H. Turner, "Electrooptic light modulators," *Appl. Optics*, vol. 5, pp. 1612–1628, Oct. 1966.
[7] I. P. Kaminow, "Measurements of the electrooptic effect in CdS, ZnTe, and GaAs at 10.6 μ," *IEEE J. Quantum Electron.*, vol. QE-4, pp. 23–26, Jan. 1968.
[8] R. Denton, F. S. Chen, and A. A. Ballman, "$LiTaO_3$ light modulators," *J. Appl. Phys.*, vol. 38, pp. 1611–1617, Mar. 1967.
[9] E. G. Spencer, P. V. Lenzo, and A. A. Ballman, "Dielectric materials for electrooptic, elastooptic and ultrasonics device applications," *Proc. IEEE*, vol. 55, pp. 2074–2109, Dec. 1967.
[10] F. S. Chen, "Modulators for optical communications," *Proc. IEEE*, vol. 58, pp. 1440–1457, Oct. 1970.
[11] W. H. Steier, "A push-pull optical amplitude modulator," *IEEE J. Quantum Electron.*, vol. QE-3, pp. 664–667, Dec. 1967.
[12] F. Hoff and B. Stadnik, "Effects of piezoelectric resonances in ADP and KDP light modulator crystals," *Electron. Letters*, vol. 2, p. 293, Aug. 1966.
[13] N. G. Theophanous, "Electrooptic modulation of a He-Ne laser beam by $Gd_2(MoO_4)_3$ and study of its electro-optic behavior," Ph.D. dissertation (in Greek), Athens Univ., Athens, Greece, 1973.
[14] S. H. Wemple, in *Laser Handbook*, F. T. Arecchi and E. O. Schulz-Dubois, Ed. Amsterdam, The Netherlands: North Holland, 1972.
[15] R. W. Ditchburn, *Light*. New York: Blackie, 1961, p. 137.
[16] I. P. Kaminow, *An Introduction to Electrooptic Devices*. New York: Academic, 1974, pp. 1–70.

Picosecond Relaxation Time Measurement from the *Q*-Switch Threshold

K. HAMAL, H. JELINKOVA, A. NOVOTNY, AND M. VRBOVA

Abstract—**A method is presented for measurement of the relaxation time of a passive *Q*-switch dye in the picosecond region which is based on the determination of the *Q*-switch threshold. The relaxation times of 24 ± 5 ps for cryptocyanine and 28 ± 5 ps for modified dicarbocyanine iodide were obtained.**

The behavior of the nonlinear absorber for *Q*-switching, mode locking, and isolation purposes is usually described by the absorption cross section and the relaxation time, or by the saturation intensity [1], [2]. The absorption cross section can be determined from the Lambert–Beer law. The picosecond relaxation time can be measured directly using a mode-locked laser [3] or it may be derived from the measurement of saturation intensity [4]. The use of direct methods requires a precise knowledge of the picosecond pulse shape. We report here a new measurement method of picosecond relaxation time of saturable dyes that does not require such knowledge. It is based on the measurement of the threshold of a *Q*-switched laser in which the measured dye acts as a passive *Q*-switch.

The dynamics of a passive *Q*-switched ruby laser can be described by three spatially averaged transport equations. The validity of the two- or three-level approximation of the description of the dye together with incoherent superposition of resonator modes is presumed [5], [6]. Two parameters, relaxation time τ and absorption cross section σ_B, specify the bleaching material. When the dye relaxation time is sufficiently short and the dye absorption cross section is very high, the set of equations is reduced using the adiabatic approximation [8]. In such a case the bleaching material is characterized by single parameter $\sigma_B\tau$ only. The equations for normalized spatially averaged light energy density x and normalized population inversion y inside the amplifying medium have the following form:

$$\frac{dx}{dt} = Axy - B\frac{x}{1+\sigma\tau x} - ax + k \tag{1}$$

$$\frac{dy}{dt} = -2xy - Dy + G \tag{2}$$

where

$$x = \sigma_R v u/(h\nu);\quad y = n/n_0;\quad A = v\mu\sigma_R n_0;$$
$$B = v\mu(-\ln T_{0S})/l;\quad a = v\mu(-\ln(T_{NS}\sqrt{R}) + \rho l)/l;$$
$$k = \sigma_R v\mu A_s \Delta\nu_g \Delta\Omega n_0/(8\pi\Delta\nu);\quad G = (2/\tau_R)$$
$$\cdot (g/(\sigma_R n_0 - g));\quad D = G + 2/\tau_R;\quad \sigma = \sigma_B/\sigma_R$$

where

u	instantaneous density of light energy inside the amplifying medium;
n_0	density of laser atoms;
n	density of population inversion;
σ_R and τ_R	stimulated emission cross section and relaxation time of laser atoms, respectively;
l, ρ	length and internal loss factor of ruby rod;
v	velocity of light in the active medium;
μ	filling factor of the resonator defined as the ratio of the optical length of the ruby rod to that of the entire resonator;
$(h\nu)$	one photon energy of laser light;
$T_{0S}, (T_{NS})$	saturable (nonsaturable) transmission of the dye cell;
R	product of laser mirrors' reflectivities;
A_s	Einstein's spontaneous emission factor;
$\Delta\nu_g$	laser linewidth;
$\Delta\nu$	luminescence linewidth;
$\Delta\Omega$	beam divergence (in steradians);
g	gain factor.

Numerical solution of (1) and (2) with initial conditions $x(0) = 0$ and $y(0) = (B + a)/A$ gave us the time dependence of inversion and that of the laser light intensity. Whenever all parameters A, B, a, k, D, G characterizing a certain laser system were evaluated carefully, the calculated pulse shape and output laser energy reproduced very closely the experimental observations. This coincidence of experimental and computer results was considered to be a confirmation of the mathematical model of the laser.

By means of repetitive solution of (1) and (2), the pulse length and peak intensity were evaluated for a range of values of a, B, and $\sigma\tau$. Naturally, in all cases the condition $(B + a)/A < G/D$ representing the above threshold action was satisfied. This condition represents the above threshold action for a free-running regime, but not necessarily the *Q*-switched action of the laser system. In the space of a and B parameters, the finite region including the parameters a and B for which the laser is *Q*-switched was found. The boundary of this region is strongly affected by the value of $\sigma\tau$. Fig. 1(a) and (b) allows the comparison. When the value of $\sigma\tau$ is very high or the pumping is very intensive, the *Q*-switch threshold and oscillation threshold approximately coincide. In the vicinity of free-running laser action threshold the monotone function representing the dependence of the *Q*-switch threshold value $B = (B)_{th}$

Manuscript received December 9, 1975; revised April 26, 1976.
The authors are with the Faculty of Nuclear Science and Physical Engineering, Prague, Czechoslovakia.

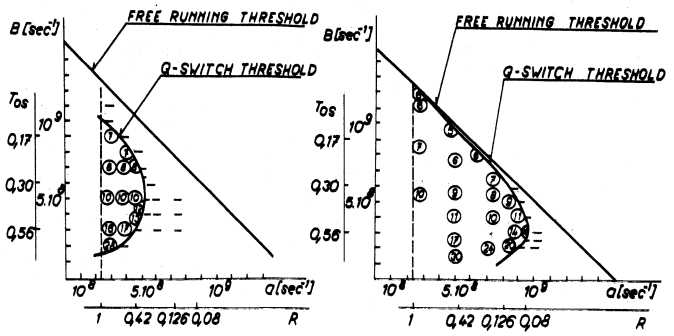


Fig. 1. Giant pulse region in a, B space. The Q-switch region was determined by the numerical integration of rate equations (1) and (2) for various values of nonsaturable loss parameter a and saturable loss parameter B. The circled numbers denote the points of the region where the laser is Q switched (and the pulse length in nanoseconds is mentioned). $-$denotes the point where the laser is not Q switched. $v\mu/l = 5 \times 10^8\ s^{-1}$, $v\mu(-\ln T_{NS} + \rho l)/l = 2.6 \times 10^8\ s^{-1}$, $A = 2.2 \times 10^9\ s^{-1}$, $G = 1350\ s^{-1}$, $D = 1950\ s^{-1}$, $k = 10^3\ s^{-1}$, (a) $\sigma\tau = 7.5 \times 10^{-7}$ s (corresponds to ruby and cryptocyanine). (b) $\sigma\tau = 2.25 \times 10^{-6}$ s (corresponds to ruby and modified dicarbocyanine iodide).

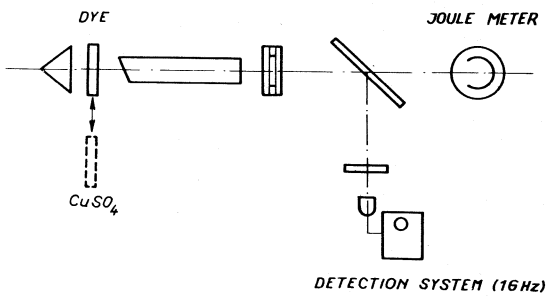


Fig. 2. Experimental setup.

on $\sigma\tau$ can be found for every value of the loss parameter a. This enables us to determine the real value $\sigma\tau$ if at least one boundary point, with coordinates $(a)_{th}$, $(B)_{th}$, is known from the experiment.

The experimental setup consisted of a laser and the photodiode, Fig. 2. The laser system consisted of a 10-mm-diam by 150-mm-long Verneuil ruby rod cut at an angle of 1°, a Porro prism, a resonant reflector, and a 10-mm-long cell. The resonant reflector consisted of two crystalline quartz plates. The cell contained either a measured saturable dye or $CuSO_4$ solution as a variable attenuator. To obtain the bleacher relaxation time this procedure was followed. The output laser pulse energy and pulse shape were examined varying either the dye transmission or the excitation energy. The boundary value of the dye transmission $(T_{0S})_{th}$ or consequent $(B)_{th}$ appropriate to a certain excitation level was found. The gain factor g, specifying the excitation level was measured using the variable attenuator instead of the bleacher cell inside the laser cavity. The parameters A, $(B)_{th}$, a, G, and D were calculated for aforementioned measured values and for $\rho = 0.02\ cm^{-1}$, $\sigma_R = 2.5 \times 10^{-20}\ cm^2$ [9], $1/\tau_R = 300\ s^{-1}$, $n_0 = 1.1 \times 10^{19}\ cm^{-3}$ [10], taking into account the geometry of our laser system. The spontaneous emission factor k was estimated to be $10^3\ s^{-1}$. Equations (1) and (2) were then integrated numerically for these known parameters and for various values of $\sigma\tau$. The dependence of pulsewidth or peak intensity on $\sigma\tau$ enabled us to determine the threshold value $(\sigma\tau)_{th}$ above which the Q switching resulted from numerical integrations. The relaxation time we measured as $\tau = (\sigma\tau)_{th}/\sigma$.

The accuracy of the result is mainly affected by the accuracy of the measurement of gain factor g, and initial dye cell transparency $T_{0S} \cdot T_{NS}$, and by the accuracy of the estimation of the spontaneous emission term k and the nonsaturable part of the dye cell transparency T_{NS}. In our case, the relative error of gain factor measured was ±0.05, the measurement accuracy of $T_{0S} \cdot T_{NS}$ was ±0.01, the estimation of T_{NS} was taken to be from 0.75 to 1 and the spontaneous emission term was varied from 10 to $10^5\ s^{-1}$. The parameters of (1) and (2) were varied according to these values and the spread of τ about ±5 ps was found.

For cryptocyanine we obtained the relaxation time 24 ± 5 ps; Duguay and Hansen [3] had obtained the value 22 ± 4 ps. Modified dicarbocyanine iodide [7] has the relaxation time 28 ± 5 ps.

References

[1] A. Laubereau and W. Kaiser, "Generation and applications of passively mode-locked picosecond light pulses," *Optoelectronics*, vol. 6, pp. 1-24, 1974.
[2] J. W. Shelton and J. A. Armstrong, "Measurement of the relaxation time of the Eastman 9740 bleachable dye," *IEEE J. Quantum Electron.* (Corresp.), vol. QE-3, pp. 696-697, Dec. 1967.
[3] M. A. Duguay and J. W. Hansen, "Direct measurement of picosecond lifetimes," *Opt. Commun.*, vol. 1, pp. 254-256, 1969.
[4] P. B. Mauer, "Q-switch dyes for neodymium lasers," *Optical Spectra*, vol. 1, pp. 61-63, 1967.
[5] "Metody rasceta opticeskih kvantovyh generatorov," vol. 2, *Nauka i Technika*, B. I. Stepanov, Ed. Minsk, USSR, 1968.
[6] A. M. Samson, K. N. Drabovitch, and V. A. Savva, "Rascet

opticeskogo kvantovogo generatora s prosvetlaiuscimsa zatvorom," *Zh. Prikl. Spektroskopya*, vol. 5, pp. 442–450, 1966.
[7] H. Jelinkova, K. Hamal, A. Novotny, and M. Vrbova, "Passive mode-locker and *Q*-switch for ruby," in *1974 Dig. Tech. Papers Quantum Electronics Conf.*, 1974, p. 48.
[8] L. E. Ericson and A. Szabo, "Behaviour of saturable-absorber giant-pulse lasers in the limit of large absorber cross section," *J. Appl. Phys.*, vol. 38, pp. 2540–2542, 1967.
[9] M. Hercher, "An analysis of saturable absorbers," *Appl. Optics*, vol. 6, pp. 947–954, 1967.
[10] Producers' communications.

Nonlinear Refractive Index Coefficient for Nd Phosphate Laser Glasses

D. MILAM AND M. J. WEBER

Abstract—**Intensity-dependent changes in the refractive index of three low-index Nd phosphate laser glasses (LHG-5, LHG-6, EV-1) and one Nd fluorophosphate laser glass were measured at 1064 nm using time-resolved interferometry. The nonlinear refractive index coefficients of these phosphate glasses are all smaller than for Nd silicate laser glass (ED-2).**

The ability to focus the energy of high-power lasers is limited by self-focusing and beam breakup arising from intensity-dependent refractive index changes in optical materials through which the laser beam propagates [1]. For long amplifier chains, such as used in neodymium glass fusion lasers, beam degradation originates in several optical elements—the lasing medium, lenses, Faraday rotators, polarizer substrates, and windows. Because of the long path length, the largest contribution usually originates in the Nd glass. Neodymium-doped phosphate glasses have recently been shown to have large stimulated-emission cross sections for the ${}^4F_{3/2} \rightarrow {}^4I$ transitions [2], [3] and higher gain coefficients [4] than for Nd-doped silicate glasses. Here we report measurements of the nonlinear refractive index for several promising Nd phosphate glasses.

The refractive index of a transparent isotropic optical material is described by

$$n = n_0 + \Delta n \tag{1}$$

where n_0 is the linear refractive index and Δn is the intensity-dependent index change. For a laser beam of intensity $I(\mathrm{W/cm^2})$ propagating through a material, the index change is given by γI or, alternatively, by $n_2\langle E^2\rangle$, where E is the amplitude of the optical electric field in electrostatic units. The nonlinear refractive index coefficients are related by

$$n_2(\mathrm{ESU}) = \left\{\frac{nc}{4\pi \times 10^{-7}}\right\} \gamma(\mathrm{cm^2/W}) \tag{2}$$

where c is the velocity of light in vacuum.

The nonlinear index was determined by time-resolved interferometry [5], [6]. Measurements were made at 1064 nm using 125-ps pulses from an Nd:YAG oscillator–amplifier system. The beam was linearly polarized and had a diameter ($1/e^2$) of ~1 cm with intensities ranging up to 25 GW/cm^2. The sample was located in one arm of a modified Michelson interferometer. Approximately 98 percent of the laser beam entering the interferometer propagated through the sample arm. A portion of this beam was combined with the weak beam propagating in the other arm to form a fringe pattern at the output of the interferometer. The fringes were imaged onto the slit of a streak camera and recorded with 10-ps time resolution. The temporal displacement of the fringes is a direct measure of the intensity-dependent refractive index and associated phase change. This method, which is described in more detail in [6], measures the actual index change during the transit of a laser beam through the material and, in contrast to other methods of determining n_2, is independent of the origin of the nonlinearity or of models for self-focusing.

Measurements were made for three Nd^{3+}-doped phosphate glasses (two from Hoya: LHG-5 and LHG-6, and one from Owens-Illinois: EV-1) and one Nd^{3+}-doped fluorophosphate glass (Sovirel A86-82 type).[1] The phosphate glass samples were rods of 25-mm diameter and 250 mm long; the fluorophosphate glass rod was 10 mm in diameter and 140 mm long. Because of the combination of a shorter length and a smaller n_2 coefficient for the fluorophosphate sample, the beam was double passed through the rod to increase the fringe shift. The neodymium content of all rods was approximately 3 weight percent (wt %). Absorption of the 1064-nm beam by Nd^{3+} due to thermal population of the ${}^4I_{11/2}$ manifold at ambient temperatures (295 K) was negligible. Samples were also examined for impurity absorption at 1064 nm using a Cary 17 spectrophotometer. A small, broad-band absorption, believed to be due to Fe^{2+}, was detected in the fluorophosphate rod and an appropriate correction [6] made for the associated loss in beam intensity. The damage thresholds of all glasses studied were >10 J/cm^2.

The measured nonlinear refractive index coefficients are given in Table I. Since experimental uncertainties in individual measurements of 20 percent or more are possible, several (5 to 10) measurements were made of each sample. The uncertainties in the tabulated values are estimated to be ±10 percent except for the fluorophosphate glass for which few measurements were made.

Also included in Table I are data for a silicate laser glass (Owens-Illinois ED-2, 1 wt % Nd_2O_3), since several measurements of n_2 for this glass are reported in the literature. Our datum is in good agreement with an earlier interferometric measurement of Bliss *et al.* [5], who employed a Mach–Zender interferometer. It is also in general agreement with a measurement obtained from intensity-dependent ellipse rotation [7] at 694 nm, when the predicted dispersion of the nonlinear susceptibility [8] is considered in comparing the results at two different wavelengths.

Our measurements were made using 125-ps pulses. Since this is much shorter than the response time for electrostrictive or thermal self-focusing, the n_2 values in Table I are attributed to the optical Kerr effect.

The values of n_2 for the phosphate glasses in Table I are all lower than for the silicate glass. The former glasses also have lower linear refractive indices and lower dispersions in the visible. The refractive index for the sodium D line and the reciprocal dispersion, given by the Abbé value ($\nu_D = n_D - 1/n_F - n_c$), are included in Table I. It has been observed that for silicate glasses, small n_2 values are correlated with low index and low dispersion [9]. The present results indicate that similar behavior is applicable to phosphate and fluorophos-

Manuscript received March 4, 1976. This work was performed under the auspices of the U.S. Research and Development Administration Contract W-7405-ENG-48.

The authors are with the Lawrence Livermore Laboratory, University of California, Livermore, CA 94550.

[1] Reference to a company or product name does not imply approval or recommendation of the product by the University of California or the U.S. Energy Research and Development Administration to the exclusion of others that may be suitable.

TABLE I
NONLINEAR REFRACTIVE INDEX COEFFICIENTS FOR ND PHOSPHATE LASER GLASSES MEASURED INTERFEROMETRICALLY USING LINEARLY POLARIZED 1064-NM LASER PULSES OF 125-PS DURATION

Glass	Type	n_D	ν_D	$n_2(10^{-13}$ esu)	$\gamma(10^{-16}$ cm^2/W)
Silicate	ED-2	1.567	54	1.41 ± 0.14	3.77 ± 0.38
Phosphate	LHG-5	1.541	63	1.16 ± 0.12	3.15 ± 0.32
Phosphate	LHG-6	1.532	66	1.01 ± 0.10	2.76 ± 0.28
Phosphate	EV-1	1.507	69	0.91 ± .09	2.53 ± 0.25
Fluorophosphate		1.492	81	0.71 ± 0.14	2.0 ± 0.4

phate glasses.[2] Therefore the use of network modifier ions which reduce the linear index and dispersion of the laser glass should in general lead to smaller nonlinear indices.

The effects of small-scale and whole-beam self-focusing in high-power laser materials grow exponentially with propagation length. The exponent for the growth in a given optical element is characterized by a beam breakup integral [1]

$$B = \frac{2\pi}{\lambda} \int_0^L \gamma I \, dl \tag{3}$$

where λ is the laser wavelength in a vacuum and the integration is over the optical path length L. For laser rods oriented perpendicular to the beam, the figure of merit to minimize B is simply proportional to $1/\gamma$. For laser disks oriented at Brewster's angle to the beam, the figure of merit has an addition factor of n due to the increased area. From Table I, the phosphate laser glasses have rod figures of merit 20–50 percent higher than ED-2 silicate laser glass. The fluorophosphate glass offers an even larger improvement of ≈90 percent higher than ED-2.

For a laser material, the gain coefficient is also important. Its relative importance depends upon whether the laser operation is pump-limited or parasitic-limited. Preliminary estimates of the gain coefficient of many phosphate glasses, obtained from spectroscopic studies [3], indicate that higher gain may be obtainable in phosphate than in fluorophosphate glass. Therefore combining the gain and nonlinear index properties, for high-power lasers phosphate glasses appear best for pump-limited staging, and fluorophosphate glasses for parasitic-limited staging. Further development and optimization of phosphate and fluorophosphate glasses are required, however, before a final selection is made.

ACKNOWLEDGMENT

We thank G. Murphy for his excellent technical assistance with these experiments and J. E. Lynch for assistance in data reduction.

REFERENCES

[1] E. S. Bliss, J. T. Hunt, P. A. Renard, G. E. Sommargren, and H. J. Weaver, "Effects of nonlinear propagation on laser focusing properties," *IEEE J. Quantum Electron.*, vol. QE-12, pp. 402–406, July 1976.
[2] R. R. Jacobs and M. J. Weber, "Induced-emission cross sections for the $^4F_{3/2} \rightarrow {}^4I_{13/2}$ transition in neodymium laser glasses," *IEEE J. Quantum Electron.*, vol. QE-11, pp. 846–847, Oct. 1975.
[3] —, "Dependence of the $^4F_{3/2} \rightarrow {}^4I_{11/2}$ induced-emission cross section for Nd^{3+} on glass composition," *IEEE J. Quantum Electron.*, vol. QE-12, pp. 102–111, Feb. 1976; also M. J. Weber (unpublished results).
[4] G. Linford, measurements of LHG-5, 6 and EV-1, Lawrence Livermore Laboratory, Livermore, CA (private communication).
[5] E. S. Bliss, D. R. Speck, and W. W. Simmons, "Direct interferometric measurements of the nonlinear refractive index coefficient n_2 in laser materials," *Appl. Phys. Lett.*, vol. 25, pp. 728–730, Dec. 1974.
[6] D. Milam and M. J. Weber, "Measurement of the nonlinear refractive index coefficient using time-resolved interferometry: Application to optical materials for high-power neodymium lasers," *J. Appl. Phys.*, vol. 47, June 1976.
[7] A. Owyoung, "Ellipse rotation studies in laser host materials," *IEEE J. Quantum Electron.*, vol. QE-9, pp. 1064–1069, Nov. 1973.
[8] M. D. Levenson and N. Bloembergen, "Dispersion of the nonlinear optical susceptibility tensor in centrosymmetric media," *Phys. Rev. B*, vol. 10, pp. 444, 1974.
[9] N. L. Boling, A. J. Glass, and A. Owyoung, "An empirical relationship for predicting nonlinear refractive index changes in optical solids," Lawrence Livermore Laboratory, Livermore, CA, Rep. UCRL 75628, Mar. 1974.

[2]Two additional measurements of n_2 for phosphate materials which are consistent with this behavior are those for FR-4 [5], a Ce phosphate Faraday rotator glass, and for KH_2PO_4 [6], a phosphate crystal.

Thermal Effects in Jet-Stream Dye Lasers

O. TESCHKE, J. R. WHINNERY, AND A. DIENES

Abstract—**The effect of temperature gradients from absorption of the pump energy in jet-stream dye lasers is investigated photographically. The pictures show definite crescent-shaped patterns (representing serious astigmatism) for the lower jet-stream velocities, and some interferences even at the highest velocities. The sources of heating are discussed and the results coordinated with theoretical predictions.**

In a recent paper [1] the authors described analysis and experiments on several effects of importance to high-power dye lasers. That paper touched upon the effects of index gradients in a jet-stream laser arising from the absorbed pump power and mentioned analysis and experiments on these effects to be presented separately. Although the importance of the thermal

Manuscript received March 5, 1976; revised April 19, 1976. This work was supported by National Science Foundation Grant ENG73-08077-A02.

O. Teschke was with the Department of Electrical Engineering, University of California, Berkeley, CA 94720. He is now with Bell Laboratories, Holmdel, NJ 07733.
J. R. Whinnery is with the Electronics Research Laboratory, University of California, Berkeley, CA 94720.
A. Dienes is with the Department of Electrical Engineering, University of California, Davis, CA 95616.

gradients is well known, most discussions have been directed toward lasers for which the dye flow is within a confined cell [2]. Recently an excellent paper [3] has analyzed the effects for jet-stream lasers. This correspondence presents an experiment which is complementary to the results of that paper, with some additional discussion on the sources of heating.

Heating of the jet-stream is both by the pump beam and the laser beam, but reabsorption of the laser beam is small so that the effect from the pump beam is dominant. From 90 to 99 percent of the pump power is absorbed in traversing jets of the type used in our experiments (rhodamine 6G dye dissolved in ethylene glycol, with streams about 0.3 mm thick streaming at velocities up to 11 m/s). A certain fraction of the absorbed pump power goes into heat through a variety of nonradiative processes. Quantum efficiency of the dye is about 90 percent but is known only within an accuracy of about 5 percent [4] so that estimates of this fraction may vary from 5 to 15 percent. Additionally, for approximately 90 percent of the pump photons converted to laser photons, heating results from the Stokes shift representing rapid thermalization from the top of a band to the bottom. This component is $(1 - \nu_{\text{laser}}/\nu_{\text{pump}})$ and of course varies appreciably with tuning of the laser. It is 11 percent for a 5145-Å pump beam and a 5800-Å laser beam. Considering all of these factors, 20 to 25 percent of the pump power is typically converted into heat.

The portion of the above arising from the Stokes shift represents the minimum possible thermal effect. The remaining portion can be minimized by maximizing laser efficiency. Reference [1] gives the optimum pump power for such maximization as a function of mirror transmission and dye-laser parameters. This optimization becomes particularly important in reducing the thermal effects for dyes of low quantum efficiency.

Analysis of the phenomenon starts with an element of the liquid moving through the Gaussian beam. The energy absorbed in each element causes a direct temperature increase since little diffuses out from the element over the time of transit across the beam, for spot sizes and flow velocities of interest. The characteristic diffusion time for ethylene glycol is about 0.6 ms [5], whereas the transit time of an element across a 30-μm beam is 6 μs for a flow velocity of 5 m/s. Diffusion is in general negligible if

$$v_0 \gg \frac{8k}{w\rho c_p} \tag{1}$$

where v_0 is stream velocity, w is spot radius and k, ρ, and c_p are, respectively, the thermal conductivity, density, and specific heat of the solvent. Integration of the heating effects then gives the temperature increase for position x, y with respect to the original beam center as

$$\Delta T(x,y) = \frac{wk_{th}I_0\sqrt{\pi}}{Jlv_0\rho c_p\sqrt{8}} \exp(-2y^2/w^2)\,[\operatorname{erf}(\sqrt{2}\,x/w) + 1] \tag{2}$$

where I_0 is intensity at the center, k_{th} is the fraction of the pump power converted into heat, and l is the thickness of the stream. J is 4.184 if thermal energy is measured in calories, and I_0 in watts per unit area. Stream velocity for the above is in the x direction. This result is consistent with the temperature equation of [3].

Index variations are then proportional to the above through the index variation with temperature, $\partial n/\partial T$. Distortions of the wave fronts of the mode may be calculated from this distribution of refractive index. In particular, deflection angles in the x and y directions for a ray at (x, y), after passing through the stream, are

$$\theta_x = \frac{l}{n}\frac{\partial n}{\partial x} = \frac{k_{th}I_0\left(\frac{\partial n}{\partial T}\right)}{Jv_0\rho c_p n} \exp[-2(x^2+y^2)/w^2] \tag{3}$$

$$\theta_y = \frac{l}{n}\frac{\partial n}{\partial y} = -\frac{4yk_{th}I_0\sqrt{\pi}\left(\frac{\partial n}{\partial T}\right)}{Jv_0\rho c_p n w\sqrt{8}} \cdot \exp\left(-\frac{2y^2}{w^2}\right)[\operatorname{erf}(\sqrt{2}x/w) + 1)]. \tag{4}$$

The maximum value of (3) occurs at $x = 0, y = 0$ and is

$$(\theta_x)_{\max} = \frac{k_{th}I_0(\partial n/\partial T)}{Jv_0\rho c_p n}. \tag{5}$$

The maximum value of (4) can be shown to occur at $y = w/2$, $x = \infty$ and is 1.5 times the above value. It is noted that (5) corresponds to a result of Gebhardt and Smith [6], [7] analyzing the effects of forced convection on a CO_2 laser beam propagating through the atmosphere. They further point out that the shift of peak intensity is three times the displacement of the central ray. Clearly if the deflection angle is appreciable compared with angles subtended by the mirrors at the cell center, important mode distortions occur. For $k_{th} = 0.20$, $w = 15$ μm, pump power = 3 W, $v_0 = 11$ m/s, and thermal parameters as given above, $3(\theta_x)_{\max} = 0.057$ rad. This angle (about 3°) is a small angle, but still measurable; as the experiments show, the main effects of convection disappear for those parameters. However for $P = 6$ W and $v_0 = 4$ m/s, conditions for which convective effects are very noticeable, $3(\theta_x)_{\max}$ is calculated as 0.288 rad or about 16.5°, an angle which subtends most of the mirror and would be expected to produce degradation of laser performance.

In order to observe the effects of thermal absorption in the moving solvent, we removed one cavity mirror from a jet-stream dye laser of the type described in [1] and observed the transmission patterns of the pump beam after passing through the dye. The pump light from a CW argon ion laser, with powers up to 6.5 W, was focused by a lens of 46.8-mm focal length onto a jet stream of 0.3-mm thickness. The speed of flow in the jet stream could be varied up to 11 m/s. Speeds were measured by collecting and measuring the liquid volume pumped in a given time through the aperture of known size.

Fig. 1 (a)–(f) corresponds to the transmission patterns measured with a stream velocity of 4 m/s and pump powers of 1.45, 3.6, 4.5, 5.1, 5.9, and 6.5 W, respectively. Note that the patterns of distortion are much like those of Gebhardt and Smith [7] measured with a beam from a CO_2 laser passing through air with an absorber added. All figures show distinct interference patterns, but those taken with higher power also show the effect of convection through a characteristic crescent pattern. In order to check the tradeoff between power and velocity predicted by (5), measurements were also made at 11 m/s with a pump power of 3 W. The deflection angle should be the same as for 1.1 W at 4 m/s, and the pattern observed was much like that of Fig. 1(a) with the crescent distortion largely removed but interference patterns remaining.

As a further check, spot size was changed by using a 16-mm focal length lens to focus the beam on the dye. The minimum spot size of a Gaussian beam is porportional to focal length [8], so we would expect minimum spot size to be reduced to about 6 μm. However the confocal distance $(\pi w_0^2/\lambda)$ is about 0.18 mm, which is comparable with the dye thickness so that the average radius is well above the minimum. The pattern with this lens and $p_p = 1.5$ W, velocity = 4 m/s corresponded approximately to Fig. 1(b) above. Increase of power to 2 W

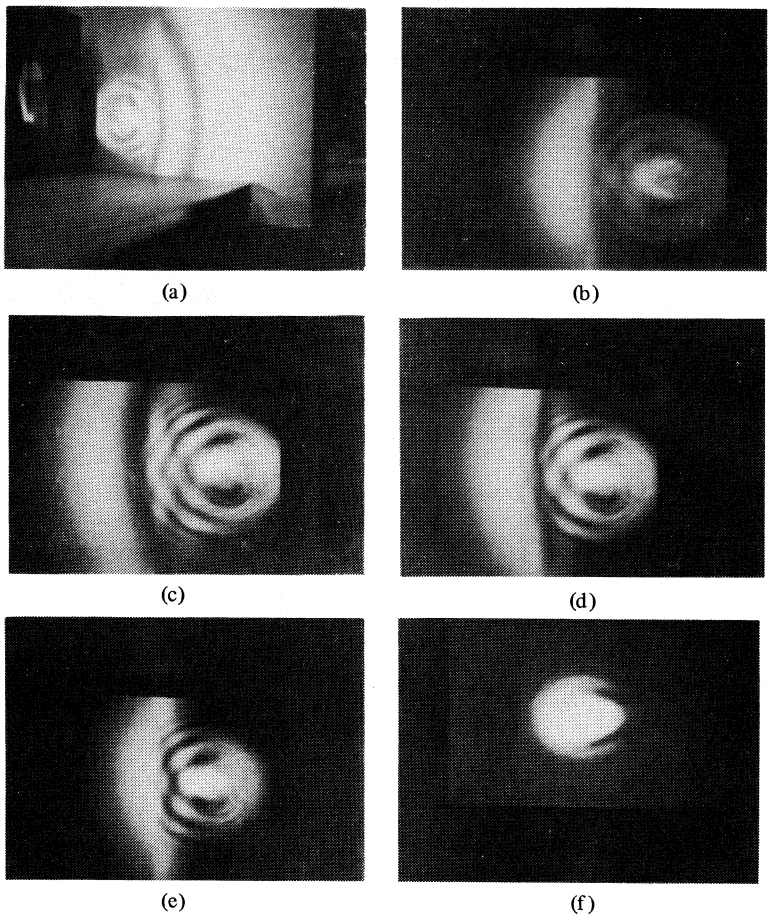


Fig. 1. Transmission patterns of the pump beam after passing through the jet stream of 0.3 mm thickness with stream velocity 4 m/s. Pump powers were (a) 1.45 W, (b) 3.6 W, (c) 4.5 W, (d) 5.1 W, (e) 5.9 W, and (f) 6.5 W. Flow in the jet stream is horizontal, from left to right. The pattern (a) shows little overall displacement but does have interference rings showing finite relative deflection of rays in different portions of the beam. Pattern (f) shows a large distortion of the pattern with displacement of the region of maximum intensity. Other patterns are intermediate to these extremes.

gave essentially the pattern of Fig. 1(f). This also is a reasonable check considering the variation of beam radius through the dye in this case.

In coordinating the pictures of Fig. 1 with operation of a laser when the mirror is back in place, we find degradation of laser performance for all velocities for which Fig. 1 clearly shows astigmatism. There is asymptotic improvement as velocity is increased, but since all pictures show some internal interferences representing small deflections, it is likely that the effects are not entirely removed even at the highest velocities.

References

[1] O. Teschke, A. Dienes, and J. R. Whinnery, "Theory and operation of high-power CW and long-pulse dye lasers," *IEEE J. Quantum Electron.*, vol. QE-12, pp. 383–395, July 1976.
[2] S. A. Tuccio and F. C. Strome, "Design and operation of a tunable continuous dye laser," *Appl. Opt.*, vol. 11, pp. 64–67, Jan. 1972.
[3] B. Wellegehausen, L. Laepple, and H. Welling, "High power CW dye lasers," *Appl. Phys.*, vol. 6, pp. 335–340, Apr. 1975.
[4] K. H. Drexhage, "Structure and properties of dye lasers," in *Dye Lasers*, F. P. Schafer, Ed. New York: Springer, 1973, p. 151.
[5] J. P. Gordon, R. C. C. Leite, R. S. Moore, S. P. S. Porto, and J. R. Whinnery, "Long-transient effects in lasers with inserted liquid samples," *J. Appl. Phys.*, vol. 36, pp. 3–8, Jan. 1965.
[6] F. G. Gebhardt and D. C. Smith, "Effects of wind on thermal defocusing of CO_2 laser radiation," *Appl. Phys. Lett.*, vol. 14, pp. 52–54, 15 Jan. 1969.
[7] ——, "Effects of diffraction of the self-induced thermal distortion of a laser beam in a crosswind," *Appl. Opt.*, vol. 11, pp. 244–248, Feb. 1972.
[8] A. E. Siegman, *An Introduction to Lasers and Masers.* New York: McGraw-Hill, 1971, p. 316.

Coaxial Sweep Scheme for Ion-Beam Lasers

JOHN F. SEELY, WILLIAM H. LOUISELL, AND RONALD R. BOUSEK

Abstract—**A coaxial sweep scheme for use in ion-beam lasers is proposed. Space charge and emittance effects which normally tend to defocus ion beams are effectively controlled.**

Manuscript received March 8, 1976. This work was supported in part by the Advanced Research Projects Agency, U.S. Army Research Office-Durham, and in part by the Applied Mathematics and Science Laboratory, B.R.L., Aberdeen Proving Ground.

J. F. Seely and W. H. Louisell are with the Departments of Physics and Electrical Engineering, University of Southern California, Los Angeles, CA 90007.

R. R. Bousek was with the Department of Physics and the Optical Sciences Center, University of Arizona, Tucson, AZ 85721. He is now with the Air Force Weapons Laboratory, Kirtland Air Force Base, NM 87117.

Due to the small spontaneous lifetimes of the excited states of short wavelength lasers, it is often necessary to sweep the region of excitation along the active medium at the speed of light. Then atoms are excited just as the laser pulse reaches them, and loss of population inversion due to spontaneous decay does not occur. In ion-beam excited lasers, the pumping mechanism may be electron pickup into an excited state of the incident ions [1], or knockout of core electrons from the target atoms [2]. Since the laser gain is proportional to the ion density on the target, focusing of the ion beam is of fundamental importance. In this correspondence we propose a coaxial deflection and focusing scheme in which the ions are initially in Harris flow [3]. This scheme has the advantage that space charge and emittance effects which normally tend to defocus the ion beam are controlled. We establish the basic equations which describe the ion beam dynamics, and show that the ions may be deflected and swept along a target at the speed of light by a voltage pulse propogating down the coaxial transmission line. We then solve the equations of motion numerically and determine the focused ion density.

Consider an axially symmetric ion beam between radii r_0 and r_1 traveling down a coaxial transmission line. Let the radial variation of the charge density be $\rho = k/r^4$ where

$$k = Ir_0^2 r_1^2/\pi(r_1^2 - r_0^2)v_0, \tag{1}$$

I is the total current, and v_0 is the axial beam velocity. To counteract the space charge fields tending to defocus the beam, we apply constant voltages V_a and V_b to the coaxial electrodes at radii r_a and r_b as in Fig. 1. The radial equation of motion of an ion at position r is

$$\ddot{r} - r\dot{\theta}^2 = (\eta k/2\epsilon_0)(r_0^{-2}r^{-1} - r^{-3}) - \eta V_A/r \tag{2}$$

where

$$\eta = q/m$$

and

$$V_A = (V_a - V_b)/\ln(r_b/r_a).$$

Since the forces are assumed to act in the radial direction only, the axial motion is uniform and the angular momentum is conserved. Thus $r^2\dot{\theta} = r_i^2\dot{\theta}(r_i)$ where r_i is the radius of the ion when it enters the coaxial line. From (2), it is apparent that $\ddot{r} = 0$ if

$$\dot{\theta}(r_i) = (\eta k/2\epsilon_0 r_i^4)^{1/2} \tag{3}$$

and

$$V_A = k/2\epsilon_0 r_0^2. \tag{4}$$

That is, if the initial angular velocity $\dot{\theta}(r_i)$ and the applied field V_A are chosen according to (3) and (4), the space charge fields tending to defocus the ion beam are canceled out across the entire beam, and an ion that enters the transmission line parallel to the axis will travel at a constant radius under the conditions of Harris flow [3]. The angular velocity $\dot{\theta} \propto r^{-2}$ may be imparted to the ion beam by having it pass through a radial magnetic field just before entering the transmission line.

In order to investigate the stability of Harris flow and the deflection of ions by a voltage pulse, we assume that the charge inside an imaginary cylinder of radius r, where r is the position of the ion under consideration, remains constant. This would be the case if the ion flow is laminar with no trajectory crossing, or if the flow of charge into the cylinder of radius r is equal to the flow out of the cylinder. Then the charge within the instantaneous radius r of the ion is equal to the charge within the initial radius r_i. Using (3) and (4), the radial equation of motion becomes

$$\ddot{r} = -\eta V_A r_0^2(r_i^{-2}r^{-1} - r^{-3}). \tag{5}$$

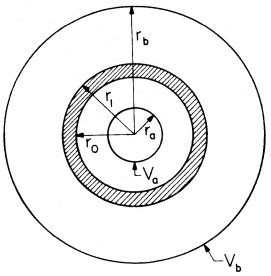


Fig. 1. The ion beam between radii r_0 and r_1 propagates down a coaxial transmission line. Voltages V_a and V_b are applied to the coaxial electrodes at r_a and r_b.

It is now easy to show that Harris flow is stable for small perturbations about the position r_i. Thus perturbations due to thermal motion or emittance of an ion beam introduce small radial oscillations about a stable equilibrium. This is in contrast to the usual beam propagation conditions where thermal spreading of the ions grows in time.

A coaxial transmission line carrying an ion beam in Harris flow will also support a voltage pulse in the form of a TEM mode. After the voltage pulse overtakes an ion at radius r_i, the radial equation of motion of the ion is

$$\ddot{r} = -\eta V_A r_0^2(r_i^{-2}r^{-1} - r^{-3}) - \eta V_p/r. \tag{6}$$

The ion is deflected toward the axis and reaches a minimum radius r_m. Using (6) and the assumption that the axial motion is uniform, it is easily shown that the axial position of the focus moves with the speed of light. That is, if a target is placed at radius r_m, then the focus of the ion beam is swept along the surface of the target with the speed of light.

Numerical solutions to the equation of motion (6) are plotted in Fig. 2. The amount of focusing is a function of the deflection parameter $\alpha = V_p/V_A$. For $\alpha = 1$, the ion density increases by more than an order of magnitude.

We now consider the production of a gas target by vaporization from a flash-heated plate. A thin layer of dense gas may be produced by resistance-heating a coated filament with a sharp voltage pulse, or by vaporization of the coating by laser radiation. In cylindrical geometry, the equations of motion and continuity of the gas layer do not have analytical solutions [4]. We have solved these equations numerically, and the evolution of the density profile is shown in Fig. 3. The slope of the density profile at the leading edge of the expanding target remains large, a feature that is important for the operation of ion-beam lasers [1]. The leading edge of the target expands at approximately the speed of sound, which is a function of the initial pressure P_0 and density ρ_0 of the target. The timing of the flash-heating of the target and the deflection of the ions by the voltage pulse must be such that the leading edge of the target is located at radius r_m when the ions arrive.

As a numerical example, consider a 0.5-keV 50-mA beam of He^+ ions in Harris flow between radii 0.5 cm and 2 cm. Using (4) and (1), the voltage which must be applied to the coaxial line to maintain Harris flow is 14 kV. Let a 14-kV pulse ($\alpha = 1$) also be applied to the coaxial transmission line. From Fig. 2 the time for the ions to reach the minimum radius at 0.27 cm is 12 ns. Now consider a filament centered on the axis of the coaxial line and coated with a 0.25-mm layer of target material such as cesium. If the filament is flash-heated to the boiling point of cesium, the vapor expands with velocity 3.2×10^4 cm/s. From Fig. 3 the time for the leading edge of the target to reach radius 0.27 cm is 6 μs. This target expansion time is much greater than the time required to focus

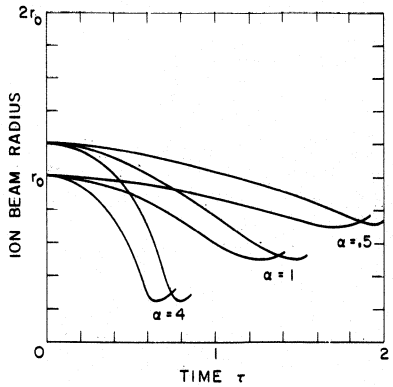


Fig. 2. Ion trajectories as a function of the focusing parameter $\alpha = V_p/V_A$. The dimensionless time is $\tau = t(\eta V_A)^{1/2}/r_0$.

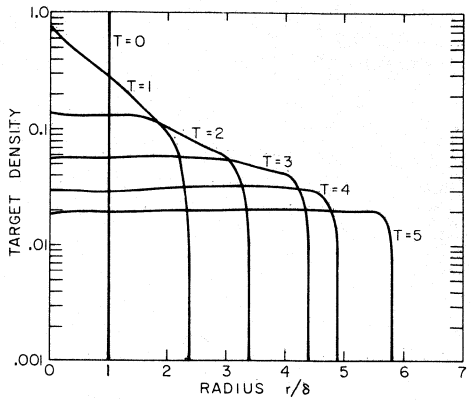


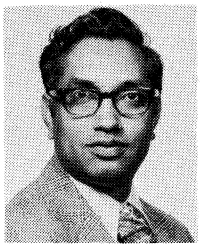
Fig. 3. Density profile of the gas target vaporized from a cylinder of radius 2δ, where δ is the initial thickness of the target coating. The dimensionless time is $T = v_s t/\delta$, where v_s is the sound velocity.

and sweep the ions with the voltage pulse. If the filament is flash-heated about 6 μs before launching the voltage pulse on the coaxial line, then the vapor target will be in the correct position when the pumping ions arrive. From Fig. 3 we see that the density of the target is about two orders of magnitude below solid density, or about 10^{19} cm^{-3}.

REFERENCES

[1] a) M. O. Scully, W. H. Louisell, and W. B. McKnight, "A soft X-ray laser utilizing charge exchange," *Optics Comm.*, vol. 9, pp. 246–248, 1973.
b) W. H. Louisell, M. O. Scully, and W. B. McKnight, "Analysis of a soft X-ray laser with charge-exchange excitation," *Phys. Rev. A*, vol. 11, pp. 989–1000, 1975.
[2] a) R. A. McCorkle, "Practicable X-ray amplifier," *Phys. Rev. Lett.*, vol. 29, pp. 982–985, 1428, 1972.
b) R. A. McCorkle and J. M. Joyce, "Threshold conditions for amplified spontaneous emission of X radiation," *Phys. Rev. A*, vol. 10, pp. 903–912, 1974.
[3] L. A. Harris, "Axially symmetric electron beam and magnetic-field systems," *Proc. IRE*, vol. 40, pp. 700–708, 1952.
[4] K. P. Stanyukovich, *Unsteady Motion of Continuous Media*. New York: Pergamon, 1960.

Contributors



Roshan L. Aggarwal was born in Salala, Punjab, India, on February 15, 1937. He received the B.Sc. (Hon. School) degree in 1957 and the M.Sc. (Hon. School) degree in 1958, both in physics, from the Punjab University College, Hoshiarpur, India. He was awarded a silver medal for obtaining the top position in the class of 1957. He received the Ph.D. degree in solid-state physics from Purdue University, Lafayette, IN, in 1965.

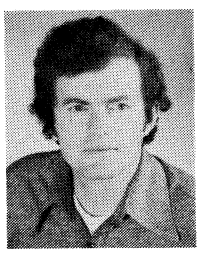
He then joined the Francis Bitter National Magnet Laboratory, Massachusetts Institute of Technology, Cambridge, where he is currently Leader of the Quantum Optics and Plasma Physics Group. Concurrently, he is a Senior Research Scientist in the Department of Physics at M.I.T. He is active in magnetooptical studies of semiconductors, light scattering in solids, and nonlinear optics.

Dr. Aggarwal is a member of the American Physical Society, the Optical Society of America, and Sigma Xi.

*

Robert D. Burnham (M'76), for a photograph and biography please see p. 88 of the February 1976 issue of this JOURNAL (Part I of Two Parts).

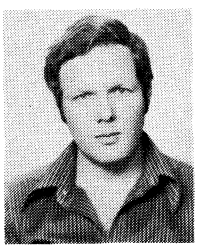
*



Robert J. Hall was born in Wilmington, DE, on July 25, 1945. He received the B.S. degree in aerospace and mechanical sciences from Princeton University, Princeton, NJ, in 1967, and the M.S. degree in aeronautics from Stanford University, Stanford, CA, in 1968.

Since 1968 he has been with the United Technologies Research Center, East Hartford, CT. His field of research is the theoretical modeling of high-power gas lasers.

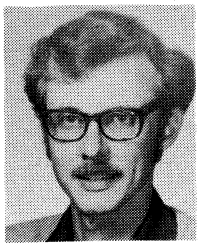
*



Mordehai Heiblum (S'74) was born in Holon, Israel, on May 25, 1947. He received the B.S. degree (honors) in electrical engineering from the Technion, Israel Institute of Technology, Haifa, in 1973, the M.S. degree from Carnegie-Mellon University, Pittsburgh, PA, in 1974, and is currently studying toward the Ph.D. degree at the University of California, Berkeley.

From 1967 to 1970 he served in the Israeli army. From 1970 to 1973 he was an Instructor with the Electronics Department of the Junior Technical High School at the Technion. He is currently with the Department of Electrical Engineering and Computer Sciences, University of California, Berkeley.

Mr. Heiblum is a member of the American Physical Society.

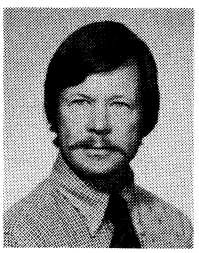


Thomas F. Johnston, Jr., was born in Ames, IA, on January 23, 1941. He received the B.A. degree in 1962 and the Ph.D. degree in 1968, both from Cornell University, Ithaca, NY, with majors in physics.

From 1967 to 1970 he was a Member of the Optical Physics Group at the General Telephone Laboratories, Bayside, NY, working on means to improve the efficiency of visible gas lasers. While at the Lansing Research Corporation, Ithaca, NY, from 1970 to 1972, he invented a device for optical alignment that produces a laser beam which pivots about a selected point in space. In 1972 he joined the Electron Dynamics Division of the Hughes Aircraft Company, Torrance, CA, and worked there on an airborne argon-ion laser, helium-cadmium lasers, and space-qualified waveguide carbon dioxide lasers. Since 1975, he has been a Member of the Engineering Staff at Coherent Radiation, Palo Alto, CA, working in the area of CW dye lasers.

Dr. Johnston is a member of the Optical Society of America and the American Physical Society.

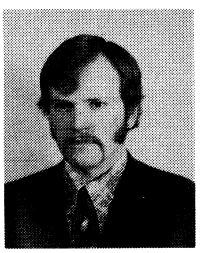
*



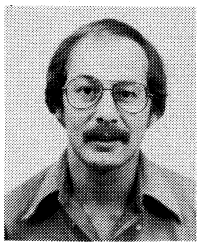
William P. Kolb was born in Ozark, AL, on February 1, 1934. He received the B.S. degree in electrical engineering from Auburn University, Auburn, AL, in 1960, and the M.S. degree in engineering from the University of Florida, Gainesville, FL, in 1965.

From 1961 to 1962, he was employed by Hughes Microwave Tube Division, where he was engaged in development work on high-powered traveling-wave tubes. From 1962 to 1965, he was a Project Engineer at Sperry Electronic Tube Division, where he was engaged in work on klystron efficiency, nonintercepting grid electron guns, and magnetic compression of electron beams. In 1965 he rejoined Hughes Aircraft Company at the Electron Dynamics Division, Torrance, CA. Since that time, he has been engaged in development work on gas lasers for commercial and military space applications. He is presently the Assistant Manager of the Laser Product Line of the Industrial Products Division with responsibility for the development of new laser products.

*



Don C. McKen was born in Yorkton, Sask., Canada on June 10, 1949. He received the B.Sc. degree with distinction in 1971 and the Ph.D. degree in 1976, both in electrical engineering, from the University of Alberta, Edmonton, Alta., Canada. He has been interested in the study of ultraviolet preionization in CO_2 TEA lasers.



Roger N. Nucho was born in Beirut, Lebanon, on March 20, 1950. He received the B.S. degree in physics in 1971 and the B.A. degree in fine arts in 1972 from the American University of Beirut, Beirut, Lebanon.

Since 1974 he has held a Research Assistantship in the Department of Physics at Massachusetts Institute of Technology, Cambridge, and is working with Prof. Peter A. Wolff. After working in the field of nonlinear optics, he is currently completing his Ph.D. degree in the area of chemical bond physics.

*

nald R. Scifres (M'74), for a photograph and biography please see p. 88 of the February 1976 issue of this JOURNAL (Part I of Two Parts).

*

Herb J. Seguin (M'71), for a photograph and biography please see p. 163 of the February 1976 issue of this JOURNAL (Part II of Two Parts).

William Streifer (S'56–M'58–SM'74), for a photograph and biography please see p. 88 of the February 1976 issue of this JOURNAL (Part I of Two Parts).

*

John Tulip, for a photograph and biography please see p. 163 of the February 1976 issue of this JOURNAL (Part II of Two Parts).

*



Peter A. Wolff was born in Oakland, CA, on November 15, 1923. He received the A.B. degree in 1945 and the Ph.D. degree in 1951, both from the University of California, Berkeley.

He served in the U.S. Army as a Combat Engineer from 1944 to 1945. From 1952 to 1963 he has been a Member of the Technical Staff at Bell Laboratories, Inc., Murray Hill, NJ, dealing with the theory of plasma waves in metals, electron multiplication in silicon and germanium, spin susceptibility of an electron gas, localized moments in metals, pair correlation in a plasma, a proposal for a cyclotron resonance laser in InSb, and Thomson and Raman scattering by mobile electrons in crystals. From 1963 to 1964 he taught at the University of California, La Jolla, as a Visiting Professor. He is currently with the Department of Physics, Massachusetts Institute of Technology, Cambridge.

Dr. Wolff is a member of the American Physics Society.

THIRD SUMMER COLLOQUIUM on ELECTRONIC TRANSITION LASERS

Wildwood Condominium Conference Center
Snowmass - in - Aspen, Colo.

SEPT. 7 - 10, 1976



Contributed papers are on the following subjects:

- Chemically pumped, electronic transition lasers
- Electrically, collision, or optically pumped electronic transition lasers
- Branching ratios and quantum yields for chemiluminescent systems
- Deactivation and quenching rates for electronically excited systems
- Spectroscopic analysis and potential curves for laser candidate molecules

Proceedings to be published



For Information & Applications Write to:
Leroy Wilson, 2932 LaVeta N.E., Albuquerque, New Mexico 87110



Sponsored by:
Chemistry Department
and Spectroscopy Laboratory, M.I.T.

Aerospace Corporation
Joint Council on Quantum Electronics

Financial Support Provided by
Air Force Office of Scientific Research

Fifth-Harmonic Generation in Isotropic Media

IVAN V. TOMOV AND MARTIN C. RICHARDSON, MEMBER, IEEE

Abstract—**This paper presents a theoretical study of fifth-harmonic generation (FHG) in an isotropic media. Two schemes are discussed—cascade generation in which the fifth harmonic results from successive nonlinear interactions in two separate elements, and direct generation where the fifth harmonic is produced in an isotropic media with third- and fifth-order nonlinear susceptibilities. In the plane-wave approximation almost full conversion of the pumping energy into the fifth harmonic is found to be possible. FHG with a focused Gaussian beam is also investigated. To determine the optimum conditions for FHG in the cascade scheme, the theory of four-wave mixing of light beams with arbitrary confocal parameters and waist locations is developed. In media with third- and fifth-order nonlinearity, the fifth harmonic results from step and direct processes. The interference between these two processes is discussed. Numerical calculations are presented for metal vapor–gas mixtures and Nd : glass laser pumping radiation.**

I. Introduction

METAL VAPORS and inert gases have recently been utilized as efficient nonlinear media for optical harmonic generation and mixing [1]-[3]. Coherent radiation in the UV and VUV has been produced and theoretical considerations predict that this technique can be extended into the soft X-ray range [1], [4]. Up to the present time, all nonlinear frequency conversion techniques have been based on the utilization of both second- and third-order nonlinear processes. However, the high power densities afforded by picosecond laser pulses permit the consideration of higher order nonlinear optical polarizabilities for the generation of still higher order harmonics with greater incremental steps through the frequency spectrum. For the improvement in the efficiencies of these processes, atomic systems should be selected in order to gain maximum advantage from specific relationships between their resonance lines and the interacting frequencies. In addition, the existence of phase-matching conditions is desirable.

It is important to note that in a system using higher order nonlinearity when phase matching for the direct process is achieved, the phase-matching conditions for the step processes produced by lower order nonlinearities as a whole are also fulfilled, even though each step is individually considerably mismatched [5], [6]. If we are interested in increasing the efficiency of higher order nonlinear conversion techniques care must be taken in considering all possible coherent interference effects between the individual step processes and the direct process.

In this paper a detailed theoretical analysis of fifth-harmonic generation (FHG) in an isotropic nonlinear medium is presented. Although FHG has already been experimentally investigated with an Nd : glass laser, relatively low conversion efficiencies have been recorded [7]-[9]. In the present case two possible methods of generation are considered. In the first, a system consisting of two separate cascades is employed to generate the fifth harmonic. In the second case, FHG in a medium having third- and fifth-order polarizabilities is investigated. Numerical calculations have been performed for the generation of the fifth harmonic ($\lambda_5 = 0.212\ \mu$) of Nd : glass laser radiation which are also applicable to the case of the Nd : YAG laser. The production of powerful radiation having a wavelength of $0.212\ \mu$ is of interest because this wavelength is close to the VUV limit, and consequently, quartz optics can be employed for further optical processing. In addition, this radiation can also be used in the generation of higher harmonics such as $\lambda_5/3 = 706.7$ Å and $\lambda_5/5 = 424$ Å.

In Section II, the phase-matching technique is discussed. It is shown that the use of a mixture of more than two gaseous components permits simultaneous phase-matching conditions to be met for more than one nonlinear process in a single cell. This would be very useful in the VUV where technical problems may arise when several different cells are used.

FHG in the cascade of two separate nonlinear conversion media is discussed in Section III. A detailed analysis is made of four-frequency mixing of Gaussian beams with arbitrary confocal parameters. The numerical results show that the most efficient case occurs when equal confocal parameters for all interacting waves are provided.

In Section IV, FHG in a medium with third- and fifth-order nonlinearity is considered. It is found that, in the plane-wave approximation, ~90-percent conversion efficiency is possible. FHG of a focused Gaussian beam is analyzed, and competing processes arising from the existence of third- and fifth-order susceptibilities are discussed.

Many of the results obtained in this paper may be extended for processes of higher order.

II. Phase-Matching Technique for Multistep Processes

In various gaseous systems, phase matching has been achieved by mixing two components, one having negative dispersion and the other positive dispersion [1]-[3]. In gases and vapors at low pressure the absorption and the variation of the refractive index is significant only in the region of spectral resonances and the continuum. Far from resonance the dispersion is weak. This permits the use of a gaseous system for frequency conversion over a wide spectral range. To date, phase-matching conditions for a single nonlinear process have been realized only for a two-gas (vapor) mixture or for a gas-vapor mixture. It is our intent to show that if a gaseous system of more than two components with suitable resonances is employed, phase-matching conditions for several successive nonlinear processes can be achieved in a single cell. Although

Manuscript received December 22, 1975.
The authors are with the Division of Physics, National Research Council of Canada, Ottawa, Ont., Canada.

the production of a homogeneous mixture of several metal vapors and gases with specific relative concentrations may pose some problems, already, some progress has been made in this area [10], [11].

Fig. 1 shows the variation of the refractive index n with wavelength for a mixture of sodium, cadmium, and xenon in the ratio 1:2.86:117.5, respectively. This mixture is simultaneously phase matched for the following processes:

$$\omega+\omega+\omega=3\omega \quad \omega+\omega+3\omega=5\omega$$
$$\omega+\omega+\omega+\omega+\omega=5\omega \tag{1}$$

where ω is the frequency of Nd:glass radiation. Note that the resonance line for Na (0.589 μ) is situated between 1.06 and 0.353 μ, and that of Cd (0.229 μ), between 0.353 and 0.212 μ. Xenon is positively dispersive over the region of interest and is added in suitable proportion to compensate for the negative dispersion of the metal vapors. Although a mixture of Na and Xe can provide phase matching for FHG (see Table I) when phase matching for THG is met, the mixture has $n_1 = n_3$ but $n_1 < n_5$ and is consequently positively dispersive from the point of view of FHG. However the addition of Cd which is negatively dispersive provides $n_1 = n_5$. At a temperature $T \simeq 555$ K, the ratio of saturated vapor densities of Cd and Na is $N_{Cd}/N_{Na} = 2.86$ and the use of a relatively simple heat pipe is required for the production of phase-matched mixtures. But at this temperature the concentration of sodium atoms, $N_{Na} \simeq 10^{14}$ atom/cm^3, is too small for good conversion efficiency. The saturated sodium vapor density is $N_{Na} = 10^{17}$ atom/cm^3 at $T \simeq 810$ K, and then $N_{Cd}/N_{Na} = 3.35$. In this case, a more complicated technique would be required for phase matching since the cadmium vapor would have to be unsaturated. In experiments where tight focusing is employed, the necessary phase-matching ratio will be variable, and some flexibility in operating parameters may be obtained by varying the temperature and focusing conditions. One can expect additional technical problems to arise when different metals are used, since not all combinations of two-metal vapors mix homogeneously [12].

In the mixture considered above, substitute vapors may be possible: sodium can be replaced with some other alkali metal (Na has the smallest absorption at 0.212 μ), cadmium can be replaced with Mg or Zn ($N_{Xe}/N_{Na} = 57$, $N_{Mg}/N_{Na} = 1.65$; $N_{Xe}/N_{Na} = 146$, $N_{Na}/N_{Zn} = 1.87$). Zn is of particular interest because its strongest line (0.2138 μ) is close to the fifth-harmonic wavelength $\lambda_5 = 0.212$ μ.

If we add argon to the mixture of Cd, Na, and Xe, simultaneous phase matching for the processes (1), and the following processes $3\omega+3\omega+3\omega=9\omega$, $\omega+3\omega+5\omega=9\omega$, $\omega+\omega+\omega+\omega+5\omega=9\omega$, and $\omega+\omega+\omega+\omega+\omega+\omega+\omega+\omega+\omega=9\omega$ is also possible. In such a mixture the single-photon absorption cross sections for the wavelengths of interest ($\lambda_1 = 1.06$ μ, $\lambda_3 = 0.353$ μ, $\lambda_5 = 0.212$ μ, and $\lambda_9 = 0.1178$ μ) are all less than 0.2 Mbn (0.2×10^{-18} cm^2). The ninth harmonic produced will result from the coherent interference of both individual step and direct processes involving odd nonlinear susceptibilities from the third to ninth order. Obviously the way these processes interfere will determine the overall efficiency of the optical convertor.

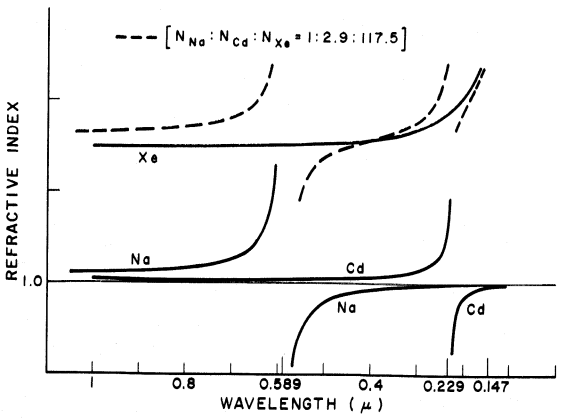


Fig. 1. Refractive indices of Na, Cd, Xe, and mixture of 1 part Na + 2.86 parts Cd + 117.5 parts Xe versus wavelength.

Finally, we note that by suitable arrangement of the configuration of the heat pipe oven, several different zones could be realized, each satisfying phase-matching conditions for different nonlinear processes. For example, in a phase-matched mixture of a metal vapor and an inert gas, the inert gas itself can be a mixture of several gases satisfying other phase-matching conditions. In addition, it may be possible to locate, in one heat pipe oven, several different, physically separated zones of metal vapor-gas mixtures.

III. FHG in Two Separate Steps

Nonlinearities of second, third, and fourth orders may be employed to generate the fifth harmonic in a cascade system [6]-[9]. Phase matching for each step is provided in separate nonlinear elements. Several combinations are possible. Here we will discuss two of them in which an isotropic nonlinear media is employed in at least the final step:

1) first step: tripling $\omega+\omega+\omega=3\omega$, and second step: mixing $\omega+\omega+3\omega=5\omega$;
2) first step: doubling $\omega+\omega=2\omega$, and second step: mixing $\omega+2\omega+2\omega=5\omega$.

For a plane-wave approximation [13]

$$E_j = A_j \exp(i\omega_j t - ik_j z). \tag{2}$$

Each one of the above processes can separately permit 100-percent conversion efficiency. To achieve maximum efficiency for the combination of two processes, additional requirements have to be met. Without detailed analysis, we will determine the conditions for full conversion of the fundamental radiation to its fifth harmonic for both schemes.

A. Plane-Wave Approximation

We assume that in both steps an optimal relation between the phases of the interacting waves exists. At the input of the two-step system it is assumed that $A_1(0) = A_{10}$, $A_2(0) = A_3(0) = A_5(0) = 0$ (here the subscripts 1, 2, 3, and 5 refer to the wave with frequencies ω, 2ω, 3ω, and 5ω, respectively).

First we discuss scheme 1). At the output of the first step ($z = L_1$) we have for the amplitudes

$$A_1(L_1) = \frac{A_{10}}{\sqrt{1+L_1^2/L_{30}^2}} \quad A_3(L_1) = \frac{A_{10}L_1/L_{30}}{\sqrt{1+L_1^2/L_{30}^2}} \tag{3}$$

where

L_1 length of the first nonlinear element;
$\sigma_3 = 18\pi\omega^2\chi^{(3)}/k_3c^2$;
c velocity of light;
$\chi^{(3)}$ nonlinear susceptibility of the third order for the process $\omega + \omega + \omega = 3\omega$;
$L_{30} = (\sigma_3 A_{10}^2)^{-1}$ characteristic interaction length;

and at $L_1/L_{30} = 3, A_3(L_1) = 0.95\,A_{10}$.

We assume linearly polarized light waves in the same direction; then the vector nature of the electric field as well as the tensor nature of the nonlinear susceptibilities may be neglected. The amplitudes of the interacting waves in the second step are described (in the slowly varying envelope approximation) by the coupled wave equations

$$\frac{dA_1}{dz} = -2\sigma_3' A_1 A_3 A_5 \quad \frac{dA_3}{dz} = -3\sigma_3' A_1^2 A_5$$

$$\frac{dA_5}{dz} = 5\sigma_3' A_1^2 A_3 \tag{4}$$

where

$$\sigma_3' = 2\pi\omega^2\chi'^{(3)}/k_1c^2.$$

It should be noted that the nonlinear susceptibilities $\chi^{(3)}$ and $\chi'^{(3)}$ may be significantly different since in the mixing process we have three different frequencies which may permit more optimum use of upper atomic levels. The features of the solution of (4) are determined by the ratio $A_1(L_1)/A_3(L_1)$. Full conversion efficiency of the two-cascade system is obtained when, at the input to the second step one has

$$A_1^2(L_1) = 0.4\,A_{10}^2 \quad A_3^2(L_1) = 0.6\,A_{10}^2. \tag{5}$$

In this case the second-step output amplitudes are

$$A_1(L_2) = \sqrt{0.4}\,\frac{A_{10}}{\sqrt{1 + L_2^2/L_{20}^2}}$$

$$A_3(L_2) = \sqrt{0.6}\,\frac{A_{10}}{\sqrt{1 + L_2^2/L_{20}^2}}$$

$$A_5(L_2) = \frac{A_{10}L_2/L_{20}}{\sqrt{1 + L_2^2/L_{20}^2}}, \tag{6}$$

here

$$L_{20} = (\sqrt{12/5}\,\sigma_3' A_{10}^2)^{-1}.$$

Obviously when $L_2/L_{20} >> 1$ one has $A_5(L_2) \simeq A_{10}$, and all fundamental wave energy is converted into its fifth harmonic.

When the same analysis is applied to the second scheme it is found that full conversion efficiency is achieved when after the first step (doubling) the amplitudes are

$$A_1^2(L_1) = 0.2\,A_{10}^2 \quad A_2^2(L_1) = 0.8\,A_{10}^2 \tag{7}$$

The physical interpretation of (5) and (7) is quite clear in photon terminology: (5) shows that at the input of the second step, the number of photons with energy $3\hbar\omega$ must be a half-integral of those with energy $\hbar\omega$, since in every elementary interaction one $3\hbar\omega$ photon is coupled with two $\hbar\omega$ photons and produces a $5\hbar\omega$ photon. Similarly, from (7), the number of photons with energy $2\hbar\omega$ should be twice those of $\hbar\omega$.

Calculated phase-matched ratios in a mixture of xenon and some metal vapors are presented in Table I for the type of interactions considered here.

B. Four-Wave Mixing by Gaussian Beams

The high power densities required for efficient higher order nonlinear processes in vapors and gases are achieved by focusing. Since second-harmonic generation (SHG) and third-harmonic generation (THG) in focused beams have been studied in detail elsewhere [14]-[17], only four-wave mixing which takes place in the second step will be treated in detail here. Bjorklund [18] has recently presented a rigorous treatment of four-wave mixing in an isotropic medium. In his analysis, identical confocal parameters and identical waist locations for all fundamental light beams were assumed. Here we extend this treatment to include the cases of interacting beams with arbitrary confocal parameters and different waist locations. In mixing experiments the wavelengths of the interacting beams may differ considerably, and with equal confocal parameters ($b_j = k_j w_{j0}^2$) the short-wavelength beam will spatially overlap a smaller region of the longer wavelength beam. This might suggest that the signal power could be increased if the volumes of the focal regions are more equal for all three beams.

In addition it is necessary to determine how critically the output signal power depends upon the mismatch between focal spot positions of the interacting beams. These two points will now be addressed for the second step of the FHG cascade.

We will study the process of four-wave mixing $\omega_\alpha + \omega_\beta + \omega_\gamma = \omega_s$ with wave vectors

$$k_\alpha + k_\beta + k_\gamma = k_s + \Delta, \quad (|\Delta| << k_j), \quad j = \alpha, \beta, \gamma. \tag{8}$$

The fundamental beams at ω_α, ω_β, and ω_γ are assumed to be lowest order Gaussian modes which propagate concentrically along the z axis oriented normally to the nonlinear media surface as in Fig. 2. The cross section of nonlinear media is considered infinite relative to the beam diameter. Similar refractive indices for both linear and nonlinear media are assumed. If a Gaussian beam passes through a thin spherical lens located at $z = 0$, then the amplitude of the beam is described by the expression

$$A_j(x, y, 0) = A_{j0} \exp\left[-(x^2 + y^2)\left(\frac{1}{w_j^2} - \frac{ik_j}{2R_j}\right)\right]. \tag{9}$$

Here w_j is the radius of the beam, R_j is the radius of the beam wavefront after passing through the lens. It is defined by the curvature of the wavefront before the lens and the focal length of the lens. The three fundamental beams propagate along the z axis and may have arbitrary confocal parameters and arbitrary waist locations. The absorption for all frequencies and the depletion of the fundamental beam amplitudes by the nonlinear process are neglected.

Under these assumptions the propagation of a Gaussian beam is described by the equation

$$\left[\frac{\partial}{\partial z} + \frac{i}{2k_j}\left(\frac{\partial^2}{\partial x^2} + \frac{\partial^2}{\partial y^2}\right)\right] A_j = 0. \tag{10}$$

The solution of (10) for the initial condition (9) is

TABLE I
THE PHASE-MATCHED[1] RATIO OF Xe TO METAL ATOMS FOR THG AND FHG OF Nd:GLASS LASER RADIATION ($\lambda_1 = 1.06\ \mu$)

	N_{Xe}/N_{metal}			
interaction / metal	$\omega+\omega+\omega = 3\omega$	$\omega+\omega+3\omega = 5\omega$	$2\omega+2\omega+\omega = 5\omega$	$\omega+\omega+\omega+\omega+\omega = 5\omega$
Li	152.7	12.6	-	33.3
Na	150.4	9.6	-	30.2
K	325.3	31.5	-	75.6
Rb	412.5	39.8	-	95.8
Cs	660.7	70.9	11.8	160.1
Ca	242.4	-	58.3	31.9
Cd	-	34.4	33.1	31.1
Mg	-	28.7	19.1	15.6
Zn	-	255.6	243.7	215.2

[1]The refractive index of Xe was derived from the Koch formula [17]; the refractive index of metal vapors was calculated from the standard Sellmeier equation and data as follows: alkali metals [17], Ca [24], Cd [25], Mg [26], Zn [27].

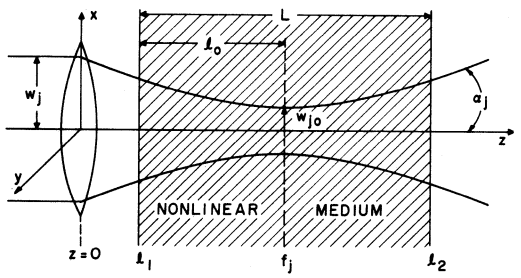


Fig. 2. Fundamental beam focused at $z = f_i$ in an isotropic nonlinear medium. Focal spot radius at f_i is w_{j0}.

$$A_j(x,y,z) = \frac{A_{j0}}{\xi_j(z)} \exp\left[-\frac{x^2+y^2}{\xi_j(z)}\left(\frac{1}{w_j^2} - \frac{ik_j}{2R_j}\right)\right] \tag{11}$$

where

$$\xi_j(z) = 1 - \frac{z}{R_j} - i\frac{2z}{k_j w_j^2}, \quad |\xi_j(z)|$$

is a dimensionless measure of the beam cross-section variation along the z axis due to focusing and diffraction. If one translates the beginning of the coordinate system to the point f_j (Fig. 2) where the beam cross section is a minimum (focal spot) with the substitution

$$\zeta_j = \frac{2}{b_j}(z - f_j) \tag{12}$$

then

$$A_j(x,y,\zeta_j) = \frac{B_{j0}}{1 - i\zeta_j} \exp\left(-\frac{k_j(x^2+y^2)}{b_j(1 - i\zeta_j)}\right) \tag{13}$$

where

$$B_{j0} = A_{j0}\left[\left(\frac{2R_j}{k_j w_j^2} - i\right)\frac{b_j}{2R_j}\right]^{-1}$$

is the electric field amplitude at the center of the focal spot $(0, 0, f_j)$ and $b_j = 4/k_j\alpha_j^2 = k_j w_{j0}^2$ is the confocal parameter, α_j being the far-field semiangular spread of the beam.

The equation describing the behavior of the signal amplitude A_s is

$$\left[\frac{\partial}{\partial z} + \frac{i}{2k_s}\left(\frac{\partial^2}{\partial x^2} + \frac{\partial^2}{\partial y^2}\right)\right] A_s = -i\sigma A_\alpha A_\beta A_\gamma \exp(-i\Delta z) \tag{14}$$

where $\sigma = 2\pi\omega_s^2\chi'^{(3)}/k_s c^2$. With the initial conditons, $A_s(x, y, l_1) = 0$, $A_j = A_j(x, y, l_1)$ at the interface $z = l_1$, the solution of (14) is

$$A_s(x,y,z) = -i\frac{\sigma A_{\alpha 0} A_{\beta 0} A_{\gamma 0}}{4} \cdot \int_{l_1}^{z} \frac{\exp\left(-\frac{x^2+y^2}{4m_1(\tau)} - i\Delta\tau\right) d\tau}{m_1(\tau) m_2(\tau)} \tag{15}$$

where

$$g_j = \frac{1}{\xi_j(\tau)}\left[\frac{1}{w_j^2} - \frac{ik_j}{2R_j}\right] \quad m_1(\tau) = \frac{1}{4(g_\alpha + g_\beta + g_\gamma)} + i\frac{\tau - z}{2k_s},$$
$$m_2(\tau) = \xi_\alpha(\tau)\,\xi_\beta(\tau)\,\xi_\gamma(\tau)\,(g_\alpha + g_\beta + g_\gamma).$$

Integrating over the intensity distribution gives the signal power P_s:

$$P_s = \frac{cn_s}{8\pi}\int_{-\infty}^{\infty}\int_{-\infty}^{\infty} A_s A_s^*\, dx\, dy = \frac{128 n_s \sigma^2 P_{\alpha 0} P_{\beta 0} P_{\gamma 0}}{c^2 n_\alpha n_\beta n_\gamma w_\alpha^2 w_\beta^2 w_\gamma^2} \times \int_{l_1}^{z} d\tau \int_{l_1}^{z} d\tau' \frac{\exp[-i\Delta(\tau - \tau')]}{m_2(\tau) m_2^*(\tau')[m_1(\tau) + m_1^*(\tau')]}. \tag{16}$$

$P_{j0} = 16 A_{j0} A_{j0}^*/cn_j w_j^2$ is the fundamental beam power at frequency ω_j.

In further calculations we will neglect the difference between indices of refraction except in the expression for Δ.

The expressions for the signal amplitude (15) and signal power (16) can be extended in a very simple way for the other four-wave interactions, such as

1) for the process $\omega_\alpha + \omega_\beta - \omega_\gamma = \omega_s$, $k_\alpha + k_\beta - k_\gamma = k_s + \Delta$ by the following replacement:

$$A_{\gamma 0} \to A_{\gamma 0}^*, \quad g_\gamma \to g_\gamma^*, \quad \xi_\gamma \to \xi_\gamma^*;$$

2) for the process $\omega_\alpha - \omega_\beta - \omega_j = \omega_s$, $k_\alpha - k_\beta - k_\gamma = k_s + \Delta$ by the following replacement:

$$A_{\beta 0} \to A_{\beta 0}^*, \quad A_{\gamma 0} \to A_{\gamma 0}^*, \quad g_\beta \to g_\beta^*, \quad g_\gamma \to g_\gamma^*,$$
$$\xi_\beta \to \xi_\beta^*, \quad \xi_\gamma \to \xi_\gamma^*.$$

Thus the formulas (15) and (16) describe the signal amplitude and the power for all types of four-wave interactions in an isotropic medium between coaxial Gaussian beams with arbitrary confocal parameters and beam waist locations on the z axis.

Simplification of these expressions must be performed explicitly for each experimental situation. It is seen that in most cases the signal is not of a lowest order Gaussian mode.

Here we present in detail the dependence of the sum-mixing power P_s on the beam confocal parameters and on the positions of the beam waists for FHG. Numerical computations have been performed for different values of the parameters of interest. In order to determine the optimum conversion efficiency for a practical system, special attention was paid to the following three situations:

1) equal confocal parameters $b_\alpha = b_\beta = b_\gamma$;
2) equal cross section of the beam waists $w_{\alpha 0} = w_{\beta 0} = w_{\gamma 0}$.
3) equal volume of the beam waist regions $b_\alpha w_{\alpha 0}^2 = b_\beta w_{\beta 0}^2 = b_\gamma w_{\gamma 0}^2$.

For the most efficient of these three configurations, the dependence of the signal power P_s on the relative beam focal spot positions f_j was studied.

For this purpose some new parameters in (16) will be introduced. If the distance between focal spot f_j and input surface (Fig. 2) of the nonlinear medium is l_0, the parameter $d = l_0/L$ will define the minimum spot size position. The focal points f_β and f_γ are on the z axis and $f_\beta - f_\alpha = \delta_{\beta 0}$, $f_\gamma - f_\alpha = \delta_{\gamma 0}$. $\delta_{\beta 0}$ and $\delta_{\gamma 0}$ are permitted to be either negative or positive depending on the positions of f_β and f_γ relative to f_α.

Substituting

$$\eta = \frac{2}{L}(\tau - f_\alpha) \tag{17}$$

(16) becomes

$$P_s = \frac{128\sigma^2 P_{\alpha 0} P_{\beta 0} P_{\gamma 0} k_\beta k_\gamma (1 + t_\beta + t_\gamma)}{c^2} \cdot q_\beta q_\gamma J_0\left(d, \frac{\Delta L}{2}, q_j, \delta_l, t_l\right) \tag{18}$$

and

$$J_0\left(d, \frac{\Delta L}{2}, q_j, \delta_l, t_l\right) = \int_{-2d}^{2(1-d)} d\eta \int_{-2d}^{2(1-d)} d\eta' \cdot \frac{\exp\left[-i\frac{\Delta L}{2}(\eta - \eta')\right]}{m_{20}(\eta) m_{20}^*(\eta')[m_{10}(\eta) + m_{10}^*(\eta')]} \tag{19}$$

where

$q_j = L/b_j$ is the focusing parameter.

When the confocal parameters are equal ($b_\alpha = b_\beta = b_\gamma$) and the focal spots coincide ($\delta_\beta = \delta_\gamma = 0$), then (19) becomes

$$J_0\left(d, \frac{\Delta L}{2}, q_\alpha, 0, t_l\right) = \tfrac{1}{2}(1 + t_\beta + t_\gamma)^{-2} \cdot \left| \int_{-2d}^{2(1-d)} \frac{\exp\left(-\frac{i\Delta L}{2}\eta\right) d\eta}{(1 - iq_\alpha \eta)^2} \right|^2 \tag{20}$$

an integral which has been investigated elsewhere [15]-[18]. It should be noted, however, that only in this case is the resulting beam in a single Gaussian mode. For any other configuration a multimode output results due to the mismatch between the size and position of confocal parameters of the interacting beams and the induced polarization.

For the evaluation of J_0 as a function of $\Delta L/2$ for various sets of other parameters we have employed a fast Fourier transform [19]. Numerical calculations of the integral (19) were performed for FHG for the interactions $\omega + \omega + 3\omega = 5\omega$ and $\omega + 2\omega + 2\omega = 5\omega$. In the expressions to follow the indices α, β, γ, and s will be replaced by 1, 2, 3, and 5 for the fundamental, second harmonic, third harmonic, and fifth harmonic, respectively. In the first interaction the two waves of the fundamental frequency are identical, thus $t_\beta = 1$, $t_\gamma = 3$, $q_1 = q_\beta$, and $\delta_\beta = 0$. We believe, as pointed out in [17], that when tight focusing is employed and the focus position is far enough from both ends of the nonlinear medium ($1/q_j < d < 1 - 1/q_j$), the value of J_0 is almost independent of the exact position of the focus. In our calculation, $d = \frac{1}{2}$ was chosen. The calculated products $q_1 q_3 J_0$ are plotted in Fig. 3 for the confocal parameter $q_1 = 20$ and the step $\delta(\Delta L/2) = \pi$. To obtain the confocal parameter configuration mentioned above the confocal parameter of the third harmonic and its waist location were changed as indicated in the corresponding curves in Fig. 3. In curve $q_3 = 20$ the maximum value occurs at $\Delta L/2 \simeq 6\pi$ which corresponds to $\Delta \simeq 2/b_1$ obtained from the analytical approximation for infinitely tight focusing. The maximum of $q_1 q_3 J_0$ at given confocal parameters moves towards smaller values of $\Delta L/2$ when $q_3 < q_1$ and towards larger values of $\Delta L/2$ when $q_3 > q_1$. In both cases its absolute value decreases.

For equal confocal parameters $q_1 = q_3 = 20$ we have calculated the influence of the focal spot mismatch on the

$$m_{10}(x) = \frac{1 + t_\beta + t_\gamma}{(1 - iq_\alpha x)^{-1} + t_\beta q_\beta / q_\alpha (1 - iq_\beta x + i\delta_\beta q_\beta) + t_\gamma q_\gamma / q_\alpha (1 - iq_\gamma x + i\delta_\gamma q_\gamma)} + iq_\alpha x$$

$$m_{20}(x) = (1 - iq_\beta x + i\delta_\beta q_\beta)(1 - iq_\gamma x + i\delta_\gamma q_\gamma) + \frac{q_\alpha}{t_\beta q_\beta}(1 - iq_\alpha x)(1 - iq_\gamma x + i\delta_\gamma q_\gamma) + \frac{q_\alpha}{t_\gamma q_\gamma}(1 - iq_\alpha x)(1 - iq_\beta x + i\delta_\beta q_\beta)$$

$$\delta_l = \frac{2\delta_{l0}}{L}, \quad t_l = \frac{k_l}{k_\alpha}, \quad (j = \alpha, \beta, \gamma, \quad l = \beta, \gamma)$$

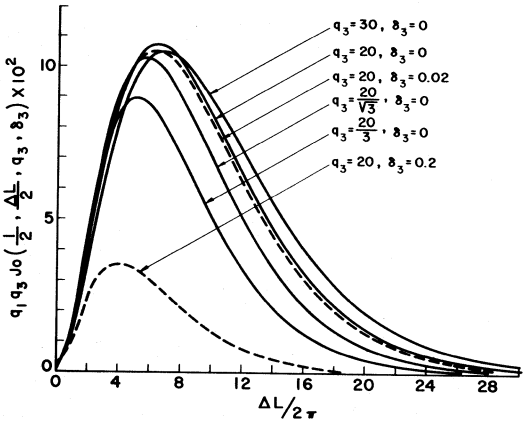


Fig. 3. Function $q_1 q_3 J_0$ versus $\Delta L/2\pi$ for sum-mixing $\omega + \omega + 3\omega = 5\omega$. $q_1 = q_3 = 20$. Curve $q_3 = 20$, corresponds to equal confocal parameters; $q_3 = 20/3$, equal cross sections of the beam waists; $q_3 = 20/\sqrt{3}$, equal beam waist volumes.

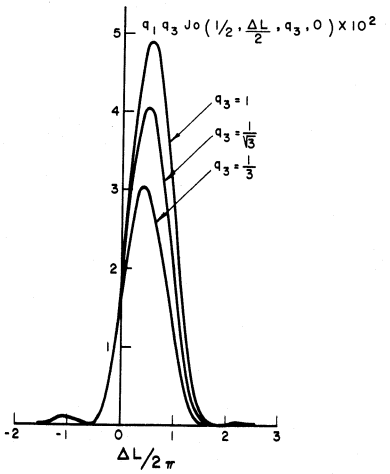


Fig. 4. Function $q_1 q_3 J_0$ versus $\Delta L/2\pi$ for sum-mixing $\omega + \omega + 3\omega = 5\omega$, $q_1 = q_3 = 1$. Curve $q_3 = 1$ corresponds to equal confocal parameters, $q_3 = \frac{1}{3}$, equal cross section of the beam waists; $q_3 = 1/\sqrt{3}$, equal beam waist volumes.

signal power. Two curves are shown in Fig. 3. For $\delta_3 = 0.02$ the maximum of $q_1 q_3 J_0$ decreases by ~3 percent and at $\delta_3 = 0.2$, $q_1 q_3 J_0$ is ~30 percent of its optimum value. From these and other calculations with different δ_3 we conclude that the accuracy of coincidence of the focal spots for ω and 3ω needs to be better than $0.1\, b_1$.

Fig. 4 presents the results for $q_1 = 1$. The maximum value of $q_1 q_3 J_0$ occurs again for equal confocal parameters $q_1 = q_3 = 1$. For weaker focusing the sidelobe structure is more evident. It was found that $q_1 q_3 J_0$ decreases less than 2 percent when a mismatch $\delta_2 = 0.2$ was included. Thus one can expect that with weaker focusing conditions the influence of focal spots mismatch will decrease.

The results for the interaction $\omega + 2\omega + 2\omega = 5\omega$ are plotted in Fig. 5. Here $t_\beta = t_\gamma = 2, q_\beta = q_\gamma = q_2$, and $\delta_\beta = \delta_\gamma$. It should be noted that the curve with $q_1 = q_3 = 20$ is the same for both interactions as follows from (20). With variation of the parameters q_2 and δ_2 the behavior of $q_2^2 J_0$ is similar to that for the interaction $\omega + \omega + 2\omega = 5\omega$. The same accuracy of focal spot coincidence as above is also required.

Thus it is seen from these calculations that the fifth-harmonic power has its maximum value for equal confocal parameters. Although we have no analytical proof we believe this to be the general case for the four-wave sum-mixing process.

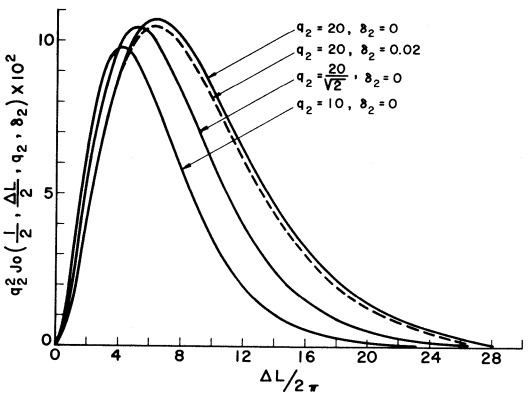


Fig. 5. Function $q_2^2 J_0$ versus $\Delta L/2\pi$ for sum-mixing $\omega + 2\omega + 2\omega = 5\omega$. $q_1 = 20$. Curve $q_2 = 20$ corresponds to equal confocal parameters; $q_2 = 10$, equal cross section of the beam waists; $q_2 = 20/\sqrt{2}$, equal beam waist volumes.

IV. FHG in Isotropic Media with Third- and Fifth-Order Nonlinearity

In this section FHG in an isotropic medium with nonlinear polarization expressed as

$$P^{NL} = \chi^{(3)} EEE + \chi^{(5)} EEEEE \tag{21}$$

will be considered.

In such a medium the fifth harmonic results from two simultaneous processes:

1) the step processes involving the third-order nonlinearity

$$\omega + \omega + \omega = 3\omega \quad \text{and} \quad \omega + \omega + 3\omega = 5\omega$$

$$k_1 + k_1 + k_1 = k_3 + \Delta_{13} \quad k_1 + k_1 + k_3 = k_5 + \Delta_{135} \tag{22}$$

2) the direct process involving the fifth-order nonlinearity

$$\omega + \omega + \omega + \omega + \omega = 5\omega,$$

$$k_1 + k_1 + k_1 + k_1 + k_1 = k_5 + \Delta_{15} \tag{23}$$

where, obviously, $\Delta_{13} + \Delta_{135} = \Delta_{15}$.

We have shown in Section II that with the use of suitable combinations of vapors and gases, it is possible to obtain different values of the wave-vector mismatch including $\Delta_{13} = \Delta_{135} = \Delta_{15} = 0$. In Section III-A it was found that when the cascade system is used it is possible to convert all the energy of the fundamental frequency to its fifth harmonic. It is therefore interesting to determine what the maximum conversion efficiency would be for only a single cell having nonlinear polarizability described by (21), under the same plane-wave approximation.

4. *Plane-Wave Approximation*

From Maxwell's equation for a lossless nonlinear medium, with a polarizability expressed by (21), the following set of differential equations for coupled amplitudes of the interacting waves are obtained [13]:

$$\frac{dA_1}{dz} = -i\sigma_1 A_1^{*2} A_3 \exp i\Delta_{13}z - i\sigma_1' A_1^{*4} A_5 \exp i\Delta_{15}z - i\sigma_1'' A_1^* A_3^* A_5 \exp i\Delta_{135}z$$

$$\frac{dA_3}{dz} = -i\sigma_3 A_1^3 \exp -i\Delta_{13}z - i\sigma_2 A_1^{*2} A_5 \exp i\Delta_{135}z$$

$$\frac{dA_5}{dz} = -i\sigma_5 A_1^5 \exp -i\Delta_{15}z - i\sigma_4 A_1^2 A_3 \exp -i\Delta_{135}z \quad (24)$$

where

$$\sigma_1 = 6\pi\omega\chi^{(3)}/cn_1, \qquad \sigma_3 = 6\pi\omega\chi^{(3)}/cn_3,$$
$$\sigma_1'' = 4\pi\omega\chi'^{(3)}/cn_1, \qquad \sigma_2 = 6\pi\omega\chi'^{(3)}/cn_3,$$
$$\sigma_4 = 10\pi\omega\chi'^{(3)}/cn_5, \qquad \sigma_1' = 10\pi\omega\chi^{(5)}/cn_1,$$
$$\sigma_5 = 10\pi\omega\chi^{(5)}/cn_5.$$

We have performed a numerical integration of (24), which has been verified by using the usual energy balance equation for a lossless medium:

$$|A_1(z)|^2 + |A_3(z)|^2 + |A_5(z)|^2 = \text{constant} \quad (25)$$

to an accuracy of better than 1 percent. Numerical integration is possible in complex numbers but, in the present case, the following procedure was adopted. Introducing the real amplitude and phase of the waves, then

$$A_j(z) = A_j'(z) \exp(i\theta_j(z)) \quad (26)$$

and through normalization

$$a_j(z) = A_j'(z)/A_1'(0) \quad \tilde{z} = z\sigma_3 A_1'^2(0) = z/L_{30}.$$

The coupled amplitude equations (24) then become

$$\frac{da_1}{d\tilde{z}} = -\sigma_{10} a_1^2 a_3 \sin\phi - \sigma_{10}' a_1^4 a_5 \sin\psi - \sigma_{10}'' a_1 a_3 a_5 \cdot \sin(\psi - \phi)$$

$$\frac{da_3}{d\tilde{z}} = a_1^3 \sin\phi - \sigma_{20} a_1^2 a_5 \sin(\psi - \phi)$$

$$\frac{da_5}{d\tilde{z}} = \sigma_{50} a_1^5 \sin\psi + \sigma_{40} a_1^2 a_3 \sin(\psi - \phi)$$

$$\frac{d\phi}{d\tilde{z}} + \tilde{\Delta}_{13} = (a_1^3/a_3 - 3\sigma_{10} a_1 a_3)\cos\phi - 3\sigma_{10}' a_1^3 a_5 \cos\psi + (\sigma_{20} a_1^2 a_5/a_3 - 3\sigma_{10}'' a_3 a_5)\cos(\psi - \phi)$$

$$\frac{d\psi}{d\tilde{z}} + \tilde{\Delta}_{15} = -5\sigma_{10} a_1 a_3 \cos\phi + (\sigma_{50} a_1^5/a_5 - 5\sigma_{10}' a_1^3 a_5) \cdot \cos\psi + (\sigma_{40} a_1^3 a_3/a_5 - 5\sigma_{10}'' a_3 a_5)\cos(\psi - \phi) \quad (27)$$

where

$$\tilde{\Delta}_{13} = \Delta_{13}/\sigma_3 A_{10}'^2, \qquad \tilde{\Delta}_{15} = \Delta_{15}/\sigma_3 A_{10}'^2,$$
$$\sigma_{10} = \sigma_1/\sigma_3, \qquad \sigma_{20} = \sigma_2/\sigma_3,$$
$$\sigma_{40} = \sigma_4/\sigma_3, \qquad \sigma_{10}'' = \sigma_1''/\sigma_3,$$
$$\sigma_{10}' = \sigma_1' A_{10}'^2/\sigma_3, \qquad \sigma_{50} = \sigma_5 A_{10}'^2/\sigma_3,$$
$$\phi = 3\theta_1 - \theta_3 - \Delta_{13}z, \qquad \psi = 5\theta_1 - \theta_5 - \Delta_{15}z.$$

These equations have been numerically integrated for parameters corresponding to a nonlinear medium consisting of a mixture of Na, Cd, and Xe. Difficulties arose in defining some of these parameters due to a lack of knowledge of the principle nonlinear susceptibilities. We assume the atomic susceptibilities $\chi_a^{(3)} = \chi_a'^{(3)} = 8.5 \times 10^{-34}$ ESU, calculated by Eicher [20] for tripling of $\lambda = 1.06\,\mu$ in Na. In addition we note that in a mixture of Na + Cd + Xe the contribution to $\chi^{(3)}$ and $\chi'^{(3)}$ from Xe atoms can be neglected but the contribution from Cd atoms might be comparable and even greater than that of Na atoms, especially in $\chi'^{(3)}$. Much more uncertainty arises in $\chi^{(5)}$. FHG in gases was reported by Harris [4] but no estimates of $\chi^{(5)}$ were given. Calculations using perturbation theory have yielded for sodium $\chi_a^{(5)} = 6.7 \times 10^{-45}$ ESU [21]. In the present case, for lack of better values, we will assume similar values for susceptibilities $\chi_a^{(3)}$, $\chi_a'^{(3)}$, and $\chi_a^{(5)}$ for Cd and Na. Thus, for a fundamental power density of 2×10^{11} W/cm^2 (limited in the case of Na by multiphoton ionization [2]) one obtains

$$\sigma_{10} = \sigma_{20} = 1, \qquad \sigma_{10}'' = 0.667,$$
$$\sigma_{40} = 1.667, \qquad \sigma_{10}' = \sigma_{50} = 0.0221,$$
$$L_{30} = (\sigma_3 A_1'^2(0))^{-1} = 6.3 \text{ cm}, \quad (N = 10^{17} \text{ atom/cm}^3),$$
$$L_{50} = (\sigma_5 A_1'^4(0))^{-1} = 283.6 \text{ cm}.$$

In addition $\sigma_{10} = \sigma_{50} = 1$ and $L_{30} = L_{50} = 0.14$ cm when the power density is 9.1×10^{12} W/cm^2.

The following initial conditions were assumed:

$$a_1(0) = 1, \quad a_3(0) = a_5(0) = 10^{-5}, \quad \phi(0) = \psi(0) = 0.$$

The solution of (27) for $\tilde{\Delta}_{13} = \tilde{\Delta}_{15} = 0$ and $\sigma_{10}' = \sigma_{50} = 0.0221$ is shown in Fig. 6(a). The third-harmonic amplitude reaches its first maximum, $a_3 = 0.6$, at $\tilde{z} = 1.3$ and the fifth harmonic reaches its first maximum, $a_5 = 0.89$, at $\tilde{z} = 7$. We have calculated the amplitudes for $\tilde{z} \leqslant 130$, but experimental conditions limit practical values of $\tilde{z} \leqslant 10$, and hence, only the dependence of the normalized amplitudes is presented for small values of $\tilde{z}$. Although there is a periodic exchange of energy between interacting waves, a simple periodic function does not always exist due to the competition of both step-wise and direct processes. For example at $\tilde{z} = 62.8$, $a_3 = 0.95$ and at $\tilde{z} = 103.2$, $a_5 = 0.97$. To compare the contribution of step and direct processes we have calculated the amplitudes for the case when $\sigma_{10}' = \sigma_{50} = 0$ (this is the situation when $\chi^{(5)} = 0$). The difference between solutions for both cases is less than 10 percent for $\tilde{z} < 10$. For larger $\tilde{z}$, significant differences exist. To explain this we note that the growth of the fifth harmonic resulting from the step processes depends on z/L_{30}, whereas the growth of the fifth harmonic resulting from the direct process depends on z/L_{50}. In Fig. 6(a), $L_{30}/L_{50} = 0.0221$ and substantial influence of the direct process will appear only at longer $\tilde{z}$.

When the power density is increased to a value permitting $\sigma_{10}' = \sigma_{50} = 1$ [(Fig. 6(b)], the normalized amplitude of the

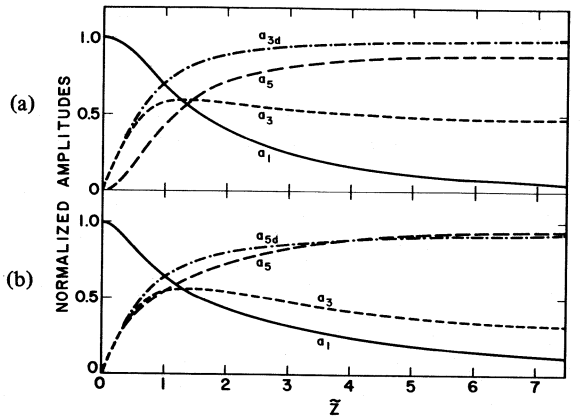


Fig. 6. Variation of normalized fundamental-, third-, and fifth-harmonic amplitudes for perfect phase matching $\tilde{\Delta}_{13} = \tilde{\Delta}_{15} = 0$. (a) $\sigma'_{10} = \sigma_{50} = 0.0221$, (b) $\sigma'_{10} = \sigma_{50} = 1$. Curves a_{3d} and a_{5d} represent the growth of the third and fifth harmonics by the direct process only. Note that $\tilde{z} = z/L_{30}$ and in (a) $L_{30}/L_{50} = 0.0221$, but in (b) $L_{30}/L_{50} = 1$.

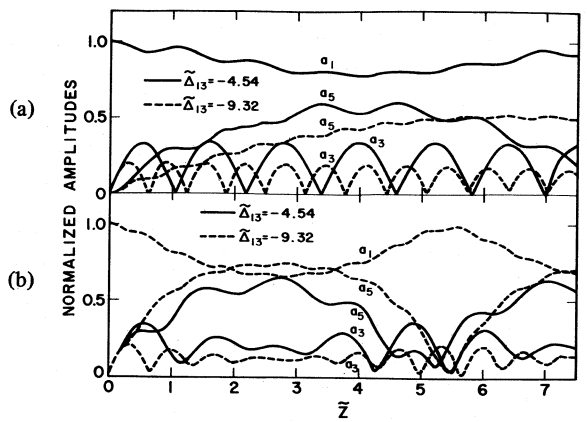


Fig. 7. Variation of the normalized amplitude of the fundamental, third, and fifth harmonics for $\tilde{\Delta}_{15} = 0$, $\tilde{\Delta}_{13} = -4.54$ and $\tilde{\Delta}_{13} = -9.32$. (a) $\sigma'_{10} = \sigma_{50} = 0.0221$, (b) $\sigma'_{10} = \sigma_{50} = 1$.

fifth harmonic is $a_5 = 0.94$ at $\tilde{z} = 7$. This corresponds to an energy conversion efficiency of 90 percent. Comparing both Fig. 6(a) and Fig. 6(b) one can observe the difference in growth of a_5 due to the different ratio of L_{30}/L_{50}. We note that the higher order harmonics are growing slower than those of lower order even in a single direct process. For example if every harmonic is generated only in a direct process then the growth of the normalized harmonic amplitude from zero with the normalized distance $\tilde{z}_n = z\sigma_n A_{10}^{n-1}$ is at $\tilde{z} < 0.5$ (and $a_{nd} < 0.4$, $a_1 > 0.9$) almost the same for all harmonics up to the fifth. However the value $a_{nd} = 0.894$ is reached for the second harmonic at $\tilde{z}_2 = 1.44$, third harmonic at $\tilde{z}_3 = 2$, fourth harmonic at $\tilde{z}_4 = 2.95$, and fifth harmonic at $\tilde{z}_5 = 4.67$. The exact functions $a_{3_d}(\tilde{z})$ and $a_{5_d}(\tilde{z})$ are shown in Fig. 6.

In Fig. 7(a) the amplitude growth for $\sigma'_{10} = \sigma_{50} = 0.0221$, $\tilde{\Delta}_{15} = 0$, $\tilde{\Delta}_{13} = -4.54$, and $\tilde{\Delta}_{13} = -9.32$ are shown. $\tilde{\Delta}_{13} = -4.54$ corresponds to a mixture of Na + Cd + Xe with $T \simeq 810$ K having saturated Na and Cd vapor concentrations with $N_{Cd}/N_{Na} = 3.35$ and $N_{Na} = 10^{17}$ atom/cm^3. $\tilde{\Delta}_{13} = -9.32$ corresponds to a Cd + Xe mixture with $N_{Cd} = 10^{17}$ atom/cm^3. In Fig. 7(b) the same parameters as in Fig. 7(a) are employed, except that $\sigma'_{10} = \sigma_{50} = 1$. In the case of Fig. 7(a) the step processes are more important and the third harmonic changes periodically. Decreasing $\tilde{\Delta}_{13}$ leads to a significant improvement in a_5. In Fig. 7(b) the direct process is comparable with the step process and even at larger $\tilde{\Delta}_{13} = -9.32$, a_5 is higher. In this case the interference between step and direct processes is substantial for the fifth-harmonic amplitude.

In a phase-matched mixture of Na + Xe for third-harmonic generation ($\tilde{\Delta}_{13} = 0$) $\tilde{\Delta}_{15} = -173.5$, the maximum value of a_5 is less than 3.5×10^{-3} and $a_3(\tilde{z}) \to 1$ when $\tilde{z} \gg 1$ following (3).

The important result from these calculations is that in a single cell of isotropic media, phase matched for step and direct processes ($\Delta_{13} = \Delta_{15} = 0$), the conversion efficiency of fundamental radiation into its fifth harmonic is comparable to that obtained in a cascade scheme. In a cell with a Cd + Na + Xe mixture with variable Xe concentration, it is possible to obtain $\Delta_{13} = 0$ and generate the third harmonic, or $\Delta_{13} = \Delta_{15} = 0$ and generate the fifth harmonic. It should be noted that in the above analysis we have not discussed the case when different signs of $\chi^{(3)}$, $\chi'^{(3)}$, and $\chi^{(5)}$ exist because of the lack of experimental or theoretical data.

B. FHG by Focused Gaussian Beam

To extend (24) for a light beam with finite cross section, transverse derivatives should be included. However, some simplifications are necessary to permit analytical solution. We will thus neglect depletion of the fundamental amplitude, (hence $A_1(z) = \text{constant}$) and also the term $\sigma_2 A_1^{*2} A_5$ in the second equation of (24) (this term describes the depletion of the third harmonic arising from its partial convertion into the fifth harmonic). Under these assumptions, FHG is described by the following set of partial differential equations:

$$\left[\frac{\partial}{\partial z} + \frac{i}{2k_1}\left(\frac{\partial^2}{\partial x^2} + \frac{\partial^2}{\partial y^2}\right)\right] A_1 = 0$$

$$\left[\frac{\partial}{\partial z} + \frac{i}{2k_3}\left(\frac{\partial^2}{\partial x^2} + \frac{\partial^2}{\partial y^2}\right)\right] A_3 = -i\sigma_3 A_1^3 \exp -i\Delta_{13} z$$

$$\left[\frac{\partial}{\partial z} + \frac{i}{2k_5}\left(\frac{\partial^2}{\partial x^2} + \frac{\partial^2}{\partial y^2}\right)\right] A_5 = -i\sigma_5 A_1^5 \cdot \exp -i\Delta_{15} z - i\sigma_4 A_1^2 A_3 \exp -i\Delta_{135} z. \quad (28)$$

The initial conditions are $A_1(x, y, o)$ from (9) and $A_3(x, y, l_1) = A_5(x, y, l_1) = 0$ (see Fig. 2).

Without focusing of the pumping beam [$R = \infty$ in (9)] and negligible diffraction for fifth-harmonic amplitude we obtain

$$A_5(x, y, z) = A_{10}^5 \exp\left(-5\frac{x^2 + y^2}{w_j^2}\right) \cdot \left[(\sigma_5 + \sigma_3\sigma_4/\Delta_{13})\frac{\exp(-i\Delta_{15}z) - 1}{\Delta_{15}} - \frac{\sigma_3\sigma_4}{\Delta_{13}}\frac{\exp(-i\Delta_{135}z) - 1}{\Delta_{135}}\right] \quad (29)$$

and therefore the effective fifth-order nonlinear susceptibility is

$$\chi_{\text{eff}}^{(5)} = \chi^{(5)} + 2\pi\chi^{(3)}\chi'^{(3)}/n_3(n_1 - n_3). \quad (30)$$

We recall that in gases and vapors it is possible that the values of $\chi^{(3)}$ and $\chi'^{(3)}$ are different. Note that the oscillator strengths among the electronic states of an atom and the resonance enhancements which are most responsible for the values of $\chi^{(3)}$ and $\chi'^{(3)}$ are also responsible for the value of $\chi^{(5)}$. A resonance of twice the pump frequency is particularly desirable since it will increase all these nonlinear susceptibilities. As seen from (20) the relative signs of $\chi^{(3)}$, $\chi'^{(3)}$, $\chi^{(5)}$, and $(n_1 - n_3)$ are important. Atoms with approximately equal absolute values of susceptibilities and dispersion, but different signs, would have different values of $\chi^{(5)}_{\text{eff}}$. For example in a mixture of Xe + Na, when $n_1 = n_5$, $n_1 - n_3 > 0$ and in a mixture of Xe + Cd, when $n_1 = n_5$, $n_1 - n_3 < 0$.

Successive solution of (28) substituting (17) gives for the fifth-harmonic amplitude

$$A_5(x, y, l_2) = -i\frac{\sigma_5 L B_{10} \exp(-i\Delta_{15} f_1)}{2(1 - iq_1)} \cdot \exp\left(-\frac{5k_1(x^2 + y^2)}{b_1(1 - iq_1)}\right) J_1 \tag{31}$$

$$J_1(\Delta_{15}L/2, \Delta_{13}L/2, W, q_1, d) = \int_{-2d}^{2(1-d)} \frac{\exp(-i\Delta_{15}L\eta/2)\, d\eta}{(1 - iq_1\eta)^4} - iWL \int_{-2d}^{2(1-d)} \frac{\exp(-i\Delta_{135}L\eta/2)\, d\eta}{(1 - iq\eta)^2} \int_{-2d}^{\eta} \cdot \frac{\exp(-i\Delta_{13}L\tau/2)\, d\tau}{(1 - iq_1\tau)^2} = J_d - iWLJ_s. \tag{32}$$

Here $W = \sigma_3\sigma_4/2\sigma_5$. Then for the fifth-harmonic power we obtain

$$P_5 = \frac{32\,768\, k_1^4 P_{10}^5 \sigma_5^2 q_1^2}{5c^4 n_1^4 b_1^2} |J_1|^2. \tag{33}$$

The fifth-harmonic power is governed by the integral (32) and its optimization will now be discussed. The first integral J_d in (32) results from the direct process and the second integral J_s from the step processes. The total value of J_1 depends also on the value and the sign of W which is the ratio between the nonlinear susceptibilities of the third and fifth orders:

$$W = 6\pi^2 N \chi_a^{(3)} \chi_a'^{(3)} / n_3 \lambda_1 \chi_a^{(5)}.$$

For $N = 10^{17}$ atom/cm^3, $\lambda_1 = 1.06 \times 10^{-4}$ cm, and the above-cited values of $\chi_a^{(3)}$, $\chi_a'^{(3)}$, and $\chi_a^{(5)}$ we obtain $W = 6.02$ cm^{-1}. For weak focusing $q_1 < 1$, and the maximum fifth-harmonic power is obtained for phase-matching conditions $\Delta_{13} = \Delta_{15} = 0$. Then the integrals in (32) may be performed to give

$$J_1 = \frac{6 - 8q_1^2(1 - 3d + 3d^2) - i12q_1(1 - 2d) - i6WL(1 - i2q_1 d)(1 - i2q_1 + i2q_1 d)}{3(1 + i2q_1 d)^3 (1 - i2q_1(1 - d))^3}. \tag{34}$$

At $d = \frac{1}{2}$, the function J_1 reaches the maximum values for both its integrals:

$$J_1 = 2(1 - q_1^3/3 - iWL(1 + q_1^2))/(1 + q_1^2)^3.$$

With strong focusing, $q_1 > 1$ because of the phase shift in the waist region for optimum conversion efficiency some wavevector mismatch Δ_{jk} should be introduced to compensate for this shift. Before evaluation of (32), some analytical approximations are possible. Here we will discuss the case when $d = \frac{1}{2}$, e.g., the focal spot is in the center of the cell.

If $\chi^{(3)} = \chi'^{(3)} = 0$ only direct FHG exists and $J_1 \equiv J_d$. For infinitely tight focusing, J_d reaches its maximum at $\Delta_{15} = 6/b_1$ [12]. $|J_d|^2$ as a function of $\Delta_{15}L/2$ is plotted in Fig. 8 for $q_1 = 20$. The optimum value for $\Delta_{15}L/2 = 19\pi$ corresponds to $\Delta_{15} \simeq 6/b_1$.

When step processes are taken into account the value of J_1 depends on J_s and W. Some consideration of the behavior of J_s will be given. J_s can be presented as a complex number:

$$J_s(\Delta_{135}L/2, \Delta_{13}L/2, q_1) = \text{Re}\, J_s + i\, \text{Im}\, J_s.$$

As seen from (32) the product $WL\, \text{Im}\, J_s$ is added to J_d and, depending on the signs, the sum should be $J_d \pm |WL\, \text{Im}\, J_s|$. It is easy to prove that the real part can be presented as ($d = \frac{1}{2}$):

$$\text{Re}\, J_s = \frac{1}{2} \int_{-1}^{1} \frac{\exp(-i\Delta_{135}\eta)\, d\eta}{(1 - iq_1\eta)^2} \int_{-1}^{1} \frac{\exp(-i\Delta_{13}\tau)\, d\tau}{(1 - iq_1\tau)^2} \tag{35}$$

and, making the substitution $x = yq_1$, we obtain for an infinite medium

$$\text{Re}\, J_s = \frac{1}{2} \int_{-\infty}^{\infty} \frac{\exp(-i\Delta_{135}b_1 x/2)\, dx}{(1 - ix)^2} \cdot \int_{-\infty}^{\infty} \frac{\exp(-i\Delta_{13}b_1 y/2)\, dy}{(1 - iy)^2}$$

$$= \tfrac{1}{2}\pi^2 b_1^2 \Delta_{13}\Delta_{135} \exp(-b_1\Delta_{15}/2), \Delta_{135} > 0, \cdot \Delta_{13} > 0.$$

$$= 0, \Delta_{135} \leqslant 0, \Delta_{13} \leqslant 0; \quad \text{or} \quad \Delta_{135} \leqslant 0; \quad \text{or} \quad \Delta_{13} \leqslant 0. \tag{36}$$

The maximum value of $\text{Re}\, J_s$ is obtained when $\Delta_{13} = \Delta_{135} = 2/b_1$ which corresponds to $\Delta_{15} = 2\Delta_{13} = 4/b_1$. For tight focusing, $\text{Re}\, J_s$ is negligible when $\Delta_{13} \leqslant 0$. This is the case for a mixture of an inert gas and Cd, Zn, or Mg. Δ_{13} is positive for a mixture of an inert gas and an alkali metal.

We did not succeed in finding a simple enough analytical approximation for the function $\text{Im}\, J_s$. However to obtain a qualitative estimation, the following procedure was adopted. For $d = \frac{1}{2}$, $q_1 = 20$, the integral J_s was numerically calculated using the same technique as for integral (19). Sets of points were found in the plane $(\Delta_{135}L/2, \Delta_{13}L/2)$ with the interval be-

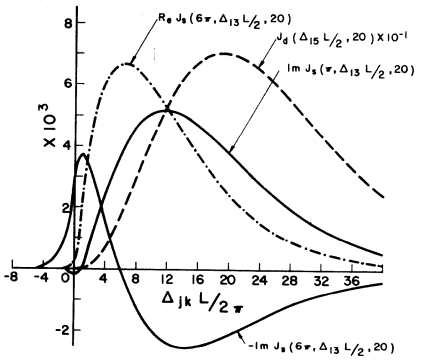


Fig. 8. Functions $J_d(\Delta_{15}L/2, 20)$, Im $J_s(6\pi, \Delta_{13}L/2, 20)$, Im $J_s(\pi, \Delta_{13}L/2, 20)$, and Re $J_s(6\pi, \Delta_{13}L/2, 20)$ versus wave-vector mismatch Δ_{jk}.

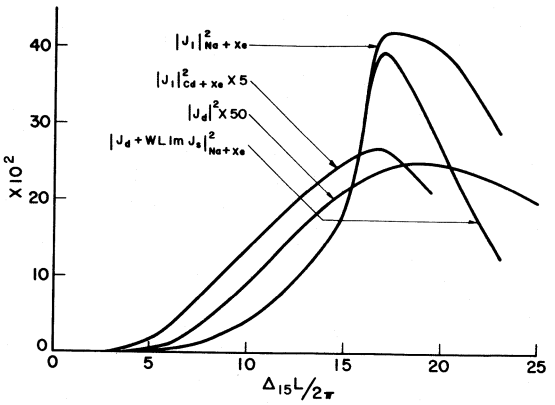


Fig. 9. Optimization of FHG power represented by $|J_1(\Delta_{15}L/2, \Delta_{13}L/2, 20)|^2$ as a function of Δ_{15} for mixture of Na + Xe and Cd + Xe. Functions $|J_d + WL \text{ Im } I_s|^2_{Na+Xe}$ and $|J_d|^2_{Na+Xe}$ are presented for comparison.

tween them $\delta(\Delta_{135}L/2) = \delta(\Delta_{13}L/2) = \pi/2$. Some of the most interesting results are shown in Fig. 8. The behavior of Re J_s corresponds to the analytical approximation obtained above. $(\text{Re } J_s)_{max}$ is achieved at $\Delta_{13}L/2 = \Delta_{135}L/2 = 6\pi$. The calculated value of $(\text{Re } J_s)_{max}$ is 0.37 percent less than the maximum analytical value derived from (36) at $\Delta_{13} = \Delta_{135} = 2/b_1$. In an area where Δ_{13} or Δ_{135} or both of them are negative, Re I_s has periodic positive and negative values and is at least three orders of magnitude less than its maximum value.

The investigation of Im I_s shows that the plane $(\Delta_{135}L/2, \Delta_{13}L/2)$ can be divided into three areas:

1) That area defined by inequalities $\Delta_{135} > 0$ and $|\Delta_{13}| < \Delta_{135}$. In this area Im $J_s < 0$ and reaches its maximum value at the point $\Delta_{135}L/2 = 12\pi$, $\Delta_{13}L/2 = \pi$. Im J_s as a function of $\Delta_{13}L/2$ at $\Delta_{135}L/2 = \pi$ and $\Delta_{135}L/2 = 6\pi$ is shown in Fig. 8.

2) That area defined by inequalities $\Delta_{13} > 0$ and $|\Delta_{135}| < \Delta_{13}$. In this area Im $J_s > 0$ and reaches its maximum at the point $\Delta_{135}L/2 = \pi$, $\Delta_{13}L/2 = 12\pi$. The areas 1) and 2) are divided by the diagonal $\Delta_{13} = \Delta_{135}$ on which Im $J_3 = 0$ (Fig. 8). The values of Im J_s in these two areas are symmetric and

$$[\text{Im } J_s(\Delta_{135}L/2, \Delta_{13}L/2)]_1 = -[\text{Im } J_s(\Delta_{13}L/2, \Delta_{135}L/2)]_2.$$

3) The rest of the $(\Delta_{135}L/2, \Delta_{13}L/2)$ plane is the third area where Im J_s is changing its sign with variations of the variables and its absolute value is at least three orders of magnitude less than $(\text{Im } J_s)_{max}$. Other calculations for different q_1 between 10 and 20 show the same behavior. They also permit us to conclude that Im $J_s(\Delta_{135}L/2, \Delta_{13}L/2)$ has a maximum absolute value at the points $(\Delta_{135}L/2 = \pi, \Delta_{13}L/2 = 4/b_1)$ and $(\Delta_{135}L/2 = 4/b_1, \Delta_{13}L/2 = \pi)$. Some use of this behavior of Re J_s and Im J_s may be exploited when the measurement of $\chi^{(5)}$ is performed.

When J_1 is calculated as a function of Δ_{15} (or Δ_{13}) for a specific mixture it should be noted that for every given value of Δ_{15} there is a corresponding exact value of Δ_{13} defined by the dispersion law of the nonlinear medium. To achieve some independence between Δ_{15} and Δ_{13} it is necessary to use a multicomponent gaseous mixture. However, such an approach would involve further practical problems.

The functions $|J_d|^2$, $|J_1|^2$, and $|J_d + WL \text{ Im } J_s|^2$ versus $\Delta_{15}L/2$ for a mixture of Na + Xe are plotted in Fig. 9. For this mixture $\Delta_{13} > 0$ when $\Delta_{15} > 0$ and Im $J_s > 0$. In the same figure, $|J_1|^2$ for Cd + Xe is plotted, for which $\Delta_{13} < 0$ and $\Delta_{15} > 0$. In this case Re $J_s = 0$ and Im $J_s < 0$. Because of the different sign of Δ_{13} the ratio

$$|J_1|^2_{Na+Xe}/|J_1|^2_{Cd+Xe} \simeq 8$$

while

$$|\text{Im } J_s|^2_{Na+Xe}/|\text{Im } J_s|^2_{Cd+Xe} \simeq 2$$

in their maxima. For both mixtures $W = 6.02$ cm^{-1} and $L = 20$ cm were adopted. With this value of W the fifth harmonic resulting from the step processes is greater than that from the direct process. Hence the maximum of $|J_1|^2$ moves towards lower $\Delta_{15}L/2$ values. The accuracy of these curves is less than that in the other figures because of the step calculations.

V. Summary

In this paper we have discussed the theory of the most promising schemes for FHG of powerful laser radiation. The plane-wave approximation has been applied to the cascade process and also to the scheme employing media with third- and fifth-order susceptibilities, to estimate the maximum conversion efficiency. Comparable efficiencies were found for both schemes.

Expressions for the signal amplitude and the power for four-wave nonlinear processes in Gaussian beams with arbitrary confocal parameters and waist locations have been derived. In the case of FHG, maximum output from the mixing step is obtained for equal confocal parameters of all the interaction beams. Thus a practical system should have a simple arrangement since SHG and THG are also optimized at equal confocal parameters. The analysis of FHG with a focused beam in a nonlinear media with third- and fifth-order susceptibility shows that consideration of interference between step-wise and direct processes is important for fifth-harmonic efficiency. For numerical estimation of various processes more data are neces-

sary, especially the nonlinear susceptibilities. A two-photon resonance will provide substantial enhancement in all nonlinear susceptibilities involved and consequently increase the conversion efficiency of the system.

Finally we note that these results are applicable to FHG with IR lasers using molecular gases as nonlinear media [22], [23]. The relatively weaker dispersion in the IR may pose less technical problems to achieve multistep phase matching.

Acknowledgment

The authors wish to thank J. Curley and R. Fedosejevs for their assistance in the preparation of the numerical programs used in this study.

References

[1] S. E. Harris, J. F. Young, A. H. Kung, D. M. Bloom, and G. C. Bjorklund, "Generation of ultraviolet and vacuum ultraviolet radiation," in *Laser Spectroscopy*, R. G. Brewer and A. Mooradian, Ed. New York: Plenum, 1973, pp. 59-75; see also references.

[2] D. M. Bloom, G. W. Bekkers, J. F. Young, and S. E. Harris, "Third harmonic generation on phase-matched alkali metal vapors," *Appl. Phys. Lett.*, vol. 26, pp. 687-689, 1975.

[3] D. M. Bloom, J. E. Young, and S. E. Harris, "Mixed metal vapor phase matching for third-harmonic generation," *Appl. Phys. Lett.*, vol. 27, pp. 390-392, 1975.

[4] S. E. Harris, "Generation of vacuum-ultraviolet and soft-x-ray radiation using high-order nonlinear optical polarizabilities," *Phys. Rev. Lett.*, vol. 31, pp. 341-344, 1973.

[5] E. Yablonovitch, C. Flytzanis, and N. Bloembergen, "Anisotropic interference of three-wave and double two-wave frequency mixing in GaAs," *Phys. Rev. Lett.*, vol. 29, pp. 865-868, 1972.

[6] a) S. A. Akhmanov *et al.*, "Direct and cascade processes in higher optical harmonic generation," in *Abstracts 7th All-Union Conf. Coherent and Nonlinear Optics* (Tashkent, USSR, May, 1974), Moscow, USSR: Moscow State Univ. Press, pp. 15-17. b) S. A. Akhmanov, A. N. Dubovik, S. M. Saltiel, I. V. Tomov, and V. G. Tunkin, "Nonlinear optical effects of fourth order in the field in a lithium formiate crystal," *ZhETF Pis. Red.*, vol. 20, pp. 264-268, 1974 (*JETP Lett.*, vol. 20, pp. 117-118, 1974).

[7] A. G. Akmanov *et al.* "Generation of coherent radiation at $\lambda = 2120$ Å by cascade frequency conversion," *ZhETF Pis. Red.*, vol. 10, pp. 244-249, 1969 (*JETP Lett.*, vol. 10, pp. 154-157, 1969).

[8] S. G. Dinev, K. V. Stamenov, and I. V. Tomov, "Generation of tunable UV radiation in the range 216-237 nm," *Optics Commun.*, vol. 5, pp. 419-421, 1972.

[9] V. G. Tunkin, T. Usmanov, and V. A. Shakizov, "Generation of fifth picosecond laser harmonic," *Kvantovaya Electronica*, vol. 11, pp. 117-118, 1972 (*Sov. J. Quant. Electron.*, vol. 2, pp. 487-488, 1973).

[10] C. R. Vidal and M. M. Hessel, "Heat-pipe oven for homogeneous mixtures of saturated and unsaturated vapors: Application to NaLi," *J. Appl. Phys.*, vol. 43, pp. 2776-2780, 1972.

[11] M. M. Hessel and T. B. Lucatorto, "The rotating heat-pipe oven: A universal device for the containment of atomic and molecular vapors," *Rev. Sci. Instrum.*, vol. 44, pp. 561-561, 1973.

[12] Laser Program Ann. Rep., Lawrence Livermore Laboratory, Univ. California, Livermore, CA, UCRL-50021-74, p. 282, 1974.

[13] J. A. Armstrong, N. Bloembergen, J. Ducuing, and P. S. Pershan, "Interactions between light waves in a nonlinear dielectric," *Phys. Rev.*, vol. 127, pp. 1918-1939, 1962.

[14] G. D. Boyd and D. A. Kleinman, "Parametric interaction of focused Gaussian light beams," *J. Appl. Phys.*, vol. 39, pp. 3597-3639, 1968.

[15] J. F. Ward and G. H. C. New, "Optical third harmonic generation in gases by a focused laser beam," *Phys. Rev.*, vol. 185, pp. 57-72, 1969.

[16] A. P. Sukhorukov and I. V. Tomov, "Wave pattern of third optical harmonic generation in isotropic and anisotropic media," *ZhETF*, vol. 58, pp. 1626-1639, 1970 (*Sov. Phys. JETP*, vol. 31, pp. 872-879, 1970).

[17] R. B. Miles and S. E. Harris, "Optical third harmonic generation in alkali metal vapors," *IEEE J. Quantum Electron.*, vol. QE-9, pp. 420-483, 1973.

[18] G. C. Bjorklund, "Effects of focusing on third-order nonlinear processes in isotropic media," *IEEE J. Quantum Electron.*, vol. QE-11, pp. 287-296, 1975.

[19] F. Abramovici, "The accurate calculation of Fourier integrals by the fast Fourier transform technique," *J. Comput. Phys.*, vol. 11, pp. 28-37, 1973.

[20] H. Eicher, "Third-order susceptibility of alkali metal vapors," *IEEE J. Quantum Electron.*, vol. QE-11, pp. 121-130, 1975.

[21] V. M. Mitev and I. V. Tomov, "Nonlinear susceptibility of the fifth-order of alkali metal vapors," presented at the Second Nat. Conf. Young Physicists, Sofia, Bulgaria, Apr. 1974.

[22] Y. Ueda and K. Shimoda, "Optical third harmonic generation by molecular vibration," *J. Phys. Soc. Japan*, vol. 28, pp. 196-207, 1970.

[23] C. Y. She and K. W. Billman, "Infrared-pumped third-harmonic and sum-frequency generation in diatomic molecules," *Appl. Phys. Lett.*, vol. 27, pp. 76-79, 1975.

[24] W. L. Wiese, A. W. Smith, and B. M. Miles, *Atomic Transition Probabilities*, vol. 2. NSRDS-NBS 22, 1969 (sodium through calcium).

[25] W. R. Newell, K. J. Ross, and J. B. Wickes, *J. Phys. B: Atom. Molec. Phys.*, vol. 4, pp. 684-689, 1971.

[26] C. J. Mitchell, *J. Phys. B: Atom. Molec. Phys.*, vol. 8, pp. 25-30, 1975.

[27] W. R. Newell, K. J. Ross, *J. Phys. B: Atom. Molec. Phys.*, vol. 5, pp. 701-709, 1972.

Antisymmetric Taper of Distributed Feedback Lasers

HERMANN A. HAUS, FELLOW, IEEE, AND CHARLES V. SHANK

Abstract—**In a distributed feedback (DFB) laser with spatial index modulation, an antisymmetric taper of the feedback parameter, κ, removes the threshold degeneracy, which is characteristic of uniform structures, and leads to one mode of particularly low threshold. Exact solutions are presented for the special case of an antisymmetric step of κ. An approximate perturbation method is developed which gives simple expressions for the threshold gains, and external Q's of some tapered distributed feedback structures. The method is tested against two exact solutions, the uniform, and the stepped-κ DFB laser. It is shown that the threshold of the stepped-κ DFB laser is the lowest of any structure with an antisymmetric taper and a prescribed maximum value of $|\kappa|$.**

I. Introduction

THE distributed feedback (DFB) laser proposed and realized by Kogelnik and Shank [1], [2] utilizes the Bragg reflection off a spatially periodic variation of index, gain coefficient, or guide thickness. Numerous other realizations of DFB lasers have been reported in the literature [3]-[7]. DFB structures have the advantage of providing better frequency stability of the mode of oscillation than cavities formed by partially transmitting mirrors at the ends of the structure.

Periodic structures with DFB have other applications. Bandpass transmission and reflection filters may be constructed using passive structures that utilize Bragg reflection [8], [9]. The reflection filter formed by such a structure is the equivalent of a mirror reflecting a band of frequencies. In surface acoustic applications [10]-[12] such "mirrors" are utilized to build high-Q cavities.

The range of application of the DFB principle motivates a study of variation of the DFB design with the purpose of achieving certain design objectives. The work reported here was initiated to achieve one particular objective. The mode spectrum of the DFB laser with index coupling as analyzed by Kogelnik and Shank [1] exhibits a gap at a "center" frequency. Modes of equal threshold occur symmetrically on the two sides of this gap. This threshold degeneracy is a disadvantage in practical applications in which single-mode operation at a predictable frequency is desired. The present work shows that tapering of the coupling coefficient or the period of the structure, which offers new degrees of design freedom, may be utilized to remove the threshold degeneracy. This is achieved with an antisymmetric taper of the periodic index (or guide height) modulation. One special case of such a taper is shown to be the insertion of a quarter-wave section between two equal uniform DFB structures. This insertion makes possible a mode of the structure within the stopband of the uniform sections. The field of the mode decays exponentially from the quarter-wave section at the center of the structure into the DFB structures on the two sides. This particular mode possesses an external Q, which can be much higher than that of the uniform structure with the same κL, where κ is the feedback parameter of Kogelnik and Shank [1], and L is the combined length of the two structures. It is a property of all structures with an antisymmetric taper of κ that they suppo[rt] a mode at the center frequency of the local stopbands. This mode has a particularly low threshold when used in a laser cavity. When the structure is used as a transmission filter, this mode is responsible for a particularly narrow transmission band.

The analysis of tapered structures can be quite complicated. Hence an effort was made to glean all essential characteristics of the tapered structure from an approximate analytic approach. The main goal of this paper is to present this approach which greatly facilitates the visualization of modes in distributed feedback structures.

In Section II we review briefly the equations of the distributed feedback laser and outline ways of producing "tapers" in the structure. We show that structures with antisymmetric tapers of κ and the Bragg parameter δ have a determinantal equation which permits modes at that frequency at which the Bragg condition is satisfied at the center of the structure. The resonance frequency of this solution is, therefore, independent of the length of the structure. As an example, we consider a special case of an antisymmetric taper, the step in $\kappa(z)$ and $\delta(z)$. Exact solutions are obtained for the thresholds and resonance frequencies of the modes of the structure.

In Section III we develop a perturbation analysis which leads to an approximate determination of thresholds and resonance frequencies. The perturbation formulas can also be used to estimate the effect upon the mode frequencies of uncontrollable perturbations of the system parameters. We test the perturbation approach against the exact analysis of the uniform DFB laser. In Section IV we present an approximate analysis of the stepped-κ structure and develop closed-form expressions for the external Q and threshold gain. In Section V we analyze a structure with a rather general antisymmetric taper of κ and δ. We prove that the stepped-κ structure gives the lowest threshold for a given maximum value of $|\kappa(z)|$. Finally, in Section VI we study the effect of uncontrollable index perturbations upon the resonance frequencies of the modes.

II. The Tapered Structure

In this section we set up the basic equations for a tapered DFB structure. We then demonstrate that a structure with an antisymmetric taper of the feedback parameter κ and the

Manuscript received January 22, 1976.

H. A. Haus was on leave at Bell Laboratories, Holmdel, NJ 07733. He is with the Department of Electrical Engineering and Computer Science and the Research Laboratory of Electronics, Massachusetts Institute of Technology, Cambridge, MA 02139.

C. V. Shank is with Bell Laboratories, Holmdel, NJ 07733.

Bragg frequency parameter δ can support a mode at a frequency within the local stopbands of the tapered structure. We apply the analysis of a structure of stepped κ and δ.

The fundamental equations of the DFB laser are [1]

$$-R' + (\alpha - j\delta) R = j\kappa S \tag{1}$$

$$S' + (\alpha - j\delta) S = j\kappa^* R. \tag{2}$$

Here α is the gain constant and δ is the "Bragg parameter" indicating deviation of the propagation constant $\beta(>0)$ from the Bragg condition

$$\delta = \beta - \frac{\pi}{\Lambda} \tag{3}$$

where Λ is the spatial period of the feedback "corrugation," and κ is the feedback parameter [1]. The condition $\delta = 0$ defines the center frequency of the "stopband." If Λ is a function of position, then the center frequency of the stopband is also a function of position.

A taper of κ is produced by variation in the height and period of the spatial index variation. A taper of δ is produced by a spatial variation of the phase velocity or by making $1/\Lambda$ depend on z. The second condition leads to analytically simpler results and hence we shall assume this to be the case. We shall show that a taper of δ is, in general, not helpful and hence the use of the simplest analytic form of a taper of δ is justified. Taking a perturbation of (3) from a frequency ω_0 to a frequency $\omega = \omega_0 + \Delta\omega$, one has

$$\delta(z) = \delta_0(z) + \frac{\Delta\omega}{v_g} \tag{4}$$

where $\delta_0(z) = \beta_0 - \pi/\Lambda$, the Bragg parameter at the frequency ω_0, and in this paper will be assumed to be antisymmetric, $\delta_0(z) = -\delta_0(-z)$. The frequency dependence of κ is usually too weak to matter.

We may derive differential equations for R and S by themselves through differentiation of (1) and (2) and elimination of S or R, respectively,

$$-R'' + \frac{\kappa'}{\kappa} R' + \left[|\kappa|^2 + (\alpha - j\delta)^2 - \frac{\kappa'(\alpha - j\delta) - (\alpha - j\delta)'\kappa}{\kappa} \right] R = 0 \tag{5}$$

and analogously for S

$$-S'' + \left(\frac{\kappa'}{\kappa}\right)^* S' + \left[|\kappa|^2 + (\alpha - j\delta)^2 + \frac{\kappa^{*\prime}(\alpha - j\delta) - (\alpha - j\delta)'\kappa^*}{\kappa^*} \right] S = 0. \tag{6}$$

Note that, according to (4), $\delta(z)$ is antisymmetric at only one frequency, the center frequency of the local stopband at the symmetry plane of the structure at $z = 0$. If the frequency differs from the center frequency, a z-independent contribution has to be added to $\delta_0(z)$, and $\delta(z)$ ceases to be antisymmetric. Denote one solution of (5) by $r(z)$. Now, $r(z)$ has associated with it a very specific dependence of the S-wave. Using (1) one has

$$S = \frac{1}{j\kappa} \{-r'(z) + (\alpha - j\delta) r(z)\}. \tag{7}$$

Denote an independent solution of (6) by $s(z)$ [i.e., $s(z)$ must not be related to $r(z)$ by (2)]. The z-dependence of the R-wave associated with the $s(z)$ solution follows from (2):

$$R = \frac{1}{j\kappa^*} \{s'(z) + (\alpha - j\delta) s(z)\}. \tag{8}$$

The general solution is a linear superposition

$$R(z) = Ar(z) + B \frac{1}{j\kappa^*} [s'(z) + (\alpha - j\delta) s(z)] \tag{9}$$

$$S(z) = A \frac{1}{j\kappa} [-r'(z) + (\alpha - j\delta) r(z)] + Bs(z). \tag{10}$$

The boundary conditions are

$$R\left(-\frac{L}{2}\right) = S\left(\frac{L}{2}\right) = 0. \tag{11}$$

They give two homogeneous linear equations in A and B whose determinant must vanish. Using (7)-(11) one obtains the determinantal equation

$$\kappa^*\left(-\frac{L}{2}\right) \kappa\left(\frac{L}{2}\right) r\left(-\frac{L}{2}\right) s\left(\frac{L}{2}\right) + [s' + (\alpha - j\delta) s]_{z=-L/2} \cdot [-r' + (\alpha - j\delta) r]_{z=L/2} = 0. \tag{12}$$

This is the determinantal equation determining the threshold gain α (assuming that α is uniform). The determinantal equation assumes a particularly simple form when $\delta(z)$ is antisymmetric, $\Delta\omega = 0$ and $\delta(z) = \delta_0(z)$. Given that $r(z)$ is a solution of (5), one can show that $s(z) = r^*(-z)$ is a solution of (6). This follows from (5) by replacing $z \to -z$, by using the antisymmetries of $\kappa(z)$ and $\delta(z)$ and taking the complex conjugate of the result. One obtains (6) with $r^*(-z)$ playing the role of s. This solution is independent of $r(z)$ in the sense defined earlier. Using the fact that $s(z) = r^*(-z)$ is a solution, introducing it into (12), and using the antisymmetry of $\delta(z)$ one obtains

$$\left|\kappa\left(\frac{L}{2}\right)\right|^2 \left|r\left(-\frac{L}{2}\right)\right|^2 - \left|-r'\left(\frac{L}{2}\right) + \left[\alpha - j\delta\left(\frac{L}{2}\right)\right] r\left(\frac{L}{2}\right)\right|^2 = 0. \tag{13}$$

The determinantal equation is *real* and hence, for a given L, can be satisfied by the choice of the *single* parameter α.

Therefore, a mode can exist at this particular frequency. Whether a solution is actually found depends upon whether the left-hand side of (13) ever crosses zero as α is raised from zero. The best way of demonstrating the existence of solutions is to look at special cases. We consider the special case of an antisymmetric taper of κ and δ, an antisymmetric step.

An antisymmetric step of κ is produced by a sign change of κ as one passes from one side of the discontinuity to the other side. We recall that κ has a reference phase that is a constant in a uniform structure. If a uniform DFB structure is cut in its

middle, a section of length equal to one half-wavelength of the corrugation removed, and then the two sections recombined, one has changed the phase of κ by 180° as one passes from one side of the structure to the other side. Another way of realizing the same effect is to produce an additional phase shift of $\pi/2$ in each of the forward and backward traveling waves, R and S. This can be done conveniently by a change of thickness of the optical guide over a length short compared with the total length of the structure. The discontinuity of the structure now allows a discontinuity of the slope of R and S.

In addition to a discontinuity of κ one may also introduce a discontinuity of δ, by, for example, stepping the spatial period Λ from one side of the structure (+ side) to the other (- side). At a particular frequency one will then have $\delta_+ = -\delta_-$ on the (+) and (-) sides of the junction.

The dispersion relation is

$$\gamma_\pm^2 = |\kappa|^2 + (\alpha - j\delta_\pm)^2 \tag{14}$$

which follows directly from (1) and (2) for the solutions on the two sides of the symmetry plane. A convenient solution for $r(z)$, which satisfies the continuity of forward and backward waves at $z = 0$, is

$$\begin{aligned} r(z) &= \sinh \gamma_+ z \qquad z > 0 \\ &= -(\gamma_+/\gamma_-) \sinh \gamma_- z \qquad z < 0. \end{aligned} \tag{15}$$

A solution for $s(z)$ is, alternately,

$$\begin{aligned} s(z) &= \sinh \gamma_+ z, \qquad z > 0 \\ &= -(\gamma_+/\gamma_-) \sinh \gamma_- z, \qquad z < 0. \end{aligned} \tag{16}$$

Introducing (15) into (13) one obtains

$$\left[-\gamma_- \coth \gamma_- \frac{L}{2} + (\alpha - j\delta_-)\right]\left[-\gamma_+ \coth \gamma_+ \frac{L}{2} + (\alpha - j\delta_+)\right] = |\kappa_+|^2. \tag{17}$$

Fig. 1 shows solutions of the determinantal equation (17) for the central mode, $\delta_+ = -\delta_-$, for different values of

$$D \equiv \left|\frac{\delta_+}{\kappa}\right| = \left|\frac{\delta_-}{\kappa}\right| \tag{18}$$

a measure of the Bragg-parameter discontinuity.

One may note the exponential decrease of the threshold gain with increase of $|\kappa|\, L/2$. Also note that the threshold gain is lowest when $D = 0$, i.e., there is no step in the Bragg parameter. In this case the mode of interest is at the center of the stopbands of both guides. The decay of the fields from the center of the structure is fastest in this case, leading to the lowest value of power escaping from the structure for a given average intensity in the structure. Fig. 2 shows the threshold gains and the frequency spacings for the different modes of the stepped-κ structure for different values of $|\kappa L|/2$. The center mode remains at $\Delta\omega = 0$ for any value of $|\kappa L|$.

Fig. 3 shows the spectrum of modes of a stepped structure with $D = 0$ and, for comparison, that of a uniform structure. Both structures are of the same overall length L, and have

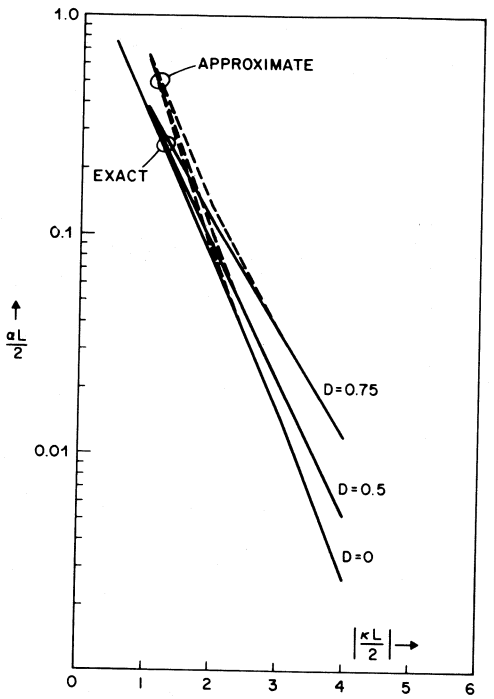


Fig. 1. A plot of the threshold gain versus DFB coupling parameter for stepped-κ and δ structure.

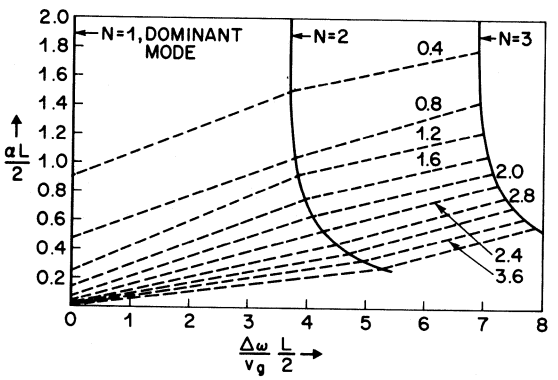


Fig. 2. Gain coefficients versus frequency deviations, with DFB coupling as parameter for stepped-κ structure.

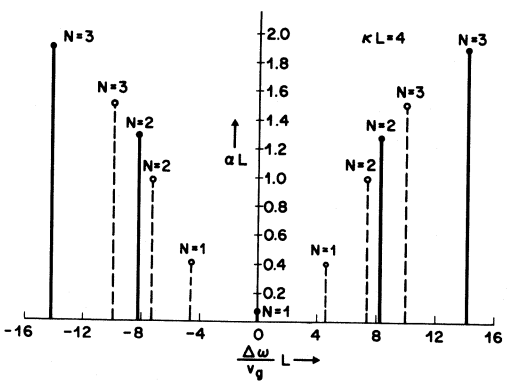


Fig. 3. The spectra of modes and their thresholds for the stepped-κ and uniform structures.

$\kappa|L| = 4$ (the value chosen in [2, Fig. 5]). It is immediately apparent that the stepped-κ structure has no threshold degeneracy, as well as a much better threshold discrimination between the fundamental mode and the first higher order mode. Also, one may note that the frequency separation between the dominant mode and the first higher order mode of the stepped structure is much greater than that of the uniform structure. In [13], the same structure was investigated, with the same conclusions. In the sequel the analysis is extended to cover general antisymmetric tapers.

III. A Perturbation Approach

In the preceding section we have shown that a structure with antisymmetric tapers of $\kappa(z)$ and $\delta(z)$ can possess a mode at the center frequency, at which $\delta(z)$ is antisymmetric. We have analyzed a special case of an antisymmetric taper and showed that such a center mode indeed exists and is characterized by an exceptionally low threshold.

It is possible to analyze other structures by computer, using the determinantal equation (13) for the modes at the center frequency, and (12) at other frequencies. This paper presents instead a perturbation approach, which provides physical insight into the behavior of tapered structures. The approach is analogous to the usual perturbation analysis of electromagnetic fields in cavities starting from Maxwell's equations in the absence of loss or gain.

The zeroth-order solutions R_0 and S_0 are defined as the solutions of (1) and (2) at some specific frequency, i.e., specific $\delta = \delta_0$, in the absence of gain.

$$-R_0' - j\delta_0 R_0 - j\kappa S_0 = 0 \tag{19}$$

$$S_0' - j\delta_0 S_0 - j\kappa^* R_0 = 0. \tag{20}$$

Now construct a perturbed solution, $R_0 + \Delta R$ and $S_0 + \Delta S$ by changing δ_0 to $\delta_0 + \Delta\delta$, κ to $\kappa + \Delta\kappa$ and α from zero to α. The perturbation obeys the equations

$$-\Delta R' - j\delta_0 \Delta R - j\kappa \Delta S = -(\alpha - j\Delta\delta) R_0 + j\Delta\kappa S_0 \tag{21}$$

$$\Delta S' - j\delta_0 \Delta S - j\kappa^* \Delta R = -(\alpha - j\Delta\delta) S_0 + j\Delta\kappa^* R_0. \tag{22}$$

The perturbations α, $\Delta\delta$, and $\Delta\kappa$ cause source terms in the equations for ΔR and ΔS which would be, otherwise, identical to the zeroth-order equations.

Note that $\Delta\delta$ plays two roles. Referring to (5), $\Delta\delta$ must be interpreted as

$$\Delta\delta = \Delta\delta_0(z) + \frac{\Delta\omega}{v_g} \tag{23}$$

a space-independent part expressing the frequency deviation, $\Delta\omega$, and a perturbation of $\delta_0(z)$ due to a perturbation of the spatial period Λ. We shall limit ourselves to the interpretation $\Delta\delta = \Delta\omega/v_g$ until Section VI, in which we discuss the effect of local perturbations in the spatial period.

By multiplying (21) by R_0^*, (22) by S_0^*, the complex conjugate of (19) by ΔR, the complex conjugate of (20) by ΔS, adding and integrating over the length of the structure from $z = z_0$ to $z = z_0 + L$, one obtains

$$-(R_0^* \Delta R - S_0^* \Delta S)\Big|_{z_0}^{z=z_0+L} = -\int_{z_0}^{z_0+L} dz\,(\alpha - j\Delta\delta) \cdot (|R_0|^2 + |S_0|^2) + j\int_{z_0}^{z_0+L} dz\,(\Delta\kappa S_0 R_0^* + \Delta\kappa^* S_0^* R_0). \tag{24}$$

This is the central equation for the perturbation analysis. To interpret equation (24) take as the zeroth-order solution the resonant transmission mode of the structure extending from $z_0 = -L/2$ to $z_0 = +L/2$. Consider the case when $\Delta\kappa = 0$. The net power escaping the structure,

$$|R_0|^2 - |S_0|^2\Big|_{z=-L/2}^{z=L/2},$$

is zero for this solution. The perturbation of the power is to first order

$$P_s = |R_0 + \Delta R|^2 - |S_0 + \Delta S|^2\Big|_{z_0}^{z_0+L} \cong 2\,\mathrm{Re}\,[R_0^* \Delta R - S_0^* \Delta S]\Big|_{z_0}^{z_0+L} \tag{25}$$

where P_s is now the power escaping the structure correct to first order in the perturbation. The real part of (24) gives (with $\Delta\kappa = 0$)

$$2\,\mathrm{Im}\,\frac{\Delta\omega}{\omega_0} = \frac{P_s - \int dz\, 2\alpha(|R_0|^2 + |S_0|^2)}{\omega_0/v_g \int dz\,(|R_0|^2 + |S_0|^2)}. \tag{26}$$

The rate of decay of the mode normalized to the resonance frequency ω_0 is equal to the difference between the power escaping the structure and the power generated in the structure divided by ω_0 times the energy storage. This is a well-known result and serves to define the Q's of the structure:

$$\frac{1}{Q_{\mathrm{ext}}} = \frac{P_s}{\omega_0 W} \tag{27}$$

and

$$\frac{1}{Q_\alpha} = \frac{\int dz\, 2\alpha(|R_0|^2 + |S_0|^2)}{\omega_0 W} \tag{28}$$

where the energy W is computed to zeroth order.

$$W = \frac{1}{v_g}\int (|R_0|^2 + |S_0|^2)\, dz. \tag{29}$$

If α is uniform along z, the threshold gain is evaluated from (26) with $\mathrm{Im}\,\Delta\omega = 0$:

$$\frac{1}{Q_\alpha} = \frac{2\alpha}{\omega_0/v_g} = \frac{1}{Q_{\mathrm{ext}}}. \tag{30}$$

Hence, the threshold gain is proportional to the inverse external Q of the resonant transmission mode.

In order to test the formalism, we present an approximate analysis of the uniform DFB laser of Kogelnik and Shank. The zeroth-order solution is the resonant mode of the structure used as a transmission cavity. This mode has $S_0 = 0$ at $z = \pm L/2$. Therefore

$$S_0 = A \cos \beta z \tag{31}$$

with

$$\beta = m \frac{\pi}{L} \tag{32}$$

where $m = 1$ for the lowest mode. Further

$$\beta^2 = \delta_0^2 - |\kappa|^2.$$

The R-wave is found from (20):

$$R_0 = -\frac{\delta_0}{\kappa^*} S_0 + jA \frac{\beta}{\kappa^*} \sin \beta z \tag{33}$$

Since $\beta \ll |\kappa|$ for a high-Q mode, the second term is much smaller than the first, and $|\delta_0/\kappa^*| \simeq 1$. Thus, $|R_0| \simeq |S_0|$. The inverse external Q of the resonant transmission mode is obtained from (27) to first order by the following argument. The energy in the structure follows from the zeroth-order solution, using (29) with $S_0 = A \cos \beta z \simeq R_0$. P_s is the power escaping the structure which is matched at both ends and excited with the mode of interest. The matches impose a node of S at $z = +L/2$ and a node of R at $z = -L/2$. From (1) we find the value of S, at a node of R:

$$S(-L/2) = \frac{j}{\kappa} \frac{dR}{dz}\bigg|_{z=-L/2} \tag{34}$$

and, correspondingly, the value of R at a node of S is from (2)

$$R(L/2) = -\frac{j}{\kappa^*} \frac{dS}{dz}\bigg|_{z=L/2}. \tag{35}$$

Since $R \simeq -S \simeq A \cos \beta z$, a good estimate of $|dS/dz|^2$ at $z = L/2$ is

$$\left|\frac{\beta A \sin \beta z}{\kappa}\right|^2 = \left|\frac{\beta A}{\kappa}\right|^2$$

and the same value is found for $|dR/dz|^2$ at $z = -L/2$. Thus

$$P_s = |S(-L/2)|^2 + |R(L/2)|^2 = 2 \frac{\beta^2 |A|^2}{|\kappa|^2} \tag{36}$$

and therefore

$$\frac{1}{Q_{\text{ext}}} = \frac{P_s}{\dfrac{\omega_0}{v_g} \displaystyle\int_{-L/2}^{L/2} dz \, (|R_0|^2 + |S_0|^2)}$$

$$= \frac{2|\beta|^2}{|\kappa|^2 (\omega_0/v_g) L} = \frac{2(m\pi)^2}{|\kappa L|^2 [(\omega_0/v_g) L]}. \tag{37}$$

The gain required to overcome the loss is obtained from (28):

$$\alpha L = \frac{m^2 \pi^2}{|\kappa L|^2}.$$

For $m = 1$, this is identical with [1, eq. (29)]. The threshold increases with increasing m, because the escaping power increases with $|\beta|^2$. The frequency of oscillation is equal to the resonance frequency of the cavity-filter-transmission. Thus, the mth frequency is given by

$$\frac{\omega_m - \omega_0}{v_g} L = \pm \sqrt{(\kappa L)^2 + m^2 \pi^2}.$$

The preceding analysis may be generalized to find solutions for the low-gain, high-Q limit of tapered DFB lasers.

1) One finds the equivalent high-Q cavity transmission mode which has a perfect standing-wave solution of R (or S) and a nonperfect standing wave of S (or R), with power entering and leaving the structure via S (or R).

2) The external Q of the actual structure, with S and R "escaping" at the two ends, is obtained from a perturbation analysis; at a node of R (or S)

$$|S|^2 \simeq |R_0'/\kappa|^2 \quad (\text{or } |R|^2 = |S_0'/\kappa|^2).$$

3) The threshold gain is determined from (30).

IV. The Step of κ and δ_0—Approximate Analysis

In order to further test the predictive power of the approximate analysis we apply the perturbation method of the preceding section to this particular structure and compare the results with those of the exact analysis. In the process we shall get a better understanding of the fields of the different modes, as well as a closed-form expression for the threshold gain.

The zeroth-order solution is obtained very simply by starting with the "lossless" mode with nodes of S at $z = \pm L/2$. Then

$$S_0 = \pm A \sinh \gamma \left(z \pm \frac{L}{2}\right) \quad \text{for} \quad z \lessgtr 0 \tag{38}$$

where

$$\gamma = |\kappa|$$

is the same on both sides. The R_0 which is associated with (38) is, according to (1) with $\delta_0 = 0$,

$$R_0 = \pm \frac{\gamma}{j\kappa^*} A \cosh \gamma \left(z \pm \frac{L}{2}\right), \quad z \lessgtr 0. \tag{39}$$

This R is continuous at $z = 0$, as it must be. Just as in the case of the uniform grating structure, the power escaping the structure is given by

$$P_s = \frac{2}{|\kappa|^2} |dS_0/dz|^2_{z=+L/2}.$$

From (27), (29), (30), and (38), and with $|R_0| \simeq |S_0|$ we obtain

$$\alpha L = \frac{|\kappa| L}{\sinh |\kappa| L - |\kappa| L}. \tag{40}$$

We can see that threshold *decreases exponentially* with increasing length. The external Q of the structure also increases exponentially with length; the structure becomes "uncoupled"

from the two end waveguides. The threshold condition (40) is shown dashed in Fig. 1.

The thresholds and frequencies of the higher order modes may be found equally simply. We consider only the case $D = 0$. Then "lossless" modes of the system are the higher order resonant transmission modes of the DFB structure used as a filter (compare the analysis in Section III). These modes can be shown to possess perfect standing wave solutions of R (or S), the transmitted power carried by the S-wave (or R-wave). The nodes are at $z = \pm L/2$ and at $z = 0$. Therefore, $\beta L/2 = m\pi$ for the mth-order mode, where $\beta = \sqrt{\delta^2 - |\kappa|^2}$. We find that

$$\alpha L = |2m\pi/\kappa L|^2. \tag{41}$$

The frequencies of the higher order modes are set by the condition $\beta L/2 = m\pi$ or

$$\frac{\omega_m - \omega_0}{v_g} L = \pm\sqrt{(2m\pi)^2 + (|\kappa|L)^2}. \tag{42}$$

The approximate frequencies and threshold values of (41) and (42) are shown in Fig. 4. Qualitatively, Fig. 4 reproduces Fig. 2. Quantitatively, the agreement is best for the lowest order mode, $N = 1$. For a given value of $|\kappa|L$, the agreement gets progressively worse the higher the order of the mode. This is to be expected, because the external Q's of the modes decrease with increasing mode number and an analysis based on a high-Q assumption is bound to fail as the Q become too small.

V. General Structures with Antisymmetric Taper

We shall now apply the approximate method of mode and threshold determination to structures with a more general antisymmetric taper. We shall demonstrate some general properties of the "lossless" high-Q mode solutions, and then obtain an expression for the Q_{ext} of these structures. Finally, we shall show that the stepped-κ structure has the highest Q_{ext} for a fixed maximum value of $|\kappa|$.

Equations (5) and (6) have simple solutions if the Wronskian $\kappa'\delta - \delta'\kappa$ vanishes. This is the case when $\delta(z)$ is proportional to $\kappa(z)$,

$$\delta(z) = D\kappa(z) \tag{43}$$

where D is a constant. Since $\delta(z)$ is a real quantity, we must limit ourselves to real values of $\kappa(z)$. Note, also, that (43) can hold only at one particular frequency, because a change of frequency changes δ, but not κ. We shall call this frequency the "center" frequency.

Equations (5) and (6), with $\alpha = 0$, can be solved by introducing the new variable

$$u \equiv \int_0^z \kappa\, dz. \tag{44}$$

Substituting (44) in (6), one has the simple differential equation

$$\frac{d^2S_0}{du^2} + (D^2 - 1)S_0 = 0. \tag{45}$$

One must satisfy the boundary condition $S_0 = 0$ at $z = L/2$ or at u equal to

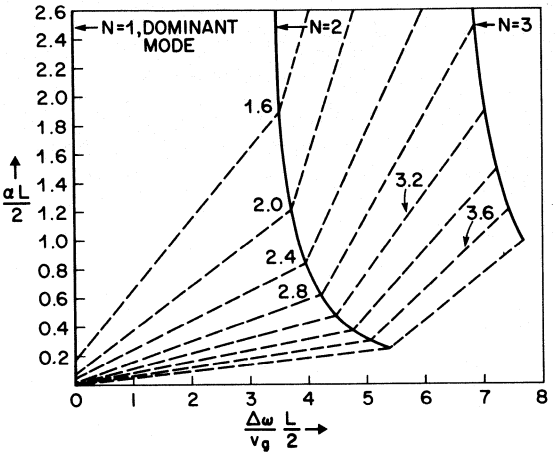


Fig. 4. The approximate gain coefficients versus frequency deviations with DFB coupling as parameter for stepped-κ structure.

$$u_0 = \int_0^{L/2} \kappa\, dz. \tag{46}$$

The solution is then

$$S_0 = A \sin\left[\sqrt{D^2 - 1}\,(u_0 - u)\right] \tag{47a}$$

for $D > 1$ and

$$S_0 = A \sinh\left[\sqrt{1 - D^2}\,(u_0 - u)\right] \tag{47b}$$

for $D < 1$.

If $\kappa(z)$ is a symmetric function of z, then u is an odd function of z. Matching the boundary conditions at $z = +L/2$ does not automatically imply a matching of the boundary condition at $z = -L/2$. Solution (47a) and (47b) must be set equal to zero at $u = -u_0$ as well. This is not possible when $D < 1$ and the hyperbolic solution applies. When $D > 1$ one must have

$$\sin\sqrt{1 - D^2}\,2u_0 = 0$$

or

$$2u_0 = m\pi(1 - D^2)^{-1/2}.$$

This condition can be met only by careful choice of system parameters. Hence a resonant mode at the "center" frequency (at which $\delta = 0$ at the center of the structure) is not automatically assured, i.e., the frequency of the central mode is not automatically selected by symmetry in terms of the fundamental parameters of the structure, *independent of the length* L.

If $\kappa(z)$ is antisymmetric, the solution is fundamentally different. Then $u(z)$ is an even function of z and matching the boundary conditions $S_0 = 0$ at $z = +L/2$, $u = u_0$, automatically satisfies the boundary condition at $z = -L/2$.

Consider first the case $D < 1$, solution (47b). The solution has a single maximum $A \sinh\sqrt{1 - D^2}\,u_0$ at $u = 0$, i.e., $z = 0$, and a solution is always found at this particular "center" frequency.

Next consider the case when $D > 1$. Then the sine functions must be taken. A solution is always found at this frequency but it does not necessarily have a single maximum. A single maximum is found only as long as

$$\sqrt{D^2-1}\int_0^{L/2}\kappa\,dz<\frac{\pi}{2}.$$

It is easy to show that the higher order modes have a spectrum symmetric around this frequency. For this purpose consider equation (6) with $\alpha=0$, κ-real, and introduce into it

$$\delta=D\kappa+\frac{\Delta\omega}{v_g}.$$

The result is, to first order in the perturbation,

$$-S_0''+\frac{\kappa'}{\kappa}S_0'+\left[\kappa^2-\left(D\kappa+\frac{\Delta\omega}{v_g}\right)^2-j\frac{\kappa'}{\kappa}\frac{\Delta\omega}{v_g}\right]S_0=0.$$

For any mode of a given complex $\Delta\omega=\Delta\omega_n$ the transformation $z\to -z$, $\Delta\omega_n\to-\Delta\omega_n^*$ and complex conjugation leads to an equation identical in form to the original equation, with $S_0^*(-z)$ playing the role of $S_0(z)$. Hence every mode at $\Delta\omega_n$ is paired with a mode at $-\Delta\omega_n^*$.

Next we study the dependence of $1/Q_{\text{ext}}$ on D and the taper of κ. We concentrate on the case of hyperbolic functions because it is the case with greatest Q_{ext}. Using the definition (27), the solutions (47b), the facts that according to (44) $dz=du/\kappa$, and that $|R|=|S_0'/\kappa|=|dS_0/du|=A$, we obtain

$$Q_{\text{ext}}=2\frac{\omega_0}{v_g}\int_0^{u_0}\frac{\sinh^2\sqrt{1-D^2}\,(u-u_0)}{1-D^2}\frac{du}{|\kappa|}. \tag{48}$$

Clearly, the integrand is the larger the smaller the value of D. The highest Q is achieved when $D=0$.

Next consider the dependence of Q_{ext} upon κ. Taking a perturbation of (48) with respect to $1/\kappa$, one has

$$\delta Q_{\text{ext}}=2\frac{\omega_0}{v_g}\left[-\int_0^{u_0}\delta u_0\frac{\sinh 2\sqrt{1-D^2}\,(u-u_0)}{\sqrt{1-D^2}}\frac{du}{|\kappa|}+\int_0^{u_0}\frac{\sinh^2\sqrt{1-D^2}\,(u-u_0)}{1-D^2}\delta\left(\frac{1}{|\kappa|}\right)du\right]. \tag{49}$$

Now from (44)

$$\int_0^{u_0}\frac{du}{|\kappa(u)|}=\frac{L}{2}$$

and thus

$$\frac{\delta u_0}{|\kappa(u_0)|}=-\int_0^{u_0}\delta\left(\frac{1}{|\kappa|}\right)du.$$

Using this relation in (49) and integrating the second term by parts, we obtain

$$\delta Q_{\text{ext}}=2\frac{\omega_0}{v_g}\left[\int_0^{u_0}-\frac{\sinh\left[2\sqrt{1-D^2}\,(u-u_0)\right]}{\sqrt{1-D^2}}\times\left\{-\left|\frac{\kappa(u_0)}{\kappa}\right|\int_0^{u_0}\delta\left(\frac{1}{|\kappa|}\right)du'-\int_0^{u}\delta\left(\frac{1}{|\kappa|}\right)du'\right\}du\right].$$

The term in wavy brackets is positive for any local $\delta(1/|\kappa|)<0$. The external Q increases with a local decrease of $(1/|\kappa|)$, or increase of $|\kappa|$, $\delta|\kappa|>0$. Therefore, $|\kappa|$ must be made as large as possible everywhere. The step function of κ yields the extremum value of Q_{ext} for a given maximum of $|\kappa|$.

These findings give some simple criteria for the construction of high-Q low-threshold laser structures.

1) In order to achieve a mode with a resonance frequency independent of the structure length one must use an antisymmetric taper of δ and κ.

2) The external Q is highest, the threshold gain lowest, when there is no taper of δ.

3) For any taper with a given maximum value of coupling coefficient κ, the antisymmetric step of κ gives the highest Q_{ext}, lowest threshold gain.

VI. Tolerances

The perturbation formula (24) serves as a convenient starting point to a study of tolerances required in a tapered structure. Suppose we have an error $\Delta\delta_0(z)$ and $\Delta\kappa(z)$ in the structure. The term $S_0^*\Delta S-R_0^*\Delta R$ involves amplitudes near the end of the structure and is small already (high Q); changes of S and R due to $\Delta\delta$ and $\Delta\kappa$ are affecting this term only to higher order and hence one may disregard it. There remains

$$\frac{\Delta\omega}{v_g}=-\frac{\int\Delta\delta_0(|R_0|^2+|S_0|^2)\,dz}{\int(|R_0|^2+|S_0|^2)\,dz}-\frac{\int(\Delta\kappa S_0R_0^*+\Delta\kappa^*S_0^*R_0)\,dz}{\int(|R_0|^2+|S_0|^2)\,dz}. \tag{50}$$

If the error is to be unimportant, then $\Delta\omega$ must be much less than the mode spacing, which is of the order of

$$\frac{\Delta\omega_m}{v_g}\frac{L}{2}\simeq\pi.$$

Thus we require that

$$\left|\frac{\int\Delta\delta_0(|R_0|^2+|S_0|^2)\,dz+\int(\Delta\kappa S_0R_0^*+\Delta\kappa^*S_0^*R_0)\,dz}{\int(|R_0|^2+|S_0|^2)\,dz}\right|\ll\frac{2\pi}{L}. \tag{51}$$

VII. Conclusions

We have shown that an antisymmetric taper of κ and $\delta(z)$ breaks the threshold degeneracy found in uniform DFB lasers. An approximate method was developed for the analysis of high-external-Q structures. The method was tested on the uniform structure and the stepped-κ structure with good results for $\kappa L>2$. Closed-form approximate expressions for the threshold gain and external Q were obtained. We found that the lowest threshold for the dominant mode is obtained with the stepped-κ structure, with no taper of δ. The threshold discrimination between the lowest order mode and first higher order mode of this structure is much better than that of the uniform structure of the same value of $|\kappa L|$ (aside from the fact that the latter structure has a threshold degeneracy). A

formula was developed for the frequency perturbation caused by perturbation of the periodic index modulation.

References

[1] H. Kogelnik and C. V. Shank, "Coupled-wave theory of distributed feedback lasers," *J. Appl. Phys.*, vol. 43, pp. 2327-2335, May 1972.

[2] —, "Stimulated emission in a periodic structure," *Appl. Phys. Lett.*, vol. 18, pp. 152-154, Feb. 1971.

[3] C. V. Shank, J. E. Bjorkholm, and H. Kogelnik, "Tunable distributed-feedback dye laser," *Appl. Phys. Lett.*, vol. 18, pp. 395-396, May 1971.

[4] M. Nakamura, A. Yariv, H. W. Yen, S. Somekh, and H. L. Garvin, "Optically pumped GaAs surface laser with corrugation feedback," *Appl. Phys. Lett.*, vol. 22, pp. 515-516, May 1973.

[5] P. R. Scifres, R. D. Burnham, and W. Streifer, "Distributed-feedback single heterojunction GaAs diode laser," *Appl. Phys. Lett.*, vol. 25, pp. 203-206, Aug. 1974.

[6] M. Nakamura *et al.*, "GaAs-$Ga_{1-x}Al_xA_s$ double-heterostructure distributed-feedback diode lasers," *Appl. Phys. Lett.*, vol. 25, pp. 487-488, Nov. 1974.

[7] F. K. Reinhart, R. A. Logan, and C. V. Shank, "GaAs-$Al_x Ga_{1-x}A_s$ injection lasers with distributed Bragg reflections," *Appl. Phys. Lett.*, vol. 27, pp. 45-47, July 1975.

[8] D. C. Flanders, H. Kogelnik, R. V. Schmidt, and C. V. Shank, "Grating filters for thin-film optical waveguides," *Appl. Phys. Lett.*, vol. 24, pp. 194-196, Feb. 1974.

[9] R. V. Schmidt, D. C. Flanders, C. V. Shank, and R. D. Standley, "Narrow-band grating filters for thin-film optical waveguides," *Appl. Phys. Lett.*, vol. 25, pp. 651-652, Dec. 1974.

[10] E. J. Staples, J. S. Schoenwald, R. C. Rosenfeld, and C. S. Hartmann, "UHF surface acoustic wave resonators," in *Proc. 1974 IEEE Ultrasonic Symp.*, Nov. 11-14, 1974, pp. 245-252.

[11] J. S. Schoenwald, R. C. Rosenfeld, and E. J. Staples, "Surface wave cavity and resonance characteristics–VHF to *L*-band," in *Proc. 1974 IEEE Ultrasonic Symp.*, Nov. 11-14, 1974, pp. 253-256.

[12] R. C. M. Li, R. C. Williamson, D. C. Flanders, and J. A. Alusow, "On the performance and limitations of the surface-wave resonator using grooved reflectors," in *Proc. 1974 IEEE Ultrasonic Symp.*, Nov. 11-14, 1974, pp. 257-262.

[13] M. Okuda and K. Kubo, "Threshold gain characteristics of the asymmetrical distributed Bragg-reflector laser," *Opt. Comm.*, vol. 13, pp. 370-374, Apr. 1975.

Discharge Pumping of Dye Vapors

PETER W. SMITH, SENIOR MEMBER, IEEE, PAUL F. LIAO, AND PATRICK J. MALONEY

Abstract–**We report the results of a study of discharge-excited dye vapors. For 20 dyes, fluorescence output was measured as a function of buffer gas, temperature, and discharge parameters. Although fluorescence efficiencies as high as 6 percent were obtained at low power levels, saturation effects limited the output fluorescence to values corresponding to gains of less than 0.2 cm^{-1}.**

I. Introduction

In an attempt to discover those conditions necessary to obtain a discharge-excited dye-vapor laser, we have made a study of the discharge-excited fluorescence from a number of dye-buffer gas systems. We find that under appropriate pulsed conditions a high efficiency of conversion of electrical input to fluorescence radiation can be obtained. Saturation effects, however, limit the excited singlet populations achievable. The maximum fluorescence power measured corresponds to gains of the order of a few tenths of a cm^{-1} for all of the dyes studied. The actual net gains are less, due both to ground-state absorption and to transient loss mechanisms induced by the electrical discharge pulse.

Preliminary experiments were performed with a pulsed longitudinal discharge using a heated discharge tube and dye reservoirs–a design similar to that used for early metal-vapor laser studies [1]. It was soon found, however, that most of the fluorescence occurred during the leading edge of the current pulse, and that significant dye decomposition was occurring at longer times. It was also found that the dye vapor increased the discharge impedance so that very large discharge voltages were required. For these reasons, and because we knew that high current densities would be required to achieve the population inversion required for laser action, we performed all further experiments on a transverse discharge arrangement capable of producing short pulses of high current densities with relatively low applied voltages.

Manuscript received March 5, 1976.
The authors are with Bell Laboratories, Holmdel, NJ 07733.

II. Apparatus

Fig. 1 shows the discharge tube and circuit used for the experiments reported in this paper. The glass discharge tube had a tungsten pin anode and nickel bar cathode separated by 5 mm, and was connected to a vacuum station to permit filling with various buffer gases. The main body of the tube containing the dye was within an oven that could be heated to ~400°C. A ~7-cm length of 3-mm ID tube extended outside the oven, and the end of this tube was closed with a normal optical window. It was found that for the dye-vapor pressures used ($\lesssim$ 10 torr), dye diffusion to the cold parts of the tube was slow when buffer gas pressures were above 200 torr.

An estimate of the current required for a given gain can be made using the data previously obtained for optically pumped POPOP vapor [2]. We found that an optical pump power of approximately 2×10^7 W/cm^3 was required to produce a gain of 1 cm^{-1}. The fluorescence efficiency was ~70 percent. For our transversely excited discharge tube, the discharge volume is ~10^{-2} cm^3. For an applied voltage of 15 kV, and assuming

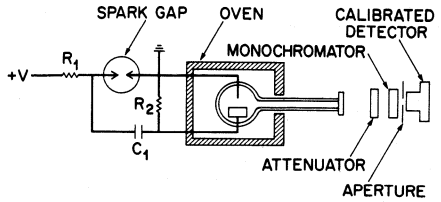


Fig. 1. Apparatus used for discharge fluorescence measurements. For most of these experiments $R_1 = 6$ MΩ, $R_2 = 1$ MΩ, and $C_1 = 260$ pF.

one-tenth of the optical pumping efficiency (7 percent), we would thus estimate a current of 130 A to achieve a gain of 1 cm^{-1}.

The discharge was excited by charging a storage capacitor (C_1) and then connecting it to the discharge tube by means of a spark gap. For most of these experiments we used a storage capacitor of 260 pF and a charging voltage of 15 kV. The resulting current pulse had a peak of ~100 A and a half-width of ~50 ns. Thus we could perform experiments with current densities of the order of those we would expect to require for laser action.

Fluorescence light was measured with a calibrated 1P28 photomultiplier tube. An aperture served to define the solid angle of the light measured, and a monochromator was used to select a portion of the fluorescence band. Calibrated neutral density filters were used to keep the input signal within the linear range of the photomultiplier, and the photomultiplier output signal was observed with a fast oscilloscope.

III. Results

For each of the dyes studied, the discharge-excited fluorescence was recorded as a function of temperature. In all cases, a saturation was observed and fluorescence power failed to increase (or increased only slowly) above a certain temperature. In Table I, we record the gain corresponding to the fluorescence power measured at this point, and the corresponding temperature. This gain is that corresponding to the measured density of excited singlet molecules and does not take account of losses due to ground-state absorption, triplet-triplet absorption, etc. It is computed from the measured fluorescence power using the formula

$$\alpha = \sigma N_1 = 3.8 \times 10^{-21} \frac{eP\tau_0}{Vh\nu} \tag{1}$$

where

- α gain in cm^{-1};
- σ cross section of the transition in cm^2;
- N_1 excited singlet population density in cm^{-3};
- ϵ molar extinction coefficient in $l \cdot mole^{-1} \cdot cm^{-1}$;
- P total fluorescence power in watts;
- τ_0 natural lifetime in seconds;
- V volume of the discharge in cm^3;
- h Planck's constant in CGS units;
- ν frequency of the transition in hertz.

In deriving this formula, we have assumed that the cross section for absorption is the same as the cross section for emission, i.e., we assume no change of molecular configuration in the excited state. This assumption should be valid for those molecules exhibiting mirror symmetry in their emission and absorption spectra.

Fig. 2 shows the saturation of output fluorescence of the dye PPF as the temperature is increased. This saturation behavior is typical of the dyes studied. We see that at high temperatures (and thus high dye-vapor pressures) a relatively smaller percentage of molecules are excited by the discharge. This may be due in part to concentration quenching, which is observed in both liquid and vapor dye lasers, but we believe the primary mechanism is the change of electron energy distribution in the discharge produced by the dye molecules themselves.

For three dyes whose vapor absorption band overlapped the strong mercury vapor resonance line at 2537 Å, experiments were performed to study resonance transfer between dye and excited Hg molecules. For 1, 1′ dinapthyl and 2,2′ dinapthyl, less fluorescence was obtained when Hg vapor was present in the discharge cell. For napthalene, a twofold increase in fluorescence was obtained with mercury vapor at 100°C. The napthalene system is not a favorable one for laser action, however, because of the long lifetime and low oscillator strength of the first excited singlet level.

In Fig. 3, the effect of buffer gases on the fluorescence output of POPOP vapor is shown. Although some other dyes showed less dependence on type of buffer gas used, we found in all cases that the maximum fluorescence signal was obtained with helium as the buffer gas. The pressure of buffer gas was not critical, little change being observed for most dyes when the pressure was varied between 200 and 800 torr.

Fig. 4 shows the variation of fluorescence as a function of input power to the discharge. The input power was taken to be $VI/2$ where V is the charging voltage on the capacitor and I is the current monitored with a current transformer. It can be seen that there is a strong saturation of fluorescence output with input power. This behavior is typical of all of the dyes tested. For POPOP, a time-dependent effect was noted, and greater fluorescence for a given input power was observed when the power was introduced in a short time (we used a small discharge capacitor charged to a high voltage). At low power inputs quite high efficiencies (ratios of peak output fluorescence power to input power) were obtained. The maximum efficiencies were: PF-6 percent; perylene-3 percent; and POPOP-1 percent.

From absorption measurements the vapor density at a given temperature can be computed with the assumption that the cross section is the same as for a liquid solution. The knowledge of the vapor density allows us to calculate the fraction of molecules pumped into the upper state at a given time. The largest values were: napthalene-8 percent; perylene-2 percent; and POPOP-1 percent.

IV. Discussion and Conclusions

We have observed two saturation phenomena which limit the intensity of discharge-excited dye-vapor fluorescence. The saturation as a function of dye vapor pressure appears to be due to the effect of the dye molecules on the discharge, although concentration quenching of fluorescence may also play a role.

TABLE I

Dye	Natural Lifetime τ_0 [3]	Peak Molar [3] Extinction Coefficient	Optical Quantum Efficiency		Gain[a]	Temp	Comments
			SOL'N [3]	Vapor			
	ns	$1 \cdot mole^{-1} \cdot cm^{-1}$			cm^{-1}	°C	
PPF	1.6	38 000	1.00		0.15	180°	- Efficiency = 6 percent (see text)
perylene	~4	~28 000	0.94	0.8[a]	0.15	280°	- Large ground state absorption (>0.20 cm^{-1}) implies net loss - Large triplet absorption
POPOP	1.5	50 000	0.93	0.6 [4] 0.7[a]	0.08	320°	- Optically-pumped vapor laser [5]
dimethyl POPOP	1.7	50 000	0.93		0.08	310°	
BBOT	1.7	58 000	0.74		0.08	320°	
PBD	1.1	48 000	0.83		0.04	320°	
napthalene	420[d]	≈200[c]	0.23	0.5 [4]	0.01	85°	- Gain increased to 0.02 cm^{-1} by addition of Hg (see text)
p-quaterphenyl	1.2	40 000	0.89		0.01	320°	- Decomposes readily
BBO	1.3	50 000	0.88[e]		0.01	300°	- Optically pumped vapor laser [5]
aNPO	3.1	25 000	0.94	0.4 [4]	0.01	275°	- Optically pumped vapor laser [5]
1-1' dinapthyl	3.4	15 000	0.77		0.01	320°	- Low ground state absorption [7]
2-2' dinapthyl	35	20 000	0.41		<0.01	320°	
p-p' diphenyl-stilbene	1.1	57 000	1.00[e]		<0.01	230°	- Low threshold for flashlamp pumping - Very weak fluorescence in vapor state
PPD	1.6	28 000	0.89	1.0 [4] 0.6[a]	<0.01	220°	
PPO	1.5	33 000	1.00	0.2 [4]	<0.01	190°	
dibutoxy POPOP[b]		72 000 [6]			<0.01	85°	- Weak T-T absorption [6] - Decomposes before appreciable vapor pressure is reached
benzo (ghi) perylene	110	1 500[f]			<0.01	290°	
p-terphenyl	1.2	34 000	0.93	1.0 [4] 0.3[a]	<0.01	240°	- Weak T-T absorption [6]
9-10 diphenyl-anthracene	~9	14 000	1.00	0.15 [4]			- Decomposes before appreciable vapor pressure is reached
bis MSB	1.3	56 000	0.94	<0.01[a]			- Very weak fluorescence in vapor state

[a] Our measurement.
[b] We would like to thank P. R. Hammond of the Naval Electronics Laboratory Center, San Diego, CA, for providing the sample of dibutoxy POPOP used for these studies.
[c] The higher peak value at 2760 Å is due to absorption into the second excited singlet state.
[d] Computed from fluorescence decay time and quantum efficiency.
[e] Computed from fluorescence decay time and natural lifetime.
[f] Data in [3] indicate a configuration change on excitation. The molar extinction coefficient used here is an estimate based on the computed value of the natural lifetime.

The saturation of fluorescence with electrical input power we ascribe to a reduction of ground-state molecules because of both decomposition and triplet pumping mechanisms. Fig. 5 shows the output fluorescence and the corresponding current pulse for PPF at 200°C. It can be seen that the fluorescence peaks well before the peak on the current pulse, and then falls off rapidly. At higher input powers, the fluorescence peaks still earlier. Such behavior is similar to the fluorescence falloff caused by decomposition which is observed in optically pumped dye vapors [8].

We have performed experiments with a 10-cm-long 50-pin transverse discharge device. Experiments with PPF, POPOP,

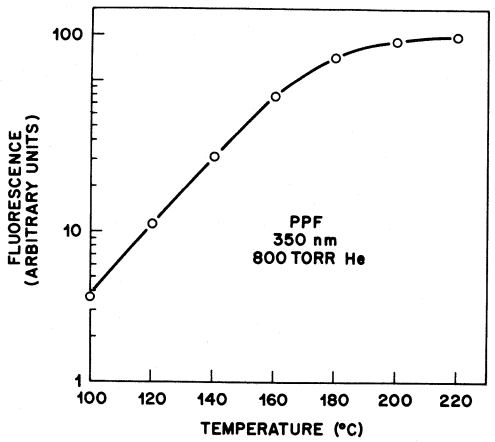


Fig. 2. Discharge-excited fluorescence of PPF vapor at 350 nm as a function of oven temperature. 800 torr He buffer gas.

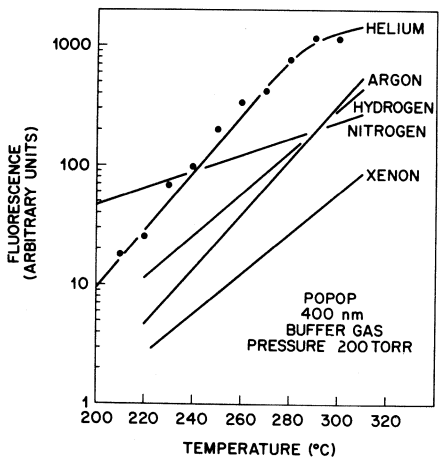


Fig. 3. Discharge-excited fluorescence of POPOP vapor at 400 nm as a function of oven temperature for various buffer gases. In each case the buffer gas pressure was 200 torr. For clarity, experimental data points are only shown for the He buffer gas curve.

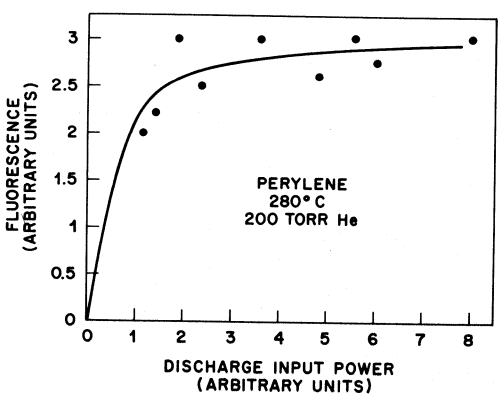


Fig. 4. Discharge-excited fluorescence of perylene vapor at 450 nm as a function of discharge input power. Data for an oven temperature of 280°C with 200 torr He buffer gas.

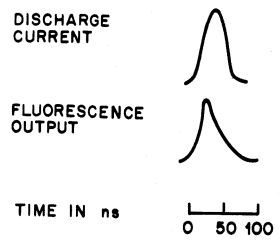


Fig. 5. Discharge current and corresponding fluorescence output of PPF vapor at 200°C as a function of time.

and perylene showed no indications of net gain or laser action. For perylene, this is due to ground-state absorption, which we measured to be larger than the discharge-produced gain. For the other two dyes, other loss mechanisms such as triplet absorption, decomposition, and beam distortion in the discharge must also play a role.

An experiment was performed to study the refractive index inhomogeneities induced by the discharge pulse. We used a discharge cell similar to that used for the dye fluorescence measurements, but with a tube extending out of each side of the cell. A probe beam from a He-Ne laser could be passed through the discharge region, and the transient loss caused by beam distortion measured by observing the transmitted beam through a pinhole located 1 m from the cell. It was found that when a current pulse of 100 A was passed through the discharge cell containing 200 torr of helium, a transient loss of the order of 10 percent was observed. This corresponds to a loss of 0.3 cm^{-1} which is greater than the largest gains recorded in Table I. Thus even without taking account of ground-state and excited-state absorption, we find that the excited singlet populations obtained with discharge pumping are below those required for positive net gain. It remains to be seen whether other excitation methods (such as electron beam excitation [9]) can be made more effective.

References

[1] W. T. Silivast, "Metal vapor lasers," *Scientific American*, pp. 88-98, Feb. 1973.

[2] P. W. Smith, P. F. Liao, C. V. Shank, C. Lin, and P. J. Maloney, "The POPOP dye vapor laser," *IEEE J. Quantum Electron.*, vol. QE-11, pp. 84-89, Feb. 1975.

[3] I. B. Berlman, *Handbook of Fluorescence Spectra of Aromatic Molecules*, 2nd ed. New York: Academic Press, 1971.

[4] Yu. Yu. Stoilov and K. K. Trusov, "Fluorescence efficiency measurements on certain complex organic molecules in the gaseous phase," *Soviet J. Quantum Electron.*, vol. 4, pp. 809-810, Dec. 1974.

[5] B. Steyer and F. P. Schäfer, "Stimulated and spontaneous emission from laser dyes in the vapor phase," *Appl. Phys.*, vol. 7, pp. 113-122 (1975).

[6] T. G. Pavlopoulos and P. R. Hammond, "Spectroscopic studies of some laser dyes," *J. Am. Chem. Soc.*, vol. 96, pp. 6568-6579, Oct. 1974.

[7] M. Post, J. Langelaar, and J. D. W. van Voorst, "The influence of the molecular conformation upon spectroscopic properties of 1,1'-binapthyl," *Chem. Phys. Letters*, vol. 32, pp. 59-62, Apr. 1975.

[8] P. F. Liao, P. W. Smith, and P. J. Maloney, "Photodecomposition in POPOP dye vapor lasers," to be published.

[9] G. Marowsky, F. P. Schäfer, J. W. Keto, and F. K. Tittel, "Fluorescence studies of electron-beam pumped POPOP dye vapor," *Appl. Phys.*, vol. 9, pp. 143-146, Feb. 1976.

Saturated Spectroscopy Applied to Xenon at 3.5 μm

JOHN NELLA, SEUNG-YAN SZETO, MEMBER, IEEE, PAUL RABINOWITZ, AND J. T. LATOURRETTE, MEMBER, IEEE

Abstract—We report the observation of the xenon isotope spectrum using saturation spectroscopy on a gain cell external to a He-Xe laser. Six resonances centered about 3.508 μm are observed over the limited tuning range of the laser. These resonances are assigned to the Xe^{128}, Xe^{130}, Xe^{131}, Xe^{132}, Xe^{134}, and Xe^{136} isotopes. The observed homogeneous linewidth is 9 ± 1 MHz, and the pressure broadening of the homogeneous linewidth is experimentally determined to be 71 ± 20 MHz/torr.

INTRODUCTION

LAMB DIP spectroscopy, or laser saturated resonance spectroscopy has been used to investigate the absorption spectrum of several gases whose transition frequencies lie within the tuning range of a laser [1]-[4]. For Doppler-broadened media, conventional spectroscopic techniques have their resolution limited to the inhomogeneous linewidth so that spectroscopic information of a finer scale is not readily obtainable. Therefore, details of the homogeneous width have to be obtained by indirect means. Lamp dip measurements provide a technique which yields spectral resolution of the homogeneous linewidth of an individual transition. Thus it is possible to do a parametric study of the homogeneous width as a function of pressure and discharge conditions and investigate the isotopic shift and hyperfine spectrum of the 3.508-μm transitions of xenon.

The experimental technique employed for the observation of the Lamb dip utilizes an external gain cell and the method is similar to that described by Rabinowitz *et al.* [1]. A cell external to the laser is used so that the widths and relative positions of the Lamb dips may be examined without the additional dispersion that exists when the cell is internal to the laser resonator. A He-Xe laser operating at 3.508 μm is used to probe a Xe gain cell. The input intensity to the gain cell is measured to assure negligible power broadening. By controlling the pressure of Xe in the gain cell, the dependence of the homogeneous linewidth on pressure is determined. An extrapolation of the linewidth to zero pressure provides a determination of the natural linewidth.

Manuscript received March 17, 1976. This work was supported in part by the Advanced Research Projects Agency and the Air Force Systems Command, RADC, under Contract F3062-72-C-0254, and in part by the Joint Services Electronics Program under Contract F44620-69-C-0047. This paper comprises part of a dissertation to be submitted to the faculty of the Polytechnic Institute of New York in partial fulfillment of the requirements for the Ph.D. degree (S. Y. Szeto).

J. Nella was with the Department of Electrical Engineering and Electrophysics, Polytechnic Institute of Brooklyn, New York, NY 11735. He is now with the Hughes Aircraft Company, Culver City, CA.

S.-Y. Szeto and J. T. LaTourrette are with the Department of Electrical Engineering and Electrophysics, Polytechnic Institute of New York, Farmingdale, NY 11735.

P. Rabinowitz was with the Department of Electrical Engineering and Electrophysics, Polytechnic Institute of New York, Farmingdale, NY, 11735. He is now with the Exxon Research and Engineering Company, Linden, NJ.

THEORY

A phenomenological description of the Lamb dip [5] has been given by Bennett in terms of hole burning in the velocity distribution of excited state atoms in a laser [6]. Basov *et al.* [7] have extended the hole burning theory to the case of the external absorption cell. More detailed treatment of this problem can be found in works by Baklanov and Chebotaev [8] and Yu [9]. One significant difference for our measurements that occurs in the external cell case is the narrowing of the dip width by a factor equal to the square root of 2. For conditions such that the gain or absorption is small, $\alpha_0 l \ll 1$, the dip width in the external cell is

$$\Delta\omega = \Delta\omega_h [(1 + I/I_s)]^{1/2}$$

where I is the circulating intensity, I_s is the saturation intensity, and $\Delta\omega_h$ is the homogeneous width of the transition. This expression is valid only when the dip width is small compared with the Doppler width, a condition always satisfied during the measurements.

The 3.508-μm transition of xenon is between the $5\,d[7/2]_3$ and $6\,p[5/2]_2$ states. Natural xenon has a number of isotopes, with mass differences sufficient to produce transition frequencies which differ by more than the homogeneous linewidth. In addition, two isotopes Xe^{129} and Xe^{131} have a nuclear magnetic moment and their transitions are further split into 3 and 9 hyperfine components, respectively. This splitting is due to the interaction of the nuclear spin, $\underline{I}$, with the total angular momentum of the electrons, $\underline{J}$. The hyperfine levels are labeled according to the resultant angular momentum, $\underline{F}$, of the upper and lower states where $\underline{F} = \underline{I} + \underline{J}$.

EXPERIMENT

The basic experimental arrangement used for this work is shown schematically in Fig. 1. Two He-Xe lasers are used having an active discharge length of 69 cm and 26 cm and an ID of 10 mm and 5 mm, respectively. The lasers are dc excited and have aluminum cold cathodes. To minimize cathophoresis effects, a nonexcited return path is provided between the anode and cathode structure. The shorter laser resonator has a length of 33.6 cm resulting in a longitudinal mode spacing of 447 MHz. The output is diffraction coupled from a 1-mm-diam gold dot on a quartz flat. The second resonator reflector is a flat mirror mounted on a piezoelectric transducer. The longer laser resonator has a 75-cm length. The resonator consists of a 50-percent transmitting flat, and a 2-m-radius reflector mounted on a piezoelectric transducer.

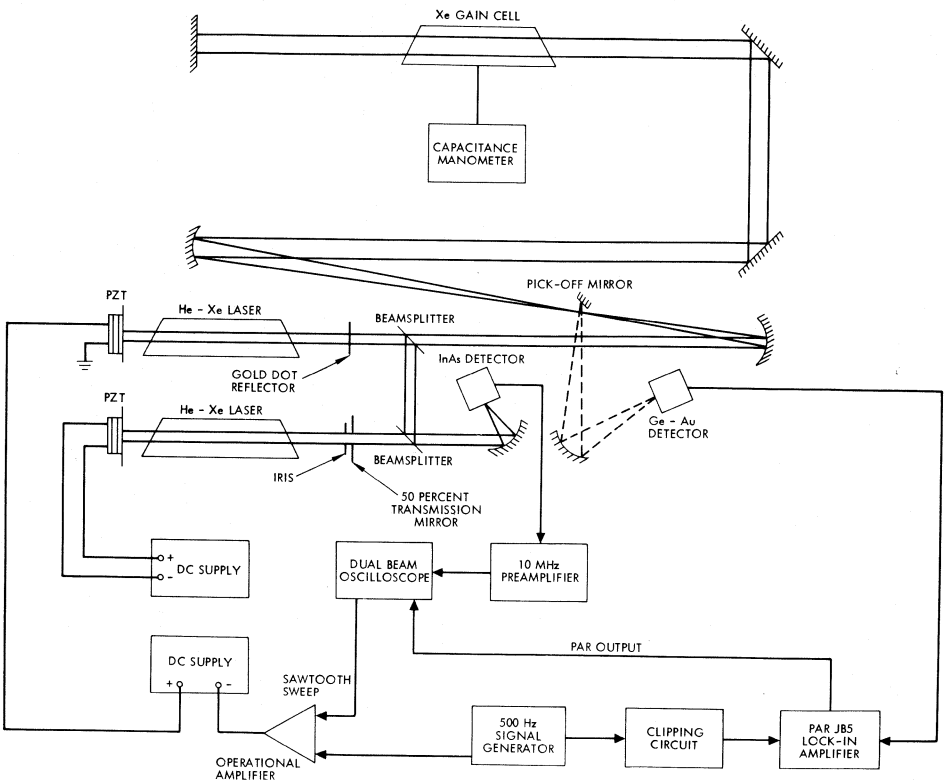


Fig. 1. Experimental apparatus for Lamb dip measurements on Xe in an external cell.

To restrict operation to the TEM_{00} mode in the longer laser, an intracavity iris is employed. The gas fills for the lasers are: 3 torr of helium and 0.08 torr of natural xenon[1] for the shorter tube, and 8 torr of He and 0.1 torr of Xe for the longer tube. Single mode operation was obtained for both lasers at low excitation currents.

Measurements were made utilizing two different gain cells. The first has an 11-cm active discharge length with a 1-cm inner diameter. The second has a 20-cm active discharge and a 5-mm inner diameter. Thermionic cathodes are used to provide for larger discharge currents and to minimize cathode sputtering. A capacitance manometer monitors the pressure in both cells.

For the Lamb dip observations, the following experimental configuration is used: the output of the shorter He-Xe laser is focused by a spherical mirror then recollimated by a second mirror before it is passed through the gain cell. A 500-Hz FM signal is applied to the laser output by driving the piezoelectric transducer. After passing through the gain cell the beam is reflected back almost upon itself and the return signal is picked off at the focus and directed toward a Ge:Au detector. The signal processing is accomplished by means of a lock-in amplifier whose output is displayed on an oscilloscope whose sawtooth voltage is used to sweep the laser frequency. The signal is observed as a discriminant of the Lamb dip features as the laser frequency is scanned across the various atomic line centers.

This technique, rather than a direct Lamb dip observation, was found to be more convenient because of its ability to discriminate against broader features of the gain profile. The discrimination was further improved by demodulating the third harmonic of the modulation frequency as opposed to the fundamental [10]. The full width of the Lamb dip is related to the peak-to-peak width of the first- and third-harmonic discriminant by

$$\Delta\omega \text{ (Lamb dip)} = \sqrt{3}\,\Delta\omega \text{ (first harmonic)}$$
$$\simeq 3.08\,\Delta\omega \text{ (third harmonic).}$$

The frequency scale for the oscilloscope trace was obtained by displaying a pair of frequency markers with a 20-MHz separation. These markers are produced by means of heterodyne detection so that a signal occurs when the two laser frequencies are separated by 10 MHz. The ratio of the frequency scale so obtained with the frequency scale obtained using the response of the PZT elements revealed a linear pulling factor of about 2 [11].

The same apparatus in a different configuration is used for the gain measurements. The laser was tuned for peak power output, and the single-pass gain through the cell was measured as a function of discharge current, pressure, and input intensity. Absolute intensity measurements were made using a calibrated Eppley thermopile. The results of these measurements allowed for an experimental determination of the satu-

[1]The natural xenon gas was from Monsanto Natural Gas Products. Xe analysis: Xe^{136}, 8.87 percent; Xe^{134}, 10.44 percent; Xe^{132}, 26.8 percent; Xe^{131}, 21.18 percent; Xe^{130}, 4.08 percent; Xe^{129}, 26.44 percent; Xe^{128}, 1.92 percent; Xe^{126}, 0.09 percent; Xe^{124}, 0.096 percent.

ration intensity which was needed to ensure that measured Lamb dip widths were not significantly power broadened.

As a final investigation, the pressure-dependent shift in the laser oscillation frequency by the addition of helium was examined using a specific xenon Lamb dip as a reference frequency.

Results and Analysis

The results of the small-signal gain and absorption measurements for naturally occurring xenon as a function of the discharge current is shown in Fig. 2. The 10-mm gain cell was used in this case. These measurements confirm and extend similar results reported by Aleksandrov *et al.* [12]. It is found that the absorption coefficient scales inversely with the tube diameter. In a manner similar to the gain situation, results for the 5-mm gain cell show a maximum absorption of 58 dB/m occurring at a pressure of 100 mtorr and a discharge current of 125 mA. For the 10-mm cell, a maximum absorption of 32 dB/m occurred at 50 mtorr and 350 mA.

The saturation intensity is determined by obtaining the dependence of the gain (or absorption) as a function of the input intensity to the gain cell. This was done over a pressure range of 10-60 mtorr and it was found that the saturation intensity varied linearly with pressure over this range, and the value

$$I_s = 3.3 \pm 1\ \mu\text{W} \cdot \text{cm}^{-2} \cdot \text{mtorr}^{-1}$$

is in fair agreement with other results [13]. There was no variation within experimental accuracy in the value of the obtained saturation intensity as the current in the gain cell was varied.

The results of the Lamb dip measurements are presented in Fig. 3. This figure is a composite drawing of the oscillograms of the third-harmonic discriminant of the six dips that were observed using natural xenon in the external cell. The scale for this figure is only for the relative spacing of the dips, and to some extent, the relative magnitude, but the widths are not to scale. The cusps indicate the end of the tuning of the laser. The dips are labeled *a* to *f* going toward lower frequency. To aid in the identification of the dips, two isotope-enriched xenon mixtures, Xe^{131} and Xe^{136} were used.[2] The Xe^{131} mixture reduced the Xe^{128}, Xe^{129}, and Xe^{130} content to approximately 0.1 percent, and with this mixture in the gain cell the dips labeled *d* and *f* were not present with the dip *c* remaining the largest. The Xe^{136} mixture did not contain any Xe^{128} or Xe^{130}, and the Xe^{131} concentration was reduced to approximately 0.4 percent. With this isotopic mixture the dips labeled *d*, *e*, and *f* were absent from the spectrum. Based on these results and with the aid of previously reported work [14]-[19], the following assignments for the various observed Lamb dips are made: *a* due to Xe^{136}, *b* to Xe^{134}, *c* to Xe^{132}, *d* to Xe^{130}, *e* to a hyperfine component of Xe^{131}, and *f* to

[2]Enriched Xe^{131} and Xe^{136} mixtures were prepared by Monsanto Gas Products. Xe^{131} mixture analysis: Xe^{136}, 4.5 percent; Xe^{134}, 16.7 percent; Xe^{132}, 38.4 percent; Xe^{131}, 40.2 percent; Xe^{130}, 0.1 percent; Xe^{129}, 0.1 percent, and Xe^{128}, 0.1 percent. Xe^{136} mixture analysis: Xe^{136}, 82 percent; Xe^{134}, 15.9 percent; Xe^{132}, 1.7 percent, and Xe^{131}, 0.4 percent.

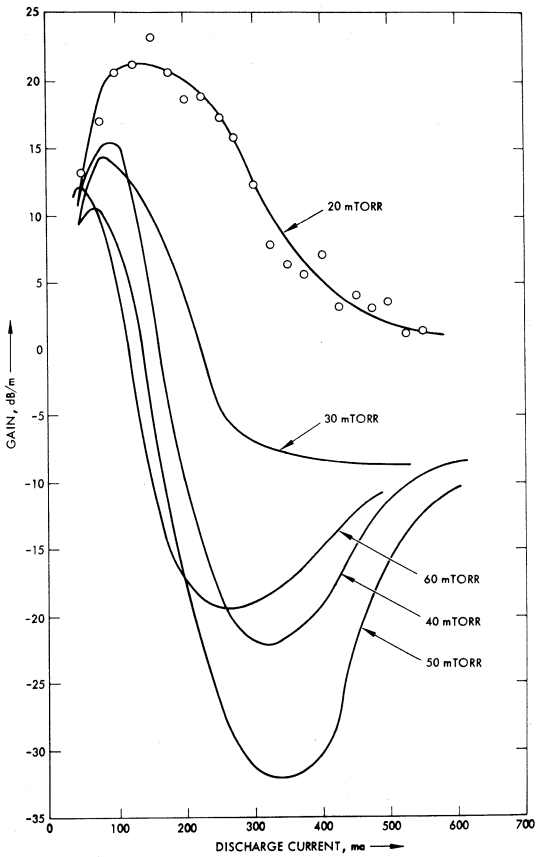


Fig. 2. Gain versus discharge current for natural Xe.

Xe^{128}. The spacing between components were determined to be

$$\Delta\nu(136\text{-}134) = 37 \pm 4\ \text{MHz}$$
$$\Delta\nu(134\text{-}132) = 43 \pm 4\ \text{MHz}$$
$$\Delta\nu(132\text{-}130) = 46 \pm 4\ \text{MHz}$$
$$\Delta\nu(130\text{-}131) = 30 \pm 6\ \text{MHz}$$
$$\Delta\nu(131\text{-}128) = 24 \pm 6\ \text{MHz}.$$

The central Lamb dip *c* attributed to Xe^{132} was found to have a larger width than any of the remaining dips. If one uses a linear interpolation of the even isotope shifts to locate the center of the Xe^{131} and Xe^{129} spectra, and makes use of the hyperfine constants given by Liberman [15], only two hyperfine components of the odd isotopes lie within the tuning range of the laser used. These components are the Xe^{129} ($F = 7/2 \rightarrow F' = 5/2$) and the Xe^{131} ($F = 9/2 \rightarrow F' = 7/2$) transitions. The Xe^{131} transition is accounted for by the observed dip *e*. The Xe^{129} component can be accounted for if its transition frequency falls within the homogeneous linewidth of another Xe transition. Aleksandrov and Kulyasov [23], using a technique different from Lamb dip spectroscopy, found that the $F = 7/2 \rightarrow F' = 5/2$ transition of Xe^{129} coincides, within 10 MHz, with the single Xe^{132} transition. Using this explanation for the broadened dip *c* and the fact that the relative abundance of Xe^{132} is almost equal to Xe^{129} in the

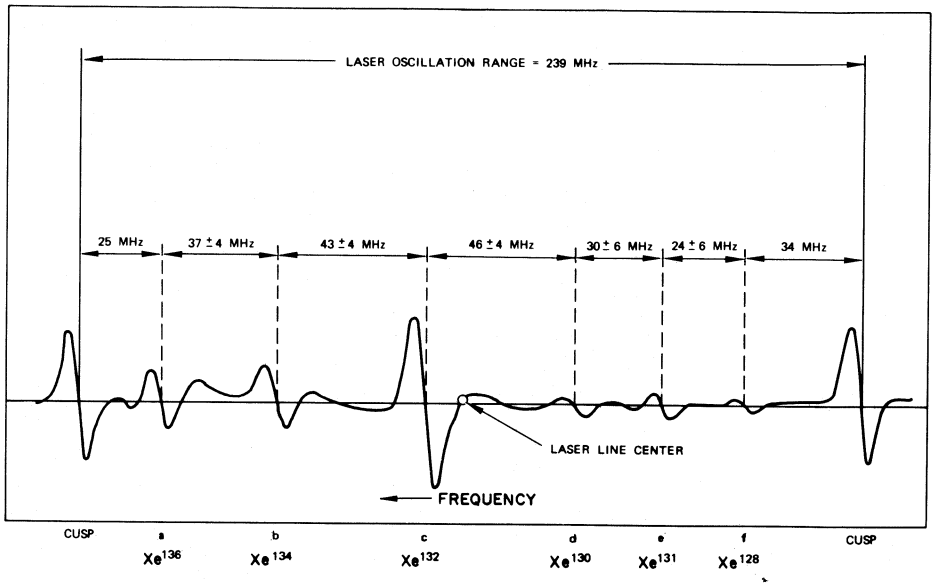


Fig. 3. Lamb dip (third-harmonic discriminant) observations of Xe at 3.508 μm (the cusps mark the limits of the range of laser oscillation).

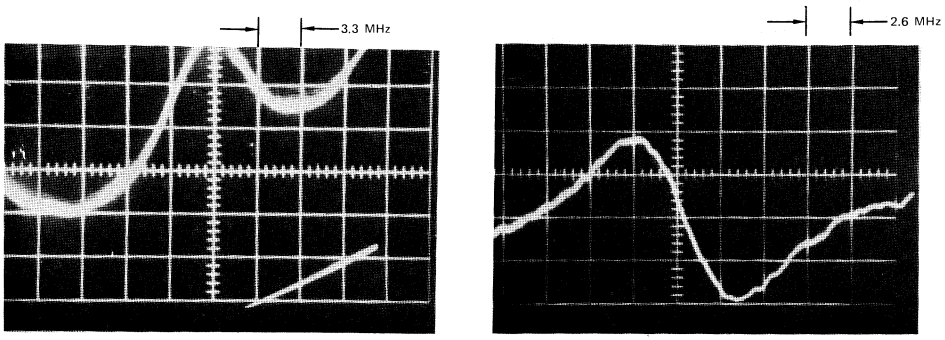


Fig. 4. Main Lamb dip: (a) Actual Lamb dip in an external Xe cell, Xe pressure 11 mtorr, and horizontal scale 3.28 MHz/div. (b) Lamb dip first-harmonic discriminant, Xe pressure 11 mtorr, horizontal scale 2.6 MHz/div.

natural xenon used, and that the strength for the Xe^{129} 7/2 to 5/2 transition is approximately 57 percent of the total 129 strength, we can conclude that the two transitions coincide to within 4 MHz or less.

An oscillogram of the Xe^{132}/Xe^{129} Lamb dip and its first harmonic discriminant is shown in Fig. 4. For this oscillogram, naturally occurring xenon was used. The pressure dependence of the discriminant was measured at 41 ± 12 MHz/torr with a zero pressure intercept of 5.8 ± 0.5 MHz. From these results the pressure broadening of the homogeneous width is found to be 71 ± 20 MHz/torr, resulting in a pressure-dependent phase interruption time ($T_2 = 1/\pi\Delta\nu_h$) of $T_2 = 4.5 \pm 1$ ns/torr. The full homogeneous linewidth is calculated from the zero pressure intercept and is found to be 10 ± 1 MHz. As mentioned above, the widths of the remaining dips were all smaller than the *c* dip, each with a resulting homogeneous linewidth of 9 ± 1 MHz. These widths agree with the reported Lamb dip widths in the output power for a monoisotopic xenon laser [20], [21].

Finally, the pressure-dependent frequency shift due to the addition of helium in the laser was measured to be 1.2 MHz/torr. The shift was toward lower frequency.

Conclusions

We have reported the Lamb dip spectrum of xenon at 3.508 μm using an external xenon cell and results of measurements on the related properties of xenon. These results can be improved by extending the tuning range of the laser and by more accurately measuring the frequency separation. A three-mirror Fox-Smith [22] type resonator can be used to scan the laser over a wider frequency range so that the entire spectrum of the xenon isotopes and hyperfine components may be observed. Accurate frequency differences may be measured by heterodyne detection of two lasers which are frequency stabi-

lized to different dips. In this way, errors due to frequency pulling effects and nonlinear response of PZT's may be avoided. These experiments are now in progress.

References

[1] P. Rabinowitz, R. Keller, and J. T. LaTourrette, "Lamb dip spectroscopy applied to SF_6," *Appl. Phys. Lett.*, vol. 14, pp. 376-378, 1969.

[2] P. H. Lee and M. L. Skolnick, "Saturated neon absorption inside a 6328A laser," *Appl. Phys. Lett.*, vol. 10, pp. 303-305, 1967.

[3] R. L. Barger and J. L. Hall, "Pressure shift and broadening of methane line at 3.39 μm studied by laser saturated molecular absorption," *Phys. Rev. Lett.*, vol. 22, pp. 4-8, 1969.

[4] P. H. Lee, "Introduction to saturated optical absorption," *IEEE Trans. Instrum. Meas.*, vol. IM-21, pp. 384-387, 1972.

[5] W. E. Lamb, Jr., "Theory of an optical maser," *Phys. Rev.*, vol. 134, pp. 1429-1450, 1964.

[6] W. R. Bennett, Jr., "Relaxation mechanisms, dissociative excitation transfer and mode pulling effects in gas lasers," in *Proc. 1963 Quantum Electronics Conf.*, Paris, France, 1963. vol. 1, p. 441.

[7] N. G. Basov *et al.*, "Investigation of narrow resonances within the Doppler line of rotational-vibrational transitions of the SF_6 molecule during absorption saturation," *Sov. Phys. JETP*, vol. 32, pp. 214-219, 1971.

[8] E. V. Baklanov and V. P. Chebotaev, "Effects of fields in resonant interaction of opposing waves in a gas," *Sov. Phys. JETP*, vol. 33, pp. 300-308, 1971.

[9] Y. B. Yu, Ph.D. dissertation, Polytechnic Institute of Brooklyn, New York, NY, 1972.

[10] A. D. White, "Frequency stabilization of gas lasers," *IEEE J. Quantum Electron.*, vol. QE-1, pp. 349-357, 1965.

[11] L. Casperson and A. Yariv, "Longitudinal modes in a high gain laser," *Appl. Phys. Lett.*, vol. 17, pp. 259-261, 1970.

[12] E. B. Aleksandrov *et al.*, "Gain at the 3.51 μm and 5.57 μm lines in a Xe^{136} discharge," *Optics and Spectroscopy*, vol. 31, pp. 170-171, 1970.

[13] L. Casperson, "Saturation and power in a high-gain gas laser," *IEEE J. Quantum Electron.*, vol. QE-9, pp. 250-252, 1973.

[14] R. Vetter, *Comptes Rendus*, Series B, vol. 267, pp. 1007-1010, 1968.

[15] S. Liberman, "Etude theoriques des configurations $Sp^1(6s + Sd)$ et $Sp^5(6p + 7P)$ du xenon I et de leur structure hyperfine," *Journal de Physique*, vol. 30, pp. 53-62, 1969.

[16] R. Vetter, "Mesure des ecarts isotopiques dans les transitions laser du xenon," *Phys. Lett.*, vol. 31A, pp. 559-560, 1970.

[17] —, *Comptes Rendus*, Series B, vol. 265, pp. 1415-1418, 1967.

[18] S. Liberman, "Sur la structure hyperfine de quelques raies laser infrarouges du xenon 129," *Comptes Rendus*, Series B, vol. 266, pp. 236-239, 1968. The spectra given are inconsistent with results updated in [15].

[19] R. Vetter, *Comptes Rendus*, Series B, vol. 268, pp. 1293-1295, 1969.

[20] S. C. Wang *et al.*, "Observation of an enhanced Lamb dip with a Pure Xe gain cell inside a 3.51 μm He-Xe laser," *Appl. Phys. Lett.*, vol. 17, pp. 120-122, 1970.

[21] L. Casperson and A. Yariv, "Gain and dispersion focusing in a high gain laser," *Appl. Optics*, vol. 11, pp. 462-466, 1972.

[22] P. W. Smith, "Stabilized single-frequency output from a long laser cavity," *IEEE J. Quantum Electron.*, vol. QE-1, pp. 343-348, 1965.

[23] E. B. Aleksandrov and V. N. Kulyasov, "Intra-Doppler spectral line structure," *Soviet Physics JETP*, vol. 29, pp. 426-428, 1969.

Correspondence

Far-Infrared Laser Oscillations from H_2CO

Y. HORIUCHI AND A. MURAI

Abstract—**Lasting laser oscillation was obtained from H_2CO vapor with a longitudinal-flow tube. Ten lasing lines, including six new lines, have been observed in the pressure range of 0.18-0.35 torr. The optimum conditions were 2.5-7.1 kV and 2.5 Hz for excitation voltage and pulse repetition rate, respectively. The pulse shape of the lines was observed by an Ni-W diode.**

It has so far been widely known that a longitudinal-flow tube is favorable for an effective and stable generation of stimulated emission in the far-IR region. Previously, Okajima and Murai found four lasing lines in the far-IR region from H_2CO vapor sealed off in a large-diameter laser tube [1]. Unfortunately, they could not obtain lasting output because of the sealed-off operation. Recently, lasting output has been successfully obtained from H_2CO at 122.8 μm by the use of a transverse-flow tube of 50 cm in active length [2]. After a detailed analysis of the experimental conditions of these works, we expected that the lasting laser oscillation would be obtained from H_2CO even in a 3-m longitudinal-flow tube, provided that a pulse repetition at a lower frequency was used in order to reduce the chance of rapid dissociation of H_2CO in the discharge. In this way, ten lasing lines, including six new lines, were detected in the far-IR region.

The experimental setup is a conventional one. The cavity consists of two mirrors of 8 cm in diameter spaced 3 m apart; one, 10 m in focal length, has a coupling hole of 4-mm bore diameter at the center and the other, 2.5 m, allows longitudinal tuning over 8 mm. Excitation is fed by discharging a 0.5-μF capacitor. The decay time of the excitation pulse is 10-40 μs. For the lasting laser oscillation from H_2CO, it is necessary that the tube be continuously filled with fresh H_2CO. H_2CO vapor was evaporated from paraformaldehyde heated to 360 K and then let into the tube which was exhausted by a 500-l/min rotary pump. A flow speed at around 2 m/s and a pulse repetition frequency (PRF) between 1 and 3 Hz are optimum. Only the 122.8- and 159.5-μm lines are detected at 7.5 Hz and none at 60 Hz. Measurements are carried out at the PRF of 2.5 Hz in the present work. An Echelette-type grating of 5

Manuscript received November 11, 1975; revised May 5, 1976.

The authors are with the Faculty of Engineering, Osaka City University, Osaka, Japan.

TABLE I
OBSERVED LASING WAVELENGTHS, INTERNAL CORRELATIONS, AND OUTPUTS

obs.λ_1(μm)	d(μm)	cal.λ_2(μm)	correlation[b]	m(%)	group	output
101.9±0.2	------			<10		0.4
119.6±0.2[a]	2330. ±60	122.75	cas.	<90	A	14
	239.1 ±5	159.46	?		B?	
122.8±0.2	------			<10	A	102
125.9±0.1[a]	2454. ±63	122.75	comp.	~70	A	1.4
155.1±0.2[a]	2799. ±78	159.52	comp.	100	B	220
157.6±0.2[a]	6797. ±160		cas.	>90	B	260
159.5±0.2	------			<10	B	154
163.8±0.2[a]	2873. ±10	155.	cas.	100	B	6.4
		159.26	comp.			
170.2±0.2	------			<10		0.6
184.4±0.2[a]	------			~40	B?	3

[a] Newly observed lines.
[b] cas.: cascade correlation; comp.: competitive one.

grooves/mm, which is calibrated against the higher order of the 28-μm line of H_2O, is used for wavelength measurement. Golay cells (UNICAM SP-50) and an Ni-W point contact diode are used as a detector.

Wavelengths of the observed lines are listed in the Table I together with the new lines denoted by superscript *a*. These lines oscillate in the range of pressure from 0.18 to 0.35 torr. There is a slight difference between the groups *A* and *B*[1] in the optimum excitation voltage. In Fig. 1(a), voltage dependence of the relative output is plotted at 0.28 torr. As for the 122.8-μm line (group *A*), 5.1 kV gives the maximum output; while 4.5 kV gives the maximum output for the 159.5-μm line (group *B*). At a given pressure the 159.5-μm line lases over still lower excitation in comparison to the 122.8-μm line, and is characterized by the narrower range of excitation voltage for oscillation. At lower pressures this tendency becomes remarkable.

Pressure dependences of the maximum output are shown in Fig. 1(b). The output of the 159.5-μm line takes a maximum value at 0.23 torr and decreases toward higher pressures. The 122.8-μm line, on the other hand, saturates at higher pressures. These typical behaviors of the 122.8- and 159.5-μm lines are also true for the other lasing lines of groups *A* and *B*, respectively. The relative output powers which are normalized against the maximum output of the H_2O 118-μm line at 0.15 torr in the present apparatus (100) are listed in Table I. The maximum output, however, is strongly affected by internal modulation. The peak power was estimated as about 30 mW to the 159.5-μm line.

Internal correlation is studied by detecting simultaneously two signals at wavelengths λ_1 and λ_2 during mirror tuning over 8 mm. A tuning curve of a line at the wavelength λ_1 often shows so-called principal maxima with spacing of *d*, in addition to subsidiary maxima spaced $\lambda_1/2$ apart. From spacing *d*, one can determine the wavelength, λ_2, of the modulating line [3].[2] The results are shown in Table I together with the degree of modulation, *m*, in percent. The signals of the strong 122.8- and 159.5-μm and very weak 101.9- and 170.2-μm lines were so insensitive to mirror tuning that

[1] We classified tentatively the observed lines into groups *A* and *B*, according to the dependence of the laser output on pressure, excitation voltage, and also to the internal correlation among the lines.

[2] In most cases, we applied the value of 1 for *p*, n_1, and n_2 in (2) of [3].

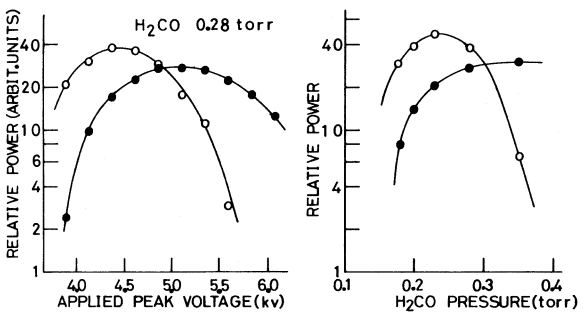


Fig. 1. Dependence of relative output of the 122.8 (closed circles) and 159.5-μm lines (open circles) on (a) applied peak voltage, (b) H_2CO pressure in torr.

we did not observe such a modulation. The 119.6-μm line seemed to couple to the 159.5-μm line as well as to the 122.8-μm line because every four subsidiary maxima were enhanced at around the principal maxima due to the 122.8-μm line. However, there still exists a possibility of the presence of adjacent lines. The 157.6-μm line relates cascadedly to the 159.5-μm line by the very long spatial period of modulation.

A tuning curve of the 163.8-μm line is shown in Fig. 2. The value of 2873 μm for *d* yields 159.26 μm, and this line couples competitively to the 159.5-μm line because these two lines do not lase simultaneously. Two small peaks that are located between two principal maxima in Fig. 2 are caused by the transverse cavity modes of the 155.1-μm line. The tuning pattern at 184.4 μm is a very complicated one and the correlation has not been clarified.

Pulse shape of the intense lines was observed by an Ni-W diode. The overall output rises in 35–60 μs after the start of the current pulse, and lasts for 15–120 μs, dependent on mirror tuning, discharge current, and pressure. The output signals at 159.5 and 122.8 μm start at almost the same time as shown in Fig. 3. The 159.5-μm line lasts a shorter duration than the 122.8-μm line and longer than the 155.1- and 157.6-μm lines. The high-frequency spiking at about 800 kHz, seen by the signal at 122.8 μm [Fig. 3(a)], appears also in a specific transverse mode of the 159.5-μm line but at a different frequency (~300 kHz).

Barry *et al.* recently reported the stimulated emission from H_2CO in the near-IR region, which was attributed to CO and

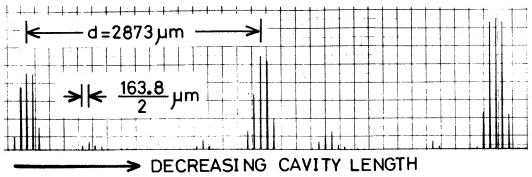


Fig. 2. Tuning curve of the 163.8-μm line. The line relates to the 155.1-μm line cascadedly and also to the 159.5-μm via the 155.1-μm line.

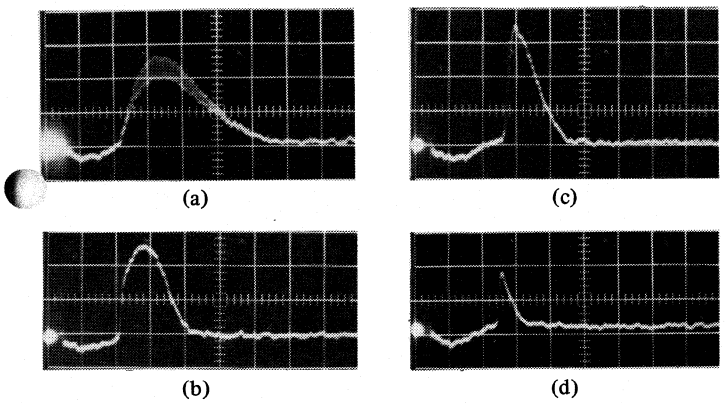


Fig. 3. Oscilloscope traces of the H_2CO laser output detected by the Ni-W point contact diode. $P_{H_2CO} = 0.30$ torr. $V = 4.6$ kV. Horizontal scale, 20 μs/div. (a) 122.8 μm, (b) 159.5 μm, (c) 155.1 μm, (d) 157.6 μm.

CO_2 [4]. We have not detected any near-IR oscillation under the optimum condition for the far-IR oscillation in the present apparatus. This may be due to the fact that the dissociation of H_2CO is suppressed as much as possible in the present apparatus.

References

[1] S. Okajima and A. Murai, "Far-infrared laser emission from H_2CO in a large gas-laser tube," *IEEE J. Quantum Electron.*, vol. QE-8, pp. 677–679, July 1972.
[2] M. Aketa, S. Okajima, N. Sokabe, and A. Murai, private communication.
[3] T. Kasuya, N. Takeuchi, A. Minoh, and K. Simoda, "Correlation between far-infrared laser oscillations in deuterium oxide vapor," *J. Phys. Soc. Japan*, vol. 26, pp. 148–154, Jan. 1969.
[4] J. D. Barry and W. E. Boney, "Near-infrared laser from HCHO," *J. Appl. Phys.*, vol. 44, pp. 1915–1916, Apr. 1973.

Optically Pumped Epitaxial GaAs Waveguide Lasers with Distributed Bragg Reflectors

CHENG-CHUNG TSENG, DAN BOTEZ, AND SHYH WANG

Abstract—**Fabrication and characteristics of epitaxial waveguide lasers with distributed Bragg reflectors are described. GaAs-(GaAl)As double-layered structures were grown by conventional liquid-phase-epitaxy (LPE) technique. Periodic corrugations were made by chemical etching through a photoresist grating mask. Laser action with clearly defined logitudinal modes was observed under optical pumping at liquid-nitrogen temperature.**

Manuscript received December 29, 1975; revised May 10, 1976. This work was supported in part by the Joint Services Electronics Program Contract F44620-71-C-0087, in part by Army Research Office Grant DAHC04-74-G0070, and in part by the Office of Naval Research Contract N00014-75-C0420.

The authors are with the Department of Electrical Engineering and the Computer Sciences and the Electronics Research Laboratory, University of California, Berkeley, CA 94720.

The work of Kogelnik and co-workers [1], [2] on distributed feedback (DFB) dye lasers has stimulated a great deal of interest in the use of Bragg scattering to provide the necessary feedback in thin-film lasers. Periodic waveguide structures suitable for solid-state and semiconductor lasers have been proposed [3]. However, the presence of periodic corrugations in the active medium of DFB lasers introduces serious disadvantages [4]. Wang [4] subsequently has proposed a new scheme of distributed Bragg-reflector (DBR) lasers, in which the Bragg-scattering region was separated from the gain medium. This novel concept was successfully demonstrated by Reinhart *et al.* [5] in their double heterostructure (DH) GaAs–(GaAl)As injection lasers with a distributed Bragg reflector at one side of the laser cavity. To reduce absorption in the reflector region, a tapered waveguide section was used for smooth transition from the active GaAs region to the reflector (GaAl)As region. Here we report the study of epitaxial GaAs waveguide lasers with two distributed Bragg reflectors at both ends of the laser cavity. As in early studies of DFB GaAs lasers [6]–[9], we used optical pumping in our preliminary study of DBR GaAs lasers. This alleviates the problem of absorption in the reflector region without using a tapered section.

A schematic drawing of the fabricated laser is shown in Fig. 1. The GaAs substrate was n-type (Si doped) with a carrier concentration of 10^{18} cm^{-3}. The optical waveguide consisted of a double-layered structure of GaAs–(GaAl)As grown on the GaAs substrate. These epitaxial layers were grown by the conventional liquid-phase-epitaxy (LPE) technique with a sliding pyrolitic graphite boat placed in ultrapure hydrogen stream. The growth temperature was 905°C and cooling rate was 0.5°C/min. The melt was supercooled 3°C before the start of growth. No intentional dopants were added during the growth. The mole fraction of Al in the (GaAl)As layer was 0.3. The thicknesses of (GaAl)As and GaAs layers were 6.5 μm and 2.0 μm, respectively. After the LPE growth, the wafer was cleaned, dried, and coated with Kodak Ortho resist (KOR). A contact mask was used to define the active and the Bragg-reflector regions. The grating mask was formed by exposing the wafer to the interference pattern of two intersecting argon laser beams and subsequently immersing the wafer in the developer. Care was taken in the exposure and development processes to ensure that the valley of the photoresist grating was developed all the way down to the substrate. The photoresist grating mask was baked at 100°C for 30 min before chemical etching was undertaken. We have found that an etching time of 30 s in a methanol solution containing 0.1 percent bromine was adequate to transfer the grating pattern to the GaAs epitaxial layer. The grating period was ~0.58 μm so that the Bragg scattering was due to the fifth-order Fourier component of the periodic corrugations.

The wafer was then saw cut at the sides and cleaved at ends to form individual bars. To minimize the reflection from the cleaved mirrors, we made no attempt to perfect the cleavages. The laser was mounted in a Dewar and then cooled down to liquid-nitrogen temperature. A nitrogen laser of output wavelength 3371 Å was used as the pumping source. The individual pumping pulses had a duration of 10 ns with a repetition rate of 100 pps and a peak power about 10 kW. A cylindrical lens was used to focus the pumping strip to 0.25 mm wide. Since the grating reflector regions, if unpumped, have high loss and low reflectivity, we pumped the sample almost from one end to the other as shown in Fig. 1. We left a small region near one end unpumped to discourage the Fabry–Perot modes

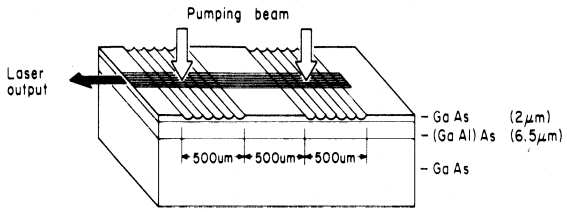


Fig. 1. Schematic diagram showing structure of an optically pumped GaAs DBR laser.

from lasing. Emission from the edge of the pumped end was passed through a Spex spectrometer and detected with a S-1 photomultiplier. The signal was further amplified and averaged with a boxcar integrator and recorded by a strip-chart recorder.

A typical emission spectrum of the lasers is shown in Fig. 2 (a). A broad spontaneous emission was centered at 8300 Å. Above a certain pumping threshold all the fabricated lasers with Bragg reflectors had a narrow stimulated peak centered near 8314 Å. The width of the stimulated emission at the half-power points ranged from 6 to 10 Å. Uniform "control" samples of the same length but without the Bragg reflectors had a stimulated peak near 8302 Å with a width of 25 Å as shown in Fig. 2(b). It is clear that the shift of the stimulated peak in our DBR lasers was due to the presence of the grating reflectors. A calculation of the guide index of refraction, using the Bragg condition for the guided wave, yields a value $n_{\text{guide}} \sim 3.6$ which is in agreement with the generally accepted value.

A high-resolution emission spectrum of the DBR laser is shown in Fig. 3. Five longitudinal modes can clearly be seen. The spacing between these longitudinal modes is about 1.40 Å which is too large for the longitudinal modes of the Fabry-Perot cavity. Theoretical prediction of the longitudinal mode spacing is given by $\Delta\lambda = \lambda_0^2/2n_{\text{eff}}L$, where λ_0 is the lasing wavelength, n_{eff} is the effective index of refraction for the waveguide taking dispersion effect into account, and L is the length of the center active region between two Bragg reflectors. Using the values of $\lambda_0 = 8314$ Å, $n_{\text{eff}} = 5.2$, and $L = 500$ μm, we find $\Delta\lambda = 1.33$ Å in good agreement with the observed value. The Fabry-Perot modes, on the other hand, would be spaced about 0.39 Å apart for $L = 1700$ μm. Therefore, the observed modes are clearly Bragg-reflector modes.

Fig. 4 shows the emission power versus pumping intensity at 8314 Å. Above the threshold, not only does the emission intensity increase abruptly, but also the radiation field becomes fully polarized in the plane of the junction. These observations together with the mode spectrum provide clear evidence of lasing. The threshold pumping intensity of 1.3×10^4 w/cm^2 was less than those previously reported [6]-[9] for optically pumped GaAs waveguide lasers. In optically pumped GaAs lasers, surface states play a very important role because most of the pumping N_2 laser beam is absorbed within a few tenths of a micron near the surface. A recent result on passivated GaAs shows that the surface recombination rate can be greatly reduced [10] by growing an oxide layer on GaAs. Furthermore, recent work on laser structures grown over preferentially etched channels [11] indicates a very interesting possibility of confining the laser beam in the lateral direction. We believe that the performance of optically pumped DBR GaAs lasers can be greatly improved by surface passivation, lateral optical confinement, and improved quality [12] of the gratings.

In conclusion, we have fabricated epitaxial GaAs waveguide lasers with distributed Bragg reflectors. Laser action was observed under optical pumping at liquid-nitrogen temperature. The Bragg-scattering effect of the grating reflectors was identified through the correlation of the emission wavelength with the corrugation period and a comparison of the laser wavelength with that of a "control" laser without the gratings. The laser action was evidenced by the simultaneous narrowing of the emission spectrum, observation of longitudinal Bragg-reflection modes, detection of strongly polarized output, and appearance of a threshold pump power.

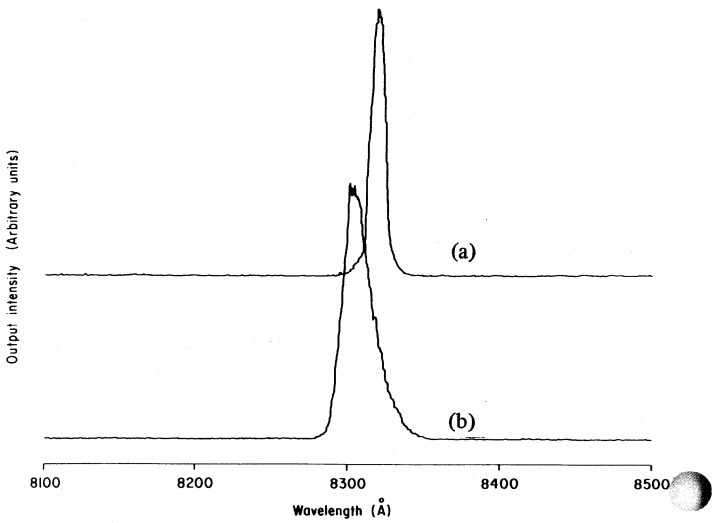


Fig. 2. Emission Spectrum of (a) a DBR laser with grating periodicity $\Lambda = 0.58$ μm and (b) a "control" laser above lasing threshold.

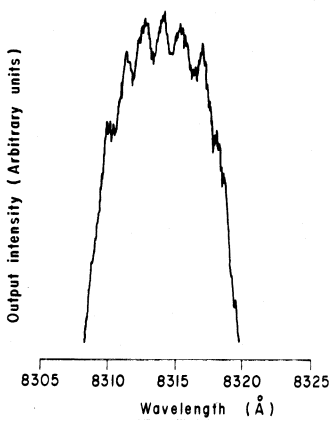


Fig. 3. High-resolution emission spectrum of a DBR laser.

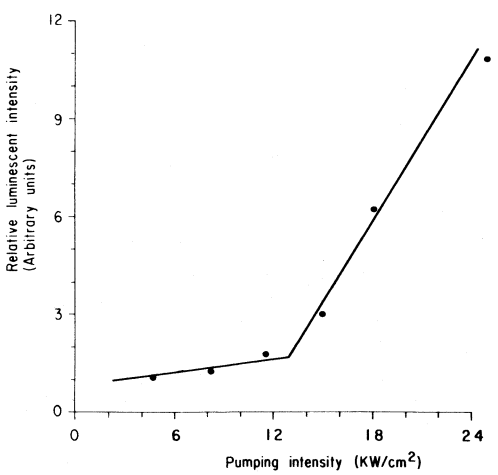


Fig. 4. Emission power as a function of pumping intensity at $\lambda = 8314$ Å for a DBR laser.

ACKNOWLEDGMENT

The authors would like to thank L. Figueroa for calibration of the power density of the N_2 laser and help with the optical experiment.

REFERENCES

[1] H. Kogelnik and C. V. Shank, "Stimulated emission in a periodic structure," *Appl. Phys. Lett.*, vol. 18, pp. 152–154, 1971.
[2] C. V. Shank, J. E. Bjorkholm, and H. Kogelnik, "Tunable distributed-feedback dye laser," *Appl. Phys. Lett.*, vol. 18, pp. 395–396, 1971.
[3] S. Wang, "Proposal of periodic layered waveguide structures for distributed lasers," *J. Appl. Phys.*, vol. 44, pp. 767–780, 1973.
[4] —, "Principles of distributed feedback and distributed Bragg-reflector lasers," *IEEE J. Quantum Electron.*, vol. QE-10, pp. 413–427, 1974.
[5] F. K. Reinhart, R. A. Logan, and C. V. Shank, "GaAs-$Al_x \cdot Ga_{1-x}As$ injection lasers with distributed Bragg reflectors," *Appl. Phys. Lett.*, vol. 27, pp. 45–48, 1975.
[6] M. Nakamura, A. Yariv, H. W. Yen, S. Somekh, and H. L. Garvin, "Optically pumped GaAs surface laser with corrugation feedback," *Appl. Phys. Lett.*, vol. 22, pp. 515–516, 1973.
[7] M. Nakamura *et al.*, "Laser oscialltion in epitaxial GaAs waveguide with corrugation feedback," *Appl. Phys. Lett.*, vol. 23, pp. 224–225, 1973.
[8] H. W. Yen, M. Nakamura, E. Garmire, S. Somekh, and A. Yariv, "Optically pumped GaAs waveguide lasers with a fundamental 0.11μ corrugation feedback," *Opt. Commun.*, vol. 9, pp. 35–37, 1973.
[9] C. V. Shank, R. V. Schmidt, and B. I. Miller, "Double-heterostructure GaAs distributed-feedback laser," *Appl. Phys. Lett.*, vol. 25, pp. 200–201, 1974.
[10] J. Y. Liou, private communication.
[11] D. Botez, W. T. Tsang, and S. Wang, "Growth characteristics of GaAs-$Ga_{1-x}Al_xAs$ structures fabricated by liquid-phase epitaxy over preferentially etched channels," *Appl. Phys. Lett.*, vol. 28, pp. 234–237, 1976.
[12] W. T. Tsang and S. Wang, "Profile and groove-depth control in GaAs diffraction gratings fabricated by preferential chemical etching in H_2SO_4-H_2O_2-H_2O system," *Appl. Phys. Lett.*, vol. 28, pp. 44–46, 1976.

A Simplified Method for Determination of the Induced-Emission Cross Section of Neodymium Doped Glasses

OTTO K. F. DEUTSCHBEIN

Abstract—**Induced-emission cross sections for the $^4F_{3/2} \rightarrow {}^4I_{11/2}$ and $^4F_{3/2} \rightarrow {}^4I_{13/2}$ transitions of Nd^{3+} in glasses can be determined with a satisfactory precision by a simplified method, based on the Judd-Ofelt theory, from the measurement of the integrated absorbance of the 750-nm band and of the effective linewidth of the fluorescence band.**

INTRODUCTION

The induced-emission cross section is an important parameter for laser materials, for it determines the laser gain for a given inversion of population.

Judd [1] and Ofelt [2] have shown that the radiative transition probabilities of the trivalent rare earths can be calculated from measurements of the oscillator strengths for the various electric dipole transitions and have given a simplified equation.

Manuscript received February 23, 1976.
The author is with the C.N.E.T., Bagneux, France.

Krupke [3] has applied this theory to the calculation of the induced-emission cross section of Nd^{3+}-doped silicate glasses at 1060 nm and found a good agreement (5 percent) with the values measured by other methods. Recently, Jacobs and Weber [4] extended this method to the laser transition at 1335 nm for silicate and phosphate glasses and claimed a precision of ±10 percent.

In this paper it will be shown that a simplified method can be used which gives a satisfactory agreement with the values obtained by a more complete calculation.

Krupke [3] calculated the absorption line strengths S of 11 transitions between the ground level and higher levels by measurements of the integrated absorbance $\int \kappa(\lambda)\, d\lambda$ according to the formula

$$\int \kappa(\lambda)\, d\lambda = \rho\, 8\pi^3\, e^2\, \lambda \eta \cdot S/3ch(2J+1) \tag{1}$$

where $\kappa(\lambda)$ is the absorption coefficient (cm^{-1}); ρ = concentration of Nd^{3+} (cm^{-3}); J = inner quantum number of the initial level; $\eta = (n^2+2)^2/9n$ is the correction factor for the local field in the dielectric medium, with n = refraction index. e, c, λ, and h are the usual symbols for charge of electron, speed of light, wavelength, and Planck's constant, respectively. It should be noted that S was initially [5] defined as the sum of the squared matrix components of the electric dipole operator $P = e \sum_i r_i$, but nowadays, several authors give S in square centimeters.[1]

From S, three phenomenological intensity parameters Ω_t (corresponding to the T_λ of Judd) had been calculated by Krupke for a number of glasses from the line strengths of 11 absorption bands, using the least squares fitting method, by the formula

$$S = \sum_{t=2,4,6} \Omega_t\, |\langle (S, L)\, J \,\|\, U^{(t)} \,\|\, (S', L')\, J' \rangle|^2 \tag{2}$$

where the $U^{(t)}$ are the matrix elements of the unit tensor operators; S, L, J and S', L', J' are the quantum numbers of the initial and the final states, respectively.

Hence, in the general case, at least three different line strengths must be determined for the evaluation of Ω_2, Ω_4, and Ω_6.

The matrix elements of the absorption transitions of Nd^{3+} and Er^{3+} have been published by Judd [1], those of the most trivalent rare earth ions by Carnall *et al.* [6]; Krupke [3] and Auzel *et al.* [7] have calculated the matrix elements for the laser transitions of Nd^{3+}. With the values of Ω_t determined by absorption measurements, the line strengths of the laser transitions can be calculated.

EXACT RELATIONS

In the case of Nd^{3+}, the comparison of the matrix elements $U^{(t)}$ of the different absorption transitions with those of the laser transitions shows a remarkable similarity of the latter with those of the absorption band at 750 nm, corresponding to the transitions $^4I_{9/2} \rightarrow {}^4F_{7/2}$ and $^4I_{9/2} \rightarrow {}^4S_{3/2}$ (which are not resolved in glasses), as seen from Table I.

The $U^{(6)}$ values are the most important for these transitions, $U^{(4)}$ are much weaker or zero, and $U^{(2)}$ are negligible or zero. According to (2), the line strengths of these transitions are determined by

$$S_{750} = \Omega_4 \times 0.045 + \Omega_6 \times 0.6597$$
$$= \Omega_6 (0.6597 + 0.045X) \tag{3a}$$

[1] With this definition, S, Ω_t, and σ_ρ have apparently the same dimension and the same order of magnitude. Thus, in the case of Nd^{3+}, according to (8) $\sigma_\rho = S_{\text{laser}}$ if $\Delta\lambda_{\text{eff}}/\lambda = 0.034$.

TABLE I
SQUARED MATRIX ELEMENTS OF Nd^{+++}

Transition	λ (nm)	$\lvert U^{(2)}\rvert^2$	$\lvert U^{(4)}\rvert^2$	$\lvert U^{(6)}\rvert^2$
$^4I_{9/2} \rightarrow {}^4F_{7/2}$ $^4I_{9/2} \rightarrow {}^4S_{3/2}$	750	0.001	0.045	0.6597
$^4F_{3/2} \rightarrow {}^4I_{11/2}$	1060	0	0.142	0.407
$^4F_{3/2} \rightarrow {}^4I_{13/2}$	1335	0	0	0.212

$$S_{1060} = \Omega_4 \times 0.142 + \Omega_6 \times 0.407$$
$$= \Omega_6 (0.407 + 0.142X) \quad (3b)$$
$$S_{1335} = \Omega_6 \times 0.212 \quad (3c)$$

with $X = \Omega_4/\Omega_6$.

Hence

$$S_{1060} = S_{750} \times 0.617\,[1 + 0.280X/(1 + 0.068X)] \quad (4a)$$
$$S_{1335} = S_{750} \times 0.321/(1 + 0.068X). \quad (4b)$$

These equations are valid for all Nd-doped materials. They show that the laser line strengths can be determined by S_{750} and X only, and that the contribution of X is quite low, for X of the order of ≈ 1. Hence errors in the estimation of X have only a reduced influence on the determination of these line strengths.

X can be determined by a second absorption line strength,[2] or by the ratio of the fluorescent branching ratios $\beta(^4F_{3/2} \rightarrow {}^4I_{11/2})$ to $\beta(^4F_{3/2} \rightarrow {}^4I_{9/2})$.

The fluorescent branching ratios for transitions originating from a specific initial manifold $|(S', L')J'\rangle$ are defined by

$$\beta[(S', L')J'; (\bar{S}, \bar{L})\bar{J}] \equiv \frac{A[(S', L')J'; (\bar{S}, \bar{L})\bar{J}]}{\sum_{\bar{S},\bar{L},\bar{J}} A[(S', L')J'; (\bar{S}, \bar{L})\bar{J}]} \quad (5)$$

where the sum is over all possible terminal manifolds $|(\bar{S}, \bar{L})\bar{J}\rangle$. A, the probability for a transition from the initial manifold to the terminal manifold, is given by

$$A[(S', L')J'; (\bar{S}, \bar{L})\bar{J}] = \frac{64\pi^4 e^2}{3h(2J' + 1)\lambda^3} n \left[\frac{(n^2 + 2)^2}{9}\right] \cdot \sum_{t=2,4,6} \Omega_t \lvert\langle (S', L')J' \| U^{(t)} \| (\bar{S}, \bar{L})\bar{J}\rangle\rvert^2. \quad (6)$$

Taking into account the matrix elements (from Table I for $^4F_{3/2} \rightarrow {}^4I_{11/2}$ and $U^{(2)} = 0$, $|U^{(4)}|^2 = 0.230$, $|U^{(6)}|^2 = 0.056$ for $^4F_{3/2} \rightarrow {}^4I_{9/2}$) and the wavelengths λ (1060 and 888 nm, respectively),

$$B = \beta(^4F_{3/2} \rightarrow {}^4I_{11/2})/\beta(^4F_{3/2} \rightarrow {}^4I_{9/2})$$
$$= (0.407 + 0.142X)/1.71(0.056 + 0.230X).$$

Hence

$$X = (1.036 - 0.245B)/(B - 0.361). \quad (7)$$

[2]Kaminskii and Li [12] proposed for the determination of X the line strengths of the transitions $^4I_{9/2} \rightarrow {}^2P_{1/2}$ and $^4I_{9/2} \rightarrow {}^4I_{15/2}$. However, the intensity parameters of these transitions are an order of magnitude weaker than those of the transitions at 750 nm and 880 nm. Therefore, about ten times greater thicknesses of the samples are necessary for the measurements.

The induced-emission cross section σ_p is related to the laser line strength by [3]

$$\sigma_p = 4\pi^2 \lambda \alpha \eta S_{\text{laser}}/3(2J + 1)\,\Delta\lambda_{\text{eff}} \quad (8)$$

where α = the fine structure constant ($=7.30 \times 10^{-3}$), $\Delta\lambda_{\text{eff}}$ = the effective linewidth of the fluorescence band, and J = the quantum number of the initial state of the laser transition.

Thus the induced-emission cross section can be determined by the measurements of the integrated absorbance at 750 nm, of the ratio of the fluorescent branching ratios $\beta_{^4F_{3/2} \rightarrow {}^4I_{11/2}}/\beta_{^4F_{3/2} \rightarrow {}^4I_{9/2}}$, and of the effective linewidth of the fluorescence band.

SIMPLIFIED EQUATIONS

Comparing the X values of twelve silicate and phosphate glasses of different compositions and one glass ceramic, only a slight variation of $X(\cong 0.9)$ was found, though the induced-emission cross sections varied by a factor of 4 (Table II).[3]

Sarkies [8] measured the branching ratios of thirty silicate glasses of different compositions and found a similar result: the branching ratios varied only slightly for different compositions:

$$\beta_{(1.06)} = 0.493 \pm 0.028 \quad \text{and} \quad \beta_{(0.88)} = 0.383 \pm 0.026.$$

Using (7), $X = 0.8$ for these glasses.

Quite recently, Jacobs and Weber [9] investigated a great number of glasses in a systematic study of different network formers: silicate, phosphate, borate, germanate, and tellurite, aluminate, titanate, and fluorophosphate glasses, with various additives: Li_2O, Na_2O, K_2O, Rb_2O, MgO, CaO, SrO, and BaO. They stated that for the glasses studied thus far, X varied over only a narrow range of approximately 0.9–1.1.

According to these experimental results, the laser line strengths and the induced-emission cross sections can be determined with a satisfactory accuracy by simplified equations taking $X = 0.9$.

Under these conditions, (4a) and (4b) become

$$S_{1060} = S_{750} \times 0.766 \quad (9a)$$
$$S_{1335} = S_{750} \times 0.301. \quad (9b)$$

Introducing these values in (8), with λ = 1060 or 1335 nm, $\eta = 1.41$, and $J = 3/2$, the induced-emission cross sections are

$$\sigma_{p1060} = 2.70 \times 10^{-6}\ \text{cm} \times S_{750}/\Delta\lambda_{\text{eff}(1060)} \quad (10a)$$
$$\sigma_{p1335} = 1.365 \times 10^{-6}\ \text{cm} \times S_{750}/\Delta\lambda_{\text{eff}(1335)}. \quad (10b)$$

In order to compare the values of the induced-emission cross section σ_{p1060} (Table II, footnote 2) obtained by the complete calculation according to Krupke with those σ_{p1060} (Table II, footnote 3) obtained by (10a), Table II shows the intensity parameters Ω_4 and Ω_6, calculated by (2) from 11 absorption bands; the measured line strengths S_{750} according to (1); the measured effective linewidths $\Delta\lambda_{\text{eff}}$, and $S_{750}/\Delta\lambda_{\text{eff}}$, for 13 glasses of different compositions, arranged by growing values of Ω_6. They cover a large range of S_{750} and σ_p.

The glasses 3669A, S33, ED-2, and LSG91H have been described and investigated by Krupke [3]; P 008 is a Nd-doped glass ceramic described by Müller and Neuroth [11]; LG650, LG700, and LG710 are commercial glasses from Jenaer Glaswerk Schott, Mainz, Germany; Sch-A to Sch-E are experimental glasses from Schott. The radiative properties of the Schott glasses have been measured and calculated by Weber

[3]For the divergent value for glass 3669A see footnote 4 in Table II.

TABLE II
INTENSITY PARAMETERS AND RADIATIVE PROPERTIES OF VARIOUS GLASSES

GLASS	3669A	LG650	SCH-A	SCH-B	P 008	LSG-91H	SCH-C	SCH-D	S 33	SCH-E	ED 2	LG700	LG710
Ω_6[1]	1.76[4]	1.89	2.53	4.04	4.49	4.59	4.69	4.74	4.79	5.02	5.18	5.43	5.72
Ω_4[1]	2.95[4]	2.40	2.00	3.78	4.03	4.79	4.24	4.06	4.47	4.87	4.68	4.99	5.84
$X = \Omega_4/\Omega_6$	1.68[4]	1.27	0.79	0.94	0.90	0.96	0.91	0.86	0.93	0.97	0.90	0.92	1.02
S_{750}[1]	1.32	1.30	1.71	2.74	3.10	3.14	3.20	3.24	3.26	3.51	3.50	3.70	3.90
$\Delta\lambda_{eff}$(nm)	33.2	33.5	37.4	38.6	35.5	34.7	30.0	30.9	33.6	28.1	33.6	26.9	23.7
$S_{750}/\Delta\lambda_{eff}$ (10^{-14} cm)	0.40	0.39	0.46	0.71	0.87	0.90	1.07	1.05	0.97	1.25	1.04	1.37	1.64
$\sigma\rho\,1060$[2,1]	1.2	1.12	1.29	1.84	2.39	2.6	3.03	2.64	2.8	3.38	2.9	3.61	4.46
$\sigma\rho\,1060$[3,1]	1.1	1.05	1.24	1.92	2.36	2.44	2.88	2.84	2.62	3.38	2.81	3.70	4.43

[1] In units of 10^{-20} cm^2.
[2] Calculated from Ω_6 and Ω_4.
[3] Calculated from (10a).
[4] These values (from [3, Table III]) are not consistent with the calculated branching ratios $\beta_{1.06} = 0.51$ and $\beta_{0.88} = 0.41$ given in [3, Table IV]) which correspond, according to (7), to $X = 0.83$. The branching ratios of this glass measured by Mann and DeShazer [10] are $\beta_{1.06} = 0.51$ and $\beta_{0.88} = 0.37$; they agree with the latter values.

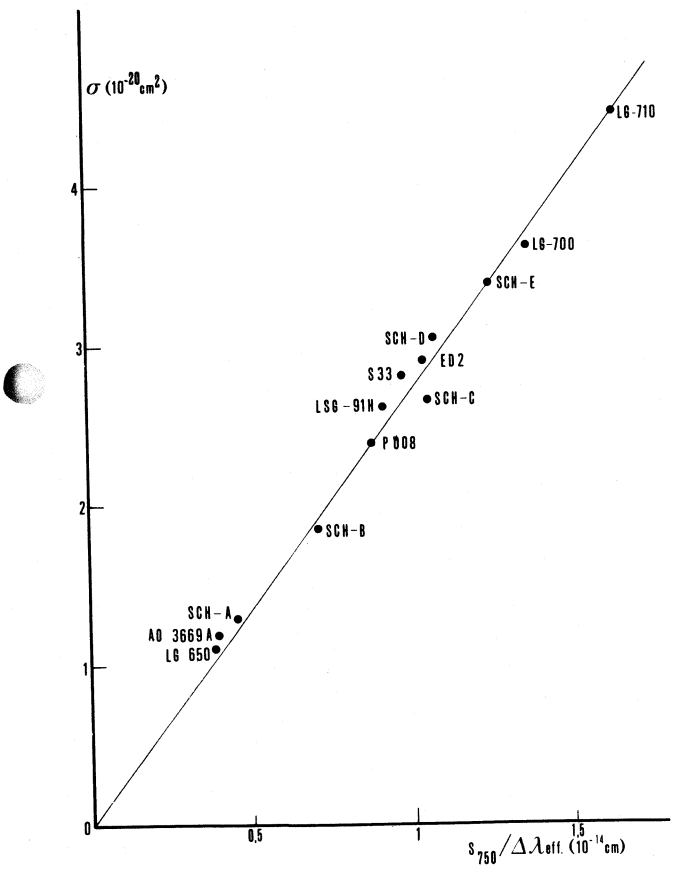


Fig. 1. Induced-emission cross sections: the straight line is obtained by (10a), the dots by the complete calculation.

TABLE III
INDUCED-EMISSION CROSS SECTIONS FOR $\lambda = 1335$ nm (IN UNITS OF 10^{-20} cm^2)

Glass	3669A	LSG-91 H	ED 2
σ_ρ Jacobs	0.30	0.65	0.72
σ_ρ (10b)	0.31	0.65	0.70

at the Lawrence Livermore Laboratory, University of California, Livermore.

In Fig. 1, the straight line is obtained by (10a) and the dots by the complete calculation.

The agreement is quite good, with an rms error of 6 percent, not much more than the errors in the Ω_t in Krupke's complete calculation (5 percent).

For the transition $^4F_{3/2} \rightarrow {}^4I_{13/2}$ at 1335 nm, Jacobs and Weber [4] published values of $\sigma_{\rho 1335}$ and $\Delta\lambda_{eff}$ for ten glasses, but not the integrated absorbance at 750 nm nor S_{750}. Hence only three glasses (3669A, ED-2, and LSG-91H) whose S_{750} had been published previously by Krupke [3] can be compared for the $\sigma_{\rho 1335}$ values obtained from (10b), see Table III.

As Jacobs estimates the uncertainty of his σ_ρ values to be ±10 percent, the agreement is wholly in these limits.

CONCLUSION

For all Nd-doped glasses studied so far, the simplified formulas (10a) and (10b) give the induced-emission cross sections with a satisfactory accuracy, within the limits of the precision of the Judd-Ofelt theory [9]. They are valuable for quick evaluations of new laser materials, especially for laboratories with limited computer facilities.

Whenever glasses should be found with fluorescent branching ratios $\beta_{1.06} \leqq 0.8\beta_{0.88}$, (4a) and (4b) must be used, with X determined by (7). However, due to the low value of $\beta_{1.06}$, such glasses would not be valuable laser materials.

ACKNOWLEDGMENT

The author wishes to thank Dr. M. Weber from the Lawrence Livermore Laboratory, University of California, Livermore, for the permission to use his measurements and calculations of the radiative properties of Schott glasses in Table II, and the

Jenaer Glaswerk Schott, Mainz, Germany, for providing these samples.

REFERENCES

[1] B. R. Judd, "Optical absorption intensities of rare-earth ions," *Phys. Rev.*, vol. 127, pp. 750–761, 1962.

[2] G. S. Ofelt, "Intensities of crystal spectra of rare-earth ions," *J. Chem. Phys.*, vol. 37, pp. 511–520, 1962.

[3] W. F. Krupke, "Induced-emission cross sections in neodymium laser glasses," *IEEE J. Quantum Electron.*, vol. QE-10, pp. 450–457, Apr. 1974.

[4] R. R. Jacobs and M. J. Weber, "Induced-emission cross sections for the $^4F_{3/2} \rightarrow {}^4I_{13/2}$ transition in neodymium laser glasses," *IEEE J. Quantum Electron.* (Corresp.), vol. QE-11 pp. 846–847, Oct. 1975.

[5] E. U. Condon and G. H. Shortley, *The Theory of Atomic Spectra*. Cambridge, England: University Press, 1935.

[6] W. T. Carnall, P. R. Fields, and K. Rajnak, "Electronic energy levels in the trivalent Lanthanide aquo ions I.," *J. Chem. Phys.*, vol. 49, pp. 4424–4442, 1968.

[7] F. Auzel and J. C. Michel, "Détermination de la force d'oscillateur de la transition $^4I_{11/2} \rightarrow {}^4F_{3/2}$ de Nd^{3+} dans la fluoroapatite, le grenat d'yttrium d'aluminium et l'ultraphosphate de néodyme," *C. R. Acad. Science Paris*, vol. 279B, pp. 187–190, 1974.

[8] P. H. Sarkies, "Cross-section measurements on neodymium laser glasses," Ph.D. dissertation, Univ. Sheffield, Sheffield, England, 1971.

[9] R. R. Jacobs and M. J. Weber, "Dependence of the $^4F_{3/2} \rightarrow {}^4I_{11/2}$ induced-emission cross section for Nd^{3+} on glass composition," *IEEE J. Quantum Electron.*, vol. QE-12, pp. 102–111, Feb. 1976.

[10] M. M. Mann and L. G. DeShazer, "Energy levels and spectral broadening of neodymium ions in laser glass," *J. Appl. Phys.*, vol. 41, pp. 2951–2957, 1970.

[11] G. Müller and N. Neuroth, "Glass ceramic–A new laser host material," *J. Appl. Phys.*, vol. 44, pp. 2315–2318, May 1973.

[12] A. A. Kaminskii and L. Li, "Analysis of spectral line intensities of TR^{3+} ions in crystal systems," *Phys. Stat. Sol.* (a), vol. 26, pp. 593–598, 1974.

Tunable Two-Wavelength Mode Locking of the CW Dye Laser

H. MAHR

Abstract–**Tunable model-locked laser output is achieved at two wavelengths with a CW dye laser containing a rhodamine 6G and a cresyl violet jet. Rhodamine 6G is pumped by a mode-locked argon laser. Output pulses of 4–5 ps duration are obtained.**

We report tunable mode-locked CW dye laser operation at two wavelengths in a cavity containing separate rhodamine 6G and cresyl violet jets. Rhodamine 6G is pumped by a mode-locked argon ion laser. The double wavelength output could be tuned from operation at 547 nm (rhodamine 6G) and 637 nm (cresyl violet) to lasing at 585 and 675 nm. CW double mode locking of these same dyes at two fixed frequencies was previously reported by Yasa and Teschke [1].

Manuscript received February 23, 1976. This work was supported in part by the U.S. Office of Naval Research under Contract N00014-75-C-0248, and in part by the National Science Foundation under Grant DMR72-03029 through the Materials Science Center, Cornell University, Tech. Rep. 2603.

The author is with the Laboratory of Atomic and Solid State Physics, Cornell University, Ithaca, NY 14853.

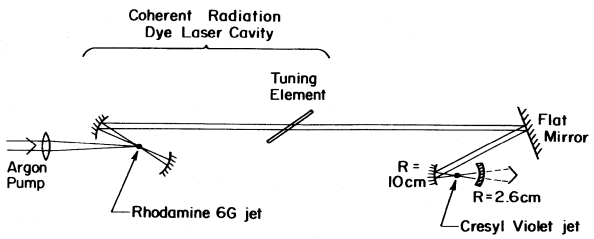


Fig. 1. Experimental setup: Two dye jets are simultaneously flowed in the doubly folded cavity shown. The laser is pumped by a mode-locked argon ion laser.

The experimental setup is shown in Fig. 1. The dye laser jet containing rhodamine 6G in ethylene glycol was pumped by a mode-locked argon ion laser with pulses of 600–800-mW average power and 200-ps duration at a 10^8-Hz repetition rate. A Coherent Radiation dye laser cavity [3] was extended in length to match the length of the argon laser for synchronous pumping. The resulting mode locking of the rhodamine 6G output was reported previously [2]. Another folded mirror extension was then added, as shown in Fig. 1, with a flow jet of cresyl violet in ethylene glycol at its intermediate focus. The mirrors were of 2.6- and 10-cm radius of curvature, respectively. The cresyl violet[1] concentration was about 5×10^{-4} molar; the concentration of rhodamine 6G was as optimized for CW operation. A single plate of birefringent sapphire of approximately 0.5-mm thickness was used as the tuning element (replacing the standard 3-plate birefringent tuning element [3] of the Coherent Radiation dye laser).

Simultaneous mode-locked laser action was observed at two wavelengths after adjustment of the total cavity length to synchronous operation. Rotation of the sapphire plate allowed us to tune the two-wavelength output from 547 nm (rhodamine 6G) and 637 nm (cresyl violet) to 585 and 675 nm, respectively. After removing the sapphire plate, fixed frequency, mode-locked, two-wavelength lasing was observed at about 580 nm and 645 nm, respectively, similar to reports by Yasa and Teschke [1].

The separation of the two lasing wavelengths is given by the birefringence Δn of the sapphire plate and its thickness 1. Output of the laser was fully mode locked and very stable. An interferometer setup, described earlier [2], was used to measure the correlation pulsewidth by monitoring the second-harmonic signal obtained from an ADP crystal. An example of a trace of the correlation output of pulses at 670 nm and showing a half-width of 7 ps is shown in Fig. 2. Care was taken to show that the pulses are completely mode locked. In our setup in which one of the two interferometer beams is chopped we observe the chopped output only. By blocking the unchopped beam an absolute zero is obtained and "shoulders" due to partial mode locking are easily detected. Pulses with rhodamine 6G alone tend to be exponential. If this were also true for the double-mode-locked pulses shown here, pulses obtained could be as short as 3.5 ps. Otherwise, pulsewidth should be 4–5 ps.

Outputs of 50 mW were observed with a 2-percent output coupler. No attempts were made to optimize the double-wavelength operation. We feel that the limit of the tuning range at 675 nm results from the use of mirrors that were not

[1] Supplier: K + K Laboratories, Plainview, NY; lot no. 5098A. Rhodamine 6G was obtained from Eastman Kodak, Rochester, NY.

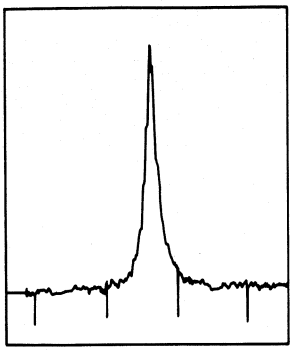


Fig. 2. Trace of the correlator output in the ultraviolet of a two-beam delayed interferometer. The marks are separated by 0.508 cm.

designed for such a broad-band use. We also feel that two-wavelength operation could be achieved with a wavelength separation quite different from the 90 nm observed here by use of different sapphire flats.

In short, this simple system provides for tunable two-wavelength operation of mode-locked pulses with a repetition rate of 10^8 Hz, pulse durations as short as 3.5–5 ps, and high average power.

References

[1] Z. A. Yasa and O. Teschke, "C.W. double mode-locking of the dye laser experiment," *Appl. Phys. Letters*, vol. 27, pp. 446–447, Oct. 15, 1975.

[2] H. Mahr and M. D. Hirsch, "An optical up-conversion light gate with picosecond resolution," *Optics Commun.*, vol. 13, pp. 96–99, Feb. 1975.

[3] J. M. Yarborough, "C.W. dye laser emission spanning the visible spectrum," *Appl. Phys. Letters*, vol. 24, pp. 639–630, June 15, 1974.

Efficient Generation of Continuously Tunable Coherent Radiation in the 2460–2650-Å Spectral Range

R. K. JAIN AND T. K. GUSTAFSON

Abstract—**Continuously tunable coherent radiation in the 2460–2650-Å spectral range has been achieved by second harmonic generation (SHG) of a dye laser in a 90° phase-matched ADP crystal, temperature tuned between −116°C and 52°C. The 8.4-percent conversion efficiency obtained at a fundamental power of 9.6 kW is approximately 5 times larger than that reported earlier for SHG at these wavelengths.**

This correspondence reports the efficient generation of coherent radiation continuously tunable between 2460 and 2650 Å, a spectral region of particular interest to photochemists and photobiologists [1]–[3]. This is achieved by 90° phase-matched second harmonic generation (SHG) of a visible dye laser in an ADP crystal, temperature tuned between

Manuscript received May 6, 1976; revised May 10, 1976. This work was supported in part by the Joint Services Electronics Program.

R. K. Jain was with the Electronics Research Laboratory, University of California, Berkeley, CA 94720. He is now with Bell Laboratories, Holmdel, NJ 07733.

T. K. Gustafson is with the Electronics Research Laboratory, University of California, Berkeley, CA 94720.

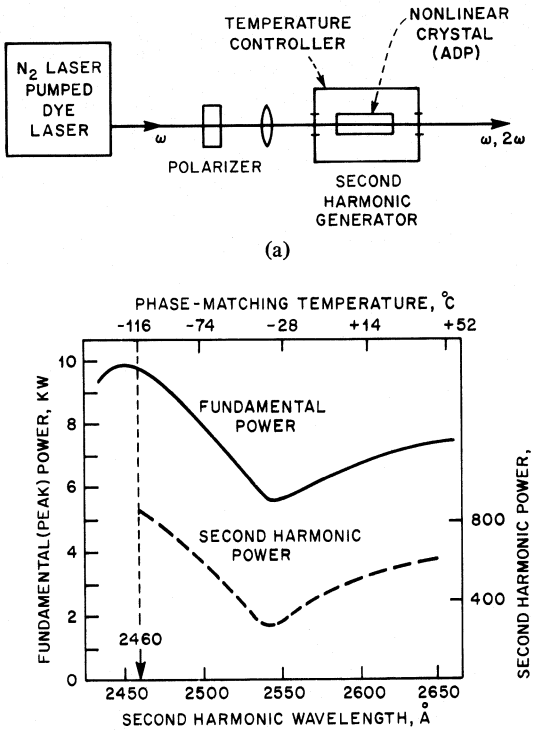


Fig. 1. (a) Basic experimental arrangement for temperature tuned 90° phase-matched SHG of the dye laser. (b) Peak fundamental and second harmonic powers versus wavelength and phase-matching temperature. The solid line is a spectral plot of available fundamental peak power, the dashed line gives the corresponding second harmonic power.

−116°C and 52°C. A conversion efficiency of 8.4 percent has been obtained with 9.6 kW of input power at a fundamental wavelength of 4920 Å. This efficiency is approximately 5 times larger than previous work [4] on SHG in this wavelength range, for which a crystal of lithium formate monohydride was used with angle-tuned phase matching.

Fig. 1(a) sketches the experimental arrangement used. This is essentially similar to that reported by Dunning *et al.* [5] for the efficient generation of radiation at wavelengths longer than 2530 Å; however, by cooling the ADP crystal down to −116°C, we have extended the tunability of this efficient SHG scheme to wavelengths as short as 2460 Å. The nitrogen laser-pumped dye laser was of the Hänsch-cavity design [6], and employed a 5×10^{-3} molar (acidic) ethanolic solution of 7-hydroxy-coumarin [7] (dye), pumped by an 80-kW N_2 laser (repetition rate = 25 pps). Output powers between 5.6 and 10 kW in a linewidth of ~1 Å were obtained over the 4900–5300-Å spectral range (Fig. 1(b), solid line), in a beam of 5-mrad divergence. The polarized beam was focused by means of a long-focal-length (15-cm) lens into a 5-cm-long 45° *z*-cut ADP crystal, mounted in a liquid-nitrogen-cooled temperature controller [8]. By varying the crystal temperature from −116°C to + 52°C (with an accuracy of 0.1°C), 90° phase-matching was obtained for each chosen dye laser wavelength [8]. As seen in the spectral plot [Fig. 1(b)] of the fundamental and second harmonic power, conversion efficiencies larger than 5 percent were obtained over the entire spectral range, with a maximum efficiency of ~8.4 percent at 4920 Å, corresponding to 9.6-kW peak power. As expected the conversion efficiency increases with fundamental power; however, due to significant depletion of the pump beam at the high power levels involved here, the proportionality and the magnitude of the conversion efficiencies cannot be compared with theory [9].

In conclusion, efficient SHG in the 2460–2650 Å spectral region has been achieved by using 90° phase-matching in ADP at temperatures as low as −116°C. The long wavelength range of this source can be extended up to ~2900 Å by the use of elevated temperatures, as demonstrated by Jennings and Varga [10]. By using the multimegawatt power level dye lasers [11] that are now commercially available [12], efficiencies of over 30 percent should be possible over the entire 2450–2900-Å wavelength range. This makes the above source very useful for several applications including atomic spectroscopy [13], isotope separation [14], and numerous photochemical [15] and biological [1]–[3], [16] studies. In particular, it should be invaluable for studies of the activity spectra of isolated nerve fibers [3], and in the selective sterilization of bacteria [17] like *E. Coli*, which are extremely vulnerable to radiation between 2500 and 2700 Å.

ACKNOWLEDGMENT

The authors thank P. K. Takahashi for his interest and encouragement.

REFERENCES

[1] W. Harm, "Effects of dose fractionation on ultraviolet survival of E. Coli," *Photochem. Photobiol.* vol. 7, pp. 73–86, 1968.
[2] a) P. K. Takahashi, "Update on the status of laser microbiological research," 1975 (unpublished).
b) P. K. Takahashi *et al.*, "Irradiation of E. Coli in the visible with a tunable dye laser source," *Appl. Microbiology*, vol. 29, pp. 63–67, 1975.
[3] E. M. Lieberman, "Ultraviolet radiation effects on isolated nerve fibers," in *Advances in Biological and Medical Physics*, vol. 13, J. H. Lawrence and J. W. Gofman, Ed. 1970, pp. 329–350.
[4] F. B. Dunning, F. K. Tittel, and R. F. Stebbings, "The generation of tunable coherent radiation in the wavelength range 2300–3000 Å using lithium formate monohydride," *Opt. Commun.*, vol. 7, pp. 181–183, 1973.
[5] F. B. Dunning, E. D. Stokes, and R. F. Stebbings, "The efficient generation of coherent radiation continuously tunable from 2500 Å to 3250 Å," *Opt. Commun.*, vol. 6, pp. 63–66, 1973. Note that the data presented here correspond to second harmonic wavelengths longer than 2530 Å. Phase-matching temperatures are not indicated.
[6] T. W. Hänsch, "Repetitively pulsed tunable dye laser for high resolution spectroscopy," *Appl. Opt.*, vol. 11, pp. 895–898, 1972.
[7] A. Dienes, R. K. Jain, and C. Lin, "Formation mechanisms in an excited-state-reaction dye laser," *Appl. Phys. Lett.*, vol. 22, pp. 632–634, 1973. For efficient lasing in the green region (5100–5400 Å), the blue-attenuating (Kodak #12) filter was inserted in the dye laser cavity.
[8] R. K. Jain and T. K. Gustafson, "Second harmonic generation of several argon-ion laser lines," *IEEE J. Quantum Electron.*, vol. QE-9, pp. 859–861, 1973 (a plot of phase-matching temperature versus wavelength is given here).
[9] G. D. Boyd and D. A. Kleinman, "Parametric interactions of focused Gaussian light beams," *J. Appl. Phys.*, vol. 39, pp. 3597–3669, 1968.
[10] D. A. Jennings and A. J. Varga, "Efficient second harmonic generation in ADP with two new fluorescein dye lasers," *J. Appl. Phys.*, vol. 42, pp. 5171–5172, 1971.
[11] E. O. Ammaann, C. D. Decker, and J. Falk, "High-peak-power 532-nm pumped dye laser," *IEEE J. Quantum Electron.*, vol. QE-10, pp. 463–465, 1974.
[12] Laser Energy Inc., Rochester, NY.
[13] J. Kuhl and H. Spitschan, "Flame-fluorescence detection of Mg, Ni and Pb with a frequency-doubled dye laser as an excitation source," *Opt. Commun.*, vol. 7, pp. 256–259, 1973.
[14] a) E. S. Young and C. B. Moore, "Isotope separation by photopredissociation," *Appl. Phys. Lett.*, vol. 21, pp. 109–111, 1972.
b) V. S. Letokhov, "Use of lasers to control selective chemical reactions," *Science*, vol. 180, pp. 451–458, 1973.
[15] a) J. T. Knudtson and E. M. Eyring, "Laser-induced chemical reactions," *Ann. Rev. Phys. Chem.*, vol. 25, pp. 255–274, 1974; see also U.S. Nat. Tech. Information Service, AD Rep. 777460/7GA, 1974.
b) L. E. Brus and J. R. McDonald, "Time-resolved fluorescence kinetics and vibronic structure in tunable ultraviolet laser excited sulfur dioxide vapor," *J. Chem. Phys.*, vol. 61, pp. 97–105, 1974.
[16] R. B. Harris, "Biological applications with tunable lasers," *Amer. Lab.*, vol. 5, pp. 93–99, 1973.
[17] P. K. Takahashi, private communication.

Controlled Energy Extraction and Sharp Nanosecond Pulses from an HF Amplifier

R. W. GETZINGER, N. R. GREINER, K. D. WARE, J. P. CARPENTER, AND R. G. WENZEL

Abstract—**We report complete spatial control of laser energy extracted from an electron-beam-initiated HF amplifier. Control was achieved by application of a weak oscillator beam, which, by extraction of all of the available energy, overcame amplified spontaneous emission. In a separate experiment, temporal control was also demonstrated. Short (4-ns) sharp (contrast ~20) amplified pulses were obtained by rapid polarization rotation and selective reflection in the amplified beam.**

INTRODUCTION

This correspondence reports the complete extraction of laser energy from a high-gain HF amplifier in a high-quality beam controlled by an HF oscillator. Unreported attempts with pulsed amplifiers and problems with parasitic modes in CW lasers have left the impression that this is hard to do with the high-gain ($n\sigma \geqslant 1$ cm^{-1}) HF medium. We show here that complete spatial control of extraction is achieved, when 1) the oscillator beam passes through the amplifier medium during the entire gain period, and 2) no parts of the amplifier medium are left out of the oscillator beam to amplify the ever-present spontaneous emission (see Fig. 1). In this work a 4×10^8-W amplified beam was controlled by a 1×10^6-W oscillator beam.

A second significant result is the successful switching of a short (4-ns) pulse from a longer (30-ns) amplified pulse with high contrast. This was accomplished by momentarily increasing the reflection (from ~0 to ~13 percent) of the amplified beam off a canted dielectric surface by the temporary rotation of the plane of polarization of the amplified beam. A 4-ns voltage pulse was applied across the electrooptic crystal shown in Fig. 2, which rotated the plane of polarization 90° for 4 ns. This pulse of rotated polarization passed successfully through the rest of the oscillator–amplifier system. At the dielectric surface, held at the Brewster angle for the unrotated polarization, none of the beam was reflected except during the rotated portion of the pulse, when ~13 percent of the extracted power was reflected into the short-pulse beam. With materials of higher refractive index, most of the power could be reflected into the short-pulse beam.

EXPERIMENTAL

The experimental configurations yielding the two principal results described in the Introduction are shown schematically

Manuscript received May 10, 1976. This work was performed under the auspices of the USERDA.

The authors are with the Los Alamos Scientific Laboratory, University of California, Los Alamos, NM 87545.

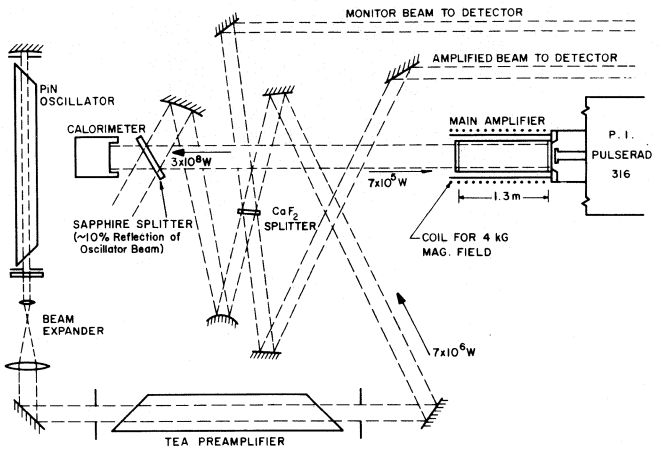


Fig. 1. Schematic of configuration for energy extraction experiments.

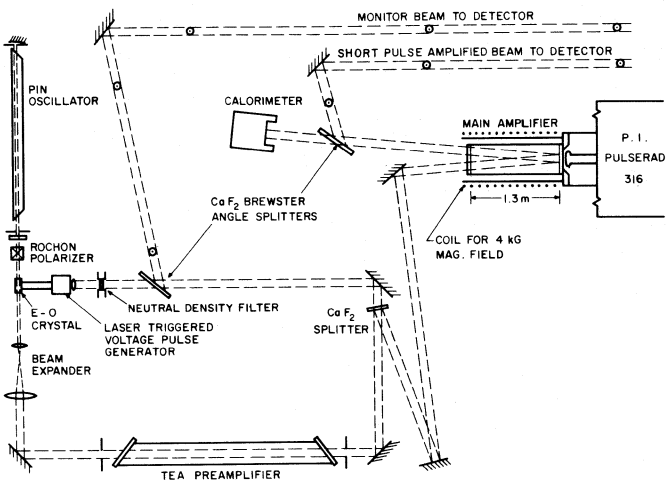


Fig. 2. Schematic of configuration for power amplification and isolation of shuttered, *s*-polarized 4-ns pulse.

in Figs. 1 and 2. The front end, consisting of the electric discharge oscillator and preamplifier fueled by SF_6 and C_2H_6, a 5X beam expander, and, in Fig. 2, a $LiNbO_3$ electrooptic crystal driven by the laser-triggered voltage pulse generator (VPG), has been described previously [1], [2]. The pilot beam leaving the TEA preamplifier is a high-quality, 100-ns FWHM pulse of HF laser radiation at 2.7 μm containing ~1 J of energy in a diameter of 20 mm. In Fig. 2, the pilot beam was *p*-polarized except for a 4-ns period of *s*-polarization produced by application of a half-wave voltage pulse from the VGP across the electrode crystal. Contrast ratios for the *s*-polarized component leaving the preamplifier, as measured by reflection off a Brewster angle CaF_2 splitter plate, were $\leqslant 90$.

The main (power) amplifier in these experiments consisted of a 1.3-m-long, 135-mm-diam, Plexiglas test chamber filled with 53 kPa of SF_6 and C_2H_6 at a ratio [3] of 10:1 excited by a 50-mm-diam, magnetically guided electron beam from a Physics International Model 316 Pulserad. A 6-μm-thick aluminized Mylar mirror, positioned immediately in front of the 127-μm-thick stainless steel anode and parallel to the 6.35-mm-thick output coupling window, served as a reflector for the incoming pilot pulse. A sapphire coupler was used in all experiments except those in Fig. 2, where polarization purity was crucial. A quartz window was employed for the short-pulse experiments in Fig. 2. Amplified spontaneous emission (ASE) energies from the amplifier, measured with a 100-mm-diam Scientech calorimeter positioned immediately outside the coupling window, were ~8 J in a FWHM pulse at ~23 ns.

In Fig. 1, the 100-ns pilot pulse was expanded to 60-mm diameter before reflection off a sapphire splitter. In this manner some 10 percent of the beam intensity was directed through the coupling window along the test chamber axis. Extracted energies were measured with the Scientech calorimeter, placed behind the sapphire splitter. Coaxial 60-mm-diam apertures at each end of the amplifier and an inner liner of flocked paper ensured pilot beam irradiation of the entire gain volume, and minimized the influence of competing ASE. A high degree of saturation was achieved by twice passing the pilot beam through the whole gain volume, using the beam doubled back on itself by reflection from the aluminized Mylar mirror.

In Fig. 2 experiments, a slightly off-axis, 20-mm-diam pilot pulse was amplified, reflected from the Mylar mirror, and directed toward a Brewster-angle splitter plate which reflected ~13 percent of the *s*-polarized component to an Au:Ge infrared detector. In this case, calorimeter measurements indicated that ~2 J of laser energy was being extracted from the main amplifier. In order to obtain time overlap between the 4-ns *s*-polarized portion of the pilot pulse and the period of positive gain within the power amplifier, careful attention was given, in particular, to optical time delays and electron-

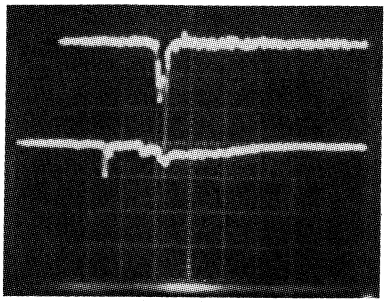


Fig. 3. Oscillogram showing 4-ns pulse leaving the main amplifier. Both traces run from left to right at 50 ns/div. Upper trace is the *s*-polarized signal leaving the main amplifier, isolated by reflection off a calcium fluoride splitter plate. Lower, monitor trace indicates that the shuttered, 4-ns pulse appeared very early in the rising pilot beam signal emerging from the TEA preamplifier.

beam jitter. Nevertheless, the desired interaction was obtained in less than 30 percent of the experiments.

Results and Discussion

With the experiment configuration shown in Fig. 1, 11.6 J of energy were extracted in a 30-ns pulse from a medium that produced an ASE output 7.7 J. We believe the extracted energy represents the total energy available from the medium and that in the absence of the pilot beam, significant energy is lost to the walls by off-axis rays developed in the ASE output. Burn patterns showed that the extracted beam was of much better quality than the ASE beam, as would be expected. The power amplification was considerable. The oscillator beam from the splitter was ~0.1 J over 100 ns. The output of 11.6 J in 30 ns represents a power amplification of ~400.

The magnitude of energy extracted in this way varies with the time in the pilot beam pulse when the amplifier gain became positive. Maximum extracted energies correlated with interaction at the beginning of the pilot pulse, and occurred under conditions where the reflecting aluminized Mylar mirror and sapphire coupling window were parallel. A ~3.6° cant of the coupling window caused the ASE to fall by more than 90 percent (to 0.7 J), and the corresponding extracted energy with the pilot beam was 4.9 J. Thus, reflection from the amplifier window is an influential factor in the competition between energy extraction and ASE.

Fig. 3 shows the result of interacting the electrooptically shuttered, 4-ns pilot pulse with the *e*-beam excited amplifier. The upper trace, the amplified beam reaching the detector, clearly shows the shuttered pulse superimposed upon the amplified *s*-polarized leakage background. The lower trace, the monitor beam signal, provides independent confirmation that the electrooptic switch fired at a point in time, relative to the amplified leakage signal, consistent with the necessary time overlap. Numerous oscillograms obtained in unsuccessful time-overlap experiments in which the shuttered pulse came either too early or too late for amplification, provide further confirmatory evidence for this conclusion. Data obtained in six successful interaction experiments are consistent with ratios of peak pulse to prepulse signal levels (contrast ratios in the absence of ASE) of 15 to 20. These results established the feasibility of isolating an amplified, nanosecond pulse after passage through the power amplifier.

These two results demonstrate that there is no fundamental problem in extracting energy from a high-gain HF amplifier. A combination of the techniques for short-pulse generation and complete irradiation of the power amplifier gain medium, coupled with an upgrading of the existing system to handle H_2–F_2 mixtures, should permit attainment of power levels of 10^{10} W in nanosecond pulses suitable for preliminary fusion target-interaction experiments.

Acknowledgment

The authors are pleased to recognize significant contributions to the progress of this work by many members of the Los Alamos Scientific Laboratory's Chemical Laser Group, including in particular, G. P. Arnold, and G. L. Schott. The assistance of R. E. Johnston and J. J. Damitz in carrying out these experiments is also gratefully acknowledged.

References

[1] R. W. Getzinger, K. D. Ware, and J. P. Carpenter, "Generation and amplification of nanosecond duration multiline HF laser pulses," presented at the SPIE/SPSE Tech. Symp. East Ultra High Power Lasers for Practicable Applications, Reston, VA, Mar. 22–23, 1976. Los Alamos Scientific Laboratory, Univ. California, Los Alamos, NM, Rep. LA-UR-76-368.

[2] a) Preamplifier construction:
G. P. Arnold and R. G. Wenzel "A double-discharge-initiated HF laser," *IEEE J. Quantum Electron.*, vol. QE-8, pp. 26–27, Jan. 1972.
——, "Improved performances of an electrically initiated HF laser," *IEEE J. Quantum Electron.*, vol. QE-9, pp. 491–493, Apr. 1973.
b) Laser-triggered VPG design:
J. F. Figueira and H. D. Sutphin, "Generation of multiband 1-ns pulses in CO_2 lasers," *Appl. Phys. Lett.*, vol. 25, pp. 661–663, Dec. 1974.
c) Coupling of an HF oscillator and preamplifier:
R. Kristal, "Pulsed HF laser holographic interferometry," *Appl. Opt.*, vol., 14, pp. 628–633, Mar. 1975.
R. G. Wenzel and G. P. Arnold, "An HF oscillator-amplifier pumped CdSe parametric oscillator tunable from 14.1 to 16.4 μm," *Appl. Opt.* (to be published).
d) Spectral composition:
N. R. Greiner, G. P. Arnold, and R. G. Wenzel, "Rapid recording of infrared spectra from pulsed chemical lasers," *J. Appl. Phys.*, vol. 44, pp. 3202–3204, July 1973.

[3] Amplifier gas mixtures were chosen to match the optimum conditions found: R. A. Gerber and E. L. Patterson, "Intense electron-beam initiation of a high-energy hydrogen fluoride (HF) laser," *IEEE J. Quantum Electron.*, vol. QE-10, pp. 333–337, Mar. 1974.

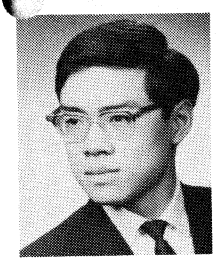
Contributors

Hermann A. Haus (S'50–A'55–SM'58–F'62), for a photograph and biography please see page 210 of the March 1976 issue of this JOURNAL.

*

J. T. LaTourrette (M'67), photograph and biography not available at the time of publication.

*

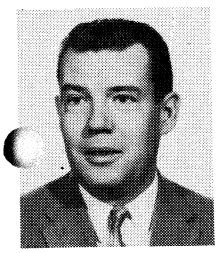


Paul F. Liao was born in Philadelphia, PA, on November 10, 1944. He received the B.S. degree in physics from the Massachussetts Institute of Technology, Cambridge, in 1966, and the Ph.D. degree in physics from Columbia University, New York, NY, in 1973.

During 1973 he was a Research Associate at the Columbia Radiation Laboratory, Columbia University. He joined Bell Laboratories, Holmdel, NJ, in September, 1973, where his interests lie in laser physics and two-photon spectroscopy.

Dr. Liao is a member of the American Physical Society and Sigma Xi.

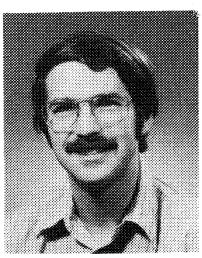
*



Patrick J. Maloney was born in New York, NY, on November 11, 1925. He received the Associate degree in applied science (electrical technology) from New York Community College, New York, NY, in 1949.

From 1950 to 1951 he was assigned to the cesium beam clock project in the Microwave Standards Section of the National Bureau of Standards, Washington, DC. From 1951 to 1953 he was engaged in experimental research with traveling-wave magnetrons at the Thermionics Branch of the Fort Monmouth Signal Corps Laboratory. From 1953 to 1961 he was employed at the IBM Thomas J. Watson Research Laboratory, New York, NY, where he worked in the fields of cryogenics, superconductivity, and thin films. He assisted Prof. C. H. Townes in the Michaelson–Morley experiment conducted at the Watson Laboratory using two ammonia masers. Since 1961 he has been assigned to the Department of Coherent Wave Physics, Bell Laboratories, Holmdel, NJ. He has been principally engaged in laser research ranging from the early ruby to the present gaseous devices.

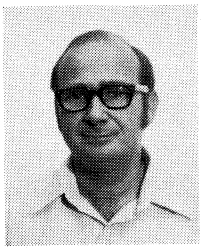
*



John Nella was born in New York, NY, on July 10, 1947. He received the B.S. degree in electrical engineering from the Polytechnic Institute of Brooklyn, New York, NY, in 1968, the M.S. degree in electrical engineering from the California Institute of Technology, Pasadena, in 1969, and the Ph.D. degree in electrophysics from the Polytechnic Institute of Brooklyn, New York, NY, in 1972.

Since 1972 he has been with the Laser Division of Hughes Aircraft Company, Culver City, CA, where he has been engaged in the development of new coherent optical sources.

*

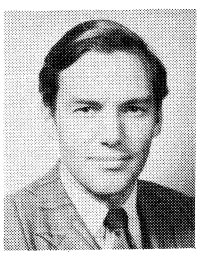


Paul Rabinowitz was born in New York, NY, in 1935. He attended Brooklyn College, New York, NY, and New York University, New York, NY, and received the Ph.D. degree in electrophysics from the Polytechnic Institute of Brooklyn, New York, NY, in 1970.

He joined TRG, Inc. as a Research Physicist in 1959 and was involved in pioneering work in the development of gas lasers, laser resonators, and laser frequency stabilization. In 1967 he joined the Polytechnic Institute of Brooklyn as a Research Associate where he directed laboratory work in quantum electronics and initiated a program of saturated resonance spectroscopy on infrared molecular systems including SF_6 and SiF_4. He is currently employed by the Exxon Research and Engineering Corporation, Linden, NJ, as a Senior Research Physicist, where he is involved in research for the development of techniques and lasers for isotope separation and laser fusion. He is the author of numerous scientific publications, and hold patents on high-loss diffraction coupled resonators and laser image amplifiers.

Dr. Rabinowitz is a member of the American Physical Society and the Optical Society of America.

*

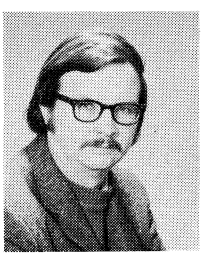


Martin C. Richardson (M'72) was born in Doncaster, England, on December 20, 1941. He received the B.Sc. degree in physics from the Imperial College, London, England, and the Ph.D. degree from London University, London, England, in 1964 and 1967, respectively.

From 1964 to 1967 he worked at the Culham Laboratory of the United Kingdom Atomic Energy Authority specializing in high-power laser techniques and nonlinear laser-plasma phenomena. Since 1967 he has been with the National Research Council of Canada, Ottawa, Ont., Canada, working in such areas as nonlinear optics, laser-induced breakdown, ultrashort pulse generation and detection. Recently his interests have centered around the development of high-power short-pulse CO_2 lasers and the interaction of such pulses with high-density plasmas of laser-fusion interest.

Dr. Richardson is a member of the Institute of Physics, the American and European Physical Societies, and the Canadian Association of Physicists.

*



Charles V. Shank received the B.S., M.S., and Ph.D. degrees from the University of California, Berkeley, in 1965, 1966, and 1969, respectively.

Since 1969 he has been a Member of the Coherent Optics Research Department at Bell Laboratories, Holmdel, NJ, where his present interests include dye lasers and waveguide devices.

Peter W. Smith (M'67-SM'76), for a photograph and biography please see page 213 of the April 1976 issue of this JOURNAL.

*



Seung-Yan Szeto (S'75-M'75) was born in Hong Kong on August 11, 1947. He received the B.S. degree in physics from the Chinese University of Hong Kong in 1969, and the M.S. and Ph.D. degrees in electrophysics from the Polytechnic Institute of New York, Farmingdale, NY, in 1972 and 1976, respectively. He was awarded a Research Fellowship by the Department of Electrical Engineering and Electrophysics while working on his doctorate. He has worked with saturated resonance spectroscopy, frequency stabilization of lasers and optical receiver systems.

Dr. Szeto is a member of the American Physical Society, the Optical Society of America and Sigma Xi.

*



Ivan V. Tomov was born in Roshkovo, Bulgaria, on January 1, 1942. He was educated at the University of Sofia, Sofia, Bulgaria, and Kharkov State University, Kharkov, USSR, and received the Diploma in radiophysics and electronics in 1966. In 1970 he received the Candidate of Science degree from Moscow State University, Moscow, USSR.

He was then appointed Assistant Professor in Physics at Sofia University continuing his research in various areas of nonlinear optics and and ultrashort pulse generation and detection. Since 1975 he has been a Research Associate at the National Research Council of Canada, Ottawa, Ont., Canada, where his interests have primarily been in the areas of high harmonic generation and the development of picosecond pulse techniques for high-density plasma diagnostics.

New Theory of Delays in Semiconductor Lasers

M. RAY, S. S. BARAL, AND D. L. BHATTACHARYYA

Abstract—**A simple model which can explain practically all important features of time delays in GaAs lasers is presented. It assumes only the presence of traps within the forbidden band and considers that the relative movement of quasi-Fermi levels of traps with temperature controls the population of the empty traps which act as saturable absorbers and thereby produce delays.**

I. Introduction

IT IS KNOWN that some GaAs semiconductor lasers pumped by current injection and electron bombardment exhibit a long time delay between the application of a current pulse and the onset of stimulated emission [1]-[8], [11]. The delay is a function of current density and the device temperature. A transition temperature T_t is found above which the delays are long (of the order of 10^{-7} s) and below which the delays are only 1 or 2 ns, the time necessary to build up the population inversion for most diodes. In some lasers the stimulated emissions occur just after the end of the current pulse, and the delay is equal to the full length of the current pulse [9]-[11]. This phenomenon is known as internal Q-switching. For injection lasers, delays are long in both homostructure [1]-[8] and single heterostructure [12]-[14] but this effect is not seen in double-heterostructure lasers [15].

After the discovery of long delay and Q-switching, many attempts have been made to explain the above two effects but no model is completely satisfactory [2], [7], [4], [6], [9], [16]-[20]. In this paper a new model has been proposed which qualitatively accounts for most of the experimental results of long delays.

The purpose of the paper is threefold: first, to discuss briefly the previous work; second, to outline the proposed theory; and third, to present results using the theory and to compare these with experimental data.

II. Previous Models

In explaining long time delay Konnerth [2] first suggested the massive trapping model. This model assumed the existence of a high density of traps ($\simeq 10^{19}$ cm^{-3}) which could capture most of the injected electrons and prevent population inversion. After a sufficient number of traps are bleached the lasing action can start. But this model cannot explain the existence of a transition temperature and a Q-switching. Another main disadvantage is that a large density of traps is required which cannot be detected by experiments. Dobson *et al.* [7] assumed that these traps were associated with the (100) minima in the conduction band rather than the (000) minimum and could explain the existence of a transition temperature. But this model cannot account for Q-switching, the wide variation of T_t from diode to diode, etc.

In 1967 Fenner [4] suggested that the traps produce the delay not by preventing population inversion, but by absorbing photons and thus causing optical losses which would prevent lasing. It was observed experimentally that traps could be bleached optically both in GaAs and in $GaAs_{1-x}P_x$ homostructure diode lasers. However, Fenner's model cannot explain the temperature dependence of time delay and the existence of the Q-switching phenomenon.

Ripper and Dyment and others [6], [9], [16]-[20] proposed the double acceptor trap model which is a modification of Fenner's optical absorption model. They proposed that the traps can be in three different states depending on the number of electrons they have captured. Initially, the traps are in a nonabsorbing state near the valence band. When they can capture electrons, the second level situated near the conduction band becomes available. In this level the trap can capture a second electron either by nonradiative transition from the conduction band or from the valence band with the absorption of a photon. Finally, when both states are occupied, the trapping level returns to a totally nonabsorbing state. At low temperatures ($T < T_t$), the Fermi level is low, the trapping level is unoccupied, and there is no saturable absorption to prevent lasing. But at high temperatures ($T > T_t$), the Fermi level is high, and the lower level is occupied and can produce the absorbing state which causes delays and Q-switching phenomena. The double acceptor model is very successful in explaining most of the experimental data in homostructure lasers, but it cannot explain the presence of long delay and Q-switching in electron-beam pumped lasers, and the absence of delay in double heterostructure lasers. Further, the physical basis of the model is obscure.

Following the suggestion by Thompson, Adams *et al.* have proposed the Nonequilibrium Impurity-Band Theory [19], [20]. They have assumed that the carriers in the impurity band tail are not in thermal equilibrium with those in the conduction band. This causes a number of empty states to be present at the top of the conduction band tail. At low temperatures ($T < T_t$) only a small number of electrons are required to reach the threshold. Transitions from the tail to the valence band cause lasing. Hence no absorbing transition is possible and there is no time delay. At higher temperatures ($T > T_t$) a higher injection level is necessary so that the transitions originate somewhere in the conduction band. The empty states are now available for absorbing photons and thus cause the long time delay. This theory also has some drawbacks: mainly, it cannot explain the Q-switching phenomenon. Secondly, it cannot predict long delays and Q-switching in

Manuscript received December 15, 1975; revised May 18, 1976.

M. Ray and S. S. Baral are with the Department of Electronics and Telecommunication Engineering, Bengal Engineering College, Howrah, India.

D. L. Bhattacharyya is with the Department of Physics, University College of Science, Calcutta, India.

n-type material where the conduction band is in thermal equilibrium.

Because of this unsatisfactory state of the theory it was felt that a new model can be profitably developed which would explain the experimental observations on the basis of simple physical considerations. The present work is the result of this effort.

III. New Theoretical Model

The model proposed is similar to that assumed by Simmons and Taylor [21], [22] for explaining the photoconductive features of amorphous semiconductors. The model assumes two trapping levels, one in the upper half of the band gap, (assumed to be acceptor type) and the other in the lower half of the band gap (assumed to be donor type). It is possible that the trap levels form groups, but for simplicity we consider only single levels. Furthermore, the theory can be generalized to multiple-trap systems, but we have concerned ourselves here with a two-trap system to keep the calculations to a minimum. Fig. 1 shows the basic model. E_1 and E_2 represent the trapping levels and E_{F0} is the equilibrium Fermi level which for a p-type GaAs will be in the lower half of the band gap. From the rate equations it can be derived that under nonequilibrium steady-state conditions the probability of occupation $f(E)$ of a trap level at an energy E in the forbidden gap is (Simmons and Taylor [21])

$$f(E) = \frac{\overline{n} + e_p}{\overline{n} + \overline{p} + e_n + e_p} \tag{1}$$

which is similar to the statistics derived by Shockley and Read for a single trap level. In (1) the parameters are as follows:

$$\overline{n} = \nu n \sigma_n, \quad \overline{p} = \nu p \sigma_p$$

$$e_p = \nu \sigma_p N_v \exp\left[(E_v - E)/KT\right]$$

$$e_n = \nu \sigma_n N_c \exp\left[(E - E_c)/KT\right]$$

where

σ_n and σ_p	electron and hole-capture cross sections for the traps;
ν	thermal velocity;
n and p	steady-state free-carrier concentrations;
N_c, N_v	effective density of states in the conduction band and in the valence band;
E_c, E_v	energy of the bottom of the conduction band and that of the top of the valence band, respectively.

For $E > E_i$, where E_i denotes the intrinsic Fermi level, $e_p \ll e_n, \overline{n}, \overline{p}$ and so

$$f(E) = \frac{\overline{n}}{e_n + \overline{n} + \overline{p}} \tag{2}$$

$$= \frac{n}{n+p}\left(\frac{1}{1 + \exp\left[(E - E_{qn})/KT\right]}\right) \tag{3}$$

where E_{qn} can be defined as the quasi-Fermi level for trapped electrons. Then E_{qn} is obtained from the relation

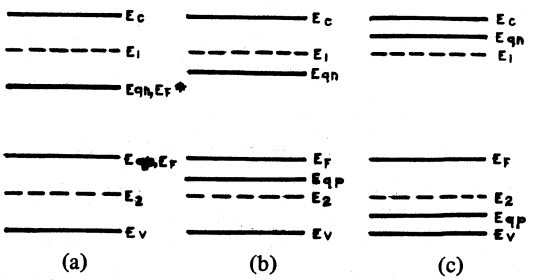


Fig. 1. Energy band diagrams (for explanation of symbols see text). (a) High temperature. (b) Intermediate temperature. (c) Low temperature.

$$N_c \exp\left[(E_{qn} - E_c)/KT\right] = n + p \tag{4}$$

where we assume $\sigma_n = \sigma_p = \sigma$ = constant. Similarly, for $E < E_i$ where $e_n \ll e_p, \overline{n}, \overline{p}$, the hole occupancy $(1 - f)$ can be expressed in the form of a modulated Fermi-Dirac function for holes

$$(1 - f) = \frac{p}{n+p}\left(\frac{1}{1 + \exp\left[(E_{qp} - E)/KT\right]}\right) \tag{5}$$

where E_{qp}, the quasi-Fermi level for trapped holes, is defined by

$$N_v \exp\left[(E_{F0} - E_{qp})/KT\right] = n + p. \tag{6}$$

Thus, following Simmons and Taylor, we have introduced here the concept of the quasi-Fermi levels for trapped electrons and trapped holes as distinct from the quasi-Fermi levels of free carriers.

In such a situation one can show that at high temperatures or low light levels the quasi-Fermi level E_{qp} of trapped holes coincides with the equilibrium Fermi level E_{F0} of the semiconductor and the quasi-Fermi level E_{qn} of the trapped electrons is at the same energy below the conduction band edge as E_{qp} is above the valence band edge. This energy is referred to as E^*_{F0}, the reflected Fermi level. Fig. 1(a) gives the energy diagram illustrating the high-temperature or low-light-level situation. When the temperature decreases or the light level increases, the quasi-Fermi level of trapped electrons and trapped holes (E_{qn}, E_{qp}) moves towards the band edges E_c and E_v. The intermediate stage when E_1 and E_2 are still between E_c and E_{qn} and E_{qp} and E_v is shown in Fig. 1(b). With further decrease of temperature or increase of light levels the trap travels are enclosed by E_{qn} and E_{qp} [Fig. 1(c)]. For very high light levels or at absolute zero of temperature it is possible to have the quasi-Fermi levels for trapped electrons and holes coincident with their respective band edges.

We now assume that the delays observed in a GaAs laser are due to saturable absorption of the laser emission. The traps near the bottom of the conduction band edge produce delays by absorbing photons and thereby cause a large optical loss which would prevent lasing. It corresponds to the optical absorption center as proposed first by Fenner and later by Dyment and Ripper.

Fig. 2(a) shows the condition when $E_{qn} > E_1$, which is valid for low temperature. The trap level is now occupied and hence there is no absorption and no appreciable time delay. At high temperature [Fig. 2(b)], when $E_{qn} < E_1$, most of the

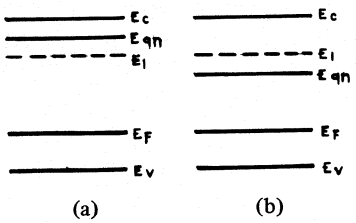


Fig. 2. Energy band diagrams showing the position of the quasi-Fermi level E_{qn} of trapped electrons for (a) low temperature ($T < T_t$) and (b) high temperatures ($T > T_t$).

traps in the E_1 state are unoccupied. They are filled either by photon-assisted capture of electrons from the valence band or by nonradiative transitions from the conduction band. As long as an appreciable number of traps remain empty, the optical losses will be higher than the gain and long delays will result. The population of the delay-producing empty traps is controlled by the relative positions of E_1 and the quasi-Fermi level of the trapped electrons, E_{qn}. The transition temperature T_t occurs when E_1 and E_{qn} are approximately equal.

It is important to point out that the experimental study of Pankove [23], [24] on the emptying of the traps in $GaAs_{1-x}P_x$ injection lasers by thermal and optical excitations offers good support for our model. In Pankove's first experiment, the quasi-Fermi level E_{qn} of the trapped electron moves downwards due to internal heating. The traps begin to be empty and return to the absorbing states which prevent lasing. But when the $GaAs_{1-x}P_x$ is irradiated optically with the output from a GaAs laser, the opposite effect (trap filling) is observed. This is due to the fact that an increase of the illumination intensity (increase of current through GaAs from 0.5 to 1.5 A) causes an increase of free-carrier densities. As a result the quasi-Fermi level of the trapped electrons moves upward toward the conduction band edge. More traps are filled and thereby reduce the optical losses for laser emission which is supported by the fact that a reduction of the time delay from 400 to 200 ns has been observed by Pankove.

We shall now give a simple theoretical treatment of the delay behavior on the basis of our model.

IV. Mathematical Development of the Model

At any heat-sink temperature T_{HS}, and under steady-state conditions, the optical gain G and the optical losses L are equal. The delay time t_d can then be calculated from the expression

$$G(T_{HS}, I, t_d) = L(T_{HS}, I, t_d) \tag{1}$$

where I is the current through the laser.

During the current pulse ($0 \leqslant t \leqslant t_p$ where t_p is the pulse length) the gain is proportional to the injection current hence we can write [25], [26]

$$G(T_{HS}, I, t) = \beta I\,[1 - \exp(-t/\tau)] \tag{2}$$

where β is a proportionality constant and τ is the time constant of the buildup of population inversion.

After the end of the current pulse ($t > t_p$) the carriers decay exponentially with a time constant τ_{sp}, the spontaneous emission lifetime. Then

$$G(T_{HS}, I, t) = \beta I\,[1 - \exp(-t_p/\tau)]\,\exp[-(t - t_p)/\tau_{sp}]. \tag{3}$$

Following Ripper [16], the optical losses can be separated into two parts. The first part is due to the normal laser losses in the absence of the traps, which vary exponentially with the junction temperature T, and the second term is due to the traps which vary in direct proportion to the effective number of empty traps at the energy state E_1.

Thus,

$$L(T_{HS}, I, t) = L_0 \exp\frac{T}{T_0} + \epsilon n_t(t, T) \tag{4}$$

where L_0, T_0, ϵ are constants and $n_t(t, T)$ is the effective number of empty traps at time t. The effective number of empty traps at time $t = 0$ is given by

$$n_t(0, T) = N_t\,[1 - f(E_1)] \tag{5}$$

where N_t is the trap density.

Let us now assume that $T < T_t$, the trapping level is fully occupied, then $n_t(0, T) = 0$, and at $T > T_t$ all traps are empty, i.e., $n_t(0, T) = N_t$. This approximation greatly simplifies the calculations. During the current pulse the rate equation can be written as

$$\frac{dn_t}{dt} = -n_t BN + \frac{n_t(0, T) - n_t(t, T)}{\tau_t} \tag{6}$$

where N is the number of injected electrons during the current pulse and varies less than linearly with the current.

Hence we can write [18]

$$N = A\,[1 - \exp(-I/I_R)] \tag{7}$$

where B and A are constants.

τ_t is the decay time constant of the trap electron and is defined by the equation

$$\tau_t^{-1} = S_0 \exp\left(-\frac{E_c - E_1}{KT}\right) \tag{8}$$

where S_0 is a constant.

At steady state,

$$\frac{dn_t}{dt} = 0. \tag{9}$$

Using these equations we find the following expressions for the threshold current I_{th}:

1) for $T < T_t$

$$I_{th} = L_0/\beta \exp\frac{T}{T_0} \tag{10}$$

2) for $T > T_t$

$$I_{th} = L_0/\beta \exp\frac{T}{T_0} + \frac{\epsilon}{\beta}\left(\frac{N_t}{1 + \tau_t BN}\right). \tag{11}$$

The corresponding delay equations are given as follows:

3) for $T < T_t$

$$t_d = \tau \ln\frac{I}{I - I_{th}} \tag{12}$$

TABLE I
VALUE OF CONSTANTS USED IN THE CALCULATIONS

	Diode A	Diode B
$\frac{\epsilon N_t}{\beta}$	8.5 amperes	14.1 amperes
I_R	9 amperes	4 amperes
$\frac{BA}{S_0}$	.0216	.1
E_1	-70 meV	-100 meV.

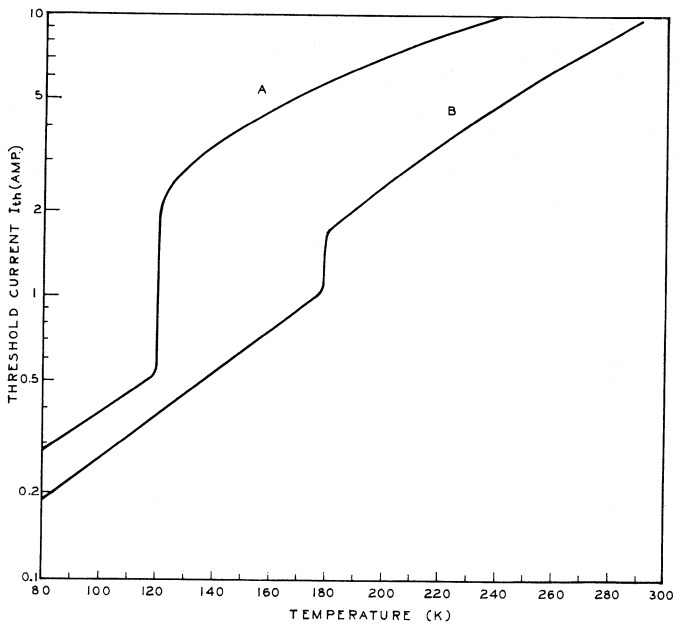


Fig. 3. Threshold curves calculated for two diodes A, and B. Transition temperatures are at 120 K and 180 K, respectively.

4) for $T > T_t$

$$t_d = \tau \ln \left[\frac{L_0}{\beta I} \exp \frac{T}{T_0} + \frac{\epsilon N_t}{\beta I(1 + \tau_t BN)} - 1 \right]. \quad (13)$$

Equations (9)-(12) are the basic relations predicted from our model which can be tested by comparison with experimental observations on real systems.

V. RESULTS

In order to compare our model with experiments we express (10)-(13) graphically and then compare them with the experimental curves obtained by previous workers. In order to compute the theoretical values we have used the parameters as given in Table I. These parameters have been obtained from those of the diodes used by Ripper and Dyment [18]. The predicted curves are shown in Figs. 3-5. The following characteristics which are in complete agreement with those derived from the experimental results of Ripper and Dyment [18] can be enumerated as follows.

1) The regions of short and long time delay are separated by the transition temperature T_t (Figs. 3, 4).

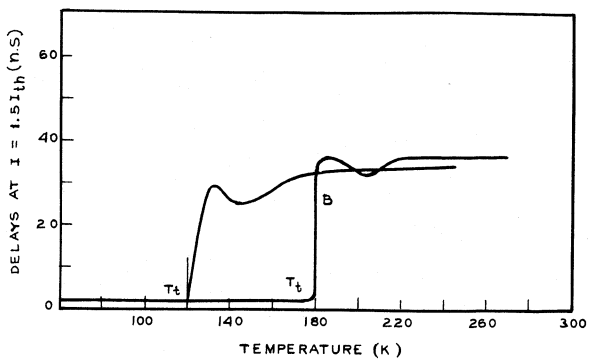


Fig. 4. Calculated variation of delays with temperature for the same two diodes as in Fig. 3 at 50 percent above threshold.

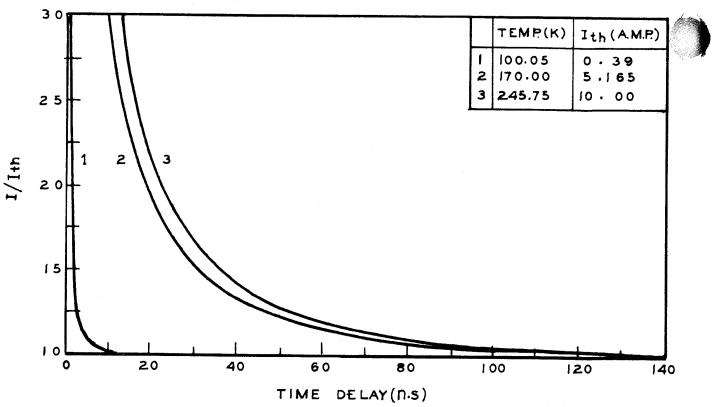


Fig. 5. Time-delays calculated for diode A for three different temperatures below and above T_t.

2) A high increase in the laser threshold current occurs at T_t (Fig. 3).

3) The transition temperature varies widely from diode to diode depending upon the fabrication procedure (Fig. 4).

Although the agreement with observation is very encouraging, there are a few points which require further investigation. It is found on approximate numerical fitting that the time constant is different below and above the transition temperature in order to secure agreement with the experimental observations. It has been suggested that time constant may be dependent on the diffusion process involved in filling and emptying the photon absorbing states (Pankove [27]).

Further we have not made any serious attempt to explain Q-switching on the basis of our model. But it may be conjectured that if lasing has not occurred after the end of the current pulse, some of the electrons (injected electrons during the current pulse) in the conduction band decay to the energy state E_1 with a fast thermalization time τ_{th}. So for $t > t_p$ we have

$$n_t(t, T) = n_t(t_p) - Bn_t(t_p) N \exp \left[- \frac{(t - t_p)}{\tau_{th}} \right].$$

On plotting we observe three distinct regions: 1) the normal lasing region for $t_d < t_p$; 2) the Q-switching region for $t_d > t_p$, which is in qualitative agreement with experiment; 3) the spontaneous emission region where Eq (1) has no solution for any t.

VI. Conclusions

The present model is thus capable of explaining, at least qualitatively, all the important features, viz., the long delays, the existence of transition temperature T_t, the wide variation of T_t from diode to diode, and the high increase of threshold current at T_t. We have not attempted to make detailed quantitative comparisons, as these involve unknown parameters like ϵ, β, T_0, B, etc.

Acknowledgment

One of us (M. R.) is grateful to the UGC for the award of a research fellowship. We thank Dr. S. N. Biswas for his interest during the progress of the work and Dr. J. I. Pankove and the referee for their constructive comments.

References

[1] N. N. Winogradaff and H. Kessler, "Light emission and electrical characteristics of epitaxial GaAs lasers and tunnel-diodes," *Solid State Commun.*, vol. 2, pp. 119–122 Apr. 1964.

[2] K. Konnerth, "Turn-on-delay in gallium arsenide lasers operated at room temperature," presented at the Solid State Devices Research Conf., Princeton, NJ, June 21–23, 1965; for abstract see —, *IEEE Trans. Electron Devices*, vol. ED-12, p. 506, Sept. 1965.

[3] R. O. Carlson, "Improved room temperature laser performance in GaAs diffused-junction diodes," *J. Appl. Phys.*, vol. 38, pp. 661–668, Feb. 1967.

[4] G. E. Fenner, "Delay of the stimulated emission in GaAs laser diodes near room temperature," *Solid State Electron.*, vol. 10, pp. 753–764, Aug. 1967.

[5] G. Guecos and M. J. O. Strutt, "Temperature dependence of the delay time between the current pulse and the laser emission of GaAs laser diodes," *Electron Lett.*, vol. 3, pp. 532–534, Dec. 1967.

[6] J. C. Dyment and J. E. Ripper, "Temperature behavior of stimulated emission delays in diodes and a proposed trapping model," *IEEE J. Quantum Electron.*, vol. QE-4, pp. 155–160, Apr. 1968.

[7] C. D. Dobson, J. Franks, and F. S. Keeble, "Characteristics of GaAs lasers near room temperature," *IEEE J. Quantum Electron.*, vol. QE-4, pp. 151–154, Apr. 1968.

[8] J. C. Marinace and K. Konnerth, "Room Temperature delay time in diffused junction GaAs injection lasers," *IBM J. Res. Develop.*, vol. 3, pp. 276–277, June 1967.

[9] J. E. Ripper, "Internal Q-switching in GaAs junction lasers," *Appl. Phys. Lett.*, vol. 12, pp. 365–367, June 1968.

[10] A. Masuyama, M. Kawabe, K. Masuda, and S. Namba, "Time-behavior of the internal Q-switching in GaAs lasers under electron beam excitation," presented at the IEEE Semiconductor Lasers Conf., Boston, MA, May 1972.

[11] J. I. Pankove, "Time delay and memory effects in $GaAs_{1-x}P_x$ injection lasers," *IEEE J. Quantum Electron.*, vol. QE-4, pp. 161–163, Apr. 1968.

[12] E. A. Ulmer, Jr., and I. Hayashi, "Internal Q-switching in GaAs · $Ga_xAl_{1-x}As$ heterostructure lasers," *IEEE J. Quantum Electron.*, vol. QE-6, pp. 297–299, June 1970.

[13] Y. Unno, M. Yamamoto, and S. Iida, "Internal Q-switching in $Ga_{1-x}Al_xAs$-GaAs heterostructure lasers," *Japan J. Appl. Phys.*, vol. 9, pp. 1181–1182, Sept. 1970.

[14] M. G. Craford, W. O. Groves, and M. Fox, "GaAs-GaAsP heterostructure injection lasers," *J. Electrochem. Soc.*, vol. 118, pp. 355–358, Feb. 1971.

[15] J. C. Dyment, J. E. Ripper, and J. P. Lee, "Measurement and interpretation of long spontaneous lifetimes in double heterostructure lasers," *J. Appl. Phys.*, vol. 43, pp. 452–457, Feb. 1972.

[16] J. E. Ripper, "Theory of Q-switching and time delays in GaAs junction lasers," in *1968 Proc. 2nd Int. Symp. GaAs: Inst. Phys.*, Phys. Soc. Conf. Series 7, pp. 91–95.

[17] —, "Time delays and Q-switching in junction lasers, I-theory," *IEEE J. Quantum Electron.*, vol. QE-5, pp. 391–395, Aug. 1969.

[18] J. E. Ripper and J. C. Dyment, "Time delays and Q-switching injection lasers: Computer calculations and comparison with experiments," *IEEE J. Quantum Electron.*, vol. QE-5, pp. 396–403, Aug. 1969.

[19] M. J. Adams, S. Gründorfer, B. Thomas, C. F. L. Davies, and D. Mistry, "Time delays and Q-switching in homostructure and heterostructure injection lasers," *IEEE J. Quantum Electron. (Part II of Two Parts: Special Issue on 1972 IEEE Semiconductor Laser Conf.)*, vol QE-9, pp. 328–337, Feb. 1973.

[20] S. Gründorfer and M. J. Adams, "Theoretical considerations of time delays in semiconductor lasers," *IEEE J. Quantum Electron.*, vol. QE-9, pp. 814–819, Aug. 1973.

[21] J. G. Simmons and G. W. Taylor, "Theory of photoconductivity in amorphous semiconductors," *J. Phys., C. Solid State Phys.*, vol. 7, p. 3051, 1974.

[22] G. W. Taylor and J. G. Simmons, "Photoconductivity and the determination of trapping parameters in amorphous semiconductors," *J. Phys., C. Solid State Phys.*, vol. 7, p. 3067, 1974.

[23] J. I. Pankove, "Lasing delay in $GaAs_{1-x}P_x$ injection lasers," presented at the 1968 Int. Conf. Physics of Semiconductors, Moscow, Russia, July 23–29, 1968.

[24] —, "Optical filling of delay-inducing traps in injection lasers," *IEEE J. Quantum Electron.*, vol. QE-4, pp. 427–429, June 1968.

[25] M. Dilkuhn and H. Rupprecht, "A relation between the current density at threshold and the length of Fabry-Perot type GaAs lasers," *Proc. IEEE* (Corresp.), vol. 51, pp. 1243–1244, Sept. 1963.

[26] K. Konnerth and C. Lanze, "Delay between current pulse and light emission of a gallium-arsenide injection laser," *Appl. Phys. Lett.*, vol. 4, pp. 120-121, Apr. 1964.

[27] J. I. Pankove, private communication.

Acoustic Waves and Heating Due to Molecular Energy Transfer in an Electric Discharge CO Laser

F. E. C. CULICK, P. I. SHEN, AND W. S. GRIFFIN

Abstract—**This paper summarizes analytical studies and the interpretation of experimental results for the compression and rarefaction waves generated in the cavity of a pulsed CO electric discharge laser. A one-dimensional analysis of acoustic waves is applied to a transversely excited laser. The influences of heating in the cathode fall, heat transfer to the cathode, flow through both the anode and cathode, and bulk heating of the plasma are included. The analysis is used to relate the bulk heating rate to observable features of the pressure and density waves. Data obtained from interferograms and reported elsewhere are used to infer the bulk heating rates in a pulsed CO laser. Results are presented for CO/Ar, CO/N_2, and N_2 plasmas. Comparison of the data with recent theoretical results for the heating due to electron/neutral collisions and the anharmonic defect associated with V-V energy transfer shows substantial differences at lower values of total energy deposition. The change of heating with E/N is in fairly good agreement with predicted values.**

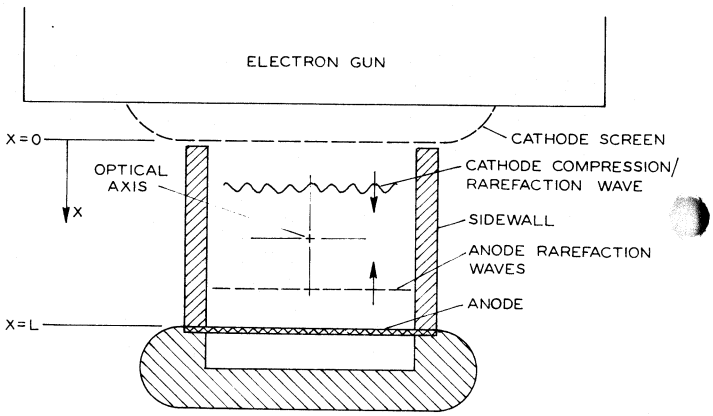


Fig. 1. Sketch of the laser cavity and acoustic waves.

I. Introduction

IN A GAS LASER excited by a pulsed electric discharge, energy is deposited nonuniformly in both space and time. One consequence is that waves of pressure, and therefore density, are excited within the laser cavity. The associated variations in the local index of refraction degrade the optical quality of the output of the device. Formation of these waves may therefore place limits on the maximum pulse length, repetition rate, energy per pulse, and output power obtainable with a specified optical quality.

The presence of waves in the cavity of an electric discharge laser of the sort considered here has been recognized and treated recently elsewhere [1]. In the present work, which was carried out independently of [1], the physical representation of the waves as a problem of acoustics is essentially the same. However, the analytical techniques used are different, and flow through porous electrodes is accounted for. The configuration analyzed is sketched in Fig. 1. Particular emphasis will be placed here on waves generated at the cathode.

As shown in Fig. 1, the optical axis of the laser is normal to the paper. The beam produced by the electron gun ionizes the gas, while a dc sustainer field, applied between the anode and the cathode, provides the electric power required to pump the molecules to vibrationally excited states. It will be assumed here that the sustainer field is constant and applied as a pulse of length t_p. During the pumping process and for some time subsequently, heating of the gas occurs. For the carbon monoxide lasers treated here, there are two important contributions to the heating in most of the cavity: ohmic dissipation associated with elastic collisions between electrons and molecules and the transfer of vibrational energy to translational energy during the process of vibrational-vibrational (V-V) energy transfer. The second arises as a result of the anharmonic defect for the vibrational levels of carbon monoxide [2].

The increase of thermal energy produces an increase of temperature and pressure. Because the electrodes are porous, some of the gas leaks out, causing rarefaction waves to propagate into the cavity. In the thin cathode sheath, the local ohmic heating rate is very high. This produces a relatively high local pressure, generating a steep-fronted compression wave which immediately precedes the rarefaction wave. At the end of the pulse of sustainer voltage, when the intense heating at the cathode ceases, a steep-fronted rarefaction wave is produced. It happens, as shown in Section II, that the rarefaction wave associated with the bulk heating (i.e., that associated with V-V transfer) and the flow through the cathode, has approximately a linear variation in space. Because the heating in the anode sheath is not intense, no sharp-fronted waves are produced there.

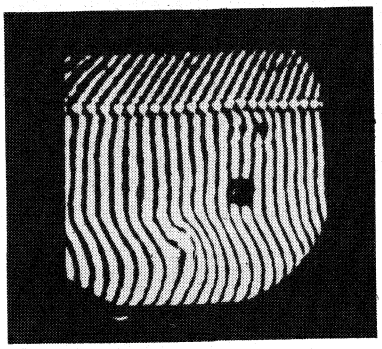
The features just described are exhibited by the interferograms shown in Fig. 2. These were taken, with a Mach-Zehnder interferometer, for a cavity 1 m long [3]. In Fig. 3, the fractional change of density is shown, based on the formula (2.27) deduced below. Note that the small number of fringe shifts in the interferograms already suggests the small changes of density depicted explicitly in Fig. 3.

Because the fluctuations of density, even in the steep portions of the waves, are not large, the problem can reasonably be treated as one of linear acoustics. Solutions for the case of nonuniform and time-varying heat addition are conveniently obtained by the use of a Green's function. This also affords

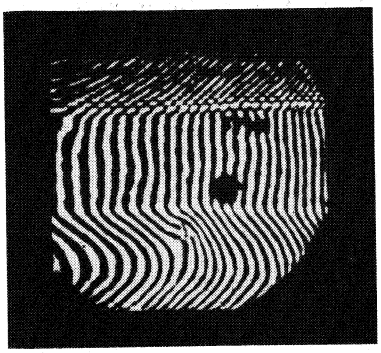
Manuscript received January 26, 1976; revised June 1, 1976. This work was supported in part by the Advanced Research Projects Agency of the Department of Defense and monitored by the Office of Naval Research under Contract N0014-72-C-0043.

F. E. C. Culick is with the Department of Engineering, California Institute of Technology, Pasadena, CA 91125.

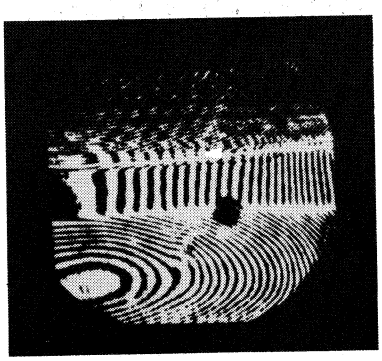
P. I. Shen and W. S. Griffin are with the Northrop Research and Technology Center, Northrop Corporation, Hawthorne, CA.



(a)



(b)



(c)

Fig. 2. Interferograms showing acoustic waves in the laser cavity for different power loadings: (a) 135 W/cm^3, (b) 400 W/cm^3, (c) 1250 W/cm^3. Pictures taken at 180 μs after the sustainer pulse.

a simple means of representing the boundary conditions of flow through the electrodes. The formulation given in this work can be used to treat more complicated cases than those treated here.

For simplicity, the heat addition within the cathode sheath is taken to be uniform in a region of thickness d. To interpret the interferograms, the limiting case of infinitesimally small d, but finite total heat addition in the sheath, is used. So far as the observed waves are concerned, these appear to be good approximations. What this really means is that the details of the processes within the sheath are smeared out or averaged in the process generating the waves.

Owing to the large temperatures which may accompany the heating near the cathode, one might expect that the heat transfer from the gas to the cathode should be substantial. This question is examined in Section III, where it is shown that the influence of the heat loss is confined to a relatively

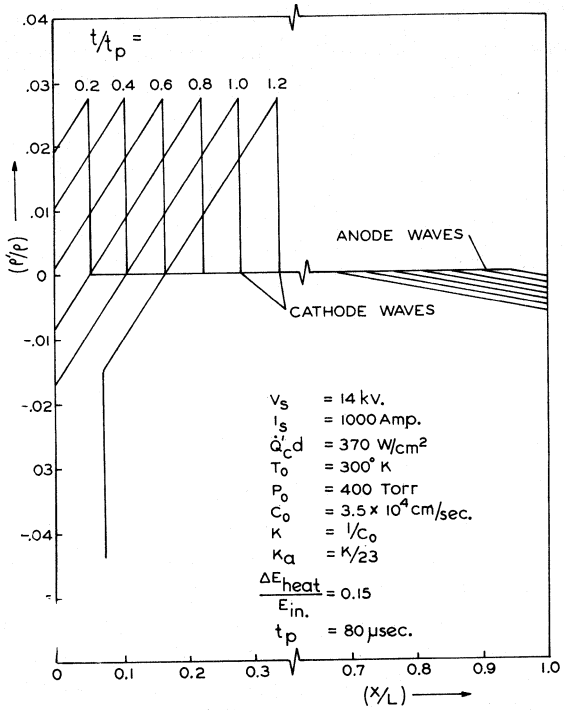


Fig. 3. Calculated density fluctuations according to (2.27). No heat loss to the cathode.

small distance behind the sharp compression wave. It can be ignored for the purposes of Section IV in which the characteristics of the rarefaction wave are used in the following way.

It is a result of the analysis of Section II that the slope of the rarefaction wave (see Fig. 3) is proportional to the bulk heating rate. The slope also depends on the permeability of the cathode, which can be estimated. One can measure the slope on interferograms and can therefore infer the bulk heating rate. The values reported in Section IV confirm the relatively low rates predicted for the CO laser [2]. However, the theoretical values for the bulk heating are substantially less than those deduced from experiments at lower values of energy deposited in the medium (less than 100 J/l) for an argon/carbon monoxide mixture. The comparison is shown in Fig. 10.

II. Analysis Without Heat Transfer to the Cathode

A. Formulation

The experimental evidence discussed above suggests that the waves may be treated as one-dimensional, small-amplitude motions. Because the gas is initially at rest, the average velocity can be taken to be zero. The equation of state is taken to be that for a perfect gas with constant specific heats, so the linearized equations of motion and state are

$$\frac{\partial \rho'}{\partial t} + \rho_0 \frac{\partial u'}{\partial x} = 0 \tag{2.1}$$

$$\rho_0 \frac{\partial u'}{\partial t} + \frac{\partial p'}{\partial x} = 0 \tag{2.2}$$

$$\rho_0 \frac{\partial T'}{\partial t} + \frac{p_0}{C_v} \frac{\partial u'}{\partial x} = \frac{\dot{Q}}{C_v} \tag{2.3}$$

$$p' = R(\rho_0 T' + T_0 \rho'). \tag{2.4}$$

The heat addition (energy/s · volume) is $\dot{Q}$. From these one can form the wave equation for the pressure fluctuations:

$$\frac{1}{c_0^2}\frac{\partial^2 p'}{\partial t^2} - \frac{\partial^2 p'}{\partial x^2} = \frac{\gamma - 1}{c_0^2}\frac{\partial \dot{Q}}{\partial t}. \tag{2.5}$$

Note that the subscript $(\,)_0$ denotes quantities for the undisturbed fluid prior to heating, and $c_0^2 = \gamma p_0/\rho_0$.

Initially, the pressure fluctuation is zero, but is changing at a rate proportional to the heat addition:

$$p' = 0, \qquad (t = 0, \text{all } x) \tag{2.6}$$

$$\frac{\partial p'}{\partial t} = (\gamma - 1)\dot{Q}. \tag{2.7}$$

The second is easily deduced from (2.5) by integrating over a small interval from $t = 0-$ to $t = 0+$.

Flow through both the cathode and anode must be accounted for. The amount of flow influences the form of the waves generated in the laser cavity itself and also produces waves which propagate in the cavities outside the porous cathode and anode. The consequent changes of pressure within the cathode and anode cavities must subsequently affect the flow through the screens; the laser cavity is obviously acoustically coupled to the cathode and anode cavities. For a more precise treatment of the problem, the pressure fluctuations within the cavities at the cathode and anode should be accounted for. Numerical calculations done as part of this work, but not included here, have shown that the influence of this refinement on the results obtained here is small; for the present it will be ignored. Further remarks on the boundary conditions are given in Section II-F.

Thus the boundary conditions at the electrodes will incorporate the approximation that the pressure is constant in the cavities outside the main laser cavity. The reasonable assumption is made, in addition, that the flow through each electrode is proportional to the pressure difference across the screen. At the cathode, for example, the fluctuation of flow outward is represented by

$$-\rho_0 u' = Kp'. \tag{2.8}$$

If (2.8) is differentiated with respect to time, then with (2.2), the boundary condition on p' is obtained:

$$\frac{\partial p'}{\partial x} = K\frac{\partial p'}{\partial t}, \qquad (x = 0, \text{all } t). \tag{2.9}$$

A similar boundary condition applies at the anode. A complete and proper description of the most general conditions would incorporate that boundary condition from the beginning. However, for most problems of practical interest, one is concerned with the behavior before the waves emanating from the cathode interact with those from the anode (see Figs. 2 and 3). Because the formulation is linear, the waves from the cathode and anode can be treated separately and the results superposed. The second boundary condition may therefore be set on the waves leaving the cathode; that far away the medium is undisturbed:

$$p' = 0, \qquad (x \to +\infty, \text{all } t). \tag{2.10}$$

Equation (2.5) with the initial conditions (2.6) and (2.7) and the boundary conditions describe linear waves issuing from the cathode. In the next section, a general solution will be given. This will be evaluated subsequently for the special case of uniform heating in the bulk of the laser cavity, and a thin region of (also uniform) intense heating at the cathode. The waves from the anode will be deduced by a simple transformation.

B. General Solution

The general solution will be constructed here by first applying the Laplace transform in time. A Green's function will be used to solve the spatial problem. In principle, then, any distribution of the heating rate $\dot{Q}$ can be accommodated. Let a tilde denote the Laplace transform (in the variable s). Then (2.5), (2.6), and (2.7) can eventually be combined to give

$$\frac{d^2\tilde{p}'(x,s)}{dx^2} - k^2\tilde{p}'(x,s) = -\frac{\gamma - 1}{c_0^2}s\tilde{\dot{Q}} \tag{2.11}$$

where

$$k = s/c_0. \tag{2.12}$$

The transform of the boundary condition (2.9) is

$$\frac{d}{dx}\tilde{p}'(x,s) = sK\tilde{p}' \qquad (x = 0) \tag{2.13}$$

and of course the condition (2.10) at infinity gives simply

$$\tilde{p}'(x,s) = 0 \qquad (x \to \infty). \tag{2.14}$$

The Green's function, appropriate to this problem, is governed by the differential equation

$$\frac{d^2}{dx^2}G(x|x_0) - k^2G(x|x_0) = \delta(x - x_0). \tag{2.15}$$

In addition to satisfying the conditions (2.13) and (2.14), $G(x|x_0)$ is subject to the usual requirements that it can be continuous at $x = x_0$, but the first derivative has a unit discontinuity. The Green's function is

$$G_- = \frac{-1}{k(k + sK)}\left[k\cosh(kx) + sK\sinh(kx)\right]e^{-kx_0} \cdot (x < x_0)$$

$$G_+ = \frac{-1}{k(k + sK)}\left[k\cosh(kx_0) + sK\sinh(kx_0)\right]e^{-kx} \cdot (x > x_0). \tag{2.16}$$

The solution for the pressure field is

$$\tilde{p}'(x,s) = -\left(\frac{\gamma - 1}{c_0^2}\right)\int_0^\infty G(x|x_0)s\tilde{\dot{Q}}dx_0. \tag{2.17}$$

C. Waves Generated by the Cathode Fall

As an approximation to the dissipation of energy in the cathode fall, assume that the heating is uniform and constant in a thin region of thickness d, for the duration t_p of the sustainer pulse:

$$\dot{Q}(x,t) = \dot{Q}_c \quad (0 < x \leq d, 0 < t \leq t_p)$$
$$= \text{otherwise.} \tag{2.18}$$

Substitution of (2.16) and (2.18) into (2.17) and inversion of the result leads to the formula for the pressure wave generated by the cathode fall:

$$\frac{p_f'(x,t)}{(\gamma-1)\dot{Q}_c} = f(t,x) - f(t-t_p,x) \tag{2.19}$$

where

$$f(t,x) = \frac{1}{2}\left(t - \frac{x-d}{c_0}\right) U\left(t - \frac{x-d}{c_0}\right) - \frac{1-Kc_0}{2(1+Kc_0)} \cdot \left(t - \frac{x+d}{c_0}\right) U\left(t - \frac{x+d}{c_0}\right) - \frac{Kc_0}{1+Kc_0}\left(t - \frac{x}{c_0}\right) U \cdot \left(t - \frac{x}{c_0}\right) \tag{2.20}$$

and $U(t-\tau)$ is the unit step function which is zero for $t < \tau$.

The function $f(t,x)$ in (2.19) represents the wave generated when the sustainer pulse is turned on, a relatively sharp-fronted compression wave. A rarefaction wave having the same shape is produced when the sustainer pulse is turned off; it is represented by $-f(t-t_p,x)$ in (2.19). At any time t, there is a wave of thickness $2d$ located in the region $c_0t - d < x < c_0t + d$. It is easy to verify that the function $f(x,t)$ represents the wave sketched in Fig. 4.

If only because the processes in the vicinity of the cathode are necessarily three-dimensional, the thickness d of the cathode region is not known precisely. It is certainly a thin zone, and it is convenient to treat this portion of the wave in the limit $d \to 0$ but $\dot{Q}_c$ finite. The wave therefore becomes a discontinuity, having amplitude proprotional to the heating, $\dot{Q}_c d$, per unit area of the cathode:

$$\lim_{d\to 0} p_f'(x,t) = (\gamma-1)\frac{\dot{Q}_c d}{1+Kc_0} \cdot \left[U\left(t - \frac{x}{c_0}\right) - U\left(t - t_p - \frac{x}{c_0}\right)\right]. \tag{2.21}$$

This simplified form will be used later in the interpretation of interferograms.

D. Waves Generated by Bulk Heating

It is a reasonable approximation that the heating of the plasma is uniform in the volume outside the thin region near the cathode. This is justified also by the observation that the fringes are relatively straight and uniformly spaced in the central areas of the interferograms in Fig. 2. Because the heating causes the pressure to rise, causing gas to flow through the cathode and anode, waves are produced at the electrodes and propagate inward.

For simplicity, the heating is assumed to be both uniform in space and constant in time, even after the pulse is turned off. The transfer of energy from vibration to translation continues as equilibrium is approached subsequent to the pulse. It is only for convenience here that $\dot{Q}_h$ is assumed to have the same value during and after the pulse. Strictly, $\dot{Q}_h$ must tend to zero for $t > t_p$. Variations in $\dot{Q}_h$ may be one reason for the curvature of the fringes behind the cathode waves shown in Fig. 2. In (2.17) the heat source is represented by

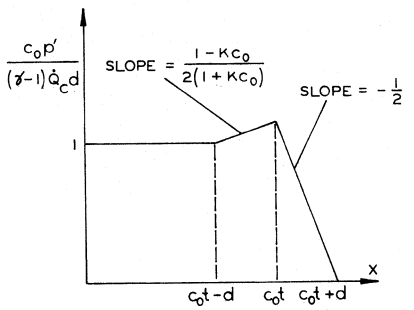


Fig. 4. Sketch of the compression wave produced in the cathode fall when the sustainer pulse is applied.

$$\dot{Q} = \begin{cases} 0, & t \leq 0 \\ \dot{Q}_h, & t > 0 \end{cases} \tag{2.22}$$

with $\dot{Q}_h$ constant. Substitution of (2.16) and (2.22) into the formula (2.17) gives

$$\tilde{p}_c'(x,s) = (\gamma-1)\dot{Q}_h \frac{1}{s^2}\left[1 - \frac{Kc_0}{1+Kc_0} e^{-sx/c_0}\right]. \tag{2.23}$$

The inverse transform is

$$\frac{p_c'(x,t)}{(\gamma-1)\dot{Q}_h} = t - \frac{Kc_0}{1+Kc_0}\left(t - \frac{x}{c_0}\right) U\left(t - \frac{x}{c_0}\right). \tag{2.24}$$

The first term represents the pressure rise which would occur in the cavity if the cathode were impermeable; the second term is the rarefaction wave produced by the flow through the cathode.

A similar result is obtained for the pressure field in the vicinity of the anode, valid before any waves from the cathode cross the cavity. Let K_a denote the permeability of the anode, and replace x by $L - x$ to obtain

$$\frac{p_a'(x,t)}{(\gamma-1)\dot{Q}_h} = t - \frac{K_a c_0}{1+K_a c_0}\left(t - \frac{L-x}{c_0}\right) U\left(t - \frac{L-x}{c_0}\right). \tag{2.25}$$

E. Density Waves in the Laser Cavity

It is the fluctuations of density in the cavity which are of primary interest, because these are directly related to fluctuations of the index of refraction, which in turn affect the laser beam. The relation between density and pressure is found by using the First Law of Thermodynamics:

$$C_v dT = \frac{dQ}{\rho} + \frac{p}{\rho^2} dp.$$

The amount of heat added to any element of gas outside the cathode fall region is simply $\dot{Q}_h t$ because $\dot{Q}_h$ is constant. Hence, with the temperature change eliminated by use of the equation of state, and with differentials replaced by fluctua-

tions, one finds

$$\rho' = \frac{p'}{c_0^2} - \frac{\gamma - 1}{c_0^2}\dot{Q}_h t. \tag{2.26}$$

The complete system of pressure waves produced in the cavity is the sum of (2.20), (2.24), and (2.25); (2.26) gives

$$\begin{aligned}\rho' = (\gamma - 1)\frac{\dot{Q}_c}{c_0^2}\Bigg[&\frac{1}{2}\left(t - \frac{x-d}{c_0}\right)U\left(t - \frac{x-d}{c_0}\right) - \frac{1 - Kc_0}{2(1+Kc_0)} \\ &\cdot\left(t - \frac{x+d}{c_0}\right)U\left(t - \frac{x+d}{c_0}\right) - \frac{Kc_0}{1+Kc_0} \\ &\cdot\left(t - \frac{x}{c_0}\right)U\left(t - \frac{x}{c_0}\right)\Bigg] \times [1 - U(t - t_p)] \\ &- (\gamma - 1)\frac{\dot{Q}_h}{c_0^2}\left[\frac{Kc_0}{1+Kc_0}\left(t - \frac{x}{c_0}\right)U\left(t - \frac{x}{c_0}\right)\right. \\ &\left. + \frac{K_a c_0}{1 + K_a c_0}\left(t - \frac{L-x}{c_0}\right)U\left(t - \frac{L-x}{c_0}\right)\right].\end{aligned} \tag{2.27}$$

For the limiting case $d \to 0$,

$$\begin{aligned}\rho' = (\gamma - 1)&\frac{\dot{Q}_c d}{c_0^3(1+Kc_0)}\left[U\left(t - \frac{x}{c_0}\right) - U\left(t - t_p - \frac{x}{c_0}\right)\right] \\ &- (\gamma - 1)\frac{\dot{Q}_h}{c_0^2}\left[\frac{Kc_0}{1+Kc_0}\left(t - \frac{x}{c_0}\right)U\left(t - \frac{x}{c_0}\right)\right. \\ &\left. + \frac{K_a c_0}{1 + K_a c_0}\left(t - \frac{L-x}{c_0}\right)U\left(t - \frac{L-x}{c_0}\right)\right].\end{aligned} \tag{2.28}$$

Note that the various terms representing the uniform rise of pressure associated with the bulk heating, $\dot{Q}_h$, cancel in the formula for the density fluctuations. The approximations used here, in particular that the flows through the cathode and anode are small, imply that the plasma is heated at essentially constant volume.

Fig. 3 is a plot of (2.28) for representative conditions. The difference in slopes of the anode and cathode waves reflects the different permeabilities ($K_a/K = 1/23$). The slopes also are proportional to the bulk heating rate, $\dot{Q}_h$; examples are shown in Fig. 5. The slope of K used is the limiting value, $1/c_0$, the inverse of the acoustic impedance for the gas. This value is only approximate and valid only for a very porous cathode. If the cathode has appreciable flow resistance, then K would be close to the value for steady-state conditions. No measured values are available. The slope of the wave after the compression front in the cathode wave is found from (2.28) to be

$$\left(\frac{\partial \rho_c'}{\partial x}\right)_t = (\gamma - 1)\left(\frac{Kc_0}{1+Kc_0}\right)\frac{\dot{Q}_h}{c_0^3}. \tag{2.29}$$

In Fig. 6, the density profile according to (2.28) is shown for comparison with the interferogram of Fig. 2(b). A heating rate of 15 percent of the input power was assumed. The slopes of the wavefronts and their relative positions in the cavity agree within a few percent. Owing to the poor resolution in the interferogram, the main region of uncertainty is at the steep front of the cathode wave.

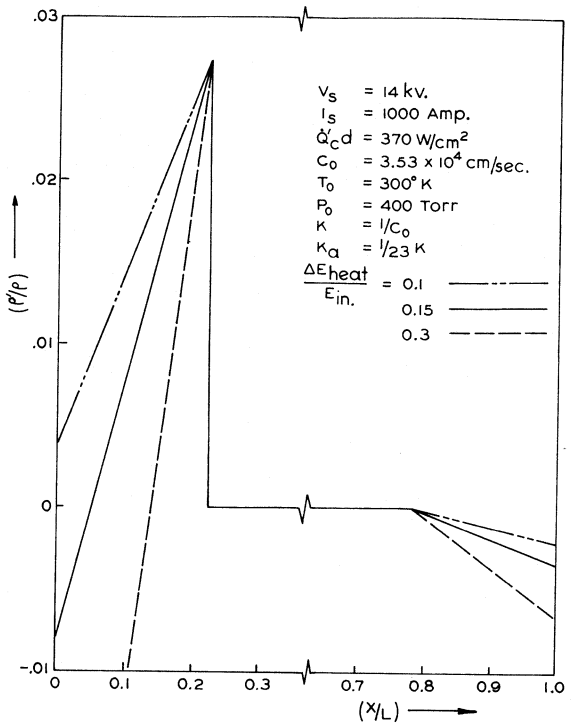


Fig. 5. Illustration of the influence of bulk heating on the cathode and anode waves.

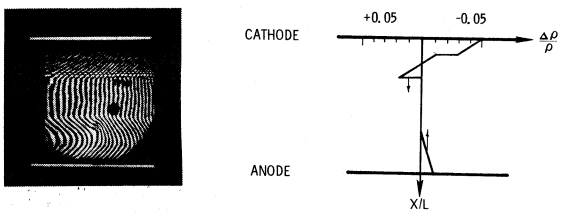


Fig. 6. Comparison of experimental and calculated density variations in a laser cavity.

It should be noted that the distribution of heat addition and the boundary conditions used here are substantially different from those used in [1]. The bulk heating was taken in that work to be nonuniform, and the influence of flow through the electrodes was not examined. If the heat addition is nonuniform in the vicinity of a rigid, impermeable surface, a wave is produced there, even in the absence of flow through the surface. In particular, the anode was apparently solid for the experiments interpreted in [1]; the analysis shows an anode wave because of nonuniform heat addition.

In view of these results, it appears that the simplified analysis constructed here is a farily good approximation for the experimental conditions to be examined here. It will be used in Section IV for inferring values of the bulk heating rate from interferograms. However, an important question arises in connection with the influence of heat transfer to the cathode from the hot gases in the cathode fall. This is examined in Section III.

F. Influence of Pressure Fluctuations in the Electrode Cavities

As remarked earlier, the expression (2.8) for the boundary condition is an approximation; the influence of pressure

changes within the cathode cavity and the finite size of the cavity are ignored. More correctly, one should use

$$-\rho_0 u' = K(p' - p_0'), \tag{2.30}$$

where p_0' is the fluctuation of pressure at the cathode, within the cathode cavity. In order to find p_0', the problem of wave motions within the cathode cavity must be solved; the solution is then matched to the solution for waves within the main laser cavity.

No essential difficulties are encountered in the solution of this problem by the techniques discussed in Section II-B. The Green's function for this case is

$$(G(x\,|\,x_0) = -\frac{1}{k(k+sK)}\left\{[k\cosh(kx) + sK\sinh(kx)]\,e^{-kx_0} + \frac{(sK)^2/(k+sK)\exp - k(x_0+x)}{\tanh(kL_c) + (sK/k+sK)}\right\} \quad (x < x_0). \tag{2.31}$$

The formula for $x > x_0$ is obtained by using the property $G(x\,|\,x_0) = G(x_0\,|\,x)$, which means simply interchanging x and x_0; L_c is the depth of the cathode cavity.

The formulas for the pressure waves are now considerably more lengthy than those found for the case $p_0' = 0$ treated above and will not be given here. For the limit $L_c \to 0$, the more general form reduces exactly to the result obtained for $p_0' = 0$. In the limit $L_c \to \infty$, one obtains the result valid before the first reflection from the far side of the cathode cavity returns to the cathode screen. Numerical calculations for that case, with $K = 1/c_0$, are practically indistinguishable from those given under the condition $p_0' = 0$. It is for that reason that the simpler results have been used to interpret the observations.

It should be noted that the complete problem accounting for the influences of the boundary conditions at the anode and cathode simultaneously can also be treated. With that solution, one may study the evolution of waves within the laser cavity subsequent to reflections from the anode and cathode. Because the behavior for long times does not appear important for practical applications, it has not been studied in detail.

III. An Approximation to the Influence of Heat Transfer at the Cathode

Because of the high heating rates, high temperatures must be expected in the region adjacent to the cathode. Suppose that the voltage drop across the cathode sheath [4] is roughly 370 V through a distance $d = 0.1$ mm, and assume that the current density is 1 A/cm^2. For a nitrogen/carbon monoxide gas mixture at 400 torr, the average heating rate in the cathode sheath is 37 000 W/cm^3. If the pulse lasts for $t_p = 100$ μs, the maximum temperature rise is roughly $\dot{Q}_c t_p/\rho_0 C_v \approx 8500$ K.

Such high temperatures cannot exist in practice, because heat is rapidly lost to the relatively cool cathode material. It is easy to estimate that if the temperature were so high, the heat transfer exceeds the rate of energy input to the cathode fall. Obviously, the loss of energy to the cathode is significant, and must affect the structure of the compression wave generated in that region.

Qualitatively, one may surmise that the influence of heat transfer is the following. At the beginning of the discharge, when the gas temperature has not changed much from the initial value, there should be little effect. In particular, one might expect that the initial amplitude of the cathode wave should be unaffected. After some time, the gas temperature has risen, heat transfer becomes important, and the compression wave should be weakened. The slope behind the front of the wave would be reduced. But if a steady state for heat conduction is reached, the slope of the compression wave may approach the value determined by the bulk heating rate and the flow through the cathode, (2.29). These ideas will be developed by analyzing the heat transfer as a boundary layer problem at the cathode, and patching the result to the adiabatic solution discussed in Section II.

The linearized energy equation with heat transfer is

$$\rho_0 \frac{\partial T'}{\partial x} + \frac{p_0}{C_v}\frac{\partial u'}{\partial x} = \frac{\dot{Q}}{C_v} + \frac{\lambda}{C_v}\frac{\partial^2 T'}{\partial x^2}, \tag{3.1}$$

and the wave equation for the pressure becomes

$$\frac{\partial^2 p'}{\partial t^2} - c_0^2\frac{\partial^2 p'}{\partial x^2} = (\gamma - 1)\frac{\partial \dot{Q}}{\partial t} + (\gamma - 1)\lambda\frac{\partial}{\partial t}\left(\frac{\partial^2 T'}{\partial x^2}\right). \tag{3.2}$$

Because of the last term in (3.2), this equation is now coupled to both the energy equation and the momentum equation (2.2). The analysis based on the Green's function, used in Section II-B, will not work here. It is for this reason that the heat transfer is treated as a separate boundary layer problem. One assumes that the influence of heat transfer is confined to a region (extending roughly a distance d from the cathode) which is small compared with the characteristic dimension of the adiabatic wave structure. The temperature profile determined in that way is then used in the last term of (3.2) and therefore appears as an additional source of pressure waves.

Two further assumptions are made: 1) the surface temperature of the cathode material does not change appreciably; and 2) the influence of convection can be ignored within the boundary layer. The first may be justified by simple estimates, and is valid because of the high density of the cathode material. The second is made initially to ease the analysis, but the results show that it is valid, principally because the heat transfer rates are much larger than energy transfer by convection within the boundary layer.

The energy equation to be solved in the cathode fall is therefore

$$\rho_0 C_v \frac{\partial T'}{\partial t} = \lambda\frac{\partial^2 T'}{\partial x^2} + \dot{Q} \tag{3.3}$$

which is now uncoupled from the pressure and velocity fields. Equation (3.3) must be solved subject to the conditions

$$\begin{aligned} T' &= 0, \quad x = 0, t > 0 \\ T' &= 0, \quad t = 0, x > 0 \\ T' &= 0, \quad x \to \infty, t > 0. \end{aligned} \tag{3.4}$$

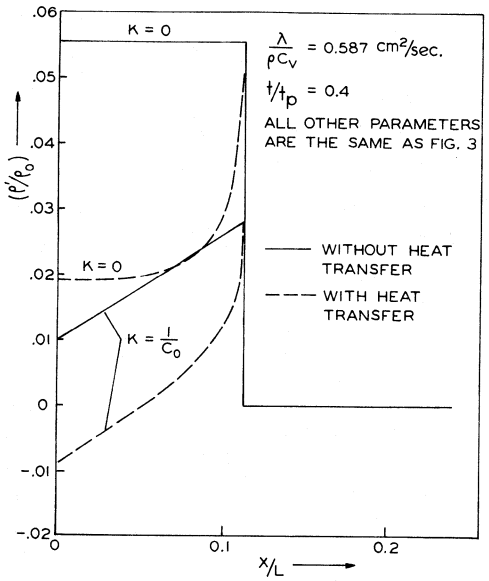


Fig. 7. Illustration of the influence of heat loss to the cathode on the density profile for the cathode wave.

The Laplace transform of (3.3) is

$$\frac{d^2\tilde{T}}{dx^2} - \beta^2\tilde{T} = -\frac{\dot{Q}}{\lambda} \tag{3.5}$$

where

$$\beta^2 = \frac{\rho C_v}{\lambda} s = \frac{s}{\alpha}. \tag{3.6}$$

The Green's function for (3.5) is

$$G = -\sqrt{\frac{\alpha}{s}} \begin{cases} \exp\left(-x_0\sqrt{\frac{s}{\alpha}}\right)\sinh\left(x\sqrt{\frac{s}{\alpha}}\right), & x < x_0 \\ \exp\left(-x\sqrt{\frac{s}{\alpha}}\right)\sinh\left(x_0\sqrt{\frac{s}{\alpha}}\right), & x > x_0 \end{cases} \tag{3.7}$$

and the temperature profile for uniform heat additions, (2.18), is

$$\tilde{T}_-(x,s) = \frac{\alpha\dot{Q}_c}{\lambda s^2}\left[\exp\left(-x\sqrt{\frac{s}{\alpha}}\right) + \frac{1}{2}\exp\left\{\sqrt{\frac{s}{\alpha}}(x-d)\right\} - \frac{1}{2}\exp\left\{-\sqrt{\frac{s}{\alpha}}(x+d)\right\} - 1\right], \quad x < d$$

$$\tilde{T}_+(x,s) = \frac{\alpha\dot{Q}_c}{\lambda s^2}\exp\left(-x\sqrt{\frac{s}{\alpha}}\right)\left[\cosh\left(\sqrt{\frac{s}{\alpha}}d\right) - 1\right], \quad x > d. \tag{3.8}$$

Note that the temperature profile decays very rapidly outside the sheath. Equation (3.8) is now used to evaluate the last term of (3.2), and the entire right-hand side appears as the source term in the solution (2.17):

$$\tilde{p}(x,s) = -\frac{\gamma-1}{c_0^2}\int_0^\infty \left[s\tilde{Q} + \lambda s\frac{d^2\tilde{T}}{dx_0^2}\right] G(x|x_0;s)\,dx_0. \tag{3.9}$$

For $x > d$, (3.9) is

$$-\frac{c_0^2}{\gamma-1}\tilde{p}(x,s) = \int_0^d \dot{Q}_c G_+ dx_0 + \lambda s\int_0^d G_+\frac{d^2\tilde{T}_-}{dx_0^2}dx_0 + \lambda s\int_d^x G_+\frac{d^2\tilde{T}_+}{dx_0^2}dx_0 + \lambda s\int_x^\infty G_-\cdot\frac{d^2\tilde{T}_+}{dx_0^2}dx_0. \tag{3.10}$$

It is a realistic assumption, which greatly simplifies the result, to take $\alpha s/c_0^2 \ll 1$. Equation (3.10) then leads to a formula which can be inverted without difficulty. The result can be separated into two parts: the first, arising from the first integral in (3.10), is the adiabatic solution (2.19); the second includes the effects of heat transfer. Denote the latter solution by p_h'; for $t < t_p$ this is

$$\frac{c_0}{(\gamma-1)\sqrt{\alpha}\dot{Q}_c}p_h'(x,t) = \frac{1}{1+KC_0}\left[\sqrt{\frac{4}{\pi}\left(t-\frac{x}{c_0}\right)}\cdot\exp\left\{-\frac{d^2}{4\alpha(t-x/c_0)}\right\} - \sqrt{t-\frac{x}{c_0}}\,U\left(t-\frac{x}{c_0}\right) - \frac{d}{\sqrt{\alpha}}\cdot\operatorname{erfc}\left\{\frac{d}{\sqrt{4\alpha(t-x/c_0)}}\right\}\right] - \frac{\sqrt{\alpha}}{c_0}\left[\frac{1}{2}\operatorname{erfc}\left(\frac{x-d}{\sqrt{4\alpha t}}\right) + \frac{1}{2}\cdot\operatorname{erfc}\left(\frac{x+d}{\sqrt{4\alpha t}}\right) - \operatorname{erfc}\left(\frac{x}{\sqrt{4\alpha t}}\right) - \frac{1}{2}U\left(t-\frac{x-d}{c_0}\right) + \frac{1}{2}\left(\frac{1-Kc_0}{1+Kc_0}\right)U\left(t-\frac{x+d}{c_0}\right) + \frac{Kc_0}{1+Kc_0}U\left(t-\frac{x}{c_0}\right)\right]. \tag{3.11}$$

The formula for the fluctuation of density can be deduced as in Section II-E.

Fig. 7 shows the profiles of the density wave for two values of K, with and without heat transfer accounted for. Note first, as argued earlier, the initial amplitude of the cathode

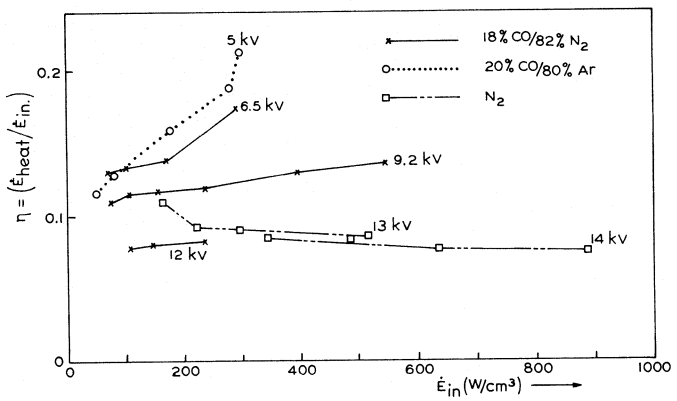


Fig. 8. Experimentally determined bulk heating rates in a 10-l laser. $p = 100$ torr, $T = 80$ K.

wave is unaffected by heat transfer. As time (or x/L) increases, an increasing proportion of the energy deposited in the cathode fall is transferred to the cathode itself, and therefore a smaller amount is available to increase the internal energy and pressure of the gas. The pressure is therefore reduced from that produced if the waves were generated with no heat transfer. But a steady state is reached rather quickly ($x/L \sim 0.05$), and at later times a fixed proportion of the energy input flows to the cathode. The slope of the wave is then the same as that when no heat transfer is accounted for.

The important conclusion of this calculation is that two observable features of the cathode wave—the maximum amplitude and the ultimate slope—can evidently be accurately represented by the result obtained when heat transfer is neglected. A relatively small portion of the wave (roughly 5 percent of the cavity depth for the example shown in Fig. 7) of the wave exhibits the effects of the heat lost to the cathode. These results justify using the simpler analysis of Section II to interpret interferograms of the flow.

IV. Determination of the Bulk Heating Rate

The formula (2.29) and the corresponding result for the anode wave have been used to infer the bulk heating rate from interferograms. It is convenient to express the bulk heating as a proportion of the total energy input:

$$\eta = \dot{Q}_h / \dot{E}_{\text{in}} . \tag{4.1}$$

Then substitution into (2.29) gives

$$\eta = \frac{2\gamma p_0 c_0}{(\gamma - 1)\dot{E}_{\text{in}}} \frac{\partial}{\partial x}\left(\frac{\rho'}{\rho_0}\right)_{\text{cathode}} . \tag{4.2}$$

The density gradient is related to the gradient dN/dx of the number of fringes in an interferogram by

$$\frac{\partial \rho'}{\partial x} = \frac{\rho_s}{\rho_0} \frac{\lambda}{\Omega L_0} \frac{dN}{dx} \tag{4.3}$$

where ρ_s is the gas density at standard conditions, L_0 is the optical path length, Ω is the Gladstone-Dale constant [5] and λ is the wavelength of the light used.

In [3], details are given for the Mach-Zehnder interferometer assembled to make observations of the density fields in the 10-l laser described there. Single- and double-pulsed interferograms have been taken for pure N_2, CO/Ar mixtures, and

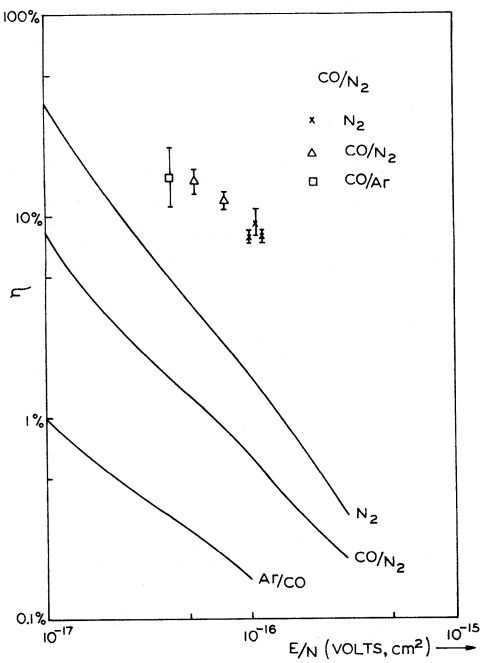


Fig. 9. Comparison of experimentally determined bulk heating rates with the heating calculated for elastic collisions only.

CO/N_2 mixtures. No optical extraction was made during those tests.

Fig. 8 shows the fractional heating rate, deduced from measurement of the fringe gradients and use of (4.3), as a function of input power for three media and several values of sustainer voltage. The data were taken at different times following initiation of the sustainer; it is often more meaningful [6] to use the total energy input, per unit volume, as the independent variable. In Fig. 9, the data are replotted, and the values of applied voltage have been converted to the more fundamental parameter E/N, where N is the total number density of neutral particles.

Computed values [7] of the total heating rate due to elastic heating only are compared in Fig. 9 with the data. The results inferred from the interferograms consistently are larger, by roughly a factor of 10, than the calculated values. This comparison suggests that other sources of heating must be acting; the most obvious is that due to the anharmonic defect in V-V energy transfer, but direct excitation of the rotational

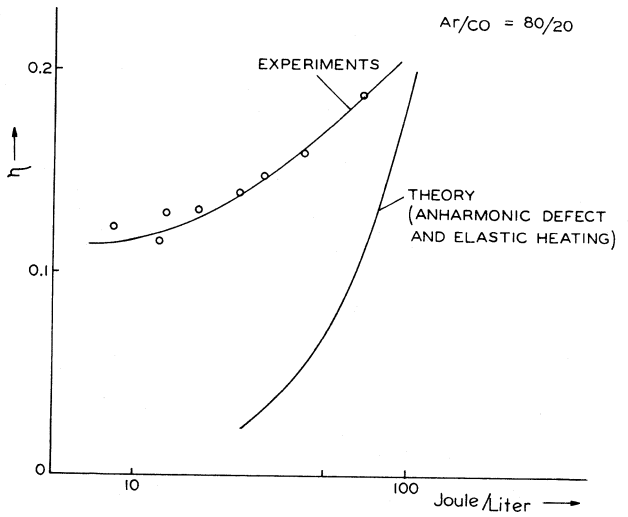


Fig. 10. Comparison of experimentally determined heating rates with the heating calculated for elastic collisions and anharmonic defect (Ar/CO mixture).

degrees of freedom by electron collisions may also contribute. It should be noted, in addition, that within the laser cavity the electric field is strongly nonuniform [7]. The values of E/N may therefore have not been correctly chosen for a valid comparison.

Finally, in Fig. 10, the fractional heating is shown as a function of the total energy deposited for a mixture of argon and carbon monoxide without optical extraction. The calculated values include both elastic heating and heating due to anharmonic defect during V-V energy transfer. Contrary to the predicted behavior, the measured values remain relatively high at the lower values of energy input, although reasonable agreement seems to be found for energies above 100 J/l. The reasons for the discrepancies are not known. A possible cause [7] is rotational excitation of carbon monoxide, which has not been accounted for in the theoretical work.

Acknowledgment

The authors thank Dr. W. B. Lacina for informative discussions, and for providing results of his calculations.

References

[1] E. R. Pugh *et al.*, "Optical quality of pulsed electron-beam sustained lasers," *Appl. Optics*, vol. 13, p. 2512, Nov. 1974.
[2] W. B. Lacina, W. W. Mann, and G. L. McAllister, "Transient oscillator analysis of a high-pressure electrically exicted CO laser," *IEEE J. Quantum Electron.*, vol. QE-9 p. 588, 1973.
[3] G. L. McAllister, R. E. Eguchi, and V. G. Draggoo, "Effects of acoustic waves on the beam quality of high energy CO lasers," *Appl. Optics*, vol. 14, p. 1290, June 1975.
[4] A. L. Ward, "Calculation of cathode-fall characteristics," *J. Appl. Phys.*, vol. 3, pp. 2789–2794, Sept. 1962.
[5] A. H. Shapiro, *The Dynamics and Thermodynamics of Compressible Fluid Flow*, vol. I. New York: Ronald Press, 1953, p. 63.
[6] M. M. Mann, "CO lasers–Design considerations," presented at the AIAA 13th Aerospace Sciences Meeting, Pasadena, CA, Jan. 1975, AIAA Paper 75-34.
[7] W. B. Lacina, private communication, to be published.

Operation-Induced Degradation of GaP Light-Emitting Diodes

AKIRA USAMI AND TOSHIO HAYASHI

Abstract—**After GaP red light-emitting diodes (LED's) had been degraded by the forward-biased operation, changes of the light output, the minority carrier lifetime, the photocurrent, and the photocapacitance were measured. There was a linear decreasing relation between the light output and the carrier lifetime. A center which was related to the degradation of the light output was observed by means of photocurrent and photocapacitance measurements. This center's energy level is about 0.8 eV from either the valence or conduction band. This center was observed to increase in concentration with degradation. However, the contribution of this center to the minority carrier lifetime is not established since the capture cross sections of the center are unknown and is not known whether the center occurs on the n-side, or the p-side, or on both sides. This center does not appear to be an oxygen donor.**

Manuscript received February 3, 1976; revised April 26, 1976 and June 9, 1976.

A. Usami is with the Department of Electronics, Nagoya Institute of Technology, Nagoya, Japan.

T. Hayashi was with the Department of Electronics, Nagoya Institute of Technology, Nagoya, Japan. He is now with the Electrical Communications Laboratory, Nippon Telegraph and Telephone Public Corporation, Tokyo, Japan.

Introduction

MANY STUDIES have been made of degradation in GaP and GaAs light-emitting diodes (LED's) under forward-biased operation ([1]-[3]). Degradation is usually caused by an increase in the bulk nonradiative recombination processes and sometimes by surface effects which are neglected in this study. As one of the nonradiative recombination centers, copper in both the GaP LED ([2]) and the GaAs LED ([3]) has been closely related to the device degradation. Two models have been proposed to explain the degradation of GaAs tunnel diodes ([4], [5]). One assumes the migration of interstitial zinc under the forward current stress, and the other assumes the formation of a Frenkel-type defect by the energy released in the nonradiative recombination processes under the

forward current stress. In most degradation experiments ([1]-[5]), the nonradiative recombination center could not be detected directly. The nonradiative defect center was presumed to be present from the device characteristic changes under the stress current. On the other hand, in other than aging experiments, oxygen donors are reported as nonradiative recombination centers in GaP LED's ([6], [9]). It has been reported that the proportion of nonradiative recombinations through oxygen donors to those through radiative zinc-oxygen pairs is 30 percent ([8]), 1.5 percent ([6], [7]), and lower than 4 percent ([9]).

The capture cross section and the energy level of the oxygen donor have been reported elsewhere ([12], [13]). From the measurement of the minority carrier lifetime of GaP LED's which were fabricated from a nonstoichiometric melt, the nonradiative Ga-vacancy concentration has been shown proportional to the inverse lifetime ([10]). The Auger recombination process could not be completely neglected as the nonradiative recombination which reduces the minority carrier lifetime in GaP LED's ([11]). The role of the oxygen donor and Ga vacancies in the process of degradation has been clarified. We have studied the nonradiative recombination center due to degradation and the oxygen donor in GaP red LED's during forward operation. We have employed light output, minority carrier lifetime, photocurrent, and photocapacitance measurements.

Experimental Procedure

The samples used in this study are GaP light-emitting diodes, TLR-103, commercially made by Toshiba Co., Ltd. Their characteristics are as follows: peak emission wavelength = 7000 A, diffusion potential = 1.5 V, concentration gradient of the junction about 5×10^{21} cm^4. Details of the fabrication process have been previously reported in Kasami's work ([11]).

The light output of the LED was measured with a silicon photodiode in the short-circuit current mode. The minority carrier lifetime of the LED was measured by the reverse recovery method ([14]). The time measured represents the lifetime of carriers in both the p- and n-sides of the diode. Pulse generator Tektronix type 109 and sampling oscilloscope Iwatsu SAS-500 were used for lifetime measurement, and the rise time of the total system was 0.5 ns. Photocurrent and photocapacitance were measured by the Takeda pA meter TR-8641 and the Boonton capacitance meter 72B-D using monochromatic light given by the Hitachi monochrometer. The samples were stressed at 60°C and 90°C under the current densities 37.5 A/cm^2 and 18.7 A/cm^2, respectively.

Intrinsic Quantum Efficiency and Lifetime

The current injection efficiency γ is defined as follows:

$$\gamma = I_{dif}/I_{tot} \tag{1}$$

where I_{dif} is diffusion current and I_{tot} is total current. The injection efficiency γ is tabulated versus aging time in Table I which is evaluated from forward I-V characteristics. The accuracy of γ is not good because of error introduced by the series resistance. Although there is relatively large scatter in γ, the degradation of injection efficiency cannot be found up to the half-degradation of light output after 1098 h of aging.

TABLE I
Intrinsic Quantum Efficiency of the GaP LED at Different Operating Times

total current / aging time	5mA	10mA	20mA
0 hours	79%	77%	84%
39	83	89	92
125	65	77	85
275	64	75	82
610	56	70	78
1098	71	80	86

Degradation of light output L is caused by degradation of the internal quantum efficiency η_i and minority carrier lifetime τ which are related by the following equation:

$$L/L_0 = \eta_i/\eta_{i0} = \tau/\tau_0\,(\tau_{r0}/\tau_r) \tag{2}$$

where the subscripts 0 and τ_r denote before aging and radiative recombination lifetime, respectively. The light output L and minority carrier lifetime which were normalized to the preaging condition are plotted in Fig. 1. The light output is proportional to minority carrier lifetime so that the results satisfy (2). Therefore the radiative recombination lifetime τ_r is constant during stress aging and the degradation of the light output results from a decrease in the minority carrier lifetime. In the following section, the nonradiative recombination center will be characterized with photocurrent and photocapacitance measurements of the LED.

Photocurrent

The photon absorption coefficient is proportional to $(h\nu - E_0)^m$, where $h\nu$ is photon energy of incident monochromatic light and E_0 is constant. In our samples, photocurrent is proportional to $(h\nu - E_0)^m$ where m is between 2 and 3. The cube root of photocurrent is plotted against photon energy in Fig. 2. Its characteristics can be approximated by three straight lines. Let it be divided into three regions and denote region I (0.8-1.8 eV), region II (1.8-2.1 eV), and region III (2.1-2.3 eV). In region I, photocurrent increases in accordance with aging time, but in the other regions (II and III) it decreases.

In order to investigate the mechanism of the photocurrent activated by the extrinsic light, the temperature dependence and bias dependence of photocurrent were measured, and these results are given in Figs. 3 and 4. Both figures show that the photocurrent of region I is independent of thermal emission and dependent on the applied voltage; the photocurrent of region II results from thermal emission whose activation energy is about 248 meV and whose photocurrent is independent of the applied voltage; the photocurrent of region III shows weak temperature dependence and no bias dependence.

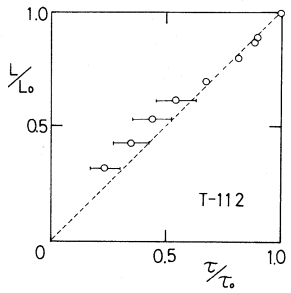


Fig. 1. Normalized light output versus normalized carrier lifetime for degraded LED.

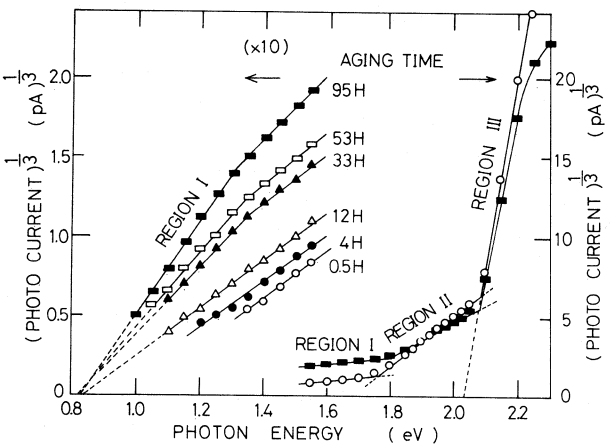


Fig. 2. Cube root photocurrent versus photon energy of degraded LED as a parameter of aging time.

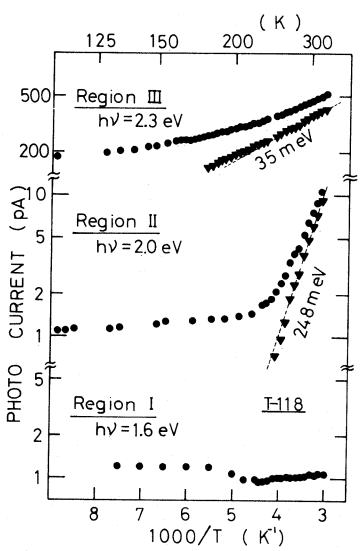


Fig. 3. Temperature dependence of photocurrent and the fractional change in photocurrent.

In Fig. 5 we illustrate the various photocurrent mechanisms corresponding to the three regions. In region I, the two-photon process can be neglected because the light source of monochromatic light is only a 40-W tungsten lamp and the Frantz-Keldish effect is also negligible because of a weakness of the electric field. Then the probable process in region I is one with tunneling through the impurity center in the forbidden band. In region II, the probable mechanism is two-

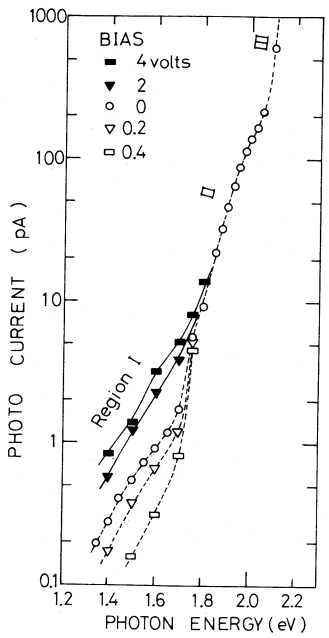


Fig. 4. Photocurrent versus photon energy of degraded LED as a parameter of applied voltage.

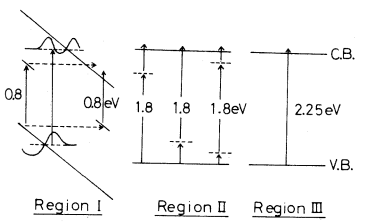


Fig. 5. Energy band model representation of photocurrent in a degraded LED. Region I, tunneling process; region II, two-step process; region III, fundamental process.

step excitations with both optical excitation and thermal emission. And in region III the photocurrent comes from the fundamental absorption edge of GaP (Fig. 5). The photocurrent in region I probably arises from impurity levels and increases with stressed aging time as shown in Fig. 2. This impurity is expected to be a nonradiative center. If so, photocurrent in region I is proportional to the nonradiative recombination rate U_{nr}, and the relation between light output and photocurrent (I_p) is given by

$$1/L = 1/K_1\,(1 + I_p/K_2\,U_r) \tag{3}$$

where K_1 and K_2 are constants given by $K_1 = L/\eta_1$ and $K_2 = I_p/U_{nr}$.

The result of the aging experiment is shown in Fig. 6 and a linear relationship was obtained between light output and photocurrent. Therefore, the above assumption that the impurity levels observed by the photocurrent are nonradiative recombination centers is reasonable. Therefore this impurity whose photoactivation energy is 0.8 eV increases with aging time and its increase degrades the output of the LED. However, the contribution of this center to the minority carrier lifetime is not established since the capture cross sections of the center are unknown and is not known whether the center occurs on the n-side, the p-side, or on both sides.

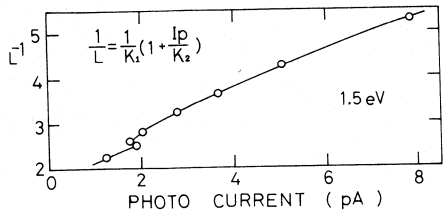


Fig. 6. Inverse light output versus photocurrent (irradiation with 1.5-eV light) of the LED during degrading processes.

The increment of the photocurrent decreases with the minority carrier lifetime. The photocurrent in region II and region III has no bias dependency so that the generation of carriers in the depletion region can be neglected, and the generation of carriers within a diffusion length of the junction is dominant. Then the photocurrent is given by

$$I_p = -e(L_p + L_n)g \tag{4}$$

where g is the rate of carrier generation per photon, e is the charge of the electron, and L_p and L_n are the hole and the electron diffusion length, respectively.

Assuming $(L_p + L_n)$ proportional to $\sqrt{D\tau}$, (4) and (2) give

$$L \propto \tau \propto (L_p + L_n)^2 \propto I_p^2. \tag{5}$$

Fig. 7 shows the relation between light output and the square of photocurrent which was measured under monochromatic light with photon energy 2.3 eV. Light output is proportional to the square of the photocurrent as was expected from (5). Since the mobility of the electron is larger than that of hole, the minority carrier diffusion length (L_n) in the p-type active region is longer than that (L_p) in the n-type region of the LED ([15]). Induced photocurrent is proportional to the inverse product of absorption coefficient and the depth from the light irradiated front surface (p-type active layer) of the LED. Then the changes of photocurrent are dominantly controlled by those of electron diffusion length, $L_n = \sqrt{D_n \tau_n}$, in the p-type active region of the LED. These decrements of diffusion length will not affect the results in region I. Because bias dependency is strong in region I and the extrapolated voltage to zero photocurrent is about plus 0.5 V and there is no generation of carriers outside of the depletion region, the model in Fig. 5 indicates that tunneling is necessary for carrier generation in a high electric field.

PHOTOCAPACITANCE

Photocapacitance measurement will give us information on the impurity generated during the aging experiment. The method is as follows (Fig. 8).

1) Before measuring the capacitance change, a forward voltage of 1.5 V must be applied to the LED. Because this LED has a stable trapping center at room temperature, by applying a forward voltage the traps in the n-type region are filled by electrons and the trapped electrons in the p-type region recombine with free holes.

2) After switching off the applied voltage a monochromatic light $(h\nu_1)$ is irradiated on the LED.

3) After turning off the first light, the second monochromatic light $(h\nu_2)$ is irradiated.

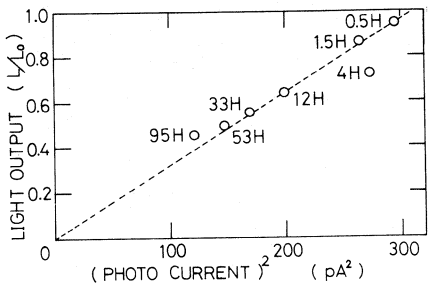


Fig. 7. Normalized light output versus the square of photocurrent (irradiation with 2.3-eV light) of the LED during degrading processes.

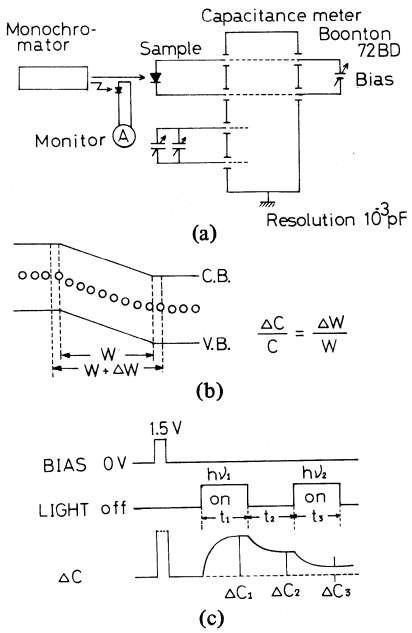


Fig. 8. Photocapacitance measurement procedures. (a) Experimental apparatus. (b) Relation between the capacitance change and the depletion region wide variation. (c) Experimental process and representation of the changing of clear pulse, irradiated light, and the capacitances.

In these processes, the capacitance change of the LED is denoted by ΔC_1, ΔC_2, and ΔC_3 as shown in Fig. 8. Characteristics of the capacitance change ΔC_2 which depends on photon energy $h\nu_1$, and ΔC_2 which depends on photon energy $h\nu_2$ are shown in Fig. 9, where the first light photon energy to measure ΔC_3 is 1.8 eV.

Our results coincide with Kukimoto's for oxygen donors in a GaP LED. He reported that the oxygen donor had three stable conditions for different photoionizing processes, i.e., e_{p1}, e_{p2}, e_{n1}, and e_{n2}. Threshold photon energy values of these three processes are tabulated in Table II. His and our values are in good agreement. The reason the threshold energy of e_{p2} cannot be measured is that we measured photocapacitance at room temperature and that the threshold is smeared by phonon broadening. Thus it seems that the capacitance change illustrated in Fig. 9 for a diode before aging results from an oxygen donor.

LED's were degraded by forward current at 60°C. After 94.5 h of aging, capacitance change is measured for lower photon energies except for capacitance change resulting from an oxygen donor (Fig. 10). Both capacitance change ΔC_1 and

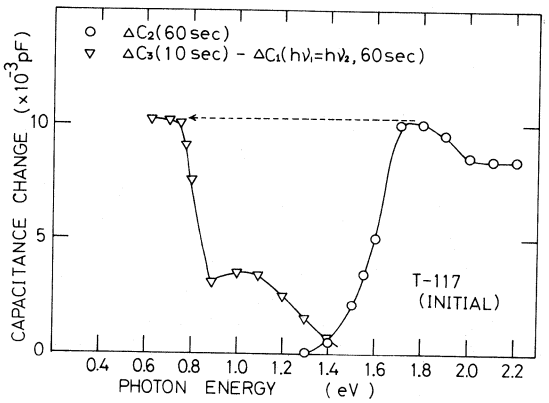


Fig. 9. Steady-state capacitance changes versus light energy. Dashed lines indicate a change in energy with the light blocked.

TABLE II
THRESHOLD ENERGY FOR PHOTOCAPACITANCE CHANGING PROCESSES OF NONDEGRADED LED

	this experiment	Kukimoto et. al
e_{p1}	1.4eV	1.42eV
e_{p2}	?	1.58
e_{n1}	0.8	0.8
e_{n2}	1.2	1.15

Note: e_{p1}, e_{p2}, e_{n1}, and e_{n2} follow Kukimoto's notation for a different ionizing process of the oxygen donor.

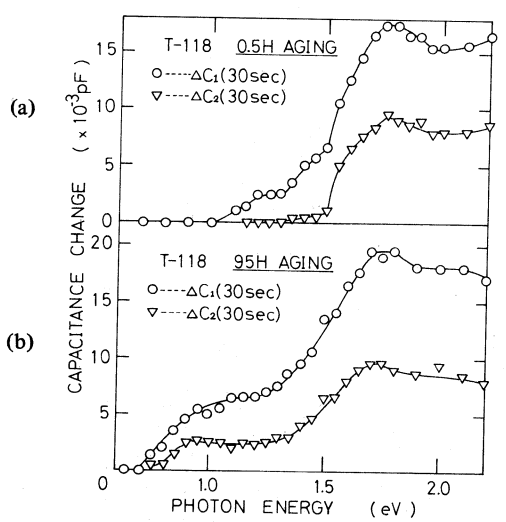


Fig. 10. Capacitance change ΔC_1 and ΔC_2 for (a) before aging and (b) after degrading the LED with irradiation of light energy.

ΔC_2 have threshold photon energy = 0.7 eV. The aging of this new capacitance change is shown in Fig. 11. Around a photon energy of 1.8 eV where capacitance change due to an oxygen donor is dominant, ΔC_1 hardly changed. That is, the concentration of oxygen is constant throughout the aging experiment and the oxygen appears independent of the degradation of the LED. On the other hand, at lower photon energy a new capacitance change emerges and increases with aging time. That is, a new trap center is created by the aging experiment.

To investigate the relation between this new trap and light

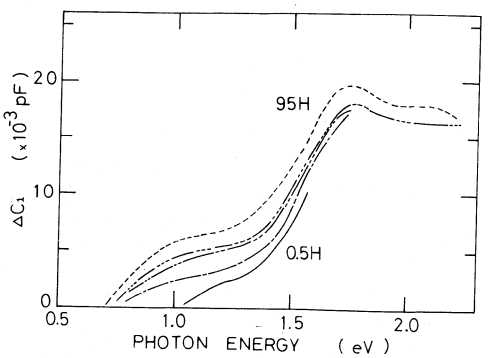


Fig. 11. Capacitance change of ΔC_1 with irradiation of light energy at different operating times.

output of the LED, the inverse of light output L^{-1} is plotted versus capacitance change at $h\nu_1 = 1.0$ eV in Fig. 12. This figure shows that the linear relation between ΔC_1 and L^{-1} is established and the relation of (5) replacing I_p by ΔC_1 is established. Therefore this new trap acts as a nonradiative recombination center.

Fig. 13 shows dependency of ΔC_1 on the depletion layer width. This is measured by changing the applied voltage V_a in Fig. 8. This result indicates that this new trap is localized within the depletion layer within 0.1-0.18 μm.

SUMMARY

Before and after degradation of GaP LED's by forward operation, light output, minority carrier lifetime, photocurrent, and photocapacitance of the LED were measured to find the nonradiative recombination center. Minority carrier lifetime measurement has made it clear that the degradation of light output by forward operation has resulted dominantly from a decrease in the internal quantum efficiency because the light output was proportional to the minority carrier lifetime. The nonradiative recombination center which degraded the internal quantum efficiency was found by photocapacitance and photocurrent measurements. Photocurrent measurement showed three different mechanisms for generating photocurrent by its dependency on photon energy. In region III ($h\nu > 2.1$ eV), photocurrent comes from fundamental absorption of GaP. In region II (1.8 eV $< h\nu <$ 2.1 eV), temperature dependency and no bias dependency of the photocurrent suggest the mechanism of two-step excitation. And in region I (0.8 eV $< h\nu <$ 1.8 eV), strong bias dependency and no temperature dependency of photocurrent show that photocurrent is generated by tunneling through a deep level in the forbidden band gap. The increasing photocurrent with aging time in region I can quantitatively explain the degradation of light output, assuming that the center concerned in region I to be a nonradiative recombination center. By means of photocapacitance measurement the oxygen donor was detected before aging samples. Though the value of capacitance change due to the oxygen donor did not change after aging, a new capacitance change due to an unidentified center different from oxygen was detected. Its threshold is 0.8 eV of photon energy, corresponding to the threshold of photocurrent in region I. This new capacitance change appeared

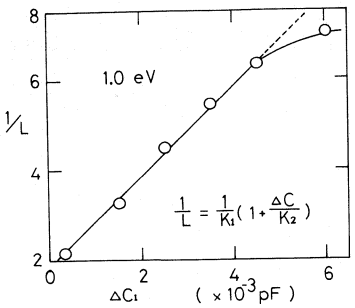


Fig. 12. Inverse light output versus capacitance changes of ΔC_1 of the LED during degrading processes.

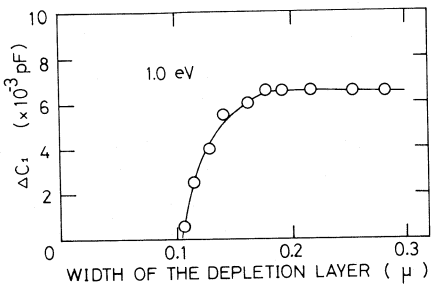


Fig. 13. Values of ΔC_1 in the depletion layer width.

after aging and increased with aging time. Assuming that this new capacitance change is due to the nonradiative recombination center (however, the contribution of this center to the minority carrier lifetime is not established), it can quantitatively explain the degradation of light output. Therefore the degradation of the LED by forward operation does not result from the oxygen donor, but from a new center which has a 0.8-eV energy level and is different from an oxygen donor.

Acknowledgment

The authors would like to express their sincere thanks to Prof. Y. Inuishi of Osaka University for his helpful encouragement during this work.

References

[1] E. S. Yang, "Degradation of zinc-diffused GaAs electroluminescent diodes," *IEEE J. Quantum Electron.*, vol. QE-7, pp. 239–244, June 1971.
[2] A. A. Bergh, "Bulk degradation of GaP red LED," *IEEE Trans. Electron Devices*, vol. ED-18, pp. 166–170, Mar. 1971.
[3] A. Bahraman and W. G. Oldham, "Role of copper in degradations of GaAs electroluminescent diode," *J. Appl. Phys.*, vol. 43, pp. 2383–2387, May 1972.
[4] R. L. Longini, "Rapid zinc diffusion in gallium arsenide," *Solid State Electron.*, vol. 5, pp. 127–130, 1962.
[5] R. D. Gold and L. R. Weisberg, "Permanent degradation of GaAs tunnel diode," *Solid State Electron.*, vol. 7, pp. 811–821, 1964.
[6] H. Kukimoto, C. H. Henry, and F. R. Merrit, "Photocapacitance studies of oxygen donor in GaP. I. Optical cross sections, energy levels and concentration," *Phys. Rev. B*, vol. 7, pp. 2486–2499, Mar. 1973.
[7] C. H. Henry, H. Kukimoto, G. L. Miller, and F. R. Merritt, "Photocapacitance studies of the oxygen donor in GaP. II. Capture cross sections," *Phys. Rev. B*, vol. 7, pp. 2499–2507, 1973.
[8] J. S. Jayson, R. Z. Bachranch, P. D. Dapkus, and N. E. Schumaber, "Evaluation of the Zn–O complex and oxygen-donor electron-capture cross sections in P-type GaP: Limits on the quantum efficiency of red-emitting (Zn, O)-doped material," *Phys. Rev.*, vol. 6, pp. 2357–2372, Sept. 1972.
[9] D. V. Lang, "Fast capacitance transient apparatus: Application to ZnO and O centers in GaP p–n junctions," *J. Appl. Phys.*, vol. 45, pp. 3014–3022, July 1974.
[10] A. S. Jordan, A. R. Von Neida, R. Caruso, and M. Didomenico, Jr., "Red photoluminecency and minority-carrier lifetime of GaP (Zn, O) pulled from nonstoichiometric melts," *Appl. Phys. Lett.*, vol. 19, pp. 394–397, Nov. 1971.
[11] K. Maeda, A. Kasami, M. Toyama, and N. Wakamatsu, "Minority carrier lifetime in GaP electroluminescent diodes," *Japan J. Appl. Phys.*, vol. 8, pp. 65–75, Jan. 1969.
[12] G. Bjorklund and H. G. Grimmeiss, "Determination of optical ionization cross sections in GaP using charge storage and impurity photovoltaic effect," *Solid State Electron.*, vol. 14, pp. 589–601, July 1971.
[13] B. L. Smith, "Background energy spectroscopy in GaP using thermal release of trapped space charge in Schottky barriers," *Appl. Phys. Lett.*, vol. 21, pp. 350–352, Oct. 1972.
[14] R. H. Dean and C. J. Nuese, "A refined step-recovery technique for measuring minority carrier lifetime and related parameters in asymmetric p–n junction diodes," *IEEE Trans. Electron Devices*, vol. ED-18, pp. 151–158, Mar. 1971.
[15] W. H. Hachett, Jr., R. H. Saul, R. W. Dixon, and G. W. Kammlott, "Scanning electron microscope characterization of GaP red emitting diodes," *J. Appl. Phys.*, vol. 43, pp. 2857–2868, June 1972.

Pump Saturation in Molecular Far-Infrared Lasers

C. O. WEISS

Abstract—**Precise absorption measurements on vibration-rotation transitions pumping far-infrared (FIR) laser transitions in HCOOH, CH_3OH, CH_3I and CH_3F were carried out using a frequency-stabilized and intensity-controlled CO_2 laser. Linear absorption coefficients and saturation intensities as a function of pressure are obtained. With the help of a rate equation model it is concluded that within the pressure range relevant for CW FIR lasers the rate of deexcitation of pumped molecules is limited by rotational relaxation. For CH_3F, limitation by diffusion of excited molecules to the cell wall is observed.**

I. Introduction

ALTHOUGH the mechanism of optically pumped far-infrared (FIR) lasers is qualitatively known, at present the quantitative understanding of the performance of these lasers is still lacking, in particular, of the generally observed low quantum efficiency. Efforts have been undertaken to establish suitable rate equation models and to compare the results with observed laser performance [1], [2]. However, as there are a number of unknown quantities in these investigations (spectroscopic and relaxation data of molecules, cavity Q, spatial distribution of pumping intensity), accurate comparisons of calculation and measurements have not been possible. It appears therefore to be useful to analyze the FIR laser cycle in more detail and to perform measurements under well-defined conditions.

The one important part of the FIR laser cycle is the vibration-rotation (V-R) transition absorbing the pump (CO_2) laser radiation and thereby populating the upper level of the FIR rotation-rotation (R-R) laser transition. Since saturation behavior and absorption coefficients of the pump transitions are important for optimizing FIR laser construction and performance, the saturated absorption of CO_2 laser radiation is investigated for the pump transitions of the strongest FIR laser lines of HCOOH and CH_3OH as well as for the well-understood symmetric-top molecules CH_3F and CH_3I. A rate equation model is set up to establish a relationship between vibration and rotation relaxation rates and the saturation intensity. Using this relationship, conclusions can be drawn on the mechanism of energy relaxation of the pumped molecules from the measured saturation intensities

II. Absorption Rate Equation Model

Fig. 1 depicts the energy levels and transitions of the laser molecule considered in the model; 1 and 2 represent rotational levels in the vibrational ground state ($v = 0$) and the first excited state ($v = 1$) which constitute the absorbing transition. Two is additionally the upper FIR laser level. The rest of the rotational levels in the $v = 0$ and the $v = 1$ state are summarized in levels 4 and 3, respectively. Radiative transitions R are induced by the pump laser between 1 and 2. Collision-induced transitions r altering the rotational quantum numbers occur between 2 and 3, and 1 and 4. Collision-induced vibrationally deexciting transitions occur from 2 to 1 and 4 and from 3 to and 4.

Collisional excitation of the $v = 1$ state can be neglected, as follows from the principle of detailed balancing. Spontaneous emission can be neglected too. The rates R_v (collisions leading from a $v = 1$ rotational level to a $v = 0$ rotational level) and R_r (altering only the rotational quantum numbers) are assumed to be independent of the rotational quantum numbers.

The rate equations for this system are [11]

$$\begin{aligned}
\frac{dn_1}{dt} &= \left(\frac{n_4}{\alpha} - n_1\right) R_r + \frac{1}{\alpha+1}(n_2+n_3)R_v + (n_2 - n_1)B\cdot q \\
\frac{dn_2}{dt} &= \left(\frac{n_3}{\alpha} - n_2\right) R_r - n_2 R_v + (n_1 - n_2)B\cdot q \\
\frac{dn_3}{dt} &= \left(n_2 - \frac{n_3}{\alpha}\right) R_r - n_3 R_v \\
\frac{dn_4}{dt} &= \left(n_1 - \frac{n_4}{\alpha}\right) R_r + \frac{\alpha}{\alpha+1}(n_2+n_3)R_v
\end{aligned} \tag{1}$$

where

- n_i densities of the levels;
- B Einstein coefficient for radiative transitions;
- q photon density;
- $(\alpha + 1)$ effective number of thermally populated levels in a vibrational state.

As the steady-state solution of (1) one obtains the number of absorbed photons per centimeters cubed and seconds:

$$(n_1 - n_2)\cdot B\cdot q = \frac{N\cdot B\cdot q}{\alpha+1}\left\{1 + B\cdot q\underbrace{\left[\frac{\alpha}{(\alpha+1)R_r} + \frac{\alpha(\alpha+1)^2R_vR_r - \alpha^2R_v^2 + 2(\alpha+1)^2R_r^2}{(\alpha+1)^2R_vR_r((\alpha+1)R_r + \alpha R_v)}\right]}_{R_E^{-1}}\right\}^{-1} \tag{2}$$

where N is the total density of molecules.

Formally this is the same expression as for a two-level system with only one energy relaxation rate [3] except that the energy relaxation rate must in this case be replaced by R_E from (2). Consequently, if the inhomogeneous broadening of the absorbing transition is allowed for, the system obeys the usual saturation formula

$$\kappa(q) = \kappa_0(1 + q/q_s)^{-1/2} \tag{3}$$

Manuscript received February 18, 1976; revised June 3, 1976.
The author is with the Physikalisch-Technische Bundesanstalt, Braunschweig, Germany.

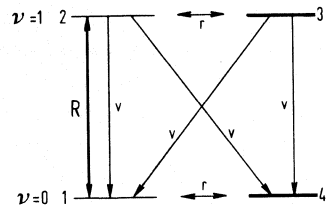


Fig. 1. Energy levels and transitions in FIR laser molecules.

with

$$q_s = \frac{\pi \cdot \Delta\nu_H \cdot R_E}{4 \cdot B \cdot h \cdot \nu} \tag{4}$$

where

κ saturated absorption coefficient;
κ_0 linear absorption coefficient;
q_s saturation photon density;
$\Delta\nu_H$ homogeneous linewidth.

Two limiting cases are of importance in an FIR laser.

1) For the case where R_E is dominated by a binary collision process, R_E is proportional to pressure p and one expects $q_s \sim p^2$ since $\Delta\nu_H \sim p$.

2) If R_E is limited by diffusion of excited molecules to the wall, $R_E \sim p^{-1}$ and q_s is expected to be independent of pressure.

III. Measurement Method

The absorption in a gas cell of length l is obtained by integrating the radiative transfer equation over the cell length, using the saturated absorption coefficient (3). This results in

$$\kappa_0 \cdot l = 2\left(\sqrt{q_0/q_s + 1} - \sqrt{q_1/q_s + 1}\right) + \ln\left[\frac{q_0\left(\sqrt{q_1/q_s + 1} + 1\right)^2}{q_1\left(\sqrt{q_0/q_s + 1} + 1\right)^2}\right] \tag{5}$$

where q_0 is the photon density in the incident beam and q_1 is the photon density transmitted through the cell. If q_0, q_1, and κ_0 are measured, q_s can be obtained by iterative solution of (5). For (5) to be valid, a constant photon density is necessary along the length of the cell. The setup shown in Fig. 2 was used for the measurements. The CO_2 laser beam is divided by a Ge beamsplitter (*BS*). One part is used to stabilize the laser frequency, the other is filtered, reduced in diameter, and attenuated before being passed through the absorption cell.

As the laser did not emit a Gaussian spatial mode (though only a single frequency, as confirmed by beating with another laser) and the beamsplitter introduced interference fringes, spatial filtering was necessary to obtain a clean, smooth beam, prerequisite for quantitative saturation measurements. Filtering is effected with the usual low-pass filter $L1$, P. The beam is recollimated by $L2$. Variable attenuation is achieved with a tilted Ge flat AT, which can be rotated about the optic axis. The radiation passing through the 20-mm-diam 1-m length absorption cell is a pure Gaussian beam of 5.8-mm diameter, the intensity of which was measured radially and axially. $L2$ was adjusted to give constant axial intensity along the cell within ±0.5 percent. Pyroelectric detector $D1$ has a sensitive area

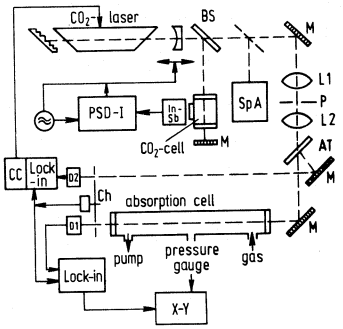


Fig. 2. Saturated absorption measurement setup. *BS*: beam splitter; *M*: mirror; $L1$: Ge lens, $f = 20$ cm; $L2$: Ge lens, $f = 10$ cm; *P*: pin-hole 0.3-mm diameter, *AT*: attenuator, tilted Ge flat; *SpA*: spectroscope for CO_2 laser line identification; InSb: 77 K InSb detector for 4.3-μm fluorescence; *PSD*, *I*: phase sensitive detector, integrator; *CC*: current control; *Ch*: chopper; *D*: pyroelectric detector.

of 0.5-mm diameter which monitors the central portion of the beam.

Because the absorption of the FIR laser gases varies appreciably with frequency within a CO_2 laser line (see, e.g., Fig. 3), the laser frequency was stabilized to the CO_2 line centers using the saturated fluorescence of CO_2 at 4.3-μm wavelength [4]. With the laser locked to the line centers, *X-Y* recordings were taken of intensity I_1 transmitted through the cell versus cell pressure. Pressure ranged from 0.1-130 Pa (1-1000 mtorr). The recordings were taken at increasing and decreasing pressure in order to have a check on errors arising from too long integration times at the lock-in amplifier, pressure gradients along the cell, and impurity leaks.

The central intensity of the incident laser beam was limited to about 800 mW/cm^2 to avoid heating of the gas, which would change the particle density in the cell in an uncontrollable manner [5]. Consequently the decrease of the absorption by saturation was quite small in some cases. As the absorption itself was small for some transitions (only 3 percent at 1 torr for 9.5-μm $CO_2P(34)$ absorption in CH_3I), it was essential to keep the laser intensity as stable as possible during the recordings. This was done by an active intensity control: multiple reflections in the Ge flat AT produce 3-4 weaker laser beams, leaving the flat in different directions since the flat is wedged. One of these weaker beams is monitored by pyroelectric detector $D2$, the output signal of which controls the discharge current through the laser tube. In this way the laser intensity was stabilized to within 0.2 percent.

Fig. 4 shows the measured absorption coefficient per unit pressure $\kappa_p = \ln(I_1/I_0) \cdot p^{-1}$ for absorption of the 9.5-μm $CO_2P(34)$ line in CH_3OH, as a function of pressure. The low-pressure part of the curve clearly shows the saturation, while the independence of κ_p of pressure at high pressure ensures that absorption is unsaturated and that the absorption line can be regarded as inhomogeneously broadened up to the highest pressure. The latter is a necessary condition for the validity of (5) and was checked for every transition. The unsaturated absorption coefficient κ_0 was determined from the pressure independent region; q_s was obtained as a function of pressure from the saturated low-pressure region using (5).

To obtain an idea about the degree of overlapping of CO_2 line and absorption line, for every transition the linear absorption versus laser frequency was measured with the free-running

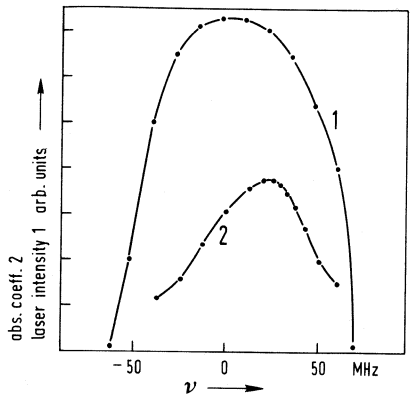


Fig. 3. 10.5-μm $P(32)$ CO_2 laser intensity (1) and linear absorption coefficient of CH_3I $R_R(15, 5)$ line (2) as functions of frequency detuning from CO_2 line center. Frequency scale is slightly nonlinear due to nonlinear piezoelement.

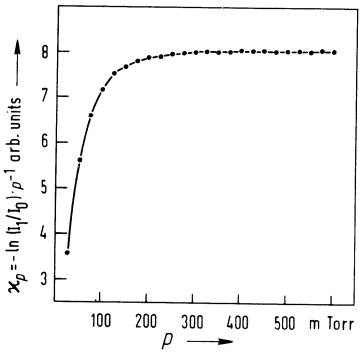


Fig. 4. CH_3OH absorption coefficient per unit pressure for 9.5-μm $CO_2P(34)$ absorption as a function of CH_3OH pressure.

laser, the piezovoltage being used as a frequency scale (see, e.g., Fig. 3).

IV. Results and Discussion

For most of the transitions investigated, the absorption line center was found to lie outside the ±50-MHz tuning range of the CO_2 laser. The only exception being the $R_R(15, 5)$ line of CH_3I, which is 30 MHz from the 10-μm $CO_2P(32)$ line center. Graner [6] calculated, in contrast, an 800-MHz frequency difference from the molecular constants of [7]. The position of the absorption lines with respect to the CO_2 lines is indicated in Table I.

In the pressure range where saturation was observable and which is of relevance for CW FIR lasers (≈ 0-100 mtorr), the pressure dependence of the saturation intensity was generally found to be quadratic. As a typical example, Fig. 5 shows a saturation intensity measurement for 9-μm $CO_2R(18)$ absorption in HCOOH in double logarithmic representation. The constant slope of 2 shows that deexcitation of the pumped molecules is limited by a binary collision process. Table I gives the measured linear absorption coefficients at the CO_2 line centers and the saturation intensities. The uncertainties of the saturation intensities are primarily due to the laser power measurements which were done with a commercial power meter. For the weakly absorbing transitions the I_s values showed larger scatter due to the residual intensity fluctuations of the laser, so that the uncertainties are larger.

Obviously, it is of importance for FIR lasers which one of the two processes, vibration or rotation relaxation, i.e., R_r or R_v determines R_E and hence I_s. To gain some insight, the rates R_E were calculated from the measured saturation intensity for the $Q_Q(12, 2)$ transition in CH_3F and the $R_R(15, 5)$ transition in CH_3I, for which the line center absorption coefficient can be measured. The thermal population of the lower absorbing levels was calculated using [8, eq. (3-48)]. From the line center absorption coefficient the spontaneous lifetime or B was then determined. The homogeneous linewidth was taken from [9]. R_E was obtained using (4). The numerical R_E values (Table II) are quite similar to one-half of the rotational relaxation rate $\pi \cdot \Delta\nu_H$ [9].

Besides this, it is known that vibrational relaxation in CH_3F is dominated by diffusion of excited molecules to the wall [10] at pressures of 0.1 torr. Since the pressure dependence of I_s for CH_3F as measured in the present experiment does not indicate diffusion domination of R_E at pressures up to 75 mtorr, one can conclude that 1) the number α of "decay channels" is very high for CH_3F; 2) the deexcitation of the pumped molecules is limited by the distribution of the pumped population on the various rotational levels in the $v = 1$ state, i.e., $(\alpha + 1)$. $R_v \gg R_r$, and R_r consequently determines R_E.

On the other hand, it is clear that at high pressure R_E is also proportional to p and $I_s \sim p^2$ because diffusion then plays no role, and R_v and R_r are both proportional to p. In an intermediate pressure range diffusion may be important, and one expects the saturation intensity to show other than the quadratic pressure dependence.

In order to check on these considerations, the saturation measurements on the $Q_Q(12, 2)$ CH_3F line were extended to the 0.1-1-torr range, which is not of direct interest for CW FIR lasers. The result of the I_s measurements shown in Fig. 6 clearly confirms the above considerations: below 75 mtorr the pressure dependence is quadratic, indicating that a binary collision process limits R_E (rotational relaxation). Between 75 mtorr and 0.5 torr the pressure dependence is weaker than linear, indicating the significance of diffusion of excited molecules to the wall. Above 0.5 torr R_E is again limited by binary collisions, diffusion is no longer important, I_s is again quadratic. The pressure dependence of R_E is also indicated in Fig. 6. It may be noted that the pressure at the minimum of R_E agrees with the minimum pressure of the vibration relaxation rate measured by laser fluorescence [10] as one would expect.

Lastly, one can obtain an estimate of the phenomenologic quantity $(\alpha + 1)$ from the quadratic high-pressure part of Fig. 6. In the limit $R_r \gg R_v$ and $\alpha \gg 1$, which seems to be a reasonable approximation for CH_3F, R_E^{-1} from (2) reduces to $R_E^{-1} = 2/R_r + 2/(\alpha \cdot R_v)$. Calculating R_E for the high-pressure region as described above and using $R_v = 590\ s^{-1} \cdot torr^{-1}$ [10], one obtains $\alpha \approx 4.10^3$ which is indeed relatively large.

As the absorption rate equations (1) are quite general and obviously give a realistic description of saturation and energy relaxation in CH_3F, it seems reasonable to extend the conclusions drawn for CH_3F to the other molecules.

1) The number α of vibration relaxation "channels" is quite high.

TABLE I
PUMP ABSORPTION PROPERTIES OF FIR LASER GASES

FIR laser molecule	CO_2 pump line	FIR laser wavelength	abs.coeff. κ_o [1] $cm^{-1}Torr^{-1}$	sat.Intens. I_s $W/(cm^2Torr^2)$	uncertainty ± %	abs.line assignment	rel. [2] position
HCOOH	9μm R(16)	446μm	$5.40 \cdot 10^{-3}$	73	10		h
HCOOH	9μm R(18)	393μm	$4.90 \cdot 10^{-2}$	48	10		h
HCOOH	9μm R(20)	433μm	$1.12 \cdot 10^{-1}$	37	10		h
CH_3OH	9μm P(36)	118μm	$1.10 \cdot 10^{-2}$	169	20		h
CH_3OH	9μm P(34)	70.5μm	$3.20 \cdot 10^{-2}$	250	10		h
CH_3OH	9μm P(32)	41.7μm	$1.46 \cdot 10^{-3}$	53	20		l
CH_3OH	9μm P(16)	570μm	$3.6 \cdot 10^{-2}$	58 [3]	20		h
CH_3I	10μm P(32)	1254μm	$9.61 \cdot 10^{-3}$	2950	10	ν_6:$^RR(15,5)$	h(+30MHz)
CH_3I	10μm P(18)	448μm	$1.06 \cdot 10^{-3}$	$6 \cdot 10^{-1}$	10	ν_6:$^RR(44,5)$	h
CH_3I	9μm R(16)	377μm	$1.1 \cdot 10^{-4}$	15	20		
CH_3I	9μm P(34)	508μm	$3.2 \cdot 10^{-4}$	760	20		
CH_3F	10μm R(32)	193μm	$6 \cdot 10^{-3}$	$3 \cdot 10^{-4}$	20	ν_3:$^QP(32,3)$	h
CH_3F	9μm P(20)	496μm	$1.75 \cdot 10^{-2}$	2300 [3] 70 [4]	20	ν_3:$^QQ(12,2)$	h

[1] Uncertainty < ± 1 percent.
[2] *h*: high frequency side; *l*: low-frequency side of CO_2 laser line.
[3] $p < 75$ mtorr.
[4] $p > 0.5$ torr.

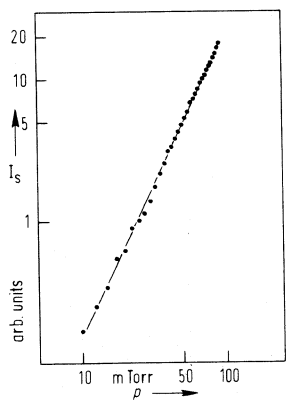


Fig. 5. HCOOH saturation intensity for 9.5-μm $CO_2R(18)$ absorption as a function of HCOOH pressure.

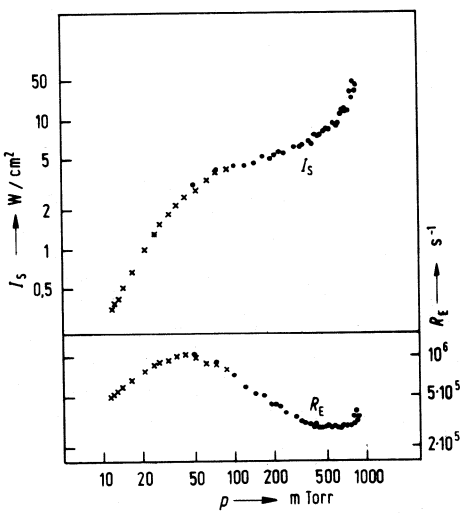


Fig. 6. Saturation intensity I_s and deexcitation rate R_E as a function of pressure for the $Q_Q(12, 2)$ CH_3F transition.

TABLE II
VALUES FOR R_E CALCULATION

	CH_3I: ν_6 ^RR (15.5)	CH_3F ν_3 ^QQ (12.2)
thermal population	$2.1 \cdot 10^{-3}$	$7 \cdot 10^{-3}$
spont. lifetime	3.5 s	2.6 s
$\pi\Delta\nu_H/2$	$6.3 \cdot 10^7$ s^{-1} $Torr^{-1}$	$6.3 \cdot 10^7$ s^{-1} $Torr^{-1}$
R_E	$6.8 \cdot 10^7$ s^{-1} $Torr^{-1}$	$3.8 \cdot 10^7$ s^{-1} $Torr^{-1}$

2) Consequently, the quadratic pressure dependence of the saturation intensity indicates that the energy relaxation of the pumped molecules is limited by the speed of distribution of the pumped population into the α rotational levels in the $v = 1$ state.

3) Diffusion may be a limiting process for the deexcitation of the pumped molecules roughly above 100 mtorr.

In summary, the absorption coefficients and saturation intensities measured allow the absorption of pump radiation in the FIR laser gases investigated to be calculated completely, including transition of inhomogeneous to homogeneous saturation resulting from radiation power broadening. In addition, it was demonstrated that measurements of the absorption saturation may well be used to obtain detailed information on relaxation processes.

ACKNOWLEDGMENT

The author would like to thank E. Musehold for the CH_3F measurements, M. Grinda for technical assistance and G. Kramer for useful discussions.

REFERENCES

[1] J. O. Hennigsen and H. G. Jensen, "The optically pumped far infrared laser: Rate equations and diagnostic experiments," *IEEE J. Quantum Electron.*, vol. QE-11, pp. 248–252, 1975.
[2] H. J. A. Bluyssen, R. E. McIntosh, A. F. van Etteger, and P. Wyder, "Pulsed operation of an optically pumped far-infrared molecular laser," *IEEE J. Quantum Electron.*, vol. QE-11, pp. 341–348, 1975.
[3] J. L. Hall, *Lectures in Theoretical Physics XII.* New York: Gordon and Breach, 1971.
[4] C. Freed and A. Javan, "Standing wave resonances in the CO_2 10.6 μ transitions observed in a low pressure room-temperature absorber gas," *Appl. Phys. Lett.*, vol. 17, pp. 53–56, 1970.
[5] C. O. Weiss and G. Kramer, "Vibrational relaxation in the HCOOH far-infrared laser," *Appl. Phys.*, vol. 9, pp. 175–177, 1976.
[6] G. Graner, "Assignment of submillimeter laser lines in CH_3I," *Opt. Comm.*, vol. 14, pp. 67–69, 1975.
[7] H. Matsmura and J. Overend, "Infrared spectra of CH_3I. The ν_6 and $\nu_3 + \nu_6$ bands at high resolution," *Spectrochim*, vol. 27A, pp. 2165–2171, 1971.
[8] C. H. Townes and A. L. Schawlow, *Microwave spectroscopy.* New York: McGraw-Hill, 1955.
[9] D. T. Hodges and J. R. Tucker, "Pump absorption and saturation in the CH_3F 496 μm laser," *Appl. Phys. Lett.*, vol. 27, pp. 667–669, 1975.
[10] E. Weitz, G. Flynn, and A. M. Ronn, "Laser excitation and equilibration of excited vibrational states in CH_3F," *J. Chem. Phys.* vol. 56, pp. 6060–6067, 1972.
[11] G. Kramer, private communication.

LED Pumped Lithium Neodymium Tetraphosphate Lasers

MASATOSHI SARUWATARI AND TATSUYA KIMURA, MEMBER, IEEE

Abstract—**Laser action in lithium neodymium tetraphosphate, $LiNdP_4O_{12}$ (LNP), crystals, pumped with $Al_xGa_{1-x}As$ electroluminescent diodes, is reported, citing both end- and side-pump configurations. The threshold incident light-emitting diode (LED) intensities at about −30°C are 14.9 W/cm^2 and 7.2 W/cm^2 for end and side pump, respectively. Temperature dependences of threshold, stimulated emission cross section, and round-trip loss were measured experimentally. Possibility of room-temperature CW operation, maximum output power, and optimum coupling are discussed. Taking account of improvements of pumping optics, crystal homogeneity and LED structure, LED intensities required for room-temperature CW operation are 35 W/cm^2 and 8.5 W/cm^2 for end and side pump, respectively.**

I. INTRODUCTION

SOLID-STATE lasers using an incoherent light-emitting diode (LED) as a pump source have been extensively studied on yttrium aluminum garnet (YAG) crystals which contain low concentrations of neodymium [1]-[4]. It is difficult, however, to improve threshold and efficiency of these lasers because of a poor pump light absorption coefficient.

Recent progress in high-neodymium-concentration materials, such as neodymium pentaphosphate, NdP_5O_{14} [5]-[7], and lithium neodymium tetraphosphate, $LiNdP_4O_{12}$ (LNP), [8], [9], has revealed possibilities of miniaturized solid-state lasers by LED pumping. Because the neodymium concentration of these crystals is about 30 times as high as Nd:YAG and the fluorescence lifetime is about half of that of Nd:YAG, a highly efficient miniaturized laser is expected at the 1.05-μm-wavelength band, which corresponds to the low-loss region of optical fibers. The present paper reports experimental results and theoretical considerations on LNP lasers, which are end-[10] and side-pumped with $Al_xGa_{1-x}As$ LED's.

Section II describes experimental components and arrangements which are used to oscillate the LED-pumped LNP lasers in both pump configurations. Experimental procedures and results, such as the temperature dependence of LNP laser threshold and output waveforms of the LNP laser pumped with LED's, are described in Section III. Threshold conditions for both pump schemes are also given. Temperature dependences of effective stimulated emission cross section and resonant round-trip loss are described in Section IV, and the experimental and theoretical pump are compared. Possibilities of decreasing the laser threshold are discussed in Section V, and the room-temperature CW threshold is estimated. The output powers of the LED-pumped LNP laser are calculated for both pump configurations. The power density of the LED required to obtain an output power of around 10 mW is estimated to be 30 W/cm^2 for the side pump, and 10^3 W/cm^2 for the end pump.

Manuscript received February 23, 1976; revised June 2, 1976.
The authors are with the Musashino Electrical Communication Laboratory, Nippon Telegraph and Telephone Public Corporation, Tokyo, Japan.

II. EXPERIMENTAL SETUP

A. LNP Crystals

The LNP crystal used for the LED end pump is a 0.3-mm-thick *a*-plate.[1] It is thick enough to absorb about half of the LED light. Both sides of the sample were optically polished in

[1] The crystal axes refer to the pseudoorthorhombic system.

parallel. On the other hand, an LNP laser, which is side-pumped with an LED array, needs a long crystal. An LNP crystal, which is 4.85 mm in length (a axis), about 4 mm wide (c axis), and 1.9 mm thick (b axis), is used as a side-pumped laser. Both the a- and b-faces are optically polished. Optical and spectroscopic data on LNP have been published in [8] and [9]. Those data, which are relevant to laser oscillation, are summarized in Table I. However, experimental results related to the temperature dependence of the LNP laser performance are not available from the above references. The temperature dependence of fluorescence intensity at 1.047 μm will be shown in Section IV.

B. LED's

Dome-type $Al_xGa_{1-x}As$ LED's [11] are used as main pump ources for both end- and side-pump schemes. Two kinds of LED's are used for both pump schemes. The characteristics of LED's are listed in Table II. The center wavelength is about 0.80 μm, which corresponds to the $^4I_{9/2} \rightarrow {}^2H_{9/2}, {}^4F_{5/2}$ transitions of neodymium ions. The full spectral width at half-intensity is 280 Å ~ 300 Å. The output power is 25 ~ 37 mW at 1-kA/cm^2 drive current density. The main differences between types A and B are due to the difference in emitting junction radius.

A single type A LED is used for the end-pump scheme. For the side-pump scheme, an array of five B LED's is used to match the LNP crystal length. Since the type B LED is mounted on a 0.9-mm-thick slab-shaped copper heat sink, the five-LED array length is 4.5 mm. The array is driven in series. All LED's were operated at room temperature throughout the following experiments.

C. Pumping Optics

In the end-pump scheme, a pair of condenser lenses with $1/F = 1.4$ were used for collecting and focusing the LED light. The condenser lens unit consists of three lenses, each surface of which is coated with antireflection films to reduce the Fresnel reflection loss. The transmission of the lens system at the LED wavelength is increased from 60 to 82 percent by the antireflection coating. The size of the image formed by the condenser lenses is the same as that of the LED in this pump system. Since the incident aperture is limited, this focusing optics scheme cannot be used for an LED array.

In the side pump, a gold-plated hemispherical reflector with 6-cm radius is used. The reflectivity of the gold-plated surface is 80 percent at 0.80 μm. The image of the LED array, focused by the reflector, has the same size as the array itself. Since the reflector radius is sufficiently large, compared to the LED array length, image distortion can be neglected.

D. End-Pumped LNP Laser Arrangement

The experimental arrangement for the end-pumped LNP laser consists of the LNP platelet, the type A LED as a pump source and an Ar ion laser as an auxiliary pump source and as alignment means, as is shown in Fig. 1(a). The 0.3-mm-thick LNP crystal a-plate is attached to a thermoelectric cooling unit with heat-sink compound. The optical resonator consists of a plane and a spherical mirror, arranged in hemispherical configuration. Plane mirror M_2 is attached to one face of the LNP crystal with silicone index-matching liquid to reduce surface reflection loss. In order to prevent the Ar laser beam from spreading, the back surface of spherical mirror M_1, with 5-cm radius of curvature, is shaped into meniscus. Both mirrors are highly reflective with more than 99.9-percent reflectivity at 1.047 μm. Transmittance is not optimized to give maximum output. Transmittances for pump beams at 0.80 and 0.5145 μm are 85 and 80 percent, respectively. To avoid problems with condensation, the entire assembly is placed within a container which is maintained under positive pressure with dry nitrogen gas. The type A LED is driven at room temperature. The LED output is focused into the LNP crystal

TABLE I
LNP SPECTROSCOPIC CHARACTERISTICS

Oscillation Wavelength	λ	1.047 μm
Laser Upper Level Fluorescence Lifetime	τ	120 μsec
Effective Emission Cross Section at Room Temperature	σ_ℓ	3.2×10^{-19} cm^2
Refractive Index	n	1.58

TABLE II
LED CHARACTERISTICS AT ROOM TEMPERATURE

		Type A	Type B
Power	P_o	25.3 mW	37.0 mW
Center Wavelength	λ_o	0.799 μm	0.802 μm
Full Width at Half Maximum	$\Delta\lambda$	280 Å	299 Å
Drive Current Corresponds to 1 kA/cm^2		120 mA	200 mA
Drive Power Corresponds to 1 kA/cm^2	P	0.34 W	0.37 W
Dome Diameter		500 μm	580 μm
Junction Diameter		120 μm	160 μm

Note: P, P_0, λ_0, and $\Delta\lambda$ values correspond to the condition that the drive current density be 1 kA/cm^2 in each type. Each value for type B expresses the average value for five diodes.

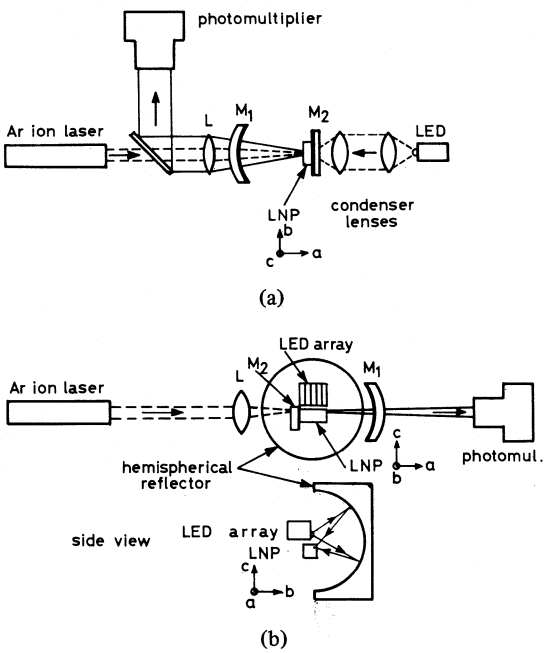


Fig. 1. Experimental setup of end- and side-pump configurations. (a) End pump. (b) Side pump.

with a pair of condenser lenses. The Ar laser beam is chopped into 1.9-ms pulsewidths at a repetition rate of 25 Hz to avoid crystal heating, and is focused into the LNP crystal with 7-cm-focal-length lens L.

E. Side-Pumped LNP Laser Arrangement

The experimental arrangement for side-pumped LNP laser is shown in Fig. 1(b). The LNP crystal is 4.85 mm long along the a axis. An auxiliary Ar laser pump beam is incident along the laser axis. The optical resonator has the same configuration as that for the end pump, except that the radius of curvature of spherical mirror M_1 is 10 cm. The output of the LED array is focused on the LNP crystal with the hemispherical reflector. The LNP sample is placed near the center of the hemisphere and the LED array is placed beside the LNP. The distance between the LED array and the LNP laser axis is about 5 mm, which is sufficiently smaller than the radius of the collecting hemisphere to avoid LED image distortion. Both the LED and LNP are kept in dry nitrogen gas ambient during operation.

III. Experimental Procedures and Results

A. End-Pump Scheme

The LNP laser is first aligned to oscillate with the Ar laser end pump. Then the transverse crystal position and mirror separation are adjusted to give minimum threshold. In order to decrease the threshold, the LNP crystal is cooled by the thermoelectric cooling unit. The absorbed Ar laser pump power at threshold versus sample temperature is shown in Fig. 2. By reducing the temperature from 22 to -35°C, the threshold Ar laser pump is reduced from 0.4 to 0.1 mW. The Ar laser beam absorption in the 0.3-mm-thick LNP depends on the sample temperature. The threshold absorbed power in Fig. 2 for the thin LNP is corrected by taking account the temperature-dependent absorption. The spot size of the focused Ar laser beam is evaluated from the beam divergence measurement to be 12.4 μm. The threshold absorbed intensities for the Ar laser pump are 46.0 and 13.2 W/cm^2 at 22 and -35°C, respectively.

The type A LED is driven by 450-μs-width current pulses, which are synchronized with the Ar laser pulses, and the output is focused into the LNP crystal. At 290-mA drive current, the LNP laser oscillates without Ar laser power. Above the threshold, the relaxation frequency increases and the delay of laser output decreases with the increase of the LED drive current, as is shown in Fig. 3.

The focused LED power density on the sample is measured by replacing the LNP crystal and the mirror M_2 with a 25-μm pinhole. Measurements of the transmitted power through the pinhole lead to the power density at the focus of the condenser lens, as shown in Fig. 4. The focused beam profile can also be measured by moving the pinhole perpendicular to the incident direction. The result shows that the profile is almost Gaussian with a diameter of 360 μm at half-intensity. Although the geometrical diameter of the emitting junction of LED is 120 μm, the effective emitting diameter is magnified with the lens effect of the dome by a factor of 3. The LED power

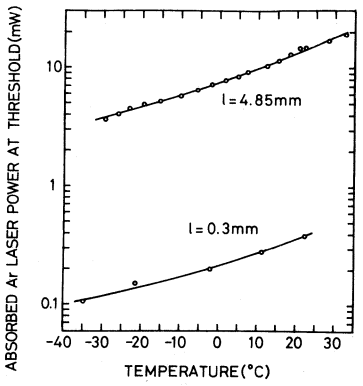


Fig. 2. Oscillation threshold temperature dependence for 0.3- and 4.85-mm crystal lengths.

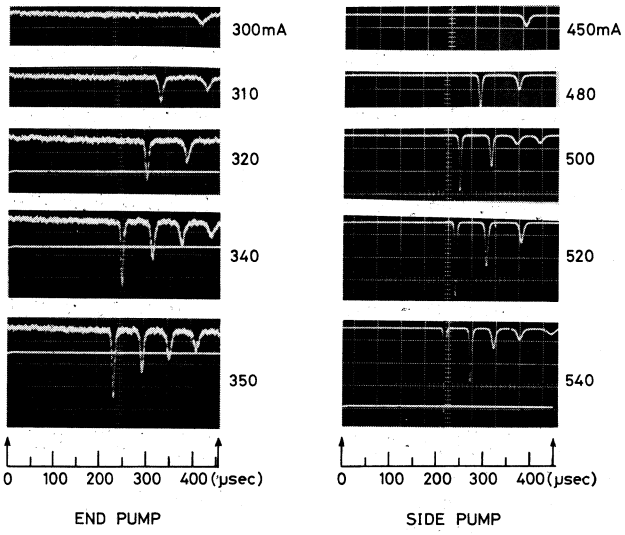


Fig. 3. LNP laser output waveforms pumped with various LED currents. Threshold drive current is 290 mA for the end pump and 440 mA for the side pump.

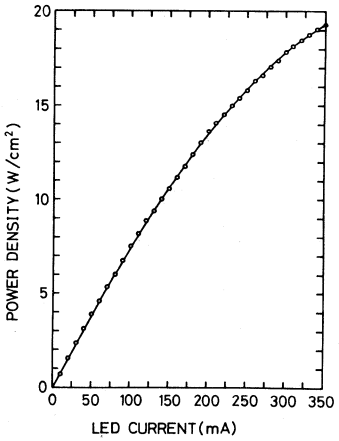


Fig. 4. LED pump power density focused with condenser lens pair in the end-pump configuration. The LED is type A.

TABLE III
END-PUMPED LNP LASER

Sample Temperature	22°C	-35°C
Incident Threshold Intensity for Ar Laser Pump[a]	75 W/cm^2	26 W/cm^2
Absorbed Threshold Intensity for Ar Laser Pump[a]	46 W/cm^2	13 W/cm^2
Incident Threshold Intensity for LED Pump	--------	15 W/cm^2
Absorbed Threshold Intensity for LED Pump	--------	8.2 W/cm^2
Theoretical Incident Threshold Intensity[b]	37.1 W/cm^2	10.9 W/cm^2
Theoretical Absorbed Threshold Intensity[b]	20.4 W/cm^2	6.0 W/cm^2
Total Round Trip Loss[c] L(T)	6.3×10^{-3}	2.5×10^{-3}
Nonresonant Round Trip Loss[d] L_o	1.75×10^{-3}	1.75×10^{-3}

Note: [a]These values are multiplied by the wavelength ratio 0.5145/0.80.
[b]Theoretical threshold is obtained by (1).
[c]Sum of theoretical resonant round-trip loss $L_r(T)$ and nonresonant round-trip loss L_0.
[d]Calculated by the threshold data at two temperatures from (2).

absorption by the 0.3-mm-thick LNP is 55 percent at 22 to -35°C. Thus the incident and the absorbed intensities at threshold for the LED end pump are 14.9 and 8.2 W/cm^2, respectively. Electrical input power at threshold is about 1.4 W. The experimental and the theoretical thresholds for the end pump are summarized in Table III. The numerical values for the Ar laser pump are reduced to the values for LED wavelength by multiplying the wavelength ratio 0.5145/0.80. The theoretical thresholds are discussed in the following section. The measured minimum spot size for the end-pumped laser is 6 μm, assuming a Gaussian mode profile.

B. Side-Pump Scheme

The LNP laser side-pumped with the LED array is also adjusted in the same way as before. However, the mirror separation to give minimum threshold is not critical in this case. The transverse crystal position is also adjusted to satisfy both the condition that the threshold power is minimal and that the oscillation axis is near the side face pumped with the LED array. This latter condition is important in realizing side-pumped laser oscillation in crystals with high pump absorption. The LNP crystal is cooled to -30°C as before. The temperature dependence of this LNP laser is also shown in Fig. 3. The threshold powers for the Ar laser end pump at 20 and -30°C are 14 and 3.7 mW, respectively. The 4.85-mm-thick LNP is long enough to absorb all the Ar laser power.

The array of the type *B* LED is driven by the same pulse condition as that for the end pump. The initial adjustment of the array position has been performed visually by observing, with an infrared image converter, the overlap between the Ar laser beam in the LNP and the image of the LED array focused by the hemispherical reflector. The fine adjustment has been performed by moving the LED array along the perpendicular directions to the laser axis in order to maximize the LNP laser output.

At a 440-mA current, the LNP laser pumped with the type B LED array oscillates without the Ar laser pump. The electrical input power at threshold is about 5 mW. The output waveforms of the side-pumped LNP laser are shown in Fig. 3 at various drive currents. The minimum spot size of the side-pumped laser is 31 μm, under the present experimental conditions. The center of the oscillating beam is located 140 μm below the pumped surface. Table IV summarizes experimental results. The numerical values for the Ar laser pump are reduced to the values for LED wavelength.

IV. Oscillating Threshold

A. End-Pump Scheme

The incident threshold power density for an end-pumped laser is given by

$$I_{\mathrm{th},e}(T) = \frac{h\nu_p}{2\tau_f \eta_e \sigma(T)} [L_r(T) + L_0] \tag{1}$$

where

τ_f fluorescence lifetime of the upper laser level;
$\sigma(T)$ effective stimulated emission cross section of the laser line [9];
$h\nu_p$ pump photon energy;
η_e absorption efficiency for the end-pump scheme;
$L_r(T), L_0$ resonant and the nonresonant round-trip losses, respectively.

The transfer efficiency of pump photons into the laser upper levels is assumed to be 1.

The theoretical threshold intensity at arbitrary temperature T can be derived from (1), if total round-trip loss $L(T) = L_r(T) + L_0$ and $\sigma(T)$ are given. Here it is assumed that τ_f is constant at -35°C to 25°C [12].

The $\sigma(T)$ is obtained from the measurement of the peak emission intensity at temperature T, assuming $\sigma(20°C) = 3.2 \times 10^{-19}$ cm^2, as shown in Fig. 5.

$L(T)$ consists of temperature-dependent $L_r(T)$ and temperature-independent L_0. Using the experimental $\sigma(T)$ value, crystal length l, and the Boltzmann distribution of the laser lower levels $N_1(T)$, $L_r(T)$ can be calculated from the relation $L_r(T) = 2l\sigma(T)N_1(T)$, as shown in Fig. 6. It is difficult to estimate L_0 directly from the cavity mirror loss, scattering loss, and so on. However, L_0 can be derived from the

TABLE IV
SIDE-PUMPED LNP LASER

Sample Temperature	22°C	-30°C
Absorbed Threshold Power for Ar Laser Pump[a]	8.3 mW	1.8 mW
Incident Threshold Intensity for LED Pump	--------	7.2 W/cm^2
Absorbed Threshold Power for LED Pump[b]	--------	2.1 mW
Theoretical Incident Threshold Intensity[c] for Side Pump Scheme	31.9 W/cm^2	6.9 W/cm^2
Theoretical Absorbed Threshold Power[d]	9.2 mW	2.0 mW
Total Round Trip Loss[e] L(T)	9.1 x 10^{-2}	2.5 x 10^{-2}
Nonresonant Round Trip Loss[f] L_o	2.0 x 10^{-2}	2.0 x 10^{-2}

Note: [a]These values are obtained by the Ar laser end pump and are reduced to the values for LED wavelength.
[b]Using the incident LED intensity, this value is calculated by (5). It is assumed that $w_0 = 31\ \mu$m, $\alpha_p = 30\ \text{cm}^{-1}$, and $d = 140\ \mu$m.
[c]Theoretical threshold intensity is obtained by (4).
[d]Theoretical threshold power is obtained by $I_{\text{th},e}(T) \times \pi w_0^2$, assuming $w_0 = 31\ \mu$m.
[e]Sum of theoretical resonant round-trip loss $L_r(T)$ and nonresonant round trip loss L_0.
[f]Calculated by the threshold data at two temperatures from (2).

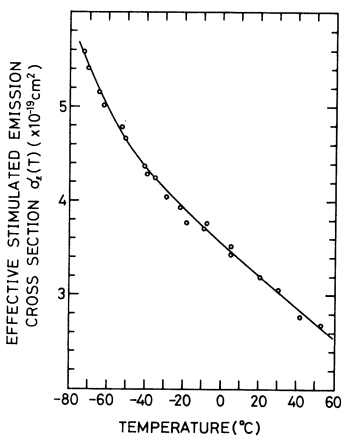


Fig. 5. Temperature dependence of effective stimulated emission cross section $\sigma(T)$ measured by fluorescence peak intensity, assuming that $\sigma(20°\text{C}) = 3.2 \times 10^{-19}\ \text{cm}^2$.

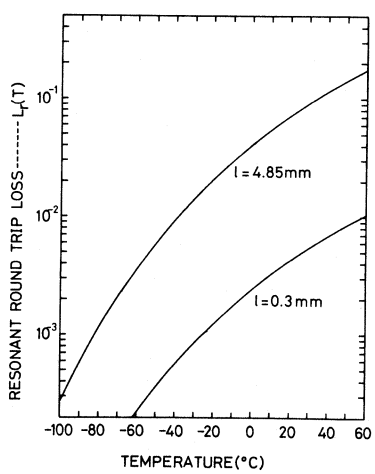


Fig. 6. Calculated resonant round trip loss $L_r(T)$ for 0.3-mm and 4.85-mm crystal lengths.

threshold data at two temperatures, as follows:

$$L_0 = L_r(T_1)\,(\alpha - \beta)/(\gamma - \alpha) \tag{2}$$

where

$$\alpha = P_{\text{th}}(T_2)/P_{\text{th}}(T_1) = I_{\text{th}}(T_2)/I_{\text{th}}(T_1),$$

$$\beta = N_1(T_2)/N_1(T_1)$$

and

$$\gamma = \sigma(T_1)/\sigma(T_2).$$

When $T_1 = 22°\text{C}$ and $T_2 = -35°\text{C}$, $\alpha = 0.287$, $\beta = 0.113$, and $\gamma = 0.75$ for an end-pumped thin LNP laser. These values lead to $L_0 = 1.75 \times 10^{-3}$. Then $L(T)$ for the end pump is calculated at an arbitrary temperature, as is summarized in Table III. The theoretical incident threshold intensity is calculated by (1) to be 37.8 and 10.9 W/cm^2 at 22 and -35°C, respectively. Total round-trip loss $L(T)$ can be estimated by measuring relaxation oscillation frequency versus relative pump power P/P_{th} [13]. This leads to almost the same value of $L(T)$ as derived by (2).

B. Side-Pump Scheme

The threshold intensity for the LED side pump cannot be experimentally measured. The total emitted power of the LED array at threshold is 340 mW. Each LED image focused by the reflector can be assumed to be the same size as the effective emitting area. Assuming the Gaussian profile of the image with the radius r_0 of 290 μm at half-intensity, the incident intensity averaged in the oscillating area $2w_0 \times l$ can be estimated by the following equation:

$$I_{\text{th}} = \frac{P_{\text{th}}}{2w_0 l}\sqrt{\frac{\ln 2}{\pi r_0^2}}\int_{-w_0}^{w_0} dy \exp\left(-\ln 2 \cdot y^2/r_0^2\right) \tag{3}$$

where w_0 is the oscillating laser spot size, l is the crystal length, and P_{th} is the focused total LED power at threshold. Here the variation of the spot size along the laser axis is ignored. Assuming that collecting efficiency by the hemispherical reflector is 64 percent, I_{th} is estimated from (3) to be 7.2 W/cm^2. Table IV shows the incident threshold intensity for the side-pumped LNP laser.

The theoretical incident threshold intensity for the side-pumped laser is given by

$$I_{\text{th},s}(T) = \frac{h\nu_p w_0}{\tau_f \sigma(T) l \eta_s}\left[L_r(T) + L_0\right], \tag{4}$$

$$\eta_s = \exp\left(-\tilde{\alpha}_p d\right)\left\{\exp\left(\tilde{\alpha}_p w_0\right) - \exp\left(-\tilde{\alpha}_p w_0\right)\right\}$$
$$\approx 2\tilde{\alpha}_p w_0 \exp\left(-\tilde{\alpha}_p d\right) \tag{5}$$

where

w_0 oscillating spot size;
η_s absorption efficiency for the side-pump scheme;
d separation between the laser axis and the pumped surface;
$\tilde{\alpha}_p$ effective absorption coefficient for LED light.

It is assumed that all the pump radiation is traveling in the direction perpendicular to the pumped surface, and that the laser beam intensity is constant within the laser beam cross section.

The effective absorption coefficient $\tilde{\alpha}_p$ depends not only on LED spectral width $\Delta\lambda$ and center wavelength λ_0, but also on d, as will be discussed in Appendix I. In order to estimate η_s, it is assumed that $\tilde{\alpha}_p = 30\ \mathrm{cm}^{-1}$, which corresponds to $\Delta\lambda$ = 300 Å, $\lambda_0 = 0.80\ \mu$m, and $d = 150\ \mu$m. As η_s is 9.6 percent using $d = 140\ \mu$m, $I_{th,s}(T)$ is calculated to be 31.1 and 6.9 W/cm^2 at 20°C and -30°C, respectively, for the side-pumped LNP laser. In the above calculation, $\sigma(T)$ and $L(T)$ are obtained by the same method as stated before. These results are summarized in Table IV.

V. Discussions

A. Theoretical and Experimental Threshold Comparison

As is shown in Tables III and IV, the experimental threshold intensities agree with theoretical values, within experimental error in determining absolute pump intensities, except for the thin LNP crystal, which is end-pumped with an Ar laser beam. This may be due to an experimental uncertainty in determining Ar pump-beam diameter and mismatch of fine beams of the Ar pump and LNP laser. As for the LED pump, the LED image focused by the pumping optics is much larger than the LNP laser spot size, so that the tolerance of the overlapping condition is not severe.

B. Homogeneity of the LNP Crystal

From the L_0 values derived from (2), LNP crystal homogeneity will be discussed. L_0 consists mainly of cavity mirror loss L_t, scattering loss L_s originated from crystal inhomogeneity, and nonresonant absorption loss L_a. In the present experiments, oscillating beam spot size w_0 for the side-pump scheme is enough smaller than beam depth d to neglect the surface scattering. Experiments have been conducted by choosing a spot to give minimum threshold in the sample. The cavity with highly reflective mirrors is estimated to have a loss L_t value of the order of 2×10^{-3}. L_0 values are 1.75×10^{-3} and 2.0×10^{-2} for thin and thick LNP's, respectively. $L_s + L_a$ for thin LNP is less than 5×10^{-4}. If $L_s + L_a$ is regarded to be proportional to crystal length, $L_s + L_a$ for thick LNP corresponds to 1.3×10^{-3}/0.3 mm. Because L_a can be regarded constant in LNP crystals, the above discrepancy may be attributed to the difference on L_s between thin and thick LNP. For a 0.3-mm-thick crystal, a homogeneous spot can be selected. However, for 4.85-mm-thick crystal, inhomogeneity of the crystal is inevitable in the present experiment.

C. Possibility of Room-Temperature CW Operation

The output power of the LED used in the present experiments is 25 mW for a single LED and 185 mW for a five-LED array under CW operation at 10^3 A/cm^2 current density. The former corresponds to 24.4 W/cm^2 and the latter corresponds to 6.2 W/cm^2, considering the effective emitting area and diode chip spacing. Under the present pumping optics, the incident intensity decreases to 7.5 W/cm^2 and 3.9 W/cm^2 for the end- and the side-pump schemes, respectively. This implies that only 20 and 15 percent of the required pump for room-temperature CW laser operation can be supplied at end and side pump, respectively.

For the end-pump scheme, incident threshold intensity is proportional to $L(T)/\eta_e$. As was discussed previously, it seems difficult to reduce total round-trip loss $L(T)$. Improvement of η_e by an elongated crystal length will result in increase of $L(T)$. The incident intensity can be increased by using lenses with small F number or using other pumping optics, such as the hemispherical reflector. As far as the hemispherical reflector used in Fig. 1(b) applied to the end-pump scheme, threshold improvement has not been observed. As the condenser lenses used have the smallest F number commercially available, the LED intensity required to oscillate the room temperature CW LNP laser is at least 120 W/cm^2, which is about five times of the present LED intensity. Therefore, in the end-pump scheme, a high-radiance LED will be needed for this purpose.

For the side-pump scheme, there are several possibilities in reducing the threshold. First, the improvement of the crystal homogeneity of LNP will reduce the threshold by about 20 percent of the present data at room temperature. Second, the required intensity will be decreased to 65 percent of the present value by reducing d, since the threshold is approximately proportional to $L(T)/l(1 - \tilde{\alpha}_p d)$. Third, the incident intensity can increase up to 1.5 times that for present pumping optics by using an elliptical reflector with high-reflection coating. From the above estimation, required LED intensity to oscillate a side-pumped LNP laser at room temperature may decrease to 35 percent of that for the present experiment. Further improvement of η_s will be possible by adopting a back-surface reflector.

D. Output Power

The output intensity of an LED required to obtain a certain laser output power will be discussed for each pump scheme. Maximum output power P_o and optimum coupling loss L_{t0} to give P_o are given by [14]

$$P_o = \pi w_0^2 I_s \frac{(\sqrt{g_0} - \sqrt{L_i})^2}{2} \tag{6}$$

$$L_{t0} = \sqrt{g_0 L_i} - L_i \tag{7}$$

where

- w_0 oscillating spot size;
- I_s saturation parameter;
- L_i nonresonant round trip loss excluding L_t;
- g_0 unsaturated round-trip gain associated with LED pump power P_{in}.

Using the calculated value of $I_s(20°\mathrm{C}) = 4.93 \times 10^3$ W/cm^2, P_o versus P_{in} can be calculated for each pump scheme, as is shown in Figs. 7 and 8. These calculations are performed based on the following assumptions.

1) Crystal lengths for end and side pump are 0.3 and 4.85 mm, respectively.

2) Beam spot size w_0 is equal to 30 μm.

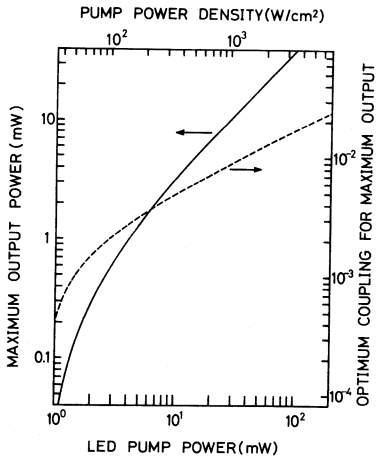


Fig. 7. Calculated maximum output power and optimum coupling, as a function of LED pump power and intensity in end pump scheme. Room temperature CW operation is assumed. Spot size, round-trip crystal loss, absorption efficiency, and crystal length are given in Table V.

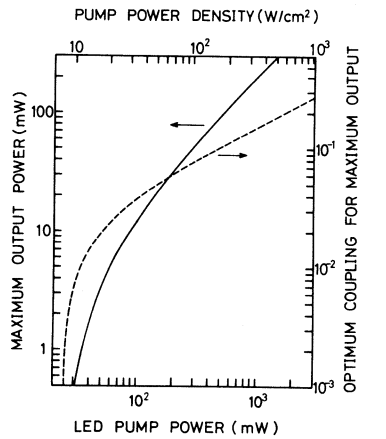


Fig. 8. Calculated maximum output power and optimum coupling as a function of LED pump power and intensity in side pump scheme. Assumptions are listed in Table V.

3) L_i is proportional to crystal length, and is equal to 5.0×10^{-4} for 0.3-mm-thick LNP.

4) The LED has a uniform flat emitting surface with area πw_0^2 and $2w_0 l$ for the end and side pump, respectively.

5) Incident pump power and size of image are equal to those for the LED.

6) η_e and η_s are equal to 0.55 and 0.30, respectively.

From these results, P_{in} required to obtain 10-mW laser output is 28 mW for end pump and 88 mW for side pump. In the above case, L_{to} values for the end and side pump are 0.85 and 3.4 percent, respectively. The required intensities in the above case are 990 and 30 W/cm^2 for the end and side pump, respectively. On the other hand, by using highly reflective mirrors, threshold pump power and intensity for the end pump are 1 mW and 35 W/cm^2, respectively, and those for the side pump are 25 mW and 8.5 W/cm^2, respectively. These results show that the threshold pump power for the end-pumped LNP laser can be made small, but increases significantly to obtain the output power on the order of milliwatts. For the side pump, large output power can be obtained by a little increase in pump power ratio.

TABLE V
LED POWER REQUIRED TO OBTAIN 10-mW OUTPUT AT ROOM TEMPERATURE

		End Pump	Side Pump
LED Power	P_{in}	28 mW	88 mW
LED Power Density	I_{in}	990 W/cm^2	30 W/cm^2
Optimum Coupling Loss	L_{to}	8.5×10^{-3}	3.4×10^{-2}
Slope Efficiency	σ_s	0.40	0.19
Assumptions			
Crystal Length	ℓ	0.3 mm	4.85 mm
Spot Size	w_o	30 μm	30 μm
Round Trip Crystal Loss	L_i	5.0×10^{-4}	8.1×10^{-3}
Pump Efficiency	η	0.55	0.30

If the values of L_t, L_{to}, η_e, and η_s are assumed to be those of the condition to obtain 10-mW output power, slope efficiency σ_s [14] is calculated to be 40 percent for the end pump and 19 percent for the side pump. Table V summarizes the above results.

VI. CONCLUSIONS

LNP lasers pumped with LED's are demonstrated in end- and side-pump configurations at reduced temperature. The theoretical thresholds for both pump schemes are calculated by measuring the temperature dependences of the effective stimulated emission cross section $\sigma(T)$ and the round-trip loss $L(T)$, and by estimating pump efficiency for the end pump experimentally and for the side pump theoretically. These results show that the present calculations explain the experimental results, such as LED intensities required to oscillate the LNP lasers and LNP laser temperature dependences for both pump schemes. In order to estimate the LED intensity required to oscillate the LNP laser at room-temperature CW operation, pump efficiency improvement and LNP crystal homogeneity are discussed. The room-temperature CW operation will be realized by using the LED side pump in the future. The LNP laser with an output power on the order of milliwatts will be needed in optical communication systems. This will be realized by the thick LNP crystal side-pumped with LED's which have a power density on the order of 10 W/cm^2.

APPENDIX
EFFECTIVE ABSORPTION COEFFICENT

The effective absorption coefficient $\tilde{\alpha}$ is related to absorption η_a of the LED power within the LNP crystal, as follows:

$$\tilde{\alpha}(\lambda_0, \Delta\lambda, x) = -\ln (1 - \eta_a(\lambda_0, \Delta\lambda, x))/x \tag{8}$$

where

$$\eta_a(\lambda_0, \Delta\lambda, x) = \int_0^\infty d\lambda \exp \left\{-\ln 2\left(\frac{2(\lambda - \lambda_0)}{\Delta\lambda}\right)^2\right\} \cdot \exp \{-\alpha(\lambda)x\}, \tag{9}$$

where

λ_0 center wavelength of the LED;
$\Delta\lambda$ full spectral width at half intensity;
x LNP crystal thickness;

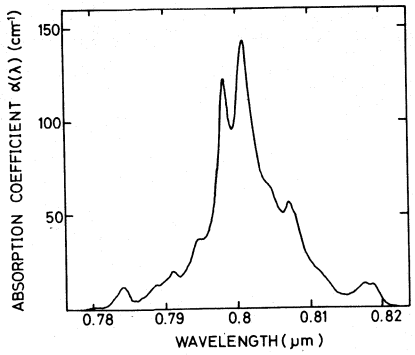


Fig. 9. Absorption coefficient $\alpha(\lambda)$ of LNP at room temperature.

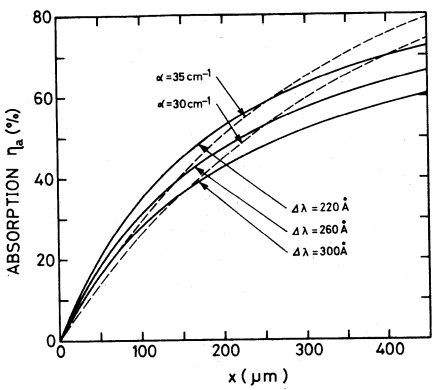


Fig. 10. Absorption η_a in LNP crystal with thickness x calculated from (9). Pump spectral profile is Gaussian with full-width $\Delta\lambda$. Broken lines show absorption for constant absorption coefficient.

$\alpha(\lambda)$ absorption coefficient of the LNP crystal at wavelength λ.

It is assumed that the LED intensity profile is Gaussian and that all the pump light is traveling in the x direction. Using the experimental data of $\alpha(\lambda)$, given in Fig. 9, η_a can be evaluated numerically for various λ_0, $\Delta\lambda$, and x values. Fig. 10 shows η_a versus x for several $\Delta\lambda$ values, when λ_0 is chosen to maximize η_a. For comparison, the broken line curves in Fig. 10 correspond to the constant absorption coefficient α. It is evident that $\tilde{\alpha}$ decreases with the increases of $\Delta\lambda$ and x.

ACKNOWLEDGMENT

The authors wish to thank Dr. N. Niizeki and Dr. S. Ohara for encouragement and discussions. They also wish to thank T. Yamada, K. Otsuka, and J. Nakano for supplying high-quality LNP crystals.

REFERENCES

[1] F. W. Ostermayer, Jr., R. B. Allen, and E. G. Dierschke, "Room-temperature CW operation of a $GaAs_{1-x}P_x$ diode-pumped Nd:YAG laser," *Appl. Phys. Lett.*, vol. 19, pp. 289–292, Oct. 1971.

[2] N. P. Barnes, "Diode-pumped solid-state lasers," *J. Appl. Phys.*, vol. 44, pp. 230–237, Jan. 1973.

[3] G. I. Farmer and Y. C. Kiang, "Low-current-density LED-pumped Nd:YAG laser using a solid cylindrical reflector," *J. Appl. Phys.*, vol. 45, pp. 1356–1371, Mar. 1974.

[4] R. B. Chesler and D. A. Draegert, "Miniature diode-pumped Nd:YA1G lasers," *Appl. Phys. Lett.*, vol. 23, pp. 235–236, Sept. 1973.

[5] H. P. Weber, T. C. Damen, H. G. Danielmeyer, and B. C. Tofield, "Nd-ultraphosphate laser," *Appl. Phys. Lett.*, vol. 22, pp. 534–536, May 15, 1973.

[6] H. P. Weber, "Nd pentaphosphate lasers," *Optics and Quantum Electronics*, vol. 7, pp. 431–442, Dec. 1975.

[7] H. G. Danielmeyer, "Stoichiometric laser materials," in *Festkörperprobleme XV, Advances in Solid State Physics.* New York: Pergamon, 1975, pp. 253–277.

[8] T. Yamada, K. Otsuka, and J. Nakano, "Fluorescence in lithium neodymium ultraphosphate single crystals," *J. Appl. Phys.*, vol. 45, pp. 5096–5097, Nov. 1974.

[9] K. Otsuka, T. Yamada, M. Saruwatari, and T. Kimura, "Spectroscopy and laser oscillation properties of lithium neodymium tetraphosphate," *IEEE J. Quantum Electron.*, vol. QE-11, pp. 330–335, July 1975.

[10] M. Saruwatari, T. Kimura, T. Yamada, and J. Nakano, "$LiNdP_4O_{12}$ laser pumped with an $Al_xGa_{1-x}As$ electroluminescent diode," *Appl. Phys. Lett.*, vol. 27, pp. 682–684, Dec. 15, 1975.

[11] a) Y. Ishioka, Y. Ono, S. Saito, and K. Kurata, presented at the 1974 Fall Meeting of the Japan Society of Applied Physics (unpublished).
b) Y. Ono, M. Mori, K. Ito, M. Morioka, and K. Kurata, presented at the 1976 Spring Meeting of the Japan Society of Applied Physics (unpublished).

[12] M. Blatte, H. G. Danielmeyer, and R. Ulrich, "Energy transfer and the complete level system of NdUP," *Appl. Phys.*, vol. 1, pp. 275–278, May 1973.

[13] T. Kimura and K. Otsuka, "Response of a CW Nd^{3+}:YAG laser to sinusoidal cavity perturbations," *IEEE J. Quantum Electron.*, vol. QE-6, pp. 764–769, Dec. 1970.

[14] A. Yariv, *Introduction to Quantum Electronics.* New York: Holt, Rinehart, and Winston, 1971.

Infrared Saturation Spectroscopy in p-Type Germanium

FRITZ KEILMANN

Abstract—We investigate spectral changes induced by high-power CO_2 laser radiation in the direct intervalence band absorption of p-type germanium. Using a model of inhomogeneously broadened two-level systems, we deduce a room-temperature saturation intensity of 4 MW/cm^2 from published observations of saturation of this absorption. The applicability of the two-level model to transitions between two electronic bands is discussed. We relate the linear absorption coefficient to the saturation intensity and the effective population difference, where the latter is obtained in a spherical band approximation. The result yields a value of 0.55 ps for the geometric mean of the phase and energy relaxation times. The meaning of these times is explained for our system, and quantitative agreement is found with published data on optical and acoustical lattice scattering probabilities.

Specifically, we find a very short phase relaxation time of 0.09 ps. This allows the prediction of a burnt-hole spectral width of 57 cm^{-1} (HWHM) at small saturation. In a preliminary experiment, we have observed the modulation of a CW CO_2 laser beam by intense nanosecond pulses of a second CO_2 laser offset in frequency by up to 140 cm^{-1}.

I. Introduction

THE ABSORPTION of light becomes a nonlinear function of light intensity for sufficiently high intensities due to various reasons depending on the system. Specifically, we consider simple two-level systems whose level populations are induced to approach one another at high intensities so that the absorption decreases.

Such bleaching of the absorber is accompanied by a drastic change in line shape. For example, let us consider an absorber whose line shape is inhomogeneously broadened, i.e., is characterized by a smooth distribution of individual absorption frequencies, such as that found in low-pressure gases due to the Doppler effect. Then bleaching occurs only within a small portion of the absorption profile centered around the saturating frequency, an effect called hole burning. The width of such a saturation hole is approximately the inverse of the dipole lifetime, i.e., the lifetime with respect to phase disturbances, T_2. Thus, lifetime information can be obtained by studying saturation-induced spectral changes.

In solids, lifetimes can be very short, from 1 ns down to 1 ps and less, so that saturation holes have sizable widths; this eases a frequency-domain lifetime measurement. On the other hand, very high intensities are needed for bleaching fast relaxing systems. As a numerical example, consider a strong transition at 10-μm wavelength, characterized by a dipole transition moment of 1 D. This corresponds to an integrated absorption cross section of $4 \cdot 10^{-6}$ cm^2/s. If now both phase and energy relaxation times are assumed to be 1 ps, an intensity of 400 MW/cm^2 is required to saturate the absorption coefficient to one-half its value (see (3) below with $n = L$). Although such intensities are well within experimental reach for many wavelengths, problems may often arise due to material damage [1].

In this paper, we describe hole burning in p-Ge at infrared wavelengths around 10 μm. The transition involved here is a direct excitation of holes from the heavy to the light valence band (Fig. 1). A very broad absorption line shape is found at room temperature (Fig. 2) [2]. Because of the continuous distribution of hole energies, the shape of the absorption spectrum does not directly reflect lifetime information. In this situation, it is fortunate that the absorption can be saturated [3] at intensities well below damaging intensities. This allows an experiment to probe the induced saturation hole from which the desired relaxation time can be determined. The calculation, however, is straightforward only if the medium can be treated as a distribution of two-level systems, which, in turn, requires knowledge of the relaxation times.

For the case of interest, we assume a two-level model applies, and calculate the product of phase and energy relaxation times from small-signal and saturated absorption data. Anisotropy in the band structure is pronounced, but we adapt an averaging procedure following Kane [4], and use a spherical band approximation to calculate the pertinent population densities.

The information on relaxation times thus obtained is further substantiated by analysis of the various interaction mechanisms that contribute to phase and energy relaxation of the two-level systems. We obtain qualitative agreement with data on optical and acoustical phonon scattering of holes, suggesting that the simple theory is applicable. Thus, on saturation, a hole-burning width of 114 cm^{-1} is expected. We attempt to verify this in a direct measurement. Experimentally we use a pulsed, self-mode-locked CO_2 laser to induce saturation, and a weak, tunable CO_2 laser for probing the saturated absorption.

II. Infrared Absorption in p-Type Germanium

In the middle infrared direct intervalence band transitions occur in p-Ge. They have been shown to constitute the dominant absorption process, at room temperature, if the total hole concentration is in the range 10^{16} cm^{-3}. Three broad bands of absorption, first observed by Kaiser *et al.* [2], exist for this process, as a consequence of the three valence bands available, as shown in Fig. 1. For the CO_2 laser region the transition from band 1 to 2 is of interest, as reproduced from [2] in Fig. 2. The absorption coefficient is quite high, $\alpha = 6.5$ cm^{-1} at 944 cm^{-1} for a total hole density of $N = 10^{16}$ cm^{-3}.

Other infrared absorption processes in germanium are briefly

Manuscript received March 16, 1976; revised May 25, 1976.

The author is with the Max-Planck-Institut für Festkörperforschung, Stuttgart, Germany.

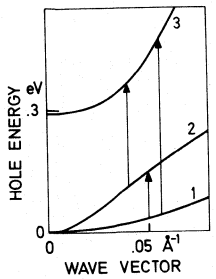


Fig. 1. Scheme of valence band structure of germanium near the center of the Brillouin zone.

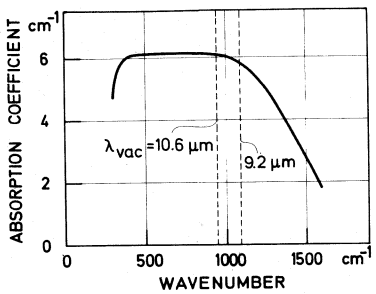


Fig. 2. Absorption line in room-temperature p-type germanium due to direct transitions between valence bands 1 and 2 (cf., Fig. 1), for a total hole concentration of 10^{16} cm^{-3}, after Kaiser *et al.* [2].

mentioned, although they are weak enough to be neglected in our experiment.

1) Intraband absorption excites a carrier into a higher state within the same band, with simultaneous generation or absorption of a phonon. This absorption follows closely the classical Drude-Zehner theory [5] yielding $\alpha \sim \nu^{-2}$ where ν is the light frequency. Quantitatively, $\alpha = 0.27$ cm^{-1} was measured at 944 cm^{-1} for a total electron density of $N = 10^{16}$ cm^{-3} [2].

2) Ionization of hydrogenic impurities occurs at energies near 0.01 eV in germanium, for indium acceptors at 0.011 eV [6]. Thus, at room temperature, these impurities are effectively ionized.

3) Lattice absorption near 1000 cm^{-1} requires cooperation of at least three phonons so that it is quite weak, $\alpha = 0.03$ cm^{-1} and 0.4 cm^{-1} at 293 K and 363 K, respectively [7].

III. Saturation in the Presence of Band Structure

In this section, we first recall basic relations for the saturation of an inhomogeneously broadened spectral line. Then we describe a range of conditions for the applicability of these relations if energy band structure, giving a continuous distribution of resonance frequencies, is the dominant cause of the linewidth. We exclude spontaneous emission and transient effects, and use results of a simplified rate equation approach dealing with level populations only.

We start out with homogeneously broadened two-level systems, i.e., a collection of absorbers of number density N, having a ground state 1, an excited state 2, a transition frequency ν_0, and a transition dipole matrix element μ. The absorption coefficient α, appearing in Beer's law $I(z) = I(0) \cdot \exp(-\alpha z)$, is then given by [8] (SI units)

$$\alpha(\nu) = \frac{2\pi^2}{\hbar \epsilon_0 c} \cdot \frac{L}{n} \cdot \frac{|\mu|^2}{3} \cdot \nu \cdot (N_1 - N_2) \cdot g(\nu) \tag{1}$$

where

ν light frequency;
c speed of light;
L Lorentz field factor;
n refractive index;
$N_{1,2}$ thermal equilibrium number densities of ground state and excited state;
$g(\nu)$ Lorentzian line factor,

$$g(\nu) = \frac{2}{\pi} \frac{1/2\pi T_2}{(\nu - \nu_0)^2 + (1/2\pi T_2)^2 \cdot (1 + I/I_s)} \tag{2}$$

where

T_2 dipole or phase relaxation time;
I light intensity;
I_s saturation intensity of the medium

$$I_s = \frac{\hbar^2 \epsilon_0 c}{2} \cdot \frac{n}{L} \cdot \frac{3}{|\mu|^2} \cdot \frac{1}{T_1 T_2} \tag{3}$$

where T_1 is the energy relaxation time of the medium discussed later.

The Lorentzian factor (2), normalized to $\int_0^\infty g(\nu) d\nu = 1$ at small intensities $I \ll I_s$, shows two dependences of steady-state saturation on intensity.

1) On resonance the absorption decreases as $g(0) \sim (1 + I/I_s)^{-1}$.

2) The Lorentzian linewidth $\Delta\nu$ (FWHM) increases, i.e., is power broadened according to

$$\Delta\nu = (1 + I/I_s)^{1/2}/\pi T_2. \tag{4}$$

Modifications occur if inhomogeneous broadening becomes important, i.e., if there exists a distribution of the resonance frequencies $\rho(\nu_0)$, as, for example, that due to the Doppler effect. Then (1) becomes

$$\alpha(\nu) = \frac{2\pi^2}{\hbar \epsilon_0 c} \cdot \frac{L}{n} \cdot \frac{|\mu|^2}{3} \cdot \nu \cdot \int_0^\infty \rho(\nu_0) \cdot g(\nu, \nu_0)\, d\nu_0 \tag{5}$$

where L, n, and μ have been taken out of the integral on the assumption they have constant values in the range of contributing frequencies. If we consider now a broad smooth distribution of resonance frequencies with width broad compared to the Lorentzian width for a given transition, we can set $\rho(\nu_0) = \rho(\nu)$, causing (5) to reduce to

$$\alpha(\nu) = \frac{2\pi^2}{\hbar \epsilon_0 c} \cdot \frac{L}{n} \cdot \frac{|\mu|^2}{3} \cdot \nu \cdot \frac{\rho(\nu)}{(1 + I/I_s)^{1/2}}. \tag{6}$$

Again, saturation reduces the absorption coefficient, but less markedly than in the homogeneous case. The physical explanation of this is that the interaction linewidth (4) increases due to power broadening allowing more and more off-resonance absorbers to contribute to the absorption, thus counterbalancing partly the reduction of absorption on resonance. From the existence of the power-broadened width $\Delta\nu$, it is clear that saturation bleaches only those absorbers having their resonance frequencies just in this range, an effect called hole burning.

Observation of the hole-burning width in an inhomogeneously broadened medium can hence give a measure of T_2 via (4). For instance, it is possible by using a second, frequency-tunable weak light beam to probe the change of absorption induced by the first, saturating beam.[1] The observed linewidth is then, in our approach, that for a convolution of the probing beam Lorentzian [(2)] with the saturated population difference [9]. According to [9, eq. (3)], this width is the sum of the power-broadened width [(4)] and the unbroadened width.

Now, we want to examine under which conditions the above analysis might be applied to transitions involving energy bands. For example, we consider free carriers in a crystal such as the holes in germanium. Due to crystal dispersion, the hole states are arranged in bands $E_i(\vec{k})$, with the energies continuously varying with momentum. Let us neglect anisotropy and consider two bands whose states can couple radiatively only if the transition is direct, i.e., the carrier momentum is conserved (the relatively small momentum of the absorbed or emitted photon is hereby neglected); all radiative transitions can then be represented by vertical arrows in a diagram, Fig. 1. If we consider only nondegenerate situations, i.e., densities low enough so that the occupation numbers are much smaller than one, we can consider the medium as an ensemble of two-level absorbers having a smooth distribution of absorption frequencies $\rho(\nu_0)$. This is then simply related to the density of thermally occupied states $\rho_{1,2}(E)$ for the two bands by $\rho(\nu_0) = (\rho_1(E_1) - \rho_2(E_2))/|1 - dE_2/dE_1|$, where $E_2 - E_1 = h\nu_0$ and $\vec{k}(E_1) = \vec{k}(E_2)$.

The system outlined can now be well described as analogous to the case of Doppler broadening in gases. If, in the same manner, we can ascertain that L, n, μ, and $\rho(\nu_0)$ are constant within a range much larger than the interaction bandwidth $\Delta\nu$ [(4)], (3) and (6) likewise apply. This means that only a small part of the band states gets radiatively populated or depopulated. These states can be visualized, in a polar diagram of the energy versus the direction of $\vec{k}$, as occupying two thin surface layers, each on a sphere in the spherical band approximation, with a layer thickness $\Delta E = h\Delta\nu$ from (4).

The problem remaining is now to link the time constants T_1 and T_2 used in this analysis to the relaxation mechanisms of the real system. All interaction processes can be thought of as contributing to phase relaxation, whereas only those give rise to level energy relaxation that cause transitions from the inside to the outside, or vice versa, of each of the spheroidal shells.

IV. Saturation Analysis of p-Type Germanium

Let us treat the 10.6-μm absorption of p-type germanium at room temperature with the model of inhomogeneously broadened two-level systems, as just outlined. Clearly, a homogeneous broadening treatment would be totally inappropriate. We thus use (3) and (6) to find

$$T_1T_2 = \frac{\pi h\nu\rho}{2\alpha_0 \cdot I_s} \tag{7}$$

where α_0 is the small-signal absorption coefficient. The saturation intensity I_s can be found from the experimental curve in [3]; by application of (6), we obtain $I_s = 4$ MW/cm^2. Now it remains to find the value of ρ, the net population density, to calculate the product of relaxation times from (7).

Details of the band structure of germanium [6, p. 381] have been analyzed by Kane [4]. We reproduce his results for the region of interest in Fig. 3. In view of the relatively small anisotropy as well as the approximations of our estimation, we average the band structure over all directions, following Kane [4], and obtain a spherical band approximation (Fig. 4). This comes out very close to the curve for the γ direction in Fig. 3. Thus, we have for the CO_2 laser transition at 10.6 μm, equivalent to 0.117 eV, $k = 5 \cdot 10^6$ cm^{-1}, $E_1 = 0.030$ eV, and $E_2 = 0.147$ eV. Note that at room temperature we have $k_BT = 0.026$ eV.

The density of available states can be easily estimated for band 1, which is parabolic with a mass of $m_h = 0.36m_e$, where m_e is the free electron mass

$$D_1(E) = E^{1/2} \cdot (2m_h)^{3/2}/2\pi^2h^3.$$

The Fermi-Dirac distribution, very well approximated by a Boltzmann distribution in our case, then gives the density of thermally populated states of the lower band

$$\rho_1(E) = 2\pi^{-1/2}N_1E^{1/2}(k_BT)^{-3/2} \exp(-E/k_BT)$$

where k_B is the Boltzmann constant and N_1 is the total number of holes in band 1 per unit volume. Taking $N_1 = 10^{16}$ cm^{-3} we find $\rho_1(E_1) = 609$ cm^{-3} · s and $\rho_1(E_1)/D_1(E_1) < 0.001$, i.e., a very small occupation number even at the lower state of the transition. In the upper state, we obtain a much smaller thermal population $\rho_2(E_2) = 2$ cm^{-3} · s, where, due to nonparabolicity of band 2, this is only a crude estimate, yielding also $N_2/N_1 = 0.1$ for the total populations of both bands. The population in band 3 (Fig. 1) can be neglected. We thus arrive at the population difference for the 10.6-μm transition of $\rho = 250$ cm^{-3} · s for a total hole concentration $N = 10^{16}$ cm^{-3}. Inserting this in (7) now gives the result $(T_1T_2)^{1/2} = 0.55$ ps.

Let us see whether this value can be related to the appropriate relaxation mechanisms, i.e., scattering of holes by holes, impurities, and phonons (see, for example [5, pp. 165 ff.]). In their analysis of room-temperature electrical conductivity, Brown and Bray [12] included ionized impurity scattering and phonon scattering, but neglected hole-hole scattering. Lattice scattering of holes is due to acoustical and optical modes, at room temperature, the optical phonon energy being 0.037 eV. The relevant deformation potentials were determined by an analysis of mobility data in [12], so that we obtain acoustical scattering times $\tau_{ac} \sim E^{-1/2}$, from [14], $\tau_{ac} = 1.25$ ps at $E = 0.03$ eV and $\tau_{ac} = 0.57$ ps at $E = 0.147$ eV. Optical phonon scattering occurs even more frequently, $\tau_{op} = 0.97$ ps at $E = 0.03$ eV and $\tau_{op} = 0.14$ ps at $E = 0.147$ eV. In this theory it is assumed that the lattice scattering probability is the same function of energy for both bands considered here. This im-

[1] Notice here that even a very weak probe beam, together with the saturating beam, produces some change in the saturation of the medium, according to spatial and temporal beatings. By this, saturation dips attain considerable structure [9], [10] which extends the usefulness of saturation spectroscopy in that various relaxation times can be individually determined [11].

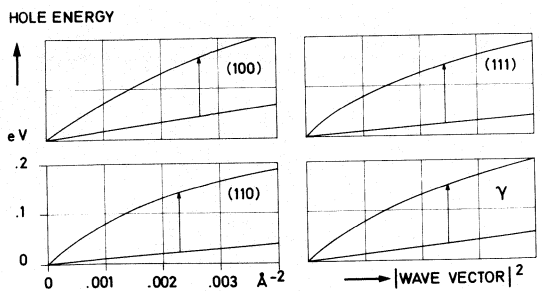


Fig. 3. Anisotropy of the two lowest valence bands in germanium after Kane [4]. The arrows mark the transitions induced by radiation at 10.6-μm wavelength. γ is a direction making equal angles with the (100), (110), and (111) directions.

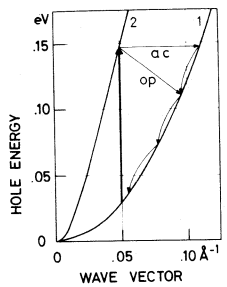


Fig. 4. Spherical approximation for the two lowest valence bands in germanium, obtained by averaging the curves in Fig. 3. The downward arrows show the most probable room-temperature routing for the relaxation of photoexcited holes by lattice scattering, 0.037 eV being the optical phonon energy.

plies that holes in band 2 are predominantly scattered into band 1, where the density of hole states is much greater.

Scattering of holes from ionized impurities, as described by the Brooks-Herring formula [5, pp. 170 ff.] seems well understood in our system. At a concentration of singly ionized impurities $N_i = 10^{16}$ cm^{-3} the scattering probability becomes relatively independent of momentum change, so that interband transitions occur as well as intraband transitions [12]. At this concentration, we obtain $\tau_i \sim E^{3/2}$ for the mean free time between scattering events, $\tau_i = 6.1$ ps for $E = 0.03$ eV in band 1 (half of this for the same energy in band 2) and $\tau_i = 32$ ps for $E = 0.147$ eV in band 2.

These numbers show that we can neglect ionized impurity scattering compared to lattice scattering. In this situation we expect that hole-hole scattering is also relatively unimportant. This is substantiated by a theoretical treatment of heat transport in nonpolar semiconductors by Appel [13].

As the last scattering mechanism, we mention hole scattering by neutral impurities, which leads to a time constant independent of hole energy $\tau_n = 25$ ps at a concentration $N_n = 10^{16}$ cm^{-3} [5, p. 167].

With this information, it is now possible to see that the most probable routing of the photoexcited holes is via two intermediate states in band 1 at energies around 0.110 and 0.073 eV back to near the ground state, as shown in Fig. 4. For steady-state irradiation the excess population of these states was calculated by Hattori *et al.* [15] and seen to give good agreement with photoconductivity measurements.

Saturation in two-level systems relaxing in a multistep cascade has been treated recently by Sargent [16]. We give here a simplified version of his treatment, using rate equations which are solved to find the steady-state solution (Fig. 5). The level populations are

$$\dot{N}_a = R(N_b - N_a) - \frac{N_a}{\tau_a}$$

$$\dot{N}_j = -\frac{N_j}{\tau_j} + \frac{N_{j+1}}{\tau_{j+1}}, \quad j = 1, \cdots, n$$

$$\dot{N}_b = -R(N_b - N_a) + \frac{N_1}{\tau_1} \tag{8}$$

where $n + 1 = a$, and $R \sim |\mu|^2 I$ is the radiative transition probability. Without resonant radiation present, we have $N_b = N$ where $N = N_a + N_b + \Sigma_1^n N_j$. Under steady-state irradiation, time derivatives of the population numbers vanish and one obtains $N_b - N_a = N/(1 + I/I_s)$ as in (2) for $\nu = \nu_0$ whereby I_s is given by (3) with $T_1 = 0.5\ (2\tau_a + \Sigma_1^n \tau_j)$. In other words, we have now a prescription of how to find T_1 given the time constants for the individual relaxation steps.

Let us now consider the resulting relaxation times for both radiatively coupled levels. For depopulation of the excited state, a single lattice scattering event suffices, leading to the upper level lifetime $\tau_a = (\tau_{ac}^{-1} + \tau_{op}^{-1})^{-1} = 0.12$ ps. While the next few steps lead to states $E < 0.037$ eV, close to the ground state in less than 1 ps, several acoustic interactions ($\tau_{ac} = 1.25$ ps) and perhaps ionized impurity interactions ($\tau_i = 6.1$ ps) seem to be necessary to restore the equilibrium. We are thus led to estimate $\Sigma_1^n \tau_j = 5$ ps. The lifetime of the population difference, i.e., the energy relaxation time of the two-level systems then becomes $T_1 = (5 + 0.24)/2 = 2.6$ ps. The phase relaxation time is given, in our case, by lattice scattering contributions of both lower and upper levels to be

$$T_2 = (1.25^{-1} + 0.97^{-1} + 0.57^{-1} + 0.14^{-1})^{-1} = 0.09 \text{ ps}.$$

Altogether, we have thus $(T_1 T_2)^{1/2} = 0.49$ ps, which we can compare to 0.55 ps as obtained from the analysis of saturated absorption above. The agreement is very good. This is somewhat unexpected in view of the assumptions made, especially since the interaction bandwidth [(4)] comes out to be 114 cm^{-1} (FWHM) which is 12 percent of the transition frequency. A correspondingly broad range of band states thus contributes to the absorption with not negligible variations in the population difference ρ as well as in the transition matrix element μ. However, the good agreement obtained suggests that the overall behavior of absorption saturation does not depend strongly on such variations. This means that simple inhomogeneous broadening theory may well provide an approximate description of the 10.6-μm absorption saturation in germanium at room temperature.

V. Hole-Burning Experiment

We set up an experiment to observe the hole-burning effect in p-type germanium at room temperature (Fig. 6). Two CO_2 laser beams were directed onto the sample. One of them was strong enough to induce saturation, the other acted as a weak but frequency-tunable probe.

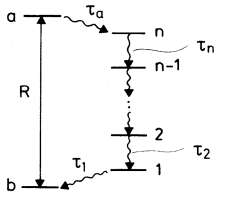


Fig. 5. Energy levels for two-level systems relaxing in a multistep cascade.

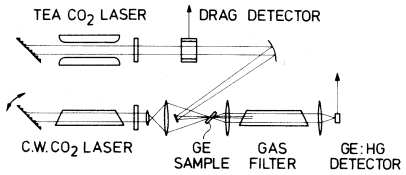


Fig. 6. Scheme of hole-burning experiment. The saturation of p-type germanium, induced by a high-power TEA CO_2 laser, is shown to drastically increase the transmission of a low-power CO_2 laser, offset in frequency by as much as 140 cm^{-1}.

The sample was indium-doped, exhibiting a resistivity of 0.40 $\Omega \cdot$ cm and a hole concentration of $7.1 \cdot 10^{15}$ cm^{-3} at 18°C. The plane-parallel disk 1.73 mm thick, showed 33-percent small-signal transmission at Brewster's angle (λ = 10.6 μm).

The saturating laser was a transversely excited CO_2 laser at atmospheric pressure, with a discharge of 60-cm length, yielding a T_{00}-mode output. The wavelength was set by an internal grating to 10.55 μm (*P*16), coupling was through a 61-percent-reflecting curved zinc selenide plate. The output energy of about 0.5 J was reproducible within 5 percent from shot to shot. The pulse showed strong self-mode-locking. Individual spikes varied in length down to a minimum of about 2 ns, as observed with a photon drag monitor with a response time below 1 ns, and an amplifier and an oscilloscope both of 400-MHz bandwidth. Since no substructure is expected in such a pulse, this in fact induces a certain steady-state population change in the sample for these few nanoseconds. Note that population transients are damped out on a picosecond time scale. A spherical mirror was used to focus the beam at 150-cm focal length to a spot diameter of about 3 mm, as measured by burn patterns in Polaroid film.

After transmission through the sample, the beam was recollimated by a BaF_2 lens and sent into a 3-m-long gas cell filled with SF_6. This served as a perfect absorber for the 10.55-μm line. Measurements showed partially saturated [17] transmission of $5 \cdot 10^{-4}$ at 0.8 torr for 1 MW/cm^2 input, from which we estimate an attenuation by about ten orders of magnitude at our working pressure of 4 torr; due to many closely overlapping SF_6 lines, strong attenuation is assured for all frequencies within the CO_2 laser gain bandwidth. At all CO_2 laser wavelengths shorter than 10.4 μm, the tube's small-signal transmission exceeded 30 percent at 4 torr. As a probe laser, we used a grating-controlled CW CO_2 laser at 12 torr. The output of about 100 mW was focused to a spot diameter about 0.5 mm at the sample, thus ensuring probing occurs in the center of the saturating beam. After passage through the SF_6 filter, the probe beam was detected by a Ge:Hg photoconductor at 4 K. The detector/amplifier combination had a response time of less than 3 ns.

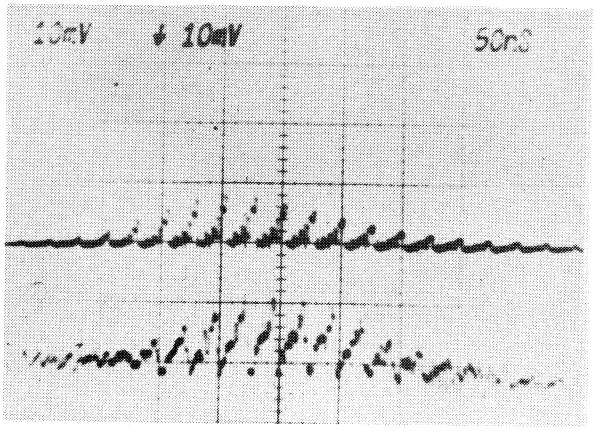


Fig. 7. Single-shot recording (Tektronix 7784 dual-beam oscilloscope) of saturating laser pulse train (upper trace) and modulated CW probe waveform (lower trace). The saturating and probing beams' wave lengths are 10.55 and 10.27 μm, respectively. The lower trace signal is delayed by 17 ns in the amplification process.

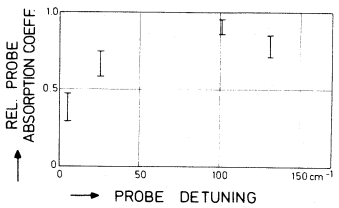


Fig. 8. Experimental hole-burning effect, evaluated for a saturating beam's intensity of 40 MW/cm^2, at 948 cm^{-1}. Probe detuning is toward higher frequencies.

Strong transmission enhancement was found to occur for the probe beam if saturating light was present. By blocking the CW laser beam, it was easily demonstrated that no measurable 10.55-μm light penetrated to the detector. In Fig. 7, the unmodulated part of the probe signal corresponds to 33-percent sample transmission, while in the peaks this is raised to approximately 55 percent. The latter value, however, is somewhat uncertain due to nonlinearity and slowness of the detector circuit's response, as well as power drift of the CW probe laser.

In Fig. 7, the probing laser was offset from the saturating laser by 25.5 cm^{-1}. In fact, the strong modulation could be observed at all wavelengths in the *R* branch of the 10.4-μm band and both *P* and *R* branches of the 9.4-μm band. The greatest frequency offset tried was 140 cm^{-1}. Even though the line shape of the saturation dip could not be determined accurately, Fig. 8 indicates that a hole of, indeed, finite width is burnt by the saturation effect, supporting the conclusion of our saturation analysis. At the time of revision, further supporting evidence from a recent experiment was kindly made available to us [20].

VI. Conclusion

We have found that the overall saturation behavior of room-temperature p-type germanium may be fairly well described in the framework of an inhomogeneously broadened two-level system. Realizing that refinements of both theory and experi-

ment will lead to more detailed insight, we may conclude here by pointing out two immediate applications. One is the passive mode-locking of CO_2 lasers to generate short pulses. Experimentally, Alcock and Walker [18] obtained a pulse duration less than 150 ps, but a further shortening (T_1 = 2.6 ps) should be in principle possible. Secondly, p-type germanium can be used for shaping and synchronization of infrared laser pulses, also down to a picosecond time scale. Due to the very fast phase relaxation, T_2 = 0.09 ps, this modulation of light by light is effective for even very large offsets between both frequencies, spanning, for example, the range of all possible CO_2 laser lines. For effective modulation, the saturating beam has to reach an intensity around 4 MW/cm^2; note that this can be obtained from a simple CW CO_2 laser. By coupling a low-power CO_2 laser to a thin germanium on gallium arsenide waveguide structure, saturation was indeed observed [19]. Still broader ranges of intermodulation open up if we include the two absorption bands centered at 2.7- and 4.5-μm coupling to the third valence band (Fig. 2). Here one has the interesting case of a three-level system with all three transition frequencies radiatively allowed.

ACKNOWLEDGMENT

It is a pleasure to thank M. Sargent, III, D.v.d. Linde, and E. O. Kane for many fruitful discussions as well as L. Genzel and H. J. Queisser for their generous support. Many thanks go to K. W. Kußmaul for his excellent technical help. The loan of the high-power CO_2 laser by the Max-Planck-Institut für Plasmaphysik, Garching, Germany is gratefully acknowledged.

REFERENCES

[1] N. Bloembergen, "Laser-induced electric breakdown in solids," *IEEE J. Quantum Electron.*, vol. QE-9, pp. 375–386, 1974.
[2] W. Kaiser, R. J. Collins, and H. Y. Fan, "Infrared absorption in p-type germanium," *Phys. Rev.*, vol. 91, pp. 1380–1381, 1953.
[3] A. F. Gibson, C. A. Rosito, C. A. Raffo, and M. F. Kimmitt, "Absorption saturation in germanium, silicon and gallium arsenide at 10.6 μm," *Appl. Phys. Lett.*, vol. 21, pp. 356–357, 1972.
[4] E. O. Kane, "Energy band structure in p-type germanium and silicon," *J. Phys. Chem. Solids*, vol. 1, pp. 82–89, 1956.
[5] See, for example, K. Seeger, "Free carrier absorption and reflection," in *Semiconductor Physics*. New York: Springer-Verlag, pp. 374–392, 1973.
[6] C. H. Kittel, *Introduction to Solid State Physics*. New York: Wiley, 1971.
[7] S. J. Fray, F. A. Johnson, J. E. Quarrington, and N. Williams, "Lattice bands in germanium," *Proc. Phys. Soc.*, vol. 85, pp. 153–158, 1965.
[8] R. H. Pantell and H. E. Puthoff, in *Fundamentals of Quantum Electronics*. New York: Wiley, 1969.
[9] E. V. Baklanov and V. P. Chebotaev, "Resonance interaction of unidirectional waves in gases," *Sov. Phys. JETP*, vol. 34, pp. 490–494, 1972.
[10] S. Haroche and F. Hartmann, "Theory of saturated-absorption line shapes," *Phys. Rev. A*, vol. 6, pp. 1280–1300, 1972.
[11] M. Sargent, III, "Laser saturation grating phenomena," *Appl. Phys.*, vol. 9, pp. 127–141, 1976.
[12] D. M. Brown and R. Bray, "Analysis of lattice and ionized impurity scattering in p-type germanium," *Phys. Rev.*, vol. 127, pp. 1593–1602, 1962.
[13] J. Appel, "Electron–electron scattering and transport phenomena in nonpolar semiconductors," *Phys. Rev.*, vol. 122, pp. 1760–1772, 1961.
[14] E. Conwell, "Lattice mobility of hot carriers," *J. Phys. Chem. Sol.*, vol. 8, pp. 234–239, 1959.
[15] H. Hattori, O. Fujitani, and M. Umeno, "Photoconductivity due to inter-valence band transition in p-type germanium," *J. Phys. Soc. Japan*, vol. 36, pp. 485–490, 1974.
[16] M. Sargent, III, "Two-level-system saturation spectroscopy with cascade relaxation," to be published.
[17] W. W. Rigrod, "Gain saturation and output power of optical masers," *J. Appl. Phys.*, vol. 34, pp. 2602–2609, 1963.
[18] A. J. Alcock and A. C. Walker, "Generation and detection of 150-psec mode-locked pulses from a multi-atmosphere CO_2-laser," *Appl. Phys. Lett.*, vol. 25, pp. 299–301, 1974.
[19] F. Bergler and R. Ulrich, "Epitaxial Ge/GaAs waveguides for 10.6 μm," Colloque sur l'Optique Guidée, Paris, France, Apr. 1975.
[20] P. J. Bishop, A. F. Gibson, and M. F. Kimmitt, "Absorption saturation in p-type germanium," to be published.

Lasing Characteristics of Distributed-Feedback GaAs–GaAlAs Diode Lasers with Separate Optical and Carrier Confinement

KUNIO AIKI, MICHIHARU NAKAMURA, AND JUN-ICHI UMEDA

Abstract—**The lasing characteristics of separate-confinement-heterostructure (SCH-structure) distributed-feedback (DFB) diode lasers are examined theoretically and experimentally. Wave propagation in five-layer SCH waveguides is analyzed to estimate such parameters as the lasing wavelength, coupling constant, and external quantum efficiency. Spectral and modal behavior are studied in the experiment and compared with the theoretical predictions. Diodes are shown to lase in a single longitudinal mode with a definite polarization. Spectral width is about 300 MHz just above the threshold, and becomes wider with increased excitation level. An output power of 40 mW with an external quantum efficiency of 5 percent is obtained under CW operation.**

Manuscript received March 24, 1976; revised June 4, 1976.
The authors are with the Central Research Laboratory, Hitachi, Ltd., Kokubunji, Tokyo, Japan.

I. INTRODUCTION

MARKED PROGRESS in distributed-feedback (DFB) diode lasers has been achieved during the last two years. Laser action has been demonstrated first of all in single-

heterostructure [1], homostructure [2], and double-heterostructure [3], [4] lasers at low temperatures. The threshold current density at 80 K was as low as 0.7 kA/cm^2 under pulse bias. At higher temperatures, however, it became increasingly difficult to operate such lasers because of rapid increase in the threshold current density with temperature.

Subsequent to these developments, studies have been carried out to achieve room-temperature operation of DFB diode lasers. It has been found that the failure of laser action at higher temperatures was due to nonradiative recombination of injected carriers at the corrugated interface between the active layer and the outer layer. This problem has been overcome by adopting a separate-confinement-heterostructure (SCH-structure), where nonradiative recombination is avoided by separating the corrugated interface from the active layer [5]. The SCH-structure DFB lasers have been fabricated by strictly controlled liquid phase epitaxy (LPE), and successfully operated at temperatures up to 370 K under pulse bias [6]. Being mounted on heatsinks, it was also possible to operate them under dc bias at room temperature [7]. The use of SCH-structure to aid in threshold reduction at higher temperatures was also reported by Casey *et al.* [8]. They realized the structure by a combination of LPE and molecular beam epitaxy. These works have contributed to a deeper understanding of lasing characteristics, and have prompted us to further explore the application of DFB lasers to various optical systems [9].

In this paper, the details of lasing characteristics of SCH-structure DFB diode lasers are described. Wave propagation in five-layer SCH waveguides is analyzed theoretically and coupling constants are estimated in Section II. The external quantum efficiency is also derived by using a Bloch formalism. Diode fabrication is briefly described in Section III. Detailed studies on spectral and modal behavior of DFB lasers are presented in Section IV. It is clearly shown that DFB lasers have such modal and spectral selectivity as predicted from theoretical analysis [10]. The external quantum efficiency is measured and compared with theoretical results.

II. Theoretical Analysis

Corrugated waveguides of a double-heterostructure DFB laser and of an SCH-structure DFB laser are schematically shown in Fig. 1. In the double-heterostructure laser, the waveguide was composed of an n-$Ga_{1-x}Al_xAs$ layer, a p-GaAs active layer, and a p-$Ga_{1-x}Al_xAs$ layer with $x \sim 0.3$. Both the injected carriers and light were confined to the p-GaAs active layer. Optical feedback was obtained by a corrugated interface which was realized by ion-milling or chemical etching.

In the SCH-structure studied here, the waveguide is composed of five layers as shown in Fig. 1(b). In this structure, the injected carriers are confined to the p-GaAs active layer, while light extends to the p-$Ga_{1-y}Al_yAs$ layer and the p-$Ga_{1-z}Al_zAs$ layer. A grating is made at the interface between the p-$Ga_{1-z}Al_zAs$ layer and the outer layer. The mole fraction of Al, y, is chosen to be ~0.17 so that the injected electrons do not reach the corrugated interface.

An alternative SCH-structure may be the one in which the grating is made on the p-$Ga_{1-y}Al_yAs$ layer [11]. In the present structure, the p-$Ga_{1-z}Al_zAs$ layer ($z \sim 0.07$) is introduced to facilitate the LPE of the p-$Ga_{1-x}Al_xAs$ layer [6].

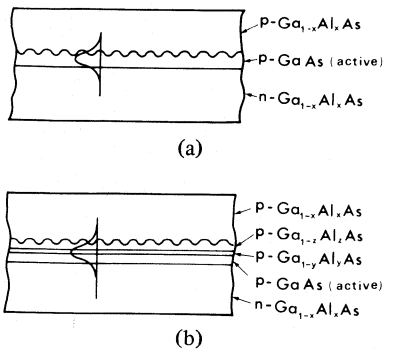


Fig. 1. Schematic drawing of DFB diode lasers. (a) Double-heterostructure laser. (b) SCH structure laser.

The electric field in a five-layer unperturbed waveguide (a waveguide without corrugation) is expressed in terms of

$$E_y^m = \mathcal{E}_m(x) \exp\,[i(\omega t - \beta_m z)], \quad (m = 0, 1, 2, \cdots) \tag{1}$$

for TE polarization, where β_m is the propagation constant of the mth transverse mode and ω is the angular frequency. In the above equation, $\mathcal{E}_m(x)$ denotes the profile in the x direction, and is given by

$$\mathcal{E}_m(x) = E_i^+ \exp\,(ik_i x) + E_i^- \exp\,(-ik_i x), \quad (i = 1, 2, \cdots, 5) \tag{2}$$

$$k_i = \sqrt{n_i^2 k_0^2 - \beta_m^2}, \quad k_0 = \frac{2\pi}{\lambda}, \quad \lambda: \text{wavelength}$$

in the ith layer in Fig. 2. The propagation constant β_m is obtained by solving an eigenvalue equation which is derived from the continuity conditions for the electric-field component E_y and the magnetic-field component H_z at each boundary.

Examples of the electric-field component calculated from (2) are shown in Fig. 3. In the calculation, the refractive index of each layer, n_i, was calculated from the semiempirical equation derived by Afromowitz [12]. It agrees well with the data given by Casey *et al.* [13], and is ~3.6 for GaAs, and ~3.38 for $Ga_{0.7}Al_{0.3}As$ at $\lambda = 0.89$ μm. In Fig. 3, the thicknesses of the GaAs active layer, the $Ga_{1-y}Al_yAs$ layer, and the $Ga_{1-z}Al_zAs$ layer were assumed to be 0.4 μm, 0.2 μm, and 0.1 μm, respectively. In this case, there are two guided modes which are denoted by $m = 0$ and $m = 1$. The effective refractive index, $\bar{n}$, defined by

$$\bar{n} = \frac{\beta_m}{k_0}$$

is 3.52 for the $m = 0$ mode and 3.44 for the $m = 1$ mode. Similar results are also obtained for TM modes, where eigenmodes are expressed by

$$H_y^m = \mathcal{H}_m(x) \exp\,[i(\omega t - \beta_m z)]. \tag{3}$$

Fig. 4 shows the effective refractive indices of TE and TM modes as functions of the active layer thickness. The thicknesses of the p-$Ga_{1-y}Al_yAs$ layer and the p-$Ga_{1-z}Al_zAs$ layer

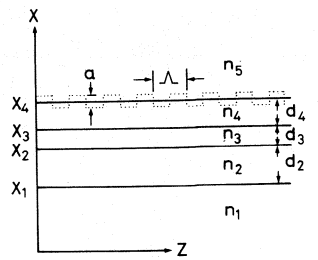


Fig. 2. SCH waveguide structure used in the theoretical analysis. The corrugation is assumed to be square-shape.

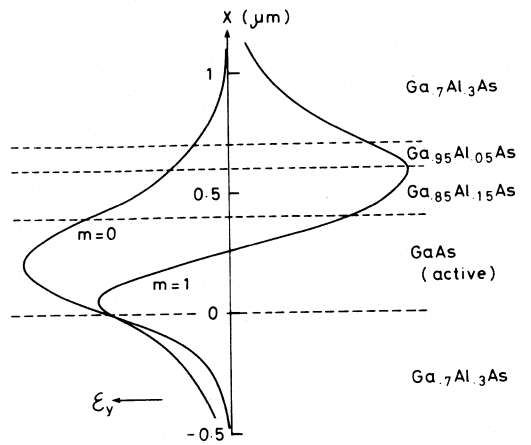


Fig. 3. Profiles of electric field component E_y for TE polarization.

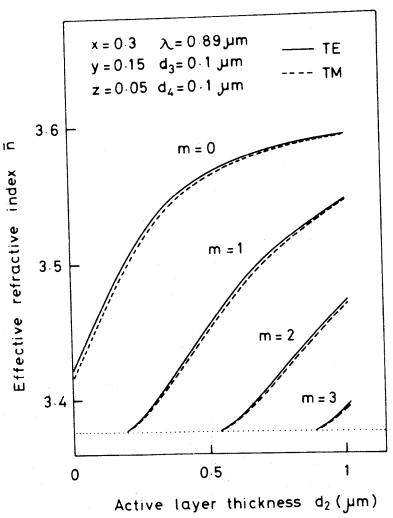


Fig. 4. Effective refractive index as a function of active layer thickness.

were both assumed to be 0.1 μm in this calculation. It is seen that TM modes have smaller propagation constants than TE modes.

In the presence of corrugation, as shown by the dotted line in Fig. 2, effective Bragg coupling takes place between forward and backward waves when

$$2\beta_m \approx \frac{2\pi}{\Lambda} l, \quad (l = 1, 2, \cdots) \tag{4}$$

where Λ is the corrugation period. The coupling constant κ is expressed approximately by

$$\kappa = \frac{\omega\epsilon_0(-1)^l}{4\pi l} \int_{-\infty}^{\infty} |\mathcal{E}_m(x)|^2 \Delta n^2(x)\, dx, \text{ (TE mode)} \tag{5}$$

$$\kappa = \frac{\omega\mu_0(-1)^l}{4\pi l} \int_{-\infty}^{\infty} |\mathcal{H}_m(x)|^2 \frac{\Delta n^2(x)}{n^2(x)}\, dx, \text{ (TM mode)} \tag{6}$$

$$\Delta n^2(x) = \begin{cases} n_5^2 - n_4^2 & \left(x_4 - \frac{a}{2} \leqslant x \leqslant x_4 + \frac{a}{2}\right) \\ 0 \end{cases}$$

for square-shape gratings with a corrugation height of a [14]. The coupling constant κ is zero for the even orders ($l = 2, 4, \cdots$) in the square-shape gratings. In the above equations, $\mathcal{E}_m(x)$ and $\mathcal{H}_m(x)$ were normalized in such a way that the power flow in the z direction is unity. More accurate expressions of κ for TM modes have recently been given by Streifer *et al.* [15], where a term proportional to $|d\mathcal{H}_m(x)/dx|^2$ has been included in the integral. Their results give a little bit smaller value for κ than those obtained here, though the difference is small.

Coupling constants calculated from (5) and (6) for $l = 3$ are shown in Fig. 5, as functions of the active layer thickness. Other parameters are the same as those used in Fig. 4. It is seen from this figure that a coupling constant as high as $\sim 100\ \text{cm}^{-1}$ is obtained in square-shape geometry. Coupling constant of TM modes are about 10 percent smaller than those of TE modes. In [16], the coupling constant κ was estimated experimentally from the field distribution along the direction of light propagation and found to be $\sim 50\ \text{cm}^{-1}$ for $l = 3$, $m = 0$, $d_2 \approx 0.3\ \mu\text{m}$, $d_3 \approx 0.1\ \mu\text{m}$, $d_4 \approx 0.1\ \mu\text{m}$, and $a \approx 0.15\ \mu\text{m}$. Therefore, one may expect that Fig. 5 gives rough estimations of κ for actual gratings, though κ depends on the corrugation shape of each diode.

The external differential quantum efficiency of a laser, η_{ext}, is given by

$$\eta_{\text{ext}} = \eta_{\text{int}} \frac{P_{\text{out}}}{P_{\text{loss}} + P_{\text{out}}} \tag{7}$$

where η_{int} is the internal quantum efficiency. In this equation, P_{loss} is the power loss in the cavity, and P_{out} is the power emitted from the laser. They are given by

$$P_{\text{loss}} = \frac{1}{2} \int_{-\infty}^{\infty} \int_0^L \epsilon\alpha v |\bar{E}_y|^2\, dxdz \tag{8}$$

and

$$P_{\text{out}} = \int_{-\infty}^{\infty} \{(\overline{\mathbf{E}\times\mathbf{H}})_z (1 - R_{\text{eff}})|_{z=L} - (\overline{\mathbf{E}\times\mathbf{H}})_z (1 - R'_{\text{eff}})|_{z=0}\}\, dx, \tag{9}$$

where $\epsilon = n^2\epsilon_0$, $v = c/\bar{n}$ (c: light velocity), and α is the total loss coefficient which includes both the absorption loss in the

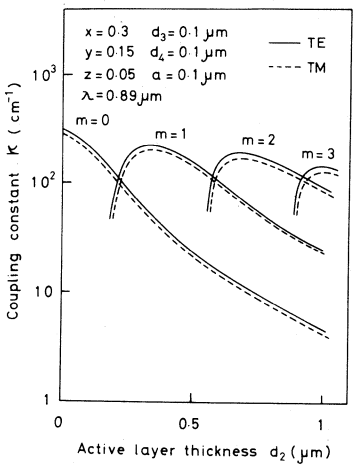


Fig. 5. Coupling constant as a function of active layer thickness.

composite waveguide and radiation loss caused by the lower order diffractions. If we express the electromagnetic field component by forward and backward Bloch waves, as was done by Wang [17],

$$E_y = [E_f \phi_f(z) \exp(\Gamma z + i\omega t) + E_b \phi_b(z) \cdot \exp(-\Gamma z + i\omega t)]\, \mathcal{E}_m(x), \tag{10}$$

the reflectivities R_{eff} and R'_{eff} in (9) are given by

$$R_{\text{eff}} = |r_{\text{eff}}|^2\, |\phi_b(L)/\phi_f(L)|^2, \tag{11}$$

$$R'_{\text{eff}} = |r'_{\text{eff}}|^2\, |\phi_f(0)/\phi_b(0)|^2, \tag{12}$$

where

$$r_{\text{eff}} = \frac{E_b}{E_f} e^{-2\Gamma L}, \tag{13}$$

$$r'_{\text{eff}} = \frac{E_f}{E_b}. \tag{14}$$

In (10), Γ is the propagation constant, E_f and E_b are the amplitudes of forward and backward Bloch waves, and $\phi_f(z)$ and $\phi_b(z)$ are periodic functions with respect to z; $\phi_f(z+\Lambda) = \phi_f(z)$ and $\phi_b(z+\Lambda) = \phi_b(z)$. If we assume that the laser is symmetric, i.e., $|\phi_f(0)| = |\phi_f(L)| = |\phi_b(0)| = |\phi_b(L)|$, and that

$$\frac{1}{\Lambda}\int_z^{z+\Lambda} |\phi_f(z)|^2\, dz = |\phi_f(0)|^2$$

$$\frac{1}{\Lambda}\int_z^{z+\Lambda} |\phi_b(z)|^2\, dz = |\phi_b(0)|^2$$

we obtain, from (7)-(14),

$$\eta_{\text{ext}} = \eta_{\text{int}} \frac{-\frac{1}{L}\ln R_{\text{eff}}}{\bar{\alpha} - \frac{1}{L}\ln R_{\text{eff}}}, \tag{15}$$

where $\bar{\alpha}$ is the effective loss coefficient given by

$$\bar{\alpha} = \frac{c\epsilon_0}{2}\int_{-\infty}^{\infty} \alpha n(x) |\mathcal{E}_m(x)|^2\, dx. \tag{16}$$

Equation (15) is a generalization of the result obtained for Fabry-Perot lasers. For the case of $\kappa > \bar{g}$ ($\bar{g}$: effective gain constant),

$$R_{\text{eff}} = R'_{\text{eff}} \approx \left(\frac{\kappa}{\sqrt{\kappa^2 + \bar{g}^2} + \bar{g}}\right)^2 \tag{17}$$

at the Bragg frequency [17]. If we assume, as an example, that $\eta_{\text{int}} \approx 70$ percent, $\kappa \approx 50\ \text{cm}^{-1}$, $\bar{g} \approx 30\ \text{cm}^{-1}$, $\bar{\alpha} \approx 30\ \text{cm}^{-1}$, and $L = 500\ \mu\text{m}$, the differential quantum efficiency η_{ext} is calculated to be ~30 percent from (17) and (15). For the output beam from one side of the laser, η_{ext} is one-half of the calculated value, i.e., ~15 percent. In the experiment, output power is obtained through a single cleaved surface as is shown in Section III. Reflection of light at the surface may result in lower external quantum efficiencies than estimated here.

III. Fabrication

The SCH-structure fabricated in the experiment is shown in Fig. 6. An n-$Ga_{0.7}Al_{0.3}As$ layer (~2 μm thick), a p-GaAs active layer (0.1 - 0.3 μm thick), a p-$Ga_{0.83}Al_{0.17}As$ layer (~0.1 μm thick), and a p-$Ga_{0.93}Al_{0.07}As$ layer (~0.2 μm thick) were successively grown on an n-GaAs (100) substrate by LPE. The n-layer was doped with Sn, and the p-layers with Ge. Next, the surface of the p-$Ga_{0.93}Al_{0.07}As$ layer was corrugated by chemical etching through a mask produced by holographic photolithography. Chemical etching was performed by using $C_2H_4(OH)_2$, H_3PO_4, and H_2O_2 (8:1:1) at 20°C. The grooves made by this etchant were composed of {111} A surfaces and a {100} bottom surface as shown in Fig. 6. The depth was ~1500 Å. The corrugation period was 0.34-0.38 μm, consequently, lasing occurred through the third-order Fourier component of corrugation. Finally a p-$Ga_{0.7}Al_{0.3}As$ layer (~2 μm thick) and a p-GaAs layer (~1 μm thick) were grown on the corrugated surface by LPE. The meltback of the corrugated surface was avoided by growing the layers at relatively low temperatures (~700°C) with a high cooling rate of 5°C/min as reported previously [18]. In such a growth condition, uniform regrowth was successfully performed on $Ga_{1-z}Al_zAs$ (z up to ~0.09).

Diodes had a mesa-stripe geometry so that injection was limited to the rectangular region as shown in Fig. 7. The stripe width was 50 μm, and the length of the excited region L was 500-700 μm. Ohmic contacts were made by evaporating Cr and Au on the p-side, and Au-Ge-Ni on the n-side. An unexcited waveguide with a length of ~2 mm was contiguous to the current excited region to eliminate optical feedback from the end surface. The output was obtained through the front surface.

In pulsed operation, current pulses with a duration of 50 ns and a repetition rate of 100 Hz were applied to the diode. In CW operation, diodes were bonded onto diamond heatsinks which were mounted on copper blocks. The thermal resistance per unit area was ~3×10^{-3} deg · cm²/W.

IV. Experimental Results

The lasing spectra of a typical DFB laser are shown in Fig. 8(a). In this figure, the lower spectrum was obtained at

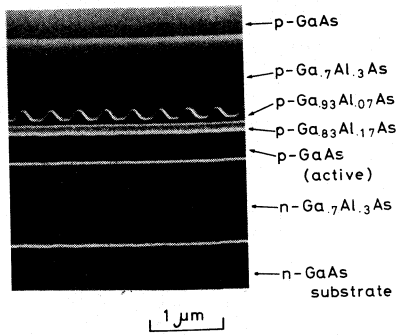


Fig. 6. An SEM photograph of the cross section of a DFB laser. The period is 3814 Å.

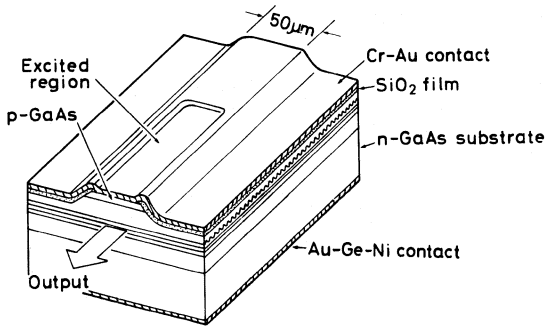


Fig. 7. Schematic structure of a DFB diode laser fabricated in the experiment.

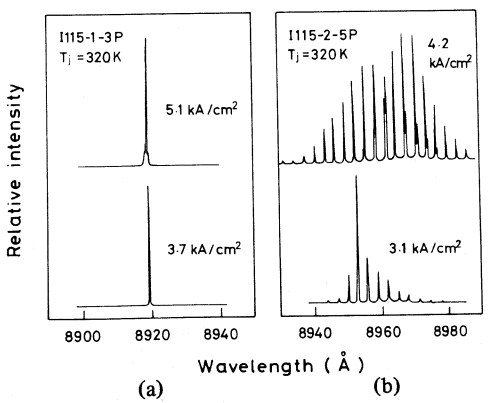


Fig. 8. Lasing spectra of two diodes. (a) a DFB laser, (b) a Fabry-Perot laser.

an excitation level of 1.1 times the threshold, and the upper one at 1.5 times the threshold. The diode had a corrugation period of 3814 Å. The thickness of the active layer, the p-$Ga_{0.83}Al_{0.17}As$ layer, and the p-$Ga_{0.93}Al_{0.07}As$ layer were 0.3 μm, 0.2 μm, and 0.15 μm, respectively. Spectra of a cleaved Fabry-Perot laser made from the same wafer are also shown in Fig. 8(b) for comparison. It is clearly seen that the DFB laser had longitudinal mode selectivity. Single longitudinal mode oscillation was observed at excitation levels up to twice the threshold. The lasing wavelength was also stable against changes in the excitation level.

The behavior of transverse modes is summarized in Fig. 9, where the threshold current density and the lasing wavelength are plotted as functions of junction temperature. Results

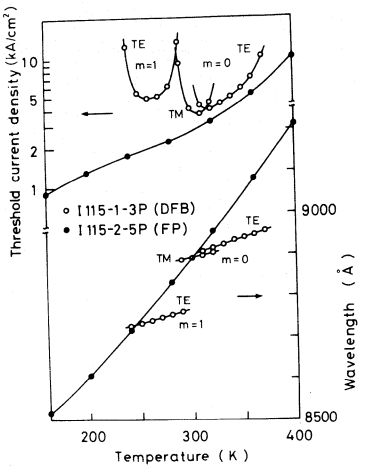


Fig. 9. Threshold current density and lasing wavelength as functions of junction temperature.

obtained in a cleaved laser are also shown in this figure. In the DFB laser, two TE modes and one TM mode were observed. At temperatures between 300 and 360 K, the diode lased in the TE $m = 0$ mode, and the threshold current density was about 20 percent higher than that of the cleaved laser. It increased rapidly below 300 K and above 360 K because of the mismatching between the Bragg frequency and the gain spectrum. The lowest threshold current density was 3.4 kA/cm² at 320 K.

The TM $m = 0$ mode and the TE $m = 1$ mode were observed at lower temperatures. These wavelengths are compared with the theoretical values calculated from (4) with good agreement, as shown in Table I. The TM $m = 1$ mode was not observed here due to its high threshold. The threshold for the $m = 1$ mode was usually higher than that for the $m = 0$ mode in the experiment, though the coupling constant calculated for the $m = 1$ mode was higher than that for the $m = 0$ mode for an active layer thickness of 0.2–0.3 μm. The higher threshold for the $m = 1$ mode may be explained by taking into account the facts that the effective gain coefficient for the $m = 1$ mode is lower and that the radiation loss caused by the corrugation is higher for the $m = 1$ mode than for the $m = 0$ mode.

It is seen in Fig. 9 that the diode lased in a single transverse mode with a definite polarization of which the wavelength was close to the peak wavelength of the gain spectrum. At transition regions, for example, the region between 310 and 320 K in this figure, both a TE mode and a TM mode were observed.

Lasing usually occurs in the multitransverse mode in the junction plane for a stripe geometry of ~50 μm. On the transverse mode, there is no selectivity specific to DFB lasers. Typical examples of far-field patterns and their spectra are shown in Fig. 10, where the diode had a corrugation period of 3648 Å and was operated at $T = 143$ K under dc bias. The threshold current density was 1 kA/cm². The diode lased in the lowest mode just above the threshold [Fig. 10(a)]. At $J \approx 1.3 J_{th}$, it lased in the lowest and the second mode as shown in Fig. 10(b), where the far-field pattern was asymmetric in the sense that one of the streaks of the second mode overlapped that of the fundamental mode. Higher modes were also observed by increasing the excitation level.

TABLE I
EFFECTIVE REFRACTIVE INDEX AND LASING WAVELENGTH OF A DFB LASER (I115-1-3P)

Mode		Calculation		Experiment	
		$\bar{n}$	λ (Å)	$\bar{n}$	λ (Å)
TE	m=0	3.516	8940	3.504	8910
	m=1	3.442	8752	3.441	8750
TM	m=0	3.514	8934	3.501	8901
	m=1	3.440	8746	-	-

Note: T_j = 300 K, Λ = 3814 Å, d_2 = 0.3 μm, d_3 = 0.2 μm, and d_4 = 0.15 μm.

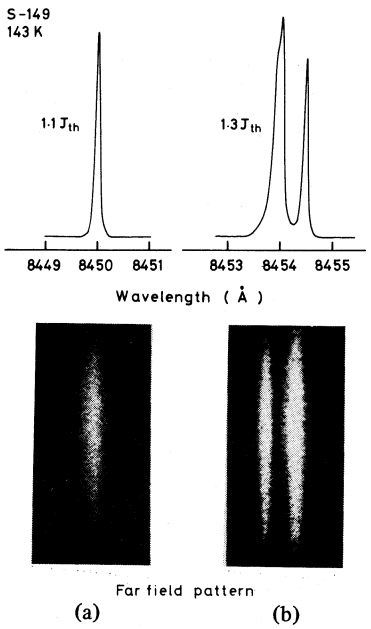


Fig. 10. Far-field pattern and lasing spectra of a DFB diode laser. (a) $J = 1.1\,J_{th}$. (b) $J = 1.3\,J_{th}$.

Spectral width of DFB lasers was examined by a Fabry-Perot etalon with a mirror distance of 1 cm. The resolution of the etalon was 45 MHz. Spectra of a typical CW laser diode are shown in Fig. 11 for three excitation levels, where the ambient temperature was 143 K. A narrow spectrum ($\Delta\nu \approx 300$ MHz, $\Delta\lambda \approx 0.01$ Å) was obtained at $J = 1.05\,J_{th}$. The peak became wider with increased exitation level, and was ~3 GHz (~0.1 Å) at $J = 1.26\,J_{th}$. In the diodes operated at room temperature, the spectral width was usually wider, typically 0.5 Å at $J = 1.5\,J_{th}$. The reason for the broadening of the spectrum is not clear now.

Fig. 12 shows the output power from a DFB laser as a function of applied current. An output power as high as ~40 mW was obtained under CW operation. The differential quantum efficiency η_{ext} was ~7 percent under pulse bias and ~5 percent under dc bias. Although it is about one-third of the roughly estimated value, it will be improved by refining the device structure including the use of first-order grating.

V. CONCLUSION

Lasing characteristics of SCH-structure DFB lasers were examined theoretically and experimentally. Single longitudinal mode oscillation was observed up to twice the threshold. The transverse modes perpendicular to the junction plane and their polarization were examined and good agreement was obtained between the theoretical predictions and experimental results. The lasing spectrum was as narrow as ~300 MHz just above the threshold and became wider with increased excitation level. An external quantum efficiency of ~5 percent was obtained under CW operation. Such lasers as described here are expected to find wide application in optical systems, especially in optical integrated circuits. Experiments concerning their integration with other components are under way.

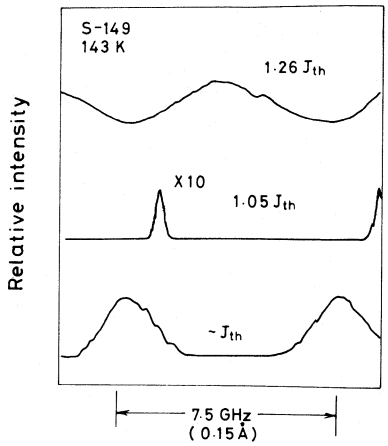


Fig. 11. Lasing spectra measured by a Fabry-Perot etalon.

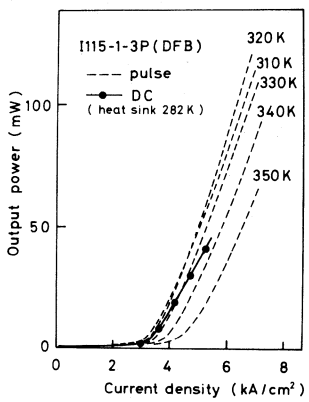


Fig. 12. Output power as a function of applied current.

ACKNOWLEDGMENT

The authors would like to thank Prof. A. Yariv of the California Institute of Technology for his helpful discussion on diode structure and lasing characteristics. They are also grateful to Dr. Y. Otomo and Dr. Y. Takeda of the Central Research Laboratory, Hitachi, Ltd., for their continuous support in this work, and S. Yamashita for his assistance in diode fabrication and SEM observations.

REFERENCES

[1] D. R. Scifres, R. D. Burnham, and W. Streifer, "Distributed feedback single heterojunction GaAs diode lasers," *Appl. Phys. Lett.*, vol. 25, pp. 203-206, Aug. 1974.

[2] H. M. Stoll and D. H. Seib, "Distributed feedback GaAs homojunction injection lasers," *Appl. Opt.*, vol. 13, pp. 1981–1982, Sept. 1974.
[3] M. Nakamura *et al.*, "GaAs-$Ga_{1-x}Al_xAs$ double heterostructure distributed feedback diode lasers," *Appl. Phys. Lett.*, vol. 25, pp. 487–488, Nov. 1974.
[4] D. B. Anderson, R. R. August, and J. E. Coker, "Distributed feedback double-heterostructure GaAs injection laser with fundamental grating," *Appl. Opt.*, vol. 13, pp. 2742–2743, Sept. 1974.
[5] An SCH-structure was previously applied to grating-coupled diode lasers for reducing the threshold current density; see, R. D. Burnham, D. R. Scifres, and W. Streifer, "Low-divergence beams from grating-coupled composite guide heterostructure GaAlAs diode lasers," *Appl. Phys. Lett.*, vol. 26, pp. 644–647, June 1975.
[6] K. Aiki *et al.*, "GaAs–GaAlAs distributed-feedback diode lasers with separate optical and carrier confinement," *Appl. Phys. Lett.*, vol. 27, pp. 145–147, Aug. 1975.
[7] M. Nakamura, K. Aiki, J. Umeda, and A. Yariv, "CW operation of distributed-feedback diode lasers at temperatures up to 300 K," *Appl. Phys. Lett.*, vol. 27, pp. 403–405, Oct. 1975.
[8] H. C. Casey, Jr., S. Somekh, and M. Ilegems, "Room temperature operation of low threshold separate confinement heterostructure injection laser with distributed feedback," *Appl. Phys. Lett.*, vol. 27, pp. 142–144, Aug. 1975.
[9] M. Nakamura and A. Yariv, "Distributed feedback semiconductor lasers," in *Digest 1976 Proc. Topical Meeting on Integrated Optics*, Jan. 1974, MA 1.
[10] H. Kogelnik and C. W. Shank, "Coupled-wave theory of distributed-feedback lasers," *J. Appl. Phys.*, vol. 43, pp. 2327–2335, May 1972.
[11] M. Nakamura and A. Yariv, "Theoretical analysis of low threshold GaAs–GaAlAs injection lasers with corrugation feedback," in *Digest 1974 Proc. Topical Meeting on Integrated Optics*, Jan. 1974, TuB 9.
[12] M. A. Afromowitz, "Refractive index of GaAlAs," *Solid-State Commun.*, vol. 15, pp. 59–63, Jan. 1974.
[13] H. C. Casey, Jr., D. D. Sell, and M. B. Panish, "Refractive index of $Al_xGa_{1-x}As$ between 1.2 and 1.8 eV," *Appl. Phys. Lett.*, vol. 24, pp. 63–65, Jan. 1974.
[14] H. Stoll and A. Yariv, "Coupled-mode analysis of periodic dielectric waveguide," *Opt. Commun.*, vol. 8, pp. 5–8, May 1973.
[15] W. Streifer, D. R. Scifres, and R. D. Bunham, "TM-mode coupling coefficients in guided-wave distributed feedback lasers," *IEEE J. Quantum Electron.*, vol. QE-12, pp. 74–78, Feb. 1976.
[16] J. Umeda, M. Nakamura, and K. Aiki, "Room temperature operation of distributed feedback diode lasers with separate carrier and optical confinement," in *Proc. 7th Conf. Solid State Devices*, Tokyo, Japan, 1975; *Japan. J. Appl. Phys.*, vol. 15 Suppl., pp. 317–320, 1973.
[17] S. Wang, "Principles of distributed feedback and distributed Bragg-refrector lasers," *IEEE J. Quantum Electron.*, vol. QE-10, pp. 413–427, June 1974.
[18] M. Nakamura *et al.*, "Liquid phase epitaxy of GaAlAs on GaAs substrate with surface corrugations," *Appl. Phys. Lett.*, vol. 24, pp. 466–468, May 1974.

Multiphoton Excitation Processes Between Vibrational States of Molecules

V. E. MERCHANT AND N. R. ISENOR

Abstract—**An approximation method has been developed to evaluate the perturbation theory expressions for the probabilities of two- and three-photon transitions among vibrational–rotational levels of diatomic and polyatomic molecules. The sum over intermediate rotational states and the degenerate quantum number M is evaluated for a general case, and the sum over intermediate vibrational states for particular cases. The molecule is taken to be a rotating anharmonic oscillator. The electrical anharmonicity and the effects of the electronic states of the molecule are considered.**

Two- and three-photon processes, with or without the presence of near-resonant intermediate states, should be observable with available infrared lasers. However, the intensities predicted for the observation of three-photon excitation would result in more dominant effects such as dissociation or gas breakdown.

I. Introduction

EXPERIMENTS and discussions of multiphoton processes in molecules have been largely concerned with dissociation or ionization involving a few quanta of energy from visible or near-infrared lasers [1]–[3]. The advent of high-power lasers at a wavelength of 10 μm has made possible multiphoton transitions between low-lying vibrational levels in the ground electronic state. However, there has been no systematic calculation of the probability of these processes. A calculation [4] of the probability of CO_2 laser-induced dissociation of molecules shows that resonant multiphoton processes have zero probability. However, this calculation neglects the anharmonicity of the molecule and the rotational contribution to the energy, both of which cause a nonzero excitation probability. Golger and Letokhov [5] investigate theoretically the two-photon resonant excitation of the fundamental vibrational band of a diatomic molecule. However, they neglected the anharmonicity which is shown in this paper to have an important effect.

This paper evaluates the multiphoton excitation probability for two- and three-photon processes in diatomic and polyatomic molecules. The terminology used is defined in the Appendix. The electrical anharmonicity results from deviations from the linear dependence of the dipole moment on the internuclear separation (A4). The mechanical anharmonicity is the deviation of the potential energy function from the

Manuscript received March 25, 1976; revised May 26, 1976. This work was supported by the National Research Council of Canada.

The authors are with the Department of Physics, University of Waterloo, Waterloo, Ont., Canada.

harmonic oscillator potential (A5). It results in irregular energy level spacings as well as affecting the transition matrix elements. The electrical and mechanical anharmonicity and the rotation of the molecule are considered explicitly.

Section II describes the division of the calculation into two parts which are called the "rotational problem" and the "vibrational problem." The rotational problem is solved for two- and three-photon processes involving linearly polarized radiation. The solution of the vibrational problem depends on the particular transition being excited. This is done in Section III for a few cases involving diatomic molecules. Section IV considers the influence of electronic states on the excitation probability, while Section V extends the results of Section III to polyatomic molecules.

Section VI considers two- and three-photon processes in systems with "quasi-resonant" intermediate states. The next section discusses the approximation involved in the calculations and the limitations of the results. This is followed by conclusions in the final section.

II. Formalism

The N photon excitation probability, evaluated by Nth-order perturbation theory, is given by

$$W = 2\pi g(N\omega_R)(2\pi\alpha_f F\omega_R)^N \sum_{M'=-J'}^{J'} \sum_{M''=-J''}^{J''} \cdot |K(N; v'', \rho''; v', \rho')|^2. \tag{1}$$

This formula follows from [6, eq. (16)]. The terms are defined as follows: α_f is the fine structure constant $(e^2/\hbar c)$; ω_R is the radiation frequency given in radians/second (as are all frequencies in this paper); F is the photon flux and $g(\omega)$ is normalized to unity by integrating over angular frequency. Primed quantities refer to the final state and double-primed quantities to the initial state. v is the vibrational quantum number, J and M are the usual rotational quantum numbers, and $\rho = \{J, \Lambda, M\}$ refers to the set of rotational quantum numbers, Λ being the component of electronic angular momentum along the molecular axis.

The composite matrix element $K(N; v'', \rho''; v', \rho')$ involves $N-1$ sums over all states of the system. Neglecting the excited electronic states, which are considered explicitly in Section IV, it is given by

$$K(N+1; v'', \rho''; v', \rho') = \sum_{v_N \rho_N} \cdots \sum_{v_1 \rho_1} \cdot [\langle gv'\rho' | \vec{\mu} \cdot \hat{p} | gv_N\rho_N\rangle \cdots \langle gv_2\rho_2 | \vec{\mu} \cdot \hat{p} | gv_1\rho_1\rangle \cdot \langle gv_1\rho_1 | \vec{\mu} \cdot \hat{p} | gv''\rho''\rangle] / (\omega_{v_N J_N} - N\omega_R) \cdots (\omega_{v_1 J_1} - \omega_R)]. \tag{2}$$

Here $\hat{p}$ is the polarization vector of the radiation, $\hbar\omega_{v_i J_i}$ is the difference in energy between the ith intermediate state and the initial state, $e\vec{\mu}$ is the dipole moment of the molecule.

If there is a state of the system whose energy is nearly equal to the energy of an integral number (less than N) of radiation quanta, then one term in the denominator will become very small and that term will dominate the sum over intermediate states. This is treated as a special case in Section VI. In what follows we assume that there are no such near resonances, and all intermediate states are treated equally.

The dipole moment matrix elements $\langle gv\rho | \vec{\mu} \cdot \hat{p} | gv''\rho''\rangle$ are discussed in the Appendix. In (A2), the first term $f(\rho, \rho'')$ determines the selection rules for changes in J and M while the second term alone determines the selection rules for the quantum number v. Hence the sums over v_i and J_i can be performed completely independently, and $K(N; v'', \rho''; v', \rho')$ can be written as

$$K(N; v'', \rho''; v', \rho') = \sum_{\rho_{N-1}} \cdots \sum_{\rho_1} f(\rho', \rho_{N-1}) \cdots f(\rho_1, \rho'') \cdot L(N; v'', v', \{J\}), \tag{3}$$

where

$$L(N; v'', v', \{J\}) = \sum_{v_{N-1}} \cdots \sum_{v_1} \frac{\langle v' | R_{gg} | v_{N-1}\rangle \cdots \langle v_1 | R_{gg} | v''\rangle}{[\omega_{v_{N-1} J_{N-1}} - (N-1)\omega_R] \cdots [\omega_{v_1 J_1} - \omega_R]}. \tag{4}$$

The evaluation of L is denoted the vibrational problem. $L(N; v'', v', \{J\})$, in general, depends on the intermediate rotational states J_i, and is assumed to have some particular functional dependence on the J_i. Then the vibrational problem for a specific case of multiphoton excitation involves evaluating the multiple sum (4) to have the particular assumed functional dependence.

The rotational problem involves substituting the general form for L into (3) and evaluating

$$\sum_{M''=-J''}^{J''} \sum_{M'=-J'}^{J'} |K(N; v'', \rho''; v', \rho')|^2.$$

Since the matrix elements $f(\rho_1, \rho'')$ are independent of the molecular parameters, the rotational problem need be performed only once for each radiation polarization.

For two-photon processes let α and γ be defined by $J' = J'' + \gamma$ and $J_1 = J'' + \alpha$. Now the energy denominator in (4) can be written as

$$\omega_{v_1 J_1} - \omega_R = \Delta\omega_{v_1} + Bb, \tag{5}$$

where $\Delta\omega_{v_1}$ contains no dependence on the rotation, B is the rotational constant, and

$$b = \alpha(2J'' + 1 + \alpha) - \tfrac{1}{2}\gamma(2J'' + 1 + \gamma).$$

The rotational contribution to the energy is taken as $BJ \cdot (J+1)$; the validity of this approximation is considered in Section VII. Then the general form for the vibrational component of the composite matrix element for two-photon excitation is given by

$$L = X + Yb + Zb^2. \tag{6}$$

For three-photon processes, α and γ are defined as before and β is defined by $J_2 = J'' + \beta$. The energy denominators in (4) are products of terms

$$\omega_{v_1 J_1} - \omega_R = \Delta\omega'_{v_1} + Bb_1$$

and

$$\omega_{v_2 J_2} - 2\omega_R = \Delta\omega''_{v_2} + Bb_2, \tag{7}$$

where

$$b_1 = \alpha(2J'' + 1 + \alpha) - \tfrac{1}{3}\gamma(2J'' + 1 + \gamma)$$

and

$$b_2 = \beta(2J'' + 1 + \beta) - \tfrac{2}{3}\gamma(2J'' + 1 + \gamma).$$

Then the general form for the vibrational component of the composite matrix element is given by

$$L = T + Ub_1 + Vb_2 + Xb_1^2 + Yb_1b_2 + Zb_2^2. \tag{8}$$

The coefficients T, U, V, X, Y, and Z depend on v', v'', and the molecular parameters. In the next section, expressions for these coefficients have been derived in particular cases.

The rotational problem involves the calculation of

$$\sum_{M''=-J''}^{J''} \sum_{M'=-J'}^{J'} |K(N; v'', \rho''; v', \rho')|^2$$

using (3) and (6) or (8). This is straightforward but tedious and has therefore been done only for linearly polarized light and for $\Lambda = 0$. Λ is the component of the electronic angular momentum along the internuclear axis, and is zero for the ground electronic state of most stable molecules. Hence the limited solution of the rotational problem corresponds to the most common experimental case.

For $\Lambda = 0$ and for linearly polarized radiation, the selection rules for the single-photon transitions are $\Delta J = \pm 1$, $\Delta M = 0$. This implies, for two-photon transitions, $\alpha = \pm 1$, $\gamma = 0, \pm 2$; and for three-photon transitions, $\alpha = \pm 1$, $\beta = 0, \pm 2$, and $\gamma = \pm 1, \pm 3$, since the composite matrix element (3) is a product of single-photon matrix elements. It also implies this restriction on M_i:

$$M' = M_{N-1} = \cdots M_1 = M''.$$

Equation (3) can now be evaluated using (A5) of the Appendix for the rotational matrix element.

It is convenient to define "rotational factors"

$$F_{NR}(\gamma) \equiv \sum_{M''=-J''}^{J''} |K(N; v'', J''; v', J')|^2$$

where $L \equiv 1$ in (3). These factors, listed in Table I, are the N photon equivalent of the Hönl-London line intensity factors. Note that

$$F_{3R}(1) \sim F_{3R}(-1) \sim 9 \times F_{3R}(3) \sim 9 \times F_{3R}(-3).$$

This is because for $\gamma = 3$ there is only one possible set of values for (α, β), namely (1, 2), whereas for $\gamma = 1$ there are three sets of values for (α, β), namely (1, 2), (1, 0), and (-1, 0). Similarly,

$$F_{2R}(0) \sim 4 \times F_{2R}(2) \sim 4 \times F_{2R}(-2).$$

Upon substituting the rotational matrix elements into (3) and solving the rotational problem, the two-photon excitation probability is

$$W = 2\pi g(2\omega_R)(2\pi\alpha_f F\omega_R)^2 (X - Y + Z)^2 F_{2R}(\gamma) \tag{9}$$

for $\gamma = \pm 2$, and

$$W = 2\pi g(2\omega_R)(2\pi\alpha_f F\omega_R)^2 \left[\left\{(X + 2Y)^2 - \frac{4Y(2X + Y)(J^2 + J)}{8J^2 + 8J + 5}\right\} F_{2R}(\gamma) + P_{XZ}XZ + P_{YZ}YZ + P_{ZZ}Z^2\right] \tag{10}$$

for $\gamma = 0$. The coefficients P_{XZ}, P_{YZ}, P_{ZZ} are complicated and are given in Table II. Obviously the solution is more attractive if $Z = 0$ is a reasonable approximation in the solution of the vibrational problem.

The three-photon excitation probability is evaluated using the general form (8) for L:

$$W = 2\pi g(3\omega_R)(2\pi\alpha_f F\omega_R)^3 [T - 2(U + V) + 4(X + Y + Z)]^2 F_{3R}(\gamma) \tag{11}$$

for $\gamma = \pm 3$, and

TABLE I
ROTATIONAL FACTORS

For $\Lambda = 0 \rightarrow \Lambda = 0$ Transitions Induced by Linearly Polarized Radiation

$$F_{2R}(2) = \frac{J+1}{15}\left[1 + \frac{1}{2J+3}\right]$$

$$F_{2R}(0) = \frac{2(2J+1)}{15}\left[1 + \frac{1}{2(2J-1)(2J+3)}\right]$$

$$F_{2R}(-2) = \frac{J-1}{15}\left[1 + \frac{1}{2J-1}\right]$$

$$F_{3R}(3) = \frac{J+2}{70}\left[1 - \frac{3}{(2J+3)(2J+5)}\right]$$

$$F_{3R}(1) = \frac{9(J+1)}{70}\left[1 + \frac{1}{(2J-1)(2J+5)}\right]$$

$$F_{3R}(-1) = \frac{9J}{70}\left[1 + \frac{1}{(2J-3)(2J+3)}\right]$$

$$F_{3R}(-3) = \frac{J-1}{70}\left[1 - \frac{3}{(2J-1)(2J-3)}\right]$$

TABLE II
COEFFICIENTS OF TERMS IN THE SOLUTION OF THE ROTATIONAL PROBLEM

Two Photon Problem:

$$P_{xz} = \frac{-8(2J+1)}{15(2J-1)^2(2J+3)^2}(8J^6+4J^5+46J^4-42J^3+43J^2+43J-15)$$

$$P_{yz} = \frac{-16(2J+1)}{15(2J-1)(2J+3)}(4J^4+2J^3+18J^2+12J-5)$$

$$P_{zz} = \frac{16(2J+1)}{15(2J-1)^2(2J+3)^2}(12J^8+8J^7-44J^6+20J^5+251J^4+238J^3-24J^2-71J+15)$$

Three Photon Problem ($\gamma = -1$):

$$P_1 = \frac{16J^2}{15}\left[T + \frac{16J^2}{9}Y + \frac{4}{3}(U+V) + \frac{8}{9}\frac{4J^2+3}{4J^2-9}(X+Z)\right]$$

$$P_2 = \frac{16J}{105(4J^2-9)}\left[(24J^4-37J^2-36)\{T + 16J^2Y/9 + 20(U+V)/9 + 4(8J^2+5)(X+Z)/9\} + 4(U+V)(4J^2-3)/9 + 28(X+Z)(2J^2-9)/9\right]$$

TABLE III
TWO-PHOTON TRANSITIONS: EXPRESSIONS FOR X, Y, Z IN PARTICULAR CASES

$(v,J) \to (v+1,J+\gamma)$	$(v,J) \to (v+3,J+\gamma)$
$X = \frac{4M_{01}^2 \{v+1\}^{1/2}}{\omega} (M_1 + M_2/3)$	$X = \frac{M_{01}^2}{\omega} \left[-8xM_2 \{(v+1)(v+2)(v+3)\}^{1/2} + 4M_1 M_{v,v+3}\right]$
$Y = -\frac{8M_{01}^2 B \{v+1\}^{1/2}}{\omega^2} \left[M_0+(v+1)(2M_1+M_2/9)\right]$	$Y = \frac{4M_{01}^2 B}{\omega^2} \left[M_2 \{(v+1)(v+2)(v+3)\}^{1/2} - 2M_{v,v+3} \{M_0+2(v+2)M_1\}/9\right]$
$Z = 0$	$Z = 0$

$$W = 2\pi g(3\omega_R)(2\pi\alpha_f F\omega_R)^3 \left[\left\{\left[T + \frac{16J^2}{9} Y + \frac{4}{3}(U+V)\right]^2 - \frac{8}{3}\frac{J^2-1}{6J^2-13}(U+V)\left[T + \frac{16J^2}{9} Y - \frac{1}{3}(U+V)\right]\right\} \cdot F_{3R}(\gamma) + (X-Z)P_1 + (X+Z)P_2\right] \quad (12)$$

for $\gamma = -1$, and a similar expression with J replaced by $J+1$ for $\gamma = +1$. P_1 and P_2 are defined in Table II. Note that U and V are found together only in the form $U+V$ and that Y is found only with T in the form

$$T + \frac{16J^2}{9} Y$$

in the expression for $\gamma = -1$, and in the form

$$T + \frac{16(J+1)^2}{9} Y$$

in the expression for $\gamma = +1$. The expressions for P_1 and P_2 are exact: they obviously simplify as $X, Z \ll T$.

III. The Vibrational Problem for Diatomic Molecules

The vibrational problem involves performing the sums over vibrational states in (4) and expressing the result in the general form (6) or (8) for two- or three-photon processes, respectively. The terminology for the matrix elements involved is described in the Appendix. The rotational contribution to the vibrational matrix elements is neglected.

As an illustration, the two-photon transition $(0,J)$ to $(1, J+\gamma)$ induced by radiation of frequency $\omega_R = (\omega + B\gamma \cdot [2J+\gamma+1])/2$ is considered. In the sum over states (4), the intermediate states $(0, J+\alpha)$ and $(1, J+\alpha)$ make the largest contribution. For these states, the energy denominators are $-\omega/2 + bB$ and $\omega/2 + bB$, respectively. Then,

$$K = \left[\frac{M_0 + M_1}{-\omega/2 + bB} + \frac{M_0 + 3M_1}{\omega/2 + bB}\right] M_{01}^2$$
$$= [4M_1/\omega - 8bB(M_0 + 2M_1)/\omega^2]\, M_{01}^2 \equiv X + Yb.$$

There are additional contributions from other intermediate states, e.g., $(2, J+\alpha)$. The expressions for some two-photon transitions are presented in Table III and those for some three-photon transitions in Table IV.

TABLE IV
THREE-PHOTON TRANSITIONS

Particular Cases of the Vibrational Problem

$(0,J) \to (1,J+\gamma)$	$T = 18M_1^2 M_{01}^3 (1-2x)^2/\omega^2 + 27M_{01}^3 x/8\omega^2$
	$Y = 81M_{01}^3 B^2 (3M_0^2+12M_0M_1+13M_1^2)/4\omega^4$
	$U+V = -81M_{01}^3 BM_1(M_0+2M_1)(1-2x)/\omega^3 - 81M_{01}^3 B/16\omega^3$
	$X = Z = 0$
$(v,J) \to (v+2,J+\gamma)$	$T = -\frac{54x}{\omega^2} \{(v+1)(v+2)\}^{1/2} M_{01}^3 [M_1+M_2/5 - (2v+3)xM_1]$
	$Y = \frac{243}{4} \{(v+1)(v+2)\}^{1/2} \frac{M_{01}^3 B^2}{\omega^4} [M_0+(2v+3)M_1 - 0.21(2v+3)M_2]$
	$U+V = \frac{81M_{01}^3 B}{4\omega^3} \{(v+1)(v+2)\}^{1/2} [2xM_0 - 4M_1 + 6x(2v+3)M_1 - \frac{13}{10} M_2]$
	$X = Z = 0$
$(0,J) \to (4,J+\gamma)$	$T = 661.4x(8x-1)M_2 M_{01}^3/\omega^2$
	$Y = 1190.5\, M_2 M_{01}^3 B^2/\omega^4$
	$U+V = 4761.8 \times M_2 M_{01}^3 B/\omega^3$
	$X = Z = 0$

In the example above, the rotational terms in the least common denominator were neglected in the first order of approximation. Alternately, the denominator can be expanded in a Taylor series to bring these rotational terms into the numerator. In this second order of approximation, all the coefficients of (6) and (8) are retained.

In every case harmonic oscillator terms in the numerator vanish; multiphoton transitions are not allowed in a harmonic oscillator. This is a consequence of the regular energy level spacings and the simple relation between matrix elements for successive transitions. A nonzero transition probability results from any effect in a real molecule which causes deviations from the energy levels or the matrix elements of the harmonic oscillator. In the example above, the only contribution for a nonrotating oscillator (i.e., $B = 0$) contains the anharmonic matrix element M_1. Other transitions may have a contribution arising from anharmonicity of the energy levels. In general, the permanent dipole moment is part of a factor $BM_0/\omega \simeq$

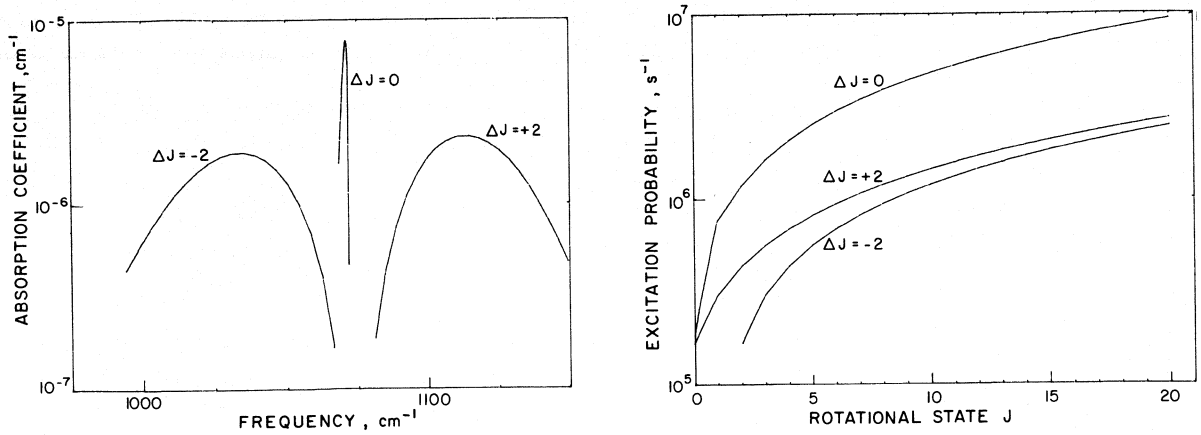


Fig. 1. Two-photon excitation of one quantum of vibration in carbon monoxide. Radiation intensity is 10^9 W/cm^2. (a) Two-photon absorption coefficient in cm^{-1} as a function of frequency in cm^{-1}. (b) Dependence of the excitation probability in s^{-1} on rotational quantum number, for $\Delta J = 0$ and $\Delta J = \pm 2$ processes. In all figures in this paper, the lines are for clarity only and do not imply that the transition probability is a continuous function of the frequency or the quantum number J.

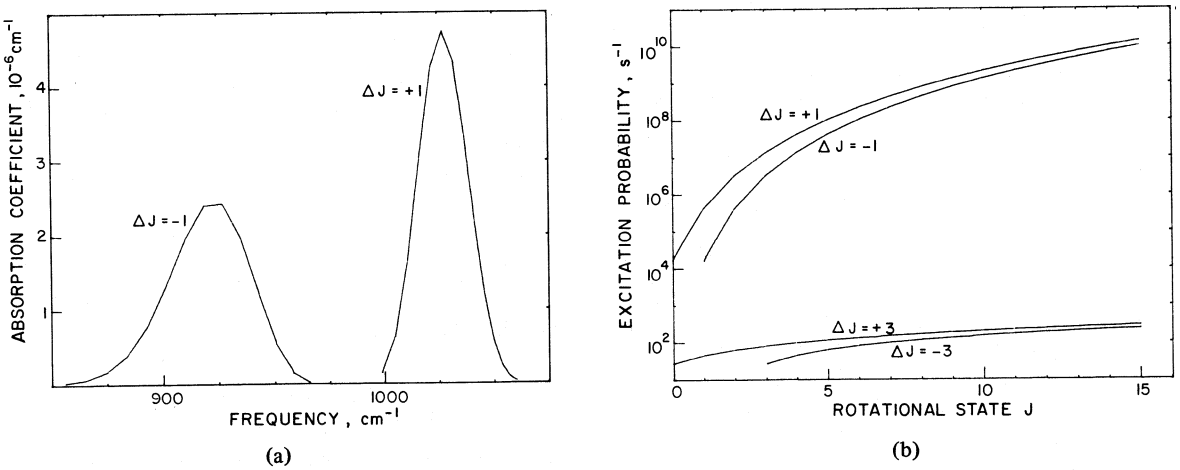


Fig. 2. Three-photon excitation of one quantum of vibration in hydrogen chloride. Radiation intensity is 10^{11} W/cm^2. (a) Three-photon absorption coefficient in 10^{-6} cm^{-1} as a function of frequency in cm^{-1}. (b) Dependence of the excitation probability in s^{-1} on rotational quantum number, for $\Delta J = \pm 1$ and $\Delta J = \pm 3$ processes.

$10^{-3}M_0$ which occurs because the rotational contributions to the energy levels result in irregular level spacings.

A previous calculation [5] of the two-photon excitation probability in molecules ignores the effects of molecular anharmonicity. This means, in the terminology presented here, $X = 0$. This neglect can lead to serious errors in the case of molecules with a small permanent dipole moment, in which $Y \ll X$. For example, the excitation probability in carbon monoxide is calculated using the method presented here to be three orders of magnitude larger than the value taking $X = 0$. The results of this paper indicate that the neglect of molecular anharmonicity always results in large errors. This occurs because the distortion of the harmonic oscillator levels due to the anharmonicity is never negligible compared to that due to the rotational contribution to the energy.

Figs. 1 and 2 examine the two-photon processes in carbon monoxide and the three-photon processes in hydrogen chloride. The excitation probability is shown in Fig. 1(b) and Fig. 2(b) for different J levels. Figs. 1(a) and 2(a) show the frequency variation of the intensity-dependent absorption coefficient. This quantity is proportional to the product of the excitation probability for a J level and the probability that the particular J level is occupied. These plots are done with the formulas (9)-(12) and with a formula from Table III for the two-photon processes. A second-order approximation expression was used for Fig. 2. The matrix elements are from [7] and [8] for CO and HCl, respectively, while spectroscopic

information is from Herzberg [9]. In both cases, a homogeneous linewidth of 10^8 s^{-1} was assumed and saturation effects were neglected.

The CO excitation spectrum contains O, Q, and S branches corresponding to $\Delta J = 2$, 0 and -2, respectively. Similarly, the HCl spectrum has $\Delta J = \pm 1$ and $\Delta J = \pm 3$ branches, but the $\Delta J \pm 3$ branches are not visible on the linear scale of Fig. 2(a). Note that the radiation intensity (10^9 W/cm^2) required for the observation of two-photon processes is typical of the focused output of a TEA laser or the unfocused output of a mode-locked TEA laser. However, for three-photon processes, a high intensity (10^{11} W/cm^2) is required.

IV. Influence of Electronic States on Two-Photon Transitions

The excited electronic states of the molecule have to this point been neglected in performing the sum over states in (2). When the summation is extended over electronic states, for two-photon transitions (2) is replaced by

$$K(2; v'', \rho''; v', \rho') = \sum_{\epsilon} \sum_{v_\epsilon} \sum_{\rho} \cdot \frac{\langle g v' \rho' | \vec{\mu} \cdot \hat{p} | \epsilon v_\epsilon \rho \rangle \langle \epsilon v_\epsilon \rho | \vec{\mu} \cdot \hat{p} | g v'' \rho'' \rangle}{\omega_{\epsilon v_\epsilon \rho} - \omega_{g v'' \rho''} - \omega_R}. \quad (13)$$

Here the intermediate state is in the electronic state ϵ and has vibrational and rotational quantum numbers denoted by v_ϵ and $\rho = \{J, \Lambda, M\}$.

With the matrix elements expressed by (A2) of the Appendix, (13) becomes

$$K(2; v'', \rho''; v', \rho') = \sum_{\epsilon} \sum_{\rho} L_e(2; v'', v', \{J\}) f(\rho', \rho) \cdot f(\rho, \rho''), \quad (14)$$

where

$$L_e(2; v'', v', \{J\}) = \sum_{v_\epsilon} \cdot \frac{\langle v' | R_{g\epsilon}(r) | v_\epsilon \rangle \langle v_\epsilon | R_{g\epsilon}(r) | v'' \rangle}{\omega_{\epsilon v_\epsilon \rho} - \omega_{g v'' \rho''} - \omega_R}. \quad (15)$$

The last summation involves a product of Franck-Condon amplitudes (FCA) divided by an energy difference. When considering excited electronic states, the FCA integrals ensure that only a few vibrational levels will contribute significantly to the summation. Because of this, and because the electronic energy is typically much greater than the vibrational and rotational contribution to the energy, the energy difference in the denominator is replaced by an average energy difference $\Delta\omega_e$ which depends only on the particular electronic state. Then the sum over vibrational levels of the excited electronic state can be performed by assuming the (bound and free) vibrational states form a complete set. The result is

$$L_e(2; v'', v', \{J\}) = \langle v' | R_{g\epsilon}(r)^2 | v'' \rangle / \Delta\omega_e, \quad \epsilon \neq g. \quad (16)$$

This expression now involves an integral of the electronic transition moment over vibrational states of the ground electronic state. These vibrational states are low lying ($v = 0, 1, 2, \cdots$) and anharmonic oscillator matrix elements are an adequate approximation.

To evaluate L_e for any particular case requires the expansion of $R_{g\epsilon}(r)$ around the equilibrium nuclear separation of the ground electronic state as in (A4). For example, for two-photon excitation of the first vibrational level,

$$L_e(2; 0, 1, \{J\}) = \frac{R_{\epsilon g}(0)}{\sqrt{2\alpha_0}\Delta\omega_e} \frac{\partial R_{\epsilon g}}{\partial \zeta} \quad (\epsilon \neq g). \quad (17)$$

For electronic states with $\Lambda = 0$, the rotational terms in (14) are identical to those previously calculated in Section II. Then the consideration of these electronic states alters the value of the parameter X previously calculated,

$$X = X' + \sum_{\epsilon \neq g} L_e. \quad (18)$$

X' is a value calculated for example by one of the formulas in Table III, and L_e is evaluated by (16). The sum over electronic states is limited to those for which $\Lambda = 0$.

The consideration of electronic states with $\Lambda \neq 0$ requires rotational matrix elements more complicated than (A1) and hence involves a new solution to the rotational problem. It has been suggested [10] that $R_{g\epsilon}(r)$ should vary more strongly for the perpendicular band systems ($\Delta\Lambda \neq 0$) in which the electron cloud changes significantly than for the parallel band systems ($\Delta\Lambda = 0$). In neither case are sufficient data for the electronic transition moment available. Using the ground-state dipole moment (R_{gg}) as a rough approximation for the electronic transition moment ($R_{g\epsilon}$) yields a value for the change in X [i.e., for (17)] which is of the same order as that calculated from Table III. Since X^2 enters into the final solutions (9) and (10) for the excitation probability, the calculations are accurate to a factor of 4. Higher accuracy may be obtained for light molecules in which the large rotational constant results in $Y > X$.

The unavailability of data for the electronic transition moment limits the accuracy of the calculations, as indicated above. These data are, in general, difficult to obtain because of lack of accurate knowledge about the potential curve for the excited electronic states [19]. Equation (16) involves an integral of the electronic transition moment over vibrational states of the ground electronic state. Since the wave functions for these states are well known, careful measurements of the multiphoton transition probabilities will result in knowledge about the electronic transition moment.

V. Polyatomic Molecules

The formalism developed in Section II is not limited to diatomic molecules. However the specific formulas developed are applicable only to molecules for which the rotational contribution to the energy is given by $BJ(J+1)$. Thus we consider only linear and spherical top molecules. There may be additional contributions to the $g(\omega)$, the density of states, from degenerate energy levels. The Coriolis coupling between degenerate states [11] is neglected in this treatment.

The formulas presented in Tables III and IV are applicable to

the multiphoton excitation of a polyatomic molecules. However, the sum over states is modified by the presence of the other modes of vibration. The largest contribution to the sum over vibrational states comes from terms which involve the harmonic oscillator matrix elements, or as few anharmonic matrix elements as possible. For example, consider two-photon excitation of the state $|v+1, 0, 0, \cdots>$ from the state $|v, 0, 0, \cdots>$. The intermediate states $|v, 1, 0, \cdots>$, etc. can now make a contribution to the summation. The result is

$$X = X' + \sum_i \frac{M_{01}^{(i)} M_{01}^{(1,i)} (v+1)^{1/2}\, 2\omega_i}{\omega_i^2 - \omega^2/4} \tag{19}$$

and

$$Y = Y' + 2B(v+1)^{1/2} \sum_i \frac{M_{01}^{(i)} M_{01}^{(1,i)}}{\omega_i^2 - \omega^2/4} \tag{20}$$

where X' and Y' are the results from Table III. The terminology for the matrix elements is explained in the Appendix. The sum extends over all the normal modes of the molecule (which have a vibrational frequency ω_i) except the particular mode being excited which has a frequency $\omega \sim 2\omega_R$. If one fundamental frequency ω_i is close to $\omega/2$, then one term in the sum over states would dominate the rest and the general formalism developed in Section II is not valid. Treatment of this special case is reserved for the next section.

We can also consider the excitation of combination modes. It is found, for example, for the two-photon excitation of $|1, 1, 0 \cdots>$ from $|0, 0, \cdots>$, that

$$X = -\frac{4M_{01}^{(1)} M_{01}^{(2)} (\omega_{1,0} + \omega_{0,1} - \omega_{1,1})}{(\omega_{1,0} - \omega_{0,1})^2} \tag{21}$$

and

$$Y = -\frac{8BM_{01}^{(1)} M_{01}^{(2)}}{(\omega_{1,0} - \omega_{0,1})^2}. \tag{22}$$

Note that X depends on the anharmonicity of the molecule and Y depends on B/ω.

Similar examples could also be derived for three-photon transitions.

VI. Quasi-Resonant Cases

A quasi-resonant case occurs when a real state of the quantum system is close enough in energy to the virtual states in the summation over states (2) for that particular state to dominate the summation. Of course if the resonance is exact, there is no N photon transition but rather two successive transitions of lower order (see, however, [11]).

The quasi-resonant case is of special interest because the small size of the energy difference can greatly increase the probability of the N photon transition. This case, however, cannot be considered by the general method of Section II, and an alternate derivation is necessary.

For two-photon processes, let g, f, and i denote the initial, final, and quasi-resonant states, respectively, and let M_{ig} and M_{fi} be the relevant vibrational matrix elements. Then

$$L = \frac{M_{fi}M_{ig}}{\Delta\omega + Bb},$$

where $\Delta\omega$ is the vibrational energy difference between the intermediate state and the midpoint between the final and initial states. It follows that

$$W = 2\pi g(2\omega_R)\,(2\pi\alpha_f F\omega_R)^2 \left(\frac{M_{fi}M_{ig}}{\Delta\omega - B}\right)^2 F_{2R}(\gamma) \tag{23}$$

for

$$\gamma = \pm 2,$$

and

$$W = \frac{2\pi g(2\omega_R)\,(2\pi\alpha_f F\omega_R)^2\,(M_{fi}M_{ig})^2}{(\Delta\omega - 2JB)^2\,(\Delta\omega + 2B(J+1))^2} \times \left[\left\{\Delta\omega^2 - 4\Delta\omega B + \frac{36(J^2+J)B^2}{(2J-1)(2J+3)}\right\} \cdot F_{2R}(\gamma) - \frac{4B(2J+1)}{3(2J-1)(2J+3)} \cdot \left\{\Delta\omega - \frac{36B(J^2+J)}{(2J-1)(2J+3)5}\right\}\right] \tag{24}$$

for

$$\gamma = 0.$$

In (24) the terms not proportional to $F_{2R}(\gamma)$ are negligible for higher values of J. The Q-branch probability becomes very large for $J \sim \Delta\omega/2B$ (or for $J = 1 - \Delta\omega/2B$ if $\Delta\omega < 0$). All the O- and S-branch transition probabilities are enhanced because of the small size of the denominator.

For three-photon processes in which there is a near resonance between the real states of the molecule and both the first and second virtual states,

$$L = \frac{M_{f2}M_{21}M_{1g}}{(\Delta\omega_2 + Bb_2)(\Delta\omega_1 + Bb_1)},$$

where

$$\Delta\omega_1 = \omega_1 - \omega_g - \frac{\omega_f - \omega_g}{3}$$

and

$$\Delta\omega_2 = \omega_2 - \omega_g - \tfrac{2}{3}(\omega_f - \omega_g).$$

Here ω_g, ω_f, ω_1, ω_2 are, respectively, the vibrational energies of the initial, final, first intermediate, and second intermediate states. M_{f2}, M_{21}, and M_{1g} are the vibrational matrix elements for one-photon transitions between the levels. Summing over rotational states yields the following results for the three-photon excitation probability:

$$W = 2\pi g(3\omega_R) \cdot (2\pi\alpha_f F\omega_R)^3 F_{3R}(-1) \cdot \left|\frac{M_{f2}M_{21}M_{1g}}{(\Delta\omega_2 - 2B)(\Delta\omega_1 - 2B)}\right|^2 F_{3R}(\gamma) \tag{25}$$

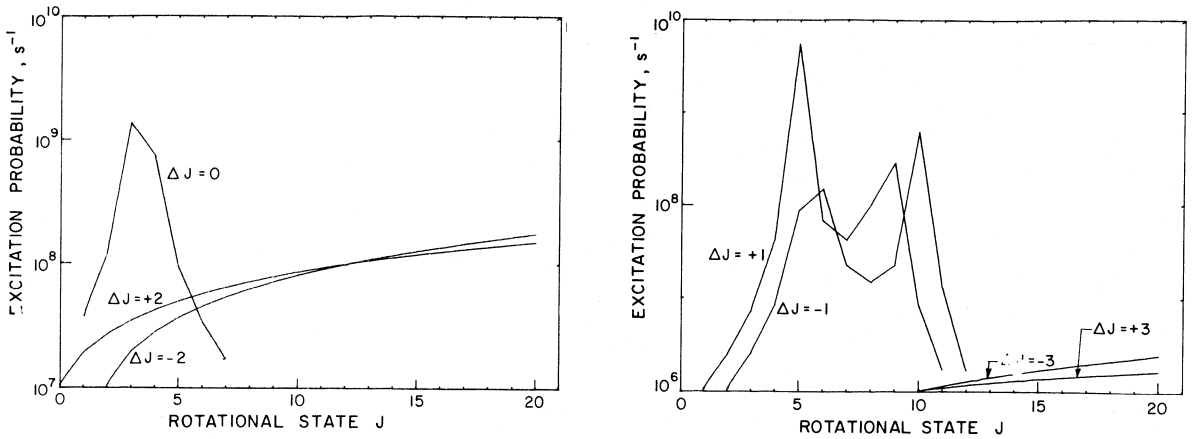


Fig. 3. Quasi-resonant excitation in carbon monoxide: dependence of the excitation probability on rotational quantum number. (a) Two-photon processes induced by radiation intensity of 10^7 W · cm^{-2}. (b) Three-photon processes induced by radiation intensity of 10^7 W · cm^{-2}.

for $\gamma = \pm 3$, and

$$W = 2\pi g(3\omega_R) \cdot (2\pi\alpha_f F\omega_R)^3 F_{3R}(-1) \cdot \left[V_1^2 - \frac{2}{3} V_1 V_2 \frac{2J^2 - 9}{6J^2 - 13} + \frac{1}{9} V_2^2 \frac{38J^2 - 45}{6J^2 - 13}\right] \Big/ \cdot \left[\left(\Delta\omega_2 + \frac{4JB}{3}\right)\left(\Delta\omega_2 + 2B - \frac{8JB}{3}\right) \cdot \left(\Delta\omega_1 - \frac{4JB}{3}\right)\left(\Delta\omega_1 + 2B + \frac{8JB}{3}\right)\right]^2 \quad (26)$$

for $\gamma = -1$, where

$$V_1 = \Delta\omega_1 \Delta\omega_2 - \tfrac{4}{3} BJ(\Delta\omega_1 - \Delta\omega_2) + B(\Delta\omega_1 + \Delta\omega_2)$$

and

$$V_2 = 4B^2 + B(\Delta\omega_1 + \Delta\omega_2).$$

The result for $\gamma = \pm 1$ is most easily found by interchanging $\Delta\omega_1$ and $\Delta\omega_2$ and replacing J by $J + 1$ in the expression for $\gamma = -1$.

Particular cases of great interest are two-photon excitation of the second vibrational level and three-photon excitation of the third vibrational level. Because of anharmonicities the vibration–rotation energies of the intermediate vibrational states will not coincide with single-photon energies. However, the transition probabilities are enhanced, as discussed above. For the two-photon transition $\Delta\omega = \omega x - 4.5\,\omega y$ and for three-photon transitions $\Delta\omega_1 = 2\omega x - 11\omega y$, $\Delta\omega_2 = 2\omega x - 65\omega y$. Here ωx is the first-order anharmonic correction to the vibrational energy and ωy is the second-order correction [9]. These two- and three-photon transitions are illustrated in Figs. 3 and 4 for carbon monoxide. The three-photon transition probabilities become very large for rotational levels such that the energy difference between the vibrational–rotational states and the virtual states is minimized. This occurs at different J values for the first and second virtual states and hence the $\Delta J = \pm 1$ branches of the transition probability each have two maxima. Note that the radiation intensities required for two- and three-photon excitation (10^7 and 10^8 W/cm^2, respectively) are considerably smaller than in the nonresonant case. It has been suggested [13] that these processes constitute the first step in the collisionless dissociation of polyatomic molecules by infrared radiation. The intensities calculated for three-photon processes agree with those employed in the experiments [14].

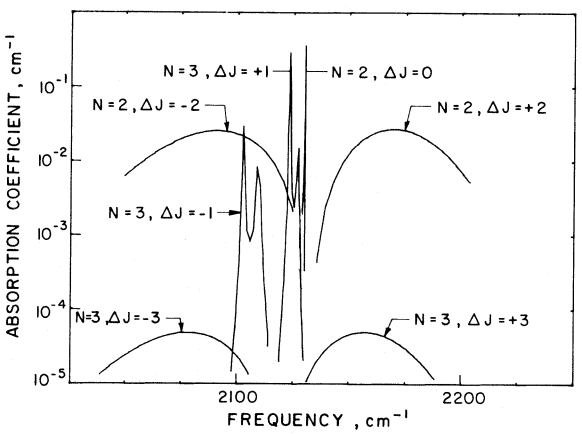


Fig. 4. Quasi-resonant excitation in carbon monoxide: absorption coefficient in cm^{-1} as a function of frequency in cm^{-1}: intensity for two-photon processes and for three-photon processes as in Fig. 3.

VII. Approximation and Limitations

An approximation consistently made in the formalism is the neglect of vibrational–rotational interaction, in particular: 1) the dependence of the rotational constant B on the vibrational state, 2) the centrifugal distortion constant, and 3) the rotational contribution to the vibrational transition matrix elements. The first point above could be considered by redefining $\Delta\omega'_{v1}$ and $\Delta\omega''_{v2}$ in (5) and (7) to include the nonequality of the rotational constants. For two-photon excitation of the first vibrational level, the resulting change in the value of X is given by

$$\frac{\Delta X}{X} = \frac{B_1 - B_0}{\omega}\left[J(J+1) + \frac{M_0}{2M_1}\gamma(2J + 1 + \gamma)\right].$$

For CO, $(B_1 - B_0)/\omega \sim 8 \times 10^{-6}$ so the change is clearly negligible. Similarly, the centrifugal distortion is expected to have a negligible effect.

The rotational contribution to the vibrational transition matrix elements was evaluated for $\Delta v = 2$ transitions from the formulas given in [8]. It was found that the rotational contribution was typically 2 percent of the contribution from mechanical and electrical anharmonicity. It was therefore neglected.

The second-order correction to vibrational level spacings $\omega y(v + \frac{1}{2})^2$ was also neglected. In cases where the largest term is proportional to x, the second-order correction can be expected to have an effect of approximately y/x. Except in the quasi-resonant case, other factors are expected to have a larger effect on the accuracy of the calculation.

A more fundamental question is whether the expressions (6) and (8) do accurately represent the sum over states (4). This was checked for two cases by comparing the approximate solutions (9)-(12) with a summation over states [(1) and (2)] performed by computer. The results are shown in Table V for three molecules, CO, HCl, and a polyatomic molecule with no permanent dipole moment. The zeroth-order approximation corresponds to neglecting all terms except the first in (6) and (8). The first-order approximation includes the terms in X and Y for two-photon processes, and the terms T, U, V, and Y for three-photon processes. The second-order approximation involves all the terms of (6) and (8), evaluated using the method of Section III.

As can be seen from Table V, the zeroth-order approximation was adequate for the polyatomic molecule with no permanent moment, for two-photon processes. HCl, which has a large dipole moment, requires a higher degree of approximation for accurate results. Generally, three-photon processes required one more degree of approximation than did two-photon processes.

The results presented in this paper are for excitation by linearly polarized light and for molecules with $\Lambda = 0$ in the ground electronic state. The extensions to circularly polarized light and to molecules with $\Lambda \neq 0$ are straightforward but expected to be algebraically tedious. Only linear and spherical top polyatomic molecules are covered, but once again, the extension to a more general case is straightforward.

The lack of any reliable data for the electronic transition moment $R_{g\epsilon}(r)$ precludes the accurate calculation of multiphoton transition probabilities in molecules, except in the quasi-resonant case. The inclusion of the data when available for transitions with $\Lambda = 0$ is described in this paper. Further work is necessary to include electronic states with $\Lambda \neq 0$.

The dependence of molecular linewidths on radiation intensity has not been considered. Such dependence can result from saturation of the multiphoton transition, a case that is easily considered but does not contribute to the physics of this problem. In addition, power broadening can result when the lifetime of the upper state of the multiphoton transition is limited by absorptive transitions to higher states. In this case, the different excitation steps are coupled [12] and cannot be treated independently. Power broadening can also result from the ac Stark shifts induced by the electric field of the radiation

TABLE V
COMPARISON OF APPROXIMATE CALCULATION WITH COMPUTER SUMMATION

Order of Approximation		Ratio of Calculated Values		
		Zeroth	First	Second
Two Photon Processes	$2\omega_R = \omega$			
Carbon Monoxide	$\gamma = 0$	0.8	1.12	
	$\gamma = -2$	1.2	1.05	
Hydrogen Chloride	$\gamma = 0$	0.15	0.94	
	$\gamma = -2$	115	2.1	
Polyatomic Molecule	$\gamma = 0$	0.99	0.99	
	$\gamma = -2$	1.03	1.03	
Three Photon Excitation	$3\omega_R = 2\omega$			
Carbon Monoxide	$\gamma = 3$	2.4	0.97	0.97
	$\gamma = -1$	0.76	1.7	0.99
Hydrogen Chloride	$\gamma = 3$	29	0.92	0.93
	$\gamma = -1$	0.49	3.5	1.02
Polyatomic Molecule	$\gamma = 3$	1.52	0.99	0.99
	$\gamma = -1$	0.83	0.92	1.00

[15]. The ac Stark shifts relax the resonant condition, increase the likelihood of the quasi-resonant case, and increase the probability of a sequential excitation to a higher level. Because of these complicating factors, the simple excitation problem presented here is not applicable for high intensity levels that produce these line-broadening effects.

VIII. CONCLUSIONS

An approximation method has been developed for evaluating the two- and three-photon transition probabilities among low-lying vibrational levels of diatomic and polyatomic molecules. The method considers explicitly the rotation of the molecule, the mechanical and the electrical anharmonicity. For the quasi-resonant case, the two-photon and three-photon excitation probabilities are given by (23)-(26). When no near resonances occur, the calculation is divided into a vibrational problem (Sections III and V) and a rotational problem [(9)-(12)].

The transition probabilities predicted by these equations for the nonresonant case are limited in accuracy by the lack of accurate values for the electronic transition moment. The results should nevertheless be reliable to an order of magnitude. For quasi-resonant excitation, the electronic states have a negligible effect and the accuracy should be limited by the reliability of the spectroscopic data.

Direct experimental observation of these effects in molecules has been limited to the quasi-resonant case [16]. The results presented here indicate that two- and three-photon processes in the absence of a near-resonant intermediate state should be observable with the output of present-day lasers.

However, the calculated intensity necessary for the occurrence of nonresonant three-photon processes is sufficiently high (10^{11} W/cm^2) for the presence of large ac Stark shifts to invalidate the calculation. Gas breakdown [17] and the

collisionless dissociation of molecules [18] occur at lower intensities. In cases where the exciting radiation does not coincide in frequency with a strong absorption band of the molecule, it is possible that multiphoton transitions to low-lying vibrational levels are involved in the initial stages of these processes. Unfortunately, CO_2-laser breakdown thresholds for "clean" polyatomic and heteropolar diatomic gases are not available.

Appendix

The purpose of the Appendix is to introduce the notation concerning the dipole moment matrix elements.

Using the Born-Oppenheimer approximation, the wave functions appearing in (2) and (13) can be written as a product of an electronic wave function $|\epsilon\rangle$, a nuclear vibration wave function $|v\rangle$, and a rotational wave function $|\rho\rangle$. v is the vibrational quantum number, or, for polyatomic molecules, refers to the set of vibrational quantum numbers $\{v_1, v_2, \cdots\}$, while ρ denotes the set of rotational quantum numbers $\{J, \Lambda, M\}$.

The dipole moment $e\vec{\mu}$ is the sum over all particles (electrons and ions) of the product of the charge of each particle and its position. To evaluate the matrix element of the dipole moment, it is necessary to transform from the laboratory frame of reference (commonly defined by the radiation polarization $\hat{p}$) to the molecular frame. The matrix element of this transformation between the rotational eigenfunctions $|\rho\rangle$ and $|\rho''\rangle$ gives rise to a factor $f(\rho; \rho'')$.[1] For the special case of a transition between two states each with $\Lambda = 0$, induced by linearly polarized light,

$$f(J''+\alpha, 0, M; J'', 0, M'') = \sqrt{\frac{(J+(1+\alpha)/2)^2 - M^2}{(2J+\alpha)(2J+2+\alpha)}} \quad \text{for } M''=M,\ \alpha=\pm 1 \qquad \text{(A1)}$$

$$= 0, \quad \text{otherwise.}$$

The matrix element of $e\vec{\mu}$ between the electronic eigenfunctions $|\epsilon\rangle$ and $|g\rangle$ results in the "dipole moment" $eR_{g\epsilon}$. Thus [19]

$$\langle \epsilon v_\epsilon \rho | \vec{\mu} \cdot \hat{p} | g v' \rho' \rangle = f(\rho; \rho') \langle v_\epsilon | R_{g\epsilon} | v' \rangle \qquad \text{(A2)}$$

where

$$R_{g\epsilon} = \hat{q} \cdot \frac{1}{e} \left[\langle \epsilon | \sum_j -e\vec{r}_j | g \rangle + \delta_{\epsilon g} \sum_i q_i \vec{R}_i \right]. \qquad \text{(A3)}$$

Here $\hat{q}$ is a unit vector along the symmetry axis of the molecule, $\vec{r}_j$ and $\vec{R}_i$ are the positions in the molecular frame of reference of the jth electron and ith ion, respectively. q_i is the charge of the ith ion.

The dipole moment $R_{g\epsilon}$ is in general a function of the internuclear separation. It is convenient to expand $R_{g\epsilon}$ around the equilibrium separation in terms of the mass weighted normal coordinate ζ. Then the dipole moment and the potential energy function of a diatomic molecule are

$$R_{g\epsilon}(\zeta) = R_{g\epsilon}(0) + \frac{\partial R_{g\epsilon}}{\partial \zeta} \zeta + \frac{1}{2} \frac{\partial^2 R_{g\epsilon}}{\partial \zeta^2} \zeta^2 \qquad \text{(A4)}$$

and

$$V = \tfrac{1}{2} \omega^2 \zeta^2 - \gamma_0 \zeta^3, \qquad \text{(A5)}$$

where

ω = angular frequency;
ζ = normal coordinate for the molecular motion;
$= \sqrt{M_R}\,(r - r_e)$ for diatomic molecules;
M_R = reduced mass of a diatomic molecule.

γ_0 is determined from the anharmonic correction to the vibrational energy levels, which is given by

$$\omega x = 15\gamma_0^2 \hbar^2 / 4\omega^4. \qquad \text{(A6)}$$

Transitions between two vibrational levels of the ground electronic state are a special case of the above. Then using anharmonic oscillator vibrational wave functions,

$$\langle n | R_{gg} | m \rangle = \left[R_{gg}(0) + \left[\frac{\hbar}{4\omega} \frac{\partial^2 R_{gg}}{\partial \zeta^2} - \frac{3\gamma_0}{2\hbar\omega} \left(\frac{\hbar}{\omega} \right)^2 \frac{\partial R_{gg}}{\partial \zeta} \right] (2n+1) \right] \delta_{mn} + \left[\frac{\gamma_0}{2\hbar\omega} \left(\frac{\hbar}{\omega} \right)^2 \frac{\partial R_{gg}}{\partial \zeta} + \frac{\hbar}{4\omega} \frac{\partial^2 R_{gg}}{\partial \zeta^2} \right] \sqrt{n(n+1)} \cdot \delta_{m-1,n+1} + \sqrt{\frac{\hbar}{2\omega}} \frac{\partial R_{gg}}{\partial \zeta} \sqrt{n+1}\, \delta_{m,n+1}. \qquad \text{(A7)}$$

In this paper, M_0, M_1, M_2 are defined as dimensionless quantities such that

$$\langle n | R_{gg} | n \rangle = M_{01} [M_0 + M_1 (2n+1)]$$

and

$$\langle n-1 | R_{gg} | n+1 \rangle = M_{01} M_2 \sqrt{n(n+1)} \qquad \text{(A8)}$$

where

$$M_{01} = \langle 0 | R_{gg} | 1 \rangle = \sqrt{\frac{\hbar}{2\omega}} \frac{\partial R_{gg}}{\partial \zeta}.$$

Note that if $\partial^2 R_{gg}/\partial \zeta^2 = 0$ then $M_1 = -3M_2$ and $M_2 = \sqrt{2x/15}$.

For a polyatomic molecule with normal coordinates ζ_i associated with modes of energy $h\omega_i$,

$$R_{gg} = R_{gg}(0) + \sum_i \frac{\partial R_{gg}}{\partial \zeta_i} \zeta_i + \sum_i \sum_j \frac{\partial^2 R_{gg}}{\partial \zeta_i \partial \zeta_j} \zeta_i \zeta_j. \qquad \text{(A9)}$$

Then

$$M_{01}^{(i)} \equiv \langle v, o, \cdots | R_{gg} | v, 1, \cdots \rangle = \sqrt{\frac{h}{2\omega_i}} \frac{\partial R_{gg}}{\partial \zeta_i},$$

and $M_{01}^{(i,j)}$ involving a simultaneous change in the quantum numbers associated with two different normal modes is defined by

[1] The Hönl–London line intensity factors [9] result from $|f(\rho; \rho'')|^2$ summed over the values of M and M''.

$$M_{01}^{i,j} = \langle v_i = v_j = 0 | R_{gg} | v_i = v_j = 1, v_k = \cdots = 0 \rangle = \sqrt{\frac{\hbar^2}{4\omega_i\omega_j}} \frac{\partial^2 R_{gg}}{\partial\zeta_i \partial\zeta_j}. \quad \text{(A10)}$$

Acknowledgment

The authors gratefully acknowledge valuable discussions with Dr. R. J. Le Roy.

Note Added in Proof: $g(\omega)$ in (1) is the density of states. α_0 in (17) is $\omega\hbar$.

References

[1] W. L. Peticolas, "Multiphoton spectroscopy," *Ann. Rev. Phys. Chem.*, vol. 18, pp. 233–260, 1967.

[2] K. B. Eisenthal, W. L. Peticolas, and K. E. Rieckhoff, "Laser induced luminescence and dissociation in biphenyl," *J. Chem. Phys.*, vol. 44, pp. 4492–4497, 1966.

[3] F. V. Bunkin and I. I. Tugov, "Multiphoton processes in heteropolar diatomic molecules," *Phys. Rev. A*, vol. 8, pp. 620–625, 1973; see also references therein.

[4] G. J. Pert, "The dissociation of molecules by intense infrared radiation," *IEEE J. Quantum Electron.*, vol. QE-9, pp. 435–444, 1973.

[5] A. L. Golger and V. S. Letokhov, "Two-photon resonant excitation of vibrational levels of diatomic molecules by laser radiation," *Sov. J. Quantum Electron.*, vol. 4, pp. 478–484, 1974.

[6] H. B. Bebb and A. Gold, "Multiphoton ionization of hydrogen and rare-gas atoms," *Phys. Rev.*, vol. 143, pp. 1–24, 1966.

[7] L. A. Young and W. J. Eachus, "Dipole moment function and vibration-rotation matrix elements for CO," *J. Chem. Phys.*, vol. 44, pp. 4195–4206, 1966.

[8] S. S. Penner, *Quantitative Molecular Spectroscopy and Gas Emissivities*. Reading, MA: Addison-Wesley, 1959.

[9] G. Herzberg, *Molecular Spectra and Molecular Structure*, Vol. I: *Spectra of Diatomic Molecules*. New York: Van Nostrand-Reinhold, 1950.

[10] R. W. Nicholls, "Laboratory astrophysics," *J. Quant. Spect. Rad. Trans.*, vol. 2, pp. 433–449, 1962.

[11] G. Herzberg, *Molecular Spectra and Molecular Structure*, vol. II: *Infrared and Raman Spectra of Polyatomic Molecules*. Princeton, NJ: Van Nostrand, 1945.

[12] P. Lambropoulos, "Theory of multiphoton ionization: Near-resonance in two-photon ionization," *Phys. Rev. A*, vol. 9, pp. 1992–2013, 1974.

[13] N. Bloembergen, "Comments on the dissociation of polyatomic molecules by intense 10.6 μm radiation," *Opt. Comm.*, vol. 15, pp. 416–418, 1975.

[14] R. V. Ambartzumian and V. S. Letokhov, "Isotopically selective photochemistry," *Laser Focus*, vol. 11, pp. 48–52, July 1975.

[15] A. M. Bonch-Bruevich and V. A. Khodovoi, "Current methods for the study of the Stark effect in atoms," *Sov. Phys. Uspekhi*, vol. 10, pp. 637–657, 1967.

[16] W. K. Bischel, P. J. Kelly, and C. K. Rhodes, "Observation of Doppler-free two-photon absorption in the υ_3 band of CH_3F," *Phys. Rev. Lett.*, vol. 34, pp. 300–303, 1975.

[17] I. P. Shkarofsky, "Review of gas-breakdown phenomena induced by high power lasers," *RCA Review*, vol. 35, pp. 48–78, 1974.

[18] N. R. Isenor, V. Merchant, R. S. Hallsworth, and M. C. Richardson, "CO_2 laser-induced dissociation of SiF_4 molecules into electronically excited fragments," *Canadian J. Phys.*, vol. 51, pp. 1281–1287, 1973.

[19] B. H. Armstrong and R. W. Nicholls, *Emission, Absorption and Transfer of Radiation in Heated Atmospheres*. Oxford, England: Pergamon, 1972, ch. 4.

The Measurement of Far-Infrared Laser Gain and Loss Using a Michelson Coupler

P. WOSKOBOINIKOW, STUDENT MEMBER, IEEE, AND W. C. JENNINGS, MEMBER, IEEE

Abstract—**It is demonstrated that small values of small-signal gain and total internal losses in far-infrared lasers can, in principle, be determined by measuring the optimum and threshold output coupling coefficients with a Michelson coupler. Experimental results show that although accurate determination of the small-signal gain can be made, only a good approximation of the internal losses is obtained by this method. The gain of the 220-μm transition of H_2O is shown to increase from 0.24 percent m^{-1} to 0.43 percent m^{-1} with the addition of helium to 0.25 torr H_2O at a discharge current of 1.8 A.**

Manuscript received March 29, 1976; revised May 26, 1976.

P. Woskoboinikow was with the Electrical and Systems Engineering Department, Rensselaer Polytechnic Institute, Troy, NY 12181. He is now with the Francis Bitter National Magnet Laboratory, Massachusetts Institute of Technology, Cambridge, MA 02139.

W. C. Jennings is with the Electrical and Systems Engineering Department, Rensselaer Polytechnic Institute, Troy, NY 12181.

SMALL-SIGNAL GAIN is an important parameter in the development and testing of laser models. In far-infrared gas discharge lasers, small-signal gain is typically on the order of 1 percent m^{-1} [1] and, therefore, is difficult to measure precisely with a gain cell. An alternate technique for determining small-signal gain is with the use of a variable output coupled laser to measure the threshold coupling or optimum coupling coefficient. Small-signal gain can then be calculated if all the losses in the laser, other than the output coupling loss, are known. Previously, small-signal gain of far-infrared lasers was determined in this way by Ulrich *et al.* [2] using a variable mesh coupler and by Bradley [3] using a Michelson coupler. In both cases an approximation was made for the other losses in the laser besides the output coupling loss. In

this paper we show that a Michelson coupled CW laser can be used to measure the threshold and optimum coupling coefficients simultaneously, allowing both the small-signal gain and the losses in the laser to be calculated. This technique is demonstrated by making some typical measurements on the 220-μm transition of a water vapor laser.

For a homogeneously broadened transition, the small-signal gain per unit length is related to the threshold and optimum coupling coefficients by the following two equations:

$$g = \frac{t_t + a}{2L} \tag{1}$$

$$g = \frac{(t_o + a)^2}{2La} \tag{2}$$

where g is the small signal gain; t_t and t_o are the threshold and optimum coupling coefficients, respectively; a represents all the other losses in the laser besides the output coupling loss; and L is the length of the discharge region. These equations are obtained by requiring that under steady-state conditions in a CW laser, the total gain is equal to the total losses. Equation (1) is for a laser oscillating at threshold and (2) is for a laser oscillating at optimum power levels.

The assumption of homogeneous broadening is not entirely correct since both homogeneous and inhomogeneous mechanisms contribute about equally to the 220-μm transition of H_2O [4]. The Doppler broadened width can be calculated to be about 5 MHz for a water vapor temperature of 500 K [5], and pressure broadening for these same conditions has also been determined to be about 5 MHz [6]. The analog of (2) for inhomogeneous broadening is

$$g = \frac{(t_o + a)^2}{2L\,(a^2 - t_o^2)^{1/2}}. \tag{3}$$

Clearly for $a^2 \gg t_o^2$, this reduces to the same expression as (2). This condition was generally true for the conditions reported here, and hence (2) was employed for all calculations presented.

Equations (1) and (2) can be combined to yield an expression for the losses in the laser, a, in terms of the coupling coefficients t_t and t_o:

$$a = \frac{t_o^2}{t_t - 2t_o}. \tag{4}$$

Thus the measurements of t_t and t_o are first used to calculate a, after which either (1) or (2) may be used to determine the small-signal gain.

The details of the Michelson coupled laser are shown in Fig. 1. It was constructed of Pyrex pipe sections with an internal diameter of 10 cm. Flat mirrors were used in the Michelson coupler and a mirror with a radius of curvature of 4.1 m was used at the other end. Two different beam splitters placed at 45° to the laser axis were used, one made of polyethylene and another made of biaxially oriented polypropylene. Table I gives their important parameters.

Moving the output coupling mirror through one-quarter of a wavelength theoretically varies the output coupling from 0 to $4|RT|^2$ where R and T are the fraction of the amplitude, polarized parallel to the plane of incidence, that would be reflected and transmitted, respectively, by the beam splitter if it were not in the Michelson coupler [7]. R and T depend on the index of refraction, the thickness, and the angle that the beam splitter makes with the laser axis. By choosing these values properly, it is possible to make $4|RT|^2$ large enough so that the laser can be tuned through both optimum and threshold coupling.

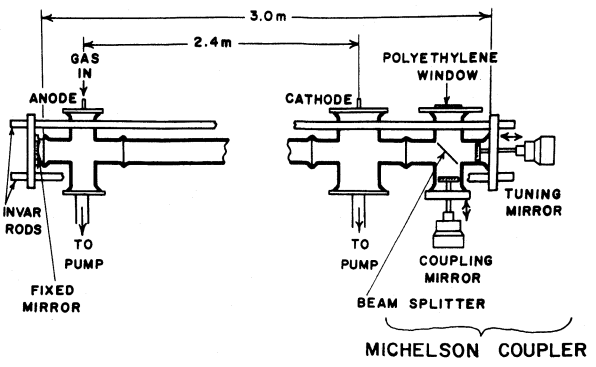


Fig. 1. Laser details.

TABLE I
BEAM SPLITTER PARAMETERS

Material	Index of Refraction	Thickness (μm)	Maximum Output Coupling, $4\|RT\|^2$ (%)
Polyethylene	1.52[1]	6.5	0.9
Polypropylene	1.50[2]	8.0	1.2

[1] See [8].
[2] Determined by measuring the Brewster angle of the beam splitter in the far infrared.

Fig. 2 shows some curves of laser output power as the coupling mirror is moved through half a wavelength. These curves were taken on the 220-μm transition of H_2O with the polyethylene beam splitter. Each successive curve from a to e was taken with an increasing amount of helium added to 0.25 torr of water vapor at a discharge current of 1.8 A. It has been shown previously [5] that the addition of helium to water vapor for these conditions causes a large increase in laser power. The coupling coefficient can be calculated by using the following relation

$$t = 4|RT|^2 \cos^2 \theta \tag{5}$$

where $\theta = 2\pi x/\lambda$ and x is the position of the coupling mirror in wavelength units. Note that for the first four curves the laser can be overcoupled to such an extent that oscillation ceases. The threshold coupling coefficient is determined from where these curves intersect the abscissa. Optimum coupling is determined from the position of the peaks. In curve e the gain of the laser had increased so much by the addition of helium that the laser could no longer be tuned through threshold, though it could be overcoupled. This did not happen with the polypropylene beam splitter. In that case, the laser could

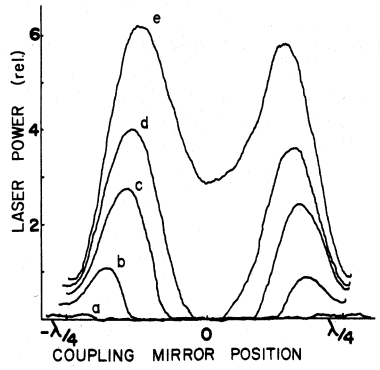


Fig. 2. Laser power versus coupling mirror position for increasing amounts of helium added to 0.25 torr H_2O at a discharge current of 1.8 A: *a* 0 torr He, *b* 0.03 torr He, *c* 0.08 torr He, *d* 0.13 torr He, *e* 0.22 torr He.

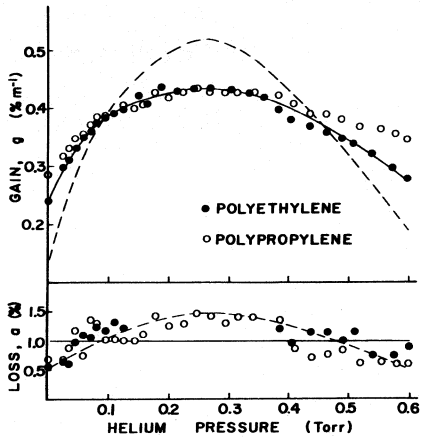


Fig. 3. Small-signal gain and laser losses versus helium pressure added to 0.25 torr H_2O at a discharge current of 1.8 A.

always be tuned through threshold because it had a higher maximum output coupling.

The results of using this technique to measure small-signal gain and laser losses are shown in Fig. 3. The measurements were made for the same discharge conditions as in Fig. 2. The small-signal gain peaks for the same mixture ratio of helium to water vapor as does the laser power, but the increase in power is about a factor of 8 while the small-signal gain is increased by less than a factor of 2 as shown. Small-signal gain was calculated by using (2) with the laser losses, a, taken to be constant at the median value of 1.0 percent. Though a shows a systematic scatter around 1.0 percent, it is not believed that it could actually vary in this way. Nevertheless, the dashed curves indicate how the small-signal gain would vary if the laser losses were allowed to vary smoothly from 0.5 to 1.5 percent as the data points seem to suggest.

The laser losses, a, are due to reflection loss at the mirrors, diffraction loss in the resonant cavity, absorption in the beam splitter, and scattering loss due to nonuniformities in the beam splitter. The latter two are believed to be the most dominant. There is no reason to believe that any of these losses would change as a function of helium pressure. A nonlinear effect in the beam splitter could explain a variation in the losses as a function of laser power, but at the low power densities 10^{-3} W · cm^{-2} maximum on the beam splitter, it was considered unlikely.

The systematic scatter in a can be explained as being inherent in the measurement technique itself. Examining the curves of Fig. 2 again, it can be seen that for minimum coupling conditions at $\pm(\lambda/4)$ the laser power output does not go to zero. This means that the Michelson coupler does not actually vary the coupling coefficient between 0 and $4|RT|^2$ but between some values larger than 0 and smaller than $4|RT|^2$. When gain is low, the optimum laser power peaks are near the minimum coupling condition, and, therefore, the calculated value for t_o is probably smaller than it actually is. The calculation of a is very sensitive to the value of t_o, since an error of only 5 percent in measuring t_o can lead to a calculation for a which is off by 50 percent. This would explain a systematic variation in a that decreases with gain.

The calculation of small-signal gain by (2) is relatively insensitive to small errors in t_o for constant a. An error in t_o of 5 percent would cause g to be off by only about 2 percent. Therefore, once a value can be established for the laser losses the calculation of small-signal gain will be fairly accurate even if there is a systematic variation in t_o.

As mentioned earlier, it is not entirely clear whether (2) or (3) is most applicable to the 220-μm transition. However, the measured values of t_o ranged from 0.2–0.4 percent, making any error introduced by the assumption of homogeneous broadening almost negligible. Other possible sources of error in determining gain and loss by this technique would be due to uncertainties in the index of refraction and thickness of the beam splitters. Such errors would have little effect on the shape of the gain curve but would displace it upward or downward. In spite of the possible sources of error this can be a fairly accurate method for determining small signal gains of less than 1 percent m^{-1} and a good way to approximate internal laser losses.

Acknowledgment

The authors wish to acknowledge C. J. Francke of Hercules Incorporated and T. Randall of the Union Carbide Corporation for providing them with the beam splitter materials.

References

[1] E. R. Mosburgh, Jr., "A study of the CW 28 μm water-vapor laser," *IEEE J. Quantum Electron.*, vol. QE-9, pp. 843–855, Aug. 1973.

[2] R. Ulrich, T. J. Bridges, and M. A. Pollack, "Variable mesh coupler for far infrared lasers," *Applied Optics*, vol. 9, pp. 2511–2516, Nov. 1970.

[3] C. C. Bradley, "Gain and frequency characteristics of a 20 mW CW water vapor laser oscillating at 118.6 μm," *Infrared Physics*, vol. 12, pp. 287–299, 1972.

[4] A. Yariv, *Quantum Electronics*, 2nd ed. New York: Wiley, 1975, ch. 8.

[5] P. Woskoboinikow and W. C. Jennings, "Improved CW laser action on the 118.6 and 220 μm H_2O transitions using helium and hydrogen," *Appl. Phys. Lett.*, vol. 27, pp. 658–660, Dec. 1975.

[6] W. S. Benedict and L. D. Kaplan, "Calculations of line widths in H_2O–H_2O and H_2O–O_2 collisions," *J. Quant. Spectrosc. Radiat. Transfer*, vol. 4, pp. 453–469, 1964.

[7] J. E. Chamberlain *et al.* "The spectral transmission at infrared wavelengths of Michelson interferometers with dielectric film beam-dividers," *Infrared Physics*, vol. 6, pp. 195–203, 1966.

[8] D. R. Smith and E. V. Loweenstein, *Applied Optics*, vol. 14, p. 1335, 1975.

Theory of Modal Character, Field Structure, and Losses for Semiconductor Lasers

DWIGHT O. NORTH, FELLOW, IEEE

Abstract—**The contemporary semiconductor laser oscillates and radiates power simultaneously in many of the characteristic modes of its cavity, perhaps only a few for the "stripe" laser near threshold, but hundreds or thousands for power lasers. This article provides a comprehensive theory of the modal characteristics: field structure, polarization, characteristic frequency, radiation pattern, and losses. A new theory is developed for cavities with a nonuniform dielectric.**

The subject matter is indispensable to understanding or use of the new nonlinear theory of laser processes. Much of it is also relevant to dielectric, optical transmission systems in general.

A CONTEMPORARY GaAs laser at room temperature, driven moderately hard, typically gives evidence that it is simultaneously oscillating and radiating appreciable power in many of the characteristic modes of its cavity, perhaps only a few for "stripe" lasers near threshold, but hundreds or thousands for power lasers. For the last five years RCA Laboratories has engaged in a wide-ranging experimental investigation of this complex process, the construction of a new nonlinear theory to describe it, and an exhaustive (and satisfying) experimental test of the theory [1], [2]. Indispensable to the construction, or use, of such a theory is a comprehensive analysis of the modal characteristics of the laser cavity: field structure, polarization, characteristic frequency, radiation pattern, and losses.

A considerable, though scattered literature dealing with some of these topics already exists. The purpose of this article is to bring a simple exposition of all into one place, primarily for the use of those concerned with semiconductor lasers. Beyond that, much of the material is relevant to understanding of dielectric, optical transmission systems in general.

I. The Laser Cavity

GaAs optical cavities come in many forms. The form (Fig. 1) most studied at RCA Laboratories [2], [3] is the power laser, which is, by design intent (if not always in fact), a rectangular parallelepiped with dimensions (D, W, L). In this paper a corresponding right-handed set of axes (x, y, z) is employed. Typically, D is a fraction, up to a few micrometers; W is a few tens, up to a few hundred micrometers; L is one hundred, up to several hundred micrometers. Typical lasing wavelength (air) is $\lambda_0 \approx 0.9$ μm. Since GaAs has a refractive index, $n_1 \approx 3.6$, typical wavelength in the cavity is $\lambda_1 \approx \frac{1}{4}$ μm. The L faces, terminating the z directions, are made by cleaving on crystal planes, providing partially transmitting windows facing air which, if left in the natural state, exhibit a (normal incidence) reflection coefficient, $R_0 = 0.32$. The W faces, facing air, are typically cut with a string saw, using submicron diamond grit. Pump current flows in the x direction; the D faces are variously formed by techniques aimed at establishing small, abrupt, controlled discontinuities of refractive index at planes precisely located in x. Thus the cavity consists of a dielectric core, n_1, bounded all around by dielectrics of smaller index. In current heterojunction structures, the D-face discontinuity, Δn, is designed to be a few percent.

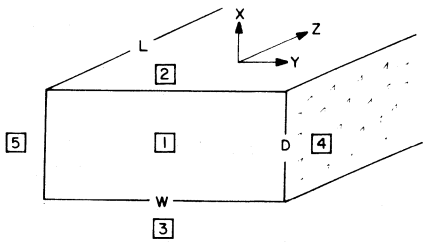


Fig. 1. Cavity geometry and nomenclature.

This is the cavity form principally analyzed in this article. Some other methods for establishing the W faces ("stripe" laser) are in current use [4]-[6], and such cavities will be discussed later in the paper.

The dissipative losses suffered by a wave in transit through the cavity are commonly expressed as a power-attenuation coefficient, $\bar{\alpha}$, the value of which, prorated over a round trip through the cavity, is typically [2] about 50 cm^{-1}. The corresponding fractional bandwidth is $\Delta\omega/\omega \approx \bar{\alpha}\lambda_1/4\pi \approx 10^{-4}$. Consequently, virtually all features of modal structure are appropriately formulated by assuming the system to be loss-free, then appending the losses as a perturbative afterthought.

II. Fresnel Theory

Consider an arbitrary unit vector, $\hat{s} = \hat{i}\alpha + \hat{j}\beta + \hat{k}\gamma$. The quantities (α, β, γ) represent the cosines of the angles which $\hat{s}$ makes with the (x, y, z) axes, likewise, the sines of the angles which it makes with the (D, W, L) faces.

$$\alpha^2 + \beta^2 + \gamma^2 = 1. \tag{1}$$

In medium n_1 $(k_1 \equiv 2\pi/\lambda_1)$, consider an unbounded, monochromatic Maxwellian plane wave, with electric field $\hat{E}$ exp $[i(k_1\hat{s}\cdot\hat{r} - \omega t)]$. Except that $\hat{E}\cdot\hat{s} = 0$, let $\hat{E}$ be arbitrarily oriented; and let its components be complex numbers (arbitrary polarization). The associated magnetic field follows deductively: $\hat{H} = n_1\hat{s}\times\hat{E}$.

Let the plane, $x = 0$, represent an unbounded interface with medium $n_2 < n_1$. Fresnel theory showed us that, with α sufficiently small, an incident wave $(\hat{E}_i; \hat{s}_i = \hat{i}\alpha + \hat{j}\beta + \hat{k}\gamma)$ is *totally* reflected $(\hat{E}_r; \hat{s}_r = -\hat{i}\alpha + \hat{j}\beta + \hat{k}\gamma)$, but the reflection is accompanied by a "skirt" wave in two-space, of the form,

Manuscript received March 29, 1976; revised May 10, 1976.
The author is with RCA Laboratories, Princeton, NJ 08540.

$$\exp\,[-k_1\mu_2 x + ik_1(\beta y + \gamma z) - i\omega t]$$

where

$$\mu_2 \equiv \sqrt{\rho_2^2 - \alpha^2}, \qquad \rho_2 \equiv \sqrt{1 - (n_2/n_1)^2}. \tag{2}$$

It showed further that:

1) If the incident $\hat{E}_i$ lies wholly in the interface,

$$\hat{E}_r = -F\hat{E}_i,$$

$$F \equiv \exp\,\{i2\,\tan^{-1}\,[\alpha/\mu_2]\} = \exp\,\{i2\,\sin^{-1}\,[\alpha/\rho_2]\}. \tag{3}$$

2) If the incident $\hat{H}_i$ lies wholly in the interface,

$$\hat{H}_r = -G\hat{H}_i, \qquad G \equiv \exp\,\{i2\,\tan^{-1}\,[(n_2/n_1)^2(\alpha/\mu_2)]\}. \tag{4}$$

It follows that an incident plane wave with arbitrary

$$\hat{E}_i \equiv \hat{i}X_i + \hat{j}Y_i + \hat{k}Z_i; \quad \alpha X_i + \beta Y_i + \gamma Z_i = 0 \tag{5}$$

yields a reflected plane wave

$$\hat{E}_r \equiv \hat{i}X_r + \hat{j}Y_r + \hat{k}Z_r; \quad -\alpha X_r + \beta Y_r + \gamma Z_r = 0 \tag{6}$$

where

$$X_r = -GX_i$$

$$Y_r = \frac{\beta^2 G - \gamma^2 F}{\beta^2 + \gamma^2} Y_i + \frac{\beta\gamma(F+G)}{\beta^2 + \gamma^2} Z_i$$

$$Z_r = \frac{\beta\gamma(F+G)}{\beta^2 + \gamma^2} Y_i + \frac{\gamma^2 G - \beta^2 F}{\beta^2 + \gamma^2} Z_i. \tag{7}$$

And we are reminded thereby that such reflection generally entails a modification of polarization character.

III. The "One-Dimensional" Waveguide

Suppose that the W faces and the L faces of the cavity are removed to infinity. This leaves a core bounded by two infinite, parallel interfaces (with media n_2 and n_3) spaced by distance D. The structure is an elementary waveguide, possessing "modes." A mode is a field structure which *preserves* the disposition of fields on a phase front as it travels.

The Fresnel theory shows us that, in the core, any such mode is describable as the sum of two plane waves $(\pm\alpha, \beta, \gamma)$, each of which transforms into the other upon reflection. Since (7) describes the transformation, we find that the component plane waves of every mode must have $\hat{E}$ lying either wholly in the interface ($E_\parallel$) or wholly at right angle ($E_\perp$) to the position of $E_\parallel$. Further, a closure (phase-match) condition must be satisfied. For $E_\parallel$, this condition takes the form $AF_2F_3 = 1$; for $E_\perp$, $AG_2G_3 = 1$; where $A \equiv \exp\,[i2k_1D\alpha]$. Explicitly,

$$E_\parallel: \quad k_1D\alpha + \tan^{-1}\,[\alpha/\mu_2] + \tan^{-1}\,[\alpha/\mu_3] = m\pi \tag{8}$$

$$E_\perp: \quad k_1D\alpha + \tan^{-1}\,[(n_2/n_1)^2(\alpha/\mu_2)] + \tan^{-1}\,[(n_3/n_1)^2(\alpha/\mu_3)] = m\pi \tag{9}$$

where m is a positive integer. The expressions simultaneously introduce a mode index number (m) and fix a corresponding value for α_m.

What if we *choose* an m so large that $\alpha_m > \rho_2$ or ρ_3? The skirt wave then becomes a radiative wave; we lose "total" reflection. We still have a mode of the waveguide; analytic continuation of (3), (4), (8), (9) suffices to define it [7]; but it is generally so very lossy that it plays no part in semiconductor laser physics. Thus we confine our discussion to a fixed range, $1 \leqslant m \leqslant M$, where M corresponds to incipient radiative loss, and represents the largest value of m for which solutions of (8), (9) exist. M can be ascertained readily. For example, suppose $\rho_2 < \rho_3$; in (8) set $\alpha = \rho_2$,

$$m = 2D\rho_2/\lambda_1 + \tfrac{1}{2} + (1/\pi)\,\sin^{-1}\,(\rho_2/\rho_3).$$

Thus we see that M rises monotonically with D/λ_1. Conversely, if $D/\lambda_1 \to 0$, eventually even the lowest mode ($m = 1$) becomes radiative; unless, perchance, $\rho_2 = \rho_3$, in which case mode 1 survives, though precariously, with huge skirts: $\mu \to \pi D\rho^2/\lambda_1$. This case, $D/\lambda_1 << 1$, has been thoroughly explored by Anderson [8].

The case, $M > 1$, is more frequently encountered or designed in laser physics. In that event, (8) can be solved approximately:

$$\alpha_m = (m\lambda_1/2D)[1 + (\lambda_1/2D\pi)(1/\rho_2 + 1/\rho_3)]^{-1}, \qquad m << M \tag{10}$$

$$M \approx 2D\rho_2/\lambda_1, \qquad \rho_2 < \rho_3. \tag{11}$$

The last term of (10) provides "end"-corrections (as in organ pipes) for D, making it *effectively* larger. In a typical, illustrative case, we choose $D = 2\ \mu$m and a 2 percent Δn, so that $\rho_2 = \rho_3 = 0.2$. We find that the end-correction is 0.2, $\alpha_m \approx m/19$, $M = 4$. Since (9) differs from (8) only by terms of order ρ^2, the approximations (10), (11) are generally adequate for either of the two permissible polarizations.

Returning to the beginning of this section, replacing D with W, α with β, we find for the simple W guide that (10) and (11) become

$$\beta_s = (s\lambda_1/2W)[1 + (\lambda_1/2W\pi)(1/\rho_4 + 1/\rho_5)]^{-1}, \qquad s << S \tag{12}$$

$$S \approx 2W\rho_4/\lambda_1, \qquad \rho_4 < \rho_5. \tag{13}$$

Since $W >> D$, the end-correction is here much smaller.

Once more, we replace D with L, α with γ, to discuss the simple L guide. Supposing (for the moment) that all modes under discussion are partially transmitted through the end-windows, we find no end-corrections, and

$$\gamma_Q = Q\lambda_1/2L, \qquad Q, \text{ a positive integer.} \tag{14}$$

IV. The "Two-Dimensional" Waveguide

We are now prepared to consider a waveguide possessing both the D and the W faces, but the L faces are removed to infinity. We expect to be able to describe its modes as the sum of *four* plane waves $(\pm\alpha, \pm\beta, \gamma)$, each of which transforms into another upon reflection from an appropriate face. Expression (7) furnishes the format for every such transformation, whence the final description would seem to entail only a little matrix algebra. Not so, and failure in the attempt is clearly traceable to the small distinction between (3) and (4). It reveals, also, that the problem has not yet been "properly put." Each skirt wave carries some of the power, not merely axially along the guide, but also peripherally around the perimeter of the $D \times W$ rectangle. And, to this point, no effort has been made either to ensure the continuity of this flow around the corners, or to

formulate the associated field-component transformations, as the flow moves from medium 2 to medium 4, etc. Indeed, one suspects that the general solution may entail a *net* flow out one pair of faces into the skirt, around the corners, and back in across the other pair.

On this last point, a clue to possible solution strategy is provided by the following observation. All of the expressions (1)-(7) still hold even though we let α, β become complex numbers, i.e., $\alpha \to \alpha + ia, \beta \to \beta + ib, \alpha a + \beta b = 0$. In this event, the core phase fronts remain plane, but the intensity is no longer uniform on them.

Ignoring peripheral continuity at corners, Marcatili [9], [10] has offered an approximate solution, leading to the conclusion that the two permissible polarizations of a mode (m, s) are such that $\hat{E}$ is predominantly either parallel D, or parallel W. The appropriateness of such a sweeping conclusion (unqualified as to $m, s, W/D$, or relative sizes of $n_1, n_2, \cdots, n_5$) is questionable. The starting, assumed (x, y)-dependence of the fields was arbitrarily restricted; certain components of the field were arbitrarily set null; and it was arbitrarily assumed that no power flowed over the faces.

Having been thwarted in the effort to formulate, simply, the fashion in which the dielectric bounds of a rectangular dielectric waveguide establish the two permissible, orthogonal polarizations for each of its modes, we now change the subject. Presently we return to the question, to discover that we do not need the answer.

V. Cavity Modes: Characteristic Frequencies

In the discussion of waveguide modes, the monochromatic frequency ω (appearing in surrogate form as λ_1) was an independent variable. It becomes fixed when we form a cavity. To study the fixation, and in the interest of clarity over precision, we drop the end-corrections, and put (10), (12), and (14) into (1):

$$(2/\lambda_1)^2 = (m/D)^2 + (s/W)^2 + (Q/L)^2. \tag{15}$$

To make this general expression immediately more useful, we rearrange it to focus attention upon that group of modes which participates in lasing. We choose a frequency ω_0 near the center of the lasing band; we choose a corresponding set of mode numbers: $s = 1, m = 1, Q = Q_0$; we define $q \equiv Q - Q_0$. Then (15) becomes

$$(\omega_\kappa - \omega_0)/\omega_0 = [2(1 - \partial \ln n_1/\partial \ln \lambda)]^{-1}[(\lambda_1/2D)^2(m^2 - 1) + (\lambda_1/2W)^2(s^2 - 1) + \lambda_1 q/L],$$
$$m = 1, 2, \cdots, M; \quad s = 1, 2, \cdots, S;$$
$$q = 0, \pm 1, \pm 2, \cdots. \tag{16}$$

Here ω_κ signifies a mode's characteristic frequency, and κ is merely shorthand for (m, s, q). For GaAs [11], the logarithmic derivative is about (-0.3).

The field structure of each cavity mode is, as we have seen, decomposable into eight plane waves $(\pm\alpha_m, \pm\beta_s, \pm\gamma_{m,s})$. A typical such wave, traveling in the z direction, has a Poynting vector inclined but slightly with respect to the z axis. In view of (10), (12), we note that the angles it makes with the D plane, W plane, and Z axis, respectively, are

$$\varphi_{m1} \approx m\lambda_1/2D, \quad \theta_{s1} \approx s\lambda_1/2W, \quad \sqrt{\varphi_{m1}^2 + \theta_{s1}^2}. \tag{17}$$

Since we have (erroneously) suppressed reference to polarization, in the formulation of (16), we must realize that the system has been artificially forced into a degeneracy. To each ω_κ correspond two modes: $(m, s, q; \pi_1)$ and $(m, s, q; \pi_2)$, where π_1, π_2 refer to two orthogonal polarization characters, yet to be determined.

We can now make, at least, an extreme upper limit estimate of the frequency splitting, $\delta\omega$, which such polarization characters will occasion. To do this, we revert to (8) and (9), to make an estimate, $\delta\alpha$, of the shift in α occasioned by switching from one to the other of the indicated polarizations:

$$\delta\alpha/\alpha \approx (k_1 D)^{-1}(\rho_2^2/\mu_2 + \rho_3^2/\mu_3) \approx (k_1 D)^{-1}(\rho_2 + \rho_3).$$

This is inserted into (16) to find the corresponding $\delta\omega$, which is then compared (Section I) with the $\Delta\omega$ associated with $\bar{\alpha}$.

$$\delta\omega/\Delta\omega \approx 2(1 - \partial \ln n/\partial \ln \lambda)^{-1}(m\lambda_1/2D)^2(\rho_2 + \rho_3)/D\bar{\alpha}.$$

Choosing $D = 2$ μm, $m = 1$, $\rho_2 = \rho_3 = 0.2$, $\bar{\alpha} = 50$ cm^{-1}, we find $\delta\omega/\Delta\omega \approx 0.2$.

We are impelled to a general conclusion concerning the GaAs laser. As with most electronic oscillators, the "pump" provides a source of power, "available" over a broad, continuous frequency range. The pump looks into a complicated network, exhibiting an input impedance continuous in frequency. It matters not at all to the pump how we characterize "normal modes," it simply delivers power at all frequencies; the power peaks at those frequencies where the *combination* of reactive and resistive impedance is least. It now appears that in the GaAs laser, the fixture of (π_1, π_2) is generally dominated by polarization-sensitive dissipation processes, rather than the reactive processes addressed in Section IV. Put another way, a field structure, of the "right" frequency will generally, on a round trip of the cavity, suffer more dissipation loss because its π-character is "wrong" than it will suffer self-interference loss on account of its "wrong" π-character. The formulation of π-character is therefore logically made a sequel to the development of dissipation theory.

VI. Radiation Features

Consider the one-dimensional D guide, terminated by an L face. Ignoring the (small?) skirt waves, we have seen that mode m can be represented by two plane waves traveling through the core towards the partially transmitting window into air, with Poynting vectors inclined, $\pm\varphi_{m1}$. The external radiation field is readily described via standard antenna theory. And if the angles, φ, of interest to an external observer are sufficiently small, then, regardless of polarization, the angular dependence of the radiation field is

$$\psi(\varphi) = \sin h_+/h_+ - (-)^m \sin h_-/h_-,$$

where

$$h_\pm(\varphi) \equiv (m\pi/2)[1 \pm \sin \varphi/n_1 \sin \varphi_{m1}].$$

Thus each plane wave produces a familiar pattern, a main lobe

("rabbit ear") flanked by lesser, satellite lobes, which carry very little of the power: $|\psi|^2$. The main lobes are inclined at angles: $\varphi_{m0} \approx \pm n_1 \varphi_{m1} \approx \pm m\lambda_0/2D$. Considered alone, without reference to its coherent neighbor, a main lobe exhibits a (half-power) width, $\Delta\varphi \approx \lambda_0/D$. The case, $m = 1$, is special; now the main lobes overlap coherently, producing a single lobe, which shows no evidence of bifurcation, points in the direction $\varphi_{10} = 0$, but exhibits about the same $\Delta\varphi$.

If the skirt waves do carry appreciable power, the description becomes a bit complex. In the first place, their reflection at the window will not be the same, thus upsetting mode stability in the reflected wave fields and complicating the description of $\psi(\varphi)$. The matter will not be elaborated here, beyond the remark that $\Delta\varphi$ will, as a rule, be appreciably diminished.

By extension, we can now formulate or visualize the radiation pattern associated with each mode of the laser itself. There are four main lobes ("fans") whose inclinations $(\varphi_{m0}, \theta_{s0})$ are like $(\pm m\lambda_0/2D, \pm s\lambda_0/2W)$. Each fan is thick in one direction, $\Delta\varphi \approx \lambda_0/D$, thin in the other, $\Delta\theta \approx \lambda_0/W$.

VII. Dissipation Theory

The available power of the laser pump is here symbolized as $g(\omega)$, a negative-attenuation coefficient (length^{-1}), continuous over a broad range of frequency. In the nonlinear theory [1], [2], the relative power appearing in each mode (κ) of the external beam is proportional to $[g(\omega_\kappa)/\bar{\alpha}_\kappa] - 1$. Here, $\bar{\alpha}_\kappa$ signifies the prorated round-trip power-attenuation coefficient for mode κ. It is therefore essential to develop a theory of $\bar{\alpha}_\kappa$, and, especially, its explicit dependence on $(m, s, q; \pi)$.

The π-dependence will be examined later. There is no dependence on q. As so often stated, provided the incidence on the two L windows is nearly normal, there is an $\bar{\alpha}(L) = (1/2L) \ln (R_a R_b)^{-1}$. GaAs example: $R_a = R_b = 0.32$, $L = 300\ \mu$m; $\bar{\alpha}(L) = 38$ cm^{-1}. This section deals with $\bar{\alpha}(m), \bar{\alpha}(s)$.

Throughout the laser structure there are always loss processes of a (quasi-) local character, e.g., free-carrier absorption, band-to-band absorption, etc. Thus the core material (n_1) might be characterized by $\bar{\alpha}_1$, whereas, across a D interface, the skirt material (n_2) might have a different characterization, $\bar{\alpha}_2$. If $\bar{\alpha}_2 << \bar{\alpha}_1$, the highest m mode might "bloom" first, and conversely.

We discuss the matter in brief. Suppose that on one side (n_3) of D the skirt is negligible. On the other side (n_2) we can readily employ the formulas of Section II to ascertain that, at the interface, the power density in the skirt wave lies below that of the incident plane wave, in the core, by approximately the factor $4\varphi_{m1}^2/\rho_2^2$. And this is negligibly sensitive to choice of polarization. By some obvious steps we deduce that, in the large-M approximation,

$$\bar{\alpha}(m) = (\bar{\alpha}_1 + \bar{\alpha}_2 G)(1 + G)^{-1}; \qquad G \equiv \frac{(m/M)^2}{\pi M \sqrt{1 - (m/M)^2}}. \tag{18}$$

[In this expression we use M, not as an integer, but as the actual cutoff value, (11).] The result is illustrated below for $M = 5.2$. Numerical values of $\bar{\alpha}(m)$ are listed, in the first line, for $\bar{\alpha}_1 = 10, \bar{\alpha}_2 = 100$, in the second line, for $\bar{\alpha}_1 = 100, \bar{\alpha}_2 = 10$.

m	1	2	3	4	5
$\bar{\alpha}(m)$	10.2	10.9	12.2	14.8	25.5
$\bar{\alpha}(m)$	99.8	99.1	97.8	94.9	84.8

Experience in this laboratory, with LOC structures, has provided qualitative confirmation [12]; with skirt $\bar{\alpha}$'s kept small, lasers have exhibited virtually single-m performance with m as large as 20 (judged by stripe count in the end-facet luminance).

We now turn to $\bar{\alpha}(s)$. If the W faces are cleaved, one is plagued by cross-lasing. Sawing eliminates this problem, and simultaneously introduces an s-dependent loss. A W face is now stochastically rough, possessing both pimples and dimples with respect to its ideal plane. Relative to this plane, the actual interface with air $(n_0 = 1)$ has a deviation, $\delta y(x, z)$. We locate the plane so that $\langle \delta y \rangle_{x,z} = 0$, and define $h^2 \equiv \langle \delta^2 y \rangle_{x,z}$. We need also to introduce two orthogonal correlation lengths (a, b), whose existence implies that, in a patch $(a \times b)$ of the surface, the deviation δy can be considered uncorrelated with that of other patches.

With respect to the norm, a patch has a volume deviation: $\delta V \equiv ab\delta y$. And the patch has an excess polarizability: $p = [(\epsilon_1 - \epsilon_0)/4\pi]\delta V$. That is, if we regard the volume as a point, immersed in an applied electric field $\hat{E}$, it develops a dipole moment: $\hat{\mu} = p\hat{E}$. On the assumption that (a, b, h) are all $<< \lambda_0$, we can estimate its radiated power, thus, finally, the attrition $\bar{\alpha}(s)$ of a core wave.

The total power (all directions) radiated by a point dipole immersed in a dielectric (ϵ) is $\mu^2\omega^4\sqrt{\epsilon}/3c^3$. The dipoles we consider are not immersed; rather, they lie near a plane interface between two dielectrics. Thus the radiated power will undoubtedly depend on dipole orientation, a matter which, at this point, we recognize only symbolically by using $\sqrt{\epsilon_\parallel}, \sqrt{\epsilon_\perp}$ to correspond with $\hat{E}$ parallel to, perpendicular to, the W plane.

How do we formulate the driving field $\hat{E}$? By ignoring the pimples and dimples, launching one of the characteristic component plane waves studied above, and describing the net field near the interface as it is reflected. When δV is positive, we must use the field just outside (air); when δV is negative, the field just inside (core).

How do we represent the plane wave in its most general form? With an eye to ultimate convenience, we elect the orthogonal TE, TM representation. A TE wave, here called "u," has $E_z = 0$; and so does each of its four plane-wave components. A TM wave, here called "v," has $H_z = 0$, and so also does each of its components. Thus, in the plane wave under discussion, we describe the (complex) amplitude of electric field (with unit absolute strength) in the most general way via the function: $\{u, v\}$. And we subject it to the condition: $uu^* + vv^* = 1$.

In employing (7), we now use all the trigonometric approximations appropriate to small (α, β). Further, we ignore $(n_0/n_1)^2$ in comparison with unity, but keep n_0/n_1. We find that the net components of the electric field just outside the interface are

$$X_0 = -i\frac{2\beta}{\sqrt{\alpha^2+\beta^2}}(\beta u + \alpha v), \quad Y_0 = -i\frac{2\beta}{\sqrt{\alpha^2+\beta^2}}(\alpha u + \beta v),$$

$$Z_0 = \frac{2\beta}{\sqrt{\alpha^2+\beta^2}}(\alpha u - \beta v). \tag{19}$$

Recalling continuity rules, we find that, just inside,

$$X_1 = X_0, \quad Y_1 = (n_0/n_1)^2 Y_0 \approx 0, \quad Z_1 = Z_0.$$

Since there are equal numbers of pimples and dimples, we form the appropriate averages:

$$|E_\parallel|^2 \equiv \langle |X|^2 + |Z|^2 \rangle = 4\beta^2 \tag{20}$$

$$|E_\perp|^2 \equiv \langle |Y|^2 \rangle = \frac{2\beta^2}{\alpha^2+\beta^2}|\alpha u + \beta v|^2. \tag{21}$$

Thus we summarize:

power radiated per patch:

$$P_0 = \left(\frac{\epsilon_1}{4\pi}\right)^2 \frac{\omega^4}{3c^3}(abh)^2 \left[\sqrt{\epsilon_\parallel}\cdot|E_\parallel|^2 + \sqrt{\epsilon_\perp}\cdot|E_\perp|^2\right] \tag{22}$$

power radiated in unit length:

$$P_r = P_0 D/ab$$

power carried in guide:

$$P_G = \frac{\sqrt{\epsilon_1}\, c}{4\pi} DW$$

power-attenuation coefficient:

$$P_r/P_G = \frac{4\pi^3}{3}\cdot\frac{\epsilon_1^{3/2}}{W}\cdot\eta^4\left[\sqrt{\epsilon_\parallel}\cdot|E_\parallel|^2 + \sqrt{\epsilon_\perp}\cdot|E_\perp|^2\right];$$

$$\eta^4 \equiv abh^2/\lambda_0^4. \tag{23}$$

In the interest of theoretical simplicity, we now introduce a guesstimate, based upon the observation that most of the power of a radiating doublet flows near its equatorial plane. Hence we use

$$\sqrt{\epsilon_\parallel} \approx \tfrac{1}{2}(n_1 + n_0), \quad \sqrt{\epsilon_\perp} \approx \sqrt{(\epsilon_1+\epsilon_0)/2},$$

and rewrite (23) as

$$\frac{A}{W}\beta^2\left[1 + B\frac{|\alpha u + \beta v|^2}{\alpha^2+\beta^2}\right] \tag{24}$$

where

$$A \equiv \frac{8\pi^3}{3}\epsilon_1^2\left(1+\frac{n_0}{n_1}\right)\eta^4; \quad B \equiv \left[\sqrt{2}\left(1+\frac{n_0}{n_1}\right)\right]^{-1}. \tag{25}$$

For GaAs

$$A = 1.8\times 10^4\cdot\eta^4, \quad B = 0.55.$$

The first term of (24) is independent of π-character. The second term is polarization sensitive, and could, at most, contribute no more than about 50 percent of the first.

We leave the second term for later, and designate the first[1] as the polarization-independent, s-dependent contribution to the power-attenuation coefficient

$$\bar{\alpha}(s) \equiv A\beta^2/W. \tag{26}$$

The term is s-dependent because, of course, the (α, β) of (19)-(24) are subject to the rules developed in Sections III-V.

To get a numerical feel for (26), suppose that $W = 100\ \mu$m, and that grit size is small enough that $\eta = O(10^{-1/2})$. An s mode, having $\alpha(s) = \alpha(L) = 38\ \text{cm}^{-1}$, has $s \approx 38$ and external radiation fans at $\theta_{s0} \approx \pm 10°$. General confirmation of (26) has repeatedly been found in the experimental work of this laboratory [1], [2].

Using entirely different mathematical methods, Suematsu and Yamada [13] obtained a result which, in its simplest expression, has the form of (26); but, for reasons unclear to me, their A depends not at all on the corrrelation lengths (a, b).

Since resolution of adjacent s modes is rarely achieved, the theory presented here suggests a smooth, symmetric θ_0 profile for the laser beam. Ragged or asymmetric profiles are occasionally encountered; presumably such features are traceable to other sources, e.g., warping of the saw cuts, or cleaving defects.

VIII. Polarization Theory

If the cleaved L window is left in its natural state, application of the Fresnel theory shows that, for near-normal incidence, the reflection coefficient is

$$R = R_0[1 \pm 2(n_1/n_0)(\alpha^2+\beta^2) + O(\alpha^2+\beta^2)^2]. \tag{27}$$

The upper sign goes with u, the lower with v. Thus, if both windows are natural,

$$(\tfrac{1}{2}L)\ln(R_a R_b)^{-1} \approx \bar{\alpha}(L) - (2/L)(n_1/n_0)(\alpha^2+\beta^2)\cdot(uu^* - vv^*).$$

We are thus, finally, enabled to formulate the total power-attenuation coefficient as

$$\bar{\alpha}_\kappa = \bar{\alpha}(L) + \bar{\alpha}(m) + \bar{\alpha}(s) + \bar{\alpha}(\pi) \tag{28}$$

where

$$\bar{\alpha}(\pi) \equiv -\frac{2}{L}\cdot\frac{n_1}{n_0}(\alpha^2+\beta^2)[|u|^2 - |v|^2] + \frac{AB}{W}\cdot\frac{\beta^2}{\alpha^2+\beta^2}\cdot|\alpha u + \beta v|^2. \tag{29}$$

In (29), α and β are, of course, determined by selection of mode numbers (m, s). We examine (29) as a function of β, with α fixed. For $\beta/\alpha \to 0$, clearly, pure u gives the lowest $\bar{\alpha}(\pi)$, whence the splitting $\Delta\bar{\alpha}(\pi)$, between the lower (TE) and the higher (TM) orthogonal polarizations is $\Delta\bar{\alpha}(\pi) = (4/L)(n_1/n_0)\alpha^2$. Thus, for GaAs, $\Delta\bar{\alpha}(\pi)/\bar{\alpha}(L) = 12.6\,\alpha^2$. (In a device for which $D = 2\ \mu$m, and $m = 1$ blooms first, $\alpha \approx \frac{1}{16}$; whence the splitting is a substantial 5 percent.) The implication is that, just above threshold, the laser should exhibit *strong* TE polarization. Such behavior has repeatedly been observed [14], [15] for double-heterojunction lasers.

As we increase β, a critical parameter enters, i.e., $\xi^2 \equiv (4n_1/n_0 AB)\cdot(W/L)$. The numerical value of ξ varies enormously with design, but in this laboratory usually $\xi << 1$. On this premise the table below points out some of the guideposts

[1] Since scattering loss can never exceed simple "walk-off" loss (completely transparent W face), (26) is inaccurate at large β. Further investigation is needed. A more accurate form might be something like $\bar{\alpha}(s) = (A\beta^2/W)(1 + A\beta)^{-1}$.

as β rises. The second column states the π-character which provides *least* loss. The third column states the loss increment, upon switching to the orthogonal polarization. (Elliptical polarization never appears.)

β/α	Least Loss	$\Delta\bar{\alpha}(\pi)$
$<<1$	$v=0, u=1$	$\frac{4}{L}\cdot\frac{n_1}{n_0}\cdot\alpha^2$
ξ	indifferent	0
1	$v=-u$	$\frac{AB}{W}\cdot\alpha^2$
$>>1$	$v=0, u=1$	$\left[\frac{4}{L}\frac{n_1}{n_0}+\frac{AB}{W}\right]\beta^2$

Further exploration of (29) is left to the reader. We see that, by and large, these lasers start up from threshold strongly TE, but quickly go "soft" when driven hard. This, too, has often been observed [14].

Designs in which D is reduced to, or below, λ_1 are not accurately described by (27). As the "Brewster window" is approached, a very strong (u, v) split of R occurs. Such designs show "hard" TE polarization. Theoretical and experimental investigations of this special case can be found elsewhere [2], [15]-[18].

IX. Generalizations

We have seen that for a particular kind of waveguide, once the π-character is designated, every mode can be *decomposed* into a number of waves, which transform into one another upon reflection from the boundaries. And, for the one-dimensional guide this number is 2; for the two-dimensional guide it is 4.

Intriguing questions arise. Can this decomposition always be accomplished, i.e., for waveguides of whatever description? Is the number of components peculiar to the description, or determined only by the dimensionality? As to the second question, dimensionality would appear to be the determinant, since every problem can be reduced to solution of an associated eigenfunction problem on the guide's cross section.

Below, these questions are by no means terminally investigated, rather, only illuminated in two illustrations.

A. Circular Metallic Guide

Consider a polarization such that $H_z \equiv 0$. It is well known [19] that, when E_z is formulated, all other field components follow as appropriate derivatives of E_z; and, for mode (m, n),

$$E_z = J_n\left(p_m\cdot\frac{r}{a}\right)\cdot\left\{\begin{matrix}\cos n\theta\\ \sin n\theta\end{matrix}\right\}\exp i(\beta_m Z - \omega t)$$

wherein $J_n(p)$ is a Bessel function; p_m, its mth root; n is an integer; $\beta_m \equiv \sqrt{k^2 - (p_m/a)^2}$, $k \equiv 2\pi/\lambda$. Suppose we select $\cos n\theta$, use its exponential expansion, hence, contemplate a pair of traveling waves of the form

$$J_n\left(p_m\cdot\frac{r}{a}\right)\exp i\left[\pm n\theta + \beta_m Z - \omega t\right].$$

We have the decomposition we sought. Using the upper sign, we find the constant-phase surface described by

$$y/x = -\tan(\beta_m Z/n),$$

and easily visualized as the surface generated by a diameter of the guide which moves forward (Z), as though on a screw, when turned clockwise. The strength of E_z is clearly not uniform on this surface. The lower sign yields the same result, but with opposite twist. Each wave transforms into the other upon reflection at the wall.

Apparently the mode under scrutiny is decomposable into only two, *not* four waves. No, we have overlooked the degeneracy (traceable solely to the circular symmetry). The $\sin n\theta$ term yields two more waves, entirely orthogonal to the first two, with phase fronts of identical character, but screwed around through an angle: $\pi/2n$.

What if the circle is now deformed, e.g., into an ellipse? Presumably the screw character and the degeneracy disappear instantly.

B. Dielectric Guide, Nonuniform Dielectric

Let us examine the "one-dimensional" guide [Fig. 2(a)] under these circumstances: 1) the waves are trapped within the core by an abrupt drop of index, n, at each boundary; 2) within the core n is a function of x only; 3) all is uniform in y, z. We seek to characterize each mode by two surfaces A, B of constant phase [Fig. 2(b)]. Both travel in the z direction with common velocity, u, without alteration of shape. Field strength (e.g., H_y) is not uniform on either A or B; and, as each wave progresses, it suffers, at every x, a continuous (partial reflection) modification because of the local variability of $n(x)$. In this fashion A and B regenerate each other, yielding a stable state, a mode. We seek the stability conditions, a description of the surfaces, and of the field strengths on them.

The allegedly stable surface will have a shape characterized by $A(x, z-ut) = \text{constant}$. As it progresses (v. Huygens) each point of the surface moves, in δt, a distance: $\delta\hat{r} = (\nabla A/|\nabla A|)v(x)\delta t$, wherein[2] $v(x) = c/n(x)$. Since the *shape* moves along z with uniform velocity, u, we have $\nabla A\cdot\delta\hat{r} = (\partial A/\partial z)u\delta t$, whence the surface is described by

$$\left(\frac{\partial A}{\partial x}\right)^2 = \left[\left(\frac{u\cdot n(x)}{c}\right)^2 - 1\right]\left(\frac{\partial A}{\partial z}\right)^2. \tag{30}$$

If we move on the surface (A invariant),

$$dz/dx = \pm\sqrt{\left(\frac{u\cdot n(x)}{c}\right)^2 - 1}. \tag{31}$$

Then the formulation we seek is

$$\begin{matrix}A\\ B\end{matrix}(x, z-ut) = \pm\int_0^x \sqrt{\left(\frac{u\cdot n(x_1)}{c}\right)^2 - 1}\;dx_1 + z - ut. \tag{32}$$

Next, we investigate the field distribution on these surfaces. Because ϵE is doubly x-dependent, we shall avoid mental confusion by studying that polarization for which $\hat{H}$ is parallel the W interfaces. We approximate in the fashion used for analysis of transmission lines with slowly varying characteristic impedance. That is, each patch of A undergoing a differential forward motion is subject to Fresnel's partial reflection. Thus,

[2]Provided we are not in a "cutoff," i.e., a skirt-wave region. Such a condition is usually more difficult to presage than to recognize when encountered.

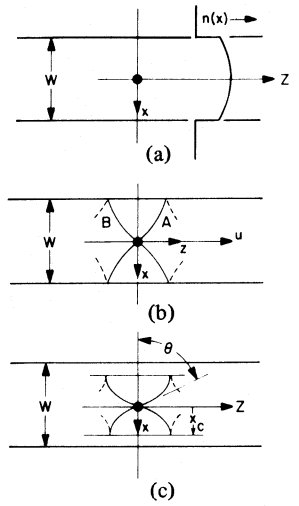


Fig. 2. Waveguide with nonuniform dielectric. (a) Dielectric distribution, (b) constant-phase surfaces (A, B) terminating at $W/2$, (c) terminating at x_c.

while it moves $\delta\hat{r}$, H suffers an alteration:

$$\delta H/H = \tfrac{1}{2}\,[1 - \cot^2\theta(x)]\,\delta n/n \tag{33}$$

where $\theta(x)$ refers to the inclination of $\delta\hat{r}$ with respect to the guide axis (z). Since $\tan\theta(x)$ is the dz/dx of (31), we obtain directly the integral of (33):

$$H(x)/H_1 = n(x)\left[\left(\frac{un(x)}{c}\right)^2 - 1\right]^{-1/4}. \tag{34}$$

This describes $H(x)$ on the A surface. The complete mode field is compounded from (32) and (34):

$$H_s(x) = H(x)\,[\exp(i\omega A/u) \pm \exp(i\omega B/u)], \tag{35}$$

where s designates a mode number, and choice of sign designates the symmetry one wishes to consider.

We pause to make connection with familiar matters. If $n(x)$ is actually a constant, n_1, (34) shows that $H(x)$ is uniform, and (32) shows that A, B are planes. Thus, two plane waves tilted at characteristic angles, $\pm\theta_s$, where $\theta_s^2 \approx (u_s n_1/c)^2 - 1$. Further, the exponential part of (35) $\rightarrow \begin{matrix}\cos\\ \sin\end{matrix}(\omega\theta_s x/u_s)$. Here we accost the final essential ingredient of mode stability: there must be closure of the phase shift after one round trip in x. Pursuit of this requirement leads straight back to Section III.

Thus we see that, in the general case, closure is an essential operation, yet to be performed, leading to a characteristic number, u_s, and characteristic shape, A_s and B_s, for each mode. We illustrate.

Suppose $n^2(x)$ to drop symmetrically and parabolically from the center [Fig. 1(a)]: $n^2(x) = n_1^2\,[1 - 2\eta(2x/W)^2]$. Suppose $\eta \ll 1$, whence $n(x) \approx n_1\,[1 - \eta(2x/W)^2]$, and η is recognized as the fractional droop, out to the point where a discrete drop occurs. In preparation for (32), introduce $\theta^2 \equiv (un_1/c)^2 - 1$, $\beta^2 \equiv 2\eta(un_1/c\theta)^2$. Thus,

$$A = (\theta W/4\beta)\,[(2\beta x/W)\sqrt{1 - (2\beta x/W)^2} + \sin^{-1}(2\beta x/W)] + z - ut. \tag{36}$$

We come now to the closure operation, and examine first that circumstance which yields the most conspicuous contrast with the case of uniform n, namely, $\beta > 1$. Inspection of (36) shows that A *terminates* (before reaching the "walls") at $x_c \equiv W/2\beta$. Beyond lies *nothing* [Fig. 2(c)]. The closure requirement is $(\omega A/u) = s\pi/2$, for $x = x_c$, $z = t = 0$. This all leads to

$$\theta\beta \approx \sqrt{2\eta}, \qquad \theta \approx [(2s\lambda_1/\pi W)\sqrt{2\eta}]^{1/2},$$
$$\beta \approx [(\pi W/2s\lambda_1)\sqrt{2\eta}]^{1/2} \qquad \lambda_1 \equiv 2\pi c/\omega n_1.$$

Further, (34) shows that, as $x \rightarrow x_c$, $H(x) \rightarrow \infty$, $H_s(x) \rightarrow 0$, and the surfaces become parallel to the x axis.

As an example, suppose $\eta = 5 \cdot 10^{-3}$, $W = 50\ \mu$m, $\lambda_1 = \frac{1}{4}\ \mu$m. Then $\theta \approx (s/3000)^{1/2}$, $\beta \approx (30/s)^{1/2}$. That is, this peculiar behavior exists for all s up to about 30. Thereafter, the discrete drops play a part, and there is a gradual transition to the familiar behavior for uniform n.

The illustration just solved is conventionally tackled in an entirely different way [4], [20], [21], i.e., the discrete drops are omitted, and Maxwell's equations are put into an approximate form, leading to expression of the fields as solutions of the Hermite-Gaussian (HG) differential equation (functions of the parabolic cylinder). In the nomenclature of this paper, such solutions take the form

$$\psi_s^{\mathrm{HG}} = Q_{s-1}\left(\sqrt{2s}\cdot\frac{x}{x_c}\right)\epsilon^{-s(x/x_c)^2} \tag{37}$$

where Q_n is the Hermite polynomial, defined by

$$Q_n(x) = (-)^n\epsilon^{x^2}\left(\frac{\partial}{\partial x}\right)^n\epsilon^{-x^2}.$$

Via (34)-(36), the solutions found in this article have the form

$$\psi_s^N = \left[1 - \left(\frac{x}{x_c}\right)^2\right]^{-1/4}\begin{matrix}\cos\\ \sin\end{matrix}\left\{s\left[\frac{x}{x_c}\sqrt{1 - \left(\frac{x}{x_c}\right)^2} + \sin^{-1}\frac{x}{x_c}\right]\right\}, \tag{38}$$

where $s = 1, 2, \cdots$; cosine goes with odd s, sine with even s.

A little comparative anatomy may be useful. In Fig. 3 these solutions can be compared for $s = 1$ and $s = 5$.

A comparison of the *radiation* fields (E) is also interesting. Apart from an unnecessary coefficient, the radiation field is formulated via

$$E = \int \psi\,\epsilon^{-ia(x/x_c)}\,d\left(\frac{x}{x_c}\right),$$

where

$$a \equiv k_0 x_c \sin\varphi,$$

φ is observer angle with respect to the window normal. It is well known that the Fourier transforms of HG functions are the same HG functions (self-transforms). In the present instance, this means that the HG curves of Fig. 3 represent *also* their radiation field, E_s^{HG}, provided the abscissa is relabeled: $x/x_c \rightarrow a/2s$.

Computing E for (38) is a little more laborious. Repeated

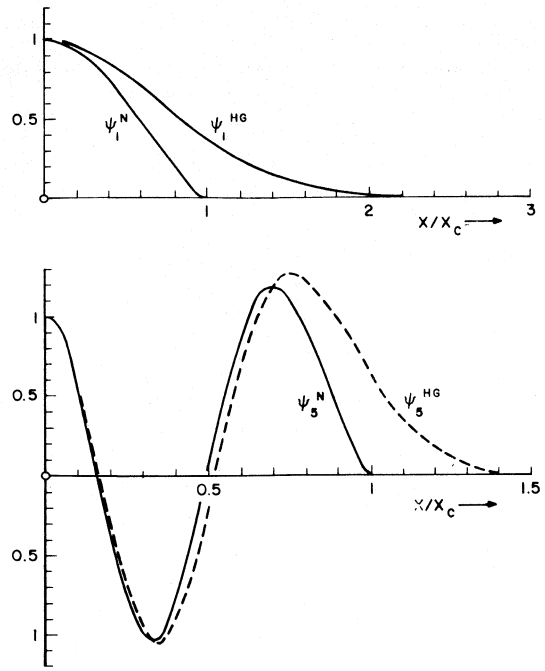


Fig. 3. Two approximate field solutions for guide with parabolic variation of dielectric; modes $s = 1$ and $s = 5$.

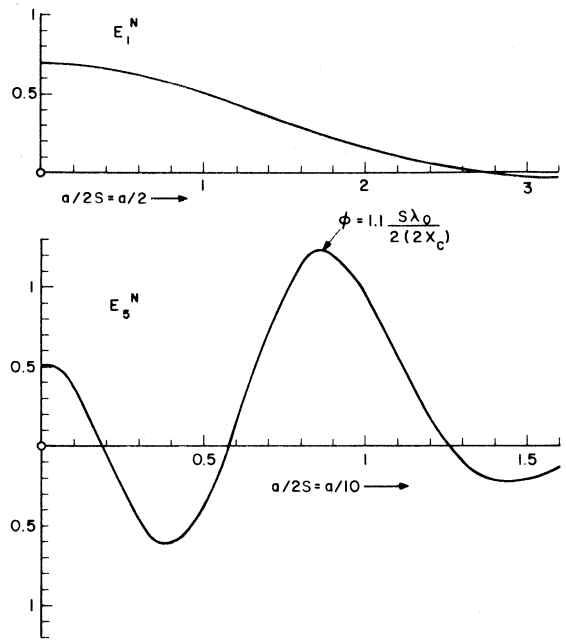


Fig. 4. Radiation fields, modes $s = 1$ and $s = 5$. When HG curves of Fig. 3 are construed as E_s^{HG} versus $a/2s$, Fig. 4 permits a direct comparison with E_s^N.

use of $\exp(iz \sin\theta) = \Sigma_{-\infty}^{\infty} J_n(z) \exp(in\theta)$, leads to

$$E_s^N \propto \sum_{\kappa} \sum_{n} J_\kappa\left(\frac{s}{2}\right) J_{2n}(a) \int_{-\pi/2}^{\pi/2} \sqrt{\cos\theta} \cdot \cos(2\kappa + 2n + s)\theta \cdot d\theta \tag{39}$$

for odd s, with a somewhat similar form for even s. Noting that $\int \sqrt{\cos\theta} \cdot \cos 3\theta \cdot d\theta = -0.14 \int \sqrt{\cos\theta} \cdot \cos\theta \cdot d\theta$, I have limited myself to only the lead term (principle of stationary phase), obtaining

$$E_s^N \approx \sum_{-\infty}^{\infty} [J(s/2) + J(s/2)] \cdot J_{2n}(a). \tag{40}$$
$$\qquad -n-\frac{1}{2}(s+1) \qquad -n-\frac{1}{2}(s-1)$$

Consequently the curves shown on Fig. 4 are claimed to be only a "sketch," but they provide many interesting comparisons. For example, E_5^N has a disposition of peak amplitudes tending away from E_5^{HG} toward that belonging to the "box" with core dielectric uniform throughout $2x_c$. The highest peak amplitude of E_5 occurs for φ's having the relative values, $\varphi^{BOX}, \varphi^{HG}, \varphi^N$: 1, 1.0, 1.1.

Maxwell's equations are: $\nabla \cdot (n^2(x)\hat{E}) = 0$, $\nabla \cdot \hat{H} = 0$, $\nabla \times \hat{E} = (i\omega/c)\hat{H}$, $\nabla \times \hat{H} = -(i\omega n^2(x)/c)\hat{E}$. The reader will find that the new technique described here satisfies all except, say, the third. The HG approximations leave both the first and the third unsatisfied. Further, the HG method fails altogether in the event of important reflections at the boundaries, $x = \pm W/2$.

The case of parabolic $n^2(x)$, with additional drops at the boundaries, is of considerable importance as the model against which to compare the performance of "stripe" lasers. Attempts to interpet such lasers in wholly HG terms often prove inadequate [4], [20], [22], [23].

The technique developed here can, of course, be used to describe the other polarization: $\hat{E}$ parallel the W interfaces. And it has showed us again how each mode of a one-dimensional guide can be decomposed into two waves. And it can be generalized to two-dimensional guides with $n(x, y)$. But perhaps its most valuable aspect is its provision of a qualitative and quantitative grasp of one's problem, whatever $n(x)$ may be.

Acknowledgment

The fund of experimental knowledge provided by virtually all members of the laser research group, led by H. Kressel, has been of great value. And among these, the endless experimental probing, the advice, and criticism supplied by H. S. Sommers, Jr., have been indispensable.

References

[1] H. S. Sommers, Jr., "Experimental properties of injection lasers: Modal distribution of laser power," *J. Appl. Phys.*, vol. 44, pp. 1263–1276, 1973.
[2] H. S. Sommers, Jr., and D. O. North, "The power spectrum of injection lasers: Theory and experiment on a non-linear model of lasing," *Solid State Electronics*, vol. 19, pp. 675–699, Aug. 1976.
[3] H. Nelson, "High-power pulsed GaAs laser diodes operating at room temperature," *Proc. IEEE*, vol. 55, pp. 1415–1419, 1967.
[4] J. C. Dyment, "Hermite-Gaussian mode patterns in GaAs junction lasers," *Appl. Phys. Lett.*, vol. 10, p. 84, 1967.
[5] J. C. Dyment *et al.*, "Proton-bombardment formation of stripe-geometry heterostructure lasers for 300 K CW operation," *Proc. IEEE*, vol. 60, pp. 726–728, 1972.
[6] H. Yonezu *et al.*, "A GaAs-$Al_xGa_{1-x}As$ double heterostructure planar stripe laser," *Jap. J. Appl. Phys.*, vol. 12, pp. 1585–1592, 1973.
[7] Thus making connection with the "walk-off," Fabry-Perot modes: A. G. Fox and T. Li, "Resonant modes in a maser interferometer," *BSTJ*, vol. 40, pp. 453–488, 1961.
[8] W. W. Anderson, "Mode confinement and gain in junction lasers,"

IEEE J. Quantum Electron., vol. QE-1, pp. 228–236, 1965.
[9] E. A. J. Marcatili, "Dielectric rectangular waveguide and directional coupler for integrated optics," *BSTJ*, vol. 48, pp. 2071–2102, 1969.
[10] D. Marcuse, *Theory of Dielectric Optical Waveguides.* New York: Academic, 1974, pp. 49–59.
[11] H. S. Sommers, Jr., "Experimental properties of injection lasers, IV: Modes of large cavity with sawed sides," *J. Appl. Phys.*, vol. 44, pp. 3601–3608, 1973.
[12] H. F. Lockwood *et al.*, "An efficient large optical cavity laser," *Appl. Phys. Lett.*, vol. 17, pp. 499–502, 1970.
[13] Y. Suematsu and M. Yamada, "Transverse mode control in semiconductor lasers," *IEEE J. Quantum Electron.*, vol. QE-9, pp. 305–311, 1973.
[14] H. S. Sommers, Jr. and H. F. Lockwood, "Experimental properties of injection lasers, III: Current dependence of polarization," *J. Appl. Phys.*, vol. 44, pp. 1902–1904, 1973.
[15] H. S. Sommers, Jr., "Experimental properties of injection lasers, V: Strong polarization," *J. Appl. Phys.*, vol. 45, pp. 237–242, 1974.
[16] F. K. Reinhart *et al.*, "Mode reflectivity and waveguide properties of double heterostructure injection lasers," *J. Appl. Phys.*, vol. 42, pp. 4466–4480, 1971.
[17] M. J. Adams and M. Cross, "Electromagnetic theory of heterostructure injection lasers," *Solid State Electronics*, vol. 14, pp. 865–883, 1971.
[18] T. Ikegami, "Reflectivity of mode at facet and oscillation mode in double heterostructure injection lasers," *IEEE J. Quantum Electron.*, vol. QE-8, pp. 470–476, 1972.
[19] H. A. Atwater, *Introduction to Microwave Theory.* New York: McGraw-Hill, 1962, pp. 65–70.
[20] T. H. Zachos and J. E. Ripper, "Resonant modes of GaAs junction lasers," *IEEE J. Quantum Electron.*, vol. QE-5, pp. 29–37, 1969.
[21] D. Marcuse, *Light Transmission Optics.* New York: Van Nostrand-Reinhold, 1972, sec. 7.3.
[22] H. S. Sommers, Jr., "Experimental properties of injection lasers, VI: Mode powering in narrow-stripe and wide sawed lasers," *J. Appl. Phys.*, vol. 46, pp. 1844–1846, 1975.
[23] H. S. Sommers, Jr., and J. K. Butler, "Coupled lateral modes in narrow stripe injection lasers," *J. Appl. Phys.*, vol. 46, pp. 2319–2322, 1975.

Experimental and Theoretical Investigation of the Nitrogen Laser

W. A. FITZSIMMONS, L. W. ANDERSON, C. E. RIEDHAUSER, AND JAN M. VRTILEK

Abstract—**We have studied several types of flat-plate-transmission-line pulse-excited nitrogen lasers. Experiments were carried over a wide variety of parameters such as laser-tube pressure, charging voltage, laser-tube inductance, transmission-line impedance, and others. A theory of the nitrogen laser is presented which treats the laser as an integrated electrooptical system. The theory is based upon the known macroscopic properties of nitrogen discharges along with the known electron impact ionization and excitation cross sections for the N_2 molecule. The theoretical predictions are in very good agreement with the experimental observations. It is suggested that this type of theoretical approach should be applicable to fast high-power discharges in many other gases.**

I. Introduction

THERE is considerable interest in the N_2 laser because of its application as a high-power ultraviolet (UV) pump for dye lasers, and because of the possible large-scale application in the area of isotope separation [1]–[9]. It is important to understand both the electrical and optical properties of this laser in order to construct N_2 lasers that operate near the maximum possible efficiency with good long-term reliability. This paper reports the results of an experimental and theoretical investigation of several types of flat-plate-transmission-line pulsed N_2 lasers. Measurements were carried out over a variety of experimental conditions such as the type of driving electrical circuit, the gas pressure in the laser tube, the laser-tube inductance, the spark-gap inductance, the characteristic impedance of the transmission line, and the charging voltage. The reliability of the laser components has been established to be of the order or greater than 100 million pulses.

A theoretical model which treats the N_2 laser as a highly integrated electrooptical system is described also. The time-dependent conductivity of the N_2 discharge is calculated in a manner that is consistent with the ability of the driving electrical circuit to deliver current to the time-dependent load. The analysis is based upon using the known electron drift velocity and Townsend ionization coefficient in N_2 to establish the electron number density, the gas conductivity, and the electron temperature as a function of the time. This is followed by calculation of the electron excitation rates for the $C^3\pi$ and $B^3\pi$ states of the N_2 molecule along with simultaneous solution of the laser rate equations. The results of the calculation are in very good agreement with the experimental observations. It is suggested that this theoretical approach should be applicable to other types of pulsed discharge lasers.

Manuscript received April 8, 1976. This work was supported in part by the National Science Foundation, and in part by the ERDA under Contract AT11-GEN7.

W. A. Fitzsimmons and L. W. Anderson are with the Department of Physics, University of Wisconsin, Madison, WI 53706.
C. E. Riedhauser was with the Department of Physics, University of Wisconsin, Madison, WI 53706. He is now with the Department of Physics, California Institute of Technology, Pasadena, CA 91109.
J. M. Vrtilek was with the Department of Physics, University of Wisconsin, Madison, WI 53706. He is now with the Department of Astronomy, Harvard University, Cambridge, MA 02138.

II. General Characteristics of the Nitrogen Lasers

In many respects the performance of an N_2 laser is determined by the type of electrical system used to ignite the discharge in the gas. We investigated two types of systems. These are the Blumlein circuit shown in Fig. 1(a), and the capacitor transfer circuit shown in Fig. 1(b). The physical construction of these two systems is shown in Fig. 2. The laser tube and spark gap are identical in both cases; and in both cases the energy-storage capacitor and transmission line are constructed from flat rectangular aluminum plates. The laser tube is attached along the edges of two of the plates, and the spark gap is connected between the appropriate two other plates at a location opposite to the laser tube. For both lasers the outermost side of the laser tube and the outermost side of the spark gap are attached to the same grounded plate. The laser is completed by putting on a top which results in a compact box 61 cm square and 5 cm thick with all outside surfaces at ground potential. The dotted lines in Fig. 2 indicate the method of doubling the electrical systems so that two parallel energy-storage and transmission-line systems are switched by the same spark gap. Table I gives the general properties of each of the two different lasers along with their doubled configurations.

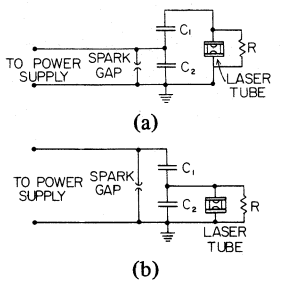


Fig. 1. (a) Equivalent circuit for the Blumlein N_2 laser high-voltage pulse generator. For the Blumlein circuit, $C_1 = C_2$. The resistance $R \approx 100\ \Omega$, which is surface resistance along the outside of the laser tube, keeps the voltage across the laser tube at zero during the charging of C_1 and C_2. (b) Equivalent circuit for the capacitor transfer N_2 laser high-voltage pulse generator. For this circuit C_1 is bigger than C_2 because of the added losses due to the fact that all the charge initially stored on the energy-storage capacitor, C_1, must be transferred through the spark gap.

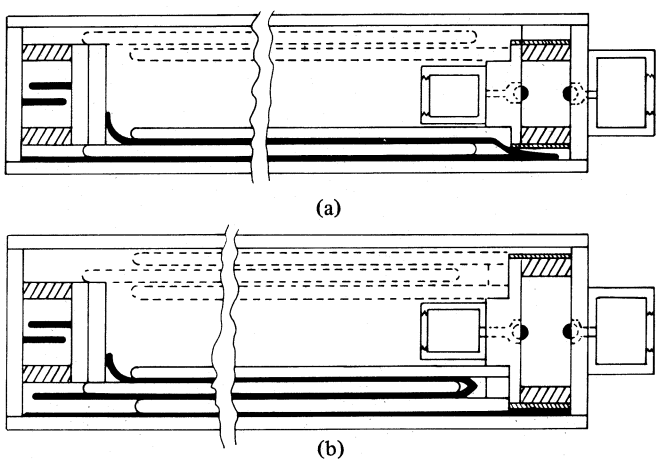


Fig. 2. (a) Physical construction of the Blumlein N_2 laser showing the locations of the spark gap and laser tube relative to the aluminum plates that comprise the energy storage capacitors and Blumlein transmission line. The dotted lines indicate the method of doubling the system so as to have two Blumleins switched by a single spark gap. (b) Physical construction of the capacitor transfer N_2 laser.

III. Details of Component Construction

A. Laser Tube

The laser tube, shown in Fig. 3, is constructed of two aluminum bars separated by Plexiglas walls. The tube is held together by screws threaded into the plastic and sealed vacuum tight with silicon rubber cement. A 0.65-cm-diam copper tube pressed into a slot in each of the aluminum bars functions as the electrodes for the discharge and also provides water cooling for the laser tube. The inside surfaces of the plastic insulators are coated with Dow Corning 3140 RTV in order to protect the plastic from damage due to the intense N_2 discharge. The high- and low-voltage sides of the laser tube are connected by two sheets of resistive paper located along the outside of the plastic insulators and extending the length of the 61-cm-long tube. The parallel resistance of the paper is about 100 Ω which is small enough to keep the voltage across the laser tube near zero during the charging of the energy-storage capacitor. Also the location of the surface resistance shorts out the fringing electric fields and thereby maintains a more uniform electric field inside the tube during the early developing stages of the discharge. The field uniformity helps prevent the arc from striking along the insulators and it also helps confine the discharge to a thickness that is approximately equal to the diameter of the electrodes.

A front-surface-aluminized mirror and a quartz feedback window are sealed with O-rings, one at each end of the laser tube. It is important that both be adjusted to be parallel to each other and perpendicular to the optical axis. The slight adjustments can be accomplished by varying the compression of the O-rings.

Laser tubes of the type shown in Fig. 3 have given satisfactory performance for many hundreds of hours of operation at a repetition rate of 60 Hz. It is important that the inductance of the laser tube be as small as possible, which means that the insulating walls are close to the discharge. The proximity of the plastic walls to the discharge in a low-inductance tube tends to limit the electrical power loading in the tube to about 10 W/cm of length. Higher power tubes require special effort to prevent overheating of the walls.

B. Gas Flow

The gas flow in the laser tube is very important, particularly during operation at high repetition rates. It is necessary that the residual ionization remaining from the previous pulsed discharge be distributed uniformly and with proper density throughout the gas in order to seed the next discharge. Too few ions or a nonuniform distribution of ions results in a nonuniform discharge. Too many ions reduces the breakdown voltage in the gas. In both cases the result is a loss of laser output. Adequate discharge conditions can be achieved by flowing the gas in a direction transverse to the optical axis. As is shown in Fig. 3, the N_2 gas is distributed by an input manifold and enters the tube from behind the copper electrode. It then flows across the tube and exits around the other electrode where it is collected by an exhaust manifold.

TABLE I
CHARACTERISTICS OF N_2 LASERS WHEN OPERATED AT 60 HZ WITH CHARGING VOLTAGE OF 19 KV

	Average Power	Peak Power	Pulse Duration	C_1	C_2	Z_o-Transmission line output
Blumlein	150mW	0.5MW	5 ns	10 nF	10 nF	0.7Ω
"Double" Blumlein	270mW	0.9MW	5 ns			0.7Ω/section
Capacitor Transfer	170mW	0.35MW	8 ns	25 nF	13 nF	0.15Ω
"Doubled" Capacitor Transfer	300mW	0.65MW	8 ns			0.15Ω/section

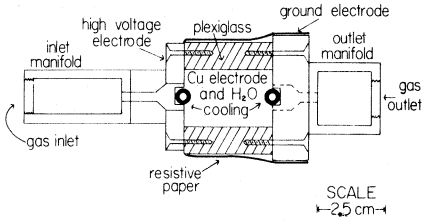


Fig. 3. Cross-section view of the laser tube showing the mechanical configuration for the gas flow, water-cooled electrodes, insulating laser tube walls, and surface resistance that is attached between the electrodes.

Sufficiently uniform gas flow can be achieved with 8 or 10 input and exit holes distributed along each electrode and located so as not to be opposite one another. At high repetition rates, for example at 60 Hz, an 8-10-ft^3/min vacuum pump is needed to adequately pump the gas. On the other hand, if the repetition rate is reduced to 5 or 10 Hz, the pump must be throttled in order that all residual ionization is not pumped away during the time between discharges. Throughout most of the experiments the lasing discharge could be observed visually in order to avoid erroneous measurements due to a nonuniform discharge.

C. The Spark Gap

The lasers described in this paper incorporate a free-running (nontriggered) two-electrode spark gap. The gap is pressurized with N_2 to about 25 lb/in^2 with the gas flowing through the gap to be used again at a reduced pressure in the laser tube. The configuration of the water-cooled aluminum end plates, the copper spark-gap electrodes, and the plastic insulator is shown in Fig. 4. The electrodes are two flat 0.65-cm-thick pieces of copper with each held by an end plate so as to be positioned with an overlapping surface area of about 2 cm × 5 cm and with a spacing of about 1.5 mm. The combination of heavy copper electrodes and water cooling results in the migration of successive sparks over the entire overlapping area of the electrodes. Because the electrode spacing is small compared to the transverse dimensions of the gap, almost all the Cu evaporated during a particular spark is redeposited elsewhere on the electrodes. Although the cathode surface may become slightly convex with prolonged use (the anode becoming slightly concave), the electrode spacing remains the same and the long-term characteristics of the gap are very stable. The lifetime characteristics of this spark gap are not yet known. After 3×10^8 pulses of switching 4 J/pulse at about 20 kV, the electrodes and insulator are still being used with relatively little wear and with little or no change in electrical characteristics of the gap. The spark gap shown in Fig. 4 has an estimated inductance of 10–15 nH when installed in the laser.

D. The Power Supply

The advantages of a two-electrode spark gap for a high-repetition-rate nitrogen laser are the relatively low cost, simple rugged construction, and long-term reliability. On the other hand two-electrode spark gaps are generally associated with erratic performance, and in a laser application this would result in fluctuations in the laser light output. However, stable repetitive operation of a two-electrode gap can be achieved with the proper type of power supply. The essential features of the power supply are shown in Fig. 5. The supply is tuned to the line frequency in the sense that the inductance located in the primary circuit may be selected by the requirement that $L = 1/C\omega^2$, where C is the laser energy-storage capacitance transformed to the primary, and ω is the circular line frequency. The operation of the supply depends upon the transient response of the nonlinear circuit to the first half and then to the second half of a complete cycle of the applied line voltage. The capacitor is charged to its maximum value in about 1/120 s. With the proper inductance in the primary, the peak capacitor charge voltage will be reached just as the applied line voltage passes through zero. Thus if the spark-gap pressure is adjusted so the gap fires at the maximum charge voltage, then the transformer can no longer deliver any significant current to the system after the gap becomes a short circuit. This reduces the current carried by the switch to be only the amount needed to discharge the capacitor, and it also ensures that the gap will open again just as soon as the capacitor is discharged. Also since the time rate of change of the charge voltage is zero at the end of the cycle, the gap will always fire at the same voltage. Depending upon the type of high-voltage transformer used in the supply, additional circuitry may be necessary to avoid saturation of the transformer core. Under proper conditions the laser output exhibits fluctuations of only about ±5 percent in intensity, and the jitter in the firing time of the gap measured relative to the line voltage is about ±100 μs.

E. Energy-Storage Capacitor and Transmission Line

The energy-storage capacitor and transmission line are constructed of 0.32-cm-thick Al plates. The outside grounded plate is 61 cm square and the interior plates are about 53 cm wide × 46 cm long. The plates are carefully polished with

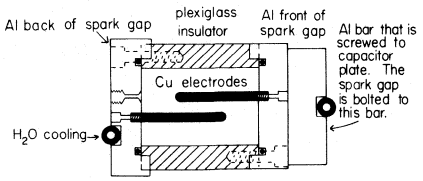


Fig. 4. Mechanical construction of spark gap.

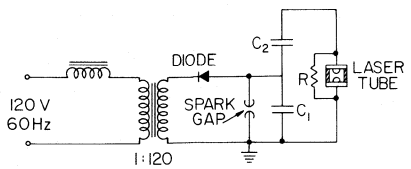


Fig. 5. Schematic of power supply. The inductance in the primary may be selected by requiring that $L = 1/C\omega^2$ where C is the total laser capacitance transformed to the primary, and ω is the circular line frequency. Depending upon the type of high-voltage transformer, additional circuitry may be necessary to avoid saturation of the core.

the edges well rounded to prevent corona. The insulation thickness was varied between 0.13 and 0.51 mm using multiple sheets of 0.13-mm-thick electrical-grade Mylar. The Mylar sheets were oiled with transformer oil and the desired thickness built up with care to exclude air from between the various sheets. The capacitor plates are firmly and rigidly held together in order to maintain a uniform spacing and to prevent mechanical flexing of the plates during the charging and discharging of the capacitor. The capacitor spacing and the capacity to ground was measured to determine the effective dielectric constant of the insulation and hence the stripline impedance. The reliability of the capacitor against high-voltage puncture was determined by many hundreds of hours of operation of the lasers at 60-Hz repetition rate along with some dc dielectric breakdown tests. The lifetime of the capacitor was found to be in excess of 10^8 pulses if the electric field in the dielectric was kept at or below 70–80 percent of the values indicated as the dielectric strength of Mylar in Dupont Bulletin M-4D.

IV. Electrical Characteristics of the Nitrogen Lasers

Both the Blumlein and capacitor transfer circuits shown in Fig. 1(a) and (b) are simply high-voltage pulse generators where the output voltage is applied across the laser tube. The lumped parameter equivalent circuits are shown in Fig. 1(a) and (b) because in both cases the output voltage is the result of the *RLC* oscillations of the circuit that begins when the spark gap breaks down. Several authors have suggested that similar flat-plate spark-gap switched systems can be used to generate a "traveling wave" excitation of the N_2 laser [8]. The condition to generate a traveling wave is that the current rise time in the spark gap, L_s/Z_0, be less than the two-way transit time on the transmission line. The switch inductance is L_s, and the characteristic impedance of the transmission line being switched is Z_0. In the case of the Blumlein system Z_0 of the switched capacitor plates is about 0.35 Ω and the two-way transit time is about 6 ns. Thus for the system to generate a steep edge traveling wave the spark-gap inductance would have to be less than about 2 nH; a value extremely difficult to achieve using a single, more or less conventional, spark gap. Thus when analyzing the voltage rise across the laser tube it is appropriate to use a lumped parameter circuit analysis. However, it is necessary to analyze the current flow in the laser tube in terms of transmission-line theory because the laser-tube inductance is of the order of 2 nH.

For the Blumlein circuit shown in Fig. 1(a) the two energy-storage capacitors are the same, and just before the spark gap breaks down, the full charging voltage V_0 appears across the spark gap while at the same time the voltage across the laser tube is near zero. At the instant the spark gap breaks down, the LC circuit composed of the capacitance C_2 and the spark-gap inductance L_s (plus all other stray inductance) begins to oscillate with the angular frequency given approximately by $\omega = (L_s C_2)^{-1/2}$. At the same time the voltage across the laser tube begins to oscillate with the same frequency, rising toward a maximum value of about $2V_0$ since one-half cycle later the voltage across C_2 is reversed. In actual operation the voltage across the laser tube will not reach $2V_0$ because the gas in the laser tube will break down at a somewhat lower voltage, usually near the value of V_0. However, if the pressure in the laser tube is purposefully set high enough, then breakdown in the tube will not occur and the open-circuit output voltage of the pulse generator can be observed. An example of such a measurement is shown in Fig. 6 for the Blumlein generator. By fitting the observed open-circuit output voltage with a damped sinusoidal oscillation of the form $V = V_0(1 - e^{-t/\tau} \cos \omega t)$ the damping time τ and the angular frequency ω can be determined. Combining these with a measurement of C_2, the switch inductance L_s and the damping resistance $R = 2L_s/\tau$ can be estimated. Typical values for L_s and R are 15 nH and 1 Ω, respectively.

Similar measurements as those discussed above were carried out for the capacitor transfer circuit also. However, the operation of the C-to-C circuit is somewhat different since the oscillatory frequency is given approximately by $\omega = [L_s C_1 C_2/(C_1 + C_2)]^{-1/2}$, and if $C_1 = C_2$ (and with no damping) the open-circuit output voltage is V_0. The effects of damping (spark-gap resistance) are somewhat more important in the C-to-C circuit then in the Blumlein circuit because all the charge stored on the energy storage capacitor is transferred through the switch. For the C-to-C laser capacitance, C_1 is therefore made somewhat larger than C_2 to compensate for the losses in the switch.

If N_2 pressure in the laser tube is adjusted to be in the range of 20–100 torr, the voltage across the laser tube reaches a peak value of about V_0 for the Blumlein laser (about $V_0/2$ for the C-to-C laser), and then falls rapidly as the discharge in the tube develops into a highly conducting plasma. This is shown in Fig. 7 for the Blumlein laser. The optical output is very accurately synchronized with respect to the voltage across the laser tube with the peak optical power occurring at a time approximatley halfway down on the falling laser tube voltage. The tight coupling between the driving electrical circuit and the optical properties of the laser is indicated by the fact that the time scales for both the optical and electrical characteristics are about the same.

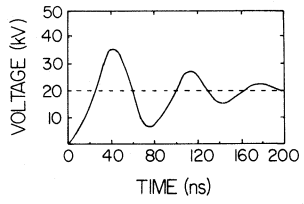


Fig. 6. Typical open-circuit output voltage for Blumlein pulse generator.

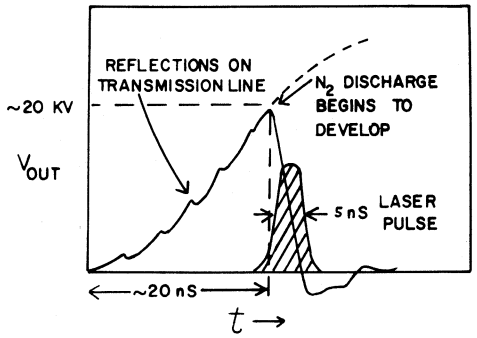


Fig. 7. Measured optical output of Blumlein laser shown relative to the measured voltage across the laser tube. The data were taken from oscilloscope photographs where the voltage across the laser tube was used to trigger the scope. Cable lengths and optical time delays were adjusted so that the center of the laser tube was the reference position for time $t = 0$.

V. Optical Characteristics of the Nitrogen Lasers

The characteristics of the nitrogen lasers when operated at a repetition rate of 60 Hz are shown in Table I. The peak power as a function of repetition rate for the Blumlein and capacitor transfer lasers is shown in Fig. 8. The average powers were determined using a Scientech Model 36-001 thermopile. The peak power is obtained by dividing the average power by the repetition rate times the duration (FWHM) of the optical pulse. Although the average powers are about the same, the Blumlein laser stores somewhat less energy and is therefore more efficient than the *C*-to-*C* configuration. The overall efficiencies as determined by dividing the average optical power by the electrical (line cord) input are about 0.07 and 0.04 percent for the Blumlein and *C*-to-*C* lasers, respectively; the efficiencies of these two systems in terms of the optical energy per pulse divided by the stored electrical energy $CV^2/2$ are about 0.085 and 0.07 percent, respectively. Because of the transverse gas flow in the laser tube, the observed fractional decrease in the average power as the repetition rate is increased is less than is observed for lasers which incorporate axial gas flow. Also the power supply, as described in Section III, charges the laser capacitor to the same voltage independent of the repetition rate. The curves in Fig. 8 correspond to optimizing the laser-tube and spark-gap pressures, as well as the gas-flow rate, for maximum laser power.

The variation of the average power for the Blumlein laser as a function of laser-tube pressure for different circuit capacitances is shown in Fig. 9. Increasing the capacitance of the circuit, which increases the rise time for the voltage across the laser tube, results in a decrease in the optimum operating pressure for the laser. The reason for this effect is that the nitrogen laser tends to work best if the fully developed discharge in the laser tube occurs when the parameter E/P is in the range of 120-140 V/cm·torr. The electric field in the laser tube at the time when the discharge becomes developed is E (in other words, E is approximately the peak electric field in the tube), and P is the laser-tube pressure in torr. As the rise time of the voltage across the laser tube is increased, one must lower the pressure in the tube to achieve the optimum condition.

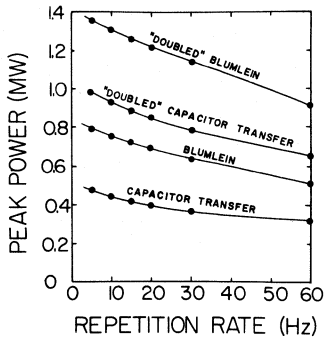


Fig. 8. Peak powers as a function of repetition rate for the Blumlein and capacitor transfer N_2 lasers and also for the "doubled" Blumlein and "doubled" *C*-to-*C* laser configurations. Note the pulse duration of the Blumlein and *C*-to-*C* lasers are 4-5 and 8 ns, respectively.

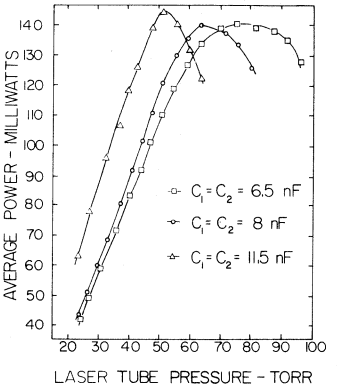


Fig. 9. Average power of Blumlein N_2 laser versus laser-tube pressure for different circuit capacitances.

The variation of the average power of the Blumlein laser for different laser-tube and spark-gap inductances is shown in Fig. 10; also shown in the figure are some of the theoretical results described in Section VI. Increasing either the switch inductance or the laser-tube inductance detracts from the performance of the device. Increasing the switch inductance also increases the rise time of the voltage across the laser tube with the result that the optimum laser-tube pressure is decreased. At pressures greater than the optimum the calculated power is somewhat greater than the measured power. This difference is probably due to the fact that at the higher pressures the discharge in the laser tube becomes nonuniform with noticeable concentrations of current flow. In the extreme limit of very high pressure the discharge degenerates into one or more sparks.

The pulse duration of the nitrogen laser decreases slightly

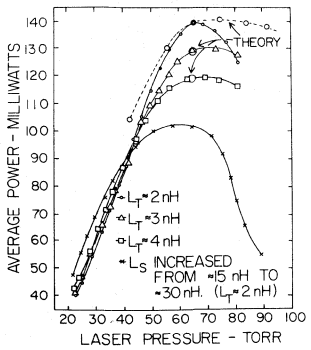


Fig. 10. Average power of Blumlein N_2 laser versus laser-tube pressure for different laser-tube inductance L_t and for different switch inductance L_s.

as the pressure in the laser tube is increased. Measurements of the optical pulse duration for the Blumlein laser are compared with the theoretical results of Section VI in Fig. 11. Measurements on the Blumlein system indicate that as the capacitance is increased from $C = 8$ nF to $C = 20$ nF (C is as indicated in Fig. 1), the pulse duration increases from 4 to 7 ns.

The measured optical power as a function of initial charge voltage is compared with the theoretical results for the Blumlein laser in Fig. 12. In order to compare with the theoretical model, the measurements shown in the figure were carried out for the single laser-tube pressure of 65 torr, with the spark-gap pressure adjusted according to the charging voltage. Increasing the charge voltage dramatically increases the power of the laser; however, it should be mentioned that increasing this voltage also dramatically decreases the lifetime of the capacitor. A Blumlein laser of this design with 3 sheets of Mylar for insulation, and with adequate protection against corona damage, can be expected to operate for of the order of 10^8 or more pulses without insulation failure for a charging voltage of 18-19 kV. Increasing the voltage to 22 or 23 kV can be expected to reduce the lifetime to about 10^6 or 10^7 pulses.

VI. Theory of the N_2 Laser

The characteristic time scale for the electrical and optical properties of a nitrogen laser is of the order of a few to 10 ns. Neither collisions between molecules nor ion recombination can be important during this short time period because the N_2 pressure in the laser tube is only about 50 torr. The ionization and excitation of the gas is almost entirely due to collisions with the electrons in the discharge, and a theoretical treatment of the laser must include an accurate description of the free electrons that are generated during the short-lived plasma.

The electrons in the nitrogen discharge may be considered to be in steady state with the instantaneous electric field since the Langevin relaxation time for the electron drift velocity, $\tau = m_e v_d\, eE$, is of the order of 10 ps, which is much less than the nanosecond time scale of the laser. Furthermore, both the growth of ionization in the gas and the production of the laser light pulse take place under conditions when the electron velocities can be described by a Maxwellian distribution

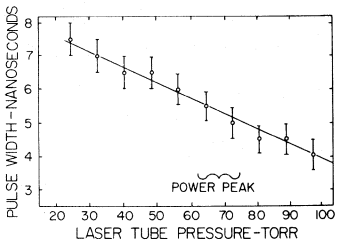


Fig. 11. Optical pulse duration (FWHM) for Blumlein laser versus laser-tube pressure.

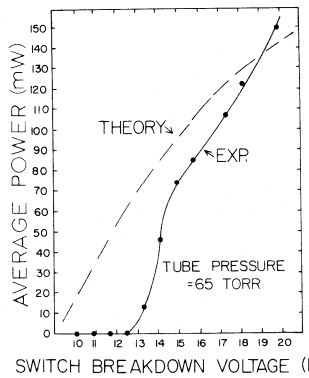


Fig. 12. Average laser output power versus Blumlein charge voltage for constant laser-tube pressure of 65 torr. The theory assumes a uniform discharge in the channel, whereas at the lower charging voltages the discharge became nonuniform, degenerating into a few sparks at very low voltages.

function. For example, Englehardt *et al.* [10], Kline and Siambis [11], and, more recently, Judd [12] have shown that the electron distribution function for a nitrogen discharge is closely approximated by a Maxwellian function when the electric field divided by the pressure exceeds about 30 to 40 V/cm·torr. This is particularly true for the high-energy tail of the distribution which is responsible for the ionization and electronic excitation of the gas molecules. It is therefore reasonable to describe the nitrogen laser plasma in terms of an electron temperature since the growth of ionization occurs when $E/P \geqslant 100$ V/cm·torr, and since the peak in the laser light output generally occurs when $E/P \approx 80$ V/cm·torr.

Within the framework of the previous discussion the electron temperature as a function of the instantaneous value of E/P can be determined by equating the ionization rates as given by the Townsend theory of ionization with the rates one would calculate from a kinetic model for the electron movement. Thus,

$$\alpha v_d = N_{\text{gas}} \int_0^\infty g(T_e, v)\, \sigma_i(v)\, 4\pi v^3\, dv \tag{1}$$

where

α	Townsend ionization coefficient;
v_d	the drift velocity;
N_{gas}	ground-state gas density;
$g(T_e, v)$	normalized Maxwell-Boltzmann distribution;
$\sigma_i(v)$	velocity-dependent ionization cross section for the nitrogen molecule.

The drift velocity v_d and the Townsend coefficient divided by the pressure α/P are each functions of (E/P). For nitrogen and for E/P between about 20 and 150 V/cm·torr (a range more than enough to describe the laser) these quantities are given to a very good approximation by

$$v_d = 2.9 \times 10^5 \left(\frac{E}{P}\right) \text{cm/s} \quad [13], [14] \tag{2}$$

$$\alpha/P = 1.4 \times 10^{-8} \left(\frac{E}{P}\right)^{3.7} \quad (\text{torr} \cdot \text{cm})^{-1} \quad [15], [16]. \tag{3}$$

The only undetermined parameter in (1) is T_e since the ionization cross section for N_2 is known [17]. This resulting point-by-point relationship gives the expression

$$kT_e = 0.11 \left(\frac{E}{P}\right)^{0.80} \text{eV} \quad (E/P \text{ in V/cm} \cdot \text{torr}). \tag{4}$$

The above procedure determines an effective electron temperature which is sufficient to predict the observed rates of ionization in nitrogen. Since the excited states associated with the laser are close to the ionization limit, one would expect the same electron temperature to closely approximate the electron excitation of these states. It is of course the difference between the excitation rates of the $C\pi$ and $B\pi$ levels that establishes the population inversion.

The above method for determining an electron temperature requires knowledge of only two macroscopic parameters, the drift velocity v_d and α/P, and knowledge of the ionization cross section. These quantities are well known for many different gases and one can expect this method to be useful in other situations. Alternative methods of estimating the electron temperature, such as solving an energy balance equation, require knowledge of all the cross sections that govern the gain or loss of energy by the electrons in this discharge. In many cases these cross sections are not all known.

In order to describe the electrical properties of a nitrogen laser it is necessary to relate the current flow in the gas to the voltage between the electrodes. This relationship must be consistent with the ability of the driving electrical circuit to deliver current to the time-dependent load. The Blumlein driven laser can be represented by the transmission-line circuit shown in Fig. 13, and in this case the current flow in the laser tube, I, is governed by the equations

$$L\frac{dI}{dt} + I(R_g + Z_0) = V_{\text{eff}} \tag{5}$$

$$V_{\text{eff}} = V_0(1 - e^{-t/\tau}\cos\omega t) - \frac{2}{C_1}\int_0^t I\,dt, \tag{6}$$

where

V_0 initial charge voltage of the system;
L inductance of the load (laser tube);
R_g time-dependent resistance of the laser discharge;
Z_0 characteristic impedance of the transmission line.

V_{eff} is the measured open-circuit voltage of the voltage-pulse generator minus a term that represents the discharge of the Blumlein capacitance.

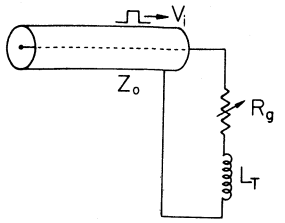


Fig. 13. Transmission-line circuit for Blumlein driven laser.

This term accounts for the voltage reflections at the spark-gap end of the transmission line and it must be included because the transmission line is of finite length.

Simultaneous with the solution of (5) and (6), one must also determine the resistance of the gas R_g. The multiplication of the electron density in the laser tube is given by the Townsend equation

$$dn_e/dt = \alpha v_d n_e. \tag{7}$$

Integration of this equation gives n_e as a function of the time. The conductivity of the gas as a function of time is given by

$$\sigma = \frac{en_e v_d}{E}. \tag{8}$$

Assuming a uniform electric field between the laser tube electrodes, the resistance of the discharge is

$$R_g = \frac{d}{s \cdot W\sigma} \tag{9}$$

where d is the 2.54-cm electrode separation, s is the thickness of the arc which is estimated to be 0.7 cm, and W is the 50-cm active length of the laser tube.

The solution of the above equations requires the electric field between the electrodes as a function of time, and this field is given by

$$E = \frac{1}{d}\left(IR_g + \epsilon L\frac{dI}{dt}\right). \tag{10}$$

The second term is that fraction of the inductive voltage across the laser tube that appears between the electrodes, ϵ is the ratio of the electrode separation d to the total perimeter length of the current flow in the tube. (This voltage is approximately 10-15 percent of the total.)

Numerical simultaneous solution of (5)-(10) was carried out using a digital computer with a time increment of 100 ps. As a test, several computations were done with an increment size of 10 ps, but there was no significant difference from the results with the 100-ps increment. The calculated voltage across the laser gap is compared with the experimentally measured voltage in Fig. 14; for the case shown the initial charge voltage is 19 kV with a laser tube pressure of 65 torr. The initial ion density at the start of the calculation was taken to be 10^8 ions/cm^3. This estimate is based on the known ion recombination coefficient for nitrogen [18] and the fact that the experiments were carried out at a laser repetition rate of 60 Hz. Reduction of the initial ion density of 10^3 ions/cm^3 (essentially zero as far as the calculations are concerned) resulted in a calculated laser energy per pulse of about twice that at 60 Hz. This is consistent with the

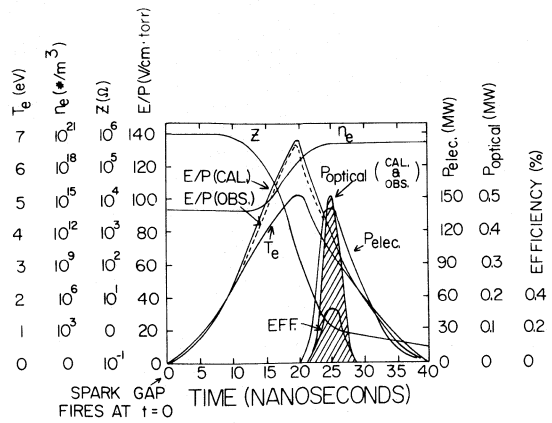


Fig. 14. Summary of measured and calculated properties of Blumlein driven N_2 laser.

observed increase of the laser output at lower repetition rates as is shown in Fig. 8.

Solution of the electrical circuit gives the growth of the electron density in the discharge, and also the time development of the electric field between the electrodes. These results are summarized in Fig. 14. Given the relationship between E/P and T_e, one can now proceed to solve the laser rate equations. The only significant processes which determine the populations of the $C\pi$ and $B\pi$ states of the nitrogen molecule during the brief laser discharge are collisions with the discharge electrons and interaction with the laser photons. It is tempting to include the possible effects of excited-state electron collisions which could alter the populations of the $C\pi$ and $B\pi$ states. However, the cross sections for these processes are not particularly well known. Furthermore these processes are not expected to be important since at the maximum plasma electron density of about $10^{14}/\text{cm}^3$, and with a typical electron temperature 4 eV (or $\bar{v}_e \approx 10^8$ cm/s), the cross section for $N_2^* - e^-$ collisions would have to be unreasonably large ($\sim 10^{-13}$ cm^2) for these reactions to be important on a nanosecond time scale. Therefore the laser rate equations are relatively simple and include only the electron excitation from the ground state to the $C\pi$ and $B\pi$ states along with the appropriate photon interactions. These rate equations are

$$\frac{dN_C}{dt} = n_e N_{\text{gas}} \int_0^\infty g(T_e, v)\sigma_{C_{v=0}}(v)4\pi v^3 dv - \sigma_{\text{stim}} n_{\text{ph}} c(N_C - N_B) - \frac{N_C}{\tau_C} \tag{11}$$

$$\frac{dN_B}{dt} = n_e N_{\text{gas}} \int_0^\infty g(t_e, v)\sigma_{B_{v=0}}(v)4\pi v^3 dv + \sigma_{\text{stim}} n_{\text{ph}} c(N_C - N_B) + \frac{N_C}{\tau_C} - \frac{N_B}{\tau_B} \tag{12}$$

$$\frac{dn_{\text{ph}}}{dt} = \sigma_{\text{stim}} n_{\text{ph}} c(N_C - N_B) - \frac{n_{\text{ph}}}{\tau_{\text{ph}}} + \gamma \frac{N_C}{\tau_C} \tag{13}$$

where N_C, N_B, n_{ph} are the number density of the $C(v = 0)$ state, the $B(v = 0)$ state, and the photons, respectively. The cross section for stimulated emission is σ_{stim}. In calculating σ_{stim} we have assumed 5 lines near 3371 Å [7]. The speed of light is c. The spontaneous lifetimes of the two laser levels are τ_C and τ_B (40 ns and 6 μs, respectively). The photon lifetime, τ_{ph}, represents the mean time a photon stays in the cavity. It is a spatial average and was taken to be the length of the cavity divided by the speed of light. The quantity γ is a geometrical factor for spontaneous photons emitted in the forward direction.

Although experimental determinations of σ_C are in relatively good agreement, the values of σ_B vary by almost a factor of 2 [19]-[22]. We have used the $C(v = 0)$ cross section as measured by Burns *et al.* [22]. We assume the same shape for the $B(v = 0)$ state with threshold and peak shifted to 6.6 eV and 10 eV, respectively. Using the upper and lower extreme value of the maximum of the σ_B cross section as compiled by Shemansky and Broadfoot [21], we calculate 100- and 290-mW average laser power for $P = 65$ torr at a repetition rate of 60 Hz. The charge voltage was taken to be the experimental value of 19 kV. The measured average power of 140 mW falls within the range predicted by the extreme values of the cross section. As a working compromise, the peak value of σ_B was taken to be 6.35×10^{-18} cm^2 in order to achieve average power agreement between experiment and theory at $P = 65$ torr. The calculated laser output power as a function of time is shown in Fig. 14. The selection of σ_B also brought the calculated optical pulse duration (FWHM) into agreement with the measurements as is shown in Fig. 14. The chosen electron excitation function for the B state has been used in all the calculations that follow.

The calculated and measured average power as a function of laser-tube pressure are compared in Fig. 10; and the calculated average power as a function of charge voltage is compared with the measured results in Fig. 12. In both cases the calculations exhibit the same qualitative characteristics as the measurements. However, for high pressure or low voltages, the calculations predict higher laser power than is observed. In both of these situations the laser discharge exhibited pronounced nonuniformities, and the difference between experiment and theory can probably be attributed to the plasma instabilities. Comparison between experiment and theory with respect to changing the laser tube inductance is shown in Fig. 10.

The calculated instantaneous electrical and optical properties of the Blumlein laser are compared with the measured E/P and optical output in Fig. 14. The calculated instantaneous electrical and optical properties of the C-to-C laser are shown in Fig. 15. Note that the time scales for the two figures differ by a factor of 2. The transmission-line analysis given by (5) and (6) was used to analyze the two different systems. However, in the case of the somewhat slower C-to-C laser, it was found that a lumped parameter analysis based upon the equivalent circuit shown in Fig. 1(b) gave essentially the same results. The curves in Fig. 15 are the result of a lumped parameter analysis that included a 1-Ω resistance associated with the spark gap. In view of the fact that the magnitude of the $B^3\pi$ excitation cross section was the only parameter adjusted to achieve agreement between the measured and predicted average power for the Blumlein laser, then the remaining

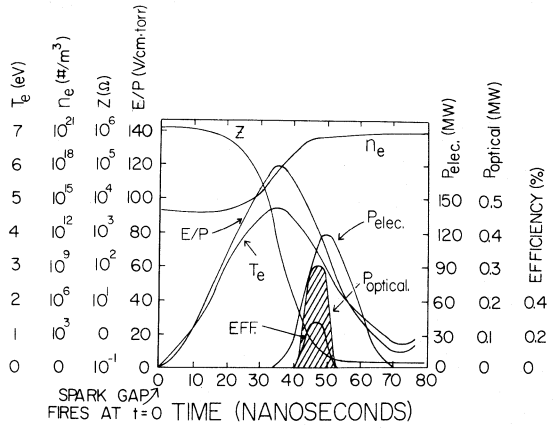


Fig. 15. Summary of calculated properties of capacitor transfer driven N_2 laser. The measured peak power and pulse duration (FWHM) of this laser were 0.35 mW and 8 ns, respectively.

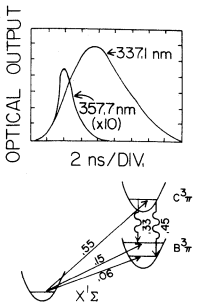


Fig. 16. Time-resolved comparison of 337.1-nm and 357.7-nm laser emission from *C*-to-*C* laser. Also shown are the relevant energy levels and Franck–Condon factors.

results of the calculation such as the optical pulse duration for the Blumlein laser, and both the peak power and the pulse duration for the *C*-to-*C* laser are in surprisingly good agreement with the experimental results.

Except for the difference in the time scales, the properties of the two lasers are very similar: the electron density increases rapidly with time only when E/P is greater than about 100 V/cm·torr, and then as the discharge begins to load the electrical circuit, E/P falls rapidly toward a very low value with the optical output occurring when E/P passes through a value of about 80 V/cm·torr ($T_e \sim 4$ eV). The general characteristic of ions being the predominate discharge product at high E/P, and then excited electronic states, the predominate product as slightly lower E/P is consistent with the previous work of Englehardt *et al.* [10] and the more recent work of Judd [12].

There are significant differences between the two lasers: for both systems the electrical power to the laser tube is a maximum when the impedance of the discharge is about equal to the impedance of the driving electrical circuit. However, for the Blumlein, the electrical power is a maximum when E/P is about 80 V/cm·torr, and thus the impedance-matching condition is reached in coincidence with the discharge conditions that are most favorable for the production of laser emission. Unfortunately, in the case of the *C*-to-*C* laser, the maximum in the electrical power is somewhat after the laser pulse. A second difference between the two lasers is indicated by when the laser pulse terminates. The optical pulse from the Blumlein laser terminates as the power to the laser tube decreases, suggesting that the optical pulse terminates because E/P (or T_e) has fallen to a value that is too low for the electrons to pump a population inversion. Of course the lasing action itself would assist this mechanism. On the other hand, for the *C*-to-*C* laser the optical pulse terminates even though E/P is still relatively high and despite the fact that the electrical power to the laser tube is still increasing. In this case the population inversion is destroyed because of the lasing action itself since the lower level is relatively long lived. Thus there appear to be two mechanisms that can result in the termination of the N_2 laser pulse. Both of these mechanisms can be observed in the *C*-to-*C* laser. For example, the lasers described in this paper were found to also exhibit weak laser emission at 357.7 nm due to the $(v = 0)C^3 \rightarrow (v = 1)B^3$ transition. Time-resolved measurements of the 337.1-nm laser emission and the much weaker laser emission at 357.7 nm are shown in Fig. 16. Also shown in the figure is an energy-level diagram for the $X^1\Sigma$, $C^3\pi$, and $B^3\pi$ states of N_2 along with the Franck–Condon factors that govern the relative electronic excitation rates to these states as well as the relative optical transitions probabilities. The fact that the Franck–Condon factor between the $(v = 0)X^1$ and $(v = 0)C^3$ states is about a factor of 10 greater than between the $(v = 0)X^1$ and $(v = 0)B^3$ states is perhaps the basic reason why N_2 is a laser at all. However there is also the possibility for a population inversion between the $(v = 0)C^3$ and $(v = 1)B^3$ states, although the conditions for this inversion are considerably less favorable than for the 337.1-nm laser transition. Thus the 357.7-nm emission would be expected to be less intense than the 337.1-nm emission, and also the 357.7-nm laser emission would be considerably more sensitive to the plasma electron temperature. For the *C*-to-*C* laser pulses shown in Fig. 16, it is very probable that the 357.7-nm pulse terminates because the electron temperature has fallen to too low a value even though this same value of T_e is still sufficiently high to continue pumping the 337.1-nm laser transition. Then as the evolution of the *C*-to-*C* discharge continues, the 337.1-nm emission terminates because of the optical transitions to the $(v = 0)B^3$ state. It is perhaps worth mentioning that for high-pressure N_2 lasers, for example, pressures in the range of 1 to several atmospheres, one might expect the 357.7-nm laser emission to be the major optical output because of collisional relaxation of the $(v = 1)B^3$ vibrational level.

VII. Summary

The properties of transmission-line pulsed-discharge excited nitrogen lasers have been investigated. The measured characteristics of the laser are described in terms of a theoretical model that treats the N_2 laser as an integrated electrooptical system. The theory is based upon the known macroscopic properties of N_2 discharges and upon the known electron impact ionization and excitation cross sections for the N_2 molecule. It is shown that the rapidly changing plasma electron temperature as well as the lasing action itself can both result in the termination of the optical output. For pulsed nitrogen laser discharges in the range of 100-torr gas pressure, the

electron density does not become high enough for excited-state-electron interactions to become competitive with ground-state-electron and excited-state-photon interactions. However, this may not be the case for higher pressure discharges. Perhaps the most important result of this investigation is the demonstration that a relatively complete and accurate description of a pulsed high-power UV laser can be achieved using methods that should be applicable to many other gases.

References

[1] H. G. Heard, "Ultra-violet gas laser at room temperature," *Nature*, vol. 200, p. 667, 1963.

[2] D. A. Lennard, "Saturation of the molecular nitrogen second positive laser transition," *Appl. Phys. Lett.*, vol. 7, pp. 4–6, 1965.

[3] E. T. Gerry, "Pulsed-molecular-nitrogen laser theory," *Appl. Phys. Lett.*, vol. 7, pp. 6–8, 1965.

[4] J. D. Shipman, Jr., "Traveling wave excitation of high power gas lasers," *Appl. Phys. Lett.*, vol. 10, pp. 3–4, 1967.

[5] A. W. Ali, A. C. Kolb, and A. D. Anderson, "Theory of the pulsed molecular nitrogen laser," *Appl. Optics*, vol. 6, pp. 2115–2119, 1967.

[6] M. Geller, D. E. Altman, and T. A. DeTemple, "Some considerations in the design of a high power pulsed N_2 laser," *Appl. Optics*, vol. 7, pp. 2232–2237, 1968.

[7] B. W. Woodward, V. J. Ehlers, and W. C. Lineberger, "A reliable, repetitively pulsed, high power nitrogen laser," *Rev. Sci. Instr.*, vol. 44, pp. 882–887, 1973.

[8] D. Bastings, F. P. Shafer, and B. Steyer, "A simple high power nitrogen laser," *Opto-Electronics*, vol. 4, pp. 43–49, 1972.

[9] J. I. Levatter and S.-C. Lin, "High power generation from a parallel-plates-driven pulsed nitrogen laser," *Appl. Phys. Lett.*, vol. 25, pp. 703–705, 1974.

[10] A. G. Englehardt, A. V. Phelps, and C. G. Risk, "Determination of momentum transfer and inelastic collision cross sections for electrons in nitrogen using transport coefficients," *Phys. Rev.*, vol. 135, pp. A1566–A1574, 1964.

[11] L. E. Kline and J. G. Siambis, "Computer simulation of electrical breakdown in gases: Avalanche and streamer formation," *Phys. Rev.*, vol. A5, pp. 794–805, 1972.

[12] O'D. P. Judd, private communication.

[13] K. H. Wagner, "Mittlere Energien und Driflgeschwindigkeiten von Elektronen in Stickstoff, Argon, und Xenon ermittelt aus Bildverstärkeraufnahmen von Elektronenlawinen," *Z. Physik*, vol. 178, pp. 64–81, 1964.

[14] P. Felsenthal and J. Proud, "Nanosecond-pulse breakdown in gases," *Phys. Rev.*, vol. 139, pp. A1796–A1804, 1965.

[15] H. Raether, *Electron Avalanches and Breakdown in Gases*. London, England: Butterworths, 1964.

[16] A. E. D. Haylen, "Townsend's first ionization coefficient in pure nitrogen," *Nature*, vol. 183, pp. 1545–1546, 1959.

[17] The electron impact ionization cross section for many gases is well known. See for example, L. J. Kieffer and G. H. Dunn, "Electron impact ionization cross section data for atoms, atomic ions, and diatomic molecules: I, Experimental data," *Rev. Mod. Phys.*, vol. 38, pp. 1–35, 1966.

[18] S. C. Brown, *Basic Data of Plasma Physics*. Cambridge, MA: MIT Press; and also New York: Wiley, 1959.

[19] M. H. Rees and R. A. Jones, "Time dependent studies of the Aurora-II spectroscopic morphology," *Planet. Sci.*, vol. 21, pp. 1213–1235, 1973.

[20] J. D. Jobe, F. A. Sharpton, and R. M. St. John, "Apparent cross sections of N_2 for electron excitation of the second positive system," *J. Opt. Soc. Am.*, vol. 57, pp. 106–107, 1967.

[21] D. E. Shemansky and A. L. Broadfoot, "Excitation of N_2 and N_2^+ systems by electrons–II, Excitation cross sections and N_2 IPG low pressure afterglow," *J. Quant. Spectroscopy and Rad.*, vol. 11, pp. 1401–1439, 1971.

[22] D. J. Burns, F. R. Simpson, and J. W. McConkey, "Absolute cross sections for electron excitation of the second positive bands of nitrogen," *J. Phys., B.*, vol. 2, pp. 52–64, 1969.

Derivative Measurements of the Current–Voltage Characteristics of Double-Heterostructure Injection Lasers

PETER A. BARNES AND THOMAS L. PAOLI, MEMBER, IEEE

Abstract—**Measurements of the electrical characteristics of double-heterostructure (DH) stripe-geometry AlGaAs junction lasers are reported. We show that the electrical characteristics of these lasers are adequately represented by a resistor in series with a p-n junction characterized by a classical diode equation, $I = I_S$ [exp $(qV_j/\eta kT) - 1$]. Devices have been measured with almost ideal junction characteristics with both the saturation current, I_S, and the exponential parameter, η, constant, while in other diodes both η and I_S exhibit a strong current dependence. Measurement of the first derivative dV/dI and the product IdV/dI is shown to be an especially useful technique for electrical characterization, yielding accurate and direct determination of the series resistance, the exponential junction parameter, and the laser threshold current. The observation of lasing threshold from an electrical measurement, instead of from the more usual optical measurement, is discussed in terms of the saturation behavior of the junction voltage at and above threshold.**

Manuscript received April 26, 1976; revised May 28, 1976.
The authors are with Bell Laboratories, Murray Hill, NJ 07974.

I. Introduction

THE electrical characteristics of semiconductor heterojunctions have been a subject of considerable interest for many years [1]. However, most heterojunctions exhibit poor lattice match of the constituent semiconductors comprising the p-n junction. This lattice mismatch creates defects and deep, electrically active levels in the depletion layer of the

heterojunction complicating considerably the electrical characteristics of the junction [1].

An exception is the AlGaAs-GaAs semiconductor system which has excellent lattice matching and thereby allows essentially defect-free heterojunctions to be grown [2]. Double heterojunctions (DH) of P:AlGaAs-p:GaAs-N:AlGaAs made possible CW, room-temperature operation of semiconductor injection lasers [3]. It is the electrical characteristics of AlGaAs-GaAs DH injection lasers, and in particular, the saturation of the junction voltage above lasing threshold, to which this paper is addressed.

In order to model the stripe-geometry, proton-bombarded DH laser for suitable analysis, an equivalent circuit is constructed based upon the physical structure of the laser. It is shown that the first derivative dV/dI of the DH laser I-V characteristic and the product $IdV/dI = dV/d(\ln I)$ allow accurate determination of the laser diode series resistance R, the exponential factor ηkT, and an electrical measurement of the laser threshold.

Historically, threshold measurements have emphasized the laser optical characteristics. However, we show that saturation of the junction voltage [4], [5] due to the onset of lasing is indicated clearly in the derivative of the device voltage dV/dI allowing accurate determination of the lasing threshold using a purely electrical measurement.

The concept of junction voltage saturation at threshold has been discussed in the early work of Eliseev *et al.* [6]. These workers reported data on dc-operated homojunction devices at 77 K in which the derivative dV/dI appears to have been determined by carefully fitting linear I-V data. These devices had four mirror surfaces, yielding totally internally reflected modes. A similar approach was used by Rode and Dawson [7] for pulsed measurements on stripe-geometry, proton-bombarded DH devices operated at room temperature. These devices had the more usual two mirror surfaces and resulting Fabry-Perot modes. Recently Walpole *et al.* [8] reported CW derivative measurements of single-heterojunction PbSnTe diode lasers at very low temperatures.

II. Diode Structure and Electrical Model

The laser diodes used in the present work were stripe-geometry, proton-bombarded [9] four-layer structures prepared by the liquid phase epitaxial process [3]. A schematic sketch of the structure is shown in Fig. 1(a). The thin active p-$Al_{0.08}Ga_{0.92}As$ layer (less than 0.4 μm) was sandwiched between layers of P-$Al_{0.36}Ga_{0.64}As$ and N-$Al_{0.36}Ga_{0.64}As$ approximately 2 μm thick. Each laser was bonded directly to a gold-plated copper heat sink allowing continuous operation at room temperature.

The electrical model for a proton-bombarded stripe-geometry junction laser follows from consideration of the physical structure of the device illustrated in Fig. 1(a). The resulting dc equivalent circuit, shown in Fig. 1(b), consists of an ideal p-n junction in series with a resistance R which accounts for the resistance of the bulk material and the contacts. Possible leakage paths around the junction, such as through the proton-bombarded material, are represented by a shunt resistance R_{sh}.

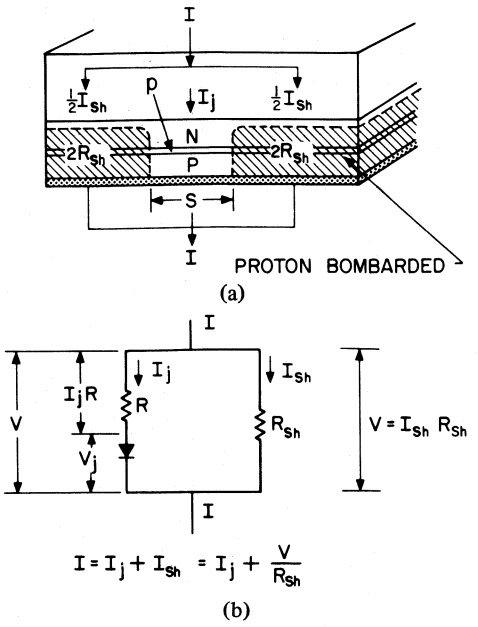


Fig. 1. Physical structure (a) and equivalent electrical circuit (b) of a stripe-geometry, proton-bombarded DH laser.

The I-V characteristic of this equivalent circuit is given by

$$I = \frac{V}{R_{sh}} + I_s \left\{ \exp \left[\left[\left(1 + \frac{R}{R_{sh}} \right) V - IR \right] / \frac{\eta kT}{q} \right] - 1 \right\} \quad (1)$$

where V is the applied voltage at the device terminals, I_s is the junction saturation current, and η is a parameter characteristic of the p-N heterojunction.

To illustrate the various regimes implicit in this I-V characteristic, we show in Fig. 2 plots of $\log I$ and I as a function of V derived from (1). The saturation current $I_s = 8.57 \times 10^{-17}$ A and $\eta kT/q = 0.0435$ V result from fitting (1) to the data of a specific DH laser to be considered in more detail in this paper. The open circles in Fig. 2 are the measured data points for this diode (diode A). Values for R of 1 to 4 Ω are typical of low- and high-resistance diodes. The resistance of diode A was 1.78 Ω. It is clear that the effect of the series resistance appears for currents in excess of 5 mA and can add from 0.1 to 0.4 V to the forward voltage near the threshold current, typically near 100 mA. The inset plot of the linear I-V shows the sensitivity of the I-V characteristic to changes in the series resistance and the lack of sensitivity to the shunt resistance. However, it is difficult to measure the series resistance from the slope of the linear I-V characteristic due to the nonlinear contribution from the junction for currents near lasing threshold. The effect of the shunt resistance is negligible for currents approaching the laser threshold, even for $R_{sh} = 10^4$ Ω, which is a value indicative of a very poor device and rarely ever seen. For typical R_{sh} of 10^7 Ω and greater, the linear region of the semilog plot is sufficient to define, from its slope, a value for $\eta kT/q$.

The I-V relation of (1) can be recast into a form more suitable for measurement of the parameters η and R.

$$V = \frac{1}{1 + R/R_{sh}} \left[IR + \frac{\eta kT}{q} \ln \left(\frac{I}{I_s} + 1 - \frac{V}{I_s R_{sh}} \right) \right] \quad (2)$$

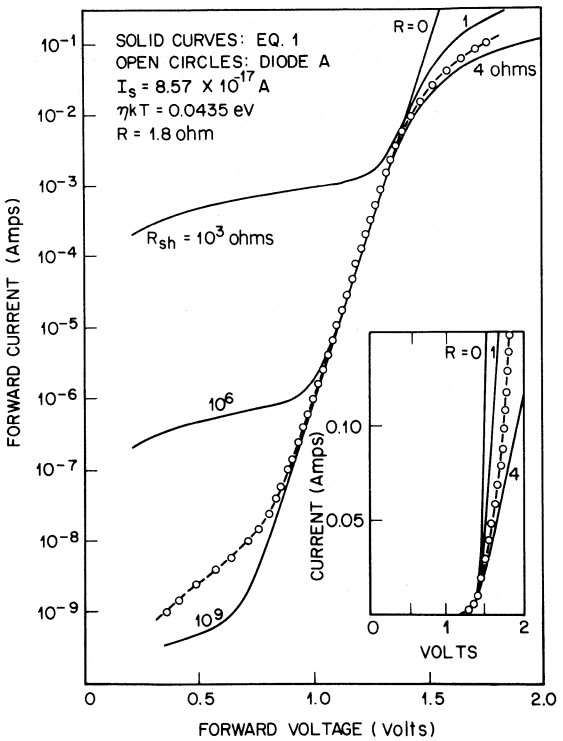


Fig. 2. Log I versus V, from a numerical fit to the equivalent circuit of Fig. 1. The parameters and data shown are for laser diode A discussed in the text.

from which the differential resistance at current I is given by

$$\frac{dV}{dI} = \frac{R + \frac{\eta kT}{q}\left(\frac{1}{I + I_s - V/R_{sh}}\right)}{\left(1 + \frac{R}{R_{sh}}\right) + \frac{\eta kT}{q}\left[\frac{1}{(I+I_s)R_{sh} - V}\right]}. \tag{3}$$

As indicated in Fig. 2, the effect of shunt resistance is usually negligible above 10^{-7} A, while the current near threshold is in the vicinity of 100 mA. Hence this cumbersome equation can be reduced to

$$\frac{dV}{dI} = R + \frac{\eta kT}{q}\frac{1}{(I+I_s)}. \tag{4}$$

Furthermore, for most cases of practical interest $I \gg I_s$, so that

$$\frac{dV}{dI} = R + \frac{\eta kT}{q}\frac{1}{I}. \tag{5}$$

Thus a plot of dV/dI versus $1/I$ is linear with a slope equal to $\eta kT/q$ and the intercept at $1/I = 0$ equal to R.

An alternate form of (5) which is also suitable for direct measurements is

$$I\frac{dV}{dI} = IR + \frac{\eta kT}{q}. \tag{6}$$

In this case, the product IdV/dI is linearly related to I with a slope equal to R and a zero-current intercept equal to $\eta kT/q$.

Finally, we consider the special features of the I-V relation for a junction laser. In an ideal laser, the separation of the electron and hole quasi-Fermi levels, and hence the junction voltage, becomes "pinned" at threshold as a result of the high rate of stimulated emission [5], [6]. The I-V relation for $I > I_{th}$ becomes

$$V = IR + V_{jth} \tag{7}$$

where V_{jth} is the junction voltage at threshold. The derivative dV/dI above threshold is therefore a constant equal to the series resistance R. Consequently at the lasing threshold, the product IdV/dI should decrease abruptly from $IR + \eta kT/q$ to IR and then continue to increase with current at a rate equal to R. Because of the linear current scale, the product representation, i.e., IdV/dI versus I, is more convenient for direct measurement of threshold than the derivative alone.

We caution the reader that the use of (1), and the derivatives which result from it, is strictly valid only below lasing threshold and without the stimulated emission process [10]. However, the experimental data to follow indicate good agreement with the model presented.

III. Experimental Technique

The technique used to measure the first derivative dV/dI is similar to well-known analog derivative techniques [11]. The procedure relies upon superimposing an ac modulation, $i\cos(\omega t)$ onto the dc bias current I applied to the laser.

If the current modulation amplitude i is kept small (relative to I) and constant, then the voltage V developed across the device terminals may be written as a Taylor power series expansion in the modulation signal,

$$\begin{aligned} V &= V[I + i\cos(\omega t)] \\ V &= V_0(I) + i\cos(\omega t)\frac{dV}{dI} + \frac{i^2\cos^2(\omega t)}{2}\frac{d^2V}{dI^2} + \cdots \\ &= \left[V_0(I) + \frac{i^2}{4}\frac{d^2V}{dI^2} + \cdots\right] + \cos(\omega t)\left[i\frac{dV}{dI} + \frac{i^3}{8}\frac{d^3V}{dI^3}\right. \\ &\quad \left. + \frac{i^5}{192}\frac{d^5V}{dI^3} + \cdots\right] + \cos(2\omega t)\left[\frac{i^2}{4}\frac{d^2V}{dI^2} + \frac{i^4}{48}\frac{d^4V}{dI^4}\right. \\ &\quad \left. + \frac{i^6}{1536}\frac{d^6V}{dI^6} + \cdots\right] + \cdots. \end{aligned} \tag{8}$$

In the discussion of the diode model, Section II, we have shown that for most practical diodes, we may assume $R_{sh} \to \infty$, and near threshold $I \gg I_s$. Thus using (5), forming the required derivatives and summing the resulting series yields

$$\begin{aligned} V = V_{dc} &+ \cos(\omega t)\left[iR + \frac{\eta kT}{q}\cdot\frac{2}{m}\left(1 - \sqrt{1-m^2}\right)\right] \\ &- \cos(2\omega t)\left[\frac{\eta kT}{q}\cdot\frac{2}{m^2}\left(1 - \tfrac{1}{2}m^2 - \sqrt{1-m^2}\right)\right] + \cdots \end{aligned} \tag{9}$$

where $m = i/I$, the modulation index. Furthermore by maintaining the modulation i much less than the bias current I ($m \ll 1$), only the leading terms of each frequency component need be retained in (8) and (9)

$$V = V_0(I) + i\frac{dV}{dI}\cos(\omega t) + \frac{i^2}{4}\frac{d^2V}{dI^2}\cos(2\omega t) + \cdots \quad (10)$$

$$= V_0(I) + \left[R + \frac{\eta kT}{q}\cdot\frac{1}{I}\right] i\cos(\omega t) - \frac{\eta kT}{q}\frac{i^2}{4I^2}\cos(2\omega t) + . \quad (11)$$

For modulation levels m less than 10 percent, the errors in approximating (8) and (9) by (10) and (11), respectively, are less than 0.25 percent for the first derivative ($\cos \omega t$) and less than 0.5 percent for the second derivative ($\cos 2\omega t$). Thus voltage detection at the fundamental frequency yields a direct indication of dV/dI and thereby the values of R and $\eta kT/q$. Similarly, the signal at 2ω can be used to measure the second derivative d^2V/dI^2. Since R is a linear element and therefore appears only in the amplitude of the fundamental signal, the second derivative yields $\eta kT/q$ directly.

The first derivative of the voltage-current characteristic of DH lasers was measured and recorded with the system illustrated in Fig. 3. The ac current modulation was provided at 10 kHz by an audio generator loaded with 250 kΩ. The modulation amplitude was set at less than 10 percent of the minimum bias current to ensure a minimal contribution from the higher order terms. The ac voltage generated across the laser was detected with a lock-in amplifier whose output was multiplied by a signal proportional to the dc current and then recorded as a function of current. The system was calibrated by replacing the laser with accurately known resistors of value 1.0 Ω and 4.3 Ω. With each linear resistor, the output of the recorder was a straight line passing through the origin with slope equal to its resistance.

A slight rearrangement of the components in Fig. 3 also allowed the derivative dV/dI to be recorded as a function of $1/I$. In this configuration, the lock-in output was sent directly to the recorder while the inverse of the current was taken by the multiplier before recording. Recording of dV/dI as a function of $1/I$ is convenient in detecting changes in $\eta kT/q$ as a function of current. A disadvantage is the nonlinear abscissa.

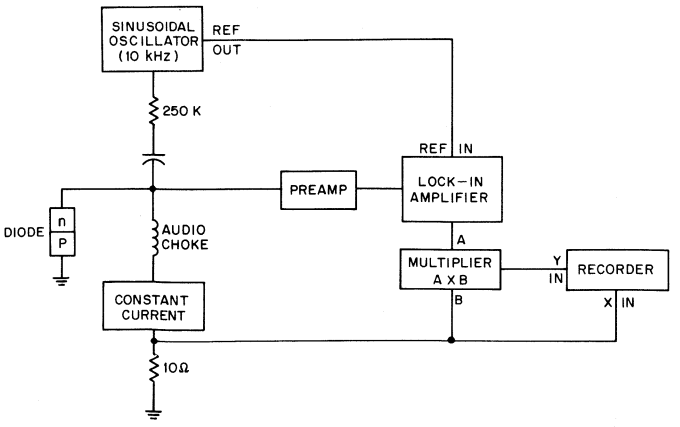


Fig. 3. Block diagram of the circuit used to measure the first derivative dV/dI of a DH laser.

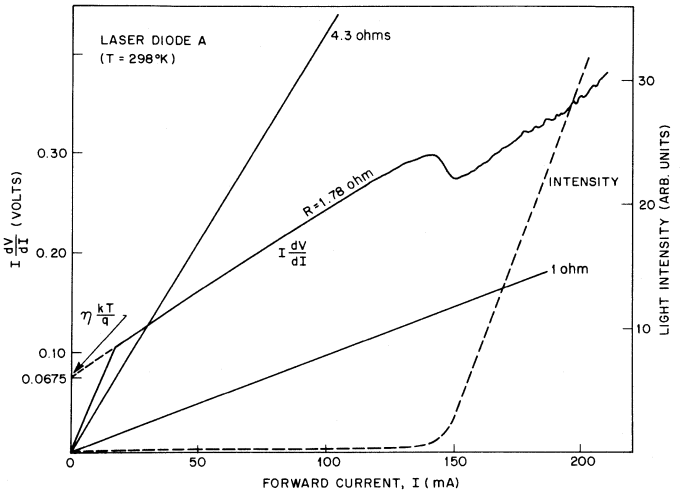


Fig. 4. $I(dV/dI)$ versus I and laser light output versus current of laser diode A, indicating voltage saturation at I_{th}.

IV. Experimental Results

An example of the experimentally observed variation of $I(dV/dI)$ with current is shown in Fig. 4 along with the corresponding light output-current characteristic. As discussed in Section II, the product $I(dV/dI)$ decreases abruptly at a current in the vicinity of the lasing threshold. For modulation levels of 10 percent or less, no change in the shape or steepness of the decrease at lasing threshold was observed. Detailed calculations of the instrument response function for an ideal laser have been recently reported by Joyce and Dixon [12]. Well below threshold, $I(dV/dI)$ varies linearly with current at a rate equal to the series resistance R, which for this laser, diode A, was 1.78 Ω. Due to clipping by the lock-in amplifier, the measurement was not accurate below about 20 mA. However, extrapolation of the linear relation to zero current yields $\eta kT/q = 0.0675$ V or a value of 2.63 for η ($T = 298$ K).

To confirm the values of R and η deduced from the product curve, the I-V characteristic of the same diode was measured directly from 10^{-9} to 0.180 A. At currents below 100 mA the diode voltage was measured on a dc basis, while above 100 mA, the diode linear I-V characteristic was measured under pulsed conditions to avoid heating. The resulting data plotted on linear scales are shown in the inset of Fig. 2. At the highest currents ($I = 180$ mA) the slope of the linear I-V gives a value for R equal to 1.8 Ω, which is in good agreement with the value obtained from the data in Fig. 4.

To obtain a value for η, the I-V data were plotted on a semilogarithmic scale as shown in Fig. 2. Equation (1) was numerically fitted to the data to determine values for R, I_s, and $\eta kT/q$. The resulting value for $R \approx 2.7$ Ω and $\eta = 1.70$ differed considerably from the values determined from the product curve ($R = 1.78$ Ω, $\eta = 2.63$) and the linear I-V curve ($R = 1.8$ Ω). Further measurements revealed that this discrepancy was the result of current dependence in η, and the subsequent change in I_s which must accompany it. The variation of η with current is clearly demonstrated in the observed variation of dV/dI with inverse current shown in Fig. 5 for the same diode. From the slope of the curve at currents between 10^{-3} and 10^{-4} A, $\eta kT/q = 0.043$ V ($\eta = 1.67$) which is in excellent agreement with the value taken from the semilog I-V characteristic over the same current range. Furthermore, as the current increases it is clear from Fig. 5 that the slope increases, indicating an increase in the value of η. Consequently,

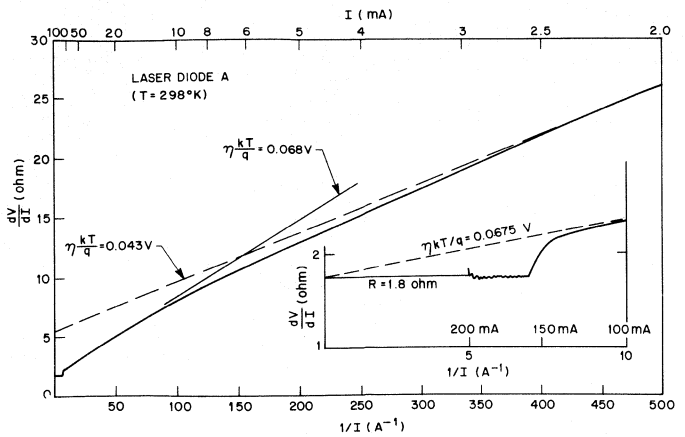


Fig. 5. dV/dI versus $1/I$ for diode A indicating the change in $\eta kT/q$ as a function of current. The rapid change in dV/dI near threshold is shown in the inset.

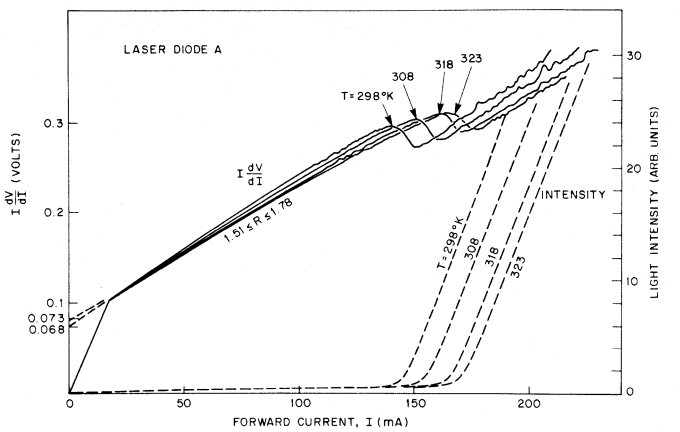


Fig. 6. $I(dV/dI)$ versus I and laser light output versus current for laser diode A, as a function of temperature, near room temperature.

at currents between 10 and 100 mA, the value of η has increased to 2.64 which agrees with the value obtained from the product curve over the same current range. Since a change in η requires a change in I_s, numerical fitting of (1) is invalid unless the functional form for η and I_s is known.

The voltage saturation which occurs at threshold is also evident in Fig. 5. As discussed in Section II, the first derivative dV/dI drops abruptly at threshold to a constant value equal to the series resistance of the diode. From Fig. 5, this value for R is 1.8 Ω which agrees with the other measurements.

To confirm that the apparent voltage saturation demonstrated in Figs. 4 and 5 was determined by the onset of lasing, several additional measurements were performed. First, the temperature of the laser was varied in order to shift the lasing threshold. The resulting $I(dV/dI)$ and light output curves are shown in Fig. 6. It is clear that the breakpoint in the curve moves to higher currents along with the laser threshold. Furthermore, over the temperature range studied, the value of $\eta kT/q$, measured by the zero-current intercept, scaled linearly with the absolute temperature, indicating a relatively constant η for 10 mA $\leqslant I \leqslant$ 100 mA. Secondly, the lasing threshold was also measured by the current at which a saturation occurred in the emission polarized orthogonally to the lasing emission [13]. Threshold measured in this way agreed accurately with the current at which the product $I(dV/dI)$ abruptly decreased. Final confirmation that this abrupt decrease is a result of the onset of lasing was obtained by operating a diode first with and then without lasing. The lasing action was inhibited by physically damaging the mirrors. As shown in Fig. 7, no evidence of an abrupt decrease in $I(dV/dI)$ was observed after the lasing was inhibited.

Not all lasers show complete voltage saturation over as large a range above threshold as illustrated in Fig. 4 for diode A. A typical example of incomplete saturation is shown in Fig. 8 along with the light-current characteristic of the laser. In this device, diode C, the product $I(dV/dI)$ varies linearly with current up to the threshold current where it exhibits the abrupt drop characteristic of the voltage saturation which occurs at threshold. However, the junction voltage remains "pinned" only for a small range of currents above threshold before con-

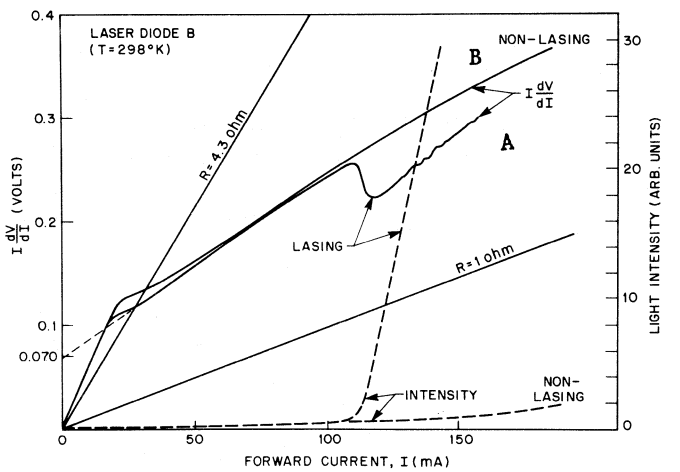


Fig. 7. $I(dV/dI)$ versus I and light output versus current for diode B. Curves A indicate voltage saturation of the product curve, and the rapid increase in light output for $I > I_{th}$. After spoiling the laser mirrors (inhibiting laser action), the voltage saturation is lost and the device does not lase as indicated in curves B.

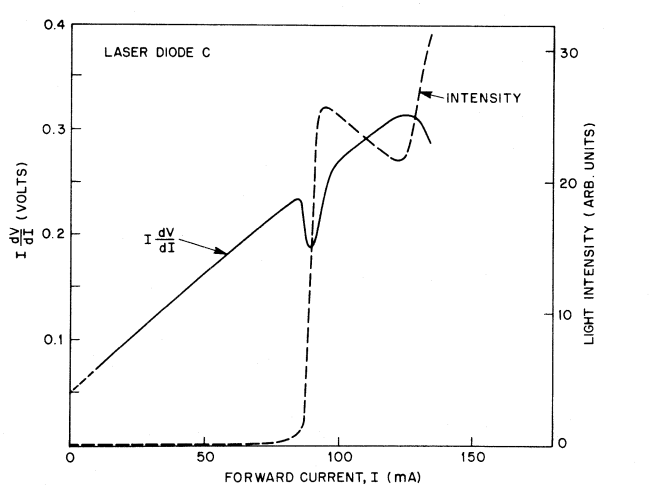


Fig. 8. $I(dV/dI)$ versus I and laser intensity versus current for diode C. The behavior of this diode indicates the response of $I(dV/dI)$ for a laser with a strong nonlinearity in the laser intensity-current characteristic which accompanies the loss of voltage saturation.

TABLE I
ELECTRICAL CHARACTERISTICS OF DOUBLE HETEROSTRUCTURE LASERS

Technique Used	R (Ω)	η		I_s (A)	I_{th} (mA)
		$I < 0.1$ mA	$I > 10$ mA		
Diode A (T = 298 K)					
I versus V	$1.9 \pm {}^{0}_{0.2}$	–	–		–
$\log I$ versus V	2.2 ± 0.5	1.69	–	$(8.6 \pm 0.2) \times 10^{-17}$	–
$I(dV/dI)$ versus I	1.78 ± 0.05	1.68	2.63		151 mA
dV/dI versus $1/I$	1.8 ± 0.1	1.68	2.64		151 mA
L versus I	–	–			146 mA
Diode C (T = 298 K)					
Technique Used					
I versus V	$2.4 \pm {}^{0}_{0.2}$				
$\log I$ versus V	2.4 ± 0.2	1.98	$\{10^{-9} \leq I < 10^{-1}$ A$\}$	$(4.26 \pm 0.5) \times 10^{-15}$	
$I(dV/dI)$ versus I	2.27 ± 0.05	1.96	1.96		89 mA
dV/dI versus $1/I$	–				–
L versus I	–				85 mA

tinuing to increase at a rate nearly equal to its prethreshold value. It is also evident that a nonlinearity in the light-current characteristic occurs at the same current at which the junction voltage begins to increase. This observation confirms studies [13], [14] which suggest that the optical gain of the laser, as indicated by its spontaneous emission, is no longer saturated at currents where the emission characteristic becomes nonlinear. This topic will be explored more completely in a future report [14].

Finally, it is useful to confirm the values for R and η determined for diode C from Fig. 8 with the values obtained from a numerical fit of (1) to the I-V characteristic as measured directly. These values are summarized in Table I along with analogous values for the laser described first in this section (diode A). The agreement between the measured values for R is good. Most interesting, however, is that the values for η for diode C are also in excellent agreement even though the measurements were performed over very different current ranges. This immediately suggests that for diode C, η does not depend on current as it did in diode A. This conclusion was also confirmed by measuring dV/dI as a function of inverse current. However, the difference in the electrical characteristics of these two devices is most vividly illustrated by plotting $\log I$ as a function of the junction voltage, $V_j = V - IR$, where R is the experimentally determined series resistance. As indicated in Fig. 9, it becomes quite evident in this way that η and I_s for diode A are changing with current, while for diode C they are constant over many decades of current.

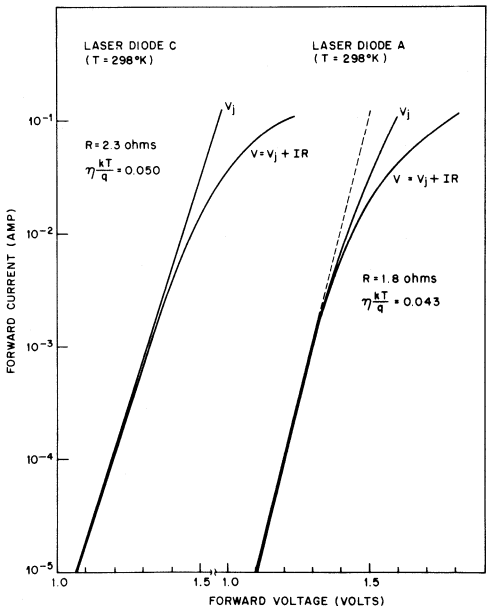


Fig. 9. Log I versus junction voltage ($V_j = V - IR$). Note that for diode C junction voltage is linear on the logarithmic plot indicative of constant η, while for diode A, the nonlinearity of V_j is indicative of a changing η.

V. CONCLUSIONS

We have demonstrated that the forward-biased electrical characteristic of a stripe-geometry DH laser diode can be adequately represented by an ideal p-n junction in which semiconductor bulk resistance and device contact resistance are accounted for by a resistance in series with the junction. A shunt resistor across the junction-series resistance pair accounts for losses around the junction, such as through the proton-bombarded area. The current through the junction was taken as exponentially dependent on voltage, $I \doteq I_s (\exp (qV_j/\eta kT) - 1)$ with $V_j = V - IR$ so that the junction is characterized by a saturation current I_s and an exponential parameter, η. Direct measurement of the I-V characteristic of currently available AlGaAs-GaAs DH laser diodes showed excellent agreement with this relation for values of η in the range of $1.6 < \eta < 3$. For many diodes η remained constant near $\eta = 2$ over 6 to 9 decades of current, while in other diodes η was observed to be constant for low values of current ($I < 1$ mA) then increasing rapidly with further increases of current. The existence of these anomalous I-V characteristics suggests that the electrical properties of DH junction diodes may provide insights into the properties of the epitaxial heterojunctions and/or the fabrication process.

In addition we have demonstrated that the first current derivative of the applied diode voltage, dV/dI, simultaneously measures the series resistance R, the junction parameter η and lasing threshold of the diode. By forming the product of the first derivative with the current and displaying this product as a function of current, the slope of the resulting linear plot determines the series resistance while the parameter η is determined from the intercept at zero current.

The technique was illustrated with measurements on presently available AlGaAs DH laser diodes. The measured values of R and η were checked against the values determined for the same devices by a numerical fit of the current-voltage relation derived for the simplified electrical model to the directly measured characteristics over eight decades of current. The agreement between these independently determined values was excellent.

Saturation of the junction voltage as a result of the onset of lasing was also easily observed with this technique. Since the threshold current determined this way coincides with the threshold measured in conventional ways, it provides an accurate and reliable method of determining threshold by a purely electrical measurement. Furthermore, loss of the voltage saturation indicates the presence of a nonlinearity in the current dependence of the lasing emission. Thus, this technique graphically and accurately reveals the range of currents over which the light output characteristic is linear and well behaved.

The results presented have been selected for two representative diode lasers, however the effects discussed are generally observed in all our DH lasers with proton delineated stripes.

Finally, we note that the simplicity of the technique, coupled with the fact that it is a purely electrical measurement, makes the method very suitable for automated routine evaluation of devices.

Acknowledgment

We gratefully acknowledge R. L. Brown and J. F. Svacek for their technical expertise in the execution of these experiments. We further acknowledge useful conversations with D. L. Rode and B. C. De Loach, Jr., and discussions of derivative techniques with R. W. Dixon.

References

[1] A. G. Milnes and D. L. Feucht, *Heterojunctions and Metal Semiconductor Junctions*. New York: Academic, 1972, ch. 2.
[2] I. Hayashi and M. B. Panish, "GaAs-$Ga_xAl_{1-x}As$ heterostructure injection lasers which exhibit low thresholds at room temperature," *J. Appl. Phys.*, vol. 41, pp. 150–163, Jan. 1970.
[3] For general reviews see M. B. Panish and I. Hayashi, "Heterostructure junction lasers," in *Applied Solid State Science*, vol. 4, R. Wolf, Ed. New York: Academic, 1974, pp. 235–328; see also H. Kressel, "Semiconductor lasers: Devices," in *Laser Handbook*. Amsterdam, The Netherlands: North Holland, 1972.
[4] G. J. Lasher and F. Stern, "Spontaneous and stimulated recombination radiation in semiconductors," *Phys. Rev.*, vol. 133, pp. A553–A563, Jan. 1964.
[5] H. Haug, "Quantum-mechanical rate equations for semiconductor lasers," *Phys. Rev.*, vol. 184, pp. 338–348, Aug. 1969.
[6] P. G. Eliseev, A. I. Krasil'nkov, M. A. Man'ko, and V. P. Strakhov, "Investigation of d.c. injection lasers," in *Physics of p-n Junctions and Semiconductor Devices*. S. M. Ryvkin and Yu. V. Shmartsev, Ed. New York: Plenum, 1971, pp. 150–159.
[7] D. L. Rode and L. R. Dawson, "Differential I/V of heterostructure correlates with laser threshold," *Appl. Phys. Lett.*, vol. 21, pp. 90–93, Aug. 1, 1973.
[8] J. N. Walpole, A. R. Calawa, R. W. Ralston, T. C. Harmon, and J. P. McVittie, "Single heterojunction $Pb_{1-x}Sn_xTe$ diode lasers," *Appl. Phys. Lett.*, vol. 23, pp. 620–622, Dec. 1973.
[9] I. Hayashi, M. B. Panish, P. W. Foy, and S. Sumski, "Junction lasers which operate continuously at room temperature," *Appl. Phys. Lett.*, vol. 17, pp. 109–111, Aug. 1970.
[10] M. J. Adams and P. T. Landsberg, "The theory of the injection laser," in *Gallium Arsenide Lasers*, C. H. Gooch, Ed. New York: Wiley-Interscience, 1969.
[11] See, for example, R. V. Coleman, R. C. Morris, and J. E. Christopher, "Experiments on electron tunneling in solids," in *Methods of Experimental Physics*, vol. 11, R. V. Coleman, Ed. New York: Academic, 1971.
[12] W. B. Joyce and R. W. Dixon, "Fundamental and harmonic response voltages of sinusoidally-current-modulated ideal semiconductor lasers," *J. Appl. Phys.*, vol. 47, pp. 3510–3514, Aug. 1976.
[13] T. L. Paoli and P. A. Barnes, "Saturation of the junction voltage in stripe-geometry (AlGa)As double-heterostructure junction lasers," *Appl. Phys. Lett.*, vol. 28, pp. 714–717, June 1976.
[14] T. L. Paoli, unpublished.

Calculation of the Minimum Repetition Rate of a Cavity-Dumped Four-Level Laser

JOSEPH M. MORAN

Abstract—**Calculations using the rate equations for an ideal 4-level laser system show that there is a minimum frequency below which efficient repetitive cavity dumping of a laser will not be stable. Expressions for the field and inversion variables are derived.**

Experimental results have been obtained using a folded cavity Nd-YAG laser that is perturbed by an intracavity acoustooptic modulator. The observed field inside the cavity is shown to behave like a damped harmonic oscillator. The minimum repetitive frequency, f, of stable operation is shown to increase with increased pumping rate and system loss and decrease with increasing laser cavity length. As a result, the minimum stable frequency depends on the strength of perturbation of the modulator since this adds loss to the system.

The range of stable operation for the Nd-YAG laser under investigation varies from 135 kHz to several megahertz.

Manuscript received May 6, 1976; revised June 17, 1976.
The author is with Bell Laboratories, Murray Hill, NJ 07974.

Introduction

CAVITY DUMPING [1], [2] is a way of obtaining high-frequency repetitive output pulses from a continuously pumped Nd-YAG laser while maintaining its full average power capability. The power is coupled out of the cavity with a fused silica acoustooptic modulator. As a result of this perturbation, the power inside the cavity varies with time and can be described by a set of rate equations.

Using cavity dumping, higher repetition rates than those achievable with Q switching [3] are possible. Q switching has a stable operating range up to 50 kHz for an Nd-YAG laser [2]. Efficient cavity dumping of an Nd-YAG laser has a stable operating range from about 100 kHz up to several megahertz [1], [2].

Instabilities at all frequencies can arise due to photons being coupled back into the laser from some external reflections [4], but these can be controlled by suitable filtering of the external laser beam.

This paper examines the inherent lower limits of stable operation of the laser and discusses the factors controlling that limit.

Theory of Cavity Dumping

The rate equations describing an ideal homogeneous four-level continuously pumped Nd-YAG laser are [3]

$$dN/dt = R - \lambda N - \beta FN \tag{1}$$

and

$$dF/dt = \beta FN - (\epsilon + T)F \tag{2}$$

where

- F number of coherent photons in the cavity multiplied by the laser transition energy E;
- N number of atoms excited to the upper laser level multiplied by E;
- R number of atoms pumped up per second multiplied by E;
- t time;
- λ spontaneous decay rate of the upper laser level.

The round-trip fractional loss inherent in the cavity is denoted by Δ, and the fractional output coupling by γ. We define $\epsilon = C\Delta/2L$ and $T = C\gamma/2L$ with C the speed of light and L the optical cavity length. β describes the stimulated emission such that $\beta = C\sigma/aLE$ where σ is the laser transition cross section and a is a constant area inside the optical cavity, over which exists a homogeneous coherent field intensity.

In the case of CW operation, the time derivatives in (1) and (2) are zero. By maximizing the output power, $P = TF$, with respect to T, and using the notation of Chesler and Maydan [3], the optimum CW values for the laser variables are obtained. They are

$$T_m = \epsilon(\varphi^{1/2} - 1) \tag{3a}$$

$$N_m = \epsilon\varphi^{1/2}/\beta \tag{3b}$$

$$F_m = \lambda(\varphi^{1/2} - 1)/\beta \tag{3c}$$

$$P_m = R(1 - 1/\varphi^{1/2})^2 \tag{3d}$$

with $\varphi \equiv R\beta/\lambda\epsilon$ (pumping rate/threshold pumping rate), and the subscript indicating P has been maximized.

In order to examine the dynamic buildup of the cavity, γ is set equal to zero. This represents the actual situation where the optical cavity mirrors are highly reflecting. Consider now a small perturbation from equilibrium given by

$$N(t) = N_0 + N_1(t), \qquad N_1 \ll N_0 \tag{4}$$

and

$$F(t) = F_0 + F_1(t), \qquad F_1 \ll F_0 \tag{5}$$

where $F_0 = \lambda(\varphi - 1)/\beta$ and $N_0 = \epsilon/\beta$ are the equilibrium solutions to (1) and (2) when $dN/dt = dF/dt = 0$ and $T = 0$. Equations (4) and (5) are substituted into (1) and (2) to yield the following:

$$\frac{dN_1}{dt} = -\epsilon F_1 - \lambda\varphi N_1 \tag{6}$$

and

$$\frac{dF_1}{dt} = \lambda(\varphi - 1)N_1. \tag{7}$$

Taking the derivative of (7) and substituting into (6) gives

$$\frac{d^2F_1}{dt^2} + \varphi\lambda\frac{dF_1}{dt} + (\varphi - 1)\lambda\epsilon F_1 = 0. \tag{8}$$

This is a differential equation describing a damped harmonic oscillator having a solution of the form

$$F_1(t) = -Ae^{-\alpha t}\cos(\omega t + \psi) \tag{9}$$

where

$$\alpha \equiv \varphi\lambda/2 \tag{10a}$$

$$\omega \equiv \sqrt{\epsilon\lambda(\varphi - 1) - (\varphi\lambda/2)^2}$$

$$\approx \sqrt{\epsilon\lambda(\varphi - 1)}, \qquad (\varphi\lambda/2)^2 \ll \epsilon\lambda(\varphi - 1). \tag{10b}$$

The predicted perturbation in the output is a damped sinusoid with a decay rate of α and a radian relaxation oscillation frequency of ω. Recalling the definitions for ϵ and φ, expressions (10a) and (10b) may be rewritten as

$$\alpha = \frac{R\sigma}{A\Delta E} \tag{11a}$$

$$\omega = \sqrt{\frac{C}{L}\left(\frac{R\sigma}{AE} - \frac{\lambda\Delta}{2}\right)}. \tag{11b}$$

ω has a weak dependence on system loss, Δ, since the pumping rate is generally large enough so that $R\sigma/AE$ dominates the $\lambda\Delta/2$ term. As a result, α and ω can be increased with increased pumping, R, while ω decreases with increasing cavity length, L, and α decreases with increasing system loss, Δ.

Fig. 1 shows the variation in internal power of a Nd-YAG cavity dump laser as a function of time when the cavity is perturbed by a low power acoustooptic pulse. It is seen to behave as a damped sinusoidal oscillator.

The full solution to the field equations may then be given by

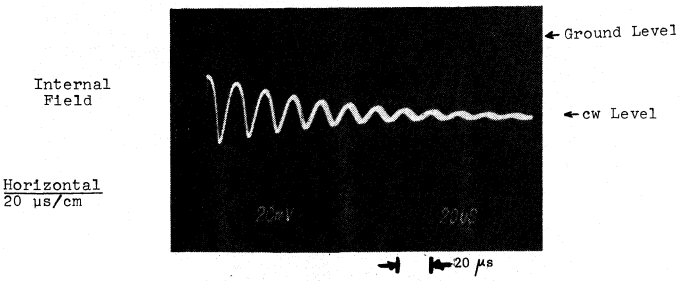


Fig. 1. Variation in internal cavity power due to small perturbation of the laser by a cavity dump pulse.

$$F = F_0 - Ae^{-\alpha t}(\cos \omega t + \psi) \tag{12}$$

in which A depends on the strength of the dumping pulse.

Equation (12) expresses the way the cavity will build up when it is perturbed by a single pulse. It is now assumed that the cavity will behave similarly when perturbed by a regular periodic pulse train.

With the short acoustooptic pulses being used to cavity dump, it can be easily calculated, from (6) and (7), that the population density (N) does not change very much (<5 percent). However, the field changes are abrupt during the perturbation which can cause large decreases in the field (F). As a result, one would then expect the field to build back up slowly after perturbation. This means the phase angle ψ, as given in (12), would be very small.

Experimental evidence supports this, in that the cavity has a repetitive behavior in the steady state and the phase angle $\psi \simeq 0$. Fig. 2 shows the field buildup in the cavity when a train of 200-ns-wide periodic (10-μs) acoustooptic pulses is suddenly applied to the laser. Initially, the cavity behavior is complicated, but after about 80 μs, steady-state conditions are apparent. The average power for the cavity is then given by

$$F_a = F_0 - \frac{1}{\tau}\int_0^{\tau} Ae^{-\alpha t} \cos \omega t \, dt, \quad F_a \leqslant F_0 \tag{13}$$

where τ is the period in seconds and F_a is the average energy in the optical cavity. F_a depends on the inherent cavity loss, Δ, as well as the loss contributed by the cavity dump modulation of the cavity. Since the acoustooptic pulse train dumps energy out of the system it is a loss which requires F_a to be less than F_0. This point is crucial to the rest of the derivation. Solving (13) gives

$$A = \frac{(F_0 - F_a)(\alpha_2^2 + \omega^2)\tau}{\alpha + e^{-\alpha\tau}(\omega \sin \omega\tau - \alpha \cos \omega\tau)} \tag{14}$$

so that the final expression for the field equation inside a weakly perturbed periodic cavity dump laser is given by

$$F = F_0 - \frac{\tau(F_0 - F_a)(\alpha^2 + \omega^2)e^{-\alpha t} \cos \omega t}{\alpha + e^{-\alpha\tau}(\omega \sin \omega\tau - \alpha \cos \omega\tau)}. \tag{15}$$

Experimental Results

A folded Nd-YAG laser cavity having an overall length, L, of 1.2 m was used in combination with a Spectra-Physics Model 135 cavity dump modulator for extracting power from the cavity (see Fig. 8). The cavity was first weakly perturbed to determine system parameters. The photon energy in the cavity, F, is shown in Fig. 1 where $\alpha = 15 \times 10^3$ s^{-1} and $\omega = 380$ krad · s^{-1}. The decay constant, λ, has a value [3], [4] of 5×10^3 s^{-1} so that $\varphi = 6$ and $\epsilon = 5.7 \times 10^6$ s^{-1}. The round-trip loss, Δ, is then calculated to be 4.5 percent which is representative for this type of laser if the rod birefringence loss as well as the loss from the Brewster angle on the cavity dump modulator is taken into account.

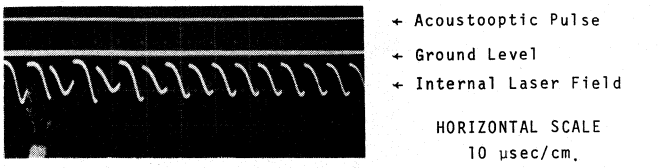


Fig. 2. Field inside the cavity when a train of acoustooptic pulses is applied to the laser. Note the steady-state condition that occurs after about 100 μs.

For the cavity configuration as well as the pump lamp level being used, the optimum power output, P_m, is 3.0 W in the TEM_{00} mode. This figure was determined using various coupling mirrors to measure optimum CW power output. Using (3), the cavity parameters are calculated to be

$$T_m = 8.3 \times 10^6 \text{ s}^{-1}$$

$$F_m = 0.363 \ \mu\text{J} \ (1.9 \times 10^{12} \text{ photons})$$

$$N_m = 698 \ \mu\text{J}.$$

It has been experimentally observed that cavity dumping below a certain frequency causes the laser cavity to become unstable. Thus, as the repetition rate is lowered, the field inside the cavity first enters a bistable mode, as shown in Fig. 3, and, as the frequency is further decreased, the laser output becomes erratic and complicated over a range of frequencies. For example, stable operation of the laser is observed from about 2 MHz down to 135 kHz. Unstable operation exists over the frequency range from 135 to about 65 kHz. Stable operation then begins again over a narrow band of about 20 kHz and this repeats again at lower frequencies. However, the area of interest is the higher frequency range since this is where cavity dumping is most efficient. Additionally, the lower frequency ranges are attainable by other means (i.e., Q switching).

If the cavity perturbations are kept small, the average energy in the cavity, F_a, will approach the value F_0 since very little loss is added to the system. Since the previously obtained relation, given by (14), requires that A be nonzero, this means that

$$\alpha + e^{-\alpha\tau}(\omega \sin \omega\tau - \alpha \cos \omega\tau) = 0 \tag{16}$$

where $f \equiv 1/\tau$ is the minimum stable repetitive frequency. If it is assumed that $e^{-\alpha\tau} \simeq 1$, (16) is solved when

$$\tan \frac{\omega\tau}{2} \simeq -\frac{\omega}{\alpha}. \tag{17}$$

For the case under consideration, $\omega/\alpha = 25.3$ so that (17) is

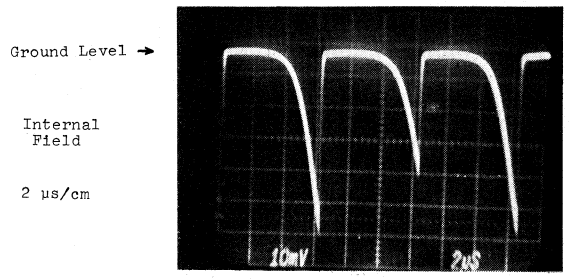


Fig. 3. Cavity power at the onset of instability. The bistable mode.

solved when

$$\tau \simeq \pi(1+2n)/\omega, \quad n = 0, 1, 2, \cdots \text{ with } \omega = 380 \text{ krad/s}. \tag{18}$$

Observing Fig. 1, it is seen that the peak power in the cavity occurs at $\tau = 8.5$ μs which is where the minimum stable frequency occurs. If τ is made larger (decreased repetition rate) this would imply gain was being added to the system ($F_a > F_0$) which is an unstable state that would be initiated by the least amount of noise or other sources. It is also at this point that cavity dumping is most efficient since maximum peak power is coupled from the laser. Therefore, for this particular laser, the minimum stable frequency for most efficient operation is 118 kHz corresponding to $n = 0$. The assumption that $e^{-\alpha\tau} \simeq 1$ is also verified. The lower frequencies ($n > 0$) also represent solutions and will give stable operation, but they are less efficient.

Equation (14) can also be solved using a computer and the sensitivity to the value of A is more apparent. If the average internal field, F_a, equals $0.99F_0$ (approximating very weak perturbation), then when $A = 0.99F_0$ the minimum frequency is 119 kHz and when $A = 0.1F_0$, the minimum calculated frequency is 129 kHz.

To verify the calculation, a repetitive (400-kHz) 200-ns pulse of low power was applied to an intracavity modulator so as to weakly perturb the laser cavity. The repetition rate was then reduced until the laser cavity became unstable. Fig. 4 shows the internal field of the laser just before going unstable and represents a minimum frequency of 135 kHz which is in good agreement with the calculated value of 129 kHz since A is measured to be about $0.1F_0$.

Although the laser does have a minimum operating frequency, the amount of power being coupled from the laser is very small since the acoustooptic pulse power is small. To couple out more power, the laser must be more strongly perturbed to the point where the output power equals the maximum CW power obtainable through a coupling mirror.

It would be desirable to apply the derived equations for small perturbations to the large perturbation case. Fig. 5 shows the cavity behavior of the field due to a single strong acoustooptic pulse perturbing the cavity. The cavity buildup does not behave exactly as a damped harmonic oscillator, but the behavior is enough like it to use the previously derived results as approximations. Using (14), computer solutions were obtained for various values of A and the results are shown in Fig. 6. The variation in F_a is plotted as a function of laser repetition frequency for fixed values of ω_0 and α. The

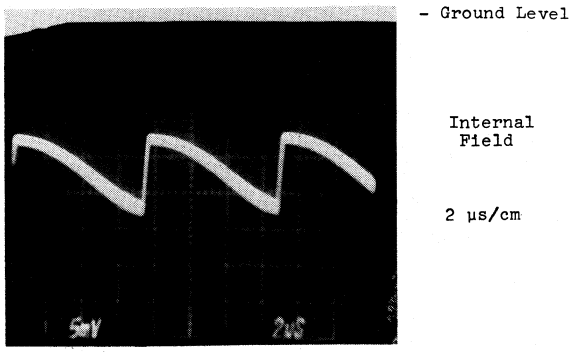


Fig. 4. Variation in cavity power at the minimum repetition rate due to a weakly perturbed laser cavity.

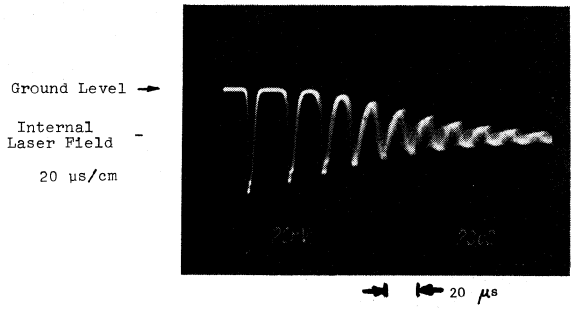


Fig. 5. Variation in cavity power due to a large perturbation of the laser cavity.

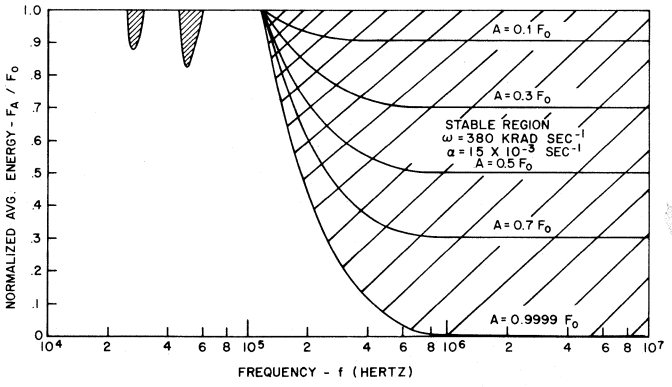


Fig. 6. Solutions to (14) with F_a/F_0 given as a function of frequency for various values of A.

shaded region represents solutions to (14) that indicate where the laser may be operated stably. Operation within a region will be determined by the repetition rate, the width of the acoustooptic pulse, and the strength of the acoustooptic pulse. A decrease in pumping light, R, by a factor of 2 would cause α to be halved and ω to decrease approximately by a factor of $\sqrt{2}$. However, (14) has a weak dependence on α so that ω is the dominant term. As a result, the shaded area would shift so that stable operation is possible at lower frequencies. The same would be true if the length of the cavity, L, is increased by a factor of 2.

With increased coupling of power from the cavity, the cavity loss will increase, causing the values of ω, α, A, and F_a to change. If A is increased, this requires an adjustment of the repetition rate upwards to satisfy the condition for a periodic solution as given by (14) and shown in Fig. 6. If the repetition

rate of the cavity dumper is increased, the cavity loss again increases which requires further increases in the minimum repetition rate. This iterative process eventually leads to a stable output since the increasing repetition rate has an everdecreasing effect on the system. As an example, consider a perturbation of the cavity such that $A = 0.9F_0$ and $F_a = 0.4F_0$. Equation (14) then predicts the minimum frequency of operation to be 229 kHz.

Fig. 7(a), (b), and (c) shows scope traces of the cavity energy, F, for increasing amounts of acoustooptic cavity perturbation (note the vertical sensitivity scales) at the minimum stable repetition rate. The slow increase corresponds to the buildup of the cavity as described in (15). The sharp decrease corresponds to cavity dumping of the laser with an acoustooptic pulse that extracts the laser power. Coupling more power out of the cavity means adding loss to the system (F_a decreases) causing the minimum stable frequency to increase. The acoustooptic perturbation pulse width remains fixed at 200 ns. For Fig. 7(a) and (b), the laser has minimum stable frequencies, respectively, of 144 and 200 kHz. The maximum perturbation possible with the present modulator yields a minimum stable frequency of 290 kHz and a power output of 3 W TEM_{00}. The internal field is shown in Fig. 7(c).

Consider, finally, the case where some further loss is introduced into the laser system (e.g., dust or damage to the optics). A rough approximation for the average power, F_a, may be given by the expression [5]

$$F_a = \frac{C(1 - \Delta - \delta)G}{\Delta + \delta} - 1 \qquad (19)$$

where δ is the coupling loss created by the periodic modulation of the laser, G is the gain coefficient of the laser, and C is a constant of the system. Let $\Delta = 0.045$, $\delta = 0.015$, and $G = 0.10$, which are representative numbers for the laser in question, so that $F_a = F_0$ when $\delta = 0$. The calculated ratio of F_a/F_0 is 0.40. If dust is introduced into the cavity for an additional $\frac{1}{2}$-percent loss, then $\Delta = 0.050$ and the ratio of $F_a/F_0 = 0.39$. This decrease in average power has also been observed experimentally. As a result, for the same amount of energy applied to the acoustooptic modulator, a less efficient laser would mean F_a would be even smaller than in the previously worked out example. Letting $A = 0.9F_0$ and $F_a = 0.39F_0$, the resulting minimum frequency, using (14), is 233 kHz. In this case it is seen that added loss increased the most efficient minimum repetition rate. This could be disastrous in a system that operates at a fixed rate that is very close to the minimum because instability would result. Care must then be taken to keep the optics as clean as possible.

If the amount of perturbation, A, as well as the length of perturbation is left fixed and the repetition rate is now increased, the cavity parameters ω, F_a, and Δ will adjust to satisfy (14) up to rates of several megahertz with no loss of stability. In this case, the operating point would fall inside the shaded area shown in Fig. 6. At some point there is sufficient loss and insufficient buildup in the cavity and the laser will no longer oscillate. The upper rate is also dependent on the speed of the modulator and this area is to be investigated and will be reported in the near future.

Fig. 8 shows the experimental laser cavity configuration used

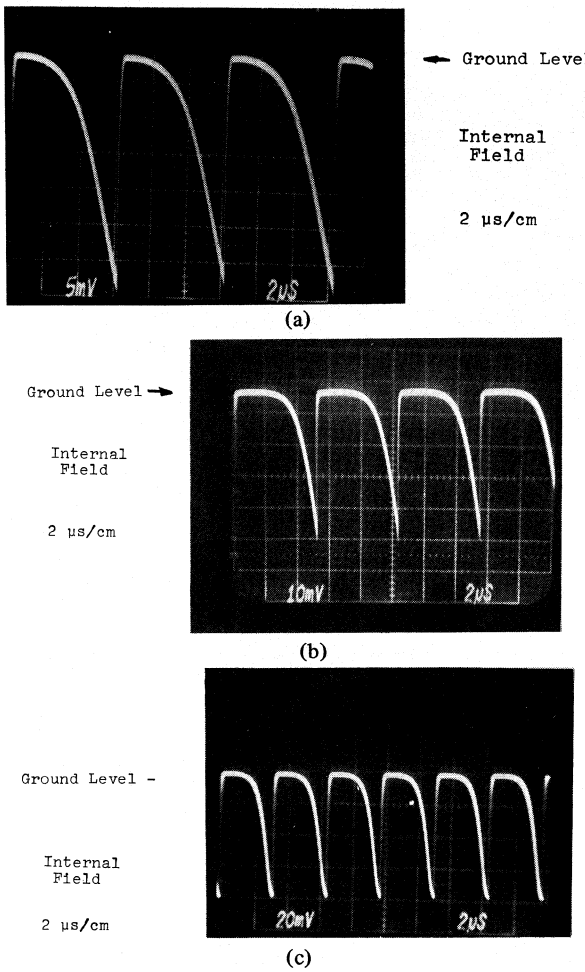


Fig. 7. (a) Internal laser field due to an acoustooptic pulse with 5-W peak power perturbing the cavity. (b) Same as (a) except 10-W peak power. (c) Same as (a) except maximum perturbation at 16-W peak power.

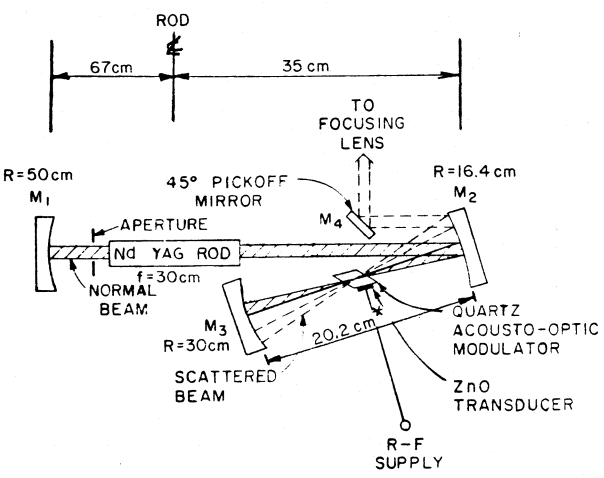


Fig. 8. Laser optical cavity. *Allows approximately 0.2 cm for the introduction of the modulator.

to make the measurements. Fig. 9 is a typical output pulse obtained from the cavity dumped laser.

Conclusion

Stable, efficient, repetitive cavity dumping can take place only within certain frequency limits. The most efficient minimum stable operating frequency of a four-level laser sys-

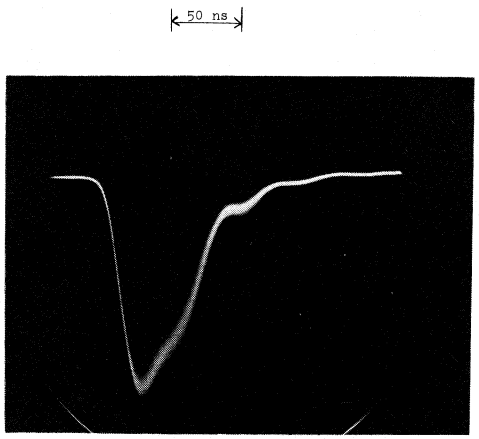


Fig. 9. Output pulse from the cavity dump laser.

tem has been shown to depend on the pumping rate of the laser, the cavity length, and the total loss in the system. This minimum frequency increases with increased loss and increased pumping rate and decreases with increased cavity length. Expressions for the field in the cavity also show that it behaves like a damped harmonic oscillator. Efficient laser repetition rates as low as 135 kHz have been obtained.

Acknowledgment

Thanks are extended to D. Maydan, R. C. Miller, and R. B. Chesler for reviewing the manuscript. Thanks also to M. Feldman, T. H. Goldstein, and J. F. Milkosky for their encouragement and assistance in this project.

References

[1] R. B. Chesler and D. Maydan, "Calculation of Nd-YAG cavity dumping," *J. Appl. Phys.*, vol. 42, pp. 1028-1030, Mar. 1971.
[2] D. Maydan and R. B. Chesler, "Q-switching and cavity dumping of Nd-YAG lasers," *J. Appl. Phys.*, vol. 42, pp. 1031-1034, Mar. 1971.
[3] R. B. Chesler, M. A. Karr, and J. E. Geusic, "An experimental and theoretical study of high repetition rate *Q*-switched Nd-YAG lasers," *Proc. IEEE*, vol. 58, pp. 1899-1914, Dec. 1970.
[4] D. Cheng, private communication.
[5] A. G. Fox and T. Li, "Effect of gain saturation on the oscillating modes of optical masers," *IEEE J. Quantum Electron.*, vol. QE-2, pp. 774-783, Dec. 1966.

Correspondence

Nonlinear Optical Susceptibilities of Solvents

J. M. CHERLOW, T. T. YANG, AND R. W. HELLWARTH

Abstract—**We have measured the nonlinear optical susceptibility coefficient governing self-induced changes in the state of elliptical polarization of a monochromatic beam in 10 common solvents. These are the first such measurements at 1060 nm. We show how our results may be used to estimate self-focusing in these solvents and to clarify other nonlinear optical properties.**

The elliptical state of polarization of a strong monochromatic beam changes as the beam propagates through a fluid or a glass. This "self-induced polarization change," or SIPC, was first predicted and observed by Maker *et al.* [1], [2]. With the advent of single- (transverse and longitudinal) mode lasers, SIPC measurements have developed into a quantitative tool for determining nonlinear optical susceptibilities [2]-[7]. We report here measurements of SIPC in 10 organic solvents at 1060 nm. These are the first SIPC measurements reported at this wavelength, and the first SIPC measurements with a single-mode laser on 8 of the 10 solvents.

To obtain the SIPC coefficient we analyzed the state of polarization of a high-power laser pulse, whose incident polarization was elliptical, after it had emerged from a cell containing the solvent. This was done with a Fresnel rhomb and Glan polarizer arranged so as to block the elliptically polarized beam at low power levels. Our apparatus was the same as that described in [7], except in the following two respects. First, we employed a 1060-nm Nd:YAG oscillator, rather than a 694-nm ruby laser. Our laser was *Q*-switched by a solution of bis (4-dimethylamino-dithiobenzil nickel) in 1, 2 dichloroethane and yielded pulses in a single transverse and longitudinal mode which were typically of 3-mJ energy and 300-kW peak power. Second, we varied the incident pulse intensity by inserting attenuating filters in a stack on the input side of the solvent sample only, rather than by transferring attenuators from the incident to output beams.

For each laser pulse we monitored the total beam power exiting the cell $I(t)$ and that part of it $P(t)$ transmitted by the

Manuscript received April 14, 1976. This work was supported in part by the U.S. Energy and Development Agency under University of California–Lawrence Livermore Laboratory Subcontract 7509105, and in part by the National Science Foundation.

J. M. Cherlow was with the Electronic Sciences Laboratory, University of Southern California, Los Angeles, CA 90007. He is now with the School of Medicine, University of California, Los Angeles, CA 90024.

T. T. Yang was with the Electronic Sciences Laboratory, University of Southern California, Los Angeles, CA 90007. He is now with the Rocketdyne Division, Rockwell International, Canoga Park, CA 91309.

R. W. Hellwarth is with the Electronic Sciences Laboratory, University of Southern California, Los Angeles, CA 90007.

TABLE I
COEFFICIENTS OF SELF-INDUCED POLARIZATION CHANGE (SIPC) NORMALIZED TO CS_2 AND REFRACTIVE INDICES OF SOME SOLVENTS

Liquid	$c_{1221}(-\omega, \omega, \omega, -\omega)/n$	n
CS_2	100	1.59
$C_6H_5NO_2$	84 ± 4[a]	1.53
	69[b]	
C_6H_5Cl	32.3 ± 2.7[a]	1.51
$C_6H_5CH_3$	24.6 ± 2.0[a]	1.48
	24[b]	
$CHBr_3$	24[c]	1.58
	16[d]	
C_5H_5N	24[d]	1.50
C_6H_6	16.8 ± 1.4[a]	1.50
	20[b]	
$(CH_2Cl)_2$	7.4 ± 0.6[a]	1.41
$CHCl_3$	5.2 ± 0.4[a]	1.43
	12[d]	
$(CH_3)_2SO$	2.8 ± 0.3[a]	1.46
CCl_4	1.4 ± 0.2[a]	1.45
	1.7 ± 0.2[e]	
	2.9[b]	
	3.0[d]	
nC_6H_{14}	2[d]	1.37
cC_6H_{12}	1.3 ± 0.2[a]	1.43
N_2 (liquid)	0.8[c]	1.21
H_2O	0.2[c]	1.33
	0.1[d]	
CH_3OH	0.1[d]	1.32

[a] This work, at 1060 nm, single mode.
[b] [4], at 694 nm, multimode.
[c] [3], at 694 nm, multimode.
[d] [1], at 694 nm, multimode.
[e] [5], at 694 nm, single mode. This value has been lowered by 15 percent because of filter error noted in [10], then raised 8 percent to correct for dispersion from 694 to 1060 nm according to procedure of [8].

final exit polarizer, displaying both on a dual-beam oscilloscope. In an ideal situation, theory predicts that $P(t) \propto I^3(t)$ [1], [2], [4]–[7]. However, in practice, imperfections in the polarizers and cell contribute a background term to $P(t)$ that is linear in $I(t)$. Therefore, we fitted the observed intensities to the relation

$$P/I = A + BI^2 \tag{1}$$

in order to determine the SIPC coefficient B.

The B coefficient of each solvent was measured relative to that for CS_2 in a series of runs. A typical run consisted of first measuring the peak value of P and I for each of 10 to 12 laser pulses of varying power propagated through the solvent cell. Then the procedure was repeated with a cell containing CS_2. For each liquid the peak value of I was varied over a range of a factor of 3 at powers below thresholds for other nonlinear effects. The peak values of P and I were fitted to (1) by a least square procedure and the value of B relative to that of CS_2 was obtained. Benzene and CCl_4 received the most study with 6 runs each.

In the useful range of I, most (~90 percent) laser shots showed values of P/I at their peaks which fell within 5 percent of the least square line fit to (1). However, approximately 10 percent of the data points fell significantly above this line. Since there were no unusually low values of P/I, we considered the high points to be anomalous and did not include them in the data analyzed.

At least one scope–trace pair from each run was also fitted to (1) as a function of time [7]. The values of B thus obtained were in good agreement with those obtained from fitting peak values. (Somewhat surprisingly, the anomalous scope–trace pairs also fit (1) as a function of time, but with anomalous values for B.)

The coefficient B in (1) is well known to be proportional to $c_{1221}(-\omega, \omega, \omega, -\omega)/n$, where n is the linear refractive index and c_{1221} is the commonly employed coefficient first defined by Maker and Terhune [2] to describe SIPC in a beam at frequency ω.

Table I lists the values for c_{1221}/n we obtained by averaging values from different runs, and normalizing them to the arbitarily chosen value of 100 for CS_2. The uncertainties quoted in Table I arise mainly from differences in the values obtained from different runs. The data from shot-to-shot (during a run) gave much more consistent values for B than that from run-to-run. From the consideration of absolute dc Kerr and Rayleigh scattering measurements discussed in [8], together with the dispersion corrections proposed there, we deduce an absolute value of $c_{1221}/n = 20 \pm 1 \times 10^{-14}$ ESU for CS_2 at 1060 nm.

For completeness we have included in Table I the results of all published SIPC measurements on liquids made to date, also normalized to CS_2. The only liquid we have measured which was also previously measured with a single-mode laser, is CCl_4 [5]. With the corrections noted in Table I, the two values agree within the experimental uncertainties. The earlier multimode values have not been corrected for dispersion since these corrections are much smaller than the experimental uncertainties.

Our results may be used to predict beam self-focusing thresholds when the solvents are used, for example, as dye solvents

for saturable absorbers, Q-switches, etc. The usual self-focusing index n_2 for a linearly polarized beam is defined as the nonlinear refractive index change divided by the mean square optical electric field. In terms of the electronic volume hyperpolarizability σ and nuclear response coefficient β defined and discussed in [5]-[9] (where it is sometimes called B_0)

$$n_2 \cong \pi(\tfrac{3}{2}\sigma + \tfrac{4}{3}\beta)/n \tag{2}$$

provided that molecular reorientation (or a mechanism with similar symmetry) is responsible for the nuclear contribution [7], [8], and electrostriction may be neglected, as here. In terms of σ and β

$$24c_{1221} = \sigma + 2\beta \cong 3nn_2\left(\frac{2+\sigma/\beta}{2+9\sigma/4\beta}\right)/2\pi \tag{3}$$

in the long-wavelength limit [5]-[9]. The value of β/σ varies from around 1 in CCl_4 to 6 in benzene and 8 in CS_2 [5], [10]. The factor in parentheses on the right-hand side of (3) is 0.71, 0.91, and 0.93 in these cases, showing that a reasonable estimate of n_2 can be made from c_{1221} without too precise a knowledge of β/σ.

Our results may also aid in determining β/σ, and hence the physical origins of n_2. This can be done by comparing our c_{1221} values with other functions of σ and β which may be determined, for example, by Kerr effect measurements [5] or Rayleigh scattering [8], [9] in the same solvent. In this connection we remark on the fact [8] that β for benzene as deduced from Rayleigh scattering measurements [11] is 50 percent higher than the value of $\beta + \sigma$ deduced from dc Kerr measurements [12]. Our value for $2\beta + \sigma$ of benzene is consistent only with the former.

ACKNOWLEDGMENT

The authors wish to thank A. Owyoung, M. Bass, and M. Levenson for helpful conversations.

REFERENCES

[1] P. D. Maker, R. W. Terhune, and C. M. Savage, "Intensity-dependent changes in the refractive index of liquids," *Phys. Rev. Lett.*, vol. 12, pp. 507-509, 1964.
[2] P. D. Maker and R. W. Terhune, "Study of optical effects due to an induced polarization third order in the electric field strength," *Phys. Rev.*, vol. 137, pp. A801-A818, Feb. 1965.
[3] P. D. McWane and D. A. Sealer, "New measurements of intensity-dependent changes in the refractive index of liquids," *Appl. Phys. Lett.*, vol. 8, pp. 278-280, 1966.
[4] C. C. Wang, "Nonlinear susceptibility constant and self-focusing of optical beams in liquids," *Phys. Rev.*, vol. 152, pp. 149-152, 1966.
[5] R. W. Hellwarth, A. Owyoung, and N. George, "Origin of the nonlinear refractive index of liquid CCl_4," *Phys. Rev. A*, vol. 4, pp. 2342-2347, Dec. 1971.
[6] A. Owyoung, R. W. Hellwarth, and N. George, "Intensity-induced changes in optical polarizations in glasses," *Phys. Rev. B*, vol. 5, pp. 628-633, Jan. 1972.
[7] A. Owyoung, "Ellipse rotation studies in laser host materials," *IEEE J. Quantum Electron.*, vol. QE-9, pp. 1064-1069, 1973.
[8] R. W. Hellwarth, *Third Order Optical Susceptibilities of Liquids and Solids*. Oxford, England: Pergamon, 1976.
[9] R. W. Hellwarth, J. M. Cherlow, and T. T. Yang, "Origin and frequency dependence of nonlinear optical susceptibilities of glasses," *Phys. Rev. B*, vol. 11, pp. 964-967, Jan. 1975.
[10] A. Owyoung, "Absolute determination of the nonlinear susceptibility via two-beam nonlinear interferometry," *Optics Comm.*, vol. 16, pp. 266-271, Feb. 1976. The value of $\beta/\sigma = 4.1$ given here for benzene has been revised, upon remeasurement, to 5.7 ± 0.5 (private communication).
[11] E. Pike, W. Pomeroy, and J. Vaughan, "Measurement of Rayleigh ratio for several pure liquids," *J. Chem. Phys.*, vol. 62, pp. 3188-3192, Apr. 1975.
[12] *Landolt-Bornstein, Zahlenwerte und Functionen II/8*. Berlin, Germany: Springer, 1962, p. 5-852.

Direct Demodulation of a 10.6-μm FM Signal with an NH_2D Stark Cell

R. L. ABRAMS AND C. K. ASAWA

Abstract—**A new technique for direct demodulation of a 10.6-μm FM signal using a Stark absorption cell is described. A Stark tunable absorption line in NH_2D is used to track the time-varying frequency of the incoming FM laser signal using a closed servo loop. The demodulated FM signal is proportional to the feedback voltage applied to the Stark cell. Demodulation at frequencies up to 5 kHz has been demonstrated, the rate being limited only by the bandwidth of the available servo electronics.**

The FM laser sources at 10.6 μm are relatively easy to build using such techniques as intracavity modulation of PZT modulation to vary cavity optical length. However, demodulation of the optical FM signal has required heterodyne detection as the first step, the heterodyne process transforming the FM optical signal into an FM RF baseband signal. A direct detection method, not requiring heterodyning, is described in this paper. The technique is an extension of a method used to Stark-cell stabilize a CO_2 laser frequency [1].

The experimental apparatus for the demonstration of direct FM demodulation is shown in Fig. 1. The Stark cell contains ~1 torr of deuterated ammonia (NH_2D) which has a resonance absorption ~1900 MHz below the $P(20)$ CO_2 laser transition and can be Stark-tuned into resonance by an applied dc field. A field of ~3.5 kV/cm is required (or ~450 V on the 0.13-cm Stark gap). This same interaction has been previously discussed in some detail and used for laser frequency stabilization of the CO_2 laser [1]. The standard ac detection scheme used here, with applied dc and ac voltages followed by phase-sensitive detection of the absorbed energy in the cell, results in detection of the first derivative of the resonance absorption line (versus dc field) and forms an ideal discriminant to be used in a feedback servo system.

For laser frequency stabilization, the detected error signal is amplified and applied to the laser PZT control, resulting in locking of the laser frequency to the Stark tunable absorption line. For FM demodulation, however, we apply the feedback signal to the Stark cell, effectively locking the absorption line to the incoming laser frequency. With the servo loop closed, the absorption line is forced to instantaneously track the incoming laser frequency and the error voltage appearing on the Stark plate is the demodulated FM signal. The absorption frequency of NH_2D has been shown to be a very linear function of applied dc field [1], resulting in a highly linear FM discriminant.

The source used for these experiments is a piezoelectrically controlled waveguide CO_2 laser. The PZT element was driven by a 1.5-V sinosoidal signal whose frequency was repetitively

Manuscript received April 26, 1976.
The authors are with the Hughes Research Laboratories, Malibu, CA 90265.

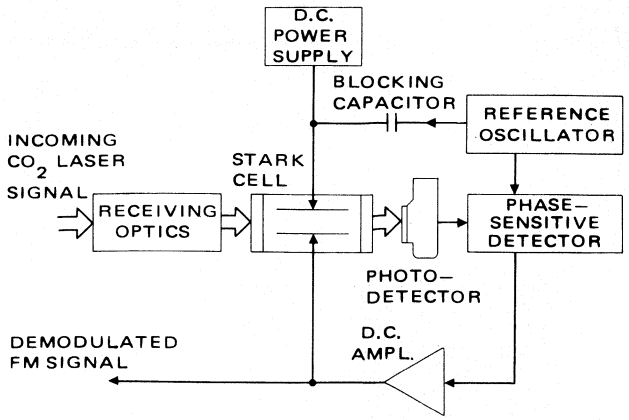


Fig. 1. FM receiver for CO_2 laser. The received signal is modulated by the Stark cell at the reference oscillator frequency, which is higher than the receiver bandwidth. A servo is used to null the modulation, locking the peak Stark-cell absorption to the incoming signal frequency. The error voltage appearing on the lower Stark plate is the demodulated signal.

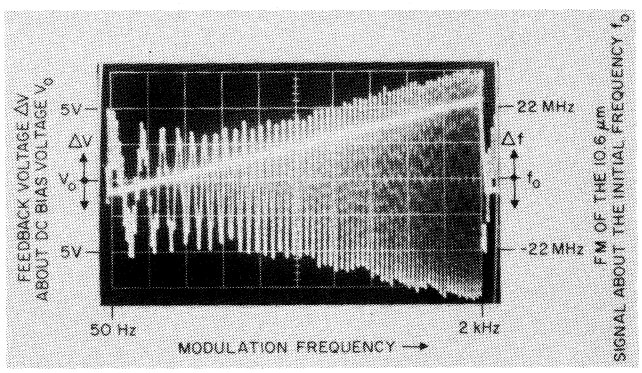


Fig. 2. Response curve for the direct demodulation of a 10.6-μm FM signal. The feedback voltage and the FM signal versus the modulation frequency is shown. The sweep oscillator ramp is also recorded; the modulation frequency is proportional to the ramp voltage.

swept from 50 Hz to 5 kHz. At a modulation rate of 2 kHz, the peak frequency deviation of the laser was 32 MHz. A HgCdTe photoconductor was used to detect the laser signal, although an uncooled pyroelectric detector would be satisfactory for low-bandwidth demodulation.

The demodulated output response curve versus the signal modulation frequency is shown in Fig. 2. The increasing response at the higher modulation frequencies is due to a piezoelectric resonance in the source transducer, resulting in greater FM excursions. The PZT-mirror assembly in the tunable CO_2 laser was resonant at 2.5 kHz. From 2.5 to 5 kHz, the response decreased slightly due to decreased source frequency excursions. It should be emphasized that the direct demodulation method is linear and that the nonlinear response of Fig. 2 is due only to the nonlinearity of the test FM source.

In conclusion, a technique for direct demodulation of an FM optical signal without heterodyne detection has been demonstrated at low modulation frequencies. The technique should be applicable to higher modulation rates, limited primarily by the response time of the servo loop.

References

[1] T. A. Nussmeier and R. L. Abrams, "Stark cell stabilization of CO_2 laser," *Appl. Phys. Lett.*, vol. 25, pp. 615-617, Nov. 1974.

Stark Effect Applicable to Optically Pumped Far-Infrared Laser

P. C. CLASPY AND K. P. KOO

Abstract—**The effect of low electric field Stark tuning on the absorption of CH_3OH gas at the $P(12)$ 9.4-μ CO_2 laser line has been studied. At the 220-mtorr CH_3OH pressure optimal for CH_3OH far-infrared (FIR) laser operation, the line center absorption coefficient increases by a factor of 5 with a Stark field of 2.3 kV/cm.**

In the past few years, a large number of molecular gases have been reported to lase in the far infrared (FIR) when optically pumped above certain thresholds by a CO_2 laser [1]. The pumping efficiency of such an optically pumped FIR laser depends on the coincidence between the pump laser frequency and the FIR laser gas absorption frequency. Since many of the FIR laser gases are known to have large permanent dipole moments in the ground vibrational state, it is possible to Stark tune the absorption components of the FIR laser gas [2] into closer coincidence with the pump laser frequency permitting the pump laser power to be more efficiently used. The range of effectively usable Stark fields in an optically pumped FIR laser gas is limited by the optimal FIR laser operating pressure. For a given gas at a given pressure, the highest electric field that can be applied across it without inducing gas breakdown follows the Parchen curve of the gas. The absorption of the $P(12)$ 9.4-μ CO_2 laser radiation has been observed to increase due to Stark tuning of CH_3OH gas over the pressure range (100–400 mtorr) reported to be optimal for CH_3OH FIR laser operation [3].

The experiment includes a series of absorption measurements at CO_2 laser frequencies as a function of Stark fields and CH_3OH gas pressures. The probe laser used is a water-cooled 2-mm-bore Pyrex waveguide CO_2 laser with an active length of 15 cm. The laser cavity is formed by a 92-percent-blaze-efficiency original diffraction grating and a 98-percent reflective Ge output mirror. The laser has a maximum output power of about 100 mW in the 10.4-μ band and about 40 mW in the 9.4-μ band. The laser beam is passed through a Stark cell with two stainless steel plates 26 cm long, 4 cm wide, and separated by 2 mm. The plate surfaces are hand polished with abrasive paper and steel wool. The transmitted laser power is detected by a Ge:Au detector using a phase-sensitive detection scheme. The detector output is then either displayed on an oscilloscope or plotted on a X–Y recorder as the laser cavity is scanned through the laser tuning curve.

A search from $P(10)$ to $P(28)$ and from $R(10)$ to $R(24)$ of the 9.4-μ CO_2 laser lines shows that CH_3OH has a number of large absorption components in near coincidence with these laser lines. Low-frequency ac Stark modulation of the CO_2 laser radiation by CH_3OH has been observed over many of these 9.4-μ CO_2 laser lines. In addition, the absorption at the $P(12)$ 9.4-μ CO_2 laser line shows a significant increase due to dc Stark tuning of the CH_3OH gas. Fig. 1 shows three oscilloscope displays for (a) the laser tuning curve alone, (b) the modified laser line shape due to 540 mtorr of CH_3OH gas in the 26-cm-long Stark cell with no Stark field, and (c) the modified laser line shape under the same conditions as (b) except for the addition of a Stark field of 2 kV/cm. It is clear from comparing Fig. 1(b) with Fig. 1(c) that there is an in-

Manuscript received May 13, 1976; revised June 29, 1976. This work has been supported in part by the National Science Foundation and the National Aeronautics and Space Administration.

The authors are with the Department of Electrical Engineering and Applied Physics, Case Western Reserve University, Cleveland, OH 44106.

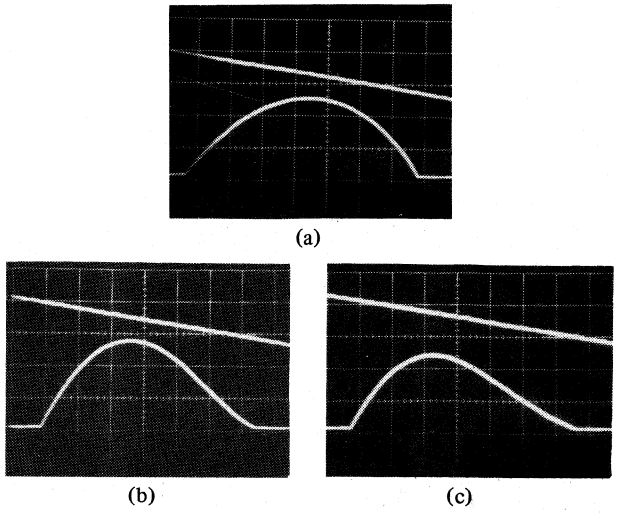


Fig. 1. Changes in the $P(12)$ 9.4-μ CO_2 laser tuning curve produced by absorption of methanol (CH_3OH). (a) Unattenuated laser tuning curve, vertical scale 0.2 V/div. (b) Laser tuning curve as modified by CH_3OH absorption (P = 540 mtorr, 26-cm absorber path length) with no external electric field, vertical scale = 0.1 V/div. (c) Same as (b) except with 2-kV/cm Stark field applied to CH_3OH.

crease in absorption due to Stark tuning of the absorbing gas. The absorption continues to increase with increasing Stark fields as shown in Fig. 2 for three CH_3OH pressures. At pressures of 220 mtorr, 480 mtorr, and 1.4 torr, the absorption coefficient at the laser line center increases, respectively, from 0.8×10^{-3} cm^{-1}, 2.1×10^{-3} cm^{-1}, and 12.8×10^{-3} cm^{-1} for no applied Stark field to 4.0×10^{-3} cm^{-1}, 7.5×10^{-3} cm^{-1}, and 24×10^{-3} cm^{-1} for a Stark field of 2.3 kV/cm. The corresponding increases in laser line center absorption coefficient due to Stark tuning are by a factor of 5, 3.7, and 1.88.

A separate first-derivative Stark spectroscopy study shows that a Stark field of 3 kV/cm tunes the line center of one of the CH_3OH Stark components into coincidence with the $P(12)$ 9.4-μ CO_2 laser tuning curve as shown in Fig. 3. These data were taken at a CH_3OH pressure of 100 mtorr. According to the Paschen law for CH_3OH, an electric field of this magnitude can be maintained only for CH_3OH pressures of 100 mtorr or less.

Optical pumping of FIR laser gas involves an induced transition of FIR laser gas molecules from a rotational energy in the ground vibrational state to a rotational level in the excited vibrational state. Stark modification of the absorption spectrum is caused by perturbing the energy levels involved in the induced transition, with the size of the perturbation in each state being determined by the rotational quantum numbers and the molecular symmetry of that state. Symmetric top and slightly asymmetric top molecules are know to have large Stark effects [4]. Since CH_3OH is a slightly asymmetric top molecule in both its ground and ν_5 vibrational states [5], [6], large Stark effects are expected. One effect is the observed increase in absorption of the CO_2 laser radiation by CH_3OH due to Stark tuning of the absorbing gas. Another possible effect is a sizable change in FIR laser transition frequency due to Stark perturbations of energy levels involved in the FIR lasing transition (usually occurring in the excited vibrational state). Although CW FIR radiation of CH_3OH has not been reported at the $P(12)$ 10.4-μ CO_2 pump laser line, FIR radiation in pulse form has been observed by Izatt *et al.* [7] when the CH_3OH is pumped by a TEA laser.

In conclusion, increased absorption due to low electric field Stark tuning of FIR laser gas has been observed at the

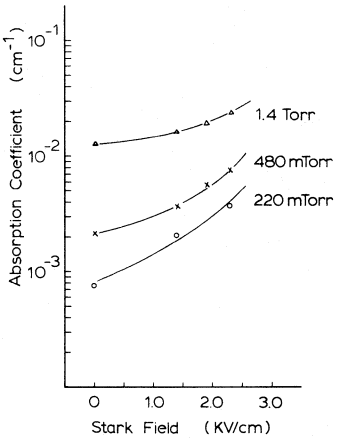


Fig. 2. Absorption coefficients of CH_3OH vapor at the $P(12)$ 9.4-μ CO_2 laser line center as a function of Stark field for three different CH_3OH pressures.

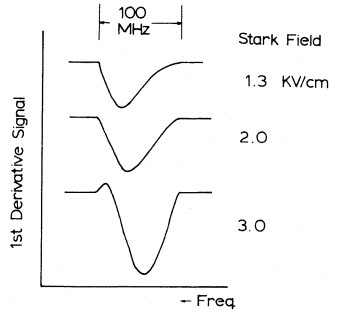


Fig. 3. First derivative Stark absorption spectra of CH_3OH within the tuning curve of the $P(12)$ 9.4-μ CO_2 laser line.

$P(12)$ 9.4-μ CO_2 laser line. This low electric field Stark tuning indicates the possibility of increasing the pumping efficiency of the CH_3OH FIR laser at its normal optimal operating pressure. It also suggests that significant Stark field induced fre-

quency modulation of the FIR laser output is possible. A FIR laser incorporating Stark electrodes is being constructed in our laboratory at this time and the effects of Stark fields upon FIR laser operation will be reported in the near future.

REFERENCES

[1] See for example the review paper by T. Y. Chang on "Optically pumped submillimeter-wave sources," *IEEE Trans. Microwave Theory Tech.*, vol. MTT-22, pp. 983–988, Dec. 1974.

[2] H. R. Fetterman, H. R. Schlossberg, and C. D. Parker, "CW submillimeter laser generation in optically pumped stark-tuned NH_3," *Appl. Phys. Lett.*, vol. 23, pp. 684–686, Dec. 15, 1973.

[3] D. T. Hodges, R. D. Reel, and D. H. Barker, "Low-threshold CW submillimeter- and millimeter-wave laser action in CO-laser-pumped $C_2H_4F_2$, $C_2H_2F_2$ and CH_3OH," *IEEE J. Quantum Electron.*, vol. QE-9, pp. 1159–1160, Dec. 1973.

[4] C. H. Townes and A. L. Schawlow, *Microwave Spectroscopy*. New York: McGraw-Hill, 1955, pp. 248–283.

[5] E. V. Ivash and David M. Dennison, "The methyl alcohol molecule and its microwave spectrum," *J. Chem. Phys.*, vol. 21, pp. 1084–1816, Oct. 1953.

[6] A. Borden and E. F. Barker, "The infra-red absorption spectrum of methyl alcohol," *J. Chem. Phys.*, vol. 6, pp. 553–544, Sept. 1938.

[7] J. R. Izatt, B. L. Bean, G. F. Candle, "One watt, far infrared CH_3OH laser," *Opt. Commun.*, vol. 14, pp. 385–387, Aug. 1975.

Contributors



Kunio Aiki was born in Aichi, Japan, in 1942. He received the B.S. degree from Kanazawa University, Kanazawa, Japan, in 1964, and the M.S. and the Ph.D. degrees in physics from Kyushu University, Fukuoka, Japan, in 1966 and 1970, respectively.

In 1969 he joined the Central Research Laboratory, Hitachi, Ltd., Kokubunji, Tokyo, Japan. He has been involved in the development of light-emitting diodes, and more recently, engaged in the realization of distributed-feedback semiconductor lasers and related thin-film optical devices.

Dr. Aiki is a member of the Physical Society of Japan, the Japan Society of Applied Physics, and the Institute of Electronics and Communication Engineers of Japan.

*



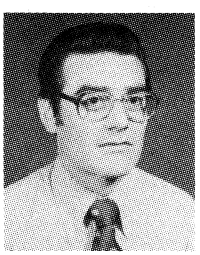
L. W. Anderson was born on December 24, 1933 in Houston, TX. He received the B.A. degree in physics from Rice Institute, Houston, TX, in 1956 and the A.M. and Ph.D. degrees in physics from Harvard University, Cambridge, MA, in 1957 and 1960, respectively.

He then joined the Faculty of the Physics Department at the University of Wisconsin, Madison, where he is currently Professor of Physics. He has conducted research in the areas of optical pumping, nuclear magnetic resonance, ferromagnetism, atomic collisions, and lasers.

Dr. Anderson is a member of Sigma Xi and is a Fellow of the American Physical Society.

S. S. Baral, photograph and biography not available at the time of publication.

*



Peter A. Barnes received the B.A.Sc. degree in engineering physics from the University of Waterloo, Waterloo, Ont., Canada, in 1963, and the M.Sc. degree in physics in 1964. After a one-year lectureship at the University of Waterloo (1964–1965) he attended Simon Fraser University, Burnaby, B.C., Canada, from which he received the Ph.D. degree in 1969. His Ph.D. dissertation involved the study of laser induced plasmas in liquids.

In 1969, he joined Bell Laboratories, Murray Hill, NJ, where he has been engaged in research related to Nd:YAG lasers, and more recently, AlGaAs injection lasers.

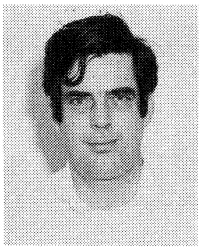
Dr. Barnes is a member of the American Physical Society and the Canadian Association of Physicists.

*

D. L. Bhattacharyya, photograph and biography not available at the time of publication.

F. E. C. Culick, photograph and biography not available at the time of publication.

*



W. A. Fitzsimmons was born on February 21, 1940, in Canton, OH. He received the B.S. degree in mechanical engineering in 1961, and the M.S. degree in physics in 1964, both from the University of Michigan, Ann Arbor. He received the M.A. and Ph.D. degrees in physics in 1966 and 1968 from Rice University, Houston, TX.

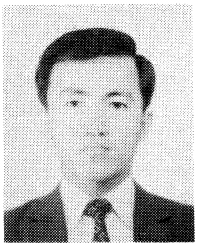
He is a Professor of Physics with the Department of Physics, University of Wisconsin, Madison. He is currently interested in studying the kinetic processes that are associated with energy transfer in high pressure laser plasmas. He is also President of the National Research Group, Inc.

Dr. Fitzsimmons is a member of the American Physical Society.

*

W. S. Griffin, photograph and biography not available at the time of publication.

*



Toshio Hayashi was born in Toyama, Japan, on January 14, 1951. He received the B.E. and M.E. degrees in electronics engineering from Nagoya Institute of Technology, Nagoya, Japan, in 1973 and 1975, respectively.

In 1975 he joined the Electrical Communication Laboratory, Nippon Telegraph and Telephone Public Corporation, Musashino, Tokyo, Japan, where he has been engaged in the research and development of high-speed bipolar memories.

Mr. Hayashi is a member of the Institute of Electronics and Communication Engineers of Japan.

*



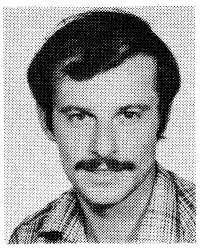
N. R. Isenor was born in Nova Scotia, Canada, on January 6, 1932. He received the B.Sc. degree in physics and mathematics from Acadia University, Wolfville, N.S., Canada, in 1954 and the Ph.D. degree from McMaster University, Hamilton, Ont., Canada, in 1959.

Since 1961, he has been a Faculty Member with the Department of Physics at the University of Waterloo, Waterloo, Ont., Canada. His current interests are multiphoton processes in atoms and molecules and laser/plasma interactions.

Dr. Isenor is a member of the Canadian Association of Physicists and the American Physical Society.

W. C. Jennings (S'66–M'70), photograph and biography not available at the time of publication.

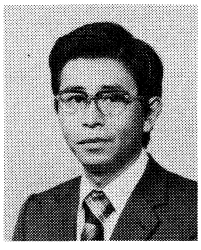
*



Fritz Keilmann was born on May 24, 1942 in Murnau, Bavaria. He received the diploma in physics as well as the Dr.rer.nat. degree from the Technical University, Munich, Germany, in 1967 and 1970, respectively. His thesis work on infrared plasma diagnostics was done at the Max-Planck-Institut für Plasmaphysik, Garching, Germany.

From 1970 to 1971, he was a Staff Scientist at the Max-Planck-Institut für Plasmaphysik investigating heterodyne detection techniques for submillimeter-wave plasma scattering. From 1972 to 1973 he was a Visiting Scientist at M.I.T. in A. Javan's laser spectroscopy lab, where he worked on precision laser frequency measurements and on optically pumped submillimeter-wave lasers. Since 1974 he has been with the Max-Planck-Institut für Festkörperforschung, Stuttgart, Germany, where he is performing saturation studies in condensed media as well as exploring the possibilities of terahertz ultrasound.

*

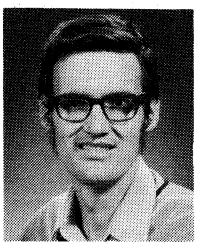


Tatsuya Kimura (S'63–M'68) was born in Oaska, Japan, on February 20, 1940. He received the B.S. degree in electrical engineering, the M.S. degree in electronics engineering and the Ph.D. degree in the field of quantum electronics, all from the University of Tokyo, Tokyo, Japan, in 1962, 1964 and 1967, respectively.

In 1967 he joined the Electrical Communication Laboratory, Nippon Telegraph and Telephone Public Corporation, Tokyo, Japan, where he is a Senior Staff Engineer. He has been engaged in work on optical communication equipment, such as light modulators, detectors, PM–AM converters, FDM filters and laser oscillators, guided millimeter-wave transmission systems, and optical fiber transmission systems.

Dr. Kimura is a member of the Institute of Electronics and Communication Engineers of Japan, the Japan Society of Applied Physics, the Physical Society of Japan, and the American Physical Society.

*



V. E. Merchant received the B.Sc. degree (first-class honors) and the M.Sc. in physics from Simon Fraser University, Burnaby, B.C., Canada, in 1969 and 1971, respectively. He is currently a student at the University of Waterloo, Waterloo, Ont., Canada, and expects to receive the Ph.D. degree in 1976. He has worked on the design of TEA lasers and their electrode configurations. He is currently investigating the CO_2 laser-induced dissociation of polyatomic molecules.

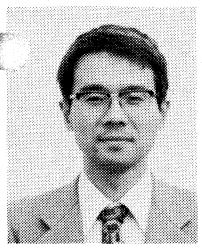
Mr. Merchant is a member of the Canadian Association of Physicists and of the American Physical Society.



Joseph M. Moran was born in New York, NY, on February 3, 1940. He received the B.E. degree in electrical engineering from the City College of New York, New York, NY, in 1965. He received the M.S. and Ph.D. degrees in electrical engineering from the University of Pennsylvania, Philadelphia, in 1967 and 1968, respectively.

He joined Bell Telephone Laboratories, Murray Hill, NJ, in 1968 as a Member of the Technical Staff in the Electron Device Laboratory where his research is currently in lasers and devices to be used for micromachining.

*



Michiharu Nakamura was born in Osaka, Japan, in 1942. He received the B.S., M.S., and Ph.D. degrees in physics from the University of Tokyo, Tokyo, Japan, in 1965, 1967, and 1975, respectively.

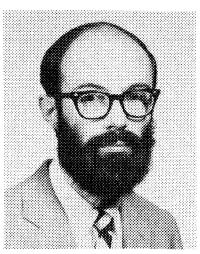
In 1967 he joined the Central Research Laboratory, Hitachi, Ltd., Kobubunji, Tokyo, Japan. He has been involved in the development of microwave semiconductor devices, and more recently, engaged in the realization of distributed-feedback semiconductor lasers and related thin-film optical devices.

Dr. Nakamura is a member of the Physical Society of Japan, the Japan Society of Applied Physics, and the Institute of Electronics and Communication Engineers of Japan.

*

Dwight O. North (A'35-M'38-F'43), for a photograph and biography please see page 262 of the April 1976 issue of this JOURNAL.

*



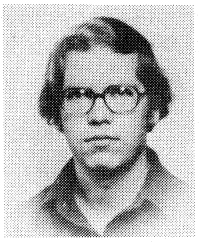
Thomas L. Paoli (S'59-M'73) was born in Springfield, IL, on May 27, 1940. He received the B.S. degree in electrical engineering and the B.A. degree, both from Brown University, Providence, RI, in 1962, and the Ph.D. degree in applied physics from Stanford University, Stanford, CA, in 1967. During the summer of 1964 he attended the Summer School of Theoretical Physics of the University of Grenoble, Les Houches, France.

He was a Research Assistant and a National Science Foundation Fellow (1962-1967) at Stanford University, working on optical coherence theory. He has also held summer positions with the Applied Research Laboratory of Sylvania Electronic Systems, where he worked on communication theory, and with the Electronic Defense Laboratory of Sylvania, where he worked on laser theory. In 1967 he joined Bell Laboratories, Murray Hill, NJ, where his research has concentrated on GaAs injection lasers.

Dr. Paoli is a member of Phi Beta Kappa, Tau Beta Pi, Sigma Xi, and the American Physical Society. He was the Guest Editor of the July 1975 Special Issue of this JOURNAL and served as a Vice-Chairman of the 1975 IEEE International Semiconductor Laser Conference.

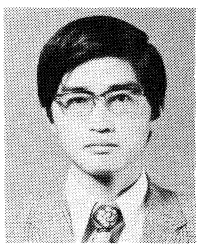
*

M. Ray, photograph and biography not available at the time of publication.



C. E. Riedhauser was born in Neenah, WI, on November 27, 1951. He received the B.S. degree in applied mathematics and engineering physics in 1974 and the M.S. degree in physics in 1975, both from the University of Wisconsin, Madison. He is currently a graduate student in theoretical physics at the California Institute of Technology, Pasadena, CA, where he is studying the theory of gravitational interactions.

*



Masatoshi Saruwatari was born in Miyazaki, Japan, on April 3, 1945. He received the B.S. degree in pure and applied science, and the M.S. degree in coordinated sciences, both from the University of Tokyo, Tokyo, Japan, in 1968 and 1970, respectively.

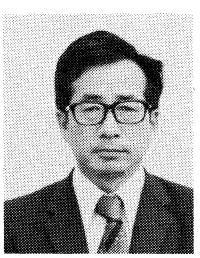
In 1970 he joined the Musashino Electrical Communication Laboratories, Nippon Telegraph and Telephone Public Corporation, Tokyo, Japan. He has been engaged in research on optical communication equipment such as optical FDM filters and solid-state laser oscillators.

Mr. Saruwatari is a member of the Institute of Electronics and Communication Engineers of Japan and the Japan Society of Applied Physics.

*

P. I. Shen, photograph and biography not available at the time of publication.

*

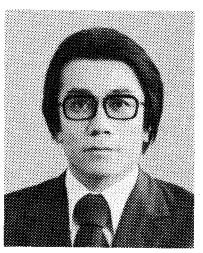


Jun-ichi Umeda was born in Mie, Japan, in 1936. He received the B.S., M.S., and Ph.D. degrees in physics from Kyushu University, Fukuoka, Japan, in 1958, 1960, and 1964, respectively.

In 1963 he joined the Central Research Laboratory, Hitachi, Ltd., Kokubunji, Tokyo, Japan. He has worked in the areas of semiconductor physics including the metal-semiconductor transition in transition metal oxides and the electric properties of intermetallic compounds; he has also been involved in the development of light-emitting diodes. He is a Senior Researcher at the same laboratory and is currently engaged in the development of semiconductor lasers and their applications including optical integration.

Dr. Umeda is a member of the Physical Society of Japan, the Japan Society of Applied Physics, and the Institute of Electronics and Communication Engineers of Japan.

*



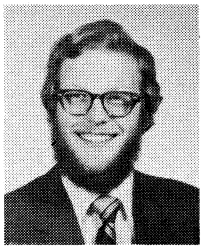
Akira Usami was born in Shimane, Japan, on October 8, 1937. He received the B.S. degree in physics from Kanazawa University, Kanazawa, Japan, in 1961. He received the Ph.D. degree in engineering from Osaka University, Osaka, Japan, in 1972.

From 1961 to 1963, he worked at General Electric Corporation, Kawasaki, Japan, in the area of semiconductor device development. Since 1963, he has been a Member of the Faculty of the Electronics Department, Nagoya Institute of Technology, Nagoya, Japan. His initial work there was the

development of the radiation-resistant silicon solar cell. His current activities are in the area of high-performance solar cell development, crystal inperfection evaluation in semiconductor crystals, and the application of the light-emitting devices to electronic measurement and control systems.

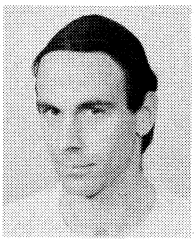
Dr. Usami is a member of the Institute of Electronics and Communication Engineers of Japan and the Japan Society of Applied Physics.

*



Jan M. Vrtilek was born in Zurich, Switzerland, on July 18, 1953. He received the B.S. degree in physics and mathematics in 1975 from the University of Wisconsin, Madison, and the A.M. degree in astronomy in 1976 from Harvard University, Cambridge, MA. He is currently a graduate student at Harvard University where he is studying the spectroscopy of supernova remnants.

Mr. Vritilek is a member of the American Astronomical Society.



C. O. Weiss attended the Technische Universität, Hannover, Germany, from 1962 to 1969. He received the physics diploma degree in 1969. From 1969 to 1973 he worked as a University Assistant in the field of plasma diagnostics with lasers at Institut für Plasmaphysik der Technischen Universität, Hannover, Germany. In 1972 he received the Dr. rer. nat. degree.

In 1973 he joined Physikalisch-Technische Bundesanstalt, Braunschweig, Germany, where he now is Head of the Infrared and Optical Frequencies Laboratory.

*

P. Woskoboinikow (S'74), photograph and biography not available at the time of publication.

5th Conference on Chemical and Molecular Lasers

The Fifth Conference on Chemical and Molecular Lasers will be held at Stouffer's Riverfront Inn, St. Louis, on April 18, 19, and 20, 1977.

Call for Papers

The scope of this conference includes research in the following areas:

1. New results on existing chemical lasers
2. New reaction systems
3. Diagnosis of chemical reactions and lasers
4. Electrically pumped lasers
5. Excitation transfer systems
6. New molecular lasers
7. Molecular relaxation, collisional quenching or electronic excitation
8. Laser controlled chemistry
9. Other

Engineering applications of lasers and specific devices lie outside the scope of this conference. Authors are encouraged to indicate on their abstracts the subject category appropriate to their paper.

Instructions for Authors

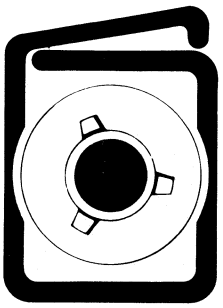
Authors are requested to submit 250 word abstracts of their papers, following the APS style for abstracts. The entire abstract (including figures) must be contained on a single side of an 8½ x 11 sheet for direct reproduction. The deadline for submission of abstracts is Jan. 10, 1977, and notices of acceptance will be sent to authors by Feb. 28, 1977. Summaries should be sent to:

Dr. W.Q. Jeffers
Helios Incorporated
P.O. Box 2190
Boulder, CO 80302

Registration Fees

Registration fee for the conference is $30.00 with a student rate of $15.00. Included in the fee is a Digest of Abstracts of the papers to be presented. A special issue of IEEE J. Quantum Electron. is planned as a conference proceedings; abstracts will be published in this issue at no additional charge.

Now—an amazing new journal with a circulation of ONE.



And that ONE is you.

It's called the ANNALS OF THE IEEE.

But please don't let the title mislead you, because the ANNALS introduces a very exciting innovation in technical journal publishing.

Technically, the ANNALS is a modified *Selective Dissemination of Information* (SDI) service. In actuality, however, it functions as a journal—but a journal with a BIG difference.

Based on the wide-ranging contents of the IEEE's 36 technical periodicals, the ANNALS permits you to . . .

. . . pick and choose and order (in advance or after original publication) only those theoretical and/or applications papers of direct interest to you, no matter in which IEEE periodical they appear.

And these are full-size reprints—not microforms—of the complete papers, including all illustrations.

Just think of the real benefits that an ANNALS subscription offers . . .

- **You receive only papers on subjects that really interest you.**
- **You greatly reduce the possibility of missing an IEEE paper that is important to you.**
- **You save costly time spent in searching periodicals.**
- **You save valuable space needed to store full issues of periodicals that might contain only one or two items you plan to read "some day."**

Considering the great number of subject-interest terms from which ANNALS subscribers may choose, we think you'll agree with the headline above. In all probability, there will be no two subscribers receiving exactly the same "journal" each month.

Subscriptions to ANNALS OF THE IEEE are available only to IEEE members at this time. If you are an IEEE member and would like to know more about the ANNALS, simply fill out the coupon below, enclose in an envelope, and mail it to the IEEE. A packet of informative literature, including a Tentative Reader Interest Profile, will be sent to you immediately.

THE INSTITUTE OF ELECTRICAL AND ELECTRONICS ENGINEERS, INC.

Mail entire coupon to:

IEEE Service Center
Annals of the IEEE
445 Hoes Lane
Piscataway, N.J. 08854



Please type or print all information requested.

IEEE Member No. _____

_____

IEEE periodicals besides Spectrum being received regularly

_____

Primary job function, eg., teaching, R&D, management, etc.

_____

Principal professional area of interest, e.g., aerospace, power, etc.

SHIPPING LABEL—please type or print.

Name _____

Address _____

City _____

State/Country _____ **Zip** _____

AN-T

SUMMER 1976 • NEW TITLES FROM THE IEEE PRESS

Each Selected Reprint book is available in clothbound and low-cost, durable, IEEE members' paperbound editions.

1. COMPUTER NETWORKING

Edited by Robert P. Blanc and Ira W. Cotton. 1976. 376 pages. ISBN — Clothbound 0-87942-071-5; Paperbound 0-87942-072-3. A Book of Selected Reprints.

Computer networks have rapidly proliferated because of their importance in many areas of industry, government, and academia. Sophisticated computer and communications technology has evolved to keep pace with the increasing range of applications. This book contains papers judged by the editors to be the most significant and up-to-date sources of information on this vital field. Specially written material provides transitional background information.

Those just entering the field of computer networking will find this collection a valuable introduction to the various facets of this important field. Experienced practitioners will find the book valuable for ready reference and review. This volume complements the book COMPUTER COMMUNICATIONS, edited by P.E. Green and R.W. Lucky and published by the IEEE PRESS in 1975.

CONTENTS: **Preface, Introduction, Network Technology, Design Considerations, Networking Examples, Network Management, Future Developments, Subject and Author Indexes. A total of 46 reprinted papers.**

	Order No.	Nonmember	Member
Clothbound	PC00646	$17.95	$13.45
Paperbound	PP00653	—	$ 8.95

2. SOLAR CELLS

Edited by Charles E. Backus, Arizona State University. 1976. 512 pages. ISBN — Clothbound 0-87942-069-3; Paperbound 0-87942-070-7. A Book of Selected Reprints.

Photovoltaic energy conversion, born in the early days of solid-state electronics, developed rapidly in the 1960's when there was a demand for electric power for space applications. The last few years have seen the photovoltaic field blossom as interest has shifted to terrestrial applications. The continuing need for alternatives to conventional energy sources will cause the solar cell to take on a future role of increasing importance.

The volume contains a specially written tutorial introduction and a wealth of reprinted papers carefully selected by the editor with the advice of prominent researchers from all over the world.

CONTENTS: **Introduction, General Review, Solar Cell Theory, Cell Fabrication, Space Systems, Terrestrial Applications, Workshop Summaries, Bibliography, Subject and Author Indexes. A total of 42 reprinted papers.**

	Order No.	Nonmember	Member
Clothbound	PC00661	$24.95	$18.70
Paperbound	PP00679	—	$12.45

3. WAVEFORM QUANTIZATION AND CODING

Edited by N.S. Jayant, Bell Laboratories. 1976. 624 pages. ISBN—Clothbound 0-87942-073-1; Paperbound 0-87942-074-X.
A Book of Selected Reprints.

This volume presents work done by over 100 authors during the past quarter century, with emphasis on the most recent and significant results. Early work concentrated on PCM with time-invariant uniform and non-uniform quantizers. The later work largely has been concerned with time-varying (adaptive) quantizers and redundancy reduction using DPCM, DM, and transform coding. The most striking applications have been in the areas of speech and picture coding. The book covers all these topics in a comprehensive manner that brings out comparisons between different waveform coding approaches and different applications.

CONTENTS: **Introduction, Basic Principles, Theoretical Work, Speech Waveforms, Picture Signals, Data Signals, Implementations and Coder Refinements, Code Conversions, Effects of Transmission Errors, Bibliography. A total of 69 reprinted papers.**

	Order No.	Nonmember	Member
Clothbound	PC00687	$29.95	$22.45
Paperbound	PP00695	—	$14.95

4. COMMUNICATIONS SATELLITE SYSTEMS: An Overview of the Technology

Edited by R. G. Gould and Y. F. Lum of the Satellite Systems Panel, IEEE Aerospace and Electronic Systems Society. 1976. 180 pages.
ISBN—0-87942-065-0.

Satellites have assumed an indispensible place in modern communication systems. This book provides an overview of past, present, and future communication satellites, including the problems they pose for system designers. Twenty-two specially written papers are included. Supplementary data on observation, scientific, tracking, and navigation satellite systems are given in an addendum.

CONTENTS: **Preface, Introduction, Notes on Usage, Communication Satellite Systems, Techniques for Expanding Communication Satellite System Capabilities, Frequency and Orbit Coordination and Utilization, Earth Station Technology, Integration of Satellite and Terrestrial Communication Networks, Addendum, Subject Index.**

	Order No.	Nonmember	Member
Clothbound	PC00703	$14.95	$11.20

5. LITERATURE SURVEY OF COMMUNICATION SATELLITE SYSTEMS AND TECHNOLOGY

Edited by J.H.W. Unger, Satellite Systems Panel, IEEE Aerospace and Electronic Systems Society. 1976. 420 pages. ISBN—0-87942-067-7.

This volume is a bibliography of over 3600 references on the technology of communication satellites and related subjects. Some early references from the 1930's are included, but the majority are from the literature of the 1960's and 1970's. Citations through 1974 and into 1975 are listed. This bibliography makes an excellent companion volume to COMMUNICATIONS SATELLITE SYSTEMS: An Overview of the Technology described above.

CONTENTS: **Preface, Introduction, List of References, Permuted Title Index, Author Index.**

	Order No.	Nonmember	Member
Clothbound	PC00729	$14.95	$11.20

INSTITUTE OF ELECTRICAL AND ELECTRONICS ENGINEERS, INC

MAIL ORDER WITH PAYMENT TO:
IEEE Service Center, 445 Hoes Lane, Piscataway, N.J. 08854

Please send me the IEEE PRESS books whose ORDER NUMBERS I have entered below. My check, made payable to IEEE, is enclosed. (Residents of New Jersey please add 5% state sales tax.)

PR-T

Book No.	Order No.	Units	Price
		Total Amount	

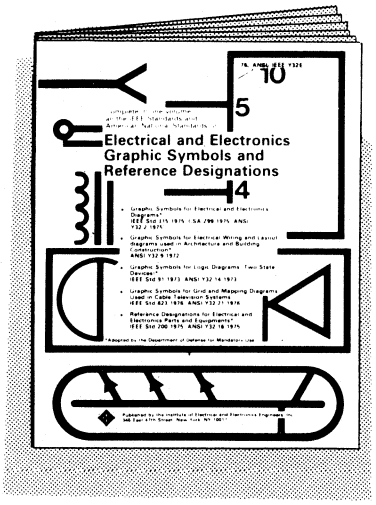
Print Name IEEE No.

Address

City State/Country Zip

A Complete, Up-to-Date Volume of Electrical and Electronics Graphic Symbols and Reference Designations

Electrical and Electronics Graphic Symbols and Reference Designations



76 ANSI/IEEE Y32E

IEEE members save $10.95

Now in one hardbound volume, a complete set of all five important documents on electrical and electronics graphic symbols and reference designations. Sold separately at a total price of $28.90, the combined package is now conveniently available to IEEE members at $17.95, a savings of nearly 40% off the list price of the individual volumes.

The five standards comprising this new volume are approved American National Standards. 76 ANSI/IEEE Y32E is the engineer's guidebook on the current shorthand used in diagram preparations. The latest developments in the state-of-the-art are reflected in this edition, an invaluable source book on equipment symbols and designations for related diagrams, schematics, parts lists, manuals, and similar publications.

Electrical and electronics diagrams are important in domestic and international trade. The use of one common symbol language ensures a clear presentation and economical diagram preparation for a wide audience of users.

These standards represent the latest development in a continuing activity to arrive at a useful series of graphic symbols and reference designations.

For a detailed listing of the five IEEE/American National Standards which comprise 76 ANSI/IEEE Y32E, please refer to the box opposite.

Order your copy today.

IEEE Member price: $17.95

These five standards on electrical and electronics graphic symbols and reference designations are contained in 76 ANSI/IEEE Y32E.

- **Graphic Symbols for Electrical and Electronics Diagrams*** IEEE Std 315-1975, CSA Z99-1975, ANSI Y32.2-1975
- **Graphic Symbols for Electrical Wiring and Layout Diagrams Used in Architecture and Building Construction*** ANSI Y32.9-1972
- **Graphic Symbols for Logic Diagrams (Two-State Devices)*** IEEE 91-1973, ANSI Y32.14-1973
- **Reference Designations for Electrical and Electronics Parts and Equipments*** IEEE Std 200-1975, ANSI Y32.16-1975
- **Graphic Symbols for Grid and Mapping Diagrams Used in Cable Television Systems** IEEE Std 623-1976, ANSI Y32.21-1976

*Adopted for mandatory use by the US Department of Defense. Drawings and diagrams in connection with military contracts will be required to conform with the provisions of the standard.

ORDER FORM

Mail to: IEEE Service Center
445 Hoes Lane
Piscataway, N.J. 08854

☐ Enclosed is $17.95. Please ship me 76 ANSI/IEEE Y32E: *Electrical & Electronics Graphics Symbols and Reference Designations* [SH06213]

Order your copies now for immediate shipment.
Payment must be included for IEEE members price.
Please make check payable to IEEE.

Name _____

IEEE Member No. _____

Address _____

_____

City & State _____ Zip _____

GS-T

A Theoretical Analysis for Gigabit/Second Pulse Code Modulation of Semiconductor Lasers

MAGNUS DANIELSEN, MEMBER, IEEE

Abstract—**Investigation of the rate equations of a semiconductor laser suggests that bit rates of 3–4 Gbit/s can be achieved. Delay, ringing transients, and charge-storage effects can be removed by adjusting the dc-bias current and the peak and width of the current pulse to values prescribed by simple analytical expressions. Also, simple approximate formulas for the light pulse maximum, width, delay, and integrated values are given.**

Introduction

PULSE modulation of a semiconductor laser presents three problems [1]–[5], when high bit rates are required: a time delay between the applied current pulse and the light pulse, ringing transients, and the charge-storage effect of preceding pulses on the light pulse form and magnitude.

This work presents a pulse modulation model which avoids these disadvantages. A dc-bias current near threshold reduces the delay. The first spike of the ringings is suggested to be exploited as a light pulse. This is done by switching off the current pulse immediately after the light pulse appeared. The influence of the charge storage, making the height of the photon pulses dependent on preceding pulses, is overcome by giving the height and duration of the applied current pulses such values that the electron and photon densities return to the start values at the end of the pulse. This makes the start condition identical for each pulse.

Numerical solutions show that the detailed current pulse form is not significant. Only the charge delivered by the current has to fulfill some requirements. Analytical formulas, derived for square current pulses, are therefore at least qualitatively applicable for a wide range of pulse forms.

The following analysis is based on the rate equations including spontaneous emission as reported in [5],

$$dn/dt = J/(ed) - n/\tau_s - gS \tag{1}$$

$$dS/dt = gS - S/\tau_p + \beta n/\tau_s \tag{2}$$

where

- n, J, S electron, current, and photon densities, respectively;
- d active layer thickness;
- e electronic charge;
- τ_s, τ_p electron and photon lifetimes.

The gain of the laser is $g = \alpha(n - N_0)$ [5], [6], where N_0 and α are constants. The factor β is the fraction of spontaneous light that goes into the the lasing modes. In [7] it has been shown that the spectrum of a narrow pulse is determined by the dc bias, and is almost independent of the current pulse height. Therefore β is taken to depend on the prebias current only and to be constant during a pulse. The value of β is estimated to be of the order of 10^{-4} when one mode is active, and is taken to be proportional to the number of active modes [8].

For simplicity, effects like mode locking, mode coupling, Q-switching, electron diffusion, and circuit parasitics have been disregarded in this analysis.

The Modulation Form

In the present modulation form, the laser is prebiased by a dc current density $J = J_0$ near threshold. This gives the start values $n = n_0$ and $S = S_0 = xS_{th}$, where S_{th} is the static photon density at threshold and x is a parameter used to describe the starting condition.

A current pulse $\Delta J(t)$, sufficiently high to give ringings [5], is superposed on J_0. The electron density n now describes an oscillating curve with a maximum and a minimum (Fig. 1). The photon density reaches a maximum S_{max} when n in its negative slope region has decreased to $n = n_c \cong 1/(\alpha\tau_p')$ where $\tau_p' = \tau_p/(1 + \alpha N_0 \tau_p)$. If the current has only small relative changes during the output of light, the pulse is nearly symmetric [5], and we have $n_{max} - n_c \simeq n_c - n_{min}$. After the minimum, the last part of the current pulse pumps n up to n_0 after which the pulse is switched off. From this moment S decays from a value only slightly higher than S_0 within 10–100 ps to this value. Another timing of the current would give the laser a longer relaxation time, up to 4 ns, due to the electron life time.

The necessary and sufficient conditions for the use of the present modulation model is expressed by the two following integrals of the current pulse $\Delta J(t) = J(t) - ed n_c/\tau_s$:

$$n_{max} - n_0 = 1/ed \int_{start}^{t(n=n_{max})} \Delta J\, dt \tag{3a}$$

$$n_0 - n_{min} = 1/ed \int_{t(n=n_{min})}^{end} \Delta J\, dt. \tag{3b}$$

These integrals follow directly from (1) and the fact that before and after the light pulse has emerged, we can neglect the term gS. Equation (3a) expresses the pumping of the electrons by the pulse necessary to give the wanted light output pulse, while (3b) expresses the pump necessary to bring the electron density back to its start value. This charge condition shows that the detailed current pulse form is not significant for the applicability of the present model.

Manuscript received October 20, 1975; revised July 1, 1976.

The author is with the Electromagnetics Institute, Technical University of Denmark, Lyngby, Denmark.

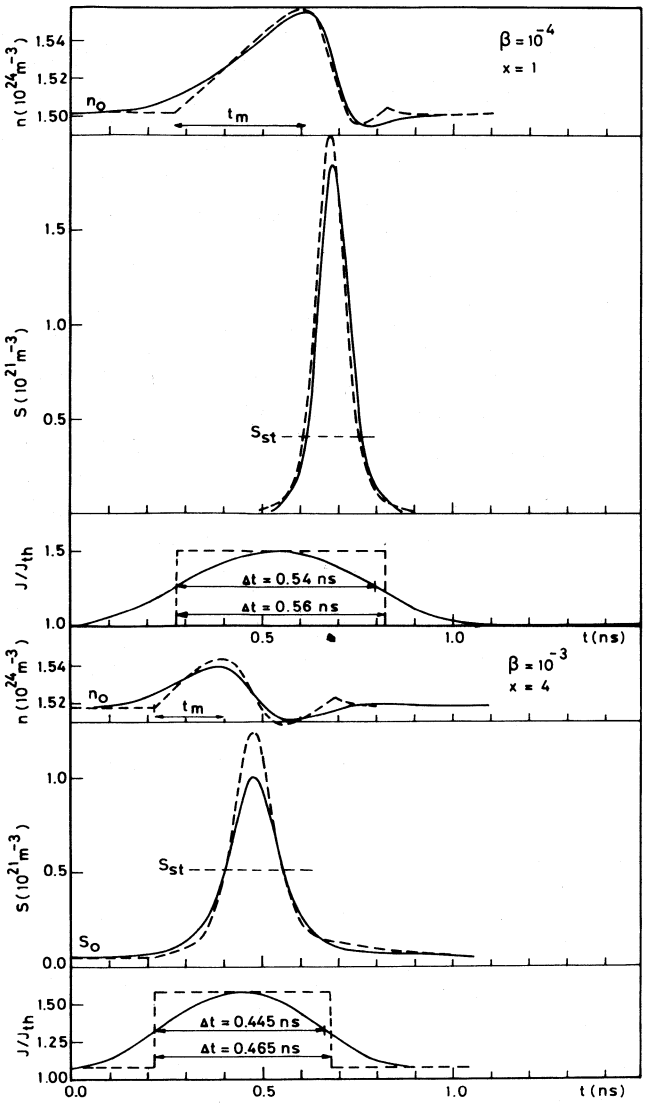


Fig. 1. Numerical results of electron and photon densities as a function of time in a pulse, calculated for a raised cosine (—) and a square (---) current pulse. The applied parameters were $\tau_p = 2.94/(1 + 2.67 \cdot 10^{-25}\, n(t))$ ps, $\tau_s = 4.0$ ns, $\alpha = 1.125 \cdot 10^{-12}$ s$^{-1} \cdot$ m^3, $N_0 = 0.11 \cdot 10^{25}$ m^{-3}, $d = 0.5$ μm, $e = 1.6 \cdot 10^{19}$ As.

Numerical Solution

Fig. 1 shows computer calculations of electron and photon densities for a square and a raised cosine pulse form. Both have the same amplitude. The half-value widths Δt of the current pulses are in both cases fitted to values according to the model. It is seen that Δt, and therefore also the charge in the pulse, is approximate independent of the current pulse form. This has been shown to be true for several sets of parameters β, x. In Fig. 1 two examples are shown where $\beta = 10^{-4}, x = 1$ and $\beta = 10^{-3}, x = 4$.

For low β and x, i.e., low start values S_0, the peak and width of the light pulse are nearly independent of the current pulse shape. For higher β and x the tendency is that the maximum decreases and the width increases, but in all cases the integrated light output is the same.

Calculations of a long row of pulses showed that no intersymbol interference was present when the correct timing of the current pulses was used, independent of the current pulse spacing down to 0.1 ns. Overtiming of the pulses gave strong intersymbol interference, while undertimed pulses with a deviation up to 10 percent gave stable light output pulses with less than 5 percent change in S_{max}.

Analytical Approximations

As a consequence of the fact that the laser response is only weakly dependent on the detailed current pulse form, and for simplicity, a square current pulse has been analyzed in order to obtain simple approximate formulas to describe the light output and the timing of the current pulse.

The computer calculations show that a square current pulse with the amplitude ΔJ causes n to vary approximately as a triangular wave with time. From the start to $n = n_{max}$ and from $n = n_{min}$ to the end of the pulse, the slope is $\Delta J' = \Delta J/(ed)$. Between $n = n_{max}$ and $n = n_{min}$, the slope was taken to be a constant $-n'$. Apparently rough, this approximation gives results which are in 5-10-percent agreement with computer calculations for all reasonable values of parameters $\Delta J/J_{th} < 2$, $10^{-4} < \beta < 5 \cdot 10^{-3}$, and $1 < x < 10$. As reference for the start condition for the pulse modulation we use the threshold values. From the definition of the threshold current density in [5] we obtain $J'_{th} = J_{th}/(ed) \simeq 1/(\alpha\tau_s\tau'_p)$. The static photon and electron densities with $J' = J'_{th}$ are given by

$$S_{th} \cong 1/(\alpha\tau_s) \cdot (\beta\tau_p/\tau'_p)^{1/2}$$

and

$$\Delta n_{th} = n_{th} - n_c \simeq -1/\alpha \cdot (\beta/\tau_p/\tau'_p)^{1/2} \tag{4}$$

where n_c is the electron density for which the gain exceeds the total photon loss in the laser. By introduction of $\Delta n = n - n_c$ in (2) we obtain

$$dS/dt = \alpha \Delta n S + \beta n/\tau_s. \tag{5}$$

The start condition is defined by $J = J_0$ giving $S = S_0 = x \cdot S_{th}$ and according to (5) $\Delta n = \Delta n_0 = \Delta n_{th}/x$. The analysis is now performed in three steps.

1) In the time interval $0 < t < t_m$, where t_m is defined by $n(t_m) = n_{max}$, an approximate solution of (5) can be written as

$$S = \{S_1(\operatorname{erf} A(t - t_0) + \operatorname{erf} At_0) + S_0 \exp(-A^2 t_0^2)\} \cdot \exp A^2(t - t_0)^2 \tag{6}$$

where $t_0 = -\Delta n_0/\Delta J'$ is the time it takes for n to grow from n_0 to n_c, and

$$S_1 = \beta/(\alpha\tau_s\tau'_p) \cdot \sqrt{\pi/(2\alpha\Delta J')} \tag{7a}$$

and

$$A = \sqrt{\alpha\Delta J'/2}. \tag{7b}$$

At $t = t_m$ we have $dn/dt = 0$. With $n_{max} \approx n_c$ in (1) we find that $S \cong S_{st}$, the stationary state value corresponding to $J = J_0 + \Delta J$. This, inserted into (6), gives in practical cases, when $A(t_m - t_0) \geq 1$,

$$t_m = t_0 + \sqrt{2B/(\alpha\Delta J')} \tag{8}$$

where

$$B = \ln (S_{st}/S_{00}) \tag{9a}$$

and

$$S_{00} = S_1(1 + \operatorname{erf} At_0) + S_0 \exp(-A^2 t_0^2). \tag{9b}$$

For pulses where $\tau_P/\tau_s \cdot x^2/\beta \cdot \Delta J'/J'_{th} > 1$, we find that

$$B \simeq \ln (\Delta J'/J_{th} \cdot x^{-1} \cdot (\tau_p/\tau'_p/\beta)^{1/2}). \tag{10}$$

A limiting condition for which the model can be applied is given by $n_{max} - n_c = n_c - n_{min}$ and $n_0 > n_{min}$, which gives $t_m \geq 2t_0$. By insertion of $t = 2t_0 \leq t_m$ into the right-hand side and $S = S_{st}$ into the left-hand side of (6), we obtain, after some calculations,

$$\Delta J/J_{th} \geq (4\tau_s^2 \tau'_p \cdot \tau_p^{-3})^{1/4} \cdot \beta^{3/4}/x^{1/2} + \tfrac{1}{2}\tau_s/\tau_p \cdot \beta/x^2 \tag{11}$$

which is in 5-percent agreement with computer simulations for all practical cases, $x > 1$ and $\beta < 5 \cdot 10^{-3}$.

2) In the time interval $t_m < t < t_{min}$, where t_{min} is defined by $n(t_{min}) = n_{min}$, we use $\Delta n = -n'\Delta t'$. Here $\Delta t' = t - t_m - \Delta n_{max}/n'$ and $\Delta n_{max} = (t_m - t_0)\Delta J'$. Equation (5) now gives

$$S = S_{max} \exp(-(\alpha n'/2)\Delta t'^2) \tag{12}$$

$$S_{max} = \tau_p \Delta J' \exp(\alpha \Delta n_{max}^2/(2n')). \tag{13}$$

The integrated photon output of one pulse is given by [5]

$$S_{out,pulse} = \frac{1}{\tau_p} \int_{t_m}^{t_{min}} S\, dt = 2\Delta n_{max} + \Delta J \cdot \Delta t_{st} \tag{14}$$

where $\Delta t_{st} = 2\Delta n_{max}/n'$ is the pulsewidth defined by points where $S = S_{st}$. From (12)-(14) an approximate proportionality between n' and $\Delta J'$ (B varies slowly) is found:

$$n'/\Delta J' = 2B/\ln(16B/\pi). \tag{15}$$

Finally we can use (15) to obtain solutions for the pulse parameters

$$S_{max} = \tau_p \Delta J' \cdot \sqrt{16B/\pi} \tag{16}$$

$$\Delta t_{st} = \sqrt{2/(\alpha \Delta J')} \ln(16B/\pi)/\sqrt{B} \tag{17}$$

and the half-power width

$$\Delta t_{1/2} = 2(2 \ln 2/\alpha/n')^{1/2} = \sqrt{2/(\alpha \Delta J')}\,(2 \ln 2 \cdot \ln(16B/\pi)/B)^{1/2}. \tag{18}$$

3) In the time interval $t_{min} < t < \Delta t$, where Δt is the current pulse length, we can approximate the slope of n by $\Delta J'$. The value of Δt for which $n(\Delta t) = n_0$ is

$$\Delta t = 2\Delta n_{max}(1/\Delta J' + 1/n') = \sqrt{2/\alpha \Delta J'} \cdot (2 + \ln(16B/\pi)/B)B^{1/2} \tag{19}$$

where we once more have used (15).

The total photon output in the pulse defined by (14) is now found by

$$S_{out,pulse} = \Delta J' \cdot \Delta t \propto \sqrt{\Delta J'}. \tag{20}$$

The essence of the last statement is that the linear variation of n leads to the result that no photon is present before and after the moments where $S = S_{st}$. The error introduced in this way is less than 20 percent, which is not serious because almost all of the 20 percent is concentrated as exponential tails at both sides of the pulse.

Conclusion

We can conclude that the formula for $S_{out,pulse}$ agreed within 20 percent, and all other formulas within 10 percent, with computer simulation for the parameters $\Delta J/J_0 < 2 \cdot 10^{-4} < \beta < 5 \cdot 10^{-3}$ and $1 < x < 10$. The variation of the times is approximately inversely proportional to $\sqrt{\Delta J'}$, while the photon pulse maximum and the integrated pulse are approximately proportional to $\Delta J'$ and $\sqrt{\Delta J'}$, respectively. These features follow from the fact that the functions of B appearing as factors in the pulse parameters vary slowly with $\Delta J'$. The only influence of β and x is also through B [(9) and (10)], which is why this influence is rather weak. The tendency is that for increasing β and x, the values of t_m, Δt, S_{max}, and $S_{out,pulse}$ decrease while $\Delta t_{1/2}$ increases. Numerical calculation shows that in all cases $\Delta t_{1/2} < 0.5\,\Delta t$. This gives good separation between the light pulses.

Correctly timed and undertimed current pulses with pulse spacings down to 0.1 ns gave no or small intersymbol interference, while overtimed current pulses gave instability and strong intersymbol interference. This suggests that the model is useful for high-speed modulation. It can also be concluded that this modulation form is most useful when the prebias is a little above threshold ($x > 1$) both because of the dynamic behavior [(11)] and because the spectrum then is narrow according to [7] (β is small). It is expected that with this model, pulse durations of $\Delta t = 0.25$-0.3 ns corresponding to bit rates 3-4 Gbit/s can be obtained with $\Delta J/J_{th} = 1.5$ which is twice the highest experimentally obtained [9]. It is believed that adjustments of the parameters Δt, ΔJ, and x to values which fit with the results of the present model have played a role in obtaining Gbit/s modulation rates in earlier experimental works. The problem of obtaining narrow current pulses ($\Delta t = 300$ ps) can, for example, be overcome by using a MESFET driver for the laser [10].

Independently of this work some experimental work has recently been performed which verifies some features of the described modulation method [11].

Acknowledgment

The author wishes to thank Dr. M. T. Vlaardingerbroek and Dr. P. Jeppesen for many fruitful discussions.

References

[1] T. P. Lee and R. M. Drosier, "Charge storage in injection lasers and its effects on high-speed pulse modulation of laser diode," *Proc. IEEE*, vol. 62, pp. 1176-1177, 1974.

[2] T. Ikegami, K. Kobayashi, and Y. Suematsu, "Transient behaviour of semiconductor lasers," *Electr. Comm. Japan*, vol. 53 B, pp. 82-89, 1970.

[3] T. Ozeki and T. Ito, "A new method for reducing pattern effects in PCM current modulation of DH-GaAlAs lasers," *IEEE J. Quantum Electron.*, vol. QE-9, pp. 532-533, 1973.

[4] M. J. Adams, "Rate equations and transient phenomena in semiconductor lasers," *Opto. Electr.*, vol. 5, pp. 201-215, 1973.
[5] P. M. Boers, M. Danielsen, and M. T. Vlaardingerbroek, "Dynamic behaviour of semiconductor lasers," *Electr. Lett.*, vol. 11, pp. 206-208, May 1975.
[6] B. W. Hakki and L. Paoli, "C. W. degradation of 300 K of GaAs double heterostructure junction lasers II," *J. Appl. Phys.*, vol. 44, pp. 4113-4119, 1973.
[7] P. R. Selway and A. R. Goodwin, "Effects of D. C. bias level on the spectrum of GaAs lasers operated with short pulses," *Elect. Lett.*, vol. 12, pp. 25-26, 1976.
[8] D. Röss, *Laser, Light Amplifiers and Oscillators.* New York: Academic p. 284, 1969.
[9] P. Russer and S. Schultz, "Direkte Modulation eines Doppelheterostrukturlasers mit einer bitrate von 2.3 Gbit/s," *A.E.U.*, vol. 27, pp. 193-194, 1973.
[10] V. Ostoich, N. Slaymaker, and P. Jeppesen, "Gbit/s modulation of DH-GaAlAs lasers with GaAs MESFET's," presented at the 1st European Conf. Opt. Fibre Comm., Sept. 1975.
[11] J. G. Farrington and J. E. Carroll, "Sub-nanosecond pulsing of GaAs stripe lasers," presented at the 1st European Conf. Opt. Fibre Comm., Sept. 1975.

Zero-Power-Gain Measurements in CW HF(DF) Laser by Means of a Fast Scan Technique

RICHARD A. CHODZKO, DONALD J. SPENCER, HAROLD MIRELS, STEPHEN B. MASON, AND DAVID H. ROSS

Abstract—**An improved technique for measuring zero power gain in a CW HF-DF chemical laser has been developed in which a CW HF(DF) single-line, frequency-stabilized TEM_{00} mode probe laser is used. Through use of a flat rotating mirror and focusing elements, the streamwise distribution of zero-power gain was scanned at a rate of ~1 mm/μs with a spatial resolution of ~1 mm. The zero-power-gain profile was observed for two arc-driven chemical-laser nozzles with both HF and DF active species. The nozzles consisted of a 36-slit array with perforated tube H_2 injectors and a 55-slit array with uniform H_2 injection. Results are presented for the variation of zero power gain with axial distance, the magnitude and location of peak gain, and the gain cutoff location for a number of transitions. Peak gain values of 15 percent/cm and 5.5 percent/cm were measured with HF and DF active species, respectively, with the 55-slit nozzle array.**

I. Introduction

SMALL-SIGNAL-GAIN measurements in an arc-driven, supersonic diffusion CW HF chemical laser have been previously made both directly by means of pulsed-probe laser [1] and indirectly by means of a chemiluminescence technique [2]. The measurements made with a pulsed-probe laser had an uncertainty in the magnitude of the gain that resulted from a lack of frequency stability in the multitransverse, multilongitudinal mode probe beam. The gain variation with distance from the nozzle exit plane x was obtained [1] by measuring the gain on the various HF vibrational rotational transitions at fixed values of x during a given arc run. The arc was then shut down, the probe beam was located at a new value of x, and the process repeated.

Clearly, real-time (fast) scans with a CW HF(DF) probe would be desirable in order to reduce run-to-run flow variations and to expedite measurements. The present work incorporates a newly developed single-transverse, single-longitudinal mode, stable CW probe laser and an optical system that permits scanning of the small-signal CW HF(DF) gain profile from the nozzle exit plane to a distance 8 cm downstream in about 0.3 ms with a 1-mm spatial resolution. Zero-power-gain distributions have been obtained by means of two different nozzle configurations with both HF and DF active species. The results are reported herein.

II. Experimental Apparatus and Method

A. Scanning Technique

The gain profile scanning technique used in the present experiments is shown in Fig. 1. A technique similar to this was used previously by Falk [3] for zero-power-gain measurements in a DF-CO_2 transfer chemical laser. The rotating mirror was located at the focal points of the focusing elements L_2 (3-m radius concave mirrors), which caused the probe beam to sweep from the nozzle exit plane to a distance 8 cm downstream while remaining parallel to the exit plane. The IR probe beam was aligned with a HeNe reference beam to the center line (vertical) of the nozzle exit. The focusing element L_3 then imaged the split probe beams on diffuse reflectors (sandblasted Al plates) viewed by the signal and reference detectors. The signal detector voltage was observed versus time with H_2/D_2 off and on. The log of the ratio of these observations defines the variation of active region gain versus

Manuscript received December 10, 1975; revised July 1, 1976. This work was supported by the Air Force Weapons Laboratory under U.S. Air Force Space and Missile Systems Organization (SAMS) Contract F04701-75-0076.

The authors are with The Aerospace Corporation, El Segundo, CA 90245.

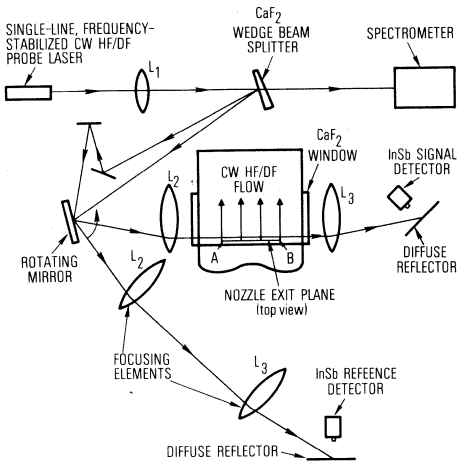


Fig. 1. CW HF(DF) zero-power-gain scanning technique.

distance downstream of the nozzle exit plane. A typical mirror rotation speed of 90 rpm implied a 280-μs scan for an 8-cm distance. The reference detector provided a signal that allowed for correction to any fluctuations in the probe output power between the $H_2(D_2)$ on and $H_2(D_2)$ off scans.

The diffuse reflectors were required to produce an InSb detector signal that was proportional to the probe beam power and independent of small variations in the direction of the probe beam. Variations in direction of the probe beam occurred because of the lack of stability of the optical elements, small variations in the window properties, and possibly refractive index variations in the probe laser active medium. Thus, the diffuse reflectors were required in order to make the reference detector and signal detector output voltages proportional to one another to within a constant factor under $H_2(D_2)$ off (no active medium) conditions. The diffuse reflectors attenuated the InSb detector signals produced by the probe laser such that electronic amplification was required, especially for the lower output power transitions. Precision current-to-voltage amplifier units of bandwidth adequate ($\simeq$1 MHz) for the rotating mirror sweep speeds were employed.

The spatial resolution of the gain scanning technique was calculated and measured [4] to be $\simeq$1 mm. The spatial resolution was measured by observing the signal detector signal while inserting a sharp-edge obstacle of known dimension at positions A and B (Fig. 1). The spatial resolution depended primarily on the width of the probe beam (TEM_{00} mode) in the gain region since the time response of the electronics was sufficiently fast. The spatial resolution was maximized by specifying (by means of L_1 and L_2) the probe beam waist to be halfway between points A and B in the gain region (Fig. 1).

B. CW HF(DF) Probe Laser

A single-frequency, single-line HF(DF) probe laser was fabricated for the gain measurements similar to the design of Hinchen [4], [5]. The stable optical cavity consisted of a concave totally reflecting mirror (R = 1 m) and a 300-line/mm grating blazed at 2.8 μm manufactured by PTR, Inc., with a 30-cm separation. The measured grating efficiency was 90 percent for the HF and 94 percent for the DF wavelength range (E vector $\perp$ to grooves). The grating was mounted in a Littrow corner reflector configuration [6] such that the direction of the zeroth-order output beam was independent of the selected line. The high grating efficiency permitted gain measurements for many ($\simeq$20) of HF and DF transitions. Peak output power levels of 1 W were measured for HF lines and 0.4 W for DF lines.

C. CW HF(DF) Active Medium

The arc-driven CW HF(DF) laser facility used here is described in [7]. Zero power gain associated with two nozzle configurations was investigated. The nozzles included a 36-slit nozzle with perforated tube $H_2(D_2)$ injectors and a 55-slit nozzle with slit $H_2(D_2)$ injectors (Fig. 2). Both nozzle arrays had a 1.25-cm exit height and a 17.8-cm active length. The nominal HF(DF) flow conditions for the 36-slit and 55-slit nozzle arrays are given in Table I. These flows yielded 1.8- and 1.7-kW peak closed-cavity power levels, respectively (HF). The DF gain measurements were made at the same molar flow rates as the HF measurements. The initial concentration of species (at the throat) calculated from the NEST computer code [8] for the 36-slit and 55-slit nozzle arrays assuming thermodynamic equilibrium are given in Table II. The plenum temperatures were computed from the hot and cold (arc off) pressures measured for the two nozzles at the flow conditions specified in Table I. Thus, from Table II, the plenum temperatures and initial F-atom concentrations for the two nozzles were not the same.

The nozzle exit pressures were $\simeq$3 torr based on Pitot total pressure measurements [9] for similar flow conditions. The active flow region was in the form of a free jet bounded by a "cavity" pressure of 6 torr. Hence, the nozzle flow was overexpanded. The pressure mismatch will generate a system of Mach waves as indicated in Fig. 3. The waves generated resulting from pressure mismatch are seen to intersect $\simeq$3 cm downstream based on nozzle segment exit height and $\simeq$0.8 cm downstream based on segment nozzle width. The major effect is expected to be an increase in static pressure from about 3 torr to about 6 torr at about 3 cm downstream of the nozzle exit. The pressure mismatch was a result of vacuum pump limitations.

III. Experimental Results

A. Typical Data

Typical data[1] obtained with the beam scanner are shown in Fig. 4. The data were obtained with the 36-slit nozzle and HF active species. Both single-scan and multiple-scan data are shown. The upper traces for the single scan data correspond to the signal detector output voltage, and the lower traces correspond to the reference detector. The upper traces show the H_2 on (gain) and H_2 off (no gain) signals. The lower traces show the H_2 on (unmodulated) and H_2 off (modulated) reference detector signals. The multiple scan data show about 10 scans over an ~10-s time interval. Thus the data are very reproducible, and the fluctuations correspond to a $\pm$3-percent variation in peak zero power gain (taking into account output

[1]The data in Fig. 4 are not the same as given in Fig. 7 since arc flow conditions and temperatures were not the same.

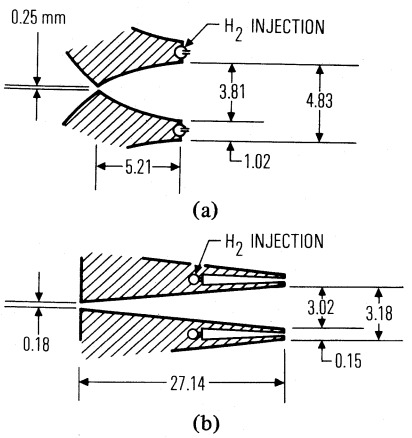


Fig. 2. Nozzle configurations for CW HF(DF) zero-power-gain measurements (12.7-mm height). (a) 36-slit contoured nozzle. (b) 55-slit, two-dimensional nozzle.

TABLE I
CW HF(DF) Flow Conditions

36-Slit Nozzle	55-Slit Nozzle
$\dot{m}_{SF_6} = 4.25$ g sec^{-1}	$\dot{m}_{SF_6} = 3.84$ g sec^{-1}
$\dot{m}_{He} = 4.50$	$\dot{m}_{He} = 4.50$
$\dot{m}_{O_2} = 0.70$	$\dot{m}_{O_2} = 0.80$
p_{cavity}[a] = 6.3 Torr	$p_{cavity} = 6.3$ Torr
$p_{plenum} = 24$ psia	$p_{plenum} = 26$ psia
Semiwidth[b] = 0.10 mm	Semiwidth = 0.15 mm
DF Active Species:	DF Active Species:
$\dot{m}_{D_2} = 1.34$ gm sec^{-1}	$\dot{m}_{D_2} = 1.30$ gm sec^{-1}
HF Active Species:	HF Active Species:
$\dot{m}_{H_2} = 0.67$ gm sec^{-1}	$\dot{m}_{H_2} = 0.65$ gm sec^{-1}

[a]Pressure measured in test section outside of nozzle flow.
[b]Half-width of individual nozzle exits.

TABLE II
Plenum Conditions

Species	36-Slit Nozzle[a] Concentration $[(mol)_i/(mol)_{total}]$	36-Slit Nozzle[a] Mass Flow (g/sec)	55-Slit Nozzle[b] Concentration $[(mol)_i/(mol)_{total}]$	55-Slit Nozzle[b] Mass Flow (g/sec)
He	0.921	4.50	0.902	4.50
F	0.050	1.15	0.075	1.78
SOF_4	0.022	3.29	0.004	0.68
SO_2F_2	0.002	0.24	0.017	2.11
Others	0.005	0.27	0.002	0.07

[a]$P = 1.81$ atm, $T = 1460$ K.
[b]$P = 1.81$ atm, $T = 1780$ K.

power variations in probe beam). The scanning rate was sufficiently fast such that the "true" gain profiles were measured since the shapes of the profiles in Fig. 4 are preserved and only the amplitude varies from scan to scan. The output power of

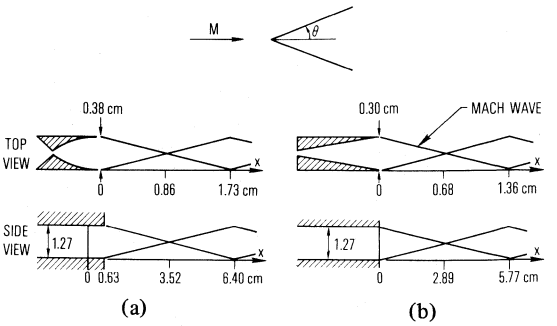


Fig. 3. Nominal Mach wave locations. $M \simeq 4.7$, $\tan\theta = (M^2 - 1)^{-1/2} \simeq 0.22$. (a) 36-slit nozzle. (b) 55-slit nozzle.

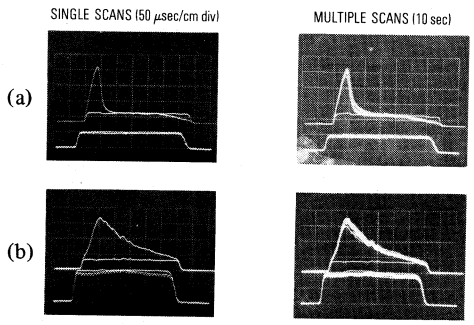


Fig. 4. Typical single- and multiple-scan zero-power-gain data. For the single-scan data, the two upper traces correspond to H_2 on (gain) and H_2 off (no gain). The lower trace (reference detector) is modulated for H_2 off and unmodulated for H_2 on. (a) $P_2(5)$ HF transition. (b) $P_1(4)$ HF transition.

the CW probe laser varied slightly from scan to scan such that corrections from the reference detector signals were required. The fine structure in the scan data is due primarily to small variations in the reflectivity of the CaF_2 windows.

The data in Fig. 4 were obtained by means of the CW HF probe laser locked on line center with a Lansing Model 80.214 electronic feedback loop. The feedback loop could be disabled and the cavity length varied by manually varying the voltage on the piezoelectric drive. It was determined, as expected, that the probe laser cavity length that produced maximum output power also gave maximum gain, i.e., line center, from the active medium. This maximum gain was the same as the gain obtained with the probe locked on line center. The probe output power was also more stable with feedback control. However, the feedback loop had a limited frequency response ($\simeq$100 Hz) and could not correct for the relatively large variations in probe output when the probe was operated on transitions with gain near threshold. Consequently, lower gain transitions, i.e., the $P_1(J)$ DF transitions, did not have as good an amplitude stability as indicated in Fig. 4 (fluctuations of up to $\pm$50 percent have been observed).

A series of gain measurements were made at the flow conditions listed in Tables I and II, with HF(DF) active species and with both the 55-slit and 36-slit nozzle arrays. Representative single-scan Polaroid photographs similar to those shown in Fig. 4 were obtained for the various $P_v(J)$ vibrational rotational HF(DF) transitions. The probe laser grating was tuned through several ($\simeq$10) lines during a single run of the arc-driven CW HF(DF) active medium. As a check of the reproducibility of the data between arc runs, gain profiles for a

fixed transition were periodically measured and compared with those obtained during previous arc runs. The gain profiles were then calculated from the relation $g_0 = l^{-1} \ln (P_1/P_0)$ and the Polaroid photographs at individual data points. P_1 and P_0 are the transmitted probe laser power levels for $H_2(D_2)$ on and $H_2(D_2)$ off conditions, respectively, after corrections are made for reference power variation and l is the gain length. Table III is a summary of the zero-power-gain data listing the transition, peak gain, position of the peak, and the cutoff (zero position).

B. 36-Slit Nozzle

The zero power gain versus distance x from the nozzle exit measured for the $P_2(J)$ HF transitions with the 36-slit nozzle is shown in Fig. 5. A peak gain ~10 percent/cm is measured at $x \simeq 6$ mm for the maximum gain $P_2(4)$ transition. Positive gain is observed at $x = 0$ within the 1-mm resolution of the scanner, which indicates possible boundary-layer separation and diffusion of HF upstream of the nozzle exit. An unexpected zero or slightly positive slope region is observed in the gain profile at a distance 4–5 cm downstream of the nozzle exit, which may be due to a repumping mechanism or the Mach wave intersection shown in Fig. 3. The zero-power-gain profiles measured for the $P_1(4)$ HF transition are nearly equal to the peak gain on the $P_2(4)$ HF transition (Fig. 6). This result is not predicted by current theoretical models such as the DESALE [10] or the BLOTTNER [11] codes, which yield $P_1(J)$ gain 2 to 3 times lower than the $P_2(J)$ gain. The equality of the peak $P_1(J)$ gain to the $P_2(J)$ gain is qualitatively consistent with a v^2 dependence (instead of v) of the vibrational translational (VT) deactivation rates that have recently been discussed by Kwok and Wilkins [12].

The zero-power-gain profiles measured for the $P_v(J)$ DF transitions with the 36-slit nozzle are shown in Figs. 7–9. A peak gain of ~3.3 percent/cm is measured at $x \simeq 7$ mm for the maximum gain $P_3(6)$ transition. The gain zones again are stretched out with a different shape at a distance $x \simeq 5$ cm in comparison to the high-gain regions at $x \simeq 1$ cm. These results are very similar to those obtained with HF except for the magnitude of the peak gain. A peak gain of ~4.7 percent/cm is measured at $x = 1$ cm for the maximum gain $P_2(6)$ transition. Unexpected local zero or positive slope region near $x \simeq 5$ cm is also observed for the $P_2(J)$ transitions. The similarity in the shapes of the gain profiles for HF and DF, i.e., the positive gain regions and the position of peak gain indicates that the HF and DF deactivation rates are not significantly different. The factor of 2 difference in peak gain may be mainly due to the difference in the Einstein coefficients [13] for the HF and DF transitions. A peak gain of ~1.7 percent/cm is measured at $x \simeq 1.5$ cm for a $P_1(9)$ DF transition. Gain measurements for $P_1(J)$ DF transitions were more difficult than for HF because of a lack of amplitude stability of the probe laser output and the low values of the gain itself. The scatter in the data is shown in Fig. 9. It was not possible, therefore, to determine the J value for maximum $P_1(J)$ DF zero power gain. However, the peak zero power gain for the $P_1(J)$ DF transitions measured is nearly three times lower than for the $P_2(J)$ DF transitions in contrast to the HF results, which may be due to the reduced chemical pumping rates for the $P_1(J)$ DF transitions in comparison with the $P_1(J)$ HF transitions.

TABLE III
ZERO-POWER-GAIN DATA

Nozzle	Lasing Molecule	Transition	Peak Gain (%/cm)	Peak Gain Location (cm)	Cutoff (cm)
36 Slit	HF	$P_2(3)$	9.0	0.50	1.75
		$P_2(4)$	10.3	0.60	2.90
		$\underline{P_2(7)}$	6.0	0.80	7.10
		$P_1(3)$	8.6	0.83	6.03
		$P_1(4)$	9.4	1.10	6.38
		$\underline{P_1(6)}$	8.3	1.30	8.28
	DF	$P_3(4)$	2.9	0.52	1.14
		$P_3(6)$	3.3	0.76	5.45
		$\underline{P_3(8)}$	2.4	0.83	>7.60
		$P_2(4)$	4.2	0.69	4.0
		$P_2(6)$	4.6	1.10	7.60
		$\underline{P_2(8)}$	3.9	1.21	>8.0
55 Slit	HF	$P_2(3)$	12.8	0.18	1.0
		$P_2(4)$	15.2	0.31	2.44
		$\underline{P_2(7)}$	9.4	0.44	5.38
		$P_1(4)$	12.76	0.50	4.36
		$\underline{P_1(6)}$	11.26	0.68	6.20
		$P_1(7)$	7.80	1.00	6.20
	DF	$P_3(5)$	2.48	0.20	2.49
		$P_3(6)$	3.54	0.30	4.19
		$\underline{P_3(7)}$	3.46	0.50	5.93
		$P_2(4)$	4.72	0.30	3.08
		$P_2(6)$	5.51	0.51	3.95
		$\underline{P_2(9)}$	3.39	0.79	5.73

Note: Underlined transitions are peak gain transitions for a given v level.

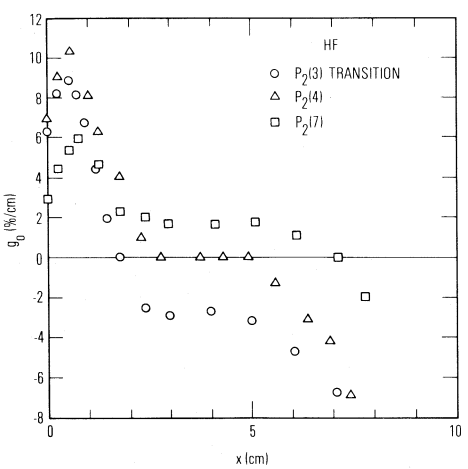


Fig. 5. Zero power gain versus distance from nozzle exit for $P_2(J)$ HF transitions and 36-slit nozzle.

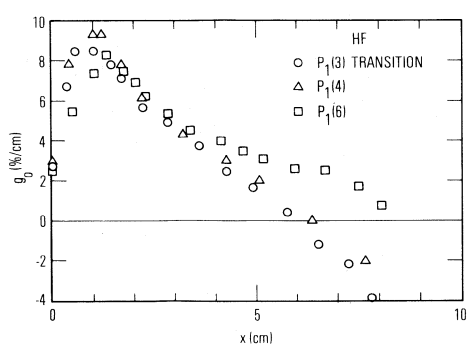


Fig. 6. Zero power gain versus distance from nozzle exit for $P_1(J)$ HF transitions and 36-slit nozzle.

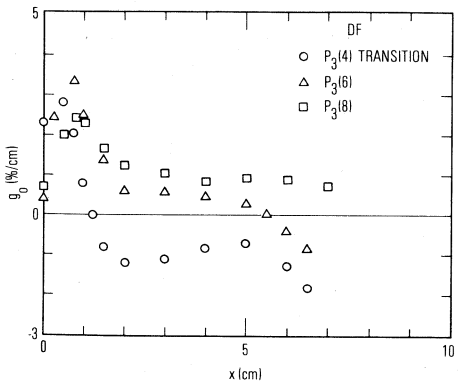


Fig. 7. Zero power gain versus distance from nozzle exit for $P_3(J)$ DF transitions and 36-slit nozzle.

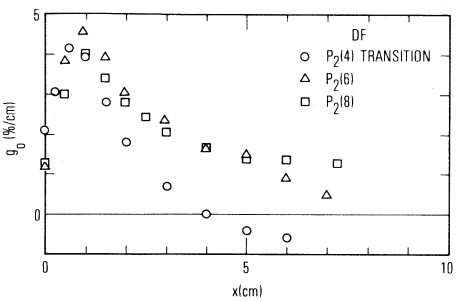


Fig. 8. Zero power gain versus distance from nozzle exit for $P_2(J)$ DF transitions and 36-slit nozzle.

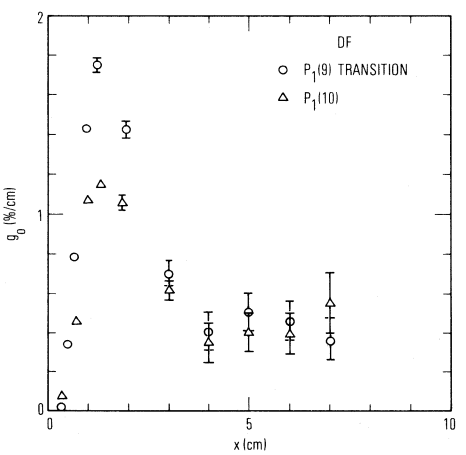


Fig. 9. Zero power gain versus distance from nozzle exit for $P_1(J)$ DF transitions and 36-slit nozzle.

C. 55-Slit Nozzle

The results of the zero-power-gain profile measurement of the $P_v(J)$ HF transitions with the 55-slit nozzle array are summarized in Table III for the flow conditions given in Tables I and II. The general shape of the HF and DF gain profiles were similar to the gain profiles observed previously with the 36-slit nozzle. The magnitude of the peak HF gain is about a factor of 3 higher than the peak DF gain for the 55-slit nozzle, compared to a factor of 2 for the 36-slit nozzle. This difference between the two nozzles is not yet understood.

IV. Conclusions

By use of a recently developed CW single-line, single-frequency, stabilized-probe laser, a technique for scanning CW HF(DF) zero-power-gain profiles in real time has been developed. The technique, for which a rotating mirror and focusing elements are employed, permits a scan of the line-center zero power gain from the nozzle exit plane to a distance $\simeq$8 cm downstream in $\sim$300 μs with a 1-mm spatial resolution. With the real-time scanning technique, experiments were initiated to compare the zero power gain associated with two CW chemical laser nozzle designs and HF* versus DF* gain. Previous CW HF zero-power-gain measurements with a pulsed-probe laser [1] had the disadvantage of not yielding the line-center zero power gain and having a reduced spatial resolution because of the nonrepeatability of the arc-flow conditions during the required sampling time, i.e., they were not real time measurements. Exact comparison between the present zero-power-gain measurements and the previous pulsed-laser experiments is not possible because the arc configuration is not the same. The magnitudes of the peak gain values ($\simeq$10 percent/cm with HF and the 36-slit nozzle) and the general shapes of the profiles, however, are in good agreement with the present results. A more detailed discussion of the present results (including the zero power gain profiles for the 55-slit nozzle) is given in [4].

References

[1] R. A. Chodzko, D. J. Spencer, and H. Mirels, "Zero power gain measurements in a CW HF laser using a pulsed-probe laser," *IEEE J. Quantum Electron.*, vol. QE-9, p. 550, May 1973.

[2] M. A. Kwok, D. J. Spencer, and R. W. F. Gross, "Chemiluminescence from the supersonic jet of a CW HF chemical laser," *J. Appl. Phys.*, vol. 45, pp. 3500–3506, Aug. 1974.

[3] T. J. Falk, *Parametric Studies of the DF-CO_2 Chemical Transfer Laser*, Air Force Weapons Lab., Kirtland AFB, NM, June 1972, Rep. AFWL-TR-71-96.

[4] R. A. Chodzko, D. J. Spencer, H. Mirels, S. B. Mason, and D. H. Ross, *Zero-Power-Gain Measurements in CW HF(DF) Laser by Means of Fast-Scan Technique*, The Aerospace Corp., El Segundo, CA, Rep. TR-0076(6605)-4, to be published.

[5] J. J. Hinchen, "Operation of a small single-mode stable CW hydrogen fluoride laser," *J. Appl. Phys.*, vol. 45, pp. 1818–1821, Apr. 1974.

[6] T. M. Hard, "Laser wavelength selection and output coupling by a grating," *Appl. Opt.*, vol. 9, pp. 1825–1830, Aug. 1970.

[7] D. J. Spencer, H. Mirels, and D. A. Durran, "Performance of CW HF chemical laser with N_2 or He diluent," *J. Appl. Phys.*, vol. 43, pp. 1151–1157, Mar. 1972.

[8] E. B. Turner, G. Emanuel, and R. L. Wilkens, *The Nest Chemistry Computer Program*, The Aerospace Corp., El Segundo, CA, Rep. TR-0059(6240-20)-1, 1970.

[9] R. L. Varwig, The Aerospace Corp., private communication.

[10] W. D. Adams, E. B. Turner, J. F. Holt, D. G. Sutton, and H. Mirels, *The RESALE Chemical Laser Computer Program*, The Aerospace Corp., El Segundo, CA, Rep. TR-0075(5530)-5, 1975.

[11] F. G. Blottner, "Finite difference methods of solution of the boundary layer equations," *AIAA J.*, vol. 8, pp. 193–205, Feb. 1970.

[12] M. A. Kwok and R. L. Wilkins, *Flow Tube Studies of Vibrational Energy Transfer*, The Aerospace Corp., El Segundo, CA, Rep. TR-0076(6603)-7, to be published.

[13] J. M. Herbelin and G. Emmanuel, "Einstein coefficients for diatomic molecules," *J. Chem. Phys.*, vol. 60, pp. 689–696, Jan. 1974.

Threshold and Rate Equation Considerations for a H^+–Cs Charge-Exchange Laser

DREW A. COPELAND, MEMBER, IEEE, H. MAHR, AND CHUNG L. TANG, SENIOR MEMBER, IEEE

Abstract—A VUV lasing scheme employing charge-exchange between H^+ ions and Cs atoms is discussed. An approximate set of rate equations is described and numerically solved to determine the conditions under which the threshold for laser action might be achieved. The required density and sharpness of both the H^+ and Cs pulses and the expected characteristics of the laser output under various initial conditions are determined from the solution of these equations.

I. Introduction

THE transfer of excitation by collisions from a donor atom to an acceptor atom leads to one of the most ubiquitous lasers available today, the He-Ne laser. McGowan and Stebbings [1] suggested the mechanism of charge-transfer from a donor atom to an excited state of an acceptor ion as another means of inverting an atomic system. The extension of this scheme towards lasing in the vacuum UV and X-ray region of the spectrum was discussed by Smirnov [2] as early as 1967. Presnyakov and Shevel'ko [3] suggested that the near-resonant transfer of electrons from the ground state of Cs atoms into the $2p$ states of H atoms could lead to an inversion population and lasing on the Lyman-α $2p$-$1s$ transition of hydrogen. Fig. 1 shows the particular scheme. At relative energies of 1 keV a cross section in excess of 10^{-15} cm^2 exists for the outer Cs electron to be transferred to the hydrogen $2p$ level while the cross section for charge-transfer to the hydrogen $1s$ level is on the order of 10^{-17} cm^2. Therefore it should be possible to obtain a hydrogen system that is temporarily inverted in its $2p$ population vis-á-vis the $1s$ ground state by this charge-transfer process.

It was pointed out by Scully *et al.* [4], Louisell *et al.* [5], and Mahr and Roeder [6] that it should be possible to obtain an inversion via charge-transfer from a suitable electron donor to H^+ or He^{++}-like ions. The absence of the Auger effect in the H atom or He^+ ion leads to reasonably long lifetimes of the lasing state and therefore reduces the demands on the pumping rate required for an inversion. Because of the availability of mirrors and coatings for many of the transitions of H and He^+, another advantage is that real cavities can be constructed thus reducing the lasing threshold densities. For the Lyman-α wavelength of 1215.67 Å, mirror coatings with 85-percent reflectivity are available; and for wavelengths from 1000 Å to about 40 Å, a method proposed by Spiller [7] promises reflectivities of about 30 to 35 percent throughout this wavelength range.

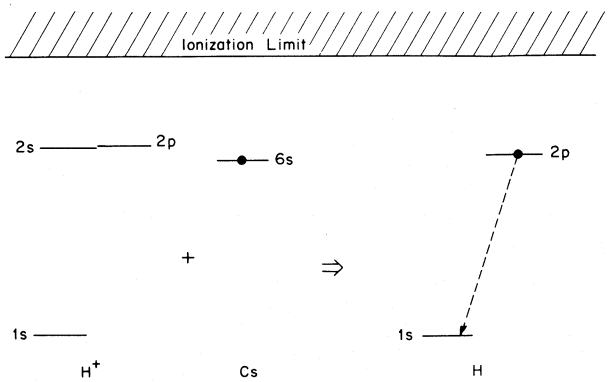


Fig. 1. Energy level diagram of charge-transfer of electrons from the ground level of a cesium atom to the $2p$ level of hydrogen. Lasing is assumed to occur on the $2p$–$1s$ transition of hydrogen.

Schemes to facilitate the fast onset of charge-exchange have also been proposed. McCorkle [8] suggested suddenly sweeping an ion beam perpendicular to its propagation direction through a foil containing the electron donors. Starting from ion beam sources, Scully *et al.* [4] and Louisell *et al.* [5] suggested mediating charge-exchange in a traveling wave fashion by sweeping the ion beam (He^{++} ions in their case) through a target of thin solid hydrogen foil or a thin hydrogen gas jet. In the present paper we discuss the use of pulsed plasma guns [9] to initiate charge-transfer. In this case a pulsed plasma beam of acceptor ions collides head-on with a stationary jet of donor atoms or ions.

Hydrogen is but the first of a large new group of potential lasing materials [4]-[6] extending the available lasing spectrum towards 100 Å and below. Hydrogen is also the easiest because of its relatively long excited-state lifetimes. In this paper we describe and analyze the rate equations for a charge-exchange laser employing a hydrogen plasma in a cesium target. Since it was desired to determine *if* an inversion population could be achieved, stimulated emission effects were not included in this model. Extensive numerical calculations were done to determine under what conditions a population inversion could be achieved with this particular scheme. The purpose of this paper was not to give a rigorous detailed analysis of a H^+–Cs charge-exchange laser, but to determine an order-of-magnitude estimate of the various major requirements, thus several simplifying assumptions have been introduced as will be discussed further below.

In Section II a brief description of the envisioned laser

Manuscript received December 12, 1975; revised July 9, 1976 and July 19, 1976. This work was supported in part by the National Science Foundation under Grant ENG-75-01389, and in part by ARPA through the Materials Science Center, Cornell University.

The authors are with the Materials Science Center, Cornell University, Ithaca, NY 14853.

system is given after which an estimate of the inversion threshold density is made. The dominant reaction processes of the hydrogen plasma and the cesium vapor are enumerated and discussed. From these considerations an approximate model of the rate equations describing the formation of the hydrogen $2p$ and $1s$ populations is derived. The method of numerically solving these partial differential equations is briefly discussed after which an expression for the total spontaneous emitted power is given. In Section III the results of the calculations are presented and discussed.

II. The Rate Equations

The proposed charge-exchange lasing scheme for Lyman-α is shown in Fig. 2. A pulse of hydrogen plasma a few centimeters in diameter and with densities ranging from 10^{15} cm^{-3} to 10^{17} cm^{-3} proceeds towards a stationary jet of cesium of a similar density. With plasma velocities in the vicinity of the equivalent of 1 keV of energy for protons, i.e., $v = 4.4 \times 10^7$ cm/s, the depth of interaction in the direction of the plasma beam is of the order of several hundred microns which is comparable to the distance that an excited hydrogen $2p$ state would travel in its lifetime. This distance, known as the decay length of the H ($2p$) states, is 0.7 mm at 1 keV. After some initial time an inversion will be achieved in the hydrogen plasma resulting in lasing if the threshold is exceeded. The cavity consists of a mirror-grating combination [10]. The grating will allow us to couple out the Lyman-α radiation without the difficulty of transmission of such short wavelength radiation.

With a given density n^{2p} of lasing $2p$ states and a density n^{1s} of ground $1s$ states the gain g for stimulated emission per centimeter of gain medium is given by

$$g = \frac{\lambda^2}{8\pi}\left[n^{2p} - n^{1s}(g^{2p}/g^{1s})\right]\frac{A_{1s2p}}{\Delta\nu}. \tag{1}$$

Here λ is the wavelength of the $2p$–$1s$ transition, g^i is the statistical weight of level i, A_{1s2p} is the relevant Einstein coefficient, and $\Delta\nu$ is the linewidth of the spontaneous emission under the conditions of the experiment. The spontaneous linewidth will be dominated by Doppler broadening due to the transverse velocity of the protons in the beam. We assume that this transverse velocity spread can be kept to about 2 eV, i.e., $v_t = 2.0 \times 10^6$ cm/s. For a cavity of gain length L and mirrors with reflectivity R, the minimum single-pass gain required to overcome the mirror losses is

$$g_{\min} \gtrsim (2.3/L)\log(1/R). \tag{2}$$

Assuming the interaction length between the cesium target and the hydrogen plasma is 4 cm and the mirror reflectivity is 0.80, we obtain $g_{\min} \gtrsim 0.056$ cm^{-1}. From (1) with the values given above we calculate a threshold inversion density of

$$n^{\text{inv}}_{\text{threshold}} \equiv \left[n^{2p} - n^{1s}(g^{2p}/g^{1s})\right] \gtrsim 2.4 \times 10^{12} \text{ cm}^{-3}.$$

Several types of reactions are important when considering the interaction of the hydrogen plasma and the cesium vapor: 1) charge-exchange between the protons and the Cs atoms, 2) collisional deactivation of the metastable H($2s$) atoms by Cs atoms, 3) electron impact excitation of the Cs atoms, 4) ionization of the Cs atoms by electron impact, and 5) spontaneous emission by the excited hydrogen and cesium atoms. These processes, our notation, and the values of the appropriate cross sections or radiative lifetimes are summarized in Table I and further discussed below.

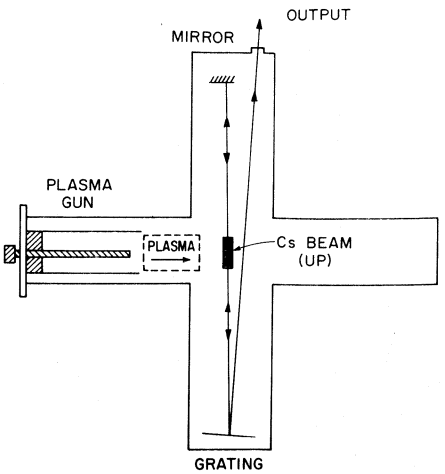


Fig. 2. Schematic diagram of a hydrogen plasma cesium charge exchange laser. The plasma gun emits pulses of high density hydrogen plasma with proton densities of 10^{15} cm^{-3} to 10^{17} cm^{-3}. The cesium jet has a depth of several hundred micrometers and a length of a few centimeters. Lasing is assumed to occur in the cavity consisting of a mirror and a grating. Output is obtained as shown.

The charge-exchange cross sections σ_{2p}, σ_{2s}, and σ_{total} between protons and unexcited cesium atoms have recently been measured by Pradel *et al.* [11] and Tuan *et al.* [12]. At proton energies of 1 keV the total cross section is dominated by electron transfer from the ground states of Cs to the near-resonant $2s$ and $2p$ levels of hydrogen. Due to the large energy defect between the unexcited Cs atoms and the hydrogen ground level, the cross section for electron transfer to the $1s$ level is considerably smaller. The value of σ_{1s} given in Table I was estimated using the theory of Rapp and Francis [13]. Charge-exchange between the protons and the excited Cs atoms was neglected in the rate equations since the slightly larger energy defects (~1 eV for the resonant Cs levels) imply smaller cross sections.

Because of the long radiative lifetime of the metastable H($2s$) states the principal destruction mechanism of these states is through collisions with Cs atoms [11]. Since collisional deactivation of the H($2s$) states proceeds primarily via transfer to the H($2p$) states [14] instead of directly to the hydrogen ground states, this provides a secondary means of creating atoms in the upper laser level. Direct collisional deactivation of the H($2p$) states to the H($1s$) level by Cs has been neglected since it is assumed that the radiative decay process is much faster in depleting the $2p$ level population. Also, collisional deactivation of the hydrogen $2s$ states by excited and/or ionized cesium atoms was ignored. Electron impact excitation and ionization of the neutral hydrogen states as well as the corresponding reverse reactions have been neglected in this model since, as is discussed in detail in the Appendix, the cross sections for these processes are small [15], [16]. For electron energies on

TABLE I
PRIMARY REACTIONS BETWEEN A HYDROGEN PLASMA AND CESIUM TARGET

Process	Reaction	Cross Section Notation	or Lifetime Value	Reference
(1) Charge-transfer	$H^+ + Cs \rightarrow H(2p) + Cs^+ + 0.49\ eV$	σ_{2p}	$6.1\times10^{-15}\ cm^2$	11
	$\rightarrow H(2s) + Cs^+ + 0.49\ eV$	σ_{2s}	2.5	11
	$\rightarrow H(1s) + Cs^+ - 9.71\ eV$	σ_{1s}	10^{-2}	13
	$\rightarrow H + Cs^+$	σ_{total}	10.0	11,12
(2) Collisional Deactivation	$H(2s) + Cs \rightarrow H(2p) + Cs$ $\rightarrow H(1s) + \hbar\omega_{2p}$	σ_c	5.0	11,14
(3) Electron Excitation	$e^- + Cs \rightarrow e^- + Cs^*$	σ_e	9.3	15
(4) Electron Ionization	$e^- + Cs \rightarrow e^- + Cs^+ + e^-$	σ_i	4.0	16
(5) Spontaneous Emission	$H(2p) \rightarrow H(1s) + \hbar\omega_{2p}$	τ_{2p}	1.6 nsec	17
	$Cs^* \rightarrow Cs + \hbar\omega_*$	τ_*	11.2	18

Note: The charge-transfer and deactivation cross sections are for proton energies of 1 keV while the electron excitation and ionization cross sections are for electron energies of a few electronvolts.

the order of a few electronvolts, that is, near the threshold for these reactions, the $2s$ and $2p$ excitation cross sections and the total ionization cross section are *no greater than* $10^{-17}\,cm^2$, $10^{-16}\ cm^2$, and $10^{-16}\ cm^2$, respectively.

Excitation and ionization of the Cs atoms by electron impact depletes the Cs ground states available for charge-exchange with the hydrogen plasma. Since the plasma pulse remains electrically neutral the small electron to proton mass ratio means that the directed plasma electron energies are on the order of a few electronvolts or about the same as the assumed electron thermal energy. At these electron energies the electron impact excitation and ionization cross sections are large since for these processes the threshold energy is on the order of a few electronvolts. The major contribution to the total cross section for excitation of unexcited Cs atoms by electrons is due to transitions from the ground state to the $6p\ ^2P_{1/2}$ and $6p\ ^2P_{3/2}$ levels since the cross sections for excitation to other levels are smaller by an order of magnitude. The total excitation cross section for Cs was obtained from the experimental data summarized in the review of electron impact excitation by Moiseiwitsch and Smith [15]. The total ionization cross section was estimated from the available data [16].

The radiative lifetime of the $H(2p)$ states was obtained from the calculations summarized by Weise *et al.* [17]. No distinction between the various excited states of cesium is made in this model. The value of τ_* in Table I was obtained by suitably averaging the radiative decay rates of the $6p\ ^2P_{1/2}$ and $6p\ ^2P_{3/2}$ Cs levels given in the compilation of experimental data by Corliss and Bozman [18].

In describing the interaction of the hydrogen plasma and the cesium target, account must be taken not only of the forward reactions listed in Table I but also of the corresponding reverse reactions with the exception of the spontaneous emission. For example, once the Cs ion density becomes appreciable, charge-exchange with the hydrogen $2p$ states will further deplete the upper laser level. Eventually, if sufficient interaction time has elapsed, steady-state densities and distributions of hydrogen $2p$ and $1s$ states will be established. In considering these reverse reactions the reverse reaction rate, $(v\sigma)_R$, was obtained from the forward reaction rate, $(v\sigma)_F$, by the condition of detailed balancing: $(v\sigma)_R = (v\sigma)_F(g^F/g^R) \cdot \exp((E_R - E_F)/kT)$ where E_i and g^i denote the energy and degeneracy of the levels involved in the reaction and T is either the electron or ion temperature as appropriate. Due to the near resonance between the $2s$ and $2p$ levels of H and the ground level of Cs, the relevant Boltzmann factors were approximated by one. In contrast, because of the large energy defect between the ground levels of H and Cs compared to the ion and Cs gas temperatures, the reverse reaction rate was about two orders of magnitude smaller than the forward reaction rate for charge-exchange; consequently, this reverse reaction was neglected in the rate equations below. Three-body electron cesium recombination was also neglected in this model since, over the range of plasma densities considered here, the recombination rate was several orders of magnitude smaller than the ionization rate [19]. Finally, in considering deexcitation of the excited cesium atoms by electrons the Boltzmann factor was again approximated by one since the energy defect ($\Delta E = 1.42$ eV, since $E_{Cs*} = -2.47$ eV and $E_{Cs} = -3.89$ eV) is small compared to the electron thermal energy which is assumed to be on the order of a few electronvolts.

From the above considerations an approximate set of rate equations describing the formation of an inversion in a H^+–Cs charge-exchange laser may be derived. For these equations the hydrogen plasma and the cesium target are assumed to be homogeneous in the direction transverse to the incident plasma pulse. We can then confine ourselves to a one-dimensional model along the plasma pulse direction. We will also suppose that the velocity spread of the incident plasma pulse along its propagation direction is negligible. A small spread in the longitudinal velocity component will not affect the charge-transfer or electron cross sections appreciably. Charge-transfer to the protons negligibly alters their incident velocity but scattering of the protons and hydrogen atoms by Cs atoms would cause deflection and additional Doppler broadening. To minimize these latter effects the Cs beam depth must be

less than the mean free collision length, l, of hydrogen in cesium. l can be estimated from

$$l \simeq 1/(n^{Cs}\sigma) \tag{3}$$

where σ is the total scattering cross section and n^{Cs} is the density of Cs. For example with [11] $\sigma \simeq 3 \times 10^{-16}$ cm^2 and $n^{Cs} = 5 \times 10^{15}$ cm^{-3}, we find l is about 7 mm, or about an order of magnitude greater than the H($2p$) decay length. Thus at these collision energies and target densities the interaction depth is limited by the decay length and not the mean free collision length.

For the calculations we adopt a coordinate system at rest relative to the Cs target. We assume that the plasma pulse is directed towards the Cs target along the x direction from the left to right as shown in Fig. 3. Let $n^i(x, t)$ be the total density of species i at time t and position x relative to the Cs rest frame. Denoting the plasma velocity by v and the degeneracy of species i by g^i ($g^{2s} = g^{Cs} = 2, g^{2p} = g^{Cs*} = 6$), the rate equations describing the interactions between a hydrogen plasma and a cesium target are

$$\left[\frac{\partial}{\partial t} + v\frac{\partial}{\partial x}\right] n^{2p} = v\sigma_{2p} n^{H^+} n^{Cs} - v\sigma_{2p}\frac{g^{Cs}}{g^{2p}} n^{2p} n^{Cs^+} + v\sigma_c n^{2s} n^{Cs} - v\sigma_c \frac{g^{2s}}{g^{2p}} n^{2p} n^{Cs} - n^{2p}/\tau_{2p} \tag{4a}$$

$$\left[\frac{\partial}{\partial t} + v\frac{\partial}{\partial x}\right] n^{2s} = v\sigma_{2s} n^{H^+} n^{Cs} - v\sigma_{2s}\frac{g^{Cs}}{g^{2s}} n^{2s} n^{Cs^+} - v\sigma_c n^{2s} n^{Cs} + v\sigma_c \frac{g^{2s}}{g^{2p}} n^{2p} n^{Cs} \tag{4b}$$

$$\left[\frac{\partial}{\partial t} + v\frac{\partial}{\partial x}\right] n^{1s} = v\sigma_{1s} n^{H^+} n^{Cs} + n^{2p}/\tau_{2p} \tag{4c}$$

$$\left[\frac{\partial}{\partial t} + v\frac{\partial}{\partial x}\right] n^{H^+} = -v\sigma_{total} n^{H^+} n^{Cs} + v\left(\sigma_{2s}\frac{g^{Cs}}{g^{2s}} n^{2s} + \sigma_{2p}\frac{g^{Cs}}{g^{2p}} n^{2p}\right) n^{Cs^+} \tag{4d}$$

$$\left[\frac{\partial}{\partial t} + v\frac{\partial}{\partial x}\right] n^{e^-} = v\sigma_i n^{e^-} n^{Cs} \tag{4e}$$

$$\frac{\partial}{\partial t} n^{Cs} = -v\sigma_{total} n^{H^+} n^{Cs} + v\left(\sigma_{2s}\frac{g^{Cs}}{g^{2s}} n^{2s} + \sigma_{2p}\frac{g^{Cs}}{g^{2p}} n^{2p}\right) n^{Cs^+} - v\sigma_i n^{e^-} n^{Cs} - v\sigma_e n^{e^-} n^{Cs} + v\sigma_e \frac{g^{Cs}}{g^{Cs*}} \cdot n^{e^-} n^{Cs*} + n^{Cs*}/\tau_* \tag{4f}$$

$$\frac{\partial}{\partial t} n^{Cs^+} = v\sigma_{total} n^{H^+} n^{Cs} - v\left(\sigma_{2s}\frac{g^{Cs}}{g^{2s}} n^{2s} + \sigma_{2p}\frac{g^{Cs}}{g^{2p}} n^{2p}\right) n^{Cs^+} + v\sigma_i n^{e^-} n^{Cs} \tag{4g}$$

$$\frac{\partial}{\partial t} n^{Cs*} = v\sigma_e n^{e^-} n^{Cs} - v\sigma_e \frac{g^{Cs}}{g^{Cs*}} n^{e^-} n^{Cs*} - n^{Cs*}/\tau_*. \tag{4h}$$

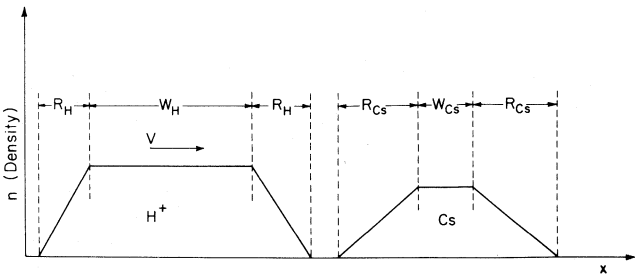


Fig. 3. The initial density distributions of the incident hydrogen plasma and the cesium target pulses in the Cs rest frame along the direction of the hydrogen plasma beam propagation.

The argument of each n^i is (x, t). In the absence of any interactions the equation $\partial n^i/\partial t = 0$ represents a stationary density while the equation $\partial n^i/\partial t + v\,\partial n^i/\partial x = 0$ represents a pulse that moves to the right with velocity v. The initial conditions for (4) require a specification of the density distributions of the incident plasma pulse and the Cs target in space along the pulse direction. One of the major questions from an experimental point of view is how sharply defined the plasma pulse and the Cs vapor must be. Therefore it is important to consider initial distributions of different shapes and sizes. We assume for the purpose of calculation that these are trapezoidal or rectangular as shown in Fig. 3. In what follows n_I^i represents the maximum density of the initial pulse distribution and the profile slope $s^i = n_I^i/R_i$ characterizes the sharpness of the initial distribution of species i.

Equations (4) were solved by an implicit centered finite difference technique and by using a straightforward iteration procedure [20]. Truncation error was minimized by taking the ratio of the space to time grid increments equal to the plasma velocity; this choice simplified the Thomas algorithm [20] for the solution of a tridiagonal system of equations. In the application of these methods to pulses of finite extent, certain terms falsely propagate after each iteration and must be zeroed out. An economical program was obtained by recognizing that at each time step the equations need to be solved only in the interaction region where the pulses actually overlap.

In addition to obtaining the spatial distributions of the population inversion $n^{inv} = n^{2p} - 3n^{1s}$ as a function of time, the total spontaneous emitted power in all directions per unit transverse area of gain medium as a function of time was computed from

$$P^i(t) = (\hbar\omega_i/\tau_i)\int n^i(x, t)\,dx, \qquad i = (2p, Cs^*) \tag{5}$$

where for the hydrogen $2p$–$1s$ transition $\hbar\omega_{2p} = 10.2$ eV; while for the excited Cs states, $\hbar\omega_* = 1.42$ eV which is a suitably averaged value for the Cs resonant transitions [18]. The spontaneous emitted power gives an order of magnitude indication of the expected laser power output when well above the threshold for lasing. The integration was performed numerically using the trapezoidal rule [21].

III. Results and Discussion

Our purpose was to ascertain the dependence of the inversion density and spontaneous power on the initial plasma and target densities and distributions in order to indicate the experimental problems that confront the development of a charge-exchange laser. There are several questions of interest.

1) For what hydrogen and cesium densities could an inversion population be achieved?

2) How does the sharpness of these density distributions affect the inversion densities which can be obtained?

3) How much contamination of the incident hydrogen plasma by H(1*s*) states will extinguish the population inversion?

4) What is the maximum spontaneous power output?

5) How long could an inversion population greater than threshold be maintained?

To answer these questions the rate equations (4) were solved to determine the inversion density and spontaneous power output for various combinations of initial shapes, dimensions, and densities assuming a neutral incident plasma and an unexcited Cs target.

In general, the solutions to equations such as (4) will exhibit both transient and steady-state behavior. As the plasma proceeds through the target, after an adequate time the forward and reverse charge-exchange reactions, the various electron reactions, and the spontaneous emission processes will equilibrate. Thus after a rapid initial transient the inversion population will reach an equilibrium distribution and remain at equilibrium for as long as fresh hydrogen plasma is incident on the cesium target. If the hydrogen pulse is so short that the reactions do not have sufficient time to equilibrate then only the transient behavior will be observed. An inversion density greater than the threshold of the hydrogen system will occur only within the leading edge of the cesium target with the peak inversion a few tenths of a millimeter from the target edge. Further downstream after a distance an excited H(2*p*) state would travel in its lifetime at 1 keV energies, the concentration of the hydrogen ground states is so large that it is impossible for the system to become inverted. It is for this reason that sharp and dense target distributions are required to achieve a significant inversion density. Fig. 4 shows a specific example of the inversion pulse and the spontaneous output power for a hydrogen plasma with an initial proton density of $n_I^{H^+} = 10^{15}$ cm^{-3} incident on a cesium target with an initial density of $n_I^{Cs} = 10^{15}$ cm^{-3}. The ramp length of each pulse was 1 mm which corresponds to a sharpness of 10^{16} cm^{-4} at these densities. In Fig. 4(a) the inversion density as a function of time and position is plotted in the cesium rest frame. The lasing threshold for the specific values of the lasing scheme of Section II is also indicated. Each line corresponds to the spatial distribution of the inversion density in units of the threshold inversion density at a particular time, the increment in time between successive steps being 0.228 ns. At each successive instant in the dark solid region of the figure the maximum inversion reached was slightly less than that of the preceding time indicating that the pulse was not quite long enough for equilibrium to be established. In the example shown the ratio of the peak inversion density to the threshold inversion density was 2.6, the time for which an inversion greater than threshold persisted was 3.2 ns, and the average length of the inversion region was 300 μm.

As the total Lyman-α output power in Fig. 4(b) clearly shows, there was insufficient time for the charge-exchange reactions to come to equilibrium in this case. The peak power at the Lyman-α line was 8.7 kW/cm^2 while the peak power at the resonant cesium line was 0.8 kW/cm^2. These correspond to a spontaneous power output of 3.5 kW and 0.3 kW, respectively,

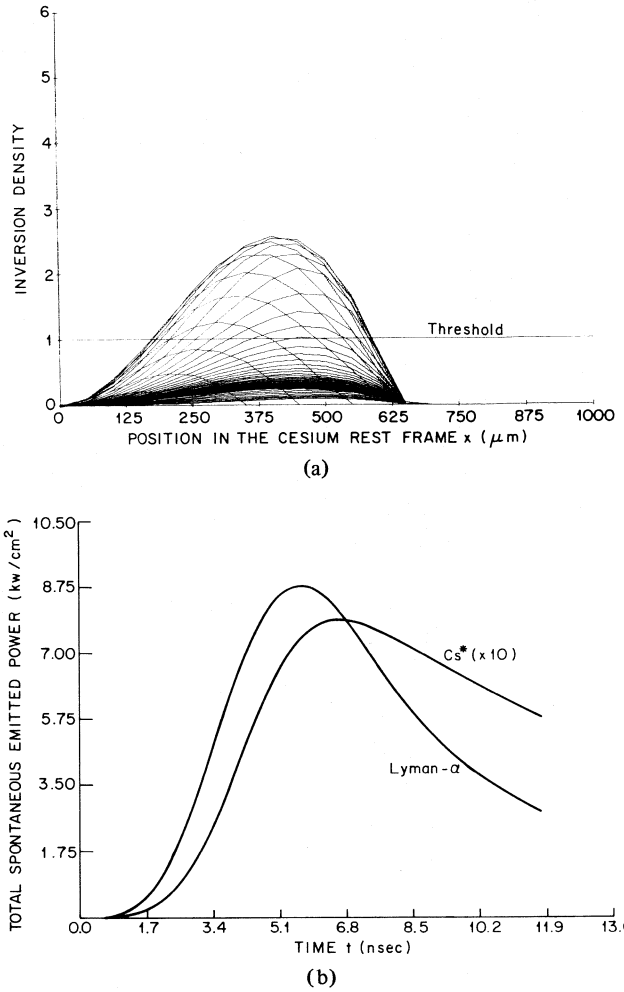


Fig. 4. (a) The inversion density n^2P–$3n^1S$ of hydrogen atoms as a function of time and position in the cesium rest frame. Each line represents the spatial distribution of the inversion population in units of the threshold inversion density at a particular time. The time increment from curve to curve is 0.228 ns. Threshold corresponds to an inversion density of 2.4 × 10^{12} cm^{-3}. The initial density of both the hydrogen plasma and cesium target was 10^{15} cm^{-3}. The cesium target had a width of W_{Cs} = 0.2 mm and a ramp length of R_{Cs} = 1.0 mm. The hydrogen plasma had a width of W_H = 3.0 mm and a ramp length of R_H = 1.0 mm. (b) The total spontaneous emitted power per unit transverse area of gain medium in all directions as a function of time. The initial pulse distributions and densities were the same as in (a). The power emitted by the excited Cs atoms has been multiplied by a factor of 10 relative to the scale shown.

for a gain medium with a length of 4 cm and a height of 0.1 cm and are indicative of the expected laser output power. Typically, the power emitted by the excited Cs atoms was about an order of magnitude less than that emitted at the Lyman-α line.

Large inversion populations and spontaneous power outputs can be expected if the cesium target and hydrogen plasma densities could be made sufficiently large. For initial hydrogen plasma densities of 10^{15} cm^{-3} and 10^{16} cm^{-3} the variation of the maximum inversion density and the peak output power at the Lyman-α line as the Cs vapor density ranges from 10^{14} cm^{-3} to 10^{16} cm^{-3} is shown in Figs. 5 and 6, respectively. While it is possible at present to obtain such high hydrogen plasma densities, it remains a serious experimental problem to practicably realize Cs densities of 10^{14} cm^{-3} or greater with suffi-

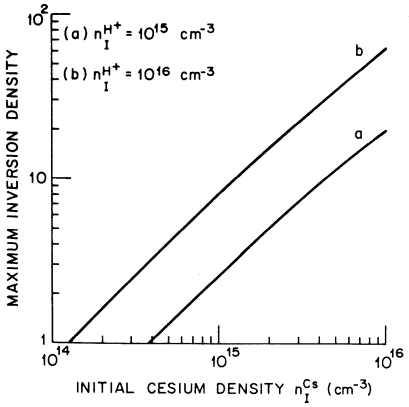


Fig. 5. The maximum inversion density in units of 2.4×10^{12} cm^{-3} as a function of the initial cesium density for a constant initial hydrogen plasma density. For curves *a* and *b* both the Cs target and hydrogen plasma configurations were identical to those of Fig. 4, except that in the present figure $W_H = 1.0$ mm.

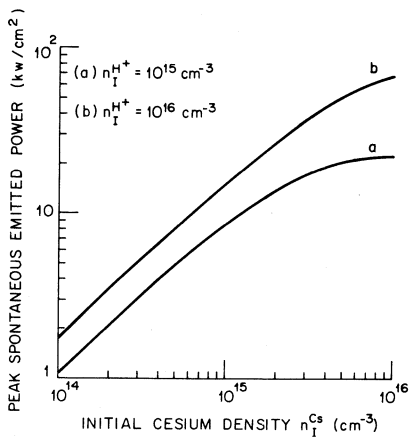


Fig. 6. The peak spontaneous emitted power at the Lyman-α line per unit transverse area of gain medium in all directions as a function of the initial cesium density for a constant initial hydrogen plasma density. For curves *a* and *b* both the Cs target and hydrogen plasma distributions were as given in Fig. 5.

cient sharpness. At these lower Cs vapor densities it is necessary that the Cs target pulse be very sharp and that the incident hydrogen plasma be quite dense. For example, as is shown in Fig. 5, for a hydrogen plasma with a density of $n_I^{H^+} = 10^{16}$ cm^{-3} and a ramp length of $R_H = 1$ mm an inversion population just barely above the lasing threshold was obtained with a Cs target having a density of $n_I^{Cs} = 1.3 \times 10^{14}$ cm^{-3} and a ramp length of $R_{Cs} = 1$ mm. For the same target parameters and plasma ramp length an inversion approximately twelve times threshold could be achieved by increasing the incident proton density to $n_I^{H^+} = 10^{17}$ cm^{-3}. Although these greater plasma densities may be realized by focusing the plasma gun such sharp target fronts may be difficult to achieve as is further discussed below.

While the peak inversion densities which can be obtained are many times threshold, the relative fraction of protons which are converted to hydrogen atoms remains very small. For curve *b* of Fig. 5, with an initial plasma density of 10^{16} cm^{-3} the maximum relative fraction of H($2p$) states formed by charge-exchange varied from 0.1 to 3.9 percent as the initial cesium density ranged from 10^{14} cm^{-3} to 10^{16} cm^{-3}. This is due to the low production efficiency of the charge-exchange process. Consequently, very little contamination of the incident plasma pulse by ground-state hydrogen atoms, typically about 1 percent for the calculations presented here, is enough to negate the inversion population achieved by charge-transfer. It is assumed that the hydrogen plasma leaving the plasma gun is completely ionized since any neutrals present in the gun would not be accelerated by the $\vec{v} \times \vec{B}$ forces. Furthermore, the collisional-radiative recombination rate for a hydrogen plasma [22] at temperatures on the order of 2 eV ($\sim 2.3 \times 10^4$ K) and densities on the order of 10^{15} cm^{-3} is about 10^{-12} cm^3/s. This corresponds to a rate of increase of neutrals of 10^{12}/cm$^3 \cdot \mu$s, or less than one-tenth of a percent recombination of the plasma per microsecond of travel of the plasma. For the same temperature at a density of 10^{16} cm^{-3} the corresponding rate is about 3 percent recombination per microsecond of travel. Hence at such higher densities the electron-proton recombination of the plasma before it strikes the cesium target downstream could be sufficient to prevent a population inversion from occurring. This imposes an upper bound on the distance between the end of the plasma gun and the target. For example, for a density of 10^{15} cm^{-3} and a recombination rate of 0.1 percent/μs, less than 0.1-percent contamination of the incident plasma beam by neutrals [H($1s$)] can be achieved with a gun-target separation of less than 44 cm at a plasma velocity of 4.4×10^7 cm/s. In a typical plasma gun the electron temperature could actually be greater than 2 eV thus making electron-proton recombination even less of a problem. Since the plasma-target interaction times are on the order of several nanoseconds, collisional-radiative recombination of the plasma was ignored in the rate equations. Thus electron-proton recombination of the plasma over the few tenths of a microsecond of travel before it strikes the cesium target should not present a serious experimental problem.

Wide cesium vapor pulses do not increase the temporal duration of the population inversion above the threshold since each H($2p$) state that is formed decays within its decay length of 0.7 mm causing large H($1s$) concentrations downstream in the cesium target. The time that the inversion remains above threshold will be greater if long hydrogen plasma pulses are incident on the target, since the various reactions will have enough time to come to equilibrium. However, only if sufficiently dense plasmas are incident on a sufficiently dense target will the reactions come to equilibrium above the threshold, otherwise only a transient output pulse will be observed regardless of the plasma pulse length. The duration of an inversion density above the threshold as a function of the plasma pulsewidth is depicted in Fig. 7 for hydrogen plasmas with initial densities of 10^{15} cm^{-3} and 10^{16} cm^{-3} incident on a cesium target with an initial density of 10^{15} cm^{-3}. At these densities an equilibrium inversion density above the threshold was not achieved. With larger target densities, although equilibrium above the threshold was not achieved, a longer transient pulse time could be attained. For example, for an initial cesium target density of $n_I^{Cs} = 10^{16}$ cm^{-3} the inversion duration was about 7 ns for plasma pulses with $n_I^{H^+} = 10^{16}$ cm^{-3}, $R_H = 1.0$ mm, and $W_H > 0.5$ mm. Such duration times are

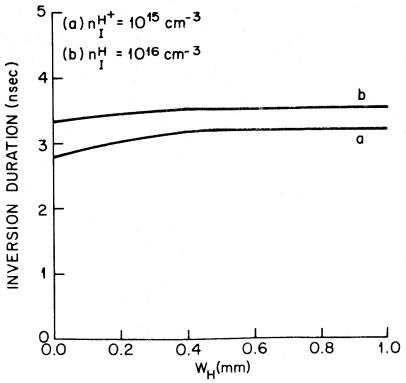


Fig. 7. The time of duration of an inversion greater than threshold as a function of the width of the hydrogen pulse for a given initial hydrogen density. The cesium target configuration and density were identical to that of Fig. 4 for both lines *a* and *b*. The hydrogen plasma ramp length was $R_H = 1.0$ mm.

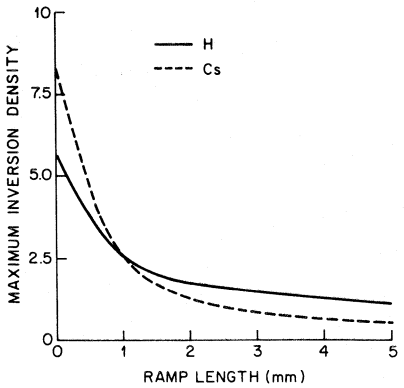


Fig. 8. Variation of the maximum inversion density in units of 2.4×10^{12} cm^{-3} with the ramp length of the leading edge of the hydrogen plasma (solid curve) and of the cesium target (dashed curve). For each curve the initial density of both the plasma and the target was 10^{15} cm^{-3} and the width of the plasma and target was $W_H = 1.0$ mm and $W_{Cs} = 0.2$ mm respectively. For solid (dashed) curve the ramp length of the cesium target (hydrogen plasma) was $R_{Cs} = 1.0$ mm ($R_H = 1.0$ mm).

larger than the single-pass travel time of the light in a sufficiently short mirror-grating cavity and would allow several passes through the gain medium.

Not only must the cesium target be dense enough that an inversion density greater than threshold could occur, but it must be sufficiently sharp so that the formation of hydrogen ground states does not prevent an inversion buildup in the leading edge of the target. With a sufficiently well-collimated cesium target it is possible that the reactions will equilibrate above the inversion threshold even though the leading edge of the hydrogen plasma is relatively diffuse. In contrast, a well-defined hydrogen plasma front incident on a sufficiently diffuse cesium target will not become inverted since ground-state contamination downstream in the high cesium density region will negate the population inversion. This is shown in Fig. 8 from which it is apparent that the inversion population falls below threshold for Cs ramp lengths of about 2.5 mm or greater. We expect the hydrogen plasma ramp length to be on the order of a few centimeters. While it is possible to obtain a well-collimated cesium vapor with ramps of about 1 mm using an effusive oven, it is difficult to achieve densities greater than 10^{12} cm^{-3} with such a technique [23]. Many-channel capillary or supersonic nozzle sources [24], [25] may provide a means of increasing the available target density by one or two orders of magnitude without significant loss of collimation. Photon-assisted nonresonant charge-transfer [26] may possibly be used to, in effect, create a sharp target front by initiating the electron transfer to the hydrogen $2p$ states after a sufficient overlap of the incident plasma and target beams has occurred. Using an electron donor with a suitable ionization potential, the unassisted nonresonant electron charge-exchange cross sections to both the H($1s$) and H($2p$) states could be made small. In the absence of the exchange initiating photon, only a small buildup of the undesirable hydrogen ground states would develop and then, when the dense regions of the plasma and target overlapped, photon initiated charge-exchange would cause an inversion.

At collision energies appreciably less than 1 keV it would be more difficult to establish an inversion population in the hydrogen system because the charge-exchange reactions no longer preferably populate the H($2p$) level. For example, at a collision energy of 100 eV, using cross sections estimated by linear extrapolation from the data of Pradel *et al.* [11], an inversion density only a few times threshold could be obtained even though $n_I^{H^+} = 10^{17}$ cm^{-3} and $n_I^{Cs} = 10^{16}$ cm^{-3} and each pulse had a ramp length of 1 mm. At best, such conditions would be difficult to achieve experimentally. An inversion above threshold was not achieved at lower cesium vapor densities. At these low relative collision energies photon-assisted enhancement of the charge-exchange cross sections could provide a means of creating an inversion as was discussed above.

From the calculations performed it can be seen that substantial population inversions and spontaneous output powers can be achieved under suitable conditions in a hydrogen system through charge-transfer of electrons from neutral cesium atoms. These results show that although a H^+–Cs charge-exchange laser is feasible, there remain difficult experimental problems to be resolved, in particular attainment of dense cesium target pulses with sufficiently sharp leading edges. Guided by these considerations we are now proceeding to test experimentally the results presented here.

Appendix

$K(2, 1)$, the rate coefficient for electron collisional deexcitation from the $n = 2$ to $n = 1$ state of atomic hydrogen, is calculated from $K(1, 2)$ by the condition of detailed balancing. $K(1, 2)$ has been numerically evaluated using the equations of Bates *et al.* [27, eq. (33)-(35)], which are based on the classical cross-section theory of Gryzinski. As Bates *et al.* [27] point out, the derived rate coefficients are unlikely to be in error by a factor greater than 3. The results are given in Table II below. Using the Saha equilibrium and detailed balancing conditions, (9) and (10), respectively, of Bates *et al.* [27], we find in their notation

$$K(2, 1) = \frac{n_E(1)}{n_E(2)} K(1, 2) \tag{A1}$$

and

TABLE II
K(1,2) AND K(2,1) FOR H AS A FUNCTION OF ELECTRON TEMPERATURE

T eV	K(1,2) cm^3/sec	K(2,1) cm^3/sec
1	1.31×10^{-12}	8.77×10^{-9}
2	2.20×10^{-10}	9.00×10^{-9}
5	4.81×10^{-9}	9.24×10^{-9}

Note: For these calculations $I_1 = 13.6$ eV, $I_2 = 3.4$ eV, $k = 8.617 \times 10^{-5}$ eV/K and 1 eV = 11 610 K.

$$\frac{n_E(1)}{n_E(2)} = \tfrac{1}{4} \exp\left[(I_1 - I_2)/kT\right]. \tag{A2}$$

Using the results of our calculation for $K(1, 2)$ and (A1) and (A2) above, values of $K(2, 1)$ for several electron temperatures are given in Table II below.

We may now estimate the electron collisional deexcitation rate for neutral H($2p$) states using these results. The rate of decrease of the density is given by the product $n(2)n(c)K(2, 1)$ (cf., footnote, Bates *et al.* [27, p. 298]), and for our purposes it is convenient to define an electron collisional rate τ_c^{-1} by

$$\tau_c^{-1} = n(c)\, K(2, 1). \tag{A3}$$

Since $K(2, 1) \simeq 10^{-8}$ cm^3/s over the temperature range considered in Table II, we find τ_c^{-1} equals 10^7 s^{-1} and 10^8 s^{-1} for electron densities of 10^{15} cm^{-3} and 10^{16} cm^{-3}, respectively. Since these rates are one to two orders of magnitude smaller than the radiative decay rate of the $2p$ state, $\tau_{2p}^{-1} = 6.3 \times 10^8$ s^{-1}, the radiative decay process is the dominant loss mechanism of the neutral H($2p$) states.

Another similar but somewhat more approximate way of looking at this is by examining the electron excitation and ionization cross section data for hydrogen [15], [16]. For electron energies on the order of a few electronvolts, that is, near the threshold for these processes, the $2s$ and $2p$ excitation cross sections and the total ionization cross section are no greater than 10^{-17} cm^2, 10^{-16} cm^2, and 10^{-16} cm^2, respectively. The electron collisional deexcitation rate is given approximately by

$$\tau_c^{-1} = n(c)\, v\sigma. \tag{A4}$$

Thus for a directed electron velocity of 4.4×10^7 cm/s and an electron density of 10^{16} cm^{-3} the rate for collisional deexcitation of the H($2p$) states is about 4.4×10^7 s^{-1} in accord with our earlier estimate.

Now consider the loss of the H($2s$) states due to collisions with the electrons. Although the corresponding collisional lifetime of the metastable $2s$ state is short compared to its radiative lifetime, $\tau_{2s} = 0.14$ s, the collisional deactivation of this state by collisions with Cs is the primary loss mechanism. Since the cross section is approximately 10^{-17} cm^2 we obtain $\tau_c^{-1} = 4.4 \times 10^6$ s^{-1} for an electron density of 10^{16} cm^{-3}. However, the cross section for collisional deactivation of the $2s$ state by Cs (see Table I of the main text) is approximately $\sigma_c \simeq 5 \times 10^{-15}$ cm^2, so that at a Cs density of 10^{15} cm^{-3} the corresponding rate is 2.2×10^8 s^{-1} and even greater at higher target densities; hence this latter process is the dominant loss mechanism of the neutral H($2s$) states.

From the preceding remarks it is clear that neglect of electron impact excitation and ionization of the neutral hydrogen states as well as the corresponding reverse reactions is a good approximation for the range of densities and temperatures in which we have modeled the H^+-Cs rate equations.

ACKNOWLEDGMENT

The authors would like to acknowledge stimulating discussions with C. Cassidy, Dr. C. Ghizoni, Dr. D. Haueisen, and Dr. P. Hartman. We also thank Dr. D. Haueisen for his valuable suggestions regarding the manuscript.

REFERENCES

[1] J. W. McGowan and R. F. Stebbings, "Charge transfer as a possible laser pumping mechanism," *Appl. Opt.* (Suppl. 2), pp. 68–72, 1965.
[2] B. M. Smirnov, "Gas laser using multiply charged ions," *JETP Letters*, vol. 6, pp. 78–80, Aug. 1967.
[3] L. P. Presnyakov and V. P. Shevel'ko, "Possibility of producing inverted population in atomic beams by charge exchange of protons with atoms," *JETP Letters*, vol. 13, pp. 203–204, Mar. 1971.
[4] M. O. Scully, W. H. Louisell and W. B. McKnight, "A soft X-ray laser utilizing charge-exchange," *Optics Commun.*, vol. 9, pp. 246–248, Nov. 1973.
[5] W. H. Louisell, M. O. Scully and W. B. McKnight, "Analysis of a soft X-ray laser with charge-exchange excitation," *Phys. Rev. A*, vol. 11, pp. 989–1000, Mar. 1975.
[6] H. Mahr and U. Roeder, "Use of metastable ions for a soft X-ray laser," *Optics Commun.*, vol. 10, pp. 227–228, Mar. 1974.
[7] E. Spiller, "Low-loss reflection coatings using absorbing materials," *Appl. Phys. Lett.*, vol. 20, pp. 365–367, May 1972.
[8] R. A. McCorkle, "Practicable X-ray amplifier," *Phys. Rev. Lett.*, vol. 29, pp. 982–985, Oct. 1972.
[9] D. Y. Cheng, "Plasma deflagration and the properties of a coaxial plasma deflagration gun," *Nucl. Fusion*, vol. 10, pp. 305–317, Sept. 1970.
[10] B. H. Soffer and B. B. McFarland, "Continuously tunable, narrow-band organic dye lasers," *Appl. Phys. Lett.*, vol. 10, pp. 266–267, May 1967.
[11] P. Pradel, F. Roussel, A. S. Schlachter, G. Spiess, and A. Valance, "Formation of H(n = 2) atoms by the nearly resonant process H^+ in Cs. Multiple collision processes," *Phys. Rev. A*, vol. 10, pp. 797–812, Sept. 1974.
[12] V. N. Tuan, G. Gautherin and A. S. Schlachter, "Formation of metastable hydrogen atoms by charge exchange of protons in cesium vapor," *Phys. Rev. A*, vol. 9, pp. 1242–1251, Mar. 1974.
[13] D. Rapp and W. E. Francis, "Charge exchange between gaseous ions and atoms," *J. Chem. Phys.*, vol. 37, pp. 2631–2645, Dec. 1962. From their equation (55) with $\gamma = (I/13.6)^{1/2}$, $I = (I_{Cs}I_{H1s})^{1/2}$, and $\omega = |I_{Cs} - I_{H1s}|$ where I is the ionization potential of species i we find $\sigma_{1s} \simeq 5.0 \times 10^{-18}$ cm^2. As they point out, this should only be used for an order of magnitude estimate, hence we take $\sigma_{1s} = 10^{-17}$ cm^2.
[14] R. E. Olson, E. J. Shipsey, and J. C. Browne, "Theoretical cross sections for H-on-Cs ionic and neutral reactions," *Phys. Rev. A*, vol. 13, pp. 180–187, Jan. 1976.
[15] B. L. Moiseiwitsch and S. J. Smith, "Electron impact excitation of atoms," *Rev. Mod. Phys.*, vol. 40, pp. 238–353, Apr. 1968.
[16] L. J. Kieffer and G. H. Dunn, "Electron impact ionization cross-section data for atoms, atomic ions and diatomic molecules: I. Experimental data," *Rev. Mod. Phys.*, vol. 38, pp. 1–35, Jan. 1966; and also, L. Goldstein, "Electrical discharge in gases and modern electronics," in *Advances in Electronics and Electron Physics, VII*, L. Marton, Ed. New York: Academic, 1955, pp. 399–503. In the review article of electron ionization by Kieffer and Dunn the lowest energy for which experimental data were available was 50 eV for which $\sigma_i \simeq 1.1 \times 10^{-15}$ cm^2. From the article by Goldstein the total recombination rate for electrons in Cs at $T = 1400$ K $\simeq 0.12$ eV was $\alpha_{Cs} = 10^{-7}$ cm^3/ion · s. Assuming the recombination cross section is approximately equal to the ionization cross section, we obtain $\sigma_i \simeq 4.9 \times 10^{-15}$ cm^2. Since the first value underestimates σ_i while the second slightly overestimates it, we take $\sigma_i = 4.0 \times 10^{-15}$ cm^2.

[17] W. L. Wiese, M. W. Smith, and B. M. Glennon, "Atomic transition probabilities, I," National Standard Reference Data Series, National Bureau of Standards, Washington, DC, May 1966.
[18] C. H. Corliss and W. R. Bozman, "Experimental transition probabilities for spectral lines of seventy elements," National Bureau of Standards, Washington, DC, Monograph 53, July 1962. The lifetimes of the resonant $6p^2P_{1/2}$ and $6p^2P_{3/2}$ levels are $\tau_{1/2}$ = 7.7 ns and $\tau_{3/2}$ = 20.8 ns, respectively. Assuming that the cross-relaxation between these levels is strong we have put $(1/\tau_*) = \frac{1}{2}(1/\tau_{1/2} + 1/\tau_{3/2})$. Similarly we have taken $\hbar\omega_*$ to be the average of $\hbar\omega_{1/2}$ = 1.39 eV and $\hbar\omega_{3/2}$ = 1.45 eV.
[19] M. Mitchner and C. H. Kruger, Jr., *Partially Ionized Gases*. New York: Wiley, 1973, pp. 78-88. The reaction rates for ionization, R_i, and three-body recombination, R_r, are given in terms of the ionization coefficient, K_i, and the recombination coefficient, K_r, by $R_i = K_i n^{e^-} n^{Cs}$ and $R_r = K_r (n^{e^-})^2 n^{Cs^+}$, respectively. From the condition of detailed balancing and the Saha equation it can be shown that the ratio of the ionization coefficient to the recombination coefficient is

$$\frac{K_i}{K_r} = \frac{2g^{Cs^+}}{g^{Cs}} \left[\frac{2\pi m_e k T_e}{h^2}\right]^{3/2} \exp\left(-E_{Cs}/kT_e\right)$$

in an obvious notation. For an electron temperature of 2 eV we find $K_r/K_i = 1.7 \times 10^{-23}$ cm^3; hence even for electron densities on the order of 10^{16} cm^{-3} the reverse reaction rate is smaller than the forward rate by several orders of magnitude.
[20] D. U. von Rosenberg, *Methods for the Numerical Solution of Partial Differential Equations*. New York: American Elsevier, 1969.
[21] L. F. Shampine and R. C. Allen, Jr., *Numerical Computing: An Introduction*. Philadelphia, PA: Saunders, 1973, p. 64.
[22] E. W. McDaniel, *Collision Phenomena in Ionized Gases*. New York: Wiley, 1964, p. 563.
[23] C. Millet and J. Millet, "Réalisation d'un jet de cesium de densité 10^{12} At · Cm^{-3}," *Entropie*, pp. 52-55, July-Oct. 1970.
[24] J. B. Anderson, R. P. Andres, and J. B. Fenn, "High intensity and high energy molecular beams," in *Advances in Atomic and Molecular Physics*, vol. I, D. R. Bates and I. Estermann, Ed. New York. Academic, 1965, pp. 345-389.
[25] E. Hundhausen and H. Harrison, "Chilled collimator for high intensity molecular beams," *Rev. Sci. Instr.*, vol. 38, pp. 131-132, Jan. 1967.
[26] D. A. Copeland and C. L. Tang, "Photon-assisted non-resonant charge-exchange: A simple molecular model," to be published in *J. Chem. Phys.*
[27] D. R. Bates, A. E. Kingston, and R. W. P. McWhirter, "Recombination between electrons and atomic ions. I. Optically thin plasmas," *Proc. Roy. Soc.* (London), vol. A267, pp. 297-312, May 1962.

Radiation Loss Coefficients of Asymmetric Dielectric Waveguides with Shallow Sinusoidal Corrugations

WILLIAM W. RIGROD, MEMBER, IEEE, AND D. MARCUSE, FELLOW, IEEE

Abstract—Kiselev [10] has solved the boundary equations for an asymmetric slab waveguide with a shallow sinusoidal corrugation, and derived explicit, closed expressions for the TE radiation loss coefficients of various waveguide geometries. For many practical applications in integrated optics, the Rayleigh assumption justifying the boundary-matching procedure and the approximations of linear perturbation analysis employed in this derivation are both satisfied. We have extended this procedure to TM modes and found that the expressions for both TE and TM modes in all of the geometries so treated agree identically with those derived by coupled-mode theory. The dependence of the TM radiation loss coefficient in each waveguide geometry on the grating period, radiation angle, refractive index profile, and mode polarization is illustrated graphically, and compared with its TE counterpart.

INTRODUCTION

THE attractiveness of corrugated surface gratings [1] as a means of coupling light beams to the guided fields in dielectric thin-film waveguides has motivated a number of analytical studies [2]-[7]. Most of these publications have been concerned with either the "aperture-matching" problem for finite area light beams, or the effects of groove shape and depth on the radiation coupling efficiency of the gratings, in each case requiring relatively intricate mathematical formalism or computational procedure which has prevented them from deriving closed expressions with widely applicable utility. By contrast, although first-order perturbation analyses are not valid for deep-groove gratings, they do permit the derivation of explicit, closed expressions for waveguides with shallow sinusoidal gratings which describe the dependence of the radiation loss coefficient upon all of the waveguide operating parameters other than the groove profile. Such closed expressions provide physical insight into the coupling mechanism of various grating-waveguide configurations, as well as a convenient means for their relative numerical assessment, which is in most cases qualitatively correct well beyond the limits of perturbation analysis.

First-order perturbation theory is based on the assumption of weak field interaction, such that none of the coupled fields

Manuscript received February 3, 1976; revised July 16, 1976.
The authors are with Bell Laboratories, Holmdel, NJ 07733.

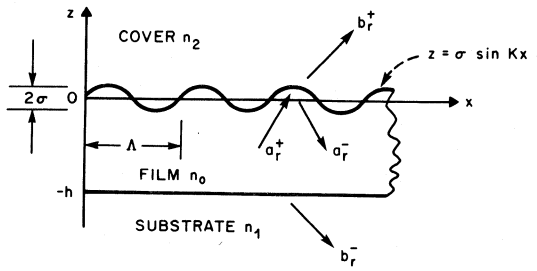


Fig. 1. Section of asymmetric slab waveguide with a shallow sinusoidal corrugation on the cover side in the notation of [10] and [11], with arrows indicating the field amplitudes.

changes appreciably over small portions of a grating, and that for a periodic perturbation only one diffraction order need be considered. Within this framework, Marcuse has used coupled-mode theory [8], [9] to derive the radiation coupling coefficients of corrugated surface gratings on asymmetric and symmetric slab waveguides, and reduced them to explicit expressions for the loss coefficients in certain special cases. More recently, Kiselev [10] has formulated the boundary value equations for an asymmetric slab guide with shallow sinusoidal corrugations, for which the Rayleigh hypothesis [4], [13] is valid, and invoked the assumptions of linear perturbation theory to solve a truncated set of these equations for TE modes. Using a first-order Taylor series expansion of the dispersion equation, he has obtained explicit expressions for the TE radiation loss coefficients of a variety of waveguide configurations: with gratings located on either the cover or substrate side of the guiding film, with radiation coupled into both of the adjacent dielectrics or into the substrate alone, and with or without a reflecting film on either the smooth or the corrugated film boundary. In a companion paper by Zlenko *et al.* [11], graphic plots of these expressions have been presented which illustrate vividly the nature of the interference phenomena affecting the dependence of the radiation loss coefficient on the wavelength, grating period and film thickness in each of these configurations.

In this paper we derive the TM-mode radiation loss coefficients from Kiselev's boundary-matching equations for each of the waveguide configurations mentioned above, in order to compare the parametric dependence of the TE and TM coefficients with each other, and to satisfy ourselves that the same expressions are obtained in each case (TE and TM) from coupled mode theory. The differences between the coupling mechanisms for TE and TM modes are illustrated by graphs, similar to those in [11], of the normalized coupling coefficient as a function of radiation angle for different waveguide geometries and refractive-index profiles.

Solution of Boundary Equations

The geometry employed by Kiselev [10] is shown in Fig. 1, with $\partial/\partial y = 0$ and a guided wave in the unperturbed waveguide. When the field pattern is decomposed into traveling wave components, the upward field component in the film n_0 is given by

$$v_0^+(x,z) = a_0^+ \exp\left[ikn^*x + i\sqrt{(n_0^2 - n^{*2})}kz\right] \exp(-i\omega t) \tag{1}$$

where $k = \omega/c$, and n^* is the effective refractive index of the guided mode. This wave is scattered by the sinusoidal boundary $z = \sigma \sin Kx$, where $K = 2\pi/\Lambda$, into an infinite set of transmitted and reflected diffraction orders. Iterative reflections of the scattered waves at the smooth lower boundary $z = -h$, followed by scattering of the reflected waves at the upper corrugated boundary of the film, cause the field in each of the media n_2, n_0, n_1 to consist of an infinite number of plane waves, of the form

$$v_2(x,z) = \sum_{r=-\infty}^{\infty} b_r^+ \exp(iN_2^{(r)}\zeta) \exp[i(n^* + rN)\xi], \qquad z > \sigma \sin Kx$$

$$v_0(x,z) = \sum_{r=-\infty}^{\infty} [a_r^+ \exp(iN_0^{(r)}\zeta) + a_r^- \exp(-iN_0^{(r)}\zeta)] \cdot \exp[i(n^* + rN)\xi], \qquad \sigma \sin Kx \geq z \geq -h,$$

$$v_1(x,z) = \sum_{r=-\infty}^{\infty} b_r^- \exp(-iN_1^{(r)}\zeta) \exp[i(n^* + rN)\xi], \qquad z < -h, \tag{2}$$

with the time dependence omitted, in which $v = E_y$ for TE waves, and $v = H_y$ for TM waves. Here $\xi = kx$, $\zeta = kz$, $N = \lambda/\Lambda = K/k$, r is the diffraction order, and

$$N_j^{(r)} = \sqrt{n_j^2 - (n^* + rN)^2}, \quad \text{with } j = 0, 1, 2.$$

This field description has been shown to be valid in the grating region for sinusoidal grooves with $K\sigma < 0.448$, when the small-slope Rayleigh assumption is satisfied [4], [13].

At the smooth boundary $z = -h$, matching of the tangential field components $v(x,z)$ and $(n_j^{-\kappa})\partial v/\partial z$ of each rth harmonic plane wave yields

$$b_r^-/a_r^- = \frac{2(n_1)^\kappa N_0^{(r)}}{(n_1)^\kappa N_0^{(r)} - (n_0)^\kappa N_1^{(r)}} \exp\left[-i(N_0^{(r)} + N_1^{(r)})kh\right] \tag{3a}$$

$$\beta_r = a_r^-/a_r^+ = \frac{(n_1)^\kappa N_0^{(r)} + (n_0)^\kappa N_1^{(r)}}{(n_1)^\kappa N_0^{(r)} - (n_0)^\kappa N_1^{(r)}} \exp\left[-2iN_0^{(r)}kh\right]. \tag{3b}$$

At the corrugated boundary $z = \sigma \sin N\xi$, each of the rth harmonic plane waves $\sim\exp[i(n^* + rN)\xi]$ is diffracted into

an infinite set of plane waves $\sim\exp[i(n^* + pN)\xi]$, where $p = 0, \pm1, \pm2$, etc. Matching $v(x, z)$ and $(n_j^{-\kappa})\,\nabla_n v$ for each of these diffracted waves yields two infinite sets of equations, respectively, each a linear combination of the field amplitudes with Bessel function coefficients. For shallow corrugations, such that $(k\sigma)^2 \ll 1$, only the incident and first-order diffracted waves need to be considered, reducing the two sets of equations to six homogeneous equations in $k\sigma$ for the six amplitudes a_r^+, b_r^+ with $r = 0$ and ±1. Of these, only the $r = 0$ and -1 waves are of interest, inasmuch as the $r = 1$ waves are evanescent, with positive imaginary propagation constants

$$kN_j^{(1)} = ik\sqrt{(n^* + N)^2 - n_j^2}.$$

With $r = p = 0$, we obtain the equations for the unperturbed waveguide,

$$a_0^+(1 + \beta_0) - b_0^+ = 0 \tag{4a}$$

$$a_0^+ N_0^{(0)}(1 - \beta_0) - b_0^+(n_0/n_2)^\kappa N_2^{(0)} = 0 \tag{4b}$$

and thereby the zeroth-order dispersion equation

$$N_0^{(0)}(1 - \beta_0) - (n_0/n_2)^\kappa N_2^{(0)}(1 + \beta_0) = 0. \tag{5}$$

With the incident field amplitude a_0^+ normalized to unity and $b_0^+ = 1 + \beta_0$; the $r = -1$ amplitudes of H_y for TM modes (with $\kappa = 2$), and those of E_y for TE modes (with $\kappa = 0$) can be written as follows:

$$a_{-1}^+ = \frac{1}{2}k\sigma(1 + \beta_0)\,\frac{\{(N_0^{(0)})^2 - (n_0/n_2)^\kappa(N_2^{(0)})^2 - [(n_0/n_2)^\kappa - 1]\,[Nn_m^* + (n_0/n_2)^\kappa N_2^{(0)}N_2^{(-1)}]\}}{[N_0^{(-1)} - (n_0/n_2)^\kappa N_2^{(-1)}]\,[1 - v_1v_2\exp(-2iN_0^{(-1)}kh)]} \tag{6}$$

$$a_{-1}^- = (a_{-1}^+)\beta_{-1} = (a_{-1}^+)v_1\exp(-2iN_0^{(-1)}kh) \tag{7}$$

$$b_{-1}^- = (a_{-1}^+)\frac{2N_0^{(-1)}}{[N_0^{(-1)} - (n_0/n_1)^\kappa N_1^{(-1)}]}\exp[-i(N_0^{(-1)} + N_1^{(-1)})\,kh] \tag{8}$$

$$b_{-1}^+ = (a_{-1}^+)[1 + v_1\exp(-2iN_0^{(-1)}kh)] - \frac{1}{2}k\sigma(1 + \beta_0)[(n_0/n_2)^\kappa - 1]\,N_2^{(0)}, \tag{9}$$

where we have defined

$$v_j = \frac{N_0^{(-1)} + (n_0/n_j)^\kappa N_j^{(-1)}}{N_0^{(-1)} - (n_0/n_j)^\kappa N_j^{(-1)}}, \qquad j = 1, 2. \tag{10}$$

For $\kappa = 2$ only, the expression for a_{-1}^+ can be expressed more compactly as

$$a_{-1}^+ = \frac{\frac{1}{2}k\sigma(1 + \beta_0)[(n_0/n_2)^2 - 1]\,[n_m^*(n_m^* - N) - N_2^{(0)}(n_0/n_2)^2N_2^{(-1)}]}{[N_0^{(-1)} - (n_0/n_2)^2N_2^{(-1)}]\,[1 - v_1v_2\exp(-2i\psi)]}, \tag{11}$$

with $\psi = N_0^{(-1)}kh$.

In deriving an expression for the loss coefficient α of TE modes, Kiselev [10] used a first-order Taylor series approximation for the dispersion equation of the perturbed waveguide to evaluate the change from n_m^* of the guided mode in the smooth waveguide to $n_m^* + \delta n_m$ of the corrugated waveguide, in which δn_m is complex. We have found this procedure to be inaccurate for TM modes, and instead use the "leaky wave" approximation

$$\alpha = (1/2P_g)(dP_g/dx) \tag{12}$$

in which P_g is the power flow in the unperturbed waveguide, and dP_g/dx the irradiance into one or both media adjacent to the guiding film n_0, over a small section of the perturbed guide.

For bound modes in thin-film waveguides, the expression for the TM power flow,

$$P_g = \frac{\beta_g}{2\omega\epsilon_0}\int_{-\infty}^{\infty}\frac{H_yH_y^*dz}{n_j^2}, \tag{13}$$

has been shown [12] to reduce to

$$P_g = \frac{|a_0^+|^2 n_m^* kh^*}{\omega\epsilon_0 n_0^2} \tag{14}$$

where $H_y = a_0^+$ in the guiding film n_0, $\beta_g = n_m^*k$, and h^* is the TM effective film thickness, defined by

$$(kh^*)_{\mathrm{TM}} = kh + \sum_{j=1,2}\frac{1}{\sqrt{(n_m^*)^2 - n_j^2}}\cdot\frac{(n_0n_j)^2}{[(n_m^*)^2(n_0^2 + n_j^2) - (n_0n_j)^2]}. \tag{15}$$

The irradiance of a plane wave diffracted into a medium of refractive index n_j adjacent to the film is

$$dP_g/dx = \frac{\beta_z H_y H_y^*}{2\omega\epsilon_0 n_j^2} \tag{16}$$

where $\beta_z = kN_j^{(-1)}$ is the propagation constant normal to the waveguide, and H_y is either b_{-1}^+ or b_{-1}^-, depending on the direction of the radiation, i.e., depending on whether $N_2^{(-1)}$ or $N_1^{(-1)}$ is real. Using $a_0^+ = 1$ as before, we obtain

$$(\alpha)_{\mathrm{TM}} = (1/4n_m^*kh^*)\cdot\mathrm{Re}\,[(n_0/n_2)^2kN_2^{(-1)}|b_{-1}^+|^2 + (n_0/n_1)^2kN_1^{(-1)}|b_{-1}^-|^2]. \tag{17}$$

In evaluating this expression for various special cases, it will be convenient to adopt an abbreviated notation, or "TM shorthand" for the $r = -1$ propagation constants, as follows:

$$N_j = (n_0/n_j)^2 N_j^{(-1)}, \quad j = 0, 1, 2. \tag{18}$$

In this notation, the TM loss coefficient (17) is given by

$$(\alpha)_{TM} = (1/4n_m^* kh^*) \cdot \mathrm{Re}[kN_2|b_{-1}^+|^2 + kN_1|b_{-1}^-|^2]. \tag{19}$$

We list below the expressions for the TM coefficient in each of 6 cases involving asymmetric, and two involving symmetric, waveguide configurations, and cite the corresponding TE loss coefficients [10], [11] in the Appendix for comparison, using the "normalized" form $(\alpha/k)(2/k\sigma)^2$ for convenience. In all cases $n_0 > n_1$, $n_0 > n_2$ and N_0 is real, but N_1 is real only when $n_1 > |n_m^* - N|$, and N_2 is real when $n_2 > |n_m^* - N|$.

Case 1: Corrugation on air (n_2) side: radiation into substrate (n_1) only. With N_1 real and $N_2 = i|N_2|$ we obtain from (8) and (11)

$$\left(\frac{\alpha_1}{k}\right)_{TM}\left(\frac{2}{k\sigma}\right)^2 = \left[\frac{n_0^2 - n_m^{*2}}{n_m^* kh^*}\right] \cdot \frac{n_2^4[n_m^*(n_m^* - N) + |N_2^{(0)}| \cdot |N_2|]^2}{[(n_m^*)^2(n_0^2 + n_2^2) - n_0^2 n_2^2][(n^* - N)^2(n_0^2 + n_2^2) - n_0^2 n_2^2]} \cdot \frac{N_1 N_0^2}{[N_0^2 - (N_0^2 - N_1^2)\cos^2(\psi - \chi_2)]}, \tag{20}$$

where $\chi_2 = \tan^{-1}(|N_2|/N_0)$ is half the phase shift angle in total internal reflection at the smooth film boundary with medium n_2, h^* is given by (15), and $N_2^{(0)} = i|N_2^{(0)}|$ for bound waveguide modes.

As indicated in the phase diagram of Fig. 2(a), the first negative order diffracted radiation can be either "forward" or "backward," relative to the guided mode n_m^*, at an angle from the normal $\theta_1 = \sin^{-1}[(n_m^* - n)/n_1]$, whose sign depends on that of $(n_m^* - N)$. The numerator term of (20) shows that α_1 is smaller for "backward" radiation, when $(n_m^* - N) < 0$. This directional asymmetry is characteristic of TM scattered radiation, and is absent from TE scattering, essentially because TM waves contain a longitudinal component of the electric field not present in TE waves, whose sign changes with the direction of propagation. (The longitudinal magnetic field of TE waves does not change sign with a change in the propagation direction.) In both cases, the longitudinal field enters the field-matching equations at the corrugated boundary.

Case 2: Corrugation on substrate (n_1) side; radiation into substrate (n_1) only, i.e., the same index relations as in Case 1, but with radiation via the corrugated boundary. From (9) and (11) with indices 1 and 2 interchanged, we obtain

$$\left(\frac{\alpha_2}{k}\right)_{TM}\left(\frac{2}{k\sigma}\right)^2 = \left[\frac{n_0^2 - n_m^{*2}}{n_m^* kh^*}\right] \frac{(n_0^2 - n_1^2)[(n_m^*)^2(n_m^* - N)^2 + N_0^2|N_1^{(0)}|^2] \cdot N_1 \cos^2(\psi - \chi_2 - \eta_1)}{[(n_m^*)^2(n_0^2 + n_1^2) - n_0^2 n_1^2)][N_0^2 - (N_0^2 - N_1^2)\cos^2(\psi - \chi_2)]}. \tag{21}$$

Here again h^* is the TM effective film thickness (15),

$$\chi_2 = \tan^{-1}(|N_2|/N_0),$$
$$|N_1^{(0)}| = \sqrt{(n_m^*)^2 - n_1^2},$$
$$\psi = N_0^{(-1)} kh,$$

and

$$\eta_1 = \tan^{-1}\left[\frac{N_0|N_1^{(0)}|}{n_m^*(n_m^* - N)}\right] \tag{22}$$

is the term expressing the directional asymmetry of TM diffracted radiation.

Case 3: Corrugation on air (n_2) side: radiation into both air (n_2) and substrate (n_1).

In this case $n_0 > n_1 > n_2 > |n_m^* - N|$, such that N_0, N_1, and N_2 as well as ν_1 and ν_2 are real quantities. The loss coefficient (19) can be conveniently expressed as the sum of two parts, representing radiation into air (or a cover dielectric) n_2 via the corrugated boundary, α_{air}, and that into the substrate n_1 via the smooth boundary, α_{sub}:

$$\alpha_3 = \alpha_{air} + \alpha_{sub} = \frac{kN_2|b_{-1}^+|^2}{4n_m^* kh^*} + \frac{kN_1|b_+^-|^2}{4n_m^* kh^*} \tag{23}$$

$$\left(\frac{\alpha_{air}}{k}\right)_{TM}\left(\frac{2}{k\sigma}\right)^2 = \left[\frac{n_0^2 - n_m^{*2}}{n_m^* kh^*}\right] \cdot \frac{(n_0^2 - n_2^2)[(n_m^*)^2(n_m^* - N)^2 + N_0^2|N_2^{(0)}|^2]}{(n_m^*)^2(n_0^2 + n_2^2) - n_0^2 n_2^2} \cdot \frac{N_2[N_1^2 + (N_0^2 - N_1^2)\cos^2(\psi - \eta_2)]}{[(N_0^2 + N_1 N_2)^2 - (N_0^2 - N_1^2)(N_0^2 - N_2^2)\cos^2\psi]} \tag{24}$$

$$\left(\frac{\alpha_{sub}}{k}\right)_{TM}\left(\frac{2}{k\sigma}\right)^2 = \left[\frac{n_0^2 - n_m^{*2}}{n_m^* kh^*}\right] \cdot \frac{(n_0^2 - n_2^2)[(n_m^*)^2(n_m^* - N)^2 + N_2^2|N_2^{(0)}|^2]}{[(n_m^*)^2(n_0^2 + n_2^2) - n_0^2 n_2^2]} \cdot \frac{N_1 N_0^2}{[(N_0^2 + N_1 N_2)^2 - (N_0^2 - N_1^2)(N_0^2 - N_2^2)\cos^2\psi]}. \tag{25}$$

The ratio of irradiance into air P_2 to that into the substrate P_1 is given by

$$\left(\frac{P_2}{P_1}\right)_{TM} = \frac{\alpha_{air}}{\alpha_{sub}} = \frac{N_2|b_{-1}^+|^2}{N_1|b_{-1}^-|^2} = \frac{N_2[N_1^2 + (N_0^2 - N_1^2)\cos^2(\psi - \eta_2)][(n_m^*)^2(n_m^* - N)^2 + N_0^2|N_2^{(0)}|^2]}{N_1 N_0^2[(n_m^*)^2(n_m^* - N)^2 + N_2^2|N_2^{(0)}|^2]}. \tag{26}$$

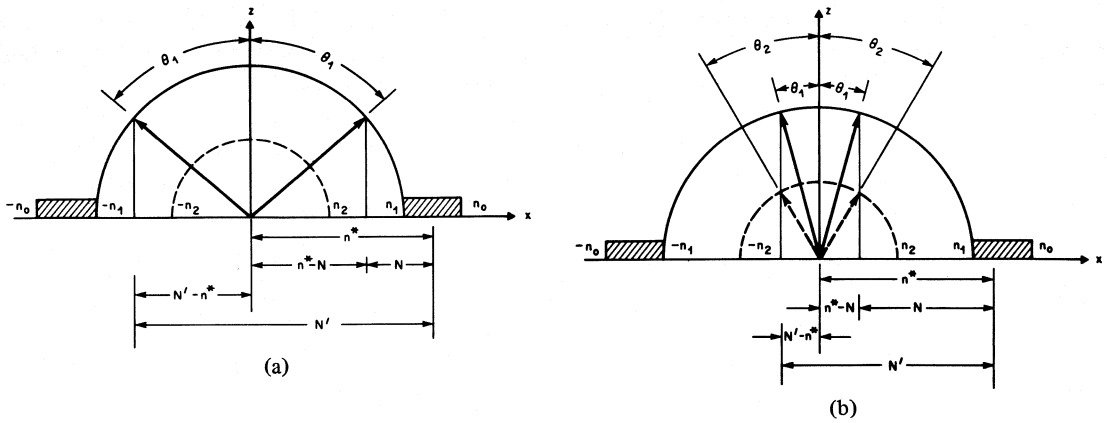


Fig. 2. Phase diagrams illustrating both forward and backward directions of negative first-order diffracted radiation ($r = -1$) for an asymmetric slab waveguide with sinusoidal corrugations on cover side. The shaded regions along the x axis denote loci of forward and backward guided modes, respectively, with effective index $n^* = \beta_g/k$, and $N = \lambda/\Lambda = K/k$ is the normalized grating constant. (a) Radiation into substrate n_1 only (Case 1), and (b) radiation into both substrate n_1 and cover dielectric n_2 (Case 3).

As shown in the phase diagram of Fig. 2(b), air radiation is emitted at an angle $\theta_2 = \sin^{-1}[(n_m^* - N)/n_2]$, and substrate radiation at an angle $\theta_1 = \sin^{-1}[(n_m^* - N)/n_1]$, from the normal, with both angles positive when $n_m^* - N > 0$ and negative when $n_m^* - N < 0$. Asymmetry in the scattered irradiance is present only in the air radiation, expressed in (24) by the angle

$$\eta_2 = \tan^{-1}\left[\frac{N_0|N_2^{(0)}|}{n_m^*(n_m^* - N)}\right]. \tag{27}$$

There is no asymmetry in the substrate radiation (25) for this case.

Case 4: Corrugation on substrate (n_1) side; radiation into both air (n_2) and substrate (n_1).

The grating condition for this case is the same as for Case 3, and the expression for the loss coefficients is obtained directly from (24)-(27) with the indices n_1 and n_2 interchanged, as well as α_{air} and α_{sub}. The ratio of irradiances is

$$\left(\frac{P_2}{P_1}\right)_{TM} = \frac{\alpha_{air}}{\alpha_{sub}} = \frac{N_2 N_0^2[(n_m^*)^2(n_m^* - N)^2 + N_1^2|N_1^{(0)}|^2]}{N_1[N_2^2 + (N_0^2 - N_2^2)\cos^2(\psi - \eta_1)][(n_m^*)^2(n_m^* - N)^2 + N_0^2|N_1^{(0)}|^2]} \tag{28}$$

where

$$\eta_1 = \tan^{-1}\left|\frac{N_0|N_1^{(0)}|}{n_m^*(n_m^* - N)}\right|. \tag{29}$$

In Cases 1-4, the effective propagation constant n_m^* is a root of the dispersion equation (5) with $\kappa = 2$ for TM modes and $\kappa = 0$ for TE modes. This equation can also be written in the form

$$khN_0^{(0)} = m\pi + \sum_{j=1,2} \tan^{-1}\left[\frac{n_0^\kappa|N_j^{(0)}|}{n_j^\kappa N_0^{(0)}}\right], \qquad m = 0, 1, 2, \cdots. \tag{30}$$

In Cases 5 and 6 below, the substrate n_1 is replaced by a perfectly reflecting conductor, and the propagation constant n_m^* is a root of the modified dispersion equation

$$khN_0^{(0)} = \left(m + \frac{1}{2}\right)\pi + \tan^{-1}\left[\frac{n_0^\kappa|N_2^{(0)}|}{n_2^\kappa N_0^0}\right], \qquad m = 0, 1, 2, \cdots. \tag{31}$$

Case 5: Reflecting film on corrugated waveguide surface; radiation into air (n_2) via smooth boundary.

The grating condition is $|n_m^* - N| < n_2$. In (20), $2\chi_2$ is the phase shift in total internal reflection at the corrugated boundary with the dielectric n_2. With a reflecting conductor at that boundary, and medium n_2 on the smooth side of the guide, the loss coefficient is obtained from (20) by interchanging the indices n_1 and n_2, and letting $(n_0/n_1)^2 = 0$ and $\chi_2 = \pi/2$:

$$\left(\frac{\alpha_5}{k}\right)_{TM}\left(\frac{2}{k\sigma}\right)^2 = \left[\frac{n_0^2 - n_m^{*2}}{n_m^* k h^*}\right]\frac{N_2 N_0^2}{[N_2^2 + (N_0^2 - N_2^2)\cos^2\psi]} \tag{32}$$

written in TM shorthand notation, with n_m^* given by (31) with $\kappa = 2$, and the effective TM film thickness h^* by

$$(kh^*)_{TM} = kh + \frac{1}{\sqrt{(n_m^*)^2 - n_2^2}}\,\frac{n_0^2 n_2^2}{[(n_m^*)^2(n_0^2 + n_2^2) - n_0^2 n_2^2]}. \tag{33}$$

It is seen that there is no directional asymmetry in TM air radiation via a smooth boundary in this case, inasmuch as the

longitudinal electric field at the corrugated boundary with the reflecting conductor is zero.

Case 6: Reflecting film on smooth waveguide surface; radiation into air (n_2) via corrugated boundary.

The grating condition is again $|n_m^* - N| < n_2$, and the loss coefficient is obtained from (21) of Case 2, with $\chi_2 = \pi/2$ and the indices n_1 and n_2 interchanged:

$$\left(\frac{\alpha_6}{k}\right)_{\mathrm{TM}} \left(\frac{2}{k\sigma}\right)^2 = \left[\frac{n_0^2 - n_m^{*2}}{n_m^* k h^*}\right] \frac{(n_0^2 - n_2^2)[(n_m^*)^2 (n_m^* - N)^2 + N_0^2 |N_2^{(0)}|^2]\, N_2 \sin^2(\psi - \eta_2)}{[(n_m^*)^2 (n_0^2 + n_2^2) - n_0^2 n_2^2]\,[N_2^2 + (N_0^2 - N_2^2)\cos^2\psi]}, \tag{34}$$

again in TM shorthand notation, with η_2 given by (27) and h^* by (33).

Case 7: Corrugated symmetric waves.

In Case 6, the perfectly reflecting surface at the smooth boundary $z = -h$ of an asymmetric slab waveguide is a plane of symmetry for the odd-numbered guided and radiation modes of a symmetric waveguide of thickness $2h$ with antisymmetrical corrugations on both boundaries with n_2 [8]. The loss coefficients α_6 of (34) and (A11) are therefore valid for radiation from both surfaces of such a symmetric guide (of thickness $2h$) with sinusoidal *bending* variations.

In a symmetric guide (of thickness $2h$), however, sinusoidal *thickness* variations couple only symmetric (even-numbered) guided modes to each other or to symmetric radiation modes [9, pp. 350–352]. In the latter case, the radiation fields correspond to those of an asymmetric corrugated waveguide of thickness h radiating into medium n_2 via the corrugated boundary, with $\chi = 0$ at the smooth boundary. The loss coefficient is then given by (21) of Case 2, with $\chi_2 = 0$, and the indices n_1 and n_2 interchanged [8, eq. (9.3-10)].

Comparison with Coupled-Mode Theory

The radiation loss coefficients listed in the preceding section can also be derived by the method of coupled-mode theory [8], [9]. Coupled-mode theory differs conceptually from the method employed in this paper. The foregoing derivation was based on calculating the scattered plane wave components at the corrugated film boundary from an incident plane wave. The total scattering loss of a guided wave in a thin film with sinusoidally deformed boundary was obtained by summing all the individual scattered wave components. Coupled-mode theory, on the other hand, uses modes of the waveguiding structure. The incident guided wave is coupled by the corrugated boundary to unbounded radiation modes that are also solutions of Maxwell's equations satisfying the boundary conditions at the refractive index discontinuities. The guided wave as well as the radiation modes are solutions of the unperturbed waveguide structure. Instead of summing over scattered wave components and keeping track of multiple reflections, the coupled-mode approach calculates coupling coefficients between the guided and the radiation modes and proceeds to determine the loss coefficients by accounting for the power that is carried away by radiation modes.

We have derived all the loss formulas presented in this paper by the methods of coupled-mode theory and have found complete agreement in every case. There is no need to present details of this calculation in this paper since the analytical method has been outlined in [9]. This comparison has shown, however, that the first order approximations of our theory are in complete agreement with the first order perturbation solutions of coupled mode theory.

Irradiance Distributions

In this section we present plots showing, for purposes of comparison, the angular variation of first-order TE and TM scattering from both low- and high-index corrugated waveguides, i.e., guides with relatively small or large asymmetries in their refractive-index profiles [14].

Zlenko *et al.* [11] have published curves of the normalized loss coefficients $(\alpha/k)\,(2/k\sigma)^2$ discussed above, for TE modes in polystyrene film waveguides on a quartz substrate at $\lambda = 0.6328\ \mu$m, for each of the Cases 1–7, as a function of the radiation angle and grating period Λ. We shall use their waveguide parameters as typical of low-index low-asymmetry waveguides, and present here both duplicates of their plots for TE(0) modes, with minor changes in format, and for comparison, similar plots for TM(0) modes.

We have indicated in Figs. 2(a) and 2(b) phase diagrams that illustrate the relationships between the propagation vectors of the incident (guided) wave and the scattered plane waves. The incident guided wave is a standing wave in z direction but it can be decomposed into two traveling plane wave components whose wave vectors have the magnitude $n_0 k$. The magnitude of the propagation vectors of the scattered plane wave is $n_2 k$ in the air space above the film and $n_1 k$ in the substrate. Phase matching requires that the projections of the propagation vectors in x directions satisfy the condition $|n^* k - n_i k \sin\theta_i| = K$, or alternatively, $|n^* - n_i \sin\theta_i| = N$, with $i = 1$ or 2. The effective propagation constant n^* of the incident wave in the film is contained in the range $n_0 \geqslant |n^*| \geqslant n_1$ that is shown hatched in the figures. Fig. 2(a) illustrates scattering into the substrate only. The two vectors represent plane waves scattered in forward or backward directions. We measure the direction from the normal to the film surface and use the symbol θ_i to indicate the angle of scattered radiation. The figure shows clearly that small values of the grating vector K (or alternatively of its effective refractive index N) result in forward scattering while large values of K (or N) are required to achieve backward scattering. Fig. 2(b) illustrates scattering into both the air space above the film and into the substrate, with the dashed arrows indicating the propagation vectors of plane waves in the air space. The figure shows that no forward-scattered air wave can exist if the magnitude of N is too small while substrate scattering is possible for very small values of N. Similar remarks apply to backward scattering which uses a more limited range of N values for the air wave.

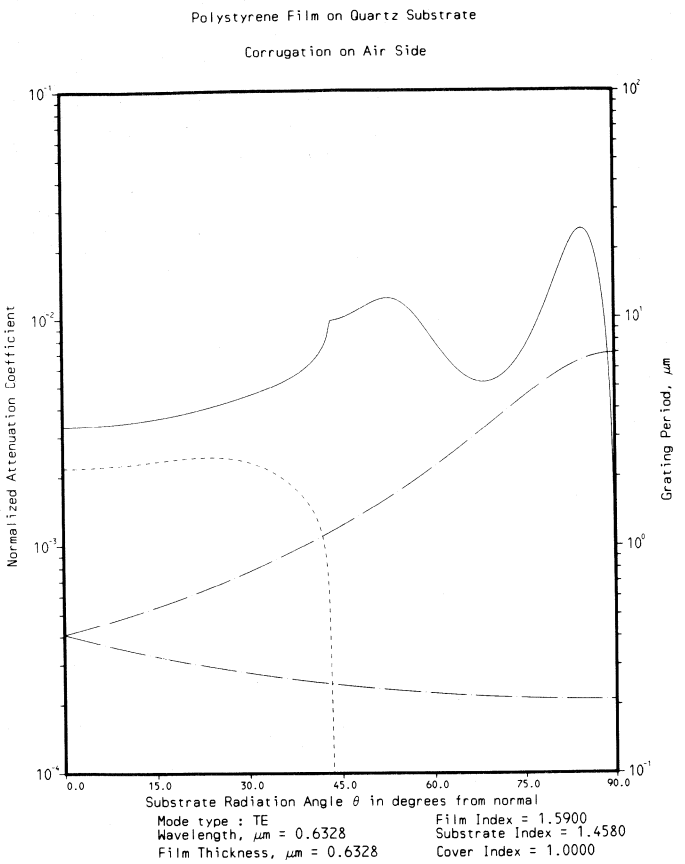


Fig. 3. The ordinates $(\alpha/k)\ (2/k\sigma)^2$ are a measure of the irradiances into the substrate (solid curve) and air (dashed curve) as a function of the radiation angle θ_1 into the substrate, for negative first-order diffraction in both the forward and backward directions. The upper chain-dotted curve defines $\Lambda(\theta_1)$ for backward radiation and the lower for forward radiation. The loss coefficients are for a TE(0) mode in a low-index waveguide corrugated on its air side. (Cases 1 and 3, and [11, fig. 2].)

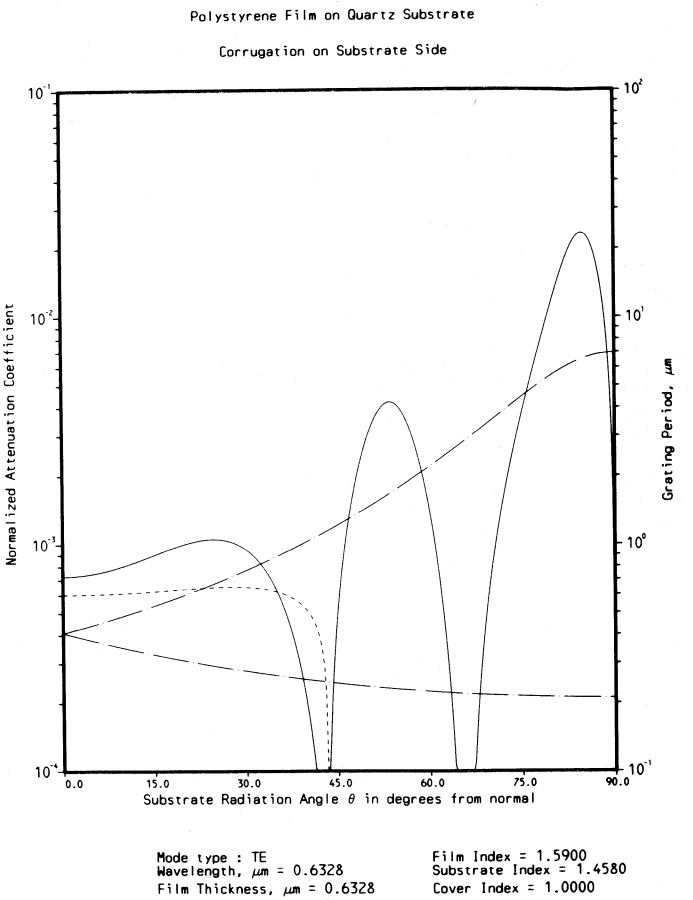


Fig. 4. The solid and dashed curves refer to the dependence of substrate and air radiation, respectively, on the substrate radiation angle (in either direction) for a TE(0) mode in the same low-index waveguide as in Fig. 3, but with its corrugation on the substrate boundary. (Cases 2 and 4, and [11, fig. 2].)

Fig. 3 shows the normalized loss coefficient for the TE(0) mode in a low-index waveguide with corrugations on the air side of the film, as a function of radiation angle into the substrate, in both the forward and backward directions. The solid curve represents radiation into the substrate, the dashed curve radiation into air, and the chain-dotted curves indicate the grating period Λ, with dimensions on the right-hand ordinate, for either forward or backward radiation (smaller or larger Λ, respectively). It should be noted that in this figure (and in all subsequent figures for TE modes), the loss coefficient has the same functional dependence on the radiation angle in both the forward and backward directions. Fig. 4 shows a similar set of curves for the same waveguide, with corrugations on the substrate side of the film. In both instances the air radiation is restricted to grating periods corresponding to substrate radiation angles $|\theta_1| < 43°$, and is somewhat stronger in Fig. 3. The substrate radiation (solid curves) tends to be stronger than air radiation, and is much more uniform over the entire range of angles and grating periods for radiation via a smooth boundary (Fig. 3) than that via a corrugated boundary (Fig. 4). As Zlenko *et al.* [11] have noted, the large changes in substrate irradiance via a corrugated boundary in the absence of air irradiance are caused by interference between waves reflected with equal intensity at the smooth film boundary. The interference effects are not as pronounced in a guide with its air boundary corrugated, as in Fig. 3, because not all of the rays suffer total internal reflection at that boundary. But even outside of the region of total internal reflection the solid curve in Fig. 4 shows much larger fluctuations than the corresponding curve in Fig. 3, because of much stronger reflection at the larger index discontinuity of the air interface.

Another illustration of the strong interference effects characterizing substrate irradiance via a corrugated boundary, when there is total internal reflection at the smooth boundary (Case 2), is shown in Fig. 5. Here the substrate irradiance (solid curve) is shown as a function of the film thickness and the effective index, for the TE(0) mode in the same low-index guide, with a fixed grating period (1.94 μm). The sensitivity of substrate radiation to small changes in film thickness has been experimentally demonstrated in [11]. In addition, as shown in [11, fig. 3], the spacing between the maxima of substrate irradiance via a corrugated boundary (with T.I.R. at the smooth boundary), as a function of radiation angle, decreases with the film thickness.

In Fig. 6, the dashed curve represents TE(0) air radiation via

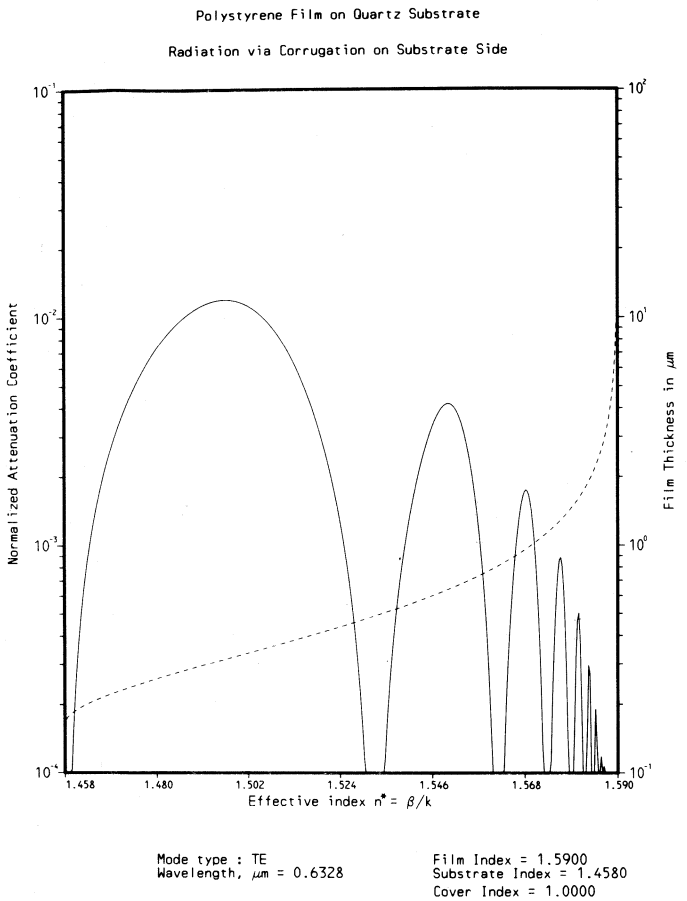


Fig. 5. The multiple maxima in the solid curve describe the sensitive variation of substrate irradiance via a corrugated boundary with the film thickness (dashed curve) and effective index. The solid curve is drawn for Case 2 (total internal reflection at the smooth boundary), for a TE(0) mode in the low-index waveguide of Figs. 3 and 4, with a fixed grating period, $\Lambda = 1.94$ μm. [11, fig. 6.]

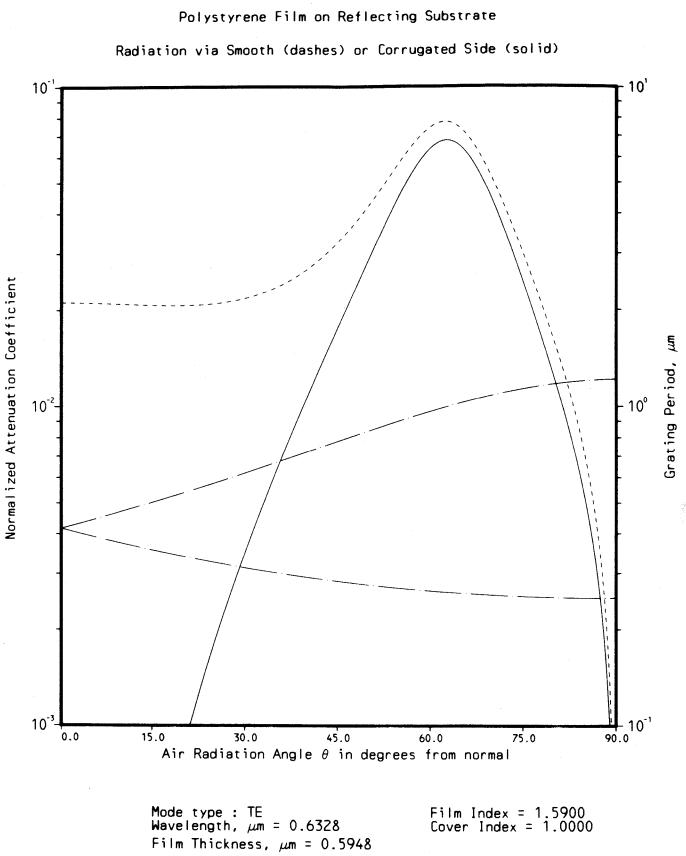


Fig. 6. Angular variation (in both the forward and backward directions) of the air irradiance from the TE(0) mode in a corrugated low-index film on a perfectly conducting substrate. The dashed curve is for the corrugation on the metallized side (Case 5), the solid curve for the corrugation on the air side (Case 6), and the chain-dotted curves define the grating period $\Lambda(\theta_2)$. The solid curve also represents the radiation loss coefficient for odd-numbered (antisymmetric) modes in a symmetrical waveguide of twice the thickness, with Λ the period of "bending" variations [8, eq. (9.3-19)].

the smooth boundary of a polystyrene film with a perfectly conducting reflector on its corrugated boundary, while the solid curve represents air radiation via the corrugated boundary of that film with a reflecting medium on its smooth side. In both cases the reflected rays are of equal intensity, but their interference effects tend to be canceled by their angular distribution when reflected at the corrugated boundary (dashed curve).

The curves of Figs. 7-9 show the first negative order irradiance distributions for a TM(0) mode in the same low-index waveguides as a function of the same parameters as for the corresponding curves for a TE(0) mode in Figs. 3-5. In Figs. 7 and 8, the solid curves represent forward substrate radiation and the dashed curves forward air radiation, whereas the dotted curves represent backward radiation—into air within the angular range $|\theta_1| \leqslant 43°$, approximately, and into the substrate in the region of substrate radiation only. (It will be recalled that there is no directional asymmetry for TM substrate radiation in Case 3.) The curves of Fig. 8, for a waveguide with its substrate side corrugated, do not show large differences for the TM(0) coupling efficiencies in the forward and backward directions, nor do they differ notably from the corresponding curves of Fig. 4 for the TE(0) mode. The greatest directional asymmetry occurs in Fig. 7, for the corrugation on the air side of the film, in the region of substrate radiation only; and this branch also differs most from the corresponding region of substrate radiation for the TE(0) mode of Fig. 3.

The multiple maxima in the variation of TM(0) substrate irradiance via a corrugated boundary, as a function of the radiation angle (or of the grating period), stem from the strong interference effects previously mentioned for TE(0) scattering in this geometry. The similarity between the curves of Figs. 4 and 8 extends to a similarity between the TM and TE curves of substrate irradiance as a function of film thickness, with a fixed grating period, such as that shown in Fig. 5.

The curves in Fig. 9 are the TM(0) counterparts of the TE(0) curves of Fig. 6, for the same polystyrene film on a perfectly conducting substrate. The dashed curve, describing TM(0) scattering into air via the smooth boundary, is the same in the forward and backward directions, as indicated in (32) Case 5, because the longitudinal electric field otherwise present

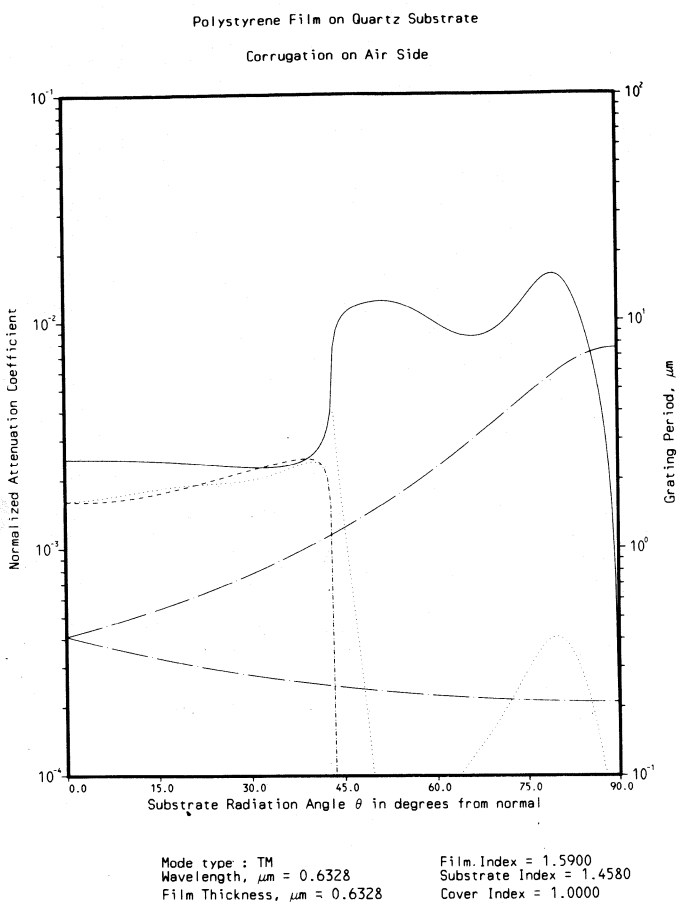


Fig. 7. Normalized loss coefficients for the TM(0) mode in the same low-index waveguide as in Fig. 3, with corrugations on its air side. The solid curve represents forward substrate radiation and the dashed curve forward air radiation, while the dotted curves represent backward radiation—into air, in the range of overlap with the dashed curve, and into the substrate in the range of overlap with the solid curve.

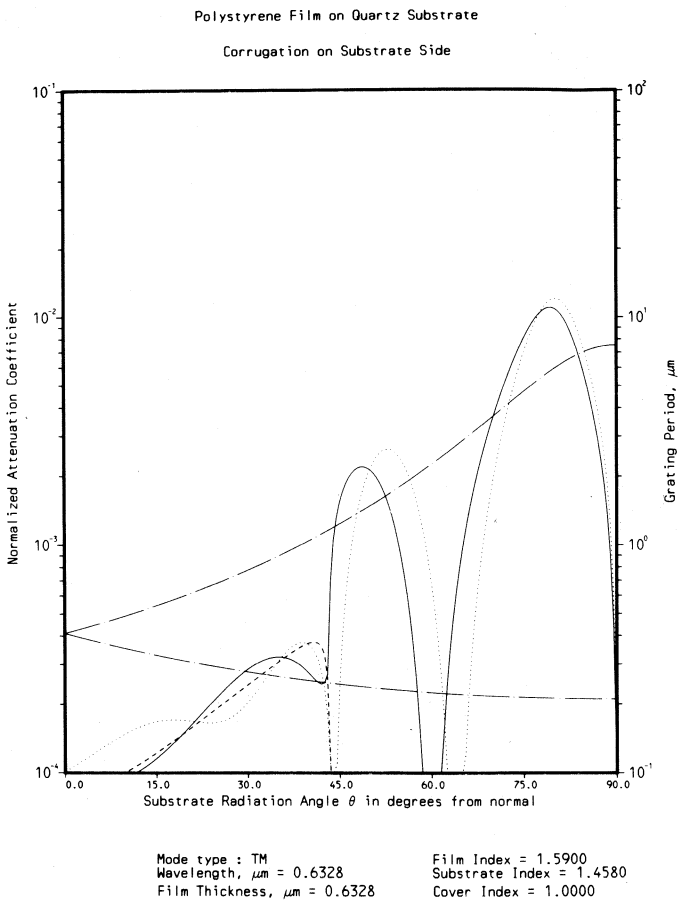


Fig. 8. Normalized loss coefficients for the TM(0) mode in the same low-index waveguide as in Fig. 4, with corrugations on its substrate side. The solid, dashed, and dotted curves have the same meanings as in Fig. 7. Unlike the curves for substrate radiation in Fig. 7, these curves do not differ appreciably in the two directions of radiation, or from the corresponding TE(0) curves of Fig. 4.

at the corrugated boundary is zero in this case. The dashed curves of Figs. 6 and 9 resemble each other closely, consistent with the resemblance between (32) and (A9) for low-index waveguides. The opposite is true of TM radiation via the corrugated boundary, which in Fig. 9 is shown by the solid curve for forward, and by the dotted curve for backward radiation. These curves differ considerably from each other and from the corresponding solid curve of Fig. 6 for TE(0) radiation.

In order to show the effects of a large asymmetry in the refractive-index profile, we have plotted in Figs. 10–15 curves of the normalized attenuation coefficients $(\alpha/k)\,(2/k\sigma)^2$ similar to those in Figs. 3–5 and Figs. 7–9, for a GaAs film on an AlGaAs substrate at $\lambda = 0.85$ μm. To make this comparison more meaningful, we have scaled down the thickness of the high-index film to values giving the same ratio n_m^*/n_0 (of the effective mode index to the film refractive index), and thereby the same obliquity of the "zig-zag" plane waves [12] comprising the guided mode in each case. This scaling procedure, resembling that in [14], results in values of the film thickness that are smaller than the free-space wavelength and are thereby somewhat restrictive on the depth of the grating corrugations, but it serves our present purpose.

Figs. 10–12 for a TE(0) mode in the high-index waveguides, are to be compared with the corresponding plots in Figs. 3, 4, and 6 for the TE(0) mode scattering in a low-index guide. The curves of Fig. 10 resemble those of Fig. 3 qualitatively, but the loss coefficients in the former are considerably larger, as might be expected from the larger index difference at the corrugated boundary. The curves of Fig. 11, however, for which the index difference is not large at the corrugated boundary, resemble those of Fig. 4 both qualitatively and quantitatively. The loss coefficients indicated by the dashed curve of Fig. 12 are almost an order of magnitude larger than those of Fig. 6, for air radiation via the smooth surface of a film with its corrugated surface metallized; and those indicated by the solid curve of Fig. 12 are much smaller than in Fig. 6, for air radiation via the corrugated surface of a film. Here again the high-index GaAs film of Fig. 12 has the equivalent of a large index difference at its corrugated boundary when that side is metallized.

In each case, the chain-dotted curves for the grating period

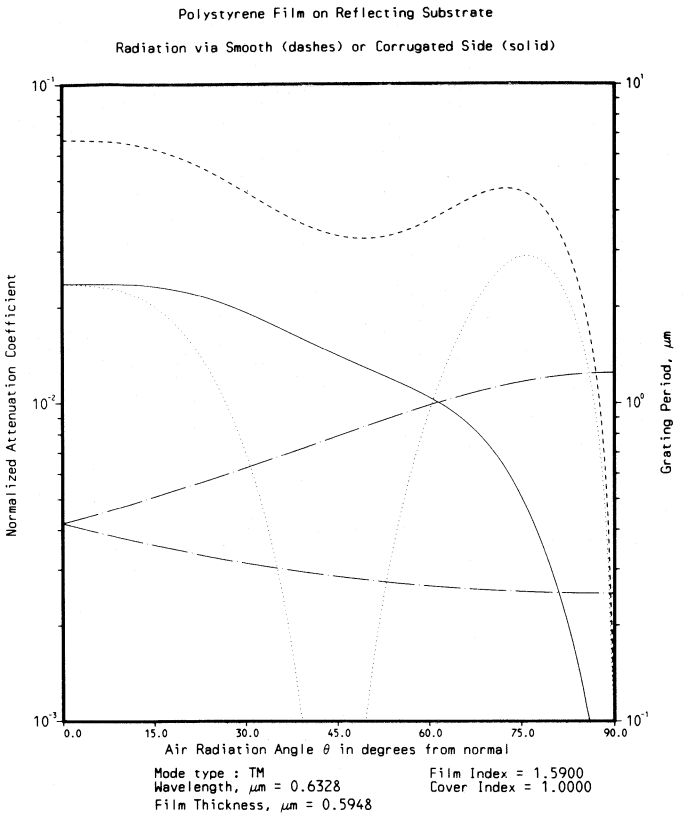


Fig. 9. Normalized loss coefficients for the TM(0) mode in the same low-index waveguide as in Fig. 6, a polystyrene film deposited on a perfectly conducting substrate. The dashed curve, describing TM(0) scattering into air via a smooth boundary, is the same in forward and backward directions, and similar to the dashed TE(0) curve of Fig. 6. The solid curve represents forward, and the dotted curve backward scattering into the air via the corrugated boundary.

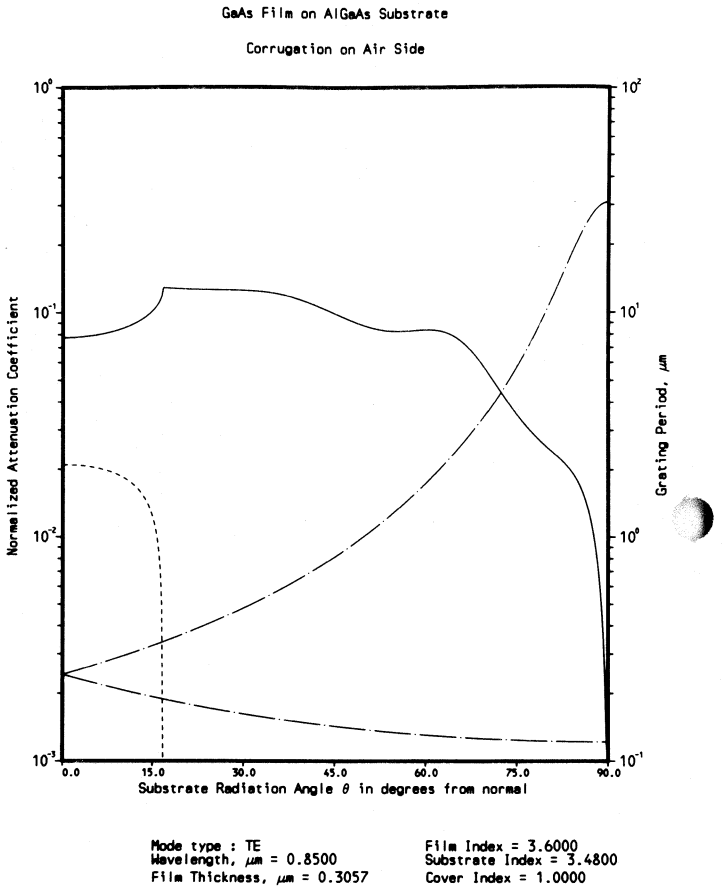


Fig. 10. Curves analogous to those of Fig. 3 for scattering from the TE(0) mode in a waveguide with highly asymmetric refractive-index profile, with its film thickness scaled to provide the same ratio n_m^*/n_0 (of effective index to film index) as in Fig. 3.

are computed from the relation $\Lambda = \lambda/(n_m^* - n_j \sin \theta_j)$, where n_m^* is the effective index of the guided mode, n_j the refractive index of either the substrate or air, and θ_j is the radiation angle in that medium, taken as positive in the forward direction. The large range of variation in Λ with substrate radiation angle in Figs. 10 and 11 for forward scattering occurs because $n^* - n_1 \ll n^*$ in the high-index waveguide.

The curves of Figs. 13-15 for TM(0) scattering from high-index waveguides are to be compared, first, with those of Figs. 10-12 for TE(0) scattering from similar waveguides, and second, with those of Figs. 7-9 for TM(0) scattering from low-index waveguides.

The TM(0) curves of Figs. 13 and 14 are seen to resemble closely their TE(0) counterparts in Figs. 10 and 11, with air radiation restricted to a narrow range of grating periods. For the high-index film on a conducting substrate, however, the TM(0) attenuation coefficients in Fig. 15 are nearly an order of magnitude greater than for TE(0) scattering in Fig. 12 via the smooth boundary (dashed curves), and unlike the TE(0) case the solid and dotted curves show that the TM(0) scattering via the corrugated boundary in both directions is nearly as large as that via the smooth boundary.

Comparison of the TM(0) curves in Figs. 13-15 with those in Figs. 7-9 shows 1) that the radiation loss coefficients of the high-index guide are about an order of magnitude greater than for the low-index guide, and 2) that there is not much difference between forward and backward TM scattering for the high-index guide.

The results of this section can be summarized as follows.

1) The radiation loss coefficients α are higher for substrate than for air radiation, and increase with the index difference at the corrugated boundary. A conducting medium behaves like a large index discontinuity at the film boundary.

2) As noted in [11], substrate radiation via a corrugated boundary in Case 2 varies sensitively with small changes in the grating period, film thickness, and effective mode index n^*; and the spacing between successive maxima and minima decreases with increasing film thickness. (This may present a difficulty if grating couplers of this type are to be used with multimode guides.) These interference effects are also present, but in lesser degree, in radiation coupling via the corrugated surface of a film deposited on a perfect conductor.

3) Except for substrate radiation in Case 3 and air radiation in Case 5, the TM loss coefficient is different in the forward and backward directions, whereas the TE loss coefficient is the same in both directions, for the same values of the propagation constants. In no case is the coupling efficiency appreciably larger in the backward direction. Therefore, unless the grating

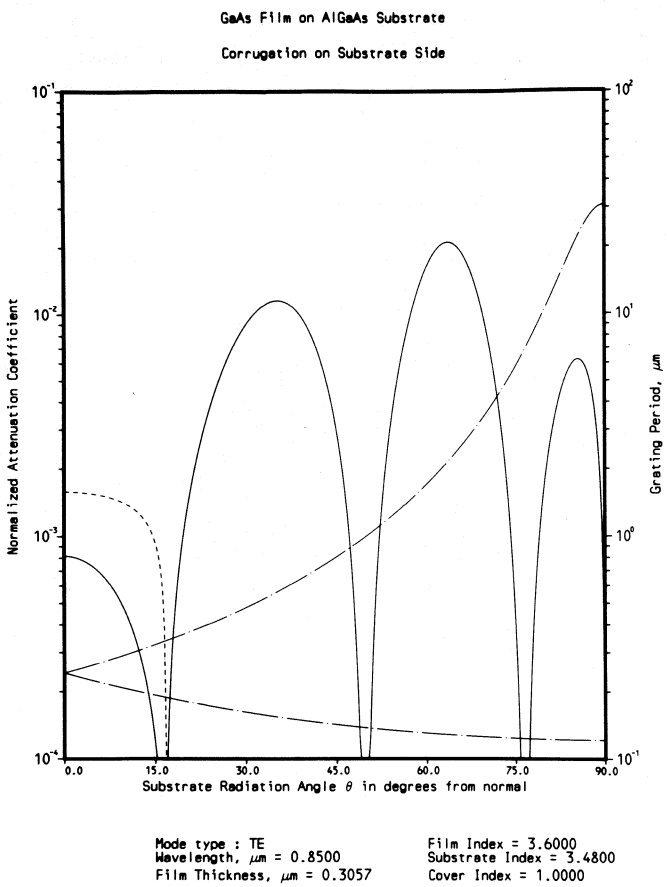


Fig. 11. Curves analogous to those of Fig. 4 for scattering from the TE(0) mode in a high-index waveguide, scaled as in Fig. 10.

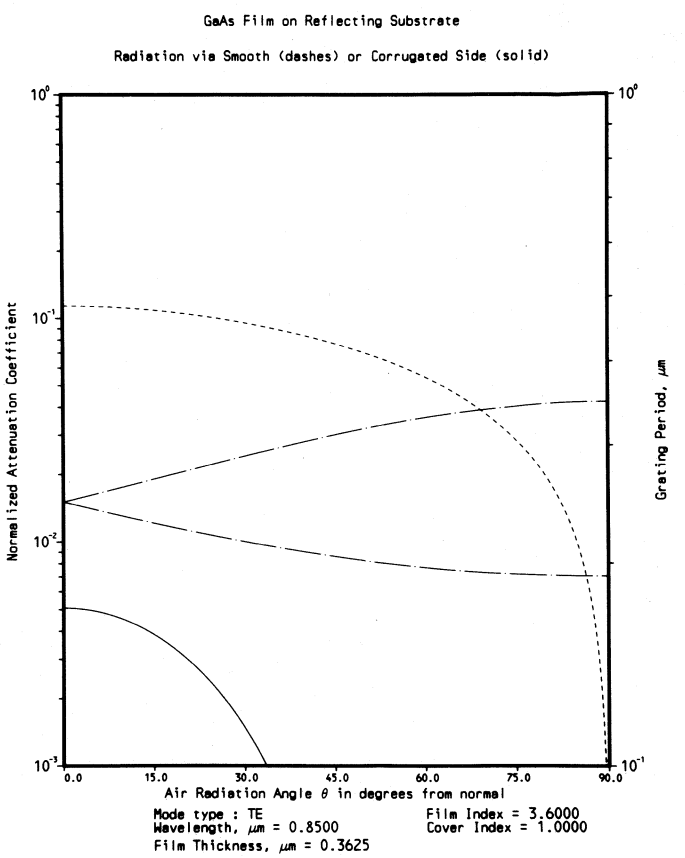


Fig. 12. Curves analogous to those of Fig. 6 for scattering from the TE(0) mode in a high-index film on a perfectly conducting substrate, scaled in thickness to provide the same ratio n_m^*/n_0 as in Fig. 6.

length required for input coupling is inconveniently large, or the corrugations so deep that higher diffraction orders become significant, it is usually advantageous to use the larger grating periods for forward diffraction, which are easier to fabricate.

4) For any given refractive index profile, the TE and TM loss coefficients tend to be about equal in magnitude in all but one case, that of a high-index film on a reflecting substrate, when the TM coefficient is considerably higher.

Conclusions

Kiselev [10] has solved the boundary-matching equations for an asymmetric slab waveguide with a shallow sinusoidally corrugated boundary to obtain explicit closed expressions for the TE radiation loss coefficients in a variety of waveguide geometries. For many practical applications in integrated optics, the Rayleigh assumption $K\sigma < 0.448$ justifying the boundary-matching procedure [4], [13] and the approximation $(k\sigma)^2 \ll 1$ of linear perturbation analysis are both satisfied. The expressions so derived, moreover, provide a good qualitative description of the first negative order scattering of such waveguides even beyond the limits of these assumptions.

We have extended Kiselev's equations to obtain the first-order TM radiation loss coefficients in each of the waveguide geometries treated, and satisfied outselves the both the TE and the TM expressions agree identically with those derived by coupled-mode theory [8], [9]. We have then sought to present the qualitative dependence of the loss coefficients for each geometry on the grating period, radiation angle, refractive index profile, and mode polarization in a number of plotted curves similar to those presented by Zlenko *et al.* [11] for TE modes in low-index guides. The TE and TM radiation loss coefficients are comparable to each other in most cases, but for a given set of propagation constants the TE coefficients are the same whether forward or backward, whereas the TM coefficients usually have directional asymmetry. The coefficients increase with an increase in the index difference at the corrugated boundary, all else equal, and display strong interference effects for substrate radiation via a corrugated boundary. The coefficient is largest for TM mode scattering by a high-index film deposited on a conducting substrate.

Appendix

Radiation Loss Coefficients for TE Modes [10], [11]

With $\psi = N_0^{(-1)}kh$, the TE propagation constant n_m^* given by (5) with $\kappa = 0$, and the TE effective film thickness h^* given by [12]

$$(kh^*)_{TE} = kh + \sum_{j=1,2} \frac{1}{\sqrt{(n_m^*)^2 - n_j^2}}, \tag{A1}$$

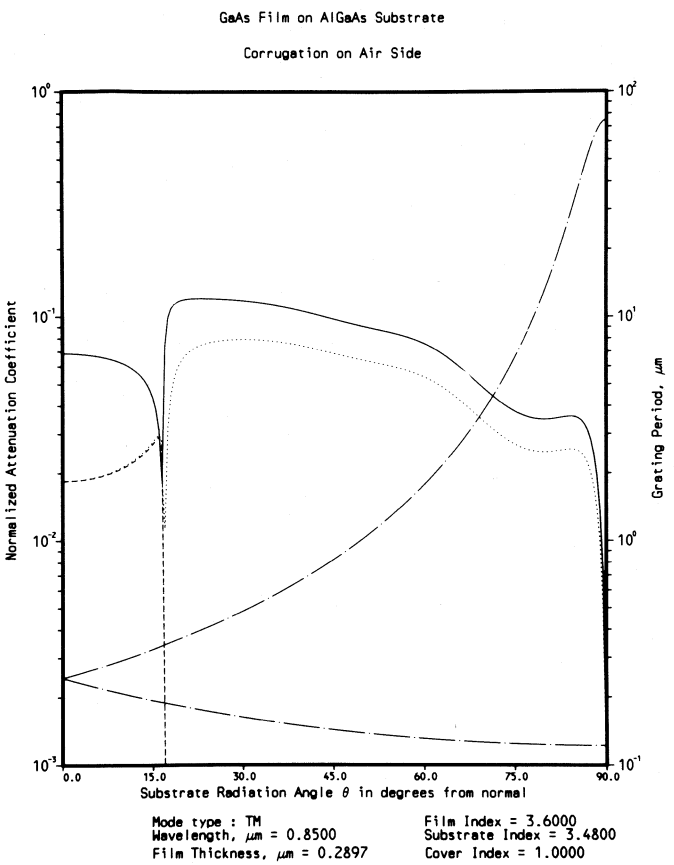


Fig. 13. Curves analogous to those of Fig. 7 for scattering from the TM(0) mode in a high-index, asymmetric-profile, waveguide with its film thickness scaled to provide the same ratio n_m^*/n_0 as in Fig. 7.

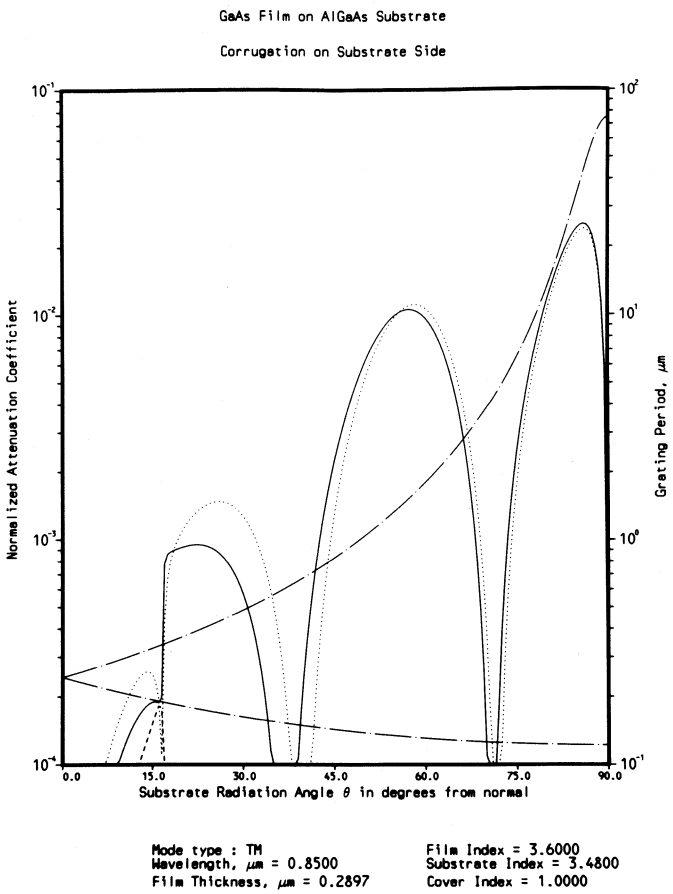


Fig. 14. Curves analogous to those of Fig. 8 for TM (0) mode scattering in the same high-index waveguide as in Fig. 13.

the TE loss coefficients for Cases 1-6 are listed here for comparison with their TM counterparts derived above.

Case 1: Corrugation on air (n_2) side: radiation into substrate (n_1) only [cf., (20)]:

$$\left(\frac{\alpha_{\text{air}}}{k}\right)_{\text{TE}}\left(\frac{2}{k\sigma}\right)^2 = \left[\frac{n_0^2 - n_m^{*2}}{n_m^* k h^*}\right] \frac{(n_0^2 - n_2^2)N_2^{(-1)}[(N_1^{(-1)})^2 + (n_0^2 - n_1^2)\cos^2\psi]}{\{[(N_0^{(-1)})^2 + N_1^{(-1)}N_2^{(-1)}]^2 - (n_0^2 - n_1^2)(n_0^2 - n_2^2)\cos^2\psi\}} \tag{A5}$$

$$\left(\frac{\alpha_{\text{sub}}}{k}\right)_{\text{TE}}\left(\frac{2}{k\sigma}\right)^2 = \left[\frac{n_0^2 - n_m^{*2}}{n_m^* k h^*}\right] \frac{N_1^{(-1)}(N_0^{(-1)})^2}{\{[(N_0^{(-1)})^2 + N_1^{(-1)}N_2^{(-1)}]^2 - (n_0^2 - n_1^2)(n_0^2 - n_2^2)\cos^2\psi\}}, \tag{A6}$$

$$\left(\frac{\alpha_1}{k}\right)_{\text{TE}}\left(\frac{2}{k\sigma}\right)^2 = \left[\frac{n_0^2 - n_m^{*2}}{n_m^* k h^*}\right] \cdot \frac{N_1^{(-1)}(N_0^{(-1)})^2}{[(N_0^{(-1)})^2 - (n_0^2 - n_1^2)\cos^2(\psi - \chi_2)]}, \tag{A2}$$

where $\chi_2 = \tan^{-1}(|N_2^{(-1)}|/N_0^{(-1)})$.

Case 2: Corrugation on substrate (n_1) side; radiation via corrugation into substrate [cf., (21)]:

$$\left(\frac{\alpha_2}{k}\right)_{\text{TE}}\left(\frac{2}{k\sigma}\right)^2 = \left[\frac{n_0^2 - n_m^{*2}}{n_m^* k h^*}\right] \cdot \frac{N_1^{(-1)}(n_0^2 - n_1^2)\cos^2(\psi - \chi_2)}{[(N_0^{(-1)})^2 - (n_0^2 - n_1^2)\cos^2(\psi - \chi_2)]} \tag{A3}$$

Case 3: Corrugation on air (n_2) side; radiation into both air (n_2) and substrate (n_1), [cf., (23)-(27)]:

$$\alpha_3 = \alpha_{\text{air}} + \alpha_{\text{sub}}, \tag{A4}$$

$$\left(\frac{P_2}{P_1}\right)_{\text{TE}} = \frac{\alpha_{\text{air}}}{\alpha_{\text{sub}}} = \frac{N_2^{(-1)}[(N_1^{(-1)})^2 + (n_0^2 - n_1^2)\cos^2\psi]}{N_1^{(-1)}(N_0^{(-1)})^2}. \tag{A7}$$

Case 4: Corrugation on substrate (n_1) side: radiation into both air (n_2) and substrate (n_1). For comparison with the TM expression (28), the ratio of TE irradiances has the form

$$\left(\frac{P_2}{P_1}\right)_{\text{TE}} = \frac{\alpha_{\text{air}}}{\alpha_{\text{sub}}} = \frac{N_2^{(-1)}(N_0^{(-1)})^2}{N_1^{(-1)}[(N_2^{(-1)})^2 + (n_0^2 - n_2^2)\cos^2\psi]}. \tag{A8}$$

Case 5: Reflecting film on corrugated waveguide surface; radiation into air (n_2) via smooth boundary [cf., (32)]:

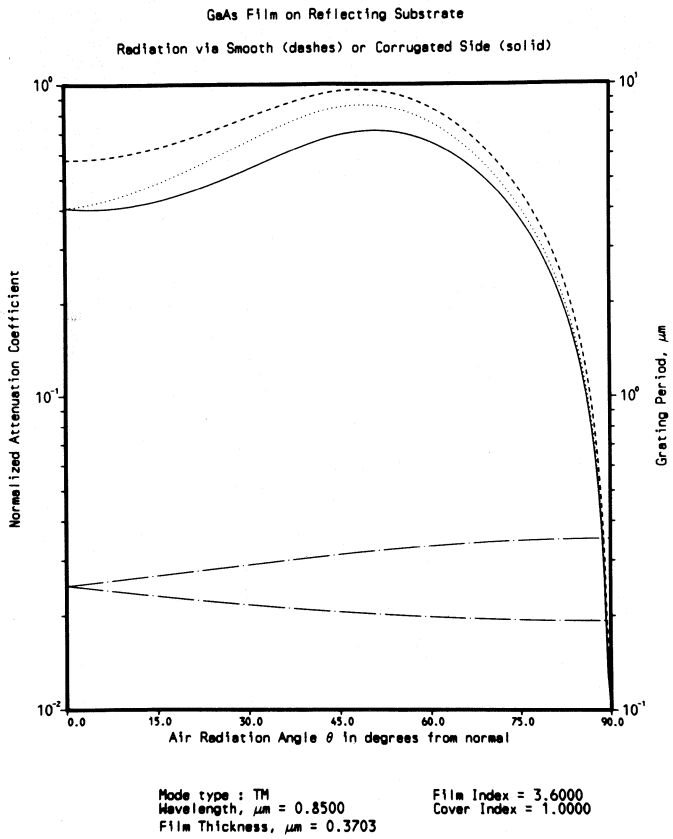


Fig. 15. Curves analogous to those of Fig. 9 for TM(0) mode scattering in a scaled-thickness high-index film on a perfectly conducting substrate.

$$\left(\frac{\alpha_5}{k}\right)_{\mathrm{TE}}\left(\frac{2}{k\sigma}\right)^2=\left[\frac{n_0^2-n_m^{*2}}{n_m^* kh^*}\right]\frac{N_2^{(-1)}(N_0^{(-1)})^2}{[(N_2^{(-1)})^2+(n_0^2-n_2^2)\cos^2\psi]}. \tag{A9}$$

Unlike Cases 1-4, we use here

$$(kh^*)_{\mathrm{TE}}=kh+\frac{1}{\sqrt{(n_m^*)^2-n_2^2}}. \tag{A10}$$

where n_m^* is a root of (31) with $\kappa = 0$.

Case 6: Reflecting film on smooth waveguide surface: radiation into air (n_2) via corrugated boundary [cf., (34)]:

$$\left(\frac{\alpha_6}{k}\right)_{\mathrm{TE}}\left(\frac{2}{k\sigma}\right)^2=\left[\frac{n_0^2-n_m^{*2}}{n_m^* kh^*}\right]\frac{(n_0^2-n_2^2)N_2^{(-1)}\sin^2\psi}{[(N_2^{(-1)})+(n_0^2-n_2^2)\cos^2\psi]} \tag{A11}$$

with h^* given by (A10), and n_m^* by (31) with $\kappa = 0$.

References

[1] M. L. Dakss, L. Kuhn, P. F. Heidrich, and B. A. Scott, "Grating coupler for excitation of optical guided waves in thin films," *Appl. Phys. Lett.*, vol. 16, pp. 523-525, June 1970.

[2] J. H. Harris, P. K. Winn, and D. G. Dalgoutte, "Theory and design of periodic couplers," *Appl. Opt.*, vol. 11, pp. 2234-1141, Oct. 1972.

[3] S. T. Peng, T. Tamir, and H. Bertoni, "Theory of periodic dielectric waveguides," *IEEE Trans. Microwave Theory Tech.*, vol. MTT-23, pp. 121-133, Jan. 1975.

[4] R. Petit, "Electromagnetic grating theories: Limitations and successes," *Nouv. Rev. Opt.*, vol. 6, pp. 129-135, 1975 (and bibliography).

[5] K. Ogawa, W. S. C. Chang, B. L. Sopori, and F. J. Rosenbaum, "A theoretical analysis of etched grating couplers for integrated optics," *IEEE J. Quantum Electron.*, vol. QE-9, pp. 29-42, Jan. 1973.

[6] C. C. Ghizoni, B. U. Chen, and C. L. Tang, "Theory and experiments on grating-couplers for thin-film waveguides," *IEEE J. Quantum Electron.*, vol. QE-12, pp. 69-73, Feb. 1976.

[7] W. Streifer, D. R. Scifres, and R. D. Burnham, "Analysis of grating-coupled radiation in GaAs:GaAlAs lasers and waveguides," *IEEE J. Quantum Electron.*, vol. QE-12, pp. 422-427, July 1976.

[8] D. Marcuse, *Light Transmission Optics.* New York: Van Nostrand-Reinhold, 1972.

[9] —, *Theory of Dielectric Optical Waveguides.* New York: Academic, 1974.

[10] V. A. Kiselev, "Diffraction coupling of radiation into a thin-film waveguide," *Sov. J. Quantum Electron.*, vol. 4, pp. 872-875, Jan. 1975.

[11] A. A. Zlenko, V. A. Kiselev, A. M. Prokhorov, A. A. Spikhal'skii, and V. A. Sychugov, "Emission of surface light waves from a corrugated part of a thin-film waveguide," *Sov. J. Quantum Electron.*, vol. 4, pp. 839-842, Jan. 1975.

[12] P. K. Tien and R. Ulrich, "Theory of prism-film coupler and thin-film light guides," *J. Opt. Soc. Am.*, vol. 60, pp. 1325-1337, Oct. 1970.

[13] R. F. Millar, "The Rayleigh hypothesis and a related least-squares solution to scattering problems for periodic surfaces and other scatterers," *Radio Sci.*, vol. 8, pp. 785-796, Aug.-Sept. 1973.

[14] H. Kogelnik and V. Ramaswamy, "Scaling rules for thin-film optical waveguides," *Appl. Opt.*, vol. 13, pp. 1857-1862, Aug. 1974.

The Efficiency of CO Vibrational Excitation in a Self-Sustained CW Glow Discharge

JOHN W. DAIBER, HERBERT M. THOMPSON, AND THEODORE J. FALK

Abstract—**The fraction of the electrical power which is placed into the vibrational energy mode of CO by a CW, aerodynamically stabilized, glow discharge has been found to decrease from 76 to 30 percent as the input energy increases from zero to 0.8 eV per CO molecule. The remaining energy is measured as being lost to gas heating within the discharge. In the first of the two experiments reported here, the vibrational energy was transferred into stream heating by collisions of the excited CO molecules with aluminum screening. The resulting heating was used to determine the energy in CO vibration. In the second experiment, the relative intensities of the spontaneous emission from the overtone bands of CO were used to determine the vibrational energy content of the CO. The results of the two measurements agreed well. The fraction of power entering vibration was found to depend on the energy loading per CO molecule, independent of He diluent concentration, total pressure, or nearness to the arcing limit. The maximum energy which can be stored in vibration for this self-sustained discharge was found to be approximately 0.25 eV/CO molecule.**

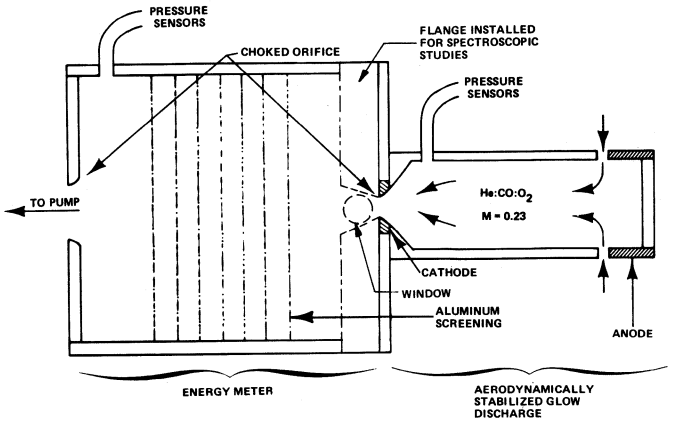


Fig. 1. Schematic diagram of the flow channels used in the experiments.

Introduction

ELECTRICAL CO lasers are of great interest because of the potentially high efficiency with which discharge power can be converted into optical power in the 5-μm spectral region. The objective of the program described in this paper was to establish the efficiency with which a discharge places energy into the vibrational manifold. The discharge chosen for study is a self-sustained one which has been demonstrated to be capable of continuous operation at pressures in excess of 1 atm [1].

The stabilization of the discharge is accomplished by a combination of radial gas injection through an annular slot adjacent to the anode [2] and a Universal Voltronics adjustable current limiter on the dc power supply [3]. The high radial velocity of the jet generates flow turbulence which increases the transport of both heat and charged particles. This helps to prevent the formation of high-temperature gas regions where high local E/N values lead to high ionization rates. The current limiter aids this process by preventing a surge in current when the incipient arcs form, thus giving time for the turbulence to dissipate the arcs. A discharge of this type has been used in the plenum of a supersonically cooled CO laser [1], [4] and as an excitation source for a CO laser with a coincident cavity and a precooled gas mixture [5].

Experimental Apparatus

A schematic diagram of the test apparatus is shown in Fig. 1. The discharge flow channel is on the right. The inner diameter was 1.5 in and the anode-to-cathode distance was 6 in. The annular gap width was typically 0.045 in and uniform around the periphery to an estimated accuracy of ±0.0005 in. With earlier versions of the anode it was found that nonuniformities in the gap spacing permitted arcs to occur at relatively low-power loadings. It was also found to be critical that the inner diameter of the discharge tube match the inner diameter of the annular injector. In one design the flow experienced a sudden doubling of diameter. This led to a large reduction in the maximum power loading, apparently caused by formation of a recirculation region with higher temperatures and locally high E/N values.

The cathode was of electrolytic copper and contained a rectangular orifice of dimensions 3 cm by 1.5 cm. The upstream portion was contoured to give a smooth entry flow. A Corning no. 9658 machinable ceramic disk was fitted over the cathode as a shield to limit the electrically active area to that washed by the accelerating subsonic flow.

The flow reached sonic velocity in the cathode-throat and then entered a channel constructed of acrylic tubing of 6.5-in inner diameter. In this channel the flow was subsonic but had a 1.763-in diameter choked orifice at the downstream end. Aluminum screening was cemented to acrylic hoops and placed inside the flow channel; this had the effect of reducing the diameter to 6 in. The total length of this flow channel was 8.625 in, and as many as 38 aluminum screens were fitted into it. The purpose of the screens was to catalyze the vibrational deactivation of the CO. This caused the energy originally stored in vibration to be transferred to stream heating. The amount of stream heating was inferred from the measured changes in gas pressure upstream of each choked orifice. The basis of this relationship is described in the next section. This flow channel is thus referred to as the vibrational energy meter.

For the overtone sidelight emissions experiments, a 2-in-thick

Manuscript received February 12, 1976; revised July 6, 1976. The experimental work was supported by the DARPA and the Air Force Weapons Laboratory (AFSC), and the interpretation of the data was carried out under a Calspan supported IR&D program.

The authors are with the Calspan Corporation, Buffalo, NY 14221.

aluminum flange was inserted between the cathode and the entrance to the energy meter. A flow channel was cut into the flange which resulted in a supersonic expansion. At the midpoint in this expansion, where the Mach number was 1.55, the spontaneous overtone emission spectrum was recorded through calcium fluoride viewing windows. The monochromator was a Jarrell-Ash $\frac{1}{4}$-m Ebert unit. A motor drive was used to turn the grating for automatic scanning. Exit optics consisted of an off-axis ellipsoidal mirror to reduce the slit height by five. This provided a better match of the area of the InSb chip in the detector to the optical system.

A photograph of the equipment used in the energy meter tests is shown in Fig. 2. The pressures were sensed with four MKS Instruments, Inc., Baratron diaphragm gauges. Two of these gauges measured the absolute pressures in the discharge and energy-meter flow channels. Two of these gauges were operated in the differential mode in which the reference side was open to a cylinder which had been filled to the flow-channel pressure when the discharge was still off. The output of these gauges was thus the increase in pressure within the discharge or energy-meter flow channels when the discharge was on.

A typical run record is shown in Fig. 3. The starting spike on the differential pressure sensor records is due to the filling of the reference volumes. The variations in the power input can be seen to be faithfully followed in the differential-pressure record for the discharge. The differential pressure in the energy meter lags a slight amount due to the time required for heating the aluminum screens. The bottom trace is the applied voltage; it remains nearly constant during a run. The power input is varied by changing the excitation current to the saturable reactor which serves as a limiter for the alternating current entering the power supply. There is no resistor in series with the discharge. The current limiter permits the discharge to operate stably even when the discharge resistance is negative. This run lasted for nearly 2 min; longer run times of up to 6 min were required to record the overtone spectrum.

Discharge Data

A summary of the discharge performance data taken at the maximum power loading condition is given in Table I. These data were taken at a discharge current setting just below that for which a large number of incipient arcs were present. The E/N ratio increased slightly with increasing input power. This is as expected because the fraction of input power going into ionization increases with E/N. Higher input powers imply a higher discharge current and consequently require a higher electron density. The lowest data trace in Fig. 3 shows the variation of the discharge voltage during a run. At low input powers the voltage increased with increasing current. A current was then reached for which the voltage decreased with further increase in the current. The number density of gas molecules is, at constant flow rate, proportional to the inverse square root of pressure. The pressure was increasing because of discharge heating, and thus the number density of gas molecules was decreasing. This lowering of number density was greater than the lowering of the electric field in the discharge so that the E/N ratio increased as the current increased. The threshold

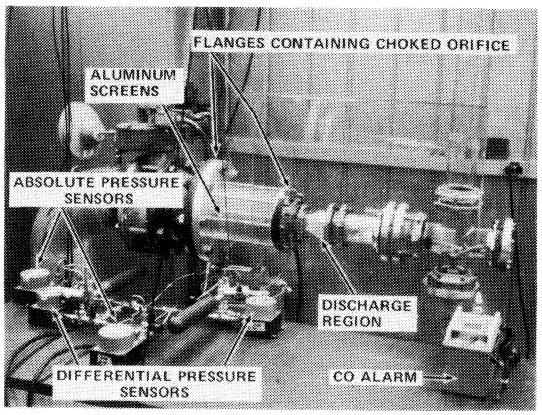


Fig. 2. Photograph of the test equipment.

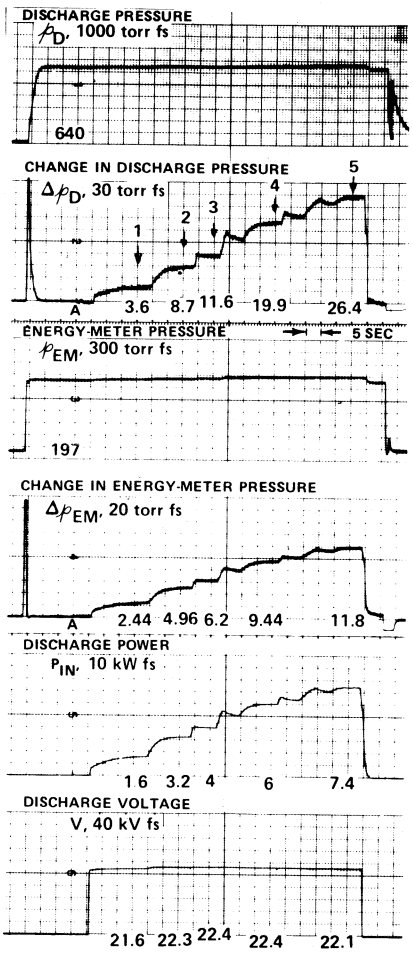


Fig. 3. Typical run records obtained with the energy meter. The number of screens is 24 for this run. The notation fs represents full scale. Time increases from left to right. At the time A the reference side of the differential pressure gauges was isolated. The gas mixture is 98.33 percent He, 1.61 percent CO, and 0.06 percent O_2. Run number 1-6-10.

E/N ratio increased linearly with the CO molar fraction X_{CO} over the range of 0.02-0.12; a fit to these data yielded $(0.07\ X_{CO} + 0.55) \times 10^{-16}$ V/cm^2. The E/N ratio at the arcing threshold also had a linear dependency on CO molar fraction; a fit to these data yielded $(0.08\ X_{CO} + 0.65) \times 10^{-16}$ V/cm^2.

The specific energy is defined as the total power deposited

TABLE I
SUMMARY OF DISCHARGE PERFORMANCE

CO MOLE FRACTION, %	DISCHARGE PRESSURE, torr	MAXIMUM POWER LOADING			
		INPUT POWER, kW	ENERGY INPUT, eV/CO	E/N RATIO, 10^{-16} V-cm^2	SPECIFIC ENERGY, kJ/lb
2.0	345	4.9	0.56	0.75	109
2.9	355	6.1	0.46	0.85	124
4.6	376	6.1	0.29	0.97	112
6.2	375	6.0	0.23	1.10	111
7.6	368	6.2	0.20	1.16	114
10.0	344	6.2	0.17	1.34	113
11.9	355	5.8	0.13	1.44	100
1.0	635	7.2	0.88	0.57	88
1.6	640	7.4	0.55	0.66	88
2.5	650	8.0	0.38	0.77	93
3.6	664	8.1	0.27	0.85	88
4.6	670	7.8	0.21	0.94	81
5.4	680	7.7	0.18	1.01	78

Note: The electrical operating parameters are such that the discharge could operate continuously; however, a slight increase in current would cause immediate constriction into an arc.

in the plasma divided by the mass flow of the gas mixture. A more meaningful correlation parameter, however, has been found to be the input energy per CO molecule. This quantity will be used as the independent variable for describing the data. The maximum input energy per molecule which could be added to the plasma before arcing occurred decreased with increasing CO partial pressure. The cause of this arcing or the dependence of the arc limit on discharge tube diameter, electrode spacing, flow mixers [5], or preionization [6] has not been investigated. It was observed that the power loading for which the glow discharge would constrict into an arc was greatly increased if oxygen was added to the flow. The maximum power loading was not critically dependent on the actual oxygen flow rate. A ratio of O_2 to CO molar fractions of 4.5 percent appeared to be nearly best and was, therefore, used for all the runs discussed in this paper. There also were random "bad bottles" of CO which had substantially lower arcing limits. This difficulty was overcome by passing the CO through an uncooled trap filled with 0.25-in-diam Alcoa H-151 activated alumina spheres [7] which had been previously conditioned by heating and pumping to remove absorbed water vapor.

Flow Heating Measurement

The heating of the flow which occurs in the discharge region and within the energy meter establishes the efficiency of the glow discharge. The power, P, which goes into heating is related to the change in temperature by

$$P = P_0\, \Delta T/T_S,$$

where P_0 is given by

$$P_0 = \dot{m}_f\, c_p\, T_S.$$

Here c_p is the specific heat at constant pressure, and T_S is the original stagnation temperature.

The changes in gas temperature within the discharge tube and energy meter can be related to the corresponding pressure changes through the conservation of mass equation. The mass flow, $\dot{m}_f$, through a choked orifice can be written [8]

$$\dot{m}_f = \rho^*\, u^*\, A^*$$

where the asterisk represents the evaluation of the density ρ, velocity u, and area A at the sonic point. The velocity at the throat is equal, by definition, to the local sound speed which is proportional to the square root of the local temperature. Using the isentropic relations, the density and temperature at the throat can be directly related to their values in the plenum chamber. The density is also proportional to the ratio of pressure to temperature. Combining these relations, it can be shown that

$$\dot{m}_f \propto p/T^{1/2}$$

where the proportionality constant depends on the specific heat ratio and the throat area.

The discharge tube and energy meter each pass a fixed mass flow and have a downstream choked orifice. Thus a change in temperature due to heat addition causes a pressure change which is proportional to the square root of the temperature change; this assumes that the heating is not enough to cause changes in gas composition and thus the specific heat ratio.

The change in pressure in the discharge tube when the discharge is turned on depends on the direct heating of the gas by the current. This is regarded as a loss to the laser not only because that energy is not available for optical extraction but also because the fraction of vibrational energy which is theoretically extractable from a CO laser decreases as the temperature increases [9]. The magnitude of this heating is seen to be given by

$$\Delta T_D/T_S = (1 + \Delta p_D/p_D)^2 - 1$$

where Δp_D is the measured change in discharge pressure p_D when the discharge is turned on.

The pressure change in the downstream flow channel is caused both by pressure changes in the discharge tube and by the relaxation of internal energy within the energy meter. Thus heating of the flow in the energy meter results in a temperature change given by

$$\Delta T_{EM}/T_S = (1 + \Delta p_{EM}/p_{EM})^2 - (1 + \Delta p_D/p_D)^2$$

from which the amount of the discharge power which has gone into exciting long-lived internal energy modes of CO can be found.

There are two internal energy modes which could have significant excitation at the E/N ratios typical of the operating conditions for this discharge, namely, vibration and electronic. Calculations were made of the relative loss process for electrons in CO-He plasmas using a discharge kinetic code [9]. The calculated energy transferred to CO vibration is of the order of eight times that transferred to the CO electronic states. The vibration-to-translation relaxation time, which is controlled by CO collisions with He, is at least 3 ms for the operating conditions [10]; this is more than four times the residence time of the gas within the discharge tube. The deactivation rate of electronically excited CO in the $a\ ^3\Pi$ state by ground state CO is fast [11], [12], requiring at most 50 ns. Consequently, nearly all of the internal energy released in the energy meter should be that which was originally stored in vibration.

Since the V-T relaxation rate for CO in helium is slow, a long flow channel would have been required to ensure complete relaxation of the vibrational energy within the energy meter. Such a long flow channel would have been subject to

heat losses to the room which could have masked the temperature increase. Therefore, aluminum screening was installed in the energy meter to shorten the flow length required for vibrational relaxation. The excited molecules transferred their energy to the screens which in turn came into thermal equilibrium with the flow.

Energy-Meter Operation

The operation of the energy meter has been modeled by considering each screen to relax a set fraction of the vibrational energy remaining in the flow as it enters that screen. The increase in translational energy is then given by

$$dE/dN = K(E_0 - E)\,\dot{n}_S/\dot{n}_{CO}$$

which has the solution

$$E/E_I = \{1 - \exp\,[-(KN\dot{n}_S/\dot{n}_{CO})]\,\}E_0/E_I \qquad (1)$$

where K is the probability that a CO molecule will be deexcited upon collision with a screen, N is the number of screens, E_0 is the initial energy in vibration, and E_I is the energy input by the discharge.

The rate at which CO molecules collide with the screen surface, $\dot{n}_S$, is given by [13]

$$\dot{n}_S = n_{CO}\,\bar{c}\,A_W/4$$

where n_{CO} is the number density of CO molecules, $\bar{c}$ is the mean velocity $(8kT/\pi m_{CO})^{1/2}$, and A_W is the total surface area of the wires $4\pi RA/S$. Here R is the wire radius, A is the flow channel area, S is the wire spacing, and m_{CO} is the mass of a CO molecule. The rate at which CO molecules pass through the screen, $\dot{n}_{CO}$, is given by

$$\dot{n}_{CO} = n_{CO}\,aMA$$

where a is the sound speed $(\gamma kT/m)^{1/2}$, M is the flow Mach number, m is the average mass of a gas particle, and γ is the specific heat ratio. The ratio of these fluxes is then

$$\dot{n}_S/\dot{n}_{CO} = (R/MS)\,(8\pi m/\gamma m_{CO})^{1/2}.$$

For the present apparatus, R is 0.013 cm, M is 0.05, S is 0.15 cm, m is 5.56, and γ is 1.64; therefore, $\dot{n}_S/\dot{n}_{CO}$ is 3.0.

The probability that a highly excited CO molecule will be deexcited upon collision with oxidized aluminum screening has not been previously measured. An estimate was made using the equation

$$K^{CO}_{Al_2O_3} = K^{CO}_{Pyrex}\,K^{N_2}_{Al_2O_3}/K^{N_2}_{Pyrex}$$

where the superscript denotes the gas and the subscript the surface. Using the values [14] $K^{N_2}_{Al_2O_3}$ equals 0.0011, K^{CO}_{Pyrex} equals 0.04, and $K^{N_2}_{Pyrex}$ equals 0.0006, an anticipated value for $K^{CO}_{Al_2O_3}$ is 0.07. The fit of (1) to the experimental data, to be shown later in Fig. 5, gives a wall deactivation coefficient for CO on Al_2O_3 of 0.03, with an estimated uncertainty of ±50 percent. This value is in reasonable agreement with the extrapolation of the prior data.

Two additional estimates were made to ensure the proper operation of the energy meter; first, that all the molecules were influenced by the screens, and, second, that the screens could come quickly into thermal equilibrium with the flow. The total flow cross section of the boundary layer on all the wires was calculated by using the growth rate for a laminar boundary layer on a flat plate of length equal to the wire radius. This area was more than half the total flow channel area. Thus, if the species boundary layer thickness is comparable to the viscous boundary layer thickness, then at least half the total number of CO molecules would be influenced by the surface of each screen. Since a minimum of 13 screens were used, it is reasonable to assume that all the molecules have many opportunities to collide with the screens.

The energy meter is designed to operate in a manner such that all of the vibrational energy entering the meter leaves in the form of translational energy. After a relatively short transient period required to heat the screens to the new gas temperature, the net heat transfer rate to the screen (excluding the effects of heat conduction to the flow channel walls) should approach zero. The duration of this transient was estimated by dividing the heat required to bring the screens to final temperature by the flux of vibrational energy into the energy meter. For typical operating conditions with 38 screens, the estimated response time is 2 s. This agrees with the relative response of the sensor measuring the differential pressure in the energy meter, shown in Fig. 3, with changes in the discharge power loading.

A source of error in the data is the heating of the flow channel walls by the gas stream. The mass of these walls is much greater than that of the screens; consequently, it is not feasible to permit the entire flow channel to approach thermal equilibrium with the gas. Thermocouples were embedded in the outer wall of the energy-meter flow channel. It was found that the wall temperature decreased when the gas flow was turned on. When the discharge was turned on, the wall temperature would slowly rise. Temperature rise over ambient exceeded 14°C at the higher power loadings when there were no screens in the energy meter, and exceeded 20°C when the screens were in place. In the no-screen runs, the heat loss exceeded the gas phase V-T heating and a negative energy in vibration was computed. This loss was around 5 percent of the input power (see Fig. 5).

Heat loss by the flow channel to the surroundings is primarily by convection, which is dependent on the temperature difference between the channel and the air. Therefore, the heat loss to the surroundings when the screens were in place was estimated by increasing the no-screen loss rate by the ratio of the wall temperature differences measured with the screens to that measured without the screens. Thus the measured energy in vibration was increased by 7 percent to account for the wall losses.

Energy-Meter Data

From the differential-pressure measurements, the fractions of input power entering translation and vibration were calculated. The reduced data for the run shown in Fig. 3 are given in Fig. 4. For each run it was found that the fraction of power entering vibration decreased, and correspondingly, the fraction of power going into translation increased with increasing input power up to the arcing limit.

The data from each run were interpolated to give the energy in vibration and translation at fixed input energy per CO

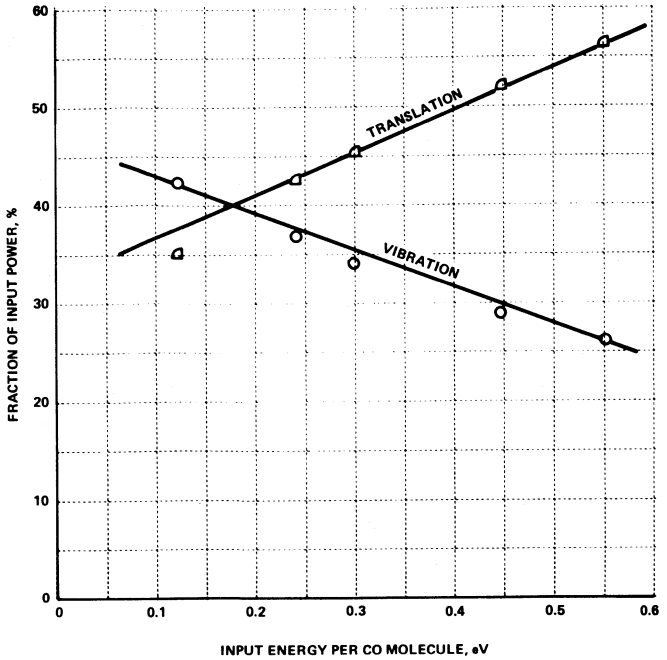


Fig. 4. Variation of the measured energy in vibration and translation with input energy. The CO molar fraction is 1.61 percent. The total discharge pressure is 640 torr. Run number 1-6-10.

molecule. These data were then plotted against the number of screens in the energy meter. All of the data for a single input energy were found to collapse onto a single curve independent of CO fraction and total pressure regardless of how close this loading is to the arcing limit. A plot of these data for an input energy per CO molecule of 0.3 eV is shown in Fig. 5.

From Fig. 5, it may be seen that the energy transferred to the flow within the energy meter increases with the number of screens. The curve through the energy-meter data is the fit of (1) referred to earlier. If the vibrational energy is extrapolated to the infinite screen limit and an additional 7 percent of input energy is added to vibration to correct for heat loss through the flow channel walls, then 93 percent of the input energy is accounted for. The remaining energy is assumed to be lost by wall and cathode heating in the discharge. A summary of the fraction of input energy entering vibration versus the total input energy is given in Table II. The vibrational energy given in this table has been corrected to the infinite screen limit and for the 7 percent wall loss.

Spectroscopic Measurements

A different technique for the measurement of the energy stored in vibration is to determine the population of molecules in each vibrational level and then sum the product of population and excitation energy. This was implemented by recording the first overtone spectrum emitted by CO at a station in a supersonic flow channel which was 1 in downstream of the cathode-throat. A computer generated spectrum was then compared to the measured spectrum [15]. Since the instrument response and slit function can be measured and calculated values of the relative transition probabilities are available [16], only the relative populations need be adjusted until a match occurs.

To obtain the relative spectral response of the system, a flat

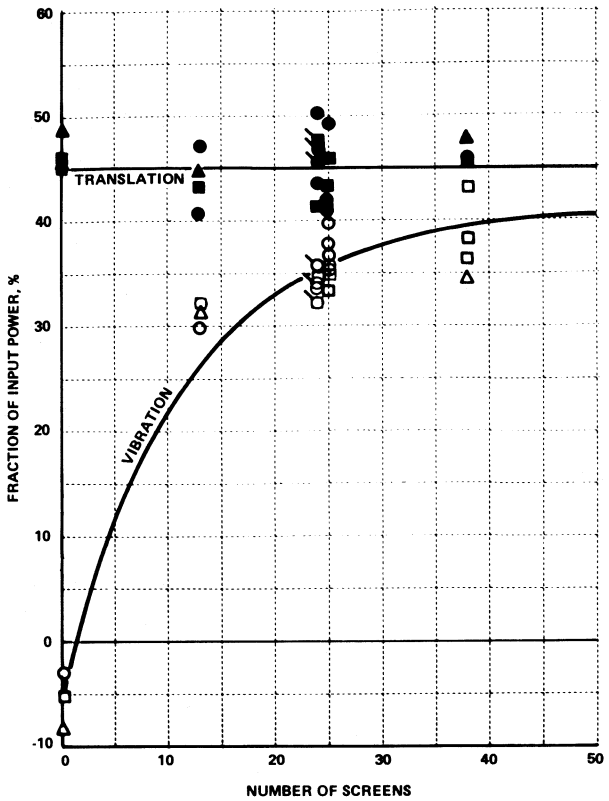


Fig. 5. Variation of vibrational (open symbols) and thermal (filled symbols) energy with number of screens in the energy meter. The data are all for a fixed input energy of 0.3 eV per CO molecule. The data symbol indicates whether the CO molar fraction is 1 to 3 percent, ○; 3 to 5 percent, □; or 5 to 7 percent, △. The total pressure was near 350 torr for the unflagged data and 650 torr for the flagged data.

TABLE II
Distribution of Electrical Energy Within the Discharge

E_I INPUT ENERGY, eV/CO	FRACTION INTO TRANSLATION, %	FRACTION INTO WALLS, %	E_V/E_I, FRACTION INTO VIBRATION, %	E_V, VIBRATIONAL ENERGY, eV/CO
0.05	24	4	72	0.036
0.1	30	6	64	0.064
0.2	39	5	56	0.112
0.3	45	7	48	0.144
0.4	51	6	43	0.172
0.5	56	5	39	0.195
0.6	59	6	35	0.210
0.7	63	6	31	0.217
0.8	66	6	28	0.224

Note: The measured vibrational energy fraction has been increased by 7 percent to correct for all wall losses. An average of 5.5 percent of input energy is unaccounted for and has been assumed to be loss in cathode and discharge wall heating.

mirror was inserted between the spherical mirror and the flow channel. A blackbody source (IR Industries, Inc.) was then placed at the image of the spectrometer entrance slit. Scans were made at several blackbody temperatures. An order-sorting filter was used in these runs to prevent the detector from viewing lower wavelength second-order radiation. The transmittance of the filter was separately measured and was subtracted from the response. Such a filter is not needed during the runs with CO and is, in fact, detrimental since it acts as a 300 K source and will swamp the weak overtone radiation. Water vapor also absorbs in the wavelength region of interest; however, all runs, CO as well as blackbody, were made in a single afternoon. It was assumed that the concen-

tration of water vapor did not change in this time, and the effect of water vapor was, therefore, left in the instrument response curve.

The overtone spectrum was selected instead of the fundamental spectrum because of self-absorption by molecules in the lower levels. The probability of absorption in the overtone is several factors of 10 less than for the fundamental. This reduction is also reflected in lower emission intensities, but this can be compensated for by using a sensitive detection technique. To verify that the overtone spectrum was indeed optically thin, a spherical mirror was placed on the back side of the flow channel to reimage the radiation back on itself. The measured transmittance of the calcium fluoride windows is 93 percent. Thus the radiation signal should have increased by 1.86 when the backside mirror was exposed. The measured increase in signal was 1.81. Because of the difficulties in alignment and the less than perfect reflectivity of the backing mirror, this value is taken as confirmation that the gas is optically thin.

Spectroscopic Data

The emission spectra and the computed spectra were carefully matched by iterating the relative populations in the levels $V = 2$ and greater. The noise level in the spectra and the quality of the match are similar to those shown in [15]. The populations of the levels $V = 2$, 3, 4, and 5 were fitted with a V-V dominated distribution [17] of the form

$$\ln (N_V/N_0) = -V(\omega_e - 2\omega_e x_e)/kT_V + V(V-1)\omega_e x_e/kT$$

where T is the translational/rotational temperature of gas at the measuring station. This analytical expression predicts accurately the relative populations of the lower vibrational levels but deviates from the predictions of more detailed calculations when the "plateau region" of the distribution is reached at higher vibrational levels. It should be accurate in the range in which it has been applied here.

The vibrational temperature, T_V, was varied until a satisfactory fit was obtained. The relative populations of the $V = 0$ and 1 levels were then obtained by solution of this equation. The extrapolation procedure was required since the overtone spectra say nothing about the populations in the lowest two levels. The error in these populations due to uncertainty in the matching procedure is at most a few percent.

The population data are summarized in Fig. 6. The populations are shown by continuous curves. These three runs resulted in an efficiency for the conversion of input energy into vibrational energy of 70 percent at 0.11 eV/CO, 65 percent at 0.18 eV/CO, and 41 percent at 0.46 eV/CO. The corresponding fractions of the input energy which went directly into heating of the gas stream within the discharge were 32 percent, 36 percent, and 51 percent, respectively. These two energy terms sum to approximately 100 percent of the input energy.

A summary of the vibrational energies determined from the energy-meter and spectroscopic data is shown in Fig. 7. The two approaches are totally independent but give nearly identical results. The estimated uncertainity in the excitation efficiency inferred from the spectroscopic data is ±5 percent. The major source of error is the extrapolation to determine the populations in the ground and first excited states. The energy-meter data suffer from uncertainity due to wall heat loss, extrapolation to the limit of complete vibrational relaxa-

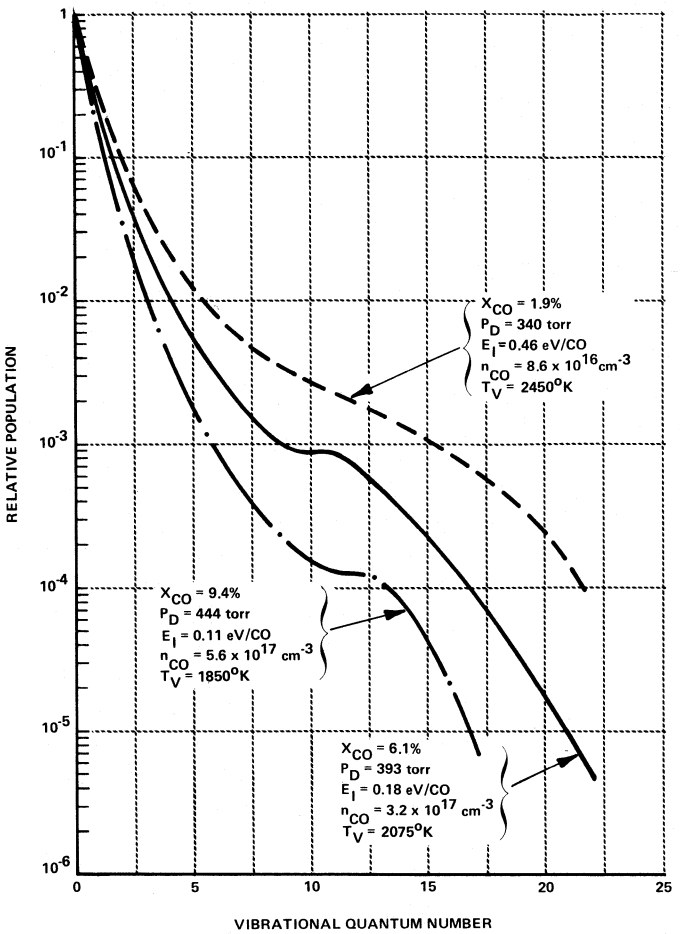


Fig. 6. Populations of the vibrational energy levels as inferred from the spectrum matching. With the curve from each run is shown the CO molar fraction, the total discharge pressure, the total input energy, the density of CO in the supersonic flow and the vibrational temperature used to extrapolate to the $V = 0$ and 1 populations. The translational temperature in the supersonic flow was 180 K for all three runs.

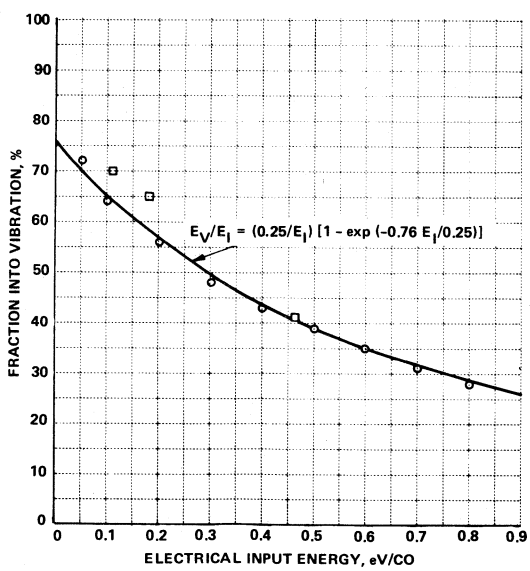


Fig. 7. Discharge performance correlation. The energy meter data are shown as ○ and the spectroscopic data are shown as □. The fit to the data is (3) given in the text.

tion, and energy storage in other modes. These are estimated to cause an error in the excitation efficiency of ±3 percent. The agreement in the vibrational energies as inferred from the two techniques is taken as confirmation that the energy meter is operating as anticipated.

Correlation Model

The variation of vibrational energy with input energy, which is shown in Fig. 7, is indicative of a loss process which has a rate that increases not only with the input energy but also with the energy in vibration. One such process involves the transfer of energy from vibration to the free electrons by superelastic collisions [18]. The importance of these collisions increases as more energy is stored in vibration and as the number of free electrons increases. Numerical calculations were made utilizing an electron kinetics code [9] which included electron energy loss to vibration and the reverse of these rates as found by detailed balancing, but did not include the affect of these superelastic collisions on the electron distribution function. The elastic and rotational processes in this code could not account for the observed fraction of input power which went into the translational heating of the discharge. However, good agreement was obtained after the code was modified to include as heating all of the power which flowed from CO back to the electrons via superelastic collisions [19]. It is possible that the electrons, which gained energy by superelastic collision, were significantly more likely to reach the energy required to excite CO electronically. The electronically excited CO then rapidly thermalized in CO–CO collisions.

A second process involves the creation of an impurity within the discharge which is a rapid relaxer of CO. A possible species is CO_2 [20]. It is plausible that the density of CO_2 would vary with the input power and thus with the electron density. The loss term, which could characterize either process, is then $BE_V n_e$. The initial rate at which the electrons pump energy into the vibrational energy is then

$$dE_V/dt = An_e - BE_V n_e.$$

The initial condition on the vibrational energy per CO molecule is that E_V is zero at t equals zero. At late times a steady state is reached. The energy in vibration at this time is denoted by E_{V_∞}. The solution of the differential equation for the vibrational energy for a fixed power loading, i.e., constant n_e, is then

$$E_V = E_{V_\infty}[1 - \exp(-An_e t/E_{V_\infty})].$$

The total energy deposited into the plasma during a molecule's residence time in the discharge can be expressed as

$$E_I = \kappa t$$

where κ is the energy addition rate. At early times the fraction of electron energy going into vibration, η, is given by

$$\eta = An_e/\kappa = An_e t/E_I.$$

Consequently, the fraction of the input energy going into vibration can be expressed as

$$E_V/E_I = [1 - \exp(-\eta E_I/E_{V_\infty})]E_{V_\infty}/E_I. \quad (2)$$

The spectroscopic and energy-meter data shown in Fig. 7 were used to determine the constants in (2). The best fit was obtained with η equaling 76 percent and E_{V_∞} equaling 0.25 eV/CO molecule. This results in the correlation equation

$$E_V/E_I = (0.25/E_I)[1 - \exp(-3.04\,E_I)]E_{V_\infty}/E_I \quad (3)$$

which is plotted in Fig. 7. This equation can be used to model discharge performance at other stable operating conditions. It is estimated that the value of the limiting energy in vibration could be in error by as much as ±20 percent because of the uncertainties in the data.

The existence of the limiting energy in vibration implies that if the same current could be passed through a longer discharge tube, then the maximum specific power of the laser device would reach 0.25 eV in vibration per CO molecule. Of course, the electrical efficiency would then be very small. Higher electrical efficiencies occur with shorter discharge tubes, but then the specific energy is low. Changing the discharge tube diameter alters the arcing limit; and this effect, if favorable, may allow more energy to be placed into the discharge and hence into the vibrational energy mode. Another method of placing more energy into vibration might be to extract it by stimulated emission within the discharge and not permit inefficiencies to limit the energy loading. This requires a coincident laser cavity and, if the lasing process is to be efficient, precooling of the gas mixture. The disadvantage of this approach is that the flow medium may not be sufficiently uniform to permit extraction of a high-brightness beam because of gradients created from discharge heating and because of turbulence generated from the transverse gas injection.

Summary

A vibrational energy diagnostic has been developed which can be used to infer the efficiency of a subsonic discharge for adding energy into the vibrational mode of a molecule. The accuracy of this diagnostic is supported by comparison with the vibrational energy determined from measurements of the overtone radiation. The efficiency with which electrical energy is converted into CO vibrational energy by an aerodynamically stabilized, self-sustained glow discharge has been found to be equal to 76 percent at vanishingly small power loadings. The efficiency decreases with increasing power loadings. The electrical-vibrational efficiency of the discharge was modeled, and from this the maximum energy which can be stored in vibration was found to be 0.25 eV per CO molecule. Future studies should be directed at elucidating the relaxant responsible for limiting the total energy storable in the CO vibrational manifold by the discharge.

Acknowledgment

The authors would like to acknowledge many informative conversations with Dr. C. E. Treanor, Dr. J. W. Rich, and Dr. J. A. Lordi.

References

[1] J. W. Rich, R. C. Bergman, and J. A. Lordi, "Electrically excited, supersonic flow carbon monoxide laser," *AIAA J.*, vol. 13, pp. 95–100, 1975.
[2] R. McLeary and W. E. K. Gibbs, "CW CO_2 laser at atmospheric pressure," *IEEE J. Quantum Electron.*, vol. QE-9, pp. 828–833, 1973.
[3] R. Lee, *Electronic Transformers and Circuits*. New York: Wiley, 1955, ch. 9, Magnetic Amplifiers, p. 259.

[4] J. W. Daiber and H. M. Thompson, "Performance of a large, CW, preexcited CO supersonic laser," *IEEE J. Quantum Electron.*, vol. QE-13, Jan. 1977, to be published.
[5] J. W. Rich and R. C. Bergman, "Demonstration of 500 W to 1 kW CO laser," Rep. AFAL-TR-74-302, Dec. 1974, unpublished.
[6] R. McLeary, P. J. Beckwith, and W. E. K. Gibbs, "Uniform continuous discharges and CO_2-laser action at atmospheric pressure by plasma injection," *IEEE J. Quantum Electron.*, vol. QE-10, pp. 649–651, 1974.
[7] R. E. Center, "High-pressure electrical CO laser," *IEEE J. Quantum Electron.*, vol. QE-10, pp. 208–212, 1974.
[8] A. H. Shapiro, *The Dynamics and Thermodynamics of Compressible Fluid Flow*. New York: Ronald Press Co., 1954.
[9] M. L. Hamilton, J. J. Kennedy, and T. J. Falk, "CO laser research program, Phase I Final Report," Rep. AFWL-TR-73-158, Sept. 1973, unpublished.
[10] D. J. Miller and R. C. Millikan, "Vibrational relaxation of carbon monoxide by hydrogen and helium down to 100°K," *J. Chem. Phys.*, vol. 53, pp. 3384–3385, 1970.
[11] G. W. Taylor and D. W. Setser, "Quenching rate constants for CO ($a\ ^3\Pi; v' = 0, 1, 2$)," *J. Chem. Phys.*, vol. 58, pp. 4840–4851, 1973.
[12] T. S. Wauchop and H. P. Broida, "Lifetime and quenching of CO ($a\ ^3\Pi$) produced by recombination of CO_2 ions in a helium afterglow," *J. Chem. Phys.*, vol. 56, pp. 330–332, 1972.
[13] J. Jeans, *An Introduction to the Kinetic Theory of Gases*. New York: Cambridge Univ. Press, 1952, p. 58.
[14] G. Black, H. Wise, S. Schechter, and R. L. Sharpless, "Measurements of vibrationally excited molecules by Raman scattering. II. Surface deactivation of vibrationally excited N_2," *J. Chem. Phys.*, vol. 60, pp. 3526–3536, 1974.
[15] J. W. Rich, R. C. Bergman, and J. W. Raymonda, "Vibration-vibration pumping of carbon monoxide initiated by an optical source," *Appl. Phys. Lett.*, vol. 27, pp. 656–658, 1975.
[16] L. A. Young and W. J. Eachus, "Dipole moment function and vibration-rotation matrix elements for CO," *J. Chem. Phys.*, vol. 44, pp. 4195–4206, 1966.
[17] C. E. Treanor, J. W. Rich, and R. G. Rehm, "Vibrational relaxation of anharmonic oscillators with exchange-dominated collisions," *J. Chem. Phys.*, vol. 48, pp. 1798–1807, 1968.
[18] J. A. Lordi, T. J. Falk, and J. W. Rich, "Analytical studies of the kinetics of electrically excited continuously operating CO flow lasers," AIAA Paper 74-563, June 17–19, 1974.
[19] J. A. Lordi, Private communication.
[20] The possibility that CO_2 could be important was pointed out to us by one of the reviewers of this manuscript.

Gas Additive Effects in CO Chemical Lasers

WILLIAM Q. JEFFERS, MEMBER, IEEE, CHARLES E. WISWALL, AND HARRIS Y. AGENO

Abstract—**The effects of gas additives on optical gain of the CO chemical laser (CL) have been measured for N_2, SO_2, H_2, HF, CF_4, CCl_2F_2, CO, OCS, N_2O, and NO. One of the more unusual additives, NO, has been used to control the output spectrum of a laser oscillator by controlled sequential quenching of the high bands. The significance of these results for total power enhancement, output spectrum control, and alternate diluent use is discussed.**

I. Introduction

MOST of the chemical kinetics and collisional energy transfer processes occurring in the CW CO chemical laser (CL) fueled by $O/O_2/CS_2$ are reasonably well understood. The O + CS reaction has been identified as the pumping reaction [1], and the primitive distribution of vibrationally excited CO (CO*) produced has been measured [2]. Direct measurements of the rate of this reaction have been recently reported [3]. The numerous additional chemical reactions possible in this system have been surveyed to attempt to produce a set of reactions which describes most of the chemistry occurring in laser devices [4]–[6]. Vibrational energy transfer processes involving CO* in collision with itself [7] and with other major species [5], [6] in the laser medium have been elucidated. All of these fundamental data have been incorporated into laser-device computer modeling codes which generally yield predictions in good agreement with experiment [6].

The CO chemical laser is generally quite tolerant of added gaseous species, in that many additives do not interfere with the basic laser reactions nor produce rapid deactivation of CO*. Thus the laser is useful for examining the effects of gas additives on the optical gain of the laser medium and on the subsequent device characteristics of laser oscillators. Suart *et al.* [8] measured the changes in output power of a longitudinal flow laser where Ar, CO_2, N_2, N_2O, CO, and OCS were added. Jeffers and Wiswall [9], [10] later investigated both total output power and output spectral changes when Ar, CO, N_2O, and NO plus N_2O were added to a transverse flow laser.

In this paper we report data which considerably extend the earlier work cited above. We have measured the effects of a large number of gas additives on the optical gain of a CO laser amplifier on transitions from $v = 3 \rightarrow 2$ to $14 \rightarrow 13$. These re-

Manuscript received March 1, 1976; revised June 30, 1976. This work was supported by the McDonnell Douglas Independent Research and Development Program.

W. Q. Jeffers was with the McDonnell Douglas Research Laboratories, McDonnell Douglas Corporation, St. Louis, MO 63166. He is now with Helios, Inc., Boulder, CO 80302.

C. E. Wiswall and H. Y. Ageno are with the McDonnell Douglas Research Laboratories, McDonnell Douglas Corporation, St. Louis, MO 63166.

sults have then been applied to the operation of a laser oscillator in which NO gas additive was used to precisely control the output vibrational band spectrum.

Gain measurements offer several significant advantages for understanding laser operation. The small-signal gain is directly related to laser optical performance, and with the high signal-to-noise ratio attainable from a probe laser beam, rapid data acquisition is possible. The gain measurements are specific to individual vibrational-rotational transitions, in contrast to chemiluminescence which normally can resolve only entire vibrational bands. Finally, with a gain experiment, optical loss as well as gain can be measured. Prediction of small-signal gain is a stringent test of computer modeling accuracy; thus, gain data are useful for comparison with modeling calculations.

II. Experimental

The CO chemical laser device used in this work has been described previously [10] and will be only briefly discussed. A cross-sectional view of the laser injectors and flow channel is shown in Fig. 1. The main stream is formed by the $O/O_2/He$ injected through the slotted glass oxygen injector. CS_2, Ar, and the test gas additive were injected through the transverse injectors. The injectors were 50 cm long in the direction of the optical axis (the y axis of the Fig. 1 insert). The probe laser beam center was positioned 1.5 cm downstream from the transverse injector slots. The spatial resolution of the gain measurements was approximately 0.5 cm, determined by apertures in the probe beam path. It was found experimentally that relatively large amounts of inert gas additives such as Ar or N_2 can be injected through the transverse injectors without significantly altering the mixing or reaction zone geometry. This was a necessary condition for separating the gas dynamic effects of additive injection from the molecular collisional effects of the additive with CO* which were of primary interest.

The most critical element in laser gain measurements is the performance of the probe laser. Over the past several years, an advanced CW electric-discharge CO probe laser has been developed [7]. The design features a triple-jacketed, liquid-nitrogen-cooled, CW discharge tube with feedback stabilization of the discharge current. The optical cavity is mounted on a massive Invar rod structure for mechanical stability. The cavity is formed by a 10-m radius of curvature, 98-percent reflective, germanium coupling mirror opposite a 150-line/mm grating selected for high efficiency in the first-order Littrow configuration. The output spectra of this device normally consist of selectable single lines on approximately six P-branch transitions of the vibrational bands $3 \rightarrow 2$ to $18 \rightarrow 17$. Apertures inside the laser cavity are adjusted to force single transverse-mode oscillation, and the cavity is stabilized to a single longitudinal mode by length tuning with a piezoelectric transducer on which the output mirror is mounted. The amplitude stability of the output beam is approximately 1 percent. The output beam intensity is less than 1 mW so that gain saturation effects are rendered negligible.

The gain measurement experiment is shown in Fig. 2. The probe beam was mechanically chopped at 1 kHz for coherent lock-in detection. The chopped beam was split by a germanium beam splitter $BS1$; the transmitted portion was analyzed

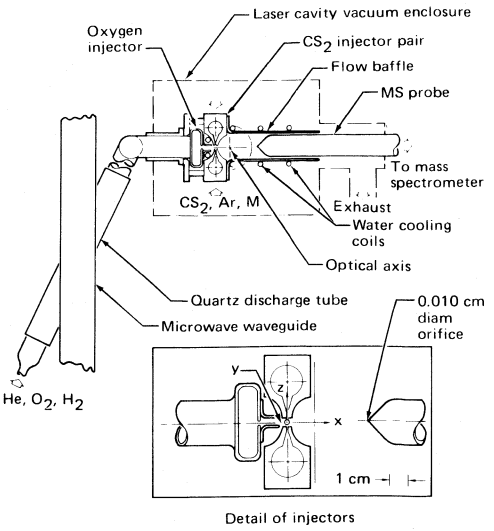


Fig. 1. Cross-sectional drawing of the CO CL. Gas additives were premixed with the CS_2 fuel and injected through the pair of transverse injectors. Gain length perpendicular to the plane of the figure was 50 cm.

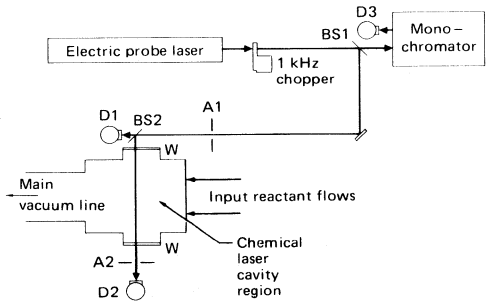


Fig. 2. Experimental arrangement for gain measurements.

with a monochromator and a detector $D3$ to identify lines and to provide feedback stabilization of the length of the probe laser. The reflected beam from $BS1$ was sent approximately 3 m through the laboratory to the chemical laser device. It passed through the aperture $A1$ to the beam splitter $BS2$, where it was split into a reference beam and a beam transmitted through the laser cavity region. The reference beam was detected by detector $D1$, and the beam through the laser cavity region was detected by detector $D2$.

Fig. 3 shows a schematic of the electronics used to acquire data. The reference beam output from detector $D1$ and the transmitted beam output from detector $D2$ were phase-sensitive detected, and the outputs of the lock-in amplifiers were fed into an analog ratio circuit. A digital voltmeter was used for visual monitoring during experiments. The analog ratio $D2/D1$ provided the Y input for an X-Y recorder; the X axis was driven by the analog output of a capacitance manometer measuring the cavity pressure. In the gas additive experiments, the initial cavity pressure was nulled with offset circuitry on the manometer; the X axis then corresponded to the partial pressure of the gas additive.

In the experiment, the ratio of transmitted-to-reference signal levels, r_0, was measured without chemical reactions by tuning off CS_2 fuel flow in the laser cavity. r_0 was set to 1.00 by adjusting beam intensities. A second measurement with reactions on produced a new ratio, r_1; the optical

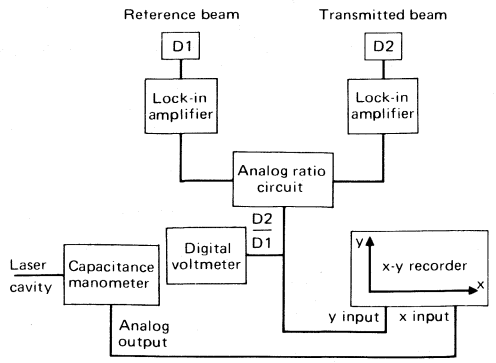


Fig. 3. Schematic diagram of electronics used in gain measurements.

gain, g_0, is then

$$g_0 = e^{\alpha_0 L} - 1 = \frac{r_1 - r_0}{r_0} \tag{1}$$

where α_0 is the gain per centimeter and L is the length of the gain region. The advantage of the ratioing technique is that any instabilities that equally affect both transmitted and reference signal levels are canceled.

The flowrate of chemically formed CO*, F_{CO^*}, was measured with a quadrupole mass spectrometer using techniques described earlier [10]. The numerical value obtained using standard flow conditions of the gas additive experiments was $F_{CO^*} = 0.45$ mmole/s. In the data presented below, the flowrate of additive, F_M, is normalized to the flowrate of CO*; thus, the dependent variable in the data is F_M/F_{CO^*}.

III. Results

Fig. 4 shows typical X-Y recorder traces of the variation in transmitted-to-reference beam ratio versus gas additive partial pressure. From these data, the change in optical gain can be calculated from (1). Since all gas additives produce a small effect on optical gain because of changes in mixing between oxidizer and fuel streams in the laser cavity, the data were analyzed to separate gas dynamic mixing effects from molecular collisional effects. The total optical gain is separated into various contributions as

$$g(F_M) = g_0\big|_{F_M=0} + \Delta g^M_{GD}(F_M) + \Delta g^M_{\text{collisional}}(F_M) + \Delta g^M_{\text{optical}}(F_M) \tag{2}$$

where

F_M	mole flowrate of additive M;
Δg^M_{GD}	gas dynamic mixing change in optical gain;
$\Delta g^M_{\text{collisional}}$	molecular collisional change in optical gain;
$\Delta g^M_{\text{optical}}$	change in optical gain resulting from absorption by the additive M.

Gain coefficients as defined in (1) can be calculated for all of the above terms and are used in presenting the data below. The mole flowrate of gas additive was chosen as the independent variable since the laser operating conditions are characterized by mole flowrates of reactants and diluents, as listed in Table I. Calibrations were performed to relate mole flowrate to cavity partial pressure of various additives. In order to separate the gas dynamic mixing effects from the molecular collisional effects (which are of prime interest), argon, whose collisional effects are known to be negligible, was used as an inert additive. The assumption was made that the gas dynamic mixing effect of any other additive would be the same at the same cavity partial pressure, Δp_c, that is,

$$\Delta g^M_{GD}(\Delta p_c) = \Delta g^{Ar}_{GD}(\Delta p_c) \tag{3}$$

where

$$\Delta p_c = p_c\big|_{F_M \neq 0} - p_c\big|_{F_M=0}. \tag{4}$$

Finally, optical absorption by the gas additive was tested experimentally and was found to be measurable in only one case: the $P_7(13)$ line using NO as the gas additive. Thus the term $\Delta g^M_{\text{optical}}(F_M)$ in (2) is usually negligible.

For comparison with other data, the gas dynamic mixing effects for Ar are shown in Fig. 5. Only three of the vibra-

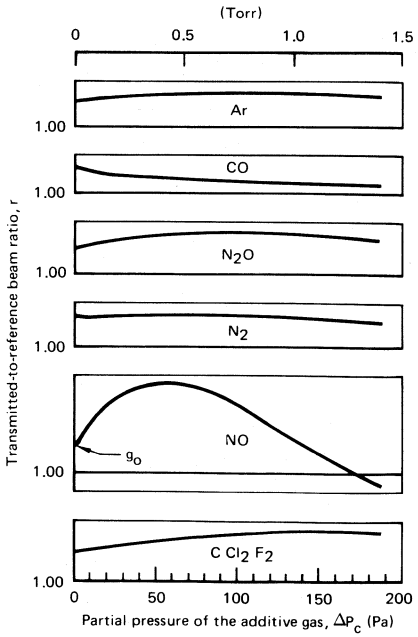


Fig. 4. Experimental traces of transmitted-to-reference beam intensity ratio for the $P_5(13)$ transition versus gas additive partial pressure. Initial ratio r_0 is 1.00 with chemical reactions off and increases to 1.04 with reactions on, additive partial pressure zero.

TABLE I
Chemical Laser Operating Conditions for Gain Measurements

Chemical laser operating conditions:		
F_{CS_2}	(transverse injectors)	0.000 559 moles/s
F_{Ar}	(transverse injectors)	0.007 150 moles/s
F_{He}	(main injector)	0.026 870 moles/s
F_{O_2}	(main injector)	0.011 220 moles/s
F_{H_2}	(main injector)	0.000 044 moles/s
p_c	(no additive)	0.67 kPa (5.0 Torr)
Gain length		50 cm
Probe laser:		
Beam position downstream from transverse injectors: 1.5 cm		
Probe lines:	$P_3(13)$, $P_4(13)$, $P_5(13)$, $P_6(13)$, $P_7(13)$, $P_8(12)$, $P_9(13)$, $P_{10}(13)$, $P_{11}(13)$, $P_{12}(13)$, $P_{13}(13)$	

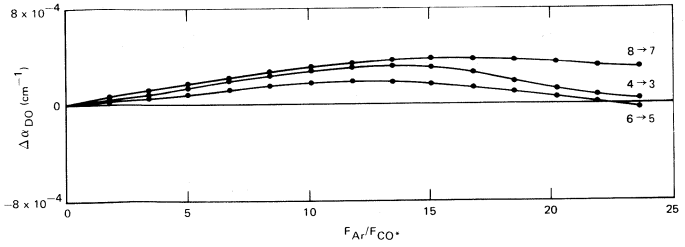


Fig. 5. Gas dynamic gain change for argon additive versus argon flowrate (normalized to the measured CO* flowrate).

tional bands are shown for clarity; the maximum effect occurs on the 8 → 7 band and is relatively small compared with molecular collisional effects of many other additives. As a second point of comparison for the data presented below, the zero-additive gain coefficients for all of the vibrational bands of interest are shown in Fig. 6.

Of the gas additives investigated, NO produces the most dramatic effects on optical gain, as shown in Fig. 7. The quenching of gain on the high bands is progressively more rapid with higher vibrational states. Conversely, in the mid and lower bands, there is a progressively larger gain enhancement. By comparison with Fig. 6, the maximum gain reached on the 3 → 2 and 4 → 3 bands with NO is about 60 percent of the maximum zero-additive gain which occurs on the 9 → 8 band.

Another additive of interest is CO itself, the data for which are shown in Fig. 8. In contrast to NO, CO causes rapid quenching of the low bands, with weak enhancement of the high bands. Data similar to those plotted in Figs. 7 and 8 were collected for 10 different gas additives. These results are summarized qualitatively in Table II.

IV. Laser Oscillator Experiments

The NO additive effects on gain shown in Fig. 7 have the unique property that the gain can be reduced to zero sequentially, starting at the highest vibrational bands. Thus, it should be possible to control the highest lasing band in a CO CL by NO additive.

To test this hypothesis, the chemical laser device used in the gain measurements was provided with optics for operation as a laser oscillator. To allow for rapid examination of the output spectra, a spectrum analyzer was used. This device incorporated a thermal image plate as a detector, allowing display of the laser output spectrum from 4.7 to 5.5 μm. The only disadvantage of the spectrum analyzer was that relatively high power (~ 0.1 W/line) was required for detection. The optical cavity was formed by a 99.5-percent reflectivity mirror opposite a 98-percent reflectivity mirror, both with 10-m radius of curvature. Optimum output coupling for this laser device is normally about 10 percent; undercoupling was used intentionally to allow low-gain transitions to lase.

It was found, as expected, that the highest lasing band could be controlled by NO gas additive. Fig. 9 shows the most important results obtained in these experiments; the total output power from the laser was measured as a function of the highest band allowed to oscillate. Concurrently, the lowest lasing band was noted. With Ar diluent and zero

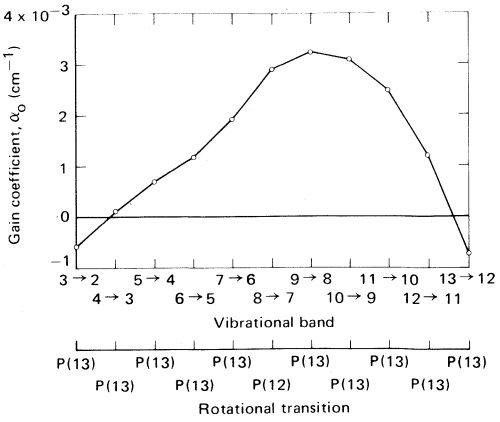


Fig. 6. Zero-additive gain coefficients.

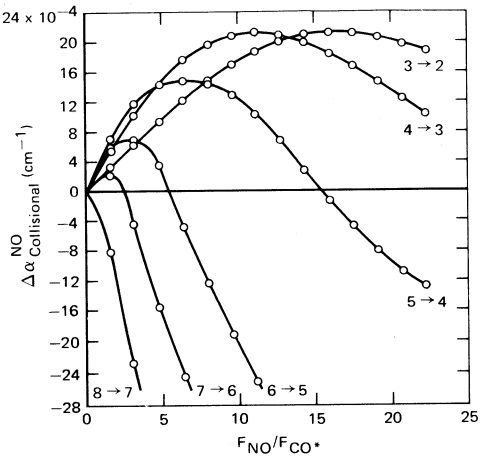


Fig. 7. Molecular collisional gain coefficient effects with NO gas additive.

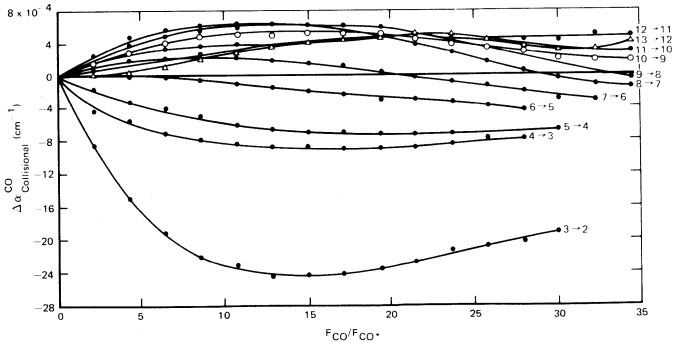


Fig. 8. Molecular collisional gain coefficient effects with CO gas additive.

NO additive, the laser produced 12.4 W while lasing on 14 → 13 through 1 → 0 [11]. By adding NO, 14 → 13 was suppressed, and 8.3 W was obtained on bands from 13 → 12 through 1 → 0. This process was continued until only 4 → 3, 3 → 2, and 2 → 1 were lasing, producing 0.2 W. The 1 → 0 band dropped below threshold when sufficient NO was added to suppress 9 → 8.

N_2O is well known as a useful gas additive for CO CL's [9]. The experiments were repeated using a constant flow of N_2O, initially adjusted to produce maximum power with

TABLE II
GAS ADDITIVE EFFECTS ON CO CHEMICAL LASER GAIN

Additive	Low bands $3\rightarrow2$ to $5\rightarrow4$	Mid bands $6\rightarrow5$ to $9\rightarrow8$	High bands $10\rightarrow9$ to $13\rightarrow12$
N_2	n	n	n
SO_2	n	n	q
H_2	n	n	q
HF	e	q to Q	Q
CF_4	e	q to Q	Q
CCl_2F_2	e	e to q	Q
CO	Q	q to e	e
OCS	Q	Q	e to Q
N_2O	e	e to n	n to q
NO	E	e to Q	Q

e = weak enhancement E = strong enhancement
n = neutral
q = weak quenching Q = strong quenching

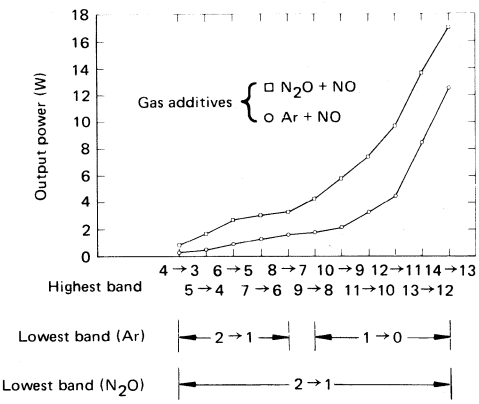


Fig. 9. Total output power versus highest upper band lasing, controlled by NO gas additive. At each power level, both the highest and lowest vibrational bands lasing are shown.

zero NO additive. As noted in the earlier publication [9], the inversion ratio enhancement effects of N_2O do not extend to the $1\rightarrow0$ band; hence with significant N_2O additive, the lowest lasing band is $2\rightarrow1$. As shown in the second set of data of Fig. 9, the bands are sequentially suppressed with increasing NO additive accompanied by a corresponding decrease in total output power. The $2\rightarrow1$ band remained in oscillation even when the higher bands were suppressed to $4\rightarrow3$.

V. DISCUSSION

The gas additive effects discussed in this paper are due primarily to inversion ratio (N_v/N_{v-1}) and total population (N_v) changes in the vibrational states of CO. The gas additives have a negligible effect on gas temperature in the laser cavity; the amounts used raise the cavity pressure typically only about 133 Pa (1 torr), starting from 0.67 kPa (5 torr); hence pressure broadening is also negligible. As discussed previously [9], if the collisional transfer probability for an additive decreases (increases) with increasing CO vibrational level, the additive will increase (decrease) the inversion ratio on the $v\rightarrow v-1$ band. Thus, the low-band inversion ratios are increased by N_2O, while the mid- and high-band inversion ratios are decreased by NO [10]. The other major effect of NO is the collisionally induced population cascade from high to low levels. This effect is specific to the O + CS pumped CO CL since the reaction pumps the higher levels more strongly than the lower levels [2].

The exception to the collisional transfer probability effect on inversion ratio is the $1\rightarrow0$ band since there is no possibility of deexciting $v=0$. Thus, all additives tend to decrease $1\rightarrow0$ inversion by deexcitation of $v=1$. Opposing this effect is the collisionally induced population cascade from higher levels into $v=1$. With the laser device used in this work, maximum $1\rightarrow0$ power was obtained without NO additive.

The gas additive results summarized in Table II illustrate the point that the CO CL is tolerant of many gas additives; therefore, this chemical laser will allow a choice of a variety of different diluents. Also, the insensitivity of CO* to optical performance degradation by most gas additives relaxes the purity requirements on reactants and diluents used to fuel the laser.

Finally, the demonstrated features of increasing total output power or controlling the output spectrum by gas additives is unique to the CO CL. N_2O will typically increase the total output power of a transverse flow laser by about 50 percent. As shown in Table II, this power increase is due to weak enhancement of low- and mid-band gain without serious quenching of the high bands. Some output spectrum modifications have been demonstrated in previous work [10]; however, the precise control of the highest lasing band and the sequential quenching by NO are new results. Fig. 9 also demonstrates a corollary result: in a multilevel cascade laser, the total power falls rapidly as the length of the cascade is shortened.

REFERENCES

[1] G. Hancock and I. W. M. Smith, "Infrared chemiluminescence from the reaction O + CS → CO + S," *Chem. Phys. Lett.*, vol. 3, pp. 573-576, Aug. 1969.
[2] H. T. Powell and J. D. Kelley, "Vibrational distribution of carbon monoxide from O + CS → S + CO(v)*," *J. Chem. Phys.*, vol. 60, pp. 2191-2192, Mar. 1974.
[3] I. R. Slagle, R. E. Graham, J. R. Gilbert, and D. Gutman, "Direct determination of the rate constant for the reaction of oxygen atoms with carbon monosulphide," *Chem. Phys. Lett.*, vol. 32, pp. 184-186, Apr. 1975.
[4] D. W. Howgate and T. A. Barr, Jr., "Dynamics of the CS_2-O_2 flame," *J. Chem. Phys.*, vol. 59, pp. 2815-2829, Sept. 15, 1973.
[5] N. A. Nielsen, Jr., "Development of a computer model for the (CS_2 + O_2) chemical laser," Ph.D. dissertation, Dep. of Chemistry, Cornell Univ., Ithaca, NY, Aug. 1975.
[6] H. V. Lilenfeld, R. F. Webbink, W. Q. Jeffers, and J. D. Kelley, "Modeling of the CW CO chemical laser," *IEEE J. Quantum Electron.*, vol. QE-11, pp. 660-669, Aug. 1975.
[7] H. T. Powell, "Vibrational relaxation of carbon monoxide using a pulse discharge. II. T = 100, 300, 500 K," *J. Chem. Phys.*, vol. 63, pp. 2635-2645, Sept. 1975.
[8] R. D. Suart, S. J. Arnold, and G. H. Kimbell, "Power enhancement of a CO chemical laser by the addition of vibrationally cool gases," *Chem. Phys. Lett.*, vol. 7, pp. 337-340, Nov. 1, 1970.
[9] W. Q. Jeffers and C. E. Wiswall, "Efficient low-band operation of a CO chemical laser," *Appl. Phys. Lett.*, vol. 23, pp. 626-627, Dec. 1, 1973.
[10] W. Q. Jeffers and C. E. Wiswall, "Experimental studies of the $O/O_2/CS_2$ CW CO chemical laser," *IEEE J. Quantum Electron.*, vol. QE-10, pp. 860-869, Dec. 1974.
[11] Detailed results on CW $1\rightarrow0$ lasing will be published elsewhere.

Optical Absorption and Fluorescence Studies in High Pressure Cesium-Xenon Mixtures

J. GARY EDEN, BLAKE E. CHERRINGTON, SENIOR MEMBER, IEEE, AND JOSEPH T. VERDEYEN, SENIOR MEMBER, IEEE

Abstract—**The pressure and temperature dependent absorption and fluorescence spectra of the cesium-xenon (CsXe) molecule have been examined. In contrast to previous investigations of the alkali-rare gas molecules, cesium atomic states that have weakly allowed optical transitions have been studied and have been shown to form excimer levels that are attractive for application as potential dissociation lasers. In particular, the (Cs[7^2S]Xe)* excimer appears promising as a source of high-energy laser radiation due to 1) its large dissociation energy (0.132 eV), 2) its stimulated emission cross section of $\simeq 10^{-17}$ cm^2, and 3) its small population threshold inversion densities ($\simeq 10^{13}$ cm^{-3}).**

I. Introduction

CURRENTLY, there is considerable interest in the alkali-rare gas molecules as potential candidates for dissociation lasers in the near infrared-visible spectral region [1]. However, the majority of past investigations of the optical properties of the alkali-rare gas molecules have concentrated on utilizing low-lying alkali P states to form the alkali-rare gas excimer. Such states may be undesirable due to their short radiative lifetimes ($\simeq$ ns).

This work summarizes the optical properties of excimer states in cesium-xenon mixtures that are characterized by relatively long radiative lifetimes, and therefore, may be much more promising as potential laser levels.

A partial energy level diagram of cesium is shown in Fig. 1. The Cs* ($6^2P_{1/2,3/2}$) atomic states are connected to ground by fast radiative transitions at 8944 and 8521 Å. The associated (CsXe)* excimers have a correspondingly rapid radiative decay which will limit the maximum attainable excimer density. However, note that the Cs* (7^2S and 5^2D)-ground atomic transitions (denoted by dashed lines) are normally forbidden due to violation of quantum mechanical selection rules. Observations to be described later demonstrate that the addition of high pressure xenon to the cesium vapor permits these transitions to occur. This atomic emission is shown to be collisionally induced by the xenon diluent which is the same mechanism responsible for the green auroral line (^1S-^1D) in oxygen-xenon mixtures [2], [3]. Association of Cs* (5^2D, 7^2S) and ground-state xenon atoms to form stable, relatively long-lived (CsXe)* complexes has also been observed by monitoring the excimer emission continua. Fluorescence from optically excited (Cs[7^2S]Xe)* excimers was also observed by Tam and co-workers [4].

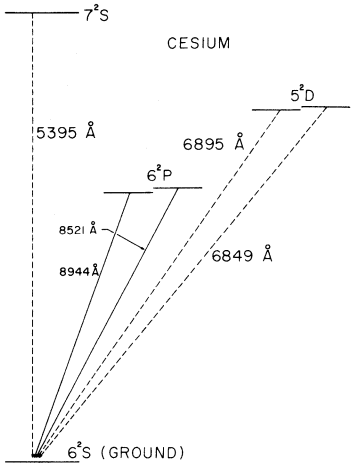


Fig. 1. Partial energy level diagram of cesium. The forbidden Cs(7^2S, $5^2D \rightarrow 6^2S$) lines at 5395, 6849, and 6895 Å are denoted by dashed lines.

In this paper, extensive measurements of the (Cs[7^2S]Xe)* and (Cs[5^2D]Xe)* molecular absorption spectra in high pressure cesium-xenon mixtures are reported. In addition, flashlamp-pumped fluorescence profiles for these long-lived ($\tau > 1$ μs) molecular states are presented. In particular, the (Cs[7^2S]Xe)* molecule is found to be attractive as a potential dissociation laser due to its large dissociation energy and stimulated emission cross section of $\sigma \simeq 10^{-17}$ cm^2. As a result, low population inversion threshold densities have been calculated for this system. The pumping requirements for population inversion, assuming a selective excitation of the 7^2S Cs state, have also been calculated taking into account the dominant effect that the rapid 7^2S-6^2P radiative transition has on the loss of the 7^2S state.

The experimental apparatus utilized to measure the Cs-Xe absorption and emission spectra is described in Section II. Typical data runs and their interpretation in terms of a possible CsXe excimer laser are presented in Section III. Finally, the results are summarized in Section IV.

II. Experimental Apparatus

The experimental apparatus used to obtain the CsXe absorption and fluorescence data is shown schematically in Fig. 2. The Pyrex absorption tubes were nominally 15.7 cm long with a 2.5-cm OD, and incorporated fused windows situated normal to the tube's axis. These Cs-Xe (doubly distilled cesium,

Manuscript received March 8, 1976; revised June 28, 1976. This work was supported by the NASA Lewis Research Center; the results have been submitted to the Graduate College of the University of Illinois in partial fulfillment of the requirements for the Ph.D. degree in Electrical Engineering (J. G. Eden).

J. G. Eden was with the Gaseous Electronics Laboratory, Department of Electrical Engineering, University of Illinois, Champaign-Urbana, IL 61801. He is now with the Laser Physics Branch, Naval Research Laboratory, Washington, DC 20375.

B. E. Cherrington and J. T. Verdeyen are with the Gaseous Electronics Laboratory, Department of Electrical Engineering, University of Illinois, Champaign-Urbana, IL 61801.

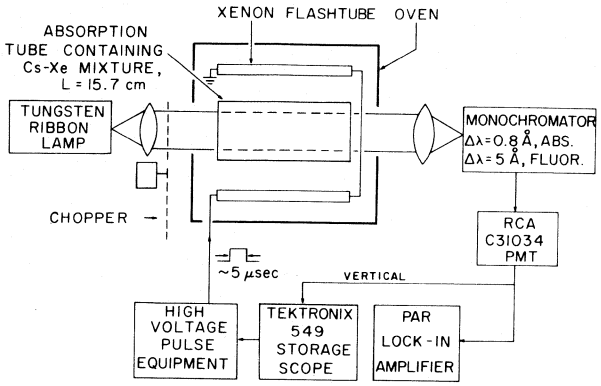


Fig. 2. Schematic diagram of the experimental apparatus used to measure the absorption and fluorescence spectra of Cs–Xe mixtures.

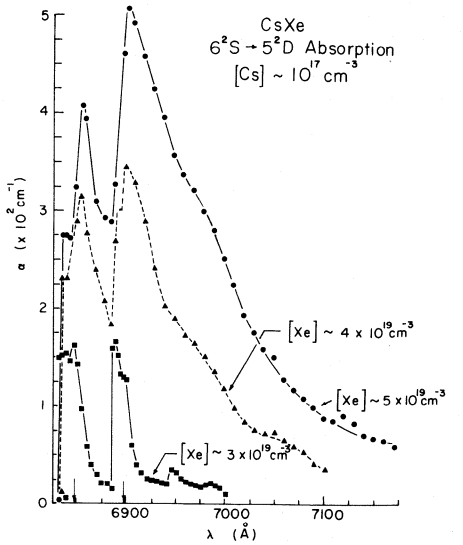


Fig. 3. Xenon density dependence of the $6^2S \rightarrow 5^2D$ atomic-molecula absorption spectrum for [Cs] $\simeq 10^{17}$ cm^{-3}. The positions of the fo bidden atomic lines at 6849 and 6895 Å are shown by arrows.

research grade xenon) filled tubes were placed at the center of a polished double elliptical cavity. This cavity was constructed so that its center coincided with one of the foci of each of the two ellipses. At the other focus of each ellipse was mounted a high intensity (≃1.5-MW output/lamp) water-cooled linear xenon flashtube. The temperature of the absorption tube was monitored using chromel-alumel thermocouples. In this way, the partial pressure of cesium could be inferred from the vapor pressure curves.

The xenon flashtubes were ignited by discharging a 0.1 μF capacitor (charged to 15 kV) through an EG & G sparkgap. The resulting 600 A current pulse had a FWHM of ≃5 μs. In addition, the flashlamps were operated in the simmer mode with a low-level dc arc (≃25 mA) maintained in the lamps. This significantly enhanced the power and radiative output repeatability of the flashlamps [5]. For absorption measurements, the broad band radiation from a standard tungsten ribbon lamp was collimated and mechanically chopped before entering the absorption cell. The resulting absorption spectrum was dispersed by a GCA-McPherson EU-700 monochromator and detected by a RCA C31034 photomultiplier. Data were obtained by scanning the monochromator and recording the synchronous output of a PAR HR-8 lock-in amplifier utilizing a strip chart recorder. The wavelength resolution of the detection system, including the effect of electronic averaging, is shown in Fig. 2 for both the absorption and fluorescence measurements.

Fluctuations in the data from run to run were <25 percent for all wavelengths. Also, due to careful calibration of the monochromator against known atomic lines in the spectral regions of interest, uncertainty in the detection wavelength was ±1 Å.

III. Experimental Results and Discussion

A. Absorption and Fluorescence Spectra of the (Cs[5²D])Xe Excimer*

Fig. 3 displays the xenon density dependence of the absorption coefficient, $\alpha(\lambda)$, for the xenon perturbed Cs (6^2S-5^2D) transition. The Cs density is kept fixed and the xenon density variation corresponds to a range of from 1 to 2 atm at room temperature.

An important point to notice is the change in the spectral shape as the Xe density is changed. (As expected, changing the Cs density at a fixed Xe pressure results in a proportiona change in absorption, but no change in spectral shape.) At lov xenon pressures, the spectrum shows collisionally induce absorption at the atomic lines. At higher xenon pressures, th red satellites emerge which peak 4–5 Å to the red side of th forbidden atomic transitions and extend for 200–300 Å. Thi spectral feature is due to the formation and subsequent bound free radiative decay of the (Cs[5^2D]Xe)* excimer. Such satellites have been reported for several alkali–rare gas mixture [6]–[9] and are analogous to those found previously fo allowed S-P transitions of the rare gas perturbed alkalis [10] In a very recent article Happer *et al.* [11] also reported ab sorption on the 6^2S-5^2D transition in CsXe, although not in as much detail as presented here. Even more recent studies by Moe *et al.* [12] have shown prominent blue-shifted absorption features of the xenon perturbed Cs(6^2S-5^2D) transition near 6376 Å. This feature is much more noticeable in absorption than in emission.

Atomic line absorption on the "forbidden" 6^2S-5^2D transitions in the presence of xenon is collisonally induced [13], [14]. That is, the Cs(5^2D) states are characterized by a transition probability A which is directly proportional to the xenon density:

$$A = K_0[\mathrm{Xe}], \tag{1}$$

where K_0 is the collisionally induced emission coefficient in cm$^3 \cdot$ s^{-1}. Fig. 4 depicts the linear variation of α as a function of xenon density ([Cs] $\simeq 10^{17}$ cm^{-3}) for the 6849-Å transition. The slope of this line is associated with K_0 which can be determined from

$$\alpha(\lambda) = \frac{\lambda^2}{8\pi}\frac{g_u}{g_l}[\mathrm{Cs}]\frac{A}{\Delta\nu} \tag{2}$$

where $\alpha(\lambda)$ is the absorption coefficient, g is the degeneracy of the appropriate level and $\Delta\nu$ is the absorption linewidth. $\Delta\nu$ was calculated from $\Delta\lambda$ where $\Delta\lambda$ was estimated from the low-Xe density absorption spectra to be approximately 20 Å.

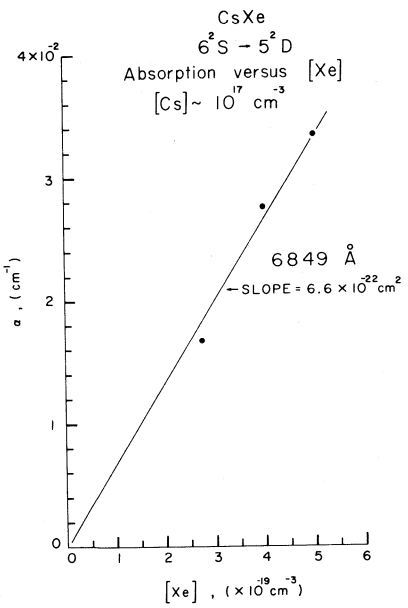


Fig. 4. Plot showing the linear dependence of the absorption coefficient (6849 Å) on xenon density.

Using (1) and (2), the collisionally induced emission coefficient is

$$K_0 \simeq 1.5 \times 10^{-17} \text{ cm}^3 \text{ (s)}.$$

Setting [Xe] = $5 \cdot 10^{19}$ cm^{-3}, then from (1), a radiative lifetime of roughly 1.4 ms is obtained for the Cs($5^2D_{5/2}$) state. Clearly then, loss of the 5^2D excited-state population due to collisionally induced radiative transitions to ground is negligible when compared to radiative 5^2D-6^2P losses ($\tau \simeq \mu$s) [15]. A similar analysis for the Cs ($5^2D_{3/2}$-$6^2S_{1/2}$) transition was not carried out since the absorption coefficient at 6895 Å shown in Fig. 3 includes a contribution due to the red wing of the 6849 Å transition. This additional absorption causes the 6895 Å absorption coefficient to deviate significantly from linearity at the higher xenon pressures. Also, by applying a similar analysis to the far red wing (molecular) absorption, the spontaneous radiative lifetime for the (Cs[5^2D] Xe)* excimer was determined to be in the microsecond regime.

Flashlamp-pumped fluorescence and absorption spectra of the (Cs[5^2D] Xe)* excimer are shown in Fig. 5. Spectrally resolved emission profiles for the (Cs[5^2D] Xe)* excimer state are shown in Fig. 6 for different Xe densities. Note that for a fixed cesium density, increasing the xenon pressure modified the spectrum contour markedly due to equilibration of the molecules within the molecular well. Yet, as might be expected, increasing the cesium density for constant xenon pressure has a negligible effect on the emission spectrum profile.

Since all of the excitation processes occurring during flashlamp pumping are not known, there is a possibility that some of the emission shown in Figs. 5 and 6 could be due to the fairly close lines radiating from higher Cs levels ($7D$-$6P$). The extent of such a contribution is unknown.

B. Spectra of the (Cs[7^2S] Xe) Molecular State*

The absorption and relative emission profiles for the (Cs[7^2S] Xe)* excimer are shown in Fig. 7. These results are

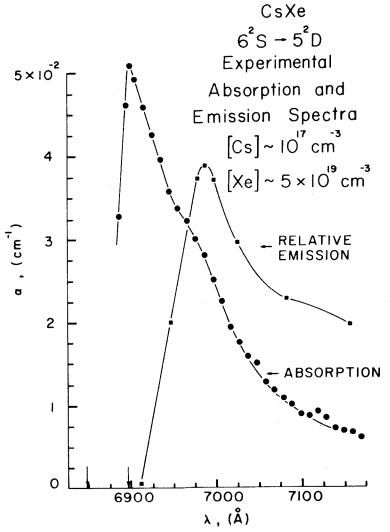


Fig. 5. Plot of Cs($6^2S \rightarrow 5^2D$) absorption and relative emission spectra for [Cs] $\simeq 10^{17}$ cm^{-3} and [Xe] $\simeq 5 \cdot 10^{19}$ cm^{-3}. The positions of the forbidden atomic lines at 6849 and 6895 Å are shown by arrows.

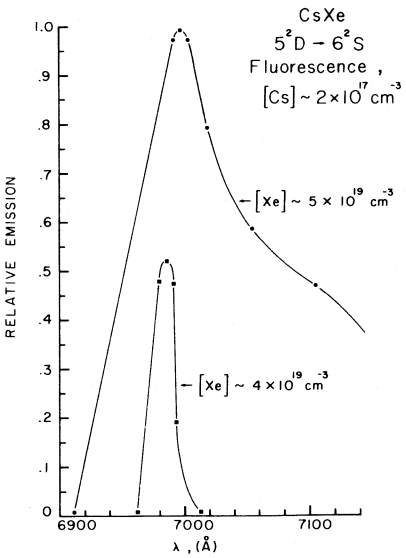


Fig. 6. Xenon pressure dependence of the (Cs[5^2D] Xe)* excimer fluorescence.

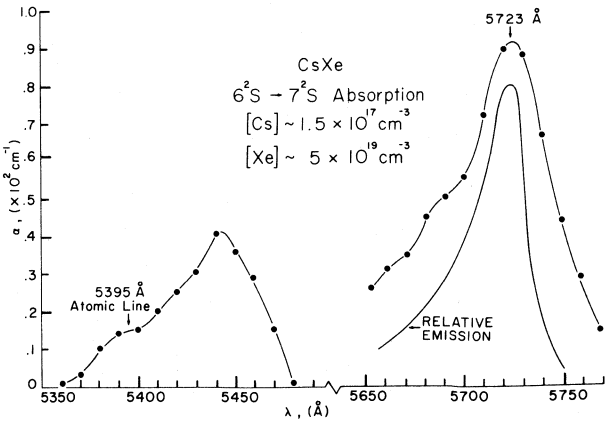


Fig. 7. Absorption and relative emission spectra of the Cs*(7^2S)-(Cs[7^2S] Xe)* atomic-molecular system.

in essential agreement with those of Happer *et al.* [11], except that they indicate almost an order of magnitude greater absorption at 5723 Å than we have observed. The fact that the dominant absorption occurs at ≃5723 Å and the far wing absorption closely follows the measured fluorescence indicates that transitions between the minimum of the (CsXe)* molecular well and the repulsive (CsXe) ground state are being observed. In addition, the shape of the (Cs[7^2S] Xe)* excimer far wing absorption profiles do not change significantly with varying cesium density (i.e., temperature). When these spectra are normalized to the cesium density, they overlap within experimental error (20 percent). This result suggests that the 5723 Å-centered molecular band terminates on a portion of the ground state that is not strongly repulsive. The conclusion implied by the data of Fig. 7 is that the (Cs[7^2S] Xe)* molecular well depth is approximately 1062 cm^{-1} = 0.132 eV. Fluorescence data, similar to those previously shown for the 5^2D excimer, are displayed in Fig. 8. Once again, varying the xenon pressure strongly affects the amplitude and slightly affects the shape of the emission profile.

C. Discussion of (Cs[7^2S] Xe)* Data

Given the experimental data and conclusions presented above, the collisional and radiative rates that are critical in depopulating the Cs*(7^2S) and (Cs[7^2S] Xe)* states have been estimated and are shown in Fig. 9. The processes considered are 1) three-body (CsXe)* excimer formation, i.e.,

$$\mathrm{Cs}^*(7^2S) + 2\mathrm{Xe} \xrightarrow{K_f} (\mathrm{Cs}[7^2S]\,\mathrm{Xe})^* + \mathrm{Xe},$$

2) atomic transitions to low-lying P states, 3) collisionally-induced atomic fluorescence, and 4) excimer spontaneous radiation to the repulsive molecular ground state. The three-body excimer formation rate shown is that determined for RbXe by Carrington and Gallagher [16]. From earlier investigations of this process in the homonuclear rare gas and alkali-rare gas molecules [17], [18], it has been shown that three-body molecular formation rates vary only slightly among the heavier molecules such as Xe_2 and RbXe. Therefore, it is expected that the value chosen here is a good approximation to the (CsXe)* formation rate. Using Carrington and Gallagher's value, the (CsXe)* three-body formation frequency is found to be $\simeq 2 \cdot 10^8$ s^{-1} for [Xe] $\simeq 5 \cdot 10^{19}$ cm^{-3}.

Secondly, the atomic Cs($7^2S \rightarrow 6^2P$) spontaneous rate shown in Fig. 9 is the sum for both the 1.47- and 1.36-μm lines (where the dipole moment for both transitions is assumed to be constant). The lifetime shown here is in close agreement to the values calculated by Stone [19].

To evaluate the collision-induced fluorescence lifetime at high xenon densities, an analysis of the Cs($6^2S \rightarrow 7^2S$) experimental absorption data shown earlier yields $\tau_{5395} \simeq 1$ ms (for [Cs] $\simeq 1.5 \cdot 10^{17}$ cm^{-3}, [Xe] $\simeq 5 \cdot 10^{19}$ cm^{-3}). Clearly then, collision-induced destruction of the Cs*(7^2S) species is negligible with respect to the other processes of interest.

The primary quantities of interest are the lifetime ($1/A$) and stimulated cross section (σ_{se}) for the (Cs[7^2S] Xe)* excimer. The use of the absorption equation

$$\alpha(\lambda) = \frac{\lambda^2}{8\pi}\frac{g_u}{g_1}\,[\mathrm{CsXe}]\; g(\lambda)\, A = \sigma_{se}[\mathrm{CsXe}], \qquad (3)$$

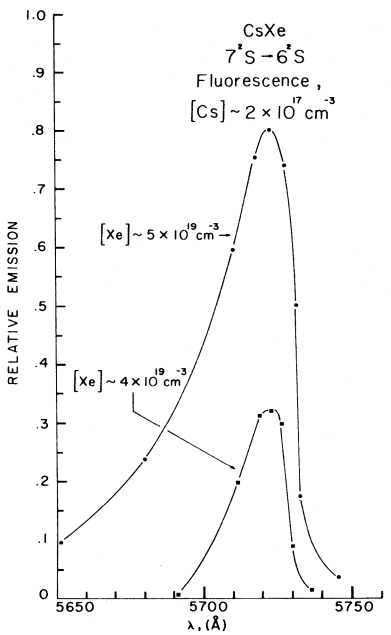


Fig. 8. Xenon pressure dependence of (Cs[7^2S] Xe)* excimer fluorescence for [Cs] $\simeq 2 \cdot 10^{17}$ cm^{-3}.

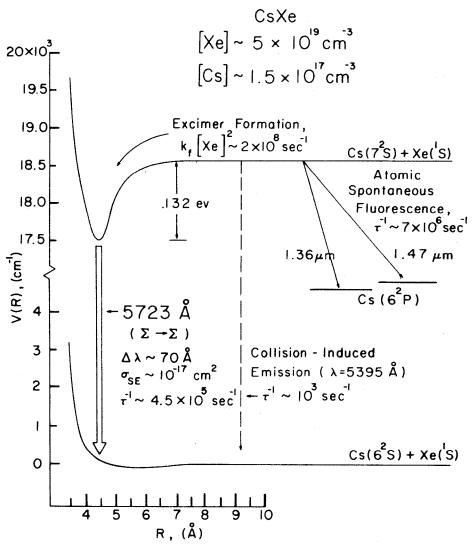


Fig. 9. Energy level diagram of the Cs*(7^2S)-(Cs[7^2S] Xe)* atomic molecular system showing collisional processes important to destroying the Cs*(7^2S) species.

where $g(\lambda)$ is the transition line shape, allows the determination of both of these quantities from the data of Fig. 7 provided that the ground state CsXe density can be estimated. The CsXe ground state molecular population at a specified interatomic radius R_0 and radial interval ΔR is given by

$$[\mathrm{CsXe}] = 4\pi R_0^2\, \Delta R\, [\mathrm{Cs}]\, [\mathrm{Xe}]\, \exp(-\Delta E/kT). \qquad (4)$$

$\Delta E = |V_I(R_0) - V_I(\infty)|$ where $V_I(R)$ is the intermolecular potential of ground state CsXe as a function of internuclear separation (R), and

T = gas temperature.

Now, of course, the estimate of [CsXe] (and of σ_{se}) depends

strongly on the shape of the CsXe potential energy curves. Although the repulsive ground state curve has been measured accurately by crossed beam [20] and fluorescence [21] experiments, only theoretical predictions are available for the bound excited molecular state. The upper state in Fig. 9 is a modification of the theoretical curve computed by Pascale and Vandeplanque [22]. To comply with our experimental observations, we deepened the potential well to 1062 cm^{-1} (they predicted a well depth of $\simeq$400 cm^{-1}). The potential minimum occurs at 4.5 Å, where the ground state is only slightly repulsive. Using this value of R_0 and setting ΔR = 0.5 Å, the molecular ground state density is found to be

$$[CsXe]\,(\text{at } R_0) \simeq 10^{15}\ cm^{-3}$$

when $[Cs] \simeq 1.5 \times 10^{17}\ cm^{-3}$ and $Xe \simeq 5 \times 10^{19}\ cm^{-3}$. Since $\alpha_{max} \simeq 0.01\ cm^{-1}$ from Fig. 7, the stimulated emission cross section

$$\sigma_{se} \simeq 10^{-17}\ cm^2.$$

It is expected that the ground state density found above is a lower limit and so the actual value of σ_{se} is possibly smaller than that given. Also, from (3), where the linewidth is approximately 60-70 Å, the lifetime of the $(Cs[7^2S]Xe)^*$ state can be found to be $\simeq 2\ \mu s$.

Given the $(Cs[7^2S]Xe)^*$ excimer absorption linewidth and radiative lifetime presented above, one can readily determine the population inversion necessary to obtain lasing from this molecule. Setting $\Delta\lambda$ = 60 Å, $\tau = 2\ \mu s$, and λ = 5723 Å, the molecular transition will exhibit gain of 1 percent/m for a population inversion of $10^{13}\ cm^{-3}$. The appropriate atomic and molecular densities necessary to produce this inversion can be estimated as follows. From (4) with R_0 = 4.5 Å, ΔR = 0.5 Å, and $kT(600\ K) \simeq 0.5$ eV,

$$[CsXe] = 1.27 \times 10^{-22}\ [Cs]\,[Xe]\ \ cm^{-3}. \tag{5}$$

For an optical gain of 1 percent/m we have

$$[CsXe]^* = [CsXe] + 10^{13}\ cm^{-3}. \tag{6}$$

The calculation of the Cs* density necessary to achieve this excimer density is probably best achieved by calculating the equilibrium constant

$$K_{eq}(T) = \frac{[CsXe]^*}{[Cs]^*[Xe]} \tag{7}$$

which is valid for thermodynamic equilibrium. The use of this constant implies that the collisional formation and destruction processes dominate over the radiative decay of the excimer, a condition which certainly is not valid if laser action occurs. Close to threshold, however, the use of the equilibrium constant should be reasonably valid. The equilibrium constant can be found by evaluating the translational, rotational, vibrational, and electronic partition functions for $(CsXe)^*$ [23], or by using the "classical" approach outlined by Hedges *et al.* [21]. Using the first approach, at 600 K

$$K_{eq} \simeq 1.46 \times 10^{-20}\ cm^3. \tag{8}$$

This approach tends to overestimate the equilibrium constant, and the second approach indicates that the equilibrium constant could be anywhere from slightly less than the value given in (8) to as much as a factor of 5 smaller if the well is assumed to be quite narrow. Keeping in mind this uncertainty, the value given in the equation will be used.

Finally, the total number of cesium atoms must be conserved. Hence,

$$[Cs] + [CsXe] + [CsXe^*] + [Cs^*] = [Cs]_{total} \tag{9}$$

where Cs_{total} is the cesium density corresponding to the gas temperature, T. Equations (5)-(7) and (9) may be solved to determine [Cs], [CsXe], [CsXe*], and [Cs*]. For $[Cs]_{total} = 1.5 \cdot 10^{17}\ cm^{-3}$ and $[Xe] = 5 \cdot 10^{19}\ cm^{-3}$,

$$[Cs] = 1.47 \cdot 10^{17}\ cm^{-3}$$

$$[CsXe] = 9.3 \cdot 10^{14}\ cm^{-3}$$

$$[CsXe^*] = 9.43 \cdot 10^{14}\ cm^{-3}$$

and

$$[Cs^*] = 1.29 \cdot 10^{15}\ cm^{-3}.$$

It is significant to note that the ground atomic state density must be depleted by $\simeq$2 percent to obtain the required population inversion.

The previous figures represent only a first-order estimate of the conditions necessary for an inversion since there are many unknowns about the system. It was assumed that the $Cs(7^2S)$ state was selectively excited by some process. In an electrical discharge, excitation would most likely occur by electron impact excitation from the $Cs(6^2P)$ state. Optical pumping would rely on exciting higher levels (7^2P) with radiative cascade down to the $Cs(7^2S)$. It is difficult to assess the density or role of the other excited atomic and molecular species that will be present other than to recognize that they will constitute an energy sink in the overall excitation process and may also enter into collisional deactivation processes. For instance $Cs(7^2S)$-$Cs(7^2S)$ collisional ionization has a presumably large cross section ($>10^{-15}\ cm^2$) [24], however, the low Cs* density causes this loss process to be negligible compared to the atomic radiative decay. Similar collisional conversion or deactivation processes may occur with CsXe*.

Another first-order method of determining the feasibility of obtaining stimulated emission from the $(Cs[7^2S]Xe)^*$ excimer is to calculate the critical fluorescence power. This is the power that must be delivered to the atomic-molecular system to attain lasing threshold (i.e., optically transparent medium). However, once stimulated emission is initiated, thermodynamic equilibrium between the [CsXe*] and [Cs*] populations is destroyed, and so any additional power delivered to the system will be converted to stimulated emission energy. The minimum critical fluorescence power may be calculated using the relation

$$P_c = h\nu_a A_a[Cs^*] + h\nu_m A_m[CsXe^*] \tag{10}$$

where the $\nu_{a,m}$ are the center frequencies of the atomic and molecular fluorescence, respectively, and the $A_{a,m}$ are the spontaneous radiative rates for the atomic and molecular

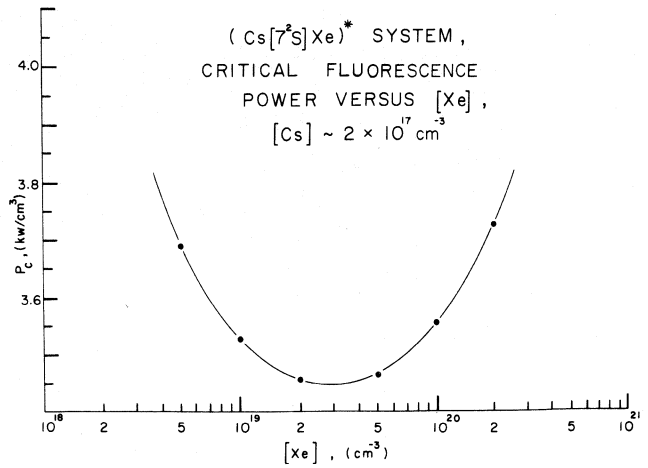


Fig. 10. Variation of the critical fluorescence power with xenon perturber density.

transitions. Setting $h\nu_a = 2.3$ eV (5395 Å), $h\nu_m = 2.17$ eV (5723 Å), $A_a = 7 \cdot 10^6$ s^{-1}, $A_m = 4.5 \cdot 10^5$ s^{-1}, [Cs*] = $1.29 \cdot 10^{15}$ cm^{-3}, and [CsXe*] = $9.43 \cdot 10^{14}$ cm^{-3}, then to attain threshold for 1 percent/m gain, the critical fluorescence power is $P_c = 3.46$ kW/cm^3.

The dependence of the critical fluorescence power density on xenon pressure for a fixed cesium density is displayed in Fig. 10. A distinct minimum of the required input energy occurs at [Xe] $\simeq 3 \cdot 10^{19}$ cm^{-3}. These minima are to be expected due to the following competing effects: 1) P_c rises at low pressures since, in this regime, the equilibrium condition favors the formation of the Cs* excited atom (rather than the excimer); and 2) P_c again climbs at increasing [Xe] since [CsXe], and hence [(CsXe)*], varies directly with the xenon density.

Even if the equilibrium constant used is too small, the increased Xe density needed to achieve the previously stated inversion conditions would not result in a greatly increased critical fluorescence power. Once again, this is a first-order estimate of the critical fluorescence power density since there is radiation from other excited states. There is also the possibility that radiation could occur from the (Cs[7^2S]Xe)* molecular state to the (Cs[6^2P]Xe)* molecular state. Presumably, the oscillator strengths would be similar to that for the Cs(7^2S)-Cs(6^2P) transition, although Σ-Σ transitions are generally favored, and so this could lead to an increase in P_c. On the other hand, the Cs(6^2P)-Cs(6^2S) transition will be heavily trapped and could act as a bottleneck for the Cs(7^2S)-Cs(6^2P) transition. This will decrease P_c. In terms of possible optical pumping, there would be an additional significant increase in P_c due to the optical branching ratio between the Cs(7^2P-7^2S) and the Cs(7^2P-5^2D) transitions (assuming the Cs(7^2P) level is optically pumped from ground).

In spite of the simplicity and limitations of the model used to describe the Cs-Xe system, the results point out the attractiveness of the (Cs[7^2S]Xe)* $\rightarrow$ (Cs[6^2S]Xe) excimer continuum as a potential laser candidate. Further studies of optically or discharge pumped Cs-Xe systems will result in an improved analysis and evaluation of such a system.

IV. Conclusions

Extensive measurements of the (Cs[7^2S]Xe)* and (Cs[5^2D]Xe)* molecular absorption and emission spectra in high-pressure cesium-xenon mixtures have been reported. In particular, the (Cs[7^2S]Xe)* molecule is found to be attractive as a dissociation laser condidate due to: 1) its large dissociation energy, 2) a high stimulated emission cross section ($\sigma \simeq 10^{-17}$ cm^2/excited molecule), and 3) a relatively long radiative lifetime (2 μs) as compared to the alkali-rare gas II states. These characteristics qualify the Cs*(7^2S)-Xe atomic-molecular system as one of the promising potential dissociation laser molecules under investigation at present.

References

[1] A. V. Phelps, "Tunable gas lasers utilizing ground state dissociation," JILA Rep. 110, Sept. 1972.
[2] D. L. Cunningham and K. C. Clark, "Rates of collision induced emission from metastable O (^1S) atoms," *J. Chem. Phys.*, vol. 61, pp. 1118-1124, 1974.
[3] H. T. Powell, J. R. Murray, and C. K. Rhodes, "Laser oscillation on the green bands of XeO and KrO," *Appl. Phys. Lett.*, vol. 25, pp. 730-732, 1974.
[4] A. Tam, G. Moe, W. Park, and W. Happer, "Strong new emission bands in alkali-noble-gas systems," *Phys. Rev. Lett.*, vol. 35, pp. 85-87, 1975.
[5] L. Noble, C. Kretschmer, R. Maynard, H. Flentz, and L. Reed, "Optical Pumps for Lasers," U.S. Army Electronics Command, Fort Monmouth, NJ, Tech. Rep. ECOM-0239-F, p. 36, 62, 1973.
[6] M. Lapp, "Collision enforced transitions in cesium," *Phys. Lett.*, vol. 23, pp. 553-554, 1966.
[7] a) M. Lapp and L. P. Harris, "Influence of alkali-vapor atmospheres on pyrometrically determined temperatures: Cesium and potassium," *J. Appl. Phys.*, vol. 34, pp. 3622-3625, 1963.
b) ——, "Absorption cross sections of alkali-vapor molecules: I CS_2 in the visible II K_2 in the red," *J. Quant. Spectrosc. Radiat. Transfer*, vol. 6, pp. 169-179, 1966. Weak absorption was observed here for the Cs(5^2D) states, but was not attributed to collision-induced absorption.
[8] F. Besombes, J. Granier, and R. Granier, "Bandes satellites observées en absorption près des raies interdites du rubidium: $5S$-$4D_{5/2,3/2}$," *Optics Comm.*, vol. 1, pp. 161-163, 1969.
[9] J. A. Gwinn, P. M. Thomas, and J. F. Kielkopf, "Satellite bands in the emission spectrum of cesium," *J. Chem. Phys.*, vol. 48, pp. 568-572, 1968.
[10] D. E. Gilbert and S. Y. Ch'en, "Pressure effects of foreign gases on the absorption lines of cesium VI intensity measurement of the cesium resonance lines and their associated satellites in the presence of various foreign gases," *Phys. Rev.*, vol. 188, pp. 40-45, 1969, and references quoted therein.
[11] W. Happer, G. Moe, and A. C. Tam, "New absorption bands observed in the CsXe system," *Phys. Lett.*, vol. 54A, pp. 405-406, 1975.
[12] G. Moe, A. C. Tam, and W. Happer, private communication.
[13] D. L. Cunningham and K. C. Clark, "Rates of collision induced emission from metastable O (^1S) atoms," *J. Chem. Phys.*, vol. 61, pp. 1118-1124, 1974.
[14] H. T. Powell, J. R. Murray, and C. K. Rhodes, "Collision induced auroral line lasers," presented at the 1975 CLEA Conf., Washington, DC, Paper 7.8.
[15] C. Tai, W. Happer, and R. Gupta, "Hyperfine structure and lifetime measurements of the second-excited D states of rubidium and cesium by cascade fluorescence spectroscopy," *Phys. Rev. A*, vol. 12, pp. 736-747, 1975.
[16] C. G. Carrington and A. Gallaher, "Teratomic recombination of excited RbXe," *J. Chem. Phys.*, vol. 60, pp. 3436-3444, 1974.
[17] R. T. Ku, J. T. Verdeyen, B. E. Cherrington, and J. G. Eden, "Decay of krypton 1 s_2 and 1 s_3 excited species in the late afterglow," *Phys. Rev. A*, vol. 8, pp. 3123-3130, 1973, and references cited therein.

[18] J. G. Eden, J. T. Verdeyen, and B. E. Cherrington, "Excimer formation rate in NaAr," *Bull. Amer. Phys. Soc.*, vol. 20, p. 247, 1975.
[19] P. M. Stone, "Cesium oscillator strengths," *Phys. Rev.*, vol. 127, pp. 1151-1156, 1962.
[20] C. J. Malerich and R. J. Cross, Jr., "High energy alkali-rare-gas scattering," *J. Chem. Phys.*, vol. 52, pp. 386-392, 1970.
[21] a) R. E. M. Hedges, D. L. Drummond, and A. Gallagher, "Extreme-wing line broadening and Cs-inert-gas potentials," *Phys. Rev. A*, vol. 6, pp. 1519-1544, 1972.
b) D. L. Drummond and A. Gallagher, "Potentials and continuum spectra of Rb-noble gas molecules," *J. Chem. Phys.*, vol. 60, pp. 3426-3435, 1974.
[22] J. Pascale and J. Vandeplanque, "Excited molecular terms of the alkali-rare gas atom pairs," *J. Chem. Phys.*, vol. 60, pp. 2278-2289, 1974.
[23] J. T. Yardley, private communication.
[24] P. A. Miller, J. T. Verdeyen, and B. E. Cherrington, "Behavior of He(2^3S) metastable atoms in weakly ionized helium plasmas," *Phys. Rev. A*, vol. 4, pp. 692-700, 1971.

Analysis of Injection Locking in Pulsed Dye Laser Systems

U. GANIEL, MEMBER, IEEE, A. HARDY, AND D. TREVES, FELLOW, IEEE

Abstract—**A pulsed dye laser system with a narrow-band signal injected into the cavity is considered. The injection starts prior to the excitation pulse. It is shown that during a transient period, injection locking can be achieved for a much wider range of parameters than under conventional CW conditions.**

The analysis is based on a set of coupled rate equations for the population densities and photon fluxes at all wavelengths. These are solved numerically with appropriate initial and boundary conditions. Analytical approximations, which are helpful for understanding the behavior of such systems, are presented. Both straight, two-mirror cavities, and ring laser cavities are discussed. The temporal evolution of the spectral components at all wavelengths is described. The range of tunability in this mode of operation and its dependence on various parameters, such as pulse length, cavity dimensions, and injection intensity are discussed.

I. Introduction

THE PROBLEM of obtaining coherent, tunable, high-power and high-energy radiation from organic dye lasers has become very important in recent years, because of the many applications that such systems find in both applied and basic research [1]. Large energy output per pulse has been achieved [2], [3], as well as considerable average power [4], but only in broad-band dye laser systems. On the other hand, line-narrowing techniques have been developed, not only for CW, but also for pulsed systems [5]-[8], leading to tunable, very narrow band operation. Line narrowing is conventionally achieved by incorporating various dispersive elements (grating, prisms, etalons, birefringent filters, or combinations thereof) in the laser cavity. As a rule, it is found that high power and narrow linewidth are somewhat contradictory requirements, because of the inevitable insertion losses introduced by every intracavity element, and because under strong pumping conditions many modes are above the oscillation threshold. One direct technique for achieving narrow-band, tunable radiation on one hand, and high output energies on the other hand, is to start from a low-power, spectrally pure laser oscillator, and use one or two laser-amplifier stages. This approach was applied by many investigators, and recently by Wallenstein and Hansch [9]. When the output of the first oscillator is high enough so that the first amplifier stage is completely saturated by the input signal, this is the most reasonable approach. In many practical cases, however, the narrow-band signal to be amplified is of very low power, and, consequently, a large fraction of the pumping energy is converted in the amplifier into broad-band fluorescence or into amplified spontaneous emission (ASE), which is undesirable [10].

An alternative technique is that of controlling the wavelength of a high-power oscillator by a tunable, narrow-band injected signal. The classical problem of locking phenomena in oscillators was analyzed long ago by Adler [11]. This work was later extended to include laser locking [12]-[13], and the effect was demonstrated by Stover and Steier [14] who achieved phase locking between two single-mode He-Ne lasers. More recently, Buczek and Freiberg [15] described frequency stabilization of a high-power CW CO_2 ring laser by locking with a stable low-power reference laser. All these investigations [12]-[15] concentrated on the behavior of the system on a CW basis. Under such conditions, the injection must be intense enough in order to extinguish the free-running fre-

Manuscript received April 12, 1976. This work was supported in part by the Israel Commission for Basic Research.

The authors are with the Department of Electronics, The Weizmann Institute of Science, Rehovot, Israel.

quency component. As we shall see later, the tuning range thus available is very narrow. In a pulsed oscillator, the tuning range which can be achieved with injection locking, during a transient period, is much wider. Such a mode of operation was reported by Bjorkholm and Danielmeyer [16] for a pulsed parametric oscillator, which was locked to an injected signal derived from a single-mode CW Nd^{3+}: YAG laser. Experiments applying the same principle to dye lasers were reported by a number of groups in recent years [17]-[22]. The purpose of this work is to present a detailed analysis of this mode of operation in dye lasers, under a wide variety of conditions.

Most authors dealing with dye laser oscillators follow the approach introduced by Sorokin *et al.* [23], in which rate equations were written for the (single-mode) photon density, the population inversion, and the triplet-state population. With various modifications, this approach was followed also by Keller [24], by Pappalardo *et al.* [25] and more recently, by Atkinson and Pace [26], who also included frequency-selective elements in their analysis. In this approach, all quantities are assumed to be uniform along the cavity. Since in many laser-pumped dye laser systems the gain is very high, and consequently, the optimum output coupling rather large [27], this approximation is not justified even at steady state [28].

In the present paper we start from a general set of rate equations which contains both the temporal and the spatial dependence of the relevant quantities. The same equations have been used previously in [10], in the analysis of ASE and amplifications in dye laser systems. We thus present a unified analytical approach which is useful for analyzing various physical situations such as ASE, amplification, and laser oscillations. These are distinguished by appropriate initial and boundary conditions on the solutions. The present analysis deals with the behavior of a pulsed dye laser system with injection of a narrow-band signal, the temporal evolution of the spectral components at all wavelengths, the tunability of the laser output as the injected wavelength is tuned across the gain curve of the dye laser, and its dependence on the injected intensity.

The behavior of a pulsed, broadly tunable system like a dye laser is governed by the overall gain curve, which is determined by the active medium parameters and the cavity losses (mainly the output coupling). The fine structure caused by the Fabry-Perot resonances of the cavity is superposed on the output spectrum. In the present analysis, this fine structure will be disregarded, since we shall be interested in broadly tunable systems. The results we shall obtain will thus describe the spectral envelope of the laser radiation. This approach is similar to the general discussion by Ambartsumyan *et al.* [29], and it also applies to the experiments described by Marowsky [30] on dye laser systems with nonresonant feedback.

In Section II we present the rate equations, define the initial and boundary conditions, and explain the details of the physical model used. Two specific numerical examples are given which illustrate the general features of an injection-locked pulsed dye laser system. Section III is devoted to a detailed analysis of the temporal period where locking takes place (the first plateau). In particular, we analyze the injection power requirements, the output intensity, the duration of the locked period, and the effects of triplet-state absorption. Both numerical results and analytical approximations are discussed. In Section IV, the temporal regime which follows the locked operation is analyzed, and again, both numerical and analytical results are presented. A short discussion is given in Section V.

II. Rate Equations

The energy level scheme we shall consider is shown schematically in Fig. 1. S_0 is the lowest vibration-rotation manifold, S_1 is the first excited singlet manifold, and T_1 is the first triplet manifold. We shall deal with two cavity configurations. One, represented in Fig. 2, is a straight two-mirror cavity. The active medium has a length L, one mirror is totally reflecting and the other mirror has reflectivity R, assumed to be nondispersive. The other configuration, represented in Fig. 3, is a ring cavity. Such a cavity is particularly convenient for operation in the injection mode, since feedback into the source of the injection is automatically avoided. The radiation is injected through the mirror with reflectivity R, which is also the output coupler. The total (optical) length of the cavity is L'.

The rate equations which govern the temporal evolution of the photon fluxes in both directions and the various level populations in the active medium are the same as in [10]

$$\frac{\partial N_1(x,t)}{\partial t} = W(t)\,N_0(x,t) - \tau^{-1}N_1(x,t) - N_1(x,t)\int\sigma_e(\lambda)[I^+(x,t,\lambda)+I^-(x,t,\lambda)]\,d\lambda + N_0(x,t)\int\sigma_{01}(\lambda)[I^+(x,t,\lambda)+I^-(x,t,\lambda)]\,d\lambda \tag{1}$$

$$\frac{\partial N_T(x,t)}{\partial t} = K_{ST}N_1(x,t) - \tau_T^{-1}N_T(x,t) \tag{2}$$

$$N_0(x,t)+N_1(x,t)+N_T(x,t)=N \tag{3}$$

$$\pm\frac{d}{dx}[I^{\pm}(x,t,\lambda)] = N_1(x,t)\,\sigma_e(\lambda)\,I^{\pm}(x,t,\lambda) + \tau^{-1}N_1(x,t)\,E(\lambda)\,g^{\pm}(x) - \sigma_{01}(\lambda)\,N_0(x,t)\,I^{\pm}(x,t,\lambda) - \sigma_T(\lambda)\,N_T(x,t)\,I^{\pm}(x,t,\lambda) \tag{4}$$

where

$$(d/dx)\,I^{\pm} = (\partial/\partial x)\,I^{\pm} \pm (\eta/c)\,(\partial/\partial t)\,I^{\pm}.$$

$W(t)$ is the pumping rate (s^{-1}) given in general by

$$W(t) = [P(t)/A]\int\sigma_a(\lambda_p)\,f(\lambda_p)(\lambda_p/hc)\,d\lambda_p \tag{5}$$

$$\sigma_e(\lambda) = [\lambda^4 E(\lambda)]/8\pi c\eta^2\tau \tag{6}$$

where

$$\int E(\lambda)\,d\lambda = \Phi$$

and all the quantities appearing in (1)-(6) are defined as in

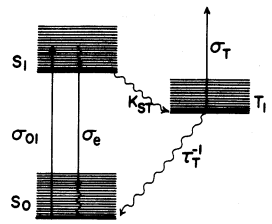


Fig. 1. Energy level scheme assumed in the calculation. Straight arrows denote radiative transitions, wiggled arrows denote radiationless transitions.

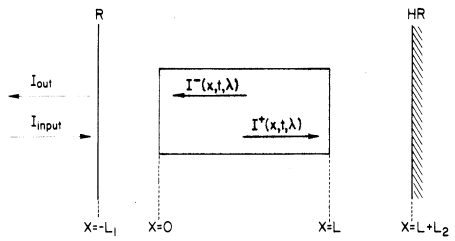


Fig. 2. Straight laser cavity.

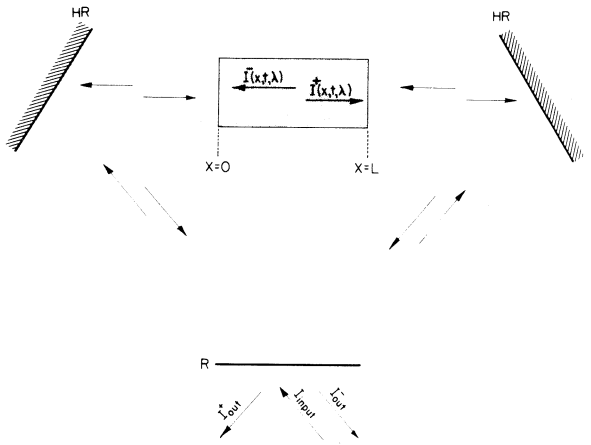


Fig. 3. Ring laser cavity.

[10] and are summarized in Table I, which also includes definitions of some symbols used frequently in this paper. In order to simplify the computation, we assume the pumping rate $W(t)$ to be uniform all over the active medium.[1] Transverse variations in the intensities and the population densities are not accounted for in this model.

The equations are written for a homogeneously broadened medium so that the same $N_i(x, t)$ $(i = 1, T)$ molecules interact with the radiation at all wavelengths within the fluorescence band. The evolvement inside the active medium was found by solving (1)-(4) numerically. Outside the medium, lossless propagation was assumed and accounted for by appropriate boundary conditions. For the straight laser cavity (Fig. 2) these are

$$I^-(L, t, \lambda) = I^+(L, t - t_2, \lambda) \tag{7a}$$

[1]Equations (1)-(4) can also be used to describe the situation for longitudinal optical pumping schemes used frequently in dye laser systems. In that case, $W(t)$ will depend also on x. Equation (4) will be used to describe $I^{\pm}(x, t, \lambda)$ at all wavelengths λ, including λ_p (the pump wavelength).

TABLE I

Symbol	Definition	Units
N	Density of dye molecules	(molecules)cm^{-3}
$N_1(x,t)$	Population density at S_1 (at time t and coordinate x)	"
$N_0(x,t)$	Population density at S_0	"
$N_T(x,t)$	Population density at T_1	"
$P(t)$	Pump power at time t	erg. sec^{-1}
A	Pumped area	cm^2
$\sigma_a(\lambda_p)$	Absorption cross section from S_0 at wavelength λ_p	cm^2
$f(\lambda_p)$	Normalized spectral distribution of pump radiation $\int f(\lambda_p)d\lambda_p = 1$	
h	Planck's constant	erg·sec
c	Velocity of light in vacuum	$cm \cdot sec^{-1}$
n	Refractive index of the active medium	-
τ	Lifetime of the S_1 state	sec
$\sigma_e(\lambda)$	Stimulated emission cross section at wavelength λ, $S_1 \rightarrow S_0$	cm^2
$\sigma_{01}(\lambda)$	Absorption cross section at wavelength λ, $S_0 \rightarrow S_1$	cm^2
$\sigma_T(\lambda)$	Absorption cross section from T_1 at wavelength λ	cm^2
K_{ST}	Inter-system crossing rate ($S_1 \rightarrow T_1$)	sec^{-1}
τ_T	Lifetime of the T_1 state	sec
$E(\lambda)$	Normalized fluorescence spectrum ($S_1 \rightarrow S_0$)	cm^{-1}
ϕ	Fluorescence quantum efficiency	-
$I^{\pm}(x,t,\lambda)$	Photon flux, per unit wavelength, at wavelength λ, propagating in the $\pm x$ direction	(photon) $cm^{-3} \cdot sec^{-1}$ -
$g^{\pm}(x)$	Geometrical factor equal to the fraction of the spontaneous emission by molecules at x, which is added to $I^{\pm}(x)$.	
$\Sigma(\lambda)$	$\Sigma(\lambda) = \sigma_e(\lambda) + \sigma_{01}(\lambda)$	cm^2
q_i	$q_i = I_{in}/WNL$	-

$$I^+(0, t, \lambda) = RI^-(0, t - t_1, \lambda) + I_{in}/\Delta\lambda_i \tag{7b}$$

where

$$I_{in} = (1 - R)\, I_{input}. \tag{8}$$

I_{input} is the injected photon flux, outside the cavity. We assume a narrow-band injection of width $\Delta\lambda_i$, i.e., $I_{input} \neq 0$ only for $\lambda_i - (\Delta\lambda_i/2) \leqslant \lambda \leqslant \lambda_i + (\Delta\lambda_i/2)$. t_2 (or t_1) represents the travel time of the wavefront from $x = L$ $(x = 0)$ to $x = L + L_2$ $(x = -L_1)$ and back. The output flux per unit wavelength at wavelength λ is given by

$$I_{out}(t, \lambda) = (1 - R)\, I^-(0, t - t_1/2, \lambda) + RI_{input}/\Delta\lambda_i \tag{9}$$

where, for cases of interest in which injection locking is achieved, the second term on the right-hand side (RHS) of (9) is negligible compared to the first. Similarly, for a ring cavity (Fig. 3) we have the boundary conditions

$$I^-(L, t, \lambda) = RI^-(0, t - t_3, \lambda) \tag{10a}$$

$$I^+(0, t, \lambda) = RI^+(L, t - t_3, \lambda) + I_{in}/\Delta\lambda_i \tag{10b}$$

where t_3 represents the travel time around the resonator outside the active medium. The output flux is given by

$$I^+_{out}(t, \lambda) = (1 - R)\, I^+(L, t - t_4, \lambda) + RI_{input}/\Delta\lambda_i \tag{11a}$$

$$I^-_{out}(t, \lambda) = (1 - R)\, I^-(L, t - t_5, \lambda) \tag{11b}$$

with t_4 and t_5 the travel times from $x = L$ and $x = 0$, respectively, to the output mirror. Clearly, under locked operation, $I^+_{out}(\lambda_i) \gg I^-_{out}(\lambda_i)$. When (1)-(6) in conjunction with the boundary conditions (7) and (9) or (10)-(11) are used to treat the laser oscillator, the fine structure due to the resonant cavity modes is clearly disregarded.[2] The initial conditions assumed for the solution are as follows: prior to the pumping

[2]The mode structure can be included in the analysis by imposing an appropriate transfer function for the intensity feedback [15], [26], which will represent the cavity resonances. This was not done here.

pulse, injection of I_{input} starts at some time, and after a few round trips a steady state is established where $I^{\pm}(x, \lambda) \simeq 0$ for all λ outside the bandwidth $\Delta\lambda_i$ of the injected radiation, and $N_0 \simeq N$, $N_1 \simeq 0$, $N_T \simeq 0$.[3] The pump pulse is then switched on. Note that if $I_{input} = 0$, we obtain the description of a laser oscillator without injection locking.

In the numerical calculations we consider a solution of the dye rhodamine 6G (R6G) in ethanol, since the material parameters for this system are well known (see Table II). A typical geometry for transversely pumped systems is considered, where the length of the active medium is appropriate for laser pumping. Depending on the pumping source and scheme, different concentrations can be used in practice. As an illustration, for a nitrogen laser pump ($\lambda_p = 337.1$ nm), $\sigma_a(\lambda_p) = 2.4 \times 10^{-17}$ cm^2, so that with a pumped strip of 1 cm × 0.04 cm, $P(t) = 1$ kW corresponds to $W(t) = 10^6$ s^{-1} [(5)]. At high pumping rates ($W \geqslant 10^7$ s^{-1} for the concentration considered here), the buildup time is short compared to the duration of the exciting pulse, and it is therefore a reasonable approximation to assume $W(t)$ to be a square wave in time, i.e., $W(t) = W$ during the excitation time.

As a basis for the discussion to follow, we plot in Fig. 4 the results of a sample calculation for $W = 10^8$ (s^{-1}), where the active medium fills the cavity ($L = 1$ cm, $L_1 = L_2 = 0$), $R = 4$ percent, $I_{input} = 5 \times 10^{20}$ (photons · cm^{-2} · s^{-1}) ($\simeq$150 W/cm^2) at $\lambda_i = 585$ nm with $\Delta\lambda_i = 5 \times 10^{-3}$ nm.[4] The effects of triplet states can be neglected here, since times much smaller than K_{ST}^{-1} are considered. The free-lasing wavelength without injection (which can be calculated from the parameters of the system, as will be shown in Section III-A) is $\lambda_l = 590$ nm. Injection starts at $t = 0$, and at $t = 1$ ns the pump is switched on. During some initial period, radiation at all wavelengths starts to build up from spontaneous emission. The behavior of the system during this period is hard to describe analytically, because of the nonlinear character of the rate equations (1)-(4). However, at high pumping rates, the buildup processes are very fast, and after a few round trips the transients die out. In the absence of injection, radiation at λ_l would reach its steady-state value and determine the population inversion (N_1) by saturation so as to have an overall closed-loop gain of unity ($G^2(\lambda_l)R = 1$, with $G(\lambda_l)$ the single-pass gain at λ_l).[5] In the example of Fig. 4, injected radiation is present in the cavity when the pump is switched on, so that the radiation at λ_i grows during the initial period with a "head start" over all other wavelengths. If $I(x, t, \lambda_i)$ reaches such a level that most of the radiation in the cavity is contained within the bandwidth of the injection ($\Delta\lambda_i$), a quasi steady state is established, and N_1 is clamped to give $G^2(\lambda_i)R = 1$.[5] We shall refer to this situation as the *first plateau*. During this period, $I(x, t, \lambda_i)$ and $N_1(x, t)$ are practically constant in time. Radiation at λ_l, however, will have excess gain (i.e., $G^2(\lambda_l)R > 1$), and will grow exponentially in time. This behavior is clearly seen in Fig. 4 (note the logarithmic scale on the ordinate). Eventually the photon flux at λ_l will approach that at λ_i, and will start to saturate $N_1(x, t)$ towards a smaller value than its value during the first plateau. The decrease in $N_1(x, t)$ will terminate the first plateau, since, after some transition period, $I(x, t, \lambda_l)$ will take over, reach its steady-state value, and $N_1(x, t)$ will then be determined so as to give $G^2(\lambda_l)R = 1$. $I(x, t, \lambda_i)$ decreases exponentially and finally settles down to a new steady state. This steady state is the *second plateau*. As another illustration, we plot in Fig. 5 the results of a similar calculation for a ring laser, of total cavity length $L' = 50$ cm, $R = 20$ percent, an active medium of length $L = 1$ cm, and all other parameters identical to those of Fig. 4. The qualitative features are similar, but the time scales involved are expanded. We shall return to this point later, in Section III-D. For broad-tuning purposes or pulsed systems, it is the first plateau which is of main interest.

TABLE II
PARAMETERS USED IN THE COMPUTATIONS

Quantity	Numerical Value	Reference
τ	5.5×10^{-9} (sec)	32
η(ethanol)	1.36	
$E(\lambda)$	Figure 9 in reference	33
$\sigma_{01}(\lambda)$	Figure 9 in reference	33
K_{ST}	3.4×10^6 (sec^{-1})	34
τ_T	2.5×10^{-7} (sec)	34
$\sigma_T(\lambda)$	Figure 7 in reference	35
N	5×10^{-3} (mole/liter) = 3×10^{18} cm^{-3}	

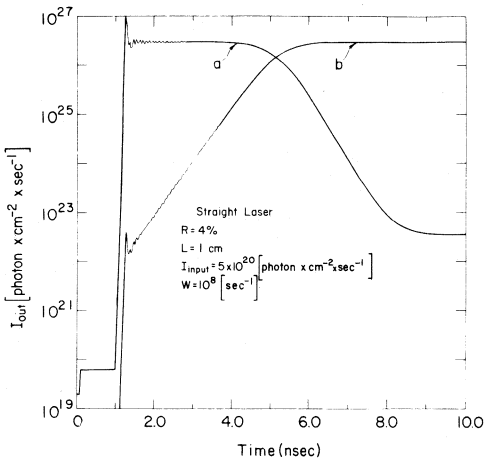


Fig. 4. Output photon flux in a straight laser with injection at $\lambda_i = 585$ nm, as a function of time: *a*–at $\lambda_i = 585$ nm; *b*–at $\lambda_l = 590$ nm, within a bandwidth of 5 nm. The geometrical factor has an average value of $g = 10^{-6}$. The pump is switched on at $t = 1$ ns. Material parameters are given in Table II.

III. The First Plateau

A. Free-Oscillation Wavelength

Since we are interested that the first plateau period be as long as possible, the injection wavelength λ_i must not be too far from the free-oscillation wavelength λ_l. λ_l is determined by the parameters of the system in the following manner. Consider a laser at steady state

[3] Some excitation of molecules from S_0 to S_1 by I_{input} takes place, but under most practical conditions it is negligible compared to the effect of the pumping radiation.

[4] In all the numerical computations the fluorescence band of R6G (520-630 nm) is divided into segments of 5 nm each. In addition, the program provides for the possibility of injection of radiation into any of these channels, at any chosen bandwidth $\Delta\lambda_i$.

[5] Actually, $G^2(\lambda_l)R$ (or $G^2(\lambda_i)R$) is somewhat smaller than 1, since the closed-loop gain, *including* the injected energy and the spontaneous emission, must be unity.

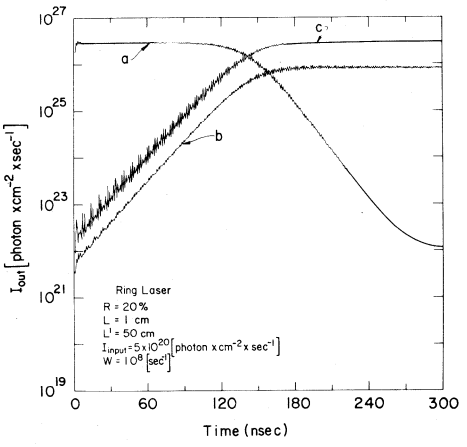


Fig. 5. Output photon flux in a ring laser with injection at $\lambda_i = 585$ nm, as a function of time. Triplet-state effects are neglected. The pump is switched on after the injected radiation of λ_i reaches steady state. *a*—at $\lambda_i = 585$ nm; *b*—at $\lambda_l = 590$ nm, in the positive direction (I_l^+); *c*—total output at $\lambda_l = 590$ nm ($I_l^+ + I_l^-$).

$$G^2(\lambda_l)R = 1 \quad \text{(straight laser)} \tag{12a}$$

or

$$G(\lambda_l)R = 1 \quad \text{(ring laser)} \tag{12b}$$

where (see [10])

$$G(\lambda) = \exp\left[\int_0^L \alpha(\xi, \lambda)\, d\xi\right] \tag{13}$$

and

$$\alpha(\xi, \lambda) = \Sigma(\lambda) N_1(\xi) + [\sigma_{01}(\lambda) - \sigma_T(\lambda)]\, N_T(\xi) - \sigma_{01}(\lambda) N. \tag{14}$$

Since no tuning element is present in the cavity,[6] λ_l will be such that $G(\lambda)$ has a maximum at $\lambda = \lambda_l$. From (13) and (14) we thus find

$$\left[\bar{N}_1 L \frac{\partial}{\partial\lambda}\Sigma(\lambda) + \bar{N}_T L\left(\frac{\partial}{\partial\lambda}\sigma_{01} - \frac{\partial}{\partial\lambda}\sigma_T\right) - NL\frac{\partial}{\partial\lambda}\sigma_{01}\right]_{\lambda=\lambda_l} = 0 \tag{15}$$

where

$$\bar{N}_i = \frac{1}{L}\int_0^L N_i(\xi)\, d\xi \qquad (i = 1, T).$$

If we concentrate on pulsed laser pump sources (nitrogen laser, Q-switched Nd^{3+}:YAG, or ruby and their harmonics, etc.) the pump pulse is much shorter than K_{ST}^{-1} so that triplet-state effects are negligible and we can assume $N_T \simeq 0$. In this case we obtain from (15), using (12)-(14)

$$\frac{1}{2}\ln(1/R)\left[\frac{\partial}{\partial\lambda}\Sigma\right]_{\lambda=\lambda_l} + NL\left[\sigma_{01}\frac{\partial}{\partial\lambda}\sigma_e - \sigma_e\frac{\partial}{\partial\lambda}\sigma_{01}\right]_{\lambda=\lambda_l} = 0 \tag{16}$$

for the straight laser, and for the ring laser the factor $\frac{1}{2}$ on the left-hand side (LHS) is replaced by 1. Equation (16) determines λ_l. For long-pulsed systems or for CW systems, where the triplet states cannot be neglected, λ_l can be found by the same reasoning. Assuming final steady-state conditions for the populations, we have from (2)

$$N_T(\xi) = K_{ST}\tau_T N_1(\xi), \tag{17}$$

and using (12)-(14) we obtain

$$\frac{1}{2}\ln(1/R)\left[\frac{\partial}{\partial\lambda}\sigma_e + (1 + K_{ST}\tau_T)\frac{\partial}{\partial\lambda}\sigma_{01} - K_{ST}\tau_T\frac{\partial}{\partial\lambda}\sigma_T\right]_{\lambda=\lambda_l} + NL\left[\sigma_{01}\frac{\partial}{\partial\lambda}\sigma_e - \sigma_e\frac{\partial}{\partial\lambda}\sigma_{01} + K_{ST}\tau_T\left(\sigma_T\frac{\partial}{\partial\lambda}\sigma_{01} - \sigma_{01}\frac{\partial}{\partial\lambda}\sigma_T\right)\right]_{\lambda=\lambda_l} = 0 \tag{18}$$

for the straight laser, and a similar equation ($\frac{1}{2} \to 1$ on the LHS) for the ring laser. The result (18) applies when the final steady state is reached, i.e., after ~ 1 μs for R6G. For fast-rise-time pump sources, after the initial buildup period, λ_l is determined by (16). If the pumping pulse lasts long enough, a wavelength sweep from that value should occur. Such effects have been observed experimentally [31].

B. Injection Power Requirements

Considering now the injected signal: we wish to establish a criterion for injection locking to take place at all, namely—what must be the magnitude of I_{in} [(7b) or (10b)] in order for the first plateau to occur? It was shown in [10] that $I_0(\lambda)$ defined by

$$I_0(\lambda) = 8\pi\eta^2 cg/\lambda^4 \qquad (g = g^+(0)) \tag{19}$$

can be identified as an equivalent noise input signal. In the case of a laser oscillator, the oscillations start from this noise. A first plateau will occur if radiation at λ_i is present in the cavity with an intensity which will determine such a growth rate that during the initial buildup most photons are emitted at λ_i. A rough estimate for the injection intensity needed to obtain this situation is given by the requirement that the photon flux at λ_i inside the cavity be larger than I_{min}, where

$$\sigma_e(\lambda_i)\, I_{min} \simeq \int_{[\delta\lambda]} \sigma_e(\lambda')\, I_0(\lambda')\, d\lambda'. \tag{20}$$

The range of integration $\delta\lambda$ is chosen so that it includes all wavelengths λ for which $G(\lambda_i) \leqslant G(\lambda)$. This criterion was checked in many numerical runs and found to be adequate. Note that (20) gives an estimate of the photon flux

[6] If the cavity contains a tuning element, as in the experiments of Turner *et al.* [20], then λ_l is determined in a similar manner, but with an additional constraint that λ_l should be inside the bandpass of that element.

(photons $\cdot s^{-1} \cdot cm^{-2}$) needed. In order to estimate I_{min} in practice, g must be known. For systems which operate in a single transverse mode (TEM_{00}), the angle of divergence is determined by $\theta = \lambda/\pi\omega_0$, with ω_0 the waist radius, and thus

$$g = \tfrac{1}{2}(1 - \cos\theta) \simeq (\lambda/2\pi\omega_0)^2. \tag{21}$$

We assume that the mode of the injected radiation is matched to the laser mode. The power P (photons/s) in a Gaussian beam is $P = \bar{I}\pi\omega_0^2$, with $\bar{I}$ an average intensity across the beam. We thus find from (19)-(21)

$$P_{in}(\text{single mode}) > P_{min} \simeq 2\eta^2 c \int_{[\delta\lambda]} [\sigma_e(\lambda')/\sigma_e(\lambda_i)]\, d\lambda'/\lambda'^2. \tag{22}$$

Equation (22) gives an estimate of the minimum injection *power* necessary for observing the first plateau in *single transverse mode* operation. Note that in this case, P_{min} does not depend on the geometry. In practice, λ_i is close to the peak of the overall gain curve, so that $\sigma_e(\lambda') \simeq \sigma_e(\lambda_i)$. Assuming, e.g., $\delta\lambda \simeq 10$ nm around $\lambda \simeq 600$ nm, we find $P_{min} \simeq 6 \times 10^{13}$ [photons/s] or $\sim 20\ \mu$W.

In the other extreme of highly multimode operation, g can be estimated as $g \simeq \Delta\Omega/4\pi$, with $\Delta\Omega$ the solid angle subtended by the output beam of the free-running laser. In such systems, $\Delta\Omega$ is determined by the geomerty, namely, $g \simeq (r/2L)^2$, where r is the radius of the excited medium and L its length. Thus if we substitute (19) in (20) and multiply by the area (πr^2) we get

$$P_{min}(\text{multimode}) \simeq 2\eta^2 c \int_{[\delta\lambda]} [\sigma_e(\lambda')/\sigma_e(\lambda_i)] \cdot (\pi r^2/\lambda' L)^2\, d\lambda'/\lambda'^2. \tag{23}$$

It is seen that in contrast with the single-mode case (22), P_{min} for the multimode case is geometry dependent and proportional to the square of the effective Fresnel number of the active medium ($F = r^2/\lambda L$). Taking a typical situation for flashlamp-pumped system ($r = 0.5$ cm, $L = 20$ cm, $\lambda = 600$ nm), $F \simeq 200$, so that we find from (23) $P_{min} \simeq 3 \times 10^{19}$ (photon/s) or ~ 10 W.

C. Output Intensity During the First Plateau

In this subsection we shall first neglect the effects of the triplet states, so that the results will apply to short enough pulses ($\Delta t \ll K_{ST}^{-1} \simeq 300$ ns for R6G). The effects of triplet states will be discussed later, in Section III-E. We assume the injection to be such that the first plateau occurs, so that most of the photon flux in the cavity is within a bandwidth $\Delta\lambda_i$ around λ_i. Starting from (1)-(4), we then find at steady state ($\partial/\partial t = 0$)

$$N_1(x) = N\left\{W + \int \sigma_{01}(\lambda)[I^+(x,\lambda) + I^-(x,\lambda)]\, d\lambda\right\} \Big/ \left\{W + \tau^{-1} + \int \Sigma(\lambda)[I^+(x,\lambda) + I^-(x,\lambda)]\, d\lambda\right\}. \tag{24}$$

Integrating (4) over λ, and writing $I^{\pm}(x) = \int I^{\pm}(x,\lambda)\, d\lambda$, we find, as was shown in detail in [10],

$$\frac{d}{dx}[I^+(x) - I^-(x)] = N_0(x)W - \tau^{-1}N_1(x) \cdot \{1 - [g^+(x) + g^-(x)]\Phi\}. \tag{25}$$

At high pumping rates, stimulated emission at the dominating wavelength is the process with the highest rate, so that

$$\int \Sigma(\lambda)[I^+(x,\lambda) + I^-(x,\lambda)]\, d\lambda \gg \tau^{-1},\ W,$$

and hence also $N_1(x) \ll N$. Thus

$$\frac{d}{dx}[I^+(x) - I^-(x)] \simeq WN. \tag{26}$$

From (4) it is also evident that for a wavelength λ at which the spontaneous emission term can be neglected, as in a laser oscillator above threshold,

$$[1/I^+(x,t,\lambda)]\frac{d}{dx}I^+(x,t,\lambda) + [1/I^-(x,t,\lambda)]\frac{d}{dx}I^-(x,t,\lambda) = 0. \tag{27}$$

From here on we shall discuss the straight laser and the ring laser separately.

1. Straight laser

During the first plateau, $I^{\pm}(x) \simeq I_i^{\pm}(x)$, where $I_i^{\pm}(x) = I_i^{\pm}(x,\lambda_i)\,\Delta\lambda_i$. Hence integration of (26) yields

$$I_i^+(x) - I_i^-(x) \simeq WNx + I_i^+(0) - I_i^-(0). \tag{28}$$

At steady state, (27) leads to

$$I_i^+(x)\, I_i^-(x) = I_i^+(0)\, I_i^-(0) = \text{const}. \tag{29}$$

Using the boundary conditions (7), we obtain from (28) and (29) the distribution of the photon flux in the active medium

$$I_i^{\pm}(x) \simeq \tfrac{1}{2} WNL\,\{\mp(L - x)/L + [(L - x)^2/L^2 + (2/(1 - R))^2(R + q_i)(1 + q_i)]^{1/2}\}. \tag{30}$$

From (24), the distribution of $N_1(x)$ along the active medium is obtained as

$$N_1(x) \simeq \{1 + \sigma_{01}(\lambda_i)NL[(L - x)^2/L^2 + (2/(1 - R))^2(R + q_i)(1 + q_i)]^{1/2}\} / L\Sigma(\lambda_i)[(L - x)^2/L^2 + (2/(1 - R))^2(R + q_i)(1 + q_i)]^{1/2}. \tag{31}$$

In Fig. 6 we plot $I_i^+(x)$ and $I_i^-(x)$ during the first plateau ($t =$ 3 ns), and in Fig. 7 we plot $N_1(x)$, both for conditions identical to those in Fig. 4. The analytical results (30), (31) were found to be in excellent agreement with the results obtained by solving (1)-(4) numerically. In particular, (30) gives

$$I_i^-(0) \simeq WNL(1 + q_i)/(1 - R)$$

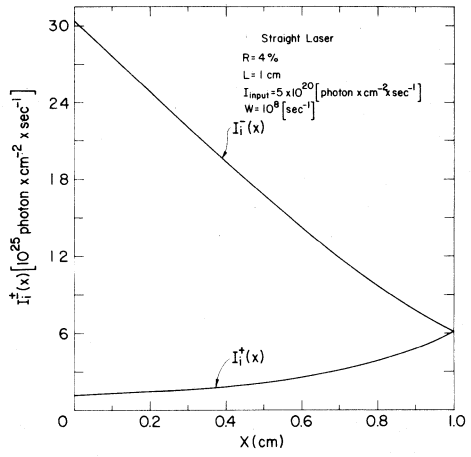


Fig. 6. Photon flux as a function of x inside the active medium in a straight laser, at the injected wavelength $\lambda_i = 585$ nm, at $t = 3$ ns (during the first plateau, see Fig. 4).

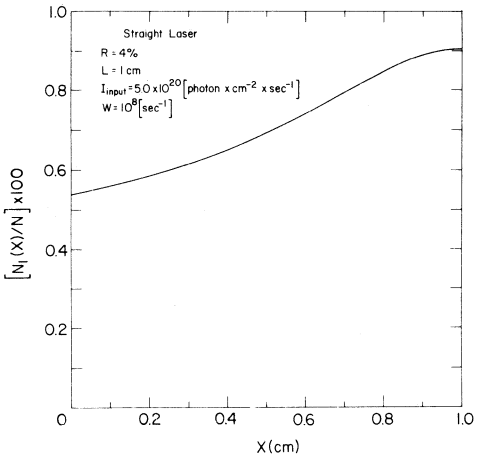


Fig. 7. Excited-state population inside the active medium ($N_1(x)$) in percents of total concentration (N), at $t = 3$ ns (during the first plateau), in a straight laser.

so that from (9)

$$I_i(\text{out}) \simeq WNL + I_{\text{input}}. \tag{32}$$

Equation (32) represents the fact that the conversion efficiency from pump to laser output photons at λ_i is close to unity, as is to be expected in a lossless situation and at high pumping rates. A similar conclusion for the case of ASE was found in [10].

We note in passing that if $I_{\text{input}} = 0$, the output will be at a wavelength λ_l determined by (16), and the results (30)-(32) apply directly to the usual case of a straight laser after λ_i is replaced by λ_l, and $I_i^{\pm}(x)$ by $I_l^{\pm}(x)$.

In actual experimental situations, the injected intensity is much smaller than the laser output, so that $q_i \ll 1$, and $I_{\text{out}} \simeq WNL$. Neglecting terms of order q_i in (31), $G(\lambda_i)$ can be calculated directly from (31) using (13) and (14). Within this approximation it is found that $G(\lambda_i) = R^{-1/2}$, as expected. (For a ring laser, a similar calculation will yield $G(\lambda_i) = R^{-1}$).

Another point which was checked in many numerical runs is the fact that the injected radiation must be present only during the initial buildup. Once the first plateau is established, I_{input} can be turned off, and the output $I_i(\text{out})$ will be $\simeq WNL$. Also the duration of the first plateau (to be discussed in Section III-D) remains the same. This fact has a direct implication in practice, since it means that a short-pulse narrow-band laser can serve as the injection source, provided it is temporally synchronized with the beginning of the second laser pulse.

2. Ring laser

Again we assume an injection intense enough for the first plateau to occur. Equation (26) is still valid inside the active medium, but since practically all the photon flux during the first plateau is included in $I_i^+(x)$, $I_i^+(x) \gg I_i^-(x)$, and (26) yields

$$I_i^+(x) \simeq WNx + I_i^+(0). \tag{33}$$

Using the boundary conditions (10b) we obtain

$$I_i^+(x) \simeq WNL\,[x/L + (1 - R)^{-1}(R + q_i)] \tag{34}$$

and from (24)

$$N_1(x) \simeq \{1 + \sigma_{01}(\lambda_i)NL[x/L + (1 - R)^{-1}(R + q_i)]\} / \{L\,\Sigma(\lambda_i)\,[x/L + (1 - R)^{-1}(R + q_i)]\}. \tag{35}$$

In Fig. 8 we plot $I_i^+(x)$ during the first plateau ($t = 30$ ns), and in Fig. 9 we plot $N_1(x)$, both for conditions identical to those in Fig. 5. Again it is found that the analytical results (34), (35) are in excellent agreement with the numerical solutions of (1)-(4). For $x = L$, (34) gives

$$I_i^+(L) \simeq WNL(1 + q_i)/(1 - R)$$

so that from (11)

$$I_i^+(\text{out}) \simeq WNL + I_{\text{input}}$$

and

$$I_i^+(\text{out}) \gg I_i^-(\text{out}) \simeq 0. \tag{36}$$

Unlike the situation for the straight laser, (34)-(36) describe only the situation during the first plateau under injection-locked operation, when $I_i^+(x)$ completely quenches $I_i^-(x)$. Without injection, $I^{\pm}(x, \lambda)$ and $N_1(x)$ are symmetric around $x = L/2$, and their spatial distributions *cannot* be deduced from (34) and (35). $N_1(x)$ and $I_l^{\pm}(x)$ for a free-running ring laser can be calculated directly using (26), (24), and the appropriate boundary conditions (10). Alternatively, we note that by symmetry,

$$I_l^+(x) = I_l^-(L - x), \qquad N_1(x) = N_1(L - x),$$

and thus the results can be read off directly from the corresponding ones for a straight laser with a medium of length $L/2$. We find

$$I_l^{\pm}(x) \simeq (\tfrac{1}{2})\,WNL\,\{\pm(x - L/2)/L + [(x - L/2)^2/L^2 + R/(1 - R)^2]^{1/2}\} \tag{37}$$

$$N_1(x) \simeq \{1 + \sigma_{01}(\lambda_l)NL[(x - L/2)^2/L^2 + R/(1 - R)^2]^{1/2}\} / \{L\,\Sigma(\lambda_l)\,[x - L/2)^2/L^2 + R/(1 - R)^2]^{1/2}\} \tag{38}$$

(ring laser, no injection).

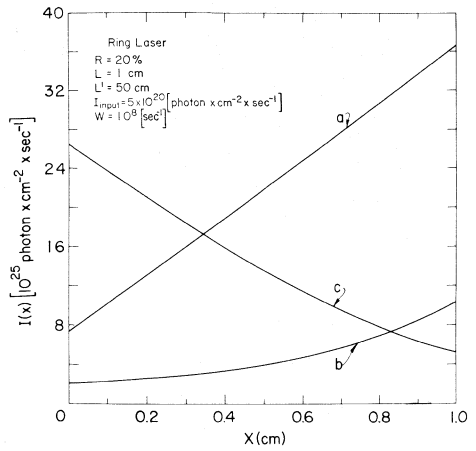


Fig. 8. Photon flux as a function of x inside the active medium in a ring laser, under conditions identical to those in Fig. 5. a—at the injected wavelength $\lambda_i = 585$ nm, at $t = 30$ ns (during the first plateau, see Fig. 5); b—at $\lambda_l = 590$ nm, in the positive direction ($I_l^+(x)$) at $t = 300$ ns (during the second plateau); c—at $\lambda_l = 590$ nm, in the negative direction ($I_l^-(x)$) at $t = 300$ ns.

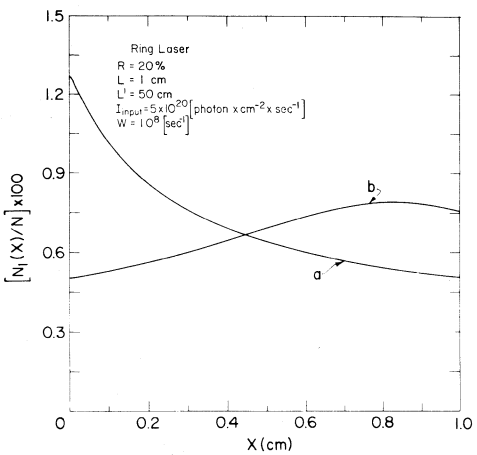


Fig. 9. Excited-state population inside the active medium ($N_1(x)$) in percent of total concentration (N), in a ring laser, under conditions identical to those in Fig. 5. a—at $t = 30$ ns.; b—at $t = 300$ ns.

D. Duration of the First Plateau

During the first plateau, the gain per pass $G(\lambda)$ is determined by $N_1(x)$ as given in (31) (or (35) for the ring laser). Radiation at λ_l will experience excess gain and its intensity will grow exponentially in time. Assume that the initial buildup period, during which $I_i(x)$ reaches the level determined by (30), lasts from the moment the pump is switched on until some $t = t_0$. Let us denote by $I_l^{\pm}(x, t_0)$ the total photon flux within the bandwidth $\delta\lambda$ as defined previously (20), i.e.,

$$I_l^{\pm}(x, t_0) = \int_{[\delta\lambda]} I^{\pm}(x, t_0, \lambda) d\lambda.$$

Since during the initial buildup period the behavior is highly nonlinear [(1)-(4)] an estimate of $I_l^{\pm}(x, t_0)$ is hard to obtain analytically. A semiqualitative argument can be as follows: λ_i is close enough to λ_l so that the overall gains, during this short period, at λ_i and at all wavelengths λ within $[\delta\lambda]$ are not very different. $I_l^{\pm}(x)$ builds up from I_{in}, whereas $I_l^{\pm}(x)$ builds up during the same period from $\int_{[\delta\lambda]} I_0(\lambda) d\lambda$. Thus a rough estimate would be

$$\frac{I_l(x, t_0)}{I_i(x, t_0)} \simeq \frac{\int_{[\delta\lambda]} I_0(\lambda) d\lambda}{I_{in}} = \frac{1}{K}; \tag{39a}$$

and in particular, for the straight laser,

$$I_l^-(0, t_0)(1 - R) \simeq WNL/K, \tag{39b}$$

or

$$[I_l^+(L, t_0) + I_l^-(L, t_0)] (1 - R) \simeq WNL/K \tag{39c}$$

for the ring laser. This assumption was checked in many computer runs and found to hold very well over a wide range of values of I_{in}, $10I_{min} \leqslant I_{in} \leqslant 10^{-2} WNL$.

The growth rate of $I_l^{\pm}(x, t)$ during the first plateau will now be considered. During the first plateau, $G(\lambda_l)$ is constant, and the contribution of the spontaneous emission to $I^{\pm}(x, t, \lambda_l)$ is negligible compared to that of the stimulated emission. For the straight laser we can write

$$I^{\pm}(x, t + \Delta t, \lambda_l) - I^{\pm}(x, t, \lambda_l) = I^{\pm}(x, t, \lambda_l)[G^2(\lambda_l)R - 1] \tag{40}$$

where Δt is one round-trip time

$$\Delta t = 2L'/c, \tag{41}$$

and L' is the optical path length of the cavity. Since the fractional growth ($\Delta I/I$) during one round trip is small ($G^2(\lambda_l) \cdot R - 1 \ll 1$), we approximate the difference equation (40) by

$$\frac{\partial}{\partial t} I^{\pm}(x, t, \lambda_l) = (c/2L')[G^2(\lambda_l)R - 1]\, I^{\pm}(x, t, \lambda_l)$$

so that during the first plateau

$$I^{\pm}(x, t, \lambda_l) = I^{\pm}(x, t_0, \lambda_l) \exp[(t - t_0)/\tau_l] \tag{42}$$

with

$$1/\tau_l = (c/2L')[G^2(\lambda_l)R - 1]. \tag{43}$$

This exponential behavior is clearly seen in Figs. 4 and 5. Note that (42) describes the average temporal behavior. On top of this are superposed fast temporal changes which occur during times shorter than one round-trip time. τ_l can be calculated explicitly from (13), (14), and $N_1(x)$ as determined by (31). After some straightforward algebra we obtain

$$1/\tau_l = F(c/L) \{\tfrac{1}{2} [\Sigma(\lambda_l)/\Sigma(\lambda_i)] \ln [(1 + q_i)/(R + q_i)] - \tfrac{1}{2} \ln (1/R) - NL [\sigma_{01}(\lambda_l) - \sigma_{01}(\lambda_i) \Sigma(\lambda_l)/\Sigma(\lambda_i)] \} \tag{44}$$

where we have defined a filling factor F by

$$F = L/L'. \tag{45}$$

For the ring laser, the calculation gives a result similar to (44), except that both factors $\frac{1}{2}$ are replaced by 1 on the RHS. Note that normally $q_i \ll 1$, so that τ_l practically does not depend on the injected intensity. Within a factor of order unity, the total photon flux within the bandwidth $\delta\lambda$ around

λ_l is given during the first plateau by

$$I_l^{\pm}(x, t) \simeq I^{\pm}(x, t, \lambda_l)\, \delta\lambda. \tag{46}$$

The first plateau will last until $I_l(x, t)$ approaches the value $I_i(x, t)$. At the output, this means that $(1 - R) I_l^{-}(0, t) \simeq WNL$. Using (39b), (42), and (46) the duration of the first plateau, $T_p = t - t_0$ can be estimated as

$$T_p \simeq \tau_l \ln \left[I_{\text{in}} / \int_{[\delta\lambda]} I_0(\lambda) d\lambda \right] = \tau_l \ln K. \tag{47}$$

In a practical situation, one is interested in as large a T_p as possible. The dependence of T_p on the injected intensity is mainly in the logarithmic factor. The more important factor in (47) is τ_l. Obviously, as T_p (or τ_l) becomes larger, the closer the injected wavelength λ_i is to λ_l. On the other hand, for systems where a wide tuning range is desired, the other factors determining T_p should be considered. For given active medium parameters (a given dye with active medium length L and concentration N), τ_l scales with $1/F$, and the duration of the first plateau will be linear with the cavity length L'. This conclusion, as well as the logarithmic dependence of T_p on I_{in}, was verified in many numerical runs.

E. Triplet-State Effects

In the discussion of the first plateau so far, the triplet-state population was neglected. This is justified only for systems which operate at short pulses. In flashlamp pumped systems, with pulses in the microsecond regime, the effect of triplet states must be considered. Fig. 10 shows the results of calculation for conditions which are identical to those in Fig. 5, except that the effect of the triplet states is now properly accounted for. This will serve to illustrate the two main effects of triplet-state absorption. First, triplet-state absorption is a loss mechanism for photons, and thus as the triplet-state population $N_T(x)$ builds up, the total photon flux slowly decreases in time, as does the conversion efficiency (pump to laser photons). Another effect is the wavelength sweep of λ_l, already mentioned earlier. Under conditions of this particular example, (16) predicts $\lambda_l = 590$ nm for short pulses, but for long pulses where triplet states are important, it is found from (18) that $\lambda_l = 585$ nm.[7] This is clearly due to the fact that $\sigma_T(590) > \sigma_T(585)$. At the beginning of the first plateau, $I_l(\lambda = 585)$ takes over as in Fig. 5, the first plateau period starts, while $I_l(\lambda = 590)$ grows as described previously. However, as $N_T(x)$ increases in time, triplet-state absorption causes $I(\lambda = 590)$ to decrease again, so that the output remains centered around $\lambda = 585$ nm. To emphasize this feature further, we show in Fig. 11 the result of a computation identical to that of Fig. 10, but the injected radiation is at $\lambda = 590$ nm. The first plateau starts in a similar fashion as in Fig. 10. During the initial buildup period $I^{\pm}(\lambda = 585)$ rises to some level and then decreases, due to ground-state absorption, since for short times (16) determines $\lambda_l = 590$ nm.

[7] These values are correct to within the resolution of our numerical computations, namely: wavelength channels of 5-nm width. The exact numbers may be somewhat different.

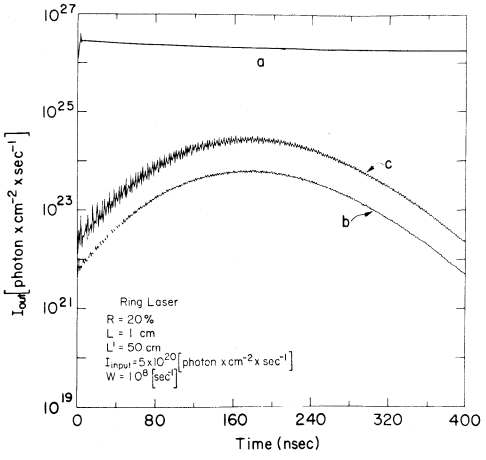


Fig. 10. Output flux in a ring laser with injection, under conditions identical to those in Fig. 5, except that triplet-state effects are properly accounted for. The notation (a, b, c) is the same as in Fig. 5.

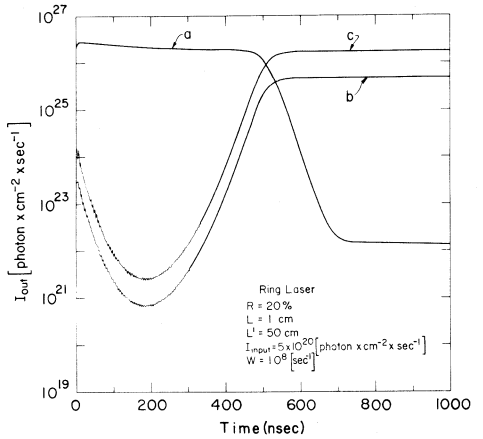


Fig. 11. Output photon flux in a ring laser with injection at $\lambda_i = 590$ nm, as a function of time. Triplet-state effects are properly accounted for. a—at $\lambda_i = 590$ nm; b—at $\lambda_l = 585$ nm, in the positive direction (I_l^{+}); c—total output at $\lambda_l = 585$ nm ($I_l^{+} + I_l^{-}$).

However, as the triplet levels start to fill up, (18) predicts $\lambda_l = 585$ nm. We thus note an exponential increase in $I^{\pm}(\lambda = 585)$ and finally the second plateau is estabilished, similar to the situation described previously, with triplet states neglected. Note that here the first plateau lasts for a longer period than in the case of Fig. 5, because of the wavelength sweeps occuring. These examples serve to demonstrate that injection locking can be ultilized to stabilize the output on a chosen wavelength, and the range in wavelengths for which injection locking is practical in long-pulse systems (~μs pulses) may even be larger than what one would estimate neglecting triplet-state effects.

IV. The Second Plateau

A. Output Intensity at λ_i and λ_l

The quasi steady state established during the first plateau lasts for a period of ~T_p. Once $I_l(x, t)$ approaches the value of $I_i(x)$, there is a transition period during which $I_i(x)$ decreases and $I_l(x, t)$ continues to increase. A new steady state is eventually established, during which most of the photon flux is

included in $I_l(x)$, the population inversion $N_1(x)$ is clamped by $I_l(x)$ to establish a gain such that $G^2(\lambda_l)R = 1$ (or $G(\lambda_l) \cdot R = 1$ for the ring laser).[8] The considerations are now analogous to the ones made for the first plateau. Considering $I_i^-(0, t)$, we write for the straight laser

$$I_i^-(0, t + \Delta t) - I_i^-(0, t) = -[1 - G^2(\lambda_i)R]\, I_i^-(0, t) + I_{in}G^2(\lambda_i). \tag{48}$$

If the fractional change $(\Delta I/I)$ during one round-trip time Δt is small, we again can approximate

$$\frac{\partial}{\partial t} I_i^-(0, t) = -(c/2L')[1 - G^2(\lambda_i)R]\, I_i^-(0, t) + (c/2L')I_{in}G^2(\lambda_i)$$

and so

$$I_i^-(0, t) = J \exp[(\theta - t)/\tau_i] + I_{in}G^2(\lambda_i)/[1 - G^2(\lambda_i)R] \tag{49}$$

with

$$1/\tau_i = (c/2L')[1 - G^2(\lambda_i)R]. \tag{50}$$

θ is some time when the exponential decrease starts, and J is determined by the value of $I_i^-(0, \theta)$. For short-pulse situations, where triplet-state effects are neglected, $1/\tau_i$ can be calculated analytically. From $G^2(\lambda_l)R = 1$ and (14) we find $\bar{N}_1$, and use it to calculate $G(\lambda_i)$. We obtain

$$1/\tau_i = F(c/L)\{[\tfrac{1}{2} \ln(1/R)][1 - \Sigma(\lambda_i)/\Sigma(\lambda_l)] + NL[\sigma_{01}(\lambda_i) - \sigma_{01}(\lambda_l)\Sigma(\lambda_i)/\Sigma(\lambda_l)]. \tag{51}$$

For the ring laser, the factor $\frac{1}{2}$ on the RHS is replaced by 1. Thus the photon flux at λ_i decreases exponentially until it reaches its final steady-state value. For a straight laser, this value is

$$I_i^-(0) = I_{in}G^2(\lambda_i)/[1 - G^2(\lambda_i)R] \tag{52}$$

and the output at λ_i during the second plateau is given by

$$I_i(\text{out}) = \{[G^2(\lambda_i) + R - 2RG^2(\lambda_i)]/[1 - G^2(\lambda_i)R]\}\, I_{\text{input}} \tag{53a}$$

where $G^2(\lambda_i)$ can be obtained from (50) and (51). Similarly, for a ring laser we consider $I_i^+(L, t)$ and obtain

$$I_i^+(\text{out}) = \{[G(\lambda_i) + R - 2RG(\lambda_i)]/[1 - G(\lambda_i)R]\}\, I_{\text{input}}. \tag{53b}$$

The coefficient of I_{input} in (53) defines the gain for an external input signal at wavelength λ_i for a laser operating at λ_l. At the second plateau, practically all the photon flux is concentrated in two wavelength channels: one at λ_i (bandwidth $\Delta\lambda_i$), and the free oscillations at λ_l. For a straight laser

$$I^{\pm}(x) = I_l^{\pm}(x) + I_i^{\pm}(x) \tag{54a}$$

but for the ring laser

$$I^+(x) = I_l^+(x) + I_i^+(x), \qquad I^-(x) = I_l^-(x). \tag{54b}$$

Using (26) and (7)–(11), we find that when triplet-state effects are neglected, the relation

$$I_{\text{out}}(\text{total}) \simeq WNL + I_{\text{input}} \tag{55}$$

holds for both the straight and the ring laser. The output at λ_l is obtained directly using (53)–(55)

$$I_l(\text{out}) = WNL - \{(1 - R)[G^2(\lambda_i) - 1]/[1 - G^2(\lambda_i)R]\}\, I_{\text{input}} \quad \text{(straight laser)} \tag{56a}$$

and

$$I_l^+(\text{out}) + I_l^-(\text{out}) = WNL - \{(1 - R)[G(\lambda_i) - 1]/[1 - G(\lambda_i)R]\}\, I_{\text{input}} \quad \text{(ring laser)}. \tag{56b}$$

Thus, during the second plateau, the output at the free-oscillation wavelength decreases linearly with I_{input}.

It may happen that the oscillation at λ_i will quench the laser oscillation at λ_l altogether. In the terms used here this means that the first and second plateaus coincide, with no transition period between them. This is the situation in CW injection locking [14], [15]. The condition for this to occur is found from the requirement that $G^2(\lambda_l)R < 1$ during the *first plateau* (or $G(\lambda_l)R < 1$ for the ring laser). Using (43) and (44), we find that if we define

$$Q = Q(\lambda_i, \lambda_l, R, N, L) = R^{-[\Sigma(\lambda_i)/\Sigma(\lambda_l)]} \cdot \exp\{2NL[\Sigma(\lambda_i)\sigma_{01}(\lambda_l) - \Sigma(\lambda_l)\sigma_{01}(\lambda_i)]/\Sigma(\lambda_l)\} \tag{57}$$

(or the same expression with 1 substituted for 2 on the RHS for the ring laser), then for

$$I_{\text{input}} > WNL(1 - QR)/[(Q - 1)(1 - R)] \tag{58}$$

the first and second plateaus coincide and all the output will be at λ_i. As an example we consider R6G under the conditions for which Fig. 5 was obtained, and find that for $I_{\text{input}} \gtrsim 1.5 \cdot 10^{25}$ (photons $\cdot$ cm^{-2} $\cdot$ s^{-1}), corresponding to ~5 MW/cm^2, the laser will lock at $\lambda_i = 585$ nm permanently, whereas without injection it would lase at $\lambda_l = 590$ nm. Note that the first plateau in Fig. 5 was obtained with only ~150 W/cm^2. The validity of the condition (58) was verified numerically.

B. Triplet-State Effects

In our treatment of the second plateau period presented so far, triplet-state effects were neglected. We already noted previously that these effects somewhat complicate the simplified model given here, but the general features of the behavior are similar, as is illustrated in Fig. 11: there is the first plateau region, where the output is locked at λ_i, then a transition period after which the output is mostly at λ_l. Clearly, the analytical approximation for $1/\tau_i$ (41) and the various intensities (53), (56), cannot be justified when triplet-state effects are included, and numerical solutions must be used. In particular, the conversion efficiency from pump to laser

[8] This equality assumes as before that spontaneous emission is negligible compared to stimulated emission at λ_l.

photons is lower than unity. This efficiency decreases continuously as $N_T(x)$ grows in time, an effect already alluded to previously. At the second plateau, when final steady state is established, we have from (1)-(3), using (17)

$$N_1(x) = N\{W + \int \sigma_{01}(\lambda)[\, I^+(x,\lambda) + I^-(x,\lambda)]\, d\lambda\} /$$

$$\{W(1 + K_{ST}\tau_T) + \tau^{-1} + \int [\sigma_{01}(\lambda)(1 + K_{ST}\tau_T) + \sigma_e(\lambda)]\, [I^+(x,\lambda) + I^-(x,\lambda)]\, d\lambda\}. \quad (59)$$

Since most of the photon flux is centered around λ_l, $\int I(x,\lambda) \cdot d\lambda \simeq I_l^{\pm}(x)$. Integrating (4) with respect to λ, we have

$$\frac{d}{dx}\,[I_l^+(x) - I_l^-(x)] = WN_0 - (N_1/\tau)\{1 - [g^+(x) + g^-(x)]\,\Phi\} - K_{ST}\tau_T N_1(x)\sigma_T(\lambda_l)[I_l^+(x) + I_l^-(x)]\,. \quad (60)$$

For a laser well above threshold, $N_1, N_T \ll N_0$, so that the spontaneous emission term can be neglected and N_0 replaced by N in (60). In the denominator of (59), W and τ^{-1} can be neglected compared to the third term, so that we find

$$\frac{d}{dx}\,[I_l^+(x) - I_l^-(x)] \simeq WN\{1 - K_{ST}\tau_T\sigma_T(\lambda_l)/[\sigma_{01}(\lambda_l) \cdot (1 + K_{ST}\tau_T) + \sigma_e(\lambda_l)]\} - N\{K_{ST}\tau_T\sigma_{01}(\lambda_l)\sigma_T(\lambda_l)/[\sigma_{01}(\lambda_l) \cdot (1 + K_{ST}\tau_T) + \sigma_e(\lambda_l)]\}\,[I_l^+(x) + I_l^-(x)]\,. \quad (61)$$

A comparison of (61) with (26), which describes the situation in the absence of triplet-state absorption, clearly demonstrates the reduction in efficiency. Equation (61) can be solved for $I_l^+(x) - I_l^-(x)$, noting that $I_l^+(x)\, I_l^-(x)$ is a constant [see (27)] if the boundary conditions (7) or (10) are used. The evaluation of $I_l^{\pm}(x)$, however, involves the solution of implicit equations and has to be performed numerically. We shall omit the details here. In particular cases where ground-state absorption at λ_l is negligible,[9] (61) simplifies to

$$\frac{d}{dx}\,[I_l^+(x) - I_l^-(x)] \simeq WN[1 - K_{ST}\tau_T\sigma_T(\lambda_l)/\sigma_e(\lambda_l)]\,. \quad (62)$$

The maximum conversion efficiency, which is unity with no triplet-state absorption, is reduced to a value equal to the coefficient of WN in (62). As an example, for a R6G laser tuned to $\lambda_l = 605$ nm, we find, using the parameters listed in Table II, that the maximum efficiency is 17 percent. We note that if (62) is applicable (i.e., $\sigma_{01}(\lambda_l) = 0$), then $I_l^{\pm}(x)$ at steady state can be calculated analytically as described previously: for the straight laser the result is obtained from (30) by writing $q_i = 0$, $I_i(x) \to I_l(x)$, and replacing WN by the RHS of (62). For a ring laser, (37) must be used, with the same substitutions. From $I_l^{\pm}(x)$, $N_1(x)$ is then obtained using (59), and $N_T(x)$ using (17).

C. Asymmetry Effects in a Ring Laser with Injection

Assuming the usual cases for which $I_{in} \ll WNL$, one would expect that once the second plateau is established, the spatial distributions of $I^{\pm}(x,\lambda)$ and $N_i(x)$ $(i = 1, T)$ will be similar to those of a free-running laser without injection. We found from many numerical runs that in a straight laser this is indeed the case.

In a free-running *ring* laser at steady state, these distributions must be symmetric around $x = L/2$. However, for a ring laser with injection during the first plateau, most of the photon flux at any point is contained in $I_l^+(x)$. Since $I_l^+(x)$ *increases* monotonically from $x = 0$ to $x = L$ (34), $N_1(x)$ *decreases* from $x = 0$ to $x = L$ (35). This results in a situation where at all wavelengths $\lambda \neq \lambda_l$ $I^+(L,\lambda) < I^-(0,\lambda)$. This was found to be true in all our computations,[10] as long as $\sigma_{01}(\lambda) \neq 0$. In particular, this situation persists while $I_l^{\pm}(x)$ grows exponentially. Hence $I_l^-(0) > I_l^+(L)$ at the second plateau, and the output from the ring laser consists of two beams of unequal intensity. This is clearly seen in Figs. 5 and 11, where the sum $I_l^+ + I_l^-$ is larger than twice I_l^+ itself, and in Fig. 8 where $I_l^+(x)$ and $I_l^-(x)$ are plotted at the second plateau ($t = 300$ ns). Once the second plateau is established, $N_1(x)$ is determined mainly by $I_l^+(x) + I_l^-(x)$, and thus $N_1(L) > N_1(0)$. This is illustrated in Fig. 9, where we plot $N_1(x)$ at the first plateau ($t = 30$ ns) and at the second plateau ($t = 300$ ns), for conditions identical to those of Fig. 5. One would expect that this asymmetric situation will evolve into a symmetric one, as in a free-running laser (37), (38). However, we found that the asymmetry described here persists for very long periods (of the order of seconds) even if the injection is turned off. The reason for this can be understood from the following arguments: unlike the situation in a straight laser, in an ideal ring laser there is no coupling between I^+ and I^- by feedback from the mirrors (7), (10). When a nonsymmetric distribution is created by the injection, and $I_l^+(L) < I_l^-(0)$, the only mechanism through which symmetry can be established is spontaneous emission. This happens because the fractional addition per pass to $I_l^+(L)$, due to ASE, is larger than the fractional addition per pass to $I_l^-(0)$ due to the same process. However, in a laser well above threshold, the contribution of the ASE is very small compared to $I_l^{\pm}$, so that the symmetrization process proceeds at a very slow rate. In practice, there may be a stronger coupling due to scattering from the mirrors or from suspended particles, in which case symmetrization will proceed at a faster rate.

V. Discussion

In previous sections, the behavior of a pulsed dye laser system with injection of an external signal was analyzed in detail. It was found that under appropriate conditions, the total output energy of a pulsed dye laser oscillator can be

[9] This is the case for dyes in which the emission and absorption bands do not overlap, as in 4-methyl-umbelliferone [32]. It can also be practical in other dyes, if the laser is forced by a dispersive element to operate at a λ_l such that $\sigma_{01} = 0$.

[10] At wavelengths for which $\sigma_{01}(\lambda) = 0$, $I^+(L,\lambda) = I^-(0,\lambda)$ already during the first plateau.

channeled into the narrow spectral band defined by the injected radiation. The conditions necessary for such locking to occur were determined.

The minimum injection power ($P_{\min}$) necessary to obtain injection locking at all, estimated using (22) and (23), obviously represents a lower limit. If the injected power equals $P_{\min}$, the growth rate of the photon flux at λ_i and at λ_l, during the initial buildup, is roughly the same, so that there is practically no locking period. In practice, therefore, injection locking will be observed if the input power is somewhat larger than $P_{\min}$. Furthermore, the analysis assumed all along that perfect spatial overlap existed between the injected radiation, the lasing mode, and the excited region. In single-mode operation this requires that the mode of the injected radiation be matched to a cavity mode [15].

As was shown in Section III-D, the duration of the locked operation (T_p) depends primarily on the proximity of λ_i to λ_l, on the cavity length, and to a lesser extent, on the injected intensity. Complete locking is obtained on a pulsed basis if T_p exceeds the pulse length. Thus the range of tunability of a given dye laser with some available injection power is determined by the pulse-length requirements. The shorter the laser pulse, the wider will the tunability range be. In the extreme, injection locking on a CW basis [14], [15] requires that λ_i be very close to λ_l, or that the injection intensity be very high (58), so that for all practical purposes the tunability range is very small.

So far we have considered the tunability in injection-locked operation around λ_l. Using a tuning element (diffraction grating or an intracavity filter, [20]), λ_l itself can be tuned across the gain curve of the free-running laser, and the injection will then serve to lock the laser into a narrow band within the bandpass of this element.

As noted earlier, the comblike structure imposed on the spectrum by the laser cavity has been neglected in our analysis. Consequently, this analysis yields the power averaged over the bandwidth of the injected radiation. If this bandwidth is narrow compared to the comb spacing as, e.g., in single-mode operation, then the overlap between the spectrum of the injected radiation and the cavity resonance must be taken into account. In practice, it will then be necessary to tune the (locked) laser cavity to the wavelength of the injected radiation. This is obviously not required in a conventional laser-amplifier.

Another point to be considered in the comparison of an amplifier with an injection-locked oscillator, is the minimum input power required in order that most of the output energy will be within the spectral band of the input signal. In the limit of multimode operation (23), the locked oscillator and the amplifier require inputs of the same order of magnitude, since for an amplifier also the factor g (19) is determined by the geometry of the active medium (see [10]). However, for single transverse mode operation (22), the input power required is reduced by several orders of magnitude, as was shown in Section III-B, and inputs of the order of ~1 mW should be adequate. Such powers are readily available from CW dye lasers, which operate in a single longitudinal and transverse mode. Thus a system consisting of a CW dye laser as the injection source and a well-designed flashlamp pumped dye laser, should deliver tens of millijoules per pulse of radiation with the spectral purity of the CW laser. Note that the "power stage" in such a system will have an effective gain of $\sim 10^8$ while single-pass gains are low ($G \sim R^{-1}$ or $R^{-1/2}$), thus avoiding parasitic oscillations. To obtain a comparable performance in a conventional amplifier would be extremely difficult due to parasitic effects. If even higher powers are needed, the output of the injection-locked oscillator can be fed into a conventional amplifier, since the powers now available will be adequate to well saturate the amplification stage. We conclude that the extra experimental complexity of mode matching and cavity tuning, necessary in the injection method, is worth the effort at least in the first stage, in obtaining medium to high powers starting from a low-power, narrow-band source.

In an experimental study performed in our laboratory [37], several of the predictions of the present model were verified. A flashlamp-pumped R6G dye laser was operated in a ring configuration without dispersive elements in the cavity. The spectral width of the free-running laser was ~5 nm. With injection of 1 mW obtained from a single-mode CW dye laser, most of the output energy of the pulsed laser was emitted within the spectral bandwidth of the injected radiation. With 100 J of electrical input, output pulses of ~50 mJ and ~350 ns duration were obtained.

Acknowledgment

We thank S. Blit for careful reading of the manuscript.

References

[1] F. P. Schafer, Ed., *Dye Lasers.* New York: Springer, 1973.
[2] F. N. Baltakov, B. A. Barikhin, and L. V. Sukhanov, "400-J pulsed laser using a solution of rhodamine -6G in ethanol," *JETP Lett.*, vol. 19, pp. 174-175, Mar. 1974.
[3] —, "Spatial and temporal characteristics of a 100J laser using a solution of rhodamine 6G in ethanol," *Sov. J. Quant. Electron.*, vol. 4, pp. 537-539, Oct. 1974.
[4] J. Jethwa and F. P. Schafer, "A reliable high average power dye laser," *Appl. Phys.*, vol. 4, pp. 299-302, 1974.
[5] T. W. Hänsch, "Repetitively pulsed tunable dye laser for high resolution spectroscopy," *Appl. Opt.*, vol. 11, pp. 895-898, Apr. 1972.
[6] R. Wallenstein and T. W. Hänsch, "Linear pressure tuning of a multielement dye laser spectrometer," *Appl. Opt.*, vol. 13, pp. 1625-1628, July 1974.
[7] G. Marowsky, "Reliable single-mode operation of a flashlamp pumped dye laser," *Rev. Sci. Instrum.*, vol. 44, pp. 890-892, July 1973.
[8] G. M. Gale, "A single mode flashlamp-pumped dye laser," *Opt. Commun.*, vol. 7, pp. 86-88, Jan. 1973.
[9] R. Wallenstein and T. W. Hänsch, "Powerful dye laser oscillator-amplifier system for high resolution spectroscopy," *Opt. Commun.*, vol. 14, pp. 353-357, July 1975.
[10] U. Ganiel, A. Hardy, G. Neumann, and D. Treves, "Amplified spontaneous emission and signal amplification in dye laser systems," *IEEE J. Quantum Electron.*, vol. QE-11, pp. 881-892, Nov. 1975.
[11] R. Adler, "A study of locking phenomena in oscillators," *Proc. IRE*, vol. 34, pp. 351-357, June 1946.
[12] R. H. Pantell, "The laser oscillator with an external signal," *Proc. IEEE*, vol. 53, pp. 474-477, May 1965.
[13] C. L. Tang and H. Statz, "Phase locking of laser oscillators by injected signals," *J. Appl. Phys.*, vol. 38, pp. 323-324, Jan. 1967.

[14] H. L. Stover and W. H. Steier, "Locking of laser oscillators by light injection," *Appl. Phys. Lett.*, vol. 8, pp. 91-93, Feb. 1966.
[15] C. J. Buczek and R. J. Freiberg, "Hybrid injection locking of high power CO_2 lasers," *IEEE J. Quantum Electron.*, vol. QE-8, pp. 641-650, July 1972; see also, C. J. Buczek, R. J. Freiberg, and M. L. Skolnik, "Laser injection locking," *Proc. IEEE*, vol. 61, pp. 1411-1431, Oct. 1973.
[16] J. E. Bjorkholm and H. G. Danielmeyer, "Frequency control of a pulsed optical parametric oscillator by radiation injection," *Appl. Phys. Lett.*, vol. 15, pp. 171-173, Sept. 1969.
[17] L. E. Erickson and A. Szabo, "Spectral narrowing of dye laser output by injection of monochromatic radiation into the laser cavity," *Appl. Phys. Lett.*, vol. 18, pp. 433-435, 1971.
[18] Q. H. F. Vrehen and A. J. Breimer, "Spectral properties of a pulsed dye laser with monochromatic injection," *Opt. Commun.*, vol. 4, pp. 416-420, Feb. Mar. 1972.
[19] G. Magyar and H. J. Schneider-Muntau, "Dye laser forced oscillator," *Appl. Phys. Lett.*, vol. 20, pp. 406-408, May 1972.
[20] J. J. Turner, E. I. Moses, and C. L. Tang, "Spectral narrowing and electrooptical tuning of a pulsed dye laser by injection locking to a CW dye laser," *Appl. Phys. Lett.*, vol. 27, pp. 441-443, Oct. 1975.
[21] M. Maeda, O. Uchino, T. Okada, and Y. Miyazoe, "Powerful narrow-band dye laser forced oscillator," *Jap. J. Appl. Phys.*, vol. 14, pp. 1975-1980, Dec. 1975.
[22] P. Burlamacchi and R. Salimbeni, "Spectral narrowing of a flashlamp-pumped, waveguide dye laser by amplification of tunable narrow-band CW radiation," *Opt. Commun.*, vol. 17, pp. 6-10, Apr. 1976.
[23] P. P. Sorokin, J. R. Lankard, V. L. Moruzzi, and E. C. Hammond, "Flashlamp pumped organic dye lasers," *J. Chem. Phys.*, vol. 48, pp. 4726-4741, May 1967.
[24] R. A. Keller, "Effects of quenching of molecular triplet states in organic dye lasers," *IEEE J. Quantum Electron.*, vol. QE-6, pp. 411-416, July 1970.
[25] R. Papalardo, H. Samelson, and A. Lempicki, "Calculated efficiency of dye lasers as a function of pump parameters and triplet lifetimes," *J. Appl. Phys.*, vol. 43, pp. 3776-3787, Sept. 1972.
[26] J. B. Atkinson and F. P. Pace, "The spectral line width of a flashlamp pumped dye laser," *IEEE J. Quantum Electron.*, vol. QE-9, pp. 569-574, June 1973.
[27] U. Ganiel and G. Neumann, "Power output coupling in a dye laser pumped by a nitrogen laser," *Opt. Commun.*, vol. 12, pp. 5-7, Sept. 1974.
[28] W. W. Rigrod, "Saturation effects in high gain lasers," *J. Appl. Phys.*, vol. 36, pp. 2487-2490, Aug. 1965.
[29] R. V. Ambartsumyan, N. G. Basov, P. G. Kryukov, and V. S. Letokhov, "Non-resonant feedback in lasers," in *Progress in Quantum Electronics*, vol. 1, J. H. Sanders and K. W. H. Stevens, Ed. New York: Pergamon, 1971, pp. 107-185.
[30] a) G. Marowsky, "Spectral narrowing in a dye laser with non-resonant feedback," *Appl. Phys.*, vol. 2, pp. 213-217, Oct. 1973.
b) ——, "Gain narrowing studies with an organic dye laser," *J. Appl. Phys.*, vol. 45, pp. 2621-2623, June 1974.
[31] F. P. Schafer, "Principles of dye laser operation," in *Dye Lasers*, F. P. Schafer, Ed. New York: Springer, 1973, pp. 1-83. See sec. 1.4.3. and references therein.
See also, N. A. Borisevich, V. V. Gruzinskii, and S. V. Davydov, "Kinetics of laser emission from lamp-pumped rhodamine 6G solutions," *Sov. J. Quantum Electron.*, vol. 4, pp. 947-951, Feb. 1975.
[32] C. V. Shank, A. Dienes, and W. T. Silvfast, "Single pass gain of exciplex 4-MU and rhodamine 6G dye laser amplifiers," *Appl. Phys. Lett.*, vol. 17, pp. 307-309, Oct. 1970.
[33] M. E. Mack, "Measurements of nanosecond fluorescence decay times," *J. Appl. Phys.*, vol. 39, pp. 2483-2485, Apr. 1968.
[34] B. B. Snavely, "Flashlamp-excited organic dye lasers," *Proc. IEEE*, vol. 57, pp. 1374-1390, Aug. 1969.
[35] J. P. Webb, W. C. McGolgin, O. G. Peterson, D. L. Stockman, and J. G. Eberly, "Intersystem crossing rate and triplet state lifetime for a lasing dye," *J. Chem. Phys.*, vol. 55, pp. 4227-4229, Dec. 1970.
[36] D. N. Dempster, T. Morrow, and M. F. Quinn, "The photochemical characteristics of rhodamine 6G-ethanol solutions," *J. Photochem.*, vol. 2, pp. 343-359, 1973-1974.
[37] S. Blit, U. Ganiel, and D. Treves, to be published.

Gain Saturation in DFB Lasers with End Reflectors

KENNETH O. HILL AND R. IAN MACDONALD

Abstract—**Results of an analysis of gain saturation in distributed feedback (DFB) lasers with end reflectors are presented. The dependence of the gain and frequency-shift eigenvalues of DFB lasers on the properties of end reflectors is reduced by gain-saturation effects. The degree of gain saturation is sensitive to the reflector properties if the distributed feedback and the reflections from the ends are of approximately equal strength.**

I. INTRODUCTION

THE optimization of practical distributed feedback (DFB) laser devices, such as GaAlAs lasers, must take account of gain saturation as well as other field-dependent nonlinear processes that may affect their operation. Nonlinear analyses of DFB lasers that include the effects of gain saturation have appeared recently in the literature [1], [2]. These allow prediction of the power output of DFB lasers and the calculation of internal irradiance levels. The gain-saturation model presented by Hill and Watanabe can be adapted readily to include other nonlinear effects. For example, calculations with this model have shown that for any given DFB structure with internal losses there exists an optimum coupling strength that maximizes the laser output power [1]. The model can also be used to treat the effects of end reflectors on DFB laser action.

End reflectors alter the operation of DFB lasers. For GaAlAs diode lasers the effect is particularly strong because the high refractive index of GaAs results in a large Fresnel amplitude reflection coefficient (0.56) at air interfaces. The response of

Manuscript received April 14, 1976.
The authors are with the Department of Communications, Communications Research Centre, Ottawa, Ont., Canada.

DFB laser threshold to both the location (with respect to the DFB structure) and reflectivity of the end reflectors has been examined recently by Chinn [3]. He showed that the frequency-selective properties of DFB lasers at threshold are degraded by symmetrically placed end reflectors and that the threshold gain is sensitive to the precise location of the reflectors. Streifer *et al.* [4], [5] considered the more general case of reflectors that are located asymmetrically with respect to the periodic feedback structure and observed that similar effects occur. End reflectors therefore affect significantly the gain and frequency eigenvalues at threshold, and it is important to determine their effect upon laser operation above threshold.

In this paper we extend our previous calculations [1] to treat the effects of gain saturation in DFB lasers with end reflectors. We show that the presence of gain saturation in symmetric DFB lasers with end reflectors stabilizes the unsaturated-gain eigenvalue [1] against variations in the complex reflectivity of the end reflectors. We show also that the degradation of the frequency selectivity of a DFB resonator resulting from end reflectors is reduced by gain-saturation effects. We note that the phase of the end reflections relative to the distributed feedback is critical in determining the operating characteristics of DFB lasers when the two types of feedback are of approximately equal strength. Because of this sensitivity to variations in phase, diode-laser designs should ensure that one form of feedback dominates. For brevity, we exclude internal losses from this treatment and leave the determination of optimum coupling strengths for future work.

II. Method

Consideration of field-dependent effects in DFB lasers leads to a set of piecewise-linear coupled-mode equations. The coupled-mode equations together with a method by which they may be solved have been given in our earlier paper [1]. The essential feature of the solution is subdivision of the laser into a sufficient number of equal segments so that the gain can be considered constant within each. The boundary conditions for each segment are expressed in terms of the complex amplitudes of the electric fields in the adjacent segment. To use the method, the complex amplitudes of the two counterrunning waves are assumed at one end of the laser and the amplitudes that result at the other end are determined by solving the coupled-mode equations in each segment in sequence. The gain coefficient α_0 in each segment is calculated from the irradiance at its initial end according to the relation

$$\alpha_0 = \frac{\alpha_u}{(1+s)} \tag{1}$$

where α_u is the unsaturated gain, and s is the irradiance in the segment measured in units of the saturation irradiance of the gain medium.

Because of symmetry, the complex amplitudes of the fields at both ends of the laser must be equal. Approximate corrections to the values assumed initially for $\alpha_u L$ and δL are determined from the difference between the computed complex amplitudes and those required by symmetry. A few serial applications of the method are usually sufficient to obtain valid solutions. The longitudinal-mode order of the solution is determined by starting conditions.

The laser structure we consider is shown in Fig. 1. The DFB periodicity is depicted as a sinusoidal corrugation and drawn to exaggerated scale to show the symmetry of the device. The end reflectors are nominally located at $x = \pm L/2$ but are in fact displaced (symmetrically) from their nominal positions by small amounts ΔL. In the computations it is assumed that the end reflectors lie at their nominal positions. Their displacements are represented by a phase shift in their complex reflectivities. The approximate equivalence of a phase change in the complex reflectivity and a displacement of the end reflectors results from the "slow growth" conditions assumed in the solution of the coupled-mode equations. The complex amplitude $E^+(x)$ of the positive-going wave is

$$E^+(x) = C^+(x) \exp j(\omega t - \beta x) \tag{2}$$

where x is the propagation direction; β is the propagation constant; $C^+(x)$ is a complex amplitude coefficient constituting a solution to the coupled-mode equations. Since, by hypothesis, $C^+(x)$ varies slowly, we can write the complex amplitude of the field at $x = L/2 + \Delta L$ as

$$E^+\left(\frac{L}{2} + \Delta L\right) \cong C^+\left(\frac{L}{2}\right) \exp j\left[\omega t - \beta\left(\frac{L}{2} + \Delta L\right)\right]. \tag{3}$$

If an end reflector of real reflectivity R is located at $x = L/2 + \Delta L$, the complex amplitude of the negative-going wave, $E^-(x)$, at position $x = L/2$ is given by

$$E^-\left(\frac{L}{2}\right) \simeq \left(C^+\left(\frac{L}{2}\right) \exp j\left[\omega t - \beta\left(\frac{L}{2} + \Delta L\right)\right] R\right) \cdot \exp j\left(\omega t + \beta \frac{L}{2}\right). \tag{4}$$

The complex reflectivity of a reflector located at $x = L/2$ that would give the same relationship between $E^+(L/2)$ and $E^-(L/2)$ is $\mathrm{Re}^{-j\beta\Delta L}$. The shift of the oscillation frequency from the Bragg frequency is generally small, so that $\beta \simeq n\pi/\Lambda$, where n is the order of the feedback and Λ is the wavelength of the feedback periodicity. A shift ΔL in reflector location is thus approximately equivalent to a phase change of $n\pi\Delta L/\Lambda$ in the complex reflectivity of a fixed reflector.

To start the computation we assume the power incident on one reflector, which we term the "internal power," P_I. We specify the internal power P_I rather than the output power for convenience. The complex amplitude of the wave impinging on this reflector is assigned zero phase at the reflector. The complex amplitude of the reflected wave is established by the complex reflectivity of the reflector. The computation then proceeds as in [1].

Since the laser structure is assumed to be symmetric, alterations in the displacement of the end reflectors result in changes in the length of the laser. Because we assume constant coupling strength κL, the computations do not, strictly speaking, refer to a single DFB structure. However, we treat phase changes only up to 2π in the reflection coefficients. Thus the laser length varies at most by four periods of the feedback structure. Practical feedback structures are many wavelengths

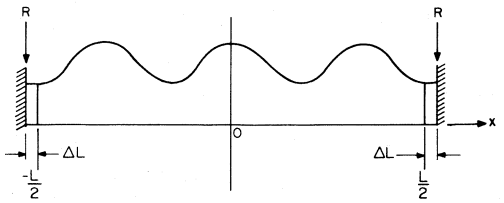


Fig. 1. DFB laser structure with end reflectors located at $\pm(L/2 + \Delta L)$.

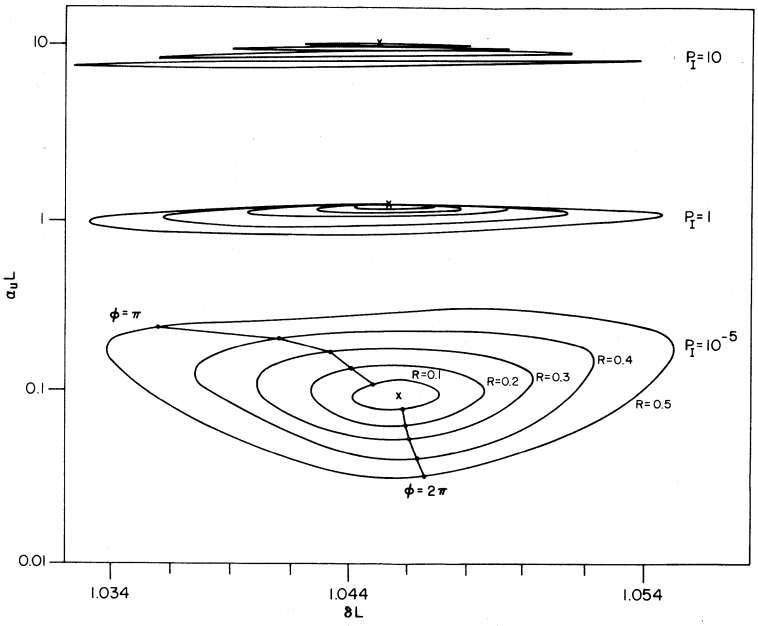


Fig. 2. Unsaturated-gain eigenvalue $\alpha_u L$ as a function of frequency-shift eigenvalue δL for an overcoupled DFB laser ($KL = 10$) with end reflectors, showing the effects of the internal power P_I, and the magnitude, R, and phase, ϕ, of the end reflections. The eigenvalues for the corresponding pure DFB lasers are shown by (x).

long so that the laser length and hence the coupling coefficient κ may be considered constant for the results presented here.

III. Results

A. Effects of Gain Saturation and End Reflectors on the Eigenvalues

Chinn [3] has pointed out that difficulty in controlling the precise location of the ends of a DFB laser, and hence the phase of end reflectors, can lead to an uncertainty in the threshold gain which can be quite large. Gain saturation reduces the relative variation in unsaturated-gain eigenvalue $\alpha_u L$ with the phase of end reflectors. This reduction is most noticeable in the overcoupled laser.

In Fig. 2 we show logarithmic plots of $\alpha_u L$ versus the frequency-shift eigenvalue δL for various internal powers P_I, end reflection magnitudes R, and phases ϕ in an overcoupled laser ($\kappa L = 10$). The small crosses in each plot show the eigenvalues of a pure DFB laser with corresponding structure and internal power. The portion of this figure corresponding to $P_I = 10^{-5}$ is comparable to [3, Fig. 5] which relates to a similar structure at threshold.

The presence of end reflectors in an overcoupled DFB laser lowers the unsaturated-gain eigenvalue under all conditions of reflector phase, provided that gain saturation occurs ($P_I = 10$, $P_I = 1$). Near threshold ($P_I = 10^{-5}$) end reflectors can act to raise the unsaturated gain under certain conditions of phase.

The *relative* variation in $\alpha_u L$ with reflector phase is much smaller in the laser under gain saturation than in the same laser near threshold. The ranges spanned by the gain eigenvalues as the reflector phases advance through 2π are about the same in absolute terms ($\Delta\alpha_u L \sim 0.3$). However, the relative variations, referred to the gain eigenvalue of the pure DFB structure, are 4.8 percent for the saturated condition and 162 percent for the unsaturated condition. The unsaturated-gain eigenvalues of DFB lasers with end reflectors are evidently stabilized against the phase of the reflectors by the effects of gain saturation.

It has been observed [3] that the presence of end reflectors reduces the frequency-selective properties of DFB lasers near threshold. Gain saturation does not seem to alter this situation substantially for the overcoupled laser. The range of δL, as the phase advances, changes little between low and high internal powers.

In Fig. 3 we show similar results for a critically coupled laser ($\kappa L = 1$). Here again it is evident that the relative variation in the unsaturated-gain eigenvalue with reflector phase is higher near threshold ($P_I = 10^{-5}$) than at greater internal powers. Near threshold the dependence of $\alpha_u L$ on phase is somewhat smaller than is the case for the overcoupled laser. In the critically coupled laser, the end reflectors are not so clearly dominated by the DFB structure, and their positions relative to it are less important. By contrast, the dependence on the magni-

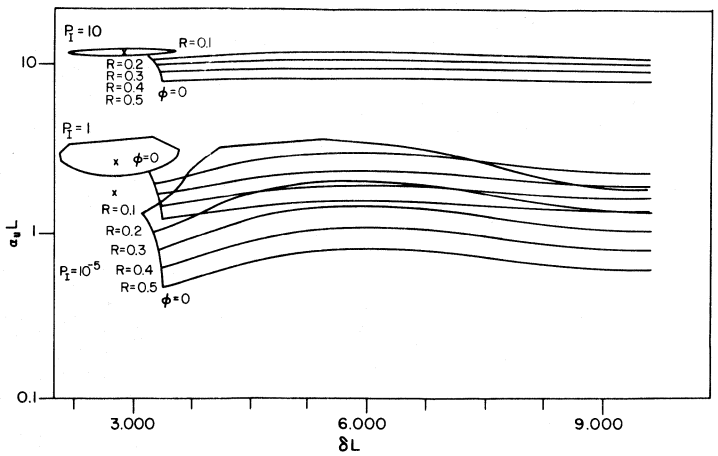


Fig. 3. Unsaturated-gain eigenvalue as a function of frequency-shift eigenvalue for a critically coupled DFB laser (KL = 1) with end reflectors. The eigenvalues for the corresponding pure DFB lasers are shown by (x).

tude of the reflection becomes more important as the Fabry-Perot cavity becomes significant in the operation of the device.

When the magnitude of the end-reflection coefficient R is high the frequency-selective properties of the critically coupled DFB laser are lost. The frequency offset advances monotonically as the reflector phase advances, and the laser is driven continuously into the region of progressively higher order modes. When R is low and the oscillation lies between two pure DFB modes the gain eigenvalue is relatively high, but as R increases even this form of frequency selection is lost and $\alpha_u L$ becomes nearly independent of δL, as in a Fabry-Perot laser.

Gain saturation has a small effect in improving the frequency selectivity of the critically coupled laser. Near threshold all of the reflection magnitudes considered are large enough that the frequency eigenvalue progresses continuously with advancing phase. At the higher internal powers (P_I = 10, 1) and with R = 0.1, the reflectors are dominated by the DFB structure and there are discrete regions of the $\alpha_u L$ versus δL diagram, associated with longitudinal mode 1 of the pure DFB structure, to which the eigenvalues are confined. The eigenvalues have a cyclic dependence on reflector phase in this region, as in the case of the overcoupled laser.

The critically coupled laser represents a transitional stage between a structure dominated by DFB and a structure dominated by end reflections. We show in the next section that competition between the two components of feedback makes it particularly unstable with respect to the reflector phase.

When the DFB laser is undercoupled ($KL = 10^{-13}$) the unsaturated gain eigenvalue $\alpha_u L$ is independent of the frequency-shift eigenvalue δL for the range of reflection-coefficient magnitudes we have considered for the end reflectors (R = 0.1 to 0.5). The Fabry-Perot cavity dominates under these conditions.

The dependence of the unsaturated-gain eigenvalue on the magnitude of the end-reflection coefficient R for fixed internal powers $P_I = 10^{-5}$ (near threshold) and P_I = 10 (with gain saturation) is shown in Fig. 4 for an undercoupled ($KL = 10^{-13}$) and an overcoupled (KL = 10) laser. The phase of the end reflectors is zero. Near threshold $\alpha_u L$ can be significantly reduced for both coupling strengths by increasing R. When gain

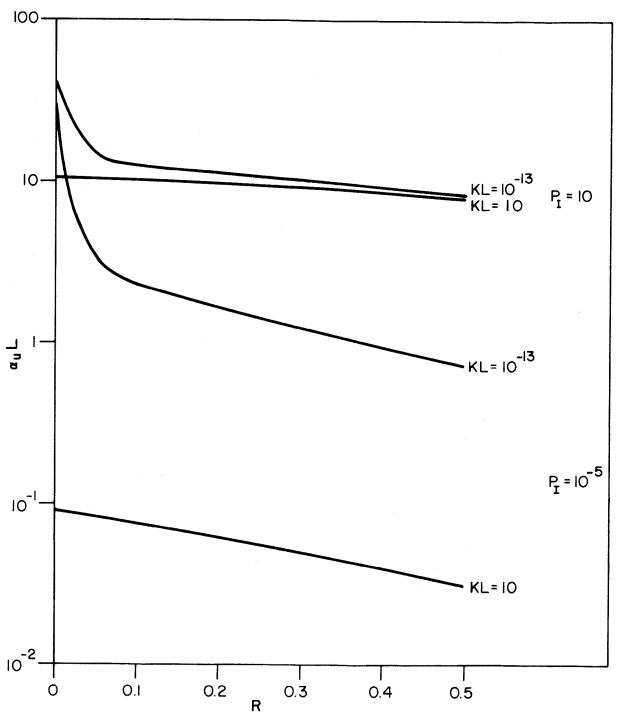


Fig. 4. Unsaturated-gain eigenvalue as a function of the magnitude R of the end reflections near threshold ($P_I = 10^{-5}$) and under gain saturation (P_I = 10) for an undercoupled ($KL = 10^{-13}$) and an overcoupled (KL = 10) DFB laser. The phase of the reflectors is zero.

saturation prevails the possible reduction in $\alpha_u L$ provided by end reflectors is considerably less than in the unsaturated laser with corresponding coupling. This behavior shows once more the stabilizing effect that gain saturation has on the unsaturated-gain eigenvalue. For the undercoupled laser the reduction in $\alpha_u L$ as R increases is initially very steep, leveling out and becoming parallel to the $\alpha_u L$ versus R dependence of the overcoupled laser for $R > 0.1$. This behavior illustrates the strong effect that even small end reflections have in altering the irradiance distribution in the undercoupled laser, reducing the strength of the endpoint spatial transient [1]. The approximately exponential dependence of $\alpha_u L$ on R for larger values of R is related to a rise in the average irradiance throughout the laser with increasing R.

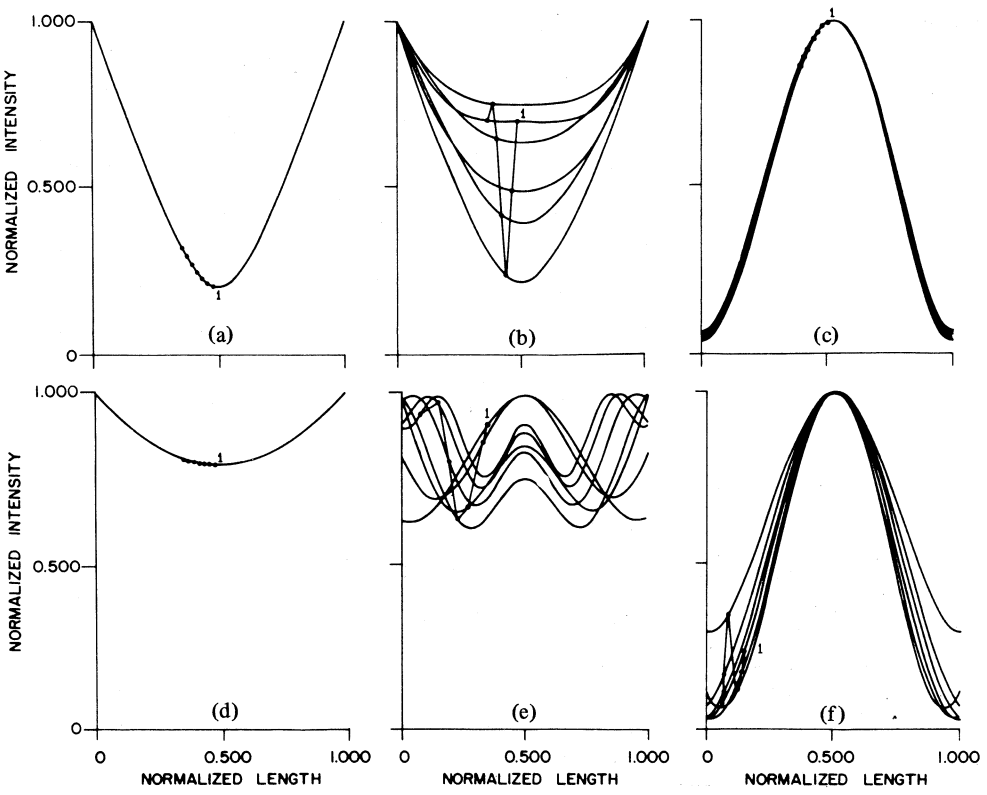


Fig. 5. Irradiance distributions under gain saturation in DFB lasers with end reflectors, for reflector phases from 0 to 360° in 60° steps. The phases can be associated with the corresponding distributions by means of the line drawn intersecting each distribution in order, beginning at the distribution corresponding to zero phase which is marked with a 1. The intersections of this line with the curves are shown by the dots. In all cases $P_I = 10$. (a) $KL = 10^{-13}$, $R = 0.1$, (b) $KL = 1$, $R = 0.1$, (c) $KL = 10$, $R = 0.1$, (d) $KL = 10^{-13}$, $R = 0.5$, (e) $KL = 1$, $R = 0.5$, (f) $KL = 10$, $R = 0.5$.

B. Irradiance Distributions

The degree of gain saturation in a laser depends on the irradiance profile within it. End reflectors strongly influence the gain saturation in a DFB laser. Their complex reflectivity plays a part in establishing the shape of the distribution of irradiance in the cavity and their transmissivity determines the absolute irradiance required at the ends for a given output power. In Fig. 5 we show irradiance distributions near mode 1 of the corresponding pure DFB lasers for lasers of three different coupling strengths ($KL = 10^{-13}$, 1, 10), two different values of the magnitude ($R = 0.1$, 0.5), and several values of the phase (ϕ from 0° to 360° in 60° intervals) of the complex reflectivity at the ends. This figure presents results for lasers with internal power $P_I = 10$. Gain saturation is established in these lasers because in all cases the irradiances are greater than the saturation irradiance throughout the laser structure. As noted in [1] the irradiance distributions are nearly independent of gain saturation except in the undercoupled device.

In the undercoupled laser [$KL = 10^{-13}$: Fig. 5 (a), (d)] the magnitude of the end reflections dominates. Their phase has no effect on the irradiance distribution, just as it has no effect on the gain eigenvalues. Their magnitude, on the other hand, determines the depth of the valley in the center of the irradiance distribution.

The critically coupled laser [$KL = 1$: Fig. 5 (b), (e)] exhibits more complex properties. Neither feedback mechanism dominates here, and the interrelation between the end reflectors and the DFB structure determines the irradiance distribution. For low reflection coefficients ($R = 0.1$), the distribution resembles that for the undercoupled case, but is strongly dependent on phase. At $R = 0.5$ the distribution is markedly altered. Near $\phi = 0$ it peaks in the center of the laser, resembling an overcoupled distribution. As the phase advances, the irradiance at the center is reduced, but two more maxima appear, so that the distribution resembles the third-order mode in a pure DFB laser. This behavior is a manifestation the noncyclic dependence of $\alpha_u L$ and δL on phase that is shown in Fig. 2.

At the high value of R the location of the minimum irradiance also depends on the phase of the reflectors. When the phase is near zero the minimum irradiance is at the ends, while near 180° phase it is at the center. When the irradiance is lowest at the ends, the irradiance throughout the rest of the laser must be higher to produce a given power at the ends than if minimum irradiance is at the center. For a fixed internal power, gain saturation is thus most complete in lasers with low irradiance at the ends. Given the difficulty of controlling the location of the ends of a DFB structure, it seems that in configurations where the DFB and end reflections compete, the degree of gain saturation will be difficult to control.

In the overcoupled laser [$KL = 10$: Fig. 5 (c), (f)] the DFB dominates the effects of end reflectors. We see by comparing Fig. 5(c) with (f) that variations in the reflection magnitude have little effect on the irradiance distribution. Furthermore, when $R = 0.1$ the phase has almost no influence on the distribution. When $R = 0.5$, the phase has some effect in determining the irradiance at the ends, but the alteration in the ratio of

the end irradiance to the irradiance at the center is small compared to the critically coupled case. The irradiance distribution, furthermore, retains a single peak as the phase advances because the dominance of the DFB structure forces the oscillation to remain near mode 1 despite the alteration in the phase of the end reflectors.

IV. Summary

We have determined the operating characteristics of gain-saturated DFB lasers with end reflectors for a range of coupling strengths and various internal power levels. End reflectors generally reduce the excitation required to produce a specified internal power. The sensitivity of the required excitation to the precise location of the end reflectors is also reduced as the laser is driven above threshold. Gain saturation also improves the frequency stability of DFB structures. We note that for a given internal power, the degree to which gain saturation prevails in the cavity is sensitive to the phase of the end reflectors if the distributed feedback and the feedback from the end reflectors compete. The efficiency of the conversion of pump power to output power depends on the degree of gain saturation when spontaneous emission losses are significant. Lasers in which distributed feedback and feedback from end reflectors compete will have variable efficiency due to the phase sensitivity, if spontaneous emission losses are not negligible.

The results of our calculations indicate the necessity of considering gain saturation effects in the design of DFB lasers with end reflectors. The threshold properties of such lasers are not always a good indication of their properties when driven above threshold. Other effects, such as those of nonuniform pumping and of losses must be considered as well as gain saturation in the optimization of a practical device. The nonlinear analysis that we have used can be extended to include these effects.

References

[1] K. O. Hill and A. Watanabe, "Envelope gain saturation in distributed-feedback lasers," *Appl. Opt.*, vol. 14, pp. 950–961, Apr. 1975.
[2] H. A. Haus, "Gain saturation in distributed feedback lasers," *Appl. Opt.*, vol. 14, pp. 2650–2652, Nov. 1975.
[3] S. R. Chinn, "Effects of mirror reflectivity in a distributed-feedback laser," *IEEE J. Quantum Electron.*, vol. QE-9, pp. 574–580, June 1973.
[4] W. Streifer, D. R. Scifres, and R. D. Burnham, "Longitudinal modes in distributed feedback lasers with external reflectors," *J. Appl. Phys.*, vol. 46, pp. 247–249, Jan. 1975.
[5] W. Streifer, R. D. Burnham, and D. R. Scifres, "Effect of external reflectors on longitudinal modes of distributed feedback lasers," *IEEE J. Quantum Electron.*, vol. QE-11, pp. 154–161, Apr. 1975.

Wavelength-Tunable Optical Mixing Experiments Between 208 nm and 259 nm

GAIL A. MASSEY, MEMBER, IEEE, AND JOEL C. JOHNSON, MEMBER, IEEE

Abstract—**Sum-frequency generation experiments in which the second harmonics of rhodamine and coumarin dye lasers are upconverted to the 208–234 nm by mixing with 1064 nm are described. The dye lasers were pumped by the second and third harmonics of a repetitively pulsed Nd:YAG laser. Both temperature-tuned and angle-tuned phase matching techniques were used with mixer crystals of ammonium dihydrogen phosphate (ADP) and potassium dihydrogen phosphate (KDP). Tunable light from 246 nm to 259 nm also was generated by mixing the output of a coumarin laser with the 532-nm harmonic of the Nd:YAG laser. Peak powers between about 500 W and 10 kW were obtained, and both theoretical and experimental tuning curves have been determined for these processes. Limitations imposed by mode beating effects in the Nd:YAG laser and by the relatively broad linewidth of the dye lasers are discussed.**

Manuscript received July 16, 1976. This work was supported by the National Science Foundation under Grant GB43630.

The authors are with the Department of Applied Physics and Electronic Science, Oregon Graduate Center, Beaverton, OR 97005.

I. Introduction

THIS paper describes experiments in which visible light from pulsed dye lasers is upconverted to the 208–259-nm spectral region by nonlinear sum-frequency generation in crystals of ammonium dihydrogen phosphate (ADP) and potassium dihydrogen phosphate (KDP). These materials have adequate second-order nonlinear susceptibilities, high resistance to ultraviolet-induced damage, and, in the best samples we have measured, absorption coefficients less that 0.05 cm^{-1} at all UV wavelengths above 200 nm. Our interest in this spectral region stems from the promise of the new technique of photoelectron microscopy [1], which requires laser sources in the 180–230-nm band to produce photoelectron emission from biological materials for high-magnification imaging of surface structure [2]. In an earlier paper [3] we presented calculations based on published refractive index data [4], [5]

showing that efficient 90° phase matched generation of UV wavelengths down to 200 nm should be possible in ADP by mixing wavelengths above 250 nm with a strong 1064-nm beam from a Nd:YAG laser. Conversion efficiencies above 50 percent were demonstrated for the special case of mixing the 266-nm fourth harmonic of the Nd:YAG laser with the fundamental to generate UV light at 212.8 nm. Here we describe some extensions of this technique which produce continuously tunable wavelengths as short as 208 nm using dye lasers pumped by the second and third harmonics of the neodymium laser that provides the 1064-nm signal for the last mixer crystal.

Two different approaches were investigated. In one group of experiments the dye laser second harmonic provided the long-wavelength UV input to the upconverter. However, available laser dyes in the 500–520-nm region are not as efficient as the best dyes in the blue and in the orange; thus it is more difficult to generate useful second harmonic power in the 250–269-nm band than at 285 nm, for example. This fact led us to carry out another group of experiments in which the long-wavelength UV was generated by mixing the dye laser output with the 532-nm second harmonic of the Nd:YAG laser. In this way it is possible to use the more efficient coumarin dyes, such as coumarin 102 [6] in methanol or 7-diethylamino-4 trifluoromethyl coumarin [7] in p-dioxane, to create the same UV wavelength range that would otherwise require a frequency-doubled dye laser oscillating near 505 nm.

II. Upconversion of Dye Laser Harmonic

A. Rhodamine Laser Experiments

Converting the output of a rhodamine laser into tunable UV between 222 nm and 235 nm requires the least equipment of the experiments described here. It can be done with all of the nonlinear crystals at room temperature using the configuration shown in Fig. 1. In our experiments the 1064-nm source was a Q-switched Nd:YAG oscillator/amplifier combination that produced 10-ns, 100-mJ pulses in the TEM_{00} mode at a pulse repetition frequency of 10 Hz. A 3-cm KDP crystal was used to generate the 532-nm harmonic with an energy conversion efficiency of 20–25 percent. The diameter of the collimated 532-nm beam was 2.3 mm; in many of our experiments in which the 532-nm beam was used as a dye laser pump, the beam diameter was reduced at the dye cell to 1 mm by inserting a lens of 500-mm focal length between the frequency doubler and the dye cell. The 532-nm beam was polarized in the plane of the diagram and separated from the 1064-nm beam by a Brewster-angle prism which also reflected a portion of the 1064-nm energy to serve as the "pump" in the ADP upconverter. A solution of rhodamine dye was circulated through a slightly tapered 2-mm gap between cell windows oriented near the Brewster angle. The 532-nm pump beam was brought into the cell at a 5° angle to the axis of the dye laser mode; in this configuration one obtains a nearly circular gain region in the dye without having to pass the pump beam through a resonator mirror. Tuning of the laser was done using two intracavity SF-4 flint glass prisms, which limit the width of the output spectrum to between 0.2 nm and 0.3 nm. An output mirror transmittance of 35 percent was used. The

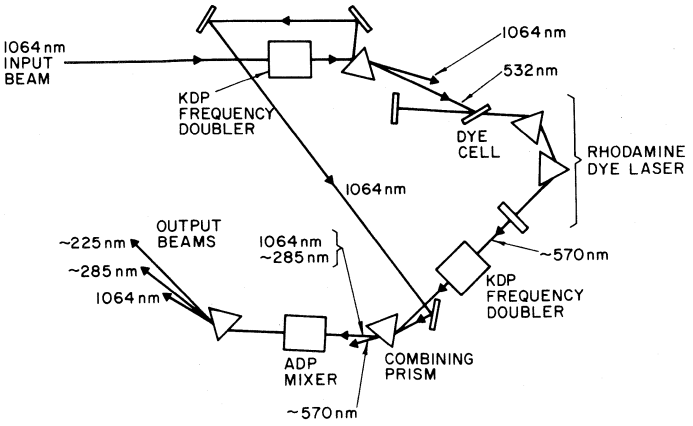


Fig. 1. Configuration for generating 222–230-nm UV by upconverting the second harmonic of a rhodamine dye laser. The dye laser is pumped by the Nd:YAG laser second harmonic.

dye solution was rhodamine 6G in methanol, with the dye concentration adjusted so that essentially all of the 532-nm light was absorbed in the cell (about 10^{-4} molar). At 565 nm, the wavelength of maximum efficiency for this laser, we obtained an energy output per pulse of 5 mJ, and we found that the wavelength tuning range of this laser was 545 nm to 585 nm. Measurements of the beam divergence with and without a unit-power telescope at the dye laser output revealed that the beam was essentially Gaussian and diffraction limited in the plane at right angles to the prism dispersion, with about three times greater divergence in the dispersion plane. There was an angular spread of output wavelengths in the latter plane. Although the dye laser mirrors were flat, the output wavefront was found to be spherically diverging, with about 5 times the angular divergence that could be achieved at the same diameter with the collimating lenses. This condition had an effect on critical phase matching for second harmonic generation when lenses were not used.

Frequency doubling of the dye laser was accomplished using a 5-cm crystal of KDP with the light propagating about 64° from the optic (z) axis in a plane at 45° from the x and y axes. The polarizations of the first and second harmonics were ordinary and extraordinary, respectively. The pulse energy conversion efficiency from 560 nm to 280 nm was between 10 percent and 15 percent when a lens of 17-cm focal length was inserted to focus the light in the region of the crystal. An additional fused silica lens was used to collimate the second harmonic light leaving the crystal. Without lenses the conversion efficiency dropped to about 2 percent, which was sufficient to allow phase matching conditions in the nonlinear crystals to be determined. The highest frequency-doubled dye laser powers we obtained were with beams focused near the optimum spot size values given by the theory of Boyd and Kleinman [8], which correspond to the focused case above. However, the power levels available in our mixing experiments usually were so high that much larger spot sizes could be used.

A beam at 1064 nm with about 10 mJ/pulse was made to propagate collinearly with the dye laser second harmonic beam by combining them in a fused silica prism placed in front of the ADP mixer crystal, as shown in Fig. 1. Care was taken to achieve synchronous arrival of the 1064 nm and dye harmonic

pulses, because we have found that the Q-switched pulses usually contain a temporal substructure with strong fluctuations down to 1 ns or less. The polished end faces of the ADP crystal were in the plane of the optic axis and 45° from the x and y crystallographic axes. Because the absorption of ADP is about 20 percent cm^{-1} at 1064 nm, and because high conversion efficiencies can be achieved in short interaction lengths by focusing the input light if necessary, we used a crystal length of only 2.2 cm. With the beams collimated in the crystal at a diameter of approximately 2.5 mm, we measured an UV upconversion efficiency of 10 percent (sum-frequency output energy near 222 nm ÷ UV input energy near 281 nm). The infrared intensity was about 20 MW/cm^2 under these conditions, about 50 times higher than the intensity suggested by the plane wave theory [9] at the same conversion efficiency. For negligible depletion of pump power P_2 in a beam of area A, this theory gives

$$P_3/P_1 = 52.2 d_{36}^2 L^2 P_2/(n_1 n_2 n_3 \lambda_3^2 A), \quad (1)$$

where L is the crystal length in centimeters, d_{36} is the nonlinear coefficient in ESU (1.36×10^{-9} ESU for ADP), P_1 is the input UV power, P_3 is the upconverted UV power at wavelength λ_3, and the n's are the appropriate refractive indices (between 1.5 and 1.6 in ADP). In the above expression the powers are in units of watts, λ_3 is in centimeters, and A is in square centimeters.

When dye lasers are used, the limited phase-matched spectral acceptance of the mixer crystal can reduce the conversion efficiency below the value indicated by (1). If the crystal is adjusted for perfect phase matching to convert a UV wavelength at λ_1 to a shorter wavelength λ_3 by mixing with a pump wavelength λ_2, the shift $\Delta\lambda_1$ from λ_1 that reduces the short-wavelength output power by a factor $4/\pi^2$ is given by

$$\Delta\lambda_1 = \frac{\lambda_1}{2L}\left[\frac{\lambda_3}{\lambda_1}\left(\frac{\partial n_3}{\partial \lambda_3} - \frac{n_3}{\lambda_3}\right) - \left(\frac{\partial n_1}{\partial \lambda_1} - \frac{n_1}{\lambda_1}\right)\right]^{-1} \quad (2)$$

according to the plane wave theory at low conversion efficiencies. If we are generating light near 210 nm by mixing long-wavelength UV with 1064 nm in ADP, (2) gives a full spectral acceptance ($2\Delta\lambda_1$) of 0.03 nm for a 1-cm crystal. At longer wavelengths the bandwidth becomes much larger as the crystal dispersion decreases rapidly toward the visible region. In addition to bandwidth considerations, there is a synchronism difficulty because of mode beating effects within the Q-switched pulse. This is discussed in more detail later in the paper.

With the dye laser wavelength set at 562 nm (as measured with a grating monochromator), corresponding to a second harmonic wavelength at 281 nm, phase-matched generation of the sum frequency at 222.3 nm occurred with the light propagating 90° to the optic axis and with the ADP crystal at 21°C. This agrees very closely with the theoretical tuning curve of [3]. From that point longer UV wavelengths can be phase matched either by raising the crystal temperature or by orienting the crystal toward smaller phase-matching angles.

Fig. 2 shows the angles required to generate wavelengths between 222 nm and 230 nm if the ADP crystal is maintained at 21°C. We were limited on the long-wavelength tuning extreme by diminishing power from the rhodamine 6G dye laser and by

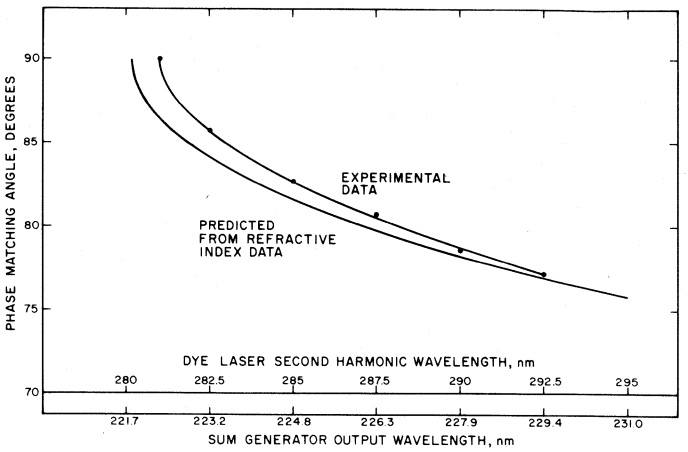


Fig. 2. Room temperature angular phase-matching characteristic for an ADP upconverter pumped at 1064 nm. The input wavelength range is 280–295 nm; these wavelengths can be obtained by frequency-doubling rhodamine 6G and rhodamine B dye lasers.

the aperture of the ADP mixer, which was cut with its length at 90° to the optic axis. The agreement between the theoretical and experimental curves is very good; we attribute most of the difference to a possible calibration error of the order of 1 nm in the monochromator used to measure the dye laser wavelengths.

When temperature tuning is not used, ADP is at a relative disadvantage because of its high-infrared absorption and sensitivity to temperature changes. We therefore substituted KDP and repeated the upconversion experiment described above. Experimental and theoretical curves for KDP at 21°C are shown in Fig. 3. Because KDP has more birefringence at room temperature, its curve extends to shorter wavelengths, and in fact all wavelengths above 215.3 nm can be reached in this material without using thermostatic controls. Rhodamine 6G was used to obtain the two points at the long-wavelength end of the curve. The short-wavelength points required the use of a fluorinated coumarin dye laser pumped by 355-nm pulses as described later in this paper. For angle matching in this wavelength band, KDP and ADP complement each other, providing continuous tuning from 215.3 nm to beyond 229 nm.

To verify the theoretical temperature tuning characteristic presented in [3], we placed the ADP crystal in a thermostatically controlled oven and repeated the frequency-doubled dye laser upconversion experiment with a fixed 90° phase-matching orientation. The longer wavelengths required the substitution of rhodamine B in place of rhodamine 6G in the laser. Fig. 4 compares the experimental and theoretical tuning characteristics for a 90° ADP upconverter with a 1064-nm pump. The experimental curve is shifted about 2 nm to the red at the extremes of the temperature range.

The highest average power achieved in these dye laser experiments was 0.5 mW at 10 pulses per second and a wavelength of 222 nm. This is to be compared to average powers between 5 and 7mW at 212.8 nm that we obtain under similar conditions by upconverting the 266-nm fourth harmonic of the Nd:YAG laser. The difference in these numbers is caused by the performance of the rhodamine dye laser and its frequency doubler. We routinely obtain 50–70 mW at 266 nm with the same 532-

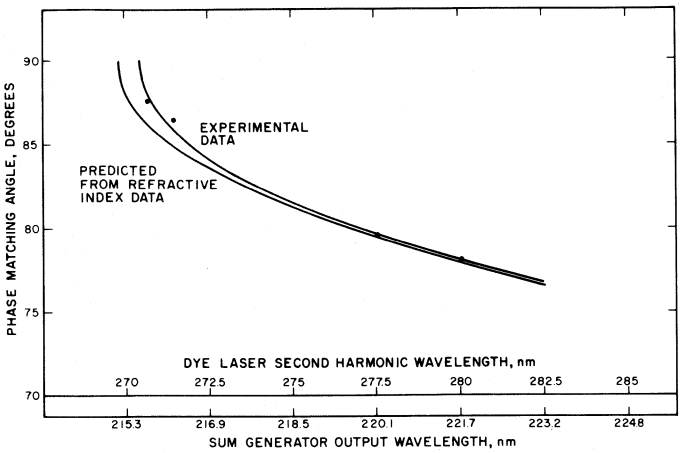


Fig. 3. Room temperature angular phase-matching characteristic for a KDP upconverter pumped at 1064 nm. UV input wavelengths from 270–280 nm are needed; they can be obtained by frequency-doubling rhodamine 6G and fluorinated coumarin dye lasers.

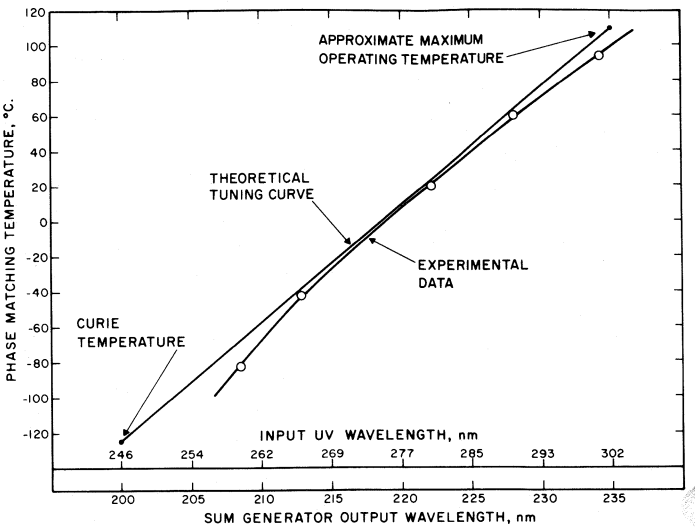


Fig. 4. Temperature tuning characteristic for 90° phase-matched upconversion in ADP using a 1064-nm pump. Wavelength extremes are set by the Curie temperature and the maximum operating temperature of the crystal.

nm power that results in 5 mW at 260 nm when the dye laser is used.

B. Coumarin Laser Experiments

To reach the shorter wavelengths of Fig. 4 the mixer crystal must be cooled. In this work we made use of a vacuum cryostat which has been described previously [10]. A frequency-doubled coumarin dye laser pumped by the Nd:YAG third harmonic at 354.7 nm was used, as shown in Fig. 5. The third harmonic was generated by passing the orthogonally polarized 1064-nm and 532-nm harmonics through a 5-cm KDP crystal oriented with the light propagating in the XZ plane at 58.3° to the Z axis. In this "Type II" phase-matching orientation [9] the 532-nm light is in an ordinary polarization along the X axis. The 355-nm pump energy produced in the TEM_{00} mode was 10 mJ per pulse; the 532–355-nm conversion is about 50 percent efficient. We used a fused silica lens of 50-cm focal length (not shown in Fig. 5) to reduce the 355-nm beam to 1-mm diameter on the dye cell. The length of the dye laser resonator was made as small as possible (about 15 cm), and the reflectance of the output mirror was 80 percent. Tuning was accomplished with prisms as in the rhodamine dye experiments.

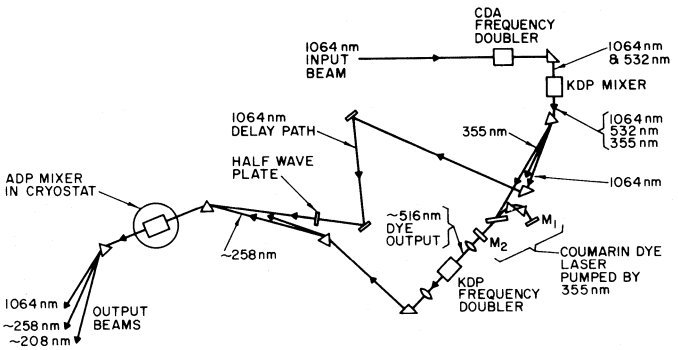


Fig. 5. Configuration for generating 208–214-nm light by upconverting the second harmonic of a coumarin laser pumped by the Nd:YAG third harmonic.

Experiments with various coumarin dyes excited by 355-nm pulses soon revealed that the behavior of these lasers is quite different from the performance of rhodamine 6G and rhodamine B lasers pumped at 532 nm. Stable efficient operation of the coumarin lasers was obtained only with very short cavity lengths and low-output coupling. We investigated several dyes, including 7 diethylamino-4-methylcoumarin, coumarin 102, coumarin 30, and coumarin 6 in methanol, as well as 7-diethylamino-4-trifluormethylcoumarin (Pilot number 481) in various solvents. All dyes were purchased from Eastman Kodak Company except the Pilot 481, which was obtained from New England Nuclear Company. With 10 mJ of UV pump energy all the dyes required output mirror reflectances of about 80 percent to reach the highest efficiencies, and the output energy was found to be a sensitive function of the cavity length. For example, the coumarin 102 dye laser provided an energy conversion efficiency of 14 percent in a linear 7-cm cavity with the wavelength selecting prisms removed, but the efficiency dropped to 6 percent when the mirror separation was increased to 10 cm and 3 percent with a 15-cm separation. This result contrasts sharply with recently published data for the same dye and pump wavelength with a 40-cm cavity length and a 10-mm dye cell thickness [11].

This cavity length limitation seriously affected the performance of coumarin dye lasers in the nonlinear optical experiments. Using prism or grating wavelength selectors, it would be desirable to insert a beam-expanding telescope to reduce the wavelength spread; however, we have found that the efficiency loss produced by the additional cavity length offsets the spectral purity advantage in nonlinear mixing.

By observing the pulse shapes of the various Nd laser harmonics and dye laser outputs with a fast vacuum photodiode and Tektronix Model 519 oscilloscope, we have determined that the cavity length problem is caused by the unexpectedly short pump pulses and by the brief excited singlet lifetimes of the coumarin dyes. The Q-switched Nd:YAG laser usually exhibits longitudinal mode beats, and these are enhanced by the nonlinear conversion to the third harmonic. When two longitudinal modes are oscillating in the Nd:YAG laser, the

dye laser pump at 355 nm consists of a train of pulses each with only 1-ns full width at half intensity. In a given Q-switched pulse there are between one and three of these nanosecond pulses carrying significant energy. Observation of the dye fluorescence with the laser mirrors removed showed that the fluorescence follows the temporal substructure of the 355-nm pump very closely; an excited-state lifetime of 1 ns is consistent with the pulse shapes we obtained. We also investigated the time required for the coumarin dye laser pulse to grow to maximum intensity. For the cavity used in our experiments, the peak of the dye laser emission was found to occur 4 ns after the first major peak in the 355-nm waveform. This delay had to be compensated in order to obtain efficient results in our upconversion experiments, which of course require synchronism between the 1064-nm pulse and the dye laser second harmonic. One last consideration in this area is the difference in dye laser and Nd:YAG laser cavity lengths imposed by the buildup time and gain limitations of the dye laser. Even if we bring the centers of the 1064 nm and dye second harmonic pulses into synchronism, the mode beating fluctuations within them are not synchronous; hence the final nonlinear upconversion process is less efficient than it would otherwise be. Use of a single-frequency master oscillator at 1064 nm, or perhaps some system of multiple delayed pump beams [12] for the dye laser, probably would improve the efficiency of the mixing process substantially.

In spite of the above difficulties we frequency-doubled the output of a 355-nm pumped Pilot 481 dye laser using a 3-cm KDP crystal at room temperature and then upconverted the second harmonic by mixing it with 1064 nm in a cooled ADP crystal. Light was focused into the doubler and then recollimated by fused silica lenses of 15-cm focal length. With the KDP doubler cut in the 90°, Type I orientation [9], we were able to produce second harmonic wavelengths from 259 nm to 268 nm by tuning the dye laser and rotating the crystal away from 90°. The energy of each second harmonic pulse was about 7 μJ when methanol was used as the dye solvent. Pilot 481 is a more efficient dye in p-dioxane, but the fluorescence maximum shifts from 530 nm to 485 nm as the methanol solvent is replaced by p-dioxane, and the latter wavelength is too short for frequency-doubling in KDP at room temperature. With mixtures of these solvents the fluorescence peak can be shifted to any wavelength of interest in this range, but the increase in efficiency obtained in pure p-dioxane is lost rapidly as small amounts of the other solvent are introduced. The second harmonic pulses were upconverted to the 208-214-nm range using the same ADP mixer and 1064-nm pump intensity as in the previous experiments, but with the mixer crystal mounted in a vacuum cryostat. With the mixer crystal at −82°C we obtained 208-nm pulses of 1.7-μJ energy and about 17-μW average power at a repetition frequency of 10 Hz. Pulsewidth measurements showed that the peak power corresponding to the above energy was about 500 W. To our knowledge 208 nm is the shortest wavelength yet attained using second-order susceptibilities in nonlinear crystals.

The wavelength limitations in these experiments were not imposed by the ADP mixer or the dye laser, but by the frequency doubler. By refrigerating the doubler crystal as well as the mixer and by adding p-dioxane to the dye solution, we should have been able to extend the lower wavelength limit down to a value between 200 and 203 nm according to the tuning characteristic curves of Fig. 4. However, to do this would have required two cryostatic systems, and only one was available in our laboratory. We did not attempt to explore the long-wavelength limits of this technique by heating the doubler crystal, since we had covered that region already in the work described earlier.

III. Mixing Dye Laser and 532-nm Light

Because large amounts of power were available at 532 nm in these experiments and because the laser dyes near 480 nm are more stable and about twice as efficient as the best dyes near 510 nm, the idea of replacing the dye laser second harmonic with the sum frequency formed by mixing the dye output with 532 nm appeared promising. In these experiments we used the Nd:YAG third harmonic to pump a coumarin 102 dye laser in a configuration similar to that of Fig. 5. Instead of taking the residual 1064-nm signal for mixing, however, we used the 532-nm beam in this case, rotating its polarization 90° and delaying it about 4 ns to bring it into synchronism with the dye laser pulse. The two beams were combined and made collinear by a Brewster-angle prism and passed through a lens of 50-cm focal length. The 90° oriented, Type I mixer (2.2 cm of ADP) described earlier was placed in the diverging beam beyond the focus, where it could be moved along the beam axis to vary the intensity. The visible beams were polarized 90° to the Z axis and 45° between X and Y in the ADP crystal, generating a sum frequency polarized along Z.

This mixing process requires cooling the crystal to temperatures between 0°C and −120°C; we therefore used the vacuum cryostat equipped with a platinum resistance thermometer to measure the phase-matching temperatures as the dye laser was tuned. Some adjustment of the optical system was needed to maintain alignment of the 532 nm and blue dye laser beams for different wavelength settings.

The phase-matching characteristic of ADP obtained in these experiments is shown in Fig. 6. The theoretical curve computed from

$$n_3/\lambda_3 = n_2/\lambda_2 + n_1/\lambda_1, \tag{3}$$

where λ_1 is the dye wavelength, $\lambda_2 = 532$ nm, λ_3 is the generated UV wavelength, and the n's are the appropriate refractive indices for the polarizations, wavelengths, [4], and temperatures [5], is also plotted in the figure. In this case the experiment shows that one can reach wavelengths almost 3 nm shorter than the published refractive index data would indicate. This is fortunate, because the Curie temperature places a −125°C limit on the lowest temperature and shortest wavelength that can be reached.

The energy per pulse at 532 nm was 10 mJ with a pulse duration of about 5 ns, corresponding to a peak power near 2 MW. The dye laser output was approximately 200 μJ at 465 nm and 490 nm, rising to about 260 μJ at the maximum, which occurred at 480 nm. At a position corresponding to a 532-nm power density of 50 MW/cm^2, the fraction of dye light converted was between 1.0 percent and 1.2 percent

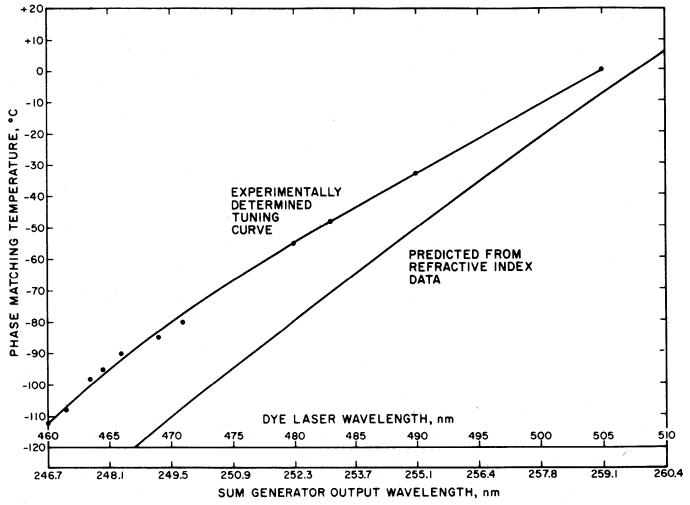


Fig. 6. Temperature tuning characteristic of a 90° phase-matched ADP upconverter pumped at 532 nm. The input wavelengths are above 460 nm, and can be obtained from various coumarin dye lasers pumped by the third harmonic of the Nd:YAG laser.

across the tuning range. The highest energy in the UV obtained in the series of measurements was approximately 3 μJ at 252 nm. This value could not be exceeded even by increasing the power density (moving the cryostat nearer to the focus) up to the crystal damage threshold. This conversion efficiency is of course far less than that predicted by (1), which indicates that 10 percent conversion should have been reached at only 0.4 MW/cm^2. The UV pulse energies obtained in these mixing experiments are about half as large as the energies we obtain by frequency-doubling the output of a Pilot 481 dye laser which provides only half as much visible light as the coumarin 102 laser. It should be noted that the frequency-doubling, as described earlier, was done with much tighter focusing, so that power densities on the nonlinear crystal were similar, and that 3 cm of KDP rather than 2.2 cm of ADP was used in the doubling.

The main point of this comparison is that we do not obtain an energy advantage by mixing as long as phase-matched harmonic generation from a comparable fundamental pulse at these power levels is possible in a similar material. We attribute the low conversion efficiency in mixing to lack of overlap of temporal substructure in the 532 nm and dye laser pulses, as well as to the excessive spectral width ($\sim$ 0.3 nm) of the dye laser compared to the phase-matching spectral acceptance of the mixer, which is 0.08 nm in this case according to (2). In harmonic generation, temporal overlap is not a factor, and there is the possibility of mixing of various spectral components whose frequencies cancel out the first-order dispersion effects of the crystal [13]. The reasons for the higher efficiencies of the very short wavelength mixing experiments described in Section II are that the 1064-nm pulses in those experiments were longer with less pronounced substructure and that the dye laser radiation had been effectively filtered through the harmonic generation process before it reached the last mixer. The advantage of greater dye stability remains with the mixing approach, however, and if the dye laser power were much less than the 10–30 kW achieved here, frequency-doubling would be less effective than mixing.

IV. Conclusions

We have described a variety of mixing experiments aimed at generating tunable coherent UV light between 200 nm and 235 nm. In one approach we have frequency-doubled the output of rhodamine and coumarin dye lasers and then mixed this long-wavelength tunable UV with a powerful 1064-nm pump to create sum frequencies in the 208–234-nm range. In a second approach the long-wavelength UV was generated by mixing the dye laser output with a strong signal at 532 nm. This permitted generation of UV between 246 nm and 259 nm. The final nonlinear crystals in these experiments were ADP and KDP, and a Nd:YAG laser was used both to pump the upconverter and to provide the power to excite the dye lasers. Most of the region between 208 nm and 259 nm was covered in these experiments, with average powers between 17 μW and 0.5 mW and peak powers up to about 10 kW. These values are compared to the 100-kW peak power, 7-mW average power that we obtain at 212.8 nm with the same equipment, using only the Nd:YAG laser harmonics. Starting with a 1064-nm beam whose pulse-to-pulse energy stability was about $\pm$ 3 percent, the fluctuations in the 212.8-nm harmonic were found to be about $\pm$ 25 percent, compared to typical fluctuations up to a factor of 2 in the upconverted signal from the coumarin dye lasers. Important limitations imposed by the mode beating effects in the 1064-nm beam as well as the spectral spread of the dye laser have been discussed.

References

[1] O. H. Griffith, G. H. Lesch, G. F. Rempfer, G. B. Birrell, C. A. Burke, D. W. Schlosser, M. H. Mallon, G. B. Lee, R. G. Stafford, P. C. Jost, and T. B. Marriott, "Photoelectron microscopy: A new approach to mapping organic and biological surfaces," in *Proc. Nat. Academy Sci.*, vol. 69, pp. 561–565, Mar. 1972.

[2] R. J. Dam, K. F. Kongslie, and O. H. Griffith, "Photoelectron quantum yields and photoelectron microscopy of chlorophyll and chlorophyllin," *Photochem. Photobiol.*, vol. 22, pp. 265–268, 1975.

[3] G. A. Massey, "Efficient upconversion of long-wavelength UV light into the 200–235 nm band," *Appl. Phys. Lett.*, vol. 24, pp.

371-373, Apr. 15, 1974.
[4] F. Zernike, Jr., "Refractive indices of ammonium dihydrogen phosphate and potassium dihydrogen phosphate between 2000 Å and 1.5 μ," *J. Optic. Soc. America*, vol. 54, pp. 1215-1220, Oct. 1964; also, *Errata*, vol. 55, pp. 210-211, Feb. 1965.
[5] R. A. Phillips, "Temperature variation of the index of refraction of ADP, KDP, and deuterated KDP," *J. Optic. Soc. America*, vol. 56, pp. 629-632, May 1966.
[6] S. A. Tuccio, K. H. Drexhage, and G. A. Reynolds, "CW laser emission from coumarin dyes in the blue and green," *Opt. Commun.*, vol. 7, pp. 248-252, Mar. 1973.
[7] E. J. Schimitschek, J. A. Trias, M. Taylor, and J. E. Celto, "New improved laser dye for the blue-green spectral region" *IEEE J. Quantum Electron.*, vol. QE-9, pp. 781-782, July 1973.
[8] G. D. Boyd and D. A. Kleinman, "Parametric interaction of focused Gaussian light beams," *J. Appl. Phys.*, vol. 39, pp. 3597-3639, July 1968.
[9] F. Zernike and J. E. Midwinter, *Applied Nonlinear Optics*. New York: Wiley, 1973.
[10] G. H. Lesch, J. C. Johnson, and G. A. Massey, "A thermostatic control system for nonlinear optical experiments at low temperatures," *IEEE J. Quantum Electron.*, vol. QE-12, pp. 83-86, Feb. 1976.
[11] K. Kato, "3547-Å pumped high power dye laser in the blue and violet," *IEEE J. Quantum Electron.*, vol. QE-11, pp. 373-374, July 1975.
[12] J. E. Lawler, W. A. Fitzsimmons, and L. W. Anderson, "Narrow bandwidth dye laser suitable for pumping by a short duration N_2 laser," *Appl. Opt.*, vol. 15, pp. 1083-1090, Apr. 1976.
[13] F. M. Johnson and M. W. Swagel, "Continuously tunable pulsed ultraviolet light source," *Appl. Opt.*, vol. 10, pp. 1624-1628, July 1971.

A Theoretical and Experimental Study of the Effect of Loss on Grating Couplers

F. T. STONE AND STEWART AUSTIN, MEMBER, IEEE

Abstract—**The effect of material absorption loss on grating-coupler performance is presented. In particular we examine grating couplers fabricated holographically in photoresist. It is shown that a total field decay constant α_T must be used in place of the leaky wave contant α whenever loss is appreciable. This total rate of field decay α_T can be obtained, to a good approximation, by adding an absorption loss factor α_{abs} to the leaky wave constant α. The absorption rate α_{abs} is calculated by considering a suitable equivalent uniform waveguide and the leaky wave constant α is obtained by neglecting all loss in the structure except that due to beam radiation. Guided wave attenuation is found to be due almost entirely to absorption in the residual resist layer left between the grating and the waveguide rather than to absorption in the grating teeth. Experiments demonstrate that grating couplers fabricated in Shipley AZ 1350B photoresist have measured properties in agreement with the lossy description described above.**

I. Introduction

SINCE the realization of the grating coupler by Dakss *et al.* [1], such devices have been recognized as a satisfactory means for coupling a beam to a surface wave while still maintaining compatibility with the concept of integrated optics. A number of techniques can be used to form the grating structure [2]. A most convenient and quick way is the direct holographic fabrication of the coupler in photoresist.

In photoresist grating couplers, the loss of the resist material itself is an important factor. Ulrich [3] showed that the coupling efficiency in the presence of loss is given by $\eta_L = \eta\alpha/(\alpha + \alpha_{abs})$ where η is the efficiency of the coupler when losses are assumed to be zero, α is the leaky wave constant of the lossless coupler, and α_{abs} describes wave attenuation due to all causes other than beam radiation. For couplers fabricated in photoresist, α_{abs} is due almost entirely to material absorption.

Despite the extensive literature on grating couplers [4], there is little quantitative experimental data on the effect of loss. Here we present theoretical and experimental results demonstrating the effect of material loss on grating couplers fabricated in Shipley AZ 1350B photoresist. These results indicate that the loss in a photoresist coupler is due almost entirely to absorption in the residual resist layer left between the grating and the waveguide. In addition, it is shown that theoretical results for lossless couplers can be modified to include loss by adding the absorption loss of an equivalent uniform waveguiding structure to the leaky wave constant obtained from a lossless analysis.

II. On the Origin of Losses in Photoresist

Guided wave attenuation by thin layers of photoresist has been noted by a number of researchers [5], [6]. Unfortunately, little quantitative information is available about the complex part of the index of refraction of photoresist n_R'' (where $n_R = n_R' + jn_R''$) which describes this optical absorp-

Manuscript received May 18, 1976; revised July 19, 1976. This work was supported in part by the Joint Services Electronics Program under Contract F44620-69-C-0047.

F. T. Stone was with the Polytechnic Institute of New York, Farmingdale, NY. He is now with Bell Laboratories, Norcross, GA 30071.

S. Austin was with the Polytechnic Institute of New York, Farmingdale, NY. He is now with the Research Laboratory for Electronics, M.I.T., Cambridge, MA 02139.

tion. However, estimates as high as 500 dB/cm at 6328 Å have been reported [6] for guided wave attenuation of submicron-thick resist films, indicating the importance of considering this factor.

Dill *et al.* [7] express the imaginary part of the index, n_R'', as $\delta\lambda/4\pi$ where $\delta = AM + B$. The wavelength-dependent A and B parameters represent the exposure-dependent and exposure-independent portions of δ, the resist absorption constant. Dissolution of the resist in developer is prevented by an inhibitor which is destroyed upon exposure. The fraction of initial inhibitor remaining, M, describes the degree of local exposure. Thus $M = 0$ corresponds to complete exposure while $M = 1$ corresponds to the unexposed case.

For Shipley AZ 1350 photoresist, A and B values have been published for $\lambda = 4047$ Å and $\lambda = 4358$ Å [8]. Using these figures we calculate as follows:

	$M = 1$	$M = 0.5$	$M = 0$
n_R'' (4047 Å) = 0.0322	0.0183	0.0043
n_R'' (4358 Å) = 0.0201	0.0116	0.0030

At our wavelength of interest, $\lambda = 6328$ Å, we expect the corresponding values of n_R'' to be smaller due to the decreased sensitivity of photoresist at longer wavelengths. Also, n_R'' may be different for Shipley AZ 1350 and AZ 1350B. The latter photoresist was used in our work. Since n_R'' is both exposure and wavelength dependent, we study the effect of absorption for a wide range of values of n_R''. We assume a fixed value of $n_R' = 1.638$ at $\lambda = 6328$ Å [5].

III. Approximate Loss Calculations for Gratings With Residual Resist Layers

Let us consider a photoresist grating with a residual layer as illustrated in Fig. 1(a). It is convenient to think of this structure as a grating of depth t_G on a two-film waveguide. The energy distribution and hence the guided wave attenuation in the five-layer structure (air, grating, resist, film, substrate) are strongly dependent on the various indices of refraction. We assume that the field attenuates rapidly enough in the grating layer so that guided wave attenuation is due predominantly to residual layer absorption. Hence initially we assume the complex surface-wave propagation constant, $\beta_{sw} = \beta_r + i\alpha_{abs}$, may be determined by considering only the uniform four-layer structure illustrated in Fig. 2(a). Here, α_{abs} describes the attenuation of the wave due to material absorption.

The transverse propagation factor in the film, $k_{ZF} = k_0 n_F \cdot \sin\theta_F$, was determined by employing a modified Newton-Raphson method to solve the transcendental equation obtained by a transverse resonance technique [9]. Here, k_0 is the free-space propagation constant, n_F is the film refractive index, and θ_F is the propagation angle in the film. The longitudinal propagation factor was then found using the dispersion relation

$$\beta_{sw} = (k_0^2 n_F^2 - k_{ZF}^2)^{1/2} \tag{1}$$

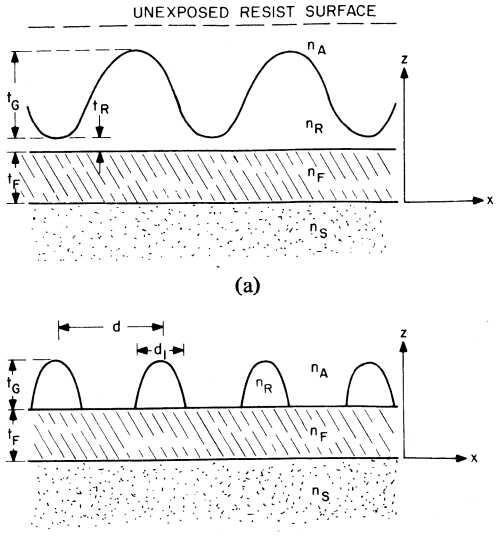


Fig. 1. Two possible photoresist grating profiles after holographic exposure and development: (a) residual resist layer and (b) residual resist layer developed away.

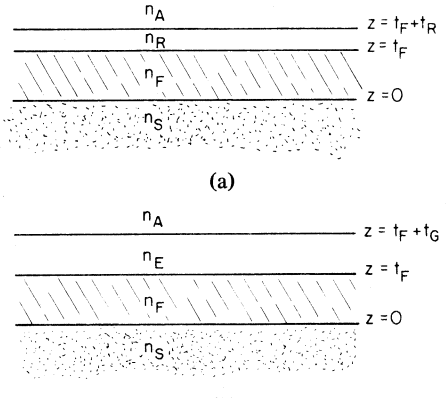


Fig. 2. Composite waveguides for calculation of absorption losses: (a) residual resist layer present (grating neglected) and (b) residual resist layer absent (grating replaced by equivalent uniform layer).

where the fields have been assumed to be invariant with respect to y. Since the energy carried by the surface wave decays as $\exp(-2\alpha_{abs}x)$, the attenuation in dB/cm can be expressed as

$$\text{attenuation (dB/cm)} = (20\,\alpha_{abs})/2.3. \tag{2}$$

Examples of the strong dependence of guided wave attenuation on film index and residual layer thickness are illustrated in Figs. 3-5. The TE_0 mode is considered, and for purposes of comparison, a fixed value of film thickness, $t_F = 5500$ Å, is used. These three cases clearly demonstrate the increase in absorption loss as the film index decreases. In addition, these figures illustrate the sharp increase in absorption with increasing residual layer thickness when the resist index is near to or greater than that of the film.

Another difficulty encountered when residual layers are present on low-index films is indicated by the dashed line in Fig. 5. At that value of residual layer thickness, the guide effective index, $n_{eff} = \beta_r/k_0$, exceeds the film index. The guided

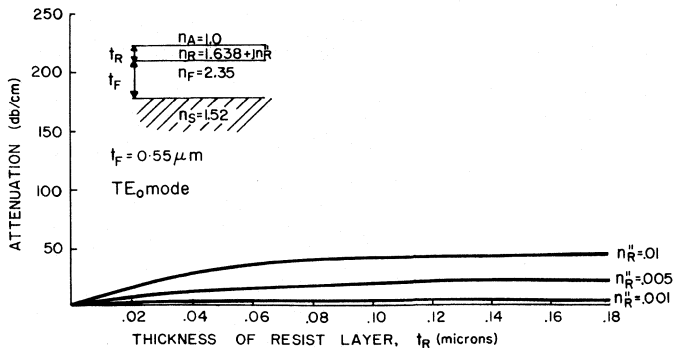


Fig. 3. Guided wave attenuation of the TE_0 mode versus residual resist thickness for various values of n''_R. Attenuation is virtually constant for $t_R > 600$ Å.

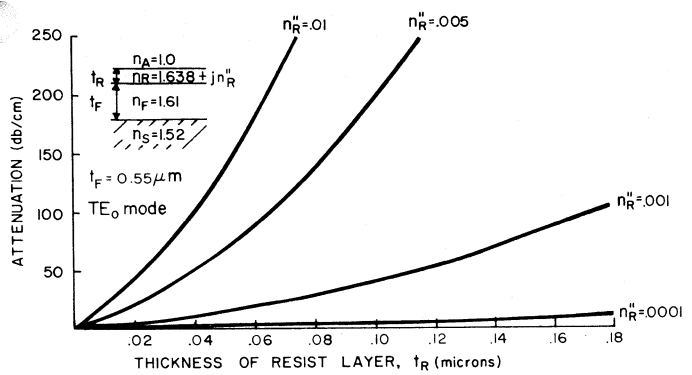


Fig. 4. Guided wave attenuation of the TE_0 mode versus residual resist thickness for various values of n''_R. Here the attenuation increases sharply as t_R increases.

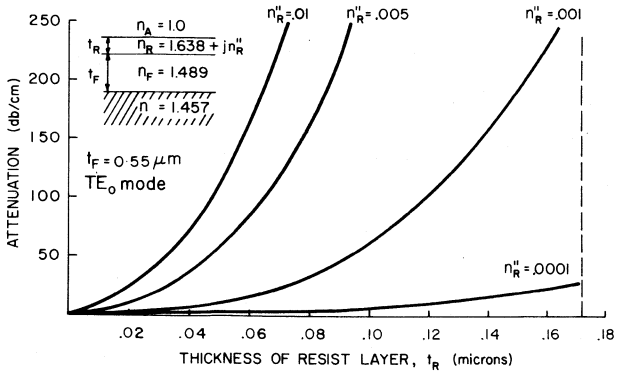


Fig. 5. Guided wave attenuation of the TE_0 mode versus residual resist thickness for various values of n''_R. For $t_R > 1700$ Å we have $n_{\text{eff}} > n_F$, hence the wave propagates only in the resist.

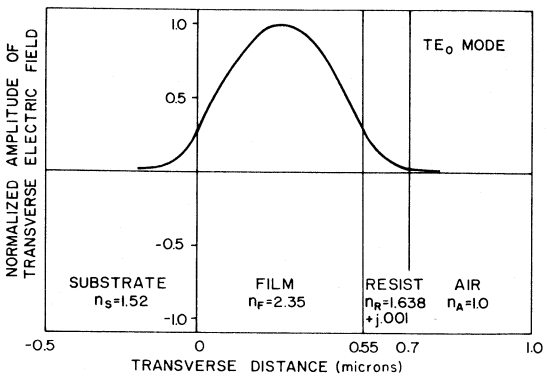


Fig. 6. Normalized amplitude of the transverse electric field, E_y, as a function of transverse position for a composite waveguide with $n_F = 2.35$. Note that the field is tightly bound to the higher index film layer so that absorption losses are small.

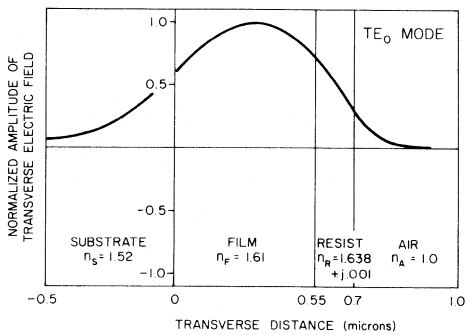


Fig. 7. Normalized amplitude of the transverse electric field, E_y, as a function of transverse position for a composite waveguide with $n_F = 1.61$. Here the wave propagates in both the film and the resist.

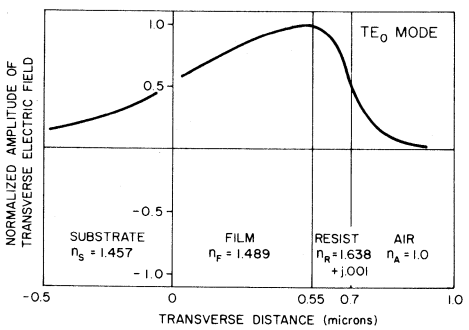


Fig. 8. Normalized amplitude of the transverse electric field, E_y, as a function of transverse position for a composite waveguide with $n_F = 1.489$. Here the field peaks near the resist layer, resulting in large absorption losses.

wave thus propagates entirely in the resist layer and is evanescent in the film. Hence, at the grating termination, most of the energy will be radiated. Obviously, this represents a severe problem for grating couplers.

Better physical insight into the problem of residual layer loss and its dependence on film index and residual layer thickness can be gained by examining the field distributions in the composite waveguides. The transverse electric field distributions for the TE_0 mode were calculated for the three cases considered above and are shown in Figs. 6-8. A fixed resist thickness of 1500 Å was used. The choice of $n''_R = 0.001$ was consistent with experimental observations to be discussed later. For the high-index film illustrated in Fig. 6, the field is seen to be tightly bound to the film layer. The field decays to e^{-1} times its magnitude at the film-resist boundary at a distance of 625 Å from the interface. Hence, increases in the resist layer thickness beyond this value have little effect on the guided wave attenuation as was shown in Fig. 3. For lower

film indices, as shown in Figs. 7 and 8, the guided energy shifts towards the higher index lossy resist layer, causing the large absorption losses illustrated in Figs. 4 and 5.

IV. Approximate Loss Calculations for Gratings With No Residual Resist Layers

The previous section demonstrated the importance of keeping residual layers as thin as possible. Here we assume that the residual layer is eliminated so that losses are present in the grating teeth only. Again we determine the absorption factor, α_{abs}, of the guided wave.

The structure under consideration is illustrated in Fig. 1(b). Such a structure is difficult to analyze. To simplify the problem, let us consider a grating with rectangular teeth of width d_1. A wave propagating in this structure then sees an average index in the periodic layer given by[1]

$$n_E = \frac{n_R d_1 + n_A(d - d_1)}{d}. \tag{3}$$

For a symmetrical grating $d_1 = d/2$ and $n_E = (n_R + n_A)/2$. By replacing the periodic layer with a uniform layer of thickness t_G and index n_E, we reduce the problem to the simpler case of the two-film waveguide shown in Fig. 2(b). Hence, β_{sw} can be evaluated as before.

An example using the above approach is illustrated in Fig. 9. A film index of 1.489 is chosen. This case was discussed previously, and the presence of a residual layer was shown to cause extremely large absorption losses. A comparison of Fig. 9 with Fig. 5 indicates the large reduction in absorption loss when residual layers are eliminated.

V. Comparison of Approximate and Exact Analyses of Lossy Grating Couplers

Gratings with absorption losses are characterized by the quantity $\alpha_T = \alpha + \alpha_{abs}$ where α is the lossless leaky wave constant. In the previous two sections, α_{abs} was calculated from equivalent uniform waveguide structures. To test the accuracy of the approximate values of α_{abs} obtained, an exact value of α_T was calculated using the rigorous techniques of Peng *et al.* [10] suitably modified to include loss. An approximate value of α_T was then calculated as the sum of the lossless leaky wave constant α [10] and the value of α_{abs} obtained from the two-film waveguide analysis of Fig. 2(a).

The accuracy of the approximate technique is indicated by Fig. 10. Clearly, the effect of absorption in the grating layer itself is negligible compared with that in the residual layer. Note that this is true even though the value of n_R'' used in Fig. 10 is ten times larger than we found experimentally. Even closer agreement between the two values of α_T could have been obtained by replacing the grating with an equivalent uniform layer and analyzing the resulting five-layer structure.

[1] As pointed out during review, it is more appropriate to average the dielectric constant instead of the refractive index, i.e., to average n^2 instead of n. For a symmetrical grating with $n_R = 1.638 + jn_R''$ and $n_A = 1.0$ this implies $n_E = 1.357 + j0.604n_R''$ (for $n_R'' << 1$) instead of $n_E = 1.319 + 0.500n_R''$. The higher real and imaginary parts of the equivalent index both increase the attenuation of the uniform waveguide. If this increased attenuation is included in Fig. 11, the approximate and exact curves almost coincide, illustrating the improvement obtained from averaging the dielectric constant, and also demonstrating the accuracy of the approximate technique presented.

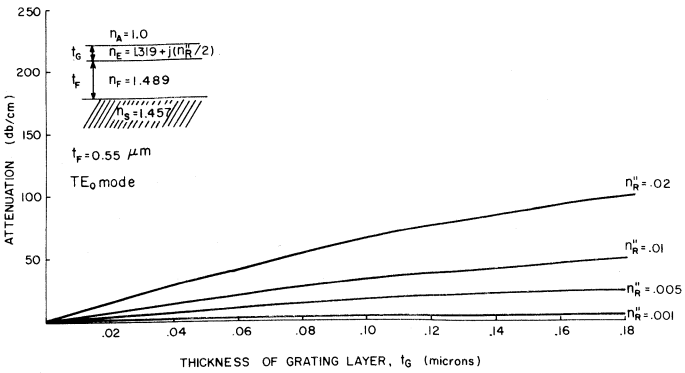


Fig. 9. Guided wave attenuation of the TE_0 mode versus grating thickness for various values of n_R''. A comparison with Fig. 5 indicates the large reduction in losses, even for relatively thick gratings, when lossy residual layers are eliminated.

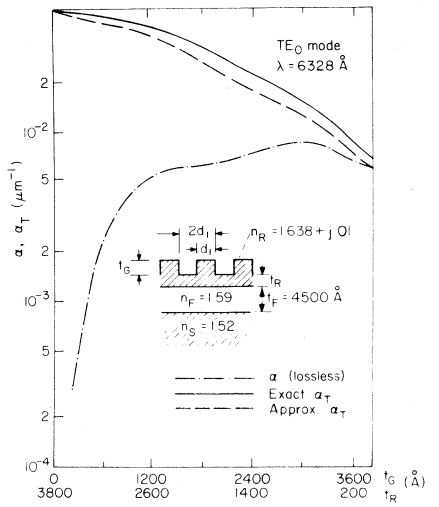


Fig. 10. Comparison of α and α_T for the structure illustrated. The approximate $\alpha_T = \alpha + \alpha_{abs}$ was determined by neglecting the grating and calculating α_{abs} for the remaining uniform four-layer structure. Comparison of the approximate α_T with that calculated using the rigorous technique demonstrates that absorption losses are due almost entirely to the residual resist layer.

Fig. 11 is a comparison of the two values for α_T for the case of no residual layer present. Here the approximate value of α_{abs} was obtained from an analysis of the structure illustrated in Fig. 2(b). Agreement is excellent even for relatively thick gratings and a value of n_R'' which is twenty times larger than that found experimentally.

VI. Experimental Results

In previous papers [11], [12] we discussed a model for fabricating a given periodic structure in photoresist. For the experiment discussed here, gratings were fabricated on thin-film waveguides with different groove depths and residual layer thicknesses. The same initial resist thickness was used for all gratings on a particular waveguide. Hence, $t_G = t_I - t_R$, where t_G and t_R are defined in Fig. 1 and $t_I = 3800$ Å.

Experimentally, the value of α_T was determined by two methods. 1) A slit was scanned across the focused radiation

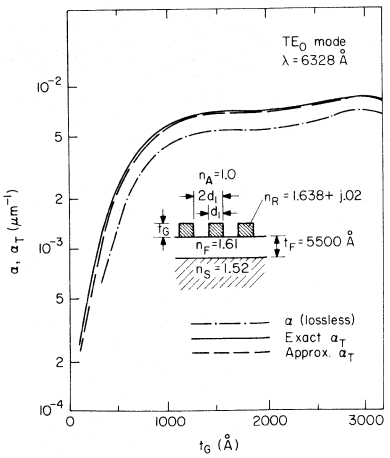


Fig. 11. Comparison of α and α_T for the structure illustrated. The approximate α_T was determined by replacing the grating layer with a uniform layer of thickness t_G and index $n_E = (n_A + n_R)/2$.

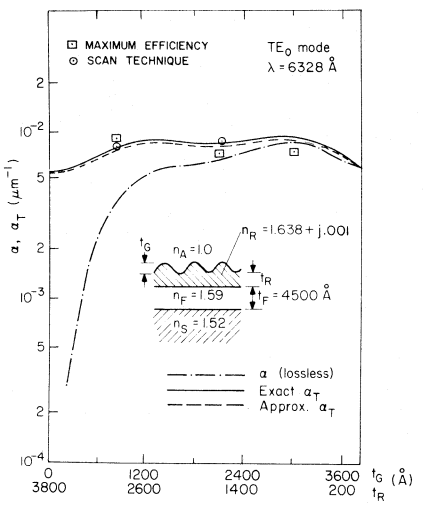


Fig. 12. A comparison of theoretical and experimental values of α_T for the structure illustrated. A square-wave approximation of the nearly sinusoidal profile was used in the calculation. Computations indicate errors less than 10 percent using this approximation.

pattern of the output coupler. This yielded a decay α_T' normal to the output beam. Thus $\alpha_T = \alpha_T' \cos\theta$ where θ is the angle between the output beam and the normal to the waveguide. 2) The efficiency of the grating acting as an input coupler was measured as a function of the exciting beam spot size. The beam radius w_0 (measured along the grating) producing the highest coupling efficiency was determined. The formula [3] $\alpha_T w_0 = 0.68$ then provided a second experimental value for α_T. Since the peak efficiency region is somewhat broad, the first method provides greater accuracy. The latter technique can be used, however, when the grating can only act as an input coupler.

Fig. 12 indicates good agreement between experimental values of α_T, and those obtained from the exact analysis. In addition, close agreement is again shown between the decay rate α_T calculated from the exact analysis, and the approximate value of α_T calculated from the uniform structure of Fig. 2(a). As can be seen from Fig. 12, the effect of the loss in the grating layer itself is negligible. The assumed loss factor, $n_R'' = 0.001$, was chosen to give a best fit to the experimental data.

Note that a plot such as in Fig. 12 determines the maximum thickness of the residual lossy layer that may be left. For example, if a 10-percent decrease in efficiency due to loss is acceptable (i.e., $\alpha_{abs} < 0.1\ \alpha_T$), a residual layer no larger than 1000 Å may be left for the parameters of Fig. 12. It is frequently desirable to leave some residual layer since the gratings so produced have greater adhesion than those in which the grooves extend down to the film surface.

The Al_2O_3 film indices were determined from a calibration of the sputter-deposition process using data obtained from multimode waveguide synchronous angle measurements [13]. Since sputtering is a reproducible deposition technique, this is quite accurate. The film thickness was obtained both from a calibration of the sputtering process and from Tolansky multiple-beam interferometry.

The photoresist profiles were determined from the calibration data of [11]. The periodicity $d = 3100$ Å. The real part of the resist index was obtained from the data of Dalgoutte and Wilkinson [5], and as mentioned before, the imaginary part was chosen to fit the experimental data. Note that this figure is in qualitative agreement with the values calculated previously, if one considers the decrease in absorption with increasing wavelength. The substrate index was determined from critical angle measurements.

VII. Conclusions

We summarize our conclusions as follows. 1) As can be seen from Fig. 10 or Fig. 12, the actual α_T differs appreciably from the lossless α even for relatively thin residual resist layers. 2) The actual efficiency of the lossy coupler will be lower than that of a similar lossless device by a factor α/α_T. It should be noted that the dip method [1] measures both radiation and absorption effects, hence actual efficiencies are lower than those found using this procedure. 3) The actual α_T, not the lossless α, must be used in determining the optimum beam spot size $w_0 = 0.68/\alpha_T$. 4) The actual α_T can be obtained from the lossless α by adding to it the absorption loss α_{abs} as calculated from the uniform waveguide structure of Fig. 2(a) or Fig. 2(b). In addition, the enhanced scattering that will be present when the resist carries an appreciable amount of energy (for instance when $n_R' > n_F$) must be taken into account. Although our results are on lossy grating couplers, the techniques discussed, particularly the approximate method of modifying lossless calculations, are applicable to many periodic integrated optical structures.

Acknowledgment

We wish to acknowledge the assistance given by Dr. S. T. Peng in the theoretical aspects of this work. In addition, we acknowledge many helpful discussions with our colleagues Prof. T. Tamir and Prof. H. L. Bertoni.

References

[1] M. L. Dakss, L. Kuhn, P. F. Heidrich, and B. A. Scott, "Grating coupler for excitation of optical guided waves in thin films," *Appl. Phys. Lett.*, vol. 16, pp. 523–525, June 1970.

[2] H. I. Smith, "Fabrication techniques for surface-acoustic-wave

and thin-film optical devices," *Proc. IEEE*, vol. 62, pp. 1361–1387, Oct. 1974.
[3] R. Ulrich, "Efficiency of optical grating couplers," *J. Opt. Soc. Am.*, vol. 63, pp. 1419–1431, Nov. 1973.
[4] T. Tamir, Ed., *Integrated Optics*. Berlin, Germany: Springer, 1975, pp. 83–137. This review article also contains an extensive bibliography on grating couplers.
[5] D. G. Dalgoutte and C. D. W. Wilkinson, "Thin grating couplers for integrated optics: An experimental and theoretical study," *Appl. Opt.*, vol. 14, pp. 2983–2998, Dec. 1975.
[6] H. W. Weber, R. Ulrich, E. A. Chandross, and W. J. Tomlinson, "Light-guiding structures of photoresist films," *Appl. Phys. Lett.*, vol. 20, pp. 143–145, Feb. 1972.
[7] F. H. Dill, J. A. Tuttle, and A. R. Neureuther, "Modelling positive photoresist," in *Proc. Kodak Microelectronics Seminar*, San Diego, CA, Oct. 1974, pp. 24–31.
[8] W. P. Hornberger, P. S. Hauge, J. M. Shaw, and F. H. Dill, "The characterization of positive photoresists," in *Proc. Kodak Microelectronics Seminar*, San Diego, CA, Oct. 1974, pp. 44–54.
[9] W. L. Weeks, *Electromagnetic Theory for Engineering Application*. New York: Wiley, 1965.
[10] S. T. Peng, T. Tamir, and H. L. Bertoni, "Theory of periodic dielectric waveguides," *IEEE Trans. Microwave Theory Tech.*, vol. MTT-23, pp. 123–133, 1975.
[11] S. Austin and F. T. Stone, "Fabrication of thin periodic structures in photoresist: A model," *Appl. Opt.*, vol. 15, pp. 1071–1074, Apr. 1976.
[12] —, "Thin periodic structures in photoresist: Fabrication and experimental evaluation," to be published in *Appl. Opt.*
[13] P. K. Tien, R. Ulrich, and R. J. Martin, "Modes of propagating light waves in thin deposited semiconductor films," *Appl. Phys. Lett.*, vol. 14, pp. 291–294, May 1969.

Correspondence

A 16-μm Source for Laser Isotope Enrichment

ROBERT L. BYER

Abstract—**A potentially efficient, high-energy 16-μm source is proposed based on stimulated rotational Raman scattering in H_2 or D_2 using a TEA CO_2 laser source.**

The calculated pump energy threshold for rotational Raman scattering on the $S(0)$ 354.33 cm^{-1} Raman line of H_2 at 77 K and 1 atm pressure is 3.1 J.

There is now considerable effort toward inventing new lasers and investigating frequency conversion methods to generate coherent radiation at 16 μm for isotope enrichment of UF_6 by a multiple photon process [1]. The proposed isotopic enrichment schemes involve selectively exciting one isotope of UF_6 to a higher vibrational level followed by photodissocation to UF_5 using either a single ultraviolet photon or many infrared photons. The latter scheme, investigated in detail by Ambartzumian *et al.* [2] appears particularly attractive since the threshold intensities for multiple photon absorption are less than 100 MW/cm^2, the photons can be at other than the primary absorption wavelength, and large separation factors are achieved for expenditures of typically 50–100 infrared photons per molecule [3]. Recently, Robinson and Jensen [4] showed that $^{235}UF_6$ and $^{238}UF_6$ spectra are clearly resolved at the 627-cm^{-1} ν_4 band for an expansion cooled gas. Furthermore, the isotope shift between the $^{235}UF_6$ Q-branch and adjacent $^{238}UF_6$ rotational lines is greater than the linewidth being on the order of 0.04 cm^{-1} or 1.2 GHz.

In this letter we propose a particularly simple scheme for generating 16-μm radiation. The method uses rotational Raman scattering in gaseous H_2 or D_2 with a CO_2 laser source. It has the important advantages of being scalable to high average powers, of being a direct conversion process with no competing nonlinear effects, and of using the already well-developed and efficient CO_2 laser source. Furthermore, the threshold intensities for stimulated Raman scattering in H_2 at the CO_2 pump wavelengths are at intensities that match the requirements for the multiple photon dissociation process.

The exponential growth for the Raman Stokes intensity is given by [5]

$$g_s = \frac{4\lambda_s^2 N(d\sigma/d\Omega)I_p}{n_s^2\,\hbar\omega_p\,\Delta\omega_R} \tag{1}$$

where N is the density, λ_s the Stokes wavelength, $(d\sigma/d\Omega)$ the Raman cross section, and $\Delta\omega_R$ the Raman linewidth.

Fortunately, the frequency shifts for H_2 and D_2 as well as the population distributions, linewidths, and Raman gain coefficients have been previously evaluated by Minck *et al.* [6] as a function of temperature for a ruby pump laser. Minck *et al.* [6] have also shown that in a cooled H_2 or D_2 gas at 77 K the stimulated Brillouin scattering gain coefficient is two orders of magnitude below the Raman gain coefficient for pressures below 1 atm. The Raman frequencies and population distributions as a function of temperature are shown in Table I for the rotational Raman transitions of H_2 and D_2.

Manuscript received May 25, 1976; revised August 2, 1976.

The author is with the Ginzton Laboratory, W. W. Hansen Laboratories of Physics, Stanford University, Stanford, CA 94305.

TABLE I
ROTATIONAL RAMAN FREQUENCY SHIFTS AND POPULATION DISTRIBUTION

		Temperature					
		25 K	50 K	75 K	100 K	200 K	300 K
H_2							
$S(0)$	354.33 cm^{-1}	0.992	0.788	0.535	0.388	0.193	0.133
$S(1)$	586.85 cm^{-1}	0.008	0.211	0.462	0.603	0.719	0.667
D_2							
$S(0)$	179.04 cm^{-1}	0.952	0.769	0.608	0.449	0.267	0.182
$S(1)$	297.52 cm^{-1}	0.047	0.208	0.291	0.313	0.260	0.205
$S(2)$	414.71 cm^{-1}	–	0.023	0.097	0.188	0.367	0.387

The CO_2 laser does not have adequate photon energy to excite the vibrational Raman transitions so that there is no competition from other Raman modes.

The linewidths for the rotational Raman lines are Doppler limited below 10^{-2}-atm pressure, show collisional narrowing [7] between 10^{-2} and 1 atm, and are pressure broadened at higher pressures. The gain increases with pressure until pressure broadening becomes important, which is between 0.1–1 atm for both H_2 and D_2. The Raman gain saturates at its maximum value for higher pressures. Since the isotope selection requires a bandwidth of 1 GHz, the CO_2 laser must operate in a single, or at most, a few axial modes within its nominal 3-GHz-gain linewidth. This can be accomplished using etalons or by incorporating a low-pressure CW CO_2 gain section within the same laser cavity [8].

The H_2 rotational Raman cross section has been accurately measured relative to the N_2 cross section by Fenner *et al.* [9] The cross section at 0.488 μm for the $Q(1)$ vibrational line is 1.6 $(d\sigma/d\Omega)_{N_2}$ where $(d\sigma/d\Omega)_{N_2} = 5.6 \pm 0.28 \times 10^{-31}$ $cm^2/sr \cdot mol$ [10]. The cross section for the hydrogen rotational Raman transition $S(1)$ is twice the vibrational Raman cross section so that at 0.488 μm the absolute rotational Raman cross section for H_2 is 1.79×10^{-30} $cm^2/sr \cdot mol$.

Scaling this cross section to the infrared by the ratio $\lambda_p(0.488)\ \lambda_S^3(0.497)/\lambda_p(10.6)\ \lambda_S^3(16) = 1.37 \times 10^{-6}$, assuming a linewidth of 0.01 cm^{-1} or 300 MHz and a hydrogen gas density of 0.95×10^{20} cm^{-3} at 1 atm pressure at 77 K we find a Raman gain coefficient from (1) of $g = 0.68 \times 10^{-4}$ cm^{-1} at a pump intensity of 1 MW/cm^2. This gain value assumes that all of the hydrogen molecules are in the $S(0)$ rotational level or parahydrogen. Experimentally, this is easy to accomplish by obtaining hydrogen gas from a liquid hydrogen source and flowing the gas into a 77 K cell where the para to ortho conversion takes place very slowly.

To achieve threshold for Raman oscillation we need $gl \approx 8$. For a 2-m cell the required input intensity is 588 MW/cm^2. To achieve this intensity a peak power of 31 MW is required if confocally focused into the 2-m cell with an area of $A = \lambda l/4$. Focusing to a smaller area does not increase the gain but does lead to the possibility of optical breakdown. For a 100-ns CO_2 TEA laser pulse the required energy to reach twice threshold is 3.1 J which is within the capability of commercial CO_2 TEA laser sources. However, this gain calculation does assume that the laser operates at a bandwidth comparable to the H_2 linewidth. The gain is invariant to cell length under confocal focusing conditions, but the intensity decreases with increasing length of the Raman cell.

For operation with lower energy lasers the Stokes wave can be resonated. The threshold reduces to $1 = R_1 R_2\, e^{gl-\alpha l}$ in the CW limit. However, for pulsed lasers a net gain of $gl = 8$ must still be reached within the time of the pump pulse. Thus for our case of a 2-m cell, sixteen passes are possible within 100 ns. The gain requirements are thus reduced to $gl = 0.5$. Equivalently, the intensity and energy required to achieve threshold are reduced to 2 MW and 193 mJ. In practice, Raman cells are found to operate more stably with near optimum conversion efficiency under single-pass superfluorescence excitation conditions.

This scheme of generating 16-μm radiation should allow over 10-percent energy conversion to the Stokes wave. The remaining 10.2-μm photons would then be available for multiple photon absorption to dissociate the selectively excited $^{235}UF_6$ molecules. Based on presently available commercial CO_2 TEA laser sources this rotational Raman generation method should allow over 1 J of 16 μm to be generated at greater than 1-pps repetition rate. Future developments in CO_2 laser technology should be able to meet the kilohertz repetition rate requirement for effective isotope separation on a commercial scale.

REFERENCES

[1] a) V. S. Letokhov and C. B. Moore, "Laser isotope separation," *Sov. J. Quantum Electron.*, vol. 6, pp. 129–150, 259–276, 1976. b) J. P. Aldridge, J. H. Birely, C. D. Cantrell, and D. C. Cartwright, "Experimental and theoretical studies of laser isotope separation," to be published in *Laser Photochemistry, Tunable Lasers and Other Topics, Physics of Quantum Electronics*, vol. 4, S. F. Jacobs, M. Sargent, III, M. O. Scully and C. T. Walker, Ed. Reading, MA: Addison-Wesley.

[2] R. V. Ambartzumian, V. S. Letokhov, E. A. Ryabov, N. V. Chekalin, "Isotopic selective chemical reaction of BCl_3 molecules in a strong infrared laser field," *JETP Lett.*, vol. 20, pp. 273–274, 1974.

[3] R. V. Ambartzumian, Yu A. Gorokhov, V. S. Letokhov, G. N. Makarov, "Separation of sulfur isotopes with enrichment coefficient $>10^3$ through action at CO_2 laser radiation on SF_6 molecules," *JETP Lett.*, vol. 21, pp. 171–172, 1975.

[4] C. Paul Robinson and Reed J. Jensen, "Some developments in laser isotope separation research at Los Alamos," presented at the Am. Phys. Soc. Meeting, Feb. 2–5, 1976, New York, NY.

[5] Y. R. Shen, "Stimulated Raman scattering," in *Light Scattering in Solids, Topics in Applied Physics*, vol. 8, M. Cardona, Ed. Berlin, Germany: Springer.

[6] R. W. Minck, E. E. Hagenlocker, and W. G. Rado, "Consideration and evaluation of factors influencing the stimulated optical scattering in gases," Ford Motor Company Tech. Rep. SL66-24, Mar. 1966; see also E. E. Hagenlocker, R. W. Minck, and W. G. Rado, "Effects of phonon lifetime on stimulated optical scattering in gases," *Phys. Rev.*, vol. 154, pp. 226–233, 1967.

[7] L. Galatry, "Simultaneous effect of Doppler and foreign gas broadening on spectral lines," *Phys. Rev.*, vol. 122, pp. 1218–1223, 1961.

[8] A. Gondhalekar, E. Holzhauer, and N. R. Heckenberg, "Single longitudinal mode operation of high pressure pulsed CO_2 lasers," *Phys. Lett.*, vol. 46A, pp. 229–230, 1973.

[9] W. R. Fenner, H. A. Hyatt, J. M. Kellam, and S. P. S. Porto, "Raman cross-sections of some simple gases," *JOSA*, vol. 63, pp. 73–77, 1973.

[10] C. M. Penney, L. M. Goldman, and M. Lapp, "Raman scattering cross-sections," *Nature* (London), Phys. Sci., vol. 235, pp. 110–112, 1972.

Laser Modulation Depth Determination by a Simple Power Measuring Technique

A. L. WAKSBERG, M. H. HUBERT, AND W. R. L. CLEMENTS

Abstract—**A simple method for measuring the depth of modulation is described. This method, which requires only power measurements, is independent of the modulation frequency and has been shown to be accurate when compared to more conventional techniques.**

In order to evaluate the performance of electrooptic crystals in laser communication systems, it is necessary to know exactly the depth of modulation. Although the measurement of the modulation depth is relatively simple at low frequencies, it is plagued with many problems as the frequency is increased (e.g., the frequency response of the detector, the determination of the driving voltage on the crystal, etc.) and hence, becomes less accurate. For meaningful results, it thus becomes necessary to take elaborate precautions to offset these problems.

We shall report a simple technique that we have successfully used in our laboratories to measure modulation depth. It requires only power measurements and has the advantage of being independent of the frequency and wavelength. It shall be referred to as the "power method." Although the technique reported here applies, strictly speaking, to modulation with an electrooptic crystal external to the laser cavity, it could be applied to other modulation techniques with a proper modification of the theoretical expression for the modulation depth.

We have verified the accuracy of our technique against more conventional methods for two separate systems: a helium–neon system operating at 0.6328 μ and a carbon dioxide system operating at 10.6 μ with excellent results.

Modulation System—Theoretical Background

For a modulation system using an electrooptic crystal external to the laser cavity, the output power P_o is given by

$$P_o = P_e \sin^2 \Gamma/2, \tag{1}$$

where P_e is the laser output power and Γ is the phase difference between the two components of the incident polarization along the electrooptic axes of the crystal. This is given by

$$\Gamma = \frac{2\pi l}{\lambda}(n_1 - n_2),$$

where l is the length of the crystal and n_1, n_2 are the effective refractive indices along the two axes. A modulation voltage $V_m(\omega) = V_m \cos \omega_m t$ applied to such a crystal would produce a modulation in the power of the laser output given by

$$P_o = CP_e\{\tfrac{1}{2}[1 - \cos(\Gamma_b)J_0(\Gamma_m)] + \sin(\Gamma_b)J_1(\Gamma_m)\cos\omega_m t + \cdots\}, \tag{2}$$

where the series is expanded only to the fundamental frequency and the other terms are assumed to be eliminated by proper filtering. J_n is the Bessel function of order n. $\Gamma = \Gamma_b + \Gamma_m \cos \omega_m t$ is the total phase difference made up of a constant bias term Γ_b and a modulated term of amplitude Γ_m at frequency ω_m. The constant term can be the result of a natural birefringence or a dc voltage applied to the crystal, while the modulated term is produced by the modulating voltage $V_m \cos \omega_m t$ according to the relation $\Gamma_m = KV_m$ with K a constant. Finally, C is the coupling coefficient of the polarization coupler which extracts the cross-polarized part of the beam.

Manuscript received June 3, 1976; revised July 13, 1976. This work was supported in part by the Canadian Government under a Defence Industrial Research Grant.

The authors are with the Research and Development Laboratories, RCA Limited, Ste-Anne-de-Bellevue, Canada.

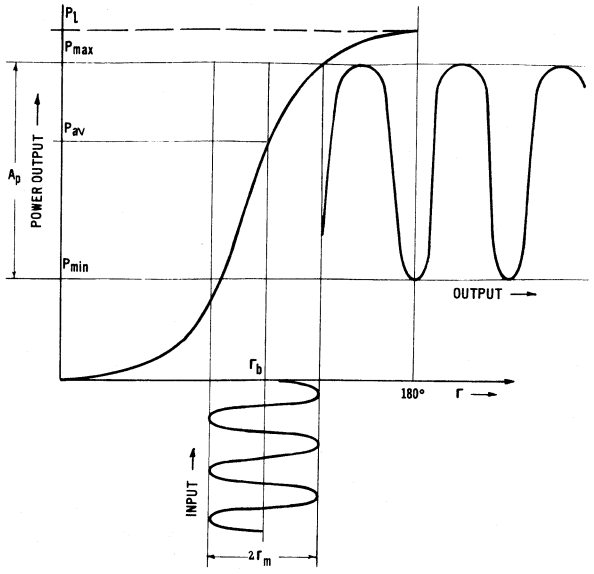


Fig. 1. Electrooptic modulation.

The most common method of determining the modulation depth, referred to as the "direct method," is as follows: the optical bias Γ_b is chosen and a drive modulation Γ_m is applied; the output power would fluctuate between $P_{\max}$ and $P_{\min}$ in a manner depicted in Fig. 1. The ratio $(P_{\max} - P_{\min})/P_{\max}$ is measured on an oscilloscope and is called the peak-to-peak modulation index m_p. This is related to Γ_m by the following relation:

$$m_p = \frac{P_{\max} - P_{\min}}{P_{\max}} = \frac{2\sin(\Gamma_b)\sin(\Gamma_m)}{1 - \cos(\Gamma_b + \Gamma_m)} \tag{3}$$

for $\Gamma_b + \Gamma_m \leqslant \pi$. Fig. 2 is a plot of m_p versus Γ_m for $\Gamma_b = 90°$.

The basis for the power method of measuring the modulation depth is based on the average dc component of the signal, which is

$$P_{o\,\mathrm{av}} = \frac{CP_e}{2}\{1 - \cos(\Gamma_b)J_0(\Gamma_m)\} \tag{4}$$

and contains the drive term Γ_m.

If we define

1) $P_{o\,\mathrm{av}}(\Gamma_b = \Pi, \Gamma_m = 0)$ as the power measured with the optical bias adjusted for a maximum output as read on the powermeter (modulation off),

2) $P_{o\,\mathrm{av}}(\Gamma_b = 0, \Gamma_m = 0)$ as the minimum power, and

3) $P_{o\,\mathrm{av}}(\Gamma_b = 0, \Gamma_m = \Gamma_m)$ as the corresponding average power with the drive (Γ_m) turned on,

then the procedure consists of making these three measurements and calculating

$$P_{o1} = P_{o\,\mathrm{av}}(\Gamma_b = \pi, \Gamma_m = 0) - P_{o\,\mathrm{av}}(\Gamma_b = 0, \Gamma_m = 0),$$

$$P_{o2} = P_{o\,\mathrm{av}}(\Gamma_b = 0, \Gamma_m = \Gamma_m) - P_{o\,\mathrm{av}}(\Gamma_b = 0, \Gamma_m = 0).$$

From (4) we see that

$$P_{o1} = CP_e \tag{5}$$

$$P_{o2} = \frac{CP_e}{2}\{1 - J_0(\Gamma_m)\}, \tag{6}$$

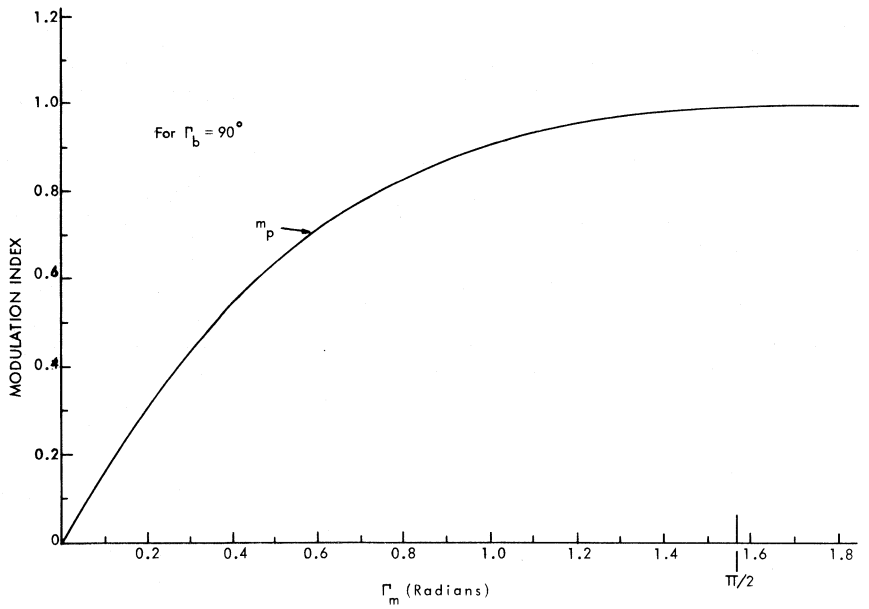


Fig. 2. Modulation index versus drive angle.

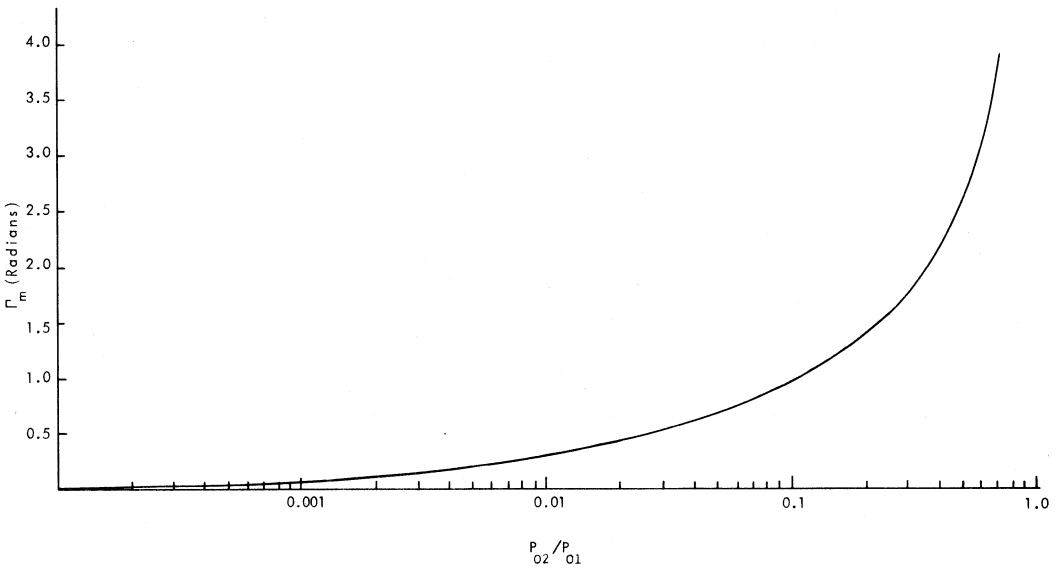


Fig. 3. Drive angle versus P_{o2}/P_{o1}.

thus,

$$\frac{P_{o2}}{P_{o1}} = \frac{1}{2}\{1 - J_0(\Gamma_m)\}. \tag{7}$$

Fig. 3 is a plot of Γ_m versus P_{o2}/P_{o1} calculated from (7). A knowledge of P_{o2}/P_{o1} thus gives Γ_m. The measurement of three average power levels on a sensitive powermeter allows a determination of the depth of modulation which is independent of the frequency and the wavelength.

When the modulation depth is relatively high and it is possible to scan the optical bias by heating, such as in the case of lithium tantalate, an alternative technique can be used. The procedure is as follows.

Step 1: The optical bias is scanned over more than 2π radians and the output of the powermeter is recorded on a chart recorder. Let the peak-to-peak amplitude of a full cycle be A_o.

Step 2: The modulation to be measured is turned on and Step 1 is repeated. Let the new peak-to-peak amplitude be A_m.

It can be shown from (4) that

$$\frac{A_m}{A_o} = J_0(\Gamma_m). \tag{8}$$

Fig. 4 is a plot of Γ_m versus A_m/A_o.

Experimental Verification

A. Carbon Dioxide System

The experimental apparatus used to measure the modulation depth included a carbon dioxide laser with a power output of 5 W, a cadmium telluride electrooptic crystal, a 70-MHz RF source followed by a high-power amplifier and a Hg CdTe detector (for measuring m_p) or a powermeter (for the power method determination). A cadmium sulphide retardation

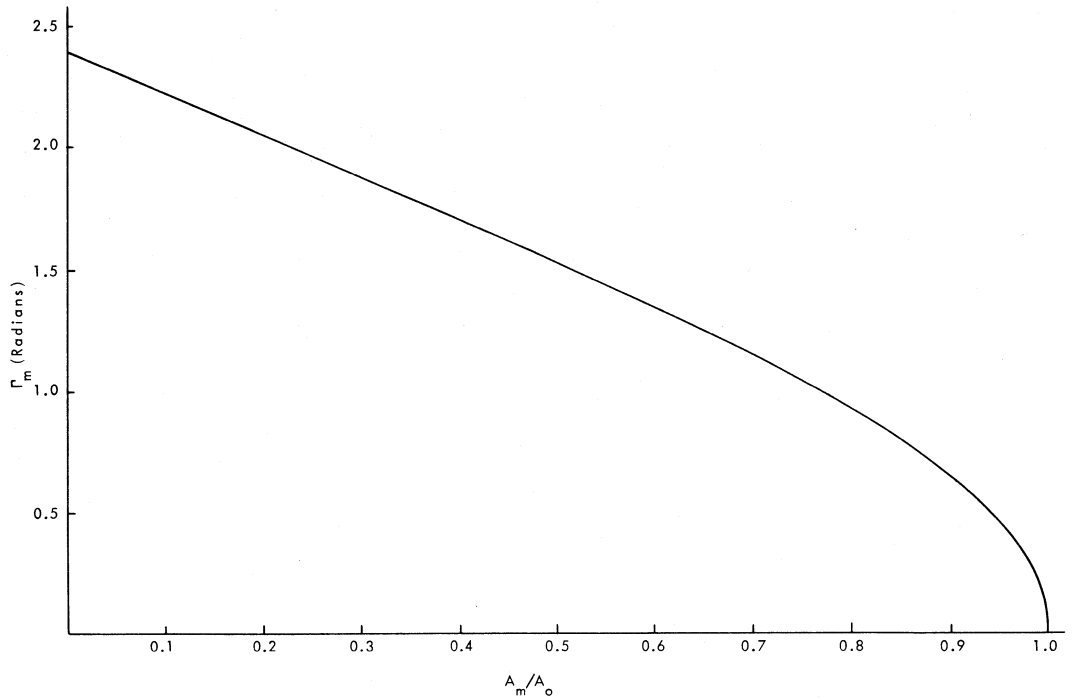


Fig. 4. Drive angle versus A_m/A_O.

TABLE I
COMPARISON OF TECHNIQUES FOR DETERMINING MODULATION DEPTH

Voltage on Crystal (VRMS)	Γ_m from m_p (radians)	Γ_m by Power Method (radians)	Percentage of Difference
43	0.1	0.09	10 percent
61	0.14	0.14	0 percent
84	0.20	0.19	5 percent

plate was used to vary the optical bias for the latter measurements. The results of the two measurement techniques for different modulating depths are given in Table I. It can be seen that the two results agree very well within the experimental accuracy, which is about 10 percent.

B. He–Ne System

In the case of the He–Ne system, it was possible to swing the optical bias over many half-wavelengths by merely heating the electrooptic crystal which was made of lithium tantalate. The amplitude of the output variation produced by the bias swing was measured with and without the 70-MHz RF modulation applied to the crystal. The resulting amplitudes A_m and A_o were used to calculate Γ_m using (8) and Fig. 4. The results were then compared with the more elaborate direct method of obtaining the modulation depth. The results gave a value of $\Gamma_m = 1.01$ rad and $\Gamma_m = 0.98$ rad for the power method and the direct method, respectively. The agreement between these two techniques is seen to be excellent and well within the experimental error which was estimated to be about 5 percent.

DISCUSSION OF RESULT

The power method of measuring depth of modulation at RF frequencies has been shown to be accurate when compared with more conventional techniques. The difference in the techniques however is that in the former method only a powermeter is required and it is therefore independent of frequency response. The measurements are fast and convenient. This should be particularly appreciated by workers in the RF field who know how difficult it is to obtain reliable results at these frequencies.

ACKNOWLEDGMENT

The authors wish to thank Dr. M. P. Bachynski for his kind support.

Comments on "Theory and Experiments on Grating Couplers for Thin-Film Waveguides"

D. G. DALGOUTTE

***Abstract*—In the above paper,[1] Ghizoni *et al.* presented results on a theoretical and experimental study of grating couplers. Some comments are given here on their discussion of previous experimental results on high-efficiency thin-grating couplers.**

In their recent paper,[1] Ghizoni *et al.* discussed a theoretical and experimental study of grating couplers. In the introduction to their paper some misleading remarks were made about some previously published results [1], [2] on high-efficiency

Manuscript received June 8, 1976; revised August 2, 1976.
The author is with Standard Telecommunication Laboratories, Ltd., Harlow, Essex, England.
[1] C. C. Ghizoni, B.-U. Chen, and C. L. Tang, *IEEE J. Quantum Electronics*, vol. QE-12, pp. 69–73, Feb. 1976.

grating couplers. The authors describe these results as being measurements of the output coupling efficiency with a consequent overestimation of the efficiency of the coupler when used as an input coupler. This is in fact erroneous. As described in [1] ([3] of Ghizoni *et al.*[1]), and previously elsewhere in the published literature [2], this measurement was made by an input coupling measurement in which the power in the single uncoupled (reflected) beam is monitored as the angle of incidence of the input beam on the coupler is varied through the coupling angle. As the authors state, this measurement will be optimistic due to scattering and reflection at the termination of the coupling structure. This, however, will be dependent on the actual structure and can be reduced by careful design. In these measurements the input beam was shaped (by focusing) to the optimum waist size for the coupler, and thus some degree of aperture matching was achieved, in contradiction to Ghizoni *et al.*[1] This dip measurement provides a useful comparison with other published coupler efficiencies. In experiments described in [1] and [2], the actual efficiency of the coupler was reported as ~60 percent. This was measured using a prism output coupler and compensating for film loss and corresponds to a loss at the coupler edge due to reflection and scattering of ~13 percent. For the coupler described, this loss was high since the grating was formed in a high-index photoresist which was removed to form the coupler termination. In the case of thin etched couplers, as described by Ghizoni *et al.*,[1] this loss would be expected to be much smaller due to the smaller discontinuity in the waveguide structure (resulting in less distortion of the guided modes by the coupling structure).

Aperture matching is very critical in obtaining accurate input coupling measurements. The aptness of output coupling measurements rather than input coupling measurements to obtain comparisons with theoretical predictions has been described elsewhere [3]. In particular, it is possible to obtain direct measurements of the coupler aperture function which can be related by reciprocity [3] to the required input beam for optimum input coupling. If the aperture function can be exactly matched by the input beam, then the input efficiency will be given by the relative power in the corresponding output beam when the coupler is acting as an output coupler. If there is nonideal aperture matching, then the input efficiency will be correspondingly less. For example, for a uniform coupler structure and a Gaussian input beam, the efficiency will be reduced by ~0.81. The effects of coupler uniformity on coupling efficiency have also been discussed [1], [4]. Small thickness variations along the coupler length can lead to considerable phase curvature of the aperture function, seriously limiting the efficiency obtainable with a plane input beam.

In conclusion, many of the experimental difficulties in measuring grating couplers are now well understood. What remains to be achieved in practice is reliable coupler design and fabrication.

References

[1] D. G. Dalgoutte, "Periodic couplers for the excitation of optical guided waves in thin films," Ph.D. dissertation, Univ. Glasgow, Glasgow, Scotland, 1973.

[2] —, "A high efficiency thin grating coupler for integrated optics," *Optics Commun.* vol. 8, pp. 124–126, June 1973.

[3] D. G. Dalgoutte and C. D. W. Wilkinson, "Thin grating couplers for integrated optics: An experimental and theoretical study," *Appl. Optics*, vol. 14, pp. 2983–2998, Dec. 1975.

[4] D. W. Fradin, P. K. Cheo, S. T. Peng, and T. Tamir, "Effects of imperfections on the efficiency of optical couplers," in *Integrated Optics* (a digest of technical papers presented at the topical meeting on Integrated Optics, Salt Lake City, UT, Jan. 12–14 1976) Paper WD2.

Authors' Reply[2]

C. C. GHIZONI, B. U. CHEN, AND C. L. TANG

1) It has been brought to our attention recently that the measured coupling efficiency of 60 percent reported by Dalgoute ([3] of our paper[1]) actually refers to an input coupling efficiency from the substrate side not an output coupling efficiency on the air side as we thought. For coupling from the substrate side, this input efficiency is quite reasonable and does not conflict with our calculated numerical results which refer to input coupling from the air side. We regret having misinterpreted his work.

2) On p. 73 of our paper,[1] the numerator on the right-hand side of the expression for T in the Appendix should read: $4n_3 \cos\phi \cdot \sqrt{1 - n_3^2 \sin^2\phi}$: there should be no minus sign in front of the square-root sign.

These corrections have no effect on the results and conclusions of the paper.

[2]Manuscript received August 12, 1976.

The authors are with the School of Electrical Engineering, Cornell University, Ithaca, NY 14853.

Radiation Losses in Distributed Feedback Lasers and Longitudinal Mode Selection

W. STREIFER, R. D. BURNHAM, AND D. R. SCIFRES

Abstract—**We show that seemingly symmetric longitudinal modes in symmetrical distributed feedback (DFB) lasers utilizing higher order Bragg reflection actually have differing thresholds and resonant wavelength shifts from the Bragg condition as a result of power radiated by the grating.**

Distributed feedback (DFB) lasers with symmetrical-shaped gratings and symmetrical boundary conditions at their ends, $z = \pm L/2$, have been shown by calculation to have longitudinal modes which are symmetric in threshold and resonant wavelength, λ_0, about the Bragg wavelength λ_b [1]–[3]. Experimentally, this is not the case [4]. One cause of this experimentally observed asymmetry is that laser medium gain and index vary with wavelength. A second, previously unnoted, factor is that otherwise symmetric longitudinal modes of DFB lasers resonating in higher Bragg orders (not the first) radiate [5]–[8] different amounts of power. Formulation and calculation of DFB longitudinal mode thresholds and resonant wavelengths, taking into account radiation losses, are given below.

Radiation from corrugated waveguides in the nonresonant case is well understood [9], [10], but the resonant situation introduces complications. The two resonant contradirectional waves are coherent and therefore their relative phases along the length of the laser must be taken into account in computing radiated power. Furthermore, the radiation reacts on the resonant waves to change the threshold and λ_0, and the overall process is dependent on the longitudinal mode structure. To understand the interactions, recall first that in the

Manuscript received August 6, 1976.

The authors are with the Xerox Palo Alto Research Center, Palo Alto, CA 94304.

nonresonant case, a wave traveling in the $+z$ direction propagates as $\exp(i\beta_0 z)$ [with $\exp(-i\omega t)$ suppressed]. This wave interacts with the grating (period Λ), whose Fourier representation is [9]

$$\sum_{\substack{q=-\infty \\ q\neq 0}}^{\infty} A_q(x) \exp i2\pi qz/\Lambda \tag{1}$$

to produce waves with

$$\beta_q = \beta_0 + 2\pi q/\Lambda. \tag{2}$$

DFB in pth Bragg order occurs if

$$\beta_p = -\beta_0 = \beta_0 + 2\pi p/\Lambda, \tag{3}$$

where $p < 0$. Waves with $p < q < 0$ generally radiate power away from the structure, whereas those with $q < p$ and $q > 0$ neither supply nor drain power directly.

In the resonant case, we let $\mathcal{E}_0(x)R(z)\exp(i\beta_0 z)$ be the TE wave traveling in the $+z$ direction and $\mathcal{E}_0(x)S(z)\exp(-i\beta_0 z)$ be the pth TE wave traveling in the $-z$ direction. $\mathcal{E}_0(x)$ is the transverse field variation and $R(z)$, $S(z)$ are the axial variations which can be shown to satisfy

$$R' + (-\alpha - i\delta - i\zeta_1)R = i(\kappa + \zeta_2)S, \tag{4a}$$

$$-S' + (-\alpha - i\delta - i\zeta_1)S = i(\kappa + \zeta_2)R, \tag{4b}$$

where κ is the coupling coefficient computed without regard to the radiating waves [9]. In (4a) and (4b), $\alpha > 0$ is the net threshold field gain,

$$\delta = \beta - \beta_0, \tag{5}$$

where $\beta = \beta(\lambda_0)$, so that δ is a measure of the shift from λ_b, i.e., $\beta_0 = \beta(\lambda_b)$, and ζ_1, ζ_2 are discussed below. Solving (4a) and (4b) subject to reflection boundary conditions at $z = \pm L/2$, determines α and δ; with no reflection $R(-L/2) = 0$ and $S(L/2) = 0$. The quantities ζ_1 and ζ_2 are zero when the effects of R and S in generating other waves ($q \neq 0$, p) are ignored. For definitiveness, R is used in the discussion. The term ζ_1 represents the first-order effect of R producing waves with $q \neq p$ and those waves reacting on R itself. Since some of the waves carry power away from the structure, they constitute a loss mechanism and so $\mathrm{Im}(\zeta_1) < 0$. The quantity ζ_2 represents the first-order effect of R generating waves with $q \neq p$ and these waves acting on S. Thus, ζ_2 is, in effect, a coupling term. $\mathrm{Re}(\zeta_2)$ acts as an index modulation whereas $\mathrm{Im}(\zeta_2)$ acts as a gain/loss modulation. These may have either sign relative to κ depending on phase. Thus, $\mathrm{Re}(\zeta_2)$ may in effect increase or decrease κ. In first Bragg order DFB, with $p = -1$, no radiating waves exist, and ζ_1, ζ_2 are both real. The calculation of ζ_1 and ζ_2 involves overlap integrals which are, in principle, similar to those for κ and α. This computation will be discussed elsewhere.

To solve (4a) and (4b) subject to the boundary conditions at $z = \pm L/2$, we write

$$R' + (-\hat{\alpha} - i\hat{\delta})R = i\hat{\kappa}S \tag{6a}$$

$$-S' + (-\hat{\alpha} - i\hat{\delta})S = i\hat{\kappa}R, \tag{6b}$$

where $\hat{\kappa} = \kappa + \zeta_2$ and

$$\alpha + i\delta = \hat{\alpha} + i\hat{\delta} - i\zeta_1. \tag{7}$$

Then we employ the methods of [3]. Generally, since ζ_2, and therefore $\hat{\kappa}$, are complex, the spectra are no longer symmetric about λ_b even if the boundary conditions are symmetric. Particular longitudinal mode thresholds may be larger or smaller than those computed with ζ_1, ζ_2 neglected. This is most evident for $|\kappa L| \gg 1$. Consider a conventional three-layer double-heterostructure GaAs:GaAlAs laser as shown in Fig. 1. With outer refractive indices of 3.4, active region thickness of $t = 1$ μm, active region index 3.6, $\lambda_0 = 0.85$ μm, $g = 1500$ Å, and $w = 0.15\ \Lambda$, $\Lambda = 4746$ Å for fourth-order Bragg DFB operation ($p = -4$), we find $\kappa = -43.45\ \mathrm{cm}^{-1}$, $\zeta_1 = -2.468 + i\ 2.004\ \mathrm{cm}^{-1}$, and $\zeta_2 = -3.1345 + i\ 1.928\ \mathrm{cm}^{-1}$, where all q with $-8 \leq q \leq 4$ have been taken into account. This truncation yields results accurate to about 1 percent. For a 1-mm long laser with no end reflectors, we obtain the results shown in Table I. Recalling that αL is the total net field gain at threshold, the total net threshold power gain at threshold is $2\alpha L$, and the actual threshold power gain, $2\alpha_{th}$, is given by

$$2\alpha_{th} = 2\alpha + 2\alpha_{ab}, \tag{8}$$

where $2\alpha_{ab}$ is the power absorption. If $2\alpha_{ab} \approx 15\ \mathrm{cm}^{-1}$ (free carrier absorption), then $2\alpha_{th} \approx 22\ \mathrm{cm}^{-1}$ for the -1 longitudinal mode and $29\ \mathrm{cm}^{-1}$ for the $+1$ longitudinal mode. Thus near threshold one would expect single longitudinal mode behavior. In the same geometry with $w = 0.85\ \Lambda$, we find $\kappa = 14.55\ \mathrm{cm}^{-1}$, $\zeta_1 = -.8471 + i\ 0.7954\ \mathrm{cm}^{-1}$, and $\zeta_2 = -1.0559 + i\ 0.7654\ \mathrm{cm}^{-1}$, and now the longitudinal modes with $\delta L < 0$ have higher thresholds than their counterparts with $\delta L > 0$. Note that with $w/\Lambda = 0.85$, the resonant period is $\Lambda = 4750$ Å because the effective guide width is slightly decreased.

Generally, the effects described above increase with increasing Bragg order resonance as one would expect. For $p = -1$, there exists no radiating wave and ζ_1, ζ_2 are real. For the laser described above with $w = 0.15\ \Lambda$ and $\Lambda = 1186$ Å, the thresholds of modes on both sides of the Bragg wavelength increase identically, and with $w = 0.85\ \Lambda$ and $\Lambda = 1188$ Å, all thresholds decrease symmetrically. In both cases, the lasing wavelengths shift asymmetrically, but this shift and the threshold changes are quite small.

The results presented herein apply to any symmetrical tooth shape. If external reflectors are employed and are asymmetric, then the thresholds are asymmetric even if radiation is not

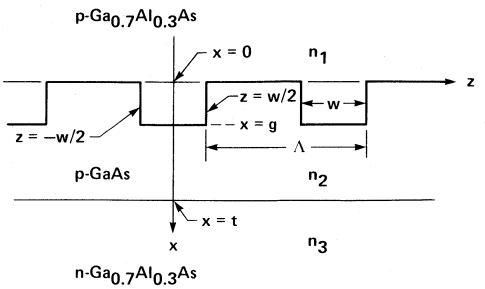


Fig. 1. Illustrating the laser geometry.

TABLE I
NET THRESHOLD GAIN AND RESONANT WAVELENGTH FOR LONGITUDINAL MODES WITH ($\zeta_1, \zeta_2 \neq 0$) AND WITHOUT ($\zeta_1, \zeta_2 = 0$) THE EFFECTS OF RADIATING WAVES

Longitudinal Mode Number	$\zeta_1, \zeta_2 = 0$		$\zeta_1, \zeta_2 \neq 0$	
	αL	δL	αL	δL
−3	1.372	−10.225	1.407	−10.077
−2	0.945	−7.485	0.954	−7.392
−1	0.374	−5.263	0.369	−5.265
+1	0.374	5.263	0.704	5.081
+2	0.945	7.485	1.199	7.965
+3	1.372	10.225	1.588	10.658

taken into account [3]. The case of asymmetric tooth shapes with or without reflectors will be discussed elsewhere.

In conclusion, we have shown that radiative losses produced by low-order Bragg scattering introduce asymmetries in longitudinal mode thresholds in otherwise symmetric DFB lasers.

References

[1] H. Kogelnik and C. V. Shank, "Coupled mode theory of distributed feedback lasers," *J. Appl. Phys.*, vol. 43, pp. 2327–2335, 1972.

[2] S. R. Chinn, "Effects of mirror reflectivity in a distributed-feedback laser," *IEEE J. Quantum Electron.*, vol. QE-9, pp. 574–580, June 1973.

[3] W. Streifer, R. D. Burnham, and D. R. Scifres, "Effect of external reflectors on longitudinal modes of distributed feedback lasers," *IEEE J. Quantum Electron.*, vol. QE-11, pp. 154–161, Apr. 1975.

[4] R. D. Burnham, D. R. Scifres, and W. Streifer, "Single heterostructure distributed-feedback GaAs-diode lasers," *IEEE J. Quantum Electron. (Part II of Two Parts)*, vol. QE-11, pp. 439–449, July 1975.

[5] Zh. I. Alferov *et al.*, "Semiconductor laser with extremely low divergence of radiation" (in Russian), *Sov. Phys.-Semicond.*, vol. 8, pp. 832–833, 1974; also (in English), *Sov. Phys.-JETP*, pp. 541, 542.

[6] P. Zory, "Laser oscillation in leaky corrugated optical waveguides," *Appl. Phys. Lett.*, vol. 22, pp. 125–128, 1973.

[7] D. R. Scifres, R. D. Burnham, and W. Streifer, "Observation of highly collimated laser beams from electrically pumped SH GaAs/GaAlAs distributed feedback lasers," *Appl. Phys. Lett.*, vol. 26, pp. 48–50, 1975.

[8] F. K. Reinhart, R. A. Logan, and C. V. Shank, "GaAs–$Al_xGa_{1-x}As$ injection lasers with distributed Bragg reflectors," *Appl. Phys. Lett.*, vol. 27, pp. 45–48, 1975.

[9] W. Streifer, D. R. Scifres, and R. D. Burnham, "Analysis of grating-coupled radiation in GaAs:GaAlAs lasers and waveguides," *IEEE J. Quantum Electron.*, vol. QE-12, pp. 422–428, July 1976.

[10] W. Streifer, R. D. Burnham, and D. R. Scifres, "Analysis of grating-coupled radiation in GaAs:GaAlAs lasers and waveguides–II: Blazing effects," *IEEE J. Quantum Electron.*, vol. QE-12, pp. 494–499, Aug. 1976.

Notes and Lines

High-Pressure Operation of a CW DF–CO_2 Transfer Laser

GEORGE EMANUEL, W. G. GASKILL, R. J. REINER, C. SHELTON, AND W. WATKINS

The DF/CO_2 CW chemically pumped transfer laser [1], [2] normally operates at cavity pressures of about 60 torr or less. This limitation applies to operation at both subsonic and supersonic flow speeds. In this correspondence, we describe high-cavity-pressure operation at a supersonic velocity. Two additional features are unique to this supersonic experiment. First, a single nozzle provides the cavity flow, instead of a nozzle array consisting of numerous small nozzles. Second, the gas in the plenum is at room temperature, in contrast to the high temperature associated with an arc or combustor for providing atomic fluorine.

A schematic of the device is shown in Fig. 1. A primary flow consisting of F_2, CO_2, and He mixes in a tube upstream of an injector for the NO and D_2 gases. The room temperature primary flow passes through a screen designed to break up large-scale eddies and then flows into a convergent–divergent nozzle, whose area ratio is 1.14. This provides a Mach number of about 1.5 from a nozzle whose exit dimensions are 1.488 × 4.445 cm with the larger dimension in the optical direction. The NO + D_2 gas mixture is injected into the primary flow at the throat through 20 small tubes (0.122-cm ID, 0.183-cm OD), each of which terminates in 17 holes of 0.024-cm diameter. These holes provide a spray pattern with a maximum angle, relative to the primary flow, of 20°. All hardware is constructed of aluminum with Teflon seals.

The jet enters a large cavity chamber which is mechanically pumped. Two water-cooled, gold-coated, 10 × 10-cm mirrors measure the "closed cavity" 10.6-μm optical power. Helium purge tubes with openings in the proximity of the jet prevent highly absorbing CO_2 (100), which is present in the hot ambient gas, from entering the optical path formed by the stable oscillator mirrors. The curved mirror could be rotated to determine the variation of power as a function of optical axis location.

Manuscript received July 12, 1976. This work was supported by the Air Force Weapons Laboratory under Contract F29601-75-C-0077.

G. Emanuel was with TRW Defense and Space Systems, Redondo Beach, CA 90278. He is now with the Los Alamos Scientific Laboratories, University of California, Los Alamos, NM 87545.

W. G. Gaskill, R. J. Reiner, and C. Shelton are with TRW Defense and Space Systems, Redondo Beach, CA 90278.

W. Watkins is with the Air Force Weapons Laboratory, Kirtland Air Force Base, NM 87117.

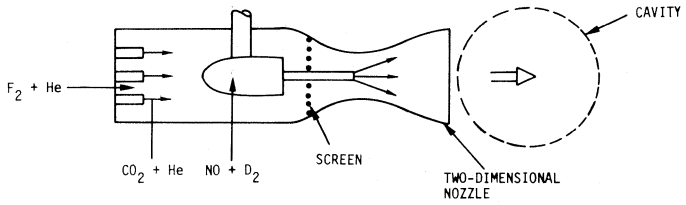


Fig. 1. Schematic of the transfer laser device.

As the NO + D_2 gas mixes with the primary flow, F atoms are produced by the reaction

$$F_2 + NO \longrightarrow F + NOF.$$

These F atoms then drive the well-known DF chain

$$F + D_2 \longrightarrow DF(v) + D$$

$$D + F_2 \longrightarrow DF(v) + F$$

and the vibrationally excited DF(v) pumps the CO_2 to the (001) state, which then lases. Efficient lasing requires the presence of a large CO_2 concentration. Without CO_2 the excited DF deexcites collisionally too rapidly for efficient lasing.

Preliminary small-signal gain measurements, at one flow condition, indicated sufficient gain (0.007 percent/cm) for a power measurement with closed-cavity optics. In a subsequent test, 1.45 kW was measured with the optical axis located 3.89 cm downstream of the nozzle exit. This power corresponds to a chemical efficiency of 1.9 percent. At this condition the plenum pressure was 631 torr and the ambient cavity pressure was 233 torr. The jet flow consisted of 5.29 g/s F_2, 57.8 g/s CO_2, 15.1 g/s He, 1.61 g/s D_2, and 1.53 g/s NO. It should be noted that these flow rates, cavity pressure, optical axis location, etc. do not represent optimum power values.

References

[1] T. A. Cool, "The transfer chemical laser: A review of recent research," *IEEE J. Quantum Electron. (Part II of Two Parts)*, vol. QE-9, pp. 72–83, Jan. 1973.

[2] G. W. Tregay, M. G. Drexhage, L. M. Wood, and S. J. Andrysiack, "DF-CO_2 Transfer Laser Development," *IEEE J. Quantum Electron. (Part II of Two Parts)*, vol. QE-11, pp. 672–678, Aug. 1975.

Contributors

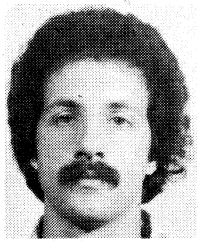


Harris Y. Ageno was born in Wailuku, Maui, Hawaii, on May 26, 1936. He received the B.S. degree in physics from the University of California, Los Angeles, in 1964.

Since 1971, he has been with the McDonnell Douglas Research Laboratories in St. Louis, MO, and is engaged in CO chemical laser research.

Mr. Ageno is a member of the Optical Society of America and the American Meteorological Society.

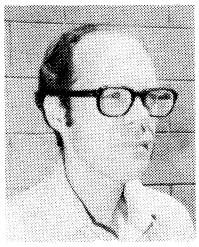
*



Stewart Austin (S'69–M'75) was born in New York, NY, on February 23, 1950. He received the B.S., M.S., and Ph.D. degrees in electrical engineering from the Polytechnic Institute of New York, NY, in 1972, 1973, and 1976, respectively.

In 1976 he became an Academic Associate in the Department of Electrical Engineering and Electrophysics at the Polytechnic Institute of New York, teaching electronics and network analysis. His early research was concerned with a variety of laser applications, including the development of an optical AGC system at 3.39 μm. More recently, his doctoral research dealt with the fabrication of periodic structures in photoresist and their use as integrated optical grating couplers. He is now working at the Lincoln Laboratory, Massachusetts Institute of Technology, Lexington, while on an appointment as a Research Associate in the Research Laboratory of Electronics at M.I.T. His work deals with optical and X-ray registration techniques for X-ray lithography.

Dr. Austin is a member of the Optical Society of America, Eta Kappa Nu, Tau Beta Pi, and Sigma Xi.

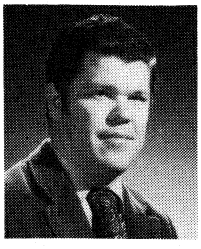


Blake E. Cherrington (S'63-M'65-SM'73) was born in Belleville, Ont., Canada, on March 16, 1937. He received the B.A. Sc. degree with honors and M.A. Sc. degree in electrical engineering from the University of Toronto, Toronto, Ont., Canada, in 1959 and 1961, respectively. He received the Ph.D. degree in electrical engineering from the University of Illinois, Urbana-Champaign.

Since 1965 he has bee a Staff Member of th Gaseous Electronics Laboratory at the University of Illinois and currently holds an appointment as Professor of Electrical Engineering and of Nuclear Engineering. He is active in the fields of gaseous electronics, quantum electronics, and plasma physics, and is presently Co-Director of five research projects in these areas.

Dr. Cherrington is a member of the American Physical Society, Sigma Xi and Eta Kappa Nu.

*



Richard A. Chodzko was born in Whittier, CA, on January 12, 1939. He received the B.A. degree in physics from the University of California, Berkeley, and the Ph.D. degree in engineering physics from the University of California, San Diego, in 1962 and 1970, respectively. His thesis work was in laser beam interactions in absorbing gases related to induced turbulence.

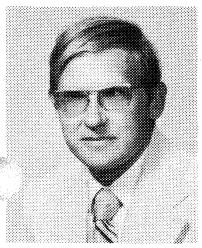
From 1962 to 1965 he worked for the Lockheed Propulsion Company in an advanced planning group on propulsion system design. He currently is a Staff Scientist in the Aerophysics Laboratory of The Aerospace Corporation, El Segundo, CA, where he has been employed since 1971. His current area of interest is in the optical aspects of CW chemical laser technology. In particular, he has worked on gain studies, line selection, unstable resonator design, beam diagnostics, and mode control in an annular gain medium for CW HF/DF chemical lasers.

Dr. Chodzko is a member of the American Institute for Aeronautics and Astronautics.

Drew A. Copeland (M'73) was born in Chicago, IL, on October 22, 1948. He received the B.S. degree in engineering physics from Cornell University, Ithaca, NY, in 1970 and the M.S. degree in physics from the University of Maryland, College Park, MD, in 1973. In 1973 he returned to Cornell University to work towards the Ph.D. degree in the area of quantum electronics.

Mr. Copeland is a student member of the American Physical Society.

*

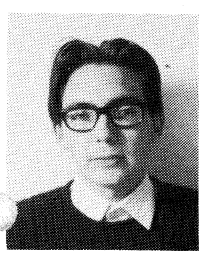


John W. Daiber was born in Doylestown, OH, on October 10, 1935. He received the B.E. degree from the University of Notre Dame, Notre Dame, IN, in 1957 and the M.E. degree from Cornell University, Ithaca, NY, in 1959, both in the field of aeronautical engineering. In 1967 he received the Ph.D. degree from the State University of New York, Buffalo, with physics as his major subject.

Since 1959 he has been employed by Calspan Corporation, formerly the Cornell Aeronautical Laboratory, in Buffalo, NY. His primary research interest lies with laser development and laser application. A related area of activity has been concerned with diagnostic measurements such as microwave interferometry, light scattering, and spectroscopy.

Dr. Daiber is a member of Sigma Xi and the American Physical Society.

*

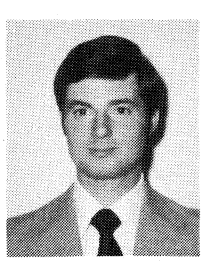


Magnus Danielsen (S'69-M'71) was born in Tórshavn, Faroes, Denmark, on August 26, 1942. He received the M.Sc. and Ph.D. degrees in electrical engineering from the Technical University of Denmark, Lyngby, in 1967 and 1972, respectively.

From 1967 to 1972 he was Assistant Professor at the Electromagnetics Institute, Technical University of Denmark. During this period he carried on research in the field of application of superconductors for microwave components, especially cavity resonators. In 1972 he was appointed Associate Professor at the Academia Færoensis Faroes, and since 1974 he has been Associate Professor at the Electromagnetics Institute.

Dr. Danielsen is a member of European Physical Society, Dansk Ingeniørforening and Verkfrøðingafelag Føroya.

*



J. Gary Eden (S'75-M'76) was born in Washington DC, on October 11, 1950. He received the B.S.E.E. degree from the University of Maryland, College Park, and the M.S. and Ph.D. degrees in electrical engineering from the University of Illinois, Urbana-Champaign, in 1972, 1973, and 1976, respectively.

Since November 1975 he has held a National Research Council Postdoctoral Research Associateship with the Laser Physics Branch of the Naval Research Laboratory, Washington, DC. His research activities have centered on electron beam excited visible and ultraviolet excimer lasers.

Dr. Eden is a member of Tau Beta Pi, Eta Kappa Nu, Phi Kappa Phi, the American Physical Society, and the American Society for Engineering Education.



Theodore J. Falk was born in Meriden, CT, on October 9, 1931. He received the B. Aero. E. degree from Rensselaer Polytechnic Institute, Troy, NY, in 1953 and the M. Aero. E. and Ph.D. degrees from Cornell University, Ithaca, NY, in 1956 and 1963, respectively.

He joined Calspan Corporation, formerly Cornell Aeronautical Laboratory, Inc., Buffalo, NY, in 1963. Since 1968 he has worked primarily in laser research. He participated in the initial development of the CW DF-CO_2 chemical transfer laser and has recently conducted analytical and experimental investigations of subsonic-flow cryogenically cooled electron-beam-ionized CW CO lasers.

*

U. Ganiel (A'71-M'72) was born in Rehovot, Israel, on September 6, 1936. He received the M.Sc. degree from the Hebrew University of Jerusalem, Jerusalem, Israel, and the Ph.D. degree from the Weizmann Institute of Science, Rehovot, Israel, both in physics, in 1963 and 1968, respectively.

He did research in the fields of atomic spectroscopy, nuclear quadrupole resonance, Mössbauer spectroscopy, and magnetism. He spent a year as a Visiting Research Physicist at Carnegie-Mellon University, Pittsburgh, PA, where he worked in Mössbauer spectroscopy. He was a Research Fellow at the California Institute of Technology for two years (1970-1971), where he worked in the field of nonlinear optics. Since 1971 he has been on the faculty of the Department of Electronics of the Weizmann Institute, where he has been working on various laser systems, problems in optical resonator theory, and specifically, on tunable dye laser systems.

Dr. Ganiel is a member of the American Physical Society and the Israel Physical Society.

*



A. Hardy was born in Hungary on February 9, 1942. He received the B.Sc. and M.Sc. degrees from the Hebrew University of Jerusalem, Jerusalem, Israel, and the Ph.D. degree in applied physics from the Weizmann Institute of Science, Rehovot, Israel, in 1966, 1969, and 1975, respectively. His Ph.D. dissertation was in the area of optical diffraction theory.

Since April 1975 he has been with the Department of Electronics, the Weizmann Institute of Science, where he has been working on dye laser systems and some problems in optical resonator theory.

*



Kenneth O. Hill was born in Guadalajara, Mexico. He received the B.Eng, M.Eng and Ph.D. degrees in engineering physics from McMaster University in Hamilton, Ont., Canada.

Following his graduate work, he joined the Communications Research Center, Ottawa, Ont., Canada, in 1968 to work on holographic memories and coherent optics. His current fields of interest include integrated optics, optical communication systems and fiber-optic lasers. Recently he was appointed Head of the Optical Communications Group at the Communications Research Center.



William Q. Jeffers (M'73) was born in Aurora, NE, on November 1, 1939. He received the S.B. degree in electrical engineering from the Massachusetts Institute of Technology, Cambridge, and the M.S. and Ph.D. degrees in electrical engineering from the University of Illinois, Urbana, in 1961, 1964, and 1967, respectively.

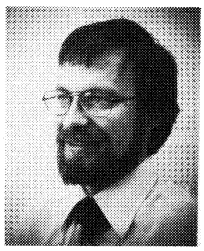
From 1961 to 1963 he was employed in the Research Division of McDonnell Aircraft Company, where he worked on microwave masers. He was in the Department of Electrical Engineering of the University of Illinois from 1963 through 1968 as a Research Assistant, Research Associate, and Assistant Professor. His thesis research at the University of Illinois was concerned with the water-vapor laser. He was associated with Hughes Research Laboratories, Malibu, CA, in 1968, and rejoined McDonnell Douglas Research Laboratories, St. Louis, MO., in 1969. He is now with Helios, Inc., Boulder, CO. His research interests have been in the field of molecular and chemical lasers. He has been active in organizing the Conference on Chemical and Molecular Lasers in St. Louis in 1969, 1972, and 1974.

Dr. Jeffers is a member of Sigma Xi and the Optical Society of America.

*

Joel C. Johnson (S'72-M'75), for a photograph and biography please see p. 161 of the February issue of this JOURNAL.

*



R. Ian MacDonald was born in Marlborough, England, on January 11, 1943. He received the B.Sc. degree in engineering physics from Queen's University, Kingston, Ont., Canada, in 1965, and the M.Eng. and Ph.D. degrees in 1972 and 1975 from Carleton University, Ottawa, Ont., Canada.

Between 1965 and 1970 he was involved in the development of microcircuits with Northern Electric Research and Development, with Microsystems International, Ottawa, and with SGS-Italia in Milan. He is currently a Research Scientist at the Communications Research Centre, Ottawa, Ont., Canada, working in optical communications.

*

H. Mahr, photograph and biography not available at the time of publication.

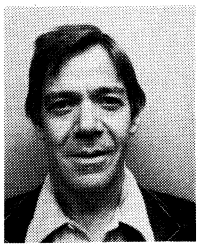
*



D. Marcuse (M'58-F'73) was born in Koenigsberg, East Prussia, Germany, on February 27, 1929. He received the degree of Diplom Physiker from the Freie Universitaet, Berlin, Germany, and the degree of Dr. Ing. from Technische Hochschule, Karlsruhe, Germany, in 1954 and 1962, respectively.

From 1954 to 1957 he worked at the Central Laboratory, Siemens and Halske, Berlin, Germany, on transmission-line problems and the development of the circular electric waveguide. In 1957 he became a member of the Technical Staff of the Bell Laboratories, Holmdel, NJ, and worked on the circular electric waveguide and masers. He is presently working on the transmission aspect of a light communications system. In addition, he is also an Adjunct Associate Professor at the University of Utah, Salt Lake City. He is the author of three books.

Dr. Marcuse is a member of the Optical Society of America.



Stephen B. Mason was born in Atlanta, GA, on October 21, 1925. He received the A.B. degree from Emory University, Atlanta, GA, in 1948, and furthered his engineering and scientific background at the Northrop Institute of Technology, Inglewood, CA. in 1952.

He was employed as an Associate Test Engineer with Vard, Inc., Pasadena, CA, from 1954 through 1956 when he joined the Caltech Wind Tunnel as an Associate Engineer in the Calibration Department. In 1958 he was employed by the Aerodynamics and Propulsion Department of what has become The Aerospace Corporation, El Segundo, CA. As a Senior Research Associate, he has assisted the Technical Staff in experimental work involving shock tunnels and laser technology.

*

Gail A. Massey (M'67), for a photograph and biography please see p. 162 of the February issue of this JOURNAL.

*



Harold Mirels was born in New York, NY, on July 29, 1924. He received the B.M.E. degree from Cooper Union, New York, NY, in 1944, the M.S.M.E. degree from Case Institute of Technology, Cleveland, OH, in 1949 and the Ph.D. degree in aeronautical engineering from Cornell University, Ithaca, NY, in 1953.

From 1944 to 1961 he was associated with the National Aeronautics and Space Administration and its predecessor, NACA. At that organization, he conducted research in the areas of linearized wing theory, hypersonic flow, and shock-tube technology. In 1961 he joined the Laboratories Division of The Aerospace Corporation, El Segundo, CA, where he is presently Head of the Aerodynamics and Heat Transfer Department. He has worked on aerodynamic and heat-transfer phenomena associated with reentry vehicles and is currently investigating the performance of continuous chemical lasers.

Dr. Mirels is a Fellow of the American Physical Society and a Fellow of the American Institute of Aeronautics and Astronautics.

*



William W. Rigrod (A'52-M'57) was born in New York, NY, on March 29, 1913. He received the B.S. degree cum laude from the Cooper Union Institute of Technology, New York, NY, in 1934, the M.S. degree from Cornell University, Ithaca, NY, in 1941, and the D.E.E. degree in electrophysics from the Polytechnic Institute of Brooklyn, New York, NY, in 1950.

From 1935 to 1939 he was engaged in the development of ionic devices at the State Electrotechnical Institute (V.E.I.), Moscow, U.S.S.R., and from 1941 to 1951 worked on pulsed and microwave electronic devices at the Westinghouse Electric Corporation, Bloomfield, NJ. Since then he has worked in the Electron Physics Research Department of Bell Laboratories, Holmdel, NJ, in various areas of microwave electronics, lasers and optics.

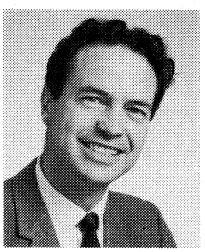
Dr. Rigrod is a member of the Optical Society of America and Sigma Xi, and has served on the ISRC Subcommittee on Cultural and Scientific Exchanges.



David H. Ross was born in Chicago, IL, on June 22, 1927. He received the B.M.E. degree from Cornell University, Ithaca, NY, in 1950. He was a Guggenheim Fellow in Jet Propulsion at the Guggenheim Institute of Jet Propulsion, Princeton University, Princeton, NJ, from 1950 to 1952, and Research Associate for Prof. Acheret, Institute for Aerodynamics, Swiss Federal Institute of Technology, Zurich, Switzerland, from 1955 to 1959.

From 1952 to 1954 he was a Research Aerodynamicist with Republic Aviation concerned with supersonic aerodynamics and propulsion and nonlinear dynamics. From 1954 to 1957, he was a Staff Engineer with the American Turbine Corporation, Anderson and Porter, Engineers, engaged in research and development of aircraft gas turbines and closed-cycle nuclear gas turbines. From 1959 to 1961 he was Assistant Professor of Mechanical Engineering, Stevens Institute of Technology, Hoboken, NJ, and Consultant on nuclear gas turbines for the General Dynamics Corporation. From 1961 to the present he has been with The Aerospace Corporation, El Segundo, CA, and is currently with the Aerophysics Laboratory, where his fields of activity include chemical laser instrumentation, laboratory, field, and airborne optoelectronic, acoustic, and flow instrumentation and studies, and the investigation of shear flow turbulence.

*

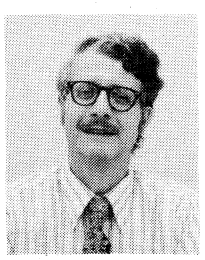


Donald J. Spencer was born in Salt Lake City, UT, on April 15, 1928. He received the B.S.E.E. degree from the University of Utah, Salt Lake City, in 1954, and the M.S. degree in applied physics from the University of California, Los Angeles, in 1956, under the Hughes Master of Science Fellowship program. He has done further graduate work at the University of Southern California, Los Angeles.

From 1954 to 1957 he was an Electronics Engineer at Hughes Aircraft Company, Culver City, CA, where he worked on test equipment design. In 1957 he joined the Ramo-Wooldrige Corporation, Los Angeles, as a Research Physicist, and in 1958 transferred to Space Technology Laboratories. Since 1960 he has been on the Research Staff of The Aerospace Corporation, El Segundo, CA, where he is now a Senior Staff Scientist in the Aerophysics Laboratory. He has done research on arc-heaters, plasma diagnostics, reentry simulation, thermochemical ablation, and gas dynamic and chemical lasers.

Mr. Spencer is a member of the American Institute of Aeronautics and Astronautics.

*



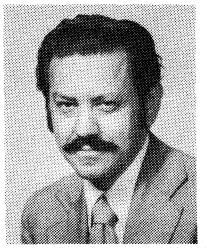
F. T. Stone was born in New York, NY, on August 14, 1938. He received the B.S. degree from Manhattan College, New York, NY, in 1960, the M.S. degree from Syracuse University, Syracuse, NY, in 1962, and the Ph.D. degree from the Polytechnic Institute of Brooklyn (now the Polytechnic Institute of New York), New York, NY, in 1970, all in electrical engineering.

From 1960 to 1962 he was Research Assistant at Syracuse University, working on cryogenic and microwave devices. From 1962 to 1976 he was Instructor, Assistant Professor, and Associate Professor at the Polytechnic Institute of New York, where his research interests included plasmas, optical communication, and integrated optics. In 1976 he joined the Staff of Bell Laboratories, Norcross, GA, where he is working on the characterization of fiber optic transmission media.

Dr. Stone is a member of the Optical Society of America, the American Vacuum Society, and Eta Kappa Nu.

*

Chung L. Tang (SM'68), for a photograph and biography please see page 88 of the February 1976 issue of this JOURNAL.



Herbert M. Thompson was born in Harrisville, WV, in 1931. He graduated from West Virginia University, Morgantown, with the B.S. degree in chemistry in 1954.

After graduation he served two years with the Air Force. In 1956 he joined the Cornell Aeronautical Laboratory now called Calspan Corporation, Buffalo, NY. His current research interests include laser heating of plasmas and gas laser development. He has utilized soft X-ray emission, spontaneous magnetic fields, and high-speed photography to study the interaction of intense laser radiation with gases. He has also participated in the development of both wall-cooled and supersonically cooled electrically excited CO lasers.

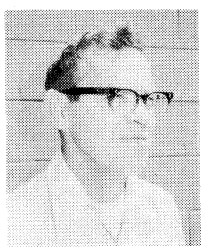
Mr. Thompson is a member of Sigma Xi.

*

D. Treves (SM'69-F'76) was born in Italy on June 29, 1930. He received the B.Sc., M.S., and Ph.D. degrees, all in electrical engineering, from the Haifa Technion, Israel, in 1953, 1956, and 1958, respectively.

Since 1953 he has been associated with the Weizmann Institute and has been involved in the study of magnetization processes; magnetic materials, magnetooptic memories, and laser systems. He spent several years in the United States as a Research Associate at Pomona College, Claremont, CA, as a member of the Technical Staff at Bell Laboratories, Murray Hill, NJ, at the Ampex Research Laboratory at Redwood City, CA, and as World Trade Exchange Fellow at IBM, San Jose, CA. At present he is a Professor with the Department of Electronics, the Weizmann Institute, Rehovot, Israel.

*



Joseph T. Verdeyen (S'59-M'63-SM'74) was born in Terre Haute, IN, on August 15, 1932. He received the B.S. degree in electrical engineering from Rose Polytechnic Institute, Terre Haute, IN, in 1954, the M.S. degree in electrical engineering from Rutgers University, New Brunswick, NJ, in 1958, and the Ph.D. degree in the field of gaseous electronics and plasmas from the University of Illinois, Urbana-Champaign, in 1962.

In 1954 he joined Bell Laboratories, where he participated in their Communications Development Training Program. In 1955 he started his two year tour of active duty in the Signal Corps at Fort Monmouth, NJ, as a Second Lieutenant. After his discharge from the Army in 1957, he returned to Bell Laboratories for the remainder of the summer and then joined the Faculty of the Department of Electrical Engineering, Rutgers University, as an Assistant Instructor. In 1958 he joined the Department of Electrical Engineering, University of Illinois, Urbana-Champaign, and currently holds an appointment as Professor of Electrical Engineering and of Nuclear Engineering. He is active in the fields of gaseous electronics, quantum electronics, and plasma physics, and presently is Director of the Gaseous Electronics Laboratory.

Dr. Verdeyen is a member of Tau Beta Pi, Sigma Xi, and the American Physical Society.

*



Charles E. Wiswall was born in Vincennes, IN, on September 16, 1938. He received the B.S. degree in engineering physics and the M.S. degree in physics from the University of Illinois, Urbana, in 1961 and 1962, respectively.

Since 1962, he has been with the McDonnell Douglas Research Laboratories, St. Louis, MO. He has worked on the theory and applications of holography, potential liquid and crystal laser materials, and is currently engaged in research of chemical lasers.

Mr. Wiswall is a member of the Optical Society of America.

5th Conference on Chemical and Molecular Lasers

The Fifth Conference on Chemical and Molecular Lasers will be held at Stouffer's Riverfront Inn, St. Louis, on April 18, 19, and 20, 1977.

Call for Papers

The scope of this conference includes research in the following areas:

1. New results on existing chemical lasers
2. New reaction systems
3. Diagnosis of chemical reactions and lasers
4. Electrically pumped lasers
5. Excitation transfer systems
6. New molecular lasers
7. Molecular relaxation, collisional quenching or electronic excitation
8. Laser controlled chemistry
9. Other

Engineering applications of lasers and specific devices lie outside the scope of this conference. Authors are encouraged to indicate on their abstracts the subject category appropriate to their paper.

Instructions for Authors

Authors are requested to submit 250 word abstracts of their papers, following the APS style for abstracts. The entire abstract (including figures) must be contained on a single side of an 8½ x 11 sheet for direct reproduction. The deadline for submission of abstracts is Jan. 10, 1977, and notices of acceptance will be sent to authors by Feb. 28, 1977. Summaries should be sent to:

Dr. W.Q. Jeffers
Helios Incorporated
P.O. Box 2190
Boulder, CO 80302

Registration Fees

Registration fee for the conference is $30.00 with a student rate of $15.00. Included in the fee is a Digest of Abstracts of the papers to be presented. A special issue of IEEE J. Quantum Electron. is planned as a conference proceedings; abstracts will be published in this issue at no additional charge.

The Influence of the Longitudinal Plasma Wave on the Propagation Characteristics of a Metal-Clad-Dielectric-Slab Waveguide

KIYOSHI NOSU AND JOJI HAMASAKI, MEMBER, IEEE

Abstract—**The influence of the longitudinal plasma wave on propagation characteristics of a metal-clad-dielectric-slab waveguide is discussed theoretically: the influences on propagating TM waves and on a surface plasma wave, respectively, appear at a wavelength shorter and longer than the plasma wavelength of the metal cladding.**

I. Introduction

SINCE metal claddings can provide electrodes for optical integrated devices, and have dielectric properties approximately characterized by negative permittivities in a low optical frequency region, characteristics of propagating waves of a metal-clad-dielectric-slab waveguide have attracted the interests of many workers [1]-[6], [11]-[13].

In the analysis of the previous papers on a metal-clad-dielectric-slab waveguide, the continuity of the normal component of the complex dielectric displacement D, defined by $\epsilon_t E^t$, is required at the metal-to-lossless-dielectric interface, where E^t and ϵ_t are an electric field and a permittivity of a transverse electromagnetic wave, respectively. In regard to the TM wave of the metal-clad-dielectric-slab waveguide whose electric field has the component normal to the metal-dielectric interface, the previous analysis did not satisfy the continuity of the normal component of the conduction current density at the metal-dielectric interface. In order to satisfy this boundary condition for the TM waves, the transverse electromagnetic wave having a divergence-free electric field E^t (div $E^t = 0$) and the longitudinal plasma wave having an irrotational electric field E^l (rot $E^l = 0$) must be taken into account in the metal [7]-[10].

In the present paper, the influences of the longitudinal plasma wave on the characteristics of TM waves of a metal-clad-dielectric-slab waveguide are analyzed theoretically to show the limits of applicability of the analysis of the previous papers.

II. Dispersion Relations of TM Waves Including the Effect of the Longitudinal Plasma Wave

At the metal-dielectric interface, the normal component of the total conduction current density, which is the sum of the conduction current density originated in the transverse electromagnetic wave and that originated in the longitudinal plasma wave, must vanish:

$$(\sigma_t E^t)_n + (\sigma_l E^l)_n = 0 \quad \text{(at the metal-dielectric interface)}, \tag{1}$$

where the suffix n means the normal component to the interface, and σ_t, σ_l are the conductivities of the transverse electromagnetic wave and the longitudinal plasma wave, respectively.

The condition for excitation of the longitudinal plasma wave is given by

$$\epsilon_l(k_l, \omega) = 0, \tag{2}$$

where ϵ_l and k_l are the permittivity and the wavenumber of the longitudinal plasma wave, respectively.

Permittivities and conductivities for the longitudinal plasma wave and the transverse electromagnetic wave can be obtained by the analysis of Melnyk and Harrison [7]. Since the longitudinal plasma wave couples only TM waves, the argument for TM waves needs to be revised.

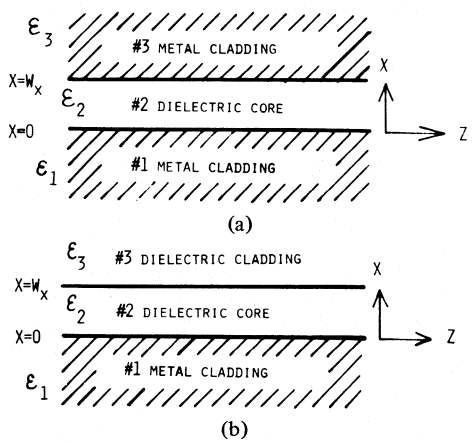


Fig. 1. Cross sections of metal-clad-dielectric slab waveguides. (a) A symmetrical waveguide. (b) An asymmetrical waveguide.

Fig. 1 (a) and (b) shows the cross sections of a symmetrical and an asymmetrical metal-clad-dielectric-slab waveguide, respectively, with associated notations. For the TM wave propagating in these waveguides, one must consider a transverse electromagnetic wave having a divergence-free electric field and a longitudinal plasma wave having an irrotational electric field in order to satisfy the boundary condition (1) at the boundary between the dielectric core and the metal cladding. Then the dispersion relation of the metal-clad waveguide is obtained.

Fig. 2 shows an interface between a dielectric core (or

Manuscript received February 26, 1976; revised August 11, 1976. This work was supported in part by the Nippon Telegraph and Telephone Public Corporation, in part by Fujitsu Laboratories, Ltd., and in part by Fujikura Cable Works, Ltd.

The authors are with the Institute of Industrial Science, University of Tokyo, Tokyo 106, Japan.

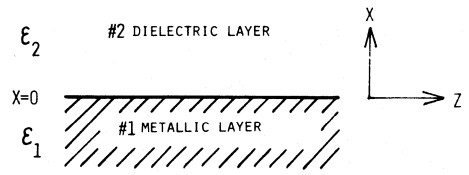


Fig. 2. Metal-dielectric (or vacuum) interface.

TABLE I
PLASMA PARAMETERS OF ALUMINUM AND POTASSIUM

	(a)	(b)	(c)	(d)	(e)			
	n (m^{-3})	$\frac{\epsilon_g}{\epsilon_0}$	ρ_0 ($\mu\Omega m$)	γ (sec^{-1})	V_F (m/sec)	ω_p (rad/sec)	λ_p (m)	λ_p (measured) (m)
Al	1.8×10^{29}	1.0	2.5×10^{2}	1.3×10^{14}	2.02×10^{6}	2.40×10^{16}	7.85×10^{-8}	8.10×10^{-8}
K	1.3×10^{28}	1.24	6.4×10^{2}	2.3×10^{13}	0.86×10^{6}	5.68×10^{15}	3.31×10^{-7}	$3.2\sim3.3\times10^{-7}$

Note: n: electron density; ϵ_g/ϵ_0: relative permittivity of metallic lattice; ρ_0: resistivity; γ: relaxation angular frequency; V_F: Fermi velocity; ω_p: plasma angular frequency; $\lambda_p = 2\pi c\omega_p^{-1}$; c: light velocity in vacuum. (a) The electron density, n, is obtained from the molar volume, the number of valence electrons, and Avogadro's number [14]. (b) From [16]. (c) From [14]. (d) The relaxation angular frequency, γ. is calculated from resistitivity, ρ_0, by the following relation: $\gamma = ne^2\rho_0\ m^{-1}$, where e and m are the charge and the mass of an electron. (e) $V_F = h(2\pi m)^{-1}(3\pi^2 n)^{1/3}$, h: Planck's constant.

vacuum) and a metal, where a surface plasma wave can propagate [11]-[13]. In order to obtain the dispersion relation for this wave, one must again consider both the transverse electromagnetic wave and the longitudinal plasma wave in the metal to satisfy the boundary condition (1). The cutoff angular frequency, ω_{sp}, of the surface plasma wave is given approximately by

$$\omega_{sp} = \omega_p\ [1 + \epsilon_2\ \epsilon_g^{-1}]^{-1/2}, \tag{3}$$

where ω_p is the plasma angular frequency of the metal, and ϵ_g is the permittivity of the metallic lattice without the effects of electron gas.

III. Numerical Calculations

Since the electronic properties of aluminum and potassium are readily explained by a free electron gas model, the influences of the longitudinal plasma wave on the characteristics of a TM wave in a metal-clad-dielectric-slab waveguide are numerically examined by using one of those metals as a cladding.

In evaluating the influences of the longitudinal plasma waves hereafter, the theoretical values obtained from the free electron gas model are used, and it is assumed that the dielectric constant of a nonmetallic material is independent of wavelength.

The plasma parameters of aluminum and potassium are listed in Table I. Fig. 3 shows the wavelength dependences of the attenuation constant, $-\mathrm{Im}\ [k_z]$, of TM_1 and TM_2 waves of symmetrical and asymmetrical waveguides of various thickness of the core ($\epsilon_2/\epsilon_0 = 3.56$) clad by aluminum. In the symmetrical waveguide, #3 dielectric cladding is assumed to be a vacuum. The solid and dashed lines in this figure show the attenuation constants including and excluding the effect

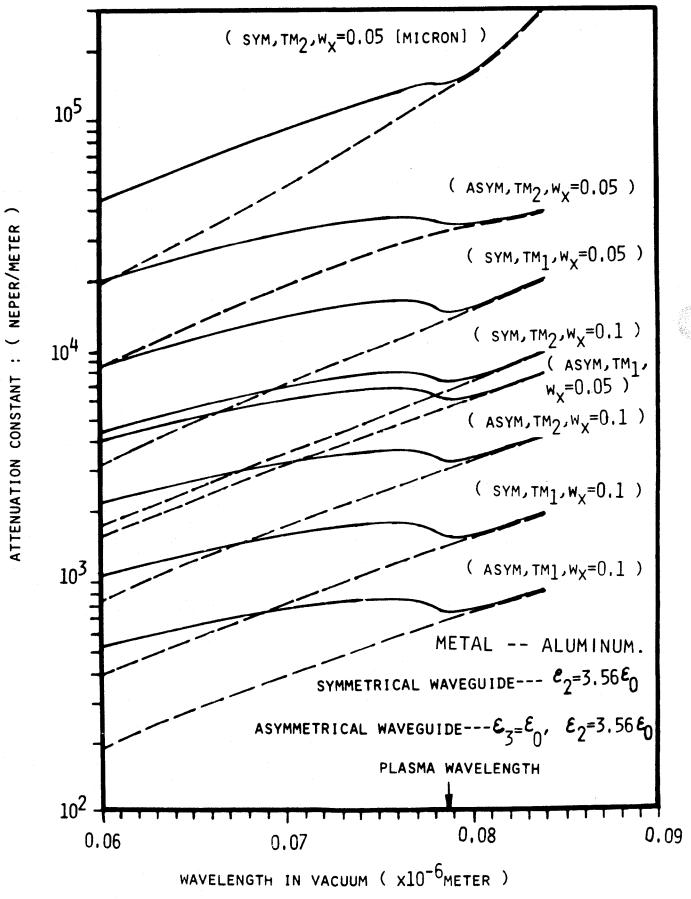


Fig. 3. Attenuation constant $-\mathrm{Im}\ [k_z]$ of TM_1 and TM_2 waves of the metal-clad-dielectric-slab waveguide versus wavelength in vacuum, λ. Solid lines indicate values including the effect of the longitudinal plasma wave; dashed lines denote values excluding the effect.

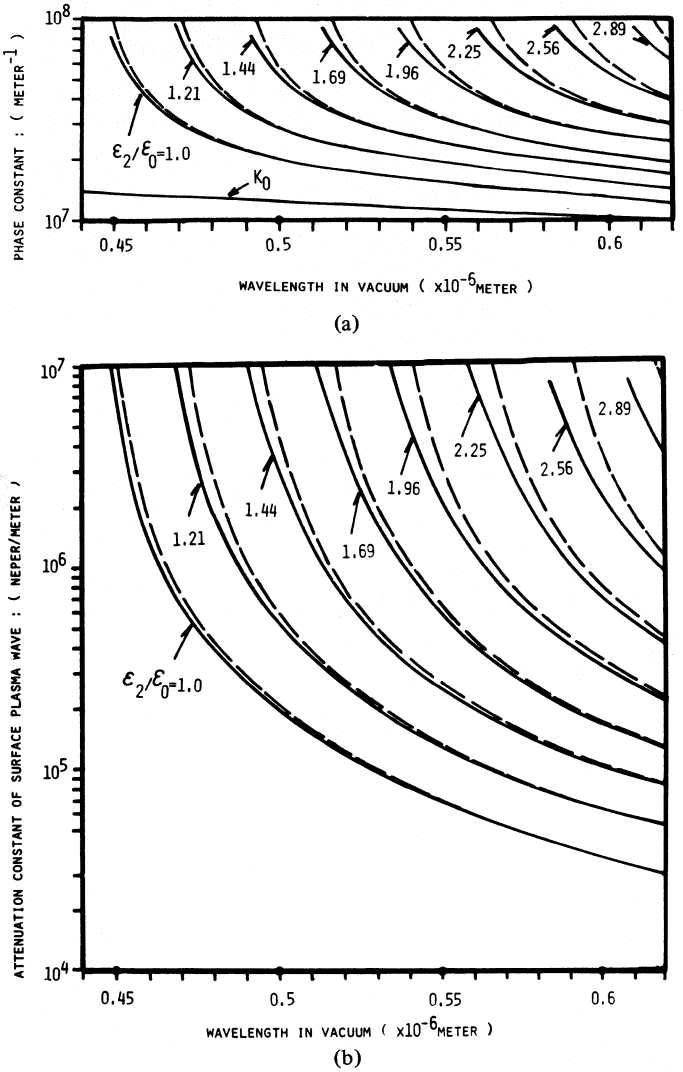


Fig. 4. Phase constant Re $[k_z]$ and attenuation constant $-\mathrm{Im}\,[k_z]$ of the surface plasma wave at the potassium-dielectric interface versus wavelength in vacuum, λ. Solid lines denote values including the effect of the longitudinal plasma wave; dashed lines denote values excluding the effect. (a) Phase constant. (b) Attenuation constant.

of the longitudinal plasma wave, respectively. Though the corresponding phase constant, Re $[k_z]$, and the field configuration do not show an appreciable difference between the waveguides including and excluding the effect of the plasma wave, the attenuation constant increases considerably by including the effect of the plasma wave at $\lambda < \lambda_p$, where the plasma wave is propagating in the metal. However, at $\lambda > \lambda_p$, no appreciable difference appears by including the effect of the plasma wave.

Fig. 4 shows dispersion relations of Re $[k_z]$ and $-\mathrm{Im}\,[k_z]$ of the surface plasma wave traveling along the interface between potassium and a lossless dielectric of which permittivity, ϵ_2, is assumed to be independent of wavelength. The surface plasma wave can exist in the region $\lambda > \lambda_{sp}$, where $\lambda_{sp} = 2\pi c\omega_{sp}^{-1}$ (c: light velocity of a vacuum). However, in contrast to the propagating waves in the metal-clad-dielectric-slab waveguides, both Re $[k_z]$ and $-\mathrm{Im}\,[k_z]$ decrease appreciably by including the effects of the longitudinal plasma wave at a wavelength slightly longer than λ_{sp}. Since λ_{sp} depends on ϵ_2, the influence of the longitudinal plasma wave appears in a visible-wavelength region if we choose a dielectric having a large ϵ_2.

IV. Conclusion

The influences of the longitudinal plasma wave on the propagating characteristics of a metal-clad-dielectric slab waveguide are examined theoretically. The following results are obtained.

1) The influences on the propagating TM waves, except for the lowest mode wave (surface plasma wave), can be neglected at a wavelength longer than the plasma wavelength of the metal cladding. Therefore, theories of the previous workers on a metal-clad-dielectric-slab waveguide are valid, when they are applied in a wavelength region longer than the plasma wavelength. (For most metals the plasma wavelengths are in the ultraviolet region.)

2) At a wavelength shorter than the plasma wavelength, however, the longitudinal plasma wave must be included in order to predict propagation characteristics of the TM waves; especially attenuation constants are considerably underestimated if the longitudinal plasma wave is not included in the theories.

3) The longitudinal plasma wave is quite influential as regards the propagation characteristics of a surface plasma wave traveling along an interface between a metal and a dielectric, even though the surface plasma wave can exist at a wavelength longer than the plasma wavelength of the metal. Both the phase and the attenuation constant are considerably overestimated if the longitudinal plasma wave is not included in the theories, especially at a wavelength slightly longer than the cutoff wavelength, λ_{sp}, of the surface plasma wave. With a high-dielectric-constant material and a proper metal, the influence of the longitudinal plasma wave will appear even in the visible-wavelength region.

Acknowledgment

The authors wish to express thanks to Dr. Lotsch for his suggestions on the longitudinal plasma waves, and to Prof. S. Saito, Prof. Y. Fujii, and Prof. H. Sakaki for their fruitful discussions.

References

[1] T. Takano and J. Hamasaki, "Propagating modes of a metal-clad-dielectric-slab waveguide for integrated optics," *IEEE J. Quantum Electron. (Part II of Two Parts: Special Issue on 1972 IEEE/OSA Conf. Laser Engineering and Applications)*, vol. QE-8, pp. 206–212, Feb. 1972.

[2] A. Reisinger, "Characteristics of optical guided modes in lossy waveguides," *Appl. Opt.*, vol. 12, pp. 1015–1024, May 1973.

[3] I. P. Kaminow, W. L. Mammel, and H. P. Weber, "Metal-clad optical waveguides: Analytical and experimental study," *Appl. Opt.*, vol. 13, pp. 396–405, Feb. 1974.

[4] J. N. Polky and G. L. Mitchell, "Metal-clad planar dielectric waveguide for integrated optics," *J. Opt. Soc. Amer.*, vol. 64, pp. 274–279, Mar. 1974.

[5] E. M. Garmire and H. Stoll, "Propagation losses in metal-film-substrate optical waveguides," *IEEE J. Quantum Electron.*, vol. QE-8, pp. 763–766, Oct. 1972.

[6] J. Hamasaki and K. Nosu, "A partially metal-clad-dielectric-slab

waveguide for integrated optics," *IEEE J. Quantum Electron.* (Corresp.), vol. QE-10, pp. 822–825, Oct. 1974.
[7] A. R. Melnyk and M. J. Harrison, "Theory of optical excitation of plasmons in metals," *Phys. Rev. B*, vol. 2, pp. 835–850, Aug. 1970.
[8] F. Sauter, "Der Einfluß von Plasmawellen auf das Reflexionsvermögen von Metallen (1)," *Z. Phys.*, vol. 203, pp. 488–494, 1967.
[9] R. Clanget, "Der Einfluß von Plasmawellen auf die optischen Eingenshaften leitender Schichten und metallischer Kolloide," *Optik*, vol. 2, pp. 180–194, Feb. 1972.
[10] H. K. V. Lotsch, "Comments on propagating modes of a metal-clad-dielectric-slab waveguide for integrated optics," *IEEE J. Quantum Electron.*, vol. QE-9, pp. 780–781, July 1973.
[11] E. N. Economou, "Surface plasmons in thin films," *Phys. Rev.*, vol. 182, pp. 539–554, June 1969.
[12] A. Otto, "Excitation of nonradiative surface plasma waves in silver by the method of frustrated total reflection," *Z. Phys.*, vol. 216, pp. 398–410, 1968.
[13] E. A. Stern and R. A. Ferrell, "Surface plasma oscillations of a degenerate electron gas," *Phys. Rev.*, vol. 120, pp. 130–136, Oct. 1960.
[14] D. E. Gray, Ed., *American Institute of Physics Handbook*, 3rd ed. New York: McGraw-Hill, 1972, sec. 6, 7, 9.
[15] K. H. Hellwege and A. M. Hellwege, Ed., "Landolt-Börnstein Zahlenwerte und Funktionen aus Physik, Chemie, Astronomie Geophysik und Technik," II. *Band, 8-Teil Optische Konstanten.* Berlin, Germany: Springer, 1962.
[16] C. Kittel, *Introduction to Solid State Physics*, 3rd ed. New York: Wiley, 1968, Chap. 8.

Dispersion Characteristics of Diffused Channel Waveguides

H. F. TAYLOR

Abstract—**A variational method is used to calculate dispersion curves for channel waveguides fabricated by masked diffusion. Composition profiles for the waveguides are obtained by numerical solution of the diffusion equation, assuming that the diffusant concentration in the unmasked region of the substrate surface is constant during the diffusion process. A linear dependence of refractive index change on diffusant concentration is assumed. The dependence of the number of guided modes on mask gap width and diffusion depth is determined as an aid to the design of modulators and switches for integrated optics.**

Introduction

THE dielectric "channel" waveguide, which exhibits two-dimensional beam confinement, has recently received considerable attention from experimentalists in integrated optics. In particular, the feasibility of producing efficient, high-speed electrooptic modulators [1], [2] and switches [3]-[5] in diffused channel waveguides has been demonstrated.

Previously, several theoretical analyses of planar diffused waveguides have been reported [6]-[10]. Although the channel waveguide is much more difficult to analyze theoretically than the planar waveguide, several methods for obtaining useful approximate solutions have been described. One approach is to approximate the field amplitude for a guided wave by a function $f(x)\ g(y)$, where f and g are fields for planar waveguide modes and it is assumed that the refractive index varies in the xy plane. This method, which has been applied to rectangular [11], rib [12], and strip-loaded [13] waveguide geometries, yields useful results for tightly bound modes. A variational method in which fields are approximated by a linear combination of orthogonal functions of the form $f_n(x)g_m(y)$ has been successfully applied to rectangular-core waveguides [14]. Another approach, useful if the refractive index varies in steps rather than continuously, is to express the electromagnetic field distribution in each region of constant refractive index as a linear combination of solutions to Maxwell's equations in that region [15]. Equations for determining linear coefficients and mode propagation constants are obtained by matching electric and magnetic fields to ensure continuity at the dielectric interfaces. The finite element method, a numerical technique which is capable, in principle, of treating arbitrary waveguide geometries [16], requires much more computation than the other methods described above [17].

This paper presents calculated dispersion characteristics for channel waveguides fabricated by masked diffusion and determines the number of guided modes as a function of diffusion depth and mask width. The calculations assume that the surface composition in the unmasked region remains constant during the diffusion process. The results were obtained using the variational method, which was selected because it provides good accuracy but requires only a moderate amount of computer time.

Spatial Variation of Diffusant Concentration and Refractive Index

The first step in analyzing the diffused waveguide is to calculate the spatial distribution of diffusant in the substrate. It assumed that the diffusant concentration c is initially zero in the substrate, and that the concentration for $t \geqslant 0$ is a con-

Manuscript received April 30, 1976; revised August 2, 1976.
The author is with the Naval Electronics Laboratory Center, San Diego, CA 92152.

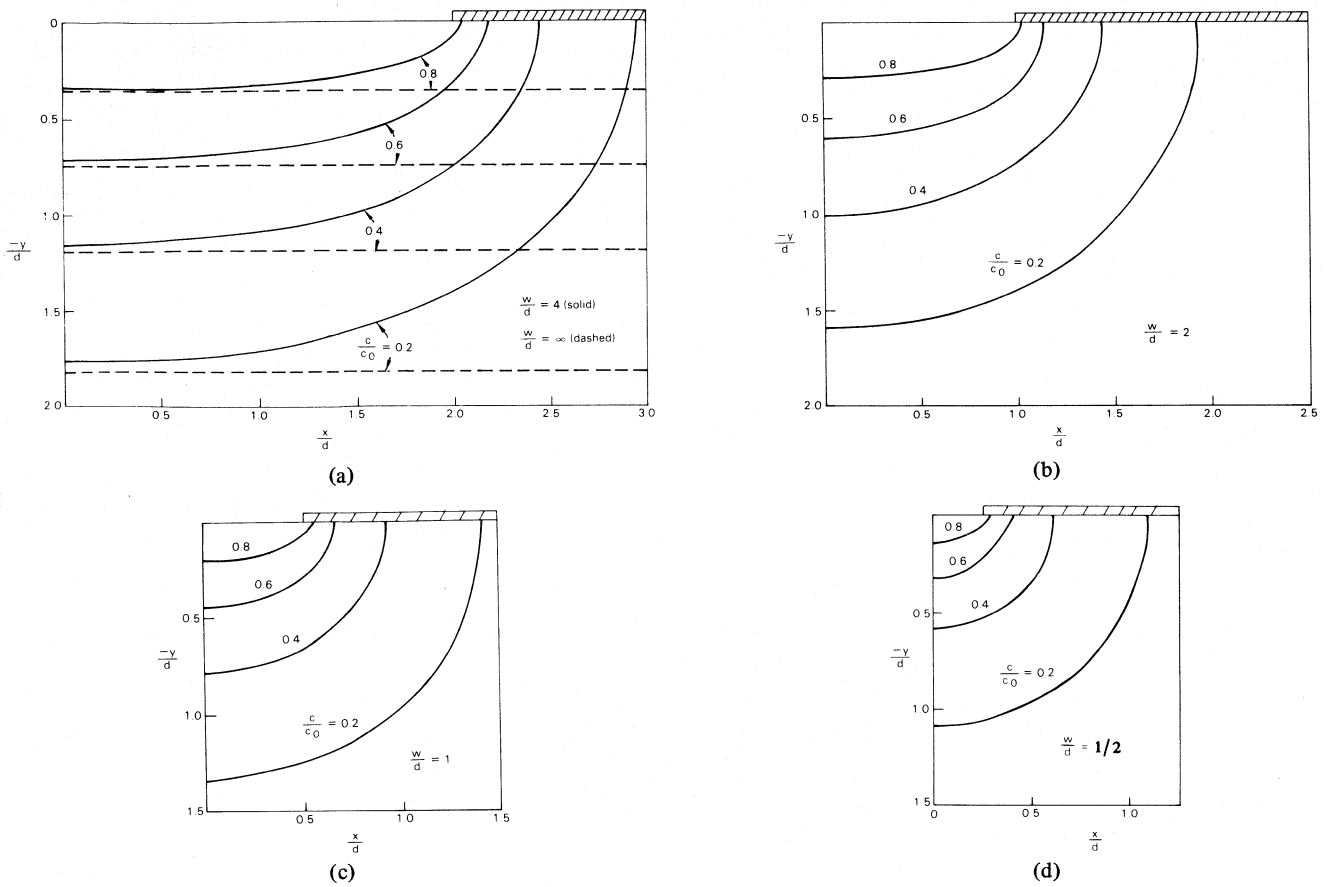


Fig. 1. Diffusant composition profiles for different ratios of mask gap width w to diffusion depth d. The dashed curve in (a) is for the planar diffused guide ($w/d \to \infty$).

stant value c_0 in an unmasked region of width w. Mathematically, the diffusion equation is written [18]

$$D\left(\frac{\partial^2 c}{\partial x^2} + \frac{\partial^2 c}{\partial y^2}\right) = \frac{\partial c}{\partial t}, \tag{1}$$

where D is the diffusion constant and the substrate is assumed to occupy the half-space $y \leqslant 0$. It is assumed that no diffusion occurs within the mask material, so that $D = 0$ for $y > 0$. The boundary conditions are

$$c = 0, \qquad t = 0, \qquad y \leqslant 0$$

$$c = c_0, \qquad -\frac{w}{2} \leqslant x \leqslant \frac{w}{2}, \qquad y = 0, \qquad t > 0.$$

Solutions to (1) obtained by standard difference-equation techniques [19] are given in Fig. 1 for various ratios of mask gap width w to diffusion depth d, defined by $d = (Dt)^{1/2}$.

It will be assumed in the following analyses that the refractive index increase in the diffused waveguide is a linear function of diffusant concentration. This assumption makes it possible to write the refractive index n for a planar guide (i.e., for $w \to \infty$) in the form

$$n = \Delta n_s \operatorname{erfc}(y/2d) + n_s \tag{2}$$

where Δn_s is the increase in index at the surface, n_s is the substrate refractive index, and erfc is the complementary error function. An index variation described by (2) has been indicated in previous experimental studies of diffused waveguides in ZnSe [20] and $LiNbO_3$ [10], [21].

Calculation of Mode Propagation Constants

It will be assumed that the diffusion mask is removed following waveguide fabrication or that it is thin enough that its effect on light propagation can be neglected. The plane $y = 0$ then represents an air-dielectric interface with large refractive-index discontinuity, while the refractive index can be assumed to vary slowly ($\lambda |\nabla n|/n \ll 1$) within the substrate. The TEM modes which this type of waveguide supports can be divided into two groups: one in which the main field components are E_x and H_y, and a second with principal field components E_y and H_x [11]. The electric field distribution E_x for a mode of the first group can be written

$$E_x = \phi(x, y)e^{-i\beta z}$$

where ϕ and ϕ_y are continuous at the interface $y = 0$, and ϕ satisfies the scalar wave equation

$$\frac{\partial^2 \phi}{\partial x^2} + \frac{\partial^2 \phi}{\partial y^2} + \left[\left(\frac{2\pi n}{\lambda}\right)^2 - \beta^2\right]\phi = 0.$$

The field distribution will be approximated by the series [14]

$$\phi = \sum_{ij} a_{ij}(2\pi\xi\eta i!j!)^{-1/2} D_i[x/\xi]\, D_j[(y - y_0)/\eta], \tag{3}$$

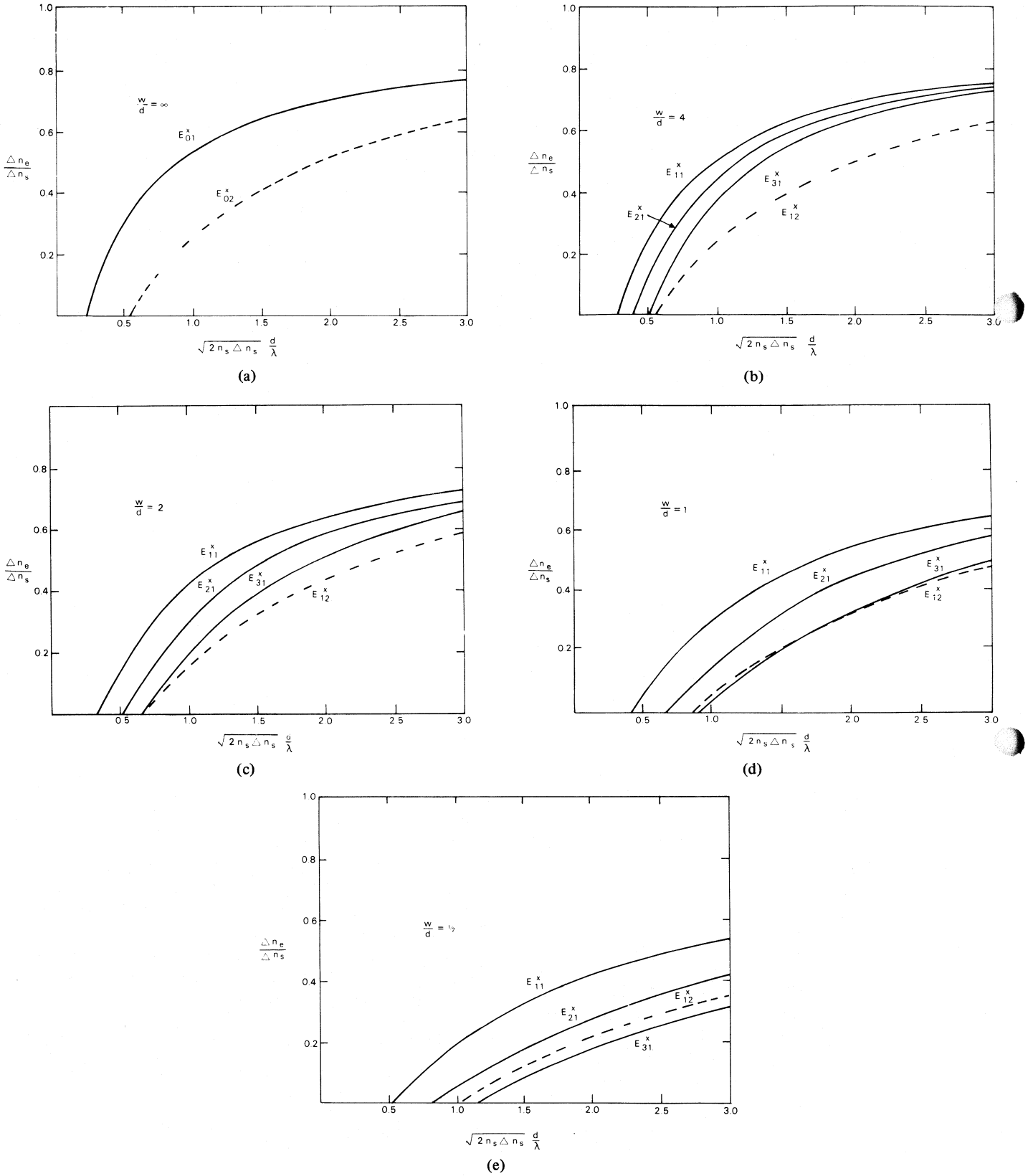


Fig. 2. Dispersion curves for diffused channel guides for various ratios of mask gap width to diffusion depth. The index change at the surface in the unmasked region is Δn_s.

where $D_n(z)$ is a parabolic cylinder function [22]. According to the variational formula, approximate values for the guided-mode propagation constants $\{\beta_n\}$ are obtained by varying the parameters ξ, η, y_0, and the a_{ij} to obtain stationary values for the quantity

$$\beta^2 = \sum_{ij}\sum_{kl} N_{ijkl}\, a_{ij}\, a_{kl} \Big/ \sum_{ij}\sum_{kl} \delta_{ik}\, \delta_{jl}\, a_{ij}\, a_{kl},$$

with

$$N_{ijkl} = (2\pi\xi\eta)^{-1}\,(i!j!k!l!)^{-1/2} \int_{-\infty}^{\infty}\int_{-\infty}^{\infty} \cdot \left\{ D_i[x/\xi]\, D_j[(y - y_0)/\eta] \left[\frac{d^2}{dx^2} + \frac{d^2}{dy^2} + \left(\frac{2\pi n}{\lambda}\right)^2 \right] \cdot D_k[x/\xi]\, D_l[(y - y_0)/\eta] \right\} dx\, dy.$$

The portion of the integral involving the term $(2\pi n/\lambda)^2$ is evaluated numerically, while the integral over terms including the second derivatives d^2/dx^2 and d^2/dy^2 is calculated from the formula

$$\frac{1}{\alpha\sqrt{2\pi\mu!\nu!}} \int_{-\infty}^{\infty} D_\mu\left(\frac{t - t_0}{\alpha}\right) \frac{d^2}{dt^2} D_\nu\left(\frac{t - t_0}{\alpha}\right) dt = -\frac{1}{2}\left(\nu + \frac{1}{2}\right)\delta_{\mu\nu} + \frac{1}{4}\sqrt{\nu(\nu - 1)}\,\delta_{\mu(\nu-2)} + \frac{1}{4}\sqrt{(\nu + 1)(\nu + 2)}\,\delta_{\mu(\nu+2)}.$$

It was found expedient in this work to choose values for ξ, η, and y_0 to maximize the lowest order matrix element, N_{0000}, and then obtain values of β_n^2 as eigenvalues of the characteristic equation

$$\sum_{ij} (N_{ijkl} - \delta_{ik}\,\delta_{jl}\,\beta^2) a_{ij} = 0. \tag{4}$$

In order to achieve convergence, a total of 21 trial functions containing products $D_i[x/\xi]\, D_j[(y - y_0)/\eta]$ were used, with $j = 0, 1, \cdots, 6$ and $i = 0, 2, 4$ for modes with even symmetry in the x direction and $i = 1, 3, 5$ for modes of odd symmetry.

Results and Discussion

Dispersion curves for various ratios of gap width to diffusion depth are given in Fig. 2. The superscript in the mode designation E^x_{pq} indicates that the main electric field component is in the x direction, and the subscripts p and q denote the number of extrema of the field in the x and y directions, respectively [11]. The effective increase in index Δn_e for a mode with propagation constant β is defined by $\Delta n_e = \beta\lambda/2\pi - n_s$. The calculations assume a 1-percent increase in index at the surface of the substrate in the unmasked region ($\Delta n_s/n_s = 0.01$) and a 60-percent decrease in index at the surface of the substrate ($n(y > 0)/n_s = 0.4$). Scaling rules introduced for highly asymmetric slab waveguides [23] should also be applicable to the diffused channel guide, so that the results of Fig. 2 are expected to be approximately correct for E^y_{pq} as well as E^x_{pq} modes, for different values of Δn_s such that $\Delta n_s/n_s \ll 1$, and for different values of surface index discontinuity, as long as $(n_s^2 - n^2(y > 0))/2n_s\Delta n_s) \gg 1$.

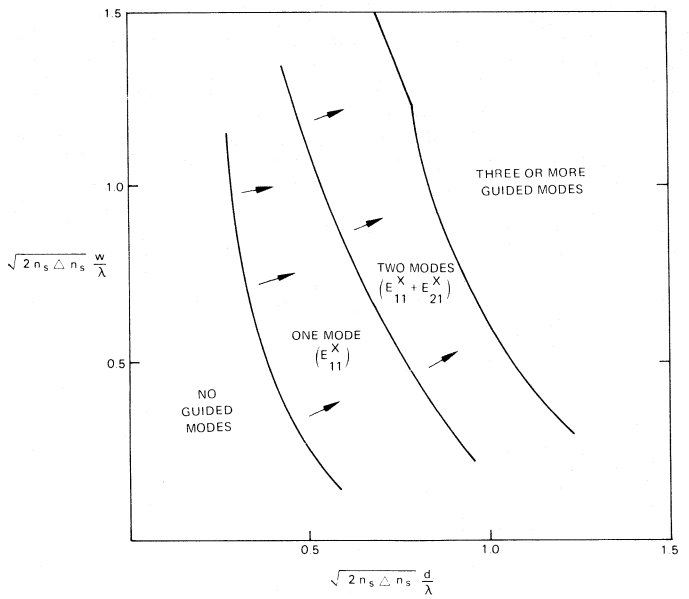


Fig. 3. Dependence of the guided mode content of a channel diffused waveguide on mask gap width and diffusion depth.

Efficient waveguide electrooptic modulators [1], [2] and directional coupler switches [4], [5] require single-mode waveguides for most efficient operation, while the interferometric switch [3] requires both single- and double-mode sections. It is important in the design of these devices to be able to select diffusion depths and mask widths to obtain the desired modal characteristics. As an aid in doing this, Fig. 3 gives the number of modes as a function of diffusion depth and gap width, plotted from the dispersion curves of Fig. 2.

Conclusions

A variational method has been used to analyze the dispersion characteristics of dielectric channel waveguides produced by masked diffusion. The results of such an analysis can aid in determining the optimum process parameters (e.g., mask width, diffusion depth) for fabricating modulators and switches for integrated optics.

References

[1] Y. Ohmachi and J. Noda, "Electrooptic light modulator with branched ridge waveguide," *Appl. Phys. Lett.*, vol. 27, pp. 544-546, Nov. 15, 1975.
[2] I. P. Kaminow, L. W. Stulz, and E. H. Turner, "Efficient strip-waveguide modulator," *Appl. Phys. Lett.*, vol. 27, pp. 555-557, Nov. 15, 1975.
[3] W. E. Martin, "A new waveguide switch/modulator for integrated optics," *Appl. Phys. Lett.*, vol. 26, pp. 562-564, May 15, 1975.
[4] M. Papuchon *et al.*, "Electrically switched optical directional coupler: Cobra," *Appl. Phys. Lett.*, vol. 27, pp. 289-291, Sept. 1, 1975.
[5] H. Kogelnik and R. V. Schmidt, "Switched directional coupler with stepped-$\Delta\beta$ reversal," presented at OSA/IEEE Topical Meeting on Integrated Optics, Salt Lake City, UT, Jan. 1976.
[6] E. M. Conwell, "Modes in optical waveguides formed by diffusion," *Appl. Phys. Lett.*, vol. 23, pp. 328-329, Sept. 15, 1973.

[7] —, "Modes in anisotropic optical waveguides formed by diffusion," *IEEE J. Quantum Electron.*, vol. QE-10, pp. 608-612, Aug. 1974.
[8] —, "Optical waveguiding in graded-indes layers," *Appl. Phys. Lett.*, vol. 25, pp. 40-42, July 1, 1974.
[9] P. K. Tien, S. Riva-Sanseverino, R. J. Martin, A. A. Ballman, and H. Brown, "Optical waveguide modes in single-crystal $LiNbO_3$-$LiTaO_3$ solid solution films," *Appl. Phys. Lett.*, vol. 24, pp. 503-506, May 15, 1974.
[10] G. B. Hocker and W. K. Burns, "Modes in diffused optical waveguides of arbitrary index profile," *IEEE J. Quantum Electron.*, vol. QE-11, pp. 270-276, June 1975.
[11] E. A. J. Marcatili, "Dielectric rectangular waveguide and directional coupler for integrated optics," *Bell Syst. Tech. J.*, vol. 48, 2071-2102, Sept. 1969.
[12] —, "Slab-coupled waveguides," *Bell Syst. Tech. J.*, vol. 53, pp. 645-674, Apr. 1974.
[13] V. Ramaswamy, "Strip-loaded film waveguide," *Bell Syst. Tech. J.*, vol. 53, pp. 697-704, Apr. 1974.
[14] M. Matsuhara, "Analysis of TEM modes in dielectric waveguides, by a variational method," *J. Opt. Soc. Amer.*, vol. 63, pp. 1514-1517, Dec. 1973.
[15] J. E. Goell, "A circular-harmonic computer analysis of rectangular dielectric waveguides," *Bell Syst. Tech. J.*, vol. 48, pp. 2133-2160, Sept. 1969.
[16] C. Yeh, S. B. Dong, and W. Oliver, "Arbitrarily shaped inhomogeneous optical fiber or integrated optical waveguides," *J. Appl. Phys.*, vol. 46, pp. 2125-2129, May 1975.
[17] —, private communication.
[18] P. G. Shewmon, *Diffusion in Solids*. New York: McGraw-Hill, 1963.
[19] L. Fox, *Numerical Solution of Ordinary and Partial Differential Equations*. Oxford, England: Pergamon, 1962.
[20] W. E. Martin, "Refractive index profile measurements of diffused optical waveguides," *Appl. Opt.*, vol. 13, pp. 2112-2116, Sept. 1974.
[21] R. V. Schmidt and I. P. Kaminow, "Metal-diffused optical waveguides in $LiNbO_3$," *Appl. Phys. Lett.*, vol. 25, pp. 458-460, Oct. 15, 1974.
[22] E. Jahnke, F. Emde, and F. Lösch, *Tables of Higher Functions*. New York: McGraw-Hill, 1960.
[23] H. Kogelnik and V. Ramaswamy, "Scaling rules for thin-film optical waveguides," *Appl. Opt.*, vol. 13, pp. 1857-1862, Aug. 1974.

A Compact Cylindrical CO_2 TEA Laser

GREGORY R. OSCHE AND HENRY E. SONNTAG

Abstract—**A cylindrical discharge scheme which utilizes a fine wire as the central electrode is investigated for compact CO_2 TEA laser applications. It is found that the strong radial dependence of electrical energy deposition into the plasma, a consequence of the large ratio of outer to inner electrode radii, produces a radial gain profile which is well localized in the center of the discharge tube. This allows for efficient matching of low-order stable optical modes to the active gain region while providing a high degree of mode selectivity in favor of these modes. Oscillation in the TEM_{01} Laguerre-Gaussian mode has been obtained at electrical efficiencies approaching 4 percent.**

Introduction

In contrast to current efforts to scale CO_2 TEA lasers to larger active volumes, certain applications, both military and commercial, require simple, compact devices. Output energies on the order of 50-100 mJ are usually sought with active volumes on the order of 10-20 cm^3. Attempts to scale down double discharge flat electrode schemes or pin electrode schemes having rectangular apertures are usually confronted with the problem of matching the more common circularly symmetric optical modes to the rectangular active area. This mismatch limits single-mode electrical efficiencies to values considerably lower than the corresponding multimode values [1]. In addition, it is observed that arcing problems become more pronounced for small-scale TEA discharges. This is attributable, at least in part, to the proportionate increase of field gradients associated with small electrodes which are fabricated to the same tolerances as larger electrodes.

This paper considers a cylindrical electrode scheme for low-energy applications which utilizes a small-diameter wire as the central electrode. Cylindrical electrodes have been investigated previously for CO_2 TEA laser applications but have always employed large-diameter rods as the central electrode [2], [3]. These devices necessarily operate in high-order transverse modes, unless special toric cavities are employed [2], and require preionization schemes similar to those of planar electrode geometries. By contrast, a highly stressed central electrode may be used simultaneously as a preionizing electrode while permitting oscillation of low-order transverse modes. In addition, the divergent nature of the current density allows one to achieve relatively high values of volumetric energy deposition in a localized region of the discharge without excessively loading the entire plasma to the point of arcing. An especially attractive feature of the device is its simplicity of construction.

Description of Electrodes

The electrodes were constructed using a 0.0127-cm- (5 mil) diam tungsten wire and a 1.524-cm ID stainless steel vacuum tube (rolled). Fig. 1 shows a schematic of the device. Other than a slight flaring of the ends of the tube which helped reduce field gradients near the edges, these materials did not require additional buffing or polishing in order to prevent arcing.

Manuscript received May 6, 1976; revised August 11, 1976.
The authors are with the U.S. Army Electronics Command, Fort Monmouth, NJ 07703.

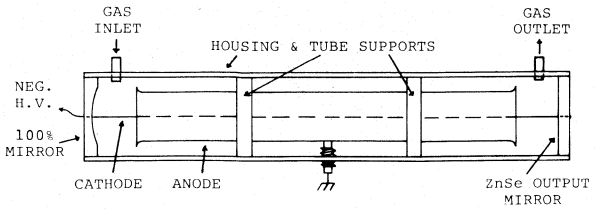


Fig. 1. Schematic of laser. Drawing is not to scale, anode ID, 1.524 cm, cathode diameter 0.0127 cm. Anode length, 48.3 cm. Output reflectivity, 89 percent.

Holes were drilled in the center of the cavity mirrors which were then used to support the wire. The entire arrangement, including cavity mirrors, was housed in a Plexiglas tube.

The pulse-forming network (PFN) is shown in Fig. 2. The main capacitor was 0.01 μF. As expected, stable discharges could only be obtained by letting the central electrode play the role of the cathode. Advantage was taken of the highly stressed nature of this electrode by series triggering the spark gap and main electrodes. A substantial degree of preionization was thereby achieved without additional trigger electrodes or circuitry. This technique had a particularly beneficial affect on the stability of the discharge at low to moderate driving voltages while greatly simplifying the overall complexity of the device.

Current and voltage waveforms were typical of pulsed TEA discharges, the current pulse being well characterized by a half-period sine wave [4], i.e.,

$$i(t) = \frac{V_p - V_0}{z_0} \sin \omega t$$

where V_p = plasma sustaining voltage, V_0 = applied voltage (on capacitors), and $Z_0 = (L/C)^{1/2}$. The current pulsewidth measured approximately 300-ns FWHM. Stable discharges could be obtained over a wide range of gas pressures (up to 2.5 atm), gas mixtures (pure N_2, CO_2, or He), and applied voltages (5-25 kV). The arcing limit of the discharge was found to occur at input energy densities of approximately 30 J/l for a variety of tube lengths (20-50 cm). Although this value is small compared to that achieved with planar electrodes it should be kept in mind that the discharge has a strong radial dependence which, as will be shown, allows one to regain the higher values in a limited region of the discharge. Subsequent data to be presented here refer to the flowing gas mixture of 1:1:3 CO_2, N_2, He at atmospheric pressure and a tube length of 48.26 cm.

Radial Gain Profile

In order to perform a meaningful comparison of the present electrode configuration with existing schemes, a detailed understanding of the radial gain profile is required. Small-signal gain measurements were made using the setup shown in Fig. 3. A 1.63-mm square aperture CO_2 waveguide laser operating at 120 torr was used as the probe laser. The laser oscillated on the $P(20)$, 10.59-μm line and had a TEM_{00} transverse mode. The beam was scanned across the radius of the discharge tube with a moving mirror. A 50-MHz bandwidth HgCdTe detector observed the scattered probe radiation from a rough-ground plate, the latter being necessary to minimize

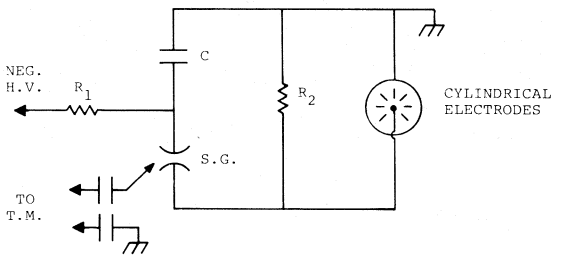


Fig. 2. Series triggered PFN. C_1 = 0.01 μF, R_1 = 1.5 MΩ R_2 = 1 MΩ, *TM* represents trigger module and *SG* the spark gap.

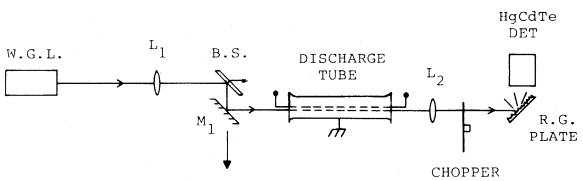


Fig. 3. Setup for measuring radial gain profile. L_1 = 33.2-cm focal length, L_2 = 5.0-cm focal length, M_1 = movable mirror, *RG* = rough ground (plate).

beam steering effects caused by thermal lensing and shock-waves. These effects appeared somewhat enhanced compared to those arising from flat electrode schemes due to the large gradients associated with the cylindrical geometry.

The maximum probe beam diameter was measured and found to be approximately 2.5 mm at the ends of the discharge tube, the beam waist after lens L_1 being located halfway into the tube and approximately 2 mm in diameter. The beam was attenuated to approximately 100 mW through a ZnSe beam splitter in order to avoid saturation effects. Since the beam diameter was a sizable fraction of the tube radius each measurement constituted an average value of the gain over the probe beam diameter. (Attempts to illuminate the entire tube radius with an expanded probe beam, while scanning the exit beam with a pin-hole/detector arrangement, proved less successful due to diffraction at the tube ends.) A chopper was placed at the focal point of lens L_2 and was synchronized with the discharge pulse so that the reference beam could be continuously monitored. This eliminated the problem of long-term amplitude stability of the probe laser. Values of gain in decibels per meter were obtained by measuring the output probe and peak gain signal $(I_2 + I_2')$ and the input probe intensity (I_1) and using the relation $(10/L) \log (I_2 + I_2'/I_1)$ where L is the active gain length (48.26 cm).

The resultant gain profile, normalized to the outer electrode radius, b, is shown in Fig. 4. Values obtained near the inner electrode surface at $r = a$ were complicated by diffraction effects arising from the partial obstruction of the probe beam by the wire and its support. However, since this data point was found to be reproducible it is included with a reasonable amount of confidence. Values obtained near $r = b$ were very low and essentially undetectable within the accuracy of the setup. Peak gains of 5-6 dB/m were observed at high input energies (2-2.5 J) in the vicinity of the central electrode.

An idealized qualitative understanding of the radial gain profile may be obtained by considering the radial dependence

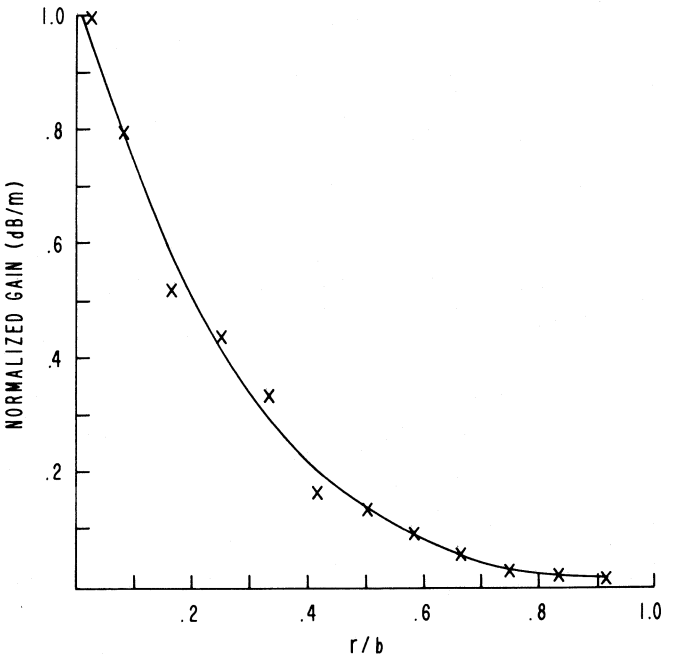


Fig. 4. Radial gain profile (decibels per meter) as given by $g = (10/L) \log (I/I_0)$. Results are normalized to peak value. Largest gains observed were 5-6 dB/m near $r = a$. Gas ratios were CO_2, N_2, He = 1:1:3.

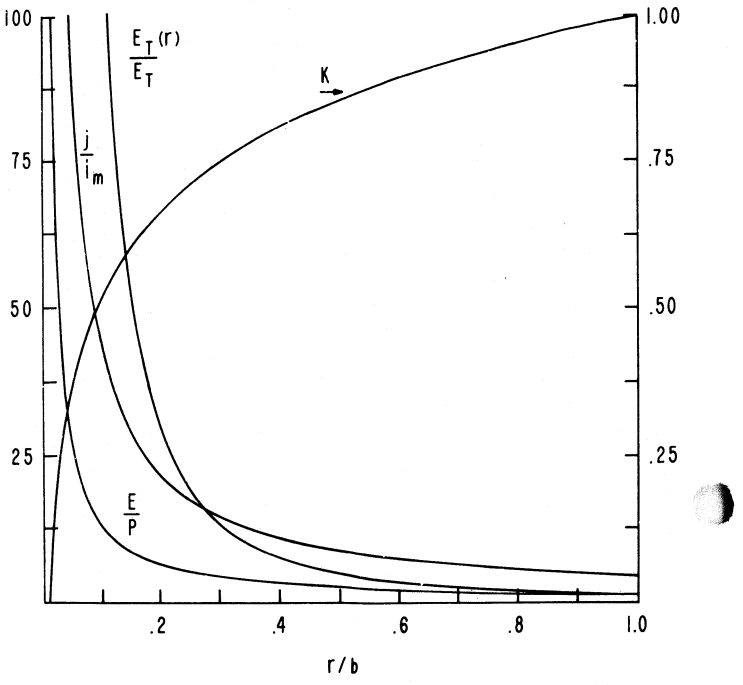


Fig. 5. Idealized curves characterizing highly stressed, coaxial discharge. $[K]$ = dimensionless, $[E/p]$ = (kV)/(cm · atm) $[j/i_m] = \text{cm}^{-2} \times 10^3$, $[E_T(r)/E_T] = 1^{-1}$. K corresponds to right ordinate. All others, the left ordinate.

of such parameters as E/p, current density j, and energy deposition jE for a cylindrical geometry. These quantities, appropriately normalized, are plotted in Fig. 5 and are discussed below.

From Gauss's law we obtain

$$\frac{E}{p} = \frac{V_p - V_c}{p \ln b/a} \cdot \frac{1}{r} \tag{1}$$

where V_c is the cathode potential drop and p is the pressure in atmospheres. Here V_p has been corrected for the cathode potential drop which was assumed to be 300 V. Possible effects due to space charge formation are neglected for simplicity. From the work of Nighan [5] and Judd [6] we see that optimum values of E/p for pumping CO_2 and N_2 exist at about $r/b = 0.25$ ($E/p = 5.2$ kV/cm · atm), while for values below $r/b \simeq 0.1$ ($E/p = 12.9$ kV/cm · atm) a significant fraction of the available electrical energy is used for electronic excitation, dissociation, and ionization. The latter is, of course, necessary in order to sustain the discharge, whereas the former two constitute a loss for the system. On the other hand, the current density

$$j(t) = \frac{i(t)}{2\pi L r} \tag{2}$$

increases rapidly below $r/b \simeq 0.15$ and more than compensates for the less efficient pumping of CO_2 and N_2 in this region. The combined effect of both E/p and j is therefore to produce a radial gain profile which is largest near the wire but which falls off slower than the r^{-2} dependence of jE (see (3) and (4) below). At higher currents it is expected that the gain curve flattens somewhat since the central regions saturate before the outer regions. This was not the case for the data points of Fig. 4, however, since they corresponded to a peak current of 200 A which, for $r/b = 0.1$, resulted in the still moderate value of 8.66 A/cm^2.

The instantaneous electrical energy deposited in the plasma is given by

$$jE = \frac{V_p(t) i(t)}{2\pi L \ln b/a} \cdot \frac{1}{r^2}. \tag{3}$$

Integrating from $0 \rightarrow \pi$, we obtain the radial distribution of the total energy, E_t, i.e.,

$$E_T(r) = \frac{E_T}{2\pi L \ln b/a} \cdot \frac{1}{r^2}. \tag{4}$$

Referring to Fig. 5, we see that relatively large input energy densities may be obtained in a localized region of the plasma. For example, at $r/b = 0.1$ and an input energy of 2 J, a value of 238 J/l is obtained with a corresponding value for E/p of 12.9 kV/cm · atm. At $r/b = 0.135$, 131 J/l is obtained at 9.6 kV/cm · atm. This should be compared with the reported results of a UV preionized laser [4], which attained a maximum value of 150 J/l at 9.5 kV/cm · atm.

The significance of the r^{-2} dependence of jE is better appreciated by integrating (4) over a cylindrical volume element extending from $r = a$ to $r = r$. Normalizing to E_t, one finds

$$K = 1 + \frac{\ln r/b}{\ln b/a} \tag{5}$$

which represents that fraction of the total energy deposited within the normalized radius r/b (see Fig. 5). One sees that, as a consequence of the large value of b/a, approximately 85 percent of the available electrical energy is deposited within $r/b = 0.5$, or within $\frac{1}{4}$ of the total gas volume. By comparison, the gain falls off by approximately 85 percent within this same radius so that the point $r/b = 0.5$ becomes a meaningful

boundary for characterizing the extent of the usable gain region. For the present device this amounts to approximately 22 cm^3 of active volume.

Laser Output Characteristics

The small active gain area associated with the present configuration suggests that the system may be efficiently matched to low-order transverse modes of stable optical cavities. In addition, the strong radial gain profile should provide some degree of mode selectivity in favor of low-order modes. In order to investigate these possibilities, a plane-concave cavity was employed which had a radius of curvature $R = 3.8$ m and a cavity length $d = 55$ cm. Coarse mirror alignment was achieved via a helium-neon laser which entered off-axis through the ZnSe output mirror. The entire mirror-wire system was considered aligned when the lowest order transverse mode appeared. At low to moderate driving voltages oscillation occured in what appeared to be the TEM_{01} Laguerre-Gaussian mode. In general, the intensity distributions of the set of Laguerre-Gaussian modes are given by [7]

$$|\psi_{mn}|^2 = \frac{2r^2}{\omega^2}\left|L_m^n\left(\frac{2r^2}{\omega^2}\right)\right|^2 e^{-2r^2/\omega^2} \tag{6}$$

where L_m^n are the generalized Laguerre polynominals of order m and index n. These modes scale according to the well-known beam parameter equations [7]

$$\omega^2(z) = \omega_0^2\left[1 + \left(\frac{\lambda z}{\pi\omega_0^2}\right)^2\right] \tag{7}$$

and

$$\omega_0^2 = \frac{\lambda}{\pi}[d(R-d)]^{1/2} \tag{8}$$

which represent the e^{-2} intensity spot sizes of the TEM_{00} mode. It is easily seen that the TEM_{01} mode is the lowest order mode capable of being sustained by an axially obstructed cavity. Fig. 6 displays the observed mode as obtained with a UV thermal imaging screen along with a 16-element pyroelectric array scan of a single pulse beam cross section. A computer plot of the TEM_{01} as predicted by (6)-(8) for a distance $z = 2.15$ m from the output mirror is overlaid on the experimental points for comparison (dotted curve). A best fit (solid curve) to the observed mode shows that the latter is well characterized by a TEM_{01} Laguerre-Gaussian mode but is slightly larger than that predicted by passive cavity theory. For the given values of z and d, the latter indicates a slight beam narrowing effect within the cavity which may be traced to the combined influences of the radial gain profile and index gradients. The resultant effect may be characterized by an effective radius of curvature (R') for the cavity of 1.89 m, which is approximately $\frac{1}{2}$ the actual value. The full-angle far-field beam divergence of the TEM_{01} mode is approximately 1.5 times that of the TEM_{00} mode [8] as measured to the outer e^{-2} points, i.e., $\theta_d = 3\lambda/\pi\omega_0$. Using R' in (8) we obtain $\theta_D = 5.9$ mrad.

It is interesting that a pure mode can be sustained by a gain profile which has a cusplike form. The reason is, of course, that the mode which oscillates has near-zero intensity in the region of the cusp. Also, the gain profile is sufficiently slowly varying in regions away from the cusp that the Gaussian-like intensity profile of the mode remains essentially unperturbed [9], [10].

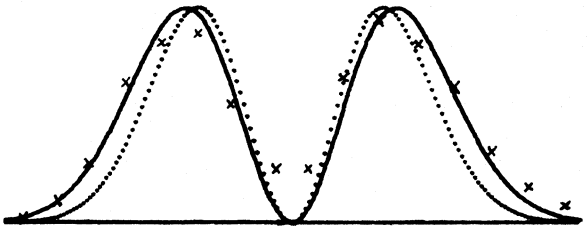


Fig. 6. Pyroelectric array scan of single pulse beam profile at $z = 2.15$ m. Distance between data points corresponds to 1.1 mm. Dotted curve represents idealized passive cavity theory. Solid curve represents best fit of passive cavity mode to experimental points. UV thermal image of beam is shown in upper right corner.

The degree to which the above mode is matched to the radial gain profile such that the optical extraction efficiency is an optimum may be estimated by considering the location of the peak intensity points of the TEM_{01} mode within the discharge tube. Noting that $d|\psi_{01}|^2/dr = 0$ at $r = \omega/\sqrt{2}$ for all z we find that the peak intensity at the output mirror for the observed mode occurs at $r = 0.120$ cm (confirmed with a UV screen), and at $r = 0.143$ cm at the rear mirror. These points correspond to the normalized radii in Fig. 4 of $r/b = 0.157$ and 0.188, respectively, which are well within the high-gain region. For additional comparison, the e^{-2} points of this mode extend to $r/b = 0.335$ and 0.398, respectively, corresponding to an optical mode volume of approximately 11 cm^3.

Higher order transverse modes could be induced by slightly misaligning the cavity (or wire) or by increasing the total input energy. It was found that cavity misalignment tended to induce modes of higher azimuthal index, n, while large input energies tended to induce modes of higher radial index, m. The former effect results from the fact that the higher order modes have a larger hole on axis and can better tolerate the misaligned cavity-wire system. The latter effect may be explained as a combination of the following: 1) flattening of the gain profile due to saturation by the pump of the central regions and 2) the extension of the usable gain region to larger values of r/b. A simple test of the latter involved increasing the radius of curvature of the cavity mirror such that the TEM_{01}-mode diameter was better matched to the larger active gain region associated with the higher input energies. For a radius of curvature of 8 m, it was found that this mode again became the more dominant one. Other modes observed included TEM_{02}, TEM_{03}, and TEM_{11}.

The laser pulse, as measured with a 50-MHz HgCdTe detector, was typical of CO_2, N_2, He TEA lasers consisting of an initial 100-ns spike followed by a 1-us tail. The energy per pulse was calculated from an average power measurement made at a rep rate of 10 Hz. The results are shown in Fig. 7. The input energy corresponds to the energy in the capacitor, $\frac{1}{2}CV_0^2$. The linear nature of the curve is assumed to be due to the nonuniform energy deposition (r^{-2}) which is capable

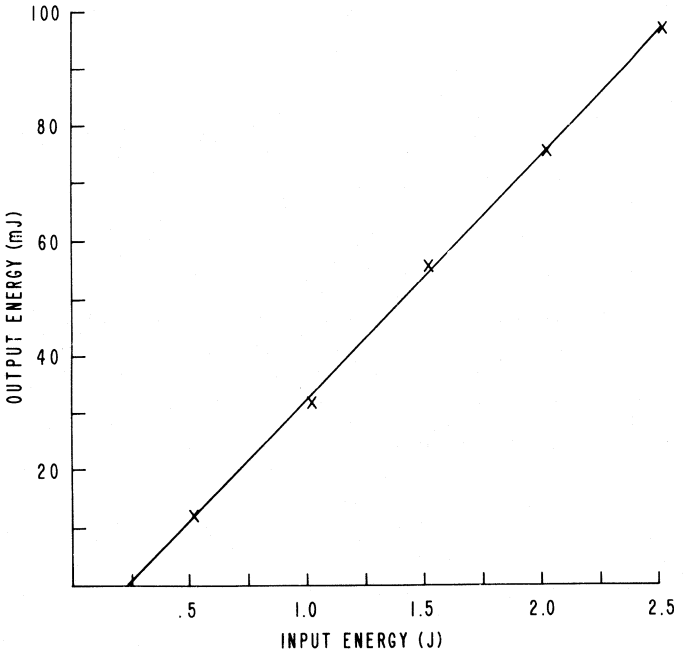


Fig. 7. Energy output versus energy input for 48.3-cm active length. Output mirror reflectivity was 89 percent. Data points were obtained with a power meter at 10 pps. Input energy = $\frac{1}{2}$ CV_0^2.

of saturating only a limited portion of the active gain region. The total electrical to optical conversion efficiency is seen to approach 4 percent at the high end of the curve. This value exceeds slightly that achieved with planar electrode geometries mainly due to the better utilization of active volume. For example, in [1] a drop in electrical efficiency from approximately 10 percent to approximately 3 percent was realized when the device was apertured for single-mode operation. The resultant optical mode volume corresponded to only 55 percent of the usable gain volume. It is expected that the values reported here could be improved still further by optimally coupling the cavity and by adjusting cavity parameters and electrode radii to further optimize the optical extraction efficiency.

Summary and Conclusions

It has been shown that a highly stressed cylindrical electrode geometry exhibits several useful characteristics for low-energy CO_2 TEA laser applications. Most important is the fact that low-order stable optical modes (TEM_{01}) may be obtained without aperturing at electrical efficiencies near 4 percent. In addition, the device is simple to construct and has demonstrated reliable arc-free operation for a minimum of electrode preparation.

Acknowledgment

The authors are particularly indebted to V. Rosati and Dr. A. Papayoanou, Dr. H. Hieslmair, and Dr. R. G. Buser for their interest and support.

References

[1] D. S. Stark, P. H. Cross, and H. Foster, "A compact sealed pulsed CO_2 TEA laser," *IEEE J. Quantum Electron.*, vol. QE-11, pp. 774–778, Sept. 1975.
[2] L. W. Casperson and M. S. Shekhani, "Mode properties of annular gain lasers," *Applied Optics*, vol. 14, pp. 2653–2661, Nov. 1975.
[3] R. K. Garnsworthy, L. E. S. Mathias, and C. H. H. Carmichael, "Atmospheric pressure pulsed CO_2 laser utilizing preionization by high energy electronics," *Appl. Phys. Lett.*, vol. 19, pp. 506–508, 1971.
[4] O. P. Judd and J. Y. Wada, "Investigations of a UV preionized electrical discharge and CO_2 laser," *IEEE J. Quantum Electron.*, vol. QE-10, pp. 12–20, Jan. 1974.
[5] W. L. Nighan, "Electron energy distributions and collision rates in electrically excited N_2, CO, and CO_2," *Phys. Rev. A*, vol. 2, pp. 1989–2000, Nov. 1970.
[6] O. P. Judd, "The effect of gas mixture on the electron kinetics in the electrical CO_2 gas laser," *J. Appl. Phys.*, vol. 45, pp. 4572–4575, Oct. 1974.
[7] H. Kogelnik and T. Li, "Laser beams and resonators," *Appl. Opt.*, vol. 5, pp. 1550–1567, Oct. 1966.
[8] R. J. Freiberg and A. S. Halsted, "Properties of low order transverse modes in argon ion lasers," *Appl. Opt.*, vol. 8, pp. 355–362, Feb. 1969.
[9] L. W. Casperson, "Gaussian light beams in inhomogeneous media," *Appl. Opt.*, vol. 12, pp. 2434–2441, Oct. 1973.
[10] H. Kogelnik, "On the propagation of Gaussian beams of light through lens like media including those with a loss or gain variation," *Appl. Opt.*, vol. 4, pp. 1562–1569, Dec. 1965.

Injection Locking and Mode Selection in TEA-CO_2 Laser Oscillators

JEAN-LOUIS LACHAMBRE, PIERRE LAVIGNE, GABRIEL OTIS, AND MICHEL NOËL

Abstract—**The injection of a master oscillator signal in a high-power TEA-CO_2 laser is analyzed and a dynamic model is formulated to represent the interaction. Based on the competition between the injected signal and the spontaneous emission, the model describes the transient evolution of the different field amplitudes and phases together with their effect on the inversion. A study over a wide range of injection levels and detuning frequencies clearly indicates three distinct regions of operation: a spontaneous oscillation zone, a mode-selection zone, and a frequency-locking zone. The main predictions of the model are compared with the results obtained with an experimental injection apparatus that assures adequate control of the TEA laser cavity length and that provides means for measuring the frequency of the output**

Manuscript received June 10, 1976; revised August 5, 1976.
The authors are with the Defence Research Establishment Valcartier, Department of National Defence, Courcelette, P.Q., Canada GOA 1R0.

pulse. While the first two zones are directly observed, it is experimentally established that, at injection levels up to 5 W/cm^2, the frequency-locking zone does not exceed, as predicted, the 3-MHz resolution limit of the apparatus.

I. Introduction

BECAUSE of its high peak power, short pulse duration, and intermediate repetition rate capabilities, the TEA-CO_2 laser fulfills most of the requirements of an optical radar transmitter in the infrared spectrum. However, for signal-to-noise considerations, an efficient radar system should operate in the coherent mode and approach the quantum limit.

To obtain these objectives with a TEA-CO_2 laser, one has to simultaneously select the laser line, the longitudinal mode of the resonator, and the frequency of that mode. Conventional means of line and mode control utilize dispersive elements [1] and selective absorbers [2], [3] or amplifiers in the cavity [4], [5]. An alternate way of doing the same thing with, hopefully, some additional control on the mode frequency consists of injecting a signal from a low-power frequency-stable master oscillator into the high-power TEA laser cavity.

In the past, this technique has been successfully used with CW and Q-switched CO_2 regenerative amplifiers [6], [7]. More recently, injection locking in a TEA-CO_2 laser has been reported at injection levels of several watts [8].

It is the purpose of this paper to present a simplified theoretical model that formulates the fundamental dynamics of the injection of a low-power laser beam in a TEA-CO_2 laser. Dealing with transient effects, the model describes the competition between the weak spontaneous noise emitted at the cavity frequency and the strong injected signal at the master oscillator frequency during the buildup of the photon density in the TEA resonator. It calculates, for various injection levels, the dependence of the output pulse shape and frequency on the cavity detuning.

The main predictions of the model are verified with an experimental injection apparatus that assures adequate control of the TEA laser cavity detuning with respect to the master oscillator and that provides means for measuring the frequency of the output pulse. The experimental findings indicate that, for all the cases studied experimentally, the model gives a satisfactory representation of the interaction.

II. Mathematical Model

A. Laser Equations

Based on arguments similar to those used by Siegman [9] and Buczek *et al.* [6], [7], the basic circuit for the cavity electric field in the presence of a field injected at one mirror is presented in Fig. 1. During a complete passage in the resonator, the cavity field $E_i(t)e^{j\omega_0 t}$ is amplified in the active medium, suffers a phase shift due to propagation, and, along with the injected amplitude $E_0(t)e^{j\omega_0 t}$, composes the new cavity field. Mathematically, this is written

$$E_i(t+2\tau) = E_i(t)\,[\sqrt{RT}e^{\alpha(t)\ell/2}\,e^{j2kL}] + E_0(t+2\tau) \qquad (1)$$

where R is the coupling mirror reflectivity and T, the power transmission of the empty cavity; $\alpha(t)$ is the power gain coefficient; ℓ denotes the active length of the amplifier; k represents the propagation constant in the resonator; $2L$ is the round-trip length of the resonator and 2τ, the time of a complete passage equal to $2L/c$ where c is the speed of light. Here the fields are defined so that their modulus $|E|^2$ represents a photon density.

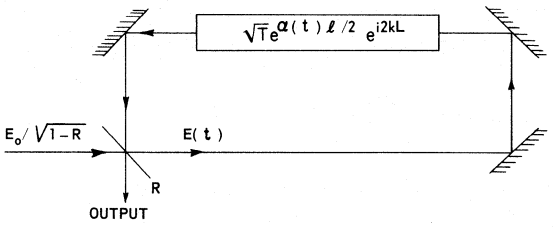


Fig. 1. Illustrating the laser cavity field $E(t)$ in the presence of an injected field E_0.

In the approximation of a slowly varying gain coefficient, it can be shown that the differential equation that correctly represents equation (1) is

$$\frac{dE_i(t)}{dt} = m(t)E_i(t) + \frac{m(t)E_0(t)}{e^{2\tau m(t)} - 1}, \qquad (2)$$

and

$$m(t) = -\frac{1}{2T_0} + \frac{c\ell\alpha(t)}{4L} + j\frac{c\phi}{2L}. \qquad (3)$$

T_0 is the photon lifetime defined as $(2\tau/\ln[1/RT])$. The detuning angle ϕ is equal to $2\pi df/\Delta f$ where Δf denotes the intermode frequency spacing, and df represents the frequency difference between the injected signal and the closest longitudinal mode of the resonator. As can be verified by integrating (2) over 2τ, the approximation used above requires only that $e^{2\tau m(t)}$ and $E_0(t)$ be almost constant during the interval t and $t+2\tau$. In the present model k is assumed constant to exclude cases where strong wave chirping arises due to active modulation or shock wave perturbations in the cavity [10].

Equation (2) represents the temporal evolution of the field that builds up in the cavity under the direct influence of the externally injected field. Concurrently, the noise present in the laser cavity at the different mode frequencies gives rise to other radiation amplitudes. The nth longitudinal mode amplitude E_s^n, which can be imagined as a field influenced by an internal injection source tuned at this mode frequency, is governed by a relation similar to (2) with $\phi = 0$ and with the injection field replaced by the noise field corresponding to one photon per resonator mode and per unit critical inversion:

$$\frac{dE_s^n(t)}{dt} = m_s(t)E_s^n(t) + \frac{m_s(t)\sqrt{\psi_N}}{e^{2\tau m_s(t)} - 1}, \qquad (4)$$

where $m_s(t)$ is the real part of $m(t)$. The one-way photon noise density ψ_N is equal to $(N_b c\sigma T_0/2V)$ per mode where N_b represents the upper level population density, σ the laser radiative cross section and V, the resonator volume [11]. It should be remembered that, because of the wide gain bandwidth of TEA-CO_2 amplifiers, the laser field that develops from spontaneous emission is a superposition of many longitudinal mode amplitudes spaced in frequency by $c/2L$. In the absence of injection, this produces a periodically pulsating laser output envelope with a periodicity of 2τ. With an external injection signal, the total cavity field is the coherent sum of all the amplitudes E_s^n and E_i. However, since only the low-frequency portion of the field envelope affects the inversion, it is convenient to define, in view of the population rate

equations, a total photon density ψ as resulting from an incoherent superposition of the different cavity amplitudes:

$$\psi = \psi_s + \psi_i = \sum_{n=1}^{N} |E_s^n|^2 + |E_i|^2. \tag{5}$$

The interaction of the active medium with the cavity photon density as well as the pumping and relaxation of its different energy levels are described by a set of differential equations based on a simplified level scheme similar to the one used by Gilbert *et al.* [12]. The CO_2-N_2-He medium is treated as a four-level system: it comprises an upper CO_2 lasing level ($00^0 1$) resonant with an energy-storage N_2 level, and a lower CO_2 lasing level ($10^0 0$) decaying to a low-energy CO_2 level ($01^1 0$) which, in turn, relaxes to the ground state. With reference to Fig. 2, the set of equations governing the different population densities (molecules/cm^3) is written

$$\frac{dN_a}{dt} = \sigma c\psi(N_b - N_a) + \gamma_{ba}N_b - \gamma_{a0}N_a + W_a,$$

$$\frac{dN_b}{dt} = -\sigma c\psi(N_b - N_a) - \gamma_{ba}N_b - \gamma_{bc}N_b + \gamma_{cb}N_c + W_b,$$

$$\frac{dN_c}{dt} = -\gamma_{cb}N_c + \gamma_{bc}N_b + W_c, \tag{6}$$

where $\sigma c\psi$ is the rate constant for stimulated emission, γ_{ij}, the collisional deactivation or exchange rate from level i to level j and W_i, the pumping source of level i. The various room-temperature collisional rates used in the model are

$$\gamma_{a0} = (10x + 4.6y + 0.56z)\ \mu s^{-1},$$

$$\gamma_{ba} = (0.27x + 0.08y + 0.06z)\ \mu s^{-1},$$

$$\gamma_{bc} = 14.5y\ \mu s^{-1},\ \gamma_{bc} = 13.2x\ \mu s^{-1}, \tag{7}$$

where x, y, z are respectively the CO_2, N_2, and He partial pressures in atmospheres. These rate constants are very close to those used by Gilbert with the exception however of γ_{a0} which, as proposed by Andrews *et al.* [13], is made equal to the measured relaxation rate of the $10^0 0$ to the $02^0 0$ level of the CO_2 molecules [14]. This minor modification permits a more precise prediction of the laser pulse shape for small-gain situations. As in Gilbert's model, the pumping rate of the upper and lower CO_2 level are made equal and assumed 2.5 times less efficient than that of the $N_2(v = 1)$ level. The following excitation pulse shape is used:

$$W_a = W_b = 0.4\,W_c = W_0 t \exp(-t/t_p), \tag{8}$$

where t_p represents the pumping pulse duration parameter and, W_0, a constant chosen to reproduce, in absence of radiation, the specified small-signal gain. Finally, the coupling of the population rate equations to the field equation is accomplished through the expression for the gain:

$$\alpha(t) = \sigma[N_b(t) - N_a(t)]\ 2L/\ell \tag{9}$$

where the effective radiative cross section σ takes the value of 5.8×10^{-20} cm^2 for TEA-CO_2 media [14]. Here σ is assumed, for the sake of simplicity, independent of both the laser mixture and the laser frequency.

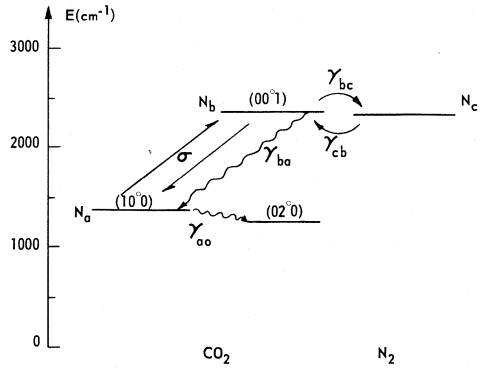


Fig. 2. Energy diagram of the CO_2 and N_2 molecules showing the pertinent vibrational levels with their optical and collisional deactivation paths.

B. Theoretical Results

Qualitatively, the injection processes in a TEA laser are very different from those of a CW laser where the injected signal forces the oscillator to operate below threshold. In a TEA-CO_2 laser, no steady-state regime occurs and two important phenomena take place, namely a competition between the noise term and the injected signal and a shifting or pulling of the injected signal carrier frequency toward the resonator mode frequency.

During the gain buildup, both the noise signal at the mode frequency and the injection signal at the master oscillator frequency circulate simultaneously in the laser cavity. Competition sets in between the two waves as to which will grow more rapidly and depopulate the active medium before the other enters into the saturation regime. In general, the injection field is stronger than the spontaneous emission; however it experiences a smaller gain because it suffers a phase change through each cavity traversal and no longer adds in phase with the injection source amplitude. Depending on the detuning angle and on the injection level, either wave may reach the saturation level first. In addition, the growing field governed by the injection signal adds vectorially to the fixed-phase injection amplitude to produce a resultant that changes in amplitude and in phase with time. This time-varying phase is equivalent to a frequency modulation that pulls the frequency of the field toward the frequency of the nearest resonator mode. The amount of pulling varies with time and depends on the instantaneous gain, on the injection level and on the detuning angle.

Quantitative results were obtained by solving the mathematical model with a Runge-Kutta integration method. The energy and peak power radiated per unit volume of laser resonator can be deduced using expressions of the form [16]

$$I_s = \frac{h\nu \ln(1/R)\psi_s}{2\tau}, \tag{10}$$

and

$$\mathcal{E}_s = \int_0^\infty I_s\, dt, \tag{11}$$

where $h\nu$ represents the energy of one photon. Here I_s and $\mathcal{E}_s$

represent, respectively, the laser power and energy per unit cavity volume, built up from the spontaneous emission in the resonator. Similar expressions are written for the output power and energy, I_i and $\mathcal{E}_i$, originating from the injection signal. Finally, since, in opposition to E_s^n, the field E_i is a complex function, it is convenient to separate it into an amplitude $|E_i|$ and a phase θ_i:

$$E_i(t) = |E_i(t)|\, e^{j\theta i(t)}. \tag{12}$$

Upon differentiation, θ_i gives the instantaneous angular frequency of the field E_i.

In view of comparing the calculated results with the experimental findings, the model parameters and the initial conditions of the set of equations have been adjusted to represent a physical situation that is realized in the laboratory. Although the present model is valid for slowly varying injection sources, we have confined the calculations to CW injection signals. Using the set of conditions listed in Table I, calculations were performed for various detuning angles and for a large range of injection levels. The oscillating mode amplitudes E_s^n are assumed equal and their number is arbitrarily fixed at $N = 12$. The photon noise density takes, at threshold, the value of 4×10^{-12} W/cm^2.

For large detuning angles, the injection signal is found to have very little influence on the laser dynamics and the output is essentially that which would be obtained without any injection signal. Such a result is presented in Fig. 3 for an injection signal of 0.5 W/cm^2 and a detuning angle of $\pi/2$. As in the case of TEA-CO_2 lasers without injection, the laser dynamics is characterized by a rapid inversion buildup interrupted by the development of a giant pulse. The pulse formation reduces the inversion towards the threshold, forcing the system to terminate the emission in a quasi-CW mode of operation. The power I_i induced by the injection signal is not represented on this figure since it is six orders of magnitude smaller than I_s.

A reduction of the detuning angle from $\pi/2$ to $\pi/8$ completely reverses the situation. In this new case, the power pulse initiated by the spontaneous emission is negligible compared to the power I_i. For this reason, I_s does not appear in Fig. 4 where the temporal evolution of the power I_i, of its instantaneous carrier frequency and of the normalized inversion are presented. From these instructive results, two major observations are made. First, the peak of the laser emission appears earlier than in the normal regime of oscillation. Since the injection signal is much more intense than the spontaneous noise signal, the saturation level is reached sooner. This early destruction of the inversion, diminishing the Q-switching effect of the system, reduces the peak power of the output pulse and lengthens its tail duration through tardy restoration of the stored energy not extracted by the main radiation spike.

As a second observation, the instantaneous frequency of the laser is that of the nearest cavity mode for the duration of the laser pulse. As seen from Fig. 4, the carrier frequency of the laser field, initially identical to the injected signal frequency, is pulled toward the mode frequency during the buildup time of the cavity field. At the instant of arrival of the main laser spike, the carrier frequency has already reached

TABLE I
SUMMARY OF ASSUMED TEA LASER OPERATING CONDITIONS

ℓ = 100 cm	α(max) = 0.04 cm^{-1}
2L = 300 cm	He = 0.7 atm.
T = 72%	CO_2 = 0.15 atm.
R = 28%	N_2 = 0.15 atm.
V = 100 cm^3	t_p = 100 ns.

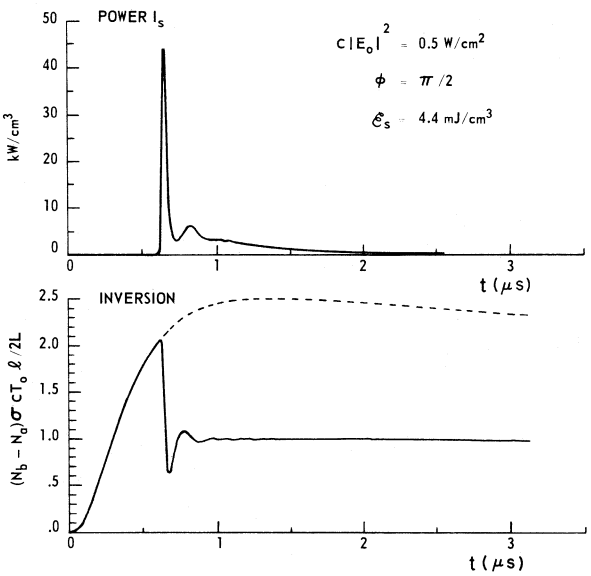


Fig. 3. Computer results showing the predicted laser output power and inversion for a typical situation where the injection signal has almost no effect. The dotted line represents the inversion that would be obtained in the absence of laser action.

the cavity mode frequency. The small sinusoidal frequency modulation, at the detuning frequency, that appears at the end of laser emission indicates the presence of two radiation fields at the cavity mode and the injection frequency, respectively. A corresponding beat is not seen on the power signal. Such a modulation would appear if the dying cavity field was comparable in amplitude to the injection signal amplified through regenerative processes. It should be noted that the laser operates near the threshold during that period. Obviously this beat signal becomes more important at higher injection levels or at smaller detuning angles for which the regenerative gain is larger. In these latter cases, a corresponding beat was found to appear on the power signal.

For larger injection fields and much smaller detuning angles, the laser field is still governed by the injection signal, but its frequency is no longer that of the TEA resonator mode. This case is represented in Fig. 5 where the laser power I_i, the radiation frequency and the laser inversion are drawn as a function of time for an injection signal of 5 kW/cm^2 and a detuning angle of $\pi/100$. The computer results indicate that the leading front of the laser radiation is significantly advanced and that the pulse duration is considerably increased at the expense of the peak power. Finally, the instantaneous frequency of the output is observed to be almost that of the injection signal for the major part of the laser emission.

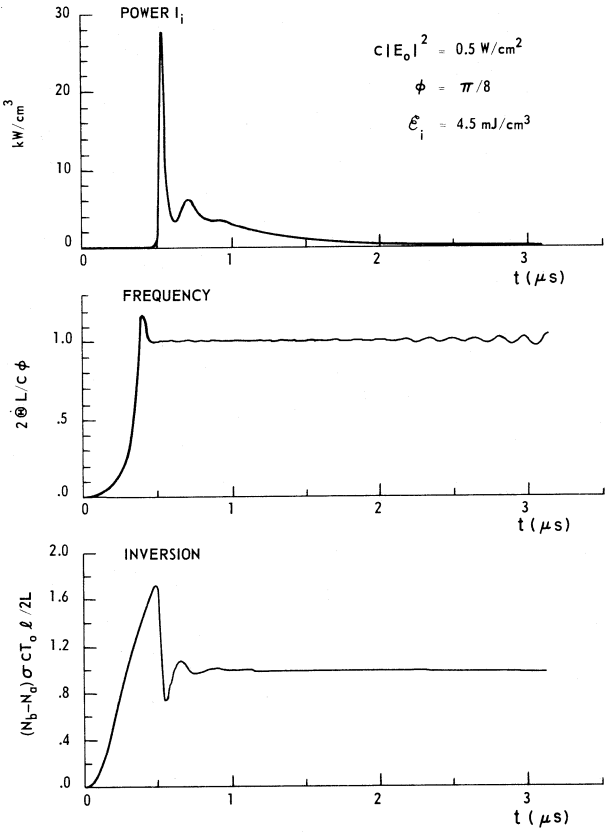


Fig. 4. Computer calculations of the laser output power, instantaneous frequency and inversion for an injection and detuning conditions that lead to the selection of a single-longitudinal mode.

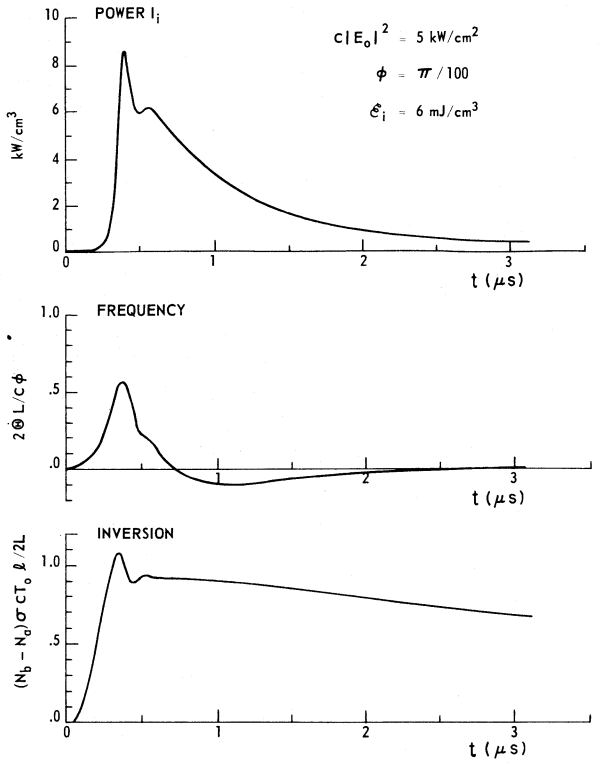


Fig. 5. Calculated time evolution of the laser output power, instantaneous frequency and inversion illustrating a frequency-locking situation.

The injected radiation starts very early to depopulate the active medium attenuating the gain-switching effect in favor of regenerative gain. Since the laser action is very early, the inversion exceeds the threshold value by a very small amount and for a very short time in such a way that the system operates below the threshold for most of the time. Except for the short period of time during which the laser is above threshold and its frequency is being pulled toward the cavity frequency, the output results mainly from stable regenerative amplification of the injected signal so that the carrier frequency is essentially the same as that of the master oscillator. This is very close to the CW-injection situation where frequency locking occurs only when the laser system is forced to operate below threshold.

In summary, from the model developed here three distinct regimes of operation are identified: a spontaneous oscillation zone at large detuning angles, a mode-selection zone at moderate detuning angles and a frequency-locking zone corresponding to small detuning angles and very large injection levels. These three zones can be quantitatively evaluated from the results of Fig. 6. For different injection levels, Fig. 6(a) shows, as a function of the detuning angle, the variation of the fraction $\mathcal{E}_i/(\mathcal{E}_i + \mathcal{E}_s)$ of the total radiated energy that is initiated by the injection field. For the various injection levels, these curves delimit precise zones of mode selection that can be measured by the detuning angle for which $\mathcal{E}_i = \mathcal{E}_s$. In general, these zones are found to diminish upon increasing either L or T_0. When the detuning angle fluctuates in a random manner, the mode-selection range represents the probability of getting a single-longitudinal-mode TEA-CO_2 laser pulse through the injection of a signal of amplitude E_0. Examination of the curves of Fig. 6(a) suggests two important remarks. First the mode selection range is not very sensitive to injection signal variations. It changes by about 20 percent over two orders of magnitude of injection levels. Second, there is a maximum range limited to less than 0.4π for realistic injection signals.

Fig. 6(b) shows the variation of the weighted laser frequency as a function of the detuning angle and of the injection level. This average frequency is defined as follows:

$$\bar{f} = \frac{\int_0^\infty I_i(t)\dot{\theta}_i(t)\,dt}{\int_0^\infty I_i(t)\,dt}, \tag{13}$$

to represent mathematically the mean frequency at which the radiation is emitted. Although this definition loses any physical meaning when $\bar{f}$ is very different from either the injection or the mode frequency, it is helpful in determining the injection-locking zone. This zone can be defined as the range of detuning angles for which the laser mean frequency $\bar{f}$ is closer to the injection frequency than to the resonator mode frequency. As seen from Fig. 6(b), the locking range is very small and reaches a value of only 0.05π for an injection power density as high as 5 kW/cm^2.

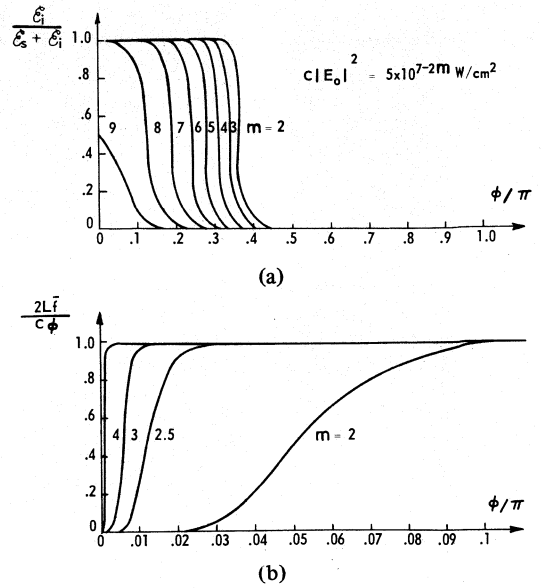


Fig. 6. (a) Effect of the detuning angle ϕ, for various injection levels, on the fraction $(\mathcal{E}_i/\mathcal{E}_i + \mathcal{E}_s)$ of the total laser energy built directly from the injected signal. Each curve delimits, for a specific injection level, a zone of single-longitudinal-mode operation. (b) Plot of the laser average frequency $\bar{f}$ relative to the detuning frequency as a function of the detuning angle ϕ for large injection levels.

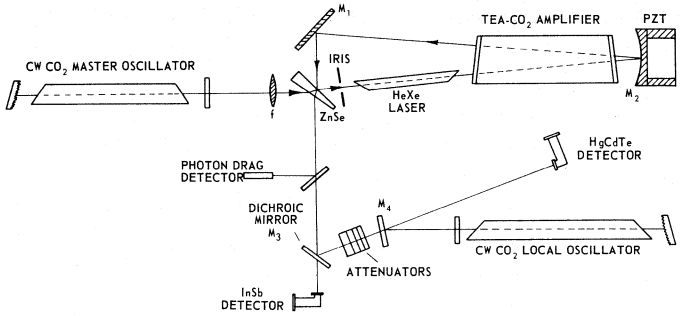


Fig. 7. Experimental apparatus used for the injection experiment.

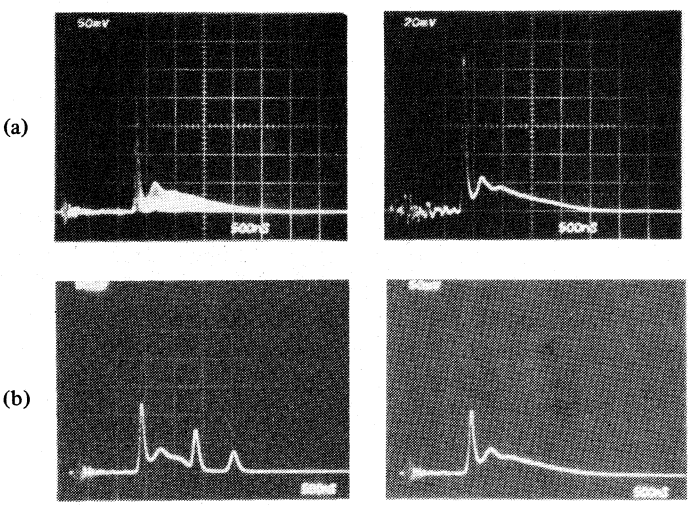


Fig. 8. (a) 500-MHz (left) and 20-MHz (right) displays of the output power pulse obtained without injection. (b) The output power pulse obtained at small detuning angles for an injection level of 5 W/cm^2.

III. Experimental Studies

A. Experimental Setup

The experimental injection setup that is used to verify the theoretical predictions of the model provides means for measuring the carrier frequency of the TEA laser output and for controlling both the TEA resonator and the master oscillator frequencies. Fig. 7 shows a schematic representation of the experimental apparatus. The TEA-CO_2 laser section is comprised of a 5 X 5 X 50 cm^3 UV-preionized double-discharge module closed at both ends with slightly tilted NaCl windows. The module is inserted in an elongated ring resonator formed by a totally reflecting curved mirror M_2 at one extremity and, at the opposite end, by two flat mirrors placed in proximity to each other at nearly 45° with respect to the optical axis. The reflection coefficient of M_1 is close to unity while that of the semitransparent mirror is 0.28 caused by the Fresnel reflection at 45° on the first surface of a ZnSe wedge used as a coupling mirror. The mirror M_2, having a radius of curvature of 20 m, is mounted on a piezoelectric ceramic for cavity tuning and scanning. In order to obtain adequate stability and reproducibility on the cavity frequency, the three mirrors are mounted on a four-bar rigid structure mechanically isolated from the main optical bench through shock-absorbing supports. With the operating He-N_2-CO_2 gas mixture set at 0.7-0.15-0.15 atm, peak gain coefficients of 0.04 cm^{-1} are obtained at an electrical excitation density of 200 J/l. In these excitation conditions, the combination of the TEA discharge amplifier and the ring resonator of Fig. 7 delivers, with a 6-mm iris, 0.75 J of radiation energy in the fundamental TEM_{00} mode on the P_{20} line of the 10.6-μm transition.

The master oscillator is a CW line-tunable CO_2 laser stabilized in frequency on the transition center by means of cavity-dithering techniques. Its 1-W output beam is injected into the TEA laser resonator through the ZnSe coupling wedge. The mode matching is realized with a 1-m focal length Ge lens placed between the two oscillators and the alignment is accomplished by superimposing independently the two beams in both the near and far field. A mode matching of better than 50 percent is claimed from the degree of superposition obtained [7]. As suggested by Buczek and Freiberg [6], the reflection of the 90-percent output mirror of the master oscillator provides, under proper alignment, a means of nonreciprocal coupling between the two directions of oscillation in the TEA laser. Consequently, this arrangement should not require, in principle, any isolation stage between the master oscillator and the TEA laser. Experimentally, with the best possible alignment, unidirectional oscillation of the TEA laser is observed with a maximum separation of 30 dB between the two directions of oscillation.

Fig. 8(a) shows the TEA laser output power typically obtained with the master oscillator turned off. These waveforms are generated by a photon-drag detector and displayed on a 7904 Tektronix oscilloscope. The left photograph is taken with a preamplifier bandwidth of 500 MHz to show the 100-MHz spontaneous beating on the laser pulse. The right oscillogram represents the same signal filtered in a 20-MHz preamplifier so as to make a clean display of the laser envelope and allow comparison with the model predictions (see Fig. 3).

With the master oscillator turned on, a smoothing of the output pulse shape is observed on a 500-MHz bandwidth display, revealing single-longitudinal-mode operation; this is realized for limited range of tuning voltages on the piezoelectric translator. As shown on the left oscillogram of Fig. 8(b), some slow spikes sometimes appear on the tail of the laser pulse. This seems to be the manifestation of higher order transverse modes enhanced by the injection beam. In practice, fine adjustments of the alignment and of the cavity iris diameter completely quench these modes and give a signal similar to that appearing on the right photograph of Fig. 8(b). In this example, the tail increases in amplitude with respect to the peak level.

A more systematic study of the effect of the detuning frequency on the injection processes requires precise control and measurement of the TEA cavity length. For this reason, an RF-excited He-Xe laser tube is inserted in the ring resonator near the coupling mirror in such a way as to allow two collinear laser beams, at 10.6 and 3.5 μm, to coexist in the same cavity. The dimension of the tube, sealed with NaCl Brewster windows, is chosen to get sufficient gain for oscillation at 3.5 μm without disturbing appreciably the TEA-CO_2 laser mode. Located behind the dichroic mirror M_3 at the TEA resonator exit, a cooled InSb detector receives the He-Xe laser signal and its temporal behavior is displayed on an oscilloscope. When a 100-ms linear ramp is applied to the piezoelectric to produce a total mirror excursion of 5.3 μm, three lobes of the He-Xe tuning curve are seen on the screen, the separation between two successive lobes corresponding to 1.755 μm [17]. A simple method to control and measure the TEA resonator length with a good reproducibility is obtained by firing the TEA-CO_2 amplifier at any desired time during the ramp and recording the triggering time superimposed on the tuning curve. A length-increment accuracy of 0.05 μm allows a 1-MHz resolution on the relative frequency of the cavity mode.

The CO_2 laser pulse frequency is measured by beating it with a local oscillator beam on a 400-MHz HgCdTe detector cooled to 77 K. In our system, the local oscillator is not derived from the master oscillator beam through acoustooptic deflection, because the coupling isolation is only 30 dB. The TEA laser signal, reflected back by the master oscillator mirror, is a few orders of magnitude larger than the injection signal. This would mask the weak heterodyne signal. To eliminate that problem, a distinct frequency-stabilized laser, identical to the master oscillator, is used as the local oscillator. Its output beam is added on mirror M_4 to the TEA-CO_2 laser beam previously attenuated through a stack of LiF and CaF_2 disks. The frequency stability of the two CW sources is experimentally measured to be ±1.5 MHz over many hours.

B. Experimental Results and Comparisons with the Model Predictions

In order to study the behavior of the laser envelope and correlate it with the frequency characteristics of the carrier, simultaneous photographs of the laser output power and of the beat signal between the laser field and that of the local oscillator are taken. Fig. 9 exhibits two pairs of oscillograms for two different detuning frequencies. The left photographs show, on a 500-MHz-bandwidth display, the output of the photon-drag detector, while the right oscillograms represent the heterodyne signal on the 400-MHz HgCdTe detector. The CW local oscillator signal is set to about 400 mV. As can be seen from these photographs, the frequency of the laser signal stays almost constant for most of the pulse duration and drifts slowly during the last portion of the tail with a chirp of about 1 MHz/μs. This late frequency shift could be explained by the small perturbation caused by shock waves to the portion of the beam passing in the vicinity of the cathode.

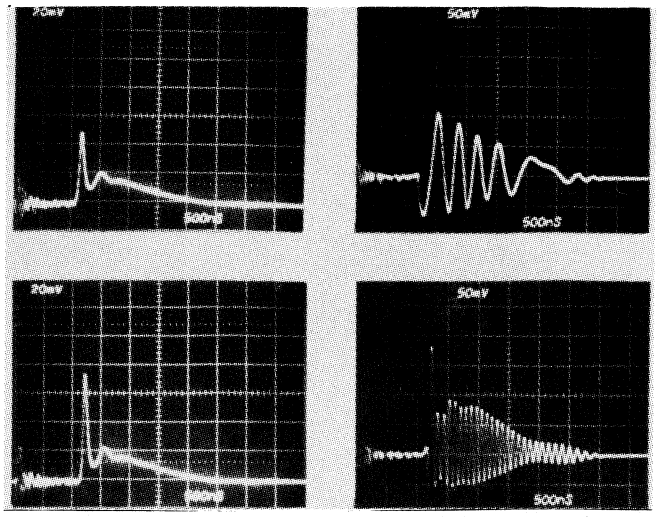


Fig. 9. Output power pulse shapes (left) and their corresponding beat signal (right) with a local oscillator on a wide-band HgCdTe detector.

A more interesting result is obtained by studying the output power and the heterodyne signal for the entire range of detuning frequencies. This is achieved by taking pairs of photographs showing these signals and by recording the 3.5-μm signal from which the corresponding relative cavity frequency is deduced. This is illustrated in Fig. 10, where the beat frequency on the HgCdTe is plotted as a function of the relative cavity frequency as measured from the He-Xe laser signal. When many beat frequencies are simultaneously present, the lowest value is retained. On this graph, the ordinate represents the difference between the TEA laser pulse frequency and the local oscillator frequency. On the abscissa, the resonator mode frequency covers the 100-MHz free spectral range ($c/2L$) with the frequency reference arbitrarily set at zero. Two consecutive runs with injection levels of 5 W/cm^2 and 10 mW/cm^2 are represented on this graph. Also shown are the two corresponding zones of single-longitudinal-mode operation of the TEA laser, as observed from the laser envelope shape measured with the photon-drag detector. The limits of these zones are determined by the detuning frequency for which the envelope modulation at 100 MHz exceeds 10 percent.

A first striking observation arises from Fig. 10: the cavity frequency and the heterodyne frequency are linearly related with unity slope. Apart from confirming the validity of the measuring apparatus, this finding claims without any ambiguity that, within the experimental errors and uncertainties, the frequency of the TEA laser pulse follows that of the TEA resonator inside as well as outside the single-longitudinal-mode zone. These observations corroborate the model predictions on the frequency-pulling effect. For all the injection

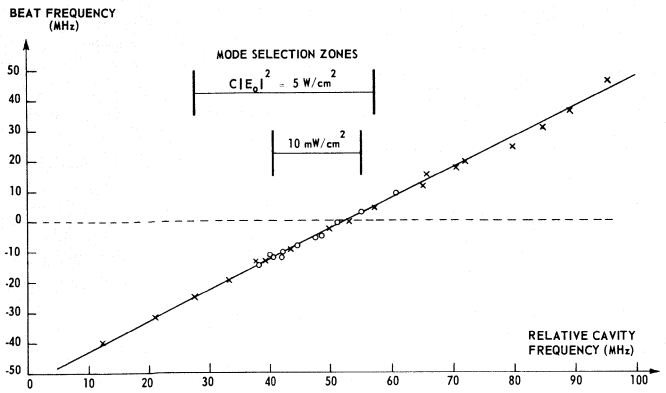


Fig. 10. Experimental plot of the beat between the TEA laser pulse and the local oscillator as a function of the relative cavity detuning frequency as measured by the He-Xe laser signal for two injection levels (× = 5 W/cm^2 and ○ = 10 mW/cm^2). The two sets of vertical bars represent, for each injection level, the detuning zone over which the TEA laser operates in a single longitudinal mode.

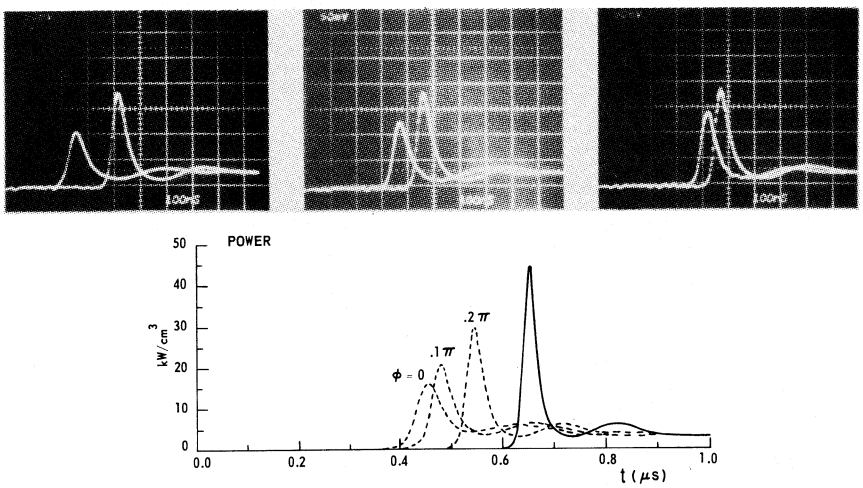


Fig. 11. Experimental power output time traces and model predictions obtained for three different detuning angles, with an injection level fixed at 5 W/cm^2. The solid-line curve on the graph and the traces to the right on the photographs represent the output power without any injection.

levels used here, the TEA laser pulse is influenced by the injection signal, but its frequency is that of the TEA cavity mode and not that of the master oscillator. The frequency-locking range is not studied here since it requires a higher frequency resolution. A second observation derived from Fig. 10 concerns the width of the single-longitudinal-mode zone: it is found to diminish by approximately one-half upon reducing the injected power by nearly three orders of magnitude. For such a change in the injection power, the mode-selection range predicted by the model [see Fig. 6(a)] would move from 33 to 28 MHz compared to 30 and 15 MHz as determined experimentally. The agreement, although not perfect, is satisfactory considering the measurement uncertainties and the approximations made to simplify the injection model.

It is also observed experimentally that the mode-selection range limits are not equally spaced on each side of the zero-beat frequency, although the model is completely symmetrical in that respect. This discrepancy cannot be explained by a displacement of the zero-detuning frequency that could be caused by heat or shock waves in the discharge. In fact, the correspondence between the zero-beat frequency and the zero-detuning frequency has been checked prior to the discharge initiation by scanning the piezoelectric translator and by identifying the resonance dip of the ring-cavity reflection curve. The selection zone is much narrower on the high-frequency side of the zero-detuning frequency where lie the higher order transverse mode frequencies. However, the present observations cannot firmly establish any influence of the transverse-mode location on these injection results.

Finally, the model is capable of correctly predicting the variation of the time advance of the laser pulse with detuning. Pulse-shape calculation results are presented on Fig. 11, together with their corresponding experimental traces for three different detuning angles. All the curves and photographs are obtained here with a fixed injection power density of 5 W/cm^2. The oscillograms displayed on a 20-MHz oscilloscope superimpose, for the same triggering origin, the laser waveforms obtained with the master oscillator alternatively turned on

and off. The right signal on these photographs represents the laser pulse obtained without any injection and corresponds to the solid line curve on the calculation results diagram. The pulse shapes predicted by the model for three different detuning frequencies are drawn on the same graph in dotted lines. It is seen both theoretically and experimentally that, upon reducing the detuning angle, the pulse leading front advances continuously and that the peak power diminishes progressively to about one-half of its maximum value. Such phenomena indicate that, for single-longitudinal-mode selection, the detuning frequency must be kept constant if pulse jittering in both amplitude and time is to be avoided.

In conclusion we have developed an injection model capable of satisfactorily describing the essential features of the interaction between a master and a TEA-CO_2 power oscillators for injection levels up to 5 W/cm^2. Extrapolation of our results to higher injection levels indicates that the frequency-locking zone is very narrow. However, these pessimistic predictions are worth being experimentally verified as new phenomena, not included in the model, could occur at very high levels of injection.

Acknowledgment

The assistance of A. Deslauriers in carrying out the experimental work is gratefully acknowledged. Thanks are also due to Dr. P. Pace for helpful discussions. The authors wish to thank A. Blanchard of the DREV Computing Center for his help with the digital computation.

References

[1] J. A. Weiss and L. S. Goldberg, "Single longitudinal mode operation of transversely excited CO_2 laser," *IEEE J. Quantum Electron.*, vol. QE-8, pp. 757-758, Sept. 1972.

[2] A. Nurmikko, T. A. DeTemple, and S. E. Schwarz, "Single-mode operation and mode locking of high-pressure CO_2 lasers by means of saturable absorbers," *Appl. Phys. Lett.*, vol. 18, pp. 130-132, Feb. 1971.

[3] J.-L. Lachambre, J. Gilbert, M. Blanchard, and F. Rheault, "Mesure des caractéristiques d'un amplificateur CO_2 TEA et l'étude expérimentale de la propagation d'une impulsion laser à front exponentiel en milieu amplificateur et absorbant à 10.6 μm," DREV R-710, 1974.

[4] A. Gondhalekar, E. Holzhauer, and N. R. Heckenberg, "Single longitudinal mode operation of high pressure pulsed CO_2 lasers," *Phys. Lett.*, vol. 46A, pp. 229-230, Dec. 1973.

[5] A. Girard, "The effect of the insertion of a CW, low-pressure CO_2 laser into a TEA CO_2 laser cavity," *Opt. Commun.*, vol. 11, pp. 346-351, Aug. 1974.

[6] C. J. Buczek and R. J. Freiberg, "Hybrid injection locking of higher power CO_2 lasers," *IEEE J. Quantum Electron.*, vol. QE-8, pp. 641-650, July 1972.

[7] C. J. Buczek, R. J. Freiberg, and M. L. Skolnick, "Laser injection locking," *Proc. IEEE*, vol. 61, pp. 1411-1431, Oct. 1973.

[8] A. R. Clobes, P. J. Berger, R. T. Brown, and C. J. Buczek, "Investigation to determine characteristics of a stable-frequency pulse regenerative-amplifier CO_2 laser transmitter," United Aircraft Research Lab. Rep. No. AD-781737, Jan. 1974.

[9] A. E. Siegman, *An Introduction to Lasers and Masers.* New York: McGraw-Hill, 1971, pp. 449-457.

[10] J. R. Izatt and C. J. Budhiraja, "Single-mode TEA-CO_2 injection laser," to be published.

[11] W. V. Smith and P. P. Sorokin, *The Laser.* New York: McGraw-Hill, 1966, pp. 71-72.

[12] J. Gilbert, J. -L. Lachambre, F. Rheault, and R. Fortin, "Dynamics of the CO_2 atmospheric pressure laser with transverse pulse excitation," *Can. J. Phys.*, vol. 50, pp. 2523-2535, 1972.

[13] K. J. Andrews, P. E. Dyer, and D. J. James, *J. Phys. E. Sci. Instrum.*, vol. 8, pp. 493-497, 1975.

[14] E. E. Stark, Jr., "Measurement of the 10°0-02°0 relaxation rate in CO_2," *Appl. Phys. Lett.*, vol. 23, pp. 335-337, Sept. 1973.

[15] J. -L. Lachambre, J. Gilbert, F. Rheault, R. Fortin, and M. Blanchard, "Performance characteristics of a TEA double-discharge grid amplifier," *IEEE J. Quantum Electron.*, vol. QE-9, pp. 459-468, Apr. 1973.

[16] B. A. Lengyel, *Introduction to Laser Physics.* New York: Wiley, 1966, pp. 235-251.

[17] D. A. Jennings, F. R. Peterson, and K. M. Evenson, "Extension of absolute frequency measurements to 148 THz: Frequencies of the 2.0 and 3.5 μm Xe laser," *Appl. Phys. Lett.*, vol. 26, pp. 510-511, May 1975.

Analysis and Design of Semileaky-Type Thin-Film Optical Waveguide Isolator

SADAHIKO YAMAMOTO, MEMBER, IEEE, YASUYUKI OKAMURA, STUDENT MEMBER, IEEE, AND TOSHIO MAKIMOTO, MEMBER, IEEE

Abstract—**This paper describes an optical waveguide isolator that utilizes the unidirectional guided-radiation mode coupling in a magneto-optic/anisotropic slab guide. The basic structure is the semileaky-type waveguide that has been previously used as a polarization mode filter. Specific features of the proposed device are its compact one-section form resulting from the inherent polarization-discrimination property and the relaxed dimensional tolerance due to the automatic phase-matching of coupled modes. Design data and a related discussion are given for the example of $LiNbO_3$/YIG/GGG layered structure operating in the 1.15-μm-wavelength region.**

Manuscript received July 1, 1976.

The authors are with the Department of Electrical Engineering, Faculty of Engineering Science, Osaka University, Toyonaka, Osaka, Japan.

I. Introduction

MODE-COUPLING phenomena in optical waveguides caused by the electrooptic, magnetooptic, or acousto-optic perturbation have been widely used in the field of guided-wave optics [1]. In particular, the magnetooptic coupling is of interest for nonreciprocal device applications. Two repre-

sentatives are the isolator and the circulator. We describe here a waveguide isolator that utilizes the coupling of orthogonally polarized guided and radiation modes in a thin-film magnetooptic waveguide with anisotropic superstrate. The basic structure is the semileaky-type slab waveguide that has originally been proposed by Sosnowski [2] for use as a polarization mode filter.

The design and construction of the waveguide isolator have been treated by several recent workers. Warner [3] has described the tandem isolator consisting of a nonreciprocal TE $\longleftrightarrow$ TM guided mode converter preceded by a polarization filter. Auracher and Witte [4] have proposed the balanced-bridge-type isolator in which two phase shifters, one of them nonreciprocal, are inserted between two hybrid couplers to form a waveguide interferometer. In comparison with these composite structures, the semileaky type isolator is in one-section form with no peripheral elements. Furthermore, it is quite insensitive to film thickness deviations since the phase matching of coupled modes is automatically achieved. The phase-matching condition frequently requires a precise film-thickness control in the guided-guided mode coupling devices.

Most of the earlier works on the guided-radiation mode coupling were concerned with the mode-excitation components such as the prism and the grating couplers. Recently, however, the application to other integrated-optical devices has received an increasing attention [5]. These include the acoustooptic scanner of Gfeller [6] and the electrooptic or the magnetooptic modulators of Marcuse [7], Lee and Wang [8], and Yamamoto and Makimoto [9], by which the present work has been motivated.

II. Basic System and Its Modal Property

The basic system that we consider is a magnetooptic/anisotropic thin-film waveguide shown in Fig. 1. The structure is two-dimensional ($\partial/\partial y = 0$) and the wave propagates along the z axis. The substrate material is isotropic with the relative permittivity K^S, whereas the film is magnetooptic with the relative permittivity tensor $[K^F]$. The thickness is d. Also the top layer material is anisotropic with $[K^T]$. In the absence of the perturbations, $[K^F]$ and $[K^T]$ are both diagonal,

$$[K^F] = \text{diag}\,[K^F_{xx}, K^F_{yy}, K^F_{zz}], \tag{1}$$

$$[K^T] = \text{diag}\,[K^T_{xx}, K^T_{yy}, K^T_{zz}]. \tag{2}$$

Materials are all assumed loss-free.

Normal modes of the layered waveguide characterized by diagonal permittivity tensors are known to be separated into TE and TM orthogonal polarizations. Here the two types of the semileaky structure are obtainable by arranging the permittivity relationship:

1) $K^T_{xx} > K^F > K^T_{yy} (>) K^S$

TE wave: guiding, TM wave: leaky

2) $K^T_{yy} > K^F > K^T_{xx} (>) K^S$

TE wave: leaky, TM wave: guiding.

As will be mentioned later, film materials with no or extremely small natural birefringence ($K^F_{xx} \simeq K^F_{yy} \simeq K^F_{zz}$) are required for the present application; hence we used the symbol K^F as the representative of three diagonal elements of $[K^F]$. Also the inequality symbol in the parentheses is set merely for our convenience in the explanation. It is sufficient in general that $K^F > K^S$ holds. The first structure applies to the construction of the TE mode isolator, while the second structure to the TM mode isolator. In the following our concern will be restricted to the first case. The second one will be treated in a quite analogous manner.

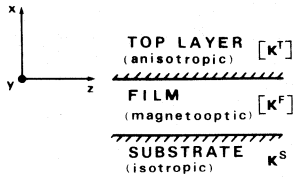


Fig. 1. Semileaky type magnetooptic/anisotropic thin-film waveguide. (Basic system with $[K^F]$ and $[K^T]$ diagonal.)

In the first structure, the normal modes for the TE polarization include the guided modes with discrete eigenvalues (the longitudinal phase constant β), whereas those for the TM polarization consist entirely of radiation modes with continuous spectrum [10]. The spectral ranges of the members of normal modes for both polarizations are comparatively shown in Fig. 2 with the effective index β/k_0 as the coordinate, where k_0 is the free-space wavenumber. Here the evanescent radiation modes belonging to the imaginary β-branch are ignored since they are of less importance in the present discussion. According to the range of the effective index, radiation modes are divided into groups with different field profiles. The top layer modes with the largest indices are peculiar to the leaky structure. Of particular importance for the mode coupling application is that the TE guided mode region is continuously covered by the TM film-top layer radiation modes. This type of radiation mode has a transverse field distribution that is sinusoidal in the film as well as in the top layer and exponentially decaying in the substrate. Although the possible β value of the guided mode depends on the film thickness, a phase-matched and orthogonally polarized radiation mode does always exist. This inherent phase matching allows us to eliminate an acoustic wave, a grating-like periodicity or an accurate film thickness control usually required for the discrete guided-guided mode interaction [1].

III. Guided-Radiation Mode Coupling in Perturbed System and Isolator Operation

An introduction of nonzero but small off-diagonal elements in the film and/or the top layer permittivity tensors leads to the coupling of otherwise independent guided and radiation modes with orthogonal polarizations of the basic system. The perturbations for TE-TM mode coupling are classified according to their paired positions in the permittivity tensor and their real/imaginary properties [11], [12]; that is, *AL:* $K_{xy} = K^*_{yx} \neq 0$ (real), *GL:* $K_{xy} = K^*_{yx} \neq 0$ (pure imaginary), *AP:* $K_{yz} = K^*_{zy} \neq 0$ (real), and *GP:* $K_{yz} = K^*_{zy} \neq 0$ (pure imaginary), where the asterisk indicates the complex conjugate. The two *A* (anisotropic) perturbations yield reciprocal coupling and can be generated by the crystal-axis rotation or the electrooptic effect, while the two *G* (gyrotropic) perturbations induced by the magnetooptic effect lead to nonreciprocal coupling.

We now consider the first semileaky structure (TE guiding, TM leaky) with the mixed perturbations, where the gyrotropic longitudinal (*GL*) perturbation is added to the film region by

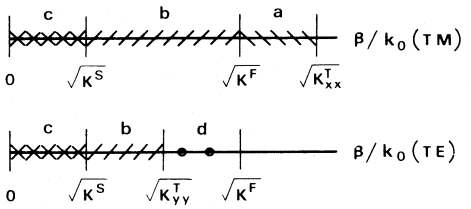


Fig. 2. Phase-constant distributions of forward propagating normal modes of the TM-leaky type semileaky structure. *a:* top layer modes, *b:* film-top layer modes; *c:* air modes (doubly degenerate); and *d:* discrete guided modes.

the external magnetic field along the z axis and the anisotropic polar (AP) perturbation is introduced in the top layer by the optic-axis rotation. The coupling of a TE guided mode ($\beta = \beta_g$) with the continuum of TM radiation modes in the mixed *GL-AP* perturbation system is described by a pair of integro-differential equations,

$$dA(z)/dz = \int_{k_0(K^S)^{1/2}}^{k_0(K^F)^{1/2}} \tilde{\kappa}(\beta)[\eta(\beta/\Delta)]\, B(\beta, z) \cdot \exp\,[-j(\beta - \beta_g)z]\, d\beta, \tag{3}$$

$$dB(\beta,z)/dz = -\tilde{\kappa}(\beta)^* A(z) \exp\,[+j(\beta - \beta_g)z], \tag{4}$$

where

$$\Delta = \eta^{1/2}(K_{xx}^T k_0^2 - \beta^2)^{1/2}, \tag{5}$$

$$\eta = (K_{zz}^T/K_{xx}^T). \tag{6}$$

In the above, A and B denote the complex normalized amplitudes of the guided and the radiation modes, respectively, for the forward ($+z$) propagation. In (3) the integration is limited to the spectral range of the film-top layer modes from the phase-matching condition. Also $\tilde{\kappa}$ is the coupling coefficient that is related to the overlap integral for the coupled modes as

$$\tilde{\kappa}(\beta) = \tilde{\kappa}_{GL}(\beta) + \tilde{\kappa}_{AP}(\beta) = (-j\omega\epsilon_0/4P)\left[\int_{-d}^{0} K_{xy}^{F*} e_y^{TE*} e_x^{TM}\, dx + \int_0^{\infty} K_{yz}^T e_y^{TE*} e_z^{TM}\, dx\right], \tag{7}$$

where $e_{x,y,z}$ represents the transverse distributions of field components and P is a real constant with the dimension of power used in the normalization [10]. Detailed field expressions of relevant modes will be presented in Appendix A.

The magnitudes of the elementary coupling coefficients $\tilde{\kappa}_{GL}$ and $\tilde{\kappa}_{AP}$, and hence the total coupling coefficient $\tilde{\kappa}$, oscillate as β varies as shown in Fig. 4 in the next section. An exact closed-form solution is not possible because of this complex β-dependence of the total coupling coefficient. Therefore, we employ an analytical method based on the Lorentzian approximation to the $|\tilde{\kappa}|^2$ curve. The details of the analysis will be presented in Appendix B. Then, unlike the periodic power exchange in the case of the guided-guided mode interaction, the power of the incident TE guided mode is found to decay monotonically as it propagates in the perturbed system,

$$P(z) = P_0 \exp(-2\alpha z). \tag{8}$$

Here the amplitude attenuation constant α due to the coupling to radiation is proportional to the squared magnitude of the total coupling coefficient evaluated at $\beta = \beta_g$,

$$\alpha = \pi\eta\,[|\tilde{\kappa}(\beta)|^2(\beta/\Delta)]_{\beta=\beta_g}. \tag{9}$$

Note that this expression for α is the same as that obtained from the perturbation method of Marcuse [10]. The validity of the above results in the order of magnitude of perturbations treated here was checked by comparing with the numerical solution based on the Runge-Kutta-Gill method. The power that is lost from the guided mode escapes into the top layer with the TM polarization, where the radiation angle with respect to the z axis is given by

$$\phi = [\tan^{-1}(\Delta/\eta\beta)]_{\beta=\beta_g}. \tag{10}$$

Essential to the isolator operation is the nonreciprocity of the mode coupling. Hence we will examine the directional property of the coupling coefficient in (7). As is seen in Appendix A, the transverse field components of normal modes are real by definition, and consequently, the longitudinal one is pure imaginary. Then noting the real/imaginary property of the individual perturbations, we see that the elementary coupling coefficients $\tilde{\kappa}_{GL}$ and $\tilde{\kappa}_{AP}$ are both real quantities. Furthermore, in the mode coupling for the backward ($-z$) propagation, the sign reversal occurs for $\tilde{\kappa}_{AP}$ while $\tilde{\kappa}_{GL}$ remains the same as the forward ($+z$) propagation [12]. This implies that when we adjust the two elementary coupling coefficients so that they are the same in magnitude but with opposite signs in the forward propagation, the radiation loss on the guided mode due to mode coupling would occur in the backward propagation only. The structure with such balanced perturbations would then behave as a TE mode isolator. Notice that there is no need of a polarization mode filter because of the spatial separation of coupled modes.

The efficiency of the proposed isolator solely depends on the amount of the backward radiation loss for the guided mode, since the guided-radiation mode interaction is generally weaker than the guided-guided mode interaction [5]. For achieving an efficient operation, the two elementary coupling coefficients should be both large and in comparable order. As to the magnetooptic perturbation in the film region, this requires the use of an isotropic film material. In this case the transverse wavenumber of the TE guided mode in the film $(K_{yy}^F k_0^2 - \beta_g^2)^{1/2}$ is matched to that of the TM film-top layer radiation mode $[(K_{zz}^F/K_{xx}^F)^{1/2}(K_{xx}^F k_0^2 - \beta^2)^{1/2}]_{\beta=\beta_g}$ with the same longitudinal phase constant yielding a sufficient field-overlap of coupled modes in the perturbed region. As to the anisotropic perturbation in the top layer, on the other hand, the transverse phase matching is essentially not possible because the guided mode field is evanescent in that direction whereas the radiation mode has a standing-wave pattern. Fortunately, however, for the *AP* perturbation in the top layer, one of the peaks of the coupling coefficient $|\tilde{\kappa}_{AP}(\beta)|$ is located in the immediate vicinity of β_g of the guided mode independent of the film thickness. (See, for example, the solid curve in Fig. 4 in the next section.) Therefore, the anisotropic coupling coefficient that is comparable to the gyrotropic one can be expected.

Another candidate leading to isolator operation is the mixed

GP-AL system in which the elementary coupling coefficients $\tilde{\kappa}_{GP}$ and $\tilde{\kappa}_{AL}$ are both pure imaginary. However, this complementary perturbation system cannot be employed since the magnitude of the anisotropic coefficient $\tilde{\kappa}_{AL}(\beta)$ at β_g is vanishingly small. Here the position of the guided mode is trapped by one of the zeros of $|\tilde{\kappa}_{AL}(\beta)|$ contrary to the preceding *GL-AP* perturbation case.

The peculiar property of the anisotropic perturbations mentioned above can be proved by showing that the determinantal equation for the extreme points of the coupling coefficient reduces to the eigenvalue equation for the guided mode with reasonable approximations or can be explained qualitatively by examining the transverse field distributions of coupled modes.

IV. Design Example and Related Discussion

Referring to several material combinations employed for the fabrication of magnetooptic waveguides in previous reports, we pick the $LiNbO_3$/YIG/GGG layered structure shown in Fig. 3. The operating wavelength is 1.15 μm (He-Ne laser). The arrangement is a modified version of that employed by Warner [3] for the nonreciprocal TE $\longleftrightarrow$ TM guided-mode converter. The difference is only that the top layer material $LiIO_3$ in the original structure is replaced here by $LiNbO_3$. Refractive indices are as follows: top layer: $LiNbO_3$ (n_o = 2.229, n_e = 2.150) [13], film: $(LaY)_3Ga_{0.33}Fe_{4.67}O_{12}$ (n = 2.178) [3]; substrate: $Gd_3Ga_5O_{12}$ (n = 1.945) [3]. The optic axis of $LiNbO_3$ is initially parallel to the y axis so that the basic structure acts as a TM-leaky-type semileaky guide. Then the *GL* perturbation is induced in the film region with the magnetization directed along the z axis, the magnitude of which is $K_{xy}^F = K_{yx}^{F*} = j3.4 \times 10^{-4}$ [3] corresponding to 280°/cm Faraday rotation. Simultaneously the AP perturbation is added to the top layer by rotating the optic axis of $LiNbO_3$ in the y-z plane as shown in Fig. 3.

In Fig. 4 are plotted the squared magnitudes of the elementary coupling coefficients $\tilde{\kappa}_{GL}$ and $\tilde{\kappa}_{AP}$ for the TE guided and TM radiation modes as functions of the effective index with the film thickness $d = 1\lambda$ and the offset angle $\theta = 1°$ for the optic axis of $LiNbO_3$. Also the chain-dotted curve in this figure applies to the total coupling coefficient [$K(\beta)$ in (B4)] for the forward (+z) propagation. Here and in what follows, the guided mode is the TE_0 mode with the longitudinal phase constant β_0, which is represented by the vertical line in Fig. 4. In this case the two elementary coupling coefficients are not equally balanced at $\beta = \beta_0$. However, it should be noticed that the location of a $|\tilde{\kappa}_{AP}|^2$ peak almost coincides with β_0 as mentioned earlier. Actually the situation is the same when β_0 moves as the film thickness varies.

Fig. 5 represents the variations of the elementary coupling coefficients evaluated at β_0 with respect to the offset angle θ for three different values of the film thickness with the fixed magnetization. Here the change of the diagonal elements of the top layer permittivity tensor $[K^T]$ due to the optic-axis rotation was taken into account. The chain-dotted curve in this figure is the trace of the operating point at which the magnitudes of elementary coefficients are equal.

Design curves for the TE_0 mode isolator using the $LiNbO_3$/YIG/GGG layered structure are presented in Fig. 6. From the required value of the backward radiation loss, the film thick-

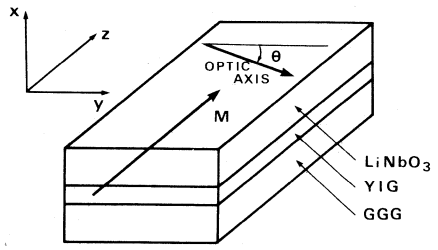


Fig. 3. $LiNbO_3$/YIG/GGG layered waveguide for TE mode one-section isolator with *GL-AP* perturbation (λ = 1.15 μm). The magnetization M is parallel to the z axis in the YIG film and the optic axis of $LiNbO_3$ lies in the y-z plane.

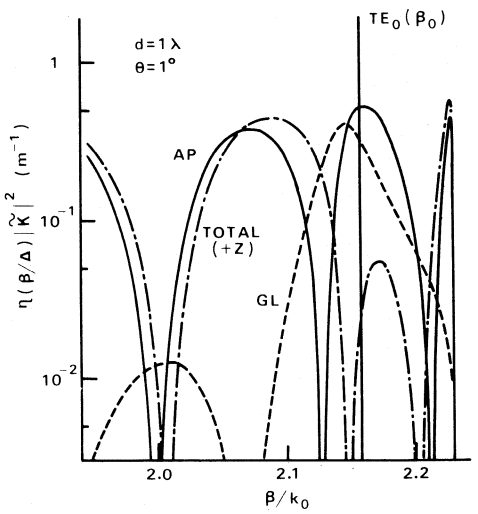


Fig. 4. Squared magnitudes of the elementary coupling coefficients $\tilde{\kappa}_{GL}$ (broken curve) and $\tilde{\kappa}_{AP}$ (solid curve) multiplied by $\eta(\beta/\Delta)$ as functions of the effective index β/k_0 for the TE_0-TM_{rad} mode coupling in the perturbed $LiNbO_3$/YIG/GGG layered waveguide, where the thickness d of the film is 1λ and the offset angle θ for the $LiNbO_3$ optic-axis is 1°. The chain-dotted curve corresponds to the total coupling coefficient [$K(\beta)$ in (B4)] for the forward (+z) propagation. The curves are drawn for the spectral range covering the top layer and the film-top layer radiation modes.

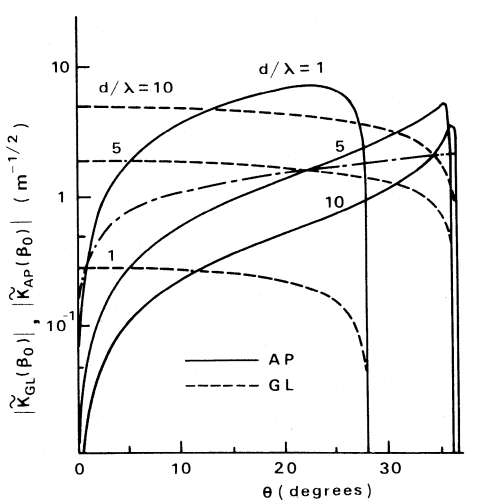


Fig. 5. Magnitudes of the elementary coupling coefficients $\tilde{\kappa}_{GL}$ and $\tilde{\kappa}_{AP}$ evaluated at $\beta = \beta_0$ as functions of the offset angle θ for the $LiNbO_3$ optic-axis for the TE_0-TM_{rad} mode coupling in the perturbed $LiNbO_3$/YIG/GGG layered waveguide with the fixed magnetooptic perturbation. The chain-dotted curve is the trace of the operating point with the balanced perturbations.

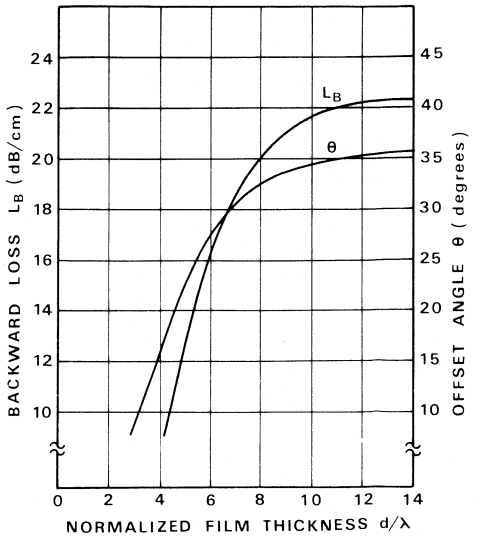


Fig. 6. Design curves for the semileaky type TE_0 mode isolator utilizing the $LiNbO_3$/YIG/GGG layered waveguide ($\lambda = 1.15\ \mu m$).

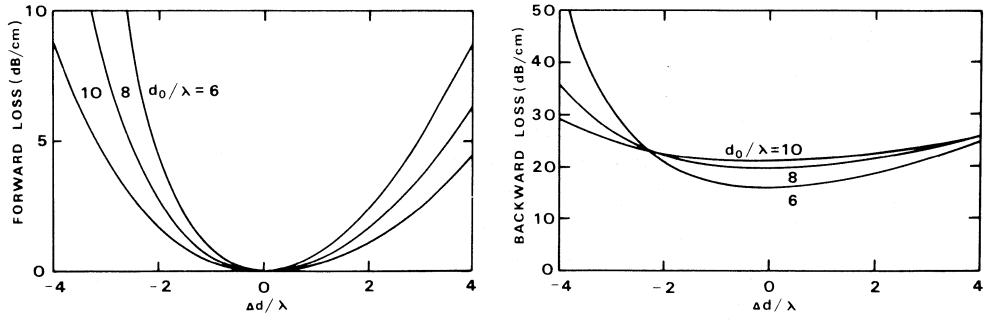


Fig. 7. Characteristics of the $LiNbO_3$/YIG/GGG layered TE_0 mode isolator when the actual film thickness d deviates from the specified one d_0. Radiation losses for (a) the forward and (b) the backward propagation as functions of the normalized film thickness deviation $\Delta d/\lambda = (d - d_0)/\lambda$.

ness and then the offset angle for the optic axis can be readily evaluated. With this structure backward loss on the order of 20 dB/cm may be gained. The efficiency of the device would be improved if one employs an anisotropic crystal that is more birefringent than $LiNbO_3$ or magnetooptic material with larger Faraday rotation than YIG. For instance, when GdIG ($n = 2.202$, $K_{xy} = j2.0 \times 10^{-3}$) [13] is used in the film region with other materials unchanged for brevity,[1] the estimated backward radiation loss reaches 100 dB/cm in the normalized film thickness near 2.5. However, as far as the authors are aware, the fabrication of the GdIG film waveguide has not been reported, and hence the YIG film guide has been adopted here.

We next discuss the dimensional tolerance for the semileaky type isolator. When the actual film thickness deviates from the specified one, the balance of the elementary coupling coefficients would be destroyed leading to the deterioration of the forward propagation characteristics. The calculated results are shown in Fig. 7 for three values of the specified film thickness. From this figure one notes that the proposed device is quite insensitive to the film thickness deviation $\Delta d(=d - d_0)$. That is, when $\Delta d \simeq \pm 1\lambda$ ($\lambda = 1.15\ \mu m$), the forward radiation loss remains on the order of 0.5 dB/cm and the backward radiation loss would be even larger than the designed value. This should be compared with the case of the guided-guided mode coupling isolator using the original $LiIO_3$/YIG/GGG layered structure [3] for which the estimated backward loss decreases to 3 dB with a slight film thickness deviation $\Delta d \simeq \pm 10^{-3}\lambda$ [15] for TE_0 mode operation or with $\Delta d \simeq \pm 3 \times 10^{-2}\lambda$ [3] for TE_2 mode operation. The relaxed tolerance of the guided-radiation mode coupling isolator is due mainly to the fact that the phase matching of coupled modes still holds even when the film thickness deviates.

In the above discussion, we have assumed an ideal situation where the structure at hand is a perfect three-layer guide. In practice, however, a thin gap is unavoidable when we attempt to optically contact the $LiNbO_3$ superstrate to the YIG film. While the presence of the fourth layer does not influence the phase-matching here, a high-index liquid has to be used to keep the polarization-discrimination property of $LiNbO_3$. The

[1] For the epitaxial growth of GdIG film, an appropriate material other than GGG has to be used since the lattice constants of GdIG and GGG are not matched to within the required accuracy [14].

contact between the YIG film and the GGG substrate raises no problem since the epitaxial growth method is usually employed [3].

V. Conclusion

As an application of the guided-radiation mode interaction to the nonreciprocal integrated-optical devices, we have discussed the design of a one-section isolator using the semileaky type magnetooptic/anisotropic layered waveguide. Specific features of the proposed device are its compact form and the relaxed film thickness tolerance compared to the previous guided-guided mode coupling isolators. The numerical calculation has been performed for the $LiNbO_3$/YIG/GGG layered structure. The previous results on the $LiIO_3$/YIG/GGG nonreciprocal TE $\longleftrightarrow$ TM guided mode converter would be useful for the present application; however, an optical contact of the superstrate crystal raises a difficult problem in fabrication. For the semileaky type isolator, the growth of a magnetooptic film directly onto an anisotropic substrate is desirable.

Appendix A

Modes of Semileaky Structure (TM-Leaky Type)

Here the film material is assumed optically isotropic with the relative permittivity K^F. As to the notations, we follow Marcuse [10].

TE guided mode $[(K^F)^{1/2} > \beta_g/k_0 > (K^T_{yy})^{1/2}]$

$$e_y = \begin{cases} N_g \exp(-\delta x), & (x > 0) \\ N_g (\cos \kappa x - \delta/\kappa \cdot \sin \kappa x), & (0 > x > -d) \\ N_g (\cos \kappa d + \delta/\kappa \cdot \sin \kappa d) \cdot \exp[\gamma(x + d)], & (-d > x) \end{cases} \tag{A1}$$

where

$$\delta = (\beta_g^2 - K^T_{yy} k_0^2)^{1/2}, \tag{A2a}$$

$$\kappa = (K^F k_0^2 - \beta_g^2)^{1/2}, \tag{A2b}$$

$$\gamma = (\beta_g^2 - K^S k_0^2)^{1/2}. \tag{A2c}$$

The amplitude coefficient is given by

$$N_g = [4\omega\mu_0\kappa^2 P/\beta_g(d + 1/\gamma + 1/\delta)(\kappa^2 + \delta^2)]^{1/2}. \tag{A3}$$

TM film-top layer mode $[(K^F)^{1/2} > \beta/k_0 > (K^S)^{1/2}]$

$$h_y = \begin{cases} N_r [(\cos \sigma d + K^F/K^S \cdot \rho/\sigma \cdot \sin \sigma d) \cos \Delta x + K^T_{zz}/K^F \cdot \sigma/\Delta \cdot (-\sin \sigma d + K^F/K^S \cdot \rho/\sigma \cdot \cos \sigma d) \sin \Delta x], & (x > 0), \\ N_r [\cos \sigma(x + d) + K^F/K^S \cdot \rho/\sigma \cdot \sin \sigma(x + d)], & (0 > x > -d), \\ N_r \exp[\rho(x + d)], & (-d > x), \end{cases} \tag{A4}$$

where

$$\Delta = (K^T_{zz}/K^T_{xx})^{1/2}(K^T_{xx} k_0^2 - \beta^2)^{1/2}, \tag{A5a}$$

$$\sigma = (K^F k_0^2 - \beta^2)^{1/2}, \tag{A5b}$$

$$\rho = (\beta^2 - K^S k_0^2)^{1/2}, \tag{A5c}$$

and

$$N_r = (4\omega\epsilon_0 K^T_{xx} P/\pi\beta)^{1/2} [(\cos \sigma d + K^F/K^S \cdot \rho/\sigma \cdot \sin \sigma d)^2 + (K^T_{zz}/K^F)^2 (\sigma/\Delta)^2 (-\sin \sigma d + K^F/K^S \cdot \rho/\sigma \cdot \cos \sigma d)^2]^{-1/2}. \tag{A6}$$

The electric field components are obtained from

$$e_x = (\beta/\omega\epsilon_0 K^i_{xx}) h_y, \tag{A7a}$$

$$e_z = (-j/\omega\epsilon_0 K^i_{zz}) \partial h_y/\partial x, \tag{A7b}$$

where $i = T, F$, or S for each region of the layered structure.

Appendix B

Solution of Coupled Mode Equations

We seek a solution of (3) and (4) subject to the boundary conditions $A(0) = A_0$ and $B(\beta, 0) = 0$; that is, the guided mode is incident at $z = 0$ on the perturbed region $z > 0$. Equation (4) then gives

$$B(\beta, z) = -\tilde{\kappa}(\beta)^* \int_0^z A(z') \exp[+j(\beta - \beta_g)z'] \, dz'. \tag{B1}$$

Substituting (B1) into (3) and changing the order of integrations, we have

$$dA(z)/dz = -\int_0^z A(z') F(z - z') \, dz', \tag{B2}$$

where $F(z)$ is defined as a finite Fourier transform,

$$F(z) = \int_{\beta_1}^{\beta_2} K(\beta) \exp[-j(\beta - \beta_g)z] \, d\beta, \tag{B3}$$

with

$$K(\beta) = \eta[|\tilde{\kappa}(\beta)|^2 (\beta/\Delta)], \tag{B4}$$

and

$$\beta_1 = k_0 (K^S)^{1/2}, \quad \beta_2 = k_0 (K^F)^{1/2}. \tag{B5}$$

Taking the Laplace transform of both sides of (B2) with respect to z leads to

$$a(p) = A_0/[p + f(p)], \tag{B6}$$

where the lower case symbols indicate the transformed quantities with p as the new variable. The direct inverse transform of $a(p)$ in (B6) is not possible because $K(\beta)$ in (B4) exhibits the oscillatory behavior as β varies. (See, for instance, the chain-dotted curve in Sec. IV, Fig. 4.) Since our concern is with the main lobe of the $K(\beta)$ curve covering the guided mode at $\beta = \beta_g$, it is approximated here by an analytically tractable Lorentzian curve as

$$K(\beta) \simeq c/[(\beta - \beta_m)^2 + b^2], \tag{B7}$$

where β_m denotes the peak position of the main lobe. The parameters b and c are to be determined by matching the two curves at $\beta = \beta_m$ as well as at $\beta = \beta_g$. Also we can safely extend the range of integration in (B3) to $-\infty < \beta < +\infty$ since the coupling of the guided mode with the radiation modes located outside the main lobe of the $K(\beta)$ curve can be neglected.

Then we obtain from (B3) and (B7)

$$F(z) = \pi(c/b) \exp [-\{b - j(\beta_g - \beta_m)\} z] \quad \text{(B8)}$$

yielding

$$f(p) = \pi(c/b)/[p + b - j(\beta_g - \beta_m)]. \quad \text{(B9)}$$

Here $a(p)$ in (B6) is rational and the inverse Laplace transform is straightforward. The final result is then, ignoring the small enough terms,

$$A(z) = A_0 \exp [-\pi(c/b)z/\{b - j(\beta_g - \beta_m)\}]. \quad \text{(B10)}$$

Hence the variation of the guided mode power is given by

$$\begin{aligned} P(z) &= |A(z)|^2 P \\ &= P_0 \exp [-2\pi\{c/[(\beta_g - \beta_m)^2 + b^2]\}z] \\ &= P_0 \exp [-2\pi K(\beta_g)z]. \end{aligned} \quad \text{(B11)}$$

The power loss coefficient is

$$2\alpha = 2\pi K(\beta_g), \quad \text{(B12)}$$

which is the same as (9).

References

[1] A. Yariv, "Coupled mode theory for guided-wave optics," *IEEE J. Quantum Electron.*, vol. QE-9, pp. 919-933, Sept. 1973.

[2] T. P. Sosnowski, "Polarization mode filters for integrated optics," *Opt. Commun.*, vol. 4, pp. 408-412, Feb./Mar. 1972.

[3] J. Warner, "Nonreciprocal magnetooptic waveguides," *IEEE Trans. Microwave Theory Tech.*, vol. MTT-23, pp. 70-78, Jan. 1975.

[4] F. Auracher and H. H. Witte, "A new design for an integrated optical isolator," *Opt. Commun.*, vol. 13, pp. 435-438, Apr. 1975.

[5] I. P. Kaminow, "Optical waveguide modulators," *IEEE Trans. Microwave Theory Tech.*, vol. MTT-23, pp. 57-70, Jan. 1975.

[6] F. R. Gfeller, "Acoustooptic scanner," presented at Top. Meeting Integrated Optics, New Orleans, LA, Jan. 1974, Paper WA11.

[7] D. Marcuse, "Electrooptic coupling between TE and TM modes in anisotropic slabs," *IEEE J. Quantum Electron.*, vol. QE-11, pp. 759-767, Sept. 1975.

[8] Y.-K. Lee and S. Wang, "Electrooptic guided-to-unguided mode converter," *IEEE J. Quantum Electron.*, vol. QE-12, pp. 273-281, May 1976.

[9] S. Yamamoto and T. Makimoto, "Semi-leaky type thin-film magnetooptic waveguide for modulator application," *J. Appl. Phys.*, to be published, Apr. 1977.

[10] D. Marcuse, *Theory of Dielectric Optical Waveguides.* New York, London: Academic, 1974.

[11] S. Wang, M. L. Shah and J. D. Crow, "Wave propagation in thin-film optical waveguides using gyrotropic and anisotropic materials as substrates," *IEEE J. Quantum Electron.*, vol. QE-8, pp. 212-216, Feb. 1972.

[12] S. Yamamoto and T. Makimoto, "Circuit theory for a class of anisotropic and gyrotropic thin-film optical waveguides and design of nonreciprocal devices for integrated optics," *J. Appl. Phys.*, vol. 45, pp. 882-888, Feb. 1974.

[13] S. Wang, J. D. Crow, and M. L. Shah, "Studies of magnetooptic effects for thin-film optical waveguide applications," *IEEE Trans. Magnetics*, vol. MAG-7, pp. 385-387, Sept. 1971.

[14] P. K. Tien, R. J. Martin, S. L. Blank, S. H. Wemple, and L. J. Varnerin, "Optical waveguides of single-crystal garnet films," *Appl. Phys. Lett.*, vol. 21, pp. 207-209, Sept. 1, 1972.

[15] S. Yamamoto and T. Makimoto, "Design considerations for nonreciprocal integrated-optical devices," *J. Appl. Phys.*, vol. 47, pp. 4056-4060, Sept. 1976.

Nonlinearities in the Emission Characteristics of Stripe-Geometry (AlGa)As Double-Heterostructure Junction Lasers

THOMAS L. PAOLI, MEMBER, IEEE

Abstract—**Significant changes in the optical and electrical properties of stripe-geometry (AlGa)As double-heterostructure junction lasers have been observed to accompany a nonlinearity in the current dependence of the lasing emission. Over the nonlinear range, the optical field of the lasing emission shifts continuously with current toward one boundary of the active stripe. Simultaneously, effective gain saturation is lost and additional transverse modes are excited. The increasing gain is believed to occur primarily in spatial regions where the optical intensity is reduced as a result of the transverse motion of the field. Additional observations suggest that this transverse motion results from an interaction between the intense lasing field and the active medium. Consequently, gain depletion is discussed as a possible cause for the transverse instability. Implications of this model for a qualitative understanding of the improved output performance recently obtained from lasers with narrow stripes are also considered.**

Manuscript received July 15, 1976; revised August 18, 1976.
The author is with Bell Laboratories, Murray Hill, NJ 07974.

I. Introduction

THE existence of nonlinearities in the current dependence of the output intensity from (AlGa)As double-heterostructure junction lasers has been noted by several authors [1]-[5]. A nonlinear emission characteristic is however an undesirable, and in some applications an unacceptable behavior for a useful junction laser operating above threshold. The presence of the nonlinearity can impose a limit on the available output power, appreciably reduce the device efficiency, and introduce severe distortion of an imposed modulating

signal, especially in an analog communication system. In addition, nonlinear regions of the emission characteristic are often observed [6] to change during accelerated aging, commonly moving to lower output powers. It is important, therefore, to understand this behavior and its controlling factors and to determine the extent to which these nonlinearities are a fundamental feature of junction laser behavior.

The present paper investigates features of the laser's characteristics which typically occur simultaneously with the onset of the nonlinearity. In this way, important effects may be identified and thereby suggest a framework for an improved understanding of the process. In general, we find that a nonlinearity is accompanied by a cessation of the effective gain saturation which occurred at threshold, the excitation of additional transverse modes, and a continuous shift of the lasing field toward one boundary of the active stripe. Observation of the position of the lasing emission on the mirror relative to that of the orthogonally polarized nonlasing field suggests that the motion is a result of an interaction between the intense lasing field and the active medium. Consequently, a spatially localized depletion of the optical gain is discussed as a possible cause of the spatial instability. Implications of this model for obtaining improved laser performance are also briefly considered.

II. Experimentally Observed Characteristics

Lasers used in this study were fabricated from conventional double-heterostructure material grown by liquid-phase epitaxy [7]. The four-layered wafers were composed of a thin (<0.4-μm) layer of $Al_{0.08}Ga_{0.92}As$ (the active layer) sandwiched between p- and n-type layers of $Al_{0.36}Ga_{0.64}As$ with a capping layer of p-GaAs on the P-AlGaAs. All devices were stripe-geometry lasers fabricated from the epitaxial wafers by proton bombardment [8]. Mirrors were formed from cleaved, uncoated facets. Gold pads, plated on the p-side before cleaving, were used as bonding pads for direct bonding to gold-plated copper studs.

A typical example of the nonlinear emission characteristics under consideration in this study is shown in Fig. 1. Although the exact shape of the light-current curve varies widely from diode to diode, nonlinearities of this type occur quite commonly at output powers (single side) below 3 mW. In fact, it is not unusual to find a significant fraction of the lasers from even a good wafer exhibit some degree of nonlinearity in their emission characteristic. In such nonlinear regions, light is usually not emitted symmetrically from the laser mirrors [5], as illustrated in Fig. 1. In fact, it is not uncommon to find the output from one mirror is increasing while the emission from the other mirror is decreasing with current. This asymmetrical emission occurs even with lasers whose output at currents below the nonlinearity is quite symmetric.

A characteristic feature of the nonlinear regime is a loss of gain saturation in the active region of the laser. The loss of saturation is directly revealed by the current-dependence of the optical emission (TM) polarized orthogonal to the lasing emission (TE). As illustrated in Fig. 2, the intensity of the TM emission typically saturates at the lasing threshold as expected

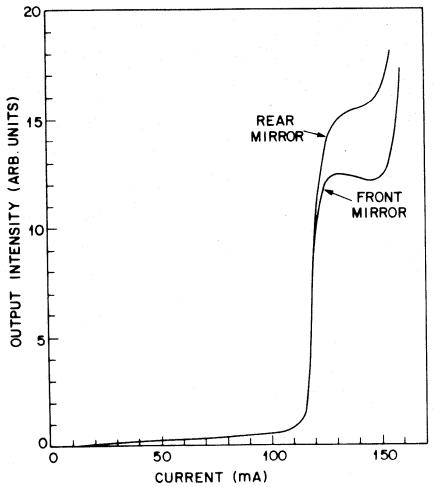


Fig. 1. Emission characteristics for the front and rear mirrors of a stripe-geometry (AlGa)As double-heterostructure junction laser operating continuously at room temperature. The curves illustrate the nonlinearities commonly observed in the current-dependence of the lasing emission. Full scale corresponds to approximately 3 mW.

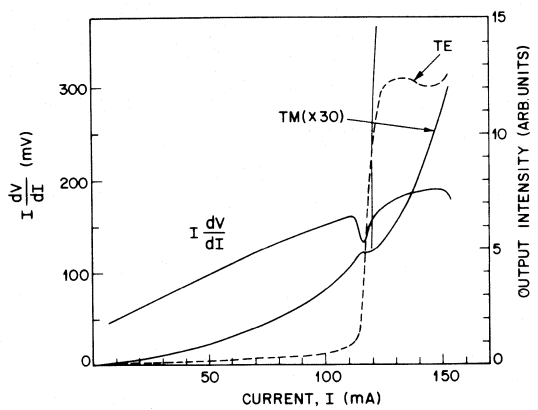


Fig. 2. Current-dependence of the derivative of the voltage and of the nonlasing emission polarized orthogonal to the lasing emission. The simultaneous variation of the lasing intensity is also shown with a dotted line. Note that the TM intensity begins to increase in the vicinity of where the lasing characteristic becomes nonlinear but at a current slightly above where the $I(dV/dI)$ shows a loss of voltage saturation.

[9] but then begins to increase at the current where the intensity of the lasing emission becomes a nonlinear function of current. Since the TM emission is a measure of the total spontaneous emission, both amplified and unamplified, increases in its intensity indicate an increasing optical gain.

An unsaturated optical gain implies that the separation of the electron and hole quasi-Fermi levels is no longer "pinned" at its threshold value. Consequently, the loss of saturation is also reflected in the above-threshold electrical characteristic of the laser diode. As described previously [10], [11], the corresponding change in the current-voltage (I-V) relation is best sensed in the variation of the product $I(dV/dI)$ with current. Fig. 2 illustrates the typical behavior of the derivative for a diode exhibiting an output nonlinearity. At the onset of lasing, an abrupt reduction occurs in the derivative as a result of the saturation of the junction voltage by the high rate of stimulated recombination. However, with further increases in current, the product $I(dV/dI)$ begins to increase, indicating

that the junction voltage does not remain saturated. As indicated in Fig. 2, the voltage saturation is lost at a current slightly below where the TM intensity also begins to increase.

The increasing above-threshold gain also manifests itself through the excitation of higher order transverse modes parallel to the junction plane. Although the fundamental mode remains dominant in the nonlinear region of the output characteristic, the presence of additional transverse modes is readily observed in the high-resolution (0.1 A or better) spectrum of the optical output [12], as shown in Fig. 3. Unfortunately, spatial resolution of the higher order modes in the near or far field is obscured by the presence of the strong fundamental mode. The excitation of additional modes suggests that increases in the population inversion are occurring at least locally along the junction plane where the intensity of these modes is large.

Measurement of the spatial distribution of the optical field on the laser mirror reveals that a transverse shift of the lasing mode accompanies the loss of a saturated gain distribution. As an example of the changes often observed, the spatial profile of the mirror illumination along the junction plane of the laser of Fig. 1 is illustrated in Fig. 4 for operation at several currents in the vicinity of the output nonlinearity. The oscilloscope traces were obtained by sweeping the magnified mirror image past a fixed aperture with a rotating mirror [13]. The traces clearly demonstrate that the optical field shifts continuously to one edge of the electrically active stripe as the current is increased through the nonlinear region of the output characteristic. In this case, the peak of the optical intensity moved 3 μm as the current was increased from threshold to 1.3 times threshold.

To demonstrate that the motion shown in Fig. 4 is not simply a result of a shifting current distribution, the mirror illuminations of the lasing (TE) and orthogonally polarized, nonlasing (TM) emission were observed under identical conditions. As illustrated in Fig. 5, the spatial distribution of the lasing emission becomes significantly displaced with respect to that of the nonlasing emission at currents within the nonlinear regime. While there is a slight distortion of the nonlasing field at high current, the position of the TM field as well as its half-power width do not change appreciably with current. The intensity of this nonlasing emission does increase markedly as shown in Fig. 2. Such spatial stability of the TM mode suggests that there is no major change in the transverse waveguiding or in the spatial distribution of at least most of the current. Consequently, the motion of the lasing emission appears to be a result of an interaction between the relatively intense lasing field and the active medium. We shall discuss this interaction further in the next section.

The correlation of the onset of a nonlinearity in the output characteristic with a transverse motion of the mirror illumination suggests that improved output characteristics may be obtained by exerting more control on the lateral location of the optical field. One way to increase the control is by narrowing the width of the electrically active stripe. Recently this approach was successfully demonstrated [5] in lasers with 8-μm-wide stripes fabricated by proton bombardment. As illustrated in Fig. 6, the output from these lasers generally

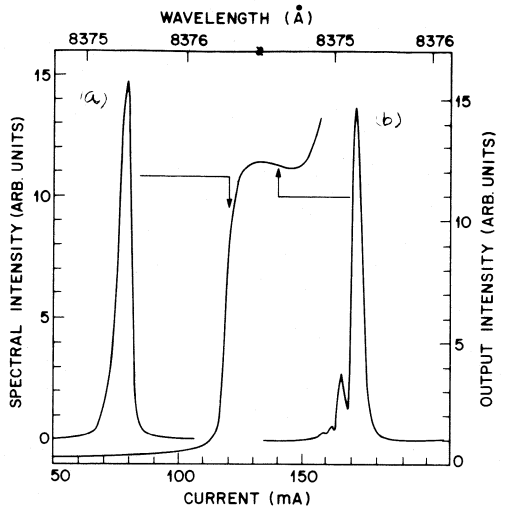


Fig. 3. High-resolution spectra of a longitudinal mode in the output of a CW laser operated in the (a) linear and (b) nonlinear regimes of its emission characteristic. Note the presence of subsidiary peaks in (b) indicating the excitation of additional modes with different spatial distributions along the junction plane.

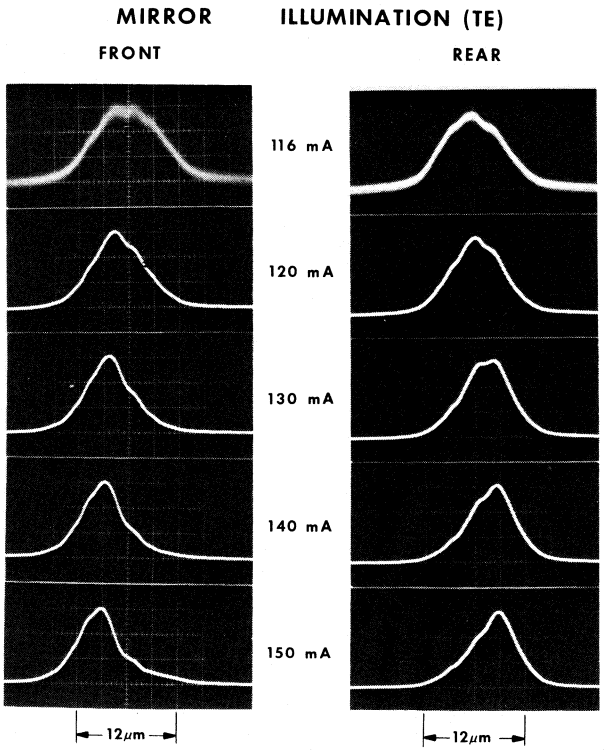


Fig. 4. The intensity distribution along the junction plane of the TE mirror illumination at selected currents from threshold into the nonlinear regime of the emission characteristic. The nominal stripe width for this laser is 12 μm. Note the shift of the peak of the field toward one edge of the stripe.

remained linear over a larger range above threshold and to a higher power level than lasers fabricated from the same wafer with 12-μm-wide stripes [14]. Furthermore, the behavior of the TM emission and the voltage derivative, illustrated in Fig. 7, demonstrates that complete gain saturation in the active region of the 8-μm laser is maintained over the entire linear range of its output characteristic. However, nonlinearities do develop at sufficiently high currents as shown in Fig. 6. As with the 12-

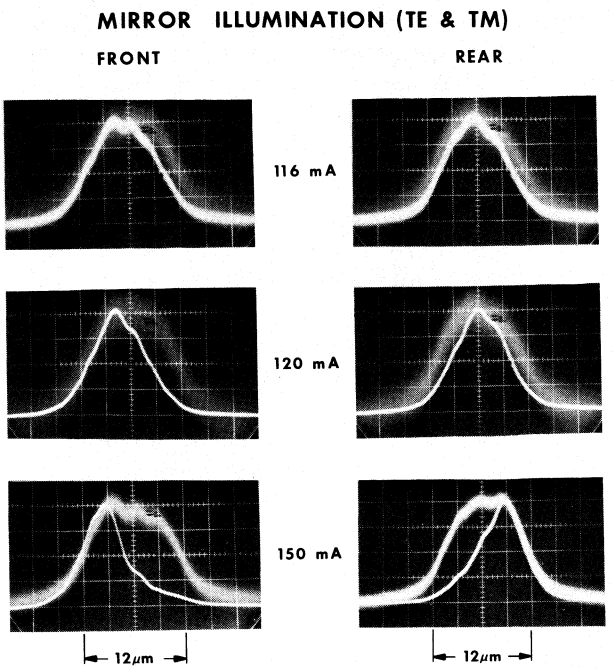


Fig. 5. The intensity distribution along the junction plane of the TE and TM mirror illuminations at selected currents for the laser of Fig. 4. Note the displacement of the TE profile with respect to the TM distribution which develops at high current. The shifts to opposite directions on the front and rear mirrors correspond to a motion of the optical field within the laser toward one edge of the stripe.

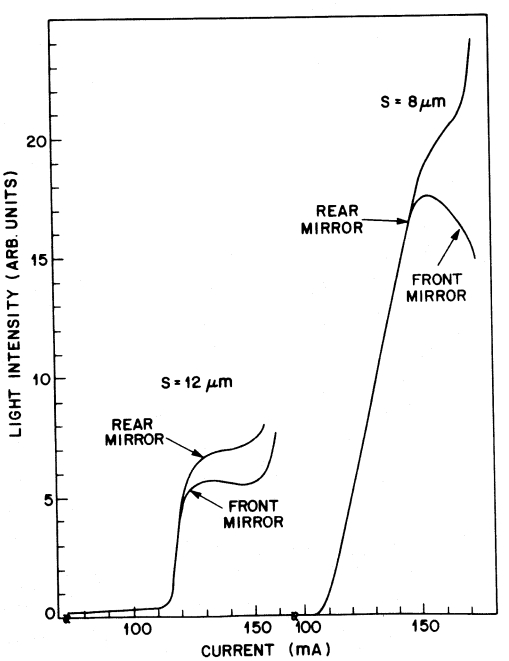


Fig. 6. Comparison of the emission characteristics for a laser with an 8-μm-wide stripe and one fabricated from the same wafer with a 12-μm stripe.

μm devices, the nonlinearity is accompanied by a loss of gain saturation which is reflected in both the voltage and nonlasing optical emission. The increasing gain also leads again to the excitation of additional transverse modes as shown in Fig. 8.

Observation of the mirror illumination in the 8-μm laser indicates that the narrow stripe exerts a significant degree of lateral control on the spatial distribution of the optical field.

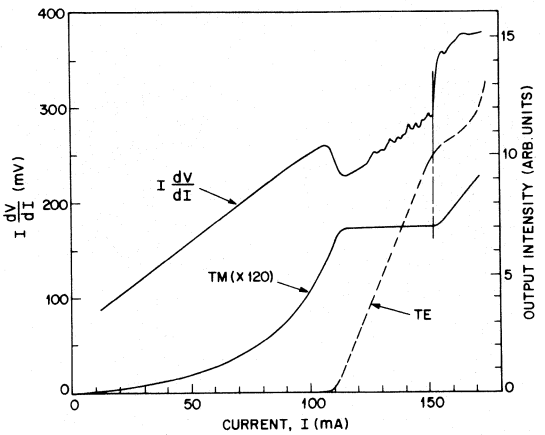


Fig. 7. Current-dependence of the nonlasing (TM) emission and the derivative of the external voltage for the 8-μm laser of Fig. 6. The simultaneous variation of the lasing intensity is also shown with a dotted line. Note the loss of saturated TM emission and voltage which accompanies the nonlinearity in the output characteristic.

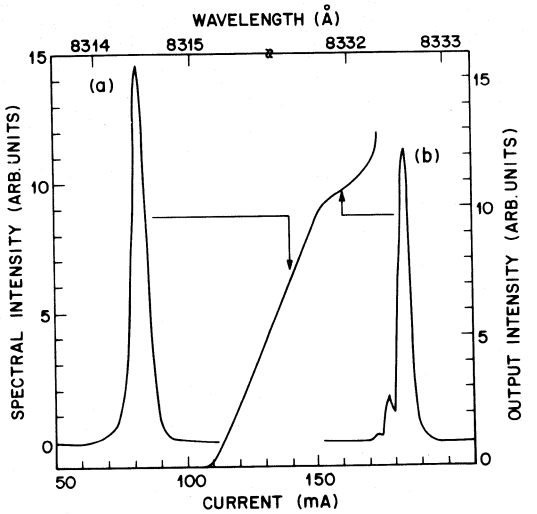


Fig. 8. High-resolution spectra of a longitudinal mode in the output of a laser with an 8-μm stripe showing the excitation of additional transverse modes which occurs when the laser is operated in the nonlinear portion of the emission characteristic.

This control is illustrated in Fig. 9 which displays the spatial profile of the mirror illumination as a function of increasing current from near threshold through the nonlinearity. For currents below 150 mA, where the nonlinearity begins, the optical field remains symmetric and fixed in position along the junction plane. However, as the current is increased into the nonlinear range, the distributions on both mirrors become distorted and shift toward one edge of the stripe, as in the case of the 12-μm laser. In this range, the distribution of the lasing emission also becomes slightly displaced with respect to that of the nonlasing emission.

Further evidence of the influence of the stripe boundary on the optical field is provided by the width and shape of the field produced in the 8-μm stripe. In general, this field is significantly narrower than that emitted by a laser with a 12-μm stripe. For example, the full width at half-power of the mirror illumination in Fig. 9 is about 3.9 μm compared to the 7.5 μm observed with the 12-μm device of Fig. 4.

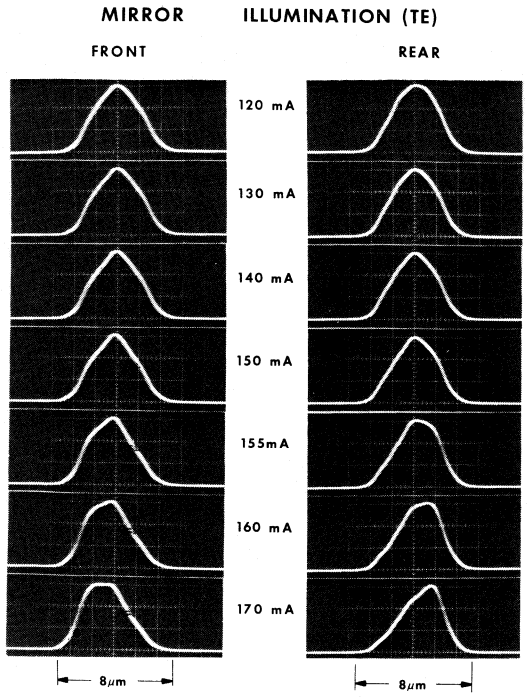


Fig. 9. The intensity distribution along the junction place of the TE mirror illumination at selected currents for the laser with a stripe width equal to 8-μm. Note the shift of the peak of the field toward one edge of the stripe at currents in the nonlinear range of the emission characteristic shown in Fig. 8.

Furthermore, the optical field shown in Fig. 9 does not extend appreciably beyond the nominal stripe width whereas with the nominally 12-μm stripe the field exhibits a comparatively long tail which evidently extends beyond the 12-μm width. The extension of the optical field beyond the stripe edges is allowed in the 12-μm device because the protons have not penetrated through its junction.[1] In the 8-μm laser, where the protons have apparently penetrated[1] through the junction, the sharp spatial cutoff of the optical field may result from the high optical loss present at the boundary defined by the proton damage.

III. Discussion

Since many of the characteristic features which accompany the nonlinearity can be understood as consequences of the transversely shifting lasing field, we begin by considering a potential cause for this spatial instability. The observed displacement of the lasing field relative to the orthogonally polarized nonlasing mode, illustrated in Fig. 5, immediately suggests a consideration of interactions between the intense field and the active medium.

Self-consistent analysis of the spatial gain in the presence of strong lasing action in a double-heterostructure laser has indicated that a spatially localized depletion of the gain tends to occur in regions where the stimulated emission is maximum [16], [17]. As a result, the gain in the wings of the spatial profile increases in order to maintain the modal gain constant and equal to the loss. Because of the spatial distribution of the optical field, relatively large increases are required at the edges of the profile (where the field is low) to compensate for a small depletion in the center of the distribution (where the field is large). The net result of this interaction is a tendency for the lasing mode to burn a spatial hole in the gain profile as the optical power increases.

The development of a hole or a depression in the spatial profile of the gain implies that the positions of peak gain and maximum optical intensity do not coincide. Under this condition, the transverse position of the optical field is not stable since any minor perturbation of the field's propagation direction will cause the peak of the field to move into the region of highest gain [18]. Consequently, it is unlikely that a gain profile with a central depression as predicted analytically [16] can exist in a real laser. Instead, formation of a local peak in the gain profile will be inhibited by increased recombination as the optical field continuously moves into the region where the increased gain is tending to occur.[2] The actual position which the field assumes is then determined by a dynamic equilibrium between field and gain in which the saturated gain of the field is maximized. Transverse motion of the field must ultimately stop as the field begins to couple strongly with the optical loss present near the edge of the electrically active region. Although this mechanism seems plausible in the light of previous analysis [16], a self-consistent treatment of the interaction between the lasing field and the gain profile allowing for transverse motion of the optical field is required to determine if such motion is in fact energetically favorable.

One obvious but important consequence of the field's motion is that the optical intensity is reduced in a region near the other edge of the active stripe. In this low-field region, the population inversion is not effectively saturated and can consequently increase with current at a rate characteristic of below-threshold operation. Increases in the carrier density imply corresponding increases in the junction voltage consistent with the observations described in Section II.

A locally increasing gain can also explain the observed increase of the TM intensity, since the intensity of the subthreshold TM mode is appreciable in the unsaturated region. Similarly, the modal gain of TE modes with nonfundamental spatial distributions along the stripe width will also increase as a result of their effective coupling to a widened gain distribution. Thus a broadening of the profile may also be expected to excite additional transverse modes as observed experimentally. However, a change in the order of the dominant transverse mode is not expected since the fundamental mode remains the most effectively coupled to the carrier profile which would exist at the same current in the absence of lasing. With further increases in current, the region of unsaturated gain can eventually lead to oscillation of a second filament or perhaps to a new, spatially wider but highly distorted, transverse mode. In either case, the onset of stimulated emission from an additional spatial region produces the increased rate

[1] This conclusion is based on the observation [15] that the zero-bias capacitance of the 12-μm laser was 66 pF, while the capacitance of the 8-μm device was only 18 pF.

[2] Note that any process which leads to a gain maximum not coincident with the maximum intensity could produce this motion provided it is close enough to the field.

of optical emission usually observed to follow a range of saturated or decreasing optical output (for example, see Fig. 1). The onset of lasing in a second filament can account for the broadened spectra of longitudinal modes which sometimes accompany the nonlinear output characteristic [5].

Incomplete saturation along the width of the electrically active stripe can account for at least some of the observed nonlinearity in the current-dependence of the light intensity. Since a portion of each increment in current goes to increasing the carrier density in the unsaturated region, the differential efficiency of the output characteristic must decrease. However, diversion of all additional current (which is unlikely) would produce a saturation of the output power but not the decreasing output which is frequently observed (see Fig. 1).

One feature of the nonlinear output characteristic which is especially difficult to understand is the commonly observed inequality of the outputs from opposite ends of the laser. As illustrated in Fig. 1, the asymmetry can sometimes be so pronounced that the output from one mirror increases while the output from the other end is decreasing. Asymmetric behavior of this nature cannot be explained by any nonuniform distribution of loss (or gain) or scattering within the active medium unless the loss depends on the propagation direction of the field or the scattering produces a substantial reflection back into the propagating mode of the waveguide. However, the possibility that the asymmetry originates at the mirrors cannot be neglected. For example, the extent to which lasing energy is coupled asymmetrically into radiation modes at the mirrors may become significant as aperturing and spatial distortion[3] of the optical field are introduced by its interaction with the edge of the stripe. Unfortunately, the experimental observations made thus far provide no clue as to the origin of this asymmetry.

IV. Conclusion

In this work, we have described significant features of the behavior exhibited by stripe-geometry (proton-delineated) (AlGa)As double-heterostructure junction lasers operating continuously in a regime where the intensity of the light output is a nonlinear function of the input current. We find that the development of a nonlinearity in the output characteristic is accompanied by a shift of the lasing optical field toward one boundary of the active stripe and by a cessation of effective gain saturation. The increasing gain is believed to occur primarily in the spatial region where the optical intensity is reduced as a result of the transverse motion of the field. Ineffective saturation is reflected by the observed increases in the junction voltage and in the subthreshold gain of the TM modes as well as by the excitation of additional transverse modes along the junction plane. At sufficiently high currents, the increased local gain can result in oscillation of a second filament or in some devices in a spatially wider but highly distorted transverse mode.

The important question which still awaits a definitive answer concerns the mechanism which causes the optical field to move. In this work, we have discussed this instability with a model in which the lasing field moves transversely in response to incipient distortions of the spatial gain profile produced by the stimulated emission. A significant feature of this interpretation is the implied inability of carrier diffusion to replenish depleted portions of the gain profile rapidly enough in the presence of appreciable stimulated emission. Since the important parameter appears [16] to be the diffusion length compared to the width of the active stripe, the improved saturation and linearity obtained by reducing the stripe width from 12 μm to 8 μm is reasonable. In addition the fact that nonlinearities do appear with the 8-μm stripes although at much higher power levels tends to support the conjecture that diffusion is the important factor in the improvement rather than the increased optical guidance provided by the narrower stripe. This observation also supports the conclusion that the process intimately involves a nonlinear interaction between the stimulated emission and the gain.

The relative importance of diffusion may also explain other observed properties of the nonlinearities. For example, the observation [2] that the critical output power at which a nonlinearity occurs tends to increase slightly with increasing temperature is consistent with a weakly increasing diffusion length. Furthermore, decreases in the linearity of the characteristic which sometimes occur during accelerated aging may be reflecting a change in the diffusion length. It seems reasonable to suspect that anything [19] which contributes to a decreased diffusion length will lead to a reduction of the optical power at which nonlinearities appear.

An alternative to making the width of the active region comparable to a diffusion length is to utilize a structure in which the optical field saturates the active medium uniformly. The utility of this approach has already been demonstrated for the direction perpendicular to the junction plane [9]. For the direction parallel to the stripe width, a structure which potentially allows uniform saturation is the buried heterostructure [20]. With this configuration, improved saturation may be obtained by allowing the optical field to spread out in both transverse directions beyond the gain region.

[3] As illustrated in Fig. 4, the distortion of the field can be different at each mirror.

Acknowledgment

The author is grateful to J. F. Svacek for his technical assistance, W. B. Joyce and F. R. Nash for useful discussions, and to R. W. Dixon and B. C. De Loach, Jr., for helpful comments on the manuscript.

References

[1] B. W. Hakki and C. J. Hwang, "Mode control in GaAs large-cavity double-heterostructure lasers," *J. Appl. Phys.*, vol. 45, pp. 2168–2173, May 1974.

[2] R. L. Hartman and R. W. Dixon, "Reliability of DH GaAs lasers at elevated temperatures," *Appl. Phys. Lett.*, vol. 26, pp. 239–242, Mar. 1975.

[3] T. L. Paoli, "Noise characteristics of stripe-geometry double-heterostructure junction lasers operating continuously–I. Intensity noise at room temperature," *IEEE J. Quantum Electron.*, vol. QE-11, pp. 276–283, June 1975.

[4] T. Kobayashi and Y. Furukawa, "Temperature distributions in the GaAs–AlGaAs double-heterostructure laser below and above the threshold current," *Jap. J. Appl. Phys.*, vol. 14, pp. 1981–1986, Dec. 1975.

[5] R. W. Dixon, F. R. Nash, R. L. Hartman, and R. T. Hepplewhite,

"Improved light-output linearity in stripe-geometry double-heterostructure (Al, Ga)As lasers," *Appl. Phys. Lett.*, Sept. 15, 1976.
[6] R. L. Hartman, Private communication.
[7] I. Hayashi, M. B. Panish, P. W. Foy, and S. Sumski, "Junction lasers which operate continuously at room temperature," *Appl. Phys. Lett.*, vol. 17, pp. 109–111, Aug. 1970.
[8] J. C. Dyment, L. A. D'Asaro, J. C. North, B. I. Miller, and J. E. Ripper, "Proton-bombardment formation of stripe-geometry heterostructure lasers for 300 K CW operation," *Proc. IEEE*, vol. 60, pp. 726–728, June 1972.
[9] T. L. Paoli, "Saturation behavior of the spontaneous emission from double-heterostructure junction lasers operating high above threshold," *IEEE J. Quantum Electron.*, vol. QE-9, pp. 267–272, Feb. 1973.
[10] T. L. Paoli and P. A. Barnes, "Saturation of the junction voltage in stripe-geometry (AlGa)As double-heterostructure junction lasers," *Appl. Phys. Lett.*, vol. 28, pp. 714–716, June 1976.
[11] P. A. Barnes and T. L. Paoli, "Derivative measurements of the current-voltage characteristics of double-heterostructure junction lasers," *IEEE J. Quantum Electron.*, vol. QE-12, pp. 633–639, Oct. 1976.
[12] T. L. Paoli, J. E. Ripper, and T. H. Zachos, "Resonant modes of GaAs junction lasers–II: High-injection level," *IEEE J. Quantum Electron.*, vol. QE-5, pp. 271–276, June 1969.
[13] Details of this system will be reported separately.
[14] Statistical evidence for this conclusion is presented in [5].
[15] F. R. Nash, Y. P. Lai, and H. M. Marcos, private communication.
[16] B. W. Hakki, "GaAs double heterostructure lasing behavior along the junction plane," *J. Appl. Phys.*, vol. 46, pp. 292–302, Jan. 1975.
[17] See also D. D. Cook and F. R. Nash, "Gain-induced guiding and astigmatic output beam of GaAs lasers," *J. Appl. Phys.*, vol. 46, pp. 1660–1672, Apr. 1975 and reference [18].
[18] This point has been emphasized by F. R. Nash, "Mode guidance parallel to the junction plane of double-heterostructure GaAs lasers," *J. Appl. Phys.*, vol. 44, pp. 4696–4707, Oct. 1973.
[19] For example, an increase in the nonradiative recombination.
[20] T. Tsukada, "Buried-heterostructure injection lasers," *J. Jap. Soc. of Appl. Phys.* (Suppl.), vol. 44, pp. 33–37, 1975.

Correspondence

Arc-Assisted Electric Discharges in High-Pressure Carbon Monoxide Gas Mixtures

R. A. CRANE, A. K. GHOSH, AND S. Y. K. TAM

Abstract—**Continuous arc-assisted electric discharges have been obtained in CO-Ar and CO-N_2-Ar gas mixtures at pressures of about 0.1 atm and with maximum discharge loadings of 7.9 and 23 kW/mole/s, respectively. The discharge technique appears suitable for adaptation to CW, high-power CO lasers.**

The substitution of helium by argon as the gas dilutent in CW, high-pressure, electric discharge CO lasers is desirable from the point of view of output efficiency [1]. This is due to the considerably longer CO vibrational lifetimes that can be obtained with Ar [2], [3]. However, in this case a greater tendency for discharge instability would be expected because of the order of magnitude lower thermal conductivity of Ar. Reported here are some exploratory discharge results in 0.1-atm mixtures of CO-Ar and CO-N_2-Ar using the arc-assisted discharge technique that was successfully applied to CO_2 laser gas mixtures [4]. In this technique a mix of thermal electrons and metastables injected from an arc source provides the independent preionization for a sustainer-type discharge in the main gas flow. Although the details of the preionization mechanism are not completely understood, it appears that metastable coupling to the electrons is a necessary feature to account for the long preionization lengths and discharge uniformity observed in both the previous [4] and present work.

Manuscript received April 9, 1976; revised July 29, 1976.

The authors are with the Research and Development Laboratories, RCA, Ltd., Ste. Anne de Bellevue, P.Q., Canada, H9X 3L3.

The arc source-discharge module, used in the present experiments, is depicted schematically in Fig. 1. The apparatus is the same as that used in previous CO_2 work [4], but with the vortex-stabilized argon arc in-line with the flow tube and a brass ring insert as the anode for the main dc supply. The glass flow tube was 1 in in diameter and the main discharge gap was fixed at 20 cm. The experiments were confined to the testing of two gas mixtures, $CO:N_2:Ar = 5.25:70$ and $CO:Ar = 10:90$, at flow rates to 10 mlb/s and pressures in the vicinity of 0.1 atm. The gas mixtures were premixed from high-purity-grade components (e.g., 99.5-percent-pure CO) and supplied in regular, high-pressure, steel cylinders. There was no gas preconditioning such as gas purification or precooling and the mixture was injected subsonically through an orifice surrounding the arc face. The discharge voltage was continuously displayed on a chart recorder with the x axis driven by the discharge current. Discharge runs were typically of 20-s duration with the uniformity assessed visually.

Continuous discharge characteristics for the triple mixture at a flow rate of 5 mlb/s (0.064 mole/s) and pressure of 85–90 torr are shown in Fig. 2 for three parametric values of arc input power. Control of the discharge by the arc source is reflected in a decreasing voltage requirement as arc power is increased from 1 to 3 kW and the fact that the discharge can be turned on or off with the arc.

The reduction in discharge loading scales only to about 10 percent with the increase in arc power, but the assessment of

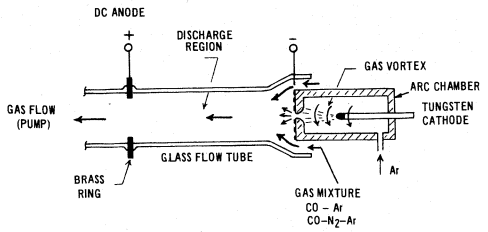


Fig. 1. Schematic of arc-preionization source-discharge module.

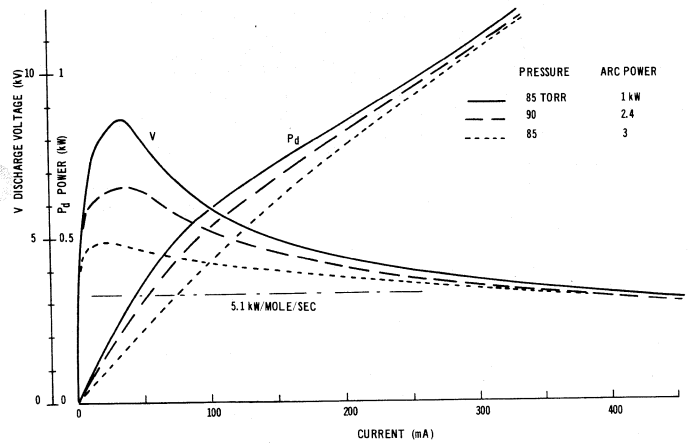


Fig. 2. Discharge voltage and loading characteristic for three values of arc input power. Gas mixture of $CO:N_2:Ar = 5:25:70$, 5-mlb/s flow rate, discharge length 20 cm, arc carrier gas Ar at 0.5 mlb/s.

this factor would have to be correlated to gain measurements which were not performed here. The 5.1-kW/mole/s reference line in Fig. 2 is the greatest reported CW discharge loading [5] and is expressed in terms of moles/second in order to compare different gas mixtures. This reference was easily surpassed with stable discharges run to the limit of the power supply, 500 mA, at which point a discharge loading of more than 23 kW/mole/s was achieved. A photograph of a typical arc-assisted discharge is shown in Fig. 3. The stability or uniformity of the discharge was qualified, visually, in terms of the absence of bright (arc) filaments and on the longitudinal and transverse uniformity of color and intensity of the plasma between the electrodes.

Fig. 4 shows the comparative difference in voltage profile when the arc gas flow is increased from 0.5 to 3 mlb/s. In the latter case the arc power requirement is reduced with 800 W being the lowest operational value for this particular arc source. In both cases a uniform discharge to the current limit of the supply was achieved with a maximum loading in excess of 15 kW/mole/s for a gas flow of 10 mlb/s.

For the $CO:Ar = 10:90$ gas mixture the results were not as successful with large-scale arc filaments occurring at some point in the discharge scans. These filaments were not disruptive of the chart trace, as was experienced with CO_2 mixtures [4], and the run could be continued to the power supply limit. Fig. 5 displays the characteristics for this mixture at a flow rate of 10 mlb/s (0.117 mole/s). For an arc gas flow of 0.5 mlb/s the voltage profile is similar to that of Fig. 2, but with an onset of arc formation just beyond the voltage rolloff. Increasing the arc power to 3 kW had little effect on the profile or the point where the arcing occurred. However, with the arc source configured for 3-mlb/s Ar flow and 800 W, the voltage assumes a profile similar to that in Fig. 4 with arcing now being initiated at a considerably greater discharge current. The maximum uniform discharge load in this case is about 7.9 kW/mole/s, a value still greater than the reference.

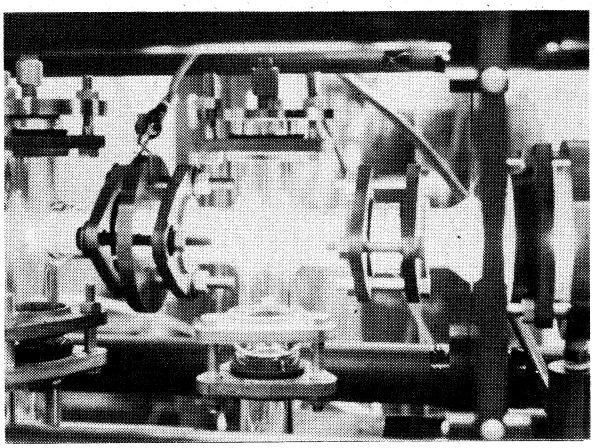


Fig. 3. Photograph of arc-assisted discharge. $CO:N_2:Ar = 5:25:70$, 10 mlb/s, 85 torr, 20-cm discharge gap.

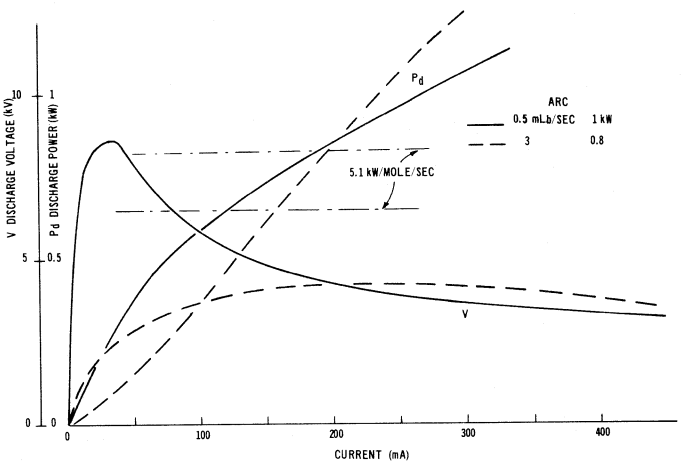


Fig. 4. Discharge characteristics for two sets of arc gas flow, power values. Gas mixture of $CO:N_2:Ar = 5:25:70$, 10 mlb/s, 85-torr pressure, and 20-cm discharge gap.

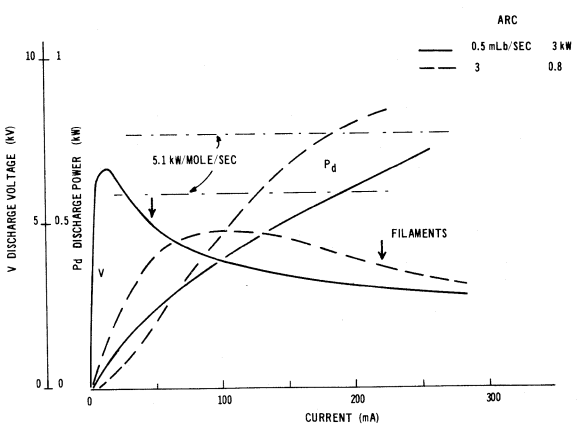


Fig. 5. Discharge characteristics for two sets of arc gas flow, power values. Gas mixture of $CO:Ar = 10:90$, 10 mlb/s, 75-torr pressure, and 20-cm discharge gap.

The carrier of the preionization has been proposed in terms of long-lived nitrogen metastables [4] and appears to be supported by the present results with the $CO–N_2–Ar$ gas mixture. In this case there was no difficulty in obtaining stable discharges with any of the arc source parameters used. As the limiting factor was the power supply, the full capability

in terms of discharge loading and gas flow rate, for this particular arc configuration, was not reached. Based on this and previous study it is expected that the arc source requirements can be reduced to less than 1 percent of the total gas flow and about 10 percent of the total system energy.

Without the presence of nitrogen in the CO–Ar mixture, the possibility of other (and shorter lived) metastables such as those of CO is proposed as the preionization carrier component. The situation with this mixture indicates a more restrictive balance between the arc power and arc gas flow. With a more proper arc source configuration one can expect somewhat similar achievements as obtained with the triple mixture.

The present experiments indicate potential for the arc-assisted electric discharge technique for high-pressure CO lasers. The preionization component is small, rugged, simple to operate, and does not require vacuum or high-voltage features. As this method has now been demonstrated for two different laser gas mixtures (CO_2 and CO) one can anticipate that this technique will also prove adaptable to other high-pressure laser systems as well, and consequently would be of interest for further study and development.

ACKNOWLEDGMENT

The technical assistance of M. Fossiez and the support of Dr. M. P. Bachynski is gratefully acknowledged.

REFERENCES

[1] C. C. Chen, "A quantitative theory of an electron-beam-excited carbon monoxide gas dynamic laser: 1. Formulation," United States Air Force Project Rand Rep. R-1321-PR, Oct. 1973, p. 54.

[2] D. J. Miller and R. C. Millikan, "Vibrational relaxation of carbon monoxide by hydrogen and helium down to 100°K," *J. Chem. Phys.* (Letters), vol. 53, pp. 3384–3385, 1970.

[3] R. C. Millikan and D. R. White, "Systematics of vibrational relaxation," *J. Chem. Phys.*, vol. 39, 3209–3212, 1963.

[4] R. A. Crane, A. K. Ghosh and S. Y. K. Tam, "Arc-assisted electric discharge technique for high pressure, CW, CO_2 lasers," *J. Appl. Phys.*, vol. 47, July 1976.

[5] T. Kan and W. Whitney, "Forced-convection-flow carbon monoxide laser," *Appl. Phys. Lett.*, vol. 21, pp. 213–215, 1972.

Notes and Lines

New Infrared Laser Transitions in Ag II

R. D. REID, W. L. JOHNSON, J. R. McNEIL, AND G. J. COLLINS

Abstract—**We have observed seven infrared laser transitions when exciting a He discharge in a silver hollow cathode. To our knowledge, five of the seven laser transitions have not been reported previously in the literature.**

Karabut [1] has reported infrared laser action on 2 transitions of Ag II, and more recently we have reported laser action on 31 laser lines of Ag II in the visible and the ultraviolet regions of the spectrum [2], [3]. We have extended our studies [2], [3] into the infrared region and have observed 5 new infrared laser transitions as well as achieving laser action on the 800.5- and 840.4-nm transitions, previously reported by Karabut [1], for a total of 7 infrared laser transitions. The upper and lower laser levels of two of these infrared transitions are shown in Fig. 1.

Table I lists all 7 infrared laser transitions observed, as well as the tentative transition assignments; CW laser action was obtained on all transitions. Because the identification of the silver spectrum is at present incomplete, we are able to *unambiguously* identify only 5 of the 7 laser transitions and the remaining 2 laser transitions are listed as "unidentified." Threshold currents for all laser transitions are given in Table I.

Manuscript received July 26, 1976. This work was supported in part by the Office of Naval Research, and in part by NASA (Lewis). This work was submitted in partial fulfillment of the requirements of the M.S. degree (W.L.J. and R.D.R.) and the Ph.D. degree (J.R.M.) at Colorado State University. J.R.M. and R.D.R. hold ERDA traineeships (Oak Ridge).

The authors are with the Department of Electrical Engineering, Colorado State University, Fort Collins, CO 80523.

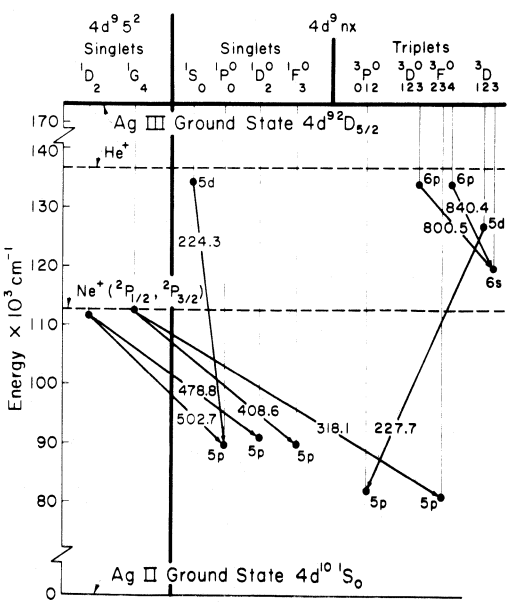


Fig. 1. A partial term diagram of Ag II indicating wavelengths of Ag II laser transitions and transition assignments. Wavelengths are given in nanometers.

It is noteworthy that the cathode fall in our device is only 250 V at 6 A, and the observed threshold currents for most of the laser transitions are below 3 A.

A silver hollow cathode of rectangular cross section (2 × 6 mm) and 50 cm in length was used to provide the active medium. This device has been described elsewhere [2], [3]. Discharge sputtering provides the silver density required for laser action. Although laser action was obtained in pure helium discharges

TABLE I
INFRARED LASER TRANSITIONS OF Ag II AND TENTATIVE LEVEL ASSIGNMENTS

λ_{air} (nm)		Transition Assignment[a]		Threshold Current[b] (A)
Measured ± 0.02 nm	Actual	Upper	Lower	
840.39[c]	8403.18	$6p\,^3F^0_4$	$6s\,^3D_3$	1.6
832.48	8324.4	$6p\,^3D^0_2$	$6s\,^3D_2$	2.4
825.47	825.47	$6p\,^3D^0_3$	$6s\,^3D_2$	3.2
800.50[c]	8005.4	$6p\,^3D^0_3$	$6s\,^3D_3$	1.4
720.45		Unidentified		1.7
660.38		Unidentified		6.0
640.43	640.27	$6p\,^3F^0_2$	$6s\,^3D_2$	1.6

[a] Identification from [4].
[b] Thresholds measured using 15 torr of He and 0.1 torr of Ar excited in a silver hollow cathode of rectangular cross section (2 × 6 mm).
[c] Previously reported by Karabut *et al.* [1].

excited in the silver hollow cathode it was found that the addition of small amounts of argon increased output power and reduced current thresholds, presumably by increasing the discharge sputtering yield [5]. Laser action occurred only with helium discharges; no laser action occurred with neon, argon, or krypton discharges.

Peak output power of 250 mW has been obtained from the 840.4-nm transition using aluminum mirrors of 90-percent reflectance (total loss of 20 percent) peaked in the 840.4-nm region. Peak power was obtained using a 200-μs-long current pulse, at a peak current of 50 A, the limit of our pulse generator. The output power of 250 mW was calculated by measuring average output power (2 mW), and dividing by the duty cycle (0.008). The output power of the 840-nm transition does not appear to saturate with increasing current. It is also noteworthy that the 840.4-nm transition possesses remarkably high gain since laser action can be obtained using a high-reflectance mirror together with an output mirror of 60-percent transmittance. The estimated gain of the 840.4-nm transition is ≈ 1 percent cm^{-1}.

REFERENCES

[1] E. K. Karabut, V. K. Kravchenko, and V. F. Papakin, "Excitation of the Ag II lines by a pulsed discharge in a mixture of silver vapor and helium," *Sov. Phys.-Tech. Phys.*, vol. 14, p. 1447, 1970.
[2] W. L. Johnson, J. R. McNeil, G. J. Collins, and K. B. Persson, "CW laser action in the blue-green spectral region from Ag II," *Appl. Phys. Lett.*, vol. 29, p. 101, 1976.
[3] J. R. McNeil, W. L. Johnson, G. J. Collins, and K. B. Persson, "Ultraviolet laser action in He-Ag and Ne-Ag mixtures," *Appl. Phys. Lett.*, vol. 29, p. 172, 1976.
[4] W. P. Gilbert, "Some higher terms in the spectrum of Ag II," *Phys. Rev.*, vol. 47, pp. 847–850, 1935.
[5] N. Laegreid and G. K. Wehner, "Sputtering yields of metals for Ar^+ and Ne^+ with energies from 50 to 600 eV," *J. Appl. Phys.*, vol. 32, p. 365, 1961.

Contributors

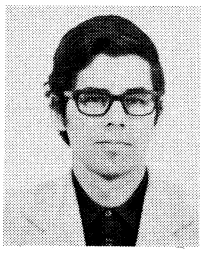


Joji Hamasaki (M'62) was born in Hiroshima, Japan, on October 25, 1931. He received the B.S., M.S., and Ph.D. degrees in electrical engineering from the University of Tokyo, Tokyo, Japan.

He has been with the Institute of Industrial Science, University of Tokyo, since 1958, and he is currently Professor of Communication Apparatus. From 1961 to 1963 he visited Bell Laboratories, Murray Hill, NJ, on leave of absence from the Institute. He has been working in the areas of microwave circuitry, microwave applications of solid-state devices, laser circuitry, and 3-D imaging and its transmission. He has also been engaged in the development of tracking radar systems for the satellite launching project of Japan.

Dr. Hamasaki is a member of the Institute of Electrical Engineers of Japan and the Institute of Electronics and Communication Engineers of Japan.

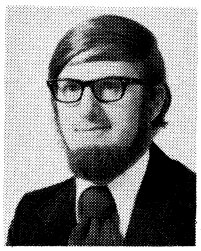
*



Jean-Louis Lachambre received the B.Sc.A. and M.Sc.A. degrees in physics from the Polytechnic School, Montreal, P.Q., Canada, in 1965 and 1967, respectively. In 1974 he received the Ph.D. degree in physics from Laval University, Quebec, P.Q., Canada.

In 1967 he joined the Defence Research Establishment Valcartier, Department of National Defence, Courcelette, Canada, where he was initially involved in the development of infrared detectors. Since 1969 he has been working in the field of molecular gas lasers. He is currently Leader of the Laser Technology Group, and his research work is concerned with CO_2 lasers and their applications to military technology.

*



Pierre Lavigne received the B.Sc. degree in physics from Laval University, Quebec, P.Q., Canada, in 1968, and the M.Sc. and Ph.D. degrees in 1970 and 1976.

He joined the Electro-Optic Division at the Defence Research Establishment Valcartier, Department of National Defence, Courcelette, P.Q., Canada, in 1973. He participated in the development of CO_2 short-pulse amplifier chains at Laval University and at DREV. His research activities have centered around TEA lasers, saturable absorbers and unstable optical resonators.

He is a member of the Optical Society of America.

*

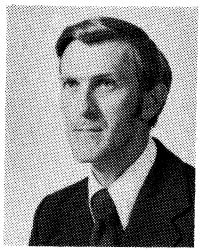


Toshio Makimoto (M'56) was born in Hiroshima, Japan, on August 30, 1916. He received the B.Eng. and D.Eng. degrees from the Tokyo Institute of Technology, Tokyo, Japan, in 1941 and 1956, respectively.

In 1941 he was employed by the Mitsubishi Electric Co., Amagasaki, Japan. From 1942 to 1945 he served in the army. In 1946 he joined the Institute of Scientific and Industrial Research, Osaka University, Osaka, Japan, and became a Professor in 1960. Since 1964 he has been with the Faculty of Engineering Science, Osaka University, as a Professor of Electrical Engineering. He has been engaged in research on microwave and millimeter-wave circuits and antennas, laser applications, integrated and fiber optics, and microwave acoustics. He is the author of four books on microwave electronics and high-frequency measurements.

Dr. Makimoto is a member of the Institute of Electrical Engineers of Japan, the Institute of Electronics and Communication Engineers of Japan, and the Institute of Television Engineers of Japan.

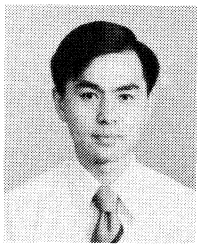
*



Michel Noël was born in St-Rédempteur, P.Q. Canada, in 1944. He graduated from the Institut de Technologie de Québec, P.Q., Canada, in 1964.

He then joined the Defence Research Establishment Valcartier, Department of National Defence, Courcelette, P.Q., Canada. He has been involved in microwave spectroscopy, and has worked on ruby and CO_2 lasers. He has taken part in the development of the first TEA-CO_2 lasers. He is currently engaged in frequency-stabilized and waveguide TEA-CO_2 lasers.

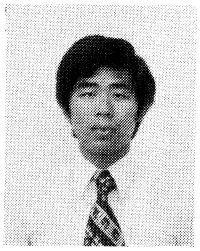
*



Kiyoshi Nosu was born in Gifu, Japan, on June 19, 1949. He received the B.S. degree in electrical engineering from Keio University, Tokyo, Japan, in 1972, and the M.S. degree in electronics engineering from the University of Tokyo, Tokyo, Japan, in 1974. He is currently interested in integrated optical circuitry.

Mr. Nosu is a member of the Institute of Electronics and Communication Engineers of Japan and the Japan Society of Applied Physics.

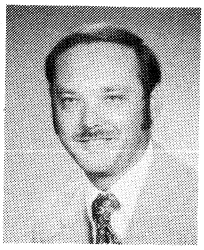
*



Yasuyuki Okamura (S'75) was born in Osaka, Japan, on September 11, 1950. He received the B.Eng. and M.Eng. degrees in electrical engineering from Osaka University, Osaka, Japan, in 1973 and 1975, respectively. He has been working toward the Ph.D. degree in electrical engineering at Osaka University; his current research interest is in the area of integrated optics.

Mr. Okamura is a member of the Institute of Electronics and Communication Engineers of Japan.

*



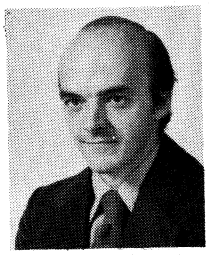
Gregory R. Osche was born in Butler, PA, on May 26, 1942. He received the B.S. degree in physics from Villanova University, Villanova, PA, in 1964, the M.S. degree in physics from Monmouth College, West Long Branch, NJ, in 1970 and the Ph.D. in physics from the Polytechnic Institute of New York, Farmingdale, NY, in 1975. His Ph.D. dissertation was theoretical involving the nonrelativistic limit of the Dirac theory of the electron.

He is currently with the U.S. Army Elec-

tronics Command, Fort Monmouth, NJ investigating CO_2 and chemical lasers for Army rangefinder/designator applications.

Dr. Osche is a member of Sigma Xi and the American Physical Society.

*



Gabriel Otis was born in Baie-St-Paul, P.Q., Canada, on November 16, 1944. He received the B.S. and Ph.D. degrees in physics, both from Université Laval, Québec, P.Q., Canada, in 1968 and 1973, respectively.

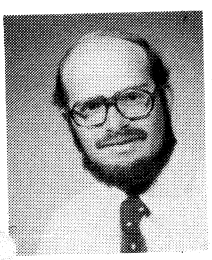
After working for a year at the Centre de Recherche Industrielle du Québec, P.Q., Canada, he joined the Defence Research Establishment Valcartier, Department of National Defence, Courcelette, P.Q., Canada, where he is currently doing research on the diffraction of laser beams and on UV preionization.

He is a member of the Optical Society of America.

*

Thomas L. Paoli (S'59-M'73), for a photograph and biography please see page 651 of the October 1976 issue of this JOURNAL.

*

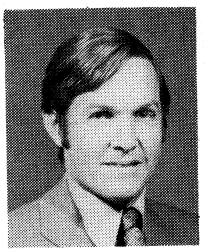


Henry E. Sonntag was born in New York, NY, on March 20, 1947. He received the B.S. and M.S. degrees in physics from the Polytechnic Institute of Brooklyn, New York, NY, in 1969 and 1972, respectively. He is currently pursuing the Ph.D. degree at the Stevens Institute of Technology, Hoboken, NJ.

In 1972 he joined the U.S. Army Electronics Command, Ft. Monmouth, NJ, where he worked primarily in optical countermeasures. He has been engaged in experimental research in CO_2 TEA lasers, optical heterodyne detection, and is currently engaged in experiments on polarization and ultraviolet atmospheric transmission.

Mr. Sonntag is a member of the Optical Society of America.

*

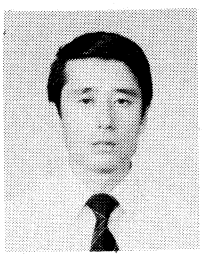


Henry F. Taylor was born in Fort Worth, TX, on September 27, 1940. He received the B.A. and Ph.D. degrees in physics from Rice University, Houston, TX, in 1962 and 1967, respectively. During 1971-72, he studied systems analysis at M.I.T., Cambridge, MA, under a Civil Service Commission fellowship.

He joined the Naval Undersea Research and Development Center, San Diego, CA, in 1967 and transferred to the Naval Electronics Laboratory Center, San Diego, CA, in 1968. From 1968 to 1970 he conducted research in the areas of color center formation in alkali halides and optically pumped semiconductor lasers. Since 1970 he has been engaged in the development of fiber optics communications systems and in research on guided-wave optical devices.

Dr. Taylor was recipient of the Naval Electronics Laboratory Center's Award for Achievement in Science in 1974, and of the American Society of Naval Engineers' Solberg Award for contributions in research and development in 1974. He is a member of the American Physical Society.

*



Sadahiko Yamamoto (S'63-M'67) was born in Osaka, Japan, on February 18, 1940. He received the B.E., M.E. and D.E. degrees in electrical communication engineering from Osaka University, Osaka, Japan, in 1962, 1964 and 1967, respectively, for studies on the transmission and network theory of multiconductor lines.

In 1967 he joined the Department of Electrical Engineering, Faculty of Engineering Science, Osaka University, where he is now an Assistant Professor. His work in that department has been concerned with inhomogeneous optical fibers and, recently, integrated optics.

Dr. Yamamoto is a member of the Institute of Electronics and Communication Engineers of Japan and the Japan Society of Applied Physics.

1976 Index
IEEE Journal of Quantum Electronics
Vol. QE-12

This index covers all items – papers, correspondence, reviews, etc. – that appeared in this periodical during 1977, and items from prior years that were commented upon or corrected in 1977. The index is divided into an Author Index and a Subject Index, both arranged alphabetically.

The *Author Index* contains the primary entry for each item; this entry is listed under the name of the first author and includes coauthor names, title, location of the item, and notice of corrections and comments if any. Cross-references are given from each coauthor name to the name of the corresponding first author. The location of the item is specified by the journal name (abbreviated), year, month, inclusive pages, and microfiche code. [The microfiche code, given in parentheses following the inclusive pages, consists of four characters to be interpreted as follows: the first character identifies the microfiche number within the set of fiches for the issue; the second character identifies the row in which the first frame of the particular item is located; and the last two characters designate the position of that frame within the row.]

The *Subject Index* contains several entries for each item, each consisting of a subject heading, modifying phrase(s), first author's name, and location of the item. For information on coauthors, title, comments and corrections if any, etc., it is necessary to refer to the Author Index. Some generic subject headings are used in this index in addition to the usual technical headings, e.g., *Books*, (books reviewed in this periodical), *Bibliographies* (both papers that are bibliographies and any other papers which contain more than 50 references), *Conferences* (technical meetings a substantial number of whose abstracts or papers have appeared in this periodical), and *Special Issues* (issues of this periodical devoted primarily to a specific subject). The Subject Index includes subject cross-references as required by the subject matter.

AUTHOR INDEX

A

Abrams, R. L., and C. K. Asawa; Direct demodulation of a 10.6μm FM signal with an NH_2D Stark cell (Corresp.); *J-QE 76 Oct* 646-647 (2C03)
Adhav, R. S., *see* Kato, K.; *J-QE 76 Jul* 443-445 (1E13)
Ageno, Harris Y., *see* Jeffers, William Q.; *J-QE 76 Nov* 693-697 (1C11)
Aggarwal, Roshan L., *see* Wolff, Peter A.; *J-QE 76 Aug* 500-504 (1D08)
Ahl, Jeffrey L., and W. R. Binns; A CS_2/O_2 electrochemical, pulsed CO TEA laser; *J-QE 76 Jan* 26-29 (1B14)
Aiki, Kunio, Michiharu Nakamura, and Jun-ichi Umeda; Lasing characteristics of distributed-feedback GaAs–GaAlAs diode lasers with separate optical and carrier confinement; *J-QE 76 Oct* 597-603 (1C11)
Alley, C. O., *see* Singh, Gurbax; *J-QE Feb* 81-82 (1B01)
An, Jyong Chi, Yoshio Cho, and Yukito Matsuo; Proposed wide-band and low-drive-power electrooptic modulators (Corresp.); *J-QE 76 Jul* 445-446 (1F01)
Anderson, L. W., *see* Fitzsimmons, W. A.; *J-QE 76 Oct* 624-633 (2A09)
Anderson, R. S., B. G. Bricks, T. W. Karras, and L. W. Springer; Discharge-heated lead vapor laser (Corresp.); *J-QE 76 May* 313-315 (1D09)
Asawa, C. K., *see* Abrams, R. L.; *J-QE 76 Oct* 646-647 (2C03)
Attwood, D. T., E. S. Bliss, E. L. Pierce, and L. W. Coleman; Laser frequency doubling in the presence of small-scale beam breakup (Corresp.); *J-QE 76 Mar* 203-204 (1C13)
Austin, Stewart, *see* Stone, F. T.; *J-QE 76 Nov* 727-732 (1F03)
Auzel, F.; Oscillator strengths of Nd^{3+} in $Nd_xLa_{1-x}P_5O_{14}$ and concentration quenching in stoichiometric rare-earth laser materials (Corresp.); *J-QE 76 Apr* 258-259 (1D06)
Avivi, P., *see* Keren, H.; *J-QE 76 Jan* 58-60 (1E04)

B

Babcock, Richard V., Irving Liberman, and W. D. Partlow; Volume ultraviolet preionization from bare sparks; *J-QE 76 Jan* 29-34 (1C03)
Baral, S. S., *see* Ray, M.; *J-QE 76 Oct* 561-565 (1A03)
Barnes, Peter A., and Thomas L. Paoli; Derivative measurements of the current–voltage characteristics of double-heterostructure injection lasers; *J-QE 76 Oct* 633-639 (2B04)
Barry, J. D.; Optical design of a frequency-doubled Nd:YAG laser (Corresp.); *J-QE 76 Apr* 254-256 (1D02)
Bass, M., and K. M. Leung; The dependence of the pulsed 10.6-μm laser damage threshold on the manner in which a sample is irradiated (Corresp.); *J-QE 76 Feb* 82-83 (1B02)
Bekkers, Gerhard W., *see* Stappaerts, Eddy A.; *J-QE 76 Jun* 330-333 (1A12)
Bethea, C. G., *see* Levine, B. F.; *J-QE 76 Jun* 367-368 (1D07)
Bezdjian, K., *see* Levine, J. S.; *J-QE 76 Jul* 437-438 (1E07)
Bhattacharyya, D. L., *see* Ray, M.; *J-QE 76 Oct* 561-565 (1A03)
Binns, W. R., *see* Ahl, Jeffrey L.; *J-QE 76 Jan* 26-29 (1B14)
Bletzinger, Peter, *see* Olson, Robert A.; *J-QE 76 May* 316-317 (1D12)
Bliss, E. S., *see* Attwood, D. T.; *J-QE 76 Mar* 203-204 (1C13)
Bliss, E. S., J. T. Hunt, P. A. Renard, G. E. Sommargren, and H. J. Weaver; Effects of nonlinear propagation on laser focusing properties; *J-QE 76 Jul* 402-406 (1B14)
Botez, Dan, *see* Tseng, Cheng-Chung; *J-QE 76 Sep* 549-551 (1C03)
Bousek, Ronald R., *see* Seely, John F.; *J-QE 76 Aug* 515-517 (1E09)
Brechignac, P., and J. P. Martin; Extension of the CW CO–N_2–He laser capabilities (Corresp.); *J-QE 76 Feb* 80-81 (1A14)
Brederlow, G., K. J. Witte, Ernst Fill, K. Hohla, and R. Volk; The Asterix III pulsed high-power iodine laser; *J-QE 76 Feb* 152-155 (2E10)
Bricks, B. G., *see* Anderson, R. S.; *J-QE 76 May* 313-315 (1D09)
Brueck, S. R. J., and A. Mooradian; External cavity CO_2-pumped InSb spin-flip laser (Corresp.); *J-QE 76 Mar* 201-202 (1C11)
Burkes, T. R., *see* Bushnell, A. H.; *J-QE 76 Jul* 447 (1F03)
Burnham, R. D., *see* Streifer, W.; *J-QE 76 Nov* 737-739 (1F13)
Burnham, Robert D., *see* Streifer, William; *J-QE 76 Feb* 74-78 (1A08)
Burnham, Robert D., *see* Streifer, William; *J-QE 76 Mar* 177-182 (1B01)
Burnham, Robert D., *see* Streifer, William; *J-QE 76 Jul* 422-428 (1D06)
Burnham, Robert D., *see* Streifer, William; *J-QE 76 Aug* 494-499 (1D02)
Bushnell, A. H., and Martin Gundersen; New far-infrared laser lines in $N^{15}H_3$ (Note); *J-QE 76 Apr* 260-261 (1D08)
Bushnell, A. H., M. Gundersen, and T. R. Burkes; *J-QE 76 Jul* 447 (1F03)
Comments on Tulip, John, Herb J. Seguin, and Wayne Faszer; High-repetition-rate TEA-laser discharge using integrated preionization and switching; *J-QE 76 Feb* 155-159 (2E13)
Butler, Jerome K., and Chung-Shu Wang; Threshold behavior of CW GaAs–AlGaAs injection lasers; *J-QE 76 Mar* 165-168 (1A03)
Byer, Robert L.; A 16-μm source for laser iostope enrichment (Corresp.); *J-QE 76 Nov* 732-733 (1F08)

C

Capelle, Gene A., and Steven N. Suchard; CN* production efficiencies from active nitrogen–hydrocarbon flames; *J-QE 76 Jul* 417-421 (1D01)
Carpenter, J. P., *see* Getzinger, R. W.; *J-QE 76 Sep* 556-558 (1C10)
Chang, T. Y., and J. D. McGee; Millimeter and submillimeter-wave laser action in symmetric top molecules optically pumped via perpendicular absorption bands (Note); *J-QE 76 Jan* 62-65 (1E08)
Chen, Bor-Uei, *see* Ghizoni, Cesar C.; *J-QE 76 Feb* 69-73 (1A03)
Chen, T. S., and W. P. White; Second-harmonic generation in $KB_5O_8{\cdot}4H_2O$ (Corresp.); *J-QE 76 Jul* 436-437 (1E06)
Cherlow, J. M., T. T. Yang, and R. W. Hellwarth; Nonlinear optical susceptibilities of solvents (Corresp.); *J-QE 76 Oct* 644-646 (2C01)
Cherrington, B. E., *see* Eden, J. G.; *J-QE 76 Nov* 698-704 (1D02)
Chinn, Stephen R., Henry Y-P. Hong, and James W. Pierce; Spiking oscillations in diode-pumped NdP_5O_{14} and $NdAl_3(BO_3)_4$ lasers; *J-QE 76 Mar* 189-193 (1B13)
Cho, Yoshio, *see* An, Jyong Chi; *J-QE 76 Jul* 445-446 (1F01)
Chodzko, Richard A., David J. Spencer, Harold Mirels, Stephen B. Mason, and David H. Ross; Zero-power-gain measurements in CW HF(DF) laser by means of a fast scan technique; *J-QE 76 Nov* 660-664 (1A06)
Claspy, P. C., and K. P. Koo; Stark effect applicable to optically pumped far-infrared laser (Corresp.); *J-QE 76 Oct* 647-649 (2C04)
Clements, W. R. L., *see* Waksberg, A. L.; *J-QE 76 Nov* 734-736 (1F10)
Cohen, Steven C.; Waveguide CO_2 laser gain: Dependence on gas kinetic and discharge properties; *J-QE 76 Apr* 237-244 (1B13)
Coleman, L. W., *see* Attwood, D. T.; *J-QE 76 Mar* 203-204 (1C13)
Collins, G. J., *see* McNeil, J. R.; *J-QE 76 Jun* 371-372 (1D11)
Collins, G. J., *see* Reid, R. D.; *J-QE 76 Dec* 778-779 (1C08)
Copeland, Drew A., H. Mahr, and Chung L. Tang; Threshold and rate equation considerations for a H^+–Cs charge-exchange laser; *J-QE 76 Nov* 665-673 (1A11)
Crane, R. A., A. K. Ghosh, and S. Y. K. Tam; Arc-assisted electric discharges in high-pressure carbon monoxide gas mixtures (Corresp.); *J-QE 76 Dec* 776-778 (1C06)
Culick, F. E. C., P. I. Shen, and W. S. Griffin; Acoustic waves and heating due to molecular energy transfer in an electric discharge CO laser; *J-QE 76 Oct* 566-574 (1A08)

D

Daiber, John W., Herbert M. Thompson, and T. J. Falk; The efficiency of CO vibrational excitation in a self-sustained CW glow discharge; *J-QE 76 Nov* 686-693 (1C04)
Dalgoutte, D. G.; *J-QE 76 Nov* 736-737 (1F12)
Comments, with author's reply, on Ghizoni, Cesar C.; Theory and experiments on grating couplers for thin-film waveguides; *J-QE 76 Feb* 69-73 (1A03)
Danielewicz, Edward J., *see* DeTemple, Thomas A.; *J-QE 76 Jan* 40-47 (1C14)

Danielsel, Magnus; A theoretical analysis for gigabit/second pulse code modulation of semiconductor lasers; *J-QE 76 Nov* 657-660 (1A03)
Davies, Richard W., and James N. Walpole; Output coupling for closely confined $Pb_{1-x}Sn_xTe$ double-heterostructure lasers; *J-QE 76 May* 291-303 (1C01)
Davis, Christopher C., Robert J. Pirkle, Ross A. McFarlane, and George J. Wolga; Output mode spectra, comparative parametric operation, quenching, photolytic reversibility, and short-pulse generation in atomic iodine photodissociation lasers; *J-QE 76 Jun* 334-352 (1B02)
DeTemple, Thomas A., and Edward J. Danielewicz; Continuous-wave CH_3F waveguide laser at 496 μm: Theory and experiment; *J-QE 76 Jan* 40-47 (1C14)
Deutsch, Thomas F., *see* Kildal, Helge; *J-QE 76 Jul* 429-435 (1D13)
Deutschbein, Otto K. F.; A simplified method for determination of the induced-emission cross section of neodymium doped glasses (Corresp.); *J-QE 76 Sep* 551-554 (1C05)
Dewey, C. Forbes, Jr., *see* Oettinger, Peter E.; *J-QE 76 Feb* 95-101 (2A09)
Dewey, Harry J.; Second-harmonic generation in $KB_5O_8 \cdot 4H_2O$ from 217.1 to 315.0 nm; *J-QE 76 May* 303-306 (1C13)
Diels, Jean-Claude, and Erwin L. Hahn; Pulse propagation stability in absorbing and amplifying media; *J-QE 76 Jul* 411-416 (1C09)
Dienes, A., *see* Teschke, O.; *J-QE 76 Aug* 513-515 (1E07)
Dienes, Andrew, *see* Teschke, O.; *J-QE 76 Jul* 383-395 (1A09)
DiLavore, P., *see* Singh, Gurbax; *J-QE Feb* 81-82 (1B01)
Dothan, F., *see* Keren, H.; *J-QE 76 Jan* 58-60 (1E04)

E

Eddleman, H. E., *see* Manes, Kenneth R.; *J-QE 76 May* 265-273 (1A03)
Eden, J. G., B. E. Cherrington, and J. T. Verdeyen; Optical absorption and fluorescence studies in high-pressure cesium-xenon mixtures; *J-QE 76 Nov* 698-704 (1D02)
Eesley, G. L., *see* Levenson, M. D.; *J-QE 76 Apr* 259-260 (1D07)
Eesley, G. L., and M. D. Levenson; Dye-laser cavity employing a reflective beam expander (Corresp.); *J-QE 76 Jul* 440-442 (1E10)
Elliott, Richard A., *see* Massey, Gail A.; *J-QE 76 Feb* 143-147 (2E01)
Emanuel, George, W. G. Gaskill, R. J. Reiner, C. Shelton, and W. Watkins; High-pressure operation of a CS DF–CO_2 transfer laser (Corresp.); *J-QE 76 Nov* 739-740 (1G01)
Ettenberg, Michael, Henry Kressel, and James P. Wittke; Very high radiance edge-emitting LED; *J-QE 76 Jun* 360-364 (1C14)

F

Fahlen, Theodore S.; Self-heated, multiple–metal–vapor laser (Corresp.); *J-QE 76 Mar* 200-201 (1C10)
Falk, T. J., *see* Daiber, John W.; *J-QE 76 Nov* 686-693 (1C04)
Faszer, Wayne, *see* Tulip, John; *J-QE 76 Feb* 155-159 (2E13)
Fill, Ernst, *see* Brederlow, G.; *J-QE 76 Feb* 152-155 (2E10)
Fink, H. J.; Propagation of waves in optical waveguides with various dielectric and metallic claddings (Corresp.); *J-QE 76 Jun* 365-367 (1D05)
Firth, William J., Brian S. Wherrett, and D. Weaire; Theory of spin-flip laser modes—Part I: Threshold modulation and tuning behavior; *J-QE 76 Apr* 218-225 (1A08)
Fitzsimmons, W. A., L. W. Anderson, C. E. Riedhauser, and Jan M. Vrtilek; Experimental and theoretical investigation of the nitrogen laser; *J-QE 76 Oct* 624-633 (2A09)
Flicker, Herbert, and Norris Nereson; Increased tuning range of $Pb_{1-x}Sn_xSe$ diode lasers using small magnetic fields; *J-QE 76 Jun* 326-330 (1A08)
Fox, A. Gardner; Editorial: Integrated optics; *J-QE 76 Jun* 321 (1A03)
Fox, A. Gardner, *Ed.*; Announcement; *J-QE 76 Apr* 213 (1A03)

G

Ganiel, U., A. Hardy, and D. Treves; Analysis of injection locking in pulsed dye laser systems; *J-QE 76 Nov* 704-716 (1D08)
Garscadden, Alan, *see* Olson, Robert A.; *J-QE 76 May* 316-317 (1D12)
Gaskill, W. G., *see* Emanuel, George; *J-QE 76 Nov* 739-740 (1G01)
George, Edward V., *see* Huber, Ernest E., Jr.; *J-QE 76 Jun* 353-359 (1C07)
Getzinger, R. W., N. R. Greiner, K. D. Ware, J. P. Carpenter, and R. G. Wenzel; Controlled energy extraction and sharp nanosecond pulses from an HF amplifier (Corresp.); *J-QE 76 Sep* 556-558 (1C10)
Ghizoni, Cesar C., Bor-Uei Chen, and Chung L. Tang; Theory and experiments on grating couplers for thin-film waveguides; *J-QE 76 Feb* 69-73 (1A03)
Comments (with author's reply) by Dalgoutte, D. G.; *J-QE 76 Nov* 736-737 (1F12)
Ghosh, A. K., *see* Crane, R. A.; *J-QE 76 Dec* 776-778 (1C06)
Glaros, Stanley S., *see* Manes, Kenneth R.; *J-QE 76 May* 265-273 (1A03)
Glenn, W. H., *see* Morey, W. W.; *J-QE 76 May* 311-313 (1D07)
Goela, J. S., and T. F. Morse; Saturation effects and Lamb-dip formation in molecular lasers; *J-QE 76 May* 281-290 (1B05)
Gonda, Shun-Ichi, *see* Mukai, Seiji; *J-QE 76 Jan* 47-53 (1D07)
Greiner, N. R., *see* Getzinger, R. W.; *J-QE 76 Sep* 556-558 (1C10)
Gribkovskii, V. P., V. K. Kononenko, G. I. Ryabtsev, and V. A. Samoilyukovich; Trapped radiation in injection lasers; *J-QE 76 Jun* 322-326 (1A04)
Griffin, W. S., *see* Culick, F. E. C.; *J-QE 76 Oct* 566-574 (1A08)
Gundersen, M., *see* Bushnell, A. H.; *J-QE Jul* 447 (1F03)
Gundersen, Martin, *see* Bushnell, A. H.; *J-QE 76 Apr* 260-261 (1D08)
Gustafson, T. K., *see* Jain, R. K.; *J-QE 76 Sep* 555-556 (1C09)

H

Haas, Roger A., *see* Manes, Kenneth R.; *J-QE 76 May* 265-273 (1A03)
Hahn, Erwin L., *see* Diels, Jean-Claude; *J-QE 76 Jul* 411-416 (1C09)
Hall, Robert J.; Rotational nonequilibrium and line-selected operation in CW DF chemical lasers; *J-QE 76 Aug* 453-462 (1A03)
Hamal, K., H. Jelinkova, A. Novotny, and M. Vrbova; Picosecond relaxation time measurement from the *Q*-switched threshold (Corresp.); *J-QE 76 Aug* 510-512 (1E04)
Hamasaki, Joji, *see* Nosu, Kiyoshi; *J-QE 76 Dec* 745-748 (1A03)
Hardy, A., *see* Ganiel, U.; *J-QE 76 Nov* 704-716 (1D08)
Harris, S. E., *see* Hsu, K. S.; *J-QE 76 Jan* 60-62 (1E06)
Harris, Stephen E., *see* Stappaerts, Eddy A.; *J-QE 76 Jun* 330-333 (1A12)
Haus, Hermann A.; Parameter ranges for CW passive mode locking; *J-QE 76 Mar* 169-176 (1A07)
Haus, Hermann A., and Charles V. Shank; Antisymmetric taper of distributed feedback lasers; *J-QE 76 Sep* 532-539 (1A14)
Hayashi, Toshio, *see* Usami, Akira; *J-QE 76 Oct* 574-579 (1B02)
Heiblum, Mordehai, and Jay H. Harris; Analysis of curved optical waveguides by conformal transformation; *J-QE 75 Feb* 75-83 (1A13)
Correction, J-QE 76 May 313 (1D09)
Heiblum, Mordehai; The prism coupler and the dielectric bend: Similarities and anomalous behavior; *J-QE 76 Aug* 463-469 (1A13)
Hellwarth, R. W., *see* Cherlow, J. M.; *J-QE 76 Oct* 644-646 (2C01)
Hill, Kenneth O., and R. Ian MacDonald; Gain saturation in DFB lasers with end reflectors; *J-QE 76 Nov* 716-721 (1E06)
Hocker, G. Benjamin; Strip-loaded diffused optical waveguides; *J-QE 76 Apr* 232-236 (1B08)
Hohla, K., *see* Brederlow, G.; *J-QE 76 Feb* 152-155 (2E10)
Hollinger, Fritz W., *see* Schwab, Adolf J.; *J-QE 76 Mar* 183-188 (1B07)
Hon, David T.; Electrooptical compensation for self-heating in CD*A during second-harmonic generation; *J-QE 76 Feb* 148-151 (2E06)
Hong, Henry Y-P., *see* Chinn, Stephen R.; *J-QE 76 Mar* 189-193 (1B13)
Horiuchi, Y., and A. Murai; Far-infrared laser oscillations from H_2CO (Corresp.); *J-QE 76 Sep* 547-549 (1C01)
Hsu, K. S., A. H. Kung, L. J. Zych, J. F. Young, and S. E. Harris; 1202.8-Å generation in Hg using a parametrically amplified dye laser (Corresp.); *J-QE 76 Jan* 60-62 (1E06)
Huber, Ernest E., Jr., Lawrence R. Jones, Edward V. George, and Robert M. Lerner; Sustainer enhancement of the VUV fluorescence in high-pressure xenon; *J-QE 76 Jun* 353-359 (1C07)
Hubert, M. H., *see* Waksberg, A. L.; *J-QE 76 Nov* 734-736 (1F10)
Huchital, David A., and George N. Steinberg; Pumping of Nd:YAG with electrodeless arc lamps; *J-QE 76 Jan 1-9* (1A03)
Hunt, J. T., *see* Bliss, E. S.; *J-QE 76 Jul* 402-406 (1B14)

I

IEEE Quantum Electronics Council; Special issue on 1975 IEEE/OSA Conference on Laser Engineering and Applications; *J-QE 76 Feb* 89-159 (2A03)
Isenor, N. R., *see* Merchant, V. E.; *J-QE 76 Oct* 603-613 (1D03)
Itzkan, Irving, *see* Janes, G. Sargent; *J-QE 76 Feb* 111-120 (2B11)
Iwasaki, Hiroshi, *see* Otsuka, Kenju; *J-QE 76 Apr* 214-217 (1A04)

J

Jacobs, Ralph R., and Marvin J. Weber; Dependence of the $^4F_{3/2} \rightarrow {}^4I_{11}d/_2$ induced-emission cross section for Nd^{3+} on glass composition; *J-QE 76 Feb* 102-111 (2B02)
Jain, R. K., and T. K. Gustafson; Efficient generation of continuously tunable coherent radiation in the 2460–2650-Å spectral range (Corresp.); *J-QE 76 Sep* 555-556 (1C09)
Janes, G. Sargent, Irving Itzkan, Charles T. Pike, Richard H. Levy, and Lawrence Levin; Two-photon laser isotope separation of atomic uranium: Spectroscopic studies, excited-state lifetimes, and photoionization cross sections; *J-QE 76 Feb* 111-120 (2B11)
Jeffers, William Q., Charles E. Wiswall, and Harris Y. Ageno; Gas additive effects in CO chemical lasers; *J-QE 76 Nov* 693-697 (1C11)
Jelinkova, H., *see* Hamal, K.; *J-QE 76 Aug* 510-512 (1E04)
Jennings, W. C., *see* Woskoboinikow, P.; *J-QE 76 Oct* 613-615 (1D13)
Johnson, J. C., *see* Lesch, G. H.; *J-QE 76 Feb* 83-86 (1B03)
Johnson, Joel C., *see* Massey, Gail A.; *J-QE 76 Feb* 143-147 (2E01)
Johnson, Joel C., *see* Massey, Gail A.; *J-QE 76 Nov* 721-727 (1E11)
Johnson, W. L., *see* Reid, R. D.; *J-QE 76 Dec* 778-779 (1C08)
Johnston, T. F., Jr.; A calibrated, knife-edge attenuator for optimization of the output mirror transmission of TEM_{00} lasers (Corresp.); *J-QE 76 May* 310-311 (1D06)
Johnston, Thomas F., Jr., and William P. Kolb; The self-heated 442-nm He–Cd laser: Optimizing the power output, and the origin of beam noise; *J-QE 76 Aug* 482-493 (1C04)
Jones, Lawrence R., *see* Huber, Ernest E., Jr.; *J-QE 76 Jun* 353-359 (1C07)
Judd, O.; On the effect of the addition of SF_6 to a N_2 electrical discharge laser (Corresp.); *J-QE 76 Feb* 78-80 (1A12)

K

Karasikov, N., and J. Shamir; Operation of TEA CO_2 lasers with rough surface electrodes (Corresp.); *J-QE 76 Apr* 257 (1D05)
Karras, T. W., *see* Anderson, R. S.; *J-QE 76 May* 313-315 (1D09)
Kashiwagi, Hiroshi, *see* Yamashita, Mikio; *J-QE 76 Feb* 90-95 (2A04)
Kasper, H. M., *see* Levine, B. F.; *J-QE 76 Jun* 367-368 (1D07)
Kato, K.; Near-infrared dye laser pumped by a carbazine-122 dye laser (Corresp.); *J-QE 76 Jul* 442-443 (1E12)
Kato, K., and R. S. Adhav; Second-harmonic generation at 0.659 μ in CD*A (Corresp.); *J-QE 76 Jul* 443-445 (1E13)
Kaufmann, Konrad, *see* Marowsky, Gerd; *J-QE 76 Mar* 207-209 (1D03)
Keilmann, Fritz; Infrared saturation spectroscopy in p-type germanium; *J-QE 76 Oct* 592-597 (1C06)
Kennedy, C. J.; A stabilizer for cavity-dumped Nd:YAG (Corresp.); *J-QE 76 Apr* 256-257 (1D04)
Keren, H., P. Avivi, and F. Dothan; Positive ion spectra in He–Co–O_2-laser discharges (Corresp.); *J-QE 76 Jan* 58-60 (1E04)
Kildal, Helge, and Thomas F. Deutsch; Infrared third-harmonic generation in molecular gases; *J-QE 76 Jul* 429-435 (1D13)
Kimura, Tatsuya, *see* Saruwatari, Masatoshi; *J-QE 76 Oct* 584-591 (1B12)
Kobayashi, Kohroh, *see* Lang, Roy; *J-QE 76 Mar* 194-199 (1C04)
Koepf, Gerhard A.; 10.6-μm amplification in metallic waveguide by external discharge pumping; *J-QE 76 Jan* 9-15 (1A11)
Kogelnik, Herwig, and Ronald V. Schmidt; Switched directional couplers with alternating $\Delta\beta$; *J-QE 76 Jul* 396-401 (1B08)
Kolb, William P., *see* Johnston, Thomas F., Jr.; *J-QE 76 Aug* 482-493 (1C04)
Kononenko, V. K., *see* Gribkovskii, V. P.; *J-QE 76 Jun* 322-326 (1A04)
Koo, K. P., *see* Claspy, P. C.; *J-QE 76 Oct* 647-649 (2C04)

Krammer, Hermann; Field configurations and propagation constants of modes in hollow rectangular dielectric waveguides (Corresp.); *J-QE 76 Aug* 505-507 (1D13)
Kreiner, W. A.; Application of laser *Q* switching for infrared spectroscopy; *J-QE 76 Jan* 16-20 (1B04)
Kressel, Henry, *see* Ettenberg, Michael; *J-QE 76 Jun* 360-364 (1C14)
Kuester, Edward F., and David C. Chang; Surface-wave radiation loss from curved dielectric slabs and fibers; *J-QE 75 Nov* 903-907 (1D07)
Correction, J-QE 76 Jun 371 (1D11)
Kumagai, Nobuaki, *see* Ohtaka, Masato; *J-QE 76 Jul* 378-382 (1A04)
Kung, A. H., *see* Hsu, K. S.; *J-QE 76 Jan* 60-62 (1E06)

L

Lachambre, J. L., P. Lavigne, G. Otis, and M. Noel; Injection locking and mode selection in TEA-CO_2 laser oscillators; *J-QE 76 Dec* 756-764 (1A14)
Lang, Roy, and Kohroh Kobayashi; Suppression of the relaxation oscillation in the modulated output of semiconductor lasers; *J-QE 76 Mar* 194-199 (1C04)
LaTourrette, J. T., *see* Nella, John; *J-QE 76 Sep* 543-547 (1B11)
Lavigne, P., *see* Lachambre, J. L.; *J-QE 76 Dec* 756-764 (1A14)
Lee, T. P., and Theresinha J. B. Serra; Characteristics of RF injection locking of self-pulsing in an AlGaAs DH junction laser (Corresp.); *J-QE 76 Jun* 368-371 (1D08)
Lee, Yong-Kyung, and Shyh Wang; Electrooptic guided-to-unguided mode converter; *J-QE 76 May* 273-281 (1A11)
Lerner, Robert M., *see* Huber, Ernest E., Jr.; *J-QE 76 Jun* 353-359 (1C07)
Lesch, G. H., J. C. Johnson, and G. A. Massey; A thermostatic control system for nonlinear optical experiments at low temperatures (Corresp.); *J-QE 76 Feb* 83-86 (1B03)
Leung, K. M., *see* Bass, M.; *J-QE 76 Feb* 82-83 (1B02)
Levenson, M. D., and G. L. Eesley; Single-mode operation of a repetitively pulsed dye laser (Corresp.); *J-QE 76 Apr* 259-260 (1D07)
Levenson, M. D., *see* Eesley, G. L.; *J-QE 76 Jul* 440-442 (1E10)
Levin, Lawrence, *see* Janes, G. Sargent; *J-QE 76 Feb* 111-120 (2B11)
Levine, B. F., C. G. Bethea, H. M. Kasper, and F. A. Thiel; Nonlinear optical susceptibility of $HgGa_2S_4$ (Corresp.); *J-QE 76 Jun* 367-368 (1D07)
Levine, J. S., K. Bezdjian, and R. Rappaport; A stacked Blumlein N_2 laser (Corresp.); *J-QE 76 Jul* 437-438 (1E07)
Levy, Richard H., *see* Janes, G. Sargent; *J-QE 76 Feb* 111-120 (2B11)
Liao, Paul F., *see* Smith, Peter W.; *J-QE 76 Sep* 539-542 (1B07)
Liberman, Irving, *see* Babcock, Richard V.; *J-QE 76 Jan* 29-34 (1C03)
Lindquist, Walter B., *see* Manes, Kenneth R.; *J-QE 76 May* 265-273 (1A03)
Louisell, William H., *see* Seely, John F.; *J-QE 76 Aug* 515-517 (1E09)
Lüthi, H. R., W. Seelig, and A. Stadler; Quasi-CW high-power mercury laser (Note); *J-QE 76 May* 317-318 (1D13)

M

MacDonald, R. Ian, *see* Hill, Kenneth O.; *J-QE 76 Nov* 716-721 (1E06)
Mahr, H.; Tunable two-wavelength mode locking of the CW dye laser (Corresp.); *J-QE 76 Sep* 554-555 (1C08)
Mahr, H., *see* Copeland, Drew A.; *J-QE 76 Nov* 665-673 (1A11)
Makimoto, T., *see* Yamamoto, S.; *J-QE 76 Dec* 764-770 (1B08)
Maloney, Patrick J., *see* Smith, Peter W.; *J-QE 76 Sep* 539-542 (1B07)
Manes, Kenneth R., Walter B. Lindquist, Paul A. Renard, H. E. Eddleman, Donald L. Smith, Stanley S. Glaros, Ted C. Stewart, and Roger A. Haas; Valkyrie: A CO_2 laser system for laser fusion experiments; *J-QE 76 May* 265-273 (1A03)
Marcuse, D., *see* Rigrod, William W.; *J-QE 76 Nov* 673-685 (1B05)
Marowsky, Gerd, and Konrad Kaufmann; Influence of spatial hole burning on the output power of a CW dye ring laser (Corresp.); *J-QE 76 Mar* 207-209 (1D03)
Martin, J. P., *see* Brechignac, P.; *J-QE 76 Feb* 80-81 (1A14)
Mason, Stephen B., *see* Chodzko, Richard A.; *J-QE 76 Nov* 660-664 (1A06)
Masopust, Otto T., Jr., *see* Saifi, Mansoor A.; *J-QE 76 Feb* 120-125 (2C06)
Massey, G. A., *see* Lesch, G. H.; *J-QE 76 Feb* 83-86 (1B03)
Massey, Gail A., Joel C. Johnson, and Richard A. Elliott; Generation of frequency-controlled nanosecond and picosecond optical pulses by high-gain parametric amplification; *J-QE 76 Feb* 143-147 (2E01)
Massey, Gail A., and Joel C. Johnson; Wavelength-tunable optical mixing experiments between 208 nm and 259 nm; *J-QE 76 Nov* 721-727 (1E11)
Matsuhara, Masanori, *see* Ohtaka, Masato; *J-QE 76 Jul* 378-382 (1A04)
Matsuo, Yukito, *see* An, Jyong Chi; *J-QE 76 Jul* 445-446 (1F01)
McArthur, David A., and Philip B. Tollefsrud; Measurement of optical gain in CO gas excited only by fission fragments; *J-QE 76 Apr* 244-253 (1C06)
McFarlane, Ross A., *see* Davis, Christopher C.; *J-QE 76 Jun* 334-352 (1B02)
McGee, J. D., *see* Chang, T. Y.; *J-QE 76 Jan* 62-65 (1E08)
McKen, Don C., Herb J. Seguin, and John Tulip; Photoionization parameters in the carbon dioxide laser gases; *J-QE 76 Aug* 470-482 (1B06)
McMurray, J. A., and C. R. Stanley; Electrooptic phase modulation in CdS optical waveguides (Corresp.); *J-QE 76 May* 307-310 (1D03)
McNeil, J. R., and G. J. Collins; Additional ultraviolet laser transitions in Cu II (Note); *J-QE 76 Jun* 371-372 (1D11)
McNeil, J. R., *see* Reid, R. D.; *J-QE 76 Dec* 778-779 (1C08)
Merchant, V. E., and N. R. Isenor; Multiphoton excitation processes between vibrational states of molecules; *J-QE 76 Oct* 603-613 (1D03)
Milam, D., and M. J. Weber; Nonlinear refractive index coefficient for Nd phosphate laser glasses (Corresp.); *J-QE 76 Aug* 512-513 (1E06)
Mirels, Harold, *see* Chodzko, Richard A.; *J-QE 76 Nov* 660-664 (1A06)
Montanarini, Marco, and Jürg Steffen; Investigations on laser welding; *J-QE 76 Feb* 126-129 (2C12)
Mooradian, A., *see* Brueck, S. R. J.; *J-QE 76 Mar* 201-202 (1C11)
Moran, Joseph M.; Calculation of the minimum repetition rate of a cavity-dumped four-level laser; *J-QE 76 Oct* 639-644 (2B10)
Moreno, J. B.; Computer solution for the traveling-wave-excited N_2 laser (Corresp.); *J-QE 76 Mar* 204-207 (1C14)
Morey, W. W., and W. H. Glenn; A 100-W-average-power flashlamp-pumped dye laser (Corresp.); *J-QE 76 May* 311-313 (1D07)
Morse, T. F., *see* Goela, J. S.; *J-QE 76 May* 281-290 (1B05)
Mukai, Seiji, and Shun-Ichi Gonda; Analysis of intensity fluctuations in a junction laser with low quantum-efficiency regions; *J-QE 76 Jan* 47-53 (1D07)
Murai, A., *see* Horiuchi, Y.; *J-QE 76 Sep* 547-549 (1C01)

N

Nakamura, Michiharu, *see* Aiki, Kunio; *J-QE 76 Oct* 597-603 (1C11)
Nella, John, Seung-Yan Szeto, Paul Rabinowitz, and J. T. LaTourrette; Saturated spectroscopy applied to xenon at 3.5 μm; *J-QE 76 Sep* 543-547 (1B11)
Nereson, Norris, *see* Flicker, Herbert; *J-QE 76 Jun* 326-330 (1A08)
Noel, M., *see* Lachambre, J. L.; *J-QE 76 Dec* 756-764 (1A14)
North, Dwight O., *see* Sommers, Henry S., Jr.; *J-QE 76 Apr* 225-232 (1B01)
North, Dwight O.; Theory of modal character, field structure, and losses for semiconductor lasers; *J-QE 76 Oct* 616-624 (2A01)
Nosu, Kiyoshi, and Joji Hamasaki; The influence of the longitudinal plasma wave on the propagation characteristics of a metal-clad-dielectric-slab waveguide; *J-QE 76 Dec* 745-748 (1A03)
Novotny, A., *see* Hamal, K.; *J-QE 76 Aug* 510-512 (1E04)
Nucho, Roger N., *see* Wolff, Peter A.; *J-QE 76 Aug* 500-504 (1D08)

O

Oettinger, Peter E., and C. Forbes Dewey, Jr.; Lasing efficiency and photochemical stability of IR laser dyes in the 710–1080-nm spectral region; *J-QE 76 Feb* 95-101 (2A09)
Ohtaka, Masato, Masanori Matsuhara, and Nobuaki Kumagai; Analysis of the guided modes in slab-coupled waveguides using a variational method; *J-QE 76 Jul* 378-382 (1A04)
Okamura, Y., *see* Yamamoto, S.; *J-QE 76 Dec* 764-770 (1B08)
Olson, Robert A., Peter Bletzinger, and Alan Garscadden; New pulsed Xe-neutral laser line (Note); *J-QE 76 May* 316-317 (1D12)
Osche, Gregory R., and Henry E. Sonntag; A compact cylinder CO_2 TEA laser; *J-QE 76 Dec* 752-756 (1A10)
Otis, G., *see* Lachambre, J. L.; *J-QE 76 Dec* 756-764 (1A14)
Otsuka, Kenju, and Hiroshi Iwasaki; Stabilization of oscillating modes in a $LiNdP_4O_{12}$ laser; *J-QE 76 Apr* 214-217 (1A04)
Otsuka, Kenju; Analysis of the response of lasers to external signal injection (Corresp.); *J-QE 76 Jul* 438-440 (1E08)

P

Paoli, Thomas L., *see* Barnes, Peter A.; *J-QE 76 Oct* 633-639 (2B04)
Paoli, Thomas L.; Nonlinearities in the emission characteristics of stripe-geometry (AlGa)As double-heterostructure junction lasers; *J-QE 76 Dec* 770-776 (1B14)
Partlow, W. D., *see* Babcock, Richard V.; *J-QE 76 Jan* 29-34 (1C03)
Petersen, F. Russell, Kenneth M. Evenson, Donald A. Jennings, Joseph S. Wells, Kenya Goto, and Juan J. Jiménez; Far infrared frequency synthesis with stabilized CO_2 lasers: Accurate measurements of the water vapor and methyl alcohol laser frequencies; *J-QE 75 Oct* 838-843 (1C08)
Correction, J-QE 76 Feb 86-87 (1B06)
Picqué, Jean-Louis; Hyperfine optical pumping of cesium with a CW GaAs laser; *J-QE 74 Dec* 892-897 (1C14)
Comments by Singh, Gurbax, P. DiLavore, and C. O. Alley; *J-QE 76 Feb* 81-82 (1B01)
Pierce, E. L., *see* Attwood, D. T.; *J-QE 76 Mar* 203-204 (1C13)
Pierce, James W., *see* Chinn, Stephen R.; *J-QE 76 Mar* 189-193 (1B13)
Pike, Charles T., *see* Janes, G. Sargent; *J-QE 76 Feb* 111-120 (2B11)
Piper, James A., and Colin Webb; High-current characteristics of the continuous-wave hollow-cathode He–I_2 laser; *J-QE 76 Jan* 21-25 (1B09)
Pirkle, Robert J., *see* Davis, Christopher C.; *J-QE 76 Jun* 334-352 (1B02)

R

Rabinowitz, Paul, *see* Nella, John; *J-QE 76 Sep* 543-547 (1B11)
Rappaport, R., *see* Levine, J. S.; *J-QE 76 Jul* 437-438 (1E07)
Ray, M., S. S. Baral, and D. L. Bhattacharyya; New theory of delays in semiconductor lasers; *J-QE 76 Oct* 561-565 (1A03)
Ready, John F.; Change of reflectivity of metallic surfaces during irradiation by CO_2–TEA laser pulses; *J-QE 76 Feb* 137-142 (2D09)
Reid, R. D., W. L. Johnson, J. R. McNeil, and G. J. Collins; New infrared laser transitions in Ag II (Corresp.); *J-QE 76 Dec* 778-779 (1C08)
Reiner, R. J., *see* Emanuel, George; *J-QE 76 Nov* 739-740 (1G01)
Renard, P. A., *see* Bliss, E. S.; *J-QE 76 Jul* 402-406 (1B14)
Renard, Paul A., *see* Manes, Kenneth R.; *J-QE 76 May* 265-273 (1A03)
Richardson, Martin C., *see* Tomov, Ivan V.; *J-QE 76 Sep* 521-531 (1A03)
Riedhauser, C. E., *see* Fitzsimmons, W. A.; *J-QE 76 Oct* 624-633 (2A09)
Rigrod, William W., and D. Marcuse; Radiation loss coefficients of asymmetric dielectric waveguides with shallow sinusoidal corrugations; *J-QE 76 Nov* 673-685 (1B05)
Ross, David H., *see* Chodzko, Richard A.; *J-QE 76 Nov* 660-664 (1A06)
Ryabtsev, G. I., *see* Gribkovskii, V. P.; *J-QE 76 Jun* 322-326 (1A04)

S

Saifi, Mansoor A., and Otto T. Masopust, Jr.; Laser-generated *RC* networks; *J-QE 76 Feb* 120-125 (2C06)
Saifi, Mansoor A., and Sotirios J. Vahaviolos; Laser spot welding and real-time evaluation; *J-QE 76 Feb* 129-136 (2D01)
Samoilyukovich, V. A., *see* Gribkovskii, V. P.; *J-QE 76 Jun* 322-326 (1A04)
Saruwatari, Masatoshi, and Tatsuya Kimura; LED pumped lithium neodymium tetraphosphate lasers; *J-QE 76 Oct* 584-591 (1B12)
Schmidt, Ronald V., *see* Kogelnik, Herwig; *J-QE 76 Jul* 396-401 (1B08)
Schwab, Adolf J., and Fritz W. Hollinger; Compact high-power N_2 laser: Circuit theory and design; *J-QE 76 Mar* 183-188 (1B07)
Scifres, Donald R., *see* Streifer, William; *J-QE 76 Feb* 74-78 (1A08)
Scifres, Donald R., *see* Streifer, William; *J-QE 76 Mar* 177-182 (1B01)
Scifres, Donald R., *see* Streifer, William; *J-QE 76 Jul* 422-428 (1D06)
Scifres, Donald R., *see* Streifer, William; *J-QE 76 Aug* 494-499 (1D02)
Scifres, D. R., *see* Streifer, W.; *J-QE 76 Nov* 737-739 (1F13)

Seelig, W., *see* Lüthi, H. R.; *J-QE 76 May* 317-318 (1D13)
Seely, John F., William H. Louisell, and Ronald R. Bousek; Coaxial sweep scheme for ion-beam lasers (Corresp.); *J-QE 76 Aug* 515-517 (1E09)
Seguin, Herb J., *see* Tulip, John; *J-QE 76 Feb* 155-159 (2E13)
Seguin, Herb J., *see* McKen, Don C.; *J-QE 76 Aug* 470-482 (1B06)
Seib, David H., *see* Stoll, Harold M.; *J-QE 76 Jan* 53-57 (1D13)
Serra, Theresinha J. B., *see* Lee, T. P.; *J-QE 76 Jun* 368-371 (1D08)
Shamir, J., *see* Karasikov, N.; *J-QE 76 Apr* 257 (1D05)
Shank, Charles V., *see* Haus, Hermann A.; *J-QE 76 Sep* 532-539 (1A14)
Shelton, C., *see* Emanuel, George; *J-QE 76 Nov* 739-740 (1G01)
Shen, P. I., *see* Culick, F. E. C.; *J-QE 76 Oct* 566-574 (1A08)
Siegman, Anthony E.; A canonical formulation for analyzing multielement unstable resonators; *J-QE 76 Jan* 35-40 (1C09)
Siegman, Anthony E.; A canonical formulation for analyzing multilement unstable resonators; *J-QE 76 Jan* 35-40 (1C09)
Correction, J-QE 76 May 315 (1D11)
Singh, Gurbax, P. DiLavore, and C. O. Alley; *J-QE 76 Feb* 81-82 (1B01)
Comments on Picqué, Jean-Louis; Hyperfine optical pumping of cesium with a CW GaAs laser; *J-QE 74 Dec* 892-897 (1C14)
Smith, Donald L., *see* Manes, Kenneth R.; *J-QE 76 May* 265-273 (1A03)
Smith, Peter W., Paul F. Liao, and Patrick J. Maloney; Discharge pumping of dye vapors; *J-QE 76 Sep* 539-542 (1B07)
Sommargren, G. E., *see* Bliss, E. S.; *J-QE 76 Jul* 402-406 (1B14)
Sommers, Henry S., Jr., and Dwight O. North; Rotation of polarization axis of injection lasers with viewing direction; *J-QE 76 Apr* 225-232 (1B01)
Sonntag, Henry E., *see* Osche, Gregory R.; *J-QE 76 Dec* 752-756 (1A10)
Spencer, David J., *see* Chodzko, Richard A.; *J-QE 76 Nov* 660-664 (1A06)
Springer, L. W., *see* Anderson, R. S.; *J-QE 76 May* 313-315 (1D09)
Stadler, A., *see* Lüthi, H. R.; *J-QE 76 May* 317-318 (1D13)
Stanley, C. R., *see* McMurray, J. A.; *J-QE 76 May* 307-310 (1D03)
Stappaerts, Eddy A., Gerhard W. Bekkers, James F. Young, and Stephen E. Harris; The effect of linewidth on the efficiency of two-photon-pumped frequency converters; *J-QE 76 Jun* 330-333 (1A12)
Steffen, Jürg, *see* Montanarini, Marco; *J-QE 76 Feb* 126-129 (2C12)
Steinberg, George N., *see* Huchital, David A.; *J-QE 76 Jan 1-9* (1A03)
Stewart, Ted C., *see* Manes, Kenneth R.; *J-QE 76 May* 265-273 (1A03)
Stoll, Harold M., and David H. Seib; Multiply resonant distributed-feedback lasers; *J-QE 76 Jan* 53-57 (1D13)
Stone, F. T., and Stewart Austin; A theoretical and experimental study of the effect of loss on grating couplers; *J-QE 76 Nov* 727-732 (1F03)
Streifer, W., R. D. Burnham, and D. R. Scifres; Radiation losses in distributed feedback lasers and longitudinal mode selection (Corresp.); *J-QE 76 Nov* 737-739 (1F13)
Streifer, William, Donald R. Scifres, and Robert D. Burnham; TM-mode coupling coefficients in guided-wave distributed feedback lasers; *J-QE 76 Feb* 74-78 (1A08)
Streifer, William, Robert D. Burnham, and Donald R. Scifres; Substrate radiation losses in GaAs heterostructure lasers; *J-QE 76 Mar* 177-182 (1B01)
Streifer, William, Donald R. Scifres, and Robert D. Burnham; Analysis of grating-coupled radiation in GaAs:GaAlAs lasers and waveguides; *J-QE 76 Jul* 422-428 (1D06)
Streifer, William, Robert D. Burnham, and Donald R. Scifres; Analysis of grating–coupled radiation in GaAs:GaAlAs lasers and waveguides—Part II: Blazing effects; *J-QE 76 Aug* 494-499 (1D02)
Suchard, Steven N., *see* Capelle, Gene A.; *J-QE 76 Jul* 417-421 (1D01)
Sutton, David G.; New laser oscillations in the N atom quartet manifold (Note); *J-QE 76 May* 315 (1D11)
Szeto, Seung-Yan, *see* Nella, John; *J-QE 76 Sep* 543-547 (1B11)

T

Tam, S. Y. K., *see* Crane, R. A.; *J-QE 76 Dec* 776-778 (1C06)
Tang, Chung L., *see* Ghizoni, Cesar C.; *J-QE 76 Feb* 69-73 (1A03)
Tang, Chung L., *see* Copeland, Drew A.; *J-QE 76 Nov* 665-673 (1A11)
Taylor, Henry F.; Dispersion characteristics of diffused channel waveguides; *J-QE 76 Dec* 748-752 (1A06)
Teschke, O., Andrew Dienes, and John R. Whinnery; Theory and operation of high-power CW and long-pulse dye lasers; *J-QE 76 Jul* 383-395 (1A09)
Teschke, O., J. R. Whinnery, and A. Dienes; Thermal effects in jet-stream dye lasers (Corresp.); *J-QE 76 Aug* 513-515 (1E07)
Theophanous, N. G.; A $Gd_2(MoO_4)_3$ longitudinal electrooptic modulator at 6328 Å (Corresp.); *J-QE 76 Aug* 507-510 (1E01)
Thiel, F. A., *see* Levine, B. F.; *J-QE 76 Jun* 367-368 (1D07)
Thompson, Herbert M., *see* Daiber, John W.; *J-QE 76 Nov* 686-693 (1C04)
Tollefsrud, Philip B., *see* McArthur, David A.; *J-QE 76 Apr* 244-253 (1C06)
Tomov, Ivan V., and Martin C. Richardson; Fifth-harmonic generation in isotropic media; *J-QE 76 Sep* 521-531 (1A03)
Treves, D., *see* Ganiel, U.; *J-QE 76 Nov* 704-716 (1D08)
Tseng, Cheng-Chung, Dan Botez, and Shyh Wang; Optically pumped epitaxial GaAs waveguide lasers with distributed Bragg reflectors (Corresp.); *J-QE 76 Sep* 549-551 (1C03)
Tulip, John, Herb J. Seguin, and Wayne Faszer; High-repetition-rate TEA-laser discharge using integrated preionization and switching; *J-QE 76 Feb* 155-159 (2E13)
Comments by Bushnell, A. H., M. Gundersen, and T. R. Burkes; *J-QE 76 Jul* 447 (1F03)
Tulip, John, *see* McKen, Don C.; *J-QE 76 Aug* 470-482 (1B06)

U

Umeda, Jun-ichi, *see* Aiki, Kunio; *J-QE 76 Oct* 597-603 (1C11)
Usami, Akira, and Toshio Hayashi; Operation-induced degradation of GaP light-emitting diodes; *J-QE 76 Oct* 574-579 (1B02)

V

Vahaviolos, Sotirios J., *see* Saifi, Mansoor A.; *J-QE 76 Feb* 129-136 (2D01)
van der Ziel, Jan P.; Effect of Fabry–Perot interference on second harmonic generation in a GaAs plate; *J-QE 76 Jul* 407-411 (1C05)
Verdeyen, J. T., *see* Eden, J. G.; *J-QE 76 Nov* 698-704 (1D02)
Volk, R., *see* Brederlow, G.; *J-QE 76 Feb* 152-155 (2E10)
Vrbova, M., *see* Hamal, K.; *J-QE 76 Aug* 510-512 (1E04)
Vrtilek, Jan M., *see* Fitzsimmons, W. A.; *J-QE 76 Oct* 624-633 (2A09)

W

Waksberg, A. L., M. H. Hubert, and W. R. L. Clements; Laser modulation depth determination by a simple power measuring technique (Corresp.); *J-QE 76 Nov* 734-736 (1F10)
Walpole, James N., *see* Davies, Richard W.; *J-QE 76 May* 291-303 (1C01)
Wang, Chung-Shu, *see* Butler, Jerome K.; *J-QE 76 Mar* 165-168 (1A03)
Wang, Shyh, *see* Lee, Yong-Kyung; *J-QE 76 May* 273-281 (1A11)
Wang, Shyh, *see* Tseng, Cheng-Chung; *J-QE 76 Sep* 549-551 (1C03)
Ware, K. D., *see* Getzinger, R. W.; *J-QE 76 Sep* 556-558 (1C10)
Watkins, W., *see* Emanuel, George; *J-QE 76 Nov* 739-740 (1G01)
Weaire, D., *see* Firth, William J.; *J-QE 76 Apr* 218-225 (1A08)
Weaver, H. J., *see* Bliss, E. S.; *J-QE 76 Jul* 402-406 (1B14)
Webb, Colin, *see* Piper, James A.; *J-QE 76 Jan* 21-25 (1B09)
Weber, Marvin J., *see* Jacobs, Ralph R.; *J-QE 76 Feb* 102-111 (2B02)
Weber, M. J., *see* Milam, D.; *J-QE 76 Aug* 512-513 (1E06)
Weiss, C. O.; Pump saturation in molecular far-infrared lasers; *J-QE 76 Oct* 580-584 (1B08)
Wenzel, R. G., *see* Getzinger, R. W.; *J-QE 76 Sep* 556-558 (1C10)
Wherrett, Brian S., *see* Firth, William J.; *J-QE 76 Apr* 218-225 (1A08)
Whinnery, John R., *see* Teschke, O.; *J-QE 76 Jul* 383-395 (1A09)
Whinnery, J. R., *see* Teschke, O.; *J-QE 76 Aug* 513-515 (1E07)
White, W. P., *see* Chen, T. S.; *J-QE 76 Jul* 436-437 (1E06)
Whitehouse, D. R., *Guest ed.*; Preface to special issue; *J-QE 76 Feb* 89 (2A03)
Whitford, B. G.; Higher order harmonics of CO_2 and N_2O laser difference frequencies (Note); *J-QE 76 Apr* 261 (1D09)
Wiswall, Charles E., *see* Jeffers, William Q.; *J-QE 76 Nov* 693-697 (1C11)
Witte, K. J., *see* Brederlow, G.; *J-QE 76 Feb* 152-155 (2E10)
Wittke, James P., *see* Ettenberg, Michael; *J-QE 76 Jun* 360-364 (1C14)
Wolff, Peter A., Roger N. Nucho, and Roshan L. Aggarwal; Coherent effects in spin–flip light scattering; *J-QE 76 Aug* 500-504 (1D08)
Wolga, George J., *see* Davis, Christopher C.; *J-QE 76 Jun* 334-352 (1B02)
Woskoboinikow, P., and W. C. Jennings; The measurement of far-infrared laser gain and loss using a Michelson coupler; *J-QE 76 Oct* 613-615 (1D13)

Y

Yamamoto, S., Y. Okamura, and T. Makimoto; Analysis and design of semileaky-type thin-film optical waveguide isolator; *J-QE 76 Dec* 764-770 (1B08)
Yamashita, Mikio, and Hiroshi Kashiwagi; Photodegradation mechanisms in laser dyes: A laser irradiated ESR study; *J-QE 76 Feb* 90-95 (2A04)
Yang, T. T., *see* Cherlow, J. M.; *J-QE 76 Oct* 644-646 (2C01)
Young, James F., *see* Stappaerts, Eddy A.; *J-QE 76 Jun* 330-333 (1A12)
Young, J. F., *see* Hsu, K. S.; *J-QE 76 Jan* 60-62 (1E06)

Z

Zych, L. J., *see* Hsu, K. S.; *J-QE 76 Jan* 60-62 (1E06)

SUBJECT INDEX

A

Absorbing media; **cf.** Infrared propagation, absorbing media; Laser absorbers; Optical propagation, absorbing media
Acoustic waves; **cf.** Carbon monoxide lasers
ADP (Ammonium dihydrogen phosphate); **cf.** Nitrogen compounds/mixtures
Aluminum alloys/compounds; **cf.** Gallium alloys/compounds
Aluminum alloys/compounds, devices
lasers; spiking oscillations in diode-pumped $NdAl_3(BO_3)_4$ lasers. *Chinn, Stephen R., J-QE 76 Mar* 189-193 (1B13)
Ammonia devices
NH_2D Stark cells; use in direct demodulation of 10.6-μm FM signal. *Abrams, R. L., J-QE 76 Oct* 646-647 (2C03)
Ammonia devices; **cf.** Gas lasers, molecular
Ammonium compounds/mixtures; **cf.** Nitrogen compounds/mixtures
Amplifiers; **cf.** Laser amplifiers; Optical amplifiers
Arcs
CO–Ar and CO–N_2Ar mixtures; continuous arc-assisted electric discharges in high-pressure mixtures. *Crane, R. A., J-QE 76 Dec* 776-778 (1C06)
Argon compounds/mixtures, devices; **cf.** Carbon monoxide lasers
Atomic frequency standards
Cs frequency standards; pumping of Cs-133 vapor using CW GaAs laser. *Picqué, Jean-Louis, J-QE 74 Dec* 892-897 (1C14) ♦
Atomic lasers; **cf.** Gas lasers

B

Beam focusing; **cf.** Laser-beam focusing
Bibliographies
I photodissociation lasers. *Davis, Christopher C., J-QE 76 Jun* 334-352 (1B02)
Boron alloys/compounds
BCl_3; optical third-harmonic generation of CO_2 laser radiation in molecular gases. *Kildal, Helge, J-QE 76 Jul* 429-435 (1D13)
Bragg scattering; **cf.** Distributed Bragg reflector lasers; Distributed feedback lasers
Breakdown; **cf.** Dielectric breakdown

C

Cadmium devices; **cf.** Gas lasers, ionic
Cadmium alloys/compounds, devices
electrooptic phase modulators using CdS thin-film optical waveguides; multilayer configuration using polycrystalline films. *McMurray, J. A., J-QE 76 May* 307-310 (1D03)

♦ Check author entry for later corrections/comments

Carbon alloys/compounds
CO; optical third-harmonic generation of CO_2 laser radiation in molecular gases. *Kildal, Helge, J-QE 76 Jul* 429-435 (1D13)
Carbon alloys/compounds, devices; **cf.** Gas lasers, molecular
Carbon dioxide lasers
CH_3CN, CH_3CCH, CH_3Cl, CH_3Br, CH_3I lasers; far infrared lines produced by CO_2-laser pumping in region of perpendicular absorption bands. *Chang, T. Y., J-QE 76 Jan* 62-65 (1E08)
far-infrared frequency synthesis using stabilized CO_2 lasers; application in measurement of laser line frequencies. *Petersen, F. Russell, J-QE 75 Oct* 838-843 (1C08) ♦
frequency measurement; generation of fourth and fifth harmonics of difference frequency between two 28-THz laser lines. *Whitford, B. G., J-QE 76 Apr* 261 (1D09)
metallic surface irradiation by CO_2–TEA lasers; changes in surface reflectivity. *Ready, John F., J-QE 76 Feb* 137-142 (2D09)
passive Q switching for infrared spectroscopy. *Kreiner, W. A., J-QE 76 Jan* 16-20 (1B04)
photoionization; volumetric preionization of CO_2–N_2–He gas mixtures by ultraviolet emission from bare sparks. *Babcock, Richard V., J-QE 76 Jan* 29-34 (1C03)
TEA lasers; compact cylindrical laser using small-diameter wire as central electrode. *Osche, Gregory R., J-QE 76 Dec* 752-756 (1A10)
TEA lasers; high-repetition-rate discharge technique using integrated ultraviolet preionization and voltage switching. *Tulip, John, J-QE 76 Feb* 155-159 (2E13) ♦
TEA lasers; injection locking and mode selection. *Lachambre, J. L., J-QE 76 Dec* 756-764 (1A14)
TEA lasers; operation with rough surface electrodes. *Karasikov, N., J-QE 76 Apr* 257 (1D05)
ultraviolet photoionization parameters in TEA lasers. *McKen, Don C., J-QE 76 Aug* 470-482 (1B06)
Valkyrie short-pulse system for laser fusion experiments. *Manes, Kenneth R., J-QE 76 May* 265-273 (1A03)
waveguide lasers; dependence of gain and tunability on gas kinetic and discharge properties. *Cohen, Steven C., J-QE 76 Apr* 237-244 (1B13)
waveguide lasers using external discharge pumping. *Koepf, Gerhard A., J-QE 76 Jan* 9-15 (1A11)
Carbon dioxide laser amplifiers
waveguide laser amplifiers; metallic waveguides using external discharge pumping. *Koepf, Gerhard A., J-QE 76 Jan* 9-15 (1A11)
Carbon dioxide lasers
DF–CO_2 transfer chemical lasers; high-cavity-pressure operation at supersonic velocity. *Emanuel, George, J-QE 76 Nov* 739-740 (1G01)
Carbon monoxide lasers
acoustic waves and heating due to molecular energy transfer in electric-discharge lasers. *Culick, F. E. C., J-QE 76 Oct* 566-574 (1A08)
chemical lasers; gas additive effects on optical gain in O–O_2–Cs_2 CW lasers. *Jeffers, William Q., J-QE 76 Nov* 693-697 (1C11)
CO–Ar and CO–N_2Ar mixtures; continuous arc-assisted electric discharges in high-pressure mixtures. *Crane, R. A., J-QE 76 Dec* 776-778 (1C06)
CO–N_2–He mixtures; CW laser action from $v=1\rightarrow v=0$ band up to $v=36\rightarrow=35$ band. *Brechignac, P., J-QE 76 Feb* 80-81 (1A14)
CO vibrational excitation efficiency in self-sustained CW glow discharge. *Daiber, John W., J-QE 76 Nov* 686-693 (1C04)
CS_2/O_2 chemical lasers; pulsed laser initiated in high-pressure double-discharge TEA system. *Ahl, Jeffrey L., J-QE 76 Jan* 26-29 (1B14)
fission-fragment-excited lasers; optical gain. *McArthur, David A., J-QE 76 Apr* 244-253 (1C06)
positive ion spectra of He–CO-laser discharges with and without O_2 addition. *Keren, H., J-QE 76 Jan* 58-60 (1E04)
Carrier processes; **cf.** Charge-carrier processes
Cavity resonators; **cf.** Laser resonators
Cesium
pumping of Cs-133 vapor using CW GaAs laser. *Picqué, Jean-Louis, J-QE 74 Dec* 892-897 (1C14) ♦
Cesium alloys/compounds
CD*A; second-harmonic generation at 0.659 μm. *Kato, K., J-QE 76 Jul* 443-445 (1E13)
Cesium alloys/compounds, devices
CD*A second harmonic generators; electrooptical compensation for self-heating. *Hon, David T., J-QE 76 Feb* 148-151 (2E06)
Cesium compounds/mixtures
CsXe; pressure- and temperature-dependent absorption and fluorescence in high-pressure Cs–Xe mixtures. *Eden, J. G., J-QE 76 Nov* 698-704 (1D02)
Cesium compounds,/mixtures, devices; **cf.** Ultraviolet lasers
Charge-carrier processes
recombination centers in GaP LEDs degraded by forward-biased operation. *Usami, Akira, J-QE 76 Oct* 574-579 (1B02)
Chemical lasers; **cf.** Gas lasers
Chemistry; **cf.** Laser applications
Computer applications, design
Nd:YAG lasers; design of optical resonators for frequency-doubled laser. *Barry, J. D., J-QE 76 Apr* 254-256 (1D02)
Conferences; **cf.** Laser Engineering and Applications Conference, 5th, Washington, DC, 1975
Copper
welding; laser welding of insulated wire to monel, phosphor bronze, and brass terminals. *Saifi, Mansoor A., J-QE 76 Feb* 129-136 (2D01)
Copper devices; **cf.** Gas lasers; Gas lasers, ionic
Copper alloys/compounds, devices
terminal posts; laser welding to insulated Cu wires. *Saifi, Mansoor A., J-QE 76 Feb* 129-136 (2D01)
Couplers; **cf.** Laser couplers; Optical couplers
Cryogenics
nonlinear optical crystals; cryostat for maintaining at temperatures between room temperature and -175°C. *Lesch, G. H., J-QE 76 Feb* 83-86 (1B03)
CU lasers
Cu II lasers; ultraviolet laser transitions at 2529, 2600, and 2707 Å. *McNeil, J. R., J-QE 76 Jun* 371-372 (1D11)

♦ Check author entry for later corrections/comments

CW lasers
AlGaAs double-heterostructure lasers; RF injection locking of self-pulsing. *Lee, T. P., J-QE 76 Jun* 368-371 (1D08)
AlGaAs–GaAs lasers; threshold gain characteristics as function of Al concentration in active region. *Butler, Jerome K., J-QE 76 Mar* 165-168 (1A03)
CH_3F waveguide lasers; conversion of CO_2 pump radiation into far-infrared 496-μm radiation. *DeTemple, Thomas A., J-QE 76 Jan* 40-47 (1C14)
CO chemical lasers; gas additive effects on optical gain. *Jeffers, William Q., J-QE 76 Nov* 693-697 (1C11)
CO lasers; arc-assisted electric discharges in CO–Ar and CO–N_2Ar high-pressure mixtures. *Crane, R. A., J-QE 76 Dec* 776-778 (1C06)
CO lasers; CW laser action in CO–N_2–He laser from $v=1\rightarrow v=0$ band up to $v=36\rightarrow=35$ band. *Brechignac, P., J-QE 76 Feb* 80-81 (1A14)
DF chemical lasers; rotational nonequilibrium and line-selected operation. *Hall, Robert J., J-QE 76 Aug* 453-462 (1A03)
DF–CO_2 transfer chemical lasers; high-cavity-pressure operation at supersonic velocity. *Emanuel, George, J-QE 76 Nov* 739-740 (1G01)
dye lasers containing separate rhodamine 6G and cresyl violet jets; tunable mode-locked operation at two wavelengths. *Mahr, H., J-QE 76 Sep* 554-555 (1C08)
dye lasers; theoretical model for CW and long-pulse lasers. *Teschke, O., J-QE 76 Jul* 383-395 (1A09)
dye ring lasers; effect of spatial hole burning on output power. *Marowsky, Gerd, J-QE 76 Mar* 207-209 (1D03)
HF–DF chemical lasers; zero-power-gain measurements using fast scan technique. *Chodzko, Richard A., J-QE 76 Nov* 660-664 (1A06)
Hg lasers; quasi-CW high-power laser action at 6501.5 Å. *Lüthi, H. R., J-QE 7[illegible] May* 317-318 (1D13)
I_2–He lasers; output characteristics of multiple-anode hollow-cathode laser for discharge currents up to 20A and quasi-continuous excitation. *Piper, James A., J-QE 76 Jan* 21-25 (1B09)
passive mode locking of homogeneously broadened lasers. *Haus, Hermann A., J-QE 76 Mar* 169-176 (1A07)
response of semiconductor lasers to external signal injection. *Otsuka, Kenju, J-QE 76 Jul* 438-440 (1E08)

D

Demodulation; **cf.** FM demodulation; Optical demodulation
Detection; **cf.** Demodulation
Deuterium alloys/compounds, devices; **cf.** Gas lasers, molecular
Deuterium compounds/mixtures; **cf.** Hydrogen compounds/mixtures
Dielectric breakdown; **cf.** Gas discharges
Dielectric radiation effects
transparent dielectric materials; threshold for pulsed 10.6-μm laser damage in ZnSe, NaCl, and Kcl. *Bass, M., J-QE 76 Feb* 82-83 (1B02)
Dielectric waveguides; **cf.** Optical waveguides
Diffraction; **cf.** Optical diffraction
Diode lasers; **cf.** Semiconductor lasers
Directional couplers; **cf.** Optical directional couplers
Dissociation of molecules; **cf.** Laser applications
Distributed Bragg reflector lasers
waveguide lasers; optically pumped epitaxial GaAs laser. *Tseng, Cheng-Chung, J-QE 76 Sep* 549-551 (1C03)
Distributed-feedback lasers
GaAs–GaAlAs diode lasers with separate optical and carrier confinement; lasing characteristics. *Aiki, Kunio, J-QE 76 Oct* 597-603 (1C11)
gain saturation in distributed-feedback lasers with end reflectors. *Hill, Kenneth O., J-QE 76 Nov* 716-721 (1E06)
longitudinal mode thresholds in symmetrical lasers; effects of radiation losses due to Bragg scattering. *Streifer, W., J-QE 76 Nov* 737-739 (1F13)
multiply resonant lasers. *Stoll, Harold M., J-QE 76 Jan* 53-57 (1D13)
tapered-structure lasers; analysis of antisymmetric tapers. *Haus, Hermann A., J-QE 76 Sep* 532-539 (1A14)
TM-mode coupling coefficients in guided-wave distributed-feedback lasers. *Streifer, William, J-QE 76 Feb* 74-78 (1A08)
Dyes
relaxation times of saturable dyes; measurement in picosecond region. *Hamal, K., J-QE 76 Aug* 510-512 (1E04)
Dye lasers
cavities using reflective beam expander. *Eesley, G. L., J-QE 76 Jul* 440-442 (1E10)
CW and long-pulse lasers; theoretical model. *Teschke, O., J-QE 76 Jul* 383-395 (1A09)
CW lasers containing separate rhodamine 6G and cresyl violet jets; tunable mode-locked operation at two wavelengths. *Mahr, H., J-QE 76 Sep* 554-555 (1C08)
CW ring lasers; effect of spatial hole burning on output power. *Marowsky, Gerd, J-QE 76 Mar* 207-209 (1D03)
high-power lasers; 100-W-average-power flashlamp-pumped laser. *Morey, W. W., J-QE 76 May* 311-313 (1D07)
high-power near-infrared dye lasers using cascade pumping. *Kato, K., J-QE 76 Jul* 442-443 (1E12)
infrared laser dyes; lasing efficiency and photochemical stability in 710–1080 nm spectral region. *Oettinger, Peter E., J-QE 76 Feb* 95-101 (2A09)
mode locking; CW passive mode locking of homogeneously broadened laser. *Haus, Hermann A., J-QE 76 Mar* 169-176 (1A07)
photodegradation of xanthene laser dyes; study using ESR detection of laser-induced triplet molecules and free radicals. *Yamashita, Mikio, J-QE 76 Feb* 90-95 (2A04)
pulsed lasers; single-mode operation of repetitively pulsed laser. *Levenson, M. D., J-QE 76 Apr* 259-260 (1D07)
pulsed laser systems with injection locking. *Ganiel, U., J-QE 76 Nov* 704-716 (1D08)
thermal effects in jet-stream dye lasers. *Teschke, O., J-QE 76 Aug* 513-515 (1E07)
ultraviolet generators, 1202.8-Å generation using resonantly enhanced four-wave optical mixing in Hg vapor. *Hsu, K. S., J-QE 76 Jan* 60-62 (1E06)
vapor lasers; discharge pumping. *Smith, Peter W., J-QE 76 Sep* 539-542 (1B07)

E

Electric discharge pumping; **cf.** Gas lasers
Electric variables measurement; **cf.** Frequency measurement
Electroluminescent devices; **cf.** Light-emitting diodes
Electromagnetic propagation
optical planar waveguides; determination of phase constant for propagating wave in metal- and dielectric-clad guide. *Fink, H. J., J-QE 76 Jun* 365-367 (1D05)
Electron-beam pumping; **cf.** Gas lasers
Electron carriers; **cf.** Charge-carrier processes
Electrooptics
self-heating compensation in CD*A second harmonic generators. *Hon, David T., J-QE 76 Feb* 148-151 (2E06)
Electrooptic modulation
$Gd_2(MoO_4)_3$ electrooptic modulators; longitudinal modulation of 6328 Å light from 100 Hz to 1 MHz. *Theophanous, N. G., J-QE 76 Aug* 507-510 (1E01)
lumped and traveling-wave modulators for wide-band and low-drive-power operation. *An, Jyong Chi, J-QE 76 Jul* 445-446 (1F01)
mode converters; electrooptic polarization conversion from guided TE wave to unguided TM wave in thin-film light guide. *Lee, Yong-Kyung, J-QE 76 May* 273-281 (1A11)
modulation depth; measurement using power method. *Waksberg, A. L., J-QE 76 Nov* 734-736 (1F10)
optical directional couplers; switched alternating-phase mismatch couplers in which complete conversion of light from one guide to another is achieved by electrical adjustment. *Kogelnik, Herwig, J-QE 76 Jul* 396-401 (1B08)
optical planar waveguide modulators; electrooptic phase modulator using CdS thin-film optical waveguides. *McMurray, J. A., J-QE 76 May* 307-310 (1D03)
Electrooptic switches
optical directional couplers; switched alternating-phase mismatch couplers in which complete conversion of light from one guide to another is achieved by electrical adjustment. *Kogelnik, Herwig, J-QE 76 Jul* 396-401 (1B08)
Excitation of lasers; **cf.** Laser excitation

F

Fabry–Perot interferometers
GaAs plane parallel plates; second-harmonic generation. *van der Ziel, Jan P., J-QE 76 Jul* 407-411 (1C05)
Fabry–Perot resonators
InSb spin-flip lasers; CO_2-laser pumped external cavity laser with output frequency determined ny Fabry–Perot modes of resonant output couplers. *Brueck, S. R. J., J-QE 76 Mar* 201-202 (1C11)
Far infrared; **cf.** Infrared (0.70–100 μm)
Feedback lasers; **cf.** Distributed-feedback lasers
Fluorescence
CsXe; pressure- and temperature-dependent fluorescence in high-pressure Cs–Xe mixtures. *Eden, J. G., J-QE 76 Nov* 698-704 (1D02)
FM demodulation
optical demodulation; direct demodulation of 10.6-μm FM signal with NH_2D Stark cell. *Abrams, R. L., J-QE 76 Oct* 646-647 (2C03)
FM signals
direct demodulation of 10.6-μm FM signal with NH_2D Stark cell. *Abrams, R. L., J-QE 76 Oct* 646-647 (2C03)
Focusing; **cf.** Laser-beam focusing
Frequency conversion; **cf.** Optical frequency conversion
Frequency measurement
infrared region; generation of fourth and fifth harmonics of difference frequency between two 28-THz laser lines. *Whitford, B. G., J-QE 76 Apr* 261 (1D09)
laser line frequency measurements; far-infrared frequency synthesis technique using stabilized CO_2 lasers. *Petersen, F. Russell, J-QE 75 Oct* 838-843 (1C08) ♦
Frequency measurement standards; **cf.** Atomic frequency standards
Frequency multiplication; **cf.** Frequency conversion
Frequency synthesizers
far-infrared frequency synthesis; application in measurement of laser line frequencies. *Petersen, F. Russell, J-QE 75 Oct* 838-843 (1C08) ♦
Fusion; **cf.** Nuclear fusion

G

Gadolinium; **cf.** Rare earths
Gallium alloys/compounds
$HgGa_2S_4$; second harmonic coefficient d_{36} and birefringence. *Levine, B. F., J-QE 76 Jun* 367-368 (1D07)
Gallium alloys/compounds, devices
GaAs–GaAlAs optical waveguides; grating-coupled radiation with rectangular-shaped gratings. *Streifer, William, J-QE 76 Jul* 422-428 (1D06)
GaAs–GaAlAs optical waveguides; grating-coupled radiation with trapezoidal-shaped gratings. *Streifer, William, J-QE 76 Aug* 494-499 (1D02)
GaAs parallel-plate Fabry–Perot structures; second-harmonic generation. *van der Ziel, Jan P., J-QE 76 Jul* 407-411 (1C05)
Gallium alloys/compounds, devices; **cf.** Gallium alloys/compounds, lasers; Light-emitting diodes
Gallium alloys/compounds, lasers
AlGaAs double-heterostructure lasers; RF injection locking of self-pulsing. *Lee, T. P., J-QE 76 Jun* 368-371 (1D08)
AlGaAs double heterostructure stripe-geometry injection lasers; electrical characteristics. *Barnes, Peter A., J-QE 76 Oct* 633-639 (2B04)
AlGaAs double-heterostructure stripe-geometry lasers; nonlinearities in emission characteristics. *Paoli, Thomas L., J-QE 76 Dec* 770-776 (1B14)
AlGaAs–GaAs lasers; threshold gain characteristics of CW lasers as function of Al concentration in active region. *Butler, Jerome K., J-QE 76 Mar* 165-168 (1A03)
GaAlAs lasers; gain saturation in distributed-feedback lasers with end reflectors. *Hill, Kenneth O., J-QE 76 Nov* 716-721 (1E06)
GaAs distributed Bragg reflector lasers; optically pumped epitaxial waveguide laser. *Tseng, Cheng-Chung, J-QE 76 Sep* 549-551 (1C03)
GaAs double heterostructure lasers; radiation losses in structure with thin GaAlAs layer between active GaAs region and GaAs substrate or superstrate. *Streifer, William, J-QE 76 Mar* 177-182 (1B01)
GaAs–GaAlAs distributed-feedback diode lasers with separate optical and carrier confinement; lasing characteristics. *Aiki, Kunio, J-QE 76 Oct* 597-603 (1C11)
GaAs–GaAlAs double-heterostructure guided-wave distributed-feedback lasers; TM-mode coupling coefficients. *Streifer, William, J-QE 76 Feb* 74-78 (1A08)
GaAs–GaAlAs lasers; grating-coupled radiation with rectangular-shaped gratings. *Streifer, William, J-QE 76 Jul* 422-428 (1D06)
GaAs–GaAlAs lasers; grating-coupled radiation with trapezoidal-shaped gratings. *Streifer, William, J-QE 76 Aug* 494-499 (1D02)
GaAs lasers; direct modulation in GHz range through suppression of relaxation oscillation in modulated output. *Lang, Roy, J-QE 76 Mar* 194-199 (1C04)
GaAs lasers; modal characteristics of laser cavity. *North, Dwight O., J-QE 76 Oct* 616-624 (2A01)
GaAs lasers; model for time delays. *Ray, M., J-QE 76 Oct* 561-565 (1A03)
GaAs lasers; multiply resonant distributed-feedback laser. *Stoll, Harold M., J-QE 76 Jan* 53-57 (1D13)
GaAs lasers; use in pumping Cs-133 vapor. *Picqué, Jean-Louis, J-QE 74 Dec* 892-897 (1C14) ♦
Gas discharges; **cf.** Ionization
Gas lasers
dye-vapor lasers; discharge pumping. *Smith, Peter W., J-QE 76 Sep* 539-542 (1B07)
ion-beam pumped lasers; coaxial deflection and focusing scheme. *Seely, John F., J-QE 76 Aug* 515-517 (1E09)
metal-vapor lasers; self-heated laser using Cu, Au, or Au–Cu mixture as active materials. *Fahlen, Theodore S., J-QE 76 Mar* 200-201 (1C10)
Gas lasers, atomic
I lasers; pulsed high power Asterix III laser for nuclear fusion experiments. *Brederlow, G., J-QE 76 Feb* 152-155 (2E10)
I photodissociation lasers; output mode spectra, comparative parametric operation, quenching, photolytic reversibility, and short-pulse generation. *Davis, Christopher C., J-QE 76 Jun* 334-352 (1B02)
N_2 lasers; laser oscillations at 1.0568, 1.0611, and 1.0623 μm in pulsed discharge of He and N_2. *Sutton, David G., J-QE 76 May* 315 (1D11)
Pb vapor lasers; discharge-heated laser with emission at 4062 and 4057 Å. *Anderson, R. S., J-QE 76 May* 313-315 (1D09)
Gas lasers, atomic; **cf.** Noble gas lasers
Gas lasers, ionic
Ag II infrared laser transitions observed in the discharges excited in Ag hollow cathode. *Reid, R. D., J-QE 76 Dec* 778-779 (1C08)
Cu II lasers; ultraviolet laser transitions at 2529, 2600, and 2707 Å. *McNeil, J. R., J-QE 76 Jun* 371-372 (1D11)
He–Cd lasers; power output and beam noise of self-heated 442-nm laser. *Johnston, Thomas F., Jr., J-QE 76 Aug* 482-493 (1C04)
Hg lasers; quasi-CW high-power laser action at 6501.5 Å. *Lüthi, H. R., J-QE 76 May* 317-318 (1D13)
I_2–He lasers; output characteristics of multiple-anode hollow-cathode laser for discharge currents up to 20A and quasi-continuous excitation. *Piper, James A., J-QE 76 Jan* 21-25 (1B09)
Gas lasers, ionic; **cf.** Noble gas lasers
Gas lasers, molecular
CH_3CN, CH_3CCH, CH_3Cl, CH_3Br, CH_3I lasers; far infrared lines produced by CO_2-laser pumping in region of perpendicular absorption bands. *Chang, T. Y., J-QE 76 Jan* 62-65 (1E08)
CH_3F lasers; conversion of CO_2 pump radiation into far-infrared 496-μm radiation in CW waveguide lasers. *DeTemple, Thomas A., J-QE 76 Jan* 40-47 (1C14)
CH_3OH far-infrared lasers; effect of low electric field Stark tuning on absorption of 9.4-μm CO_2 laser radiation. *Claspy, P. C., J-QE 76 Oct* 647-649 (2C04)
CN chemical lasers; active N_2–hydrocarbon reactions in supersonic flow system. *Capelle, Gene A., J-QE 76 Jul* 417-421 (1D01)
DF chemical lasers; rotational nonequilibrium and line-selected operation in CW lasers. *Hall, Robert J., J-QE 76 Aug* 453-462 (1A03)
H_2CO lasers; far-infrared laser oscillations from H_2CO vapor in longitudinal-flow tube. *Horiuchi, Y., J-QE 76 Sep* 547-549 (1C01)
H_2O, D_2O, and CH_3OH lasers; measurement of line frequencies using far-infrared frequency synthesis technique. *Petersen, F. Russell, J-QE 75 Oct* 838-843 (1C08) ♦
HCOOH, CH_3OH, CH_3I, and CH_3F far-infrared lasers; saturated absorption of CO_2 laser radiation in pump transitions. *Weiss, C. O., J-QE 76 Oct* 580-584 (1B08)
N_2 lasers; compact high-power laser. *Schwab, Adolf J., J-QE 76 Mar* 183-188 (1B07)
N_2 lasers; computer solution for excitation by longitudinal relativistic electron beam. *Moreno, J. B., J-QE 76 Mar* 204-207 (1C14)
N_2 lasers; experimental and theoretical study of transmission-line pulse-discharge excited lasers. *Fitzsimmons, W. A., J-QE 76 Oct* 624-633 (2A09)
N_2 lasers; fast-rise-time, large-volume electrical-discharge excitation using stacked Blumlein transmission lines. *Levine, J. S., J-QE 76 Jul* 437-438 (1E07)
N_2O lasers; passive Q switching for infrared spectroscopy. *Kreiner, W. A., J-QE 76 Jan* 16-20 (1B04)
NH_3 lasers; transitions in ND_3, ND_2H, NH_2D, and $N^{15}H_3$. *Bushnell, A. H., J-QE 76 Apr* 260-261 (1D08)
saturation effects and Lamb-dip formation. *Goela, J. S., J-QE 76 May* 281-290 (1B05)
SF_6–N_2 gas mixtures; electron distribution function in electrical discharge laser. *Judd, O., J-QE 76 Feb* 78-80 (1A12)
Gas lasers, molecular; **cf.** Carbon dioxide lasers; Carbon monoxide lasers; Hydrogen halide lasers; Noble gas lasers
Germanium
infrared absorption; saturation-induced spectral changes. *Keilmann, Fritz, J-QE 76 Oct* 592-597 (1C06)
Germanium devices
output couplers for InSb spin-flip lasers. *Brueck, S. R. J., J-QE 76 Mar* 201-202 (1C11)

Glass
Nd-doped laser glasses; tailoring for specific applications by compositional changes. *Jacobs, Ralph R., J-QE 76 Feb* 102-111 (2B02)
Nd phosphate laser glasses; nonlinear refractive index coefficients. *Milam, D., J-QE 76 Aug* 512-513 (1E06)
Glass devices; **cf.** Neodymium:glass lasers; Solid lasers
Gold devices; **cf.** Gas lasers

H

Harmonic generation; **cf.** Optical harmonic generation
Heating; **cf.** Plasma heating
Helium; **cf.** Noble gases
Helium compounds/mixtures, devices; **cf.** Carbon dioxide lasers; Carbon monoxide lasers; Gas lasers, ionic; Noble gas lasers
Hole carriers; **cf.** Charge-carrier processes
Hydrogen compounds/mixtures, devices
ADP parametric amplifiers; generation of frequency-controlled ns and ps visible pulses by high-gain parametric amplification. *Massey, Gail A., J-QE 76 Feb* 143-147 (2E01)
Hydrogen compounds/mixtures, devices; **cf.** Gas lasers, molecular; Ultraviolet lasers
Hydrogen halide lasers
HF–DF CW chemical lasers; zero-power-gain measurements using fast scan technique. *Chodzko, Richard A., J-QE 76 Nov* 660-664 (1A06)

I

IEEE Quantum Electronics Council
appointment of associate editors. *Fox, A. Gardner, Ed., J-QE 76 Jul* 377 (1A03)
editorial staff change. *Fox, A. Gardner, Ed., J-QE 76 Apr* 213 (1A03)
integrated-optics special issue of IEEE J-QE. *Fox, A. Gardner, J-QE 76 Jun* 321 (1A03)
Indium alloys/compounds
InSb; Raman-induced IR spin resonance radiation. *Wolff, Peter A., J-QE 76 Aug* 500-504 (1D08)
Indium alloys/compounds, devices; **cf.** Semiconductor lasers
Infrared (0.70–100 μm); **cf.** Submillimeter-wave (300–3000 GHz)
Infrared generation
far-infrared generation; generation of fourth and fifth harmonics of difference frequency between two 28-THz laser lines. *Whitford, B. G., J-QE 76 Apr* 261 (1D09)
far-infrared generation; Raman-induced coherent spin resonance radiation from InSb. *Wolff, Peter A., J-QE 76 Aug* 500-504 (1D08)
Infrared lasers
Ag II laser transitions observed in He discharges excited in Ag hollow cathode. *Reid, R. D., J-QE 76 Dec* 778-779 (1C08)
CH_3CN, CH_3CCH, CH_3Cl, CH_3Br, CH_3I lasers; far infrared lines produced by CO_2-laser pumping in region of perpendicular absorption bands. *Chang, T. Y., J-QE 76 Jan* 62-65 (1E08)
CH_3F lasers; conversion of CO_2 pump radiation into far-infrared 496-μm radiation in CW waveguide lasers. *DeTemple, Thomas A., J-QE 76 Jan* 40-47 (1C14)
CH_3OH far-infrared lasers; effect of low electric field Stark tuning on absorption of 9.4-μm CO_2 laser radiation. *Claspy, P. C., J-QE 76 Oct* 647-649 (2C04)
dye lasers; high-power near-infrared laser using cascade pumping. *Kato, K., J-QE 76 Jul* 442-443 (1E12)
H_2O, D_2O, and CH_3OH lasers; measurement of line frequencies using far-infrared frequency synthesis technique. *Petersen, F. Russell, J-QE 75 Oct* 838-843 (1C08) ♦
HCOOH, CH_3OH, CH_3I, and CH_3F far-infrared lasers; saturated absorption of CO_2 laser radiation in pump transitions. *Weiss, C. O., J-QE 76 Oct* 580-584 (1B08)
He–Xe TEA lasers; laser transitions at 2.03, 2.65, 3.43, 3.65, and 4.02 μm. *Olson, Robert A., J-QE 76 May* 316-317 (1D12)
N_2 lasers; laser oscillations at 1.0568, 1.0611, and 1.0623 μm in pulsed discharge of He and N_2. *Sutton, David G., J-QE 76 May* 315 (1D11)
N_2O lasers; passive Q switching for infrared spectroscopy. *Kreiner, W. A., J-QE 76 Jan* 16-20 (1B04)
NH_3 lasers; transitions in ND_3, ND_2H, NH_2D, and $N^{15}H_3$. *Bushnell, A. H., J-QE 76 Apr* 260-261 (1D08)
Pb–Sn–Se diode lasers; increased current tuning range using small magnetic fields. *Flicker, Herbert, J-QE 76 Jun* 326-330 (1A08)
Raman lasers; 16-μm source for isotope enrichment using rotational Raman scattering in gaseous H_2 or D_2 with CO_2 laser source. *Byer, Robert L., J-QE 76 Nov* 732-733 (1F08)
small-signal gain and total internal losses in far-infrared lasers; measurement using Michelson coupler. *Woskoboinikow, P., J-QE 76 Oct* 613-615 (1D13)
Infrared lasers; **cf.** Carbon dioxide lasers; Dye lasers; Neodymium:solid lasers
Infrared propagation, absorbing media
CH_3OH gas; effect of low electric field Stark tuning on absorption of 9.4-μm CO_2 laser radiation. *Claspy, P. C., J-QE 76 Oct* 647-649 (2C04)
Ge; saturation-induced spectral changes. *Keilmann, Fritz, J-QE 76 Oct* 592-597 (1C06)
Infrared signal detection
direct demodulation of 10.6-μm FM signal with NH_2D Stark cell. *Abrams, R. L., J-QE 76 Oct* 646-647 (2C03)
Infrared spectroscopy
detection of near coincidences between fixed-frequency CO_2 and N_2O lasers and molecular absorption lines using passive Q switching. *Kreiner, W. A., J-QE 76 Jan* 16-20 (1B04)
Ge; saturation absorption-induced spectral changes. *Keilmann, Fritz, J-QE 76 Oct* 592-597 (1C06)
Injection lasers; **cf.** Semiconductor lasers
Integrated circuits; **cf.** Integrated optics
Integrated optics
proposed special issue. *Fox, A. Gardner, J-QE 76 Jun* 321 (1A03)
Integrated optics; **cf.** Optical planar waveguides; Optical strip waveguides
Interferometry; **cf.** Fabry–Perot interferometers
Iodine devices; **cf.** Gas lasers, atomic; Gas lasers, ionic
Ion-beam pumping; **cf.** Gas lasers
Ionization
molecules; multiphoton excitation processes between vibrational states. *Merchant, V. E., J-QE 76 Oct* 603-613 (1D03)
Ionization; **cf.** Photoionization
Ion lasers; **cf.** Gas lasers; Solid lasers
Isolators; **cf.** Optical isolators
Isotope separation; **cf.** Laser applications, chemistry

J

Junction lasers; **cf.** Semiconductor lasers
Junctions; **cf.** Semiconductor junctions

L

Lamb dip; **cf.** Laser tuning
Lamps; **cf.** Laser excitation
Lanthanum; **cf.** Rare earths
Lasers; **cf.** CW lasers; Distributed-feedback lasers; Dye lasers; Gas lasers; Infrared lasers; Pulsed lasers; Raman lasers; Ring lasers; Semiconductor lasers; Solid lasers; Submillimeter-wave lasers; Traveling-wave lasers; Ultraviolet lasers; Visible lasers; Waveguide lasers
Laser absorbers
optical pulse propagation, stability in absorbing and amplifying media. *Diels, Jean-Claude, J-QE 76 Jul* 411-416 (1C09)
saturable dyes; measurement of relaxation times in picosecond region. *Hamal, K., J-QE 76 Aug* 510-512 (1E04)
Laser amplifiers
controlled energy extraction and sharp ns pulses from HF amplifier. *Getzinger, R. W., J-QE 76 Sep* 556-558 (1C10)
optical pulse propagation, stability in absorbing and amplifying media. *Diels, Jean-Claude, J-QE 76 Jul* 411-416 (1C09)
Laser amplifiers; **cf.** Carbon dioxide laser amplifiers
Laser applications
dissociation and ionization of molecules; multiphoton excitation processes between vibrational states. *Merchant, V. E., J-QE 76 Oct* 603-613 (1D03)
Nd:glass lasers; tailoring of glass for specific applications by compositional changes. *Jacobs, Ralph R., J-QE 76 Feb* 102-111 (2B02)
Laser applications; **cf.** Optical measurements
Laser applications, chemistry
isotope enrichment; 16-μm source for enrichment of UF_6. *Byer, Robert L., J-QE 76 Nov* 732-733 (1F08)
isotope separation; selective two-step excitation and photoionization of atomic U vapor. *Janes, G. Sargent, J-QE 76 Feb* 111-120 (2B11)
Laser applications, materials processing
integrated *RC* network generation. *Saifi, Mansoor A., J-QE 76 Feb* 120-125 (2C06)
metallic surfaces; reflectivity changes during irradiation by CO_2–TEA lasers. *Ready, John F., J-QE 76 Feb* 137-142 (2D09)
Laser applications, nuclear fusion
CO_2 lasers; Valkyrie short-pulse system. *Manes, Kenneth R., J-QE 76 May* 265-273 (1A03)
I lasers; Asterix III pulsed high-power laser. *Brederlow, G., J-QE 76 Feb* 152-155 (2E10)
Laser applications, welding
difficult to weld, dissimilar materials; welding process using fundamental mode laser pulses. *Montanarini, Marco, J-QE 76 Feb* 126-129 (2C12)
insulated Cu wires to terminal posts; real-time weld evaluation using stress-wave emission. *Saifi, Mansoor A., J-QE 76 Feb* 129-136 (2D01)
Laser-beam focusing
nonlinear propagation effects. *Bliss, E. S., J-QE 76 Jul* 402-406 (1B14)
self-focusing in solvents; estimation. *Cherlow, J. M., J-QE 76 Oct* 644-646 (2C01)
Laser cavity resonators; **cf.** Laser resonators
Laser couplers
GaAs–GaAlAs lasers; grating-coupled radiation with rectangular-shaped gratings. *Streifer, William, J-QE 76 Jul* 422-428 (1D06)
GaAs–GaAlAs lasers; grating-coupled radiation with trapezoidal-shaped gratings. *Streifer, William, J-QE 76 Aug* 494-499 (1D02)
InSb spin-flip lasers; CO_2-laser pumped external cavity laser with output frequency determined ny Fabry–Perot modes of resonant output couplers. *Brueck, S. R. J., J-QE 76 Mar* 201-202 (1C11)
Michelson coupled lasers for measurement of far-infrared laser gain and loss. *Woskoboinikow, P., J-QE 76 Oct* 613-615 (1D13)
Pb–Sn–Te double-heterostructure lasers; output coupling for closely confined laser. *Davies, Richard W., J-QE 76 May* 291-303 (1C01)
Laser diodes; **cf.** Semiconductor lasers
Laser Engineering and Applications, Conference on, 5th, Washington, DC, 1975
selected papers, *J-QE 76 Feb* 89-159 (2A03)
selected papers; foreword to special issue. *Whitehouse, D. R., Guest ed., J-QE 76 Feb* 89 (2A03)
Laser excitation; **cf.** *Specific type of laser*
Laser machining; **cf.** Laser applications, materials processing
Laser measurements
electrooptic modulation; measurement of modulation depth using power method. *Waksberg, A. L., J-QE 76 Nov* 734-736 (1F10)
HF–DF CW chemical lasers; zero-power-gain measurements using fast scan technique. *Chodzko, Richard A., J-QE 76 Nov* 660-664 (1A06)
induced-emission cross sections of Nd^{3+}-doped glasses. *Deutschbein, Otto K. F., J-QE 76 Sep* 551-554 (1C05)
laser line frequency measurements; far-infrared frequency synthesis technique using stabilized CO_2 lasers. *Petersen, F. Russell, J-QE 75 Oct* 838-843 (1C08) ♦
optimum output mirror transmission, output power at optimum transmission, and small-signal gain of TEM_{00}-mode lasers. *Johnston, T. F., Jr., J-QE 76 May* 310-311 (1D06)
small-signal gain and total internal losses in far-infrared lasers; measurement using Michelson coupler. *Woskoboinikow, P., J-QE 76 Oct* 613-615 (1D13)

♦ Check author entry for later corrections/comments

Laser modes
CO_2 TEA lasers; injection locking and mode selection. *Lachambre, J. L., J-QE 76 Dec* 756-764 (1A14)
distributed-feedback lasers; effects of radiation losses on longitudinal mode thresholds in symmetrical lasers. *Streifer, W., J-QE 76 Nov* 737-739 (1F13)
GaAs–GaAlAs double-heterostructure guided-wave distributed-feedback lasers; TM-mode coupling coefficients. *Streifer, William, J-QE 76 Feb* 74-78 (1A08)
InSb spin-flip lasers; threshold intensity and output frequency as function of magnetic field. *Firth, William J., J-QE 76 Apr* 218-225 (1A08)
stabilization of oscillating modes in $LiNdP_4O_{12}$ lasers. *Otsuka, Kenju, J-QE 76 Apr* 214-217 (1A04)
Laser modes; **cf.** Mode-locked lasers
Laser modulation; **cf.** Optical modulation
Laser noise
He–Cd lasers; power output and beam noise of self-heated 442-nm laser. *Johnston, Thomas F., Jr., J-QE 76 Aug* 482-493 (1C04)
junction lasers with low quantum-efficiency regions; intensity fluctuation spectra in output due to quantum shot noise. *Mukai, Seiji, J-QE 76 Jan* 47-53 (1D07)
Laser processing applications; **cf.** Laser applications, materials processing
Laser pulses; **cf.** Optical pulses
Laser radiation effects
metallic surfaces; reflectivity changes during irradiation by CO_2–TEA lasers. *Ready, John F., J-QE 76 Feb* 137-142 (2D09)
transparent dielectric materials; threshold for pulsed 10.6-μm laser damage in ZnSe, NaCl, and Kcl. *Bass, M., J-QE 76 Feb* 82-83 (1B02)
Laser radiation effects; **cf.** Laser applications; Laser thermal factors
Laser resonators
dye-laser cavity using reflective beam expander. *Eesley, G. L., J-QE 76 Jul* 440-442 (1E10)
GaAs lasers; modal characteristics of laser cavity. *North, Dwight O., J-QE 76 Oct* 616-624 (2A01)
Nd:YAG lasers; design of optical resonators for frequency-doubled laser. *Barry, J. D., J-QE 76 Apr* 254-256 (1D02)
unstable resonators; canonical formulation for analyzing multielement resonators. *Siegman, Anthony E., J-QE 76 Jan* 35-40 (1C09) ♦
Laser thermal factors
CD*A second harmonic generators; electrooptical compensation for self-heating. *Hon, David T., J-QE 76 Feb* 148-151 (2E06)
CO lasers; acoustic waves and heating due to molecular energy transfer in electric-discharge lasers. *Culick, F. E. C., J-QE 76 Oct* 566-574 (1A08)
dye lasers; effect of temperature gradients from absorption of pump energy in jet-stream lasers. *Teschke, O., J-QE 76 Aug* 513-515 (1E07)
Laser tuning
CW dye lasers containing separate rhodamine 6G and cresyl violet jets; tunable mode-locked operation at two wavelengths. *Mahr, H., J-QE 76 Sep* 554-555 (1C08)
Lamb-dip formation in molecular lasers. *Goela, J. S., J-QE 76 May* 281-290 (1B05)
Pb–Sn–Se diode lasers; increased current tuning range using small magnetic fields. *Flicker, Herbert, J-QE 76 Jun* 326-330 (1A08)
Laser welding; **cf.** Laser applications, welding
Lead devices; **cf.** Gas lasers, atomic
Lead alloys/compounds, devices
Pb–Sn–Se diode lasers; increased current tuning range using small magnetic fields. *Flicker, Herbert, J-QE 76 Jun* 326-330 (1A08)
Pb–Sn–Te double-heterostructure lasers; output coupling for closely confined laser. *Davies, Richard W., J-QE 76 May* 291-303 (1C01)
Light; **cf.** Optical
Light-beam focusing; **cf.** Laser-beam focusing
Light-emitting diodes
(AlGa)As double-heterojunction edge-emitting diode with very high radiance. *Ettenberg, Michael, J-QE 76 Jun* 360-364 (1C14)
GaP diodes; operation-induced degradation of forward-biased diode. *Usami, Akira, J-QE 76 Oct* 574-579 (1B02)
laser pumping; $LiNdP_4O_{12}$ lasers using AlGaAs LED side or end pumps. *Saruwatari, Masatoshi, J-QE 76 Oct* 584-591 (1B12)
Liquid lasers; **cf.** Dye lasers
Lithium alloys/compounds, devices
lasers; stabilization of oscillating modes in $LiNdP_4O_{12}$ lasers. *Otsuka, Kenju, J-QE 76 Apr* 214-217 (1A04)
$Ta_2O_5/LiTaO_3$ electrooptic polarization converters. *Lee, Yong-Kyung, J-QE 76 May* 273-281 (1A11)
Lossy media; **cf.** Absorbing media
Lumped-element microwave circuits
electrooptic modulators for wide-band and low-drive-power operation. *An, Jyong Chi, J-QE 76 Jul* 445-446 (1F01)

M

Machining; **cf.** Materials processing
Magnetics
InSb spin-flip lasers; threshold intensity and output frequency as function of magnetic field. *Firth, William J., J-QE 76 Apr* 218-225 (1A08)
Pb–Sn–Se diode lasers; increased current tuning range using small magnetic fields. *Flicker, Herbert, J-QE 76 Jun* 326-330 (1A08)
Masers
Cs-133 vapor; pumping using CW GaAs laser. *Picqué, Jean-Louis, J-QE 74 Dec* 892-897 (1C14) ♦
Materials processing; **cf.** Laser applications
Measurement; **cf.** Electric variables measurement; Laser measurements; Optical measurements
Measurement standards; **cf.** Frequency measurement standards
Mercury devices
ultraviolet generators, 1202.8-Å generation using resonantly enhanced four-wave optical mixing in Hg vapor. *Hsu, K. S., J-QE 76 Jan* 60-62 (1E06)
Mercury devices; **cf.** Gas lasers, ionic
Mercury alloys/compounds
$HgGa_2S_4$; second harmonic coefficient d_{36} and birefringence. *Levine, B. F., J-QE 76 Jun* 367-368 (1D07)
Metal radiation effects
laser radiation effects on metallic surface reflectivity. *Ready, John F., J-QE 76 Feb* 137-142 (2D09)
Metal vapor lasers; **cf.** Gas lasers
Methyl compounds/mixtures, devices; **cf.** Gas lasers, molecular
Microwave (3–30 GHz); **cf.** Millimeter-wave (30–300 GHz)
Microwave circuits; **cf.** Lumped-element microwave circuits
Millimeter-wave (30–300 GHz); **cf.** Microwave (3–30 GHz); Submillimeter-wave (300–3000 GHz)
Millimeter-wave devices
lasers; far-infrared lines in CH_3CN, CH_3CCH, CH_3Cl, CH_3Br, and CH_3I lasers produced by CO_2-laser pumping in region of perpendicular absorption bands. *Chang, T. Y., J-QE 76 Jan* 62-65 (1E08)
Mixers; **cf.** Optical mixers
Mode-locked lasers
CW dye lasers containing separate rhodamine 6G and cresyl violet jets; tunable mode-locked operation at two wavelengths. *Mahr, H., J-QE 76 Sep* 554-555 (1C08)
CW passive mode locking of homogeneously broadened lasers. *Haus, Hermann A., J-QE 76 Mar* 169-176 (1A07)
Modes; **cf.** Laser modes
Modulation; **cf.** Optical modulation; Pulse modulation
Molecular dissociation; **cf.** Laser applications
Molecular lasers; **cf.** Gas lasers
Moving media; **cf.** Relativistic effects

N

Near infrared; **cf.** Infrared (0.70–100μm)
Neodymium alloys/compounds, lasers
$LiNdP_4O_{12}$ lasers; stabilization of oscillating modes. *Otsuka, Kenju, J-QE 76 Apr* 214-217 (1A04)
NdP_5O_{14} and $NdAl_3(BO_3)_4$ lasers; spiking oscillations in diode-pumped lasers. *Chinn, Stephen R., J-QE 76 Mar* 189-193 (1B13)
$Nd_xLa_{1-x}P_5O_{14}$ lasers; oscillator strengths of Nd^{3+} and concentration quenching. *Auzel, F., J-QE 76 Apr* 258-259 (1D06)
Neodymium:glass lasers
glass; tailoring for specific applications by compositional changes. *Jacobs, Ralph R., J-QE 76 Feb* 102-111 (2B02)
induced-emission cross sections of Nd^{3+}-doped glasses; determination. *Deutschbein, Otto K. F., J-QE 76 Sep* 551-554 (1C05)
phosphate laser glasses; nonlinear refractive index coefficients. *Milam, D., J-QE 76 Aug* 512-513 (1E06)
Neodymium:solid lasers
$LiNdP_4O_{12}$ lasers; end- and side-pumping with AlGaAs LEDs. *Saruwatari, Masatoshi, J-QE 76 Oct* 584-591 (1B12)
output pulses; effects of small-scale beam breakup in laser on frequency multiplication in narrow acceptance angle crystals. *Attwood, D. T., J-QE 76 Mar* 203-204 (1C13)
Neodymium:YAG lasers
cavity-dumped lasers; minimum repetition rate for stable operation. *Moran, Joseph M., J-QE 76 Oct* 639-644 (2B10)
frequency-doubled lasers; design of optical resonator. *Barry, J. D., J-QE 76 Apr* 254-256 (1D02)
mode locking; CW passive mode locking of homogeneously broadened laser. *Haus, Hermann A., J-QE 76 Mar* 169-176 (1A07)
pumping with electrodeless arc lamps. *Huchital, David A., J-QE 76 Jan 1-9* (1A03)
relaxation oscillations in cavity-dumped lasers; suppression by intracavity frequency doubler. *Kennedy, C. J., J-QE 76 Apr* 256-257 (1D04)
welding using high-repetition-rate pulsed lasers. *Saifi, Mansoor A., J-QE 76 Feb* 129-136 (2D01)
Networks; **cf.** *RC* networks
Nickel alloys/compounds, devices
terminal posts; laser welding to insulated Cu wires. *Saifi, Mansoor A., J-QE 76 Feb* 129-136 (2D01)
Nitrogen devices; **cf.** Gas lasers, atomic; Gas lasers molecular
Nitrogen compounds/mixtures, devices
ADP parametric amplifiers; generation of frequency-controlled ns and ps visible pulses by high-gain parametric amplification. *Massey, Gail A., J-QE 76 Feb* 143-147 (2E01)
Nitrogen compounds/mixtures, devices; **cf.** Carbon dioxide lasers; Carbon monoxide lasers; Gas lasers; Gas lasers, molecular
Noble gases
Xe isotope spectrum; Lamb dip spectrum at 3.508 μm. *Nella, John, J-QE 76 Sep* 543-547 (1B11)
Noble gas lasers
I_2–He lasers; output characteristics of multiple-anode hollow-cathode laser for discharge currents up to 20A and quasi-continuous excitation. *Piper, James A., J-QE 76 Jan* 21-25 (1B09)
Noble gas lasers, atomic
He–Xe TEA lasers; pulsed Xe-neutral laser line at 4.02 μm. *Olson, Robert A., J-QE 76 May* 316-317 (1D12)
Xe lasers; vacuum ultraviolet fluorescence from high-pressure Xe excited by low-energy, high-repetition-rate electron beam with and without sustainer discharge. *Huber, Ernest E., Jr., J-QE 76 Jun* 353-359 (1C07)
Noble gas lasers, molecular
(CsXe)* excimer lasers; optical absorption and fluorescence of CsXe in high-pressure Cs–Xe mixtures. *Eden, J. G., J-QE 76 Nov* 698-704 (1D02)
Xe lasers; vacuum ultraviolet fluorescence from high-pressure Xe excited by low-energy, high-repetition-rate electron beam with and without sustainer discharge. *Huber, Ernest E., Jr., J-QE 76 Jun* 353-359 (1C07)
Noise; **cf.** Laser noise
Nonlinear optics; **cf.** Optical propagation, nonlinear media
Nonlinear wave propagation; **cf.** Optical propagation, nonlinear media
Nuclear fusion; **cf.** Laser applications

O

Optical amplifiers; **cf.** Laser amplifiers; Optical parametric amplifiers

Optical couplers
GaAs–GaAlAs waveguides; grating-coupled radiation with rectangular-shaped gratings. *Streifer, William, J-QE 76 Jul* 422-428 (1D06)
GaAs–GaAlAs waveguides; grating-coupled radiation with trapezoidal-shaped gratings. *Streifer, William, J-QE 76 Aug* 494-499 (1D02)
Optical couplers; cf. Laser couplers; Optical directional couplers; Optical planar waveguide couplers; Optical strip waveguide couplers
Optical demodulation
FM demodulation; direct demodulation of 10.6-μm FM signal with NH_2D Stark cell. *Abrams, R. L., J-QE 76 Oct* 646-647 (2C03)
Optical diffraction gratings; cf. Optical couplers
Optical directional couplers
switched alternating-phase mismatch couplers in which complete conversion of light from one guide to another is achieved by electrical adjustment. *Kogelnik, Herwig, J-QE 76 Jul* 396-401 (1B08)
Optical fiber waveguides
surface-wave radiation loss for all modes. *Kuester, Edward F., J-QE 75 Nov* 903-907 (1D07) ♦
Optical frequency conversion
frequency multiplication of intense laser pulses in nonlinear crystals of narrow acceptance angle; effects of small-scale beam breakup. *Attwood, D. T., J-QE 76 Mar* 203-204 (1C13)
Nd:YAG lasers; suppression of relaxation oscillations by intracavity frequency doubler. *Kennedy, C. J., J-QE 76 Apr* 256-257 (1D04)
two-photon-pumped converters; conversion efficiency. *Stappaerts, Eddy A., J-QE 76 Jun* 330-333 (1A12)
Optical frequency conversion; cf. Optical harmonic generation; Optical mixers
Optical harmonic generation
far-infrared generation; generation of fourth and fifth harmonics of difference frequency between two 28-THz laser lines. *Whitford, B. G., J-QE 76 Apr* 261 (1D09)
fifth-harmonic generation in isotropic media. *Tomov, Ivan V., J-QE 76 Sep* 521-531 (1A03)
second harmonic generation in CD*A crystals; electrooptical compensation for self-heating. *Hon, David T., J-QE 76 Feb* 148-151 (2E06)
second-harmonic generation in $KB_5O_8 \cdot 4H_2O$ from 217.1 to 315.0 nm. *Dewey, Harry J., J-QE 76 May* 303-306 (1C13)
second harmonic generation in GaAs plates; effect of Fabry–Perot interference. *van der Ziel, Jan P., J-QE 76 Jul* 407-411 (1C05)
second-harmonic generation in $KB_5O_8{\cdot}4H_2O$. *Chen, T. S., J-QE 76 Jul* 436-437 (1E06)
second-harmonic generation at 0.659 μm in CD*A. *Kato, K., J-QE 76 Jul* 443-445 (1E13)
second-harmonic generation of visible dye laser in ADP crystal; generation of continuously tunable coherent radiation in 2460-2650 Å spectral range. *Jain, R. K., J-QE 76 Sep* 555-556 (1C09)
third harmonic generation of CO_2 laser radiation in SF_6, BCl_3, and CO. *Kildal, Helge, J-QE 76 Jul* 429-435 (1D13)
Optical isolators
optical planar waveguide isolators using unidirectional guided-radiation mode coupling in magnetooptic/anisotropic slab guide. *Yamamoto, S., J-QE 76 Dec* 764-770 (1B08)
Optical measurements; cf. Laser measurements; Optical spectroscopy
Optical mixers
wavelength-tunable mixing between 208 nm and 259 nm. *Massey, Gail A., J-QE 76 Nov* 721-727 (1E11)
Optical modulation; cf. Electrooptic modulation
Optical parametric amplifiers
optical pulse generation; generation of frequency-controlled nanosecond and picosecond visible pulses by high-gain parametric amplification. *Massey, Gail A., J-QE 76 Feb* 143-147 (2E01)
Optical planar waveguides
bend losses in curved guides; conformal transformation analysis. *Heiblum, Mordehai, J-QE 75 Feb* 75-83 (1A13) ♦
curved guides; comparison of guiding characteristics to those of prism couplers. *Heiblum, Mordehai, J-QE 76 Aug* 463-469 (1A13)
electromagnetic wave propagation in dielectric- and metal-clad guides; determination of phase constant using graphic method. *Fink, H. J., J-QE 76 Jun* 365-367 (1D05)
propagation characteristics of metal-clad-dielectric-slab waveguides; effect of longitudinal plasma wave. *Nosu, Kiyoshi, J-QE 76 Dec* 745-748 (1A03)
strip-loaded diffused waveguides. *Hocker, G. Benjamin, J-QE 76 Apr* 232-236 (1B08)
surface-wave radiation loss for TE modes in asymmetric slab guides. *Kuester, Edward F., J-QE 75 Nov* 903-907 (1D07) ♦
Optical planar waveguide components
electrooptic phase modulators; multilayer structure using polycrystalline CdS film. *McMurray, J. A., J-QE 76 May* 307-310 (1D03)
isolators using unidirectional guided-radiation mode coupling in magneto-optic/anisotropic slab guide. *Yamamoto, S., J-QE 76 Dec* 764-770 (1B08)
mode converters; electrooptic polarization conversion from guided TE wave to unguided TM wave. *Lee, Yong-Kyung, J-QE 76 May* 273-281 (1A11)
Optical planar waveguide couplers
grating couplers; effect of material absorption loss on performance. *Stone, F. T., J-QE 76 Nov* 727-732 (1F03)
grating couplers for thin-film waveguides. *Ghizoni, Cesar C., J-QE 76 Feb* 69-73 (1A03) ♦
prism couplers; comparison of guiding characteristics to those of curved planar guides. *Heiblum, Mordehai, J-QE 76 Aug* 463-469 (1A13)
Optical planar waveguides
TM-mode radiation loss coefficients of asymmetric slab guides with shallow sinusoidal corrugations. *Rigrod, William W., J-QE 76 Nov* 673-685 (1B05)
Optical propagation; cf. Infrared propagation; Optical transient propagation; Optical waveguides
Optical propagation, absorbing media
CsXe; pressure- and temperature-dependent absorption in high-pressure Cs–Xe mixtures. *Eden, J. G., J-QE 76 Nov* 698-704 (1D02)
Optical propagation, nonlinear media
$HgGa_2S_4$; second harmonic coefficient d_{36} and birefringence. *Levine, B. F., J-QE 76 Jun* 367-368 (1D07)
laser-beam focusing; nonlinear propagation effects. *Bliss, E. S., J-QE 76 Jul* 402-406 (1B14)
Nd:solid lasers; degradation of output pulse by small-scale beam breakup in laser. *Attwood, D. T., J-QE 76 Mar* 203-204 (1C13)
nonlinear optical crystals; cryostat for maintaining at temperatures between room temperature and -175°C. *Lesch, G. H., J-QE 76 Feb* 83-86 (1B03)
nonlinear optical susceptibility coefficient governing self-induced polarization changes of monochromatic beam in solvents. *Cherlow, J. M., J-QE 76 Oct* 644-646 (2C01)
Optical propagation, nonlinear media; cf. Optical frequency conversion
Optical pulses
laser pulses; effects of small-scale beam breakup in Nd:solid laser on frequency multiplication in narrow acceptance angle crystals. *Attwood, D. T., J-QE 76 Mar* 203-204 (1C13)
Optical pulse generators
visible frequency-controlled nanosecond and picosecond pulses; generation by pulsed high-gain parametric amplification. *Massey, Gail A., J-QE 76 Feb* 143-147 (2E01)
Optical pulse propagation; cf. Optical transient propagation
Optical pumping; cf. Laser excitation
Optical radiation effects; cf. Laser radiation effects; Ultraviolet radiation effects
Optical reflection
metallic surfaces; reflectivity changes during irradiation by CO_2–TEA lasers. *Ready, John F., J-QE 76 Feb* 137-142 (2D09)
Optical refraction
glasses; nonlinear refractive index coefficients of Nd phosphate laser glasses. *Milam, D., J-QE 76 Aug* 512-513 (1E06)
Optical resonators; cf. Fabry–Perot resonators; Laser resonators
Optical scattering; cf. Raman scattering
Optical signal detection; cf. Infrared signal detection
Optical spectroscopy
Xe; isotope spectrum at 3.508 μm using laser saturated resonance spectroscopy. *Nella, John, J-QE 76 Sep* 543-547 (1B11)
Optical spectroscopy; cf. Infrared spectroscopy
Optical strip waveguides
dispersion characteristics for diffused channel waveguides. *Taylor, Henry F., J-QE 76 Dec* 748-752 (1A06)
slab-coupled guides; analysis of waveguiding properties using vector variational method. *Ohtaka, Masato, J-QE 76 Jul* 378-382 (1A04)
Optical strip waveguide couplers
optical directional couplers; switched alternating-phase mismatch couplers in which complete conversion of light from one guide to another is achieved by electrical adjustment. *Kogelnik, Herwig, J-QE 76 Jul* 396-401 (1B08)
Optical surface waves
radiation loss from asymmetric slab waveguides and optical fibers. *Kuester, Edward F., J-QE 75 Nov* 903-907 (1D07) ♦
Optical transient propagation
stability conditions for pulse propagation in two-level systems with linear scattering and combined homogeneous and inhomogeneous broadening. *Diels, Jean-Claude, J-QE 76 Jul* 411-416 (1C09)
Optical waveguides
GaAs–GaAlAs waveguides; grating-coupled radiation with rectangular-shaped gratings. *Streifer, William, J-QE 76 Jul* 422-428 (1D06)
GaAs–GaAlAs waveguides; grating-coupled radiation with trapezoidal-shaped gratings. *Streifer, William, J-QE 76 Aug* 494-499 (1D02)
hollow rectangular dielectric guides; field configurations and propagation constants of linearly polarized low-loss modes. *Krammer, Hermann, J-QE 76 Aug* 505-507 (1D13)
Optical waveguides; cf. Optical fiber waveguides; Optical planar waveguides; Optical strip waveguides
Organic dye lasers; cf. Dye lasers
Oxygen
He–Co-laser discharges; positive ion spectra with and without O_2 addition. *Keren, H., J-QE 76 Jan* 58-60 (1E04)

P

Parametric amplifiers; cf. Optical parametric amplifiers
PCM
abbr. of Pulse-code modulation
semiconductor lasers; Gbit/s pulse-code modulation. *Danielsel, Magnus, J-QE 76 Nov* 657-660 (1A03)
Periodic structures; cf. Optical diffraction gratings
Phase modulation; cf. PM
Photoionization
isotope separation; selective laser two-step excitation and photoionization of atomic U vapor. *Janes, G. Sargent, J-QE 76 Feb* 111-120 (2B11)
Photoionization; cf. Gas lasers
Plasma heating
CO lasers; acoustic waves and heating due to molecular energy transfer in electric-discharge lasers. *Culick, F. E. C., J-QE 76 Oct* 566-574 (1A08)
Plasma waves
optical planar waveguides; effect of longitudinal plasma wave on propagation characteristics of metal-clad-dielectric-slab guide. *Nosu, Kiyoshi, J-QE 76 Dec* 745-748 (1A03)
PM
abbr. of Phase modulation
optical planar waveguide modulators; electrooptic phase modulator using CdS thin-film optical waveguides. *McMurray, J. A., J-QE 76 May* 307-310 (1D03)
Potassium alloys/compounds
$KB_5O_8 \cdot 4H_2O$; second-harmonic generation between 217.1 and 315.0 nm. *Dewey, Harry J., J-QE 76 May* 303-306 (1C13)
$KB_5O_8{\cdot}4H_2O$; optical second-harmonic generation. *Chen, T. S., J-QE 76 Jul* 436-437 (1E06)
KCl; threshold for pulsed 10.6-μm laser-induced surface and bulk damage. *Bass, M., J-QE 76 Feb* 82-83 (1B02)
Propagation; cf. Electromagnetic propagation; Optical propagation
Proton radiation effects
AlGaAs double heterostructure lasers; electrical characteristics of proton bombarded stripe-geometry injection lasers. *Barnes, Peter A., J-QE 76 Oct* 633-639 (2B04)

♦ Check author entry for later corrections/comments

Pulse amplifiers; **cf.** Laser amplifiers
Pulse-code modulation; **cf.** PCM
Pulsed lasers
AlGaAs double-heterostructure lasers; RF injection locking of self-pulsing. *Lee, T. P., J-QE 76 Jun* 368-371 (1D08)
CO_2 lasers; Valkyrie short-pulse system for laser fusion experiments. *Manes, Kenneth R., J-QE 76 May* 265-273 (1A03)
CS_2/O_2 chemical, CO laser initiated in high-pressure double-discharge TEA system. *Ahl, Jeffrey L., J-QE 76 Jan* 26-29 (1B14)
dye lasers; single-mode operation of repetitively pulsed laser. *Levenson, M. D., J-QE 76 Apr* 259-260 (1D07)
dye lasers; theoretical model for CW and long-pulse lasers. *Teschke, O., J-QE 76 Jul* 383-395 (1A09)
dye laser systems with injection locking. *Ganiel, U., J-QE 76 Nov* 704-716 (1D08)
He–Xe TEA lasers. *Olson, Robert A., J-QE 76 May* 316-317 (1D12)
HF amplifiers; controlled energy extraction and sharp ns pulses from electron-beam-initiated amplifier. *Getzinger, R. W., J-QE 76 Sep* 556-558 (1C10)
I lasers; pulsed high power Asterix III laser for nuclear fusion experiments. *Brederlow, G., J-QE 76 Feb* 152-155 (2E10)
I photodissociation lasers; short-pulse generation. *Davis, Christopher C., J-QE 76 Jun* 334-352 (1B02)
Pulsed lasers; **cf.** Mode-locked lasers; *Q*-switched lasers
Pulse generators; **cf.** Optical pulse generators
Pulse modulation; **cf.** PCM
Pumping of lasers; **cf.** Laser excitation

Q-switched lasers
infrared spectroscopic applications of N_2O and CO_2 lasers. *Kreiner, W. A., J-QE 76 Jan* 16-20 (1B04)
saturable dyes; measurement of relaxation times in picosecond region. *Hamal, K., J-QE 76 Aug* 510-512 (1E04)
Quantum Electronics Council; **cf.** IEEE Quantum Electronics Council

R

Radiation effects
CO lasers; optical gain in fission-fragment-excited lasers. *McArthur, David A., J-QE 76 Apr* 244-253 (1C06)
Radiation effects; **cf.** Dielectric radiation effects; Laser radiation effects; Metal radiation effects; Optical radiation effects; Proton radiation effects; Semiconductor device radiation effects
Radioactive materials; **cf.** Uranium
Raman lasers
InSb spin-flip lasers; CO_2-laser pumped external cavity laser with output frequency determined ny Fabry–Perot modes of resonant output couplers. *Brueck, S. R. J., J-QE 76 Mar* 201-202 (1C11)
InSb spin-flip lasers; threshold intensity and output frequency as function of magnetic field. *Firth, William J., J-QE 76 Apr* 218-225 (1A08)
rotational Raman scattering in gaseous H_2 or D_2 with CO_2 laser source; 16-μm source for isotope enrichment. *Byer, Robert L., J-QE 76 Nov* 732-733 (1F08)
Raman scattering
coherent IR radiation from InSb at spin resonance frequency. *Wolff, Peter A., J-QE 76 Aug* 500-504 (1D08)
Rare earth alloys/compounds, devices
$Gd_2(MoO_4)_3$ electrooptic modulators; longitudinal modulation of 6328 Å light from 100 Hz to 1 MHz. *Theophanous, N. G., J-QE 76 Aug* 507-510 (1E01)
Rare earth ion lasers; **cf.** Solid lasers
***RC* networks**
integrated networks produced by laser machining. *Saifi, Mansoor A., J-QE 76 Feb* 120-125 (2C06)
Reflection; **cf.** Optical reflection
Refraction; **cf.** Optical refraction
Relativistic effects
N_2 laser excitation by longitudinal relativistic electron beam. *Moreno, J. B., J-QE 76 Mar* 204-207 (1C14)
Relaxation processes
saturable dyes; measurement of relaxation times in picosecond region. *Hamal, K., J-QE 76 Aug* 510-512 (1E04)
Resonators; **cf.** Fabry–Perot resonators; Laser resonators
Rib waveguides; **cf.** Optical strip waveguides
Ring lasers
CW dye lasers; effect of spatial hole burning on output power. *Marowsky, Gerd, J-QE 76 Mar* 207-209 (1D03)

S

Scattering; **cf.** Optical scattering
Second-harmonic generation; **cf.** Optical harmonic generation
Self-focusing; **cf.** Laser-beam focusing
Semiconductor charge carriers; **cf.** Charge-carrier processes
Semiconductor device radiation effects
AlGaAs double heterostructure lasers; electrical characteristics of proton bombarded stripe-geometry injection lasers. *Barnes, Peter A., J-QE 76 Oct* 633-639 (2B04)
Semiconductor heterojunctions; **cf.** Gallium alloys/compounds; Semiconductor lasers
Semiconductor junctions; **cf.** Semiconductor heterojunctions
Semiconductor lasers
direct modulation in GHz range; suppression of relaxation oscillation in modulated output using light injection. *Lang, Roy, J-QE 76 Mar* 194-199 (1C04)
Gbit/s pulse-code modulation. *Danielsel, Magnus, J-QE 76 Nov* 657-660 (1A03)
InSb spin-flip lasers; CO_2-laser pumped external cavity laser with output frequency determined ny Fabry–Perot modes of resonant output couplers. *Brueck, S. R. J., J-QE 76 Mar* 201-202 (1C11)
InSb spin-flip lasers; threshold intensity and output frequency as function of magnetic field. *Firth, William J., J-QE 76 Apr* 218-225 (1A08)
intensity fluctuation spectra due to quantum shot noise in output from junction lasers with low quantum-efficiency regions. *Mukai, Seiji, J-QE 76 Jan* 47-53 (1D07)

♦ Check author entry for later corrections/comments

Pb–Sn–Se diode lasers; increased current tuning range using small magnetic fields. *Flicker, Herbert, J-QE 76 Jun* 326-330 (1A08)
Pb–Sn–Te double-heterostructure lasers; output coupling for closely confined laser. *Davies, Richard W., J-QE 76 May* 291-303 (1C01)
polarization axis of injection lasers; rotation with viewing direction. *Sommers, Henry S., Jr., J-QE 76 Apr* 225-232 (1B01)
response of CW lasers to external signal injection. *Otsuka, Kenju, J-QE 76 Jul* 438-440 (1E08)
stimulated emission threshold and power in injection lasers; effect of trapped radiation. *Gribkovskii, V. P., J-QE 76 Jun* 322-326 (1A04)
Semiconductor lasers; **cf.** Gallium alloys/compounds, lasers
Semiconductor materials; **cf.** Gallium alloys/compounds; Germanium; Indium alloys/compounds; Lead alloys/compounds
SF_6
optical third-harmonic generation of CO laser radiation in molecular gases. *Kildal, Helge, J-QE 76 Jul* 429-435 (1D13)
SF_6 lasers; **cf.** Gas lasers, molecular
Signal detection; **cf.** Optical signal detection
Silver devices; **cf.** Gas lasers, ionic
Slab waveguides; **cf.** Optical planar waveguides
Sodium devices
optical frequency converters; conversion efficiency of two-photon-pumped converters. *Stappaerts, Eddy A., J-QE 76 Jun* 330-333 (1A12)
Sodium alloys/compounds
NaCl; threshold for pulsed 10.6-μm laser-induced surface and bulk damage. *Bass, M., J-QE 76 Feb* 82-83 (1B02)
Solid lasers; **cf.** Neodymium... lasers; Semiconductor lasers
Special issues
Laser Engineering and Applications, Conference on, 5th, Washington, DC, 1975; selected papers, *J-QE 76 Feb* 89-159 (2A03)
Spectroscopy; **cf.** Optical spectroscopy
Spin-flip lasers; **cf.** Raman lasers
Standards; **cf.** Measurement standards
Stark effect
CH_3OH far-infrared lasers; effect of low electric field Stark tuning on absorption of 9.4-μm CO_2 laser radiation. *Claspy, P. C., J-QE 76 Oct* 647-649 (2C04)
NH_2D Stark cells; use in direct demodulation of 10.6-μm FM signal. *Abrams, R. L., J-QE 76 Oct* 646-647 (2C03)
Stimulated emission
injection lasers; effect of trapped radiation on stimulated emission threshold and power. *Gribkovskii, V. P., J-QE 76 Jun* 322-326 (1A04)
Submillimeter-wave (300–3000 GHz); **cf.** Infrared (0.70–100 μm); Millimeter-wave (30–300 GHz)
Submillimeter-wave lasers
CH_3CN, CH_3CCH, CH_3Cl, CH_3Br, CH_3I lasers; far infrared lines produced by CO_2-laser pumping in region of perpendicular absorption bands. *Chang, T. Y., J-QE 76 Jan* 62-65 (1E08)
CH_3OH far-infrared lasers; effect of low electric field Stark tuning on absorption of 9.4-μm CO_2 laser radiation. *Claspy, P. C., J-QE 76 Oct* 647-649 (2C04)
H_2CO lasers; far-infrared laser oscillations from H_2CO vapor in longitudinal-flow tube. *Horiuchi, Y., J-QE 76 Sep* 547-549 (1C01)
H_2O, D_2O, and CH_3OH lasers; measurement of line frequencies using far-infrared frequency synthesis technique. *Petersen, F. Russell, J-QE 75 Oct* 838-843 (1C08) ♦
H_2O vapor lasers; measurement of small-signal gain and total internal losses in Michelson-coupled far-infrared lasers. *Woskoboinikow, P., J-QE 76 Oct* 613-615 (1D13)
HCOOH, CH_3OH, CH_3I, and CH_3F far-infrared lasers; saturated absorption of CO_2 laser radiation in pump transitions. *Weiss, C. O., J-QE 76 Oct* 580-584 (1B08)
Sulfur hexafluoride; **cf.** SF_6
Surfaces
laser damage threshold in NaCl, KCl, and ZnSe. *Bass, M., J-QE 76 Feb* 82-83 (1B02)
metallic surface reflectivity changes during irradiation by CO_2–TEA laser. *Ready, John F., J-QE 76 Feb* 137-142 (2D09)
Surface waves; **cf.** Optical surface waves
Switches; **cf.** Electrooptic switches

T

Tantalum alloys/compounds, devices
$Ta_2O_5/LiTaO_3$ electrooptic polarization converters. *Lee, Yong-Kyung, J-QE 76 May* 273-281 (1A11)
TEA lasers; **cf.** Gas lasers
Thermal factors; **cf.** Laser thermal factors
Thin-film waveguides; **cf.** Optical planar waveguides
Tin alloys/compounds, devices
Pb–Sn–Se diode lasers; increased current tuning range using small magnetic fields. *Flicker, Herbert, J-QE 76 Jun* 326-330 (1A08)
Pb–Sn–Te double-heterostructure lasers; output coupling for closely confined laser. *Davies, Richard W., J-QE 76 May* 291-303 (1C01)
terminal posts; laser welding to insulated Cu wires. *Saifi, Mansoor A., J-QE 76 Feb* 129-136 (2D01)
Transversely excited lasers; **cf.** Gas lasers
Traveling-wave devices
electrooptic modulators for wide-band and low-drive-power operation. *An, Jyong Chi, J-QE 76 Jul* 445-446 (1F01)
Traveling-wave lasers
N_2 lasers; traveling-wave excited laser. *Moreno, J. B., J-QE 76 Mar* 204-207 (1C14)
Traveling-wave lasers; **cf.** Ring lasers
Tunable lasers; **cf.** Laser tuning

U

Ultraviolet generation
continuously tunable coherent radiation in 2460–2650 Å spectral range; generation by second-harmonic generation of visible dye laser in ADP crystal. *Jain, R. K., J-QE 76 Sep* 555-556 (1C09)

optical mixing; wavelength-tunable mixing between 208 nm and 259 nm. *Massey, Gail A., J-QE 76 Nov* 721-727 (1E11)
resonantly enhanced four-wave optical mixing generation of 1202.8 Å radiation in Hg vapor. *Hsu, K. S., J-QE 76 Jan* 60-62 (1E06)
second-harmonic generation in $KB_5O_8 \cdot 4H_2O$ from 217.1 to 315.0 nm. *Dewey, Harry J., J-QE 76 May* 303-306 (1C13)

Ultraviolet lasers
Cu II lasers; ultraviolet laser transitions at 2529, 2600, and 2707 Å. *McNeil, J. R., J-QE 76 Jun* 371-372 (1D11)
H^+–Cs charge-exchange lasers; rate equations and threshold. *Copeland, Drew A., J-QE 76 Nov* 665-673 (1A11)
N_2 lasers; experimental and theoretical study of transmission-line pulse-discharge excited lasers. *Fitzsimmons, W. A., J-QE 76 Oct* 624-633 (2A09)
N_2 lasers; fast-rise-time, large-volume electrical-discharge excitation using stacked Blumlein transmission lines. *Levine, J. S., J-QE 76 Jul* 437-438 (1E07)
Pb vapor lasers; discharge-heated laser with emission at 4062 and 4057 Å. *Anderson, R. S., J-QE 76 May* 313-315 (1D09)
Xe lasers; vacuum ultraviolet fluorescence from high-pressure Xe excited by low-energy, high-repetition-rate electron beam with and without sustainer discharge. *Huber, Ernest E., Jr., J-QE 76 Jun* 353-359 (1C07)

Ultraviolet radiation effects
CO_2 lasers; photoionization parameters in TEA lasers. *McKen, Don C., J-QE 76 Aug* 470-482 (1B06)
CO_2 lasers; volumetric photoionization in CO_2–N_2–He gas mixtures by ultraviolet emission from bare sparks. *Babcock, Richard V., J-QE 76 Jan* 29-34 (1C03)
TEA CO_2 lasers; high-repetition-rate discharge techniques using integrated ultraviolet preionization and voltage switching. *Tulip, John, J-QE 76 Feb* 155-159 (2E13) ♦

Uranium
isotope separation; selective two-step excitation and photoionization of atomic U vapor. *Janes, G. Sargent, J-QE 76 Feb* 111-120 (2B11)

Uranium alloys/compounds
UF_6; -μm source for laser isotope enrichment. *Byer, Robert L., J-QE 76 Nov* 732-733 (1F08)

V

Visible lasers
CW dye lasers containing separate rhodamine 6G and cresyl violet jets; tunable mode-locked operation at two wavelengths. *Mahr, H., J-QE 76 Sep* 554-555 (1C08)
He–Cd lasers; power output and beam noise of self-heated 442-nm laser. *Johnston, Thomas F., Jr., J-QE 76 Aug* 482-493 (1C04)
Hg lasers; quasi-CW high-power laser action at 6501.5 Å. *Lüthi, H. R., J-QE 76 May* 317-318 (1D13)
metal-vapor lasers; self-heated laser using Cu, Au, or Au–Cu mixture as active materials. *Fahlen, Theodore S., J-QE 76 Mar* 200-201 (1C10)

Visible-light generation
second-harmonic generation at 0.659 μm in CD*A. *Kato, K., J-QE 76 Jul* 443-445 (1E13)

W

Waveguides; **cf.** Optical waveguides

Waveguide lasers
CH_3F lasers; conversion of CO_2 pump radiation into far-infrared 496-μm radiation in CW lasers. *DeTemple, Thomas A., J-QE 76 Jan* 40-47 (1C14)
CO_2 lasers; dependence of gain and tunability on gas kinetic and discharge properties. *Cohen, Steven C., J-QE 76 Apr* 237-244 (1B13)
CO_2 lasers using external discharge pumping. *Koepf, Gerhard A., J-QE 76 Jan* 9-15 (1A11)
distributed Bragg reflector lasers; optically pumped epitaxial GaAs laser. *Tseng, Cheng-Chung, J-QE 76 Sep* 549-551 (1C03)

Wave propagation; **cf.** Propagation

Welding; **cf.** Laser applications

X

Xenon; **cf.** Noble gases

Xenon compounds/mixtures
CsXe; pressure- and temperature-dependent absorption and fluorescence in high-pressure Cs–Xe mixtures. *Eden, J. G., J-QE 76 Nov* 698-704 (1D02)

Y

YAG lasers; **cf.** Neodymium:YAG lasers; Solid lasers

Z

Zinc alloys/compounds
ZnSe; threshold for pulsed 10.6-μm laser-induced surface and bulk damage. *Bass, M., J-QE 76 Feb* 82-83 (1B02)

Zinc alloys/compounds, devices
terminal posts; laser welding to insulated Cu wires. *Saifi, Mansoor A., J-QE 76 Feb* 129-136 (2D01)